

Encyclopedia of Nanoscience and Nanotechnology

Volume 1 Number 1 2004

- [▶ view](#) Aligned Carbon Nanotubes 1
Xianbao Wang; Yunqi Liu; Daoben Zhu
- [▶ view](#) Alkanethiol Self-Assembled Monolayers 17
J. Justin Gooding
- [▶ view](#) Analytical Characterization of Single Wall Carbon Nanotubes 51
Sivaram Arepalli; Pasha Nikolaev; Olga Gorelik
- [▶ view](#) Analytical Ultracentrifugation of Nanoparticles 67
Helmut Cölfen
- [▶ view](#) Applications of Electrodeposited Nanostructures 89
G. Palumbo; J. L. McCrea; U. Erb
- [▶ view](#) Applications of Focused Ion Beam in Nanotechnology 101
V. J. Gadgil; F. Morrissey
- [▶ view](#) Atomic Manipulation by Scanning Tunneling Microscopy 111
K.-F. Braun; G. Meyer; F. Moresco; S.-W. Hla; K. Morgenstern; S. Fölsch; J. Repp; K.-H. Rieder
- [▶ view](#) Atomic Structure of Defects in Semiconductors 135
I. Yonenaga
- [▶ view](#) Atomic Structure of Diamond Surfaces 147
J. M. Perez; R. E. Stallcup II
- [▶ view](#) Atomic Wires 169
I. N. Yakovkin
- [▶ view](#) Augmented Waves for Nanomaterials 191
Pavel N. D'yachkov
- [▶ view](#) Bimetallic Ferrofluids 213
Michael Hilgendorff
- [▶ view](#) Biocompatible Core-Shell Nanoparticles for Biomedicine 235
Xiaoxiao He; Xia Lin; Kemin Wang; Liang Chen; Ping Wu; Yin Yuan; Weihong Tan
- [▶ view](#) Bioconjugated Silica Nanoparticles for Bioanalysis 255
Xiaojun Zhao; Lisa R. Hilliard; Kemin Wang; Weihong Tan
- [▶ view](#) Biodoped Sol-Gel Polymer Nanocomposites 269
Iqbal Gill

▶ view Biogenic Nanoparticles	<u>293</u>
<i>Joseph M. Slocik; Marc R. Knecht; David W. Wright</i>	
▶ view Biological Molecules in Nanodevices	<u>309</u>
<i>Stephen C. Lee; Mark A. Ruegsegger; Mauro Ferrari</i>	
▶ view Bionanodevices	<u>329</u>
<i>Thomas Schalkhammer</i>	
▶ view Bionanomotors	<u>361</u>
<i>Dmitri Grigoriev; Dieter Moll; Jeremy Hall; Peixuan Guo</i>	
▶ view Bismuth Nanostructured Materials	<u>375</u>
<i>Joshua T. Moore; Charles M. Lukehart</i>	
▶ view Boron-Carbon Nitride Nanohybrids	<u>383</u>
<i>Yoke Khin Yap</i>	
▶ view Boron Nitride Nanotubes	<u>395</u>
<i>Dmitri Golberg; Yoshio Bando</i>	
▶ view C ₆₀ -Based Materials	<u>409</u>
<i>J. G. Hou; A. D. Zhao; Tian Huang; Shan Lu</i>	
▶ view Calixarenes	<u>475</u>
<i>Chebrolu P. Rao; Mishtu Dey</i>	
▶ view Cantilever-Based Sensors	<u>499</u>
<i>D. Then; C. Ziegler</i>	
▶ view Carbon Nanomaterials	<u>517</u>
<i>Maheshwar Sharon</i>	
▶ view Carbon Nanostructures for Cold Electron Sources	<u>547</u>
<i>P. Gröning; L. Nilsson; P. Ruffieux; R. Clergereaux; O. Gröning</i>	
▶ view Carbon Nanotube Growth by Chemical Vapor Deposition	<u>581</u>
<i>M. Meyyappan</i>	
▶ view Carbon Nanotube Sensors	<u>591</u>
<i>Jun Li; Hou Tee Ng</i>	
▶ view Carbon Nanotubes: Synthesis by Arc Discharge Technique	<u>603</u>
<i>Yoshinori Ando</i>	
▶ view Carbon Nanotube-Based Field Emitters	<u>611</u>
<i>Seong Chu Lim; Hee Jin Jeong; Kay Hyeok An; Dong Jae Bae; Young Hee Lee; Young Min Shin; Young Chul Choi</i>	
▶ view Carbon Nanotube-Based Supercapacitors	<u>625</u>
<i>Young Hee Lee; Kay Hyeok An; Ji Young Lee; Seong Chu Lim</i>	

▶ view Carbon Nanotubes in Composite Materials <i>Ch. Laurent; A. Peigney</i>	<u>635</u>
▶ view Catalysis by Gold Nanoparticles <i>Masatake Haruta</i>	<u>655</u>
▶ view Catalytic Synthesis of Carbon Nanotubes and Nanofibers <i>Kenneth B. K. Teo; Charanjeet Singh; Manish Chhowalla; William I. Milne</i>	<u>665</u>
▶ view Ceramic Nanoparticle Synthesis <i>Xiangdong Feng; Michael Z. Hu</i>	<u>687</u>
▶ view Ceramic Nanopowders <i>Yong S. Cho; Howard D. Glicksman; Vasantha R. W. Amarakoon</i>	<u>727</u>
▶ view Charge Carrier Dynamics in Nanoparticles <i>Christian D. Grant; Thaddeus J. Norman Jr.; Jin Z. Zhang</i>	<u>745</u>
▶ view Chemical Derivatization of Carbon Nanotube Tips <i>Vladimir A. Basiuk; Elena V. Basiuk (Golovataya-Dzhymbeeva)</i>	<u>761</u>
▶ view Chemical Synthesis of Nanoparticles <i>H. Bönemann; K. S. Nagabhushana</i>	<u>777</u>
▶ view Chemically Prepared Magnetic Nanoparticles <i>M. A. Willard; L. K. Kurihara; E. E. Carpenter; S. Calvin; V. G. Harris</i>	<u>815</u>
▶ view Chemistry of Carbon Nanotubes <i>V. N. Khabashesku; J. L. Margrave</i>	<u>849</u>
▶ view Chiral Macrocycles <i>Suk Joong Lee; Wenbin Lin</i>	<u>863</u>

Copyright © 2004 American Scientific Publishers

Aligned Carbon Nanotubes

Xianbao Wang, Yunqi Liu, Daoben Zhu

Chinese Academy of Sciences, Beijing, People's Republic of China

CONTENTS

1. Introduction
2. Carbon Nanotubes and Their Preparation Methods
3. Alignments and Patterns of Multiwalled Carbon Nanotubes
4. Alignments of Single-walled Carbon Nanotubes
5. Properties and Applications of Aligned Carbon Nanotubes
6. Summary
Glossary
References

1. INTRODUCTION

Significant progress has been made in the science of carbon nanotubes (CNTs) since the publication of Iijima's milestone paper in 1991 [1]. If there is one thing which has characterized fullerene and nanotube sciences, it is serendipity [2]. The discovery of buckminsterfullerene itself was a wonderful accident, and nanotubes were an unanticipated by-product of the bulk synthesis of C_{60} . CNTs have captured the imagination of physicists, chemists, and materials scientists alike. Their intriguing electronic, magnetic, optical, and mechanical properties, coupled with their unusual molecular shape and size, have made CNTs very promising as functional components for building molecular-based electronics, nanomachines, and nanoscale biomedical devices as well as composites as structural materials. Physicists have been attracted to their extraordinary electronic properties, chemists to their potential as "nanotest-tubes," and materials scientists to their amazing stiffness, strength, and resilience. Nanotechnologists, mostly from the three aforementioned areas, have discussed and explored possible nanotube-based nanodevices such as nanogears, nanobearings, single electron transistors, quantum computers, and so on. Many review articles [3–9], books [2, 10–14], and special issues of journals [15–17] have been devoted to this topic to collect the

new developments and concepts in this rapidly developing interdisciplinary field.

Following the discovery of CNTs, single-walled carbon nanotubes (SWNTs) reported simultaneously by Iijima and Ichihashi [18] and Bethune et al. [19] in 1993, which are ideal models of one-dimensional materials with unique structural and electronic properties, have generated great interest for use in a broad range of potential nanodevices. Perhaps the largest volume of research into nanotubes has been devoted to the electronic properties, of which the field emission study was extensive, profound, and highly near to a practicable product. CNTs are known to be very good electron emitters. This is why since their discovery there has been a lot of speculation and experiments about the use of nanotubes in the construction of flat panel devices. The first study on CNT field emission (FE) properties was carried out by Rinzler et al. [20] from Rice University. They found that field emission of electrons from individually mounted CNTs has been dramatically enhanced when the nanotube tips are opened by laser evaporation or oxidative etching. A short time-hereafter, the field emission from a film of postsynthesized reduced CNT alignments was made by de Heer and co-workers [21]. However, a prerequisite for a major breakthrough in the area would be the perfect alignments of CNTs on a suitable surface.

This chapter is mainly focused on the synthesis and applications of aligned carbon nanotubes, including SWNTs and multiwalled carbon nanotubes (MWNTs). The organization of this chapter is as follows: Section 2 first considers three classical methods for synthesizing nanotubes, including arc discharge, laser ablation, and chemical vapor deposition (CVD), especially comparing the advantages and disadvantages of each synthesis method, and then presents the new preparation techniques developed in the last two years. In Section 3, the fabrications of various alignments and patterns are discussed in detail for MWNTs, and the emphasis in this section is on the controllable fabrication of nanotube alignments. Alignments of SWNTs are described in Section 4. Section 5 gives a discussion of properties and application of aligned CNTs, and the FE properties are of great concern. Finally, future research consideration and challenges are presented in Section 6.

2. CARBON NANOTUBES AND THEIR PREPARATION METHODS

A carbon nanotube consists of one or more seamless cylindrical shells of graphitic sheets. The nanotube is typically closed at each end, according to Euler's theorem [22], by the introduction of pentagons in the hexagonal network. A theoretical model of a CNT with two closed ends was simulated by Endo and Kroto [23]. However, an experimental observation of the tube with both ends closed has seldom been reported for two main reasons. One is that most CNTs, regardless of the synthesis methods (such as arc discharge, laser ablation, and catalyst decomposition of hydrocarbon), are attached by either open ends, or one closed carbon cap, or ends capped with metal particles. The other is that the large length/diameter ratio (>1000) prevents one from simultaneously observing two ends of the tubes in the same field of vision under a transmission electron microscope (TEM), though tubes with two caps exist in the product. In an earlier report [24], it was also noticed that nanotubes produced using the arc discharge technique can be fairly short, and these structures with two capped ends can be observed under high resolution transmission electron microscopy. However, the structure is so small and asymmetric, with a diameter of at most 40 nm, that it should be precisely defined as an elongated nanoparticle of graphitic carbon rather than a well-defined CNT with capped ends. We reported a perfect carbon nanotube with two graphitic caps observed in the products by pyrolysis of metal phthalocyanine [25]. Such a large CNT with capped ends is of great interest for the formation mechanism of nanotubes.

CNTs are most attractive because of their fascinating features. What makes nanotubes so special is the combination of dimension, structure, and topology that translates into a whole range of superior properties. The basic constitution of the nanotube lattice is the C–C covalent bond (as in graphite planes) which is one of the strongest in nature. The perfect alignment of the lattice along the tube axis and the closed topology endow nanotubes with in-plane properties of graphite such as high conductivity, excellent strength and stiffness, chemical specificity, and inertness together with some unusual properties such as the electronic structure, which is dependent on lattice helicity and elasticity. In addition, the nanodimensions provide a large surface area that could be useful in mechanical and chemical applications. The surface area of MWNTs has been determined by BET techniques and is $\sim 10\text{--}20\text{ m}^2/\text{g}$, which is higher than that of graphite but small compared to activated porous carbons. This value for SWNT is expected to be an order of magnitude higher. Similarly, due to the relatively large hollow channels in the center of nanotubes, their density should be very low compared to graphite. Rough estimates suggest that SWNT density could be as small as $0.36\text{ g}/\text{cm}^3$, and MWNT density could range between 1 and $2\text{ g}/\text{cm}^3$ depending on the constitution of the samples [7].

2.1. Classical Synthesis Methods

Nanotubes are not always perfect seamless shells of graphite. Their quality depends on the method used to generate them and the exact conditions of the particular method. Making

nanotubes is simple, but making good quality samples with high yields and highly graphitized shells is not trivial.

There are several methods to produce CNTs, but three classical methods including arc discharge, laser ablation, and a catalytic technique remain the most practical for scientific purposes and realistic applications. The arc method [26, 27] remains by far the best technique for the synthesis of high-quality nanotubes simply because the process has a very high temperature of 4000 K. However, this method suffers from a number of disadvantages [14]. First, it is labor intensive and requires some skill to achieve a satisfactory level of reproducibility. Second, the yield is rather low, since most of the evaporated carbon is deposited on the walls of the vessel rather than on the cathode, and the materials that are formed in the deposit contain substantial amounts of nanoparticle and other graphitic debris. Third, it is a batch rather than a continuous process, and it does not easily lend itself to scale-up. The amount of nanotubes that can be produced is limited. Progress in this direction has been hampered somewhat by a lack of understanding of the growth mechanism of tubes in the arc.

The laser evaporation technique developed by Smalley's group [28–30] appears to produce the highest yield and best quality materials, but the high powered lasers required for this method will obviously not be available in every laboratory. The synthesis of MWNTs in this way has been carried out by a pure graphite target [29]. In 1995, they reported the development of the laser synthesis technique which enabled them to prepare SWNTs with a target of a metal–graphite composite instead of pure graphite [28]. Subsequent refinements to this method led to the production of SWNTs with unusually uniform diameter [30].

CVD of hydrocarbon over metal catalyst has been another classical method to produce carbon materials. Various forms of carbon fibers, filaments, and MWNTs have been synthesized by this technique in the past [31–34]. In general, metal catalytic particles are exposed to a medium containing hydrocarbon gaseous species, and the formation of nanotubes is catalyzed [35]. During growth, good uniformity in size of the tube is achieved by controlling the size of the seeded catalyst particles, and the process can be easily scaled up to produce large amounts of materials. In some cases, when the catalysts are prefabricated into patterned arrays, well-aligned nanotube assemblies are produced, which will be discussed in detail (Section 3). This seems a promising direction for further research. However, the quality of tubes produced in this way has been rather poor compared with the arc and laser methods. As shown in Figure 1, a nanotube prepared by a catalytic pyrolysis of iron phthalocyanines is a structure with lots of topological defects in a wall [36].

There is a further serious weakness of all these techniques for preparing nanotubes; they produce a wide range of the size and structures. This may not be a problem for some applications, but it could be a drawback in areas where specific tube structures with uniform properties are needed, such as in nanoelectronics. Progress in this direction has been hampered somewhat by a lack of understanding of the growth mechanism of tubes. Although a number of theories [37–40] have been put forward, none of which has gained universal acceptance, most questions remain unanswered and the uncertainty surrounding nanotube growth

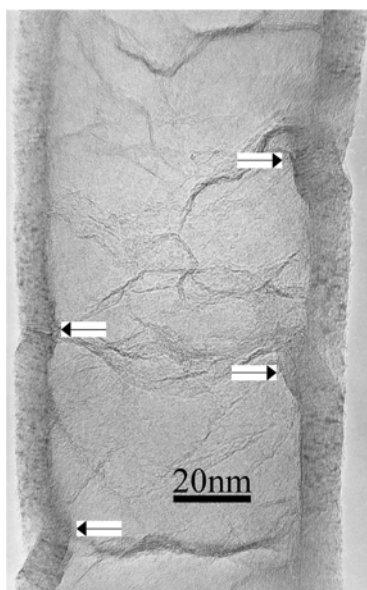


Figure 1. A carbon nanotube with many topological defects synthesized by chemical vapor deposition. Reprinted with permission from [37], M. Endo and H. W. Kroto, *J. Phys. Chem.* 96, 6941 (1992). © 1992, Elsevier Science.

mechanisms has impeded progress in the development of more controlled synthesis techniques.

2.2. Preparation Methods of Nanotubes

In the last two years, a few new synthesis methods were developed to produce CNTs to solve one or more problems during the conventional preparation process. These ways take respective advantages over the conventional methods to a certain extent and were of important potential for basic research as a new route to produce CNTs. However, the samples of the nanotubes produced by all those new methods existed in lower quality and less perfect structures than the classical ones. A number of experimental conditions should be optimized before these synthesis methods are developed to produce nanotubes with high quantity and desirable structures to meet scientific research and practical applications.

2.2.1. Hydrothermal or Solvothermal Synthesis

The oxidative effect of hot water on amorphous carbon is currently used for purification of CNTs by hydrothermal treatment (immersion in water at moderate and high temperatures and pressures) [41, 42]. It was found that the hydrothermal processing method could be developed to synthesize nanostructural carbon [43, 44]. Recently, MWNTs have been synthesized in the absence of metal catalyst by hydrothermal treatment of amorphous carbon in pure water at 800 °C and 100 MPa [45]. The hydrothermal nanotubes are free of amorphous carbon after treatment. The homogeneity of hydrothermal processes and availability of amorphous carbon materials, without the need for catalyst, are

advantages favoring the scaling-up of this new method. However, this method suffers from harsh synthesis conditions (a high temperature of 800 °C, a high pressure of 100 MPa, and a long time of 48 h), and electron microscopy observations revealed that very short multiwalled tubes (hundreds of nanometers) exist together with the aggregates of needle-like and polygonal nanoparticles.

Compared with this method, a solvothermal route to MWNTs has been developed under a lower temperature (350 °C) and shorter time (8 h) [46]. This catalyst-assembly benzene-thermal route was carried out to produce CNTs using reduction of hexachlorobenzene by metallic potassium in the presence of Co/Ni catalyst. The synthesis temperature was low, but the quantity of the nanotubes was poor.

2.2.2. Supercritical CO₂ Technique

Carbon dioxide is nonflammable, essentially nontoxic, and environmentally benign [47]. Motiei et al. [48] reported the structures of graphitic concentric shells grown by supercritical CO₂. It is found that MWNTs and nested fullerenes could be prepared from dry ice in the presence of Mg by heating the precursors in a closed vessel at the autogenic pressure of the mixture. This method avoids the complexities of using a flowing gas at controlled pressures and high temperature and requires no technically complex equipment.

2.2.3. Solid-State Metathesis Reaction

The solid-state metathesis reaction has been developed over the past few years into a simple and effective route to materials that are difficult to synthesize by conventional methods [49–51]. These highly exothermic and self-propagating reactions initiated by a heated filament often use molecular precursors to produce crystalline products. An exchange reaction between carbon halides and lithium acetylide catalyzed by cobalt dichloride enables the rapid synthesis of CNTs by the following equation [52]: $C_2Cl_6 + 3 Li_2C_2 \rightarrow 8 C$ (nanotubes) + 6 LiCl.

Without a catalyst, only graphitic and amorphous carbon forms. These reactions, once optimized, will likely require cheaper precursors, more preparation, and less expensive equipment than existing methods. However, along with multi- and single walled nanotubes, graphite-encapsulated cobalt nanoparticles, free carbons, and cobalt metals were found. These shortages should be overcome before the extensive application of this method.

2.2.4. Flame Synthesis

Combustion is widely used in industrial processes for large-scale materials synthesis, such as for carbon black and metal oxides [53, 54]. These flame processes are well known for their many desirable features including continuous processing and energy efficiency. Recent investigations have sought to take advantages of these advantages to synthesize SWNTs in aerosol form [55, 56]. It was found that SWNTs could be produced by a binary or ternary gas mixture of CO/C₂H₂/H₂ with a metal catalyst at 700 °C in a two-stage flame. This flame system afforded the advantage that the catalyst formation step could be separated from the nanotube growth steps, which allowed investigations of catalyst particle size

dependencies upon nanotube growth unlike methods that employ *in-situ* generation and concurrent growth.

Apart from the methods presented previously, there are many other methods such as a gas phase synthesis [57], a reduction catalysis route at a low temperature of 200 °C [58], and a solar approach [59], although these methods to produce nanotubes suffer from different drawbacks.

3. ALIGNMENTS AND PATTERNS OF MULTIWALLED CARBON NANOTUBES

CNTs are the most promising materials anticipated to impact future nanoscience and nanotechnology. Their unique structural and electronic properties have generated great interest for use in a broad range of potential nanodevices [60, 61]. Most of these applications will require a fabrication method capable of producing CNT alignments or patterns with uniform structures and periodic arrangements to meet device requirements. Therefore, the ability to controllably obtain ordered or patterning CNT architectures is important to both fundamental characterizations and potential applications [62]. Controlled synthesis involving CVD has been studied as an effective strategy to order or pattern CNTs on a variety of surfaces [63–67]. This has been stimulated by its simplicity, its ability to yield structures that are two- or three-dimensional (2D or 3D) periodic over large area, and its potential to be much less expensive than other synthesis methods such as an arc discharge and a laser ablation. In these early attempts, most of the works to date have focused on fabricating 2D CNT alignments or patterns over large areas because of their paramount importance for obtaining scale-up functional devices. However, in contrast to these efforts, little research on the preparation of 3D CNT alignments or patterns has been reported because of many technical difficulties, although the 3D structures show more unique and potential applications such as photonic devices [68, 69], data storage [70, 71], and ultrahydrophobic materials [72, 73]. In this section, various fabricating methods are discussed for alignments and patterns of MWNTs, including 2D or 3D structures.

3.1. Preparation of 2D Nanotube Alignments on Different Substrates

Alignments or patterns of CNTs are particularly important for fabricating functional devices such as field emitters and nanoelectronics. Earlier attempt to manipulate nanotubes for these application have been made by postgrowth methods such as cutting a polymer resin–nanotube composite [74] or drawing a nanotube–ethanol suspension through a ceramic filter [75]. In the past few years, a great quantity of research on the fabrication of 2D CNT alignments has been reported [63–67, 76–78]. Although all these 2D CNT alignments were synthesized by CVD, different technical routes were adopted by different research groups. The main differences of these synthesis methods may be summarized as the following factors: a substrate and a precursor. The substrates that are used to support the CNTs alignments may be put into two categories: porous templates (mesoporous

silica [63], nanochannel alumina [76], etc.) and plain plates (quartz glass [77], single crystal silicon plate [78], glass [65], etc.). As far as the precursor is concerned, there are two main materials: hydrocarbons [66, 76] and metal organic compounds [77]. When hydrocarbons are used as precursors, metal catalysts (such as Fe, Co, Ni) should be added to grow CNTs. However, as for metal organic compounds no additional metal catalyst is necessary since these precursors contain both the metal catalyst and carbon source required for CNT growth.

The following discussion is mainly focused on the substrates where the nanotube alignments grow.

3.1.1. Planar Substrate

Quartz glass is a good planar substrate for growing well-aligned nanotubes [64, 77, 79]. Terrones et al. [64] described a method for generating aligned nanotubes by pyrolysis of 2-amino-4, 6-dichloro-triazine over thin films of a cobalt catalyst patterned on a silica substrate by laser etching. We have grown well-aligned nanotubes with large diameters on quartz glass substrate by pyrolysis of a metal phthalocyanine under Ar/H₂ flow at a temperature of 950 °C [77]. We investigated the influence of the growth time and precursor level on the structures of MWNTs. It was found that both the outer diameter and length of aligned nanotubes increased with increasing growth time and precursor level. The outer diameters of well-aligned nanotubes range from 25 to 250 nm, and the length ranges from 1 to 500 μm. However, the microstructures of aligned nanotubes are independent of the growth temperature and the Ar/H₂ flow rate in our case.

Figure 2a is a scanning electron microscopy (SEM) image showing a large area of well-aligned CNTs with uniform diameter and length. Figure 2b is a typical TEM image of the bamboo-shaped nanotubes [80] produced by pyrolysis of 0.5 g iron phthalocyanine in 12 min. The graphite sheath sliding out from the Fe particle surface accounts for the formation of the compartments of bamboolike CNTs. The driving force of the sliding was caused by the stress accumulated

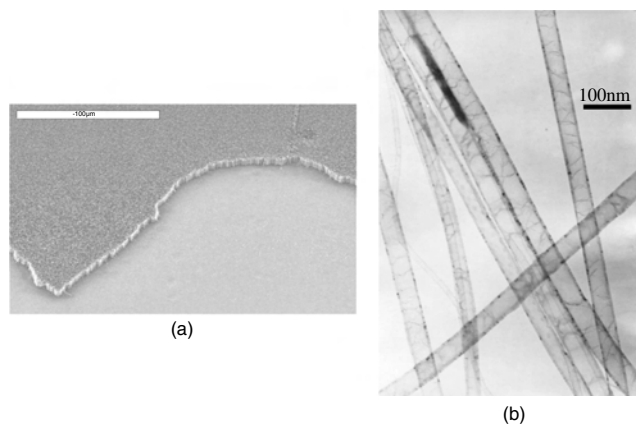


Figure 2. A SEM micrograph showing large area well-aligned CNTs perpendicular to the surface of the substrate. (b) A typical TEM image of the CNTs produced by pyrolysis of 0.5 g FePc in 12 min. Reprinted with permission from [77], X. B. Wang et al., *Chem. Phys. Lett.* 340, 419 (2001). © 2001, Elsevier Science.

in the graphite sheath due to the segregation of carbon atoms from the inside of the sheath [80].

Apart from quartz glass, we can produce aligned nanotubes on various substrates made of other materials such as single crystalline silicon, iron plate, nickel plate, cobalt plate, and so on.

Glass is the most common material for panel display. The ability to prepare aligned nanotubes over a glass substrate makes them more suitable for electron emission applications. Recently, Ren et al. [65, 81] reported the growth of large scale well-aligned CNT arrays on nickel-coated glass at temperatures below 666 °C by plasma-enhanced hot filament CVD. Acetylene gas was used as the carbon source and ammonia gas was used as a catalyst and dilution gas. It was found that NH_3 plays a crucial catalytic role together with the nickel layer to promote the growth of the nanotubes, and nickel thickness plays a very important role in determining the diameters.

Nickel wafers were found to be another good substrate for producing nanotube alignments. Chen et al. have grown aligned graphitic nanofibers on single crystalline Ni (100) [82] and polycrystalline Ni substrate [83] via plasma assisted hot filament CVD using a gas mixture of nitrogen and methane. Small Ni particles on the substrate surface generated by the plasma acted as a catalyst for the growth of nanofibers.

3.1.2. Porous Template

Mesoporous silica containing iron nanoparticles was used as a substrate when well-aligned CNTs were first synthesized by Xie et al. [63]. The mesoporous silica was prepared by a sol-gel process from tetraethoxysilane hydrolysis in iron nitrate aqueous solution [84]. This method to produce large areas of highly ordered, isolate long nanotubes is based on CVD. The tubes are up to about 50 μm long and well graphitized. The growth direction of the nanotubes can be controlled by the pores from which the nanotubes grow.

Porous silicon, a light-emitting material [85, 86], is an ideal substrate for growing organized nanotubes. Fan et al. [60] have prepared porous silicon patterned with Fe film by electron beam evaporation through shadow masks and then on this substrate carried out the synthesis of self-oriented regular arrays of CNTs by catalyst decomposition of ethylene at 700 °C. Porous silicon substrate exhibits an important advantage over plain silicon for synthesizing nanotubes. The investigation showed that the nanotubes grew at a higher rate on porous silicon than on silicon. The well-ordered nanotubes can be used as electron FE arrays. Scaling-up of the synthesis process should be compatible with the existing semiconductor processes and allows the development of nanotubes devices integrated into silicon technology.

Highly ordered arrays of CNTs can be grown by pyrolysis of acetylene on cobalt within a hexagonal close-packed nanochannel alumina template at 650 °C [76]. The method is based on template growth. An illustration of a typical fabrication process flow is shown in Figure 3a. The process begins with the anodization of high purity (99.999%) alumina on a desired substrate. The next step is to deposit electrochemically a small amount of cobalt catalyst into the bottom of the template channels. The ordered arrays of nanotubes (Fig. 3b)

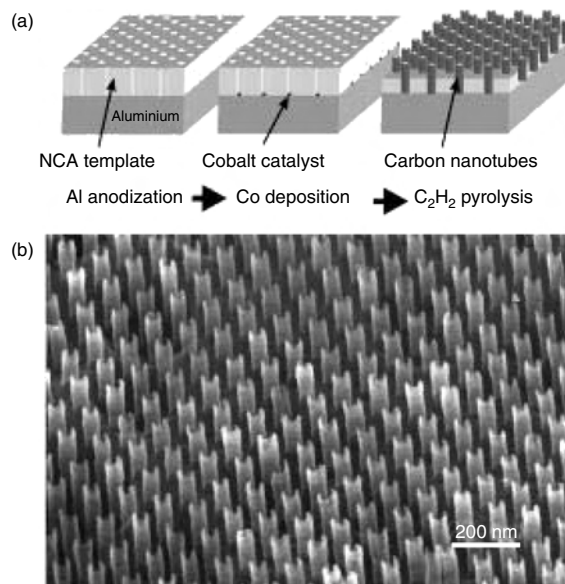


Figure 3. (a) Schematic of fabrication process. (b) SEM image of the resulting ordered arrays of CNTs synthesized using the nanochannel alumina template. Reprinted with permission from [76], J. Li et al., *Appl. Phys. Lett.* 75, 367 (1999). © 1999, American Institute of Physics.

are grown in a flow of a mixture of 10% acetylene in nitrogen. There are several features in this fabrication technique [87, 88]. First, each pore of the template is filled with one nanotube, which defines the tube diameter, and the tube diameter distribution throughout the arrays is narrow. Second, the controlled variation of the nanotube size, density, and array spacing depends on easily adjustable parameters such as the anodizing voltage, electrolyte composition, and temperature. Tube lengths of up to 100 μm can be obtained by varying the length of the pores in the alumina template, which can be achieved by varying the time of anodization. Finally, the method allows inexpensive production of large arrays of ordered nanotubes.

3.2. Controllable Fabrication of CNT Alignments

3.2.1. Selective Positioning Growth for Patterns

Selective positioning growth of CNT patterns is arousing a wide range of research interest [89–91]. In the past few years, several methods have been developed to site-selectively grow nanotubes.

Photolithographic Approach Wei et al. [89, 90] have used a CVD method with gas-phase catalyst delivery to direct the assembly of CNTs in a variety of predetermined orientations onto silicon/silica substrates, of which patterning was generated by photolithography followed by a combination of wet and/or dry etching. Figure 4 shows some striking examples of organized nanotube patterns grown on preselected substrate sites by the photolithographic approach. There is no nanotube grown on silicon, but the aligned nanotubes grow readily on silica in a direction that is normal to the substrate surface [90]. The preference of nanotubes to grow

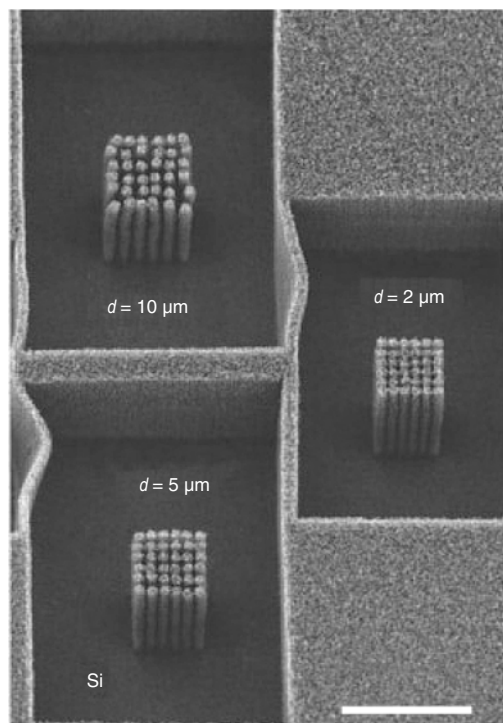


Figure 4. SEM images of organized nanotube patterns grown on pre-selected substrate sites by a photolithographic approach. Scale bars, 100 μm . Reprinted with permission from [89], B. Q. Wei et al., *Nature* 416, 495 (2002). © 2002, Nature Publishing Group.

selectively on and normal to silica surfaces allows the sites of nucleation and the direction of growth to be controlled. Yang et al. [67] have also reported the fabrication of patterns of perpendicularly aligned nanotubes with resolution down to μm scale by pyrolysis of iron phthalocyanines onto a quartz substrate prepatterned with a photoresist film.

Electron Beam Lithographic Approach With a electron beam lithographic technique, patterned growth of freestanding nanotubes on nickel dots on silicon can be achieved by plasma-enhanced hot filament CVD [92]. The thin film nickel pattern as a catalyst for growing nanotubes was fabricated on a silicon wafer by a standard microlithographic method and metal evaporators. Well-separated, single MWNTs grew on each dot of an array of ~ 100 nm nickel dots under an acetylene/ammonia mixture at below 660 $^{\circ}\text{C}$. The diameter and height depend on the nickel dot size and growth time, respectively. Using this method, devices requiring freestanding vertical CNTs such as scanning probe microscopy, FE flat panel displays, etc. can be fabricated.

Soft Lithographic Approach Most microfabrication methods mentioned start with photolithography to form a pattern in a photoresist on the substrate. Although these techniques are very widely used, they are incompatible for solution such as gels, some polymers, some organic and organometallic species, and biological molecules. To pattern these materials successfully, the patterned photoresist must be impermeable to the reagents used and the deposited materials should not be compromised by solvents used for the liftoff. Methods other than photolithography

often involve a shadow mask formed from a rigid metal. The air gap between the mask and substrate makes the use of rigid shadow masks to pattern materials from solution impossible [60].

One micropatterning technique that circumvents some of these drawbacks is soft lithography [93–95], which uses a patterned elastomer fabricated from poly(dimethylsiloxane) as the mask, stamp, or mold. Because the elastomer can conform to and seal reversibly against the contours of a surface, it can be used as a mask or a stamp. Soft lithography has become a very promising technique for micro/nanostructuring a wide range of materials. Various strategies, including microcontact printing (μCP) [96–98] and micromolding [99], have been developed for nanoscale patterning.

Kind et al. [96] elucidated some important aspects of using μCP to pattern silicon substrate with catalysts followed by the growth of CNTs on the activated regions. In brief, a patterned and inked elastomeric stamp is used to print a catalyst as a pattern onto a substrate (Fig. 5). The growth of MWNTs follows from the catalytic decomposition of acetylene on the printed pattern of the catalyst. Changing the concentration of the catalyst in the ink solution allows one to tune the density of the nanotubes from single, randomly oriented nanotubes to densely packed arrays of nanotubes oriented normal to the substrate.

This approach relied on rigid solid-state substrates such as silicon and alumina to achieve aligned nanotubes, which

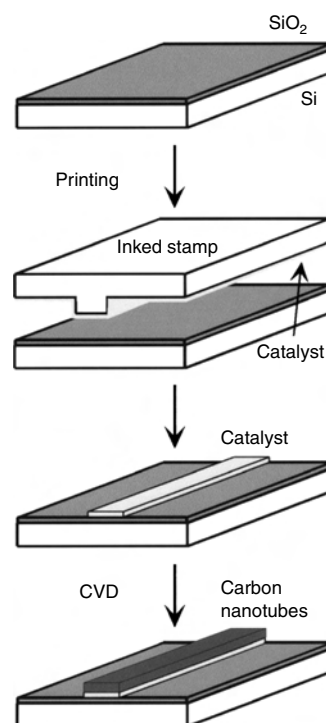


Figure 5. Procedure for the patterned growth of carbon nanotubes by microcontact printing a Fe(III)-based catalyst precursor onto silicon wafers. The stamp is inked with an ethanolic solution of Fe(III) and then printed onto the substrate. The growth of carbon nanotubes proceeds by the catalytic decomposition of acetylene. Reprinted with permission [96], H. Kind et al., *Langmuir* 16, 6877 (2000). © 2000, American Chemical Society.

may limit its wider scope of application. Hence, it would be interesting and challenging to investigate the possibility of performing *in-situ* selective growth on a novel substrate such as polymers and its direct integration with elastomeric polymers to fabricate practical devices. Ng et al. [98] have recently reported the combination of soft-lithography-mediated growth and surface wettability manipulation of an elastomeric polymer to achieve *in-situ* highly site-selective growth of multiwalled nanotubes arrays on elastomeric substrates patterned with catalyst precursors. The realization of this approach may provide new methodologies for flexible FE display, implantable sensors, etc.

Biased Growth Approach The investigations by Avigal and Kalish [100] showed that patterns of MWNTs could be obtained by positively biasing the substrate during growth. Growth was performed in a flowing mixture of 7% CH₄ in Ar onto Co covered Si held at 800 °C with and without the presence of an electric field. It was found that the tube alignment occurs only when a positive bias is applied to the substrate whereas no aligned growth occurs under negative bias and no tube growth is observed with no field. Therefore, selective area biasing may permit selected area growth of vertically aligned CNTs, a process that may find many applications.

Fabrication of micropatterned nanotubes remains both scientific and technically challenging. Many methods have been presented in preceding parts of this section to produce nanotube patterns. However, these synthetic methods suffer from complex pre- or postsynthesis manipulation. In 2000, we have developed a simple method [101] for large-scale synthesis of CNTs (up to several square centimeters) aligned in a direction normal to the substrate surface (typically, quartz glass plates). Unexpectedly, we found honeycomblike aligned CNTs by pyrolysis of nickel-cobalt phthalocyanine (designated as Ni-CoPc), which was synthesized by roasting the mixtures of metal salts, phthalanlione, urea, and ammonium molybdate.

A typical experimental procedure is as follows: a clean quartz glass plate (4 × 2 × 0.1 cm) was placed in a flow reactor consisting of a quartz glass tube and a furnace fitted with an independent temperature controller: A flow of Ar-H₂ (1:1, v/v, 20 cm³ min⁻¹) was then introduced into the quartz tube during heating. After the central region of the furnace reached 950 °C, a quartz boat with 0.5 g Ni-CoPc was placed in the region where the temperature was about 500–600 °C. After 5 min heating, CNTs grew in a direction normal to the substrate surface.

Figure 6 is a set of SEM micrographs showing the honeycomblike shape of CNTs. As can be seen in Figure 6a, the honeycomblike CNTs are close together, and the diameters of the honeycombs range from 15 to 80 μm. Figure 6b is a higher magnification image of an area in Figure 6a and clearly shows the size and distribution uniformity of honeycombs. Figure 6c is a magnification image of a typical honeycomb shown in Figure 6a (square frame). The external diameter of the honeycomb is 80 μm, which contains a hollow inner cavity with diameter of 30 μm. The CNTs, forming the honeycombs, grow out from the inner cavity perpendicular uniformly to the substrate surface and then extend all around from the opening of the inner cavity, and finally twin with those of other honeycombs along its outside line.

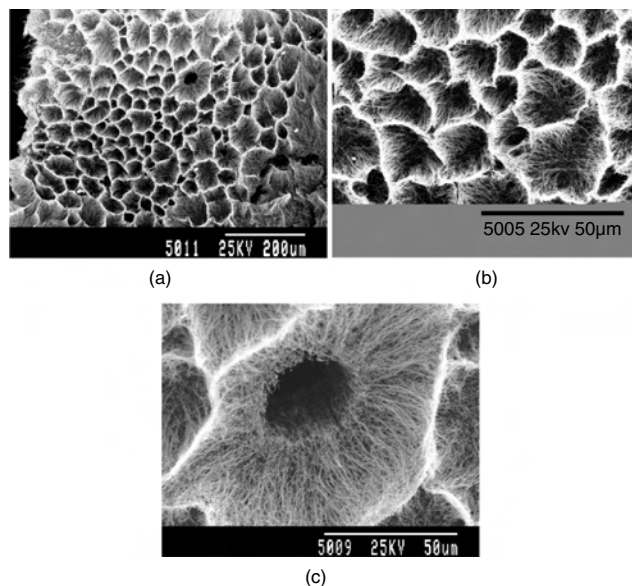


Figure 6. (a) SEM micrograph of honeycomblike aligned CNTs. (b) A higher magnification image of honeycomblike aligned CNTs. (c) Magnification image of a typical honeycomb shown in Figure 2a. Reprinted with permission from [101], X. B. Wang et al., *Appl. Phys. A* 71, 347 (2000). © 2000, Springer-Verlag.

It is interesting that the same patterns of honeycomblike CNTs, two years later, were synthesized by prolysis of ferrocene and xylene on thermally oxidized silicon wafers [102].

3.2.2. Controllable Growth of Structures and Density of Aligned Nanotubes

Controllable Growth of Diameters and Lengths Since nanotubes were first discovered in 1991, several advances in synthesis have led to the production of tubes in larger quantities [63, 103] and higher purities [104–106]. Different diameter, length, and chairality of nanotubes give rise to diverse physical and mechanical properties [10, 107, 108]. However, controlling diameter, length, and chirality has never been easy. Recently, several approaches for controlling diameters of SWNTs have been made. As far as the arc discharge method is concerned, the diameter of SWNTs can be changed by selecting metal catalysts [109] and ranging the pressure of helium gas [110]. For the laser ablation method, the diameters of SWNTs can be controlled by varying the furnace temperature [111] and laser pulse power [112]. However, the research on controlled growth of MWNTs, especially aligned CNTs, falls behind in contrast with that of SWNTs.

Choi et al. [113] have synthesized aligned CNTs on Ni-deposited Si substrate using microwave plasma-enhanced CVD. They found that the diameter, growth rate (length), and density of CNTs could be controlled systematically by the grain size of Ni thin films. With decreasing the grain size of Ni thin films, the diameter of the nanotubes decreased, whereas the growth rate and density increased. The grain size of Ni films varied with the radio frequency (rf) power density during the rf magnetron sputtering process.

As mentioned in Section 3.1.1, we can control the diameters and lengths of aligned CNTs by varying the growth time and the precursor level. Research results show that

the length of the aligned nanotubes increases with the increase of the growth time, and the mean diameters does sharply, too. The diameter distribution width (a difference of between the largest and smallest diameter of a sample) shifts systematically to larger region with increasing growth time, which indicates that the outer diameters of nanotubes become inhomogenous in longer growth time.

The template approach, shown in Section 3.1.2, can control effectively the diameter and length of aligned nanotubes by changing the nanochannel size and the thickness of template substrate, respectively. Recently, Jeong et al. [114] reported nanotube alignments with a narrow length distribution by etching the aluminum oxide template away. Sonication of aligned nanotubes on the template in an acetone solution cut the overgrown tubes effectively, resulting in short MWNTs.

Site Density Controlling of Aligned CNTs Although the diameter and the length of aligned nanotubes can be easily controlled by changing the catalyst particle size, the growth time, etc., control of the site density is still challenging. For well-aligned nanotubes, tuning of site density is very important for certain applications, such as FE, nano-electronic arrays, etc., because of the shielding effect of the dense arrays. Previous methods used to induce the site density include electron beam lithography [92], photolithography [115], microcontact printing [96], shadow mask [60], etc. However, all these methods either require expensive equipment and intensive labor or cannot control the site density in large area.

Recently, research efforts to control the site density have been successful. Pulse-current electrochemical deposition has been used to prepare Ni nanoparticles that are used as the catalysts for the growth of aligned CNTs [116]. The nucleation site density of the Ni nanoparticles was controlled by changing the magnitude and duration of the pulse current. The site density of the aligned nanotubes varied from 10^5 to 10^8 cm^{-2} (Fig. 7).

3.3. 3D Alignments and Patterns of CNTs

In the preceding part of this section, we gave a wide coverage on the fabrication of alignments and patterns of 2D nanotubes with selective positioning and controlled growth. However, in sharp contrast to the research enthusiasm for 2D aligned CNTs, the research on 3D alignment and patterns of nanotubes is sparse.

We have developed a simple method for the large-scale synthesis of 3D aligned CNT patterns on quartz glass substrate [62, 117]. A typical experimental procedure is as follows: a flow reactor, consisting of a quartz tube and a furnace fitted with an independent temperature controller, was heated to 950 $^{\circ}\text{C}$ under a flow of Ar/H_2 (1:1, v/v, 20 cm^3 min^{-1}). Almost immediately after the transfer of a quartz glass plate ($4 \times 2 \times 0.1$ cm) from acetone solution to the central region (950 $^{\circ}\text{C}$) of the furnace, a quartz boat with 0.5 g of FePc was placed in the region where the temperature was 550 $^{\circ}\text{C}$. After 5 min CNTs grew in a direction normal to the substrate surface.

Figure 8a shows an SEM image of 3D regular arrays of nanotubes aligned along the direction perpendicular to the

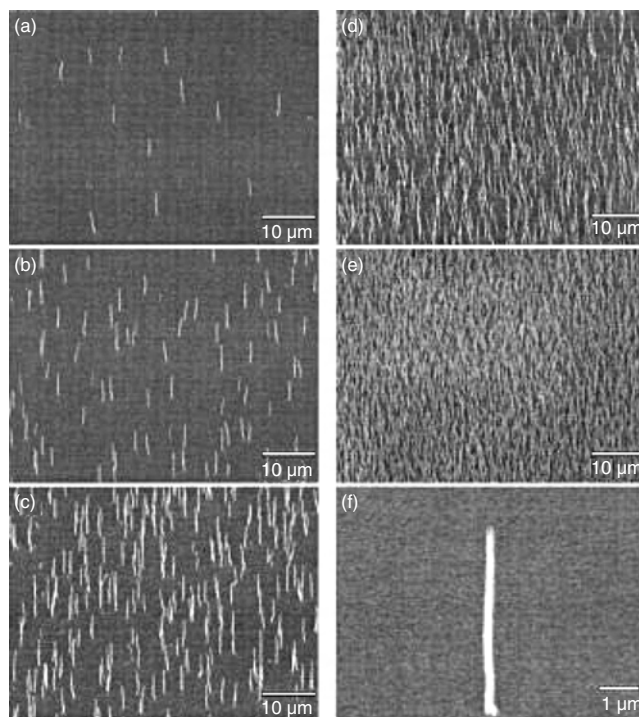


Figure 7. SEM images of aligned CNTs with site densities of (a) 7.5×10^5 (b) 2×10^6 , (c) 6×10^6 , (d) 2×10^7 , and (e) 3×10^8 cm^{-2} , and (f) a single standing CNT. Reprinted with permission from [116], Y. Tu et al., *Appl. Phys. Lett.* 80, 4018 (2002). © 2002, American Institute of Physics.

substrate surface. A few pillar-shaped structures of CNTs grow out from the 2D alignments in a well-distributed mode, which characterizes the 3D CNT alignments. The CNT posts with a diameter of about 3.4 μm are 7.8 μm higher

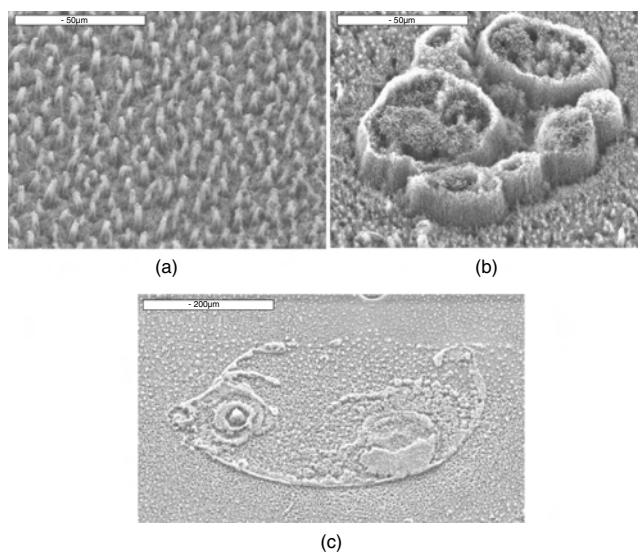


Figure 8. (a) SEM images of 3D regular arrays of nanotubes aligned along the direction perpendicular to the substrate surface. SEM images of 3D nanotube patterns: (b) ringlike castles and (c) a 490 - μm -long crucian carp without a tail and fins. Reprinted with permission from [117], X. B. Wang et al., *Chem. Commun.* 8, 751 (2001). © 2001, The Royal Society of Chemistry.

than the 2D nanotube alignments, whose height is mainly $6\ \mu\text{m}$ from the quartz substrate. In addition to the pillar-shaped 3D nanotube alignments, most interesting patterns made of nanotubes arrays, such as ringlike castles (Fig. 8b) and a $490\text{-}\mu\text{m}$ -long crucian carp without a tail and fins (Fig. 8c), were observed under similar experimental conditions. Although the growth mechanism for these patterns is incomplete at present, we think that the substrate should be responsible for their formation. At the original stage, acetone soaked on the quartz glass substrate was rapidly carbonized at high temperature before volatilization to form the patterns. The resulting carbon, together with iron atom by pyrolysis of FePc, generates metal carbide, which is a more activated catalyst to grow CNTs than metal [80]. Thus, the CNTs in the pattern region formed by metal carbide grow more rapidly than those by metal. This accounts for the formation of alignments and patterns of 3D CNTs. Apart from this, both the strong van der Waals interactions between the tubes and the high surface density of the growing nanotubes serve as additional advantages for the constituent nanotube to be “uncoiled” and allow the aligned nanotubes to develop on the quartz substrate.

In spite of the interesting patterns of 3D nanotubes, the results were unexpected. On the basis of the previous experiments, we have recently realized the controllable fabrication of 3D nanotubes patterns with features of high resolution by a vacuum deposition technique through shadow masks [118]. Using SEM, we observed 3D aligned CNTs, consisting of two streaked ribbons with widths of 6.5 and $8.4\ \mu\text{m}$, respectively (Fig. 9), by pyrolysis of FePc for 5 min. The nanotubes in the ribbon area are about $1.4\ \mu\text{m}$ higher than those of 2D alignments (beyond the ribbon region). The growth rates of the nanotubes in and beyond the ribbon region were about 25 and $20.3\ \text{nm/s}$, respectively. It is only the difference of growth rates that results in the formation of 3D nanotube alignment. These 3D micropatterns of well-aligned

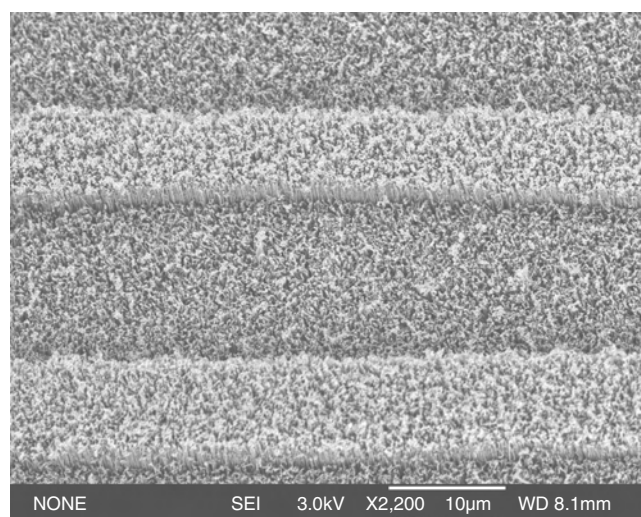


Figure 9. SEM images of 3D nanotube alignments consisting of two ribbonlike structures (6.5 and $8.5\ \mu\text{m}$). The nanotubes in the ribbon region are $1.4\ \mu\text{m}$ higher than those elsewhere. Reprinted with permission from [118], X. B. Wang et al., *Adv. Mater.* 14, 1557 (2002). © 2002, Wiley-VCH.

nanotubes were also prepared on photolithographically prepatterned substrates by the same method [119]. This opened the way for fabricating 3D nanotube micropatterns and thus developing novel nanoelectronic devices.

4. ALIGNMENTS OF SINGLE-WALLED CARBON NANOTUBES

Alignments of SWNTs have been envisioned to enhance performance of various technologically important devices such as sensors [120], field emitters, and organic light-emitting diodes [121]. Immobilizing the random SWNTs into a controlled orientation would be an extremely important step for these real device application of the nanotubes. However, the creation of SWNT alignments has fallen far behind MWNT arrays because of the technical difficulty in handling or aligning individual SWNTs to ideal locations.

4.1. Chemical Alignments

Chemical alignment is an effective method to order SWNTs perpendicular to the substrate by shortening SWNTs in an oxidizing environment, followed by chemical modification of the carboxyl end groups. Short and long SWNTs have exhibited considerable affinity for amine-functionalized substrates, although they tend to orient parallel to the substrate [122, 123]. Thiol functionalization of SWNTs resulted in better alignment on gold substrate; nevertheless, this system was plagued by low surface coverage and long adsorption time [124]. Recently, Wu et al. developed an alternative method for the assembly of oxidatively shortened SWNTs on silver surfaces [125]. This technique is based on the spontaneous adsorption (self-assembly) of the $-\text{COOH}$ groups at the open ends of CNTs onto silver surfaces. Their studies revealed that most of the SWNTs (ca. 80%) assembled on silver surfaces have a bundle size of $6.5 \pm 0.5\ \text{nm}$, possibly suggesting the selective adsorption of SWNTs on silver.

More recently, dense arrays of monolayer and multilayer assemblies of shortened SWNTs have been demonstrated using a metal assisted organization process from nonaqueous media [126]. The self-assembly, which was performed on a substrate such as glass, silicon (110) wafers with native oxide and quartz crystal microbalance resonator, consisted of sequential dipping in an aqueous solution of FeCl_3 followed by immersion in DMF dispersed shortened SWNTs and separated by intermedia washing in DMF. A monolayer of densely packed, needlelike domains was obtained after 30 min immersion in nonaqueous dispersions of shortened SWNTs. This geometry is believed to be the result of a high concentration of carboxy groups on the severed edges of shortened SWNTs, hydroxy functionalization of Fe^{3+} -decorated surfaces, and strong hydrophobic interactions between adjacent shortened SWNTs.

4.2. Alignments by an Electrical or Magnetic Field

Applying an electrical or magnetic field may be a simple and alternative method to align CNTs. Bubke et al. [127] reported that MWNTs dispersed in ethanol can be aligned by an electrical field. Due to the orientation of these elongated particles, the nanotube alignments exhibited optical

anisotropy. Thick films of aligned SWNTs and ropes have been produced by filtration/deposition from suspension in strong magnetic field [128, 129]. Recently, Chen et al. [130] aligned SWNTs on Si/SiO₂ substrate with an alternating current electrical field. Highly oriented SWNT samples were prepared when an electric field with a frequency of 5 MHz was applied. The alignment of the SWNTs demonstrated significant dependencies on the frequency and the magnitude of the electric field. The results suggested that the alignment degree of CNTs was reduced gradually with the decrease of the frequency of the electric field, and the concentration of the aligned SWNTs decreased with the decrease of magnitude. However, SWNT samples oriented by the dc electric field did not demonstrate the apparent orientation. Zhang et al. [131] also demonstrated electric field directed growth of SWNTs over the quartz substrate with prepatterned polysilicon films by CVD. Highly aligned suspended SWNTs can be fabricated along the electric field direction in the range of 0.5–2 V/ μm .

4.3. *In-Situ* Self-Assembly of Aligned SWNTs

Both chemical alignment and alignment by an electrical/magnetic field were obtained by a postprocessing technique, which suffered from the difficulty of local position and complex postsynthesis manipulation. So *in-situ* preparation of aligned SWNTs is of paramount importance for basic research and many potential applications.

Schlitter et al. [132] reported the self-assembly of single crystal SWNTs using thermolysis of alternate layers of C₆₀ and Ni precursors. It is exciting that each crystal is composed of an ordered array of tubes with identical diameters and chirality, although these properties vary between crystals. The structures produced are almost perfect rodlike crystals of SWNTs preferentially oriented normal to the surface of a molybdenum substrate. The perfection of the crystals of SWNTs and the observation that they are all physically identical within any given crystal containing up to several thousand individual nanotubes are unexpected from the point of view of previous results and synthetic approaches in the field.

Zhu et al. [133] directly synthesized the long strands of ordered SWNTs by catalyst CVD with a floating catalyst method in a vertical furnace, where *n*-hexane in combination with thiophene, ferrocene, and hydrogen is catalytically pyrolyzed. The long nanotube strands up to several centimeters in length, consisting of aligned SWNTs, are an alternative to the fibers and filaments spun from nanotube slurries. The research on mechanical and electrical properties indicated that the aligned nanotube strand would be a candidate for practically useful nanotube-based macroscale cables.

However, well-defined alignments of SWNTs synthesized *in-situ* on a substrate were not fabricated until Botti et al. reported the latest results [134]. It was found that well-aligned SWNTs on heated Si substrates could be self-assembled from the carbon nanosized particles without a catalyst by a simple spraying technique. By increasing the substrate temperature, the density of the SWNTs increases and the nanotubes with a uniform length are oriented perpendicularly to the substrate. Although the aligned tubes are bundles of tightly interlaced SWNTs with different chirality

and mean diameter 1.1 ± 0.3 nm, this report opens a route to prepare aligned SWNTs.

5. PROPERTIES AND APPLICATIONS OF ALIGNED CARBON NANOTUBES

Carbon nanotubes are known for their superior mechanical strength and low weight [135], good heat conductance [136], varying electronic properties depending on their helicity and diameter [12], large surface area useful for adsorption of hydrogen or other gas [137], and their ability to emit a cold electron at relatively low voltages due to high aspect ratios and nanometer size tips [20]. Therefore, many future applications have been found in a wide range of fields for being used as field emitters for flat panel displays, vacuum microelectronic devices like microwave power amplifier tubes, nanofield effect transistors [138, 139], nanotube circuits [140], ultrasensitive electrometers [120, 141, 142], nanotweezers [143], nanothermometers [144], and so on.

For aligned CNTs, considerable attention is mainly focused on their excellent FE properties. In this section, apart from the FE properties, we will present other potential properties and applications such as the anisotropic electrical transport property, the superamphiphobic property, and energy storage.

5.1. Field Emission Properties

Earlier than FE, thermionic emission of electron guns had been a key concept in the electron-beam technique. In thermionic electron emission, the solid electron source (i.e., the cathode) is heated above 2000 °C to allow free electrons to escape from the surface [145]. The greatest advantage of this so-called “hot cathode,” usually a heated tungsten (W) filament, is that it works even in non-ultra-high-vacuum (non-UHV) ambiances, which contain vast numbers of gaseous molecules. However, hot cathodes are prone to chemically react with residual water and oxygen to produce tungsten oxides and get thinner and thinner over a long duration through the sublimation of the oxides. In addition, hot cathodes require a power supply for heating, thus making it difficult to construct a compact electron-beam tool.

In the mid 1950s, these disadvantage of hot cathodes were be overcome by replacing them with a FE or “cold cathode” [146]. Unfortunately, the electron emission from a FE cathode is exponentially affected by the chemical and morphological states of the electron emitting area, resulting in instability of emitted currents in non-UHV ambiances. This is particularly true of metallic cathodes, which strongly interacted with residual gaseous molecules.

Chemically, carbon is far more stable, and hence more robust in non-UHV, than metals. Indeed, great effort has been made to develop field emitters based on carbon-containing materials such as diamond, diamondlike carbon, and tetrahedral-amorphous carbon [147, 148]. The high expectations and promise held by these materials, however, have not yet been matched by their performances.

CNTs have emerged as one of the most promising electron field emitters. The power of CNTs as electron sources for displays and lighting devices was amply demonstrated in

the last few years. The superior aspect ratio, good chemical stability, high thermal conductivity, and mechanical stiffness of CNTs are advantageous over conventional semiconductor and metal emitters [149–151]. The investigation of FE properties of individual CNTs and aligned CNT films was originally reported by Rinzler et al. [20] and de Heer et al. [21], respectively. From then on, many research techniques, including improving the method to fabricate CNT alignments, introducing gaseous adsorbates, and controlling the CNT density, have been developed to reduce the operating voltage, enhance the emission current, decrease the field-screening effect, lengthen the device lifetimes, increase the stability of electron emission, etc.

It is worth noticing that the Samsung CNT FE displays represent an impressive feat and an important milestone toward a fully functional device [152, 153]. They work up to now in diode configuration, which implies that the brightness of a pixel is controlled by varying the potential between emitter and phosphor screen, which is on the order of several kilovolts. Conversely, a triode configuration incorporates a control electrode located near the emitter, and the brightness of the pixel is then controlled by adjusting the potential between cathode and control electrode.

Many good FE properties of aligned CNTs have been obtained by different groups although they are still far from practical. Thong et al. [154] reported the emission current density up to 130 mA/cm^2 could be reached at an average field strength of $1.925 \text{ V}/\mu\text{m}$. This emission current was found to be very stable, with short-term fluctuations of no more than $\pm 1.5\%$, while the current drifted less than 1.5% . A turn-on field of $1.2 \text{ V}/\mu\text{m}$ and emission currents of 1 mA/cm^2 at $3 \text{ V}/\mu\text{m}$ were achieved on well-aligned CNT emitters [115]. A test of cathode-ray tube lighting elements underway suggested a lifetime of exceeding 10,000 h.

5.1.1. Effect of Gas Adsorbates on FE Properties

The FE properties are correlated with the electronic structure of the CNTs, and intrinsic properties such as electrical resistivity, thermoelectric power, and thermal conductivity can be modified by adsorption and desorption of gas adsorbates [120, 142, 155]. Therefore, one way to achieve good emission properties is to introduce adsorbates that might effectively lower the ionization potential and facilitate the extraction of electrons.

Many studies have reported the effects of gases on the FE of CNTs [156–159]. Recent experiments done at Motorola [160] indicated that water molecules adsorbed on CNT tips significantly enhance FE current, while O_2 and H_2 not affect the FE behavior appreciably. The first principles density functional theory calculations [161] showed that the water-nanotube interaction under emission conditions at the tube tip can increase the binding energy appreciably, thereby stabilizing the adsorbate, and lower the ionization potential, thereby making it easier to extract electrons.

Wadhawan et al. [162] compared the effects of O_2 , Ar, and H_2 gases on the FE properties of SWNTs and MWNTs. They found that H_2 and Ar gases do not significantly affect the FE properties of SWNTs or MWNTs. O_2 exposure temporarily increased the turn-on field of SWNTs by 22% and decreased

the FE current by two orders of magnitude. However, the FE properties completely recover after 40 h of FE operation in UHV. For MWNTs, the higher voltage O_2 exposure leads to a 43% increase of the turn-on field and reduction of FE current by three orders of magnitude. The recovery in UHV is only partial, indicating that the MWNTs suffer from permanent structural degradation [163]. Kung and Huang [164] demonstrated that the emission current of the CNT arrays treated by O_2 and O_3 was increased $\sim 800\%$ along with a decrease of the onset FE voltage from 0.8 to $0.6 \text{ V}/\mu\text{m}$.

However, a contrary experimental result has been reported by Lee et al. [165] due to different measurement methods of FE properties. Their investigations showed that the turn-on voltages of O_2 and N_2 gases first decreased and saturated at large gas exposure times, whereas that of H_2 gas decreased initially and increased to saturation at large gas exposures. They considered this behavior to be being strongly correlated with the difference of electronegativity of the adsorbed gases. FE is a highly selective process and is extremely sensitive to small variations in the chemical nature and shape and or surroundings of the emitter [166, 167]. This makes a comparison of the results obtained by different groups delicate since the growth, purification, film preparation techniques, and experimental setups differ significantly.

5.1.2. Field-Screening Effect

It is known that the FE properties of the tubes could be affected by a field screening effect provoked by the proximity of neighboring tubes. The field screening effect is determined by various factors relative to the nanotube arrays, including the density, the height, and the diameter. According to the prediction of Nilsson et al. [168], the FE will become maximum when the height of the tubes is about one-half the intertube distance, and arrays with medium densities ($\sim 10^7$ emitters/ cm^2) show the highest emitted current densities. The experiments by Suh et al. [169] suggested that the FE was optimal when the tube height was similar to the intertube distance. This is a little deviation from the prediction. Teo et al. [170] have demonstrated that the density of carbon nanofibers can be decreased to enhance the FE properties of vertically aligned carbon nanofiber emitters, and the arrays of individual, vertically standing nanofibers spaced twice their height apart had the most desirable FE characteristics and the highest apparent field enhancement factor. Therefore, we can tune the FE properties of CNT film emitters by varying the nanotube density [171]. The optimized field emitter can also be achieved by changing the tube diameter according to the result of the first principle calculations [172].

5.2. Anisotropic Electrical Transport Properties

The electrical resistivities of aligned CNTs are anisotropic, being smaller along the tubes than normal to them, because of corresponding differences in the electrical transport [173]. Chauvet et al. [174] observed magnetic anisotropies of the aligned CNTs as well. Recently, electrical, thermal, and structural anisotropies of magnetically aligned single wall CNT films have been obtained by Fischer's et al. [128, 129].

However, all of these aligned CNT films are not as-grown, either they were transferred to a Teflon surface [173, 174] or deposited on a nylon filter membrane [128, 129], which results in a deviation of experimental results. Moreover, these CNT films are imperfectly aligned with some entanglement or curvature of individual tubes (ropes). The disadvantageous factors make the observed results no real reflections of intrinsic properties of those partly aligned CNT films. However, to date the measurements of anisotropic electrical transport properties have not been carried out on as-grown aligned CNT films due to the difficulty in obtaining electrical resistance parallel to the tube axis.

Recently, we have developed a simple technique to measure anisotropic electrical transport properties of as-aligned carbon nanotube films [175]. The temperature dependence of relative electrical resistance suggests that most of the well-aligned carbon nanotubes are semiconductive in both directions parallel and perpendicular to the tube axis. The anisotropy (R_{\perp}/R_{\parallel}) of electrical resistance increases with decreasing temperature T , reflecting the difference in the longitudinal and transverse hopping rates. The differences of the electrical properties in both directions could be explained by a difference degree of localization of charge carriers. The plot of the logarithm of relative resistance against powers of the reciprocal temperature $1/T$ is closely fitted by three-dimensional variable range conduction. After annealing and Br_2 -doping treatments the resistivities of the aligned carbon nanotube films decreased by two orders of magnitude, resulting from the fewer defects and the greater carrier density, respectively.

5.3. Super-“amphiphobic” Properties

Wettability is an important factor for a material. Dujardin et al. have studied the wettability of CNTs in detail and found they could be wet and filled by different substances [176, 177]. In general, wettability of solid surfaces is controlled by the chemical composition and the geometrical structures of the surfaces, and it is usually enhanced by surface roughness [178], especially by fractal structures [181]. Recently, superhydrophobic or superlipophobic surfaces, that is, those with a contact angle of water or oil, respectively, that is higher than 150° [178, 179], have attracted much interest due to practical applications. These surfaces have been commonly prepared through the combination of surface roughening and lowering of the surface energy. However, few reports were concerned with super-“amphiphobic” surfaces [180], which appear to have both superhydrophobic and superlipophobic properties. As the structure of aligned CNT films is similar to that of these superhydrophobic surfaces, the films are expected to show special wettability features.

We reported that the aligned CNT films appear to have super-“amphiphobic” properties; namely, the contact angles for both water and oil are larger than 160° [72]. We demonstrated that the as-grown CNT films are superhydrophobic and superoleophilic. The contact angles for water and rapeseed oil are $158.5 \pm 1.5^\circ$ and $0 \pm 1.0^\circ$, respectively. However, the contact angle for water on a film of CNTs lying flat on a surface is $136.5 \pm 7.0^\circ$, which shows that the aligned

structure of the CNT films is responsible for the superhydrophobic properties.

A low free energy surface is required for a superoleophobic surface to be obtained, and this can be realized by modifying the aligned CNT films with fluorinated compounds. Since the surface of CNTs is rather inert, it is very difficult to modify the surface directly. The hot concentrated H_2SO_4 and HNO_3 mixture (1:1 v/v) was employed to oxidize the aligned CNTs for further chemical modification. The contact angle for water on the aligned CNT film was $128 \pm 3.0^\circ$ after oxidation. It has been reported that some functional groups, such as hydroxyl and carboxyl, can be realized on the surface of CNTs through chemical oxidation treatments. Hence, the oxidized films were modified through immersion in a methanolic solution of hydrolyzed fluoroalkylsilane. After this modification the aligned CNT films contained fluoroalkylsilane groups, which repel both water and oil. The contact angles for water and rapeseed oil on the films were $171 \pm 0.5^\circ$ and $161 \pm 1.0^\circ$ respectively. Hence the film shows both superhydrophobic and superoleophobic properties; namely, it is a super-“amphiphobic” surface. The water droplets move spontaneously and do not come to rest, even when there is little or no apparent tilt of the surface ($<1^\circ$), while the rapeseed droplets remain pinned in one place.

5.4. Hydrogen Storage

The use of CNTs for hydrogen storage has attracted more and more attention due to their high storage capability and potential applications in the next generation energy source. Different types of nanotubes, as well as nanofibers, have been studied for this purpose. In the experimental report published, high hydrogen pressure (up to 100 atm), [181] subambient temperature [183], and alkali-metal doping [184] are applied to achieve hydrogen adsorption. Recently, aligned CNTs were employed for hydrogen adsorption experiments in their as-prepared and pretreated states [185]. The hydrogen storage capacity of 5–7 wt% could be achieved reproducibly at room temperature under modest pressure (10 atm) for the as-prepared samples. Pretreatments, which include heating the samples to 300°C and removing the catalyst tips, can increase the capacity up to 13 wt% and decrease the pressure required for storage. The release of the adsorbed hydrogen can be achieved by heating the samples up to 300°C .

6. SUMMARY

In this account, we have given a brief survey of experimental work directed toward the synthesis and properties of aligned CNTs. In last few years, significant progress has been made for fabricating various alignments and patterns of CNTs, especially MWNTs. However, there still remain many fundamental and fascinating issues about their synthesis, for example, the formational mechanism of aligned CNTs, the controllable synthesis of CNT structures, and so on. The solution of these problems promises to be an exciting and challenging area of nanoscale physics and chemistry in the future. For the properties and applications of aligned CNTs, extensive research interest is only focused on the FE

although the properties of superamphiphobicity and hydrogen storage start to arouse research enthusiasm. There must be wide room, we believe, to explore the potential properties of aligned CNTs in future applications. We are still in the early days of the field, and many surprises undoubtedly lie ahead.

GLOSSARY

Aligned carbon nanotube A film made of an alignment by carbon nanotubes.

Anisotropic electrical transport The electrical resistivities of aligned carbon nanotubes are smaller along the tubes than normal to them.

Carbon nanotube Carbon nanotubes can be thought of as graphitic sheets with a hexagonal lattice that have been wrapped up into a seamless cylinder.

Chemical vapor deposition (CVD) CVD is a chemical reaction which transforms gaseous molecules, called precursor, into a solid material, in the form of thin film or powder, on the surface on a substrate. The process is widely used to fabricate semiconductor devices.

Controllable fabrication of carbon nanotubes Diameter, length, and position are controllable in preparation of carbon nanotubes.

Superamphiphobic The contact angles between the surfaces of a material with water and oil are higher than 150 °C.

ACKNOWLEDGMENTS

The authors gratefully acknowledge financial support from the National Natural Science Foundation of China, the Major State Basic Research Development Program, and the Chinese Academy of Sciences.

REFERENCES

1. S. Iijima, *Nature* 354, 56 (1991).
2. P. J. F. Harris, "Carbon Nanotubes and Related Structures: New Materials for the Twenty-First Century," p. 3. Cambridge Univ. Press, Cambridge, UK, 1999.
3. T. W. Ebbesen, *Annu. Rev. Mater. Sci.* 24, 235 (1994).
4. T. W. Ebbesen, *Phys. Today* 49, 26 (1996).
5. M. S. Dresselhaus, *Annu. Rev. Mater. Sci.* 27, 1 (1997).
6. M. S. Dresselhaus, *Phys. World* (January 1998).
7. P. M. Ajayan, *Chem. Rev.* 99, 1787 (1999).
8. M. Terrones, W. K. Hsu, H. W. Kroto, and D. R. M. Walton, *Top. Current Chem.* 190 (1999).
9. A. Huczko, *Appl. Phys. A* 74, 617 (2002).
10. M. S. Dresselhaus, G. Dresselhaus, and P. C. Eklund, "Sciences of Fullerenes and Carbon Nanotubes." Academic Press, New York, 1996.
11. T. W. Ebbesen, "Carbon Nanotubes: Preparation and Properties" CRC Press, Boca Raton, FL, 1997.
12. R. Saito, M. S. Dresselhaus, and G. Dresselhaus, *Physical Properties of Carbon Nanotubes.* World Scientific, New York, 1998.
13. M. S. Dresselhaus, G. Dresselhaus, and P. Avouris, "Carbon Nanotubes: Synthesis, Structure, Properties, and Application." Springer, Heidelberg, 2001.
14. A. M. Rao, in "Nanotubes and Related Materials Symposium," 27–30, November 2000, Boston, Mas. Materials Research Society, Warrendale, PA, 2001.
15. Special issues on carbon nanotubes, *Carbon* 33, 873 (1995).
16. Special issues on carbon nanotubes, *Appl. Phys. A* 67 (1998).
17. Special issues on carbon nanotubes, *J. Mater. Res.* 13 (1998).
18. S. Iijima and T. Ichihashi, *Nature* 363, 603 (1993).
19. D. S. Bethune, C. H. Kiang, M. S. DeVries, G. Gorman, R. Savoy, and R. Beyers, *Nature* 363, 605 (1993).
20. A. G. Rinzler, J. H. Hafner, P. Nikolaev, L. Lou, S. G. Kim, D. Tomanek, P. Nordlander, D. T. Colbert, and R. E. Smalley, *Science* 269, 1550 (1995).
21. W. A. de Heer, A. Chatelain, and D. Ugarte, *Science* 270, 1179 (1995).
22. B. T. Dunlap, *Phys. Rev. B* 49, 5643 (1994).
23. M. Endo and H. W. Kroto, *J. Phys. Chem.* 96, 6941 (1992).
24. P. M. Ajayan, T. Ichihashi, and S. Iijima, *Chem. Phys. Lett.* 202, 384 (1993).
25. X. B. Wang, Y. Q. Liu, and D. B. Zhu, *J. Nanosci. Nanotech.* 2, 33 (2002).
26. T. W. Ebbesen and P. M. Ajayan, *Nature* 358, 220 (1992).
27. T. W. Ebbesen, in "Carbon Nanotubes: Preparation and Properties," p 139. CRC Press, Boca Raton, FL, 1997.
28. T. Guo, P. Nikolaev, A. Thess, D. T. Colbert, and R. E. Smalley, *Chem. Phys. Lett.* 243, 49 (1995).
29. T. Guo, P. Nikolaev, A. G. Rinzler, D. Tomanek, D. T. Colbert, and R. E. Smalley, *J. Phys. Chem.* 99, 10694 (1995).
30. A. Thess, R. Lee, P. Nikolaev, H. Dai, P. Petit, J. Robert, C. Xu, Y. H. Lee, S. G. Kim, A. G. Rinzler, D. T. Colbert, G. E. Scuseria, D. Tomanek, J. E. Fischer, and R. E. Smalley, *Science* 73, 483 (1996).
31. G. G. Tibbetts, in "Carbon Fibers, Filaments and Composites," pp. 73–94. Kluwer Academic, Amsterdam, 1999.
32. G. G. Tibbetts, *Appl. Phys. Lett.* 42, 666 (1983).
33. M. Endo, *Chemtech* 18, 568 (1988).
34. R. T. K. Baker and N. M. Rodrigue, in *Mater. Res. Soc. Symp. Proc.* 349, 251 (1994).
35. S. Amelinckx, X. B. Zhang, D. Bernaerts, X. F. Zhang, V. Ivanov, and J. B. Nagy, *Science* 265, 635 (1994).
36. X. B. Wang, Z. G. Wang, Y. Q. Liu, C. Wang, C. L. Bai, and D. B. Zhu, *Chem. Phys. Lett.* 339, 36 (2001).
37. M. Endo and H. W. Kroto, *J. Phys. Chem.* 96, 6941 (1992).
38. A. Maiti, C. J. Brabec, C. M. Roland, and J. Bernholc, *Phys. Rev. Lett.* 73, 2468 (1994).
39. J. C. Charlier, A. De Vita, X. Blase, and R. Car, *Science* 275, 646 (1997).
40. E. G. Gamaly and T. W. Ebbesen, *Phys. Rev. B* 52, 2083 (1995).
41. J. Liu, A. G. Rinzler, H. Dai, J. H. Hafner, R. K. Bradley, P. J. Baul, A. Lu, T. Iverson, K. Shelimov, C. B. Huffman, F. Rodriguez-Macias, Y. S. Shon, T. R. Lee, D. T. Colbert, and R. E. Smalley, *Science* 280, 1253 (1998).
42. K. Tohji, T. Goto, H. Takahashi, Y. Shinada, N. Shimizu, B. Jeyadevan, I. Matsuoka, Y. Saito, A. Kasuya, T. Ohsuna, K. Hiraga, and Y. Nishina, *Nature* 383, 679 (1996).
43. J. M. Calderon-Moreno, S. Swamy, T. Fujina, and M. Yoshimura, *Chem. Phys. Lett.* 329, 317 (2000).
44. J. M. Calderon-Moreno, T. Fujina, and M. Yoshimura, *Carbon* 39, 618 (2001).
45. J. M. Calderon-Moreno and M. Yoshimura, *J. Am. Chem. Soc.* 123, 741 (2001).
46. Y. Jiang, Y. Wu, S. Zhang, C. Xu, W. Yu, Y. Xie, and Y. Qian, *J. Am. Chem. Soc.* 122, 12383 (2000).
47. P. S. Shah, S. Husain, K. P. Johnston, and B. A. Korgel, *J. Phys. Chem. B* 105, 9433 (2001).
48. M. Motiei, Y. R. Hacoen, J. Caderon-Moreno, and A. Gedanken, *J. Am. Chem. Soc.* 123, 8624 (2001).
49. J. B. Wiley and R. B. Kaner, *Science* 255, 1093 (1992).

50. P. R. Bonneau, R. F. Jarvis, and R. B. Kaner, *Nature* 349, 510 (1991).
51. I. P. Parkin, *Chem. Soc. Rev.* 25, 199 (1996).
52. J. L. O'Loughlin, C. H. Kiang, C. H. Wallace, T. K. Reynolds, L. Rao, and R. B. Kaner, *J. Phys. Chem. B* 105, 1921 (2001).
53. J. B. Donnet, R. C. Bansal, and M. J. Wang, "Carbon Black Science and Technology," 2nd ed. Dekker, New York, 1993.
54. G. D. Ulrich, *Combust. Sci. Technol.* 4, 45 (1971).
55. R. L. V. Wal and T. M. Tich, *J. Phys. Chem. B* 105, 10249 (2001).
56. R. L. V. Wal, G. M. Berger, and L. J. Hall, *J. Phys. Chem. B* 106, 3564 (2001).
57. H. Ago, S. Ohshima, K. Uchida, and M. Yumura, *J. Phys. Chem. B* 105, 10453 (2001).
58. X. Wang, J. Lu, Y. Xie, X. Guo, and S. Zhang, *J. Phys. Chem. B* 106, 933 (2002).
59. D. Laplaze, P. Bernier, W. K. Maser, G. Flamant, T. Guillard, and A. Loiseau, *Carbon* 36, 685 (1998).
60. S. Fan, M. G. Chapline, N. R. Franklin, T. W. Tombler, A. M. Cassell, and H. Dai, *Science* 283, 512 (1999).
61. W. B. Choi, D. S. Chung, J. H. Kang, H. Y. Kim, Y. W. Jin, I. T. Han, Y. H. Lee, J. E. Jung, N. S. Lee, G. S. Park, and J. M. Kim, *Appl. Phys. Lett.* 75, 3129 (1999).
62. X. B. Wang, Y. Q. Liu, and D. B. Zhu, *Adv. Mater.* 14, 165 (2002).
63. W. Z. Li, S. S. Xie, L. X. Qian, B. H. Chang, B. S. Zou, W. Y. Zhou, R. A. Zhao, and G. Wang, *Science* 274, 1701 (1996).
64. M. Terrones, N. Grobert, J. Olivares, J. P. Zhang, H. Terrones, K. Kordatos, W. K. Hsu, J. P. Hare, P. D. Townsend, K. Prassides, A. K. Cheetham, H. W. Kroto, and D. R. M. Walton, *Nature* 388, 52 (1997).
65. Z. F. Ren, Z. P. Huang, J. W. Xu, J. H. Wang, P. Bush, M. P. Siegal, and P. N. Provencio, *Science* 282, 1105 (1998).
66. Z. P. Huang, J. W. Xu, Z. F. Ren, J. H. Wang, M. P. Siegal, and P. N. Provencio, *Appl. Phys. Lett.* 73, 3845 (1998).
67. Y. Yang, S. Huang, H. He, A. W. H. Mau, and L. Dai, *J. Am. Chem. Soc.* 121, 10832 (1999).
68. D. J. Norris and Y. A. Vlasov, *Adv. Mater.* 13, 371 (2001).
69. Y. Lu, Y. Yin, and Y. Xia, *Adv. Mater.* 13, 415 (2001).
70. D. Routkevitch, A. A. Tager, J. Haruyama, D. Almalawi, M. Moskovits, and J. M. Xu, *IEEE Trans. Electron Devices* 43, 1646 (1996).
71. R. J. Tonucci, B. L. Justus, A. J. Campillo, and C. E. Ford, *Science* 258, 783 (1992).
72. H. J. Li, X. B. Wang, Y. L. Song, Y. Q. Liu, Q. S. Li, L. Jiang, and D. B. Zhu, *Angew. Chem. Int. Ed.* 40, 1743 (2001).
73. D. Öner and T. J. McCarthy, *Langmuir* 16, 7777 (2000).
74. P. M. Ajayan, O. Stephan, C. Colliex, and D. Trauth, *Science* 265, 1212 (1994).
75. W. A. de Heer, W. S. Bacs, A. Chatlain, T. Gerfin, R. Humphrey-Baker, L. Forro, and D. Ugarte, *Science* 268, 845 (1995).
76. J. Li, C. Papadopoulos, J. M. Xu, and M. Moskovits, *Appl. Phys. Lett.* 75, 367 (1999).
77. X. B. Wang, Y. Q. Liu, and D. B. Zhu, *Chem. Phys. Lett.* 340, 419 (2001).
78. Y. C. Choi, Y. M. Shin, Y. H. Lee, B. S. Lee, G. S. Park, W. B. Choi, N. S. Lee, and J. M. Kim, *Appl. Phys. Lett.* 76, 2367 (2000).
79. S. Huang, L. Dai, and A. W. H. Mau, *J. Phys. Chem. B* 103, 4223 (1999).
80. X. B. Wang, W. P. Hu, Y. Q. Liu, C. F. Long, Y. Xu, S. Q. Zhou, D. B. Zhu, and L. M. Dai, *Carbon* 39, 1533 (2001).
81. Z. P. Huang, J. W. Xu, Z. F. Ren, J. H. Wang, M. P. Siegal, and P. N. Provencio, *Appl. Phys. Lett.* 73, 3845 (1998).
82. Y. Chen, Z. L. Wang, J. S. Yin, D. J. Johnson, and R. H. Prince, *Chem. Phys. Lett.* 22, 178 (1997).
83. Y. Chen, S. Patel, Y. Ye, D. T. Shaw, and L. Guo, *Appl. Phys. Lett.* 73, 2119 (1998).
84. B. M. Novak, *Adv. Mater.* 5, 422 (1993).
85. L. T. Canham, *Appl. Phys. Lett.* 57, 1046 (1990).
86. R. T. Collins, *Phys. Today* 50, 24 (1997).
87. T. Iwasaki, T. Motol, and T. Den, *Appl. Phys. Lett.* 75, 2044 (1999).
88. J. S. Suh and J. S. Lee, *Appl. Phys. Lett.* 75, 2047 (1999).
89. B. Q. Wei, R. Vajtal, Y. Jung, J. Ward, R. Zhang, G. Ramanath, and P. M. Ajayan, *Nature* 416, 495 (2002).
90. Z. J. Zhang, B. Q. Wei, R. Vajtal, G. Ramanath, and P. M. Ajayan, *Appl. Phys. Lett.* 77, 3764 (2000).
91. J. I. Sohn, S. Lee, Y. H. Song, S. Y. Choi, K. I. Cho, and K. S. Nam, *Appl. Phys. Lett.* 78, 901 (2001).
92. Z. F. Ren, Z. P. Huang, D. Z. Wang, J. G. Wen, J. W. Xu, J. H. Wang, L. E. Calvet, J. Chen, J. F. Klemic, and M. A. Reed, *Appl. Phys. Lett.* 75, 1086 (1999).
93. Y. Xia and G. M. Whitesides, *Angew. Chem. Int. Ed. Engl.* 37, 551 (1998).
94. A. Kumar and G. M. Whitesides, *Appl. Phys. Lett.* 63, 2002 (1993).
95. E. Delamar, H. Schmid, A. Bietsch, N. B. Larsen, H. Rothuizen, B. Michel, and H. Biebuyck, *J. Phys. Chem. B* 102, 3324 (1998).
96. H. Kind, J. M. Bonard, L. Forro, K. Kern, K. Hernadi, L. O. Nilsson, and L. Schlappbach, *Langmuir* 6, 6877 (2000).
97. A. M. Cassell, S. Verma, L. Delzeit, M. Meyyappan, and J. Han, *Langmuir* 17, 260 (2001).
98. H. T. Ng, M. L. Foo, A. Fang, J. Li, G. Xu, S. Jaenicke, L. Chan, and S. F. Y. Li, *Langmuir* 18, 1 (2002).
99. S. Huang, A. W. H. Mau, T. W. Turney, P. A. White, and L. Dai, *J. Phys. Chem. B* 104, 2193 (2000).
100. Y. Avigal and R. Kalish, *Appl. Phys. Lett.* 78, 2291 (2001).
101. X. B. Wang, Y. Q. Liu, and D. B. Zhu, *Appl. Phys. A* 71, 347 (2000).
102. Z. Zhang, B. Wei, and P. M. Ajayan, *Chem. Commun.* 9, 962 (2002).
103. C. Journet, W. K. Maser, P. Bernier, A. Loiseau, M. L. Chapelle, S. Lefrant, P. Deniard, R. Lee, and J. E. Fischer, *Nature* 388, 756 (1997).
104. S. Niyogi, H. Hu, M. A. Hamon, P. Bhowmik, B. Zhao, S. M. Rozenzhak, J. Chen, M. E. Itkis, M. S. Meier, and R. C. Haddon, *J. Am. Chem. Soc.* 123, 733 (2001).
105. J. M. Moon, K. H. An, Y. H. Lee, Y. S. Park, D. J. Bae, and G. S. Park, *J. Phys. Chem. B* 105, 5677 (2001).
106. R. Marphy, J. N. Coleman, M. Cadek, B. McCarthy, M. Bent, A. Drury, R. C. Barklie, and W. J. Blau, *J. Phys. Chem. B* 106, 3087 (2002).
107. N. Humada, S. Sawata, and A. Oshiyama, *Phys. Rev. Lett.* 68, 1579 (1992).
108. R. A. Jishi, M. S. Dresselhaus, and G. Dresselhaus, *Phys. Rev. B* 48, 11385 (1993).
109. A. Kasuya, Y. Sasaki, Y. Saito, K. Tohji, and Y. Nishina, *Phys. Rev. Lett.* 78, 4434 (1997).
110. Y. Saito, Y. Tani, and A. Kasuya, *J. Phys. Chem. B* 104, 2495 (2000).
111. S. Bandow, S. Asaka, Y. Saito, A. M. Rao, L. Grigorian, E. Richter, and P. C. Eklund, *Phys. Rev. Lett.* 80, 3779 (1998).
112. C. Dillon, P. A. Parilla, J. L. Alleman, J. D. Perkins, and M. J. Heben, *Chem. Phys. Lett.* 316, 13 (2000).
113. Y. C. Choi, Y. M. Shin, Y. H. Lee, B. S. Lee, G.-S. Park, W. B. Choi, N. S. Lee, and J. M. Kim, *Appl. Phys. Lett.* 76, 2367 (2000).
114. S. H. Jeong, O. J. Lee, and K. H. Lee, *Chem. Mater.* 14, 1859 (2002).
115. H. Murakami, M. Hirakawa, C. Tanaka, and H. Yamakawa, *Appl. Phys. Lett.* 76, 1776 (2000).
116. Y. Tu, Z. P. Huang, D. Z. Wang, J. G. Wen, and Z. F. Ren, *Appl. Phys. Lett.* 80, 4018 (2002).
117. X. B. Wang, Y. Q. Liu, and D. B. Zhu, *Chem. Commun.* 8, 751 (2001).
118. X. B. Wang, Y. Q. Liu, P. A. Hu, G. Yu, K. Xiao, and D. B. Zhu, *Adv. Mater.* 14, 1557 (2002).
119. Q. Chen and L. Dai, *J. Nanosci. Nanotech.* 1, 43 (2001).

120. P. G. Collins, K. Bradley, M. Ishigami, and A. Zettl, *Science* 287, 1801 (2000).
121. J. E. Riggs, Z. Guo, D. L. Carrol, and Y. P. Sun, *J. Am. Chem. Soc.* 122, 5879 (2000).
122. J. Liu, M. J. Casavant, M. Cox, D. A. Walters, P. Boul, W. Lu, A. J. Smith, D. T. Colbert, and R. E. Smalley, *Chem. Phys. Lett.* 303, 125 (1999).
123. M. Burghard, G. Duesberg, G. Philipp, J. Muster, and S. Roth, *Adv. Mater.* 10, 584 (1998).
124. Z. Liu, Z. Shen, T. Zhu, S. Hou, L. Ying, Z. Shi, and Z. Gu, *Langmuir* 16, 3569 (2000).
125. B. Wu, J. Zhang, Z. Wei, S. Cai, and Z. Liu, *J. Phys. Chem. B* 105, 5075 (2001).
126. D. Chattopadhyay, I. Galeska, and F. Papadimitrakopoulos, *J. Am. Chem. Soc.* 123, 9451 (2001).
127. K. Bubke, H. Gnewuch, and M. Hempstead, *Appl. Phys. Lett.* 71, 1906 (1997).
128. B. W. Smith, Z. Benes, D. E. Luzzi, J. E. Fischer, D. A. Walters, M. L. Casavant, J. Schmidt, and R. E. Smalley, *Appl. Phys. Lett.* 77, 663 (2000).
129. J. Hone, M. C. Lagune, N. M. Nemes, A. T. Johnson, J. E. Fischer, D. A. Walters, M. J. Casavant, J. Schmidt, and R. E. Smalley, *Appl. Phys. Lett.* 77, 666 (2000).
130. X. Q. Chen, T. Saito, H. Yamada, and K. Matsushige, *Appl. Phys. Lett.* 78, 3714 (2001).
131. Y. Zhang, A. Chang, J. Cao, Q. Wang, W. Kim, Y. Li, N. Morris, E. Yenilmez, J. Kong, and H. Dai, *Appl. Phys. Lett.* 79, 3155 (2001).
132. R. R. Schlittler, J. W. Seo, J. K. Gimzewski, C. Durkan, M. S. M. Saifullah, and M. E. Welland, *Science* 292, 1136 (2001).
133. H. W. Zhu, C. L. Xu, D. H. Wu, B. Q. Wei, R. Vajtal, and P. M. Ajayan, *Science* 296, 884 (2002).
134. S. Botti, R. Ciardi, M. L. Terranova, S. Piccirillo, V. Sessa, M. Rossi, and M. Vittori-Antisari, *Appl. Phys. Lett.* 80, 1441 (2002).
135. M. M. Treachy, T. W. Ebbesen, and J. M. Gibson, *Nature* 381, 678 (1996).
136. R. S. Ruoff and D. C. Lorents, *Carbon* 33, 925 (1995).
137. C. Liu, Y. Y. Fan, M. Liu, H. T. Cong, H. M. Cheng, and M. S. Dresselhaus, *Science* 286, 1127 (1999).
138. H. W. Ch. Postma, T. Teeppen, Z. Yao, M. Grifoni, and C. Dekker, *Science* 293, 76 (2001).
139. A. Bachtold, P. Hadley, T. Nakanishi, and C. Dekker, *Science* 294, 1317 (2001).
140. P. G. Collins, M. S. Arnold, and P. Avouris, *Science* 292, 706 (2001).
141. L. Roschier, R. Tarkiainen, M. Ahlskog, M. Paalanen, and P. Hakonen, *Appl. Phys. Lett.* 78, 3295 (2001).
142. J. Kong, N. R. Franklin, C. Zhou, M. G. Chapline, S. Peng, K. Cho, and H. Dai, *Science* 287, 622 (2000).
143. P. Kim and C. M. Lieber, *Science* 286, 2148 (1999).
144. Y. Gao and Y. Bando, *Nature* 415, 599 (2002).
145. R. A. Reaghead, J. P. Hobson, and E. V. Kornelsen, "The Physical Basis of Ultrahigh Vacuum," Ch. 2. Chapman and Hall, London, 1968.
146. W. P. Dyke and W. W. Dolan, *Adv. Electron. Electron Phys.* 8, 169 (1956).
147. F. S. Baker, A. R. Osborn, and J. Williams, *Nature* 239, 96 (1972).
148. C. Lea, *J. Phys. D* 6, 1105 (1973).
149. Q. H. Wang, A. A. Setlur, J. M. Lauerhaas, J. Y. Dai, E. W. Seeling, and R. P. H. Chang, *Appl. Phys. Lett.* 73, 918 (1998).
150. E. W. Wong, P. E. Sheehan, and C. M. Lieber, *Science* 277, 1972 (1997).
151. Z. Yao, C. L. Kane, and C. Dekker, *Phys. Rev. Lett.* 84, 2941 (2000).
152. W. B. Choi, D. S. Chung, J. H. Kang, H. Y. Kim, Y. W. Jim, I. T. Han, Y. H. Lee, J. E. Jung, N. S. Lee, G. S. Park, and J. M. Kim, *Appl. Phys. Lett.* 75, 3129 (1999).
153. D. S. Chung, S. H. Park, H. W. Min, S. H. Cho, M. J. Yoon, J. S. Lee, C. K. Lee, J. H. Yoo, J. M. Kim, J. E. Jung, Y. W. Jin, Y. J. Park, and J. B. You, *Appl. Phys. Lett.* 80, 4045 (2002).
154. J. T. L. Thong, C. H. Om, W. K. Eng, W. D. Zhang, and L. M. Gan, *Appl. Phys. Lett.* 79, 2811 (2001).
155. G. U. Sumanasekera, C. K. W. Adu, S. Fang, and P. C. Eklund, *Phys. Rev. Lett.* 85, 1096 (2000).
156. J. M. Bonard, J. P. Salvetat, T. Stockli, and W. A. de Heer, *Appl. Phys. Lett.* 73, 918 (1998).
157. J. M. Bonard, F. Maier, T. Stockli, A. Chatelain, W. A. de Heer, J. P. Salvetat, and L. Forro, *Ultramicroscopy* 73, 7 (1998).
158. D. S. Chung, *J. Vac. Sci. Technol. B* 18, 1054 (2000).
159. K. A. Dean and B. R. Chalamala, *Appl. Phys. Lett.* 75, 3017 (1998).
160. K. A. Dean, P. von Allmen, and B. R. Chalamala, *J. Vac. Sci. Technol. B* 17, 1959 (1999).
161. A. Maiti, J. Andzelm, N. Tanpipat, and P. von Allmen, *Phys. Rev. Lett.* 87, 155502 (2001).
162. A. Wadhawan, R. E. Stalleup II, K. F. Stephens II, and J. M. Perez, *Appl. Phys. Lett.* 79, 1867 (2001).
163. T. Kuzumaki, Y. Takamura, H. Ichinose, and Y. Horiike, *Appl. Phys. Lett.* 78, 3699 (2001).
164. S. C. Kung and K. C. Huang, *Appl. Phys. Lett.* 80, 4819 (2002).
165. Y. H. Lee, N. S. Lee, and J. M. Kim, *Adv. Mater.* 13, 1563 (2001).
166. J. M. Bonard, J. P. Salvetat, T. Stockli, L. Forro, and A. Chatelain, *Appl. Phys. Lett.* 69, 245 (1999).
167. D. N. Davydov, P. A. Sattari, D. AlMawlawi, A. Osika, T. L. Haslett, and M. Moskovits, *J. Appl. Phys.* 86, 3983 (1999).
168. L. Nilsson, O. Groening, C. Emmenegger, O. Kuettel, E. Schaller, and L. Schlapbach, *Appl. Phys. Lett.* 76, 2071 (2000).
169. J. S. Suh, K. S. Jeong, J. S. Lee, and I. Han, *Appl. Phys. Lett.* 80, 2392 (2002).
170. K. B. K. Teo, M. Chhowalla, G. A. J. Amaratunga, W. I. Milne, G. Pirio, P. Legagneux, F. Wyczisk, D. Pribat, and D. G. Hasko, *Appl. Phys. Lett.* 80, 2011 (2002).
171. J. M. Bonard, N. Weiss, H. Kind, T. Stockli, L. Forro, K. Kern, and A. Chatelain, *Adv. Mater.* 13, 184 (2001).
172. G. Zhou, W. Duan, and B. Gu, *Appl. Phys. Lett.* 79, 836 (2001).
173. W. A. de Heer, W. S. Bacsas, A. Châtelain, T. Gerfin, R. Humphrey-Baker, L. Forro, and D. Ugarte, *Science* 268, 845 (1995).
174. O. Chauvet, L. Forro, W. Bacsas, D. Ugarte, B. Doudin, and W. A. de Heer, *Phys. Rev. B* 52, R6963 (1995).
175. X. B. Wang, Y. Q. Liu, G. Yu, C. Y. Xu, J. B. Zhang, and D. B. Zhu, *J. Phys. Chem. B* 105, 9422 (2001).
176. E. Dujardin, T. W. Ebbesen, H. Hiura, and K. Tanigaki, *Science* 265, 1850 (1994).
177. E. Dujardin, T. W. Ebbesen, A. Krishnan, and M. M. J. Treacy, *Adv. Mater.* 10, 1472 (1998).
178. A. Nakajima, A. Fujishima, K. Hashimoto, and T. Watanabe, *Adv. Mater.* 11, 1365 (1999).
179. K. Sujii, T. Yamamoto, T. Onda, and S. Shibuichi, *Angew. Chem. Int. Ed. Engl.* 36, 1011 (1997).
180. L. Jiang, R. Wang, B. Yang, T. J. Li, D. A. Trigk, A. Fujishima, K. Hashimoto, and D. B. Zhu, *Pure Appl. Chem.* 72, 73 (2000).
181. C. Liu, Y. Y. Fan, H. T. Cong, H. M. Cheng, and M. S. Dresselhaus, *Science* 286, 1127 (1999).
182. A. C. Dillon, K. M. Johns, T. A. Bekkedahl, C. H. Klang, D. S. Bethune, and M. J. Heben, *Nature* 386, 377 (1997).
183. Y. Ye, C. C. Ahm, C. Witham, B. Fultz, J. Liu, A. G. Rinzler, D. Colbert, K. A. Smith, and R. E. Smalley, *Appl. Phys. Lett.* 74, 2307 (1999).
184. P. Chen, X. Wu, J. Lin, and K. L. Tan, *Science* 285, 91 (1999).
185. Y. Chen, D. T. Shaw, X. D. Bai, E. G. Wang, C. Lund, W. M. Lu, and D. D. L. Chung, *Appl. Phys. Lett.* 78, 2128 (2001).

Alkanethiol Self-Assembled Monolayers

J. Justin Gooding

The University of New South Wales, Sydney, Australia

CONTENTS

1. Introduction
 2. Preparation and Properties of Alkanethiol Self-Assembled Monolayers
 3. Applications of Self-Assembled Monolayers
 4. Concluding Remarks
- Glossary
References

1. INTRODUCTION

1.1. Self-Assembly in Nanotechnology

Nanotechnology involves making useful devices with nanometer control in at least one dimension. Nanometer control infers that nanotechnology involves fabrication from molecular components. Therefore, in nanotechnology different molecular components must be integrated into a functional device. Such integration requires the precise positioning of individual molecules. To create this molecular organization, the fabrication of nanostructures can be achieved with either the “top-down” or the “bottom-up” fabrication methods. The potential drawbacks of top-down methods, include the materials used, usually have little chemical diversity and the approach is limited in the number of nanodevices that can be fabricated at one time [1]. Therefore, bottom-up fabrication from molecular components possesses far more promise in enabling the nanotechnology revolution to be fully realized.

Bottom-up fabrication can be achieved either through the physical placement of individual atoms and molecules, or via self-assembly. The former invokes images of either molecular assemblers, which have been elegantly demonstrated by the iron corrals and molecular abacus assembled by the IBM research labs [2], or the single placement of phosphorous atoms on silicon surfaces as part of the development of silicon-based quantum computers [3]. In common with top-down fabrication, the physical placement of individual atoms, or molecules, has the disadvantage of low throughput of devices. Therefore, self-assembly appears to be the most likely strategy for developing a generic approach to the fabrication of functional nanodevices [1].

Self-assembly is how nature makes molecular machines. From linear sequences of amino acids, nanomachines like enzymes and ion channels form through spontaneous folding (sometimes with a little chaperoning) into functional conformations. The essence of self-assembly is that no external intervention is required once the process has started. That is, the rules for organization are encoded into the molecular structure and the conditions used [4]. The self-organization inevitably means the structures are thermodynamically stable, relative to other conformations, in conditions similar to those in which they were formed. Achieving such spontaneous assembly requires exquisite control over the noncovalent interactions involved as the nanomachines are formed. Frequently, different subunits of a protein or ion channel, derived from different linear chains of amino acids, will be combined to give the final functional device [5]. The combination of the subunits favors the production of a symmetrical molecule. The joining of subunits reflects two of the key features of self-assembly in natural systems. First, the molecules must have a strong affinity for each other. This affinity exploits molecular recognition to ensure that the binding of subunits is not only strong but also selective. This gives the second key feature, which is that predictable structures are formed when the subunits associate. These two features are demonstrated in the formation of a DNA duplex when two complementary single strands are self-assembled.

1.2. Self-Assembled Monolayers (SAMs)

Self-assembly directed by human hands is a long way removed from the complex nanomachines that nature produces, although impressive control has been demonstrated with self-assembled monolayers and other surfactant systems. Self-assembled monolayers (SAMs) are ordered monomolecular films, which are spontaneously formed from immersing a solid substrate into a solution containing amphifunctional molecules (see Fig. 1). The amphifunctional molecule has a head group, which usually has a high affinity for the solid surface, a tail—typically an alkyl chain—and a terminal group that can be used to control the surface properties of the resultant monolayer. The molecular

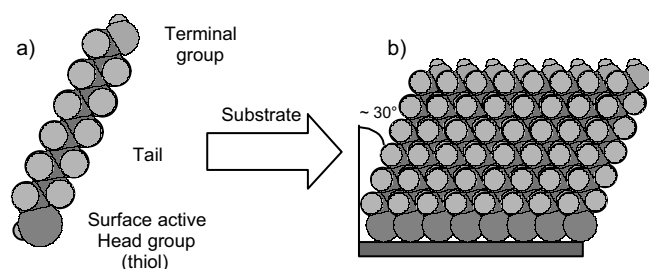


Figure 1. a) A self-assembling molecule with a surface active head group (in this case, a thiol group), an alkyl chain tail, and a terminal group. The terminal group is represented as an amine but could be any functional group; b) an alkanethiol SAM formed on an Au(111) surface with the characteristic 30° tilt from normal.

forces between the tails are chiefly responsible for the order of the monolayer. So SAMs have the two key features of self-assembly in biological systems, namely, that molecules have high affinity for each other and predictable structures are formed when the molecular units are associated. The ability to tailor both head groups and tail groups of the self-assembling molecules makes control over the self-assembly behavior possible. This control is important both for nanoscience and nanotechnology. With regards to nanoscience, SAMs provide an opportunity to increase the fundamental knowledge about self-organization, structure-function relationships, and interfacial phenomena [6]. From the perspective of nanotechnology, SAMs allow accessible molecular level control for bottom-up fabrication in at least two dimensions. Furthermore, because molecular level assembly frequently occurs on macroscopic surfaces, SAMs also provide a reasonably simple way of interfacing the nanodevices with the macroscopic human world.

The potential applications of SAMs in nanotechnology span a diverse range. From the simplest case of the assembly of a single component on a surface to give functional surface coatings (such as in corrosion or wear protection) [7–9] to complicated integrated molecular systems used in chemical and biosensing (where the biomimetic and biocompatible nature of SAMs is particularly attractive) [10–13] and in molecular electronics [14], where the addressing of functional molecules to each other and to the outside world is so important.

1.3. Organosulfur SAMs

The most extensively studied self-assembled monolayers are silanes, which are used to modify hydroxyl terminated surfaces, and organosulfur compounds, which exploit the affinity of sulfur for coinage metals (such as gold, platinum, and silver) [15]. The formation of SAMs of organosulfur compounds on metal surfaces was first described by Nuzzo and Allara [16] in 1983 with the adsorption of a di-*n*-alkyl disulfide onto gold surfaces. Since this time the research into organosulfur adsorbates has been exceedingly active. Apart from alkanethiols and di-*n*-alkyl disulfide [16–20] a number of other surface organosulfur compounds which form monolayers on gold have been reported including di-*n*-alkyl sulfides [19, 21–26], thiophenes [27–29] and alkyl xanthates [30–33] (see Fig. 2). Representative spectroscopic data and

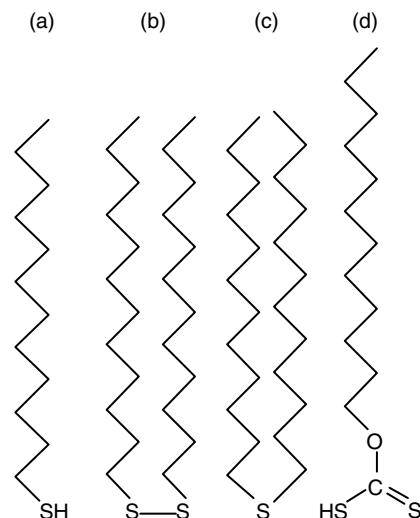


Figure 2. The chemical structures of representative organosulfur compounds that can form self-assembled monolayers on coinage metal surfaces, a) *n*-decanethiol, b) di-dodecyl-*n*-disulfide, c) di-*n*-dodecyl sulfide, d) dodecyl xanthic acid.

physical properties for each class of organosulfur SAM are outlined in Table 1.

An alkanethiol has a thiol (-SH) head group and a tail that is usually an alkyl chain. At the end of the tail is the terminal group, which in a well-packed monolayer, determines the properties of the surface of the monolayer. *n*-Alkanethiols and di-*n*-alkyl disulfide self-assemble on coinage metals to form well-organized monolayers, where the formation of a bond between the thiolate head group and the metal surface anchors the organosulfur molecules to the surface and interactions between the alkyl chains give the monolayer its order (see Fig. 1). Both alkanethiols and di-*n*-alkyl disulfide give alkanethiolate surfaces. The other organosulfur compounds give different surface structures (see Fig. 2). (There has recently been debate as to whether carbon sulfur cleavage occurred in the self-assembly of the dialkylsulfides [19, 34–36], but it has been confirmed that both alkyl chains remain bonded to the sulfur [36, 37]). The vast majority of research has concentrated on alkanethiols and disulfides and hence are the focus of this chapter. As they produce the same surface

Table 1. Physical and spectroscopic data on some representative organosulfur compounds.

Compound	MP (°C)	¹ H NMR Data	Ref.
Dodecanethiol	—	400 MHz (C ₆ D ₆): 2.17 (m, 2 H), 1.4–1.05 (m, 20 H), 0.91 (t, 3 H)	[134]
di- <i>n</i> -dodecyl disulphide	—	200 MHz (CD ₂ Cl ₂): 3.58 (t, 2 H), 2.65 (t, 4 H), 1.68 (m, 2 H), 1.54 (m, 4 H), 1.45–1.25 (m, 32 H), 0.87 (t, 3 H)	[20]
di- <i>n</i> -dodecyl sulphide	40.0–41.5	300 MHz (CDCl ₃): 2.50 (t, 4 H), 1.57 (m), 1.26 (m), 0.88 (t, 6 H)	[21]
Dodecyl xanthic acid	—	400 MHz (CDCl ₃): 5.49 (s, 1 H), 4.42 (t, 2 H), 1.67–1.73 (m, 2 H), 1.20–1.32 (m, 18 H), 0.81 (t, 3 H)	[33]

attached species—an alkanethiolate—throughout this chapter the term alkanethiol or alkanethiol SAMs will refer to SAMs formed from either, unless explicitly stated.

Alkanethiols and related compounds are popular for the formation of SAMs for a number of reasons. First, preparation of alkanethiol SAMs is relatively easy. Assembly does not require vacuum or anaerobic conditions and the solvent has minimal effect on the assembly process. Furthermore, the assembly process still occurs despite some surface impurity (although there will be an influence of the kinetics of SAM formation and the number of defects), as organic matter will be displaced by the alkanethiol as a consequence of the affinity of thiols for the metal. This affinity provides the second reason for the popularity of alkanethiol SAMs—namely, they are reasonably stable. The stability is demonstrated by the fact that alkanethiol SAMs survive prolonged exposure to vacuum used during many surface characterization experiments [15] and that the SAMs withstand a broad range of potentials applied to the underlying metal surface (typically between +1.0 and -1.0 V versus SCE) [38–40]. The third reason is that a variety of functional groups can be incorporated into the SAM without disrupting the self-assembly process. Finally, mixed SAMs can be prepared either through simultaneous deposition [41] or sequentially by a place-exchange reaction [42]. These final two reasons are a crucial feature in molecular level fabrication. Being able to direct the type and spacing of terminal groups of the SAM provides control over what is built upon a surface.

Applications of alkanethiolate modified surfaces include making surfaces biocompatible [43, 44], mimicking biological membranes [45], using SAMs to obtain fundamental information regarding electron transfer processes [46], in the fabrication of sensors [10, 11, 47], and as a “molecular glue” for fabricating nanostructures [48]. As coinage metals form good electrodes, the assembly of alkanethiol SAMs onto these surfaces has seen many of the applications involving alkanethiols being electrochemical [4, 10–12, 46, 49–51]. Typically, the SAM is used to alter the performance of the electrode, such as making it selective for an analyte [10–12], passivating it [46, 52, 53], or making the surface biocompatible [43, 44, 49, 54]. Synthesizing novel alkanethiols, which can act as molecular wires or conduits for electron transfer, allows SAMs to be used for fundamental research into electron transfer in nature [46, 55, 56] and for molecular electronics [57, 58]. The alkyl chains of the SAMs also allow bilayer structures to be formed so the interface mimics a biological membrane [45, 59, 60]. Self-assembled monolayers can also provide the base layer upon which a multilayer system with molecular level control is fabricated [61, 62]. The molecular level control of the modification of the interface provides a foundation which other nanoscale building blocks, such as nanoparticles [48, 63–65], nanotubes [66–68], and DNA [69–74], can be built upon.

There are a number of detailed reviews on SAMs, which the interested reader is referred to that address single issues in more detail. Reviews that are available address topics such as SAM formation and structure [6, 15], simulation of SAMs [15, 75, 76], their characterization using electrochemical [46], scanning tunneling microscopy [77], and atomic force microscopy [78, 79] techniques, their applications to

the fabrication of biosensors [11–13, 80], and electrochemical sensors [10, 47, 51], providing controlled surface properties [43, 44, 49, 54, 81, 82], patterning SAMs [81, 83–86], SAMs on nanoparticles [87, 88], and providing unique reaction environments [89]. The purpose of this chapter is to give an overall outline of the basic features of alkanethiol SAMs and then to review some applications of SAMs in sensing and nanofabrication.

2. PREPARATION AND PROPERTIES OF ALKANETHIOL SELF-ASSEMBLED MONOLAYERS

In this section, the formation of SAMs, their structure, and important variables in their preparation will be discussed. As there are many types of organosulfur molecules that self-assemble on a variety of metal surfaces (all of which can give subtle differences in SAM structure), SAM preparation procedures and so on, the discussion below will refer to long chain aliphatic alkanethiols (typically either dodecanethiol or hexadecanethiol) adsorbed onto gold surfaces unless otherwise stated.

2.1. Methods of Assembly

2.1.1. Solution Assembly

Alkanethiols adsorb spontaneously from solution onto the surface of coinage metals. Gold is the most frequently used. The thiol groups chemisorb onto the gold surface via the formation of a gold-thiol bond [6, 90] to produce a densely packed, highly ordered monolayer. Gold is the most popular metal surface for reasons of ease of handling. It is generally thought not to have a stable oxide under ambient conditions, and it can withstand harsh cleaning procedures that are often required in SAM preparation [91]. A stable oxide can, in fact, be formed on gold when exposed to ultraviolet (UV) light and in the presence of ozone to produce Au_2O_3 [92]. Ron et al. [93] have actually used the gold oxidation as a surface cleaning procedure, removing the gold oxide in ethanol, the most popular solvent for preparation of SAMs. The ethanol reduces the gold oxide to give a fresh gold surface for self-assembly. Soaking in pure ethanol for at least 10 min prior to adding alkanethiol is required to ensure all the oxide is removed [94]. Failure to completely remove the gold oxide will result in SAMs first assembling onto the bare gold and then onto the oxidized gold surfaces during the later stages of the self-assembly [94, 95]. Noncontact atomic force microscopy (AFM) shows that the SAMs formed on the oxide regions are less stable than the gold-thiol SAM [94].

As with the ozone treatment to clean gold surfaces, other cleaning procedures involve the oxidation of the gold surface and removal of this oxide. More common cleaning procedures for gold include etching the gold surface in dilute aqua regia [42], oxidizing organic contaminants using “piranha” (a 1:3 mixture of 30% hydrogen peroxide and concentrated sulfuric acid at 100 °C; **Warning** a mixture that reacts violently with organic material and has been known to explode when stored in closed containers) or electrochemical cleaning in 1 M sulfuric acid using cyclic voltammetry between

−0.3 and +1.5 V versus Ag/AgCl. Electrochemical cleaning involves oxidizing the gold surface during the positive potential sweep and reductively removing the oxide during the negative scan. As the area under the reduction peak allows the calculation of the number of gold atoms oxidized, the electrochemical cleaning procedure allows the simultaneous measurement of the active surface area of the gold [96, 97]. The importance of cleaning the gold surface is well recognized for bulk gold surfaces (either polycrystalline or single crystal), but frequently, thin film deposited gold surfaces are not cleaned prior to assembly of the SAM. The consequence of poorly cleaned surfaces with minor amounts of organic matter on the surface is a deleterious influence on the kinetics of SAM formation rather than the prevention of the assembly process altogether [46, 97]. More defects are expected on contaminated surfaces.

Typically alkanethiols are assembled onto gold surfaces from dilute solutions (millimolar concentrations). Common solvents are ethanol for shorter alkanethiols or hexane. Two distinct adsorption stages are observed in the assembly—a rapid stage within the first few minutes by which time the contact angle is close to its limiting value and the thickness is 80–90% of the maximum [98]. The length of this stage is dependant on the alkanethiol concentration, taking only a few minutes at a concentration of 1 mM but about 100 min at 1 μ M [99, 100]. The second slow stage occurs over several hours as the contact angle and thickness reach their final value [98]. During the latter stage, the molecules in the SAM undergo a slow reorganization equivalent to surface crystallization [101]. The growth rate of the SAM is dependant on the number of vacant sites in agreement with simple first-order Langmuirian kinetics [100, 102–104]. The kinetics of SAM formation was initially studied by *ex-situ* techniques such as external reflectance FTIR, optical ellipsometry [21, 98], contact angle measurements [21, 98], and radioisotope labeling [105], but more recently, *in-situ* quartz crystal microbalance measurements have been used [100, 104, 106]. Due to the slow reorganization of the SAM, many workers typically allow 12 to 24 hr for SAM formation prior to use.

2.1.2. Assembly by Printing

The process of microcontact printing, developed by Xia and Whitesides et al. [86, 107] for patterning surfaces, can also be used to form alkanethiol SAMs on metal surfaces in only a few seconds. A polydimethylsiloxane stamp is “inked” with a thiol solution. Typically, the solvent is evaporated and the inked stamp is contacted with the metal. The low surface energy and flexibility of the elastomeric stamp have advantages with regards to allowing the stamp to conform to the shape of the metal surface. Depending on the amount of alkanethiol placed on the stamp, the SAMs produced can be of equivalent integrity and structure as a solution-assembled SAM despite no time being allowed for the slow organization of the alkanethiols after deposition onto the surface [108–110]. Evaluation of the printed SAMs was performed using scanning tunnel microscopy (STM) [108] and electrochemistry [110]. To obtain equivalent SAMs to solution assembly requires the surface loading of the alkanethiol ink to exceed a threshold value (20 nmol mm^{−2} of

hexadecanethiol) [110]. The length of time the stamp is in contact with the surface does not, however, appear to be important [108]. Self-assembled monolayers of dialkylsulfides prepared by printing were also found to be of similar quality to decanethiol SAMs with regards to order and etch resistance [111].

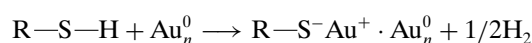
2.1.3. Other Deposition Methods

A variety of other methods of preparing self-assembled monolayers have been less commonly employed. With volatile alkanethiols, deposition can be achieved from the vapor phase, both at ambient pressures [102, 112–117] and under vacuum [115, 118–120]. Alkanethiol monolayers have also been formed using the Langmuir–Blodgett film technique [121–123]. One technique, which is important for ensuring that the alkanethiol is deposited on a reduced metal surface, is to use potentially assisted deposition of the alkanethiol. At highly cathodic potentials, alkanethiols desorb from the underlying metal surface. As the potential is scanned back anodically, alkanethiols can reabsorb onto the electrode [124]. Shifting the potential positively has also been shown to accelerate the rate of alkanethiol adsorption [125, 126].

2.2. Structure and Properties of Alkanethiol Monolayers

2.2.1. Monolayer Structure

The exact nature of the bond that forms between the gold and the sulfur is still not clear, but in the case of alkanethiols it can be considered as an oxidative addition of the S—H bond to the gold surface followed by a reductive elimination of hydrogen [6]



Evidence for H₂ leaving has been hard to come by, but the presence of a thiolate (RS[−]) has been confirmed by XPS [17, 127–129], FTIR [130], electrochemistry [90], and other techniques [131–133]. A recent study by Hasan et al. [134], using NMR and gold nanoclusters, shows that the loss of hydrogen can be prevented if there is no easy reaction pathway for hydrogen removal. The Au—S bond strength is about 40 kcal mol^{−1} [131] and the free energy change for the adsorption of alkanethiolates on gold is approximately −5.5 kcal mol^{−1} [105]. The equivalent Au—S bond is also formed from a disulphide [6].

On an Au(111) surface, the alkanethiols form a ($\sqrt{3} \times \sqrt{3}$)R30° hexagonal lattice with an average spacing of 5 Å between alkanethiol chains (see Fig. 2) [135, 136]. The alkane chains are in the all trans configuration with very few gauche defects. The chains typically tilt between 20 and 30 degrees from normal to the surface (see Fig. 1). The tilt angle is dictated by the spacing of adsorption sites on the metal surface and is a consequence of the chains establishing van der Waals contact [6, 15].

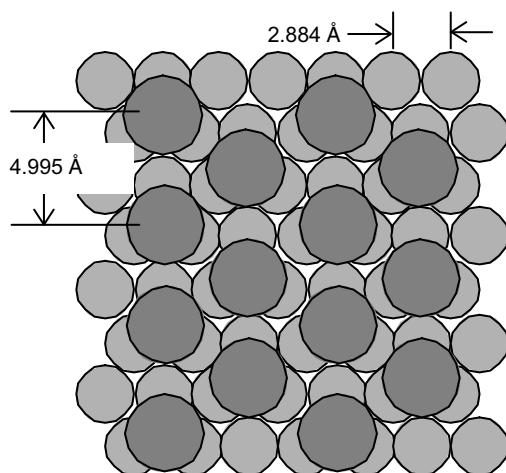


Figure 3. Model of an alkanethiol SAM (large circles) on an Au(111) surface (small circles) where the SAM forms the $(\sqrt{3} \times \sqrt{3})R30^\circ$ lattice.

2.2.2. Important Factors in Determining the Structure and Function of Organosulfur Monolayers

The structure discussed in Section 2.2.1 refers to the ideal structure observed with long chain aliphatic alkanethiols on an Au(111) surface. There are a number of factors that influence the SAM structure, and hence function, including the surface upon which the SAM is formed, the chain length, the terminal group of the alkanethiol, and having a mixture of components in the SAM. For example, attractive van der Waals forces between the alkyl chains affect the stability and level of defects within a SAM [98]. Defects in SAMs are important in determining a SAM. The consequence of a defect is either a pinhole (a hole in the SAM where there is direct access to the metal) in the SAM or a collapsed site. In both cases, the blocking ability of the SAM will be reduced. The decrease in blocking may be an advantage, such as in an electrochemical system where the underlying electrode is required to be electrochemically accessible [137–140], or may be a disadvantage if the function of the SAM is to block access to the metal [38, 86, 141, 142]. Therefore, any factor that increases or decreases the van der Waals forces will alter the order of the resultant SAM. Some of these variables will be discussed below.

The Underlying Metal Surface Alkanethiol SAMs can be formed on a number of coinage metal surfaces apart from gold including platinum, silver, and copper, as well on different crystal faces of these metals. Turning our attention to gold first, the gold surface can be polycrystalline, single crystal, or thin film deposited. Single crystal surfaces are attractive for fundamental studies [143–145], as the surface is well defined, but are not compatible with the bulk manufacture of a large number of devices in the same way that deposited thin films are. Because of the influence of van der Waals forces on SAM integrity and stability, smoother surfaces produce more ordered and robust SAMs with higher integrity (i.e., less defects) than those with rougher surfaces [42, 109, 146–150]. The influence of the gold surface roughness on the energy required to remove a hexadecane SAM [109] is shown in Figure 4. Figure 4 shows the portion of a cyclic

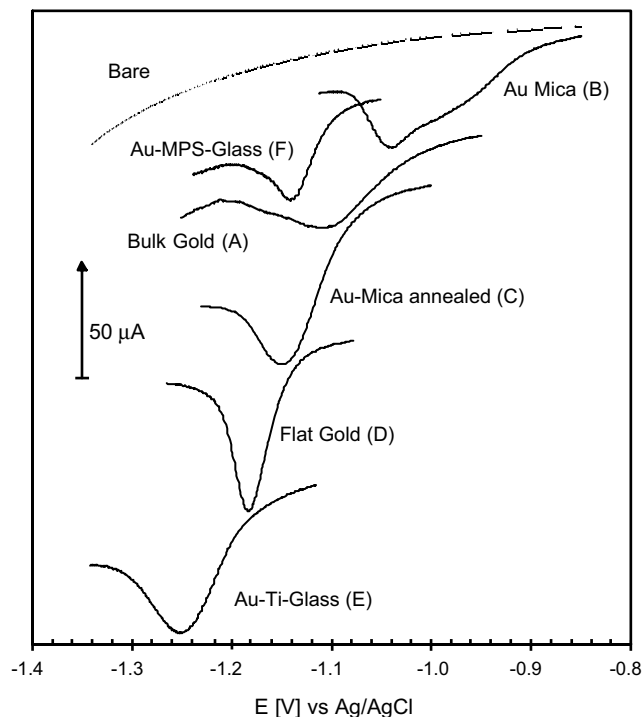


Figure 4. Reductive desorption CV peaks for various gold substrates coated with SAM (first cycle). All recorded in 0.5 M KOH at scan speeds of 100 mV s^{-1} , except Au-MPS glass (F) which is recorded at 5 mV s^{-1} . Reprinted with permission from [109], D. Losic et al., *Langmuir* 17, 3307 (2001). © 2001, American Chemical Society.

voltammogram where the alkanethiol is reductively desorbed for six different gold surfaces. With the exception of one surface, the peak potential shifts to more cathodic (negative) potentials the smoother the surface. Higher potentials mean the SAM is more difficult to remove. The smoothness of the gold is even more important for microcontact printed SAMs than solution-assembled SAMs because the alkanethiol is only deposited where the stamp contacts the surface [109]. Of equal importance when preparing defect-free SAMs, however, is the purity of the gold [147].

In nanofabrication, it is important to recognize that often the variation in height of a gold surface is of a similar or greater scale than the size of the adsorbate. Therefore, schematics of molecular assembly frequently seen in the literature where molecules are arranged onto a perfectly flat surface only depict an idealized molecular assembly rather than reality. Methods of fabricating gold surfaces that are atomically flat over large regions have been developed using template stripping of the metal surface from mica [151–155]. Although such strategies have not been applied to other metals, there is no reason to assume such strategies would not also render molecularly smooth surfaces.

Different gold crystal faces have different metal atom spacing and, therefore, the resultant SAM has a different structure. For example, on a Au(100) face, the tilt angle is only 5° rather than the 30° seen on an Au(111) face [6]. The interest in Au(111) is a consequence of it being the most thermodynamically stable surface because it has the highest atomic surface density. Therefore, vacuum evaporation and

gold annealing typically give surfaces that are predominantly Au(111).

As stated above, apart from gold, SAMs can be formed on other metal surfaces, such as silver [7, 105, 156–159], copper [7, 8, 105, 160–164], nickel [165], platinum [21, 139, 166–168], and palladium [169–172] as well as on metal composite surfaces like gallium arsenide [173–176]. Schlenoff et al. [105] have shown that the surface coverage on a variety of surfaces decreases in the order $\text{Cu} > \text{Ag} > \text{Pt} > \text{Au} > \text{GaAs}$. The higher surface coverage on silver relative to gold is a consequence of the SAM structure. On Ag, the SAMs are very similar structurally to on Au(111) but with a lower tilt angle (12° compared to 30° for Au) and a smaller chain-chain distance (4.1 \AA for Ag and 5.0 \AA for Au) [177]. The SAMs on copper are structurally more complex and very sensitive to the surface preparation of the metal [177]. On platinum, in contrast to Au, Ag, and Cu, the SAM shows a number of gauche transformations which can reversibly be eliminated at both positive and negative potentials [166]. Surfaces where underpotential deposition is employed to deposit a monolayer of one metal onto a gold surface have also been modified with organosulfur SAMs [7, 178]. The underpotential deposition of silver onto gold has been shown to give a more stable SAM than on gold alone [7].

Chain Length The order and stability of alkanethiol monolayers are very sensitive to the length of the alkyl chain. Porter et al. [128] investigated the influence of alkyl chain length using electrochemistry, optical ellipsometry, and infrared spectroscopy. For carbon chains over 11 carbon atoms, the monolayer is densely packed and crystal-like [128]. As the chain length decreases, the structure becomes increasingly disordered with lower packing density and coverage. The transition between crystal-like and disordered occurs between 5 and 11 carbon atoms depending on the measurement technique and surface used. Electrochemical measurements, with the long-chain SAMs, show that the monolayers provide substantial barrier properties to electron transfer and are strongly resistant to ion penetration [128].

An additional influence of chain length on monolayer properties in highly ordered SAMs comes from the so-called “odd-even” effect where the orientation of the terminal group, and the structure of the SAM [179], depends on the number of carbons in the alkyl chain. The orientation of the terminal group has been shown to influence the electrochemical stability of biphenyl terminated SAMs [180], the reactivity of the SAM [181, 182], wetting [183, 184], and its tribological [184] properties.

As the densely packed monolayers of long-chain alkanethiols (10 or more alkyl carbons) passivate electrode surfaces, the choice of alkyl chain length is dictated by the application of the SAM. If the SAM is required to prevent access to the underlying gold, then a long-chain alkanethiol is required [185]. However, in many sensing applications, where electrochemistry must occur at the metal below the SAM, either short-chain alkanethiols are required [12] or the order of a long-chain SAM must be disrupted [139, 186, 187]. The consequence of a shorter chain SAM, however, is poorer electrochemical and thermal stability. Recently, Markovich and Mandler [188] have shown that

long-chain SAMs can be disrupted through the incorporation of amphiphilic molecules during deposition of the SAM.

The Influence of the Terminal Group If only one terminal group was available with alkanethiols, they would be of limited utility. Part of the power of alkanethiol chemistry is the ability to relatively easily tailor the chemistry of the self-assembly molecules to a particular application [189]. Altering the terminal group is perhaps the most important aspect of this ability as it allows the building onto the surface of additional components and controls the surface properties of the SAM-modified interface.

The influence of the terminal group on SAM structure depends very much on the size of the terminal group. Terminal groups such as $-\text{CH}_3$, $-\text{OH}$, $-\text{CO}_2\text{H}$, $-\text{NH}_2$, $-\text{CONH}_2$, $-\text{CO}_2\text{CH}_3$, where the cross-sectional area is smaller than that of the alkyl chain ($\sim 20 \text{ \AA}$) [98], do not interfere with the packing of the hydrocarbon chains. Hence, these monolayers present a single homogeneous functionality at the exposed surface. In contrast, SAMs with bulky terminal moieties, such as sulfonates and oligo(ethyleneoxides) [190], show significant deviation from the $(\sqrt{3} \times \sqrt{3})R30^\circ$ hexagonal lattice due to disruption of the hydrocarbon packing [191, 192]. A consequence of disruption of the chain-chain packing is that no longer does the surface present homogeneous functionality. In the case of oligo(ethyleneoxide)-terminated surfaces their ability to be wetted is affected as a result [189].

Similarity of structure does not necessarily imply a similar function. An example of this relates to how the terminal influences the interactions of the terminal surface of the SAM with the surroundings. Methyl-terminated SAMs present low-surface free energy, hydrophobic surfaces while the high-surface free energy, alcohol-terminated surface is hydrophilic. Furthermore, the properties of the surface can be altered, depending on the terminal group, through changing solution conditions. The effect of solution conditions is demonstrated by a carboxylic acid-terminated SAM, which can be either negatively charged or neutral depending on the pH [193]. The change in the charge state of the interface will then greatly influence the blocking ability of the SAM on a surface. The variation in blocking ability with pH was used by Zhao et al. [194] to measure the surface pK_a of (3-mercaptopropionic acid). A pK_a titration was performed by electrochemically measuring the decreased ability of ferricyanide to penetrate the carboxylic acid-terminated SAM with increasing pH (as the surface changing from neutral to negatively charged). It is important to note that the surface pK_a can be significantly different than the pK_a of the molecule in bulk solution [195, 196]. Similar tailoring surface properties have been very important in using SAM-modified surfaces for tasks such as restricting protein adsorption [43, 197], orientating the approach of biomolecules [198, 199], controlled wetting [41, 200], controlling crystal growth [201], and influencing the surface friction [193, 202].

2.2.3. Stability of Alkanethiol Monolayers

The application of SAMs to anything other than fundamental studies requires the resultant modified surface to be stable. Self-assembled monolayers have good stability over a

wide range of conditions. Variation in stability between different SAMs is a function of the chain-chain interactions as the gold-thiolate bond is the same. Therefore, any factor that increases the integrity of the SAM will ultimately also improve the stability of the SAM.

Thermal stability of aliphatic alkanethiol SAMs has been the subject of several studies. The SAMs have been reported to begin desorbing from gold at temperatures from 75 °C for butanethiol [203] to above 100 °C for dodecanethiol [204]. There is some inconsistency in the reported desorption temperatures and rates for a given alkanethiol, because of the influence of parameters, such as the smoothness of the gold surface and the method of determining the loss of the alkanethiol. For example, Nuzzo et al. [17] have reported hexadecanethiol desorbs in a range between 170–230 °C using X-ray photoelectron spectroscopy and infrared spectroscopy, while Schlenoff et al. [105] use radiolabelling to show complete loss of the SAM at 210 °C which began at 100 °C. The greater the forces of interaction between the tails of the SAM-forming molecules, the greater the thermal stability of the SAM. Therefore, monolayers where there is hydrogen bonding [205] or π - π bonding [206] between the alkyl chains exhibit better thermal stability than aliphatic hydrocarbons. Similarly, repulsive forces between terminal groups such as carboxylic acids and sulfonates will result in a lower stability than the equivalent methyl-terminated SAM. The impact of these repulsive terminal interactions will again be influenced by the alkyl chain length, where the influence of the terminal group is diluted as the alkyl chain increases in length.

For many applications the electrochemical stability of alkanethiol SAMs is particularly important. Self-assembled monolayers have been shown to be stable to potentials between approximately +1.0 and -1.0 V versus SCE, although this potential window depends on chain length, terminal group, and the quality of the underlying gold surface [38, 40, 207]. Such a potential window is compatible with most electrochemical applications. Outside this range, the thiols are either oxidatively or reductively desorbed [33, 39, 124, 146, 150, 180, 208–210]. The instability at high potentials, however, can be used to control the order of the SAM during formation [124]. Self-assembled monolayers with high integrity and few defects are more stable, requiring more positive or negative potentials to desorb, because ordered regions, where there is a high level of bonding between alkyl chains, require whole sheets of the SAM to be removed at a time rather than individual alkanethiols [109, 150]. The influence of the gold surface on the stability of SAMs is demonstrated in Figure 5 with hexadecanethiol SAMs assembled on gold surfaces with different roughness [109]. The three gold surfaces are gold evaporated onto mica with no annealing (A), polycrystalline bulk gold (B), and atomically smooth gold prepared by template stripping (C) [155]. The roughness of the gold surfaces decreases from surface A to C. The higher the roughness of the surface, the poorer the packing between the alkyl chains and hence the greater the number of defect sites where pinholes, where bare gold is exposed to solution. Figure 5 shows the number of pinholes in the SAM formed on each surface. The pinhole fraction is measured by performing a cyclic voltammogram between -0.5 and 1.5 V versus Ag/AgCl in 0.1 M

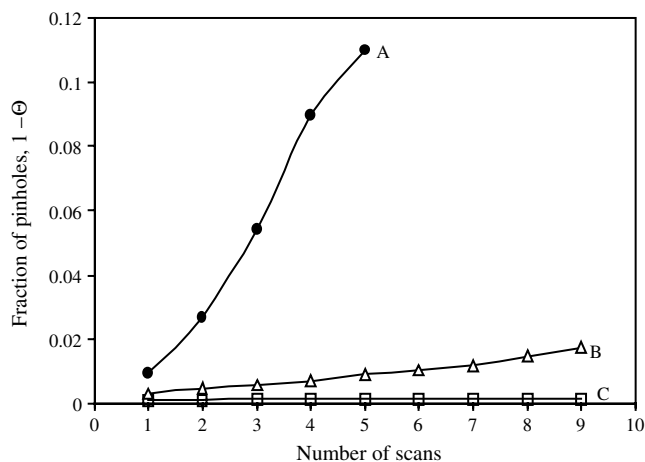


Figure 5. The variation in the fraction of the SAM surface covered in pinholes as a function of the number of cycles in a cyclic voltammogram on three gold surfaces. The surfaces are (A) gold evaporated onto mica with no annealing, (B) polycrystalline bulk gold, and (C) atomically smooth gold prepared by template stripping. The roughness of the gold surfaces decreases from surface A to C. The number of pinholes in each SAM is measured by performing a cyclic voltammogram between -0.5 and 1.5 V versus Ag/AgCl in 0.1 M H₂SO₄. During this measurement there is a minor amount of further disruption of the SAM. The increase in pinhole fraction with the number of scans gives an indication of the SAM robustness with SAMs formed on smoother surfaces being more robust.

H₂SO₄, the same conditions used for the electrochemical cleaning of gold. In this experiment, as the potential is swept positive, any exposed gold from pinholes will be oxidized. Upon sweeping negative, this gold oxide is reduced and the area under the reduction peak allows the quantification of the amount of pinholes. During this measurement, there is a minor amount of further disruption of the SAM. This is evident in Figure 5 where the pinhole fraction increases as the number of scans increases. Note, however, with the smoother surfaces, where there are larger sheets of the SAM with more chain-chain interactions, the SAM is far more robust to this repeated cycling.

The long-term storage stability of SAMs is less well understood. Horn et al. [211] have used reflection-absorption IR spectroscopy (RAIRS) to monitor changes in structure of aliphatic alkanethiols over a 6-month period. Changes in the symmetric and asymmetric CH₂ stretching modes observed with the RAIRS are attributed to chemical oxidation of the thiolate species at the point of attachment to the gold. Upon oxidation of the thiolate to either sulfonates ($-\text{SO}_2^-$) or sulfonates ($-\text{SO}_3^-$), the SAM is less strongly bound to the gold as determined by their ability to desorb from the surface in solution [212]. The oxidative loss of alkanethiols is particularly problematic for applications that employ short chain alkanethiols, where oxygen and other oxidants can easily access the gold-thiolate bond [213]. The rate of oxidation of the thiol to a sulfonate has been shown to be dependent on the alkyl chain length [213, 214], as well as the terminal group of the SAM [214]. In the case of the terminal group, the rate constant for photo-oxidation has a ratio of 4:2:1 for CH₃:OH:COOH for both long and short chain SAMs [214].

In practice, the problem of oxidation can be reduced by storing devices in oxygen-free environments such as vacuum packs.

With the depiction of alkanethiol SAMs as ordered, stable, and static monolayers on surfaces, it is easy to forget that SAMs are dynamic systems in which the alkanethiols are capable of moving about on the surface, as is evident from the kinetic studies where after adsorption the SAM slowly reorganizes itself. The dynamic behavior of SAMs is demonstrated by two key observations. First, when a SAM modified gold surface is placed in a different alkanethiol solution, exchange occurs at the grain boundaries of the underlying metal surface [40, 42, 77, 105]. This is called a place exchange reaction. Second, the alkanethiol in a SAM have been shown to surface diffuse to heal gaps of exposed gold [210]. This healing process occurs over the time span of several hours [9, 215–217]. The rate to which defects are healed is independent of the chain length of the alkanethiol, which suggests the head group dominates the adsorption and desorption steps [215] and that the first layer of gold atoms are involved in the monolayer movement [9].

2.2.4. Mixed Monolayers

To use SAM surfaces as the base upon which nanofabrication can be performed requires more than one component to be incorporated within the SAM. The formation of homogeneous SAMs from mixtures of alkanethiols would allow the construction of integrated molecular systems where several components are incorporated within a single monolayer. For example, mixed monolayers can allow either large recognition elements or nanoscale building blocks to be spaced apart from each other if necessary. Furthermore, through varying the composition of a mixed SAM the density of attachment points, and hence the surface loading of added components, can be controlled.

Mixed monolayers have commonly been produced through the use of a mixture of alkanethiols in the solution to which the substrate is immersed, although place exchange reactions have also been used [40, 42, 105, 169, 218–226]. In a place exchange reaction the exchange is greater in SAMs with more defects [42].

A mixed SAM formed from two components in solution has been regarded as being a reasonably homogeneous mixture of the components [41, 227–229] rather than phase segregation into “islands” as has been observed in Langmuir–Blodgett films [15]. There is some controversy as to whether phase segregation occurs or not. Homogeneity was determined via wetting studies [41], which is supported by STM measurements that suggested no segregation occurs on the scale of greater than 50 nm [230]. However, on a smaller scale some phase segregation has been reported to occur [231]. Scanning tunneling microscopy studies indicate domain-rich regions of individual components of nanometer dimensions can be observed [232, 233]. This phase separation is believed to occur by adsorption/desorption followed by movement. Differences in length and chemical functionality certainly play a key role in any phase separation [231]. For example, Atre et al. [231] showed using wetting studies, FTIR and XPS, with a mixture of $\text{HS}(\text{CH}_2)_{15}\text{CH}_2\text{OH}$ and $\text{HS}(\text{CH}_2)_{(15+m)}\text{CH}_3$ with m increasing systematically from

–6 to +6, that the monolayer underwent structural change from randomly placed protruding —OH-terminated chains at low m to phase segregated at high m . However, in contrast to studies that show phase separation STM studies by Takami et al. [234] do not show phase separation even at the nanometer level for mixtures of azobenzene-terminated SAMs and dodecanethiol. This contradictory evidence highlights the many differences in SAM studies such as the surface upon which assembly occurs, the alkanethiol used, and the measurement technique, which play a role in the conclusions reached. With regards to phase separation in mixed SAMs, it appears that generally mixed SAMs form a 2-dimensional alloy, which can decompose into a heterogeneous distribution particularly when the two components are significantly different [118].

When forming mixed SAMs by solution assembly, the ratio of the components in the SAM can be adjusted by varying the ratio of the components in solution. Note, however, that the mole fraction of components in solution is not necessarily the same as the two components on the surface. In the two-component mixture, the more alike the two components the closer the mole fraction in the SAM will be to the mole fraction in solution. If the two components are quite different, the surface mole fraction can be very different to the solution mole fraction. For example, Offord et al. [18, 235] have looked at mixed SAM of octadecyl mercaptan **1** with either butyl mercaptan **2** or tert-butyl mercaptan **3** and a variety of different ratios in solution. Time-of-flight secondary ion mass spectrometry showed that the adsorption efficiency of **1–3** varied in the order $\mathbf{1} > \mathbf{2} \gg \mathbf{3}$. In the case of a 1:1 mixture of butyl to octadecyl adsorbate in solution, there was a 3–4 fold excess of **1** to **2** and a 40–100 fold excess of **1** to **3** [18]. These excesses are dependent on the solvent used [235]. Therefore, it is clear that the relative solubility of the two adsorbates has an influence on the surface mole fractions. Similar results have also been observed with thermal desorption mass spectrometry [236].

A novel exploitation of the phase separation of mixed SAMs to control the surface loading of a recognition element has recently been developed by Satjapipat et al. [210] (see Fig. 6). They formed a mixed SAM of 3-mercaptopropionic acid (MPA) and mercaptohexanol (MCH). As the two alkanethiols are reasonably different chemically, they tended to separate into domains rich in each of the two components. As MPA desorbs at a lower potential than MCH, MPA was selectively removed through reductive desorption. The result was a surface that contained some bare regions. Before the remaining adsorbed MCH could diffuse across the surface to cover the bare regions, the substrate was placed in a solution of thiolated DNA which assembled onto these regions. This approach represents one method of fabricating interfaces with discrete domains of different components; in essence, this is patterning a SAM. More controlled methods of patterning SAMs are discussed in Section 2.3.

2.3. Patterning of SAMs

Many applications in nanotechnology require patterning of the surface chemistry, and hence the controlled positioning of the different components used to modify the surface.

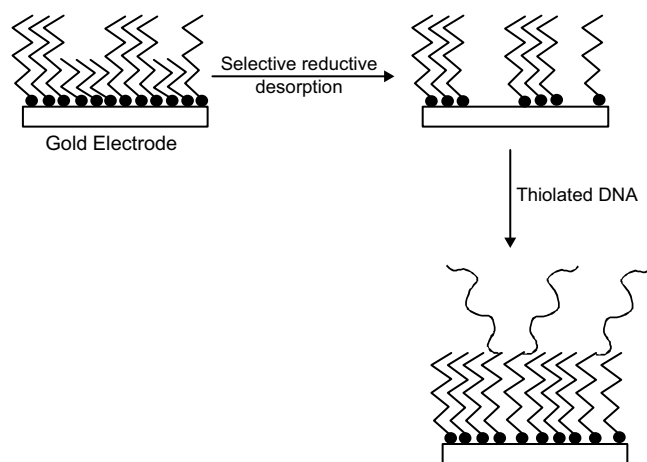


Figure 6. Schematic representation of the procedure used by Satjapit et al. [210] to fabricate a DNA recognition interface. A mixed SAM of MCH and MPA is formed. The electrode potential is scanned until the MPA is reductively desorbed to leave bare gold. The electrode is then placed in thiolated DNA which adsorbs onto the bare regions.

Applications include biosensors, microelectronics, and optical devices such as displays and waveguides. Many of these applications require the patterns to be as small as possible. Controlled positioning of different components can be achieved using a variety of techniques for patterning SAMs, which have recently begun being developed where resolution can vary from centimeters down to as low as 20 nm [237]. Approaches to patterning of SAMs can be divided into composition methods where the SAM is patterned during its assembly and decomposition methods, where parts of a complete SAM are removed to allow a second component to be added [238]. Decomposition methods, such as photolithography, electron beam writing, and micromachining, have traditionally been more popular for patterning SAMs. New decomposition methods like nanoshaving [237, 239] and a proximity printing technique using focused ion beams developed by Golzhauser et al. [240] have also been developed. However, in recent times with the advent of microcontact printing [43, 81, 83, 84, 86, 107–111, 171, 172, 197, 201, 241–254] and dip-pen lithography [73, 255–261], composition methods are moving to the fore.

2.3.1. Decomposition Methods

Photolithography The wide applicability of photolithography in creating features and devices on the microscale has inevitably seen it also used for patterning SAMs. The photo-oxidation of alkanethiolate can be achieved directly upon exposure of the SAM to UV radiation in the presence of oxygen [262, 263]. Using a chrome mask patterned to allow selective exposure of the surface to UV radiation, patterning of the SAM can be achieved [264, 265]. The oxidized thiols can easily be desorbed from the surface and then a second alkanethiol can be assembled onto the bare surface. Alternatively, the remaining SAM can act as a chemical resist that blocks the access of etchants to the underlying surface: Therefore, exposure of the patterned surface to an etchant will result in the bare surface being etched away, with the SAM-covered regions remaining, to give a microstructure.

Patterns down to 100 nm have been achieved with photolithography by Behm et al. [266] using a microscope to focus the light in projection lithography. Although photolithography is an efficient method of patterning substrates to make microstructures, it has a number of limitations in nanofabrication, especially with regards to developing new nanodevices. First, it requires expensive specialist equipment and clean room facilities. Second, the shallow depth of field requires that only planar substrates can be patterned that limits the range of materials upon which nanostructures can be built. Finally, and perhaps most importantly, the ultimate resolution is dependent on the wavelength of light. This final limitation appears to restrict photolithographical patterning to defining regions on a surface where nanofabrication can occur rather than being involved in the precise positioning of molecular components in nanofabrication.

Beam Lithography Beam lithography is a decomposition method that uses beams such as atoms, ions, or electrons to remove the alkanethiolates. Selectivity is again achieved with a mask. The best resolutions appear to be achieved using neutral beams [267, 268]. Berggren and Younkun et al. [267, 269] have patterned features smaller than 100 nm on gold and silicon using neutral cesium beams. Berggren et al. [268] have also shown nanometer resolution in patterning alkanethiols using argon beams. In common with photolithography, different alkanethiols show different susceptibility to the decomposition source, and therefore some tailoring of the technique is required for individual systems.

Nanoshaving Truly nanometer-size features can be patterned onto SAMs using one of several scanning probe microscope (SPM) techniques [239, 255] collectively called scanning probe lithography. “Nanoshaving,” developed by Xu and Liu et al. [237, 239] (Fig. 7) involves displacing the adsorbate on a SAM-modified surface using an AFM tip. The tip is scanned at a load higher than the displacement threshold. In this way, patterns of bare metal with feature sizes down to 20 nm can be produced. If the nanoshaving is performed in a solution containing a second alkanethiol, the exposed metal will be modified by the second component; this is called nanografting. An equivalent nanofabrication

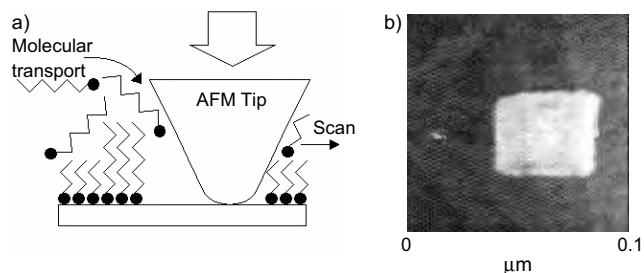


Figure 7. The principles of nanoshaving where a) AFM tip is dragged across an alkanethiol modified surface with sufficient force to remove the alkanethiol from the surface. If this nanoshaving is performed in a solution containing a second alkanethiol, then a surface patterned with two alkanethiols can be produced. Feature sizes as small as 20 nm have been fabricated; b) shows a 50 nm wide island of octadecanethiol patterned into a decanethiol SAM. Reprinted with permission from [237], S. Xu and G. Y. Liu, *Langmuir* 13, 127 (1997). © 1997, American Chemical Society.

method using STM has also been developed, where the tip potential is sufficiently high to cause thiol desorption. Nanoshaving has also been used for fabricating semiconducting nanowires [270] and to characterize the thickness of novel alkanethiol SAMs [271].

2.3.2. Composition Methods of Patterning

Microcontact Printing Microcontact printing is one of a suite of soft-lithography methods for patterning surfaces developed by Xia and Whitesides [86]. The basic principles of microcontact printing are shown in Figure 8. A stamp with relief structure is prepared from a master. The master can be any structure with the appropriate relief. In fact, Deng et al. have shown how a master can simply be made using a normal computer printer and transparencies [253]. The stamp is coated with alkanethiol ink which is evaporated onto the stamp so the printing process is essentially dry. Upon contact of the inked stamp with the surface, a SAM formed at the points of contact. As the SAM only forms where the stamp contacts the surface, the pattern of the stamp is transferred to the solid substrate. In this way, features as small as 100 nm have been fabricated [245].

Placing the patterned surface into a solution containing a different alkanethiol allows a two-component system to be fabricated, which could be used to give either controlled wetting/dewetting [243] locations where the underlying electrode is passivated and others where access is maintained, provide specific sites for crystal nucleation [201] or allow the selective deposition of other materials such as polymers [247] and cells [107, 197]. Rather than deposit a second alkanethiol onto the exposed metal surface, it could be used either as a microelectrode array [252], or the printed SAM could be used as an ultra-thin chemical resist for selective etching to remove the exposed metal surface [244, 250].

The essential advantages of microcontact printing are that it is cheap and easy to set up. Existing fabricated devices can be used as the masters for new stamps and, with some

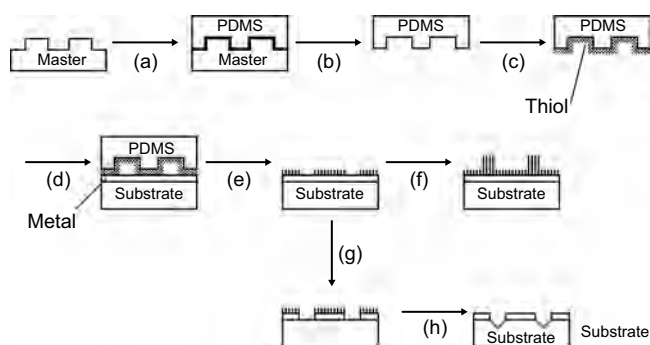


Figure 8. Schematic of the process of microcontact printing where: (a) a master which contains a relief structure is coated with the elastomer PDMS, (b) the PDMS is removed from the master and becomes the stamp, (c) the stamp is inked with an alkanethiol, and (d) contacted with a the surface to be patterned, (e) the alkanethiol is transferred to the metal surface at the points of contact. The result is a patterned surface with exposed metal and metal covered in alkanethiol. Either (f) the patterned surface is placed in another alkanethiol solution to give a surface patterned with two different alkanethiols or alternatively in (g) the exposed metal is etched away, using the alkanethiol as a resist, followed by (h) the removal of the remaining alkanethiol.

creativity, quite sophisticated devices can be fabricated. The low cost is because no special clean room facilities or expensive masks are required. One of the reasons that clean room facilities are not required relates to the stamp itself. Typically, it is made of polydimethylsiloxane (PDMS) which is an elastomer with a low surface energy. If the surface to be patterned is contaminated by a speck of dust (which would be a big problem in photolithography), the stamp will conform around the dust particle and the mobility of the alkanethiols may even allow assembly onto the part of the surface covered by the dust particle.

Microcontact printing has been performed on nonplanar substrates [242] and even inside tubes [246]. With this emerging technique, issues that have been addressed include how to decrease the size of the pattern [245], what dimensions give a stable stamp that does not collapse upon itself [86, 248], the order of the printed SAM relative to solution assembled monolayers [108], methods of inking the stamp [251], how the ink is dispersed from the stamp to the substrate [249], the influence of the topography of the gold surface [109], and the amount of alkanethiol applied to the stamp [110] on the integrity of the printed SAM.

“Dip-Pen” Lithography “Dip-Pen” lithography is an ingenious approach to nanofabricating SAM-based structures with an AFM developed by Piner and Hong et al. (Fig. 9) [255, 272]. Dip-pen lithography exploits the water meniscus that travels with an AFM tip when contacting a surface under ambient conditions. By coating the tip in an alkanethiol, the water meniscus solubilizes some of the alkanethiol and transfers it to the solution substrate upon which it is traveling. In this way, line widths of 30 nm resolution have been achieved. Dip-pen generated templates of DNA have been used to orthogonally assemble nanoparticle building blocks, thus allowing nanofabrication in a third dimension [73]. This was achieved by patterning a gold surface with 16-MCH acid to which a sequence of DNA was attached. Gold nanoparticles were modified with thiolated complementary DNA. Exposure of the patterned surface to the complementary DNA allowed ordered arrays of nanoparticles to be fabricated onto the original gold surface. A similar approach has been used to pattern amine modified polystyrene spheres, which were bound to the MCH-patterned surface via electrostatic interactions [257]. Dip-pen lithography has now been extended beyond alkanethiols to sol-gel based inks [258].

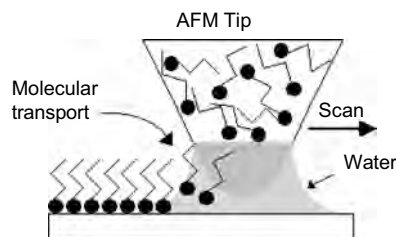


Figure 9. Dip-pen lithography where an AFM tip coated in alkanethiol is scanning across a surface under ambient conditions. The meniscus of water that travels with the tip solubilizes the alkanethiol, transferring it to the metal surface to produce patterns.

An earlier variant of dip-pen lithography, which produced patterned features of size greater than $10\ \mu\text{m}$, is microwriting [273, 274]. In microwriting, neat alkanethiol is dispensed from the tip of a fine capillary directly onto the gold surface. Control over the distance between the tip and the surface gives some control over line widths that are achieved.

2.3.3. Controlled Positions of Alkanethiol Deposition

Controlling the location where a particular alkanethiolate SAM is deposited has also been achieved electrochemically. This is done using an electrode array where the elements of the array are held at different potentials, depending on whether they are to be modified by the SAM in solution or not. Such an approach is important in controlling the modification of different elements of an electrode array with different recognition species. The first demonstration of using electrode potential to control the deposition of alkanethiols was by Tender et al. [275], where interdigitated electrodes were first all coated with $\text{HO}(\text{CH}_2\text{CH}_2\text{O})_6(\text{CH}_2)_{11}\text{SH}$. Sufficient potential was applied to one of the interdigitated electrodes to selectively desorb the SAM. The microelectrodes were then placed into 16-mercaptohexadecane (MHD) to coat the now bare electrode. The MHD-coated electrode allowed selective adsorption of proteins. The crucial aspect of this technology is that different elements in an electrode array can be selectively coated without requiring any alignment [276]. Wang et al. [125] have used the complete opposite approach to selectively coating individual electrodes in an array. By placing a negative potential on the electrode to be coated, the adsorption of the SAM from ethanolic solution onto that electrode is accelerated. The other electrodes, held at open-circuit potential, are modified much more slowly and therefore are only partially coated. Hsueh et al. [277] have also used potential to control which elements in an electrode array are modified with a SAM. The primary difference to the approach of Tender is, rather than use alkanethiols, the electrochemical oxidation of alkylthiosulfates (Bunte salts) to certain electrodes is used. The oxidation of the Bunte salts produces either a disulfide or an alkylsulfide radical at the electrode which is then trapped on the electrode surface to produce a gold-thiolate bond.

3. APPLICATIONS OF SELF-ASSEMBLED MONOLAYERS

As stated above there are a host of applications to which SAM modified surfaces have been applied including surface coatings, sensing, molecular electronics, and nanofabrication with nanoscale building blocks. We shall discuss each of these applications in turn.

3.1. Surface Coatings

The affinity of alkanethiols for coinage metal surfaces and their subsequent self-assembly onto the surface made use of alkanethiols as surface coatings for metal surfaces an obvious application. One of the attractive features of using alkanethiol chemistry is that the surface coating can be achieved with nanometer control. The alkanethiol surface coatings have been used to give metal surfaces corrosion resistance,

changing the frictional properties of surfaces, making them hydrophobic or hydrophilic, giving controlled environments for crystal growth, making surfaces that resist fouling and preparing surfaces for controlled protein and cell growth. Many of these surface-coating technologies lead to further applications, such as surfaces for controlled protein adsorption can then be used for the development of biosensors.

3.1.1. Corrosion Resistance

Since metal surfaces can be passivated using close-packed alkanethiol monolayers, several workers have used these monolayers to protect copper [7, 8, 160, 161, 164, 278–284], iron [285–288], and gold [216, 242, 289] surfaces from species in solution. It is the ability of alkanethiol monolayers to protect an underlying metal surface, which is used in microcontact printing to allow etching of exposed gold and not gold coated by the SAM [86, 242, 244, 246]. Laibinis and Whitesides [290] first attempted to prevent the oxidation of copper surfaces coated with alkanethiols when in the presence of atmospheric oxygen. XPS measurements showed that the rate of oxidation was inversely proportional to the alkanethiol chain length. The resistance to corrosion was much greater with alkanethiols where the chain length was greater than 12 carbons due to more closely packed SAMs being formed [281]. In aqueous solutions of NaSO_4 , however, even octadecanethiol did not prevent corrosion [291]. As a consequence, further modification of the alkanethiol was required to reduce the coatings permeability [160, 164, 207, 278–280, 283–285]. As example of this approach is by Itoh et al. [160], where copper surfaces were modified with 11-mercapto-1-undecanol. The alkanethiol was then reacted with an alkyltrichlorosilane to form an alkylsiloxane polymer. The formation of a polymer on the copper surface improved the corrosion resistance of the coating.

3.1.2. Surfaces for Controlled Crystal Growth

The terminal moiety of a SAM, and the ease to which this can be modified, provides a method of controlling the chemistry of a surface upon which crystallization occurs [201, 292–300]. The ability to easily pattern the SAM using microcontact printing allows the controlled position on a surface where nucleation of crystals occurs. This was elegantly demonstrated by Aizenberg et al. [201], where a SAM of an alkanethiol that promoted crystal growth (symbolized as $\text{HS}(\text{CH}_2)_{15}\text{X}$ and which was mercaptohexanoic acid X is COOH) was patterned into dots using microcontact printing onto a metal surface (gold, silver, or palladium). The rest of the surface was coated with MCH. Placing this patterned surface into a CaCl_2 solution exposed to carbon dioxide and ammonia vapor resulted in calcite crystals forming predominantly on the $\text{HS}(\text{CH}_2)_{15}\text{X}$ parts of the SAM. Not only can the position of crystal growth on a surface be dictated but also control over whether many or only a single crystal grew at each location was afforded by judicious choice of the feature size, as well as the density and concentration of the crystallization solution. Even more exciting was the demonstration that different X groups in $\text{HS}(\text{CH}_2)_{15}\text{X}$ resulted in crystal growth from different crystal faces. The ability to control the position of the growth of single crystals on a

surface, and also to be able to control the type of crystal, could be exceedingly useful for fabricating ordered arrays of nanoparticles. This concept has already been realized by Qin et al. [301] with arrays of a variety of crystals being grown including CdCl_2 and Nile red.

3.1.3. Biological Surfaces

Surfaces that interact with biological environments have enormous numbers of applications in a large number of fields ranging from biological implants, drug development, to biosensors. An important aspect of these applications is an understanding of how biological molecules and organisms interact with the man-made surfaces to which they are exposed. There is a huge amount of research in these fields which fills many volumes. In this section, the role alkanethiol SAMs have played in these fields will be discussed.

Proteins Adsorption The adsorption to proteins to surfaces is exceedingly complex, and although there has been considerable research into the field there is yet to be a complete molecular level understanding [302–306]. Self-assembled monolayers are therefore important in understanding and using proteins adsorption, because they are model systems where the surface properties are well defined and can easily be altered in a known way [43, 49, 238, 307]. Furthermore, protein adsorption mediates subsequent cell adhesion which is important in implants [308, 309] and in controlled growth of cells on surfaces [49, 107, 307]. The adsorption of proteins while retaining the protein's configuration and activity is also important in the development of biosensors [11, 44, 81, 310]. As direct contact between a metal surface and proteins will cause denaturing of the protein, and hence in the fabrication of protein surfaces, SAMs play a role in not only allowing molecular level control over the immobilization of the protein but also insulate the protein from the metal. For controlled adsorption of proteins onto surfaces, however, nonspecific adsorption needs to be eliminated. Nonspecific adsorption of proteins occurs on many different SAM end groups [190, 238, 309, 311–314] and appears to correlate with the hydrophobicity of the surface [311, 314]. Some end groups, however, have been shown to resist nonspecific adsorption of proteins onto surfaces [190]. The most widely used [107, 197, 315–320] and successful terminal group that resists protein adsorption has been poly(ethylene glycol) with between two and seven ethylene glycol units (see Fig. 10). The polyethylene glycol head group has been shown to resist nonspecific adsorption of a number of proteins with a range of molecular weights and isoelectric points under a wide range of solution conditions [321, 322]. Self-assembled monolayers that resist protein adsorption then allow specific adsorption of a protein of interest, as well as patterning a surface so that the protein adsorbs at well-defined locations.

Specific adsorption of a protein for the development of biosensors has most commonly been performed via covalent attachment where either the protein is first derivatized with an alkanethiol and attached to the surface, or alternatively, the surface is modified with a SAM and covalently linking the protein to the SAM (see Section 3.2.1 and Figure 14 for an example of this strategy). An alternative approach is to use biospecific recognition of the protein for a ligand.

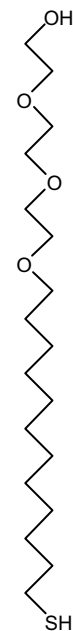


Figure 10. Structure of an ethylene glycol-terminated alkanethiol that resists protein adsorption. The number of ethylene glycol repeat units typically ranges from 2 to 7.

To achieve the biospecific recognition requires the substrate to restrict nonspecific binding to the surface so that the ligand can interact with the desired protein. The classic example of such an approach in nature is the biotin-avidin affinity reaction. There have been, however, some elegant examples developed in recent years. The Whitesides group prepared a mixed SAM of ethylene glycol end groups and a benzo-sulfonamide ligand for the specific adsorption of carbonic anhydrase. In a similar strategy, Sigal et al. [315] prepared a mixed SAM terminated with ethylene glycols and nitrilotriacetic acid (NTA). The NTA chelates with Ni(II) to form a complex with two vacant sites on the Ni(II) center. This surface can now selectively bind proteins prepared with a histidine tag as confirmed via surface plasmon resonance. Schlereth et al. [323] have also used a biospecific binding to immobilize the enzyme lactate dehydrogenase onto electrodes where the ligand is a triazine dye. One of the attractive features of the specific adsorption of proteins using biospecific ligands is that the protein is immobilized with control over its orientation. The specific adsorption of proteins onto surfaces not only opens up the opportunity for well-controlled immobilization for biosensors but also provides a surface upon which cell adhesion can occur.

Cell Adhesion The analysis of individual cultured cells, and how they interact with target molecules, is important in screening target drugs in genetic engineering and in assessing the toxicological effects of compounds. To use individual cells for any of these applications requires the isolation of large numbers of cells, controlling their distribution, and position in space. The obvious way of achieving ordered arrays of individual cells is to immobilize them on the surface. The adhesion of cells onto surfaces is mediated by proteins of the extracellular matrix (ECM) such as fibronectin, laminin, heparin, vitronectin, and collagen. Therefore, to

promote controlled cell adhesion, one approach is to first adsorb one or more of these proteins to the surface [81]. Both hydrophilic [324, 325] and ionic [326] SAMs have been used for this purpose; they afford poor control over the adsorption process.

A more nanotechnological approach to controlled cell adhesion is to exploit the fact that the attachment of the cells to the extracellular matrix is controlled by specific interactions between the integrin receptors on the cell membranes and peptide sequences of the ECM proteins [327]. As specific peptide motifs are involved in the cell adhesion, surfaces terminated with the appropriate motif, such as Arg-Gly-Asp, can be used to promote adhesion. Forming a mixed SAM with an ethylene glycol-terminated component and a peptide-terminated component can promote cell adhesion while limiting nonspecific adsorption [316, 328].

Achieving the desired outcome of arrays of individual cells of defined shape, size, and distribution has been achieved using patterned SAMs [329] (see Fig. 11). The substrates, upon which individual cells of a defined shape were cultured, were prepared using microcontact printing. The metal surface was stamped with hexadecanethiol ($\text{HS}(\text{CH}_2)_{16}\text{CH}_3$) to form the islands upon which the cells were grown. The rest of the gold surface was coated with $\text{HS}(\text{CH}_2)_{11}(\text{OCH}_2)_3\text{OH}$

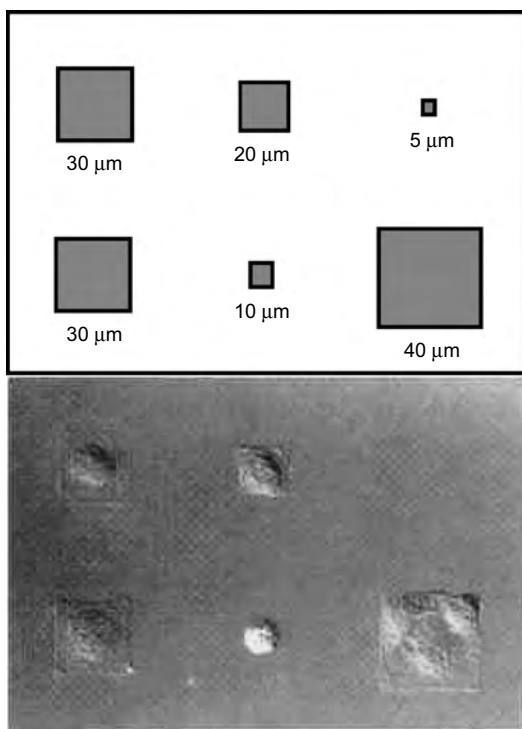


Figure 11. Demonstration of the ability to grow ordered arrays of individual cells of a defined size and shape by forming islands upon which cells will adhere using microcontact printing. Initially, the surface is patterned with a $-\text{CH}_3$ -terminated SAM with the rest of the surface coated in an ethylene glycol-terminated SAM. As extracellular matrix proteins will only adsorb to the $-\text{CH}_3$ surface, these are the only locations to which the cells will adhere. The size of the cell islands was shown to influence whether the cells proliferated or underwent apoptosis. Adapted with permission from [329], C. S. Chen et al., *Science* 276, 1425 (1997). © 1997, American Association for the Advancement of Science.

to prevent protein adsorption. The islands were coated with appropriate ECM proteins. Cells cultured on the surfaces spread to the size and shape of the island. The size of the islands were shown to influence cell life or death with apoptosis increasing with decreasing island size.

3.2. Sensors

The vast majority of the applications of SAMs, which involve nanofabrication, have been in diagnostic devices [10, 11, 44, 51, 81, 87, 310, 330], in particular electrochemical sensors, where a number of elegant nanostructures or integrated molecular systems have been fabricated. The focus on electrochemical sensing is partly related to organosulfur SAMs being formed on an electrode material—gold. Typically, a sensor requires a recognition molecule integrated with a signal transducer. Usually the recognition molecule, which gives the sensor its selectivity, is immobilized over the signal transducer. This arrangement is depicted in Figure 12. The signal transducer determines the extent of the recognition reaction and outputs the signal to an end user. Examples of recognition species include macrocyclic or other types of ligands, enzymes, antibodies, DNA, and even whole cells or tissues. An array of approaches to transduction have been employed including electrochemical [10, 47, 331], acoustic wave [332], optical [333], calorimetric [334], changes in surface force [335–338] or stress [330, 339, 340].

The immobilization of the recognition molecule is the critical step in the fabrication of a sensor. The most common immobilization strategy is to either entrap or covalently attach the recognition molecule within a polymer membrane. Although highly versatile as an approach, the control over the location and density of recognition molecules is poor [331].

Furthermore, if the analyte to be detected is large, then only recognition molecules at the surface of the polymer will interact with the analyte. In contrast, the modification of gold with a SAM can be achieved with molecule level control over the interface, and hence the position of the recognition molecules in space can also be controlled with molecular level precision. That is, the sensing interface can be fabricated using the bottom-up principle of nanotechnology.

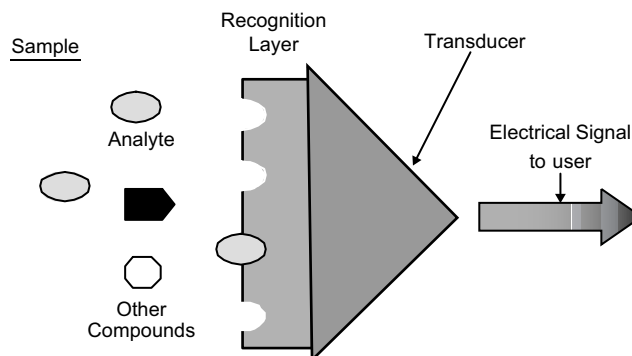


Figure 12. Schematic of a sensor showing the recognition layer that gives the sensor its selectivity for the target analyte despite the presence of other molecules in the sample. The transducer determines the extent of the reaction between the recognition component and the analyte and converts this to an electronic signal which can be outputted to the end user.

The simplest sensors based on alkanethiols are monolayers that either provide selective access to the underlying transducer surface [341, 342] or incorporate a recognition molecule attached to the SAM-modified transducer [10–13]. Slightly more complicated examples include controlling the spacing of the recognition molecule on the surface [343, 344] or using mixed monolayers to control the micro-environment of the recognition molecule [343]. Controlling the micro-environment may serve the purpose of orientating the recognition molecule [70], preventing adsorption of electrode fouling species [43, 201, 345], or providing a charge exclusion layer to prevent interferences interacting with the electrode [52, 216, 252, 346, 347]. Using the initial monolayer as the base for layer-upon-layer fabrication allows this molecular level control to be extended into a third dimension. This extension into the third dimension may be with a single recognition element [61, 62, 348–357] or with more than one type of recognition molecule that operate cooperatively [348, 358]. The number of roles that the SAM can play in the development of a sensing interface, in many ways represents the level of control afforded by SAMs in nanofabrication as several molecular components are integrated in a controlled way to fulfill a variety of functions. The sophistication to which nanofabrication, using SAMs, is perhaps best demonstrated by enzyme biosensors.

3.2.1. Catalytic (Enzyme) Biosensors

Basics of Enzyme Electrodes Enzyme biosensors employ an enzyme as the recognition element. Typically, the enzyme is a redox enzyme, which either oxidize or reduce its substrate. As the enzyme reaction is a catalytic reaction, enzyme biosensors are often classed as *catalytic sensors*. In an enzyme biosensor, the substrate is the analyte of interest. The analyte reacts with the enzyme and produces a product. Transduction is achieved by monitoring either a molecule consumed in the enzyme reaction or one that is produced. The classic example is a glucose biosensor which uses the enzyme glucose oxidase (GOD) to oxidize glucose in the presence of a mediator to produce gluconolactone and a reduced form of the mediator (see Fig. 13).

The role of the mediating species is to complete the catalytic cycle. The enzyme in its oxidized form is reduced as the glucose is oxidized. Therefore, the mediator oxidizes the reduced form of the enzyme and in the process is itself reduced. In nature, the mediator is oxygen with hydrogen peroxide being produced while many of the commercial glucose biosensors use redox species such as ferrocene or ferricyanide [359]. As there are changes in oxidation state in the recognition reaction, it is common for the transduction of enzyme reactions to be electrochemical. In a conventional enzyme biosensor, the reduced form of the mediator is detected amperometrically at the electrode with the current being proportional to the amount of glucose in the sample. These principles can be extended to many other enzymes, where all that is required is an enzyme specific for the analyte and a product of the enzyme reaction that can be transducer. The commercial glucose meters that arise from these ideas usually immobilize the enzyme in a polymer layer over the electrode [360]. Immobilization of enzymes in polymers, however, gives poor control over where the enzyme

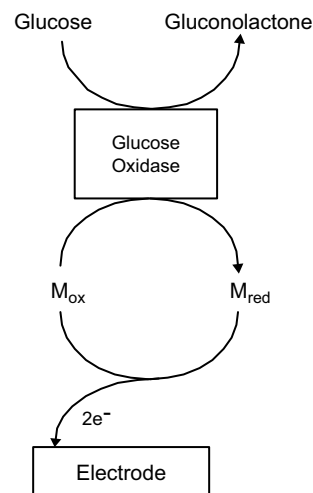


Figure 13. Schematic of an electrochemical glucose biosensor, where glucose is oxidized by the enzyme glucose oxidase to produce gluconolactone. In the process, the enzyme is reduced. The reduced enzyme is reoxidized by a mediator. In nature, this mediator is oxygen with hydrogen peroxide being produced as the reduced form of the mediator. The reduced form of the mediator is oxidized at the electrode to give a current proportional to the amount of glucose in the sample.

is in space, which is partly responsible for reproducibility problems associated with enzyme electrodes [361].

Fabricating the Biorecognition Interface Enzyme electrodes fabricated using SAMs have been studied extensively with a view to providing more controlled enzyme immobilization [12, 13, 62, 70, 140, 155, 348–350, 354, 358, 361–379]. The simplest enzyme electrodes fabricated using SAMs involve the covalent attachment of a single enzyme on a SAM as represented schematically in Figure 14. In this case, the SAM is prepared from 3-MPA and the enzyme is GOD [361, 376]. The reasons for using MPA are two-fold. First, the short chain alkanethiol produces a disordered SAM, which makes the underlying gold electrode electrochemically accessible. Second, the carboxylic acid functionality allows covalent attachment of the enzyme via the formation of a peptide bond after activation. In Figure 14, the activation is achieved using 1-ethyl-3-(3-dimethylaminopropyl) carbodiimide hydrochloride (EDC) and *N*-hydroxysuccinimide (NHS), which yields a succinimide ester intermediate that

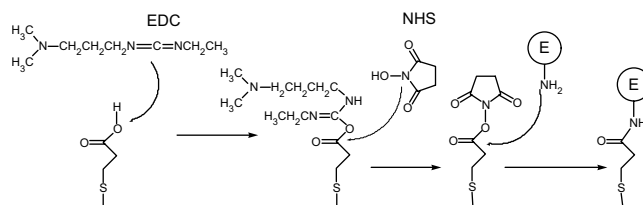


Figure 14. Reaction scheme for the immobilization of enzymes and other biomolecules onto a carboxylic acid-terminated SAM. In this case, the SAM is composed of 3-mercaptopropionic acid. The carboxylic acid terminated-SAM is activated using EDC and NHS. The succinimide ester-terminated SAM is now susceptible to nucleophilic attack from amines such as found on the surface of biomolecules. The result of the nucleophilic attack is a peptide bond.

is susceptible to nucleophilic attack from amines such as those found on proteins. This is perhaps the most common method of attaching enzymes, although other methods of immobilizing enzymes onto SAMs include other methods of covalent attachment [380, 381], electrostatic adsorption [62], using biotinylated enzymes bound to streptavidin [350, 382–384], using antibody-antigen binding [349, 363–368] and cross-linking [139, 351, 385–391]. Apart from the glutaraldehyde approach, which results in the uncontrolled formation of multilayers of enzyme and hence loses the advantage of controlled immobilization using SAMs, the other methods give a monolayer of enzyme immobilized on the SAM surface that exhibit good reproducibility [376, 378]. Many of the important issues in molecular level fabrication of enzyme electrodes have been reviewed elsewhere [12, 13, 376, 377]. Importantly, for this work on simple SAM-based enzyme electrodes are that the SAM provides a generic base upon which many different enzymes, and other biomolecules, can be immobilized.

Examples of SAM-Based Enzyme Electrodes That Employ Nanofabrication

From the platform of a single enzyme-modified SAM, quite complicated molecular constructs have been fabricated with multiple functionality integrated into a single layer or multilayer. Multilayers of enzyme systems can be fabricated using a variety of strategies with molecular level control [61, 62, 348, 349, 382]. Riklin and Willner [348] have shown that multiple enzymes can be incorporated into an enzyme electrode with a layer-by-layer approach. Importantly, however, Gooding et al. [358] have shown that in a bienzyme amplification system, using glucose oxidase and glucose dehydrogenase, the response of the final enzyme electrode is sensitive to the relative spatial organization of the two enzymes (see Fig. 15). In this bienzyme system, the glucose is converted into gluconolactone by the glucose oxidase, and the glucose dehydrogenase reduces the gluconolactone back to glucose to create an amplification cycle. In each cycle where the glucose is oxidized to gluconolactone, the mediator a *p*-benzoquinone is reduced to hydroquinone. The hydroquinone is then detected at the electrode. When the enzyme electrode was made in two layers, one containing glucose oxidase and the other gluconolactone, a different linear range and gain was observed depending on whether GOD was in the inner layer directly adjacent to the electrode or on the outer layer.

Improving and/or controlling the transduction of the biorecognition reaction has been the objective of considerable attention with SAM-modified enzyme electrodes [140, 370, 372, 373, 388, 392, 393]. In many examples of SAM-based enzyme electrodes, a redox mediator is used either in the sample solution or attached to the enzyme [12]. Blonder and Willner et al. [372, 388] modulated the access of the mediator to the enzyme interface using nitrospiropyran. Reversible photoisomerism of nitrospiropyran to the cationic nitromerocyanine can be achieved by irradiating with UV light, switching back to nitrospiropyran using light of wavelengths greater than 475 nm. By covalently attaching nitrospiropyran to the enzyme, the access of the charged mediator—ferrocene monocarboxylic acid—can be modulated through charge exclusion by switching between the

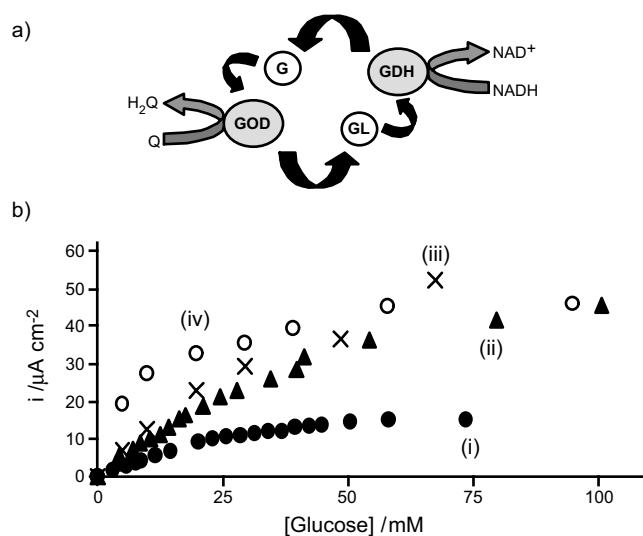


Figure 15. The bienzyme electrode fabricated by Gooding et al. [358], which employs the two enzymes GOD and glucose dehydrogenase (GDH) to create an enzyme amplification cycle as shown in a) where the analyte glucose (G) is oxidized to gluconolactone (GL) by GOD in the presence of the mediator benzoquinone (Q). During the oxidation, the B is reduced to hydroquinone (H_2Q). The GL is reduced back to G by GDH, in the presence of the enzyme cofactor, reduced nicotinamide adenine dinucleotide (NADH), to complete the amplification cycle; b) shows the influence of the enzyme electrode geometry on the amplification gain where (i) is an enzyme electrode fabricated with glucose alone, (ii) contains both enzymes in the same layer, (iii) the GOD is in the inner layer and the GDH is immobilized in a second layer over the GOD, and (iv) GDH is in the inner layer and GOD in the outer layer. Reprinted with permission from [358], J. J. Gooding et al., *Electrochem. Commun.* 2, 217 (2000). © 2000, Elsevier Science.

two photoisomers [388]. Improved exclusion of the mediator, and hence improved switching, was achieved by attaching the nitrospiropyran directly to the redox active center of GOD—flavin adenine dinucleotide (FAD) [372].

As the enzyme reaction involves a change in oxidation state, the ultimate goal of enzyme electrode research is to obviate the need for a mediator by oxidizing and reducing the enzyme directly at the electrode. The attractiveness of SAM technology for achieving direct electron transfer is that the enzymes can be immobilized close to the electrode in a highly controlled manner. Furthermore, with judicious choices of self-assembling molecules, the SAM-forming molecule can be used to facilitate the electron transfer [55, 56, 394–397].

Direct electron transfer has been achieved with SAM-based enzyme electrodes where peroxidase enzymes are used [198, 373, 393, 398]. Lötzbeyer et al. [371, 373] have investigated the distance dependence of long-range electron transfer by using hydrogen peroxide-reducing enzymes of different size which are a covalent attachment to short chain alkanethiol SAM-modified electrodes. The focus on peroxidase enzymes is a consequence of their redox active sites being located close to the enzyme surface [398]. With most enzymes, however, the redox active centers are located a sufficient distance from the surface of the glycoprotein to prevent direct electron transfer [399]. For example, in the case of glucose oxidase, the closest approach of the redox active center—FAD—to the enzyme surface is 13 Å

[400]. Willner et al. [392] have spanned this 13 Å gap with an electrically wired enzyme electrode where a mediator—pyrroloquinoline quinone (PQQ)—was covalently attached to a cystamine-modified gold electrode using EDC. The PQQ-terminated SAM was then bonded to a derivatized version of the FAD cofactor for GOD, *N*⁶-(2-aminoethyl)-FAD, to form a diad. The PQQ/FAD diad was treated with *apo*-glucose oxidase to provide a glucose enzyme electrode mediated by PQQ. This enzyme electrode had an extremely large linear range—up to 80 mM—consistent with efficient turnover of enzyme [358, 361], and an exceedingly high sensitivity of $300 \pm 100 \mu\text{A cm}^{-2}$.

The elegant-wired enzyme electrode of Willner et al. still represents a mediated enzyme electrode where the ultimate intimate relationship between the enzyme and the mediator is achieved via molecule level fabrication. The transport of electrons between the enzyme and the electrode is still achieved via hopping from the FAD to the PQQ and then to the electrode. Liu et al. [401] are extending this principle to achieve electron tunneling directly to the electrode from the FAD (see Fig. 16). This electrode construct requires the synthesis of norbornylogous bridge-based SAMs as the connector between the electrode and the FAD. Norbornylogous bridges have been shown to allow efficient electron transfer over long distances via the super-exchange mechanism [55, 402, 403]. *N*⁶-(2-aminoethyl)-FAD is attached to the end of the bridge and the *apo*-GOD reconstituted over FAD to give active enzyme. In this case, despite the enzyme active on the FAD being embedded within the protein, and being 108° from the electrode, direct electron transfer between the FAD and the electrode is still observed.

3.2.2. Affinity Biosensors

Basics of Affinity Biosensors Affinity biosensors rely on a binding reaction between the biorecognition molecule and the analyte. Typical biorecognition molecules used

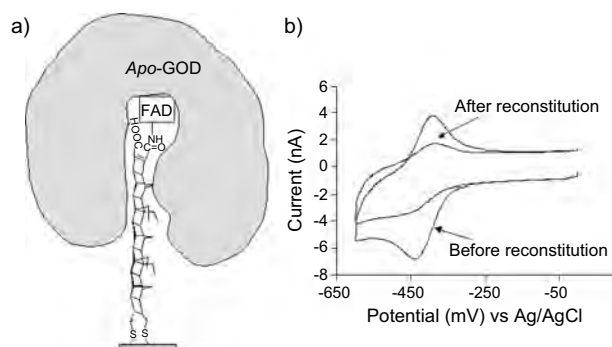


Figure 16. Electrode construct designed to achieve direct electron transfer to enzymes such as glucose oxidase. In a) an 18 Å long norbornylogous bridge SAM is formed with the redox active center of glucose oxidase FAD, attached to the end of the bridge, which serves as a conduit for electron transfer between the electrode and the redox active center of the enzyme. Subsequently, the *apo*-glucose oxidase (*apo*-GOD) is reconstituted over the FAD to form the active enzyme; b) shows the electrochemistry of the FAD before and after reconstitution. The characteristic FAD electrochemistry shows that FAD 18 Å from the electrode can still be interrogated before and after the active enzyme is reconstituted. This illustrates direct electron transfer to the redox active center of glucose oxidase.

in affinity biosensors are antibodies, sequences of DNA (oligonucleotides) or peptides. Frequently, the analyte to be bound is also a protein or sequence of DNA, although the molecule to be bound can also be a small molecule. Once the binding reaction has occurred, there is still the need to transduce the biorecognition event. Unlike catalytic biosensors, where the biorecognition event produces a molecule that can then be detected, in affinity sensors the analyte simply binds. To transduce such biorecognition events either requires labels, so familiar in the myriad of immunoassay formats, or a transduction method that can detect the change that occurs at the interface. The two most popular methods that allow label-free transduction of affinity biosensors are evanescent wave techniques such as surface plasmon resonance (SPR) [81, 220, 315, 318, 404–425] and piezoelectric acoustic wave devices such as the quartz crystal microbalance (QCM) [31, 320, 332, 422, 425–451], although a variety of other transduction methods that may involve labels have been employed including electrochemical [433, 452–468], and microcantilever [330, 340, 469, 470].

Surface plasmon resonance is an optical method where a thin film of gold or silver (~50 nm thick) is deposited over one face of a prism. It is this metal film that forms the sensing surface and will be modified with a SAM. When light is launched into the film, such that it is reflected off the prism face coated with the metal layer, the light is coupled into the surface plasmon-polaritons. The surface plasmon-polaritons occur at the outer surface of the metal. The adsorption of molecules onto this surface causes a change in the refractive index of the interface, which affects the amount of light coupled into the surface plasmon mode, and hence a change in the intensity of light reflected into the detector. To use this phenomenon for affinity sensing, the metal surface is modified with the biorecognition molecule. The binding of the analyte causes a change in the surface plasmons and hence transduction is achieved without any labels [359, 471]. Examples of simple SPR transduction for monitoring bioaffinity reactions include peptides for recognizing antibodies [407–409] or lipoproteins [318, 410, 411], DNA to detect specific sequences of DNA [220, 412, 413, 415, 416, 419–421], and proteins to detect other proteins and small molecules as in immunosensors [315, 320, 406, 408, 409, 414, 422, 424, 425, 450, 451, 472].

Transduction using a QCM is achieved using an oscillating piezoelectric AT cut quartz crystal. The deposition of electrodes, gold in most cases, onto both faces of the quartz slice allows an alternating current to be applied to the crystal. The alternating current causes the crystal to oscillate at a frequency characteristic of the thickness of the crystal slice. Adsorption or desorption of molecules from the crystal surface cause a change in the frequency of oscillation with picogram sensitivity. Thus, by immobilizing the biorecognition molecule onto the surface of one of the gold electrodes, the bioaffinity reaction is transduced by a decrease in the frequency of the QCM [11, 332]. In a similar manner to SPR, affinity biosensors employing QCM transduction have been developed for DNA recognition [426–428, 430, 431, 435–439, 442] and for monitoring antibody-antigen binding [422, 425, 429, 432, 433, 440, 441, 443–449].

Fabricating the Biorecognition Interface In a bioaffinity sensor, the recognition molecule must be free to bind with the analyte. Therefore, immobilizing the biorecognition molecule such that it is accessible for binding is exceedingly important. The molecular level control afforded over, not only the immobilization of biomolecules but also the environment in which they are immobilized, makes SAMs very attractive for fabricating bioaffinity interfaces. An example of the control afforded over biomolecule immobilization is the SAM interface used for the immobilization of DNA by Levicky and Steel et al. [70, 473–475] (see Fig. 17).

In a DNA sensor, typically a single strand of DNA (ss-DNA) is immobilized onto the transducer surface. This immobilized ss-DNA is referred to as the probe strand and is the biorecognition molecule. Hybridization of the immobilized probe DNA with the complementary sequence in solution (the target strand) is the binding reaction that is to be transduced. Levicky et al. [70] synthesized probe DNA with a mercaptohexyl linker at the 5' end of the DNA. With the thiol linker only located at one end, end point immobilization of the probe DNA is achieved via self-assembly onto a gold surface. The idea of the end-point immobilization was to minimize the decrease in configurational freedom caused by the hybridization. Such minimization is particularly important in DNA biosensors, as the probe and target must be free to rotate around each other for hybridization to

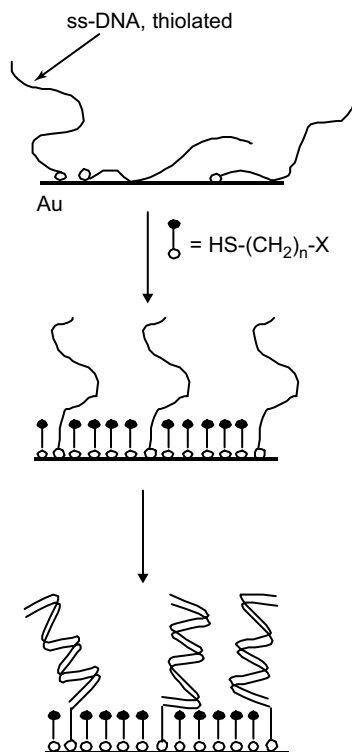


Figure 17. Steps involved in the fabrication of the DNA recognition interface prepared by Levicky et al. [70], which allows efficient hybridization of DNA where one of the strands is immobilized onto a gold surface using alkanethiol chemistry. Efficient hybridization is achieved by having endpoint immobilization of the DNA and preventing nonspecific binding of the DNA to the gold electrode by using a diluent layer of 6-MCH.

occur. Neutron reflectivity studies, however, indicated that the ss-DNA was lying flat on the gold surface with multiple adsorption points due to the DNA bases complexing with the gold [70, 210, 476, 477]. The resultant hybridization efficiency was low—10% or less. Hybridization efficiency was improved to almost 100% by preventing the nonspecific adsorption of the DNA bases. This was achieved by exposing the DNA-modified surface to 6-mercaptohexanol (MCH). The MCH not only lifted the nonspecifically adsorbed DNA off the surface but the net negative dipole of the alcohol terminus repelled the negatively charged DNA backbone, thus helping to project the probe strand out into solution.

Synthesizing a biorecognition molecule with a thiol linker is not always the simplest strategy for immobilizing biorecognition molecules. However, there are a number of reasonably generic methods of fabricating recognition interfaces for affinity sensors which provide favorable conditions for the recognition reaction to occur. One is to use a similar strategy to that used for enzyme biosensors (Fig. 14), where the gold surface is modified with a carboxylic acid-terminated SAM and carbodiimide coupling is used to attach the biorecognition molecule. Such an approach has been used for oligonucleotides [379, 478, 479], antibodies [405, 440], and peptides [480–482].

An alternative generic interfacial structure first developed by Häussling, Schmitt, and Spinke et al. [483–485] involves using a biotin-terminated SAM. Biotin has an exceedingly high affinity for avidins, such as streptavidin ($K_{\text{aff}} = 10^{15}$ M), making the binding virtually irreversible. As each avidin has four binding sites, the ‘plug-and-socket’ aspect of the avidin-biotin system makes it a very important molecular building block for nanofabrication. The usefulness of the avidin-biotin system is enhanced further by the ease of modifying other molecules with biotin. In the case of SAM-based affinity sensors the avidin is bound to the biotinylated monolayer and subsequently biotinylated biorecognition molecules are bound. Such a strategy has been used for the immobilization of antibodies [319, 485], DNA [319, 413, 430], peptides [319, 486] and even enzymes [382–384]. The accessibility of the biorecognition molecule can be controlled by forming mixed SAMs, where a long-chain alkanethiol acts as a spacer to keep the biotin group away from the monolayer surface, and the shorter alkanethiol spaces the biotin coupling points apart [485].

Examples of Affinity Biosensors Relevant to Nanotechnology

There have been many examples where SAMs have been employed to make affinity biosensors, primarily because of the ability to control the accessibility for binding of the biorecognition molecule and the compatibility with the SPR and QCM transduction systems. Among these examples are some of the most exquisite examples of nanofabrication that have thus far been realized. We shall discuss a few of these examples in turn.

The first example is the fabrication of a simple immunosensor for *Salmonella paratyphi*, where transduction is achieved using a quartz crystal microbalance [447]. The biorecognition interface is fabricated as in Figure 14 by modifying the gold electrodes on the 10 MHz quartz crystal with 3-MPA followed by activation with EDC and NHS to allow by covalent attachment of antibodies specific for the

S. paratyphi bacteria. After immobilization of the antibody, the rest of the crystal was coated in bovine serum albumin to prevent nonspecific binding to the crystal surface. The resultant sensor could differentiate between *S. paratyphi* and other bacteria, including *E. coli* and other serogroups of *Salmonella* with a detection limit of 1.7×10^2 cells/mL.

A sensor for low-density lipoproteins (LDLs) by Gaus and Hall et al. [318, 410, 411] provides an example where multiple molecule components are incorporated in the one interface to allow differentiation between LDLs and oxidized LDLs. Initial work used a heparin-modified surface to detect LDL adsorption to the interface via surface plasmon resonance, but this lacked the specificity to differentiate between LDLs and the more harmful oxidized LDLs. To improve the ability to differentiate between LDLs and oxidized LDLs, the fifth ligand repeat unit (LR5) of the LDL receptor was genetically engineered and attached to a mercaptoundecanoic acid SAM using EDC/NHS chemistry [410]. Unfolded LR5 was ineffective as an affinity ligand, but refolded LR5 showed a high affinity for native LDLs but little affinity for oxidized LDLs (see Fig. 18). This study showed the potential for using small peptide sequences—40 amino acids in this case—as highly selective affinity ligands. The one drawback was the instability of the refolded LR5 ligand. To overcome the instability of the affinity ligand, Gaus and Hall investigated a library of short peptide ligands (three to five amino acids long) related to conserved peptide sequences of the LR5 receptor [318, 411]. A more sophisticated recognition interface was used comprised of a mixed SAM of mercaptoundecanoic acid for coupling the amino acids and 1-mercapto-octyl-hexa(ethylene glycol) to resist nonspecific adsorption. Amino acids were coupled

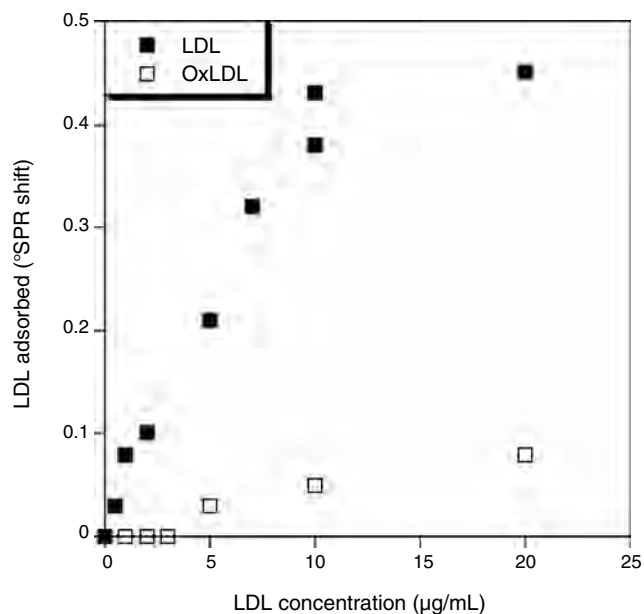


Figure 18. The surface plasmon resonance response to low-density lipoproteins and oxidized low-density lipoproteins to a SAM-modified interface with the LR5 ligand attached. The SPR response shows the good selectivity of the LR5 ligand for LDLs over oxidized LDLs. Adapted with permission from [410], K. Gaus et al., *Analyst* 126, 329 (2001). © 2001, The Royal Society of Chemistry.

to the SAM on the SPR chip one amino acid at a time to enable *in-situ* synthesis of peptide sequences by step-wise elongation. Using this combinatorial approach, a library of peptides was assessed for their affinity to LDLs and oxidized LDLs. The short peptide sequences GlyCystineSerAspGlu and GlyLysLys-OH were found to be the most effective for the selective binding of LDLs and oxidized LDLs, respectively, although detection limits were not quite as low as the LR5 ligand. The variation in LDL binding with oxidation levels of the peptide sequences provides a powerful approach to detecting the LDL oxidation levels in an unknown sample which could provide a sensing system to assess a patient's atherosclerosis risk [411].

The above example illustrates a recognition interface involving combinatorial synthesis of the recognition element and multiple functionalities incorporated within the recognition interface. The DNA sensor developed by clinical microsensors (CMS) [345], which is illustrated in Figure 19, shows a recognition interface where nanofabrication using SAMs enables the recognition interface to also fulfill several functions. The SAM recognition interface contains two other components apart from thiolated DNA. The majority of the SAM is composed of polyethylene glycol terminated alkanethiol, designed not only to resist nonspecific binding of DNA and proteins, but also to insulate the electrode [107, 190, 316]. Oligophenylethynyl thiols are also present in the SAM. The function of the oligophenylethynyl thiols is to allow communication with the electrode, as these molecules are efficient molecular wires. Upon hybridization between a target nucleic acid and the capture probe, transduction is achieved by also hybridizing a reporter sequence of DNA with the target. The reporter sequence is modified with ferrocene labels. The molecular wires allow oxidation of the

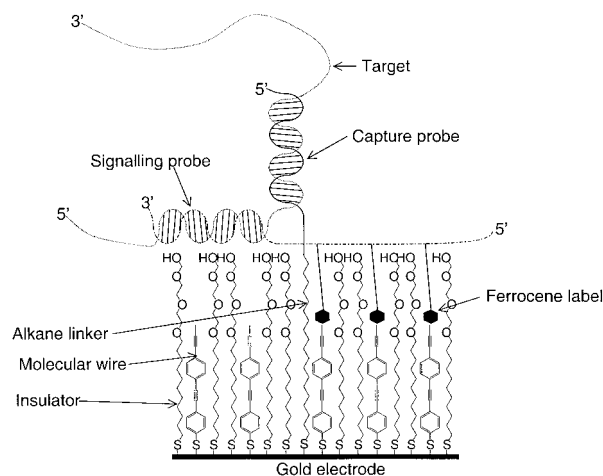


Figure 19. Schematic of the DNA biosensor of Umek et al. [345]. The SAM is composed of polyethylene glycol-terminated alkanethiol, which resist nonspecific binding of DNA and insulates the electrode, oligophenylethynyl thiols, which act as molecular wires to allow communication with the electrode and thiolated probe DNA molecules. Upon hybridization between a target nucleic acid and the capture probe, transduction is achieved by also hybridizing a reporter sequence of DNA with the target. The reporter sequence is modified with ferrocene labels. The molecular wires allow oxidation of the ferrocene labels. Therefore, recognition of the target strand is transduced by the occurrence of a current signal.

ferrocene labels. Therefore, recognition of the target strand is transduced by the occurrence of a current signal.

The final example is the ion-channel biosensor currently being commercialized by AMBRI [45, 317, 487–493]. The ion-channel biosensor can arguably be claimed to be the first real nanomachine with moving components. The recognition interface is comprised of a lipid bilayer which is anchored to an underlying gold electrode using alkanethiol chemistry (see Fig. 20). The lipid bilayer contains 10 or more components including gramicidin ion channels. The ion channels in the lower layer of the bilayer are fixed to the electrode while those in the upper layer float free. The ion channels in the upper layer are derivatized to allow transduction of a biorecognition event. In one variant of the biosensor, the upper ion channel is modified with antibody Fab' fragments. The other half of the antibody-binding site is locked into its position in the bilayer using a thiol-terminated membrane-spanning lipid. When there is no analyte present, the floating gramicidin channel moves through the top layer of the bilayer allowing a complete ion channel to form. Opening of the ion channel results in a flow of ions through the bilayer and there is a large increase in conductivity. When analyte is present, the two halves of the Fab-binding site bind to the analyte. This binding event locks the ion channel in a closed position; thus the conductivity decreases. The particularly elegant aspects of this design we first, utilize not only biological molecules for detecting but mimic cellular approaches to transduction and second, the transduction method can be applied to a wide variety of different types of analytes. The system has been used to detect small molecules such as digoxin, hormones, bacteria, and even sequences of DNA [45, 494].

3.2.3. Chemical Sensors

The differentiation between a biosensor and a chemical sensor can be made according to the recognition element. In a chemical sensor, the recognition element is of nonbiological origin and therefore refers to a ligand of some sort. There have been many SAM-based chemical sensors and in this section only a few that are interesting examples of nanofabrication will be discussed.

Hickman et al. [137] developed the first electrochemical SAM-based pH sensor that contained two terminals: a quinone was used as the pH indicator (having pH sensitive electrochemistry) and pH insensitive ferrocene as a reference electrode. The two redox species were coimmobilized onto a SAM. The oxidation and reduction peaks of the quinone shifted linearly with pH, which allowed accurate measurement of pH between pH 1–11. Beulen et al. [495] elegantly extended this principle to where the different components of a SAM act cooperatively. Rather than form a mixed SAM, a carboxylic acid-ferrocene sulfide was synthesized to give a bifunctional monolayer adsorbate. The normally pH independent electrochemistry of the ferrocene unit became pH dependent due to through space interactions with the adjacent carboxylic acid. Deprotonation of the adjacent carboxylic acid stabilized the oxidized state of the ferrocene resulting in a pH sensitive cathodic shift.

Electrochemical sensors for metal ions have been the subject of considerable interest. A sophisticated example involving SAMs is reported by Rubinstein et al. [186], where SAMs

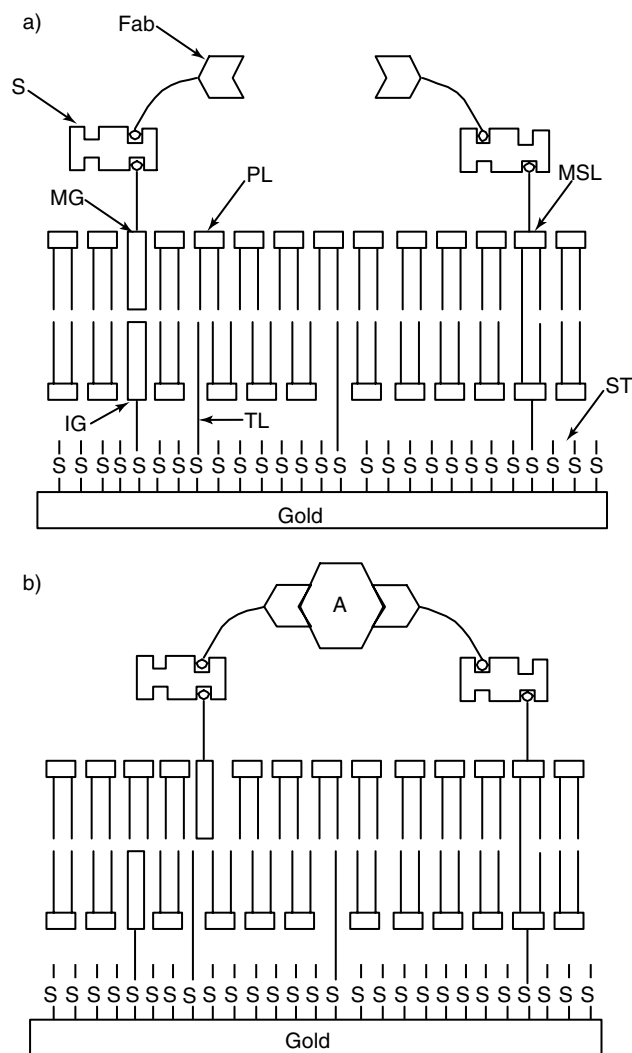


Figure 20. The ion-channel biosensor based on a suspended lipid bilayer developed by AMBRI. The self-assembled monolayer consists of spacer thiols (ST), which define an ionic reservoir under the bilayer composed of phospholipids (PL). The bilayer is anchored to the gold electrode using tethered lipids (TL), which span into the lower half of the bilayer. Incorporated within the lower part of the bilayer are immobilized gramicidins (IG), which are immobilized to the electrode with a thiol. In the open state, the IG are associated with mobile gramicidins with pendant biotin groups (MG) in the top part of the bilayer. Membrane spanning lipids (MSL), also with pendant biotin, span across both halves of the bilayer. Biotinylated antibody fragments are attached to both the MG and the MSL using streptavidin (S) as a molecular building block. When there is no analyte (A) present, the MG can move across the bilayer. a) When the MG and IG coincide, there is a large increase in conductivity as ions can pass across the bilayer. b) When the analyte binds to the two Fab antibody fragments, the gramicidins can no longer diffuse freely through the bilayer and the ion channels are closed. The result is a low conductivity.

were used to selectively detect Cu^{2+} in the presence of Fe^{3+} . This was achieved using the ligand 2,2'-thiobisethyl acetoacetate (TBEA). The thiol group allows the assembly onto a gold electrode while the tetradentate ligand satisfied the four coordinate complexation preference of $\text{Cu}(\text{II})$. The metal ion sensors were prepared with a mixed SAM of

octadecylmercaptan (OM) and TBEA. The OM passivated the electrode, while the TBEA provided defect sites where the Cu^{2+} was bound and amperometrically detected. As the Fe^{3+} did not effectively bind to the TBEA and the OM prevented direct access to the electrode, Cu^{2+} could effectively be detected despite the presence of the other metal species.

Many other metal ion sensors have been developed where ligands such as crown ethers [496–499], oligoethylene glycols [500–502], and calixarenes [503] are attached to an electrode using SAMs. Calixarenes have also been reported as selective recognition elements for organic molecules such as steroids [404, 456, 504]. The key drawback of using selective ligands is the need to design and synthesize a new ligand for each analyte. Therefore, a simple generic synthetic strategy is required if arrays of sensors are to be developed. Yang and Gooding et al. [481, 482, 505, 506] have addressed this issue using amino acids [505], oligopeptides [482], and polypeptides [481] as the selective ligands for metal ions. A high degree of selectivity for Cu^{2+} with very low detection limits has been achieved. An attractive feature of this approach is that similar, simple synthetic protocols can be used for most peptide sequences desired. Thus, the amino acids act as the alphabet from which a library of receptor ligands with varying selectivity can be synthesized.

An interesting approach to the fabrication of chemical sensors for organic molecules using SAMs has recently been developed, which is analogous to molecular imprinting [507–510]. In molecular imprinting, an artificial receptor is prepared by forming a polymer or sol-gel in the presence of the analyte of interest. The analyte is then removed to produce a three-dimensional porous structure where the cavities match the molecular structure of the analyte. With SAMs of alkanethiols, the same principle can be applied to give two-dimensional receptor sites (Fig. 21) [51, 511–516]. Typically, the binding of the analyte into the receptor site was transduced by a change in capacitance of the interface [513] or the restricted access of an electroactive species to the underlying electrode [512]. One of the difficulties that must be overcome with imprinting receptor sites in SAMs is the mobility of the alkanethiols [216, 217]. Initial attempts to imprint receptor sites resulted in the loss of the receptor property after a single adsorption/desorption cycle [513]. To overcome this problem, a templating molecule with the same shape as the analyte was adsorbed to the surface with a long-chain alkanethiol. The templating molecule was maintained on the surface with pores defined by the long-chain alkanethiols available for binding the analyte. The binding of the analyte is transduced by a decrease in the interfacial capacitance of the electrode. The molecular imprinting approach has been demonstrated for cholesterol [511, 512, 515], barbiturates [513], quinines [516], phenothiazines [511], and adenine triphosphate (ATP) [51].

3.3. Electron Transfer and Molecular Electronics

Electron transfer through alkanethiol SAMs, or even individual molecules, has potential applications in improving our fundamental understanding of electron transfer processes [46], molecular electronics [517], and in sensing [458]. Alkanethiol SAMs have a number of advantages that make

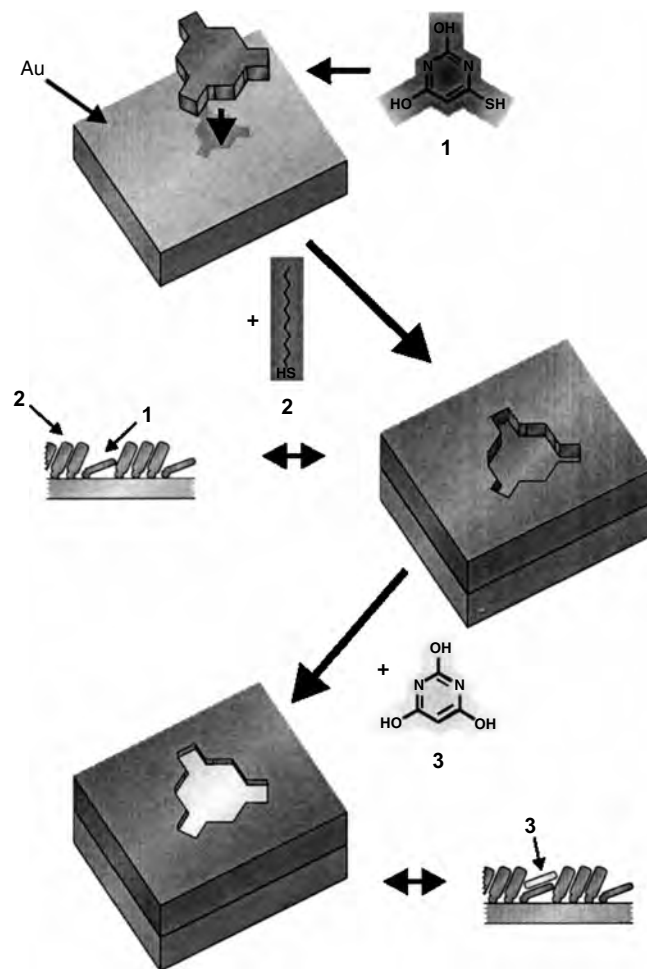


Figure 21. The alkanethiol SAM-based artificial chemoreceptor. The binding sites are formed by adsorbing the template thiobarbituric acid **1** onto a gold surface in the presence of the matrix molecule **2** which was dodecanethiol. The template must be a similar shape to the analyte and must be able to bind strongly to the gold surface so that it is not displaced by the matrix molecule. When the analyte barbituric acid **3** is exposed to the surface, it can bind in the clefts in the SAM formed by the templating molecule. Reproduced, with permission from [513], V. M. Mirsky et al., *Angew. Chem.-Int. Edit.* 38, 1108 (1999). © 1999, Wiley-VCH.

them suitable for studying and exploiting long-range electron transfer. These advantages include those that have already been discussed, such as densely packed SAMs giving well-defined distance relationships, the formation of mixed SAMs allowing the spacing of redox centers, the low number of defects or pinholes in well-prepared SAMs ensuring that tunneling processes are probed, and the ease of altering their chemical structure allowing simple exploration of structure-function relationships. A further advantage is that the thiol functionality is ideal for connecting “molecular wires” to bulk materials and hence allowing a connection to the surroundings. Thus, the organosulfur molecules act as the “glue” between electronic materials in molecular devices. Such electronic materials could be bulk surfaces or quantum particles. The alkyl chain or unsaturated conjugated system acts as the conduit for electron transfer.

Thus, the electron movement can be through σ -bonding systems, which are the most frequently investigated systems so far. In the case of σ -bonding systems, the electron transfer occurs through a superexchange mechanism [403]. Alternatively, electron movement can be through a π -bonding system via a typical electron transport mechanism. The actual nature of the chemical connection is exceedingly important and a subject of considerable interest. If the influence of the actual contact can be understood, then the potential to tailor the connection in organic-conductor/semiconductor hybrid systems is greatly expanded and the behavior of the devices will be better controlled.

Our understanding of the influence of the contact is poor at this stage but improving rapidly through a number of elegant experiments involving alkanethiol molecules. Cui et al. [518] demonstrated the importance of an alkanethiol having a bond to both electronic materials. A gold surface was modified with either an octadecanedithiol or an octadecanethiol SAM. To the other end of the SAM was bound gold nanoparticles. So in the case of the dithiol, a gold-thiol bond formed with the nanoparticle while in the monothiol case the nanoparticle simply adsorbed onto the methyl terminal of the SAM. The current-voltage (I - V) properties of these molecular constructs were measured using a conducting probe AFM. There was increase in current of up to four orders of magnitude for a given tip bias when the dithiol was used relative to the monothiol. A similar increase in conductivity was also observed by Selzer et al. [519] with the addition of a bond, in this case between a mercury and a semiconductor surface. The influence of different types of bonds on the conductivity was investigated by Holmlin et al. [520]. A gold surface modified with one alkanethiol SAM and a mercury electrode modified with a second SAM are brought into contact and the I - V behavior measured. With judicious choice of the monolayers, they compare electron transfer across bilayers that form either covalent, hydrogen, or van der Waals bonds. The conclusion was that tunneling rates increased in the order van der Waals < hydrogen bonds < covalent bonds. It is clear from these studies using alkanethiols how important the junction between the organic molecule and the electronic material is. The actual contact resistance of a gold-thiol bond has been estimated at $10^4 \Omega$ by Wold et al. [521] using a similar conducting AFM-type experiment to Cui et al. [518] but without the gold colloid.

The research into tunneling through alkanethiol SAMs has been dominated, not by measuring the influence of the link between the organic molecule and the electronic material, but by the distance dependence of the rate of electron transfer through the organic molecules. Distance dependence has typically been measured using redox monolayers, where a redox active group attached to the terminus of a SAM is probed electrochemically. This approach is well covered in a review by Finklea [46] and in a number of excellent papers since (see, for example, [56, 142, 522, 523]). A wide variety of electroactive groups and redox proteins have been investigated [46]. A number of electrochemical methods allow the measurement of rates in the range of 10^{-2} – 10^5 s^{-1} including cyclic voltammetry [524], AC impedance spectroscopy [525] or voltammetry [526], square wave voltammetry [527], and chronoamperometry [528].

The distance dependence of the rate of electron transfer can be described using Marcus theory [529], which relies on the overlap of donor and acceptor energy levels in the redox molecule and the electrode. The important parameters in the theory include the reorganization energy (λ), the energy needed to change the redox center's structure and solvation sphere during the change in oxidation state, and tunneling parameter β . The tunneling parameter is a structure dependent constant, which describes how the electronic coupling decays, as seen in the equation describing the electron transfer rate constant, k_{ET} ,

$$k_{ET} = k_0 \exp[-\beta d]$$

where k_0 is the rate constant at zero overpotential and d is the distance between the donor and acceptor in this case (the redox species and the electrode). A remarkable consistency in the dependence of the electron transfer with rate is beginning to emerge for aliphatic hydrocarbons. Despite the different redox active species that have been investigated, the value of β is found to be between 0.8–1.1 \AA^{-1} . Similar values for β are also found when the I - V characteristic of alkanethiol SAMs are measured using conducting AFM [521, 530] or the bilayer approach of Holmlin et al. [520, 531]. Although the presence of different coupling chemistry to a redox active species does not appear to significantly alter the value of β [523], large structural rearrangements in the molecule during the electron transfer, such as found with azobenzenes, do cause increases [532]. Conjugation on the other hand definitely causes a decrease in the value of β , indicating less decay in the electron transfer rate with distance. Values for β that have been quoted for conjugated systems include for oligo(phenylethynyl) "molecular wire" bridges β of 0.36 \AA^{-1} , around 0.4 \AA^{-1} for oligophenylenevinylene bridges [394], 0.41 \AA^{-1} [521] or 0.61 \AA^{-1} [520] for oligophenylenes, and 0.67 \AA^{-1} [520] for benzyl derivatives of oligophenylene. These lower decay constants indicate useful molecular wires could be developed with conjugated systems.

3.4. Nanofabrication with Other Nanobuilding Blocks

In recent times, SAMs have been used as the foundation upon which nanofabrication into the third dimension is achieved using nanoscale building (nanobuilding) blocks such as nanoparticles, nanotubes, and dendrimers.

3.4.1. Nanoparticles

Monolayer-protected gold nanoparticles have received considerable attention since a simple synthetic strategy for their production was described by Brust et al. [63]. The gold nanoparticles are typically of the order of 1 to 3 nm (which represents 50 to a few hundred gold atoms) with an alkanethiol coating that serves to stabilize the colloidal solution. The quality of the SAM on the nanoclusters appears to be very similar to SAMs formed on planar surfaces with a similar number of gauche defects [533, 534]. Self-assembled monolayers on nanoclusters are important from a nanoscience perspective as they can be regarded as three-dimensional

SAMs. As these three-dimensional SAMs can be investigated in bulk solution, the SAMs can now be investigated using a range of analytical techniques not available to the two-dimensional variety.

The alkanethiol coating, however, also provides the opportunity to add specific chemical functionality to the clusters. The first example of functionalized monolayer-protected clusters (MPCs) used a place exchange reaction to substitute ω -ferrocenyl groups for simple aliphatic alkanethiols [535, 536]. Each cluster contains multiple redox sites which were not strongly electronically coupled with each other. If the clusters are probed electrochemically, under hydrodynamic control with a rotating disk electrode, the voltammograms indicate that nanoclusters are electronically charged in solution so as to equilibrate the potential of the metal-like Au cores of the clusters with the electrode. This double layer charging of the clusters means they are, in fact, nanoelectrodes. As the size of the nanoelectrodes decreases, their double layer charging behavior undergoes a transition from metal-electrolyte interfaces to exhibiting redox chemical behavior [537], which means the cluster capacitance changes from being dominated by electrostatic processes to one dominated by binding interactions.

Nanoparticles certainly have the potential to be used as structural components in the fabrication of three-dimensional nanostructures. Gold and silver nanoclusters have been used to produce surfaces with well-defined nanostructure and roughness [536], as well as to produce electrodes using an entirely wet process [64]. Connecting nanoclusters together in a well-defined way has been demonstrated by Mirkin et al. [69], where two batches of gold colloidal particles were modified with noncomplementary DNA. Upon addition of an oligonucleotide duplex, with ends complementary to the two sequences attached to the nanoparticles, the nanoparticles self-assemble into aggregates. An attractive feature of this assembly technique is that denaturing of the duplexes allows the aggregates to be redispersed. Oligonucleotide modified gold colloids have also been used by Alivisatos and Loweth et al. [538, 539] where with judicious choices of oligonucleotide sequence, DNA-based assembly of the colloids can be used to produce highly ordered linear assemblies of colloids (Fig. 22). Alternative approaches to nanoparticle assembly have used biotin-modified colloids connected using avidin [540] while Murray's group have also assembled clusters using Cu^{2+} to connect gold colloids, which are modified with ω -carboxylate alkanethiols [65, 541]. These aggregates are surface bound using a carboxylate or thiol-terminated surface. Thermal decomposition of the surface bound MPCs produces films of the core metal.

Nanoparticles are beginning to find utility in a variety of applications in sensing, either as the sensors or as labels. An example where the nanoparticle is used as the label is in the detection of DNA hybridization by the Mirkin group, using nanoparticle modified oligonucleotides in the transduction of hybridization [535, 536], and by the Willner group [71]. A recent development by the Mirkin group [74] employed oligonucleotide-modified gold nanoparticles and nanofabrication to transduce DNA hybridization by forming a connection between two gold electrodes. This is achieved using two types of capture probes.

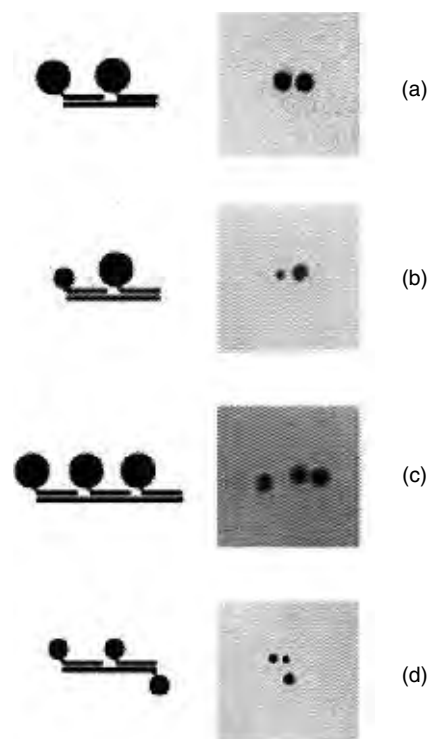


Figure 22. Schematic illustrations and representative transmission electron microscopy images of DNA/gold nanoparticle structures [539]. Image (a) shows a 10-nm homodimer; (b) shows a 10-nm/5 nm heterodimer; (c) shows a 10-nm homotrimer; and (d) shows a 5-nm homotrimer. Reproduced with permission from [539], C. J. Loweth et al., *Angew. Chem. Int. Ed.* 38, 1808 (1999). © 1999, Wiley-VCH.

One set of capture probes is immobilized in a line in the gap between two microelectrodes. The second set of capture probes is attached to the surface of the gold nanoparticles in solution. A longer target strand is introduced in solution which is complementary to both capture probes. Therefore, hybridization of the target to the surface immobilized probes allows the oligonucleotide-tethered gold colloids to align in the gap between the two microelectrodes, thus increasing the conductivity between the two electrodes. The increase in conductivity can be amplified markedly by the addition of Ag(I) and hydroquinone to give a sensor that can detect concentrations of as low as 0.5 pM.

The application of nanoparticles as the platform upon which nanosensors are developed has been demonstrated for fluorescence-based nanosensors, which are capable of detecting metal ions and molecular oxygen within mammalian cells [542–545]. Such sensors use polymer nanoparticles rather than exploit alkanethiol SAMs but they do highlight an application in which three-dimensional monolayers could be employed. A recent example of nanoparticle-based sensors that rely on alkanethiol chemistry is by Maxwell et al. [546]. In this biosensor, single strands of DNA are attached to gold nanoparticles using an alkanethiol linker. To the other end of the DNA is attached a fluorophore, which is attracted to the gold surface. The adsorption of the fluorophore onto the gold quenches the fluorescence. Hybridization with the complementary sequence forces the fluorophore away from the gold

nanoparticle with a concomitant increase in fluorescence. Alkanethiol-modified gold nanoparticles are also used by Storhoff et al. [547] in a DNA assay where hybridization causes the aggregation of oligonucleotide-modified gold nanoparticles. With the aggregation, there is a color change from the ruby red of individual nanoparticles to the blue to purple of the aggregated particles.

3.4.2. Carbon Nanotubes

The discovery of buckminsterfullerene in 1985 [548] was the first example of the third form of carbon. The equally serendipitous discovery of carbon nanotubes by Ijima [549] followed in 1991. The two discoveries have led to whole research fields focused on nanocarbon [550]. Nanocarbon structure, and in particular carbon nanotubes, serve as important building blocks in nanofabrication and possibly the fabrication of nanocircuits. Carbon nanotubes can be thought of as graphene sheets rolled up into cylinders. They can be classified into multi-walled nanotubes (MWNT) or single-walled nanotubes (SWNT) depending on the number of graphene sheets that make up the cylinder. Diameters range from 1 nm to tens of nanometers. The MWNT are generally perceived as concentric SWNT of different diameters arranged inside each other [550], although there is electron microscopy evidence that some tubes have a scroll-like structure [551]. The interest in carbon nanotubes from many diverse fields is stimulated by their unique properties, those being that they are relatively defect-free, highly conductive, and the strongest materials known. Because of their relatively structural simplicity, SWNT have been the subject of most attention with regards to an understanding and prediction of nanotube properties, although MWNT are simpler to manufacture [550]. With regards to the electrical properties, which are the source of much interest in molecule electronics, SWNT can be metallic or semiconducting depending on the helices index. The helices index refers to the way the graphene sheet is rolled up [552].

So what of the integration of carbon nanotubes with SAMs? Liu et al. [553] have controlled the deposition of individual nanotubes which is important in the fabrication of molecule circuit components such as the nanotube field effect transistor developed by Huang et al. [554, 555]. To achieve this, silicon surfaces were modified with a tetramethylsilane (TMS) SAM. The TMS is selectively removed using e-beam or AFM lithography and replaced with an amine-terminated SAM. Nanotubes are shown to selectively adsorb onto the amino-functionalized surface. This technique has been used to demonstrate a single nanotube connecting two gold electrodes.

The integration of carbon nanotubes with alkanethiol SAMs is at its very beginning. Liu et al. [66–68, 556] have developed a number of methods for organizing SWNT normal to a surface. All these methods involve the shortening of the tubes in a combination of nitric and sulfuric acids. These oxidizing acids attack defects in the walls of SWNT causing a breakage. The now open end of the tube contains carboxylic acid moieties. These ends have then been modified with an alkanethiol, and self-assembled onto a gold surface [66], or aligned directly onto silver surfaces using the affinity of carboxylic acids for Ag^+ [67].

More recently, aligned nanotubes have been covalently attached to a cysteamine-modified gold surface using carbodiimide coupling to form a peptide bond between the amine-terminated SAM and the carboxylic acid terminated tubes [68, 556]. Yang et al. [557] have formed the same molecular construct, but to the free ends of the nanotubes they have attached microperoxidase MP-11 and shown that direct electron transfer to the enzyme can be achieved. These represent initial experiments into using carbon nanotubes as molecular wires for sensing applications.

3.4.3. Dendrimers

Dendrimers are regularly branched, monodispersed macromolecules that have attracted extensive scientific interest of late because of their unusual architecture and properties [558–561]. An example of a dendrimer is the poly(amidoamine) (PAMAM) dendrimer shown in Figure 23. The globular structures have three distinct regions. There is a central core, then a repetitive branching region and finally the terminal moieties [562]. The structure can be precisely controlled at the molecule level and the dendrimer properties can easily be altered by changing the type of core, the amount of branching, and the functionality at the termini. Furthermore, the dendrimers have a low mass density in the interior and are highly permeable to small molecules [562]. It is therefore clear that dendrimers have enormous promise as nanoscale building blocks in supramolecular devices. Applications proposed for dendrimers include catalysis [563], encapsulation and controlled release of drugs [564], chemical sensors [565, 566], and biomimetic materials [567].

Integrating dendrimers with SAMs to give three-dimensional structures projecting from a surface has recently attracted some interest. An early example by Tokuhiwa and Zhao et al. involved using the molecular gating capabilities of PAMAM dendrimers [562, 568]. The dendrimers were

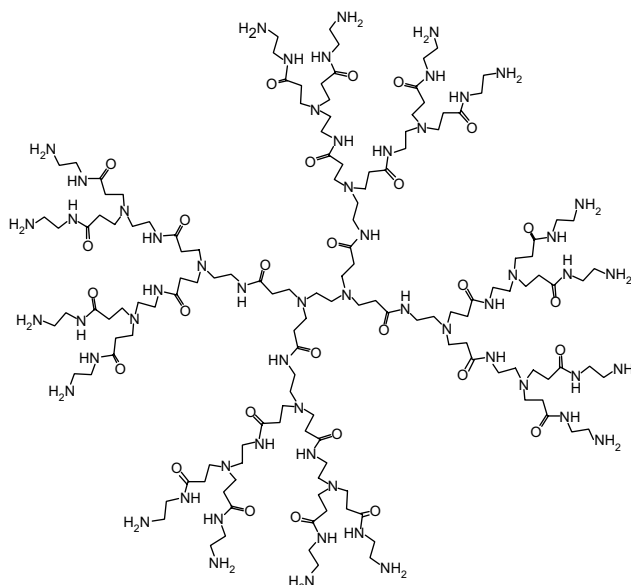


Figure 23. Chemical structure of a second generation the PAMAM dendrimer.

adsorbed directly onto a gold surface where they tended to spread out. If a SAM of hexadecanethiol was adsorbed onto the dendrimer-modified surface, the dendrimers were confined into a more compact structure. Apart from confining the dendrimers, the hexadecanethiol SAM had a second function of passivating the electrode not covered by the dendrimers. The dendrimers were used to prevent access of positively charged ruthenium (III) hexamine complex to the electrode at neutral pH, at which the dendrimer is positively charged. At the same pH, the access of negatively charged ferricyanide was barely impeded by the dendrimer. Altering the pH to 11.0 made the dendrimers neutral and allowed the $\text{Ru}(\text{NH}_3)_6^{3+}$ to pass through the dendrimer and react at the underlying electrode. To confirm that the gating was through the dendrimer rather than defects in the SAM, the terminal amine functionality of the PAMAM dendrimer was converted to 4-(trifluoromethyl)benzamido groups. With these modified dendrimers, the ferricyanide was now prevented from accessing to electrode but the ruthenium hexamine could pass through the dendrimers. Dendrimers have also been coated onto gold nanoparticles by converting some of the amine terminals of the PAMAM into thiols [569]. Dendrimers have been used to assemble nanoparticles onto a planar surfaces in a controlled way [570] and have been patterned onto SAM surfaces using microcontact printing [254]. Dendritic SAMs have also been synthesized and assembled on gold electrodes where the organothiol is the focal point of the dendrimer [571–573].

Early examples of the application of dendrimer-modified surfaces are again beginning to emerge in the field of sensing. Yoon et al. [457] have developed an affinity sensor for the detection of avidin using PAMAM dendrimers, which are modified with biotin as the recognition element for avidin and ferrocene for transduction of the affinity reaction. The amine-terminated dendrimers were covalently attached to a gold electrode modified with 3,3-dithiopropionic acid bis-*N*-hydroxysuccinimide ester. Glucose oxidase in solution is used as a diffusional tracer. The ferrocene-labeled dendrimer mediates the glucose oxidase reaction with glucose, thus providing a current. Binding of the avidin onto the electrode surface reduces the ability of the glucose oxidase to access the dendrimer, and therefore a reduction in current is observed. The purpose of using dendrimers to fabricate sensors is that they provide a spatially ordered and compact sensing surface. In the example by Yoon et al. [457], the enzyme layer had a surface coverage of 2.5 pmol cm^{-2} . This enzyme loading is 2.5 times higher than that achieved with enzyme attached directly to a SAM [375], which suggests that attaching enzymes to a dendrimer may allow more sensitive monolayer enzyme electrodes to be developed.

4. CONCLUDING REMARKS

The application of SAMs of alkanethiols on surfaces has seen some exquisite and complicated examples of integrated molecule systems developed in pursuit of novel surface coatings, sensors, and molecular electronics. Many of these elegant examples represent the very edge of what has been achieved thus far in nanotechnology with bottom-up fabrication. What has been achieved so far clearly demonstrates that alkanethiol SAMs have the potential to enable

the fabrication of many useful nanodevices by self-assembly in sufficiently large volume and with sufficient control to be commercially viable. In fact, two of the most complicated affinity sensors discussed in this review, which are perhaps some of the best examples of molecular level fabrication of useful devices, namely, the AMBRI biosensor and the CMS DNA sensor, are close to or have already been commercialized.

Regardless of the success of the AMBRI and CMS sensors, SAMs have enabled a considerable amount of fundamental nanoscience to be conducted which drives much of the current nanotechnological developments and enables many other nanotechnological dreams to be realized. Furthermore, what we learn about self-assembly and how to control molecular level fabrication from alkanethiol monolayers will be exceedingly valuable in developing other self-assembly systems. This brings us to the future. The author believes the research into SAMs will follow two key directions. First, more advanced integration of nanoscale building blocks such as the nanoparticles, nanotubes, and dendrimers, with SAMs will certainly be developed. Second, alternative self-assembly systems will be developed that have the many attractive features of alkanethiol chemistry outlined throughout this article but which solve the long-term stability problems that alkanethiol chemistry have. Certainly, some researchers are already directing their attention to the problem of stability through new alkanethiols which increase the forces of attraction between the alkyl chains [205–207] or through self-assembly systems which form more robust bonds with the underlying substrate using more attachment points [499] or different chemistry [574]. So the application of SAMs is expected to grow in the future.

GLOSSARY

Alkanethiol The family of compounds of the general formula $\text{HS}-(\text{CH}_2)_n-\text{X}$ where the thiol headgroup self-assembles onto coinage metal surfaces to form self-assembled monolayers, the aliphatic chain contributes to the order of the monolayer, and the X terminal group defines the surface properties of the monolayer.

Biosensor A portable analytical device that integrates a biorecognition molecule, such as an enzyme, an antibody, or DNA, with a signal transducer. The biorecognition molecule gives the biosensor the selectivity for the analyte while the transducer determines the extent of the biorecognition reaction and converts this to an electronic signal which is outputted to the user.

Microcontact printing A method of patterning self-assembled monolayers where a stamp that is patterned with the desired relief is inked with self-assembling molecules and contacted with a substrate to give a patterned self-assembled monolayer on the substrate surface.

Scanning probe lithography The suite of techniques for patterning self-assembled monolayers using atomic force microscopy, scanning tunneling microscopy or associated techniques.

Self-assembled monolayer (SAM) Ordered monomolecular film that is spontaneously formed upon immersion of a solid into a solution of an amphifunctional molecule.

ACKNOWLEDGMENTS

I would like to thank Dr. Jason Harper for reading this article so carefully. His contribution improved it considerably. I would also like to thank Dr. Katharina Gaus for useful discussion and assistance with the figures.

REFERENCES

1. N. C. Seeman and A. M. Belcher, *Proc. Natl. Acad. Sci. U. S. A.* 99, 6451 (2002).
2. IBM Research: Atomic and Nano Technology <http://www.research.ibm.com/atomic>
3. J. L. O'Brien, S. R. Schofield, M. Y. Simmons, R. G. Clark, A. S. Dzurak, N. J. Curson, B. E. Kane, N. S. McAlpine, M. E. Hawley, and G. W. Brown, *Phys. Rev. B* 64, 1401 (2001).
4. D. L. Allara, *Biosens. Bioelectron.* 10, 771 (1995).
5. D. S. Goodsell, in "American Scientist," Vol. 88, p. 230. 2000.
6. A. Ulman, *Chem. Rev.* 96, 1533 (1996).
7. G. K. Jennings and P. E. Laibinis, *Colloid Surf. A-Physicochem. Eng. Asp.* 116, 105 (1996).
8. M. Ishibashi, M. Itoh, H. Nishihara, and K. Aramaki, *Electrochim. Acta* 41, 241 (1996).
9. G. E. Poirier and M. J. Tarlov, *J. Phys. Chem.* 99, 10966 (1995).
10. D. Mandler and I. Turyan, *Electroanalysis* 8, 207 (1996).
11. T. Wink, S. J. van Zuilen, A. Bult, and W. P. van Bennekom, *Analyst* 122, 43R (1997).
12. J. J. Gooding and D. B. Hibbert, *TrAC* 18, 525 (1999).
13. I. Willner and E. Katz, *Angew. Chem.-Int. Edit.* 39, 1181 (2000).
14. D. Cahen and G. Hodes, *Adv. Mater.* 14, 789 (2002).
15. A. Ulman, "An Introduction to Ultrathin Organic Films From Langmuir-Blodgett to Self-Assembly." Academic Press, London, 1991.
16. R. G. Nuzzo and D. L. Allara, *J. Am. Chem. Soc.* 105, 4481 (1983).
17. R. G. Nuzzo, F. A. Fusco, and D. L. Allara, *J. Am. Chem. Soc.* 109, 2358 (1987).
18. D. A. Offord, C. M. John, and J. H. Griffin, *Langmuir* 10, 761 (1994).
19. C. Jung, O. Dannenberger, Y. Xu, M. Buck, and M. Grunze, *Langmuir* 14, 1103 (1998).
20. Y. S. Shon, C. Mazzitelli, and R. W. Murray, *Langmuir* 17, 7735 (2001).
21. E. B. Troughton, C. D. Bain, W. G. M., D. L. Allara, and M. D. Porter, *Langmuir* 4, 365 (1988).
22. E. Katz, N. Itzhak, and I. Willner, *J. Electroanal. Chem.* 336, 357 (1992).
23. H. Y. Lee, Z. L. He, C. L. Hussey, and D. L. Mattern, *Chem. Mat.* 10, 4148 (1998).
24. J. Noh, T. Murase, K. Nakajima, H. Lee, and M. Hara, *J. Phys. Chem. B* 104, 7411 (2000).
25. H. Schonherr and G. J. Vancso, *Langmuir* 15, 5541 (1999).
26. M. H. Schoenfish and J. E. Pemberton, *Langmuir* 15, 509 (1999).
27. M. H. Dishner, J. C. Hemminger, and F. J. Feher, *Langmuir* 12, 6176 (1996).
28. T. Nakamura, H. Kondoh, M. Matsumoto, and H. Nozoye, *Langmuir* 12, 5977 (1996).
29. T. Ishida, N. Choi, W. Mizutani, H. Tokumoto, I. Kojima, H. Aze-hara, H. Hokari, U. Akiba, and M. Fujihira, *Langmuir* 15, 6799 (1999).
30. A. Ihs, K. Uvdal, and B. Liedberg, *Langmuir* 9, 733 (1993).
31. M. Niwa, M. Date, and N. Higashi, *Macromolecules* 29, 3681 (1996).
32. P. Talonen, G. Sundholm, S. Floate, and R. J. Nichols, *PCCP Phys. Chem. Chem. Phys.* 1, 3661 (1999).
33. K. V. Gothelf, *J. Electroanal. Chem.* 494, 147 (2000).
34. C. J. Zhong and M. D. Porter, *J. Am. Chem. Soc.* 116, 11616 (1994).
35. J. L. Trevor, K. R. Lykke, M. J. Pellin, and L. Hanley, *Langmuir* 14, 1664 (1998).
36. M. W. J. Beulen, B. H. Huisman, P. A. vander Heijden, F. van Veggel, M. G. Simons, E. Biemond, P. J. de Lange, and D. N. Reinhoudt, *Langmuir* 12, 6170 (1996).
37. C. J. Zhong, R. C. Brush, J. Anderegg, and M. D. Porter, *Langmuir* 15, 518 (1999).
38. H. O. Finklea, S. Avery, M. Lynch, and T. Furtch, *Langmuir* 3, 409 (1987).
39. M. M. Walczak, D. D. Popenoe, R. S. Deinhammer, B. D. Lamp, C. Chung, and M. D. Porter, *Langmuir* 7, 2687 (1991).
40. W. R. Everett, T. L. Welch, L. Reed, and I. Fritsch-Fauler, *Anal. Chem.* 67, 292 (1995).
41. C. D. Bain and G. M. Whitesides, *J. Am. Chem. Soc.* 110, 6560 (1988).
42. S. E. Creager, L. A. Hockett, and G. K. Rowe, *Langmuir* 8, 854 (1992).
43. M. Mrksich and G. M. Whitesides, *Annual Reviews of Biophysical Biomolecular Structures* 25, 55 (1996).
44. S. Ferretti, S. Paynter, D. A. Russell, K. E. Sapsford, and D. J. Richardson, *Trac-Trends Anal. Chem.* 19, 530 (2000).
45. B. A. Cornell, V. L. B. Braach-Maksvytis, L. G. King, P. D. J. Osman, B. Raguse, L. Wiczorek, and R. J. Pace, *Nature* 387, 580 (1997).
46. H. O. Finklea, *Electroanal. Chem.* 19, 109 (1996).
47. J. J. Gooding, F. J. Mearns, W. Yang, and J. Liu, *Electroanalysis* 15, 81 (2003).
48. M. Bartz, N. Weber, J. Kuther, R. Seshadri, and W. Tremel, *Chem. Commun.* 2085 (1999).
49. M. Mrksich, *Chem. Soc. Rev.* 29, 267 (2000).
50. D. Hernandez-Santos, M. B. Gonzalez-Garcia, and A. C. Garcia, *Electroanalysis* 14, 1225 (2002).
51. V. M. Mirsky, *Trac-Trends Anal. Chem.* 21, 439 (2002).
52. I. Bontidean, C. Berggren, G. Johansson, E. Csoregi, B. Mattiason, J. A. Lloyd, K. J. Jakeman, and N. L. Brown, *Anal. Chem.* 70, 4162 (1998).
53. V. Braach-Maksvytis and B. Raguse, *J. Am. Chem. Soc.* 122, 9544 (2000).
54. M. Mrksich, *Curr. Opin. Chem. Biol.* 6, 794 (2002).
55. T. T. Wooster, P. R. Gamm, W. E. Geiger, A. M. Oliver, A. J. Black, D. C. Craig, and M. N. Paddon Row, *Langmuir* 12, 6616 (1996).
56. S. Creager, C. J. Yu, C. Bamdad, S. O'Connor, T. MacLean, E. Lam, Y. Chong, G. T. Olsen, J. Luo, M. Gozin, and J. F. Kayyem, *J. Am. Chem. Soc.* 121, 1059 (1999).
57. F. R. F. Fan, J. P. Yang, L. T. Cai, D. W. Price, S. M. Dirk, D. V. Kosynkin, Y. X. Yao, A. M. Rawlett, J. M. Tour, and A. J. Bard, *J. Am. Chem. Soc.* 124, 5550 (2002).
58. F. R. F. Fan, J. P. Yang, S. M. Dirk, D. W. Price, D. Kosynkin, J. M. Tour, and A. J. Bard, *J. Am. Chem. Soc.* 123, 2454 (2001).
59. A. L. Plant, M. Gueguetchkeri, and W. Yap, *Biophys. J.* 67, 1126 (1994).
60. J. K. Cullison, F. M. Hawkrige, N. Nakashima, and S. Yoshikawa, *Langmuir* 10, 877 (1994).
61. E. J. Calvo, C. Danilowicz, and A. Wolosiuk, *J. Am. Chem. Soc.* 124, 2452 (2002).
62. J. Hodak, R. Etchenique, E. J. Calvo, K. Singhal, and P. N. Bartlett, *Langmuir* 13, 2708 (1997).
63. M. Brust, M. Walker, D. Bethell, D. J. Schiffrin, and R. Whyman, *J. Chem. Soc.-Chem. Commun.* 801 (1994).
64. M. D. Musick, D. J. Pena, S. L. Botsko, T. M. McEvoy, J. N. Richardson, and M. J. Natan, *Langmuir* 15, 844 (1999).
65. W. P. Wuelfing, F. P. Zamborini, A. C. Templeton, X. G. Wen, H. Yoon, and R. W. Murray, *Chem. Mat.* 13, 87 (2001).
66. Z. F. Liu, Z. Y. Shen, T. Zhu, S. F. Hou, L. Z. Ying, Z. J. Shi, and Z. N. Gu, *Langmuir* 16, 3569 (2000).

67. B. Wu, J. Zhang, Z. Wei, S. M. Cai, and Z. F. Liu, *J. Phys. Chem. B* 105, 5075 (2001).
68. X. Nan, Z. N. Gu, and Z. F. Liu, *J. Coll. Interface Sci.* 245, 311 (2002).
69. C. A. Mirkin, R. L. Letsinger, R. C. Mucic, and J. J. Storhoff, *Nature* 382, 607 (1996).
70. R. Levicky, T. M. Herne, M. J. Tarlov, and S. K. Satija, *J. Am. Chem. Soc.* 120, 9787 (1998).
71. F. Patolsky, K. T. Ranjit, A. Lichtenstein, and I. Willner, *Chem. Commun.* 1025 (2000).
72. E. M. Boon, D. M. Ceres, T. G. Drummond, M. G. Hill, and J. K. Barton, *Nat. Biotechnol.* 18, 1096 (2000).
73. L. M. Demers, S. J. Park, T. A. Taton, Z. Li, and C. A. Mirkin, *Angew. Chem.-Int. Edit.* 40, 3071 (2001).
74. S. J. Park, T. A. Taton, and C. A. Mirkin, *Science* 295, 1503 (2002).
75. J. I. Siepmann and I. R. McDonald, in "Self-Assembled Monolayers of Thiols," Vol. 24, p. 206. Academic Press, New York, 1998.
76. S. Y. Jiang, *Mol. Phys.* 100, 2261 (2002).
77. G. E. Poirier, *Chem. Rev.* 97, 1117 (1997).
78. G.-Y. Liu, S. Xu, and S. Cruchon-Dupeyrat, in "Self-Assembled Monolayers of Thiols," Vol. 24, p. 82. Academic Press, New York, 1998.
79. D. A. Smith, C. Robinson, J. Kirkham, J. Zhang, and M. L. Wallwork, *Rev. Anal. Chem.* 20, 1 (2001).
80. N. K. Chaki and K. Vijayamohanam, *Biosens. Bioelectron.* 17, 1 (2002).
81. M. Mrksich and G. M. Whitesides, *TIBTECH* 13, 228 (1995).
82. N. B. Bowden, M. Weck, I. S. Choi, and G. M. Whitesides, *Acc. Chem. Res.* 34, 231 (2001).
83. Y. N. Xia, X. M. Zhao, and G. M. Whitesides, *Microelectron. Eng.* 32, 255 (1996).
84. H. A. Biebuyck, N. B. Larsen, E. Delamarche, and B. Michel, *IBM J. Res. Develop.* 41, 159 (1997).
85. D. Qin, Y. N. Xia, J. A. Rogers, R. J. Jackman, X. M. Zhao, and G. M. Whitesides, in "Microsystem Technology in Chemistry and Life Science," Vol. 194, p. 1. 1998.
86. Y. Xia and G. M. Whitesides, *Angew. Chem. Int. Ed.* 37, 551 (1998).
87. A. N. Shipway, E. Katz, and I. Willner, *Chem. Phys. Chem.* 1, 18 (2000).
88. M. Brust and C. J. Kiely, *Colloid Surf. A-Physicochem. Eng. Asp.* 202, 175 (2002).
89. V. Chechik, R. M. Crooks, and C. J. M. Stirling, *Adv. Mater.* 12, 1161 (2000).
90. Y. Li, J. Huang, R. T. McIver, Jr., and J. C. Hemminger, *J. Am. Chem. Soc.* 114, 2428 (1992).
91. H. O. Finklea, in "Encyclopaedia of Analytical Chemistry." John Wiley & Sons, New York, 2000.
92. D. E. King, *J. Vac. Sci. Technol. A-Vac. Surf. Films* 13, 1247 (1995).
93. H. Ron, S. Matlis, and I. Rubinstein, *Langmuir* 14, 1116 (1998).
94. J. T. Woodward, M. L. Walker, C. W. Meuse, D. J. Vanderah, G. E. Poirier, and A. L. Plant, *Langmuir* 16, 5347 (2000).
95. C. Yan, A. Golzhauser, M. Grunze, and C. Woll, *Langmuir* 15, 2414 (1999).
96. D. A. J. Rand and R. Woods, *J. Electroanal. Chem.* 31, 29 (1971).
97. J. C. Hoogvliet, M. Dijkstra, B. Kamp, and W. P. van Bennekom, *Anal. Chem.* 72, 2016 (2000).
98. C. D. Bain, E. B. Troughton, Y.-T. Tao, J. Evall, G. M. Whitesides, and R. G. Nuzzo, *J. Am. Chem. Soc.* 111, 321 (1989).
99. H. Schessler, D. S. Karpovich, and G. J. Blanchard, *J. Am. Chem. Soc.* 118, 9645 (1996).
100. W. Pan, C. J. Durning, and N. J. Turro, *Langmuir* 12, 4469 (1996).
101. D. S. Karpovich, H. Schessler, and G. J. Blanchard, in "Self-Assembled Monolayers of Thiols," Vol. 24, p. 44. Academic Press, New York, 1998.
102. R. C. Thomas, L. Sun, R. M. Crooks, and A. J. Ricco, *Langmuir* 7, 620 (1991).
103. M. Buck, M. Grunze, F. Eisert, J. Fischer, and F. Trager, *J. Vac. Sci. Technol. A* 10, 926 (1992).
104. D. S. Karpovich and G. J. Blanchard, *Langmuir* 10, 3315 (1994).
105. J. B. Schlenoff, M. Li, and H. Ly, *J. Am. Chem. Soc.* 117, 12528 (1995).
106. D. S. Karpovich and G. J. Blanchard, *J. Chem. Educ.* 72, 466 (1995).
107. R. Singhvi, A. Kumar, G. P. Lopez, G. N. Stephanopoulos, D. I. C. Wang, G. M. Whitesides, and D. E. Ingber, *Science* 264, 696 (1994).
108. N. B. Larsen, H. Biebuyck, E. Delamarche, and B. Michel, *J. Am. Chem. Soc.* 119, 3017 (1997).
109. D. Lolic, J. J. Gooding, and J. G. Shapter, *Langmuir* 17, 3307 (2001).
110. D. Lolic, J. G. Shapter, and J. J. Gooding, *Electrochem. Commun.* 3, 722 (2001).
111. M. Liebau, J. Huskens, and D. N. Reinhoudt, *Adv. Funct. Mater.* 11, 147 (2001).
112. O. Chailapakul, L. Sun, C. Xu, and R. M. Crooks, *J. Am. Chem. Soc.* 115, 12459 (1993).
113. M. H. Dishner, J. C. Hemminger, and F. J. Feher, *Langmuir* 13, 2318 (1997).
114. H. Morgner, *Langmuir* 13, 3990 (1997).
115. H. Kariis, E. Smela, K. Uvdal, M. Wirde, U. Gelius, and B. Liedberg, *J. Phys. Chem. B* 102, 6529 (1998).
116. M. H. Dishner, P. Taborak, J. C. Hemminger, and F. J. Feher, *Langmuir* 14, 6676 (1998).
117. T. Y. B. Leung, M. C. Gerstenberg, D. J. Lavrich, G. Scoles, F. Schreiber, and G. E. Poirier, *Langmuir* 16, 549 (2000).
118. G. E. Poirier and E. D. Pylant, *Science* 272, 1145 (1996).
119. G. E. Poirier, *J. Vac. Sci. Technol. B* 14, 1453 (1996).
120. Y. W. Yang and L. J. Fan, *Langmuir* 18, 1157 (2002).
121. R. Bilewicz and M. Majda, *Langmuir* 7, 2794 (1991).
122. P. Krynski, R. V. Chamberlain II, and M. Majda, *Langmuir* 10, 4286 (1994).
123. R. Bilewicz, T. Sawaguchi, R. V. Chamberlain II, and M. Majda, *Langmuir* 11, 2256 (1995).
124. D. E. Weisshaar, B. D. Lamp, and M. D. Porter, *J. Am. Chem. Soc.* 114, 5860 (1992).
125. J. Wang, M. Jiang, A. M. Kawde, and R. Polsky, *Langmuir* 16, 9687 (2000).
126. F. Y. Ma and R. B. Lennox, *Langmuir* 16, 6188 (2000).
127. M. M. Walczak, C. Chung, S. M. Stole, C. A. Widrig, and M. D. Porter, *J. Am. Chem. Soc.* 113, 2370 (1991).
128. M. D. Porter, T. B. Bright, D. L. Allara, and C. E. D. Chidsey, *J. Am. Chem. Soc.* 109, 3559 (1987).
129. C. D. Bain, H. Biebuyck, and G. M. Whitesides, *Langmuir* 5, 723 (1989).
130. R. G. Nuzzo, B. R. Zegarski, and L. H. Dubois, *J. Am. Chem. Soc.* 109, 733 (1987).
131. R. G. Nuzzo, L. H. Dubois, and D. L. Allara, *J. Am. Chem. Soc.* 112, 3145 (1990).
132. M. A. Bryant and J. E. Pemberton, *J. Am. Chem. Soc.* 113, 3629 (1991).
133. M. A. Bryant and J. E. Pemberton, *J. Am. Chem. Soc.* 113, 8284 (1991).
134. M. Hasan, D. Bethell, and M. Brust, *J. Am. Chem. Soc.* 124, 1132 (2002).
135. C. E. D. Chidsey, G. Y. Liu, P. Rowntree, and G. Scoles, *J. Chem. Phys.* 91, 4421 (1989).
136. C. A. Alves, E. L. Smith, and M. D. Porter, *J. Am. Chem. Soc.* 114, 1222 (1992).
137. J. J. Hickman, D. Ofer, P. E. Laibinis, W. G. M., and M. S. Wrighton, *Science* 252, 688 (1991).
138. G. Wittstock, R. Hesse, and W. Schuhmann, *Electroanalysis* 9, 746 (1997).

139. X.-D. Dong, J. Lu, and C. Cha, *Bioelectrochem. Bioenerg.* 36, 73 (1995).
140. J. J. Gooding, V. Praig, and E. A. H. Hall, *Anal. Chem.* 70, 2396 (1998).
141. H. O. Finklea and D. D. Hanshew, *J. Am. Chem. Soc.* 114, 3173 (1992).
142. K. Weber, L. Hockett, and S. Creager, *J. Phys. Chem. B* 101, 8286 (1997).
143. D. F. Yang and M. Morin, *J. Electroanal. Chem.* 441, 173 (1998).
144. D. F. Yang, C. P. Wilde, and M. Morin, *Langmuir* 12, 6570 (1996).
145. D. F. Yang and M. Morin, *J. Electroanal. Chem.* 429, 1 (1997).
146. M. M. Walczak, C. A. Alves, B. D. Lamp, and M. D. Porter, *J. Electroanal. Chem.* 396, 103 (1995).
147. L. H. Guo, J. S. Facci, G. McLendon, and R. Mosher, *Langmuir* 10, 4588 (1994).
148. Z. Hou, N. L. Abbott, and P. Stroeve, *Langmuir* 14, 3287 (1998).
149. Z. Hou, S. Dante, N. L. Abbott, and P. Stroeve, *Langmuir* 15, 3011 (1999).
150. S.-S. Wong and M. D. Porter, *J. Electroanal. Chem.* 485, 135 (2000).
151. M. Hegner, P. Wagner, and G. Semenza, *Surface Science* 291, 39 (1993).
152. P. Wagner, M. Hegner, H. J. Guntherodt, and G. Semenza, *Langmuir* 11, 3867 (1995).
153. P. Wagner, F. Zaugg, P. Kernén, M. Hegner, and G. Semenza, *J. Vac. Sci. Technol. B* 14, 1466 (1996).
154. J. Mazurkiewicz, F. J. Mearns, D. Losic, C. Rogers, J. G. Shapter, and J. J. Gooding, *J. Vac. Sci. Technol. B* 20, 2265 (2002).
155. D. Losic, J. G. Shapter, and J. J. Gooding, *Aust. J. Chem.* 54, 643 (2001).
156. G. Gillen, J. Bennett, M. J. Tarlov, and F. Burgess, *Anal. Chem.* 66, 2170 (1994).
157. G. Gillen, S. Wight, J. Bennett, and M. J. Tarlov, *Appl. Phys. Lett.* 65, 534 (1994).
158. S. C. Chang, I. Chao, and Y. T. Tao, *J. Am. Chem. Soc.* 116, 6792 (1994).
159. A. Ulman, *J. Mat. Ed.* 11, 205 (1989).
160. M. Itoh, H. Nishihara, and K. Aramaki, *Journal of the Electrochemical Society* 141, 2018 (1994).
161. Y. Q. Feng, W. K. Teo, K. S. Siow, Z. Q. Gao, K. L. Tan, and A. K. Hsieh, *Journal of the Electrochemical Society* 144, 55 (1997).
162. J. Scherer, M. R. Vogt, O. M. Magnussen, and R. J. Behm, *Langmuir* 13, 7045 (1997).
163. H. Ron, H. Cohen, S. Matlis, M. Rappaport, and I. Rubinstein, *J. Phys. Chem. B* 102, 9861 (1998).
164. R. Haneda and K. Aramaki, *Journal of the Electrochemical Society* 145, 2786 (1998).
165. Z. Mekhalif, J. Riga, J. J. Pireaux, and J. Delhalle, *Langmuir* 13, 2285 (1997).
166. M. A. Hines, J. A. Todd, and P. Guyotsonnest, *Langmuir* 11, 493 (1995).
167. P. Lang, Z. Mekhalif, B. Rat, and F. Garnier, *J. Electroanal. Chem.* 441, 83 (1998).
168. H. O. Finklea, K. Yoon, E. Chamberlain, J. Allen, and R. Haddox, *J. Phys. Chem. B* 105, 3088 (2001).
169. F. P. Zamborini, S. M. Gross, and R. W. Murray, *Langmuir* 17, 481 (2001).
170. J. C. Love, D. B. Wolfe, M. L. Chabinyc, K. E. Paul, and G. M. Whitesides, *J. Am. Chem. Soc.* 124, 1576 (2002).
171. A. Carvalho, M. Geissler, H. Schmid, B. Michel, and E. Delamar, *Langmuir* 18, 2406 (2002).
172. D. B. Wolfe, J. C. Love, K. E. Paul, M. L. Chabinyc, and G. M. Whitesides, *Appl. Phys. Lett.* 80, 2222 (2002).
173. C. W. Sheen, J.-X. Shi, J. Maartensson, A. N. Parikh, and D. L. Allara, *J. Am. Chem. Soc.* 114, 1514 (1992).
174. H. Ohno, L. A. Nagahara, S. Gwo, W. Mizutani, and H. Tokumoto, *Jpn. J. Appl. Phys. Part 2—Lett.* 35, L512 (1996).
175. T. Baum, S. Ye, and K. Uosaki, *Langmuir* 15, 8577 (1999).
176. Q. Zhang, H. Z. Huang, H. X. He, H. F. Chen, H. B. Shao, and Z. F. Liu, *Surface Science* 440, 142 (1999).
177. P. E. Laibinis, G. M. Whitesides, D. L. Allara, Y. T. Tao, A. N. Parikh, and R. G. Nuzzo, *J. Am. Chem. Soc.* 113, 7152 (1991).
178. S. Y. Lin, T. K. Tsai, C. M. Lin, C. H. Chen, Y. C. Chan, and H. W. Chen, *Langmuir* 18, 5473 (2002).
179. T. W. Li, I. Chao, and Y. T. Tao, *J. Phys. Chem. B* 102, 2935 (1998).
180. Y. T. Long, H. T. Rong, M. Buck, and M. Grunze, *J. Electroanal. Chem.* 524, 62 (2002).
181. V. J. Angelico, S. A. Mitchell, and V. H. Wysocki, *Anal. Chem.* 72, 2603 (2000).
182. K. V. Wolf, D. A. Cole, and S. L. Bernasek, *Langmuir* 17, 8254 (2001).
183. R. Colorado, R. J. Villazana, and T. R. Lee, *Langmuir* 14, 6337 (1998).
184. S. Lee, A. Puck, M. Graupe, R. Colorado, Y. S. Shon, T. R. Lee, and S. S. Perry, *Langmuir* 17, 7364 (2001).
185. M. Ohtani, T. Sunagawa, S. Kuwabata, and H. Yoneyama, *J. Electroanal. Chem.* 429, 75 (1997).
186. I. Rubinstein, S. Steinberg, Y. Tor, A. Shanzer, and J. Sagiv, *Nature* 332, 426 (1988).
187. T. Nagaoka, Z. D. Chen, H. Okuno, M. Nakayama, and K. Ogura, *Anal. Sci.* 15, 857 (1999).
188. I. Markovich and D. Mandler, *Analyst* 126, 1850 (2001).
189. P. E. Laibinis, B. J. Palmer, S.-W. Lee, and G. K. Jennings, in "Self-Assembled Monolayers of Thiols," Vol. 24, p. 1. Academic Press, New York, 1998.
190. K. L. Prime and G. M. Whitesides, *J. Am. Chem. Soc.* 115, 10714 (1993).
191. S.-C. Chang, I. Chao, and Y. T. Tao, *J. Am. Chem. Soc.* 116, 6792 (1994).
192. S. D. Evans, U. E., A. Ulman, and N. Feris, *J. Am. Chem. Soc.* 113, 4121 (1991).
193. D. V. Vezenov, A. Noy, L. F. Rozsnyai, and C. M. Lieber, *J. Am. Chem. Soc.* 119, 2006 (1997).
194. J. W. Zhao, L. Luo, X. Yang, E. K. Wang, and S. J. Dong, *Electroanalysis* 11, 1108 (1999).
195. S. E. Creager and J. Clarke, *Langmuir* 10, 3675 (1994).
196. K. Kim and J. Kwak, *J. Electroanal. Chem.* 512, 83 (2001).
197. M. Mrksich, C. S. Chen, Y. N. Xia, L. E. Dike, D. E. Ingber, and G. M. Whitesides, *Proc. Nat. Acad. Sci. U.S.A.* 93, 10775 (1996).
198. L. Jiang, C. J. McNeil, and J. M. Cooper, *Angew. Chem. Int. Ed. Engl.* 34, 2409 (1995).
199. J. Wei, H. Y. Liu, H. Yamamoto, Y. He, and D. H. Waldeck, *J. Am. Chem. Soc.* 124, 9591 (2002).
200. C. D. Bain and G. M. Whitesides, *Science* 240, 62 (1988).
201. J. Aizenberg, A. J. Black, and G. M. Whitesides, *Nature* 398, 495 (1999).
202. C. D. Frisbie, L. F. Rozsnyai, A. Noy, M. S. Wrighton, and C. M. Lieber, *Science* 265, 2071 (1994).
203. N. Sandhyarani and T. Pradeep, *Vacuum* 49, 279 (1998).
204. E. Delamar, B. Michel, H. Kang, and C. Gerber, *Langmuir* 10, 4103 (1994).
205. R. S. Clegg, S. M. Reed, and J. E. Hutchinson, *J. Am. Chem. Soc.* 120, 2486 (1998).
206. K. Murty, M. Venkataramanan, and T. Pradeep, *Langmuir* 14, 5446 (1998).
207. T. Kim, K. C. Chan, and R. M. Crooks, *J. Am. Chem. Soc.* 119, 189 (1997).
208. C. A. Widrig, C. Chung, and M. D. Porter, *J. Electroanal. Chem.* 310, 335 (1991).
209. T. Ito, *J. Electroanal. Chem.* 495, 87 (2001).
210. M. Satjapipat, R. Sanedrin, and F. M. Zhou, *Langmuir* 17, 7637 (2001).
211. A. B. Horn, D. A. Russell, L. J. Shorthouse, and T. R. E. Simpson, *J. Chem. Soc. Faraday Trans.* 92, 4759 (1996).

212. R. D. English, M. J. Van Stipdonk, R. C. Sabapathy, R. M. Crooks, and E. A. Schweikert, *Anal. Chem.* 72, 5973 (2000).
213. D. A. Hutt and G. J. Leggett, *J. Phys. Chem.* 100, 6657 (1996).
214. E. Cooper and G. J. Leggett, *Langmuir* 14, 4795 (1998).
215. R. L. McCarley, D. J. Dunaway, and R. J. Willicut, *Langmuir* 9, 2775 (1993).
216. F. P. Zamborini and R. M. Crooks, *Langmuir* 14, 3279 (1998).
217. J. K. Schoer and R. M. Crooks, *Langmuir* 13, 2323 (1997).
218. S. W. Tamchang, H. A. Biebuyck, G. M. Whitesides, N. Jeon, and R. G. Nuzzo, *Langmuir* 11, 4371 (1995).
219. M. S. Fleming and D. R. Walt, *Langmuir* 17, 4836 (2001).
220. E. A. Smith, M. J. Wanat, Y. F. Cheng, S. V. P. Barreira, A. G. Frutos, and R. M. Corn, *Langmuir* 17, 2502 (2001).
221. T. Kakiuchi, K. Sato, M. Iida, D. Hobara, S. Imabayashi, and K. Niki, *Langmuir* 16, 7238 (2000).
222. S. W. Chen, *J. Phys. Chem. B* 104, 663 (2000).
223. A. Ishida and T. Majima, *Chem. Commun.* 1299 (1999).
224. C. Chung and M. Lee, *J. Electroanal. Chem.* 468, 91 (1999).
225. K. Kajikawa, M. Hara, H. Sasabe, and W. Knoll, *Jpn. J. Appl. Phys. Part 2—Lett.* 36, L1116 (1997).
226. R. W. Zehner and L. R. Sita, *Langmuir* 13, 2973 (1997).
227. C. D. Bain, J. Evall, and G. M. Whitesides, *J. Am. Chem. Soc.* 111, 7155 (1989).
228. C. D. Bain, J. Evall, and G. M. Whitesides, *J. Am. Chem. Soc.* 111, 7164 (1989).
229. A. Ulman, S. D. Evans, Y. Shnidman, R. Sharma, J. E. Eilers, and J. C. Cheng, *J. Am. Chem. Soc.* 113, 1499 (1991).
230. E. Delamarche, B. Michel, B. H. A., and C. Gerber, *Adv. Mater.* 8, 719 (1996).
231. S. V. Atre, B. Liedberg, and D. L. Allara, *Langmuir* 11, 3882 (1995).
232. S. J. Stranick, A. N. Parikh, Y.-Y. Tao, D. L. Allara, and P. S. Weiss, *J. Phys. Chem.* 98, 7636 (1994).
233. D. Hobara, S. Takayuki, S.-I. Imabayashi, and T. Kaiuchi, *Langmuir* 15, 5073 (1999).
234. T. Takami, E. Delamarche, B. Michel, H. Wolf, and H. Ringsdorf, *Langmuir* 11, 3876 (1995).
235. D. A. Offord, C. M. John, M. R. Linford, and J. H. Griffin, *Langmuir* 10, 883 (1994).
236. T. Shibue, T. Nakanishi, T. Matsuda, T. Asahi, and T. Osaka, *Langmuir* 18, 1528 (2002).
237. S. Xu and G.-Y. Liu, *Langmuir* 13, 127 (1997).
238. S. W. Tam-Chang and I. Iverson, in "Adsorption and Its Applications in Industry and Environmental Protection. Vol I: Applications in Industry," Vol. 120, p. 917. Elsevier, Amsterdam, 1999.
239. G. Y. Liu, S. Xu, and Y. L. Qian, *Acc. Chem. Res.* 33, 457 (2000).
240. A. Golzhauser, W. Geyer, V. Stadler, W. Eck, M. Grunze, K. Edinger, T. Weimann, and P. Hinze, *J. Vac. Sci. Technol. B* 18, 3414 (2000).
241. A. Kumar and G. M. Whitesides, *Science* 263, 60 (1994).
242. R. J. Jackman, J. L. Wilbur, and G. M. Whitesides, *Science* 269, 664 (1995).
243. Y. N. Xia and G. M. Whitesides, *J. Am. Chem. Soc.* 117, 3274 (1995).
244. E. Kim, A. Kumar, and G. M. Whitesides, *J. Electrochem. Soc.* 142, 628 (1995).
245. Y. Xia and G. M. Whitesides, *Ad. Mater.* 7, 471 (1995).
246. J. A. Rogers, R. J. Jackman, and G. M. Whitesides, *J. Microelectromech. Sys.* 6, 184 (1997).
247. Z. Huang, P.-C. Wang, A. G. Mac Diarmid, Y. Xia, and G. M. Whitesides, *Langmuir* 13, 6480 (1997).
248. E. Delamarche, H. Schmid, B. Michel, and H. Biebuyck, *Ad. Mater.* 9, 741 (1997).
249. E. Delamarche, H. Schmid, A. Bietsch, N. B. Larsen, H. Rothuizen, B. Michel, and H. Biebuyck, *J. Phys. Chem. B* 102, 3324 (1998).
250. A. J. Black, K. E. Paul, J. Aizenberg, and G. M. Whitesides, *J. Am. Chem. Soc.* 121, 8356 (1999).
251. L. Libiouille, A. Bietsch, H. Schmid, B. Michel, and E. Delamarche, *Langmuir* 15, 300 (1999).
252. H. X. He, Q. G. Li, Z. Y. Zhou, H. Zhang, S. F. Y. Li, and Z. F. Liu, *Langmuir* 16, 9683 (2000).
253. T. Deng, H. K. Wu, S. T. Brittain, and G. M. Whitesides, *Anal. Chem.* 72, 3176 (2000).
254. P. Ghosh, W. M. Lackowski, and R. M. Crooks, *Macromolecules* 34, 1230 (2001).
255. R. D. Piner, J. Zhu, F. Zu, S. Hong, and C. A. Mirkin, *Science* 283, 661 (1999).
256. Y. Li, B. W. Maynor, and J. Liu, *J. Am. Chem. Soc.* 123, 2105 (2001).
257. L. M. Demers and C. A. Mirkin, *Angew. Chem.-Int. Edit.* 40, 3069 (2001).
258. M. Su, X. G. Liu, S. Y. Li, V. P. Dravid, and C. A. Mirkin, *J. Am. Chem. Soc.* 124, 1560 (2002).
259. Y. Li, M. Ben, and J. Liu, *China J. Inorg. Chem.* 18, 75 (2002).
260. J. Hyun, S. J. Ahn, W. K. Lee, A. Chilkoti, and S. Zauscher, *Nano Lett.* 2, 1203 (2002).
261. Y. M. Jung, S. J. Ahn, E. R. Kim, and H. Lee, *J. Korean Phys. Soc.* 40, 712 (2002).
262. M. J. Tarlov, R. F. Donald, J. Burgess, and G. Gillen, *J. Am. Chem. Soc.* 115, 5305 (1993).
263. J. Huang and J. C. Hemminger, *J. Am. Chem. Soc.* 115, 3342 (1993).
264. L. F. Rozsnyai and M. S. Wrighton, *Chem. Mater.* 8, 309 (1996).
265. L. F. Rozsnyai and M. S. Wrighton, *Langmuir* 11, 3913 (1995).
266. J. M. Behm, K. R. Lykke, M. J. Pellin, and J. C. Hemminger, *Langmuir* 12, 2121 (1996).
267. K. K. Berggren, R. Younkin, E. Cheung, M. Prentiss, A. J. Black, G. M. Whitesides, D. C. Ralph, C. T. Black, and M. Tinkham, *Adv. Mater.* 9, 52 (1997).
268. K. K. Berggren, A. J. Bard, J. L. Wilbur, J. D. Gillaspay, A. G. Helg, J. J. McClelland, S. L. Rolston, W. D. Phillips, M. Prentiss, and G. M. Whitesides, *Science* 269, 1255 (1995).
269. R. Younkin, K. K. Berggren, K. S. Johnson, M. Prentiss, D. C. Ralph, and G. M. Whitesides, *Appl. Phys. Lett.* 71, 1261 (1997).
270. A. B. Chwang, E. L. Granstrom, and C. D. Frisbie, *Adv. Mater.* 12, 285 (2000).
271. T. L. Brower, J. C. Garno, A. Ulman, G. Y. Liu, C. Yan, A. Golzhauser, and M. Grunze, *Langmuir* 18, 6207 (2002).
272. S. H. Hong, J. Zhu, and C. A. Mirkin, *Langmuir* 15, 7897 (1999).
273. A. Kumar, H. A. Biebuyck, N. L. Abbott, and G. M. Whitesides, *J. Am. Chem. Soc.* 114, 9188 (1992).
274. A. Kumar, N. L. Abbott, E. Kim, H. A. Biebuyck, and G. M. Whitesides, *Acc. Chem. Res.* 28, 219 (1995).
275. L. M. Tender, R. L. Worley, H. Y. Fan, and G. P. López, *Langmuir* 12, 5515 (1996).
276. L. M. Tender, K. A. Opperman, P. D. Hampton, and G. P. López, *Adv. Mater.* 10, 73 (1998).
277. C. C. Hsueh, M. T. Lee, M. S. Freund, and G. S. Ferguson, *Angew. Chem.-Int. Edit.* 39, 1228 (2000).
278. R. Haneda, H. Nishihara, and K. Aramaki, *Journal of the Electrochemical Society* 144, 1215 (1997).
279. M. Itoh, H. Nishihara, and K. Aramaki, *Journal of the Electrochemical Society* 142, 3696 (1995).
280. R. Haneda and K. Aramaki, *Journal of the Electrochemical Society* 145, 1856 (1998).
281. G. K. Jennings, J. C. Munro, T. H. Yong, and P. E. Laibinis, *Langmuir* 14, 6130 (1998).
282. O. Azzaroni, M. Cipollone, M. E. Vela, and R. C. Salvarezza, *Langmuir* 17, 1483 (2001).
283. D. Taneichi, R. Haneda, and K. Aramaki, *Corrosion Sci.* 43, 1589 (2001).

284. Z. L. Quan, S. H. Chen, and S. L. Li, *Corrosion Sci.* 43, 1071 (2001).
285. K. Nozawa, H. Nishihara, and K. Aramaki, *Corrosion Sci.* 39, 1625 (1997).
286. K. Nozawa and K. Aramaki, *Corrosion Sci.* 41, 57 (1999).
287. K. Aramaki and T. Kikuchi, *Journal of the Electrochemical Society* 147, 1734 (2000).
288. K. Aramaki, *Corrosion Sci.* 41, 1715 (1999).
289. I. Touzov and C. B. Gorman, *Langmuir* 13, 4850 (1997).
290. P. E. Laibinis and G. M. Whitesides, *J. Am. Chem. Soc.* 114, 9022 (1992).
291. Y. Yamamoto, H. Nishihara, and K. Aramaki, *J. Electrochem. Soc.* 143, 436 (1993).
292. M. Tanahashi and T. Matsuda, *J. Biomed. Mater. Res.* 34, 305 (1997).
293. A. Y. Lee, A. Ulman, and A. S. Myerson, *Langmuir* 18, 5886 (2002).
294. P. Jiang, Z. F. Liu, and S. M. Cai, *Langmuir* 18, 4495 (2002).
295. A. M. Travaille, J. Donners, J. W. Gerritsen, N. Sommerdijk, R. J. M. Nolte, and H. van Kempen, *Adv. Mater.* 14, 492 (2002).
296. R. A. Fischer, U. Weckenmann, C. Winter, J. Kashammer, V. Scheumann, and S. Mittler, *J. Phys. IV* 11, 1183 (2001).
297. J. Kuther, M. Bartz, R. Seshadri, G. B. M. Vaughan, and W. Tremel, *J. Mater. Chem.* 11, 503 (2001).
298. J. Aizenberg, *J. Chem. Soc.-Dalton Trans.* 3963 (2000).
299. C. Winter, U. Weckenmann, R. A. Fischer, J. Kashammer, V. Scheumann, and S. Mittler, *Chem. Vapor Depos.* 6, 199 (2000).
300. J. Aizenberg, A. J. Black, and G. M. Whitesides, *J. Am. Chem. Soc.* 121, 4500 (1999).
301. D. Qin, Y. Xia, B. Xu, H. Yang, C. Zhu, and G. M. Whitesides, *Ad. Mater.* 11, 1433 (1999).
302. J. J. Ramsden, *Chem. Soc. Rev.* 24, 73 (1995).
303. V. P. Zhdanov and B. Kasemo, *Surf. Rev. Lett.* 5, 615 (1998).
304. N. D. Spencer, *Chimia* 52, 598 (1998).
305. J. Talbot, G. Tarjus, P. R. Van Tassel, and P. Viot, *Colloid Surf. A-Physicochem. Eng. Asp.* 165, 287 (2000).
306. A. R. Halperin and D. E. Leckband, *C. R. Acad. Sci. Ser. IV-Phys. Astrophys.* 1, 1171 (2000).
307. K. Bhadriraju and C. S. Chen, *Drug Discovery Today* 7, 612 (2002).
308. B. D. Ratner, *J. Biomed. Mater. Res.* 27, 837 (1993).
309. M. Lestelius, B. Liedberg, and P. Tengvall, *Langmuir* 13, 5900 (1997).
310. N. K. Chaki and K. Vijaymohan, *Biosens. Bioelectron.* 17, 1 (2002).
311. K. L. Prime and G. M. Whitesides, *Science* 252, 1164 (1991).
312. M. Mrksich, L. E. Dike, J. Tien, D. E. Ingber, and G. M. Whitesides, *Exp. Cell Res.* 235, 305 (1997).
313. R. R. Seigel, P. Harder, R. Dahint, M. Grunze, F. Josse, M. Mrksich, and G. M. Whitesides, *Anal. Chem.* 69, 3321 (1997).
314. G. P. Lopez, H. Biebuyck, R. Harter, A. Kumar, and G. M. Whitesides, *J. Am. Chem. Soc.* 115, 10774 (1993).
315. G. B. Sigal, C. Bamdad, A. Barberis, J. Strominger, and G. M. Whitesides, *Anal. Chem.* 68, 490 (1996).
316. C. Roberts, C. S. Chen, M. Mrksich, V. Martichonok, D. E. Ingber, and G. M. Whitesides, *J. Am. Chem. Soc.* 120, 6548 (1998).
317. G. Krishna, J. Schulte, B. A. Cornell, R. Pace, L. Wiczorek, and P. D. Osman, *Langmuir* 17, 4858 (2001).
318. K. Gaus and E. A. H. Hall, *Anal. Chim. Acta* 470, 3 (2002).
319. M. Riepl, K. Enander, B. Liedberg, M. Schaferling, M. Kruschina, and F. Ortigao, *Langmuir* 18, 7016 (2002).
320. C. F. Wang, H. Wang, Z. Y. Wu, G. L. Shen, and R. Q. Yu, *Anal. Bioanal. Chem.* 373, 803 (2002).
321. M. Mrksich, G. B. Sigal, and G. M. Whitesides, *Langmuir* 11, 4383 (1995).
322. G. B. Sigal, M. Mrksich, and G. M. Whitesides, *J. Am. Chem. Soc.* 120, 3464 (1998).
323. D. D. Schlereth and K. R. P. H., *J. Electroanal. Chem.* 431, 285 (1997).
324. G. P. Lopez, W. M. Albers, S. L. Schreiber, R. Carroll, E. Peralta, and G. M. Whitesides, *J. Am. Chem. Soc.* 115, 5877 (1993).
325. S. Margel, E. A. Vogler, F. L., T. Watt, S. Haynie, and D. Y. Sogah, *J. Biomed. Mater. Res.* 27, 1463 (1993).
326. D. Kleinfeld, K. H. Kahler, and P. E. Hockberger, *J. Neurosci.* 8, 4098 (1988).
327. D. D. Schlaepfer and T. Hunter, *Trends Cell Biol.* 8, 151 (1998).
328. B. T. Houseman and M. Mrksich, *J. Org. Chem.* 63, 7552 (1998).
329. C. S. Chen, M. Mrksich, S. Huang, G. M. Whitesides, and D. E. Ingber, *Science* 276, 1425 (1997).
330. R. Raiteri, M. Grattarola, H. J. Butt, and P. Skladal, *Sens. Actuator B-Chem.* 79, 115 (2001).
331. E. A. H. Hall, J. J. Gooding, and C. E. Hall, *Mikrochim. Acta* 121, 119 (1995).
332. C. K. O'Sullivan and G. G. Guilbault, *Biosens. Bioelectron.* 14, 663 (1999).
333. "Optical Biosensors: Present and Future." Elsevier, Amsterdam, 2002.
334. B. Danielson and K. Mosbach, in "Biosensors: Fundamentals and Applications," p. 575. Oxford University Press, Oxford, 1987.
335. D. R. Baselt, G. U. Lee, M. Natesan, S. W. Metzger, P. E. Sheehan, and R. J. Colton, *Biosens. Bioelectron.* 13, 731 (1998).
336. O. Lioubashevski, F. Patolsky, and I. Willner, *Langmuir* 17, 5134 (2001).
337. M. M. Miller, P. E. Sheehan, R. L. Edelstein, C. R. Tamana, L. Zhong, S. Bounnak, L. J. Whitman, and R. J. Colton, *J. Magn. Magn. Mater.* 225, 138 (2001).
338. R. L. Edelstein, C. R. Tamana, P. E. Sheehan, M. M. Miller, D. R. Baselt, L. J. Whitman, and R. J. Colton, *Biosens. Bioelectron.* 14, 805 (2000).
339. R. Berger, E. Delamar, H. P. Lang, C. Gerber, J. K. Gimzewski, E. Meyer, and H.-J. Güntherodt, *Science* 276, 2021 (1997).
340. A. M. Moulin, S. J. O'Shea, and M. E. Welland, *Ultramicroscopy* 82, 23 (2000).
341. A. Abdelghani, J. M. Chovelon, N. JaffrezicRenault, C. Ronot Trioli, C. Veillas, and H. Gagnaire, *Sens. Actuator B-Chem.* 39, 407 (1997).
342. V. M. Mirsky, M. Vasjari, I. Novotny, V. Rehacek, V. Tvarozek, and O. S. Wolfbeis, *Nanotechnology* 13, 175 (2002).
343. A. J. Guimar, J. T. Guthrie, and S. D. Evans, *Langmuir* 15, 1198 (1999).
344. S. Takenaka, K. Yamashita, M. Takagi, Y. Uto, and H. Kondo, *Anal. Chem.* 72, 1334 (2000).
345. R. M. Umek, S. W. Lin, J. Vielmetter, R. H. Terbruggen, B. Irvine, C. J. Yu, J. F. Kayyem, H. Yowanto, G. F. Blackburn, D. H. Farkas, and Y. P. Chen, *J. Mol. Diagn.* 3, 74 (2001).
346. M. J. Giz, B. Duong, and N. J. Tao, *J. Electroanal. Chem.* 465, 72 (1999).
347. I. Bontidean, J. R. Lloyd, J. L. Hobman, J. R. Wilson, E. Csoregi, B. Mattiasson, and N. L. Brown, *J. Inorg. Biochem.* 79, 225 (2000).
348. A. Riklin and I. Willner, *Anal. Chem.* 67, 4118 (1995).
349. C. Bourdillon, C. Demaille, J. Moiroux, and J.-M. Savéant, *Acc. Chem. Res.* 29, 529 (1996).
350. P. G. He, J. N. Ye, Y. Z. Fang, J. Anzai, and T. Osa, *Talanta* 44, 885 (1997).
351. S. Kim, S.-E. Yun, and C. Kang, *Electrochem. Commun.* 1, 151 (1999).
352. C. Danilowicz, E. Corton, F. Battaglini, and E. J. Calvo, *Electrochim. Acta* 43, 3525 (1998).
353. E. S. Forzani, M. Otero, M. A. Perez, M. L. Teijelo, and E. J. Calvo, *Langmuir* 18, 4020 (2002).
354. E. J. Calvo, R. Etchenique, L. Pietrasanta, A. Wolosiuk, and C. Danilowicz, *Anal. Chem.* 73, 1161 (2001).
355. E. J. Calvo, F. Battaglini, C. Danilowicz, A. Wolosiuk, and M. Otero, *Faraday Discuss.* 47 (2000).

356. E. S. Forzani, V. M. Solis, and E. J. Calvo, *Anal. Chem.* 72, 5300 (2000).
357. E. J. Calvo and R. Etchenique, *J. Phys. Chem. B* 103, 8944 (1999).
358. J. J. Gooding, L. Pugliano, D. B. Hibbert, and P. Erokhin, *Electrochem. Commun.* 2, 217 (2000).
359. R. L. Earp and R. E. Dessy, in "Commercial Biosensors," Vol. 148, p. 99. John Wiley and Sons, New York, 1998.
360. T. P. Henning and D. D. Cunningham, in "Commercial Biosensors," Vol. 148, p. 304. John Wiley and Sons, New York, 1998.
361. J. J. Gooding, E. A. H. Hall, and D. B. Hibbert, *Electroanalysis* 10, 1130 (1998).
362. I. Willner, A. Riklin, B. Shoham, D. Rivenzon, and E. Katz, *Adv. Mater.* 5, 912 (1993).
363. C. Bourdillon, C. Demaille, J. Guerin, J. Moiroux, and J.-M. Savéant, *J. Am. Chem. Soc.* 115, 12264 (1993).
364. C. Bourdillon, C. Demaille, J. Moiroux, and J.-M. Savéant, *J. Am. Chem. Soc.* 116, 10328 (1994).
365. C. Bourdillon, C. Demaille, J. Moiroux, and J.-M. Saveant, *J. Am. Chem. Soc.* 117, 11499 (1995).
366. O. Pierrat, N. Lechat, C. Bourdillon, and J.-M. Laval, *Langmuir* 13, 4112 (1997).
367. N. Anicet, C. Bourdillon, J. Moiroux, and J.-M. Saveant, *J. Phys. Chem.* 102, 9844 (1998).
368. N. Anicet, C. Bourdillon, J. Moiroux, and J. M. Saveant, *Langmuir* 15, 6527 (1999).
369. L. Jiang, C. J. McNeil, and J. M. Cooper, *J. Chem. Soc. Chem. Commun.* 1293 (1995).
370. A. Riklin, E. Katz, I. Willner, A. Stocker, and A. F. Bückmann, *Nature* 376, 672 (1995).
371. T. Lötzbeyer, W. Schuhmann, and H.-L. Schmidt, *Sensors Actuators B* 33, 50 (1996).
372. R. Blonder, E. Katz, I. Willner, V. Wray, and A. F. Bückmann, *J. Am. Chem. Soc.* 119, 11747 (1997).
373. T. Lötzbeyer, W. Schuhmann, and H.-L. Schmidt, *Bioelectrochem. Bioenerg.* 42, 1 (1997).
374. G. Wittstock and W. Schuhmann, *Anal. Chem.* 69, 5059 (1997).
375. J. J. Gooding, M. Situmorang, P. Erokhin, and D. B. Hibbert, *Anal. Comm.* 36, 225 (1999).
376. J. J. Gooding, P. Erokhin, and D. B. Hibbert, *Biosensors Bioelectronics* 15, 229 (2000).
377. J. J. Gooding, P. Erokhin, D. Losic, W. R. Yang, V. Policarpio, J. Q. Liu, F. M. Ho, M. Situmorang, D. B. Hibbert, and J. G. Shapter, *Anal. Sci.* 17, 3 (2001).
378. D. Losic, J. J. Gooding, J. G. Shapter, D. B. Hibbert, and K. Short, *Electroanalysis* 13, 1385 (2001).
379. K. Kerman, D. Ozkan, P. Kara, B. Meric, J. J. Gooding, and M. Ozsoz, *Anal. Chim. Acta* 462, 39 (2002).
380. E. Katz, A. Riklin, and I. Willner, *J. Electroanal. Chem.* 354, 129 (1993).
381. I. Willner, E. Katz, B. Willner, R. Blonder, V. Heleg-Shabtai, and A. F. Bückmann, *Biosens. Bioelectron.* 12, 337 (1997).
382. Q. Chen, Y. Kobayashi, H. Takeshita, T. Hoshi, and J. Anzai, *Electroanalysis* 10, 94 (1998).
383. J. Anzai, H. Takeshita, Y. Kobayashi, T. Osa, and T. Hoshi, *Anal. Chem.* 70, 811 (1998).
384. C. Mousty, J. L. Bergamasco, R. Wessel, H. Perrot, and S. Cosnier, *Anal. Chem.* 73, 2890 (2001).
385. Y. Kajiya, T. Okamoto, and H. Yoneyama, *Chemistry Letters* 2107 (1993).
386. S. E. Creager and K. Olsen, *Anal. Chim. Acta* 307, 277 (1995).
387. M. Imamura, T. Haruyama, E. Kobatake, Y. Ikariyama, and M. Aizawa, *Sensors Actuators B* 24–25, 113 (1995).
388. I. Willner, M. Lion-Dagan, S. Marx-Tibbon, and E. Katz, *J. Am. Chem. Soc.* 117, 6581 (1995).
389. T. Nakaminami, S. Ito, S. Kuwabata, and H. Yoneyama, *Anal. Chem.* 71, 1068 (1999).
390. I. D. Karalemas and D. S. Papastathopoulos, *Anal. Lett.* 31, 913 (1998).
391. C. Ruan, F. Yang, C. Lei, and J. Deng, *Anal. Chem.* 70, 1721 (1998).
392. I. Willner, V. HelegShabtai, R. Blonder, E. Katz, and G. L. Tao, *J. Am. Chem. Soc.* 118, 10321 (1996).
393. H. Zimmermann, A. Lindgren, W. Schuhmann, and L. Gorton, *Chem.-Eur. J.* 6, 592 (2000).
394. H. D. Sikes, J. F. Smalley, S. P. Dudek, A. R. Cook, M. D. Newton, C. E. D. Chidsey, and S. W. Feldberg, *Science* 291, 1519 (2001).
395. S. O. Kelley, N. M. Jackson, M. G. Hill, and J. K. Barton, *Angew. Chem. Int. Ed.* 38, 941 (1999).
396. R. E. Holmlin, P. J. Dandliker, and J. K. Barton, *Angew. Chem. Int. Ed. Engl.* 36, 2714 (1997).
397. F. Lisdat, B. Ge, and F. W. Scheller, *Electrochem. Commun.* 1, 65 (1999).
398. T. Ruzgas, E. Csoregi, J. Emneus, L. Gorton, and G. Marko-Varga, *Anal. Chim. Acta* 330, 123 (1996).
399. A. Heller, *Acc. Chem. Res.* 23, 128 (1990).
400. H. J. Hecht, D. Schomburg, H. Kalisz, and R. D. Schmid, *Biosens. Bioelectron.* 8, 197 (1993).
401. J. Liu, M. N. Paddon-Row, and J. J. Gooding, unpublished results.
402. A. J. Black, T. T. Wooster, W. E. Geiger, and M. N. Paddon-Row, *J. Am. Chem. Soc.* 115, 7924 (1993).
403. M. N. Paddon-Row, *Acc. Chem. Res.* 27, 18 (1994).
404. B. H. Huisman, R. P. H. Kooyman, F. vanVeggel, and D. N. Reinhoudt, *Adv. Mater.* 8, 561 (1996).
405. D. M. Disley, D. C. Cullen, H. X. You, and C. R. Lowe, *Biosens. Bioelectron.* 13, 1213 (1998).
406. D. M. Disley, P. R. Morrill, K. Sproule, and C. R. Lowe, *Biosens. Bioelectron.* 14, 481 (1999).
407. C. Duschl, A. F. Sevin Landais, and H. Vogel, *Biophys. J.* 70, 1985 (1996).
408. R. P. H. Kooyman, D. J. Vandenheuvel, J. W. Drijfhout, and G. W. Welling, *Thin Solid Films* 244, 913 (1994).
409. I. Vikholm, E. Gyorvary, and J. Peltonen, *Langmuir* 12, 3276 (1996).
410. K. Gaus, A. Basran, and E. A. H. Hall, *Analyst* 126, 329 (2001).
411. K. Gaus and E. A. H. Hall, *Biosens. Bioelectron.* 18, 151 (2003).
412. K. A. Peterlinz, R. M. Georgiadis, T. M. Herne, and M. J. Tarlov, *J. Am. Chem. Soc.* 119, 3401 (1997).
413. C. E. Jordan, A. G. Frutos, A. J. Thiel, and R. M. Corn, *Anal. Chem.* 69, 4939 (1997).
414. A. J. Haes and R. P. Van Duyne, *J. Am. Chem. Soc.* 124, 10596 (2002).
415. M. Boncheva, L. Scheibler, P. Lincoln, H. Vogel, and B. Åkerman, *Langmuir* 15, 4317 (1999).
416. J. M. Brockman, A. G. Frutos, and R. M. Corn, *J. Am. Chem. Soc.* 121, 8044 (1999).
417. P. D. Gershon and S. Khilko, *J. Immunological Methods* 183, 65 (1995).
418. K. Gaus and E. A. H. Hall, *J. Coll. Interface Sci.* 194, 364 (1997).
419. S. Sawata, E. Kai, K. Ikebukuro, T. Iida, T. Honda, and I. Karube, *Biosens. Bioelectron.* 14, 397 (1999).
420. A. J. Thiel, A. G. Frutos, C. E. Jordan, R. M. Corn, and L. M. Smith, *Anal. Chem.* 69, 4948 (1997).
421. H. J. Watts, D. Yeung, and H. Parkes, *Anal. Chem.* 67, 4283 (1995).
422. I. Vikholm, T. Viitala, W. M. Albers, and J. Peltonen, *Biochim. Biophys. Acta-Biomembr.* 1421, 39 (1999).
423. C. A. Rowe-Taitt, J. J. Cras, C. H. Patterson, J. P. Golden, and F. S. Ligler, *Anal. Biochem.* 281, 123 (2000).
424. W. M. Mullett, E. P. C. Lai, and J. M. Yeung, *Methods* 22, 77 (2000).
425. T. Liu, J. Tang, H. Q. Zhao, Y. P. Deng, and L. Jiang, *Langmuir* 18, 5624 (2002).

426. J. Wang, P. E. Nielsen, M. Jiang, X. Cai, J. R. Fernandes, D. H. Grant, M. Ozsoz, A. Beglieter, and M. Mowat, *Anal. Chem.* 69, 5200 (1997).
427. H. Zhang, R. Wang, T. H., L. Nie, and S. Yao, *Talanta* 46, 171 (1998).
428. H. Zhang, H. Tan, R. Wang, W. Wei, and S. Yao, *Anal. Chim. Acta* 374, 31 (1998).
429. B. A. Cavic, G. L. Hayward, and M. Thompson, *Analyst* 124, 1405 (1999).
430. F. Caruso, E. Rodda, D. N. Furlong, K. Niikura, and Y. Okahata, *Anal. Chem.* 69, 2043 (1997).
431. Y. Okahata, Y. Matsunobu, K. Ijio, M. Mukae, A. Murakami, and K. Makino, *J. Am. Chem. Soc.* 114, 8299 (1992).
432. I. Ben Dov, I. Willner, and E. Zisman, *Anal. Chem.* 69, 3506 (1997).
433. Y. Cohen, S. Levi, S. Rubin, and I. Willner, *J. Electroanal. Chem.* 417, 65 (1996).
434. M. Minunni, M. Mascini, G. G. Guilbault, and B. Hock, *Anal. Lett.* 28, 749 (1995).
435. L. M. Furtado and M. Thompson, *Analyst* 123, 1937 (1998).
436. T. Hianik, V. Gajdos, R. Krivanek, T. Oretskaya, V. Metelev, E. Volkov, and P. Vadgama, *Bioelectrochemistry* 53, 199 (2001).
437. E. Huang, M. Satjapipat, S. B. Han, and F. M. Zhou, *Langmuir* 17, 1215 (2001).
438. Y. Okahata, M. Kawase, K. Niikura, F. Ohtake, H. Furusawa, and Y. Ebara, *Anal. Chem.* 70, 1288 (1998).
439. S. Storri, T. Santoni, and M. Mascini, *Anal. Lett.* 31, 1795 (1998).
440. R. D. Vaughan, C. K. O'Sullivan, and G. G. Guilbault, *Fresenius J. Anal. Chem.* 364, 54 (1999).
441. X. D. Su, F. T. Chew, and S. F. Y. Li, *Anal. Biochem.* 273, 66 (1999).
442. R. B. Towery, N. C. Fawcett, P. Zhang, and J. A. Evans, *Biosens. Bioelectron.* 16, 1 (2001).
443. J. Horacek and P. Skladal, *Anal. Chim. Acta* 347, 43 (1997).
444. S. Susmel, C. K. O'Sullivan, and G. G. Guilbault, *Enzyme Microb. Technol.* 27, 639 (2000).
445. X. C. Zhou and L. Cao, *Analyst* 126, 71 (2001).
446. Z. Y. Wu, C. P. He, S. P. Wang, G. L. Shen, and R. Q. Yu, *Chem. J. Chin. Univ.-Chin.* 22, 542 (2001).
447. Y. S. Fung and Y. Y. Wong, *Anal. Chem.* 73, 5302 (2001).
448. S. F. Chou, W. L. Hsu, J. M. Hwang, and C. Y. Chen, *Anal. Chim. Acta* 453, 181 (2002).
449. A. J. C. Eun, L. Q. Huang, F. T. Chew, S. F. Y. Li, and S. M. Wong, *J. Virol. Methods* 99, 71 (2002).
450. R. Saber, S. Mutlu, and E. Piskin, *Biosens. Bioelectron.* 17, 727 (2002).
451. C. C. Wang, H. Wang, Z. Y. Wu, G. M. Zeng, G. H. Huang, G. L. Shen, and R. Q. Yu, *Acta Chim. Sin.* 60, 1284 (2002).
452. E. Katz and I. Willner, *J. Electroanal. Chem.* 418, 67 (1996).
453. C. Berggren and G. Johansson, *Anal. Chem.* 69, 3651 (1997).
454. R. Blonder, I. Ben Dov, A. Dagan, I. Willner, and E. Zisman, *Biosens. Bioelectron.* 12, 627 (1997).
455. C. Berggren, B. Bjarnason, and G. Johansson, *Biosens. Bioelectron.* 13, 1061 (1998).
456. A. Friggeri, F. van Veggel, and D. N. Reinhoudt, *Chem.-Eur. J.* 5, 3595 (1999).
457. H. C. Yoon, M.-Y. Hong, and H.-S. Kim, *Anal. Biochem.* 282, 121 (2000).
458. J. Yan, L. M. Tender, P. D. Hampton, and G. P. López, *J. Phys. Chem. B.* 105, 8905 (2001).
459. M. Riepl, V. M. Mirsky, I. Novotny, V. Tvarozek, V. Rehacek, and O. S. Wolfbeis, *Anal. Chim. Acta* 392, 77 (1999).
460. H. Aoki, P. Buhlmann, and Y. Umezawa, *J. Electroanal. Chem.* 473, 105 (1999).
461. V. P. Y. Gadzekpo, K. P. Xiao, H. Aoki, P. Buhlmann, and Y. Umezawa, *Anal. Chem.* 71, 5109 (1999).
462. M. Liu, Q. X. Li, and G. A. Rechnitz, *Electroanalysis* 12, 21 (2000).
463. M. Dijkema, B. Kamp, J. C. Hoogvliet, and W. P. van Bennekom, *Anal. Chem.* 73, 901 (2001).
464. C. Berggren, B. Bjarnason, and G. Johansson, *Electroanalysis* 13, 173 (2001).
465. R. J. Pei, Z. L. Cheng, E. K. Wang, and X. R. Yang, *Biosens. Bioelectron.* 16, 355 (2001).
466. L. Alfonta, A. Bardea, O. Khersonsky, E. Katz, and I. Willner, *Biosens. Bioelectron.* 16, 675 (2001).
467. Z. Liron, L. M. Tender, J. P. Golden, and F. S. Ligler, *Biosens. Bioelectron.* 17, 489 (2002).
468. C. M. Ruan, L. J. Yang, and Y. B. Li, *Anal. Chem.* 74, 4814 (2002).
469. H. F. Ji, E. Finot, R. Dabestani, T. Thundat, G. M. Brown, and P. F. Britt, *Chem. Commun.* 457 (2000).
470. K. M. Hansen, H. F. Ji, G. H. Wu, R. Datar, R. Cote, A. Majumdar, and T. Thundat, *Anal. Chem.* 73, 1567 (2001).
471. J. Homola, S. S. Yee, and D. Myszka, in "Optical Biosensors: Present and Future," p. 207. Elsevier, Amsterdam, 2002.
472. S. Busse, V. Scheumann, B. Menges, and S. Mittler, *Biosens. Bioelectron.* 17, 704 (2002).
473. A. B. Steel, T. M. Herne, and M. J. Tarlov, *Anal. Chem.* 79, 4670 (1998).
474. A. B. Steel, T. M. Herne, and M. J. Tarlov, *Bioconjugate Chem.* 10, 419 (1999).
475. A. B. Steel, R. L. Levicky, T. M. Herne, and M. J. Tarlov, *Biophys. J.* 79, 975 (2000).
476. C. Xu, L. Sun, L. J. Kepley, and R. M. Crooks, *Anal. Chem.* 65, 2102 (1993).
477. D. V. Leff, L. Brandt, and J. R. Heath, *Langmuir* 12, 4723 (1996).
478. E. Huang, F. M. Zhou, and L. Deng, *Langmuir* 16, 3272 (2000).
479. D. Ozkan, E. A., K. Kerman, P. Kara, J. J. Gooding, P. E. Nielsen, and M. Ozsoz, *Electrochem. Commun.* 4, 796 (2002).
480. B. L. Frey and R. M. Corn, *Anal. Chem.* 68, 3187 (1996).
481. W. Yang, J. J. Gooding, and D. B. Hibbert, *Analyst* 126, 1573 (2001).
482. W. Yang, D. Jaramillo, J. J. Gooding, D. B. Hibbert, R. Zhang, G. D. Willett, and K. J. Fisher, *Chem. Commun.* 1982 (2001).
483. L. Häussling, H. Ringsdorf, F. J. Schmitt, and W. Knoll, *Langmuir* 7, 1837 (1991).
484. F. J. Schmitt, L. Häussling, H. Ringsdorf, and W. Knoll, *Thin Solid Films* 201/211, 815 (1992).
485. J. Spinke, M. Liley, H. J. Guder, L. Angermaier, and W. Knoll, *Langmuir* 9, 1821 (1993).
486. H. Matsui, P. Porrata, and G. E. Douberly, *Nano Lett.* 1, 461 (2001).
487. P. D. J. Osman, V. L. B. Braach-Maksytytis, B. A. Cornell, L. G. King, R. J. Pace, B. Raguse, and L. Wiczorek, *Biophys. J.* 72, TH291 (1997).
488. B. A. Cornell, G. Krishna, P. D. Osman, R. D. Pace, and L. Wiczorek, *Biochem. Soc. Trans.* 29, 613 (2001).
489. G. Woodhouse, L. King, L. Wiczorek, P. Osman, and B. Cornell, *J. Mol. Recognit.* 12, 328 (1999).
490. G. E. Woodhouse, L. G. King, L. Wiczorek, and B. A. Cornell, *Faraday Discuss.* 247 (1998).
491. B. Raguse, V. L. B. Braach-Maksytytis, B. A. Cornell, L. G. King, P. D. J. Osman, R. J. Pace, and L. Wiczorek, *Langmuir* 14, 648 (1998).
492. V. L. B. Braach-Maksytytis, B. A. Cornell, L. G. King, P. D. J. Osman, R. J. Pace, B. Raguse, and L. Wiczorek, *Biophys. J.* 72, TH288 (1997).
493. B. A. Cornell, V. L. B. Braach-Maksytytis, L. G. King, P. D. J. Osman, R. J. Pace, B. Raguse, and L. Wiczorek, *Biophys. J.* 72, TH289 (1997).
494. S. W. Lucas and M. M. Harding, *Anal. Biochem.* 282, 70 (2000).
495. M. W. J. Beulen, F. C. J. M. van Veggel, and D. N. Reinhoudt, *Chem. Commun.* 503 (1999).

496. S. Flink, H. Schonherr, G. J. Vancso, F. A. J. Geurts, K. G. C. van Leerdam, F. van Veggel, and D. N. Reinhoudt, *J. Chem. Soc.-Perkin Trans. 2*, 2141 (2000).
497. S. Flink, B. A. Boukamp, A. van den Berg, F. C. J. M. van Veggel, and D. N. Reinhoudt, *J. Am. Chem. Soc.* 120, 4652 (1998).
498. A. J. Moore, L. M. Goldenberg, M. R. Bryce, M. C. Petty, A. P. Monkman, C. Marengo, J. Yarwood, M. J. Joyce, and S. N. Port, *Adv. Mater.* 10, 395 (1998).
499. H. Y. Liu, S. G. Liu, and L. Echegoyen, *Chem. Commun.* 1493 (1999).
500. K. Bandyopadhyay, L. H. Shu, H. Y. Liu, and L. Echegoyen, *Langmuir* 16, 2706 (2000).
501. K. Bandyopadhyay, H. Y. Liu, S. G. Liu, and L. Echegoyen, *Chem. Commun.* 141 (2000).
502. K. Bandyopadhyay, S. G. Liu, H. Y. Liu, and L. Echegoyen, *Chem.-Eur. J.* 6, 4385 (2000).
503. T. D. Chung, J. Park, J. Kim, H. Lim, M. J. Choi, J. R. Kim, S. K. Chang, and H. Kim, *Anal. Chem.* 73, 3975 (2001).
504. A. Friggeri, F. van Veggel, D. N. Reinhoudt, and R. P. H. Kooyman, *Langmuir* 14, 5457 (1998).
505. W. Yang, J. J. Gooding, and D. B. Hibbert, *J. Electroanal. Chem.* 516, 10 (2001).
506. J. J. Gooding, D. B. Hibbert, and W. Yang, *Sensors* 1, 75 (2001).
507. B. Sellergren, *Trac-Trends Anal. Chem.* 16, 310 (1997).
508. S. A. Piletsky and A. P. F. Turner, *Electroanalysis* 14, 317 (2002).
509. H. Asanuma, T. Hishiyama, and M. Komiyama, *Adv. Mater.* 12, 1019 (2000).
510. S. A. Piletsky, T. L. Panasyuk, E. V. Piletskaya, I. A. Nicholls, and M. Ulbricht, *J. Membr. Sci.* 157, 263 (1999).
511. Z. P. Yang, J. M. Kauffmann, M. I. A. Valenzuela, and S. Ozkan, *Mikrochim. Acta* 131, 85 (1999).
512. S. A. Piletsky, E. V. Piletskaya, T. A. Sergeeva, T. L. Panasyuk, and A. V. El'skaya, *Sens. Actuator B-Chem.* 60, 216 (1999).
513. V. M. Mirsky, T. Hirsch, S. A. Piletsky, and O. S. Wolfbeis, *Angew. Chem.-Int. Edit.* 38, 1108 (1999).
514. M. Lahav, E. Katz, A. Doron, F. Patolsky, and I. Willner, *J. Am. Chem. Soc.* 121, 862 (1999).
515. Z. P. Yang, I. Engquist, B. Liedberg, and J. M. Kauffmann, *J. Electroanal. Chem.* 430, 189 (1997).
516. H. L. Zhang, M. Chen, and H. L. Li, *J. Phys. Chem. B* 104, 28 (2000).
517. D. Cahen and G. Hodes, *Ad. Mater.* 14, 789 (2002).
518. X. D. Cui, A. Primak, X. Zarate, J. Tom Fohr, O. F. Sankey, A. L. Moore, T. A. Moore, D. Gust, G. Harris, and L. S. M., *Science* 294, 571 (2001).
519. Y. Selzer, A. Salomon, and D. Cahen, *J. Am. Chem. Soc.* 124, 2886 (2002).
520. R. E. Holmlin, R. F. Ismagilov, R. Haag, V. Mujica, M. A. Ratner, M. A. Rampi, and G. M. Whitesides, *Angew. Chem. Int. Ed.* 40, 2316 (2001).
521. D. J. Wold, R. Haag, M. A. Rampi, and C. D. Frisbie, *J. Phys. Chem. B* 106, 2813 (2002).
522. S. E. Creager and G. K. Rowe, *J. Electroanal. Chem.* 420, 291 (1997).
523. J. J. Sumner, K. S. Weber, L. A. Hockett, and S. E. Creager, *J. Phys. Chem. B* 104, 7449 (2000).
524. E. Laviron, *J. Electroanal. Chem.* 101, 19 (1979).
525. E. Laviron, *J. Electroanal. Chem.* 97, 135 (1979).
526. S. E. Creager and T. T. Wooster, *Anal. Chem.* 70, 4257 (1998).
527. J. H. Reeves, S. Song, and E. F. Bowden, *Anal. Chem.* 65, 683 (1992).
528. C. E. D. Chidsey, *Science* 251, 919 (1991).
529. R. A. Marcus and N. Sutin, *Biochim. Biophys. Acta* 811, 265 (1985).
530. D. J. Wold and C. D. Frisbie, *J. Am. Chem. Soc.* 123, 5549 (2001).
531. M. A. Rampi and G. M. Whitesides, *Chem. Phys.* 281, 373 (2002).
532. Z. H. Yu, H. B. Shao, Y. Luo, H. L. Zhang, and Z. F. Liu, *Langmuir* 13, 5774 (1997).
533. M. J. Hostetler, J. J. Stokes, and R. W. Murray, *Langmuir* 12, 3604 (1996).
534. C. S. Weisbecker, M. V. Merritt, and G. M. Whitesides, *Langmuir* 12, 3763 (1996).
535. M. J. Hostetler, S. J. Green, J. J. Stokes, and R. W. Murray, *J. Am. Chem. Soc.* 118, 4212 (1996).
536. K. C. Grabar, K. J. Allison, B. E. Baker, R. M. Bright, K. R. Brown, R. G. Freeman, A. P. Fox, C. D. Keating, M. D. Musick, and M. J. Natan, *Langmuir* 12, 2353 (1996).
537. S. W. Chen, R. S. Ingram, M. J. Hostetler, J. J. Pietron, R. W. Murray, T. G. Schaaff, J. T. Khoury, M. M. Alvarez, and R. L. Whetten, *Science* 280, 2098 (1998).
538. A. P. Alivisatos, K. P. Johnsson, X. G. Peng, T. E. Wilson, C. J. Loweth, M. P. Bruchez, and P. G. Schultz, *Nature* 382, 609 (1996).
539. C. J. Loweth, W. B. Caldwell, X. Peng, A. P. Alivisatos, and P. G. Schultz, *Angew. Chem. Int. Ed.* 38, 1808 (1999).
540. S. Mann, W. Shenton, M. Li, S. Connolly, and D. Fitzmaurice, *Adv. Mater.* 12, 147 (2000).
541. F. P. Zamborini, J. F. Hicks, and R. W. Murray, *J. Am. Chem. Soc.* 122, 4514 (2000).
542. J. P. Sumner, J. W. Aylott, E. Monson, and R. Kopelman, *Analyst* 127, 11 (2002).
543. H. A. Clark, M. Hoyer, M. A. Philbert, and R. Kopelman, *Anal. Chem.* 71, 4831 (1999).
544. H. A. Clark, R. Kopelman, R. Tjalkens, and M. A. Philbert, *Anal. Chem.* 71, 4837 (1999).
545. H. A. Clark, S. L. R. Barker, M. Brasuel, M. T. Miller, E. Monson, S. Parus, Z. Y. Shi, A. Song, B. Thorsrud, R. Kopelman, A. Ade, W. Meixner, B. Athey, M. Hoyer, D. Hill, R. Lightle, and M. A. Philbert, *Sens. Actuator B-Chem.* 51, 12 (1998).
546. D. J. Maxwell, J. R. Taylor, and S. M. Nie, *J. Am. Chem. Soc.* 124, 9606 (2002).
547. J. J. Storhoff, R. Elghanian, R. C. Mucic, C. A. Mirkin, and R. L. Letsinger, *J. Am. Chem. Soc.* 120, 1959 (1998).
548. H. W. Kroto, J. R. Heath, S. C. O'Brien, R. F. Curl, and R. E. Smalley, *Nature* 318, 162 (1985).
549. S. Iijima, *Nature* 354, 56 (1991).
550. S. Subramoney, *Ad. Mater.* 10, 1157 (1998).
551. V. P. Dravid, X. Lin, Y. Wang, X. K. Wang, A. Yee, J. B. Ketterson, and R. H. P. Chang, *Science* 259, 1601 (1993).
552. J. Berholc, D. Brenner, M. Buongiorno Nardelli, V. Meunier, and C. Roland, *Annu. Rev. Mater. Res.* 32, 347 (2002).
553. J. Liu, M. J. Casavant, M. Cox, D. A. Walters, P. Boul, W. Lu, A. J. Rimberg, K. A. Smith, D. T. Colbert, and R. E. Smalley, *Chem. Phys. Lett.* 303, 125 (1999).
554. Y. Huang, X. F. Duan, Y. Cui, L. J. Lauhon, K. H. Kim, and C. M. Lieber, *Science* 294, 1313 (2001).
555. Y. Huang, X. F. Duan, Q. Q. Wei, and C. M. Lieber, *Science* 291, 630 (2001).
556. P. Diao, Z. F. Liu, B. Wu, X. Nan, J. Zhang, and Z. Wei, *Chem. Phys. Chem.* 3, 898 (2002).
557. J. J. Gooding, R. Wibowo, J. Liu, W. Yang, D. Lusic, S. Orbons, F. J. Mearns, J. G. Shapter and D. B. Hibbert, *J. Am. Chem. Soc.* 125, 9006 (2003).
558. J. M. Fréchet, *Science* 263, 1710 (1994).
559. D. A. Tomalia, A. M. Naylor, and W. A. Goddard III, *Angew. Chem. Int. Ed.* 29, 138 (1990).
560. J. Issberner, R. Moors, and F. Voegtle, *Angew. Chem. Int. Ed.* 33, 2413 (1994).
561. D. A. Tomalia and H. D. Durst, *Top. Curr. Chem.* 165, 193 (1993).
562. H. Tokuhisa, M. Q. Zhao, L. A. Baker, V. T. Phan, D. L. Dermody, M. E. Garcia, R. F. Pez, R. M. Crooks, and T. M. Mayer, *J. Am. Chem. Soc.* 120, 4492 (1998).

563. J. W. J. Knapen, A. W. van der Made, J. C. D. Wilde, W. van Leeuwen, P. Wijkens, D. M. Groves, and G. van Koten, *Nature* 372, 659 (1994).
564. J. F. G. A. Jansen, E. M. M. de Brabander-van den Berg, and E. M. Meijer, *Science* 266, 1226 (1994).
565. M. Wells and R. M. Crooks, *J. Am. Chem. Soc.* 118, 3988 (1996).
566. H. Tokuhisa and R. M. Crooks, *Langmuir* 13, 5608 (1997).
567. J. Kukoska-Latallo, A. N. Bielinska, J. Johnson, R. Spindler, D. A. Tomalia, and J. R. Baker, Jr., *Proc. Nat. Acad. Sci. U.S.A.* 93, 4897 (1996).
568. M. Q. Zhao, H. Tokuhisa, and R. M. Crooks, *Angew. Chem.-Int. Edit.* 36, 2596 (1997).
569. V. Chechik and R. M. Crooks, *Langmuir* 15, 6364 (1999).
570. A. Friggeri, H. J. van Manen, T. Auletta, X.-M. Li, S. Zapotoczny, H. Schönher, G. J. Vancso, J. Huskens, F. C. J. M. van Veggel, and D. N. Reinhoudt, *J. Am. Chem. Soc.* 123, 6388 (2001).
571. C. B. Gorman, R. L. Miller, K. Y. Chen, A. R. Bishop, R. T. Haasch, and R. G. Nuzzo, *Langmuir* 14, 3312 (1998).
572. L. Zhang, F. W. Huo, Z. Q. Wang, L. X. Wu, X. Zhang, S. Hop-pener, L. F. Chi, H. Fuchs, J. W. Zhao, L. Niu, and S. J. Dong, *Langmuir* 16, 3813 (2000).
573. A. Friggeri, H. Schonherr, H. J. van Manen, B. H. Huisman, G. J. Vancso, J. Huskens, F. van Veggel, and D. N. Reinhoudt, *Langmuir* 16, 7757 (2000).
574. F. Effenberger, G. Gotz, B. Bidlingmaier, and M. Wezstein, *Angew. Chem. Int. Ed.* 37, 2462 (1998).

Analytical Characterization of Single Wall Carbon Nanotubes

Sivaram Arepalli, Pasha Nikolaev, Olga Gorelik

G. B. Tech./NASA-Johnson Space Center, Houston, Texas, USA

CONTENTS

1. Introduction
2. Analytical Techniques
 - Glossary
 - References

1. INTRODUCTION

During the last few years, interest in the study of single wall carbon nanotubes (SWCNTs or SWNTs) has grown exponentially because of their extraordinary properties [1, 2]. Some of the possible applications include flat panel displays, superstrong fibers and panels, multifunctional materials, nanoelectronics and sensors, supercapacitors, and fuel cells [3–5]. The large aspect ratio (nanometer diameter and several micrometer length) adds tremendous appeal to the SWCNTs as reinforcing materials for composites. Also, the large surface areas available from individual tubes provide possible means for energy storage. The anisotropic nature allows enhanced properties along the length of the tube such as directed thermal energy transfer. The applications depend heavily on the diameter, length, chirality, and bundle size as well as on the amount and extent of impurities existing in the nanotube material. These impurities are inherent to the production process and change in character with the processing and purification steps used.

The carbon nanotubes can be produced by a variety of techniques including carbon arc, laser ablation, chemical vapor deposition, and carbon monoxide disproportionation [6–9] using metal catalysts. In addition to SWCNTs, the produced product may contain multiwall tubes with inferior properties. The as-produced material is known to be inhomogeneous and contain a variety of impurities including graphite coated metal clusters, amorphous carbon, and other carbon compounds including fullerenes. The type and extent of these impurities change with the production method used. The production process also influences the length, diameter,

chirality, and surface moiety of the nanotubes (and nanotube bundles). It is indeed a challenge to determine all these impurity levels and characterize this material to a reasonable extent using the available analytical techniques. Also, the purification processes used to improve the percentage of SWCNTs in the material tend to alter the nanotubes by adding functional groups, damaging and cutting the tubes [10–13]. For some applications, it is indeed necessary to add functional groups at specific locations and therefore requires additional sophisticated analytical tools for characterization.

The SWCNT material seems to behave similar to carbon soot and may require additional precautions while handling because of its submicrometer size dimensions. It is therefore necessary to assess all possible hazards involved in handling and address the toxicological effects of the nanotubes [14].

This chapter addresses the analytical tools and techniques used to characterize the SWCNT material. Most of the aforementioned aspects are covered in general and the reader may like to follow the cited references for further detailed information. Some of these techniques which are qualitative in nature can be used for quantitative estimates by using calibrated standards and procedures. Each technique is described briefly and its application to SWCNTs is shown by providing one or two measurements as examples.

2. ANALYTICAL TECHNIQUES

The analytical techniques are divided into subgroups based on general operating principles. The first group is based on electron microscopy and encompasses techniques such as scanning electron microscopy (SEM), transmission electron microscopy (TEM), scanning tunneling microscopy (STM), and atomic force microscopy (AFM). The second group is related to spectrophotometry (absorption and emission) in the ultraviolet-visible-infrared (UV-VIS-IR) regions and includes Raman methods. The third group is focused on mass spectrometry [gas chromatography (GC) and time-of-flight (TOF) mass spectrometry (MS)] and chromatography [high pressure liquid chromatography (HPLC)] that use size-selection processes to characterize the material. The fourth

group is based on X-ray excitations such as X-ray diffraction (XRD), X-ray photoelectron spectroscopy (XPS), and extended X-ray absorption fine structure (EXAFS). Magnetic resonance methods such as electron paramagnetic resonance (EPR) and nuclear magnetic resonance (NMR) constitute the fifth group. The sixth group covers the thermal methods such as thermogravimetric analysis (TGA), temperature programmed oxidation (TPO), and differential scanning calorimetry (DSC).

2.1. Electron Microscopy

2.1.1. TEM

Transmission electron microscopy remains one of the best tools to characterize nanotubes and related nanostructures. Historically, both multiwall [15] and single-wall [16] carbon nanotubes were discovered on the TEM micrographs of the cathode deposit and soot formed in the arc-discharge fullerene generator. Figures 1 and 2 show high resolution TEM images of single wall carbon nanotubes produced by two different processes. A number of other nanostructured carbons, like bucky peapods [17] and carbon nanohorns [18], were also discovered and studied in TEM.

TEM works on the same principle as optical microscope, except photons (typical wavelength 200–800 nm) are replaced with electrons (typical wavelength 0.0025 nm at 200 kV accelerating voltage). Numerical aperture of TEM is much smaller than that in the optical microscope (35° compared to $\sim 70^\circ$). Electron beam optics is essentially free of chromatic aberrations, while spherical aberrations are severe. Theoretical resolution is determined by electron wavelength and numerical aperture and is very high, while in practice it does not exceed ~ 0.3 nm and is limited by spherical and diffraction aberrations.

Imaging in TEM is strongly dependent on the type of the electron source. There are three common types: tungsten filament, lanthanum hexaboride (LaB_6) crystal, and field-emission gun (FEG). Tungsten filament creates a source of relatively large size, low brightness, and low coherence and is hardly used anymore. A LaB_6 source is the most common

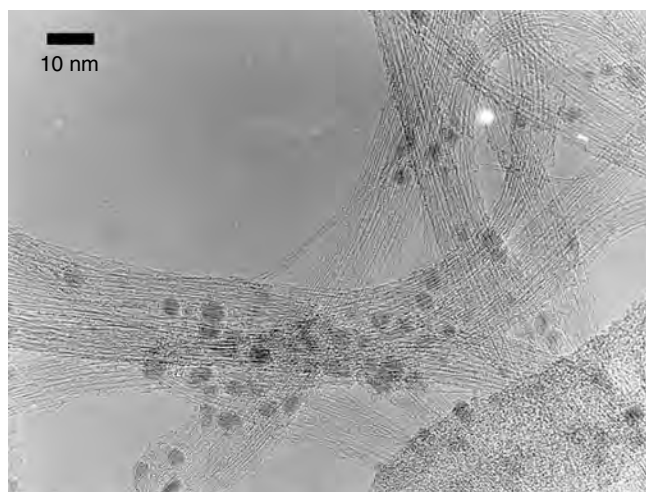


Figure 1. High-resolution TEM image of a SWCNT produced by the HiPco process.

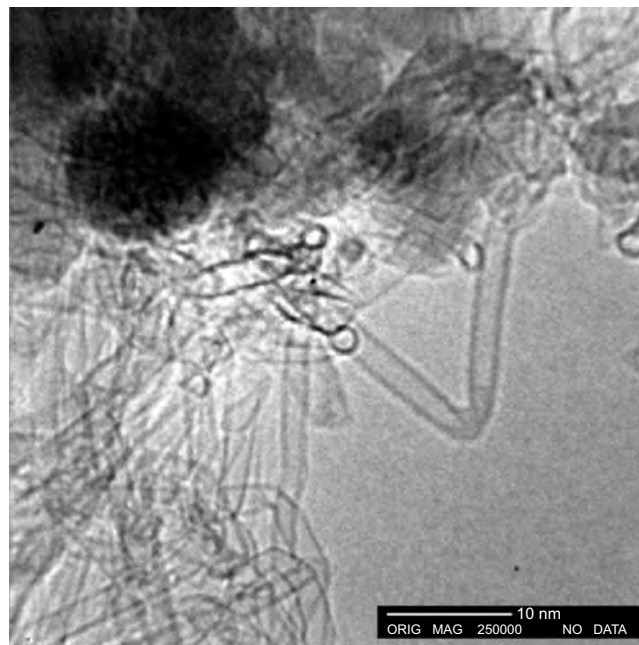


Figure 2. High-resolution TEM image of single wall carbon nanotubes produced from carbon monoxide feedstock using Fe–Mo catalyst supported on silica particles.

these days and provides much better coherence, brightness, and size while still being a relatively inexpensive option. There are few field-emission-type TEMs available, which are significantly more expensive than other options. Source size and beam coherence in FEG systems are excellent, which significantly improves resolution. But brightness of the FEG source exceeds that of LaB_6 by 1–2 orders of magnitude, which creates much higher fluence of the electron beam illuminating the sample. Therefore a TEM equipped with a FEG source quickly produces significant e-beam damage of the nanotube samples. The authors have observed nanotubes literally falling apart in a matter of minutes. FEG TEM has to be used with the understanding that nanotubes can be damaged very quickly.

Another important factor in TEM imaging is the accelerating voltage. The common range is 100–200 kV, but modern TEMs can achieve up to 800 kV–1 MV. In theory higher accelerating voltage allows one to achieve higher resolution, since electron wavelength is smaller. In practice, however, TEM imaging is always a trade-off between resolution and contrast. Carbon atoms are relatively light and do not scatter high-energy electrons well. Scattering cross-section decreases quickly at higher accelerating voltages, and image contrast becomes very small. Defocusing can be used to increase contrast, but then resolution suffers. It is believed that accelerating voltage in the range of 100–160 kV is optimal for imaging nanotube samples.

The most common way to prepare TEM specimens is to disperse nanotubes in organic solvent (alcohol, acetone, etc.) and then place a droplet of suspension on the TEM grid lying on tissue paper. The solvent is adsorbed by the tissue, and the nanotubes lay flat on the grid and coat it more or less uniformly. The thickness of the carbon film on the commercially available grids is around 50–100 nm. This means that individual nanotubes and small bundles (1–10 nm in

thickness) cannot be imaged effectively sitting directly on the support film. It is necessary to use “holey” or “lacey” grids, with plenty of holes in the support film, in order to image nanotubes bridging the holes.

There are more exotic ways to prepare TEM specimens. For example, TEM can be used to measure nanotube diameters. But nanotubes exist almost exclusively as bundles, which makes it nearly impossible to distinguish walls of each nanotube in the bundle lying flat on the support film in order to measure the diameter of each nanotube. Moreover, if a triangular lattice of a well-ordered nanorope is positioned a certain way with respect to the electron beam, line spacing observed on the TEM image represent either $\frac{\sqrt{3}}{2}(d+a)$ or $\frac{1}{2}(d+a)$, where d is nanotube diameter and a is van der Waals interwall spacing in the nanorope [19]. Figure 3 shows the same nanorope rotated 0 and 60 degrees around its axis, and interline spacing follows this expression. However, if the bundle loops through the focal plane of the TEM so that nanotubes are parallel to the electron beam, one can image the cross-section of the bundle with nanotubes represented as circles (Fig. 4). It is easy to determine the diameters of a large number of nanotubes on such an image. There is a simple technique to prepare a specimen with a large number of cross-sectional views of SWNT bundles, which works well on dry and fluffy as-made nanotubes. One can place a small chunk of dry nanotube material on a TEM grid and wet it with a droplet of alcohol. The nanotube chunk becomes compressed by capillary forces and sticks to the support film. In the process SWNT bundles at the chunk extremities fold onto themselves and create loops, most of which are in-plane or at some angle to the e-beam. A small fraction of the loops, however, is parallel to the e-beam, which creates the aforementioned cross-sectional images. To make measurements of the diameters of a large number of circles easier, Nikoalev has written a simple program [20] which allows one to superimpose a circle over a nanotube image, adjust its size and position to achieve the best fit, and then record its diameter. About 200–300 circles can be accurately measured in an hour (Fig. 5).

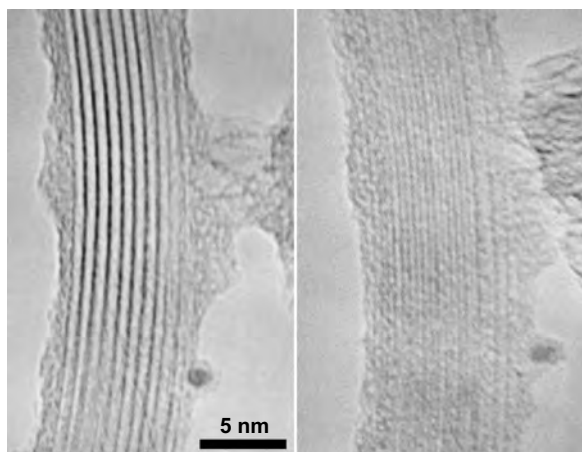


Figure 3. TEM images of crystalline SWCNT nanorope rotated around its axis by 0° and 60°. Interline spacing changes according to the particular view of the triangular lattice of the nanorope. Reprinted with permission from [7] A. Thess et al., *Science* 273, 483 (1996). © 1996, American Association for Advancement of Science.

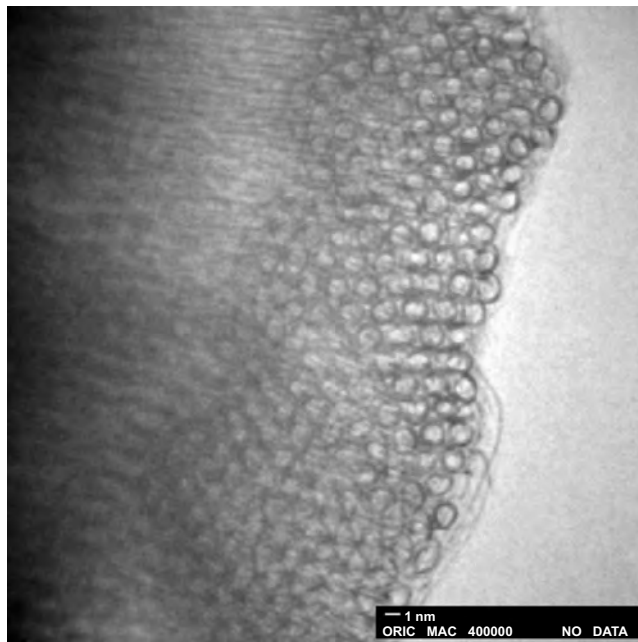


Figure 4. Cross-sectional view of SWCNT nanorope. Reprinted with permission from [63], A. G. Rinzler et al., *Appl. Phys. A* 67, 29 (1998). © 1998, Springer-Verlag.

Amorphous carbon is a major impurity in the SWNT. It is not well understood, and there is no single analytical technique which can reliably discriminate between nanotubes and other forms of carbon. TEM observations are often used to estimate the purity of SWNT materials, although such estimates are very subjective. TEM is also frequently used to determine dimensions of various nanostructures.

2.1.2. SEM

Scanning electron microscopy is another common tool used to study nanotubes and related nanostructures (Fig. 6). Modern SEMs utilize the same electron sources as TEMs, tungsten, LaB₆, and field emission guns, FEG providing the

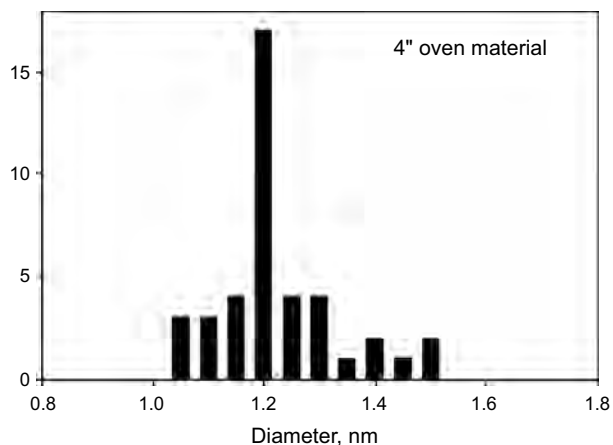


Figure 5. Diameter distribution of SWCNT shown in Figure 4, measured from TEM micrographs. Reprinted with permission from [63], A. G. Rinzler et al., *Appl. Phys. A* 67, 29 (1998). © 1998, Springer-Verlag.

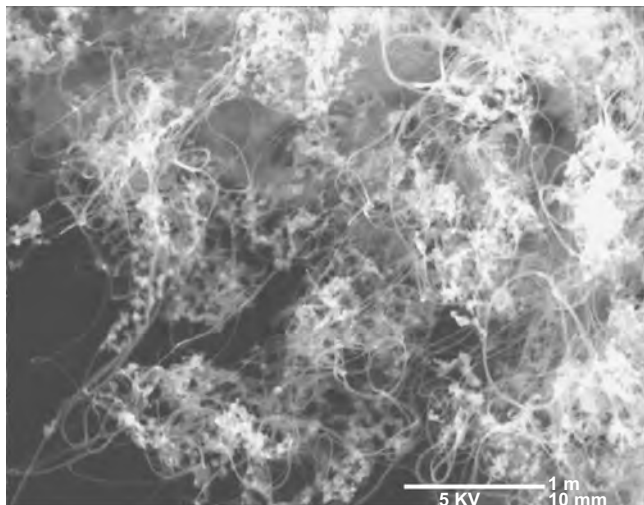


Figure 6. SEM image of unpurified dry SWCNT.

best brightness and coherence. SEMs detect either backscattered or secondary electrons. There are no reports on using backscattered electron detectors in nanotube imaging, so all discussion will concentrate on secondary electrons (although backscattered electrons can be used to image nanocomposites, i.e., nanotubes embedded in polymers). Resolution of SEM depends on the beam diameter, which is usually 3–5 nm, but is not determined by it. This happens because electrons penetrate into the surface of the specimen, and observed secondary electrons are emitted from the pear-shaped volume within the sample which can extend up to a micrometer below the surface. This means that generally SEM cannot detect individual nanotubes, but only bundles of at least 3–5 nm in diameter. Sample preparation for SEM is fairly simple—a small piece of nanotube material is mounted on the double-sided carbon tape or glued to the substrate with silver paint, in order to assure good electrical contact. Nanotube samples are generally conductive enough to prevent charge buildup, but in rare cases it is necessary to coat samples with a thin layer of platinum to improve conductivity. The most common use of SEM is to estimate the purity of nanotube samples, although, just like in TEM, such estimates are very subjective.

2.1.3. Energy-Dispersive Spectroscopy

EDS stands for energy-dispersive spectroscopy. TEMs and SEMs are frequently equipped with EDS detectors, which are able to detect characteristic X-rays generated by various elements when irradiated with high-energy electrons. The EDS spectra indicate the relative amounts of metals and other noncarbon elements in SWCNT material (Figs. 7 and 8). While EDS is good in determining relative amounts of heavy elements, it is notoriously unreliable in determining carbon concentration because of hydrocarbon contamination present in all SEMs and TEMs, and poor sensitivity of EDS detectors in the low-energy end of spectrum, where the carbon peak is found. In addition, EDS spectra taken in TEM usually show large copper peaks coming from copper TEM grids and apertures in the column, and TEM grids are frequently contaminated with silicone grease during manufacturing, producing a weak silicon signal. While the former

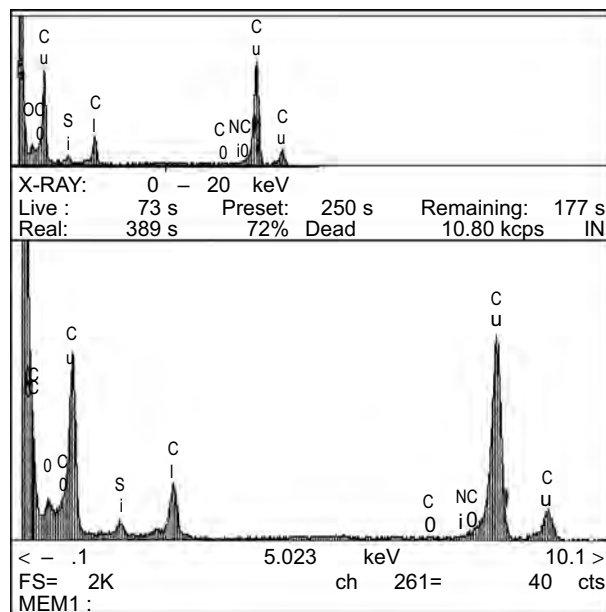


Figure 7. EDS spectrum of purified HiPco SWCNT obtained in TEM. Iron particles have been removed. The large Cu signal comes from the TEM grid and apertures. A small Si peak can appear due to impurities in SWCNTs as well as silicone grease contaminating the TEM grid.

is largely irrelevant since nanotubes do not normally have any copper in them, the latter is a problem, since silicon is frequently present in nanotube samples. EDS utilizes the same samples as TEM and SEM; therefore we refer reader to Sections 2.1.1 and 2.1.2 for sample preparation.

2.1.4. Microprobe

An electron beam microprobe operates on the same principle as EDS, except the beam current is much higher and X-ray detectors are different. Microprobe instruments are

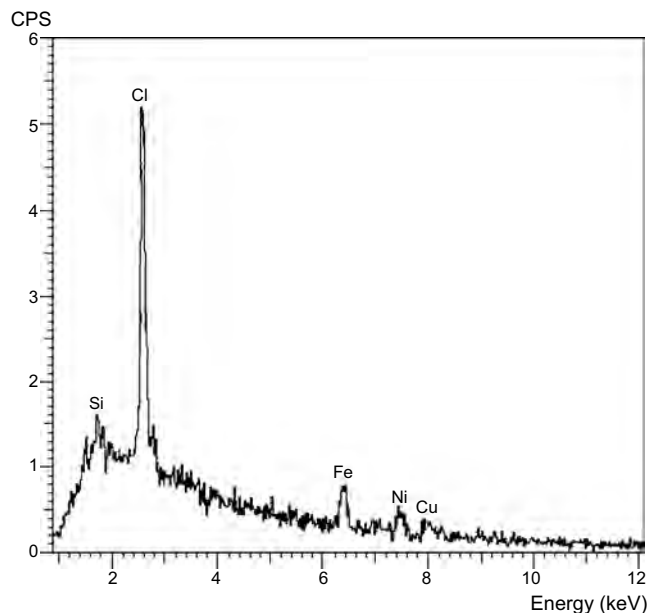


Figure 8. EDS spectrum of the same purified HiPco SWCNT as in Figure 7, obtained in SEM.

better equipped to produce elemental maps with larger lateral span and better resolution. Sample preparation for microprobe measurements is similar to SEM sample preparation, described in the relevant section. The microprobe is usually calibrated before each use using standard samples. Accuracy of the microprobe measurements is sensitive to the precise focusing of the electron beam. Therefore, the sample surface has to be very smooth and level in order to produce meaningful elemental maps, which is rarely achieved with buckypaper-type samples. Concentration measurements performed with a stationary beam are therefore more accurate, but sample composition in one spot may not be representative of the whole specimen due to inhomogeneity of nanotube material. Figure 9 shows the elemental maps of a target material (graphite with 1% Co and Ni) used for production of nanotubes by laser ablation. The microprobe suffers from the same hydrocarbon contamination problems as EDS, and measured carbon concentration is prone to overestimation. The microprobe has been used in the past to measure the amount of fluorine in fluorinated nanotubes [21], but for the reasons mentioned and in the absence of independent verification, the accuracy of such measurements remains questionable.

2.1.5. AFM

Atomic force microscopy is used to determine the topography of flat samples. A sharp tip is scanned over the sample surface, and either tip deflection or change in the amplitude of the tip oscillation serves as feedback in the vertical direction. Accuracy of the height measurement is tremendous, approaching 0.01 nm. Lateral resolution, on the other hand, is determined by the tip diameter and is typically 15–30 nm. Nanotubes have to be deposited onto a suitable smooth substrate for AFM imaging (Fig. 10). The easiest way is

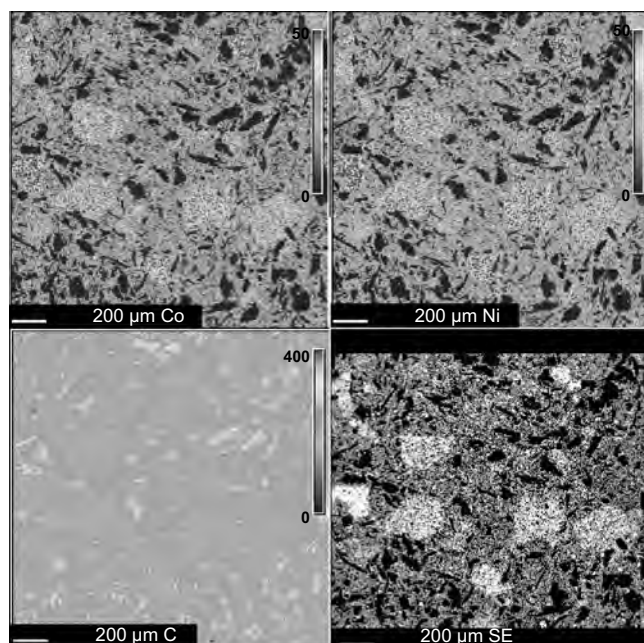


Figure 9. E-beam microprobe elemental maps and secondary electron image of a polished surface of carbon/Co/Ni target used for SWCNT production in a laser oven.

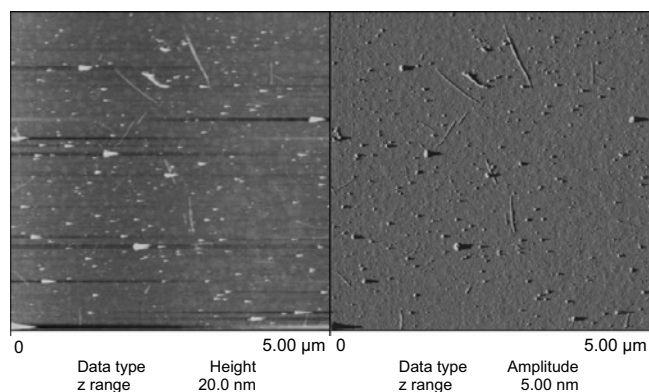


Figure 10. Tapping mode AFM image of a SWCNT wrapped in PVP (polyvinyl pyrrolidone) and deposited on amine-functionalized silicon oxide surface.

to disperse nanotubes in organic solvent or in water with surfactant, and spin-coat or dry on silicon, mica, graphite (HOPG, or highly oriented pyrolytic graphite), or even glass coverslip. AFM is often used to assess how well nanotubes are dispersed in the solvent, so it could be important to preserve the state of dispersion as nanotubes are transferred to the substrate and dried. For example, nanotubes can be electrodeposited onto a HOPG surface in the DMF suspension [22]. Another approach is to coat silicon surface with a positively charged amine-terminated self-assembled monolayer and dip such substrate in nanotubes dispersed in water in the presence of sodium dodecyl sulphate (SDS), an anionic surfactant giving nanotubes a net negative charge [23]. Other surfactants or polymers [24] can also be used. Arepalli et al. have reported nanotubes being deposited onto polished fused silica substrates directly in the laser oven, as they are produced, bypassing the solvents altogether [25]. Figure 11 shows tapping mode AFM image of nanotubes deposited onto quartz substrate this way. AFM is often used to measure diameters and lengths of nanotubes and nanoropes (nanotube bundles). It is important to mention that because of the poor lateral resolution AFM can only measure height, rather than diameter, of a nanostructure. Therefore it is impossible to distinguish one individual nanotube

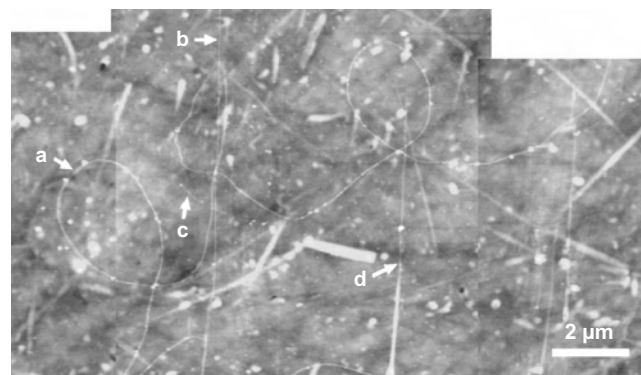


Figure 11. Tapping mode AFM image of a SWCNT deposited on a fused silica substrate directly in the laser oven. Reprinted with permission from [25], S. Arepalli et al., *Appl. Phys. Lett.* 78, 1610 (2001). © 2001, American Institute of Physics.

and a small bundle of nanotubes lying flat on the substrate, having the same height. Nanotube length measurement is straightforward for short tubes not exceeding a few micrometer in length. But if nanotubes are longer and exist in bundles, it becomes impossible to find both ends of a particular nanotube, and one can only estimate nanotube lengths.

2.1.6. STM

Scanning tunneling microscopy is similar to AFM, except that tunneling current between the sample and the sharp metal tip is utilized as a feedback signal. Therefore STM samples have to conduct electric current, which limits substrates to HOPG, heavily doped silicon, and metals. Otherwise the sample preparation is similar to that of AFM samples. The tunneling current is limited to a few atoms on the tip closest to the sample, since its intensity drops exponentially with the distance from the sample. Because of that, lateral resolution of STM is much higher than in AFM and allows one to achieve atomic resolution, which usually calls for measurements in high vacuum and at low temperatures. While AFM probes actual topography of the specimen, STM probes local density of electronic states in the sample, which varies with the distance from the Fermi level. Therefore SEM images taken with different bias between sample and tip are different. STM also allows scanning tunneling spectroscopy measurements, in which the tip is kept stationary above the sample, and bias is varied in order to probe the density of states above and below the Fermi level. Such measurements, combined with helicity measurements from the atomically resolved images [26], have provided the first proof of the relationship between nanotube geometry (helicity and diameter) and electronic structure (Fig. 12).

2.2. Spectroscopy

2.2.1. UV-VIS-NIR Absorption and Emission

The age-old spectrophotometry is used to measure absorption and transmission of SWCNT samples in the solution phase as well as thin films. The measurements are done a double beam apparatus by comparing the transmission with a reference solvent [27–29] in the wavelength range of 200 to 2000 nm. Figure 13 shows changes of the optical spectra with oxidation and annealing of single wall carbon nanotubes. Recently, excitation spectra and fluorescence of individual SWCNTs (Fig. 14) were also recorded [30]. This measurement is used to identify the chirality and the “ n, m ” designation of the semiconducting tubes in the raw HiPco material (Fig. 15). The procedure involves extensive sonication of the material in a surfactant (SDS) followed by very high level centrifuging (200,000 g) which yields very short (couple of hundred nm long) individual tubes wrapped with surfactant. The energy levels responsible for the sharp absorption and fluorescence features arise from “van Hove” singularities in the electronic density of states [31]. Metallic tubes can be monitored in the absorption spectrum only and no fluorescence can be observed because the conduction band provides a way for rapid nonradiative relaxation. The features from the semiconducting tubes can be used to determine the primary (S11), secondary (S22), as well as tertiary (S33) transitions. Fluorescence is only observed from individual

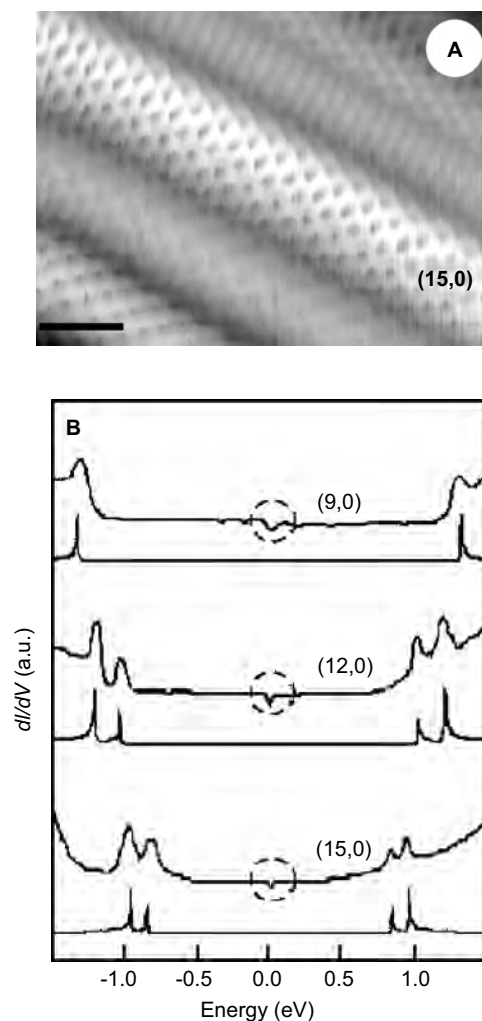


Figure 12. (A) Typical atomically resolved STM image of a (15, 0) SWCNT. The image was recorded in the constant-current mode with bias voltage of 0.65 V and current 0.15 nA. Scale bar, 1 nm. (B) Tunneling conductance data, dI/dV , for different zigzag SWCNTs, with corresponding calculated densities of state shown below each experimental curve. Reprinted with permission from [81], M. Ouyang et al., *Science* 292, 702 (2001). © 2001, American Association for Advancement of Science.

tubes and disappears when bundling takes place [30]. However, absorption can still be noticed and it may be possible to determine the bundle size from the width of the spectral features.

The absorption spectra of the SWCNTs can also be used to determine the stability of nanotube suspensions. If the nanotubes tend to bundle up, flocculate, and fall out of the solution, the absorption decreases and this change in the absorptivity as function of time is used to assess the dispersion stability [32].

Atomic Absorption and Inductively Coupled Plasma

These two techniques are used for qualitative as well as quantitative estimation of metals in materials. Atomic absorption (AA) uses selective absorption of “fingerprint” spectral lines either from a broadband source or from sharp hollow-cathode lamp sources that provide very sharp atomic

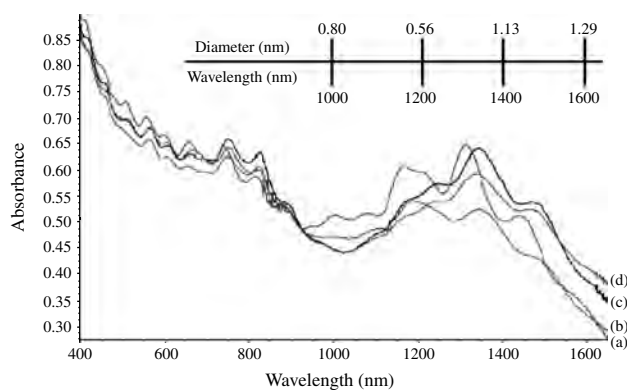


Figure 13. UV-visible-near IR absorption spectra of SWCNT: (a) raw HiPco tubes, (b) after 225 °C oxidation step, (c) after 325 °C oxidation step, (d) after 425 °C oxidation step. Each oxidation step is completed by HCl sonication, vacuum-drying, and annealing at 800 °C in Ar for 1 hour. Spectra have been normalized at 925 nm and scale bar shows adjusted tube diameter. Reprinted with permission from [11], I. W. Chiang et al., *J. Phys. Chem. B* 105, 8297 (2001). © 2001, American Chemical Society.

line radiation emission. Hollow cathode lamps and multi-detector arrays are used with spectrometers operating in “echelle” modes to provide simultaneous detection of several elements with high sensitivity [33]. High temperature furnaces are used to vaporize the material with a short heat pulse and thereby provide gas phase atoms for AA study. Current AA methods extend from VUV to IR wavelength regions and use laser sources to provide atomic radiations. This is especially true in the IR where solid state diode lasers are used with very high resolution and increased sensitivity.

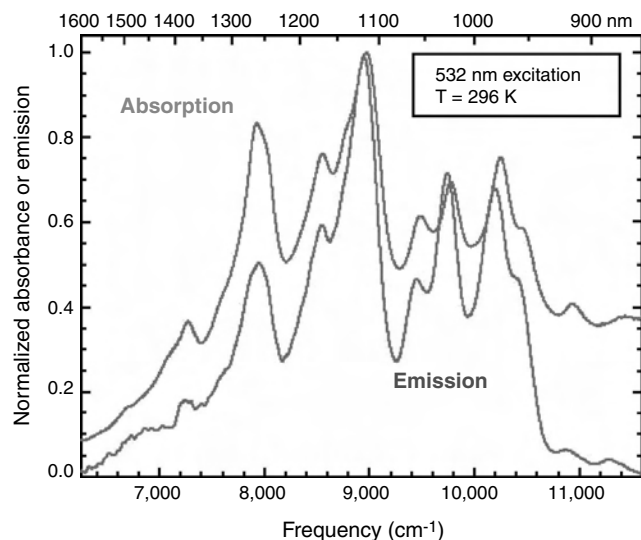


Figure 14. Emission spectrum (red) of individual fullerene nanotubes suspended in SDS micelles in D₂O excited by 8 ns, 532 nm laser pulses, overlaid with the absorption spectrum (blue) of the sample in this region of first van Hove bandgap transitions. The detailed correspondence of absorption and emission features indicates that the emission is band gap photoluminescence from a variety of semiconducting nanotube structures. Reprinted with permission from [30a], M. J. O’Connell et al., *Science* 297, 593 (2002). © 2002, American Association for Advancement of Science.

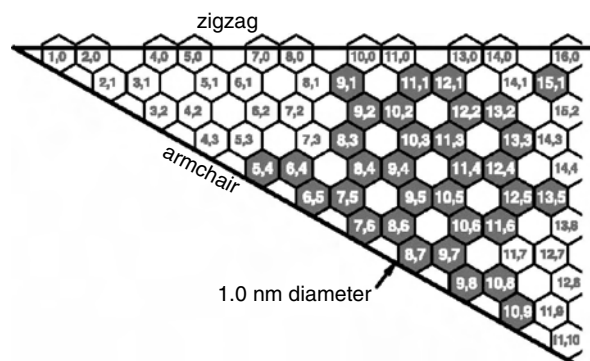


Figure 15. Results from the deduced spectral assignment. Observed nanotube structures marked as green hexagons with white (n, m) labels on a graphene lattice. Other structures have blue or red labels for $(n - m) \bmod 3 = 1$ or 2 , respectively. Reprinted with permission from [30b], S. M. Bachilo et al., *Science* 298, 2361 (2002). © 2002, American Association for Advancement of Science.

The inductively coupled plasma (ICP) technique involves injecting the material as a spray into a plasma torch which vaporizes the material. This process pumps the atoms to excited states which emit “fingerprint” spectral lines and can be used for quantitative elemental analysis of the material. This technique coupled with a mass spectrometer is useful for a complete elemental analysis for even organic compounds including polymers.

Both of these techniques have been used to monitor the metal contents in SWCNT material [34]. It is to be understood that metals encapsulated in graphite may be difficult to detect by ICP and the quantification of the metal content determined by this method may be underestimated.

2.2.2. IR Absorption and Emission

The absorption and emission in the infrared region (2 to 20 micrometer) arise from vibrational modes of the molecules constituting the material. The spectra arising from vibrational energy of the molecular bonds such as C—C, C=C, C—H, C—H₂, CH₃, C—F, C—N, O—H, N—H, etc. are commonly used as “fingerprints” of the material. In principle, the Kramer–Kronig relationship can be used to deduce the dielectric function of the material from the IR spectrum [35]. Data collection in the IR region normally done in double beam spectrometers can be done faster with fourier transform spectrometers and the capabilities are easily extended to very small solid samples using accessories. The IR region of the SWCNT is very very weak because of the low absorption cross-section of the carbon nanotubes (Fig. 16). In the recent work on SWCNT films and suspensions IR is used to monitor the functional groups attached to the SWCNTs (Fig. 17) as well as the effect of surfactants [35–38]. The IR spectrum is also used to analyze the condensable gases that are released when the material is heated (for example in conjunction with TGA [39]).

2.2.3. Raman

Raman spectroscopy is a powerful spectroscopic tool in providing “fingerprint” spectra of the molecular vibrational modes of the material [40]. The Raman spectra can be obtained in any wavelength region using different laser

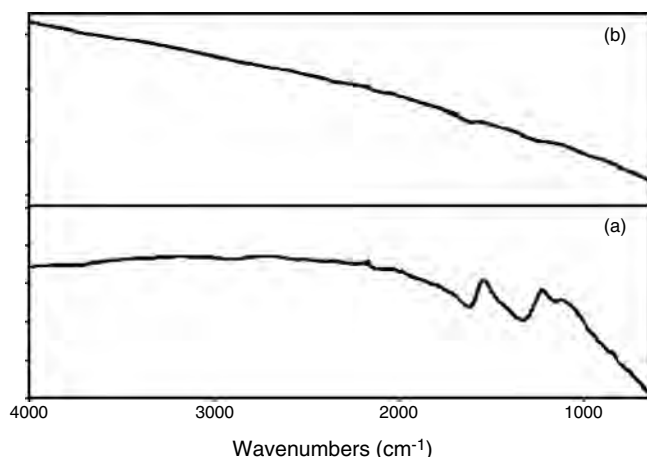


Figure 16. ATR-IR spectra of the SWCNT. (A) SWCNT fluorinated to $\sim C_3F$ stoichiometry. (B) Cut SWCNT. Reprinted with permission from [39b], Z. Gu et al., *Nano Lett.* 2, 1009 (2002). © 2002, American Chemical Society.

wavelengths. The recent advances that include FT Raman and confocal micro-Raman provide rapid data acquisition of even micrometer size materials in addition to the normal solid, liquid, and gas phase studies. The Raman spectra of SWCNTs can be separated as three distinctive regions (Fig. 18), one in the small wavenumber region called radial breathing mode (RBM), the second in the intermediate wavenumber region called transverse mode (TM), and the third at higher wavenumber regions emanating from harmonics and combinations of these two fundamental modes [41, 42]. The RBM modes are resonantly enhanced because of van Hove singularities and can be used to monitor the changes in the diameter distribution of SWCNTs [43]. The TM (*G*-Mode) region also shows spectral features that can be attributed to amorphous carbon (*D*-mode). The intensity ratio of the *D*-band and *G*-band ("*D/G*" ratio) is used by many researchers to determine the relative purity of the SWCNT material [44, 45]. However, it is noted that the

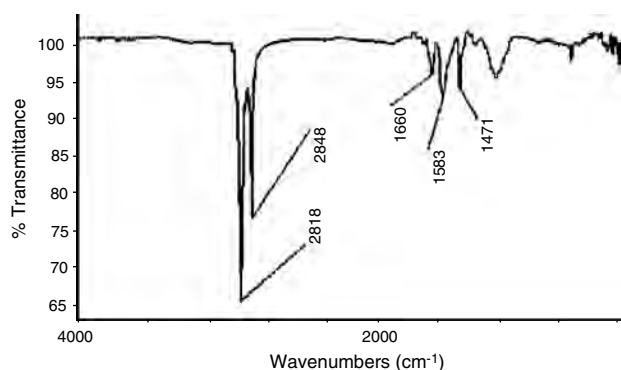


Figure 17. Mid-IR spectrum of functionalized SWCNT (thin film on quartz substrate). *s*-SWCNT-CONH(CH₂)₁₇CH₃ showed peaks at 2918 and 2845 [$\nu(C-H)$ stretch modes of the alkyl chain], 1660 [$\nu(C=O)$ stretch of the amide], 1583 [$\nu(C=C)$ stretch of the SWCNTs], and 1471 cm^{-1} [$\delta(C-H)$ bend of the alkyl chain]. Reprinted with permission from [82], M. A. Hamon et al., *Chem. Phys. Lett.* 347, 8 (2001). © 2001, Elsevier.

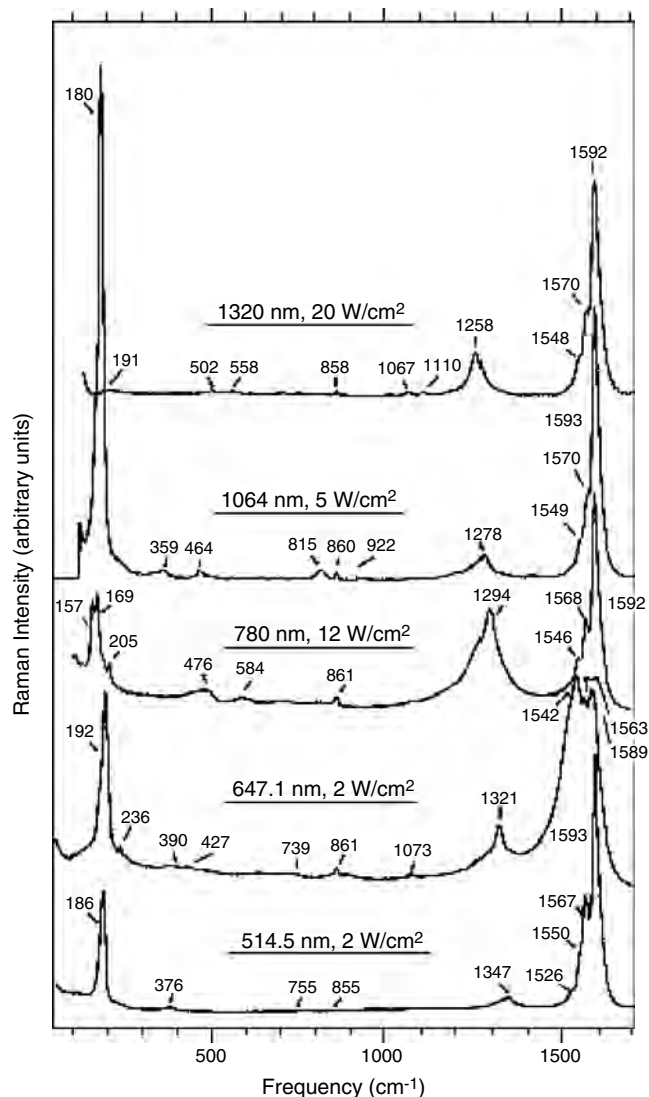


Figure 18. Room-temperature Raman spectra of purified SWCNTs excited at five different laser frequencies. The laser frequency and power density for each spectrum is indicated, as are the vibrational frequencies. Reprinted with permission from [41b], A. M. Rao et al., *Science* 275, 187 (1997). © 1997, American Association for Advancement of Science.

broad "*D*-band" becomes sharper with increasing "purification" and may therefore contain a SWCNT signature. This also occurs when the nanotubes are functionalized. Recent Raman work is focused on monitoring isolated SWCNTs (Fig. 19) and their chiralities [46]. Polarized Raman studies are used to assess the alignment of SWCNT fibers by changing the polarization of the laser with respect to the fiber axis [47, 48]. There is a preferential enhancement when the polarization axis is parallel to the nanotube axis and this "parallel to perpendicular" ratio is used to estimate the extent of alignment. Raman is also used to monitor strain (Fig. 20) in the SWCNT fibers and their load transfer to the composite matrices [49]. Temperature variation studies of Raman spectra are also used to assess the intrinsic nature and their dependence of the vibrational modes [50].

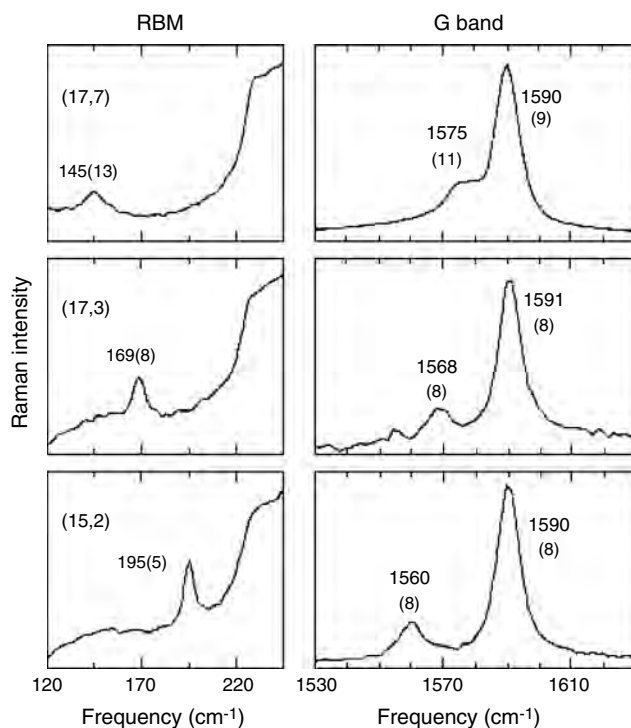


Figure 19. The RBM and G-band Raman spectra for three isolated semiconducting SWCNTs resonant with E_{laser} ; that is, $E_{\text{laser}} = 2.41$ eV for the spectrum in the top, labeled (17, 7), and $E_{\text{laser}} = 2.54$ eV for the other two spectra, labeled (17, 3) and (15, 2). The spectra are taken at three different spots on the substrate. The frequencies (linewidths) of the principal peaks for the RBM, ω_G^- and ω_G^+ features, are displayed in cm^{-1} . The shoulder observed to the right side of the RBM spectral feature comes from the Si substrate. Reprinted with permission from [83], A. Jorio et al., *Phys. Rev. B* 65, 155412 (2002). © 2001, American Physical Society.

2.2.4. Surface Characterization Tools

A variety of techniques are available [XPS, electron energy loss spectroscopy (EELS), etc.] to monitor the surface characterization of thin films consisting of SWCNTs. The techniques are all based on monitoring electrons or photons emitted from the material when excited with high energy electrons or X-rays. Photoelectron spectroscopy utilizes photoionization and energy-dispersive analysis of the emitted photoelectrons [51]. This is useful for the study of the composition as well as the electronic state of the surfaces. In X-ray photoelectron spectroscopy, the photon is absorbed by an atom in a molecule or solid, leading to ionization and the emission of a core (inner shell) electron. By contrast, ultraviolet photons can be used to probe valence levels.

The kinetic energy (KE) distribution of the emitted photoelectrons is measured using an electron energy analyzer and allows one to deduce the binding energy (BE) of the electron:

$$A + h\nu \longrightarrow A^+ + e^-$$

$$KE = h\nu - BE$$

The exact binding energy of an electron varies with the oxidation state as well as chemical environments giving rise to

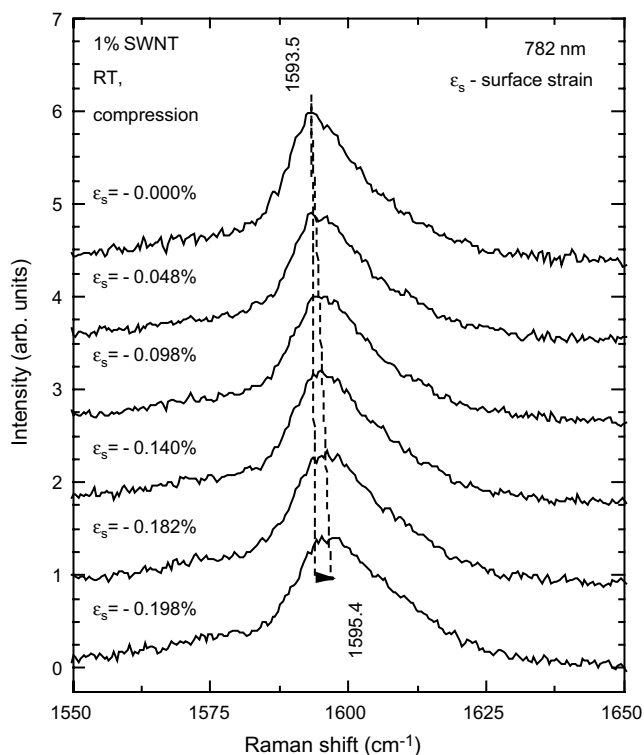


Figure 20. Raman spectra (782 nm excitation) of composite sample (1% SWCNT embedded in epoxy). G-mode frequency increases proportionally to the applied compressive stress (ϵ_s).

“chemical shifts.” An XPS spectrum of a nanotube film is shown in Figure 21.

Another technique that can be used to determine the atomic neighbors is extended X-ray absorption fine structure. The modulations noticed in the X-ray absorption spectrum arise from interference of the outgoing photon with the reflections from the neighboring atoms. This spectrum can then be used to determine the size and distances of the neighboring atoms from the atom of interest. Herrera et al. used EXAFS and X-ray absorption near edge structures

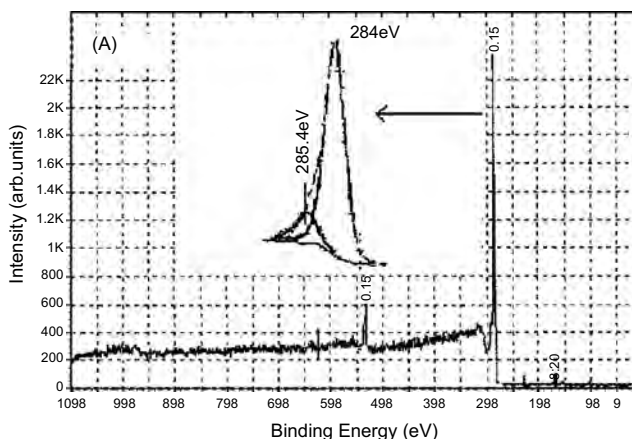


Figure 21. XPS of as-prepared SWCNT film. Reprinted with permission from [84], T. V. Sreekumar et al., *Chem. Mater.* 15, 175 (2003). © 2003, American Chemical Society.

(XANES) to monitor the production of SWCNTs under varying catalyst concentrations [52]. The XANES spectra are shown in Figure 22. The EELS technique has also been used to assess the valence state of carbon atoms [53].

2.3. Chromatography

Chromatographic based techniques are used for solubilized SWCNTs to separate different components and constituents of SWCNT material. Different mass fractions can be identified with mass spectrometry in conjunction with gas chromatography and matrix desorption. This information in turn can be utilized to establish the nature and extent of the derivatization of the SWCNT materials and matrices with SWCNTs. Early successes are achieved in “purification” of the SWCNT material by using HPLC columns [54]. Recently, HPLC has been used to separate the SWCNT tubes and ropes by their lengths [55].

2.3.1. GC MS and TOF MS

The identification and quantification of trace organic constituents of the SWCNT material extractable by water or any organic solvent are done by gas chromatographic methods. In gas chromatography, a mobile phase (a carrier gas such as nitrogen or helium) and a stationary phase (capillary column coating) are used to separate individual compounds. When the sample solution is introduced into the column, the organic compounds are vaporized and moved through the column by the carrier gas. They travel through the column at different rates, depending on differences in partition coefficients between the mobile and stationary phases. The electrolytic conductivity detector is used to monitor halocarbons and nitrogen containing compounds. The electron

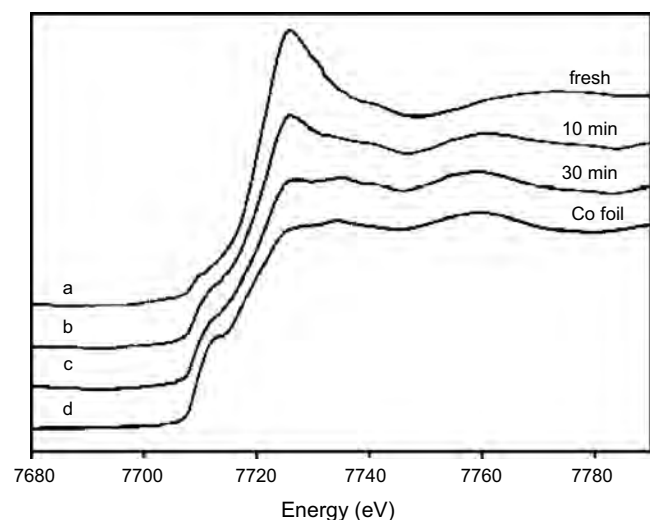


Figure 22. Near edge spectra XANES obtained at the K edge of Co ($E_0 = 7.709$ eV) on a fresh Co : Mo/SiO catalyst (Co : Mo = 1 : 2), pretreated in H_2 (500 °C) /He(700 °C), and after the growth of carbon nanotubes by decomposition of 50% CO/He at 700 °C for reaction periods of 10 and 30 min. The XANES of a Co foil is included for comparison. Reprinted with permission from [66], W. E. Alvarez et al., *Carbon* 39, 547 (2001). © 2001, Elsevier.

capture detector usually is used for the analysis of compounds that have high electron affinities such as halogens, peroxides, quinines, and nitro groups. The flame ionization detector is also widely used because of its high sensitivity to organic carbon-containing compounds. Mass analysis of the large fullerenes found in the SWCNT material is carried out using a time-of-flight mass spectrometric detector connected to a matrix assisted laser desorption/ionization (MALDI) system as shown in Figure 23 [56].

2.3.2. HPLC

This method is used for identification and quantification of trace organic constituents and soluble fullerenes extractable by organic solvents like toluene, dichlorobenzene, carbon disulfide, and others. High performance liquid chromatography is an analytical technique in which a liquid mobile phase transports a sample through a column containing a stationary phase. Selection of a suitable column is very crucial and the researchers used columns including Styragel HMW7, C_{18} , and Plgel Mixed-A columns. The interaction of the sample with the stationary phase selectively retains individual compounds and permits separation of sample components. Of special concern for HPLC is the masking of the absorbance region of the HPLC mobile phase and its additives. This may reduce the range and sensitivity of the detector to sample components. This test method is applied for the determination of monoaromatic, diaromatic, and polyaromatic hydrocarbon contents in toluene extracted solutions from raw nanotube material produced by arc, laser, or HiPco methods [57]. The total aromatic content in % m/m is calculated from the sum of the individual aromatic hydrocarbon types (Fig. 24). This test method is calibrated for distillates containing from 4 to 40% (m/m) monoaromatic hydrocarbons, 0 to 20% (m/m) diaromatic

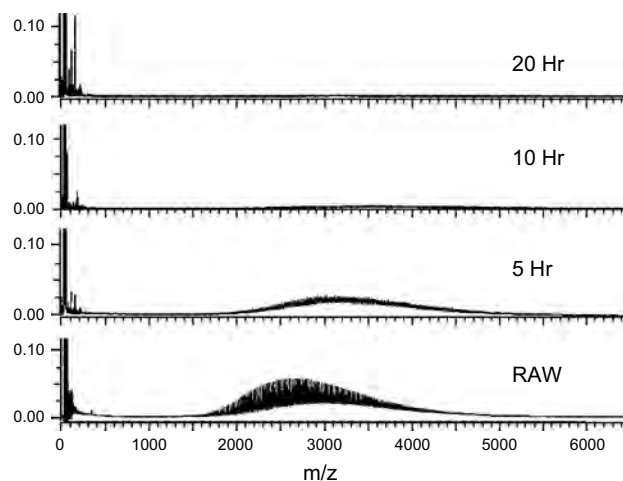


Figure 23. LDI-TOF mass spectral patterns recorded under identical conditions on HiPco raw samples soft baked for varying times. The raw sample showed a mass spectral span of 1800–4500 amu with the maximal intensity at 2600 amu. The masses were evenly separated at a spacing of 24 amu. Note that the mass number for maximal intensity has shifted to higher mass numbers in the oxidized samples indicating a lower threshold for low-molecular weight carbonaceous species. Reprinted with permission from [56], S. Ramesh et al., *J. Phys. Chem. B* 107, 1360 (2003). © 2003, American Chemical Society.

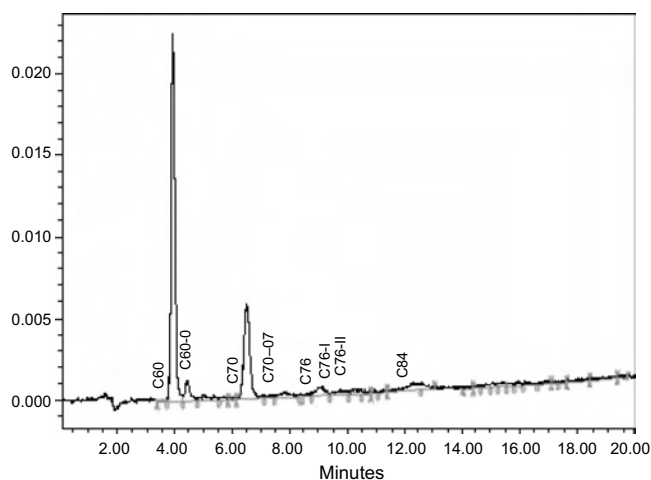


Figure 24. HPLC chromatogram of toluene extract of SWCNTs produced in a laser oven. The Y-axis is absorption at 316 nm wavelength. This sample has ~4% by weight of C₆₀ and C₇₀, plus a small amount of higher soluble fullerenes (C₇₆, C₇₈, and C₈₄).

hydrocarbons, 0 to 6% (m/m) polycyclic aromatic hydrocarbons, and 4 to 65% (m/m) total aromatic hydrocarbons. The precision of this test method has been established for an extract of soluble fullerenes and their blending components, containing from 4 to 40% (m/m) monoaromatic hydrocarbons, 0 to 20% (m/m) diaromatic hydrocarbons, 0 to 6% (m/m) polycyclic aromatic hydrocarbons, and 4 to 65% (m/m) total aromatic hydrocarbons.

2.4. Magnetic Resonance

Two of the prominent magnetic resonance techniques are electron spin resonance (ESR) and nuclear magnetic resonance. In the case of ESR, one monitors the precession of the valence electron in a strong magnetic field. The ESR spectrum can be used to study the effect of ligands and chemical environments by monitoring the shape, symmetry, width, and splitting of the ESR lines. Figure 25 shows that ESR spectral features change during purification. Petit et al. [58] reported microwave resistivity and ESR of laser grown SWCNTs and observed that the system remained metallic even at low temperatures. Theoretical work by DeMartino et al. [59] successfully explained the double-peak nature of the ESR spectrum to spin-charge separation.

The nuclear magnetic resonance methods are used to measure the hydrogen content (from ¹H NMR) and carbon content (by the ¹³C NMR). Kleinhammes et al. [60] studied the hydrogen adsorption in carbon nanotubes by following the kinetics of adsorption and desorption as a function of temperature and pressure. The electronic structures of the SWCNTs are also determined by relaxation times of ¹³C NMR signals [61]. The fast relaxing component is attributed to metallic tubes. Figure 26 shows the effect of spinning (MAS stands for magic angle spinning) on the NMR spectra of SWCNT samples. It was found to account for one-third of the sample which is consistent with random chirality of the SWCNTs. It is also noted that exposure to small amounts of oxygen can drastically change the relaxation behavior of the

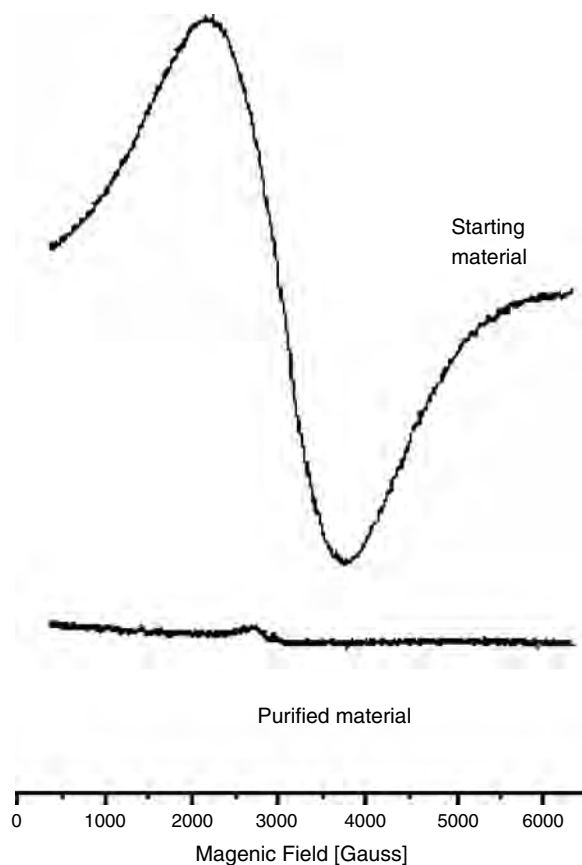


Figure 25. Electron spin resonance signal of unpurified and purified SWCNTs recorded at 9 GHz and at 300 K as a function of the static magnetic field. The former shows the huge ferromagnetic resonance line coming from the catalytic particles, while this signal is almost absent on the latter. Reprinted with permission from [86], Le T-N et al., *Nano Lett.* 2, 1349 (2002). © 2002, American Chemical Society.

NMR signals. The proximity of paramagnetic or ferromagnetic impurities (catalysts used in SWCNT production) may cause broadening of the NMR linewidths [62].

2.5. Thermal Methods

The following thermal methods rely on monitoring the weight, heat content, and reactivity of the SWCNTs as a function of elevated temperatures. These constitute one set of analytical techniques where the sampled material is destroyed or altered permanently. However, these can be used for quantitative estimation of purity of SWCNT samples and also yield very crucial information on thermal stability of these materials. The change in heat content is monitored by DSC where the phase transformations from crystalline to amorphous and/or glassy states are recorded.

2.5.1. TGA and TPO

Thermogravimetric analysis is used to monitor the changes in weight of the sample with increasing temperature [63]. Normally, this is done in air and at a ramp rate of 5 to 10 degrees per minute. The effects of compacting, ramp rate of the furnace, and type of gas used for TGA are discussed

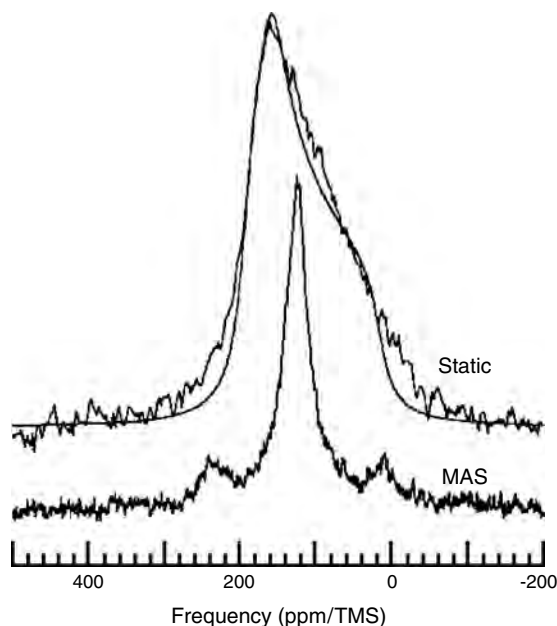


Figure 26. The static and MAS (spun at 11.7 kHz) ^{13}C spectra of SWCNT. The isotropic shift is 124 ppm based on the MAS spectrum. The fit is the powder pattern of a chemical shift tensor with $\sigma_{11} = 195$ ppm, $\sigma_{22} = 160$ ppm, and $\sigma_{33} = 17$ ppm. Reprinted with permission from [61], X.-P. Tang et al., *Science* 288, 492 (2000). © 2000, American Association for Advancement of Science.

in a recent presentation [64]. A faster ramp rate is observed to result in premature combustion and excessive compacting reduces the extent of oxidation (Figs. 27, 28). The peak of the derivative (dm/dT) plotted in Figure 27 is now regarded as indicative of the temperature of oxidation. For SWCNTs, this will shift to lower temperatures for small diameter tubes and derivatized tubes (which can burn easily). At temperatures beyond 1073 K, the ash content can be attributed to metal oxides and therefore can be used to estimate the metal content of the SWCNT material. This technique is one of the few quantitative techniques that can be used to compare different purification methods (by comparing the metal contents of the samples).

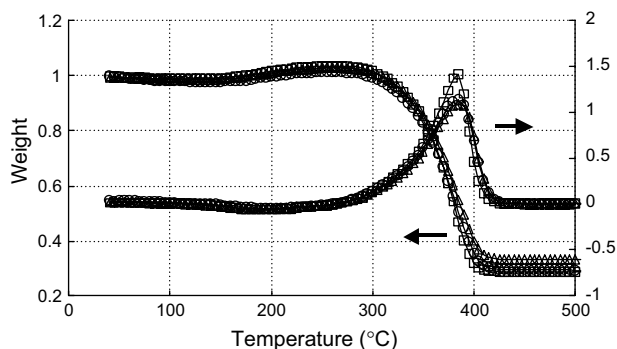


Figure 27. TGA traces of unpurified HipCO nanotubes (100 sccm air, 2.5 °C/min ramp rate; the same sample was measured three times). Small differences in the TGA traces are attributed to the inhomogeneity of the sample.

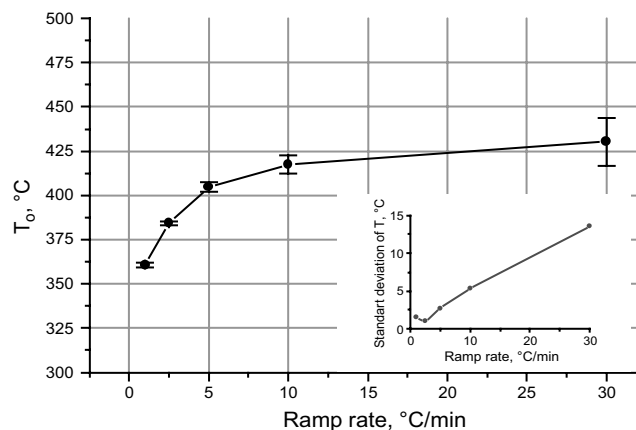


Figure 28. Burning temperature (T_0 , defined as a maximum in the weight loss rate) and its standard deviation dependence on the ramp rate in TGA. Run parameters and samples are similar to those in Figure 28. T_0 increases by ~ 70 °C as heating rate goes from 1 to 30 °C/min. Standard deviation of T_0 also increases, due to uncontrolled combustion above 5 °C/min.

Also, the shape and size of the derivative signals used are indicative of the “temperature of oxidation.” The oxidation temperature is noted to decrease with smaller diameter tubes and also when the nanotubes have extensive derivatization and/or defects [65].

In the temperature programmed oxidation technique, the material is submitted to a programmed temperature increase in an oxidizing mixture of gas (small percentage of oxygen in inert gas) and the reduction or oxidation rates are continuously measured by monitoring the change in composition by chemical means or by weight. In general, TPO studies are carried out under low partial pressure of the reactive gas. In this way it is possible to observe the intermediate reactions, depending on analytical conditions such as temperature rate, flow rate, and concentration of reactive gas. Alvarez et al. used this to separate out the peaks in the TGA data (Fig. 29)

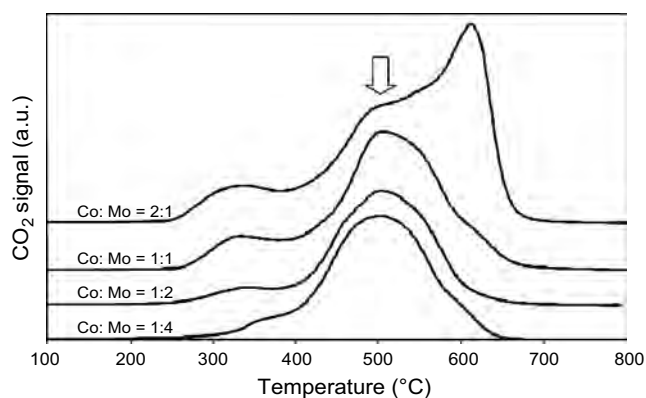


Figure 29. TPO traces of SWCNTs produced by decomposition of CO on Co:Mo catalyst of varying composition. A continuous flow of 5% O_2 in He is passed over the material while the temperature is linearly increased at 11 °C/min ramp rate. The evolution of CO_2 produced by the oxidation of the carbon species is monitored by a mass spectrometer. The arrow indicates the center of the peak corresponding to the oxidation of the SWCNT. Reprinted with permission from [87], B. Kitiyanan et al., *Chem. Phys. Lett.* 317, 497 (2000). © 2000, Elsevier Science.

and could identify and estimate the different types of carbon in the SWCNT sample [66].

2.5.2. DSC

Differential scanning calorimetry uses an indirect method of estimating the heat content of the sample as a function of temperature. The DSC spectrum can be used to monitor exothermic and endothermic reactions, and transition temperatures between different phases. This becomes especially useful when nanotubes are used to make composite materials for strength or conductivity enhancements. Also, peaks in the derivative signals of DSC can be used to determine curing temperatures, glass transition temperatures, and crystallization temperatures [67].

2.6. Miscellaneous Methods

2.6.1. XRD

One of the early methods used to monitor the extent of crystallinity was X-ray diffraction of SWCNT material [68]. The sharpness of the peaks at low angles increases with increased purity and crystallinity (Fig. 30). The broad background in the XRD spectrum at larger angles is attributed to the extent of amorphous content. This technique has also been used for estimating the diameter distribution [69] and the phonon density of states of SWCNTs [70].

2.6.2. Optical Microscopy

Resolution of the optical microscope is limited by numerical aperture and wavelength of light and does not exceed 400–500 nm. So it is not useful for imaging nanotubes and even large bundles. But optical microscopy has been utilized to assess nanotube dispersion in polymer films [71]. Nanotubes were dispersed in polyimide, and optical transmission micrographs of the resulting films were used to compare the degree of nanotube dispersion (Fig. 31). Dispersion of purified nanotube material in DMF is studied by drying a

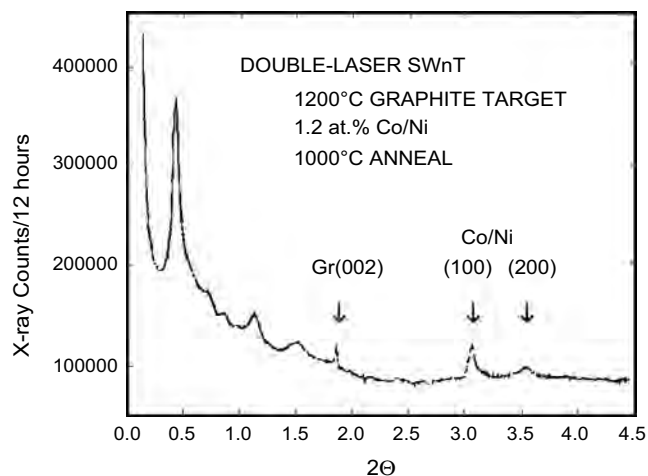


Figure 30. X-ray diffraction pattern of laser oven SWCNTs annealed in vacuum at 1000 °C. Reprinted with permission from [7], A. Thess et al., *Science* 273, 483 (1996). © 1996, American Association for Advancement of Science.

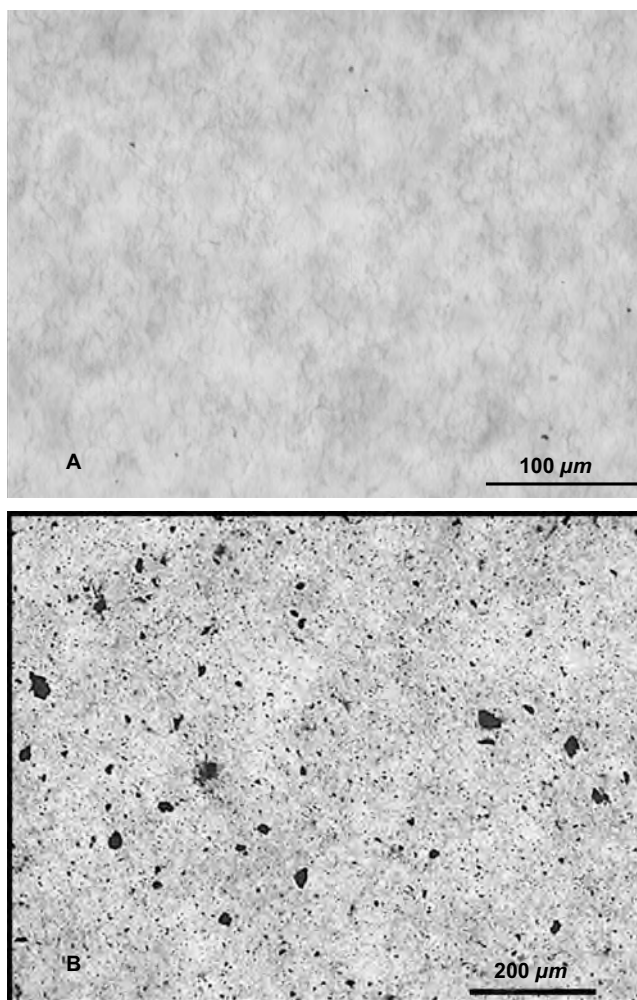


Figure 31. Optical transmission images of a SWCNT (0.05%) dispersed relatively well (A) and worse (B) in polyimide film.

drop of nanotubes suspended in DMF on a glass slide. For a quantitative comparison, one can resort to algorithms that can count the size and number of aggregates in the image. It is to be noted that the drying process may alter the state of aggregation of nanotube material. Optical microscopy is more useful for dispersability study when higher concentrations of nanotubes (>0.1 mg/mL) are used. For low concentrations (0.01 mg/mL), normal transmission study may be sufficient for this evaluation (see Section 2.2.1).

2.6.3. Surface Area and Surface Energy Measurements

A variety of applications including supercapacitors and rechargeable batteries depend on the availability of the large surface area of the SWCNTs. It is to be noted that the available surface area varies with the functional groups attached to the nanotubes as well as the number of dangling bonds. This in turn determines the surface energy of the nanotube material that affects the extent of adhesion of the SWCNTs to the surrounding matrix material. The BET surface area analyzer estimates the specific external surface of a solid by determining the volume of a specific gas that is absorbed

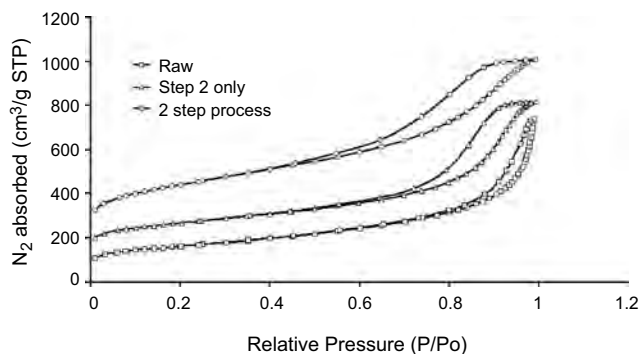


Figure 32. N_2 adsorption isotherms (77.6 K) for the raw SWCNTs and a sample purified using the complete two-step process. Isotherm for a sample which skipped Step 1 (DMF/EDA treatment) and was subjected only to the HCl treatment/wet oxidation (Step 2) is also shown for comparison. Reprinted with permission from [77], M. Cinke et al., *Chem. Phys. Lett.* 365, 69 (2002). © 2002, Elsevier Science.

under controlled conditions [72]. Surface area and pore volume can be determined using a commercial instrument such as a BET COULTER SA 3100. The method consists of one-hour gas evacuation at 393 K and of determination of the pore volume introducing helium gas, followed by adsorption of nitrogen at the temperature of liquid nitrogen (77 K). The system performs automatic single-point and multipoint BET surface area, full adsorption and desorption isotherms, and pore volume distributions. One can use other gases such as krypton, hydrogen, carbon dioxide, and saturated hydrocarbons. A typical single-point surface area analysis takes a few hours, while a full adsorption/desorption isotherm can take up to 3 days to complete (Fig. 32).

The surface areas of SWCNTs are reported to be in the range of 300 to 3000 m^2/g . Early work on the surface area determination of SWCNTs was prompted by the possibility of high hydrogen adsorption [73–75]. Other applications such as supercapacitors and catalysts required precise surface area and pore size measurements [76, 77]. Improved performance of supercapacitors using single walled CNT electrodes was reported by Young Hee Lee of Sung Kyun Kwan University, Korea. The heat treatment at high temperature was necessary to increase the capacitance and reduce the CNT-electrode resistance. The increased capacitance was well explained by the enhancement of the specific surface area and the abundant pore distributions at lower pore sizes of 30 to 50 angstroms estimated from the BET (N_2) measurements [78].

Direct measurement of surface energy can use inverse gas chromatography (Hans Darmstadt, Univ. Laval [79]). Surface energy of the SWCNTs can also be estimated by measuring the contact angle with different solvents and surfaces. Initial experiments seem to indicate low contact angle with water and other common solvents [80].

GLOSSARY

Bucky peapods Nanoscale material consisting of string of buckyballs (cage-like carbon clusters) enclosed inside carbon nanotube.

Chemical vapor deposition Chemical process based on catalytically assisted decomposition of gas-phase precursor molecules.

Chirality Property of an object that is not superimposable on its mirror image.

Chromatic aberrations Wavelength-dependent artifacts in imaging that occur because the refractive index of the lens material varies with wavelength.

Field emission electron gun (FEG) Electron source based on extremely sharp tip. Electric field in the tip vicinity is high enough to allow electron emission without thermal assistance (or with very low thermal assistance).

Nanohorns Nanoscale material made of graphene sheets rolled into capped cones.

Nanorope Term used to describe a bundle of nanotubes held together by Van der Waals forces. Nanoropes are not twisted, unlike real ropes.

Numerical aperture The sine of the vertex angle of the largest cone of meridional rays that can enter or leave an optical system or element, multiplied by the refractive index of the medium in which the vertex of the cone is located.

Spherical aberrations Imaging artifact caused because a spherical lens does not focus parallel rays to a point, but along a line.

ACKNOWLEDGMENTS

The authors acknowledge financial support from NASA contract NAS9-19100 to Lockheed Martin and encouragement from NASA-JSC carbon nanotube group members.

REFERENCES

1. M. S. Dresselhaus, G. Dresselhaus, and P. C. Eklund, in "Science of Fullerenes and Carbon Nanotubes." Academic Press, New York, 1996.
2. B. I. Yakobson and R. E. Smalley, *Am. Sci.* 85, 324 (1997).
3. C. Dekker, *Physics Today* 22 (1999).
4. L. Yowell, B. Files, C. Scott, B. Mayeaux, E. Sullivan, S. Arepalli, P. Nikolaev, O. Gorelik, W. Holmes, and V. Hadjiev, AIAA IAC-02-IAA.12.1.01 (2002).
5. "Carbon Nanotubes: Synthesis, Structure, Properties and Applications" (M. S. Dresselhaus, G. Dresselhaus, and P. Avouris, Eds.), Topics in Applied Physics, Vol. 80. Springer-Verlag, Heidelberg, 2001.
6. C. Journet, W. K. Maser, P. Bernier, A. Loiseau, M. Lamy de la Chapelle, S. Lefrant, P. Deniard, R. Lee, and J. E. Fischer, *Nature* 388, 756 (1997).
7. A. Thess, R. Lee, P. Nikolaev, D. Hongjie, P. Petit, J. Robert, C. Xu, Y. H. Lee, S. G. Kim, A. G. Rinzler, D. T. Colbert, G. E. Scuseria, D. Tománek, J. E. Fischer, and R. E. Smalley, *Science* 273, 483 (1996).
8. H. Dai, J. Kong, C. Zhou, N. Franklin, T. Tombler, A. M. Cassell, S. Fan, and M. Chapline, *J. Phys. Chem.* 103, 11246 (1999).
9. P. Nikolaev, M. J. Bronikowski, R. K. Bradley, F. Rohmund, D. T. Colbert, K. A. Smith, and R. E. Smalley, *Chem. Phys. Lett.* 313, 91 (1999).
10. O. Gorelik, P. Nikolaev, and S. Arepalli, NASA contractor report, NASA/CR-2000-208926, 2001.
11. I. W. Chiang, B. E. Brinson, A. Y. Huang, P. A. Willis, M. J. Bronikowski, J. L. Margrave, R. E. Smalley, and R. H. Hauge, *J. Phys. Chem. B* 105, 8297 (2001).

12. J. L. Margrave, J. L. Zimmerman, R. K. Bradley, C. B. Huffman, and Robert H. Hauge, *Chem. Mater.* 12, 1361 (2000).
13. A. C. Dillon, T. Gennett, K. M. Jones, J. L. Alleman, P. A. Parilla, and M. J. Heben, *Adv. Mater.* 11, 1354 (1999).
14. R. F. Service, *Science* 300, 243 (2003).
15. S. Iijima, *Nature* 354, 56 (1991).
16. D. S. Bethune, C. H. Kiang, M. S. de Vries, G. Gorman, R. Savoy, J. Vazguy, and R. Beyer, *Nature* 363, 605 (1993).
17. B. W. Smith, M. Monthieux, B. W. Smith, M. Monthieux, and D. E. Luzzi, *Nature* 396, 323 (1998).
18. S. Iijima, M. Yudasaka, R. Yamada, S. Bandow, K. Suenaga, F. Kokai, and K. Takahashi, *Chem. Phys. Lett.* 309, 165 (1999).
19. A. Thess, R. Lee, P. Nikolaev, H. J. Dai, P. Petit, J. Robert, C. H. Xu, Y. H. Lee, S. G. Kim, A. G. Rinzler, D. T. Colbert, G. E. Scuseria, D. Tomanek, J. E. Fischer, and R. E. Smalley, *Science* 273, 483 (1996).
20. P. Nikolaev, Gas Phase Production Of Single-Walled Carbon Nanotubes, Ph.D. Thesis, Rice University, Houston, TX, 2000.
21. E. T. Mickelson, C. B. Huffman, A. G. Rinzler, R. E. Smalley, R. H. Hauge, and J. L. Margrave, *Chem. Phys. Lett.* 296, 188 (1998).
22. J. Liu, A. G. Rinzler, H. J. Dai, J. H. Hafner, R. K. Bradley, P. J. Boul, A. Lu, T. Iverson, K. Shelimov, C. B. Huffman, F. Rodriguez-Macias, Y. S. Shon, T. R. Lee, D. T. Colbert, and R. E. Smalley, *Science* 280, 1253 (1998).
23. J. Liu, M. J. Casavant, M. Cox, D. A. Walters, P. Boul, W. Lu, A. J. Rimberg, K. A. Smith, D. T. Colbert, and R. E. Smalley, *Chem. Phys. Lett.* 303, 125 (1999).
24. M. J. O'Connell, P. Boul, L. M. Ericson, C. Huffman, Y. H. Wang, E. Haroz, C. Kuper, J. Tour, K. D. Ausman, and R. E. Smalley, *Chem. Phys. Lett.* 342, 265 (2001).
25. S. Arepalli, P. Nikolaev, W. Holmes, and B. S. Files, *Appl. Phys. Lett.* 78, 1610 (2001).
26. T. W. Odom, J. L. Huang, T. W. Odom, J. Huang, P. Kim, and C. M. Lieber, *Nature* 391, 62 (1998).
27. W. Chiang, B. E. Brinson, R. E. Smalley, J. L. Margrave, and R. H. Hauge, *J. Phys. Chem. B* 105, 1157 (2001).
28. O. Jost, A. A. Gorbunov, W. Pompe, T. Pichler, R. Friedlein, M. Knupfer, M. Reibold, H.-D. Bauer, L. Dunsch, M. S. Golden, and J. Fink, *Appl. Phys. Lett.* 75, 2217 (1999).
29. M. E. Itkis, S. Niyogi, M. E. Meng, M. A. Hamon, H. Hu, and R. C. Haddon, *Nano Lett.* 2, 155 (2002).
30. (a) M. J. O'Connell, S. M. Bachilo, C. B. Huffman, V. C. Moore, M. S. Strano, E. H. Haroz, K. L. Rialon, P. J. Boul, W. H. Noon, J. Ma, R. H. Hauge, R. B. Weisman, and R. E. Smalley, *Science* 297, 593 (2002). (b) S. M. Bachilo, M. S. Strano, C. Kittrell, R. H. Hauge, R. E. Smalley, and R. B. Weisman, *Science* 298, 2361 (2002).
31. J. W. G. Wilder, L. C. Venema, A. G. Rinzler, R. E. Smalley, and C. Dekker, *Nature* 391, 59 (1998).
32. S. Arepalli, P. Nikolaev, O. Gorelik, V. Hadjiev, W. Holmes, B. Files, and L. Yowell, submitted for publication.
33. J. R. Dean and D. J. Ando, "Atomic Absorption and Plasma Spectroscopy," 2nd ed. Wiley, New York, 1997.
34. K. L. Strong, D. P. Anderson, K. Lafdi, and J. N. Kuhn, *Carbon* 41, 1477 (2003).
35. T. Pichler, M. Knupfer, M. S. Golden, J. Fink, A. Rinzler, and R. E. Smalley, *Phys. Rev. Lett.* 80, 4729 (1998).
36. F. Pompeo and D. E. Resasco, *Nano Lett.* 2, 369 (2002).
37. J. Sun, *J. Colloid Interface Sci.* 260, 89 (2003).
38. P. J. Boul, J. Liu, E. T. Mickelson, C. B. Huffman, L. M. Ericson, I. W. Chiang, K. A. Smith, D. T. Colbert, R. H. Hauge, J. L. Margrave, and R. E. Smalley, *Chem. Phys. Lett.* 310, 367 (1999).
39. (a) Y. S. Lee, T. H. Cho, B. K. Lee, J. S. Rho, K. H. An, and Y. H. Lee, *J. Fluor. Chem.* 120, 99 (2003). (b) Z. Gu, H. Peng, R. E. Smalley, and J. L. Margrave, *Nano Lett.* 2, 1009 (2002).
40. R. L. McCreery, "Raman Spectroscopy for Chemical Analysis." Wiley Interscience, New York, 2000.
41. (a) A. M. Rao, E. Richter, S. Bandow, B. Chase, P. C. Eklund, K. A. Williams, S. Fang, K. R. Subbaswamy, M. Menon, A. Thess, R. E. Smalley, G. Dresselhaus, and M. S. Dresselhaus, *Science* 275, 187 (1997). (b) P. H. Tan, Y. Tang, Y. M. Deng, F. Li, Y. L. Wei, and H. M. Cheng, *Appl. Phys. Lett.* 75, 1524 (1999).
42. V. W. Brar, Ge. G. Samsonidze, M. S. Dresselhaus, G. Dresselhaus, R. Saito, A. K. Swan, M. S. Unlu, B. B. Goldberg, A. G. Souza Filho, and A. Jorio, *Phys. Rev. B* 66, 155418 (2002).
43. S. Farhat, M. Lamy de La Chapelle, A. Loiseau, C. D. Scott, S. Lefrant, C. Journet, and P. Bernier, *J. Chem. Phys.* 115, 6277 (2001).
44. Bandow, A. M. Rao, K. A. Williams, A. Thess, R. E. Smalley, and P. C. Eklund, *J. Phys. Chem. B* 101, 8839 (1997).
45. P. H. Tan, Y. Tang, Y. M. Deng, F. Li, Y. L. Wei, and H. M. Cheng, *Appl. Phys. Lett.* 75, 1524 (1999).
46. D. Chattopadhyay, I. Galeska, and F. Papadimitrakopoulos, *J. Am. Chem. Soc.* 125, 3371 (2003).
47. D. A. Walters, M. J. Casavant, X. C. Qin, C. B. Huffman, P. J. Boul, L. M. Ericson, E. H. Haroz, M. J. O'Connell, K. Smith, D. T. Colbert, and R. E. Smalley, *Chem. Phys. Lett.* 338, 14 (2001).
48. S. Reich and C. Thomsen, *Phys. Rev. Lett.* 85, 3544 (2000).
49. V. G. Hadjiev, M. N. Iliev, S. Arepalli, P. Nikolaev, and B. S. Files, *Appl. Phys. Lett.* 78, 3193 (2001).
50. V. A. Karachevtsev, A. Yu. Glamazda, U. Dettlaff-Weglikowska, V. S. Kurnosov, E. D. Obratsova, A. V. Peschanskii, V. V. Eremenko, and S. Roth, *Carbon* 41, 1567 (2003); M. Iliev, A. P. Litvinchuk, S. Arepalli, P. Nikolaev, and C. D. Scott, *Chem. Phys. Lett.* 316, 217 (2000).
51. S. Hufner, "Photoelectron Spectroscopy," 3rd Ed. Springer-Verlag, Heidelberg, 2003.
52. J. E. Herrera, L. Balzano, A. Borgna, W. E. Alvarez, and D. E. Resasco, *J. Catal.* 204, 129 (2001).
53. T. Hertel, R. Fasel, and G. Moos, *Appl. Phys. A* 75, (2002); M. Kociak, L. Henrard, O. Stephan, K. Suenaga, and C. Colliex, *Phys. Rev. B* 61, 13936 (2000).
54. G. S. Duesberg, J. Muster, V. Kristic, M. Burghard, and S. Roth, *Appl. Phys. A* 67, 117 (1998); S. Niyogi, H. Hu, M. A. Hamon, P. Bhowmik, B. Zhao, S. M. Rozenzhak, J. Chen, M. E. Itkis, M. S. Meier, and R. C. Haddon, *J. Am. Chem. Soc.* 123, 733 (2001).
55. C. Huffman, Ph.D. Thesis, Rice University, 2003.
56. S. Ramesh, B. Brinson, M. Pontier Johnson, Z. Gu, R. K. Saini, P. A. Willis, T. Marriotti, W. E. Billups, J. L. Margrave, R. H. Hauge, and R. E. Smalley, *J. Phys. Chem. B* 107, 1360 (2003).
57. O. Gorelik, P. Nikolaev, and S. Arepalli, NASA Contractor Report, NASA/CR-2000-208926 (2001).
58. P. Petit, E. Jouguelet, J. E. Fischer, A. G. Rinzler, and R. E. Smalley, *Phys. Rev. B* 56, 9275 (1997).
59. A. DeMartino, R. Egger, K. Hallberg, and C. A. Balseiro, *Phys. Rev. Lett.* 88, 206402 (2002).
60. A. Kleinhammes, C. Bower, O. Zhou, and Y. Wu, BAPS MAR 98, I19.05 (1998).
61. X. P. Tang, A. Kleinhammes, H. Shimoda, L. Fleming, K. Y. Bennoune, S. Sinha, C. Bower, O. Zhou, and Y. Wu, *Science* 288, 492 (2000).
62. S. Latil, L. Henrard, C. G. Bac, P. Bernier, and A. Rubio, *Phys. Rev. Lett.* 86, 3160 (2001).
63. A. G. Rinzler, J. Liu, H. Dai, P. Nikolaev, C. B. Huffman, F. J. Rodriguez-Macias, P. J. Boul, A. H. Lu, D. Heymann, D. T. Colbert, R. S. Lee, J. E. Fischer, A. M. Rao, P. C. Eklund, and R. E. Smalley, *Appl. Phys. A* 67, 29 (1998).
64. P. Nikolaev, O. Gorelik, and S. Arepalli, TGA Measurement uncertainties for SWCNT sample evaluation. Private Communication, 2003.
65. J. L. Bahr, J. P. Yang, D. V. Kosynkin, M. J. Bronikowski, R. E. Smalley, and J. M. Tour, *J. Amer. Chem. Soc.* 123, 6536 (2001).

66. W. E. Alvarez, B. Kitiyanan, A. Borgna, and D. E. Resasco, *Carbon* 39, 547 (2001).
67. B. McMorrow, R. Chartoff, and D. Klosterman, in "SAMPE 2003 Proceedings," Long Beach, CA, May 2003.
68. A. Thess, R. Lee, P. Nikolaev, D. Hongjie, P. Petit, J. Robert, C. Xu, Y. H. Lee, S. G. Kim, A. G. Rinzler, D. T. Colbert, G. E. Scuseria, D. Tománek, J. E. Fischer, and R. E. Smalley, *Science* 273, 483 (1996).
69. S. Rols, A. Righi, L. Alvarez, E. Anglaret, R. Almairac, C. Journet, P. Bernier, J. L. Sauvajol, A. M. Benito, W. K. Maser, E. Munoz, M. T. Martinez, G. F. de la Fuente, A. Girard, and J. C. Ameline, *Eur. Phys. J. B* 18, 201 (2000).
70. J. Hone, B. Batlogg, Z. Benes, A. T. Johnson, and J. E. Fischer, *Science* 289, 1730 (2000).
71. C. Park, Z. Ounaies, K. A. Watson, R. E. Crooks, J. Smith, Jr., S. E. Lowther, J. W. Connell, E. J. Siochi, J. S. Harrison, and T. L. St. Clair, *Chem. Phys. Lett.* 364, 303 (2002).
72. B. C. Lippens and J. H. deBoer, *J. Catal.* 4, 319 (1965); J. P. M. Syvitski, "Principles, Methods, and Application of Particle Size Analysis." Cambridge Univ. Press, Cambridge, UK, 1991.
73. Y. Ye, C. C. Ahn, C. Witham, B. Fultz, J. Liu, A. G. Rinzler, D. Colbert, K. A. Smith, and R. E. Smalley, *Appl. Phys. Lett.* 74, 2307 (1999).
74. C. C. Ahn, J. J. Vajo, B. Fultz, R. Yazami, D. W. Brown, and R. C. Brown, DOE Hydrogen Program Review, NREL/CP-610-32405, 2002.
75. K. Pradhan, A. Harutyunyan, D. Stojkovic, P. Zhang, M. W. Cole, V. Crespi, H. Goto, J. Fujiwara, and P. C. Eklund, *Mater. Res. Soc. Symp. Proc.* 706 (2002).
76. P. Ajayan and O. Zhou, "Carbon Nanotubes: Synthesis, Structure, Properties and Applications" (M. S. Dresselhaus, G. Dresselhaus, and Ph. Avouris, Eds.), Topics in Applied Physics, Vol. 80. Springer-Verlag, Berlin, 2001.
77. M. Cinke, J. Li, B. Chen, A. Cassell, L. Delzeit, J. Han, and M. Meyyappan, *Chem. Phys. Lett.* 365, 69 (2002).
78. K. H. An, K. K. Jeon, J. K. Heo, S. C. Lim, D. J. Bae, and Y. H. Lee, *J. Electrochem. Soc.* 149, A1058 (2002).
79. H. Darmstadt, C. Roy, S. Kaliaguine, and H. Cormier, *Rubber Chem. Technol.* 70, 759 (1997).
80. R. Krishnamoorthy, University of Houston, private communication.

Analytical Ultracentrifugation of Nanoparticles

Helmut Cölfen

Max-Planck-Institute of Colloids and Interfaces, Golm, Germany

CONTENTS

1. Introduction
 2. Instrumentation
 3. Basic Experiments
 4. Analysis of Nanoparticles
 5. Current Trends in Analytical Ultracentrifugation
 6. Availability of Free Evaluation Software
 7. Conclusion
- Glossary
References

1. INTRODUCTION

Analytical ultracentrifugation (AUC) is a powerful fractionating technique for polymer and particle characterization and has played a significant part in the understanding of colloidal but especially macromolecular systems starting with the pioneering work of Svedberg and co-workers [1, 2] who initially invented this technique for the characterization of particle sizes [1, 3]. However, it soon turned out that the technique was also well suited to the study of macromolecules, especially biopolymers, so that interest shifted almost exclusively to the study of macromolecules. One important result of the early work was the proof that macromolecules truly exist and that they are not aggregates of small molecules as was heavily debated at the time. Since that time, analytical ultracentrifugation has gained importance and become one of the most important characterization techniques for polymers mainly in biophysics/biochemistry. By 1970, there were about 1500 analytical ultracentrifuges in operation throughout the world. However, evaluation of the experimental results was tedious and time consuming in many cases because the results had to be derived from photographic records. With the advent of faster, cheaper, and more convenient techniques such as light scattering (LS), the importance

of the analytical ultracentrifuge decreased so that, by the end of the 1980s, only a few old instruments were still in use. The use of this technique for nanoparticle characterization appeared forgotten and only a few specialized, mainly industrial laboratories, still applied AUC for particle characterization.

However, in the beginning of the 1990s, Beckman Instruments released a new analytical ultracentrifuge—the Optima XL-A—equipped with a scanning absorption optical system [4]. This modern and fully computer controlled instrument led to a resurrection of analytical ultracentrifugation as the data acquisition was much simplified so that, nowadays, modern computer technology and powerful software can be applied for fast and rigorous evaluation (e.g., fitting experimental data to a model, handling of multiple data sets, etc.).

Analytical ultracentrifugation is an absolute method requiring no standards and covering a broad application range of molar masses between 200 and 10^{14} g/mol and particle sizes between less than 1 and 5000 nm. The power of the technique lies in the fractionation of the sample into its components either according to their molar masses/particle sizes or to their structure/density without the need for any stationary phase as required in many chromatographic methods. The fractionation enables the measurement of distributions of molar masses, particle sizes, and densities, and different types of basic experiments with the same instrument can yield complementary physicochemical information. Also, sedimentation equilibrium analysis is based on solid thermodynamics. Often, analytical ultracentrifugation is the only applicable technique if complex mixtures are to be investigated. For example, a unique feature of the technique is that interactions between molecules and/or particles can be investigated over a wide range of concentrations without perturbing the chemical equilibrium [5]. This is important for the study of biologically relevant relatively weak interactions ($K \approx 10\text{--}100\text{ M}^{-1}$) but can, in analogy, be adapted to any kind of interaction such as macromolecule–particle.

The range of samples that can be investigated by analytical ultracentrifugation is extremely wide and includes all systems that consist of a solvent and a dispersed or dissolved

substance spanning from gels to microgels and dispersions and emulsions to solutions. Also, there are no limitations on the choice of solvent even at extreme pH. This results in a whole variety of applications, and although the technique has already existed for about 80 years, there are still new methods and applications coming up. This review will give the basics of the technique but will also discuss the modern applications and recent trends of the last few years. Here, the methods that have been developed for polymer analysis but are, in principle, adaptable to nanoparticle analysis are also mentioned to give the reader the full array of available experimental or evaluation methods.

2. INSTRUMENTATION

An analytical ultracentrifuge is an ultracentrifuge with one or several optical detection systems that allow for the observation of a sedimenting sample in a centrifugal field of up to 290,000-fold the gravitational force (see Fig. 1). The sample is placed in a single- or double-sector cell (see Fig. 1) where the sector shape prevents convection during sedimentation due to the radially sedimenting sample. In addition to the two optical systems that modern machines are equipped with (see Fig. 1) and that detect the radially changing concentration in the cell, the Schlieren optical system, which detects the refractive index/concentration gradient, can also be applied. It delivers the first derivative of the radial concentration gradient and is thus well suited to watch sedimenting boundaries during sedimentation velocity experiments. The typical Schlieren peak is probably the most well known experimental output of an analytical ultracentrifuge. All three optical systems have their special advantages. The UV-absorption optics combines sensitivity with selectivity due to the variable detection wavelength, whereas the Rayleigh interference optics yields accurate experimental data due to the acquisition of a number of interference fringes, which are then evaluated via a fast Fourier transformation. However, the interference optics can only determine relative concentration changes with respect to a fixed point, which is usually the meniscus air/solution. The Schlieren

optics is well suited for high concentration or density gradient work and all kinds of experiments where a derivative of the concentration gradient is needed for the evaluation (e.g., the determination of the z-average molar mass from sedimentation equilibrium). The Schlieren optics is similar to the setup of the Rayleigh interferometer in Figure 1 but has a phase plate or knife edge in the focus of the condenser lens as an additional element.

The Schlieren optics was widely considered to be the least sensitive of the three detection systems, but it was shown that the sensitivity equals that of the Rayleigh interferometer [7]. An ultrasensitive Schlieren optical system has also been described [8]. However, despite the equipment of many ultracentrifuges with video cameras to save the photographic evaluation of the experimental traces, fully automated evaluation of the images was very difficult and only reported in one case [9] until the recent introduction of an on-line Schlieren optical system [10].

The typical optical patterns derived by the three detection systems are shown in Figure 2. For an extensive description of these optical systems, see [11]. For modern ultracentrifuges, only the Rayleigh interferometer (as an on-line detector) and the absorption optics are still available although the Schlieren optics was recently adapted for use in the Beckman Optima XL/XL-I [12]. Other detection systems include a fluorescence detector [13] and a turbidity detector specially designed for particle size analysis mainly of latexes [14–17].

The fluorescence optical system is extremely sensitive and allows for the selective investigation of components with concentrations as low as 10 ng/mL even in mixtures with a much larger amount of other components. A prototype

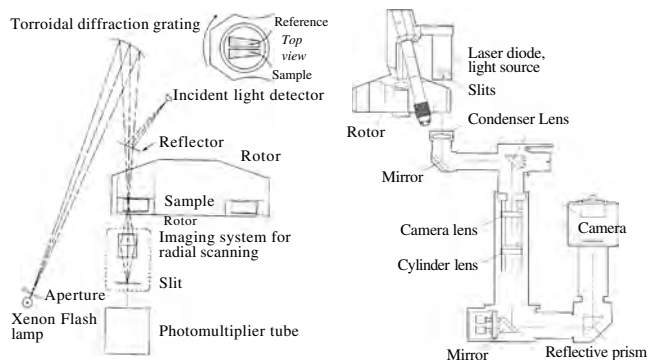


Figure 1. Optical detection systems of the Optima XL-I analytical ultracentrifuge. Left: UV/vis absorption optics. Right: Rayleigh interference optics based on the construction of Laue [6]. Reprinted with permission from G. Ralston, *Introduction to Analytical Ultracentrifugation*, Beckman Instruments, Fullerton, CA. (1993). © 1993, Beckman Coulter.

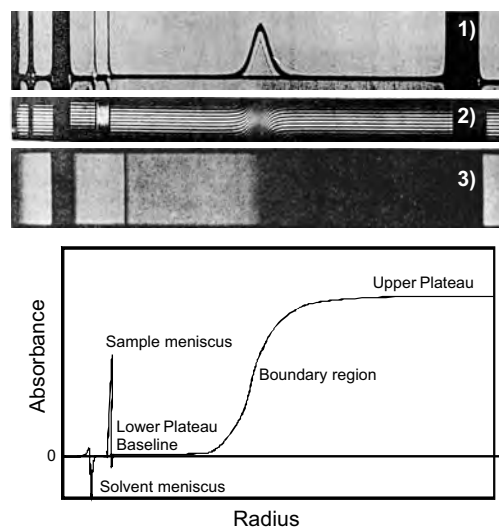


Figure 2. Photographically recorded optical data obtained from the different detection optics of an analytical ultracentrifuge for the same sample. (1) Schlieren optics, (2) Rayleigh interference optics, and (3) absorption optics. The lower diagram presents the output for scanning absorption optics. Reprinted with permission from [19], H. K. Schachman, *Ultracentrifugation in Biochemistry*, 1959, Academic Press, © 1959, Academic Press and with permission from G. Ralston, *Introduction to Analytical Ultracentrifugation* 1993, Beckman Instruments, © 1993, Beckman Coulter.

fluorescence detector for the Optima XL-I ultracentrifuge has recently been constructed [18] so that now a third detector is commercially available, which can be simultaneously used in a modern analytical ultracentrifuge. The turbidity optics, on the other hand, proves its virtues for the analysis of particle size distributions, even if they span the entire colloidal range; as with the appropriate correction of the particle concentration for MIE scattering, even weakly scattering small particles can be precisely characterized in the presence of strongly scattering large particles.

It is generally advantageous to combine several optical systems. In particular, the combination of the Rayleigh interference optics and the ultraviolet/visible (UV/vis) absorption optics can yield important information about complex systems where, for example, an absorbing component is selectively detected with the absorption optics, whereas the Rayleigh interferometer detects all components. For examples, see [20] or Figure 18.

3. BASIC EXPERIMENTS

There are four basic types of experiments that can be performed with an analytical ultracentrifuge. Each of them can deliver its own range of physicochemical information on the sample. The different experimental approaches will be treated in the following section. Table 1 outlines the characteristics of each experiment type and the most important accessible parameters.

3.1. Sedimentation Velocity Experiment

A sedimentation velocity experiment is carried out at high centrifugal fields and is the most important AUC technique for nanoparticle characterization. Here, the molecules/particles sediment according to their mass/size, density, and shape without significant back diffusion according to the generated concentration gradient. Under such conditions, a separation of mixture components takes place and one can detect a steplike concentration profile in the ultracentrifuge cell usually exhibiting an upper and a lower plateau (see Fig. 2, lower trace). Each step corresponds to one species. If one detects the radial concentration gradient in certain time intervals, the sedimentation of the

molecules/particles can be monitored. This is demonstrated in Figure 3a.

From the velocity of the sedimenting boundary, one can determine the sedimentation coefficient s according to

$$s = \frac{\ln(r/r_m)}{\omega^2 t} \quad (1)$$

where r is the position of the midpoint or second-moment point of the moving boundary, r_m the radial distance of the meniscus, t the time, and ω the angular velocity of the rotor. The sedimentation coefficient is a concentration- and pressure-dependent quantity that can be taken into account by appropriate correction or by extrapolation of a concentration series to zero concentration. A plot of $\ln(r/r_m)$ vs. $\omega^2 t$ is a line in which the slope s is equal to the sedimentation coefficient (see Fig. 3b). The sedimentation coefficient is measured in svedbergs (S) where $1 \text{ S} = 10^{-13} \text{ s}$. If the diffusion coefficient D is known from other experiments (light scattering, ultracentrifugation, etc.), one can calculate the molar mass of the sample according to the Svedberg equation:

$$M = \frac{sRT}{D(1 - \bar{v}\rho)} \quad (2)$$

where M is the molar mass of the sample, R the gas constant, T the thermodynamic temperature, \bar{v} the partial specific volume, and ρ the solvent density. The partial specific volume is a critical value, but it can be determined with good precision in a density oscillation tube if enough sample material is available. For hybrid particles in mixtures with different compositions, \bar{v} cannot be measured as only the average over all particles in the mixture is obtained. Here, the workaround of reasonable assumptions must be applied or quantitative density gradient experiments can yield the average density from the density distribution.

In general, sedimentation velocity experiments offer a good possibility for the rapid determination of particle size distributions and molar mass but also of equilibrium constants of interacting systems, which is especially advantageous for unstable systems that cannot be subjected to sedimentation equilibrium experiments due to possible sample degradation during the experiment [22].

Table 1. Basic experiment types in analytical ultracentrifugation and their characteristics and basic accessible parameters.

Experiment	Operative term in the Lamm equation (8)	Characteristics of experiment	Main accessible physicochemical parameter
Sedimentation velocity (3.1)	Sedimentation term prevails over diffusion term	High rotational speed	Sedimentation coefficient
Synthetic boundary experiment (3.4)	Only diffusion term operative	Low rotational speed, synthetic boundary cell	Diffusion coefficient
Sedimentation equilibrium (3.2)	Both terms operative, equilibrium between sedimentation and diffusion	Low to moderate rotational speed	Molar mass, equilibrium constants, and stoichiometries of interacting systems
Density gradient (3.3)	Both terms operative, equilibrium between sedimentation and diffusion	Moderate to high rotational speed, establishment of a radial solvent density gradient	Density

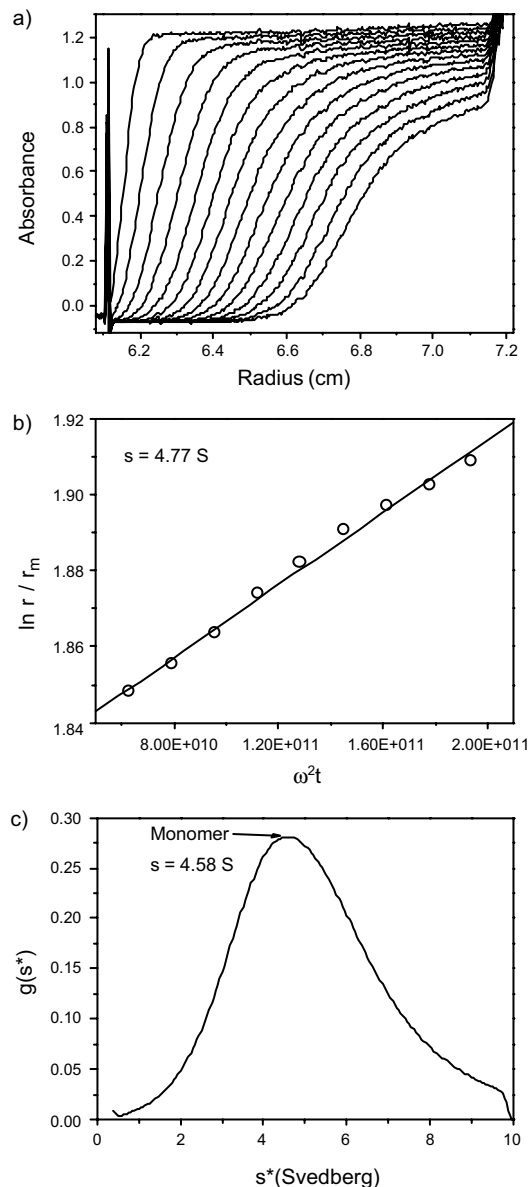


Figure 3. Sedimentation velocity experiment on bovine serum albumin in 0.5 N NaCl at 50,000 rpm and 20 °C. (a) Experimental raw data acquired with scanning absorption optics at 280 nm. Scan interval 10 min. Radius means the radial distance to the center of rotation. (b) Sedimentation coefficient calculated from (1). (c) sedimentation coefficient distribution from the time derivative method (3) and [21].

3.1.1. Moving-Boundary Method

Many procedures for the determination of s from sedimentation velocity data are available which cannot all be named here. Some of them like the moving-boundary method [23] allow an evaluation of the diffusion coefficient from the spreading of the boundary during the proceeding experiment [24] and thus a calculation of M . However, the calculation of D from the boundary spreading suffers from the requirement of reasonably monodisperse or at least reasonably separated samples because polydispersity leads to a boundary spreading proportional to time whereas diffusion goes only with the square root of time. If the whole boundary

spreading is only attributed to the diffusion spreading for polydisperse samples, the determined diffusion coefficient can be found to be significantly too high. Whereas polydispersity is often not an issue for biopolymers, it can be serious in nanoparticle analysis in that it can lead to erroneous results if the diffusion coefficient is determined by this method. Therefore, in nanoparticle analysis, the diffusion coefficient should be determined by other methods such as dynamic light scattering or flow-field-flow fractionation.

3.1.2. van Holde–Weischet Method

A problem arising from the diffusion broadening of boundaries is that the boundaries of several components can be smeared so that the overall boundary appears to be that of a single component. An approach to removing the effects of boundary spreading by diffusion and thus enabling calculation of the integral diffusion-corrected s distribution $G(s)$ was introduced by van Holde and Weischet [25]. This is done by selecting a fixed number of data points from one experimental scan that are evenly spaced between the baseline and the plateau. Then, an apparent sedimentation coefficient s^* is calculated for each of the data points and plotted versus the inverse root of the run time, yielding the typical van Holde–Weischet plot (see Fig. 4).

If a linear fit of the corresponding s^* (one slice) is performed, the integral diffusion-corrected sedimentation coefficient distribution $G(s)$ can be obtained from the y values at infinite time in the van Holde–Weischet plot. In the case of a single monodisperse component, the lines intersect in one point (see Fig. 4). For multiple components, the corresponding number of intersects is obtained whereas the intersection point is shifted to times less than infinity in the case of nonideality. Therefore, the van Holde–Weischet analysis is a rigorous test for sample homogeneity or nonideality [25–31].

3.1.3. Time Derivative Method

In many cases, particles are polydisperse or one detects a multimodal distribution. In such cases, it is of interest to determine the sedimentation coefficient distribution $G(s)$ or the differential form thereof $g(s)$. Although this is, in principle, possible by the van Holde–Weischet method, a

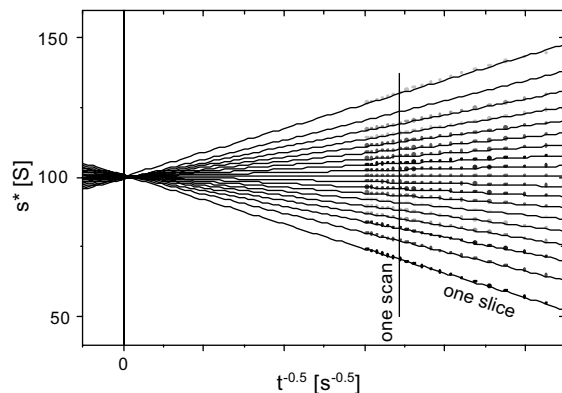


Figure 4. Typical van Holde–Weischet plot of a sedimentation velocity experiment with a monodisperse system. Reprinted with permission from [26], K. Schilling, Ph.D. thesis, Potsdam (1999).

better suited method for the determination of $g(s)$ is the time derivative method [21, 32, 33], which determines the time derivative of the radial scans acquired at different times according to

$$g(s^*)_t = \left(\frac{\partial \{c(r, t)/c_0\}}{\partial t} \right) \left(\frac{\omega^2 t^2}{\ln(r_m/r)} \right) \left(\frac{r}{r_m} \right)^2 \quad (3)$$

where $g(s^*)$ equals the true distribution $g(s)$ in cases where diffusion can be ignored. An example for bovine serum albumin is given in Figure 3c. An important advantage of this procedure is significant improvement in the signal-to-noise ratio of the experimental data because two scans are subtracted from each other so that systematic errors in the optical patterns cancel out and the random noise decreases. This approach takes advantage of the rapid data acquisition of modern analytical ultracentrifuges (Rayleigh interference optics) where 100 or more scans per velocity experiment are no longer an experimental problem. Hence, even scans for very diluted solutions where the sedimenting boundary can hardly be seen in the raw scans can be evaluated with the time derivative method. By that means, concentrations as low as 10 $\mu\text{g/mL}$ can be investigated so that interacting macromolecules and particles can be addressed in a concentration range previously not accessible with the analytical ultracentrifuge. However, a drawback of the time derivative method is that only scans from a relatively narrow time interval can be used for a single evaluation so that, in fact, no full advantage is taken of the possibility to scan several hundreds of experimental scans throughout an experiment.

If diffusion is significant, extrapolation of the $g(s^*)$ curves calculated for different times to infinite time yields the true distribution. The diffusion coefficient can also be derived from the $g(s^*)$ distribution using the maximum of the $g(s^*)$ curve [21]:

$$g(s^*)_{\max} = \left(\frac{s}{2\pi D} \right)^{1/2} (\omega^3 r_m) \left(\frac{t}{\sqrt{1 - e^{-2\omega^2 s t}}} \right) \quad (4)$$

and thus a plot of $g(s^*)_{\max}$ vs. $t/\sqrt{1 - e^{-2\omega^2 s t}}$ yields a line with a slope proportional to the square root of s/D so that the Svedberg equation can be applied to derive the molar mass

$$M = \frac{2\pi RT}{(1 - \bar{v}\rho)\omega^6 r_m^2} (\text{slope})^2 \quad (5)$$

However, for heterogeneous systems, the molar mass can be underestimated by 10–20%.

Another way of determining D from $g(s^*)$ is to look at the standard deviation σ of a Gaussian distribution fitted to $g(s^*)$:

$$D = \frac{(\sigma\omega^2 r_m)^2}{2t} \quad (6)$$

If a solution is analyzed where just different conformations of the same molecule or different particle shapes with the same molar mass or small amounts of aggregates are present, M and thus s/D can be fixed in the Svedberg equation for each component [Eq. (2)] to give the basis for a

very sensitive analysis—the so-called conformational spectra (CON-SPEC) [34]. Combining (2) and (6) with the equation for the Gaussian distribution function yields

$$g(s^*) = \frac{A}{\sqrt{2g(s^*)_{\max}\pi J}} \exp\left(\frac{-(s^* - g(s^*)_{\max})^2}{2(g(s^*)_{\max}J)^2}\right) \quad (7)$$

where A is the amount of the considered species and

$$J = \frac{2RTt}{(\omega^2 t r_m)^2 (1 - \bar{v}\rho)M}$$

is the collection of all known terms in the analysis. As M has to be known, J can be calculated so that only A and s can vary in (7). When σ in the Gaussian distribution function is replaced with the value of the standard error of the determination of $g(s^*)_{\max}$, a sort of mass spectrum is obtained where broad sedimentation coefficient distributions are replaced by sharp error-related distributions. This gives a very sensitive analysis for marginal differences in s even in the second digit for different components (see Fig. 5).

The determination of $g(s^*)$ can yield a lot of important information besides the sample homogeneity and number of components. In the case of interacting systems, for example, interaction constants can be derived [35–37]. If multiple Gauss curves with a maximum at fixed s are fitted to $g(s)$, then each of them corresponds to one component [38]. By that means, the aggregation state as well as the corresponding concentration of the different aggregates can be determined for aggregating systems so that the equilibrium constant and thus the free enthalpy of the association steps is accessible. An example of the advantageous application of this technique was reported for the precrystallization aggregation of lysozyme, which yielded the smallest oligomer capable of forming a crystal [39].

3.1.4. Fitting to Approximate or Finite-Element Solutions of the Lamm Equation

One new and recently much investigated approach has proved useful for the determination of s and D and thus M as well as the concentrations of individual components from sedimentation velocity data as in Figure 3a. This is the fit

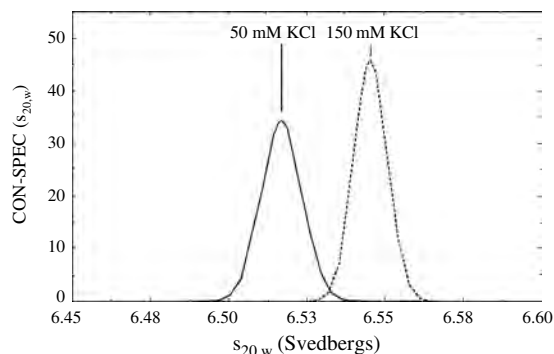


Figure 5. CON-SPEC ($s_{20,w}$) for α -actinin showing a modest conformational change upon an increase in salt concentration from 50 to 150 mM KCl. That the change is only marginally significant can be seen from the slight overlap of the two functions. Reprinted with permission from [34], N. Errington, et al., *Biophys. Chem.* 80, 189 (1999). © 1999,

of a series of radial concentration profiles to approximate solutions of the Lamm [40] differential equation of the ultracentrifuge [41–46] or finite-element solutions of the Lamm equation [47–50]:

$$\frac{\partial c}{\partial t} = \underbrace{D \left(\frac{\partial^2 c}{\partial r^2} + \frac{1}{r} \frac{\partial c}{\partial r} \right)}_{\text{Diffusion term}} - \underbrace{\omega^2 s \left(r \frac{\partial c}{\partial r} + 2c \right)}_{\text{Sedimentation term}} \quad (8)$$

As the Lamm equation (8) is the fundamental equation in analytical ultracentrifugation capable of describing all types of ultracentrifuge experiments, fitting of experimental data to this equation is a potentially very powerful approach. However, a drawback is that this method is clearly model dependent. Nevertheless, it is widely applicable and can quite accurately determine the sedimentation and diffusion coefficients even in mixtures of up to three components as long as the proper fitting function is used, the individual components are reasonably monodisperse (see the discussion about boundary broadening), and the individual components have differences in s of a factor of 1.5 or more. For smaller s differences, the van Holde–Weischet method is better suited. In the case of unknown samples, the van Holde–Weischet method can be used first to determine the type of system under investigation so that the correct model can be used for fitting the Lamm equation.

If mixtures of more than three components have to be analyzed, the s and D values of some components have to be known in order to get reliable fitting results. The fitting of experimental data to solutions of the Lamm equation has its special merits for small macromolecules or nanoparticles that sediment so slowly ($s < 1$ S) that they do not clear the meniscus. Furthermore, such approaches permit the rapid determination of molar masses with an accuracy of 10% within 15–30 min after the start of a sedimentation equilibrium experiment using a modified Archibald approach [50]. This is especially important for unstable samples that have to be characterized rapidly.

Very recently, the requirement of monodisperse samples for fitting of the Lamm equation was overcome so that now even the sedimentation coefficients and molar mass distributions of polydisperse samples can be investigated [51]. However, this approach suffers from the necessary prior knowledge of \bar{v} (no serious problem) and the frictional ratio f/f_0 of the sample (f is the frictional coefficient and f_0 is the frictional coefficient of the spherical particle having the same mass and \bar{v} as the sample under consideration). If the frictional ratio is not known, it can also be fitted, which, in turn, allows conclusions about the particle shape.

The most significant advantage of this approach for nanoparticle analysis is the possibility to correct for the effects of diffusion on the broadening of the sedimenting boundary so that diffusion-corrected sedimentation coefficient distributions can be obtained reflecting the true sample polydispersity. The method was recently shown to yield reliable results for different model systems [52].

3.2. Sedimentation Equilibrium Experiment

In contrast to the sedimentation velocity run, a sedimentation equilibrium experiment is carried out at moderate centrifugal fields. Here, the sedimentation of the sample

is balanced by a back diffusion according to Fick's law caused by the established concentration gradient. After the equilibrium between these two transport processes is achieved, an exponential concentration gradient has formed in the ultracentrifuge cell (see Fig. 6a, which represents a true thermodynamic equilibrium). Therefore, the sedimentation equilibrium analysis is based on solid thermodynamics. The time of equilibrium attainment considerably depends on the column height of the solution [53] so that short column techniques with solution columns of about 1 mm are common practice nowadays where even a rapid equilibrium within 1–2 h or less is desired [54].

The concentration gradient contains information about the molar mass of the sample, the second osmotic virial coefficient, or the interaction constants in the case of interacting systems independently of the particle shape. An advantage is that the detection of the concentration gradient is possible without disturbing the chemical equilibrium even of weak interactions. Sedimentation equilibrium is of more value for polymeric systems, because the molar mass of particles can already be too high to allow a significant diffusion counteracting the particle sedimentation. Nevertheless, for smaller down to the smallest nanoparticles, or even subcritical clusters and complexes, it can also be applied successfully as shown for the example of complexes of Zr(IV) and Hf(IV) formed by hydrolytic polymerization in an acidic medium [55, 56]. Various procedures exist for the evaluation of

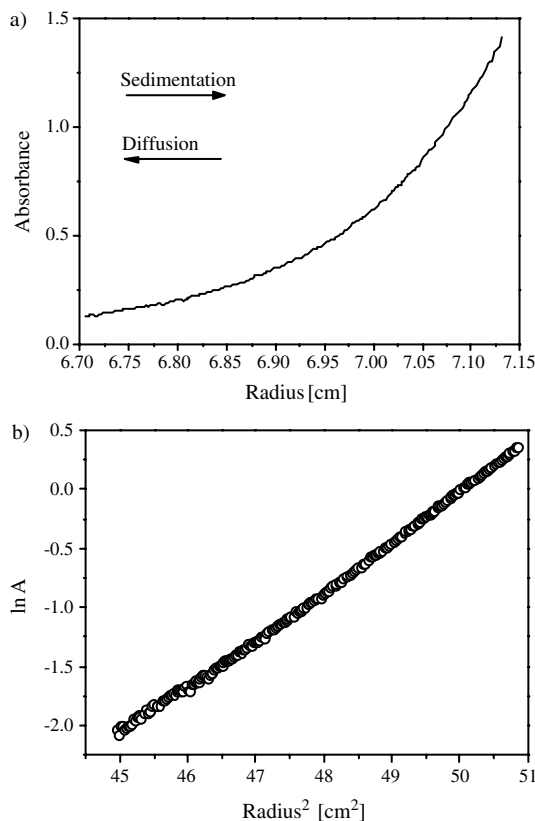


Figure 6. Sedimentation equilibrium experiment on bovine serum albumin in 0.5 N NaCl at 20 °C and 10,000 rpm. (a) Experimental raw data acquired with scanning absorption optics. (b) Plot of $\ln(\text{absorbance } A)$ vs. r^2 to evaluate $M_{w,app}$ from the slope.

sedimentation equilibrium experiments which are discussed in the following.

3.2.1. Classical Approaches

The classical approach to the evaluation of sedimentation equilibrium concentration gradients is to plot $\ln c$ vs. r^2 to obtain the weighted-average molar mass M_w from the slope according to the following equation (see Fig. 6b):

$$M_{w, \text{app}} = \frac{2RT}{(1 - \bar{v}\rho)\omega^2} \frac{d(\ln c)}{dr^2} \quad (9)$$

It must be noted that these M_w values have apparent character because they are calculated for finite sample concentrations. Consequently, they are denoted $M_{w, \text{app}}$. The true M_w can be obtained by an extrapolation of a concentration series to infinite dilution. The evaluation according to (9) works well for monodisperse ideal samples because, in such cases, the $\ln(c)$ vs. r^2 plot is linear. However, in many cases, this plot is curved, which yields erroneous $M_{w, \text{app}}$ values from linear regression. Nevertheless, the curvature indicates whether the sample is nonideal (downward curvature) or heterogeneous or self-associating (upward curvature). One advantage of (9) is that it allows for the computation of local $M_{w, \text{app}}(r)$ values for every acquired data point. $1/M_{w, \text{app}}(r)$ can be plotted against the corresponding concentrations to yield M_w and the second osmotic virial coefficient A_2 due to

$$\frac{1}{M_{w, \text{app}}(r)} = \frac{1}{M_w} + 2A_2 c(r) \quad (10)$$

From the radial concentration gradient (Fig. 6a) and the local $M_{w, \text{app}}(r)$ values, the apparent z-average molar mass $M_{z, \text{app}}(r)$ can also be obtained according to (11) if the data set is of good quality (double differentiation of the experimental raw data) [57]:

$$\begin{aligned} M_{z, \text{app}}(r) &= M_{w, \text{app}}(r) + \frac{2RT}{(1 - \bar{v}\rho)\omega^2} \left[\frac{d \ln M_{w, \text{app}}(r)}{d(r^2)} \right] \\ &= \frac{2RT}{(1 - \bar{v}\rho)\omega^2} \frac{d}{d(r^2)} \ln \left(\frac{1}{r} \frac{dc(r)}{dr} \right) \end{aligned} \quad (11)$$

An alternative evaluation procedure was described by Lansing and Kraemer [58]:

$$M_{w, \text{app}} = \frac{2RT}{(1 - \bar{v}\rho)\omega^2} \frac{c_b - c_m}{c_0(r_b^2 - r_m^2)} \quad (12)$$

where the indices b and m denote bottom and meniscus, respectively. This procedure also allows for the calculation of $M_{z, \text{app}}$ [59, 60]:

$$\begin{aligned} M_{z, \text{app}} &= \frac{RT}{(1 - \bar{v}\rho)\omega^2} \frac{1}{(c_b - c_m)} \\ &\times \left[\frac{1}{r_b} \left(\frac{dc(r)}{dr} \right)_b - \frac{1}{r_m} \left(\frac{dc(r)}{dr} \right)_m \right] \end{aligned} \quad (13)$$

Equations (12) and (13) yield average molar masses for the whole cell and no local values. A significant disadvantage of this evaluation is that it completely relies on the correct determination of the concentration at the meniscus and the

cell bottom where there might be considerable uncertainty. Furthermore, the obtained molar masses can be strongly influenced by impurities being much smaller (c_m influenced) or larger (c_b influenced) than the sample due to the evaluation of a whole-cell average molar mass.

3.2.2. Fitting Concentration Gradients to a Model

An approach for the analysis of sedimentation equilibrium data greatly facilitated by cheap and commonly available computers is the fit of the radial equilibrium concentration gradient to a theoretical model using nonlinear least squares analysis [61, 62]. This approach is highly popular today, and a whole variety of programs is available for this purpose, commercial as well as public-domain software [61, 63]. Furthermore, such fitting routines can easily be set up on commercial software platforms, offering freely definable functions for the curve-fitting process. In general, the radial equilibrium concentration gradient in the ultracentrifuge is described as the exponential form of (9) for a single-ideal component, as a modified exponential equation in the case of nonideality [see Eq. (14)], or as a sum of exponentials for different components in a mixture or in an interacting system [see Eq. (15)]. For a nonideal one-component system, the radial concentration gradient $c(r)$ can be described by

$$c(r) = c(r_{\text{ref}}) \exp \left(\frac{\omega^2}{2RT} M(1 - \bar{v}\rho)(r^2 - r_{\text{ref}}^2) - A_2 M(c(r) - c(r_{\text{ref}})) \right) \quad (14)$$

where r_{ref} is the chosen reference radius.

$$\begin{aligned} c(r) &= c_{\text{mon}}(r_{\text{ref}}) \exp \left(\frac{\omega^2}{2RT} M_{\text{mon}}(1 - \bar{v}\rho)(r^2 - r_{\text{ref}}^2) \right) \\ &+ c_{\text{mon}}(r_{\text{ref}})^{n_2} K_2 \exp \left(\frac{\omega^2}{2RT} n_2 M_{\text{mon}}(1 - \bar{v}\rho)(r^2 - r_{\text{ref}}^2) \right) \\ &+ \dots + c_{\text{mon}}(r_{\text{ref}})^{n_i} \\ &\times K_i \exp \left(\frac{\omega^2}{2RT} n_i M_{\text{mon}}(1 - \bar{v}\rho)(r^2 - r_{\text{ref}}^2) \right) \end{aligned} \quad (15)$$

For an ideal self-associating system of the type n monomer $\rightarrow n$ -mer with $K = c(n\text{-mer})/c(\text{monomer})^n$, the first two exponentials in (15) can be used as a fitting function, whereas for a more complicated self-associating system with several n -mers, the sum of the exponentials in the form of (15) can be applied. By such an approach, the quantitative determination of the association constant(s), stoichiometries, and second virial coefficients for self-associating systems is possible [64–69].

One can think of many more models for a system that can be used to fit the experimentally detected radial concentration gradient. However, the case of a polydisperse and often highly nonideal system—colloid chemists are very often confronted with—is not yet covered by a model in the commonly available programs. Therefore, in this case, the models for a monodisperse system must be applied knowing

that the obtained values for the polydisperse system are only averages.

Very often, a baseline absorbance that originates from nonsedimenting but light-absorbing material is used as a fitting parameter for data derived from absorption optics just by adding a variable to the right-hand side of (14) and (15). This can have an enormous influence on the results and extreme care has to be taken when allowing the baseline absorbance to be a fitting variable. Wherever possible, one should determine the baseline absorbance using the so-called overspeeding technique where the sample is sedimented to the cell base, leaving only the nonsedimenting material behind. If the Rayleigh interference optics is applied, which yields interference fringe shifts relative to the meniscus, it is recommended to apply synthetic boundary experiments in order to determine the fringe shifts at the meniscus for low-speed equilibrium experiments [70]. Another possibility is to use the so-called high-speed equilibrium technique, which applies such high speeds that the meniscus is cleared of the sample, leaving an exponential radial concentration gradient. Whereas this technique works well for relatively monodisperse samples, in highly polydisperse systems the high-molecular-weight material has sedimented to the cell bottom already and is thus lost for detection, resulting in a molar mass that is found to be too low.

The advantage of fitting the radial equilibrium concentration gradient to a model is that the experimental data can directly be analyzed without differentiation, an operation that amplifies experimental noise. Furthermore, multiple data sets can be fitted to one model, allowing for an analysis with better statistical significance. On the other hand, a possible danger of every fitting process that the least squares fit just corresponds to a side minimum can become serious even if the fitted curve well describes the experimental data. The fact that sums of exponentials have to be used for the analysis of the equilibrium concentration gradient limits the analysis of multicomponent systems considerably to three or four components [71] because the fitting parameters of the exponentials are badly determined by the data. A further serious disadvantage is that a model has to be known prior to the fitting process; that is, one must already have information about the system from other sources. However, one does not often know anything about the sample under investigation. In such cases, several models can lead to answers of similar accuracy from the statistical viewpoint. This requires either other independent techniques to seek more information or applying model-independent approaches such as the M^* function (see below) or an evaluation using a classical approach to learn something about the system of interest prior to fitting.

3.2.3. Model-Independent Approaches

There are two main model-independent approaches to evaluate sedimentation equilibrium data. The first one is the so called M^* function [72] defined as

$$M^*(r) = \frac{c(r) - c_m}{\Phi c_m (r^2 - r_m^2) + 2\Phi \int_{r_m}^r r [c(r) - c_m] dr} \quad \text{with}$$

$$\Phi = \frac{(1 - \bar{v}_i \rho) \omega^2}{2RT} \quad (16)$$

The most useful property of the M^* function is that it equals $M_{w, \text{app}}$ at the cell bottom. This means that one can get a cell average molar mass by extrapolating $M^*(r)$ to r_b . The M^* function has been combined with the classical evaluation according to (9) in evaluation algorithms [73, 74] to yield the whole-cell average $M_{w, \text{app}}$ via $M^*(r)$ as well as the local $M_{w, \text{app}}(r)$ via (9) to allow detailed insight into the kind of system under investigation besides the evaluation of $M_{w, \text{app}}$. Afterwards, the selection of a model for fitting the radial concentration gradient should lead to realistic results in coincidence with those already derived for $M_{w, \text{app}}$, allowing more detailed insight into the system under consideration (e.g., concentration of different components in a mixture, equilibrium constants of interacting systems, etc.).

The second model-independent approach—the Ω function [75, 76] or (in a recently derived form) ψ function [77]—is particularly well suited for interacting systems. The Ω function is a transformed type of the concentration distribution at sedimentation equilibrium:

$$\Omega_i(r) = \frac{c(r)}{c(r_{\text{ref}})} \exp \left[\frac{(1 - \bar{v}_i \rho) \omega^2}{2RT} M_i (r_{\text{ref}}^2 - r^2) \right]$$

$$= \frac{a_i(r_{\text{ref}}) c(r)}{a_i(r) c(r_{\text{ref}})} \quad (17)$$

where M_i is the molar mass of the smallest sedimenting species i (1 in the beginning of the evaluation). M_i usually has to be determined in a separate experiment using routines like MSTAR [74]. a_i is the thermodynamic activity of the smallest sedimenting species i equal to the concentration in the ideal case. If $\Omega_i(r)$ is plotted vs. $c(r)$, the intercept (or, realistically, the extrapolated intercept) equals the ratio of $a_i(r_{\text{ref}})/c(r_{\text{ref}})$, where $c(r_{\text{ref}})$ is known from the experimental data. The activity/concentration at the reference radius then allows for the calculation of the concentration gradient using the integrated form of (9) [see also (14) or (15) in the form for an ideal noninteracting one-component species]. Then, a revised radial concentration gradient [$c(r) - c_i(r)$] can be calculated, and the analysis is repeated for the next smaller sedimenting component. This unraveling of the total concentration gradient into those of the individual components is illustrated in Figure 7.

From the concentration gradients of the individual species, one can calculate the equilibrium constants. The elegance of this model-independent approach is that it avoids any differentiation/integration, the former being especially sensitive to the amplification of experimental noise. Furthermore, it allows for the calculation of activity distributions, giving a rigorous thermodynamic treatment of nonideal systems. However, one difficulty is still the curvature in the $\Omega(r)$ vs. $c(r)$ plots, especially for low $c(r)$, which are important for the extrapolation to infinite dilution to give the correct intercept (see Fig. 7a). Therefore, the Ω function was modified giving the ψ function [77], which shows a much better linearity when plotted as $c(r)/\psi_i(r)$ (y axis) versus ψ_{i+1}/ψ_i on the x axis and thus allows a safer determination of the intercept and $c_i(r_{\text{ref}})$, where $\psi_i(r)$ is defined as

$$\psi_i(r) = \exp \left[\frac{(1 - \bar{v}_i \rho) \omega^2}{2RT} M_i (r^2 - r_{\text{ref}}^2) \right] \quad (18)$$

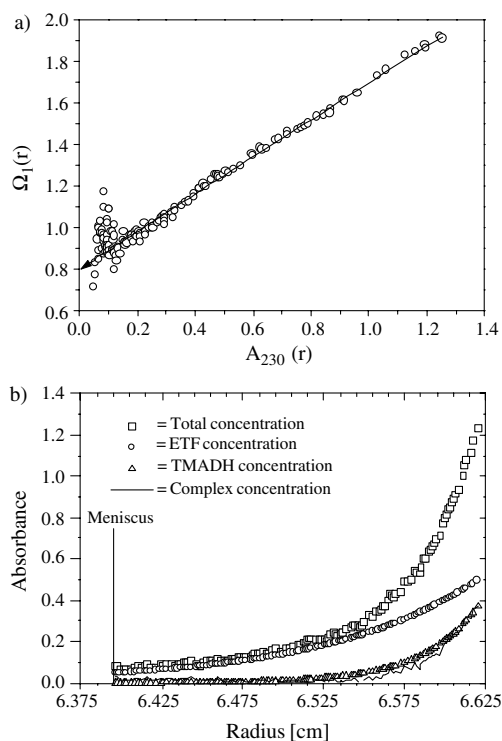


Figure 7. Interacting system between trimethylamine dehydrogenase (TMADH) and the corresponding electron transfer flavoprotein (ETF): (a) shows the Ω function for ETF in relation to the concentration in absorbance units to demonstrate a typical example; (b) shows the individual concentration gradients of all components in the mixture which allow the calculation of interaction constants for each set of corresponding data points.

Then, the calculation of the concentration distribution of i can be performed using $c_i(r) = c_i(r_{\text{ref}})\psi_i(r)$ and the analysis is repeated for the next smaller sedimenting species. This evaluation was recently implemented in a computer program [78]. Such analysis is especially useful if nothing is known about the kind of interaction taking place in a complicated mixture (homogeneous or heterogeneous interaction) and in which several components are involved [79]. If the interaction is found to be homogeneous, the total concentration gradient $c(r)$ can be fitted to simple polynomials of $c_1(r)$ of the form

$$c(r) = c_1(r) + K_2[c_1(r)]^2 + K_3[c_1(r)]^3 + \dots \quad \text{or}$$

$$c(r) = c_1(r) + K_n[c_1(r)]^n \quad \text{for monomer} \rightarrow n\text{-mer} \quad (19)$$

This allows for the analysis of complicated self-associations with a general polynomial fit or of monomer \rightarrow n -mer interactions using the second part of (19).

The Ω resp. ψ function has several other useful features. One is a sensitive diagnostic test for the discrimination between polydispersity and self-association. If $\Omega(r)$ is plotted for different cell-loading concentrations but a common $c(r_{\text{ref}})$, the plots will be superimposed in the case of self-associating systems, whereas they will not be superimposed in the case of a polydisperse or impure system. This test is more sensitive than the commonly applied plot of $M_{w,\text{app}}(r)$ vs. $c(r)$ for different cell-loading concentrations [80].

3.3. Density Gradient Experiment

The second principal possibility of separation in an analytical ultracentrifuge is the separation due to the chemical structure expressed in different solute densities in a density gradient. To generate a continuous density gradient in the ultracentrifuge cell, either a high-density salt (CsCl, etc.) or a substance like sucrose is dissolved in water or a mixture of two organic solvents with very different densities is applied. Under the action of the centrifugal field, the salt or the more dense solvent sediments toward the cell bottom and thus changes the density of the solution continuously toward the cell bottom. If a sample is placed into the density gradient, it will sediment/float to a position where its density matches that of the gradient. In the case of a mixture, this leads to a banding of the components due to their chemical structure/density. The range of densities that can be covered using density gradients is limited (0.8–2.0 g/mL) [14] but sufficient for the separation of purely polymeric substances. However, inorganic or organic–inorganic hybrid colloids have a density that is, in most cases, too high for the successful application of a density gradient. Also, the high salt concentrations in aqueous density gradients may be a problem for the analysis of electrostatically stabilized colloids. Furthermore, these so-called static density gradient experiments take a long time, usually on the order of several days (see Fig. 8), due to the slow banding of the sample. Also, potential solvent binding of the sample in a density gradient may be a problem. Nevertheless, density gradients are an excellent tool for the investigation of structural differences in mixtures and have especially proven to be an invaluable tool for the analysis of polymer latexes [14].

The separation capabilities of a static density gradient are demonstrated in Figure 8 for the separation of a mixture of an acrylonitrile–vinylacetate copolymer in a DMF/CHBr₃

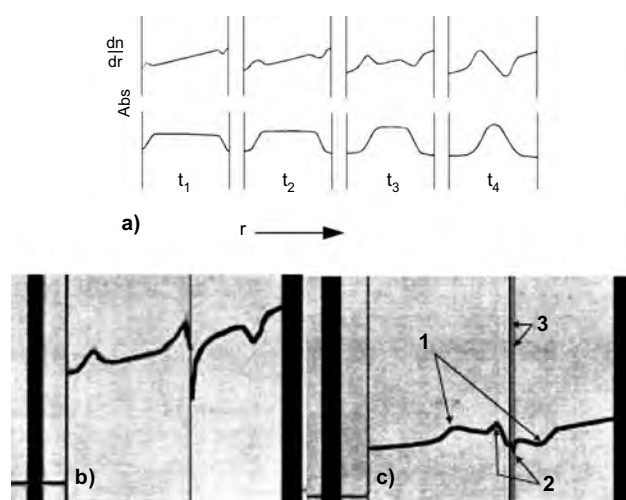


Figure 8. Static analytical density gradient. (a) Banding of a sample in a density gradient observed with Schlieren optics (upper) or absorption/Rayleigh interference optics (lower) at different times. (b) Acrylonitrile–vinylacetate copolymer in a DMF/CHBr₃ (136 g/L) density gradient after 35 h at 33,450 rpm. Fractions 1 and 2 are separated already. (c) After 108 h at 33,450 rpm (equilibrium). Figure adapted with permission from [81], R. Buchdahl et al., *J. Polym. Sci., Part C 1*, 143 (1963). © 1963, John Wiley.

density gradient. The sample consists of three fractions that could be successfully separated: (1) linear polymer (0.5×10^6 g/mol, $\rho = 1.0347$ g/mL), (2) highly branched polymer (25×10^6 g/mol, $\rho = 1.0365$ g/mL), and (3) weakly cross-linked polymer (75×10^6 g/mol, $\rho = 1.0371$ g/mL). If one looks at the densities of the separated components, one sees that the resolution of the separation is in the fourth digit of the density.

Much of the theory for the analysis of analytical density gradient experiments was established in the classical papers of Meselson, Hermans and Ende [82–85]. However, the Hermans–Ende equation was restricted to ideal systems, which can result in serious errors in the calculation of the radial density profile. Therefore, it was recently improved for real systems [86–88]. The basic equations that allow for the calculation of the density of the gradient at every point in the ultracentrifuge cell can be found in these references. From the width σ of the Gaussian concentration profile of the sample, the molar mass can be calculated [82]. The accuracy is much smaller, however, than that of the molar mass derived by sedimentation equilibrium experiments so that it can realistically only serve as an estimate.

The disadvantage of the prolonged experimental times for static density gradient experiments can be overcome by using the so-called dynamic density gradients [89, 90]. Here, a layer of H_2O is usually layered upon D_2O in a synthetic boundary experiment (see the corresponding section for details of this technique) establishing the fast formation of a dynamic H_2O/D_2O density gradient within a few minutes. Although the density range of this type of gradient is rather limited (1.0–1.1 g/mL), it is well suited for the fast characterization of latexes—especially polystyrene—and can be extended to 0.85–1.25 g/mL under certain circumstances [89]. An example is given in Figure 9 where an 11-component latex mixture with different densities is subjected to an H_2O/D_2O density gradient. As five latexes have a density in the density range between H_2O and D_2O , the gradient selectively separates these components, whereas the other six components are not detected although their density is partly quite close to the solvent. This example illustrates how fast information on the structural composition of a mixture can be derived. After only 2 min of centrifugation, four of the five latexes are already separated; after 4 min, all

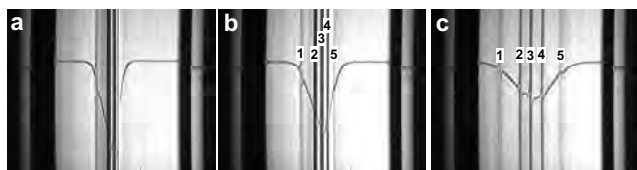


Figure 9. Formation of a dynamic H_2O/D_2O density gradient with a mixture of 11 different ethyl hexylacrylate/methylacrylate (EHA/MA) copolymer lattices that have been polymerized separately ($w[MA] = 0/10/20/30/40/50/60/70/80/90/100$ wt%). All particles had approximately the same diameter of 200 nm and exhibit the following densities: 0.980/1.000/1.021/1.043/1.066/1.089/1.114/1.167/1.196/1.225/1.140 g/mL. Just five of these are in the density range between 0.997 (pure H_2O) and 1.095 g/mL (pure D_2O). Run conditions: 40,000 rpm, 25 °C. (a) 2 min, (b) 4 min, and (c) 16 min. Reprinted with permission from [12], W. Mächtle, *Prog. Colloid Polym. Sci.* 113, 1 (1999) © 1999, Springer-Verlag.

five components are separated; and the separation is further improved within the next 12 min. Therefore, dynamic density gradients are the fastest technique to learn about the structural heterogeneity of mixtures as long as the particles have densities in the limited range for this type of density gradient.

3.4. Synthetic Boundary Experiment

In a synthetic boundary experiment, changes of a boundary between solution and solvent with time are observed at low centrifugal fields where no sedimentation of the sample occurs. Such experiments require special cells where the solvent is layered upon the solution column under the action of a certain centrifugal field. This is achieved by capillaries that connect the solvent compartment with the solution compartment and that allow a flow at a certain hydrostatic pressure. At $t = 0$, a sharp boundary comparable

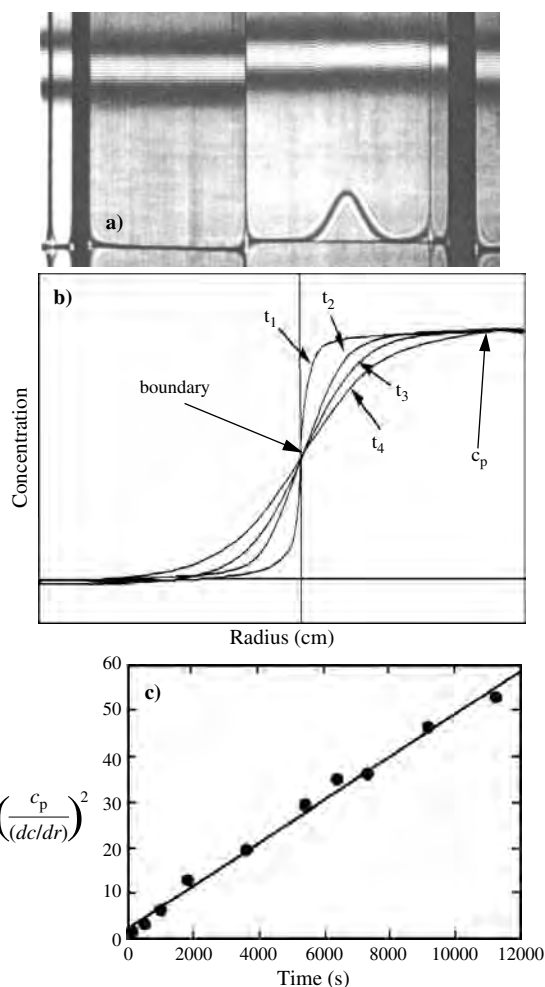


Figure 10. Synthetic boundary experiment. (a) Optical patterns from Rayleigh interference optics (upper) and Schlieren optics (lower) derived at time t . (b) Schematic radial concentration profiles at different times where $t_4 > t_3 > t_2 > t_1$. (c) Plot of $(c_p/(dc/dr))^2$ vs. time to derive the diffusion coefficient from the slope of the regression line. Reprinted with permission from G. Ralston, *Introduction to Analytical Ultracentrifugation 1993*, Beckman Instruments. © 1993, Beckman Coulter.

to the meniscus is obtained (see Fig. 10b). Within seconds, this boundary spreads by diffusion according to Fick's law due to the high concentration gradient at the boundary. The spreading of the boundary with time is monitored (see Fig. 10b and c). Now the plateau concentration of the upper plateau c_p as well as (dc/dr) at the boundary position can be determined. A plot of $(c_p/(dc/dr))^2$ vs. time yields a line with a slope equal to $4\pi D$. It is also possible to derive the dependence of D on the polymer concentration in a single synthetic boundary experiment [92]. A pseudo synthetic boundary experiment can be constructed from a normal sedimentation velocity experiment if $G(s)$ is obtained by the van Holde–Weischet method and subtracted from the experimental scans at various times [93]. This has the advantage that any layering imperfections that can occur in a conventional synthetic boundary experiment are avoided and, furthermore, samples that sediment at even the low speeds of a conventional synthetic boundary experiment can be investigated. However, compared to dynamic light scattering, a synthetic boundary experiment is more tedious and time consuming for the determination of the particle diffusion coefficient, so that, here, dynamic light scattering is the method of choice. Nevertheless, if aggregates are present in a sample, the light-scattering results can be seriously obstructed, whereas the synthetic boundary experiment will be unaffected as the aggregates will sediment even at the low applied speeds.

4. ANALYSIS OF NANOPARTICLES

There are numerous examples of information derived by one of the four basic experiments or combinations thereof using an ultracentrifuge. They cannot be treated completely here, but the selected applications will show that analytical ultracentrifugation is a universal absolute technique for the characterization of polymers or colloids, especially in mixtures. The examples given here have been chosen in such a way that the range of information obtained by AUC is as broad as possible and the emphasis of the selected examples is more on the methods of how to derive information on a nanoparticle system by AUC rather than on how precisely this information can be obtained for a specific nanoparticle system. At the end of this section, a table is presented which will give the reader an overview of the primary literature for specific systems.

4.1. Particle Size Distributions

The application of analytical ultracentrifugation for the determination of particle sizes and their distributions to address problems of colloid analysis was already realized by the pioneers of this technique because sedimentation velocity experiments provide a sensitive fractionation due to particle sizes/molar masses [3, 94–96]. Nevertheless, it appears that the potential of this application is still not yet commonly recognized. It is relatively straightforward to convert a sedimentation coefficient distribution, which can be calculated using (1) for every data point (a) r_i (if a radial scan has been acquired at a specified time) or (b) t_i (if a concentration detection at a specified radius has been performed in dependence of time), to a particle size distribution. Assuming the

validity of Stokes' law (e.g., the sample is spherical), the following derivative of the Svedberg equation (2) is obtained

$$d_i = \sqrt{\frac{18\eta s_i}{\rho_2 - \rho}} \quad (20)$$

where d_i is the particle diameter corresponding to s_i , ρ_2 is the density of the *sedimenting* particle (including solvent/polymer, etc., adhering to the sample), and η is the solvent viscosity. If the particles are not spherical, only the hydrodynamically equivalent diameter is obtained unless form factors are applied if the axial ratio of the particles is known from other sources such as transmission electron microscopy (TEM).

The conversion of a sedimentation coefficient distribution to a particle size distribution highly relies on the knowledge of the density of the sedimenting particle. For hybrid particles or very small nanoparticles less than 5 nm, this issue can be a severe problem, especially in the case of mixtures, as the density of the particles is usually not known. Measurements of the average particle density in the mixture can lead to erroneous results so that in such cases the correlation of the sedimentation coefficient distribution with a distribution obtained from a density-insensitive method such as flow–field–flow fractionation or dynamic light scattering is meaningful. This can, in turn, yield the particle density, which can give information about the relative amount of materials building up the hybrid particle [97]. But even an apparent particle size distribution that is calculated within the limits of reasonable particle densities can already yield very valuable information [98].

However, in the case of industrially important latexes, the particle density is usually exactly known from the chemistry of particle formation/polymerization. Thus, the determination of particle size distributions with the analytical ultracentrifuge is a rapid technique providing a high statistical accuracy (e.g., every sedimenting particle is detected) in contrast to transmission electron microscopy (TEM), which delivers information about the particle shape but often suffers from drying artifacts. Determination of a particle size distribution from TEM images requires counting hundreds/thousands of particles. This problem has only partly been diminished by the advent of commercially available picture evaluation algorithms. A recent test dedicated to particle size analysis by the Bayer group in 17 laboratories, confirmed the view that TEM and/or analytical ultracentrifugation are the best techniques for the determination of particle size distributions [99] as discussed above. A combination of TEM, AUC, and X-ray diffraction techniques can provide a complete insight into a colloidal system [100]. Analytical ultracentrifugation in combination with electron microscopy in its various forms can be considered the most powerful characterization approach for particle size distributions and particle morphologies known to date. The following examples illustrate the fractionation power of the analytical ultracentrifuge for latexes [14, 101, 102] (see Fig. 11a) and especially for inorganic colloids [103].

In the case of latexes, the accessible size range is between 10 and 5000 nm with a baseline resolution for monodisperse components differing just by 10% in diameter [105], whereas for inorganic colloids, analytical ultracentrifugation separates dispersions with an almost atomic resolution. The

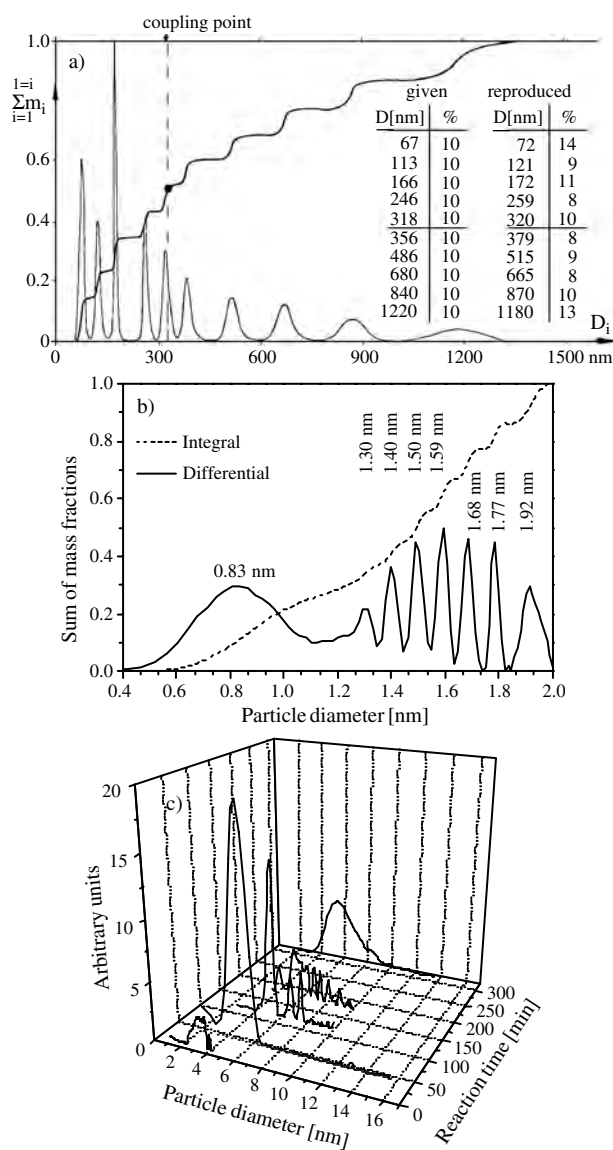


Figure 11. Examples of particle size distributions determined with the analytical ultracentrifuge. (a) 10-component mixture of polystyrene standard latexes corrected for MIE scattering. Reprinted with permission from [17], W. Mächtle, "Analytical Ultracentrifugation in Biochemistry and Polymer Science," p. 147, Royal Society of Chemistry, Cambridge, UK, 1992. © 1992, Royal Society of Chemistry. (b) Pt colloid during particle growth. Reprinted with permission from [103], H. Cölfen and T. Pauck, *Colloid Polym. Sci.* 275, 175 (1997). © 1997, Springer-Verlag. (c) Particle growth of ZnO. Reprinted with permission from [104], H. Cölfen et al., *Prog. Colloid Polym. Sci.* 107, 136 (1997). © 1997, Springer-Verlag.

smallest reported species that could be detected was a ZrO_2 precursor just 0.4 nm in diameter [98], which shows the potential of the analytical ultracentrifuge for the analysis of the smallest nanoparticles or subcritical complexes. This means that particle size distributions derived by ultracentrifugation can well be used to investigate particle growth mechanisms [98, 103] from its initial stages/the critical crystal nucleus, especially if the growth is slow enough to detect time-dependent particle growth as in the example of ZnO (see Fig. 11c) [103, 104].

For very small particles, diffusion becomes significant so that it must be corrected. This is possible by extrapolation to infinite time, but, recently, another method was suggested which is based on the calculation of the diffusion coefficient from the particle size [106]. From this, the diffusion broadening of the sedimenting boundary can be calculated and subtracted from the measured concentration distribution, giving the diffusion-corrected particle size distribution. This procedure works best for monomodal and relatively narrow distributions, whereas it becomes less accurate for broad and/or multimodal distributions. An alternative is the diffusion correction of the sedimentation coefficient distribution by fitting the experimental concentration profiles to approximate solutions of the Lamm equation [51].

Another substance class rapidly gaining importance is the hybrid colloids between polymers and inorganic matter. Here, analytical ultracentrifugation shows all its merits for the investigation of transformations, aggregation processes, and so on. For example, the encapsulation of a molybdenum cluster with a surfactant could be characterized as well as the aggregation of the primary clusters in different solvents with high resolution [107]. An example of monitoring a restructuring process of a complex hybrid colloid in solution is given in Figure 12. Here, calcium phosphate was synthesized within functional polymeric aggregates so that a very unusual neuron-like crystal morphology was obtained within the polymeric aggregates. This neuron-like morphology is slowly transformed into a more compact spherical structure (see photos from left to right), which could be monitored by analytical ultracentrifugation so that the relative proportions of each species could be determined [108]. Since the

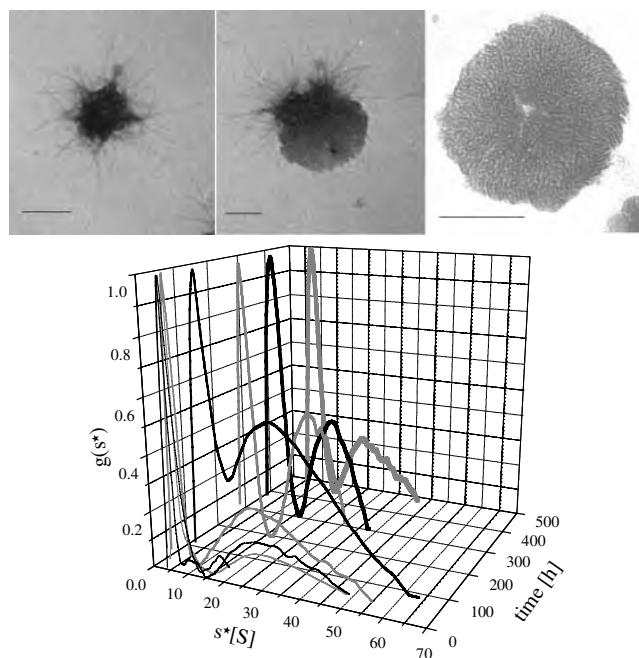


Figure 12. Transformation of "neuron-like" calcium phosphate into a more compact spherical form and the time-resolved observation of this process by analytical ultracentrifugation. The ultracentrifuge data reproduced with permission from [108], M. Antotietti et al., *Chem. Eur. J.* 4, 2493 (1998). © 1998, Wiley-VCH.

particle density is not known, only the consideration of the sedimentation coefficient distributions makes sense.

From the sedimentation coefficient distributions, the whisker structure is evident in the species with the lower sedimentation coefficient, whereas the dense spherical structure can be identified by its high sedimentation coefficients. The formation of the dense species has a clear maximum before its amount decreases again due to macroscopic precipitation. The observation of such transformation in solution enhances the visual information from TEM and shows the potential of ultracentrifuge experiments combined with a TEM investigation.

A combined particle size and density gradient analysis is a powerful tool for the analysis of very complex mixtures where the particle sizes as well as the densities of the components are different. This is illustrated in Figure 13. Here, a mixture of four different polybutylacrylate (PBA) latexes was grafted with a styrene/acrylonitrile (SAN) copolymer which has a higher density than PBA [14].

In the density gradient, the four grafted particles are clearly resolved, indicating that the degree of grafting is different for every particle size. From the particle size distributions of the ungrafted and grafted PBA particles, it becomes obvious that the mass fraction of the smaller particles increases after grafting. This allows the conclusion that the amount of grafting is proportional to the particle surface.

Another possibility for obtaining the density of unknown particles is to run two velocity experiments in chemically similar solvents with different densities (e.g., H_2O/D_2O) [101, 109]. This allows us to simultaneously determine particle sizes and density distributions. The method works best for particles with densities less than 1.5 g/mL but requires

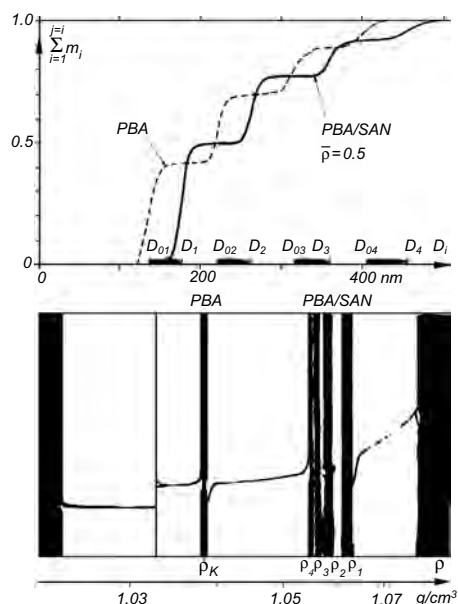


Figure 13. Particle size distribution and density gradient of a four-modal ungrafted and a SAN-grafted PBA dispersion (40 : 30 : 20 : 10 wt% mixture). D refers to the particle diameter; the index $0i$ to ungrafted and i to the grafted latex. Reprinted with permission from [17], W. Mächtle, "Analytical Ultracentrifugation in Biochemistry and Polymer Science," p. 147, Royal Society of Chemistry, Cambridge, UK, 1992. © 1992, Royal Society of Chemistry.

rather good data quality. Recently, a diffusion correction has been implemented into this method, which is especially important for small particles/molecules so that even complex mixtures become accessible by this method [110].

4.2. Characterization of Emulsions

In analogy to dispersions, emulsions, respectively mini- or microemulsions, can be characterized by the particle size distribution of the dispersed phase if flat centerpieces are used which permit the passage of light to the detector through the turbid emulsion as the emulsion cannot be diluted in contrast to a dispersion. One such example was reported for water/AOT/heptane water in oil microemulsions [111]. Furthermore, it is possible to force the coalescence of the emulsion by the ultracentrifugal field which can easily be detected as the formation of a new phase by any optical detection system of the ultracentrifuge. This is a fast and effective measure to look at the stability of emulsions in a qualitative way by determining either the centrifugal field necessary for spontaneous coalescence or the time until coalescence occurs at a given centrifugal field [112–114]. From experimental parameters such as the rotational speed and density, a coalescence pressure can be calculated as a more quantitative measure [112].

4.3. Characterization of Microgels

The analytical ultracentrifuge has proved to be very useful for characterization of the thermodynamic and elastic properties of gels and microgels as reviewed in [115, 116]. In the case of microgels in a thermodynamically good solvent, the degree of swelling Q can be determined from sedimentation velocity experiments [117]. If the microgel contains un-crosslinked polymer, two components are resolved in the sedimentation coefficient distribution calculated via (1). From $G(s)$ (see Fig. 14), the amount of each component can be

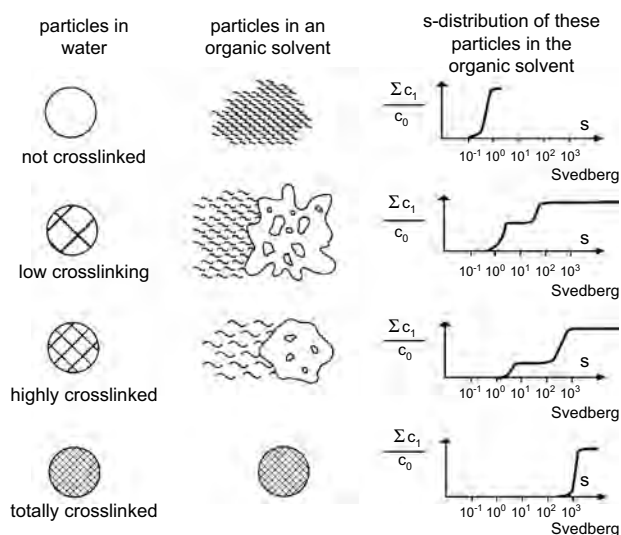


Figure 14. Sedimentation coefficient distributions for lattices with different degrees of cross-linking. Reprinted with permission from [117], H. G. Müller et al., *Prog. Colloid Polym. Sci.* 86, 70 (1991). © 1991, Springer-Verlag.

derived. The swelling degree Q can then be calculated using

$$Q = \frac{bd^2}{s} - \frac{\rho_2 - \rho}{18\eta} \quad (21)$$

where d is the diameter of the compact, unswollen particle, ρ_2 is the density of the compact, unswollen particle, ρ is the density of the dispersion medium, and η is the viscosity of the diluted dispersion. b is a factor according to $m_r = b \cdot m$ where the mass of the particle m_r reduced by the soluble part is related to the mass m of the particle consisting of soluble and insoluble components. It can be derived from interference optical traces.

The particle diameter of the unswollen sample has to be determined in a nonsolvent in a separate experiment. The swelling degree can be related to the molar mass of the elastically effective network chains and thus to the elastic properties of the microgel applying the Flory–Rehner theory. Such experiments not only allow the characterization of microgels but can furthermore be used to investigate the efficiency of cross-linking reactions by specifying the amount and physicochemical properties of the un-cross-linked polymer [118]. Figure 14 shows the sedimentation coefficient distributions that are derived for different cross-linking degrees of latexes. One can now easily compare samples from different cross-linking reactions.

4.4. Observation of Chemical Reactions

It is possible to perform chemical reactions in the analytical ultracentrifuge with a synthetic boundary experiment using a special cell (see Fig. 15a). In biochemistry, this kind of centrifugation is called “active enzyme centrifugation” [119], but the principle can be applied to every chemical reaction. In the synthetic boundary cell (Fig. 15a), a small amount

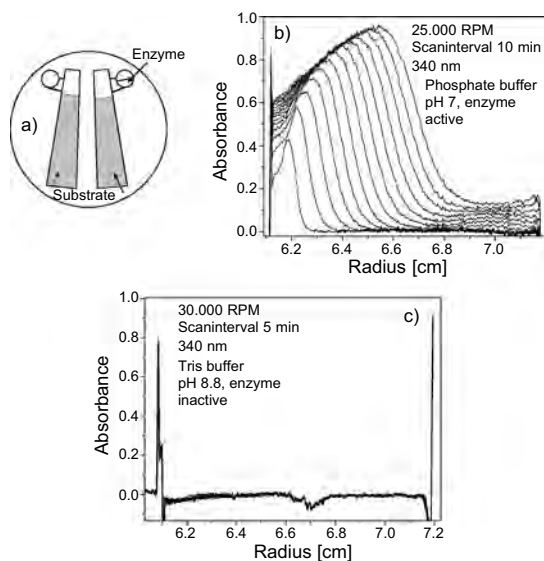


Figure 15. (a) Synthetic boundary cell with small sample compartments. (b) Sedimentation velocity profile of a glutamate dehydrogenase mutant enzyme which reacts with its substrate. (c) Sedimentation velocity profile of the same enzyme at a different pH. The enzyme is now inactive and no chemical reaction takes place.

of a reactant (usually 10–15 μL) is layered onto a column of the second reactant while the centrifuge is speeded up to about 3000 rpm. Thus, a reaction boundary is established. The detection wavelength of the absorption optics is set to a wavelength where the reaction product (here the enzyme–substrate complex) absorbs. One can then observe the product formation and sedimentation as visualized in Figure 15b. The absorbance increases with the time of sedimentation, indicating that the sedimenting enzyme is reacting continuously. Such experiments can yield sedimentation and diffusion coefficients of the enzyme in its catalytically active state which enables detection of differences in polymerization state, hydration, or conformation with the non-reacting enzyme. If the extinction coefficient of the reaction product is known, the product concentration in relation to time can be calculated. Figure 15c shows that a slight change in pH can turn the enzyme to its inactive state. An advantage of the application of synthetic boundary cells of the type shown in Figure 15a is that only a few microliters corresponding to a few micrograms/nanograms of reactant are required.

This type of synthetic boundary experiment was recently adapted to carry out crystallization reactions inside the spinning cell of the ultracentrifuge and was named “synthetic boundary crystallization ultracentrifugation” [120, 121]. Here, a small amount of Na_2S was layered upon a solution of CdCl_2 containing a stabilizer. A fast reaction to CdS with subsequent stabilization of the small nanoparticles takes place according to the scheme shown in Figure 16. [121].

The advantages of this technique lie in the fast chemical reaction within the very small reaction zone and the quenching of additional particle growth in lack of the second reaction partner as soon as the particles move out of the reaction zone by sedimentation or diffusion processes. These particles are then fractionated according to their size and density and a particle size distribution can be determined as discussed above. However, as the formed nanoparticles are very small, they show significant diffusion so that they can diffuse back into the reaction boundary and grow further, thus forming the second growth generation of particles. This process is repeated until the reaction partner in the reaction zone is used up (which usually occurs within a few minutes), so that the particles only sediment due to their size/density with the usual diffusion broadening of the boundary. By this technique, different growth stages of nanoparticles can be

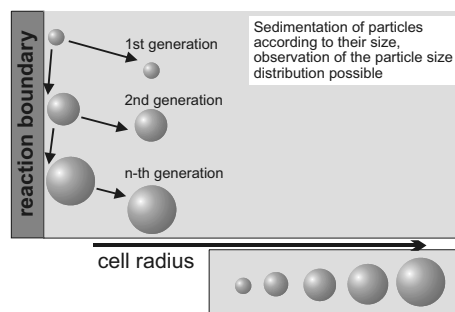


Figure 16. Schematic representation of synthetic boundary crystallization ultracentrifugation.

investigated. However, due to the extensive diffusion of the particles, the individual particle size distributions become extensively smeared so that they are only detected as a continuous distribution. Nevertheless, even such data can show the different stabilizer capabilities with a resolution in the Angström range as shown for CdS in Figure 17 [120, 121].

Another elegant way to observe reactions with a synthetic boundary technique was introduced by Wandrey and Bartkowiak [122]. They were able to observe the formation of polyelectrolyte complex membranes between two oppositely charged polyelectrolytes and the influence of parameters such as pH, ionic strength, component ratio, and temperature. Also, the membrane formation kinetics could be detected as overlaying of the two polymer solutions resulted in the formation of a thin membrane at the solution interface which could be precisely detected and its thickness measured.

4.5. Determination of Sample Homogeneity, Efficiency of Chemical Reactions, and Determination of Extinction Coefficients

In many fields of polymer or colloid chemistry, complicated complexes or hybrid colloids are synthesized. It is often desirable to have a quick and convenient check for the efficiency of the reaction as well as a check of sample homogeneity. Sedimentation velocity experiments can be used very advantageously here due to the fractionation without any stationary phase as is demonstrated for the case of iron oxyhydroxide particles partly stabilized in a self-assembling microgel of κ -carrageenan (Fig. 18) [123]. If one component selectively absorbs light (FeOOH) and the second does not (κ -carrageenan), one can selectively detect the absorption of the iron oxide in the polymeric superstructures with absorption optics, whereas all components together are detected by the simultaneously used Rayleigh interference optics. Here it must be stated that most colored inorganic compounds have a high extinction coefficient and are thus almost exclusively detected in the UV/vis absorption optics, whereas

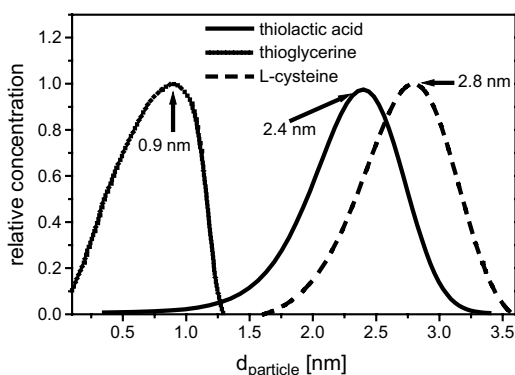


Figure 17. Apparent particle size distributions of CdS in the presence of different stabilizer molecules as detected by synthetic boundary crystallization ultracentrifugation. Reprinted with permission from [121], L. Börger et al., *Colloids Surf., A* 163, 29 (2000). © 2000, Elsevier Science.

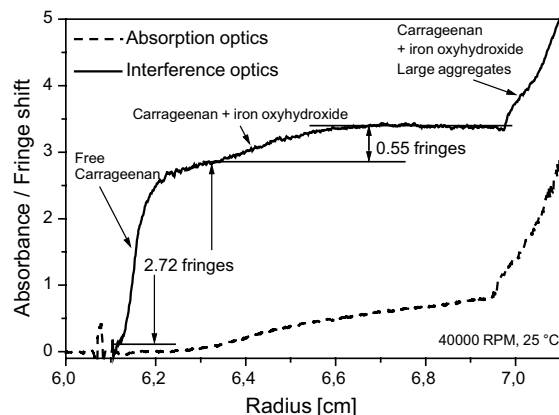


Figure 18. Iron oxyhydroxide in κ -carrageenan microgels. Detection of the different species by combination of UV/vis and refractive index detection. Reprinted with permission from [123], F. Jones et al., *Colloid Polym. Sci.* 278, 491 (2000). © 2000, Springer-Verlag.

the simultaneously applied interference optics almost exclusively represents the local polymer concentrations which can be converted to the real concentrations via the refractive index increment and the known refractive index of the solvent. From Figure 18, three species are clearly quantitatively detected: free unbound κ -carrageenan, κ -carrageenan + iron oxyhydroxide microgels, and larger cross-linked aggregates. The control of efficiencies of chemical reactions was also reported for complicated complexes between oppositely charged polyelectrolytes [124].

If the change in the refractive index of a sample (Rayleigh interference optics) is simultaneously detected with its absorption at a specified wavelength, extinction coefficients can be determined [125]. This is not particularly interesting if a single component is considered, but for mixtures the analytical ultracentrifuge is often the only method capable of determining the extinction coefficient of a specified component in a complicated mixture. The extinction coefficient can be calculated from a concentration reading in the Rayleigh interference scan which must be converted to the concentration unit of desire using the refractive index increment and the corresponding absorption. Figure 19 demonstrates this for ZnO prepared in polystyrene–polymethacrylic acid (PS–PMAA) micelles.

An extinction coefficient based on an absorption reading taken in a spectrophotometer under the assumption that all Zn^{2+} have reacted to ZnO delivers a low extinction coefficient of less than $1000 \text{ L mol}^{-1} \text{ cm}^{-1}$ due to the majority of UV/vis inactive species. Therefore, it is of interest to detect which amount of the sample is the spectroscopically active ZnO. Figure 19a shows the results and confirms that only a minor amount of the mixture is responsible for the detected light absorption. From the interference scans in Figure 19a, it can be seen that the component with a similar sedimentation velocity as the ZnO-filled micelles detected by the corresponding UV-absorption scans has only a concentration of 0.18 fringes. The major part is a considerably slower sedimenting component (micelles with unreacted Zn^{2+}). A third component (polymer or empty micelles) is also detected.

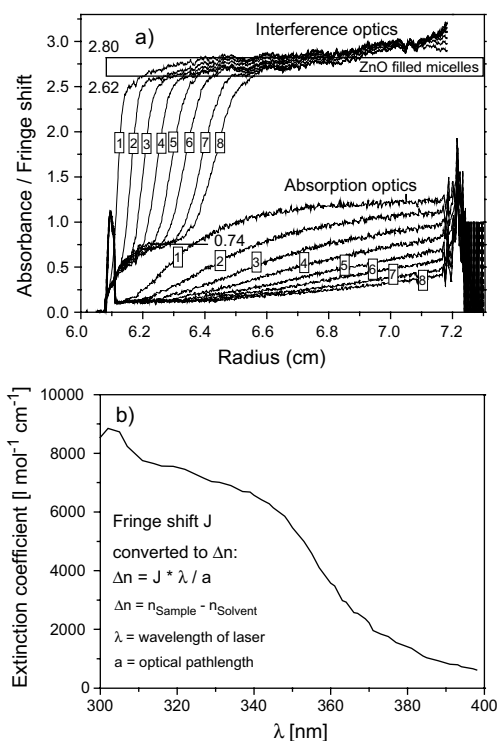


Figure 19. Determination of the extinction coefficient of ZnO in PS-PMAA micelles [104]. (a) Sedimentation velocity profiles acquired simultaneously with Rayleigh interference and absorption optics (315 nm). Run parameters: 20,000 rpm, scan interval 2 min. The numbers represent the corresponding interference and absorption scans. (b) Wavelength dependence of the extinction coefficient for ZnO prepared in PS-PMAA micelles. The particle diameter of the ZnO (from TEM) is 3.2–6.7 nm. The diameter of the micelles (from light scattering) is 64.4 ± 33.9 nm. Reprinted with permission from [104], H. Cölfen et al., *Prog. Colloid Polym. Sci.* 107, 136 (1997). © 1997, Springer-Verlag.

The interference fringe shift of the ZnO-filled micelles can be converted to a concentration and this can be related to a spectrum of the ZnO in the ultracentrifuge cell, giving the wavelength dependence of the ZnO extinction coefficient (Fig. 19b). The extinction coefficient is found to reach about $9000 \text{ L mol}^{-1} \text{ cm}^{-1}$. This illustrates how important the separation is to determine the spectral properties of the optically active component in a complicated mixture. Many more variations of such experiments are possible, showing that the separation capability of the AUC can be used not only to determine the concentrations of the individual compounds but also to elicit their spectral properties if they absorb light.

4.6. Analytical Ultracentrifugation of Nanoparticles Sorted by Systems

Table 2 gives some examples of nanoparticle systems that have been investigated by AUC with references to the original literature. The table is by no means exhaustive or representative and is just meant to guide the reader to the original literature if solutions for a particular nanoparticulate system are sought.

5. CURRENT TRENDS IN ANALYTICAL ULTRACENTRIFUGATION

The current trends in analytical ultracentrifugation can be divided into three subcategories: (a) improvement of data evaluation methodologies, (b) new detection systems, and (c) application of analytical ultracentrifugation to novel systems apart from the classical biomolecules.

5.1. Improvement of Data Evaluation Methodologies

Progress in computer and electronic technology has greatly facilitated the analysis capabilities of analytical ultracentrifugation and catalyzed the rebirth of this technique. Nowadays, it is relatively simple to apply fitting functions for all kinds of experimental output and, furthermore, it is possible to acquire data fast and conveniently even when simultaneously using several different methods of detection. Therefore, a major current trend in analytical ultracentrifugation is the development of better evaluation methodologies and algorithms. One example is the simultaneous radial and wavelength analysis of sedimentation equilibrium experiments possible with the Optima XL-I ultracentrifuge [153]. A complicated interacting system exhibiting three different chromophores and consisting of the Band3 membrane protein, a small ligand, oxyhemoglobin, and the complexes between these components—an 11-component system overall—could be successfully analyzed. These investigations are also applicable to complicated colloid mixtures. This amounts to seven more components than possible before when analyzing a concentration profile acquired at a single wavelength. The increase in components that can be resolved is achieved by the acquisition of as much experimental information as possible—in this case wavelength scans at different radii as well as radial scans at different wavelengths. From this information, it is possible to create a two-dimensional data surface in a radius–wavelength–absorption space which allows a proper analysis by fitting procedures. Therefore, it is not surprising that more and more scientists are using the capability of scanning at multiple wavelengths [154, 155]. A further enhancement of the data space is achieved by the application of several rotational speeds in the experiments. As this increases the experimental time, so-called short-column techniques [156, 157], which considerably decrease the time to reach the sedimentation equilibrium by the application of a shorter solution column in the ultracentrifuge cell, are becoming popular as long as the resolution of the optical system is still sufficient for the short solution column. However, for the mainly polydisperse nanoparticles, such an approach is restricted.

Significant effort has also been put into other efficient analyses of ultracentrifuge data which generally increases the sensitivity of ultracentrifuge experiments. Nowadays, components can be identified, which are almost not visible in the experimental raw data and thus could not be recognized in the old days of analytical ultracentrifugation. As the Rayleigh interference system of the XL-I ultracentrifuge allows a rapid acquisition of large data sets, the confidence intervals of fitting procedures in general can be

Table 2. Application of AUC to different nanoparticulate systems.

System	Experiment type/quantity	Ref.
Latex dispersions	Sedimentation velocity/particle size distribution; static and dynamic density gradient/particle density	Polystyrene [14]; polystyrene, polybutylacrylatestyrene, polybutadiene, polyethylacrylate [15]; polystyrene [16]; polystyrene, polybutylacrylate (also styrene and acrylonitrile grafted), polybutadiene, acrylic homopolymer and copolymer dispersions [17]; polychloropropene [96]; polystyrene, polystyrene/polybutadiene, polystyrene-co-butadiene, polychloropropene [99]; polystyrene, polystyrene-co-butadiene, styrene, and acrylonitrile grafted polybutadiene [101]; polystyrene [102]; polyurethane [105]; polystyrene [106]; polystyrene, polybutadiene, Polybutylacrylate-co-butadiene [109]
Inorganic nanoparticles	Sedimentation velocity/particle size distribution	Au [3]; Au [94]; ZrO ₂ [98]; Au ₅₅ cluster [100]; Pt, ZnO [103]; ZnO, Au, CdS, Pt [104]; CdS [105]; silica [106]; β -FeOOH [109]; CdS [120]; CdS [121]; iron oxide [126]; surfactant-encapsulated (NH ₄)[H ₃ Mo ₅₇ V ₆ (NO)(6)O-183 H ₂ O(18)] [127]
Inorganic complexes	Sedimentation equilibrium/molar mass	Zr complexes [55]; Zr complexes [56]
Magnetic fluids	Sedimentation velocity	Fe ₃ O ₄ [128]; Fe ₃ O ₄ [129]
Microgels	Sedimentation velocity/composition and density	Styrene-butadiene [117]; acrylic acid [118]; polystyrene-poly-4-vinylpyridine microgels [130]
Gels	Sedimentation velocity and equilibrium/swelling degree and pressure, amount of soluble compounds	Gelatin, κ -carrageenan, agar, casein [116]; gelatin, κ -carrageenan, agar, casein [131]; other systems (reviews)
Emulsions	Sedimentation equilibrium	SDS-stabilized <i>n</i> -decane in water [112]; food emulsions [113]; Legumin-stabilized <i>n</i> -decane in water [114]; legumin-stabilized <i>n</i> -decane in water [132]
Supramolecular assemblies and polymers	Sedimentation equilibrium/molar mass, sedimentation velocity/particle size	Co-coordination arrays [133]; Co-coordination arrays [134]; Fe-coordination polymers [135]; Co-coordination arrays [136]
Polyelectrolyte complexes	Sedimentation velocity/particle size and composition, sedimentation equilibrium/molar mass and interaction and membrane characteristics; synthetic boundary/membrane formation	Alginate/chitosan [122]; polysyrenesulfonate/polydiallyldimethylaminchlorid acrylamide [124]
Micelles	Sedimentation velocity/composition; dynamic density gradient/composition	Polymampholyte/fluorinated and hydrogenated dodecanoic acid [137]; lipid and detergent micelles [138]; review, different systems [139]; polystyrene- <i>b</i> -polyisoprene, polystyrene- <i>b</i> -poly(ethylene-co-propylene) [140]; polylactide-co-polyethyleneglycol [141]; enzymes in reverse micelles [142]
Dendrimers	Sedimentation velocity and sedimentation equilibrium/hydrodynamics	Carbohydrate-coated polypropyleneimine dendrimers [143]; lactosylated polyamidoamine dendrimers [144]
Hybrid colloids	Sedimentation velocity/composition/particle size	Au/polystyrenesulfonate microgels, CdS or Au in polystyrene- <i>b</i> -poly-4-vinylpyridin micelles, Pt in polyethyleneoxide-polymethacrylic acid [104]; Calcium phosphates in alkylated polyethyleneoxide- <i>b</i> -polymethacrylic acid [108]; FeOOH, NiOOH, and CoOOH in κ -carrageenan microgels [123]; review of various systems [145]; CdS in reverse micelles [146]; Pt and Pd in polystyrene- <i>b</i> -polyethyleneoxide/cetylpyridiniumchloride mixed micelles [147]; Au, Pt, and Pd in poly-2-vinylpyridine- <i>b</i> -polyethyleneoxide micelles [148]; Pt, Pd, Rh, and Cu in polyethyleneoxide- <i>b</i> -polyethyleneimine [149]
Organic colloids	Sedimentation equilibrium; sedimentation velocity/composition, molar mass	Cu-phtalocyanine [102]; κ -casein particles [150]; κ -casein particles [151]
Nanocapsules	Sedimentation velocity, density gradient/composition	Oil-filled polybutylcyanoacrylate nanocapsules [152]

significantly improved. However, the interference data contain time-invariant and radial-invariant noise components in addition to the random noise so that an efficient algebraic method was developed for the elimination of the time- and radial-invariant noise [158]. This leads to a high sensitivity of Rayleigh interference data even for such experiments where the sedimentation boundary can only barely be traced due to the noise components. The so-improved data sets can then be used for fitting to approximate analytical and numerical solutions of the Lamm equation. It is also possible to eliminate systematic noise components in the interference data of sedimentation equilibrium profiles by extraction of the time-invariant noise during the approach to equilibrium [159]. It turned out by this approach that the sensitivity of the Rayleigh interference optics for sedimentation equilibrium experiments can be improved by an order of magnitude so that equilibrium experiments with concentrations as low as 50 $\mu\text{g/mL}$ are no problem for Rayleigh interference detection. Very recently, the described systematic noise decomposition method [158] has been applied for linear least squares modeling of the sedimenting boundary by a superposition of $g(s)$ of ideal nondiffusing components [160]. This approach turned out to be especially advantageous for data acquired during a large time interval so that, in such cases, an improved resolution could be achieved especially for heterogeneous mixtures. A very recent advance is the determination of molar mass distributions from the fitting of finite-element solutions of the Lamm equation (8) paired with regularization algorithms as discussed before [51]. However, the range of successful application still needs to be explored.

5.2. New Detection Systems for the XL-I Ultracentrifuge

Computer-based picture evaluation allows the on-line capture of Schlieren patterns, enabling the fast and efficient evaluation of these records, which previously had to be photographed [9, 10, 161, 162]. The on-line digitization and picture evaluation of these optical records rely on the proper detection of the zeroth-order Fresnel fringe, which is the detected Schlieren curve in Figure 2a. Either by means of picture manipulation performed in order to facilitate a proper detection of the Schlieren curve even with a nonuniformly illuminated picture or by additional consideration of higher order Fresnel fringes, the concentration gradient curve can be properly detected automatically. Especially with the system built at the University of Leicester/Nottingham [10], high rates of data acquisition can be achieved with good data quality so that the on-line Schlieren system proves its virtues. This system is currently being adapted to the XL-I ultracentrifuge. Also, the Schlieren optics was set up on a preparative ultracentrifuge [12]. A potentially interesting optical system that should also be adaptable to XL ultracentrifuges is the Lebedev interferometer, which gives an interference pattern but with a Schlieren peak for a sedimenting boundary [163]. Therefore, the fast evaluation algorithms developed for the Rayleigh interferometer should be applicable here as well, resulting in high-quality Schlieren images.

Another system that is currently commercially available on the XL-I ultracentrifuge is the fluorescence detector developed by Schmidt and Riesner [13] and adapted to the XL-I by MacGregor and Laue [18]. These systems are designed to be simultaneously applicable with the present absorption and Rayleigh interference optics with the exception of the Schlieren optics, which uses the optical path of the interference optics. Further current approaches toward the faster detection of UV/vis data are under way in the laboratories of Laue and Cölfen [164].

5.3. Application of Analytical Ultracentrifugation to Novel Systems

Apart from biological systems, analytical ultracentrifugation is more and more being applied to complicated synthetic systems, for example, supramolecular assemblies and polymers [133–136], colloidal clusters [127], smallest colloids and their interactions with stabilizers [100, 120, 121, 127], synthetic polyelectrolytes [165–169] and complexes thereof [124], micelles [139–141], components inside micelles [142], dendrimers [143, 144], and hybrid colloids between organic and inorganic matter [108, 148, 149]. In most of these applications, advantage is taken of the simultaneous acquisition of Rayleigh interference and UV/vis absorption data. Insofar, it can be speculated how much a simultaneous application of additional detectors could yield further information and thus would open further applications. A visionary paper about future requirements in ultracentrifuge methodology and detection systems was published by Mächtle [170] more than 10 years ago, and it can at least be stated that the simultaneous application of as many detectors as possible as already realized in size exclusion chromatography is advantageous and will open up new applications for AUC.

6. AVAILABILITY OF FREE EVALUATION SOFTWARE

In general, most of the best evaluation software for analytical ultracentrifugation experiments is still free and shared among different user groups.

To download free evaluation software, one can use several offers: <ftp://bbri.harvard.edu/dka200/anonymous/rasmb/spin/> at the Boston Biomedical Research Institute or <http://www.cauma.uthscsa.edu/software> at the University of Texas Center for Analytical Ultracentrifugation of Macromolecular Assemblies. At both sites, one can find a comprehensive collection of the freely available evaluation software.

Furthermore, there is a user group called RASMB (Reversible Associations in Structural and Molecular Biology), which is a discussion platform for the study of interacting systems and analytical ultracentrifugation. However, do not hesitate to be included on this list if you are not directly working in the field of biochemistry/biophysics as many general aspects of analytical ultracentrifugation are addressed on this discussion platform. To be included on the e-mail list, check out <http://rasmb-email.bbri.org/mailman/listinfo/rasmb>. On the RASMB, there are further links to all relevant Internet sites related to AUC.

7. CONCLUSION

Analytical ultracentrifugation is one of the most universally applicable and variable physicochemical techniques for characterization of colloidal or polymeric systems in solution, dispersion, or emulsion. The power of analytical ultracentrifugation lies in the fractionation of the sample due to either the molar mass/size (sedimentation velocity/sedimentation equilibrium) or the chemical structure (density gradient) in the solvent and therefore the possibility to measure distributions without the interaction with any stationary phase or solvent flows as occurs in current chromatographic techniques. Wherever information is sought for the individual components in a mixture, analytical ultracentrifugation is among the first techniques of choice. On the other hand, the sedimentation equilibrium is an equilibrium well described by thermodynamics. Thus, it is possible to derive information even on complicated or interacting systems on an absolute basis and without disturbing this equilibrium. There are many different physicochemical quantities that can be determined. However, simple investigations such as those of sample homogeneity can provide much information on a system. But a complete physicochemical characterization is also possible, often with information that cannot be obtained by other techniques. Similar to other analytical techniques, the rapid computer and electronics development of the past years was of benefit for analytical ultracentrifugation. This development provides many new applications, improved sensitivity of the experiments, and even the realization of evaluation approaches not possible so far. Briefly stated, not only has the amount of experimental data from an ultracentrifuge experiment been increased but also the amount of information. This has led to a resurgence of interest in this technique. Especially if multidetection systems can be realized on ultracentrifuge platforms, new dimensions of analytical information will be available from a single sedimentation velocity experiment. Therefore, a synergy between ultracentrifuge hardware and methodology development can be expected which will lead to an increasing number of applications.

In biochemistry/biophysics, analytical ultracentrifugation is once again gaining importance after a slowdown in the 1980s. The same trend is not unlikely for the field of polymer or colloid chemistry although so far many chemists are not yet aware of the potential of analytical ultracentrifugation.

GLOSSARY

Analytical ultracentrifugation Analytical observation of sedimentation processes at speeds up to 60000 RPM.

Density gradient Separation of a binary mixture to a continuous concentration and thus density gradient in the ultracentrifugal field.

Lamm equation The basic equation of analytical Ultracentrifugation which describes the transport process by sedimentation and diffusion in the centrifugal field.

Partial specific volume The volume change in ml if one gram of pure sample is added to an infinite amount of solvent.

Sedimentation coefficient Detected Sedimentation velocity normalized to gravitational force.

Sedimentation equilibrium experiment Particle sedimentation at moderate speed where sedimentation is balanced by counter diffusion to yield the absolute molar mass.

Sedimentation velocity experiment Particle sedimentation at very high speeds to determine the sedimentation coefficient.

Synthetic boundary experiment Overlaying of a solvent onto a solution to create a liquid interface.

REFERENCES

1. T. Svedberg and J. B. Nichols, *J. Am. Chem. Soc.* 45, 2910 (1923).
2. T. Svedberg and K. O. Pedersen, "The Ultracentrifuge." Clarendon, Oxford, 1940.
3. T. Svedberg and H. Rinde, *J. Am. Chem. Soc.* 46, 2677 (1924).
4. R. Giebler, in "Analytical Ultracentrifugation in Biochemistry and Polymer Science" (S. E. Harding, A. J. Rowe, and J. C. Horton, Eds.), p. 16. Royal Society of Chemistry, Cambridge, UK, 1992.
5. H. Kim, R. C. Deonier, and J. W. Williams, *Chem. Rev.* 77, 659 (1977).
6. T. M. Laue, in "Analytical Ultracentrifugation in Biochemistry and Polymer Science" (S. E. Harding, A. J. Rowe, and J. C. Horton, Eds.), p. 63. Royal Society of Chemistry, Cambridge, UK, 1992.
7. A. Rowe, S. Wynne Jones, D. G. Thomas, and S. E. Harding, in "Analytical Ultracentrifugation in Biochemistry and Polymer Science" (S. E. Harding, A. J. Rowe, and J. C. Horton, Eds.), p. 49. Royal Society of Chemistry, Cambridge, UK, 1992.
8. H. Cölfen and W. Borchard, *Proc. SPIE* 2136, 307 (1994).
9. U. Klodwig and W. Mächtle, *Colloid Polym. Sci.* 267, 1117 (1989).
10. A. C. Clewlow, N. Errington, and A. J. Rowe, *Eur. Biophys. J.* 25, 311 (1997).
11. P. H. Lloyd, "Optical Methods in Ultracentrifugation, Electrophoresis and Diffusion." Oxford Univ. Press, 1974.
12. W. Mächtle, *Prog. Colloid Polym. Sci.* 113, 1 (1999).
13. B. Schmidt and D. Riesner, in "Analytical Ultracentrifugation in Biochemistry and Polymer Science" (S. E. Harding, A. J. Rowe, and J. C. Horton, Eds.), p. 176. Royal Society of Chemistry, Cambridge, UK, 1992.
14. H. J. Cantow, *Makromol. Chem.* 70, 130 (1964).
15. W. Scholtan and H. Lange, *Kolloid Z. Z. Polym.* 250, 782 (1972).
16. H. G. Müller, *Colloid Polym. Sci.* 267, 1113 (1989).
17. W. Mächtle, in "Analytical Ultracentrifugation in Biochemistry and Polymer Science" (S. E. Harding, A. J. Rowe, and J. C. Horton, Eds.), p. 147. Royal Society of Chemistry, Cambridge, UK, 1992.
18. L. K. MacGregor and T. M. Laue, *Biophys. J.* 76, A357 (1999).
19. H. K. Schachman, "Ultracentrifugation in Biochemistry." Academic Press, New York, 1959.
20. A. Böhm, S. Kielhorn Bayer, and P. Rossmann, *Prog. Colloid Polym. Sci.* 113, 121 (1999).
21. W. F. Stafford, in "Analytical Ultracentrifugation in Biochemistry and Polymer Science" (S. E. Harding, A. J. Rowe, and J. C. Horton, Eds.), p. 359. Royal Society of Chemistry, Cambridge, UK, 1992.
22. J. C. Lee and S. Rajendran, in "Modern Analytical Ultracentrifugation" (T. M. Schuster and T. M. Laue, Eds.), p. 138. Birkhäuser, Boston, 1994.
23. R. J. Goldberg, *J. Phys. Chem.* 57, 194 (1953).
24. N. Muramatsu and A. P. Minton, *Anal. Biochem.* 168, 345 (1988).
25. K. E. van Holde and W. O. Weischet, *Biopolymers* 17, 1387 (1978).
26. K. Schilling, Ph.D. thesis, Potsdam, 1999.
27. B. Demeler, H. Saber, and J. C. Hansen, *Biophys. J.* 72, 397 (1997).
28. J. Geiselmann, T. D. Yager, S. C. Gill, P. Camettes, and P. H. von Hippel, *Biochemistry* 31, 111 (1992).

29. S. C. Gill, T. D. Yager, and P. H. von Hippel, *J. Mol. Biol.* 220, 325 (1991).
30. J. C. Hansen and D. Lohr, *J. Biol. Chem.* 268, 5840 (1993).
31. J. C. Hansen, J. Ausio, V. H. Stanik, and K. E. van Holde, *Biochemistry* 28, 9129 (1989).
32. D. A. Yphantis, *Biophys. J.* 45, 324a (1984).
33. W. F. Stafford, *Anal. Biochem.* 203, 295 (1992).
34. N. Errington, O. Byron, and A. J. Rowe, *Biophys. Chem.* 80, 189 (1999).
35. W. F. Stafford, *Biophys. J.* 66, A280 (1994).
36. W. F. Stafford, *Biophys. J.* 74, A301 (1998).
37. W. F. Stafford, in "Modern Analytical Ultracentrifugation" (T. M. Schuster and T. M. Laue, Eds.), p. 119. Birkhäuser, Boston, 1994.
38. J. Behlke and O. Ristau, *Eur. Biophys. J.* 25, 325 (1997).
39. J. Behlke and A. Knespel, *J. Cryst. Growth* 158, 388 (1996).
40. O. Lamm, *Ark. Math. Astron. Fysik B* 21, 1 (1929).
41. L. A. Holladay, *Biophys. Chem.* 10, 187 (1979).
42. J. Behlke and O. Ristau, *Prog. Colloid Polym. Sci.* 107, 27 (1997).
43. L. A. Holladay, *Biophys. Chem.* 11, 303 (1980).
44. J. Philo, in "Modern Analytical Ultracentrifugation" (T. M. Schuster and T. M. Laue, Eds.), p. 156. Birkhäuser, Boston, 1994.
45. J. Behlke and O. Ristau, *Biophys. J.* 72, 428 (1997).
46. J. Philo, *Biophys. J.* 72, 435 (1997).
47. B. Demeler and H. Saber, *Biophys. J.* 74, 444 (1998).
48. P. Schuck, C. E. McPhee, and G. J. Howlett, *Biophys. J.* 74, 466 (1998).
49. P. Schuck, *Biophys. J.* 75, 1503 (1998).
50. P. Schuck and D. B. Millar, *Anal. Biochem.* 259, 48 (1998).
51. P. Schuck, *Biophys. J.* 78, 1606 (2000).
52. P. Schuck, M. A. Perugini, N. R. Gonzales, G. J. Howlett, and D. Schubert, *Biophys. J.* 82, 1096 (2002).
53. K. E. van Holde and R. L. Baldwin, *J. Phys. Chem.* 62, 734 (1958).
54. D. A. Yphantis, *Ann. N.Y. Acad. Sci.* 88, 586 (1960).
55. K. A. Kraus and J. S. Johnson, *J. Am. Chem. Soc.* 75, 5769 (1953).
56. J. S. Johnson and K. A. Kraus, *J. Am. Chem. Soc.* 78, 3937 (1956).
57. J. M. Creeth and R. H. Pain, *Prog. Biophys. Mol. Biol.* 17, 217 (1967).
58. W. D. Lansing and E. O. Kraemer, *J. Am. Chem. Soc.* 57, 1369 (1935).
59. H. Fujita, "Foundations of Ultracentrifugal Analysis." Wiley, New York, 1975.
60. M. D. Lechner, in "Analytical Ultracentrifugation in Biochemistry and Polymer Science" (S. E. Harding, A. J. Rowe, and J. C. Horton, Eds.), p. 295. Royal Society of Chemistry, Cambridge, UK, 1992.
61. M. L. Johnson, J. J. Correia, D. A. Yphantis, and H. R. Halvorson, *Biophys. J.* 36, 575 (1981).
62. M. L. Johnson and S. G. Frazier, in "Methods in Enzymology" (C. H. W. Hirs and S. N. Timasheff, Eds.), Academic Press, San Diego, 1985.
63. D. K. McRorie and P. J. Voelker, "Self-Associating Systems in the Analytical Ultracentrifuge." Beckman Instruments, Fullerton, CA, 1993.
64. D. A. Yphantis and T. Arakawa, *Biochemistry* 26, 5422 (1987).
65. N. G. Dolinnaya, E. H. Braswell, J. A. Fossella, H. Klump, and J. R. Fresco, *Biochemistry* 32, 10263 (1993).
66. P. B. Harbury, T. Zhang, P. S. Kim, and T. Alber, *Science* 262, 1401 (1993).
67. J. Liu, T. M. Laue, H. U. Choi, L. H. Tang, and L. Rosenberg, *J. Biol. Chem.* 269, 28366 (1994).
68. T. M. Laue, M. A. Starovasnick, R. E. Klevit, and H. Weintraub, *Proc. Natl. Acad. Sci. U.S.A.* 92, 11824 (1995).
69. C. G. Lon, E. H. Braswell, D. Zhu, J. Apigo, J. Baum, and B. Bodsky, *Biochemistry* 32, 11688 (1993).
70. D. R. Hall, S. E. Harding, and D. J. Winzor, *Prog. Colloid Polym. Sci.* 113, 62 (1999).
71. D. Schubert and P. Schuck, *Prog. Colloid Polym. Sci.* 86, 12 (1991).
72. J. M. Creeth and S. E. Harding, *J. Biochem. Biophys. Methods* 7, 25 (1982).
73. S. E. Harding, J. C. Horton, and P. J. Morgan, in "Analytical Ultracentrifugation in Biochemistry and Polymer Science" (S. E. Harding, A. J. Rowe, and J. C. Horton, Eds.), p. 275. Royal Society of Chemistry, Cambridge, UK, 1992.
74. H. Cölfen and S. E. Harding, *Eur. Biophys. J.* 25, 333 (1997).
75. B. K. Milthorpe, P. D. Jeffrey, and L. W. Nichol, *Biophys. Chem.* 3, 169 (1975).
76. D. J. Winzor and P. R. Wills, in "Modern Analytical Ultracentrifugation" (T. M. Schuster and T. M. Laue, Eds.), p. 66. Birkhäuser, Boston, 1994.
77. P. R. Wills, M. P. Jacobsen, and D. J. Winzor, *Biopolymers* 38, 119 (1996).
78. H. Cölfen and D. J. Winzor, *Prog. Colloid Polym. Sci.* 107, 36 (1997).
79. P. R. Wills, M. P. Jacobsen, and D. J. Winzor, *Prog. Colloid Polym. Sci.* 107, 1 (1997).
80. G. B. Ralston and M. B. Morris, in "Analytical Ultracentrifugation in Biochemistry and Polymer Science" (S. E. Harding, A. J. Rowe, and J. C. Horton, Eds.), p. 253. Royal Society of Chemistry, Cambridge, UK, 1992.
81. R. Buchdahl, H. A. Ende, and L. H. Peebles, *J. Polym. Sci., Part C* 1, 143 (1963).
82. M. Meselson, F. W. Stahl, and J. Vinograd, *Proc. Natl. Acad. Sci. U.S.A.* 43, 581 (1957).
83. J. J. Hermans and H. A. Ende, *J. Polym. Sci., Part C* 1, 161 (1963).
84. J. J. Hermans, *J. Polym. Sci., Part C* 1, 179 (1963).
85. H. A. Ende, *Makromol. Chem.* 88, 159 (1965).
86. M. D. Lechner, *Macromol. Rapid Commun.* 18, 781 (1997).
87. M. D. Lechner, W. Mächtle, and U. Sedlack, *Prog. Colloid Polym. Sci.* 107, 148 (1997).
88. M. D. Lechner and W. Borchard, *Eur. Polym. J.* 35, 371 (1999).
89. H. Lange, *Colloid Polym. Sci.* 258, 1077 (1980).
90. W. Mächtle, *Colloid Polym. Sci.* 262, 270 (1984).
91. L. Börger, *Eur. Biophys. J.*, to appear.
92. P. M. Budd, *Prog. Colloid Polym. Sci.* 94, 107 (1994).
93. H. Cölfen and K. Schilling, *Prog. Colloid Polym. Sci.* 113, 44 (1999).
94. H. Rinde, The Distribution of the Sizes of Particles in Gold Sols, Ph.D. Thesis, Upsala, 1928.
95. J. B. Nichols, *Physics* 1, 254 (1931).
96. J. B. Nichols, E. O. Kramer, and E. D. Bailey, *J. Phys. Chem.* 36, 326 (1932).
97. H. Cölfen, Habilitation Thesis, Potsdam, 2001.
98. H. Cölfen, H. Schnablegger, A. Fischer, F. C. Jentoft, G. Weinberg, and R. Schlögl, *Langmuir* 18, 3500 (2002).
99. H. Lange, *Part. Part. Syst. Charact.* 12, 148 (1995).
100. D. H. Rapoport, W. Vogel, H. Cölfen, and R. Schlögl, *J. Phys. Chem. B* 101, 4175 (1997).
101. H. G. Müller and F. Herrmann, *Prog. Colloid Polym. Sci.* 99, 114 (1995).
102. W. Mächtle, *Biophys. J.* 76, 1080 (1999).
103. H. Cölfen and T. Pauck, *Colloid Polym. Sci.* 275, 175 (1997).
104. H. Cölfen, T. Pauck, and M. Antonietti, *Prog. Colloid Polym. Sci.* 107, 136 (1997).
105. H. G. Müller, *Prog. Colloid Polym. Sci.* 107, 180 (1997).
106. M. D. Lechner and W. Mächtle, *Prog. Colloid Polym. Sci.* 113, 37 (1999).
107. D. G. Kurth, P. Lehmann, D. Volkmer, H. Cölfen, M. J. Koop, A. Müller, and A. DuChesne, *Chem. Eur. J.* 6, 385 (2000).
108. M. Antonietti, M. Breulmann, C. G. Göltner, H. Cölfen, K. K. W. Wong, D. Walsh, and S. Mann, *Chem. Eur. J.* 4, 2493 (1998).
109. W. Mächtle, *Makromol. Chem.* 185, 1025 (1984).
110. K. Schilling and H. Cölfen, *Prog. Colloid Polym. Sci.* 113, 50 (1999).
111. P. M. Budd, R. K. Pinfield, and C. Price, *Prog. Colloid Polym. Sci.* 107, 189 (1997).
112. K. Strenge and A. Seifert, *Prog. Colloid Polym. Sci.* 86, 76 (1991).

113. A. Seifert, K. Strengge, M. Schultz, and H. Schmandtke, *Nahrung* 9, 989 (1991).
114. A. Seifert and K. D. Schwenke, *Prog. Colloid Polym. Sci.* 99, 31 (1995).
115. H. Cölfen, *Colloid Polym. Sci.* 273, 1101 (1995).
116. H. Cölfen, *Biotechnol. Genet. Eng.* 16, 87 (1999).
117. H. G. Müller, A. Schmidt, and D. Kranz, *Prog. Colloid Polym. Sci.* 86, 70 (1991).
118. W. Mächtle, G. Ley, and J. Streib, *Prog. Colloid Polym. Sci.* 99, 144 (1995).
119. R. Cohen, *C. R. Acad. Sci. Paris* 256, 3513 (1963).
120. L. Börger and H. Cölfen, *Prog. Colloid Polym. Sci.* 113, 23 (1999).
121. L. Börger, H. Cölfen, and M. Antonietti, *Colloids Surf., A* 163, 29 (2000).
122. C. Wandrey and A. Bartkowiak, *Colloids Surf., A* 180, 141 (2001).
123. F. Jones, H. Cölfen, and M. Antonietti, *Colloid Polym. Sci.* 278, 491 (2000).
124. N. Karibyants, H. Dautzenberg, and H. Cölfen, *Macromolecules* 30, 7803 (1997).
125. P. Voelker, *Prog. Colloid Polym. Sci.* 99, 162 (1995).
126. J. B. Nichols, E. O. Kramer, and E. D. Bailey, *J. Phys. Chem.* 36, 326 (1932).
127. D. G. Kurth, P. Lehmann, D. Volkmer, H. Cölfen, M. J. Koop, A. Müller, and A. Du Chesne, *Chem. Eur. J.* 6, 385 (2000).
128. A. Seifert, N. Buske, and K. Strengge, *Colloids Surf.* 57, 267 (1991).
129. A. Seifert and N. Buske, *J. Magn. Magn. Mater.* 122, 115 (1993).
130. E. E. Remsen, K. B. Thurmond, and K. L. Wooley, *Macromolecules* 32, 3685 (1999).
131. H. Cölfen, *Colloid Polym. Sci.* 273, 1101 (1995).
132. J. P. Krause, R. Wustneck, A. Seifert, and K. D. Schwenke, *Colloids Surf., B* 10, 119 (1998).
133. D. Schubert, J. A. van den Broek, B. Sell, H. Durchschlag, W. Mächtle, U. S. Schubert, and J. M. Lehn, *Prog. Colloid Polym. Sci.* 107, 166 (1997).
134. C. Tziatzios, H. Durchschlag, B. Sell, J. A. van den Broek, W. Mächtle, W. Haase, J. M. Lehn, C. H. Weidl, C. Eschbaumer, D. Schubert, and U. S. Schubert, *Prog. Colloid Polym. Sci.* 113, 114 (1999).
135. M. Schütte, D. G. Kurth, M. R. Linford, H. Cölfen, and H. Möhwald, *Angew. Chem., Int. Ed. Engl.* 37, 2891 (1998).
136. D. Schubert, C. Tziatzios, P. Schuck, and U. S. Schubert, *Chem. Eur. J.* 5, 1377 (1999).
137. A. F. Thünemann, K. Sander, W. Jaeger, and R. Dimova, *Langmuir* 18, 5099 (2002).
138. A. Lustig, A. Engel, and M. Zulauf, *Biochim. Biophys. Acta* 1115, 89 (1991).
139. R. W. Roxby, in "Analytical Ultracentrifugation in Biochemistry and Polymer Science" (S. E. Harding, A. J. Rowe, and J. C. Horton, Eds.), p. 609. Royal Society of Chemistry, Cambridge, UK, 1992.
140. M. Pacovska, K. Prochazka, Z. Tuzar, and P. Munk, *Polymer* 34, 4585 (1993).
141. S. A. Hagan, A. G. A. Coombes, M. C. Garnett, S. E. Dunn, M. C. Davies, L. Illum, and S. S. Davis, *Langmuir* 12, 2153 (1996).
142. N. A. Chebotareva, B. I. Kurganov, and A. A. Burlakova, *Prog. Colloid Polym. Sci.* 113, 129 (1999).
143. G. M. Pavlov, E. V. Korneeva, K. Jumel, S. E. Harding, E. W. Meijer, H. W. I. Peerlings, J. Fraser Stoddart, and S. A. Nepogodiev, *Carbohydr. Polym.* 38, 195 (1999).
144. G. M. Pavlov, E. V. Korneeva, R. Roy, N. A. Michailova, P. C. Ortega, and M. A. Perez, *Prog. Colloid Polym. Sci.* 113, 150 (1999).
145. H. Cölfen, Habilitation Thesis, Potsdam, 2001.
146. B. H. Robinson, T. F. Towey, S. Zourab, A. J. W. G. Visser, and A. Vanhoek, *Colloids Surf.* 61, 175 (1991).
147. L. M. Bronstein, D. M. Chernychov, G. I. Timofeeva, L. V. Dubrovina, P. M. Valetsky, E. S. Obolonkova, and A. R. Khokhlov, *Langmuir* 16, 3626 (2000).
148. L. H. Bronstein, S. N. Sidorov, P. M. Valetsky, J. Hartmann, H. Cölfen, and M. Antonietti, *Langmuir* 15, 6256 (1999).
149. S. N. Sidorov, L. M. Bronstein, P. M. Valetsky, J. Hartmann, H. Cölfen, H. Schnablegger, and M. Antonietti, *J. Colloid Interface Sci.* 212, 197 (1999).
150. H. M. Farrell, E. D. Wickham, H. J. Dower, E. G. Piotrowski, P. D. Hoagland, P. H. Cooke, and M. L. Groves, *J. Protein Chem.* 18, 637 (1999).
151. H. M. Farrell, T. F. Kumosinski, P. H. Cooke, P. D. Hoagland, E. D. Wickham, J. J. Unruh, and M. L. Groves, *Int. Dairy J.* 9, 193 (1999).
152. M. Wohlgemuth, W. Mächtle, and C. Mayer, *J. Microencaps.* 17, 437 (2000).
153. P. Schuck, *Prog. Colloid Polym. Sci.* 94, 1 (1994).
154. M. S. Lewis, R. I. Shrager, and S. J. Kim, in "Modern Analytical Ultracentrifugation" (T. M. Schuster and T. M. Laue, Eds.), p. 94. Birkhäuser, Boston, 1994.
155. A. P. Minton, *Prog. Colloid Polym. Sci.* 107, 11 (1997).
156. K. E. van Holde and R. L. Baldwin, *J. Phys. Chem.* 62, 734 (1958).
157. J. J. Correia and D. A. Yphantis, in "Analytical Ultracentrifugation in Biochemistry and Polymer Science" (S. E. Harding, A. J. Rowe, and J. C. Horton, Eds.), Royal Society of Chemistry, Cambridge, UK, 1992.
158. P. Schuck and B. Demeler, *Biophys. J.* 76, 2288 (1999).
159. P. Schuck, *Anal. Biochem.* 272, 199 (1999).
160. P. Schuck and P. Rossmanith, *Biopolymers* 54, 328 (2000).
161. H. Cölfen and W. Borchard, *Prog. Colloid Polym. Sci.* 94, 90 (1994).
162. D. Kisters and W. Borchard, *Prog. Colloid Polym. Sci.* 113, 10 (1999).
163. P. Lavrenko, V. Lavrenko, and V. Tsvetkov, *Prog. Colloid Polym. Sci.* 113, 14 (1999).
164. T. M. Laue and H. Cölfen, "Presentations on Advances in AUC and Hydro Meeting," 2002.
165. P. M. Budd, in "Analytical Ultracentrifugation in Biochemistry and Polymer Science" (S. E. Harding, A. J. Rowe, and J. C. Horton, Eds.), Royal Society of Chemistry, Cambridge, UK, 1992.
166. E. Görnitz, M. Hahn, W. Jaeger, and H. Dautzenberg, *Prog. Colloid Polym. Sci.* 107, 127 (1997).
167. G. J. Timofeeva, S. A. Pavlova, C. Wandrey, W. Jaeger, M. Hahn, K. J. Linow, and E. Görnitz, *Acta Polym.* 41, 479 (1990).
168. C. Wandrey and E. Görnitz, *Acta Polym.* 43, 320 (1992).
169. M. Hahn, E. Görnitz, and H. Dautzenberg, *Macromolecules* 31, 5616 (1998).
170. W. Mächtle, *Prog. Colloid Polym. Sci.* 86, 111 (1991).

RELATED LITERATURE

Although the primary literature cited above will give the reader an appropriate insight into the AUC analysis of nanoparticle systems, a selection of related literature follows which contains textbooks and books about recent AUC developments together with a short description. This is mainly for the reader who wants to learn more about AUC.

GENERAL TEXTBOOKS

There are several general books in the English language on analytical ultracentrifugation. All of them are quite out of date, but are nevertheless still useful both for the beginner and for the more experienced user if they are still available.

171. T. Svedberg and K. O. Pedersen, "The Ultracentrifuge." Clarendon, Oxford, 1940. The classical textbook about analytical ultracentrifugation still with much impact today.

172. H. K. Schachman, "Ultracentrifugation in Biochemistry." Academic Press, New York, 1959. A compact and useful book covering experimental and theoretical aspects.
173. C. H. Chervenka, "A Manual of Methods for the Analytical Ultracentrifuge." Spinco Division, Beckman Instruments, Palo Alto, CA, 1969. A very useful compilation of classical evaluation methods with examples.
174. T. J. Bowen and A. J. Rowe, "An Introduction to Ultracentrifugation." Wiley, London, 1970. An introduction for the beginner.
175. J. W. Williams, "Ultracentrifugation of Macromolecules." Academic Press, New York, 1972. A compilation of seminars covering polydisperse solute and self-associating systems in more detail.
176. H. Fujita, "Foundations of Ultracentrifugal Analysis." Wiley, New York, 1975. An exhaustive description of the mathematical theory behind analytical ultracentrifugation, not recommended for the beginner.

NEW BOOKS WITH RECENT DEVELOPMENTS

177. S. E. Harding, A. J. Rowe, and J. C. Horton, Eds., "Analytical Ultracentrifugation in Biochemistry and Polymer Science." Royal Society of Chemistry, Cambridge, UK, 1992. The most comprehensive modern book about analytical ultracentrifugation. A very good overview about methods and techniques of analytical ultracentrifugation and a valuable source of modern applications.
177. T. M. Schuster and T. M. Laue, Eds., "Modern Analytical Ultracentrifugation." Birkhäuser, Boston, 1994. A compilation of some modern trends in analytical ultracentrifugation.

SYMPOSIUM BOOKS WITH RECENT TRENDS IN ANALYTICAL ULTRACENTRIFUGATION OF THE LAST DECADE

178. W. Borchard, *Prog. Colloid Polym. Sci.* 86 (1991). Papers from the Seventh Symposium on Analytical Ultracentrifugation, Duisburg, 1991.
179. M. D. Lechner, *Prog. Colloid Polym. Sci.* 94, (1994). Papers from the Eighth Symposium on Analytical Ultracentrifugation, Osnabrück, 1993.
180. J. Behlke, *Prog. Colloid Polym. Sci.* 99 (1995). Papers from the Ninth Symposium on Analytical Ultracentrifugation, Berlin, 1995.
181. R. Jaenicke and H. Durchschlag, *Prog. Colloid Polym. Sci.* 107 (1997). Papers from the 10th Symposium on Analytical Ultracentrifugation, Regensburg, 1997.
182. H. Cölfen, *Prog. Colloid Polym. Sci.* 113 (1999). Papers from the 11th Symposium on Analytical Ultracentrifugation, Potsdam, 1999.
183. W. Borchard and A. Straatmann, *Prog. Colloid Polym. Sci.* 119 (2002). Papers from the 12th Symposium on Analytical Ultracentrifugation, Duisburg, 2001.

Applications of Electrodeposited Nanostructures

G. Palumbo, J. L. McCrea

Integran Technologies Inc., Toronto, Ontario, Canada

U. Erb

University of Toronto, Toronto, Ontario, Canada

CONTENTS

1. Introduction
 2. Synthesis and Structure of Electrodeposited Nanostructures
 3. Properties of Electrodeposited Nanostructures
 4. Applications of Electrodeposited Nanostructures
 5. Summary
- Glossary
References

1. INTRODUCTION

The concept of a new class of materials with an ultrafine grain structure possessing unique properties was first introduced by Gleiter [1] about two decades ago. Originally referred to as “interfacial materials,” the main characteristic of these materials is the enhanced volume fraction of their interface component (i.e., grain boundaries, triple junctions, quadruple nodes [2, 3]) compared with their polycrystalline counterpart as a consequence of the ultrafine grain structure. With the large proportion of atoms located at interfacial regions, it was suggested that the atomic and electronic structures of such a material might be different from the structures found in compositionally equivalent material in the amorphous or polycrystalline states. Today these materials are referred to as nanocrystalline or nanostructured materials and are generally defined as materials with a characteristic length scale (e.g., grain size, particle size, film thickness, structure size) less than 100 nm. In the case of bulk nanostructured materials this length scale is the grain size. In recent years, bulk nanostructured materials have generated much excitement in

the scientific community due to the many enhanced properties associated with the nanoscale grain structure, which have led to many new industrial applications.

Many synthesis techniques have been developed over the past 20 years to produce bulk nanostructured materials, including: physical and chemical vapor phase processing, mechanical attrition, consolidation of nanophase powders, crystallization of amorphous precursors, as well as chemical and electrochemical methods (e.g., [4, 5]). A common feature of most synthesis techniques is that they operate far from equilibrium conditions to favor nucleation of new grains and reduce growth of existing grains, thus promoting a nanocrystalline grain structure. Unlike many other synthesis techniques, electrodeposition is a single-step process that produces fully dense material without the need for secondary consolidation of powders or annealing of amorphous precursors. The focus of this chapter presented here is on electrodeposited nanostructures.

Over the past decade, electrodeposited nanostructures have advanced rapidly to commercial application because of the following factors: (1) an established industrial infrastructure (i.e., electroplating and electroforming industries), (2) a relatively low cost of application whereby nanomaterials can be produced by simple modification of bath chemistries and electrical parameters used in current plating and electroforming operations, (3) the capability in a single-step process to produce metals, alloys, and metal–matrix composites in various forms (i.e., coatings, freestanding complex shapes), and most importantly (4) the ability to produce *fully dense* nanostructures free of extraneous porosity. From the outset, the fully dense nanomaterials have displayed *predictable* material properties based upon their increased content of intercrystalline defects. This “predictability” in ultimate material performance has accelerated the adoption of electrodeposited nanomaterials by industry, whereby such

extreme grain refinement simply represents another metallurgical tool for microstructural optimization.

The development of a thorough understanding of the structure–property relationships of electrodeposited nanostructured materials over the years has enabled the “optimization” (rather than simple minimization) of the grain size of various nanostructured materials for specific industrial applications. In this chapter, current and emerging practical applications for electrodeposited nanostructured materials are presented and discussed in light of the enhanced properties relevant to the specific application.

2. SYNTHESIS AND STRUCTURE OF ELECTRODEPOSITED NANOSTRUCTURES

Electrodeposition is likely the simplest method of producing nanostructured materials. However, the earliest systematic studies on the use of electrodeposition to produce nanocrystalline materials were only published in the late 1980s [6, 7]. Potentially, any metal or alloy can be modified to yield nanocrystalline deposits during the electrodeposition procedure. Important processing parameters include bath composition, pH, temperature, overpotential, bath additives, etc. To date, a large number of systems (pure metals, alloys, composites, and ceramics) have been electrodeposited with average grain sizes less than 100 nm. For example, the literature contains numerous examples giving electrochemical processing windows for the synthesis of nanocrystalline pure metals (e.g., Ni [8–11], Co [12], Pd [13], Cu [12]), binary alloys (e.g., Ni–P [6, 7], Ni–Fe [14, 15], Zn–Ni [16, 17], Pd–Fe [18], Co–W [19]) and ternary alloys (e.g., Ni–Fe–Cr [20–22], Co–Fe–P [23]). Even multilayered structures or compositionally modulated alloys (e.g., Cu–Pb [24], Cu–Ni [25, 26], Ag–Pd [27], Ni–P [28]), metal–matrix composites (e.g., Ni–SiC [10, 23, 29], Ni–Al₂O₃, Ni–MoS₂ [23]), ceramics (e.g., ZrO₂ [30]), and ceramic nanocomposites (e.g., Ti_aPb_bO_c [31]) have been successfully produced by electrodeposition methods.

Electrodeposited bulk nanostructures, in the as-deposited condition, are fully dense materials, with negligible porosity (as determined by density [32] and position annihilation [33] measurements), unless deliberately produced in powder form. High-resolution electron microscopy has demonstrated that grain boundary structures in electrodeposited bulk nanostructures are similar to structures found in conventional polycrystalline materials [34]. Grain size measurements commonly show log normal grain size distributions [8] when the materials are deposited with an equiaxed grain structure. Average grain size and crystallographic texture can be controlled by various plating parameters, including but not limited to bath pH, current density, pulse parameters, and bath additions. Cross-sectional examination of thin (<3 μm) and thick (>1 mm) coatings has shown that the nanocrystalline structure is fully established right at the interface with the substrate and that the grain size is independent of coating thickness [35], in contrast to conventionally produced electrodeposits which often show considerable grain coarsening with increasing coating thickness [36]. Binary and ternary alloys typically show extended

solid solubility ranges, compared to materials produced under thermodynamic equilibrium conditions (for example, in Ni–P [6, 7] Zn–Ni [16], Co–W [19]).

Various coatings with thicknesses up to ~100 μm electrodeposited onto substrates to modify specific surface properties are probably the most widely known applications of electrodeposition technologies. It should be noted, however, that several other methods (e.g., brush plating, electrowinning, and electroforming) are used to produce bulk nanostructured materials as thick coatings (several mm thick) or as freestanding material in the form of sheet, foil, tubes, wire, mesh, plate, and foam. Table 1 lists examples of shapes and the corresponding applications of commonly produced electrodeposited and electroformed products.

3. PROPERTIES OF ELECTRODEPOSITED NANOSTRUCTURES

Many detailed investigations have focused on identifying the important structure–property relationships of nanocrystalline materials, attempting to correlate the distinct structure of these materials with various physical, chemical, mechanical, electrical, and magnetic properties. For example, extensive studies of fully dense nanocrystalline nickel produced by electrodeposition have indicated that the structure–property relationships can be categorized into two basic groups: (i) those that exhibit a strong dependence on grain size and (ii) those with weak grain size dependence. A summary of the various grain size dependent and independent properties is given in Table 2 [37]. Detailed descriptions

Table 1. Various shapes and applications of electrodeposited and electroformed products.

Shapes	Applications
Thin coatings (on substrates)	surface modification for wear and corrosion resistance; catalytic surfaces
Thick coatings (on substrates)	electrosleeve™; repair of worn components
Sheet, foil (freestanding)	gaskets; pressure control membranes; hydrogen purification membranes; thermal barriers; solar energy absorbers; microfoils; soft magnets
Tubes, wire (freestanding)	surgical tools; missile guidance systems; miniature gamma radiation sources
Mesh (freestanding)	filters; precision sieve screens; razor foils; printing screens; centrifuge screens
Plate (freestanding)	structural applications
Foam (freestanding)	filters; electromagnetic shielding; battery electrodes; catalyst carriers
Molds (freestanding)	CD stampers; embossing tools for holograms; compression, injection and pattern molds
Free forms	precision bellows; erosion shields for helicopters; trust chambers for rocket engines; components for micromagnetic motors, micro-optics, microactuators and microfiltration; shaped charge liners; precision reflectors and mirrors; nozzles
Powder	catalysts; reinforcements

Table 2. Grain size dependent and independent properties of electrodeposited nanocrystalline nickel.

Grain size dependent properties	
Property	Observation
Solid solubility	greatly enhanced
Hydrogen solubility	greatly enhanced
Localized corrosion	nearly eliminated
Corrosion potential	shifted to more noble potential
Defect structure in passive layer	higher defect density
Thermal stability	greatly reduced
Hydrogen diffusivity	greatly enhanced
Coefficient of friction	reduced by a factor of 2
Wear resistance	greatly enhanced
Strength	increased by a factor of 3 to 10
Ductility	greatly reduced
Hardness	increased by a factor of 5
Electrical resistivity	increased by a factor of 3
Grain size independent properties	
Property	Observation
Bulk density	reduced by <1%
Thermal expansion	unchanged
Young's modulus	unchanged
Adhesion to substrate (for coatings)	unchanged
Thickness of passive layer	same as polycrystalline (1.3 nm)
Resistance to salt spray environment	unchanged
Saturation magnetization	reduced by ~5%

Source: Adapted with permission from [37], A.-M. El-Sherik and U. Erb, in "Nickel-Cobalt 97" (F. N. Smith, Ed.), Vol. 4, p. 257. The Metallurgical Society of CIM, Montreal, 1997. © 1997, The Metallurgical Society of CIM.

of the enhanced properties associated with electrodeposited bulk nanostructured materials, relevant to specific industrial applications, will be given in the following section.

4. APPLICATIONS OF ELECTRODEPOSITED NANOSTRUCTURES

The starting point for the development of a particular application of electrodeposited bulk nanostructured materials is the realization that different properties scale differently with grain size. In this context material design and selection involves the optimization of all important property requirements, which then dictates the final grain size for a particular application. Other microstructural parameters, such as grain shape, crystallographic texture, grain boundary character distribution, alloying additions, and second phase particles, can also be further modified (if necessary) to design the final material. The development of a thorough understanding of the various material properties as a function of grain size over the years has led to the successful implementation of various electrodeposited bulk nanostructured materials for specific industrial applications. In the subsequent sections, several structural and functional applications

are discussed along with the relevant material properties integral for the application.

4.1. Structural Applications

As would be expected from Hall-Petch considerations, numerous practical applications for nanocrystalline materials are based upon opportunities for high strength structural components. Table 3 displays mechanical properties of nanocrystalline nickel (99.99%) with grain sizes of 10 and 100 nm, in comparison to conventional polycrystalline (10 μm) nickel. Remarkable increases in hardness, yield strength, and ultimate tensile strength are observed with decreasing grain size. It is also interesting to note that the work hardening coefficient decreases with decreasing grain size, to a negligible value at a grain size of 10 nm [38]. The ductility of the material decreases with decreasing grain size from 50% elongation to failure in tension for conventional material to 15% at 100 nm grain size and approximately 1% at 10 nm grain size. Ductility in bending was generally observed to be somewhat greater than in uniaxial tension. As is also shown in this table, the fatigue performance of the 100 nm material is fully consistent with that of the conventional Ni. Compared to conventional polycrystalline Ni, nanocrystalline Ni electrodeposits exhibit drastically reduced wear rates and lower coefficient of friction as determined in dry air pin-on-disk tests [37].

In a recent study on the tensile properties of electrodeposited nanocrystalline cobalt [39], the yield (0.2%) and ultimate tensile strengths for materials with an average grain size of approximately 12 nm were reported to be 1000–1100 and 1750–1950 MPa, respectively, while maintaining considerable ductility with elongation values ranging between 4 and 8%. For direct comparison, the yield (0.2%) and ultimate tensile strength for a coarse-grained polycrystalline cobalt counterpart with an average grain size larger than 1 μm were reported to be 370–400 and 760–860 MPa, respectively, with elongation values between 7 and 18%.

Table 3. Mechanical properties of conventional and nanocrystalline nickel.

Property	Nano-Ni		
	Conventional ^a 10 μm	100 nm	10 nm
Yield strength, MPa (25 °C)	103	690	>900
Ultimate tensile strength, MPa (25 °C)	403	1100	>2000
Tensile elongation, % (25 °C)	50	>15	1
Elongation in bending, % (25 °C)	—	>40	—
Modulus of elasticity, GPa (25 °C)	207	214	204
Vickers hardness, kg/mm ²	140	300	650
Work hardening coefficient	0.4	0.15	0.0
Fatigue strength, MPa (10 ⁸ cycles/air/25 °C)	241	275	—
Wear rate (dry air pin on disk), $\mu\text{m}^3/\mu\text{m}$	1330	—	7.9
Coefficient of friction (dry air pin on disk)	0.9	—	0.5

Source: "ASM Metals Handbook," Vol. 2. ASM International, Materials Park, OH, 1993.

4.1.1. Steam Generator Repair

One of the first large-scale structural applications of a bulk nanostructured material is the use of an electrodeposited nanocrystalline nickel microalloy as an *in-situ* repair technique for nuclear steam generator tubing [40, 41]. This so-called electrosleeve process [42] has been successfully implemented in both Canadian and U.S. pressurized water reactors and has been incorporated as a standard procedure for pressure tubing repair [43], wherein a thick coating (0.5–1.0 mm) of nanostructured Ni microalloy (80–100 nm grain size) is electrodeposited on the inside surface of steam generator tubes to form a complete structural repair at sites where the structural integrity of the original tube has been compromised (e.g., corrosion, stress corrosion cracking, etc.). Figure 1 shows a cutaway of an alloy 600 nuclear steam generator tube repaired with the electrosleeve process. The high strength and good ductility of the 100 nm grain size microalloy allows for an appropriate thickness (0.5–1 mm) for which the impact on fluid flow and heat transfer in the steam generator tube is minimized.

4.1.2. Wear and Corrosion Resistant Coatings

Also as a result of Hall–Petch strengthening, nanocrystalline materials display significant increases in hardness and strength relative to their coarser grained counterparts. Hardness increases on the order of 500% to 700% are typically observed [6, 44–49]. Deviations from Hall–Petch behavior have been noted at extremely fine grain sizes (i.e., <20 nm) and were attributed to the breakdown of dislocation pile-up mechanisms [49] and the potential for alternative “softening” mechanisms such as room temperature Coble creep [45] and triple line disclination processes [44, 50]. Table 4 summarizes the nanocrystalline grain sizes and corresponding hardness values for several nanocrystalline metals and alloys synthesized by electrodeposition.

The general relationship between wear performance and material hardness is often expressed by Archard’s law [51], which demonstrates that the volume loss due to wear should

Table 4. Typical hardness values achieved with electrodeposited bulk nanostructured materials.

Coating composition	Average grain size (nm)	Hardness (VHN)
Ni	11	660
Ni–7 wt% Mo	14	620
Ni–0.5 wt% P	<5	>1100
Ni–20 wt% Fe	15	690
Ni–15 wt% Cr–10 wt% Fe	12	890
Co	13	650
Co–1 wt% P	<10	680
Co–5 wt% P	<10	745
Co–30 wt% Fe–3 wt% P	15	890
Co–45 wt% Fe–10 wt% Zn	10	650
Co–12 wt% W	<100 nm	550
Zn–13 wt% Ni	60	425
Zn–20 wt% Ni	<100 nm	540

be inversely proportional to the hardness of the material. The applicability of this law to nanocrystalline materials has recently been demonstrated [52] where the grain size dependence of abrasive wear performance was examined using the commonly used Taber wear technique [53].

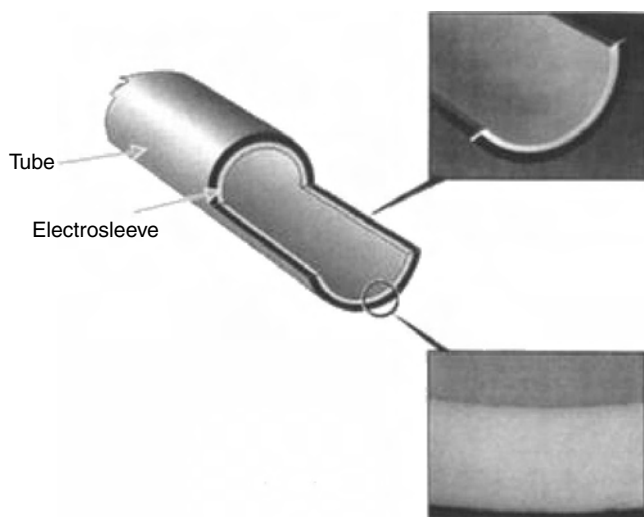


Figure 1. Cutaway view of an alloy 600 nuclear steam generator tube repaired with the electrosleeve process.

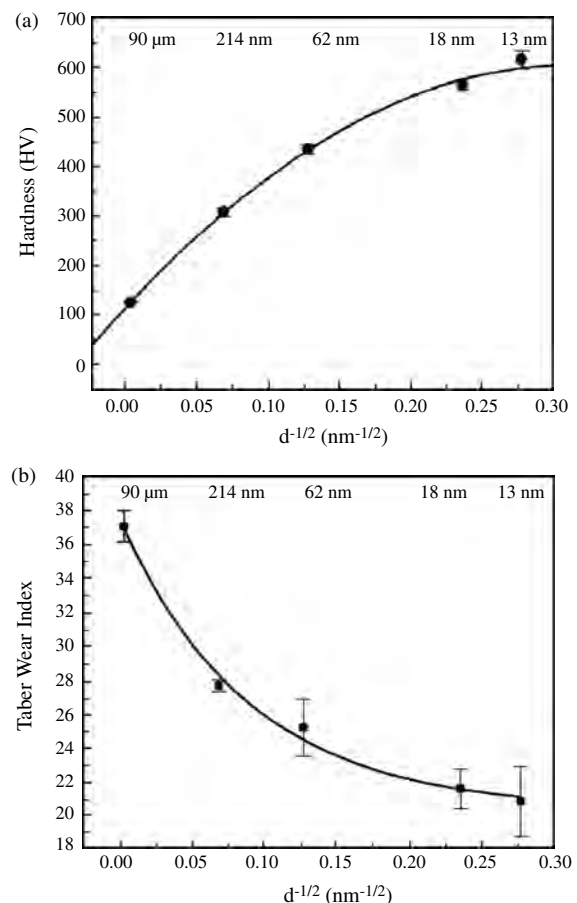


Figure 2. (a) Hardness as function of grain size for Ni. (b) Taber wear index as function of grain size for Ni. Adapted with permission from [52], D. H. Jeong et al., *Scripta Mater.* 44, 493 (2001). © 2001, Elsevier Science.

Figure 2 shows the effect of average grain size on both the hardness and Taber wear index (a measure of volume loss due to wear) for nickel. As shown, decreasing the grain size of Ni from 90 μm to 13 nm results in hardness increases from 125 to 625 VHN; commensurately, the Taber wear index is reduced from approximately 37 to 21.

Figure 3 shows the pin-on-disk (POD) volume wear loss for various nanocrystalline Co alloys relative to those obtained with mild steel, tool steel, and hard chrome. As noted in this figure, the wear resistance is no longer a simple function of the material hardness. When tested under identical conditions, the wear resistance of most of the nanocrystalline deposits exceeded that of hard chrome, even though their hardness values were lower. The POD volume wear loss values for nanocrystalline cobalt decreased with the addition of phosphorus (Co-4% P) and with precipitation hardening (Co-4% P, HT). The addition of iron results in a further decrease in the wear loss.

4.1.3. Environmentally Benign Replacements for Hard Chrome Electroplating

Electrodeposited hard chromium coatings (0.25 to 10 mil thick) are commonly used in both industrial and military applications [54–57] for imparting wear and erosion resistance to components. This is because of their intrinsic high hardness (600–1000 VHN) and low friction coefficient (<0.2) [58]. The most common (and most practical) means of depositing such hard chromium deposits has been through the use of chromic acid baths. However, health risks associated with the use of hexavalent chromium baths have been recognized since the early 1930s [59], wherein skin irritation and inflammation, particularly in the nasal passages, were identified. More recently, such hexavalent Cr baths have been shown to enhance the risk of cancer of the lung and nose [60]. Although significant progress has been made in

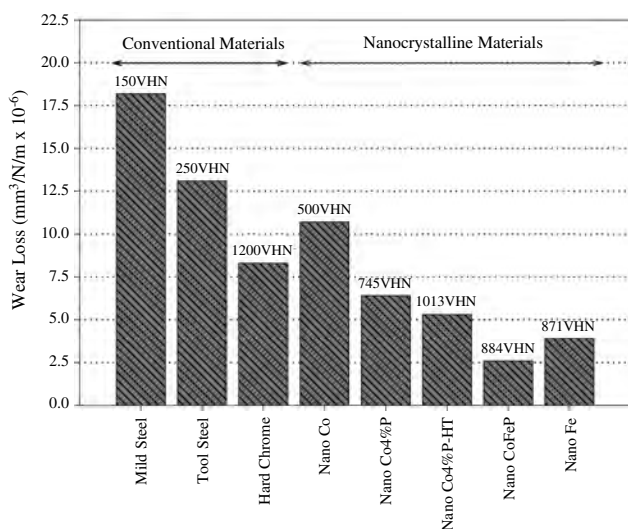


Figure 3. POD wear loss values for various nanocrystalline materials along with mild steel, tool steel, and hard chromium. The Vicker's microhardness value is given on top of the bar for each material on the chart.

the development of less harmful “trivalent Cr” plating processes (e.g., [61]), a reliable industrial process has yet to emerge.

In addition to the health risks associated with Cr plating, there are several other technical drawbacks to this technology. As a result of the relatively low electrolytic efficiency of Cr plating processes, deposition (or build) rates are relatively low compared to the plating of other metals and alloys (e.g., 20–50 μm per hour for Cr versus >200 μm per hour for nickel) [62]. As a further consequence of this low Cr-plating efficiency, high rates of hydrogen co-generation occur and precautions must be taken to prevent hydrogen embrittlement of susceptible substrate materials (e.g., high strength steels) [56]. Moreover, the intrinsic brittleness of hard chromium deposits (i.e., $<0.1\%$ tensile elongation [63]) invariably leads to micro- or macrocracked deposits. These “cracks,” which do not compromise wear and erosion resistance, are wholly unsuitable for applications where corrosion resistance is required. In these applications, an electrodeposited underlayer of more ductile and corrosion resistant material (usually Ni) must be applied [63].

Electrodeposited bulk nanostructured nickel and cobalt alloys have been recently developed as environmentally benign replacements of hard chrome electroplating [23, 64, 65]. It is important to note that although the wear performance of some of these single phase nanocrystalline coatings currently only approaches that of hard chrome, there exist significant benefits for many of these nanocrystalline coatings, which already render them a superior alternative for specific applications. For example, the significant ductility of nanocrystalline materials relative to hard chromium, and the absence of microcracking, provides significant advantages in fatigue and corrosion performance. Also, the high current efficiencies associated with the deposition of these nanocrystalline materials mitigates problems associated with hydrogen embrittlement. Furthermore, as will be outlined, these nanocrystalline single-phase systems can provide a hard but still relatively ductile matrix for incorporation of second phase particles, which can impart even greater hard-facing improvements.

Further increases in hardness and wear resistance may be achievable through the incorporation of second phase particulates in the nanocrystalline metal/alloy matrix. Two approaches can be used to accomplish this. The first is alloy deposition followed by heat treatment to precipitate a finely dispersed second phase, and the second is to co-deposit particulate during the deposition process. Significant increases in hardness have been achieved by precipitation of phosphates in electrodeposited Co-P [64, 65], Co-Fe-P [23], and Ni-P [66] to values exceeding those commonly found for hard chromium coatings (800–1200 VHN). Figure 4 shows precipitation hardening in the nanocrystalline cobalt-iron-phosphorus alloy, whereby hardness is plotted as a function of annealing time at 300, 400, and 500 $^{\circ}\text{C}$ for up to 100 hours. The Co-Fe-P deposits show an increase in hardness with annealing time at all temperatures, passing through a maximum after approximately 1 hour, followed by a slow decrease with increasing time. The subsequent decrease in hardness is believed to be due to the over-ripening of the precipitates. The additional loss in hardness during annealing at 500 $^{\circ}\text{C}$ to values below that of the

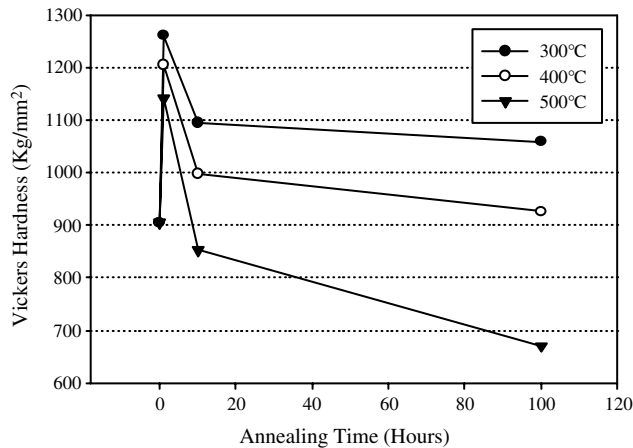


Figure 4. Effect of annealing time at 300, 400, and 500 °C on the hardness of a nanocrystalline Co-Fe-P alloy.

as-deposited material is due to the onset of grain growth, resulting in a loss of the Hall-Petch strengthening.

Nanocomposite coatings can also be produced by co-deposition during the electroplating process, whereby the second phase particulate is kept in suspension in the plating bath. In this manner, insoluble second phases of metals, alloys, ceramics, or polymers can be uniformly distributed in the host nanocrystalline metal or alloy matrix. Figure 5a shows an example of nanocrystalline nickel (13 nm avg. grain size) containing a uniform dispersion of aluminum oxide particles, produced by electrodeposition. Figure 5b presents a bright field transmission electron microscope (TEM) image of two Al_2O_3 particles and the surrounding nanocrystalline nickel showing that the nanocrystalline matrix structure continues up to the particle/matrix interface.

The benefits of utilizing nanocrystalline metal-ceramic composites is shown in Figure 6 for Ni-SiC [67]. Significant increases in hardness, yield strength, and ultimate tensile strength are achieved by utilizing a nanocrystalline rather than a conventional nickel matrix. In this work [67], it was also noted that, for low concentrations of SiC, the nanocrystalline composite possessed significantly improved ductility compared with nanocrystalline nickel of the same grain size but without SiC particles.

In addition to the potential for co-depositing hard second phase particles, there exists the opportunity to also incorporate second phases with functional properties. For example, hard-facing coatings with self-lubricating properties are highly desirable in certain applications. These properties can be achieved through the use of dry lubricant particles such as graphite, polytetrafluoroethylene, etc. Such co-deposited systems are already commercially available with a conventional grain size matrix (e.g., Ni). However, a hard nanocrystalline matrix extends the usage of these coatings to more severe industrial conditions, since by application of the rule of mixtures, the relatively “soft” lubricating second phase can be incorporated to larger volume fractions without significant compromise of the overall hardness of the coating.

Figure 7a and b shows parallel and through-thickness scanning electron microscope (SEM) micrographs, respectively, of a nanocrystalline Ni-P matrix containing hexagonal

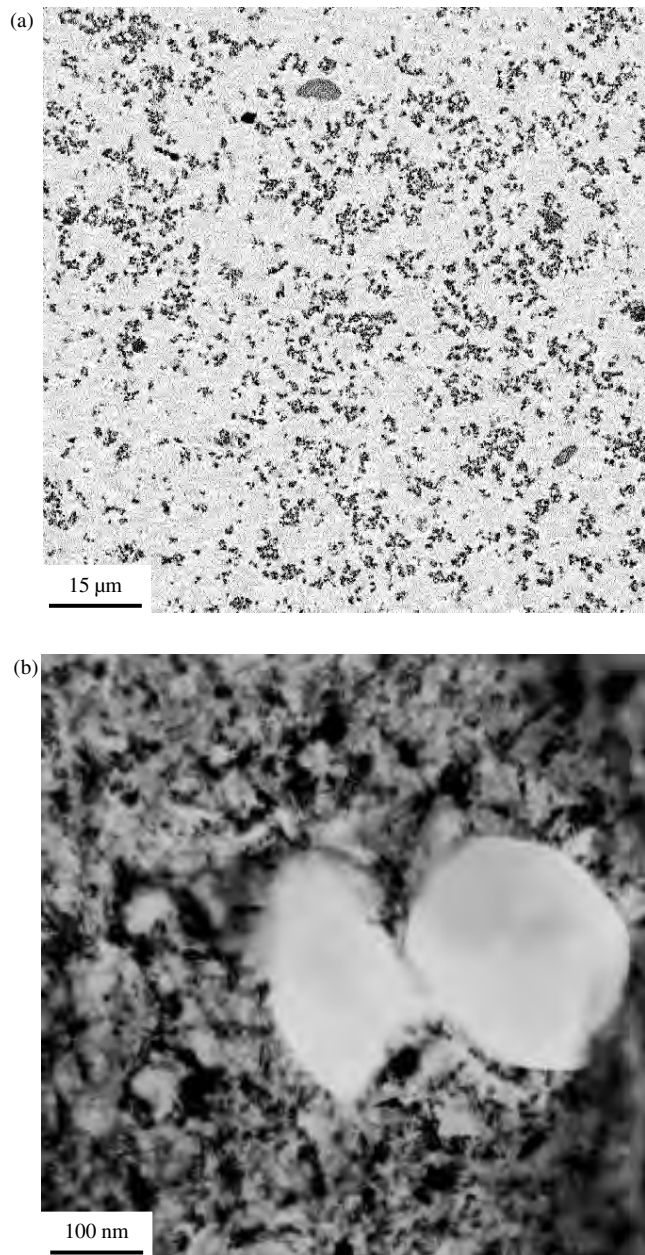


Figure 5. (a) Scanning electron micrograph (backscattered electron image) of nanocrystalline nickel (13 nm average grain size) matrix containing Al_2O_3 particulate (black). (b) Bright field TEM micrograph of nanocrystalline Ni- Al_2O_3 deposit showing the interface between the matrix and the Al_2O_3 particle.

boron nitride (BN) particles (mean particle size $\sim 10 \mu\text{m}$). The presence of the BN particles in the material results in a coating that “self-lubricates” during wear. Figure 8 shows a photograph of hydraulic expansion mandrels, coated with a nanocrystalline Ni- MoS_2 composite, which utilize the self-lubricating mechanism in order to extend their service life.

4.1.4. Microelectromechanical Devices

Rapid growth in the demand for microelectromechanical structures (MEMS) has resulted in the development of suitable fabrication techniques for micrometer-scale

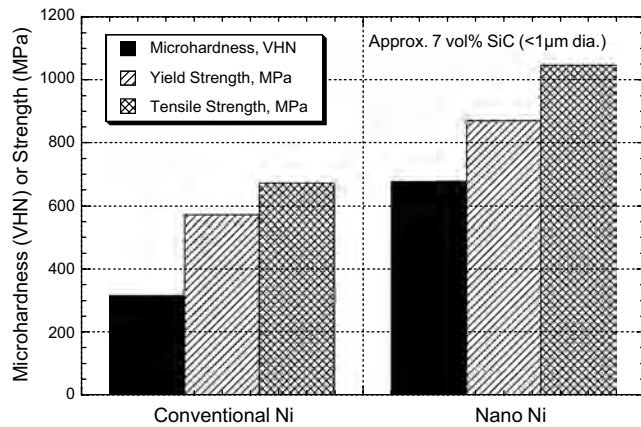


Figure 6. Summary of mechanical properties for Ni-SiC composites produced by electrodeposition. Adapted with permission from [67], A. Zimmerman et al., *Mater. Sci. Eng. A* 328, 137 (2002). IOP Publishing Ltd. © 2002,

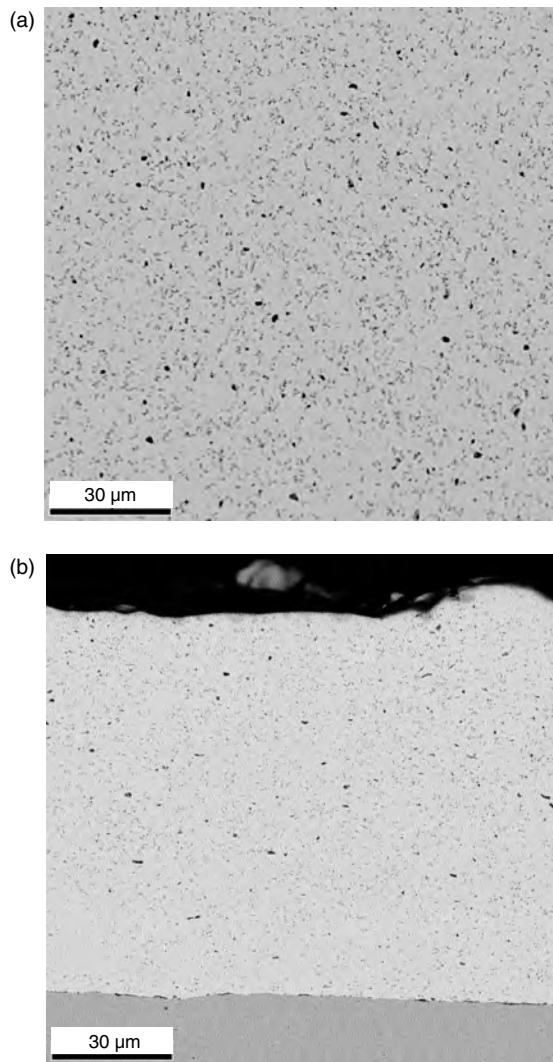


Figure 7. Parallel (a) and through-thickness (b) SEM micrographs of a nanocrystalline Ni-P matrix with BN particles.



Figure 8. Self-lubricating nanocrystalline nickel + molybdenum disulfide composite coating on hydraulic expansion mandrels.

components. One of the most commonly used fabrication techniques for metallic MEMS components is molding by electrodeposition (through-mask electroplating or LIGA, originally developed in Germany). The LIGA technique makes use of photoresist technology to allow for the fabrication of high aspect ratio structures (e.g., [68]). Conventionally produced LIGA and other electrodeposits, however, have been shown to suffer from severe reliability problems in terms of unpredictable properties (e.g., [69, 70]). Properties such as Young's modulus, yield strength, ultimate tensile strength, fatigue strength, and creep behavior have been shown to be extremely sensitive to processing parameters. Using conventional electroplating, columnar grain structure with varying crystallographic texture and large grains (in the micrometer range) are typically found in LIGA Ni, which is the main cause of the unreliability issue, as not all material properties are isotropic. Another critical factor in these devices is the fact that the grain size of conventionally electroformed MEMS structures approaches the length scale of the actual structure compromising the overall strength of the components. Initial studies have shown that the concerns with current LIGA structures can be alleviated by adopting electrodeposition parameters that yield nanocrystalline deposits [8, 9] with controllable and reproducible grain shape and crystallographic texture.

4.1.5. Other Applications

The exceptional specific strengths displayed by electrodeposited nanocrystalline metals and alloys have led to the development of a cost-effective, corrosion resistant, multi-layer nanocomposite which can form the basic building unit for armor laminate panels or complex laminate components for lightweight armor applications. By providing specific strengths >850 kpsi/(lb/cu.in.), intrinsic energy absorption and dissipation capability, and multiple round projectile blunting capability a broad range of threats can be defeated. Table 5 summarizes the specific strengths of electrodeposited nanocrystalline nickel, cobalt, and iron. As shown in this table, cobalt and iron, which can be produced in a cost-effective manner, already exhibit the lightweight structural

Table 5. Summary of specific strength properties of nanocrystalline metals produced by electrodeposition (NanoPlate™).

Material	Grain size (by XRD)	Crystal structure	Density (lb/cu. in.)	Tensile strength (kpsi)	Specific strength
NanoPlate™ Ni	17 nm	fcc	0.32	175	547
NanoPlate™ Co	12 nm	hcp	0.32	283	884
NanoPlate™ Fe	10 nm	bcc	0.28	484	1729

properties desired for the lightweight armor applications. Further increases in the specific strength can be achieved by incorporating lightweight ceramic phases.

Recent geometric models and experimental findings [71, 72] have shown that nanostructured materials can possess a high resistance to intergranular cracking processes, including creep cracking. Several emerging applications for nanocrystalline materials possessing high intergranular cracking resistance include lead-acid battery (positive) grids and shape charge liners (Cu, Pb, Ni) for military and industrial applications (e.g., demolition, oil well penetrators, etc.). In these applications, durability and performance of conventional polycrystalline materials are frequently compromised by premature intergranular failure.

4.2. Functional Applications

4.2.1. Soft Magnetic Films and Foils

The magnetic properties of ferromagnetic materials are strongly dependent upon parameters such as composition, crystallographic texture, internal stress, grain shape anisotropy, and the grain size distribution [73–75]. The magnetic properties of interest for nearly all applications can be divided into two categories: intrinsic and extrinsic magnetic properties. The fundamental intrinsic properties are generally independent of structure, such as the saturation magnetization (M_S) and the Curie temperature (T_C). The extrinsic magnetic properties are those that depend in some way on microstructure, such as permeability (μ), coercivity (H_C), and remnant magnetization (M_R).

Over the years, tailoring the chemistry and optimizing microstructure have resulted in significant improvements in the intrinsic and extrinsic magnetic properties of ferromagnetic materials. For soft magnetic applications, ranging from electromagnetic shielding, transformer materials, read–write heads, high efficiency motors, or emerging microelectromechanical system components, magnetic materials that exhibit small hysteresis losses per cycle are required. More specifically, materials with: (i) high permeability (the parameter which describes the flux density in very small fields), (ii) low coercivity, (iii) high saturation and remnant magnetization, (iv) high electrical resistivity (to minimize losses due to eddy current formation), and (v) high Curie temperatures are required. High strength is also of concern in particular for very thin foils or wires as is high corrosion and wear resistance, if these materials are used as a coating on softer substrates.

In nanocrystalline materials, the grain size approaches or decreases below the critical magnetic length scales found in conventional materials such as the domain (Bloch) wall

thickness or the ferromagnetic exchange length. As a result, considerable changes in the magnetic behavior can occur. In conventional polycrystalline materials (grain sizes >100 nm), the coercivity is found to be inversely proportional to the grain size. In this case, the grain size exceeds the domain wall thickness and the grain boundaries effectively act to pin magnetic domain wall motion, resulting in magnetically harder materials with decreasing grain size.

However, when the crystal size is reduced to the extent that the domain wall thickness is comparable to the average grain diameter the magnetic structure in relation to the microstructure is not well understood. For a series of nanostructured materials produced by crystallization from amorphous precursors it was found that the coercivity decreased by several orders of magnitude for grain sizes less than about 50 nm, following a D^6 relationship, where D is the grain size of nanocrystals (e.g., [76]). This observation was explained in terms of a random anisotropy model. Although this effect is not observed for all nanocrystalline materials, recent results have demonstrated that materials prepared by electrodeposition [77] show similar trends.

Early studies on the saturation magnetization of ultrafine particles and nanocrystalline materials made by gas condensed nanocrystalline powders found the M_S to be reduced, by as much as 40%, when compared to their compositionally equivalent polycrystalline counterparts [78–81]. Studies on the M_S of electrodeposited nanocrystalline materials, however, showed a decrease in M_S by no more than 5% [82–85]. Initially the reduced M_S in consolidated nanocrystalline powders was explained in terms of the structural disorder of the interfaces, in which atoms located at the interfaces were estimated to possess only half the magnetic moment of the atoms located within the grains [81]. However, in later work involving higher purity material [86], the previously reported reduction in M_S was attributed to oxygen contamination. Recent detailed calculations on the magnetic properties of grain boundaries [87, 88] revealed that the local magnetic moment in nickel is rather insensitive to the amount of disorder present in the structure, varying at most by 20%, for only certain sites in the boundary, thereby agreeing with the measured M_S values from nanocrystalline materials made by electrodeposition [82–85].

The Curie temperature of nanocrystalline materials has also been the subject of debate over the years. While a considerably reduced Curie temperature has been reported for nanocrystalline nickel made by consolidated nanocrystalline powders [89], no major reduction has been observed for nanocrystalline nickel produced by electrodeposition [90].

Nanocrystalline Fe- and Co-based soft magnetic materials made from devitrified amorphous alloys are currently being used in industry. The rapid solidification production technique of the amorphous precursor alloys, however, requires substantial alloying with metalloids such as boron and/or phosphorus. Therefore improvement in some of the soft magnetic properties, such as coercivity and permeability as a result of the ultrafine grain size, comes at the expense of the saturation magnetization of the base material (Fe or Co). In the case of electrodeposited nanocrystalline materials, the ultrafine grain size is accomplished without the need for alloying, such that saturation magnetization is not sacrificed, as shown in Figure 9.

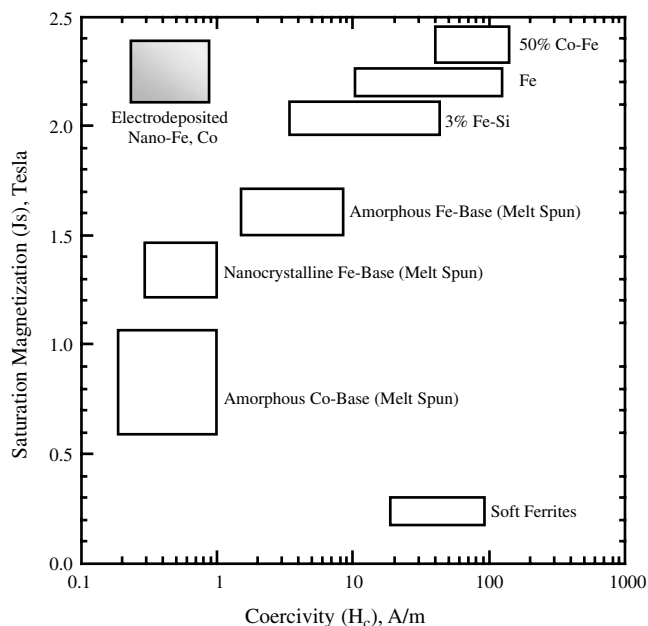


Figure 9. Saturation magnetization as a function of coercivity for targeted electrodeposited materials (white boxes) along with various commercial materials (grey box).

The industrial use of these high performance ferromagnetic materials in motor, transformer, and shielding applications was accelerated by the development of a drum plating process (shown in Fig. 10) for cost-effectively producing large quantities of sheet, foil, and wire in nanocrystalline form.

4.2.2. Copper Foil for Printed Circuit Boards

Line etchability of copper foil for printed circuit board applications is strongly dependent on the crystallographic orientation of the crystals in the foil [91]. Nonuniform line etching has become a severe issue as the linewidth continues to decrease to dimensions close to the grain size in conventional polycrystalline copper foils produced by electrodeposition. In an effort to improve the line etchability, a nanocrystalline Cu foil was recently developed [92]

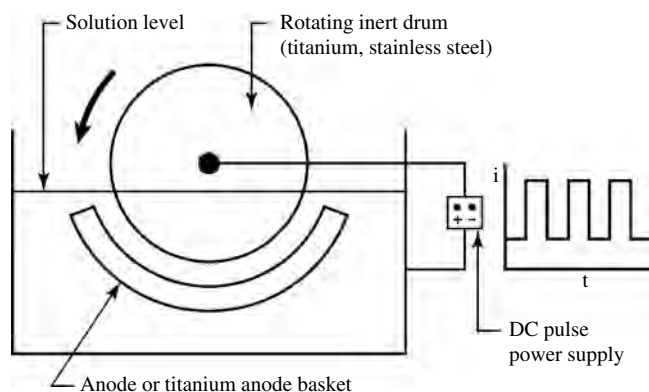


Figure 10. Prototype drum-plater for producing nanocrystalline sheet, foil, and wire products.

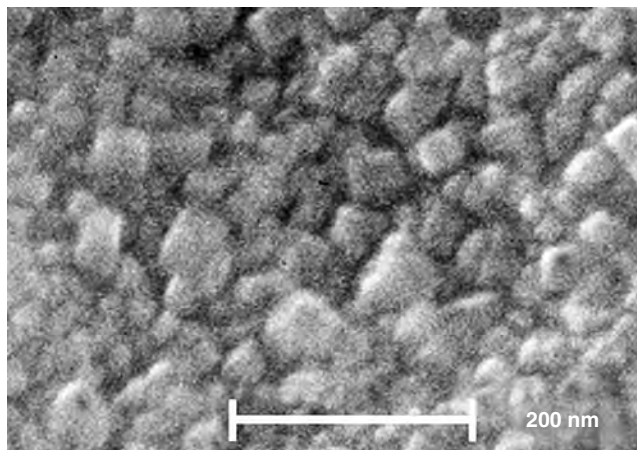


Figure 11. Field emission scanning electron micrograph of electrodeposited nanocrystalline Cu foil having an average grain size of 50 nm.

with grain sizes in the 50–100 nm range. Although further grain size reduction would be beneficial in terms of strength advantage and etchability, the associated increase in electrical resistivity would be unacceptable for this particular application [93]. Figure 11 shows a cross-sectional field emission scanning electron micrograph of nanocrystalline Cu foil produced for this application.

4.2.3. Catalytic and Energy Storage Applications

The high density of intercrystalline defects present within the bulk and intersecting the free surface of nanostructured materials provides considerable opportunity in catalytic and hydrogen storage applications. Hydrogen transport rates and storage capacity in nanocrystalline Ni have been shown to be significantly enhanced over that observed in conventional material [94, 95]; 6- to 10-fold increases in hydrogen diffusivity and 60-fold increases in hydrogen storage capacity have been determined at room temperature. In addition, higher electrocatalytic behavior has been noted with regard to the hydrogen evolution reaction for alkaline water electrolysis at room temperature [95]. Several applications are being developed for the use of these materials in nickel metal hydride battery systems and as alkaline fuel cell electrodes.

5. SUMMARY

Bulk nanostructured materials produced by electrodeposition exhibit excellent mechanical, wear, corrosion, catalytic, and magnetic properties. Several economically viable electrodeposition technologies are already available to produce large quantities of various pure metals, alloys, and composites in many different forms and shapes including thin and thick coatings, freestanding foil, sheet, tubes, and wires as well as complex geometries. Based on the outstanding properties and the established industrial infrastructure a number of advanced applications for electrodeposited nanostructures have been developed over the past decade, which have herein been presented.

GLOSSARY

Co-deposition The deposition of more than one species during electrodeposition. For example, if two metals are co-deposited at the same time the resulting material is an alloy. Metal matrix composites can be produced by co-depositing a second phase particle (e.g., ceramic, polymer, or intermetallic particles) with a metallic matrix.

Electrodeposition The deposition of a metal, ceramic, semiconductor, or polymer from an aqueous, or organic solution, or a molten salt.

Interfacial material A fully dense polycrystalline material such as a metal, alloy, ceramic or semiconductor with crystal sizes less than 100 nm. These materials have large volume fractions of interfaces (i.e., grain boundaries or phase boundaries) and, therefore, their properties quite different from those observed for their amorphous or conventional polycrystalline counterparts.

Nanocomposite A composite material in which at least one of the phases is nanocrystalline with a crystal size less than 100 nm.

REFERENCES

- H. Gleiter, Deformation of polycrystals: Mechanisms and microstructures, in Proc. 2nd Riso Int. Symp. on Metallurgy and Materials Science, Riso National Laboratory, Roskilde, Denmark, 1991, Vol. 15.
- G. Palumbo, S. J. Thorpe, and K. T. Aust, *Scripta Metall. Mater.* 24, 1347 (1990).
- N. Wang, G. Palumbo, Z. Wang, U. Erb, and K. T. Aust, *Scripta Metall. Mater.* 28, 253 (1993).
- "Proc. 3rd Int. Conference on Nanostructured Materials" (M. L. Trudeau et al., Eds.), *Nanostr. Mater.* 9, 1–771 (1997).
- "Proc. 4th Int. Conference on Nanostructured Materials" (M. Muhammed and K. V. Rao, Eds.), *Nanostr. Mater.* 12, 1–1188 (1999).
- G. McMahon and U. Erb, *Microstr. Sci.* 17, 447 (1989).
- G. McMahon and U. Erb, *J. Mater. Sci. Lett.* 8, 865 (1989).
- U. Erb and A. M. El-Sherik, U.S. Patent 5, 352, 266, 1994.
- U. Erb, A. M. El-Sherik, C. Cheung, and M. J. Aus, U.S. Patent 5, 433, 797, 1995.
- U. Erb, A. M. El-Sherik, G. Palumbo, and K. T. Aust, *Nanostr. Mater.* 2, 383 (1993).
- I. Bakonyi, E. Toth-Kadar, T. Tarnoczi, L. K. Varga, A. Cziraki, I. Gerocs, and B. Fogarassy, *Nanostr. Mater.* 3, 155 (1993).
- I. Bakonyi, E. Toth-Kadar, J. Toth, T. Tarnoczi, and A. Cziraki, in "Processing and Properties of Nanocrystalline Materials" (C. Suryanarayana et al., Eds.), TMS, Warrendale, 1996.
- R. Würschum, S. Gruss, B. Gissibl, H. Natter, R. Hempelmann, and H. E. Schäfer, *Nanostr. Mater.* 9, 615 (1997).
- D. L. Grimmitt, Ph.D. Thesis, University of California, Los Angeles, 1988.
- C. Cheung, F. Djuanda, U. Erb, and G. Palumbo, *Nanostr. Mater.* 5, 513 (1995).
- A. M. Alfantazi, A. M. El-Sherik, and U. Erb, *Scripta Metall. Mater.* 30, 1245 (1994).
- A. M. Alfantazi and U. Erb, *J. Mater. Sci. Lett.* 15, 1361 (1996).
- K. J. Bryden and J. Y. Ying, *Nanostr. Mater.* 9, 485 (1997).
- D. Osmola, E. Renaud, U. Erb, L. Wong, G. Palumbo, and K. T. Aust, *Mater. Res. Soc. Symp. Proc.* 286, 161 (1993).
- C. Cheung, U. Erb, and G. Palumbo, *Mater. Sci. Eng. A* 185, 39 (1994).
- C. Cheung, P. Nolan, and U. Erb, *Mater. Lett.* 20, 135 (1994).
- C. Cheung, G. Palumbo, and U. Erb, *Scripta Metall. Mater.* 31, 735 (1994).
- G. Palumbo, U. Erb, J. L. McCrea, G. D. Hibbard, I. Brooks, F. Gonzalez, and K. Panagiotopoulos, *AESF SUR/Fin Proc. Q*, 204 (2002).
- A. R. Despic and V. D. Jovic, *J. Electrochem. Soc.* 134, 3004 (1987).
- D. S. Lashmore and M. P. Dariel, *J. Electrochem. Soc.* 135, 1218 (1988).
- D. Tench and J. White, *Metall. Trans.* 15A, 2039 (1994).
- U. Cohen, F. B. Koch, and R. Sand, *J. Electrochem. Soc.* 130, 1987 (1983).
- A. Haseeb, B. Blanpain, G. Wouters, J. P. Celis, and J. R. Roos, *J. Mater. Sci. Eng. A* 168, 137 (1993).
- A. F. Zimmerman, D. G. Clark, K. T. Aust, and U. Erb, *Mater. Lett.* 52, 85 (2002).
- M. Shirkhazadeh, *Mater. Lett.* 16, 189 (1993).
- J. A. Switzer, *Nanostr. Mater.* 1, 43 (1992).
- T. R. Haasz, K. T. Aust, G. Palumbo, A. M. El-Sherik, and U. Erb, *Scripta Metall. Mater.* 32, 423 (1999).
- T. Turi, Thermal and Thermodynamic Properties of Fully Dense Nanocrystalline Ni and Ni-Fe Alloys, Ph.D. Thesis, Queen's University, Kingston, Ontario, Canada, 1997.
- S. C. Mehta, D. A. Smith, and U. Erb, *Mater. Sci. Eng. A* 204, 227 (1995).
- U. Erb, K. T. Aust, and G. Palumbo, in "Nanostructured Materials" (C. C. Koch, Ed.), p. 179. Noyes, Norwich, NY, 2002.
- H. K. Merchant, in "Defect Structure, Morphology and Properties of Deposits" (H. D. Merchant, Ed.), TMS, Warrendale, 1995.
- A. M. El-Sherik and U. Erb, in "Nickel-Cobalt 97" (F. N. Smith, Ed.), p. 257. The Metallurgical Society of CIM, Montreal, 1997.
- N. Wang, Z. Wang, K. T. Aust, and U. Erb, *Mater. Sci. Eng. A* 237, 150 (1997).
- A. A. Karimpoor, U. Erb, K. T. Aust, Z. Wang, and G. Palumbo, *Mater. Sci. Forum* 386–388, 415 (2002).
- G. Palumbo, F. Gonzalez, A. M. Brennenstuhl, U. Erb, W. Shmayda, and P. C. Lichtenberger, *Nanostr. Mater.* 9, 737 (1997).
- F. Gonzalez, A. M. Brennenstuhl, G. Palumbo, U. Erb, and P. C. Lichtenberger, *Mater. Sci. Forum* 225–227, 831 (1996).
- G. Palumbo, P. C. Lichtenberger, F. Gonzalez, and A. M. Brennenstuhl, U.S. Patents 5, 527, 445, 1996; 5, 516, 415, 1996; 5, 538, 615, 1996.
- ASME Code Case 96-189-BC96-206 Case N-569; Section XI, Division 1; Alternative Rules for Repair by Electrochemical Deposition of Class 1 and 2 Steam Generator Tubing, 1996.
- G. Palumbo, U. Erb, and K. T. Aust, *Scripta Metall. Mater.* 24, 2347 (1990).
- A. H. Chokshi, A. H. Rosen, J. Karch, and H. Gleiter, *Scripta Metall. Mater.* 23, 1679 (1989).
- G. W. Nieman, J. R. Weertman, and R. W. Siegel, *Nanostr. Mater.* 1, 18 (1992).
- K. Lu, W. D. Wei, and J. T. Wang, *Scripta Metall. Mater.* 24, 2319 (1990).
- T. Christman and M. Jain, *Scripta Metall. Mater.* 25, 767 (1991).
- N. Wang, Z. Wang, K. T. Aust, and U. Erb, *Acta Metall. Mater.* 43, 51 (1995).
- E. M. LeHockey, G. Palumbo, K. T. Aust, U. Erb, and P. Lin, *Scripta Mater.* 39, 341 (1998).
- J. F. Archard, *J. Appl. Phys.* 24, 981 (1953).
- D. H. Jeong, F. Gonzalez, G. Palumbo, K. T. Aust, and U. Erb, *Scripta Mater.* 44, 493 (2001).

53. D. T. Gawne and U. Ma, *Wear* 129, 123 (1989).
54. MIL-C-7460A NOT 1 (March 19, 1993).
55. DOD-STD-2182 (January 29, 1985).
56. MIL-P-6871 (2) (July 27, 1955).
57. MIL-P-19419A (August 21, 1989).
58. D. T. Gawne, *J. Vac. Sci. Tech. A* 3 (6), 2334 (1985).
59. UK Chromium Plating Regulations 1931 (amended in 1973), HMSO (1073).
60. "The Toxicity of Chromium and Inorganic Chromium Compounds," HSE Toxicity Review TR31, HMSO (1989).
61. P. Benaben, U.S. Patent 4, 612, 091, 1986.
62. "Metals Handbook" (H. E. Boyer and T. L. Gall, Eds.). ASM, Metals Park, OH, 1985.
63. J. K. Dennis and T. E. Such, "Nickel and Chromium Plating," 3rd ed., Woodhead, Cambridge, UK, 1993.
64. J. L. McCrea, G. Palumbo, F. Gonzalez, A. Robertson, K. Panagiotopoulos, and U. Erb, *AESF SUR/Fin Proc. D* (2001).
65. J. L. McCrea, G. Palumbo, M. Marcoccia, U. Erb, and D. E. Lee, *AESF WEEK Proc. L* (2002).
66. U. Erb, G. Palumbo, and K. T. Aust, in "Proc. of the NATO Advanced Research Workshop on Nanostructured Films and Coatings," Santorini, Greece (G.-M. Chow, I. A. Ovid'ko, and T. Tsakalakos, Eds.). Kluwer Academic, Dordrecht, 2000.
67. A. Zimmerman, G. Palumbo, K. T. Aust, and U. Erb, *Mater. Sci. Eng. A* 328, 137 (2002).
68. S. M. Spearing, *Acta Mater.* 48, 179 (2002).
69. H. R. Last, K. J. Hemker, and R. Witt, *Mater. Res. Soc. Symp. Proc.* 605, 191 (2000).
70. Z. L. Xie, D. Pan, H. Last, and K. J. Hemker, *Mater. Res. Soc. Symp. Proc.* 605, 197 (2002).
71. G. Palumbo, P. J. King, K. T. Aust, U. Erb, and P. C. Lichtenberger, *Scripta Metall.* 25, 1775 (1991).
72. G. Palumbo, E. M. Lehouckey, P. Lin, U. Erb, and K. T. Aust, *Mater. Res. Soc. Symp. Proc.* 458, 273 (1997).
73. E. C. Stoner, "Magnetism and Matter." Methun and Co. Ltd., London, 1934.
74. A. E. Berkowitz and E. Kneller, "Magnetism and Metallurgy." Academic Press, New York, 1969.
75. R. M. Bozorth, "Ferromagnetism." IEEE Press, New York, 1978.
76. G. Herzer, in "Handbook of Magnetic Materials" (K. H. J. Bushchow, Ed.), Vol. 10, Ch. 3, p. 415. Elsevier Science, Amsterdam, 1997.
77. C. Cheung, M. J. Aus, U. Erb, J. L. McCrea, and G. Palumbo, in "Proceedings of the 6th International Conference on Nanostructured Materials (NANO2002)," Orlando, FL, 16–21 June 2002, in press.
78. H. Gleiter, *Progr. Mater. Sci.* 33, 223 (1989).
79. W. Gong, H. Li, Z. Zhao, and J. Chen, *J. Appl. Phys.* 69 (1991).
80. S. Gangopadhyay, G. C. Hadjipanayis, B. Dale, C. M. Sorenson, and K. J. Klabunde, *Nanostr. Mater.* 1, 77 (1992).
81. H. E. Schaefer, H. Kisker, H. Kronmüller, and R. Würschum, *Nanostr. Mater.* 1, 523 (1992).
82. M. J. Aus, Ph.D. Thesis, Queen's University, Kingston, Ontario, Canada, 1999.
83. M. J. Aus, C. Cheung, and B. Szpunar, *J. Mater. Sci. Lett.* 17, 1867 (1998).
84. M. J. Aus, B. Szpunar, U. Erb, G. Palumbo, and K. T. Aust, *Mater. Res. Soc. Symp. Proc.* 318, 173 (1993).
85. M. J. Aus, B. Szpunar, A. M. El-Sherik, U. Erb, G. Palumbo, and K. T. Aust, *Scripta Metall.* 27, 1639 (1992).
86. H. Kisker, T. Gessman, R. Würschum, H. Kronmüller, and H. E. Schaefer, *Nanostr. Mater.* 6, 925 (1995).
87. B. Szpunar, R. Zurgic, U. Erb, and L. J. Lewis, *Can. Metall. Quart.* 34, 281 (1995).
88. B. Szpunar, U. Erb, G. Palumbo, K. T. Aust, and L. J. Lewis, *Phys. Rev. B* 53, 5547 (1996).
89. H. E. Schaefer, *NATO Adv. Stud. Inst. Ser. E* 233 (1992).
90. J. L. McCrea, M. J. Aus, B. Szpunar, T. Turi, J. Szpunar, and U. Erb, submitted for publication.
91. J. W. Dini, "Electrodeposition," p. 170. Noyes, Park Ridge, NJ, 1993.
92. A. Robertson, U. Erb, and G. Palumbo, *Nanostr. Mater.* 12, 1035 (1999).
93. J. L. McCrea, The Effect of Temperature on the Electrical Resistivity of Electrodeposited Nanocrystalline Materials, Ph.D. Thesis, University of Toronto, Toronto, Ontario, Canada, 2001.
94. G. Palumbo, D. M. Doyle, A. M. El-Sherik, and U. Erb, *Scripta Metall. Mater.* 25, 679 (1991).
95. D. M. Doyle, G. Palumbo, K. T. Aust, A. M. El-Sherik, and U. Erb, *Acta Metall. Mater.* 43, 3027 (1991).

Applications of Focused Ion Beam in Nanotechnology

V. J. Gadgil

University of Twente, Enschede, The Netherlands

F. Morrissey

FEI Company, Eindhoven, The Netherlands

CONTENTS

1. Introduction
 2. Interaction of Ions with Matter
 3. Principles of Focused Ion Beam
 4. Focused Ion Beam Equipment
 5. Applications of Focused Ion Beam
in Nanotechnology
 6. Summary
- Glossary
References

1. INTRODUCTION

Focused ion beam (FIB) systems and technology were developed about 20 years ago in the early 1980s. As the applications increased and demand for commercial equipment increased, commercial instruments became available on the market [1]. Today FIB systems are being widely used in semiconductor research and processing, failure analysis, and chip design. The technology makes it possible to carry out localized milling and deposition of conductors and insulators with high precision. Because of this FIB application has become possible in device modification, mask repair, process control, and failure analysis [2–6]. The possibility to image at high magnification and milling at a very specific site has made possible preparation of specimens for transmission electron microscopy (TEM). The FIB technique is also being used in production processes like trimming of thin-film magnetoresistive heads (for magnetic storage disks) [7]. Recently a number of reports have appeared in the literature about the use of FIB in micromachining applications

for microelectromechanical structures [8–10]. This powerful tool shows a promising future in nanotechnology and nanofabrication. The FIB is based on the interactions of an ion beam with surfaces and molecules. It is therefore important to cover how ions interact with matter.

2. INTERACTION OF IONS WITH MATTER

Ion implantation for integrated circuit manufacture is a well established technique. It has been widely studied and there is a considerable amount of literature available in this area. Typical energies used in ion implantation are in the 10 to 200 keV range, while typically the commercially available FIB systems use around 30–50 keV. The incident ion loses its energy when it strikes the surface of the specimen. This energy is partially lost to the electrons and partially to the atoms itself. Due to Coulomb interaction the ion excites the electrons in the solid to bound states or to continuum states. This is a predictable process. The loss of energy to the atom is more complicated. This is because of the finite number of random collisions with significant energy loss. The development of the theory of an ion slowing in a solid has been difficult because the problem of describing both the ion and the target is complex. Once the ion penetrates a solid, it is quickly stripped of some of its electrons, and its charge state becomes a function of the target. The target feels the ion coming, and its electrons polarize around the moving ion. The charge state of the ion is modified by the polarized target, which then further affects the target. Some of the target atoms penetrate through the ion's electron cloud causing quantum exclusions of available states. Finally, all of these effects depend on the constantly changing ion velocity. When an ion strikes the surface of a solid, the ion is deflected from its path and the atom is displaced from its original

position. The ions penetrate the solid to a depth R_p called penetration depth or range. If a Gaussian curve is fitted to the distribution of ions at a depth Z it has the form $\exp[-(Z - R_p)^2/2(\Delta R_p)^2]$ where ΔR_p is called range straggle. In addition to this the collisions also produce uncertainty in the transverse position of the ion in the solid. This is described as ΔR_t or transverse straggle. Plots of R_p , ΔR_p , and ΔR_t for silicon are available in the literature [11].

More recently computer simulations are available on the internet called the stopping and range of ions in matter. The simulation has used a vast number of data points available in the literature. The software claims to be accurate to about 10% of the available data.

The ion causes various effects when it is incident on the specimen surface. A schematic diagram of the interactions can be seen in Figure 1.

1. The ions produce radiation damage. This is a result of displacement of atoms from their lattice sites due to collisions with ions. The cumulative effect of the damage can result in formation of an amorphous layer. For example, after an implantation dose of 10^{14} As⁺ ions/cm² such an amorphous layer is formed in silicon. Light ions such as B⁺ do not form such a layer. The depth and distribution of the damage follows the distribution of the ions.
2. The ions striking the surface can cause sputtering. This is removal of atoms from the substrate. This occurs at low energies of 50–1000 eV. The removal of atoms from the substrate is dependent on the energy of the incident ions. The yield or the number of atoms removed increases with energy up to about 100 keV and then decreases. Typical yield is about 1 to 10 atoms per ion. The sputtered ions leave the surface with a few eV of energy.
3. When the ion strikes the surface, electrons are emitted. About 1–10 electrons are emitted per ion with typical energies of a few eV. In a FIB system these electrons called secondary electrons are used to image the surface.

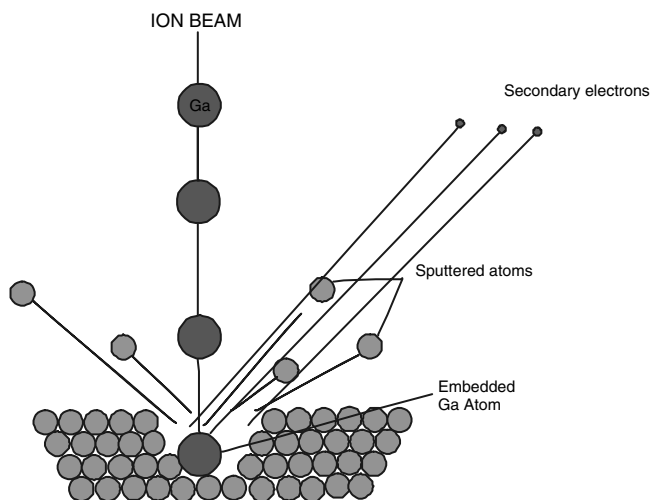


Figure 1. Interaction of ion beam with specimen.

4. Chemical effects are also produced by ions. These are because of the ion–electron interactions as well as ion–atom interaction. When a photoresist is exposed to the ions, the molecules are changed because of the ions. They can either make the resist soluble or insoluble in developer. Ions can also break molecules into parts. A typical example is an organic gas molecule carrying a metal atom. The ions can break the molecule causing deposition of the metal on the surface. Another example is ion assisted etching where a gas is used in combination with the ion source.

3. PRINCIPLES OF FOCUSED ION BEAM

A modern dual beam FIB system has two separate columns, one for the electron beam and the other for the ion beam. The ion beam interacts with the specimen and has two important functions, namely milling of material and deposition of material. Interaction of the ion beam with the sample surface can also be used for imaging. The principal components and functions of FIB are the following:

1. ion source
2. ion column
3. imaging
4. milling
5. deposition

3.1. Ion Source

Focused ion beam machines make use of a liquid metal ion source or LMIS. This consists of a blunt field emitter with an end radius of around $10 \mu\text{m}$ which is coated with a metal film that has a high surface tension and a low vapor pressure at its melting point. The field emitter is heated to the melting point of the metal so that the metal forms a liquid film on the emitter. A high electric potential is applied to the field emitter relative to an electrode in its proximity called an extractor electrode. The positive voltage is in the range of 2–10 kV. The magnitude of the voltage is dependent on the distance between the field emitter and the extractor electrode. The liquid film experiences two kinds of forces: the surface tension of the liquid and the electrostatic field. Depending on the balance between these forces the liquid film is drawn into a conical shape. The radius of the tip of the cone is about 5 nm. The small radius and high electric field cause the formation of ions by field evaporation. Because of the high field the potential barrier against evaporation is lowered and the atoms can evaporate. The evaporated atoms then ionize in the electric field. At low ion currents this is the dominating mechanism. At high ion currents ions are formed by field ionization of metal atoms which are in the vapor state. Several elements have been used as ion sources. These are Al, As, Au, B, Be, Cs, Cu, Ga, Ge, Fe, In, Pb, P, Pd, Si, Sn, U, and Zn. The LMIS is more complicated to describe mathematically than a solid source, because unlike the solid source, the liquid tip is the emitter. The shape of the tip is determined by the forces acting on the liquid. As mentioned, these are the surface tension and the electrostatic force. The balance of these forces

maintains the liquid in a conical form. It is therefore necessary to have an accurate description of the electric field that maintains the liquid in a conical form in the presence of the space charge. The space charge is highly dependent on the field because of the field evaporation process. The situation is further complicated by the fact that the pressure in the interior of the cone is altered because of flow of liquid through it to replace the evaporated atoms. The flow is dependent on the rate of evaporation, which is dependent on the current. A LMIS source is a device where sufficiently high electric field can be applied to the liquid metal so that it forms the conical shape when the surface tension just balances the stress caused by the electric field. This is known as the Taylor cone.

Some of the most important properties of the LMIS sources are the highly nonlinear current–voltage characteristics. The LMIS source also displays variation in the energy distribution of the beam and composition of the ions dependent on the current.

3.2. Ion Column

The ion column is quite similar to the electron column of a scanning electron microscope (SEM). However, in a SEM an electron beam is manipulated using electromagnetic lenses, while in an FIB ion column, the ion beam is manipulated using electrostatic lenses. A typical ion column can be seen in Figure 2. The LMIS functions in vacuum and the entire column is maintained at about 1×10^{-7} mbar. The ion beam from the LMIS is in the form of a cone and first a spray aperture limits the shape of the beam. The first electrostatic lens then condenses the beam. The beam stigmatism is adjusted by the first octopole. The ion beam has energy of about 10–50 kV. The beam currents vary between 1 and 10,000 pA. The beam current is controlled by introducing variable apertures. Small currents are used for imaging while large currents are used for milling. Typical beam currents in FEI FIB equipment are 1, 4, 11, 70, 150, 350, 1000, 2500, 6000, and 11,000 pA. There is another octopole below the apertures. This is used to scan the surface of the sample as in a SEM. The beam also can be blanked using a blanking mechanism. A second electrostatic lens focuses the beam to a fine spot. This can give a resolution of up to 5 nm.

3.3. Imaging

As described previously, when energetic ions hit the surface of a solid sample, they lose their energy to the electrons of the solid as well as the atoms. The electrons in the solid leave the surface of the sample and are called secondary electrons. These electrons are collected on a multichannel plate (MCP) detector. This detector can be positively biased to collect the secondary electrons. When the ion beam rasters the surface of the sample, the secondary electrons produce the image of the surface of the sample. The energetic ions can also cause the atoms on the surface of the sample to leave the surface as ions. These are called secondary ions. These ions can be collected by the MCP when it is negatively biased. These can also be used to image the sample surface. Nonconducting samples pose a problem.

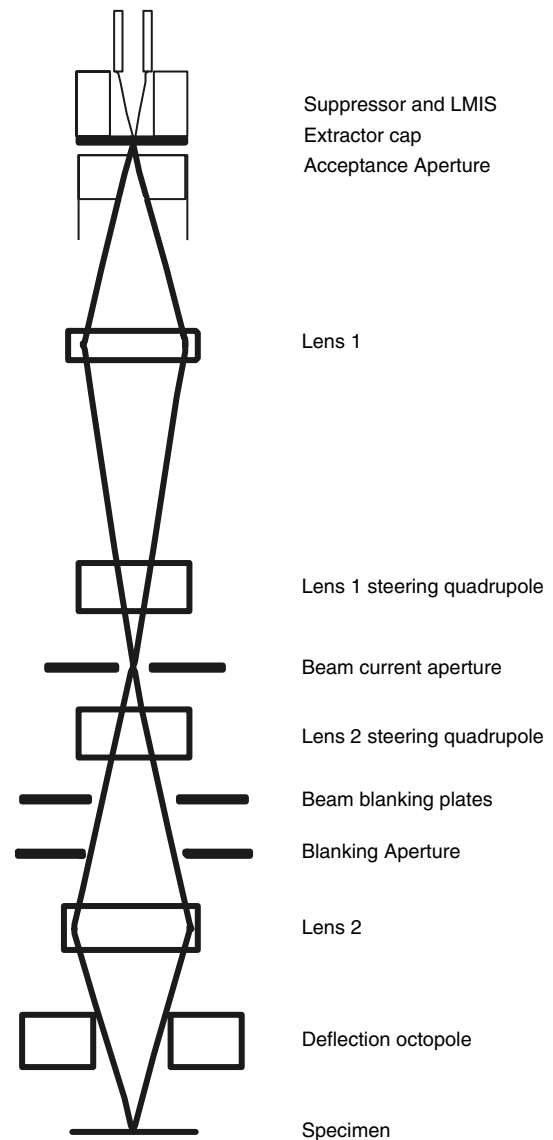


Figure 2. Typical ion column.

The surface builds up positive charge because of the ions. This interferes with the imaging of the sample surface. This problem is overcome using a separate electron source to flood the surface with electrons. In a dual beam machine it is possible to use the electron column for this purpose.

The traditional single-beam ion system has some limitations. The imaging process in a FIB system results in the ion beam continuously removing material from the sample. If the feature or defect being imaged is small, under 0.1 mm, the feature will be damaged or altered in the time needed to collect a high-resolution image. This has led to the development of a dual-column FIB system. A well-designed dual-column system is able to integrate the ion beam's milling and deposition capabilities with the electron beam's high-resolution, nondestructive imaging, without compromise to either column's performance. A system that provides these qualities can be used like a dedicated SEM for defect inspection and, when needed, provide three-dimensional (3D) inspection of particles, buried defects, or metrology.

The best resolution achieved by FIB machines using an ion beam is dependent on the spot size of the beam. This is typically of the order of 5 nm in modern equipment. In a dual beam machine of course the resolution is same as that of a SEM.

There is another effect of the ions when they strike a material like aluminum and copper. The ions penetrate to some depth in these materials. The depth of penetration varies because of channelling along the open columns in the lattice structure. The penetration depth therefore depends on the orientation of the crystal with respect to the incident beam. Since secondary electron emission is dependent on the depth of penetration, the image reveals differences in orientation of the crystals [12]. When the specimen is tilted, it is possible to see changes in brightness of the grains due to changes in channeling conditions as the angle between the grains and the incident ion beam changes.

3.4. Milling

The main purpose of FIB equipment is milling of materials. The energetic ions striking the surface of the specimen eject the atoms on the surface. This results in milling of the specimen surface. As mentioned, removal of atoms from the substrate is dependent on the energy of the incident ions. The yield or the number of atoms removed increases slowly with energy, flattens out, and then decreases at about 50 keV [13]. With Focused ion beams, the characteristics of milling, such as yield, are geometry dependent. When an ion beam is scanned on the surface as a line, a trench develops which has a Gaussian shape as expected from the beam profile. However, when the dose is increased, the trench becomes sharp, narrowly V shaped, and deep [14, 15]. In addition, the shape of a milled feature is also dependent on whether it is obtained with a single scan or repetitive scans even though the total dose is kept the same [15, 16]. The yield has to be defined in such a way that the geometric effects are avoided such as repetitive scanning over an area where the lateral dimensions are much larger than the depth milled. Thus if the material has a density ρ (atoms/cm³) and an ion dose Δ (ions/cm²) mills the material to a depth d (cm), then the yield can be defined as

$$Y = (\rho d / \Delta) \quad (\text{atoms/ion})$$

Since in focused ion beams milling ions can be buried in the material, and other phenomena such as redeposition can also take place, the actual yield may not correspond exactly to the atoms removed per ion. Typical implantation depth and sputtering yield for Ga⁺ ions in silicon dioxide (SiO₂) and aluminum (Al) at normal incidence is given in Table 1 [12]. The sputtering yield is also dependent on the angle of incidence. It roughly increases with $1/\cos(\theta)$, with θ the angle between the surface normal and the ion beam direction.

In order to speed up the milling process, or to increase the selectivity toward different materials, an etching gas can be introduced into the work chamber during milling. It will increase the etching rate and the selectivity toward different materials by chemically facilitating the removal of reaction products. This technique is called gas assisted etching

Table 1. Typical implantation depth and sputtering yield for Ga⁺ ions in silicon dioxide (SiO₂) and aluminum (Al).

Ga ion energy	Implantation depth			Sputtering yield		
	Si	SiO ₂	Al	Si	SiO ₂	Al
10 keV	13 ± 5	12 ± 4	11 ± 4	1.46	Si: 0.62; O: 2.23	2.59
20 keV	20 ± 7	19 ± 6	17 ± 6	1.87	Si: 0.64; O: 2.34	2.98
30 keV	27 ± 9	25 ± 8	23 ± 8	1.98	Si: 0.67; O: 2.25	2.91
40 keV	33 ± 11	31 ± 10	29 ± 10	2.04	Si: 0.77; O: 2.54	3.54
50 keV	39 ± 14	38 ± 11	35 ± 12	2.01	Si: 0.67; O: 2.39	3.48

(GAE). Typical etching gases and their milling rate enhancement factors are shown in Table 2 [12]. One of the advantages of GAE is that the reaction products are volatile and this prevents redeposition and permits high aspect ratio structures to be fabricated [17–19]. With increasing use of copper, GAE of copper is gaining importance. Recently several studies on GAE of copper have been reported using SiCl₄ and BCl₃ [20–23]. A 12-fold increase in milling rates has been reported [17]. More recently water has been added to the arsenal of gases for FIB chemical etching. FIB water etching is especially rapid with polymers (including photoresist). The enhancement factor for poly(methyl methacrylate), for example, can exceed 10x, which may have value for resist lithography purposes. Presently FIB water etching has been employed to cross-section photoresist for SEM analysis [24]. Recently, selective etching has made progress. New machines offer up to four etching chemistries:

- enhanced etch: milling rate enhancement for materials such as silicon, aluminum, and gallium arsenide
- selective carbon mill: removes photoresist and other polymers
- insulator enhanced etch: removes insulating materials used in the IC manufacturing process
- delineation etch: enables the imaging of various materials and oxide layers exposed in a FIB cross-section

3.5. Deposition

For many years people have used FIB systems for beam induced deposition of metals and insulators onto device surfaces. As can be seen in Figure 3, the deposition of materials is accomplished by introducing metal or insulating atoms as a part of a carrier molecule, very close to the sample surface where they collide with gallium ions from the primary ion beam and are forced onto the sample surface. The principle is chemical vapor deposition (CVD). As the ion beam can be focused to a very small spot size, the deposition is

Table 2. Typical GAE gases and their etch rate enhancement factors on various materials.

	Al	W	Si	SiO ₂ , Si ₃ N ₄	Photoresist; polyimide
Cl ₂	10–20	—	10	—	—
Br ₂	10–20	—	6–10	—	—
ICl	8–10	2–6	4–5	—	—
XeF ₂	—	10	10–100	6–10	3–5

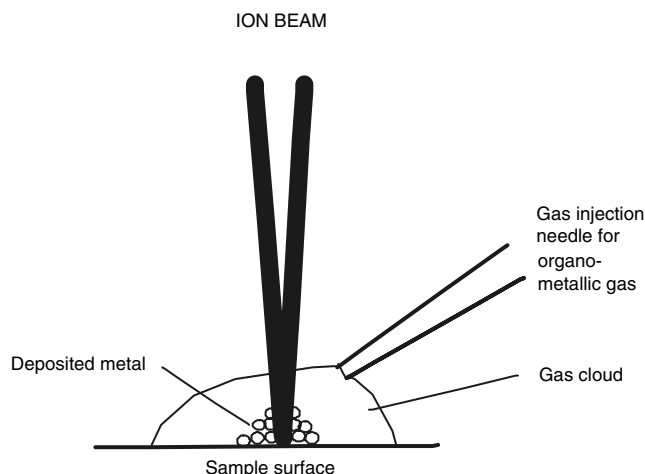


Figure 3. Schematic diagram showing metal deposition.

very localized. The beam can be made to follow a preprogrammed pattern and this results in deposition of the metal in the desired form. The carrier molecule is in vapor form and is introduced through a needle which is brought in close proximity to the sample surface. The gas is adsorbed on the surface of the specimen. The ion beam dissociates the carrier molecule as it collides with it. The dissociated products are volatile and are removed by the vacuum system while the desired reaction products carrying the metal atoms remain attached to the surface. The deposited metal is not pure as it also contains Ga and parts of the carrier organic molecule. The most common metals deposited in commercially available machines are Pt and W. In case of W the organometallic gas is $W(CO)_6$. Insulating material like SiO_2 can also be deposited. In this case 1,3,5,7-tetramethylcyclotetrasiloxane and oxygen or water vapor is used as a precursor. A wide range of metals have also been deposited for research purposes such as Ta [25], Au [26, 27], C [28], Fe, and Al [29]. The smallest feature that can be deposited by conventional FIB is of the order of <100 nm. Traditionally these depositions are mainly used to connect or isolate wires when doing device edit operations.

A new application for metal deposition is to deposit a layer of metal in order to protect the features of small particle defects during ion beam cross-sectioning. If the particle is exceedingly small ($>0.20 \mu m$) the ions used for depositing the protective metal layer can still damage the particle during initial exposure. In a dual-column system the electron beam can be used to do the initial deposition of metal, generally a thin layer less than $0.1 \mu m$ thick. Once this initial layer is deposited, the ion beam can be used to finish the deposition without affecting the particle. The slow milling rate of the metal also gives a clean face to the cross-section while preserving the particle's important physical and compositional characteristics.

4. FOCUSED ION BEAM EQUIPMENT

A modern two-beam FIB workstation like the one marketed by made by the FEI Corporation is typically used for research, design modification, defect characterization, process control, and site specific TEM specimen preparation.

A schematic diagram showing the configuration of a two-beam FIB is shown in Figure 4. With a dual beam, the sample can be viewed by SEM while it is being processed by the ion beam. This makes it possible to make slice-by-slice, 3D images of features of interest. The samples that are processed by FIBs are mounted on a motorized five-axis stage, mounted inside the specimen chamber. There are two types of specimen stages. For highly accurate navigation the specimen stage has laser interferometers. The stage is much more rigid. This, however, limits freedom of movement in tilt. Accuracy of such a stage is about 5 nm. The specimen stage with five-axis freedom has less accuracy. Under normal operating conditions, 10^{-7} mbar vacuum is maintained. A system of vacuum pumps is needed to maintain the vacuum inside the specimen chamber. A fore pump is used in combination with a turbo pump for pumping the specimen chamber. The ion column and the electron column are provided with additional ion pumps. Loading of samples in FEI machines is done by opening the whole front of the specimen chamber. This enables large samples to be loaded so that the maximum size of the specimen chamber can be exploited.

As discussed, gas assisted milling and deposition of various metals requires that there is a possibility to introduce these gases in the specimen chamber. The gas containers are outside the specimen chamber. The gas sources are connected with appropriate piping to the specimen chamber. The gases have to be delivered very close to the specimen itself. This is achieved by retractable needles which can be lowered to the specimen surface when required. This is necessary so that the specimen can first be manipulated without the hindrance of the needle.

A computer system governs all the operations. Imaging is also digital and displayed on a computer monitor. The new machines have powerful navigation software. A specimen can be positioned to within 5 nm of the desired location. The system can read CAD files for positioning which are the same files used for preparation of masks.

5. APPLICATIONS OF FOCUSED ION BEAM IN NANOTECHNOLOGY

There is a very large number of applications of FIBs reported in the literature in this area. The most successful application of FIBs in semiconductor technology is in failure analysis. In addition a lot of information can be obtained

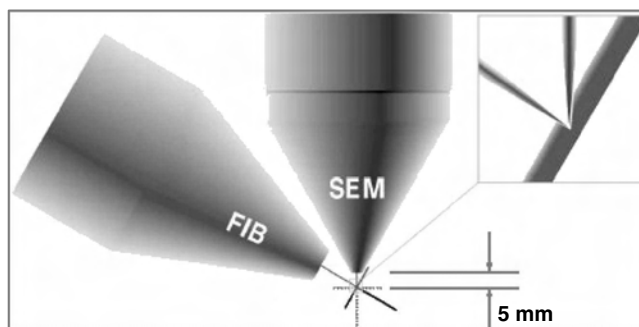


Figure 4. Dual beam configuration.

for process control. Furthermore, the capability of cross-sectioning makes the FIB a powerful tool to make site specific TEM samples. Now with the considerable activity in the nanotechnology FIB has found new role in nanofabrication.

5.1. Making Site Specific Cross-Sections

A FIB system has the ability to image a specimen and then to select a specific feature of interest on the surface. This feature can be milled with the ion beam. After the milling operation, the specimen can be tilted to view the cross-section. This gives a unique opportunity to make and examine site specific cross-sections. A FIB milled cross-section of a “surface defect” is shown in Figure 5. The cross-section reveals that the surface defect is in fact an underlying defect.

5.2. Milling of Optical Fibers

A new emerging field is near field optical microscopy. The light field at the surface of an object actually contains more information—higher spatial frequencies—than we can image by using a “far-field” lens system. Only the spatial frequencies that reach the imaging lens (pass through the numerical aperture) are “seen.” These are the propagating, low frequencies. Higher spatial frequencies exist at the sample surface but decay exponentially within a distance less than the wavelength, so they never reach the detector. These high spatial frequencies are the “near field” (NF; the detector must be very near to see them). These are detected using a very small aperture to illuminate the object in the NF. An optical fiber is drawn to a sharp point. This is then coated with Al. The end is trimmed and an aperture is made by FIB milling. Figure 6 shows such probes fabricated using a FIB.

5.3. Trimming and Shaping of Magnetic Disk Heads

An industrial use of FIB micromachining is trimming and shaping of thin-film magnetic disk heads [7]. FIB milling is used to reduce the pole width of giant magnetoresistive heads to 100 nm. Such narrow gaps increase the magnetic resolution of the heads up to areal densities of 100 Gb in⁻². Manufacturers now offer dedicated machines for this purpose. The main advantage is that the existing production facilities can be used while greatly reducing the critical

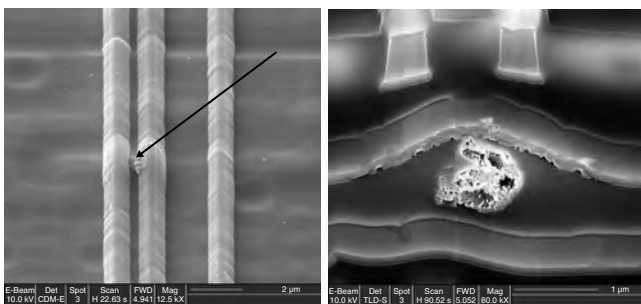


Figure 5. Cross-sectioning of a “surface defect” revealing that it is in fact below the surface.

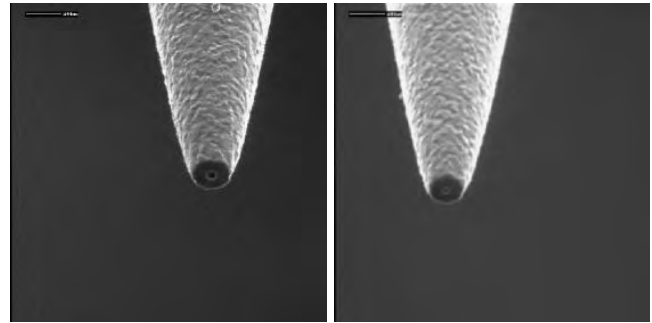


Figure 6. Near-field optical microscopy probes trimmed with FIB. The diameter of the tip is about 450 nm and the aperture is about 50 nm. Images courtesy of F. B. Segerink, MESA+, University of Twente.

dimensions. The process is fully automated using pattern recognition software. The magnetic heads can be trimmed on wafers and lapped rowbars. Typical cycle times are of the order of 2 to 5 sec/head.

5.4. Nanofabrication with Wet Etching

It has been reported in the literature that Ga⁺ ions in silicon act as an etch stop [30]. This is particularly effective in an etchant like KOH. This phenomenon can be used to fabricate micro- and nanomechanical elements in silicon. FIB ions have relatively low energy compared to the ion implantation process. As a result only a very thin layer is implanted with Ga⁺ ions. This layer is thinner than 50 nm. It is found that the critical dose for the etch stop to be effective is about 1×10^{15} ions cm⁻². This dose is easily obtained using a current of 100 pA in a few seconds of exposure. The implanted regions are amorphous. Using this method cantilevers of nanometer sizes can be fabricated. Sidewall doping can also be used to fabricate nanostructures in combination with wet etching.

5.5. Mask Repair

One of the first uses of FIB technology was photomask repair. To repair opaque defects, the undesired metal, for example, Cr, can simply be milled away [31]. The milling ions do embed themselves in the glass. This can lead to some loss in transmission of light. Clear defects can be repaired by milling a light scattering structure in the material. A grating or a prism, for example, acts to scatter light and appears opaque when viewed in transmission. The new technology uses extreme ultraviolet photolithography for nanoscale devices. Based on 70 nm node, the minimum space between features on a 4X mask is 280 nm. The minimum mask feature size is 180 nm (corresponding to a 45 nm gate length on wafer). The minimum printable defect size is 55 nm. For such a mask the repair process has the following requirements: etching dimension <280 nm, deposition dimension <180 nm, resolution required to repair small defects <55 nm, edge placement precision 35 nm, and the repair must not damage multilayer. FIB has been shown to be successfully applied to meet all the requirements [32].

5.6. Site Specific TEM Specimen Preparation

The FIB is ideally suited for making site specific TEM specimens. These are of great importance in the semiconductor industry for defect characterization and process control. FIB specimen preparation has been used to investigate several failure mechanisms, for instance of gate oxide defects, overalloyed contacts, various kinds of particles, notches in metal lines, electromigration failures, implant damage, and other site specific problems [33]. There is considerable literature about application of FIB for making TEM specimens [34–36]. TEM specimen preparation can be seen in Figure 7. Now FIB has also found applications in nano technology. The FIB specimen preparation technique has been used to investigate carbon nanotube/metal junctions [37].

5.7. Fabrication and Trimming of Nanotips

Atomic force microscopes (AFMs) are fabricated using a Si or Si_3N_4 tip with a metallic or a well conducting film. AFM measurements of semiconductors with conventional pyramid shaped tips can lead to problems. The feature of interest may be in proximity to a large step and the region next to the step cannot be reached. To overcome this, tips with high aspect ratios are of importance. A FIB is used to trim the pyramid shaped all diamond tips to obtain high aspect ratio tips. Tips with a height of 700 nm, a tip radius of 30 nm, and an aspect ratio of 1:7 have been reported. Still higher values of aspect ratios can be obtained [38]. The field ion microscope (FIM) is a powerful tool for analysis and imaging at atomic scale. However, the material to be observed

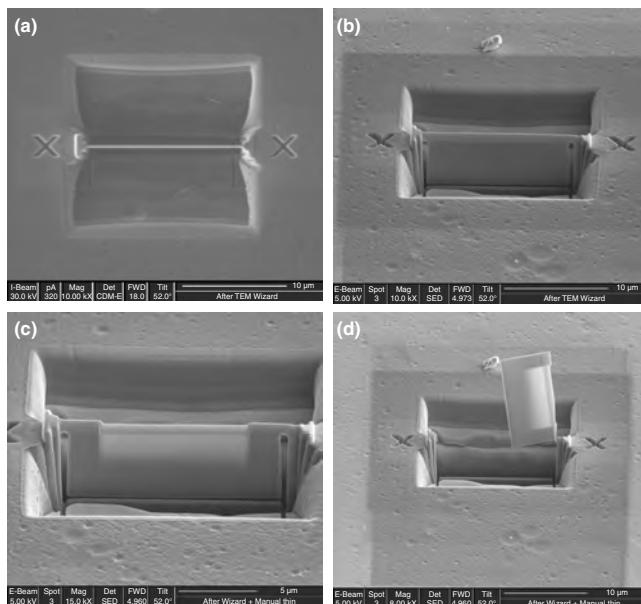


Figure 7. Sequence of TEM sample preparation using a FIB. (a) Initial mills to make section. (b) Release of bottom and sides. (c) Final thinning. (d) Section.

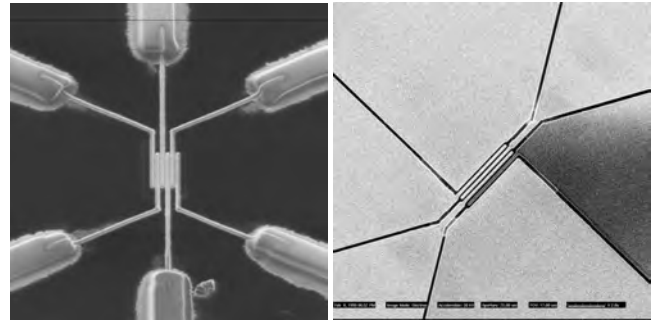


Figure 8. Nanofabrication for measuring electrical properties of carbon nanotubes using CVD deposition.

has to be in the form of a sharp needle with a tip radius of around 30 nm. The FIB has been successfully used to make FIM specimens from various materials like TiAl alloy, Cu–Co alloy, and even multilayer film devices [39].

5.8. Nanofabrication

Electron beam (EB) equipment and FIBs have both been successfully used to fabricate nanoscale devices. These include single electron transistors and metal-oxide semiconductor transistors with nanometer gate length. Commercially available FIB workstations can form 10 nm structures with beam diameters of 5–10 nm and a high resolution photoresist. The deposition of FIB CVD is much higher than EB CVD because of the difference in the mass of the ions compared to electrons. The penetration depth of the ions is smaller than electrons allowing fabrication of nanostructures [40]. Examples of such devices are shown in Figure 8. The facility of milling patterns in FIB has made it possible to use this technique to fabricate photonic devices. Examples of such structures milled in a chromium film can be seen in Figures 9 and 10. The shape of the holes and the pitch can

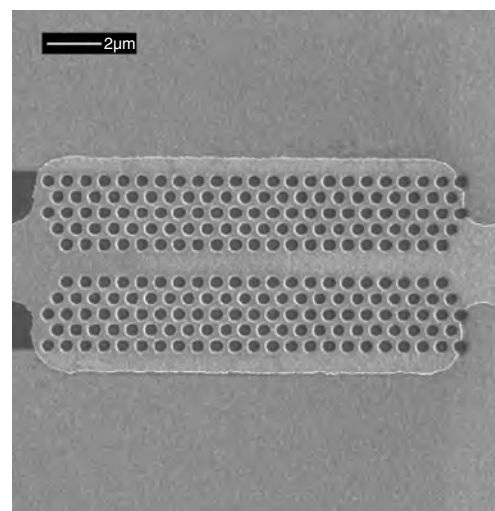


Figure 9. Pattern etched in Cr layer on Si for fabrication of a waveguide.

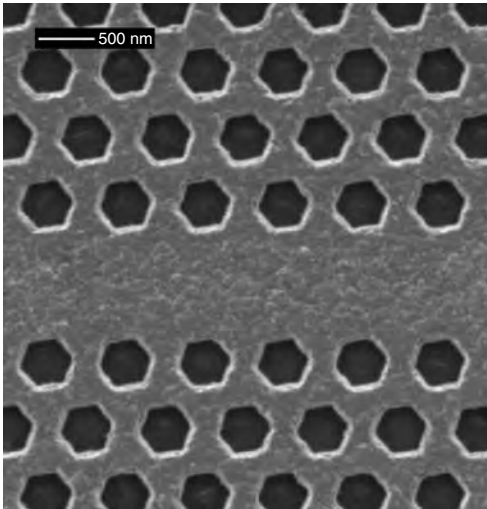


Figure 10. Hexagonal holes milled in a Cr layer on Si.

be varied freely. Typical milling current is 70 pA and milling time is 7 min.

5.9. Device Modification and Prototyping

The ability to mill any material and to deposit conductors as well as insulators can be used to carry out device modification and prototyping. In many cases a part of the circuit needs to be modified and tested. This can be achieved by cutting through the connects then milling through the via. The circuit can be reconfigured by laying new connects. In a modern machine it can also be tested using probes present inside the specimen chamber. An example of the modification is shown in Figures 11–14.

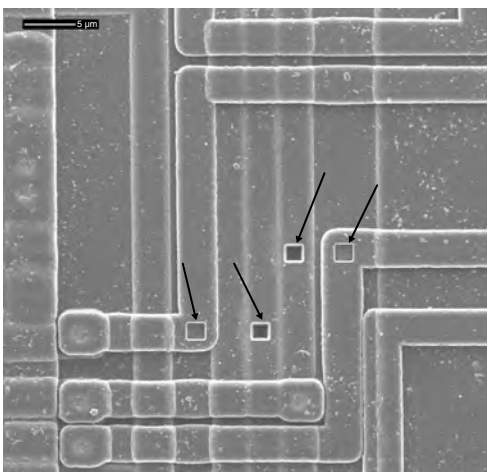


Figure 11. Cutting vias for device modification.

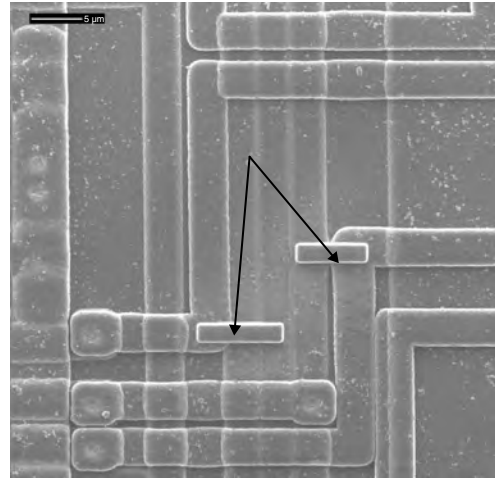


Figure 12. Platinum connects deposited for modification.

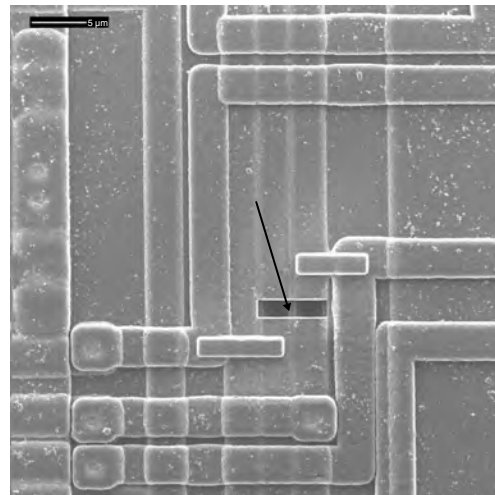


Figure 13. Metal lines cut by ion milling for circuit modification.

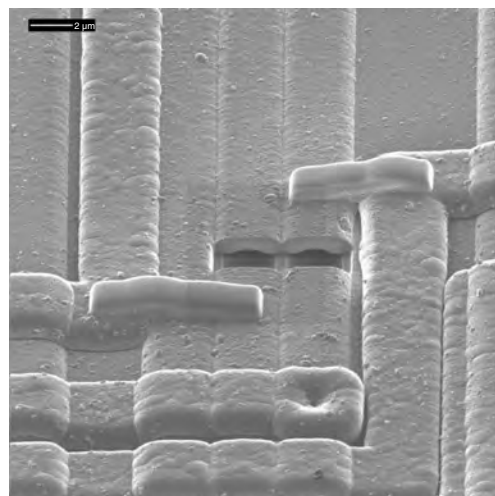


Figure 14. Modified device viewed by tilting.

6. SUMMARY

We have seen that the FIB has evolved from an implantation device to a flexible and versatile equipment. There are ever increasing applications of FIBs in the semiconductor industry, materials science, and nanotechnology. The developments have led to smaller beam diameters, better positioning hardware and software, and a greater number of materials that can be deposited. A greater number of gases for GAE and selective etching are also being made available. Over the years the FIB has become a powerful tool in mask repair, defect analysis, and TEM specimen preparations. The FIB remains the only tool that can be used for device modification and prototyping. Further developments in detectors has made it possible to use FIB also as an analytical tool. In the field of nanotechnology the FIB has very important applications in making near-field optical probes, sensors, photonic devices, and nanostructures by deposition of material. The FIB is now also used in production specially of magnetic heads. It is not, however, suitable for mass throughput fabrications. It remains a relatively slow process. Despite the drawbacks the applications show a great promise in path breaking technologies in nanotechnology. It is clear that FIB technology will play a central role in the coming years.

GLOSSARY

Amorphous layer Layer which does not display a regular ordered structure seen in crystals.

Coulomb interactions Electrical interactions in charged particles.

Failure analysis When a semiconductor device or any component fails, the causes of failure are investigated. The factors leading to the failure are analyzed.

Ion implantation Ions directed at a surface of a material, with high energy embed themselves in the material. This is used to change the properties of the material by adding another species to the material.

Magnetoresistive heads The magnetoresistive heads used for information storage are made from a ferromagnetic alloy whose resistance changes as a function of an applied magnetic field. This phenomenon was discovered by Lord Kelvin in 1857 and today is called the anisotropic magnetoresistance effect.

Mask repair Photolithography depends on masks which are used to expose a photoresist to light. The pattern of the mask is thus transferred to the photoresist.

Raster Scan.

Sputtering Removal of atoms from the surface of a material due to impact of incident atoms.

ACKNOWLEDGMENTS

Figure 6 showing near-field optical microscopy probes is courtesy of F. B. Segerink of MESA+ Institute, University of Twente. Circuit modification shown in Figures 11–14 is courtesy of Maser Engineering of Enschede, The Netherlands.

REFERENCES

1. J. Melngailis, *J. Vac. Sci. Technol. B* 5, 469 (1987).
2. D. K. Stewart, L. A. Stern, G. Foss, G. Hughes, and P. Govil, *Proc. SPIE* 1263, 21 (1990).
3. J. Glanville, *Solid State Technol.* 32, 270 (1989).
4. S. Reyntjens, D. De Bruyker, and R. Puers, in "Proc. 1998 Microsystem Symp.," Delft, The Netherlands, 1998, p. 125.
5. B. W. Ward, N. P. Economou, D. C. Shaver, J. E. Ivory, M. L. Ward, and L. A. Stern, *Proc. SPIE* 923, 92 (1988).
6. J. F. Walker, J. C. Reiner, and C. Solenthaler, in "Proc. Microsc. Semicond. Mater. Conf.," Oxford, 20–23 March 1995, p. 629.
7. G. J. Athas, K. E. Noll, R. Mello, R. Hill, D. Yansen, F. F. Weners, J. P. Nadeau, T. Ngo, and M. Siebers, *Proc. SPIE* 3223, 198 (1997).
8. J. H. Daniel and D. F. Moore, *Sensors Actuators A* 73, 201 (1999).
9. J. Brugger, G. Beljakovic, M. Despont, N. F. de Rooij, and P. Vettiger, *Microelectron. Eng.* 35, 401 (1997).
10. G. Thornell and S. Johansson, *J. Micromech. Microeng.* 8, 251 (1998).
11. S. K. Ghandi, "VLSI Fabrication Principles." Wiley, New York, 1985.
12. S. Reyntjens and R. Puers, *J. Micromech. Microeng.* 11, 287 (2001).
13. N. Matsunami, Y. Yamamura, Y. Itikawa, N. Itoh, Y. Kazumata, N. Miyagawa, K. Morita, R. Shimatzu, and H. Tawara, *At. Data Nucl. Data Tables* 31, 1 (1984).
14. R. L. Kubena, R. L. Seliger, and E. H. Stevens, *Thin Solid Films* 92 (1982).
15. H. Yamaguchi, A. Shimase, S. Haraichi, and T. Miyauchi, *J. Vac. Sci. Technol. B* 3, 71 (1985).
16. H. Marimoto, Y. Sasaki, Y. Watanabe, and T. Kato, *J. Appl. Phys.* 159 (1985).
17. K. Edinger, *J. Vac. Sci. Technol. B* 17, 60 (1999).
18. R. J. Young, J. R. A. Cleaver, and H. Ahmed, *J. Vac. Sci. Technol. B* 11, 234 (1993).
19. J. D. Casey Jr., A. F. Doyle, R. G. Lee, and D. K. Stewart, *Microelectron. Eng.* 24, 43 (1994).
20. K. Ohmo, M. Sato, and Y. Arita, *Jpn. J. Appl. Phys.* 2 28, L1070 (1989).
21. S. K. Lee, S. S. Chun, C. Y. Hwang, and W. J. Lee, *Jpn. J. Appl. Phys.* 1 36, 50 (1997).
22. K. Ohmo, M. Sato, and Y. Arita, *J. Electrochem. Soc.* 143, 4089 (1996).
23. B. J. Howard and Ch. Steinbruchel, *Appl. Phys. Lett.* 59, 914 (1991).
24. T. J. Stark, G. M. Shedd, J. Vitarelli, D. P. Griffis, and P. E. Russell, *J. Vac. Sci. Technol. B* 13, 2565 (1990).
25. D. K. Stewart, A. F. Doyle, and J. D. Casey, Jr., *Proc. SPIE* 2437, 276 (1995).
26. P. G. Blauner, J. S. Ro, Y. Butt, and J. Melngailis, *J. Vac. Sci. Technol. B* 7, 609 (1989).
27. I. Utke, P. Hoffmann, B. Dwir, K. Leifer, E. Kapon, and P. Doppelt, *J. Vac. Sci. Technol. B* 18, 3168 (2000).
28. J. P. Levin, P. G. Blauner, and A. Wagner, *Proc. SPIE* 1263, 2 (1990).
29. R. L. Kubena and F. P. Stratton, *J. Vac. Sci. Technol. B* 6, 1865 (1988).
30. B. Schmidt, L. Bischoff, and J. Teichert, *Sensors Actuators A* 61, 369 (1997).
31. J. Orloff, M. Utlaut, and L. Swanson, "High Resolution Focused Ion Beams: FIB and Its Applications." Kluwer Academic/Plenum, New York, 2003.
32. T. Liang, A. Stivers, R. Livengood, P.-Y. Yan, G. Zhang, and F.-C. Lo, *J. Vac. Sci. Technol. B* 18 (2000).
33. F. Altmann and D. Katzer, *Thin Solid Films* 343, 609 (1999).

34. G. Majni, *Thin Solid Films* 125, 71 (1985).
35. T. Shimozaki, T. Narishige, Y. Wakamatsu, and M. Onishi, *Mater. Trans. JIM* 35, 868 (1994).
36. R. M. Langford, C. M. Reeves, and J. G. Goodall, *J. Vac. Sci. Technol. B* 18, 100 (2000).
37. B. Wei, P. Kohler-Redlich, U. Bader, B. Heiland, R. Spolenak, E. Artzt, and M. Ruhle, *Ultramicroscopy* 85, 93 (2000).
38. A. Olbrich, B. Ebersberger, C. Bolt, Ph. Niedermann, W. Hanni, J. Vancea, and H. Hoffmann, *J. Vac. Sci. and Technol. B* 17, 1570 (1999).
39. D. J. Larson, D. T. Foord, A. K. Petford-Long, T. C. Anthony, I. M. Rozdilsky, A. Cerezo, and G. W. D. Smith, *Ultramicroscopy* 75, 147 (1998).
40. S. Matsui, T. Kaito, J-I. Fujita, M. Komuro, K. Kanda, and Y. Haruyama, *J. Vac. Sci. Technol. B* 18, 3181 (2000).

Atomic Manipulation by Scanning Tunneling Microscopy

K.-F. Braun, G. Meyer, F. Moresco, S.-W. Hla, K. Morgenstern, S. Fölsch,
J. Repp, K.-H. Rieder

Free University, Berlin, Germany

CONTENTS

1. Introduction
 2. Scanning Tunneling Microscopy
 3. Lateral Manipulation
 4. Pulling, Pushing, and Sliding of Atoms and Small Molecules
 5. Vertical Manipulation
 6. Vibrational Spectroscopy with the Scanning Tunneling Microscopy (STM)
 7. Effects Due to Electron Current
 8. Chemistry with the STM Tip
 9. Manipulation of Large Molecules
 10. Intramolecular Mechanics During the Manipulation of a Large Molecule
 11. Physics with Artificial Structures
 12. Toward Manipulation on Thin Insulating Films
 13. Summary
- Glossary
References

1. INTRODUCTION

The scanning tunneling microscope (STM) was initially intended for imaging surfaces and has proven its unique abilities in producing images down to atomic resolution. Soon it was realized that, due to its close proximity to the surface atoms, the STM tip often influences and modifies the surface due to tip-induced migration of surface particles. This obvious disadvantage for imaging was, however, readily turned into a positive prospect by realizing that the tip–substrate interactions as well as electrical field and current can be used to induce modifications of the surface. Pertinent studies proved that the STM tip–surface forces indeed offer startling possibilities to move single atoms and molecules in a desired way

on the atomic scale [1–6]. Thus, the longstanding dream of building man-designed functional nanostructures and creating new material combinations or even new materials in an atom-by-atom manner appears to have come into realistic reach.

To modify a surface by means of a STM tip, one can use three different parameters: the electrical field between tip and substrate, the tunneling current, and the forces between tip and surface (Fig. 1) [1,2,5]. Although field and current effects can be used for surface modifications, these parameters yield mainly gross changes like attraction or repulsion of charged particles or particles carrying a dipole moment from a region under the tip by applying corresponding tip biases [7–11] or electron current induced desorption due to local heating [4]. Reliable atomic scale precision for manipulation is achieved mainly by soft manipulation, where only the tip–substrate forces are employed. These forces can be tuned by changing the distance between the tip and the manipulated particle (Fig. 1). On working with single atoms and molecules, lateral and vertical manipulation modes are distinguished. In the former mode, a particle on the surface is moved along the surface to the desired place without losing contact with the substrate (Fig. 2), while in the latter mode a particle is deliberately picked up to the tip and then released back to the surface (Fig. 2).

2. SCANNING TUNNELING MICROSCOPY

The controlled manipulation of single atoms and molecules demands a higher stability and lower thermal drift of the microscope than necessary for imaging surfaces. Most experiments up to now have been performed at low temperatures since instrumental effects like piezo creep, hysteresis, and thermal drift are then negligible. STMs cooled by liquid helium show usually a drift of less than a few Å within 24 hours, making it possible, for example, to manipulate single atoms from hexagonal close packed (hcp) to face-centered cubic (fcc) sites—a distance of only 1.6 Å. Furthermore, at low temperatures the sample surface can be

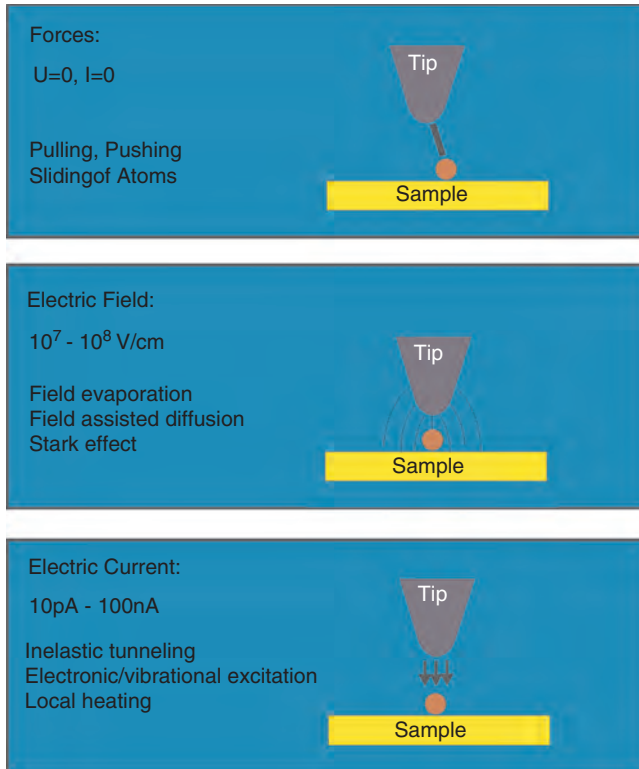


Figure 1. Schematic image of the basic tip-sample interaction mechanism for atomic scale modification of surfaces.

kept clean for many days since the surrounding radiation shieldings act as cryogenic pumps and create ideal vacuum conditions—a necessary condition for the time consuming creation of larger artificial structures. Descriptions of instruments capable of operating at low temperature can be found in [12–21].

For the lateral manipulation the control unit is required to be able to (1) position the tip over the adparticle, (2) switch the feedback loop to the manipulation parameters, (3) move the tip (with the adparticle) to the final position, and (4) retract the tip back to the initial imaging height (Fig. 2). Alternatively the feedback loop can be switched off during

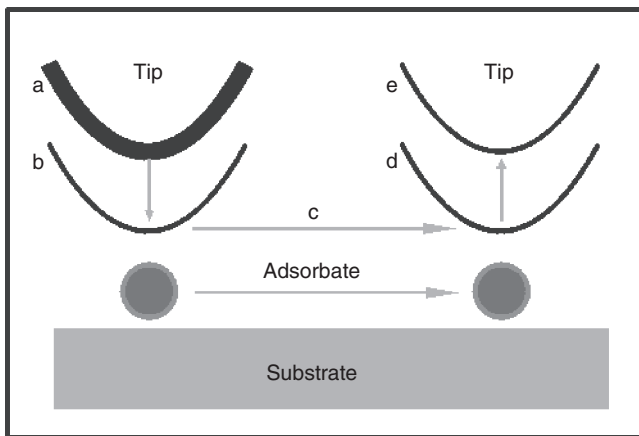


Figure 2. Schematic sketch of the lateral manipulation procedure of single atoms or molecules on a surface.

the manipulation to work in the constant height modus [22]. Recording simultaneously the feedback loop signal or the tunneling current gives information about the manipulation process itself. Software lacking these possibilities can be used for tip induced migration only. Automated software for the lateral manipulation including the determination of the initial position has been used in [23]. For the vertical processes the tip needs to be positioned over the adparticle and the voltage and/or distance is then varied with the feedback loop on or off. For tunneling spectroscopy the first or second derivative measured with a lock-in technique is recorded together with the current. For extended datasets or in case of low signals repeated measurements have been acquired using an automatized tracking procedure to keep the tip over the adparticle [24].

Adparticle-surface systems suitable for lateral manipulation experiments should not exhibit thermally activated diffusion of the adparticles but need to have binding energies low enough that the counterforces acting on the tip do not alter the tip apex instead. As substrates for the manipulation experiments mainly low index noble metal surfaces like Cu(111), Ag(111), Ag(110), Cu(100), and Cu(211) were widely employed, the latter being a regularly stepped surface consisting of (111) nanofacets separated by (100) steps of monoatomic height. The crystal surfaces have to be cleaned in ultrahigh vacuum by several cycles of sputtering with noble gas ions and annealing at elevated temperatures. Desired very small coverages of gaseous adsorbates are dosed at low temperature either through very fine holes to the sample located in the STM or in separate preparation chambers. Metals and heavier molecules are evaporated from Knudsen cells in analogous ways.

Due to the aforementioned requirements attempts to do lateral manipulation at room temperature achieved a much lower precision in the experiments than at low temperatures. Nevertheless vertical manipulation can be done with atomic precision at room temperature too.

3. LATERAL MANIPULATION

Figures 3 and 4 prove the ability to create artificial structures by lateral manipulation. Figure 3 shows the first structures by the first two groups who have succeeded in showing manipulation on atomic scale. In the upper part, the name of their company was written by Eigler and Schweizer using 35 Xe atoms with a 4K-STM [25]. In the lower part, the Berlin group of Meyer et al. formed at 25 K the two letters F and U with a total of 20 CO molecules, which designate the abbreviation of their university [26]. Notice that at this elevated temperature the CO molecules were still so mobile that it was impossible to keep them in the desired places due to irregular thermally induced jumps. In contrast to this, at temperatures of 15 K structures can be built with CO with atomic precision, as proven in Figure 4, where the Brandenburg Gate of Berlin is reproduced on the nanometer scale. The structure was built by manipulating 47 CO molecules laterally on Cu(211). At 15 K, the molecules are frozen to a sufficient degree that precise working is possible with a rather large number of particles and the artificial structure remains stable for a long time. An impression concerning different stages of the buildup work of an artificial

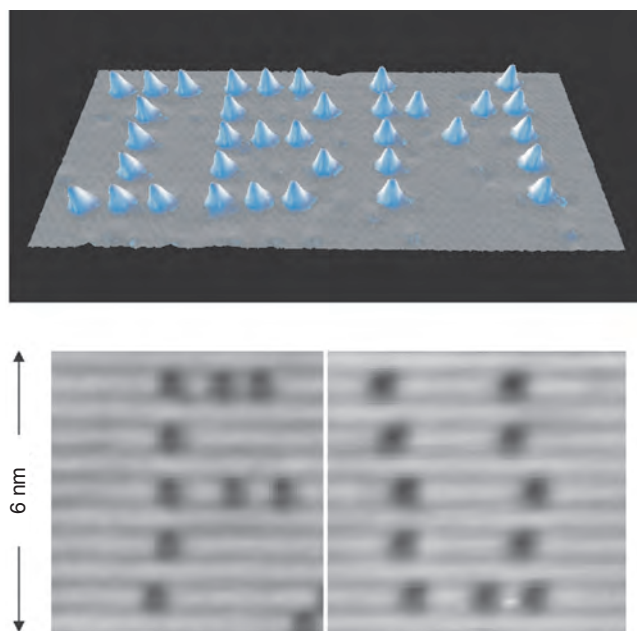


Figure 3. The first successful works of artificial atomic structures created by manipulation with a STM. Upper: The IBM logo written with single Xe atoms on Ni(110). Reprinted with permission from [25], D. Eigler and E. Schweizer, *Nature* 344, 524 (1990). © 1990, Nature Publishing Group. Lower: CO molecules forming the letters FU on Cu(211). Reprinted with permission from [26], G. Meyer et al., *Appl. Phys. A* 60, R343 (1995). © 1995, Springer-Verlag.

structure is given in Figures 4, 5, 8, and 41. Although all experiments presented here are performed at low temperature, tip-induced diffusion at room temperature of Br atoms strongly bound on Cu(001) (Fig. 6) has already been demonstrated [27]. The construction of atomically perfect struc-

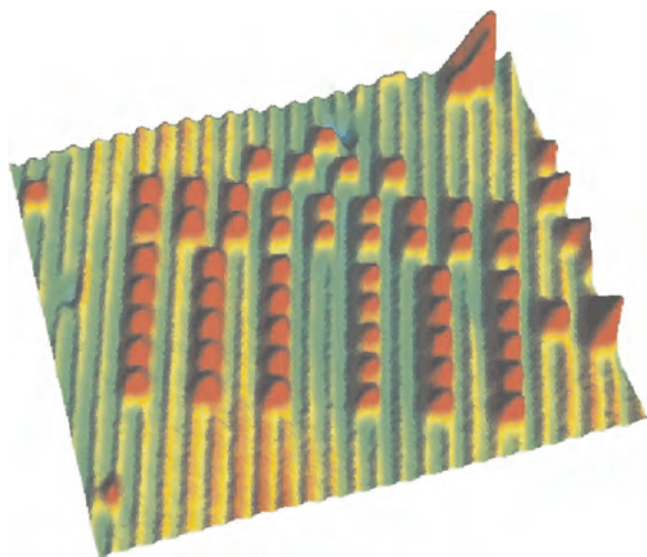


Figure 4. STM image of the Brandenburg Gate, as an example of artwork on an atomic scale employing lateral manipulation of CO molecules deposited on Cu(211). The substrate temperature was 15 K. Reprinted with permission from [127], F. Moresco et al., *Chinese Phys.* 10, S10 (2001). © 2001, Institute of Physics.

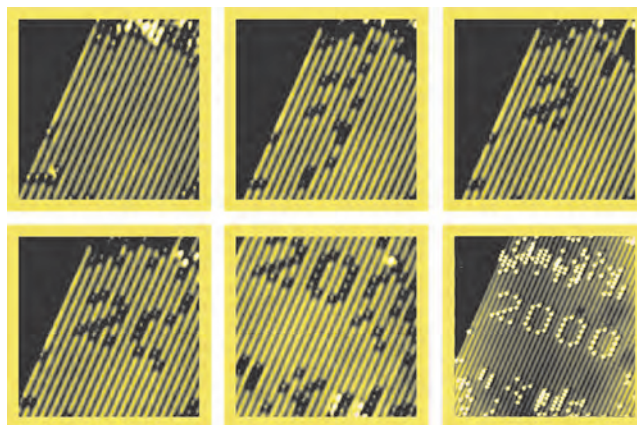


Figure 5. Sequence of STM pictures showing the gradual buildup of the millennium number “2000” with 47 CO molecules on a Cu(211) substrate. Notice that an area free from any CO molecules had to be prepared at the beginning. Reprinted with permission from [127], F. Moresco et al., *Chinese Phys.* 10, S10 (2001). © 2001, Institute of Physics.

tures with many atoms or molecules is, however, to date bound to low temperatures.

As demonstrated, the first successful manipulation experiments were performed with Xe atoms [1] and small molecules like CO and C₂H₄ [26]; manipulations of metal atoms like Pb, Cu, and Ag followed [12]. It was observed that increasing forces have to be applied in the respective order. With still increasing forces, it was shown on Cu(211) that it is also possible to release native substrate atoms from sixfold coordinated kink sites (Fig. 7a–c) and even from sevenfold coordinated regular step-edge sites (Fig. 7d–f) [26]. This important result opens the way for structuring the surface itself with the promising prospect that also deeper lying substrate layers may be included in the buildup of artificial

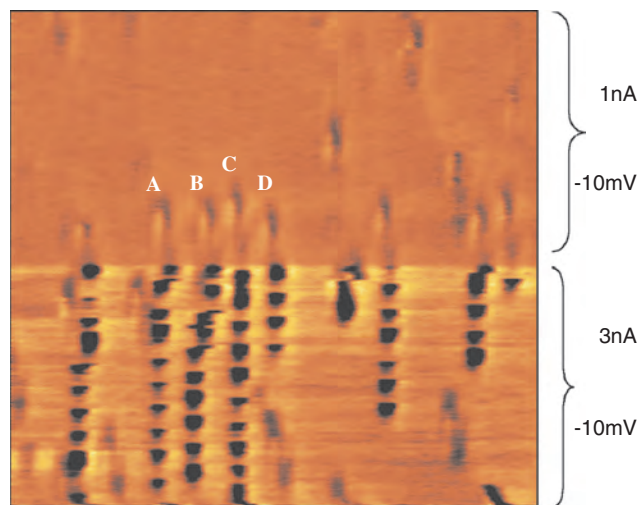


Figure 6. STM image ($60 \times 60 \text{ \AA}$) of Br on Cu(100) at RT. The tunnel current is reduced halfway up the image. The tracks in the 3 nA (lower half) area are single atoms hopping from site to site. When the current is reduced the bromine atoms stop moving, for example, those marked A, B, C, and D. Reprinted with permission from [27], T. Fishlock et al., *Nature* 404, 743 (2000). © 2000, Macmillan Magazines Ltd.

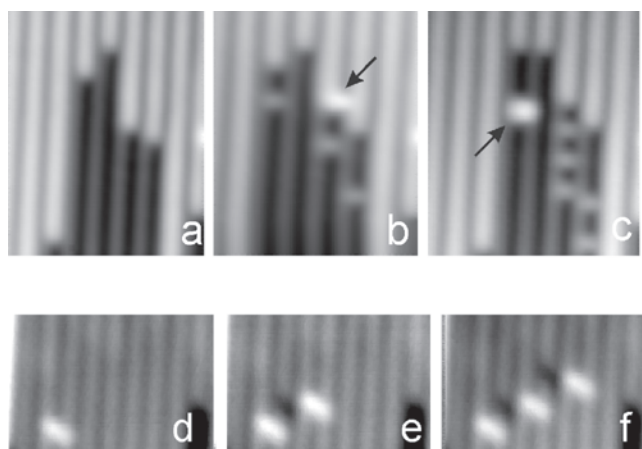


Figure 7. Manipulation of native Cu atoms from sixfold coordinated kink sites out of defect steps (a–c) and out of sevenfold coordinated regular step sites (d–f) on Cu(211). Notice the appearance of adatom/vacancy pairs in the latter case. Reprinted with permission from [28], G. Meyer et al., *Phys. Rev. Lett.* 78, 1512 (1997). © 1997, American Physical Society.

prototype structures. It could also be shown that vacancies at step edges of regularly stepped surfaces like Cu(211) can be “healed out” by manipulating single atoms into them. Interestingly, a larger force is required for this purpose than for manipulation along defect-free step edges, indicating that a local barrier due to atom relaxations around the vacancy has to be surmounted [28]. The manipulation of “native” substrate atoms on Cu(211) to different positions allowed determination of adsorbate adsorption sites [29]. Manipulation of Cu atoms perpendicular to the step edges on Cu(211) can also lead to particle exchange at the steps [30]. Data storage employing adatoms and vacancies with writing, reading, and deleting capabilities thus can constitute the utmost limit of storage density [26].

The structure presented in Figure 8 shows the formation of an artificial metallic structure. By lateral manipulation 36 Ag atoms have been positioned in a circle with diameter of 31.2 nm on a Ag(111) surface [23]. The electrons of the surface state are scattered at the adatoms resulting in an energy dependent interference pattern as well, visible in Figure 8. The closed scattering geometry results in an (imperfect) confinement of the electrons inside of the quantum corral as has been demonstrated by Crommie et al. [31]. Experiments with quantum corrals are discussed in Section 11. For more examples of lateral manipulation see references in Table 1.

4. PULLING, PUSHING, AND SLIDING OF ATOMS AND SMALL MOLECULES

In manipulation experiments performed with Cu atoms, Pb atoms, and CO molecules on Cu(211) different manipulation modes, depending on the applied tip–particle force (qualitatively measured by the tunneling resistance), could be distinguished [5,23]. These manipulation modes are shown in Figure 9. Pb (and also Cu and other metal) atoms could be manipulated via attractive tip–adatom interactions in a way in which they follow the tip discontinuously by hopping from one adsite to the next (pulling mode, Fig. 9a, b,

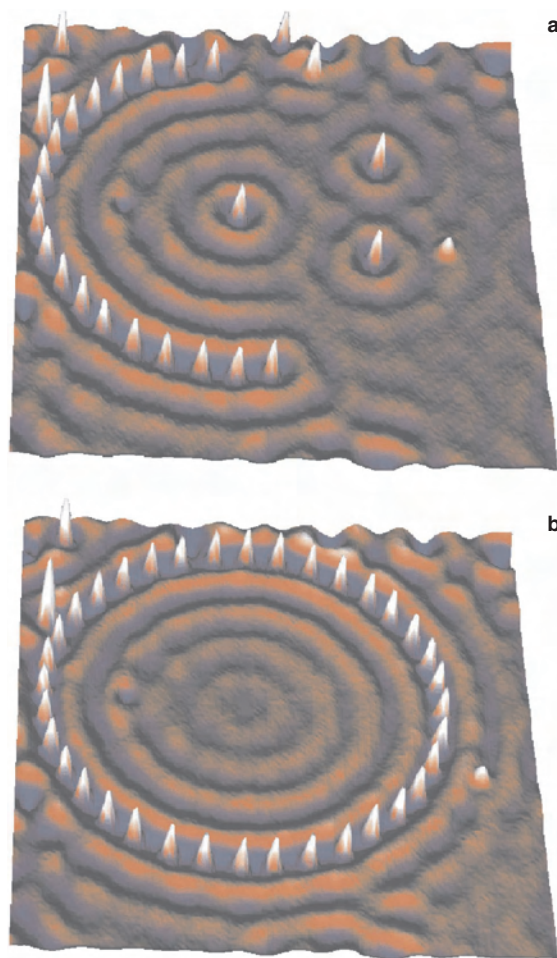


Figure 8. Series of images displaying the formation of a circular quantum corral consisting of 36 native Ag atoms on a Ag(111) surface by lateral manipulation. Circular standing electron waves result from the scattering of the surface electrons with the adatoms. The diameter of the corral is 31.2 nm. Reprinted with permission from [23], S.-W. Hla et al., *Phys. Rev. B* (2003). © 2003, American Physical Society.

e–g). Upon application of larger forces than for pulling, Pb atoms could also be manipulated attractively in a continuous way (sliding mode, Fig. 9c); in this mode the tip–particle interaction is increased so strongly that the tip–particle–system scans the corrugation of the substrate, while the particle–substrate interaction is still strong enough to keep the particle on the substrate. Finally, single CO molecules as well as rows of several CO molecules could reliably be manipulated via repulsive interaction (pushing mode, Fig. 8d), whereby the intrinsic step edges, on top of which the CO molecules are bound, act as railway trails [5]. Using tip induced migration Ag atoms were moved on a Ag(100) surface as can be seen in Figure 10. Depending on the applied voltage the atoms were moved in a pushing or pulling mode along the closed packed rows or across the rows respectively [32,33]. By use of tip induced motion of Ag atoms on the same surface the adsorption site of PTCDA has been determined [34].

On the closed-packed metal surface the direction of the adparticle movement can be chosen freely and here the manipulation mode additionally depends upon the direction.

Table 1. Selected references on lateral manipulation.

System	Temperature	Junction resistance	Ref.
Ag/Ag(111)	5 K	$<(210 \pm 19) \text{ k}\Omega$	[23]
Au/Ag(111)	5 K	$<164 \text{ k}\Omega$	[132]
Au/Ni(111)	5 K	$<(1.14 \pm 0.10) \text{ M}\Omega$	[132]
TBPP/Cu(100)	300 K	10 M Ω	[82]
Pb/Cu(211)	30 K	100–190 k Ω	[5]
Pb dimers/Cu(211)	30 K	100–190 k Ω	[5]
CO/Cu(211)	30 K	1 M Ω	[26]
Cu/Cu(211)	4 K	500–700 k Ω	[28]
Xe/Ni(111)	4 K	5 M Ω	[25]
C ₅ H ₅ /Ag(100)	300 K	$\sim 200 \text{ M}\Omega$	[83]
Zinc-porphirin/HOPG ^a	300 K	10 M Ω	[85]
(1-Nitronaphthalene) ₁₀ /Au(111)	50 K	25 M Ω	[87]
HtBDC/Cu(110)	$<160 \text{ K}$	1 M Ω	[88]
Lander molecules C ₉₀ H ₉₈ /Cu(110)	100–200 K	50 M Ω	[89,90]
Au/NiAl(110)	12 K	200 k Ω	[107,133]
CO/Pt(111)	4 K	200 k Ω	[1,134]
Phosphangulene/Ag(111)	6 K	0.5–10 M Ω	[91]
C ₆₀ /Si(100)-2 × 1	300 K	$\sim 2 \text{ G}\Omega$	[86]

^a HOPG—highly oriented pyrolytic graphite.

The manipulation curves from the lateral manipulation of Ag atoms on a Ag(111) surface therefore display additional features. A continuous transition from pulling along the closed-packed [110] direction to sliding along the [211] direction has been observed [23].

The tunneling resistance necessary to move a Ag atom on a Ag(111) surface was determined by systematically varying the manipulation parameters over a wide range. An extensive set of several thousand computer-automated manipulations has been taken for this purpose. The atom manipulations were performed by using tunneling current values ranging from 8 to 950 nA and tunneling voltages ranging from ± 10 to ± 55 mV. Figure 11a shows a plot for the probability of a successful atom manipulation versus tunneling current at -45 mV bias. At this bias, the probability of a successful atom manipulation changes from ~ 0 below 147 nA to ~ 1 above 250 nA and an average threshold current is determined as 200 nA. The entire measurement procedure is repeated for a wide range of bias voltages. Evaluation of these measurements yields the minimum current necessary to move the atom as a function of the tunneling voltage averaged over all surface directions. Figure 11b depicts the results, which clearly display a linear dependence between the tunneling voltage and the threshold current, independent of the bias polarity. In this low bias regime, influence of electric field effects in the manipulation process is negligible. From the slope of the curve in Figure 11b, a tunneling resistance of $(210 \pm 19) \text{ k}\Omega$ has been measured. This linear relationship unambiguously reveals that the tunneling resistance is the ultimate parameter to move an atom within the bias range used in this experiment. This tunneling resistance value corresponds to a tip–atom distance of $(1.3 \pm 0.2) \text{ \AA}$ before the formation of an ohmic point contact, as can be determined from I – Z spectra. The lateral center-to-center distance between the apex atom and the adatom was measured to be typically 3.5–4.2 \AA ,

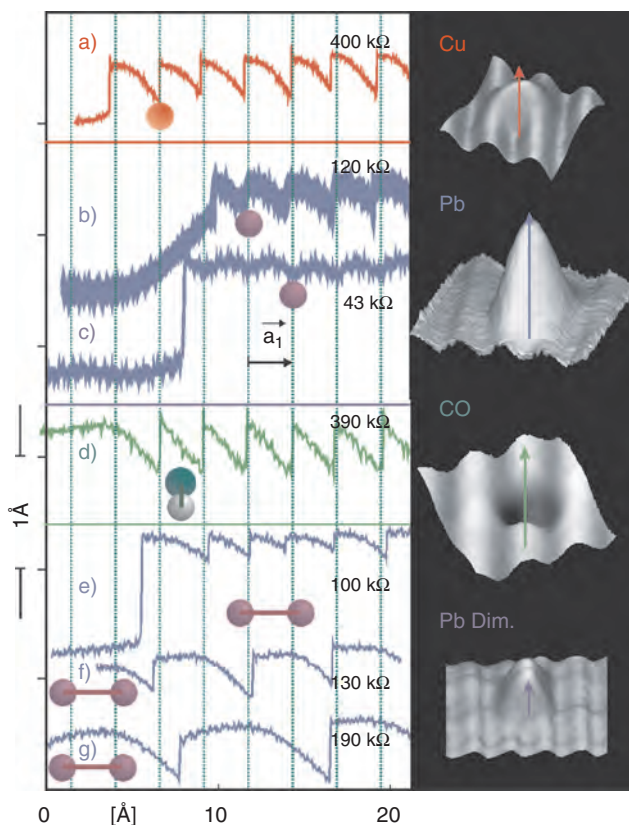


Figure 9. Tip height curves during manipulation of (a) a Cu atom, (b, c) a Pb atom, (d) a CO molecule, and (e–g) a Pb dimer along step edges on Cu(211). The tip is moved from left to right and respective tunneling resistances are indicated. The vertical dotted lines correspond to fcc sites next to the step edge. The initial sites of the manipulated particles are indicated. Notice that in the attractive manipulation modes (a, b, e–g: pulling and c: sliding) the particles first hop toward the tip and then follow it, whereas in the repulsive mode (d: pushing) the particle performs hops away from the tip [5]. Image courtesy of L. Bartels.

depending on the exact path of the atom as discussed in detail in [23]. Since this is a distance where the tip and manipulated atom wavefunctions are overlapping to form bonds, the chemical nature of tip–atom interaction is proven to be the main force in the lateral manipulation process. Theoretical calculations have been made for the pulling of a Cu atom adsorbed at a Cu step edge only. The calculated threshold distances are in fair agreement with the experimental findings for the pulling of Ag atoms on a Ag(111) surface. The calculated force necessary to move a Cu atom is estimated to be 10–100 pN [35].

5. VERTICAL MANIPULATION

Vertical manipulation was first reported by Stroscio and Eigler [1], who demonstrated an atomic switch by transferring repeatedly a Xe atom from the surface to the tip and vice versa. Other experiments with Xe used another method to prove successful transfer of Xe to the tip: A Xe atom was picked up to the tip apex and used for imaging the same area as before with the bare tip. The markedly improved resolution proved that the single Xe atom “sharpens” the

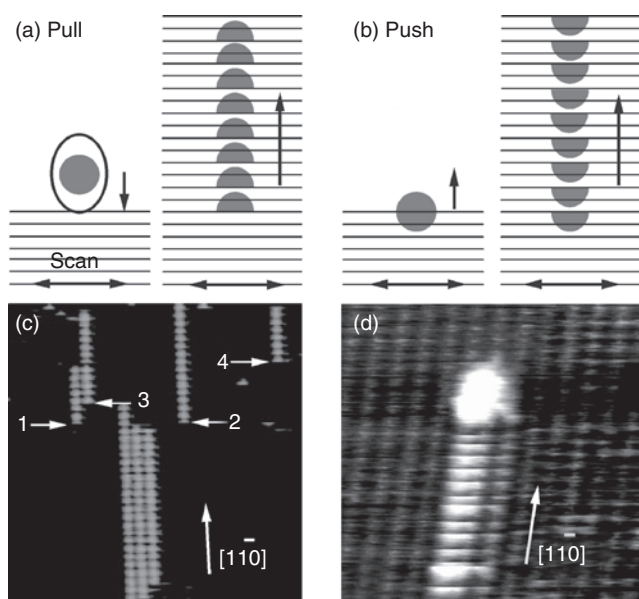


Figure 10. Schematic representation of the STM image resulting from (a) attractive or (b) repulsive tip-atom interaction during tip-induced diffusion of Ag atoms on Ag(110). Experimental observations for pulling (c) and pushing (d) (the slow scan direction is pointing from bottom to top). Reprinted with permission from [33], J. Li et al., *Appl. Phys. A* 66, 675 (1998). © 1998, Springer-Verlag.

tip [36]. Theoretical calculations for the manipulation of Xe atoms can be found in [10,37–40].

The pickup of single CO molecules to the tip is interesting, as it is well known that CO stands upright on metal surfaces with the carbon atom binding to the substrate. Upon transfer to the tip, the molecule consequently has to turn around (Fig. 12a). A reliable experimental procedure for transferring single CO molecules to the tip apex and back to a Cu surface was found to require ramping of the tunneling voltage and simultaneous decrease of the tip–CO distance [5]. While the vertical transfer of a Xe atom at higher voltages is attributed to a polarizing effect of the electric field, the transfer of CO is caused by tunneling into an electronic resonance; See section 7.

An advantageous by-product of the ability to deliberately transfer CO to the tip is demonstrated in Figure 12b. As one can see in Figure 12b, all species imaged with a clean metal tip appear as depressions. When a CO molecule (denoted in this case by the white arrow) is transferred to the tip apex, all CO molecules change their appearance to protrusions (Fig. 12b, left), whereas the oxygen atom in the upper left part of Figure 12b (right) retains its appearance [5]. Thus, chemical contrast in STM imaging is achieved, a phenomenon very useful for the analytic abilities of the STM.

The dependence of STM images on parameters like the chemical constitution of the tip or the density of adsorbed species on the surface is, however, still an open problem, as can be realized from Figure 13 [41]. In Figure 13a we show a regular adlayer of CO on Cu(211) with (3×1) periodicity. With the knowledge that the coverage is $2/3$ of a monolayer, a structural model like the one illustrated in Figure 13b, where CO molecules occupy on-top and bridge sites, thus maximizing their mutual distance, appears

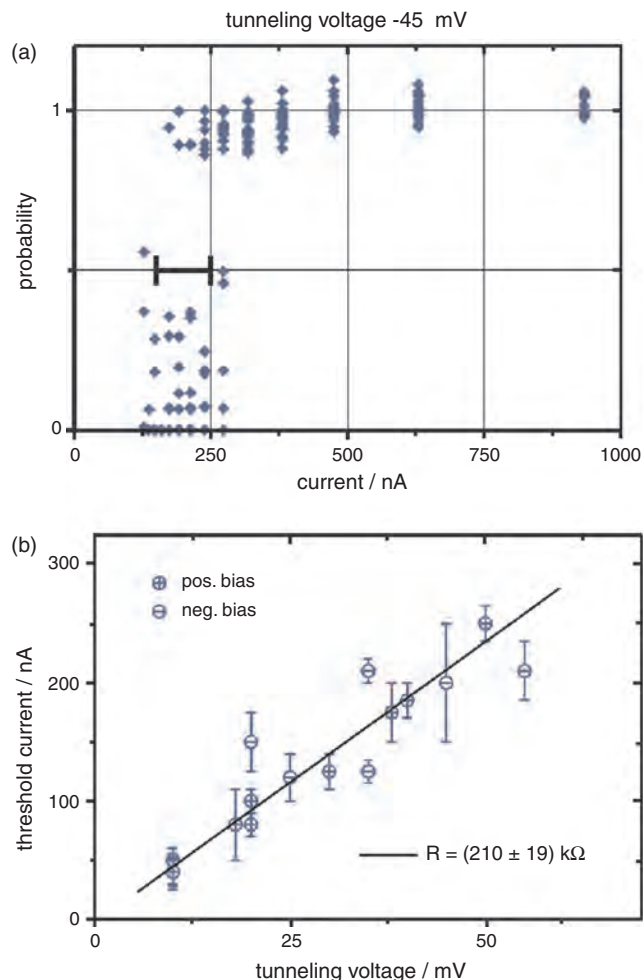


Figure 11. Threshold tunneling current and resistance for a successful atom manipulation. (a) The probability for an Ag atom to move along with the STM tip versus the tunneling current at a fixed voltage of -45 mV. (b) The threshold current between ± 10 to ± 55 mV determined by 3857 automated atomic manipulations shows a linear dependence on the tunneling voltage [23]. Image courtesy of K.-F. Braun.

plausible. Figure 13c–e shows, however, that laterally manipulating together two CO molecules into adjacent on-top sites changes the image from two minima into one maximum located between the two on-top sites. Thus, upon formation of a CO “dimer,” a dramatic change in the appearance of the two CO molecules has occurred (Fig. 13d). By separating the two CO molecules their appearance changes to the initial shape. Using the lateral manipulation technique also an extended domain of the (3×1) structure was formed (Fig. 13f) leading to the conclusion that the model depicted in Figure 13g is the proper one and has to replace that of Figure 13b.

Single atoms have been extracted from semiconductor surfaces with a related technique: The tip is brought close to the surface to induce a strong chemical bond and a voltage pulse of several volts induces field evaporation of the substrate atom (“chemically assisted field evaporation” [42] or “transfer on contact”). Using this technique, Becker et al. [43] were the first to report in 1987 the creation

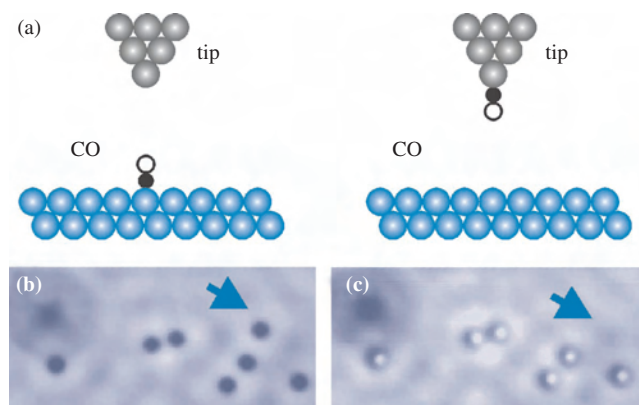


Figure 12. (a) Schematic picture demonstrating the flipping of a CO molecule upon vertical transfer from the substrate to the tip. (b) Demonstration that chemical contrast is obtained for CO molecules with a CO tip, whereas oxygen remains unaffected. The blue arrow denotes the CO molecule, which was transferred deliberately towards the tip. Reprinted with permission from [59], L. Bartels et al., *Appl. Phys. Lett.* 71, 213 (1997). © 1997, American Institute of Physics.

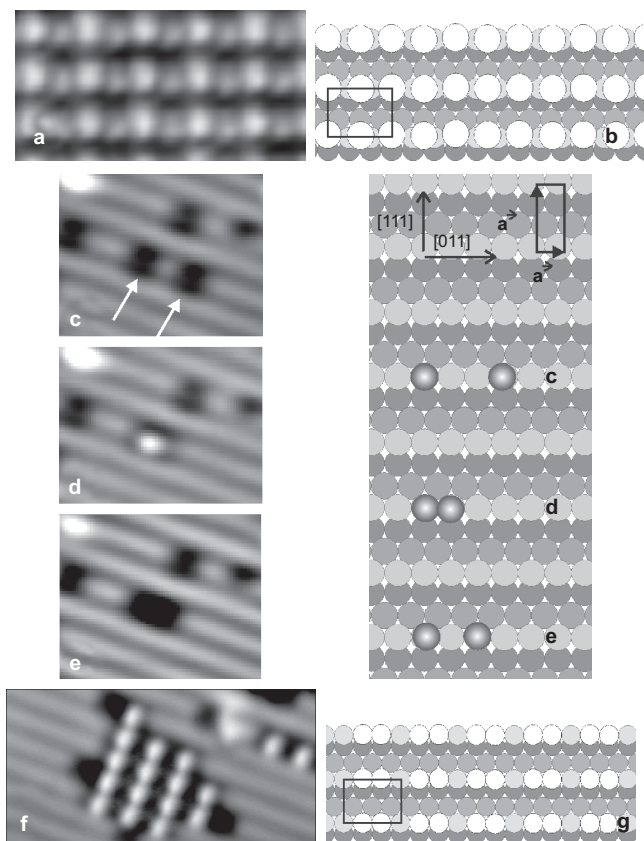


Figure 13. (a) STM image of a regular adlayer of CO on Cu(211) with (3×1) periodicity. The coverage is $2/3$ of a monolayer. (b) Naive model of the (3×1) structure. The CO molecules occupy on-top and bridge sites. (c–e) STM images and corresponding sphere models of the manipulation of two CO molecules to shortest lateral distance and apart again. Notice that a dramatic change in the appearance of the two CO molecules occurs when their mutual distance changes. (f) Local CO (3×1) domain formed by lateral manipulation. (g) Correct model of the CO (3×1) structure. Reprinted with permission from [41], S. Zöphel et al., *Chem. Phys. Lett.* 310, 145 (1999). © 1999, Elsevier Science.

of an atomic-scale “bit” by removing single Ge atoms from Ge(111). The mechanism was investigated by Lyo and Avouris upon experimenting with Si(111) 7×7 [42]. Using the same surface Ushida et al. [44] found that center atoms in the 7×7 reconstruction are more frequently removed than atoms near corner holes and concluded that the latter are more strongly bound by 0.1 eV. Similar conclusions for Ge(111) 2×8 were reported by Molinas-Mata et al. [45]. Very recently, the removal of Si atoms from a Si(111) 5×2 -Au surface at room temperature (RT) as a memory application has been discussed [46]. An artificial structure using this technique was made by Hosoki et al. [47] on the MoS₂ surface by extracting sulfur atoms (see Fig. 14).

6. VIBRATIONAL SPECTROSCOPY WITH THE SCANNING TUNNELING MICROSCOPY

Whereas spectroscopy of electronic states employing the STM has been used since for more than 10 years, vibrational spectroscopy was pioneered only in 1998, when Stipe et al. [48] showed that the C–H stretch mode could be observed on single C₂H₂ molecules adsorbed on a Cu(100) surface. A pronounced isotope effect from 358 to 256 meV was observed when using C₂D₂. Noticeably, with C₂HD, the individual ends of the molecule could be determined by measuring the vibrational energies at the respective parts of the mixed isotope molecule (Fig. 15) [24]. In a fascinating extension of this work, Ho performed *vibrational microscopy* of the C–D stretch mode in C₂HD by tuning the voltage to the energy of the C–D stretch (Fig. 16) [24]. In STM inelastic electron tunneling spectroscopy (IETS), the sample bias is increased and when it crosses the threshold for excitation of

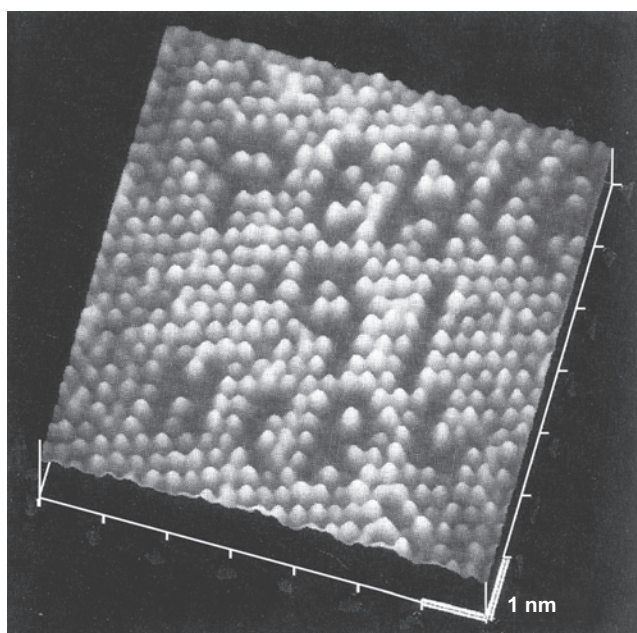


Figure 14. STM image of a MoS₂ surface after extracting single sulfur atoms by applying voltage pulses with the tip. Reprinted with permission from [47], S. Hosoki et al., *Appl. Surf. Sci.* 60/61, 643 (1992). © 1992, Elsevier Science.

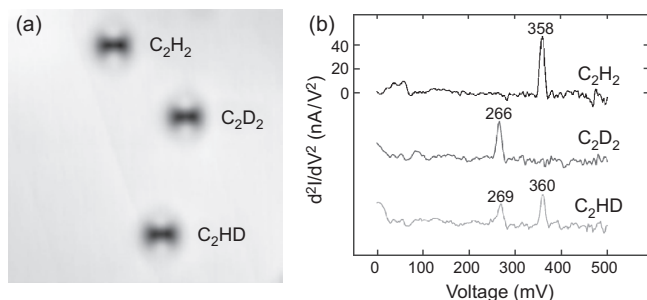


Figure 15. (a) Three $56 \text{ \AA} \times 56 \text{ \AA}$ STM topographical images and (b) single molecule vibrational spectra via STM-IETS of three acetylene isotopes on Cu(001) at 8 K. Reprinted with permission from [24], W. Ho, *J. Chem. Phys.* 117, 11033 (2002). © 2002, American Institute of Physics.

a vibrational mode, a new inelastic tunneling channel opens, giving rise to a change in conductance dI/dV . To make this change clearly visible the second derivative d^2I/dV^2 is measured using lock-in techniques.

The CO frustrated translational and rotational modes [49] as well as the internal stretching mode on Cu(100) and Cu(110) [50] were observed soon after. In Figure 17

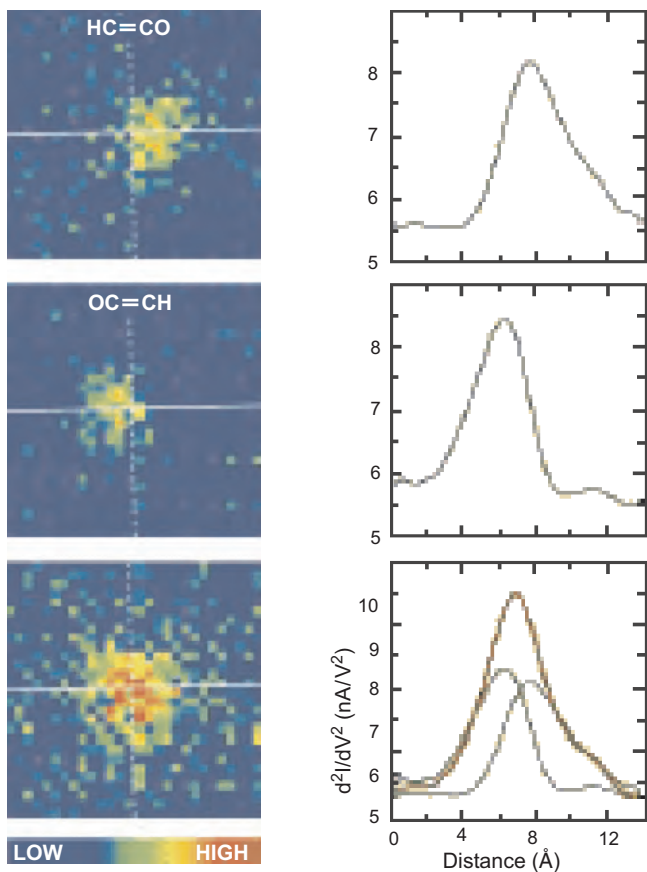


Figure 16. Vibrational microscopy of the C–D stretch in the mixed isotope of acetylene (C_2HD) on Cu(001) at 9 K. The sum of the two C–D stretch intensity distributions is found to agree with the C–D stretch intensity distribution for C_2D_2 . Reprinted with permission from [24], W. Ho, *J. Chem. Phys.* 117, 11033 (2002). © 2002, American Institute of Physics.

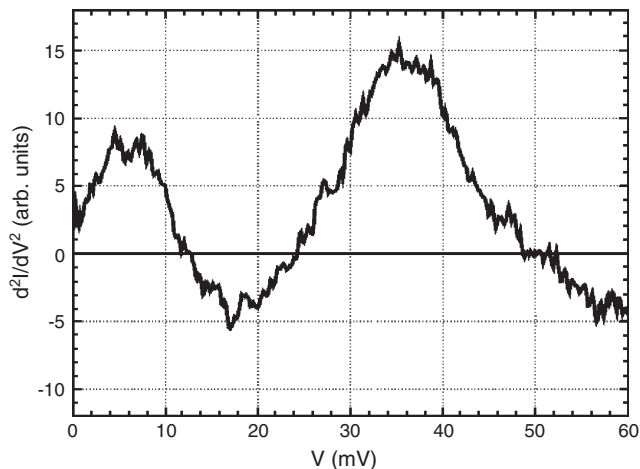


Figure 17. Vibrational spectroscopy with a CO-functionalized tip. The d^2I/dV^2 spectrum of a single CO molecule on Cu(111) exhibits the frustrated translational and rotational modes. Reprinted with permission from [51], F. Moresco et al., *Mod. Phys. Lett. B* 13, 709 (1999). © 1999, World Scientific.

results related to the frustrated low energy modes are shown, which have been obtained after having transferred a single CO molecule on the tip by vertical manipulation; the frustrated rotational and vibrational modes of CO on Cu(211) are observed at energies of 5.8 and 35.9 meV, respectively [51].

Inelastic tunneling spectra with a CO or ethylene modified tip have been taken on O_2 and CO on a Ag(110) surface [52]. A number of systems have been characterized by vibrational spectroscopy including larger molecules such as ethioporphyrin-I on Cu(001) [53] as well as single atoms like H and D on Cu(001) [54]. Inelastic tunneling electrons can excite rotational or translational degrees of freedom of a molecule (see Section 7) or even break chemical bonds (see Section 8). Vibrational spectra of water have been taken on Ag(111) [55] and Cu(111) [56]. The excitation of a fullerene cage vibrational mode by inelastic tunneling electrons has been observed with d^2I/dV^2 spectroscopy along with vibrational maps on single C_{60} molecules adsorbed on Ag(110). The inelastic signal showed strong variations depending on the molecular orientation which is attributed to the different degrees of symmetry of the adsorbed molecule [57].

7. EFFECTS DUE TO ELECTRON CURRENT

A detailed analysis of the vertical transfer mechanism of CO molecules on Cu(111) [58] showed that a minimum tunneling bias of 2.4 V is required to excite a molecule. This corresponds to the onset of the CO derived $2\pi^*$ level of the CO/Cu(111) system as known from two photon photoelectron spectroscopy. The hopping rate depends linearly on the tunneling current, which indicates that a one-electron process is the basis of the excitation mechanism. The probability per tunneling electron to induce a hop of a CO molecule depends on the applied bias and has a value below 10^{-10} , if the bias does not exceed 3 V. A strong isotope effect for the quantum yield of the hopping process can be found using

$^{12}\text{C}^{16}\text{O}$ and $^{13}\text{C}^{18}\text{O}$. Within the framework of the Menzel–Gomer–Redhead model this isotope effect can be used to estimate a per excitation probability for a hop of a CO molecule of 5×10^{-9} and a fraction of 0.5% of the electrons making up the tunneling current passing through the $2\pi^*$ level of the CO molecules; the lifetime of the electrons in the antibonding $2\pi^*$ level is as short as 0.8–5 femtoseconds [58]. Thus, the CO transfer depends on an effect induced by the electrons provided by the tunneling current. The approach of the tip in the pickup procedure just increases the probability that the molecule is “caught” at or near the tip apex [59].

Electrons tunneling inelastically through molecules can also be used to induce rotational or translational motion, although the injection at high symmetry points does not result in a preferential direction. The current induced lateral hopping of CO molecules on Pd(110) has been demonstrated recently by Komeda et al. [60]. Detailed studies of the rotation of oxygen molecules on a Pt(111) surface and acetylene molecules on a Cu(100) surface have been done by Stipe et al. [61,62]. The electron induced hopping and desorption of hydrogen on a Ge(111)- $c(2 \times 8)$ surface has been investigated by Dujardin et al. [63]. Hydrogen on Si(100) can be desorbed by resonant electronic excitation as well as by multiple vibrational excitation [64,65]. The specific desorption of lines of hydrogen from a hydrogen terminated Si(100) surface followed by the adsorption of Ga constitutes the first example of an artificially formed metallic wire with a diameter of one atom [66] (Fig. 18).

STM investigations of the adsorption of water on Cu(111) at low temperatures (Fig. 19) showed that starting from the adsorbed monomers, the formation of small water clusters

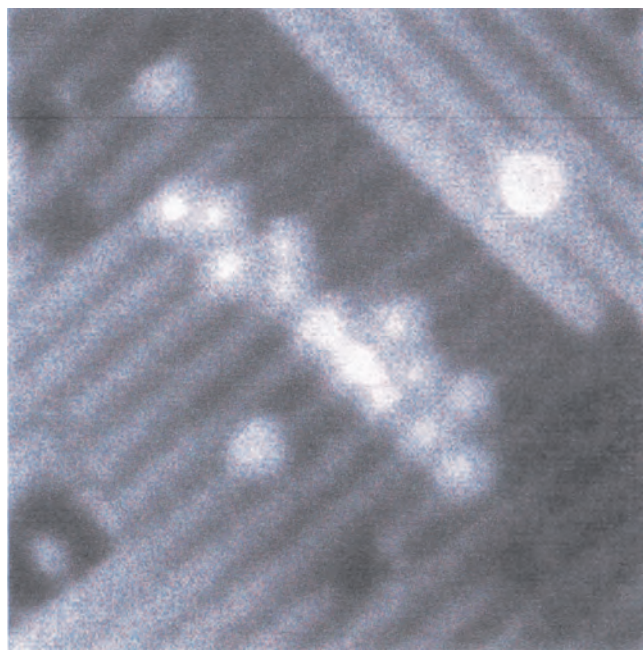


Figure 18. The specific desorption of lines of hydrogen from a hydrogen terminated Si(100) surface followed by the adsorption of Ga results in an artificially formed metallic wire with a diameter of one atom. Reprinted with permission from [66], Y. Wada, *Surf. Sci.* 386, 265 (1997). © 1997, Elsevier Science.

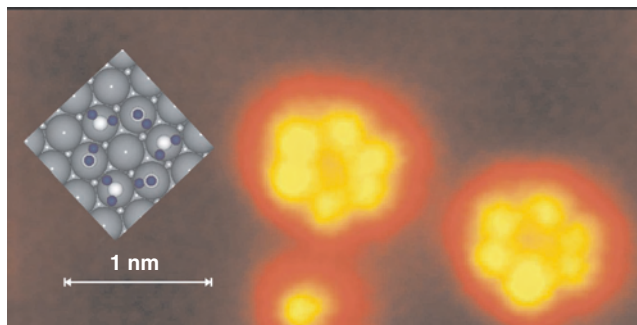


Figure 19. Small crystalline ice clusters formed from monomers via excitation of vibrational modes of the water molecules. Reprinted with permission from [56], K. Morgenstern and K.-H. Rieder, *J. Chem. Phys.* 116, 5746 (2002). © 2002, American Institute of Physics.

and of the cyclic hexamer could be induced by exciting vibrational modes of the molecule with electrons from the STM tip [56]. Crystallization, dissociation, and substrate oxidation can be induced with electrons of higher energy [67].

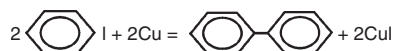
The hopping movements of Cl atoms on a Si(111)- (7×7) surface can be induced by electron injection with a STM tip positioned laterally displaced from the atom. Thereby electrons can be trapped resonantly by the antibonding orbital associated with a Cl atom, leading to an instabilization of the bond and a diffusion of the Cl atom. The radial probability of the hopping exhibits an anisotropic spread with an oscillatory dependence on the distance from the tip position. This result is interpreted in terms of a coherent wave packet propagation of electrons in a surface resonance band [68].

8. CHEMISTRY WITH THE STM TIP

The combination of several manipulation techniques makes it possible to do surface chemistry at the atomic level which involves dissociation of the parent molecules, lateral manipulation (to account for the diffusion steps), and synthesis of the reactants. The dissociation of a molecule with a STM was first investigated by Dujardin et al. [69]. By scanning $\text{B}_{10}\text{H}_{15}$ molecules adsorbed on a Si(111)- (7×7) surface with a tunneling voltage ≥ 4 V dissociation into a variety of fragments was observed. O_2 molecules on a Si(111)- (7×7) surface have been dissociated by electron injection into unoccupied adsorbate levels with tunneling voltages above 6 V [70]. Dissociation by vibrational heating of O_2 molecules on a Pt(111) surface was done at much lower voltages. Here multiple intramolecular vibrational excitations via a resonant inelastic electron tunneling process resulted in bond breaking [71]. HS and DS molecule fragments on Si surfaces can be dissociated at low voltages as well as at high voltages [72,73].

It was recently shown that it is possible to induce all steps of a complex chemical reaction with the STM tip at such low temperatures, at which the reaction would not proceed naturally. Specifically, all elementary steps of a century old basic aromatic ring coupling mechanism known as the Ullmann reaction [74] were induced on single molecules using

the STM tip at 20 K on a Cu(111) substrate. The synthesis of biphenyl out of iodobenzene on copper



essentially consists of three steps: Dissociation of iodobenzene ($\text{C}_6\text{H}_5\text{I}$) to phenyl (C_6H_5) and iodine, diffusion of phenyl to find another phenyl as a reaction partner, and their chemical association to form biphenyl ($\text{C}_{12}\text{H}_{10}$). Figure 20 shows the steps of the reaction sequence. First, the iodine atoms originating from two $\text{C}_6\text{H}_5\text{I}$ molecules adsorbed at a Cu(111) step (Fig. 20a) have been separated from the parent molecules by injecting 1.5 eV energy tunneling electrons from the tip (Fig. 20b). The iodine (smaller hills) and phenyl (larger hills) are further separated with the tip (Fig. 20c). Then, the iodine atom placed between the two phenyls has been removed to the lower terrace by using lateral manipulation (Fig. 20d). The left phenyl is then repositioned close to the right phenyl by pulling with the tip and then the injection tunneling electrons with an energy of 500 meV is needed for the chemical association of the phenyl couple (Fig. 20e). The formation of biphenyl is verified by pulling the synthesized molecule from its front end with the tip [75]. In this image sequence, the top and bottom images exactly represent the left and right side of the Ullmann equation.

The CO oxidation reaction was induced with STM in two ways on Ag(110) by Hahn and Ho [76]. Oxygen atoms were prepared by dissociation of single oxygen molecules using tunneling electrons of a certain energy [71], whereby the two oxygens remain close to each other (Fig. 21a). Then a CO molecule was manipulated toward an oxygen atom pair by repeatedly applying sample bias pulses over the CO until a

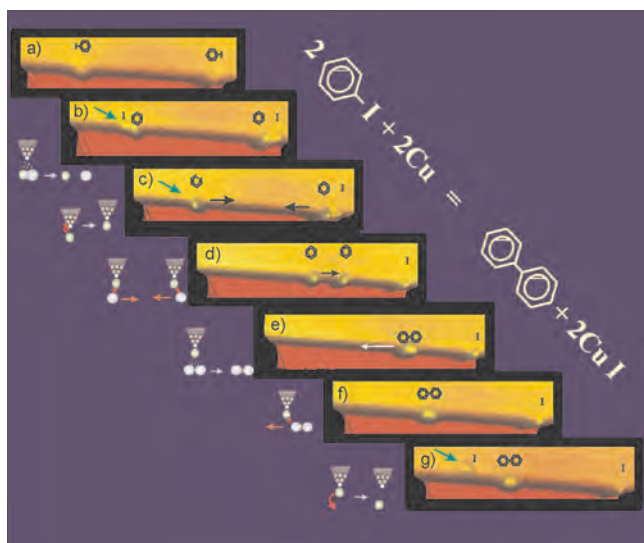


Figure 20. STM tip-induced single-molecule Ullmann reaction sequence on a Cu(111) substrate at 20 K. All reaction steps including dissociation of parent iodobenzene molecules, motion of phenyl reactants and iodine by-products, and association of phenyl reactants to the final product, biphenyl, are induced with the STM tip. Reprinted with permission from [128], S.-W. Hla and K.-H. Rieder, *Superlatt. Microstruct.* 31, 63 (2002). © 2002, American Physical Society.

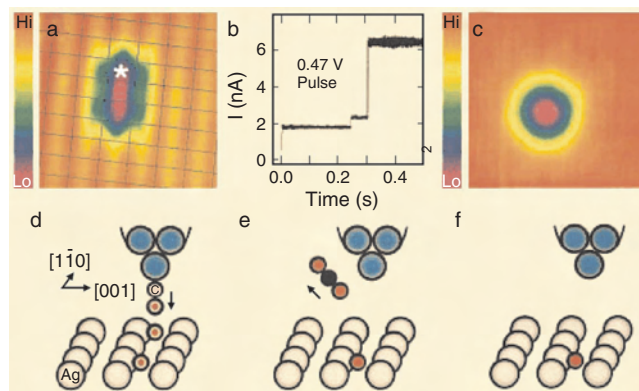


Figure 21. Reaction of CO molecule released from CO-functionalized tip with an O atom adsorbed at the Cu(100) surface. Reprinted with permission from [24], W. Ho, *J. Chem. Phys.* 117, 11033 (2002). © 2002, American Institute of Physics.

O–C–O complex was formed, which could be recognized due to its characteristic STM appearance. With a further pulse over the CO in the complex, formation of CO was induced, whereby the product immediately desorbed. In the second variant (Fig. 21d–f), a CO molecule was picked up to the tip apex and transferred back to the surface over an oxygen atom thus inducing CO_2 formation again with immediate desorption of the product leaving only one of the initial oxygen atoms at the surface (Fig. 21c). The product formation was recognized via a sudden change of the tunneling current (Fig. 21f) [24].

An interesting mechanism for an STM induced single molecule reaction was reported by Kim et al. [77]. The molecule *trans*-2-butene (C_4H_8) was transformed into 1,2-butadiene (C_4H_6) by inducing electrons of sufficient energy to excite a specific vibrational mode to an amplitude such that two hydrogens were shaken off. The parent molecule as well as the product were identified by both their appearance in the STM images (Fig. 22) and their vibrational spectra (Fig. 23).

Vertical manipulation has been used to transfer CO molecules between a Ag(110) surface and the tip. By transferring the CO molecules from the Ag surface to the tip and back to single Fe atoms deposited on the surface with the technique discussed in Section 7 the formation of iron-carbonyl complexes $\text{Fe}(\text{CO})_n$ (with $n = 1, 2$) could be induced (Fig. 24) [78].

Okawa and Aono [79] recently showed that a diacetylen chain polymerization can be induced in a self-assembled monolayer of 10,12-nonacosadiyonic acid on graphite under ambient conditions (Fig. 25a). After creation of an artificial defect with the STM tip by applying a positively pulsed sample bias, the polymerization of a single diacetylene monolayer chain was initiated at another surface location with an opposite voltage pulse. After progression of the chain reaction, the polymer chain was terminated at the artificial defect site. This experiment combines the advantage of topochemical reactions for nanoscale patterning of surfaces with the ability to induce reactivity locally.

Lopinski et al. [80] generated molecular lines on H-terminated Si(100) by creating dangling bonds at the surface and exposing them to styrene vapor, whereby a benzyl

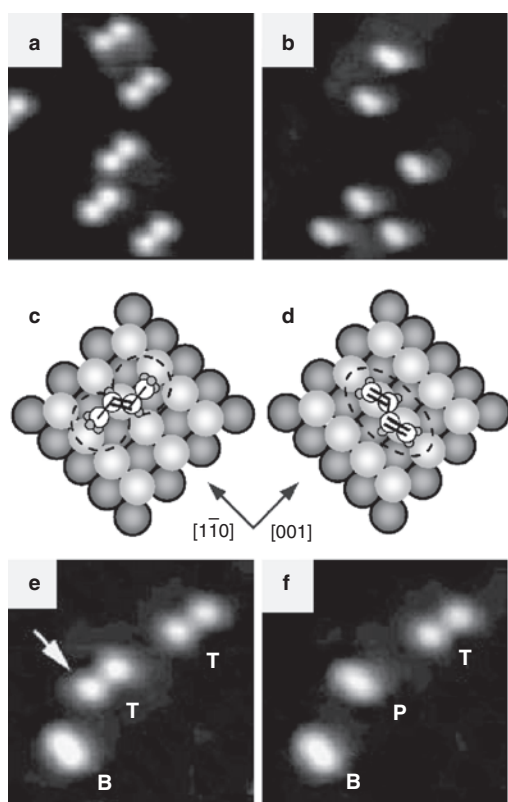


Figure 22. Hydrogen stripping reaction induced by exciting a high energy vibrational mode in 1,3 butadiene on Pd(110) using tunneling electrons. The product is *trans*-2-transbutene. Reprinted with permission from [77], Y. Kim et al., *Phys. Rev. Lett.* 89, 126104 (2002). © 2002, American Physical Society.

radical is formed which is stabilized by H abstraction from the neighboring Si–H site. Thus, the propagating species, the dangling bond, is regenerated. The process leads to the formation of lines with potential use as molecular wires by planting individual phenyls on the surface that line up in a typical π – π stacking (Fig. 25b).

9. MANIPULATION OF LARGE MOLECULES

The investigation of organic molecules is of interest from both fundamental and technological viewpoints. Due to their complexity and high number of internal degrees of freedom large molecules display more variety for manipulation than atoms and small molecules.

Cu–TBPP molecules (Fig. 26b) adsorbed on a Cu(100) surface at RT do not exhibit thermally activated diffusion and are therefore suitable for manipulation experiments. These molecules can be imaged at large tunneling resistances of several G Ω and exhibit tip-induced molecular flexure at tunneling resistances of the order of several hundred M Ω . At even smaller junction resistances of about 10 M Ω it is possible to laterally move the molecules without rupture or fragmentation of intramolecular bonds. Elastic scattering quantum chemistry (ESQC) calculations revealed an uncorrelated motion of the four ligands in a stick-slip

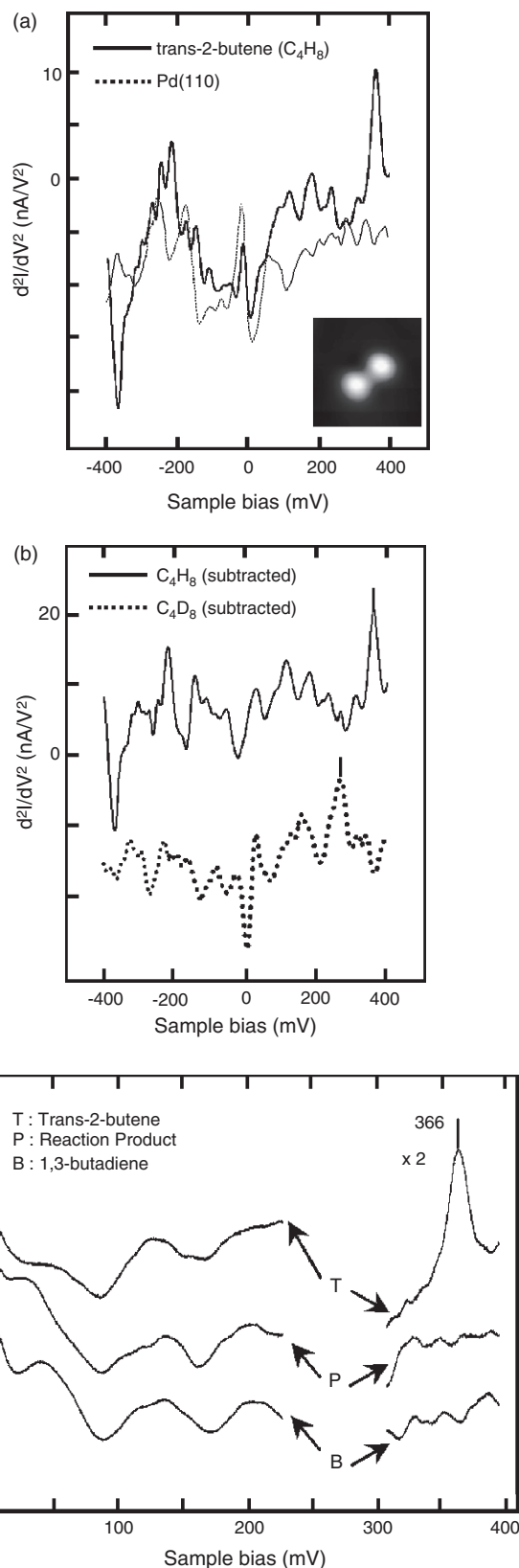


Figure 23. The products of the H-stripping reaction shown in Figure 22 are identified by STM-IETS. Reprinted with permission from [77], Y. Kim et al., *Phys. Rev. Lett.* 89, 126104 (2002). © 2002, American Physical Society.

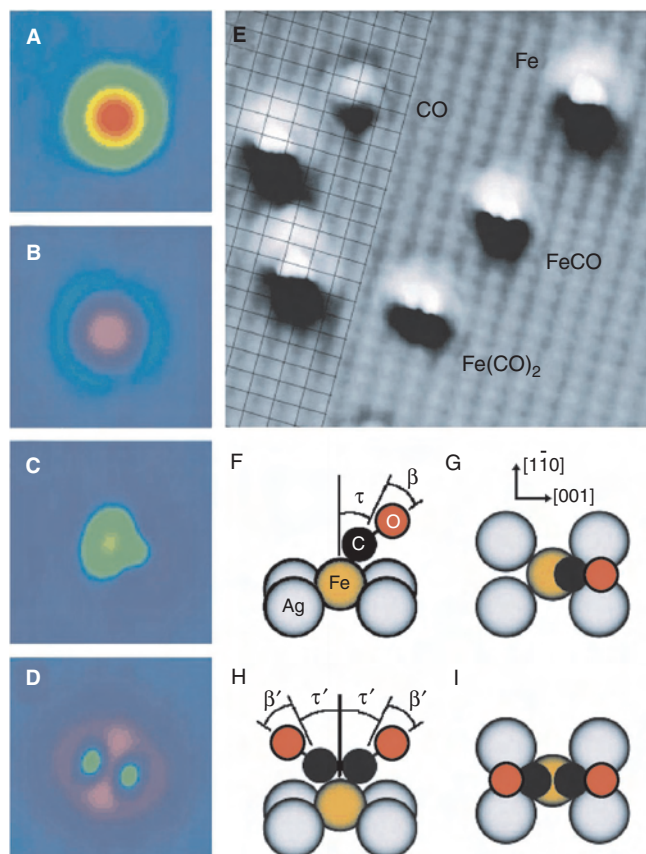


Figure 24. Producing iron carbonyl entities $\text{Fe}(\text{CO})$ and $\text{Fe}(\text{CO})_2$ by releasing CO molecules from the tip to the preadsorbed Fe atoms. The technique relies on the vertical manipulation techniques shown in Figure 12. Reprinted with permission from [78], H. Lee and W. Ho, *Science* 286, 1719 (1996). © 1996, American Association for the Advancement of Science.

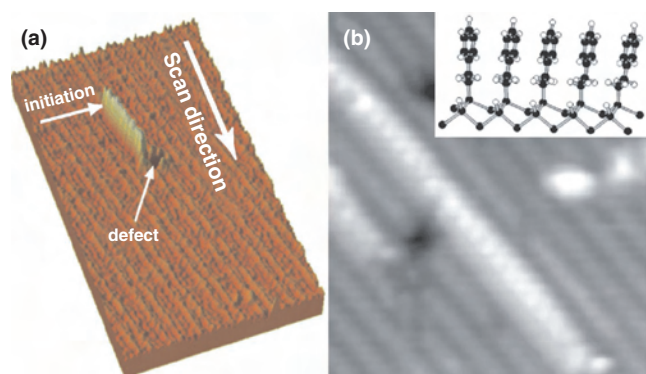


Figure 25. (a) STM induced production of a nanostructure via a chain reaction. Diacetylen polymerization in a self-assembled monolayer of graphite, initiated by a voltage pulse of -4 V and terminated at an intentionally produced defect (voltage pulse $+5$ V). Reprinted with permission from [79], Y. Okawa and M. Aono, *Nature* 409, 619 (2001). © 2001, Nature Publishing Group. (b) Artificially produced nanostructure: Self-directed growth of styrene lines on H-terminated Si(100) initiated by tip-created surface dangling bonds. Reprinted with permission from [80], G. Lopinski et al., *Nature* 406, 48 (2000). © 2000, Macmillan Magazines Ltd.

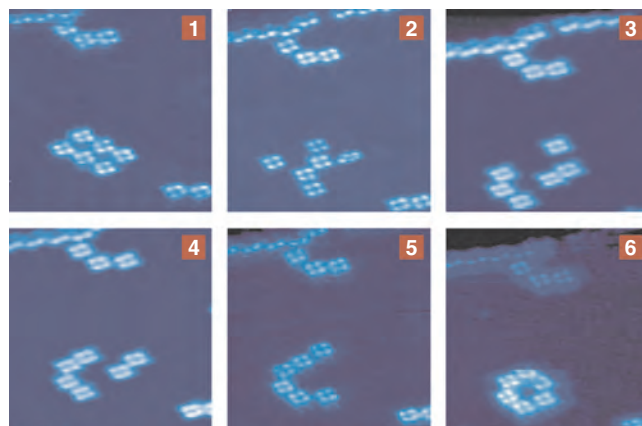


Figure 26. Sequence of images that illustrate the positioning of individual TBPP molecules on a Cu(100) surface at RT. Reprinted with permission from [129], T. Jung et al., *Science* 271, 181 (1996). © 1996, American Association for the Advancement of Science.

motion. The molecule is moved in the pushing mode while the tip–surface distance is controlled with a closed feedback loop [81,82]. The lateral manipulation in the constant-height mode at low temperature has been analyzed in detail and will be described in Section 10.

Whereas benzene molecules exhibit high thermal mobility on metal surfaces at RT, this is not the case for the structurally related cyclopentadienyl C_5H_5 . This strongly chemisorbed radical can be moved by tip-induced migration at RT. At gap resistances of ~ 200 M Ω the molecule starts to migrate parallel to the $\langle 110 \rangle$ direction independent of the polarity (Fig. 27, middle). The images reveal a repulsive interaction between tip and molecule which moves in steps of one lattice constant in length (Fig. 27, right). It is proposed that the molecule is tilted upright before jumping to the next site thereby reducing the motion barrier [83].

Benzoate molecules adsorb upright on a Cu(110) surface at RT and form a $c(8 \times 2)$ superstructure. Imaging this surface with a STM induces molecular motion which has been analyzed quantitatively. A model is proposed describing the vibrational excitation via a negative ion intermediate state involving a field-induced shifting of the resonance [84].

Self-assembled stripes of zinc porphyrin molecules can be formed by deposition from solution onto the surface of graphite. This system can be imaged at RT under ambient

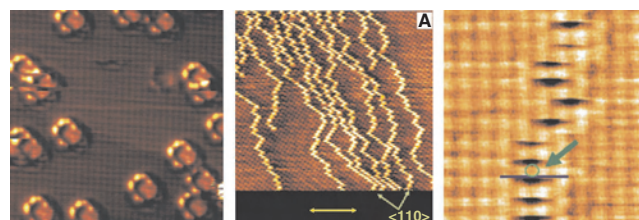


Figure 27. Left: STM image showing cyclopentadienyl C_5H_5 molecules on a Ag(110) at RT. Middle: At gap resistances of ~ 200 M Ω the molecule starts to migrate parallel to the $\langle 110 \rangle$ directions. Right: The images reveal a repulsive interaction between tip and molecule which moves in steps of one lattice constant in length (slow scan direction from down to top). Reprinted with permission from [83], W. Pai et al., *Surf. Sci.* 393, L106 (1997). © 1997, Elsevier Science.

conditions with a gap resistance of 70 M Ω . At a reduced gap resistance of 10 M Ω the molecules can be moved laterally to create breaks in such a stripe [85].

C₆₀ molecules are covalently bound on a Si(100)2 \times 1 surface and have been laterally manipulated at RT. The molecules can be pulled, thereby moving in 1–3 lattice constants steps (Fig. 28a). At smaller tip–surface distances the tip–molecule interaction is repulsive and the C₆₀ molecules

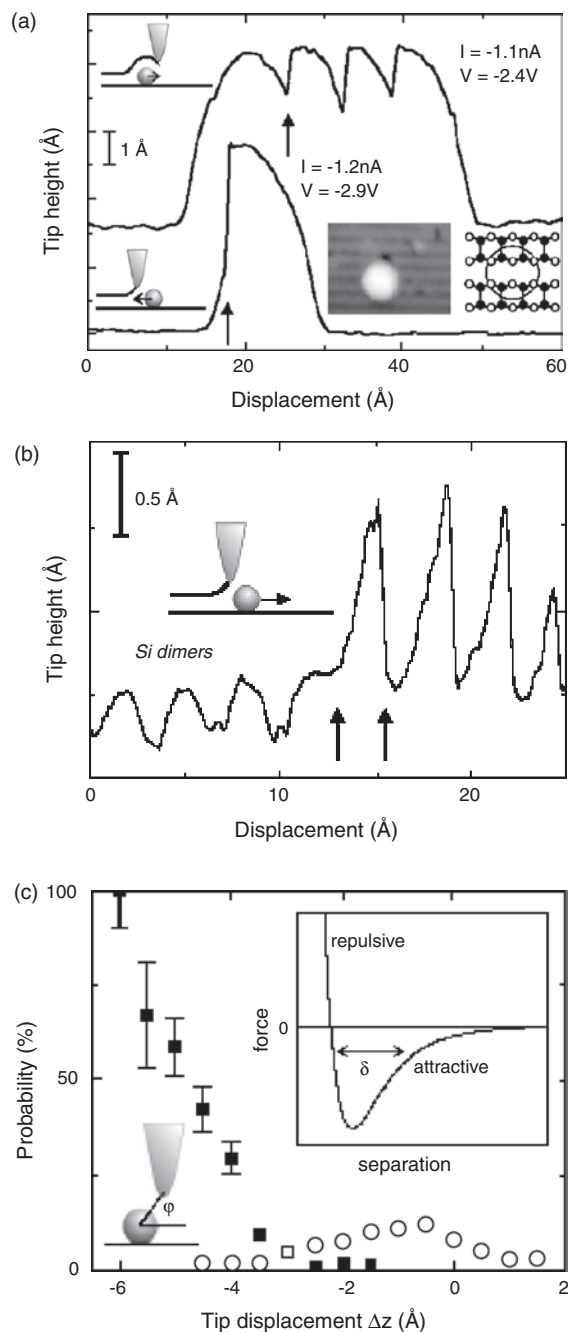


Figure 28. Manipulation curves of C₆₀ molecules on a Si(100)-2 \times 1 surface demonstrating (a) pulling and (b) pushing mode. (c) Probability distribution for successful attempts as a function of relative tip–surface separation (initial parameters $U = -3$ V and $I = -0.1$ nA). Reprinted with permission from [86], D. Keeling et al., *Chem. Phys. Lett.* 366, 300 (2002). © 2002, Elsevier Science.

are moved in a pushing mode in single lattice constant steps (Fig. 28b). The probability for a successful manipulation can in this case reach $\sim 100\%$ (Fig. 28c). In spite of rather high electric fields (tunneling voltages ranging from -1 to -5 V) chemical forces are suggested to dominate [86].

The polar molecule 1-nitronaphtalene forms self-assembled decamers on a Au(111) surface due to its electrostatic interaction. At 50 K these decamers can be stably imaged with a gap resistance of 60 G Ω and laterally moved at a reduced tunneling resistance of 25 M Ω without changing their internal structure [87].

By using lateral manipulation it became possible to reveal the restructured metal surface beneath adsorbed HtBDC molecules. These molecules form a self-assembled double-row structure on a Cu(110) surface at RT (Fig. 29ab). At temperatures < 160 K the thermally activated diffusion is suppressed and the surface can be imaged with a tunneling gap of about 1 G Ω . The adsorbed molecules can then be removed at a tunneling resistance of 1 M Ω by changing the tunneling current or voltage or both (Fig. 29c). It is found that $\cong 14$ Cu atoms are expelled from the surface in

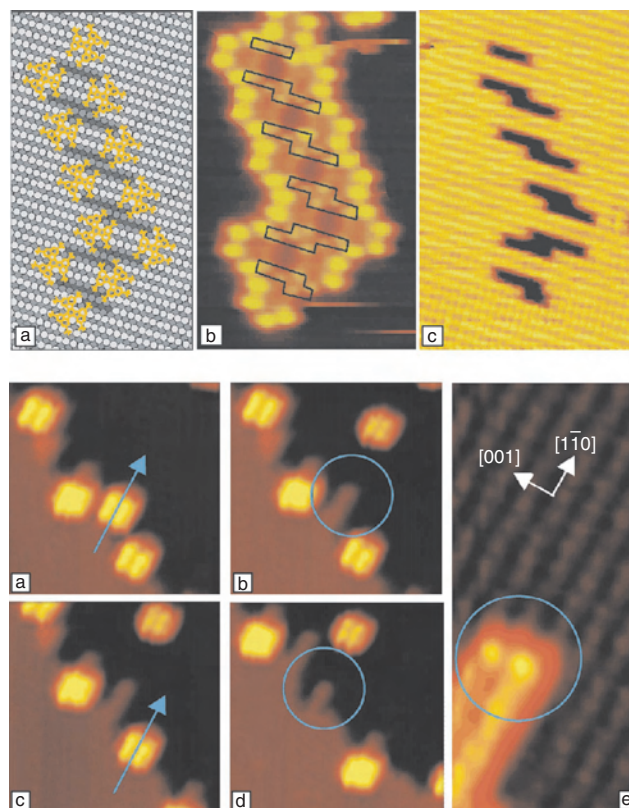


Figure 29. Upper images: (a) Model of the (b) self-assembled double-row structure of HtBDC molecules adsorbed on a Cu(110) surface. (c) The trenches in the surface layer beneath become visible after removal of the molecules by tip-assisted diffusion [88]. Image courtesy of M. Schunack. Lower images: (a–d) Manipulation sequence of the Lander molecules from a step edge on Cu(110). (e) Zoom-in smooth-filtered STM image showing the characteristic two-row width of the toothlike structure (right corner) after removal of a single Lander molecule from the step edge. The Cu rows are also visible. Reprinted with permission from [90], F. Rosei et al., *Science* 296, 328 (2002). © 2002, American Association for the Advancement of Science.

two adjacent $[1\bar{1}0]$ rows, forming a base for anchoring of the molecules which is the driving force of the self-assembly [88].

A similar effect was revealed upon adsorption of so-called lander molecules $C_{90}H_{98}$ onto a Cu(110) surface at RT. Subsequent images and manipulation experiments were performed between 100 and 200 K. Figure 29 shows a manipulation sequence where a molecule is removed from a step edge thereby making a double row of Cu atoms visible. The molecule diffuses toward the step edges at RT and reshapes the fluctuating Cu step adatoms into a toothlike structure. Theoretical calculations showed a higher energy gain for this conformation than the energy required for the creation of the Cu rows [89,90].

The manipulation of the polar molecule phosphangulene adsorbed on a Ag(111) surface was investigated in detail at low temperature. By lateral and vertical manipulation the molecule could be switched between three different conformations which were identified by ESQC calculations. The lateral manipulation of the three-lobed type is shown in Figure 30a, b. Whereas at tunneling resistances of 0.5 M Ω pushing, sliding, and pulling were observed, at higher resistances up to 10 M Ω only pulling was possible. Experiments with different polarity indicated that the molecular dipole has a minor effect on the lateral manipulation. Usually the lateral displacement was accompanied by a rotation of the molecule also visible in Figure 30. The interconversion between different conformations is possible with lateral manipulation as well (Fig. 30) [91].

The manipulation at low temperature of a single TBPP molecule offers the opportunity to demonstrate the principle of a conformational molecular switch [92]. Lateral and vertical manipulation were used to selectively modify the

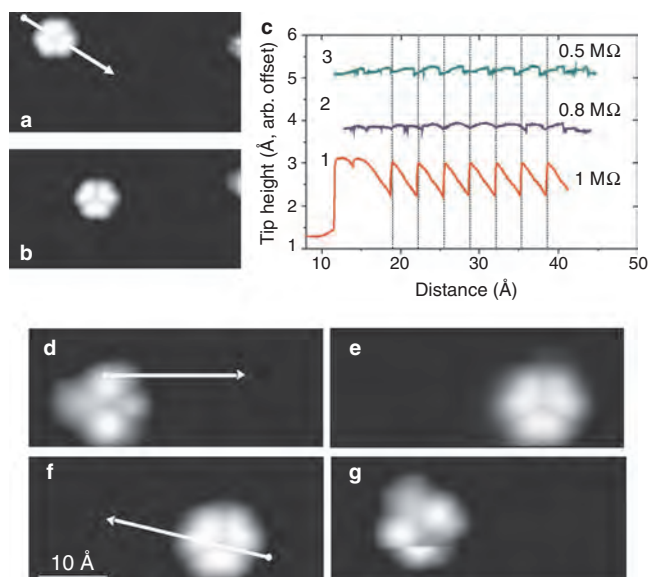


Figure 30. The upper image shows the lateral manipulation of a phosphangulene molecule which usually results in a rotation at the same time. The tip-height curves recorded during the manipulation process show pulling, sliding, and pushing behavior at the indicated threshold resistances. The lower images show the interconversion between different conformations induced by lateral manipulation. Reprinted with permission from [91], R. Lin et al., *Surf. Sci.* 477, 198 (2001). © 2001, Elsevier Science.

molecular conformation, by rotating single legs in and out of the porphyrin plane.

STM images of single TBPP molecules deposited on the stepped Cu(211) surface are shown in Figure 31a. The molecules show eight lobes, corresponding to four legs oriented nearly flat on the surface [93]. In a few cases (Fig. 31b), a single brighter lobe appears among the double lobes, indicating that one leg is rotated nearly perpendicular to the plane of the substrate.

Calculations show that in the case of flat legs (Fig. 31a) a tilt angle of 10° relative to the surface is present, while in the case of Figure 31b one leg is rotated by 55° . Molecular models (Fig. 31c and d) roughly visualize the two different conformations of the molecule.

A further step toward the implementation of a molecular switch is to use manipulation techniques to reversibly modify the molecular conformation. The switching of a single leg in and out of the porphyrin plane is possible by lateral and vertical movement of the tip to push the leg down.

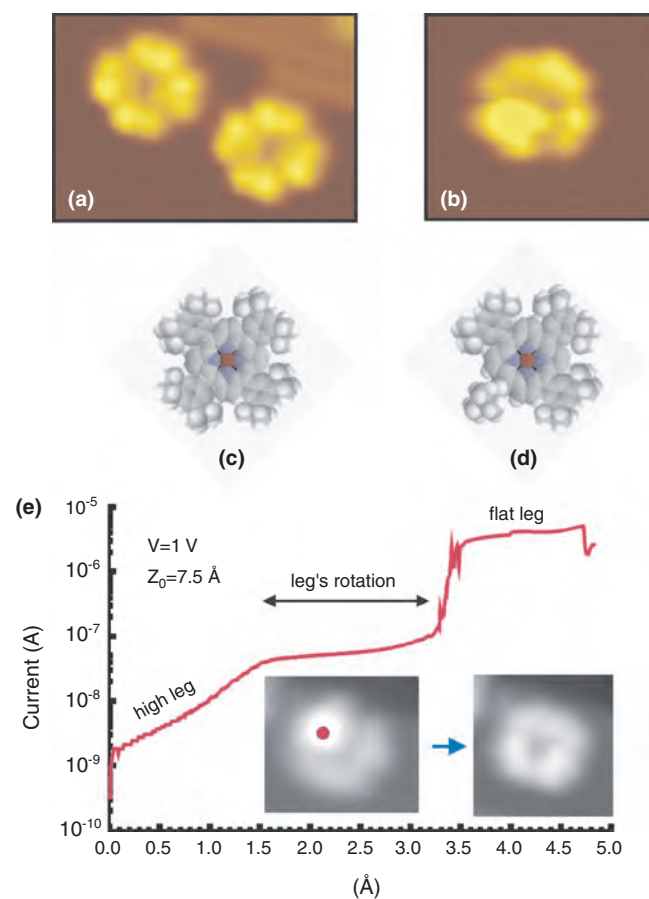


Figure 31. (a) STM image of a Cu-TBPP molecule on Cu(211) lying flat on the surface and oriented parallel to the intrinsic step edges. (b) STM image of a Cu-TBPP molecule on Cu(211) showing one leg rotated out of the porphyrin plane. (c) and (d) Sketch of the approximate molecular conformation for (a) and (b). (e) Current through a single leg versus the tip-surface distance during a vertical manipulation process leading to a leg's rotation. STM images of the molecule before and after the manipulation are shown in the inset. The black dot in the left image shows the exact position of the tip during the vertical manipulation [92]. Image courtesy of F. Moresco.

To experimentally demonstrate the principle of the molecular switch, the interaction between tip apex and leg during a vertical manipulation sequence was quantitatively investigated, as shown in Figure 31e. By measuring the current passing through a single leg in real time during its rotation it could be shown that the tunneling current through one leg strongly depends on the extent of its rotation. Molecular mechanics calculations show that a rotation of 90° should induce a change in resistance of over six orders of magnitude.

It recently became possible to directly determine the energy required to rotate a leg of a Cu-TBPP molecule adsorbed on a Cu(100) surface at RT by using noncontact atomic force microscopy (AFM). Figure 32a shows frequency–distance curves recorded above the molecule and the bare surface. The subtracted curve (Fig. 32b) can be converted into short-range tip–molecule force (Fig. 32c). In combination with theoretical calculations an upper limit of 100 zJ required to rotate a di-phenyl-butyl leg was deduced [94].

10. INTRAMOLECULAR MECHANICS DURING THE MANIPULATION OF A LARGE MOLECULE

The technique of single particle manipulations by means of the STM can also be applied to the controlled displacement of large molecules at room temperature [81,83]. To understand and control the process, it is, however, necessary to experimentally measure the intramolecular movement during the manipulation by recording the feedback signal in real time. To assure a low noise level and high stability this experiment was performed at low temperature.

Single TBPP molecules deposited on different Cu substrates were manipulated at low temperature (Fig. 33). Due to the complicated structure of the molecules and their high conductance, controlled lateral manipulation was performed in constant height mode [22]. As shown in Figure 33a, TBPP on Cu(100) shows four bright lobes with some lateral residual echoes, while the porphyrin ring is hardly visible [92]. Calculations of the STM image show that each lobe corresponds to a leg oriented nearly perpendicular to the surface, at an angle of about 80° .

TBPP molecules were manipulated by pushing at one of the legs. The exact path followed by the tip is shown in Figure 33c. The recorded manipulation signal is presented in Figure 33d. The sequence reflects first of all the Cu(100) lattice periodicity, but details in each period do not resemble the regular sawtooth signals recorded during STM manipulations of atoms and diatomic molecules. Zoomed parts of the signal show a specific intraperiod signature, peculiar to this specific type of manipulation.

To extract from the manipulation signal the details about the intramolecular mechanics occurring during a manipulation sequence, calculations and computer simulations were performed, revealing that the main contributor to the signal is the leg which directly interacts with the tip apex and that a minor contribution comes from the leg in front of the tip. The movements are very small; oscillations of the legs amount only to a few half degrees. Such a very fine analysis

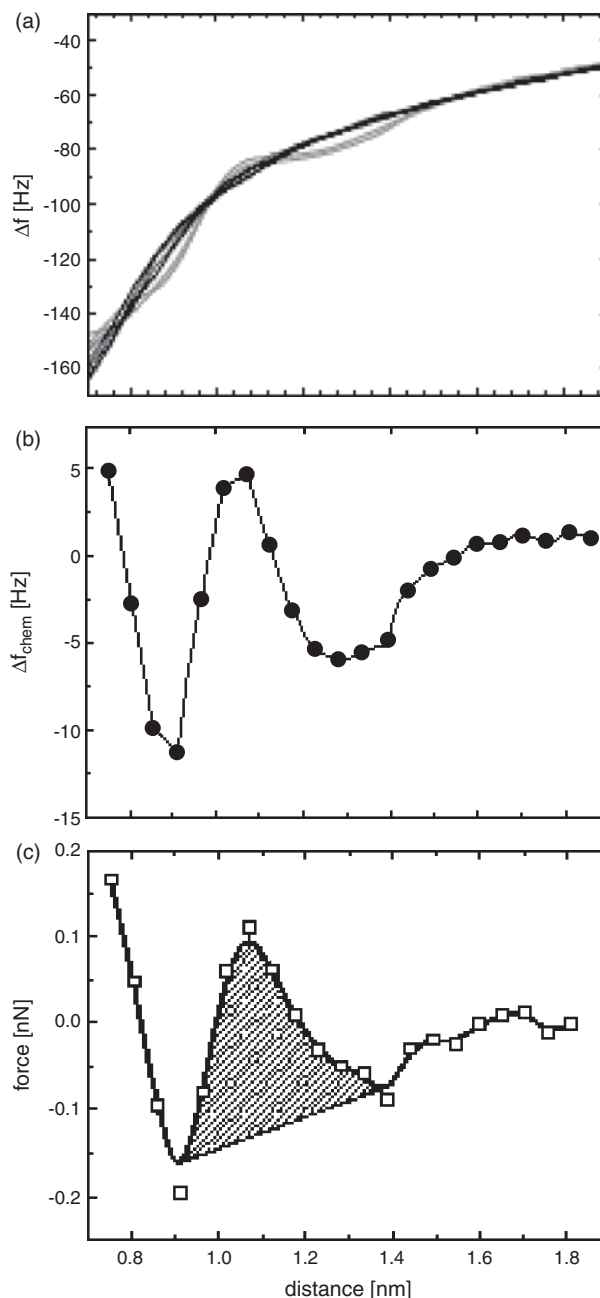


Figure 32. (a) Frequency–distance curves recorded via noncontact AFM above Cu-TBPP molecules and the bare Cu(100) surface at RT. The subtracted curve (b) can be converted into the short-range tip–molecule force (c) during the rotation of one leg of a Cu-TBPP molecule [94]. Image courtesy of Ch. Loppacher.

demonstrates, however, that detailed “on line” information on the internal mechanics of a molecule can be extracted from $I(x)$ during many periods [95].

11. PHYSICS WITH ARTIFICIAL STRUCTURES

The lateral manipulation technique has been used to investigate the coupling between magnetic atoms exhibiting Kondo resonances. A Kondo resonance occurs when a magnetic

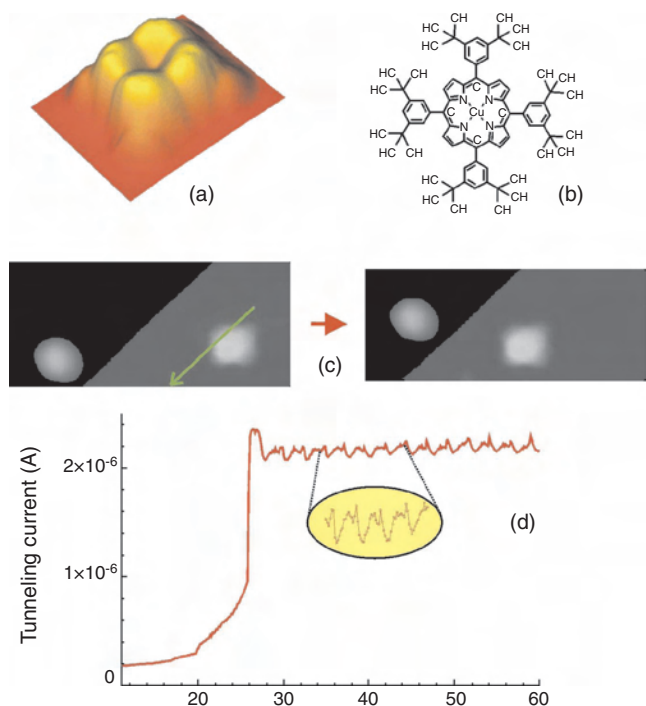


Figure 33. (a) STM image of a TBPP molecule deposited on Cu(100) and (b) its chemical structure. The image was taken at a tunneling current of 400 pA and a bias voltage of 300 mV. (c) A TBPP molecule recorded before and after the manipulation process. The arrow on the left image indicates the exact path followed by the tip. (d) Experimental $I(x)$ (current versus distance) curve recorded during the manipulation. Details of the signal are displayed in the inset [95]. Image courtesy of F. Moresco.

impurity in a metal couples to surrounding conduction electrons. This coupling causes conduction electrons to form a highly correlated nonmagnetic ground state screening the magnetic moment of the impurity and leads to a narrow Kondo resonance at the Fermi energy. dI/dV spectra taken over single Ce atoms on Ag(111) at low temperature show a clear antiresonance at the Fermi energy [96]. The probing of a localized state immersed in a continuum by STM can proceed either through the localized state or directly into the continuum leading to quantum interference. In the limit where the transition into the localized state approaches zero ($q \approx 0$) this results in the observed antiresonance as first elucidated by Fano [97]. Similar results were obtained from Co atoms on Au(111) shown in Figure 34. Here the higher transition rate into the localized state ($q \approx 0.7$) results in an asymmetric lineshape [98]. Artificially created Co dimers on the other hand showed an abrupt disappearance at separations less than 6 Å resulting from a reduced exchange coupling between Au conduction electrons and ferromagnetic Co dimers [99]. Using lateral manipulation Cr dimers and trimers were fabricated on the same surface. The measurements showed that only one of the trimer configurations exhibits a Kondo resonance [100].

An elliptic quantum corral has been constructed by Manoharan et al. [101,102] as a mirror for electron waves. By dI/dV spectroscopy the Kondo resonance of a magnetic atom located in one focus was detected at the other focus. Figure 35 shows an elliptical quantum corral made of 36

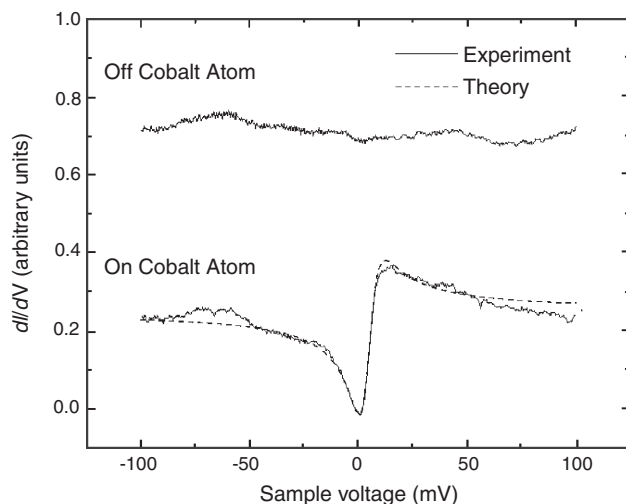


Figure 34. The dI/dV spectra of a single Co atom adsorbed on a Au(111) surface is displaying a Kondo resonance. The dashed line denotes a calculation with a modified Fano theory ($q \approx 0.7$). Reprinted with permission from [98], V. Madhavan et al., *Science* 280, 569 (1998). © 1998, American Association for the Advancement of Science.

cobalt atoms positioned on a copper [111] surface. When a magnetic cobalt atom is placed at a focus point of an elliptical corral (upper left), the Kondo resonance also appears at the other focus (lower left) while it does not when the atom is moved out of the focus. The projection of information from an atom to another place where there is no atom is named the “quantum mirage” effect; a possible application

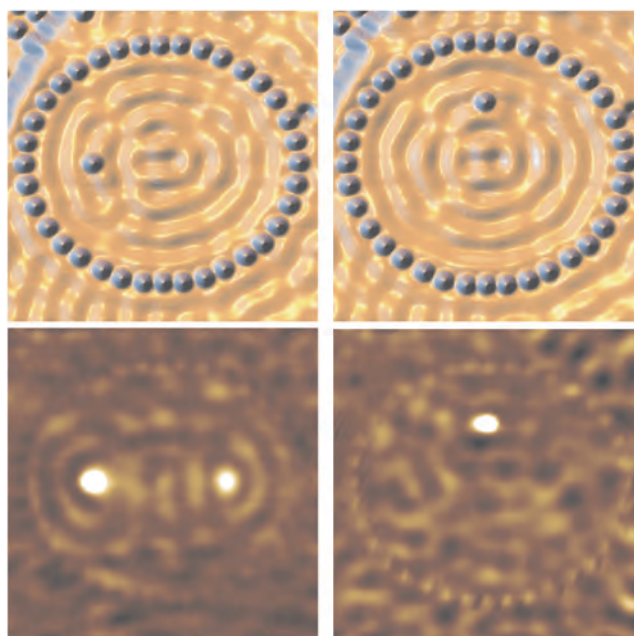


Figure 35. The upper STM images show the topography of an elliptical arrangement of 36 cobalt atoms positioned on a Cu(111) surface; the lower images are the associated dI/dV maps at the Kondo resonance. When a Co atom is placed at a focus the resonance appears at the other focus too (left image) while it does not when it is moved out of the focus. Reprinted with permission from [101], H. Manoharan et al., *Nature* 403, 512 (2000). © 2000, Macmillan Magazines Ltd.

for data transfer in future nanoscale electronics is discussed [101,102].

The formation of closed-packed metallic atomic structures is possible as well. Figure 36 shows a single Cu atom within two parallel closed-packed atomic Cu chains at a distance of 3.5 nm on a Cu(111) surface. At a temperature of 12 K the single Cu atom starts a thermally activated diffusion while the atomic lines remain stable. The surface-state mediated interaction [103] of the single Cu atom with the atomic lines results in an anisotropic movement, guided by the electron standing wave pattern of the atomic lines [104,105].

Large functionalized structures of CO molecules on a Cu(111) surface were assembled by manipulation with a STM recently by Heinrich et al. [106]. Thereby a cascade effect was employed where the motion of one CO molecule caused the subsequent motion of another CO molecule which itself caused a further CO molecule to move and so on. Linear arrangements of such a cascade can serve to transport one bit of information from one place to another. The crossed combination of several cascades made it possible to built logical gates and other devices.

The base unit consists of three CO molecules initially arranged in a bent line; see Figure 37. This configuration decays to an energetically favorable triangular arrangement. The underlying process was identified to be quantum tunneling and temperature independent below 6 K. At higher temperatures the hopping rate was thermally activated with an anomalously low Arrhenius prefactor, resulting from tunneling from an excited vibrational state. The hopping rate is furthermore sensitive to other surrounding adsorbates or defects and also dependent on the direction. These units,

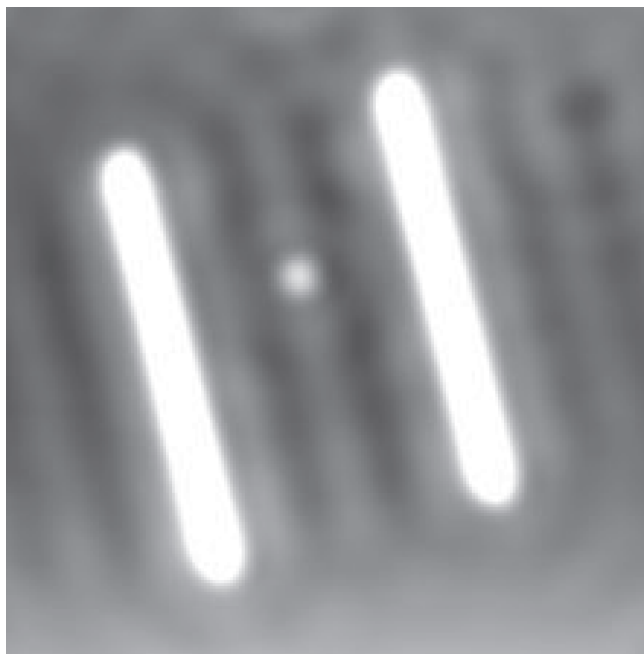


Figure 36. Two parallel dense-packed Cu rows on Cu(111) were formed by lateral manipulation of 44 Cu adatoms for the construction of an open quantum box. The single Cu adatom put into the center was used for studies of its thermal motion in the confined structure [104]. Image courtesy of J. Repp.

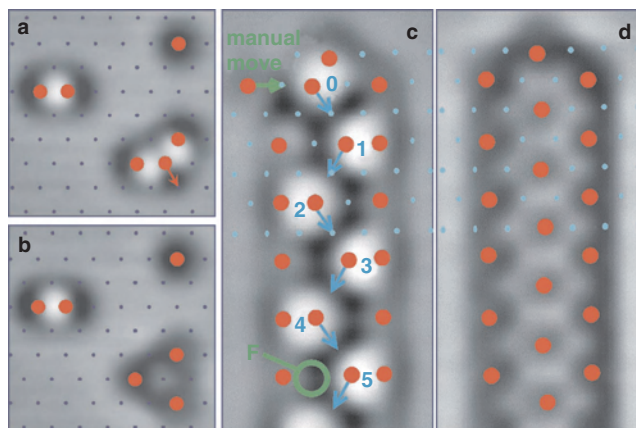


Figure 37. STM images showing CO molecules on a Cu(111) surface at 5 K. Solid red circles denote locations of CO molecules and blue dots surface-layer Cu atoms. (a) An isolated CO molecule, a dimer, and a trimer are shown. (b) After a few minutes the trimer has decayed into a new configuration. A molecule cascade (c) before and (d) after being manually initiated. Reprinted with permission from [106], A. Heinrich et al., *Science* 298, 1381 (2002). © 2002, American Association for the Advancement of Science.

called “chevrons,” can then be combined into a linear arrangement yielding a cascade and with two cascades logical gates can be constructed; see Figure 38. The combination of basic logical units then made it possible to construct a two-input sorter and a three-input sorter, consisting of 545 CO molecules (Fig. 39). The decay time of a single chevron is typically 5 minutes at 5 K resulting in an operating time

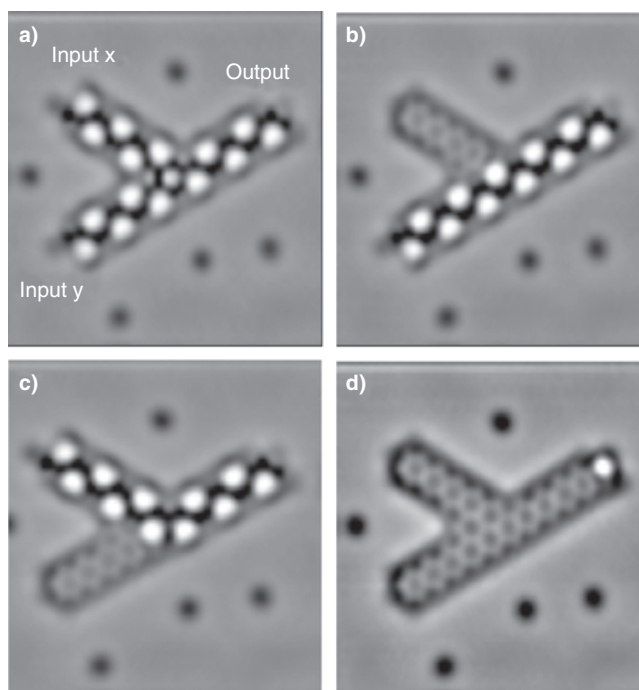


Figure 38. (a) Initial setup of a logic AND gate. Either first input x or input y can be triggered (b) or (c) and subsequently the other input, resulting in a logic 1 at the output (d). Reprinted with permission from [106], A. Heinrich et al., *Science* 298, 1381 (2002). © 2002, American Association for the Advancement of Science.

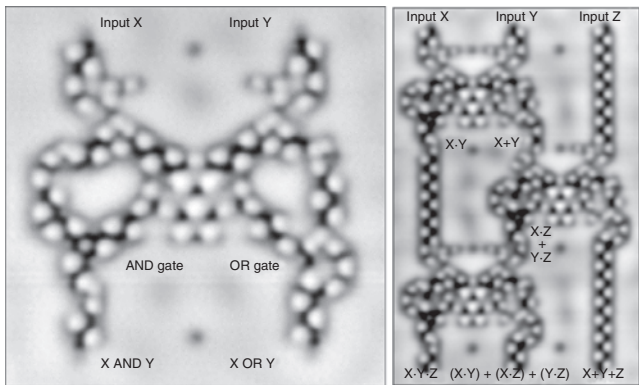


Figure 39. STM images showing a two-input sorter (left) and a three-input sorter (right) in the initial setup. Reprinted with permission from [106], A. Heinrich et al., *Science* 298, 1381 (2002). © 2002, American Association for the Advancement of Science.

of about 1 hour for the three-input sorter. After the one-time operation the device needs to be reset by moving the CO molecules back into their initial position which typically needs several hours.

Next to the image mode STM has provided means to probe the electronic properties of surfaces locally by scanning tunneling spectroscopy (STS). Thereby the tip is held fixed in position and the tunneling voltage is swept over the range of interest. By a lock-in technique the first derivative of the tunneling current dI/dV is recorded which is a direct measure of the local density of states (LDOS). STS performed at a fixed energy over an area records the LDOS in dI/dV maps. The construction of artificial atomic structures alters the LDOS strongly locally and can therefore ideally be investigated by STS and dI/dV mapping.

Au atoms adsorbed on a NiAl(110) surface were laterally manipulated to form compact chains 2–20 atoms in length. The Au atoms could reproducibly be moved at a junction resistance of 200 k Ω and attached or detached from the end of the chain with the same tunneling resistance. Single Au atoms show an electronic resonance at 1.95 eV above the Fermi energy resulting from an unoccupied Au state hybridized with the NiAl states. Moving the atoms together results in the evolution of one-dimensional electronic density oscillations. Figure 40 shows dI/dV maps of an 11-atom chain taken at different voltages. The measurement of the varying wavelength yields an effective electronic mass of 0.4 ± 0.1 [53,107].

The LDOS inside a triangular quantum corral has been analyzed carefully yielding the electron lifetime as a major property of surfaces [108]. Electron lifetimes have been measured with a STM on the defect-free terrace on Ag(111) by Li et al. [109] at the dispersion minimum of the surface state and as a function of energy by Bürgi et al. [110] and Bauer et al. [135]. Values for other noble metal surfaces have been determined [111] as well inside a Mn atom resonator [112].

By means of lateral manipulation 51 Ag atoms have been precisely positioned at a distance of five lattice constants to form a triangle with a base length of 245 Å as shown in Figure 41. The electrons of the surface state present on the Ag(111) surface are scattered by these Ag adatoms, resulting in a complex standing wave pattern. Energy resolved

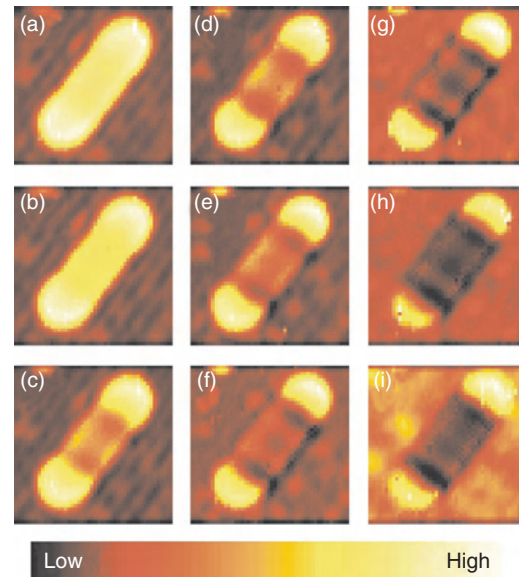


Figure 40. dI/dV images of an 11 Au atom chain taken at 0.1 V intervals between (a) +1.1 and (i) +1.9 V [53]. Image courtesy of M. Wallis.

data ranging from -55 to $+796$ meV with respect to the Fermi level were taken in the spectroscopic mode as shown in Figure 42. The displayed images were recorded at energies where the wavelength of the electrons is in resonance with the triangle resulting in a strong enhancement of the intensity.

Calculations of the wave pattern have been performed based on a multiple scattering approach [113]. Adjusting the calculations to the data yields the parameters of the scatterers on the one hand and the phase-relaxation length of the electrons on the other hand. The phase-relaxation length of an electron is the distance an electron can travel without losing its phase information [114] and is directly related to the lifetime of an electron. The spatial decay of the quantum mechanical interference pattern is influenced by the loss of coherence which is expressed in the phase-relaxation length and which is measured here.

Figure 43 depicts the result of the evaluations for the electron lifetime as a function of energy. The measurements clearly show a sharp maximum at the Fermi energy in accordance with Fermi liquid theory for a two-dimensional electron gas. Furthermore two pronounced edgelike features show up in the data at $+65$ and $+300$ meV as indicated in Figure 43. These features can be attributed to the dispersion minimum of the surface state and the transition of the surface state into the projected bulk states. Below these energies the inelastic scattering of surface electrons with other electrons is increased resulting in the observed decrease of the electron lifetime. Finally a fine structure can be observed which has to be attributed to the influence of the triangle [108].

The controlled atomic manipulation allows the design of arbitrary scattering geometries and on the basis of a deeper understanding of the electron lifetimes it should become possible to even engineer the lifetimes which are a key quantity in quantum computing and quantum transportation.

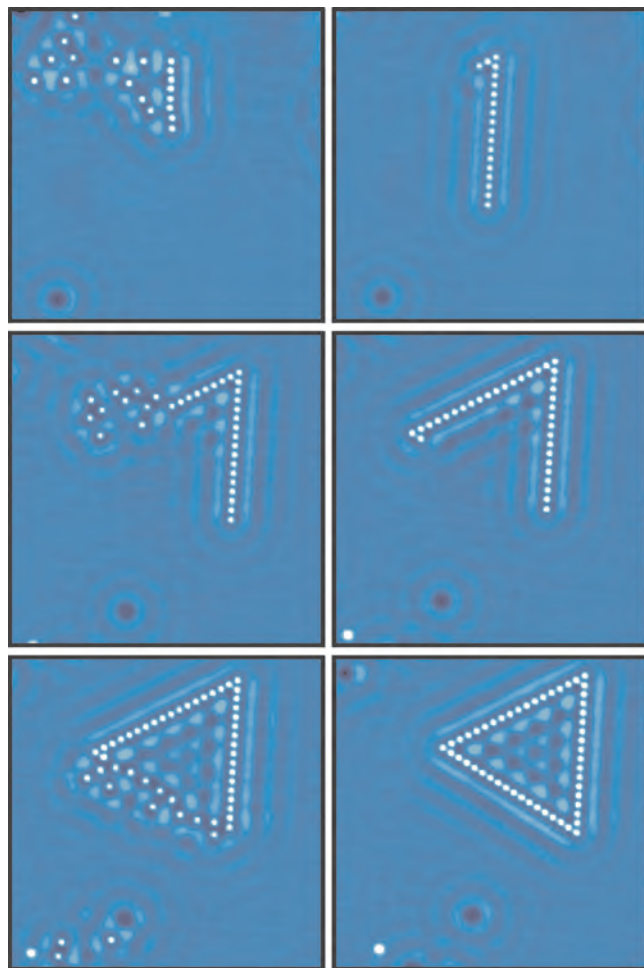


Figure 41. Series of images showing the construction of the triangle consisting of 51 Ag atoms on a Ag(111) surface ($49.3 \text{ nm} \times 49.3 \text{ nm}$, $U = +39 \text{ mV}$, $I = 1.1 \text{ nA}$). Reprinted with permission from [108], K.-F. Braun and K.-H. Rieder, *Phys. Rev. Lett.* 88, 096801 (2002). © 2002, American Physical Society.

12. TOWARD MANIPULATION ON THIN INSULATING FILMS

The prospects of atomic/molecular manipulation lie in the formation of electronic and mechanical devices on the atomic scale. These range from monomolecular devices [115] to atomic scale structures built up atom by atom. A device of the last kind has been proposed by Wada et al. and is called an atomic relay (Fig. 44) [66,116,117]. This and similar devices are characterized by a switching which incorporates the movement of only a single atom. These atomic relays can be integrated to build up complex logic networks including memory cells.

With regard to the existing atomic manipulation experiments, one important problem arises. When an atom or molecule is adsorbed on a metallic surface it has a strong electronic interaction with the metallic reservoir of electrons. Therefore the electronic and mechanical properties of adsorbates are strongly disturbed on metal substrates. With regard to applications it will be very important to electronically decouple adsorbates from the substrate or to be able to

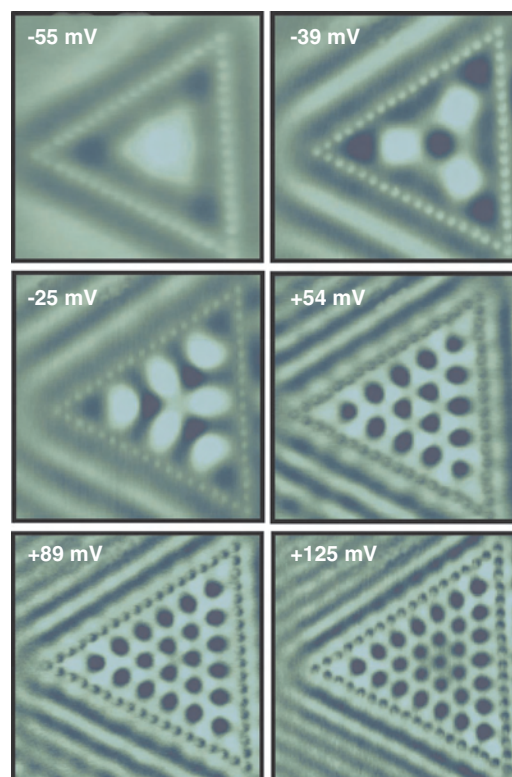


Figure 42. dI/dV maps displaying the local density of states at energies where the wavelength of the electrons is in resonance with the triangular quantum corral. Reprinted with permission from [108], K.-F. Braun and K.-H. Rieder, *Phys. Rev. Lett.* 88, 096801 (2002). © 2002, American Physical Society.

vary the strength of the electronic coupling. This decoupling from the substrate is obviously indispensable for devices like atomic relays, but it is certainly very important for a lot of other systems.

Ultrathin films of insulating materials represent a convenient way to perform these kind of experiments. Not only can the molecules be significantly decoupled with varying degrees from the substrate by changing the thickness of the insulating layers, but at same the time it is still possible to continue to use STM to perform the experiments. For bulk insulators certainly AFM would be necessary, a technique which has been improved amazingly during the last decade, but its application in atomic manipulation especially at low temperatures is still very difficult. Transfer of the STM manipulation techniques is therefore presently pursued to thin films of insulators like alkali halides and simple oxides.

The ability of the STM to operate on insulating films relies on the fact that a finite density of electronic states extending from the metal substrate through the insulating film into the vacuum exists, high enough to support a very small but still measurable tunneling current. For example insulating layers of NaCl of up to a thickness of 4 ML can be routinely imaged with the STM [118]. Even atomic resolution has been observed on these films. As has been shown these NaCl films can be grown in a surprisingly perfect and defect-free manner on different metal substrates, with islands several micrometers in size extending smoothly even

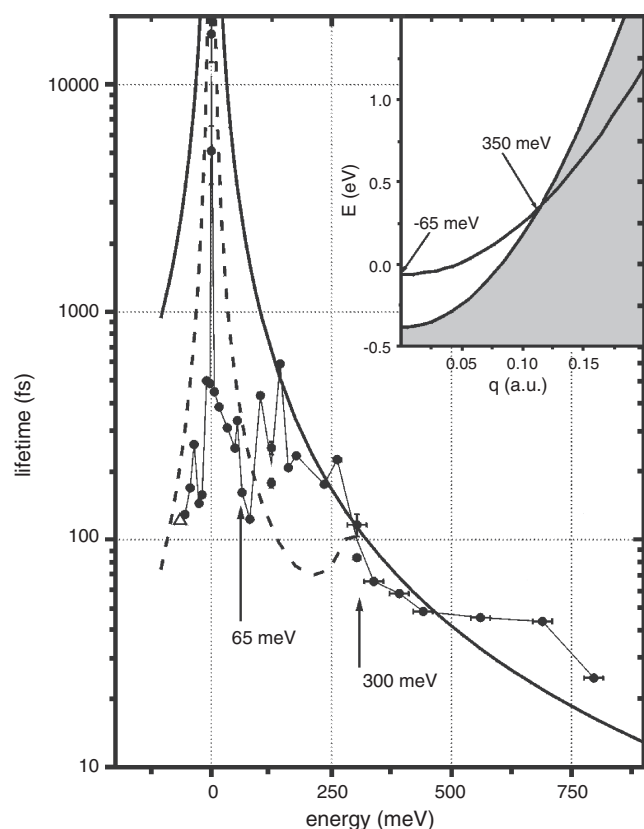


Figure 43. The full circles connected by straight lines denote the measured lifetimes. The open triangle is a measured value on a defect-free terrace [109,111] and the solid line represents an extrapolation of the measurements in [110] taken above 1 eV. The dashed line is an adaptation to the theoretical calculation for Cu(111) [130]. Reprinted with permission from [108], K.-F. Braun and K.-H. Rieder, *Phys. Rev. Lett.* 88, 096801 (2002). © 2002, American Physical Society.

across substrate defect steps (known as carpet growth mode) [118–123]. As has been shown by photoemission, NaCl layers of a thickness equal to or higher than two monolayers show a bandgap with a width similar to bulk material.

The system NaCl on Cu(211) is interesting for several reasons. For substrate temperatures below 200 K the growth of chainlike NaCl islands with monoatomic height is observed as modeled in Figure 45a. An atomically resolved image (Fig. 45b) reveals that only the anions are observed. Figure 45c–e proves that these chains can be cut by lateral manipulation, whereby the NaCl entities are pushed (Fig. 45f).

If the growth temperature exceeds ~ 300 K [i.e., in the range of emerging kink site mobility for bare Cu(211)], the initially flat (211) surface drastically reorganizes upon NaCl submonolayer deposition. This behavior is in sharp contrast to the common growth features of alkali halides on close-packed metal surfaces [118] which is characterized by weak interactions between the inert overlayer and the metal substrate. On Cu(211) a regular one-dimensional (1D) hill-and-valley structure is formed which is composed of (311) and (111) facets [120] (Fig. 46a,b). The facet arrangement relative to the Cu(211) surface is visualized schematically in Figure 46d (top view) and e (side view). The facets are

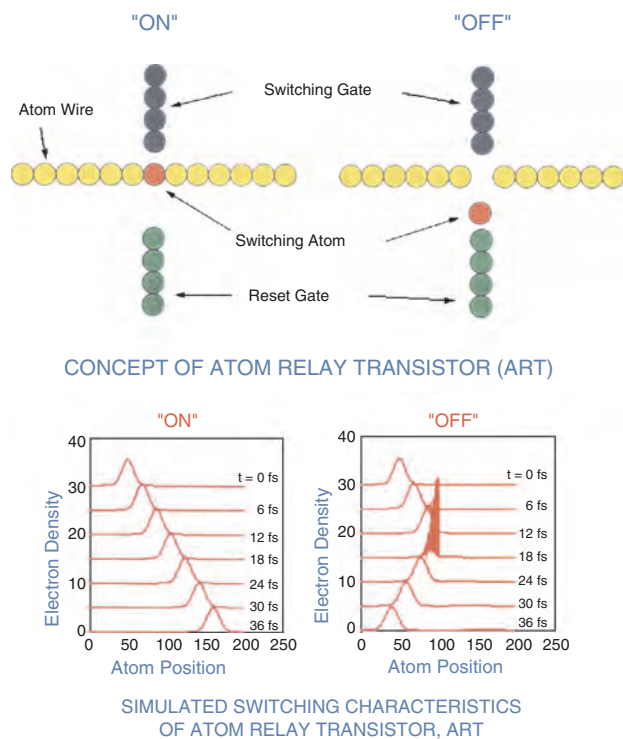


Figure 44. A proposed atomic scale device called an atomic relay by Wada et al. [66,116,117]. This device is characterized by a switching which incorporates the movement of only a single atom. These atomic relays can be integrated to build up a complex logic network including memory cells. Reprinted with permission from [66], Y. Wada, *Surf. Sci.* 386, 265 (1997). © 1997, Elsevier Science.

built up by incorporating additional Cu atom rows along the intrinsic step direction. Note that the resulting (311) facet is also a stepped plane, which exhibits a reduced step separation of 4.23 \AA . It is important to notice that NaCl grows selectively on the (311) facets only and thereby creates a regular surface pattern with alternating stripes of NaCl-covered areas and bare metal facets. This is evident from the STM topograph in Figure 46b which shows discrete stripes with a pronounced corrugation of cubic symmetry according to (100)-terminated NaCl. The characteristic size of this surface pattern (i.e., the periodic facet separation) can be adjusted by the growth temperature and ranges from $\sim 30 \text{ \AA}$ at 300 K to 230 \AA at 600 K [121]. The restructuring process observed here is driven by an exceptionally high energetic stability of the NaCl(100)-covered (311) facets, which is due to Coulomb interactions between the ionic charges of the alkali halide layer and electrostatic dipoles associated with the steps of the metal template [122] (the step dipoles arise from the well known Smoluchowski smoothing effect of the electron charge [124]). This 1D patterning process is also applicable to other ionic insulator/metal combinations since it is based on a stability criterion with rather general requirements, namely (i) a charge-modulated template (this is an inherent feature of stepped and kinked metal surfaces) [124] and (ii) lattice matching between the ions of the film and the charge modulation of the metal template. Due to the selectivity of the alkali halide-induced faceting process a modulation in surface chemical composition is established.

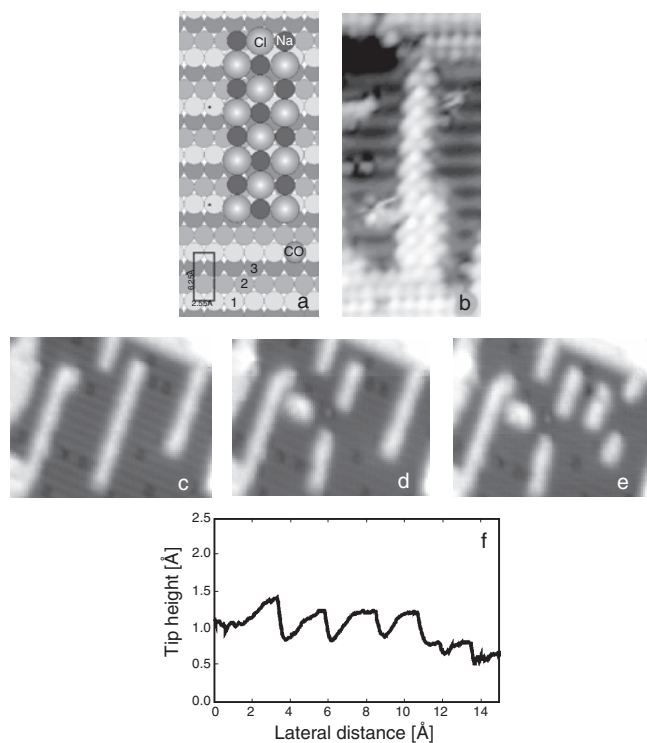


Figure 45. (a) Model of a NaCl chain oriented perpendicularly to an intrinsic step on a Cu(211) surface. (b) Atomically resolved STM image of a NaCl chain. (c–e) Cutting of two NaCl chains by lateral manipulation with the STM tip. (f) Tip–height curves demonstrating that the NaCl clusters are pushed. Reprinted with permission from [131], G. Meyer et al., *Single Molecules* 1, 79 (2000). © 2000, Wiley-VCH.

Hence, one obtains a nanoscale masking effect of the surface which can be controlled by the growth temperature. This gives at hand a prerequisite substrate for the lateral structuring of subsequently deposited material by selective decoration [125]. The formation of regular pyramids starting from a regularly kinked vicinal Cu(532) surface was demonstrated recently; therefore 2D regular patterning can be achieved too. Only two sides of the pyramids are covered with NaCl leaving a 2D array of metallic areas, which can be used for further reactions [41].

These examples have important implications for further manipulation work: They show (1) that the insulator films can be machined and (2) that self-assembly can give rise to regular structures with alternating insulating and metallic parts, so that, for example, a conducting molecule could be manipulated to lie on the insulator with one end touching the metal and by using the STM tip as second electrode conductivity measurements may become feasible along the molecule.

While no lateral manipulation experiments on insulators have been reported to date, theoretical studies have been performed. In the case of NaCl(001), the manipulation of a Au atom and the formation of Au dimers and trimers on this surface have been investigated by Bouju et al. [126]. Already several of the future difficulties common to manipulation on insulators have been addressed in this work. So one of the major problems will be that the binding energy between metal atoms is in general much higher than the

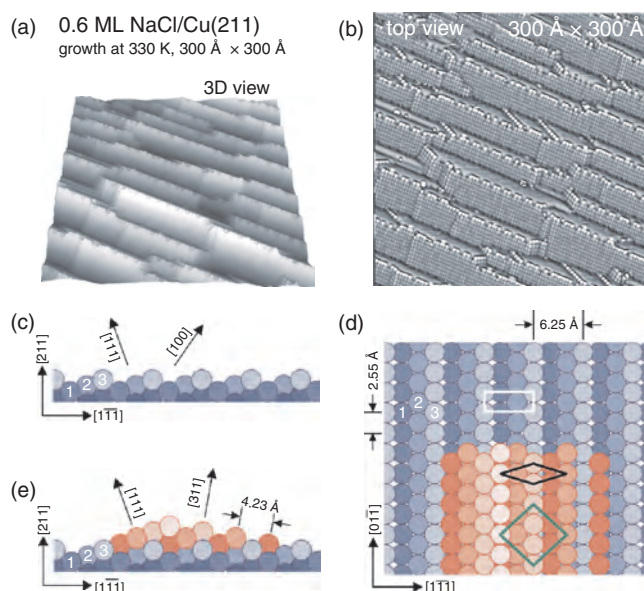


Figure 46. (a, b) STM topographs (1.1 nA, –330 mV) visualizing the mesoscopic faceting effect in 3D view representation (a) and in top view after depositing 0.6 ML NaCl on Cu(211) at 330 K (b). The image on the right shows that NaCl-covered (311) facets (cf. corrugation with cubic symmetry) alternate with bare Cu(111) facets. (c)–(e) Sphere model of the Cu(211) substrate surface in side view along the intrinsic (100) steps (c) and in top view [upper part of (d)]. The primitive rectangular unit cell is denoted by the white line and nonequivalent surface atoms are numbered. The lower part of the top view scheme (d) and the side view in (e) shows a ridge built up by a (111)/(311) facet pair. The rhombic unit cell of the Cu(311) plane (full black line) and the cubic unit cell of the NaCl(100) layer (omitted in the scheme) containing two molecules are also shown [120]. Image courtesy of S. Fölsch.

binding between the metal atoms and the insulator substrate. This results in the problem that the formation of metastable structures like atomic wires will be more difficult than on metallic substrates. An analogous problem will be the strong attractive interaction between the STM tip apex and the adsorbates, which might result in an unwanted transfer of the metal atom to the tip even before the lateral force is large enough to move the adatom.

This underpins the necessity to uncover the basic adsorbate–substrate interaction properties by manipulation/diffusion experiments. Certainly future successful manipulation experiments and the buildup of atomic scale structures will strongly rely on the right selection of the insulating film materials.

13. SUMMARY

In this chapter, lateral manipulation of atoms and molecules and the buildup of artificial nanoscale structures on metallic surfaces is discussed using the technique of “soft manipulation,” in which basically only tip–particle forces are employed. Such structures can be used as quantum laboratories, which allow detailed investigations of important physical quantities like electron lifetimes. Vertical manipulation experiments show that besides tip/particle forces electronic effects are also important for the transfer of particles like CO and Xe from the substrate to the tip

and vice versa. Electric current effects play also dominant roles in STM-induced chemical modifications of molecules like dissociation. A combination of all parameters (forces, current, field) is required to associate several species and to form new chemical entities. Moreover, manipulation of single large molecules opens the route to the creation of electronic devices at the nanoscale and to the ability to control the internal mechanics of a molecule by the STM tip. Engineering with single molecules and single atoms offers in combination with self-organization processes the ability to create novel man-designed artificial entities. Consequently engineering of functional structures including construction elements formed in an atom-by-atom manner certainly no longer belongs to the realm of mere utopia.

GLOSSARY

Lateral manipulation An adparticle on the surface is moved with the STM tip along the surface to the desired place without losing contact with the substrate. In lateral manipulation three basic different modes can be discerned: (1) pulling where the adparticle discontinuously follows the tip from one adsorption site to another due to attractive forces; (2) pushing where the adparticle moves discontinuously in front of the tip due to repulsive interaction; and (3) sliding where the adparticle is trapped under the tip and follows its motion instantaneously and continuously. See also Sections 3 and 4.

Manipulation curve Tip height recorded during the lateral manipulation in the constant current mode. The manipulation curve yields information about the tip–adparticle and the adparticle–surface interaction. See Section 4. If the lateral manipulation is performed in the constant height mode the current is recorded instead. See Section 10.

Quantum corral An artificial atomic structure arranged in a closed geometry (e.g., triangle, circle etc.). The scattering of surface electrons results in confinement with a strongly altered electronic structure. See Sections 4 and 11.

Soft manipulation Mainly the tip–adparticle forces are employed for the manipulation which can be tuned by changing the distance between the tip and the manipulated particle. Only in this regime can adparticles be moved with atomic precision. See Sections 3 and 4.

Tip-induced migration/diffusion Taking along a particle with the tip in an uncontrolled, accidental manner. Obviously, this variant does not allow the buildup of artificial structures in a particle-by-particle manner with atomic precision. See Section 3.

Vertical manipulation An adparticle is deliberately picked up with STM tip and then released back to the surface. See Section 5.

REFERENCES

1. J. Stroscio and D. Eigler, *Science* 254, 1319 (1991).
2. P. Avouris, *Acc. Chem. Res.* 28, 95 (1995).
3. R. Nyffenegger and R. Penner, *Chem. Rev.* 97, 1195 (1997).
4. A. Baski, "Advanced Semiconductor and Organic Nano-Techniques." Academic Press, San Diego, 2002.
5. L. Bartels, G. Meyer, and K.-H. Rieder, *Phys. Rev. Lett.* 79, 697 (1997).
6. S. Gauthier, *Appl. Surf. Sci.* 164, 85 (2000).
7. L. Whitman, J. Stroscio, R. Dragoset, and R. Celotta, *Science* 251, 1206 (1991).
8. J. Zhang, J. Liu, L. Huang, P. Kim, and C. Lieber, *Science* 274, 757 (1996).
9. Y. Mo, *Science* 261, 886 (1993).
10. N. Mingo and F. Flores, *Thin Solid Films* 318, 69 (1998).
11. N. Mingo and F. Flores, *Surf. Sci.* 395, 342 (1998).
12. G. Meyer, *Rev. Sci. Instrum.* 67, 2960 (1996).
13. Y. Kondo, E. Foley, and T. Amakusa, *Rev. Sci. Instrum.* 72, 2977 (2001).
14. L. Petersen, M. Schunack, B. Schaefer, T. Linderoth, P. Rasmussen, P. Sprunger, E. Laegsgaard, I. Stensgaard, and F. Besenbacher, *Rev. Sci. Instrum.* 72, 1438 (2001).
15. N. Moussy, H. Courtois, and B. Pannetier, *Rev. Sci. Instrum.* 72, 128 (2001).
16. E. Foley, A. Kam, and J. Lyding, *Rev. Sci. Instrum.* 71, 3428 (2000).
17. B. Stipe, M. Rezaei, and W. Ho, *Rev. Sci. Instrum.* 70, 137 (1999).
18. S. Pan, E. Hudson, and J. Davis, *Rev. Sci. Instrum.* 70, 1459 (1999).
19. O. Pietsch, A. Kubetzka, and D. Haude, *Rev. Sci. Instrum.* 71, 424 (2000).
20. J. Ferris, J. Kushmerick, J. Johnson, M. Y. Youngquist, R. Kessinger, H. Kingsbury, and P. Weiss, *Rev. Sci. Instrum.* 69, 2691 (1998).
21. K.-F. Braun, Ph.D. Thesis, Freie Universität Berlin, 2001.
22. F. Moresco, G. Meyer, K.-H. Rieder, H. Tang, A. Gourdon, and C. Joachim, *Appl. Phys. Lett.* 78, 306 (2001).
23. S.-W. Hla, K.-F. Braun, and K.-H. Rieder, *Phys. Rev. B* (2003).
24. W. Ho, *J. Chem. Phys.* 117, 11033 (2002).
25. D. Eigler and E. Schweizer, *Nature* 344, 524 (1990).
26. G. Meyer, B. Neu, and K.-H. Rieder, *Appl. Phys. A* 60, R343 (1995).
27. T. Fishlock, A. Oral, R. Egdell, and J. Pethica, *Nature* 404, 743 (2000).
28. G. Meyer, L. Bartels, S. Zöphel, E. Henze, and K.-H. Rieder, *Phys. Rev. Lett.* 78, 1512 (1997).
29. G. Meyer, S. Zöphel, and K.-H. Rieder, *Phys. Rev. Lett.* 77, 2113 (2000).
30. J. Schulz, R. Koch, and K.-H. Rieder, *Phys. Rev. Lett.* 84, 4597 (2000).
31. M. Crommie, C. Lutz, and D. Eigler, *Nature* 262, 218 (1993).
32. J. Li, R. Berndt, and W.-D. Schneider, *Phys. Rev. Lett.* 76, 1888 (1996).
33. J. Li, W.-D. Schneider, and R. Berndt, *Appl. Phys. A* 66, 675 (1998).
34. M. Böhringer, W.-D. Schneider, K. Glöckler, E. Umbach, and R. Berndt, *Surf. Sci.* 419, L95 (1998).
35. U. Kürpick and T. Rahman, *Phys. Rev. Lett.* 83, 2765 (1999).
36. B. Neu, G. Meyer, and K.-H. Rieder, *Mod. Phys. Lett. B* 9, 963 (1995).
37. X. Bouju, C. Joachim, C. Girard, and P. Sautet, *Phys. Rev. B* 47, 7454 (1993).
38. X. Bouju, C. Joachim, and C. Girard, *Phys. Rev. B* 59, R7845 (1999).
39. X. Bouju, C. Joachim, C. Girard, and H. Tang, *Phys. Rev. B* 63, 085415 (2001).
40. A. Buldum, S. Ciraci, and S. Erkoç, *J. Phys. Cond. Matt.* 7, 8487 (1995).
41. S. Zöphel, J. Repp, G. Meyer, and K.-H. Rieder, *Chem. Phys. Lett.* 310, 145 (1999).
42. I. Lyo and P. Avouris, *Science* 253, 173 (1991).
43. R. Becker, R. Golovchenko, and B. Schwarzenruber, *Nature* 325, 419 (1987).
44. H. Ushida, D. Huang, F. Grey, and M. Aono, *Phys. Rev. Lett.* 70, 2040 (1993).

45. P. Molinas-Mata, A. Mayne, and G. Dujardin, *Phys. Rev. Lett.* 80, 3101 (1998).
46. R. Bennewitz, J. Crain, A. Kirakosian, J.-L. Lin, J. McChesney, D. Petrovykh, and F. Himpsel, *Nanotechnology* 13, 499 (2002).
47. S. Hosoki, S. Hosaka, and T. Hasegawa, *Appl. Surf. Sci.* 60/61, 643 (1992).
48. B. Stipe, A. Rezaei, and W. Ho, *Science* 280, 1732 (1998).
49. B. Briner, unpublished.
50. L. Lauhon and W. Ho, *Phys. Rev. B* 60, R8525 (1999).
51. F. Moresco, G. Meyer, and K.-H. Rieder, *Mod. Phys. Lett. B* 13, 709 (1999).
52. J. Hahn and W. Ho, *Phys. Rev. Lett.* 87, 196102 (2001).
53. T. Wallis, X. Chen, and W. Ho, *J. Chem. Phys.* 113, 4837 (2000).
54. L. Lauhon and W. Ho, *Phys. Rev. Lett.* 85, 4566 (2000).
55. K. Morgenstern and J. Nieminen, *Phys. Rev. Lett.* 88, 066102 (2002).
56. K. Morgenstern and K.-H. Rieder, *J. Chem. Phys.* 116, 5746 (2002).
57. J. Pascual, J. Gomez-Herrero, D. Sanchez-Portal, and H.-P. Rust, *J. Chem. Phys.* 117, 9531 (2002).
58. L. Bartels, G. Meyer, K.-H. Rieder, D. Velic, E. Knoesel, A. Hotzel, M. Wolf, and G. Ertl, *Phys. Rev. Lett.* 80, 2004 (1998).
59. L. Bartels, G. Meyer, and K.-H. Rieder, *Appl. Phys. Lett.* 71, 213 (1997).
60. T. Komeda, Y. Kim, M. Kawai, B. Persson, and H. Ueba, *Science* 295, 2055 (2002).
61. B. Stipe, M. Rezaei, and W. Ho, *Science* 279, 1907 (1998).
62. B. Stipe, M. Rezaei, and W. Ho, *Phys. Rev. Lett.* 81, 1263 (1998).
63. G. Dujardin, A. Mayne, and F. Rose, *Phys. Rev. Lett.* 89, 036802 (2002).
64. T.-C. Shen, C. Wang, G. Abeln, J. Tucker, J. Lyding, Ph. Avouris, and R. E. Walkup, *Science* 268, 1590 (1995).
65. P. Avouris, R. Walkup, A. Rossi, H. Akpati, P. Nordlander, T.-C. Shen, G. Abeln, and J. Lyding, *Surf. Sci.* 363, 368 (1996).
66. Y. Wada, *Surf. Sci.* 386, 265 (1997).
67. K. Morgenstern and K.-H. Rieder, *Chem. Phys. Lett.* 358, 250 (2002).
68. Y. Nakamura, Y. Mera, and K. Maeda, *Phys. Rev. Lett.* 89, 266805 (2002).
69. G. Dujardin, R. Walkup, and P. Avouris, *Science* 255, 1232 (1992).
70. R. Martel, P. Avouris, and I.-W. Lyo, *Science* 272, 385 (1996).
71. B. Stipe, M. Rezaei, W. Ho, S. Gao, M. Persson, and B. Lundqvist, *Phys. Rev. Lett.* 78, 4410 (1997).
72. M. Rezaei, B. Stipe, and W. Ho, *J. Chem. Phys.* 110, 3549 (1999).
73. M. Rezaei, B. Stipe, and W. Ho, *J. Chem. Phys.* 109, 6075 (1999).
74. F. Ullmann, G. Meyer, O. Loewenthal, and O. Gilli, *Liebigs Ann. Chem.* 331, 38 (1904).
75. S.-W. Hla, L. Bartels, G. Meyer, and K.-H. Rieder, *Phys. Rev. Lett.* 85, 2777 (2000).
76. J. Hahn and W. Ho, *Phys. Rev. Lett.* 87, 166102 (2001).
77. Y. Kim, T. Komeda, and M. Kawai, *Phys. Rev. Lett.* 89, 126104 (2002).
78. H. Lee and W. Ho, *Science* 286, 1719 (1996).
79. Y. Okawa and M. Aono, *Nature* 409, 619 (2001).
80. G. Lopinski, D. Wayner, and R. Wolkow, *Nature* 406, 48 (2000).
81. T. Jung, R. Schlittler, J. Gimzewski, and C. Joachim, *Science* 283, 1683 (1999).
82. J. Gimzewski, T. Jung, M. Cuberes, and R. Schlittler, *Surf. Sci.* 386 (1997).
83. W. Pai, Z. Zhang, J. Zhang, and J. Wendelken, *Surf. Sci.* 393, L106 (1997).
84. B. Frederick, A. Munz, T. Bertrams, Q. Chen, C. Perry, and N. Richardson, *Chem. Phys. Lett.* 272, 438 (1997).
85. P. Thomas, N. Berovic, P. Laitenberger, R. Palmer, N. Bampos, and J. Sanders, *Chem. Phys. Lett.* 294, 229 (1998).
86. D. Keeling, M. Humphry, P. Moriarty, and P. Beton, *Chem. Phys. Lett.* 366, 300 (2002).
87. M. Böhrringer, K. Morgenstern, W.-D. Schneider, and R. Berndt, *J. Phys. Cond. Mat.* 11, 9871 (1999).
88. M. Schunack, L. Petersen, A. Kühnle, E. Laegsgaard, I. Stensgaard, I. Johannsen, and F. Besenbacher, *Phys. Rev. Lett.* 86, 456 (2001).
89. M. Schunack, F. Rosei, Y. Naitoh, P. Jiang, A. Gordon, E. Laegsgaard, I. Stensgaard, C. Joachim, and F. Besenbacher, *J. Chem. Phys.* 117, 6259 (2002).
90. F. Rosei, M. Schunack, P. Jiang, A. Gordon, E. Laegsgaard, I. Stensgaard, C. Joachim, and F. Besenbacher, *Science* 296, 328 (2002).
91. R. Lin, K.-F. Braun, H. Tang, U. Quaade, F. Krebs, G. Meyer, C. Joachim, K.-H. Rieder, and K. Stokbro, *Surf. Sci.* 477, 198 (2001).
92. F. Moresco, G. Meyer, K.-H. Rieder, H. Tang, A. Gourdon, and C. Joachim, *Phys. Rev. Lett.* 86, 672 (2001).
93. F. Moresco, G. Meyer, K.-H. Rieder, J. Ping, H. Tang, and C. Joachim, *Surf. Sci.* 499, 94 (2002).
94. C. Loppacher, M. Guggisberg, O. Pfeiffer, E. Meyer, M. Bammerlin, R. Lüthi, R. Schlittler, J. Gimzewski, H. Tang, and C. Joachim, *Phys. Rev. Lett.* 90, 066107 (2003).
95. F. Moresco, G. Meyer, K.-H. Rieder, H. Tang, A. Gourdon, and C. Joachim, *Phys. Rev. Lett.* 87, 088302 (2001).
96. J. Li, W.-D. Schneider, R. Berndt, and B. Delley, *Phys. Rev. Lett.* 80, 2893 (1998).
97. U. Fano, *Phys. Rev.* 124, 1866 (1961).
98. V. Madhavan, W. Chen, T. Jamneala, M. Crommie, and N. Wingreen, *Science* 280, 569 (1998).
99. W. Chen, T. Jamneala, V. Madhavan, and M. Crommie, *Phys. Rev. B* 60, R8529 (1999).
100. T. Jamneala, V. Madhavan, and M. Crommie, *Phys. Rev. Lett.* 87, 256804 (2001).
101. H. Manoharan, C. Lutz, and D. Eigler, *Nature* 403, 512 (2000).
102. H. Manoharan, C. Lutz, D. Eigler, G. Fiete, J. Hersch, and E. Heller, *Phys. Rev. Lett.* 86, 2392 (2001).
103. J. Repp, F. Moresco, G. Meyer, and K.-H. Rieder, *Phys. Rev. Lett.* 85, 2981 (2000).
104. J. Repp, Ph.D. Thesis, Free Universität Berlin, 2002.
105. C. Joachim and S. Gauthier, *Pour la science* 30 (2001).
106. A. Heinrich, C. Lutz, J. Gupta, and D. Eigler, *Science* 298, 1381 (2002).
107. N. Niluis, T. Wallis, and W. Ho, *Science* 297, 1853 (2002).
108. K.-F. Braun and K.-H. Rieder, *Phys. Rev. Lett.* 88, 096801 (2002).
109. J. Li, W.-D. Schneider, R. Berndt, O. Bryant, and S. Crampin, *Phys. Rev. Lett.* 81, 4464 (1998).
110. L. Bürgi, O. Jeandupeux, H. Brune, and K. Kern, *Phys. Rev. Lett.* 82, 4516 (1999).
111. J. Kliewer, R. Berndt, E. Chulkov, V. Silkin, P. Echenique, and S. Crampin, *Science* 288, 1399 (2000).
112. J. Kliewer, R. Berndt, and S. Crampin, *New J. Phys.* 3, 22 (2001).
113. E. Heller, M. Crommie, C. Lutz, and D. Eigler, *Nature* 369, 464 (1994).
114. S. Datta, "Electronic Transport in Mesoscopic Systems." Cambridge Univ. Press, Cambridge, UK, 1995.
115. C. Joachim, J. Gimzewski, and A. Aviram, *Nature* 408, 541 (2000).
116. Y. Wada, T. Uda, M. Lutwyche, S. Kondo, and S. Heike, *J. Appl. Phys.* 74, 7321 (1993).
117. Y. Wada, "Atomic and Molecular Wires," p. 197. Kluwer Academic, Dordrecht, 1997.
118. W. Hebenstreit, J. Redinger, Z. Horzova, M. Schmid, R. Podloucky, and P. Varga, *Surf. Sci.* 424, L321 (1999).
119. R. Bennewitz, A. Foster, L. Kantorovich, M. Bammerlin, C. Loppacher, S. Schär, M. Guggisberg, E. Meyer, and A. Shluger, *Phys. Rev. B* 62, 2074 (2000).
120. S. Fölsch, A. Helms, S. Zöphel, J. Repp, G. Meyer, and K.-H. Rieder, *Phys. Rev. Lett.* 84, 123 (2000).
121. S. Fölsch, A. Helms, A. Riemann, J. Repp, G. Meyer, and K.-H. Rieder, *Surf. Sci.* 497, 113 (2002).

122. J. Repp, S. Fölsch, G. Meyer, and K.-H. Rieder, *Phys. Rev. Lett.* 86, 252 (2001).
123. S. Fölsch, A. Riemann, J. Repp, G. Meyer, and K.-H. Rieder, *Phys. Rev. B* 66, 16140(R) (2002).
124. R. Smoluchowski, *Phys. Rev.* 60, 661 (1941).
125. F. Himpsel, A. Kirakosian, J. Crain, J.-L. Lin, and D. Petrovykh, *Solid State Commun.* 117, 149 (2001).
126. X. Bouju, C. Joachim, and C. Girard, *Phys. Rev. B* 50, 7893 (1994).
127. F. Moresco, S. Hla, J. Repp, K.-F. Braun, S. Fölsch, G. Meyer, and K. Rieder, *Chinese Phys.* 10, S10 (2001).
128. S.-W. Hla and K.-H. Rieder, *Superlatt. Microstruct.* 31, 63 (2002).
129. T. Jung, R. Schlittler, J. Gimzewski, H. Tang, and C. Joachim, *Science* 271, 181 (1996).
130. P. Echenique, J. Osma, M. Machado, V. Silkin, E. Chulkov, and J. Pitarke, *Progr. Surf. Sci.* 67, 271 (2001).
131. G. Meyer, J. Repp, S. Zöphel, K.-F. Braun, S. Hla, S. Fölsch, L. Bartels, F. Moresco, and K.-H. Rieder, *Single Molecules* 1, 79 (2000).
132. K.-F. Braun, S.-WHla, N. Pertaya, H.-W. Soe, C. F. J. Flipse, and K.-H. Rieder, Proceeding of the conference on scanning tunneling microscopy. Eindhoven 2003.
133. T. Wallis, N. Nilius, and W. Ho, *Phys. Rev. Lett.* 89, 236802 (2002).
134. P. Zeppenfeld, C. Lutz, and D. Eigler, *Ultramicroscopy* 128, 42 (1992).
135. A. Bauer, A. Mühlig, D. Wegner, and G. Kaindl, *Phys. Rev. B* 65, 075421 (2002).

Atomic Structure of Defects in Semiconductors

I. Yonenaga

Tohoku University, Sendai, Japan

CONTENTS

1. Introduction
 2. Crystal Structure
 3. Dislocations
 4. Dislocation Interaction
 5. Dislocation Climb
 6. Defect Complexes
 7. Numerical Estimation of Atomic Displacement Around the Defects
 8. Formation Mechanism of the Central stacking fault Observed in Z-Shaped Dipoles
- Glossary
References

1. INTRODUCTION

The increasing nano and atomic scale miniaturization and large scale integration of advanced semiconductor devices demand improved understanding of structural defects such as dislocations, impurity-defect complexes, etc., which play a vital role in the device function. Thus, their atomic and electronic structures have been the subject of intense theoretical and experimental investigation (for example, [1–3]). Various *ab initio* calculations have been reported on the assumption of the atomic structure of the defects (for example, [4–8]). Experimentally, high resolution electron microscopy (HREM) [9, 10], scanning tunneling microscopy, and Z-contrast (high-angle annular dark field) imaging in scanning transmission electron microscopy [11] are valuable techniques which lead structural information on defects in real space to be ascertained on the nano and atomic scale. Generally, the atomic arrangements in the vicinity of structural defects within semiconductor materials have been determined from projected end-on images and Z-contrast imaging. A number of reports on the defects within semiconductors have been published (e.g., [12–16]). However,

such structural defects are generally unstable under the electron beam and are susceptible to change the structure or dynamic motion during observation and a complete understanding of the microstructure of such defects has not been achieved. To date, there have been several detailed quantitative reports of atom positions and displacements around such defects using HREM (e.g., [17–25]).

This chapter reviews the current knowledge of fundamental defects, mainly dislocations and stacking faults, typically observed in deformed GaAs by HREM and the numerical evaluation of their atomic structure. After preliminary description of the structure of semiconductor materials in Section 2, atomic structure and HREM images of perfect and dissociated dislocations and misfit dislocations at the thin film/substrate interfaces are shown in Section 3, and then, defects induced through dislocation interaction, climb of dislocations, and defect complexes derived by point defect and impurity agglomerations are described in subsequent Sections 4, 5, and 6. In Section 7, the recent development of the direct determination of the atomic positions and their displacements is shown for a 60° dislocation and a Z-shaped dipole. Finally, the formation mechanism of the Z-shaped dipole is discussed in Section 8. Only some limited examples of typical HREM and Z-contrast images will be shown from a huge number of reports in the present field.

Here, it should be noted that high resolution electron microscopy for end-on imaging and Z-contrast imaging is a powerful technique to understand the detailed structure of defects quantitatively though the results should be verified with numerical simulations from geometrical models [11, 23, 26].

2. CRYSTAL STRUCTURE

Tetrahedrally coordinated semiconductors crystallize in the diamond-cubic (e.g., diamond, Si, Ge), sphalerite (zincblende) (GaAs, InP, CdTe, ZnSe, etc.), or wurtzite structure (GaN, ZnO, etc.). Each atom possesses four nearest neighbors with covalent and ionic nature bonding depending on its electronic affinity. Crystals can be considered as

an assembly of corner-sharing tetrahedra. The diamond-cubic structure of elemental semiconductors consists of two interpenetrating face-centered cubic (fcc) basis lattices, displaced from one another by one-quarter of the cubic diagonal length. Deducing the stacking order of the closed packed planes ... ABCABC... in fcc structure, the {111} planes stack as ... AaBbCcAaBbCc... by doubling the atoms in the stacking sequences, as shown in Figure 1a. Here A, B, C and a, b, c notes the atoms on the basis sublattices, respectively. Thus, Aa, Bb, and Cc show the positions of [111] bonds connecting the basis sublattices. In III-V and II-VI compound semiconductors the two different atoms of the basis lattices are of different natures, which gives sphalerite and wurtzite structure in the case of the cubic [... AaBbCcAaBbCc... stacking of (111) planes] and hexagonal [... AaBbAaBb... stacking of (0001) planes] symmetry, respectively. Figure 1b shows the atomic arrangement of the stacking of {111} planes in III-V or II-VI sphalerite structure. The (111) atomic planes to be occupied only by III (II) atoms and those only by V (VI) atoms are stacked alternatively, repeating a wide and a narrow interatomic plane also alternatively. The ratio of the two

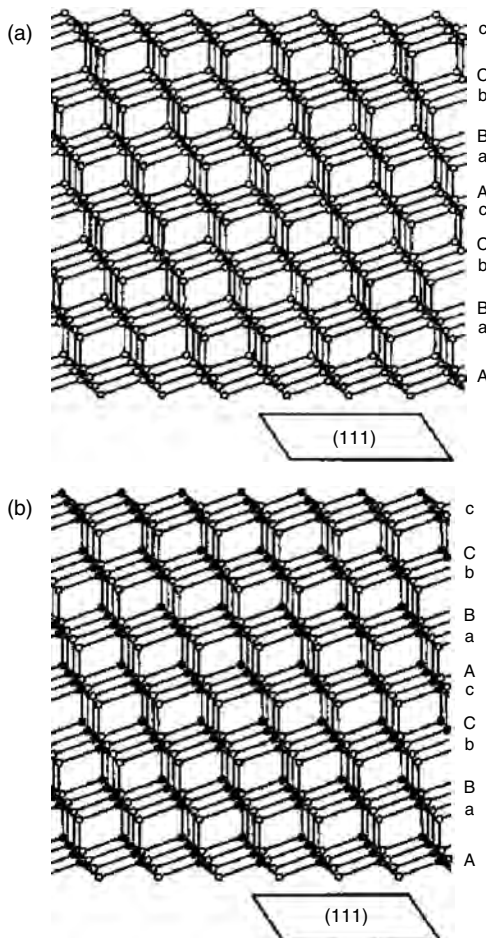


Figure 1. Atomic arrangement of the stacking of {111} planes (a) in diamond-cubic structure and (b) in III-V or II-VI sphalerite structure. In sphalerite structure open circles represent group III (II) atoms and solid circles group V (VI) atoms.

interatomic-plane distances is 3:1 in the stacking of {111} planes in sphalerite structure and (0001) planes in wurtzite structure. SiC is a typical poly-type material, possessing various crystal structures called 3C, 4H, 6H, and 15R. According to the Ramsdell [27] notation, the number gives the periodicity of the tetrahedral stacking along the axis perpendicular to the basal plane (0001) and the letter (C, H, and R) indicates the symmetry of the resulting structure (cubic, hexagonal, and rhombohedral) [28]. The sphalerite and wurtzite structures are 3C and 2H, respectively, in the notation.

3. DISLOCATIONS

3.1. Perfect Dislocations

Dislocation is a defect controlling the plasticity of crystals by the glide motion and plays a detrimental role in the efficiency of various semiconductor devices. Originating from their basis lattices, the diamond-cubic and sphalerite structure crystals have the dislocation Burgers vectors $a/2[110]$ on the slip planes {111} as fcc crystals, whereas the wurtzite structure crystals have $a/3[1\bar{2}10]$ on (0001). These dislocations are called *perfect type*. Due to a high Peierls stress dislocations in a semiconductor with the diamond or sphalerite structure are energetically stable when they lie parallel to the $\langle 110 \rangle$ directions on the {111} planes whereas dislocations in wurtzite structure crystals are stable when they lie parallel to the $a/3 \langle 1\bar{2}10 \rangle$ on (0001). Thus, the shape of a stable dislocation loop is hexagonal with two opposite screw segments and four 60° segments as seen in Figure 2a. These are such types of dislocations that the dislocation lines make angles of 60° and 0° , respectively, with the Burgers vector [29]. A dislocation lying along some direction deviated from the $\langle 110 \rangle$ may be regarded as comprising a number of $\langle 110 \rangle$ segments connected by kinks. Figure 2b and c show the atomic arrangements around 60° and screw dislocations in a sphalerite structure crystal. Here, the dislocation

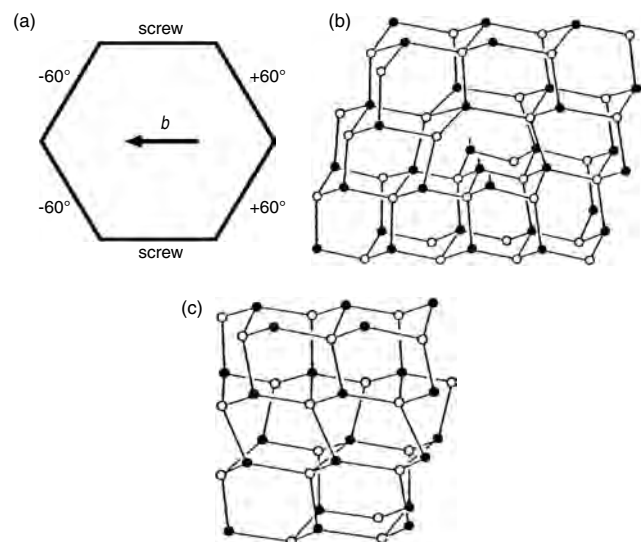


Figure 2. (a) A dislocation loop on a slip plane and atomic arrangements around perfect (*shuffle set*) dislocations in a sphalerite structure crystal. (b) A 60° dislocation and (c) screw dislocation.

is a perfect one and terminates at the wide-type $\{111\}$ interatomic planes, called a *shuffle set* in the terminology of Hirth and Lothe [30]. Differing from the diamond structure crystal, 60° dislocations have geometrical dangling bonds emerging from either group III (II) or V (VI) atoms at the core in III–V (II–VI) compound crystals with the sphalerite or wurtzite structure. The former type of dislocation is termed α -type and the latter β -type, showing the different dynamic properties.

Figure 3a shows a HREM image of a dislocation within plastically deformed GaAs. The image was obtained with the incident electron beam parallel to $[01\bar{1}]$ (see [24]). The white spots in the HREM image were found to correspond to columns of the Ga and As atom pairs, that is, the *dumbbells* with a short separation (0.14 nm) in the $[01\bar{1}]$ projection. Careful measurement of the image with a Burgers circuit around the defect confirms that the dislocation is a perfect-type 60° dislocation. An extra half-plane due to the edge component of the dislocation can be seen clearly as indicated by an arrow. The atomic structure is schematically shown in Figure 2b. Even now there is controversy over whether such a shuffle-set dislocation moves through the wide-type $\{111\}$ interatomic planes during a plastic deformation [31–33]. However, the configuration is indispens-

able to cross-slip in dislocation multiplication process during plastic deformation [34].

Figure 3b shows a high resolution Z-contrast image of a threading dislocation viewed along the $[0001]$ c -axis direction within wurtzite GaN film grown by metal-organic vapor phase epitaxy [35]. The bright spots are atomic columns of alternating Ga and N atoms determined by intensity distribution. From drawing the Burgers circuit around the dislocation the dislocation core is known to have an edge Burgers vector component of $a/3[11\bar{2}0]$. Two extra half-planes $\{10\bar{1}0\}$ meeting at the core at an angle of 60° between them can be seen clearly. The eightfold ring structure can be seen, meaning the formation of dimers at the core. The core structure, sketched in Figure 3c, well corresponds to the model proposed by theoretical calculation [36]. Sixty degree perfect dislocations with a Burgers vector of $a/3[11\bar{2}0]$ on the basal plane were found in pulverized GaN at room temperature [37]. Perfect screw dislocations with a Burgers vector perpendicular to the basal plane were observed in GaN [35]. Screw dislocations with a large magnitude of the Burgers vector are considered to be associated with the formation of hollow tubes 5–25 nm across (micropipe and nanotube) [38]. Micropipes are typically observed in GaN heteroepitaxially grown sapphire substrates [39, 40].

3.2. Dissociated Dislocations

Generally a glide dislocation in a semiconductor with the diamond or sphalerite structure is dissociated into two Shockley-type partial dislocations bounding a strip of intrinsic stacking fault by following the reaction

$$(a/2)[1\bar{1}0] = (a/6)[1\bar{2}1] + (a/6)[2\bar{1}\bar{1}] \quad (1)$$

In the terminology of Hirth and Lothe [30], the dislocation is of the *glide set* and moves through the narrow-type $\{111\}$ interatomic planes. Thus, in the hexagonal shape of a stable dislocation loop, the 60° segment consists of a 90° Shockley partial and a 30° Shockley partial bounding a strip of stacking fault, while the screw segment consists of two 30° Shockley partials as seen in Figure 4a. Dislocations have geometrical dangling bonds emerging from either group III (II) or V (VI) atoms at the core in the narrow-type interatomic plane in III–V (II–VI) compounds. Contrary to the shuffle set dislocations, the former type of dislocation is termed β -type and the latter α -type in the glide set. A 60° dislocation marked α in Figure 4a consists of a 90° Shockley partial and a 30° Shockley partial both of α -type as drawn in Figure 4b. A dislocation segment located on the opposite side of an α -type segment in the same hexagonal loop is always of β -type. Figure 4c shows that a 60° dislocation of β -type consists of a 90° Shockley partial and a 30° partial, both of β -type. A screw dislocation consists of a 30° Shockley partial of α -type and a 30° Shockley partial of β -type, as shown in Figure 4d. No distinction of α and β type is available in the diamond-type semiconductor. The difference in the core structure of α and β dislocations leads to the different effects of impurities on them in compound semiconductors. In the wurtzite structure a dislocation on the basal plane dissociates into two partial dislocations in

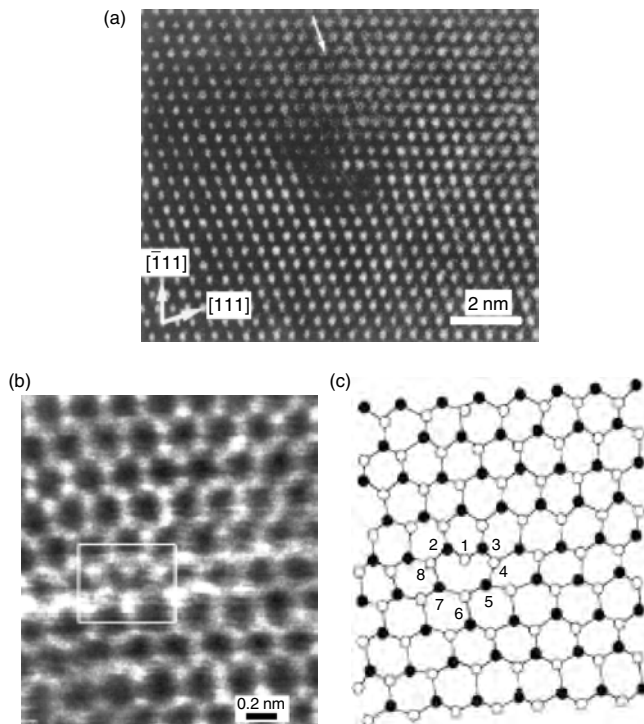


Figure 3. (a) HREM image of a perfect 60° dislocation in plastically deformed GaAs. (b) High resolution Z-contrast image of an edge dislocation viewed along the $[0001]$ c -axis direction within wurtzite GaN film grown by metal-organic vapor phase epitaxy. (c) Atomic arrangement of the core indicated by numbers 1 to 8. (a) Reprinted with permission from [24], I. Yonenaga et al., *Mater. Sci. Eng. A* 309–310, 125 (2001). © 2001, Elsevier Science. (b) and (c) Reprinted with permission from [35], Y. Xin et al., *Appl. Phys. Lett.* 72, 2680 (1998). © 1998, American Institute of Physics.

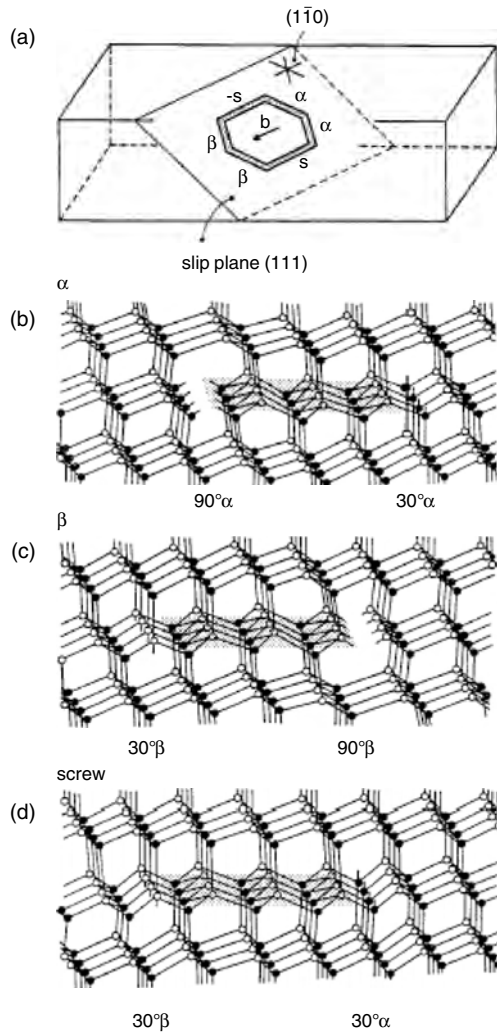


Figure 4. (a) A dislocation loop on a slip plane, and atomic arrangements at the core of (b) an α dislocation, (c) a β dislocation, and (d) a screw dislocation (*glide set*) in a III–V (II–VI) compound. The shaded regions denote an intrinsic stacking fault. In diamond-cubic structure open and solid circles all represent group IV atoms and there is no distinction between an α dislocation and a β dislocation. In sphalerite structure open circles represent group III (II) atoms and solid circles group V (VI) atoms.

a similar way. Here, it is commonly accepted that the geometrical dangling bonds are reconstructed to make bonds between two atoms neighboring each other along the dislocation line [41].

Figure 5a shows a typical HREM image of a 60° dislocation in deformed GaAs in the $[01\bar{1}]$ projection. In the image, differing from that in Figure 3a, the 60° dislocation is known to dissociate into two partial dislocations of 30° and 90° , denoted A and B, respectively, bounding a strip of intrinsic stacking fault. The type of the dislocation, whether α or β , corresponding to Figure 4b or c, was not clarified. Figure 5b shows a HREM image of a screw dislocation, dissociated into two 30° partials, in GaAs, corresponding to Figure 4d. The difference of the dissociation width originates from the dislocation nature. The width of the stacking fault is typically of the order of 6–10 nm in elemental and III–V compound

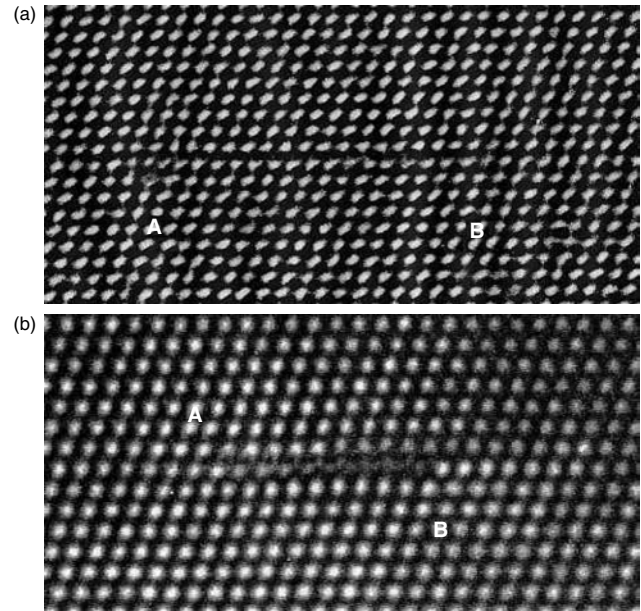


Figure 5. End-on HREM images of (a) a 60° and (b) a screw dislocation in deformed GaAs in the $[01\bar{1}]$ projection. Normally the 60° dislocation dissociates into two partial dislocations of 30° and 90° , denoted A and B respectively, and the screw dislocation dissociates into two 30° partials, A and B, bounding a strip of intrinsic stacking fault.

semiconductors such as Si, Ge, GaAs, InP, CdTe, ZnSe, etc. The width can be applied for estimating the stacking fault energy in various semiconductors together with their ionicity [42] as shown in Table 1 [28, 37, 43–55].

Figure 6 shows a plane-view image of a dissociated 60° dislocation in Si [18]. Shockley partial dislocations of 90° and 30° were observed to be dissociated by a stacking fault

Table 1. The structure, the magnitude b of the Burgers vector, the ionicity f , and the stacking fault energy γ of various semiconductors.

Crystal	Structure	b (nm)	f [42]	γ (mJ/m ²)	Ref.
C	diamond-cubic	0.252	0	285	[43]
Si	diamond-cubic	0.384	0	55	[44]
Ge	diamond-cubic	0.400	0	60	[45]
Ge _{0.6} Si _{0.4}	diamond-cubic	0.394	0	57	[46]
SiC	3C, 4H, 6H, 15R ^a	0.308	0.18	2.9–15	[28]
AlN	wurtzite	0.311	0.45	220	[47]
GaN	wurtzite	0.318	0.50	20	[37]
GaP	sphalerite	0.385	0.33	43	[48]
GaAs	sphalerite	0.400	0.31	45	[49]
GaSb	sphalerite	0.431	0.26	53	[50]
InP	sphalerite	0.415	0.42	18	[50]
InAs	sphalerite	0.427	0.36	30	[50]
InSb	sphalerite	0.458	0.32	38	[50]
ZnO	wurtzite	0.325	0.62	100	[47]
ZnS	sphalerite	0.384	0.623	<6	[51]
ZnSe	sphalerite	0.401	0.63	13	[52]
ZnTe	sphalerite	0.430	0.61	16	[53]
CdS	wurtzite	0.414	0.685	8.7	[54]
CdSe	wurtzite	0.430	0.699	14	[55]
CdTe	sphalerite	0.458	0.72	9	[53]

^a SiC: typical polytypes.

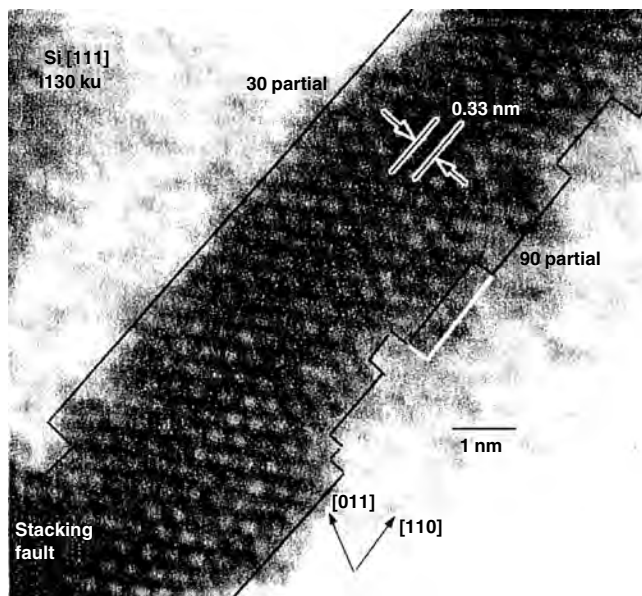


Figure 6. Plane-view HREM image of a dissociated 60° dislocation in Si in the $[111]$ projection. The 90° and 30° partial dislocations with kinks are shown by black lines. Reprinted with permission from [18], H. R. Kolar et al., *Phys. Rev. Lett.* 77, 4031 (1996). © 1996, American Physical Society.

in width of 5.8 nm. Such a kind of a plane-view image can be obtained under the condition of forbidden reflections arising from the stacking fault that separates partial dislocations [56]. On the 90° partial dislocation, kinks can be seen clearly. The dynamic motion of kinks was observed directly in an atomic scale during *in situ* observation at 600°C . Such a direct observation addressed the understanding of the elementary process of dislocation motion. Such a plane-view observation has been attempted also for Ge and GaAs [57, 58].

In addition to the direct observations of partial dislocations by the plane-view imaging, the investigation of the electronic structure of the partial dislocations has been conducted in Si by electron energy loss spectroscopy (EELS) [59] and by convergent beam electron diffraction (CBED) [60] to clarify the core reconstruction of dislocations as mentioned previously. It is thought that the geometrical dangling bonds make bonds between neighboring atoms in a single or double period along the dislocation line [61, 62].

Here it might be noted that as seen in Figures 3a and 5a, dislocations are found both in undissociate (perfect) and dissociate states in some semiconductors [15, 24]. In GaN, for example, 60° undissociate (perfect) and dissociate dislocations with a Burgers vector of $a/3[11\bar{2}0]$ on the basal plane were reported [37]. There is controversy over which type of dislocation plays a detrimental role in plastic deformation [31]. It is necessary to discuss their energetic stability in motion and in rest [63, 64].

In semiconductor crystals the dislocation velocity v is described using the empirical equation as a function of the stress τ and temperature T

$$v = v_0(\tau/\tau_0)^m \exp(-Q/k_B T) \quad (2)$$

where $\tau_0 = 1$ MPa. k_B is the Boltzmann constant. The constants v_0 , m , and Q are experimentally determined constants. The different types of dislocations in any compound semiconductors have different mobilities and show different physical characteristics in a variety of interactions with impurities [65–68]. Thus, the determination of the dislocation type, α or β , is important to understand the dislocation activities originating from the atomic structure of dislocation cores. For the determination of dislocation type the CBED technique [69] is useful as will be shown. The type of partial dislocation, α or β , in SiC was distinguished by the evaluation of the image contrast of the large difference in atomic number of the constituents [70].

3.3. Misfit Dislocations

Epitaxial semiconductor films are important and lead to various applications in the present microelectronics and optoelectronics technology. The lattice parameter difference between the grown thin film and substrate leads to the generation of misfit dislocations in the interface when the film thickness exceeds a certain critical magnitude. There has been a lot of effort to observe such interfacial dislocations and twins in various epitaxial semiconductor systems. At the interface an array of Lomer dislocations and 60° dislocations has been observed in the heteroepitaxial interface of, for example, ZnTe on GaAs by HREM [71, 72] and of CdTe on GaAs by high resolution Z-contrast imaging [16]. Lomer dislocations are generated by the mutual interaction of dislocations as will be described. Figure 7 shows a Z-contrast image of 60° dislocation at the interface of GaAs on Si and plausible atomic structure [73]. The ellipse-like white spots in the image correspond to columns of the Ga and As atom pairs (i.e., the *dumbbells*). The dislocation core was known to have dangling bonds emerging from As atoms at the interface. Sources for misfit dislocation were found at

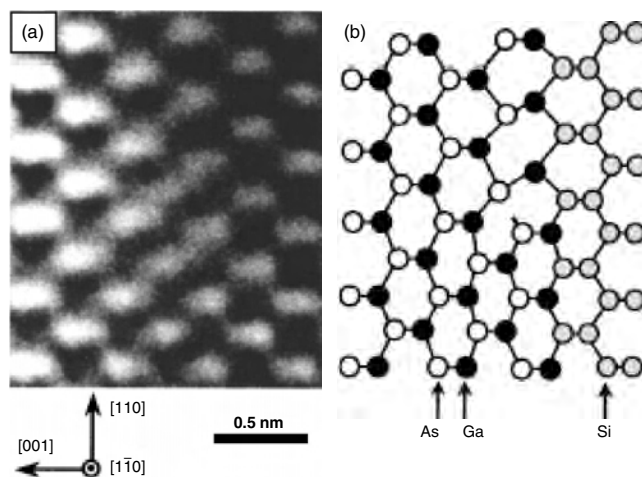


Figure 7. (a) High resolution Z-contrast image of a 60° misfit dislocation viewed along the $[110]$ direction at GaAs/Si and (b) the atomic structure model of the dislocation core. The epitaxial-grown GaAs appears brighter than the substrate Si in the Z-contrast imaging since GaAs is heavier than Si. Reprinted with permission from [73], S. Loptin et al., *Appl. Phys. Lett.* 81, 2728 (2002). © 2002, American Institute of Physics.

surface ripple troughs in InGaAs on GaAs heteroepitaxy [74]. The electronic structure of 60° dissociate misfit dislocations generated at the heteroepitaxial interface of GeSi on Si has been investigated by the EELS method to clarify the core reconstruction [75]. The EELS method and Z-contrast imaging are successfully applied to evaluate quantitatively the composition and also the compositional variation at the interfaces of Si/GeSi/Si multiepitaxial layers [76].

4. DISLOCATION INTERACTION

4.1. Lomer–Cottrell Dislocation

Reaction between two dislocations gliding on the intersecting slip planes can lead some types of dislocation junctions, among which a *Lomer–Cottrell* dislocation is well known. Lomer–Cottrell dislocations are found in Si [77] and in sub-boundaries and heteroepitaxial interfaces in GaAs on Si [73, 78] and ZnTe on GaAs [17]. Figure 8a shows a HREM end-on image of a Lomer–Cottrell dislocation within bulk GaAs deformed plastically. Two extra half $\{111\}$ planes, emerging at the core at an angle of 55° between them, can be seen. The image is consistent with the asymmetrical structure as shown in Figure 8b, where the stacking fault extends slightly only on one $\{111\}$ glide plane [79]. Lomer–Cottrell dislocations are sessile since the Burgers vector $a/2[110]$ perpendicular to the dislocation line $[110]$ is not on the slip plane and acts as a strong barrier for the motion of other dislocations, leading a strong work-hardening of materials.

4.2. Z-Shape Faulted Dipole

Figure 9a is a high-resolution image of a Z-shape defect within deformed GaAs recorded with the incident electron beam parallel to $[011]$. The three intrinsic stacking faults and four partial dislocations (i.e., two stair-rod and two 90° Shockley partial dislocations) delineating the defect can be seen clearly [21, 80]. A stair-rod partial dislocation is sessile since the Burgers vector $a/6(110)$ perpendicular to the dislocation line is not on a slip plane. A Burgers circuit around the whole defect shows no closure error, which confirms the defect to be a faulted dipole. Schematic illustration of the

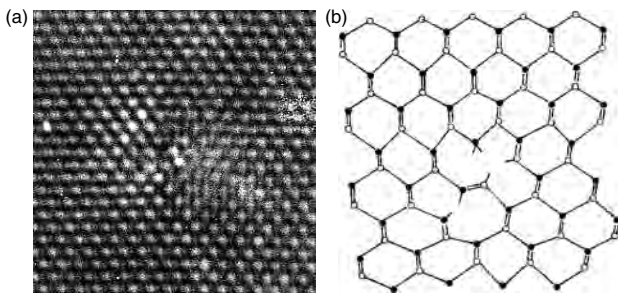


Figure 8. (a) HREM image of a Lomer–Cottrell dislocation within bulk GaAs deformed plastically. The images are consistent with the asymmetrical structure as shown in Figure 6b. Single and double lines mean that an atom located at the corner of hexagons puts out one or two interatomic bonds.

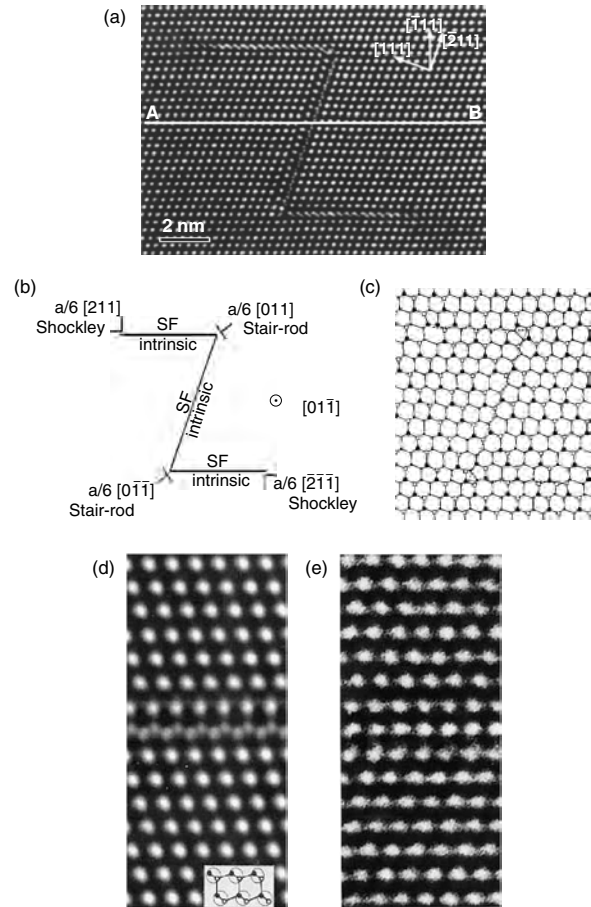


Figure 9. (a) HREM image of a Z-shape faulted dipole in deformed GaAs. (b) Schematic illustration showing the configuration of intrinsic stacking faults and partial dislocations which form the Z-shape faulted dipole. (c) Atomic arrangements around a Z-shaped faulted dipole. (d) and (e) Enlarged images of the central stacking fault and the lower stacking fault in the Z-shape faulted dipole, respectively, obtained with defocus conditions different from that of (a). (a) Reprinted with permission from [24], I. Yonenaga et al., *Mater. Sci. Eng. A* 309–310, 125 (2001). © 2001, Elsevier Science. (b) Reprinted with permission from [23], D. Shindo et al., *Mater. Characterization* 44, 375 (2000). © 2000, Elsevier Science.

configuration of the intrinsic stacking faults and partial dislocations that form the Z-type faulted dipole is shown in Figure 9b. Figure 9c shows the atomic arrangement around a Z-shaped faulted dipole. The contrast from the stacking faults is consistent with them being of the intrinsic, while extra half-planes located at the top and bottom stacking fault also imply this to be a vacancy-type defect [13]. By the CBED technique it was found that the partial dislocations at the top of this Z-shape defect are to be of the α -type, while those at the bottom of the defect are β -type [81]. Z-shape defects are generated following the interaction of dissociated α and β dislocations, having opposite Burgers vectors and moving on parallel slip planes, and become a stable Z-shape configuration, confined to lie along $\langle 1\bar{1}0 \rangle$ directions [82, 83]. Z-shape faulted dipoles are sessile. Similar Z-shape dipoles are also reported in Ge [84] and Si [85].

Figure 9d and e shows an enlarged image of the central stacking fault, lying between the two stair-rod partial dislocations, and the lower stacking fault between the stair-rod dislocation and 90° Shockley partial dislocation in the Z-shape faulted dipole, respectively. The white spots in the HREM image were confirmed to correspond to columns of the Ga and As atom pairs in the [011] projection. By drawing the line AB in the central region between the two stair-rod dislocations of the defect in Figure 9a, the white spots (dumbbells) in the region are found to be displaced parallel to the (111) plane asymmetrically on either side of the defect. In addition, it is remarkable to see splitting of the white spots on the central stacking fault in contrast to the lower and upper stacking faults. These aspects of the central stacking fault are quite distinct and very different from the atomic arrangement of other stacking faults.

5. DISLOCATION CLIMB

It is well known that dislocations can glide easily on their slip plane during electron microscope observation. The phenomenon is termed *recombination enhanced motion* of a dislocation and is considered to be caused by nonradiative electron-hole recombination at the dislocation [86]. The energy released by recombination is converted to a lattice vibration and can affect the elementary process of dislocation motion. Also, after prolonged electron irradiation, dislocations climb by absorbing or eliminating intrinsic point defects. Figure 10 shows a high resolution image of the faulted dipole modified during the irradiation [87]. Even though the whole image shows signs of irradiation damage, it is clearly seen that both β - and α -type 90° Shockley partial dislocations (A and D, respectively) have climbed from the stacking fault plane a few atomic distances in length to the position A' and D'. This means that the 90° partials have climbed through absorption of both Ga and As interstitials. However, it is noted that the β partial dislocation has climbed over a longer distance than the α partial.

From these observations, we can consider a climb process of a 90° Shockley partial dislocation as follows. During electron irradiation, the same number of Ga and As interstitials are generated, and these migrate and collapse to form perfect dislocation loops on the partial dislocations. This is in

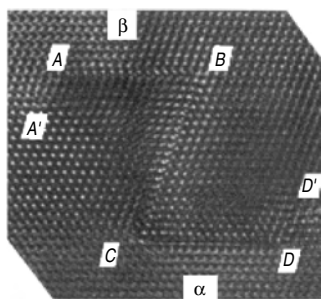


Figure 10. HREM image of a Z-shape faulted dipole showing the modification by the prolonged electron irradiation. The 90° partial dislocations A and D have climbed to A' and D', respectively, during irradiation. Reprinted with permission from [87], I. Yonenaga et al., *Mater. Sci. Eng. A* 253, 148 (1998). © 1998, Elsevier Science.

good accordance with a model based on the observations by weak-beam transmission electron microscopy [88]. Climb of dissociated dislocations was also reported in Si [89].

The force necessary to nucleate a perfect dislocation loop AA' of size l is given by the interaction force between a partial dislocation (A) and a perfect dislocation (A'),

$$F_{AA'} = -(3/16)Ga^2/\pi l \quad (3)$$

where a is the lattice constant and G is the shear modulus. The osmotic force for dislocation climb due to an interstitial concentration is given by the equation [29]

$$F_O = (\sqrt{6}/4)kTa\Omega^{-1} \ln(c/c_0) \quad (4)$$

where c_0 is the equilibrium concentration and Ω is the atomic volume. For nucleation of a perfect dislocation loop on a partial dislocation, the osmotic force due to the saturation of interstitials is balanced with the elastic interaction force between the relevant dislocations:

$$F_{AA'} + F_O = 0 \quad (5)$$

Accordingly, at room temperature, the required supersaturation of interstitials should be of the order of 10^7 cm^{-3} which will be obtained by irradiation.

6. DEFECT COMPLEXES

In semiconductor crystals various kinds of defect complexes have been found by transmission electron microscopy including HREM. Here a few typical examples of HREM observations are shown. Figure 11a shows a HREM image of a hydrogen-induced platelet in Si viewed along the [110] direction [90]. The size is a few tens of nanometers. The image with one extra row of bright dots inserted into the {111} stacking planes is due to hydrogen atoms breaking the [111] atomic bonds and saturating the broken bonds between the adjacent wide-type interatomic (111) planes. The structure shown in Figure 11b has been derived theoretically from the energetic calculation [91]. The defect acts as a nucleation site of {111} cleavage in the *smart cut* technique in hydrogen implantation.

In implanted or irradiated Si wafers rodlike defects running along $\langle 110 \rangle$ directions are generated. Figure 12 shows a HREM image of a rodlike defect with a {311} habit plane [92]. The defects are generated by precipitation of excess interstitials on {311} planes as a single layer of hexagonal Si.

HREM investigations of atomic structure of impurity precipitates, especially NiSi_2 , CoSi_2 , Cu_3Si , etc., in Si, have been applied to relate to their electronic structures for the harmful degradation of the devices [93].

7. NUMERICAL ESTIMATION OF ATOMIC DISPLACEMENT AROUND THE DEFECTS

Quantitative evaluation of the atomic displacement around the defects has been attempted in a perfect 60° dislocation [24] and a central stacking fault of the Z-shape defect [21].

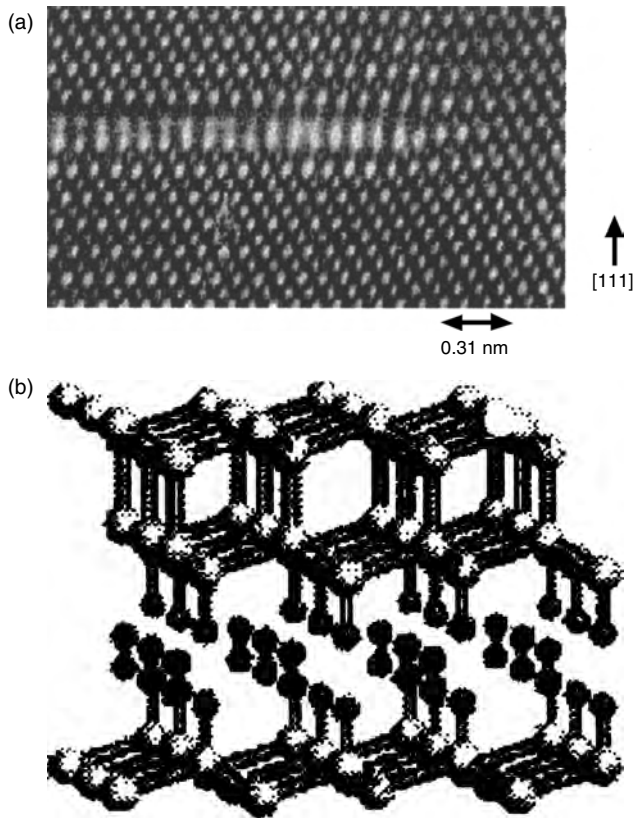


Figure 11. (a) HREM image of a hydrogen-induced platelet in Si viewed along the [110] direction [90]. (b) Atomic structure of the defect derived theoretically [91]. Open circles represent Si and solid circles H atoms. (a) Reprinted with permission from [90], S. Muto et al., *Philos. Mag. A* 72, 1057 (1995). © 1995, Taylor & Francis Ltd. (b) Reprinted with permission from [91], Y.-S. Kim and K. J. Chang, *Physica B* 308–310, 143 (2001). © 2001, Elsevier Science.

Figure 13 shows the variation of the displacement of the (111) layers along the [111] direction (i.e., the component of the displacement perpendicular to the extra half-plane) as a function of distance from the dislocation core for the perfect 60° dislocation in Figure 3a. Here, the displacement is defined as a difference between the (111) layer spacing and that of the perfect crystal. The displacement of the white spots is essentially zero in the region far from the dislocation core in the left side. The displacement of the white spots becomes large gradually through the following ~15 (111) layers (≈ 5 nm) from the dislocation core. The upper layers above the glide plane show negative displacement while the

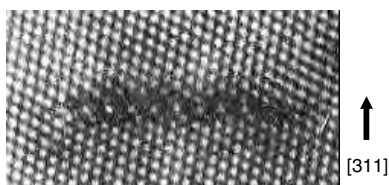


Figure 12. HREM image of a rodlike defect with a {311} habit plane in Si. Excess interstitials agglomerate on {311} planes as a single hexagonal layer. Reprinted with permission from [92], D. J. Egelsham et al., *Appl. Phys. Lett.* 65, 2305 (1994). © 1994, American Institute of Physics.

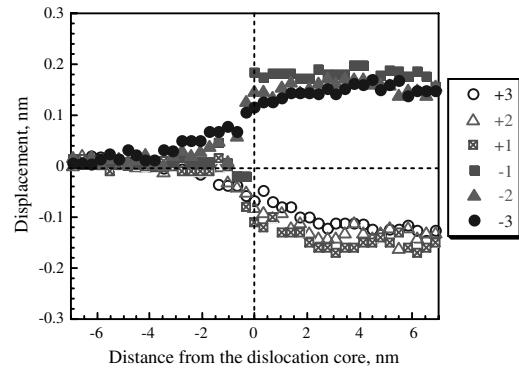


Figure 13. Variation of the displacement of white dots from the (111) planes along the [111] direction plotted against distance from the 60° perfect dislocation core in Figure 3a. The displacements of white dots on the three layers closest to the glide plane (111), either upper or lower side, are given with various symbols.

lower layers below that show positive displacement, which mean the existence of compressive and expansive strain of the dislocation with an edge component. On the right side the changes of the displacement of the upper and lower layers decrease from ~15 (111) layers away from the dislocation core. Finally the total difference of the displacement of the upper and lower layers is 0.326 nm, corresponding to the displacement by one perfect dislocation.

Figure 14a shows the deviation of the white spots from the line AB along the [211] direction, that is, the component of the deviation parallel to the central stacking fault of the Z-shape defect in Figure 7a, as a function of distance from the stacking fault. The deviation of the white spots is essentially zero in the regions far from the stacking fault and increases in an antisymmetric manner from both sides. The extent of deviation of the white spots then decreases gradually through the following ~10 (111) layers (≈ 3.3 nm). Such deviations were almost homogeneously distributed along the central stacking fault. Figure 14b shows the changes of the displacement of the (111) layers, which is defined as a difference between the (111) layer spacing and that of the perfect crystal. The predominant deviations of the white spots occur along the direction parallel to the central stacking fault along [211], which means the central stacking fault was generated by a shear process. That is, the motion of a Shockley partial dislocation between the two 30° Shockley partials of an original dislocation dipole results in the formation of one stacking fault and two stair-rod dislocations [94, 95].

8. FORMATION MECHANISM OF THE CENTRAL stacking fault OBSERVED IN Z-SHAPED DIPOLES

Furthermore, the atomic arrangement around the central stacking fault of the Z-shape defect and the formation process have been discussed in comparison with theoretical simulation [21]. First, an intrinsic stacking fault can be generated into a perfect crystal, with Ga and As atoms on the (111) planes in the perfect crystal being displaced at a narrower interatomic plane ... CcAa/BbCc... according to the faulting procedure in a sphalerite structure as shown in

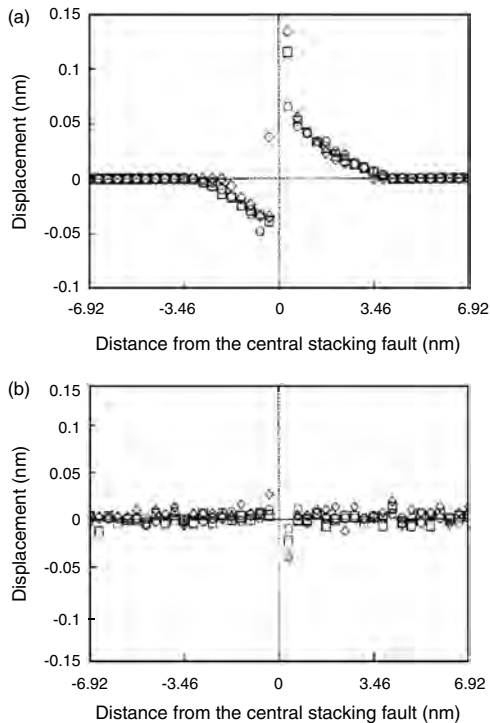


Figure 14. (a) Variation of the displacement of white dots on the $(\bar{1}11)$ plane in the vicinity of the central stacking fault from $(\bar{1}11)$ along the $[211]$ direction and (b) from the (111) planes along the $[111]$ direction plotted against distance from the stacking fault observed in the Z-shape faulted dipole in Figure 9a. Circles, squares, and diamonds correspond to measurements from HREM images with different defocus conditions. Reprinted with permission from [24], I. Yonenaga et al., *Mater. Sci. Eng. A* 309–310, 125 (2001). © 2001, Elsevier Science.

Figure 15a and b. Ga and As atoms combined at a wide-type interatomic plane displace as a unit (e.g., Aa, Bb...). The faulting between the 30° Shockley partial dislocations of a dislocation dipole is induced through shear displacement of $(a/6)[11\bar{2}]$ or $(a/6)[\bar{1}21]$ type dislocations (inclined to the plane of the page). Thus, the pair Bb of Ga and As atoms above a narrow-type (111) interatomic plane and that Aa below the plane, resulting in the intrinsic stacking fault, are displaced by components $(a/24)[2\bar{1}\bar{1}]$ and $(a/24)[\bar{2}11]$ in opposite directions parallel to the plane of the page. The extent of displacement of Ga and As atom pairs located at successive planes decreases away from the stacking fault. However, no explicit splitting of the Ga and As atom pairs along the central stacking fault was obtained in the consideration of shear mode.

In order to reproduce the observed splitting of the white spots, the As and Ga atoms combined at the stacking fault plane in the model of Figure 15b were shifted in the range of 20–50% in $[211]$ and $[2\bar{1}\bar{1}]$ directions, respectively, along the stacking fault plane as shown in Figure 15c. The shift of the As and Ga atoms was given as the percentage of the increased distance between Ga and As atoms, relative to that of the perfect crystal, at the intrinsic stacking fault plane in the model. Essentially the stacking fault width of a dissociated dislocation is given by the balance between the interaction force of

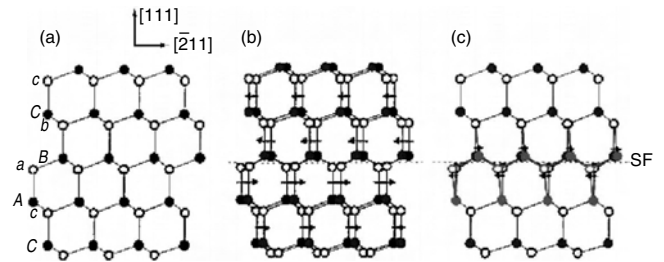


Figure 15. Model of atomic structure and formation of (a) a perfect sphalerite crystal viewed along $[01\bar{1}]$. (b) Schematic indicating the faulting procedure required to create an intrinsic stacking fault SF. (c) The atomic shift to reproduce the splitting of white spots corresponding to the observed central stacking fault in the Z-shape faulted dipole. The arrows in (b) and (c) denote the atomic shifting to create an intrinsic stacking fault and the splitting of white spots, respectively. Open and solid circles in the figures correspond to Ga and As atoms, respectively.

two partial dislocations and the interfacial energy of the stacking fault. Conversely, the central stacking fault of a Z-shape defect is induced by the motion of a $(a/6)[112]$ Shockley partial dislocation between a pre-existing dipole of two dissociated dislocations. Generally, the mutual interaction of two stair-rod partial dislocations is weaker than that of two Shockley partial dislocations, and the width of the former might become narrower if the two stair rods are mobile. The induced stacking fault in a Z-shape defect thus may show some relaxation due to these competing interaction energies, thereby giving it a nature different from that of an intrinsic stacking fault.

GLOSSARY

Burgers vector A translation vector of the crystal lattice representing the displacement of the material to create a defect such as a dislocation, stacking fault, etc.

Defect An irregularity (imperfection) of the atomic arrangement in the crystalline structure (point, line, and planar defects).

Dislocation A line defect running along the certain directions in which there is an atomic displacement from the regular arrangement in the crystalline structure.

Misfit dislocation A dislocation induced by the difference of the lattice constants at the epitaxial film and substrate interface.

Recombination enhanced motion A promotion of dislocation motion induced by the optical and electrical excitations.

stacking fault A planar defect in the crystal structure in which there is a change from the regular sequence of positions of atomic planes in the crystal structure.

ACKNOWLEDGMENTS

The author expresses his gratitude to Professor D. Shindo of Tohoku University, Dr. P. D. Brown of University of Nottingham, and Professor C. J. Humphreys of University of Cambridge for their collaboration.

REFERENCES

1. H. Alexander and H. Teichler, in "Electronic Structure and Properties of Semiconductors" (W. Schröter, Ed.), p. 249. VCH, Weinheim, 1991.
2. K. Sumino, in "Handbook on Semiconductors" (S. Mahajan, Ed.), Vol. 3, p. 73. Elsevier Science, Amsterdam, 1994.
3. A. George, *Mater. Sci. Eng. A* 233, 88 (1997).
4. P. Sitch, R. Jones, S. Öberg, and M. I. Heggie, *Phys. Rev. B* 50, 17717 (1994).
5. V. V. Bulatov, S. Yip, and A. S. Argon, *Philos. Mag. A* 72, 453 (1995).
6. C. P. Ewels, R. Jones, S. Öberg, J. Miro, and P. Deák, *Phys. Rev. Lett.* 77, 865 (1996).
7. N. Lehto and M. I. Heggie, in "Properties of Crystalline Silicon" (R. Hull, Ed.), p. 357. INSPEC, London, 1999.
8. R. Jones and A. T. Blumenau, *Scripta Mater.* 45, 1253 (2001).
9. J. C. H. Spence, "Experimental High-Resolution Electron Microscopy." Oxford Univ. Press, London, 1988.
10. G. R. Anstis and J. L. Hutchison, in "Dislocations in Solids" (F. R. N. Nabarro, Ed.), Vol. 9, p. 1. North-Holland, New York, 1992.
11. S. J. Pennycook, in "Advances in Imaging and Electron Physics" (P. W. Hawkes, Ed.), Vol. 123, p. 173. Academic Press, San Diego, 2002.
12. J. C. H. Spence and H. Kolar, *Philos. Mag. A* 39, 59 (1979).
13. A. Olsen and J. C. H. Spence, *Philos. Mag. A* 43, 945 (1981).
14. M. Tanaka and B. Jouffrey, *Philos. Mag. A* 50, 733 (1984).
15. D. Gerthsen, F. A. Ponce, and G. B. Anderson, *Philos. Mag. A* 59, 1045 (1989).
16. D. Shindo and K. Hiraga, "High-Resolution Electron Microscopy for Materials Science." Springer-Verlag, Tokyo, 1998.
17. A. J. McGibbon, S. J. Pennycook, and J. E. Angelo, *Science* 269, 519 (1995).
18. H. R. Kolar, J. C. H. Spence, and H. Alexander, *Phys. Rev. Lett.* 77, 4031 (1996).
19. G. Möbus, R. Schweinfest, T. Gemminug, T. Wagner, and M. Rühle, *J. Microsc.* 190, 109 (1998).
20. W. E. King, G. H. Campbell, S. M. Foiles, D. Cohen, and K. M. Hanson, *J. Microsc.* 190, 131 (1998).
21. S.-H. Lim, D. Shindo, I. Yonenaga, P. D. Brown, and C. J. Humphreys, *Phys. Rev. Lett.* 81, 5350 (1998).
22. J. C. H. Spence, *Mater. Sci. Eng.* R26, 1 (1999).
23. D. Shindo, Y. Ikematsu, S.-H. Lim, and I. Yonenaga, *Mater. Characterization* 44, 375 (2000).
24. I. Yonenaga, S.-H. Lim, C.-W. Lee, and D. Shindo, *Mater. Sci. Eng. A* 309–310, 125 (2001).
25. S. Kret, P. Ruterana, A. Rosenauer, and D. Gerthsen, *Phys. Status Solidi B* 227, 247 (2001).
26. S. P. Beckman, X. Xu, P. Specht, E. R. Weber, C. Kisielowski, and D. C. Chrzan, *J. Phys.: Condens. Matter* 14, 12673 (2002).
27. L. S. Ramsdell, *Amer. Mineralogist* 32, 64 (1947).
28. M. H. Hong, A. V. Samant, and P. Pirouz, *Philos. Mag. A* 80, 919 (2000).
29. J. Hornstra, *J. Phys. Chem. Solids* 5, 129 (1956).
30. J. P. Hirth and J. Lothe, "Theory of Dislocations." Wiley, New York, 1982.
31. M. S. Duesbery and B. Joós, *Philos. Mag. Lett.* 74, 253 (1996).
32. T. Suzuki, T. Yasutomi, T. Tokuoka, and I. Yonenaga, *Philos. Mag. A* 79, 2637 (1999).
33. J. Rabier, P. Cordier, T. Pondellier, J. L. Demenet, and H. Garem, *J. Phys.: Condens. Matter* 12, 10059 (2000).
34. I. Yonenaga and T. Suzuki, *Philos. Mag. Lett.* 80, 511 (2000).
35. Y. Xin, S. J. Pennycook, N. D. Browning, P. D. Nellist, S. Sivananthan, F. Omnés, B. Beaumont, J. P. Faurie, and P. Gibart, *Appl. Phys. Lett.* 72, 2680 (1998).
36. J. Elsner, R. Jones, P. K. Sitch, V. D. Porezag, M. Elsner, Th. Frauenheim, M. I. Heggie, S. Öberg, and P. R. Briddon, *Phys. Rev. Lett.* 79, 3672 (1997).
37. K. Suzuki and S. Takeuchi, *Philos. Mag. Lett.* 79, 423 (1999).
38. D. Cherns, W. T. Young, and F. A. Ponce, *Mater. Sci. Eng. B* 50, 76 (1997).
39. X. J. Ning, F. R. Chien, P. Pirouz, J. W. Yang, and M. Asif Khan, *J. Mater. Res.* 11, 580 (1996).
40. Z. Liliental-Weber, Y. Chen, S. Ruvimov, and J. Washburn, *Phys. Rev. Lett.* 79, 2835 (1997).
41. S. Markland, *Phys. Status Solidi B* 100, 77 (1980).
42. J. C. Phillips, "Bonds and Bands in Semiconductors." Academic Press, New York, 1973.
43. P. Pirouz, D. J. H. Cockayne, H. Shimada, P. Hirsch, and A. R. Long, *Proc. Roy. Soc. London Ser. A* 386, 241 (1983).
44. H. Gottschalk, *J. Phys.* 40, C6-127 (1979).
45. D. J. H. Cockayne, P. B. Hirsch, and V. Vitek, *Philos. Mag.* 31, 105 (1975).
46. I. Yonenaga, S.-H. Lim, and D. Shindo, *Philos. Mag. Lett.* 80, 193 (2000).
47. K. Suzuki, M. Ichimura, and S. Takeuchi, *Jpn. J. Appl. Phys.* 33, 1114 (1994).
48. P. L. Gai and A. Howei, *Philos. Mag.* 30, 939 (1974).
49. D. Gerthsen and C. B. Carter, *Phys. Status Solidi A* 136, 29 (1993).
50. H. Gottschalk, G. Patzer, and H. Alexander, *Phys. Status Solidi A* 45, 207 (1978).
51. A. V. Zaretskii, Y. A. Osipyan, V. F. Peterenko, G. K. Strukova, and I. I. Kohdos, *Philos. Mag. A* 48, 279 (1983).
52. V. V. Aristov, A. V. Zaretskii, Y. A. Osipyan, V. F. Peterenko, G. K. Strukova, and I. I. Kohdos, *Phys. Status Solidi A* 75, 101 (1983).
53. G. Lu and D. J. H. Cockayne, *Philos. Mag. A* 53, 307 (1986).
54. D. J. H. Cockayne, A. Hons, and J. C. H. Spence, *Philos. Mag. A* 42, 773 (1980).
55. K. Suzuki, S. Takeuchi, M. Shino, K. Kanaya, and H. Iwanaga, *Trans. Jpn. Inst. Metals* 24, 435 (1993).
56. H. Alexander, J. C. H. Spence, D. Shindo, H. Gottschalk, and N. Long, *Philos. Mag. A* 53, 627 (1986).
57. K. Maeda, M. Inoue, K. Suzuki, H. Amasuga, M. Nakamura, and E. Kanematsu, *J. Phys. III (France)* 7, 1451 (1997).
58. M. Inoue, K. Suzuki, H. Amasuga, Y. Mera, and K. Maeda, *J. Appl. Phys.* 83, 1953 (1998).
59. P. E. Batson, *Phys. Rev. Lett.* 83, 4409 (1999).
60. J. Spence and C. Koch, *Scripta Mater.* 45, 1273 (2001).
61. A. Valladares, A. K. Petford-Long, and A. Sutton, *Philos. Mag. Lett.* 79, 9 (1999).
62. C. J. Fall, J. P. G. Goss, R. Jones, P. R. Briddon, A. T. Blumenau, and T. Frauenheim, *Physica B* 308–310, 577 (2001).
63. K. Edagawa, H. Koizumi, Y. Kamimura, and T. Suzuki, *Philos. Mag. A* 80, 2591 (2000).
64. L. Pizzagalli, P. Beauchamp, and J. Rabier, *J. Phys.: Condens. Matter* 14, 12681 (2002).
65. I. Yonenaga and K. Sumino, *J. Appl. Phys.* 65, 85 (1989).
66. I. Yonenaga, *J. Phys. III (France)* 7, 1435 (1997).
67. I. Yonenaga, *J. Appl. Phys.* 84, 4209 (1998).
68. K. Sumino and I. Yonenaga, *Solid State Phenom.* 85/86, 145 (2002).
69. W. G. Burgess, A. R. Preston, G. A. Botton, N. J. Zaluzec, and C. J. Humphreys, *Ultramicroscopy* 53, 276 (1994).
70. M. Lancin, C. Ragaru, and C. Godon, *Philos. Mag. B* 81, 1633 (2001).
71. P. D. Brown and C. J. Humphreys, *Mater. Sci. Tech.* 11, 54 (1995).
72. P. D. Han and J. Zou, *Appl. Phys. Lett.* 72, 2424 (1998).
73. S. Lopatin, S. J. Pennycook, J. Narayan, and G. Duscher, *Appl. Phys. Lett.* 81, 2728 (2002).
74. A. G. Cullis, A. J. Pidduck, and M. T. Emeny, *Phys. Rev. Lett.* 75, 2368 (1995).

75. P. E. Batson, *Phys. Rev. B* 61, 16633 (2000).
76. T. Walther and C. J. Humphreys, *J. Cryst. Growth* 197, 113 (1999).
77. A. Bourret, J. Desseaux, and A. Renault, *Philos. Mag. A* 45, 1 (1982).
78. A. Vilà, A. Cornet, J. R. Morante, P. Ruterana, M. Loubradou, R. Bonnet, Y. González, and González, *Philos. Mag. A* 71, 85 (1995).
79. F. Louchet and J. Thibault-Desseaux, *Rev. Phys. Appl.* 22, 207 (1987).
80. I. Yonenaga, P. D. Brown, W. G. Burgess, and C. J. Humphreys, *Inst. Phys. Conf. Ser.* 146, 87 (1995).
81. A. T. Winter, S. Mahajan, and D. Brasen, *Philos. Mag. A* 37, 315 (1978).
82. B. C. De Cooman and C. B. Carter, *Appl. Phys. Lett.* 50, 40 (1987).
83. B. C. De Cooman and C. B. Carter, *Phys. Status Solidi A* 112, 41 (1988).
84. S.-W. Chiang, C. B. Carter, and D. L. Kohlstedt, *Philos. Mag. A* 42, 103 (1980).
85. M. Sato, K. Sumino, and K. Hiraga, *Phys. Status Solidi A* 68, 567 (1981).
86. K. Maeda and S. Takeuchi, in "Dislocations in Solids" (F. R. N. Nabarro and M. S. Duesbery, Eds.), Vol. 10, p. 443. North-Holland, Amsterdam, 1996.
87. I. Yonenaga, P. D. Brown, and C. J. Humphreys, *Mater. Sci. Eng. A* 253, 148 (1998).
88. D. Cherns and G. Feuillet, *Philos. Mag. A* 51, 661 (1985).
89. J. Thibault-Desseaux, H. O. K. Kirchner, and J. L. Putaux, *Philos. Mag. A* 60, 385 (1989).
90. S. Muto, S. Takeda, and M. Hirata, *Philos. Mag. A* 72, 1057 (1995).
91. Y.-S. Kim and K. J. Chang, *Physica B* 308–310, 143 (2001).
92. D. J. Egelsham, P. A. Stolk, H.-J. Gossmann, and J. M. Poate, *Appl. Phys. Lett.* 65, 2305 (1994).
93. F. Riedel, H. Hedemann, and W. Schröter, *Nucl. Instrum. Methods A* 476, 596 (2002).
94. C. B. Carter, *Philos. Mag.* 36, 147 (1977).
95. M. Sato, *Phys. Status Solidi A* 75, 107 (1983).

Atomic Structure of Diamond Surfaces

J. M. Perez

University of North Texas, Denton, Texas, USA

R. E. Stallcup II

Zyvex, Inc., Richardson, Texas, USA

CONTENTS

1. Introduction
 2. Development of Chemical Vapor Deposition (CVD) Diamond Techniques
 3. CVD Growth of Diamond
 4. Scanning Tunneling Microscopy
 5. Atomic Structure of Diamond Surfaces
 6. Conclusions
- Glossary
References

1. INTRODUCTION

Diamond films grown by chemical vapor deposition (CVD) have a great number of potential applications in nanotechnology including electronic devices, sensors, field emission (FE) electron sources, and microelectromechanical systems (MEMS). Current commercial applications include cutting tools, heat spreaders, optical windows, and speaker diaphragms. These applications utilize the unique bulk and surface properties of diamond such as extreme hardness, high thermal conductivity, wide bandgap, optical transparency from infrared to ultraviolet wavelengths, high FE current, and low frictional coefficient. There are numerous good books [1–5], conference proceedings [6–7], and review articles [8–16] on the CVD growth and properties of diamond films. Our focus in this review article, however, is to present a comprehensive and up-to-date description of the atomic structure of diamond surfaces as determined using scanning tunneling microscopy (STM) in air and ultra-high vacuum (UHV). We emphasize the diamond (100) surface and UHV STM techniques. In Section 2, we describe the development of CVD diamond growth techniques and the basic properties and applications of diamond films. In Sections 3 and 4 we describe the CVD diamond growth and STM techniques, respectively. In Section 5, we describe

the atomic structure of diamond (100), (111), and (110) surfaces.

STM in UHV has been extensively used to study the surface structure and epitaxial growth of Si and other semiconductors at the atomic scale [17–19]. However, UHV STM has not been extensively used to study diamond [20–24]. Most STM studies of diamond have been performed in air where sample preparation is limited to room temperature techniques and usually a hydrogen-terminated surface [25–33]. A recent study reported that STM was not possible in UHV because the diamond surface was not conductive enough until it was exposed to air [33]. One would like to see UHV STM results of diamond comparable in quality to those that have been reported for Si. The STM techniques described in this review article can be used to study adsorbates and processes such as etching, diffusion, and growth with atomic resolution. Such studies are crucial in understanding the growth and properties of diamond surfaces, which are currently not well understood. Earlier reviews of diamond surfaces describe structure and chemistry [34, 35], electronic properties [36, 37], and tribological properties [38].

2. DEVELOPMENT OF CHEMICAL VAPOR DEPOSITION DIAMOND TECHNIQUES

2.1. Historical Development

Diamond is metastable at atmospheric pressure and transforms into a stable form, graphite, when heated above 1700 °C in vacuum [39]. In the past, diamond has been used exclusively as a gemstone and cutting material. In 1955, General Electric reported a technique to produce diamond from solid carbon in a liquid melt by using high temperatures (1500–2000 °C) and high pressures at which diamond is stable (50–100 kbar) [40]. Although this process has been extensively used to produce diamond for commercial applications such as abrasives and cutting tools [41], it has proven to be limited in electronic applications because diamond

crystal sizes are small and the temperatures needed would melt most materials on which it would be useful to deposit diamond. During the 1970s and 1980s, the growth of diamond at high rates using CVD at low substrate temperatures (700–1000 °C) and low pressures (30 Torr) was developed [42–45]. This process uses atomic hydrogen and a gas such as methane (CH_4) that contains carbon. Although diamond is metastable under these conditions, it is believed that atomic hydrogen etches away stable graphitic forms of carbon, and promotes diamond growth by terminating the diamond surface in an sp^3 configuration. However, the exact growth mechanism is not well understood. CVD is compatible with microfabrication techniques and scalable to large areas. In addition, CVD growth conditions such as gas species, substrate temperature, and bias can be controlled, resulting in a variety of carbon-based films with useful properties, such as amorphous diamond, amorphous carbon, tetrahedral amorphous carbon, diamond-like carbon, and nanocrystalline diamond films [46–53]. During the past two decades, there has been considerable worldwide interest in the growth and properties of such carbon films.

The history of the development of CVD diamond growth techniques has been described in detail [42, 43, 45, 54]. In 1952, W. G. Eversole at the Union Carbide Corporation demonstrated CVD growth of diamond on diamond seeds using carbon monoxide (CO) at temperatures of 900–1000 °C and pressures of 100–300 atmospheres [42, 55]. He also grew diamond using hydrocarbons and other carbon-containing gases and used a cyclic growth/etch process to remove codeposited graphite. Independently, B. V. Spitsyn and B. V. Deryagin in the Soviet Union grew diamond on diamond seeds using carbon tetrabromide (CBr_4) and carbon tetraiodide (CI_4) [43]. In these experiments, growth rates were less than $0.001 \mu\text{m/hr}$, too low for commercial applications. During the 1960s, research on CVD diamond growth techniques was continued by a few researchers including Angus in the United States and Deryagin's group [42, 43, 54]. Angus developed a cyclic process that consists of a growth cycle followed by an etching cycle in which only atomic hydrogen was used to efficiently remove graphite. The atomic hydrogen was produced by using a hot-tungsten filament to dissociate molecular hydrogen (H_2); however, growth rates remained too low. In the mid-1970s and early 1980s, the Soviet group made significant advances by using both a carbon source and atomic hydrogen during growth, which increased the growth rate to on the order of $1 \mu\text{m/hr}$ and nucleated diamond on nondiamond substrates [43, 44]. During the early 1980s, Setaka's group in Japan developed CVD techniques that used a hot-tungsten filament [45, 56] or microwaves [57] to dissociate a hydrocarbon gas and H_2 . Positively biasing the substrate was found to increase the diamond nucleation density and growth rate [45]. In Japan, other CVD techniques were developed, including low pressure DC and RF plasma techniques with growth rates of $20 \mu\text{m/hr}$; atmospheric pressure techniques using DC, RF, and microwave plasmas with growth rates of up to $900 \mu\text{m/hr}$; and oxygen-acetylene combustion flame techniques with growth rates of $100 \mu\text{m/hr}$ [45]. These techniques share in common the use of a carbon containing gas and hydrogen or oxygen, which are activated at high temperatures. In atmospheric and combustion flame

techniques, the growth rate is higher because the gas temperature is higher; however, the film quality is lower.

These innovations triggered considerable research in the United States, Europe, and the rest of the world in CVD diamond synthesis. Since the late 1980s, the cost of growing diamond films has decreased from \$5,000/carat to below \$5/carat [58]. It is now possible to grow polycrystalline diamond films on a variety of substrates including Si, W, Ta, Mo, Ni, Cu, and SiO_2 , and to produce high-quality free-standing films that are on the order of 2 mm thick and 6 inches in diameter [59, 60].

In the early 1990s, it was predicted that by the year 2000 diamond films would be extensively used in a wide range of technological applications from cutting tools to electronic devices, and the market for diamond films would be \$2 billion per year [13]. Several companies currently produce diamond films for heat spreaders, tool coatings, optical windows, and other applications [61–68]. However, market predictions have not been met mainly due to the high cost of growing thick films and the inability to grow single-crystal films on nondiamond substrates [13]. Heat spreaders and optical windows require thick high-quality polycrystalline films having a low concentration of nondiamond carbon phases and other defects. Widespread commercial use of these products has been limited by the high cost of growing and polishing such films [58].

Applications in coatings for cutting tools have been limited by poor film adhesion and roughness [9, 58]. Poor film adhesion is due to the difference in thermal expansion coefficient between diamond and tool materials and the dissolution of carbon in Co, Ni, and Fe at high temperatures. Film adhesion has been improved by lowering the growth temperature and using diffusion barriers. Several companies currently produce polycrystalline diamond coated drills, end mills, etc. for the cutting of nonmetallic materials, such as graphite and plastic composites, and nonferrous materials such as aluminum and copper [61–64, 67, 68]. For applications that require precise cutting of aluminum, such as in the automobile industry, diamond coatings with small crystallite size are being investigated [9].

Applications in electronic devices have been limited by grain boundaries in polycrystalline films and by the lack of dopants having low activation energies. Although p -type doping with B is possible, the large activation energy of 0.37 eV results in room-temperature conductivities that are low and highly temperature dependent [69–72]. N -type doping with P has been reported [69, 70, 73, 74]. However, phosphorus has a large activation energy of 0.5 eV and electron mobilities of doped films are low. Sulfur has been predicted to have an activation energy of 0.2 eV, and is currently being investigated [69].

Although applications that require thick high-quality polycrystalline or single crystal diamond films have been limited, there are a number of applications in areas that use thin polycrystalline films, such as ultraviolet photodetectors [11, 75, 76], pressure and acceleration sensors [77, 78], electrodes [79], surface-acoustic-wave (SAW) devices [71], field emitters [80], MEMS [81–85], probes for atomic force microscopy [86], and X-ray lithography masks [87]. In addition, research in CVD diamond growth has generated considerable interest in the growth of smooth hard films such

as diamondlike carbon, nanocrystalline diamond, and boron- and nitrogen-containing films [8, 46–50, 81]. Such films have low wear rates and frictional coefficients that have applications in MEMS and coatings for medical implants and hard disks.

2.2. Basic Properties of Diamond

Diamond crystallizes in the face-centered cubic (fcc) unit cell structure with a basis at each lattice site consisting of two carbon atoms at $(0,0,0)$ and $(1/4,1/4,1/4)$ [88]. There are eight atoms per unit cell. A schematic of the unit cell in three dimensions is shown in Figure 1. In the bulk, each atom is covalently bonded to four nearest neighbors, and the bonds form a regular tetrahedron centered about the atom. The tetrahedral bonding configuration is due to the directional nature of the covalent bonds and also occurs in Si and Ge. The side of the unit cell in diamond measures 3.56 \AA , making diamond the material with the highest atomic density. For comparison, the side of the unit cell in Si and Ge is 5.43 and 5.65 \AA , respectively. The high atomic density of diamond is responsible in part for its excellent frictional coefficient, thermal conductivity, hardness, and optical transparency.

The surface of a crystal often has an atomic structure that is different than that of the bulk. Figures 2–4 show schematics of the bulk-terminated diamond (100), (111), and (110) surfaces, respectively, in which atoms at the surface have the same atomic structure as atoms in the bulk. As shown in Figures 2–4, atoms at the surface are bonded to fewer than four atoms, resulting in dangling bonds. The atoms near the surface reposition themselves to form stable energy configurations. As a result, atoms from the top-most layer to a few atomic layers in the bulk participate in surface reconstructions. The reconstructions result in different atomic structures and electronic states from those of the bulk. Many solid-state phenomena such as etching, epitaxial growth, adsorption, oxidation, diffusion, and phase transformations take place near the surface and are determined by near-surface atomic configurations [17, 18]. Therefore, studying the surface of materials and understanding the nature of structures and reactions of surface atoms has been a primary aim of researchers around the world for

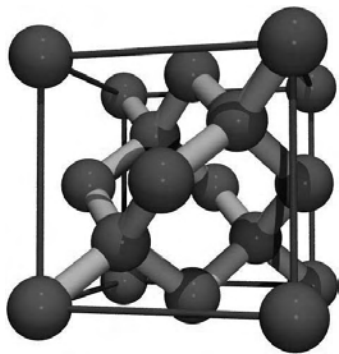


Figure 1. Schematic of the unit cell of the diamond lattice. Spheres are carbon atoms.

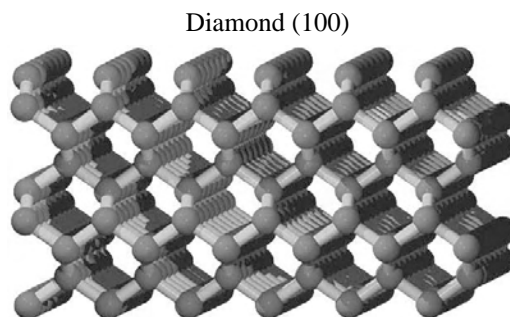


Figure 2. Schematic of the diamond (100) surface.

decades. Diamond surfaces are known to be hydrogen terminated after growth. Annealing at $1,000 \text{ }^\circ\text{C}$ in UHV removes the hydrogen termination and produces a clean surface. The reconstructions of diamond surfaces are described in detail in Section 5.

The properties listed in Table 1 are what make diamond such an attractive material for nanotechnology applications. Diamond is the hardest material known. It has a high carrier mobility, high dielectric breakdown field, and room-temperature thermal conductivity that is five times greater than that of copper. These properties make single crystal diamond an excellent semiconductor for high power and high speed applications [89]. Diamond has a wide bandgap of 5.45 eV , and is inert and tolerant to high energy radiation, which makes it ideal for applications in harsh environments such as high temperature, chemical, and space environments [77, 90].

Electronic applications of polycrystalline diamond films include ultraviolet photodetectors, high energy particle detectors, gas sensors, accelerometers, electrodes, SAW filters, and FE sources. Due to its wide bandgap of 5.45 eV , diamond absorbs radiation at wavelengths $<200 \text{ nm}$ and is insensitive to radiation at wavelengths $>230 \text{ nm}$. These properties have applications in solar blind ultraviolet detectors [11, 75, 76], such as those used in space missions. The wide bandgap, high carrier mobility, and high dielectric breakdown field of diamond has applications in high-energy particle detectors having low leakage noise and a large collection distance [91]. Diamond films have been utilized in hydrogen, oxygen, and carbonmonoxide gas sensors that operate at high temperatures and in harsh environments [77, 92, 93]. Such sensors consist of a catalytic film of Pd or

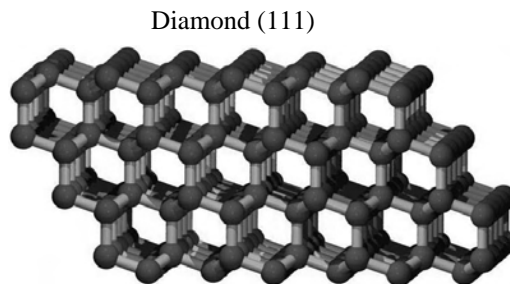


Figure 3. Schematic of the diamond (111) surface.

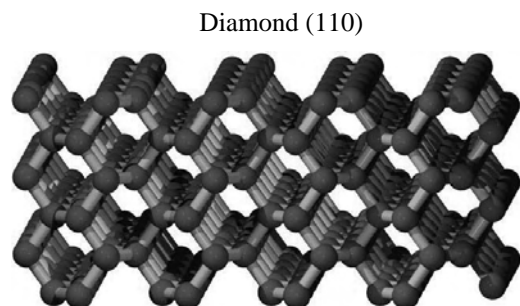


Figure 4. Schematic of the diamond (110) surface.

SnO_x that is deposited on an insulating diamond film that is grown on a boron-doped diamond film.

Boron-doped diamond films have an electrical resistance that varies with mechanical strain. This property, called piezoresistance, is due to the lifting of the degeneracy between light and heavy holes by strain. Piezoresistive diamond films have been utilized in pressure and acceleration sensors [77, 78]. Boron-doped diamond films also have excellent electrochemical properties such as stability and wide potential window [79]. These properties can be used in electrodes for biomedicine, harsh environments, and reactions involving high cathodic potentials. The high velocity of sound in diamond has applications in high-frequency SAW filters for cell phones [71]. In addition, CVD diamond films and diamond-coated microtips are being investigated for use as electron field emitters in flat panel displays, miniature X-ray sources, and other vacuum microelectronics applications [94–97]. These applications utilize the high FE current observed from diamond films. The high FE was initially

thought to be due to the negative electron affinity (NEA) of the hydrogen-terminated surface. It is now thought that other mechanisms play a role in FE such as defects, surface conductivity, and local field enhancement due to microstructures on the surface, back contact, or in the bulk [80, 94]; however, the exact mechanism is not known.

The surface properties of diamond are also unique and have many potential applications. Hydrogen-terminated diamond surfaces are inert and have *p*-type conductivity with a low activation energy of approximately 0.05 eV [74]. Oxygen-terminated surfaces are nonconducting. These properties can be used to fabricate field effect transistors. Clean diamond surfaces are highly reactive and can be functionalized with organic molecules for applications in chemical and biological sensors and molecular electronics [98–100]. Hydrogen-terminated diamond, nanocrystalline diamond, and diamond-like carbon films have low wear rates and frictional coefficients [38, 46–51, 81, 101–104]. Such films are currently being investigated as a material for MEMS and coatings for medical implants.

2.3. UHV STM of Diamond

CVD diamond films are typically grown from a mixture of a hydrocarbon gas, such as CH_4 , and H_2 that is broken by a hot-tungsten filament or microwaves into hydrocarbon radicals and atomic hydrogen [1–5]. The ratio of H_2 to hydrocarbon gas is about 1–2%. The mechanism for CVD diamond growth and the role of atomic hydrogen in this process are not well understood. Understanding the CVD diamond growth process at the atomic level is crucial in successfully growing films at high growth rates with reliable properties. A basic assumption concerning the CVD diamond growth

Table 1. Properties of diamond.

Property	Value	Units
Hardness	1.0×10^4	Kg/mm ²
Strength, tensile	>1.2	Gpa
Strength, compressive	>110	Gpa
Coefficient of friction (dynamic)	0.03	Dimensionless
Sound velocity	1.8×10^4	m/s
Density	3.52	g/cm ³
Young's modulus	1.22	Gpa
Poisson's ratio	0.2	Dimensionless
Thermal expansion coefficient	1.1×10^{-6}	K ⁻¹
Thermal conductivity	20.0	W/cm-k
Thermal shock parameter	3.0×10^8	W/m
Debye temperature	2,200	K
Optical index of refraction (@591nm)	2.41	Dimensionless
Optical transmissivity (from nm to far IR)	225	Dimensionless
Dielectric constant	5.7	Dimensionless
Dielectric strength	1.0×10^7	V/cm
Electron mobility	2,200	cm ² /V-s
Hole mobility	1,600	cm ² /V-s
Electron affinity	NEA	eV
Band gap	5.45	eV
Electron saturated velocity	2.7×10^7	cm/s
Hole saturated velocity	1.0×10^7	cm/s
Resistivity	10^{13} – 10^{16}	Ω -cm
Graphitization temperature (vacuum)	>1,700	°C

Source: Reprinted with permission from [3], K. E. Spear and J. P. Dismukes, Eds., "Synthetic Diamond: Emerging CVD Science and Technology." John Wiley & Sons, New York, 1994. © 1994 John Wiley & Sons.

process is that it involves the formation of carbon complexes on the growth surface. Atomic hydrogen is well known to etch graphitic forms of carbon and diamond. Also, the etch rate of diamond is much slower than that of graphite. Therefore, it is believed that the graphitic forms of carbon are removed during the CVD growth process, thus leaving the diamond by selective etching. In addition, atomic hydrogen is believed to play a role in the formation of sp^3 bonded carbon precursors on the growth surface.

By using UHV STM one can investigate the surface of a conducting material and resolve the atomic structure [105]. This technique has been instrumental in understanding the atomic surface structure and the etch and growth processes of other semiconducting materials such as Si and Ge [17–19]. Other techniques such as X-ray diffraction and ion channeling give information about the bulk properties of crystalline materials [106]. Although low-energy-electron-diffraction (LEED) and transmission electron microscopy are used extensively in materials analysis [107], neither give real spatial information about a sample surface. STM is unique in that it has the ability to give real spatial locations of atoms at the atomic scale, thus revealing vacancies, adatoms, adsorbates, and bond length.

Since the surface of a material is the location where deposition of other atoms and chemical reactions occur, it is important that the surface be the focus of study when one wants to understand in detail crystal etching, growth, and other processes. In the case of diamond, it is important to understand the role of atomic hydrogen and its reaction with the diamond surface during CVD diamond production. There is no better way to understand this and other processes than at the atomic scale where one can observe by UHV STM the results of a physical process or chemical reaction atom-by-atom.

UHV STM has many advantages over STM in air such as sample surface cleanliness, ability to prepare the surface, the possibility of the use of electrochemically etched tungsten tips that result in sharper images, and *in-situ* tip cleaning. Tunneling current versus voltage (I - V) spectroscopy using STM is also more reliable in UHV [18]. Originally, when diamond (100) was studied by STM it was done in air [25–33]. This was on the assumption that diamond is a relatively inert material and that the diamond (100) surface would be minimally contaminated by air. Also, air experiments limited the STM to PtIr or gold tips, as well as prevented reliable tip cleaning. Consequently, the air experiments were limited to the inert hydrogen-terminated diamond surface, and the image quality was poor and unreliable.

3. CVD GROWTH OF DIAMOND

3.1. Growth Techniques

The most widely used CVD techniques to grow diamond films are the hot-tungsten filament and microwave plasma techniques. Figure 5 shows a picture of a hot-tungsten filament reactor in which an epitaxial diamond film is being grown on a synthetic diamond (100) substrate. There are four main parameters for diamond growth: gas mixture,

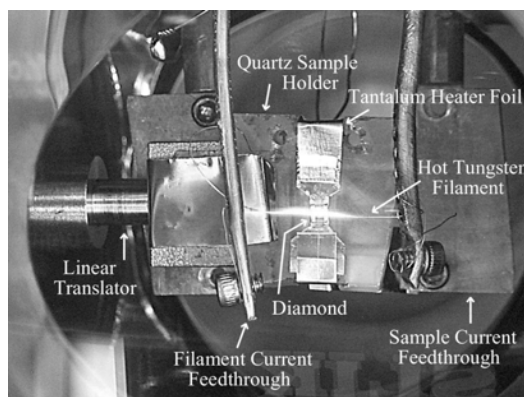


Figure 5. Picture inside a hot-filament CVD diamond growth system. The sample holder is on a linear translator for translation into a UHV STM system.

gas pressure, substrate temperature, and filament temperature. Typical growth conditions are H_2 and CH_4 flow rates of about 200 and 1 standard cubic centimeters per minute (scm), respectively, pressures of approximately 30–100 Torr, sample temperatures of 800–1000 °C, and a filament temperature of about 2,000 °C. To grow diamond on Si requires that the substrate be pretreated by scratching it with diamond powder or using bias enhanced nucleation techniques in which the substrate is negatively biased under a hydrocarbon plasma for about 20 minutes.

In order to produce high quality diamond via CVD, the vapor quality must be controlled. It is imperative that the ratio of the main constituent gasses (hydrogen, the catalyst, and methane, the carbon source) be closely monitored in order to produce a consistent crystal morphology. By varying the ratio, one can choose the dominant growth of low index faces in polycrystalline films. Typically, this is done by a combination of gas flow meters and metering valves. To increase the electrical conductivity of films at room temperature, doping with boron at high concentrations is carried out. For example, diborane (B_2H_6) gas is introduced during growth at concentrations on the order of 10 ppm relative to H_2 . The conductivity is due to impurity bands or hopping mechanisms [72].

Figure 6 shows an atomic force microscopy (AFM) image of a polycrystalline diamond film grown on a Si substrate for 12 hours using the hot-tungsten filament technique. The sample temperature was 900 °C and the CH_4/H_2 concentration was 1%. As shown in Figure 6, the film has crystallites with exposed square {100} and triangular {111} faces and oriented with the $\langle 110 \rangle$ direction normal to the substrate. Such a film is defined to have a {100}{111} $\langle 110 \rangle$ texture [108]. In Figure 6, the {111} faces are rough and micro-faceted, and the {100} faces are smooth.

3.2. Texture of Polycrystalline Diamond Films

The texture of polycrystalline diamond films can be understood using the primary bonded chain (PBC) [109, 110] and Van der Grift [111] models. The PBC model is used to explain differences in the growth velocities of crystallographic faces. The growth velocity of a crystallographic

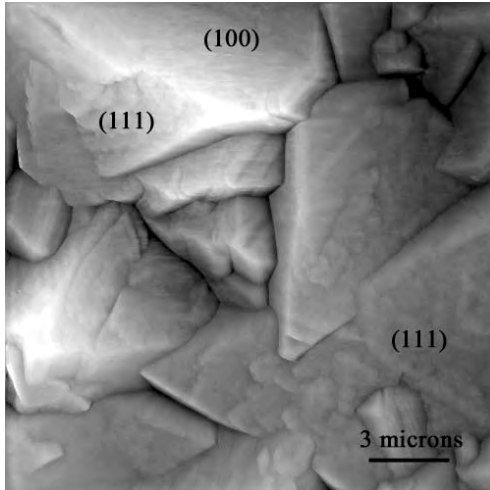


Figure 6. AFM image of a CVD grown polycrystalline diamond film showing $\{100\}$ and $\{111\}$ faces oriented in the $\langle 110 \rangle$ direction.

face is defined as the growth rate normal to the surface. A PBC consists of a linear chain of atoms that grows preferentially along the chain. The diamond lattice has only one PBC, which consists of a zig-zag linear chain of atoms in the $\langle 110 \rangle$ direction (see Fig. 4). The diamond $\{111\}$ faces contain three PBCs in nonparallel directions, the diamond $\{110\}$ and all faces in the $\langle 110 \rangle$ zone except the $\{111\}$ faces contain one PBC, and the diamond $\{400\}$ and all other faces contain no PBCs [110, 112]. Therefore, $\{111\}$ faces have slow growth velocities, and $\{110\}$ and $\{100\}$ faces have significantly faster growth velocities. Faces with fast growth velocities grow themselves out to a point or edge and, consequently, are not observed in crystallites. As a result, diamond crystallites should have an octahedral shape with $\{111\}$ faces. Most natural diamond crystals are observed to have this shape [112]. However, CVD grown diamond crystallites are observed to have shapes that range from cubic to cubo-octahedral to octahedral depending on growth conditions. The range of shapes that occurs during CVD growth shows that the growth velocity of $\{100\}$ faces is comparable to that of $\{111\}$ faces. This is thought to occur as a result of the introduction of additional PCBs on the (100) surface by a hydrogen-terminated 2×1 reconstruction or an adsorbate layer [112].

Figure 7 shows the shape of diamond crystallites as a function of the ratio of growth velocities of $\{100\}$ and $\{111\}$ faces. In Figure 7, the growth parameter $\alpha = \sqrt{3}V_{100}/V_{111}$, where V_{100} and V_{111} are the $\{100\}$ and $\{111\}$ growth velocities, respectively. At $\alpha = 1$, crystallites are cubic with $\{100\}$ faces and corners in the $\langle 111 \rangle$ direction; at $\alpha = 1.5$, they are cubo-octahedral with square $\{100\}$ and triangular $\{111\}$ faces and corners in the $\langle 110 \rangle$ direction; and, at $\alpha = 3$, they are octahedral with $\{111\}$ faces and corners in the $\langle 100 \rangle$ direction. By varying CVD growth conditions, this range of shapes can be observed. The value of α for a growth experiment is difficult to predict because it depends on various conditions such as sample temperature, CH_4/H_2 concentration, and reactor geometry. The value of α can be determined after growth by measuring the dimensions of isolated

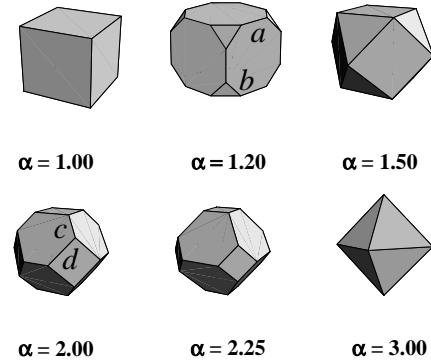


Figure 7. Shape of diamond crystallites as a function of α that is proportional to the ratio of growth velocities of $\{100\}$ and $\{111\}$ faces.

crystallites and using the equations,

$$\alpha = \frac{a + \sqrt{2}b}{a + 2/3\sqrt{2}b} \quad \text{for } 1 \leq \alpha \leq 1.5$$

$$\alpha = 3 \frac{c + d}{c + 2d} \quad \text{for } 1.5 \leq \alpha \leq 3$$

where a , b , c , and d are as shown in Figure 7. It is generally observed that α decreases as the substrate temperature increases and the CH_4 concentration decreases [9, 112].

The Van der Grift model [111] provides an explanation for the development of texture in polycrystalline films in terms of evolutionary competition between crystallites that have nucleated on the substrate. This model assumes that crystallites nucleate on the substrate with random orientations. During growth, crystallites oriented such that the fastest growth direction is normal to the substrate will overgrow all other crystallites. Crystallites oriented with their fastest growth direction normal to the substrate will have specific faces that are exposed on the surface, such as shown in Figure 7. Eventually, such crystallites cover the surface of the film resulting in a specific texture. As a result of this process, the film also has a columnar cross-sectional structure.

The Van der Grift model describes polycrystalline film growth for conditions that are consistent with the model's assumptions that diffusion does not affect crystallite shape and new phases and orientations do not form during growth. These assumptions are met for a range of CVD diamond growth conditions, allowing texture to be controlled by varying growth conditions [9, 108]. However, at high CH_4 concentrations and high temperatures, nondiamond carbon phases develop. In addition, twinning easily occurs on $\{111\}$ faces, and penetration twins occur on $\{100\}$ and $\{111\}$ faces. These processes have a significant effect on the morphology and growth rate of polycrystalline diamond films [113, 114]. For example, at low temperatures, twinning on $\{111\}$ faces frequently occurs and films develop a $\{111\}\langle 110 \rangle$ texture independent of methane concentration [9].

For a given α , multiply twinned diamond crystallites form with untwinned crystallites. Untwinned crystallites have shapes shown in Figure 7. Figure 8a and b show scanning electron microscopy (SEM) images of multiply twinned

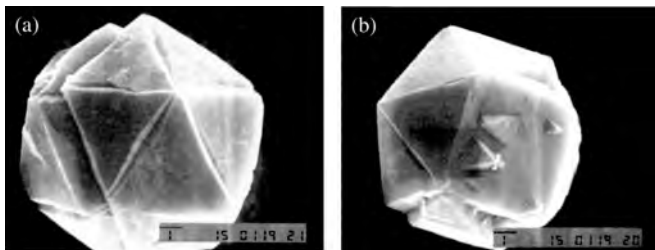


Figure 8. SEM image of multiply twinned diamond crystallites. (a) Icosahedra with 20 $\{111\}$ faces. (b) Decahedra with ten $\{111\}$ and 5 $\{100\}$ faces. Bar denotes 1 μm .

diamond crystallites that have icosahedral and decahedral shapes, respectively. The icosahedra has twenty $\{111\}$ faces, and the decahedra has ten triangular $\{111\}$ faces and five square $\{100\}$ faces. These shapes are due to the formation of five $\Sigma = 3$ twins [114]. Depending on α , multiply twinned crystallites show reentrant grooves between $\{111\}$ and $\{100\}$ faces [115], as observed in Figure 8. Reentrant grooves between $\{111\}$ faces have enhanced growth and greatly increase the growth rate of $\{111\}$ faceted crystals [116].

Polycrystalline diamond films having a specific texture are grown by varying growth conditions such as sample temperature and CH_4/H_2 concentration. For example, by setting growth conditions such that $1.56 < \alpha < 1.73$, diamond films with a $\{100\}\{111\}\langle 110 \rangle$ texture were grown [108]. By increasing α to slightly greater than 1.73, films with $\{100\}$ faces in a near $\langle 100 \rangle$ direction were grown [108]. By increasing α further, films with a $\{100\}\{111\}\langle 100 \rangle$ texture were grown [108]. With α increased to about 2.60, films with a $\{111\}\langle 100 \rangle$ texture were grown [108].

4. SCANNING TUNNELING MICROSCOPY

4.1. Principle of Operation

The experimental techniques used to characterize surfaces are often based on different physical phenomena. Prior to the invention of STM, the atomic structure of surfaces was characterized using LEED and other techniques that gave indirect and incomplete information. Not until STM [105] and other scanning probe techniques were invented was a detailed understanding of the atomic structure of surfaces possible.

The basic principle of STM is quantum mechanical tunneling of electrons between a conducting tip and sample. Quantum tunneling is the transmission of electrons through a potential barrier higher than the energy of the electrons. Tunneling can be observed when a tip under bias is positioned above a sample at a distance of approximately 10 \AA . The direction that the electrons flow, tunneling into unoccupied states or from occupied states on the surface, is controlled by the polarity of the tip. The tunneling current at small bias is described by the following equation [18]

$$I \propto (V/s) \exp(-A\phi^{1/2}s)$$

where $A = (2m/h^2)^{1/2} = 1.025/(\text{eV}\text{\AA})$, I is the tunneling current, V is the bias voltage applied between the tip and

sample, ϕ is the local barrier height, s is the tip-to-sample distance, and m is the mass of the free electron. This equation shows that I decreases exponentially as s increases. Assuming a barrier height of about 4 eV, I decreases by about an order of magnitude for every 1 \AA increase in s . The order of magnitude change in I with changes in s on the order of 1 \AA is responsible for atomic resolution in STM.

To obtain an image using STM requires positioning the tip into tunneling range and scanning the tip above the surface with atomic resolution. This requires highly precise control of tip positioning and isolation of the STM system from external vibrations. In the early years of STM, achieving atomic resolution was hindered by these difficulties. When G. Binnig et al. [105] published the first STM image of the Si (111) 7×7 surface reconstruction in 1983, the results were not widely accepted because only a few groups were able to reproduce them [117–119].

Tip positioning is accomplished using a piezoelectric material that changes length under the application of a voltage. Piezoelectric scanners can be designed to have a resolution less than 1 \AA in the x - and y -directions and 0.05 \AA in the z -direction, and movement that is approximately independent along each axis and linearly proportional to the applied voltage. A common design is the tube scanner [120], which consists of a hollow piezoelectric tube, as shown in Figure 9. The tube scanner has a scanning range on the order of microns that is determined by the diameter and length of the tube, and is compact and rigid for vibration isolation. The inner surface of the tube is coated with a single silver electrode, and the outer surface is coated with four electrodes arranged in opposing pairs, as shown in Figure 9. To perform x - and y -motion, voltages are applied to the appropriate electrodes to bend the tube. To perform z -motion, the same voltage is added to all four electrodes. Figure 10 shows a schematic of a commercial STM head consisting of a tube scanner mounted in an inchworm motor [121]. The inchworm motor moves the tube scanner over a distance of several millimeters with a step size on the order of a micron. As shown in Figure 10, the motor is composed of piezoelectric actuators that move the inchworm by using a controlled sequence in which clamps 1 and 3 are activated and deactivated, and segment 2 is contracted and extended [121]. The inchworm motor and tube scanner move the tip from a distance of millimeters from the sample to within tunneling range. The STM head is mounted on a base plate

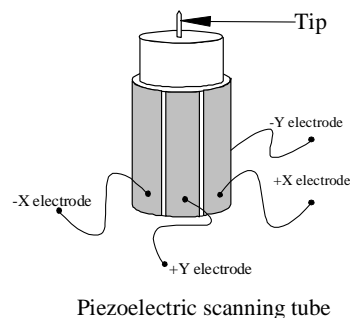


Figure 9. Schematic of a piezoelectric tube scanner with an STM tip attached.

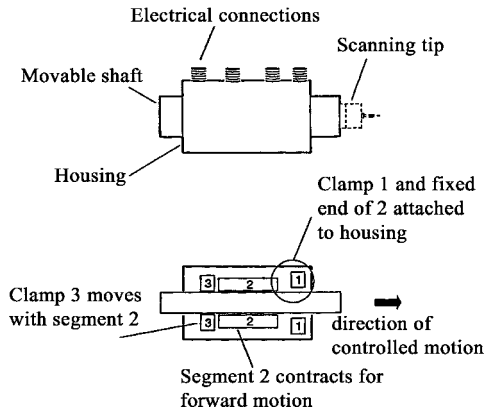


Figure 10. Schematic of a tube scanner as the movable shaft of an inchworm motor. The bottom schematic shows the locations of piezoelectric clamps that are used to move the shaft. Reprinted with permission from [121], ARIS 6000 Instruction Manual, Burleigh Instruments, 1994. © 1994, Burleigh Instruments.

that is isolated from vibrations by springs. For UHV applications, the STM head is mounted on a UHV flange, as shown in Figure 11. Other piezoelectric devices for moving the tip and scanner to within tunneling distance are inertial sliders that use the stick-slip principle [18].

After the tip is positioned within tunneling distance, a digital or analog feedback loop is used to maintain a constant tip-to-sample distance to keep the tip from crashing into the surface. As shown in Figure 12, the tunneling current is converted to a voltage using a current-to-voltage converter. The voltage is compared with a reference value that is set by the user. The feedback loop minimizes the difference between the measured and reference voltages by adjusting the *z*-position of the tip. Digital feedback loops have the

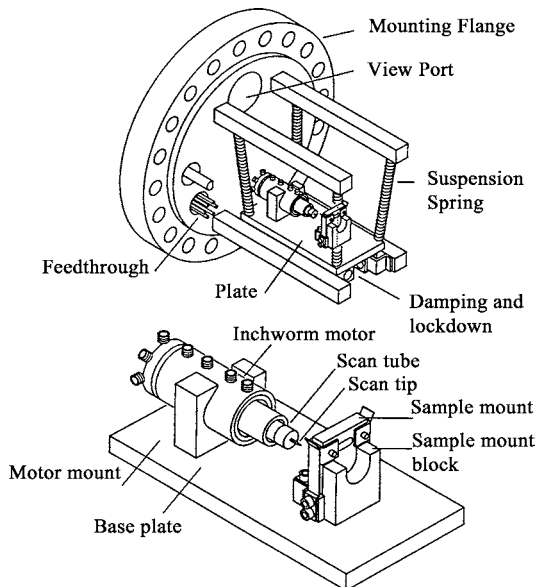


Figure 11. Schematic of an STM head mounted on a flange for UHV operation. Reprinted with permission from [121], ARIS 6000 Instruction Manual, Burleigh Instruments, 1994. © 1994, Burleigh Instruments.

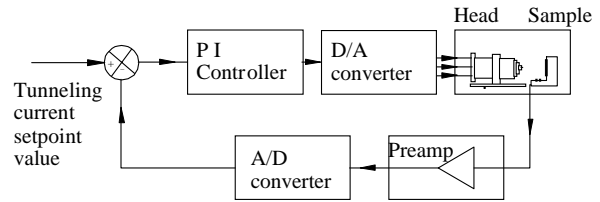


Figure 12. Block diagram of a digital feedback loop of an STM system.

advantages that they are assembled using standard boards and are flexible. In a digital feedback loop, the difference voltage is sent to a conventional proportional and integral controller, as shown in Figure 12. The integral gain controls the speed of the feedback response. If the integral gain is set too low, feedback operation is slow and the tip will crash. If it is set too high, the tip will oscillate. Proportional gain controls how far the tip is advanced for a given difference value.

To obtain an STM image, the tip is moved across the surface by modulating the scanner in the *x*- and *y*-direction, as depicted in Figure 13. Typical tunneling currents are between 0.1 and 1.0 nA with a bias on the order of a volt. Depending on which mode of operation the STM system is in, the feedback is either on or off. With the feedback

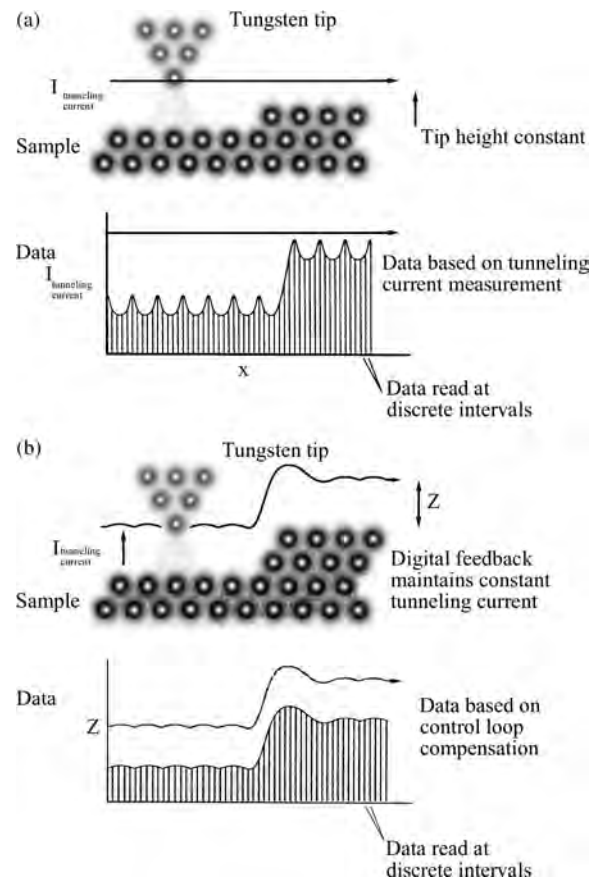


Figure 13. Schematic illustration of the two modes of STM operation. (a) Constant height with feedback off. (b) Constant current with feedback on. Reprinted with permission from [121], ARIS 6000 Instruction Manual, Burleigh Instruments, 1994. © 1994, Burleigh Instruments.

off, the tunneling current between the sample and tip is recorded as the tip is scanned in the x - and y -directions. With the feedback on, the tunneling current is held constant by maintaining a constant tip-to-sample separation by also modulating the z -direction as the tip is scanned in the x - and y -directions. This second mode of operation, called topographic, is the most common and produces a three-dimensional image of the surface.

In addition to imaging, STM can be used to measure the local surface density of states and barrier height with atomic resolution. These techniques involve measuring at a specific atomic location I as a function of V at fixed s , and I as a function of s at fixed V [18]. These techniques are referred to as I - V and I - Z spectroscopy, respectively.

4.2. Preparation of the STM Tip

The tip is one of the most critical parts of an STM system. The shape and material of the tip influences imaging and spectroscopic measurements. Multiple tips can result in superimposed images. The best images are obtained when a single sharp tip scans over a flat surface. The most widely used tip materials are platinum-iridium (Pt-Ir) and tungsten (W). Pt-Ir tips are stable in air and can be easily prepared by cutting a Pt-Ir wire using a wire cutter. They can also be electrochemically etched in a molten CaCl solution. W tips form a thin oxide layer in air, and can only be used in UHV after the oxide layer has been removed by heating. The advantages of W tips are that they can be made ultrasharp by using electrochemical etching techniques [122] and can be cleaned in UHV resulting in reliable imaging and spectroscopic measurements.

Ultrasharp W tips have been reported to produce clear large-area atomic resolution STM imaging of clean boron-doped epitaxial diamond (100) films [21]. Figure 14a is an SEM image of an ultrasharp STM tip. The tip was made by electrochemically etching a 0.020 inch diameter tungsten wire in a 1 molar solution of NaOH [24]. Figure 14b shows a schematic for electrochemically etching ultrasharp tungsten tips. The drop technique [123] shown in Figure 14b is employed because it gives the best tip geometry. Also, the drop section of the tungsten wire provides an event that can be electronically detected and used to signal that the etch process has completed. The electronic control box provides the bias voltage and the circuitry to detect the drop and terminate the etching process by opening the electrical circuit. It is important that the voltage be controlled electronically because a manually operated switch cannot be opened quickly enough in order to obtain an ultrasharp tip. It is also possible to shut off the bias voltage too soon. If that occurs then the tip will have a stretched and curved tail, as shown in Figure 15a. The curvature is probably due to recoil of the tip as the drop section falls and no longer supplies tension to the submicron tip. A small delay after the drop section has fallen, on the order of a few microseconds, is necessary to etch away the tail portion. If the shut off delay is too long, the tip sharpness rapidly decreases. Figure 15b shows the sharpest tip that typically can be obtained using a manual cutoff.

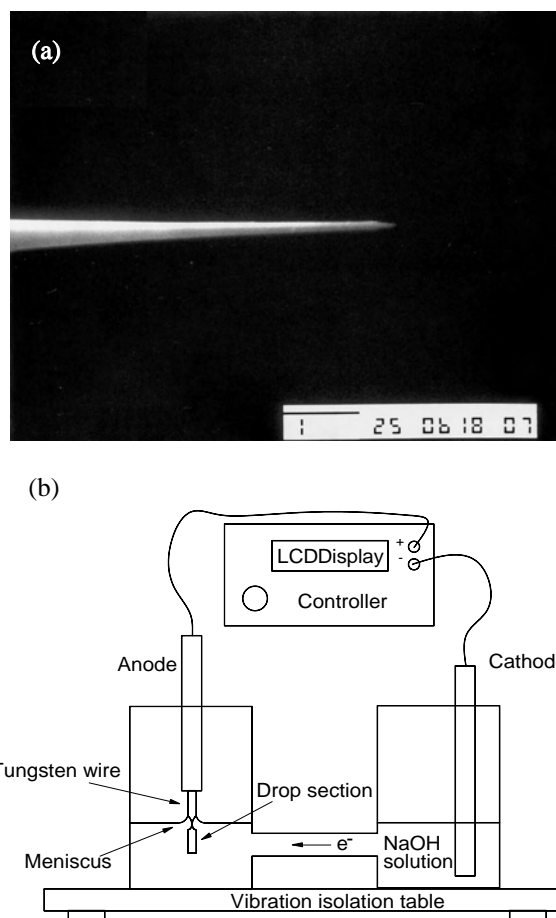


Figure 14. (a) SEM image of an ultrasharp STM tungsten tip. (b) Block diagram of the electronic shut-off system used to etch the tip in (a). Bar denotes 1 μm .

5. ATOMIC STRUCTURE OF DIAMOND SURFACES

5.1. Diamond (100) Surface

5.1.1. Air and UHV STM Results

STM imaging of diamond film is possible by increasing the conductivity of the surface by doping the film with boron or terminating the surface with hydrogen. The first reports of STM imaging of diamond were carried out in air using a Pt-Ir tip. Turner et al. [25] reported STM imaging of boron-doped polycrystalline diamond films with nanometer resolution. Everson and Tamor [26] imaged boron-doped polycrystalline diamond films with near-atomic resolution.

The first atomic resolution imaging of diamond was reported by Tsuno et al. [27] who imaged epitaxial diamond (100) films in air using a Pt-Ir tip. The epitaxial films were grown on high pressure/high temperature (HPHT) grown synthetic diamond (100) substrates using the microwave plasma technique. A $2 \times 1/1 \times 2$ dimer reconstruction was observed with anisotropic extension of dimer rows. The 2×1 reconstruction after growth is known to be monohydride terminated [34], and is denoted as diamond (100)- 2×1 :H. Figure 16 shows an air STM image of the diamond

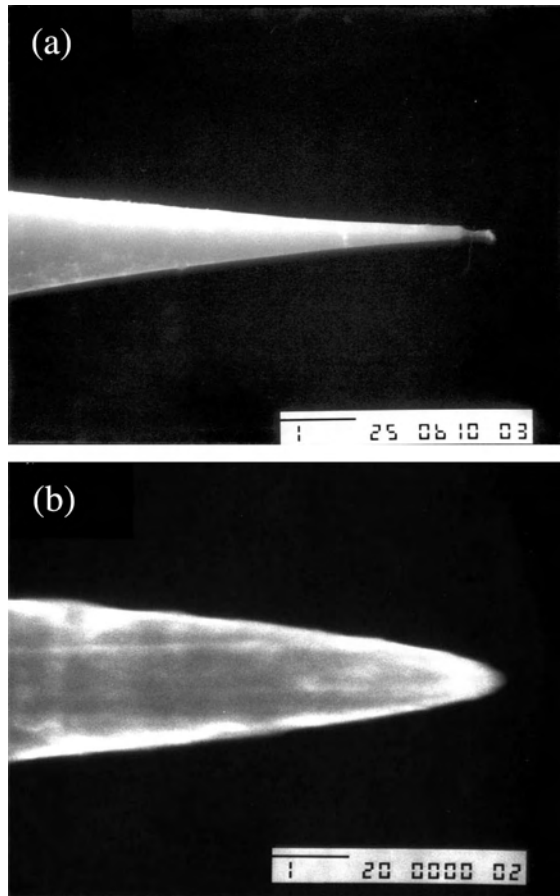


Figure 15. (a) SEM image of a tungsten tip made with an electronic system that was shut off too soon showing a curved end. (b) SEM image of the sharpest tungsten tip that can typically be made using a manual shut-off. Bar denotes 1 μm .

(100)- 2×1 :H surface from [30]. The surface consists of atomic planes with dimer rows rotated in the xy -plane 90° relative to the dimer rows in the upper or lower atomic planes. Each carbon atom in a dimer is attached to one hydrogen atom. In Figure 16, there are two different types

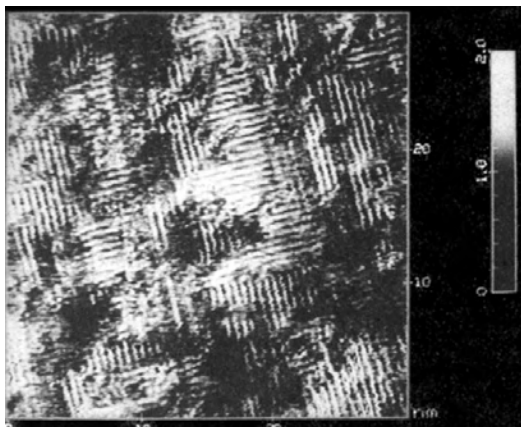


Figure 16. Atomic resolution air STM image of the diamond (100)- 2×1 :H surface. Reprinted with permission from [30], Th. Frauenheim et al., *Phys. Rev. B* 48, 18189 (1993). © 1993, American Physical Society.

of steps, denoted S_A and S_B . S_A and S_B steps are single atomic layer steps that have dimer rows parallel and perpendicular to the step edge, respectively. D_A and D_B steps are double atomic layer steps that have dimer rows parallel and perpendicular to the step edge, respectively. Figures 17a–c show schematic representations of the hydrogen-terminated diamond (100)- 1×1 , 2×1 , and 3×1 reconstructions, respectively.

Tsuno et al. [31] also used air STM to study epitaxial diamond (100) films grown on synthetic diamond substrates that were misoriented 4.3° from $\langle 001 \rangle$ towards $\langle 110 \rangle \pm 3^\circ$. The films were grown using the microwave plasma technique at CH_4 to H_2 concentrations from 2–6%. The films were not annealed in a hydrogen plasma after growth. At a methane concentration of 2%, a single domain 2×1 surface was observed consisting of D_A steps. The formation of D_A steps was attributed to a step flow growth mode in which dimer rows preferentially grow in the direction of the dimer rows. At a methane concentration of 6%, $2 \times 1/1 \times 2$ domains were observed using LEED indicating the formation of two-dimensional islands.

Kuang et al. [32] used air STM to study boron-doped epitaxial diamond (100) films that were grown on natural diamond substrates using the microwave plasma technique. After growth, the films were annealed in a hydrogen plasma for 10 minutes at 875°C . Observed were D_B steps, local hydrogen-terminated 3×1 reconstructions, antiphase boundaries, and dimer vacancies. The D_B steps were thought to be nonbonded. As shown schematically in Figure 17c, the hydrogen-terminated diamond (100)- 3×1 reconstruction, denoted as diamond (100)- 3×1 :1.3H, consists of alternating rows of dihydride and monohydride terminated subunits. It was thought that the diamond (100)- 3×1 :1.3H reconstruction exists only locally due to strong steric repulsion between hydrogen atoms [32]. In contrast, the Si (100)- 3×1 :1.3H reconstruction is observed over large areas using STM [19].

Polycrystalline diamond films have also been used to study the diamond (100) surface with atomic resolution. Busmann et al. [28] imaged polycrystalline diamond films with nanometer resolution using a mechanically prepared Pt-Ir tip. Observed were disordered structures of clusters 5–30 nm in size. Zimmermann-Edling et al. [29] studied polycrystalline diamond films at the micron and atomic scale, and observed a diamond (100)-(2×1):H reconstruction on the $\{100\}$ faces of crystallites. In the above experiments, the films were not intentionally doped and the

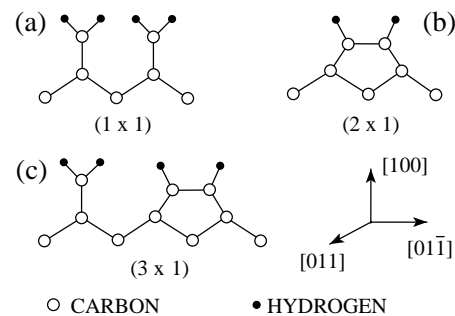


Figure 17. Schematics of the hydrogen-terminated diamond (100) surface. (a) 1×1 :2H. (b) 2×1 :1H. (c) 3×1 :1.3H.

conductivity was due to hydrogen-termination or amorphous carbon regions. Busmann et al. [33] carried out a detailed investigation of the atomic structure of $\{100\}$ faces of polycrystalline films as a function of morphology and texture. The morphology and texture was varied by changing only the substrate temperature during growth. At $\alpha = 2.8$, a rough surface was observed that could not be imaged with atomic resolution. At $\alpha = 1.5$, a diamond (100)- 2×1 :H reconstruction with islands was observed. At $\alpha = 1.3$, a diamond (100)- 2×1 :H reconstruction was observed with a clear atomic step structure in which S_B steps were broader than S_A steps. This was attributed to a step-flow growth mode in which dimer rows grow in the direction of the rows. At $\alpha = 1.2$, a 2×1 reconstruction was observed with strongly asymmetric islands that was attributed to a nonhydrogen terminated diamond (100)- 2×1 reconstruction.

Using LEED, Marsh and Farnsworth [124] and Lurie and Wilson [125] showed that polished diamond (100) substrates display a 1×1 pattern. The diamond (100)- 1×1 :2H reconstruction is shown schematically in Figure 17a. Since this surface is not observed using STM, it is believed that the 1×1 LEED pattern is due to a rough surface consisting of a distribution of dihydride and monohydride units [34]. Annealing of polished substrates in UHV at temperatures >1000 °C results in a 2×1 LEED pattern [125] that is due to the clean diamond (100)- 2×1 surface. This surface is described in detail in the next section. Exposure of the clean diamond (100)- 2×1 surface to atomic hydrogen results in a 2×1 LEED pattern that is due to the diamond (100)- 2×1 :H surface [34]. Theoretical studies show that the most stable configuration for the clean and hydrogen-terminated diamond (100) surfaces is the 2×1 reconstruction with symmetric dimers [34]. For clean and hydrogen-terminated diamond (100)- 2×1 surfaces, theoretical studies predict that single and double layer steps are nonbonded [126].

Air STM has also been used to image natural and synthetic diamond (100) substrates. In these studies, the conductivity was due to boron doping. Couto et al. [127] studied the morphology of HPHT grown type IIb diamond (100) substrates after polishing along easy and difficult directions. Different polishing mechanisms were observed. Nutzenadel et al. [128] studied natural doped diamond (100) substrates that were etched in a hydrogen plasma, and observed a diamond (100)- 2×1 :H reconstruction and large atomically flat terraces.

UHV STM is required to study clean diamond surfaces because such surfaces are highly reactive. In UHV, the surface can be prepared in a controlled manner making possible detailed studies of adsorbates, diffusion, etching, and growth. Tsuno et al. [20] used UHV STM to study clean boron-doped epitaxial diamond (100) films and observed a diamond (100)- 2×1 reconstruction. Stallcup et al. [22, 23] used UHV STM to study hydrogen-terminated epitaxial diamond (100) films after growth. The surfaces of the films were observed to be amorphous at the atomic scale. After 5 minutes of exposure to atomic hydrogen, the surfaces were observed to consist mostly of 2×1 :H regions. Stallcup and Perez [21] also used UHV STM to study anisotropic etching of boron-doped epitaxial diamond (100) films by atomic hydrogen, as described in detail in the next section. Recently,

Bobrov et al. [129] used UHV STM to image clean insulating natural diamond (100) substrates with atomic resolution using resonant electron injection into the conduction band. In these experiments, the tip-to-sample bias was approximately 5.4 V, corresponding to an energy higher than the work function of diamond of 5.3 eV. At such a high bias, the STM operates in the near-field emission regime that typically has a resolution on the order of 3 nm. In the case of diamond, it was thought that atomic resolution is possible due to the large dz/dV slope at resonance. It was thought that the sample conducted the tunneling current due to the long diffusion lengths in diamond of 150–250 μm .

5.1.2. Anisotropic Etching

The diamond (100) surface is of particular interest because epitaxial diamond (100) films grow smooth at substrate temperatures of approximately 1000 °C, unlike epitaxial diamond (111) and (110) films that grow rough [2]. The growth of smooth diamond (100) films is not well understood. Surface diffusion of adsorbates, which is responsible for the growth of most smooth films, is not widely accepted as responsible for the growth of smooth diamond (100) films because the hydrogen-terminated surface prevents diffusion [129]. Diffusion on the diamond (100) surface during growth has been modeled as occurring along surface sites where hydrogen has been removed by abstraction [131]. However, recent theoretical models have shown that the addition of surface diffusion to models would lead to higher growth rates than are experimentally observed [132]. Other mechanisms that have been proposed to explain the growth of smooth diamond (100) films are anisotropic etching [133] and preferential etching of undercoordinated atoms [132]. Using UHV STM, Stallcup and Perez [20] found that etching by atomic hydrogen is highly temperature dependent resulting in a rough and pitted surface at $T \approx 200$ °C and $T \approx 500$ °C, respectively. At $T \approx 1000$ °C, etching results in a smooth surface and is highly anisotropic occurring predominantly in the direction of dimer rows. This observation supports recent theoretical models that propose anisotropic etching as the mechanism for the growth of smooth diamond (100) films.

Previous STM results on the hydrogen-terminated diamond (100)- 2×1 :H surface [22, 23] were limited to small area scans due to tunneling instabilities resulting from physisorbed hydrogen and carbon on the sample surface. Imaging such a surface with loosely bound atoms was problematic and short-lived but necessary in order to study the CVD diamond growth process. Scanning tips did not last long because of contamination from the surface to the tip. During instances of tunneling current instabilities caused by this contamination, “tip crashes” would occur and often this resulted in rendering the tip useless. In this case, a “tip crash” is when the STM feedback overcorrects or undercorrects as a result of the current instabilities and the tip comes into hard contact with the sample surface, usually deforming the tip.

The results in [21] are without these problems because of three factors. The first important factor is that the samples were etched by atomic hydrogen after growth for at least five minutes, thereby removing the excess and

loosely bound carbon from the surface. The second factor is that desorbing the loosely bound hydrogen from the surface by heating the substrate to 800 °C for one minute resulted in improvement of the tunneling current stability, which produced clearer STM images. Further heating to 1000 °C removed the hydrogen-terminated surface and further enhanced the STM image quality. These techniques for cleaning the diamond surface can only be performed in UHV. The third and very important factor was the use of ultrasharp tungsten tips that were described in Section 3. These factors make possible atomic resolution STM imaging over large areas measuring $80 \times 80 \text{ nm}^2$. From images of large areas, both the atomic structure and large-scale morphology of the surface resulting from etching, growth, and other processes can be studied.

The CVD diamond films were grown epitaxially on $2 \text{ mm} \times 2 \text{ mm} \times 0.25 \text{ mm}$ type 2b (100) diamond substrates. The films were grown for two hours in a UHV compatible hot tungsten filament CVD reactor and were approximately 2 microns thick. The films were doped with boron during growth to increase their conductivity for STM studies. Without the incorporation of boron, the diamond surface would have become highly insulating when the hydrogen was desorbed by heating in UHV. The CVD growth pressure was 30 Torr with the hydrogen, methane, and diborane gases having flow rates of 200 sccm, 0.5 sccm, and 6.0 sccm, respectively. The substrates were resistively heated to 900 °C using a tantalum heater foil. The tungsten filament temperature was that typically used for CVD diamond growth of 2200 °C. The growth process was terminated by shutting off the methane flow and maintaining all of the other parameters for 5 minutes. This step was a post-growth etch with atomic hydrogen. The filament was then turned off followed by the sample heater and then the hydrogen flow being turned off. After the growth process was terminated, the CVD reactor was evacuated to 1×10^{-8} Torr and the samples were transferred to the UHV STM chamber via a linear translator without exposure to air.

After verifying by STM that the diamond films were of good quality, the samples were returned to the CVD reactor, via the linear translator, for additional exposure to atomic hydrogen. The hydrogen flow rate, pressure, and filament temperature were 200 sccm, 30 Torr, and 2200 °C, respectively. These parameters were the same as those for the CVD diamond growth to ensure that the diamond surface was exposed to the same amount of atomic hydrogen flux as during growth. From this point on, two different groups of experiments were done. In Group A, the sample temperature was a constant of 500 °C and the atomic hydrogen exposure times were 2, 7, 12, and 17 minutes. After each additional exposure, the sample was translated to the UHV STM and analyzed to determine if additional etching had an effect on the surface morphology. In the group B experiments, the exposure time was held constant, 5 minutes, with the substrate temperature being the variable and having the values of 200 °C, 500 °C, and 1000 °C. Each diamond sample was then returned to the UHV STM to determine whether the atomic surface structure had changed as a result of the atomic hydrogen etching at the different temperatures. Tunneling currents of 1 nA with a sample bias of -1 to -1.5 V were used.

Figure 18 shows a UHV STM image of a CVD grown boron doped epitaxial diamond (100) film after exposure to atomic hydrogen for 5 minutes at a sample temperature of 500 °C. As previously discussed, the diamond (100)- 2×1 surface exposed to atomic hydrogen is known to be monohydride terminated. In Figure 18, unmarked arrows indicate regions where S_A steps are etched perpendicular to the rows resulting in islands marked I. The islands are believed to be due to etching and not the growth process because the islands were not observed until the 500 °C etching. The islands have a 3×1 reconstruction consisting of a wide monohydride-terminated row and a narrow dihydride-terminated row, as indicated in Figure 18. The 3×1 reconstruction on diamond (100) has been previously observed along step edges [32]. There are many antiphase boundaries in Figure 18 marked Φ , and these boundaries are necessary in order for a terrace to accommodate both 2×1 and 3×1 reconstructions.

Figure 19 shows a UHV STM image of an epitaxial diamond (100) film after exposure to atomic hydrogen for 10 min at 500 °C. A square etch pit several atomic layers deep and containing a bright circular structure having a diameter of approximately 2.5 nm is observed. Other regions of the film showed similar etch pits with bright structures. The bright structures are conjectured to be etch byproducts or groups of hydrogen atoms because the structures disappear after the sample is heated to 1000 °C, as shown in Figure 20a and b. It is well known that hydrogen can be stored in carbon nanotubes and nanostructured carbon materials. Similar sized bright structures have been observed in etched Si and attributed to etch byproducts [19]. The pit in Figure 19 is pyramidal in shape and has $\{111\}$ faces. This shows that, at 500 °C, the etch rate in the $\{111\}$ direction is slower than that in the $\{100\}$ and $\{110\}$ directions.

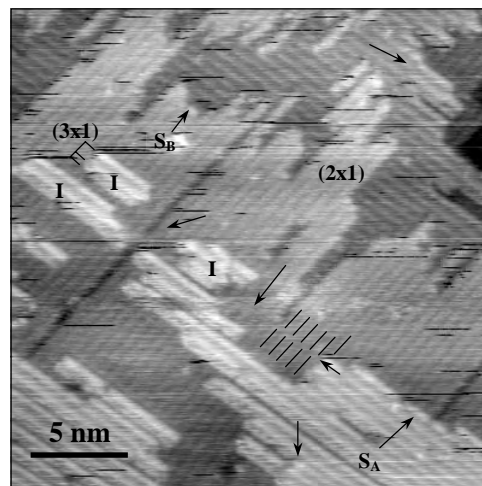


Figure 18. Atomic resolution UHV STM image of the diamond (100)- 2×1 :H surface after etching by atomic hydrogen for 5 min at 500 °C obtained using an ultrasharp tungsten tip. Observed are 2×1 and local 3×1 reconstructions, islands marked I, and dimer phase shifts marked Φ . Both S_A and S_B steps are rough. Reprinted with permission from [21], R. E. Stallcup and J. M. Perez, *Phys. Rev. Lett.* 86, 3368 (2001). © 2001, American Physical Society.

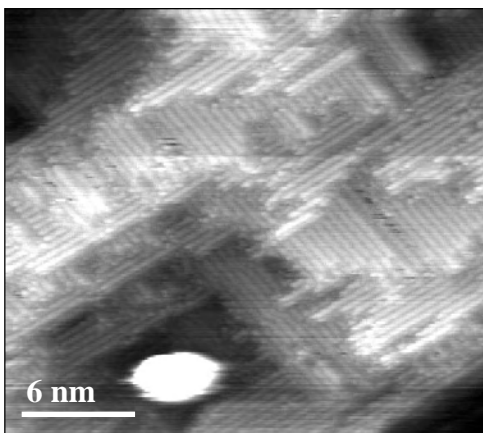


Figure 19. UHV STM image of the diamond (100)- 2×1 :H surface after exposure to atomic hydrogen for 10 min at 500 °C showing an etch pit containing a bright circular structure. Reprinted with permission from [21], R. E. Stallcup and J. M. Perez, *Phys. Rev. Lett.* 86, 3368 (2001). © 2001, American Physical Society.

In order to further explore pit formation and how pits evolve, the previously mentioned Group A experiments were done. Figure 20a and b show the results of the 500 °C time exposure experiments of Group A. These results show

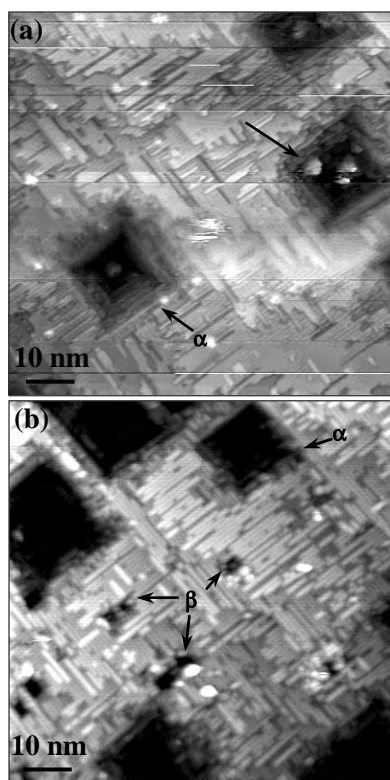


Figure 20. UHV STM image of a CVD epitaxial diamond (100) film after sequential exposures to atomic hydrogen at 500 °C showing the evolution of pits. (a) After a total of 7 min of exposure. (b) After exposure to 0.001 Torr of oxygen for 1 min and an additional 5 min atomic hydrogen etch for a total of 12 min. The unmarked arrows indicate hydrogen that has aggregated in the etch pits. α indicates the original nucleated etch pits, and β indicates the new etch pits that were nucleated by the oxygen.

that the pit nucleation density does not significantly change with added exposure to atomic hydrogen. But, with increasing exposure time, the pits increase in area and depth, which is what one might expect with additional surface etching. Although the pits are becoming larger with additional atomic hydrogen exposure, the pits on each new surface are about the same size relative to each other. The small variation in pit size indicates that over time no new pits are being nucleated. The arrows marked α in Figure 20a and b are indicating the original pits. Only until exposure to oxygen and then further etching with atomic hydrogen are new pits nucleated, as indicated in Figure 20b by the arrows marked β . It is unknown what the cause of nucleation is for the first group of pits, but it is hypothesized that they are the result of lattice dislocations. It is well known that etch pits on crystal surfaces are nucleated on lattice dislocations [88]. Figure 20a and b show the dramatic improvement in the STM imaging of diamond (100) after annealing in UHV. Figure 20a is a UHV STM image of the hydrogen saturated 2×1 surface before annealing in UHV. Figure 20b shows the sample after it was heated to 1000 °C for 1 minute, resulting in desorption of all the hydrogen in the etch pits and removal of the hydrogen that terminated the 2×1 surface. Note the dramatic improvement in image quality shown in Figure 20b after the 1000 °C anneal.

Figures 21–24 show UHV STM images of the Group B variable temperature experiments in which the diamond (100)- 2×1 surface was exposed to atomic hydrogen for 5 minutes at substrate temperatures of 200, 500, and 1,000 °C. In these images, the diamond (100) surface was heated to 1000 °C for 1 minute in UHV after the atomic hydrogen exposure in order to desorb the hydrogen physisorbed and chemisorbed on the surface. Using LEED and electron-energy-loss spectroscopy, it has been reported that desorption of hydrogen at 1,000 °C in UHV results in a nonhydrogen terminated diamond (100)- 2×1 surface [34], in agreement with Figures 21–24. The stability of the

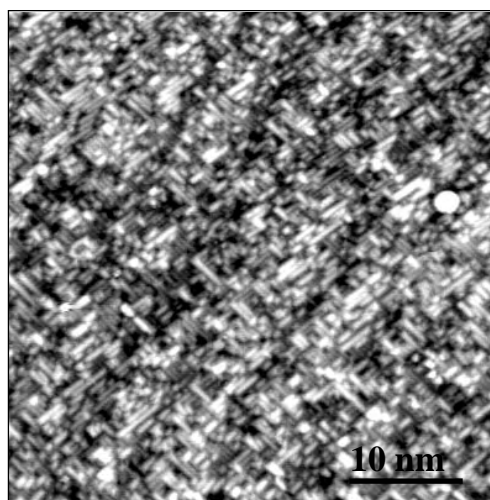


Figure 21. Nonhydrogen terminated diamond (100)- 2×1 surface after atomic hydrogen exposure for 5 min at 200 °C. Reprinted with permission from [21], R. E. Stallcup and J. M. Perez, *Phys. Rev. Lett.* 86, 3368 (2001). © 2001, American Physical Society.

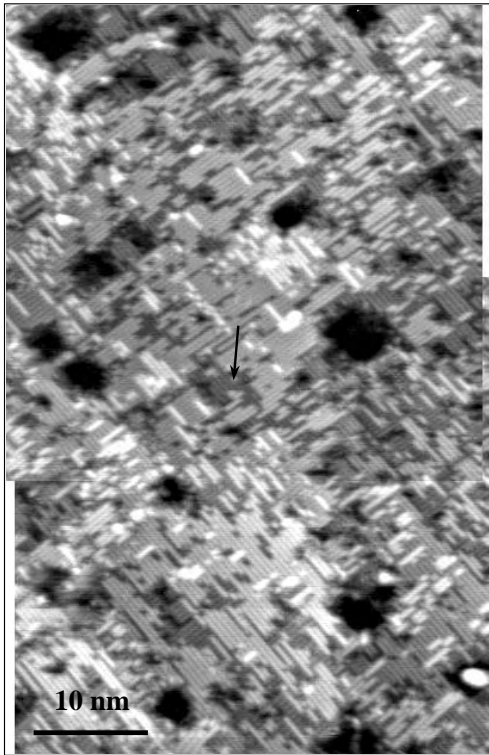


Figure 22. Nonhydrogen terminated diamond (100)- 2×1 surface after atomic hydrogen exposure for 5 min at 500 °C. Unmarked arrow indicates vacancy island. Reprinted with permission from [21], R. E. Stallcup and J. M. Perez, *Phys. Rev. Lett.* 86, 3368 (2001). © 2001, American Physical Society.

tunneling current was found to increase after the hydrogen desorption. For example, Figures 22 and 23 show tiled STM images obtained one after the other showing excellent reproducibility. As shown in Figures 21–24, the diamond (100)- 2×1 surface has dimer rows that are narrower than those in the diamond (100)- 2×1 :H surface. In addition, in the diamond (100)- 2×1 surface, individual dimers are not observed.

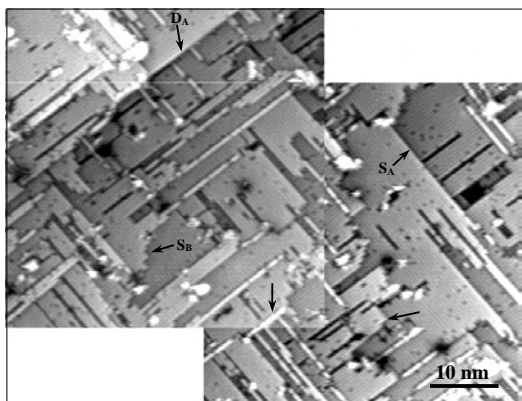


Figure 23. Nonhydrogen terminated diamond (100)- 2×1 surface after atomic hydrogen exposure for 5 min at 1000 °C. Observed are S_A , S_B , and D_A steps. Reprinted with permission from [21], R. E. Stallcup and J. M. Perez, *Phys. Rev. Lett.* 86, 3368 (2001). © 2001, American Physical Society.

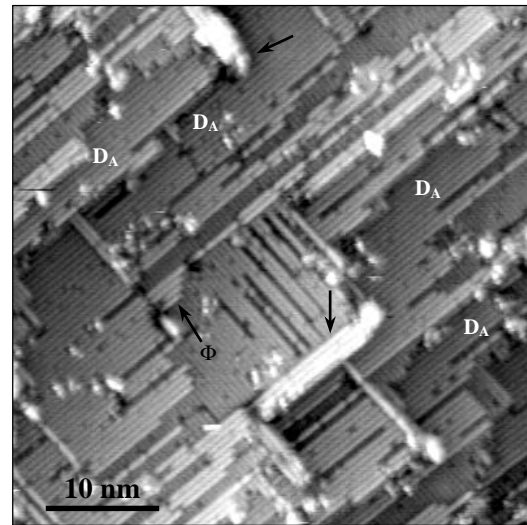


Figure 24. Nonhydrogen terminated diamond (00)- 2×1 surface after atomic hydrogen exposure for 5 min at 1000 °C. Observed are various D_A steps. Reprinted with permission from [21], R. E. Stallcup and J. M. Perez, *Phys. Rev. Lett.* 86, 3368 (2001). © 2001, American Physical Society.

Figures 21–24 show that the temperature of the surface during exposure to atomic hydrogen had a significant effect on the resulting morphology. It was found that the morphologies shown in Figures 21–24 are due to the atomic hydrogen exposure at the various temperatures instead of the subsequent annealing at 1,000 °C in UHV. For example, additional annealing of the surface at 1,000 °C in UHV for 15 minutes did not result in any observable changes in morphology. In addition, films with any one of the three different morphologies shown in Figures 21–24 could be converted to any of the two other morphologies by simply etching at that specific temperature. For example, a film with the smooth morphology of Figure 24 was exposed to atomic hydrogen with a sample temperature of 200 °C and resulted in producing a surface morphology like that of Figure 21. The observed morphology was then changed back to the smooth morphology by etching at 1,000 °C.

As shown in Figure 21, exposure at 200 °C results in a very rough surface at the atomic scale. The rough surface shows that etching at 200 °C is isotropic. No large pits are observed, and the largest domain size is about 6.25 nm^2 . As shown in Figure 22, exposure at 500 °C results in a surface that is smoother at the atomic scale with larger domains measuring about 100 nm^2 . In addition, this surface contains large single atomic layer vacancy islands, single height steps, and deep pits. The pits have a pyramidal shape, as was previously discussed in the Group A experiments. The vacancy islands have an average length along the dimer rows that is 2.1 times greater than the average length perpendicular to the dimer rows. This shows that etching at 500 °C is anisotropic and that it is 2.1 times more likely to occur along the dimer rows than perpendicular to them. Shown in Figures 23 and 24, exposure at 1,000 °C results in a smooth surface with single and double atomic steps, and the largest domains of the three experiments measuring approximately 350 nm^2 .

The step morphology in Figures 23 and 24 shows that S_B steps, in which the dimer rows are perpendicular to the steps, are very rough. However, S_A steps, in which the dimer rows are parallel to the steps, are very smooth. In contrast, the 500 °C etched sample shown in Figure 22 has rough S_A steps. In addition, S_A steps having a few dimer rows above them are not etched, as shown by the unmarked arrow in Figure 24. In Figures 23 and 24, vacancy islands consist mainly of single row vacancies and no large pits, and there are D_A steps in which the middle S_B step has been completely etched. These observations show that etching at 1000 °C is highly anisotropic with the etch rate along the dimer rows much greater than that perpendicular to the rows.

The anisotropic etching in the direction of dimer rows supports recent theoretical models of the growth of smooth diamond (100) films. Figure 25 shows a schematic of the diamond (100)- 2×1 :H surface. In theoretical models, growth on this surface occurs by the adsorption of CH_3 on surface sites where hydrogen has been abstracted [130]. The adsorbates then form methylene bridges and dimers. In the anisotropic etching model described in [133], extension of the dimer row at atoms 1 and 2 in Figure 25 can occur as long as hydrocarbons have not adsorbed at the dimer bonds to their right. For example, the presence of a methylene bridge between atoms 3 and 4 will prevent adsorption of CH_3 at atoms 3 or 1 due to steric repulsion, and growth will wait until this methylene bridge is etched. Growth of dimers at S_A steps, corresponding to atoms 5 and 6 in Figure 25, is not kinematically stable against etching because all dimers grown at S_A steps are similar to dimers at the ends of S_B steps and can be etched [133]. In contrast, only the last dimer in a row of an S_B step has a high probability of being etched. For example, atoms 7 and 8 can be etched only after atoms 9 and 10 are etched. Therefore, growth at S_B steps can proceed via dimer row extension and produce a continuous monolayer. The UHV STM results described above provide direct evidence for this model. A recent model that considers the preferential etching of undercoordinated atoms predicts the observed growth rate and a smooth surface [132].

5.1.3. Steps and Defects

Steps and defects on the surface play an important role in the growth of films and nanostructures. As previously described, the diamond (100)- 2×1 :H surface is inert and

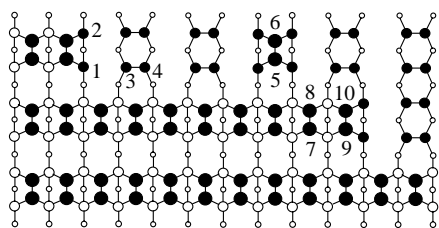


Figure 25. Schematic of the diamond (100)- 2×1 surface. The large, intermediate, and small circles represent the top, second, and third layer carbon atoms, respectively. The shaded carbon atoms are hydrogen terminated. Reprinted with permission from [21], R. E. Stallcup and J. M. Perez, *Phys. Rev. Lett.* 86, 3368 (2001). © 2001, American Physical Society.

consists of single- and double-layer steps, local 3×1 reconstructions, phase shifts, and dimer vacancies. The clean diamond (100)- 2×1 surface is reactive and has been investigated as a substrate for metal films [134], buckyballs [135], functionalized organic molecules [98–100], and mechano-synthesis of nanostructures [136]. Stallcup and Perez [137] studied the atomic structure of steps and defects on the diamond (100)- 2×1 surface using UHV STM and found that single- and double-layer steps are rebonded. The main types of defects observed were single, multiple, and row dimer vacancies, and antiphase boundaries. Buckling of dimers was not observed, in agreement with theoretical predictions that dimers are symmetric [138].

Figure 26 shows schematics of single S_A and S_B , and double D_A steps on the diamond (100)- 2×1 surface. As shown in Figure 26, rebonded S_B steps have edge atoms on the bottom plane that are bonded. For such steps, the distance from edge dimers on the upper plane to the nearest dimer row on the bottom plane is $3d$, where d is the lattice constant of the unreconstructed 1×1 surface. For nonbonded S_B steps, the distance from edge dimers to the nearest dimer row on the bottom plane is $2d$. D_A steps consist of an S_A step on an S_B step, and have edge atoms on the bottom plane that are rebonded or nonbonded in a manner similar to that of S_B steps. For the Si (100)- 2×1 surface, UHV STM studies have shown that S_B and D_A steps are rebonded [17, 18]. Theoretical studies of this surface have shown that rebonded steps are more energetically favorable than nonbonded steps because they have fewer dangling bonds per step length [139]. In contrast, for the diamond (100)- 2×1 surface, theoretical studies predict that S_B and D_A steps are nonbonded because carbon dimers form strong double bonds that effectively reduce the number of dangling bonds [126].

Boron-doped epitaxial diamond (100) films were grown and imaged using UHV STM as described in the section on anisotropic etching. After growth, the films were exposed to atomic hydrogen for 10 minutes at 900 °C to produce a smooth surface. Figure 27 shows a UHV STM image of a clean diamond (100)- 2×1 film showing S_B , S_A , and D_A steps. Figure 28a is a higher resolution image of the same

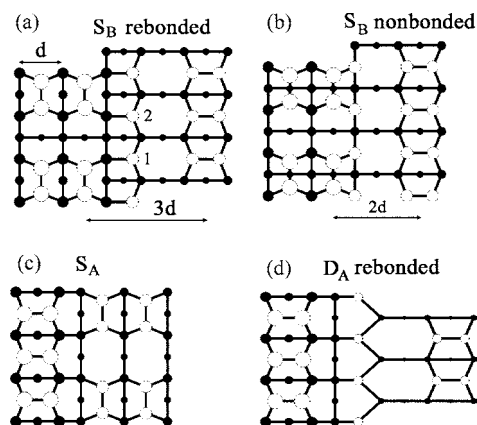


Figure 26. Schematic representations of S_B , S_A , and D_A steps. Reprinted with permission from [137], R. E. Stallcup and J. M. Perez, *Appl. Phys. Lett.* (In press.) © 2002, American Institute of Physics.

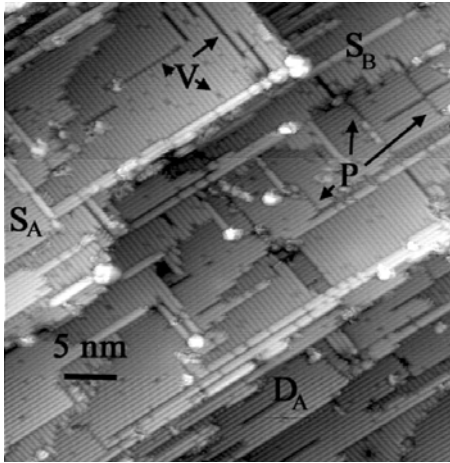


Figure 27. UHV STM image of the clean diamond (100)- 2×1 surface showing the atomic structure of steps and defects. Reprinted with permission from [137], R. E. Stallcup and J. M. Perez, *Appl. Phys. Lett.* (In press.) © 2002, American Institute of Physics.

film showing rebonded S_B steps near regions marked “R.” Figure 28b shows a high-resolution image of the S_B step near the center of Figure 28a and a superimposed schematic of a rebonded S_B step. As shown in Figure 28b, the distance from edge dimers on the upper plane to the nearest

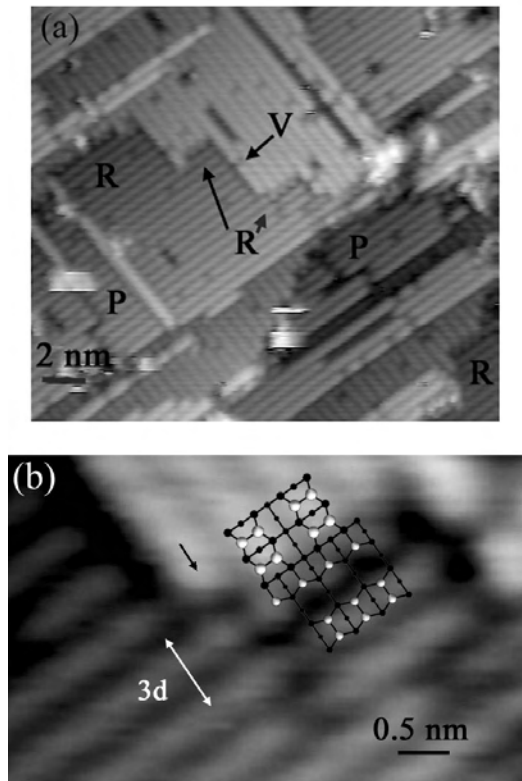


Figure 28. (a) UHV STM image of the diamond (100)- 2×1 surface showing rebonded S_B steps. (b) High resolution UHV STM image of the S_B step near the center of (a) and a superimposed schematic of a rebonded S_B step. Reprinted with permission from [137], R. E. Stallcup and J. M. Perez, *Appl. Phys. Lett.* (In press.) © 2002, American Institute of Physics.

full dimer row on the bottom plane is $3d$. In Figure 28b, the dimer row indicated by the unmarked arrow forms a local nonbonded step. On the Si (100)- 2×1 surface, local nonbonded steps are thought to be stabilized by vacancies [17, 18]. Therefore, the nonbonded step in Figure 28b is attributed to vacancy V indicated by the arrow in Figure 28a. Figure 29 shows a UHV STM image of a rebonded D_A step in which the bonding configuration of edge atoms on the bottom plane is similar to that of rebonded S_B steps. The observation of rebonded steps on the diamond (100)- 2×1 surface contradicts recent theoretical predictions that single- and double-layer steps are nonbonded [126].

Also observed in Figures 27 and 28 are defects consisting of dimer vacancies indicated by V that are single, multiple, and arranged in rows parallel and perpendicular to dimer rows. The density of single and multiple vacancies is about $8 \times 10^{12}/\text{cm}^2$. In addition, a large number of antiphase boundaries indicated by P are observed on type A steps. The antiphase boundaries occur such that the phase shift is accommodated at a step edge, or vacancy row that is perpendicular to the boundary and has a width of d and $2d$ on either side of the boundary. It is thought that antiphase boundaries are formed during exposure to atomic hydrogen and remain after desorption of hydrogen at 1000°C . Evidence of buckled dimers or stabilization of buckled dimers by steps and vacancy defects was not observed. On the Si (100)- 2×1 surface, buckled dimers are stabilized by such structures at room temperature [17, 18]. These observations are consistent with theoretical predictions that the diamond (100)- 2×1 surface has symmetric dimers and the Si (100)- 2×1 surface has asymmetric dimers [138].

5.2. Diamond (111) Surface

STM studies of the diamond (111) surface have been carried out in air using polycrystalline [33, 140, 141] and homoepitaxial [142] diamond (111) films. To our knowledge, UHV STM studies of the clean diamond (111) surface have not been reported. Large-area air STM studies of diamond (111) films show that the surface is rough with islands having $\{111\}$ faces [33, 140, 141]. Figure 30 shows a large-area UHV STM image of an epitaxial diamond film grown on a synthetic diamond (111) substrate [143]. The film was not annealed in UHV after growth. In Figure 30, the derivative of the data, dz/dx , is shown in order to accentuate steps. Observed are triangular islands oriented in the $\langle 111 \rangle$ direction, mono-atomic steps, and screw dislocations [143]. While the film is defective, it is in atomic registry with the crystalline substrate.

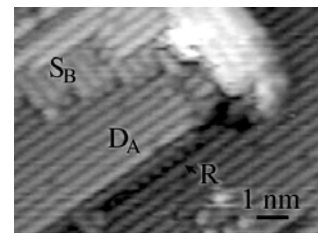


Figure 29. UHV STM image of the diamond (100)- 2×1 surface showing a rebonded D_A step. Reprinted with permission from [137], R. E. Stallcup and J. M. Perez, *Appl. Phys. Lett.* (In press.) © 2002, American Institute of Physics.

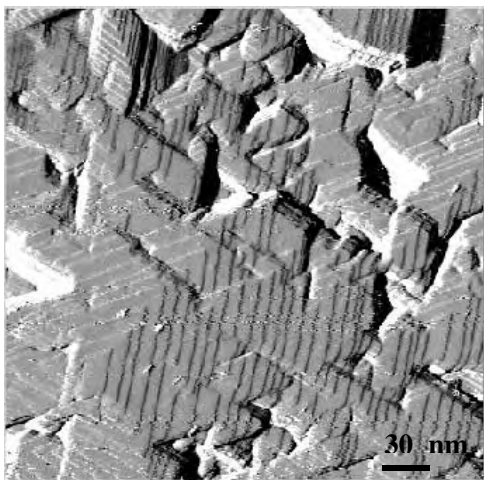


Figure 30. Large-area UHV STM image of an unannealed epitaxial diamond (111) film.

Atomic resolution studies of diamond (111) films show coexisting regions having 1×1 , 2×1 , 2×2 , and $\sqrt{3} \times \sqrt{3} R30^\circ$ reconstructions [30, 33, 140–142]. Figure 31 shows an atomic resolution UHV STM image of an unannealed epitaxial diamond (111) film showing a 1×1 reconstruction [143]. Theoretical calculations show that the only stable 1×1 structure is the diamond (111)- 1×1 :H surface [30], shown schematically in Figure 32. Therefore, this surface is thought to be the surface observed using STM [33]. Calculations also show that the hydrogen-terminated 2×1 single chain and Pandey [144] reconstructions are stable [30], as shown in Figure 33a and b. The diamond (111)- 2×1 surface observed using STM is thought to be either of these two reconstructions [33]. The diamond (111)- 2×2 and $\sqrt{3} \times \sqrt{3} R30^\circ$ reconstructions observed using STM are thought to be due to adsorbed hydrocarbon radicals [33]. Calculations also predict that the clean diamond (111)- 2×1 single chain and Pandey reconstructions, and clean and hydrogen-terminated $\sqrt{3} \times \sqrt{3} R30^\circ$ reconstructions are

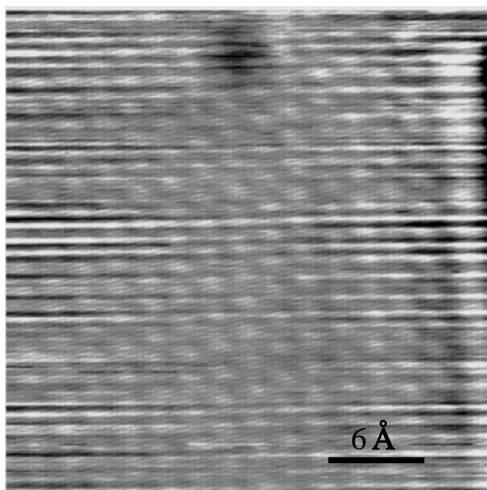


Figure 31. Atomic resolution UHV STM image of an unannealed epitaxial diamond (111) film showing a 1×1 structure.

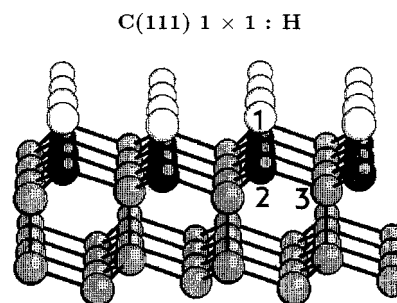


Figure 32. Schematic representations of stable hydrogen-terminated diamond (111)- 1×1 surface. Reprinted with permission from [30], Th. Frauenheim et al., *Phys. Rev. B* 48, 18189 (1993). © 1993, American Physical Society.

stable [30]. However, STM imaging of such surfaces has not been reported. LEED studies have shown that the diamond (111) surface annealed in UHV at temperatures higher than $1,000^\circ\text{C}$ shows a 2×1 pattern [34, 145]. This 2×1 surface changes to a 1×1 surface after exposure to atomic hydrogen [34, 145].

5.3. Diamond (110) Surface

Few STM studies of the diamond (110) surface have been reported. Mercer et al. [146] used AFM to study diamond (110) substrates after exposure to atomic hydrogen at

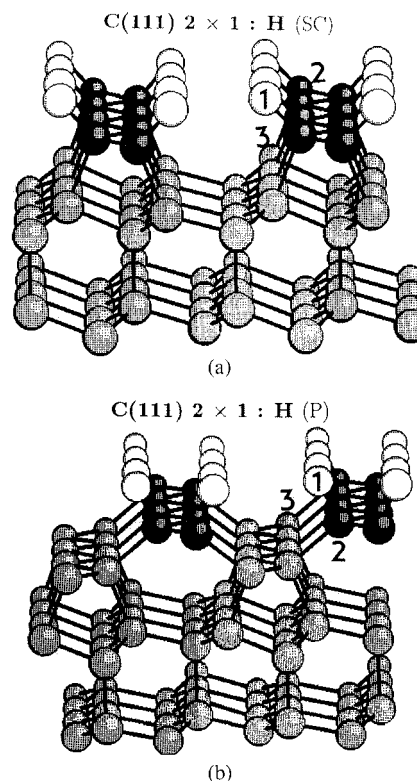


Figure 33. Schematic representations of stable hydrogen-terminated diamond (111)- 2×1 reconstructions. (a) 2×1 single chain. (b) 2×1 Pandey. Reprinted with permission from [30], Th. Frauenheim et al., *Phys. Rev. B* 48, 18189 (1993). © 1993, American Physical Society.

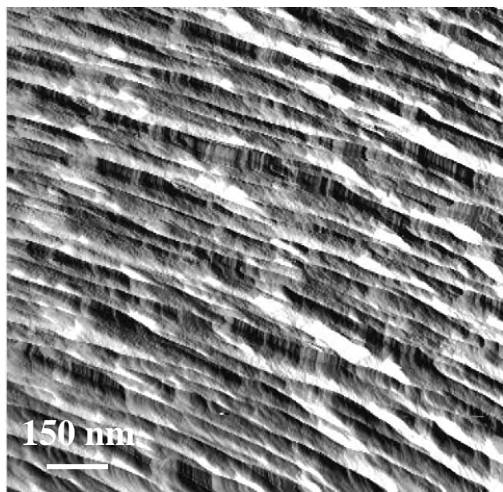


Figure 34. Large area UHV STM image of an epitaxial diamond film grown on a synthetic diamond (110) substrate. Observed is a rough surface having striations.

a temperature of 900 °C. They observed that atomic hydrogen exposure results in a very rough surface at the micron scale with deep pits having {111} faces. They also observed that polished diamond (110) substrates have pits with {111} faces. Lim et al. [147] used UHV STM to study epitaxial diamond films grown on a synthetic diamond (110) substrate. The epitaxial films were not annealed in UHV after growth. The surface of the film was observed to consist of striations with {111} faces on the side and {100} faces on top, as shown in Figure 34. Using LEED, Lurie and Wilson [125] observed a 1×1 pattern for polished diamond (110) substrates and no reconstructions after annealing the substrate at 1000 °C in UHV. Cheng et al. [148] used LEED to study the etching of diamond (110) substrates by atomic hydrogen and found that {111}-oriented facet formation occurs.

As shown in Figure 4, the bulk-terminated diamond (110) surface consists of zig-zag chains of atoms having one dangling bond per atom. For the clean and hydrogen-terminated surface, theoretical studies of Davidson and Pickett [149] predict weak dimerization of the chains. Calculations of Alfonso et al. [150] predict a buckling of nondimerized chains for the clean surface and bulk-like nondimerized chains for the hydrogen-terminated surface. Kern and Hafner [151] recently predicted no buckling or dimerization and an inward shift of the top layer for the clean surface and a bulk-like structure for the hydrogen-terminated surface. Using UHV STM, Lim et al. [147] observed isolated regions on unannealed epitaxial diamond (110) films showing a zig-zag atomic structure that was ascribed to the hydrogenated (110) surface.

6. CONCLUSIONS

In conclusion, the atomic structure of diamond surfaces has been successfully studied using STM. Although diamond is an insulator, STM imaging is possible by increasing the

surface conductivity by doping the film with boron or hydrogen terminating the surface. UHV STM results of diamond comparable in quality to those that have been reported for Si are possible by cleaning the surface in UHV and using ultrasharp tungsten tips. For the diamond (100) surface, air STM has been used to study the atomic structure of the hydrogen-terminated surface. UHV STM studies of the clean surface have revealed the atomic-scale properties of steps, defects, and the atomic hydrogen etching mechanism. For the diamond (111) surface, air STM studies have shown various reconstructions of the hydrogen-terminated surface. There have been no reports of studies of the clean surface using UHV STM. For the diamond (110) surface, there have been few STM studies, mainly because the surface is very rough. The UHV STM techniques described can be used to study etching, adsorbates, growth, and other processes at the atomic scale that are crucial in understanding the growth and properties of diamond.

GLOSSARY

Diamond film Diamond deposited as a film using chemical vapor deposition with hydrogen and a carbon-containing gas such as methane. Typical substrate temperatures and gas pressures are 700–900 °C and 30 Torr, respectively.

Diamondlike carbon film An amorphous and typically hydrogenated carbon film.

Epitaxial film A single crystal film in atomic registry with the substrate.

Nanocrystalline diamond Carbon film having nanometer-size grains and mostly sp^3 bonding. Such films are made using buckyballs or a carbon containing gas and Ar or N gas that are activated using a microwave plasma or laser.

Polycrystalline film A film composed of crystallites having different orientations and separated by grain boundaries.

Scanning tunneling microscopy (STM) A technique for imaging the surface of a conductor with atomic resolution that uses tunneling between the surface and a sharp tip that is scanned across the surface using a piezoelectric device.

Surface reconstruction Rearrangement of atoms in the near surface region from their bulk positions.

Ultrahigh vacuum (UHV) A vacuum having a pressure $<10^{-9}$ Torr.

ACKNOWLEDGMENTS

We gratefully acknowledge Dr. Seong Lim and Dr. Kenny Stephens for useful discussions; graduate students Gary Woodard, Jeremy Hansen, Roberto Failla, and Danekar Koustubh for drawing figures and finding references; and Dr. Atul Wadhawan and graduate student Ryan Cottier for careful readings of the manuscript. This work was supported by the National Science Foundation under Award No. DMR-0074636 and the Texas Advanced Technology Program under Award No. 003594-0048-99.

REFERENCES

1. M. H. Nazare and A. J. Neves, Eds., "Properties, Growth and Applications of Diamond." INSPEC, London, 2001.
2. M. A. Prelas, G. Popovici, and L. K. Bigelow, Eds., "Handbook of Industrial Diamonds and Diamond Films." Marcel Dekker, New York, 1998.
3. K. E. Spear and J. P. Dismukes, Eds., "Synthetic Diamond: Emerging CVD Science and Technology." John Wiley & Sons, New York, 1994.
4. J. E. Field, Ed., "The Properties of Natural and Synthetic Diamond." Academic Press, New York, 1992.
5. R. E. Clausing, L. L. Horton, J. C. Angus, and P. Koidl, Eds., "Diamond and Diamond-Like Films and Coatings." Plenum Press, New York, 1991.
6. See, for example, J. T. Glass, R. Messier, and N. Fujimori, Eds., "Diamond, Silicon Carbide and Related Wide Bandgap Semiconductors," Materials Research Society Symposium Proceedings vol. 162, MRS, Pittsburgh, 1990.
7. See, for example, R. Messier, J. T. Glass, J. E. Butler, and R. Roy, Eds., "Proceedings of the Second International Conference New Diamond Science and Technology," MRS, Pittsburgh, 1991.
8. A. Badzian, *Mater. Chem. Phys.* 72, 110 (2001).
9. A. Gicquel, K. Hassouni, F. Silva, and J. Achard, *Current Appl. Phys.* 1, 479 (2001).
10. T. A. Railkar, W. P. Kang, H. Windischmann, A. P. Malshe, H. A. Naseem, J. L. Davidson, and W. D. Brown, *Critical Review of Solid State and Materials Science* 25, 163 (2000).
11. A. Mainwood, *Semicond. Sci. Technol.* 15, 55 (2000).
12. A. P. Malshe, B. S. Park, W. D. Brown, and H. A. Naseem, *Diamond Relat. Mater.* 8, 1198 (1999).
13. D. M. Gruen and I. Buckley-Golder, Eds., "Diamond Films: Recent Developments," *MRS Bull.* 23 (1998).
14. J. E. Butler and R. L. Woodin, *Phil. Trans. R. Soc. Lond., Ser. A* 342, 205 (1993).
15. J. C. Angus, Y. Wang, and M. Sunkara, *Annu. Rev. Mater. Sci.* 21, 221 (1991).
16. F. G. Celii and J. E. Butler, *Annu. Rev. Phys. Chem.* 42, 643 (1991).
17. See, for example, J. Dabrowski and H. J. Mussig, "Silicon Surfaces and Formation of Interfaces," World Scientific, Singapore, 2000.
18. See, for example, J. Strocioc and W. Kaiser, Eds., "Scanning Tunneling Microscopy," Academic, Boston, 1993.
19. J. J. Boland, *Surf. Sci.* 262, 17 (1992).
20. T. Tsuno, T. Imai, S. Shikata, and N. Fujimori, in "Advances in New Diamond Science and Technology" (S. Saito, Ed.), p. 241. MYU, Tokyo, 1994.
21. R. E. Stallcup and J. M. Perez, *Phys. Rev. Lett.* 86, 3368 (2001).
22. R. E. Stallcup, L. M. Villarreal, S. C. Lim, I. Akwani, A. F. Aviles, and J. M. Perez, *J. Vac. Sci. Technol., B* 14, 929 (1996).
23. R. E. Stallcup, A. F. Aviles, and J. M. Perez, *Appl. Phys. Lett.* 66, 2331 (1995).
24. R. E. Stallcup, Ph.D. dissertation, University of North Texas, 2000.
25. K. F. Turner, Y. M. LeGrice, B. R. Stoner, J. T. Glass, and R. J. Nemanich, *J. Vac. Sci. Technol., B* 9, 914 (1991).
26. M. P. Everson and M. A. Tamor, *J. Vac. Sci. Technol., B* 9, 1570 (1991).
27. T. Tsuno, T. Imai, Y. Nishibayashi, K. Hamada, and N. Fujimori, *Jpn. J. Appl. Phys.* 30, 1063 (1991).
28. H.-G. Busmann, H. Sprang, I. V. Hertel, W. Zimmermann-Edling, and H. J. Guntherodt, *Appl. Phys. Lett.* 59, 295 (1991).
29. W. Zimmermann-Edling, H.-G. Busmann, H. Sprang, and I. V. Hertel, *Ultramicroscopy* 42-44, 1366 (1991).
30. Th. Frauenheim, U. Stephan, P. Blaudeck, D. Porezag, H. G. Busmann, W. Zimmermann-Edling, and S. Lauer, *Phys. Rev. B* 48, 18189 (1993).
31. T. Tsuno, T. Tomikawa, S. Shikata, T. Imai, and N. Fujimori, *Appl. Phys. Lett.* 64, 572 (1994).
32. Y. Kuang, Y. Wang, N. Lee, A. Badzian, T. Badzian, and T. T. Tsong, *Appl. Phys. Lett.* 67, 3721 (1995).
33. H.-G. Busmann and I. Hertel, *Carbon* 36, 391 (1998).
34. M. P. D'Evelyn, in "Handbook of Industrial Diamonds and Diamond Films," p. 89. Marcel Dekker, New York, 1998.
35. J. M. Thomas, in "The Properties of Diamond" (J. E. Field, Ed.), p. 211. Academic Press, London, 1979.
36. B. B. Pate, *Surf. Sci.* 165, 83 (1986).
37. B. B. Pate, in "Diamond: Electronic Properties and Applications" (L. S. Pan and D. R. Kania, Eds.), p. 31. Kluwer, Boston, 1995.
38. M. N. Gardos, *Surf. Coat. Technol.* 113, 183 (1999).
39. A. V. Khomich, V. G. Ralchenko, A. V. Vlasov, R. A. Khmel'nitskiy, I. I. Vlasov, and V. I. Konov, *Diamond Relat. Mater.* 10, 546 (2001).
40. F. P. Bundy, H. T. Hall, H. M. Strong, and R. H. Wentorf, *Nature* 176, 51 (1955).
41. D. Choudhary and J. Bellare, *Ceramics International* 26, 73 (2000).
42. J. C. Angus, in "Synthetic Diamond: Emerging CVD Science and Technology," p. 21. John Wiley & Sons, New York, 1994.
43. D. V. Fedoseev, in "Synthetic Diamond: Emerging CVD Science and Technology," p. 41. John Wiley & Sons, New York, 1994.
44. B. V. Spitsyn, L. L. Bouilov, and B. V. Derjaguin, *J. Cryst. Growth* 52, 219 (1981).
45. N. Setaka, in "Synthetic Diamond: Emerging CVD Science and Technology," p. 57. John Wiley & Sons, New York, 1994.
46. J. Robertson, *Mater. Sci. Eng., A* 37, 129 (2002).
47. A. Erdemir, G. R. Fenske, A. R. Krauss, D. M. Gruen, T. McCauley, and R. T. Csencsits, *Surf. Coat. Technol.* 120-121, 565 (1999).
48. D. M. Gruen, in "Diamond Films: Recent Developments," p. 32. *MRS Bull.* 23 (1998).
49. F. Z. Cui and D. J. Li, *Surf. Coat. Technol.* 131, 481 (2000).
50. A. Grill, *Diamond Relat. Mater.* 8, 428 (1999).
51. C. Donnet, *Surf. Coat. Technol.* 100-101, 180 (1998).
52. P. J. Gielisse, in "Handbook of Industrial Diamonds and Diamond Films," p. 49. Marcel Dekker, New York, 1998.
53. A. Grill and B. S. Meyerson, in "Synthetic Diamond: Emerging CVD Science and Technology," p. 91. John Wiley & Sons, New York, 1994.
54. R. C. DeVries, A. Badzian, and R. Roy, *MRS Bull.* 21, 65 (1996).
55. W. G. Eversole, U. S. Patents 3,030,187 and 3,030,188 (1962).
56. S. Matsumoto, S. Y. Sato, M. Kamo, and N. Setaka, *Jpn. J. Appl. Phys.* 21, 183 (1982).
57. M. Kamo, Y. Sato, S. Matsumoto, and N. Setaka, *J. Cryst. Growth* 62, 642 (1983).
58. J. E. Butler and H. Windischmann, in "Diamond Films: Recent Developments," p. 22. *MRS Bull.* 23 (1998).
59. M. Thumm, *Diamond Relat. Mater.* 10, 1692 (2001).
60. S. E. Coe and R. S. Sussmann, *Diamond Relat. Mater.* 9, 1726 (2000).
61. Beijing Tiandi Orient Superhard Materials Co., Ltd., Beijing, P. R. China (www.td-diamond.com.cn).
62. Crystallume, Inc., Santa Clara, CA (www.crystallume.com).
63. De Beers Industrial Diamond Division Ltd., Ascot, Surrey, UK (www.debid.co.uk).
64. Diamond Tool Coating, North Tonawanda, NY (www.diamondtc.com).
65. Diamonex, Allentown, PA (www.diamonex.com).
66. P1 Diamond, Inc., Santa Clara, CA (www.p1diamond.com).
67. sp³, Inc, Mountain View, CA (www.sp3inc.com).
68. Technodiamant, Almere, The Netherlands (www.technodiamant.nl).
69. R. Kalish, *Diamond Relat. Mater.* 10, 1749 (2001).
70. R. Kalish, *Carbon* 37, 781 (1999).
71. J. T. Glass, B. A. Fox, D. L. Dreifus, and B. R. Stoner, "Diamond Films: Recent Developments," p. 49. *MRS Bull.* 23 (1998).
72. J. L. Davidson, in "Synthetic Diamond: Emerging CVD Science and Technology," p. 355. John Wiley & Sons, New York, 1994.

73. S. Koizumi, M. Kamo, Y. Sato, H. Ozaki, and T. Inuzuka, *Appl. Phys. Lett.* 71, 1065 (1997).
74. S. Shikata, in "Diamond Films: Recent Developments," p. 61. *MRS Bull.* 23 (1998).
75. J. Wei and J. Ahn, *Cryst. Res. Technol.* 34, 133 (1999).
76. R. D. McKeag and R. B. Jackman, in "Lasers in Synthesis, Characterization, and Processing of Diamond, Proceedings of the SPIE," 3484, 182 (1997).
77. J. L. Davidson, W. P. Kang, Y. Gurbuz, K. C. Holmes, L. G. Davis, A. Wisitsora-at, D. V. Kerns, R. L. Eidson, and T. Henderson, *Diamond Relat. Mater.* 8, 1741 (1999).
78. J. L. Davidson, D. R. Wur, W. P. Kang, D. L. Kinser, and D. V. Kerns, *Diamond Relat. Mater.* 5, 86 (1996).
79. G. M. Swain, A. B. Anderson, and J. C. Angus, in "Diamond Films: Recent Developments," p. 56. *MRS Bull.* 23 (1998).
80. W. Zhirnov and J. J. Hren, in "Diamond Films: Recent Developments," p. 42. *MRS Bull.* 23 (1998).
81. J. P. Sullivan, T. A. Friedman, and K. Hjort, in "Microelectromechanical Systems: Technology and Applications" (D. Bishop, A. Heuer, and D. Williams, Eds.), p. 309. *MRS Bulletin*, April, 2001.
82. E. Kohn, P. Gluche, and M. Adamschik, *Diamond Relat. Mater.* 8, 934 (1999).
83. R. Ramesham, C. D. Ellis, J. D. Olivas, and S. Bolin, *Thin Solid Films* 330, 62 (1998).
84. M. N. Touzelbaev and K. E. Goodson, *Diamond Relat. Mater.* 7, 1 (1998).
85. J. L. Davidson, R. Ramesham, and C. Ellis, *J. Electrochem. Soc.* 137, 3206 (1990).
86. T. Shibata, Y. Kitamoto, K. Unno, and E. Makino, *J. Microelectromech. Syst.* 9, 47 (2000).
87. J. T. Sheu, G. Y. Yang, and B. R. Huang, "Materials and Device Characterization in Micromachining," *Proc. SPIE-Int. Soc. Opt. Eng.* 3512, 173 (1998).
88. See, for example, C. Kittel, "Introduction to Solid State Physics," seventh edition, John Wiley & Sons, New York, 1996.
89. J. S. Goela, N. E. Brese, M. A. Pickering, and J. E. Graebner, *MRS Bull.*, June, 458 (2001).
90. P. R. Chalker, *Thin Solid Films* 343-344, 616 (1999).
91. S. Schnetzer et al., (RD42 Collaboration), *IEEE Trans. Nucl. Sci.* 46, 193 (1999).
92. Y. Gurbuz, W. P. Kang, J. L. Davidson, and D. V. Kerns, *Sens. Actuators, B* 49, 115 (1998).
93. W. P. Kang, Y. Gurbuz, J. L. Davidson, and D. V. Kerns, *Sens. Actuators, B* 24-25, 421 (1995).
94. P. H. Cutler, N. M. Miskovsky, P. B. Lerner, and M. S. Chung, *Appl. Surf. Sci.* 146, 126 (1999).
95. B. C. Djubua and N. N. Chubun, *IEEE Trans. Electron Devices* 38, 2314 (1991).
96. C. Wang, A. Garcia, D. C. Ingram, and M. E. Kordesh, *Electron. Lett.* 27, 1459 (1991).
97. M. W. Geis, N. N. Efremov, J. D. Woodhouse, M. D. McAleese, M. Marchywka, D. G. Socker, and J. F. Hochedez, *IEEE Electron Device Lett.* 12, 456 (1991).
98. J. S. Hovis, S. K. Coulter, and R. J. Hamers, *J. Am. Chem. Soc.* 122, 732 (2000).
99. J. N. Russell, J. E. Butler, G. T. Wang, S. F. Bent, J. S. Hovis, R. J. Hamers, and M. P. D'Evelyn, *Mater. Chem. Phys.* 72, 147 (2001).
100. T. Strother, T. Knickerbocker, J. N. Russel, J. E. Butler, L. M. Smith, and R. J. Hamers, *Langmuir Lett.* 18, 968 (2002).
101. M. N. Gardos, *Tribol. Lett.* 4, 175 (1998).
102. M. N. Gardos, in "Protective Coatings and Thin Films" (Y. Pauleau and P. B. Barna, Eds.), p. 185. Kluwer, New York, 1997.
103. M. N. Gardos, *Tribol. Lett.* 2, 173 (1996).
104. M. N. Gardos and B. L. Soriano, *J. Mater. Res.* 5, 2599 (1990).
105. G. Binning, H. Rohrer, Ch. Gerber, and E. Welbel, *Phys. Rev. Lett.* 49, 57 (1982).
106. L. C. Feldman and J. W. Mayer, "Fundamentals of Surface and Thin Film Analysis," North-Holland, New York, 1986.
107. G. A. Somorjai, "Introduction to Surface Chemistry and Catalysis," John Wiley & Sons, New York, 1994.
108. R. E. Clausing, L. Heatherly, and E. D. Specht, in "Diamond and Diamond-Like Films and Coatings," pp. 611-618, (Ref. [5]).
109. P. Hartman and W. G. Perdock, *Acta Crystallogr.* 8, 49, 521, 525 (1955).
110. P. Hartman, *Z. Kristallogr.* 121, 78 (1965).
111. A. van der Drift, *Philips Res. Rep.* 22, 267 (1967).
112. R. E. Clausing, in "Handbook of Industrial Diamonds and Diamond Films," p. 19. Marcel Dekker, New York, 1998.
113. C. Wild, R. Kohl, N. Herres, W. Mueller-Sebert, and P. Koidl, *Diamond Relat. Mater.* 3, 373 (1994).
114. M. A. Tamor and M. P. Everson, *J. Mater. Res.* 9, 1838 (1994).
115. J. Buhler and Y. Prior, *J. Cryst. Growth* 209, 779 (2000).
116. J. C. Angus, M. Sunkara, S. R. Sahaida, and J. T. Glass, *J. Mater. Res.* 7, 3001 (1992).
117. R. S. Becker, J. A. Golovchenko, and B. S. Swartzentruber, *Phys. Rev. Lett.* 54, 2678 (1985).
118. R. M. Feenstra and A. P. Fein, *Phys. Rev. B* 32, 1394 (1985).
119. R. M. Tromp, R. J. Hamers, and J. E. Demuth, *Phys. Rev. Lett.* 55, 1303 (1985).
120. G. Binnig and D. P. E. Smith, *Rev. Sci. Instrum.* 57, 1688 (1986).
121. Burleigh Instruments, ARIS 6000 Instruction Manual, 1994.
122. Y. G. Kim, E. H. Choi, S. O. Kang, and G. Cho, *J. Vac. Sci. Technol., B* 16, 2079 (1998).
123. P. J. Bryant, H. S. Kim, Y. C. Zheng, and R. Yang, *Rev. Sci. Instrum.* 58, 1115 (1987).
124. J. B. Marsh and H. E. Farnsworth, *Surf. Sci.* 1, 3 (1964).
125. P. G. Lurie and J. M. Wilson, *Surf. Sci.* 65, 453 (1977).
126. M.-H. Tsai and Y.-Y. Yeh, *Phys. Rev. B* 58, 2157 (1998).
127. M. Couto, W. J. P. van Enckevort, B. Wichman, and M. Seal, *Appl. Surf. Sci.* 62, 263 (1992).
128. C. Nutzenadel, O. M. Kuttel, L. Diederich, E. M. Schaller, O. Groning, and L. Schlapbach, *Surf. Sci.* 369 L111 (1996).
129. K. Bobrov, A. J. Mayne, and G. Dujardin, *Nature* 413, 616 (2001).
130. D. Goodwin and J. Butler, in "Handbook of Industrial Diamonds and Diamond Films," p. 527. (Ref. [2]).
131. M. Frenklach and S. Skokov, *J. Phys. Chem. B* 101, 3025 (1997).
132. C. Battaile, D. J. Srolowitz, and J. E. Butler, *J. Chem. Phys.* 111, 4291 (1999).
133. M. Zhu, R. H. Hauge, J. L. Margrave, and M. P. D'Evelyn, in "Proceedings of the Third International Symposium on Diamond Materials" (J. Dismukes and K. Ravi Eds.), p. 138. The Electrochemical Society, Pennington, 1993.
134. P. K. Baumann and R. J. Nemanich, *Diamond Relat. Mater.* 7, 612 (1998).
135. Y. Ma, Y. Xia, Y. Mu, S. Li, H. Zhang, M. Zhao, and R. Wang, *Nucl. Instr. Methods Phys. Res., Sect. B* 168, 169 (2000).
136. S. P. Walch and R. C. Merkle, *Nanotechnology* 8, 149 (1997).
137. R. E. Stallcup and J. M. Perez, *Appl. Phys. Lett.* 18, 4538 (2002).
138. P. Kruger and J. Pollmann, *Phys. Rev. Lett.* 74, 1155 (1995).
139. J. D. Chadi, *Phys. Rev. Lett.* 59, 1691 (1987).
140. H. G. Busmann, W. Zimmermann-Edling, H. Sprang, H. J. Guntherodt, and I. V. Hertel, *Diamond Relat. Mater.* 1, 979 (1992).
141. H. G. Busmann, S. Lauer, I. V. Hertel, W. Zimmermann-Edling, H. J. Guntherodt, Th. Frauenheim, P. Blaudeck, and D. Porezag, *Surf. Sci.* 295, 340 (1993).
142. H. Sasaki and H. Kawarada, *Jpn. J. Appl. Phys.* 32, L1771 (1993).
143. S. C. Lim, Ph.D. dissertation, University of North Texas, 1998.
144. K. C. Pandey, *Phys. Rev. B* 25, 4338 (1982).
145. J. J. Lander and J. Morrison, *Surf. Sci.* 4, 241 (1966).

146. T. W. Mercer, J. N. Russell, and P. E. Pehrsson, *Surf. Sci.* 392, L21 (1997).
147. S. C. Lim, R. E. Stallcup, I. Akwani, and J. M. Perez, in "Materials Issues in Vacuum Microelectronics," Materials Research Society Symposium Proceedings, Vol. 509, p. 165. MRS, Warrendale, PA, 1998.
148. C. L. Cheng, H. C. Chang, J. C. Lin, K. J. Song, and J. K. Wang, *Phys. Rev. Lett.* 78, 3713 (1997).
149. B. N. Davidson and W. E. Pickett, *Phys. Rev. B* 49, 11253 (1994).
150. D. R. Alfonso, D. A. Drabold, and S. E. Ulloa, *Phys. Rev. B* 51, 14669 (1995).
151. G. Kern and J. Hafner, *Phys. Rev. B* 56, 4203 (1997).

Atomic Wires

I. N. Yakovkin

National Academy of Sciences of Ukraine, Kiev, Ukraine

CONTENTS

1. Introduction
 2. Atomic Wires on Semiconductor Surfaces
 3. The Nonmetal-to-Metal Transition
in Free Monolayers
 4. Atomic Wires on Furrowed Transition
Metal Surfaces
 5. Conclusion
- Glossary
References

The variety of atomic wires can now be synthesized on furrowed and stepped surfaces, which provides opportunities for systematically tailoring surface properties. One of the most important issues for investigators in the field is the metallicity of the atomic wires and how one can control this metallicity. Hence, the nature of nonmetal-to-metal transition is a key problem. The different ways of casting the explanation of the nonmetal-to-metal transition (NMT) has provoked the classification of the NMT into types such as the Mott-Hubbard, the Wilson, and the Peierls transitions. In fact this complexity is illusionary; there is a single phenomenon, which is revealed by the gap at E_F , which is characteristic for a dielectric state, and closing this gap leads to the NMT.

In the present article, the NMT is analyzed from the viewpoint of transformation of band structure. This approach provides results that can be directly justified by angle-resolved photoemission (ARUPS) and other techniques that allow band structure mapping to be undertaken near the Fermi level. This is illustrated by the example of Mg atomic wires adsorbed on a Mo(112) surface, one archetypal example much exploited in this review. The band structure approach to explaining the NMT in monovalent crystals is brought into sharp perspective through the consideration of a coupling of adjacent atoms (Peierls' distortion) that results in a lowering of the total energy and affects an even number of valence electrons in the unit cell.

At low coverages, alkali, alkaline earth, and rare earth layers adsorbed on furrowed transition metal surfaces—such as the Mo(112) surface—demonstrate a quite unusual behavior. In contrast to well-known formation of one-dimensional wires lying in furrows of reconstructed surfaces of semiconductors and noble metals, these metals adsorbed on the W(112), Mo(112), and Re(1010) surfaces tend to form commensurate linear structures built of mono-atomic chains directed across the furrows. Monte Carlo simulations of the increasing disorder of the chains with increasing temperature provide a transparent presentation of typical fluctuations in such linear structures. Such studies provide insight into the parameters of indirect interaction that are the basis for the formation of the atomic wires. As with most “metallic” wires on semiconductor surfaces, the linear alkaline earth chains on the furrowed transition metal surfaces do not exhibit strong metallic character but, rather, may be considered as dielectric atomic chains. Such a behavior results from interaction with the substrate, which “ties up” the valence electrons in the adsorption bonds. The local character of these bonds is replaced by a metallic one when the lattice period of the adsorbed layer becomes incoherent with the substrate period along the furrows. In this coverage range, both theory and experiment indicate a Wilson-type NMT transition in the adsorbed layers. Atomic wires, adsorbed on furrowed transition metal surfaces, seem very attractive for the study of fundamental physical problems such as NMT in overlayers.

1. INTRODUCTION

“Wires” call to mind an association with something long and thin and definitely metallic. To this end, atomic chains built from atoms of a metal represent a limiting case of a wire. When adsorbed on stepped or reconstructed surfaces, many metals tend to form long linear or zigzag chains lying in the troughs of the substrate surface. This feature may be considered the “self-assembly” of adsorbed atoms into atomic wires, supported by a “steering effect” along substrate furrows or step edges.

The great interest in the quite special behavior of atomic wires [1–19], in large part, has been caused by the potential

for the creation of conductors of the smallest possible dimensions. The investigation of such systems provides a unique perspective on the limits of nanotechnology [17–28]. The present capabilities of modern techniques, such as scanning tunneling microscope (STM) atomic manipulation, gives the experimentalist precise control of the formation of atomic wires on various substrates. It is now becoming possible to create both single atomic chains and arrays of atomic wires with desirable electronic properties. This opens a new branch of nanotechnology—nanoelectronics [17–28].

Electronic properties of atomic chains depend substantially on the substrate. The Si(111) surface is a particularly convenient substrate, not only for achieving metallic character, but also for obtaining straight and regular step arrays. Thus, stepped (vicinal) Si surfaces, with a slight misfit from the low-index crystallographic plane, form suitable templates for the fabrication of atomic wires [18–26]. The distance between the atomic wires can be adjusted in a wide range by controlling the preparation parameters, and thus the fabrication, by design, of a wide range of novel artificial materials is possible.

To obtain good templates for tailoring atomic wires, one can also explore vicinal surfaces of transition metals, for example, Pt(997), a highly stepped Pt(111) surface [19]. More suitable substrates, however, are the inherently furrowed (112) surfaces of W or Mo and (10 $\bar{1}$ 0) faces of hexagonal close-packed (hcp) Re [29, 30]. These surfaces have very similar structures, which can be described as built from close-packed (2.73–2.76 Å) atomic rows with rather large spacing between them (4.43–4.45 Å). Here the surface potential is corrugated, and one can expect similar formations of the chains of adsorbed alkali or alkaline earth atoms lying in the deep furrows. In fact, at low coverages, the adlayers usually form chains orthogonal to the expected direction. Increasing coverage results in a decrease in spacing between the adatoms due to compression of the films along the furrows, which leads to dramatic transformations of the electronic structure of the overlayers [29, 30]. Hence, at a complete monolayer coverage, the films may be better characterized as metallic chains lying along the substrate furrows. In the case of adsorption of rare earths, the situation is more complicated because of strong interaction with the transition metal surface, which can cause, at elevated temperature, reconstruction of the substrate surface. Nevertheless, in the second layer of Gd on a Mo(112) surface [31], well-developed self-assembled arrays of atomic wires have been found (Fig. 1).

It should be clarified what is actually implied when we speak about the metallicity of adsorbed layers [32, 33]. Of course, metallic wires must be conductive. However, there are inherent problems with direct measurement of the conductance of adsorbed wires [14, 24–27]. Apart from obvious technical complications, any extrinsic contact would unavoidably affect the properties of adsorbed layers, and therefore only limited information could be obtained. On the other hand, a metal can be characterized by the absence of a gap at the Fermi energy and, to some extent, by collective electronic excitations [29, 30, 34]. If we accept these criteria of metallicity, the state of the adsorbed films can be probed (at least in principle) by electron spectroscopy techniques such as ultraviolet photoelectron spectroscopy

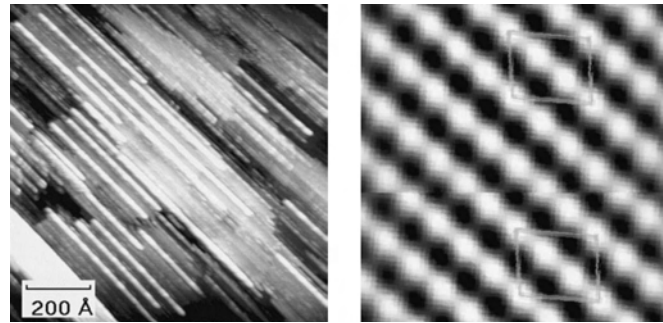


Figure 1. Gd atomic wires on the Mo(112) surface. STM images, obtained for two different scales, illustrate a “self-assembly” forming atomic wires (Courtesy of Ya. B. Losovyj, private communication).

(UPS) [35, 36], inverse photoelectron spectroscopy (IPES) [37], STS (scanning tunneling spectroscopy) [38–40], and electron energy loss spectroscopy (EELS) [34, 41–43]. From the theory side, a metallic state can be better characterized by bands crossing E_F , which also provides a nonzero density of states at the Fermi energy.

Strange as it may sound, in most cases “metallic” wires demonstrate dielectric behavior. For example, STM, core-level and valence-band UPS, and IPES studies of Cs on various $A_{III}B_V$ semiconductor surfaces (GaAs(110), InAs(110), and InSb(110)) reveal the dielectric state of the adsorbed Cs film, even at complete monolayer coverages [44–50].

The issue of metallicity of adsorbed atomic wires is further complicated by the presence of the substrate surface. In many experiments, it is not always clear whether just the adsorbed layer or the semiconductor surface attains a metallic character. In the case of a metallic substrate the situation becomes even more involved. Nevertheless, there are several examples of such adsorption systems for which a NMT has been observed by UPS and EELS [51–57]. The evidence of metallization of adsorbed layers in such experiments is obtained from the increase in the density of states at the Fermi energy (UPS), the appearance of bands crossing E_F (ARUPS), and the appearance of characteristic losses that can be attributed to plasmon excitations.

Actually, our understanding of the electronic structure of atomic wires is based on certain model descriptions of adsorption systems. The more realistic the model, the better the explanation of various phenomena at the surface. To this end, it should be noted that the term “atomic wires” inherently implies a model treatment of wires as free atomic chains. Hence, to learn more about the metallicity of atomic wires, it seems reasonable to study the experimental data within a framework of certain theoretical models, such as a one-dimensional chain or a free monolayer.

The quasi-“one-dimensional” outlook of atomic wires provokes a number of theoretical considerations of electronic structure that are both interesting and exciting, but applying these ideas to real adsorption systems, in terms of a model one-dimensional system, must be done with extreme care. Predictions for one-dimensional electron systems are very exotic [1–18, 58–60]. The increasing amount of correlation between electrons in one dimension results in different

statistics for quasi-particles. In three dimensions the electronic and optical properties of metals are well described by the Fermi liquid theory. In one-dimensional metallic systems the electron-phonon interaction leads to the Peierls instability, whereas the electron-electron interaction may lead to Luttinger liquid behavior. In a Luttinger liquid [58], the electron loses its identity and separates into two quasi-particles, a spinon that carries spin without charge and a holon that carries the positive charge of a hole without spin. It seems possible (in principle) to visualize a holon in a Luttinger liquid as a charge density wave and a spinon as a spin density wave, which might allow one to justify the theory through experimental confirmation from electron spectroscopies applied to atomic wires [9–11, 59, 60].

However, we live in a three-dimensional world, and therefore for real material systems such one-dimensional concepts, as well as main statements based on these theoretical concepts, must be accepted very cautiously. In fact, an atomic wire is not a one-dimensional system. Indeed, atomic size in a wire is compatible with the period and, in many cases, with the length of the wire. The “degree” of the one-dimensionality becomes a challenge when possible mechanisms of the NMTs in atomic wires are considered.

The issue of “dimensionality” emphasizes a fundamental problem of relation between many-body and one-particle approaches in solid-state physics. Usually all discrepancies in calculated band structures with experiment are attributed to limitations of local density approximation (LDA) or, furthermore, density functional theory (DFT) [61–64]. Of course, the band structure rigorously describes only the ground state of an electronic system and cannot treat coherent excitations (plasmons). However, the modern understanding of the band structure [61] implies that it is pertinent to one-particle excitations, that is, for quasi-particles (still called “electrons”), which are not just the “real” electrons as in the Hartree-Fock method. This means that the band structure approach can be applicable to the interpretation, in large measure, of photoemission and inverse photoemission spectra. In spite of many limitations, theory does often give the correct physical picture of surface electronic structure. We will revisit the well-known failure to describe the NMT in the case of monovalent metals, which implies involving many-body effects through the Mott-Hubbard scheme [65], as discussed in some detail below.

In the following sections, we will first consider several examples of real atomic wires built on various semiconductor surfaces (Section 2). The metallicity of atomic wires, which is a focus of this chapter, requires consideration of various types of NMTs and their applicability to the transformations of the electronic structure of adsorbed layers. These issues are discussed in Section 3. The band structure approach to the NMT is the perspective from which this chapter has been prepared. An example of the power of this approach is Mg overlayers on Mo(112), and both band mappings by ARUPS and calculated band structures of this system are presented in Section 4.

2. ATOMIC WIRES ON SEMICONDUCTOR SURFACES

Metals on semiconductors generate a large variety of low-dimensional surface structures with interesting electronic properties. There have been reports of correlation effects destroying the metallicity of surfaces despite an odd electron count per unit cell [66–70], which is somewhat related to the anomalous surface corrugation by charge density waves or by large atomic displacements [71–75]. There has also been mention of metallic nanowires [76–78], of a surface state with mixed dimensionality [19], of spin-charge separation in a Luttinger liquid [1, 2, 60, 79–81], and of a surface with an even electron count becoming metallic [20]. Theory predicts a variety of exotic phases in such low-dimensional systems, which are generated by the increased interactions and subsequent correlations that electrons experience when they are confined.

2.1. Alkali Metal Chains on Reconstructed Si Surfaces

Alkali metal adsorption on a Si(100) surface is among the most heavily investigated systems in surface physics and surface science. The Si(100) surface reconstructs, as a result of dimer formation, and this 2×1 surface has been the substrate of choice for many alkali metal overlayer studies. The adsorption of alkali metals on Si(100) is supposed to lead to the formation of a metallic overlayer with increasing coverage, and the Si(100) 2×1 reconstructed surface is considered nonreactive with respect to alkali metal adsorption. Yet this system remains controversial. Details of charge transfer to the substrate and the overlayer structure are not completely resolved and call into question whether the substrate or the alkali metal overlayer undergo the nonmetal-to-metal phase transition [82].

The 2×1 reconstruction of the Si(100) surface has been characterized by a variety of techniques [82, 83], including STM studies [84]. The buckling of the surface remains a subject of controversy, particularly with respect to the charge distribution of the buckled dimer [85], though recent photoemission studies indicate that the surface dimers are essentially covalent [86]. One problem with the symmetric 2×1 reconstruction of the Si(100) surface is that the surface is metallic in the one-electron picture [87–89]. However, a metallic surface is inconsistent with experiment [90–92]; thus the addition of spin considerations is necessary theoretically to open up a gap [87, 89].

The issue of the adsorption site for alkali metals, which is important with regard to the possible metallicity of atomic wires, is further complicated by the fact that under some circumstances alkali metals will induce 3×2 or 4×1 reconstruction of the Si(100) surface [93–97]. While there have been some theoretical and experimental indications that initial adsorption at least partly favors the highly coordinated sites [93, 94, 98–108], recent STM studies indicate adsorption into T sites [84, 109, 110], largely consistent with LEED intensity analysis [111]. On the other hand, it is important to realize that the theoretically derived “most stable” binding sites are dramatically affected by the choice of the basis function cutoff used in the calculation [112].

There is a general consensus [88, 98–103, 113–126] that at one-half monolayer coverage, the alkali metal overlayer on Si(100) is one-dimensional rows of atoms, that is, atomic wires, with a spacing of 3.84 Å and with the rows more widely separated by some 7.68 Å. Aruga et al. [113] reported a metallic state of K linear chains adsorbed on the reconstructed Si(001) 2×1 surface. Evidence for metallization [113, 119–126] of the K wires, lying on top of the rows of the reconstructed substrate, was derived from the overlayer plasmon dispersion in a K adlayer measured by angle-resolved electron energy loss spectroscopy. At saturation coverage, the intraband plasmon mode was observed, which could identify a metallic character of the K chains. It was proposed that “the K chains adsorbed on Si(001) are in the nature of a one-dimensional metal.” (It should be mentioned here that nature does not provide any example of a real one-dimensional material!)

However, according to suggested estimates [113] of the dipole moments of adsorbed K atoms, the adlayer must be strongly polarized, if not ionized. This follows from a decrease in the work function as well as from the significantly reduced (17%) interatomic distance between adjacent K atoms (3.84 Å along the chain, and the K diameter is 4.62 Å). Therefore, the K valence electrons must all be essentially localized to provide a polar covalent bonding with the semiconductor surface and can hardly be considered as nearly free electrons that are the signature of the metallic state for simple metals. Such a behavior has been reported for Mg layers adsorbed on the Cr₂O₃(111) surface [127]. In contrast to the expected metallic state for a complete Mg monolayer, metallization of the film starts only with the formation of the second layer. Again, a dielectric state of the Mg monolayer results from a strong polar covalent bonding with the substrate. This feature seems typical for adsorption on dielectric and semiconductor surfaces and, unfortunately, prevents observation of metallization within the first monolayer or lesser coverage for alkali metals on silicon [32, 69].

Work with Si(111) [128] suggests that alkali metal interaction with the silicon substrate results in different amounts of charge transfer to the surface as a consequence of changes in the extent of electron occupancy of the gap states at the surface. For clean Si(111), alkali metal adsorption appears to be covalent as in the case of Si(100); indeed there are results obtained with metastable (He*) deexcitation spectroscopy (MDS) studies of cesium adsorption on Si(111) [129] and lithium on Si(111) [130] that are similar to those obtained with Si(100). There are differences between alkali metal adsorption on Si(100) and Si(111) nonetheless.

Total energy calculations [99–102] suggest that alkali metal adsorption induces a substantial surface reconstruction on Si(111), though calculated band structures can still be compared to the photoemission results for Cs on Si(111) [131]. Na [132] and Li [133] adsorption on Si(111) destroys the 2×1 reconstruction on Si(111) [99]. Cs adsorption, on the other hand, changes the 2×1 reconstruction to a $(\sqrt{3} \times \sqrt{3})$ -R30 reconstruction [134], whereas K adsorption preserves the 2×1 reconstruction [135].

Band structure measurements from Reihl and co-workers [132–135] suggest that for Cs, Na, and Li adsorption, the surface remains semiconducting to quite high alkali metal coverages close to one monolayer, in contrast to the total

energy calculation [115] for K on Si(111). Jeon et al. [136] have also used the STM in the microscopy and spectroscopy modes to show that the Na/Si(111) system is a Mott insulator and that a Mott-Hubbard transition occurs as the second layer begins to form at a coverage greater than 2/3. The problem with these measurements, as pointed out by Weiering and Perez [137], is that an STM cannot tell the difference between a Si atom and a Na atom. The 1×3 structure, which Jeon et al. [136] believed to be a third of a monolayer of sodium, is, in fact, reconstructed Si, with a sodium coverage as low as 0.1 of a monolayer, as this is all that is required to reconstruct the Si(111) [137, 138].

The charge transfer from the adsorbed alkali metal to the silicon dangling bond is also uncertain. The calculated charge densities [99–104, 114–116, 126] suggest a nearly complete charge transfer to the silicon dangling bond, indicative of a fairly ionic bond. Ishida and Terakura [126] and others [103, 104] suggest that the adatom is essentially neutral if the electron density is averaged in the alkali adatom sphere. The brightly imaged Li, K, or Cs adatoms on Si(100) in STM pictures have suggested that the alkali adatoms are not completely ionized upon adsorption [84], though the appearance of the lobes of charge density perpendicular to the Si(100) dimer rows for lithium adatoms has been taken as evidence of a charge redistribution due to the silicon-lithium interaction [109, 110].

The degree of charge transfer may in fact be a problem of definition, and the degree of charge transfer may depend solely upon how space is assigned to the alkali metal atoms or silicon dangling bonds [102, 126]. Hybridization between the semiconductor substrate and the alkali metal s,p states undoubtedly plays a role, but relating hybridization to charge transfer, with all of the problems associated with image plane location and atomic locations and size, is difficult at best.

With the large charge transfer to the surface, theory [99–103, 108, 126] predicts that the Si(100) surface becomes metallic at a half-monolayer alkali metal coverage. In the picture where there is a large charge transfer to the silicon, the Si(100) surface has a half-filled band at half-monolayer alkali metal coverage. The silicon surface becomes semiconducting as this band fills completely, which would occur at one monolayer coverage of alkali metal. This is consistent with the increase and subsequent decrease of the apparent density of states with increasing alkali metal coverage, as observed both in MDS [139] and photoemission [140, 141]. In this scheme it is the silicon surface, not the alkali metal overlayer, which becomes metallic. In fact, in this picture, the alkali metal overlayer has no free electron band below the Fermi energy since there is, after all, a depletion of electrons from the alkali metal layer, and therefore the overlayer is essentially nonmetallic [99–103, 126]. Indeed, in the experimental band structure [141–143], the electronic structure of the Si(100)- 2×1 potassium overlayer resembles a semiconductor consistent with this picture.

There is evidence that the surface of Si(100) does not become semiconducting with alkali metal coverages greater than half a monolayer. Inverse photoemission studies [144] provide strong indications that the high-coverage potassium overlayers are metallic, at coverages where the MDS and photoemission intensities at the Fermi energy are no longer

at a maximum. Other band structure studies also suggest an onset to metallicity at close to one monolayer of coverage. On this basis of changes in band structure, Reihl et al. [133] suggested that the NMT occurs at one monolayer, in agreement with Tikhov et al. [145]. The energies of potassium desorption [146] also indicate that for coverages greater than half a monolayer, the adlayer is metallic. The core level shift data from Soukiassian et al. [147] for Na 2p and Cs 4d also indicate an onset of metallicity, but well above half a monolayer. The appearance of a plasmon loss near the alkali metal core-level feature was interpreted to mean that it is the alkali metal overlayer, not the substrate, which goes metallic [147]. In addition, core-level binding energy shifts [148] and second-harmonic generation signals [149] suggest that the onset of metallicity occurs at very low alkali metal coverages (0.25) and the surface remains metallic to saturation (monolayer coverage), as is also indicated by the plasmon-induced electron energy loss [120, 121]. It should be noted that the plasmon data are complicated by the presence and persistence of a clean Si(100) electron energy loss feature at 1.7 eV due to single particle excitations [90, 121, 150–153], and some results indicate the onset of metallicity at relatively low coverages.

2.2. Fabrication of Metallic Atomic Wires

In recent years, several metallic chain structures have been found on semiconductor surfaces [1–28]. The Si(111) substrate has been particularly useful as a substrate, not only as a laboratory for achieving metallic character in surfaces and ultrathin overlayers, but also as a surface for obtaining particularly straight and regular step arrays.

Beyond the flat Si(111) surface, there are opportunities for using stepped Si(111) surfaces to produce tailored, one-dimensional structures with exotic electronic states [18–21, 24–28, 74]. Low step densities, formed with a miscut angle of about 1° , stabilize a single domain of the one-dimensional 532 structure. High miscut angles, such as 9.5° for Si(557) [18–21], create a whole new category of one-dimensional structures that incorporate a step into the unit cell (Fig. 2).

Several of the structures induced by Au on flat and stepped Si(111) have been reported to be metallic [18–21]. Another metallic chain structure is formed by In on Si(111) [79]. One-dimensional structures of Au on Si(111) give a nice example of the options for tailoring electronic states. The number of atomic chains can be modified by adding steps and by varying the Au coverage. This affects the electron count in the unit cell and is critical for metallic versus insulating character.

Gold adsorbed on stepped (vicinal) Si(111) surfaces forms two distinct one-dimensional structures: highly stepped Si(557)-Au (metallic) and flat Si(111) 5×2 -Au (semiconducting) [18, 19]. Both exhibit the chains along the $\langle 110 \rangle$ direction. The Si(111) 5×2 -Au surface contains two rows of Au atoms separated by a single Si row spacing, according to transmission electron microscopy and diffraction. The Si(111)532-Au surface contains one such chain per unit cell, and the Si(557)-Au contains two chains with a spacing of two rows. In addition, the electron count differs in these two structures [19]. The Si(557)-Au surface, with an even

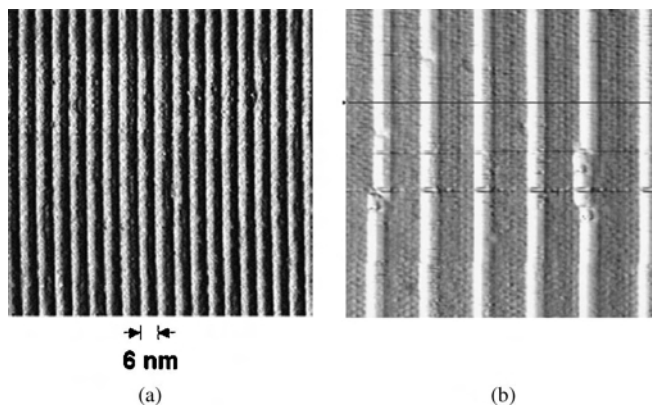


Figure 2. Templates for atomic wires. The images have been obtained with STM with the method of step decoration. (a) Stepped Si surface decorated by CaF_2 adsorbed molecules. (b) Ag wires provide bright decoration of the step edges on Pt(997), a highly stepped Pt(111) surface. Reproduced with permission from [18], F. J. Himpsel et al., *J. Phys.: Condens. Matter* 13, 11097 (2001). © 2001, IOP Publishing Ltd.

electron count, is metallic and seems to defy the conventional wisdom that an even electron count produces a semiconductor and an odd count a metal. Si(111) 5×2 -Au, on the other hand, exhibits a pseudo-gap where the “parabolic” free electron-like band abruptly loses spectral weight before reaching the Fermi level [18, 19].

Metallic behavior is deduced from the observation that the bands extend all the way up to the Fermi level E_F for Si(557)-Au, as in a metal. By way of contrast, the flat Si(111)-Au surface shows a band that does not reach E_F . Another metallic chain structure is formed by In on Si(111) [18, 19]. Vicinal Si surfaces, with adsorbed Au atomic wires, can, in turn, serve as a template for fabrication of mesoscopic wires of Pb [23]. The spontaneous formation of mesoscopic Pb wires, on a 4° off-cut Si(001) vicinal surface, Si(755), Si(533), and Si(110) substrates, was studied by low-energy electron microscopy. Before the deposition of Pb the substrates were modified by predeposition of a submonolayer amount of Au followed by annealing. The Au-induced reconstruction creates quasi-one-dimensional facets and superstructures. Their widths ranged from several hundred nanometers, in the case of the vicinal Si(001) surfaces, down to atomic-scale dimensions, for the Si(110) surface. The best-developed arrays of parallel aligned mesoscopic wires were obtained during the deposition of Pb on substrates cooled slightly below room temperature [23]. Wires with length-to-width ratios reaching 130 were produced on the Si(755) and the Si(533) substrates. The width of these nanowires was uniform over the whole substrate and was about 60 nm. The driving forces for the formation of the mesoscopic wires are the anisotropic strain due to the large misfit between the Pb and the Si lattice and one-dimensional diffusion of Pb.

2.3. Surface Plasmon Modes and Metallicity of Overlayers

The work discussed above raises the issue of what is a metallic state [32, 33] and whether the appearance of the plasmon peak is indeed indicative for the NMT in adsorbed layers. If

we accept the concept of a one-dimensional K metal [121, 131], derived from anisotropy in the plasmon dispersion, it is then quite difficult to explain a dielectric state for adsorbed Cs films. Furthermore, plasmons can be excited in semiconductors, such as silicon, and not just metallic systems. Hence, identification of a metallic state of films and adlayers by EELS needs additional justification.

In general, the EEL spectra contain information about one-particle and collective excitations in bulk as well as in the surface region [154–162]. It is not easy to distinguish the yields from surface and bulk, especially in the presence of an adsorbed layer. Therefore, it is essential to characterize the excitations from the substrate and the adsorbed layer.

A true surface plasmon is a monopole sheet of charge, whose field at $q = 0$ penetrates infinitely into the bulk, that is, the surface plasmon depends upon the bulk charge density [32, 33, 163–165]. This means that such a mode cannot directly characterize excitations just in the adsorbed layers. At submonolayer coverages, there exists so-called multipole surface plasmon mode [32, 33, 163–170] that is dipolar in character and, consequently, because of a fast decay of the field along both vacuum and the bulk directions, develops in very thin films [164, 165]. Thus, the multipole mode of collective excitations is extremely well localized within the surface region, so that its energy, which is usually about 0.6–0.8 of the bulk plasmon energy, is roughly determined by a local electronic density at the surface [164, 165]. A detailed analysis of the collective excitations in thin adsorbed films has shown [163, 164] that with increasing density and thickness of the overlayer film, these modes transform into ordinary surface and bulk plasmons characteristic for the adsorbate.

With an oscillating electrostatic field normal to the surface, this multipole mode (MM), in contrast to a “regular” surface plasmon, can be excited directly by incident photons, which will lead to a strong absorption resonance of the incident light. This occurs when the energy of the incident radiation is close to the energy of the multipole mode [33, 164–170]. The excitation and subsequent decay of the multipole surface plasmons [163–170] are intimately related to enhanced surface photoemission—the surface photoeffect [29, 165–168, 171–177] predicted by Makinson [178].

Obviously, a bulk plasmon as well as a multipole surface plasmon, once excited, can contribute to the photoemission intensity to the extent that each decays to a single-particle excitation with a final-state electron that can escape from the solid [164, 165]. A bulk plasmon that propagates away from the surface also results in strong absorption that can contribute to the photoemission, as in the special cases of a strong coupling of the plasmon with interband transitions in d-metals [164], but generally this is not pronounced. In contrast, the multipole modes are located just at the surface. Therefore, the decay of the MM to electronic excitations gives rise to the resonance in the intensity of the surface photoemission. It should be mentioned, however, that a detailed description of induced electromagnetic fields near the surface (suggested by Feibelman [177]) does not require the MM excitation but provides, nonetheless, explanation of the surface photoeffect in excellent agreement with results of photoemission studies from simple metal surfaces and thin films [165–168, 171, 172, 179–181].

The multipole modes have been directly observed by EELS for surfaces of simple metals [168]. For transition metals, a strong decay of the plasmons due to a high density of states, provided by the d bands, makes the EELS spectra too involved to detect the multipole modes unambiguously. Thus it is not surprising that, for transition metal surfaces, the surface photoeffect has been observed only for Mo(112) [182].

2.4. The “One-Dimensional” Concept and the Free Monolayer Model

While it might appear that the multipole modes might be described as “two-dimensional excitations,” it should be emphasized that these excitations imply a polarization in direction normal to the surface. This feature makes multipole modes, in fact, three-dimensional objects. This is in contrast with inherently one-dimensional Luttinger liquid [58].

It has been put forth that the Luttinger liquid is the proper model for describing an interacting one-dimensional electron system without a gap in the spin or charge excitation channel [2–10]. The characteristics of these excitations must be significantly different from those of the Fermi liquid model for 3D systems. It is one of the peculiarities of Luttinger liquids that elementary excitations are not quasiparticles with charge e and spin $\frac{1}{2}$, but collective charge and spin density fluctuations with bosonic character, so-called spinons and holons. These spin and charge excitations propagate with different velocities, which leads to the separation of spin and charge [2–10, 18].

It was suggested that angle-resolved photoemission studies [3, 4] on “one-dimensional” SrCuO₂ and CuO chains revealed excitations that could not be explained within the conventional band theory, but required a picture in which the spin and charge degrees of freedom for a single electron were separated. Using the one-particle Green function approach for the Tomonaga–Luttinger model of one-dimensional interacting fermions, Meden and Schönhammer [17] have obtained spectral functions that determine photoemission and inverse-photoemission spectra. With this theory, the dispersion relationship can be explained by underlying spinon and holon branches, indicating separated spin and charge excitations [3, 4, 17].

The possibility of the opening of a pseudo-gap that could affect the metal-to-nonmetal transition was questioned by Lieb and Wu [6]. The ground-state energy, wave function, and chemical potentials, obtained with the short-range, one-band model for electron correlations in a narrow energy band, suggested that the ground state should not exhibit the conductor-insulator transition with increasing correlation strength.

Apart from the spin-charge separation, suppression of spectral weight at the Fermi energy E_F is a characteristic feature of a Luttinger liquid. Such a suppression of spectral weight has been reported for a number of quasi-1D compounds (for example, “Berchgaard salts”) by photoemission experiments [59]. Another example is the atomic Au wires on vicinal Si(111). With this system Segovia et al. [2] found collective excitations in photoemission spectra, as one could expect for one dimensional systems. On the other hand,

interpretation of these experiments is still ambiguous. Thus, for Au on the Si(557) surface, Altmann et al. [19] have found that the observed band splitting at E_F rules out the spinon-holon splitting suggested as its origin initially [9, 10, 17]. Indeed, spinon and holon bands are to converge at E_F , and therefore a natural interpretation of the splitting is a closely spaced doublet of ordinary bands crossing E_F .

As commonly recognized, in three dimensions the electronic and optical properties of metals are qualitatively described by the Fermi-liquid theory. There is no reason for the existence of inherently one-dimensional systems, with the associated exotic behavior, in our three-dimensional world. We note that the suggested transformation of electronic excitations into spinons and holons, that is, bosonic excitations, ultimately negates any meaning of a Fermi energy and therefore all related electronic phenomena. Hence, to get exotic behavior one must study extremely exotic systems, but not atomic wires on semiconductor surfaces, which may be better characterized as real objects, with strong anisotropy of electronic properties.

As is evident from the above arguments, the appearance of a loss peak that corresponds to plasmon mode excitations cannot, by itself, prove the existence of a metallic state, nor prove, in particular, the existence of metallic character in the adsorbed layer. Therefore, it is quite important to also explore another approach to determining the presence or absence of metallic character, namely, band structure measurements and calculation.

In the band structure picture, a nonmetal must have a gap at the Fermi energy, while a metallic state could be convincingly characterized by bands crossing the Fermi level. Unfortunately, in reality, the situation is very complicated because of strong complex interactions in the system, and therefore interpretation of the results is not always as straightforward as one would expect. Thus, there is only qualitative agreement between the experimental [140–142] and the theoretical band structures. The theory does not agree with the dispersion relationship for the unoccupied bands, determined by inverse photoemission [88, 133, 144], or the dispersion relationship obtained from photoemission for the occupied bands [102, 140]. The occupied density of states seen in metastable deexcitation spectroscopy [130] and photoemission [140, 141] does resemble the calculated density of states in some calculations [116, 126] but not others [104, 108].

A free monolayer, possible only in model calculations [182–187], avoids the complications caused by the influence of a substrate surface. Obviously, such a simplification can provide only a qualitative description of the electronic structure of adsorbed layers (specifically, atomic wires). Nevertheless, as will be illustrated below by several examples, the free monolayer approach is really capable of explaining many important features of metallic films adsorbed on transition metal surfaces, in particular, the NMT in alkaline earth films with increasing coverage [187]. Application of this idealized model to metal films adsorbed on semiconductor surfaces, however, is rather ambiguous because of a localized character of adsorption bonds, which results in substantial redistribution of valence electrons within the surface region. To this end, it may be noted that it was suggested [18] that interaction with a semiconductor surface should be less

important than that with a metal surface. This statement, it was argued, is in line with empirical considerations, by the lack of the band hybridization that should occur when the bands of the adsorbed metallic layer appear in the energy gap of the substrate. In fact, the situation is just opposite. Usually, in semiconductors, there are narrow bands of surface states in the vicinity of the Fermi energy, which provide strong polar covalent bonding to the adsorbed metal atoms. These bonds remain of a local character even at a complete monolayer coverage, which prevents metallization of the adsorbed films [127]. In the case of a metal substrate, while at low adsorbate coverages the bonding should be somewhat similar (i.e., localized), near a complete monolayer, because of metallization of the overlayer [29, 30, 51–54], the bonding attains a metallic (delocalized) character. Hence, the film acquires a certain “independence,” which makes the free monolayer approximation more realistic.

3. THE NONMETAL-TO-METAL TRANSITION IN FREE MONOLAYERS

Because of strong interaction of the Fermi electrons with phonons, structural instability is characteristic of low-dimensional metals [188]. Hence, unsupported linear metallic atomic wires must be unstable, and therefore the interaction with the substrate surface is essential for the appearance of the appropriate film structures, particularly linear or zigzag atomic chains. Nevertheless, many important properties of the atomic wires can be learned by studying the electronic structure of free, unsupported monolayers. This simple model allows for rigorous band structure calculations for various spacings between atoms. We can describe the dramatic changes in the state of the system, NMT, which must take place with increasing density of a crystal built from atoms of “nominal” metal.

To calculate electronic structure, one may choose, depending on the type of interactions between adsorbed atoms, between quantum-chemical calculations for clusters and the crystal-based band structure approach that is valid for infinite periodic monolayers [182–187]. Each approach has its place. That is, when the attraction between adsorbed particles results in the growth of islands [189–192], it is worthwhile to simulate the onset of metallicity by increasing the cluster size [192–194]. On the other hand, when metallization is caused by a compression of adlayers with repulsion between adatoms, which is mostly the case for alkali and alkaline earth layers adsorbed on smooth transition metal surfaces [29, 30], the calculations for free periodic monolayers with decreasing lattice period [186, 187] seem to be more appropriate for simulating the adsorbed film. In each case, there is the essential issue of what a metal is. Comparison between approaches makes the question rather critical. Thus, a metal may be considered a piece of matter that exhibits conductivity, in other words, that has a certain density of states in the vicinity of the Fermi energy. Such a metal may be a cluster of sufficient size, a liquid or a fluid. Alternatively, a metal is associated with a metallic band structure, whose existence necessarily implies periodicity that is characteristic for crystals. In the literature, this distinction

between the two possible definitions of a metal is usually obscured, thus leaving the reader to guess which approach is actually adopted.

The system studied by the widest variety of approaches, perhaps, is mercury [32, 195–200]. The evolution of the electronic structure of adsorbed films of mercury shows different behavior on different substrates. Various experimental and theoretical approaches have been applied, giving a comprehensive description of the role of a strain in adsorbed Hg layers [195, 196], as well as the critical volume and coordination number [197–200] in the NMT. While fully metallic behavior in Hg clusters occurs for free clusters 70 to 110 atoms [197, 198] in size, corresponding to a coordination number of 9 to 20, the deviation from nonmetallic behavior and the transition toward metallic behavior begins at a coordination number of about 6. A similar cluster approach for Cs overlayers on GaAs [199] has revealed the critical coordination number to be about 3.

What we underscore here is that the cluster-based calculations definitely suggest a nonmetallic state for a coordination number of 2. This means that this approach precludes dielectric behavior in atomic wires for any spacing between atoms.

We will consider the NMT from the point of view of the crystal-based approach, and therefore the complex issues of the “degree” of metallicity (which appears in sufficiently large but still finite sized clusters), density of impurities, and finite temperatures (better described by Anderson transition, but in only three dimensions [201–203]) remain beyond the scope of this chapter. In other words, we will deal with perfect infinite crystals at zero temperature limit to outline basic principles of the NMT resulted from increasing density.

3.1. The Wilson Transition

Most handbooks on solid-state physics associate NMT with the names Mott and Hubbard [65, 204–208] (Mott-Hubbard transition) but sometimes omit Wilson [209, 210], who first (in 1931) described NMT for divalent atoms in a two-band model. The Wilson transition is illustrated in Figure 3 by results of model calculations for free Mg monolayers with a square lattice. When spacing between divalent atoms in

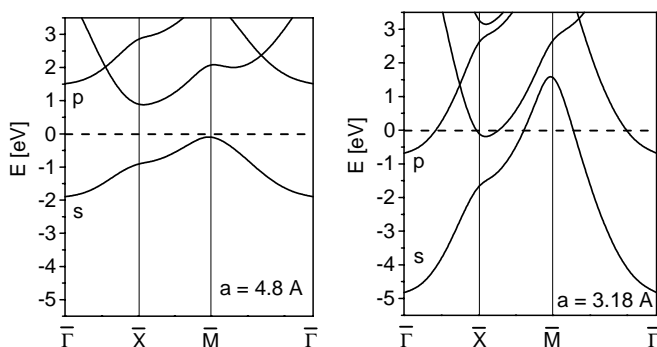


Figure 3. The Wilson transition in a Mg monolayer with a square lattice. A decreasing lattice constant results in a metallic state, which is evident from closing of the gap at E_F .

a crystal is large, the lower s-band is filled and the upper p-band is empty. This results in a dielectric state (at $T = 0$, in the most rigorous definition, the Fermi level locates at the topmost occupied level that is the edge of the s band, as shown in Fig. 3). As the spacing decreases, increasing overlap of atomic orbitals is followed by increasing width of the bands and their hybridization. The gap at E_F vanishes and the crystal becomes metallic.

Wilson’s NMT does not need any special transformation of the structure, and, thus, with decreasing spacing between adsorbed alkaline earth atoms, the NMT is revealed by the rise in the density of states at the Fermi level, which can be observed by ultraviolet photoelectron spectroscopy (UPS) [51–54]. Obviously, a metallic substrate complicates the study of the NMT in adsorbed layers but, on the other hand, provides a unique opportunity to change the density of the adlayer over a rather wide range. To this end, it is important to understand how the changing spacing, between atoms in a free monolayer film, would be revealed in the evolution of the electronic structure. This can be performed by band structure calculations for various structures and lattice densities.

Wimmer [183, 184] and Boettger and Trickey [185] calculated the band structure, density of states (DOS), and cohesive energies for close-packed monolayers of free alkali and alkaline earth. Both studies reported a metallic state in monolayers for lattice spacings that were chosen to be equal to experimental bulk lattice constants or related to the minimum in total energies. According to these calculations, a hexagonal lattice structure has the lowest total energy and, therefore, is the most probable structure for free alkaline earth monolayers.

Transformations of the band structure of alkaline earth free hexagonal monolayers [187] with increasing lattice periods have been studied by the LAPW method for thin films. Results of these calculations revealed a Wilson-type transition that occurs at certain critical spacings between alkaline earth atoms. Thus, when interatomic spacing is large, a dielectric state of Be, Mg, or Ca layers is evident from the band gap at E_F , separating s and p bands (the predominantly s and p characters of the bands are derived from the partial DOS). As the density increases, the bands gradually become wider and hybridization makes the gap close. For close-packed monolayers, the band structure clearly shows a metallic state with two parabolic bands crossing the Fermi level. A rather high DOS at E_F is provided by both the s and p partial densities, which indicates that the metallic state is established because of the s-p band hybridization. This is characteristic of the Wilson NMT. Such a behavior is typical also for Sr and Ba, apart from the substantial contribution of d states to the DOS at E_F .

The issues concerning the role of the coordination number in the NMT have been investigated by calculating the evolution of band structures for bulk Ba and various monolayer structures of Ba as a function of increasing lattice constant [211]. Among the alkaline earth metals, Ba is attractive for model studies because it is rather close in size and behavior to Hg, of which metallization with decreasing spacing is a classic example of the NMT [65]. The calculations were performed by the scalar relativistic (film-) LAPW method [212], assuming a bcc structure for the bulk Ba and hexagonal,

square, and diluted linear structures for monolayers. In the latter case, a rectangular lattice with a longer period of 10 Å was employed to simulate the absence of electron density overlap between the linear chains, while the atomic spacing along the chains was varied. Using essentially the same methods for the bulk and the monolayers, the role of the coordination and dimensionality of the system has been studied by comparing, for each different lattice geometry, the interatomic spacing that corresponds to a sharp rise of DOS at E_F .

The main result in comparing the nearest-neighbor distances between Ba atoms, which is related to the critical NMT point [211], can be summarized as follows. The transition point for bcc Ba corresponds to the nearest-neighbor distance of 7.9 Å, which is much greater than the value of 5.7 Å for the NMT in the monolayers with a hexagonal or square lattice. There is a generally larger critical spacing associated with the larger coordination number in the bulk (8 for bcc Ba), as compared with 6 for hexagonal, 4 for square, and 2 for linear lattices. However, the comparison shows that the critical spacing does not scale as a simple inverse function of the coordination number.

Hence, quasi-one-dimensional atomic wires can be metallic provided that the interatomic spacing is small enough—the NMT in these wires must occur at much smaller lattice periods than in a bulk crystal. This feature may be a reason why Yamada [24] claimed that one-dimensional Mg chains are always nonmetallic. Indeed, apart from well-known limitations of the tight-binding approach when used for simple metals, these calculations do not address the possibility of a small compression of the wires, which is typical for adsorbed layers. For example, in the $(1 \times 1)\text{Mg}/\text{Mo}(112)$ structure [29, 52–54], the distance between Mg atoms in the furrows is 2.73 Å, which is approximately 14% less than the distance between Mg atoms in a bulk crystal. Figure 4 shows the results of model self-consistent LAPW calculations of one-dimensional band structures for linear Mg wires at various characteristic distances between atoms.

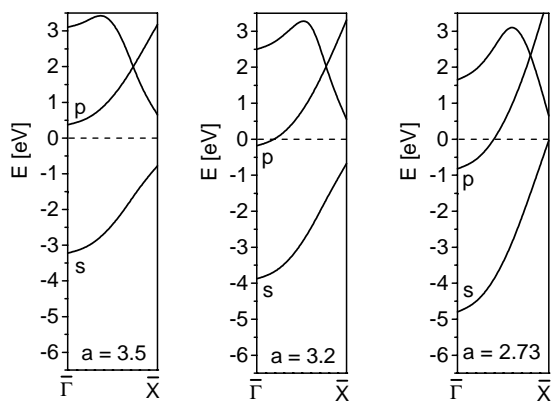


Figure 4. The Wilson transition in linear Mg chains. While for $a = 3.5$ Å the Mg chain is dielectric, at $a = 3.2$ Å, which is about the bulk lattice period of hcp Mg, the wire becomes metallic. For the $p(1 \times 1)\text{Mg}/\text{Mo}$, the distance between Mg atoms located in the furrows is 2.73 Å, and the wires are definitely metallic.

Whereas for $a = 3.5$ Å the chain is obviously dielectric, at $a = 3.2$ Å, which is about the bulk lattice period of hcp Mg, the wire becomes metallic. It should be noted that the position of the Fermi level is determined here from the density of states evaluated while accounting for other chains, which form a rectangular unit cell of the monolayer. In other words, despite of negligible overlap of wave functions of the atoms in neighboring chains (with 10 Å spacing), the system, in fact, still remains three-dimensional (in the direction of the normal to the model monolayer, wave functions are evaluated by numerical integration).

3.2. Mott-Hubbard Transition and the “Failure” of Band Theory

No ghost “many-body effects” are needed to describe the Wilson transition—this can be done solely in terms of electronic band structure transformations resulting from the increasing density of the crystal. This mechanism evidently fails to directly explain the NMT in alkali crystals. Indeed, in considering one-electron (per atom) systems, it seems that the crystal must be metallic, because the lower s band is half-filled, regardless of the lattice constant. For this reason, it has been claimed that a band structure approach should be invalid for the case of strongly localized valence electrons. Thus, it has become a conventional wisdom that the DFT needs certain many-body corrections to account for enhanced correlations that appear in Mott insulators and ferromagnets. To date, it is generally believed that while the NMT in divalent crystals still can be explained as a Wilson transition (that is, in terms of hybridization of the s and p bands), the NMT in monovalent metals unavoidably involves many-body effects and therefore must be attributed to the Mott-Hubbard transition [32, 33, 61, 65, 126, 213–220].

Mott and Hubbard [65, 204–208] suggested a semiempirical picture of the transformation from metallic to insulating phase based on considerations of the gain in total energy. Using atomic ionization potential, affinity, and Hubbard interaction energies U , they have obtained a rather transparent explanation of the transition from localized to delocalized states of valence electrons with decreasing spacing between alkali atoms.

Let us consider two well-known explanations of the Mott-Hubbard transition with changing spacing between monovalent atoms. When the spacing is large, a transfer of an electron from an atom to a neighboring atom would be very unfavorable because of the large increase U in the total energy, which can be roughly estimated as the difference between the ionization potential and the electron affinity of the atom. This is a dielectric state, and valence electrons stay bounded with their atoms. Such a state is described by two narrow Hubbard bands (or several bands in some more sophisticated approaches) that originate from atomic occupied (ns^1) and empty states, separated by an energy U . With decreasing lattice period, increasing overlap of atomic wave functions leads to an increase in the widths B_{upper} and B_{lower} of the upper and lower Hubbard bands, respectively. The resulting increase in widths leads to band tail overlap, which corresponds to the transition to a metallic state. Establishment of a metallic state results in a decrease in

total energy, which largely compensates for the lost U , and electrons gain some freedom (delocalize). The criterion of the NMT [32, 65] may be roughly estimated from the relationship between U and the widths of Hubbard bands as

$$(B_{\text{upper}} + B_{\text{lower}})/2 = U$$

This interpretation of the NMT, in general, seems very reasonable. Indeed, there must be a transition to a dielectric state when the spacing between monovalent atoms becomes large. What is questionable here, however, is validity of the linear combination of atomic orbitals (LCAO) approach based on tight-binding approximation. Such an approach might be more or less justified for describing the dielectric state but becomes, obviously, rather poor for attempting to describe the nearly free electron bands in a simple metal.

Another popular explanation of the Mott-Hubbard transition is based on the consideration of screening (which is a many-body effect) and its dependence on electron density [32, 65]. The screening parameter l_s (inverse screening length) is introduced through the Thomas-Fermi approximation:

$$V(r) = (-e^2/r) \exp(-l_s r)$$

When the screening length exceeds the distance between monovalent atoms, the crystal will be metallic; otherwise the electrons will remain bounded to the ions and therefore the crystal will be a dielectric. Such a description presents an attempt to explain NMT by starting from a metallic state, for which the Thomas-Fermi approximation is acceptable. However, near the transition point and for a dielectric state, the system must be very far from a free-electron gas, and thus macroscopic parameters of screening can lose their physical meaning.

Another challenge with regard to the Mott-Hubbard transition is the order of transition and related transformations in the magnetic state. Though it is generally believed that the Mott-Hubbard transition must be of the first order [32, 65], the situation with magnetic transition is still unclear. Mott [65, 204, 205] considered an array of hydrogen atoms at zero temperature fixed rigidly on a lattice. The ground state of this system can be characterized as follows. At very high density the system will be a paramagnetic metal, while at low densities it will be an insulator and probably antiferromagnetic. Between these two limits there must be a transition from metallic to insulating behavior and from paramagnetic to antiferromagnetic behavior. Thus, Mott [65] suggested that with a decreasing lattice constant, there will occur, at some critical interatomic distance, the dielectric-metal and magnetic transitions (that is, in fact, a single transition). In contrast, the Hubbard model [207] predicted two separate phase transitions that should occur at two different distances between monovalent atoms.

This problem was studied by Rose et al. [221], who used tight-binding band calculations to describe a hydrogen crystal at various interatomic spacings. They also found two separate transitions that originated from the indirect overlap of the spin-split bands. As the spacing decreases, first, the second-order transition from a spin-ordered (ferromagnetic) state to a paramagnetic state occurs. Then, second, with a

further decrease in the spacing, the first-order phase transition from the dielectric state to the metallic state occurs.

For atomic wires, the picture seems even more complicated because of enhanced correlations in a one-dimensional case [1, 32]. Using the short-range one-band model for electron correlations in a narrow energy band, Lieb and Wu [6] have found the ground-state energy, wave function, and chemical potentials in the one-dimensional case. Based on these results, they have found that the ground state exhibits no conductor-insulator transition as the correlation strength is increased.

In contrast, on the basis of self-consistent DFT calculations, Zabala et al. [16] predicted that three-dimensional nanowires of simple metals should undergo a transition from a spin-polarized magnetic state at critical radii. Noteworthy here is that the wires are considered as three-dimensional objects, for which an inherently one-dimensional description, pertinent to excitations in Luttinger liquid [1], is not applicable.

To find a guideline in this quite involved situation and to gain a clear description of the NMT, we will adopt the band structure approach. The present understanding of band structure [61] precludes assigning true one-electron meaning to the bands, as suggested by the Hartree-Fock approach. Rather, the bands should be treated as energies of quasi-particles that may be considered as electrons combined with exchange-correlation holes. Therefore, the many-body effects are in fact included in the band structure (apart from coherent excitations that cannot be treated in the model of quasi-particles with weak interaction). These ideas, first suggested by Wigner and Slater [222–224], have found their justification in the famous Hohenberg-Kohn-Sham DFT [225–227] as well as in a number of experiments. It is the introduced effective exchange correlation potential that has connected the many-body effects to the band structure, thus unavoidably changing its original one-electron meaning.

In some special cases, however, the applicability of the DFT approach was questioned. It was established that the local spin density approximation (LSDA) fails to describe correctly the electronic structure of strongly correlated systems such as Mott insulators, insulator ferromagnets, and 4f metals [228–230]. The inability of LSDA to correctly describe 4f metals occurs mainly because of the incorrect position of spin up $f\uparrow$ and spin down $f\downarrow$ bands if the 4f electrons are treated as bands (not as core states) [231–233]. The increasingly compelling evidence that gadolinium was a local moment system with correlated electrons [234, 235] provoked the development of an improved version of the LSDA method by including the Hubbard U , taken from the mean-field approach to the many-body problem [228, 229]. To date, the LSDA + U method is widely recognized and has proved fruitful in recent calculations of the bulk and surface electronic structure of Gd [236–238]. Because of a better accounting of the intra-atomic correlations, the 4f minority band rises away from the Fermi level, while the 4f majority band increases in binding energy to the correct position [236]. Implementation of the LSDA in the LAPW method for thin films has been accomplished [237], and calculated self-consistent densities of states for Gd(0001) surface provide a reasonable positioning of the occupied 4f

band. Again, inclusion of the Hubbard U allowed for a correct estimation of the magnetic moment as well as of the width of the s-d valence band (above 4 eV) [238]. Nonetheless, the correlation U remains something of a “fudge” factor even in *ab initio* calculations.

On the other hand, the LSDA + U results ultimately predict the existence of the spin minority unoccupied band approximately at +2 eV above E_F . This band originates from the Gd 4f spin minority localized “atomic” state and therefore is very narrow (0.5 eV [236, 238]). This band results in an extremely sharp peak in the unoccupied DOS (the “pure” LSDA approach puts this peak on E_F [236]). The challenge here is that for the Gd surface, such a peak is very difficult to observe in angle-resolved inverse photoemission [239], and the existing assignment cannot be completely definitive.

An alternative approach to the rare earths, with consideration of 4f states as core states, has been argued [240] to be relevant, because of a strong localization of the 4f electrons within the Gd core. It has been suggested [233] that the “first-principle” (pure) LSDA approach can be rescued and resuscitated, provided that the 4f states are treated as core states. Bylander and Kleinman [231, 232], in considering 4f states, proposed that the key to the problem is that exchange and correlation should be treated differently for core states and for bands. Thus, LSDA must be adequate for valence electrons in the band states, whereas for core electrons the Hartree-Fock approximation seems more appropriate. It should be mentioned also that the authors have questioned the validity of the LSDA + U approach in providing a correct electronic structure of Gd.

The example of Gd electronic structure illustrates the essential issues concerning the validity of band structure for strongly correlated systems. Indeed, regardless of the actual description of the system, to obtain some physical picture one needs consideration of the bands. Having the “tentative” band structure, it is possible to estimate certain “many-body corrections” such as the Hubbard U [228, 229] and the inner potential, which is roughly equal to one-half of the bandwidth [32, 182]. However, it is this method, but not the band structure, that has inherent problems, because if the bands are invalid, they cannot be used to properly evaluate the corrections. To this end, using LSDA in a slab model, the electronic structure of the Gd(0001) surface has been obtained in good agreement with spin-resolved ARUPS and IPES results [241], which indicates the validity of the band structure approach, even in the case of localized 4f states.

For the sake of completeness, the very recent evidence of limitations of DFT should be mentioned as well. Using a number of the most sophisticated calculational techniques, Feibelman et al. [112] have suggested that DFT total energy calculations are incapable of predicting correct atomic structures. This tends to negate the value of all total energy calculations performed to date and does not open any new options as an alternative either. The only hope that remains is that, in fact, increasing matrix size (used to achieve a unique convergence) could result in unexpected mathematical problems with numerical stability and applicability of standard diagonalization procedures. In any case, fortunately, this issue concerns only total energy, but not band structure calculations.

Hence, the band structure approach, buttressed with the density functional theory, gives a *correct* description of the ground state of a crystal. Therefore, it must explain the NMT in alkali crystals as well. Indeed, increasing the lattice spacing cannot cancel the band structure because its formation is determined only by the periodicity of a crystal. As the spacing increases, the local density approximation becomes worse, but the challenge is to obtain a qualitative picture of the transition rather than achieve great accuracy in band structure calculations. If, for divalent atoms, the band approach is valid, how can such calculations be completely invalid for monovalent metals?

3.3. Peierls Transition

A natural explanation of the dielectric state of an expanded alkali chain is the Peierls’ distortion [188]—a charge wave that provides a coupling of adjacent atoms (Fig. 5). This coupling leads to a doubling of the period along the chain and thus to an associated decrease in the Brillouin zone. Then the Fermi level falls within the gap that opens at the new edges of the zone, which gives rise to a dielectric state.

The Peierls instability is induced by strong electron-phonon interactions, enhanced by so-called nesting—overlap of parts of the Fermi surface as a result of a translation, $|\mathbf{k}| = 2k_F$. For a spherical Fermi surface of a simple metal, the nesting is negligible and therefore the metal can be stable. In contrast, for a single one-dimensional metallic chain of atoms, the Fermi surface consists of two points, $k = +k_F$ and $k = -k_F$, which results in a perfect nesting and thus leads to instability of the chain. This is why the Peierls distortion is usually considered as a characteristic of essentially one-dimensional metals. However, substantial nesting appears also for a three-dimensional, periodic sequence of noninteracting (or weakly interacting) chains [2–4, 8–17]. In this case, the Fermi surface is very flat and can be approximated by two parallel planes that are perpendicular to the chain direction and can be shifted onto each other by the translation $|\mathbf{k}| = 2k_F$. Hence, the Peierls instability results from the strong anisotropy of metallic chains (wires) rather than from just one-dimensional properties of the system.

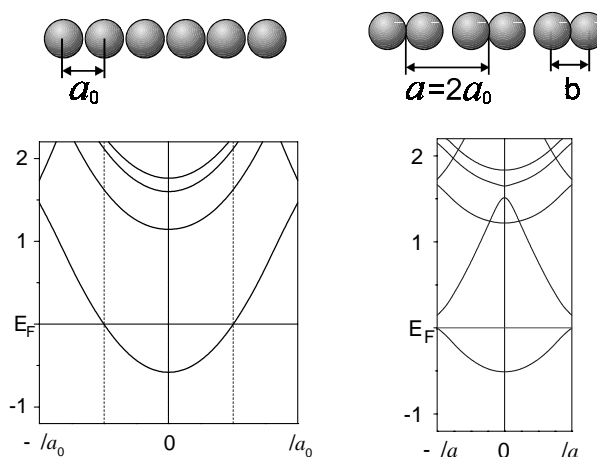


Figure 5. The Peierls transition. Coupling of the atoms in the metallic chain opens the gap at E_F .

It is this behavior that allows one to expect the Peierls distortion and related opening of the gap at E_F for real atomic wires.

In other words, an atomic wire must be unstable toward static periodic lattice distortions due to lowering of the total energy when the gap opens. On the other hand, such a distortion increases the phonon energy, and, hence, the instability of the metallic chain will occur below the Peierls temperature.

In spite of the expectation of dielectric character (due to Peierls instability), some of the atomic wires, such as Au on stepped a Si(557) surface, were found to be metallic [18, 19]. To explain this result, it was suggested [18] that the metal atoms at a silicon surface were locked into the silicon crystal lattice. This provides a means for “anchoring” the chain to prevent dimerization.

3.4. Zigzag Structures and the “Gapless” Peierls Transition

It has been noticed that various adsorbates tend to form zigzag chains when adsorbed to metal or semiconductor surfaces. For example, Cs on $A_{III}-B_V(110)$ surfaces (GaAs and InSb) forms stable one-dimensional zigzag chains extending for several hundred angstroms along the [110] direction [44–46] (Fig. 6), as observed in scanning tunneling microscopy (STM). At 40% of saturation coverage, the quasi-linear chain phase evolves into a 2D cluster layer. Over this whole coverage range, the 1D chains and 2D clusters are found to be insulating. The measured tunneling gap, which narrows with the transition from the 1D to the 2D film structure, provides strong evidence for a band gap and the insulating state of Cs at coverages below a monolayer [44]. The metallic character is observed only with formation of the second Cs overlayer [44].

Such zigzag structures can be a result of Peierls-like distortions but are accomplished by a transverse displacement of every other atom in the chain, and one might expect that this distortion could open up a gap at the Fermi energy. This idea was very attractive, in particular, in the picturesque explanation of a dielectric state of zigzag Cs chains on GaAs. However, purely transverse displacement of the atoms in alkali metal chains will not open a gap at the zone edge, as

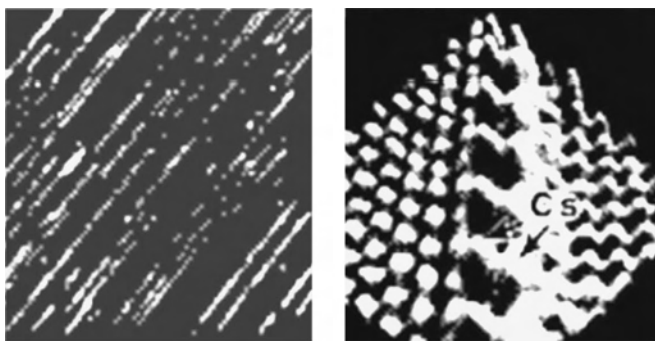


Figure 6. Zigzag Cs wires on GaAs. STM images of Cs chains on the GaAs(110) surface at $\theta = 0.03$. Left: Overview ($1370 \times 1370 \text{ \AA}$). Right: A single Cs zigzag chain ($70 \times 70 \text{ \AA}$). Reprinted with permission from [44], L. J. Whitman et al., *Phys. Rev. Lett.* 66, 1338 (1991). © 1991, American Physical Society.

illustrated by Figure 7. Such a behavior has been explained by Batra [99, 100], who has found that a transverse distortion does not lift the degeneracy at the Brillouin zone edge. Hence, in spite of lowering energy, a transverse distortion, the “gapless Peierls transition,” cannot result in a dielectric state of the Cs atomic wire. This is why the nonmetal state of zigzag Cs chains on GaAs was suggested to be an example of a Mott insulator [47, 48, 100–102, 213–220, 242–248].

These ideas have provoked a number of investigations focused on the search for the gapless Peierls transition in adsorbed atomic wires. For alkali metals on Si(100), the long chains of alkali metal atoms for the metallic half-monolayer coverage surface could potentially exhibit a Peierls-like phase distortion. Longitudinal distortions for such chains are unlikely (spacing distortions along the chain) because of the close spacing between alkali atoms, and in general these “steric” effects favor transverse distortion [102, 104]. However, strong interaction with a semiconductor surface complicates interpretation, and the results obtained thus far are not clearly indicative of the Peierls transition. A more fruitful approach in seeking the evidence for the Peierls transition [100] has been investigation of the trivalent metal overlayers, like Al, Ga, and In, on reconstructed semiconductor and metal (Cu(110) [248–250]) surfaces.

Symmetric dimer formation, rather than the more conventional transverse bulking of the gapless Peierls phase, has been proposed for the 3×2 (third of a monolayer), 2×2 (half monolayer), and other structures observed by low-energy electron diffraction for gallium overlayers on Si(100) [143, 251–253]. Similar results from STM studies [251] tend to confirm that the structures formed by gallium on Si(100) are either more akin to a conventional Peierls distortion (as opposed to a transverse distortion) or a dimer row formation. This is supported by photoemission [143]. Such structures are, in fact, different from both the expected longitudinal and transverse Peierls phase distortions. In Figure 7 (on the right), model band structure calculations are shown to illustrate the opening of the gap in this more complex situation.

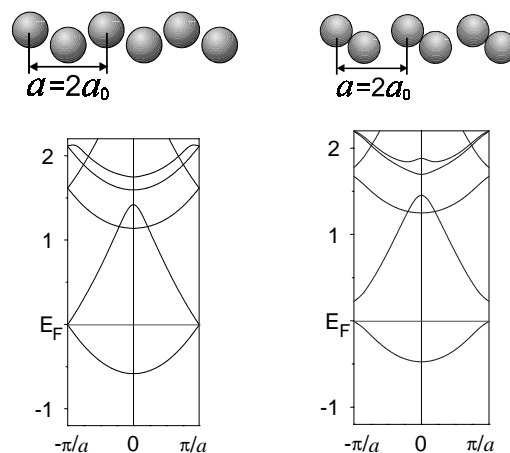


Figure 7. The “gapless” Peierls transition. While a transverse distortion does not open the gap at E_F , rotation of the pairs of monovalent atoms in the chain leads to a dielectric state.

Arsenic overlayers are also seen to form symmetric dimer rows on Si(100) [82, 254–256]. The results for As on Ge(100) 2×1 reconstructed surfaces are very similar [57]. Again, the increasing binding energy of the surface state bands for As on Si(100) [201–203] is not consistent with a gapless, purely transverse Peierls phase transition. Unlike the clean Si(100) reconstructed surface, the dimers of arsenic on Si(100) form filled bonding and antibonding surface states, though these states are not resolved in photoemission [254, 256].

The deposition of indium tends to result in metallic indium island formation [258], but symmetric dimer formation is also observed with submonolayer coverages [258–260]. Given the tendency for indium to aggregate into islands, this overlayer system may not be particularly suitable for investigating a Peierls phase transition. Antimony presents a similar complication, with the observed tendency for the formation of Sb₄ tetramers on top of a chemisorbed Sb layer on Si(100) [261, 262]; nonetheless it is clear that Sb on Si(100) will form dimer rows at submonolayer coverages [260, 263, 264]. As a consequence of the Sb filling of the dangling bond states, a suppression of the silicon surface band structure is seen with Sb adsorption [259].

In adsorbed layers, the Peierls transition from the metallic to the dielectric state has indeed been reported for trivalent Tl and In wires on furrowed $p(1 \times 2)$ Si and GaAs(110) semiconductor surfaces [79]. This mechanism of NMT must be valid for alkali wires [216–218] as well and indicates the importance of further experimental investigations of electronic states of atomic alkali chains for elucidation of this fundamental phenomenon. In particular, the NMT in adsorbed alkali layers with increasing density must be accompanied by a structural phase transition—in the quasi-one-dimensional case of the linear chains, by the change from the coupled to the uniform distribution of atoms along the chains.

Concerning the gapless Peierls transition, it should be noted that though a purely transverse distortion does not lift degeneracy at the Brillouin zone edges, a rotation of pairs of metal atoms in the chain (that is, complex longitudinal-transverse distortion) does result in an opening of the gap (Fig. 7). Experimentally, it will be very difficult to distinguish between purely transverse and such complex distortions. Nevertheless, this task is quite interesting and therefore is worthy of some effort.

In summary, identification of Peierls-like transitions in atomic wires may be characterized as a cornerstone problem in the experimental confirmation of the theory of NMT. By considering Peierls-like distortions, one can reduce the Mott-Hubbard transition to a picture with Wilson-like hybridization, and thus it can be addressed with the band structure approach.

4. ATOMIC WIRES ON FURROWED TRANSITION METAL SURFACES

As follows from previous sections, direct application of theory to atomic wires on semiconductor surfaces is complicated by strong local adsorption interactions, particularly by the localized bonds with possible charge transfer. To this

end, another kind of substrate may be more appropriate—namely, furrowed transition metal surfaces. It might be surprising that a metallic substrate, with its huge bath of free electrons, would provide a better substrate than a good dielectric, but this is indeed the case. We can expect that near a monolayer of coverage the adsorption bonds will be smeared out, giving rise to metallic bonding with the surface. Hence the films will acquire a certain degree of “independence,” which means that the free monolayer model would provide a much better description of the band structure of adsorbed layers than in the case of semiconductor substrate surfaces.

On the other hand, a metal substrate complicates the experimental determination of both metallic and nonmetallic states of an adsorbed metal layer. In photoemission, evidence for the metallization of overlayers can be obtained from an increase in the density of states at Fermi energy and, in the case of angle-resolved photoelectron spectroscopy, from the appearance of surface bands crossing the Fermi level [32]. However, the identification of such a behavior in the photoelectron spectra is not always an easy task, and this is where a comparison with the calculated band structure is essential. Additional evidence for the metallization of overlayers can be obtained with EELS [29, 30, 32–34]. In contrast to semiconductor substrate surfaces, energies of surface and bulk plasmons for transition metals are usually far larger than the plasmon energies in alkali or alkaline earth overlayers. This facilitates identification of the electron losses.

To study the transformation of the state of the overlayers it is reasonable to use, as a substrate, those transition metals that have a low bulk density of states at E_F , such as W or Mo [212, 265]. The (112) surface of these bcc metals, as well as (10 $\bar{1}0$) faces of hexagonal close-packed (hcp) structures, has a furrowed structure built from close-packed (2.73–2.76 Å) atomic rows with rather large spacing between them (4.43–4.45 Å). Here the surface potential is corrugated, and one can expect a similar formation of the chains of adsorbed atoms lying in the deep furrows. In fact the adlayers form chains orthogonal to the expected direction. Thus, as found by LEED studies, at low coverages, many alkali, alkaline earth, and rare earth metals form linear chains—wires—directed across the furrows [29, 30, 51–57, 266–279] (Fig. 8). Increasing coverage can result either in a decrease in the spacing between the chains or in the destruction of the chain structure, depending on the size and dipole moment of adatoms. Evolution of electronic structure with increasing coverage has been the most extensively studied for Mg on the Mo(112) surface [51–54]. Mg atoms at low coverages form such chains with little lateral overlap between valence orbitals of adjacent atoms. At these low coverages, it is now an issue whether these wires are metallic or dielectric. Near the completion of a monolayer, the spacing between Mg atoms along the furrows (2.73 Å for the $p(1 \times 1)$ structure) becomes smaller than that across the furrows (4.45 Å), and, with increasing coverage, one may presume dramatic changes in electronic structure resulting from the compression of the Mg wires along the furrows.

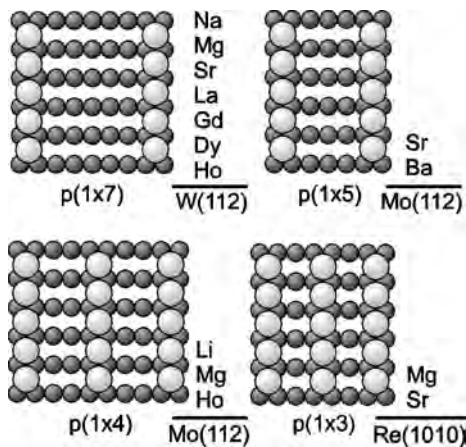


Figure 8. Linear structures on the furrowed transition metal surfaces. Note that preferable distances between various atomic chains depend on the substrate, in spite of the same atomic structures of the surfaces. Reprinted with permission from [30], I. N. Yakovkin, *J. Nanosci. Nanotech.* 1, 357 (2001), © 2001, American Scientific Publishers.

4.1. Lateral Interaction and Formation of Linear Structures

Formation of the commensurate $p(1 \times n)$ linear structures originates from substrate-mediated “indirect” interaction [266, 280–287]. While the distances between the chains in these structures correspond to n periods of the substrate along the furrows, the period along the chains is dictated by the width of the furrows.

Gurney’s model [288] suggests a partial transfer of a valence electron of an adsorbed atom, ideally a simple metal, to the metal or semiconductor substrate surface. The adatom acquires a positive charge, which, together with its image in the substrate, forms a dipole. At low coverages, increasing density of the dipoles leads to a linear decrease of work function. For higher coverages, mutual depolarization of the dipoles results in a gradual decrease of the charge transfer within the double electrical layer, and the film becomes “neutral.” This can be associated with the metallization of the overlayer. This simple description of the charge transfer from the adsorbed layer to the surface has recently been questioned [124–126], causing an extensive discussion [148, 289–306] on the nature of adsorption bonding. For example, from the calculated charge distribution for Cs on W(110) [306], it appears more appropriate to speak about a strong polarization of the adatom rather than charge transfer. However, these results better demonstrate that importance of the covalent part of the adsorption bonding (even for alkali metals) than prove the absence of the charge transfer because of the lack of a definition of the position of the surface plane, which may be arbitrarily chosen.

Regardless of which description is adopted, the decrease of work function reveals the dipole moment μ of adsorbed alkali and alkaline earth atoms, which can be derived through the Helmholtz equation. Lateral interaction between the dipoles with a parallel orientation is repulsive with energy

$$E_{d-d} = 2\mu^2/r^3$$

where r is the distance between adatoms, and the factor of 2 is due to the location of the screening electrons at the surface but not at the position of the image [280]. For example, taking a typical value of the initial dipole moment of Sr on a Mo(112) surface of 2.9 Debyes [270], one can estimate the energy of the dipole-dipole interaction between Sr atoms in adjacent furrows to be about 119 meV. This is why the formation of the linear wires directed across the furrows is so surprising! Hence, there must also be another, strong interaction that can provide the effective attraction between the adatoms in spite of their substantial polarization.

Indirect interaction between adsorbed atoms on a metal surface [280–284] is intimately related to the oscillations in electron density that occurs during screening for an impurity in the volume of a metal [285–287]. The energy of the substrate-mediated (indirect) interaction E_{in} at the surface [266] can asymptotically be estimated as

$$E_{in} \sim r^{-n} \cos(2k_F r + \eta)$$

This energy of the indirect interaction oscillates with distance (Fig. 9), whereas the period is determined by the Fermi vector k_F . Indeed, as illustrated by Figure 8, various adsorbates on the W(112) form a $p(1 \times 7)$ linear structure [266], which indicates the minimum in potential of the indirect interaction between the chains at a distance of 7 periods of the substrate along the furrows.

For Mo(112), presumably because of the smaller size of the Fermi surface, the period of oscillations of the potential seems to fall between 4 and 5 periods of the substrate. Of course, at such a large spacing between the chains, indirect interactions cannot provide any significant displacement of the adatoms from adsorption sites, which is evident from the formation of the coherent (that is, with periods related to several periods of a substrate) linear structures. Therefore, in this situation, the preferable distance between the chains can be 4 or of 5 periods of the Mo(112) surface along the furrows, which is consistent with LEED-derived results

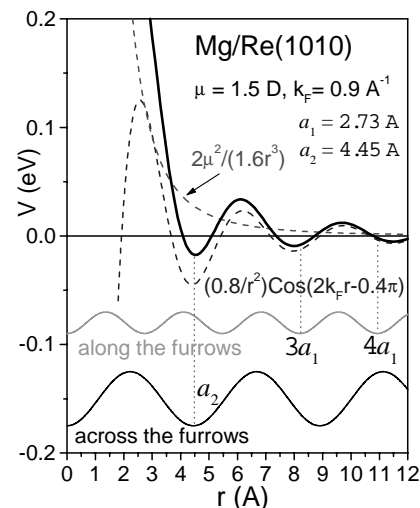


Figure 9. The lateral interactions between adsorbed atoms. The effective potential (solid line) is the sum of indirect and dipole-dipole interactions. Formation of the film structures also depends on the surface corrugation, shown schematically at the bottom.

[269–277]. For example, at low coverages, Li and Mg on Mo(112) form the $p(1 \times 4)$ structure, while Sr and Ba form the $p(1 \times 5)$ structure. On the Re(10 $\bar{1}0$) surface, the effective minimum in the potential of the lateral interaction occurs at the distance between Mg chains of 3 periods of the surface [272]. Hence, despite the quite similar geometry of the substrates, spacing between adsorbed chains is different for these surfaces, which is most likely a consequence of the differences in surface electronic structure that places the pertinent Fermi wave vectors k_F at different values (for each surface).

The effectiveness of the interaction depends on the decay length, which is determined by a power law functional of the distance between the adatoms [266, 287]. It is intuitively clear that the strength of the interaction must depend on the number of electrons that take part in the Friedel oscillations, in other words, density of states at Fermi energy and direction in k -space. Thus, a spherical Fermi surface provides a strong screening and an unfavorable r^{-5} decay, whereas flat electronic jacks lead to much better r^{-2} behavior [266], which is much better for interactions on a longer length scale. The most effective decay function, r^{-1} , for the indirect interaction was predicted for the case of surface bands crossing the Fermi level [266]. Because of a deep minimum in the bulk density of states for W or Mo at the Fermi energy [212, 265], it is just such surface states that can provide the quantity of electrons required for the formation of the chains.

The existence of the surface bands crossing the Fermi level has been confirmed, for the Mo(112) surface, by UPS and IPES experiments [51–54, 182, 307–309] as well as by the band structure calculations [182, 265, 309]. For the Mo(112), “true” surface states occur only in the vicinity of the $\bar{\Gamma}$ point and presumably lie within a gap that relates to d states of different symmetry [182]. Nonetheless, the surface resonance bands crossing the E_F , found from calculations, can facilitate the formation of the linear chains of adsorbed alkali and alkaline earth layers.

Such a band crossing the Fermi level is essential for possible surface reconstruction [310–322] that causes a relative gap to open at Fermi energy, thus decreasing the total energy of the system. This mechanism was suggested for the reconstruction of the Mo(112) surface induced by hydrogen, oxygen, or carbon adsorption [308]. In particular, oxygen adsorption on Mo(112) leads to a surface reconstruction. However, it is still possible to obtain a $p(1 \times 2)$ linear structure of the oxygen layer on an unreconstructed surface of Mo(112). This feature, due to conservation of the Brillouin zone size in the $\bar{\Gamma}\bar{Y}$ direction (that is, across the furrows), has permitted direct identification of the Mo(112) surface bands through the study of the changes in position and dispersion of the bands both with and without oxygen adsorption. Recent IPES (inverse photoemission spectroscopy) data, combined with band structure calculations and symmetry assignments for the surface states [309], supplements our understanding of the electronic structure of the Mo(112) surface, derived from extensive UPS and EELS studies [51–54, 182, 307, 308].

Because of d electrons in the valence band, rare earth adsorbates generally exhibit stronger bonding with transition metal surfaces. Thus, adsorption of rare earth metals [55–57,

278, 279] at elevated temperatures causes a reconstruction of the Mo(112) surface. In particular, a small amount of Dy will drive a compound reconstruction [279] of the Mo(112) surface that can be assigned to a “glassy” state. This means that the Mo(112) surface is not rigid enough to provide a template for the formation of robust rare earth wires across the furrows. In contrast, the rare earths La, Sm, Gd, Dy, and Ho do form the $p(1 \times 7)$ structure on the W(112) surface [266].

No reconstruction of the Mo(112), W(112), or Re(10 $\bar{1}0$) surfaces has been reported with the adsorption of alkali or alkaline earth metals. Having almost identical atomic structures, these surfaces do allow for comparative studies of the influence of the electronic structure of the substrate on the properties of adsorbate.

4.2. Monte Carlo Simulations of the Order–Disorder Transition in Overlayers

Strength of the lateral interaction can be roughly estimated by studying the disordering of the structures of adsorbed layers with increasing temperature. A structure that is well ordered at low temperature can undergo disordering as the temperature increases. This order–disorder transition [267] is due to thermal fluctuations, which can be related to atoms “jumping” to neighboring adsorption sites. The transition point T_{tr} corresponds to the temperature for which the energy of the fluctuations $k_B T$ reaches the energy of the lateral interaction. Then, through measurement of the temperature dependence of the intensity of the LEED reflections related to the overlayer structure, the energies of interaction between the adatoms can be derived. The value of T_{tr} is usually determined by the inflection point in the $I(T)$ plot.

In the case of linear structures, however, the $I(T)$ dependence is of a gradual character [266, 269–272], which can be attributed to a strong anisotropy in the lateral interactions [272]. Generally one presumes that the indirect interaction along a wire must be much stronger than the interaction between the wires. This feature can result in two sequential stages of the disordering with increasing temperature [272]. In the first stage, characteristic fluctuations correspond to adatoms shifted along the furrows from their position in the chains to adjacent adsorption sites (transverse distortions). Increasing the number of these displaced adatoms leads to the formation of fragments of linear chains shifted relative to their initial position. Therefore, the first stage is the loss of coherence in the interchain distances. The second stage is characterized by a disruption of the chains.

Justification of such a picture of the order–disorder transition in linear structures can be obtained from Monte Carlo simulations [323–328] of the distribution of adatoms at various temperatures. Within the lattice gas model, dynamical equilibration of a structure is achieved by moving randomly chosen particles to neighboring sites along the furrows. The probability of each replacement (one “jump”) of the particle is determined by the partition function $\exp(-\Delta E/k_B T)$ or, if the replacement leads to a decrease in the total energy, that is, $\Delta E < 0$, the probability is taken to be unity. As a result of such an equilibration procedure (typically 10–20 jumps per particle are required), at low temperatures,

well-ordered structures of adlayers are formed, whereas at higher temperatures, the adlayers become disordered. The relative intensity of the corresponding LEED reflections can then be evaluated in kinematic approximation, which gives the model $I(T)$ plot required for comparison with experiment. Consideration for the experimental parameters, particularly the typical coherence width for LEED, makes one inclined to choose the size of the matrix to be about $100 \times 100 \text{ \AA}^2$, with periodic boundary conditions. Obviously, formation of the actual overlayer structure depends on the coverage and assumed lateral interactions that can be introduced as parameters that are determined from comparison with experiment. In the case of alkali and alkaline earth adsorption on furrowed surfaces, apart from a long-range dipole-dipole repulsion (which requires one to take into account all particles located at the sites within a rather large circle around the one particle under consideration), the indirect interaction is described by parameters E_1 , the energy of attraction between adjacent atoms in a chain, and E_2 , effective attraction along the furrows at favorable distances derived from LEED experiments.

Shown in Figure 10 are results of the Monte Carlo simulation [328] for $\theta = \frac{1}{4}$ at $T < T_{tr}$ and $T > T_{tr}$. As seen from the top panel, apart from several typical defects, at low temperature, a well-ordered $p(1 \times 4)$ structure is formed, representing the structure of Sr layers on Re(10 $\bar{1}0$) or Na on Mo(112). Though increasing the temperature of the system leads to disordering of the $p(1 \times 4)$ structure, as seen in the bottom panel of Figure 10, at $T \approx 1.5 \cdot T_{tr}$ some fragments

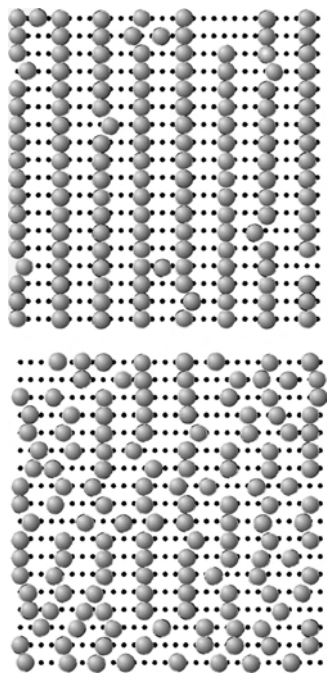


Figure 10. “Snapshots” of the distributions of adsorbed atoms [328] for $\theta = 0.25$. At low temperature, $T < T_{tr}$ (top), a well-ordered $p(1 \times 4)$ structure is formed, representing the structure of Sr layers on Re(10 $\bar{1}0$) or Na on Mo(112). At $T \approx 1.5 \cdot T_{tr}$ (bottom), the film is disordered, but some fragments of the chains still exist, thus revealing a two-stage transition. Reprinted with permission from [30], I. N. Yakovkin, *J. Nanosci. Nanotech.* 1, 357 (2001). © 2001, American Scientific Publishers.

of the chains still exist, thus confirming the above suggestion concerning the character of the typical thermal excitations in the linear structures. It is the possibility of fitting experimental $I(T)$ plots not only at the transition point but over a wide temperature range that allows for an independent determination of the parameters of lateral interaction. For example, the energy of attraction between adjacent atoms in Li chains on Mo(112) has been found to be 20 meV, which is consistent with recent evaluations [278] obtained by adopting the Ising model for the approximation of nearest-neighbor interactions.

From the simulations [328], the most important trends in the lateral interaction can be derived. First, the effective attraction along the chains of alkaline earth adatoms substantially exceeds that obtained for alkalis. This enhanced strength of the alkaline earth wires becomes even more evident if we recall that this indirect interaction must compete with the dipole-dipole repulsion between the adatoms. Then, second, among alkaline earth adsorbates (as well as among alkalis), the strength of the wires increases with a decrease in the dipole moment. It is also worth mentioning that the indirect interaction between atoms of transition metals, reported in an ion field microscopy study of migrations of atomic pairs and clusters [284], much exceeds effective attraction between alkaline earth adatoms, which can be attributed to the significant role of d orbitals in the indirect interaction.

4.3. Nonmetal-to-Metal Transition in Mg Layers Adsorbed on the Mo(112) Surface

Nearly free electrons in simple metals have a parabolic energy dependence (dispersion) on the wave vector. In contrast, a dielectric state is characterized by a flat valence band that does not cross the Fermi level. Hence, the postulated NMT in adsorbed alkaline earth films must be accompanied by a significant transformation of the band structure. In particular, a decreasing distance between linear Mg chains on Mo(112) with increasing coverage should be followed by evolution of the bands from a flat to a parabolic shape along the $\bar{\Gamma}-\bar{X}$ direction in the Brillouin zone (BZ) that in real space corresponds to the direction along the furrows (Fig. 11). Such a transformation must result in the appearance of a band crossing the Fermi level, thus proving that metallization of the film occurs.

These ideas have been confirmed in a detailed ARUPS study of the band transformations with increasing Mg coverage on the Mo(112) surface conducted by Zhang et al. [53, 54]. For the commensurate $p(1 \times 2)$ structure, the distance between the chains (5.46 \AA) substantially exceeds the diameter of the Mg atom (3.20 \AA). Therefore, at $\theta \leq 0.5$, there should be no significant coupling between the Mg chains. The dispersion along $\bar{\Gamma}-\bar{X}$ of the surface resonance (SR) band of -1.6 eV (here and below, the bands are denoted by their energy at $\bar{\Gamma}$ point relatively to the Fermi level) is rather weak (a “flat” band that is characterized by a large effective mass [54]). As the coverage increases, this band gradually attains the parabolic shape inherent for nearly free electrons. For coverages above one monolayer, this SR band is similar to that reported for the Mg(0001) surface [304, 329].

Presented in Figure 11 are the results of self-consistent calculations (performed with the linearized augmented

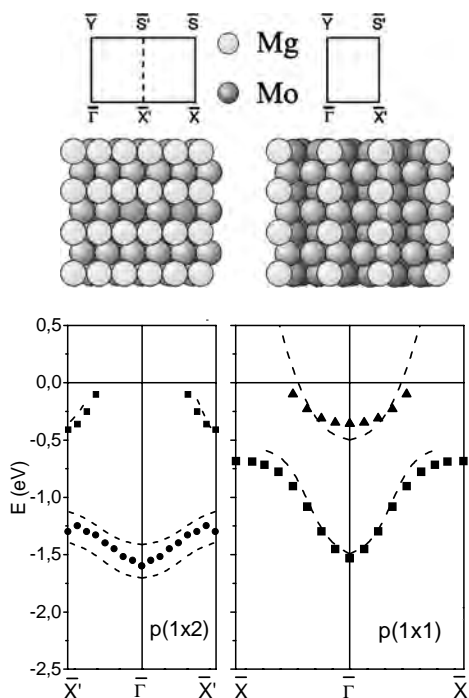


Figure 11. The surface bands [330] along the $\bar{\Gamma}$ - \bar{X} for the $p(1 \times 2)$ (left) and $p(1 \times 1)$ (right) Mg/Mo(112) (dashed lines). The experimental data by Zhang et al. [53] for surface sensitive bands for the Mg/Mo(112) are shown by solid dots. Increasing Mg coverage results in increasing dispersion of the bands and in the band crossing of the Fermi level.

plane wave method for thin films) of the electronic structure of Mg layers, adsorbed on the Mo(112) surface [330], for two characteristic coverages: $\theta = 0.5$, when the alkaline earth films are believed to be dielectric, and $\theta = 1$, when the films are metallic. The states with predominantly surface weight—surface states and resonances—are marked by dashed lines.

As the coverage increases, the one-dimensional compression of the Mg layer along the furrows results in increasing dispersion of the bands and in an increase in the local density of states within the Mg layer. The most convincing evidence of the metallization of adsorbed Mg film is the appearance of the -0.5 eV surface resonance band, which, having a parabolic shape, crosses the Fermi level along the $\bar{\Gamma}$ - \bar{X} direction related to the direction along the furrows (see Fig. 11). Such a behavior is typical for nearly free electrons in simple metals and is therefore indicative of metallicity. Indeed, for the $p(1 \times 2)$ Mg/Mo(112) adsorption system, this band is absent both in ARUPS data [53, 54] (shown by symbols in the Fig. 11) and in the calculated band structure. It is the one-dimensional compression of the Mg layer along the Mo(112) furrows that leads to a loss in coherence with the substrate and attainment of the metallic state of the film.

The increasing density of the adsorbed layer leads to noticeable changes in the charge distribution of the resonances. Thus, for the $p(1 \times 1)$ Mg, the -1.5 eV surface resonance attains certain “metallic” features, such as a more pronounced s character of the charge distribution [330]. In other words, the polar covalent bonding at low coverage transforms to a more delocalized electron “state,”

that is, metallic adsorption bonding at higher coverages. Indeed, on breaking bonds with the substrate, which results from the commensurate-incommensurate phase transition, the valence electrons are largely restored to the Mg film and thus provide the basis for the overlayer film metallization. In this situation the adsorbed films attain a certain independence from the substrate, and the free-monolayer model can give a qualitatively correct description of the surface electronic structure.

5. CONCLUSION

A variety of atomic wires can now be synthesized on furrowed and stepped surfaces, which provides opportunities to systematically tailor the surface properties. These almost one-dimensional systems can be formed by both self-assembly and artificial preparation with STM techniques for a wide variety of adsorbate and substrate combinations. The very unusual electronic features of such systems provide for new possibilities in atomic chain electronics.

For further progress in this new field of nanotechnology, much of the underlying physics remains to be investigated. One of the most important issues here is the metallicity of the atomic wires and how one can control this metallicity. Hence, the nature of the NMT is a key problem to be investigated. Strange as it sounds, but after half a century of study of this fundamental problem of solid state physics, there is no general consensus about mechanisms of the NMT. In large measure, this situation has been provoked by the huge variety of approaches—such as many-body considerations, band structure methods, growing clusters within “first-principle” quantum chemical calculations, and so on—that have, thus far, failed to provide a unified picture.

In this chapter, the NMT is analyzed from the viewpoint of transformation of the band structure. The reason for this choice is simple. The atomic wires are real, that is, three-dimensional, material objects. This implies that exotic one-dimensional theories need not necessarily be involved for an explanation of their behavior. With regard to a many-body approach, it should be mentioned that, aside from its recognized validity in all possible cases, little gain in understanding can be extracted from this quite sophisticated view. Understanding means that a clear picture of a phenomenon is evident. It is very possible that such simple insights can be drawn with semiempirical mean-field approximations that include a variety of parameters such as Hubbard’s U . Nature requires a natural explanation, which, for NMT, can be obtained in terms of transformations of the band structure.

The different ways of describing the NMT have provoked the classification of the NMT into different types, such as the Mott-Hubbard, Wilson, and Peierls. In fact, there is a single phenomenon, revealed in the closing of the gap at E_F , which is characteristic for a dielectric state. Obviously, the gap implies the existence of at least two bands—one below and one above E_F . Whether these bands are called Hubbard bands (that appear through a semiempirical tight-binding approach while claiming to account for many-body effects) or ordinary bands (which can be obtained by using band structure calculation techniques) obviously depends on the approach and view one wishes to apply. Whereas the

former method allows, at best, only qualitative comparison with experiment, the latter provides results that can be directly justified by ARUPS and other techniques that allow band structure mapping, as illustrated in this chapter for Mg atomic wires adsorbed on a Mo(112) surface.

In this context, the issue of the ability of the band structure approach to explain NMT in monovalent crystals is of particular importance. This challenge has provoked much discussion about the interplay between a classical solid-state many-body consideration and the band structure approach. However, there is a simple argument that leads one to advocate the band method. If many-body effects can be avoided in explaining the NMT in divalent crystals, which follows from excellent agreement with experiment, how many body effects could be crucial for the case of monovalent metals? No compelling reason has yet been given, though the suggestion that it is essential has been implicit in many theoretical arguments to date. Hence, there should be another explanation of the nonmetallic state that extends to monovalent crystals. The coupling of adjacent atoms, which results in a lowering of the total energy, affects an even number of valence electrons in the unit cell and could be the unifying idea extending a band structure picture to monovalent systems. Such a coupling is not a particularly one-dimensional effect that can only be attributed to the Peierls distortion, but also occurs in adsorbed films (charge density waves) and in bulk crystals (recall the Jones model for semimetal properties of Bi).

Speaking about the metallicity of atomic wires, we should keep in mind that in reality there must always be present a substrate surface, which unavoidably affects the properties of the overlayers. The interaction with a semiconductor surface can be strong enough even to effect “anchoring” of adsorbed atomic wires, and therefore arguments based on a one-dimensional approach or free monolayer model may be suspect. The success of the application of the free monolayer models in describing atomic wires on furrowed transition surfaces seems to occur because of the nonlocal (metallic) character of adsorption bonding at coverages near a complete monolayer. It should be mentioned here that the classical example of NMT in Hg overlayers has been observed so clearly because of rather weak interaction (as derived from a small heat of adsorption) with a metal surface.

Alkali, alkaline earth, and rare earth atomic wires on furrowed transition metal surfaces, which at low coverages are directed across the furrows, are a consequence of indirect interaction between adsorbed atoms. These wires are robust enough to provide, at room temperature, well-ordered commensurate linear structures observed by LEED. The parameters of the indirect interaction can be evaluated by comparison of experimental results and dependences of LEED intensity derived from Monte Carlo simulations with increasing temperature that causes disordering of the adlayer structures.

As with most “metallic” wires on semiconductor surfaces, the linear alkaline earth chains on the furrowed transition metal surfaces do not exhibit metallicity, but, rather, they may be considered as dielectric atomic chains. Such a behavior results from the interaction with the substrate, which “ties up” the valence electrons in the adsorption bonds. The local character of these bonds is replaced by a metallic

one when the lattice period of the adsorbed layer becomes incoherent with the substrate period along the furrows. In this coverage range, both theory and experiment indicate a Wilson-type NMT in the adsorbed layers.

In summary, recent achievements in the fabrication of atomic wires on semiconductor surfaces, particularly metallic Au wires on stepped Si surfaces, provide a basis for the development of novel materials and thus open new perspectives for nanoelectronics. On the other hand, atomic wires, adsorbed on furrowed transition metal surfaces, still seem to be more attractive for the study of fundamental physical problems such as NMT in overlayers. The author’s viewpoint here is that a theory should not break with experiment, and, hence, direct comparison of the obtained theoretical results with experiment—such as has been demonstrated in the band structure approach—is an essential ingredient for progress.

GLOSSARY

Angle-resolved ultraviolet photoelectron spectroscopy (ARUPS) (synonyms: angle-resolved photoemission, valence band spectroscopy). The major technique for mapping surface and bulk electronic band structures.

Indirect interaction Lateral interaction between adsorbed atoms which is accomplished through electrons of the substrate. Potential of this kind of interaction oscillates with distance between adsorbed atoms and therefore may result in effective attraction at rather large spacings.

Inverse photoelectron spectroscopy (IPES) Efficient method for investigation of “empty” electronic states above the Fermi level.

Linear augmented plane waves (LAPW) Linearized modification (1975) of Slater’s augmented plane wave method (1937) for band structure calculations. Linearization provides a gain in computation time (about 10^2) and thus allows for self-consistent calculations.

Monte Carlo simulations Effective method for the “computer experiment” which provides, in particular, a clear illustration for ordering of adsorbed atoms.

Scanning tunneling microscope (STM) A recently developed device which allows for viewing the surface with atomic resolution. Because of the possibility of atomic manipulation, it gives the experimentalist precise control of the formation of atomic wires on various substrates.

Scanning tunneling spectroscopy (STS) Electron spectra are obtained by using electronic derivation of the tunneling current in STM.

Self-assembling A popular term which implies that ordering of a system can be gained through its own potential (or Providence). Because of thus introduction of a certain mystification, it is better avoided in scientific publications.

Ultraviolet photoelectron spectroscopy (UPS) (usually, angle-integrated).

ACKNOWLEDGMENT

The author thanks P. A. Dowben for many fruitful discussions and helpful comments on the manuscript.

REFERENCES

1. J. Voit, *Rep. Prog. Phys.* 58, 977 (1995).
2. P. Segovia, D. Purdie, M. Hengsberger, and Y. Baer, *Nature* 402, 504 (1999).
3. C. Kim, Z.-X. Shen, N. Motoyama, H. Eisaki, S. Uchida, T. Tohyama, and S. Maekawa, *Phys. Rev. B* 56, 15589 (1997).
4. C. Kim, A. Y. Matsuura, Z.-X. Shen, N. Motoyama, H. Eisaki, S. Uchida, T. Tohyama, and S. Maekawa, *Phys. Rev. Lett.* 77, 4054 (1996).
5. Z.-X. Shen and D. S. Dessau, *Phys. Rep.* 253, 1 (1995).
6. E. H. Lieb and F. Y. Wu, *Phys. Rev. Lett.* 20, 1445 (1968).
7. Z. Zou and P. W. Anderson, *Phys. Rev. B* 37, 627 (1988).
8. T. N. Todorov, J. Hoekstra, and A. P. Sutton, *Phys. Rev. Lett.* 86, 3606 (2001).
9. R. Claessen, U. Schwingenschloegl, M. Sing, C. S. Jacobsen, and M. Dressel, *Physica B* 312–313, 660 (2002).
10. R. Claessen, G.-H. Gweon, F. Reinert, J. W. Allen, W. P. Ellis, Z.-X. Shen, C. G. Olson, L. F. Schneemeyer, and F. Levy, *J. Electron Spectrosc. Relat. Phenom.* 76, 121 (1995).
11. B. Dardel, D. Malterre, M. Grioni, P. Weibel, Y. Baer, and F. Levy, *Phys. Rev. Lett.* 67, 3144 (1991).
12. A. Sekiyama, A. Fujimori, S. Aonuma, H. Sawa, and R. Kato, *Phys. Rev. B* 51, 13899 (1995).
13. N. Motoyama, H. Eisaki, and S. Uchida, *Phys. Rev. Lett.* 76, 3212 (1996).
14. C. C. Wan, H. Guo, and J. Wang, *Phys. Rev. B* 58, 13138 (1998).
15. C. C. Wan, J.-L. Mozos, J. Wang, and H. Guo, *Phys. Rev. B* 55, R13393 (1997).
16. N. Zabala, M. J. Puska, and R. M. Nieminen, *Phys. Rev. Lett.* 80, 3336 (1998).
17. V. Meden and K. Schönhammer, *Phys. Rev. B* 46, 15753 (1992).
18. F. J. Himpsel, K. N. Altmann, R. Bennewitz, J. N. Crain, A. Kirakosian, J.-L. Lin, and J. L. McChesney, *J. Phys.: Condens. Matter* 13, 11097 (2001).
19. K. N. Altmann, J. N. Crain, A. Kirakosian, J.-L. Lin, D. Y. Petrovykh, F. J. Himpsel, and R. Losio, *Phys. Rev. B* 64, 035406 (2001).
20. R. Losio, K. N. Altmann, and F. J. Himpsel, *Phys. Rev. Lett.* 85, 808 (2000).
21. R. Losio, K. N. Altmann, A. Kirakosian, J.-L. Lin, D. Y. Petrovykh, and F. J. Himpsel, *Phys. Rev. Lett.* 86, 4632 (2001).
22. F. Yamaguchi and Y. Yamamoto, *Solid State Commun.* 102, 779 (1997).
23. M. Jalochowski and E. Bauer, *Surf. Sci.* 480, 109 (2001).
24. T. Yamada, *J. Vac. Sci. Technol., B* 15, 1019 (1997).
25. T. Yamada, *J. Vac. Sci. Technol., A* 17, 1463 (1999).
26. T. Yamada, C. W. Bauschlicher, and H. Partridge, *Phys. Rev. B* 59, 15430 (1999).
27. T. Yamada, *J. Vac. Sci. Technol., A* 15, 1280 (1997).
28. T. Yamada and Y. Yamamoto, *Phys. Rev. B* 54, 1902 (1996).
29. I. N. Yakovkin, G. A. Katrich, A. T. Loburets, Yu. S. Vedula, and A. G. Naumovets, *Prog. Surf. Sci.* 59, 355 (1998).
30. I. N. Yakovkin, *J. Nanosci. Nanotechnol.* 1, 357 (2001).
31. Ya. B. Losovyj, I. N. Yakovkin, S. D. Barrett, Takashi Komesu, and P. A. Dowben, *Surf. Sci.*, in press.
32. P. A. Dowben, *Surf. Sci. Rep.* 40, 151 (2000).
33. E. W. Plummer and P. A. Dowben, *Prog. Surf. Sci.* 42, 201 (1993).
34. M. Rocca, *Surf. Sci. Rep.* 22, 1 (1995).
35. E. W. Plummer and W. Eberhard, *Adv. Chem. Phys.* 49, 533 (1982).
36. F. J. Himpsel, *Adv. Phys.* 32, 1 (1983).
37. F. J. Himpsel, *Surf. Sci. Rep.* 12, 1 (1990).
38. Ph. Ebert, M. G. Lagally, and K. Urban, *Phys. Rev. Lett.* 70, 1437 (1993); H. Uchida, D. Huang, F. Grey, and M. Aono, *Phys. Rev. Lett.* 70, 2040 (1993).
39. D. M. Eigler and E. K. Schweizer, *Nature* 344, 524 (1990).
40. M. F. Crommie, C. P. Lutz, and D. M. Eigler, *Science* 262, 218 (1993).
41. P. Nozieres and D. Pines, *Phys. Rev.* 113, 1254 (1959).
42. N. R. Avery, *Surf. Sci.* 111, 358 (1981).
43. J. A. D. Matthew and S. Parker, *Surf. Rev. Lett.* 3, 1345 (1996).
44. L. J. Whitman, J. A. Stroscio, R. A. Dragoset, and R. J. Celotta, *Phys. Rev. Lett.* 66, 1338 (1991).
45. L. J. Whitman, J. A. Stroscio, R. A. Dragoset, and R. J. Celotta, *J. Vac. Sci. Technol., B* 9, 770 (1991).
46. L. J. Whitman, J. A. Stroscio, R. A. Dragoset, and R. J. Celotta, *Phys. Rev. B* 44, 5951 (1991).
47. N. J. DiNardo, J. M. Wong, and E. W. Plummer, *Phys. Rev. Lett.* 65, 2177 (1990).
48. M. G. Betti, V. Corradini, G. Bertoni, S. Gardonio, C. Mariani, L. Gavioli, R. Belkhou, and A. Taleb-Ibrahimi, *Surf. Sci.* 422, 35 (2001).
49. K. O. Magnusson and B. Reihl, *Phys. Rev. B: Solid State* 40, 5864 (1989).
50. J. A. Stroscio and D. M. Eigler, *Science* 254, 1319 (1991).
51. G. A. Katrich, V. V. Klimov, and I. N. Yakovkin, *Ukr. J. Phys.* 37, 429 (1992).
52. G. A. Katrich, V. V. Klimov, and I. N. Yakovkin, *J. Electron Spectrosc. Relat. Phenom.* 68, 369 (1994).
53. J. Zhang, D. N. McIlroy, and P. A. Dowben, *Phys. Rev. B* 49, 13780 (1994).
54. J. Zhang, D. N. McIlroy, and P. A. Dowben, *Phys. Rev. B* 52, 11380 (1995).
55. Ya. B. Losovyj, *Vacuum* 48, 195 (1997).
56. Ya. B. Losovyj, *Vacuum* 54, 19 (1999).
57. Ya. B. Losovyj and N. T. Dubyk, *Vacuum* 54, 25 (1999).
58. J. M. Luttinger, *J. Math. Phys.* 4, 1154 (1963).
59. M. Grioni and J. Voit, in “Electron Spectroscopies Applied to Low-Dimensional Materials” (H. Starnberg and H. Hughes, Eds.). Kluwer, Dordrecht, 2000, p. 209.
60. M. Grioni, I. Vobornik, F. Zwick, and G. Margaritondo, *J. Electron Spectrosc.* 100, 313 (1999).
61. M. Imada, A. Fujimori, and Y. Tokura, *Rev. Mod. Phys.* 70, 1040 (1998).
62. S. L. Sondhi, S. M. Girvin, J. P. Carini, and D. Shahar, *Rev. Mod. Phys.* 69, 315 (1997).
63. H.-L. Lee, J. P. Carini, D. V. Baxter, and G. Grüner, *Phys. Rev. Lett.* 80, 4261 (1998).
64. S. Bogdanovich, M. P. Sarachik, and R. N. Bhatt, *Phys. Rev. Lett.* 82, 137 (1999).
65. N. F. Mott, “Metal-Insulator Transitions.” Taylor & Francis, London, 1974.
66. G. Santoro, S. Scandolo, and E. Tosatti, *Phys. Rev. B* 59, 1891 (1999).
67. F. Flores, J. Ortega, and R. Perez, *Surf. Rev. Lett.* 6, 411 (1999).
68. H. H. Weitering, J. Chen, N. J. DiNardo, and E. W. Plummer, *Phys. Rev. B* 48, 8119 (1993).
69. H. H. Weitering, X. Shi, P. D. Johnson, J. Chen, N. J. DiNardo, and K. Kempa, *Phys. Rev. Lett.* 78, 1331 (1997).
70. V. Ramachandran and R. M. Feenstra, *Phys. Rev. Lett.* 82, 1000 (1999).
71. J. M. Carpinelli, H. H. Weitering, E. W. Plummer, and R. Stumpf, *Nature* 381, 398 (1996).
72. J. M. Carpinelli, H. H. Weitering, M. Bartkowiak, R. Stumpf, and E. W. Plummer, *Phys. Rev. Lett.* 79, 2859 (1997).
73. J. Avila, A. Mascaraque, E. G. Michel, M. C. Asenio, G. Lelay, J. Ortega, R. Perez, and F. Flores, *Phys. Rev. Lett.* 82, 442 (1999).
74. K. Yoo, S. J. Tang, P. T. Sprunger, I. Benito, J. Ortega, F. Flores, P. C. Snijders, M. C. Demeter, and H. H. Weitering, *Surf. Sci.* 514, 100 (2002).
75. A. Mascaraque, J. Avila, J. Alvarez, M. C. Asensio, S. Ferrer, and E. G. Michel, *Phys. Rev. Lett.* 82, 2524 (1999).
76. S. C. Erwin and H. H. Weitering, *Phys. Rev. Lett.* 81, 2296 (1998).
77. F. Pedreschi, J. D. O’Mahony, P. Weightman, and J. R. Power, *Appl. Phys. Lett.* 73, 2152 (1998).

78. I. G. Hill and A. B. McLean, *Phys. Rev. Lett.* 82, 2155 (1999).
79. H. W. Yeom, S. Takeda, E. Rotenberg, I. Matsuda, K. Horikoshi, J. Schaefer, C. M. Lee, S. D. Kevan, T. Ohta, T. Nagao, and S. Hasegawa, *Phys. Rev. Lett.* 82, 4898 (1999).
80. N. Shannon and R. Joynt, *J. Phys.: Condens. Matter* 8, 10 493 (1996).
81. M. G. Zacher, E. Arrigoni, W. Hanke, and J. R. Schrieffer, *Phys. Rev. B* 57, 6370 (1998).
82. R. I. G. Uhrberg and G. U. Hansson, *Crit. Rev. Solid State Mater. Sci.* 17, 133 (1991).
83. D. Haneman, *Rep. Prog. Phys.* 50, 1074 (1987).
84. T. Sakurai, T. Hashizume, I. Kamiya, Y. Hasegawa, N. Sano, H. W. Pickering, and A. Sakai, *Prog. Surf. Sci.* 33, 3 (1990).
85. G. K. Wertheim, D. M. Riffe, J. E. Rowe, and P. H. Citrin, *Phys. Rev. Lett.* 67, 120 (1991).
86. D.-S. Lin, T. Miller, and T.-C. Chiang, *Phys. Rev. Lett.* 67, 2187 (1991).
87. E. Artacho and F. Yudurain, *Phys. Rev. Lett.* 62, 2491 (1989).
88. I. P. Batra, *Phys. Rev. B* 41, 5048 (1990).
89. A. Redondo and W. A. Goddard, *J. Vac. Sci. Technol.* 21, 344 (1982).
90. H. H. Farrell, F. Stuki, J. Anderson, D. J. Frankel, G. J. Lapeyre, and M. Levinson, *Phys. Rev. B* 30, 721 (1984).
91. F. J. Himpsel and D. E. Eastman, *J. Vac. Sci. Technol.* 16, 1297 (1979).
92. F. J. Himpsel and Th. Fauster, *J. Vac. Sci. Technol., A* 2, 815 (1984).
93. T. Abukawa and S. Kono, *Phys. Rev. B* 37, 9097 (1988).
94. T. Abukawa and S. Kono, *Surf. Sci.* 214, 141 (1989).
95. G. S. Glander and M. B. Webb, *Surf. Sci.* 222, 64 (1989).
96. R. Holtom and P. M. Gundry, *Surf. Sci.* 63, 263 (1977).
97. Y. W. Mo, R. Kariotis, B. S. Swartzentruber, M. B. Webb, and M. G. Lagally, *J. Vac. Sci. Technol., A* 8, 201 (1990).
98. M. C. Asenio, E. G. Michel, J. Alvarez, C. Ocal, R. Miranda, and S. Ferrer, *Surf. Sci.* 211–212, 31 (1989).
99. I. P. Batra and S. Ciraci, *Phys. Rev. B* 37, 8432 (1988).
100. I. P. Batra, *Phys. Rev. B* 41, 9162 (1990).
101. I. P. Batra, *J. Vac. Sci. Technol., A* 8, 3425 (1990).
102. I. P. Batra, *Phys. Rev. B* 43, 12322 (1991).
103. K. Kobayashi, Y. Morikawa, K. Terakura, and S. Blugel, *Phys. Rev. B* 45, 3469 (1992).
104. Y. Ling, A. J. Freeman, and B. Delley, *Phys. Rev. B* 39, 10144 (1989).
105. T. Makita, S. Komoto, and A. Ishimaya, *Surf. Sci.* 242, 65 (1991).
106. Y. Ma, J. I. Rowe, G. M. Meigs, and C. T. Chen, *Bull. Am. Phys. Soc.* 37, 224 (1992).
107. P. Pervan, E. Mitchel, G. R. Castro, R. Miranda, and K. Wandelt, *J. Vac. Sci. Technol., A* 7, 1885 (1989).
108. R. Ramirez, *Phys. Rev. B* 40, 3962 (1989).
109. S. Hasegawa and S. Ino, *Phys. Rev. Lett.* 68, 1192 (1992).
110. T. Hashizume, T. Sakurai, H. Tochihara, M. Kubota, and Y. Murata, *Phys. Rev. B* 41, 9688 (1990).
111. C. M. Wei, H. Huang, S. Y. Tong, G. S. Glander, and M. B. Webb, *Phys. Rev. B* 42, 11284 (1990).
112. P. J. Feibelman, B. Hammer, J. K. Norskov, F. Wagner, M. Scheffler, R. Stumpf, R. Watwe, and J. Dumesic, *J. Phys. Chem.* B 105, 4018 (2001).
113. T. Aruga, H. Tochihara, and Y. Murata, *Phys. Rev. Lett.* 53, 372 (1984).
114. S. Ciraci and I. P. Batra, *Phys. Rev. Lett.* 56, 877 (1986).
115. S. Ciraci and I. P. Batra, *Phys. Rev. Lett.* 58, 1982 (1987).
116. S. Ciraci and I. P. Batra, *Phys. Rev. B* 37, 2995 (1988).
117. J. D. Levine, *Surf. Sci.* 34, 90 (1973).
118. E. M. Oellig and R. Miranda, *Surf. Sci.* 177, L947 (1986).
119. A. J. Smith, W. R. Graham, and E. W. Plummer, *Surf. Sci.* 243, L37 (1991).
120. H. Tochihara and Y. Murata, *J. Phys. Soc. Jpn.* 51, 2920 (1982).
121. H. Tochihara, *Surf. Sci.* 126, 523 (1983).
122. T. Aruga, H. Tochihara, and Y. Murata, *Phys. Rev. B* 34, 8237 (1986).
123. T. Aruga and Y. Murata, *Prog. Surf. Sci.* 31, 61 (1989).
124. H. Tsukada, H. Ishida, and N. Shima, *Phys. Rev. Lett.* 53, 376 (1984).
125. H. Ishida, M. Shima, and M. Tsukada, *Phys. Rev. B* 32, 6246 (1985).
126. H. Ishida and K. Terakura, *Phys. Rev. B* 40, 11519 (1989).
127. M. Bender, I. N. Yakovkin, and H.-J. Freund, *Surf. Sci.* 365, 394 (1996).
128. Y. Ma, J. I. Rowe, E. E. Chaban, C. T. Chen, R. L. Headrick, G. M. Meigs, S. Modesti, and F. Sette, *Phys. Rev. Lett.* 65, 2173 (1990).
129. S. Nishigaki, N. Oishi, S. Matsuda, N. Kawanishi, and T. Sasaki, *Phys. Rev. B* 39, 8048 (1989).
130. S. Nishigaki, M. Ohara, A. Murakami, S. Fukui, and S. Matsuda, *Appl. Surf. Sci.* 35, 121 (1988).
131. H. Tochihara, M. Kubota, M. Miyao, and Y. Murata, *Surf. Sci.* 158, 497 (1985).
132. B. Reihl, S. L. Sorensen, R. Dudde, and K. O. Magnusson, *Phys. Rev. B* 46, 1838 (1992).
133. B. Reihl, R. Dudde, L. S. O. Johansson, and K. O. Magnusson, *Appl. Phys. A* 55, 449 (1992).
134. K. O. Magnusson and B. Reihl, *Phys. Rev. B* 39, 10456 (1989).
135. B. Reihl and K. O. Magnusson, *Phys. Rev. B* 42, 11839 (1990).
136. D. Jeon, T. Hashizume, T. Sakurai, and R. F. Willis, *Phys. Rev. Lett.* 69, 1419 (1992).
137. Weitering and Perez, *Phys. Rev. Lett.* 71, 1619 (1993).
138. W. C. Fan and A. Ignatiev, *Phys. Rev. B* 41, 3592 (1990).
139. S. Nishigaki, S. Matsuda, T. Sasaki, N. Kawanishi, Y. Ikeda, and H. Takeda, *Surf. Sci.* 231, 271 (1990).
140. Y. Enta, T. Kinoshita, S. Suzuki, and S. Kono, *Phys. Rev. B* 36, 9801 (1987).
141. Y. Enta, T. Kinoshita, S. Suzuki, and S. Kono, *Phys. Rev. B* 39, 1125 (1989).
142. Y. Enta, S. Suzuki, S. Kono, and T. Sakamoto, *Phys. Rev. B* 39, 5524 (1989).
143. Y. Enta, S. Suzuki, and S. Kono, *Surf. Sci.* 242, 277 (1991).
144. L. S. O. Johansson and B. Reihl, *Phys. Rev. Lett.* 67, 2191 (1991).
145. M. Tikhov, G. Boishiu, and L. Surnev, *Surf. Sci.* 241, 103 (1991).
146. C. R. Castro, P. Pervan, E. G. Michel, R. Miranda, and K. Wandelt, *Vacuum* 41, 564 (1990).
147. P. Soukiassian, M. H. Batshi, Z. Hurych, and T. M. Gentle, *Surf. Sci.* 221, L759 (1989).
148. D. M. Riffe, G. K. Wertheim, J. E. Rowe, and P. H. Citrin, *Phys. Rev. B* 45, 3532 (1992).
149. S. Arekat, S. D. Kevan, and G. L. Richmond, *Europhys. Lett.* 22, 337 (1993).
150. S. Ciraci, R. Butz, E. M. Oellig, and H. Wagner, *Phys. Rev. B* 30, 711 (1984).
151. H. Ibach and J. I. Rowe, *Phys. Rev. B* 10, 710 (1974).
152. S. Maruno, H. Iwasaki, K. Horiaka, S. T. Li, and S. Nakamura, *Phys. Rev. B* 27, 4110 (1983).
153. J. E. Rowe and H. Ibach, *Phys. Rev. Lett.* 32, 451 (1976).
154. J. A. D. Matthew and S. Parker, *Surf. Rev. Lett.* 3, 1345 (1996).
155. P. Soukiassian, R. Rivan, and Y. Borensztein, *Solid State Commun.* 44, 1375 (1982).
156. D. L. Seymour, C. F. McConville, D. P. Woodruff, and J. E. Inglesfield, *Surf. Sci.* 214, 57 (1989).
157. N. R. Avery, *Surf. Sci.* 111, 358 (1981).
158. W. J. Pardee, G. D. Mahan, D. E. Eastman, R. A. Pollak, L. Ley, F. R. McFeely, S. P. Kowalczyk, and D. Shirley, *Phys. Rev. B* 11, 3614 (1975).
159. M. Rocca, *Surf. Sci. Rep.* 22, 1 (1995).
160. P. Nozieres and D. Pines, *Phys. Rev.* 113, 1254 (1959).
161. J. H. Weaver, D. W. Lynch, and C. G. Olson, *Phys. Rev. B* 10, 501 (1974).

162. Y. Ballu, J. Lecante, and H. Rousseau, *Phys. Rev. B* 14, 3201 (1976).
163. A. Liebsch, *Phys. Rev. Lett.* 67, 2858 (1991).
164. A. Liebsch, "Electronic Excitations at Metal Surfaces." Plenum Press, New York and London, 1997.
165. E. W. Plummer, *Solid State Commun.* 84, 143 (1992).
166. R. T. Sprunger, G. M. Watson, and E. W. Plummer, *Surf. Sci.* 269/270, 551 (1992).
167. J. A. Gaspar, A. G. Eguluz, K.-D. Tsuei, and E. W. Plummer, *Phys. Rev. Lett.* 67, 2854 (1991).
168. K. D. Tsuei, E. W. Plummer, A. Liebsch, E. Pehlke, K. Kempa, and P. Bakshi, *Surf. Sci.* 247, 302 (1991).
169. J. J. Quinn, *Phys. Rev.* 126, 1453 (1962).
170. A. Eguluz, S. C. Ying, and J. J. Quinn, *Phys. Rev. B* 11, 2118 (1975).
171. G. A. Katrich and I. N. Yakovkin, *Ukr. Fiz. Zh.* 38, 767 (1993).
172. G. A. Katrich, V. V. Klimov, N. V. Petrova, and I. N. Yakovkin, *Izv. Russ. Ac. Sci., Ser. Phys.* 58, 7 (1994).
173. K. L. Kleiwer, in "Photoemission and the Electronic Properties of Surfaces." Wiley, New York, 1978, p. 45.
174. P. Apel, *Phys. Scr.* 25, 57 (1982).
175. L. Wallden, *Phys. Rev. Lett.* 54, 943 (1985).
176. C.-H. Solterbeck, D. Samuelsen, A. Yang, and W. Schattke, *J. Electron Spectrosc. Relat. Phenom.* 68, 321 (1994).
177. P. J. Feibelman, *Prog. Surf. Sci.* 12, 287 (1982).
178. A. Makinson, *Proc. R. Soc. London, Ser. A* 162, 367 (1937).
179. H. J. Levinson, E. W. Plummer, and P. J. Feibelman, *Phys. Rev. Lett.* 43, 952 (1979).
180. A. Schwartz and W. L. Schaich, *Phys. Rev. B* 30, 1059 (1984).
181. K. Kempa and R. Gerhards, *Solid State Commun.* 53, 579 (1985).
182. I. N. Yakovkin, Jiandi Zhang, and P. A. Dowben, *Phys. Rev. B* 63, 11540 (2001).
183. E. Wimmer, *J. Phys. F* 13, 2313 (1983).
184. E. Wimmer, *J. Phys. F* 14, 681 (1984).
185. J. C. Boettger and S. B. Trickey, *J. Phys.: Condens. Matter* 1, 4323 (1989).
186. H. J. F. Jansen, A. J. Freeman, M. Weinert, and E. Wimmer, *Phys. Rev. B* 28, 593 (1983).
187. I. N. Yakovkin, *Surf. Sci.* 442, 431 (1999).
188. R. E. Peierls, "Quantum Theory of Solids." Clarendon, Oxford, 1955.
189. Y. Q. Cai, A. M. Bradshaw, Q. Guo, and D. W. Goodman, *Surf. Sci.* 399, L357 (1998).
190. G. Lilienkamp, C. Koziol, and E. Bauer, *Surf. Sci.* 226, 358 (1990).
191. J. Kolaczkiwicz and E. Bauer, *Phys. Rev. Lett.* 53, 485 (1984).
192. J. A. Rodriguez and M. Kuhn, *Surf. Sci.* 330, L657 (1995).
193. G. Angonoa, J. Koutecky, and C. Pisani, *Surf. Sci.* 121, 355 (1982).
194. M. G. Mason, *Phys. Rev. B* 27, 748 (1983).
195. P. A. Dowben, D. LaGraffe, D. Li, G. Vidali, J. Zhang, L. Dottle, and M. Onellion, *Phys. Rev. B* 43, 10677 (1991).
196. P. A. Dowben, S. Varma, Y. J. Kime, D. R. Mueller, and M. Onellion, *Z. Phys. B: Condens. Matter* 73, 247 (1988).
197. N. K. Singh and R. G. Jones, *Surf. Sci.* 232, 229 (1990).
198. N. K. Singh, *Phys. Rev. B* 49, 4954 (1994).
199. G. R. Freeman and N. H. March, *J. Chem. Phys.* 98, 9486 (1994).
200. E. Tosatti, in "Electronic Surface and Interface States on Metallic Systems" (E. Bertel and M. Donath, Eds.), p. 6. World Scientific, Singapore, 1995.
201. P. W. Anderson, *Phys. Rev.* 109, 1492 (1958).
202. P. W. Anderson, E. Abrahams, and T. V. Ramakrishnan, *Phys. Rev. Lett.* 43, 718 (1979).
203. P. W. Anderson, *Phys. Rev. B* 23, 4828 (1981).
204. N. F. Mott, *Philos. Mag.* 6, 287 (1961).
205. N. F. Mott, *Philos. Mag.* 13, 989 (1966).
206. J. Hubbard, *Proc. R. Soc. London, Ser. A* 243, 336 (1957).
207. J. Hubbard, *Proc. R. Soc. London, Ser. A* 276, 238 (1963).
208. J. Hubbard, *Phys. Rev. B: Solid State* 17, 494 (1968).
209. A. H. Wilson, *Proc. R. Soc. London, Ser. A* 134, 277 (1931).
210. A. H. Wilson, *Physica* 24, 98 (1958).
211. I. N. Yakovkin and P. A. Dowben, *J. Chem. Phys.* 46, 143 (2000).
212. M. Posternak, H. Kraraue, A.-J. Freeman, and D. D. Koelling, *Phys. Rev. B* 21, 5601 (1980).
213. F. Bechstedt and M. Scheffler, *Surf. Sci. Rep.* 18, 145 (1993).
214. J. Hebenstreit, M. Heineman, and M. Scheffler, *Phys. Rev. Lett.* 67, 10134 (1991).
215. J. Hebenstreit and M. Scheffler, *Phys. Rev. B* 92, 1031 (1992).
216. O. Pankratov and M. Scheffler, *Phys. Rev. Lett.* 70, 351 (1993).
217. O. Pankratov and M. Scheffler, *Phys. Rev. Lett.* 71, 2797 (1993).
218. O. Pankratov and M. Scheffler, *Surf. Sci.* 287/288, 584 (1993).
219. T. Kennedy and E. H. Lieb, *Phys. Rev. Lett.* 59, 1309 (1987).
220. C. Y. Fong, L. H. Yang, and I. P. Batra, *Phys. Rev. B* 40, 6120 (1989).
221. R. Rose, H. B. Shore, and L. M. Sander, *Phys. Rev. B* 21, 3037 (1980).
222. E. P. Wigner, *Trans. Faraday Soc.* 34, 678 (1938).
223. E. P. Wigner, *Phys. Rev.* 46, 1002 (1934).
224. J. C. Slater, *Phys. Rev.* 51, 846 (1937).
225. P. Hohenberg and W. Kohn, *Phys. Rev.* 136, 864 (1964).
226. W. Kohn and L. J. Sham, *Phys. Rev. A* 140, 1133 (1965).
227. L. J. Sham and W. Kohn, *Phys. Rev. B* 145, 561 (1966).
228. V. I. Anisimov, J. Zaanen, and O. K. Andersen, *Phys. Rev. B* 44, 943 (1991).
229. B. N. Harmon, V. P. Antropov, A. I. Liechtenstein, I. V. Solovyev, and V. I. Anisimov, *J. Phys. Chem. Solids* 56, 1521 (1995).
230. D. J. Singh, *Phys. Rev. B* 44, 7451 (1991).
231. D. M. Bylander and L. Kleinman, *Phys. Rev. B* 50, 1363 (1994).
232. D. M. Bylander and L. Kleinman, *Phys. Rev. B* 49, 1608 (1994).
233. O. Eriksson, R. Ahuja, A. Ormeci, J. Tregg, O. Hjorstam, P. Soderlind, B. Johansson, and J. M. Willis, *Phys. Rev. B* 52, 4420 (1995).
234. P. A. Dowben, D. N. McIlroy, and Dongqi Li, in "Handbook on the Physics and Chemistry of Rare Earths" (K. A. Gschneidner and LeRoy Eyring, Eds.), Vol. 24, Chap. 159, p. 1. North-Holland, Amsterdam, 1997.
235. P. A. Dowben, D. N. McIlroy, and Dongqi Li, in "Magnetism and Electronic Correlations in Local Moment Systems" (M. Donath, P. A. Dowben, and W. Nolting, Eds.). World Scientific, Singapore, 1998.
236. R. F. Sabirianov and S. S. Jaswal, *Phys. Rev. B* 55, 4117 (1997).
237. A. B. Shick, A. I. Liechtenstein, and W. E. Pickett, *Phys. Rev. B* 60, 10763 (1999).
238. A. B. Shick, W. E. Pickett, and C. S. Fadley, *Phys. Rev. B* 61, R9213 (2000).
239. Dongqi Li, C. W. Hutchings, P. A. Dowben, C. Hwang, Rong-Tzong Wu, M. Onellion, A. B. Andrews, and J. L. Erskine, *J. Magn. Magn. Mater.* 99, 85 (1991).
240. R. Wu, C. Li, A. J. Freeman, and C. L. Fu, *Phys. Rev. B* 44, 9400 (1991).
241. I. N. Yakovkin, T. Komesu, and P. A. Dowben, *Phys. Rev. B* 66, 035406 (2002).
242. P. N. First, R. A. Dragoset, J. A. Stroschio, R. J. Celotta, and R. M. Feenstra, *J. Vac. Sci. Technol., A* 7, 2868 (1989).
243. A. Calzolari, C. A. Pignedoli, R. Di Felice, C. M. Bertoni, and A. Catellani, *Surf. Sci.* 457, 207 (2000).
244. S. Modesti, A. Falasca, M. Polentarutti, M. G. Betti, V. De Renzi, and C. Mariani, *Surf. Sci.* 133, 447 (2000).
245. J. Ortega and F. Flores, *Phys. Rev. Lett.* 63, 2500 (1989).
246. F. Flores and J. Ortega, *Europhys. Lett.* 17, 619 (1992).
247. F. Flores, *Surf. Rev. Lett.* 2, 513 (1995).
248. C. Binns and C. Norris, *Surf. Sci.* 115, 395 (1982).
249. C. Binns and C. Norris, *J. Phys.: Condens. Matter* 3, 5425 (1991).
250. C. Binns, M. G. Barthes-Labrousse, and C. Norris, *J. Phys. C* 17, 1465 (1984).
251. A. A. Baski, J. Nogami, and C. F. Yates, *J. Vac. Sci. Technol., A* 8, 245 (1990).

252. B. Bourguignon, K. L. Carleton, and S. R. Leone, *Surf. Sci.* 204, 455 (1988).
253. T. Sakamoto and H. Kawanami, *Surf. Sci.* 111, 177 (1981).
254. R. D. Bringans, R. I. G. Uhrberg, M. A. Olmstead, and R. Z. Bachrach, *Phys. Rev. B* 34, 7447 (1986).
255. H. Niehus, K. Mann, B. N. Eldridge, and M. L. Yu, *J. Vac. Sci. Technol., A* 6, 625 (1988).
256. R. I. G. Uhrberg, R. D. Bringans, R. Z. Bachrach, and J. E. Northrop, *J. Vac. Sci. Technol., A* 4, 1259 (1986).
257. J. F. Morar, U. O. Karlsson, R. I. G. Uhrberg, J. Kanski, P. O. Nilsson, and H. Qu, *Appl. Surf. Sci.* 41/42, 312 (1989).
258. L. Knall, J. E. Sundgren, G. V. Hansson, and J. E. Greene, *Surf. Sci.* 166, 512 (1986).
259. D. H. Rich, T. Miller, C. E. Franklin, and T.-C. Chiang, *Phys. Rev. B* 39, 1438 (1989).
260. D. H. Rich, F. M. Leibsle, A. Samsavar, E. S. Hirschorn, T. Miller, and T.-C. Chiang, *Phys. Rev. B* 39, 12758 (1989).
261. S. A. Barnett, H. F. Winter, and G. E. Greene, *Surf. Sci.* 165, 303 (1986).
262. W. F. J. Slijkerman, P. M. Zagwijn, J. F. van der Veen, D. J. Gravensteijn, and G. F. A. van der Walle, *Surf. Sci.* 262, 25 (1992).
263. J. Nogami, A. A. Baski, and C. F. Quate, *Appl. Phys. Lett.* 58, 475 (1991).
264. M. Richter, J. C. Woicik, J. Nogami, P. Pianetta, K. E. Miyano, A. A. Baski, T. Kendelevicz, C. E. Bouldin, W. E. Spicer, C. F. Quate, and I. Lindau, *Phys. Rev. Lett.* 65, 3417 (1990).
265. I. N. Yakovkin, *Surf. Sci.* 389, 48 (1997).
266. O. M. Braun and V. K. Medvedev, *Sov. Phys. Usp.* 32, 328 (1989).
267. I. F. Lyuksyutov, A. G. Naumovets, and V. Pokrovsky, "Two-Dimensional Crystals." Academic, Boston, 1992.
268. J. M. Chen and C. A. Papageorgopoulos, *Surf. Sci.* 21, 377 (1970).
269. V. K. Medvedev and I. N. Yakovkin, *Fiz. Tverd. Tela* 20, 928 (1978).
270. V. K. Medvedev and I. N. Yakovkin, *Fiz. Tverd. Tela* 21, 313 (1979).
271. V. K. Medvedev and I. N. Yakovkin, *Fiz. Tverd. Tela* 23, 669 (1981).
272. I. F. Lyuksyutov, V. K. Medvedev, and I. N. Yakovkin, *JETP* 81, 2452 (1981).
273. V. K. Medvedev and I. N. Yakovkin, *Poverkhnost'* 5, 112 (1982).
274. M. S. Gupalo, V. K. Medvedev, B. M. Palyukh, and T. P. Smereka, *Fiz. Tverd. Tela* 34, 368 (1973).
275. F. M. Honchar, V. K. Medvedev, T. P. Smereka, Ya. B. Losovyj, and H. V. Babkin, *Sov. Phys. Sol. State* 21, 568 (1979).
276. V. K. Medvedev, A. G. Naumovets, and T. P. Smereka, *Surf. Sci.* 34, 368 (1973).
277. F. M. Honchar, V. K. Medvedev, T. P. Smereka, Ya. B. Losovyj, and H. V. Babkin, *Fiz. Tverd. Tela* 29, 2833 (1987).
278. A. Fedorus, D. Kalthoff, V. Koval, I. Lyuksyutov, A. Naumovets, and H. Pfnuer, *Phys. Rev. B* 62, 2852 (2000).
279. A. G. Fedorus, V. P. Koval, A. G. Naumovets, and H. Pfnuer, *Fiz. Nizkikh Temperatur* 27, 68 (2001).
280. T. L. Einstein, *CRC Crit. Rev. Solid State Mater. Sci.* 7, 261 (1978).
281. T. B. Grimley, *Proc. Phys. Soc.* 90, 751 (1967).
282. T. B. Grimley, *J. Am. Soc.* 90, 3016 (1968).
283. J. Kuppers, *Vacuum* 21, 393 (1971).
284. T. T. Tsong, *Phys. Rev. B* 6, 417 (1972).
285. J. Friedel, *Philos. Mag.* 43, 153 (1952).
286. K. H. Lau and W. Kohn, *Surf. Sci.* 75, 69 (1978).
287. A. M. Gabovich, L. G. Il'chenko, E. A. Pashitskiy, and Yu. A. Romanov, *JETP* 75, 249 (1978).
288. R. W. Gurney, *Phys. Rev.* 47, 479 (1935).
289. H. Ishida, *Phys. Rev. B* 38, 8006 (1988).
290. H. Ishida, *Phys. Rev. B* 39, 5492 (1989).
291. P. Soukiassian, T. Kendelewicz, and Z. D. Hurych, *Phys. Rev. B* 40, 12570 (1989).
292. P. Soukiassian, P. Robin, J. Cousty, R. Riwan, and J. Lecante, *J. Phys. C* 18, 4785 (1985).
293. P. Soukiassian, R. Rivan, J. Lecante, E. Wimmer, S. R. Chubb, and A. J. Freeman, *Phys. Rev. B* 31, 4911 (1985).
294. S. A. Lindgren and L. Wallden, *Surf. Sci.* 257, L619 (1991).
295. S. A. Lindgren and L. Wallden, *Surf. Sci.* 211/212, 394 (1989).
296. M. Gautier, E. Marteaux, J. P. Duraud, A. Brenac, and D. Spanjaard, *J. Vac. Sci. Technol., A* 5, 550 (1987).
297. N. Memmel, G. Rangelov, E. Bertel, and V. Dose, *Phys. Rev. B* 43, 4693 (1991).
298. R. Wu, K. Chen, D. Wang, and N. Wang, *Phys. Rev. B* 38, 3180 (1988).
299. E. Lewa and W. Schmickler, *Chem. Phys. Lett.* 160, 75 (1989).
300. T. K. Sham and J. Hrbek, *J. Chem. Phys.* 89, 1188 (1988).
301. B. N. J. Persson and E. Zaremba, *Phys. Rev. B* 30, 5669 (1984).
302. V. O. Karlsson, G. V. Hansson, P. E. S. Persson, and S. A. Flodstrom, *Phys. Rev. B* 26, 1852 (1982).
303. R. A. Bartynski, E. Jensen, T. Gustafsson, and E. W. Plummer, *Phys. Rev. B* 32, 1921 (1985).
304. R. A. Bartynski, R. H. Gaylord, T. Gustafsson, and E. W. Plummer, *Phys. Rev. B* 33, 3644 (1986).
305. J. Bormet, J. Neugerbauer, and M. Sheffler, *Phys. Rev. B* 49, 17242 (1994).
306. S. R. Chubb, E. Wimmer, A. J. Freeman, J. R. Hiskes, and A. M. Karo, *Phys. Rev. B* 36, 4112 (1987).
307. C. Waldfried, D. N. McIlroy, J. Zhang, P. A. Dowben, G. A. Katrich, and E. W. Plummer, *Surf. Sci.* 363, 296 (1996).
308. T. McAvoy, J. Zhang, C. Waldfried, D. N. McIlroy, P. A. Dowben, O. Zeybek, T. Bertrams, and S. D. Barrett, *Eur. Phys. J. B* 14, 747 (2000).
309. H.-K. Jeong, T. Komesu, I. N. Yakovkin, and P. A. Dowben, *Surf. Sci.* 494, L773 (2001).
310. M. I. Holmes and T. Gustafsson, *Phys. Rev. Lett.* 47, 443 (1981).
311. J. S. Campusano, J. E. Inglesfield, D. A. King, and C. Somerton, *J. Phys. C* 14, 3099 (1981).
312. M. Methfessel, D. Hennig, and M. Sheffler, *Phys. Rev. B* 46, 4816 (1992).
313. H. Krakauer, *Phys. Rev. B* 30, 6834 (1984).
314. S. Ohnishi, A. J. Freeman, and M. Weinert, *Phys. Rev. B* 29, 5267 (1984).
315. M. Weinert, A. J. Freeman, and S. H. Ohnishi, *Phys. Rev. B* 56, 2295 (1986).
316. P. C. Stephenson and D. W. Bullet, *Surf. Sci.* 1391 (1984).
317. J. Cousty, R. Riwan, P. Soukiassian, and F. Mila, *J. Phys. C* 19, 2383 (1986).
318. S. L. Weng, E. W. Plummer, and T. Gustafsson, *Phys. Rev. B* 18, 1718 (1978).
319. L. D. Roelofs, R. L. Park, and T. L. Einstein, *J. Vac. Sci. Technol.* 16, 478 (1979).
320. C. Waldfried, D. N. McIlroy, and P. A. Dowben, *J. Phys.: Condens. Matter* 9, 10615 (1997).
321. R. C. Kittler and K. H. Bennemann, *Solid State Commun.* 32, 403 (1979).
322. T. M. Lu, G. C. Wang, and M. G. Lagally, *Phys. Rev. Lett.* 39, 411 (1977).
323. G. Ertl and M. Plancher, *Surf. Sci.* 48, 364 (1975).
324. V. K. Medvedev and I. N. Yakovkin, *Fiz. Tverd. Tela* 19, 1587 (1977).
325. E. D. Williams, S. L. Cunningham, and W. H. Weinberg, *J. Chem. Phys.* 68, 4688 (1978).
326. H. C. Kang and W. H. Weinberg, *J. Chem. Phys.* 90, 2824 (1980).
327. T. T. Tsong, *Surf. Sci.* 122, 99 (1982).
328. I. N. Yakovkin, *Surf. Sci.* 282, 195 (1993).
329. E. V. Chulkov, V. M. Silkin, and E. N. Shirykalov, *Surf. Sci.* 188, 287 (1987).
330. I. N. Yakovkin, *Surf. Sci.* 488, 7 (2001).

Augmented Waves for Nanomaterials

Pavel N. D'yachkov

Russian Academy of Sciences, Moscow, Russia

CONTENTS

1. Introduction
 2. One-Electron Orbitals and Secular Equations
 3. Identities for the Radial Wave Function Inside the Muffin-Tin (MT) Spheres
 4. Linear Augmented Plane-Wave Method
 5. Linear Augmented Cylindrical-Wave Method
 6. Cluster Linear Augmented Spherical-Wave Method
 7. Applications
- Glossary
References

1. INTRODUCTION

It is now generally accepted that in-depth knowledge of the electronic structure and properties of nanomaterials is of great scientific and technological importance. We are now being confronted with the acute problem of first-principle calculation of nanomaterial characteristics. For bulk solids, an augmented plane-wave (APW) method was developed by Slater back in 1937 [1–3]. After a time, the computationally faster linear-APW (LAPW) formalism was presented [4–10]. During the past decades, the techniques for APW and LAPW calculations have reached the point at which, with the aid of large computers, a solution of the band structure problem may be obtained for particular crystals, including those with heavy metals [11, 12]. There is good reason to believe that the LAPW method is one of the most accurate computational schemes in bulk solid-state electronic structure theory. These developments have challenged the generalization of the LAPW approach to low-dimensional systems such as nanofilms, nanowires, nanotubes, and clusters.

In this review, we give a brief overview of the linear augmented wave (LAW) methods for the electronic structure of nanomaterials. These methods are based on a generalization of the bulk LAPW approach. In common with the standard and most simple bulk LAPW (3D-LAPW) technique, the one-electron potential is used and is constructed using a

muffin-tin (MT) approximation. In the MT approximation, a one-electron potential is spherically symmetric in the atomic region and constant in the interstitial region [13]. The constant potential can be taken as the origin for measurements of energy. However, the electronic potential of the nanomaterials differs drastically from that of the bulk system [14, 15]. In reality, the infinite motion of electrons is possible in any direction in crystals, but it is obviously limited in the case of nanomaterials by their size and shape. For example, in the case of nanofilm, there are two vacuum regions above and below the film. The film and vacuum regions are separated by the essentially impenetrable approximately planar potential barriers that are obviously absent in the case of bulk crystal. The term film-MT potential is taken to mean that the one-electron potential is spherically symmetric in the atomic regions and constant in the interstitial region up to the planar potential barriers. In the case of nanotubes with approximately cylindrical symmetry, the cylindrical-MT potential is constant in the interstitial region up to the cylindrical potential barrier. For an approximately spherical nanocrystal, quantum dot, or cluster, the system to be studied and vacuum regions are separated by the spherical potential barrier (spherical-MT potential), and so on.

There are procedures to account for potential variations between the interstitial and vacuum regions; however, for the sake of simplicity, we suggest here that the interstitial and vacuum regions are separated by the step potential barriers. For the same reason, we do not discuss here the full-potential version of the LAW methods, in which one takes into account the one-electron potential variations in the intersphere regions, as well as a nonspherical part of the potential in the MT regions.

The characteristic feature of the LAW methods is that the basis functions in the interstitial regions (where variations in the potential are relatively smooth) are augmented inside the MT spheres by the functions constructed from the exact solutions in these spheres (where variations in the potential are large and the potential is approximately equal to the atomic one). The basis functions in the interstitial regions are different in various materials due to a variety of boundary conditions. These functions are the plane waves in the case of bulk crystals, the cylindrical waves in the case of nanotubes, the spherical waves in the case of

spherical nanocrystals and quantum dots, and so on. In line with the type of basis functions in the interstitial regions, one obtains the 3D-LAPW method for crystals, the linear augmented cylindrical-wave (LACW) method for nanotubes, the linear augmented spherical-wave (LASW) method for spherical systems, and so forth.

2. ONE-ELECTRON ORBITALS AND SECULAR EQUATIONS

In the LAW methods, the concept of one-electron orbitals is used [2, 3, 16–18]. It is assumed that separate electrons in a polyatomic system are characterized by wave functions of their own, or spin orbitals. Each spin orbital ψ_i represents a function of spatial coordinates of the electron and its spin. It is assumed in the simplest approach that spin orbitals can be written as products of spatial and spin functions $\psi_i(\mathbf{r})\alpha$ and $\psi_i(\mathbf{r})\beta$, where α and β are the spin functions of electrons with spins “up” and “down,” respectively. The spatial function $\psi_i(\mathbf{r})$ is called an orbital. A study of the electronic structure of a multiatomic system therefore reduces to a study of its orbitals. These orbitals are functions defined in three-dimensional space and are therefore easy to visualize. The $\psi_i(\mathbf{r})$, together with the corresponding one-electron energies E_i , are found by solving the one-electron Schrödinger equation

$$\hat{H}\psi_i(\mathbf{r}) = E_i\psi_i(\mathbf{r}) \quad (1)$$

with effective one-electron Hamiltonian (in atomic rydberg units)

$$\hat{H} = -\left(\frac{\partial^2}{\partial x^2} + \frac{\partial^2}{\partial y^2} + \frac{\partial^2}{\partial z^2}\right) + U \equiv -\Delta + U \quad (2)$$

This Hamiltonian contains the electron kinetic energy operator, $-\Delta$, and the operator U describing the summed action on the electron in consideration of all the other electrons in the system and all its nuclei α . Finding U is a nontrivial task, which is solved by different quantum chemical methods. For instance, in the Hartree–Fock approximation, U is a non-local operator [16]. In the LAW methods, the local density approximation $U = U(\mathbf{r})$ is commonly used [19–21]:

$$U(\mathbf{r}) = -2 \sum_{\alpha} \frac{Z_{\alpha}}{|\mathbf{r} - \mathbf{R}_{\alpha}|} + 2 \int \frac{\rho(\mathbf{r}')}{|\mathbf{r} - \mathbf{r}'|} dr' + V_{X\alpha}(\mathbf{r}) \quad (3)$$

where Z_{α} and \mathbf{R}_{α} are the nuclear charge and coordinate and $\rho(\mathbf{r})$ is the electron density. The first term in (3) describes attraction between the electrons and nuclei, the second one corresponds to the mutual repulsion of electrons, and $V_{X\alpha}(\mathbf{r})$ is the exchange correlation potential. A frequently used equation for $V_{X\alpha}(\mathbf{r})$ is [2, 3]:

$$V_{X\alpha}(\mathbf{r}) = -6\alpha \left(\frac{3}{8\pi}\rho(\mathbf{r})\right)^{1/3} \quad \alpha = 2/3 \quad (4)$$

In the MT approximation in (3), Z_{α} is substituted for the MT-sphere effective charge and the integral over all space is exchanged for the integral over the intersphere region.

In all LAW methods, the basis functions $\varphi_n(\mathbf{r})$ are everywhere continuous and differentiable, and the Rayleigh–Ritz

variational principle is then easily applied. Expanding the electronic wave functions

$$\psi_i(\mathbf{r}) = \sum_n c_{i,n} \varphi_n(\mathbf{r}) \quad (5)$$

and applying the variational principle then yield the secular equations:

$$\det\|\langle\varphi_n|\hat{H}|\varphi_m\rangle - E\langle\varphi_n|\varphi_m\rangle\| = 0 \quad (6)$$

$$\sum_n [\langle\varphi_n|\hat{H}|\varphi_m\rangle - E_i\langle\varphi_n|\varphi_m\rangle]c_{i,n} = 0 \quad (7)$$

where $\langle\varphi_n|\hat{H}|\varphi_m\rangle$ and $\langle\varphi_n|\varphi_m\rangle$ are the Hamiltonian \hat{H} and overlap matrix elements, respectively. The most important feature of the LAW secular equations (6) and (7) is that the Hamiltonian and overlap matrices are energy independent, which permits the simultaneous determination of the eigenvalues E_i and eigenvectors $c_{i,n}$.

3. IDENTITIES FOR THE RADIAL WAVE FUNCTION INSIDE THE MUFFIN-TIN SPHERES

Let us consider a single MT sphere and derive some formulas common to all LAW methods [4, 5]. Inside the MT sphere α , the Hamiltonian \hat{H} is spherically symmetric. The radial wave function $u_{l,\alpha}(E_{l,\alpha}, r)$ is taken to be the solution of the radial Schrödinger equation with energy $E_{l,\alpha}$:

$$\hat{H}u_{l,\alpha}(r) = E_{l,\alpha}u_{l,\alpha}(r) \quad (8)$$

In the LAW formalism, $E_{l,\alpha}$ is kept fixed within some energy region. In rydberg units, this equation takes the form:

$$\frac{1}{r} \frac{\partial^2}{\partial r^2} (ru_{l,\alpha}) + \left[E_{l,\alpha} - V_{\alpha}(r) - \frac{l(l+1)}{r^2} \right] u_{l,\alpha} = 0 \quad (9)$$

where $V_{\alpha}(r)$ is the local density spherically symmetric potential in the region of the MT sphere α and $E_{l,\alpha}$ are the constant-energy parameters. The functions $u_{l,\alpha}(E_{l,\alpha}, r)$ are normalized inside the MT spheres with radius r_{α} as

$$\int_0^{r_{\alpha}} u_{l,\alpha}^2 r^2 dr = 1 \quad (10)$$

$$\int_0^{r_{\alpha}} u_{l,\alpha} \hat{H} u_{l,\alpha} r^2 dr = E_{l,\alpha} \quad (11)$$

Differentiating (8) and (9) with respect to energy yields a differential equation for the radial energy derivative functions $\dot{u}_{l,\alpha}(E_{l,\alpha}, r) = \partial u_{l,\alpha}(E_{l,\alpha}, r) / \partial E_{l,\alpha}$:

$$\hat{H}\dot{u}_{l,\alpha}(r) = u_{l,\alpha}(r) + E_{l,\alpha}\dot{u}_{l,\alpha}(r) \quad (12)$$

$$\frac{1}{r} \frac{\partial^2}{\partial r^2} (r\dot{u}_{l,\alpha}) + u_{l,\alpha} + \left[E_l - V_{\alpha}(r) - \frac{l(l+1)}{r^2} \right] \dot{u}_{l,\alpha} = 0 \quad (13)$$

The functions $u_{l,\alpha}(E_l, r)$ and $\dot{u}_{l,\alpha}(E_l, r)$ will be orthogonal as can be seen by differentiating (10) with respect to energy

$$\int_0^{r_{\alpha}} u_{l,\alpha} \dot{u}_{l,\alpha} r^2 dr = 0 \quad (14)$$

and

$$\int_0^{r_\alpha} \dot{u}_{l,\alpha} \widehat{H} u_{l,\alpha} r^2 dr = 0 \quad \int_0^{r_\alpha} u_{l,\alpha} \widehat{H} \dot{u}_{l,\alpha} r^2 dr = 1 \quad (15)$$

$$\int_0^{r_\alpha} \dot{u}_{l,\alpha} \widehat{H} \dot{u}_{l,\alpha} r^2 dr = E_{l,\alpha} N_{l,\alpha}$$

where

$$N_{l,\alpha} = \int_0^{r_\alpha} (\dot{u}_{l,\alpha})^2 r^2 dr \quad (16)$$

Multiplying (9) by $r^2 \dot{u}_{l,\alpha}$ and (13) by $r^2 u_{l,\alpha}$, subtracting (13) from (9), and integrating $\int_0^{r_\alpha} dr$ then yield the identity:

$$\int_0^{r_\alpha} r \left(\dot{u}_{l,\alpha} \frac{\partial^2}{\partial r^2} (r u_{l,\alpha}) - u_{l,\alpha} \frac{\partial^2}{\partial r^2} (r \dot{u}_{l,\alpha}) \right) dr = 1 \quad (17)$$

Moreover, we have

$$\int r \left(\dot{u}_{l,\alpha} \frac{\partial^2}{\partial r^2} (r u_{l,\alpha}) - u_{l,\alpha} \frac{\partial^2}{\partial r^2} (r \dot{u}_{l,\alpha}) \right) dr$$

$$= r^2 \left(\dot{u}_{l,\alpha} \frac{\partial}{\partial r} u_{l,\alpha} - u_{l,\alpha} \frac{\partial}{\partial r} \dot{u}_{l,\alpha} \right) \quad (18)$$

Finally, from (17) and (18), we obtain

$$r^2 [\dot{u}_{l,\alpha}(r) u'_{l,\alpha}(r) - u_{l,\alpha}(r) \dot{u}'_{l,\alpha}(r)]|_{r=r_\alpha} = 1 \quad (19)$$

where $u'_{l,\alpha} = \partial u_{l,\alpha} / \partial r$ and $\dot{u}'_{l,\alpha} = \partial \dot{u}_{l,\alpha} / \partial r$ are radial derivatives of the $u_{l,\alpha}$ and $\dot{u}_{l,\alpha}$ functions.

4. LINEAR AUGMENTED PLANE-WAVE METHOD

4.1. Bulk LAPW Method

It is instructive to start with the 3D-LAPW method for a bulk crystal [4, 5].

4.1.1. Forming the Bulk Basis Functions

In the interstitial region (Ω_{II}), the one-electron potential is constant, and the basis functions $\varphi_n(\mathbf{r})$ (5) are the plane waves

$$\varphi_{II,n}(\mathbf{k}, \mathbf{r}) = (1/\Omega)^{1/2} \exp(i\mathbf{K}_n \mathbf{r}) \quad (20)$$

which are the solutions of the Schrödinger equation with Hamiltonian $\widehat{H} = -\Delta$. Here, Ω is the volume of the unit cell, $\mathbf{K}_n = \mathbf{k} + \mathbf{k}_n$, \mathbf{k} is the reduced wave vector, and \mathbf{k}_n is the reciprocal lattice vector.

Inside the muffin-tin spheres (Ω_I), the basis function $\varphi_n(\mathbf{r})$ is a linear combination of spherical solutions. In the local spherical coordinate system $\rho = \{\rho, \theta, \varphi\}$, it takes the form

$$\varphi_{I\alpha,n}(\rho, \theta, \varphi) = \sum_{lm} [A_{lm,\alpha}^n u_{l,\alpha}(E_{l\alpha}, \rho) + B_{lm,\alpha}^n \dot{u}_{l,\alpha}(E_{l\alpha}, \rho)] Y_{lm}(\hat{\rho}) \quad (21)$$

where $\sum_{lm} \equiv \sum_{l=0}^{\infty} \sum_{m=-l}^l$ and $Y_{lm}(\hat{\rho}) \equiv Y_{lm}(\theta, \varphi)$. The plane wave (20) can be written in terms of the local coordinate system $\{\rho, \theta, \varphi\}$:

$$\varphi_{II,n}(\rho, \theta, \varphi) = (1/\Omega)^{1/2} \exp(i\mathbf{K}_n \mathbf{R}_\alpha) \exp(i\mathbf{K}_n \rho) \quad (22)$$

Here, $\mathbf{R}_\alpha = (X_\alpha, Y_\alpha, Z_\alpha)$ is the position vector of the α th atom in the unit cell and $\mathbf{r} = \mathbf{R}_\alpha + \rho$. The joining condition across the muffin-tin-sphere boundary results from expanding the plane wave in terms of spherical harmonics [16]:

$$\exp(i\mathbf{K}_n \rho) = 4\pi \sum_{lm} i^l j_l(|\mathbf{K}_n| \rho) Y_{lm}^*(\widehat{\mathbf{K}}_n) Y_{lm}(\hat{\rho}) \quad (23)$$

and requiring that each angular momentum term be continuous with continuous derivative. This gives the coefficients $A_{lm,\alpha}^n$ and $B_{lm,\alpha}^n$:

$$A_{lm,\alpha}^n = 4\pi r_\alpha^2 \Omega^{-1/2} i^l \exp(i\mathbf{K}_n \mathbf{R}_\alpha) Y_L^*(\widehat{\mathbf{K}}_n) a_{l,\alpha}(n) \quad (24)$$

$$B_{lm,\alpha}^n = 4\pi r_\alpha^2 \Omega^{-1/2} i^l \exp(i\mathbf{K}_n \mathbf{R}_\alpha) Y_L^*(\widehat{\mathbf{K}}_n) b_{l,\alpha}(n) \quad (25)$$

Here, j_l is a spherical Bessel function of order l , $\widehat{\mathbf{K}}_n = \mathbf{K}_n / |\mathbf{K}_n|$ and $\hat{\rho} = \rho / |\rho|$ are unit vectors, and

$$a_{l,\alpha}(n) = j'_l(K_n r_\alpha) \dot{u}_{l,\alpha}(r_\alpha) - j_l(K_n r_\alpha) \dot{u}'_{l,\alpha}(r_\alpha) \quad (26)$$

$$b_{l,\alpha}(n) = j_l(K_n r_\alpha) u'_{l,\alpha}(r_\alpha) - j'_l(K_n r_\alpha) u_{l,\alpha}(r_\alpha) \quad (27)$$

where we used (19).

4.1.2. Bulk LAPW Hamiltonian and Overlap Matrices

The basis functions (20)–(27) satisfy the cellular boundary conditions and connectivity across the muffin-tin spheres. We can now apply this basis set to form a trial function (5) and calculate matrix elements in the secular equations (6) and (7). The overlap matrix is given by

$$\langle \varphi_m | \varphi_n \rangle = U_{m,n} + \frac{4\pi}{\Omega} \sum_{\alpha} r_\alpha^4 \exp[i(\mathbf{k}_m - \mathbf{k}_n) \mathbf{R}_\alpha] \times \sum_{l=0}^{\infty} (2l+1) P_l(\widehat{\mathbf{K}}_m \widehat{\mathbf{K}}_n) S_{l,\alpha}^{m,n} \quad (28)$$

where

$$U_{m,n} = \delta_{m,n} - \frac{4\pi}{\Omega} \sum_{\alpha} r_\alpha^2 \frac{j_1(|\mathbf{k}_m - \mathbf{k}_n| r_\alpha)}{|\mathbf{k}_m - \mathbf{k}_n|} \times \exp[i(\mathbf{k}_m - \mathbf{k}_n) \mathbf{R}_\alpha] \quad (29)$$

$$S_{l,\alpha}^{m,n} = a_{l,\alpha}(m) a_{l,\alpha}(n) + N_{l,\alpha} b_{l,\alpha}(m) b_{l,\alpha}(n) \quad (30)$$

In (28), the $U_{m,n}$ is the contribution from the interstitial region, and the second term is the contribution from all the MT spheres. To calculate the overlap integral (28) and (29), we take into account that

$$\int_{\Omega_\alpha} \exp[i(\mathbf{k}_m - \mathbf{k}_n) \rho] d\rho = 4\pi r_\alpha^2 \frac{j_1(|\mathbf{k}_m - \mathbf{k}_n| r_\alpha)}{|\mathbf{k}_m - \mathbf{k}_n|} \quad (31)$$

A spherical harmonic sum rule

$$\sum_{m=-l}^l Y_{lm}(\widehat{K}_m) Y_{lm}^*(\widehat{K}_n) = \frac{(2l+1)}{4\pi} P_l(\widehat{K}_m \widehat{K}_n) \quad (32)$$

has been used to obtain the Legendre polynomials $P_l(\widehat{K}_m \widehat{K}_n)$, where $\widehat{K}_m \widehat{K}_n$ is a scalar product of the unit vectors \widehat{K}_m and \widehat{K}_n .

Similarly,

$$\begin{aligned} \langle \varphi_m | \widehat{H} | \varphi_n \rangle &= \mathbf{K}_n \mathbf{K}_m U_{m,n} + \frac{4\pi}{\Omega} \sum_{\alpha} r_{\alpha}^4 \exp[i(\mathbf{k}_m - \mathbf{k}_n) \mathbf{R}_{\alpha}] \\ &\times \sum_{l=0}^{\infty} (2l+1) P_l(\widehat{K}_m \widehat{K}_n) (E_{l,\alpha} S_{l,\alpha}^{m,n} + \gamma_{l,\alpha}^{m,n}) \end{aligned} \quad (33)$$

where

$$\begin{aligned} \gamma_{l,\alpha}^{m,n} &= \left\{ \dot{u}_{l,\alpha}(r) u'_{l,\alpha}(r) [j'_l(K_m r) j_l(K_n r) + j_l(K_m r) j'_l(K_n r)] \right\}_{r=r_{\alpha}} \\ &- [\dot{u}'_{l,\alpha}(r) u_{l,\alpha}(r) j_l(K_m r) j_l(K_n r) \\ &+ \dot{u}_{l,\alpha}(r) u_{l,\alpha}(r) j'_l(K_m r) j'_l(K_n r)]_{r=r_{\alpha}} \end{aligned} \quad (34)$$

4.2. Film LAPW Method

A thin film with one or several monoatomic layers is a two-dimensional nanomaterial. The film LAPW (2D-LAPW) method was developed in [7, 22–25] and applied to systems such as transition metal layers. The film is periodic in the x – y plane. The potential is spherically symmetric inside the MT spheres Ω_I and it is constant in the interstitial region Ω_{II} . For the sake of simplicity, we suggest that the interstitial and vacuum regions be separated by the two impenetrable planar step potential barriers Ω_{III} so that the wave function is equal to 0 on the boundaries at $z = \pm \frac{1}{2}d$. A distance d is to be chosen in such a way that an essential part of the electronic density of a system is located between the potential walls.

4.2.1. Forming the Film Basis Functions

In analogy with the bulk LAPW method, in the interstitial region the basis function is the product of a two-dimensional plane wave in the x – y plane and a one-dimensional symmetrized plane (standing) wave in the z direction:

$$\varphi_{nm}^{\pm}(\mathbf{k}, \mathbf{r}) = (2/\Omega)^{1/2} \exp[i(\mathbf{k} + \mathbf{k}_m) \mathbf{r}] \times \begin{cases} \cos(k_n z); & (+) \\ \sin(k_n z); & (-) \end{cases} \quad (35)$$

Here, (+) and (–) denote states, which are, respectively, symmetric and antisymmetric with respect to the z reflection; \mathbf{k} is a two-dimensional crystal momentum vector, \mathbf{k}_m is a two-dimensional reciprocal lattice vector, Ω equals the volume of the unit cell between $z = \pm \frac{1}{2}d$, and k_n is defined as

$$k_n = \begin{cases} (n+1/2)2\pi/d; & (+) \\ n2\pi/d; & (-) \end{cases} \quad n = 0, 1, 2, \dots \quad (36)$$

thus forcing a node at $z = \pm \frac{1}{2}d$ for both (+) and (–) states.

Inside the α th MT sphere in the unit cell, the basis function is expanded in spherical harmonics times a radial function and its energy derivative

$$\begin{aligned} \varphi_{l\alpha, nm}^{\pm}(\rho, \theta, \varphi) &= \sum_{lm} [A_{lm,\alpha}^{\pm} u_{l,\alpha}(E_l, \rho) + B_{lm,\alpha}^{\pm} \dot{u}_{l,\alpha}(E_l, \rho)] \\ &\times Y_{lm}(\theta, \varphi) \times \begin{cases} i^l; & (+) \\ i^{l-1}; & (-) \end{cases} \end{aligned} \quad (37)$$

Here, as distinct from the analogous equation (21) in the 3D-LAPW method, the phase coefficients i^l and i^{l-1} for states (+) and (–) are added to simplify the equations. Using (23), the $A_{lm,\alpha}^{\pm}$ and $B_{lm,\alpha}^{\pm}$ coefficients are determined by matching (37) onto the symmetrized plane-wave basis function equation (35) so that the basis function and its derivative are continuous across the MT-sphere boundary:

$$A_{lm,\alpha}^{\pm}(nm) = 4\pi r_{\alpha}^2 \Omega^{-1/2} e^{i\mathbf{K}_m \mathbf{R}_{\alpha}} a_{l,\alpha}(nm) Y_{L,\alpha}^{\pm}(nm) \quad (38)$$

$$B_{lm,\alpha}^{\pm}(nm) = 4\pi r_{\alpha}^2 \Omega^{-1/2} e^{i\mathbf{K}_m \mathbf{R}_{\alpha}} b_{l,\alpha}(nm) Y_{L,\alpha}^{\pm}(nm) \quad (39)$$

where

$$\begin{aligned} Y_{lm,\alpha}^{\pm}(nm) &= 2^{-1/2} [\exp(ik_n Z_{\alpha}) Y_{lm}(\mathbf{K}_m + \mathbf{k}_n) \\ &\pm \exp(-ik_n Z_{\alpha}) Y_{lm}(\mathbf{K}_m - \mathbf{k}_n)] \end{aligned} \quad (40)$$

and

$$a_{l,\alpha}(nm) = j'_l(G_{nm} r_{\alpha}) \dot{u}_{l,\alpha}(r_{\alpha}) - j_l(G_{nm} r_{\alpha}) \dot{u}'_{l,\alpha}(r_{\alpha}) \quad (41)$$

$$b_{l,\alpha}(nm) = j_l(G_{nm} r_{\alpha}) u'_{l,\alpha}(r_{\alpha}) - j'_l(G_{nm} r_{\alpha}) u_{l,\alpha}(r_{\alpha}) \quad (42)$$

Here, $\mathbf{K}_m = \mathbf{k} + \mathbf{k}_m$, $\mathbf{k}_n = k_n \hat{z}$, and $G_{nm} = |\mathbf{K}_m + \mathbf{k}_n| = |\mathbf{K}_m - \mathbf{k}_n|$.

4.2.2. Film LAPW Hamiltonian and Overlap Matrices

The overlap matrix in the basis (35)–(37) is the sum of the contributions from the interstitial region and from all the MT spheres:

$$\begin{aligned} \langle \varphi_{n'm'}^{\pm} | \varphi_{nm}^{\pm} \rangle &= U_{n'm', nm}^{\pm} + \frac{4\pi}{\Omega} \sum_{\alpha} r_{\alpha}^4 \exp[-i(\mathbf{k}_m - \mathbf{k}_{m'}) \mathbf{R}_{\alpha}] \\ &\times \sum_{l=0}^{\infty} (2l+1) S_{l,\alpha}^{n'm', nm} P_{l,\alpha}^{\pm} \end{aligned} \quad (43)$$

$$\begin{aligned} U_{n'm', nm}^{\pm} &= \delta_{n'm', nm} \epsilon_n^{\pm} - \frac{4\pi}{\Omega} \sum_{\alpha} r_{\alpha}^2 \exp[-i(\mathbf{k}_m - \mathbf{k}_{m'}) \mathbf{R}_{\alpha}] \\ &\times \{ \cos[(k_n - k_{n'}) Z_{\alpha}] J_{\alpha}(G_{n'm'}^+, G_{nm}^+) \\ &\pm \cos[(k_n + k_{n'}) Z_{\alpha}] J_{\alpha}(G_{n'm'}^+, G_{nm}^-) \} \end{aligned} \quad (44)$$

The quantities in (43) are defined as follows:

$$S_{l,\alpha}^{n'm', nm} = a_{l,\alpha}(n'm') a_{l,\alpha}(nm) + N_{l,\alpha} b_{l,\alpha}(n'm') b_{l,\alpha}(nm) \quad (45)$$

$$\begin{aligned} P_{l,\alpha}^{\pm} &= \{ \cos[(k_n - k_{n'}) Z_{\alpha}] P_l(\widehat{G}_{n'm'}^+ \widehat{G}_{nm}^+) \\ &\pm \cos[(k_n + k_{n'}) Z_{\alpha}] P_l(\widehat{G}_{n'm'}^+ \widehat{G}_{nm}^-) \} \end{aligned} \quad (46)$$

with $J_{\alpha}(\mathbf{x}, \mathbf{y}) = j_1(|\mathbf{x} - \mathbf{y}|/r_{\alpha})/|\mathbf{x} - \mathbf{y}|$, $\epsilon_n^- = 1$, $\epsilon_n^+ = (1 + \delta_{n,0})$, and $\mathbf{G}_{nm}^{\pm} = \mathbf{K}_m \pm k_n \hat{z}$.

The Hamiltonian matrix is given as the sum of two terms

$$\langle \varphi_{n'm'}^{\pm} | \widehat{H} | \varphi_{nm}^{\pm} \rangle = G_{n'm'}^2 U_{n'm',nm}^{\pm} + \frac{4\pi}{\Omega} \sum_{\alpha} r_{\alpha}^4 \exp[-i(\mathbf{k}_m - \mathbf{k}_{m'}) \mathbf{R}_{\alpha}] \times \sum_{l=0}^{\infty} (2l+1) (E_{l,\alpha} S_{l,\alpha}^{n'm',nm} + \gamma_{l,\alpha}^{n'm',nm}) P_{l,\alpha}^{\pm} \quad (47)$$

where

$$\begin{aligned} \gamma_{l,\alpha}^{n'm',nm} = & \dot{u}_{l,\alpha}(r) u'_{l,\alpha}(r) [j'_l(G_{n'm'} r) j_l(G_{nm} r) \\ & + j_l(G_{n'm'} r) j'_l(G_{nm} r)] \Big|_{r=r_{\alpha}} \\ & - [\dot{u}'_{l,\alpha}(r) u'_{l,\alpha}(r) j_l(G_{n'm'} r) j_l(G_{nm} r) \\ & + \dot{u}_{l,\alpha}(r) u_{l,\alpha}(r) j'_l(G_{n'm'} r) j'_l(G_{nm} r)] \Big|_{r=r_{\alpha}} \quad (48) \end{aligned}$$

4.3. Bar LAPW Method

The LAPW formalism for one-dimensional systems of a nanosize cross section having a translation symmetry in one direction (bar LAPW method or 1D-LAPW) is developed in [26–28] and applied to a series of nanomaterials, including conjugated carbon polymers and carbon nanotubes intercalated with transition metals [29, 30]. This approach is a further extension of the bulk and film LAPW theory to nanowires with specific geometry.

As infinite motion of electrons is only possible in one direction (along the z axis) and it is limited to perpendicular directions, we suggest that the system be confined between four plane impenetrable barriers, so that the wave function is equal to 0 on this boundary. An essential part of the electronic density of a system is located in the infinite bar with an $a \times b$ cross section.

4.3.1. Forming the Bar Basis Functions

In the interstitial region, the basis functions are the solutions of a wave equation for motion of a free electron in the potential bar with dimension $a \times b \times \infty$. Here, the basis function $\varphi_{m^{\pm}n^{\pm}p}(k, \mathbf{r})$ is a product $\psi_m^{\pm}(x)\psi_n^{\pm}(y)\psi_p(z, k)$. For the z direction, we have

$$\begin{aligned} \psi_p(z, k) = & c^{-1/2} \exp(iK_p z) \\ K_p = & k + k_p, k_p = p(2\pi/c), p = 0, \pm 1, \pm 2, \dots \quad (49) \end{aligned}$$

where c is a lattice constant for the z direction, k is a one-dimensional crystal momentum, $-\pi/c \leq k \leq \pi/c$. For the directions x and y , the solutions take a form of standing waves

$$\begin{aligned} \psi_m^{\pm}(x) = & (2/a)^{1/2} \\ & \times \begin{cases} \cos(k_m x); & (+), \\ m=1, 3, 5, \dots & \\ \sin(k_m x); & (-), \\ m=2, 4, 6, \dots & \end{cases} \quad k_m = (\pi/a)m \quad (50) \end{aligned}$$

$$\begin{aligned} \psi_n^{\pm}(y) = & (2/b)^{1/2} \\ & \times \begin{cases} \cos(k_n y); & (+), \\ n=1, 3, 5, \dots & \\ \sin(k_n y); & (-), \\ n=2, 4, 6, \dots & \end{cases} \quad k_n = (\pi/b)n \quad (51) \end{aligned}$$

Inside the α th MT sphere, the basis function is written as

$$\varphi_{l\alpha, mnp}^{\pm, \pm} = \sum_{lm} [A_{lm, \alpha}^{m^{\pm}n^{\pm}p} u_{l, \alpha}(E_l, \rho) + B_{lm, \alpha}^{m^{\pm}n^{\pm}p} \dot{u}_{l, \alpha}(E_l, \rho)] Y_{lm}(\hat{\rho}) i^f \quad (52)$$

Here, $f = l$ for $(+, +)$, i^{l-1} for $(+, -)$ and $(-, +)$, and i^{l-2} for $(-, -)$. The coefficients $A_{lm, \alpha}^{m^{\pm}n^{\pm}p}$ and $B_{lm, \alpha}^{m^{\pm}n^{\pm}p}$ are readily calculated from the expansion of the waves (49)–(51) in terms of Y_{lm} (22):

$$A_{lm, \alpha}^{m^{\pm}n^{\pm}p} = 4\pi r_{\alpha}^2 \Omega^{-1/2} e^{iK_p Z_{\alpha}} a_{l, \alpha}(m, n, p) Y_{lm, \alpha}^{m^{\pm}n^{\pm}p} \quad (53)$$

$$B_{lm, \alpha}^{m^{\pm}n^{\pm}p} = 4\pi r_{\alpha}^2 \Omega^{-1/2} e^{iK_p Z_{\alpha}} b_{l, \alpha}(m, n, p) Y_{lm, \alpha}^{m^{\pm}n^{\pm}p} \quad (54)$$

Here,

$$\begin{aligned} Y_{lm, \alpha}^{m^{\pm}n^{\pm}p} = & (1/2) \{ \exp[i(\mathbf{k}_m + \mathbf{k}_n) \mathbf{R}_{\alpha}] Y_{lm}^*(\mathbf{k}_m + \mathbf{k}_n + \mathbf{K}_p) \\ & + \delta_1 \exp[i(\mathbf{k}_m - \mathbf{k}_n) \mathbf{R}_{\alpha}] Y_{lm}^*(\mathbf{k}_m - \mathbf{k}_n + \mathbf{K}_p) \\ & + \delta_2 \exp[i(-\mathbf{k}_m + \mathbf{k}_n) \mathbf{R}_{\alpha}] Y_{lm}^*(-\mathbf{k}_m + \mathbf{k}_n + \mathbf{K}_p) \\ & + \delta_3 \exp[i(-\mathbf{k}_m - \mathbf{k}_n) \mathbf{R}_{\alpha}] Y_{lm}^*(-\mathbf{k}_m - \mathbf{k}_n + \mathbf{K}_p) \} \quad (55) \end{aligned}$$

where $\delta_1 = \delta_2 = \delta_3 = 1$ for $Y_{lm, \alpha}^{m^+n^+p}$, $\delta_1 = \delta_3 = -1$ and $\delta_2 = 1$ for $Y_{lm, \alpha}^{m^+n^-p}$, $\delta_2 = \delta_3 = -1$ and $\delta_1 = 1$ for $Y_{lm, \alpha}^{m^-n^+p}$, $\delta_1 = \delta_2 = -1$ and $\delta_3 = 1$ for $Y_{lm, \alpha}^{m^-n^-p}$. Finally,

$$a_{l, \alpha}(mnp) = j'_l(G_{mnp} r_{\alpha}) \dot{u}_{l, \alpha}(r_{\alpha}) - j_l(G_{mnp} r_{\alpha}) \dot{u}'_{l, \alpha}(r_{\alpha}) \quad (56)$$

$$b_{l, \alpha}(mnp) = j_l(G_{mnp} r_{\alpha}) u'_{l, \alpha}(r_{\alpha}) - j'_l(G_{mnp} r_{\alpha}) u_{l, \alpha}(r_{\alpha}) \quad (57)$$

where $G_{mnp} = |\mathbf{K}_p \pm \mathbf{k}_m \pm \mathbf{k}_n|$.

4.3.2. Bar LAPW Hamiltonian and Overlap Matrices

Using the basis (49)–(57), we obtain the overlap matrix:

$$\begin{aligned} \langle \varphi_{m'n'p'}^{\pm, \pm} | \varphi_{mnp}^{\pm, \pm} \rangle = & U_{m'n'p', mnp}^{\pm, \pm} + \frac{4\pi}{\Omega} \sum_{\alpha} r_{\alpha}^4 \exp[-i(k_p - k_{p'}) Z_{\alpha}] \\ & \times \sum_{l=0}^{\infty} (2l+1) S_{l, \alpha}^{m'n'p', mnp} \\ & \times \sum_{i=1}^4 x_{i\alpha}^{m^{\pm}n^{\pm}, m^{\pm}n^{\pm}} P_{i, l}^{m'n'p', mnp} \quad (58) \end{aligned}$$

where

$$\begin{aligned} U_{m'n'p', mnp}^{\pm, \pm} = & \delta_{m^{\pm}n^{\pm}p', m^{\pm}n^{\pm}p} - \frac{4\pi}{\Omega} \sum_{\alpha} r_{\alpha}^2 \exp[-i(k_p - k_{p'}) Z_{\alpha}] \\ & \times \sum_{i=1}^4 x_{i\alpha}^{m^{\pm}n^{\pm}, m^{\pm}n^{\pm}} J_{\alpha}(G_i^{m'n'mn, p-p'}) \quad (59) \end{aligned}$$

The $x_{i\alpha}^{m^{\pm}n^{\pm}, m^{\pm}n^{\pm}}$ coefficients are presented in Table 1, where $A_1 = X_{\alpha}(k_m + k_{m'})$, $B_1 = Y_{\alpha}(k_n + k_{n'})$, $A_2 = X_{\alpha}(k_m - k_{m'})$, $B_2 = Y_{\alpha}(k_n - k_{n'})$, $A_3 = X_{\alpha}(k_m + k_{m'})$, $B_3 = Y_{\alpha}(k_n - k_{n'})$, $A_4 = X_{\alpha}(k_m - k_{m'})$, and $B_4 = Y_{\alpha}(k_n + k_{n'})$.

In (59), $J_{\alpha}(G_i) = j_1(|G_i|/r_{\alpha})/|G_i|$, where

$$\begin{aligned} \mathbf{G}_1^{m'n'mn, p-p'} &= \mathbf{k}_m + \mathbf{k}_{m'} + \mathbf{k}_n + \mathbf{k}_{n'} + \mathbf{k}_p - \mathbf{k}_{p'} \\ \mathbf{G}_2^{m'n'mn, p-p'} &= \mathbf{k}_m - \mathbf{k}_{m'} + \mathbf{k}_n + \mathbf{k}_{n'} + \mathbf{k}_p - \mathbf{k}_{p'} \\ \mathbf{G}_3^{m'n'mn, p-p'} &= \mathbf{k}_m + \mathbf{k}_{m'} + \mathbf{k}_n - \mathbf{k}_{n'} + \mathbf{k}_p - \mathbf{k}_{p'} \\ \mathbf{G}_4^{m'n'mn, p-p'} &= \mathbf{k}_m - \mathbf{k}_{m'} + \mathbf{k}_n - \mathbf{k}_{n'} + \mathbf{k}_p - \mathbf{k}_{p'} \end{aligned} \quad (60)$$

Finally,

$$S_{l,\alpha}^{m'n'p', mnp} = a_{l,\alpha}(m'n'p')a_{l,\alpha}(mnp) + N_{l,\alpha}b_{l,\alpha}(m'n'p')b_{l,\alpha}(mnp) \quad (61)$$

$$P_{i,l}^{m'n'p', mnp} = P_i(K_i^{m'n'p', mnp}/G_{n'm'p'}G_{mnp}) \quad (62)$$

$$\begin{aligned} K_1^{m'n'p', mnp} &= -k_mk_{m'} - k_nk_{n'} + K_pK_{p'} \\ K_2^{m'n'p', mnp} &= k_mk_{m'} - k_nk_{n'} + K_pK_{p'} \\ K_3^{m'n'p', mnp} &= -k_mk_{m'} + k_nk_{n'} + K_pK_{p'} \\ K_4^{m'n'p', mnp} &= k_mk_{m'} + k_nk_{n'} + K_pK_{p'} \end{aligned} \quad (63)$$

The Hamiltonian matrix elements have the form:

$$\begin{aligned} &\langle \varphi_{m'n'p'}^{\pm, \pm} | \hat{H} | \varphi_{mnp}^{\pm, \pm} \rangle \\ &= (k_m^2 + k_n^2 + K_p^2) \delta_{m^{\pm}n^{\pm}p', m^{\pm}n^{\pm}p} \\ &\quad - \frac{4\pi}{\Omega} \sum_{\alpha} r_{\alpha}^2 \exp[-i(k_p - k_{p'})Z_{\alpha}] \\ &\quad \times \sum_{i=1}^4 x_{i\alpha}^{m^{\pm}n^{\pm}, m^{\pm}n^{\pm}} J_{\alpha}(G_i^{m'n'mn, p-p'}) K_i^{m'n'p', mnp} \\ &\quad + \frac{4\pi}{\Omega} \sum_{\alpha} r_{\alpha}^4 \exp[-i(k_p - k_{p'})Z_{\alpha}] \end{aligned}$$

Table 1. The coefficients $x_{i\alpha}^{m^{\pm}n^{\pm}, m^{\pm}n^{\pm}}$ [26].

$x_{i\alpha}^{m^{\pm}n^{\pm}, m^{\pm}n^{\pm}}$	$i = 1$	$i = 2$	$i = 3$	$i = 4$
m^+n^+, m^+n^+	$\cos A_1 \cos B_1$	$\cos A_2 \cos B_2$	$\cos A_3 \cos B_3$	$\cos A_4 \cos B_4$
m^+n^+, m^+n^-	$\cos A_1 \sin B_1$	$\cos A_2 \sin B_2$	$\cos A_3 \sin B_3$	$\cos A_4 \sin B_4$
m^+n^+, m^-n^+	$\sin A_1 \cos B_1$	$\sin A_2 \cos B_2$	$\sin A_3 \cos B_3$	$\sin A_4 \cos B_4$
m^+n^+, m^-n^-	$\sin A_1 \sin B_1$	$\sin A_2 \sin B_2$	$\sin A_3 \sin B_3$	$\sin A_4 \sin B_4$
m^+n^-, m^+n^+	$\cos A_1 \sin B_1$	$\cos A_2 \sin B_2$	$-\cos A_3 \sin B_3$	$-\cos A_4 \sin B_4$
m^+n^-, m^+n^-	$-\cos A_1 \cos B_1$	$-\cos A_2 \cos B_2$	$\cos A_3 \cos B_3$	$\cos A_4 \cos B_4$
m^+n^-, m^-n^+	$\sin A_1 \sin B_1$	$\sin A_2 \sin B_2$	$-\sin A_3 \sin B_3$	$-\sin A_4 \sin B_4$
m^+n^-, m^-n^-	$-\sin A_1 \cos B_1$	$-\sin A_2 \cos B_2$	$\sin A_3 \cos B_3$	$\sin A_4 \cos B_4$
m^-n^+, m^+n^+	$\sin A_1 \cos B_1$	$-\sin A_2 \cos B_2$	$\sin A_3 \cos B_3$	$-\sin A_4 \cos B_4$
m^-n^+, m^+n^-	$\sin A_1 \sin B_1$	$-\sin A_2 \sin B_2$	$\sin A_3 \sin B_3$	$-\sin A_4 \sin B_4$
m^-n^+, m^-n^+	$-\cos A_1 \cos B_1$	$\cos A_2 \cos B_2$	$-\cos A_3 \cos B_3$	$\cos A_4 \cos B_4$
m^-n^+, m^-n^-	$-\cos A_1 \sin B_1$	$\cos A_2 \sin B_2$	$-\cos A_3 \sin B_3$	$\cos A_4 \sin B_4$
m^-n^-, m^+n^+	$\sin A_1 \sin B_1$	$-\sin A_2 \sin B_2$	$-\sin A_3 \sin B_3$	$\sin A_4 \sin B_4$
m^-n^-, m^+n^-	$-\sin A_1 \cos B_1$	$\sin A_2 \cos B_2$	$\sin A_3 \cos B_3$	$-\sin A_4 \cos B_4$
m^-n^-, m^-n^+	$-\cos A_1 \sin B_1$	$\cos A_2 \sin B_2$	$\cos A_3 \sin B_3$	$-\cos A_4 \sin B_4$
m^-n^-, m^-n^-	$\cos A_1 \cos B_1$	$-\cos A_2 \cos B_2$	$-\cos A_3 \cos B_3$	$\cos A_4 \cos B_4$

$$\begin{aligned} &\times \sum_{l=0}^{\infty} (2l+1) [S_{l,\alpha}^{m'n'p', mnp} E_{la} + \gamma_{l,\alpha}^{m'n'p', mnp}] \\ &\times \sum_{i=1}^4 x_{i\alpha}^{m^{\pm}n^{\pm}, m^{\pm}n^{\pm}} P_{i,l}^{m'n'p', mnp} \end{aligned} \quad (64)$$

where

$$\begin{aligned} \gamma_{l,\alpha}^{m'n'p', mnp} &= \dot{u}_{l,\alpha} u'_{l,\alpha} [j'_l(G_{m'n'p'}r) j_l(G_{mnp}r) \\ &\quad + j_l(G_{m'n'p'}r) j'_l(G_{mnp}r)]|_{r=r_{\alpha}} \\ &\quad - [\dot{u}'_{l,\alpha} u'_{l,\alpha} j_l(G_{m'n'p'}r) j_l(G_{mnp}r) \\ &\quad + \dot{u}_{l,\alpha} u_{l,\alpha} j'_l(G_{m'n'p'}r) j'_l(G_{mnp}r)]|_{r=r_{\alpha}} \end{aligned} \quad (65)$$

4.4. Cluster LAPW Method

The cluster LAPW method (0D-LAPW or linear augmented standing-wave method, LASTW) is a final extension of the LAPW theory to low-dimensional systems. Consider an important case of a tetragonal nanocrystal or cluster and assume that the multiatomic system is confined in an impenetrable potential box with dimension $\Omega = a \times b \times c$ so that an essential part of the electronic density is located in the box and the cluster wave function is equal to 0 on the boundary.

4.4.1. Forming the Cubic Cluster Basis Functions

In the interstitial region, the basis function $\varphi_{m^{\pm}n^{\pm}p^{\pm}}(k, \mathbf{r})$ is a product $\psi_m^{\pm}(x)\psi_n^{\pm}(y)\psi_p^{\pm}(z)$ of three standing waves

$$\begin{aligned} \psi_m^{\pm}(x) &= (2/a)^{1/2} \\ &\times \begin{cases} \cos(k_mx); & (+), \\ m=1, 3, 5, \dots \\ \sin(k_mx); & (-), \\ m=2, 4, 6, \dots \end{cases} \quad k_m = (\pi/a)m \quad (66) \end{aligned}$$

$$\psi_n^\pm(y) = (2/b)^{1/2} \times \begin{cases} \cos(k_n y); & (+), \\ n=1, 3, 5, \dots \\ \sin(k_n y); & (-), \\ n=2, 4, 6, \dots \end{cases} \quad k_n = (\pi/b)n \quad (67)$$

$$\psi_p^\pm(z) = (2/c)^{1/2} \times \begin{cases} \cos(k_p z); & (+), \\ p=1, 3, 5, \dots \\ \sin(k_p z); & (-), \\ p=2, 4, 6, \dots \end{cases} \quad k_p = (\pi/a)p \quad (68)$$

Inside the α th MT sphere, the basis function can be written as

$$\varphi_{l\alpha, mnp}^{\pm, \pm, \pm} = \sum_{lm} [A_{lm, \alpha}^{m^\pm n^\pm p^\pm} u_{l, \alpha}(E_l, \rho) + B_{lm, \alpha}^{m^\pm n^\pm p^\pm} \dot{u}_{l, \alpha}(E_l, \rho)] Y_{lm}(\hat{\rho}) i^f \quad (69)$$

Here, $f = l$ for $(+, +, +)$; i^{l-1} for $(-, +, +)$, $(+, -, +)$, and $(+, +, -)$; i^{l-2} for $(+, -, -)$, $(-, +, -)$, and $(-, -, +)$; and i^{l-3} for $(-, -, -)$. The coefficients $A_{lm, \alpha}^{m^\pm n^\pm p^\pm}$ and $B_{lm, \alpha}^{m^\pm n^\pm p^\pm}$ are readily calculated from the expansion of the waves in terms of Y_{lm} (22):

$$A_{lm, \alpha}^{m^\pm n^\pm p^\pm} = 4\pi r_\alpha^2 \Omega^{-1/2} a_{l, \alpha}(m, n, p) Y_{lm, \alpha}^{m^\pm n^\pm p^\pm} \quad (70)$$

$$B_{lm, \alpha}^{m^\pm n^\pm p^\pm} = 4\pi r_\alpha^2 \Omega^{-1/2} b_{l, \alpha}(m, n, p) Y_{lm, \alpha}^{m^\pm n^\pm p^\pm} \quad (71)$$

Here,

$$\begin{aligned} Y_{lm, \alpha}^{m^\pm n^\pm p^\pm} = & (8)^{-1/2} \{ \delta_1 \exp[i(k_m X_\alpha + k_n Y_\alpha + k_p Z_\alpha)] \\ & \times Y_{lm}^*(\mathbf{k}_m + \mathbf{k}_n + \mathbf{k}_p) \\ & + \delta_2 \exp[i(-k_m X_\alpha + k_n Y_\alpha + k_p Z_\alpha)] \\ & \times Y_{lm}^*(-\mathbf{k}_m + \mathbf{k}_n + \mathbf{k}_p) \\ & + \delta_3 \exp[i(k_m X_\alpha - k_n Y_\alpha + k_p Z_\alpha)] \\ & \times Y_{lm}^*(\mathbf{k}_m - \mathbf{k}_n + \mathbf{k}_p) \\ & + \delta_4 \exp[i(-k_m X_\alpha - k_n Y_\alpha + k_p Z_\alpha)] \\ & \times Y_{lm}^*(-\mathbf{k}_m - \mathbf{k}_n + \mathbf{k}_p) \\ & + \delta_5 \exp[i(k_m X_\alpha + k_n Y_\alpha - k_p Z_\alpha)] \\ & \times Y_{lm}^*(\mathbf{k}_m + \mathbf{k}_n - \mathbf{k}_p) \\ & + \delta_6 \exp[i(-k_m X_\alpha + k_n Y_\alpha - k_p Z_\alpha)] \\ & \times Y_{lm}^*(-\mathbf{k}_m + \mathbf{k}_n - \mathbf{k}_p) \\ & + \delta_7 \exp[i(k_m X_\alpha - k_n Y_\alpha - k_p Z_\alpha)] \\ & \times Y_{lm}^*(\mathbf{k}_m - \mathbf{k}_n - \mathbf{k}_p) \\ & + \delta_8 \exp[i(-k_m X_\alpha - k_n Y_\alpha - k_p Z_\alpha)] \\ & \times Y_{lm}^*(-\mathbf{k}_m - \mathbf{k}_n - \mathbf{k}_p) \} \quad (72) \end{aligned}$$

The values of δ_i are presented in Table 2.

Table 2. Values of δ_i in (72).

	δ_1	δ_2	δ_3	δ_4	δ_5	δ_6	δ_7	δ_8
$m^+ n^+ p^+$	1	1	1	1	1	1	1	1
$m^- n^+ p^+$	1	-1	1	-1	1	-1	1	-1
$m^+ n^- p^+$	1	1	-1	-1	1	1	-1	-1
$m^+ n^+ p^-$	1	1	1	1	-1	-1	-1	-1
$m^- n^- p^+$	1	-1	-1	1	1	-1	-1	1
$m^- n^+ p^-$	1	-1	1	-1	-1	1	-1	1
$m^+ n^- p^-$	1	1	-1	-1	-1	-1	1	1
$m^- n^- p^-$	1	-1	-1	1	-1	1	1	-1

Finally,

$$a_{l, \alpha}(mnp) = j_l'(g_{mnp} r_\alpha) \dot{u}_{l, \alpha}(r_\alpha) - j_l(g_{mnp} r_\alpha) \dot{u}'_{l, \alpha}(r_\alpha) \quad (73)$$

$$b_{l, \alpha}(mnp) = j_l(g_{mnp} r_\alpha) u'_{l, \alpha}(r_\alpha) - j_l'(g_{mnp} r_\alpha) u_{l, \alpha}(r_\alpha) \quad (74)$$

where $g_{mnp} = |\mathbf{k}_p \pm \mathbf{k}_m \pm \mathbf{k}_n|$.

4.4.2. Cluster LAPW Hamiltonian and Overlap Matrices

Using the standing-wave basis, we obtain the overlap matrix:

$$\begin{aligned} \langle \varphi_{m'n'p'}^{\pm, \pm, \pm} | \varphi_{mnp}^{\pm, \pm, \pm} \rangle = & U_{n'm'p', nmp}^{\pm, \pm, \pm, \pm, \pm, \pm} \\ & + \frac{4\pi}{\Omega} \sum_{\alpha} r_{\alpha}^4 \sum_{l=0}^{\infty} (2l+1) S_{l, \alpha}^{m'n'p', mnp} \\ & \times \sum_{i=1}^8 x_{i\alpha}^{m^\pm n^\pm p^\pm, m^\pm n^\pm p^\pm} P_{i, l}^{m'n'p', mnp} \quad (75) \end{aligned}$$

where

$$\begin{aligned} U_{n'm'p', nmp}^{\pm, \pm, \pm, \pm, \pm, \pm} = & \delta_{m^\pm n^\pm p^\pm, m^\pm n^\pm p^\pm} - \frac{4\pi}{\Omega} \sum_{\alpha} r_{\alpha}^2 \sum_{i=1}^8 x_{i\alpha}^{m^\pm n^\pm p^\pm, m^\pm n^\pm p^\pm} \\ & \times J_{\alpha}(g_i^{m'n'p', mnp}) \quad (76) \end{aligned}$$

The $x_{i\alpha}^{m^\pm n^\pm p^\pm, m^\pm n^\pm p^\pm}$ coefficients are presented in Table 3, where

$$\begin{aligned} A_1 = X_{\alpha}(k_m + k_{n'}) & \quad B_1 = Y_{\alpha}(k_n + k_{n'}) & \quad C_1 = Z_{\alpha}(k_p + k_{p'}) \\ A_2 = X_{\alpha}(k_m - k_{n'}) & \quad B_2 = Y_{\alpha}(k_n + k_{n'}) & \quad C_2 = Z_{\alpha}(k_p + k_{p'}) \\ A_3 = X_{\alpha}(k_m + k_{n'}) & \quad B_3 = Y_{\alpha}(k_n - k_{n'}) & \quad C_3 = Z_{\alpha}(k_p + k_{p'}) \\ A_4 = X_{\alpha}(k_m - k_{n'}) & \quad B_4 = Y_{\alpha}(k_n - k_{n'}) & \quad C_4 = Z_{\alpha}(k_p + k_{p'}) \\ A_5 = X_{\alpha}(k_m + k_{n'}) & \quad B_5 = Y_{\alpha}(k_n + k_{n'}) & \quad C_5 = Z_{\alpha}(k_p - k_{p'}) \\ A_6 = X_{\alpha}(k_m - k_{n'}) & \quad B_6 = Y_{\alpha}(k_n + k_{n'}) & \quad C_6 = Z_{\alpha}(k_p - k_{p'}) \\ A_7 = X_{\alpha}(k_m + k_{n'}) & \quad B_7 = Y_{\alpha}(k_n - k_{n'}) & \quad C_7 = Z_{\alpha}(k_p - k_{p'}) \\ A_8 = X_{\alpha}(k_m - k_{n'}) & \quad B_8 = Y_{\alpha}(k_n - k_{n'}) & \quad C_8 = Z_{\alpha}(k_p - k_{p'}) \quad (77) \end{aligned}$$

Table 3. The $x_{i\alpha}^{m^{\pm} n^{\pm} p^{\pm}}, m^{\pm} n^{\pm} p^{\pm}$ coefficients. Here, $cA_i = \cos A_i$, $sA_i = \sin A_i$, $cB_i = \cos B_i$, $sB_i = \sin B_i$, etc.

$x_{i\alpha}^{m^{\pm} n^{\pm} p^{\pm}}, m^{\pm} n^{\pm} p^{\pm}$	$i = 1$	$i = 2$	$i = 3$	$i = 4$
+++ , +++	$cA_1 cB_1 cC_1$	$cA_2 cB_2 cC_2$	$cA_3 cB_3 cC_3$	$cA_4 cB_4 cC_4$
+++ , ++-	$cA_1 cB_1 sC_1$	$cA_2 cB_2 sC_2$	$cA_3 cB_3 sC_3$	$cA_4 cB_4 sC_4$
+++ , +-+	$cA_1 sB_1 cC_1$	$cA_2 sB_2 cC_2$	$cA_3 sB_3 cC_3$	$cA_4 sB_4 cC_4$
+++ , +--	$cA_1 sB_1 sC_1$	$cA_2 sB_2 sC_2$	$cA_3 sB_3 sC_3$	$cA_4 sB_4 sC_4$
+++ , -++	$sA_1 cB_1 cC_1$	$sA_2 cB_2 cC_2$	$sA_3 cB_3 cC_3$	$sA_4 cB_4 cC_4$
+++ , -+-	$sA_1 cB_1 sC_1$	$sA_2 cB_2 sC_2$	$sA_3 cB_3 sC_3$	$sA_4 cB_4 sC_4$
+++ , -+-	$sA_1 sB_1 cC_1$	$sA_2 sB_2 cC_2$	$sA_3 sB_3 cC_3$	$sA_4 sB_4 cC_4$
+++ , ---	$sA_1 sB_1 sC_1$	$sA_2 sB_2 sC_2$	$sA_3 sB_3 sC_3$	$sA_4 sB_4 sC_4$
++- , +++	$cA_1 cB_1 sC_1$	$cA_2 cB_2 sC_2$	$cA_3 cB_3 sC_3$	$cA_4 cB_4 sC_4$
++- , ++-	$-cA_1 cB_1 cC_1$	$-cA_2 cB_2 cC_2$	$-cA_3 cB_3 cC_3$	$-cA_4 cB_4 cC_4$
++- , +-+	$cA_1 sB_1 sC_1$	$cA_2 sB_2 sC_2$	$cA_3 sB_3 sC_3$	$cA_4 sB_4 sC_4$
++- , +--	$-cA_1 sB_1 cC_1$	$-cA_2 sB_2 cC_2$	$-cA_3 sB_3 cC_3$	$-cA_4 sB_4 cC_4$
++- , -++	$sA_1 cB_1 sC_1$	$sA_2 cB_2 sC_2$	$sA_3 cB_3 sC_3$	$sA_4 cB_4 sC_4$
++- , -+-	$-sA_1 cB_1 cC_1$	$-sA_2 cB_2 cC_2$	$-sA_3 cB_3 cC_3$	$-sA_4 cB_4 cC_4$
++- , ---	$sA_1 sB_1 sC_1$	$sA_2 sB_2 sC_2$	$sA_3 sB_3 sC_3$	$sA_4 sB_4 sC_4$
+-+ , +++	$-sA_1 sB_1 cC_1$	$-sA_2 sB_2 cC_2$	$-sA_3 sB_3 cC_3$	$-sA_4 sB_4 cC_4$
+-+ , ++-	$cA_1 sB_1 sC_1$	$cA_2 sB_2 sC_2$	$cA_3 sB_3 sC_3$	$cA_4 sB_4 sC_4$
+-+ , +-+	$cA_1 cB_1 cC_1$	$-cA_2 cB_2 cC_2$	$cA_3 cB_3 cC_3$	$cA_4 cB_4 cC_4$
+-+ , +--	$-cA_1 cB_1 sC_1$	$-cA_2 cB_2 sC_2$	$cA_3 cB_3 sC_3$	$cA_4 cB_4 sC_4$
+-+ , -++	$sA_1 sB_1 cC_1$	$sA_2 sB_2 cC_2$	$-sA_3 sB_3 cC_3$	$-sA_4 sB_4 cC_4$
+-+ , -+-	$sA_1 sB_1 sC_1$	$sA_2 sB_2 sC_2$	$-sA_3 sB_3 sC_3$	$-sA_4 sB_4 sC_4$
+-+ , ---	$-sA_1 cB_1 cC_1$	$-sA_2 cB_2 cC_2$	$sA_3 cB_3 cC_3$	$sA_4 cB_4 cC_4$
+-- , +++	$-sA_1 cB_1 sC_1$	$-sA_2 cB_2 sC_2$	$sA_3 cB_3 sC_3$	$sA_4 cB_4 sC_4$
+-- , ++-	$cA_1 sB_1 sC_1$	$cA_2 sB_2 sC_2$	$-cA_3 sB_3 sC_3$	$-cA_4 sB_4 sC_4$
+-- , +-+	$-cA_1 sB_1 cC_1$	$-cA_2 sB_2 cC_2$	$cA_3 sB_3 cC_3$	$cA_4 sB_4 cC_4$
+-- , +--	$-cA_1 cB_1 sC_1$	$-cA_2 cB_2 sC_2$	$cA_3 cB_3 sC_3$	$cA_4 cB_4 sC_4$
+-- , ---	$cA_1 cB_1 cC_1$	$cA_2 cB_2 cC_2$	$-cA_3 cB_3 cC_3$	$-cA_4 cB_4 cC_4$
-++ , +++	$-sA_1 sB_1 sC_1$	$-sA_2 sB_2 sC_2$	$sA_3 sB_3 sC_3$	$sA_4 sB_4 sC_4$
-++ , ++-	$-sA_1 sB_1 cC_1$	$-sA_2 sB_2 cC_2$	$sA_3 sB_3 cC_3$	$sA_4 sB_4 cC_4$
-++ , +-+	$-sA_1 sB_1 sC_1$	$-sA_2 sB_2 sC_2$	$sA_3 sB_3 sC_3$	$sA_4 sB_4 sC_4$
-++ , +--	$-sA_1 cB_1 cC_1$	$-sA_2 cB_2 cC_2$	$sA_3 cB_3 cC_3$	$sA_4 cB_4 cC_4$
-++ , -++	$-cA_1 cB_1 cC_1$	$cA_2 cB_2 cC_2$	$-cA_3 cB_3 cC_3$	$cA_4 cB_4 cC_4$
-++ , -+-	$-cA_1 cB_1 sC_1$	$cA_2 cB_2 sC_2$	$-cA_3 cB_3 sC_3$	$cA_4 cB_4 sC_4$
-++ , ---	$-cA_1 sB_1 cC_1$	$cA_2 sB_2 cC_2$	$-cA_3 sB_3 cC_3$	$cA_4 sB_4 cC_4$
-+- , +++	$-cA_1 sB_1 sC_1$	$cA_2 sB_2 sC_2$	$-cA_3 sB_3 sC_3$	$cA_4 sB_4 sC_4$
-+- , ++-	$-cA_1 cB_1 cC_1$	$cA_2 cB_2 cC_2$	$-cA_3 cB_3 cC_3$	$cA_4 cB_4 cC_4$
-+- , +-+	$-cA_1 cB_1 sC_1$	$cA_2 cB_2 sC_2$	$-cA_3 cB_3 sC_3$	$cA_4 cB_4 sC_4$
-+- , +--	$-cA_1 sB_1 cC_1$	$cA_2 sB_2 cC_2$	$-cA_3 sB_3 cC_3$	$cA_4 sB_4 cC_4$
-+- , -++	$sA_1 cB_1 sC_1$	$sA_2 cB_2 sC_2$	$-sA_3 cB_3 sC_3$	$-sA_4 cB_4 sC_4$
-+- , -+-	$sA_1 cB_1 cC_1$	$sA_2 cB_2 cC_2$	$-sA_3 cB_3 cC_3$	$-sA_4 cB_4 cC_4$
-+- , ---	$sA_1 sB_1 sC_1$	$sA_2 sB_2 sC_2$	$-sA_3 sB_3 sC_3$	$-sA_4 sB_4 sC_4$
--- , +++	$-sA_1 sB_1 cC_1$	$-sA_2 sB_2 cC_2$	$sA_3 sB_3 cC_3$	$sA_4 sB_4 cC_4$
--- , ++-	$-sA_1 sB_1 sC_1$	$-sA_2 sB_2 sC_2$	$sA_3 sB_3 sC_3$	$-sA_4 sB_4 sC_4$
--- , +-+	$-sA_1 cB_1 cC_1$	$-sA_2 cB_2 cC_2$	$sA_3 cB_3 cC_3$	$-sA_4 cB_4 cC_4$
--- , +--	$-sA_1 cB_1 sC_1$	$-sA_2 cB_2 sC_2$	$sA_3 cB_3 sC_3$	$-sA_4 cB_4 sC_4$
--- , -++	$cA_1 cB_1 cC_1$	$-cA_2 cB_2 cC_2$	$-cA_3 cB_3 cC_3$	$cA_4 cB_4 cC_4$
--- , -+-	$cA_1 cB_1 sC_1$	$-cA_2 cB_2 sC_2$	$-cA_3 cB_3 sC_3$	$cA_4 cB_4 sC_4$
--- , ---	$cA_1 sB_1 cC_1$	$-cA_2 sB_2 cC_2$	$-cA_3 sB_3 cC_3$	$cA_4 sB_4 cC_4$

continued

In (76), $J_\alpha(g_i) = j_1(|\mathbf{g}_i|r_\alpha)/|\mathbf{g}_i|$, where

$$\begin{aligned} \mathbf{g}_1^{m'n'p',mnp} &= \mathbf{k}_m + \mathbf{k}_{m'} + \mathbf{k}_n + \mathbf{k}_{n'} + \mathbf{k}_p + \mathbf{k}_{p'} \\ \mathbf{g}_2^{m'n'p',mnp} &= \mathbf{k}_m - \mathbf{k}_{m'} + \mathbf{k}_n + \mathbf{k}_{n'} + \mathbf{k}_p + \mathbf{k}_{p'} \\ \mathbf{g}_3^{m'n'p',mnp} &= \mathbf{k}_m + \mathbf{k}_{m'} + \mathbf{k}_n - \mathbf{k}_{n'} + \mathbf{k}_p + \mathbf{k}_{p'} \\ \mathbf{g}_4^{m'n'p',mnp} &= \mathbf{k}_m - \mathbf{k}_{m'} + \mathbf{k}_n - \mathbf{k}_{n'} + \mathbf{k}_p + \mathbf{k}_{p'} \\ \mathbf{g}_5^{m'n'p',mnp} &= \mathbf{k}_m + \mathbf{k}_{m'} + \mathbf{k}_n + \mathbf{k}_{n'} + \mathbf{k}_p - \mathbf{k}_{p'} \\ \mathbf{g}_6^{m'n'p',mnp} &= \mathbf{k}_m - \mathbf{k}_{m'} + \mathbf{k}_n + \mathbf{k}_{n'} + \mathbf{k}_p - \mathbf{k}_{p'} \\ \mathbf{g}_7^{m'n'p',mnp} &= \mathbf{k}_m + \mathbf{k}_{m'} + \mathbf{k}_n - \mathbf{k}_{n'} + \mathbf{k}_p - \mathbf{k}_{p'} \\ \mathbf{g}_8^{m'n'p',mnp} &= \mathbf{k}_m - \mathbf{k}_{m'} + \mathbf{k}_n - \mathbf{k}_{n'} + \mathbf{k}_p - \mathbf{k}_{p'} \end{aligned} \quad (78)$$

Finally,

$$S_{l,\alpha}^{m'n'p',mnp} = a_{l,\alpha}(m'n'p')a_{l,\alpha}(mnp) + N_{l,\alpha}b_{l,\alpha}(m'n'p')b_{l,\alpha}(mnp) \quad (79)$$

$$P_{i,l}^{m'n'p',mnp} = P_i(k_i^{m'n'p',mnp}/g_{m'n'p'}g_{mnp}) \quad (80)$$

$$\begin{aligned} k_1^{m'n'p',mnp} &= -k_mk_{m'} - k_nk_{n'} - k_pk_{p'} \\ k_2^{m'n'p',mnp} &= k_mk_{m'} - k_nk_{n'} - k_pk_{p'} \\ k_3^{m'n'p',mnp} &= -k_mk_{m'} + k_nk_{n'} - k_pk_{p'} \\ k_4^{m'n'p',mnp} &= k_mk_{m'} + k_nk_{n'} - k_pk_{p'} \\ k_5^{m'n'p',mnp} &= -k_mk_{m'} - k_nk_{n'} + k_pk_{p'} \\ k_6^{m'n'p',mnp} &= k_mk_{m'} - k_nk_{n'} + k_pk_{p'} \\ k_7^{m'n'p',mnp} &= -k_mk_{m'} + k_nk_{n'} + k_pk_{p'} \\ k_8^{m'n'p',mnp} &= k_mk_{m'} + k_nk_{n'} + k_pk_{p'} \end{aligned} \quad (81)$$

The Hamiltonian matrix elements have the form:

$$\begin{aligned} &\langle \varphi_{m'n'p'}^{\pm,\pm,\pm} | \hat{H} | \varphi_{mnp}^{\pm,\pm,\pm} \rangle \\ &= (k_m^2 + k_n^2 + k_p^2) \delta_{m^\pm n^\pm p^\pm, m^\pm n^\pm p^\pm} - \frac{4\pi}{\Omega} \sum_\alpha r_\alpha^2 \\ &\times \sum_{i=1}^8 x_{i\alpha}^{m^\pm n^\pm p^\pm, m^\pm n^\pm p^\pm} J_\alpha(g_i^{m'n'p',mnp}) k_i^{m'n'p',mnp} \\ &+ \frac{4\pi}{\Omega} \sum_\alpha r_\alpha^4 \sum_{l=0} (2l+1) [S_{l,\alpha}^{m'n'p',mnp} E_{la} + \gamma_{l,\alpha}^{m'n'p',mnp}] \\ &\times \sum_{i=1}^8 x_{i\alpha}^{m^\pm n^\pm p^\pm, m^\pm n^\pm p^\pm} P_{i,l}^{m'n'p',mnp} \end{aligned} \quad (82)$$

where

$$\begin{aligned} \gamma_{l,\alpha}^{m'n'p',mnp} &= \dot{u}_{l,\alpha} u'_{l,\alpha} [j'_l(g_{m'n'p'}r) j_l(g_{mnp}r) \\ &\quad + j_l(g_{m'n'p'}r) j'_l(g_{mnp}r)] \Big|_{r=r_\alpha} \\ &- [\dot{u}'_{l,\alpha} u'_{l,\alpha} j_l(g_{m'n'p'}r) j_l(g_{mnp}r) \\ &\quad + \dot{u}_{l,\alpha} u_{l,\alpha} j'_l(g_{m'n'p'}r) j'_l(g_{mnp}r)] \Big|_{r=r_\alpha} \end{aligned} \quad (83)$$

5. LINEAR AUGMENTED CYLINDRICAL-WAVE METHOD

The synthesis of nanotubes [31], which represent graphite layers convoluted in cylinders, as well as implanting metal atoms in such cylinders [32], opens the way to producing a new class of nanowires [33, 34]. For theorists, the basic challenge is interpreting and predicting the properties of these cylindrical systems.

5.1. Rod LACW Method

The rod LACW method is an extension of the 1D-LAPW method to cylindrical nanowires [35–37]. In the LACW theory under consideration, we use the step cylindrical-MT one-electron potential; that is, we consider that the potential is spherically symmetric in the vicinity of atoms Ω_I and constant in the Ω_{II} space among them and that the system is confined in an impenetrable potential box of cylindrical shape Ω_{III} . The radius a of the cylinder is chosen so that the cylinder includes a significant portion of the electron density of the nanorod.

5.1.1. Forming the Rod Basis Functions

To form the basis functions (linear augmented cylindrical waves, LACWs), the solutions of the wave equation for the cylindrical interstitial and MT regions should be sewn together so that the resulting LACWs and their first derivatives are continuous. In the interstitial region, the LACWs are the solutions of the Schrödinger equation for free electron movement in a cylinder of size $\pi a^2 \times \infty$. When expressed in cylindrical coordinates Z , R , and Φ , this equation takes the form:

$$\begin{aligned} &\left\{ -\left[\frac{1}{R} \frac{\partial}{\partial R} R \frac{\partial}{\partial R} + \frac{1}{R^2} \frac{\partial^2}{\partial \Phi^2} + \frac{\partial^2}{\partial Z^2} \right] + U(R) \right\} \Psi(Z, R, \Phi) \\ &= E \Psi(Z, R, \Phi) \end{aligned} \quad (84)$$

where the potential $U(R) = 0$ at $R \leq a$ and $U(R) = \infty$ at $R > a$. Let

$$\Psi(Z, R, \Phi) = \Psi_p(Z, k) \Psi_M(\Phi) \Psi_{|M|,N}(R) \quad (85)$$

be the solutions of (84). As in the bar-LACW method, the $\Psi_p(Z, k)$ function describes the movement of an electron along the z axis in the one-dimensional system, (49). The function

$$\Psi_M(\Phi) = (2\pi)^{-1/2} \exp(iM\Phi) \quad M = 0, \pm 1, \pm 2, \dots \quad (86)$$

corresponds to the axial component, and $\Psi_{|M|,N}(R)$ corresponds to the transverse component of the wave function that is the solution of the equation

$$\begin{aligned} &\left(-\frac{1}{R} \frac{d}{dR} R \frac{d}{dR} + \frac{M^2}{R^2} \right) \Psi_{|M|,N}(R) \\ &+ U(R) \Psi_{|M|,N}(R) = E_{|M|,N} \Psi_{|M|,N}(R). \end{aligned} \quad (87)$$

$$a_{lm,\alpha}(PMN) = I_2(r_\alpha) \dot{u}_{l,\alpha}(r_\alpha) - I_1(r_\alpha) \dot{u}'_{l,\alpha}(r_\alpha) \quad (100)$$

$$b_{lm,\alpha}(PMN) = I_1(r_\alpha) u'_{l,\alpha}(r_\alpha) - I_2(r_\alpha) u_{l,\alpha}(r_\alpha) \quad (101)$$

Here, I_1 and I_2 are integrals of the augmented Legendre polynomials $P_l^{|m|}$:

$$I_1 = 2 \int_0^{\pi/2} \exp[i(K_P r_\alpha \cos \theta)] J_m(\kappa_{|M|, N} r_\alpha \sin \theta) P_l^{|m|}(\cos \theta) \sin \theta d\theta \quad (102)$$

$$I_2 = 2 \int_0^{\pi/2} \exp[i(K_P r_\alpha \cos \theta)] [iK_P \cos \theta J_m(\kappa_{|M|, N} r_\alpha \sin \theta) + (1/2)\kappa_{|M|, N} \sin \theta] [J_{m-1}(\kappa_{|M|, N} r_\alpha \sin \theta) - J_{m-1}(\kappa_{|M|, N} r_\alpha \sin \theta)] P_l^{|m|}(\cos \theta) \sin \theta d\theta \quad (103)$$

5.1.2. Rod LACW Hamiltonian and Overlap Matrices

With the use of the equations for the basis functions, we can calculate the overlap and Hamiltonian matrices:

$$\begin{aligned} & \langle \Psi_{P'M'N'} | \Psi_{PMN} \rangle \\ &= \delta_{P'M'N', PMN} + 2\pi [\Omega |J'_{|M'|}(\kappa_{|M'|, N'} a) J_{|M|}(\kappa_{|M|, N} a)]^{-1} \\ & \times (-1)^{M+M'} \sum_{\alpha} \exp\{i[(k_P - k_{P'})Z_{\alpha} + (M - M')\Phi_{\alpha}]\} \\ & \times \sum_{m=-\infty}^{\infty} J_{m-M'}(\kappa_{|M'|, N'} R_{\alpha}) J_{m-M}(\kappa_{|M|, N} R_{\alpha}) \\ & \times \left\{ I_3 - r_{\alpha}^4 \sum_{l=|m|}^{\infty} \frac{(2l+1)[(l-|m|)!]}{2[(l+|m|)!]} S_{lm,\alpha}^{P'M'N', PMN} \right\} \quad (104) \end{aligned}$$

$$\begin{aligned} & \langle \Psi_{P'M'N'} | \hat{H} | \Psi_{PMN} \rangle \\ &= (K_{P'} K_P + \kappa_{|M'|, N'} \kappa_{|M|, N}) \delta_{P'M'N', PMN} \\ & - 2\pi [\Omega |J'_{|M'|}(\kappa_{|M'|, N'} a) J_{|M|}(\kappa_{|M|, N} a)]^{-1} (-1)^{M+M'} \\ & \times \sum_{\alpha} \exp\{i[(k_P - k_{P'})Z_{\alpha} + (M - M')\Phi_{\alpha}]\} \\ & \times \sum_{m=-\infty}^{\infty} J_{m-M'}(\kappa_{|M'|, N'} R_{\alpha}) J_{m-M}(\kappa_{|M|, N} R_{\alpha}) \\ & \times W_{\alpha m}^{P'M'N', PMN}, \quad (105) \end{aligned}$$

where

$$\begin{aligned} W_{\alpha m}^{P'M'N', PMN} &= K_{P'} K_P I_3 + \kappa_{|M'|, N'} \kappa_{|M|, N} I_3' + m^2 I_4 \\ & - r_{\alpha}^4 \sum_{l=|m|}^{\infty} \frac{(2l+1)[(l-|m|)!]}{2[(l+|m|)!]} \\ & \times (E_{l\alpha} S_{lm,\alpha}^{P'M'N', PMN} + \gamma_{lm,\alpha}^{P'M'N', PMN}), \quad (106) \end{aligned}$$

$$I_3 = 2 \int_0^{\pi/2} \int_0^{r_{\alpha}} \cos[r(k_P - k_{P'}) \cos \theta] J_m(\kappa_{|M'|, N'} r \sin \theta) \times J_m(\kappa_{|M|, N} r \sin \theta) \sin \theta r^2 d\theta dr$$

$$I_3' = 2 \int_0^{\pi/2} \int_0^{r_{\alpha}} \cos[r(k_P - k_{P'}) \cos \theta] J'_m(\kappa_{|M'|, N'} r \sin \theta) \times J'_m(\kappa_{|M|, N} r \sin \theta) \sin \theta r^2 d\theta dr$$

$$I_4 = 2 \int_0^{\pi/2} \int_0^{r_{\alpha}} \cos[r(k_P - k_{P'}) \cos \theta] J_m(\kappa_{|M'|, N'} r \sin \theta) \times J_m(\kappa_{|M|, N} r \sin \theta) (\sin \theta)^{-1} d\theta dr \quad (107)$$

$$S_{lm,\alpha}^{P'M'N', PMN} = a_{lm,\alpha}^*(P'M'N') a_{lm,\alpha}(PMN) + N_{l,\alpha} b_{lm,\alpha}^*(P'M'N') b_{lm,\alpha}(PMN) \quad (108)$$

$$\gamma_{lm,\alpha}^{P'M'N', PMN} = (I_2^* I_1 + I_1^* I_2) \dot{u}_{l,\alpha} u'_{l,\alpha} - I_2^* I_2 \dot{u}_{l,\alpha} u_{l,\alpha} - I_1^* I_1 \dot{u}'_{l,\alpha} u'_{l,\alpha} \quad (109)$$

We calculated integrals I_1 – I_4 by numerical methods.

5.2. Tube LACW Method

In the LACW method with the rod-MT approximation, the electron potential of a polyatomic system is assumed to be constant in the interatomic space up to an impenetrable cylindrical potential barrier. Thus, electrons are allowed to move throughout the interior of the potential cylinder; that is, the interior of a nanopolymer of near-cylindrical shape is free of cavities as, for example, in intercalated carbon nanotubes. On the other hand, a number of important polymeric systems have near-cylindrical symmetry and an interior cylindrical hole. Among these systems are, for example, original all-carbon and boron nitride nanotubes and MX₂ nanotubes (M = W, Mo; X = S, Se). Here, we extend the LACW method to nanotubes with an interior hole [41–43].

5.2.1. Forming the Tube LACW Basis Functions

We assume that the effective one-electron potential is constant in the interspherical region up to the two cylindrical potential barriers: the exterior cylinder of radius a and the interior cylinder of radius b . In this region, the basis functions are the solutions of the Schrödinger equation for free electron movement inside an infinite tube with outer radius a and inner radius b . This equation has the same form (84) as in the case of a nanorod; however, the potential is

$$U(R) = \begin{cases} 0, & b \leq R \leq a \\ \infty, & R < b, R > a \end{cases} \quad (110)$$

Because of the cylindrical symmetry of the potential $U(R)$, the wave function has the form (85), where $\Psi_{|M|, N}(R)$ is the solution of the Bessel equation (89) with new boundary conditions $\Psi_{|M|, N}(a) = \Psi_{|M|, N}(b) = 0$. Any solution of the Bessel equation can be represented as a linear combination of its partial solutions—cylindrical Bessel functions of the first J_M and second Y_M kinds

$$\Psi_{M, N}(R) = C_{M, N}^J J_M(\kappa_{|M|, N} R) + C_{M, N}^Y Y_M(\kappa_{|M|, N} R) \quad (111)$$

Here, $C_{M, N}^J$ and $C_{M, N}^Y$ are the constants chosen in such a way as to ensure the normalization of the $\Psi_{|M|, N}(R)$ function

$$\int_b^a \Psi_{M, N}^2(R) R dR = 1 \quad (112)$$

and its vanishing at the interior and exterior potential barriers:

$$\Psi_{M,N}(a) = C_{M,N}^J J_M(\kappa_{|M|,N} a) + C_{M,N}^Y Y_M(\kappa_{|M|,N} a) = 0 \quad (113)$$

$$\Psi_{M,N}(b) = C_{M,N}^J J_M(\kappa_{|M|,N} b) + C_{M,N}^Y Y_M(\kappa_{|M|,N} b) = 0 \quad (114)$$

[Note that, for a cylinder without a hole, the coefficient $C_{M,N}^Y$ in (111) vanishes, because the function $Y_M(\kappa_{|M|,N} R)$ has a singularity at $R = 0$; however, we are interested in the solutions of the Schrödinger equation that are finite and continuous everywhere over the region.] From the set of equations (113) and (114), we can easily derive the equation for finding $\kappa_{|M|,N}$:

$$J_M(\kappa_{|M|,N} a) Y_M(\kappa_{|M|,N} b) = J_M(\kappa_{|M|,N} b) Y_M(\kappa_{|M|,N} a) \quad (115)$$

In our work, we solve this equation numerically (we determine the segments containing at least one root, which was found by bisecting the segment). From (113) and (114), the relationship between $C_{M,N}^J$ and $C_{M,N}^Y$ can be found:

$$C_{M,N}^Y = -C_{M,N}^J \frac{J_M(\kappa_{|M|,N} a)}{Y_M(\kappa_{|M|,N} a)} \quad (116)$$

To calculate the integral (112), let us use the equation

$$\begin{aligned} & \int z F_M(\kappa z) G_M(\kappa z) dz \\ &= \frac{z^2}{2} F_M(\kappa z) G_M(\kappa z) - \frac{z^2}{4} [F_{M-1}(\kappa z) G_{M+1}(\kappa z) \\ & \quad + F_{M+1}(\kappa z) G_{M-1}(\kappa z)] \quad (117) \end{aligned}$$

for an indefinite integral and the recurrence formulas

$$z F_{M-1}(z) = z F'_M(z) + M F_M(z) \quad (118)$$

$$-z F_{M+1}(z) = z F'_M(z) - M F_M(z) \quad (119)$$

where F_M and G_M are any two cylindrical functions, in particular, J_M and Y_M . Then,

$$\frac{R^2}{2} [C_{MN}^J J'_M(\kappa_{|M|,N} R) + C_{MN}^Y Y'_M(\kappa_{|M|,N} R)]^2 \Big|_b^a = 1 \quad (120)$$

Finally, the basis function $\Psi_{II,PMN}(Z, R, \Phi)$ in the region Ω_{II} in the general cylindrical coordinate system takes the form:

$$\begin{aligned} & \Psi_{II,PMN}(Z, R, \Phi) \\ &= \frac{1}{\sqrt{2\pi c}} \exp[i(K_P Z + M\Phi)] [C_{M,N}^J J_M(\kappa_{|M|,N} R) \\ & \quad + C_{M,N}^Y Y_M(\kappa_{|M|,N} R)] \quad (121) \end{aligned}$$

Here, the $\kappa_{|M|,N}$ values are found from (115), and $C_{M,N}^J$ and $C_{M,N}^Y$ are derived from the set of equations (120) and (116).

Inside the MT sphere α in the local spherical coordinate system, the LACW has the same form as in the case of bulk

or nanorod. In order to determine the coefficients A_{lm}^{PMN} and B_{lm}^{PMN} , let us again use the theorem of addition for cylindrical functions (Figs. 1 and 2). In the local spherical coordinate system, the function $\Psi_{II\alpha,PMN}(\rho, \theta, \varphi)$ for a cylinder with a hole takes the form:

$$\begin{aligned} & \Psi_{II\alpha,PMN}(\rho, \theta, \varphi) \\ &= (2\pi c)^{-1/2} \exp[i(K_P Z_\alpha + M\Phi_\alpha)] \exp(iK_P \rho \cos \theta) (-1)^M \\ & \quad \times \sum_{m=-\infty}^{\infty} [C_{M,N}^J J_{m-M}(\kappa_{|M|,N} R_\alpha) + C_{M,N}^Y Y_{m-M}(\kappa_{|M|,N} R_\alpha)] \\ & \quad \times J_m(\kappa_{|M|,N} \rho \sin \theta) e^{im\varphi} \quad (122) \end{aligned}$$

Finally, we obtain that the A_{lm} and B_{lm} coefficients can be calculated from (97) and (98) with

$$\begin{aligned} D_{lm,\alpha}^{PMN} &= \frac{1}{\sqrt{2c}} \left\{ \frac{(2l+1)[(l-|m|)!]}{[(l+|m|)!]} \right\}^{1/2} (-1)^{[0.5(m+|m|+l)]} i^l \\ & \quad \times \exp[i(K_P Z_\alpha + M\Phi_\alpha)] \\ & \quad \times (-1)^M [C_{M,N}^J J_{m-M}(\kappa_{|M|,N} R_\alpha) \\ & \quad + C_{M,N}^Y Y_{m-M}(\kappa_{|M|,N} R_\alpha)] \quad (123) \end{aligned}$$

5.2.2. Tube LACW Hamiltonian and Overlap Matrices

The overlap and Hamiltonian matrices in this case have the form:

$$\begin{aligned} \langle \Psi_{P'M'N'} | \Psi_{PMN} \rangle &= \delta_{P'M'N',PMN} - \frac{1}{c} (-1)^{M+M'} \\ & \quad \times \sum_{\alpha} \exp\{i[(K_P - K_{P'})Z_\alpha + (M - M')\Phi_\alpha]\} \\ & \quad \times \sum_{m=-\infty}^{\infty} [C_{M',N'}^J J_{m-M'}(\kappa_{|M'|,N'} R_\alpha) \\ & \quad + C_{M',N'}^Y Y_{m-M'}(\kappa_{|M'|,N'} R_\alpha)] \\ & \quad \times [C_{M,N}^J J_{m-M}(\kappa_{|M|,N} R_\alpha) \\ & \quad + C_{M,N}^Y Y_{m-M}(\kappa_{|M|,N} R_\alpha)] \\ & \quad \times \left\{ I_3 - r_\alpha^4 \sum_{l=|m|}^{\infty} \frac{(2l+1)[(l-|m|)!]}{2[(l+|m|)!]} \right. \\ & \quad \left. \times S_{lm,\alpha}^{P'M'N',PMN} \right\}, \quad (124) \end{aligned}$$

$$\begin{aligned} \langle \Psi_{P'M'N'} | \hat{H} | \Psi_{PMN} \rangle &= (K_{P'} K_P + \kappa_{|M'|,N'} \kappa_{|M|,N}) \delta_{P'M'N',PMN} \\ & \quad - \frac{1}{c} (-1)^{M+M'} \sum_{\alpha} \exp\{i[(K_P - K_{P'})Z_\alpha + (M - M')\Phi_\alpha]\} \\ & \quad \times \sum_{m=-\infty}^{\infty} [C_{M',N'}^J J_{m-M'}(\kappa_{|M'|,N'} R_\alpha) \\ & \quad + C_{M',N'}^Y Y_{m-M'}(\kappa_{|M'|,N'} R_\alpha)] \\ & \quad \times [C_{M,N}^J J_{m-M}(\kappa_{|M|,N} R_\alpha) \\ & \quad + C_{M,N}^Y Y_{m-M}(\kappa_{|M|,N} R_\alpha)] W_{\alpha m}^{P'M'N',PMN} \quad (125) \end{aligned}$$

5.3. LACW Method for Nanoporous System

The pore LACW method can be developed to study the characteristic electron states of the pores in nanoporous system with cylindrical nanocavities in a bulk material [44, 45]. Again, we use the step cylindrical-MT electron potential. In this case, an impenetrable cylindrical step potential separates an unattainable for electron cylindrical region from the rest of the system.

In this case in the interstitial region, the LACW

$$\Psi_{II, PMN}(Z, R, \Phi) = [\sqrt{\Omega}|Y'_M(\kappa_{|M|, N}b)|]^{-1} \times \exp[i(K_p Z + M\Phi)]Y_M(\kappa_{|M|, N}R) \quad (126)$$

is a solution of the Schrödinger equation (84) with the potential $U(R) = 0$ at $R \geq b$ and $U(R) = \infty$ at $R < b$. The condition of the vanishing of the wave function at the impenetrable barrier $\Psi_{|M|, N}(b) = Y_M(\kappa_{|M|, N}b) = 0$ determines the corresponding energy spectrum through the roots of the Bessel functions of the second kind. Here, $\Omega = \pi cb^2$.

In the local spherical coordinate system $\rho, \theta,$ and $\varphi,$ we have

$$\Psi_{II\alpha, PMN}(\rho, \theta, \varphi) = [\sqrt{\Omega}|Y'_M(\kappa_{|M|, N}a)|]^{-1} \times \exp[i(K_p Z_\alpha + M\Phi_\alpha)] \exp(iK_p \rho \cos \theta)(-1)^M \times \sum_{m=-\infty}^{\infty} Y_{m-M}(\kappa_{|M|, N}R_\alpha) J_m(\kappa_{|M|, N}\rho \sin \theta) e^{im\varphi} \quad (127)$$

When (127) is compared with analogous equations (96) for a nanorod or (122) for a nanotube, the overlap and Hamiltonian matrix elements are readily obtained from (104) and (105) or (124) and (125):

$$\begin{aligned} &\langle \Psi_{P'M'N'} | \Psi_{PMN} \rangle \\ &= \delta_{P'M'N', PMN} + 2\pi[\Omega|Y'_{|M'|}(\kappa_{|M'|, N'}b)Y'_{|M|}(\kappa_{|M|, N}b)|]^{-1} \\ &\quad \times (-1)^{M+M'} \sum_{\alpha} \exp\{i[(k_p - k_{p'})Z_\alpha + (M - M')\Phi_\alpha]\} \\ &\quad \times \sum_{m=-\infty}^{\infty} Y_{m-M'}(\kappa_{|M'|, N'}R_\alpha) Y_{m-M}(\kappa_{|M|, N}R_\alpha) \\ &\quad \times \left\{ I_3 - r_\alpha^4 \sum_{l=|m|}^{\infty} \frac{(2l+1)[(l-|m|)!]}{2[(l+|m|)!]} S_{lm, \alpha}^{P'M'N', PMN} \right\}, \quad (128) \end{aligned}$$

$$\begin{aligned} &\langle \Psi_{P'M'N'} | \hat{H} | \Psi_{PMN} \rangle = (K_p K_{p'} + \kappa_{|M'|, N'} \kappa_{|M|, N}) \delta_{P'M'N', PMN} \\ &\quad - 2\pi[\Omega|Y'_{|M'|}(\kappa_{|M'|, N'}b)Y'_{|M|}(\kappa_{|M|, N}b)|]^{-1} (-1)^{M+M'} \\ &\quad \times \sum_{\alpha} \exp\{i[(k_p - k_{p'})Z_\alpha + (M - M')\Phi_\alpha]\} \\ &\quad \times \sum_{m=-\infty}^{\infty} Y_{m-M'}(\kappa_{|M'|, N'}R_\alpha) Y_{m-M}(\kappa_{|M|, N}R_\alpha) \\ &\quad \times (\kappa_{|M|, N}R_\alpha) W_{\alpha m}^{P'M'N', PMN} \quad (129) \end{aligned}$$

6. CLUSTER LINEAR AUGMENTED SPHERICAL-WAVE METHOD

In this section, a cluster linear augmented spherical-wave (C-LASW or 0D-LASW) method for spherical nanocrystals or polyatomic clusters such as fullerene C_{60} is presented

[46, 47]. The C-LASW model is based on the 3D-LASW method for crystals [48] and the multiple-scattering model for polyatomic molecules [49–51]. We use the spherical-MT approximation here; that is, we assume that the effective one-electron potential is spherically symmetric with large radial variation in the vicinity of atoms Ω_I and constant in the Ω_{II} space among them up to the impenetrable spherical potential barrier Ω_{III} . In the general case considered here that a molecule such as C_{60} has an inner spherical hole, there must be two spherical potential barriers with radii a and b , between which the major part of the electron density is located.

6.1. Forming the Basis Cluster LASW Functions

Here, the basis function is called a linear augmented spherical wave (LASW). In the spherical interatomic region, it is a solution of the wave equation with constant potential. In the general spherical coordinates $R, \Theta,$ and Φ (Fig. 3), the Schrödinger equation for free electron movement in a spherical layer takes the form:

$$\left\{ -\frac{1}{R^2} \frac{\partial}{\partial R} R^2 \frac{\partial}{\partial R} - \frac{\Lambda}{R^2} + U(R) \right\} \Psi(R, \Theta, \Phi) = E \Psi(R, \Theta, \Phi) \quad (130)$$

where

$$\Lambda = \frac{1}{\sin \Theta} \left[\frac{\partial}{\partial \Theta} \left(\sin \Theta \frac{\partial}{\partial \Theta} \right) + \frac{\partial^2}{\sin \Theta \partial \Phi^2} \right] \quad (131)$$

For a spherical cluster with a spherical hole, $U(R) = 0$ for $a \leq R \leq b$ and $U(R) = \infty$ outside the step potential barriers (110). The solution of (130)

$$\begin{aligned} \Psi_{II, NLM}(R, \Theta, \Phi) &= f_{N, L}(R) Y_{L, M}(\Theta, \Phi) \\ &\equiv f_{N, L}(R) Y_{L, M}(\hat{R}) \quad (132) \end{aligned}$$

is called the spherical wave. The radial function $f_{N, L}(R)$ is the solution of the equation

$$\left(\frac{d^2}{dR^2} + \frac{2}{R} \frac{d}{dR} + \kappa_{N, L}^2 - \frac{L(L+1)}{R^2} \right) f_{N, L}(R) = 0 \quad (133)$$

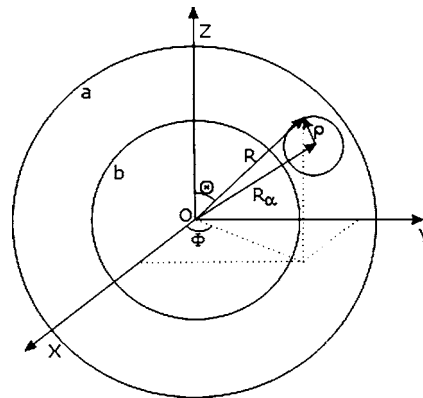


Figure 3. General and local spherical coordinate systems and illustration of the theorem of expansion for spherical waves.

where $\kappa_{N,L} = \sqrt{E}$. Any solution of this equation is a linear combination of its partial solutions—spherical Bessel functions of the first j_L and second y_L kinds

$$f_{N,L}(R) = c_{N,L}^j j_L(\kappa_{N,L}R) + c_{N,L}^y y_L(\kappa_{N,L}R) \quad (134)$$

Using the normalization

$$\int_b^a f_{N,L}^2(R) R^2 dR = 1 \quad (135)$$

and boundary conditions $f_{N,L}(a) = f_{N,L}(b) = 0$, we obtain three equations

$$j_L(\kappa_{N,L}a)y_L(\kappa_{N,L}b) = j_L(\kappa_{N,L}b)y_L(\kappa_{N,L}a) \quad (136)$$

$$c_{N,L}^y = -c_{N,L}^j \frac{j_L(\kappa_{N,L}a)}{y_L(\kappa_{N,L}a)} \quad (137)$$

$$\begin{aligned} \frac{R^3}{2} [(c_{N,L}^j)^2 j_{L-1} j_{L+1} + (c_{N,L}^y)^2 y_{L-1} y_{L+1} \\ + c_{N,L}^j c_{N,L}^y (j_{L-1} y_{L+1} + j_{L+1} y_{L-1})] \Big|_a^b = 1 \end{aligned} \quad (138)$$

for $\kappa_{N,L}$, $c_{N,L}^j$, and $c_{N,L}^y$. Here, $j_{L-1} = j_{L-1}(\kappa_{N,L}R)$, $j_{L+1} = j_{L+1}(\kappa_{N,L}R)$, \dots . To obtain (138) from (135), we used (117) and the relationship between spherical and cylindrical Bessel functions

$$\begin{aligned} j_L(z) &= \sqrt{\frac{\pi}{2z}} J_{L+1/2}(z) \\ y_L(z) &= \sqrt{\frac{\pi}{2z}} J_{-L-1/2}(z) (-1)^{L+1} \end{aligned} \quad (139)$$

Inside the MT sphere α in the local spherical coordinate system, the basis function $\Psi_{I\alpha,NLM}(\rho, \theta, \varphi)$ is expanded in spherical harmonics according to (21) with the coefficients $A_{lm,\alpha}^{NLM}$ and $B_{lm,\alpha}^{NLM}$ determined by matching the basis function Ψ_{NLM} and its derivative over the boundary of MT spheres.

Using an expansion theorem (Fig. 3) for the spherical wave [49], according to which

$$\begin{aligned} \frac{n_L(\kappa R) Y_{LM}(\hat{R})}{4\pi} &= \sum_{l'm'} \sum_{l''m''} i^{l'+l''-L} I_{l''m''}(LM, l'm') n_L(\kappa R_\alpha) \\ &\times Y_{l'm'}(\hat{R}_\alpha) j_{l''}(\kappa r) Y_{l''m''}(\hat{r}) \end{aligned} \quad (140)$$

where n_L is the spherical Bessel function of the first j_L or second y_L kind and κ is an arbitrary complex number, we express the $\Psi_{II,NLM}(R, \Theta, \Phi)$ function through the general spherical coordinates R_α , Θ_α , and Φ_α of the center of the α th sphere and through the local spherical coordinates ρ , θ , and φ :

$$\begin{aligned} \Psi_{II\alpha,NLM} &= 4\pi \sum_{l'm'} \sum_{l''m''} i^{l'+l''-L} I_{l''m''}(LM, l'm') \\ &\times [c_{N,L}^j j_{l''}(\kappa_{N,L}R_\alpha) + c_{N,L}^y y_{l''}(\kappa_{N,L}R_\alpha)] \\ &\times Y_{l'm'}(\hat{R}_\alpha) j_{l''}(\kappa_{N,L}\rho) Y_{l''m''}(\hat{\rho}) \end{aligned} \quad (141)$$

where the Gaunt integral

$$\begin{aligned} I_{l''m''}(LM, l'm') &= \int_0^\pi \int_0^{2\pi} Y_{l''m''}(\theta, \varphi) \\ &\times Y_{LM}^*(\theta, \varphi) Y_{l'm'}(\theta, \varphi) \sin \theta d\theta d\varphi \\ &= \sqrt{\frac{(2l''+1)(2l'+1)}{4\pi(2L+1)}} C_{l''0l'0}^{L0} C_{l''m''l'm'}^{LM} \end{aligned} \quad (142)$$

over triple products or spherical harmonics is easily computed in terms of products of Clebsch–Gordan coefficients $C_{l''0l'0}^{L0}$ and $C_{l''m''l'm'}^{LM}$ [52].

From the equality of the function $\Psi_{I\alpha,NLM}$ of the type (21) and $\Psi_{II\alpha,NLM}$ (141) and of their derivatives at the MT-sphere boundary, we have

$$A_{lm,\alpha}^{NLM} = r_\alpha^2 D_{lm,\alpha}^{NLM} a_{lm,\alpha}(NL) \quad (143)$$

$$B_{lm,\alpha}^{NLM} = r_\alpha^2 D_{lm,\alpha}^{NLM} b_{lm,\alpha}(NL) \quad (144)$$

where

$$\begin{aligned} D_{lm,\alpha}^{NLM} &= 4\pi \sum_{l'm'} i^{l'+l-L} I_{lm}(LM, l'm') [c_{N,L}^j j_l(\kappa_{N,L}R_\alpha) \\ &+ c_{N,L}^y y_l(\kappa_{N,L}R_\alpha)] Y_{l'm'}(\hat{R}_\alpha) \end{aligned} \quad (145)$$

$$a_{lm,\alpha}(NL) = j_l'(\kappa_{N,L}r_\alpha) u_{l,\alpha}'(r_\alpha) - j_l(\kappa_{N,L}r_\alpha) u_{l,\alpha}'(r_\alpha) \quad (146)$$

$$b_{lm,\alpha}(NL) = j_l(\kappa_{N,L}r_\alpha) u_{l,\alpha}'(r_\alpha) - j_l'(\kappa_{N,L}r_\alpha) u_{l,\alpha}(r_\alpha) \quad (147)$$

6.2. Cluster LASW Hamiltonian and Overlap Matrices

The overlap matrix in this method has the form:

$$\begin{aligned} \langle \Psi_{N_2L_2M_2} | \Psi_{N_1L_1M_1} \rangle &= \delta_{N_2L_2M_2, N_1L_1M_1} - (4\pi)^2 \sum_{l''m''} \sum_{l'm'} i^{l'-l''-L_1+L_2} \\ &\times \sum_{\alpha} [c_{N_2,L_2}^j j_{l''}(\kappa_{N_2,L_2}R_\alpha) \\ &+ c_{N_2,L_2}^y y_{l''}(\kappa_{N_2,L_2}R_\alpha)] Y_{l''m''}^*(\hat{R}_\alpha) \\ &\times [c_{N_1,L_1}^j j_{l'}(\kappa_{N_1,L_1}R_\alpha) + c_{N_1,L_1}^y y_{l'}(\kappa_{N_1,L_1}R_\alpha)] Y_{l'm'}(\hat{R}_\alpha) \\ &\times \sum_{lm} I_{lm}(L_2M_2, l''m'') I_{lm}(L_1M_1, l'm') \\ &\times [I_{1,l\alpha} - r_\alpha^4 S_{l\alpha}^{N_2L_2, N_1L_1}] \end{aligned} \quad (148)$$

where

$$I_{1,l\alpha} = \int_0^{r_\alpha} j_l(\kappa_{N_2,L_2}r) j_l(\kappa_{N_1,L_1}r) r^2 dr \quad (149)$$

$$\begin{aligned} S_{l\alpha}^{N_2L_2, N_1L_1} &= a_{lm,\alpha}(N_2L_2) a_{lm,\alpha}(N_1L_1) \\ &+ N_{l\alpha} b_{lm,\alpha}(N_2L_2) b_{lm,\alpha}(N_1L_1) \end{aligned} \quad (150)$$

The Hamiltonian matrix is

$$\begin{aligned}
& \langle \Psi_{N_2 L_2 M_2} | \hat{H} | \Psi_{N_1 L_1 M_1} \rangle \\
& = \kappa_{N_2, L_2} \kappa_{N_1, L_1} \delta_{N_2 L_2 M_2, N_1 L_1 M_1} - (4\pi)^2 \sum_{l_2 m_2} \sum_{l_1 m_1} i^{l_1 - l_2 - L_1 + L_2} \\
& \quad \times \sum_{\alpha} [c_{N_2, L_2}^j j_{l_2}(\kappa_{N_2, L_2} R_{\alpha}) + c_{N_2, L_2}^y y_{l_2}(\kappa_{N_2, L_2} R_{\alpha})] Y_{l_2 m_2}^*(\hat{R}_{\alpha}) \\
& \quad \times [c_{N_1, L_1}^j j_{l_1}(\kappa_{N_1, L_1} R_{\alpha}) + c_{N_1, L_1}^y y_{l_1}(\kappa_{N_1, L_1} R_{\alpha})] Y_{l_1 m_1}(\hat{R}_{\alpha}) \\
& \quad \times \sum_{lm} I_{lm}(L_2 M_2, l_2 m_2) I_{lm}(L_1 M_1, l_1 m_1) \\
& \quad \times \{ I_{2, l\alpha} + l(l+1) I_{3, l\alpha} \\
& \quad \quad - r_{\alpha}^4 (E_{l\alpha} S_{l\alpha}^{N_2 L_2, N_1 L_1} + \gamma_{l\alpha}^{N_2 L_2, N_1 L_1}) \} \quad (151)
\end{aligned}$$

where

$$I_{2, l\alpha} = \int_0^{r_{\alpha}} \frac{dj_l(\kappa_{N_2, L_2} r)}{dr} \frac{dj_l(\kappa_{N_1, L_1} r)}{dr} r^2 dr \quad (152)$$

$$I_{3, l\alpha} = \int_0^{r_{\alpha}} j_l(\kappa_{N_2, L_2} r) j_l(\kappa_{N_1, L_1} r) dr \quad (153)$$

$$\begin{aligned}
\gamma_{l\alpha}^{N_2 L_2, N_1 L_1} & = \dot{u}_{l, \alpha} u'_{l, \alpha} [j'_l(\kappa_{N_2, L_2} r) j_l(\kappa_{N_1, L_1} r) \\
& \quad + j_l(\kappa_{N_2, L_2} r) j'_l(\kappa_{N_1, L_1} r)] |_{r=r_{\alpha}} \\
& \quad - [\dot{u}'_{l, \alpha} u'_{l, \alpha} j_l(\kappa_{N_2, L_2} r) j_l(\kappa_{N_1, L_1} r) \\
& \quad + \dot{u}_{l, \alpha} u_{l, \alpha} j'_l(\kappa_{N_2, L_2} r) j'_l(\kappa_{N_1, L_1} r)] |_{r=r_{\alpha}} \quad (154)
\end{aligned}$$

For the special case that there is no inner spherical hole in a cluster, the overlap and Hamiltonian matrices can easily be found from these equations. In this case, $c_{N, L}^y = 0$, $f_{N, L}(R) = c_{N, L}^j j_L(\kappa_{N, L} R)$, $\kappa_{N, L}$ are to be obtained from the equation $j_L(\kappa_{N, L} a) = 0$, and

$$c_{N, L}^j = \left[\frac{a^3}{2} (j_L^2(\kappa_{N, L} a) - j_{L-1}(\kappa_{N, L} a) j_{L+1}(\kappa_{N, L} a)) \right]^{-1/2} \quad (155)$$

7. APPLICATIONS

Presently, there are not too many applications of the LAW theory to nanomaterials. The majority of the studies are related to 1D and 2D systems such as nanotubes, nanowires, and films. In terms of the LAW formalism, we studied nanotubes and nanowires, and these data are briefly described below. Here, the applicability of the LAW formalism to nanomaterials will be demonstrated by examples of our calculations of one-dimensional systems: polymers, transition metal nanowires, and pure and 3d-metal intercalated carbon and boron nitride nanotubes. As to the applications of the LAW theory to nanoporous crystals and spherical and tetragonal clusters, the development of computer codes is in progress.

7.1. Polymers

Carbyne is a linear chain of carbon atoms with alternating bond lengths of 1.34 and 1.20 Å. It is the most simple carbon nanowire. The results of the 1D-LAPW calculations of this system are presented in Figure 4 [27–29]. The calculations are in close agreement with the experimental data for carbyne: the experimental bandgap width is 1–2.2 eV, the width of the valence π band is 5–6 eV, and the width of the σ band is 6–7 eV [53].

Figure 5 shows the 1D-LAPW calculated electron dispersion curves together with the total (N_T) and partial densities of the 1s(H), 2s(C), and 2p(C) states of poly(*para*-phenylene) broadened by the gauss with a half-width of 0.25 eV. In this figure, the calculated results are compared with photoelectron spectroscopy (PES) data [54]. In agreement with experiment, the calculated total valence band width equals 18 eV. The three PES bands in the range from 0 to –7 eV are to be assigned to the $2p_{\pi}$ (C) states. The positions of these peaks virtually coincide with those of the peaks of the total and $2p$ (C) states. The 2s(C) and 1s(H) states dominate in a structure below –9 eV with peaks at –10, –13, and –16 eV. The $2p_{\pi}^*$ (C) states dominate in the conduction band in a region between 0 and 4 eV. The energy gap is equal to 1 eV and corresponds to a direct $p_{\pi}^* - p_{\pi}$ transition. The bands located above 5 eV include contributions of the 2s(C) and $2p_{\sigma}$ (C) states with significant admixture of the 1s(H) states at energies exceeding 7.5 eV.

As seen from a comparison of the densities of the valence states and PES [54] of the polyethylene (Fig. 6), the valence band width and positions of the experimental and theoretical peaks near –14 and –21 eV coincide completely. The dip in the experimentally PES is represented by the gap in the band structure in the range from –14 to –11.5 eV. The set of theoretical peaks spreading from the valence band edge to about –11.5 eV with the most intensive maximum at –7 eV is observed experimentally as a band with a peak at the same energy. The energy gap between the conduction and valence bands corresponds to a direct transition near $k = (2/3)(\pi/c)$. The 1D-LAPW band structure of polyethylene seems to reproduce the PES of this system somewhat better than the results of *ab initio* calculations by the molecular orbital linear combination of atomic orbitals (MO LCAO) method [55, 56].

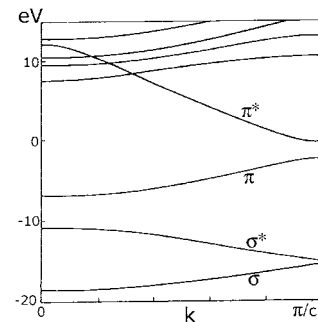


Figure 4. Band structure of carbyne with permission from [27], A. V. Nikolaev et al., *Dokl. Chem.* 348, 91 (1995).

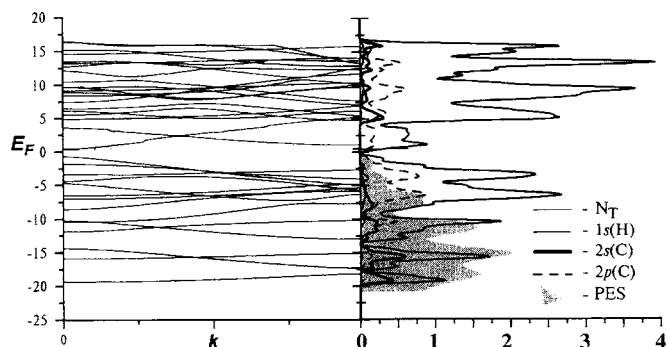


Figure 5. Electron structure of poly(*para*-phenylene). Reprinted with permission from [29].

7.2. Carbon Nanotubes

The electronic structure of all-carbon nanotubes was predicted by *ab initio* and Hückel quantum-chemical calculations in the early 1990s [57–60]. This prediction has been later corroborated by electric conductivity measurements and spectra. At the present time, a great body of theoretical and experimental information on the electronic structure of such nanotubes is available [61–65]. Therefore, we believe that they are best suited for testing the LACW method [41, 42, 66].

As is known, all carbon nanotubes with the armchair configuration have a metal-type electronic structure. The Fermi level is located at the intersection of two π bands at the point $k = (2/3)(\pi/c)$. This is also reproduced by the LACW method, as follows from our calculations of the (n, n) nanotubes (Fig. 7).

The carbon $(n, 0)$ nanotubes with a zigzag configuration, depending on their diameter parameter n , can be both semiconductors with a direct gap in the center of the Brillouin zone (at $k = 0$) and semimetals when the top of the valence band and the bottom of the conductivity band touch each other at $k = 0$. If n is a multiple of 3, the nanotubes are semimetals (Fig. 8); otherwise, they are semiconductors (Fig. 9), which is clearly reproduced by the LACW method.

7.3. 3d-Metal Atomic Wires

Intercalating different metals inside nanotubes opens the way to producing metal nanowires. Similar superthin metal wires have also been produced upon implanting metal atoms

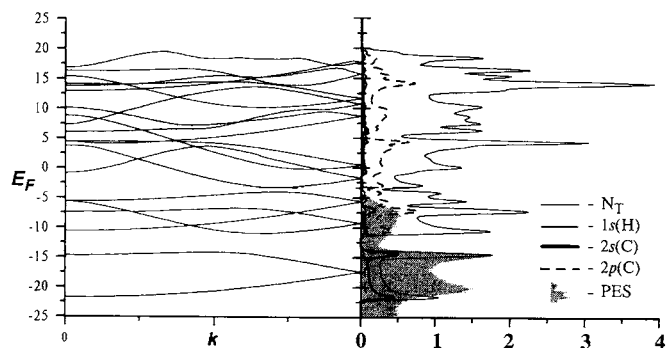


Figure 6. Electron structure of polyethylene. Reprinted with permission from [29].

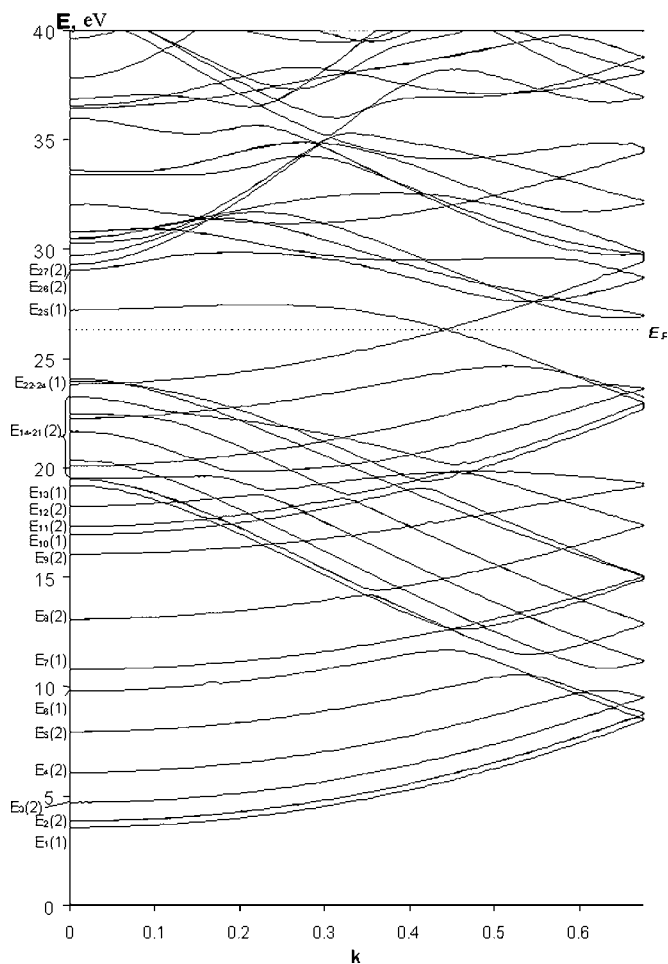


Figure 7. Band structure of carbon $(5, 5)$ nanotube. Reprinted with permission from [41].

in zeolite [67, 68]. Metal nanowires were observed on the crystal surfaces and sandwiched between the leads [69–71].

The rod-LACW method was used to calculate the electronic structure of nanowires consisting of third-period atoms from potassium to zinc [35, 36]. The chains (M_∞) and $(M_2)_\infty$ with, respectively, equal and alternating short and long M–M bonds were calculated.

Figure 10 shows that all the (M_∞) chains without alternating, except for those formed by Ca and Zn, exhibit the metal-type band structure. The $(K)_\infty$ chain is a one-dimensional metal, since the nondegenerate $4s$ band is half-filled with valence electrons. The $(Ca)_\infty$ chain represents a one-dimensional dielectric with a completely filled nondegenerate $4s$ band, whose top is located at the edge of the Brillouin zone. The band gap is 2.2 eV and corresponds to the indirect transition into the doubly degenerate band dominated by the $4p_x$ and $4p_y$ states.

In the low-energy region, the dispersion curves of all $3d$ transition metals have much in common. As in the case of $4s$ metals, their origin can be interpreted in terms of the MO LCAO method and related to the MOs of the M_2 diatomic molecules of transition metals [72]. In all cases, the nondegenerate $E_1(1)$ and $E_1(2)$ bands in the (M_∞) chains without bond alternation represent bonding and antibonding combinations of the $4s$ - and $3d_{z^2}$ -metal states. In all transition

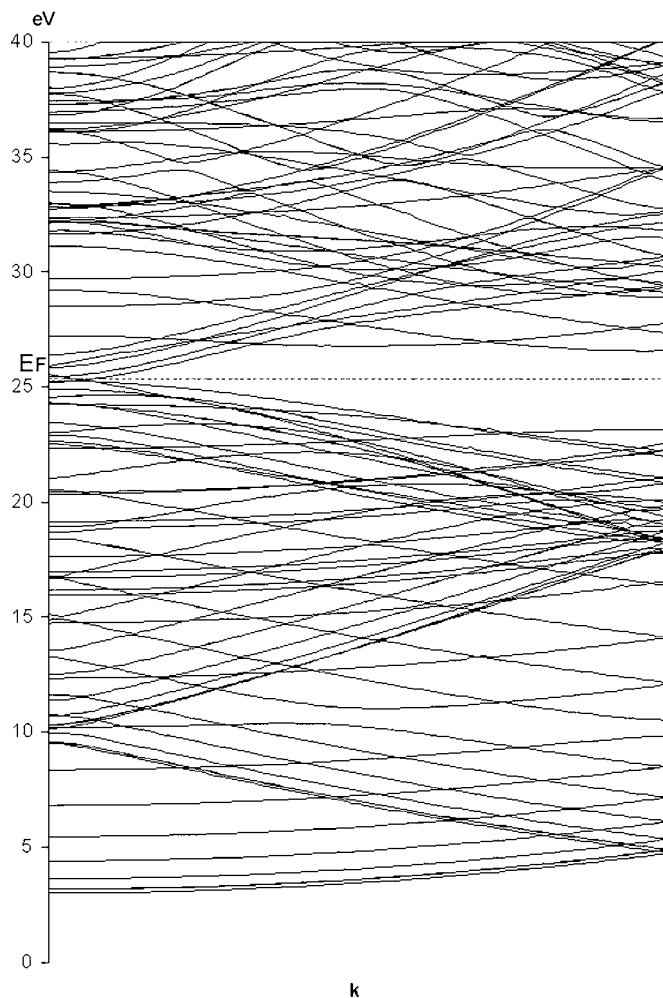


Figure 8. Band structure of carbon (12, 0) nanotube. Reprinted with permission from [41], P. N. D'yachkov and D. V. Kirin, *Dokl. Chem.* 369, 326 (1999).

metals, the $E_1(1)$ band is completely filled with electrons. An increase in the atomic number of a transition metal is accompanied first by an increase and then by a decrease in the bandwidth. The doubly degenerate narrow band $E_2(1)$, located between the $E_1(1)$ and $E_1(2)$ bands, is formed by the $3d_{x^2-y^2}$ and $3d_{xy}$ functions. Orientation of these functions indicates that this band is a δ -bonding band. In the $(M)_\infty$ chains from Sc to V, the Fermi level intersects this band; hence, conductivity in these chains should occur with participation of δ -type states. The doubly degenerate $E_2(2)$ and $E_2(3)$ bands are higher in energy. One of these bands can be related to the π states formed by the $3d_{xz}$ and $3d_{yz}$ functions of a metal. The origin of the other (higher energy) band is not interpreted in terms of the MO LCAO method. This band can be associated with metallic conducting states with electron transfer over the interspherical region.

Beginning with the $(Cr)_\infty$ chain, the $E_2(3)$ band is gradually filled with electrons. The whole $E_2(2)$ band lies higher than the upper occupied level in all the metal chains, except for the copper one. The $(Zn)_\infty$ chain with the completely filled $E_1(1)$, $E_2(1)$, $E_1(2)$, and $E_2(3)$ bands represents a

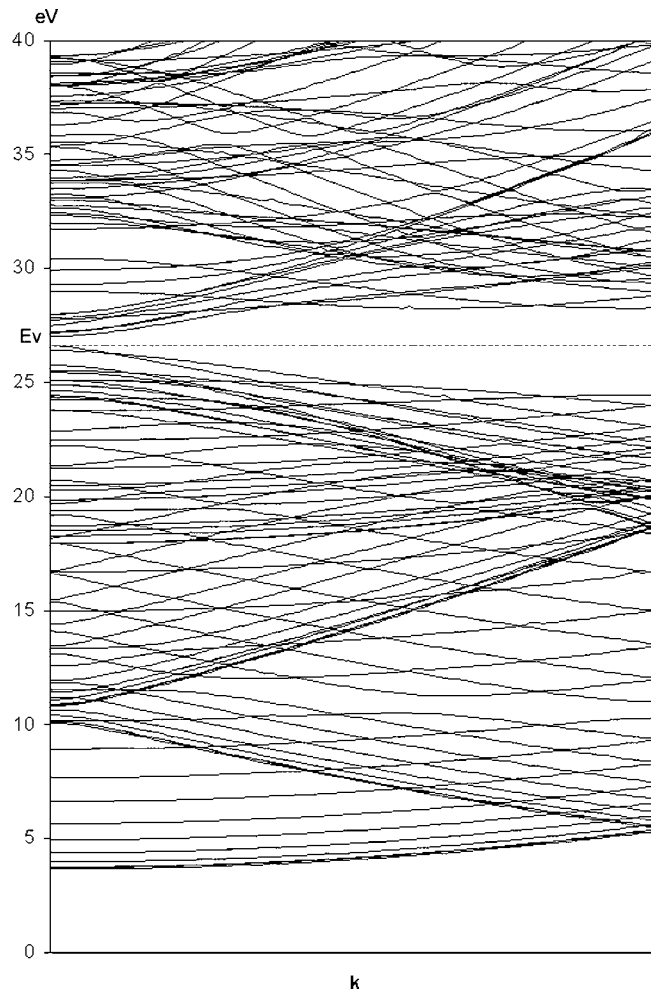


Figure 9. Band structure of carbon (16, 0) nanotube. Reprinted with permission from [41], P. N. D'yachkov and D. V. Kirin, *Dokl. Chem.* 369, 326 (1999).

narrow-gap semiconductor with a direct gap of 0.19 eV at the edge of the Brillouin zone.

The $(Sc)_\infty$ and $(Sc_2)_\infty$ [73] chains are characterized by a virtually flat upper partially filled band and, correspondingly, by a high density of states at the Fermi level, which can lead to a high conductivity of these nanowires.

Let us discuss the chemical bond strength in $3d$ -metal chains, taking into account the bonding and antibonding character of the bands and their filling with electrons. In all cases, the bonding σ band $E_1(1)$ is completely filled; therefore, its influence leads to the equal stabilization of all the systems. In the series Sc–Ti–V–Cr, the bonding δ band $E_2(1)$ becomes broader and is gradually filled with electrons. The broader the band, the stronger the metal–metal δ interactions; the greater the filling of this band with electrons, the stronger the bond between the atoms in the chain. Therefore, we can predict an increase in stability of the chains to metal–metal bond dissociation in the series Sc–Cr. Beginning with a chain of manganese atoms, the antibonding σ band $E_1(2)$ is filled, which should result in a weakening of the chemical bond. In the chains of Ni, Cu, and Zn atoms, σ antibonding neatly compensates for σ bonding;

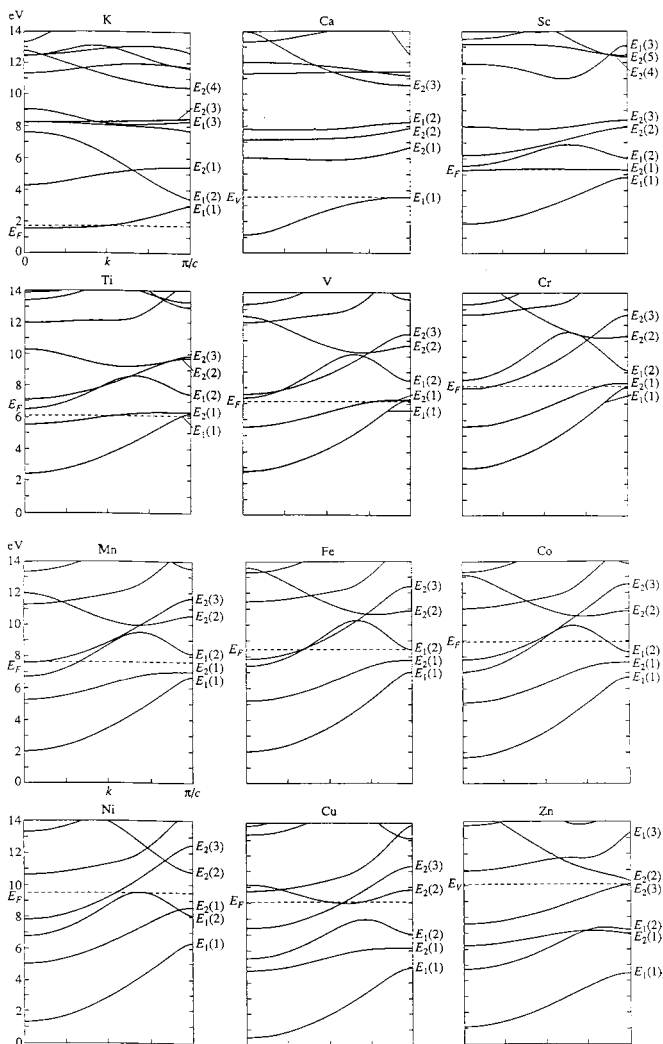


Figure 10. Band structure of metal chains without bond alternation. Reprinted with permission from [35].

hence, these chains should be unstable, since they are stabilized only by weak δ interactions. The chain of copper atoms is additionally destabilized because of a partial filling of the antibonding $d(\pi)$ band $E_2(2)$. The filling of the $E_2(2)$ band, which we associate with predominant electron transfer across the interspherical region, should not result in stabilization of the chains formed by late 3d metals. Therefore, upon an increase in the atomic number of a transition metal, the stability of the $(M)_\infty$ chains should first increase and then decrease.

7.4. 3d-Metal Intercalated Carbon Nanotube

Using the LACW method, we calculated the band structures of the 3d-metal doped carbon nanotube $(M@C_{20})_\infty$ with a (5, 5) armchair carbon network and metal atoms located on the tube axis [35, 37, 42, 74]. Figure 11 shows a typical example of the $(Mn@C_{20})_\infty$ nanotube band structure.

Comparison with the calculation results of the $(C_{20})_\infty$ tube indicates that the bands $E_1(1)$ – $E_8(1)$ and $E_1(2)$ – $E_{16}(2)$ are

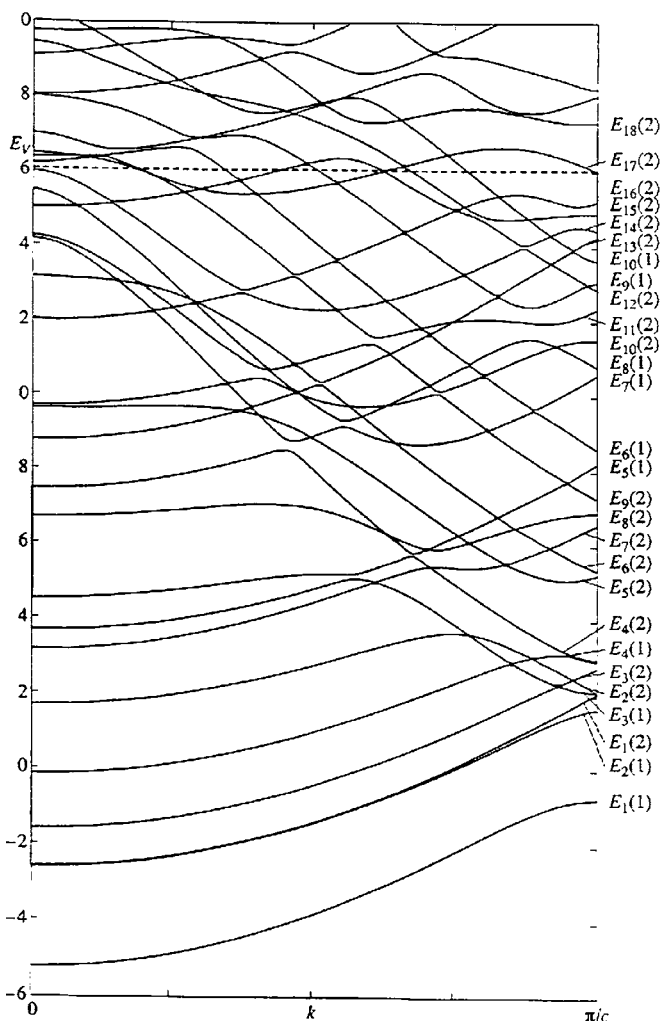


Figure 11. Band structure of the $(Mn@C_{20})$ nanotube. Reprinted with permission from [35].

similar to those observed for the pure carbon tube. The bands $E_9(1)$, $E_{10}(1)$, $E_{17}(2)$, and $E_{18}(2)$ are similar to the 4s and 3d bands of $(Mn)_\infty$. In the vicinity of the Fermi level, the dispersion curves of the carbon and metal subsystems intersect, which points to their considerable interaction and joint participation in conductivity. The most important are the narrow bands that intersect the Fermi level. They can be assigned to the 3d(Mn) and 4s(Mn) states. In the pure carbon armchair nanotube, the Fermi level is known to be located in the dip of the electron density of states. Intercalation of metals fills the dip (Fig. 12), which results in growth of the electron density of states in the Fermi level and, consequently, in a considerable increase in the conductivity of the carbon nanotube.

7.5. Pure and Intercalated BN Nanotube

Figures 13 and 14 show the influence of Ti atoms located in the tube cavity on the properties of the boron nitride (5, 5) tube [42, 43]. The pure tube is a wide-gap semiconductor in agreement with the LCAO data with parametrization based

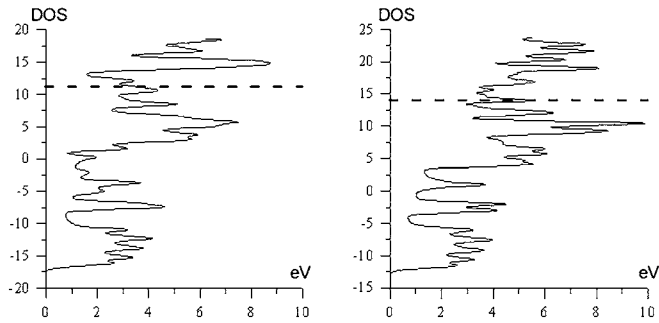


Figure 12. Total densities of states of the $(\text{Sc}@C_{20})_{\infty}$ (left) and $(\text{Cu}@C_{20})_{\infty}$ (right) nanotubes. Reprinted with permission from [74].

on the band structure of hexagonal BN [75, 76]. Introducing Ti atoms changes the type of conductivity from semiconducting to metallic. This can be used to create wide-gap semiconductor–metal heterojunctions and various nanoelectronic setups based on them. For example, to design a diode, it suffices to fill one half of the tube with metal, while the other half should remain unfilled. In such a system, the current will only flow in one direction: from the metallic end to the semiconducting one.

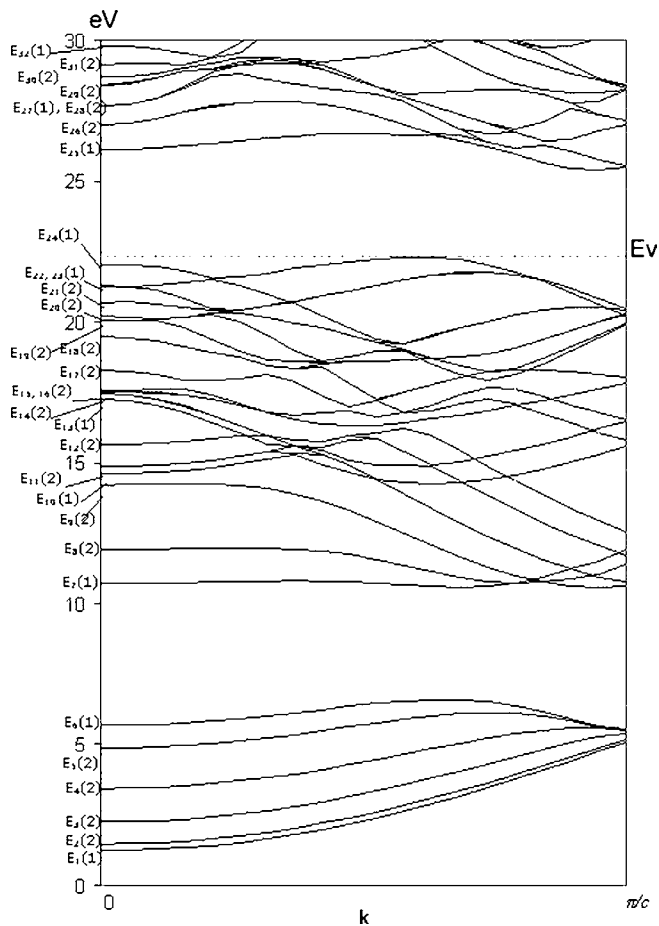


Figure 13. Band structure of boron nitride (5, 5) nanotube. Reprinted with permission from [43].

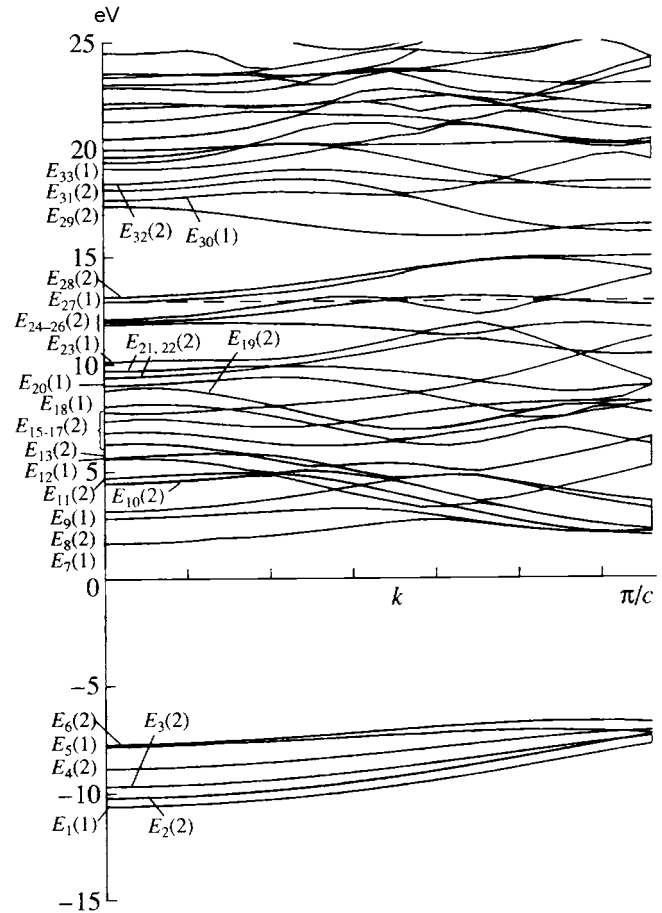


Figure 14. Band structure of $[\text{Ti}@\text{BN}]_{\infty}$. Reprinted with permission from [43].

GLOSSARY

Augmented wave Basis function for electronic structure calculations in terms of the LAPW, LACW, LASW, etc. methods.

Cylindrical-MT potential This term is taken to mean that the one-electron potential is spherically symmetric in the atomic region and constant in the interstitial region up to the cylindrical potential barrier that separates, for example, the nanotube and the vacuum region.

Film-MT potential This term is taken to mean that the one-electron potential is spherically symmetric in the atomic region and constant in the interstitial region up to the planar potential barrier that separates the film and the vacuum region.

Linear augmented cylindrical-wave method (LACW) First-principle techniques in the electronic structure theory applicable to cylindrical multiatomic systems such as nanotubes, nanowires, and porous systems with cylindrical nanocavities.

Linear augmented plane-wave method (LAPW) First-principle techniques in the electronic structure theory applicable to bulk and nanocrystals, nanofilms, polymers, nanowires, and clusters.

Linear augmented spherical-wave method (LASW) First-principle techniques in the electronic structure theory applicable to spherical multiatomic systems such as quantum dots, spherical clusters, and porous systems with spherical nanocavities.

Muffin-tin potential (MT potential) A model one-electron potential spherically symmetric in the atomic region and constant in the interstitial region.

Spherical-MT potential This term spherical-MT potential is taken to mean that the one-electron potential is spherically symmetric in the atomic region and constant in the interstitial region up to the spherical potential barrier that separates, for example, the spherical cluster or quantum dot and the vacuum region.

ACKNOWLEDGMENTS

The author is grateful to A. V. Nikolaev, O. M. Kepp, and D. V. Kirin for their long-standing cooperation. The work was supported by the Russian Foundation for Basic Research (Grant 00-03-32968). The work was part of the Russian Scientific and Engineering Program “Actual Problems in Solid State Physics.”

REFERENCES

1. J. C. Slater, *Phys. Rev.* 51, 846 (1937).
2. J. C. Slater, “Quantum Chemistry of Molecules and Crystals,” Vol. 1. McGraw-Hill, New York, 1963.
3. J. C. Slater, “Quantum Chemistry of Molecules and Crystals,” Vol. 4. McGraw-Hill, New York, 1974.
4. O. K. Andersen, *Phys. Rev. B* 12, 3060 (1975).
5. D. D. Koelling and G. O. Arbman, *J. Phys. F: Metal Phys.* 5, 2041 (1975).
6. T. Takeda and J. Kübler, *J. Phys. F: Metal Phys.* 9, 661 (1979).
7. H. Krakauer, M. Posternak, and A. J. Freeman, *Phys. Rev. B* 19, 1706 (1979).
8. E. E. Krasovskii and W. Schattke, *Phys. Rev. B* 56, 12874 (1997).
9. A. V. Nikolaev and P. N. D'yachkov, *Int. J. Quantum. Chem.* 86, 58 (2002).
10. D. Singh, *Phys. Rev. B* 43, 6388 (1991).
11. L. F. Mattheiss, J. H. Wood, and A. C. Switendick, in “Methods of Computational Physics” (B. Alder, S. Fernbach, and M. Rotenberg, Eds.), Vol. 8, p. 64. Academic Press, New York, 1968.
12. D. J. Singh, “Planewaves, Pseudopotentials and the LAPW Method.” Kluwer Academic, Boston, 1994.
13. J. M. Ziman, “Principles of the Theory of Solids.” Cambridge University Press, Cambridge, UK, 1972.
14. J. Smoliner and G. Ploner, in “Handbook of Nanostructured Materials and Nanotechnology” (H. S. Nalwa, Ed.), Vol. 3, pp. 1–91. Academic Press, San Diego, 2000.
15. L. R. Ram-Mohan, I. Vurgftman, J. R. Meyer, and D. Dossa, in “Handbook of Nanostructured Materials and Nanotechnology” (H. S. Nalwa, Ed.), Vol. 2, p. 707. Academic Press, San Diego, 2000.
16. L. D. Landau and E. M. Lifshitz, “Quantum Mechanics, Nonrelativistic Theory.” Pergamon, Oxford, 1977.
17. L. I. Schiff, “Quantum Mechanics.” McGraw-Hill, New York, 1968.
18. A. A. Levin and P. N. D'yachkov, “Heteroligand Molecular Systems.” Taylor & Francis, London/New York, 2002.
19. R. M. Dreizler and E. K. U. Gross, “Density Functional Theory: An Approach to the Quantum Many-Body Problem.” (Springer-Verlag, Berlin, 1990).
20. P. Hohenberg and W. Kohn, *Phys. Rev. B* 136, 864 (1964).
21. W. Kohn and L. J. Sham, *Phys. Rev.* 140, 1133 (1966).
22. O. Jepsen, J. Madsen, and O. K. Andersen, *Phys. Rev. B* 18, 605 (1979).
23. E. E. Krasovskii, *Phys. Rev. B* 56, 12866 (1997).
24. I. N. Yakovkin, *Surf. Sci.* 406, 57 (1998).
25. V. N. Antonov and B. Yavorski, *J. Phys.: Condens. Matter* 10, 4093 (1998).
26. P. N. D'yachkov and A. V. Nikolaev, *Dokl. Chem. (Engl. Transl.)* 344, 235 (1995).
27. A. V. Nikolaev and P. N. D'yachkov, *Dokl. Chem. (Engl. Transl.)* 348, 91 (1995).
28. P. N. D'yachkov and A. V. Nikolaev, *J. Mol. Mater.* 8, 135 (1996).
29. O. M. Kepp and P. N. D'yachkov, *Chem. Phys. Rep.* 17, 1179 (1998).
30. P. N. D'yachkov, *Z. Phys. Chem.* 200, 165 (1997).
31. S. Iijima, *Nature (London)* 351, 56 (1991).
32. A. Liiseau, N. Demoncey, O. Stephan, C. Colliex, and H. Pascard, in “Science and Application of Nanotubes” (D. Tomanek and R. J. Enbody, Eds.), p. 1. Kluwer Academic/Plenum, New York, 2000.
33. T. W. Ebbesen, *Phys. Today* 49, 26 (1996).
34. C. Dekker, *Phys. Today* 52, 22 (1999).
35. P. N. D'yachkov, O. M. Kepp, and A. V. Nikolaev, *Dokl. Chem. (Engl. Transl.)* 365, 67 (1999).
36. P. N. D'yachkov, O. M. Kepp, and A. V. Nikolaev, *Macromol. Symp.* 136, 17 (1998).
37. P. N. D'yachkov and O. M. Kepp, in “Science and Application of Nanotubes” (D. Tomanek and R. J. Enbody, Eds.), p. 77. Kluwer Academic/Plenum, New York, 2000.
38. G. N. Watson, “A Treatise on the Theory of Bessel Functions.” 1945.
39. G. A. Korn and T. M. Korn, “Mathematical Handbook for Scientists and Engineers.” McGraw-Hill, New York, 1961.
40. M. Abramowitz and I. A. Stegun, Eds. “Handbook of Mathematical Functions.” Dover, New York, 1972.
41. P. N. D'yachkov and D. V. Kirin, *Dokl. Chem. (Engl. Transl.)* 369, 326 (1999).
42. P. N. D'yachkov and D. V. Kirin, *Ital. Phys. Soc. Conf. Proc.* 74, 203 (2000).
43. D. V. Kirin and P. N. D'yachkov, *Dokl. Chem. (Engl. Transl.)* 373, 115 (2000).
44. T. J. Pinnavaia and M. N. Thorpe, Eds., “Access in Nanoporous Materials.” Kluwer Academic/Plenum, New York, 1996.
45. F. Thomas, in “Handbook of Nanostructured Materials and Nanotechnology” (H. S. Nalwa, Ed.), Vol. 4, p. 159. Academic Press, San Diego, 2000.
46. P. N. D'yachkov, unpublished manuscript.
47. V. I. Klimov, in “Handbook of Nanostructured Materials and Nanotechnology” (H. S. Nalwa, Ed.), Vol. 4, p. 451. Academic Press, San Diego, 2000.
48. A. R. Williams and J. Kübler, *Phys. Rev. B* 19, 6094 (1979).
49. K. H. Johnson, *Adv. Quantum Chem.* 7, 143 (1973).
50. K. H. Johnson, *J. Chem. Phys.* 45, 3085 (1966).
51. J. C. Slater and K. H. Johnson, *Phys. Rev. B* 5, 844 (1972).
52. E. U. Condon and G. H. Shortley, “The Theory of Atomic Spectra.” Cambridge University Press, Cambridge, UK, 1967.
53. Yu. P. Kudryavtsev, M. B. Evsyukov, and M. B. Guseva, *Izv. Akad. Nauk, Ser. Khim.* 3, 450 (1993).
54. G. Beamsom and D. Biggs, “High Resolution XPS of Organic Polymers. The Scienta ESCA 300 Database.” Wiley, Chichester, 1992.
55. J. M. Andre, J. Delhalle, and J. Ladik, “Quantum Theory of Polymers.” Kluwer Academic, Dordrecht, 1978.
56. A. Karpfen, *J. Chem. Phys.* 75, 243 (1981).
57. J. W. Mintmire, B. I. Dunlap, and C. T. White, *Phys. Rev. Lett.* 68, 631 (1992).
58. R. Saito, M. Fujita, G. Dresselhaus, and M. S. Dresselhaus, *Phys. Rev. B* 46, 1804 (1992).
59. H. Ajiki and T. Ando, *J. Phys. Soc. Jpn.* 64, 4382 (1995).
60. H. Ajiki and T. Ando, *Jpn. J. Appl. Phys.* 34, 107 (1995).

61. J. W. Wildöer, L. C. Venema, A. G. Renzler, R. E. Smalley, and C. Dekker, *Nature (London)* 391, 59 (1998).
62. M. S. Dresselhaus, G. Dresselhaus, and P. C. Ecklund, "Science of Fullerenes and Carbon Nanotubes." Academic Press, New York, 1996.
63. R. Saito, G. Dresselhaus, and M. S. Dresselhaus, "Physical Properties of Carbon Nanotubes." Imperial College Press, London, 1998.
64. T. W. Odom, J. L. Huang, P. Kim, and C. M. Lieber, *Nature (London)* 391, 62 (1998).
65. P. M. Ajajan, in "Handbook of Nanostructured Materials and Nanotechnology" (H. S. Nalwa, Ed.), Vol. 5, p. 375. Academic Press, San Diego, 2000.
66. P. N. D'yachkov, H. Hermann, and D. V. Kirin, *Appl. Phys. Lett.* 81, 5228 (2002).
67. K. Schmidt and M. Springborg, *Solid State Commun.* 104, 633 (1997).
68. S. Romanov, *J. Phys.: Condens. Matter* 5, 1081 (1993).
69. G. Cuniberti, G. Fagas, and K. Richter, *Ital. Phys. Soc. Conf. Proc.* 74, 185 (2000).
70. G. Fagas, G. Cuniberti, and K. Richter, *Phys. Rev. B* 63, 045416 (2001).
71. V. R. Misko, V. M. Fomin, and J. T. Devreese, *Phys. Rev. B* 64, 014517 (2001).
72. A. P. Klyagina and A. A. Levin, *Koord. Khim.* 10, 579 (1984).
73. O. M. Kepp and P. N. D'yachkov, *Dokl. Chem. (Engl. Transl.)* 365, 62 (1999).
74. P. N. D'yachkov, *Russ. J. Inorg. Chem. (Engl. Transl.)* 46, 92 (2001); 47, S1 (2002).
75. A. Rubio, J. Corkill, and M. L. Cohen, *Phys. Rev. B* 49, 508 (1994).
76. V. V. Pokropivny, V. V. Skorokhod, and G. S. Oleinik, *J. Solid State Chem.* 154, 214 (2001).

Bimetallic Ferrofluids

Michael Hilgendorff

Research Center Caesar, 14109 Berlin, Germany

CONTENTS

1. Introduction
 2. Methods
 3. Magnetism
 4. Results
 5. Concluding Remarks
- Glossary
References

1. INTRODUCTION

Inorganic colloidal solutions are in the first kinetically stable dispersions of nanoscale clusters or fine particles, which can be crystalline or amorphous, in a solvent [1–4]. If the dispersed material is known to exhibit ferromagnetic behavior in the bulk material, colloidal solutions thereof are generally called ferro fluids or magnetic fluids [5–8]. Magnetorheological fluids are ferrofluids with special hydrodynamic behavior for the colloidal solution [9, 10].

Inorganic colloids are of interest in many applications, primarily as a result of their promising size-dependant electronic properties, known generally as the “quantum-size effect.” Moreover, they find applications as the colloidal dispersion itself or for the preparation of assembled particle layers on different substrates by applying inexpensive deposition techniques, that is, Langmuir–Blodgett (LB) [11, 12], layer-by-layer (LBL) assembly [13–16], dip-coating, spin-coating, spraying, or simply drying (for an overview, see, for example, [17–23]).

There have been many reports describing application of mechanical (LB), electrical [24], and magnetic [25, 26] external forces during deposition that influence the symmetry, as well as the properties, of the as-deposited particulate layers. Different deposition techniques demand different properties for the parent colloidal solution, for example, viscosity, and different surface properties for the dispersed nanoparticles, for example, charge. Moreover, each application requires different properties for the dispersed material, for example, biocompatibility for applications in cancer therapy or drug delivery. The availability of different colloidal dispersed

materials for different applications is limited mainly by the surface chemistry of the dispersed materials [27, 28].

It is widely appreciated that the surface-to-volume ratio of nanoparticles increases with the decreasing particle size, for example, the surface chemistry of fine particles dispersed in a solvent becomes more and more important with decreasing particle diameter, thus determining the materials properties. The main properties that are influenced by the size of magnetic nanoparticles are their chemical reactivity, the occurrence of superparamagnetism, and an enhanced magnetic moment per atom [29–33]. Such increased reactivity decreases the oxidative stability of the materials, especially as ferromagnetic materials in general comprise nonnoble metal materials, for example, Fe, Co, Ni. Moreover, the decreasing size causes structural changes compared to bulk materials, which have been well documented in the past [34–37]. In addition, drastically decreased melting points [38, 39] have been observed, as well as the formation of metastable alloy phases of elements (for example, behavior not found for bulk materials) like FeCu [40], FeAg [41], or CoAg [42, 43], which have been theoretically predicted and experimentally verified for nanoscale materials. The latter is not surprising, as inorganic nanoparticles are usually prepared under conditions far from those approaching thermodynamic equilibrium, used to obtain binary alloys of bulk materials [44].

Generally, it is necessary to surface-passivate colloidal nanoparticles with a protecting shell consisting of inorganic and/or organic materials to decrease their reactivity. The important role of the stabilizing organic shell is to overcome the dipole-dipole interactions (magnetic [45–47] and van der Waals [48, 49]) and hinder aggregation and precipitation processes. Solubility and the wetting behavior of such nanoparticles are additionally tailored by the chemical nature of the organic shell material, while the particle properties are mainly determined by their core-shell interaction [50–54]. The increasing reactivity with decreasing size of nanoparticles, as well as the core-shell interaction is of interest in catalysis [55–58]. Of particular interest is the production of extremely small particles covered with chemical compounds which can further enhance the particles catalytic activity.

Single crystals of ferromagnetic nanoparticles, small enough to be a single domain particle, show superparamagnetic behavior above a critical temperature called the blocking temperature T_B [5, 7]. Single domain size and critical temperature are material-dependant properties. The preparation of polycrystalline ferromagnetic nanoparticles ($d <$ single domain diameter) each consisting of several smaller single-crystalline subunits has been reported [59].

Therefore, superparamagnetic behavior limits the number of applications of ferrofluids to those that do not require ferromagnetic behavior for the dispersed material. The determination of the orbital-to-spin ratio of the magnetic moment in fine particle systems via sophisticated characterization methods, for example, studies using synchrotron radiation, may lead to a better understanding of magnetism in the nanoscale. Most properties of inorganic colloids are functions of the particular material(s), particle size, and synthetic procedure due to the different interactions between the nanoparticles and their environment.

In summary, ferrofluids have received much attention in the past several decades for their interesting properties, which can be exploited to develop new technologies such as new refrigerators that employ the magneto-caloric effect [60–63], novel inks for inkjet printers [64, 65], new spin valves [66], or within areas of cancer therapy (such as hyperthermia [67] and apheresis [68]), as well as for the investigation of enhanced surface effects and magnetism in these nanoscale materials [29–33]. An extensive list of references and patents describing syntheses of ferrofluids and the investigation of their properties and applications can be found in the magnetic fluid bibliographies [69–74]. It is interesting to note that most articles in the literature concern magnetite (Fe_3O_4) or maghemite ($\gamma\text{-Fe}_2\text{O}_3$). This may reflect the fact that they can both be easily prepared in aqueous solutions and doped with Co, Mn, Zn, or Ni, the latter which allows manipulation of the magnetic hardness of the material.

Many possible applications of ferrofluids necessitate two material prerequisites—high remanent magnetization and high anisotropy at room temperature for the dispersed particles. High remanent magnetization is a characteristic property of soft ferromagnetic materials. Moreover, high anisotropy is a characteristic feature of ferromagnetic three-dimensional elements alloyed with noble metal elements of the platinum group (hard magnetic materials) [75–77]. Soft ferromagnetic materials embedded in a metallic matrix of Cu, Ag, or Au exhibit a technologically important property known as the giant magneto-resistance effect (GMR) [78]. In addition to these properties, the syntheses of colloidal bimetallic magnetic particles may be directed to yield materials with increased stability to oxidative processes. Another desirable feature is the ability to manipulate magnetic particles like noble metal particles upon appreciation of their surface chemistry, and to investigate the combination of optical and magnetic properties. To achieve oxidative stability under applicable conditions is a major problem that has yet to be resolved for nonnoble metal colloidal systems.

The preparation of ferromagnetic/noble metal alloys or core-shell particles is therefore a challenge, as evidenced by the small number of articles (mainly motivated by catalytic applications and ground state investigations of nanomagnetism), which were published in the last century [79–94].

The most important breakthrough came in 2000, through the publication of results by Sun et al. in *Science* on the synthesis and self-assembly of FePt nanoparticle alloys [95]. Since then, interest in the colloidal chemical preparation of bimetallic ferrofluids has been renewed. The as-described syntheses of well-ordered layers of particles are expected to yield novel systems for the preparation of devices with increased data storage capacity, to define a new application of bimetallic ferrofluids [96–129]. Alloys of FeMo [106], prepared by thermal *in-situ* decomposition of zerovalent metal-organic compounds and CoMo alloys [108], prepared in reverse micelles, have been investigated as catalysts for the growth of single- and multiple-walled carbon nanotubes, thus demonstrating a further new application of bimetallic magnetic fluids.

A major issue that remains for bimetallic ferrofluids is a comprehensive investigation of the nanoparticle structure and morphology. Structure and morphology of bimetallic noble metal clusters and colloidal alloys—as well as core shell particles, have been unambiguously determined using combinations of ultraviolet/visible/infrared (UV/VIS/IR), X-ray powder diffraction (XRD), high-resolution transmission electron microscopy (HRTEM), energy filtered energy-dispersive X-ray spectroscopy (EDX) and electron energy loss spectroscopy (EELS), X-ray photoelectron spectroscopy (XPS), X-ray absorption near edge spectroscopy (XANES), and extended X-ray absorption fine structure (EXAFS) [19, 56, 130, 131]. By contrast, the determination of structure and morphology of as-prepared bimetallic *ferrofluids* often remain ambiguous, because of the amorphous character of the particles and an increased reactivity of the materials compared to noble metal particles.

2. METHODS

Wet chemical syntheses, based on a bottoms-up approach, of mono- and bimetallic noble metal nanoparticles, alloys, and core-shell particles are well documented and have been thoroughly reviewed in the past [19, 56, 57]. Nonnoble three-dimensional monometallic particles such as Fe [55, 102, 132–134], Co [26, 36, 37, 45, 55, 102, 135–143], or Ni [55, 102, 144–147], have been successfully synthesized by electrochemical reduction [138, 147], chemical reduction by Li [144], hydroborides [55, 137, 141, 142], or alcohols [56] (denoted hereafter as polyols) of metal salts; thermal decomposition (initiated conventionally [26, 36, 45, 132–136, 139, 140, 143–145] or by ultrasound [134]) of zerovalent metal-organic compounds in organic solvents in the presence of bulky stabilizers such as

- (i) fatty acids (in combination with organic amines or phosphines) [26, 37, 102, 141];
- (ii) polymers [36, 56, 133, 139, 140, 143];
- (iii) tensides (often called surfactants) [29–31, 45, 55, 56, 59, 133, 137, 142].

In the case of (i), the fatty acids act as stabilizing compounds, i.e., to overcome oxidation and dipole-dipole interactions, while the amines or phosphines control the particle growth. Tensides can be used as stabilizers tetra-octylammonium bromide (TOAB), sodium-bis-2-ethyl-hexyl sulfosuccinate (AOT), sodium-dioctyl sulfosuccinate (MOT),

N-methyl-*N*-(1-oxo)-9-octadecenyl glycine (SO) for inorganic nanomaterials dispersed in organic solvents or as compounds sodium-dodecyl sulfate (SDS) forming stable micelles in heterogeneous oil-in-water systems. Other tensides didodecyl-dimethyl-ammonium bromide (DDAB), cetyl-trimethyl-ammonium bromide (CTAB), (AOT) form a stable emulsion of water droplets in hydrophobic solvents (reverse micelles).

Morphology, size, and size deviation of the particles are controlled by stabilizers. General observations for these systems are increasing particle sizes with decreasing concentrations and decreasing chain length of the stabilizers, and increasing size distributions with increasing particle size. As one challenge of syntheses is to achieve a narrow-size distribution, the reverse micelle technique and the so-called "hot injection" technique have been successfully applied, especially for the preparation of larger particles (diameters > 5 nm–15 nm). Using the latter method, standard size deviations <10% have been experimentally demonstrated (standard size deviations of ca. 5% have been predicted theoretically by choosing a proper combination of solvent and stabilizers [148]). Moreover, the hot-injection technique has been employed to facilitate a further growth of primary prepared particles (seed particles [149–151]) by reactive precipitation of precursors on the surface of seed particles.

The main differences between noble metal and nonnoble ferromagnetic colloidal materials are crystallinity and reactivity. Noble metal colloids are usually highly crystalline and are resolved in their bulk modification or form well-defined polyhedrons [152, 153]. Ferromagnetic colloids, however, are often amorphous, polycrystalline, and/or crystallize in structures not known for bulk materials (depending on the applied synthetic procedure). As a result, determinations of structures by XRD are often ambiguous, except for particles post-treated at high temperatures (at least above 250 °C), which of course results in structural changes and size development of as-prepared particles.

The increased reactivity of nonnoble metal nanoparticles requires the use of chemisorbed rather than physisorbed stabilizers [45], resulting in an increased mass of stabilizers remaining on dried particle surfaces, which further increases the (inelastic) radiation damage in transmission electron microscopy (TEM) investigations and necessitates TEM specific spectroscopy, for example, EDX, in the nanoprobe mode (spot sizes of only a few nm) [154]. The micelle technique, as well as methods producing polymer stabilized particles, results in products with enhanced amounts of organic compounds compared to other techniques. Additionally, the micelle, ferritin, and some polyol reduction techniques (**M**, **R**, **F**, and **P** (see Table 1)) employing aqueous media assist surface oxidation processes. The latter remains a problem for all syntheses and further hinders the determination of structure and morphology. A typical morphology found for nonnoble colloidal particles consists of a core, an inner oxidation layer, and an outer shell of stabilizers, as depicted in Figure 1.

The development of bimetallic ferrofluid syntheses has been based on existing synthetic procedures for monometallic ferrofluids. In general, alloys have been produced by *in-situ* reduction of metal salts or thermal decomposition of zero-valent monometallic metal-organic compounds,

or combinations thereof, as well as by decomposition of bimetallic zero-valent metal-organic compounds (see Table 1). *In-situ* reactions require similar reaction kinetics for both metal components, which are mainly determined by the difference in redox potentials. With increasing differences, the reactions will become successive and this is expected to form core-shell particles. Thus, core-shell particles have been produced by the precipitation of metal atoms on the surface of initial seed particles (successive reduction, successive decomposition, or combinations thereof [56]). It has been reported that successive reduction is also dependant on the difference in redox potential between seed particles and successively added metal compounds. With increasing redox potential difference, the reduction of metal salts by seed particles becomes an increasing concurrent reaction, to the metal salt reduction by an additional added reductant. The reaction between preformed particles and added compounds results in the formation of ionic compounds of the seed particles material, which, subsequently, may be further reduced by the reducing agent. This mechanism has been rationalized to explain the formation of bimetallic noble metal alloys produced by successive reduction [56].

Stabilizers are known to change the redox potential of particles and compounds. Thus, the formation of inverse core shell particles, that is, consisting of a core of successively grown compounds covered with a shell of the seed particle material, by an improper (or proper, if desired) choice of surfactants and solvents, cannot be excluded. Comparisons of documented surface tensions of different bulk materials have been taken into account to explore the possibility of formation of Fe, Co, or Ni particles covered with an Au or Ag shell. Reported data of the element surface tensions were usually derived under conditions far from those pertaining to the colloidal syntheses.

A second important parameter determining the formation of bimetallic colloids is the lattice mismatch between both elements. It has been observed to be the main reason for the formation of separated monometallic particles in several syntheses. The possibility of separated particle formation increases with increasing lattice mismatch [56].

In summary, bimetallic noble metal particles form alloys, core-shell particles, or clusters in cluster particles [155], all dependant largely, but not exclusively, on reaction kinetics. Applied methods and comments are summarized in Table 1. Figure 2 provides a schematic overview of possible morphologies. A gallery showing TEM images representing typical results obtained from colloidal systems by various methods is presented in Figure 3.

The Li reduction of metal salts in naphthalene (known as the Rieke method [156]) and the ultrasound decomposition of zero-valent metal-organic compounds (the sonochemical approach developed by Suslick [157]) have been cited as a route to bimetallic ferrofluids. Kirkpatrick et al. has published the preparation of high reactive stabilizer free powders of MgCo alloy [158]. Suslick et al. presented the preparation of Fe-ferrofluids [134], as well as the preparation of bimetallic nanocrystalline FeCo powders [159]. The preparation of bimetallic ferrofluids has not been forthcoming to date. It should be mentioned that Gonsalves and Rangarajan used Suslick's method for the preparation

Table 1. Overview and comments about applied routes to bimetallic ferrofluids.

Synthesis	Materials	Comments	Ref.
D Decomposition:			
D ₁ Thermal decomposition of zero valent bimetallic metal-organic compounds in organic solvents stabilized by the surfactants Duomeen, Solsperse, (FeCo) MOT, or SO (FeNi).	FeCo and FeNi alloys	Noncommercially available compounds; particle composition did not equal compound composition for FeNi; problems of magnetic diameter calculations were discussed.	[79, 80]
D ₂ Thermal <i>in-situ</i> decomposition of zero valent monometallic metal-organic compounds in tetrahydrofuran stabilized by polymer (PVP).	CoRh and CoPt alloys	Noncommercially available, carbonyl free compounds; synthesis under 3 bar H ₂ pressure; ground-state magnetic surface physics; sophisticated investigation methods.	[101, 115, 126]
D ₃ Thermal <i>in-situ</i> decomposition of zero valent metal carbonyls in octyl ether.	FeMo alloy	Particle size increases with increasing stabilizer amount; carbon nanotube growth.	[106]
E Electrolysis: Electrochemical <i>in-situ</i> reduction of metal ions in tetrahydrofuran stabilized by tetraoctylammonium ions.	FeCo, FeNi, and NiPd alloys	Metal ions were preformed by oxidation of the desired electrode pair within the same electrolysis cell; tetraoctylammonium bromide was electrolyte; catalysis.	[82]
F Reduction in apoferritin: Sodium borhydride <i>in-situ</i> reduction of metal salts in the cavities of demineralized ferritin (apoferritin).	CoPt alloy		[100]
R Reverse Micelles:			
R ₁ Sodium borhydride <i>in-situ</i> reduction of metal salts in water-in-oil reverse micelles formed by different surfactants (AOT, CTAB, DDAB).	FeCu, CoPt, and CoMo alloys	Aggregated particles for FeCu and CoPt; sophisticated investigation methods for FeCu; carbon nanotubes grown on CoMo.	[84, 90, 116]
R ₂ As R ₁ but successive reduction.	Co _{clusters} Ag _{Host} , Au@Fe@Au, and Fe@Au	H ₂ reduction of Co in CoAg at moderate 100 °C; Au coating of FeAu particles is ambiguous; different magnetic properties for <i>similar prepared</i> FeAu particles were not discussed.	[81, 85, 89, 90, 96–98, 109–112, 125]
R ₃ Combination of R ₁ and R ₂ .	FePt@Au and CoPt@Au	The existence of Au at the surface was again not unambiguously verified.	[90, 98, 110, 113]
M Micelles: Sodium borhydride co reduction of metal salts in oil-in-water micelles formed by the surfactant sodium dodecyl sulfate (SDS).	FeCu alloy	Elongated and coagulated particles; sophisticated investigation methods.	[86]
O Organohydroborate Reduction: Successive reduction of metal salts by tetraoctylammonium triethylborhydride (TOAEt ₃ BH) in tetrahydrofuran.	Fe, Co, and Ni covered with Pd, Ag, Pt, or Au	Mainly noncommercially available reducing compound; principle stabilizer was tetraoctylammonium salt; core-shell morphology is expected but remains ambiguous; catalysis.	[92]
P Polyol Reduction:			
P ₁ <i>In-situ</i> reduction of metal salts stabilized by PVP.	CoPt and NiPd alloys	Catalysis; sophisticated investigation methods for NiPd.	[83, 94]
P ₂ Successive reduction of metal salts stabilized by PVP.	Pd@Ni	“Core-shell” morphology for particles prepared by <i>in-situ</i> reduction; catalysis.	[87, 88, 93]
C Combination:			
C ₁ Decomposition of metal carbonyls combined with <i>in-situ</i> polyol reduction of metal salts in high boiling solvents.	FePd, FePt, FeCoPt, CoPt, and CoSm alloys	Chen and Nikles used the diol reduction of Co(acac) ₂ for the synthesis of FeCoPt [120], and the thermolysis of the more expensive Co(CO) ₃ NO for the synthesis of CoPt [121], both instead of the thermolysis of dicobalt octacarbonyl.	[95, 103, 104, 119–123]
C ₂ Decomposition/transmetallation.	Ag@Co, Co@Pt, and CoPt alloy	Sophisticated investigation methods for AgCo. Co@Pt core-shell morphology remains ambiguous.	[107, 127–129]
C ₃ Organoborhydride reduction/transmetallation.	Fe@Au, Co@Pt, and Co@Au	Noncommercially available compounds; core-shell morphology was expected but remains ambiguous.	[91, 107]

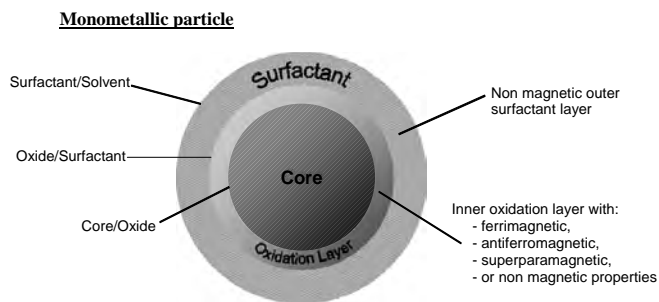


Figure 1. Representation of a magnetic nanoparticle prepared via typical colloidal chemical synthesis. The desired core material is covered with an inner oxidation layer of the core material and an outer surfactant layer, necessary to overcome attractive forces. As a result, three interfaces are present, which determine the nanoparticles properties. Adapted with permission from [27], M. Hilgendorff and M. Giersig, "Nanoscale Materials," 2002. © 2002, Kluwer Academic Publishers.

of M50-type steel fluids consisting of 4.0% Cr, 4.5% Mo, 1.0% V, 0.8% C, and 0.3% Mn [160]. The desired crystalline phase could be only obtained after post-treatment of dried particles at high temperatures. Similar results have been reported for the colloid chemical preparation of ternary compounds, such as yttrium iron garnet [161, 162] or barium hexaferrite [163, 164]. The results reflect the fact that "multinary" systems can be well prepared by colloid chemistry, but the extent of amorphous components in the materials increases with increasing components in the systems. Thus, post-treatments that reduce the particle solubility in aqueous or organic solvents are required to obtain the desired materials.

Bimetallic particles

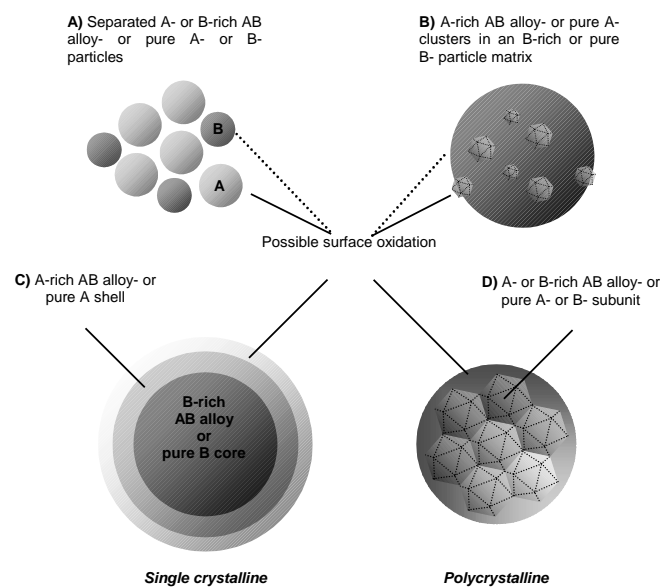


Figure 2. Schematic of possible results of colloidal AB bimetallic ferrofluid preparation. (A) separated particles; (B) small clusters embedded in a nanoparticulate matrix; (C) core-shell particle obtained by either synthesis or segregation; (D) polycrystalline nanoparticle. **B** is denoted to be the heavier element and represented by darker contrast as found typically in TEM investigations.

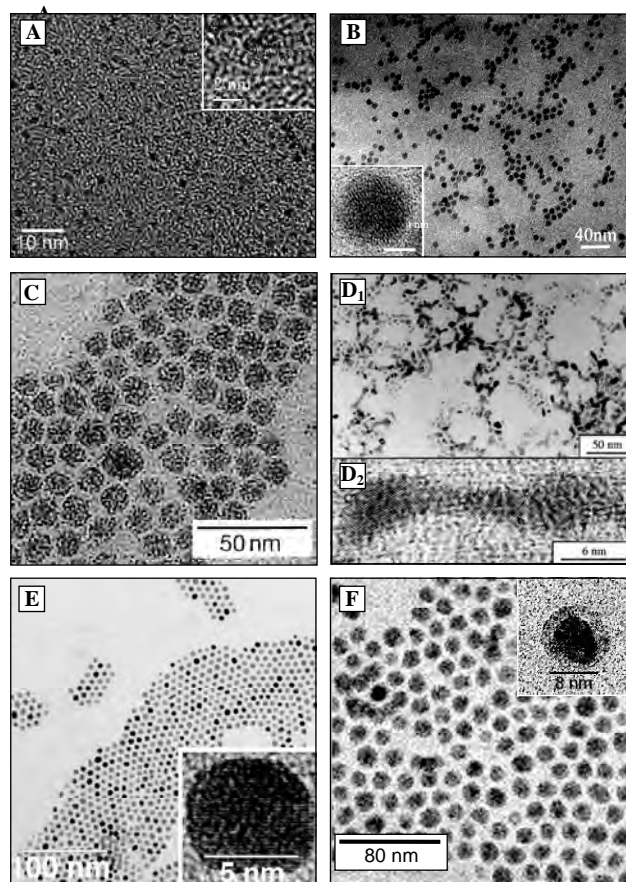


Figure 3. TEM gallery of bimetallic ferrofluids. (A)–(C) and (E) represent typical micrographs of nanoparticles obtained by different routes; (D) and (F) are special cases (see text for details). (A) Adapted with permission from [126], D. Zitoun et al., *Phys. Rev. Lett.* 89, 037203 (2002). © 2002, American Physical Society. (B) Adapted with permission from [106], Y. Li et al., *Chem. Mater.* 13, 1008 (2001). © 2001, American Chemical Society. (C) Adapted with permission from [116], H. Ago et al., *J. Phys. Chem. B* 105, 10453 (2001). © 2001, American Chemical Society. (D) Adapted with permission from [86], N. Duxin et al., *Langmuir* 14, 1984 (1998). © 1998, American Chemical Society. (E) Adapted with permission from [120], E. V. Shevchenko et al., *J. Am. Chem. Soc.* 124, 11480 (2002). © 2002, American Chemical Society.

Consideration of both the multiple morphology of bimetallic noble metal colloids versus synthetic methods (as mentioned above) and segregation phenomenon of bimetallic bulk alloys prepared under thermodynamic equilibrium conditions [165] leads to the following conclusions. It is clear that bimetallic ferromagnetic nanoparticles, generally prepared under conditions of kinetic control, are rather complicated materials. Thus, the determination of structure and morphology requires the combination of different investigation methods, as well as their careful interpretation.

3. MAGNETISM

The critical discussion of magnetic properties is rather complicated because of a large number of systems and units. In the field of nanoscale magnetic colloids, the confusion is enhanced because of the size dependence of material properties—that is, physical parameters like ϵ_0 , μ_0 , ρ , etc.,

defined as constants in descriptions of bulk material properties, become size dependant. In other words, changing the size of nanoscale materials produces new materials. Moreover, different results have been obtained from measurements on different physically conditioned samples, that is, fluids, powders, or assembled layers, because of different degrees of interaction [166, 167].

The first detailed description of magnetism was developed around 1900 using the electromagnetic cgs unit system. Two different systems are still in use—the irrational system, where μ_0 is set to unity (implying that μ_0 does not exist), and the rationalized system, where $\mu_0 = 4\pi$. Both systems rely on different basic equations. Subsequently, the mks-based SI system was developed and is widely employed. The central and unambiguous conversion between cgs and mks in magnetism is based on the relation

$$1 \text{ T} = 10^4 \text{ G.} \quad (1)$$

The translation of the two cgs systems in mks units produced at least two different mks systems, which differ by the factor $4\pi \times 10^{-7}$. The systems and their differences are represented schematically in Figure 4. A more detailed summary and critical discussion of existing systems and units and their relation can be found by Scholten [168]. Misconceptions and misinterpretations of hysteresis curves in textbooks and scientific literature have been reviewed by Sung and Rudowicz [169]. An extensive list of tables describing the transformation between different magnetic units is available via the internet [170].

Nowadays, the SI system is the only legally allowed system that has to be used by engineers and teachers. However, many scientists in the field of magnetism still employ cgs units. The advent of smart materials has led to renewed interest in the investigation and interpretation of magnetic properties. Thorough descriptions of magnetism in textbooks, developed about 30 years ago, increasingly provide descriptions of nanomagnetism. One main difference in contemporary works is the tendency to present magnetic properties in units of energy per atom [171], or in reduced (dimensionless) units, for example, M_R/M_S versus T/T_B , to facilitate the comparison between particle assemblies with different blocking temperatures and saturation magnetizations or to circumvent the confusion of using different systems. In the present review, however, results presented are generally given in cgs units. This holds for M versus H hysteresis loops, as well as for M versus T (or χ versus T)

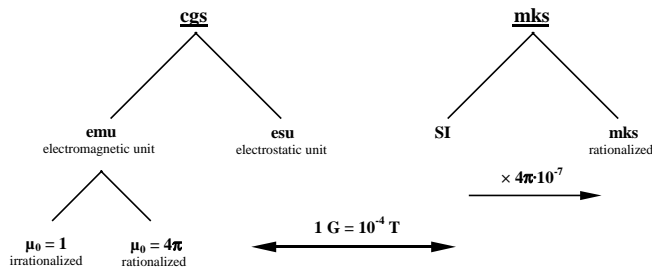


Figure 4. Schematic drawing of systems and units used in magnetic literature, and how they are related.

field cooled/zero field cooled (FC/ZFC) curves. The determination of the susceptibility $\chi \equiv dM/dB$ for $B \rightarrow 0$ and χ versus T easily allows one to distinguish between ferro-, para-, and diamagnetic properties of materials. Susceptibilities of diamagnetic materials are negative and temperature-independent. Susceptibilities of paramagnetic materials are positive and decrease with increasing temperature, according to the Curie law. Both susceptibilities are independent of the applied magnetic field strength and very small ($|\chi| \ll 1$). In ferromagnetic materials, the susceptibility is defined differently, since dM/dB is infinite for a single-domain ferromagnet; in other words, there exists a remanent magnetization without an applied magnetic field B . It is generally accepted to use M/B as a measure of the susceptibility which is positive. The “ferromagnetic susceptibility” decreases with increasing temperature, dependant on the applied magnetic field strength, and is orders of magnitudes enlarged (about 100–1000 times) compared to susceptibilities of dia- and paramagnetic materials ($|\chi| \gg 1$). Typical shapes and important parameters obtained from magnetic hysteresis loops and FC/ZFC curves are qualitatively presented in Figure 5.

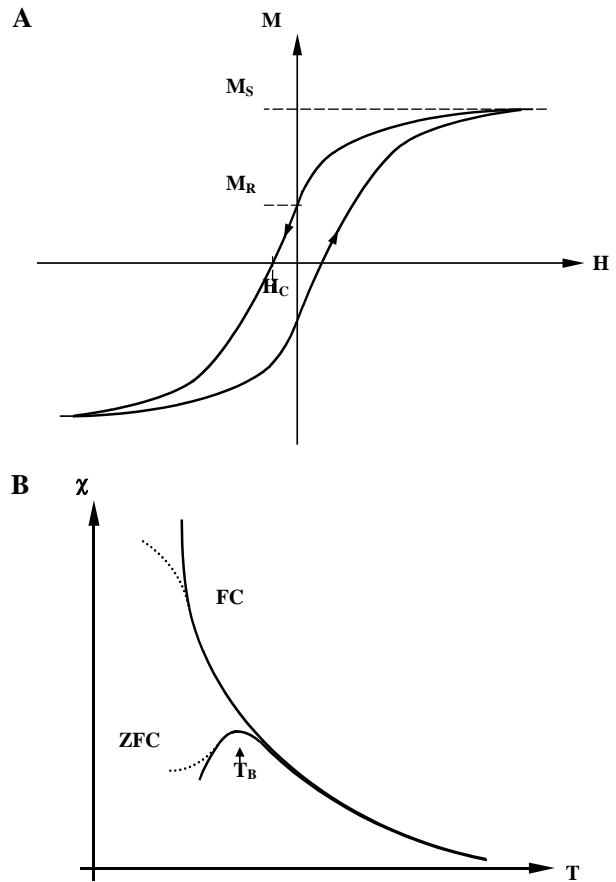


Figure 5. Qualitative presentation of important parameters obtainable from (A) M versus H hysteresis loops, and (B) ZFC/FC χ versus T plots. Saturation magnetization M_S , remanent magnetization M_R , coercivity H_C , and blocking temperature T_B , are shown. The shape of the dashed lines indicates deviations from the assumption that particles have uniaxial anisotropy.

Hysteresis loops allow the determination of H_C , M_R , and M_S , which all depend on the applied temperature. One observation in magnetic colloid science is that magnetization remains often unsaturated even at high fields. Furthermore, hysteresis loops sometimes remain unclosed within the range of the applied magnetic field. Values of M_R and H_C obtained from those loops (minor or inner loops) are then decreased, compared to values obtained from closed loops because of incomplete alignment of magnetic domains within the sample. Temperature-dependant ZFC curves are usually determined in order to define the blocking temperature T_B , which decreases with increasing applied magnetic fields. Below T_B , measurements sometimes show a decreased change of the curves shape with decreasing temperature, which often reach a plateau (dashed lines in Figure 5B). The results are rationalized in terms of a failure of the assumption of uniaxial anisotropy. Otherwise, the curves follow the shape of the solid lines in Figure 5B. Quantitative descriptions of these observations are still not available. T_B is commonly determined to calculate the effective anisotropy constant K_{eff} from the Néel equation:

$$K_{\text{eff}}V = \ln(\tau/\tau_0)k_B T_B \quad (2)$$

where τ is the relaxation time of magnetization over an energy barrier $\Delta E = K_{\text{eff}}V$ (assuming uniaxial anisotropy), τ_0 an attempt time, typically set between 10^{-12} s– 10^{-9} s, and V , the magnetic volume. In dc susceptibility experiments over a time range of $t = 100$ s, $\ln(t/\tau_0)$ has values, therefore, in the 25–32 range. Hence, the magnetization of a material will relax within the measurement time t if $\tau \leq t$. More detailed information is available by Leslie-Pelecky and Rieke [8] and Binns [165]. The following relations between SI and cgs units were found to be valid in the literature reviewed here [79–129]:

$$H [\text{Oe}] = 10^{-4}H [\text{T}] \quad (3)$$

$$M [\text{emu/g}] = M [\text{Am}^2/\text{kg}] = M [\text{J}/(\text{Tkg})] \quad (4)$$

$$K_{\text{eff}} [\text{erg/cm}^3] = 0.1K_{\text{eff}} [\text{J/m}^3] \quad (5)$$

Critical is the particular term of M given in emu per mass, per unit volume, or as μ_B/atom . Measurements of M by standard methods gives only emu (or 10^{-3} Am²). The exact determination of magnetic mass or volume is therefore required. The same holds for calculations of K_{eff} requiring V . Magnetic moments can be divided into orbital and spin moments. General observations of nanoscale materials showed enhanced orbital-to-spin ratios of magnetic moments for colloids with increasing degrees of freedom, indicating that the enhanced orbital magnetic moment is mainly effected by the orbital magnetic moment of surface atoms. Thus, one can conclude that the degree of freedom of the orbital magnetic moment of surface atoms is rather influenced by interactions with the particles environment, while the spin moment of colloids is mainly a function of the size of inner core atoms.

It is well known that oxidatively sensitive colloids consist of a magnetic core and a nonmagnetic (that is, dia-, para-, or antiferromagnetic) shell. This is reflected by the fact that particle diameters are always found to be smaller compared

to TEM diameters when calculated from magnetic measurements. The first method for magnetic diameter determination of nanoparticles was developed by Chantrell et al. and published in 1978 [172]. More recently, Berkov et al. developed a new method for the determination of the particle magnetic moment distribution in a ferrofluid [173, 174], and Wiedenmann et al. presented magnetic_{core}-nonmagnetic_{shell} determinations by small-angle scattering investigations of ferrofluids using polarized neutrons [175, 176].

The shell typically consists of a nonmagnetic outer shell of stabilizers and probably a second inner shell (Fig. 1). The outer shell defines the solubility of the colloid and may impart some stability to oxidation, which increases with increasing binding energy of the stabilizer, that is, chemisorption > physisorption. Existence and composition of the inner shell depends on two factors, the interaction of stabilizers with the particle surface and the extent to which surface oxidation is excluded during syntheses. The interaction between stabilizer and particle surface is mainly determined by the stabilizers electron σ -donation capability, which increases with its increasing electron density. On the other hand, the binding energy between stabilizer and particle is determined by the stabilizers π -electron acceptor ability (electron back donation from the metal particle to the stabilizer), which decreases as the stabilizers electron density increases [177]. It has been reported that electron injection into the colloid surfaces results in quenching of the particle surface atoms orbital magnetic moment [51, 52]. A “dead” magnetic surface layer will be formed if the quenching is complete.

Reduced binding energies between stabilizer and colloid enhance the potential for particle oxidation, that is, the formation of different sized oxide surface layers becomes more and more possible. The oxide surface layer can therefore reveal ferrimagnetic (in the case of iron oxide) or antiferromagnetic (in the case of cobalt oxide) properties, which further enhances the uncertainty of magnetic volume determinations from magnetization curves. Furthermore, the formation of oxide layers changes the interaction with stabilizers (electron back donation) and the occurring oxide_{shell}/particle_{core} interaction must be further take into account. Generally, a progress in anisotropy is observed in oxide-covered monometallic ferrofluids, as well as an exchange bias causing a shift of FC hysteresis loops to negative applied fields.

Commonly employed methods for investigations of concentration in colloids are atomic absorption spectroscopy (AAS) and EDX. Volumes are then calculated using TEM diameters, which can be extremely different if the real particle structure is unsolved because of different surface-to-volume ratios (see Fig. 6). The calculation of “dead” surface layers therefore remains ambiguous. The techniques of AAS and EDX do not allow one to distinguish between different oxidation states of elements, thus rendering the exact determination of magnetic volumes.

Different results have been obtained while investigating different physically conditioned samples. The reasons cited are different magnetic dipole-dipole interactions in fluids, powders, or assembled layers. Cooling a liquid to low temperatures produces a frozen liquid, that is, particles embedded in a solid matrix. The degree of interaction is then

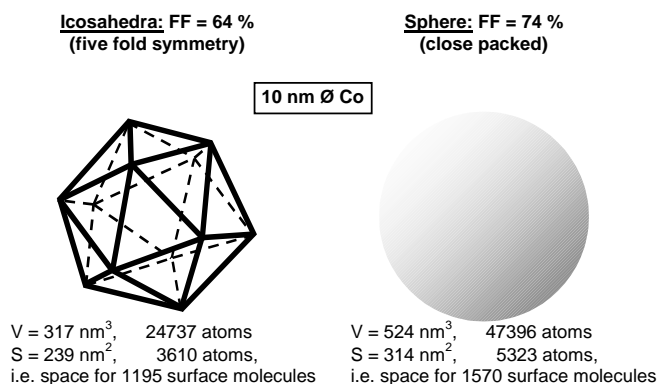


Figure 6. Calculation of the surface-to-volume ratio and the surface area of Co nanoparticles, 10 nm in diameter, for two different geometries with the fill-factor FF. Adapted with permission from [27], M. Hilgendorff and M. Giersig, "Nanoscale Materials," 2002. © 2002, Kluwer Academic Publishers.

dependant on concentration. Available results showed that dipole-dipole interaction is more affected by particle size than by volume fraction, that is, interaction will increase faster with increasing particle size than with decreasing interparticle distance [166, 167].

In conclusion, one has to accept that the magnetic properties presented here are, in principle, only qualitatively comparable for particles prepared by similar methods.

4. RESULTS

A detailed description of different methods applied for the preparation of bimetallic ferrofluids, their catalytic and magnetic properties, and conclusions on determination of structure and morphology of dispersed materials will be given below. The results are discussed separately by applied methods and are summarized in Table 2.

4.1. D: Decomposition

The thermal decomposition of organic compounds provides the advantage of gaseous by-products which are not present in the final fluids. Oxide and carbide formation at the surface of monometallic colloids prepared from metal carbonyls has been observed.

4.1.1. D₁: Decomposition of Bimetallic Metal-Organic Compounds

The first successful route to bimetallic magnetic fluids, prepared in hydrocarbons by thermal decomposition of non-commercially available zero-valent bimetallic metal organic compounds under inert gas conditions, was published by Lambrick et al. FeCo-containing fluid was reported in 1985 [79] and synthesized by thermal decomposition of the binuclear precursor $[(\pi\text{-C}_5\text{H}_5)\text{Fe}(\text{CO})_2\text{Co}(\text{CO})_4]^-$ in toluene in the presence of commercially available surfactants (Duomeen-T, Duomeen-TDO, or the polymeric hyperdispersant Solsperse 3000). The precursor was prepared by reaction of $[(\pi\text{-C}_5\text{H}_5)\text{Fe}(\text{CO})_2\text{Cl}]$ and $[\text{Co}(\text{MeOH})_6]^{2+} [\text{Co}(\text{CO})_4]^-$ at room temperature (RT) over 16 h in methanol (MeOH) [178]. The compounds $[(\pi\text{-C}_5\text{H}_5)\text{Fe}(\text{CO})_2\text{Cl}]$ and

$[\text{Co}(\text{MeOH})_6]^{2+} [\text{Co}(\text{CO})_4]^-$ have been prepared by Piper et al. [179] and by the disproportionation of $\text{Co}_2(\text{CO})_8$ in MeOH at $\sim 30^\circ\text{C}$. Typical starting concentrations of the precursor were 100 g/l and 150 g/l, corresponding to a range where such colloids show magnetorheological behavior. The ratio precursor/surfactant was adjusted to either 1 wt% or 0.5 wt%. Transmission electron microscopy investigations showed particles with diameters between 5 nm and 8 nm with a narrow size distribution. The formation of the ordered 1:1 alloy phase of FeCo has been concluded from HRTEM.

Magnetic investigations have been done under different conditions using a vibrating sample magnetometer. Room temperature measurements show that M_S (in the order of $1\text{--}3 \text{ JT}^{-1}\text{kg}^{-1}$) varies with the preparative conditions. Magnetic particle diameters obtained by applying the method of Chantrell et al. [172] were smaller than the TEM diameters. Magnetization measurements in the frozen state showed no coercivity and remanence. More generally, it was concluded that Solsperse 3000 provided better, but not complete, protection against oxidation, while Duomeen-TDO provided better protection against sedimentation. Carbide formation was not discussed. It was mentioned that no alloy formation could be observed under similar conditions by *in-situ* decomposition of iron and cobalt carbonyls.

FeNi-containing fluid [80] was prepared by thermal decomposition of the trinuclear bimetallic cluster $[\pi\text{-}(\text{C}_2\text{H}_5)_2\text{Ni}_2\text{Fe}(\text{CO})_5]$, which has been prepared, as described by Hsieh and Knight [180]. Methyl naphthalene or petroleum ether were used as solvents. The particles were stabilized by MOT or SO. The weight ratio of compound/surfactant was adjusted between 1.08 and 1.65. Typical concentrations of the bimetallic compounds in the starting solutions were 44–70 g/l. This again is in a range where such colloids show magnetorheological behavior. The structure of the particles was determined from HRTEM investigations (images were not shown). The authors presented average diameters of 7 nm, and concluded from lattice spacings, the formation of the L_{12} phase of ordered Ni_3Fe , which was different from the starting composition of the bimetallic precursor (Ni_2Fe). These results were rationalized in terms of the greater reactivity of Fe to oxygen and surfactants, reflecting the fact that oxidation remains a problem in these materials. Carbide formation was not discussed.

Magnetic investigations have been done under a variety of conditions using a vibrating sample magnetometer. Room temperature measurements show that M_S (in the order of $0.3\text{--}0.5 \text{ JT}^{-1}\text{kg}^{-1}$) varies with the TEM diameter and does not saturate in applied fields up to 1 T. T_B is $>4.2 \text{ K}$ and $<77 \text{ K}$, H_C at 4.2 K is 13 mT. Particle sizes have also been calculated from magnetic measurements using the method of Chantrell et al. [172], showing again the typical result that the magnetic diameter is smaller than the TEM diameter. Problems of the accuracy of this calculation and calculations of K_{eff} (in the order of some 10^6 erg/cm^3) concerning uncertainties in concentration determination were discussed.

4.1.2. D₂: Decomposition of Monometallic Metal-Organic Compounds

CoRh [115, 126] and CoPt [101] alloys have been successfully prepared by *in-situ* thermal decomposition of carbonyl-free, zero-valent, metal-organic compounds $\text{Co}[(\eta^3\text{-C}_8\text{H}_{13})$

Table 2. Properties of as-prepared or moderately post-treated (<250 °C) bimetallic magnetic particles synthesized by various routes.

Material	Synthesis	Diameter [nm] (Method)	Type	Applied Investigation Methods	Magnetization M_s { M_R } (T)	Coercivity (T)	K_{eff} [erg/cm ³]	T_B [K] (H)	Ref.
FeCo	D ₁	5–8 (TEM), 4–5 Chantrell	A	TEM (<i>not shown</i>), VSM	1–3 JT ⁻¹ kg ⁻¹ (?T)	—	—	<77	[79]
FeCo	E	2.5–3 (TEM)	A	TEM	—	—	—	—	[82]
FeNi	D ₁	7 (TEM), 4 (Chantrell)	A	TEM (<i>not shown</i>), VSM	0.318 JT ⁻¹ kg ⁻¹ (RT, 6T)	13 mT (4.2 K)	3 × 10 ⁶	>4, 2	[80]
FeNi	E	2.5–3 (TEM)	A	TEM	—	—	—	—	[82]
Fe _x Cu _{1-x}	R ₁	5–15 (TEM)	A	XRD, TEM, EDX, EELS, Mössbauer, GFM	51 {18} emu/g (RT, $x = 0.7$)	531 Oe (RT)	—	>RT (1.8 T)	[84]
Fe _x Cu _{1-x}	M	6.6 × ~40 (TEM)	A	XRD, HRTEM, EDX, EELS, Mössbauer, SQUID	40 emu/g (1.8 K, $x = 0.14$)	250 Oe (1.8 K)	2 × 10 ⁵	9.5 (20 Oe)	[86]
FeMo	D ₃	3.5–14 (TEM)	A	HRTEM, EDX, AFM	—	—	—	—	[106]
FePd	C ₁	11 (TEM)	A	TEM, EDX, GFM	—	12 Oe (RT)	—	—	[122]
FePt	C ₁	4–6 (TEM)	A	XRD, SAXS, HRTEM, SQUID	—	0 Oe (RT)	—	20–30 (10 Oe)	[95]
FePt	C ₁	4.5 (TEM)	A	XRD, HRTEM, SQUID	~30 (5 K)	~800 Oe (5 K)	1 × 10 ⁶	14 (200 Oe)	[119]
FePt	C ₁	4.2 (TEM)	A	TEM, SQUID	—	—	—	—	[103]
FeCoPt	C ₁	3.5 (TEM)	A	TEM	—	—	—	—	[121]
FePtAu	R ₃	10 (TEM)	CS	TEM, SQUID	{2,3} emu/g (2 K)	500 Oe (2 K)	—	70 (100 Oe)	[110, 113]
FeAu	R ₂	10 (TEM)	CS	UV/Vis, XRD, HRTEM, SQUID, XANES	{13,67} emu/g (2 K)	400 Oe (2 K)	—	50 (1 kG)	[98, 110–112, 125]
AuFeAu	R ₂	12 (TEM, XRD)	CS	TEM, SQUID, RF, XRD, EDX (<i>not shown</i>)	11.5 {3,6} emu/g (10 K)	420 Oe (10 K)	—	50–52 (1 kG)	[96, 97, 110, 125]
FeAu	C ₃	2 (TEM)	CS	TEM (<i>not shown</i>), SQUID, Mössbauer	<2.24 μ_B (bulk value)	0.1 T (2.5 K)	8 × 10 ⁶	10 (100 Oe)	[91]
FeAu	O	2 (TEM)	CS	—	—	—	—	—	[92]
CoMo	R ₁	10.8 (TEM)	A	TEM, XPS (<i>not shown</i>)	—	—	—	—	[116]
CoRh	D ₂	1.8, 2.6 (TEM)	A	WAXS, HRTEM, SQUID	~1.9 μ_B /Co-atom (4.2 K)	—	1.0 × 10 ⁷ , 6 × 10 ⁶	11, 13.5 (1 mT)	[115, 126]

continued

Table 2. Continued

Material	Synthesis	Diameter [nm] (Method)	Type	Applied Investigation Methods	Magnetization M_s { M_R } (T)	Coercivity (T)	K_{eff} [erg/cm ³]	T_B [K] (H)	Ref.
CoAg	R₂	10–15 Ag (TEM, XRD) 10 atoms Co cluster (magnetometry)	CS	AES, XRD, TEM, EPR, VSM (later SQUID)	646 emu/cm ³ (as prepared) 1700 emu/cm ³ (p.t., 2 K)	—	2.0×10^7 (as prepared) 8.5×10^7 (p.t.)	<2 (as prepared) 6 (p.t., 50 Oe)	[81, 85, 89]
CoAg	C₂	8–15 (TEM)	CS	UV/VIS, HRTEM, EDX, EELS, XMCD, SQUID	—	—	—	>90	[127–129]
CoPt	P₂	1.7–2.2 (TEM, XRD)	A	XRD, TEM	—	—	—	—	[83]
CoPt	F	~3.5	A	TEM	—	—	—	—	[100]
CoPt	C₁	7 (TEM)	A	TEM, EDX, GFM	—	0 (RT)	—	—	[122]
CoPt	C₂	1.8 (TEM)	A	UV/VIS/IR, (HR)TEM, SQUID, EDX (supp.)	—	6.9 kOe (5 K)	—	20 (75 Oe)	[107]
CoPt	C₁	6.3 (TEM)	CS	UV/VIS/IR, (HR)TEM, SQUID, EDX (supp.)	—	0.33 kOe (5 K)	—	15 (75 Oe)	[107]
CoPt	D₂	1–1.5 (TEM)	A	IR, WAXS, HRTEM, SQUID	1.3–1.95 μ_B / Co-atom (5 K)	0.2–1 T (5 K)	—	10–20 (1 mT)	[101]
CoPt	C₁	1.5–7.2 (TEM, XRD)	A	(HR)TEM, XRD, SQUID (supp.)	6 emu/g (RT, 6.2 nm)	~1.2 kOe (5 K)	—	~35 (100 Oe)	[120]
CoPt	R₁	15 (TEM)	A	XRD, TEM, SQUID	$\mu_{\text{eff}} = 0.06$ emu/g (2 K)	2700 G (2 K)	—	140 (1 kG)	[90]
CoPtAu	R₃	18 (TEM)	CS	XRD, TEM, SQUID	$\mu_{\text{eff}} = 0.017$ emu/g (2 K)	1000 Oe (2 K)	—	80 (100 Oe)	[90, 110]
CoAu	R₂	15 (TEM)	CS	XRD, TEM, SQUID	—	20 Oe (10 K)	—	60 (100 Oe)	[90, 110]
CoAu	C₃	2.8 (TEM)	CS	TEM (not shown), SQUID, Mössbauer	1.77 μ_B /atom (5 T)	—	2.6×10^6	~8 (100 Oe)	[91]
CoSm	C₁	9 (TEM)	A	TEM, SQUID	2 emu/g (RT)	50 Oe (RT)	—	>RT	[123]
NiPd	P₁	2.5 (TEM, XRD)	CS	XRD, (HR)TEM, SQUID, XPS, ESR	0.21–0.64 μ_B / atom (1.8 K)	—	—	—	[87, 88, 94]
NiPd	P₂	2.5 (TEM)	A	XRD, (HR)TEM XPS, XANES, EXAFS	—	—	—	—	[93]
NiPd	E	2.5–3.5 (TEM)	A	TEM	—	—	—	—	[82]

A: Alloy, CS: Core-shell.

p.t.: post-treated (H₂, 100 °C, 2 h).

Comments and results presented as supporting information (supp.) to cited references are given in italics. For details see text.

($\eta^4\text{-C}_8\text{H}_{12}$) and $\text{Rh}[(\text{acac})(\eta^4\text{-C}_8\text{H}_{12})]$ or $\text{Co}[(\eta^3\text{-C}_8\text{H}_{13})(\eta^4\text{-C}_8\text{H}_{12})]$ and $\text{Pt}_2(\text{dba})_3$, respectively. Syntheses have been performed using tetrahydrofuran (THF) as the solvent. Particles were stabilized by poly-(N-vinyl-2-pyrrolidone) (PVP) and the precursors were decomposed at room temperature under a H_2 pressure of 3 bar during 15 h–64 h. The motivation for using carbonyl free metal-organic compounds and PVP as a stabilizer was that the surface properties of the final particles remain unchanged.

The compound $\text{Co}[(\eta^3\text{-C}_8\text{H}_{13})(\eta^4\text{-C}_8\text{H}_{12})]$ has been prepared by Otsuka and Rossi [181], while $\text{Pt}_2(\text{dba})_3$ has been prepared using the method of Moseley and Maitlis [182], both with minor modifications. Information on the synthesis of $\text{Rh}[(\text{acac})(\eta^4\text{-C}_8\text{H}_{12})]$ was not given. The final particle compositions reflected the precursor compositions and were adjusted by varying the ratio of the metal-organic compounds, that is, Co_3NM , CoNM , and CoNM_3 ($\text{NM} = \text{Rh}, \text{Pt}$). Typical concentrations of the metal-organic compounds in the starting solution were ~ 8 g/l. Structural investigations were performed by HRTEM and wide-angle X-ray scattering (WAXS). The latter method shows bimetallic bonds within the particles, thus verifying the formation of alloys. The degree of ordering decreased with increasing Co content, and the authors described Co_3NM and CoNM particles as consisting of a crystalline NM rich core surrounded by a disordered Co rich shell. Transmission electron microscopy and HRTEM analysis showed extremely small particles (1 nm–2.6 nm in diameter) with a small size distribution. The presented TEM and HRTEM images were consistent with those expected for small bimetallic colloids prepared by different methods, that is, \mathbf{D}_2 , \mathbf{E} , \mathbf{O} , \mathbf{P} , and \mathbf{C}_2 (for alloy formation). In particular, TEM and HRTEM (insert) of CoRh particles dried from a solution on a carbon-coated Cu-grid, representing morphology and size deviation of several nanoparticles $d < 3$ nm and prepared by various methods, can be viewed in Figure 3A.

Super-conducting interference device (SQUID) measurements showed an increase of T_B for CoPt and a decrease of T_B for CoRh with increasing noble metal (NM) content in a range between 10 K and 20 K. T_B was calculated from ZFC/FC versus T curves. The magnetization for all particles does not saturate at 5 T. H_C and magnetic moments are increased compared to pure Co colloids. H_C and magnetic moments per Co atom of $\text{Co}_{1-x}\text{Pt}_x$ particles increase with increasing x . Estimated values were 0.518 T, 1.76 T, and 2.057 T of H_C ($T = 0$) and $1.35 \mu_B$, $1.5 \mu_B$, and $1.95 \mu_B$ of the magnetic moments (5 K, 5 T) for $x = 0.25, 0.5$, and 0.75 . $\text{Co}_{0.5}\text{Rh}_{0.5}$ colloids have been estimated to show a magnetic moment per Co atom of $1.9 \mu_B$ (5 T) and K_{eff} was found to be $1 \times 10^6 \text{ Jm}^{-3}$. The differences in fine particle magnetism with the corresponding materials bulk magnetism was discussed.

4.1.3. \mathbf{D}_3 : Decomposition of Monometallic Metal-Organic Carbonyls

The *in-situ* thermal decomposition of commercially available metal carbonyls has been used for the preparation of FeMo ferrofluids [106]. Synthesis has been achieved by refluxing a solution of $\text{Mo}(\text{CO})_6$ and $\text{Fe}(\text{CO})_5$ in dioctylether for 30 min, in the presence of equimolar amounts of octanoic

acid and/or ethyl hexyl amine as stabilizers under an inert atmosphere. Typical carbonyl concentrations of the starting solutions were 45 g/l and the Fe/Mo molar ratio was adjusted to 5/1. A structural investigation was conducted by HRTEM and compositional analysis by EDX. The former was consistent with highly crystalline particles. Energy-dispersive X-ray spectroscopy analyses gave a mole-atom ratio for the final particles of $\text{Fe/Mo} = 96/4$. This result was explained in terms of the lower decomposition rate of $\text{Mo}(\text{CO})_6$ compared to $\text{Fe}(\text{CO})_5$. However, presented EDX spectra showed K- and L-edge signals from Fe and L-edge signals from Mo, although the composition calculations from EDX were not explained. Different particle sizes were achieved by varying the nature and concentration of stabilizers. One surprising result of this work was the fact that the particle size increases with increasing octanoic acid concentration, which represents a reversal of many published results. The authors explained their observations by assuming a lowering of the reaction rate for carbonyl moieties in the presence of octanoic acid, which means a lower number of nuclei were formed initially. Different reaction kinetics for the $\text{Fe}(\text{CO})_5$ or $\text{Mo}(\text{CO})_6$ decomposition in the presence of stabilizers, which may explain both the observed reversal and the discrepancy between initial precursor composition and the composition found by EDX, were not considered. However, it was agreed that more work was necessary in order to clarify discussion of presented results. Nevertheless, TEM and HRTEM images as shown represent typical images of bimetallic nanocrystals prepared by various methods, that is, \mathbf{D}_1 , \mathbf{D}_3 , and \mathbf{C}_1 . An image of 8.5 nm particulate alloys is given in Figure 3B. Magnetic properties were not investigated. The particles were used as a catalyst for the growth of single-walled carbon nanotubes (SWNT). The results appear to indicate that an upper limit of particle size exists to grow SWNT.

4.2. E: Electrolysis

This novel procedure was developed by Reetz et al. and differs greatly from other conventional techniques [82]. The method is based on the *in-situ* electrochemical reduction of metal salts in THF under inert gas conditions. Metal ions were preformed by oxidation of the desired metal electrode pair in the presence of 0.1 M TOABr, which acts as a stabilizer and electrolyte. Oxidation of the electrodes and reduction of the preformed metal salts occurs in a commercially available electrolysis cell (volume of 80 mL). By employing this configuration, Ni_xPd_y ($x/y = 0.25, 0.32$, and 5.25), $\text{Fe}_{74}\text{Co}_{26}$, and $\text{Fe}_{72}\text{Ni}_{28}$ particles have been prepared, which may be redispersed in THF (concentrations of 1 M [82]). Typical particle sizes as determined by TEM were 2.5–3.5 nm for NiPd and 2.5–3.0 nm for FeCo and FeNi. Alloy formation was expected.

4.3. F: Reduction in Apoferritin

A further unusual approach for preparation of bimetallic ferrofluids has been developed by Warne et al. (NanoMagnetics Ltd.) [100]. The synthesis is based on the *in-situ* reduction of metal salts by NaBH_4 within the empty cavities of the demineralized protein ferritin (apoferritin). Demineralization has been done according to the method of

Funk et al. [183]. The synthesis allows for the preparation of monodisperse, biocompatible, aqueous, magnetic fluids, and post-annealing of assembled layers thereof, in reductive atmosphere, result in carbon protected nanoparticulate films. Carbon protection is the result of reductive protein decomposition. NanoMagnetics Ltd. hold the patent for the preparation of a large range of materials prepared via this method [184]. In the case of bimetallic ferrofluids, only the preparation of CoPt has been published.

CoPt was prepared by *in-situ* reduction of ammonium tetrachloroplatinate and cobalt acetate-loaded, aqueous protein solution by NaBH_4 . The as-prepared particles ($d \sim 3.5$ nm) were amorphous, as could be revealed by electron diffraction. Further investigations have only been done after the annealing of dried powders in hydrogen at 650°C for 1 h.

4.4. R: Reverse Micelles

The water-in-oil reverse micelle technique is very popular and has been applied for the preparation of a large number of colloidal materials. Importantly, this technique has provided well-separated colloidal particles with diameters up to 15 nm or more with narrow size distributions. Figure 3C is representative of typical images of particles prepared via this method. A further advantage of the procedure is the possibility of controlling the size of colloids by controlling the size of micelles, which is dependant on the H_2O /surfactant ratio.

4.4.1. R_1 : In-Situ Reduction

FeCu alloys have been prepared by Duxin et al. [84] by NaBH_4 *in-situ* reduction of $\text{Fe}(\text{AOT})_2$ and $\text{Cu}(\text{AOT})_2$ in isoctane under inert atmosphere. Initial compositions were reported as 30% (70%) $\text{Fe}(\text{AOT})_2$ and 70% (30%) $\text{Cu}(\text{AOT})_2$. The total concentration was maintained at 0.1 M. Structural characterization was achieved by XRD, TEM, EDX, EELS, and Mössbauer experiments. Transmission electron microscopy showed aggregated particles, 5–15 nm in diameter, with a broad-size distribution for both starting compositions. This observation is not typical for this method. The final composition obtained from EDX (spectrum not given) was similar to the starting composition for Cu-rich samples and different for Fe-rich samples. The former gave rise to alloy formation, the latter to the formation of pure Fe and alloy composites. These assumptions have been confirmed by XRD, showing a single reflection for α -Fe for Fe-rich samples and by EELS. Results from EELS on the $L_{2,3}$ -edges of Fe and Cu and the K-edge of B of dried samples revealed a homogeneous distribution of the three elements in Cu-rich and a heterogeneous distribution in Fe-rich samples. The authors concluded from this investigation that the procedure led to the formation of FeCuB alloys. Mössbauer spectra were consistent with a metallic alloy. Fe^{3+} and Fe^{2+} in the Cu-rich sample and mainly α -Fe and Fe^{3+} in Fe-rich samples could be detected. It was expected that Fe^{3+} is derived from iron oxide and Fe^{2+} results from incomplete reduction. Super-conducting interference device magnetometry of Cu-rich (Fe-rich) samples at RT showed M_S , and H_C of 1.1 emu/g (51 emu/g), and 24 Oe (531 Oe), respectively.

CoPt colloids have been prepared by NaBH_4 reduction of the metal chlorides in reverse micelles formed by CTAB in octane under inert atmosphere [90]. The Co concentration was chosen to be 10 mM. Initial compositions were CoPt and CoPt_5 , and final compositions were not published. The colloids were investigated by XRD and TEM; the former revealed good crystallinity and no formation of ordered alloys. The size distribution cannot be deduced from the as-presented results. Boride formation is not discussed. A SQUID magnetometer was used for magnetization measurements. T_B was obtained from ZFC plots in a field of 1 kG. H_C was determined from M versus H curves recorded at 2 K. Values of T_B , H_C , and μ_{eff} for CoPt (CoPt_5) were reported as 140 K (130 K), 2700 Oe (2000 Oe), and 0.0598 emu/g (0.0357 emu/g), respectively.

CoMo colloids have been prepared by NaBH_4 reduction of the metal chlorides in reverse micelles formed by DDAB in toluene under inert gas conditions [116]. Typical concentrations were 60 g/L. The initial metal composition was equimolar and only slightly changed during reaction (determined by XPS; spectra not given). Transmission electron microscopy data presented well-separated particles (the typical image of colloids prepared by this technique (see Fig. 3C)), possessing an average diameter of 8.5 nm. The colloids were used for the growth of SWNTs and it was pointed out that nanoparticles as small as the diameter of SWNTs are not necessary for the nanotube growth.

4.4.2. R_2 : Successive Reduction

The formation of Co@Ag core-shell particles [81, 85, 89] has been realized by a process involving successive reduction of a 10-fold molar excess of Ag^+ ions on the surface of Co nanoparticles, in reverse micelles formed by AOT in n-heptane. The reduction of Ag^+ was carried out by UV irradiation or NaBH_4 treatment. A typical starting concentration of cobalt salt was 0.1 M. Transmission electron microscopy investigations show well-separated monodisperse particles of about 10 nm in diameter. Only fcc Ag reflections were recorded in the XRD pattern.

Super-conducting interference device magnetometry and electron paramagnetic resonance (EPR) measurements were applied for investigation of magnetic properties. The as-prepared particles remain superparamagnetic down to 2 K measured in a field of 50 Oe. M_S and K_{eff} were calculated from high-field magnetization data ($H > 30$ kOe) at different temperatures and determined to be 646 emu/g and 2×10^7 erg/cm³, respectively. The formation of CoO was extrapolated from the obtained inverse susceptibility data which indicated antiferromagnetic interactions. Calculation of the magnetic volume resulted in a Co cluster size of only 10 atoms, that is, the synthesis has produced small Co clusters embedded in a nanoparticulate Ag matrix (see Fig. 2B). After moderate post-treatment of the particles in H_2 at 100°C for 2 h, values for M_S and K_{eff} increased to 1700 emu/g and 8.5×10^7 erg/cm³, respectively, indicating the reduction of CoO to metallic Co. It is worthy to note that the value of M_S was higher than the bulk value for Co. The observation is well known for small Co clusters. However, the question remains as to whether the reduction is limited to Co clusters near the surface of the Ag matrix, as depicted in Figure 2B.

The successful synthesis of Fe@Au core-shell particles has also been reported. The procedure involves successive NaBH₄ reduction of HAuCl₄ on the surface of Fe particles, in reverse micelles formed by CTAB in octane [98, 110–112, 125]. Metal concentrations of 0.1 M were typically employed. Investigations of structure and morphology were performed using UV/VIS, XRD, HRTEM, and later XANES (2002) [125]. X-ray powder diffraction data revealed good crystallinity. The results of TEM were indicative of aggregated particles with a core-shell structure. Surprisingly, the core had a dark contrast, while the shell was shiny. This observation was contrary to existing theory and in published results of core-shell particles, the disparity was not discussed by the authors. Conventional wisdom would expect a darker contrast for the heavier Au shell and a lower contrast for the lighter Fe core. Such observations have been made and published for bimetallic noble metal core-shell colloids. Moiré patterns, visible in HRTEM investigations, verify a core-shell structure [112]. Interpretations of XANES experiments revealed that the Fe in these particles consisted mainly of iron oxide, demonstrating unsuccessful protection of the Fe core by the Au shell. The authors suggested that the Fe core was not centered in the Au shell and thus parts of the core were not covered by a protective Au layer. Incomplete coverage through Au island formation on the Fe surface, as well as alloy formation of FeB, FeAu, and FeAuB that is possible under these preparation conditions, were not discussed.

Due to these many factors, different magnetic properties must be expected for different samples prepared in a similar way. Values for T_B (1 kOe), H_C (2 K), and M_R (2 K) have been reported as 50 K, 400 Oe, and 13.67 emu/g, respectively.

Formation of Au@Fe@Au core-shell particles has been achieved using similar strategies to those used for the Fe@Au particles presented above. Au@Fe particles were first prepared vice versa to Fe@Au particles in similar concentrations in reverse micelles formed under identical conditions. Subsequently, these have been used as the core material for the preparation of Au@Fe@Au onions [96, 97, 109, 110, 125]. The techniques of TEM, XRD, and EDX have been applied for structural investigations. Again, XRD demonstrated only crystallinity (diagram not presented). Transmission electron microscopy showed aggregated particles with an untypical broad-size distribution. The particles consisted of a dark core of Au and a shiny shell of Fe, as expected from theory. The outer second shell of Au could not be resolved. Results from EDX measurements in the nanoprobe mode (spot size = 2 nm) were consistent with Au enrichment at the surface (spectra not available). The authors did not discuss their results with respect to the XANES investigations of Au@Fe@Au colloids, as well as the possible alloy formation of FeB, FeAu, and FeAuB. Similar rationales were not discussed with reference to magnetic properties. Values for T_B (1 kOe), H_C (10 K), and M_R (10 K) were reported as 50 K, 420 Oe, and 3.6 emu/g, respectively.

Co@Au particles [90, 110] were prepared in a similar fashion to Fe@Au, although detailed investigation of structure, morphology, and composition were not revealed. T_B (100 Oe) and H_C (10 K) were determined by SQUID magnetometry to be 60 K and 20 Oe.

4.4.3. R₃: Combination of In-situ and Successive Reduction

FePt@Au and CoPt@Au have been prepared by reduction of HAuCl₄ on the surface of preformed bimetallic particles, prepared similarly to CoPt particles presented in Section 4.4.1 and by the same group [90, 98, 110, 113]. Initial compositions of the core particles were CoPt and CoPt₃, and Fe₂Pt, FePt, and FePt₃. Final compositions were stated to be similar to the starting composition. FePt₃ was characterized as a homogeneous alloy and as an intermetallic compound. Transmission electron microscopy images showing core-shell particles were not presented. Oxide and boride formation was not discussed.

A detailed discussion of magnetic properties requires a detailed knowledge of structures. The results of magnetic measurements of references [90, 96–98, 109–113] presented in Table 2, will therefore only be given for completeness.

4.5. M: Micelles

Syntheses of ferromagnetic colloids by NaBH₄ reduction of metal salts in oil-in-water micellar solutions have been reported. The synthesis of elongated FeCu alloys (alloy formation in bulk materials is not known under conditions of thermodynamic equilibrium) published by Duxin et al. is the only example of bimetallic ferrofluids prepared by this method [86].

FeCu alloys have been synthesized by *in-situ* NaBH₄ reduction of 30% Fe(DS)₂ and 70% Cu(DS)₂, forming ellipsoidal shaped micelles of 2.7 nm hydrodynamic diameter at critical micellar concentrations of 1.34 mM (synthesis under inert atmosphere). Typical structure, morphology, and composition of the resulting particles have been investigated by XRD, HRTEM, EDX, EELS, and Mössbauer experiments. Transmission electron microscopy showed coagulated networks of elongated particles of 6.6 nm average diameter (Fig. 3D). X-ray powder diffraction (XRD), electron diffraction (ED), and fast fourier transformation (FFT) of HRTEM revealed good crystallinity, and calculations thereof were in good agreement with the [111] lattice spacing for bulk fcc Cu. Neither an oxide phase nor the α -Fe phase could be detected. Alloy formation was concluded from Mössbauer experiments. The average composition was determined by EDX, employing a 35 nm spot (spectra not shown), giving compositions of 14% Fe and 86% Cu. The authors explained this result in terms of incomplete reduction of Fe(DS)₂. Electron energy loss spectroscopy (EELS) on the L_{2,3} edges of Fe and Cu showed Fe enrichment at the surface of the particles. The pattern of results was consistent with the formation of a heterogeneous FeCu alloy. Moreover, the presence of interstitial boron, well known for colloid preparations by NaBH₄ reduction of metal salts in the presence of water and investigated in detail by Glavec et al., [137, 185] was expected.

Magnetic properties have been determined by SQUID magnetometry. The magnetization at 1.8 K did not saturate in applied fields up to 50 kOe. M_S was calculated by extrapolation to zero at 40 emu/g. A value for H_C of 250 Oe was determined. T_B was determined from ZFC curves at various applied fields, showing a decrease of T_B with increasing H. The values were 9.5 K, 8.5 K, and 7.5 K for applied

fields of 20 Oe, 50 Oe, and 100 Oe, respectively. K_{eff} has been estimated from the Neel equation and reported as $\sim 10^5$ erg/cm³. Uncertainty in the value was explained in terms of the colloidal particle shape, which makes the determination of the particle volume rather difficult.

4.6. O: Organohydroborate Reduction

This method has been developed by Bönemann more than 10 years ago for the preparation of highly dispersed mono- and bimetallic particles, with typical diameters < 5 nm, in organic solvents [55]. This nonaqueous method additionally produces boron-free final product materials. Typical starting concentrations for the metal salt were ~ 25 mM. The method's success based on the preformation of novel, non-commercially available reducing agent TOAEt₃BH (synthesized in THF by the reaction of KEt₃BH with TOABr). KEt₃BH was used rather than the more commonly employed Li analogue (super hydride), because KBr is insoluble in THF and can be separated from the product. As a result, the synthesis leads to products free of impurities derived from the reducing agent. Parallels to the approach are found in work developed by Reetz (E).

Fink et al. [186] provided evidence that both the tetraoctyl-ammonium (TOA) cation, as well as the counterion from the reduced metal salt, comprise the stabilizing shell on the surface of noble metal nanoparticles. The inner shell consists of counterions and the outer shell is formed by TOA⁺. These investigations were later confirmed by Bucher et al. [187] using XANES and metastable impact electron spectroscopy (MIES), correcting earlier assumptions by Bönemann and Reetz of a vice versa stabilizing shell composition.

The preparation of nanoparticulate Fe, Co, and Ni passivated with a protecting layer of Ag, Au, Pd, and Pt has been reported in the patent literature [92]. The procedure involves addition of solutions of noble metal salts in THF to mixtures of preprepared Fe, Co, or Ni nanoparticles and excess strong reducing compounds (e.g., superhydride, modified superhydride, or trialkyl aluminium hydride) in THF or toluene over a period of several hours (14 h–16 h). The particles thus obtained showed an increased stability of magnetization compared to both unpassivated seed particles and particles covered with Au by successive transmetalation ([91], see C₃). The decreased stability of particles prepared via C₃ was ascribed to island formation of the protecting noble metal shell. Detailed structural and morphological investigations, as well as differences in magnetic properties of different compositions were not presented.

4.7. P: Polyol Reduction

Polyols have been used as moderate reducing compounds for the preparation of colloids for several years [188]. One advantage of this method is that alcohols with one, two, or more hydroxyl groups are oxidized to aldehydes or ketones during reaction, that is, they do not form ionic by-products. Moreover, this method allows for the preparation of colloids in hydrophilic, as well as hydrophobic media, by choosing alcohols with corresponding properties. The polyol method

has been modified for the preparation of bimetallic micron-sized particles [189]. The modification is based on the hydrolysis of mixed metal salts prior to reduction, resulting in the formation of hydroxides.

4.7.1. P₁: In-situ Reduction

CoPt The modified polyol process has been applied to produce CoPt alloy colloids [83]. Cobalt chloride and hexachloroplatinic acid were dissolved in a 4/1 mixture of ethylene glycol/diethylene glycol, hydrolyzed by adding aqueous NaOH, and heated to reflux for 2 h under N₂ in the presence of poly-(*N*-vinyl-2-pyrrolidone) (PVP). A typical starting concentration of 0.4 M in Pt was employed, the Pt/Co ratio adjusted to 3 and the PVP concentration (as monomeric residue) maintained at ~ 50 mM.

The final colloidal dispersion has been investigated by TEM and XRD. Transmission electron microscopy exhibits isolated particles of ~ 1.7 nm average diameter. X-ray powder diffraction showed rather broad reflections due to the small size of the particles. The authors concluded from XRD that the colloid consisted of CoPt₃ particles or a mixture of CoPt and Pt. An unambiguous structural determination from XRD was not possible because of overlapping reflections for CoPt_x and Pt, further complicated by the broadening effect due to the small particle size. Magnetic properties were not investigated. The colloid was applied as catalyst for the hydrogenation of cinnamaldehyde showing high selectivity and conversion. The particles were found to withstand the hydrogenation reaction at 333 K and 4 MPa.

NiPd A minor modification to the (modified) polyol process has been found to be suitable for the preparation of NiPd alloy colloids [94]. Palladium acetate and nickel sulfate were chosen instead of hexachloroplatinic acid and nickel acetate; Pd acetate was dissolved in dioxane prior to use. Initial reaction concentrations were 4 mM (total concentration of metal salts at various Ni/Pd ratios). Synthesis was performed by refluxing the hydrolyzed metal salts in ethylene glycol for 3 h under N₂ in the presence of 14.3 times molar excess of PVP (as monomeric unit). Investigations by TEM and HRTEM revealed well-separated crystalline particles with an average diameter of about 2 nm. Interpretation of XPS, XANES, and EXAFS measurements resulted in a Pt-rich random alloy structure of the particles. The colloids have been found to be an excellent catalyst for the hydrogenation of nitrobenzene. Maximum activity was found for a composition of Ni₂Pd₃.

4.7.2. P₂: Successive Reduction

A successive polyol method was described in 1999 for the preparation of Pd@Ni core-shell particles stabilized by PVP [93]. It is necessary to point out that the authors published the procedure previously, but the work concerned the formation of alloys while applying the same investigation methods (TEM, XRD, XPS) [87, 88]. The synthetic procedure is based on the prepreparation of PVP-stabilized Pd particles and involves reflux of 0.16 mmol H₂PtCl₄ and 1.6 mmol PVP (as a monomeric unit) in a mixture of 640 ml H₂O and 160 ml ethanol for 3 h. The preformed Pd particles (initial concentration of ~ 8 mM Pd (atoms); $d = 2.5$ nm) were then

refluxed in 1-propanol, together with various amounts of Ni acetate for 3 h under N_2 . As a result, monodisperse colloids possessing particle diameters in the range 2.5–2.8 nm were formed by using a Ni/Pd ratio up to 1 (the theoretical thickness of the Ni shell for a ratio of 1 is about 1.5 layers). Further increases in the Ni/Pd ratio led to a remarkable increase of the particles diameter along with a broadening of their size distribution. Super-conducting interference device measurements at 1.8 K showed a remarkable increase of the magnetic moment above a Ni/Pd ratio of ~ 0.07 . It is concluded that the anomalous increase of the magnetization may correspond to the giant magnetic moment effect in ultrafine Pd particles [190].

4.8. C: Combination

Thermal decomposition of zerovalent metalorganic Fe or Co compounds, combined with polyol reduction or redox transmetallation [191] of Ag, Sm, Pd, or Pt salts, have been reported to be suitable methods for the preparation of bimetallic ferrofluids. The transmetallation, first adapted by Paulus et al. for the preparation of Co@Au and Fe@Au colloids [91], is based on the reduction of noble metal salts by surface atoms of preformed colloids (C_3) of nonnoble metal elements.

4.8.1. C_1 : Decomposition/Polyol Reduction

FePt A notable success in this field of research was the seminal report in *Science* by Sun et al. on the preparation of bimetallic FePt ferrofluids [95]. The authors combined the polyol reduction of a noble metal salt, described by the 1,2-hexadecanediol reduction of $Pt(acac)_2$, with the thermal decomposition of $Fe(CO)_5$ at high temperatures in the presence of two stabilizers (*vis oleic acid and octylamine*). As a result, monodisperse alloy particles were fabricated. Initial concentrations of 25 mM $Pt(acac)_2$ were employed. The particle size distribution could be narrowed by applying the hot injection technique using a high boiling solvent (octyl ether or phenyl ether) followed by a size-selective precipitation using, for example, ethanol as the nonsolvent [192]. The reaction was initiated by adding $Fe(CO)_5$ to a solution of $Pt(acac)_2$ at 100 °C (hot injection) and continued under reflux conditions for 30 min under N_2 . The composition could be adjusted by varying the starting Fe/Pt ratio. Primary particle diameters were 3 nm, which could be increased to 10 nm by successive addition of desired precursor ratios to a solution containing the 3 nm seed particles.

Investigations by TEM of as-prepared 4 nm particles revealed a typical fcc structure of the particles which were substantiated by XRD. Super-conducting interference device measurements showed superparamagnetic behavior for those particles at room temperature and blocking temperatures between 20 K and 30 K in a field of 10 Oe. Further investigations have been only applied on sintered films of self-assembled particles, showing a transformation to the $L1_0$ phase above 500 °C, which was concomitant with an increase of coercivity.

The method of Sun et al. has been reproduced [103, 119] and adapted for the preparation of FePd [122], Fe [103, 104, 117] (Yamamuro, Farrell, and Chamberlin et al. used seed Pt clusters to obtain monodisperse Fe particles by

successive growth. The Pt concentration was less than 1%), FeCoPt [121], CoSm [123], and CoPt [122] ferrofluids, and modified for the synthesis of $CoPt_3$ [120] by several groups. The work by Shevchenko et al. [119] showed a blocking temperature of 14 K in a field of 200 Oe for as prepared 4.5 nm particles. Applying the Néel equation by assuming $\ln(\tau/\tau_0)$ to be 25, leads to a value for the anisotropy constant $K_{eff} = 1 \times 10^6$ erg/cm³.

FePd Chen and Nikles adapted the described method by substituting $Pt(acac)_2$ with $Pd(acac)_2$ [122]. The resultant particles showed an average diameter of 11 nm, which is increased in comparison to FePt, in addition to a relative broad-size distribution. Both observations are indicative of different reaction kinetics. The particles were found to be ferromagnetic at RT ($H_C = 12$ Oe). Further investigations have been performed only on annealed self-assembled films, showing that FePd particles do not transform to the $L1_0$ phase within the applied temperature range up to 700 °C.

FeCoPt Chen and Nikles have adapted Sun's method for the synthesis of ternary FeCoPt alloys by adding $Fe(CO)_5$ to a mixture of $Pt(acac)_2$ and $Co(acac)_2$ in dioctyl ether [121]. Investigations have only been done on sintered self-assembled layers. The main result from these studies was that the measured coercivity of the annealed particles decreases with increasing Co content.

CoSm Ono et al. adapted Sun's method using $Sm(acac)_3$ and $Co_2(CO)_8$ instead of $Pt(acac)_2$ and $Fe(CO)_5$, respectively [123]. The final particles had an average diameter of 9 nm as determined by TEM and showed a decreased Sm content, compared to the starting composition of the metal salts (determined by EDX). This result may be due to an incomplete reduction of Sm^{3+} as was discussed by Pileni for iron in FeCu particles. Magnetic measurements indicated a coercivity of 50 Oe and a saturation magnetization $M_S = 2$ emu/g at RT. These values are different from pure Co particles prepared in a similar way indicating a 3d–4f electron interaction. A discussion of electronic interaction is still outstanding.

CoPt $CoPt_3$ and $Co_{48}Pt_{52}$ have been synthesized by substituting $Co(CO)_3NO$ for $Fe(CO)_5$ [122]. Issues concerning the use of $Co(acac)_2$ or $Co_2(CO)_8$, instead of $Co(CO)_3NO$, were discussed. Investigations have been focused on $Co_{48}Pt_{52}$. The colloids showed an average particle diameter of 7 nm and were superparamagnetic at RT. Further investigations were only applied on annealed films.

CoPt₃ A modified procedure has been developed by Shevchenko et al. for the preparation of $CoPt_3$ colloids by thermolysis of $Co_2(CO)_8$ and polyol reduction of $Pt(acac)_2$ [120]. The modifications were as follows: (i) use of mixtures of highly coordinating solvents, that is, diphenyl ether/hexadecylamine, diphenyl ether/tetradecylphosphonic acid, or hexadecanol/hexylamine; (ii) replacement of oleic acid by adamantanecarboxylic acid or adamantanacetic acid. Use of different hot injection temperatures and reaction times for solutions of $Co_2(CO)_8$ in dichlorobenzene have also been thoroughly investigated. The best results concerning size distribution, crystallinity, and reproducibility were obtained for

syntheses involving mixtures of diphenyl ether/HDA (hexadecylamine) and diphenylether/TDPA (tetradecylphosphonic acid) in the presence of ACA (adamantanecarboxylic acid). A typical starting concentration of 8 g/l $\text{Pt}(\text{acac})_2$ was employed. Primary particle sizes were in the range of 3 nm–5.5 nm. The success of procedures using ACA as a stabilizer was explained in terms of protection of free surface sites from coordination by ligand molecules. This would be expected to increase the free surface energy of the particles, leading to growth and larger dimensionality compared to systems using fatty acids. Moreover, this method allowed the further growth of alloys without remarkable changes in size distributions for one and two additional precursor injections. However, experiments with pure $\text{Co}_2(\text{CO})_8$ were not successful when using ACA as a stabilizer.

High-resolution transmission electron microscopy and XRD investigations showed well-separated single crystalline particles consisting of the CoPt_3 intermetallic L_{12} phase. A (HR)TEM image of the particles, representing a micrograph typical for successive-growth colloids prepared via C_1 , is presented in Figure 3E. The authors emphasized that segregation and core-shell formation could not be excluded, but was not expected from their results. Some explanations concerning their expectations were given.

Results of magnetic measurements on ~ 6.2 nm particles are available as supporting information to [120]. M versus H curves were measured at 5 K and 300 K, and ZFC/FC M versus T plots measured in a field of 100 Oe. Exact values of characteristic magnetic properties were not given. The presented curves reveal that the colloids are superparamagnetic at RT. T_B , M_S (5 K), and H_C (5 K) can be estimated from the figures to be ~ 35 K, ~ 10 emu/g, and ~ 1200 Oe, respectively.

4.8.2. C_2 : Decomposition/Transmetallation

Ag@Co A procedure has been described to produce Ag@Co colloids, involving the thermal decomposition of $\text{Co}_2(\text{CO})_8$ in the presence of anhydrous AgClO_4 (reduced *in-situ* by $\text{Co}_2(\text{CO})_8$ via transmetallation) in toluene, using oleic acid and tridodecylamine as stabilizers [127–129]. A typical starting concentration of 25 mM AgClO_4 is employed. The thickness of the Co shell could be increased by increasing the amount of $\text{Co}_2(\text{CO})_8$ from 24 mM to 56 mM, while keeping the Ag concentration constant. As a result, Ag particles of a diameter of 8 nm and covered with a Co shell of lower TEM contrast were found (see insert in Figure 3F), in addition to some unpassivated pure Ag particles of a smaller size. The final compositions have been determined from corresponding edges by EDX.

Ultraviolet/VIS spectrometry showed an increasing blue shift and quenching of the Ag surface plasmon band with increasing Co content, that is, increasing shell thickness, indicating a strong electronic interaction for both elements in these composite particles (Fig. 7A). Similar observations have been reported for Ag particles coated with an Au shell [193]. A comparison with the optical spectra for mixtures of pure Co and Ag colloids (Fig. 7B) indicated neither a Ag/Co-ratio dependant blue shift nor a broadening of the Ag plasmon wavelength. Structural investigations by (HR)TEM revealed a multiple twinning or “polycrystalline” structure

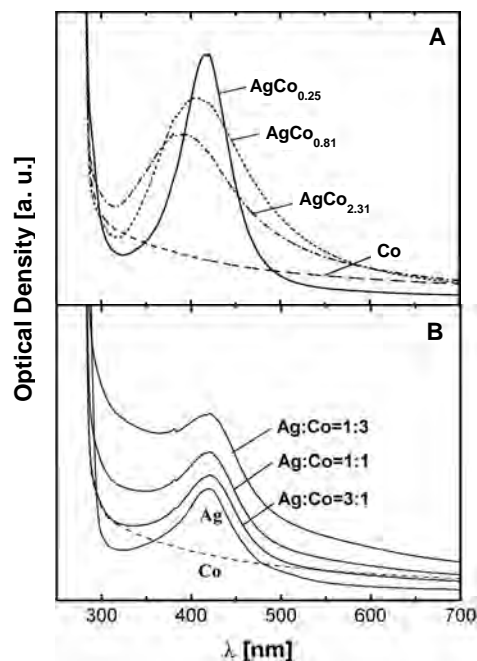


Figure 7. (A) Blue shift and quenching of the Ag plasmon band with increasing Co content for composite particles of constant Ag concentration in solution. The stoichiometric ratio is given as AgCo_x . (B) Optical density of different mixtures of pure Ag and Co particles. The size of the Ag particles (8 nm) is the same as in (A). Reprinted with permission from [127], N. S. Sobal et al., *Nano Lett.* 2, 621 (2002). © 2002, American Chemical Society.

of particles consisting of fcc phase subunits of both elements. Energy-filtered EELS analysis on the Ag $M_{4,5}$ and Co $L_{2,3}$ edges verified that Ag was present mainly in the center, while Co was preferentially located in the particles shell. Calculations from EELS measurements on Ag@Co particles having a thin shell (< 2 nm) suggest no surface oxidation of the Co shell. It was concluded that the latter result again reflects a strong electronic interaction of both elements in the nanocrystals. Superconducting interference device [127, 128] and X-ray magnetic circular dichroism (XMCD) [129] measurements were applied to obtain information concerning magnetic properties of the material. Available magnetization experiments showed superparamagnetic behavior at RT and ferromagnetic behavior at 90 K. H_C (90 K), and M_R/M_S (90 K) were found to be 0.07 T and 0.32, respectively. X-ray magnetic circular dichroism difference spectra on the $L_{2,3}$ edge of Co allowed the calculation of the orbital-to-spin ratio of the magnetic moment after ion etching of a deposited film under grazing incident conditions (to remove the stabilizers from the surface). The ratio was found to be 0.24, that is, a threefold increase compared to bulk fcc Co (0.08). Detailed discussions of these results were not given.

CoPt Park and Cheon reported on the preparation of CoPt and CoPt_3 alloy colloids by *in-situ* thermal decomposition of $\text{Co}_2(\text{CO})_8$ in the presence of platinum hexafluoroacetylacetonate, $\text{Pt}(\text{hfacac})_2$ (that is, transmetallation) in toluene, using oleic acid as stabilizer [107]. Hot injection

of a $\text{Co}_2(\text{CO})_8$ /toluene dispersion was used to obtain a narrow particle size distribution. The expensive, commercially available $\text{Pt}(\text{hfacac})_2$ has been prepared by the method of Okeya and Kawaguchi [194]. A typical initial concentration of 50 mM $\text{Pt}(\text{hfacac})_2$ was used. The procedure resulted in the formation of well-resolved crystalline particles having an average diameter of ~ 1.9 nm, determined by (HR)TEM. Lattice spacing was found to be in the range of known data for the corresponding bulk materials. Different compositions for the colloids were obtained by changing the ratio of starting compounds. Energy dispersive X-ray spectroscopy investigations revealed a final particle composition close to compositions expected from the starting ratio of metal compounds. Super-conducting interference device magnetometry was used for magnetization experiments. For CoPt_3 (CoPt) colloids, as powders incorporated in gelatin capsules, blocking temperatures T_B of 75 Oe at 20 K (15 K) and coercivities H_C at 5 K of 6900 Oe (5300 Oe) were determined.

Co@Pt The synthesis of Co@Pt core-shell nanocrystals, by reduction of $\text{Pt}(\text{hfacac})_2$ in a redox transmetallation reaction on Co nanoparticle surfaces, has been published by the same authors [107]. The reaction was carried out in nonane solvent in the presence of (noncommercially available) dodecane isocyanide as a stabilizer. The stabilizer was prepared by the method of Weber and Gokel [195]. As a result, well-defined particles with an average diameter of 6.4 nm and a relatively broad-size distribution ($\sigma = 0.54$) were obtained. Micrographs from HRTEM investigations showed two particles with a homogeneous contrast throughout, having lattice fringes whose distances correspond to typical distances of bulk Pt. A core-shell structure was not visible. Magnetic measurements were done using a SQUID magnetometer. T_B (75 Oe) and H_C (5 k) were determined to be 15 K and 330 Oe, respectively. The authors mentioned that these values are close to values for pure Co particles, having diameters similar to those estimated for the Co core in Co@Ag colloids (T_B and H_C values of pure Co can be found in [12]). The possible formation of disordered alloys or a mixture of Pt and PtCo or Co particles was not discussed.

4.8.3. C_3 : Organoborohydride Reduction/Transmetallation

Fe@Au particles have been formed by successive reductive transmetallation of AuCl_3 on the surface of preformed Fe particles [91]. Measured diameters of prepared particles, determined by TEM (images not shown), were determined to be 2 nm and 5 nm. Structure and morphology, inferred from SQUID magnetometry and Mössbauer experiments, were consistent with those expected for FeAu alloy formation. Magnetization curves showed an increase of T_B compared to pure Fe particles. Applying the Néel expression, K_{eff} was found to be increased to 8×10^6 erg/cm³. An Au coating would be predicted to yield a reduced anisotropy.

Co@Au particles were prepared and investigated similarly to Fe@Au particles described above [91]. Transmission electron microscopy diameters of the particles were close to 3 nm. Alloy formation was not concluded from magnetization measurements. Super-conducting interference device

magnetometry showed a saturation magnetization M_S (5 K, 5 T) of $1.77 \mu_B/\text{atom}$, which is close to the bulk value of Co. T_B (100 Oe) was decreased compared to pure Co particles. K_{eff} , calculated from the Néel equation, was reduced to 2.6×10^6 erg/cm³, the bulk value of Co. The authors concluded that the additional surface anisotropy, usually found in small Co particles, was reduced by Au coating.

5. CONCLUDING REMARKS

The presented results showed that colloid chemistry is rather complex. The complexity enhances with the number of parameters, which, in general, comprise the number of elements. Small changes in preparative conditions have been shown to lead to completely different results. The main reason for this observation is the enhanced surface-to-volume ratio of nanoparticles. Thus, the properties of nanoparticles are mainly determined by the interaction of surfaces and interfaces. In particular, in the case of nonnoble materials, the enhancement of the surface-to-volume ratio means an increased reactivity that ensures that such materials are comparatively difficult to handle. Moreover, the increased reactivity highlights the discrepancies that exist between the environments of basic research (high expense, for example, ultra-high vacuum) and industrial scale development (low capital costs are desirable).

The development of materials for new applications is clearly a dynamic process. Investigations in novel colloid syntheses for technological applications often rise to serendipitous developments and new applications. In summary, work on bimetallic ferrofluids will be a challenge for many scientists from different fields for at least the next decade.

GLOSSARY

Colloidal nanoparticles Kinetically stable dispersion of nanoparticles in a solvent.

Electron energy loss spectroscopy (EELS) Electron energy loss spectroscopy analyses the inelastically scattered electrons present in the beam of a TEM after it has been transmitted through the sample. The spectra can be used to obtain information about the chemical composition and electronic structure of the sample.

Electron paramagnetic resonance (EPR) Spectroscopic technique that relies on the detection of microwave-induced transitions between the split sublevels of a certain paramagnetic defect.

Energy dispersive X-ray spectroscopy (EXDS) Generally used in conjunction with the electron microscope and allows relative concentrations of particular elements within a sample to be measured.

Extended X-ray absorption fine structure (EXAFS) XAFS measurements in the region up to 1000 eV past the absorption edge to yield information about bond lengths, coordination numbers, and structural disorder.

Ferrofluid Ferrofluids or magnetic liquids, are colloidal ferromagnetic nanoparticles.

Metastable impact electron spectroscopy (MIES) Based on the energy analysis of electrons originating from collisions of metastable He^* (2^3S) atoms with the surface, and

can be used for probing the spatial distribution of surface species.

Micelle A spherical assembly of appropriate surfactants in solution.

Microemulsion A stable dispersion of two immiscible liquids containing appropriate amounts of different surfactants.

Nanoparticle A material with dimensions in the lower nm (10^{-9} m) region.

Superconducting quantum interference devices (SQUID)

The most sensitive devices available for magnetometry. The detector consists of a superconducting loop and one or two Josephson junctions.

Superparamagnetism Paramagnetic behavior of low dimensional ferromagnetic materials (nanoparticles) above a size dependant temperature T_b but with giant magnetic moments compared to paramagnetic materials.

Surfactants Are organic molecules, which have two ends with different polarities, and can serve as a capping or protecting agent for nanoparticles against external forces.

Transmission electron microscopy (TEM) Used to obtain images of nanoparticles for shape and size analysis. Electron diffraction patterns provide structural information, while chemical analysis is possible by EDX or EELS.

X-ray absorption fine structure (XAFS) An XAS analytical technique that uses the small variations in absorption (fine structure) above the absorption edge to extract information regarding oxidation states and coordination symmetry (XANES) or bond lengths, coordination numbers, and structural disorder (EXAFS).

X-ray absorption near-edge fine structure (XANES)

XAFS measurements in the region near the absorption edge (within several 10 eV) to determine the oxidation states and the coordination symmetries of the elements in the sample.

X-ray absorption spectroscopy (XAS) Measures the degree of X-ray absorption of a sample as a function of X-ray energy. XAS energy spectra are characteristic of both the elements and their electronic energy levels.

X-ray diffraction (XRD) An X-ray beam can be diffracted by the lattices planes of atoms in samples of sufficient crystallinity.

ACKNOWLEDGMENTS

The author gratefully acknowledges the financial support provided by the DFG (AZ.: II C10 SPP 1072), as well as helpful discussions with Dr. M. Giersig, Hahn-Meitner-Institut, Berlin, Germany (electron microscopy) and Dr. M. Farle, Universität Duisburg-Essen, Germany (magnetic studies). The author also thanks Dr. D. Smyth-Boyle, Manchester Materials Science Centre, UK, for his useful comments and revision of the manuscript.

REFERENCES

1. M. Faraday, *Phil. Trans. Roy. Soc.* 147, 145 (1857).
2. T. Graham, *Phil. Trans. Roy. Soc.* 151, 183 (1861).
3. W. Ostwald, *Die Welt der vernachlässigten Dimensionen*, Steinkopf, Dresden, 1915, (in German).
4. J. Turkevich, P. C. Stevenson, and J. Hillier, *Disc. Faraday Soc.* 11, 55 (1951).
5. E. C. Stoner and E. P. Wohlfahrt, *Philos. Trans. R. Soc. London, Ser. A* 240, 599 (1948).
6. L. R. C. Néel, *Acad. Sci.* 228, 664 (1949).
7. W. F. Brown, *Phys. Rev.* 130, 1677 (1963).
8. D. L. Leslie-Pelecky and R. D. Rieke, *Chem. Mater.* 8, 1770 (1996).
9. R. E. Rosensweig, *Magnetic Fluids, Sci. Am.* 247, 124 (1982).
10. R. E. Rosensweig, "Ferrohydrodynamics." Dover Publishing, New York, 1998.
11. S. A. Iakovenko, A. S. Trifonov, M. Giersig, A. Mamedov, D. K. Nagesha, V. V. Hanin, E. C. Soldatov, and N. A. Kotov, *Adv. Mater.* 11, 388 (1999).
12. T. Fried, G. Shemer, and G. Markovich, *Adv. Mater.* 13, 1158 (2001).
13. M. A. Correa-Duarte, M. Giersig, N. A. Kotov, and L. M. Liz-Marzán, *Langmuir* 14, 6430 (1998).
14. F. G. Aliev, M. A. Correa-Duarte, A. Mamedov, J. W. Ostrander, M. Giersig, L. M. Liz-Marzán, and N. A. Kotov, *Adv. Mater.* 11, 1006 (1999).
15. F. Caruso, M. Spasova, A. Susha, M. Giersig, and R. A. Caruso, *Chem. Mater.* 13, 109 (2001).
16. E. L. Bizdoaca, M. Spasova, M. Farle, M. Hilgendorff, and F. Caruso, *J. Magn. Magn. Mater.* 240, 44 (2002).
17. C. J. Brinker and G. W. Scherer, "Sol-Gel Science." Academic Press, San Diego, 1990.
18. H.-D. Dörfler, "Grenzflächen- und Kolloidchemie." VCH, Weinheim, 1994, (in German).
19. G. Schmid (Ed.), "Clusters and Colloids." VCH, Weinheim, 1994.
20. J.-H. Fendler (Ed.), "Nanoparticles and Nanostructured Films." Wiley-VCH, Weinheim, 1998.
21. H. S. Nalwa (Ed.), "Handbook of Surfaces and Interfaces of Materials." Academic Press, San Diego, 2001.
22. P. Moriarty, *Rep. Prog. Phys.* 64, 297 (2001).
23. New Aspects of Nanocrystal Research, *Mater. Res. Soc. Bull.* 26 (2001).
24. M. Giersig and P. Mulvaney, *J. Phys. Chem.* 97, 6334 (1993).
25. M. Giersig and M. Hilgendorff, *J. Phys. D: Appl. Phys.* 32, L111 (1999).
26. M. Hilgendorff, B. Tesche, and M. Giersig, *Aust. J. Chem.* 54, 497 (2001).
27. M. Hilgendorff and M. Giersig, in "Nanoscale Materials" (L. M. Liz-Marzán and P. Kamat, Eds.), p. 335. Kluwer Academic Publishers, Boston, 2002.
28. M. Hilgendorff and M. Giersig, in "NATO Science Series II, Vol. 91, Low-Dimensional Systems: Theory, Preparation, and Some Applications" (M. Giersig and L. M. Liz-Marzán, Eds.), p. 151. Kluwer Academic Publishers, Dordrecht, 2003.
29. S. Gangopadhyay, G. C. Hadjipanayis, B. Dale, C. M. Sørensen, and K. J. Klabunde, *Nanostruct. Mater.* 1, 77 (1992).
30. F. Bødeker, S. Mørup, and S. Linderorth, *Phys. Rev. Lett.* 72, 282 (1994).
31. J. P. Chen, C. M. Sørensen, K. J. Klabunde, and G. C. Hadjipanayis, *Phys. Rev. B* 51, 11527 (1995).
32. T. Taniyama, E. Ohta, T. Sato, and M. Takeda, *Phys. Rev. B* 55, 977 (1997).
33. T. Shinohara, T. Sato, T. Taniyama, and I. Nakatani, *J. Magn. Magn. Mater.* 196–197, 94 (1999).
34. L. Katsikas, A. Eichmüller, M. Giersig, and H. Weller, *Chem. Phys. Lett.* 172, 201 (1990).
35. I. G. Dance, R. G. Garbutt, and T. D. Bailey, *Inorg. Chem.* 29, 603 (1990).
36. M. Respaud, J. M. Broto, H. Rakoto, A. R. Fert, L. Thomas, B. Barbara, M. Verelst, E. Snoeck, P. Lecante, A. Mosset, J. Osuna, T. Ould Ely, C. Amiens, and B. Chaudret, *Phys. Rev. B* 57, 2925 (1998).

37. D. P. Dinega and M. G. Bawendi, *Angew. Chem.* 111, 1906 (1999); *Angew. Chem. Int. Ed.* 38, 1788 (1999).
38. Y. Xue, Q. Zhao, and C. Luan, *J. Colloid Interface Sci.* 243, 388 (2001).
39. M. Zhao, X. H. Zhou, and Q. Jiang, *J. Mater. Res.* 16, 3304 (2001).
40. A. R. Yavari, P. J. Desré, and T. Benameur, *Phys. Rev. Lett.* 68, 2235 (1992).
41. M. K. Roy, P. M. G. Nambissan, and H. C. Verma, *J. Alloys Compd.* 345, 183 (2002).
42. Z. C. Li, X. Q. Cheng, and B. X. Liu, *J. Alloys Compd.* 327, L1 (2001).
43. J. B. Liu, Z. F. Li, J. X. Zhang, B. X. Liu, G. Kresse, and J. Hafner, *Phys. Rev. B* 64, 54102 (2001).
44. T. B. Massalski, "Binary Alloy Phase Diagrams." ASM International, Materials Park, OH, 1990.
45. N. Buske, H. Sonntag, and T. Götze, *Colloids and Surfaces* 12, 195 (1984).
46. D. Y. C. Chan, D. Henderson, J. Barojas, and A. M. Homola, *J. Res. Develop.* 29, 11 (1985).
47. A. P. Philipse, M. P. B. van Bruggen, and C. Pathmamanoharan, *Langmuir* 10, 92 (1994).
48. J. N. Israelachvili, "Intermolecular and Surface Forces." Academic Press, San Diego, 1992.
49. R. Tadmor, *J. Phys.: Condens. Matter* 13, L195 (2001).
50. M. J. Yacamán, S. Fuentes, and J. M. Dominguez, *Surf. Sci.* 106, 472 (1981).
51. N. Rösch and G. Pacchioni, in "Clusters and Colloids" (G. Schmidt, Ed.), p. 5. VCH, Weinheim, 1994.
52. D. A. van Leeuwen, J. M. van Ruitenbeek, L. J. de Jongh, A. Ceriotti, G. Pacchioni, O. D. Häberlen, and N. Rösch, *Phys. Rev. Lett.* 73, 1432 (1994).
53. J. Guevara, A. M. Llois, and M. Weissmann, *Phys. Rev. Lett.* 81, 5306 (1998).
54. S. Krüger, M. Stener, and N. Rösch, *J. Chem. Phys.* 114, 5207 (2001).
55. H. Bönemann, W. Brijoux, R. Brinkmann, E. Dinjus, T. Jousen, and B. Korall, *Angew. Chem.* 103, 1344 (1991); *Angew. Chem. Int. Ed.* 30, 1344 (1991).
56. N. Tushima and T. Yonezawa, *New. J. Chem.* 1179 (1998).
57. H. Bönemann and R. M. Richards, *Eur. J. Inorg. Chem.* 2455 (2001).
58. N. Tushima, Y. Shiraishi, T. Teranishi, M. Miyake, T. Tominaga, H. Watanabe, W. Brijoux, H. Bönemann, and G. Schmidt, *Appl. Organometal. Chem.* 15, 178 (2001).
59. X. M. Lin, C. M. Sørensen, K. J. Klabunde, and G. C. Hadjipanayis, *Langmuir* 14, 7140 (1998).
60. J. A. Barclay, *J. Appl. Phys.* 53, 2887 (1982).
61. V. K. Pecharsky and K. A. Gschneidner, Jr., *J. Magn. Magn. Mater.* 200, 44 (1999).
62. T. A. Yamamoto, M. Tanaka, Y. Misaka, T. Nakagawa, T. Nakayama, K. Niihara, and T. Numazawa, *Scr. Mater.* 46, 89 (2002).
63. M. P. Annaorazov, M. Ünal, S. A. Nikitin, A. L. Tyurin, and K. A. Asatryan, *J. Magn. Magn. Mater.* 251, 61 (2002).
64. M. Ronay, *IBM Technol. Discl. Bull.* 19, 2753 (1976).
65. C. Kormann, E. Schwab, F.-W. Raulfs, and K. H. Beck, U.S. Patent 5, 500, 141, 1996.
66. J. C. Lodder, D. J. Monsma, R. Vlutters, and T. Shimatsu, *J. Magn. Magn. Mater.* 198–199, 119 (1999).
67. A. Jordan, R. Scholz, P. Wust, H. Schirra, T. Schiestel, H. Schmidt, and R. Felix, *J. Magn. Magn. Mater.* 194, 185 (1999).
68. M. Y. Mapra, I. J. Körner, M. Hildebrandt, R. Bargou, D. Krahl, P. Reichardt, and B. Dörken, *Blood* 89, 337 (1997).
69. S. W. Charles and R. E. Rosensweig, *J. Magn. Magn. Mater.* 39, 192 (1983).
70. S. Kamiyama and R. E. Rosensweig, *J. Magn. Magn. Mater.* 65, 403 (1987).
71. E. Blum, R. Osols, and R. E. Rosensweig, *J. Magn. Magn. Mater.* 85, 305 (1990).
72. V. Cabuil, S. Neveu, and R. E. Rosensweig, *J. Magn. Magn. Mater.* 122, 439 (1993).
73. S. P. Bhatnagar and R. E. Rosensweig, *J. Magn. Magn. Mater.* 149, 199 (1995).
74. L. Vékás, V. Sofonea, and O. Balau, *J. Magn. Magn. Mater.* 201, 454 (1999).
75. R. D. Shull and L. H. Bennet, *Nanostruct. Mater.* 1, 83 (1992).
76. G. R Harp, S. S. P. Parkin, W. L. O'Brian, and B. P. Tonner, *Phys. Rev. B* 51, 12037 (1995).
77. G. Moraitis, H. Dreyssé, and M. A. Khan, *Phys. Rev. B* 54, 7140 (1996).
78. M. N. Baibich, J. M. Broto, A. Fert, F. N. van Dau, F. Petroff, P. Etienne, G. Creuzet, A. Friederich, and J. Chazelas, *Phys. Rev. Lett.* 61, 2472 (1988).
79. D. B. Lambrick, N. Mason, N. J. Harris, G. J. Russell, S. R. Hoon, and M. Kilner, *IEEE Trans. Magn.* MAG-21, 1891 (1985).
80. D. B. Lambrick, N. Mason, S. R. Hoon, and M. Kilner, *J. Magn. Magn. Mater.* 65, 257 (1987).
81. J. Rivas, R. D. Sánchez, A. Fondado, C. Izco, A. J. García-Bastida, J. García-Otero, J. Mira, D. Baldomir, A. González, I. Lado, M. A. López-Quintela, and S. B. Oseroff, *J. Appl. Phys.* 76, 6564 (1994).
82. M. T. Reetz, W. Helbig, and S. A. Quaiser, *Chem. Mater.* 7, 2227 (1995).
83. W. Yu, Y. Wang, H. Liu, and W. Zheng, *J. Mol. Catal. A* 112, 105 (1996).
84. N. Duxin, N. Brun, P. Bonville, C. Colliex, and M. P. Pileni, *J. Phys. Chem. B* 101, 8907 (1997).
85. A. J. García-Bastida, R. D. Sánchez, J. García-Otero, J. Rivas, A. González-Penedo, J. Solla, and M. A. López-Quintela, *Mater. Sci. Forum* 269–272, 919 (1998).
86. N. Duxin, N. Brun, C. Colliex, and M. P. Pileni, *Langmuir* 14, 1984 (1998).
87. N. Nunomura, T. Teranishi, M. Miyake, A. Oki, S. Yamada, N. Tushima, and H. Hori, *J. Magn. Magn. Mater.* 177–181, 947 (1998).
88. N. Nunomura, H. Hori, T. Teranishi, M. Miyake, and S. Yamada, *Phys. Lett. A* 249, 524 (1998).
89. R. D. Sánchez, M. A. López-Quintela, J. Rivas, A. González-Penedo, A. J. García-Bastida, C. A. Ramos, R. D. Zysler, and S. Ribeiro-Guevara, *J. Phys.: Condens. Matter* 11, 5643 (1999).
90. E. E. Carpenter, C. T. Seip, and C. J. O'Connor, *J. Appl. Phys.* 85, 5184 (1999).
91. P. M. Paulus, H. Bönemann, A. M. van der Kraan, F. Luis, J. Sinzig, and L. J. de Jongh, *Eur. Phys. J. D* 9, 501 (1999).
92. H. Bönemann, W. Brijoux, R. Brinkmann, and M. Wagener (to Studiengesellschaft Kohle m.b.H.) WO 99/41758 (1999).
93. T. Teranishi and M. Miyake, *Chem. Mater.* 11, 3414 (1999).
94. P. Lu, T. Teranishi, K. Asakura, M. Miyake, and N. Tushima, *J. Phys. Chem. B* 103, 9673 (1999).
95. S. Sun, C. D. Murray, D. Weller, L. Folks, and A. Moser, *Science* 287, 1989 (2000).
96. E. E. Carpenter, A. Kumbhar, J. A. Wiemann, H. Srikanth, J. Wiggins, W. Zhou, and C. J. O'Connor, *Mater. Sci. Eng. A* 286, 81 (2000).
97. J. Wiggins, E. E. Carpenter, and C. J. O'Connor, *J. Appl. Phys.* 87, 5651 (2000).
98. E. E. Carpenter, J. A. Sims, J. A. Wiemann, W. L. Zhou, and C. J. O'Connor, *J. Appl. Phys.* 87, 5615 (2000).
99. H. Bönemann, U. Endruschat, B. Tesche, A. Ruffinska, C. W. Lehmann, F. E. Wagner, G. Filoti, V. Părvulescu, and V. I. Părvulescu, *Eur. J. Inorg. Chem.* 819 (2000).
100. B. Warne, O. I. Kasyutich, E. L. Mayes, J. A. L. Wiggins, and K. K. W. Wong, *IEE Trans. Magn.* 36, 3009 (2000).

101. T. Ould Ely, C. Pan, C. Amiens, B. Chaudret, F. Dassenoy, M.-J. Casanove, A. Mosset, M. Respaud, and J.-M. Broto, *J. Phys. Chem. B* 104, 695 (2000).
102. C. B. Murray, S. Sun, H. Doyle, and T. Betley, *Mater. Res. Soc. Bull.* 26, 985 (2001).
103. S. Yamamuro, D. Farrell, K. D. Humfeld, and S. A. Majetich, *Mater. Res. Soc. Symp. Proc.* 636, D.10.8.1 (2001).
104. D. Farrell, S. Yamamuro, and S. A. Majetich, *Mater. Res. Soc. Symp. Proc.* 674, U.4.4.1 (2001).
105. K. D. Humfeld, A. K. Giri, E. L. Venturini, and S. A. Majetich, *IEEE Trans. Magn.* 37, 2194 (2001).
106. Y. Li, J. Liu, Y. Wang, and Z. L. Wang, *Chem. Mater.* 13, 1008 (2001).
107. J.-I. Park and J. Cheon, *J. Am. Chem. Soc.* 123, 5743 (2001).
108. H. Ago, S. Oshima, K. Uchida, and M. Yumura, *J. Phys. Chem. B* 105, 10453 (2001).
109. H. Srikanth, E. E. Carpenter, L. Spinu, J. Wiggins, W. L. Zhou, and C. J. O'Connor, *Mater. Sci. Eng. A* 304–306, 901 (2001).
110. C. J. O'Connor, V. Kolesnichenko, E. Carpenter, C. Sangregorio, W. Zhou, A. Kumbhar, J. Sims, and F. Agnoli, *Synth. Met.* 122, 547 (2001).
111. J. Lin, W. Zhou, A. Kumbhar, J. Wiemann, J. Fang, E. E. Carpenter, and C. J. O'Connor, *J. Solid State Chem.* 159, 26 (2001).
112. W. L. Zhou, E. E. Carpenter, J. Lin, A. Kumbhar, J. Sims, and C. J. O'Connor, *Eur. Phys. J. D* 16, 289 (2001).
113. C. J. O'Connor, J. A. Sims, A. Kumbhar, V. L. Kolesnichenko, W. L. Zhou, and J. A. Wiemann, *J. Magn. Magn. Mater.* 226–230, 1915 (2001).
114. H. Bönemann, in "Handbook of Surfaces and Interfaces of Materials" (H. S. Nalwa, Ed.), Vol. 3, p. 41. Academic Press, San Diego, 2001.
115. M. C. Fromen, A. Serres, D. Zitoun, M. Respaud, C. Amiens, B. Chaudret, P. Lecante, and M. J. Casanove, *J. Magn. Magn. Mater.* 242–245, 610 (2001).
116. H. Ago, S. Oshima, K. Uchida, and M. Yumura, *J. Phys. Chem. B* 105, 10453 (2001).
117. R. V. Chamberlin, K. D. Humfeld, D. Farrell, S. Yamamuro, Y. Ijiri, and S. A. Majetich, *J. Appl. Phys.* 91, 6961 (2002).
118. S. Yamamuro, D. Farrell, and S. A. Majetich, *Phys. Rev. B* 65, 224431 (2002).
119. E. V. Shevchenko, D. V. Talapin, A. Kornowski, F. Wiekhorst, J. Kötzler, M. Haase, A. L. Rogach, and H. Weller, *Adv. Mater.* 14, 287 (2002).
120. E. V. Shevchenko, D. V. Talapin, A. L. Rogach, A. Kornowski, and H. Weller, *J. Am. Chem. Soc.* 124, 11480 (2002).
121. M. Chen and D. E. Nikles, *Nano Lett.* 2, 211 (2002).
122. M. Chen and D. E. Nikles, *J. Appl. Phys.* 91, 8477 (2002).
123. K. Ono, Y. Kakefuda, R. Okuda, Y. Ishii, S. Kamimura, A. Kitamura, and M. Oshima, *J. Appl. Phys.* 91, 8480 (2002).
124. J. Fang, L. D. Tung, K. L. Stokes, J. He, D. Caruntu, W. L. Zhou, and C. J. O'Connor, *J. Appl. Phys.* 91, 8816 (2002).
125. B. Ravel, E. E. Carpenter, and V. G. Harris, *J. Appl. Phys.* 91, 8195 (2002).
126. D. Zitoun, M. Respaud, M. C. Fromen, M. J. Casanove, P. Lecante, C. Amiens, and B. Chaudret, *Phys. Rev. Lett.* 89, 037203 (2002).
127. N. S. Sobal, M. Hilgendorff, H. Möhwald, M. Giersig, M. Spasova, T. Radetic, and M. Farle, *Nano Lett.* 2, 621 (2002).
128. M. Spasova, T. Radetic, N. Sobal, M. Hilgendorff, U. Wiedwald, M. Farle, M. Giersig, and U. Dahmen, *Mater. Res. Soc. Symp. Proc.* 721, E 2.3.1 (2002).
129. U. Wiedwald, M. Ulmeanu, M. Farle, N. S. Sobal, M. Giersig, A. Fraile-Rodriguez, and D. Arvanitis, *MAX-Lab Activity Report 2001*, 372 (2002).
130. A. S. Bommannavar, P. A. Montano, and M. J. Yacamán, *Surf. Sci.* 156, 426 (1985).
131. K. Siepen, H. Bönemann, W. Brijoux, J. Rothe, and J. Hormes, *Appl. Organometal. Chem.* 14, 549 (2000).
132. T. W. Smith and D. Wychick, *J. Phys. Chem.* 84, 1621 (1980).
133. J. Rivas, M. A. López-Quintela, M. G. Bonome, R. J. Duro, and J. M. Grenèche, *J. Magn. Magn. Mater.* 122, 1 (1993).
134. K. S. Suslick, M. Fang, and T. Hyeon, *J. Am. Chem. Soc.* 118, 11960 (1996).
135. P. H. Hess and P. H. Parker, Jr., *J. Appl. Polym. Sci.* 10, 1915 (1966).
136. E. Papirer, P. Horny, H. Balard, R. Anthore, C. Petipas, and A. Martinet, *J. Colloid Interface Sci.* 94, 207 (1983).
137. G. N. Glavee, K. J. Klabunde, Ch. M. Sørensen, and G. C. Hadjipanayis, *Inorg. Chem.* 32, 474 (1993).
138. J. A. Becker, R. Schäfer, R. Festag, W. Ruland, J. H. Wendorff, J. Pebler, S. A. Quaiser, W. Helbig, and M. T. Reetz, *J. Chem. Phys.* 103, 2520 (1995).
139. J. Osuna, D. de Caro, C. Amiens, B. Chaudret, E. Snoeck, M. Respaud, J.-M. Broto, and A. Fert, *Synthesis, J. Phys. Chem.* 35, 14571 (1996).
140. Ch. Pathmanoharan and A. P. Philipse, *J. Colloid. Inter. Sci.* 205, 340 (1998).
141. S. Sun and C. B. Murray, *J. Appl. Phys.* 85, 4325 (1999).
142. C. Petit, A. Taleb, and M. P. Pileni, *J. Phys. Chem. B* 103, 1805 (1999).
143. J. P. Stevenson, M. Rutnakornpituk, M. Vadala, A. R. Esker, S. W. Charles, S. Wells, J. P. Dailey, and J. S. Riffle, *J. Magn. Magn. Mater.* 225, 47 (2001).
144. D. L. Leslie-Pelecky, S.-H. Kim, M. Bonder, X. Q. Zhang, and R. D. Rieke, *Chem. Mater.* 10, 164 (1998).
145. A. S. R. Hoon, M. Kilner, G. J. Russell, and B. K. Tanner, *J. Magn. Magn. Mater.* 39, 107 (1983).
146. N. Cordente, M. Respaud, F. Senocq, M.-J. Casanove, C. Amiens, and B. Chaudret, *Nano Lett.* 1, 565 (2001).
147. M. T. Reetz, M. Winter, R. Breinbauer, T. Thurn-Albrecht, and W. Vogel, *Chem. Eur. J.* 7, 1084 (2001).
148. D. V. Talapin, A. L. Rogach, M. Haase, and H. Weller, *J. Phys. Chem. B* 105, 12278 (2001).
149. K. R. Brown and M. J. Natan, *Langmuir* 14, 726 (1998).
150. N. R. Jana, L. Gearheart, and C. J. Murphy, *Chem. Mater.* 13, 2313 (2001).
151. H. Yu, P. C. Gibbons, K. F. Kelton, and W. E. Buhro, *J. Am. Chem. Soc.* 123, 9198 (2001).
152. W. Neumann and J. Komrska, *Phys. Stat. Sol. A* 150, 113 (1995).
153. Z. L. Wang, *Adv. Mater.* 10, 13 (1998).
154. L. Reimer, "Transmission Electron Microscopy." Springer, Berlin, 1997.
155. N. Toshima, M. Harada, Y. Yamazaki, and K. Asakura, *J. Phys. Chem.* 96, 9927 (1992).
156. R. D. Rieke, *Top. Curr. Chem.* 59, 1 (1975).
157. K. S. Suslick, *Science* 247, 1493 (1990).
158. E. M. Kirkpatrick, D. L. Leslie-Pelecky, S.-H. Kim, and R. D. Rieke, *J. Appl. Phys.* 85, 5375 (1999).
159. R. Bellissent, G. Galli, T. Hyeon, S. Magazu, D. Majolino, P. Migliardo, and K. S. Suslick, *Phys. Script. T* 57, 79 (1995).
160. K. E. Gonsalves and S. P. Rangarajan, *J. Appl. Polym. Sci.* 64, 2667 (1997).
161. A. G. Teijeiro, D. Baldomir, J. Rivas, S. Paz, P. Vaqueiro, and M. A. López-Quintela, *J. Magn. Magn. Mater.* 140–144, 2129 (1995).
162. P. Vaqueiro, M. A. López-Quintela, J. Rivas, and J. M. Grenèche, *J. Magn. Magn. Mater.* 169, 56 (1997).
163. S. Castro, M. Gayoso, C. Rodríguez, J. Mira, J. Rivas, S. Paz, and J. M. Grenèche, *J. Magn. Magn. Mater.* 140–144, 2097 (1995).
164. S. Castro, M. Gayoso, J. Rivas, J. M. Grenèche, J. Mira, and C. Rodríguez, *J. Magn. Magn. Mater.* 152, 61 (1996).

165. C. Binns, in "Handbook of Surfaces and Interfaces of Materials" (H. S. Nalwa, Ed.), Vol. 2, p. 357. Academic Press, San Diego, 2001.
166. C. Djurberg, P. Svedlindh, P. Nordblad, M. F. Hansen, F. Bødeker, and S. Mørup, *Phys. Rev. Lett.* 79, 5154 (1997).
167. S. Taketomi and R. D. Shull, *J. Appl. Phys.* 91, 8546 (2002).
168. P. C. Scholten, *J. Magn. Magn. Mater.* 57, 149 (1995).
169. H. W. F. Sung and C. Rudowicz, *J. Magn. Magn. Mater.* 260, 250 (2003).
170. http://www.magwerks.com/information/magnetic_units.htm. Inserting the term "units for magnetic properties" in common search engines results in a suitable number of addresses.
171. M. Farle, *Rep. Prog. Phys.* 61, 755 (1998).
172. R. Chantrell, J. Popplewell, and S. W. Charles, *IEEE Trans. Magn. MAG-14*, 975 (1978).
173. D. V. Berkov, A. Daum, P. Görnert, N. Buske, C. Gansau, J. Mueller, M. Giersig, W. Neumann, and D. Su, *IEE Trans. Magn.* 35, 4064 (1999).
174. D. V. Berkov, P. Görnert, N. Buske, C. Gansau, J. Mueller, M. Giersig, W. Neumann, and D. Su, *J. Phys. D: Appl. Phys.* 33, 331 (2000).
175. A. Wiedenmann, *J. Appl. Cryst.* 33, 428 (2000).
176. A. Wiedenmann, A. Hoell, and M. Kammel, *J. Magn. Magn. Mater.* 252, 83 (2002).
177. N. N. Greenwood and A. Earnshaw, Pergamon Press, Oxford, 1985, p. 360.
178. A. R. Mannig, *J. Chem. Soc. A* 2321 (1971).
179. T. S. Piper, F. A. Cotton, and G. Wilkinson, *J. Inorg. Nuclear Chem.* 1, 165 (1955).
180. A. T. T. Hsieh and J. Knight, *J. Organometal. Chem.* 26, 125 (1971).
181. S. Otsuka and M. Rossi, *J. Chem. Soc. A* 2630 (1968).
182. K. Moseley and P. M. Maitlis, *Chem. Comm.* 982 (1971).
183. F. Funk, J. P. Lenders, R. R. Crighton, and W. Schneider, *Eur. J. Biochem.* 152, 167 (1985).
184. E. Mayes, WO 01/39217 A1 (2001).
185. G. N. Glavee, K. J. Klabunde, Ch. M. Sørensen, and G. C. Hadjipanayis, *Langmuir* 9, 162 (1993).
186. J. Fink, C. J. Kiely, D. Bethell, and D. J. Schiffrin, *Chem. Mater.* 10, 922 (1998).
187. S. Bucher, J. Hormes, H. Modrow, R. Brinkmann, N. Waldöfner, H. Bönemann, L. Beuermann, S. Krischock, W. Maus-Friedrich, and V. Kemper, *Surf. Sci.* 497, 321 (2002).
188. F. Fiévet, J. P. Lagier, and M. Figlarz, *Mater. Res. Soc. Bull.* 14, 29 (1989).
189. G. Viau, F. Ravel, O. Archer, F. Fiévet-Vincent, and F. Fiévet, *J. Appl. Phys.* 76, 6570 (1994).
190. A. J. Cox, J. G. Louderback, S. E. Apsel, and L. A. Bloomfield, *Phys. Rev. B* 49, 12295 (1994).
191. W. Lin, C. W. Benjamin, R. G. Nuzzo, and G. S. Girolami, *J. Am. Chem. Soc.* 115, 11644 (1993).
192. A. Chemseddine and H. Weller, *Ber. Bunsenges. Phys. Chem.* 97, 636 (1993).
193. P. Mulvaney, M. Giersig, and A. Henglein, *J. Phys. Chem.* 97, 7061 (1993).
194. S. Okeya and S. Kawaguchi, *Inorg. Synth.* 20, 65 (1980).
195. W. P. Weber and G. W. Gokel, *Tetrahedron Lett.* 13, 1637 (1972).

Biocompatible Core–Shell Nanoparticles for Biomedicine

Xiaoxiao He, Xia Lin, Kemin Wang,
Liang Chen, Ping Wu, Yin Yuan

Hunan University, Changsha 410082, People's Republic of China

Weihong Tan

University of Florida, Gainesville, Florida, USA

CONTENTS

1. Introduction
 2. Configuration of the Biocompatible Core–Shell Nanoparticles
 3. Synthesis of Biocompatible Core–Shell Nanoparticles
 4. Characteristics of the Biocompatible Core–Shell Nanoparticles
 5. Applications of the Biocompatible Core–Shell Nanoparticles in Biomedicine
 6. Conclusions
- Glossary
References

1. INTRODUCTION

The investigation range of life science has reached the level of single cells, subcells, and even single molecular (such as nerve glia) and single base pairs of nucleotide acid, as shown in Figure 1. Traditional analysis methods and techniques such as optical fiber sensors or electroanalytical sensors, even submicrometer optical fiber sensors or micro-machined electroanalytical sensors for obtaining biological and chemical information [1–3], are confronted with great challenges. How to analyze and detect trace analytes of life science in the microlevel, *in-situ*, *in vivo*, and in real time to understand the relationship between biological molecule structure and its function is the focus of the challenges. With the fast development of nanotechnology in 1990s, new thoughts and opportunities have appeared for deep research of biomedicine and resolution of the aforementioned key problem. As the revolutionary effect of the microelectronic

integrating technology on the electronics industry, the development of nanotechnology has had considerable impact on biotechnology and biomedicine systems [4, 5]. Because particle size approaches the molecular dimension, all properties of the materials will change to some extent; however, some of them are wonderful for use in particular biological applications [6]. The fact that the nanoparticles are similar to many common biomolecules with respect to size magnitude permits them to have widespread use in biotechnological systems. The broad fields of biotechnology and medicine, such as diagnosis of disease, drug delivery, gene repair, dispensing, gene therapy, and so on, are all correlative with the nanotechnology [7–11].

Especially with the implementation and accomplishment of the human genome project, it becomes much more crucial to resolve the abundant data to find the pivotal genes that control or dominate the versatile functions of life through nanotechnology techniques than before. Nanoparticles, with high surface-to-volume ratio and ultrasmall in size, are potential alternative materials to obtain biological information inside or outside of living specimens, and provide an excellent analysis system for biotechnology and biomedicine. Given the particularity of living life, biocompatible core–shell nanoparticles have been developed and attracted much attention from all over the world. And a new growth point of modern analytical chemistry has been formed under the combination of nanotechnology, analytical chemistry, materials science, and biotechnology. Especially carrying out research and application of bionanotechnology and developing modern analytical methods and techniques for obtaining related biochemical information *in-situ*, *in vivo*, in real time, and in nanolevel is one of the new research directions of current chemistry and biology.

In this chapter, we will first introduce the general configuration and the synthesis of biocompatible core–shell nanoparticles. The unique properties of biocompatible core–shell nanoparticles for bioanalytical chemistry,

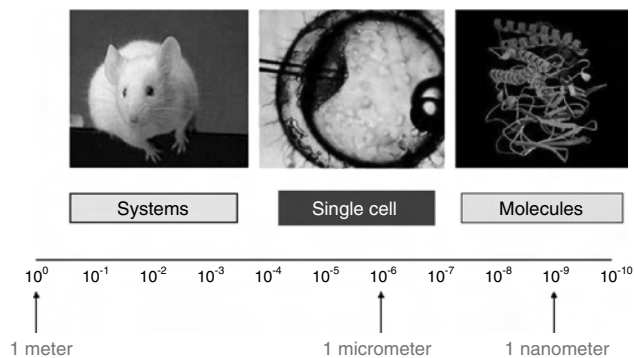


Figure 1. The size of our research objects is from big to small in the life science.

bioseparation, and bioimaging have been summarized. At the same time, several successful examples of biocompatible nanoparticles that have been integrated with biomolecular species and applied to relevant problems in biotechnology have been introduced. The use of biocompatible nanoparticles as biological labels will be discussed. The novel bioseparation method based on biocompatible nanoparticles, the novel delivery for genes and drugs based on biocompatible nanoparticles, will also be described. The objective of this chapter is to introduce the magical and extremely valuable biocompatible core–shell nanoparticles to biologists and analytical chemists and to encourage them to consider biocompatible core–shell nanoparticles in their own research and projects.

2. CONFIGURATION OF THE BIOCOMPATIBLE CORE–SHELL NANOPARTICLES

Universally particles with at least one dimension (d) \leq 100 nm can be considered nanoparticles; the biocompatible core–shell nanoparticles are of course a kind of nanomaterial with diameter of $1 \text{ nm} < d < 100 \text{ nm}$. In contrast to normal nanoparticles, the outstanding advantage of the biocompatible core–shell nanoparticles lies in the typical core–shell structure and favorable biocompatibility. Generally speaking, biocompatible core–shell nanoparticles are composed of a functionalized core, a modifiable shell, and the biomolecules modified on the surface of the nanoparticles [12], as shown in Figure 2. The three parts all make prominent contributions to their application of biomedicine.

2.1. Biocompatible Core–Shell Nanoparticles with Different Cores

The different functionalized biocompatible core–shell nanoparticles can be prepared by using different core materials. There are many kinds of materials that can be used as core materials, such as luminescent, electronic, magnetic, and thermal materials and so on. Prepared core–shell nanoparticles with different core material possess various properties and functions and so play an important role in a wide range of biotechnology and nanotechnology, especially

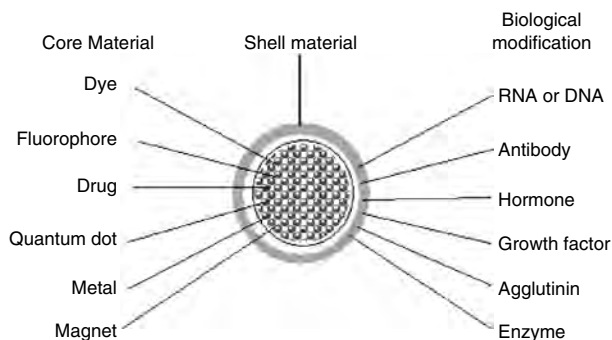


Figure 2. The schematic diagram of the biocompatible core–shell nanoparticles.

in biomedicine. For example, core–shell fluorescent nanoparticles encapsulating fluorescent dyes, like the inorganic dye [tris(2,2'-bipyridyl) dichlororuthenium(II) hexahydrate (RUBY)] [13–15] have been widely studied in fluorescent labeling of biomolecules and tissue because their intensified fluorescent signals are agreeable and their fluorescence characteristics are protected due to the high degree of insulation from the environment. Core–shell semiconductor nanoparticles, also called quantum dots (QDs) with CdSe as core material [16, 17], are used for the preparation of sensors with multidimensional response signals, because QD labels exhibit size-tunable, narrow-band luminescent emission and high resistance to photodegradation. Core–shell magnetic nanoparticles with Fe_3O_4 as core [18], according to their peculiar superparamagnetism (i.e., magnetized in the presence of a magnetic field while nonpermanent in the absence of a magnetic field), can easily be operated in magnetic or electromagnetic fields, so they are commonly utilized in the separation and enrichment of biological analytes. Core–shell drug nanoparticles [19] can perform the targeted delivery of drugs and avoid the side effects of drugs as much as possible, because drugs are encapsulated in the core of nanoparticles, which can be concentrated around the suffering tissues under the exterior guide and greatly increase therapy efficiency. Core–shell gene nanoparticles [20] make the higher efficient transfection realized compared with other materials or tools for the same usage and present great promise in gene therapy and related application.

There is another interesting structure [21] which widens our views on nanoparticles. In this model, the core is a single living yeast cell. It has been encapsulated by the alternate adsorption of oppositely charged polyelectrolytes. Its fluorescent images showed the integrity of the core and shell structure after the coating procedure (Fig. 3). The most significant result is that after encapsulation, cells preserve their metabolic activities and are still able to divide (Fig. 4), which provides evidence of its interesting foreground for biophysical studies.

Sometimes, single and simple core material is not sufficient to form completely perfect nanoparticles with core–shell structure, for they may leach through netlike shells with pores. Hence, many researchers attempted to encapsulate the conjugates of desired material with other macromolecules, thus protecting useful core material from

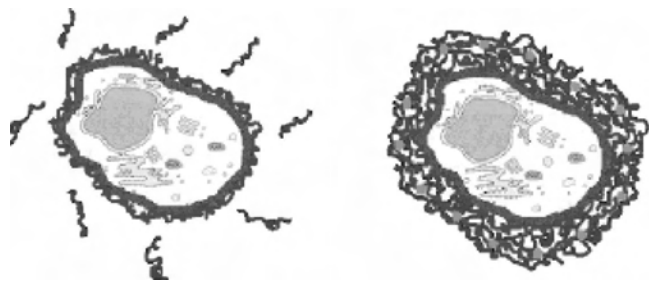


Figure 3. Confocal images of fresh by coated shells. Vignette of the encapsulation process, consecutive adsorption of the polycation PAH (red) and the polyanion PSS (blue) onto a single living cell. To provide evidence of a successful coating, one or two layers are FITC-labeled PAH (green). Reprinted with permission from [21], A. Diaspro et al., *Langmuir* 18, 5047 (2002). © 2002, American Chemical Society.

bleaching. In normal conditions, free fluoresceine isothiocyanate (FITC) and rhodamine are difficult to entrap into silica shells. These situations can be dramatically improved by forming fluorescent dye complexes. Our studies have found that the FITC–IgG complexes could be encapsulated into silica nanoparticles with a much higher entrapment efficiency, greatly increased compared to that of free FITC [22]. The entrapment efficiency of FITC–dextran conjugate has also been studied, but it did not offer as good results as that of FITC–IgG, maybe because of the different structures of dextran and IgG, and their different effects on FITC. To control permeability, polydextran aldehyde, incorporated into the particle core, was used to enable physiologic cross-linking and long-term retention of substances that would otherwise rapidly leak out of the nanoparticles [23]. Results of cross-linking experiments clearly demonstrated that the release rate could be substantially reduced, depending on the degree of cross-linking.

In addition, complex core materials can be utilized for more functions and better performance. Lai et al. reported [24] the preparation of novel two-photon dye encapsulated silica nanobubbles with enhanced luminescent

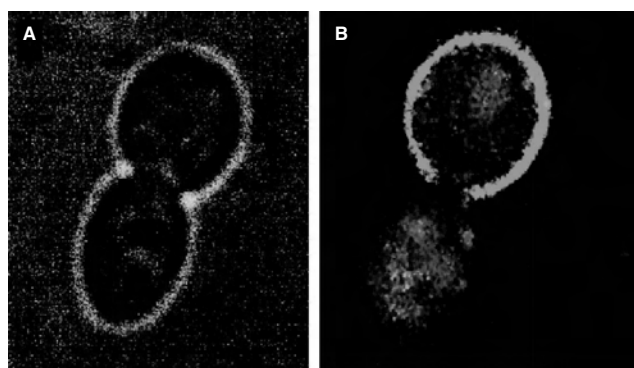


Figure 4. Transmission image (A) of a duplicating cell. This is confirmed by the fluorescence image (B) where the lack of green fluorescence in the mother cell coating reveals where the bud has formed. The DAPI-labeling of the DNA distribution allows the imaging of both mother and uncoated daughter cell. Reprint with permission from [21], A. Diaspro et al., *Langmuir* 18, 5047 (2002). © 2002, American Chemical Society.

properties and pleasing bioimaging applications. It is a zinc sulfide-ASPI-SH dye (homemade)–silica layered heterostructure. As they showed, two-photon processes have drawn considerable interest for thorough application in two-photon laser scanning microscopy. Mitra et al. [19] have conjugated the anticancer drug Doxorubicin (OXR) with dextran (the latter was found to minimize the undesirable side effects of the drug while making the drug retain its antitumor activity in the conjugate) and then encapsulated this drug conjugate in hydrogel nanoparticles for tumor targeted delivery.

2.2. Biocompatible Core–Shell Nanoparticles with Different Shells

A number of shell materials exist nowadays. Generally, nanoparticles are classified according to the shell materials into inorganic nanoparticles, organic nanoparticles (polymer nanoparticles), metal nanoparticles, and semiconductor nanoparticles. Silica shell as inorganic material is extensively studied for the reason of its superiorities. Compared with liposomes, it is not subject to microbial attack and will be resistant to bile salts and lipases encountered in the gastrointestinal tract and physical stress during aerosolization, and it should also withstand autoclaving in principle. In contrast to polymers, there is little concern about its toxicity [25]. Moreover, silica is chemically inert and therefore does not affect the redox reaction at the core surface. This shell is optically transparent too. Organic nanoparticles of cholesterol, rhovanil, and rhodiarome have been synthesized [26]. And the common organic shell material is chitosan, a polysaccharide known to be a favorable pharmaceutical material and a kind of ideal hydrophilic material because of its biocompatible and biodegradable properties. Coating chitosan on a magnetite nanoparticle surface will render the nanoparticles water soluble, more stable, and biocompatible and will provide the nanoparticles with functional amino and hydroxyl groups on their surfaces. There is also broad interest in semiconducting matrixes. Han et al. prepared ZnS-capped CdSe quantum dots [27] whose emission colors varies from blue to red with the change of nanoparticle size, excited by the same excitation wavelength (as shown in Fig. 5).



Figure 5. Ten distinguishable emission colors of ZnS-capped CdSe QDs excited with a near-ultraviolet lamp. From left to right (blue to red), the emission maxima are located at 443, 473, 481, 500, 518, 543, 565, 587, 610, and 655 nm. Reprinted with permission from [27], M. Y. Han et al., *Nat. Biotechnol.* 19, 631 (2001). © 2001, Macmillan Magazines Ltd.

2.3. Biocompatible Core–Shell Nanoparticles Modified with Different Biomolecules

Core–shell nanoparticles may still lack adequate biocompatibility to be applied in biomedicine or cannot perform the required bioanalysis exclusively. Through the design of the biomolecule linked to the nanoparticles (biological modification on the surface of nanoparticles), the biocompatibility of the nanoparticles will be strikingly heightened and their application will be widely expanded. In particular, the biomolecules modified always play an indispensable part in biological applications.

Well-studied single strand DNA or RNA-complementary DNA or RNA, biotin–streptavidin, antibody–antigen, and other ligand–receptor reactions are commonly used to realize biological chemical detection and related studies. Therefore, DNA or RNA and proteins including antibody or antigen and enzymes are usually conjugated with nanoparticles. Other biomolecules like hormone, growth factor, and agglutinin are suitable in specific experiments. The most beneficial aspect of the modification of biomolecules lies in the specific recognition and targeting effect. The biocompatible core–shell nanoparticles with Fe_3O_4 as core and different materials as shell and modified with different biomolecules prepared in our lab are shown in Table 1.

3. SYNTHESIS OF BIOCOMPATIBLE CORE–SHELL NANOPARTICLES

The synthesis and preparation of biocompatible core–shell nanoparticles is crucial for applications in biomedicine. Because of the complexity of the biological system, the dimension of the nanoparticles might as well be controlled in the range of $1 \text{ nm} \leq (d) \leq 100 \text{ nm}$ and with narrow distribution. At the same time, the functionalized biomolecules should be easily immobilized on the surface of nanoparticles with high bioactivity. Thus, it is required to carefully choose effective methods to synthesize biocompatible core–shell nanoparticles. There are three key techniques for the preparation of the biocompatible core–shell nanoparticles [28].

3.1. Nucleation of the Core–Shell Nanoparticles

Selection of appropriate method to prepare the core of the nanoparticles is of first importance. The size and the distribution of the nanoparticles will be mainly affected by using

Table 1. Core–shell magnetic nanoparticles with different shell materials and surface modification.

Batch	Shell material	Surface modification	Applications
1	SiO_2	DNA	separation of DNA
2	gelose	antibody	enrichment of liver cells
3	dextran	sorbent	purification of enzymes
4	chitosan	enzyme	immobilization of enzymes
5	polylactic acid	antineoplastic drugs	targeting therapy of cancer cells
6	polystyrene	concanavalin A	environmental protection

different methods of nanoparticle preparation. The preparation techniques of nanoparticles are usually classified into gas phase, liquid phase, sol–gel, etc., methods. Among these methods, the microemulsion method that belongs to the liquid phase method has played a vital part in the preparation of nanoparticles [29–31]. A microemulsion is an isotropic and thermodynamically stable single-phase solution formed with least three components: two of them immiscible, such as oil and water, and a surfactant with amphiphilic behavior. As for the water-in-oil microemulsion, the water core of the microemulsion is akin with a nanocontainer for core materials and a nanoreactor for the formation of shell (Fig. 6). The dimension of the nanoreactor can straightly control the size and the distribution of the nanoparticles through selection of an appropriate microemulsion system. The nanoparticles are uniform in size and well dispersed when prepared by this method. Many nanoparticles with different cores such as fluorescent dye, magnetic material, drug, and gene have been successfully prepared by this method and are widely used in biomedicine.

3.2. Shell Coating of the Nanoparticles

The shell coating technique is also important to realize the conformation of the core–shell nanoparticles. A coating shell is built up around the core materials to increase their chemical stability, intensify their functions, improve their biocompatibility compared with bare core materials, confer specific properties, such as optical, magnetic, or mechanical properties on the core material, and so on. Organic material and inorganic material can both used as shell material. One typical example of such nanoparticles is a silica coated biocompatible nanoparticle. The synthesis of silica nanoparticles with controlled diameters and size distribution has been extensively studied by Osseo-Asare and Arriagada [32, 33]. The technique involves the base-catalyzed controlled hydrolysis of tetraethoxysilane (TEOS), with short-chain nonionic surfactants as stabilizer and ammonia as catalyst. Following a synthetic procedure similar to that of Osseo-Asare and Arriagada, a silica coating can be also performed in the nanoreactor of a water-in-oil microemulsion, as shown in Figure 7. We have prepared a series of silica coated functionalized nanoparticles

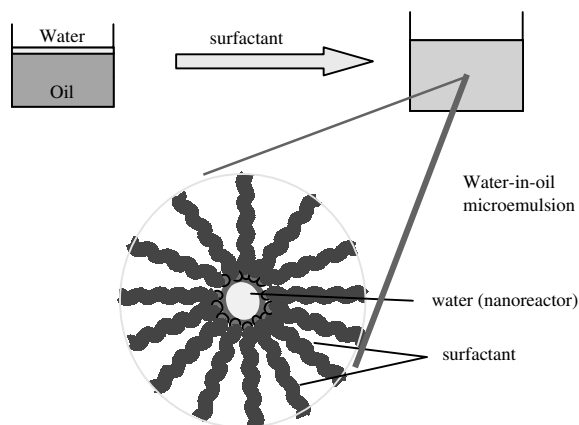


Figure 6. Schematic diagram of nucleation of the nanoparticles.

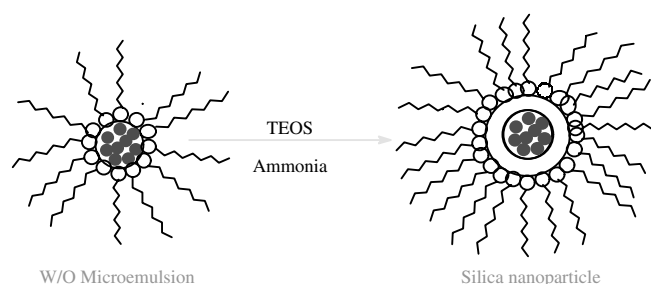


Figure 7. Shell coating of nanoparticles.

through the hydrolysis of TEOS in the nanoreactor of the microemulsion. But we found that not all water-soluble material can be doped in the silica shell. A great breakthrough in the synthesis theory and techniques of core–shell nanoparticles has been obtained. The results have testified that the charges of the shell materials and core materials will dominate whether the stable core–shell structure forms or not, by employing the silica shell formed through the hydrolysis of TEOS and the core formed by microemulsion. Figure 8 shows transmission electron microscope (TEM) images of silica coated nanoparticles that we have prepared.

On the other hand, a variety of trialkoxysilane molecules with vinyl, thiol, amino, or methacryloxy functionalities were introduced into the nanoreactor of the microemulsion along with TEOS to produce functionalized silica shell coated nanoparticles, which will be engaged for further application in biomedicine [34]. Based on this theory, a synchronous technique for preparation of amino-modified silica nanoparticles has been developed in our study.

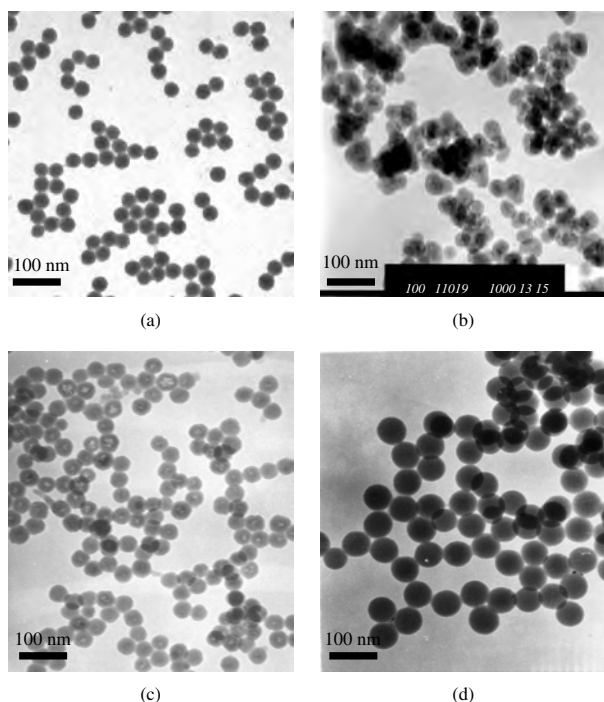


Figure 8. TEM images of silica coated nanoparticles. (a) RuBPY doped silica nanoparticles, (b) silica coated magnetic nanoparticles, (c) TRITC doped silica nanoparticles, (d) RuBPY doped silica nanoparticles.

Amino-modified silica nanoparticles are directly synthesized using the synchronous hydrolysis of tetraethoxysilane and *N*-(β -aminoethyl)- γ -aminopropyltriethoxysilane in water-in-oil microemulsion [35].

3.3. Biological Modification of the Nanoparticles

The surface properties of core–shell nanoparticles play outstandingly significant roles from both a theoretical and a practical point of view. For instance, modified quantum dots are capable of purifying and binding to the targeted chemical or biological agents. At the same time they provide visible evidence of the binding event, such as a change in color or light diffraction capabilities of the sample, and represent a promising alternative to organic dyes for a variety of fluorescence-based applications in biosensing. However, bare quantum dots are difficult to apply in biological assay due to their poor biocompatibility. Biological modification of the nanoparticles is generally rated as an absolutely necessary step to reduce cytotoxicity and immunogenicity both *in vitro* and *in vivo*. Functionalization of the surface makes it possible to obtain the fine biocompatibility of nanoparticles. By selecting the desirable functional modification, the application of nanoparticles is expanded and extended extensively in many biological fields such as gene transfection and therapy immunoassay, enzyme immobilization, cell recognition, biological separation, and biosensing.

Modifying biomolecules onto the ultrasmall surface of nanoparticles while least affecting their activities is a prime goal for the nanoparticles used in biomedicine. At the present time, modification of the surface can be done via three methods. One is performed *in-situ* during the nanoparticle synthesis. As described, amino-modified silica nanoparticles are prepared by the synchronous hydrolysis of TEOS and AEAPS. The simple synthesis process provides the formation of silica nanoparticles and the modification of the amino group as well. The other two first synthesize the nanoparticles and then treat them with adequate biomolecules. One is physical absorption such as electrostatic binding. In this case the modified biomolecules are susceptible to removal from the surface under certain conditions such as high salt and high temperature and so are restrained in a relatively narrow application areas. The other is widely used chemical modification. Chemical modification is mainly done by a variety of covalent coupling the activated functional group on the nanoparticle surface, such as hydroxyl, carboxyl, amino groups, and so on, with that of biomolecules, the same as the modification of microspheres [36], as shown in Figure 9. Biotin–streptavidin, antibody–antigen, and other ligand–receptor reactions are commonly selected to realize the biological chemical modification. This modification is not necessarily finished in one step. Multistep modification has been reported. Following are some modification methods of silica nanoparticles. The first is achieved by using a cyanogen bromide (CNBr) method [18]. Dried silica coating nanoparticles were suspended with sodium carbonate solution of appropriate concentration by ultrasonication for 15 min. Solution of CNBr in acetonitrile (2 mg/ml) was then added dropwise to the nanoparticle suspension under stirring for 10 min at

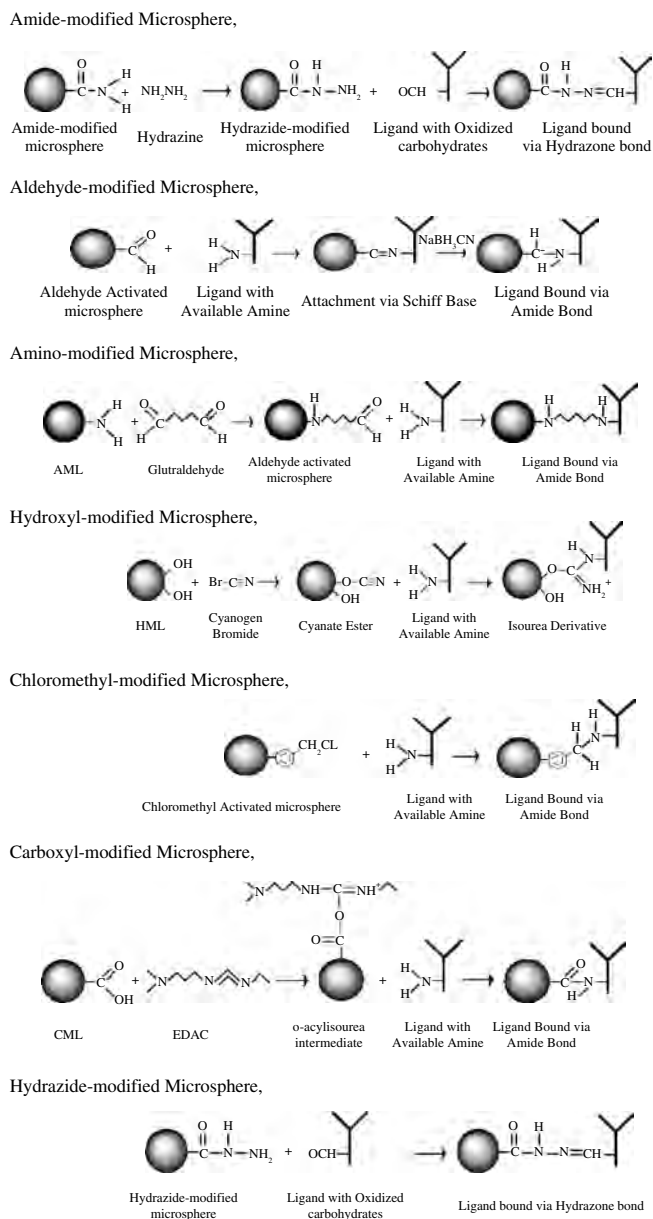


Figure 9. Biological modification of activated microspheres. Reprinted with permission from [36], Bangs Laboratories, Inc., Covalent Coupling, Tech Note 205, 1999. © 1999, Bangs Laboratories, Inc.

room temperature. The active particles then were washed twice with iced water and twice with PBS buffer (pH 7.6) and resuspended in PBS buffer. In this way, modified nanoparticles were prepared for the experiments. In the second method [15], silanization was performed by immersion in freshly prepared 1% (v/v) solution of distilled DETA and 1 mM acetic acid for 30 min at room temperature. The DETA modified silica nanoparticles were thoroughly rinsed with deionized water to remove excess DETA and then were treated with 10% succinic anhydride in dimethylformamide solution under an argon atmosphere and stirred for 6 h. The resulting carboxylate modified nanoparticles were washed with water and centrifuged several times; then the whole modification procedure for pure silica nanoparticles was finished.

4. CHARACTERISTICS OF THE BIOCOMPATIBLE CORE–SHELL NANOPARTICLES

Because of the unique core–shell structure, biocompatible core–shell nanoparticles are more superior in biocompatibility, photochemical stability, and ultrasensitivity in detection in comparison with other materials.

4.1. Least Toxicity

Many nanoparticle materials with optic, electric, thermal, and magnetic properties have been widely used in optics, catalysis, microelectronics, and so on. However, their application in biomedicine is restrained because of their lack of biocompatibility. When they are applied in biological fields, they may disturb the normal metabolism and functions of biological system or cells, due to some side effects occurring by the physical and chemical properties of themselves. Finally, they present toxicity to some extent. The problem is remarkably solved using these functional materials as core. When these materials are encapsulated as functional core materials, the biocompatible shell forms an excellent barrier. The side effects will be reduced because the core materials are separated from the cellular environment and do not have contact with the system or cell directly. Anticancer drugs for cancer therapy are good examples, because when the anticancer drugs are taken by the system, the drugs will also play their role in the normal tissues, and anticancer drugs presently are widely limited for use in clinic therapy. However, there are many reports focusing on drug delivery and disease therapy by use of core–shell nanoparticles. By encapsulation of drugs in biocompatible nanoparticles, one can not only protect the integrity of drugs during their transport in blood circulation but also protect the normal nontarget tissues from the toxicity of drugs. In our study, we have studied the biocompatibility of the silica coated fluorescent nanoparticles *in vivo* and *in vitro*. The fluorescent nanoparticle was injected into the tail vein of a mouse and incubated with different times. The result indicated that the fluorescent silica nanoparticles could be eliminated quickly, as shown in Figure 10. We also have studied the biocompatibility of the silica coated fluorescent nanoparticles with cells. The HNE1 cells were seeding in the cell-dish with medium. For biocompatibility, the cells were incubated with nanoparticles and cultured for a time. Then the cells were subcultured four times. The results showed that the cells could endocytosize the nanoparticles effectively and were biocompatible with the nanoparticles. The cell-endocytosized silica nanoparticles not only grow well but also have normal shapes. There is no obvious difference with the cells in the control experiment [35], as shown in Figure 11.

4.2. Photochemical Stability

Because of the protection of the shell, another special advantage of the core–shell structure is its photochemical stability. The shell acts as a stabilizer, limiting the effect of the outside environment on the core material, such as photo-bleaching, oxidation, biodegradation, and so on. This is particularly

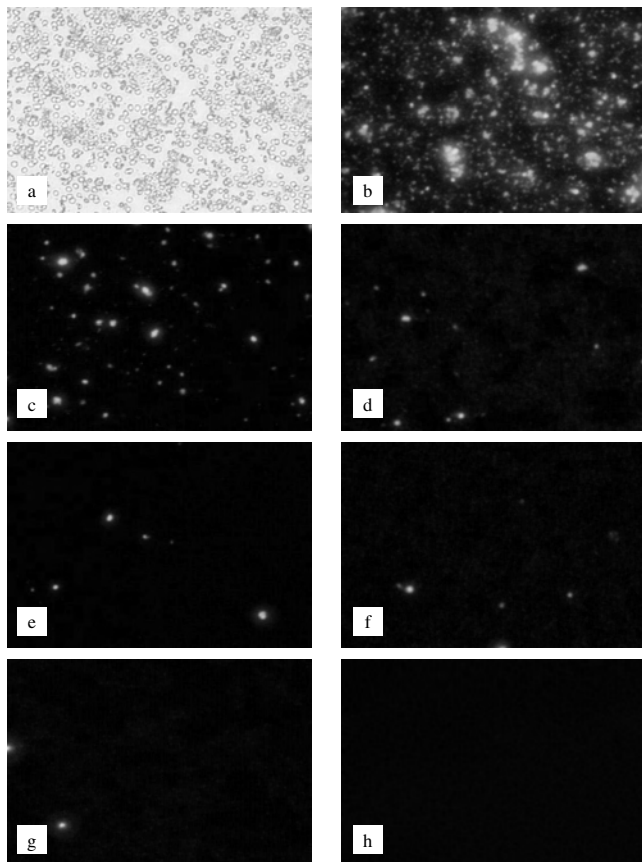


Figure 10. Images of the blood. (a) Optical image of blood cells taken at 15 min. (b)–(h) Fluorescence images of blood cells taken at 15, 30, 45, 60, 75, 90, and 105 min.

important for dyes, genes, and drug nanoparticles. For example, there are many quenching substances such as oxygen that may affect the fluorescence of the fluorophore [37]. And genes can be digested or degraded by enzymes before they reach the desired organs or tissues. For drugs, they are affected as far blood clearance and immunogenicity are concerned. The shell provides a protective obstacle to penetration of external substances, thereby not only making the dyes more photostable [37, 38] (Figs. 12 and 13) but also making

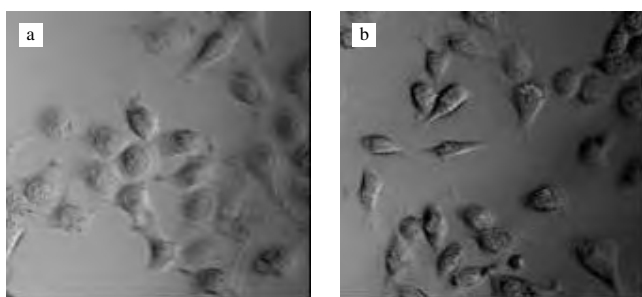


Figure 11. Biocompatibility of the inorganic silica nanoparticles with HNE1 cells. (a) HNE1 cells without endocytosis of core-shell biofluorescent nanoparticles. (b) HNE1 cells that endocytosed core-shell biofluorescent nanoparticles. Reprinted with permission from [35], X. X. He et al., *Chinese Sci. Bull.* 48, 223 (2003). © 2003, Chinese Science Bulletin.

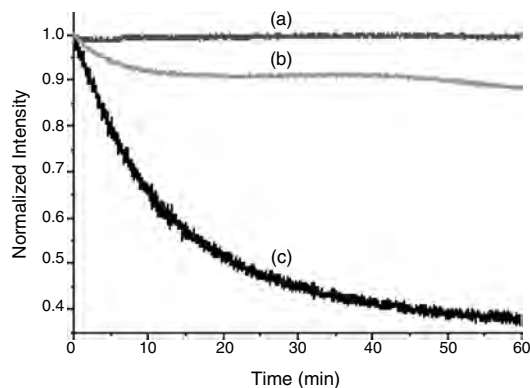


Figure 12. Photostability of silica coated fluorescent nanoparticles. (a) Silica coated fluorescent nanoparticles with two layers of shell. (b) Silica coated fluorescent nanoparticles with one layer of shell. (c) Fluorescence dye in the solution.

the genes and drugs more stable in biological milieu before they are released at target sites.

4.3. Ultrasensitivity in Detection

Increased surface area caused by the size effect of nanoparticles results in two advantages, more biomolecules modified onto the surface of core-shell nanoparticles and the amplification characteristic derived from the encapsulation of functionalized core materials by the core-shell structure. Both lead to highly increased sensitivity when core-shell nanoparticles are used for biomedicine detection and determination.

In our research, the emission intensity of the labeled cell by the fluorescent nanoparticles and FITC label was recorded [39]. The results indicate that the fluorescent nanoparticle label provided more sensitivity in comparison with the FITC label method. We think the number of dye molecules coupled to the antibody is the most important reason for this. There are only a few dye molecules coupled to one antibody through the amine group in the FITC label method [40]. However, the fluorescent nanoparticle label was achieved by coupling the antibody to the shell of the fluorescent nanoparticles. We have roughly estimated there

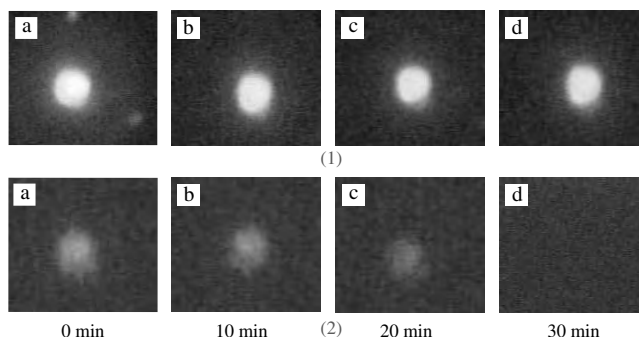


Figure 13. Photostability comparison of (1) the fluorescent nanoparticles labeled target cells and (2) the FITC labeled target cell. The cell images were taken every 10 minutes. Reprinted with permission from [38], X. X. He et al., *J. Nanosci. Nanotech.* 2, 317 (2002). ©2002, American Scientific Publishers.

were about 8000 dye molecules in a single nanoparticles of 30 nm. In this way, one antibody can be coupled to about 8000 dye molecules. The detection sensitivity was thus greatly improved. See Figure 14.

5. APPLICATIONS OF THE BIOCOMPATIBLE CORE–SHELL NANOPARTICLES IN BIOMEDICINE

Biocompatible core–shell nanoparticles emerged under the combination of nanotechnology and biotechnology and have already exhibited potential applications as nanosensors in cell imaging and biochemical information determination, biological separators, drug and gene carriers, or other types of analysis measurements. Biocompatible core–shell nanoparticles have been proven to be efficient and effective tools for biomedical research. Details are described as follows.

5.1. Biochemical Information Obtained Based on Biocompatible Nanoparticles

The development of highly sensitive nonisotopic detection systems for obtaining biochemical information has received considerable attention in biology and medicine research fields. At present, nonisotopic detection methods, such as organic reporter molecules that undergo enzyme-linked color changes, and luminescent, electrochemical, and fluorescent methods, have been applied in these fields [41–43]. Among these methods, the fluorescence is an important nonisotopic detection method. The fluorophores as fluorescent biological labels play an important role in the field of biomedicine, such as the detection of materials inside or outside of the cell [44, 45], hybridization and sequencing of the nucleic acid [46, 47], clinic diagnostics at the early stage,

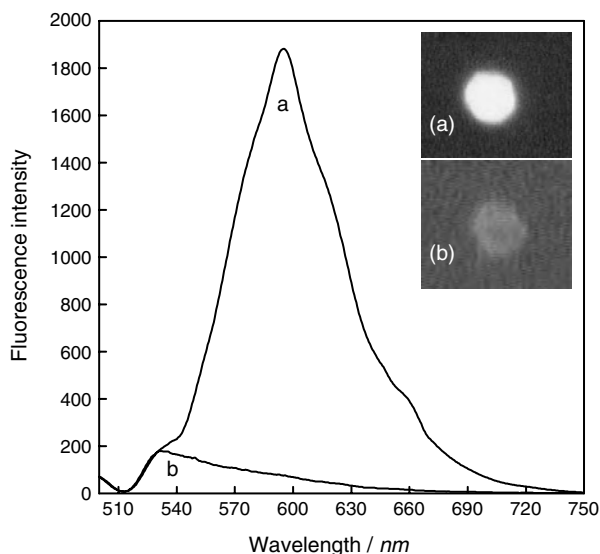


Figure 14. The emission spectra and image (1000 \times) of the labeled SmIgG⁺ B lymphocytes. (a) Recognized by the fluorescent nanoparticles label. (b) Recognized by the FITC label. Reprinted with permission from [39], X. X. He et al., *Chinese Sci. Bull.* 46, 1962 (2001). © 2001, Chinese Science Bulletin.

and so on [48]. But the conventional fluorescent labels may be restricted in some fields of biological application because of the following limitations. Some fluorophores are easy to photobleach, which will affect the emission intensity. The toxin of some fluorophores is harmful to living things or cells. The detection sensitivity is not very high because only a few fluorophores can be coupled to one biomolecule in the conventional fluorescent label methods. Recently, significant progress has been achieved in fluorescent labeling by the use of core–shell nanoparticles that are induced by analyte binding as the sensing mechanism, as shown in Figure 15.

5.1.1. Bioconjugate Quantum Dots as Fluorescent Biological Labels

Semiconductor quantum dots are highly light absorbing, luminescent nanoparticles whose absorbance onset and emission maximum shift to higher energy with particle size, due to quantum confinement effects [16]. These nanoparticles are in the size range of 2–8 nm in diameter. Unlike molecular fluorophores, which typically have very narrow excitation spectra, semiconductor quantum dots absorb light over a very broad spectral range, as shown in Figure 5. This makes it possible to optically excite a broad spectrum of quantum dot colors using a single excitation laser wavelength, which enables one to simultaneously probe several markers. Bruchez et al. [17] and Chan and Nie [16] reported the synthesis of highly luminescent semiconductor quantum dots (zinc sulfide-capped cadmium selenide), which can be covalently coupled to biomolecules for use in ultrasensitive biological detection. In comparison with organic dyes such as rhodamine, this kind of luminescent label is 20 times as bright, 100 times as stable against photobleaching, and one-third as wide in spectral linewidth. After biological modification on the QDs, formed nanometer-sized conjugates are water soluble and biocompatible. Results showed that quantum dots that were labeled with the protein transferrin underwent receptor-mediated endocytosis in cultured Hela cells, while those dots that were labeled with immunomolecules recognized specific antibodies or antigens. Their further research was to use two luminescent QDs emitting red and green lights separately for simultaneous detection of murine actin fibers and cell nuclei (Fig. 16) [17]. In order to analyze a large number of molecules at the same time, Han et al. have invented a way to barcode DNA using tiny light-emitting quantum dots to obtain molecular ID codes [27]. By embedding such quantum dots in polystyrene microbeads bearing short strands of DNA, these created labels can recognize particular DNA molecules of interest

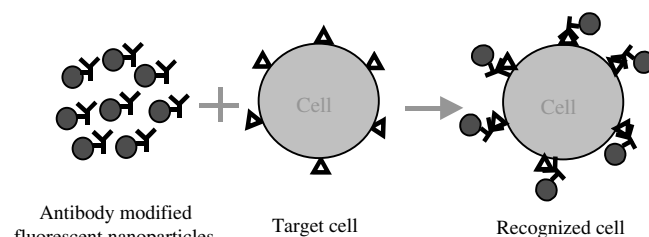


Figure 15. The principle recognition target cell using fluorescent labeling.



Figure 16. Semiconductor nanocrystals as fluorescent biological labels. Reprinted with permission from [17], M. J. Bruchez et al., *Science* 281, 2013 (1998). © 1998, American Association for the Advancement of Science.

by tagging them with a unique identification code (Fig. 17). Uniquely coded beads are built using different combinations of colors and intensity levels and visualizing various fluorescent signals. Ultimately, it is expected that the codes should be easily be tagged onto both nucleic acids and proteins—facilitating research in many areas of biomedical research, including drug screening, gene expression studies, and clinical diagnostics.

Similarly, Chen et al. [49] presented fluorescent markers made from semiconductors only 5 nanometers in size, which could help detect tumor cells. This particular semiconductor is manufactured with a core of cadmium and selenium crystals, encapsulated in a shell made from a zinc-sulfur compound. These materials all have properties conducive to semiconductors. At 5 nanometers, the structure can display varied fluorescent coloring depending on the size when binding with other molecules. The QDs have demonstrated good ability at targeting specific molecules on tumor cells and provide an enhanced method of detecting cancer and other diseases. They have previously developed an approach to conjugate biotinylated or nonbiotinylated antibodies to CdSe–ZnS core shell QDs via molecular adaptor proteins that have been electrostatically bound to nanocrystals capped with dihydrolipoic acid ligands.

Mattoussi et al. [50] showed results of studies that employed QD–protein conjugates in immuno- and fluorescence-based quenching assays to detect low levels of toxin analytes and explosives in solution environments. In particular they showed that these QD–antibody conjugates exhibit high specificity and stability in both surface and

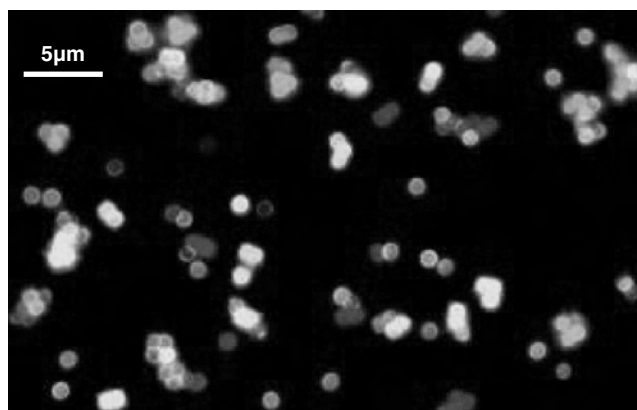


Figure 17. Fluorescence micrograph of a mixture of CdSe/ZnS QD-tagged beads emitting single-color signals at 484, 508, 547, 575, and 611 nm. Reprinted with permission from [27], M. Y. Han et al., *Nat. Biotechnol.* 19, 631 (2001). © 2001, Macmillan Magazines Ltd.

flow displacement immunoassays. These QD bioconjugates are used in live cell labeling and show that QD–antibody conjugates can selectively label cells and regions within cells that express proteins of interest. These approaches enable us to use luminescent QDs for simultaneously studying growth and development of multiple cells over extended time periods.

In short, combining the advantages of capped CdSe–ZnS or other kinds of quantum dots, such as photochemical stability and narrow band tunable emission through the visible, with the simple binding approach, these hybrid bioinorganic conjugates represent a very promising tool for use in biotechnological applications especially in biosensing and biolabeling.

5.1.2. Fluorescent Dye Doped Nanoparticles as Biolabels

At present time, rapid and sensitive molecular techniques for the detection of particular microorganisms (e.g., pathogens and biological warfare agents) in environmental sources serve as an important means of warning and prevention. Fluorescence sensing systems are the most commonly used means for the current methods but are limited to the availability of specific targets and the number of targets simultaneously examined. The use of fluorescent dye doped nanoparticles as the sensing system has emerged as a promising approach since it provides better specificity than fluorescence dyes, can be seen under visible light (low equipment cost), and allows specific targets to be examined.

Tan et al. [51, 52] reported the development of novel luminescent nanoparticles composed of inorganic luminescent dye, tris(2,2'-bipyridyl) dichlororuthenium (II) hexahydrate, doped inside a silica network. These dye doped silica (DDS) nanoparticles all are suitable for biomarker application since they are much smaller than cellular dimension. The luminophores are well protected from the environmental oxygen because they are doped inside the silica network. These nanoparticles are highly photostable in comparison to most commonly used organic dyes. Generally speaking, the silica surface of DDS nanoparticles is available to covalently bind with biomolecules for surface modification and bioconjunction. For demonstration as a biomarker, the DDS nanoparticle surface has been biochemically modified to attach membrane-anchoring groups and applied successfully to stain human leukemia cells. As an example, they used an antibody for leukemia cell recognition. The antibody was first immobilized onto the luminophore-doped nanoparticle through silica chemistry and then was used for leukemia cell identification by a fluorescent microscopy imaging technique. The leukemia cells were identified easily, clearly, and with high efficiency using these antibody-coated nanoparticles.

In our research, a method for cell recognition of system lupus erythematosus (SLE) patients using photostable luminescent nanoparticles as biological labels was reported too [38]. The luminescent silica nanoparticles are prepared and are covalently immobilized with goat anti-human immunoglobulin G (IgG), which can recognize SmIgG⁺ B lymphocytes. Using antibody-conjugated nanoparticles, target SmIgG⁺ B lymphocytes isolated from the circulating

blood of SLE patients were recognized. It has been observed that the bioassay based on fluorescent nanoparticle labeling can identify target cells selectively and efficiently (Fig. 18). According to these experimental results, this cell recognition method based on fluorescent nanoparticle labeling was an effective diagnosis of the SLE diseases. Based on the same technology, HepG liver cancer cells have been recognized selectively.

Soukka et al. [53–55] introduced a detection technology improving sensitivity in miniature that relies on the use of europium (III) nanoparticles and time-resolved fluorometry to improve the detection limit of biochemical assays and to visualize individual molecules in a microtiter plate format. Streptavidin was covalently coated on 107 nm nanoparticles containing >30,000 europium molecules entrapped with P-diketones. In a model assay system, these nanoparticles were used to trace biotinylated prostate-specific antigen in a microtiter plate format. As a conclusion, the universal streptavidin-coated europium (III) nanoparticle label is suitable for detection of any biotinylated molecule either in solution or on a solid phase. The europium (III) nanoparticle labeling technology is applicable to many areas of modern biochemical analysis, such as immunochemical and multianalyte DNA-chip assays as well as histochemistry and cytochemistry to improve detection sensitivities.

5.1.3. Colorimetric Assay Based on Gold Nanoparticles

The use of gold colloid in biological applications began in 1971, when Faulk and Taylor invented the immunogold staining procedure. Since that time, the labeling of targeting molecules, especially proteins, with gold nanoparticles has revolutionized the visualization of cellular or tissue components by electron microscopy [56] because the high density of gold makes them appear dark in a transmission electron microscope image. Site-specific staining is obtained by labeling the nanogold particles with antibodies directed against a protein in the region of interest. Recently, gold nanoparticle conjugation was applied to polynucleotide detection based on a colorimetric method. The characteristic red of gold colloid has long been known to change to a bluish-purple color upon colloid aggregation. When a single-stranded target oligonucleotide was introduced into solution, a polymer network was formed consisting of the target

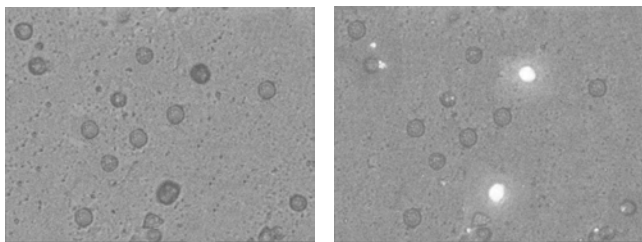


Figure 18. Detection of System Lupus Erythematosus diseases based on fluorescent nanoparticle labeling (400 \times). (a) Optical image, (b) Fluorescent image. Reprinted with permission from [38], X. X. He et al., *J. Nanosci. Nanotech.* 2, 317 (2002). © 2002, American Scientific Publishers.

oligonucleotide and the conjugated nanoparticles. This condensed network brought the nanoparticles into close enough vicinity to induce a dramatic red-to-blue macroscopic color change. Mirkin et al. [57–60] have developed selective colorimetric detection of DNA, scanometric DNA array, and array-based electrical detection of DNA by the use of gold nanoparticles.

5.1.4. Other Nanoparticles as Biolabels

Biological binding reactions play a key role in biology and medicine. Their detection is usually achieved by labeling one of the reaction components with radioisotopes, enzymes, or fluorescence dyes. In particular, assays, using the specificity of the reaction between antibodies and antigens, are of outstanding importance. Most of these assays are hampered by the drawback that the label generates a signal that is not influenced by the binding reaction. Therefore, separation procedures between bound and unbound reaction components are mostly inevitable. The use of superconducting quantum interference device (SQUID)-based magnetic nanoparticle relaxation measurement has been [61] presented as a novel tool for the quantitative determination of biological binding reactions, where magnetic nanoparticles are used as labels to antibodies. The rotational diffusion of the label is hindered by the binding of the antibody to the antigen, which is adsorbed to the sample tube wall. As a result, the observed relaxation of its magnetization is driven by the internal reorientation of the magnetic moment of the nanoparticles. The measured signal is specific for the magnetically labeled antibody bound to the antigen. It was shown that already at a very early stage of technical development SQUID-based magnetic nanoparticle relaxation shows a higher sensitivity than a comparable standard assay technique, enzyme linked immunosorbent assay.

5.1.5. Nanosensor Probe Single Living Cells Based on Biocompatible Nanoparticles

Rapid advances in the biomedical field pose new challenges to analytical chemistry in the field of chemical and biological sensors and real-time, noninvasive analysis of biochemical processes inside live cells and their suborgans. In recent years, the submicrometer-sized sensors have widely been used for getting biochemical information, with applications including pH, Ca, Na, K, O, Mg, glucose, glutamate, and so on [62–71]. However, the submicrometer optical fiber or a micropipet tip was still limited in biological research, particularly in the field of single cell analysis where the sensor has to be inserted into a single cell through the cell membrane. Then the measurement technique is as not as invasive as conventional cellular fluorescence labeling. Furthermore, this technique is not feasible when a large population of cells needs to be detected at the same time. Recently sensors based on biocompatible nanoparticles have been in development. Nanosensors based on biocompatible nanoparticles can overcome these problems. Clark et al. have reported a kind of nanosensor which is called PEBBLES (probes encapsulated by biological localized embedding). They introduced a unique approach for

the fabrication of nanosized optochemical probes in which the fluorescent dye is entrapped in nanosized phospholipid vesicles. The PEBBLEs can be delivered to viable cells and these cells can be observed in a time resolved manner, responding to changes in their environment [72–74]. Rosenzweig et al. have developed the dye-encapsulating liposome as a fluorescence-based oxygen nanosensor, and for the first time one can quantify an analyte-molecular oxygen [75].

We have synthesized a novel fluorescent core–shell nanoparticle which has been developed by encapsulating the conjugation of FITCs modified with protein IgG into a silica shell for use as fluorescent pH-sensitive nanoparticles, and we carried out its application in intracellular pH measurements in real time [76]. These nanoparticles can measure the change of intracellular pH value after phagocytosis by murine macrophages, and they show excellent stability and high reproducibility when used as pH optical sensors, as shown in Figure 19.

5.2. Separation of Biomolecules or Cells Using the Nanocapturer

The separation of biological cells and life active species is a basic technique in biomedicine, such as the separation of fetal cells, separation of disease cells, classification of cells, and so on [77–80]. Biocompatible core–shell nanoparticles offer a novel tool and means for the separation of cells and biological species. Magnetic bioseparation, for example, is a powerful and versatile diagnostic technique in biology and medicine. The basic concept in magnetic bioseparations is to selectively bind the biomaterial of interest (e.g., a specific cell, protein, or DNA sequence) to a magnetic particle and then separate it from its surrounding matrix using a magnetic field. They could find a large range of applications for the separation of DNA and other intermediate-size objects such as cells, proteins, organelles, and so on. Nanoparticles of Fe_3O_4 with diameters in the 5–100 nm range are typically used for such separations. These particles are “superparamagnetic,” meaning that they are attracted to a magnetic field but retain no residual magnetism after the field is removed [80]. Then the superparamagnetic nanoparticles coupled with specific analytes can be easily and rapidly isolated from the original sample solution. A common use of superparamagnetic nanoparticles is for immunospecific cell separations. Exploiting coating protein A on the surface of magnetic nanoparticles, followed by modifying the specific antibody to the antigen on the surface of cells, Sonti and Bose realized the immunoseparation of chick red blood corpuscles [81]. One hospital in London applied magnetic polystyrene nanoparticles (50 nm) with the modification of antinerval cellular tumor monoclonal antibody to cure cancer by successfully separating cancer cells from human marrow [82].

In our research, silica coated magnetic nanoparticles, employing Fe_3O_4 as core and silica as shell, have been prepared by using a water-in-oil microemulsion technique. The procedure was first done using synthesis of aqueous magnetic ferrofluid with the precipitation of the chloride mixture with the base. Then the silica coating was done using a

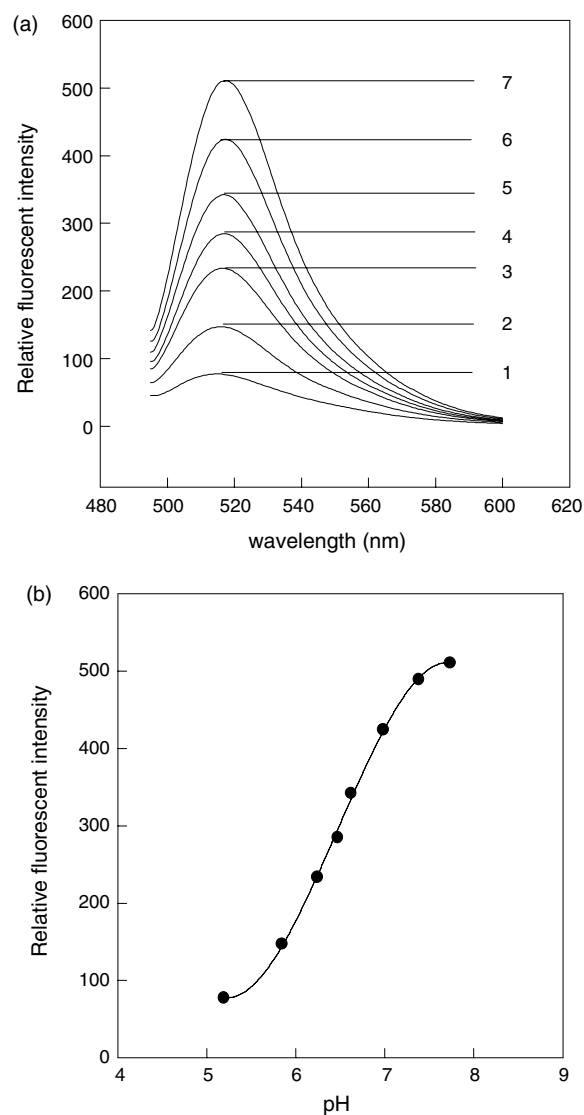


Figure 19. (a) pH sensitivity of fluorescent core–shell nanoparticles, (1) pH = 5.19; (2) pH = 5.84; (3) pH = 6.24; (4) pH = 6.47; (5) pH = 6.62; (6) pH = 6.98; (7) pH = 7.73. (b) Fluorescence pH response of fluorescent core–shell nanoparticles.

water-in-oil microemulsion technique. The magnetic nanoparticles are also superparamagnetic, as shown in Figure 20. A nanocapturer has been developed using the superparamagnetic [18]. Based on the special recognition and combination between the biomolecules modified on the magnetic nanoparticles and analyzed substances, superparamagnetic nanocapturers have been developed for biological separation. Zhao et al. report the development of a genemagnetic nanocapturer using magnetic nanoparticles functionalized with MBs [83]. The high sequence selectivity and excellent detection sensitivity of MBs are combined with the superior separation capability of the magnetic nanoparticles for the separation of trace amounts of DNA/mRNA strands with a single base difference. Single base mismatched DNA has been easily separated, collected, and determined from perfectly matched complementary DNA by applying a magnetic field and controlling the temperature.

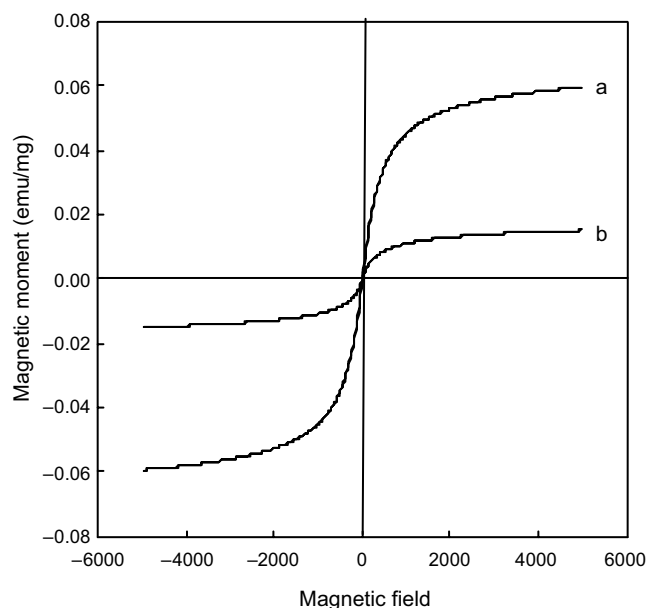


Figure 20. Magnetization versus field at room temperature for magnetic nanoparticles. (a) Magnetic core (1 mg). (b) Silica coated magnetic nanoparticles (1 mg). Reprinted with permission from [84], K. M. Wang et al., *Chem. J. Chinese Univ.* 24, 40 (2003). © 2003, Chem. J. Chinese Univ.

Under the special combination of biotin and avidin, a superparamagnetic DNA nanoseparator has been built through modification of single strand oligonucleotide probes labeled with biotin onto the surface of these nanoparticles. Complementary oligonucleotide labeled with streptavidin was efficiently separated (Fig. 21) with high selectivity and the characteristics of the separated DNA were not affected (Fig. 22) [84].

The biological separation method based on superparamagnetic particle captures has also been developed to separate trace biological active substances [85, 86]. Guo et al. prepared the superparamagnetic particle and modified it with rhIL-2 monoclonal antibody and further purified and

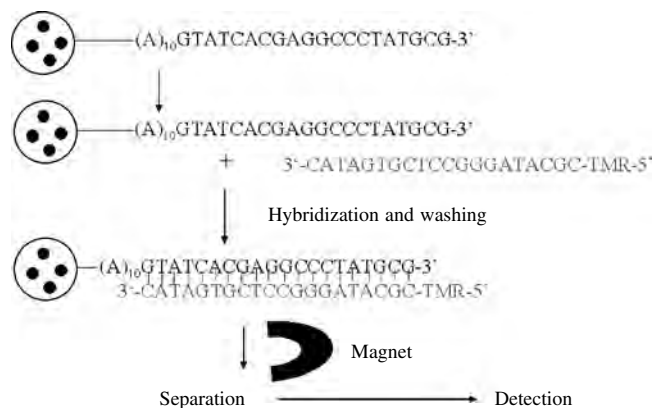


Figure 21. Schematic diagram of separation of oligonucleotide by use of superparamagnetic DNA nanocaptor. Reprinted with permission from [84], K. M. Wang et al., *Chem. J. Chinese Univ.* 24, 40 (2003). © 2003, Chem. J. Chinese Univ.

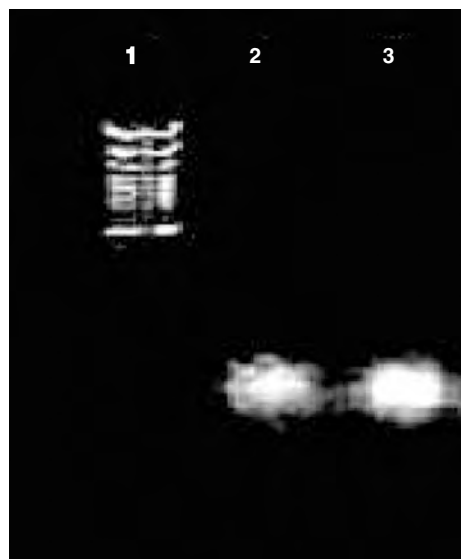


Figure 22. Agarose gel electrophoresis of captured ssDNA. Lane 1; a standard marker DNA (100 bp). Lane 2; target ssDNA (20 bp). Lane 3; dissociated target ssDNA after being captured (20 bp). Reprinted with permission from [84], K. M. Wang et al., *Chem. J. Chinese Univ.* 24, 40 (2003). © 2003, Chem. J. Chinese Univ.

enriched rhIL-2 with a purity of 93%, thus providing a simple and rapid separation method for proteins [87].

A flow-through quadrupole magnetic cell separator [88, 89] has been designed and built using a cell model system of human peripheral T lymphocytes [CD4(+), CD8(+), and CD45(+)] cells. It was accomplished using a sandwich of mouse antihuman monoclonal antibody conjugated to fluorescein isothiocyanate and rat antimouse polyclonal antibody conjugated to colloidal magnetic nanoparticles for the immunomagnetic labeling. The magnetically labeled cells could be separated from the nonlabeled. The maximum throughput of the quadrupole magnetic cell separator was 7040 cells/s (CD45 cells, initial purity of 5%). Theoretical calculations showed that the throughput could be increased to 10^6 cells/s by a scale-up of the current prototype. Paramagnetic nanoparticles conjugated to antibodies that target specific cell surface molecules are consequently commonly utilized as an excellent cell separation method.

5.3. Drug Delivery Based on Nanoparticles

With development of biotechnology and genomics, many new chemical drugs have been synthesized. Among the drugs being synthesized, proteins and peptides represent the major part. But these drugs are often poorly permeable, poorly soluble, and unstable in physiological fluids, with rapid drug metabolism *in vivo* and unfavorable pharmacokinetics. Biocompatible core-shell nanoparticles are promising technologies that can be used to overcome most of the problems of protein/peptide delivery and stability. These delivery systems offer numerous advantages compared to conventional dosage forms, including improved efficacy, reduced toxicity,

uptake by the cells through the cell membrane, and the ability to cross the blood–brain barrier and to target specific cells.

Furthermore, most anticancer drugs have difficulties and limitations in clinical administration due to their poor solubility and/or other unfavorable properties. They usually require the aid of an adjuvant, which often causes serious side effects. Moreover, intravenous injection and infusion are unavoidably associated with considerable fluctuation of drug concentration in the blood. Therefore, the drugs can only be administered over a limited dosage and time period. Their efficacy is far from satisfactory and the diseases of the patients greatly deteriorate. By microencapsulating drugs in nanosphere matrices to form biodegradable and/or biocompatible core–shell nanoparticles, the release of drugs can be controlled without reaching toxic levels. By further targeting the drugs to be concentrated in the tumor tissue, toxicity can be selectively reduced with a concurrent increase in therapeutic index. The nanoparticle delivery systems offer the advantage of targeted or site-specific delivery of chemotherapeutics and other drugs to affected cells over an extended period, thereby increasing efficacy while reducing toxic side effects.

5.3.1. Polymeric Nanoparticles as Drug Carriers

Many carrier systems for the treatment of brain tumors and nervous system disorders have been developed using polymeric nanoparticles recently. Nanosphere drug targeting systems allow any drug to cross the blood–brain barrier (BBB). Advectus Life Sciences, Canada, has completed the first phase of a study to determine the effectiveness of its Nanocure nanoparticles (P80DOX-NP) for delivering cancer-fighting drugs to brain tumors, which is a novel method for delivering the drug doxorubicin across the blood–brain barrier—a network of blood vessels and cells that protect the brain and prevent certain molecules from passing through. This nanocure consists of a nanoparticles of poly(butylcyanoacrylate) (PBCA) polymer coated with a layer of doxorubicin and a layer of polysorbate-80. Once nanocure enters the bloodstream, the polysorbate-80 coating attracts apolipoproteins. These proteins coat the nanoparticles and, as a result, the blood–brain barrier treats the particles. Results showed there was an excellent dose–response curve for all cancer cell lines tested and that doses delivered as doxorubicin and doses delivered as nanoparticles were equally effective, indicating that the drug did not lose its effectiveness during nanoparticle formulation or shipping.

It has recently been suggested that the PBCA nanoparticle drug delivery system has a generalized toxic effect on the BBB and that this effect forms the basis of an apparent enhanced drug delivery to the brain. Kreuter et al. [90] explored more fully the mechanism by which PBCA nanoparticles could deliver drugs to the brain. Both *in vivo* and *in vitro* methods have been applied to examine the possible toxic effects of PBCA nanoparticles and polysorbate-80 on cerebral endothelial cells using human, bovine, and rat models. It is confirmed that at concentrations of PBCA nanoparticles and polysorbate-80 that achieve significant drug

delivery to the brain, there is little *in vivo* or *in vitro* evidence to suggest that a generalized toxic effect on the BBB is the primary mechanism for drug delivery to the brain.

Paclitaxel, one of the best antineoplastic drugs found from nature in recent decades, will be used as a prototype drug due to its excellent efficacy against a wide spectrum of cancers and its great commercial success in the world market. American Pharmaceutical Partners has developed a protein-based paclitaxel nanoparticle currently in clinical studies for metastatic breast cancer. Their product, dubbed ABI-007, leverages the attributes of nanotechnology by encapsulating paclitaxel in an albumin-based paclitaxel nanoparticle approximately a hundredth of the size of a single red blood cell. It poses drug-delivery challenges to solid tumors without using the solubilizing reagent which can be very toxic.

As mentioned, an increasing amount of attention to the use of polymeric nanoparticles as drug carriers is arising both in academia and industry. The development of suitable delivery systems for protein drugs with high molecular weights and short half-lives is of current interest. In conclusion, nanoparticles have a number of potential applications in drug and vaccine delivery.

Prokop et al. [23] featured a new production technology for nanoparticles comprised of multicomponent polymeric complexes that are candidates for delivery vehicles of biological molecules such as proteins and drugs. This novel technology is extensively discussed in contrast to other technologies, primarily those that are water- and organic solvent-based. The usefulness is demonstrated using several examples, evaluating protein and small drug delivery.

Kim and Kim [91] reported polymeric nanoparticles synthesized from a sugar-containing conjugate for liver-specific drug delivery. The conjugate was composed of lactobionic acid, diamine-terminated poly(ethylene glycol), and cholic acid. In aqueous media, the conjugate can self-assemble to form core–shell type nanoparticles. Clonazepam (CNZ) was used as a model hydrophobic drug and was incorporated into the hydrophobic core of the nanoparticles. CNZ was released more slowly at a higher drug loading due to drug crystallization, so these polymeric nanoparticles can be used as drug carriers.

5.3.2. Chitosan Nanoparticles as Drug Carriers

Chitosan (CS), an aminopolysaccharide, has extensive applications as a new drug or gene delivery carrier because it is nontoxic, bioabsorbable, and biodegradable. Recently it has become of consequence to develop hydrophilic nanoparticle carriers for water-soluble natural macromolecules, such as peptides, proteins, and polynucleotides. Calvo and Remunan-López [92] reported a new approach for the preparation of nanoparticles based on an ionic gelation process between CS and a diblock copolymer of PEO–PPO and polyanion sodium tripolyphosphate. These new nanoparticles have great protein loading capacity and provide a continuous release of the entrapped protein for up to 1 week.

Poly(ethylene glycol)-grafted chitosan (PEG-g-chitosan) was found [93] to form nanoparticles through intermolecular

hydrogen bonding in an aqueous solution. PEG-g-chitosan nanoparticles can be expected to incorporate water-soluble, polar, or anionic molecules, which can then interact with chitosan by hydrogen bonds or electrostatic interactions. Therefore Ohya et al. investigated the incorporation of a peptide hormone, insulin, as a model peptide drug into PEG-g-chitosan nanoparticles. PEG-g-chitosan nanoparticles incorporated a certain quantity of insulin molecules spontaneously which depended on the degree of introduction of PEG chain on chitosan, as did the release rate. PEG-g-chitosan nanoparticles have much possibility to be applied as delivery vehicles for peptide drugs.

Polymeric vesicles based on glycol chitosan have been prepared to encapsulate drugs and control the release of drugs, making them suitable for use as drug carriers. Wang et al. [94] reported that the size of the polymeric vesicles might be controlled by the polymer molecular weight. This is not possible with the existing nanoparticles and liposome carriers. The chitosan amphiphile used to make the liposome encapsulating polymeric vesicles is also capable of increasing the transport of drugs across mucous membranes [95]. The incorporation of targeting ligands into polymeric vesicles increases the specific uptake of a drug by mammalian cells [96]. A simple carbohydrate polymer glycol chitosan has been investigated for its ability to form polymeric vesicle drug carriers [97]. Glycol chitosan modified by attachment of fatty acid pendant groups assembles into uniform polymeric vesicles with a mean size of 200 nm in the presence of cholesterol. These polymeric vesicles are found to be biocompatible and capable of entrapping water-soluble drugs, such as bleomycin, which can be efficiently loaded on to these polymeric vesicles to yield a bleomycin-to-polymer ratio of 0.5 units mg^{-1} .

Some anticancer drugs such as doxorubicin (DXR) produce undesirable side effects such as cardiotoxicity. To minimize these, attempts have been made to couple the drug with dextran (DEX) and then to encapsulate this drug conjugate in chitosan nanoparticles [98]. The size of nanoparticles, found to be 100 ± 10 nm diameter, favors the enhanced permeability and retention effect as observed in most solid tumors. The tumor targeted delivery of encapsulated DEX–DXR conjugate using chitosan nanoparticles not only reduces the side effects but also improves its therapeutic efficacy in the treatment of solid tumors.

A novel delivery system based upon chitosan has obtained increasing attention for nasally administered vaccines due to its enhancement to the immune response of nasally administered vaccines. Illum and co-workers [99–103] have exploited the chitosan concept for the delivery of a variety of pharmacological agents, to include peptide and protein drugs such as insulin, calcitonin, etc. Chitosan-based formulations can greatly improve the absorption of drugs from the nasal cavity and products for the treatment of migraine and cancer pain have reached Phase II clinical evaluation. Investigations in cell culture (CaCo-2) as well as in animal models have demonstrated that chitosan is due not only to improved adhesion between the formulation and the nasal tissues, but also to a transient effect of chitosan on paracellular transport process [104].

5.4. Nonviral Gene Carrier Based on the Nanoparticles

Nonviral gene delivery systems based upon plasmid DNA/chemical complexes have gained increasing attention for their potential in avoiding problems inherent in viral gene vectors. With the development of nanotechnology, nanoparticle gene vectors brought about new hope to safely and efficiently transfer foreign DNA into cells. In view of biocompatible and biodegradable natures and flexibility in design and fabrication with chemical or molecular biology methods, biocompatible core shell nanoparticles provide an excellent and relevant material to form DNA nanoparticles while endosomal lysis and nuclear uptake domains may be included for further improvement in the efficiency of DNA based gene therapy.

At present, nonviral gene therapy has been growing rapidly in two directions. One concerns the synthesis of DNA-encapsulated nanoparticles. The other deals with the DNA modification of the core–shell nanoparticles with diverse functions. Nevertheless, both delivery systems are designed to provide opportunities for DNA targeted delivery.

5.4.1. DNA-Doped Nanoparticles as Gene Carriers

Cui and Mumper [20] reported a pDNA-nanoparticle delivery system developed by entrapping hydrophobized pDNA inside nanoparticles engineered from oil-in-water microemulsion precursors. *In vitro*, hepatocyte transfection studies in Hep G2 cells showed that pullulan (a hepatocyte targeting ligand) coated DNA nanoparticles resulted in enhanced luciferase expression, compared to both pDNA alone and uncoated nanoparticles. Preincubation of the cells with free pullulan inhibited the transfection. Finally, 30 min after tail vein injection to Balb/C mice to monitor *in vivo* biodistribution of the nanoparticles containing I-125 labeled pDNA, only 16% of the “naked” pDNA remained in the circulating blood compared to over 40% of the entrapped pDNA. Due to the apparent stability of these pDNA-entrapped nanoparticles in the blood, potential of these nanoparticles for systemic gene therapy applications requiring cell and/or tissue-specific delivery is assumed.

Ultralow size, highly monodispersed DNA doped calcium phosphate nanoparticles reported by Roy et al. [105] presented a unique class of nonviral vectors, which can serve as efficient and alternative DNA carriers for targeted delivery of genes too. The DNA encapsulated inside the base is protected from the external DNaseI environment and could be used safely to transfer the encapsulated DNA under *in vitro* and *in vivo* conditions after suitably modifying these nanoparticles by adsorbing a highly adhesive polymer like polyacrylic acid followed by conjugating the carboxylic groups of the polymer with a ligand such as *p*-amino-1-thio-beta-galactopyranoside using 1-ethyl-3-(3-dimethylamino-propyl)-carbo diimide hydrochloride as a coupling agent. The modified calcium phosphate nanoparticles have been used *in vivo* to target genes specifically to the liver.

Kabbaj and Phillips [106] demonstrated a possible material for mycobacterium phlei (*M. phlei*) DNA delivery.

Although *M. phlei* DNA inhibits cancer cell division but is susceptible to degradation by DNaseI, incorporation of DNA within chitosan nanoparticles significantly decreases the degradation of DNA. They have characterized chitosan-DNA based formation, determined DNaseI susceptibility, and evaluated their antiproliferative activity. In their results, the ability of *M. phlei* DNA-chitosan nanoparticles to inhibit melanoma cell division was determined relative to *M. phlei* DNA and a cationic Liposomal *M. phlei* DNA formulation. *M. phlei* DNA had antiproliferative activity (MTT reduction, IC₅₀ = 0.9 mg/ml) without intrinsic cytotoxicity (LDH release, ED₅₀ > 50 µg/ml). Cationic polyphosphate chitosan nanoparticles were inert (antiproliferative IC₅₀ > 1 mg/ml, ED₅₀ > 1 mg/ml). *M. phlei* DNA-chitosan nanoparticles were 20-fold more potent than *M. phlei* DNA. Cationic DOTAP/DOPE liposomes were cytostatic (IC₅₀ = 49 µg/ml) and cytotoxic (ED₅₀ = 87 µg/ml), and complexation of *M. phlei* DNA resulted in a significant reduction of antiproliferative activity. Chitosan nanoparticles may therefore be appropriate delivery vehicles for *M. phlei* DNA.

Extensive studies examining the interaction between chitosan and DNA were conducted [107, 108] and it was found that it is possible to produce a range of nanoparticles of size from 20 to 500 nm, carrying different surface charges. These nanoparticles have been proven to be appropriate for *in vitro* cell transfection as well as for optimal performance *in vivo*.

5.4.2. DNA-Conjugated Nanoparticles as Gene Carriers

Besides DNA-encapsulated nanoparticles as nonviral gene carriers, there are many reports about DNA-nanoparticle conjugates used in gene delivery.

In the research of Zhu et al. [109], silica nanoparticles (SiNP) were synthesized first in a microemulsion system, polyoxyethylene nonylphenyl ether (OP-10)/cyclohexane/ammonium hydroxide, and then poly-L-lysine (PLL) was linked on the surface of SiNP by nanoparticle surface energy and electrostatically bound. Lastly a novel complex nanomaterial—poly-L-lysine-silica—was prepared to conjugate with DNA. Their cell transfection showed that PLL-SiNP could efficiently transfer PEGFPC-2 plasmid DNA into HNE1 cell lines, which indicated that PLL-SiNP was a novel nonviral nanoparticle gene vector and would probably play an important role in gene structure and function research as well as gene therapy.

Recently we have developed a novel DNA enrichment technology based on the amino-modified silica nanoparticles which have been prepared by the controlled synchronous hydrolysis of tetraethoxysilane and *N*-(β-aminoethyl)-γ-aminopropyl-triethoxy silane in water nanodroplets of water-in-oil microemulsion. Due to the presence of amino groups on the surface of the nanoparticles, nanoparticle-plasmid DNA complexes (DNA-NP) can easily form through electrostatic binding between the positive charges of the amino-modified silica nanoparticles and the negative charges of the plasmid DNA. As shown in Figure 23, lanes 2 and 4, plasmid DNA moved in the electric field, and amino-modified silica nanoparticle-plasmid DNA complexes

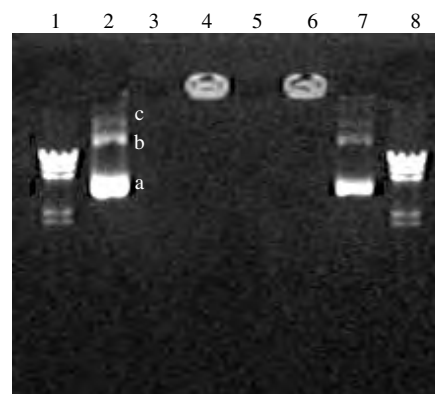


Figure 23. Agarose gel electrophoresis of plasmid DNA and DNA-NP complexes. Lane 1 is DNA marker (λ DNA is cleaved by HindIII). Lane 2 is undigested free plasmid DNA. (a) Superhelix DNA, (b) linear DNA, and (c) open circular DNA are the three forms of the plasmid DNA. Lane 3 is digested free plasmid DNA. Lane 4 is plasmid DNA-NP complexes. Lane 5 is pure silica NP after incubation with plasmid DNA. Lane 6 is plasmid DNA-NP complexes digested with DNaseI. Lane 7 is the DNA released from the DNA-NP complexes that have been digested with DNaseI. Lane 8 is DNA marker (λ DNA is cleaved by HindIII). Reprinted with permission from [110], X. X. He et al., *J. Am. Chem. Soc.* 125, 7168 (2003). © 2003, American Chemical Society.

were retained around the sample well. The reason the DNA-NP complexes did not move toward the positive electrode lies in the charge and the large size of the complexes. In a control experiment, pure silica nanoparticles with negative zeta potential at neutral pH could not enrich plasmid DNA. As shown in lane 5, there was no DNA shown in the lane after the incubation of the pure silica nanoparticles with plasmid DNA. This clearly shows that it is necessary to have amino-modified NP for DNA binding. And the results also suggested the plasmid DNA enriched on the nanoparticles could be protected from DNaseI cleavage and keep its integration function, due to the large surface and pore structures of the nanoparticles. As shown in Figure 23, lanes 3 and 6, free plasmid DNA was degraded completely when incubated with DNaseI, while plasmid DNA-NP complexes were visualized around the sample pore after the same digestion process, and the intensity is quite similar to the plasmid DNA-NP complexes without digestion of DNaseI (lane 4). And the properties of the plasmid DNA in the DNA-nanoparticle complexes were not changed after digestion with DNaseI. It was clear that the DNA released from the DNA-NP complexes gave the same three bands (lanes 2 and 7) as those from the free plasmid DNA. The relative intensities of the bands are different for lanes 2 and 7, and the possible reason is that not all the plasmid DNA is released from the nanoparticles. These results have shown that DNA-NP complex formation was indeed efficient to provide protection against enzymatic cleavage [110].

Based on the aforementioned advantages of the amino-modified silica nanoparticles, a nonviral protective gene carrier has been developed. By using these nanoparticles, the plasmid DNA can successfully cross various systemic barriers to COS-7 cells as well as mediate high expression of the green fluorescence protein gene in cells (Fig. 24).

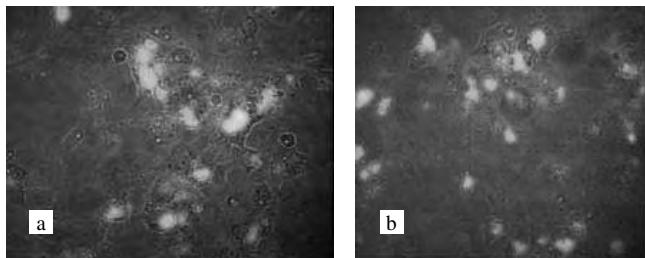


Figure 24. Transfection of plasmid DNA in COS-7 cells based on (a) amino-modified silica nanoparticle gene carrier, (b) amino-modified silica coated magnetic nanoparticle gene carrier.

Keneuer et al. developed a nonviral DNA delivery system also based on surface modified silica nanoparticles which can efficiently transfect genes into cells *in vitro* [111]. In their study, the galactosidase expression plasmid DNA pCMV/ β was immobilized on the nanoparticle surface and efficiently transfected COS-1 cells. The transfection activity was accompanied by very low cytotoxicity, with LD_{50} values in the milligrams per milliliter range.

Efforts to influence the biology of blood vessels by gene delivery have been hampered by a lack of targeting vectors specific for endothelial cells in diseased tissues. Hood et al. [112] aimed to solve this and their results showed that a cationic nanoparticle (NP) coupled to an integrin α v β 3-targeting ligand could deliver genes selectively to angiogenic blood vessels in tumor-bearing mice. The therapeutic efficacy of this approach was tested by generating NPs conjugated to a mutant Raf gene, ATP(μ)-Raf, which blocks endothelial signaling and angiogenesis in response to multiple growth factors. Systemic injection of the NP into mice resulted in apoptosis of the tumor-associated endothelium, ultimately leading to tumor cell apoptosis and sustained regression of established primary and metastatic tumors.

5.4.3. Significant Factors in Gene Delivery

During the gene delivery process, some factors predominantly contribute the transfection of biocompatible core-shell nanoparticles.

The size of the nanoparticles may be considerably related to transfection efficiency. As for nanoparticles formulated from biodegradable polymers [113], such as poly(lactic acid) and poly(D,L-lactide-co-glycolide), extensively investigated as nonviral gene delivery systems due to their sustained release characteristics and biocompatibility, the smaller sized nanoparticles showed a 27-fold higher transfection than the larger sized nanoparticles in the COS-7 cell line and a 4-fold higher transfection in the HEK-293 cell line.

Different DNA–nanoparticle complexes as well as nanoparticles conjugated with different biomolecules may result in better or worse transfection efficiency. The transfection efficiency of chitosan–DNA nanoparticles prepared using a complex coacervation process was cell-type dependent [114]. Typically, it was three to four orders of magnitude, in relative light units, higher than the background

level in HEK293 cells, and 2–10 times lower than that achieved by LipofectAMINE(TM)–DNA complexes. The present study also developed three different schemes to conjugate transferrin or KNOB protein to the nanoparticle surface. The transferrin conjugation only yielded a maximum 4-fold increase in their transfection efficiency in HEK293 cells and HeLa cells, whereas KNOB conjugated nanoparticles could improve the gene expression level in HeLa cells 130-fold.

6. CONCLUSIONS

In this chapter, we have described the structure, synthesis, characteristics, and applications in biomedicine of biocompatible core–shell nanoparticles. Different core material and different shell material can be used to construct varieties of core–shell nanoparticles. Biomolecules immobilized on the surface of nanoparticles make them more biocompatible for the application in biomedicine. By exploiting the nucleation and coating techniques, nanoparticles can be synthesized with a typical core–shell structure. Further biological modification on their surface in one-step or multistep reactions extend the range of functions and provide access to a new sort of smart functional nanoparticle for particular applications.

Due to their marvelous core–shell structure, nanometric size, and high surface to volume ratio, these core–shell nanoparticles are least toxic, highly stable, and highly sensitive compared with conventional materials or tools used in biological analysis. Based on these excellent characteristics, core–shell nanoparticles have been used in biosensing, cell recognition, bioseparation, drug delivery, gene transfection, and so on. Desirable results have been obtained and so much attention has focused on their further research.

Although the core–shell nanoparticle research has veritably exploded over the last few years and a few remarkable attempts have already been made, there is no doubt that ever-increasing advancements of science and technology, such as nanotechnology, biotechnology, materials science, medicine, and the combination of them, should allow the development of new core–shell nanoparticles with amazing properties and offer bright prospects that the applications of core–shell nanoparticles are almost unlimited.

GLOSSARY

Biocompatibility The property of being biologically compatible by not producing a toxic, injurious, or immunological response in living tissue.

Bioimaging Visualization of internal bodily organs, tissues, or cavities using specialized instruments and techniques, such as fluorescent microscopy, for diagnostic purposes.

Biomedicine The branch of medical science that deals with the ability of human beings to tolerate environmental stresses and variations and detects trace analytes of life science to understand the relationship between biological molecule structure and its function.

Biosensing Detecting a specific biological molecule, system of biological molecules, or biologically produced signal with a device.

Bioseparation Develops new and improved technologies for isolation of biomolecules or cells (e.g., proteins).

Core-shell nanoparticles A kind of nanomaterial with diameter of $1 \text{ nm} < d < 100 \text{ nm}$ and possessing typical core-shell structure.

DNA A nucleic acid that carries the genetic information in the cell and is capable of self-replication and synthesis of RNA. DNA consists of two long chains of nucleotides twisted into a double helix and joined by hydrogen bonds between the complementary bases adenine and thymine or cytosine and guanine. The sequence of nucleotides determines individual hereditary characteristics.

Drug delivery A device or material to transport drugs actively directed to the target cell, actively translocated across the cell membrane, and specifically to intervene with a particular function in the cell.

Gene delivery A device or material introducing DNA or RNA into cells, tissues, or organisms, in order to study regulation and function of genes and proteins.

Nanocapturer A nanodevice designed to obtain or separate the desired materials and information.

Nanosensor A nanodevice designed to detect specific biological molecules, chemical molecules, system of biological molecules, or biologically produced signal or other chemical process and so on.

Nucleation A process in which some material condenses into clusters or particles in settlements of increasing size and density.

Quantum dot A nanoscale crystalline structure made from cadmium selenide that absorbs white light and then reemits it a couple of nanoseconds later in a specific color. The quantum dot has been around since the 1980s when scientists were looking into the technology as a way to build nanoscale computing applications where light is used to process information. More recently, however, the technology is being used in medicine. The crystals are one ten-millionth of an inch in size and can be dissolved in water. When illuminated, they act as molecule-sized light-emitting diodes and can be used as probes to track antibodies, viruses, proteins, or DNA within the human body.

Real time The actual time in which a physical process, chemical process, or a biological process under control occurs.

Ribonucleic acid (RNA) A naturally occurring polymer composed of ribonucleotides. Although commonly found in its single-stranded form, it can adopt two- and four-stranded forms having a variety of shapes.

ACKNOWLEDGMENTS

This work was supported by the Pre-Key Project of Basic Research of the Sci. and Tec. Ministry of China (2001-51), the Key Project of the Natural Science Foundation of the People's Republic of China (20135010), the Leading Teacher Foundation of the China Education Ministry (2000-65), the Overseas Youth Scholar Co-research Foundation of the

People's Republic of China (20028506), and the National Key Basic Research Program (2002CB513100).

REFERENCES

1. W. H. Tan, Z. Y. Shi, and S. Smith, *Science* 778, 781 (1992).
2. C. D. T. Bratten, P. H. Cobbold, and J. M. Cooper, *Anal. Chem.* 70, 1164 (1998).
3. J. Corderk, X. W. Wang, and W. H. Tan, *Anal. Chem.* 71, 1529 (1999).
4. L. Jean-Marc, C. H. Joel, and T. Daniel, *Tibetech November Rev.* 13, 470 (1995).
5. C. R. Martin and D. T. Mitchell, *Anal. Chem. News Features* 70, 322A (1998).
6. B. C. Crandall, MIT Press, Cambridge, MA, 1996.
7. L. Jean-Marc, C. H. Joel, and T. Daniel, *Tibetech November Rev.* 13, 470 (1995).
8. L. W. Jennifer and J. H. Naomi, *Commentary* 11, 215 (2000).
9. R. L. Christopher, *Eng. Design* 10, 428 (2000).
10. R. C. Merkle, *Tibtech* 17, 271 (1999).
11. A. Zimmer, *A Companion Methods Enzymol.* 18, 286 (1999).
12. X. X. He and K. M. Wang, *Chinese Commun. Biomed. Res.* 31, 2 (2002).
13. W. H. Tan, S. Santra, and P. Zhang, U.S. Patent 09/572, 469, 2001.
14. S. Santra, P. Zhang, K. M. Wang, R. Tapeç, and W. H. Tan, *Anal. Chem.* 73, 4988 (2001).
15. M. Qhobosheane, S. Santra, P. Zhang, and W. H. Tan, *Analyst* 126, 1274 (2001).
16. W. C. W. Chan and S. M. Nie, *Science* 281, 2016 (1998).
17. M. J. Bruchez, M. Moronne, P. Gin, S. Weiss, and A. P. Alivisatos, *Science* 281, 1313 (1998).
18. X. X. He, K. M. Wang, and W. H. Tan, *Proc. SPIE* 394, 4414 (2001).
19. S. Mitra, U. Gaur, P. C. Ghosh, and A. N. Maitra, *J. Control. Release* 74, 317 (2001).
20. Z. R. Cui and R. J. Mumper, *Bioconjugate Chem.* 13, 1319 (2002).
21. A. Diaspro, D. Silvano, S. Krol, O. Cavalleri, and A. Gliozzi, *Langmuir* 18, 5047 (2002).
22. J. H. Duan, K. M. Wang, W. H. Tan, X. X. He, C. M. He, B. Liu, and D. Li, *Chem. J. Chinese Univ.* 24, 255 (2003).
23. A. Prokop, E. Kozlov, G. Carlesso, and J. M. Davidson, *Adv. Polym. Sci.* 160, 119 (2002).
24. M. Lai, L. Levy, K. S. Kim, G. S. He, X. Wang, Y. H. Min, S. Pakatchi, and P. N. Prasad, *Chem. Mater.* 12, 2632 (2000).
25. C. Kneuer, M. Sameti, E. G. Haltner, T. Schiestel, H. Schirra, H. Schmidt, and C. M. Lehr, *Int. J. Pharm.* 196, 257 (2000).
26. F. Debuigne, L. Jeuniau, M. Wiame, and J. B. Nagy, *Langmuir* 16, 7605 (2002).
27. M. Y. Han, X. H. Gao, J. Z. Su, and S. M. Nie, *Nat. Biotechnol.* 19, 631 (2001).
28. K. M. Wang, W. H. Tan, and D. Xiao, Chinese Patent 1342515, 2002.
29. M. A. López-Quintela and J. Rivas, *J. Colloid Interf. Sci.* 158, 446 (1993).
30. W. Y. Kim, T. Hanaoka, and M. Kishida, *Appl. Catal. A* 155, 283 (1997).
31. J. A. L. Perez, M. A. L. Quintela, J. Mira, J. Rivas, and S. W. Charles, *J. Phys. Chem. B* 101, 8045 (1997).
32. K. Osseo-Asare and F. J. Arriagada, *Colloid Surface Sci.* 50, 321 (1990).
33. K. Osseo-Asare and F. J. Arriagada, *J. Colloids Surf.* 69, 105 (1992).
34. E. Bourgeat-Lami, *J. Nanosci. Nanotech.* 2, 1 (2002).
35. X. X. He, K. M. Wang, W. H. Tan, B. Liu, X. Lin, S. S. Huang, D. Li, C. M. He, and J. Li, *Chinese Sci. Bull.* 48, 223 (2003).

36. Bans Laboratories, Inc., Covalent Coupling, Tech Note 205, 1999.
37. K. P. McNamara and Z. Rosenzweig, *Anal. Chem.* 70, 4853 (1998).
38. X. X. He, K. M. Wang, W. H. Tan, J. Li, X. H. Yang, S. S. Huang, and D. Li, *J. Nanosci. Nanotech.* 2, 317 (2002).
39. X. X. He, K. M. Wang, W. H. Tan, D. Xiao, J. Li, and X. H. Yang, *Chinese Sci. Bull.* 46, 1962 (2001).
40. R. J. Winchester, *J. Immunol.* 114, 1210 (1975).
41. P. G. Issac, Humana, Totowa, NJ, 1994.
42. E. P. Diamandis and T. K. Christopoulos, "Immunoassay." Academic Press, New York, 1996.
43. L. J. Kricka, Academic Press, New York, 1995.
44. J. D. Bui, T. Zelles, H. J. Lou, V. L. Gallion, M. I. Phillips, and W. H. Tan, *J. Neurosci. Meth.* 89, 9 (1999).
45. W. H. Tan, V. Parpura, P. G. Haydon, and E. S. Yeung, *Anal. Chem.* 67, 2575 (1995).
46. F. Sanger, S. Nicklen, A. R. Coulson, *Proc. Natl. Acad. Sci. USA* 74, 5463 (1977).
47. J. C. Fung, W. F. Marshall, A. D. Dernburg, D. A. Agard, and J. W. Sedat, *J. Cell Biol.* 141, 5 (1998).
48. D. J. Bornhop, D. S. Hubbard, M. P. Houlne, C. Adair, G. E. Kiefer, B. C. Pence, and D. L. Morgan, *Anal. Chem.* 71, 2607 (1999).
49. C. C. Chen, C. P. Yet, H. N. Wang, and C. Y. Chao, *Langmuir* 15, 6845 (1999).
50. H. J. Mattoussi, J. M. Mauro, E. R. Goldman, G. P. Anderson, V. C. Sundar, F. V. Mikulec, and M. G. Bawendi, *J. Am. Chem. Soc.* 122, 12142 (2000).
51. R. Tapeç, J. L. Zhao, and W. H. Tan, *J. Nano. Nanotech.* 3, 405 (2002).
52. S. Santra, K. M. Wang, R. Tapeç, and W. H. Tan, *J. Biomed. Opt.* 6, 160 (2001).
53. H. Harma, T. Soukka, and T. Lovgren, *Clin. Chem.* 47, 561 (2001).
54. T. Soukka, K. Anttonen, H. Harma, A.-M. Pelkkikangas, P. Huhtinen, and T. Lövgren, *Clin. Chem. Acta* 328, 45 (2003).
55. T. Soukka, H. Harma, J. Paukkunen, and T. Lovgren, *Anal. Chem.* 73, 2254 (2001).
56. "Colloidal Gold, Principles, Methods and Applications" (M. Hayat, Ed.). Academic Press, San Diego, 1989.
57. R. Elghanian, J. J. Storhoff, R. C. Mucic, R. L. Letsinger, and C. A. Mirkin, *Science* 277, 1078 (1997).
58. S. J. Park, T. A. Taton, and C. A. Mirkin, *Science* 295, 1503 (2002).
59. T. A. Taton, C. A. Mirkin, and R. L. Letsinger, *Science* 289, 1757 (2000).
60. Y. W. C. Cao and C. A. Mirkin, *Science* 297, 1536 (2002).
61. A. Abedi, J. J. Fellenstein, A. J. Lucas, and J. P. Wikswo, *Rev. Sci. Instrum.* 70, 4640 (1999).
62. S. McCullochs and D. Uttamchandani, *Opto. Electron.* 144, 162 (1997).
63. J. Corderk, X. W. Wang, and W. H. Tan, *Anal. Chem.* 71, 1529 (1999).
64. J. Li and Z. Rosenzweig, *Anal. Chim. Acta* 397, 93 (1999).
65. S. L. R. Barker and R. Kopelman, *Anal. Chem.* 70, 971 (1998).
66. S. L. R. Barker, B. A. Thorsrud, and R. Kopelman, *Anal. Chem.* 70, 100 (1998).
67. Z. Rosenzweig and R. Kopelman, *Anal. Chem.* 68, 1408 (1996).
68. M. Shortreed, E. Bakker, and R. Kopelman, *Anal. Chem.* 69, 2656 (1996).
69. X. Liu and W. H. Tan, *Mikrochim. Acta* 131, 129 (1999).
70. M. Shortreed, R. Kopelman, M. Kuhn, and B. Hoyland, *Anal. Chem.* 68, 1414 (1996).
71. J. Lou, G. Yao, and T. Drake, *OE Mag.* 22, 23 (2002).
72. H. A. Clark, M. Hoyer, M. A. Philbert, and R. Kopelman, *Anal. Chem.* 71, 4831 (1999).
73. H. A. Clark, M. Hoyer, M. A. Philbert, and R. Kopelman, *Anal. Chem.* 71, 4837 (1999).
74. H. A. Clark, S. L. R. Barker, M. Brasuel, M. T. Miller, E. Monson, S. Parus, Z. Y. Shi, A. Song, B. Thorsrud, R. Kopelman, A. Ade, W. Meixner, B. Athey, M. Hoyer, D. Hill, R. Lightle, and M. A. Philbert, *Sens. Actuators B* 51, 12 (1998).
75. J. Ji, N. Rosenzweig, I. Jones, and Z. Rosenzweig, *Anal. Chem.* 73, 3521 (2001).
76. J. H. Duan, K. M. Wang, and X. X. He, *Acta Human Univ.*, in press.
77. V. V. Schonfeldt, H. Krishnamurthy, L. Foppiani, and S. Schlatt, *Biol. Reprod.* 61, 582 (1999).
78. L. A. Herzenberg, D. W. Bianchi, and J. Schroder, *Proc. Nat. Acad. Sci. USA* 76, 1453 (1997).
79. O. W. Mueller, C. S. Hawes, and A. E. Wright, *Lancet* 336, 197 (1990).
80. P. D. Rye, *Bio/Technology* 14, 155 (1996).
81. S. V. Sonti and A. Bose, *J. Colloid. Interf. Sci.* 170, 575 (1995).
82. L. D. Zhang and J. M. Mou, "Nano-material." Liaoning Science Press, Shenyang, China, 1994.
83. X. J. Zhao, R. Tapeç-Dytioco, and K. M. Wang, *Anal. Chem.*, in press.
84. X. X. He, K. M. Wang, W. H. Tan, B. Liu, D. Li, and S. S. Huang, *Chem. J. Chinese Univ.* 24, 40 (2003).
85. I. J. Bruce, M. J. Davies, K. Howard, D. Smethurst, and M. Todd, *Pharm. Pharmacol.* 48, 147 (1996).
86. T. Hawkins, *DNA Seq.* 3, 65 (1992).
87. L. A. Guo, W. Q. Chen, and B. Q. Zhu, *Chinese J. Cell. Mol. Immunol.* 1, 1 (1999).
88. K. E. McCloskey, K. Comella, J. J. Chalmers, S. Margel, and M. Zborowski, *Biotech. Bioeng.* 75, 642 (2001).
89. L. P. Sun, M. borowski, and L. R. Moore, *J. Cytom.* 33, 469 (1998).
90. J. Kreuter, P. Ramge, V. Petrov, S. Hamm, S. E. Gelperina, B. Engelhardt, R. Alyautdin, H. von Briesen, and D. J. Begley, *Pharmaceut. Res.* 20, 409 (2003).
91. L. S. Kim and S. H. Kim, *Int. J. Pharm.* 245, 67 (2002).
92. P. Calvo and C. Remunan-López, *Pharm. Res.* 14, 1431 (1997).
93. Y. Ohya, R. Cai, H. Nishizawa, and T. Ouchi, *STP Pharma Sci.* 10, 77 (2000).
94. W. Wang, A. McConaghy, L. Tetley, and I. F. Uchegbu, *Langmuir* 17, 631 (2001).
95. D. McPhail, C. Dufes, L. Tetley, C. Dufes, and I. F. Uchegbu, *Int. J. Pharm.* 200, 73 (2000).
96. R. L. Christopher, *Eng. Design* 10, 428 (2000).
97. C. Dufes, A. G. Schätzlein, L. Tetley, A. I. Gray, J. C. Olivier, W. Couet, and I. F. Uchegbu, *Pharm. Res.* 17, 1250 (2000).
98. I. F. Uchegbu, A. G. Schätzlein, L. Tetley, J. Sludden, S. Siddique, and E. Masha, *J. Pharm. Pharmacol.* 50, 453 (1998).
99. L. Illum, I. Jabbal-Gill, M. Hinchcliffe, A. N. Fisher, and S. S. Davis, *Adv. Drug Delivery Rev.* 51, 81 (2001).
100. I. Jabbal-Gill, A. N. Fisher, R. Rappuoli, S. S. Davis, and L. Illum, *Vaccine* 16, 2039 (1998).
101. A. Bacon, J. Makin, and P. J. Sizer, *Infect. Immun.* 68, 5764 (2000).
102. L. Illum, P. Watts, and A. N. Fisher, *STP Pharma* 10, 89 (2000).
103. E. McNeela, D. O'Connan, I. Jabbal-Gill, L. Illum, S. S. Davis, M. Pizza, S. Peppoloni, R. Rappuoli, and K. H. G. Mills, *Vaccine* 19, 1188 (2000).
104. V. Dodane, M. A. Khan, and J. R. Merwin, *Int. J. Pharm.* 182, 21 (1999).
105. I. Roy, S. Mitra, and A. Maitra, *Mozumdar Int. J. Pharm.* 250, 25 (2003).
106. M. Kabbaj and N. C. Phillips, *J. Drug Targeting* 9, 317 (2001).
107. F. C. MacLaughlin, R. J. Mumper, J. Wang, J. M. Tagliaferri, I. Gill, M. Hinchcliffe, and A. P. Rolland, *J. Control. Release* 56, 259 (1998).
108. K. Roy, H. Q. Mao, S. K. Huang, and K. W. Leong, *Nat. Med.* 5, 387 (1999).

109. S. G. Zhu, H. B. Lu, J. J. Xiang, and G. Y. Li, *Chinese Sci. Bull.* 47, 654 (2002).
110. X. X. He, K. M. Wang, W. H. Tan, B. Liu, X. lin, C. M. He, D. Li, S. S. Huang, and J. Li, *J. Am. Chem. Soc.* 125, 7168 (2003).
111. C. Keneuer, M. Sameti, U. Bakowsky, T. Schiestel, H. Schirra, H. Schmidt, and C.-M. Lehr, *Bioconjugate Chem.* 11, 926 (2000).
112. J. D. Hood, M. Bednarski, R. Frausto, S. Guccione, R. A. Reisfeld, R. Xiang, and D. A. Cheresh, *Science* 296, 2404 (2002).
113. S. Prabha, W. Z. Zhou, J. Panyam, and V. Labhasetwar, *Int. J. Pharm.* 244, 105 (2002).
114. H. Q. Mao, K. Roy, V. L. Troung-Le, K. A. Janes, K. Y. Lin, Y. Wang, J. T. August, and K. W. Leong, *J. Control. Release* 70, 399 (2001).

Bioconjugated Silica Nanoparticles for Bioanalysis

Xiaojun Zhao, Lisa R. Hilliard, Kemin Wang, Weihong Tan

University of Florida, Gainesville, Florida, USA

CONTENTS

1. Introduction
 2. Synthesis and Characterization
 3. Bioconjugation
 4. Applications
 5. Conclusions
- Glossary
References

1. INTRODUCTION

Nanotechnology in combination with biomedical and other biotechnological developments promises to produce major breakthroughs and revolutionary tools in bioanalysis. One of the best ways to link biomolecules and nanotechnology is through the generation of bionanomaterials. Recently, nanoparticles have been rapidly developed and show great potential for use as efficient bionanomaterials [1–10]. Among them, luminescent nanoparticles have demonstrated great promise as optical probes in bioanalysis due to their unique optical properties and high surface-to-volume ratio [11–20]. In comparison with traditional fluorescence labeling techniques, which usually use fluorescent dye molecules to signal target bioconjugation and other biological interactions, the luminescent nanoparticle labeling method provides enhanced detectable signal and reproducibility. This advancement in luminescent techniques makes direct and rapid detection of trace amounts of biomolecules possible. To effectively use nanoparticle probes in various bioassays, conjugation of biomolecules to the luminescent probes is critically important. The most convenient and effective surface bioconjugation can be done using well established silica surface chemistry if the nanoparticle has a silica surface. As a result, silica nanoparticles can be routinely modified

to bionanomaterials suitable for various bioanalytical studies. Thus, this chapter focuses on luminescent silica nanoparticles for biomedical applications and begins with a brief review of the recent developments in the field of luminescent nanomaterials.

Several important nanoluminescent materials, including quantum dots [21–27], gold and silver nanoparticles [28, 29], and dye-doped nanoparticles [30], have demonstrated excellent signaling capabilities in the detection of trace amounts of target biomolecules. Quantum dots are remarkable luminescent nanocrystals that show great promise for simultaneous detection of multiple analytes, with a single excitation wavelength, as a result of their narrow emissions based on size. Basically, the emission energies of quantum dots shift to higher energies as the size of the quantum dots (QDs) decreases due to quantum confinement. A clear difference in emission peaks is observed with a 1–2 nm difference in QD size. Some efforts have been made to improve the solubility of quantum dots in aqueous solution in order to use them in biological environments. The recent development of water-soluble silica coated quantum dots shows promise in the bioconjugation of QDs with biomolecules [31, 32]. So far, quantum dots have been employed to label several biomolecules including proteins and oligonucleotides for cell recognition, anisotropy studies, and DNA detection. Nie and others have achieved great success in the development and applications of quantum dots [33–39]. The unique advantage of QDs with narrow emissions offers new capabilities for multicolor optical coding in gene expression studies, high-throughput screening, and medical diagnostics.

Gold nanoparticles are another attractive nanomaterial for merging nanotechnology with biotechnology due to the high affinity of the gold atom toward thiol modified molecules. Ultrasensitive analyses of oligonucleotides, proteins, and other bioanalytes have been achieved using gold nanoparticles as biomarkers [40–46]. Mirkin et al. have done extensive work in this area [47–60], especially in DNA analysis using gold nanoparticles as signaling probes. Principally, as the target biomolecules bind to the

probe molecules linked to gold nanoparticles, the formation of polymeric gold nanoparticle/polybiomolecule aggregates leads to changes in the sample's emission wavelength. The resultant fluorescence intensity reflects the amount of target molecules. Gold nanoparticles have also been extended to biomolecule detection in the solid phase. In a sandwich-based array method, a DNA-labeled gold nanoparticle hybridizes with a target sequence that has also formed a duplex with a capture sequence immobilized to a solid support. Signal is obtained from the bound gold nanoparticle probe and is further amplified by silver reduction of the gold nanoparticle probe. By utilizing different light scattering properties of oligonucleotide-capped particles, a method has also been developed for multicolor labeling and imaging of DNA arrays, which shows an ability to distinguish two different DNA targets.

Dye-doped nanoparticles provide highly luminescent signals due to the very high quantum yield of dye molecules as compared to other luminescent materials. Various organic dye-doped polymer microparticles have been developed [61–64]. Due to their hydrophobic properties, organic dye molecules are easily incorporated inside polymer matrices to form luminescent polymer particles. Some commonly used fluorophores in traditional fluorescence labeling techniques, such as fluorescein isothiocyanate and rhodamine isothiocyanate, have been applied to generate luminescent polymer particles. Polystyrene and poly(tert-butylacrylate) are polymer materials that are frequently employed to produce uniform polymer particles through the microemulsion method. The resultant particles emit high luminescence intensity. However, most biomolecule reactions take place in aqueous solutions, making polymer nanoparticles unsuitable for bioanalysis due to their hydrophobicity and bioincompatibility. Core–cell luminescent microparticles, including organosilicon microgels [65–67], have also been reported [68–71].

To develop highly effective nanoluminescent probes, we have produced dye-doped silica nanoparticles for easy bioconjugation, significant signal amplification, and excellent

reproducibility. The dye-doped silica nanoparticle contains thousands of dye molecules in a matrix of water soluble silica [30, 72–74]. Due to the large number of dye molecules (with a high quantum yield), the dye-doped silica nanoparticles provide highly luminescent signals when used as optical probes. Also, the silica matrix protects the dye molecules from environmental oxygen, and thus the dye-doped nanoparticles give highly photostable fluorescent signals. Moreover, silica is an excellent biocompatible and versatile substrate for the immobilization of biomolecules. In this chapter, we will discuss the synthesis, characterization, bioconjugation, and applications of various silica nanoparticles [61–80], including core–shell fluorescent silica particles and microgels, silica coated metal nanoparticles and quantum dots, and dye-doped silica nanoparticles. Polymer fluorescent particles and magnetic silica nanoparticles will also be briefly discussed [81–84].

It is our intent in this chapter to mainly focus on dye-doped silica nanoparticles and their utilization in biomedicine. We believe that each one of the biolabeling reagents listed in Table 1 has its own advantages and can be preferably used in unique applications in order to best exploit the strengths of each probe.

2. SYNTHESIS AND CHARACTERIZATION

There are two major silica nanoparticle synthesis methods, Stöber [83] and reverse microemulsion [94–96], which provide a silica matrix by hydrolysis and polymerization of tetraethylorthosilicate (TEOS). The Stöber method requires a shorter synthesis time than the microemulsion method but results in relatively large, nonuniform nanoparticles. In contrast, the reverse microemulsion method provides monodisperse and smaller sized silica nanoparticles. Thus, the majority of the silica nanoparticles discussed here is synthesized using the reverse microemulsion method.

The reverse microemulsion method, also called water-in-oil (W/O) microemulsion, is based on an isotropic and thermodynamically stable, single-phase system that consists

Table 1. Comparison of fluorescence labeling reagents for bioanalysis.

Characteristics	Dye-doped NP	Fluorophores	Quantum dots
Signal amplification	Extremely high, up to 100,000 × 1 Fluorophore	Low	<20× of 1 Fluorophore
Photostability	Excellent without photobleaching	Poor	Excellent with minimal photobleaching
Ability to bioconjugate	Easy and universal	Easy, but nonuniversal	Still under investigation and progress being made
Aqueous solubility	Excellent	Mostly excellent, but some low	Low
Multiplex analysis capability	Possible and under investigation	Difficult	Excellent
Toxicity	None	Severe	Minimal
Environmental influence	None	Severe	Minor
Manufacturing	Easy and batch production possible	N/A	Difficult
Compatibility with existing detection system	Excellent	Excellent	Very good
Overall feasibility for bioanalysis	Great potential	Good	Great potential, still under investigation

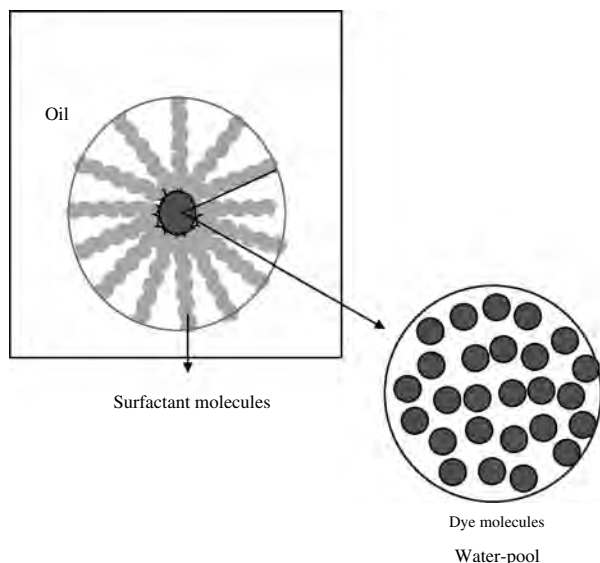


Figure 1. Schematic diagram of water-in-oil microemulsion system for synthesis of silica nanoparticles.

of small amounts of water, a large volume of oil, and a surfactant. The surfactant molecules lower the interfacial tension between water and oil, resulting in the formation of a transparent solution. Water nanodroplets (also called water pools) are formed in the bulk oil phase and serve as nanoreactors for the synthesis of nanoparticles from various materials (Fig. 1). The size of the water pool influences the size of the nanoparticles. By changing the molar ratio of water to surfactant (W_0 value), the size of the spherical nanoparticles is controllable. In general, the higher the value of W_0 , the larger the particle size will be. The excess base in the microemulsion initiates the polymerization reaction through hydrolysis of TEOS and finally forms the network silica matrix [97]. The rate of the polymerization is much slower in the microemulsion in comparison to that in a bulk aqueous solution. Therefore, as the polymerization reaction proceeds, monodisperse silica nanoparticles are formed.

The Stöber method is based on hydrolysis and polymerization of TEOS using either base or acid in a bulk ethanol solution. Using this method, different sizes of silica particles are obtained ranging from 100 nm to 1 μm in diameter. The size of the particles can be tuned by changing the experimental conditions, such as temperature, polymerization time, and silica precursor (TEOS) concentration. Although this method is relatively simple and easy to carry out in only a few hours, it is limited by the nonuniformity of the produced nanoparticles. Consequently, this method is usually used as an alternative procedure for the preparation of large silica nanoparticles.

Using the W/O microemulsion method, the produced silica nanoparticles have very uniform size, which is characterized by scanning electron and transmission electron microscopy (SEM and TEM) (Fig. 2). Inorganic and organic dye-doped silica nanoparticles show the same size distribution. Given the different applications for bioanalysis, various sized silica nanoparticles can be obtained by controlling the W_0 value and using different surfactants. For example

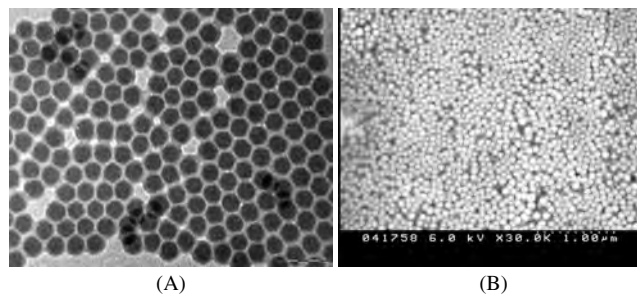


Figure 2. SEM images (A) and TEM images (B) of synthesized silica nanoparticles using the reverse microemulsion method.

at $W_0 = 10$, the nanoparticle size is 60 ± 3 nm in diameter; RuBpy-doped silica nanoparticles of this size have been used in applications for cell recognition and bacteria detection [76, 78].

2.1. Pure Silica Nanoparticles and Core-Shell Silica-Polymer Particles

To take advantage of the high surface to volume ratio of the nanoparticles, pure silica nanoparticles were synthesized for application as effective solid supports in bioanalysis. Both Stöber and reverse microemulsion methods were used as will be described.

Very uniform pure silica nanoparticles were synthesized using the W/O microemulsion method. In an organic solvent solution, cyclohexane, surfactant (Triton X-100), and a co-surfactant (*n*-hexanol) were mixed. A small volume of water (amount dependent upon the desired nanoparticle size) was then added to the system to form an isotropic and thermodynamically stable single phase. In the presence of TEOS, a polymerization reaction was initiated by adding a small amount of NH_4OH (28–30 wt%). The reaction was allowed to proceed for 24 hours with continuous stirring. After the reaction was completed, the silica nanoparticles were isolated from the solution using acetone to break the single phase of the microemulsion system, followed by washes in ethanol and acetone to remove any surfactant molecules. The resultant nanoparticles were air-dried at room temperature.

The Stöber method was also used to obtain pure silica nanoparticles [80]. The synthesis process was carried out in a bulk of ethanol solution with various amounts of TEOS. The solution was cooled to 0 $^\circ\text{C}$ in an ice cooled ultrasonicator. Ammonium hydroxide (NH_4OH , 28–30 wt%) was added to the solution with ultrasonication. After reacting for 1 hour, the nanoparticles were separated from the solution, washed 5–6 times with water and acetone, and air-dried.

The pure silica nanoparticles obtained from the W/O microemulsion method were small and uniform while the nanoparticles from the Stöber method were relatively large. Both pure silica nanoparticles demonstrated good support when used as a solid substrate for DNA detection and enzyme catalyzed reactions in aqueous solutions [79, 80].

The silica particles can be further coated with various polymers to form core-shell silica-polymer particles that may have different applications in material science and biomedicine [84], such as the stabilization of pigments in

paints and drug delivery. So far, several core-shell particle synthesis methods have been reported, including copolymerization of hydrophobic monomer core-hydrophilic shells [85], and different self assembly approaches [86–90]. Among various assembly methods, a colloidal assembly of polystyrene shell on the silica particle surface is simple and attractive [84]. As shown in Figure 3, the colloidal assembly process was controlled by either specific chemical or biochemical interactions. For the chemical reaction, the amine-modified particles were first activated by glutaraldehyde followed by chemical binding with amine-modified polystyrene nanoparticles. For the biochemical reaction, the glutaraldehyde-activated silica particles were coated with avidin; then biotin-labeled polystyrene nanoparticles were assembled onto the silica particle surfaces. The assembled polymer particles on the silica particle surface were subsequently heated at temperatures above the glass transition of the polymer nanoparticles, allowing the polymer to flow over the silica particle surface and resulting in a uniform core-shell composite (Fig. 4). Due to the stability of the

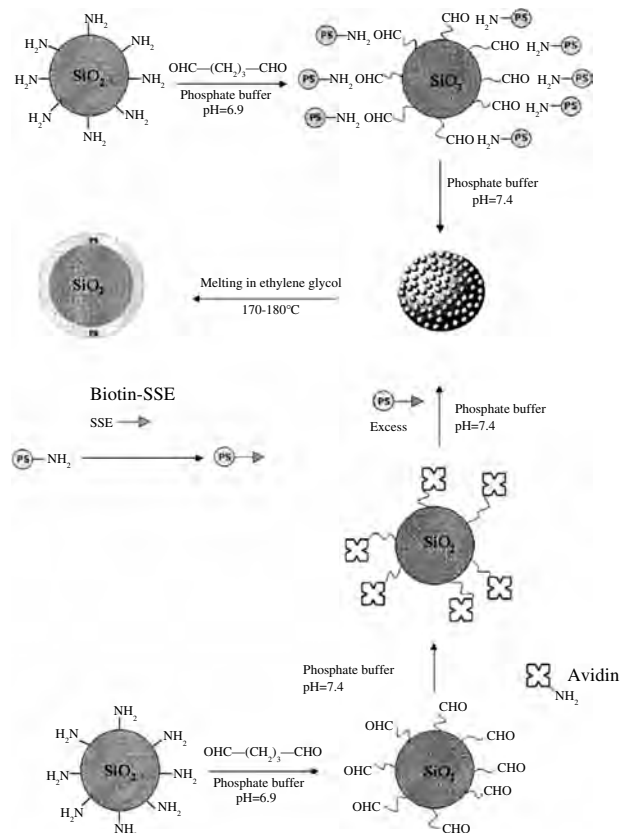


Figure 3. Reaction scheme for assembling composite materials via both glutaraldehyde chemistry and biospecific interactions. The top section illustrates assemblies starting with amine-labeled silica. Glutaraldehyde treatment of the labeled silica is followed by reaction with amine-modified polystyrene nanoparticles. The resultant material is heated to melt the polystyrene and form the polymer shell. The bottom section illustrates assembly of biotin-labeled polystyrene nanoparticles onto avidin coated silica microspheres. Reprinted with permission from [84], M. S. Fleming et al., *Chem. Mater.* 13, 2213 (2000). © 2000, American Chemical Society.

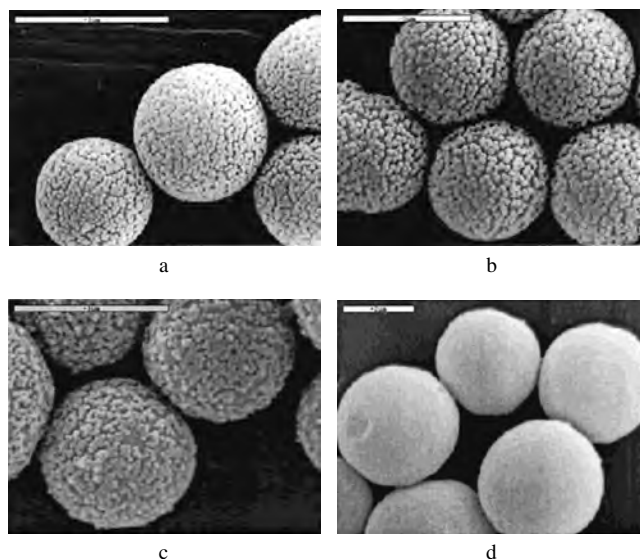


Figure 4. (a) Three μm silica particles assembled with 100 nm polystyrene particles; (b) 5 μm silica particles assembled with 200 nm polystyrene particles; (c) 5 μm silica particles assembled with 100 nm polystyrene particles. (d) Resultant polymer coated silica particles after heating of the assembled material. Reprinted with permission from [84], M. S. Fleming et al., *Chem. Mater.* 13, 2214 (2000). © 2000, American Chemical Society.

bonds between the polymer and silica, a wide range of pHs, ionic strengths, and solvents can be applied in the assembly process.

2.2. Core-Shell Fluorescent Silica Particles

To obtain highly fluorescent, photostable, and biocompatible nanoparticles for bioanalysis, several fluorescent silica nanoparticles were developed [30, 72–74]. The basic idea was to entrap a large number of dye molecules inside a single nanoparticle so that each individual nanoparticle would emit a strong fluorescent signal and thus serve as a highly fluorescent probe.

A core-shell fluorescent silica particle is one type of highly fluorescent material that consists of an organosilica fluorescent core and a silica shell, which was developed by van Blaaderen et al. [68–70] and recently reviewed by Schärftl [71]. The fluorescent molecules, such as fluorescein isothiocyanate and rhodamine isothiocyanate, were covalently attached to the silane coupling agent 3-(aminopropyl)triethoxysilane (APS). The reaction product between APS and fluorescent dyes was incorporated into a silica core via polymerization of the TEOS (Stöber method). The resultant fluorescent silica core was further coated with another silica shell by a second polymerization of TEOS. The nonfluorescent shell of the particles did not block the fluorescence of the core. Moreover, with efficient shell thickness, the fluorescence signals of the individual particles were clearly separated in the fluorescence images even though the concentration of the particles was very high. This property makes the core-shell fluorescent particles very useful for generating a highly concentrated colloidal system for bioanalysis.

Organosilicon microgels with a dye-labeled core and a protective nonfunctionalized shell are a novel type of core-shell fluorescent particle developed by Schärfl et al. [71]. This particle has larger porosity and a lower density than other core-shell silica particles. The synthesis process is schematically illustrated in Figure 5. A reactive core was first formed by condensation of trimethoxymethylsilane (TMOMS) and chlorobenzyltrimethoxysilane. The core was then coated with a nonfunctional shell of pure TMOMS. To avoid chemical aggregation, the particle surface was reacted with monosilane. Finally, the produced core-shell particles were converted to functional dye-labeled microgels by dissolving the particles in tetrahydrofuran, and using the $-\text{CH}_2\text{Cl}$ groups for esterification with the carboxylate group of a dye molecule, which diffuses through the micropores of the TMOMS shell into the reactive core. Several fluorescent dye molecules containing COO^- groups, such as coumarin 343 and pyrene, have been incorporated into the microgels. The dye molecules remained inside the microgel network without leakage, making the fluorescent microgels a stable optical tracer for bioanalysis.

2.3. Dye-Doped Silica Nanoparticles

2.3.1. Inorganic Dye-Doped Silica Nanoparticles

Inorganic dye-doped silica nanoparticles were first developed using the W/O microemulsion method. The synthesis method is effective because of the electrostatic attraction between the positively charged metal ions in the inorganic dye molecules and the negatively charged silica matrix of the nanoparticles. Due to the hydrophilic property of inorganic dye molecules, they are easily dissolved in aqueous solution and retained in the water pool during the TEOS polymerization reaction. Thus, after the negatively charged silica matrix forms, the inorganic dye molecules are trapped inside by electrostatic interactions, resulting in inorganic dye-doped silica nanoparticles.

A commonly used inorganic dye molecule, tris(2,2'-bipyridyl) dichlororuthenium (II) (RuBpy), was employed

as a dopant in the W/O microemulsion [30]. The synthesis procedure was similar to the pure silica nanoparticle synthesis method using the W/O microemulsion system described earlier. Instead of the pure water, dye in aqueous solution was added to the water pool. The resultant dye-doped nanoparticles contain tens of thousands of dye molecules. However, the luminescence intensities of the dye-doped nanoparticles were not proportional to the amounts of loaded dye molecules. As the loaded dye amount increases, the luminescence intensity of the nanoparticles increases up to a certain dye concentration limit. Approximately 20 wt% loading of dye molecules is an optimal amount, indicated by maximum luminescence intensity of the nanoparticles. Further dye loading reduced the luminescent signal due to self-quenching of the dye molecules. To make the nanoparticle size compatible with biomolecules for more effective use in bioanalysis, much smaller sized nanoparticles, ranging from 10 to 90 nm in diameter, were prepared using different surfactant types and W_0 values (Fig. 6).

2.3.2. Organic Dye-Doped Silica Nanoparticles

Given the higher quantum yield of organic dyes than inorganic ones, the doping of organic dyes inside silica nanoparticles is an improved alternative for obtaining highly fluorescent probes. Inspired by the success of the inorganic dye-doped silica nanoparticle synthesis, we then focused on the development of organic dye-doped silica nanoparticles. However, it was difficult to trap organic dye molecules inside the silica matrix using either the W/O microemulsion or the Stöber method. Two factors hindered the retention of the organic dye molecules inside the silica matrix in the synthesis process of the silica nanoparticles. One is the hydrophobic property of the organic compounds. Some organic dye compounds cannot dissolve in aqueous solution; some partially dissolve in the water solution but their solubility in organic reagents is much higher than in the aqueous solution. Thus, even though they first dissolve in the water pool in the W/O microemulsion system, they quickly transfer to the

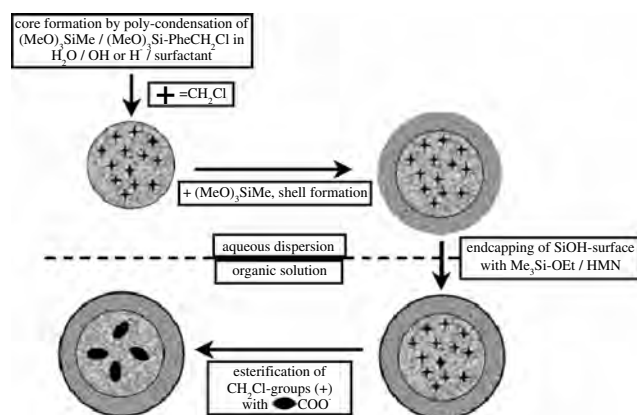


Figure 5. Preparation of organosilicon microgels with dye-labeled and nonfunctional protective shell (HMN = hexamethyldisilazane). Reprinted with permission from [71], W. Schärfl, *Adv. Mater.* 12, 1903 (2000). © 2000, Wiley.

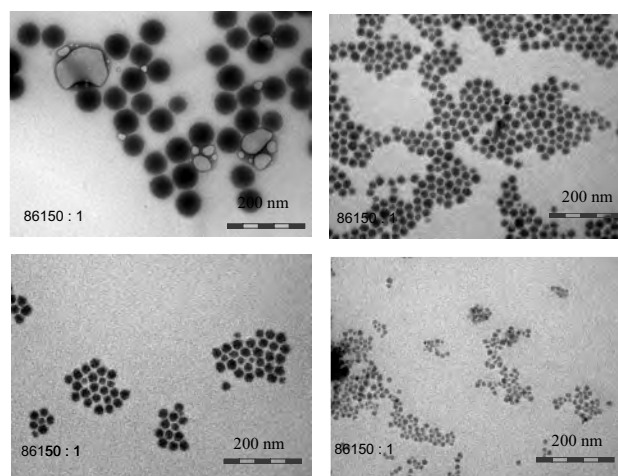


Figure 6. TEM images of various sizes of RuBpy-doped silica nanoparticles synthesized with different types of surfactants and water to surfactant ratios.

organic phase, resulting in pure silica nanoparticles. The second reason is the lack of attraction force between organic molecules and the silica matrix. Unlike RuBpy, most organic dye molecules have neutral charges, and thus there is no electrostatic attraction to retain the dye molecules inside the silica matrix. Thus, water solubility and positive charge are two essential requirements for obtaining dye-doped silica nanoparticles using the W/O microemulsion and Stöber methods. All the methods to be described for the synthesis of organic dye-doped silica nanoparticles focus on the exploration of novel approaches based on these two requirements.

Rhodamine 6G (R6G) and tetramethylrhodamine (TMR) are commonly used organic fluorophores in bioanalysis due to their high quantum yield and suitable excitation and emission wavelengths for most conventional optical sources and instrumental detection systems. Therefore, these two dye molecules were chosen to explore new synthesis methods for organic dye-doped silica nanoparticles.

R6G-Doped Silica Nanoparticles The goal of this Stöber-based synthesis approach was to reduce the hydrophilicity of the silica matrix so that the highly hydrophobic R6G molecules would be trapped inside the nanoparticle matrix [72]. TEOS was still used as a hydrophilic silica precursor in the system. In addition, a relatively hydrophobic silica compound, phenyltriethoxysilane (PTES), was also added to the system as a second precursor to aid in trapping the organic fluorophores. Since the matrix was changed to a mixed medium of hydrophilic and hydrophobic components, R6G was more retained in this matrix, resulting in R6G-doped silica nanoparticles. This method was previously used for the synthesis of hydrophobic-dye-doped microspheres [88]. The silica nanoparticle formation was a three-step process: (a) hydrolysis of the silica precursors TEOS and PTES to silanols, (b) polymerization, and (c) nanoparticle formation. For the preparation of the R6G-doped nanoparticles, a dye solution in ethanol was mixed with PTES. Hydrochloric acid or ammonium hydroxide was added to the resulting solution to start the hydrolysis of the PTES. The completion of the reaction was indicated by the formation of a one-phase system after a few hours. TEOS, which also hydrolyzes in the presence of ammonium hydroxide, was then added to the system. The reaction proceeded for 1 hour at 0 °C with continuous sonication and frequent vortexing. An excess amount of acetone was then added to stop the growth of the nanoparticles. The size of R6G silica nanoparticles can be controlled by the polymerization time.

The amount of PTES was an important factor for the entrapment of R6G in the silica nanoparticles. An increase in the amount of PTES resulted in a corresponding increase in the amount of doped dye molecules. The assumed driving force for the entrapment of the dye molecules is the affinity between the hydrophobic dye molecules and PTES. At high PTES concentrations, the produced nanoparticles possess a high degree of hydrophobicity and thus hinder subsequent nanoparticle surface biomodification.

Nanoparticles obtained through this approach exhibited high fluorescent intensity, excellent photostability, and minimal dye leakage after prolonged storage in aqueous solution. Applications of the R6G-doped silica nanoparticles

illustrated their utility as fluorescent probes for ELISA-like assays in BSA determination and as biosensors in glutamate analysis [72].

TMR-Doped Silica Nanoparticles The obtained R6G-doped silica nanoparticles are relatively large and nonuniform due to the employment of the Stöber-based method. To obtain a better organic dye-doped silica nanoparticle, a different synthesis approach was explored. The new design for the synthesis of TMR-doped silica nanoparticles was based on the W/O microemulsion method. Unlike the scheme of the synthesis of R6G-doped silica nanoparticles which altered the composition of the silica matrix, the aim of this approach was to change the property of the water pool in the microemulsion system to make the TMR molecules meet the two requirements for the synthesis of organic dye-doped silica nanoparticles [73].

Since TMR molecules are neither positively charged nor hydrophilic compounds, more than one modification procedure was initially needed to trap TMR molecules inside the silica matrix. To avoid complicated synthesis procedures, a novel approach was designed to complete the two objectives within one step using the W/O microemulsion method. The basic idea employs a special binary compound to form the bulk of water pool; this compound has both organic and inorganic properties and acts as an aqueous solvent to dissolve and retain the TMR molecules inside the water pool. Moreover, this compound also provides enough protons to induce positive charges on the TMR molecules. Acetic acid (HAc) is an ideal compound that meets all the requirements. First, acetic acid acts as an organic reagent capable of dissolving the TMR molecules. Second, TMR-HAc remains in the water pool in the W/O microemulsion system because in the presence of both water and oil, HAc has a greater affinity for the water phase than the oil phase. Third, acetic acid provides protons for the TMR and makes it positively charged. Thus, TMR molecules can be trapped inside the silica matrix using acetic acid as a solvent to form TMR-doped silica nanoparticles; this approach is simple and easy to carry out. Compared to inorganic dye-doped nanoparticles, the TMR-doped silica nanoparticles provide much higher fluorescent signals. Preliminary results show that these TMR-doped silica nanoparticles, despite the formation of aggregates, can be used as highly fluorescent biomarkers for cancer cell recognition and detection.

TMR-Dextran Doped Silica Nanoparticles An alternative approach for the synthesis of TMR-doped silica nanoparticles was also developed using a TMR-dextran complex [74]. By linking a highly hydrophilic dextran molecule to a TMR molecule, the TMR was converted to a hydrophilic molecule and thus could be trapped inside the water pool in the microemulsion system. However, due to the lack of a combination force between the TMR-dextran complex and the silica matrix, the TMR-dextran easily leaked out from the silica matrix when it was used in an aqueous solution. To efficiently trap TMR molecules inside the silica, TMR-dextran complex needed to become positively charged. By adding a low pH hydrochloric acid solution to the water phase in the microemulsion system, the TMR molecules were firmly entrapped in the silica matrix,

resulting in highly fluorescent TMR-doped silica nanoparticles (Fig. 7). TMR-dextran-doped silica nanoparticles showed excellent capability as a highly fluorescent probe for detection of DNA molecules [77].

2.3.3. Signal Amplification and Photostability of Dye-Doped Silica Nanoparticles

To evaluate the effect of the signal amplification of three types of dye-doped silica nanoparticles described, a series of comparisons of the fluorescent intensities between the dye-doped nanoparticles and the corresponding dye molecules was carried out in aqueous solution using a spectrofluorometer. The results showed that the fluorescence intensity of one dye-doped nanoparticle was approximately 10^4 times higher than that of one dye molecule when each dye-doped nanoparticle is observed at its maximum fluorescence intensity. For TMR-dextran-doped silica nanoparticles, the dextran molecules did not affect the nanoparticle fluorescence intensity as compared to TMR-doped silica nanoparticles because excessive loading of TMR molecules reduces fluorescent intensity of the nanoparticles due to TMR molecule self-quenching effect. Thus, one dye-doped nanoparticle contains approximately 10^4 effective dye molecules. This result is the foundation for the extremely high signal enhancement provided by dye-doped nanoparticles when they are used as fluorescent probes for bioanalysis (Fig. 7).

The excellent photostability of dye-doped silica nanoparticles was proven by the following comparisons. Solutions of three types of dye-doped silica nanoparticles and corresponding dye molecules were prepared. For each comparison, a pair of samples with the same fluorescent intensity, a dye solution and a dye-doped nanoparticle solution, were continuously irradiated with excitation light for 1000 seconds. The fluorescence intensity of the pure RuBpy molecules was reduced by 81%, while the fluorescence intensity of RuBpy-doped silica nanoparticles remained constant (Fig. 8).

To further verify the RuBpy-doped silica nanoparticle's optical stability, a different experiment was carried out by varying the oxygen level during excitation. It is known that oxygen greatly quenches RuBpy, and thus RuBpy is used as an oxygen sensing reagent. However, RuBpy-doped silica nanoparticles showed great stability to oxygen at high oxygen concentrations up to 8 psi. The reason for the high

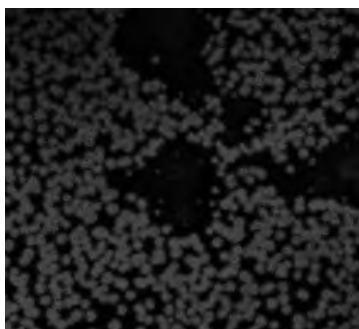


Figure 7. Fluorescence image of TMR-dextran-doped silica nanoparticles.

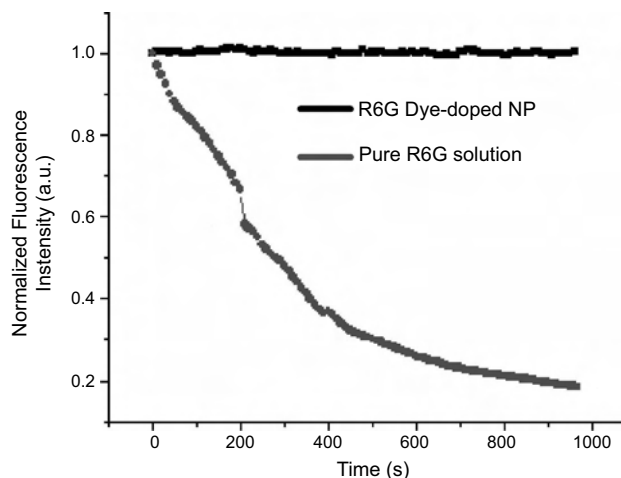


Figure 8. Comparison of photostability of dye-doped silica nanoparticles vs pure dye molecules. Reprinted with permission from [72], R. Tavec et al., *J. Nanosci. Nanotech.* 2, 3–4, 405 (2002). © 2002, American Scientific Publishers.

photostability of dye-doped silica nanoparticles is the protective function of the silica matrix, which acts as a shield to isolate dye molecules from environmental oxygen, thus allowing the dye molecules inside silica to provide a constant fluorescence signal in various environments. This high photostability of the nanoparticles provides a foundation for precise and reproducible analytical measurements when nanoparticles are used as fluorescent probes.

2.4. Silica Coated Metal Particles

2.4.1. Silica Coated Luminescent Metal Nanoparticles and Quantum Dots

As discussed in the Introduction, quantum dots and metal nanoparticles, such as gold and silver, are attractive luminescent nanomaterials. To use these nanomaterials in different systems, silica shell coated gold clusters and quantum dots were developed [91, 92]. The shell of the silica does not change the optical and electrical properties of the metal particles. Moreover, the silica shell stabilizes the individual particles by reducing metal particle aggregation (Fig. 9) [93]. The synthetic principle is to provide a silane coupling agent for the metal surface and then the agent is used as an anchor point for chemical deposition of active silica [84]. The development of this sort of silica coated metal material has been systematically reviewed by Schärtl [71].

2.4.2. Silica Coated Magnetic Nanoparticles

Magnetic nanoparticles are very important in the separation of a variety of biomolecules [99, 100]. However, the inherent property of nanoparticle aggregation and the biodegradation of biomolecules restrict magnetic nanoparticle's bioapplications. A suitable coating prevents these limitations and makes the magnetic nanoparticles more practical for bioanalysis. Based on this idea, silica coated magnetic nanoparticles were developed using the W/O microemulsion method [82].

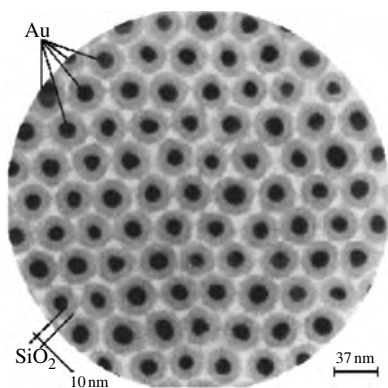


Figure 9. TEM micrograph of silica coated gold clusters. Reprinted with permission from [93], M. Giersig et al., *Adv. Mater.* 9, 572 (1997). © 1997, Wiley-VCH.

Two separate microemulsions (ME1 and ME2) were prepared using each surfactant, Brij-97, Igepal CO-520, and Triton X-100, respectively. ME1 contained the iron salts, FeSO_4 or FeCl_2 and FeCl_3 , whereas ME2 contained the base, either NaOH or NH_4OH . All aqueous solutions were prepared with deoxygenated pure water. ME2 was allowed to stir for an hour and then was added to ME1. The resultant microemulsion was further reacted for 12 hours, and the water droplets collided and coalesced to form the nanoparticles. Nitrogen gas was used to continuously purge the mixture when NaOH was used. The formation of pure magnetic nanoparticles was visually recognized by a change in color of the microemulsion mixture to dark brown [101]. To form a silica coating layer outside the magnetic core, TEOS was added to the system. The base-catalyzed hydrolysis of TEOS produced silica acid, which undergoes polymerization to produce the silica coating layer. Resultant silica coated magnetic nanoparticles were isolated after 24 hours of aging using acetone and ethanol washes.

The produced magnetic nanoparticles were characterized using TEM, X-ray electron diffraction, and superconducting quantum interference device magnetometry. The results showed that the size of the nanoparticles was ultrasmall and the magnetic property was very strong, close to that of pure superparamagnetic materials. The silica coating layer provided a convenient biocompatible surface that allowed the conjugation of various biomolecules to the magnetic nanoparticles. These silica coated magnetic nanoparticles have the potential to be useful in biomolecule separation and drug delivery.

2.5. Polymer Fluorescent Particles

Synthesis techniques for polymer fluorescent particles have been widely developed. Various commercial polymer fluorescent particles, which are loaded with different dye molecules, are available. [Molecular Probes (Eugene, OR) is one of the biggest suppliers of a wide variety of polystyrene fluorescent beads [102].] The fluorescent intensity of the polymer beads is sufficient to allow visualization of single particles. Meanwhile, the polymer particles show good photostability when they are excited with the intense illumination required for fluorescence microscopy. So far, the

smallest size of polystyrene fluorescent beads produced by Molecular Probes is 20 nm in diameter. In order to apply the fluorescent beads to bioanalysis, several different functional groups have been linked to the bead surface, including carboxylates, sulfates, aldehyde-sulfates, amines, and avidin/biotin.

Fluorescent polymer particles are synthesized with different polymers. Polymerization of methyl methacrylate (MMA) loading dye molecules to form fluorescent particles is one example. Passirani et al. [103] prepared such fluorescent nanoparticles by random copolymerization of MMA and *N*-vinyl carbazole (NVC). The NVCs were covalently linked to PMMA, resulting in fluorescent nanoparticles that can be used as *in vivo* monitor targets.

3. BIOCONJUGATION

Simple and reliable bioconjugation is very important for nanoparticle applications. The silica-based nanoparticles can be useful in bioanalysis only when they are conjugated to recognition biocomponents which contain special elements that selectively interact with target analytes. Silica surface chemistry has been well established for bioconjugation of various molecules when used as a solid support. Most of these surface modification methods are easily adapted to attach biomolecules to the silica nanoparticle surface. The bioconjugation methods to be discussed are based on previously reported silica surface immobilization knowledge [104–109].

Using various biochemical binding approaches, the nanoparticle surface can be modified to contain functional groups that are useful for subsequent surface modification and biomolecule immobilization. Some commonly used functional groups biochemically added to the silica nanoparticle surface include amines, carboxyls, and thiols. The most frequently used biomolecule linking bridge, the avidin–biotin linkage, was also adapted for bioconjugation of probe molecules onto the silica nanoparticles. Various biomolecules including oligonucleotides, enzymes, antibodies, and other proteins have been immobilized onto the nanoparticles using this method, clearly demonstrating the advantage of the silica matrix in providing bioversatility.

3.1. Avidin–Biotin Linking Bridge

The affinity constant between avidin and biotin is 10^{15} l/mol, which is 10^5 – 10^6 times higher than that of regular antibody–antigen. Therefore, the avidin–biotin linkage is a great conjugation approach to bind biomolecules onto the silica nanoparticles, which has been used for immobilization of biomolecules on the glass substrate [108]. Usually, biotin easily links to biomolecules to form recognition agents, and thus many biotinylated biomolecules are commercially available. As long as avidin molecules are immobilized to the nanoparticles, upon avidin–biotin binding, the recognition biomolecules steadily remain on the nanoparticle surface for subsequent binding and identification of target biomolecules.

This avidin immobilization process is very simple mainly based on electrostatic attraction. The silica surface of the

nanoparticles is negatively charged, which allows the positively charged avidin to passively adsorb on the silica surface. By incubating appropriate concentrations of avidin with the silica nanoparticles for 12 hours at 4 °C, the avidin is adsorbed on the nanoparticle surface. To stabilize the adsorption, a cross-linking step is followed using 1% glutaraldehyde solution, which has two carboxyl groups at both ends of the molecule. The remaining unbound carboxyl groups can be blocked by reacting them with a buffer containing primary amine groups (Tris-HCl) for 3 hours. The resulting avidin-coated silica nanoparticles conjugate to biotinylated molecules via a strong avidin–biotin affinity (See Fig. 10).

3.2. Disulfide-Coupling Chemical Binding

Disulfide-coupling chemistry has proven to be an efficient method for the immobilization of oligonucleotides to a substrate [109]. Unlike most of the other covalent attachment processes, this method does not require preactivation or reduction of the disulfide groups to generate more reactive, however, unstable thiol species. The disulfide-modified oligonucleotides are directly coupled to the silane-activated silica surface without any pretreatment. Potential side reactions are minimized due to the specificity of the thiol/disulfide exchange reaction.

To covalently attach oligonucleotides, the silica nanoparticles were silanized with 1% 3-mercaptopropyltrimethoxy-silane in 95% ethanol and 16 mM acetic acid (pH 4.5) for 30 minutes at room temperature and rinsed with ethanol and acetic acid. Then, the nanoparticles were cured for approximately two hours in a vacuum oven at 150 °C, forming functional thiol groups on the silica nanoparticle surfaces. A disulfide-modified oligonucleotide was used as a probe DNA attached onto the nanoparticle surface through disulfide-coupling. This process was performed by directly adding disulfide-modified oligonucleotide to the silane-activated silica nanoparticles and incubating for 15–21 hours in a humid chamber. The immobilized nanoparticles were then washed in a buffer containing 0.05% Tween 20. Using this process, a probe DNA sequence was bioconjugated to the silica nanoparticles through disulfide-coupling chemical binding [79].

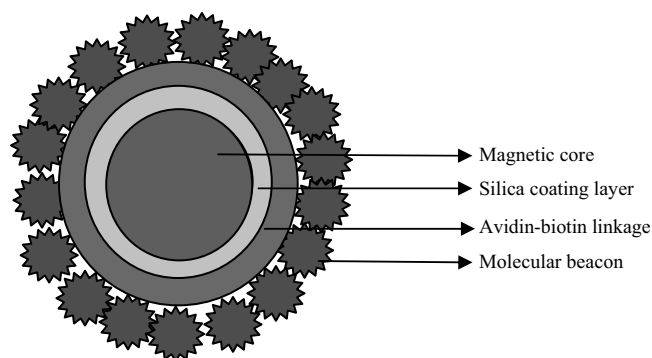


Figure 10. Schematic diagram of genomagnetic nanocapturer.

3.3. Amino-Group Derivatization Linkage

An effective bioconjugation approach for the immobilization of proteins, such as enzymes and antibodies, onto the silica nanoparticles is to chemically link amino groups on the nanoparticle surface. Then, the amino groups on the surface of the proteins can replace the same group on the nanoparticle, leading to chemically bound proteins on the silica nanoparticles. The procedure used in this method is more complicated than the other two methods described. The advantage of this approach is a more stable binding between the silica nanoparticles and proteins that can last until the proteins become inactive [80].

The silica nanoparticles were silanized by immersion in 1% (v/v) solution of distilled trimethoxysilylpropyldiethylenetriamine (DETA) and 1 mM acetic acid for 30 minutes at room temperature (23 °C). The DETA modified silica nanoparticles were thoroughly rinsed with deionized water to remove excess DETA. The silanized particles were then treated with 10% succinic anhydride in dimethylformamide solution under an argon atmosphere and stirred for 6 hours [110]. The resulting carboxylate modified particles were washed with deionized water. Two different approaches were used, based on Bangs Labs [111] protocols, to further modify the nanoparticle. The first approach used carbodimide hydrochloride in an activation buffer to produce *o*-acylisourea intermediate on the nanoparticle surface. Then, the proteins with available amine groups were bound to the modified silica nanoparticles through amine bonds by immersion of the nanoparticles in a suitable concentration of protein solution. The nanoparticles were subsequently washed and ultrasonicated to remove any physically adsorbed protein molecules on the silica surface. The second approach was to add a water-soluble *N*-hydroxysuccinimide along with carbodimide hydrochloride to the carboxyl modified silica nanoparticles. The active ester intermediate formed by the *N*-hydroxy compound replaced the *o*-acylisourea intermediate, which was more stable for hydrolysis, and thus the coupling efficiency of proteins to the nanoparticles was increased. After probe protein immobilization on the nanoparticle surface, 1% BSA was used to block unreacted functional groups to prevent non-specific binding in later reactions with target biomolecules.

An alternative approach also provided effective bioconjugation of proteins to the silica nanoparticles by activating the nanoparticles with sodium carbonate [111]. A solution of cyanogen bromide in acetonitrile was added to the nanoparticle suspension to yield –OCN groups on the nanoparticle surface. The produced modified nanoparticles can directly bind to the biomolecules containing free amino groups [78]. Using the aforementioned conjugation methods, the produced bioconjugated silica nanoparticles well retain the original activity of the biomolecules.

4. APPLICATIONS

Several significant bioapplication areas have been exploited using the three types of developed silica nanoparticles, including pure silica nanoparticles [79, 80], dye-doped silica nanoparticles [30, 72–78], and magnetic nanoparticles [81].

This section focuses on how dye-doped silica nanoparticles have shown great signal amplification as fluorescent biomarkers for trace bioanalysis. In addition, silica coated magnetic nanoparticles have been used for biomolecule separations, and pure silica nanoparticles have served as solid support substrates for bioanalysis.

4.1. Cell Recognition

Luminescent nanoparticles are novel labeling probes that offer highly enlarged detectable signals in bioanalysis. Generally, identification and detection of bioanalytes are carried out with labeling technologies that use fluorescent dyes to provide a detectable signal [112]. Of the various available fluorescent materials, organic dye molecules are frequently used due to their high quantum yield [113]. However, the sensitivity of methods using organic dyes is limited by a low number of recognizable components in trace amounts of biosamples; thus, there are not enough detectable fluorescent signals. In addition, all dye molecules suffer from rapid photobleaching [114], resulting in unstable and inaccurate fluorescence signals. In contrast, newly developed dye-doped silica nanoparticles contain a large number of dye molecules for signaling targets and have excellent photostability due to the silica matrix protection. Therefore, dye-doped silica nanoparticles are ideal fluorescent probes because they provide significantly amplified and photostable signals. The following three applications of dye-doped silica nanoparticles have shown this promise in bioanalysis and biotechnology.

RuBpy-doped silica nanoparticles were first used in bioanalysis to identify leukemia cells with antibody–nanoparticle conjugates through fluorescent imaging [78] (see Fig. 11). A special antibody, mouse antihuman CD10 antibody, was used as a recognition element in the system, which was covalently immobilized onto the nanoparticle surface using CNBr pretreated nanoparticles. The mononuclear lymphoid cells with a round shape were incubated with CD10-immobilized nanoparticles. Unbound nanoparticles were washed away with PBS buffer. The cell suspension was then imaged using both optical microscopy and fluorescence microscopy (Fig. 11). The leukemia cells were well recognized as bright fluorescent areas in the fluorescence images, which correlated well with the optical images. Control experiments were done using bare RuBpy-doped silica nanoparticles without labeling probe antibody and with PTK2 cells, cells that do not have a surface antigen on the

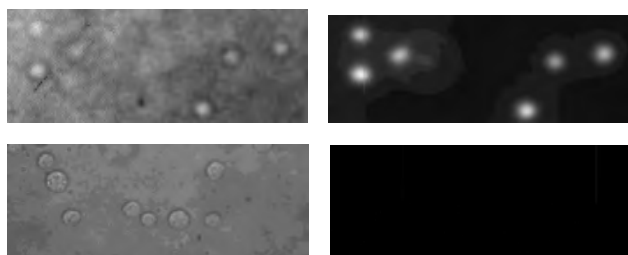


Figure 11. Recognition of target cells using RuBpy-doped silica nanoparticle probes. Fluorescent image (A) and optical image (B). Reprinted with permission from [78], S. Santra et al., *Anal. Chem.* 73, 4992 (2001). © 2001, American Chemical Society.

cell membrane for CD10 antibody. The resulted fluorescent images showed no fluorescent signals, indicating that the nanoparticle conjugate is able to selectively identify cells when using a fluorescence imaging system.

4.2. Bacteria Determination

A rapid bioassay for the precise determination of a single bacterium was developed using bioconjugated nanoparticles. Rapid and sensitive detection of pathogenic bacteria is extremely important for food safety, clinical diagnosis, and the inactivation of bioterrorism agents. Traditional methods for the detection of trace amounts of bacteria require amplification or enrichment of the bacteria in the sample. These methods tend to be laborious and time-consuming due to complicated assay procedures [115–120]. Recently, many attempts have been made to improve the sensitivity of bacterial detection without the need for target amplification and pre-enrichment [121–123]. However, rapid bacterial detection at the single cell level in a large volume sample has not been possible.

Using the nanoparticles and their conjugation with bacterium specific antibody, a novel bionanotechnology has been developed for fast, ultrasensitive, and accurate detection of single bacterial cells without any amplification or enrichment. The antibody conjugated nanoparticles offer significant signal amplification in bacterium bioanalysis [76]. A potentially lethal bacterium, *E. coli* O157:H7 [124–126], was selected as the object for detection. The antibodies against *E. coli* O157:H7 were conjugated to the RuBpy-doped silica nanoparticle to form a nanoparticle–antibody complex that was used to bind the antigen on the *E. coli* O157:H7 surface and thus give fluorescence signals. In comparison with a conventional immunoassay, where an antibody–antigen binding event brings only a few dye molecules for signaling, dye-doped nanoparticles contained approximately 10^4 dye molecules to signal one antibody–antigen binding event and provided significant signal amplification. Meanwhile, there were many *E. coli* O157:H7 surface antigens for the antibody specific recognition. Thus, thousands of nanoparticles bound to one bacterium to greatly amplify detectable signals. This bioassay is rapid (<20 minutes from sampling to detection and analysis), convenient, and highly selective. Furthermore, since multiple samples can be analyzed simultaneously, this assay is adaptable to high-throughput bioanalysis. This study clearly demonstrates the excellent utility of biologically conjugated nanomaterials in biological studies and biotechnology.

4.3. Probing Single Strand DNA Sequences

TMR-doped silica nanoparticles have much higher fluorescent intensity than RuBpy-doped silica nanoparticles [72, 73]. For cell or bacteria analysis, there are many surface binding sites on each target and that means many nanoparticles can link to one target; thus, the RuBpy nanoparticles are good enough for signal amplification [76, 78]. However, for DNA detection based on hybridization, each probe sequence can bind to only one target, and a much stronger fluorescent probe is needed

to achieve excellent detection limits. TMR-doped silica nanoparticles can overcome this limitation.

An ultrasensitive DNA analysis has been developed using TMR-dextran-doped silica nanoparticle probes [77]. Usually, a fluorophore labeled probe DNA sequence hybridizes to the target DNA in conventional DNA analysis, the fluorescence intensity is detected, and then it reflects the amount of the target DNA. Each target DNA molecule is represented by only one dye molecule. In comparison with the dye molecule labeled method, dye-doped nanoparticle labeled assay can give approximately 10^4 dye molecules to represent one target DNA sequence, which means that the signal is enlarged by 10^4 times. Therefore, a single hybridization event is highly indicated, making the trace amount of target DNA detection possible. Based on this principle, using a highly fluorescent TMR-doped silica nanoparticle probe and a high resolution confocal microscope, an ultrasensitive DNA analysis was achieved.

This DNA analysis assay was carried out using a typical sandwich method in which a capture DNA sequence was immobilized on a glass substrate [59], a probe DNA sequence was attached to a dye-doped silica nanoparticle, and a target DNA sequence was complementary to the capture DNA and the probe sequence. In a two-step hybridization procedure wherein the target DNA hybridizes to the capture DNA and the probe DNA, the target DNA was recognized and signaled by the fluorescent nanoparticle probe. An imaging system was used to measure the fluorescence signal of the surface-bound nanoparticle probes. The number of fluorescent particle spots, proportional to the concentration of the target DNA, was counted on the images. A detection limit of 5 fM was achieved in this assay.

Polymer fluorescent nanoparticles have also been covalently linked to DNA binding proteins to probe specific sequences on single DNA molecules [16] as shown in Figure 12; 20 nm latex fluorescent nanoparticles were used as biomarkers. The results showed that attached proteins maintain specific DNA binding and cleavage activities, while the nanoparticles emit intense and stable fluorescent signal. The use of fluorescent nanoparticle bioconjugates solves the problems associated with single fluorophores, such as rapid photobleaching and blinking. The results of target specific sequences on single DNA molecules suggested that it is possible to observe real-time DNA-protein binding and enzymatic dynamics.

4.4. Biomolecular Separation

Magnetic separation has been widely used in bioanalysis and biotechnology for purification and separation of various biomolecules [127–129]. Based on newly developed silica coated magnetic nanoparticles [82], a novel genomagnetic nanocapturer (GMNC) was designed for the collection and detection of trace amounts of DNA/mRNA molecules from a complex matrix such as a mixture or cells [81].

The GMNC was constructed with a magnetic nanoparticle core, a silica coating layer, a biotin–avidin linking bridge, and a biotinylated molecular beacon DNA probe (Fig. 10). The two key elements, the magnetic nanoparticle

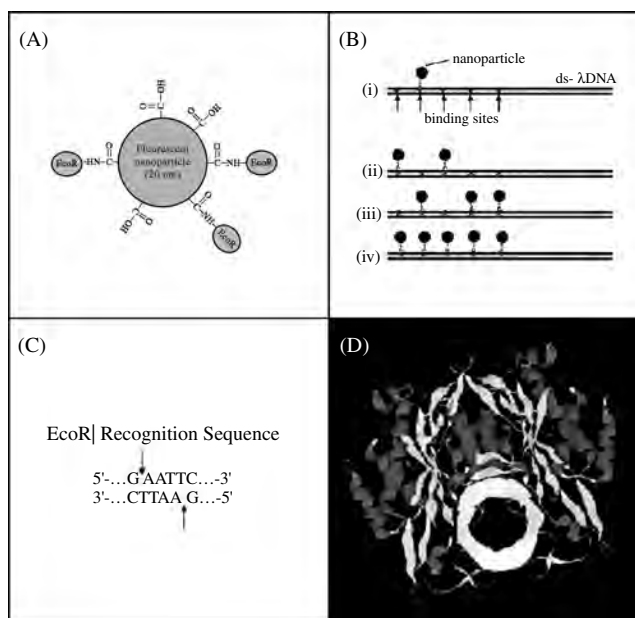


Figure 12. Illustration of (A) EcoRI molecules covalently conjugated to a 20 nm fluorescent nanoparticle. (B) Single DNA molecules bound at specific sites. (C) DNA sequence recognized by EcoRI. (D) EcoRI dimer bound to double-stranded DNA. Reprinted with permission from [16], J. R. Taylor et al., *Anal. Chem.* 72, 1982 (2000). © 2000, American Chemical Society.

and MB, provide the GMNC with unique properties; the nanocapturer acts as an effective molecule separator and carrier and serves as a highly selective and sensitive gene probe for the recognition and detection of specific DNA sequences. The excellent sequence selectivity of the GMNC is a result of the MB's special stem-loop structure [130–135], which is critical for single base mismatch discrimination. Meanwhile, the nanoparticles in the GMNC structure further enhance the utility of the MB by altering the MB's melting temperature curve. The melting temperature profiles of the MB on the GMNC surface shift to a higher temperature when the MBs are immobilized onto the GMNC surface, resulting in an optimal temperature for separation of the different target DNA sequences with high collection efficiency.

The GMNC's strong target collection ability was demonstrated by specific hybridization and collection of trace amounts of perfectly complementary DNA vs a single base mismatched DNA sequence in the presence of nontarget DNA sequences and proteins. By subjecting the mixture to a magnetic field, the GMNC was removed from the system, resulting in separation of the target DNA from the rest of the matrix. In addition, a specific mRNA sequence in living cells was selectively collected using the GMNC. The capture ability of the GMNC was also showed in the trace amount of DNA/RNA collected from a large sample volume. With adequate hybridization time, the GMNC collected as low as 0.3 pM target sequences in aqueous solution with high specificity and collection efficiency. Moreover, real-time monitoring of the DNA hybridization can be performed by recording fluorescent signals of the GMNC as the hybridization takes proceeds.

5. CONCLUSIONS

The development of various luminescent silica nanoparticles has been summarized in this chapter. Among them, dye-doped silica nanoparticles demonstrate great signaling ability when they act as fluorescent probes in trace bioanalysis. Three major advantages of dye-doped silica nanoparticles—high fluorescence intensity, excellent photostability, and good biocompatibility—make the dye-doped silica nanoparticles ideal fluorescent biomarkers for use in bioanalysis and biotechnology. The bioconjugation approaches provide simple ways to modify the silica nanoparticles for biomolecule recognition and detection. The examples of real applications for fluorescent silica nanoparticles described in this chapter show great promise in the advancement of fluorescent labeling techniques.

Many theoretical and technical problems still have to be solved—from understanding the contrast mechanisms and the nanofabrication of smaller sized particles, to the control of bioconjugation for applications with biologically active molecules. We believe that bionanotechnologies will be highly useful for bioimaging of cells and cellular components, bioassays targeted at biologically relevant diseases, detection probes used in neurochemical monitoring, and mRNA/DNA detection techniques based on nanoparticle arrays.

GLOSSARY

Bioconjugation Immobilization of biomolecules onto a substrate or solid support.

Dye-doped silica nanoparticle A silica nanoparticle in which a large number of dye molecules are trapped inside a silica matrix.

Nanoparticle A spherical particle with a diameter in the range of 1–100 nanometers.

Polymer fluorescent particle A polymer sphere in which a number of dye molecules are trapped inside a polymer matrix.

Silica coated magnetic nanoparticles A silica nanoparticle in which the core of the particle is made from magnetic materials and the shell is a layer of silica.

ACKNOWLEDGMENTS

We thank our colleagues at the University of Florida for their collaborative work. This work was partially supported by NIH GM66137, NIH NCI CA92581, a Packard Foundation grant, and NSF 0304569.

REFERENCES

1. C. Kneuer, M. Sameti, U. Bakowsky, T. Schiestel, H. Schirra, H. Schmidt, and C. M. Lehr, *Bioconjugate Chem.* 11, 926 (2000).
2. C. Kneuer, M. Sameti, U. Bakowsky, T. Schiestel, H. Schirra, H. Schmidt, and C. M. Lehr, *Int. J. Pharm.* 196, 257 (2000).
3. H. Q. Mao, K. Roy, V. L. Troung-Le, K. A. Janes, K. Y. Lin, Y. Wang, J. T. August, and K. Leong, *J. Control. Release* 70, 399 (2001).
4. S. R. Sershen, S. L. Westcott, N. J. Halas, and J. L. West, *J. Biomed. Mater. Res.* 51, 293 (2001).

5. S. Kubitschko, J. Spinke, T. Bruckner, S. Pohl, and N. Oranth, *Anal. Biochem.* 253, 112 (1997).
6. E. V. Shevchenko, D. V. Talapin, A. L. Rogach, A. Kornowski, M. Haase, and H. Weller, *J. Am. Chem. Soc.* 124, 11480 (2002).
7. C. Mangeney, F. Ferrage, I. Aujard, V. Marchi-Artzner, L. Jullien, O. Ouari, E. D. Rekaï, A. Laschewsky, I. Vikholm, and J. W. Sadowski, *J. Am. Chem. Soc.* 124, 5811 (2002).
8. A. Nelson, L. H. Bennett, and M. J. Wagner, *J. Am. Chem. Soc.* 124, 2979 (2002).
9. T. Hyeon, S. S. Lee, J. Park, Y. Chung, and N. H. Bin, *J. Am. Chem. Soc.* 123, 12798 (2001).
10. M. K. Corbierre, N. S. Cameron, M. Sutton, S. G. J. Mochrie, L. B. Lurio, A. Ruhm, and R. B. Lennox, *J. Am. Chem. Soc.* 123, 10411 (2001).
11. G. T. Gillies, S. W. Allison, and B. M. Tissue, *Nanotechnology* 13, 484 (2002).
12. X. X. He, K. M. Wang, W. H. Tan, J. Li, X. H. Yang, S. S. Huang, D. Li, and D. Xiao, *J. Nanosci. Nanotech.* 2, 317 (2002).
13. L. Josephson, M. F. Kircher, U. Mahmood, Y. Tang, and R. Weissleder, *Bioconjugate Chem.* 13, 554 (2002).
14. P. Calvo, B. Gouritin, H. Villarroya, F. Eclancher, C. Giannavola, C. Klein, J. P. Andreux, and P. Couvreur, *Eur. J. Neurosci.* 15, 1317 (2002).
15. C. Pan, K. Pelzer, K. Philippot, B. Chaudret, F. Dassenoy, P. Lecante, and M. J. Casanove, *J. Am. Chem. Soc.* 123, 7584 (2001).
16. J. R. Taylor, M. M. Fang, and S. M. Nie, *Anal. Chem.* 72, 1979 (2000).
17. E. Kumacheva, O. Kalinina, and L. Lilje, *Adv. Mater.* 11, 231 (1999).
18. M. H. Nayfeh, N. Barry, J. Therrien, O. Akcakir, E. Gratton, and G. Belomoin, *Appl. Phys. Lett.* 78, 1131 (2001).
19. M. H. Lee, S. G. Oh, and S. C. Yi, *J. Colloid. Interf. Sci.* 226, 65 (2000).
20. K. J. Ziegler, R. C. Doty, K. P. Johnston, and B. A. Korgel, *J. Am. Chem. Soc.* 123, 7797 (2001).
21. B. O. Dabbousi, J. Rodriguez-Viejo, F. V. Mikulec, J. R. Heine, H. Matoussi, R. Ober, K. F. Jensen, and M. G. Bawendi, *J. Phys. Chem. B* 101, 9463 (1997).
22. A. P. Alivisatos, *J. Phys. Chem.* 100, 13226 (1996).
23. W. C. W. Chan and S. M. Nie, *Science* 285, 2016 (1998).
24. S. R. Emory and S. M. Nie, *J. Phys. Chem. B* 102, 493 (1998).
25. M. Han, X. Gao, J. Z. Su, and S. Nie, *Nat. Biotechnol.* 19, 631 (2001).
26. M. J. Bruchez, M. Moronne, A. P. Alivisatos, and S. Weiss, *Science* 281, 2013 (1998).
27. M. Dahan, T. Laurence, F. Pinaud, D. S. Chemla, A. P. Alivisatos, M. Sauer, and S. Weiss, *Opt. Lett.* 26, 825 (2001).
28. J. Hranisavljevic, N. M. Dimitrijevic, G. A. Wurtz, and G. P. Wiederrecht, *J. Am. Chem. Soc.* 124, 4536 (2002).
29. Y. W. Cao, R. Jin, and C. A. Mirkin, *J. Am. Chem. Soc.* 123, 7961 (2001).
30. S. Santra, K. Wang, R. Tapeç, and W. Tan, *J. Biomed. Opt.* 6, 160 (2001).
31. D. Gerion, F. Pinaud, S. C. Williams, W. J. Parak, D. Zanchet, S. Weiss, and A. P. Alivisatos, *J. Phys. Chem. B* 105, 8861 (2001).
32. A. Schroedter, H. Weller, R. Eritja, W. E. Ford, and J. M. Wessels, *Nano. Lett.* 13 (2002).
33. D. J. Maxwell, J. R. Taylor, and S. M. Nie, *J. Am. Chem. Soc.* 124, 9606 (2002).
34. S. M. Nie, *Cytometry* 25, 11 (2002).
35. W. C. W. Chan, D. J. Maxwell, X. H. Gao, R. E. Bailey, M. Y. Han, and S. M. Nie, *Curr. Opin. Biotech.* 13, 40 (2002).
36. S. M. Nie, *Absta. Papam. Chem. S* 221, 472 (2001).
37. C. Y. Zhang, H. Ma, Y. Ding, L. Jin, D. Y. Chen, Q. Miao, and S. M. Nie, *Chem. J. Chinese U* 22, 34 (2001).

38. C. Y. Zhang, H. Ma, S. M. Nie, Y. Ding, L. Jin, and D. Y. Chen, *Analyst* 125, 1029 (2000).
39. J. T. Krug, G. D. Wang, S. R. Emory, and S. M. Nie, *J. Am. Chem. Soc.* 121, 9208 (1999).
40. D. Zanchet, C. M. Micheel, W. J. Parak, and A. P. Alivisatos, *Nano. Lett.* 1, 32 (2001).
41. Y. Weizmann, F. Patolsky, and I. Willner, *Analyst* 126, 1502 (2001).
42. G. R. Souza and T. J. Miller, *J. Am. Chem. Soc.* 123, 6734 (2002).
43. J. Reichert, A. Csaki, M. Kohler, and W. Fritzsche, *Anal. Chem.* 72, 6025 (2000).
44. B. Dubertret, M. Calame, A. P. Alivisatos, and J. Y. Libchaber, *Nat. Biotechnol.* 19, 365 (2001).
45. O. Siiman, K. Gordon, A. Burshteyn, J. A. Maples, and J. K. Whitesell, *Cytometry* 41, 365 (2000).
46. A. Gole, C. Dash, C. Soman, S. R. Sainkar, M. Rao, and M. Sastry, *Bioconjugate Chem.* 12, 684 (2001).
47. J. J. Storhoff, R. Elghanian, R. C. Mucic, C. A. Mirkin, and R. L. Letsinger, *J. Am. Chem. Soc.* 120, 1959 (1998).
48. Y. W. C. Cao, R. C. Jin, and C. A. Mirkin, *Science* 297, 1536 (2002).
49. S. J. Park, T. A. Taton, and C. A. Mirkin, *Science* 295, 1503 (2002).
50. R. A. Reynolds, C. A. Mirkin, and R. L. Letsinger, *Pure Appl. Chem.* 72, 229 (2000).
51. J. J. Storhoff and C. A. Mirkin, *Chem. Rev.* 99, 1849 (1999).
52. H. Cai, C. Xu, P. He, and Y. Fang, *J. Electroanal. Chem.* 510, 78 (2001).
53. C. A. Mirkin, R. L. Letsinger, R. C. Mucic, and J. J. Storhoff, *Nature* 382, 607 (1996).
54. L. M. Demers, C. A. Mirkin, R. C. Mucic, R. A. Reynolds, R. L. Letsinger, R. Elghanian, and G. Viswanadham, *Anal. Chem.* 72, 5535 (2000).
55. K. J. Watson, J. Zhu, S. T. Nguyen, and C. A. Mirkin, *Pure Appl. Chem.* 72, 67 (2000).
56. K. J. Watson, J. Zhu, S. T. Nguyen, and C. A. Mirkin, *J. Am. Chem. Soc.* 121, 462 (1999).
57. R. L. Letsinger, C. A. Mirkin, R. Elghanian, R. C. Mucic, and J. J. Storhoff, *Phosphorus Sulfur* 146, 359 (1999).
58. R. Elghanian, J. J. Storhoff, R. C. Mucic, R. L. Letsinger, and C. A. Mirkin, *Science* 277, 1078 (1997).
59. T. A. Taton, C. A. Mirkin, and R. L. Letsinger, *Science* 289, 1757 (2000).
60. R. A. Reynolds, C. A. Mirkin, and R. L. Letsinger, *J. Am. Chem. Soc.* 122, 3795 (2000).
61. C. L. Zhou, Y. Zhao, T. C. Jao, M. A. Winnik, and C. Wu, *J. Phys. Chem. B* 106, 1889 (2002).
62. S. S. Kwon, Y. S. Nam, J. S. Lee, B. S. Ku, S. H. Han, J. Y. Lee, and I. S. Chang, *Colloid Surface A* 210, 95 (2002).
63. S. Ito, H. Yoshikawa, and H. Masuhara, *Appl. Phys. Lett.* 78, 4046 (2001).
64. D. QuintanarGuerrero, E. Allemann, and F. E. Doelker, *Colloid Polym. Sci.* 275, 640 (1997).
65. C. Graf, W. Schärfl, M. Maskos, and M. Schmidt, *J. Chem. Phys.* 112, 3031 (2000).
66. C. Graf, W. Schärfl, K. Fischer, N. Hugenberg, and M. Schmidt, *Langmuir* 15, 6170 (1999).
67. W. Schärfl, C. Graf, C. Roos, and M. Schmidt, *Progr. Colloid. Polym. Sci.* 112, 214 (1999).
68. A. van Blaaderen and A. Virj, *J. Colloid Interface. Sci.* 156, 1 (1993).
69. A. van Blaaderen, J. Peetermans, G. Maret, and J. K. G. Dhont, *J. Chem. Phys.* 96, 4591 (1992).
70. A. van Blaaderen, A. Imhof, W. Hage, and A. Virj, *Langmuir* 8, 1514 (1992).
71. W. Schärfl, *Adv. Mater.* 12, 1899 (2000).
72. R. Tapeç, X. J. Zhao, and W. Tan, *J. Nanosci. Nanotech.* 2, 405 (2002).
73. X. J. Zhao, R. Tapeç, T. Drake, and W. Tan, unpublished results.
74. X. J. Zhao, R. Bagwe, and W. Tan, submitted for publication.
75. X. X. He, K. M. Wang, W. H. Tan, B. Liu, X. Lin, S. S. Huang, D. Li, C. M. He, and J. Li, *Chin. Sci. Bull.* 48, 223 (2003).
76. X. Zhao, L. R. Hilliard, Y. Wang, S. Jin, and W. Tan, unpublished results.
77. X. Zhao, R. Tapeç, L. R. Hilliard, and W. Tan, submitted for publication.
78. S. Santra, P. Zhang, K. M. Wang, R. Tapeç, and W. H. Tan, *Anal. Chem.* 73, 4988 (2001).
79. L. R. Hilliard, X. Zhao, and W. Tan, *Anal. Chim. Acta* 470, 51 (2002).
80. M. Qhobosheane, S. Santra, P. Zhang, and W. Tan, *Analyst* 126, 1274 (2001).
81. X. Zhao, R. Tapeç-Dytioco, K. Wang, and Weihong Tan, *Anal. Chem.*, 75, Web Release June 3 ASAP Article (2003).
82. S. Santra, R. Tapeç, N. Theodoropoulou, J. Dobson, A. Hebard, and W. Tan, *Langmuir* 17, 2900 (2001).
83. W. Stöber, A. Fink, and E. Bohn, *J. Colloid Interface Sci.* 26, 62 (1968).
84. M. S. Fleming, T. K. Mandal, and D. R. Walt, *Chem. Mater.* 13, 2210 (2000).
85. J. H. Lee, T. G. Park, and H. K. Choi, *J. Microencapsulation* 16, 715 (1999).
86. T. Serizawa, S. Takehara, and M. Akashi, *Macromolecules* 33, 1759 (2000).
87. S. A. Jenekhe and X. L. Chen, *Science* 279, 1903 (1998).
88. X. L. Chen and S. A. Jenekhe, *Langmuir* 15, 8007 (1999).
89. T. K. Mandal, M. S. Fleming, and D. R. Walt, *Chem. Mater.* 12, 3481 (2000).
90. T. von Werne and T. E. Patten, *J. Am. Chem. Soc.* 121, 7409 (1999).
91. M. Kerker, "The Scattering of Light and Other Electromagnetic Radiation." Academic, New York, 1969.
92. C. F. Bohren and D. F. Huffman, "Absorption and Scattering of Light by Small Particles." Wiley, New York, 1983; M. A. Correa-Duarte, M. Giersig, and L. M. Liz-Marzan, *Chem. Phys. Lett.* 286, 497 (1998).
93. M. Giersig, T. Ung, L. M. Liz-Marzan, and P. Mulvaney, *Adv. Mater.* 9, 570 (1997).
94. E. Stathatos, P. Lianos, F. DelMonte, D. Levy, and D. Tsiourvas, *Langmuir* 13, 4295 (1997).
95. S. Shiojiri, T. Hirai, and I. Komasa, *Chem. Commun.* 14, 1439 (1998).
96. D. O. Shah, "Micelles, Microemulsions, and Monolayers—Science and Technology," p. 19. Dekker, New York, 1998.
97. H. E. Bergna, "The Colloid Chemistry of Silica" (H. E. Bergna, Ed.), p. 9. Am. Chem. Soc., New York, 1994.
98. S. Shibata, T. Taniguchi, T. Yano, and M. Yamane, *J. Sol-Gel Sci. Tech.* 10, 263 (1997).
99. L. Babes, B. Denizot, G. Tanguy, J. J. Le, P. J. Jeune, and P. Jallet, *J. Colloid Interface Sci.* 212, 474 (1999).
100. V. Tchikow, S. Schütze, and M. K. J. Kronke, *Magn. Mater.* 194, 242 (1999).
101. C. Liu, B. Zou, A. J. Rondinone, and Z. J. Zhang, *J. Phys. Chem. B* 104, 1141 (2000).
102. <http://www.molecularprobe.com>.
103. C. Passirani, L. Ferrarini, G. Barratt, J. P. Devissaguet, and D. Labarre, *J. Biomater. Sci. Poly. Ed.* 10, 47 (1999).
104. F. Kleinjung, S. Klussman, V. A. Erdmann, F. W. Scheller, J. P. Furst, and F. F. Bier, *Anal. Chem.* 70, 328 (1998).
105. L. A. Chrisey, G. U. Lee, and C. E. O'Ferral, *Nucleic Acids Res.* 24, 3031 (1996).
106. Y. Rogers, P. Jiang-Baucom, Z. Huang, V. Bogdanov, S. Anderson, and M. Boyce-Jacino, *Anal. Biochem.* 266, 23 (1999).
107. M. A. Osborne, W. S. Furey, D. Klenerman, and S. Balasubramanian, *Anal. Chem.* 72, 3678 (2000).
108. G. Bonnet, S. Tyagi, A. Libchaber, and F. R. Kramer, *Proc. Natl. Acad. Sci. USA* 96, 6171 (2000).

109. Y. H. Rogers, P. Jiang-Baucom, Z. J. Huang, V. Bogdanov, S. Anderson, and M. T. Boyce-Jacino, *Anal. Biochem.* 266, 23 (1999).
110. M. Mascini, S. Fortunati, D. Moscone, G. Pallexchi, M. Benedetti, and P. Fabietti, *Clin. Chem.* 31, 451 (1985).
111. Bangs Laboratories Inc., 9025 Technology Drive Fishers, IN 46038-2866, USA, 1-800-387-0672.
112. J. R. Lakowicz, "Principles of Fluorescence Spectroscopy," 2nd ed. Kluwer/Plenum, New York, 1999.
113. J. Bui, T. Zelles, H. Lou, V. Gallion, M. I. Phillips, and W. Tan, *Eurosci. Methods* 89, 9 (1989).
114. D. Gerion, F. Pinaud, S. C. Williams, W. J. Parak, D. Zanchet, S. Weiss, and A. P. Alivisatos, *J. Phys. Chem. B* 105, 8861 (2001).
115. S. S. Iqbal, W. M. Mayo, J. G. Bruno, B. V. Bronk, and C. A. Batt, *Biosensors Bioelec.* 15, 549 (2000).
116. G. W. Beran, H. P. Shoeman, and K. F. Anderson, *Dairy Food Environ. Sci.* 11, 189 (1991).
117. "Immunoassays: Essential Data" (R. Edwards, Ed.), p. 84. Wiley, New York, 1996.
118. "Antibody Applications: Essential Techniques" (R. J. Delves, Ed.), p. 43. Wiley, New York, 1995.
119. K. L. Cao, G. P. Anderson, F. S. Ligler, and J. Ezzel, *J. Clin. Microbiol.* 33, 336 (1995).
120. M. M. Brett, *J. Appl. Microbiol. Symp. Suppl.* 84, 110S (1998).
121. A. G. Gehring, D. I. Patterson, and T. Si, *Anal. Biochem.* 258, 293 (1998).
122. S. M. Paffard, R. J. Milwa, C. R. Clark, and R. G. Price, *J. Immunol. Methods* 192, 133 (1996).
123. I. Abdel-Hamid, D. Ivnitcki, P. Atanasov, and E. Willkins, *Biosensors Bioelec.* 14, 309 (1999).
124. P. S. Mead, P. M. Griffin, B. Swaminathan, and R. V. Tauxe, "Outbreaks caused by Shiga toxin-producing *Escherichia coli*, Summary of 2001 Surveillance Data," Available at <http://www.cdc.gov/foodborneoutbreaks/ecoli/CSTEletter2001.pdf>.
125. P. S. Mead, P. M. Griffin, B. Swaminathan, and R. V. Tauxe, <http://www.cdc.gov/ncidod/dbmd/outbreak/ecoli00summary.pdf>.
126. J. P. Nataro and J. B. Kaper, *Clin. Microbiol. Rev.* 11, 142 (1998).
127. Y. R. Chela, H. L. Grossman, Y. Poon, R. Mcdermott, R. Stevens, M. D. Alper, and J. Clark, *Proc. Natl. Acad. Sci. USA* 26, 14268 (2000).
128. I. Safarik and M. Safarikova, *J. Chromatogr. B* 722, 33 (1999).
129. V. S. Srinivas and B. Arijit, *Colloids Surfaces B* 8, 1999 (1997).
130. S. Tyagi, D. P. Bratu, and F. R. Kramer, *Nat. Biotechnol.* 16, 49 (1998); S. Tyagi and F. R. Kramer, *Nat. Biotechnol.* 14, 303 (1996).
131. X. Fang, J. Li, J. Perlette, K. Wang, and W. Tan, *Anal. Chem.* 72, 747A (2000).
132. L. G. Kostrikis, S. Tyagi, M. M. Mhlanga, D. D. Ho, and F. R. Kramer, *Science* 279, 1228 (1998).
133. J. Li, X. Fang, S. Schuster, and W. Tan, *Angew. Chem. Int. Ed.* 39, 1049 (2000).
134. X. Fang, J. J. Li, and W. Tan, *Anal. Chem.* 72, 1979 (2000).
135. X. Fang, X. Liu, S. Schuster, and W. Tan, *J. Am. Chem. Soc.* 121, 2921 (1999).

Biodoped Sol–Gel Polymer Nanocomposites

Iqbal Gill

BioSynTech, Nutley, New Jersey, USA

CONTENTS

1. Nanotechnology and Biologicals
 2. Sol–Gel Technology and Bionanocomposites
 3. Biological Materials and Bioencapsulation
 4. Practical Aspects of Sol–Gel Bioencapsulation
 5. Sol–Gel Precursors and Matrices
 6. The Structure and Functioning of Sol–Gel Bioencapsulates
 7. Applications of Sol–Gel Bioencapsulates
 8. Future Developments in Sol–Gel Nanobioencapsulation
- Glossary
References

1. NANOTECHNOLOGY AND BIOLOGICALS

1.1. Nanotechnology

The last two decades have witnessed spectacular advances in the biological, chemical, and materials sciences, with rapid progress being made in the elucidation of the functioning of living systems and the organization of natural and synthetic materials and the development of physicochemical techniques for the study and manipulation of matter. In the vanguard of these advances is nanotechnology, a highly interdisciplinary science which seeks to comprehend and control phenomena at the atomic to macromolecular scale (1–100 nm) and therein create nanostructures and assemble them into larger architectures with the aim of devising materials, devices, and systems that have novel properties and functions by virtue of their nanoscale size and/or organization [1–5].

Areas that are receiving particular attention in this respect are the understanding of the nanoscale organization and functioning of biosystems and the application of this knowledge to the construction of bio-inspired systems and the

interfacing of biological macromolecules and assemblages with synthetics to create hybrid materials with novel properties [1–12]. This interest derives from a number of unique properties of biological molecules [13–16]:

- (a) Biomolecules, especially polymers such as nucleic acids (DNA and RNA), proteins, and oligosaccharides, are typically highly functionalized and spatially organized, and this gives rise to defined molecular structures with unique properties, such as chirality, amphiphilicity, and aggregation behavior.
- (b) Biomolecules such as oligosaccharides, proteins, and nucleic acids exhibit hierarchical structural organization by virtue of their modular form and precise intra- and intermolecular interactions.
- (c) Functionality, hierarchical structure, and chirality enable highly specific molecular recognition interactions, such as the binding of ligands by antibodies and nucleic acids, and catalysis by enzymes and catalytic RNA.
- (b) Biological molecules and macromolecules can assemble into two-dimensional (2D) and three-dimensional (3D) architectures and form multifunctional assemblies, for example, vesicles, membranes, 2D and 3D crystals, colloids, fibers, and networks.

As a result, biomolecules such as lipids and macrocyclics, macromolecules including natural, engineered, and synthetic proteins, polypeptides, oligosaccharides, DNA and RNA, as well as macromolecule assemblies have found unique nanotechnical applications in areas as diverse as catalysis, sensors, diagnostics, medical imaging, electronics, optics, drug discovery, controlled delivery, and high-performance coatings [6–25].

1.2. Nanostructured Bioencapsulated Solid-State Materials

The realization of the aforementioned applications depends critically on enabling technologies, of which the production of solid-state materials in which the requisite biosystems are

organized onto synthetic surfaces or incorporated into polymers to form composites have gained a special significance [17–26]. The need for such solid-state biomaterials derives from several factors:

- (a) Biological materials are often characterized by their lability—thus, proteins and nucleic acids are readily degraded by various biotic and abiotic processes and are sensitive to a host of environmental perturbances (pH, temperature, salts, solvents, pressure, etc.), all of which can result in the partial or complete loss of biological properties. Immobilization onto/within a rigid polymer matrix often substantially stabilizes the biological by anchoring the molecular structure and protecting it from bio/chemical attack, and the ability to engineer the physicochemistry of synthetic materials enables the tailoring of the immobilization method to the biological and its application.
- (b) Although many biological materials can be obtained in the solid state, for example 2D/3D protein crystals and DNA/RNA colloids and thin films, these materials tend to have poor physicochemical attributes (solubility in water, resistance to solvents, storage stability, mechanical properties, etc) and cannot be utilized in their native form. Immobilization allows for the fixation of biologicals on or encasement within robust synthetic polymers that endow the resultant materials with their distinctive physicochemical properties which can be readily engineered.
- (c) Many applications require the isolation of biological components, their interfacing with other biosystems and/or with synthetic polymers, and/or their spatial organization in a reproducible manner. Immobilization addresses all these issues, since it allows for the matrix isolation of biologicals in defined physicochemical environments, enables the simultaneous or sequential immobilization of multiple biosystems, and by virtue of the controllable functionality of synthetic surfaces and polymers also permits the site-specific and ordered anchoring of biologicals.

The importance of bio-immobilization is clear from the many commercial technologies and research fronts that rely on immobilized biologicals for molecular assembly, recognition, catalysis, and transduction functions [13–26]. Thus, the production of many lipids, amino acids, peptides, mono- and oligosaccharides, antibiotics, and numerous food ingredients, cosmetics, pharmaceuticals, agrochemicals, and fine chemicals depends on heterogeneous biocatalysts that can function efficiently under a variety of operating conditions and are stable to long-term usage [13–19]. Similarly, biosensors for detecting and monitoring analytes such as sugars, hydroxyacids, amino acids, sterols, nitric oxide, mycotoxins, pesticides, antigens, antibodies, and pathogenic organisms in clinical, environmental, industrial, and consumer settings depend critically on bioimmobilizates, which must be highly discriminating and responsive, operate reliably for extended periods, and be amenable to miniaturization and mass fabrication [20–35]. Likewise, bioarrays employing peptides, proteins, and nucleic acids anchored on/within polymers for the detection and profiling of ligands, proteins, DNA and RNA, and biooptics and bioelectronics devices utilizing chromatic,

photoactive, and electroactive proteins encapsulated within polymers require biologicals immobilized in defined and reproducible orientations/conformations and materials that can be readily microfabricated [33–46].

Many of the above applications are served by biocomposite materials comprising the biological entrapped at the nanoscale level within a polymer framework, the latter being a purely inorganic lattice, an organometallic material, an organic polymer, or a combination thereof [47]. The result is a material that marries at the nanoscale level the molecular structures of the biological and the host polymer to form a hybrid material endowed with the functional, recognition, organizational, and/or catalytic attributes of the biological together with the bulk functional, physicochemical, and mechanical properties of the host polymer [47].

In the field of bio-nanocomposite materials, the technique of sol–gel encapsulation has achieved pre-eminence as a generic platform for the production of bionanocomposites.

2. SOL–GEL TECHNOLOGY AND BIONANOCOMPOSITES

2.1. Classical Sol–Gel Technology

Classic sol–gel technology is based upon the striking observation early in the last century that silica glasses can be produced via a simple room temperature synthetic process [47–53]. In its simplest form, the protocol consists of the following:

- (a) A silica precursor, namely an ester of orthosilicic acid such as tetramethyl orthosilicate (tetramethoxy silane, TMOS) or tetraethyl orthosilicate (tetraethoxysilane, TEOS) is mixed with water and methanol or ethanol as cosolvent.
- (b) The addition of a strong organic or mineral acid catalyst results in the rapid hydrolysis of the orthosilicate ester to form a solution containing partial esters such as trimethyl orthosilicic acid and dimethyl orthosilicic acid, which upon extended reaction ultimately afford fully hydrolyzed orthosilicic acid.
- (c) The partial silicic acid esters and silicic acid can undergo condensations to form soluble oligomeric species, reactions that are catalyzed by acids and especially by bases such as fluoride, amine, and hydroxide.
- (d) The soluble oligomers condense to form colloids composed of macromeric species, and this is accompanied by a sharp increase in viscosity of the reaction mixture.
- (e) Further condensation of collidal macromers results in the formation of a polymer network and bulk phase separation, which is observed as gelation of the reaction mixture and the formation of a friable and transparent hydrated gel, the hydrogel.
- (f) Upon standing, the hydrogel undergoes further condensation and crosslinking, resulting in contraction of the hydrated polymer and the extrusion of interstitial liquid from the pore network, a phenomenon known as syneresis.

- (g) Drying of the aged hydrogel results in further shrinkage (up to 80%) and pore collapse and furnishes a rigid and transparent nano- to mesoporous silica glass, the xerogel.

By substituting metal alkoxides and organofunctional silicon alkoxides for simple silicic acid esters, it has proven possible to prepare a wide range of main group and transition metal oxides, metallosilicates, organically modified silicates (Ormosils), various composite materials, and highly structured nano- to macroporous inorganic and hybrid organic-inorganic polymers with an astounding range of chemical characteristics [48–56].

2.2. Sol-Gel Bioencapsulation

A critical feature of sol-gel technology that was discerned at an early stage is that small molecules, such as transition metal complexes and organic dyes, could be encapsulated within sol-gel polymers to form doped materials. Research has shown that the entrapped molecules largely retain their native chemical characteristics within the polymers, and this combined with high optical transparency and porosity to low molecular weight molecules enables their use as optical materials, chemical sensors, or catalysts [47–56]. In view of the the aqueous chemistry of the sol-gel method, efforts were undertaken to extend sol-gel encapsulation to biological molecules. Thus, in 1984 Venton et al. [57] showed that antiprogesterone antibodies could be immobilized within silica-poly(3-aminopropylsiloxane) xerogels and, crucially, that they therein retained to a large degree their binding affinity for progesterone, thus demonstrating for the first time that sensitive biologicals could be encapsulated via silicon alkoxide sol-gel chemistry. One year later, Glad et al. [58] expanded upon these observations with the disclosure that the enzymes glucose oxidase, horseradish peroxidase, trypsin, and alkaline phosphatase could be immobilized within silica-poly[*N,N*-bis(2'-hydroxyethyl)-3-aminopropylsiloxane) sol-gels and that the resulting nanocomposites efficiently catalyzed oxidation and hydrolysis reactions typical of the native enzymes. These groups utilized aminoalkyl- and aminohydroxyalkyl-substituted alkoxy silanes rather than tetraalkoxy silanes as precursors, thus forming organically modified silicates (Ormosils) rather than pure silicas, in the belief that alkoxy silanes bearing functional organic ligands were requisite for efficient bioencapsulation and that simple precursors such as TMOS and TEOS were not suitable.

Although these two groups proved the fundamental concept underpinning bioencapsulation, perhaps the most significant advances leading to its establishment as a mainstream research field derived from the efforts of Avnir et al. [59], who in 1990 reported that the proteins alkaline phosphatase, chitinase, aspartase, and α -glucosidase could indeed be encapsulated into pure silica sol-gels using modified protocols with TMOS and TEOS as precursors. This was followed in 1992 with the disclosure by Ellerby et al. [60] that the metalloproteins copper-zinc superoxide dismutase, cytochrome *c*, and myoglobin could similarly be entrapped within silica xerogels [60]. Reinforcing the findings of Avnir et al., this group showed that the bioencapsulated

nanocomposites displayed the catalytic, metal-exchange, oxidation-reduction, and ligand-binding reactions typical of the free, soluble proteins.

These investigations unequivocally demonstrated that labile biological molecules with catalytic, recognition, and transduction functions could be incorporated into sol-gel materials with minor modifications in protocols [47, 61–75]. Explorations of the arena since then have proven the broad applicability of the technique, and to date proteins, polypeptides, antibodies, antigens, DNA, RNA, cell fractions, organelles, and whole cells have been encapsulated in a range of inorganic, organic, and hybrid polymers [47, 61–75]. The focus of bioencapsulation is mainly on highly selective, sensitive, and robust biosensor platforms for industrial, biomedical, and environmental analysis [47, 67–75], but there is also increasing awareness of the applicability of the approach to generating high-performance biocatalysts and materials for bioelectronics [47, 74].

3. BIOLOGICAL MATERIALS AND BIOENCAPSULATION

3.1. The Properties of Proteins

Before discussing the practical aspects of sol-gel bioencapsulation, it is instructive to review some relevant features of biological materials, in particular proteins [76–79]:

- (a) Proteins are typically linear polymers composed of amino acids with a variety of pendant functionalities and with molecular weights ranging from $\sim 5,000$ to $>400,000$, corresponding to sizes of ~ 1 – 15 nm [76], which is in the pore size range of mesoporous materials [61–66].
- (b) The constituent amino acids of proteins possess neutral, hydrophilic, hydrophobic, basic, and acidic functionalities, and these are typically organized in a hierarchical fashion to form ordered assemblies that are critical to binding, catalysis, dynamics, and stability [76–79]. A variety of physicochemical factors, such as pH, solutes, solvents, and liquid or solid interfaces that interact with these assemblages can influence the ionization state, hydration and hydrophobicity, dynamics, and ligand partitioning and have an impact upon biomolecule structure, solubility, aggregation, and activity [76–79].
- (c) Proteins are hierarchical nanostructures: the primary structure (amino acid sequence) is ordered into a topologically defined secondary structure (β -turns, β -sheets, α -helices, etc.), which is itself spatially organized into a (monomeric) tertiary structure (α - α packed helices, β - β barrels, etc.) which may further associate with other monomers to form homo- or hetero-oligomeric assemblies (cylinders, toroids, sheets, etc.) that comprise quaternary structures [76, 77]. Critical to molecular recognition and catalysis is the binding site, a specific spatial and functional arrangement of amino acids, which is complemented by complexed metal centers and/or photo-/redox-active cofactors in more complex proteins. The components of the active site interact

among themselves as well as the surrounding protein residues and solvent environment in a precise fashion to create a topologically and physicochemically defined chiral microenvironment, the structure and dynamics of which dictate the selectivity and efficiency of recognition and catalysis [76, 77]. Therefore, the maintenance of the various levels of short- and long-range structural order is a prerequisite to protein functioning, and pH, solutes, solvents, polymers, and interfaces that interact with organization can dramatically influence biomolecule function [76–79].

- (d) Proteins are highly dynamic systems: local and/or global conformational motions impart a high degree of local and/or global conformational flux, and this feature is central to the dynamic processes which accompany ligand channelling, orientation, and binding and the resulting cascade of recognition, transduction, and catalytic event(s) [76, 77]. Such dynamics can range from relatively small structural changes restricted largely to the binding site and its immediate surroundings as in proteases, to the movement of secondary structures such as α -helices and β -sheets as observed in lipases and cutinases, and the large-scale concerted supramolecular movements of oligomeric assemblies that characterize multicomponent photoactive and membrane protein systems. Here again, any environmental factors (solvents, interfaces, etc.) that impact upon the kinetics and/or thermodynamics of such structural transitions can profoundly impact protein functioning.

3.2. Considerations for the Bioencapsulation of Proteins

When one considers the above attributes of proteins, one can identify several critical aspects that must be factored in when the sol–gel bioencapsulation of such biomolecules is contemplated [47, 61–67, 74]:

- (a) The encapsulation of proteins must proceed in conditions resembling their native environments—that is, aqueous solutions, crystalline products, or some suitably “protected” forms: (i) aqueous solutions or suspensions, assemblies with synthetic surfactants, natural lipids, membranes or protein arrays, or solid-supported nano-sized dispersions [47, 74, 79]; (ii) pure protein crystals or co-crystals with suitable protein or polymer dopants; (iii) proteins which are modified by conjugation to surfactants, polyethylene glycol (PEG), functional siloxanes, silica or acrylates [80].
- (b) The bioencapsulation procedure and any subsequent processing must be biocompatible—that is [47, 61–74]: (i) aqueous protocols must employ ambient/sub-ambient temperatures, in the biological pH and redox and ionic strength range, and with the minimal use of solvents or other organic species which can cause protein unfolding/denaturation, aggregation, or precipitation; (ii) nonaqueous media permit the use of more aggressive conditions due to the increased stability of the biomolecule conjugates employed therein, and solvents, surfactants, and polymerization initiators can be used.

- (c) The encapsulating polymer structure must allow sufficient access to the entrapped protein as well as freedom for conformational mobility to enable efficient protein functioning, while also preventing the solubilization and leaching of protein molecules from the matrix [47, 61–74]. A 3D continuous mesoporous structure with unrestricted entry to the protein is clearly essential for realizing native protein–target molecule interactions, as is a spacious entrapment cavity to permit the requisite molecular movements. However, this must be balanced against sufficient constraint, in the form of gross physical embedding and/or more specific physicochemical protein–polymer interactions, to prevent the escape of the protein from the polymer matrix.

These types of considerations are especially critical for multimeric proteins and those that are part of larger-scale assemblies such as bilayers, vesicles, and membranes, because the gross structural integrity and hierarchical structural transitions of these structures are especially sensitive to perturbation and require careful preservation [79, 81, 82].

4. PRACTICAL ASPECTS OF SOL–GEL BIOENCAPSULATION

The first publications in the arena of sol–gel bioencapsulation established some critical features that form the basis of the present day technology [47, 61–75]:

- (a) Classical aqueous sol–gel protocols can be modified and used to encapsulate biomolecules to form bioencapsulated nanocomposites.
- (b) The careful selection of experimental conditions enables bioencapsulation under conditions that are mild enough to permit proteins to largely retain their native structure, dynamics, and molecular recognition and catalytic functions, in both hydrogels and xerogels.
- (c) The mesoporous structure and high pore volume of sol–gel matrices enable the diffusion of low to medium molecular weight species (up to 20,000 depending upon sol–gel type) and their free interaction with entrapped biomolecules.
- (d) The mesoporosity, physical rigidity, functionality, and specific host matrix-entrapped protein interactions prevent the leakage of entrapped biomolecules, while also stabilizing their structure.

When one considers these attributes, it becomes apparent that the technology offers some singular benefits in the immobilization of proteins [47, 61–75]:

- (a) Sol–gel bioencapsulation offers the only truly generic route discovered to date for efficiently incorporating biomolecules into polymers to form nanocomposite materials.
- (b) The great flexibility of sol–gel chemistry allows bioencapsulation in a very diverse range of inorganic, hybrid organic–inorganic, and composite materials.
- (c) Many bioencapsulated sol–gel polymers can be produced as ultraviolet (UV)–visible(VIS) transparent materials suitable for optical applications.

- (d) Conducting, redox-active, and photoactive sol–gels can be accessed by utilizing transition metal (Mo, W, Zn, Ti, and Sn) oxides as bulk sol–gels or as dopants and/or by incorporating graphite, noble metals (Au, Pt, and Pd), metallocenes (ferrocene, nickelocene, titanocene, etc), biological redox cofactors (nicotinamide, flavins, plastoquinones, etc.), photoactive proteins (rhodopsin, phytochromes, etc.) and others, therein allowing the fabrication of electrochemical and optochromic devices.
- (e) Standard sol–gel fabrication methods can be used to produce bioencapsulates as monolithic materials, nano-, micro-, and macroparticulates, and deposited, spun, screen-printed, and stamped thin and thick films.
- (ii) The precursor sol obtained is mixed with a buffered (typically pH 5–9, 10–200 mM buffer) solution or suspension of the biological. Fluoride, hexafluorosilicate, or amine catalysts, and drying control additives such as formamide and glycerol. Poly(vinyl alcohol) (PVA), PEG, and alginate, and fumed silica, clays, glass powder, and graphite can also be included as structure modifiers and reinforcing fillers, respectively. The catalysts and/or elevated pH of the buffer initiate a series of condensation and crosslinking reactions which lead to the formation, growth, and aggregation of oligomeric species and in an increase in viscosity, culminating in the observed sol–gel transition (that is, viscous solution transforming into a stiff gel) and bulk gelation, all this occurring within a time frame of seconds to hours.

4.1. The Technique of Sol–Gel Bioencapsulation

The practical procedure used for bioencapsulation parallels that of the sol–gel entrapment of abiotic materials in many respects, except that protocols must be adapted to ensure that encapsulation and ensuing processing operations are conducted under biocompatible conditions (Fig. 1) [47, 61–75]:

- (i) An aqueous solution (sol) containing partially or fully hydrolyzed alkoxysilanes is prepared as follows:
- Alkoxysilanes such as TMOS, TEOS, or methyltrimethoxysilane (MeTrMOS) are 50–100% hydrolyzed under acid and/or surfactant catalysis in water or water–alcohol (ethanol or methanol) mixtures to furnish solutions of poly(alkoxysiloxanes), poly(alkyl silicates) or poly(silicic acids), which may be partially or fully evaporated to reduce or remove alcohols [47, 61–75].
 - Alkoxysilanes are subjected to 50–75% hydrolysis with the stoichiometric amount of water in an alcoholic solvent (ethanol or methanol) and then transesterified (one pot) with glycerol under acid, basic, or alkoxide catalysis to form water-soluble and isolable poly(glyceryl silicates) and poly(glyceroxysiloxanes), which can be isolated and dissolved in water to furnish aqueous solutions [47, 74].

The identity of the precursor sol can range from a mixture of linear, branched, and cyclic poly(silicates)/poly(siloxanes) with degrees of polymerization of 3–16 for partially hydrolyzed sols to colloidal solutions of nano-sized macromers for fully hydrolyzed and aged sols. The exact composition depends upon the structure of the precursor silane (number and types of alkoxy groups, functionality of nonhydrolyzable moieties, whether the silane is monomeric or a disiloxane, etc.), its concentration, the catalyst, cosolvent, water content, and temperature used for hydrolysis, and how the sol is stored/aged [61, 64, 65, 74].

- Exogenously added catalysts as well as surface amine, amide, hydroxy, thiol, and carboxy residues of the protein and any functional additives accelerate the hydrolytic, condensation, and crosslinking reactions.
- The adsorption of sol–gel oligomers onto biomolecule surfaces via ionic, H-bonding, and/or hydrophobic interactions results in soluble protein–macromer complexes and the biomolecule-directed evolution of oligomer/polymer growth and morphology. Functional additives such as PEG and PVA can act in a similar fashion.
- This biomolecule surface-templated development of the polymer framework results in the physical embedding of the protein via the overgrowth of biomolecule–macromer complexes and/or their coalescence to form colloidal nanoparticles.
- The further growth and coalescence results in phase separation of the nanoparticles to form nano-sized aggregates which fuse to form large-scale nano- or microparticle frameworks, this transition coinciding with bulk gelation and the formation of the hydrated mesoporous polymer framework.

It is critical to minimize the use of cosolvents in this stage: 0–30% v/v of lower alcohols and ketones can lead to reversible aggregation and inhibition of proteins, while higher concentrations often cause irreversible denaturation and precipitation with corresponding losses in biological activity [61–65, 74]. The hydrogels produced are typically brittle or semi-flexible, compressible gels that contain some 50–80% interstitial solvent, with pore volumes of 0.9–3.4 mL g⁻¹, pore distributions of 4–200 nm, and surface areas of 600–2,100 m² g⁻¹. The extent of protein encapsulation depends upon the nature of the biomolecule, the type of sol–gel precursor used, and the gelation conditions: generally, silicates and hydrophilic siloxanes give near-quantitative immobilizations (80–100%), whereas the corresponding figures for hydrophobic siloxanes can be as low as 30%

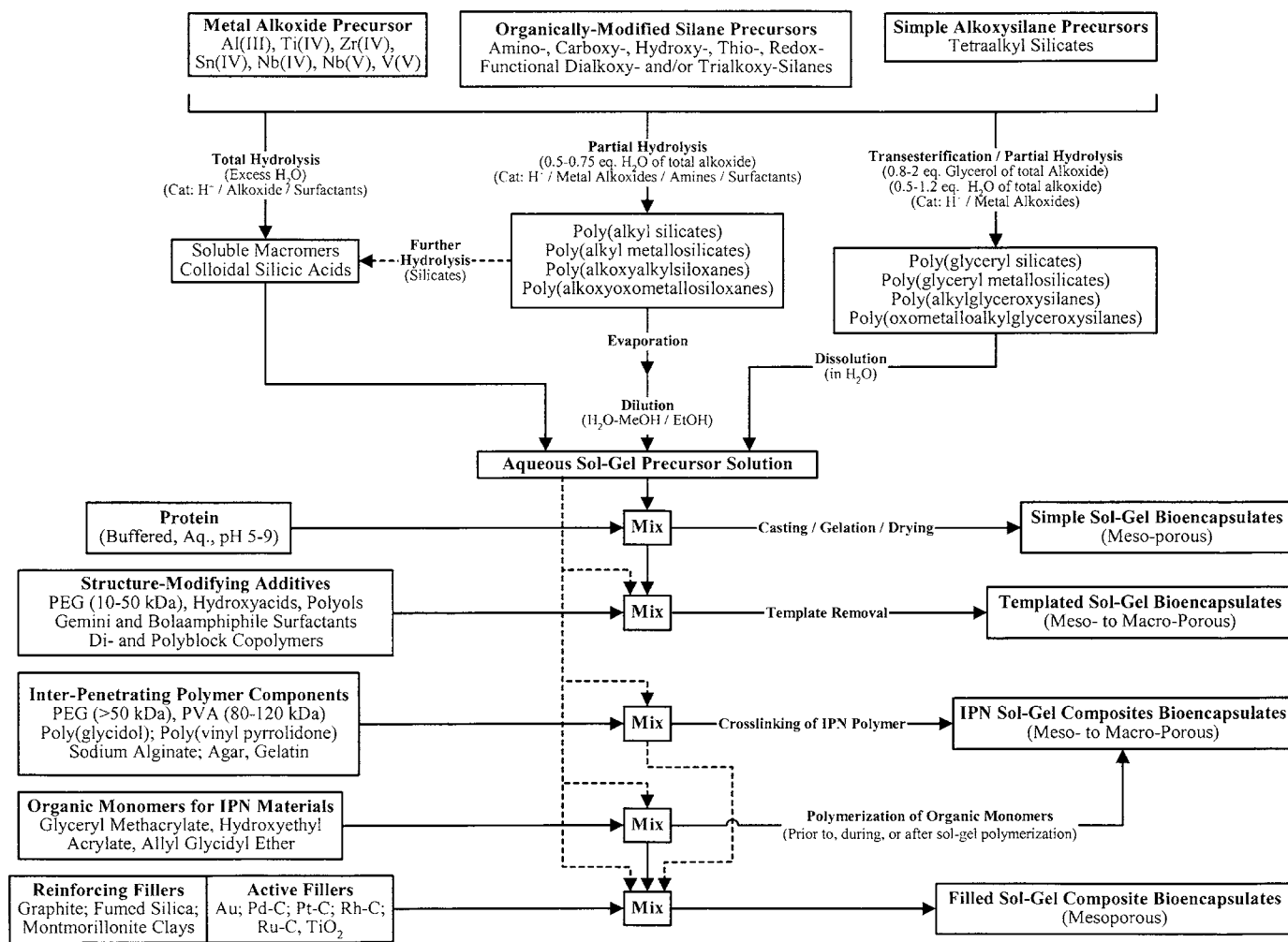


Figure 1. Standard protocols for the sol-gel bioencapsulation of proteins.

due to phase separation effects, resulting in substantial entrainment of the protein in the interstitial solvent phase. Due to the high degree of hydration and elevated porosity of these materials, biomolecules typically display 60–100% of their native activities within such freshly prepared hydrogels [47, 61–65, 74].

- (iii) The hydrogel is then typically aged in the wet state for 12–72 h to allow for the completion of condensation reactions, particle growth/fusion, and the maturation of the polymer framework. This results in bulk shrinkages of 5–30% and the contraction of the pore network and resultant expulsion of entrained liquid (syneresis). Aged hydrogels range from brittle glassy gels (silicates and hydrophobic siloxanes) to semiflexible hydrogels (hydrophilic siloxanes and composites with PVA, PEG, alginate, etc.), with typical pore volumes of 0.4–3.1 mL g⁻¹, pore sizes of 3–150 nm, and surface areas of 600–1,700 m² g⁻¹. Aging can reduce biomolecule activities by 0–20% from those observed in fresh hydrogels [47, 61–65, 74].
- (iv) The aged hydrogel is conditioned by washing with buffer and then dried, resulting in the loss of most of the remaining water, further crosslinking

and structural consolidation, pore collapse, and bulk shrinkage. Controlled dehydration, via freeze-drying or pinhole drying, may be required to avoid the structural collapse that accompanies the removal of the interstitial solvent and the ensuing loss of porosity, an occurrence that can result in a severe loss of biomolecule viability. The incorporation of drying control additives or the use of glyceroxysilane precursors can substantially reduce pore collapse effects and speed up the drying process and therein enable the recovery of high levels of biomolecule activity [47, 74]. The final xerogels can range from optically clear brittle silicate glasses to rigid or semiflexible siloxane plastics and rubbers, which contain up to 30% of bound water, show pore volumes of 0.3–2.7 mL g⁻¹, pore sizes of 0.5–100 nm, and surface areas of 400–1,300 m² g⁻¹. Due to their dehydrated state and resulting pore collapse and matrix compression, up to 80% of biomolecule viability can be lost in the final xerogel. Rehydration of xerogels can result in a considerable expansion of the pore framework and the recovery of up to 30% of biomolecule activity, especially in the case of materials derived from hydroxylated siloxanes, and composites containing

hydrophilic modifiers such as PVA, PEG, alginate, gelatin and poly(hydroxyethyl acrylate).

5. SOL-GEL PRECURSORS AND MATRICES

Although most studies of sol-gel bioencapsulation have utilized silica matrices derived from tetraalkyl silicates such as TMOS and TEOS because of their facile preparation, reasonable physicochemical robustness, and good optical transparency, a variety of other more exotic sol-gel polymer chemistries have been explored (Tables 1–3, Fig. 1) [47, 61–75, 83]:

- (a) *Inorganic oxide/hydroxide sol-gels*. These include aluminum, titanium, zirconium, tantalum, niobium, tin, vanadium, iron and molybdenum oxides, their mixed oxides with silica, as well as polyoxomolybdate-silicas. The hydrogels are friable and compressible gels while the corresponding xerogels are hard transparent glasses that are micro- to meso-porous and chemically robust, have good optical clarity, but are limited by their inherent brittleness, limited porosity, and lack of modifiable chemical functionality.
- (b) *Organically modified silica sol-gels (Ormosils)*. In this case, the precursor silanes are monomeric or dimeric and bear one or two organic groups attached by hydrolytically stable Si-C bonds, and furnish poly(organosiloxanes) upon hydrolysis/polymerization. The resultant polymers marry an inorganic siloxane backbone with pendant organic moieties, the attached functions ranging from simple alkyl, alkenyl, and aryl moieties to those additionally bearing functional amino, amido, carboxy, hydroxy, thiol, and mixed groups, as well as redox-active metallocenes, nicotinamides, flavins, quinones, and phthalocyanines. These matrices are very utilitarian because they offer tailorable hydrophilic, hydrophobic, ionic, and H-bonding capacities, as well as specific functionalities such as electrochemical activity. Although the hydrogels and xerogels display a broad mesoporosity, they are relatively fragile, of limited optical transparency, and less robust than the inorganic matrices.
- (c) *Hybrid sol-gels*. These materials are derived from amino- and/or hydroxy-functional homopolymers and di-block copolymers, such as polymethylsiloxane, polydimethylsiloxane, poly(alkene oxide), polyurethane/polyurea, polyacrylate, polyphosphazene, and polydimethylsiloxane-co-poly(alkene oxide), which are modified on the main chain or termini with alkoxy silanes [47, 74, 83]. Polymerization leads to siloxane-crosslinked dendritic or comb architectures, which combine the physicochemical attributes of the contributing polymer components. This leads to rigid, semirigid, rubber, and plastic materials with good mechanical properties, variable hydrophobic-hydrophilic balances, and a wide range of porosities, but with poor optical properties.
- (d) *Interpenetrating polymer network (IPN) composite sol-gels*. These composite polymers are obtained by the

following methods [47, 74, 83]. (1) A solution of sol-gel precursor is combined with that of a water-soluble polymer such as alginate, carrageenan, gelatin, agar, PVA, PEG, poly(vinylpyrrolidone), or poly(glycidol), followed by initiation of sol-gel polymerization, which is often followed by phase separation of the organic component by ionotropic crosslinking (alginate or carrageenan) or cryo-phase separation (PVA, gelatin, agar, or gelatin). (2) Solutions of nonhydrolyzed or partially hydrolyzed sol-gel precursors are infused into organic hydrogels, such as calcium alginate, potassium carrageenan, agar, gelatin, PVA cryogels, poly(glycerol methacrylate), poly(hydroxyethyl acrylate), poly(acrylamide), and polyurethane, and sol-gel polymerization is allowed to proceed therein. (3) Organic monomers such as glycerol and hydroxyethyl acrylates are infiltrated into preformed sol-gels, and the organic component is polymerized via standard free radical, UV, or redox initiation processes. Whichever method is used, the resultant composites contain 20–80% w/w of organic component and display varying degrees of phase separation, thereby forming rigid plastics, elastic hydrogels and flexible rubbers with meso- to macro-pore networks. A unique attribute of these materials is that they combine the respective attributes of the component polymers—thus, the sol-gel phase transforms otherwise soft organic hydrogels that readily imbibe water and/or are liquefied by chelating agents or elevated temperatures into rigid glassy materials that are resistant to swelling and structural collapse, due to the supporting action of the supporting sol-gel framework. Such composites are notable for their high biocompatibility and are highly suited to the entrapment of very labile biologicals such as multi-component enzymes and membrane proteins;

- (e) *Reinforced/filled composite sol-gels*. All of the aforementioned materials can be reinforced with inert nano- or microparticulate materials such as native and oxidized graphite powder, hydrophilic and hydrophobic fumed silicas, clays, zeolites, cellulose, and esters thereof [47, 61–75, 83]. The fillers may be incorporated at levels of up to ~75% w/w and substantially improve the mechanical properties and processing attributes of the sol-gel polymers. In addition, active fillers such as gold, palladium, and platinum, and palladium-graphite can be used where conducting and redox-active materials are required.
- (f) *Templated sol-gels*. The simple sol-gel systems (a–b) can be templated with a variety of compounds which act to direct the evolution of the pore structure and the supporting structural framework [84–96]. Templating agents include polyols, hydroxyacids, PEG, monovalent surfactants, multivalent gemini and bolaamphiphile surfactants and surface-active di- and polyblock copolymers. These compounds form nanostructured assemblies such as microemulsions and vesicular and liquid crystalline phases that act as chemical and topological templates for guiding the sol-gel process. Removal of the templates after aging

Table 1. Sol-gel oxide polymers used for bioencapsulation and their precursors.

Sol-gel oxides	Precursors	Bulk properties	Chemical attributes
Silica (SiO_2)	Tetraalkyl silicates: $\text{Si}(\text{OMe})_4$; $\text{Si}(\text{OEt})_4$; $\text{Si}(\text{O}i\text{Pr})_4$ Poly(alkyl silicates): $[\text{SiO}_{1-1.4}(\text{OMe})_{1.2-2}]_n$ Poly(glyceryl silicates): $[\text{SiO}_{1-1.2}\text{Gl}_{0.8-1}]_n$	Hard, brittle Clear, transparent UV-VIS	Hydrophilic to semihydrophobic Stable to pH 2-9 Degraded by fluorides
Alumina ($\text{Al}_2\text{O}_3 \cdot x\text{H}_2\text{O}$)	Aluminium(III) alkoxides: $\text{Al}_2(\text{OEt})_6$; $\text{Al}_2(\text{O}i\text{Pr})_6$; $\text{Al}_2(\text{O}t\text{Bu})_6$	Hard, brittle Clear, transparent UV-VIS	Hydrophilic Stable to pH 2-14
Alumina-silica	Aluminium(III) alkoxides + poly(alkyl silicates), etc.		
Zirconia ($\text{ZrO}_2 \cdot x\text{H}_2\text{O}$)	Zirconium(IV) alkoxides: $\text{Zr}(\text{OEt})_4$; $\text{Zr}(\text{O}i\text{Pr})_4$; $\text{Zr}(\text{O}t\text{Bu})_4$	Hard, brittle Clear, transparent UV-VIS	Hydrophilic Resistant to pH 2-14
Zirconia-silica	Zirconium(IV) alkoxides + poly(alkyl silicates), etc.		
Titania ($\text{TiO}_2 \cdot x\text{H}_2\text{O}$)	Titanium(IV) alkoxides: $\text{Ti}(\text{OEt})_4$; $\text{Ti}(\text{O}i\text{Pr})_4$; $\text{Ti}(\text{O}t\text{Bu})_4$	Hard, brittle Clear, transparent UV-VIS	Hydrophilic Photoactive Stable to pH 2-14
Titania-silica	Titanium(IV) alkoxides + poly(alkyl silicates), etc.		
Niobia ($\text{NbO}_2 \cdot x\text{H}_2\text{O}$)	Niobium(IV) alkoxides: $\text{Nb}(\text{OEt})_4$	Hard, brittle Clear, transparent UV-VIS	Hydrophilic Chromic, photoactive Stable to pH 2-11
Niobium(V) oxide (Nb_2O_5)	Niobium(V) alkoxides: $\text{Nb}(\text{OEt})_5$		
Tin(IV) oxide ($\text{SnO}_2 \cdot x\text{H}_2\text{O}$)	Tin(IV) alkoxides: $\text{Sn}(\text{OEt})_4$; $\text{Sn}(\text{O}i\text{Pr})_4$; $\text{Sn}(\text{O}t\text{Bu})_4$ Tin(IV) alkoxides + poly(alkyl silicates), etc.	Hard, brittle Clear, semitransparent UV-VIS	Hydrophilic Conductive, redox-active, photoactive Stable to pH 4-10
Vanadium(V) Oxide (V_2O_5)	Vanadium(V) oxide trialkoxides: $\text{VO}(\text{OEt})_3$; $\text{VO}(\text{O}i\text{Pr})_3$ Vanadium(V) oxide trialkoxides + poly(alkyl silicates), etc.	Hard, brittle Clear, colored, opaque UV-VIS	Hydrophilic Conductive, redox-active, photochromic Stable to pH 3-9
Molybdenum(V) oxide (Mo_2O_5)	Molybdenum(V) alkoxides: $\text{Mo}(\text{OEt})_5$; $\text{Mo}(\text{O}i\text{Pr})_5$; $\text{Mo}(\text{O}t\text{Bu})_5$	Hard, brittle Clear, colored, opaque UV-VIS	Hydrophilic Conductive, redox-active, photoactive Stable to pH 4-10
Polyoxometallates-silicates-siloxanes	Phosphomolybdic acid and phosphotungstomolybdic acids + tetraalkyl silicates, poly(alkyl silicates), etc.	Hard, brittle Clear, colored, opaque UV-VIS	Hydrophilic to semihydrophobic Redox-active, photoactive Stable to pH 3-9

Table 2. Organically modified silicate sol-gels used for bioencapsulation and their precursors.

Sol-gel	Precursors	Bulk properties	Chemical attributes
Alkylsiloxanes	Trialkoxyalkylsiloxanes: SiR'(OR) ₃ Dialkoxodialkylsiloxanes: Si(R') ₂ (OR) ₂ Tetraalkoxydialkylsiloxanes: [OSiR'(OR) ₂] ₂ Bis(trialkoxysilyl)alkanes: (C _n H _{2n}) ₂ Si(OR) ₃ ₂ (R' = CH ₃ to C ₁₈ H ₃₇ , cyclohexyl; R = Me, Et, Pr, glyceryl)	Soft, semiflexible, hard, brittle Clear, translucent, opaque Semitransparent UV-VIS	Hydrophobic Stable to pH 2–10
Alkylsiloxanes	Trialkoxyalkenylsiloxanes: SiR'(OR) ₃ Dialkoxoalkenylsiloxanes: SiR'R''(OR) ₂ Tetraalkoxydialkenylsiloxanes: [OSiR'(OR) ₂] ₂ N-Acryloylaminoalkyltrialkoxysilanes: CH ₂ CHCONHC ₃ H ₆ Si(OR) ₃ (R' = vinyl, allyl, propargyl; R'' = Me, Et; R = Me, Et, glyceryl)	Soft, semiflexible, hard to brittle Clear, translucent, opaque Semitransparent UV-VIS	Semihydrophobic Stable to pH 2–10
Arylsiloxanes	Trialkoxyarylsiloxanes: SiAr(OR) ₃ Bis(trialkoxysilyl)arenes: Ar[Si(OR) ₃] ₂ (Ar = Ph, PhCH ₂ , C ₆ H ₄ , C ₆ H ₄ (CH ₂) ₂ ; R = Me, Et)	Soft, semiflexible, hard, brittle Clear, translucent, opaque Semipaque UV-VIS	Hydrophobic Stable to pH 2–11
Aminosiloxanes	Aminoalkyltrialkoxysilanes: NH ₂ C ₃ H ₆ Si(OR) ₃ N,N-Bis(aminoalkyl)aminoalkyltrialkoxysilanes: (NH ₂ C ₂ H ₄) ₂ NC ₃ H ₆ Si(OR) ₃ N-(Aminoacyl)aminoalkyltrialkoxysilanes: AAc-NHC ₃ H ₆ Si(OR) ₃ (AAc = 2-aminoacyl; R = Me, Et, Pr, glyceryl)	Semiflexible Clear, semitransparent UV-VIS	Hydrophilic Basic, zwitterionic Stable to pH 6–11
Amidoalkylsiloxanes	N-Acylaminoalkyltrialkoxysilanes: R'CONHC ₃ H ₆ Si(OR) ₃ Ureidoalkyltrialkoxysilanes: NH ₂ CONHC ₃ H ₆ Si(OR) ₃ (R'CO = Ac, TFAC, higher acyl; R = Me, Et, Pr, glyceryl)	Semiflexible, brittle Hydrogels Clear, semitransparent UV-VIS	Hydrophilic to hydrophobic Basic, neutral Stable to pH 4–11
Carboxyalkylsiloxanes	Carboxyalkyltrialkoxysilanes: HO ₂ CC ₃ H ₆ Si(OR) ₃ N-(Carboxyalkyl)aminoalkyltrialkoxysilanes: HO ₂ CCH ₂ CONHC ₃ H ₆ Si(OR) ₃ (R = Me, Et, Pr, glyceryl)	Semiflexible, brittle Hydrogels Clear, semitransparent UV-VIS	Hydrophilic Acidic Stable to pH 2–11
Hydroxyalkylsiloxanes	Dihydroxyalkyltrialkoxysilanes: HOCH ₂ (HOCH)OC ₃ H ₆ Si(OR) ₃ N,N-Bis(hydroxyalkyl)aminoalkyl: (HOC ₂ H ₄) ₂ NHC ₃ H ₆ Si(OR) ₃ N-(Polyhydroxyalkyl)aminoalkyltrialkoxysilane: R'CONHC ₃ H ₆ Si(OR) ₃ Hydroxyalkylureidoalkyltrialkoxysilane: HOC ₂ H ₄ NHCONHC ₃ H ₆ Si(OR) ₃ (R'CO = δ-gluconyl, pantoyl; R = Me, Et, Pr, glyceryl)	Flexible, semiflexible, rigid Hydrogels Clear, semitransparent UV-VIS	Hydrophilic Neutral to Basic Stable to pH 4–11
Meraptoalkylsiloxanes	Thioalkyltrialkoxysilanes: HSC ₃ H ₆ Si(OR) ₃ Bis(trialkoxysilyl)alkyl)disulfides: [SC ₃ H ₆ Si(OR) ₃] ₂ (R = Me, Et, Pr, glyceryl)	Flexible, semiflexible, rigid Hydrogels Clear, semitransparent UV-VIS	Hydrophilic Neutral, slightly acidic Redox-active Stable to pH 4–9
Redox-active siloxanes	Ferrocenylalkyltrialkoxysilanes: N-ferroceneacetyl-NHC ₃ H ₆ Si(OR) ₃ Nicotinamidoalkyltrialkoxysilanes: [NAD-/NADP-CONH]-COC ₃ H ₆ Si(OR) ₃ Flavinamidoalkyltrialkoxysilanes: [FAD-NH]-COC ₃ H ₆ Si(OR) ₃ (R = Me, Et, Pr)	Flexible, semiflexible, rigid Clear, colored Semitransparent UV-VIS	Hydrophilic Redox-active Stable to pH 5–9

Table 3. Composite sol–gels used for bioencapsulation and their precursors.

Sol–gel	Precursors	Bulk properties	Chemical attributes
Polydimethylsiloxanes–silicates–siloxanes	Bis(alkoxyalkylsiloxy)polydimethylsiloxane: $[\text{Si}(\text{OR})_2\text{O}]_2[\text{Me}_2\text{SiO}]_n$ Bis[poly(alkoxyalkylsiloxy)polydimethylsiloxane: $\{(\text{SiO}_x\text{R}'(\text{OR}))_{m-2}[\text{Me}_2\text{SiO}]_n$ ($\text{R}' = \text{aminoalkyl, hydroxyalkyl, etc; R} = \text{Me, Et, Pr, glyceryl}$)	Flexible, semiflexible to rigid Translucent, opaque Semitransparent UV-VIS	Hydrophobic Stable to pH 4–11
Polymethylsiloxane–silicates–siloxanes	Poly[(trialkoxysilyl ethylene)methylsiloxane]: $\{(\text{OR})_3\text{SiC}_2\text{H}_4[\text{Si}(\text{Me})\text{O}]\}_n$ ($\text{R} = \text{Me, Et, Pr, glyceryl}$)	Flexible, semiflexible, rigid Translucent, opaque Semitransparent UV-VIS	Hydrophobic to hydrophilic Surface-active Stable to pH 4–11
Poly(alkene oxides)–silicates–siloxanes	Bis(alkoxyalkylsiloxy)poly(ethylene oxide): $[\text{Si}(\text{OR})_2\text{C}_3\text{H}_6\text{NHCH}_2(\text{CHOH})]_2$ -PEO Bis(alkoxyalkylsiloxy)-(PEO-co-PDMS): $[\text{Si}(\text{OR})_2\text{C}_3\text{H}_6\text{NHCH}_2(\text{CHOH})]_2$ -(PEO-co-PDMS) ($\text{R} = \text{Me, Et, Pr, glyceryl}$)	Flexible, semiflexible, rigid Translucent, opaque Semitransparent UV-VIS	Hydrophobic, hydrophilic Surface-active Stable to pH 4–10
Poly(acrylates)–silicates–siloxanes	Poly[(trialkoxysilyl)alkylaminocarboxy]ethylmethacrylate): $[\text{Si}(\text{OR})_3\text{C}_3\text{H}_6\text{NHCO}_2\text{C}_2\text{H}_4\text{O}_2\text{C}(\text{Me})\text{CH}]_n$ ($\text{R} = \text{Me, Et, Pr, glyceryl}$)	Flexible Hydrogels	Hydrophilic Stable to pH 4–10
Polyurethanes–silicates–siloxanes	Bis(trialkoxysilylalkyl)-[poly(propylene glycol)-diurea]: $[\text{Si}(\text{OR})_3\text{C}_3\text{H}_6\text{NHCONH}(\text{MeC}_6\text{H}_3)\text{NHCO}(\text{CH}(\text{Me})\text{CH}_2)]_n$ ($\text{R} = \text{Me, Et, Pr, glyceryl}$)	Clear, Semitransparent UV-VIS	Hydrophilic Stable to pH 4–10
Polyureas–silicates–siloxanes	Tris[(trialkoxysilylalkylureido)poly(propylene glycol)]glycerol: $[\text{CHO}-(\text{CH}_2\text{O})_2-]_3[\text{CH}_2\text{CH}(\text{MeO})\text{CONHC}_3\text{H}_6\text{Si}(\text{OR})_3]_3$ ($\text{R} = \text{Me, Et, Pr, glyceryl}$)	Clear, translucent Semiopaque UV-VIS	Hydrophilic Stable to pH 4–10
Poly(phosphazenes)–silicates–siloxanes	Poly[bis(trialkoxysilylalkylamino)phosphazenes]: $[\text{NP}(\text{NHC}_3\text{H}_6\text{Si}(\text{OR})_3)_2]_n$ ($\text{R} = \text{Me, Et, Pr, glyceryl}$)	Flexible Clear, translucent Semitransparent UV-VIS	Hydrophilic Stable to pH 4–10

Note: PEO, poly(ethylene oxide); PDMS, poly(dimethyl siloxane).

and drying provides meso- to macroporous materials with highly structured pore frameworks, which despite the dearth of bioencapsulation applications, hold great promise for accessing highly ordered and porous bioencapsulated sol-gels [83, 96].

In general, the physicochemical properties of hybrid and composite sol-gel materials are often significantly improved over those of the constituent sol-gel polymers due to the reinforcing action of the partnering phase [74, 83]. In a similar vein, xerogels are usually superior in terms of mechanical properties and chemical resistance to hydrogels by virtue of greater crosslinking and densification [61–65]. However, the drying of hydrogels inevitably reduces porosity and increases steric compression effects and diffusional limitations, thereby resulting in reduced protein functionality, especially in the case of oxide-based sol-gels [61–65].

6. THE STRUCTURE AND FUNCTIONING OF SOL-GEL BIOENCAPSULATES

On the surface, the (gross) morphology of bioencapsulated sol-gels can appear very similar to that of undoped materials, but this belies that fact that the entrapped biomolecules can substantially affect sol-gel nanostructure by modifying the development of the polymer network. Thus, as outlined above, acidic/basic and charged residues influence the mechanism and rates of alkoxy silane hydrolysis and condensation, and charged, hydrophilic, hydrophobic, and H-bonding domains can act as interfacial templates to direct the branching pattern, functionality, growth, topology, and aggregation of developing polysilicate/polysiloxane colloids [65–74, 84–92].

The avenue via which large oligomeric proteins (>100,000 molecular weight) and micron-sized biologicals such as membrane fragments that are larger than the pore structure can be readily explained by bulk capture by the developing polymer framework. However, the mechanism of entrapment and retention of smaller biomolecules whose dimensions are smaller than the pore size of the sol-gel is less obvious. For example, proteins with molecular weights as low as ~8,000 (globular size ~1 nm) can be irreversibly encapsulated in sol-gels with mesopore networks spanning 2–6 nm, which otherwise allow the infiltration of molecules with masses of 2000–200,000. Thus, polylysine with a molecular weight 150,000 can penetrate into silica and metallosilicate xerogels and therein inhibit trypsin [89, 97], and cytochrome *c* and myoglobin are able to diffuse through *N,N*-bis(3-siloxypropyl)ethylenediamine xerogels [98]. Similarly, RNase enzymes can penetrate silica xerogels and bind to encapsulated dinitrophenyl (DNP)-poly(adenylate) [99], and immunoglobulin antibodies can diffuse into silica hydrogels and bind to encapsulated antigenic proteins and cells [100]. Intriguingly, high-porosity sol-gels prepared via special gelation and templating procedures to display pore sizes of 2–20 nm (xerogels) and 4–100 nm (hydrogels) have been used to fractionate proteins with molecular weights of 14,000–77,000 [101]. Even more striking, it has been shown that intact 50–100 nm influenza virus particles can access and bind to sialic acid-coated liposomes encapsulated in silica hydrogels [102].

The few investigations undertaken to date on this aspect of sol-gel bioencapsulation suggest that entrapment derives from a combination of physical embedding of the protein within sol-gel nanoparticles and strong binding interactions between the biomolecule and surrounding (templated) sol-gel surfaces. Studies indicate that small to midsized biomolecules (5000–100,000 molecular weight) are fully or partially encased by sol-gel surfaces that substantially conform to the topology of the hydrated biologicals, thereby essentially halting their large-scale lateral diffusion [61–74]. However, while global biomolecule dynamics are restricted as a result of this confinement, it appears that the encapsulating sol-gel structures of most hydrogels and xerogels are sufficiently loose to allow for local rotational and translational motions [61–63].

UV-VIS, fluorescence, Fourier transform infrared, Raman, circular dichroism, electron spin resonance, and nuclear magnetic resonance studies of proteins encapsulated in sol-gels have provided some insights into biomolecular dynamics in these restricted environments. Thus, investigations on myoglobin, hemoglobin, cytochrome *c*, cytochrome *c* peroxidase, catalase, monellin, oncomodulin, glutamate dehydrogenase, glucose oxidase, and nitrobenzoxadiazole- and acryloidan-labeled bovine and human albumins entrapped in a variety of silica and siloxane hydrogels and xerogels suggest that the proteins are confined to 3–10 nm pockets wherein they substantially retain nanosecond and subnanosecond dynamics and at least partial rotational and translational mobility, akin to the species in solution [103–124]. For instance, fluorescence studies of silica-entrapped glucose oxidase demonstrate that the rotational mobility of the enzyme is ~50% of that in solution, that the folding kinetics of the flavin (redox) moiety are greatly reduced, but surprisingly, that the local motions of the active site pocket are similar to those in solution [113, 122]. Similarly, UV-VIS probing of ferricytochrome *c* encased in silica sol-gels indicates that active site dynamics are not repressed per se, but that sol-gel confinement does modify them in the sense of creating local heterogeneity [125]. Similarly, the photoactive proton pump bacteriorhodopsin shows decreased dynamics as reflected in a drop in the rate of decay of the excited M state, but retains sufficient global mobility to change its conformational state and therefore function in silica hydrogels and xerogels [126–130].

In addition to modifying biomolecular motions, the polymer surface can also physically block recognition/catalytic sites. For example, studies with myoglobin, albumins, and glucose oxidase have demonstrated that the active sites of subpopulations of the silica-entrapped proteins reflect highly restricted environments that are essentially not-accessible to their corresponding substrates/ligands [104–108, 122]. Not surprisingly, the chemical functionality of the enveloping sol-gel surface can also strongly affect protein function [61–74], as demonstrated by the observation that glucose oxidase retains most of its activity when entrapped in silica, while glycolate and lactate oxidases lose most of their functioning [131, 132]. It has been suggested that the structures of the active sites as well as redox functioning of the flavin cofactor in the latter enzymes are disrupted via electrostatic interactions between their positively charged binding channels and the anionic silica matrix, while the zwitterionic nature of the

binding cleft in glucose oxidase protects the former protein from such effects.

From the above, one can envisage the following structure for bioencapsulated sol-gels [61–74]:

- (a) The biological is embedded within the body of the polymer matrix and/or its pore structure, the two defining a bicontinuous framework of fused nano- or microparticles.
- (b) Depending upon the biological and the composition and mode of preparation of the sol-gel, the biomaterial is distributed homogeneously as matrix-isolated molecules, may self-associate/precipitate during gelation to form aggregates, or may be nano- or micro-compartmentalized at the surface of sol-gel particles or into the pore structure due to interfacial/phase separation effects.
- (c) The biological is in contact with a partially or fully enclosing polymer shell, and the contact surface is templated to conform topologically and chemically to the hydrated surface of the biomolecule.
- (d) A low-mobility H-bonded layer of water molecules is trapped between the biomolecule and polymer surface.
- (e) Global biomolecule mobility and segmental motions are diminished, depending upon the degree of compliance of the biomolecule and polymer surfaces, the type and magnitude of their interactions, and the amount and mobility of the water layer.
- (f) There is sufficient accessibility between the recognition sites of a portion of the biomolecule population and the surrounding pore structure and enough freedom for local conformational transitions to enable the entry and recognition/reaction of ligands.

7. APPLICATIONS OF SOL-GEL BIOENCAPSULATES

7.1. Sol-Gel Biosensors

By far the most investigated area of application of sol-gel bioencapsulates has been the realm of biosensors [47, 61–74]. This has resulted from the pressing need for rugged, miniaturized, and portable biosensing devices for applications such as clinical medicine, diagnostics, bioprocess monitoring, food and environmental analysis, food and drug quality control, drug discovery, genomics, and proteomics [133–144]. The great attraction of sol-gel biosensing platforms lies in the generic nature of the technology together with the ability to readily produce materials with diverse chemistries and fabricate them in a variety of formats.

Most work on sol-gel biosensors has focused on glucose sensors based around the flavoprotein glucose oxidase (GOx), which mediates the air oxidation of glucose to gluconolactone with concomitant generation of hydrogen peroxide (Table 4) [145–183]. In this context it should be noted that despite 30 years of development work, robust biosensor platforms for glucose determination in consumer and clinical settings have as yet to be devised. The enzyme has been encapsulated in silica, metal oxides, metallosilicates, Ormosils, and composite sol-gels and the materials

fabricated as monolithic, passive-deposited thin and thick film and spin-coated optical sensors, and monolithic and passive-deposited thin and thick-film electrodes and electrode coatings. Optical biosensors function via the UV-VIS or fluorescence monitoring of the redox state of the chromophoric flavin cofactor, while amperometric platforms measure oxygen levels via Clarke electrodes or oxygen-sensitive rhodium(II)/(III) complexes, or monitor the redox cycling of the active site of GOx via electrochemical coupling to the electrode surface using suitable electron transfer mediators. Interestingly, the active site of GOx can also be directly “wired” to an electrode by modification of the enzyme with a ferrocene derivative or via the co-dispersion/co-polymerization of dye, transition metal complex, or metallocene redox mediators in the sol-gel, and the activity monitored amperometrically [146, 147, 155, 160, 163–166].

A significant development in amperometric GOx biosensors has been the advent of carbon composite electrodes wherein graphite together with mediators is incorporated into GOx-Ormosil sol-gels, thereby furnishing highly sensitive and robust wired configurations, which can be mass produced by screen printing [146–148, 156, 157, 160, 166, 171, 175–177]. In these materials, the carbon phase provides electrical conductivity, porosity, and mechanical reinforcement, while the Ormosil sol-gel framework provides modifiable chemical functionality for fine tuning the catalytic properties and stability of GOx, as well as controlling the hydrophobicity and wetting behavior of the composite. This configuration enables the surface of monolithic and thick film electrodes to be renewed as required by simple polishing to exposing fresh biosensor surface, once sensor performance declines due to surface fouling and/or enzyme inactivation. In a further modification, the inclusion of electrocatalytically active graphite-supported palladium, platinum and ruthenium, or gold nanocrystals in place of graphite provides mediator-free electrodes that are highly sensitive, selective, and stable [147, 149, 155, 169, 172, 174]. Mediator-free amperometric configurations can also be constructed by coupling GOx with horseradish or soybean peroxidases, which mediate the reduction of hydrogen peroxide [145, 147, 155–157, 171].

The generic applicability of sol-gel biosensor platforms has been amply demonstrated with its extension to a wide variety of oxidoreductases ranging from peroxidases, alcohol, amine, polyol and hydroxyacid oxidases and dehydrogenases, phenol oxidases, and hydroxylases to nitrite and nitrate reductases (Table 5) [184–210]. These biosensors have been applied to the determination of hydrogen peroxide, aliphatic alcohols and aldehydes, sugars, lactate, amines, phenols, organophosphates, competitive enzyme inhibitors such as cyanide and organophosphates, nitrates, nitrites, and polar organic solvents.

Whereas optical and amperometric configurations are readily constructed for chromoproteins and oxidoreductases, other proteins can also be applied, providing that the substrate/product can be monitored optically/electrochemically. Thus, the sol-gel entrapped hydrolases cholinesterase, acetylcholinesterase, butyrylcholinesterase, phosphodiesterase, urease, and penicillinase have been used as direct and inhibition-based biosensors for the optical and potentiometric monitoring of acetylcholine, organophosphate

Table 4. Glucose oxidase and glucose oxidase–horseradish peroxidase sol–gel optical and electrochemical biosensors.

Precursors	Bioencapsulated sol–gel	Sensor type	Ref.
TMOS	[GOx ± HRP + 1,1'-dimethylferrocene]–carbon–silica xerogels	Amperometric	[145]
TEOS	[GOx ± HRP]–[Pd-graphite]–siloxane or [GOx-ferrocene]–graphite–siloxane xerogels		[146, 155]
MeTMOS	[GOx]–carbon–silica xerogels	Amperometric	[147, 148]
TEOS	[GOx]–Au–siloxane xerogels		[149]
MeTMOS, TEOS	[GOx]–carbon–siloxane xerogels		[151]
3-FAPTOS	[GOx]–silica xerogels		[153]
TEOS, TMOS	[GOx]–silica xerogels		[154]
TEOS, 3-FAPTOS	[GOx + HRP]–graphite–siloxane xerogels		[157]
3-APTEOS, 2-ECETOS	[GOx]–siloxane hydrogels crosslinked with glyoxal		[162]
ATIP	[GOx]–alumina xerogels		[162]
MeTEOS	[GOx]–[poly(vinylpyrrolidone)-Os(bpy) ₂]–siloxane xerogels		[163]
TMOS	[GOx + Co(II) phthalocyanine + ferrocene + DPTC]–carbon–silica xerogels		[166]
TMOS	[GOx]–silica–siloxane hydrogels		[167]
3-APTOS, MeTEOS, TEOS	[GOx]–[Pd-carbon]–siloxane xerogels		[168]
MeTMOS	[GOx]–[poly(vinyl alcohol)-g-poly(4-vinylpyridine)]–silica xerogels		[169]
TEOS	[GOx ± HRP]–graphite–PEG–siloxane or [GOx]–PEG–siloxane hydrogels		[170]
3-APTEOS, 2-ECETOS	[GOx]–[Rh-graphite]–silica xerogel		[156, 171]
MeTMOS	[GOx]–silica xerogel		[172]
MeTMOS	[GOx]–[Ru-graphite]–silica xerogels		[173]
TEOS	[GOx]–graphite–siloxane xerogels	[174]	
MeTMOS, 3-FAPTOS	[GOx]–graphite–siloxane xerogels	[147, 175]	
MeTMOS, 3-APTOS, 3-FAPTOS	[GOx]–siloxane hydrogels and xerogels	[176, 177]	
TMOS	[GOx]–Ir–silica hydrogel and xerogel	[178]	
TMOS	[GOx]–ferrocene–polyelectrolyte–silica hydrogels	[179]	
3-APTEOS, 2-ECETOS	[GOx]–siloxane hydrogels	[180]	
TMOS	[GOx]–silica hydrogels and xerogels	[181]	
ATIP	[GOx]–bovine serum albumin–alumina hydrogels	[182]	
TMOS	[GOx]–graphite–silica	Luminescence	[183]
TEOS	[GOx]–silica xerogels		[158]
MeTMOS, TMOS	[GOx]–siloxane xerogel	[159]	
TMOS	[GOx-fluorescein/Texas Red/Cy5 bioconjugates]–silica hydrogels	Fluorescence	[160]

Note: 3-APTOS, 3-aminopropyltrimethoxysilane; ATIP, aluminum triisopropoxide; 2-ECETOS, 2-(3,4-epoxycyclohexyl)ethyltrimethoxysilane; 3-FAPTOS, 3-ferroceneacetamidopropyltrimethoxysilane; HRP, horseradish peroxidase; MeTEOS, methyltriethoxysilane; MeTMOS, methyltrimethoxysilane; TEOS, tetraethoxysilane; TMOS, tetramethoxysilane.

pesticides, penicillin, and urea (Table 6) [221–228]. Of particular interest is the construction of coupled optical sensors using bacteriorhodopsin together with urease, acetylcholine esterase, or penicillinase—the action of the hydrolase alters the pH and thus the protonation state of and hence the rate of decay of the photoactive M state of bacteriorhodopsin [230].

A variety of noncatalytic proteins that selectively bind metal ions and gaseous oxygen and oxides have also been utilized for optical sol–gel biosensing (Table 6). Thus, the luminescent protein has been used to construct sol–gel sensors for calcium, and the chromophoric metalloproteins hemoglobin, myoglobin, cytochrome *c*, and superoxide dismutase have been applied to the solution- and gas-phase detection/quantification of oxygen, carbon monoxide, carbon dioxide, and nitrogen monoxide. In particular, the heme proteins have proved to be excellent model systems for sol–gel bioencapsulation, because the proteins are chromophoric and can be de-readily metallated and metal-exchanged, and their conformation, molecular motions, and ligand binding

can be easily monitored via spectroscopic probing of the active centers [83, 157, 231–240].

There is particular interest in the medical, food, drug, and environmental sectors for developing biosensors for the detection and quantification of antibody–antigen interactions, and sol–gel materials have been explored with some success on this front. Thus, monoclonal and polyclonal antibodies to fluorescein, nitroaromatics, and organophosphates have been encapsulated in silica sol–gels and used for the optical, electrochemical, and coupled enzyme-linked immunosorbent assay (ELISA) detection of the corresponding antigens (Table 6) [241–246]. The reverse configuration, that is, the entrapment of antigens in sol–gels has been used for constructing optical biosensors for detecting the presence of antibodies to disease-causing parasites in human blood [248, 249].

Photoactive proteins, which are of interest for photocatalyst and optoelectronics applications, have also been entrapped for envisaged application as solid-state optical devices and transducers. Thus, the membrane-associated proteins bacteriorhodopsin, phycocyanin, allophycocyanin,

Table 5. Oxidoreductase-based sol–gel optical and electrochemical biosensors.

Precursors	Bioencapsulated sol–gel	Analyte(s)	Sensor type	Ref.
Peroxidase				
TEOS	[Enz]–silica hydrogel	H ₂ O ₂	Luminescence	[184, 185]
TMOS	[Enz + ferrocene]–silica hydrogel	H ₂ O ₂	Amperometric	[185]
TEOS	[Enz]–[PVA- <i>g</i> -poly(4-vinylpyridine)]–silica hydrogels	H ₂ O ₂	Amperometric	[186]
TEOS	[Enz]–[PVA- <i>g</i> -poly(4-vinylpyridine)]–silica hydrogels	H ₂ O ₂	Amperometric	[187]
MeTMOS, 3-MPTMOS	[Enz]–[PVA- <i>g</i> -poly(4-vinylpyridine)]–siloxane–hydrogels	H ₂ O ₂	Amperometric	[188]
TMOS	[Enz]–silica hydrogels	H ₂ O ₂ , RO ₂ H, RO ₂ R'	Amperometric	[190]
TMOS	[Enz]–silica hydrogels	H ₂ O ₂	Amperometric	[191]
TEOS	[Enz]–[poly(vinyl alcohol)- <i>g</i> -poly(4-vinylpyridine)]–silica hydrogels	H ₂ O ₂	Amperometric	[192]
MeTEOS	[Enz]–[poly(vinylpyrrolidone)-Os(bpy) ₂]–siloxane xerogels	H ₂ O ₂	Amperometric	[193, 194]
TEOS	[Enz]–[Pd-graphite]–silica xerogels	CN [−] , H ₂ O ₂	Amperometric	[195]
TMOS, MTMOS, PTMOS	[Enz]–silica/siloxane–ABTS hydrogels and xerogels	H ₂ O ₂	UV-VIS	[196]
TMOS	[Enz]–silica hydrogels	Phenols, naphthol, coumarate, H ₂ O ₂	Luminescence	[197]
TMOS	[Enz]–silica hydrogels	H ₂ O ₂	Luminescence	[198]
TMOS	[Enz]–silica-poly(ester sulfonate) hydrogels	H ₂ O ₂	Amperometric	[199]
TMOS	[Enz]–PVA–PVP–silica hydrogels	H ₂ O ₂	Amperometric	[200]
Glucose, galactose, lactate oxidases + peroxidase				
PGS, 3-HEAGS	[Enzymes]–poly(vinyl alcohol)–siloxane hydrogels	Glucose, galactose, lactose, lactate	UV-VIS	[83]
Lactate oxidase				
MeTMOS	[Enz]–[Pd-carbon]–siloxane xerogels	Lactate	Amperometric	[147, 169]
MeTEOS	[Enz]–[poly(vinylpyrrolidone)-Os(bpy) ₂]–siloxane xerogels	Lactate	Amperometric	[201]
TMOS	[Enz]–graphite-cellulose ester–silica hydrogels	Lactate	Amperometric	[216]
Oxalate oxidase				
TMOS	[Enz]–silica xerogels	Oxalate	UV-VIS	[202]
Xanthine oxidase				
MeTMOS	[Enz]–graphite–siloxane xerogel	Hypoxanthine	Amperometric	[203]
Polyphenol oxidase				
TEOS, MeTMOS	[Enz]–PVA- <i>g</i> -poly(4-vinylpyridine)–siloxane hydrogels	MeCN, <i>i</i> -PrOH, <i>n</i> -BuOH	Amperometric	[104, 209]
TEOS, MeTMOS, 3-APTMS	[Enz]–PEG-siloxane or [PPOx]-poly(vinyl alcohol)–siloxane hydrogels	Phenol, catechol, <i>p</i> -cresol	Amperometric	[205]
ATIP	[Enz]–alumina xerogel	Phenol, catechol, cresols	Amperometric	[206]
TMOS	[Enz]–silica hydrogels	Phenol, amino-, chloro- and nitro-	Amperometric	[207,]
ATIP	[Enz]–alumina xerogels	Phenols, catechol, cresols	Amperometric	[208–210]
Phenol hydroxylase				
TMOS	[Enz]–silica hydrogels	Phenol, amino-, chloro-fluoro-, carboxy- and methylphenols, catechol, resorcinol	Amperometric	[211]
Laccase				
TMOS	[Enz]–silica hydrogels	Phenol, resorcinol, aniline	UV-VIS	[212]
Cytochrome P450_{cam}				
MeTEOS	[Enz + bovine serum albumin]–glutaraldehyde–siloxane xerogels	Camphor, pyrene	Amperometric	[213]
Choline oxidase + acetylcholine esterase				
PGS, 3-GAPS	[Enzymes]–poly(vinyl alcohol)–[Pd-graphite]–siloxane hydrogels	Acetylcholine, choline	Amperometric	[83]
Lactate dehydrogenase				
TEOS	[Enz]–silica xerogels	Lactate, pyruvate	UV-VIS	[214]
TMOS	[Enz]–silica hydrogels and xerogels	Lactate	Fluorescence	[215]
Malate dehydrogenase				
TMOS	[Enz]–graphite-cellulose ester–silica hydrogels	Malate	Amperometric	[216]

continued

Table 5. Continued

Precursors	Bioencapsulated sol–gel	Analyte(s)	Sensor type	Ref.
Glucose-6-phosphate dehydrogenase				
PGS, 3-APGS	[Enz]–poly(vinyl alcohol)–siloxane hydrogel	Glucose-6-phosphate	UV-VIS	[83]
TMOS	[Enz]–silica hydrogels	Glucose-6-phosphate	Fluorescence	[217]
Alcohol dehydrogenase				
TMOS	[Enz + NADH]–silica xerogels	Ethanol, 1-propanol, acetaldehyde, propionaldehyde	Fluorescence	[218]
Nitrate and nitrite reductases				
TMOS	[Enz]–silica hydrogels	Nitrate	UV-VIS	[219]
TMOS	[Enz]–silica hydrogels and xerogels	Nitrite	UV-VIS	[220]

Note: ABTS, 2,2'-azinobis (3-ethylbenzothiazoline)-6-sulfonic acid; 3-APTMS, 3-aminopropyltrimethoxysilane; Enz, enzyme; 3-GAPS, 3-gluconamidopropylsiloxane; 3-HEAGS, 3-(1'-hydroxy-2'-(2'-hydroxyethylamino)ethoxy)-propylglyceroxysiloxane; MeTEOS, methyltriethoxysilane; MeTMOS, methyltrimethoxysilane; 3-MPTMS, 3-mercaptopropyltrimethoxysilane; PGS, poly(glyceryl silicate); TEOS, tetraethoxysilane; TMOS, tetramethoxysilane.

Table 6. Optical, electrochemical, and immunochemical sol–gel biosensors.

Biological(s)	Precursor	Bioencapsulated sol–gel	Analyte(s)	Sensor type	Ref.
Cholinesterase	TMOS	[Enz]–silica xerogel	Fenitrothion, azinphos-ethyl, methidathion, naled, mecarbam	Fluorescence	[221]
Butyrylcholinesterase	TMOS	[Enz]–silica xerogel	BADAPP, cognex	UV-VIS	[222, 223]
Acetylcholinesterase	TMOS	[Enz]–silica and [Enz]–PEG-silica hydrogels	Omethoate, carbaryl, diazinon,	UV-VIS	[223]
	TMOS	[Enz]–silica hydrogel	Malathion, methamidophos, chlorpyrifos,	Amperometric	[224]
	TMOS	[Enz]–silica hydrogel	Methidathion, dichlorvos, acetylcholine	Fluorescence	[225]
Parathion hydrolase	TMOS	[Enz]–silica xerogel	Parathion	UV-VIS	[226]
Urease	TMOS	[Enz]–silica hydrogels	Urea	Potentiometric	[227, 229]
	TEOS	[Enz]–silica hydrogel	Urea	Potentiometric	[228]
Bacteriorhodopsin + acetylcholine esterase or penicillinase or urease	TMOS	[Enzymes]–silica hydrogels	Acetylcholine, penicillin, urea	UV-VIS	[230]
Aequorin	TMOS	[Enz]–silica hydrogels	Ca ²⁺	Luminescence	[231]
Cytochrome <i>c</i>	TMOS	[Prot]–silica xerogels and hydrogels	CO, O ₂ , NO	UV-VIS	[231–236]
Cytochrome <i>c'</i>					
Hemoglobin	TMOS	[Prot]–silica xerogels and hydrogels	CO, O ₂ , NO	UV-VIS Fluorescence	[232, 237]
Myoglobin	TMOS	[Prot]–silica xerogels and hydrogels	CO, CO ₂ , O ₂ , NO	UV-VIS	[232, 233,]
Mn–myoglobin				Fluorescence	[238, 239]
Cu–Zn–superoxide dismutase	TMOS	[Prot]–silica hydrogels and xerogels	CN [−]	UV-VIS	[227]
	PGS				
Polyclonal antibodies to fibrin antigens	TMOS	[Antibody–fluorescein conjugates]–silica hydrogels	Fibrin D dimer antigens	Fluorescence	[241]
Anti-fluorescein antibodies	TEOS	[Antibody]–silica xerogels	5-/6-Carboxy-4',5'-dimethylfluorescein	Fluorescence	[242]
	TMOS	[Antibody]–silica hydrogels and xerogels	Fluorescein	Fluorescence	[243]
Anti-nitroaromatic antibodies	TMOS	[Antibody]–silica hydrogels and xerogels	1,3-Dinitrobenzene, 2,6-Dinitrophenylhydrazine	UV-VIS	[244]
Anti-atrazine antibodies	TMOS	[Antibody]–silica xerogels	Atrazine	ELISA	[245, 246]
Immunoglobulin (IgG)	TEOS	[IgG]–hydroxypropylcellulose–graphite-silica xerogels	Goat anti-rabbit IgG antibodies	Amperometric	[247]
Antigens					
<i>Echinococcus</i> parasite	TMOS	[Antigens]–silica hydrogels and xerogels	Human sera anti- <i>Echinococcus</i> antibodies	UV-VIS	[248]

continued

Table 6. Continued

Biological(s)	Precursor	Bioencapsulated sol–gel	Analyte(s)	Sensor type	Ref.
Hydatid cyst antigens <i>Leishmania</i> parasite	TMOS	[Antigens]–silica hydrogels and xerogels	Human sera anti- <i>Leishmania</i> antibodies	UV-VIS	[249]
Promastigote antigens Bacteriorhodopsin	TMOS PGS HEAGS	[Prot]–silica hydrogels and xerogels	Phototransduction	UV-VIS	[250–254]
Calmodulin + melittin	TMOS	[Prot]–silica hydrogels	Antagonists	Fluorescence	[256]
Phycocerythrin	TMOS	[Prot]–silica hydrogels and xerogels	Phototransduction	UV-VIS	[255]
Phycocyanin				Fluorescence	
Allophycocyanin					

Note: BADAPP, 1,5-bis(4-allyldimethylammoniumphenyl)pentan-3-one dibromide; ENZ, enzyme; 3-HEAGS, 3-(1'-hydroxy-2'-(2''-hydroxyethylamino)ethoxy)propylglycerosiloxane; PGS, poly(glyceryl silicate); Prot, protein; TEDS, tetraethoxysilane; TMOS, tetramethoxysilane.

and phycocerythrin have been entrapped in silica hydrogels and xerogels and shown to retain their proton pumping and photoactive properties [149–154].

7.2. Sol–Gel Biocatalysts

A sphere of application that has received rather less attention but that also offers considerable commercial promise is sol–gel biocatalysts (Table 7). With the increasing application of biological catalysts to synthetic chemistry and industrial processes has come the growing need for high-performance immobilized biological catalysts that are efficient, are stable to long-term operations under a variety of operating conditions, and can be fabricated on a large scale [13–15, 257–260]. Initial work in this arena was restricted to the encapsulation of model hydrolases such as trypsin and acid phosphatase with little prospect for industrial applications, but more attention has been focused on this arena recently. Thus, Reetz et al. [261–267] established the general practical utility of sol–gel immobilized biocatalysts with their studies on the encapsulation of lipase enzymes in Ormosils and composite sol–gels. The maximal activity of many lipases, as well as that of phospholipases and cutinases, requires the operation of a lid mechanism, whereby the contact with a hydrophobic interface displaces a mobile section of the tertiary structure to expose the binding site, thereby “activating” the enzyme toward its substrate [108]. Reetz et al. [261–267] reasoned that it might be possible to use hydrophobic Ormosils to both encapsulate and activate lipases and showed that a variety of lipases could indeed be stably activated and entrapped in micro-phase-separated poly(alkylsiloxanes), hybrid poly(alkylsiloxane)–polydimethylsiloxane sol–gels, and magnetite–Ormosil composites. The method has since been extended to functional Ormosils and filled composite sol–gels, and it appears that the technique is generically applicable to many lipases, phospholipases, and cutinases [268–277]. The technique provides particulate and thick film materials that display aqueous and organic-phase activities of 60–130% and 140–1,400% of those of the soluble enzymes. The biocatalysts have been used to catalyze the regio-, chemo- and enantio-selective hydrolysis, esterification, and transesterification of carboxylic acids, alcohols, and esters and the acylation of amines in aqueous and aqueous–

organic media and organic solvents. Fluka offers these catalysts for laboratory-scale trials, and Novo Nordisk markets several poly(alkoxysiloxane)–lipase immobilizates for industrial catalysis.

Various other hydrolases have also been encapsulated in inorganic, Ormosil, hybrid, filled, and IPN sol–gels (Table 7). Esterase, serine, cysteine, and metallo-proteases, α - and β -glycosidases, acid and alkaline phosphatases, phospholipases, and organophosphorus hydrolases have been successfully entrapped in hydrogels and xerogels and applied to the hydrolysis of model compounds and the synthesis of bioactive peptides, glycosides, oligosaccharides, lipids, etc. [83, 226, 279–283].

Sol–gel biocatalysts have also been fabricated for lyase enzymes, which are of great interest for asymmetric synthesis by virtue of their ability to stereospecifically form C–C bonds [13–15, 257–260]. Enzymes such as aldolases, aldolase catalytic antibodies, oxynitrilase, and ketoacid decarboxylases have been successfully entrapped in oxide and siloxane sol–gels and applied to the asymmetric aldol condensation, hydrocyanation, and addition of aldehydes and ketones [83, 284, 285]. Similarly, sol–gel immobilized oxidoreductases, including lipoxygenases, tyrosinases, the heme proteins, cytochrome *c*, hemoglobin, myoglobin, and horseradish peroxidase, and alcohol and polyol oxidases and dehydrogenases have likewise been used for the synthesis of polyunsaturated fatty acid hydroperoxides, the hydroxylation of aromatics, oxidative polymerization of phenolics, the *S*-oxidation of sulfides, and the regio- and enantio-selective oxidation of alcohols [83, 286, 287].

The power of sol–gel encapsulation is perhaps best demonstrated with its application to the preparation of multienzyme biocatalysts (Table 7) [83, 288]. Thus, it has been clearly demonstrated that the co-entrapment of enzymes that catalyze consecutive reactions in sol–gels can lead to an enhancement in overall catalytic efficiency and productivity, presumably due to the proximity of catalytic centers resulting in the efficient transfer of reaction intermediates between enzymes, effectively enhancing their local concentration. Thus, a system of the six proteins—sialic acid aldolase, myokinase, pyruvate kinase, pyrophosphatase, CMP-sialate synthase, and α -(2,6)-sialyl transferase—has been trapped in Ormosil–metallo-silicate matrices and applied to the continuous synthesis of the

Table 7. Enzyme-based sol–gel biocatalysts.

Proteins	Precursor(s)	Bioencapsulated sol–gel	Reaction catalyzed	Ref.
Lipases:	TMOS	[Enz]–siloxane xerogels	Hydrolysis and transesterification of glycerolipids	[83, 261–278]
<i>Candida rugosa</i>	TEOS	[Enz–ferrite]–siloxane xerogels	Hydrolysis and transesterification of esters	
<i>Candida antarctica</i>	MeTMOS	[Enz]–magnetite–siloxane xerogels	Esterification of alcohols and carboxylic acids	
<i>Candida lipolytica</i>	PrTMOS	[Enz]–PVA–siloxane xerogels	Enantioselective hydrolysis of esters	
<i>Aspergillus niger</i>	BuTMOS	[Enz]–gelatin–siloxane xerogels		
<i>Aspergillus oryzae</i>	HxTMOS	[Enz]–graphite–siloxane xerogels		
<i>Aspergillus awamori</i>	OcTMOS	[Enz]–phyllosilicate–siloxane xerogels		
<i>Rhizomucor miehei</i>	ODcTMOS			
<i>Mucor javanicus</i>	PGS			
<i>Pseudomonas cepacia</i>	TMOS + MeTMOS			
<i>Pseudomonas fluorescens</i>	TMOS + PrTMOS			
<i>Penicillium roquefortii</i>	PrTMOS + 3-APTMOS			
<i>Rhizopus arrhizus</i>	TMOS + PDMS			
<i>Humicola lanuginosa</i>	MeTMOS + PDMS			
Wheat germ	TEOS + 3-MPTEOS			
Porcine pancreas	PrGS + PDMS-PGS			
Pig liver esterase	PMeMS + PMZrS MeGS + PGZrS	[Enz]–siloxane xerogels (Thick films on sintered clay, and powders)	Enantioselective hydrolysis of esters	[83]
Proteases	TMOS	[Enz]–siloxane hydrogels and xerogels	Hydrolysis of amides	[83, 279]
Trypsin	TEOS	[Enz]–metallo-silicate xerogels	Hydrolysis of N-protected amino acid esters	
Proteinase K	PGZrS		Transesterification of unprotected amino acid esters	
Carboxypeptidase Y	VnGS + PGS		Synthesis of dipeptides and oligopeptides	
α -Chymotrypsin	MeGS + PGS			
Subtilisin	GAPS + PGAIS			
Glycosidases	TMOS	[Enz]–siloxane hydrogels and xerogels	Hydrolysis of model and natural β -glucosides	[83, 280, 281]
Rice α -galactosidase	PMS	[Enz]–alginate–silica hydrogels and xerogels	Synthesis of alkyl and hydroxyalkyl α -galactosides	
Almond β -glucosidase	PGS		Synthesis of sterol β -glucuronides	
<i>Sulfolobus</i> β -glucosidase	PGS + GAPS			
Bovine β -glucuronidase	PDMS-PGS			
Phospholipase D	PMeGS + PGZrS	[Enz]–siloxane hydrogels and xerogels	Hydrolysis and transesterification of phospholipids	[83]
Acid phosphatase	PMS PGS	[Enz]–silica hydrogels and xerogels	Hydrolysis of phenyl phosphate	[83]
<i>Pseudomonas</i> atrazine	TMOS	[Enz]–siloxane hydrogels and xerogels	Hydrolysis of atrazine	[282, 283]
Chlorohydrolase	TMOS + MeTMOS			
Organophosphorus hydrolases	TMOS	[Enz]–siloxane hydrogels and xerogels	Hydrolytic detoxification of paraoxon and parathion	[83, 226]
<i>Pseudomonas</i> paraoxonase	PGS			
<i>Pseudomonas</i> parathion Hydrolase	PDMS-PMS PDMS-PGS			
Aldolase catalytic antibodies (abzymes)	TMOS	[Antibody]–silica xerogel	Aldol condensation of aldehydes and ketones	[284]
Aldolases	PMS	[Enz]–silicate hydrogels and xerogels	Aldol condensations of aldehydes and ketones	[83, 285]
Rabbit muscle aldolase	PGS			
Sialic acid aldolase	PGTiS			

continued

Table 7. Continued

Proteins	Precursor(s)	Bioencapsulated sol–gel	Reaction catalyzed	Ref.
Almond α -hydroxynitrile Lyase (oxynitrilase)	PMS GAPS + PGS GAPS + PGS + MeGS	[Enz]–siloxane hydrogels and xerogels	Hydrolysis of α -hydroxynitriles Asymmetric hydrocyanation of aldehydes	[83]
Pyruvate decarboxylase	PGAIS	[Enz]–silicate hydrogels and xerogels	Synthesis of phenylacetyl carbinol	[286]
Soybean lipoxygenase I	TMOS	[Enz]–siloxane hydrogels and xerogels	Hydroperoxidation of linoleic and linolenic acids	[83, 286]
	PMS MeGS + PGS	[Enz]–alginate-silica hydrogels and xerogels		
Mushroom tyrosinase (polyphenol oxidase)	PMS PGS + GAPS	[Enz]–phyllsilicate-silica xerogels [Enz]–siloxane hydrogels and xerogels	Hydroxylation of phenols and tyrosine derivatives	[83]
Heme proteins	TMOS	[Enz]–silica hydrogels and xerogels	Oxidative polymerization of phenols	[83, 287]
Cytochrome <i>c</i>	PMS		<i>S</i> -Oxidation of dibenzothiophene	
Hemoglobin	PGS		<i>S</i> -Enantioselective sulfoxidation of sulfides	
Myoglobin				
Horseradish peroxidase				
Alcohol oxidoreductases	PMS	[Enz]–siloxane hydrogels and xerogels	Oxidation of glucose to gluconate	[83]
Glucose oxidase	PGS		Oxidation of glycerol-3-phosphate to glyceraldehyde-3-phosphate	
Glycerol-3-phosphate oxidase	PGZrS		Enantioselective oxidation of primary alcohols	
Alcohol dehydrogenase	PMeMS + PMS PMeGS + PGS		Asymmetric reduction of aldehydes	
Sialic acid aldolase + sialyl transferase + myokinase + pyruvate kinase + CMP sialate synthase + pyrophosphatase	3-APGS + PGZrS	[Enzymes]–siloxane xerogels	Synthesis of the bioactive sialylated trisaccharide α -(2,6)-sialyl- <i>N</i> -acetylactosamine	[83]
Formate dehydrogenase + formaldehyde dehydrogenase + alcohol dehydrogenase	TMOS	[Enzymes]–silica hydrogels	Conversion of carbon dioxide to methanol	[288]

Note: 3-APGS, 3-aminopropylglyceroxysilane; 3-APTMS, 3-aminopropyltrimethoxysilane; BuTMOS, butyltrimethoxysilane, 3-GAPS, 3-gluconamidopropylsiloxane; 3-HEAGS, 3-(1'-hydroxy-2'-(2''-hydroxyethylamino)ethoxy)propylglyceroxysiloxane; HxTMOS, hexyltrimethoxysilane; MeGS, methylglyceroxysilane; MeTEOS, methyltriethoxysilane; MeTMOS, methyltrimethoxysilane; 3-MPTMS, 3-mercaptopropyltrimethoxysilane; OcTMOS, octyltrimethoxysilane; ODcTMOS, octadecyltrimethoxysilane; PDMS, silanol-terminated polydimethylsiloxane; PGAIS, poly(glyceryl aluminosilicate); PGS, poly(glyceryl silicate); PGZrS, poly(glyceryl zirconosilicate); PMS, poly(methyl silicate); PMeGS, poly(methylglyceroxysilane); PMeMS, poly(methylmethoxysilane); PMZrS, poly(methyl zirconosilicate); PrTMOS, propyltrimethoxysilane; TEOS, tetraethoxysilane; TMOS, tetramethoxysilane; VnGS, vinylglyceroxysilane.

bioactive oligosaccharide α -(2,6)sialyl-*N*-acetylactosamine [83]. Similarly, formate dehydrogenase, formaldehyde dehydrogenase, and alcohol dehydrogenase, have been co-encapsulated in silica and used for the remarkable conversion of carbon dioxide to methanol [288].

8. FUTURE DEVELOPMENTS IN SOL–GEL NANOBIOENCAPSULATION

The last decade has witnessed an increasing interest in sol–gel bio-nanocomposites, and studies to date have uncovered some remarkable features of these materials [47, 61–74]:

- Sol–gel bioencapsulation is generic—a remarkably diverse range of enzymes, noncatalytic proteins, DNA, RNA, organelles, and even live cells have been encapsulated.
- Although, as expected, encapsulation within a sol–gel polymer matrix modifies the functioning of the biological, the native activity can be largely retained therein.

- Inorganic, hybrid, and composite materials with exotic physicochemical properties can be utilized for bioencapsulation.
- Bioencapsulation enables the conversion of labile biological materials into reusable and physicochemically robust nanocomposites, which can be fabricated and manipulated using conventional sol–gel processing procedures.
- Biomolecules encapsulated in sol–gel polymers are protected from biological degradation, and are often considerably stabilized to chemical and thermal inactivation.
- Sol–gel bioencapsulates can be interfaced with spectroscopic, optical, and electrochemical platforms to generate biosensing devices.

However, studies have also exposed substantial hurdles that need to be overcome for the widespread adoption of the technology [47, 61–74]:

- The biocompatibility of sol–gel protocols needs to be refined: although advances have been made with

alcohol-free solutions and glyceroxysilane precursors, difficulties are still encountered with certain classes of biologicals, especially oligomeric biomolecules, membrane proteins, organelles, and live cells.

- (b) Pore collapse during xerogel preparation remains a major issue: as well as being the single most important cause of bioactivity decline upon encapsulation, this can also lead to structural defects in films and monoliths and complicate fabrication procedures. Although some amelioration can be achieved via the application of special drying regimens, drying control additives, templating and pore-forming compounds, and glyceroxysiloxane precursors, a generic, practical, and scalable method for minimizing structural collapse has as yet to be devised.
- (c) The porosity of current generation bioencapsulates is not optimal: low pore size and volume and the presence of a disordered/semicontinuous pore structure give rise to biomolecule subpopulations, which are inaccessible to analytes, reduce biomolecule dynamics and inhibit functioning, and cause internal diffusional limitations. The availability of ordered mesocellular materials with large pore dimensions above 10 nm would considerably ease the fabrication of efficient materials for fast-biosensing and high-throughput biocatalysis. Most likely, this could be achieved via the application of structure-directing surfactants and polymers, and the use of self-templating precursors.
- (d) Present day bioencapsulates generally show poor mechanical attributes: brittleness and a low resistance to mechanical stress are typical, and this poses a limit on many bulk applications. Unfortunately, here one is at odds with porosity—in general, the greater the pore size and volume the more fragile and deformable the polymer is and vice versa. A possible partial solution is the synthesis of sol–gels with ordered mesopore or hierarchical pore assemblies, the honeycomb structures of which are known to enhance mechanical stability. Alternatively, mechanical properties can be improved by using dendritic- or comb-type macromeric precursors, IPN composites, and the use of reinforcing fillers.

In spite of the many substantial hurdles facing sol–gel bioencapsulation, the rapid advances that have been made in the past decade in improving encapsulation protocols and diversifying applications have been remarkable. Indeed, sol–gel nanoencapsulation offers the single most facile, generic, and promising methodology for the entrapment and stabilization of biological materials. With this in mind, one can foresee some future directions for sol–gel nanocomposite bioencapsulates:

- (a) *Combinatorial discovery.* Recently developed methods for generating sol–gel polymer and heterogeneous catalyst libraries will be applied to the discovery of novel matrices, the optimization of sol–gel compositions, and the screening of sensor and catalyst libraries for particular applications [289, 290].
- (b) *Bioencapsulation in transition metal alkoxides.* The use of bulk transition metal oxides and co-encapsulated

oxometallates and metal oxide colloids with conducting, catalytic and/or chromic properties may pave the way to novel bioencapsulated electro- and photocatalytic and electrochromic devices for novel biosensors, photobioelectronics, etc. [291–297].

- (c) *Engineering of Ormosils.* The appendage of moieties that can be directly wired to the active centers of oxidoreductases and photoproteins and interfaced with co-encapsulated conducting or photoactive polymers would enable the construction of integrated electrosensor and optical devices. Similarly, the adaptation of strategies for the co-entrapment of transition metal catalysts will allow the execution of multicatalytic reaction cascades [298–300].
- (d) *Advanced hybrids and composites.* Novel organic–inorganic sol–gels, IPN and filled composites, and multilayered architectures are expected to contribute to the development of highly responsive and rugged biosensors and biocatalysts that can be used in extreme environments, and self-supporting catalytic membranes, as well as enable the use of novel fabrication methods [301, 302].
- (e) *Templated sol–gels.* The development of biocompatible templating methods based upon self-assembling mercaptosiloxanes and long-chain alkyl siloxanes, polyblock siloxane copolymers, and exogenous pore-forming additives should give access to encapsulates with highly ordered pore morphologies and chemical functionalities. Furthermore, the deployment of molecular imprinting techniques should allow the addition of highly specific recognition functions to sol–gel biosensors and thereby improve selectivity, response and resistance to interference and fouling [303–308].
- (f) *Microfabrication methods.* Recently developed microstamping, soft lithography, microspotting, and ink-jet printing technologies [309–311] are expected to be applied to sol–gel bioencapsulates to the fabrication arrays for drug screening, genomics, proteomics, and combinatorial synthesis [312–316] and the production of microsensors, microreactors, and bioelectronic devices [317–321].

Although still in its infancy, sol–gel bio-nanocomposites should significantly advance a range of disciplines that interface with biology, from the production of biosensors, biocatalysts, and bioartificial organs to the fabrication of high-density bioarrays and bioelectronic devices. Indeed, it is expected that the coming years will witness the realization of a variety of research and industrial applications, especially those aimed at the catalysis, sensing/monitoring, diagnostics, biotechnology, and biocomputing sectors.

GLOSSARY

Biological or biosystem A material of biological origin, for example, a protein, deoxyribonucleic acid (DNA), living cell, or some part thereof.

Biocatalyst A biological material, typically an enzyme (protein) or collection of enzymes, that is able to catalyze a chemical reaction in a highly specific manner.

Bioencapsulation The process whereby a biological such as a protein is physically entrapped within a polymeric material, for example, a sol-gel, during the synthesis of the latter.

Biosensor A sensor that utilizes a biological molecule such as protein as a highly specific material for the recognition of the target analyte.

Electrochemical (bio)sensor A (bio) sensor that generates an electrical signal in the presence of the corresponding analyte. The signal is typically measured and quantified using an electrochemical cell.

Nanocomposite A solid-state material that consists of two or more components, at least one of which is polymeric, and the structure of which is derived from the nanoscale (typically 1–50 nm) interaction and organization of the contributing components.

Optical (bio)sensor A (bio)sensor that generates an optical signal in the presence of the corresponding analyte, typically in the ultraviolet-visible region. The signal is usually measured and quantified by visual or spectroscopic methods.

Sensor A solid-state material that can specifically recognize one or more chemical compounds (analytes) in its environment and generates a response which can be measured and used to determine the concentration of the analyte(s).

Siloxane A polymer of silicon or a precursor thereof, which is characterized by the presence of stable covalent Si–O–Si bonds as well as Si–C bonds.

Sol-gel An inorganic silicon or metal oxide-based polymer or a derivative thereof that is produced using a unique room-temperature aqueous protocol (sol-gel technology) based upon the controlled hydrolysis of specific chemical precursors.

REFERENCES

- C. N. R. Rao and A. K. Cheetham, *J. Mater. Chem.* 11, 2887 (2001).
- G. M. Whitesides, "Nanotechnology: Art of the Possible," Technology Review. Cambridge, MA, 1998.
- R. W. Seigel, E. Hu, and M. C. Roco, "Nanostructure Science and Technology," National Science and Technology Council Report. Kluwer Academic, Boston, 1999.
- M. C. Rocco, R. S. Williams, and A. P. Alivisatos, "Nanotechnology Research Directions," National Science and Technology Council Report, Kluwer Academic, Boston, 2000.
- Issues in Nanotechnology, *Science* 290, 1523 (2000).
- J. M. Laval, J. Chopineau, and D. Thomas, *Trends Biotechnol.* 13, 474 (1995).
- D. E. Morse, *Trends Biotechnol.* 17, 230 (1999).
- N. C. Seeman, *Annu. Rev. Biophys. Biomol. Struct.* 27, 225 (1998).
- N. C. Seeman, *Nano Lett.* 1, 22 (2001).
- T. Sawitowski, S. Franzka, N. Beyer, M. Levering, and G. Schmid, *Adv. Funct. Mater.* 11, 169 (2001).
- R. C. Merkle, *Trends Biotechnol.* 17, 271 (1999).
- N. C. Seeman, *Trends Biotechnol.* 17, 437 (1999).
- R. N. Patel, "Stereoselective Biocatalysis," Marcel Dekker, New York, 2000.
- K. Drauz and H. Waldmann, "Enzyme Catalysis in Organic Synthesis," VCH, Weinheim, 2002.
- C. H. Wong and G. M. Whitesides, "Enzymes in Synthetic Organic Chemistry," Tetrahedron Organic Chemistry Series, Vol. 12. Elsevier Science, Oxford, 1994.
- E. Kress-Rogers, "Handbook of Biosensors and Electronic Noses," CRC Press, Boca Raton, FL, 1996.
- G. F. Bickerstaff, "Immobilization of Enzymes and Cells," Humana Press, Totowa, NJ, 1997.
- T. Cass and F. S. Ligler, "Immobilized Biomolecules in Analysis," Oxford University Press, Oxon, UK, 1998.
- M. Reiss and W. Hartmeier, in "Biotechnology" (H. J. Rehm, Ed.), Vol. 11a, pp. 125–140. VCH, Weinheim, 2002.
- L. Campanella and M. Tomassetti, *Food Technol. Biotechnol.* 34, 131 (1996).
- J. R. Woodward and R. B. Spokane, *Chem. Anal.* 148, 227 (1998).
- A. F. Collings and F. Caruso, *Rep. Prog. Phys.* 60, 1397 (1997).
- M. B. Swindells and J. P. Overington, *Drug. Discovery Today* 7, 516 (2002).
- S. A. W. Gruner, E. Locardi, E. Lohof, and H. Kessler, *Chem. Rev.* 102, 491 (2002).
- P. Meers, *Adv. Drug Delivery Rev.* 53, 265 (2001).
- R. R. Breaker, *Curr. Opin. Biotechnol.* 13, 31 (2002).
- F. W. Scheller, U. Wollenberger, A. Warsinke, and F. Lisdat, *Curr. Opin. Biotechnol.* 12, 35 (2001).
- R. L. Rich and D. G. Myszka, *J. Mol. Recognit.* 14, 273 (2001).
- C. L. Baird and D. G. Myszka, *J. Mol. Recognit.* 14, 261 (2001).
- A. Janshoff, H. J. Galla, and C. Steinem, *Angew. Chem., Int. Ed. Engl.* 39, 4004 (2000).
- R. L. Rich and D. G. Myszka, *J. Mol. Recognit.* 13, 388 (2000).
- D. J. Winzor, *J. Mol. Recognit.* 13, 279 (2000).
- K. Rekha, M. S. Thakur, and N. G. Karanth, *Crit. Rev. Biotechnol.* 20, 213 (2000).
- T. Weimar, *Angew. Chem., Int. Ed. Engl.* 39, 1219 (2000).
- I. Karube and Y. Nomura, *J. Mol. Catal. B* 10, 177 (2000).
- C. C. Wang and Y. Cheng, *Adv. Biotechnol.* 18, 35 (2000).
- N. L. van Berkum and F. C. P. Holstege, *Curr. Opin. Biotechnol.* 12, 48 (2001).
- C. A. Harrington, C. Rosenow, and J. Retief, *Curr. Opin. Microbiol.* 3, 285 (2000).
- C. B. Epstein and R. A. Butow, *Curr. Opin. Biotechnol.* 11, 36 (2000).
- H. Zhu and M. Snyder, *Curr. Opin. Chem. Biol.* 5, 40 (2001).
- E. T. Fung, V. Thulasiraman, S. R. Weinberger, and E. A. Dalmasso, *Curr. Opin. Biotechnol.* 12, 65 (2001).
- T. Kodadek, *Chem. Biol.* 8, 105 (2001).
- I. Willner and B. Willner, *Trends Biotechnol.* 19, 223 (2001).
- N. Hampp, *Chem. Rev.* 100, 1755 (2000).
- I. Willner, *Acc. Chem. Res.* 30, 347 (1997).
- I. Willner and E. Katz, *Angew. Chem., Int. Ed. Engl.* 39, 1180 (2000).
- I. Gill, *Chem. Mater.* 13, 3404 (2001).
- L. L. Hench and J. K. West, *Chem. Rev.* 90, 33 (1990).
- J. E. Mark, *Heterog. Chem.* 3, 307 (1996).
- D. Avnir, *Acc. Chem. Res.* 28, 328 (1995).
- N. Hüsing and U. Schubert, *Angew. Chem. Int. Ed. Engl.* 37, 22 (1998).
- C. G. Guizard, A. C. Julbe, and A. J. Ayril, *J. Mater. Chem.* 9, 55 (1999).
- A. Huczko, *Appl. Phys. A* 70, 365 (2000).
- C. Sanchez, F. Ribot, and F. Lebeau, *J. Mater. Chem.* 9, 35 (1999).
- P. M. Price, J. H. Clark, and D. J. Mcquarrie, *J. Chem. Soc. Dalton Trans.* 101 (2001).
- E. W. McFarland and W. H. Weinberg, *Trends Biotechnol.* 17, 107 (1999).
- D. Venton, K. Cheesman, R. Chatterton, and T. Anderson, *Biochim. Biophys. Acta* 797, 343 (1984).
- M. Glad, O. Norrlöw, B. Selligren, N. Siegbahn, and K. Mosbach, *J. Chromatogr.* 347, 11 (1985).
- S. Braun, S. Rappoport, R. Zusman, D. Avnir, and M. Ottolenghi, *Mater. Lett.* 10, 1 (1990).
- L. M. Ellerby, C. R. Nishida, F. Nishida, S. A. Yamanaka, B. Dunn, J. S. Valentine, and J. I. Zink, *Science* 255, 1113 (1992).

61. D. Avnir and S. Braun, "Biochemical Aspects of Sol-Gel Science and Technology." Kluwer, Hingham, MA, 1996.
62. J. C. Livage, *R. Acad. Sci. Ser.* 322, 417 (1996).
63. D. Avnir, S. Braun, O. Lev, and M. Ottolenghi, *Chem. Mater.* 6, 1605 (1994).
64. B. C. Dave, B. Dunn, J. S. Valentine, and J. I. Zink, *Anal. Chem.* 66, 1120A (1994).
65. J. Lin and C. W. Brown, *Trends Anal. Chem.* 16, 200 (1997).
66. J. C. Livage, F. Beteille, C. Roux, M. Chatry, and P. Davidson, *Acta Mater.* 46, 743 (1998).
67. A. Walcarius, *Electroanalysis* 10, 1217 (1998).
68. J. Lin and C. W. Brown, *Trends Anal. Chem.* 16, 200 (1997).
69. M. E. Tess and J. A. Cox, *J. Pharm. Biomed. Anal.* 19, 55 (1999).
70. B. Dunn, J. M. Miller, B. C. Dave, J. S. Valentine, and J. I. Zink, *Acta Mater.* 46, 737 (1998).
71. J. Wang, *Anal. Chem. Acta* 399, 21 (1999).
72. E. H. Lan, B. C. Dave, J. M. Fukuto, B. Dunn, J. I. Zink, and J. S. Valentine, *J. Mater. Chem.* 9, 45 (1999).
73. H. J. Böttcher, *Prakt. Chem.* 342, 427 (2000).
74. I. Gill and A. Ballesteros, *Trends Biotechnol.* 18, 282 (2000).
75. W. Jin and J. D. Brennan, *Anal. Chem.* 461, 1 (2002).
76. A. M. Lesk, "Protein Architecture." IRL Press, Oxford, 1991.
77. M. Sinnott, "Comprehensive Biological Catalysis," Vols. 1-3. Academic Press, San Diego, 1998.
78. A. Gómez-Puyou, "Biomolecules in Organic Solvents." CRC Press, Boca Raton, FL, 1992.
79. Y. Llov and H. Möhwald, "Protein Architecture: Interfacing Molecular Assemblies and Immobilization Biotechnology." Marcel Dekker, New York, 2000.
80. I. Gill and A. Ballesteros, *Trends Biotechnol.* 18, 469 (2000).
81. R. F. Taylor, "Protein Immobilization," Marcel Dekker, New York, 1991.
82. T. Cass and F. S. Ligler, "Immobilized Biomolecules in Analysis," Oxford University Press, New York, 1998.
83. I. Gill and A. Ballesteros, *J. Am. Chem. Soc.* 120, 8587 (1998).
84. S. Mann, S. L. Burkett, S. A. Davis, C. E. Fowler, N. H. Mendelson, S. D. Sims, D. Walsh, and N. T. Whilton, *Chem. Mater.* 9, 2300 (1997).
85. G. A. Ozin, *Acc. Chem. Res.* 30, 17 (1998).
86. C. G. Göltner, S. Henke, M. C. Weissenberger, and M. Antonietti, *Angew. Chem., Int. Ed. Engl.* 37, 613 (1998).
87. P. Schmidt-Winkel, W. W. Lukens, D. Zhao, P. Yang, B. F. Chmelka, and G. D. Stucky, *J. Am. Chem. Soc.* 121, 254 (1999).
88. D. Zhao, Q. Huo, J. Feng, B. F. Chmelka, and G. D. Stucky, *J. Am. Chem. Soc.* 120, 6024 (1998).
89. M. Templin, A. Franck, A. Du Chesne, H. Leist, Y. Zhang, R. Ulrich, V. Schädler, and U. Weisner, *Science* 278, 1795 (1997).
90. A. Imhof and D. J. Pine, *Nature* 389, 948 (1997).
91. M. X. Wu, T. Fujii, and G. L. Messing, *J. Non-Cryst. Solids* 121, 407 (1990).
92. P. T. Tanev and T. J. Pinnavaia, *Science* 271, 1267 (1996).
93. S. A. Bagshaw, E. Prouzet, and T. J. Pinnavaia, *Science* 269, 1242 (1995).
94. Y. Wei, J. Xu, Q. Feng, H. Dong, and M. Lin, *Mater. Lett.* 44, 6 (2000).
95. Y. Wei, D. Jin, T. Ding, W.-H. Shih, X. Liu, S. Z. D. Cheng, and F. Qiang, *Adv. Mater.* 3, 313 (1998).
96. Y. Wei, J. Xu, H. Dong, J.-H. Dong, K.-Y. Qiu, and S. A. Jansen-Varnum, *Chem. Mater.* 11, 2023 (1999).
97. S. Sheltzer, S. Rappoport, D. Avnir, M. Ottolenghi, and S. Braun, *Biotechnol. Appl. Biochem.* 15, 227 (1992).
98. M. S. Rao and B. C. Dave, *J. Am. Chem. Soc.* 120, 13270 (1998).
99. U. Narang, P. N. Prasad, F. V. Bright, A. Kumar, N. D. Kumar, B. D. Malhotra, M. N. Kamalasanan, and S. Chandra, *Anal. Chem.* 67, 1935 (1995).
100. J. Livage, C. Roux, J. M. DaCosta, I. Desportes, and J. F. Quinson, *J. Sol.-Gel Sci. Technol.* 7, 45 (1996).
101. Y.-J. Han, G. D. Stucky, and A. Butler, *J. Am. Chem. Soc.* 121, 9897 (1999).
102. R. Zusman, *Anal. Biochem.* 201, 103 (1992).
103. K. Flora and J. D. Brennan, *Analyst* 124, 1455 (1999).
104. L. Zheng, W. R. Reid, and J. D. Brennan, *Anal. Chem.* 69, 3940 (1997).
105. L. Zheng and J. D. Brennan, *Analyst* 123, 1735 (1998).
106. C. L. Wambolt and S. S. Saavedra, *J. Sol.-Gel Sci. Technol.* 7, 53 (1996).
107. P. L. Edmiston, C. L. Wambolt, M. K. Smith, and S. S. Saavedra, *J. Colloid Interface Sci.* 163, 395 (1994).
108. M. Gerstein, A. M. Lesk, and C. Chothia, *Biochemistry* 33, 6739 (1994).
109. H. W. Hellinga and J. S. Marvin, *Trends Biotechnol.* 16, 183 (1998).
110. K. A. Giuliano, P. L. Post, K. M. Hahn, and D. L. Taylor, *Annu. Rev. Biophys. Biomol. Struct.* 24, 405 (1995).
111. J. D. Jordan, R. A. Dunbar, and F. V. Bright, *Anal. Chem.* 67, 2436 (1995).
112. J. D. Brennan, *Appl. Spectrosc.* 53, 106A (1999).
113. A. M. Hartnett, C. M. Ingersoll, G. A. Baker, and F. V. Bright, *Anal. Chem.* 71, 1215 (1999).
114. B. Dunn and J. I. Zink, *Chem. Mater.* 9, 2280 (1997).
115. B. C. Dave, H. Soyey, J. M. Miller, B. Dunn, J. S. Valentine, and J. I. Zink, *Chem. Mater.* 7, 1431 (1995).
116. D. S. Gottfried, A. Kagan, B. M. Hoffman, and J. M. Friedman, *J. Phys. Chem. B* 103, 2803 (1999).
117. G. A. Baker, J. D. Jordan, and F. V. Bright, *J. Sol.-Gel Sci. Technol.* 11, 43 (1998).
118. L. Zheng, C. W. V. Hogue, and J. D. Brennan, *Biophys. J.* 71, 157 (1998).
119. C. Shen and N. M. Kostić, *J. Am. Chem. Soc.* 119, 1304 (1997).
120. C. Shen and N. M. Kostić, *J. Electroanal. Chem.* 438, 61 (1997).
121. N. Husing, *J. Sol.-Gel Sci. Technol.* 15, 57 (1999).
122. P. Audebert and C. Demaille, *Chem. Mater.* 5, 911 (1993).
123. D.-M. Liu and I.-W. Chen, *Acta Mater.* 47, 4535 (1999).
124. D. K. Eggers and J. S. Valentine, *J. Mol. Biol.* 314, 911 (2001).
125. M. G. Santangelo, M. Levantino, E. Vitrano, and A. Cupane, *Biophys. Chem.*, (2003) in press.
126. P. C. Pandey, S. Singh, B. Upadhyay, H. H. Weetall, and P. K. Chen, *Sens. Actuators, B* 35-36, 470 (1996).
127. H. H. Weetall, *Biosens. Bioelectron.* 11, 327 (1996).
128. H. H. Weetall, *Appl. Biochem. Biotechnol.* 49, 241 (1994).
129. H. H. Weetall, B. Robertson, D. Cullin, J. Brown, and M. Walch, *Biochim. Biophys. Acta* 1142, 211 (1993).
130. H. Jin-An, L. Samuelson, L. Li, J. Kumar, and S. K. Tripathy, *Adv. Mater.* 11, 435 (1999).
131. Q. Chen, G. L. Kenausis, and A. Heller, *J. Am. Chem. Soc.* 120, 4582 (1998).
132. J. Heller and A. Heller, *J. Am. Chem. Soc.* 120, 4586 (1998).
133. I. R. Lauks, *Acc. Chem. Res.* 31, 317 (1998).
134. G. S. Wilson and Y. Hu, *Chem. Rev.* 100, 2693 (2000).
135. K. Schügerl, B. Hitzmann, H. Jurgens, T. Kullick, R. Ulber, and B. Weigal, *Trends Biotechnol.* 14, 21 (1996).
136. J. H. T. Luong, P. Bouvrette, and K. B. Male, *Trends Biotechnol.* 15, 369 (1997).
137. H. H. Thorp, *Trends Biotechnol.* 16, 117 (1998).
138. H. A. Fishman, D. R. Greenwald, and R. N. Zare, *Annu. Rev. Biophys. Biomol. Struct.* 27, 165 (1998).
139. K. Ramanathan, M. Rank, J. Svitel, A. Dzgoev, and B. Danielsson, *Trends Biotechnol.* 17, 499 (1999).
140. C. R. Lowe, *Curr. Opin. Chem. Biol.* 3, 106 (1999).
141. K. A. Giuliano and D. L. Taylor, *Trends Biotechnol.* 16, 135 (1998).
142. R. J. Leatherbarrow and P. R. Edwards, *Curr. Opin. Chem. Biol.* 3, 544 (1999).
143. H. Y. Aboul-Enein and R. I. Stefan, *Crit. Rev. Anal. Chem.* 28, 259 (1998).

144. S. Ramanathan, M. Ensor, and S. Daunert, *Trends Biotechnol.* 15, 500 (1997).
145. J. Wang, D. S. Park, and P. V. Pamidi, *J. Electroanal. Chem.* 434, 185 (1997).
146. P. V. Pamidi, D. S. Park, and J. Wang, *J. Polym. Mater. Sci. Eng.* 76, 513 (1997).
147. S. Sampath, I. Pankratov, J. Gun, and O. Lev, *J. Sol.-Gel Sci. Technol.* 7, 123 (1996).
148. J. Wang, P. V. Pamidi, and D. S. Park, *Anal. Chem.* 68, 2705 (1996).
149. J. Wang and P. V. Pamidi, *Anal. Chem.* 69, 4490 (1997).
150. S. Bharathi and O. Lev, *Anal. Commun.* 35, 29 (1998).
151. J. Gun and O. Lev, *Anal. Chim. Acta* 336, 95 (1997).
152. J. Li, L. S. Chia, N. K. Goh, and S. N. Tan, *J. Electroanal. Chem.* 460, 234 (1999).
153. S. Yang, Y. Lu, P. Atanossov, and E. Wilkins, *Talanta* 47, 735 (1999).
154. T. Yao and K. Takashima, *Biosens. Bioelectron.* 13, 67 (1998).
155. S. Sampath and O. Lev, *Electroanalysis* 8, 1112 (1996).
156. P. C. Pandey, *Electroanalysis* 11, 59 (1999).
157. L. Coche-Guerente, S. Cosnier, and P. Labbe, *Chem. Mater.* 9, 1348 (1997).
158. X. Wu, M. M. F. Choi, and D. Xiao, *Analyst* 125, 157 (2000).
159. O. S. Wolfbeis, I. Oehme, N. Papkovskaya, and I. Klimant, *Biosens. Bioelectron.* 15, 69 (2000).
160. S. De Marcos, J. Galindo, J. F. Sierra, J. Galbán, and J. R. Castillo, *Sens. Actuators, B* 57, 227 (1999).
161. P. C. Pandey, S. Upadhyay, and H. C. Pathak, *Sens. Actuators, B* 60, 83 (1999).
162. Z. Liu, B. Liu, M. Zhang, J. Kong, and J. Deng, *Anal. Chim. Acta* 392, 135 (1999).
163. J. Li, S. Chia, N. K. Goh, and S. N. Tan, *J. Electroanal. Chem.* 460, 234 (1999).
164. U. Kuenzelmann and H. Boettcher, *Sens. Actuators, B* 39, 222 (1997).
165. T. M. Park, E. I. Iwuoha, M. R. Smyth, and B. D. MacCraith, *Anal. Commun.* 33, 271 (1996).
166. Y. Guo and A. R. Guadalupe, *Sens. Actuators, B* 46, 213 (1998).
167. J. Li, L. S. Chia, N. K. Goh, S. N. Tan, and H. Ge, *Sens. Actuators, B* 40, 135 (1997).
168. U. Künzelmann and H. Böttcher, *Sens. Actuators, B* 38–39, 222 (1997).
169. S. Sampath and O. Lev, *Anal. Chem.* 68, 2015 (1996).
170. B. Wang, B. Li, Q. Deng, and S. Dong, *Anal. Chem.* 70, 3170 (1998).
171. P. C. Pandey, S. Upadhyay, and H. C. Pathak, *Electroanalysis* 11, 59 (1999).
172. S. Sampath and O. Lev, *J. Electroanal. Chem.* 426, 131 (1997).
173. S. Sampath and O. Lev, *Adv. Mater.* 9, 410 (1997).
174. J. Wang, P. V. A. Pamidi, and D. S. Park, *Electroanalysis* 9, 52 (1997).
175. I. Pankratov and O. Lev, *J. Electroanal. Chem.* 393, 35 (1995).
176. J. Gun and O. Lev, *Anal. Chim. Acta* 336, 95 (1996).
177. J. Gun and O. Lev, *Anal. Lett.* 29, 1933 (1996).
178. F. Tian and G. Zhu, *Sens. Actuators, B* 86, 266 (2002).
179. J. Niu and J. Y. Lee, *Sens. Actuators, B* 82, 250 (2002).
180. C. M. Couto, A. N. Araujo, C. M. Montenegro, J. Rohwedder, I. Raimundo, and C. Pasquini, *Talanta* 56, 997 (2002).
181. Y. Wei, H. Dong, J. Xu, and Q. Feng, *Chem. Phys. Chem.* 9, 802 (2002).
182. X. Chen, Y. Hu, and G. S. Wilson, *Biosens. Bioelectron.* 17, 1005 (2002).
183. L. Zhu, Y. Li, F. Tian, B. Xu, and G. Zhu, *Sens. Actuators, B* 84, 265 (2002).
184. J. Li, K. M. Wang, X. H. Yang, and D. Xiao, *Anal. Commun.* 36, 195 (1999).
185. S. L. Chut, J. Li, and S. N. Tan, *Analyst* 122, 1431 (1997).
186. B. Wang and S. Dong, *Talanta* 51, 565 (2000).
187. B. Wang, J. Zhang, G. Cheng, and S. Dong, *Anal. Chim. Acta* 407, 111 (2000).
188. J. Zhang, B. Li, Z. Wang, G. Cheng, and S. Dong, *Anal. Chim. Acta* 388, 71 (1999).
189. A. N. Díaz, M. C. R. Peinado, and M. C. T. Minguéz, *Anal. Chim. Acta* 363, 221 (1998).
190. J. Li, S. N. Tan, and J. T. Oh, *J. Electroanal. Chem.* 448, 69 (1998).
191. J. Li, S. N. Tan, and H. Ge, *Anal. Chim. Acta* 335, 137 (1996).
192. B. Wang, B. Li, Z. Wang, G. Xu, Q. Wang, and S. Dong, *Anal. Chem.* 71, 1935 (1999).
193. T. M. Park, *Anal. Lett.* 32, 287 (1999).
194. T. M. Park, E. I. Iwuoha, and M. R. Smyth, *Electroanalysis* 9, 1120 (1997).
195. E. N. Kadnikova and N. M. Kostic, *J. Mol. Catal. B* 18, 39 (2002).
196. M. C. Ramos, M. C. Torijas, and A. N. Diaz, *Sens. Actuators, B* 73, 71 (2002).
197. B. Li, Z. Zhang, and Y. Jin, *Sens. Actuators, B* 72, 115 (2001).
198. X. Chen, J. Zhang, B. Wang, G. Chen, and S. Dong, *Anal. Chim. Acta* 434, 255 (2001).
199. X. Chen, B. Wang, and S. Dong, *Electroanalysis* 13, 14 (2001).
200. J. Wang, P. V. A. Pamidi, and D. S. Park, *Anal. Chem.* 68, 2705 (1996).
201. T. M. Park, E. I. Iwuoha, M. R. Smyth, R. Freaney, and A. J. McShane, *Talanta* 44, 973 (1997).
202. S. A. Yamanaka, N. P. Ngyen, B. Dunn, J. S. Valentine, and J. I. Zink, *J. Sol.-Gel Sci. Technol.* 7, 117 (1996).
203. J. Niu and J. Y. Lee, *Sens. Actuators, B* 62, 190 (2000).
204. B. Wang, J. Zhang, G. Cheng, and S. Dong, *Chem. Commun.* 2123 (2000).
205. B. Wang and S. Dong, *J. Electroanal. Chem.* 487, 45 (2000).
206. Z. Liu, J. Deng, and D. Li, *Anal. Chim. Acta* 407, 87 (2000).
207. J. Li, L. S. Chia, N. K. Goh, and S. N. Tan, *Anal. Chim. Acta* 362, 203 (1998).
208. Z. Liu, B. Liu, J. Kong, and J. Deng, *Anal. Chem.* 72, 4707 (2000).
209. B. Wang, B. Li, G. Xu, Q. Wang, and S. Dong, *Anal. Chem.* 71, 1935 (1999).
210. S. A. Kane, E. Iwuoha, and M. Smyth, *Analyst*, 123, 2001 (1998).
211. J. Metzger, M. Reiss, and W. Hartmeier, *Biosens. Bioelectron.* 13, 1077 (1998).
212. R. A. Simkus, *Anal. Lett.* 29, 1907 (1996).
213. E. I. Iwuoha, S. Kane, C. O. Ania, M. R. Smyth, P. R. Ortiz de Montellano, and U. Fuhr, *Electroanalysis* 12, 980 (2000).
214. K. Ramanathan, M. N. Kamalasanan, B. D. Malhotra, D. R. Pradhan, and S. Chandra, *J. Sol.-Gel Sci. Technol.* 10, 309 (1997).
215. C. I. Li, Y. H. Lin, C. L. Shih, J. P. Tsaour, and L. K. Chau, *Biosens. Bioelectron.* 17, 323 (2002).
216. M. Albarreda-Sirvent and A. L. Hart, *Sens. Actuators, B* 4342, 1 (2002).
217. S. A. Yamanaka, B. Dunn, J. S. Valentine, and J. I. Zink, *J. Am. Chem. Soc.* 117, 9095 (1995).
218. A. K. Williams and J. T. Hupp, *J. Am. Chem. Soc.* 120, 4366 (1998).
219. J. W. Aylott, D. J. Richardson, and D. A. Russell, *Analyst* 122, 77 (1997).
220. S. Ferretti, S. K. Lee, B. D. MacCraith, A. G. Oliva, D. J. Richardson, D. A. Russell, K. E. Sapsford, and M. Vidal, *Analyst* 125, 80 (1993).
221. A. N. Díaz and M. C. R. Peinado, *Sens. Actuators, B* 38–39, 426 (1997).
222. F. Akbarian, A. Lin, B. S. Dunn, J. S. Valentine, and J. I. Zink, *J. Sol.-Gel Sci. Technol.* 8, 1067 (1997).
223. M. Altstein, G. Segev, N. Aharonson, O. Ben-Aziz, A. Turniansky, and D. Avnir, *J. Agric. Food Chem.* 46, 3318 (1998).
224. S. Andreescu, L. Barthelmebs, and J. L. Marty, *Anal. Chim. Acta* 464, 171 (2002).
225. R. A. Doong and H. C. Tsai, *Anal. Chim. Acta* 434, 239 (2001).

226. C. Dosoretz, R. Armon, J. Starosvetzky, and N. J. Rothschild, *J. Sol.-Gel Sci. Technol.* 7, 7 (1996).
227. W. Y. Lee, S. R. Kim, T. H. Kim, K. S. Lee, M. C. Shin, and J. K. Park, *Anal. Chim. Acta* 404, 195 (2000).
228. K. Ogura, A. Nakaoka, M. Nakayama, M. Kobayashi, and A. Fujii, *Anal. Chim. Acta* 384, 219 (1999).
229. W. Y. Lee, K. S. Lee, T. H. Kim, M. C. Shin, and J. K. Park, *Electroanalysis* 12, 78 (2000).
230. P. C. Pandey, S. Singh, B. Upaghyay, H. H. Weetall, and P. K. Chen, *Sens. Actuators, B* 36, 470 (1996).
231. D. J. Blyth, J. W. Aylott, J. W. Moir, D. J. Richardson, and D. A. Russell, *Analyst* 121, 1975 (1996).
232. D. J. Blyth, J. W. Aylott, J. W. Moir, D. J. Richardson, and D. A. Russell, *Analyst* 124, 129 (1999).
233. D. J. Blyth, J. W. Aylott, D. J. Richardson, and D. A. Russell, *Analyst* 120, 2725 (1995).
234. Q. Ji, C. R. Lloyd, W. R. Ellis, and E. M. Eyring, *J. Am. Chem. Soc.* 120, 221 (1998).
235. J. M. Miller, B. Dunn, J. S. Valentine, and J. I. Zink, *J. Non-Cryst. Solids* 202, 279 (1996).
236. J. W. Aylott, D. S. Richardson, and D. A. Russell, *Chem. Mater.* 9, 2261 (1997).
237. S. L. R. Barker, R. Kopelman, T. E. Meyer, and S. A. Cusanovich, *Anal. Chem.* 70, 971 (1998).
238. N. Shibayama and S. Saigo, *J. Mol. Biol.* 251, 203 (1995).
239. M. F. McCurley, G. J. Bayer, and S. A. Glazier, *Sens. Actuators, B* 36, 491 (1997).
240. K. E. Chung, E. H. Lan, E. S. Davidson, B. Dunn, J. S. Valentine, and J. I. Zink, *J. Am. Chem. Soc.* 67, 1505 (1995).
241. S. A. Grant and R. S. Glass, *IEEE Trans. Biomed. Eng.* 46, 1207 (1999).
242. J. D. Jordan, R. A. Dunbar, and F. V. Bright, *Anal. Chim. Acta* 332, 83 (1996).
243. R. Wang, U. Narang, P. Prasad, and F. V. Bright, *Anal. Chem.* 65, 2671 (1996).
244. N. Aharonson, M. Altstein, G. Avidan, D. Avnir, A. Bronshtein, A. Lewis, K. Liberman, M. Ottolenghi, Y. Poleyeva, C. Rottman, J. Samuel, S. Shalom, A. Strinkovski, and A. Turniansky. *Mater. Res. Soc. Symp.* 346, 519 (1994).
245. A. Turniansky, D. Avnir, A. Bronshtein, N. Aharonson, and M. Altstein, *J. Sol.-Gel Sci. Technol.* 7, 135 (1996).
246. A. Bronshtein, N. Aharonson, D. Avnir, A. Turniansky, and M. Altstein, *Chem. Mater.* 9, 2632 (1997).
247. J. Wang and P. V. Pamidi, *Anal. Commun.* 70, 1171 (1998).
248. C. Roux, J. Livage, K. Farhati, and L. Monjour, *J. Sol.-Gel Sci. Technol.* 8, 663 (1997).
249. J. Livage, C. Roux, J. M. Costa, I. Desportes, and J. F. Quinson, *J. Sol.-Gel Sci. Technol.* 7, 45 (1996).
250. H. H. Weetall, *Biosens. Bioelectron.* 11, 327 (1996).
251. H. H. Weetall, *Appl. Biochem. Biotechnol.* 49, 241 (1994).
252. J. I. Zink, J. S. Valentine, and B. Dunn, *New J. Chem.* 18, 1109 (1994).
253. S. Wu, L. M. Ellerby, J. S. Cohan, B. Dunn, M. A. El-Sayed, J. S. Valentine, and J. I. Zink, *Chem. Mater.* 5, 115 (1993).
254. H. H. Weetall, B. Robertson, D. Cullin, J. Brown, and M. Walch, *Biochim. Biophys. Acta* 1142, 211 (1993).
255. Z. Chen, D. L. Kaplan, K. Yang, J. Kumar, K. A. Marx, and S. K. Tripathy, *J. Sol.-Gel Sci. Technol.* 7, 99 (1996).
256. K. K. Flora, T. Keeling-Tucker, C. W. Hogue, and J. D. Brennan, *Anal. Chim. Acta*, (2003) in press.
257. R. N. Patel, "Stereo-selective Biocatalysis." Marcel Dekker, New York, 2000.
258. C.-H. Wong and G. M. Whitesides, "Enzymes in Synthetic Organic Chemistry." Elsevier Science, New York, 1994.
259. A. Liese, K. Seelbach, and C. Wandrey, "Industrial Biotransformations." Wiley-VCH, Weinheim, 2000.
260. W. Tischer and V. Kasche, *Trends Biotechnol.* 17, 326 (1999).
261. M. T. Reetz, *Adv. Mater.* 9, 943 (1997).
262. M. T. Reetz, A. Zonta, and J. Simpelkamp, *Angew. Chem., Int. Ed. Engl.* 34, 301 (1995).
263. M. T. Reetz, A. Zonta, and J. Simpelkamp, *Biotechnol. Bioeng.* 49, 527 (1996).
264. M. T. Reetz, A. Zonta, J. Simpelkamp, and J. Könen, *Chem. Commun.* 1397 (1996).
265. M. T. Reetz, R. Wenkel, and D. Avnir, *Synthesis* 6, 781 (2000).
266. M. T. Reetz, A. Zonta, V. Vijayakrishnan, and K. Schimossek, *J. Mol. Catal. A* 134, 251 (1998).
267. M. T. Reetz, A. Zonta, J. Simpelkamp, A. Rufinska, and B. Tesche, *J. Sol.-Gel Sci. Technol.* 7, 35 (1996).
268. K. Kawakami and S. Yoshida, *Biotechnol. Tech.* 8, 441 (1994).
269. S. Sato, T. Murakata, M. Ochifuji, M. Fukushima, and T. J. Suzuki, *Chem. Eng. Jpn.* 27, 732 (1994).
270. T. Antczak, J. Mrowiec-Bialon, S. Bielecki, A. B. Jarzebski, J. J. Malinowski, A. I. Lachowski, and E. Galas, *Biotechnol. Tech.* 11, 9 (1997).
271. G. Kuncova and M. Sivel, *J. Sol.-Gel Sci. Technol.* 8, 667 (1997).
272. G. Kuncova, M. Guglielmi, P. Duubina, and B. Safar, *Collect. Czech. Chem. Commun.* 60, 1573 (1995).
273. M. Heidt, U. Bornscheuer, and R. D. Schmid, *Biotechnol. Tech.* 10, 25 (1996).
274. K. Kawakami and S. Yoshida, *J. Ferment. Bioeng.* 82, 239 (1997).
275. K. Kawakami and S. Yoshida, *Biotechnol. Tech.* 9, 701 (1995).
276. A. Pierre and P. Buisson, *J. Mol. Catal. B* 11, 639 (2001).
277. A. F. Hsu, T. A. Foglia, and S. Shen, *Biotechnol. Appl. Biochem.* 31, 179 (2000).
278. C. B. Park and D. S. Clark, *Biotechnol. Bioeng.* 78, 229 (2002).
279. S. Sheltzer, S. Rappoport, D. Avnir, M. Ottolenghi, and S. Braun, *Biotechnol. Appl. Biochem.* 15, 227 (1992).
280. O. Heichal-Segal, S. Rappoport, and S. Braun, *Biotechnology* 13, 798 (1995).
281. O. Ariga, *J. Ferment. Bioeng.* 82, 341 (1996).
282. C. Kauffmann and R. T. Mandelbaum, *J. Biotechnol.* 62, 169 (1998).
283. C. G. Kauffmann and R. T. Mandelbaum, *J. Biotechnol.* 51, 219 (1996).
284. D. Shabat, F. Grynszpan, S. Saphier, A. Turniansky, D. Avnir, and E. Keinan, *Chem. Mater.* 9, 2258 (1997).
285. I. Gill and A. Ballesteros, *Proc. N.Y. Acad. Sci.* 799, 697 (1996).
286. A. F. Hsu, E. Wu, S. Shen, T. A. Foglia, and K. Jones, *Biotechnol. Appl. Biochem.* 3, 245 (1999).
287. S. Wu, J. Lin, and S. I. Chan, *Appl. Biochem. Biotechnol.* 47, 11 (1994).
288. R. Obert and B. C. Dave, *J. Am. Chem. Soc.* 121, 12192 (1999).
289. B. Jandeleit, D. J. Schaefer, T. S. Powers, H. W. Turner, and W. H. Weinberg, *Angew. Chem., Int. Ed. Engl.* 38, 2495 (1999).
290. S. Senkan, *Angew. Chem., Int. Ed. Engl.* 40, 313 (2001).
291. B. Alonso, J. Maquet, B. Vina, and C. Sanchez, *New J. Chem.* 935 (1998).
292. W. Cheng, B. Baudrin, B. Dunn, and J. I. Zink, *J. Mater. Chem.* 11, 92 (2001).
293. F. Chen, Z. Shi, and M. Liu, *Chem. Commun.* 2095 (2000).
294. T. Hirai, H. Okubo, and I. J. Komasa, *Mater. Chem.* 10, 2592 (2000).
295. I. Willner, *Acc. Chem. Res.* 30, 347 (1997).
296. I. Willner and E. Katz, *Angew. Chem., Int. Ed. Engl.* 39, 1180 (2000).
297. N. Hampp, *Chem. Rev.* 100, 1755 (2000).
298. B. K. Das and J. H. Clark, *Chem. Commun.* 605 (2000).
299. D. Juwiler, J. Blum, and R. Neumann, *Chem. Commun.* 1123 (1998).
300. A. J. Sandee, L. A. van der Veen, J. N. H. Reek, P. C. J. Kamer, M. Lutz, A. L. Spek, and P. W. N. van Leeuwen, *Angew. Chem., Int. Ed. Engl.* 38, 3231 (1999).
301. C. G. Guizard, A. C. Julbe, and A. Ayral, *J. Mater. Chem.* 9, 55 (1999).

302. C. Sanchez, F. Ribot, and B. Lebeau, *J. Mater. Chem.* 9, 35 (1999).
303. K. Haupt and K. Mosbach, *Trends Biotechnol.* 16, 468 (1998).
304. O. Ramström and K. Mosbach, *Curr. Opin. Chem. Biol.* 3, 759 (1999).
305. S. Al-Kindy, R. Badía, J. L. Suárez-Rodríguez, and M. E. Díaz-García, *Crit. Rev. Anal. Chem.* 30, 291 (2000).
306. K. Haupt and K. Mosbach, *Chem. Rev.* 100, 2495 (2000).
307. S. Dai, M. C. Burleigh, Y. Shin, C. C. Morrow, C. E. Barnes, and Z. Xue, *Angew. Chem., Int. Ed. Engl.* 38, 1235 (1999).
308. R. Makote and M. M. Collinson, *Chem. Commun.* 425 (1998).
309. C. C. Liu and Z. Jin, *Trends Biotechnol.* 15, 213 (1997).
310. W. M. Zhao, Y. Xia, and G. M. Whitesides, *J. Mater. Chem.* 7, 1069 (1997).
311. Y. Xia and G. M. Whitesides, *Angew. Chem., Int. Ed. Engl.* 37, 550 (1998).
312. C. A. Harrington, C. Rosenow, and J. Retief, *Curr. Opin. Microbiol.* 3, 285 (2000).
313. C. C. Xiang and Y. Chen, *Biotechnol. Adv.* 18, 35 (2000).
314. G. Walter, D. Büssow, D. Cahill, A. Lueking, and H. Lehrach, *Curr. Opin. Microbiol.* 3, 298 (2000).
315. D. J. Graves, *Trends Biotechnol.* 17, 127 (1999).
316. P. C. Michels, Y. L. Khmel'nitsky, J. S. Dordick, and D. S. Clark, *Trends Biotechnol.* 16, 210 (1998).
317. J. W. Grate, *Chem. Rev.* 100, 2627 (2000).
318. R. I. Stefan, J. F. van Staden, and H. Y. Aboul-Enein, *Crit. Rev. Anal. Chem.* 29, 133 (1999).
319. S. H. DeWitt, *Curr. Opin. Chem. Biol.* 3, 350 (1999).
320. C. De Bellefon, N. Tanchoux, S. Caravieilhès, P. Grenouillet, and V. Hessel, *Angew. Chem., Int. Ed. Engl.* 39, 3442 (2000).
321. N. G. Wilson and T. McCreedy, *Chem. Commun.* 733 (2000).

Biogenic Nanoparticles

Joseph M. Slocik, Marc R. Knecht, David W. Wright

Vanderbilt University, Nashville, Tennessee, USA

CONTENTS

1. Introduction
 2. Biosynthesis of Zero-Valent Noble Metals (Ag⁰ and Au⁰)
 3. Biomineralization of Metal Oxides (Fe₃O₄ and SiO₂)
 4. Biomineralization of Metal Sulfide Nanoclusters (CdS, ZnS, and Ag₂S)
- Glossary
References

1. INTRODUCTION

Biological systems offer an unparalleled level of molecular control over the biosynthesis of inorganic materials, either as a means of metal detoxification (Ag⁰, Au⁰, ZnS, CdS, and Ag₂S) or cellular integration of a functional component (Fe₃O₄, Fe₃S₄, and SiO₂). Detoxification processes include the bioreduction and/or precipitation of toxic metal ions into insoluble nontoxic nanoclusters. Alternatively, the controlled biosynthesis of magnetite and silica involves oxidative and condensative associated processes. As a result, the collection of biogenic particles display exquisite structural assemblies (diatom frustules), morphologies (tetragonal Ag⁰ particles), functionality (Fe₃O₄ as an internal magnet and SiO₂ as a protective barrier), quality (24 carat bacterioform gold), crystallinity, and monodispersity.

2. BIOSYNTHESIS OF ZERO-VALENT NOBLE METALS (Ag⁰ AND Au⁰)

Noble metals are naturally present in the environment at various abundances in sea water (ng amounts), rock (ng amounts), the atmosphere (ng amounts), and soil (μg amounts). A wealth of documented examples of microbial-metal interactions and bioaccumulation of noble metals in everything from unicellular organisms to animals and even in humans has been documented [1]. At trace amounts, noble metals are toxic to many organisms. Consequently, the survival of the organism is dependent upon the detoxification of

noble metal ions by either bioreduction and/or mineralization processes. For example, bacterial cells detoxify Ag⁺ by evolving silver resistant encoded plasmids that enable Ag⁰ production in exquisitely shaped particles [2–4]. Interestingly, it is believed that microbial-metal based interactions involving gold deposits by bacteria date back to over 2.8 billion years [5]. The following examples provide a detailed survey of the organisms and mechanisms of biogenic synthesis of gold and silver nanoparticles (summarized in Table 1).

2.1. Biomineralization of Ag⁰ Nanocrystals

2.1.1. Classification of Silver Resistance by Organisms

Several bacterial cultures of *Pseudomonas stutzeri* [2–4], *Escherichia coli* [6, 7], *Enterobacter cloacae* [8], and *Citrobacter intermedius* B6 [9, 10] are resistant to the antimicrobial effects of silver. Silver ions primarily act by poisoning respiratory enzymes and electron transport components through interference with DNA and/or in combination by blocking the permeability of the outer membrane, thereby inhibiting growth [7]. Organisms have developed mechanisms to compensate for this toxicity via precipitation of less toxic silver salts (Ag₂PO₄, AgCl, or Ag₂S), possession of silver resistant plasmids (silver ion efflux or other energy dependent process), and/or bioreduction of silver ions to nanocrystals [6, 12].

Genetically encoded silver resistance is common to all of these organisms and is the most likely silver detoxification mechanism. However, with the exception of *Pseudomonas stutzeri*, studies of most species of bacteria have only reported the biological ramifications of silver and not the physical characterization of these deposits. The resistance of *Citrobacter intermedius* B6 [9, 10] and *Escherichia coli* [6, 7] was conferred by an ion efflux pump and a lack of an outer membrane permeability barrier [7].

Pseudomonas stutzeri A259 was the first bacteria shown to produce silver nanocrystals [3]. Isolated near a silver mine in Utah, silver resistance in *Pseudomonas stutzeri* was linked directly to the DNA plasmid of pKK1 (molecular weight 49.4 MD), one of three known plasmids (pKK1, pKK2, and

Table 1. Summary of biogenic particles.

Name	Organism	Product	Size	Conditions	Ref.
<i>Pseudomonas stutzeri</i>	Bacteria	Ag ⁰	<200 nm	Grown in AgNO ₃	[2]
<i>Medicago sativa</i>	Alfalfa plant	Au ⁰	2–20 nm	Active uptake Au ⁰	[18, 19]
<i>Pedomicrobium</i> -Like	Budding bacteria	Au ⁰	~1 μm	Natural mineralization	[5, 21]
<i>Verticillium sp.</i>	Fungus	Au ⁰	20 nm	Intracellular reduction	[17]
<i>Verticillium sp.</i>	Fungus	Ag ⁰	25 nm	Intracellular reduction	[15]
<i>Lactobacillus</i> strains	Bacteria (buttermilk)	Au ⁰	25–50 nm	Exposure to HAuCl ₄	[14]
<i>Lactobacillus</i> strains	Bacteria (buttermilk)	Ag ⁰	15–500 nm	Exposure to AgNO ₃	[14]
<i>Fusarium oxysporum</i>	Fungus	Au ⁰	20–40 nm	Extracellular reduction	[22]
<i>Cylindrotheca fusiformis</i>	Diatom	SiO ₂	500–700 nm	Exposure to Si(OH) ₄	[70, 71]
<i>Coscinodiscus granii</i>	Diatom	SiO ₂	Undefined	Exposure to Si(OH) ₄	[69]
<i>Aquaspirillum</i>	Bacteria	Fe ₃ O ₄	25–55 nm	2–7 μM oxygen	[44]
<i>A. Magnetotacticum</i>	Bacteria	Fe ₃ O ₄	Undefined	2–7 μM oxygen	[47, 48]
Undesignated	Magnetotactic bacteria	Fe ₃ S ₄	69 nm	Anaerobic	[56]
<i>Schizosaccharomyces pombe</i>	Yeast	CdS	1.8 nm	Peptide mediated/Cd ²⁺	[86]
<i>Candida glabrata</i>	Yeast	CdS	2.0 nm	Peptide mediated/Cd ²⁺	[86]
<i>Fusarium oxysporum</i>	Yeast	CdS	5–20 nm	Extracellular reduction	[89]
<i>Klebsiella aerogenes</i>	SO ₄ ²⁻ reducing bacteria	CdS	20–200 nm	Exposure to Cd ²⁺ /SO ₄ ²⁻	[90]
<i>Pseudomonas stutzeri</i>	Bacteria	Ag ₂ S	Undefined	Grown in AgNO ₃	[2]
<i>Desulfobacteriaceae</i>	Bacterial biofilm	ZnS	2–5 nm	pH 7.2–8.6/(0.1 ppm Zn)	[107]

pKK3) [3]. The existence of pKK1 in the resistant strain was substantiated by its omission in a silver-sensitive bacterial colony, forming the basis for a comparative study. However, this interpretation is controversial.

Slawson et al. [4] first described the accumulation of silver between the resistant and sensitive strains as occurring rapidly within the first eight minutes of exposure and with comparable amounts of silver (300 mg of silver per gram of dry weight of bacteria) through an energy dependent pathway. Similarly, both the resistant and sensitive strains exhibited silver binding and deposition localized predominantly at the cell surface. The silver was deposited at the surface in the insoluble form of Ag₂S as dense conglomerates in response to high levels of H₂S produced by the cell [4]. The release of H₂S was observed to occur at higher concentrations in the Ag-resistant strain than in the Ag-sensitive ones, thus accounting for differing degrees of resistance to silver [4].

In an alternate mechanism for silver resistance, Haefeli et al. [3] speculated that a molecule analogous to metallothionein forms an inert complex with Ag⁺, thereby protecting the bacteria. This was supported by the lack of silver reduction upon exposure to light. Additionally, Haefeli et al. [3] reported the reduction capabilities of *Pseudomonas stutzeri* A259 and the silver resistant strain A256 with the common reagents of methylene blue and resazurin, establishing a plausible bioreduction mechanism for Ag⁺. They emphasize that this reductive capacity may or may not have a connection to silver resistance as evidenced by similar results with A256 and A259 [3].

2.1.2. Biomimetic Approaches to Microbial-Induced Ag⁰ Nanocrystals

Characterization of Ag⁰ Particles by *Pseudomonas stutzeri* Another microbial pathway of detoxification involves the production of silver nanocrystals by *Pseudomonas stutzeri* under laboratory conditions and cultured

in media enriched with AgNO₃. Recently, Klaus et al. [2] characterized these particles by TEM, EDX, and electron diffraction. The majority of silver was deposited as particles in vacuole-like granules (ranging from a few to 200 nm in diameter) between the outer and plasma membranes, with higher concentrations located at the cell poles (Fig. 1) [2]. At these cellular binding/accumulation sites, different crystal morphologies displayed in the TEM micrographs were distributed throughout the periplasmic space of the cell in the form of triangular, hexagonal, and spheroidal silver containing particles [2]. The shape selectivity of the triangular and hexagonal forms was presumed to result from the confined space available for plate-like morphology, in addition to the crystallographic plane bearing the highest atomic density [12]. It is known that plate morphology is preferred

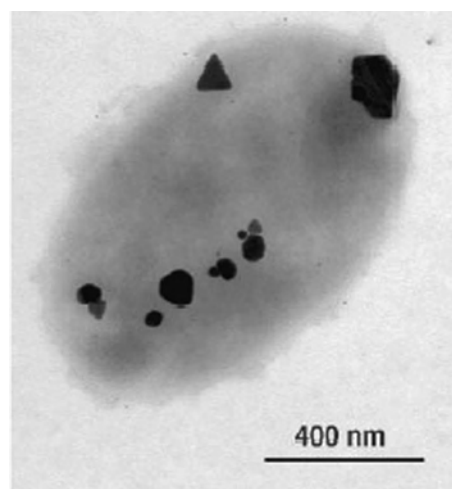


Figure 1. TEM image of whole uncontrasted cell enriched with Ag⁺. Reprinted with permission from [2], T. Klaus et al., *Proc. Natl. Acad. Sci.* 96, 13611 (1999). © 1999, National Academy of Sciences, U.S.A.

during crystal growth due to the faster rate of accumulation relative to spherical growth. This results from a high aspect ratio (edge size to thickness) of about 100/1 for a flat crystallite, which provides a surface to volume ratio two orders of magnitude larger than at equilibrium for plates versus spheres [12].

From electron diffraction measurements, three different crystal phases were observed within the cell's boundary: a face-centered cubic structure for metallic silver, a monoclinic crystalline α -form of Ag_2S , and an undeterminable phase [2]. From a representative sample, the metallic form was present in the highest abundance followed by a small number of Ag_2S particles. The third crystal type was unidentified crystallographically [2].

Joerger et al. [13] have further developed a biomimetic approach of transforming bio-composites of nanocrystalline silver and bacteria into optically functional thin-film coatings. The films were simply produced by thermally treating the composites to yield a functional carbonaceous material [13]. The optical properties were characterized by strong wavelength selective absorption in regions where the matrix weakly absorbed, and strong reflectance in spectral regions where the matrix strongly absorbed [13].

Formation of Ag^0 Particles by *Lactobacillus* Bacterial strains of *Lactobacillus* isolated from buttermilk produced Ag^0 clusters *in-situ* when treated with AgNO_3 and whey within 12 hours of exposure [14]. The harvested silver deposits exhibited a bimodal distribution in sizes centered around 15 nm and 500 nm, with the larger particles resulting from coalescence [14]. The subsequent coalescence of the larger particles inside the bacterium forced a structural change observed by a protrusion of particles into the cell wall lining [14]. The crystallinity of these Ag^0 products was inconsistent with metallic silver and Ag_2S by XRD, but likely represented a composite with a silver-rich core externally shielded by various organic species at the surface [14].

2.1.3. Fungal-Mediated Ag^0 Biosynthesis

Verticillium fungal cells exhibited intracellular surface reduction of silver [15]. Mukherjee et al. [15] cultured cells for 72 hours at concentrations of 10^{-4} M Ag^+ , producing silver nanoparticles that were uniformly distributed on the cell surface with average sizes of 25 ± 12 nm. The specific location of the silver deposits was confined to both the cell wall (external boundary) and cytoplasmic membrane (internal boundary), thus providing credence for the biosynthetic mechanism [15]. The mechanism controlling nanocluster formation was dominated by surface trapping of the Ag^+ ions through electrostatic interactions between the Ag^+ and the negatively charged carboxylate groups of cellular enzymes (not specified) [15]. After trapping the silver ions, they are reduced by enzymes in the cell wall to silver nuclei, which further nucleate to clusters [15]. The authors also reported the successful multiplication of cells over a week in the presence of Ag^+ showing no detrimental effects on cell growth. In contrast to the *Pseudomonas* biosynthesized Ag^0 nanoparticles, the crystal morphologies were primarily spheroidal shapes [15].

2.2. Biomineralization of Au^0 Deposits and Nanoclusters

Gold ions in general are less toxic than silver ions. Consequently, an array of examples of organisms which can effectively biomineralize metallic gold particles has been observed. As a result of gold's properties (lower toxicity), organisms do not require essential resistance encoded plasmids as they did for Ag^+ , but in turn must be more robust (physical features of the cell) to counteract the increased density of mineralized gold. *Bacillus cereus* [16], *Verticillium sp.* [17], *Medicago sativa* [18, 19], and *Pedomicrobium*-like bacteria [5, 20], have the ability to biomineralize gold.

2.2.1. Mechanism and Characterization of Microbial-Produced Gold

Pedomicrobium-like bacteria are commonly associated with the oxidation of iron and manganese. They represent the first known system to biologically produce gold particles (termed bacterioform gold) at a quality of 24 carats [5]. They have been discovered anchored on gold placer deposits at several geographical sites including Alaska, northwestern China, and regions of South Africa [21]. Common among all three sites are locally high concentrations of Au^+ and Au^{3+} complexes of $\text{Au}(\text{CN})_2^-$, $\text{Au}(\text{OH})\text{Cl}_3^-$, and AuCl_4^- amenable to bioaccumulation processes [5]. Additionally, the bacteria exhibited characteristics suitable for deposition processes such as a direct budding behavior and an inclination towards colonization advantageous to the continuous mineralization of gold [5, 21].

The mineralization of gold begins with accumulation in the cell wall through electrostatic binding of the anionic gold complexes with positively charged residues (RNH_3^+ , R_4N^+) and/or ligation with coordinating ligands (RSH , R_2S) of polypeptides [5]. Aggregates of these sulfur-rich/cationic peptides then serve as nucleation sites for gold. Upon binding at the surface, electron transfer processes induce sufficient reduction to metallic Au^0 and crystal growth occurs [5]. This suggests that the high purity (24 carats) isolated from gold deposits are consequences of both highly selective binding and the redox properties of the cell.

The formation of gold particles is controlled and limited by the morphological characteristics of the cells. These bacteria lack spatially delineated compartments that can restrict the dimensions of crystal growth, so the mineralized gold products result in structurally ill-defined, physically heterogeneous, and spatially disorganized forms [5]. This structural incontinuity is clearly apparent in the SEM images obtained from representative samples of bacterioform gold [5, 21]. Additionally, coatings of open diffuse colonies of *Pedomicrobium* produced gold deposits that are described as ranging in appearance from extended lacelike networks to oval, spheroidal, and/or kidney shaped structures approximately 1 μm in size [21]. Samples imaged by SEM also showed a core region that was significantly compacted, indicative that the gold layers episodically grew outwards [21]. This intricate architecture of thin gold layers develops from the complex growth patterns of budding cells, their symbiotic role in the colony, and possibly a hierarchy order. These colonies consisted of branching, axial, and lateral direct budding cells

capable of mineralizing gold in all directions to different extents, evident in the micrographs in which budding assemblages are joined by slender gold metallized stalks and hollow tubules [21]. It is the budding nature of these cells that enables the colony to remain a step ahead of irrevocable entombment by the gold shell.

Watterson [21] confirmed the involvement of *Pedomicrobium*-like bacteria in bacterioform gold by using electron-beam heating experiments. The incident electron beam causes pyrolytic swelling and other textural changes in the substrate material identifying its composition [21]. From the experiments, the results established that the deposits were not solid gold objects, but they possessed an organic substrate interior [21].

The strain of *Lactobacillus*, already shown to produce Ag^0 particles, analogously crystallized Au^0 under the same experimental conditions [14]. Parallel to Ag^0 , the growth of Au^0 crystals pushed and/or possibly ruptured the cell wall, but preserved the integrity of the bacterial contour [14]. The Au^0 products belonged to the two size domains of 20–50 nm and greater than 100 nm [14]. The TEM micrograph (Fig. 1) illustrated these two distinct sizes along with the cellular distribution. An abundance of Au^0 clusters resided clearly outside the delineation of the bacterial contour; however within the defined contour were predominantly large Au^0 crystals resulting from coalescence [14].

2.2.2. Eukaryotic Biomineralization of Au^0

Eukaryotic organisms are also a source of biologically derived gold particles. The synthesis of gold particles was recently achieved with the silver bioreducing fungus, *Verticillium sp.*, under the same laboratory conditions utilized for Ag^0 [14, 17]. Upon exposure of AuCl_4^- to *Verticillium* fungal cells and after an incubation period of 72 hours, monodispersed gold nanoparticles successfully formed [17]. The isolated nanoparticles, averaging 20 nm in size, were characterized by a distinguishable plasmon absorption resonance at 540 nm and intense diffraction peaks for the (111), (200), and (220) crystal planes of face-centered cubic gold [17].

The fungal cells bioprocess gold by surface trapping AuCl_4^- ions at the cell wall and through cytoplasmic membrane binding interactions analogous to Ag^+ [17]. The bound gold ions are subsequently reduced by enzymes within the cell wall, resulting in the aggregation of metal atoms and formation of nanoparticles [17]. Mukherjee et al. [17] arrived at this conclusion by examining the sugars in the cell wall and the surrounding media for extracellular reduction of Au^{3+} . A survey of the cell shows a distribution of nanoparticles between the two boundaries, with a higher abundance of gold nanoparticles on the cytoplasmic membrane than the cell wall. Through examination of the TEM micrographs, a few but large gold particles were also present in the cytoplasm with random triangular and hexagonal shaped particles observed.

Contrary to the intracellular synthesis of Au^0 by *Verticillium*, Mukherjee et al. [22] demonstrated the extracellular reductive capacity of an atypical genera of fungus, *Fusarium oxysporum*. In solution, the fungal cells released agents which reduced AuCl_4^- to nanoclusters of Au^0 [22]. Four proteins (molecular masses 10 kDa–66 kDa) were identified as

being released in the solution according to gel electrophoresis [22]. One of the proteins was speculated as being responsible for the Au^{3+} reduction, while the other proteins might bind and stabilize the Au^0 nanoclusters against aggregation [22]. The gold products were characterized by FTIR and TEM. The results from FTIR spectroscopy revealed unchanged amide I and II bands relative to native proteins, suggesting that the secondary structure was not affected by reacting with the gold ions nor binding the gold nanocluster surface [22]. The TEM images showed particles 20–40 nm in size with spherical and triangular morphologies [22]. The implications of extracellular gold reduction impact a proposed harvesting process and affords commercial viability [22].

2.2.3. Phytosynthesis and Remediation of Au^0 Particles

The active uptake and mineralization of gold by plants was first described by Anderson et al. [23] with *Brassica juncea* or common mustard plant. It was shown to hyperaccumulate gold as high as 57 μg of gold per gram of dry biomass when complemented with different concentrations of thiocyanate [23]. More recently, gold biomineralization was reported with *Medicago sativa* alfalfa plants [18, 19, 21]. Previously, Gardea-Torresday et al. showed that inactivated alfalfa biomass can reduce Au^{3+} ions to Au^0 nanoparticles in solution [18, 20]. In more recent studies, live alfalfa plants grown in a gold enriched agar were examined for nanocluster formation. The experiments were carried out at different concentrations of gold (0, 5, 10, 20, 40, 80, 160, and 320 ppm) and harvested after two weeks of growth [19]. The harvested plants were characterized by EXAFS (X-ray absorption fine structure) measurements and TEM analysis [19]. From EXAFS, it was determined that the Au^{3+} was reduced to Au^0 in the agar solid media prior to active uptake by the alfalfa [19].

Analysis of the plant components by TEM (Fig. 2) revealed areas of aggregated gold nanoparticles in the plant

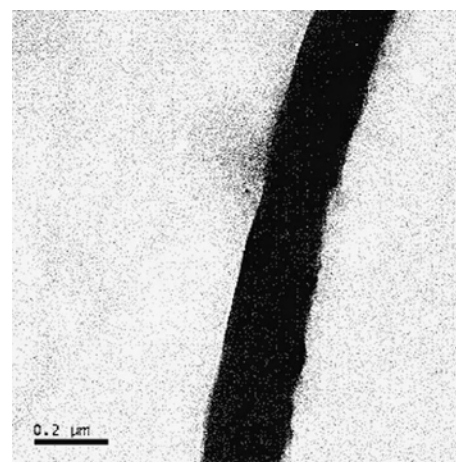


Figure 2. Low magnification TEM micrograph of alfalfa shoot showing aggregates of gold nanoparticles. Reprinted with permission from [19], J. L. Gardea-Torresday et al., *Nano Lett.* 2, 397 (2002). © 2002, American Chemical Society.

shoots and roots with a negligible concentration in the stems. This suggested that nucleation of the gold atoms inside the plants occurred in preferential zones [19]. The plant samples displayed a broad distribution of nanoparticles with sizes ranging from 2 to 20 nm in diameter [19]. Gardea-Torresdey et al. [19] claimed that the difference in sizes is a consequence of nanoparticles being formed at different times during the transport of gold atoms through the roots and shoots network. This particle size then affected the final crystal phase of the gold, such that an icosahedron structure was adopted by a 4 nm gold particle and a face centered cubic twinned structure crystallized for particles 6–10 nm in size [19]. The icosahedron structure was the most common, as it represents the lowest energy configuration for gold [19].

The bioreduction of noble metals is a viable mechanism utilized by biological systems to control the formation of zero-valent metal particles resulting from the stress of toxic metal ions present in the environment. Specific organisms process metal particles differently; however the exact function that metal particles serve for the organisms besides that of a detoxification product remains elusive. It is speculated that silver particles may possibly function in cellular activity with parallel multifunctionality to magnetite [12]. Additionally, it is alleged that bacteria could use silver ions as part of an electron transport process in its reduction to metallic silver [12].

3. BIOMINERALIZATION OF METAL OXIDES (Fe₃O₄ AND SiO₂)

3.1. Magnetite Bioproducing Bacteria

3.1.1. Discovery and Classification of Bacterium

In 1975, aquatic bacteria were discovered to have the ability to biomineralize the magnetically responsive mineral magnetite (Fe₃O₄). The bacterium was originally seen in the light of its magnetotaxis during cell culturing. The cells in the culture were able to translocate inside the culture based upon the orientation of the magnetite crystals with respect to the earth's geomagnetic field [24]. Since then, biogenic magnetite has been discovered in a wide variety of organisms, including algae, insects, mollusks, fish, birds, and in the human brain [25–30]. Recent research has focused on improving the understanding of the uptake of iron and formation of magnetite, and its bioapplications will be reviewed.

The largest group of organisms that biologically produce magnetite are bacteria. While there exists an extremely broad range of bacteria that can produce biogenic magnetite, all are gram-negative prokaryotes [31]. Isolated freshwater magnetotactic bacterial strains include *Magnetospirillum gryphiswaldense* (Fig. 3), *Magnetospirillum* sp. AMB-1, *Magnetospirillum magnetotacticum* MS-1, and *Magnetospirillum* sp. MGT-1 [32–35]. These organisms generally reside in river sediments and/or in low oxygen concentrated aquatic environment. Specifically, Bazylinski et al. [36] have discovered live magnetotactic bacteria in the Pettaquamscutt River Estuary from depths of 2.25 m to a total depth of 6.5 m. Other populations of bacteria were discovered at

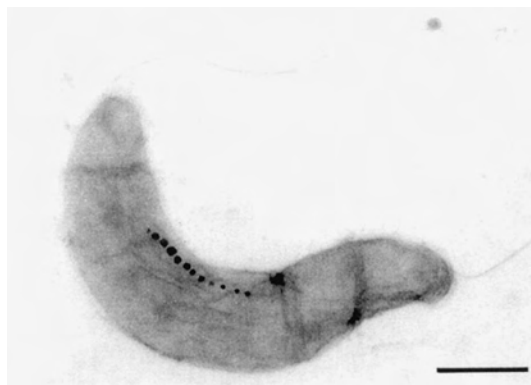


Figure 3. Electron micrograph of *Magnetospirillum gryphiswaldense*. Bar = 0.5 μ m. Reprinted with permission from [102], D. Schüller and R. B. Frankel, *Appl. Microbiol. Biotechnol.* 52, 465 (1999). © 1999, Springer-Verlag.

depths between 3.5 and 4.7 m below sea level in a region known as the Oxic-Anoxic Transition Zone (OATZ) with a maximum number of living motile cells located between 4.4 and 4.7 m [36]. The OATZ is a region of the estuary in which both molecular oxygen and hydrogen sulfide exist, but at minimal concentrations. Below the OATZ region is the anoxic zone where concentrations of hydrogen sulfide exist, but molecular oxygen does not. Schüller et al. [37] elucidated that the oxygen concentration range for which bacterial magnetite formation occurs is between 2 to 7 μ M, although cells are able to proliferate at higher concentrations of molecular oxygen [37].

Bacterial cells are able to use the magnetite to wade through their native aquatic environments with respect to the earth's magnetic fields [24]. The crystals are single-domain in nature and form chains along the interior of the cell wall [24]. The orientation of the chains aids the cell in direction and motion, which is termed magnetotaxis. Researchers have capitalized on this mobility to isolate magnetite-producing cells from samples by using a magnet to extract these specific cells to an area separate from the other cells [38, 39].

The internalized compass that the bacterial cells possess allows them to determine which direction to move and for what reason. The motility of the cells is directly linked to other environmental factors, especially the concentration of transition metals in the ambient surroundings. Studies have been conducted of cell motility in aqueous environments to understand the effects of the metal concentrations. Concentrations of 1, 10, and 100 parts per million were used as a factor in the study. Copper, cobalt, and zinc were shown to completely inhibit the motility of the cells at any concentration, while other transition metals showed no inhibition of the cell motility [41].

3.1.2. Iron in Bioprocessing

Iron uptake is the first step in the formation of magnetite as illustrated in Figure 4. Matsunaga and Takeyama [42] discovered and cloned the MagA transport protein from the magnetotactic bacterium *Magnetospirillum* into *E. coli* cells using previously employed techniques [49]. This protein exhibits a high degree of hydrophobicity and is oriented in

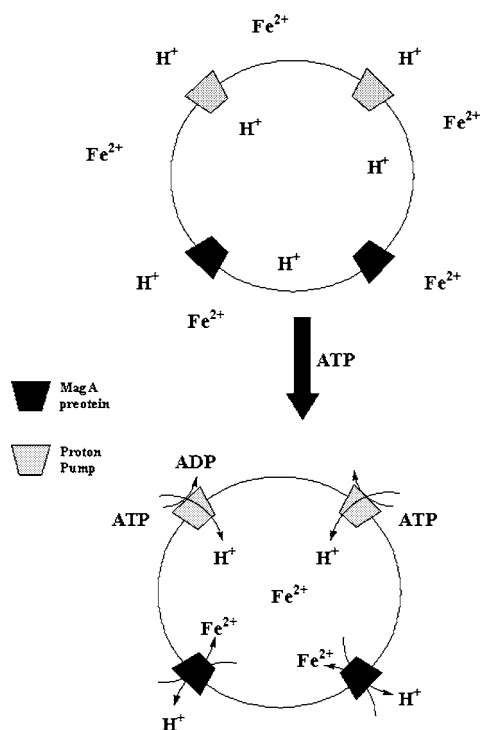


Figure 4. Dynamic scheme of Fe uptake by magnetotactic bacteria.

the phospholipids bilayer with both the N and C terminals directed towards the interior of the cell. Interestingly, MagA does not possess the ATPase gene and binding site for ATP, thereby supporting the theory of it being used as a transporter protein for iron. Iron uptake is directly linked to ATP consumption away from the MagA site. Upon addition of ATP to the cloned *E. coli* cultures isolated with the proteins, the cloned cells immediately began uptake of ^{59}Fe , which was terminated upon the addition of CCCP (carbonylcyanide *m*-chlorophenyl-hydrazone), a metabolic phosphorylation inhibitor [42].

Inside the cell, the iron is used as a substrate for the building of magnetic particles. While the detailed mechanism of biomineralization has not been elucidated, two different modes have been proposed. Round et al. [48] have speculated that iron is taken up by the cell, and chemically adjusted to hydrous ferric oxide (Fe_2O_3) as a precursor to magnetite (Fe_3O_4). The cell utilizes the magnetosome, a highly developed lipid and protein layer that envelops the magnetite crystal [38], to direct the crystallization and/or precipitation of the aqueous ferric oxide precursor to a specific location in the bacterial cell. Mann observed under high resolution transmission electron microscopy (HRTEM) in *A. magnetotacticum* that nucleation of the precursor occurs at many locations in the cell. There existed a primary site of nucleation for the single domain crystals to grow. Since precipitation of the precursor occurred outside the primary site, he speculated that this precipitated precursor needed to be dissolved and reprecipitated at the primary site. Mann et al. [47] also observed that the amorphous precursor is kinetically more stable than the final product of magnetite crystals. Consequently, once crystallization has begun the magnetite (Fe_3O_4) will be the more thermodynamically stable product relative to the ferric oxide precursor [38].

The second method of controlled growth is envisioned as a solid state rearrangement at a solution front between the amorphous precursor and the crystalline magnetite. As crystals of magnetite grow in the bacterial cell, they form large conglomerates of the amorphous ferric oxide that is used to form the crystal phase magnetite. It has been speculated that the amorphous phase encounters a solution front causing the solid state rearrangement of the substrate of ferric oxide to form the magnetite. In the *A. magnetotacticum* cell, amorphous material has been observed in high association with the Fe_3O_4 crystals, suggesting that the rearrangement of the amorphous ferric oxide occurs to form the magnetite crystals. It is unlikely that precipitation of the precursor occurs in the second method of solid state rearrangement to form the crystal because of this high degree of associativity between the precursor and crystalline phases [38].

3.1.3. The Magnetosome

While studying magnetite in *Aquaspirillum*, Balkwill et al. conjectured that the magnetite particles are probably enveloped by a lipid bilayer, known as the magnetosome [49]. They were, however, unable to visualize the lipid bilayer because of the high electron density of the magnetite core that the bilayer surrounded. Gorby et al. [38] attempted to prove the existence of the lipid layer by removing it using standard biochemical techniques and characterizing the composition of the layer. Magnetotactic cells were cultured and lysed so that the magnetite particles were able to be magnetically separated. Once separated, the lipid layer of the magnetosome was extracted and analyzed [35]. The composition was determined to consist of three components. The first fraction made up of neutral lipids and free fatty acids amounted to eight percent of the total structure. The second fraction, consisting of thirty percent of the lipid layer, was made of glycolipids, sulfolipids, and phosphatides, while phospholipids accounted for sixty-two percent of the lipid layer by weight was the third fraction. None of the neutral lipids, fatty acids, or glycolipids were identified, while the phospholipids were identified as either phosphatidyl-ethanolamine or phosphatidylserine by thin layer chromatography [38].

Further research by Okudu et al. [45] has led to the isolation of three unique proteins associated with the magnetosome. These proteins include a 12 kDa protein (MAM12), a 22 kDa protein (MAM22), and a 28 kDa protein (MAM28). Interestingly, MAM22 shows a significant degree of homology with numerous proteins of the tetratricopeptide repeat protein family. MAM22 is believed to be located on the surface of the magnetosome and electrostatically interacts with the cytoplasm [45]. Although there has been some speculation that the MAM 22 protein may have a receptor-like function, to date there has been no evidence to support this theory.

3.1.4. Crystal Dimensions and Morphology

In magnetotactic cells, there exist many different morphologies of magnetite crystals that are based specific to different species of magnetotactic bacteria (Fig. 5). The main technique for identifying the structures is HRTEM. Through this

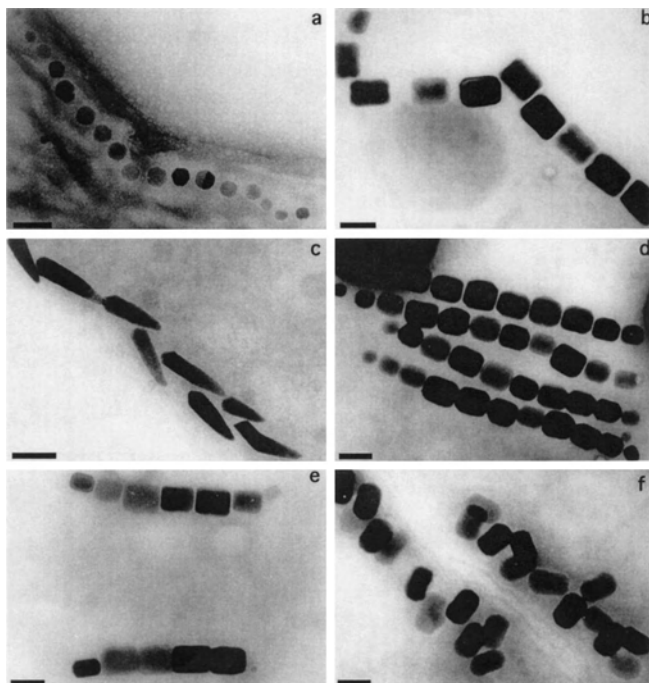


Figure 5. Morphologies of bacterially produced magnetite. Morphologies include (a) cubo-octahedral, (b, d, e, f) elongated hexagonal prismatic, and (c) bullet shaped. Reprinted with permission from [104] D. Schüller and R. B. Frankel, *Appl. Microbiol. Biotech.* 52, 466 (1999). © 1999, Springer-Verlag.

method, researchers have been able to identify a wide variety of structures including parallelepipeds ($40 \times 40 \times 60$ nm) [46], hexagonal prisms truncated by the $\{111\}$ plane [40], and octahedral with faces truncated by the $\{111\}$ and $\{100\}$ faces [47].

Along with varying shapes of the crystal structures, the crystals themselves have defined size values that are species dependent. The overall space constraints within the cell probably dictate the final size of the crystals of magnetite [48]. For instance, Balkwill et al. [44] studied the dimensions of the magnetite mineralized in cells from the genus *Aquaspirillum*. These cells possessed magnetite with a monomodal size range of 25 to 55 nm in diameter (average of 42 nm) and 39 to 49 nm in length [44]. This particular genus of bacteria has a distinct cell size that is determined through mitotic division. When any cell is reproduced, size constraints are dictated by the genetic makeup of that particular cell. Due to this rigid cell size, the biological magnetite can only be produced to a size that can actually fit within the physical space of the cell, leading to crystal size conformity of the magnetite in individual cells of any genera.

3.2. Biological Production of Magnetite in Salmon

While bacterial cells are the most abundant sources of biogenic magnetite, other organisms are able to mineralize magnetite and use it as an internal compass. A notable example is salmon, which employs magnetotaxis to “hone in” on a specific location to spawn without celestial recognition [49]. Biogenic magnetite has been discovered deep in

the recesses of the salmon (*Oncorhynchus nerka*) brain in the ethmoid region [50, 51]. Mann et al. [50] studied the composition and orientation of these magnetite crystals. The chains were straight and continuous, disrupted, or folded upon themselves and looped around other magnetite chains [50]. Previously, other chains were found in bacterial magnetite sources that are typically straight and continuous. In Mann’s analysis, sample preparation could have caused the discrepancies in the salmon chains [50]. Overall, the chain makeup contained between 13 and 45 magnetite crystals with modal length groups of 21 to 25 crystals and 35 to 40 crystals. The median of the chain groups fell within a range of 21 to 25 particles in length [50].

The chain arrangements and lengths are not as significant as the morphology of the crystals. As stated earlier, bacterial magnetite has always been highly associated with an amorphous iron layer that surrounds the crystallized material. In salmon, the magnetite is not associated with any amorphous material and in fact has no structural irregularities or edge dislocations [50]. All of the crystals studied were cubo-octahedral and had the $[111]$ face of the adjacent crystals perpendicular to the axis of the crystal chain. The average size of the crystals studied was 25 to 60 nm with a mean value of 48 nm. Elemental analysis showed iron as the only inorganic source in the crystals [50].

The ethmoid region of the adult salmon brain shows an intense magnetic moment. The intensity of the magnetization of the ethmoid tissue was 130 ± 75 pT while the ethmoid cartilage had an intensity of 281 ± 77 pT [52]. This high level of magnetization enables the salmon to translocate using earth’s geomagnetic field. The magnetite that is found in the salmon increased throughout the entire lifespan of the fish (fry, yearling, smolt, and adult) [52]. From theoretical calculations, it is believed that salmon in the fry stage of life are able to respond to magnetic changes. Salmon in the smolt stage of life have been shown to be able to detect small magnetic changes in a magnetic field and use this information as a magnetoreceptor [52]. The brain is not the only source of magnetic material for the salmon. Magnetic material, not characterized as magnetite, has been found in other tissues, of salmon such as eye, skin, and olfactory tissues, which do not function in magnetoreception [52].

3.3. Biological Production of Magnetite in the Human Brain

Magnetite has also been found in human brain tissues [30]. Kirschvink [52] exposed magnetite crystals in human cadaver brain tissue 12 to 24 hours post mortem. They found trace amounts of ferromagnetic material homogeneously throughout the meninges and entire brain, including all cerebral lobes, the cerebellum, basal ganglia, and the midbrain [30]. In the meninges, the magnetite crystal concentration was around 70 ng of magnetite per 1 g of tissue, while in brain tissue concentrations were approximately 4 ng of magnetite per 1 g of tissue. Dobson and Grassi [52] have also studied the distribution of magnetite in the brain, observing higher concentrations of 3.0 to 7.2 ng/g for human brain tissue and 54 to 109 ng/g for meninges tissue. The primary difference between the studies is that Dobson and Grassi’s were obtained from living samples and frozen in liquid nitrogen

immediately, while Kirschvink's samples were attained post mortem [53]. It seems possible that post mortem degradation or fragmentation from sample preparation of the overall crystal structures may explain the difference in particle concentration and size.

Cerebral magnetite crystals have an oddly prismatic morphology, unlike the more typical octahedral crystals found in geological samples. This bolsters the argument that magnetite formed in the brain is of biogenic origin [30]. The grain sizes of the magnetite are bimodal with a population of crystals between 10 to 70 nm in length, and another population between 90 and 200 nm in length [30]. Due to this large distribution of sizes, the crystals are not likely to be used as a magnetic field detector in humans [54]. Currently, a physiological use for these crystals is unknown. In the study of the human brain crystals, they are remarkably similar to other biogenic crystals of magnetite from other organisms in shape and morphological content [30].

An interesting aside is the fact that there does exist a difference between magnetite crystal bioproduction in human males and females. Male subjects have shown an increased concentration of neural magnetite crystals with age. The data trend has a slope of positive 1.48 for the increase of magnetite as the male ages. In fact, the data is significant at the 90% confidence interval [55].

3.4. Greigite Bioproducing Bacteria

3.4.1. Discovery of Bacterium

While the organisms mentioned above are able to mineralize magnetic particles of Fe_3O_4 , other bacterial organisms are able to biomineralize a different magnetic iron particle. Bacteria that reside in anaerobic environments are able to biologically produce crystals of greigite, Fe_3S_4 . This bacterium commonly resides in sulphidic rich, brackish water and river sediments [56].

3.4.2. Crystal Composition

Originally, Mann et al. [56] discovered these undesigned magnetotactic bacteria with a mixture of particles containing greigite (Fe_3S_4) and pyrite (FeS_2). The samples that were used were collected from marine environments with high sulphidic concentrations. Upon separation of the crystals, powder patterns returned d-spacings for pyrite from this magnetic material that was irregular in structure. This finding gives support to the fact that in these samples, greigite was a minor component. Greigite was certainly in the sample, though, because strong diffraction contrasts indicated a crystalline structure consistent with Fe_3S_4 [56].

3.4.3. Crystal Morphology and Distribution

Since this initial finding of greigite, more structurally pronounced crystals have been uncovered from bacterial specimens. From sulphidic environments, two different unclassified rod-shaped, single-cell, greigite-producing bacteria have been shown to synthesize highly regulated crystals of greigite. The first bacterial strain is able to produce highly organized chains of rectangular prismatic greigite, up to 57 crystals in length, with crystal dimensions of 69×50 nm. The second strain of bacteria is able to biomineralize chains

of 26 well-defined cubo-octahedral crystals with an average length of 67 nm. All particles analyzed contained only iron and sulfur with no oxygen atoms present [57].

Bazylinksi et al. [36] continued this research of greigite producers to find the environment that they inhabited. Researchers located magnetotactic greigite producing bacteria in the OATZ (Oxic-Anoxic Transition Zone) region and in the anoxic region below the OATZ that is completely sulfidic in nature. These organisms are logically found in this region because of their need of sulfur sources for the biogenic production of greigite. From the OATZ and anoxic regions, magnetotactic bacteria were uncovered that contained both greigite (Fe_3S_4) and magnetite (Fe_3O_4). The deeper into the OATZ region that the samples were produced, the more likely the crystals were to be solely greigite. Finally, once the anoxic region was reached, the bacteria contained only greigite crystals [36].

3.5. Silica Bioproduction

Biogenic silica, SiO_2 , has been found in a vast array of creatures in the plant kingdom. Stunning examples of these organisms include single celled diatoms (of the order *Bacillariophyceae*) [58]. These fascinating creatures can bioproduce an estimated 240 ± 40 teramoles of silicon per year in breathtaking arrays of siliceous structures resulting from the uptake and conversion of silicic acid present in dilute concentrations of the earth's oceans [61].

3.5.1. Diatoms

Diatoms, classified under genera *Nitzschia* or *Hantzschia*, are single-celled organisms that biogenically produce amorphous silica as structural elements of their cell wall, commonly referred to as a frustule [59]. Diatoms have two different cell structures, which give rise to different cell shapes. The pinnate diatoms are long and narrow with an axis that spans the length of the diatom and parallel to the plane of symmetry. The centric diatoms have radial symmetry around an axis that is located through the center of the cell lengthwise [60]. Figure 6 provides an example of a centric diatom.

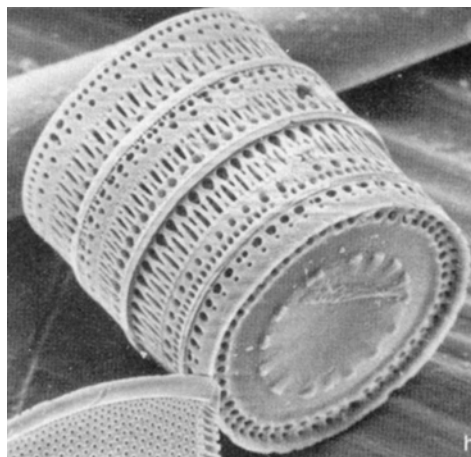


Figure 6. The diatom *P. sulcata*. Reprinted with permission from [59], F. E. Round et al., "The Diatoms: Biology and Morphology of the Genera," Cambridge Univ. Press, New York, 1990.

Recently, studies have begun to focus on the biochemical pathways that give rise to biogenic silica. The likely precursor of biogenic silica is silicic acid ($\text{Si}(\text{OH})_4$), which exists in concentrations of $70 \mu\text{M}$ throughout the world's oceans [61]. Transport proteins from the cell walls of the diatom *Cylindrotheca fusiformis* have been putatively identified as active silicic acid transporters [62]. To date, five different transporter proteins have been found. Active uptake of silicic acid is coupled with sodium ion transport [63, 64]. For frustule formation, the cell must have enough silicic acid for complete formation of the frustule. If there is not enough precursor, the frustule cannot be completely formed. Consequently, it is believed that uptake of silicic acid by the diatom is completed just before frustule formation is performed [62].

Diatom Cell Division The rigid and amorphous silica cell wall of the diatom causes cell formation to undergo different steps of morphogenesis, different than cells with a phospholipid bilayer cell wall. This specialized cell division actually causes the biodeposition of silica to form this unique diatom cell wall. The silica frustule forms a Petri dish like structure that encapsulates the interior of the cell and protects it from external forces. The top portion of the frustule is the epitheca, which overlaps the bottom portion known as the hypotheca. With cell division, each newly formed cell must develop a new portion of the frustule, either the epitheca or hypotheca. The new cells are able to retain the opposite theca from the original cell from which cell division began [60, 65, 66].

Once the cell begins the division process, a specialized valve is developed in association with each daughter cell. This valve, known as the silica deposition vesicle (SDV), is used for the biodeposition of silica to form the new frustule half. The SDV is used in exocytosis of the silica held within it to form a hypovalve on the exterior of the two daughter cells where the silica frustule is not located. This eventually is turned into the hypotheca of new cells [60, 65, 66].

With the hypovalve developed, the daughter cells separate from each other to form two new cells. The girdle bands, the overlapping bands of the Petri dish like structure, continue to develop fully into the frustule. During this point of division, each newly formed cell uses two SDVs to form the overlapping girdle bands, completing the cell division process [60, 65, 66]. Ironically, such a specialized cell division process eventually reaches a point of diminishing terms. Each resulting daughter cell is smaller than the original cell from which it was derived. Due to this mitotic division, the size distribution of the cell over time will become smaller. Eventually, when mitotic reproduction reaches a 30% to 40% reduction in cell size proportions, the diatoms will engage in sexual reproduction, leading to the return of the larger sized diatomic cells [67, 68].

Diatom Frustule Each species of diatom has a different silica frustulitic structure leading to an astounding variety of morphologies. Noll et al. [69] have studied the frustulitic morphological structure of the diatom *Coscinodiscus granii* using scanning electron microscopy (SEM), as seen in Figure 7, and atomic force microscopy (AFM). From these micrographs, the inner surface of the sample appeared smooth and featureless between the craters in the silica formation. The right side of the image has been disrupted

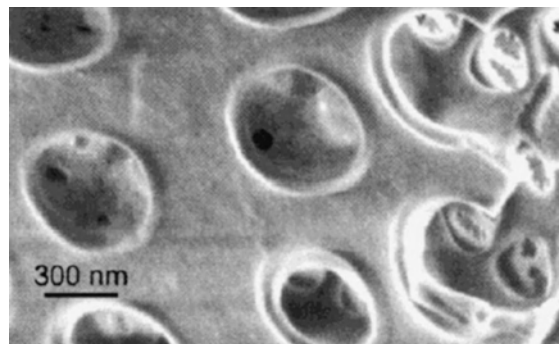


Figure 7. SEM micrograph of the valves from the diatom *C. granii*. The right side of the image has been disrupted by the purification process. Reprinted with permission from [69], F. Noll et al. *Nano Lett.* 2, 91 (2002). © 2002, American Chemical Society.

by the purification process. The diameter of the craters is approximately 400 nm [69].

The surface of the *C. granii* diatomic frustule took on new definition when it was analyzed using an AFM. While the gross morphologies of the frustule were similar in both AFM and SEM, more defined structures were revealed by AFM. Granular structures, on the order of tens of nanometers, were clearly observable between the craters as well as on the rim of the craters shown in Figure 8. The crater heights were measured to be on the order of 80 nm from the surface of

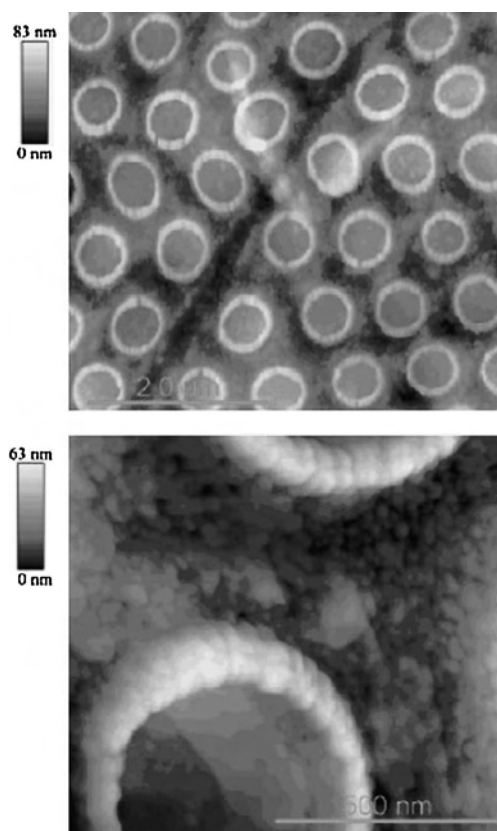


Figure 8. AFM image of the valves from the diatom *C. granii*. Reprinted with permission from [69], F. Noll et al., *Nano Lett.* 2, 91 (2002). © 2002, American Chemical Society.

the valve [69]. It is interesting to note that these individual spherule sizes were similar to those observed in experiments with the silica precipitating peptides, the silaffins.

3.5.2. Silica Precipitating Peptides

During frustule formation, silicic acid that has been transported to the SDV must be hydrolyzed to silica and deposited. In their pioneering study, Kröger et al. [70] demonstrated that diatoms have specific peptides associated with the biogenic synthesis of silica. Extracted from the frustule of *C. fusiformis*, the silaffin peptide was shown to mediate the direct precipitation of silica from silicic acid solutions [70]. Terminal amino acid sequencing indicated a high degree of homology between all of the silica precipitating peptides. The primary amino acid sequence was ultimately determined to be SSKKSGSYSGKSGSKRRIL with extensive post-translational modifications of the lysine residues by polyamines. Additionally, the application of more mild purification methods coupled with ^{31}P NMR studies revealed that the serines were post-translationally modified as phosphoserines. This interpretation was confirmed by mass spectrometry, which definitively demonstrated that all of the serines were in fact phosphoserines [71].

Post-translational modifications of the lysine and serine residues of the R5 peptide are of particular interest (Fig. 9). These modifications include phosphorylation of the serine residues and long chain polyamine derivatives of the lysine residues [70, 71]. Studies from different species have shown these modifications to be species-specific [70, 71]. The polyamines are highly associated with the frustule and have been shown to precipitate silica *in vitro* from solutions of silicic acid [72]. The process by which these polyamines generate silica remains unknown. A likely process would occur via interactions of the amine moieties with the silicic acid driving the hydrolysis of the precursor into the formation of silica. Kröger et al. have shown in comparisons between silaffin and the R5 peptide from *C. fusiformis* (with lysines not chemically modified) that there exists a significant difference in the pH profiles for silica deposition. While the nonmodified R5 peptide precipitated silica with a maximum activity at pH 7.0, silaffins have been shown to have optimal silica precipitation activity at pH 5.0 (Figure 10).

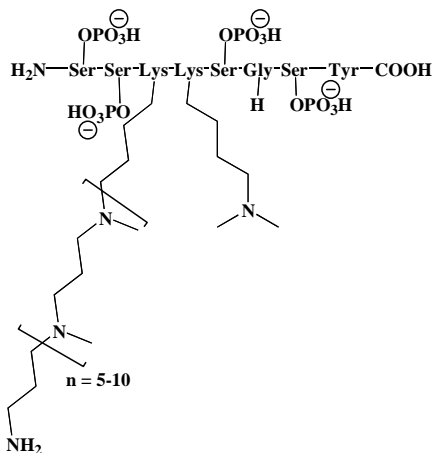


Figure 9. Silaffin with modified lysine residues.

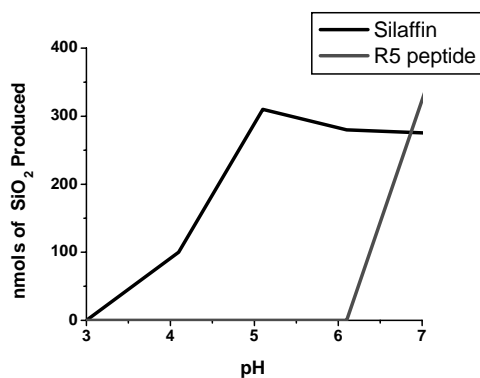


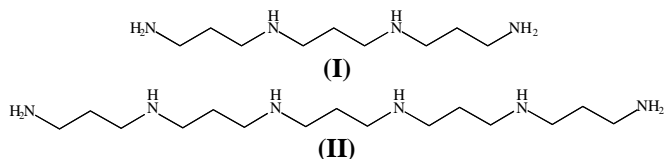
Figure 10. pH dependence of silaffin vs. R5 peptide.

This suggests that the polyamine modifications are important in the biologically relevant precipitation of silica [70]. Recently, it has been suggested that the phosphorylation of the serine residues allows for the formation of supramolecular peptide assemblies with locally high concentrations of polyamine moieties to drive silica formation [71].

3.5.3. Biogenic Silica Morphology

Biogenic silica from silaffins and the related R5 peptide is of interesting morphology. *In vitro* precipitated silica forms tiny nanospheres of amorphous silica that aggregate together to form larger particles with a size distribution of 500–700 nm [69, 71]. These nanospheres of amorphous silica are the building blocks of the cell wall frustule.

The morphology of silica precipitated from amine containing polymers has also been investigated. Noll et al. [69] studied the effects of using tripropylenetetramine (I) and pentapropylenehexamine (II) on silica precipitation. These polyamines partially mimicked the post-translational modifications made to the silaffin peptide lysine side chains. Upon addition of these linear chain polyamines to silicic acid solutions, precipitation of silica was immediate. Interestingly, the amorphous silica that was produced had similar aggregate spherical morphology to that produced by silaffins but yielded different sizes. The spheres produced by the polyamine (I or II) possessed a diameter of only 400 nm [69], which is smaller than those produced from silaffins. Poly-L-lysine has also been shown to be active in the precipitation of silica. The nucleophilic amine of each side chain showed similar precipitation activity to the nucleophilic lysine of the R5 peptide. The resultant silica had a particle size distribution of 40–600 nm with a majority of the particles between 200–400 nm [73]. This wide variation in particle size can be attributed to the statistical distribution of amine moieties within the polymer's composition.



4. BIOMINERALIZATION OF METAL SULFIDE NANOCCLUSERS (CdS, ZnS, AND Ag₂S)

The biomineralization of cadmium sulfide and zinc sulfide nanoparticles is well known in plants, certain fungi, yeasts, and sulfate reducing bacteria. As with many metal ions, Cd²⁺ and Zn²⁺ are toxic to these organisms at high levels [74]. In response to these metals, organisms have developed a variety of specific detoxification mechanisms: (1) alteration of membrane transport systems reducing entry of Cd²⁺ into cell, (2) intracellular or extracellular sequestration and precipitation, (3) an energy-dependent ion efflux process, and (4) enzymatic oxidation or reduction of metal ion to a less toxic form [75]. An example of CdS biomineralization utilized by plants and yeasts is a biotransformation mechanism consisting of a metal triggered biosynthetic pathway, metal ion sequestration by small selective peptides, and then coprecipitation with inorganic sulfide to form nontoxic metal sulfide clusters (Figure 11) [74]. A description of the mechanisms will be provided as well as examples of characterized metal sulfide clusters mineralized from different organisms.

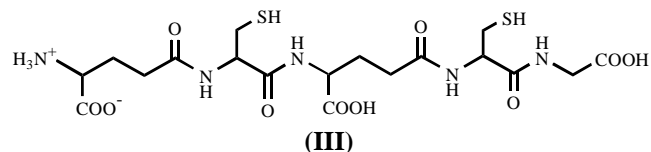
4.1. Metal Detoxification by Chelating Peptides

The main feature of metal detoxification (plants and yeast) is the incorporation of small thiol-rich peptides of the general form of (γ-Glu-Cys)_n-Gly called phytochelatins (PC_n), which can strongly bind Cd²⁺ or Zn²⁺ ions [74, 76–80]. Conversely, a minor function of these peptides is associated with maintaining the homeostasis of the organism by balancing its essential micronutrients [80]. The importance of the peptide, however, originates from the unique binding capacity utilized by the organism in controlling the metal toxicity. These sequences can contain anywhere from 2 to 11 repeating units, *n*, depending upon concentration, duration of metal exposure, and species [81]. Usually, organisms possess a heterogeneous mixture of peptides of various lengths [82]. This peptide has been identified in a number of biological systems such as *Silene cucubalus* [76], *Pisum sativum* L. [81], *Schizosaccharomyces pombe* [74, 77], *Candida glabrata* [77], and in all plants.

The utility of the phytochelatin peptides results only after a metal induced trigger mechanism of a specific biosynthetic pathway is initiated. Exposure of Cd²⁺ ions induces cellular synthase of an enzyme of γ-glutamylcysteine dipeptidyl transpeptidase, termed phytochelatin synthase [82]. It was

observed that Cd²⁺ is the strongest inducer of this pathway requiring only low concentrations to trigger the enzyme, whereas Cu²⁺, Zn²⁺, Pb²⁺, and Ni²⁺ are less effective and must be present at higher external levels for induction [84]. Binding of Cd²⁺ into a metal recognition domain induces a conformational shift of the protein to assemble the active site. The activated enzyme catalyzes the transpeptidation of γ-glutamylcysteine moieties of GSH onto another GSH molecule of the growing phytochelatin peptide [78]. This catalyzed reaction terminates when the newly synthesized phytochelatin peptide reaches an intracellular concentration such that free phytochelatin removes Cd²⁺ bound to PCs.

After synthesis of the peptide template, the available metal ions coordinate to the peptide, forming a metal-phytochelatin complex in accordance with an S₄ coordination environment [79]. Johanning and Strasdeit [79] studied the dynamic nature of this complex in terms of thermodynamic stability and its subsequent equilibria by implementing a model system of Cd²⁺/(PC₂) to ascertain its biological significance. PC₂, (III), was chosen since it represents the simplest phytochelatin and a pentabasic acid [79]. Two categories of complexes were observed: complexes with the same number of ligands and Cd²⁺ ions (log *K*^{Cd} = 9.9–13.3) and those with more ligands than metal ions (log *K*^{Cd} = 16.3–19.3) [79]. They reported at a plant physiological pH of 7.3, typical of the pH in the cytoplasm of higher plants, the complex of [Cd₂(H₂L)(HL)₂]⁷⁻ predominates [79]. Additionally at this pH, at least 0.5% of the cadmium was uncomplexed and in the free +2 ionic state indicating that these complexes are by no means extremely stable [79]. Meanwhile, at a pH of 5.4 in the vacuoles of higher plants, the Cd²⁺/(PC₂) system liberates 62% of the cadmium [79]. Thus at a basic pH, Cd²⁺ is chelated by the peptide, but in the acidic environment of the vacuole, the complexes entirely dissociate to cadmium. This is reminiscent of a storage/transport mechanism, such that the peptide temporarily binds and stores the Cd²⁺ metal ions in the plant cytosol until transported into the vacuole whereby the complexes dissociate and the peptide releases unbound Cd²⁺ [79]. It is suggested that this complex dissociation also allows the plant to recover the phytochelatin peptides [79].



An additional component of the metal-phytochelatin complex is the integration of acid labile sulfide into the resultant nanocluster. Reactive sulfide ions are believed to originate via one of two biochemical pathways—either from a cadmium-induced mechanism that leads to cellular sulfide generation (source of sulfide is unknown) or as a consequence of the functionality of sulfate reducing bacteria. It is known, however, that the generated S²⁻ ions and H₂S readily react with the Cd²⁺/(PC_n) complex to form insoluble CdS particles coated with the phytochelatin peptides. The sulfide content of the cell invariably increases the binding capacity of the peptide, controls the size of crystallites, and also can

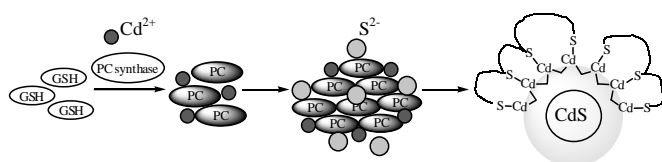


Figure 11. Biotransformation mechanism to CdS involving phytochelatin synthesis, formation of metal-phytochelation complex, incorporation of labile sulfide, and mineralization of CdS with a surface coat representative of PC₃ and PC₄ peptides.

vary the composition of the peptide coat. The binding capacity was shown to increase for PC₂ from 0.5 mole equivalents of Cd²⁺ in the absence of sulfide to 5 mole equivalents of Cd²⁺ per peptide when the sulfide level was increased [85].

4.2. Biosynthesis of CdS Crystallites by Plants and Yeasts

As recently as 1989, CdS crystallites produced in yeasts were discovered by Dameron and Winge [86]. The importance of the discovery established a method of preparing small monodisperse CdS clusters that offer unique semiconductor properties (high discrete excited electronic states and optimal quantum yields) and are stable against Ostwald ripening and oxidation as compared to synthetic crystals [87]. For example, the yeasts *Schizosaccharomyces pombe* and *Candida glabrata* produced intracellular 1.8 nm and 2.0 nm CdS clusters respectively, with approximately 85 CdS units encapsulated with 30 PC₂ peptides [86]. The presence of a peptide coat was a significant observation in the biological formation of CdS, as it protected and passivated the surface. Also extracellular production of 2.9 ± 0.5 nm sized CdS crystallites yielded clusters of undefined stability [86].

Williams et al. studied the batch cultivation of CdS by *Schizosaccharomyces pombe* during different growth phases for optimal crystallite production. They reported that during early-exponential growth, cellular metabolism is affected and there is an increased efflux of Cd²⁺ ions from the cell, resulting in minimal formation of CdS. The addition of cadmium during the mid-exponential growth phase produced a maximal amount of CdS. Williams et al. concluded that the timing of cultivation harvest and the saturation factor of the biomass are critical for batch production, but production would also be feasible with a fed-batch culture of increased biomass cells [88].

4.2.1. Extracellular Enzymatic Formation of CdS

In a separate study, exposure of aqueous Cd²⁺ and SO₄²⁻ to the fungus *Fusarium oxysporum* (see Section 1.2) resulted in the first reported case of extracellular fungal synthesis of CdS by a purely enzymatic process [89]. The active mechanism operating in the CdS crystallization was the extracellular secretion of sulfate reductase enzymes, which slowly reduced the sulfate over 12 days and formed CdS nanoclusters 5–20 nm in size [89]. Analysis of the fungal mediated synthesis by UV-vis and polyacrylamide gel electrophoresis (PAGE) confirmed the presence of proteinaceous material consisting of the active enzyme and auxiliary proteins (PAGE indicated 4 protein bands) [89]. These auxiliary proteins possibly afforded a degree of stability to the CdS nanoparticles by binding to the cluster surface and preventing aggregation of the colloidal solution [89].

Anaerobic sulfate reducing bacteria presents another enzymatic source of labile sulfide, which has been recognized for years and implicated in the biomineralization of CdS particles. Examples include *Klebsiella aerogenes* [90] and *Clostridium thermoaceticum* [91] type bacteria. *Klebsiella aerogenes* grown in the presence of Cd²⁺ was documented to mineralize extracellular CdS crystallites (20–200 nm) on

the cell surface with a total cellular content of labile sulfide and cadmium between 0.5–2.0 molar ratio of Cd:S [90]. For *Clostridium thermoaceticum*, CdS synthesis was energy dependent and driven by the ability of a cysteine desulfhydrase enzyme to catalyze the release of H₂S from cysteine [91]. In order for CdS precipitation to occur, an essential source of cysteine and Cd²⁺ was required. In cultures containing Cd²⁺, it was observed that the total sulfide increased fourfold and twofold with respect to the amount of extracted protein [91].

4.2.2. Biomimetic Approaches to Encapsulated CdS Clusters

As expected, it is not surprising that different species process and synthesize CdS crystallites to differing degrees and sizes over a range of conditions. The composition of the CdS peptide coat is therefore also likely to be modified. Barbas et al. [91] and Dameron et al. [92] studied the surface coat of *Candida glabrata* derived CdS clusters under different growth and nutrient conditions. They reported a time/sulfide content dependent conversion of an entirely glutathione-coated cluster to a phytochelatin coated surface [91]. The preference of higher order and more elongated phytochelatin peptides offering a multidentate binding mode to the surface are undoubtedly more stable [91]. When cultured in rich nutrients, the CdS particles had a heterogeneous surface composition of both glutathione and γ -glutamylcysteine. In synthetic minimal medium, clusters formed with only polymerized γ -glutamylcysteine peptides as the coating surface [92].

The phytochelatin driven biomineralization of CdS *in vivo* has directed the progression towards new biomimetic approaches. These involve mimicking the phytochelatin peptide template with synthetic analogues. The native CdS crystallites isolated from *Candida glabrata* were systematically compared with clusters formed *in vitro* with synthetic phytochelatin peptides ($n = 2-4$) and a metallothionein hexapeptide [82]. Results indicated that the synthetically produced CdS crystals (coated with phytochelatin peptides or metallothioneins) exhibited a red-shifted electronic transition to 318 nm in the UV-Visible absorption spectrum analogous to the properties of the native CdS formed *in vivo* [82].

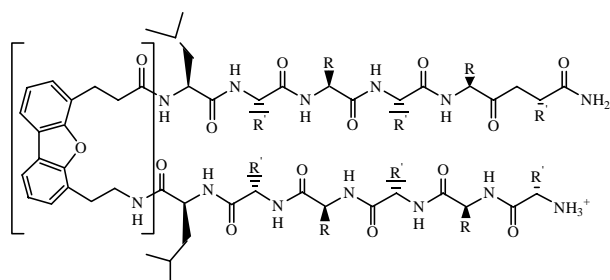
Spreitzer et al. [93] and Whitling et al. [94] have recently developed a spatially addressable combinatorial library based on an n₃ phytochelatin skeleton structure, X-Cys-Y-Cys-Z-Cys-Gly, to investigate the stabilization of CdS nanoclusters. Five possible natural and non-natural amino acids of α -Glu, γ -Glu, γ -aminobutyric acid (GABA), SerGly, and ϵ -aminohexanoic acid (ϵ -Ahx) were permuted over the X, Y, and Z spacer positions, thus generating a library consisting of 125 peptidomimetic ligands [94]. Results from screening the library showed peptides that stabilized discrete populations of CdS clusters ranging from 1.9 to 2.6 nm in diameter [93]. Spreitzer et al. [93] attributed the difference in sizes to the number of spacer bonds between cysteine residues.

Bae and Mehra [95] synthesized CdS-(GSH) clusters under laboratory conditions to yield a homogeneous GSH surface. They reported size distributions of CdS-(GSH)

ranging from 2.14 nm to 4.06 nm upon varying the $\text{Cd}^{2+}/\text{GSH}$ ratio and the $\text{S}^{2-}/\text{Cd}^{2+}$ molar ratio [95]. In contrast, the phytochelatin-stabilized CdS clusters at various sulfide/ Cd^{2+} ratios resulted in a uniform crystallite distribution with similar optical properties. The optical properties of CdS-(GSH) were highly affected by the GSH content, whereby the largest sized particles formed at the highest sulfide concentration generated the least GSH capping material and showed a reduced fluorescence (λ_{max} emission = 490 nm) [95]. The extreme case representing clusters with the highest GSH content also exhibited low fluorescence [95]. Additionally, the CdS-(GSH) clusters were shown to reduce methylviologen accounting for its semiconductor properties.

In a parallel experiment, Mehra and coworkers [81], examined the stability of surface bound glutathione ligands around the CdS core. They effectively demonstrated that the titration of phytochelatin peptides with CdS-(GSH) nanoclusters led to a complete ligand exchange on the CdS surface with the phytochelatin peptides and no apparent change in cluster size [82]. This exchange reaction was monitored and detected by following the emission at 480 nm, fractionated on a Sephadex G-25 column, and then analyzed by a cyclic assay [82]. The displacement of GSH conclusively established the higher affinity of CdS for phytochelatin peptides.

Aside from peptide template controlled CdS synthesis, a divergent biomimetic approach is involved in the implementation of an organic matrix mediated process to CdS biosynthesis. Nayar et al. [96] exploited the quaternary structure of bovine serum albumin for its role in CdS mineralization. The applicability of bovine serum albumin resulted from the 35 available cysteine moieties for binding Cd^{2+} and a spherical protein cage with a 5–10 nm cavity suited for crystal growth [96]. According to the SEM image, particles of CdS precipitated out in the appearance of a branched star structure and were arranged in a helical manner along each branch indicative of a denatured protein structure [96]. The CdS crystal sizes were representative of the protein structure and confined to the dimensions of the cavity (5–10 nm CdS clusters).



(IV)

Similarly, a peptidomimetic matrix (IV) above was designed to nucleate CdS clusters along the $\{01.0\}$ crystal face by Bekele et al. [97]. The ligand was chosen because of its propensity to nucleate β -hairpin folding (bracketed structure) and inclination to self-assemble into β -sheet monolayers [97]. The resultant peptidomimetic two-dimensional monolayer effectively nucleated the crystal growth of CdS

(2.5–5.0 nm in width and length) in a wurtzite lattice structure oriented roughly in the same direction on the monolayer [97]. The driving force for the site specific nucleation was predominantly a consequence of the monolayer organization and the $\{01.0\}$ CdS crystal plane [97]. In the $\langle 001 \rangle$ direction of CdS, the Cd-Cd distance was 6.72 Å, which correlated with the atom separation distance of glutamic acid $\text{C}_\alpha\text{-C}_\alpha$ of 6.9 Å within a single β -strand [97].

4.3. ZnS Biomineralization and Biomimetic Design

Biogenic ZnS nanoparticles are analogous to CdS particles with respect to the crystal lattice structures that they can accommodate (wurtzite and zinc blend), photo-physical properties, semiconductor properties, bioprocessing/mineralization mechanism, and, to a lesser extent, their binding behaviors and affinities. For these reasons, the examples of biomineralized ZnS crystallites are limited in contrast to CdS produced clusters. However, the biological production of ZnS crystals are by no means less important. The following examples will be focused on biomimetic techniques and unique aspects to the stabilization and control of ZnS particles.

Mehra and colleagues studied a collection of metal-chelating bioligands of cysteine [98, 99], glutathione [100, 101], and histidine [102] in the formation of ZnS crystals. All of the ZnS nanoclusters were synthesized under a variety of conditions based on a modified colloidal synthetic procedure that mimicked the *in vivo* biomineralization of eukaryotic organisms. Essentially, the strategy involved preforming a $\text{Zn}(\text{ligand})_n$ complex and then subsequently reacting the complex with inorganic sulfide [98]. The presence of inorganic sulfide along with the stabilizing ligand prompted a competition for metal binding, thus promoting ligand displacement and cluster formation entirely controlled and tailored by the amounts of reactants added and various binding affinities of ligands/ S^{2-} for Zn^{2+} [98–102]. For example, the dissociation constant of a zinc-cysteine complex is 1.5×10^{-18} and the K_d for ZnS is 1.1×10^{-24} confirming the preference to form ZnS [99].

According to this bio-inspired synthesis, cysteine capped ZnS nanoclusters were successfully produced on a gram quantity scale [99]. The isolated ZnS clusters exhibited many highly desired characteristics such as a large shelf life (stable for more than 30 months as a powder and against Ostwald ripening), an average particle size of around 6.08 ± 0.76 nm determined from TEM, photocatalytic activity with *p*-nitrophenol, enhanced optical properties (absorbance $\lambda_{\text{max}} = 257\text{--}277$ nm), and cost effectiveness [99].

The analogue to cysteine is the cysteine containing tripeptide of glutathione, already reported for the stabilization of CdS nanocrystals. The biosynthesis of ZnS-(GSH) crystals was carried out by the above procedure and characterized by a cluster size of 3.45 ± 0.5 nm (TEM) [100]. Absorbance maxima ranging from $\sim 250\text{--}290$ nm were reported for ZnS-(GSH) clusters synthesized from ratios of sulfide varying from 0.25 to 5.0 [95, 98]. In comparison to ZnS-(Cys),

the glutathione stabilized clusters were more disperse in size possibly as a result of the higher stability of the Zn^{2+} -Cys complex [98].

The use of histidine as a capping agent yielded hexagonal ZnS(His) clusters (average size 4.2 nm from TEM) stabilized through surface coordination of the imidazole moiety [102]. Characterization of the resultant clusters by UV-visible spectroscopy revealed a dual peak absorption at ~ 260 nm and ~ 290 nm indicative of two ZnS populations. A significant enhancement in the fluorescence of the histidine encapsulated clusters by tenfold was achieved relative to the ZnS-(Cys) clusters, likely due to the charge delocalization within the imidazole ring [102]. It was suggested that histidine may serve as a more efficient ligand than cysteine or glutathione in surface passivation by preventing deep trap surface states from nonradiative recombination [102].

4.4. Biosynthesis of Ag_2S Particles

The previously described bacterial strain of *Pseudomonas stutzeri* was documented to produce intracellular zero-valent silver nanoclusters, but also was capable of biogenically producing complementary silver sulfide particles [2, 4]. The extent of silver sulfide precipitation by the bacterial cell varied between reported examples, but Klaus et al. suggested that the difference in results was due to the experimental conditions [2].

Brelle et al. [103] have used the ligands of cysteine and glutathione once again in the biomimetic synthesis of silver sulfide particles. For both glutathione and cysteine capped Ag_2S clusters, the average particle diameter was determined to be around 9 nm (TEM) [103]. Also, it was observed that Ag_2S showed a lack of strong absorption, characteristic of an indirect band gap semiconductor [103].

4.5. Bacterial Biofilms

Bacterial biofilms exist naturally as distinct communities of bacteria located near the vicinity of mineral deposits. The formation of biofilms proceed through several stages: attachment of individual bacterial cells to (abiotic or biotic) surfaces, colonization of bacteria, quorum sensing, and growth of a mature biofilm [104]. Quorum sensing allows bacterial cells to participate in cell-cell communication, which synchronizes the activities of the organized biofilm community [104]. The classification of biofilms and their relationship to metals are sparsely reported in the literature. An excellent example of a biofilm mediated mineralization process was demonstrated in the prefossilization of *Platanus* and *Taxodium* leaves by ferrihydrite [105]. It was discovered that terrestrial leaf fossils originate from leaves coated with an iron oxide surface; however, the leaves are covered by a hydrophobic waxy cuticle, which is impervious to metal binding [105]. In aquatic environments, leaves are quickly colonized by iron oxidizing bacteria (*Pseudomonas* sp. and other gram negative rods) that form biofilms featuring an anionic surface amenable to metal binding [105]. It was claimed that as much as 10^7 colony forming units per square centimeter of leaf can inhabit a single leaf [105]. Upon exposure of the biofilm coated leaf to FeCl_3 , within a period of 10–15 minutes the leaf became encrusted with Fe_2O_3 [105]. This

encrustation by iron oxide accelerated the conversion from mineralized leaves to completely fossilized fauna buried in the sediment over time [105].

Another type of bacterial biofilm mass was identified near acid mine drainage sites at Iron Mountain in northern California [106]. The biofilm was classified as a new species of Archaea, representing a prokaryote population of *Ferroplasma acidarmanus* anchored within pyritic sediments forming dense slime streamers [106]. Uniquely, this Archaeon was observed to grow under harsh conditions of pH 0.5 and 40°C as a result of the composition and structural construction of the cytoplasmic membrane [106]. The extremely low pH, although not particularly suited for microbial growth, supported high metal concentrations in solution (iron has been measured as high as 111 g/L) [106]. The nucleation and characterization of mineral deposits originating from the archaeon biofilm were not reported.

Natural biofilms are also associated with the sulfate-reducing bacteria family of *Desulfobacteriaceae* [107]. Labrenz et al. [105] have shown that these biofilms can preferentially mineralize ZnS spherical particles of 2–5 nm with micrometer sized aggregates (SEM) based on a sphalerite lattice structure in more ambient conditions (pH 7.2–8.6). The mineralization of ZnS occurs under moderately reducing conditions accompanied by the accumulation of sulfide generated by the biofilm mass. Additionally, it was apparent that the biofilms concentrated zinc by 10^6 times that of groundwater [107].

4.6. Summary

This collection of organisms best exemplifies the biomineralization of zero-valent metal, metal oxides, and metal sulfide nanoclusters. These bioproduced nanocrystals exhibit superior quality (i.e., 24 carat gold), morphology, crystallinity, and monodispersity to synthetic laboratory-grown clusters as a result of highly orchestrated detoxification mechanisms. The uses of such organisms to biomimetically control the nucleation of nanoclusters under laboratory conditions was successful with a number of biological systems. For instance, the fungus *Fusarium oxysporum* generated Au^0 and CdS nanocrystals extracellularly in good yields. Inspired by these systems, a variety of innovations and approaches toward nanocluster synthesis has evolved, such as the implementation of different nucleating domains ranging in complexity from peptides to proteins to polymers. These biomolecules have added a degree of control to the subsequent nanocluster growth along with providing a stabilization component to the nanocluster surface. For example, CdS crystal-lites were synthesized with the capping ligands of cysteine, glutathione, and phytochelatin peptides. Additionally, such biomolecules will play an important role in alternative fabrication methods involving the surface derivatization of nanoclusters with antibodies, antigens, or viruses.

GLOSSARY

Bacterioform gold Gold particles originating via microbial processes.

Diatoms Unicellular marine plant life able to biomineralize a rigid silica frustule.

Ethmoid region Area of the salmon brain responsible for magnetic field sensing.

Magnetotaxis Movement of organisms based upon responses to earth's geomagnetic field.

Oxic anoxic transition zone (OATZ) Sediment level of fresh water sources in which the transition from the aerobic region to anaerobic region occurs.

Phytochelatins Class of small metal-binding peptides (γ EC)_nG found in yeast, fungi, and all plants.

Silver resistant plasmids Small circular DNA molecules that possess genes encoding resistance to silver.

ACKNOWLEDGMENTS

Funding was provided by an NSF CAREER Award (CHE-0093829). J.S. and M.K. thank the Vanderbilt Institute of Nanoscale Science and Engineering for support. Also, we graciously thank Lisa Pasierb for her assistance in proof-reading the manuscript.

REFERENCES

- R. R. Brooks, Ed., "Noble Metals and Biological Systems," CRC Press, Ann Arbor, MI, 1992.
- T. Klaus, R. Joerger, E. Olsson, and C.-G. Granqvist, *Proc. Natl. Acad. Sci.* 96, 13611 (1999).
- C. Haefeli, C. Franklin, and K. Hardy, *J. Bacteriol.* 158, 389 (1984).
- R. M. Slawson, J. T. Trevors, and H. Lee, *Arch. Microbiol.* 158, 398 (1992).
- S. Mann, *Nature* 357, 358 (1992).
- M. E. Starodub and J. T. Trevors, *J. Med. Microbiol.* 29, 101 (1989).
- X.-Z. Li, H. Nikaido, and K. E. Williams, *J. Bacteriol.* 179, 6127 (1997).
- A. T. Hendry and I. O. Stewart, *Can. J. Microbiol.* 25, 915 (1979).
- P. A. Goddard and A. T. Bull, *Appl. Microbiol. Biotechnol.* 31, 308 (1989).
- P. A. Goddard and A. T. Bull, *Appl. Microbiol. Biotechnol.* 31, 314 (1989).
- J. T. Trevors, *Enzyme Microb. Technol.* 9, 331 (1987).
- M. Sarikaya, *Proc. Natl. Acad. Sci.* 96, 14183 (1999).
- R. Joerger, T. Klaus, and C.-G. Granqvist, *Adv. Mater.* 12, 407 (2000).
- B. Nair and T. Pradeep, *Crystal Growth & Design* 2, 293 (2002).
- P. Mukherjee, A. Ahmad, D. Mandal, S. Senapati, S. Sainkar, M. I. Khan, R. Parishcha, P. V. Ajaykumar, M. Alam, R. Kumar, and M. Sastry, *Nano Lett.* 1, 515 (2001).
- T. J. Beveridge and R. G. E. Murray, *J. Bacteriol.* 141, 876 (1980).
- P. Mukherjee, A. Ahmad, D. Mandal, S. Senapati, S. R. Sainkar, M. I. Khan, R. Ramani, R. Parishcha, P. V. Ajaykumar, M. Alam, M. Sastry, and R. Kumar, *Angew. Chem., Int. Ed. Engl.* 40, 3585 (2001).
- J. L. Gardea-Torresdey, K. J. Tiemann, G. Gamez, K. Dokken, I. Cano-Aguilera, L. R. Furenlid, and M. W. Renner, *Environ. Sci. Technol.* 34, 4392 (2000).
- J. L. Gardea-Torresdey, J. G. Parsons, E. Gomez, J. Peralta-Videa, H. E. Troiani, P. Santiago, and M. Jose-Yacamán, *Nano Lett.* 2, 397 (2002).
- J. L. Gardea-Torresdey, K. J. Tiemann, G. Gamez, K. Dokken, S. Tehuacanero, and M. Jose-Yacamán, *J. Nanopart. Res.* 1, 397 (1999).
- J. R. Watterson, *Geology* 20, 315 (1991).
- P. Mukherjee, S. Senapati, D. Mandal, A. Ahmad, M. I. Khan, R. Kumar, and M. Sastry, *Chem. Bio. Chem.* 5, 461 (2002).
- C. W. N. Anderson, R. R. Brooks, R. B. Stewart, and R. Simcock, *Nature* 395, 553 (1998).
- R. Blakemore, *Science* 190, 377 (1975).
- F. F. Torres de Araujo, M. A. Pires, R. B. Frankel, and C. E. M. Bicudo, *Biophys. J.* 50, 375 (1986).
- B. A. Maher, *Proc. R. Soc. London, Ser. B* 265, 733 (1998).
- H. A. Lowenstam, *Science* 211, 1126 (1981).
- S. Mann, N. H. C. Sparks, M. M. Walker, and J. L. Kirschvink, *J. Exp. Biol.* 140, 35 (1998).
- R. Wiltshcko and W. Wiltshcko, "Magnetic Orientation in Animals," Springer, New York, 1995.
- J. L. Kirschvink, A. Kobayashi-Kirschvink, and B. J. Woodford, *Proc. Natl. Acad. Sci.* 89, 7683 (1992).
- R. P. Blakemore, N. A. Blakemore, D. A. Bazylinski, and T. T. Moench, *Magnetotactic Bacteria*, 3, 1882 (1989).
- K. H. Schleifer, D. Schüller, S. Spring, M. Weizenegger, R. Amann, W. Ludwig, and M. Kohler, *Syst. Appl. Microbiol.* 14, 379 (1991).
- T. Matsunaga, T. Sakaguchi, and F. Tadokora, *Appl. Microbiol. Biotechnol.* 35, 651 (1991).
- R. P. Blakemore, D. Maratea, and R. S. Wolfe, *J. Bacteriol.*, 140, 720 (1979).
- T. Matsunaga, F. Tadokoro, and N. Nakamura, *IEEE Trans. Magn.* 26, 1557 (1990).
- D. A. Bazylinski, R. B. Frankel, B. R. Heywood, S. Mann, J. W. King, P. L. Donaghay, and A. K. Hanson, *Appl. Environ. Microbiol.* 61, 3232 (1995).
- D. Schüller and E. Baeuerlein, *J. Bacteriol.* 180, 159 (1998).
- Y. A. Gorby, T. J. Beveridge, and R. P. Blakemore, *J. Bacteriol.* 170, 834 (1988).
- A. M. Spormann and R. S. Wolfe, *FEBS Microbiol. Lett.* 22, 171 (1984).
- T. Matsuda, J. Endo, N. Osakabe, A. Tonomura, and T. Arii, *Nature* 302, 411 (1983).
- A. S. Bahaj, P. A. B. James, and I. W. Croudace, *IEEE Trans. Magn.* 30, 4707 (1994).
- T. Matsunaga and H. Takeyama, *Supramolec. Sci.* 5, 391 (1998).
- T. Matsunaga, C. Nakamura, J. G. Burgess, and K. J. Sode, *J. Bacteriol.* 174, 2748 (1992).
- D. L. Balkwill, S. Maratea, and R. P. Blakemore, *J. Bacteriol.* 141, 1399 (1980).
- Y. Okudu, K. Denda, and Y. Fukumori, *Gene* 171, 99 (1996).
- D. A. Bazylinski, R. B. Frankel, and H. W. Jannash, *Nature* 334, 518 (1988).
- S. Mann, R. B. Frankel, and R. P. Blakemore, *Nature* 310, 405 (1984).
- F. E. Round, R. M. Crawford, and D. G. Mann, in "Magnetite Biomineralization and Magnetoreception in Organisms," S. Mann, Ed., Plenum Press, New York, 1985.
- R. Wiltshcko and W. Wiltshcko, "Magnetic Orientation in Animals," Springer, New York, 1995.
- S. Mann, N. H. C. Sparks, M. W. Walker, and J. L. Kirschvink, *J. Exp. Biol.* 140, 35 (1988).
- M. W. Walker, T. P. Quinn, J. L. Kirschvink, and C. Groot, *J. Exp. Biol.* 140, 51 (1988).
- J. L. Kirschvink, *Bioelectromagnets* 17, 187 (1996).
- J. Dobson and P. Grassi, *Brain. Res. Bull.* 39, 255 (1996).
- J. R. Dunn, M. Fuller, J. Zoeger, J. Dobson, F. Heller, J. Hammann, E. Caine, and B. M. Moskowitz, *Brain Res. Bull.* 36, 149 (1995).
- J. Dobson, *Experimental Brain Research* online (2002).
- S. Mann, N. H. C. Sparks, R. B. Frankel, D. A. Bazylinski, and H. W. Jannasch, *Nature* 343, 258 (1990).
- B. R. Heywood, D. A. Bazylinski, A. Garratt-Reed, S. Mann, and R. B. Frankel, *Naturwissenschaften* 77, 536 (1990).
- T. L. Simpson and B. E. Volcani, "Silicon and Siliceous Structures in Biological Systems," Springer, New York, 1981.

59. F. E. Round, R. M. Crawford, and D. G. Mann, "The Diatoms: Biology and Morphology of the Genera," Cambridge Univ. Press, New York, 1990.
60. N. Kröger and M. Sumper, in "Biomineralization: From Biology to Biotechnology and Medical Applications," E. Baeuerlein, Ed., Wiley-VCH, Weinheim, 2000.
61. P. Tréguer, D. M. Nelson, A. J. Van Bennekom, D. J. DeMaster, A. Leynaert, and B. Quéguiner, *Science* 268, 375 (1995).
62. M. Hildebrand, K. Dahlin, and B. E. Volcani, *Mol. Gen. Genet.* 260, 480 (1998).
63. C. W. Sullivan, *J. Phycol.* 12, 390 (1976).
64. P. Bhattacharyya and B. E. Volcani, *Proc. Natl. Acad. Sci. USA*, 77, 6386 (1980).
65. C. Zurzolo and C. Bowler, *Plant Physiol.* 127, 1339 (2001).
66. J. Pickett-Heaps, A. M. M. Schmid, and L. A. Edgar, "The Cell Biology of Diatom Valve Formation," Biopress, Bristol, U.K., 1990.
67. D. G. Mann, *Hydrobiologia*, 269/270, 11 (1993).
68. C. Van Den Hoak, D. G. Mann, H. M. Johns, "Algae: An Introduction to Phycology," Cambridge Univ. Press, New York, 1997.
69. F. Noll, M. Sumper, and N. Hampp, *Nano Letters* 2, 91 (2002).
70. N. Kröger, R. Deutzmann, and M. Sumper, *Science* 286, 1129 (1999).
71. N. Kröger, S. Lorenz, E. Brunner, and M. Sumper, *Science* 298, 584 (2002).
72. N. Kröger, R. Deutzmann, C. Bergsdor, and M. Sumper, *Prod. Natl. Acad. Sci.* 97, 14133 (2000).
73. S. V. Patwardhan, N. Mukherjee, and S. J. Clarson, *J. Inorgan. & Organomet. Polymers* 11, 193 (2002).
74. P. Perego and S. B. Howell, *Toxicol. Appl. Pharmacol.* 147, 312 (1997).
75. D. P. Cunningham and L. L. Lundie, Jr., *Appl. Environ. Microbiol.* 59, 7 (1993).
76. M. Friederich, R. Kneer, and M. H. Zenk, *Phytochemistry* 49, 2323 (1998).
77. A. Al-Lahham, V. Rohde, P. Heim, R. Leuchter, J. Veeck, C. Wunderlich, K. Wolf, and M. Zimmermann, *Yeast* 15, 385 (1999).
78. S. Klapheck, S. Schlunz, and L. Bergmann, *Plant Physiol.* 107, 515 (1995).
79. J. Johanning and H. Strasdeit, *Angew. Chem., Int. Ed. Engl.* 37, 2464 (1998).
80. R. Kneer and M. H. Zenk, *Phytochemistry* 31, 2663 (1992).
81. S. Klapheck, W. Fliegner, and I. Zimmer, *Plant Physiol.* 104, 1325 (1994).
82. C. T. Dameron and D. R. Winge, *Inorg. Chem.* 29, 1343 (1990).
83. R. K. Mehra and D. R. Winge, *J. Cell. Biochem.* 45, 30 (1991).
84. E. Grill, S. Löffler, E.-L. Einnacker, and M. H. Zenk, *Proc. Natl. Acad. Sci. USA* 84, 439 (1987).
85. R. K. Mehra, E. B. Tarbet, W. R. Gray, and D. R. Winge, *Proc. Natl. Acad. Sci. USA* 85, 8815 (1988).
86. C. T. Dameron and D. R. Winge, *Nature* 338, 596 (1989).
87. P. Williams, E. Keshavarz-Moore, and P. Dunhill, *Enzyme Microb. Technol.* 19, 208 (1996).
88. P. Williams, E. Keshavarz-Moore, and P. Dunhill, *J. Biotechnol.* 48, 259 (1996).
89. A. Ahmad, P. Mukherjee, D. Mandal, S. Satyajyoti, M. I. Khan, R. Kumar, and M. Sastry, *J. Am. Chem. Soc.* 124, 12108 (2002).
90. J. D. Holmes, P. Smith, R. Evans-Gowing, D. J. Richardson, D. A. Russell, and J. R. Sodeau, *Arch. Microbiol.* 163, 143 (1995).
91. J. Barbas, V. Santhanagopalan, M. Blaszczynski, W. R. Ellis Jr., and D. R. Winge, *J. Inorg. Biochem.* 48, 95 (1992).
92. C. T. Dameron, B. R. Smith, and D. R. Winge, *J. Biol. Chem.* 264, 17355 (1989).
93. G. Spreitzer, J. M. Whiting, J. D. Madura, and D. W. Wright, *Chem. Commun.* 209 (2000).
94. J. M. Whiting, G. Spreitzer, and D. W. Wright, *Adv. Mater.* 12, 1377 (2000).
95. W. Bae and R. K. Mehra, *J. Inorg. Biochem.* 69, 33 (1998).
96. S. Nayar, A. Sinha, S. Das, S. K. Das, and P. R. Rao, *J. Mat. Sci. Lett.* 20, 2099 (2001).
97. H. Bekele, J. H. Fendler, and J. W. Kelly, *J. Am. Chem. Soc.* 121, 7266 (1999).
98. W. Bae and R. K. Mehra, *J. Inorg. Biochem.* 70, 125 (1998).
99. R. Kho, C. L. Torres-Martinez, and R. K. Mehra, *J. Colloid Interface Sci.* 227, 561 (2000).
100. C. L. Torres-Martinez, L. Nguyen, R. Kho, W. Bae, K. Bozhilov, V. Klimov, and R. K. Mehra, *Nanotechnology* 10, 340 (1999).
101. W. Bae, R. Abdullah, D. Henderson, and R. K. Mehra, *Biochem. Biophys. Res. Comm.* 237, 16 (1997).
102. R. Kho, L. Nguyen, C. L. Torres-Martinez, and R. K. Mehra, *Biochem. Biophys. Res. Comm.* 272, 29 (2000).
103. M. C. Brelle, J. Z. Zhang, L. Nguyen, and R. K. Mehra, *J. Phys. Chem. A* 103, 10194 (1999).
104. S. Kjelleberg and S. Molin, *Current Opinion in Microbiology* 5, 254 (2002).
105. K. A. Dunn, R. J. C. McLean, G. R. Upchurch Jr., and R. L. Folk, *Geology* 25, 1119 (1997).
106. K. J. Edwards, P. L. Bond, T. M. Gihring, and J. F. Banfield, *Science* 287, 1796 (2000).
107. M. Labrenz, G. K. Druschel, T. Thomsen-Ebert, B. Gilbert, S. A. Welch, K. M. Kemner, G. A. Logan, R. E. Summons, G. De Stasio, P. L. Bond, B. Lai, S. D. Kelly, and J. F. Banfield, *Science* 290, 1744 (2000).

Biological Molecules in Nanodevices

Stephen C. Lee, Mark A. Ruegsegger, Mauro Ferrari

Dorothy M. Davis Heart and Lung Research Institute, Columbus, Ohio, USA

CONTENTS

1. Introduction
 2. Nucleic Acids in Nanobiological Devices
 3. Proteins in Nanodevices
 4. Conclusions
- Glossary
References

1. INTRODUCTION

1.1. Nanotechnology, Biotechnology and Nanobiological Devices

Nanotechnology aims to satisfy desired objectives using materials and devices whose valuable properties owe to some specific nanometer-scale element of their structures. This definition puts no restrictions on the overall dimensionality of nanotechnologically derived constructs, but merely requires involvement of some precise-structure nanoscale feature in function. Thus, devices and structures of even macroscale dimensionality assembled from, or containing, functional nanoscale components can be legitimately gathered under the nanotechnology umbrella. As a second corollary to the definition, biotechnology must be considered a subdiscipline of nanotechnology. The function of biological macromolecules (proteins, nucleic acids) depends on their precise nanoscale structures, so inclusion of aspects of biotechnology relating to macromolecule engineering under the nanotechnology rubric is legitimate. Individual biological macromolecules (proteins, nucleic acid molecules, supramolecular complexes, etc.) often exhibit the coordinated, modular multifunctionality that is characteristic of purpose-built devices.

The topic of this article is nanodevices containing functional biological molecules, rather than nanomaterials *per se*, and device design and operational properties will be discussed in preference to discussion of novel physical, chemical, or electrical properties of nanomaterials and structures.

For instance, both nanomaterials used as drug formulation excipients (pharmacologically inert materials included in formulations that modulate pharmacophore uptake, biodistribution, pharmacokinetic, handling, storage, or other properties) and single molecule nanomaterials with therapeutic activity (as are most protein drugs), while important in their own contexts, will rightly be excluded from discussion of nanodevices here. The logic of this auctorial choice is clear, but is supported by another less obvious consideration that is gradually gaining broad acceptance. Unlike nanotechnology practice in most nonmedical contexts, access to novel physical properties associated with the nanosize regime (for instance, quantum effects) is not primary, or even significant, motivation for most nanotherapeutic design. The impetus to ultra-small and nanotherapeutics lies in the related desires for minimally invasive therapies and therapeutics which provide high densities of multi-faceted functionality in very small packages. In addition, nanotherapeutics generally must interface with biological nanocomponents of the patient (protein, nucleic acids, etc.), a goal frequently best satisfied by functional biological components (protein, nucleic acids, etc.) of nanodevices. Clearly, quantum and other physical effects, typically associated with other aspects of nanotechnology are not the primary drivers of the function of most biological macromolecules. This logic suggests that for the near future, and perhaps indefinitely, many nanotherapeutic devices will contain (or be primarily composed of) biological macromolecules. The argument is most persuasive in the cases of nanodevices used *in vivo*.

Devices are integrated functional structures which exhibit desirable emergent properties that are inherent in (and are the object of) their design. These properties emerge as the result of a spatial/temporal organization of components, as well as a coordination action of individual components. The organization of components in devices is the critical factor that allows them to perform cogent work processes and differentiates devices from admixtures of their constituent components. In the early 21st century, availability of synthetic functional nanocomponents is problematic. While some nanoscale catalysts, electrical components, and functional structures are available, current technology

does not allow the combination of precise nanoscale control of structure and chemistry coupled with high manufacturing throughput necessary to satisfy plenipotent nanodevice technology. Again, logic and circumstance dictate a critical role for biological macromolecules in nanotechnology.

In as much as biotechnology can be considered a subdiscipline of nanotechnology, it is fitting that biotechnology should provide a critical source of functional components for nanodevices. The diversity of chemical activity of proteins and nucleic acids in the biological world is vast and well beyond the capability of the most advanced current materials science to duplicate with synthetic materials. Furthermore, production and engineering of biological macromolecules is facile (see [1] for a review of protein engineering approaches for nanotechnological device construction) and relatively inexpensive. In the absence of a capacity to produce corresponding nanocomponents by synthetic means, incorporation of engineered or native biomolecules as functional components is a logical approach to functional nanodevices in which one or more protein species (or nucleic acid species) is organized around or within a synthetic nanostructure that causes the aggregate manifestation of the activities of the biomolecules to add to a useful outcome. As we will see, this can occur as the result of the coordination of disparate biological activities to nanoscale proximity, or by organization of functional components such that they interact in a controlled manner, leading to a desired result.

This said, biotechnology historically has focused on production of individual soluble protein and nucleic acid molecules for pharmaceutical use, paying only limited attention to functional supramolecular structures [1–6]. The bias towards free molecules on the part of the biotechnology industry has been driven by the marketplace. Single protein drugs are among the easiest biotechnological therapeutics to realize from both technical and regulatory perspectives. However, this commercially driven bias flies in the face of the importance of supramolecular structures in the biological world. Within even the least complex biological entities, biological macromolecules are aggregated into supramolecular assemblages performing concerted functions that cannot be achieved without such organization. Virtually all organismal activities and functions ultimately emerge from the activities and interactions of such supramolecular complexes, which themselves function as the result of the combined activities of individual nanoscale macromolecules. Viewed from this perspective, the biological world is populated with naturally occurring nanodevices, a fact that provides additional motivation for the incorporation of biomolecules in nanodevices used in therapeutic contexts. Hybrid nanodevices can interact with patients on multiple levels, ranging from organismal to molecular, but it is reasonable to expect that most nanotherapeutics will interface with patients at the nanoscale at least to some extent [1–4, 7–12]. This translates to interaction between therapeutic devices and patient biological macromolecules, supramolecular structures, and organelles. As previously discussed, this consideration often dictates the incorporation of biological macromolecules and other biostructures into nanodevices [2, 3, 11–13].

Until recently, incorporation of biomolecules into functional supramolecular structures (devices) has been technically difficult, and used only in special cases. However, synthetic materials derived using micro/nanotechnology techniques afford the opportunity to complement and transcend the (self-imposed) limits of biotechnology to the production of individual soluble macromolecules. These materials can provide scaffolds that support higher-level organization of multiple biomolecules into devices. The organization of functional components provided by nanoscale scaffolds allows nanodevices to perform work activities that mixtures of their protein components as soluble molecules cannot. Such supramolecular structures have been variously called nanobiotechnological devices [14], nanobiological devices [1–6, 15], or hybrid or semi-biological nanodevices.

1.2. Design of Nanobiological Devices

Construction of hybrid nanodevices involve incorporation of prefabricated biological components, an activity which presents distinctive challenges that are seldom encountered in other aspects of engineering. For instance, since native biological macromolecules are not made to human design, their properties are often much less well understood than are those of purpose-built synthetic structures. Additionally, the activities of biological molecules are often multifaceted (so-called pleiotropic activities), though this may not be immediately apparent to an engineer wishing to use a particular protein or nucleic acid sequence as a device component. These and other factors make design and prototyping of biological nanodevices highly iterative and empirical processes [1, 3, 4, 12].

First, the biological components of nanobiological devices must retain their function in new (*i.e.*, device) contexts. The specific bounds of a biological component in a semi-biological device are defined by the requirements of the component for function, and therefore identification of the minimal unit requires at least rudimentary knowledge of the biochemistry of the protein or nucleic acid involved. In some cases, incorporation of intact biological macromolecules is not necessary to satisfy device functions (see Figs. 1 and 2). For instance, specific molecular recognition functions can be useful for either nanodevice assembly or tissue targeting. Such recognition functions can be conveniently derived from antibodies, though it is not usually necessary to incorporate entire 150,000 atomic mass unit (AMU) antibody molecules into devices. Specific antigen recognition is conferred by a 20,000 AMU antibody fragment [16–18] and this antibody fragment is sufficient to confer specific recognition properties to nanoparticles or devices (Fig. 1B).

In other cases, desired functionalities are not inherent in a single molecule and multimolecular complexes must be incorporated into devices. Most biological molecular motor systems function as multiprotein complexes, and multiprotein complexes sometimes must be incorporated into functional nanostructures to impart motility upon them (Fig. 2). Rotary motors, such as the F-ATPase [19, 20] and the bacterial flagellar cap [21–25] are obligately multiprotein complexes to accommodate their rotary action.

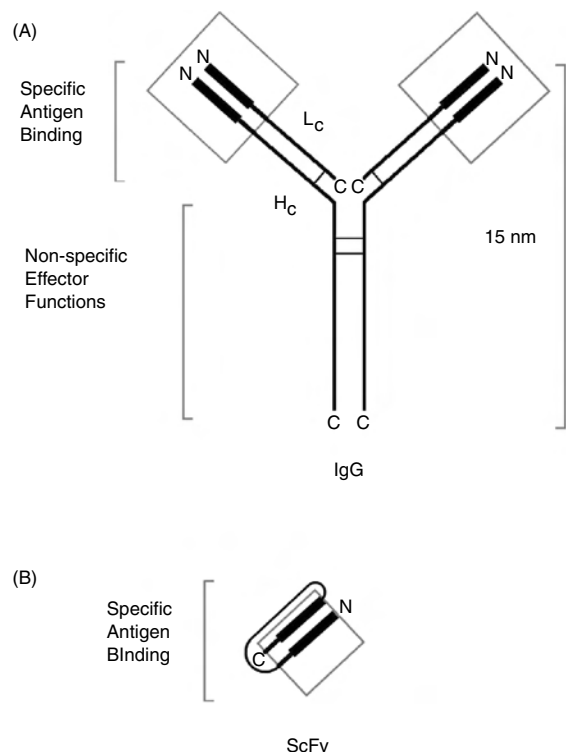


Figure 1. Many biological macromolecules are multifunctional and essentially modular: distinct molecular functions are performed by discrete regions of the molecules. Here individual polypeptide chains of an immunoglobulin G molecule (IgG) (Fig. 1A) and an engineered derivative of an IgG (Fig. 1B) are represented as lines with amino- and carboxy-ends of the polypeptide chains are indicated by N and C, respectively. IgGs are monospecific, bivalent molecules composed of two low molecular weight light chains (L_c), two higher molecular weight heavy chains (H_c), covalently linked by intrachain disulfide linkages (crosshatches). IgGs perform a number of activities, some of which are antigen-specific (antigen recognition), and some of which are not (nonspecific effector functions including complement fixation, recognition of macrophage surface receptors, etc.). Individual activities are delimited to specific regions (domains) of the protein. For instance, specific antigen binding is mediated by a domain containing elements of the light chain and the heavy chain which are proximal in the three dimensional structure of IgG (boxed, bold lines). Amino acid sequence in this domain, variously called the variable region (Fv) or complementarity determining region (CDR), varies from one IgG molecule to the next, conferring on each individual IgG its exquisitely specific antigen recognition properties. Nonspecific effector functions are common to all IgGs, and are also mediated by domains that are proximal to each other in space and whose amino acid sequences are highly conserved in all IgG molecules. Nonspecific effector regions are clustered in the so-called constant region or Fc of IgG. Engineered immunoglobulins (in this case, a single-chain Fv or ScFv) illustrate how the modularity of proteins can be exploited by technologists (Fig. 1B). Each CDR accounts for less than one-seventh of IgG molecular weight, but confers all of the antigen-specific recognition properties of the antibody. Since the CDR consists of both a H_c and L_c component, ScFvs are conveniently synthesized as a single molecule by incorporation of a short flexible peptide region between the H_c and L_c versions of the CDR, using standard protein engineering methods. ScFvs confer the exquisitely specific antigen recognition properties of their parent IgGs to any molecule or nanostructure to which they are appended.

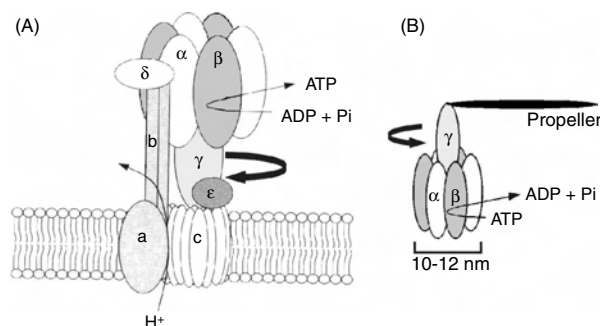


Figure 2. Some biological functions are performed by concerted action of oligomeric macromolecular complexes, rather than single macromolecules. Unlike the polypeptide chains of immunoglobulins, the individual polypeptides of such complexes are typically not covalently bound to one another. Here an oligomeric protein complex, F-ATPase (Fig. 2A), and an engineered derivative of it (Fig. 2B), provide examples of complexes of multiple proteins that act in concert to perform a single function. In this representation, individual polypeptides are presented as ovals, representing their globular natures and to more accurately represent the organization of the complex. F-ATPase also illustrates how nanotechnologists can isolate functionalities of interest from larger biological structures, provided they have sufficient biochemical and ultrastructural information. F-ATPase is an integral membrane mechanoenzyme complex that harvests energy from transmembrane proton gradients to synthesize ATP. Adenosine triphosphate synthesis involves the rotation of part of the complex (indicated by the clockwise arrow), driven by energy harvested from the proton gradient. The holoenzyme complex contains eight distinct protein species, and about 20 individual protein molecules, but only the α , β , and γ subunits are required for rotary motion. The potential for the relevant portions of F-ATPase (α , β , and γ subunits) to act as molecular motors has been recognized by both cell biologists and nanotechnologists, and the α , β , and γ subunits of the mechanoenzyme complex have been isolated and assembled with a propeller (either an actin filament or a micromachined structure) linked to the γ subunit (2b). If the α and β subunits are attached to a substrate, ATP hydrolysis by the structure results in rotation of the γ subunit and the propeller attached to it. The α , β , and γ subunits-propeller assembly can provide motive force to nanomaterials to which it is attached (see [19, 86–89]).

As previously described, device function emerges from the summed activities of device components. Coordination of component activities into a cogent work process occurs as the result of the organization of the components relative to each other that is imposed in device design. As Figure 2 shows, motor complexes require precise spatial positioning of individual protein subunits to allow them to interact productively, and impart motion to the nanodevice. Similarly, the spatial relationships between protein that do not interact with each other but interact with other nanoscale molecules and structures (such as auxiliary proteins or receptor beds present in various cell types or tissue spaces) can be critical to device function and properties. This has also been observed in cases in which growth factors and cytokines have been deployed on solid surfaces and the resulting structures have been used to trigger cell proliferation [26–29]. The magnitude of proliferation and other parameters of biological responses are intensely sensitive to the specific geometries of protein presentation on the proliferative surface, as will be discussed subsequently.

The bacmid (or Bac-to-Bac™) molecular cloning system exemplifies how specific arrangements of functional

biological components support device function, as will be discussed later. However, bacmid exhibits another critical property of nanobiological devices: the potential for such devices to perform functions without precedent in the natural world. Other nanobiological devices, for example, systems incorporating motor proteins, particularly those derived from F1 ATPase and similar supramolecular structures, also illustrate the potential to cause biological structures to perform functions that are other than those they perform in their native settings as the result of careful design and assembly of nanobiological devices. Nanobiological device designers are thus not limited to merely recapitulating naturally occurring supramolecular systems, as is described later in a discussion of specific supramolecular devices.

Some design guidelines for hybrid biosynthetic nanodevices, particularly for therapeutic applications, have been formulated [1, 3, 4, 10–13, 30–32]. One vision of nanoscale therapeutic platforms arose from collaboration between the National Cancer Institute (NCI) and the National Aeronautics and Space Agency (NASA) [3, 11, 13, 30]. National Space and Aeronautics Agency is concerned with minimal mass therapeutics, driving their interest in compact, multifunctional therapeutics. National Cancer Institute is interested in early detection of disease and non-invasive therapy to improve prognosis. Since this requires screening of a population of predominantly healthy patients, the screening mode must be minimally invasive. The interests of the two agencies are complementary and can be met both with ultra-small (micro- or nanoscale), multifunctional hybrid biosynthetic devices. Additionally, the proposed therapeutic entities are not only expected to remediate undesired physiological conditions, but also to recognize (sense) and report them. Extensive capability for molecular recognition and communication with external clinicians/operators is integral to the NASA/NCI vision and is eminently feasible using hybrid nanodevices. These capacities would allow controlled provision of therapeutic intervention, maximizing benefits and minimizing side effects, thereby yielding “smart” therapeutics (see the discussion of targeting and triggering). The authors have named these supramolecular entities therapeutic platforms, denoting their multifunctionality and differentiating them from conventional small molecule and protein drugs.

While substantial progress has been made in device design and realization, no multipotent nanoscale hybrid therapeutic platform has yet been commercialized. However, segregation of individual therapeutic functions into individual modules allowed in the therapeutic platform paradigm is potentially very powerful. Classes of broadly similar devices could be tailored by interchanging modules (targeting modules, sensing modules, drug dispensing modules, etc.) of the hybrid device as appropriate to particular disease states or therapeutic courses. Standardization and interchangeability of functional modules may eventually allow tuning of nanotherapeutics to needs of individual patients or conditions. Standardization of modules could potentially mitigate regulatory burdens for variants of individual therapeutic platforms.

A dendritic polymer-based therapeutic platform design incorporating independent, fungible component modules, is

illustrated in Figure 3. This structure represents a class of devices that have been termed “cluster agents” by their inventors. The device is a supramolecular complex built by exploitation of dendrimer self-assembly properties [33, 34]. This particular cluster agent is intended for cancer chemotherapy, and exhibits many of the canonical features postulated in the NCI/NASA vision [11, 13]. Individual functions (sensing, triggering targeting, drug delivery, etc.) are delimited to individual device subunits (*i.e.*, individual dendrimers) that can be interchanged as needed to address therapeutic exigencies. For instance, many tumor types overexpress folate receptor on their surfaces, and so targeting/tethering to such tumors can be accomplished via a folic acid residue covalently linked to the targeting module. For other tumor types, folate might not be the appropriate molecular targeting moiety, and a different module would be used (for instance, one decorated with glycoproteins or cytokine molecules preferentially recognized by the target tumor type). Similar tuning could be applied to the specific drug and therapeutic delivery module, to best accommodate the drug sensitivities of individual tumors. As genomics and proteomics are applied increasingly to individual patients, the modularity of cluster agents and similar nanobiological devices may allow very nimble, personalized

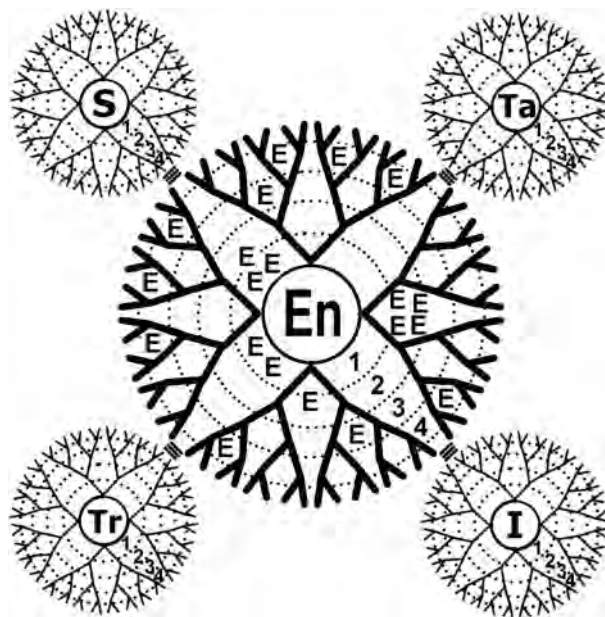


Figure 3. Synthetic materials can be used to organize functional biological molecules into modules that can be assembled into therapeutic devices and modules can be interchanged to tune activity of the devices. Shown is a schematic of a modular “cluster agent” for cancer therapy [13, 33, 34, 163] consisting of multiple derivatized PAMAM dendrimers. PAMAM dendrimers are fractal nanoscale polymers grown in discrete steps called generations (indicated by numbers) from a central initiator core. Activities/subroutines of this cluster agent include tissue targeting (Ta), sensing of the local environment (S), encapsulation of therapeutic payload (En, encapsulated drug indicated as E), and triggering of therapeutic action (Tr). These activities, and the biomolecules responsible for them, are localized to the surfaces or internal spaces of the indicated dendrimer subunits. The modularity of the design allows the cluster agents to be configured as is appropriate for a number of related but distinct clinical circumstances.

therapeutic responses to disease leading to potentially vast improvements in individual therapeutic outcome.

2. NUCLEIC ACIDS IN NANOBIOLOGICAL DEVICES

2.1. Nucleic Acid Hybridization: Structure and Assembly

The base pair hybridization, specific sequence recognition, and replication properties of nucleic acids (Fig. 4A and 4B) and associated enzymes are potentially attractive properties for incorporation in semi-synthetic nanodevices and are often exploited by nanodevice designers [35–38]. For instance, reversible self-assembly by DNA hybridization is used to control the assembly and relative positions of nanomaterials conjugated to nucleic acids in many nanodevices. Seeman et al. [35] and Shchepinov, Niemeyer, and Seeman et al. [39–43] have demonstrated that careful control of DNA sequence and hybridization conditions can generate nanoscale nucleic acid structures with extremely complex topographies (Fig. 4C). Because double-stranded DNA segments greater than 100 base pairs (a few nanometers) in length are quite flexible, these exquisitely defined topographies do not produce comparably well-defined geometries.

The inability to control the geometry of nucleic acid constructs can limit their utility for organizing pendent nanoscale components in three-dimensional patterns. However, nucleic hybridization can be used to bring individual nanocomponents into proximity, allowing them to interact efficiently (Fig. 5A). This principal is exploited in hybridization-driven photonic devices [44–46]. Fluorescence transfer (FT) between a photonic excited donor molecule and an acceptor can only occur when they are in very close (less than five nanometers) proximity. Donor and acceptor can be brought into the requisite proximity if each is pendent to oligonucleotides that hybridize to adjacent regions of a complementary, single-stranded nucleic acid target. Fluorescence transfer devices can be used in biosensors to detect target DNA segments, for instance the DNA of a pathogen. In the absence of pathogen (target) DNA, the donor and acceptor oligonucleotides cannot assemble, FT does not occur, and light emitted from the device is at the characteristic emission wavelength of the donor molecule D. If pathogen (target) DNA is present, the target DNA supports assembly of donor and acceptor oligonucleotides, bringing D and A into proximity, allowing FT to occur, and light is emitted at the emission wavelength determined by A. The shift in emission wavelength is easily detected and quantitated.

A highly analogous prodrug strategy has been developed [37, 47]. Prodrugs are pharmaceuticals that are administered in a form that has little or no pharmacologic effect until the prodrug is activated as the result of intrinsic conditions at the site of action or in response to a stimulus provided by an external operator. This delimits the action of the therapeutic in time, space, or both, and is useful for potentially toxic therapeutics. In this particular prodrug system, hybridization to a target single-stranded nucleic acid strand brings a hydrolytic catalyst linked to one oligonucleotide in sufficiently close proximity with a prodrug linked to another

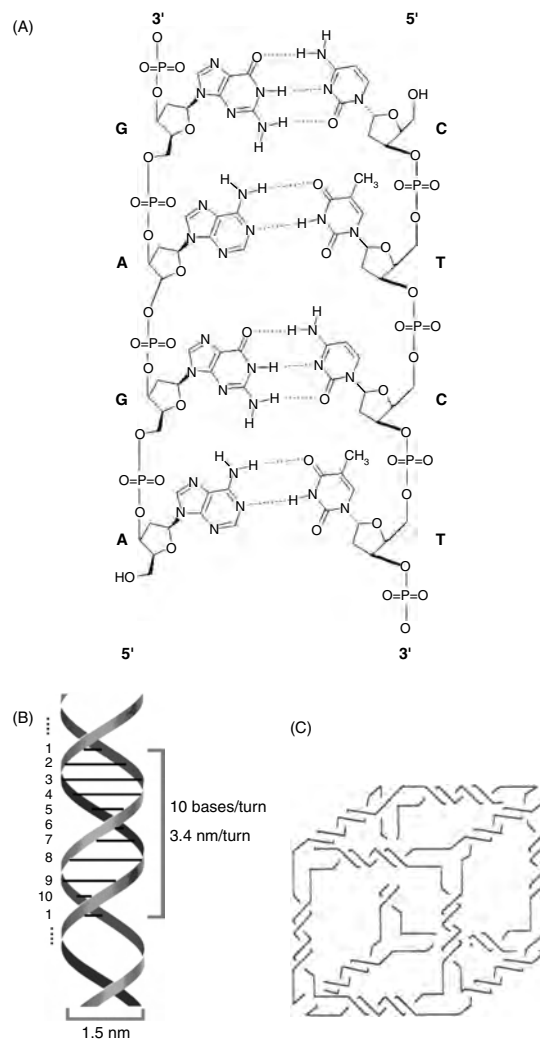


Figure 4. DNA self-assembly is driven by noncovalent interactions between the nitrogenous bases of DNA strands. DNA is a linear polymer that arrays nucleotide bases, (purines: adenine (A), guanine (G), and pyrimidines: thymine (T), cytosine (C)) in specific order along a phosphodiester polymer backbone (Fig. 4A). Bases have specific hydrogen-bonding preferences (G for C, A for T) which allow base-pairing between bases of different DNA strands, and in aggregate, allow DNA strands with complementary nucleotide sequences to hybridize into a double-stranded (ds) complex. Note that DNA strands are vectorial in that they are synthesized from the 5' end of the strand to the 3' end of the strand only (5' and 3' referring to the specific phosphoester linkages of the phosphodiester backbone). Specific nucleotide sequences were chosen arbitrarily for illustration purposes. 5' and 3' at strand ends are as indicated, so that hybridizing DNA strands are arranged in an anti-parallel fashion. DNA strands wrap around each other to form an anti-parallel double helix (Fig. 4B) with a periodicity of 10 base pairs/turn (about 3.4 nm) and a width slightly larger than 1 nm. Lines between DNA strands indicate base pairs. Judicious choice of DNA sequence can allow the construction of nanostructures with highly defined, complex topographies by hybridization-driven self-assembly [41]. A schematic of a cubic topography achieved by hybridization of six designed DNA oligonucleotides is shown in Figure 4C. While the structure exhibits the connectivity of a cube, it is not rigid and can adopt multiple three-dimensional conformations. The base-paired double-helical regions that drive assembly of the controlled topography are as indicated.

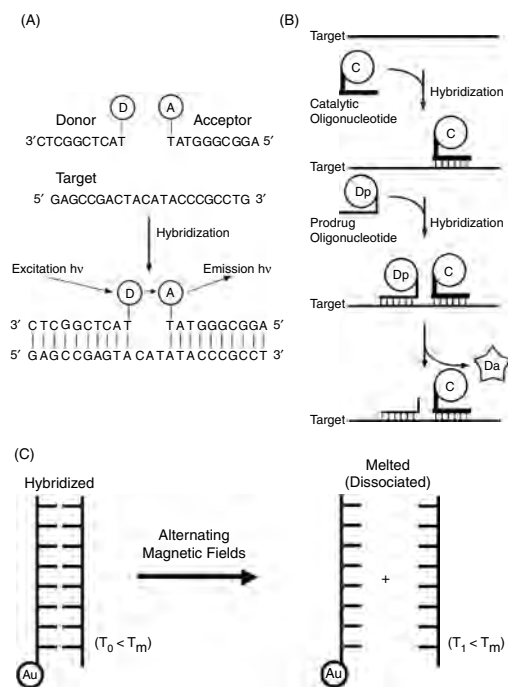


Figure 5. DNA hybridization can be exploited to construct self-assembled functional nanostructures. Shown in Figures 5A and 5B are two nanodevices that depend on DNA hybridization to bring components into sufficient proximity to allow them to interact and provide device function. When shown, specific DNA sequences were chosen arbitrarily for purposes of illustration. In Figure 5A is a fluorescence transfer (FT) device consisting of a target DNA segment and two oligonucleotides complementary to it (donor and acceptor), but not to each other [35–38]. The donor oligonucleotide is conjugated to a small molecule (D) that can absorb a chosen (excitation) wavelength of light and the acceptor oligonucleotide is conjugated to second distinct small molecule (A) that can accept energy from the donor molecule in a quantum process and emit that energy at still another (emission) wavelength. FT between D and A molecules requires they be in close proximity and that condition is satisfied when the donor and acceptor oligonucleotides hybridize to the target oligonucleotide. Configured as illustrated, the distance between D and A is about a nanometer. Figure 5B shows an analogous therapeutic nanodevice that depends on hybridization to trigger controlled release of bioactive drug [37, 47]. In this case, one oligonucleotide is conjugated to a catalyst C (the catalytic oligonucleotide) and a second oligonucleotide is conjugated to a drug molecule (D_p) that is inactive in the conjugate state (the prodrug oligonucleotide). C catalyzes the breakage of the linkage between D_p and the prodrug oligonucleotide, liberating active drug (D_a), indicated with a star. The nucleic acid hybridization of devices of Figures 5A and 5B is intensely sensitive to environmental conditions (pH, salt concentration, temperature, etc.) at the site of hybridization. Figure 5C illustrates a strategy by which a local condition critical for hybridization (temperature) might be manipulated by a remote or external operator. In this system, a nanogold particle (Au) is conjugated to one of two complimentary oligonucleotides. The two oligonucleotides hybridize when the initial temperature (T_0) is below the melting temperature (T_m) for the hybridized species. Application of an alternating magnetic field by a remote operator produces eddy currents in the nanogold particle that produce Joule heating. When heating raises the local temperature to a T_1 that is above T_m , the double-stranded sequence melts and the two oligonucleotides dissociate. The process is potentially reversible, and might be applied controlling the assembly and activity of nucleic acid nanodevices [48].

oligonucleotide also hybridizing to the same target strand to cause the efficient release of active drug (Fig. 5B). Assembly of catalytic oligonucleotide and prodrug oligonucleotide on target nucleic acid brings catalyst in close proximity with its substrate, efficiently hydrolyzing the linkage between drug and prodrug oligonucleotide. Locally high concentration of catalysts results in the release of active drug (D_a) preferentially at sites where the target nucleic acid is present in relative abundance. Theoretically, such a system could allow preferential release of a cytotoxin or other drugs at tissues or sites expressing specific RNA (for instance, tumors) or containing specific DNA sequences (for instance, virally infected cells).

DNA hybridization is a reversible process that can be controlled by manipulation of the immediate chemical and physical environments of hybrids. Environmental salt and/or chaotropic concentrations and temperature, as well as the G + C content, length, extent, and position of base pair mismatches in hybridizing strands can all be controlled to manipulate the association of hybridizing nucleic acid strands. Control of hybridization for nanobiological device assembly by sequence parameters as previously described occurs at the level of device design, and may not be easily amenable to manipulation of nanodevice component assembly over time by a remote device operator. Similarly, change of the chemical composition of the device operating environment may not be a practical means to control the association state of nanobiological devices assembled by nucleic acid hybridization. However, in *in-vivo* applications, environmental temperature may be the variable most amenable to manipulation by an outside clinician/operator. For instance, externally applied magnetic fields can be used to control the association of hybridized nucleic acid structures that are conjugated to nanometallic particles (Fig. 5C). Eddy currents induced by alternating magnetic fields can heat the particles and their immediate vicinity [48]. Colloidal gold particles are covalently conjugated to biomolecules (nucleic acids or proteins) and alternating magnetic fields are used to induce heating sufficient to cause dissociation of hybridized nucleic acid structures or denaturation of three-dimensional protein structures. Nucleic acid duplex hybridization and melting are fully reversible processes, and protein denaturation is reversible to some degree in some cases. This and other methods to control temperature in the nanobiological device operating environment [49–52] may allow remote, reversible activation/inactivation of nanobiological therapeutic devices.

2.2. Biologically Functional Nucleic Acid Nanodevices

As the foregoing shows, the physical-chemical properties of oligonucleotides can be exploited to assemble and control the activity of nanodevices in biologic or nonbiologic contexts. These applications primarily exploit nucleic acid hybridization properties without reference to the genetic functions inherent in some nucleic acid sequences. Both the genetic toggle switch (Fig. 6A) and the bacmid (or Bac-to-Bac™ molecular cloning system) (Fig. 6B) previously mentioned, provide examples of nanodevices that exploit the

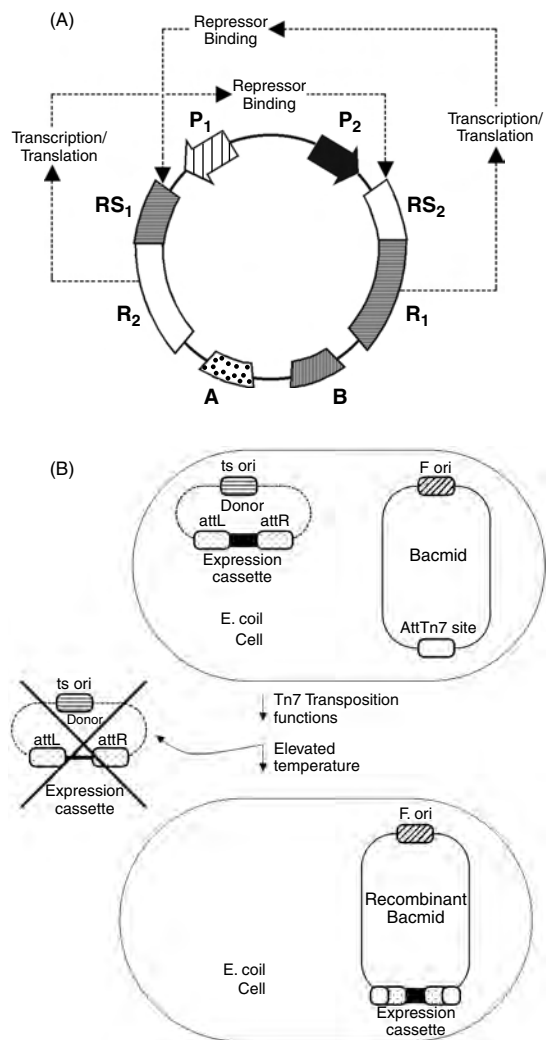


Figure 6. Biological components can be isolated from their native contexts, organized by a designer into a nanodevice whose function is unprecedented in nature, illustrated here by nucleic acid nanodevices that perform preselected tasks in biological environments. A prototypical toggle switch plasmid is shown in Figure 6A [53]. For simplicity sake, only those genetic elements directly involved in regulated switching behavior are shown. This device contains two distinct, divergently transcribed promoters (diagonally striped or black arrowheads: P₁, P₂). Overlapping each promoter is a distinct repressor binding site (RS₁: cross-hatched box; RS₂: open box). When the cognate repressor (encoded by the R₁ gene: horizontally cross-hatched box or encoded by R₂ gene: open box) binds its repressor binding site (R₁ repressor to RS₁, or R₂ repressor to RS₂, indicated by arrows), expression from P₁ or P₂, respectively, are repressed. Expression of functional repressor from one promoter decreases expression from the other promoter, so the system exists in one of two highly stable states where expression from P₂ or P₁ dominates. Control input for switching is provided by modulating the concentration of active R₁ or R₂ repressor. This can be done by induction of one of the promoters with a chemical substance that increases the efficiency of expression from one of the two promoters specifically. Alternatively, if R₁ or R₂ are temperature sensitive (that is, not functional at elevated or reduced temperature), temperature shift can be used as the control input. One utility of this bistable switching system could be to provide the ability to remotely control which of two (or more) genetic programs is followed by a target microorganism. Here two different genes, or blocks of genes, A (polka dotted box)

biological functionalities of their constituent nucleic acid components in a biological context [53–55].

Prokaryotic plasmids (circular, autonomously replicating DNA segments) with the ability to switch between two alternative stable states in response to a control input have been used to control the physiological properties (protein expression) of bacteria [53, 54]. These systems configure genetic elements (promoters, repressor binding sites, positive control elements, transposition sites, etc.) to manipulate the physiology of host microbes. A bistable “toggle switch” plasmid is shown in Figure 6A. The toggle plasmid operates in an *Escherichia coli* cell and contains two distinct promoters (DNA sequences that direct the transcription of mRNA from the genes downstream of them on DNA segments), each promoter directing the synthesis of a distinct repressor (a protein that blocks transcription from its cognate promoter by binding to or near the promoter). Each promoter has a repressor-binding site positioned such that repressor binding represses transcription from the cognate promoter. Promoters and repressor binding sites are configured so that the repressor synthesized under the control of one promoter represses the promoter directing the synthesis of the second repressor.

The system exists in one of two states, corresponding to repression of one of the two promoters, and relatively unimpeded transcription of the other. In the absence of control input, these states are highly stable and persist through tens

and B (vertically crosshatched box), each representing a discrete genetic program, is expressed or not depending on whether P₂ or P₁, respectively, are repressed. Multiplexing of these and other control architectures may eventually lead to remote control of their biosynthetic and biodegradative activities, potentially expanding the utility of microorganisms in industrial, manufacturing, and bioremediation applications. The bacmid molecular cloning system (Fig. 6B) is a multi-component molecular device that allows efficient production of recombinant insect viruses (baculovirus) in *E. coli* cells [55, 164, 165]. Baculovirus (solid line) is replicated in *E. coli* by the F plasmid origin of replication (F ori: cross-hatched box), and is called a bacmid. The bacmid also includes an engineered transposable DNA element 7 (Tn7) attachment site isolated from the chromosome of an enteric bacteria (AttTn7: open box). AttTn7 can recombine with Tn7 elements transposed from other cellular locations. A donor plasmid (donor: dashed line) is replicated by a temperature-sensitive plasmid pSC101 origin of replication (ts ori: box with lines). The donor also incorporates a protein expression cassette containing both the gene encoding a protein of interest for ultimate expression in insect cells and a selectable genetic marker operable in *E. coli* (black box). The expression cassette is flanked by DNA sequences (attL and attR) that are derived from Tn7 and are recognized by the Tn7 transposition machinery. Tn7 transposition machinery resides elsewhere in the same *E. coli* cell (not shown). When donor plasmid is introduced into *E. coli* containing bacmid, Tn7 transposition machinery causes the physical relocation of the expression cassette from donor plasmid to bacmid. Unreacted donor plasmid is conveniently eliminated by elevating the incubation temperature, causing the ts pSC101 replicon to cease to function, with the result that the donor plasmid is lost. If selection for the genetic markers within the expression cassette is applied at this point, the only *E. coli* that survive are those containing recombinant bacmid (that is, those that have received the gene for insect cell expression by transposition from the donor). Recombinant bacmid are conveniently isolated from *E. coli* and introduced into insect cell culture, where expression of the gene of interest occurs (not shown).

of *E. coli* generations. In the configuration of Figure 6A, control input for switching is provided by inactivation of one of the repressors or exogenous induction of one of the promoters (wherein the level of induction is sufficient to overcome ground state repression of the corresponding promoter). Currently, these systems can mimic the behavior of simple physical-chemical switches and oscillators, but programming more complex activities will doubtless be possible in the future. Ultimately, these sorts of control strategies may allow programming of microorganisms to manufacture specific structures, compounds, or macroscale architectures.

The toggle switch is an example of a device in which the engineered, functional genetic components are linked into a single DNA molecule. Other devices incorporate multiple DNA molecules that interact to produce a desired work product. The work product of bacmid is recombinant baculovirus to be used for expression of foreign proteins in insect cells. The system allows construction of recombinant baculoviruses for insect cell expression in about a week (four- to six-fold faster than other available methods) using *E. coli* molecular genetic methods.

The bacmid molecular cloning system replicates an engineered insect cell (baculo-) virus in a nonnative environment (the *E. coli* cytosol) by linkage of the *E. coli* F plasmid (self-replicating DNA sequence) and origin of replication (ori). This construct is referred to as a “bacmid,” and will replicate stably and indefinitely in *E. coli*. The bacmid itself contains additionally a DNA sequence, the *attTn7* site, which can accept the insertion of transposable elements related to bacterial transposon Tn7. The insect cell expression cassette to be inserted into the *att* site of bacmid is carried on a second plasmid (the donor plasmid) in the same *E. coli* cell. The expression cassette is flanked by DNA sequences *attL* and *attR*, which together with the *attTn7* site of bacmid, are recognized by Tn7 transposition enzymes. These are provided *in trans*, and mediate the physical relocation (transposition) of the expression cassette from the donor plasmid to bacmid, generating recombinant bacmid. Recombinant bacmid is harvested directly from *E. coli*, introduced into insect cells, and used to generate recombinant protein.

The bacmid system illustrates many of the canonical properties of nanobiological devices previously described. Specifically, the constituent nucleic acid segments of the bacmid system are harvested as intact functional modules from multiple biological sources (the *E. coli* genome, bacterial plasmids and transposons, and insect viruses). The specific arrangement of the elements (linkages between baculovirus and the F ori and the *attTn7* site, the flanking of the expression cassette by *attL* and *attR*, the provision of Tn7 transposition machinery *in trans*, etc.) is imposed in device design and drives device function. Critical changes in these structural relationships result in loss of device activity. For example, failure to link the mini-F origin of replication to the baculovirus would preclude its maintenance in *E. coli*, and failure to incorporate an *attTn7* site in bacmid would preclude bacmid as a possible destination for the transposed expression cassette. Bacmid also hints at the vast potential of nanobiological devices to provide novel activities. Bacmid has spawned a series of highly similar nanobiological systems for generating recombinant eukaryotic viruses in bacteria

[56–60]. As discussed previously, no naturally occurring system creates eukaryotic viruses in prokaryotes, so bacmid and derivative systems demonstrate that nanobiological devices are not limited to recapitulation of natural systems, but can represent novel devices whose functions are truly new under the sun.

3. PROTEINS IN NANODEVICES

This discussion has emphasized the importance of the structure of nanobiological devices from the standpoint of the impact of the specific arrangement of functional biological components on device function. When considering nucleic acids in nanodevices, the relationships of interest can usually be satisfied in the order of genetic elements along a linear nucleic acid strand (but not always; consider the three-dimensional DNA topographies previously discussed). Protein-containing nanobiological devices are at least as sensitive to the configuration of their functional components as are nucleic acid-containing devices; but in this case, three-dimensional arrays of protein components, as opposed to simple linear arrays of genetic elements, are often required to support function.

Biological macromolecules undergo self-assembly at multiple levels, and like all such processes, biological self-assembly is driven by thermodynamic forces. Some biomolecules undergo intramolecular self-assembly (*e.g.*, protein folding from linear peptide sequences). Also, higher order structures are constructed by the intermolecular self-assembly of smaller self-assembled subunits (for instance, structures assembled by hybridization of multiple oligonucleotides, enzyme complexes, etc.).

Proteins are copolymers of 20 chemically distinct amino acid (aa) subunits [61]. Linear polypeptide chains form specific secondary structures via interactions between aa side chains. These secondary structures themselves associate to form tertiary (and quaternary) structures that constitute final folded protein structure(s). This self-assembly process generates consistent nanostructures that derive their biological properties from their strict control of the deployment of chemical specificities (the aa side chains) in three-dimensional space.

The biological diversity of proteins isolatable from nature is immense, and is augmented by the capacity to engineer proteins to suit in many applications (see [4] for discussion of protein engineering methods for nanobiological device applications). In fact, the number of potential nanobiological device functions that can be accommodated with engineered or native proteins is vastly beyond the capacity of any single treatise to fully enumerate. However, there are some particular applications of nanobiological devices that are widely used, even at this very early point in the development of the technology.

3.1. Polypeptide Affinity Reagents: Targeting, Triggering, and Assembly

Much like nucleic acid molecules, proteins can be used as affinity reagents to drive assembly of nanostructures, either as free molecules or when conjugated to heterologous nanomaterials. As discussed in the context of antibodies, the

domains of proteins responsible for specific molecular recognition of cognates are often sufficiently small, contiguous, and discrete to be abstracted from their native context as modules. Thus, binding domains of proteins (such as the variable regions of antibodies) can be appended to nanomaterials to drive specific nanostructure assembly. This can be applied to the delivery/tethering of nanostructures to sites containing the cognates of specific binding proteins in any number of contexts, including therapeutic settings.

In the simplest case, proteinaceous affinity reagents can be made as translational fusions with, or bioconjugates to, protein or small molecule drugs (Fig. 7). Immunotoxins are primarily anti-tumor therapeutics which append all or part of an antibody to a cytotoxic therapeutic to maximize toxicity to the tumor while minimizing systemic toxicity, based on the specific recognition of a tumor-associated antigen by the antibody portion of the conjugate [62–66]. This same strategy can be used to tether nanomaterials such as polymer therapeutics to disease sites [9, 10, 31, 32, 67–77]. Linear polymers or supramolecular polymer structures such as micelles can be tethered to desired sites using affinity reagents (Fig. 7).

The purpose of all therapeutic targeting is to delimit therapeutic action in space to minimize undesired side effects. The specificity of action of targeted therapeutics can be further enhanced if their actions are triggered, either by intrinsic conditions at the site of action (such as in the nucleic acid prodrug system discussed above), or by a stimulus provided by a clinician/device operator. Much as the three-dimensional conformation of, and therefore the function of,

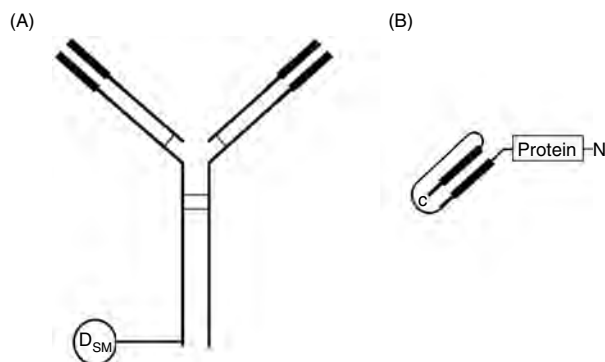


Figure 7. Biological affinity reagents are commonly used to tether other materials to their cognate antigens. This strategy is typically, but not solely, used to target therapeutics or imaging reagents to sites of interest *in vivo*. Figure 7A shows a bioconjugate composed of an IgG molecule, as in Figure 1, and a covalently linked small-molecule drug (D_{sm}). Bioconjugates, as in Figure 7A, are not synthesized in a single step, but rather the individual constituents (in this case, the antibody and the small molecule) are made separately and covalently linked to one another in a subsequent conjugation reaction. A wide variety of molecules and nanostructures can be conjugated to antibodies to confer the specific binding/assembly properties of the antibody to the construct. Figure 7B shows a fusion protein consisting of a ScFv (as in Fig. 1) fused to a second protein, which might be a protein therapeutic of some description (a cytotoxin, cytokine, etc.). Such fusion protein constructs exhibit the specific antigen recognition properties of their parent antibodies. Unlike the bioconjugate of Figure 7A, this molecule is made as a single molecule because the construct is synthesized from a single gene, engineered by standard molecular biology means.

proteins (as well as nucleic acid hybrids) can be controlled by external triggering strategies [48], proteins can be engineered to make their conformations sensitive to intrinsic conditions at their desired sites of activity. For instance, diphtheria toxin (DT) has been engineered to require a passage at low pH to achieve its toxic configuration. When the variant DT is associated with a receptor ligand, it can only be taken up and transported into low-pH lysosomal vesicles by cells with the appropriate counter-receptor on their surfaces [78]. Thus, toxicity of the variant DT is triggered only in cells expressing the appropriate receptor. Enzyme-activated delivery (EAD) is another triggering approach in which the properties of a nanoscale drug delivery vehicle are altered at the site of action by an endogenous enzymatic activity [72]. Enzyme-activated delivery involves a liposomal or micellar nanostructure from which synthetic pendant groups can be cleaved by metabolic enzymes (alkaline phosphatase, phospholipases, proteases, glycosidic enzymes, etc.) that are known to be highly expressed at the site of therapy. Nanostructures are designed so that cleavage of the pendant group causes a conformational or electrostatic change in the polymeric components of the delivery device, rendering the micellar structure fusogenic, leaky, or causing partial or complete dissociation of the structure to release its therapeutic payload at preselected sites [10]. Therapeutic administration by EAD approaches can be employed with or without a concomitant tissue-specific affinity targeting.

Obviously, affinity-mediated, tissue-specific delivery requires the presence of tissue-specific surface features (usually proteins or glycoproteins called tissue-specific antigens). Principal challenges in the search for tissue-specific antigens for drug targeting are specificity (few antigens are uniquely present in any single tissue) and availability (some tissues may not have their own unique antigenic signature or markers, or they may not be accessible from the vasculature). The recent discovery of a vascular address system [79–81] is exciting.

The vascular address system was identified by intravenous administration of a peptide phage display library (see [82] for a discussion of display technology) to animals, resecting individual organs from the animals and extracting phage from the vasculature of the isolated organs (Figs. 8A and 8B) [79–81]. The vasculature of individual organs was found to present unique constellations of receptors that could be recognized by short (10 amino acids or less) peptide sequences from the phage display library. Furthermore, the affinity-selected peptides can tether nano- to micro-scale particles to their cognate vasculature tissue-specific antigens, as illustrated in Figure 8C by the binding phage particles presenting the peptides to specific vascular locations. The vascular address system has been used to target a specific organ (the prostate) for destruction *in vivo* [83], establishing the utility of the address system in drug delivery [83, 84]. Mapping of the vascular address system is underway [81] and it remains to be seen whether each organ (or disease site) has a single molecular marker constituting its address which will be amenable to delivery of drugs tethered to the cognate peptide(s). Vascular addresses deliver materials to the organ vasculature—extravasation and access of organ tissue spaces by nanotherapeutics remains a separate issue.

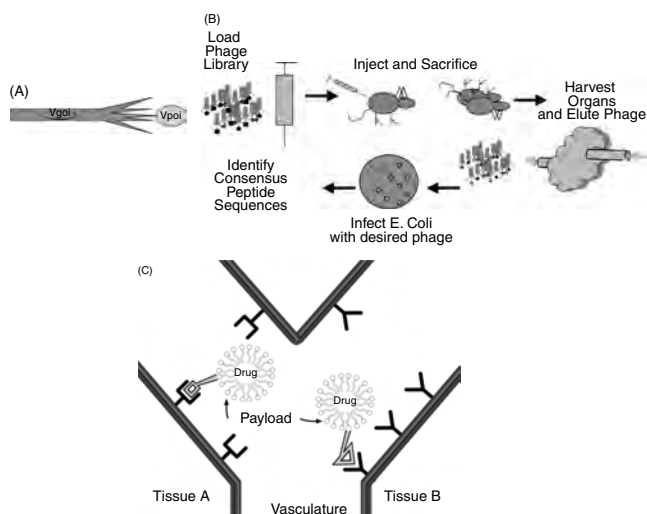


Figure 8. Biological affinity reagents can be derived *de novo* for a broad variety of molecules and nanomaterials using display technology. Figure 8A presents a schematic of an individual filamentous phage particle from a phage display library. Each particle contains a variant gene of interest (VgoI) as a part of the replicable phage DNA (circle, replicable in *E. coli*) and presents on its surface the corresponding variant protein of interest (Vpoi). The linkage between protein and the gene encoding it afforded by phage display methods allows simultaneous sorting of proteins of interest and the replicable genetic elements encoding them. Sorting is based on the relative affinities of the variant proteins presented for a target counter-receptor. Figure 8B shows an overview of a procedure by which reagents that recognize tissue-specific vascular “addresses” can be identified using phage display libraries. Phage are depicted as in Figure 8A, and the diverse Vpoi (peptides presented on surfaces of phage of a library are represented by various shaded shapes presented by the phage). A phage library presenting a vast number (up to 10^{12} different species) of variant peptides is injected intravenously into an animal, whereupon individual phage bind the vasculature of different tissues by virtue of the affinity of the peptide they present for tissue-specific vascular receptors (addresses). The animals are sacrificed and organs of interest (represented by the irregular shape) are harvested. Phage particles bound to receptors of vasculature of individual organs are perfused with an eluent buffer, releasing phage from the vasculature, *E. coli* is infected with the eluted phage particles and clonally propagated (symbolized by a schematic of bacterial colonies growing on a culture plate), ultimately allowing the identification of specific peptide sequences that recognize specific receptors on the vasculature of the organ or tissue involved. Usually one or more consensus peptide groups, rather than a single peptide species, are isolated after such an experiment. Members of consensus groups vary in amino acid sequence, but have some common sequence properties. Particularly, they exhibit one or more conserved or chemically similar amino acids at specific positions in the peptide sequence, defining the consensus. Display methods have been used to identify peptides which recognize many nanostructures and materials of both biological and synthetic origin. Typically, peptidic binding determinants selected, using phage display, are modular, and when isolated away from the parent phage, retain the specific recognition properties of the parent phage. Figure 8C shows therapeutic payloads (drugs or therapeutic nanodevices: payload) delivered to tissue-specific receptors by virtue of the affinity of peptidic reagents selected from a display library as in Figure 8B. Specific targeting peptides (square and triangle) tether a drug or other therapeutic nanodevice to their cognate receptors on vascular surfaces. Schematized here is a micelle containing a drug for targeted delivery to Tissue A or Tissue B, depending on which affinity reagent (square or triangle) is appended to the surface of the nanostructure [79–81].

3.2. Mechanoenzymes in Nanobiological Devices

Motor proteins (mechanoenzymes) excite significant attention from the engineering perspective, in part because of their striking resemblance to macroscale engineered structures. Furthermore, the value of imparting motility to device components is well understood in the context of macroscale devices, also contributing to the interest in the potential use of motor proteins in nanobiological devices. Consideration of motor proteins in nanodevices can be initiated most productively with consideration of the classes and distinct properties of available mechanoenzymes. Motor proteins may be divided into four major classes based on their mechanisms of action: rotary motors, linear (track) motors, polymerization/depolymerization motors, and lastly, a loose group of several mechanoenzymes with diverse structures, mechanisms, and functions that do not fit into the other groups. Both rotary and track motors have been used in nanobiotechnology to date.

3.2.1. Biological Rotary Motors

The chemiosmotic theory [85] maintains that bacterial cells utilize the electrochemical potential generated by cellular transmembrane proton gradients to produce adenosine triphosphate (ATP) (ATP is the major energy storage molecule found in living things). The bacterial protein complex responsible for interconversion of electrochemical potentials to chemical energy is the F-ATPase (Fig. 2A) [19, 20]. To generate ATP, protons passing through this pump induce conformational changes in the enzyme’s α and β subunits. These conformational changes result in the rotation of these subunits around a spindle (the gamma subunit), concomitant with ATP biosynthesis. Fortuitously, this process is fully reversible in the case of the F-ATPase, allowing the motor to hydrolyze ATP to ADP and inorganic phosphate to drive subunit rotation and proton transport. Because it possesses this property of reversibility, the F-ATPase offers an ATP-driven rotary motor for convenient use in nanobiological devices. Based on the “toroid and spindle” morphology of its assembled α , β , and γ subunits, the rotary mechanism of the F-ATPase had long been suspected. This mechanism was confirmed using a nanobiological device similar to the one shown in Figure 2B [86–88].

The device consists of a complex of the F-ATPase subunit α with modified versions of the β and γ subunits oriented on a metallic (nickel) stage which, in the presence of ATP, drives the rotation of an actin filament appended to the γ subunit. The α and modified β and γ subunits spontaneously self-assemble into the required toroid and spindle structure. This structure is oriented on the nickel surface by interaction between the metal and polyhistidine domains (polyhistidine sequences are known to bind metals), engineered as translational fusions to the β subunit. A biotin (a small organic molecule) is appended to the γ subunit, and a second biotin is appended to an actin filament using standard bioconjugation methods. The γ protein and the actin filament are linked by a streptavidin complex (streptavidin is a tetrameric protein complex that binds biotins with high affinities in interactions that are nearly as stable as covalent bonds). In

the presence of ATP, rotation of the actin filament “propeller” is detected by microscopic methods. A modification of this device has also been presented [19, 20]. There, the polyhistidine-beta subunit translational fusion protein orients the α - β - γ complex on a micro-machined, nickel-topped post. The actin filament is replaced with a biotinylated, micro-machined rod of approximately one micrometer. This version of the device may be marginally closer to the configuration we might expect for the use of the F-ATPase rotary motor in more complex nanobiological devices, but in its essential aspects, it is identical to the device of Noji et al. [86–90].

The devices of Noji and Soong [20, 87, 89] exhibit design features common to other nanobiological devices in that the relative positions and stoichiometries of assembled components are absolutely critical to device function. Furthermore, the toroid and spindle assembly sufficient for use as a nanoscale motor consists of only a small portion of the F-ATPase holoenzyme complex. The intact complex contains over 20 individual protein molecules, and eight distinct protein species [91, 92]. Additionally, the motor activity of the F-ATPase devices is incidental to the primary function of the enzyme complex, which is ATP biosynthesis. Thus, the designers of the devices of Figure 2B have caused modified biological components to perform a function (providing motive force) entirely dissimilar to their functions in their native biological contexts, by virtue of the designer’s control of the constituents and assembly of the devices, and providing yet another example of a nanobiological device design which extracts an unprecedented functionality from prefabricated biological components.

Other reasonably well-characterized, biological rotary motors include the V-ATPases and the bacterial flagellar motor. The V-type ATPases are ion transporters and are structurally similar to and operate by similar mechanisms as the F-ATPase [93, 94]. V-type ATPases occur throughout the biological world, from Archaeobacteria to higher eukaryotes. The F-ATPase and V-ATPases are attractive for use in nanotechnology by virtue of their compact sizes and high efficiencies. The efficiency of conversion of chemical energy into mechanical energy by these mechanoenzymes has been estimated to be between 60–100%, almost an order of magnitude greater than the efficiencies of myosin, dynein, and kinesin motor systems [90].

Bacterial flagellar motors utilize transmembrane proton gradients to power flagellar rotation, but they are structurally and genetically distinct from the F-ATPase and its relatives [95]. Though their prokaryotic origin should make flagellar motors convenient to genetically engineer and produce in quantity, their use in nanobiotechnological applications lags behind that of the F-ATPase for multiple reasons. For one thing, flagellar motors contain more distinct protein subunits and are more structurally complex than either F- or V-ATPases-derived rotary motors. Unlike the rotary motor structures of the V and F-type ATPases, parts of the flagellar motors transit the cell membrane, the peptidoglycan cell wall, and for Gram-negative bacteria, the outer membrane. The hydrophobicity of the domains involved in crossing hydrophobic structures (the cell and outer membranes) may

present challenges in incorporating the motor into semi-synthetic structures. Additionally, the specific structure and organization of flagellar motors also vary in different bacterial species. The diversity of flagellar motors may ultimately offer the nanotechnologist a selection of similar, yet distinct, rotary motors from which the best-suited motor could be chosen for any given application. However, with the possible exception of the flagellar motor of the Enterobacteriaceae (*E. coli* and related organisms), most flagellar motors have not yet been studied in sufficient detail to allow reasoned selection.

3.2.2. Biological Linear (Track) Motors

Linear motors such as myosin [96–99], dynein [100–116], and kinesin [117–138] are multi-protein complexes that migrate along a track of cytoskeletal protein. Myosin migrates along actin filaments, whereas both dynein and kinesin move along microtubules. Nucleotide hydrolysis (generally ATP) is the chemical energy source for all of these motor systems, so the motor proteins themselves are technically all ATPases, though they exhibit varying degrees of structural and functional analogy to one another. To date, only the kinesin/microtubule system has been put to extensive use in nanobiological devices.

All the linear motors discussed here migrate along a preformed polypeptide track. In nanotechnological applications, this allows the path, the motor unit, and any attached cargo will take to be determined by the specific deployment of the track protein. Actin filaments are double-stranded homopolymers of monomeric actin configured as a left-handed double helix [139, 140]. The diameter of a double-stranded actin filament is only very slightly in excess of 5.5 nanometers, which is the diameter of an actin monomer. The actin monomer is asymmetrical, and the filaments are polar, with so-called plus and minus ends. Most myosins migrate towards the plus end of filaments. Kinesin (Fig. 9A) and dynein migrate along microtubules, which are themselves supramolecular nanostructures of significant complexity [139, 141]. Individual microtubules are rigid, hollow tubes of 24 nanometers in diameter composed of left-handed double helices, one helix composed of α -tubulin and the other of β -tubulin (Fig. 9B). One end of the microtubule, the plus (+) end, terminates with β -tubulin while the minus (–) end terminates with α -tubulin. As was the case with myosin migration on actin filaments, individual kinesin species migrate towards either the plus or minus end of the microtubule. To date, only dynein species that migrate from plus to minus on microtubules have been described [139].

Movement of a mechanoenzyme along a biological linear polymer (such as the protein tracks previously described, but also nucleic acid strands, in the case of enzymes involved in DNA and RNA metabolism) in stable association with the linear polymer (*i.e.*, without falling off the polymer track) is called processive. Various linear molecular motors vary in their extents of processivity. All currently known kinesins and dyneins are highly processive, whereas many myosins require ultrastructural features in addition to the actin filament in order to exhibit appreciable processivity. In applications in which a nanodevice is intended to deliver a cargo to a preselected site, the processivity of the mechanoenzyme

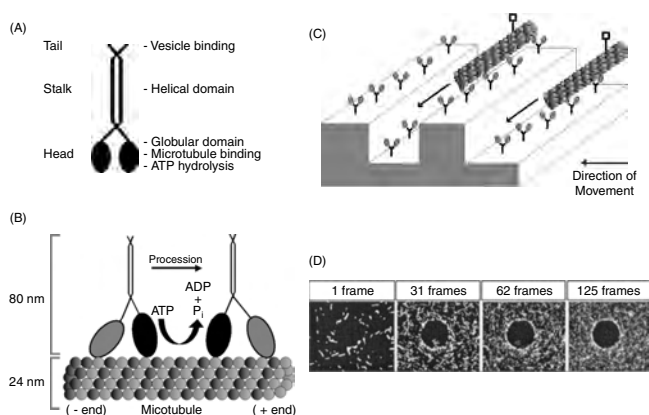


Figure 9. Linear “track” mechanoenzymes responsible for moving organelles to specific locations in the cell can be exploited by nanotechnologists. The kinesin linear motor protein contains an extended helical domain and tail domains that can bind specific intracellular vesicles (Fig. 9A). At the opposite end of the helical domains are globular locomotor domains that bind microtubules and hydrolyze ATP to move along them. The structure of myosin is analogous, though the primary nucleotide sequences of myosin is quite different from that of tubulin. Figure 9B shows – to + processive of kinesin along a microtubule. Microtubules are vectorial left-handed helices of α and β tubulin monomers (black and white dots). Kinesins have been described which migrate from the plus to minus and the minus to plus end of microtubules, but all native kinesins described to date can move in only one direction along the microtubule. Locomotion of kinesin resembles nothing so much as bipedal walking of kinesin along the microtubule and is powered by ATP hydrolysis. Myosin locomotion along actin filaments proceeds by a similar mechanism. Figure 9C illustrates incorporation of kinesin and microtubules into a device [119, 120, 147, 148]. In this configuration, the motor protein is deposited on a micromachined (grooved) surface that acts as a guiding channel (either in the grooves or on the ridges between them) for a microtubule shuttle. Shuttles can be derivatized with payloads (box appended to shuttles) that will process along paths determined by the deployment of kinesin and surface topography. Figure 9D shows an application of this configuration [118]. A substrate with microfeatures (polyurethane posts) was imaged. Kinesin was deployed on the substrate, and 1.5 micrometer fluorescently-tagged microtubulin shuttles were deposited on the substrate, and ATP was provided. The shuttles move along areas of the substrate containing kinesin, but cannot access the tops of the polyurethane posts due to microtubule rigidity. Movement of the shuttles is confined to the regions of the substrate other than the polyurethane posts. Superposition of multiple photomicrographs of shuttle fluorescence resulted in the image of the polyurethane posts shown in Figure 9D. This imaging method may be applied to other microstructures. Reprinted with permission from [149], H. Hess et al., *Nano Letters* 2, 113 (2002). © 2002, American Chemical Society.

is clearly critical. Mechanoenzymes with insufficient processivity with respect to the biological polymer could simply dissociate from the track prior to delivering their payloads to their targets, defeating the purpose of the device. Alternatively, the requirement for ultrastructures in addition to the track might be exploited by device designers to build delivery systems that are functional in some environments (chosen or selected by the designer), but not in others.

Kinesins are a superfamily of highly related eukaryotic motor proteins. They were originally identified as a motor protein that moved vesicles in extracts along microtubules directionally from slow-growing to fast-growing ends, though

kinesin species that locomote in the opposite direction along the tubules have also been discovered [121–125, 127, 131–134]. The kinesin holoenzyme is a heterotetramer consisting of two heavy chains and two light chains (Fig. 9A) [126]. The motor domain is located in the so-called head of kinesin, and consists of a 320-amino-acid catalytic core with both a microtubule and nucleotide triphosphate (ATP) binding site. Appended to each head is a flexible neck domain that connects the head to the stalk and tail. Cargos carried along the microtubule are bound to the kinesin tail. Kinesin head and tail morphology is similar to that of myosin and, in fact, both myosin and kinesin exhibit similar modularity. The motor domains of both kinesins and myosins are highly conserved (though the kinesin and myosin motor domains are dissimilar to one another), and the specific tail-domain, amino acid sequence dedicates the kinesin or myosin to particular transport functions. The identity of the tail module determines the cargo the motor can carry and which diverse cellular process the kinesin (or actin) contributes to. In the case of kinesin, the protein participates in diverse cell processes such as vesicular transport [135], and associates with the scaffolding proteins of signal transduction pathways [136] and kinetochores [137, 138].

Kinesins function by binding to a specific site on microtubules and undergoing an ATP-dependent conformational change that is linked to release from the tubule. Since kinesin is a dimer, at least one kinesin monomer contacts the microtubule at all times. Adenosine triphosphate hydrolysis causes one of the kinesin heads to release the microtubule and swivel to recontact the microtubule downstream of its original position. The power stroke cycle completes with rebinding to the microtubule by the head. The second head of the complex then completes an identical power stroke (Fig. 9B) and the kinesin dimer literally walks along the microtubule in the presence of ATP. The overall mechanism is highly similar to that of myosin locomotion on actin filaments [142].

Locomotion of native kinesins is unidirectional, so ATP hydrolysis causes kinesin to ratchet vectorially along the length of microtubules. Minus to plus (– to +) kinesin and plus to minus (+ to –) kinesin share essentially identical structures, but their polarity of motion on microtubules can be attributed to small structural differences in the neck domain [128, 129]. Indeed, a single point mutation in the neck region of kinesin renders the protein capable of movement in both directions on microtubules [130].

About 40 distinct myosin genes are recognized in humans [96], so like kinesins, myosins are a large superfamily of ATP-hydrolyzing mechanoenzymes. Unlike kinesin, myosins migrate along actin microfilaments [96–99]. Despite the fact that the two superfamilies are genetically quite distinct, myosin and kinesin share similar morphologies and mechanisms of action [142], as well as similar modularity if their tail domains that dedicate specific motor proteins to specific tasks. Myosin and actin are involved in various important physiological processes including organelle trafficking, muscle contraction, and cell division [143].

Dyneins are a third superfamily group of eukaryotic, linear mechanoenzymes associated with eukaryotic cilia and flagella [100, 101], and are also expressed in the cytoplasm where they are involved in vesicle and organelle transport

and reorganizations of the nuclear spindle during cytokinesis [100, 101]. Dynein is the largest of the linear cytoskeletal motor proteins, consisting of 4600 amino acids making it twice the size of myosin and four times the size of kinesin. Fully 3000 amino acids of this protein comprise the enormous motor domain, containing six tandemly iterated ATPase domains [107–109]. Like kinesin, dynein moves along microtubules, but the mechanism of dynein movement is thought to differ from those of myosin and kinesin [108, 115, 116]. The large size and relatively poor biochemical definition of dynein mechanism and activity may make it less attractive in nanobiological application in the near future.

Other biological linear track motors include all of the template-dependent oligonucleotide polymerases involved in replication, transcription, reverse transcription, and repair [144, 145]. In the course of oligonucleotide polymerization, these enzymes migrate along an oligonucleotide substrate (the template) synthesizing a second strand that is the reverse complement of the template. The energy for the motive-force generation ultimately comes from hydrolysis of nucleotide triphosphates, which are incorporated into the nascent oligonucleotide strand. This class of mechanoenzymes has yet to see extensive application in nanobiological devices, though they have potentially interesting features and properties. In particular, short nucleic acid segments are quite flexible, as discussed above. This flexibility allows oligonucleotides to be deployed to conform to nanoscale features considerably smaller than those to which rigid microtubules can.

The capacity of linear track motors to move along predetermined pathways is potentially attractive for use in nanobiological devices to shuttle carried materials or to actuate devices. The carried materials can be quite large relative to the linear motor proteins. For instance, microscale myosin-coated beads move on isolated actin filaments in an ATP-dependent manner [146].

Of the three major linear motors discussed, only the kinesin-microtubule system has enjoyed the extensive use in nanobiological devices. The system can be deployed with the track (microtubulin) adherent to a substrate, and the motor protein moving along the track. Alternatively, active motor proteins can be coupled to a substrate, and a segment of the track can be used as the shuttle [147, 148]. This expedient helps mitigate limitations imposed by the rigidity of microtubules. Microtubules can only be used to guide motors around features of five millimeters and greater, corresponding to the persistence length of the microtubules [118, 120]. However, deployed motor proteins are not similarly restricted, and when used with a textured surface featuring a guiding channel with the kinesin deployed in them, microtubule shuttles can describe complex paths with micrometer, and potentially greater, resolution in an ATP-dependent fashion (Fig. 9C).

Fluorescently labeled microtubule shuttles have put to novel use to image an elevated and recessed pattern on a surface decorated one micrometer polyurethane posts (Fig. 9D) [149] in a method that takes advantage of the high rigidity of microtubules. Kinesin was deployed densely and evenly across an 85×68 micrometer-patterned surface and approximately 600 fluorescently labeled 1.5 micrometer microtubule shuttles were deposited at random on the

surface. In the presence of 1mM ATP, the shuttles commenced random motion on the surface. Owing to their rigidity, the microtubulin fragments could not traverse the raised posts from the recessed surface, despite the presence of active kinesin on those posts. Consequently, superposition of fluorescence photomicrographs revealed the fluorescence of the recessed surface while the raised posts appeared as dark regions. In this experiment, the image was collected in about five seconds. Effectively, the fluorescent microtubulin shuttles act as autonomous probes of the surface (“self-propelled robot probes”), and the investigators suggest their use as a highly fault-tolerant alternative to force microscopy imaging approaches.

3.3. Immobilized Growth Factors: Ex-vivo Cell Expansion

Cytokines and similar growth-promoting proteins are typically soluble proteins secreted by one cell to trigger the proliferation and/or the metabolic activity of itself (autocrine stimulation) or another cell (endocrine, paracrine, or juxtacrine stimulation) [28, 150]. In applications involving *ex-vivo* cell expansion (for instance, for hematopoietic reconstruction or other tissue engineering applications) it can be useful to immobilize such factors on solid surfaces to direct cellular colonization of a synthetic structure or to modulate the expansion of a cell product. Ultimately, these approaches may allow cultivation of cells in a media containing no proteins in solution [151–154]. Particularly in cases in which the expanded cell product is to be readministered to patients, these approaches can minimize the coadministration potentially inflammatory, immunogenic, or toxic-dissolved proteins along with the therapeutic cell product.

Insulin is a familiar example of a protein with both mitogenic and physiological regulatory properties: it not only stimulates conversion of glucose to glycogen to maintain normoglycemia, but it also only triggers proliferation of many cell types. Insulin, as well as other polypeptide growth factors like interleukin-2 (IL-2) and epidermal growth factor (EGF), can retain its biological activity when coupled to solid surfaces [26, 29, 151–156]. Not surprisingly, coimmobilizing accessory proteins (such as cell adhesion molecules) stabilize cell binding to the growth-promoting surfaces and enhance proliferative responses [26, 27, 157]. More remarkably, as shown in Figure 10A, the mitogenic specific activity of these proteins (their cell expansion activity expressed as a function of the concentration or absolute amount of the mitogen: a measure of potency) of these factors is increased by as much as one to two orders of magnitude in certain bioconjugates [26, 157, 158].

Though the bioconjugates in question are polyvalent (that is, present multiple individual growth factor molecules), and polyvalency might play some role in their enhanced activity, the primary mechanism of enhancement of proliferative activity is apparently related to the size of the bioconjugates (Fig. 10B). Bioconjugates large enough to prevent the cellular uptake associated with growth factor receptor cycling and ligand degradation seem to trigger prolonged cytokine signal transduction, resulting in enhanced proliferation [26, 157, 158]. This phenomenon may figure into the potent juxtacrine stimulation effects observed *in vivo* and *ex vivo* with

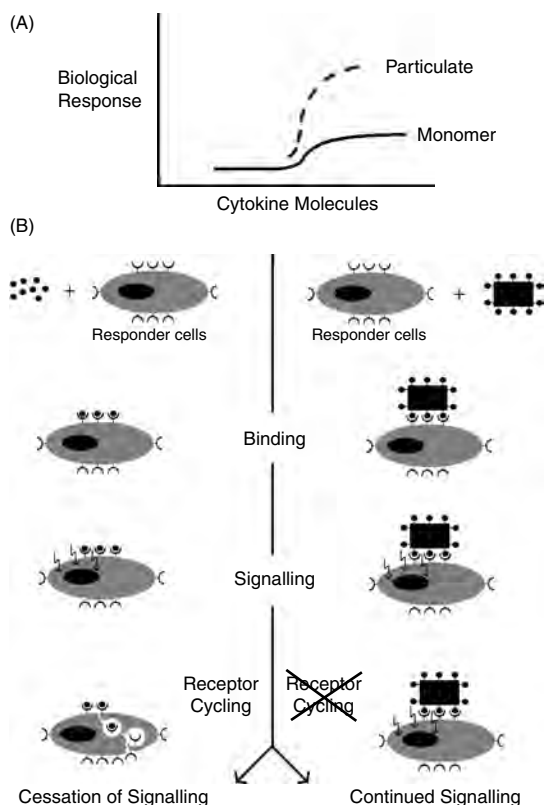


Figure 10. Deployment of biological signaling molecules on synthetic micro and nanosurfaces can enhance their activities. Figure 10A shows how the activity of cytokines and other signaling proteins (typically cell proliferative activity, but also other physiological activities may be similarly effected), normalized to their concentration, can increase when signaling proteins are provided to responder cells as a bioconjugate to nano- and microscale materials. Responses to appropriately sized bioconjugates can be supramaximal relative to responses to free monomeric protein (that is, giving responses higher than can be attained with any concentration of free protein). This suggests that signal transduction or response mechanisms associated with such bioconjugates somehow differ from those associated with free-signaling proteins, and a potential mechanism is shown in Figure 10B. Protein-signaling molecules, such as insulin and interleukins, (circles) bind receptors on the surface of responder cells (Y-shaped structures on cell surfaces), resulting in a signal (to proliferate, to differentiate, lightning bolt) being sent to the cell nucleus. To allow the cells to respond to subsequent waves of signaling molecules, receptors with bound signaling molecules are endocytosed (internalized) in vesicles, wherein the signaling molecules are degraded, and the receptors are subsequently returned to the surface. This process is referred to as receptor cycling, and individual signaling molecules cease to provide signals to responder cells when they undergo receptor cycling. It is hypothesized that bioconjugates to particles that are too large to be endocytosed (the box decorated with circles) are unable to participate in receptor cycling, and therefore provide a signal to responder cells for a much longer duration than do individual signaling protein molecules. This is thought to result in a higher magnitude proliferative and physiological response. The size range necessary to trigger the enhanced responses is currently poorly defined, and may vary with the signaling molecules, the responder cell, and particle topography and chemistry [26, 157, 158].

cell membrane-bound forms of protein growth factors [150]. The size limit that precludes uptake and leads to enhanced mitogenesis is not well defined, but sizes approximating the size of the cell taking the material up would seem to be logical. This would place the critical dimensionality for juxtacrine effects somewhere in the micrometer range. In the case of EGF, the density of the growth factors on the surface clearly impact proliferative activity [26]. Studies of a micropatterned surface with EGF deployed in stripes at various distances from one another revealed that optimal proliferation is supported when stripes of growth factors are considerably closer to each other than the medium length of individual cells. Taken together, these data show that it is possible to build nano- to micro-scale devices to support more efficient cell proliferation than can soluble growth factors. Such proliferative devices will feature growth factors and accessory proteins deployed on microscale surfaces at micrometer or submicrometer distances from one another.

4. CONCLUSIONS

The initial formulation of the nanobiological approach to device construction was driven by expediency. No technology was then available to make a selection of synthetic nanocomponents with ranges of activities as broad as those represented by biological macromolecules. In the years since this notion was first promulgated, there have been incremental improvements in nanocomponent construction, but incorporation of functional biomolecules often remains the only feasible approach to build many specific functional nanostructures of interest. Fortunately, the diversity of proteins available in the biological world and achievable by genetic engineering methods is practically inexhaustible.

Successful nanobiological devices exhibit some common features. Knowledge of the biology, chemistry, and mechanism of action of biomolecular components is critical for their incorporation into a functional nanostructure. Such knowledge allows designers to deal with biocomponents as modules, and to incorporate all biological features needed for the function in question, while minimizing the incorporation of extraneous features (Figs. 1, 2, 6–8). This assures that device components can perform the subroutines for which they were selected and mitigates the possibility that undesired activities and functions might be introduced into devices. Incorporating the minimal biological unit needed for function may also increase device stability, since minimizing the size of the components, also minimizes the number of possible enzymatic cleavage sites for proteases and nucleases that might contribute to component (and device) degradation.

Components are often abstracted from multiple, potentially phylogenetically distant biological sources, as the bacmid system illustrates in its incorporation of both prokaryotic and eukaryotic genetic elements in a single device. In most contexts, incorporation of components from disparate sources presents no barrier to device function, though device function requires the concerted or sequential action of multiple device components and emerges from this summed activity of components. The activities of components are able to sum to a desired result as the result of physical/temporal organization imposed by device design

rather than by component phylogenetic relationships. The necessity of coordinated action of multiple molecular components to nanobiological device function and the role of designed, specific structure to support function is apparent in virtually every nanodevice discussed herein. An important differentiation between fully synthetic and semi-biological hybrid devices is that the full range of properties of biological components are often more complex and less well understood than are those of purpose-designed synthetic components. Operationally, this means that nanobiological device design and synthesis is often a highly iterative business involving rapid prototyping and assay, followed by redesign, resynthesis, and re-assay until a version of the device with the desired properties is achieved. The iterative nature of nanobiological device design makes facile synthesis and sensitive assay of device function and properties immensely valuable.

Finally, nanobiological devices are not limited to biomimetic structures. The range of possible functions that nanobiotechnology can realize are less dependent on precedents from the biological world than on the ingenuity of device designers. At one level or another, virtually every structure described here presses one or more biological component into a service that is distinct from the actions those biomolecules perform in their native contexts. Specific device functionalities are implicit in the organization provided in design, and not inherent in the biological components themselves.

Nanodevices are potentially highly congruent with applications in drug delivery, *in vivo* sensing, and diagnostics [1, 3, 4, 11, 12, 30]: disease states involving aberrant behavior of nanoscale components (proteins, nucleic acids, other biological macromolecules, and supramolecular structures) must often be addressed with dimensionally appropriate (nanoscale) therapeutics. The drive to medical device miniaturization is also supported by the desire for minimally invasive therapeutic interventions (or in NASA's case, the desire for low-mass therapeutics). At some point, the distinction between materials science and pharmacology begins to blur, but the nanoscale therapeutic devices are differentiated from more conventional drugs by their multifaceted activities and by the potentially complex physiological services such devices might someday deliver. Though nanobiological approaches were initially devised as a stopgap, therapeutic nanodevices may represent a special case that will always be best served by incorporation of biomolecules, regardless of advances in materials science, microfabrication, and polymer chemistry which might support fully synthetic nanotherapeutics. Biomolecules can potentially provide a compositionally and dimensionally appropriate interface between nanodevices and biological systems (patients).

Realization of the potential of nanobiological devices for human therapy will require meeting numerous technological challenges, some of which attach to nanobiological devices in any context, and some of which apply primarily to nanobiological devices in therapeutic use. In the former category, the means to deal with the lability of the biological components of nanobiological devices are required. The lability of biomolecules delimits those environments and conditions under which nanobiological devices can function. Biomolecule lability also delimits the processing and

assembly conditions available for nanobiological device realization. Not only must processing methods preserve the structural and functional integrity of biological components, but those methods must be massively parallel and require limited direct operator intervention. Annual demand for individual therapeutic devices could be in excess of tens of moles of devices in some cases, so manufacture must be highly reproducible, cheap, and facile.

With specific regard to therapeutic nanobiological devices *in vivo*, the biocompatibility and immunogenicity of the devices are critical concerns. Currently, there is no reliable means to eliminate opsonization, inflammatory, foreign body and wound-healing responses to nano-microscale implants. Ultimately, these responses compromise the efficacy of many macroscopic therapeutic implants, and are likely to similarly impact the function of nanobiological therapeutics [159]. Furthermore, it is becoming clear that many synthetic nanomaterials can sometimes trigger specific immune responses. For instance, carbon nanotubes and PAMAM dendrimers trigger specific antibody responses under some circumstances [6, 160–162]. Antibody responses can neutralize the therapeutic properties of protein and small molecule drugs, and have the potential to produce similarly negative impacts on the action of nanobiological therapeutic devices [6, 160–162].

This does not represent an exhaustive list of the challenges lying between current technology and robust nanobiotechnology, but rather represents a sampling of some of the most pressing issues. Doubtless, as yet unimagined challenges will manifest themselves as the technology matures. Still, nanobiotechnology offers vast technological power and opportunity. The extent of possibility can best be glimpsed from a survey of the diversity of function, the economy of action, and the sheer magnitude of the synthetic capability manifest in the biological world. This constitutes a motivation sufficient to justify the expenditure of resources that will be necessary to fully realize nanobiotechnology and associated nanobiological devices.

GLOSSARY

Antibody A soluble immune effector protein induced in response to and capable of recognizing a specific epitope. There are multiple types of antibodies, with IgG, occurring in serum, being the most commonly encountered. IgG molecules are bivalent but monospecific antibodies.

Bacmid A baculovirus containing a bacterial plasmid origin of replication, capable of replicating in bacteria and insect cells.

Baculovirus One of a family of viruses (nuclear polyhedrosis viruses) that infect insects, and which are used as cloning vectors for heterologous protein production in insect cell culture.

Cytokine One of a class of typically soluble protein growth factors involved in the growth, differentiation and activation of hematopoietic cells.

Dendrimer cluster agents A class of therapeutic platform consisting of multiple dendritic polymers, each individual dendritic polymer derivatized to perform a specific device function *in vivo*. Cluster agents are constructed using dendritic polymer self-assembly properties.

Diphtheria toxin (DT) Toxin of the bacterial pathogen *Corynebacterium diphtheriae*.

Enzyme activated delivery (EAD) A prodrug strategy typically involving drugs carried in nonfusogenic liposomes in which the liposomes are rendered fusogenic with cell membranes (and therefore delivering their pharmacological payloads) by the action of cell-membrane enzymes at their desired sites of action.

Epitope A molecular feature recognized by a specific immune effector, such as an antibody.

Ex vivo cell expansion Directed proliferation of cells (often hematopoietic precursors) isolated from a living thing, typically done with the intent to readminister the expanded cells.

Growth factors Specific substances that direct growth and differentiation of specific cell populations.

Hematopoiesis The process of generating cellular components of blood.

Mechanoenzymes Enzymes that transduce energy (from ATP or transmembrane ion gradients) into mechanical energy.

Mitogen A substance that causes the proliferation of cells.

Nanobiological device A nanodevice containing both synthetic and biological components in which the components are organized to perform a desired work process.

Nanodevice A structure whose function is mediated by some precise nanoscale feature or component.

Nucleic acid hybridization The propensity of complementary nucleic acid sequences to associate with each other non-covalently via inter-strand hydrogen bonding interactions.

Plasmid An autonomously replicating, nonchromosomal DNA sequence of prokaryotes or eukaryotes, typically a double-stranded, circular nucleic acid molecule.

Prodrug A drug moiety with no or minimal pharmacological activity upon administration, but which is processed to an active form *in vivo*.

Therapeutic platform A multifunctional therapeutic nano-to microscale device or diagnostic, typically for *in vivo* use, that incorporates the capacity to be modified to address specific disease states or patients.

Transposon A genetic element capable of moving from one specific DNA site to another.

ACKNOWLEDGMENTS

The authors gratefully acknowledge many friends and colleagues whose input helped shape this article. Particularly, we acknowledge Beth S. Lee for many, many helpful discussions and unflagging support. We acknowledge Phil Streeter for many of the same services, performed in the office of friend, rather than spouse. SL acknowledges the support and encouragement of Robert Jansson, which helped make his early nanotechnology career possible. This article is dedicated in loving memory of Mildred A. Lee, Antonio Ferrari, Marialuisa Ferrari, and the innumerable others whose lives have been so tragically touched by cancer, with the commitment that nanotechnology shall be used to help wrest from the disease its terrible power over human life.

REFERENCES

1. S. C. Lee, in "Biological Molecules in Nanotechnology: The Convergence of Biotechnology, Polymer Chemistry and Materials Science" (S. C. Lee and L. Savage, Eds.), p. iv. IBC Press, Southborough, MA, 1998.
2. S. C. Lee, *Trends Biotechnol.* 16, 239–240 (1998).
3. S. C. Lee, in "Biological Molecules in Nanotechnology: The Convergence of Biotechnology, Polymer Chemistry and Materials Science" (S. C. Lee and L. Savage, Eds.), pp. 3–14. IBC Press, Southborough, MA, 1998.
4. S. C. Lee, in "Biological Molecules in Nanotechnology: The Convergence of Biotechnology, Polymer Chemistry and Materials Science" (S. C. Lee and L. Savage, Eds.), pp. 67–74. IBC Press, Southborough, MA, 1998.
5. S. C. Lee, R. Parthasarathy, and K. Botwin, *Polymer Preprints* 40, 449–450 (1999).
6. S. C. Lee. "A Biological Nanodevice for Drug Delivery." National Science and Technology Council. IWGN Workshop Report: Nanotechnology Research Directions, Baltimore, MD, International Technology Research Institute, World Technology Division. Kluwer Academic Publishers, 2000.
7. J. Baish, Y. Gazit, D. Berk, M. Nozue, and L. T. Baxter, *Microvasc. Res.* 51, 327–346 (1996).
8. J. R. Baker, Jr., in "Biological Molecules in Nanotechnology: The Convergence of Biotechnology, Polymer Chemistry and Materials Science" (S. C. Lee and L. Savage, Eds.), pp. 173–183. IBC Press, Southborough, MA, 1998.
9. R. Duncan, *J. Drug Targeting* 5, 1–4 (1997).
10. R. Duncan, S. Gac-Breton, R. Keane, R. Musila, Y. N. Sat, R. Satchi, and F. Searle, *J. Controlled Release* 74, 135–146 (2001).
11. D. S. Goldin, C. A. Dahl, K. L. Olsen, L. H. Ostrach, and R. D. Klausner, *Science* 292, 443–444 (2001).
12. S. C. Lee, in "Dendrimers and Other Dendritic Polymers" (D. Tomalia and J. Frechet, Eds.), pp. 548–557. John Wiley & Co., London, 2001.
13. J. R. Baker, Jr., A. Quintana, L. Piehler, M. Banazak-Holl, D. Tomalia, and E. Racka, *BMMD* 3, 61–69 (2001).
14. L. Jelinski, in "Nanostructure Science and Technology" (R. W. Siegel, E. Hu, and M. C. Roco, Eds.), pp. 113–130. Kluwer Academic Publishers, Dordrecht, 1999.
15. A. Prokop, in "Bioartificial Organs III: Tissue Sourcing, Immunoisolation, and Clinical Trials," Vol. 944, pp. 472–490, 2001.
16. F. Breitling and S. Dubel, "Recombinant Antibodies." John Wiley & Sons, London, 1998.
17. E. Harlow and D. Lane, "Antibodies: a Laboratory Manual." Cold Spring Harbor Press, Cold Spring Harbor, 1989.
18. C. A. Janeway, P. Travers, M. Walport, and J. D. Capra, "Immunobiology." Elsevier Science, London, 1999.
19. C. Montemagno and G. Bachand, *Nanotechnology* 10, 225–231 (1999).
20. R. K. Soong, G. D. Bachand, H. P. Neves, A. G. Olkhovets, H. G. Craighead, and C. D. Montemagno, *Science* 290, 1555–1558 (2000).
21. K. Yonekura, S. Maki, D. G. Morgan, D. J. DeRosier, F. Vonderviszt, K. Imada, and K. Namba, *Science* 290, 2148–2152 (2000).
22. K. Yonekura, S. Maki-Yonekura, and K. Namba, *J. Structural Biology* 133, 246–253 (2001).
23. D. Walz and S. R. Caplan, *Bioelectrochemistry* 55, 89–92 (2002).
24. T. Atsumi, *J. Theoret. Biol.* 213, 31–51 (2001).
25. G. H. Deng, Q. W. Xu, J. K. Liu, and Y. G. Cong, *Prog. Biochem. Biophysics* 27, 612–615 (2000).
26. G. P. Chen, Y. Ito, and Y. Imanishi, *Bioconjugate Chemistry* 8, 106–110 (1997).
27. Y. Ito, *Nanotechnology* 9, 200–204 (1998).
28. Y. Ito, *Mater. Sci. Eng. C-Biomimetic Mater. Sens. Systems* 6, 267–274 (1998).

29. G. P. Chen and Y. Y. Ito, *Biomaterials* 22, 2453–2457 (2001).
30. S. C. Lee, in “Dendrimers and Other Dendritic Polymers” (D. Tomalia and J. Frechet, Eds.). John Wiley & Co., London, 2001.
31. R. Duncan, J. K. Coatsworth, and S. Burtles, *Hum. Exper. Toxicol.* 17, 93–104 (1998).
32. R. Duncan, *Chem. Industry* 7, 262–264 (1997).
33. J. Li, D. R. Swanson, D. Qin, H. M. Brothers, L. T. Piehler, D. Tomalia, and D. J. Meier, *Langmuir* 15, 7347–7350 (1999).
34. D. A. Tomalia, H. M. Brothers, L. T. Piehler, H. D. Durst, and D. R. Swanson, *Proc. Natl. Acad. Sci. USA* 99, 5081–5087 (2002).
35. N. C. Seeman, J. Chen, Z. Zhang, B. Lu, H. Qiu, T.-J. Fu, Y. Wang, X. Li, J. Qi, F. Liu, L. A. Wenzler, S. Du, J. E. Mueller, H. Wang, C. Mao, W. Sun, Z. Shen, M. H. Wong, and R. Sha, in “Biological Molecules in Nanotechnology: The Convergence of Biotechnology, Polymer Chemistry and Materials Science” (S. C. Lee and L. Savage, Eds.), pp. 45–58. IBC Press, Southborough, MA, 1998.
36. M. J. Heller, in “Biological Molecules in Nanotechnology: The Convergence of Biotechnology, Polymer Chemistry and Materials Science” (S. C. Lee and L. Savage, Eds.), pp. 59–66. IBC Press, Southborough, MA, 1998.
37. Z. C. Ma and J. S. Taylor, *Proc. Natl. Acad. Sci. USA* 97, 11159–11163 (2000).
38. R. C. Merkle, *Trends Biotechnol.* 17, 271–274 (1999).
39. M. S. Shchepinov, K. U. Mir, J. K. Elder, M. D. Frank-Kamenetskii, and E. M. Southern, *Nucleic Acids Res.* 27, 3035–3041 (1999).
40. C. M. Niemeyer, *Appl. Phys. A-Mater. Sci. Proc.* 68, 119–124 (1999).
41. N. C. Seeman, *Nano Letters* 1, 22–26 (2001).
42. N. C. Seeman and A. M. Belcher, *Proc. Natl. Acad. Sci. USA* 99, 6451–6455 (2002).
43. A. Carbone and N. C. Seeman, *Proc. Natl. Acad. Sci. USA* 99, 12577–12582 (2002).
44. J. T. Mascarello, A. R. Brothman, K. Davison, G. W. Dewald, M. Herrman, D. McCandless, J. P. Park, D. L. Persons, K. W. Rao, N. R. Schneider, G. H. Vance, and L. D. Cooley, *Arch. Pathol. Lab. Med.* 126, 1458–1462 (2002).
45. M. J. Heller, *Ann. Rev. Biomed. Eng.* 4, 129–153 (2002).
46. J. Shaughnessy, E. Tian, J. Sawyer, J. McCoy, G. Tricot, J. Jacobson, E. Anaissie, M. Zangari, A. Fassas, F. Muwalla, C. Morris, and B. Barlogie, *Brit. J. Haematology* 120, 44–52 (2003).
47. Z. C. Ma and J. S. Taylor, *Bioorganic Med. Chem.* 9, 2501–2510 (2001).
48. K. Hamad-Schifferli, J. J. Schwartz, A. T. Santos, S. Zhang, and J. M. Jacobson, *Nature* 415, 152–155 (2002).
49. C. Y. Li and M. W. Dewhirst, *Internat. J. Hyperthermia* 18, 586–596 (2002).
50. S. R. Dixon, R. J. Whitbourn, M. W. Dae, E. Grube, W. Sherman, G. L. Schaer, S. Jenkins, D. S. Baim, R. J. Gibbons, R. E. Kuntz, J. J. Popma, T. T. Nguyen, and W. W. O’Neill, *J. Am. College Cardiology* 40, 1928–1934 (2002).
51. V. Chytrý and K. Ulbrich, *J. Bioactive Compatible Polymers* 16, 427–440 (2001).
52. L. Lundgren-Eriksson, R. Hultborn, and R. Henriksson, *Anti-cancer Res.* 21, 3275–3280 (2001).
53. T. Gardner, C. R. Cantor, and J. J. Collins, *Nature* 403, 339–342 (2000).
54. J. Hasty, F. Isaacs, M. Dolnik, D. McMillen, and J. J. Collins, *Chaos* 11, 207–220 (2001).
55. S. C. Lee, M. S. Leusch, V. A. Luckow, and P. Olins (1994). Method of producing recombinant viruses in bacteria. *U.S. Patent and Trademark Office* 5,348,886.
56. L. K. Hawkins, N. R. Lemoine, and D. Kirn, *Lancet Oncology* 3, 17–26 (2002).
57. L. Stevceva, A. G. Abimiku, and G. Franchini, *Genes Immunity* 1, 308–315 (2000).
58. S. Zoppi, D. R. Allman, R. D. Gerard, and M. J. McPhaul, *J. Molecular Endocrinology* 27, 321–328 (2001).
59. H. Mizuguchi, M. A. Kay, and T. Hayakawa, *Adv. Drug Delivery Rev.* 52, 165–176 (2001).
60. B. C. Horsburgh, M. M. Hubinette, D. Qiang, M. L. E. MacDonald, and F. Tufaro, *Gene Therapy* 6, 922–930 (1999).
61. D. J. A. Crommelin and R. D. Sindelar, “Pharmaceutical Biotechnology.” Harwood Academic Publishers, Amsterdam, 1997.
62. R. Hassan, J. L. Viner, Q. C. Wang, I. Margulies, R. J. Kreitman, and I. Pastan, *J. Immunotherapy* 23, 473–479 (2000).
63. Y. Reiter and I. Pastan, *Trends in Biotechnology* 16, 513–520 (1998).
64. Y. Reiter, U. Brinkmann, B. K. Lee, and I. Pastan, *Nature Biotechnology* 14, 1239–1245 (1996).
65. E. Mansfield, P. Amlot, I. Pastan, and D. J. Fitzgerald, *Blood* 90, 2020–2026 (1997).
66. C. G. L. Lee, W. D. Vieira, I. Pastan, and M. M. Gottesman, *Human Gene Therapy* 12, 945–953 (2001).
67. M. E. Akerman, W. C. W. Chan, P. Laakkonen, S. N. Bhatia, and E. Ruoslahti, *PNAS* 99, 12617–12621 (2002).
68. K. M. Bernt, D. S. Steinwaerder, S. H. Ni, Z. Y. Li, S. R. Roffler, and A. Lieber, *Cancer Res.* 62, 6089–6098 (2002).
69. Z. G. Gao, A. N. Lukyanov, A. Singhal, and V. P. Torchilin, *Nano Letters* 2, 979–982 (2002).
70. C. Allen, D. Maysinger, and A. Eisenberg, *Coll. Surf. B-Biointerfaces* 16, 3–27 (1999).
71. P. M. Loadman, M. C. Bibby, J. A. Double, W. M. Al-Shakhaa, and R. Duncan, *Clin. Cancer Res.* 5, 3682–3688 (1999).
72. P. Meers, *Adv. Drug Delivery Rev.* 53, 265–272 (2001).
73. N. G. Patrick, S. C. W. Richardson, M. Casolaro, P. Ferruti, and R. Duncan, *J. Control Rel.* 77, 225–232 (2001).
74. R. Satchi, T. A. Connors, and R. Duncan, *Brit. J. Cancer* 85, 1070–1076 (2001).
75. H. Wang, H. Song, and V. C. Yang, *J. Cont. Release* 59, 119–122 (1999).
76. X. J. Wu, X. P. Tang, M. Xian, and P. G. Wang, *Tetrahedron Lett.* 42, 3779–3782 (2001).
77. S. Spiwongsitanont and M. Ueno, *Chem. Pharmaceutical Bull.* 50, 1238–1244 (2002).
78. V. Raso, M. Brown, and J. McGrath, *J. Biol. Chem.* 272, 27623–27628 (1997).
79. M. Kolonin, R. Pasqualini, and W. Arap, *Curr. Opin. Chem. Biol.* 5, 308–313 (2001).
80. E. Ruoslahti, *Pharmaceutical News* 7, 35–40 (2000).
81. W. Arap, M. Kolonin, M. Trpel, J. Lahdenranta, M. Cardovila, R. Giordano, P. J. Mintz, P. Ardel, V. Yao, C. Vidal, L. Chen, A. Flamm, H. Valtanen, L. M. Weavind, M. E. Hicks, R. Pollock, G. H. Botz, C. D. Bucana, E. Koivunen, D. Cahil, P. Troncosco, K. A. Baggerly, R. D. Pentz, K.-A. Do, C. Logothetis, and R. Pasqualini, *Nature Med.* 8, 121–127 (2002).
82. B. K. Kay, “Phage Display of Peptides and Proteins.” Academic Press, San Diego, 1996.
83. W. Arap, W. Haedicke, M. Bernasconi, R. Kain, D. Rajotte, S. Krajewski, M. Ellerby, R. Pasqualini, and E. Ruoslahti, *Proc. Natl. Acad. Sci. USA* 99, 1527–1531 (2002).
84. M. Essier and E. Ruoslahti, *Proc. Natl. Acad. Sci. USA* 99, 2252–2257 (2002).
85. P. Mitchell, *FEBS Lett.* 56, 1–6 (1975).
86. Y. Hirono-Hara, H. Noji, M. Nishiura, E. Muneyuki, K. Y. Hara, R. Yasuda, K. Kinoshita, and M. Yoshida, *Proc. Natl. Acad. Sci. USA* 98, 13649–13654 (2001).
87. K. Adachi, H. Itoh, T. Nishizaka, H. Noji, R. Yasuda, M. Yoshida, and K. Kinoshita, *Biophys. J.* 80, 655–663 (2001).
88. R. Yasuda, H. Noji, M. Yoshida, K. Kinoshita, and H. Itoh, *Nature* 410, 898–904 (2001).
89. H. Noji, R. Yasuda, M. Yoshida, and K. Kinoshita, *Nature* 386, 299–302 (1997).

90. K. J. Kinoshita, R. Yasuda, H. Noji, and K. Adachi, *Philos. Trans. R. Soc. Lond. B Biol. Sci.* 355, 473–489 (2000).
91. M. Yoshida, E. Muneyuki, and T. Hisabori, *Nat. Rev. Mol. Cell Biol.* 2, 669–677 (2001).
92. I. Arechanga and P. C. Jones, *FEBS Lett.* 494, 1–5 (2001).
93. T. Nishi and M. Forgac, *Nat. Rev. Mol. Cell Biol.* 3, 94–103 (2002).
94. S. L. Gluck, B. S. Lee, S. P. Wang, D. Underhill, J. Nemoto, and L. S. Holliday, *Acta Physiol. Scand. Suppl.* 643, 203–212 (1998).
95. R. M. Berry and J. P. Armitage, *Adv. Microb. Physiol.* 41, 291–337 (1999).
96. J. S. Berg, B. C. Powell, and R. E. Cheney, *Mol. Biol. Cell* 12, 780–794 (2001).
97. J. P. Baker and M. A. Titus, *Curr. Opin. Cell Biol.* 10, 80–86 (1998).
98. E. D. Korn, *Proc. Natl. Acad. Sci. USA* 97, 12559–12564 (2000).
99. M. S. Mooseker and R. E. Cheney, *Ann. Rev. Cell. Dev. Biol.* 11, 633–675 (1995).
100. D. J. Asai and M. P. Koonce, *Trends Cell Biol.* 11, 196–202 (2001).
101. I. R. Gibbons, *Cell. Motil. Cytoskel.* 32, 136–144 (1995).
102. D. Salina, K. Bodoor, D. M. Eckley, T. A. Schroer, J. B. Rattner, and B. Burke, *Cell* 108, 97–107 (2002).
103. D. L. Dujardin and R. B. Vallee, *Curr. Opin. Cell Biol.* 14, 44–49 (2002).
104. J. V. Shah and D. W. Cleveland, *Curr. Opin. Cell Biol.* 14, 58–62 (2002).
105. A. Habura, I. Tikhonenko, R. L. Chisolm, and M. P. Koonce, *J. Biol. Chem.* 274, 15447–15453 (1999).
106. S. H. Tynan, M. A. Gee, and R. B. Vallee, *J. Biol. Chem.* 275, 32769–32774 (2000).
107. M. Samsó, M. Radermacher, J. Frank, and M. P. Koonce, *J. Mol. Biol.* 276, 927–937 (1998).
108. R. D. Vale, *J. Cell Biol.* 150, F13–19 (2000).
109. S. M. King, *J. Cell Sci.* 113, 2521–2526 (2000).
110. B. H. Gibbons and I. R. Gibbons, *J. Biol. Chem.* 262, 8354–8359 (1987).
111. U. Goodenough and J. E. Heuser, *J. Mol. Biol.* 180, 1083–1118 (1984).
112. I. R. Gibbons, B. H. Gibbons, G. Mocz, and D. J. Asai, *Nature* 352, 640–643 (1991).
113. M. P. Koonce, *J. Biol. Chem.* 272, 19714–19718 (1997).
114. M. A. Gee, J. E. Heuser, and R. B. Vallee, *Nature* 390, 636–639 (1997).
115. G. Mocz and I. R. Gibbons, *Structure* 9, 93–103 (2001).
116. H. Sakakibara, H. Kojima, Y. Sakai, E. Katayama, and K. Oiwa, *Nature* 400, 586–590 (1999).
117. L. Limberis, J. J. Magda, and R. J. Stewart, *Nano Letters* 1, 277–280 (2001).
118. H. Hess, J. Clemmens, C. M. Matzke, G. D. Bachand, B. C. Bunker, and V. Vogel, *Appl. Phys. A-Mater. Sci. Proc.* 75, 309–313 (2002).
119. H. Hess, J. Howard, and V. Vogel, *Nano Letters* 2, 1113–1115 (2002).
120. J. R. Dennis, J. Howard, and V. Vogel, *Nanotechnology* 10, 232–236 (1999).
121. R. D. Vale, T. S. Reese, and M. P. Sheetz, *Cell* 42, 39–50 (1985).
122. R. D. Vale, B. J. Schnapp, T. J. Mitchison, E. Steuer, T. S. Reese, and M. P. Sheetz, *Cell* 43, 623–632 (1985).
123. J. M. Scholey, M. E. Porter, P. M. Grissom, and J. R. McIntosh, *Nature* 318, 483–486 (1985).
124. S. P. Gilbert, R. D. Allen, and R. D. Sloboda, *Nature* 315, 245–248 (1985).
125. R. D. Allen, D. G. Weiss, J. H. Hayden, D. T. Brown, H. Fujiwaka, and M. Simpson, *J. Cell Biol.* 100, 1736–1752 (1985).
126. G. Woehlke and M. Schliwa, *Nat. Rev. Mol. Cell Biol.* 1, 50–58 (2000).
127. T. Hasson and R. E. Cheney, *Curr. Opin. Cell Biol.* 13, 29–35 (2001).
128. R. B. Case, D. W. Pierce, N. Hom-Booher, C. L. Hart, and R. D. Vale, *Cell* 90, 959–966 (1997).
129. U. Henningsen and M. Schliwa, *Nature* 389, 93–96 (1997).
130. S. A. Endow and H. Higuchi, *Nature* 406, 913–916 (2000).
131. I. Arnal, F. Metoz, S. DeBonis, and R. H. Wade, *Curr. Biol.* 6, 1265–1270 (1996).
132. K. Hirose, A. Lockhart, R. A. Cross, and L. A. Amos, *Proc. Natl. Acad. Sci. USA* 93, 9539–9544 (1996).
133. F. J. Kull, E. P. Sablin, R. Lau, R. J. Fletterick, and R. D. Vale, *Nature* 380, 550–555 (1996).
134. E. P. Sablin, F. J. Kull, R. Cooke, R. D. Vale, and R. J. Fletterick, *Nature* 380, 555–559 (1996).
135. M. Setou, T. Nakagawa, D. H. Seog, and N. Hirokawa, *Science* 288, 1796–1802 (2000).
136. K. J. Verhey and T. A. Rapoport, *Trends Biochem. Sci.* 26, 545–550 (2001).
137. H. Funabiki and A. W. Murray, *Cell* 102, 411–424 (2000).
138. A. A. Levesque and D. A. Compton, *J. Cell Biol.* 154, 1135–1146 (2001).
139. J. Howard, “Mechanics of Motor Proteins and the Cytoskeleton.” Sinauer Associates, Sunderland, MA, 2001.
140. P. B. Moore, H. E. Huxley, and D. J. DeRosier, *J. Mol. Biol.* 50, 279–295 (1970).
141. J. Fan, A. D. Griffiths, A. Lockhart, R. A. Cross, and L. A. Amos, *J. Mol. Biol.* 259, 325–330 (1996).
142. J. A. Spudich, *Nat. Rev. Mol. Cell Biol.* 2, 387–392 (2001).
143. H. Lodish, D. Baltimore, A. Berk, S. L. Zipursky, P. Matsudaira, and J. Darnell, in “Molecular Cell Biology,” pp. 999–1050. Scientific American Books, NY, 1995.
144. A. Kornberg and T. A. Baker, “DNA Replication.” W. H. Freeman, New York, 1991.
145. D. A. Clayton, *Ann. Rev. Biochem.* 53, 573–594 (1984).
146. J. A. Spudich, S. J. Kron, and M. P. Sheetz, *Nature* 315, 584–586 (1985).
147. A. J. Hunt and J. Howard, *Proc. Natl. Acad. Sci. USA* 90, 11653–11657 (1993).
148. T. Yanagida, M. Nakase, K. Nishiyama, and F. Oosawa, *Nature* 307, 58–60 (1984).
149. H. Hess, J. Clemmens, J. Howard, and V. Vogel, *Nano Letters* 2, 113–116 (2002).
150. J. Massague and A. Pandiella, *Ann. Rev. Biochem.* 62, 515–541 (1993).
151. Y. Ito, J. Zheng, and Y. Imanishi, *Biotechnology and Bioengineering* 45, 144–148 (1995).
152. Y. Ito, T. Uno, S. Q. Liu, and Y. Imanishi, *Biotechnology and Bioengineering* 40, 1271–1276 (1992).
153. Y. Ito, G. P. Chen, and Y. Imanishi, *Biotechnology Progr.* 12, 700–702 (1996).
154. Y. Ito, J. Zheng, Y. Imanishi, K. Yonezawa, and M. Kasuga, *Proc. Natl. Acad. Sci. USA* 93, 3598–3601 (1996).
155. J. I. Horwitz, M. Toner, R. G. Tompkins, and M. L. Yarmush, *Mol. Immun.* 30, 1041–1048 (1993).
156. Y. Ito, J. S. Li, T. Takahashi, Y. Imanishi, Y. Okabayashi, Y. Kido, and M. Kasuga, *J. Biochem.* 121, 514–520 (1997).
157. Y. Ito, J. Zheng, and Y. Imanishi, *Biomaterials* 18, 197–202 (1997).
158. B.-X. Chen, S. R. Wilson, M. Das, D. J. Coughlin, and B. F. Erlanger, *Proc. Natl. Acad. Sci. USA* 95, 10809–10813 (1998).
159. M. Rueggeger and R. Marchant, *J. Biomed. Mater. Res.* 56, 159–167 (2001).
160. S. C. Lee, R. Parthasarathy, K. Botwin, D. Kunneman, E. Rowold, G. Lange, J. Zobel, T. Beck, T. Miller, and C. F. Voliva, *PMSE* 84, 824–825 (2001).
161. S. C. Lee, R. Parthasarathy, T. Duffin, K. Botwin, T. Beck, G. Lange, J. Zobel, D. Jansson, D. Kunneman, E. Rowold, and C. F. Voliva, in “Dendrimers and Other Dendritic Polymers”

- (D. Tomalia and J. Frechet, Eds.), pp. 559–566. John Wiley & Co., London, 2001.
162. S. C. Lee, R. Parthasarathy, K. Botwin, D. Kunneman, E. Rowold, G. Lange, J. Zobel, T. Beck, T. Miller, and C. F. Voliva, in “Functional Condensation Polymers” (C. Carraher and G. Swift, Eds.), pp. 31–41. Kluwer Publishers, New York, 2002.
163. A. Quintana, E. Raczka, L. Piehler, I. Lee, A. Myc, I. Majoros, A. K. Patri, T. Thomas, J. Mule, and J. R. Baker, Jr., *Pharm. Res.* 19, 1310–1316 (2002).
164. M. S. Leusch, S. C. Lee, and P. O. Olins, *Gene* 160, 191–194 (1995).
165. V. A. Luckow, S. C. Lee, G. F. Barry, and P. O. Olins, *J. Virol.* 67, 4566–4579 (1993).

Bionanodevices

Thomas Schalkhammer

*Technical University of Delft, Delft, The Netherlands
Attophotonics Bioscience-Schalkhammer KG, Alland, Austria*

CONTENTS

1. Bionanotechnology
2. Nanocluster-Based Technology
3. Nanocluster and Field Effects
 - Glossary
 - References

1. BIONANOTECHNOLOGY

Nanotechnology is the technology embedded and determined by the world of atoms, molecules, and clusters at the nanometer scale. Whereas machining and handling accuracy at the nanometer level is already state of the art for the advanced semiconductor industry, a number of new phenomena become important in this ultrasmall world. Bionanotechnology aims at developing the techniques of characterizing, processing, and organizing ordered molecular structures via biomolecules and biomolecular recognition principles, which can be used in fabricating molecular functional elements and molecular circuits.

The main research activities are the molecular manipulation and organization made by the self-assembly of molecules, bioinduced alignment techniques, LB films, the development of biomolecule-nanoparticle structures with unique opto- and electronic activities, ordered assembly techniques for nanoparticles, nanowaveguides, techniques of nanoscale fabrication by, for example, electron beam or scanning probe microscope, novel bioanalytic techniques, fundamental studies on biooptoelectronic processes on the molecular level, selection and characterization of functional molecules, and, last but not least, modeling and prediction of bionanoscale structures. These goals are summarized by the following list:

- **Bio-system.** Characterization of biological recognition, biomolecular assembly, and molecular motors.
- **Production of nanomaterials.** Quantity, quality, properties, and production.
- **Production of assembled nanomaterials.** Autoassembly via (bio)interactions.

- **Characterization at both atomic and bulk scales.** Fundamental mechanical, electrical, magnetic, and optical properties.
- **Modeling and simulation.** Prediction of properties and behavior from macroscale to nanoscale.
- **Applications development.** Tools and techniques for applications of nanotechnology. Verification of predicted behavior/performance in actual environments. Systems analysis to guide technology development

Critical Bionanotechnology Areas:

- Materials with programmable optical/thermal/mechanical/other properties.
- 3D-biomolecular self-assembly and processing.
- Bio-inspired adaptable, self-healing systems.
- Low-power, integrable nanodevices.
- Quantum devices and systems for ultrasensitive detection.
- Materials with embedded sensing.
- Lab-on-a-chip for *in-situ* life science.
- *In vivo* analysis or analyses in small volume or small entity (e.g., subcellular).
- Noninvasive diagnostic tools.
- Molecular signature for early detection.

1.1. Bionanomachines

Eukaryotic and prokaryotic cells are nanoscale machines. Organisms work via protein nanostructures to shuffle material within the cell, to slide over surfaces, to drive themselves, and sometimes even to move biomolecules distances of inches to meters (e.g., within the axons of nerve cells). Muscles make use of the molecular motor myosin (only 10 nm in size) to move along the filaments made of a protein called actin. Microtubules, a cylinder of only 25 nm, moves DNA to the two daughter cells during cell division.

In developing nanodevices it will be critical to take stock of the nanomachines already existing in nature. Thus, nature is an essential component of bionanotechnology that enables us to learn how to build nanosystems.

Bionanotechnology offers novel ways to fabricate artificial biological structures, artificial cells, and even artificial tissues, as well as new ways to enhance the performance and functionality of existing devices. Whereas simple planar structures are produced via enhanced lithography, complex artificial tissues (such as the sophisticated structures of organs) are fabricated by biological self-organization, which is effective for three-dimensional networks.

E-beam and laser-based direct writing as well as techniques that use beams for moving and positioning microscale and nanoscale biological particles (e.g., living cells, bacteria, bioactive nanoclusters) are explored and are fundamental elements of such applications.

Cell-based nanodevices offer new chances. Encapsulation of, for example, pancreatic cells in microcapsules with nanopores will permit the treatment of diabetes in a curative approach. Nanopore materials are vital for preventing the body's immune cells from rejecting implanted cells or biocatalysts.

Assembly, nanolithography, and template-based building and etching techniques are of fundamental importance in creating these nanofilters. The combination of nanofabrication techniques and nanofilters will be essential for such implantable microdevices.

Biomedical nanosensors will play an important role in the future of medicine. The ability to detect biological molecules via small and fully automated devices is central to many advanced diagnostic techniques. *In-situ* detection of cancer is only possible by tracing cells and metabolites within the living organism. Novel detection principles based on the interaction of nanomarkers and nanoreceptors are essential to these novel devices (e.g., multicantilever biochips for sensitive force, magnetic field, or friction measurement represent a promising approach). Increased resolution via carbon nanotube tips allows identification of single bimolecular particles because of their shape. Novel tips with selective transducers recognize molecules based on their mechanical, magnetic, or electrical characteristics.

The gain in functionality of current analytical devices by nanotechniques is ideal for modifying the surface of implantable devices that rely on many surface interactions with the biological host tissue and the host immune system. Tuned surfaces at the nanoscale level allow high performance in biocompatibility and biocorrosion resistance.

Synergy between chip technology and biosciences allows micro- and nanobiodevice fabrication. While static biodevices, such as biosensors, DNA, and protein arrays, are already established in the field, much has to be done to develop dynamic nanobiodevices. Of these biodevices, microfluidic devices, for example, are already available but still are large and not real nanodevices but more or less microdevices. On the other hand, all other dynamic bionanodevices are in the state of infancy because of the novel surface effects that must be understood and mastered at the nanometer scale.

Molecular motors based on proteins (rotary and linear) are ideal tools for the fabrication of bionanomachines. For successful application much must be done to understand their operation and their behavior in artificial environments. Direct methods have been developed, such as laser trapping and atomic force microscopy, and successfully applied to

actin-myosin and kinesin-tubulin motors. Know-how gained from these experiments supplies engineering information that is necessary for the fabrication of future nanodevices based on these motors.

Nanofabricated devices are expensive in the first run but ultimately are more affordable. Whereas laser trapping offers zero-D confinement probing, nanofabricated structures offer the possibility to confine biological motors at the 1D, 2D, and 3D levels, and thus, at flat surfaces, in channels, on ridges, in wells, or on pillars. In the most advanced form, arrow-shaped microchannels have been used for example, to statistically enforce the directionality of the movement of tubulin filaments (Fig. 1). Whereas flat-surface 1D structures are easiest to fabricate, a 3D confinement in nanowells gives the highest level of information and control—for example, converting a molecular motor into a directional pump, or coupling two enzymes into a synthesizing cascade.

1.2. Nanoparticles

Nanoparticles or nanocluster research makes use of the strong size dependence of the physical and chemical properties of nanometer-sized particles. Clusters are well-defined building blocks for the construction of materials and devices with novel mechanical, electrical, and optical properties.

We define clusters as a number of atoms bound or arranged together, without specifying the size, shape, or property of this assembly. Within the state of matter described by cluster-type behavior we define a nanocluster, nano-island, precipitate, colloid particle, or whatever name is used for these assemblies as a nanoparticle composed of between 2 and 10^8 atoms (Fig. 2).

A cluster can be formed from a wide variety of materials. Even biomolecules such as DNA oligomers and proteins are essentially nanoparticles in the nanometer size range. These bionanoparticles are either biosynthesized or made by, for example, electrospraying technique, followed by electrostatic classification or manipulation.

To achieve efficient collective behavior and thus resonance of the electrons, these particles are preferably composed of a conducting metal such as gold, silver, indium, or tin or semiconductors such as cadmium sulfide or cadmium selenide. Clusters made of a few atoms still exhibit more molecular than cluster-type behavior. Large particles composed of more than 10^8 atoms exhibit macroscopic behavior, such as metallic luster or conductivity for micrometer-sized metallic particles. Thus, clusters cover an extremely wide range between a few and up to nearly a billion atoms [1–4] (Figs. 3–5).

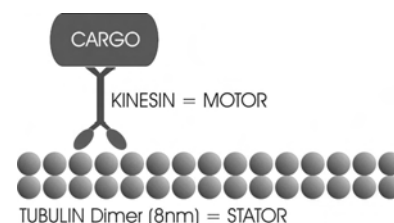


Figure 1. Nanomotor based on tubulin filaments.

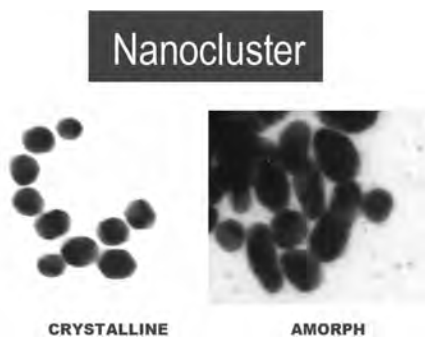


Figure 2. EM of metal nanoparticles (~10–20 nm).

A field of increasing interest is the use of nanoclusters for novel (bio)electronic and (bio)optical devices. Attempts to reduce the size of electronic devices with current technologies will encounter insurmountable barriers within one or two decades. The use of nanoparticles as building blocks for new devices is a new route for overcoming these barriers and building highly integrated, three-dimensional electronic circuits. Manufacturing these devices will require the development of completely new approaches to the manipulation and localization of nanoparticles on substrates.

To describe fundamental properties we will be dealing with isolated clusters first and later on will upgrade to more complex cluster–cluster, cluster-molecule, and cluster-resonator systems. Systems made up of a plurality of clusters are often referred to as cluster matter, nanocrystalline materials, or mesoscopic systems.

The history of clusters dates back hundreds of years and includes such scientific highlights as the work of Faraday, Ostwald, Mayer, Mie, Seitz, Svedberg, and Zsigmondy. Within the last decade the cluster as a base for nanotechnology, nanoengineering, and nanodevices has assumed a central role in the upswing caused by STM and AFM techniques followed by the nano-boom. Clusters are not a fifth state of matter but combine rather specific properties of metals, semiconductors, and surface and particle plasmons, to name just a few.

Quite often effects are divided into intrinsic and extrinsic behaviors. The first is, for example, chemical reactivity, ionization potential, or crystallographic structure, the second is collective electron gas and lattice resonance, often cited as Mie resonance. The scheme of electron energy levels and its relation to cluster size and cluster shape are often

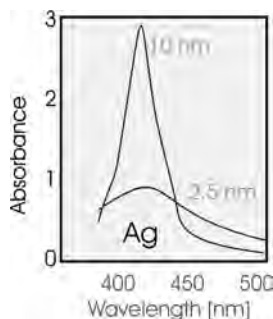


Figure 3. Spectral signal of the Mie resonance of a silver nanocluster.

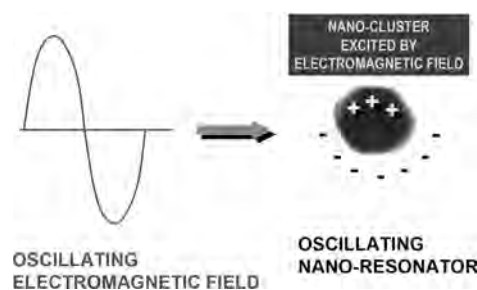


Figure 4. Cluster and light.

cited as quantum or quantum-size effects. A fundamental change in behavior is the transition from macroscopic metals to semiconductor-type clusters and, farther on, to isolating atoms or atom assemblies. This transition to the isolating state for most metals, such as Au or Hg, is observed between 10^1 and 10^2 atoms. Some unique states are obtained if the magic number is reached and defect-free nanocrystals are obtained. Gold in a perfect nanocrystal is stable against any oxidation, even more stable than any macroscopic gold metal sheet.

Surface effects such as SERS (surface-enhanced Raman spectroscopy), SEA (surface-enhanced absorption), SEF (surface-enhanced fluorescence), or catalytic effects are novel phenomena of nanoscopic systems. The high surface-to-volume ratio of nanoparticulate matters offers the opportunity to use otherwise inefficient surface-confined energy transduction pathways.

Last but not least, a great number of clusters are found in everyday life, such as silver centers in photographic films, red-colored glass, aerosols, exhausts, precipitates, or just dust and dirt.

For small clusters the boundary region penetrates to whole grains, thus influencing the state of every atom in a more or less distinct way. Even clusters containing 1000 or more atoms still contain up to 25% surface-modified material. At more than 100,000 atoms the behavior can be described by the bulk property because less than 1% of the atoms are at or near the surface.

Clusters have been synthesized by various means as particles that are free, surface-bound, embedded in a material, or in the form of a nanopowder. Electrical and optical properties are modified by shape, by surface-bound molecules, as well as by the surrounding medium. Although clusters can be made by size reduction of macroscopic matter (e.g., grinding

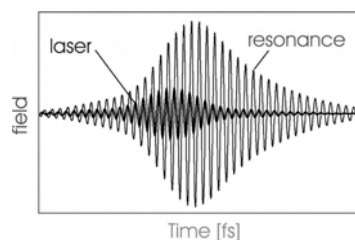


Figure 5. Resonance of the cluster driven by a laser pulse at resonant frequency.

or milling), most techniques use the synthetic approach to build clusters from the bottom up.

Ultrasmall clusters built from a few atoms can be modeled with quantum-based *ab initio* methods. In contrast to this, large clusters can be described using solid-state physics.

Ultrasmall clusters (a few to 10^3 atoms) are often examined with high-vacuum beam techniques because of their chemical reactivity, based on their high surface-to-volume ratio. Within this size regime order structures with “magic numbers” are targets of major interest. Quite often mass spectrometry is used to obtain insight into the size and setup of these small particles. A variety of techniques can be applied to study fundamental properties, including photoionization, magnetic moment, polarizability, or optical spectra.

Surface-supported systems or clusters obtained via chemical reduction of metals are usually “big” clusters with more than 10^4 atoms. To study these clusters, electron microscopy, surface tunneling microscopy, atomic force microscopy, or optical near-field techniques offer the chance to directly access size, shape, and electrooptical properties of individual clusters.

To describe the electrodynamics of clusters the standard approach may be used for “big” clusters, whereas for small particles the optical functions become size dependent. Simplified models can be set up for ideal clusters from sodium, for example; nevertheless, these calculations are of reduced practical value because none of these clusters can be used in any technical setup under ambient temperatures, in air or in a humid atmosphere.

1.3. Nanocluster Devices

Clusters as optical signal transducers of molecular binding are chosen because of their significantly higher extinction coefficients compared with any organic or inorganic chromophores. These nanoparticles are more intensely colored than the most intensive phthalocyanine dyes used for staining. With the use of cluster-based assays it is possible to visualize the binding of biomolecules at a given surface by a bound layer of modified metal clusters. A similar direct approach of detection with chromophores turns out to be very insensitive without the use of an additional amplification by an enzyme (ELISA).

Since the introduction of gold and silver colloid staining methods, signal transduction by metal nanoclusters has undergone an enormous evolution. A wide variety of techniques have been developed to synthesize clusters by physical and chemical means.

The narrow size distribution and surface ligand modification permit the application of nanoparticles as transducers of biorecognitive binding and molecular structure.

The success of these methods has been and is based on preparation as monodisperse particles by chemical synthesis, efficient stabilization and coating with various biomolecules, and electron-dense matrix, highly resonant plasmons, direct visualization, enhancement by deposition of other metals (e.g., silver), and signal stability (contrary to chromophores and fluorophores). In recent years the nanocluster has become the basis of new devices

employing cluster resonance, cluster field enhancement, and cluster–cluster interactions:

<i>Nanospecific property:</i>	<i>Used for:</i>
Formation of ultrafine pores	Molecular filters
Large surface area	Heat-exchange materials
Lower sintering temperature	Fabrication via sintering
Single magnetic domain	Magnetic recording, data encryption
Small mean free path of electrons	Designing conductors
High and selective optical absorption	Biochips, colors, filters, solar absorbers, photovoltaics
Mixture of clusters	New materials
Grain size too small for dislocation	High strength and hardness
Large specific surface area	Catalysis, sensors
Plastic behavior of ceramics	Ductile ceramics
Cluster coating and metallization	Special sensors
Multishell particles	Optical devices, catalysts

Not only spherical clusters but rod-shaped metal particles or tubes are the tools for bionanodevices. A research group explored the transport properties of membranes that contain a parallel collection of gold nanotubules that span the complete thickness of the membrane.

These nanotube doped membranes are prepared via a template method using deposition of Au within the pores of a polycarbonate template membrane. It was proved that the inside diameters of Au nanotubules can be adjusted down to molecular dimensions by controlling the metal deposition time. Because nanotubules have inside diameters of molecular dimensions, these membranes can be used to cleanly separate small molecules on the basis of molecular size, in contrast to standard biomembranes, which suffer from biological limitations.

For the construction of a nanoanalytical device, nanotube membranes are placed in a salt solution, and a constant potential is applied across the membrane. The transmembrane current is based on the migration of ions through the nanotubes. When an analyte molecule of dimensions comparable to the inside diameter of the nanotubes (e.g., a DNA molecule or a protein) is added these molecules enter the nanotubes and occlude the pathway for ion conduction across the membrane and the transmembrane current drops. To achieve the desired selectivity a biochemical molecular recognition agent is bound to the channel. In essence this approach is an artificial cell membrane gate similar to a ligand-gated ion channel. AC impedance and a potential-step method have been used to investigate the change in conductivity of gold nanochannels.

1.4. Nanobiotechnology

With respect to biotechnology, artificial nanostructured material is either a template for assembling biological materials, or the other way around. The biochemistry

included in this field is broad, ranging from fundamental bioorganic processes, to DNA and other biopolymers, and farther on to living cells

The use of nucleic acids as a matrix and means of self-assembly of nanoparticles (Fig. 6)(clusters, tubes (Fig. 7), molecules) into programmable arrangements provides the basis for manufacturing nanobiodevices. Contrary to top-down lithography, in which features are written onto a structure by a lithographic process, the bottom-up approach makes use of the base pairing in DNA molecules for assembly. The ability to set up three-dimensional structures enables DNA (RNA or PNA) nanotechnology to construct nanoscale assemblies far exceeding those created with lithographic techniques and is able to provide building blocks for applications in nanoelectronics, nanorobotics, and nanomaterials (Fig. 8).

Artificial nanostructured materials are a novel support for natural materials, such as living tissue. These structures mimic the natural properties of natural objects. One core element of nature is nanofibers—thus nanofibrils of bioorganic substances are a useful construction element for building soft biomaterials such as polymeric nanogels with molecular recognition capabilities (e.g., for rapid sensing) or ultrastrong but reactive nanolinkers.

While inorganic matrices such as silica surfaces or rare elements are generally not considered to interact specifically with biological systems, novel biological molecules built via phage display or ribosome selection techniques are a novel means of biomechanical interfacing. Dow-Corning announced a joint venture with Genencor International, putting \$35 million into silicon biotechnology nanofabrication.

1.5. Bionanoelectronic Devices

With the ever driving need for greater capacity in information storage and ultra-high-speed information processing, the usability of conventional lithographic technologies is approaching its limit. Novel techniques for decreasing structure width in pattern formation down to the nanometer scale are directly correlated with an increase in storage capacity. Nevertheless, advancement in data processing and data storage will require not only a better performance in lithography, but new design concepts as well.

Research is focused on the possible use of nanoclusters as a basic element of novel electronic and optical devices. A nanocluster can serve, for example, as the gate in a nanoscale field effect transistor (Fig. 9), as an optical switch in a nanooptical waveguide (Fig. 10), or as the storage point in a high-speed memory. The use of clusters for waveguides and storage dots addresses scaling issues of conventional

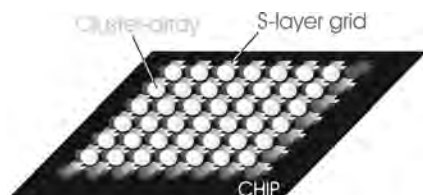


Figure 6. Array of nanoclusters arranged via bio-self-assembly.

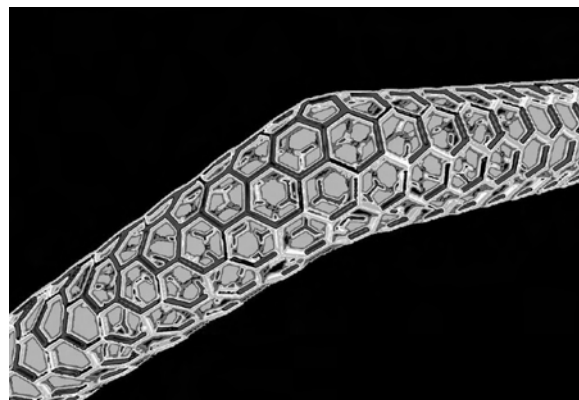


Figure 7. Carbon nanotube.

devices. Electron and surface plasmon tunneling effects at nanodistances offer novel gateways for processing information, using principles based on nonlinear systems fundamentally different from conventional computer systems, and are more related to the neural networks within living organisms.

As a well-established tool in nanoscience carbon nanotubes (around 2 nm in diameter) or metal-(or metal cluster)-coated DNA or protein filaments exhibit semiconducting and metallic properties. These basic elements can be engineered via biological recognition systems to serve as nanoscale tunneling junctions, nanoscale field-effect transistors, and other electronic devices. Although this research is still poorly developed, these construction elements have a bright future. Small but highly promising industrial research activities have already been begun in these areas by Lucent Technologies and Motorola.

Areas of interest are improving direct electron transfer to and between molecules, nanoclusters, and metallic



Figure 8. Coupling and assembly of DNA-functionalized clusters.

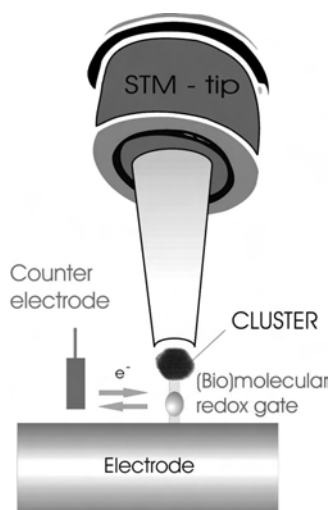


Figure 9. Cluster-based nanocluster device for electronic readout.

electrodes; the characterization of transport properties in nanostructured and clustered molecular systems; and the development of nanoclusters and quantum dots with useful electrical characteristics (magnetic nano storage dots, cluster laser, etc.).

Application in the coming years will be found in forms of information storage technologies, including hard drives, tapes, and optical media, where the critical parameter, bit density, will be optimized via biologically arranged magnetic and opto-switching nanoparticles.

1.6. Molecular Positioning and Dispensing

A major area of research is controlling the position and motion of macromolecules, DNA/RNA, proteins, and nanoparticles to enable functional processes such as molecular recognition, biochemical reactions, and, later, the self-assembly of nanoscale devices. A number of techniques have been developed

One way to handling sensitive biological species makes use of fluid streams on a chip. A key goal is the creation of nanofluidic technologies to handle nanoscale particles and molecules in microscale reactors. A fundamental understanding of the interactions between individual

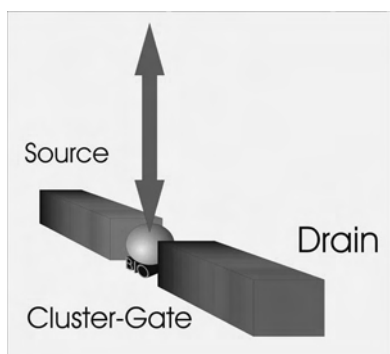


Figure 10. Cluster-based biotransistor.

molecules and a single molecule with the quite large surface of the device is vital. Tunable forces provide a path for developing efficient nanofluidic technologies. Ultimately, nanofluidics forms the backbone for a wide spectrum of bionano-applications. Fluidic processes include delivery of minute amounts of fluid, mixing/separation, and surface property control through functional molecules.

A way to deliver subpicoliter fluid droplets uses an e-jet (similar to MS injection techniques, but at ambient pressure) or microthermal actuation in a cavity. Single liquid droplets with volumes of less than a picoliter can be ejected through a metal fiber or nozzle (Fig. 11). In thermal actuation devices the actuator controls the pressure gradient and solves the satellite droplets problem, which has troubled industry for the last two decades. In e-jet devices a potential around 1–1.5 kV drives picodroplets along the field lines (in a 200- μm gap) to the chip surface.

The ability to move molecules and to guide them on a chip surface plays a vital role in the efficiency of micron-size biochemical reactors. Among the techniques of interest, electrokinetic, hydrodynamic, or magnetic forces can overcome surface forces and drive the fluid to chaotic mixing (significantly shortening the reaction time). An electrokinetic force-based focusing device that focuses negatively charged DNA into a region the size of tens of nanometers is now established and commercially available from Nanogen or November AG, for example. The surface-to-volume ratio increases dramatically in nanodevices. Thus, a large portion of molecules will interact with the surface in these devices. Well-designed molecules placed on the surface of a nanofluidic circuit can either recognize certain molecules or suppress nonspecific adsorption. In this way either the analyte of interest is lost or more positively selective filters are available.

In recent years the group around Chad Mirkin [5] has developed a nanopen. It writes on a flat gold surface, using a standard atomic force microscope (AFM) tip as the nib of the pen. The ink is loaded onto the nib by dipping into an evaporating sulfur-containing compound. Although the principle had been discussed years ago, the breakthrough relies on the formation of a meniscus of water between the tip and the gold surface, drawing the ink off the nib onto the surface. The relative humidity allows control of the flow of ink off the tip. Lines are well controlled down to a width of a few molecules. The use of 1-octadecanethiol or 16-mercaptohexadecanoic acid allows patterning or overwriting of lines. Biomolecules are easily attached to the patterned surface with the appropriately functionalized thiols.

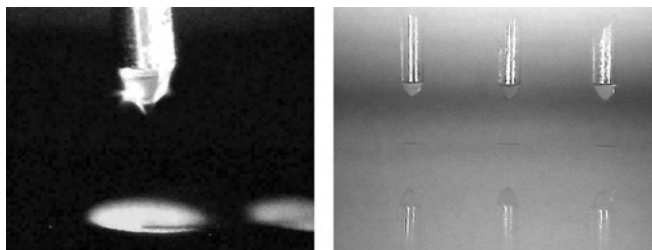


Figure 11. E-spray device with pl-precision.

Another nanotool within the necessary kit developed at Harvard University [6] is the “nanotweezer.” Nanotweezers consist of carbon nanotubes attached to electrodes made, for example, on glass micropipettes. When a voltage is applied to the electrodes the tubes bend, and thus the ends of the nanotubes open or close. With the tweezer it is possible to pick up nanoobjects or move tiny structures. First experiments proved that the nanotubes are suited for gripping a cluster of nanospheres from a support. At 0 V, the tweezers are fully open. Applying a voltage closes the tweezers. At around 10 V, they are closed. Nanotweezers introduce the possibility of manipulating delicate objects, such as individual biological cells or subcellular elements. Improvements to the nanotweezers may lead to the ability to move single atoms.

Several groups have investigated the effect of dc and ac electric fields on fiber-type biological molecules such as DNA in aqueous solution. The electric fields are generated between parallel electrodes lithographically patterned on the chip. For easy manipulation, the gap between the electrodes is chosen to be less than 10 μm . The ac electric field applied is up to 1,000,000 V/m, with frequencies around 100 kHz. The field polarizes the DNA molecules and leads to an orientation of the DNA parallel to the electric field lines. If an electric field gradient is present, the polarized molecules are attracted to regions of higher field strength. DNA aggregates in the gap between the electrodes. If the ac electric field is switched off after a few seconds, the molecules diffuse out into the solution. If the field is left on for a few minutes, the DNA molecules adhere to the contacts with their ends and keep spanning the contacts when the ac electric field is switched off. It turns out, however, that the high voltages applied during the orientation procedure lead to an electrolysis of the water and a redeposition of metal between the contacts. Thus, the above orientation procedure is feasible only for small voltages but high electric fields, requiring an electrode spacing of less than 100 nm.

1.7. Single (Bio)molecule Conductivity

Ultimately electronics will consist of networks of individual molecules carrying electrical currents of a few electrons. Single-molecule conductivity measurement was first achieved with the use of a scanning tunneling microscope (STM) tip positioned above a molecule adsorbed to a metallic or semiconducting surface [7]. These experiments proved the viability of the concept of molecular electronics by measuring the conductivity of individual molecules. However, this method is limited by its lack of mechanical stability. Furthermore, it is impossible to determine whether a substrate-molecule-tip contact really occurs, and it is difficult to maintain a long molecule perpendicular to the surface. Nevertheless, the experiments marked a step toward single-molecule electronics.

In recent years a number of research groups have passed electricity through single molecules ranging from DNA to organic molecules often less than 1 nm long. Measurements of DNA conductivity were recently obtained by several groups [8, 9]. Currently most groups use a technique based on breaking a gold bridge around 50 nm wide and 50 nm thick. The first real metal-molecule-metal junctions

were the mechanically controllable break (MCB) junctions, created by Reed and used then in France by Bourgoin and Magoga [10, 11]. They used molecules with a sulfur atom at either end. The sulfur atoms at the ends of a molecule precisely bonded to the two gold electrodes to form the electrical contacts. Nevertheless, it should be noted that the sulfur atoms introduce additional electron barriers.

Varying the voltage across the gap made it possible to characterize the behavior of the single molecule trapped within. When researchers varied the voltage across asymmetric molecules, the current changes turned out to be asymmetric. At least part of that asymmetry arose from changes in the asymmetric distribution of molecular orbitals across the molecule.

A number of groups focus on the development of nanojunctions separated by a sub-50-nm gap for the electrical characterization of biomolecules. The gap is filled by a few (one to five) deposited biomolecules. The objective is either single-molecule science or the study of interactions between a greater number of molecules (e.g., a nanocluster) and a single molecule. These experiments are essential for refining the models and an understanding of charge transfer phenomena at the molecular scale in biomolecules. Nano-electrodes must be ultrasharp. Moreover, it must be possible to verify *in-situ* the quality of the gap and of the metal-molecules-metal junction with an atomic force microscope (AFM).

Recently, electric conduction in double-stranded lambda-DNA has been studied at room temperature with the use of low energy electron point source (LEEPS) imaging. For this purpose, the DNA molecule was strained over a perforated conducting membrane. The measurements indicated a surprisingly large electrical conductivity. This result suggests that DNA-based biomolecules can be applied to electric circuits, for example, as electric sensors with recognition capabilities.

Microtubules are essential in cell architecture and cellular transport. Single-molecule experiments were carried out with the use of microstructured electrode surfaces and microtubules between the electrodes. Arrays of electrode pairs are built from a $\sim 100\text{-nm}$ gold layer (primed with a titanium layer) on a thermally oxidized silicon wafer according to standard photolithographic techniques. Microtubules are purified from brain by three cycles of temperature-dependent disassembly/reassembly and stabilized with 20 mM taxol. For adsorption experiments, the assemblies are applied to a substrate of microstructured gold lines on oxidized silicon.

A new approach to the wiring of nanostructures is linking metallized DNA or microtubules to prestructured microelectrodes. Briefly, the protein structures are activated by the adsorption of Pt-catalyst particles with the use of K_2PtCl_4 solution, followed by a metallization with Ni acetate [12]. Similar metallization techniques are well established for gold or silver coating. Electron beam-induced deposition (EBD) was used for the structuring of connecting gold lines as nanoelectrodes, which wire a single microtubule to microelectrodes created by photolithography. A metallized microtubule yielded a resistance below 50 Ohm over the length of 1 μm .

EBD line writing is an add-on to simplify the electrical connection of single molecules (Fig. 12). Repeated line scan induces the polymerization of amorphous carbonaceous material along the path of the electron beam on the substrate, which appears as a black line in the SEM contrast. A prerequisite for successful EBD lines is a minimal drift of the SEM; otherwise a broadening of the lines occurs. The conductivity of the substrate enhances the growth. This phenomenon is explained by charging effects suppressing the EBD effect. Localization, EBD line writing, and a first characterization of the created line structures can be obtained by SEM in about an hour.

1.8. Scanning Probe Microscopes

Imaging and manipulation of nanometer-sized objects, single molecules, or individual atoms are the playground for bionanoscience and nanobiotechnology. Whereas classical macroscopic techniques rely on molecular ensembles, averaging over all possible molecular conformations, single-molecule techniques make it possible to address and observe molecular individuals in their individual shapes and activities.

The field of novel scanning probe techniques is enormous and cannot be covered—even to a minor extent—in this bionanotechnology summary (Fig. 13). The applicability of, for example, atomic force microscopy for imaging biological molecules in their native environment was demonstrated shortly after the invention of this technique. Through time AFM has become a successful tool that complements other structural techniques such as NMR, X-ray crystallography, and electron microscopy. AFM is applicable not only for the visualization of biomolecules and surfaces, but also for the manipulation of nanostructures such as proteins, DNA, or nanoclusters. To make use of the AFM to monitor biological molecules, a number of techniques have been developed. The three main modes of operation are contact mode (CM),

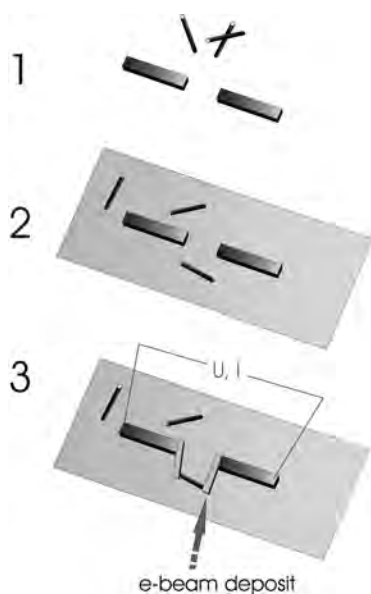


Figure 12. E-beam line writing to contact nanotubes or metal-coated DNA strands.

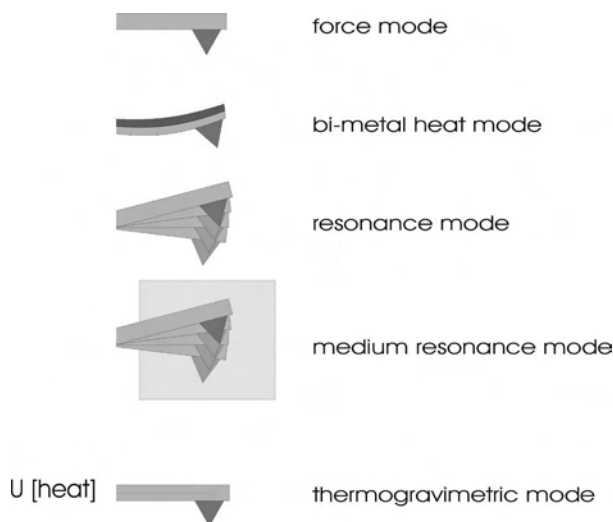


Figure 13. A few novel techniques of the large family of surface scanning microscopes.

noncontact mode (C), and tapping or intermittent contact mode (IC). The principles by which the AFM works are very simple. An atomically sharp tip is scanned over a surface with feedback mechanisms that enable the piezoelectric scanners to maintain the tip at a constant force (to obtain height information) or height (to obtain force information) above the sample surface. Other “scanning probe” techniques use a wide variety of parameters to obtain this feedback (e.g., scattering of light, fluorescence, magnetic field, thermo current, etc.).

Just to illustrate the use of AFM: it permitted the detailed study of the intra- and intermolecular forces of the DNA double helix, which are central to understanding its structure and rich functional behavior. DNA exhibits very interesting biophysical and physicochemical properties that are essential for a proper functioning of the biomolecular processes involved. Interaction forces between single strands of DNA are conveniently determined via atomic force microscopy. The ability to measure the force between the tip and the sample is an additional important feature of the atomic force microscope. The cantilever on which the tip is mounted is moved toward the sample, and, after touching it, the tip is pulled back from the surface of the sample. The attractive force of the sample, which holds the cantilever back by pulling it away from it, is displayed as a diagram (Fig. 14).

Already around 1994 DNA oligonucleotides were covalently attached to the probe and surface. Adhesive forces had been measured between complementary oligonucleotides (~20 bases). Data exhibit several distinct force distributions, which are associated with the rupture of the interchain interaction between a single pair of molecules, which involves breaking of short fragments. When a third long DNA molecule was coupled between complementary surfaces, both intra- and interchain forces were observed. The intrachain interaction resulting from the molecule’s elasticity manifested itself as a long-range cohesive force. Fundamental phenomena like molecular elasticity, binding to proteins, supercoiling, and electronic conductivity also depend on the

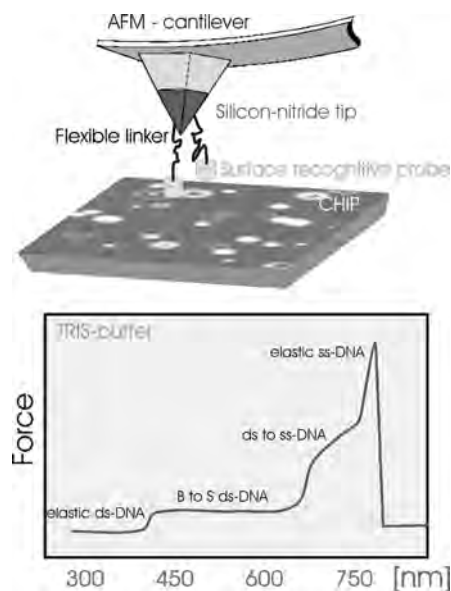


Figure 14. Force curve obtained by unwinding a DNA double strand from an AFM tip.

numerous possible DNA conformations and can currently be investigated on the single-molecule level.

Similar experiments had been done with proteins as, for example, antigen-antibody complexes. The antigen is immobilized covalently via, for example, a long hydrophilic spacer of polyethylene glycol to the silicon nitride PM tip. Closely related antibody molecules differing in only one amino acid at their binding site can be distinguished via the measurement of binding forces.

Experiments with single molecules were reported with scanning tunneling microscopy [13], fluorescence microscopy [14], fluorescence correlation spectroscopy [15], optical tweezers [16, 17], bead techniques in magnetic fields [18, 19], optical microfibers [20], low-energy electron point sources (electron holography) [21], and atomic force microscopy (AFM) [22].

Whereas standard scanning microscopes are tabletop instruments, novel devices shrink the scanner equipment down to the millimeter scale, thereby increasing the resonance frequency of the scanner. Cantilever sensors rely on well-known and simple transduction principles and have attracted interest (Fig. 15). This is due, at least in part, to the combination of silicon fabrication techniques and surface modification biochemistry with the development of multicantilever sensing methods. Interest in microfabricated cantilevers has grown since the development of the AFM in 1986. Cantilever sensor techniques allow direct measurement of specific interactions between surfaces at the molecular scale. A micro-AFM measures the tiny forces acting on a sharp tip of a multicantilever chip. By shrinking the cantilever structure to a microscopic size one obtains a low spring constant (high sensitivity), a high resonant frequency, fast response times, and high immunity to external mechanical noise. Miniaturization and mass production are achieved by taking advantage of silicon micromachining techniques developed for IC process technology.

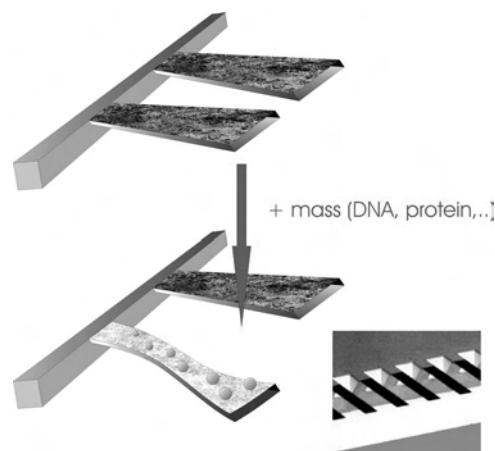


Figure 15. Sketch of a cantilever sensor.

With a microcantilever operated in the oscillating mode, it is possible to count the number of bacteria adsorbed to an antibody-coated cantilever. The specific binding of a herbicide to an antibody-coated cantilever causes a significant shift in resonance frequency. It was proved that this chip differentiates between the adsorption of low-density lipoproteins and oxidized lipoproteins bound to a heparin surface. Coating the cantilever surface with specific receptors and labeling the analyte with the beads will yield an extremely sensitive single-molecule sensor. Cantilever sensors also show great potential in genomics. One hot topic is the detection of single nucleotide polymorphisms (SNPs), the origin of biological diversity and diseases.

A common modification of the AFM is the scanning electrochemical microscope (SECM) (Fig. 16). The microscope requires an almost completely insulated AFM tip, leaving the minimum area possible (conductingly) exposed at the end. This metal or carbon tip forms the working electrode in an electrochemical cell. This nanomicroelectrode is scanned across a surface, and the current is measured as a function of position to acquire an electrochemically topographic map of the chip. The ultimate detection limit of the single molecule has already been achieved.

The scanning near-field optical microscope (SNOM) is realized by scanning a small spot of “light” over the specimen and detecting the reflected, scattered, or transmitted light. The SNOM principle relies on optical tunneling, which is a quantum phenomenon resulting from photon delocalization that allows light to cross propagation barriers. The resolution of the SNOM image is defined by the size of

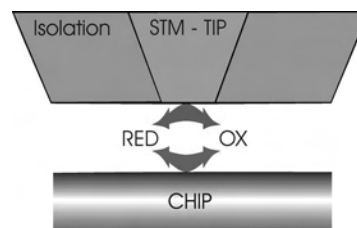


Figure 16. Electrochemical scanning microscope (the redox signal is obtained by cycling a redox-active molecule in the nanometric electrode gap).

the aperture. SNOM utilizes nanoapertures with a diameter in the range of ~ 50 nm. Typically such apertures are prepared in the metal coating of pulled fibers. The optical near-field decays exponentially with distance. Scanning the aperture at a typical distance of ~ 10 nm from the sample produces a high-resolution optical image. A detection limit of a single molecule is achievable. The single molecules most often detected and characterized in the literature are dye molecules on DNA fragments.

A new member of the scanning probe microscope family and one of the most prominent of the emerging nanoelectromechanical systems technologies is magnetic resonance force microscopy (Fig. 17). The energy separation of useful magnetic sublevels within a molecule ranges from μeV to meV and is detectable by either nuclear or electron spin resonance.

2. NANOCUSTER-BASED TECHNOLOGY

As could be deduced from the summary of technologies, the use of nanoparticles is one of the most promising areas of bionanoscale research. Unique behavior in the interaction with electromagnetic fields and radiation is among the most exciting properties (Fig. 18). This article will focus on nanoclusters, start with their intrinsic properties, and later on focus on potential bioapplications in the field.

2.1. Properties

In an extended metal unconfined electron movement is possible, resulting in strong, unspecific reflectivity, well known as metallic luster. In contrast, for clusters of any size or geometry the optical spectra are primarily determined by the strongest oscillation process. Resonance of metal clusters is dominated by collective oscillation of the electron gas within the cluster, forming either plasmons or plasmon-polaritons. We will mainly focus on electronic excitation from visible light to IR and add some basic phenomena of vibration and Raman spectroscopy.

Optical spectroscopy of metal clusters is best described by electrodynamics. It is appropriate to apply a quasi-static regime only for a cluster smaller than 10–20 nm for visible light. Within a static regime phase shifts in the particle are small enough and thus might be neglected. This simplifies the excitation of the cluster to an oscillating dipole.

For real clusters the resonance is smeared out because of clustersize and shape distribution. Furthermore, the influence of matrix boundaries, as well as a finite penetration of the electromagnetic wave, has to be considered.

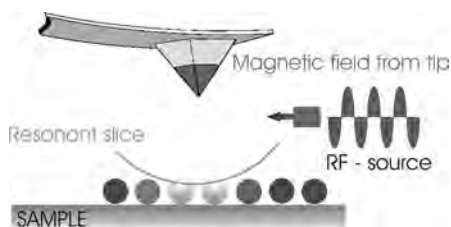


Figure 17. Nano-NMR scanning microscope.

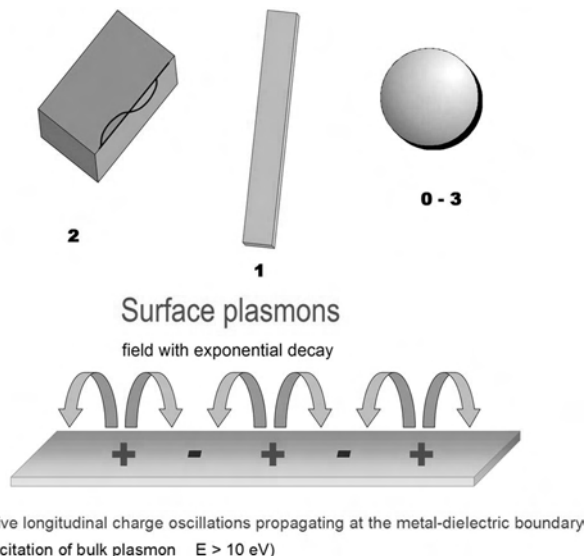


Figure 18. Preferred plasmon propagation within nanoscale structures.

The electron mean free path plays a key role in modifying the optical properties of metal clusters. Whereas for small clusters the field attenuation is small, in larger clusters (> 30 nm) only surface regions are excited by the field. The skin depth (at 2 eV) is 24 nm for Ag, 13 nm for Al, 31 nm for Au, 30 nm for Cu, and 38 nm for Na.

To apply electromagnetic theory, the negative charges are allowed to move when they are excited by an external field. In contrast, the positive charges are more or less immobile. Metals that exhibit strong optical effects are free-electron metals, based on the fact that most of the electronic properties are caused by conduction electrons. These metals have completely filled valence bands and partially filled conduction bands. For free electron metals the optical response is based on the conduction electron band, whereas other metals exhibit various interband transitions.

Noble or seminoble metals such as silver, gold, or copper exhibit both free electron and interband transition behavior, depending on the frequency range. For basic studies alkali metals proved to be very useful. Because of their instability in an ambient environment, noble metals are the only clusters studied in aqueous solvents.

The response of a metal cluster to an exciting electromagnetic field is based on the dielectric function $\epsilon(\omega)$ of Drude-Lorentz-Sommerfeld. The internal field of a metal cluster is calculated by adding the boundaries of the sphere surface. Thus the static electric polarizability of a spherical cluster of radius r is given by $\alpha_{cl} = 4\pi\epsilon_0 r^3 \cdot (\epsilon - \epsilon_m)/(\epsilon + 2\epsilon_m)$. This formula is suited for small metal clusters. It is not applicable for large nanoparticles.

Thus for a small ϵ_2 a resonance is given at $\epsilon_1 = -2\epsilon_m$ with a resonance frequency (at $\epsilon_m = 1$) of $\omega = \sqrt{(e^2/(m_e 4\pi\epsilon_0 R^3))}$. Often ω is interpreted as the plasmon frequency; nevertheless, it is a resonance (and polarization) of a particle. To sum up, the conduction electrons in clusters act as an oscillator system, whereas those in a bulk metal act as a relaxator system with no excitation at the eigenfrequency ω .

Realistic coupling of the electron gas with the ion core can be described by refinement procedures (e.g., by introducing an effective optical mass instead of the electron mass) and was first introduced by Mie-Gans-Happel based on a solution of Maxwell's equations with appropriate boundary conditions. Mie divided the problem into two parts: the electromagnetic one and the one based on material properties he excluded by using a dielectric function $\varepsilon(\omega, R)$.

The dielectric function is an average of all electronic and atomic behavior of the cluster as dipolar, multipolar, or magnetic modes of absorption and scattering. The success of this theory is based on extracting data from experiments.

Basic data are gained by correlating ε_1 with $\Delta\lambda_{\max}$, the peak height with ε_2 , and the bandwidth with n . Thus, a steep $\varepsilon_1(\omega)$ results in a narrow resonance peak, whereas a flat $\varepsilon_1(\omega)$ results in a broad band.

2.2. Cluster and Quantum Dots

In the visible spectral region the dipolar surface plasmon is dominating for alkali metals since damping is small. In contrast, noble metals (mainly Ag, Au, and Cu) show significant deviation from free electron behavior due to interband transitions. These transitions influence the spectra in the visible region. The plasmon energy limit shifts from the free electron value of 9 eV to less than 4 eV! The threshold in eV is 3.9 for Ag, 1.5 for Al, 2.4 for Au, 1.3 for Ba, 2.1 for Cu, 0.9 for Cs, 1.3 for K, >6 for Mg, and ~ 2 for Na.

Thus, this resonance cannot be regarded as a free electron resonance but is a cooperative effect based on conduction and d electrons. Whereas silver is even the less pronounced member of the group of noble metals cited above, in copper the plasmon energy limit shifts from more than 9 eV to around 2 eV.

Only Ag has a well-developed resonance near 400 nm. Gold has a peak around 520 with an shoulder to higher energy. Copper exhibits no resonance in embedding media with ε_m around one, but a sharp resonance peak can be found in media of higher refractive index.

Resonance of Pt clusters is damped away in the visible region of the spectrum but is useful in the near-IR. Metals like Ti and Ta exhibit plasmons combined with various elementary excitations of the metal.

Advances in nanotechnology have led to the development of highly sensitive cluster-nanoprobes, which have had a large impact on fundamental biology research and medical diagnostics. These semiconductor clusters, quantum dots, exhibit visible room-temperature photoluminescence that is shifted to higher energies compared with bulk materials because of quantum confinement. Even indirect bandgap materials such as silicon, molybdenum sulfide, and pyrite, which show no significant PL at room temperature, can have intense room-temperature luminescence in nanocluster form.

Quantum dots are nanometer-size colloidal particles with dimensions smaller than the exciton Bohr radius. In comparison with traditional organic probes, semiconductor quantum dots are 20 times brighter and 100 times more stable against photobleaching.

At present, the use of quantum dots for multicolor staining, homogeneous assays, and imaging for tissues is already

established. Bioassays are accomplished by modifying the surface of quantum dots with hydrophilic molecules and conjugating selectively interacting biomolecules onto the surface.

Colloidal gold is orange, red, or red-violet, depending on the preparation method. Colloidal gold is prepared by catalytic deposition of metallic gold produced by the reduction of gold salts with numerous reagents. The most common are phosphorus, tannic acid, ascorbic acid, and sodium citrate. Depending on the method used, colloidal gold preparations vary in particle size and size variability expressed as the coefficient of variation of the gold particle diameter in a sol. Such a sol is called monodisperse when the coefficient of variation is smaller than 15%.

A new route to the synthesis of colloidal Au clusters with diameters between 30 and 100 nm is described by Brown and Natan [23]. On the basis of surface-catalyzed reduction of Au^{3+} by NH_2OH , the approach is used to grow existing nanoparticles into larger particles of a size determined solely by the initial particle diameter and the amount of Au^{3+} added. The resulting clusters exhibit improved monodispersity relative to those prepared in one step by the reduction of Au^{3+} by citrate. Surface-bound Au clusters can also be enlarged with this method. Thus, this technique provides an attractive route to colloidal Au monolayers with variable interparticle spacing.

The colloid preparation is one of the major methods employed for the purposes of cytochemistry, especially staining of electron microscopic samples [24, 25].

2.2.1. Techniques for Preparing Nanoclusters

- One of the most well-known methods (due to Frens) provides monodisperse colloidal gold. In short: a solution of gold chloride is diluted in double-distilled water, the solution is heated to boiling, trisodium citrate is added quickly, and the solution is boiled gently until an orange red color develops. The size of the clusters between 6 and 60 nm can be adjusted by adding varying amounts of reducing agent.
- Another well-known method provides monodisperse colloidal silver. In short: AgNO_3 solution is diluted double-distilled water, tannic acid solution is added, the mixture is heated to 80 °C, sodium citrate is added under rapid stirring, and the solution is kept at 80 °C until the colloidal color becomes yellow. Colloid formation can be followed via an absorption peak at around 400 nm. The colloids prepared in this way are polydisperse, with an average particle diameter of 30 nm.
- Graphite-encapsulated metal nanoclusters are synthesized with high-temperature electric arc techniques. Carbon and the metal of interest are coevaporated by producing an electric arc between a tungsten cathode and a graphite/metal composite anode. The encapsulation occurred *in-situ*.
- CdS and PbS colloids of nanometer dimension are synthesized by controlled precipitation of the metal sulfide in water and acetonitrile solution. These colloids exhibit quantum size effects but have a broad size distribution.

- CdS nanocluster can be synthesized within the pore structure of zeolite. The coordination of Cd atoms with the framework of the zeolite leads to the formation of stable nanoclusters with a structural geometry superimposed by the host matrix.
- Metal nanoclusters are prepared by solution-phase thermolysis of molecular precursor compounds.
- Nanoclusters of CdSe have been synthesized with the use of organometallic reagents in an inverse micellar solution. Precipitation in reverse micelles gives a semiconductor lattice and *in-situ* molecular modification of the cluster surface.
- Gold nanoclusters might be fabricated with metal vapor deposition techniques. In this method, gold is codeposited with, for example, liquid styrene or methylmethacrylate.
- Block copolymers are used to fabricate metal nanoclusters with the deposition of metal on the surface of a microphase separated PS-PMMA diblock copolymer. After deposition, the film is annealed. The shape and size of the nanoclusters are determined by the microphases of the polymer mixture.
- Researchers at MIT synthesized metal nanoclusters inside the microphases of diblock copolymers. Nanoclusters within these copolymer show 3D ordering, and the density of nanoclusters is high enough for commercial applications.

In the absence of stabilizing agents, aqueous dispersions are inherently unstable. All will form aggregates. The strong tendency is caused by attractive van der Waals forces, which basically always act at short distances. For submicrometer clusters, the primary van der Waals minimum is much deeper than the thermal energy, and therefore two particles that collide by Brownian motion will stick to each other.

The rate of cluster formation was calculated by von Smoluchowski a century ago. A more detailed description is based on the hydrodynamic resistance and the finite range of the van der Waals attraction. Nevertheless, dispersed colloidal particles will inevitably aggregate within seconds unless some stabilizing mechanism is available. The most basic process in colloidal stability is the dimer formation in an initially stable dispersion. Aggregation may be triggered by an increase in the ionic strength, changes in the solution pH, or by the addition of flocculants like polymers or surfactants.

A dispersion of charged nanoclusters is usually stable at low salt concentrations. It can be destabilized by mixing with a salt solution of higher concentration. At a high concentration of salt ions, the particle charge is screened, and the repulsive electrostatic force is overcome by the attractive van der Waals force and the particles precipitate.

2.3. Nonspherical, Core-Shell, and Phase-Boundary Clusters

Based on the theory of Mie, several modified concepts deal with nonspherical cluster shape and core shell particles. Based on the quasi-static approach, various geometric forms have been treated (e.g., oblates, ellipsoids, cubes, and cylinders).

The axial ratio a/b as a main parameter is suitable for calculation extending the polarization to L_i , where $i = a, b, c$ and $\sum L_i = 1$ (for spheroids $L_a = L_b = L_c$). To treat samples with arbitrarily oriented ellipsoids the signal has to be averaged over all orientations. Clusters of a single size and eccentricity exhibit a splitting of the peak to three more or less distinct peaks. Clusters of a continuous distribution correspond to a flat and broad peak (Fig. 19) [26].

Clusters set up from more than one metal can often be treated by combining the functions of pure metals. Often one observes broad-band and multiplex spectra. For very thick layers spectra converge to the spectra of the top-layer metal (Fig. 20). Especially amorphous metal can significantly modify long-wave absorption of metal-cluster films.

Already monomolecular surface layers exhibit pronounced effects. In the visible region even small ad-layers of sulfides, iodides, oxides, or borates lead to a significant deformation of the spectra [27] (Fig. 21).

Ordered arrays of metal columns deposited on or etched out of a substrate surface exhibit similar or even enhanced effects. High local fields permit efficient signal generation with SERS.

Of particular interest is chemically confined growth or catalytic growth, in which the catalyst is used to direct highly anisotropic growth. Methods using a catalyst cluster with a diameter in the 10-nm size range permit the growth of nanocolumns and wires. Nanowire growth is initiated after generated clusters become supersaturated.

Bimetallic nanostructures act as unidirectional light pipes. The effect is attributed to plasmon propagation. This optical analog to the diode may be used to directly construct optically addressable memory elements, logic devices, and sensors at the nanoscale.

As a straightforward approach silver-gold core-shell clusters are synthesized via gold nucleated silver-deposition. In short: Au colloids are diluted in water, the solution is heated, AgNO_3 and trisodium citrate are added, in intervals, additional aliquots of AgNO_3 are added, and finally trisodium citrate is also added to complete the reduction. The resulting solution has an absorbance maximum around 329 nm (typical for Ag). The two types of particles can readily be separated by centrifugation.

Whereas a simple discussion of $\epsilon(\omega)$ depicts the setup of single spherical clusters in an isotropic material, it has to be extended for anisotropic phase boundary systems. Clusters on surfaces are influenced by the adjacent medium. In a

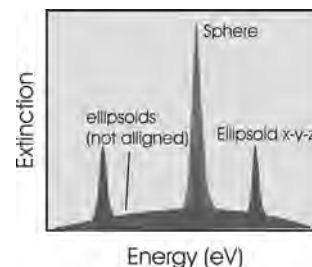


Figure 19. Splitting of the plasmon resonance peak into three distinct peaks in an aspherical cluster.

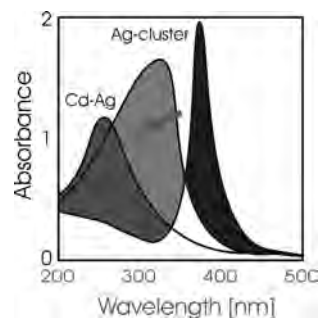


Figure 20. Shift of plasmon frequency of single-metal and dual-metal clusters.

very simple case ϵ_m can be replaced by an averaged dielectric ϵ of the surrounding media, giving reasonable results (Fig. 22). In a more complex description an oblate cluster shape induces a well-defined splitting of the polarization. Thus, by choosing the appropriate polarization of the exciting beam, selective excitation of modes can be accomplished. Moreover, the cluster plasmon peak will split up into at least two defined peaks, one shifting slightly to shorter wavelengths, the other quickly moving to red and infrared.

2.4. Magnetic Clusters and Magnetodendrimers

Magnetic nanoclusters are monodomains. Thus, one expects that in magnetic nanophase materials the grains also correspond to domains. Very small clusters have special atomic structures with discrete electronic states, which give rise to special properties in addition to superparamagnetism.

Studies of magnetism in small nickel clusters have found them to be highly magnetic. The moments per atom exceed the bulk value per atom. These observations support theoretical predictions of enhanced magnetization in systems with reduced dimensionality.

This effect extends throughout the transition metals. Cobalt and iron clusters are also more magnetic than the bulk, and clusters of rhodium (nonmagnetic transition metal) exhibit strong magnetic moments.

While the surfaces of clusters show enhanced magnetizations, such surface effects are difficult to observe. A large surface-to-volume ratio and an absence of nearest neighbors

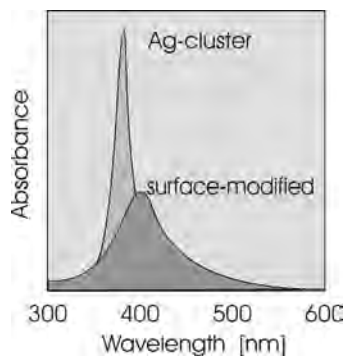


Figure 21. Coating of a silver cluster with a monolayer of iodine and a strong damping of the plasmon peak.

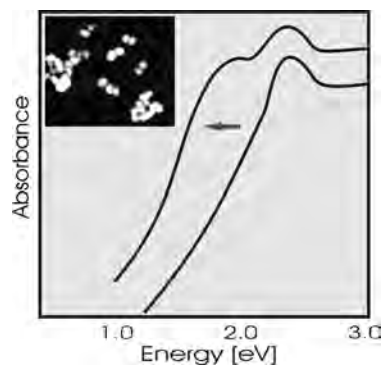


Figure 22. Spectral change induced by cluster aggregation.

induce rapid rotation of the magnetic field. As a result, the clusters appear to be macroscopically nonmagnetic, and only at a very low temperature is the rotation frozen.

In bulk materials, surface magnetism is hard to separate from bulk magnetism. Since small clusters are more or less entirely on the surface, they are ideal to study surface magnetism. The very smallest clusters, which have no internal atoms at all, are thus extremely magnetic, in agreement with theoretical predictions.

Thus, most nanoclusters are considered to be isolated single-domain ferromagnetic materials. Magnetic resonance (MR) and magnetic scanning microscope (MSM) imaging offers both high resolution and large area imaging capability. To be visualized, structures must be labeled with a nanoscale marker that can be detected by MR imaging. Superparamagnetic iron oxide nanoparticles currently provide the highest sensitivity when used as a MR contrast agent.

A new type of iron oxide nanoparticle, magnetodendrimers, have excellent magnetic and NMR relaxation-enhancing properties, and, because of their coating with a dendrimer as a transfection agent and their nanosize, they are efficiently taken up by a number of mammalian cells. The magnetodendrimers exhibit a high saturation magnetization of ~ 100 emu g/Fe, no magnetic hysteresis at 300 K, and T2 relaxivities of $200 \text{ mM}^{-1}\text{s}^{-1}$ (at 37°C), with a rapid approach to saturation at magnetic field strengths well below 1.5 Tesla. Magnetically tagged cells show a high degree of cellular uptake and thus intracellular labeling, with the cytoplasm containing large numbers of iron-containing vesicles and endosomes. Magnetodendrimers represent a new class of cellular nano-contrast agents that can be used efficiently for magnetic cellular labeling and *in vivo* tracking of cells down to the molecular scale.

2.5. Cluster-Cluster Interaction

Standard electromagnetic theory can only be applied as long as no significant coagulation of the clusters takes place. The origin of the two peaks observed on aggregate formation can be deduced from experiments clearly showing that the low-frequency peak is reduced with increasing p-polarization, in contrast to high-energy peaks, which are nearly insensitive to a change in polarization of light. Thus, the low-frequency peak is caused by longitudinal mode excitation, whereas the high-frequency peaks correspond to the transverse mode of the system.

The stability of a cluster system against coagulation and, furthermore, on coalescence is due to electrostatic repulsion of the clusters (see above). Repulsion, sometimes combined with added steric inhibitors such as polymers, blocks cluster-cluster contact. This prevents a metal-to-metal contact induced by thermal motion.

A color change results from the formation of aggregates of the nanoclusters, or the precipitation of the aggregated nanoclusters (from red to violet and, farther on, blue for Au-colloids). This color change may be observed with the naked eye or spectroscopically (Fig. 22).

Aggregation of nanoclusters can be quantified by EM or light scattering. A color change can be more readily observed against a background of a contrasting color. The observation of a color change is facilitated by spotting a sample on a solid white surface of an RP-18 TLC plate. Upon drying at room temperature, a blue spot develops if the nanoparticle conjugates are linked by biochemical interactions; otherwise the spot appears red-pink. The results can be stored in this format.

Conventional silver enhancement kits greatly increase the sensitivity of the reaction.

2.6. Coating Clusters with Biomolecules

Gold clusters are unstable as sols in the presence of electrolytes. It is believed that the gold nanocluster has a gold-0 core and a gold-1 shell, because of incomplete reduction at the outer surface. The coreagent used in synthesis coats the surface with citrate or chloride ions, for example. When salts are added to a cluster sol the color turns to blue, and the clusters precipitate. However, if proteins are added under proper conditions, these bind spontaneously to the gold cluster surface. Surfaces are modified and the sols remain stable in the presence of added electrolytes.

The binding of proteins to metal clusters is more or less irreversible. Most of the proteins retain their biological activities, at least in part. This property makes nanoclusters highly useful as transducers.

Because of their high reproducibility and robustness, cluster-based assays are useful tools in protein assays and high-throughput profiling of the proteome. The degree to which biological activity is lost depends upon the structural integrity of the protein. The degree to which conformational changes are vital for the proper function of the protein depends on how tightly the protein is bound to the surface. Furthermore, the pH during immobilization versus isoelectric point of the protein is important.

No general rule can easily be obtained for the degree to which biological function is retained, but mostly it is better than or at least comparable to other covalent immobilization techniques.

On the average one 14-nm colloid is covered with 25–100 proteins 3 nm in diameter. Therefore even poor immobilization results in sufficient biological activity of the cluster reagent.

Binding of protein to the gold clusters is pH-dependent. Stable complexes are achieved at a pH 0.5–1 units higher than the isoelectric point of the protein to be immobilized.

The pH of the colloidal clusters can be adjusted by the addition of 0.1 M NaOH or by the addition of 0.1 N HCl.

The pH is measured with pH paper or with gel-filled electrodes. Glass electrodes are coated by colloids and thus might be modified in their response.

In the case where very tiny amounts of protein are available for coating the gold sol it is important to estimate the minimum amount of protein needed to stabilize the sol. To provide optimal conditions for protein binding, the ionic strength should be low, since salt induces cluster aggregation (a red gold sol turns blue).

Particle sizes	Unconjugated colloidal gold sols, 2–50 (250) nm
Aggregation	80–90% singles with no clusters greater than triplets
Stability	Gold conjugates with 20% glycerol are stable if stored at ≤ -25 °C.
Storage buffer	20 mM Tris-base, 20 mM Na ₂ S ₂ O ₃ , 200 mM NaCl, pH 8, +1% BSA, 20% glycerol
Assay buffer	20 mM Tris buffer, 200 mM NaCl, pH 8.2

Gold conjugates with protein ~100 kDa

Size (nm)	OD (520 nm)	Protein concentration (μ g/ml)	Proteins/cluster
1	—	50	1
5	3	36	3
10	3	30	~10
15	4	30	~30
20	4	30	~50
30	5	15	~100

Gold colloids are coated with protein in a 2–3-fold excess for several hours. Excess protein has to be removed by washing. Coating can take place with reduced amounts of the desired or any other protein if, in addition to the functional protein, in a second step an unreactive protein is applied for the stabilization of colloids. In a similar way other proteins can be attached to the colloid surface, considering their isoelectric points.

Monolayers of the polypeptide poly-L-lysine are useful for controlling the specific adsorption of proteins onto gold cluster surfaces. A poly-L-lysine monolayer modified with biotin is electrostatically adsorbed onto a gold cluster coated with a self-assembled monolayer of a carboxylated thiol (e.g., 11-mercaptoundecanoic acid). The immobilized biotin groups act as specific biorecognition sites for avidin. By varying the percentage biotinylation of poly-L-lysine, it is possible to control the surface coverage of avidin to create either full or partial monolayers (4.1 nm). The poly-L-lysine monolayer and any adsorbed avidin can be rinsed from the surface with a low- or high-pH solution to allow quantitation of the adsorbed molecules.

2.7. AFM Imaging

For HT-biomolecular screening, novel comparative techniques permit rapid identification of modified genomic DNA molecules. Specific DNA sequences are labeled with

conductive reagents such as colloidal gold particles, and the position of conductive reagents along DNA contours is detected via nanofabricated electromechanical devices.

Individual DNA molecules are labeled with colloidal gold particles by hybridization of synthetic nucleotides conjugated with biotin into human genomic DNA fragments and subsequent coupling with colloidal gold particles coated with avidin. DNA, labeled with colloidal gold particles, is straightened and immobilized on the silicon surface. Electromagnetic force, surface tension, or hydrodynamic force is used to uncoil and stretch DNA molecules. The positions of colloidal gold particles are detected by AFM or other scanning probe microscopy techniques along the straightened DNA molecule.

Direct imaging can be done in ultralarge biomolecular assemblies, such as the extremely large ribonucleoproteins (RNPs), the molecular mass of which may be several million Daltons. For such polymorphic assemblies, visualization by electron microscopy provides structural information at a resolution that is difficult to obtain in any other way. Yet, localization and tracing of RNA within RNP complexes are not straightforward. A novel way to accomplish these is through the synthesis of RNA molecules that are covalently derivatized with gold nanoclusters, which thereby can be visualized by EM or by atomic force microscopy.

2.8. Immunocluster Techniques

Conjugates, prepared by coupling of antibodies on colloidal gold particles, were used in a homogeneous sol particle immunoassay for various proteins. Most assays are based on cluster coagulation, resulting in color reduction. The best results were obtained with big particles of 50 nm or more near the stability limit. The addition of polymers sometimes increased the agglutination rate considerably. The influence of temperature on the agglutination is small. Higher concentrations resulted in steeper calibration curves. The dose-response curves in buffer or urine are almost identical, and the reproducibility in biological fluids is fine. Homogeneous aggregation assays have a high practicability and are easy to automate. A disadvantage might be the method's moderate sensitivity.

Based on well-known colloid labeling, various semiquantitative flow-immunoassay methods for the detection of antibodies or antigens have been developed. The label is a colored colloidal particle such as gold (red), carbon (black), silica (several colors), or latex (several colors) for direct visualization of the immune reaction. In practice, colloidal gold particles or gold nanoclusters with a diameter of 25–40 nm are the most commonly applied labels in strip tests. The colloidal particles are coated with an organic reagent, which, in turn, is attached to the antibody by covalent bonds. Appropriate antibodies or antigens for a sandwich-type immune assay are immobilized on the cluster surface and on chromatography paper or in a nanochannel in the most advanced devices.

Thus, a typical strip test device consists of a test strip that is mounted in a plastic cassette (housing). The test strip is made up of a number of components, including a sample pad, a conjugate pad, an absorbent pad, and a membrane that contains the capture reagents. The paper strips

are developed with an appropriate immuno-gold reagent in a plastic tube in the presence of urine (e.g., pregnancy) or serum [28, 29]. The mixture migrates up the strips toward the test band. A purple band develops, which indicates the presence of the corresponding antigen or antibody. About 50 mIU of hCG in urine can be detected in 5 min or less.

These test kits are simple and rapid and require no complicated or costly instruments. A disadvantage may be the limited sensitivity of the assay and lack of multidimensional multianalyte capabilities. This immunoassay format is also known as the strip test, one-step strip test, immunochromatographic test, rapid flow diagnostic, rapid immunoassay, lateral flow immunoassay (LFI), on-site test or assay, or near-patient test.

To prepare large gold nanoclusters (40 nm) for immuno-strip tests, heat 100 ml of 0.01% (w/v) tetrachloroauric[III]acid trihydrate ($\text{HAuCl}_4 \cdot 3\text{H}_2\text{O}$) to boiling under reflux conditions, and add 1 ml of 1% (w/v) trisodium citrate dihydrate under constant stirring. In about 25 the slightly yellow solution will turn faintly blue and nuclei are formed. After approximately 1 min the blue color changes to dark red, indicating the formation of spherical clusters. The solution is boiled for another 5 min. The optical density, measured at 540 nm, will be about 1. Add 0.05% (w/v) sodium azide for storage.

A standard immuno protocol might be done as follows: Blocking for 30 min at room temperature; primary antibody for 30–60 min at room temperature or 37 °C; rinse 1 with buffer; gold conjugate incubation for 30–45 min at room temperature or 37 °C; rinse 2 with buffer +2 M NaCl; rinse 3 with buffer; rinse 4 with distilled water. The binding is monitored in real time by observation of a developing absorption peak in a setup with a 125- μm aqueous top layer. Because any compound penetrating the polymer film will potentially react with the metal mirror layer (e.g., Ag mirror and chloride ions) and alter its optical and adhesive properties, care has to be taken to obtain distance layers without pinholes or cracks.

2.9. Assembly of Functionalized Nanoclusters and Nano-Objects

Any standard hybridization test can be done with metal cluster aggregation. It should be noted that the formation of particle arrays gives a very sharp signal due to the large number of interactions between different particles. However, this cooperative effect limits the dynamic range of the reaction. Because nanoclusters assemble only in the presence of a complementary DNA strand, the change in material properties induced by assembly can be used as an indicator of whether a particular sequence is present in a sample or not. Such signatures include the changing optical, mechanical, and electrical properties.

Based on the appearance of the second peak on cluster aggregation, a new analytical device was developed by Mirkin et al. [30–34]. The method is based on colorimetric detection of DNA and RNA based on mercaptoalkyl-coated oligonucleotide-modified gold nanoclusters. Introduction of a hybridizing oligonucleotide into a solution containing the modified particles results in the formation of a polymeric network of clusters. This aggregation of clusters

can be directly monitored as a red-to-purple-violet shift of the solution. Transfer of the aggregated cluster net to a silica matrix results in a shift of the signal to a clearly visible blue spot. The assay can detect femtomoles of oligonucleotides.

First assays (e.g., targeting anthrax bacteria) are extending now to clinical DNA detection. DNA arrays with DNA-functionalized gold nanoparticles assemble metal cluster arrays onto a sensor surface induced by the complementary target. The procedure even permits the detection of single base-pair mismatches. Gold nanoclusters are chosen as the major building block because of the ease of synthesis from tetrachloroaurate and citrate.

In a novel process, even small DNA-modified optoelectronic components are transported to the surface of a microelectrode by electrophoresis, whereupon sequence-specific oligonucleotide interactions direct component localization and binding. This biologically inspired method of component localization is a new approach to circuit fabrication. It provides self-assembly-based manufacturing methods as a substitute for pick-and-place technology.

The attachment of short synthetic oligonucleotides to gold nanoparticles in particular follows rules slightly different from those of the attachment of proteins or larger polyelectrolytes, which is due to the linear nature of the species. A preparation as cited above (Au colloids, 12 nm in diameter, 17 nM in particle concentration) is reacted with a 200-fold excess of a thio-functionalized oligonucleotide (3.5 μM) in water. The reaction is allowed to stand for 24 h at room temperature to allow reorientation at the surface and provide optimal space filling. About 80 molecules are assumed to immobilize to the surface of a 12-nm particle. The excess of oligonucleotides is removed by centrifugation. The particles show very good stabilities at high salt concentrations. However, to provide temperature stability at 70 °C and higher the linking group has to be modified. Either a multivalent thiol linker is applied or the particles are derivatized with an alkylsiloxane. The oligonucleotides can then be bound covalently to functional groups in the surface of the coated particle. The test itself leads to the aggregation of nanocluster arrays. Two types of particles are coated with two sequences specific for the same target molecule. Upon addition of the target the particles bind to the target. Since any particle bears a large number of identical sequences, aggregation of particles will occur. The formation of these 3D arrays gives a detectable change that occurs upon hybridization of the oligonucleotides on the nanoparticles to the nucleic acid; this is a color change from red to blue.

To set up ordered nanostructures at chip interfaces, nanoarrays based on cluster monolayers became a growing area of experimental and theoretical research. Metal colloids and nanoparticles such as biopolymers, bioparticles, or even small polymer spheres in the size range from a few nanometers up to 5 μm have been used to form lithographic masks on surfaces. The masks consist of (often hexagonally) arranged monolayers of these particles.

When a droplet of the colloidal suspension is placed on a substrate, the masks form independently via a self-organized process. The deformation of the liquid film causes an attractive force between the nanoparticles: the lateral capillary force. Protruding nanoparticle caps deform the surface of the fluid and induce an attractive force between the

nanoparticles, which exceeds the thermal energy, kT . Often a nonmiscible solvent is used and the nanostructure forms upon solvent evaporation at the interface. With a floating technique, for example, the masks can be transferred to almost any arbitrary substrate. These nanoarrays have been utilized, for example, as masks for vacuum deposition of metal cluster arrays, plasma etching, or masters for nanoprinting.

Current research focuses on catalytic and chemical properties of nanodot arrays and the potential application of cluster monolayer lithography for the production of optical and electronic switches, guides, and memories.

2.10. Nanocluster Arrays by Biotemplating

Aggregated nanoclusters are excellent tools. A variety of analytical techniques use them to detect fluorescence, Raman scattering, atomic and magnetic force, and electrical conductivity. Hybridization of DNA is an excellent tool for directly and precisely assembling nanometer-sized structures. This methodology allows for the fabrication of materials with defined nanodevices to be used, for example, biomolecule sensing and separation technologies. The strategy is applicable to the synthesis of new nanostructured materials made from metals, semiconductors, and inorganic and polymer insulators. Nanosized assemblies are designed by changing the DNA linker and the particle composition and controlled construction and deconstruction of the materials by hybridization and dehybridization.

Nanotechnology is severely needed for lithographic methods applicable to pattern inorganic material at the nanometer-length scale. The nanoapproach for the fabrication of molecularly engineered nanostructures is the method of biotemplating [35–37]. This technique makes use of the well-defined structural, physical, and chemical properties of self-assembled biological macromolecular complexes.

Well-defined bilayers are used as templates for the buildup of organic and inorganic nanoassemblies. Thus, the bottom-up approach allows the setup of nanometer fabrication facilities via molecular engineering.

Biomolecular templating focuses on two different aspects:

- The geometrical shape of the template is employed for the fabrication of artificial nanostructures such as metallic nanowires, for example, by coating the specimens with thin metal.
- Large macromolecular assemblies built from identical subunits possess a regular structure.

The periodicity arises from the self-organization of biomolecules into ordered molecular arrays [38]. These layers are a precise spatial modulation of chemical surface that can be used to accomplish site-specific chemistry. In contrast to standard lithography, such as electron beam lithography, templating techniques provide the advantage of parallel fabrication. A well-defined deposition of metal and semiconductor clusters onto a 2D protein template was demonstrated by several groups. In a further processing step the metal is used for example, to set up a regular array of holes. The topology of the pattern is determined by the geometry of the template used. Thus, the deposited layer represents the intrinsic spatial structure of the underlying

protein monolayer. The protein template that is most often used is a bacterial surface layer (S-layer). These layers are regular protein crystals that form the outermost cell envelope component of many prokaryotes exhibiting different kinds of lattice symmetry (p1, p2, p3, p4, and p6). S-layers are 5 to 15 nm thick. The spacing between structural units varies from 3 to 30 nm. Isolated S-layers are suspended in a buffer solution (e.g., 50 mM sodium phosphate, pH 7.5, 1 mM MgCl₂, and 0.02% sodium azide) at a concentration of ~2 mg/ml and stored at 4 °C. The possibility of coating two-dimensional arrays with perfect uniformity on solid surfaces or at liquid–air interfaces makes them an ideal biological template. A variety of clusters have been deposited on these films, including gold, silver, platinum, or cadmium sulfide. Well-defined sites are decorated with metal particles deposited from the aqueous or gas phase.

In the presence of protein, cluster formation is strongly accelerated compared with the reaction in pure solution. For *in-situ* generation of clusters on S-layer surfaces the protein is often activated by molecular deposition of metal catalyser, such as Au, Pd, or Pt from a metal salt solution. After activation the S-layer suspension turned from colorless to light yellow, becoming darker with increasing reaction time and thereby indicating metal deposition on the protein template. The activation kinetics were studied by recording the optical absorption of the solution. The chemical deposition of metal on the S-layer leads to the formation of highly ordered arrays of metal clusters. Well-separated, clusters are aligned along the crystalline structure of the protein template, reproducing the symmetry of the S-layer.

The usability of biological templates for such purposes has been proved not only for nucleic acids and S-layers, but even for microtubules and viruses.

Microtubules are highly ordered protein polymers consisting of regularly arranged α - β -tubulin dimers, which have a length of about 8 nm and a diameter of ~5 nm. Microtubules are useful templates for assembling small metal clusters. The surface of the tubulin molecules exposes a defined pattern of amino acid residues that provides a wide variety of active sites for nucleation, organization, and binding of metal clusters. Clusters formed organized arrays, ordered chains, and defined patterns, reflecting the regular arrangement of the tubulin subunits within the microtubule. Taxol-stabilized Zn induced two-dimensional tubulin sheets. It was shown that histidines are centrally located on α -tubulin. These histidines are easily accessible and correspond to the pattern of the metal clusters. Thus, it is assumed that these histidines are candidates for chelating noble metal clusters.

2.11. *In-Situ* Assembly of Clusters on Electrodes

Biosensors can be set up by *in-situ* assembly of colloidal particles on micropatterned electrodes. Microspheres or nanospheres from suspension are collected via electrophoresis or dielectrophoresis in the micrometer-sized gaps between planar electrodes. The assembled particulate patches are fixed by changing the colloidal interactions to induce coagulation, for example. Biorecognitive molecules on the nanoparticle surface bind the analyte molecules. A direct electric conductivity readout is made after labeling

with colloidal gold particles and, if necessary, by further enhancement with silver nucleation. The method is a basis for setting up disposable on-chip arrays for specific proteins, DNA, or other biomolecules [39].

Chip substrates are set up, bearing photolithographically fabricated metal electrodes with micrometer gaps between them. Nanospheres are suspended in a low-electrolyte aqueous medium and are collected in the gaps between the electrodes. A nonuniform alternating electric field is used to drive the particles via dielectrophoresis. Aggregated microspheres, however, do not exhibit enough signal and disassemble when the field is turned off. The critical step for binding the nanoparticles is to decrease the repulsive interactions and to coagulate the particles. Particles that are stabilized by electrostatic repulsion can be coagulated on an oppositely charged surface; particles stabilized by polymers or surfactants are deposited by washing away the protective layer. The detection is carried out by immunological tagging of colloidal gold clusters to the nanosphere layer. Before the test results are read, the gold particles might be enlarged and fused together via catalyzed deposition of a silver enhancement.

The readout is carried out by measuring the resistance between the electrodes. In the case of a positive immunological reaction, the electrodes become connected via thin metal bridges.

2.12. SPR Transduction

Surface plasmon excitation is obtained when photons are coupled into a metal/dielectric interface. These plasmons are resonant charge density oscillations at that surface of the metal. The wave is a perturbation of the electron plasma or, more precisely, a surface plasmon-polariton extending several tens of nanometers into the metal and up to 500 nm into the adjacent medium. The plasmon exhibits an exponential electromagnetic decay of the field perpendicular to the interface.

For SPR coupling the light must be at a well-defined angle to the interface. Any coating of the surface of the metal with an overlayer of varying ϵ will change the coupling angle of the resonant system. This change induces a shift in resonant angle up to a few degrees. Based on this principle and related techniques, various devices are commercially available directly (mostly without any label) that can transduce biochemical binding into a variation of resonant angle [40–42].

Although a direct transduction is very useful for basic interaction studies, its overall sensitivity is low. Thus based on the large difference in $\epsilon_{\text{H}_2\text{O}}$ and ϵ_{metal} , a significant increase in assay sensitivity was obtained by adding a metal nanocluster label to the assay.

The significant increase in sensitivity by nanoclusters has to be evaluated against the disadvantage of labeling the analyte.

2.13. Clusters as Nanoswitches

In recent years a first step has been taken toward synthesizing reversible molecular switches and integrating these switches into electronic circuits. Any digital microelectronic

device is based on switches known as transistors and diodes. Complex elements, such as flip-flops, are created from a combination of these simple elements. Two transistors are combined, for example, to set up a Schmitt trigger. A Schmitt trigger defines a bit of binary information as either zero or one.

In a recent development novel nanocluster-based devices turned the conductivity on and off by changing the oxidation state of a single molecule. Some organic molecules contain a redox-active center where reduction or oxidation can be achieved more or less reversibly. If they are sandwiched as molecules between electrical contacts they support quite large currents. The phenomenon is based on resonant tunneling, when the electron energy bands of the molecule overlap with those of the metal.

The effect has previously been shown with layers of an organic molecule containing the bipyridinium group (bipy). In a nano-approach, a molecule sandwiched between a gold electrode and a gold nanocluster serves as the molecular switch. A convenient setup can be obtained by attaching thiols to each end of the redox switch (one thiol at the gold electrode, the other at the gold nanocluster). To obtain a simple readout the tip of a scanning tunneling microscope might be used to record the current through the nanocluster.

New results show that changing the redox state of the bipy molecule can control electron transport between the gold electrode and the nanocluster. A switch based on these clusters might work with fewer than 30 electrons. When the molecule is in the reduced state, large currents flow through the device; when a certain threshold voltage is applied, the tunneling current decreases markedly. The threshold voltage corresponds to the redox state of the molecule used as a switch. A molecular trigger would operate too slowly and have insufficient gain to be applied as an electronic circuit.

Nevertheless, biointeractions coupled to a nanoparticle allow a novel type of biosensor to be set up. Such a device can detect single molecules or single chemical reactions. The system reported by Schiffrin adds a novel switch to a rapidly expanding list of switchable nanoelectronic devices.

In a related setup it had been shown that individual gold nanoclusters can be controlled by adding protons to molecules bound at the cluster surface. Future bioelectronic devices may thus be related to flip-flops well established in the microelectronic field.

2.14. Resonant Cavities

When a point defect is created in a regular cluster array, it is possible for that defect to pull a light mode into the band gap. Because such a state is forbidden from propagating in the bulk layer, it is trapped. The mode decays exponentially into the bulk.

Such a point defect, or resonant cavity, can be utilized to analyze biorecognitive interactions by opening or closing these defined spots via biorecognitive interactions. For example, such an array can be coupled with a pair of waveguides to produce a very sharp filter through resonant tunneling. Through a change in the size or the shape of the defect, its frequency can easily be tuned to any value within the band gap. Moreover, the symmetry of the defect can also be tuned. Point defects are already the heart of many other

non-biodevices, such as channel drop filters or resonant cavities, and enhance the efficiency of lasers.

2.15. Electroluminescence

To produce ultrasmall clusters, a thin film of silver oxide is treated with an electrical current of about 1 A. This creates a thin line of silver clusters of two to eight atoms. Under the influence of an alternating current these clusters exhibit electroluminescence, emitting light at a frequency that depends on their size. Experiments have shown that a high-frequency (>100 MHz) alternating current produces an electroluminescence response that is 10,000 times as great as that produced by a direct current. Whereas bulk materials cannot respond quickly enough to an alternating current, the alternating current creates rapid electron-hole recombination within single molecules in nanoclusters in a very narrow section of the sample. Similar fluorescence emission phenomena have been observed with nanoclusters of copper atoms.

3. NANOCLUSTER AND FIELD EFFECTS

3.1. Surface-Enhanced Optical Absorption

The optical properties of metal island films are used in surface-enhanced optical absorption (SEA), the so-called anomalous absorption. An absorbing cluster layer positioned at a defined distance from a metal mirror represents a special kind of reflection interference system. At a certain distance of the cluster from the mirror the electromagnetic field reflected by the mirror has the same phase at the position of the absorbing layer as the incident fields, and thus by this feedback mechanism the effective absorption coefficient of the absorbing layer is strongly enhanced. Since for a given interlayer distance the optimum phase is only given for a defined wavelength, the system is characterized by a spectrally narrow reflection minimum. The spectral position shifts sensitively with the cluster-mirror distance [43, 44] (Fig. 23).

The optical characteristics of the sensor can be modeled by either the stratified medium theory or the CPS theory developed by Chance, Prock, and Silbey. These theories focus either on optical thin films or on a cluster in proximity to a metal surface.

The stratified medium theory (SMT) can be applied for the calculation of any cluster films, whereas the CPS model

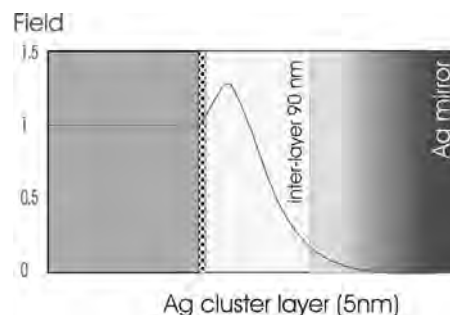


Figure 23. Field within SEA chip.

is best suited for single clusters. Application of the SMT is based on the complex optical constants in all three layers. Whereas optical constants of mirror metals (Ag, Au, Al) can be found in the literature, the optical constants of island films are strongly dependent on preparation parameters. Mostly they must be found experimentally. Standard methods for the determination of optical constants are based on independent measurements of the cluster film reflection and transmission. A (relative!) maximum of the signal can be obtained if the mean mass thickness of gold or silver clusters is around 5 nm. Depending on the number of bound clusters, the reflection varies by several orders of magnitude. With the use of optimized equipment, even single clusters close to the surface are visible as color dots.

Similar to interference-based systems, there are several regimes of reflectivity change. According to the selected cluster-mirror distance, the desired dynamic range of the system, the optimum wavelength, and the layer thickness can be tuned (Figs. 24 and 25). The spectral reflectivity minimum strongly depends on the cluster distance, and thus a thickness change of any interlayer will be visually observable upon white-light illumination by the altered color impression of the reflected light.

Resonance-enhanced absorption of nanoclusters is a novel means by which nucleic acids, enzymes, or binding proteins can be detected in a simple and reproducible way. The analytes induce binding or dissociation of metal clusters, which have been or will be bound at a defined distance from a reflecting, preferentially electron-conducting substrate surface. The binding or dissociation is transduced into a clearly detectable optical signal through resonant enhancement of clusters interacting with their mirror dipoles. Metal clusters or colloids are chosen with a diameter smaller than 100 nm, preferentially around 40–50 nm to suppress multiple peaks in the spectrum, to enhance diffusion and to avoid precipitation and coagulation during storage.

The setup is more cost effective than standard ELISA tests and reduces handling time through a novel one-step test procedure. Rapid and sensitive one-step test kits for clinical and lab use can be set up based on this technology. Possible fields of application include the diagnosis of urinary tract infections; screening of allergens; detection

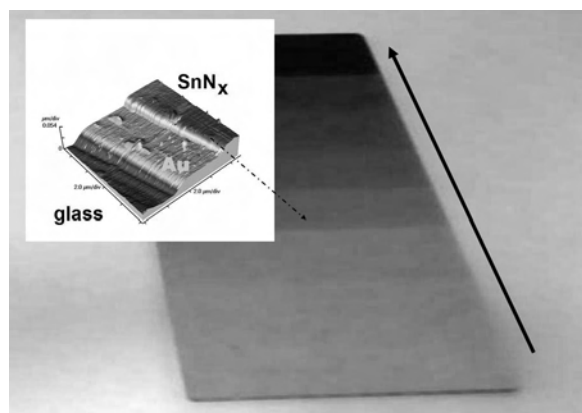


Figure 24. Chip surface versus coating time of the interlayer (glass-type SnN_x).

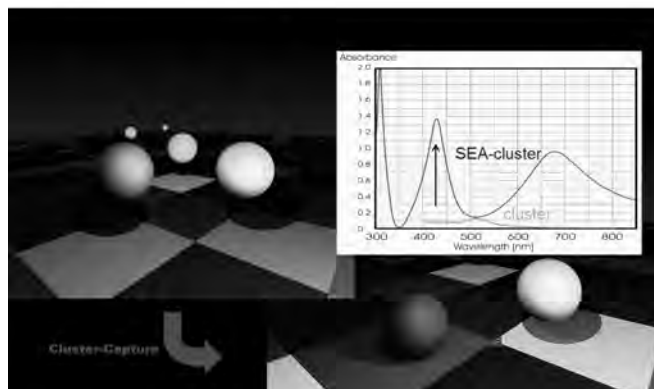
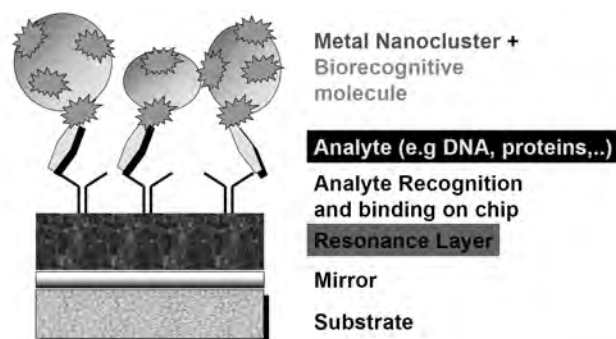


Figure 25. Capture assay and cluster approaching the surface.

and quantification of pathogenic bacteria, glucose, and C-reactive protein; food identification, etc.

If the analyte interacts with the chip, it

- induces changes in the packing density of the cluster layer or
- induces changes in the spatial arrangement of bound clusters,

both leading to characteristic changes of the optical appearance of the sensor surface. The color of the surface is altered because of binding, catalytic activity, or a structural rearrangement of the analyte or a biorecognitive active component added to the mixture.

Given an optimized setup, the spectral position is highly dependent on the spatial arrangement, especially

- the distance of the cluster layer from an electron-conducting surface and
- the local variation in ϵ_m .

Moreover, the sensor setup can transduce changes in the extent of surface coverage with bound clusters into a clearly visible optical signal, by

- a strong change in absorption at a defined wavelength or
- a spectral shift of an absorption maximum.

To estimate the ultimate sensitivity of the chip, clusters with a diameter of 40 nm were arranged in a two-dimensional lattice of 150 nm, at an optical resolution of 1/200 mm, inducing a change of 10% of the signal, equal to 400 molecules. This sensitivity has been proved with an antigen–antibody setup that detects proteins. Decreasing the

optical field to around $1\ \mu\text{m}$ permits monitoring of the resonance of single metal clusters bound to the chip surface.

The application of catalytically active analytes or labels such as urease is another way to increase the sensitivity significantly and allows single molecule detection.

Clusters (preferentially silver or gold cluster) can be bound by means of a variety of biochemical linkers at a defined distance from a mirror. A detectable signal will result if these linkers are either formed or cut by biochemical recognition or by catalysis, or if their spatial arrangement is altered. According to the setup, oligonucleotides, for example, are applied as linkers, which can then be cut by specific restriction enzymes from microorganisms. Many pathogenic microorganisms express specific restriction endonucleases and can therefore be detected by means of the new sensor without expensive instrumentation.

Because of their particle structure cluster films do not form a barrier of diffusion to gases or fluids. The analyte concentration can be measured with high sensitivity via visual inspection of the sensor surface. The intensity of the absorption band is directly proportional to the number of interacting clusters. Any reduction of the number of clusters results in a lowering of the absorption of the system at a high surface coverage in a spectral shift due to a change in cluster-cluster interactions.

Reduction of nonspecific background absorption of the sample measurement can be carried out at two angles of observation. Whereas absorption of chromophores is independent of the angle of observation, the specific signal shifts strongly, depending on the angle. Thus by simple subtraction of both signals the background resulting from matrix effects can be eliminated.

In addition to the cluster-based color, a thin film color might show up, based on the extent of phase difference of the multilayer system. This color depends on the thickness and refractive index of the interlayer film, the angle at which the light strikes the film surface, and the color of the light. If for a particular color the two reflected rays are in phase with each other when they rejoin, then they will combine to produce a constructive interference. If they are out of phase, they will eliminate each other and a strong color will appear.

3.1.1. SEA Biochips

Surface-enhanced absorption is an increased optical absorption of clusters in nanometric proximity to a wave-reflecting surface. Total enhancement in absorption of spherical metal colloids is at least 8-fold, and relative adsorption enhancement is more than 100-fold and independent of the method of application of sputtered clusters but depends on the attachment of clusters under given conditions [45–50].

A SEA biochip consists of a mirror layer on a substrate surface (mostly metal), an inert distance layer, deposited by spin coating or chemical vapor deposition, on top of which individual biorecognitive molecules are arrayed.

After incubation with the analyte, clusters are bound with protein or DNA-coated colloidal particles. This binding step can be monitored in real time if required. Such direct and sensitive kinetic monitoring makes it possible to transduce a number of molecular binding events into an macroscopic optical signal visible to the eye.

To relate the number of individual clusters to the optical signal obtained, scanning techniques based on STM and AFM are employed. An interlayer deposited via spin coating of polymers and activation of the sensor surface by plasma chemistry permits cost-efficient, small-series production. For large numbers and high quality, interlayers deposited by sputter or CVD techniques are an excellent choice.

Any conventional ELISA can be adapted to the new detection protocol transducing various antigen-antibody interactions (Figs. 24 and 25). To test for *Escherichia coli* proteins as impurities in commercial drug produced via genetic engineering in *E. coli*, anti-*E. coli* (IgG) was coated on gold colloids. *E. coli* proteins are microdotted onto the chip SEA surface. Upon incubation of *E. coli*-covered sensor surfaces, the anti-*E. coli*-coated colloids bound to the sensor surface and the proteins developed a color visible to the eye. The detection limit of *E. coli* protein was in range of fmol/mm^2 . For the study of multistep interactions, antibody detection with recombinant protein G-coated clusters proved to give excellent sensitivity.

A significant advantage of surface-enhanced optical sensors is the ultrahigh density that can be achieved with printing techniques on surfaces similar to a CD-ROM or DVD (digital versatile disk). Areas of $1 \times 1\ \mu\text{m}$ can easily be read out with rather cheap and simple devices based on a commercial CCD camera chip at prices as low as 1–2 Euro.

Because of the ultraflat, high-quality surface, array-based sensor chips are easily set up by photolithography, microdotting, or inkjet printing. With these techniques thousands of molecules, such as ligands, proteins, or oligonucleotides, are immobilized in a well-defined array on a SEA chip fully compatible with glass-slide-based systems (Fig. 25).

It should be noted that up to a wavelength of 600 nm the optical properties of SEA sensor chips covered with chemically synthesized clusters are equivalent to chips covered with sputtered metal clusters. At any wavelength substantially above 600 nm sputtered cluster layers show optical properties dramatically different from those of crystalline colloids attached to the polymer surface via affinity interactions. This results from the difference in shape as well as from varying degrees of crystalline nanostructure.

During a gold colloid synthesis based on the procedure of Frens, significant changes in the color of the reaction mixture occur. Upon the addition of the reducing agent to a boiling yellow gold solution, the color changes within minutes from black to dark blue to violet and finally shifts suddenly to red. By comparing the absorption spectra of the reaction mixture as a function of time during the synthesis, one finds that the characteristic sharp absorption peak of nanocrystalline colloidal gold develops only slowly. Earlier stages of the synthesis absorb light also substantially above 600 nm, which can be isolated by a rapid cool-down or the addition of metal ions blocking crystallization of the gold cluster.

If such glass-type noncrystalline colloids are applied, in a surface-enhanced absorption setup resonance enhancement at $\lambda > 600\ \text{nm}$ is significant. This makes it possible to shift the desired absorption peak all over the visible spectrum to IR and therefore to wavelengths favorable for technical reasons of measurement, such as matrix absorption or light source.

Summing up, a direct, even kinetic monitoring of biomolecular interactions is achieved by transforming a molecular binding event into an optical signal visible to the eye. The optical sensor permits the setup of one-step assays because detection does not necessitate any extra incubation steps. Surface-enhanced absorption transduces changes in surface coverage of submonomolecular cluster layers.

As substrates glass slides (e.g., Corning or Menzel), aluminum foils and polycarbonate or polyethyleneterephthalate sheets (Goodfellow-UK) hydrophilized by oxygen-plasma etching proved to be suitable.

On a polymer chip the deposition of a mirror layer is necessary. Silver, aluminum, gold, or gold-palladium is deposited by DC or RF sputter-coating. Under conditions of glow discharge, ion bombardment of the cathode will occur; this results in the erosion of the cathode material and the subsequent omnidirectional deposition of the sputtered atoms, forming coatings of the cathode material. The most common arrangement for sputter coating is to make the negative cathode the target material to be sputtered and the location of the chip the anode so that the chip is effectively at "ground" potential; for high-throughput coating a low-frequency AC double-electrode source should be used. The pressure is obtained by a rotary pump (if necessary combined with a turbomolecular pump). For metal coating argon is bled into the chamber. Sputtering has to be optimized for the optical quality of the metal film (highest possible reflection) as well as adhesion of the metal film on the support and applicability of the metal film for spinning of varying polymer dilutions. Attachment of silver, gold, or gold-palladium on glass is rather poor; thus, adhesion layers of tungsten, chromium, or titanium are required. At lab scale sputtering is carried out in a sputter coater, for 60–120 s, at 0.1 mbar argon and a power of up to 500 W.

As prefabricated mirror substrates, aluminated or titanium coated polyethyleneterephthalate can be applied instead of the above substrates. Moreover, highly polished metal foils or sheets can be used provided that their surfaces are sufficiently reflective. The chemical stability of the mirror is excellent for gold, whereas Ag darkens quickly and Al is often etched in an aqueous environment if the solvent can penetrate the protecting distance layer. Please note that chloride-based buffers easily dissolve standard adhesion layers used for gold or silver mirrors such as chromium or tungsten.

To obtain the desired resonance an interlayer tuned to the appropriate optical thickness is coated on the mirror. One way to achieve this is by spin-coating of polymer layers. Adhesion of the polymer film on the metal or mirror surface is critical for chip stability. A nanoscale film of hexylpolymethacrylate (with an average molecular weight of 400,000) (Aldrich) is applied by spin-coating at 4000 rpm with varying dilutions of the polymer in AZ 1500 Photothinner (Hoechst) and *n*-decane (Sigma). The appropriate solvent for the polymer should be chosen depending on the molecular coating of the metal film. The thickness of the interlayer is best studied with atomic force microscopy.

For further chemical derivation the etching of polymer layers by oxygen plasma is vital. The polymer surface is etched, for example, with oxygen plasma for 10 s at 45 mA

at an oxygen pressure of 0.1 mbar. Strong hydrophilicity is observed by exposure to oxygen plasma.

Another method of chemical activation of the polymer and attachment of biomolecules is the chemical breakdown of the polymer surface. A way to create functional -COOH groups at the surface of an ester polymer is to hydrolyze the bonds of the polymer. Hydrolysis is achieved by incubation with 2–4 N KOH. To limit polymer damage by total ester hydrolysis, reaction time should be less than 10 min. No substantial deterioration of film stability is observed; however, a slight film hydrophilization is observed. For application the protein is coupled covalently to carbodiimide-activated surfaces or is bound via noncovalent absorption to a plasma-etched polymer. For most applications simple adsorption is sufficient to bind the ligand layer to the polymer surface, adapting know-how from ELISA technology.

Most polymer-based chips need an oxygen plasma treatment to achieve sufficient adhesion of metal or polymer layers to the chip. The surfaces of the chips are functionalized by oxidation in plasma. The latter step greatly increases the hydrophilicity of the surface and allows better handling in combination with any standard assay format. The chip is inserted into the substrate holder inside the vacuum chamber of the sputter coater. The chamber is evacuated, and after the chamber is washed with oxygen (or air) at a pressure of 1 mbar, the pressure is adjusted to 0.1 mbar. Next, around 8 kV (AC, 20 kHz) is applied, which results in the ignition of a plasma. A plasma is formed between an aluminum target and the metal wall of the sputter coater ($P = 35$ W). The activated oxygen atoms bombard the chip surface and perform an oxidation reaction there. Thereby surfaces can be cleaned from organic substances and polymers can be rendered hydrophilic. In the case of polymers the oxidation reaction results in a wide variety of oxidized forms of carbon: hydroxyl, carbonyl, and carboxyl groups. Carboxyl groups are generated only at a minor percentage of the whole number of reactive groups formed at the surface of such plasma-activated polymers.

To functionalize the interlayer so that DNA, proteins, or thin films can be covalently attached, silane derivatives can be bound and cross-linked to form a stable monolayer or thin film by backing the chips at 105 °C. A silane layer serves as an adhesion layer for a variety of polymer, ceramics, glasses, and even nanocluster films. For vapor phase-coating techniques the silanes need a considerable vapor pressure to guarantee a sufficient adsorption rate. Two techniques might be employed to coat the chip with a stable silane layer.

Vapor coating is done to achieve a very homogeneous coverage. The chip surfaces are cleaned by subsequent washing with isopropanol, ethanol, and water or under reactive oxygen plasma. Both the chips and the silane or silane solution are placed in a vacuum chamber, to which a vacuum is applied with a membrane pump for several minutes. After the pump is turned off, silane fills the evacuated chamber and attaches to all of the surfaces therein. The adsorption process takes about 4 to 6 h but is usually done overnight. Subsequently, the chips are heated for 1 h to 60 °C or 10 min at 105 °C. Heating is necessary to cross-link silane molecules with each other and the surface by condensation.

To obtain a thick and cross-linked silane layer the coating is done from solution. The surfaces to be coated are cleaned

by washing with isopropanol, ethanol, and water. The silanes are diluted in ethanol at concentrations from 0.01% to 5%, and an equivalent amount of distilled water is added to the solution. Depending on how fast the reaction should occur (maximum of a few minutes in 5% solution) and how much a monolayer is desired (a few hours in 0.01% solution), the concentrations and periods of immersion in the silane solutions are chosen. Thereafter, the chips can be dried directly, strongly increasing the tendency to form multilayers, or the chips are washed with isopropanol to remove access silane. Then the chips are heat-treated as given above.

The gold clusters are labeled with proteins by first dissolving the protein in 200 μl of water at 1 mg/ml. Serial dilutions (1:5 to 1:10) of the protein in distilled water are prepared with 100 μl of each. Five hundred microliters of the pH-adjusted gold sol is added to each tube, and after 10 min 100 μl of 10% NaCl in distilled water is added. Tubes that contain enough protein to stabilize the gold sol maintain a red color even in the presence of electrolytes, and the red color turns to violet and blue. The amount of protein considered sufficient corresponds to the second tube containing more protein than the one whose color changes to blue. The success of conjugation can of course be followed spectrophotometrically. The maximum absorption of the colloidal solution is at $\lambda = 520$ nm. Once the optimal pH and amount for adsorption has been determined, large-scale protein-gold complex preparation (500 ml to $\times 1$) is carried out. The optimally stabilizing amount of protein plus about 10% is dissolved in distilled water and filtered through a 0.2–0.45- μm filter. The pH of colloidal gold is adjusted, and then the sol is added to the protein solution. The mixture is incubated overnight. The cluster is washed by centrifugation the next day, and thereby the excess of protein is removed. After cluster particles are pelleted, they can be resuspended in a small volume for the preparation of more concentrated solutions.

Most protein-gold conjugates retain their biological activity for months in the refrigerator at 4 °C with 0.02% sodium azide added to the buffer solution. Good bioactivity preservation for a longer period is also obtained upon storage at –20 °C in the presence of 45% glycerol.

To set up a polymer-interlayer SEA biochip, the following protocol might be employed. Onto mirror-coated glass chips or metallized plastic a 6% solution of polyhexyl metacrylate is applied by spin coating (5000 rpm). The surface of the thin film is functionalized under oxygen plasma. Capture proteins are bound via adsorption or EDC coupling (2 h, RT). After several washing cycles the chip is incubated with the analyte for 1 min (analyte at mmol/liter) to several hours (analyte at nmol– μmol /liter). Gold colloids 14–40 nm in diameter, coated with the secondary capture protein, are added and bind to the analyte at the surface. Aggregation of clusters or nonspecific binding is prevented by the addition of 0.1% Tween 20. The reaction is followed visually or via a CCD camera (Fig. 26). The chip is scanned in direct reflection mode (no standard scanner applicable!).

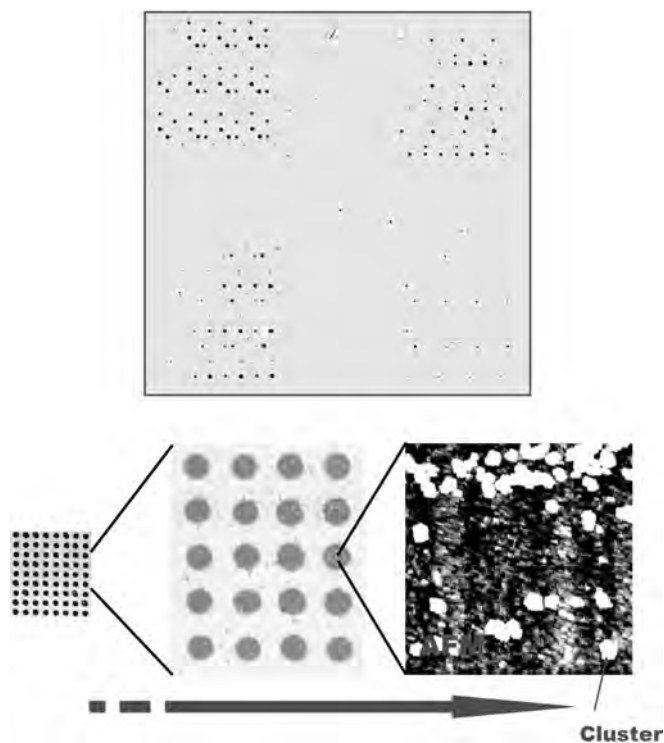


Figure 26. Optical and AFM scan of a cluster biochip.

3.1.2. Nanodistance Transduction via SEA Biochips

The “metal island coated on reactive interlayer system” (MICORIS) is an optical thin-layer system consisting of a mirror, a transparent interlayer (in this case represented by the active analyte-induced swelling or shrinking macromolecule), and a metal cluster (island) film as the topmost layer.

Because of the special optical behavior of the cluster film and the special layer design, this system shows a characteristic spectral reflection behavior cited above. Thus the setup is strongly dependent on the thickness of the transparent interlayer (Fig. 27).

The visual impression obtained by observation of the reflected light upon diffuse white light illumination of MICORIS in the interlayer optical thickness ranges up to

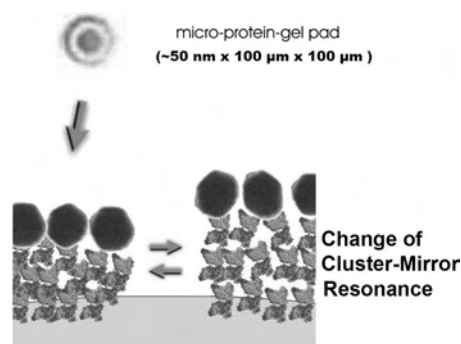


Figure 27. Shift in optical response induced by a change in the reactive interlayer.

1 μm of optical thickness (thickness \times refractive index). There is sufficient color contrast for visually distinguishing thickness changes of a few nanometers, and with elaborate equipment even sub-nanometer changes are easily detected. Swelling or shrinking of the interlayer molecule is equivalent to changing the cluster-mirror distance.

The response of a MICORIS sensor induced by different analytes is fully reversible if the interlayer can perform a reversible conformational change. Thus, for example, the spectra obtained upon variation of ions in a number of polymer layers can be compared with calculated spectra and calibrated in effective thickness. The increase in absorbance (which corresponds to a decrease in reflectance) at a certain wavelength is an appropriate measure for the interlayer thickness change. For small changes a linear relation between absorbance and thickness change can be assumed.

As a typical polymer, polyvinylpyrrolidone cross-linked with sulfonated bisazidostilbenes exhibits ion-dependent shrinking and swelling, which can be observed by using this polymer as an interlayer polymer in a MICORIS device. The response of the sensor depends on the type, the charge, and the concentration of the ion. It is fully reversible and, because of the direct exposure of the very thin swelling polymer layer to the analyte, a fast volume change. As a chemical sensor the MICORIS system was used to monitor different ions, pH, organic solvents, and polyphenols [51–56].

Moreover, with this device, it could be proved that polyvinylpyrrolidone is an excellent model for protein behavior. Because of its related polyamide structure the effects of chaotropic agents on polyvinylpyrrolidone polymers and on proteins are very similar. Chaotropic agents not only interact with the surface of a polymer, but increase the free volume of polymer chains. A comparative study of the ion effect with a cross-linked polyvinylpyrrolidone polymer demonstrated a fundamental correlation of the polymer swelling properties with the “Hofmeister series” of chaotropic agents. The ion effects are in good accordance with the molecular theory of chaotropic agents. The experiments showed, moreover, that the device can directly and dynamically monitor volume changes in polymer layers with a thickness of only one or several molecules.

A wide variety of polymers or biopolymers cross-linked for gel formation are suitable sensory materials. Cross-linking has to be adapted to the chemical properties of the polymer. In most cases a distinct reversible color change is observed when the concentration of an ion in a buffered solution is changed.

For medical applications ion variations are established with a buffer system similar to that of human blood. Variations of chloride induced within the pathological concentration range are transduced by cross-linked polyvinylpyrrolidone after the exclusion of large proteins from the polymer. No or only minor pH-induced changes were observed at blood pH. Thus between pH 5 and pH 8 ion effects can be well separated from pH effects. The volume response of the sensor induced by different ions is fully reversible over more than 500 cycles.

Regarding a wide concentration range, a sigmoid logarithmic calibration curve of polymer-based sensor is obtained with monovalent cations and anions. Bivalent cations induce a more complex behavior of the polymer gel. The calibration

curve for Ca^{2+} is an overlay of the sigmoid logarithmic shrinking curve with a swelling effect at high ionic concentrations. Because of the direct exposure of the active swelling polymer layer to the analyte, an immediate response (within seconds) to changes in ionic environment can be observed.

Similar to a polymer, any protein is a suitable sensor layer [57, 58]. However, since most proteins do have a globular shape it is necessary to cross-link protein to form a thin-film gel pad without destruction of the three-dimensional structure. Thus the proteins should undergo volume changes but never dissolve. To build a sensor array various proteins representing a spectrum of properties can be chosen and applied to the chip. To coat the total chip surface with a homogeneous protein gel layer, a spin coating of proteins is superior.

Covalent layer-by-layer immobilization has distinct disadvantages in reproducibility and in the degree of cross-linking. An ordered protein film with a high degree of cross-linking turned out to have less flexibility of chain folding and thus less response.

To obtain a protein conformation array, protein gel pads have to be deposited via a microarrayer. Similar to spin coating, a cross-linking procedure within the deposited protein dot leads to the formation of a small (0–250 μm) gel pad. In contrast to microdotting for binding assays, the concentration of the protein solution microdotted as 1-nl microdots is reasonably high, with up to about 5%. Cross-linking is achieved similar to spin-coated layers.

In addition to the direct techniques described above, surface-enhanced optical sensors can also transduce the action of an enzymatic label, for example, by application of a pH- or ion-sensitive distance layer performing reversible volume changes upon, for example, a pH shift.

A setup can be as follows. Proteins to be assayed for their binding of pharmaceuticals are immobilized to the sensor. Urease is coupled to an anti-protein antibody as a label. Binding to receptors on the sensor surface occurs in a narrow compartment. Upon incubation with urea the enzyme will produce ammonium and carbonate, which will lead to local pH and ion changes that are reversibly transduced into a macroscopic optical signal. This setup offers the highest spatial resolution and the direct use of ELISA protocols.

In the following some experimental protocols should ease the application of this promising technology:

Coating of a polymer interlayer: Any solid surface with sufficient optical flatness can be used as a support. The supports are carefully cleaned by sonication in a detergent and washing in ultrapure water for 24 h. Immediately before the first deposition step the supports are treated in a plasma cleaner (nitrogen or oxygen plasma) to remove any organic contaminations. Deposition of the mirror layer is performed by evaporation or sputtering of about 200 nm of a gold/chromium or silver/tungsten sandwich. The swelling polymer has to be deposited with sufficient thickness precision and uniformity. This is best done by spinning (3000–5000 rpm). If a dip coating method is used, the formation of crystals from the cross-linker must be avoided by lowering the crosslinker concentration. A universal swelling polymer is synthesized according to the following procedure: stock solutions containing 2.5%

(w/v) PVP (polyvinylpyrrolidone, MW = 360,000) or 5% (w/v) MA-PVP (polyvinylpyrrolidone-dimethylaminoethyl methacrylate quaternized) in distilled water and 0.75% (w/v) DIAS (4,4'-diazidostilbene-2,2'-disulfonic acid disodium salt tetrahydrate) in distilled water are mixed (3:2 v/v). The sensor support is coated and dried. Cross-linking is done by exposing the chip to the light of a UV 50-W Hg medium-pressure lamp for 5 s. Over-cross-linking will induce cracks in the layer; insufficient cross-linking will result in dissolution of the film. Finally, a metal cluster film is deposited, for example, by evaporation of gold onto the polymer surface. The mechanism of island growing strongly depends on the mobility of single metal atoms on the support surface. For PVP this criterion is widely fulfilled. If necessary the metal cluster film can be replaced by covalent or adsorptive coupling of colloids to the polymer surface.

Spin-coating and microdotting of proteins: To set up an appropriate resonance interlayer it is vital to deposit a polymer film by spin-coating or microdotting. For low-resolution-low-price applications, highly polished aluminum chips (diameter: 12 mm; thickness: 0.5 mm) served both as support and mirror layer in a polymer-based chip design; for high-performance applications sputter-coated chips are used. Typically, a nanoscale film of protein is coated onto the surface by spin-coating of a solution of the protein (5%) at 4000 rpm for 30 s. For microdotting the solution given below is dotted onto the chip with the use of, for example, a pin and ring arrayer. Care is necessary to avoid excessive illumination during microdotting; otherwise the protein is already cross-linked in solution and thus precipitates.

Cross-linking of reactive proteins: Some proteins are applied with a 5% (w/v) solution of the protein in deionized H₂O. Cross-linking is done by exposing the chip to the UV light of a Stratagene DNA cross-linker at 25 mJ for 5 min. At the wavelength employed (about 300 nm) aromatic amino acids (Tyr, Trp, Phe) and thiols on the outside of the protein are activated and thus couple to other proteins as well as to the surface of the support. Finally, either a gold cluster film (mass thickness ~5 nm) is deposited by sputter coating (0.1 mbar Ar) onto the protein surface with the use of a sputter coater, or clusters are coated from aqueous solution via chemisorption.

Cross-linking of standard proteins: Most proteins, such as glucose oxidase (GOD) and urease, require reactive photo-cross-linking. Stock solutions containing 5% (w/v) protein and a solution of 3% (w/v) 4,4'-diazidostilbene-2,2'-disulfonic acid disodium salt tetrahydrate (DIAS) solutions in distilled water are mixed in a 10:1 ratio (v/v). The solution containing protein and cross-linker are spin-coated on the chip and activated with a monolayer of an adhesion promoter as 1-(3-aminopropyl)-methyl-diethoxysilane. Silanization of aluminum-coated chips is done via gas-phase silanization with amino-silane in a vacuum desiccator overnight. The chips are baked at 100 °C for 30 min to cross-link the amino-silane. To remove unbound amino-silane the chips are washed with methanol and dried. Cross-linking of the spin-coated film is done by irradiation of the chips with UV light for 30 s (350 nm, 60 W). It is not recommended to use a DNA cross-linker because its emission near 300 nm causes DIAS decomposition. The gold cluster film is deposited by covalent coupling or adsorptive binding of

colloids synthesized in solution via citric acid according to the method described by Frens. Chemically synthesized clusters of 9–40 nm are concentrated (20-fold) via centrifugation and resuspension in H₂O and deposited by adsorption to the protein surface (1–3 min). Sensors are rinsed with H₂O.

Spin-coating of DNA: A 5% solution of herring sperm DNA is dissolved under vigorous stirring in deionized water. one hundred microliters of this solution is mixed with 40 μ l of 3% 4,4'-diazidostilbene-2,2'-disulfonic acid disodium salt tetrahydrate (DIAS), spin-coated directly onto the chip surface at 4000 rpm for 30 s, and dried. The chip surface must be hydrophilized with oxygen plasma to increase the surface density of hydroxyl groups. The chips are activated with 1-(3-aminopropyl)-methyl-diethoxysilane. Silanization of aluminum-coated chips can be done via gas-phase silanation in a vacuum desiccator overnight. The chips are baked at 100 °C for 30 min to cross-link the amino-silane. To remove unbound amino-silane the chips are washed with methanol and dried. Cross-linking of the spin-coated film is done by irradiation of the chips with UV light for 60 s (350 nm, 60 W). A metal cluster film is deposited by sputter coating under high vacuum onto the chip surface with a turbo molecular pump (Varian, 10 s, mass thickness 3–5 nm). To increase stability, the chips are incubated with saturated NaCl for 30 min. This step is necessary to reach a more stable conformation of the polymer. In the last step the chips are washed with deionized water.

3.2. Resonance-Enhanced Fluorescence

Nanoresonant multilayer films have the potential to amplify the local field and thus to enhance the fluorescence signal of labeled biomolecules on biochip surfaces. Fluorophores are bound at a well-defined distance within the field of the resonant structure, resulting in enhanced absorption and emission of the fluorophore driven by the resonant field.

This amplification of fluorescence makes the system highly useful to the study of any type of interaction, including those of RNA, DNA, proteins, peptides, or any pharmacological ligand. Often biochips suffer from insufficient absolute signal or a low signal-to-noise ratio. Thus chips are limited to molecules of medium to high abundance, or long incubation times are needed to bind molecules from a large volume. Novel approaches are needed for the identification of regulatory proteins or low-copy RNA.

Enhanced fluorescence is a new technique that is useful for a variety of biorecognitive interaction systems strongly enhancing any fluorescence signals at a biochip surface. Compared with standard fluorescence assays, both the signal-to-noise ratio and the fluorescent intensity are considerably higher in this field boosting technology [45–67]. The novel approach of signal amplification is based on surface enhancement of the field and a direct influence on the excitation-deexcitation pathways (Fig. 28).

There are several setups, including nanoparticle layers, rough surfaces, surface plasmons in thin metal films, or multilayer waveguides—some with a microstructured surface—providing increased local field, resulting in a fluorescence amplification from 2 to 200 times.

Novel biochips based on nanoresonant layers of metal particles are among the best in enhancing fluorescence by

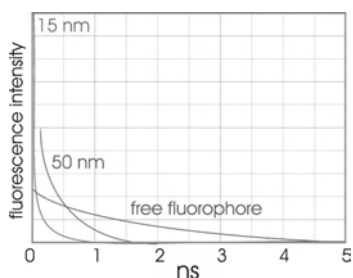


Figure 28. Decay of a fluorophore near a metal surface.

coupled resonant field effects. They are set up by a cluster layer deposited at the surface of the chip. By coating a second transparent nonmetal layer on top of the cluster film, the fluorophores are easily positioned at a certain defined distance from the resonant structure. A resonant interlayer is used to couple the energy from the metal film into the fluorophore. Two to three enhancement zones are found at well-defined distances from the resonant cluster film located at multiples of the wavelength of the desired fluorophore (Fig. 29).

To set up a REF chip, the substrate surface has first to be covered by metal clusters, which can be done by sputter or evaporation coating or by adsorption of metal colloids from an aqueous solution.

A cluster enhanced resonant chip is set up by

1. A layer consisting of a plurality of nanometric clusters, islands, or colloids of electrically conductive material (silver or gold for best plasmons!), which is applied to the surface of a substrate,
2. An inert interlayer tuned to the optical thickness which allows a resonance at the desired wavelength (thickness and refractive index are important!),
3. A biorecognitive layer at the surface, and
4. Biorecognitive molecules that are labeled with fluorophores.

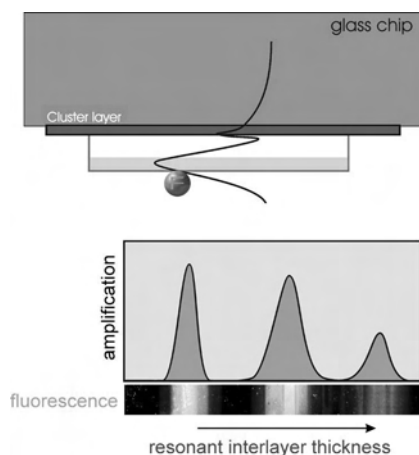


Figure 29. Electromagnetic field in a multilayer system and fluorescence amplification in a Ag-cluster layer– SnN_x -interlayer system (0–700 nm).

A method for measuring the concentration of an analyte in a sample comprises the following steps:

- a. Contacting the sample with a biorecognitive sensor layer.
- b. Contacting the sample with an analyte-specific fluorescent compound.
- c. Binding the analyte-specific fluorescent compound to the analyte, which in turn is bound by the biorecognitive layer.
- d. Radiating excitation radiation which is suitable for exciting of the analyte-specific fluorescent compound (the quantum yield per molecule and per time of the analyte-specific fluorescent compound increase strongly in the vicinity of the cluster layer).
- e. Determining the fluorescence radiation emitted by the bound analyte-specific fluorescent compound as a measure of the analyte concentration.

Fluorophores at the resonant distance (see above) show a significant gain in fluorescence compared with fluorophores in the bulk solution. Therefore discrimination between surface-bound and free fluorophores is possible.

Fluorescence is a two-step process: with absorption of light at wavelength A and emission of light at wavelength B. Steps a and b are driven upon interaction between the resonant film and the fluorophore. In absorption fluorophores and metal plasmons are oscillators driven by irradiated light. In emission, the fluorophore is the origin of radiation. The molecule is an oscillator with a resonant structure in its vicinity.

Multilayer resonant films exhibit a much stronger interaction with light than the fluorophore. Thus, the fluorophore is no longer directly driven by the irradiated light, while the excitation field distribution is strongly modified.

In surface plasmon resonance devices (SPRs) thin metal films are used as sensor elements. The field strength of the incoming light is enhanced by a factor of about 8-fold because of the resonant excitation of surface plasmon (not Mie) modes at the interface with the analyte solution. Irradiation of a cluster layer drives surface plasmons and Mie plasmons at their oscillation resonance wavelength. The intensity of this resonance strongly exceeds the intensity of the original light field without the cluster layer. Most energy is coupled into the Mie plasmon, whereas only about 1/10 is driving the surface plasmon of the film. The resonant interlayer is now driven by the plasmons. In a second step the fluorophore feels the enhanced light field of the interlayer and has consequently an enhanced absorption probability.

In photon emission, the fluorophore is a radiating dipole. The oscillator is influenced by the resonant layer nearby. Thus, an additional charge is induced and the emission process is enhanced. The influence of the layer can be considered as the buildup of a more efficient fluorophore antenna, leading to better radiation efficiency.

Fluorophores feel more laser light than standard glass slide-based chips and emit more photons per unit time. Given a good fluorophore, such as Cy3, Cy5, or fluorescein, the signal amplification will reach up to 8 on smooth films. In contrast to these smooth metal films, significantly larger enhancement factors of around 200 times have been observed for cluster structures. In these clustered films more

energy can be coupled because of Mie and surface plasmons. For a layer of silver a surface plasmon propagation length of more than a millimeter is found; nevertheless, this value is significantly reduced in stripe-like structures.

Annealing of metal films deposited on a glass substrate leads to self-organized metal cluster films (Fig. 30). As proved by Aussenegg, Schalkhammer, and recently Strekal et al., these films work for REF as well as SERS. Surprisingly, annealing at higher temperatures (300–400 °C) seems to drive SERS, whereas annealing at 200 to 300 °C drives REF.

To attach biomolecules to the chip (interlayer) surface all standard processes of immobilization can be used. Layers of various molecules such as polylysine or SAM of pentane-thiol are beneficial for binding molecules at the ideal distance for REF well out of the quenching field of the metal surface.

In a special setup excitation of the cluster layer can be done with an incidental beam in attenuated total reflection (ATR) geometry. ATR geometry results in high background suppression of signals generated by molecules in the bulk solution, since a zone of just about 100 nm adjacent to the surface is irradiated. The enhancement effect of the metal particles contributes to this bulk suppression and further increases the signal-versus-background ratio of the method.

A modified protocol for REF in microtiter plates has been developed. This microtiter-plate-based REF setup performs kinetic single-step biorecognition assays with fluorophore-labeled compounds, using the fluorescence enhancement properties of well-bound silver clusters. Silver clusters are bound to standard microplates, mostly via silanization of the plastic surface. The use of standard microplates makes this method fully compatible with conventional microplate processing and reading devices. Neither excitation with coherent laser light nor ATR geometry is required; the measurement is performed in a standard fluorescence microplate reader.

Methods are adapted to coat clusters into microplates and set up the interlayer for fluorescence enhancement. In a standard protein bioassay the detection limit is in the picomolar range. The ease of colloid-surface preparation and the high sensitivity make fluorescence enhancement at colloid-coated microplates a valuable tool for studying reaction kinetics and performing rapid single-step immunoassays.

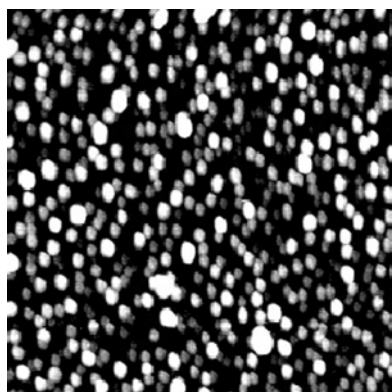


Figure 30. AFM scan of a silver cluster layer prepared via thermal curing at 225 °C.

According to the optical spectra, the absorption maxima of the different silver colloid preparations shift to higher wavelengths with increasing silver concentration used for synthesis of the colloids. This shift of the absorption maximum of Ag clusters from 400 nm to 470 nm reflects the increase in particle size and the multipolar modes of silver-cluster film prepared at higher silver concentration. Concurrent with the shift of the absorption maximum, broadening of the spectra is observed. This indicates multipolar modes and a loss of spherical shape at higher silver concentrations (around 6 mM silver; see protocols below).

The coating of clusters to amino microplates is followed by reading the absorption around 400 nm. The amount of colloid bound to the microtiter plate surface strictly increases with time. On incubation with 2–4 mM colloid solutions, saturation of the surface is achieved after 1 h. Colloidal clusters prepared from 6 mM silver solution need more time for adsorption and showed an almost linear increase for at least 2 h. The colloid adsorbed at the surface with respect to a given incubation time should not be linearly correlated between preparations of different sizes because of diffusion speed and agglomeration degree. To study the quality of the structure and the relative silver amount at the surface of the colloid films, scanning electron microscopy or atomic force microscopy is necessary. A homogeneous surface coating with silver clusters and a few larger crystallites should be obtained.

With a sputter coater a number of metals can be deposited as cluster layers, including silver, gold, palladium, copper, tin, and indium. These metals have rather low evaporation temperatures and can therefore be sputtered even at low energies. Metal is deposited as atoms, and if the surface temperature is high enough they migrate and finally assemble into clusters on the surface. These clusters usually are small, often flat, and asymmetrical. At higher coating thickness most clusters are interconnected after sputtering. Upon heating to 100–350 °C (Au up to 600 °C) the clusters melt and thus form round, noninterconnected nanoclusters. The sputter process itself is carried out in an inert or semi-inert plasma with an argon or nitrogen plasma. Standard targets are used, the chamber is evacuated to a vacuum of less than 10^{-2} mbar, and after the chamber is purged extensively with argon, the pressure is adjusted to 10^{-2} to 10^{-1} mbar. Please note that these pressure data vary depending on machine, metal, and size of chamber. Next a pulsed DC field is applied to ignite the plasma. The metal is deposited on the substrate. The thickness of the metal layer is adjusted by sputter time, pressure, and current.

Three modes are found:

- *Layer-by-layer growth mode.* The interaction between substrate and layer atoms is stronger than that between adjacent layer atoms;
- *Island growth.* The interaction between neighboring film atoms exceeds the overlayer substrate interaction, leading to an island growth; and
- *Layer-plus-island growth.* An intermediate case.

After formation of a layer, island formation occurs and islands grow on top of the first layer.

Thus, formation of islands or layers is dependent on both the metal and the surface. Furthermore, the nanostructure is

influenced by temperature and sputter gas. For example, silver on glass will preferably form islands, whereas chromium will form an adherent film.

To set up a cluster-layer-enhanced fluorescence chip, use standard microscope slides. The slides are coated with silver or gold clusters by absorption (see part on adsorption) or with a silver or gold cluster layer deposited by a sputter process. Nitrogen (Ag) or argon (Au) is used as the sputter gas. To “cluster” the film, curing at a temperature of 200 to 600 °C is required. (silver near 200–300 °C, gold around 400–600 °C). For increased adhesion of silver or gold to glass, a sublayer of an adhesion promoter is often required. Chromium, tungsten, titanium, or palladium (or a bilayer) is coated beyond the resonant cluster layer. By sputter-coating, an inert and hard distance layer is applied to the metal cluster film. Among other things silicon dioxide or tin nitride might be used. For tin nitride use tin as a target material and nitrogen as a sputter gas. Aging in air for several days is necessary to produce an adsorptive surface for tin nitride interlayers. Apply atomic force microscopy to study the surface of the film. For chip enhancement calibration, bovine serum albumin (BSA) (Sigma) is used to coat the entire surface at a concentration of 1 mg/ml in phosphate-buffered saline (PBS) (pH 7.4). Alternatively, 0.1% of polylysine can be used. After 20 min of incubation, the chip is washed with MQ water, and the surface is dried with air. Ten mg/ml *N*-(3-dimethylaminopropyl)-*N*-ethylcarbodiimide hydrochloride (EDC · HCl) is used to cross-link and activate the BSA surface (20 min, fresh!). Single-stranded DNA, amino-modified at its 3' end, is diluted to 5 pmol/ μ l in PBS (pH 5.4) and microdotted at the chip (on EDC-activated surface within a few minutes after activation!). Polylysine is able to bind DNA without EDC activation via a strong ionic interaction. After microdotting, the chips are kept wet in a humidity chamber for at least 20 min (best inverted over a bath of warm water, small droplets should form were the microdots are!). The chip is washed with MQ water and dried. Adsorbed DNA is further stabilized by cross-linking with UV light. The analyte DNA is hybridized in SSC or Dig Easy hybridization buffer (1–16 h). Complementary DNA, Cy3, Cy5, or rhodamine labeled, is diluted in Dig Easy hybridization or SSC buffer to 2 pmol/ μ l and incubated for 15 min to 3 h. The chip surface is washed with 10 mM MgCl₂, 5% glycerol. The chips are dried and used for scanning.

For aminosilanization of polystyrene chips the chip is covered with \sim 300 μ l 10% (v/v) aqueous solution of 3-aminopropyltriethoxysilane. The substrate is protected via a lid and incubated for 60 min at 50 °C in a convection oven. The aminosilane solution is poured off and the chip is dried for 60 min at 50 °C without a lid. Excess aminosilane is removed by three subsequent washing steps with deionized water. Chips are dried in a dry air stream.

To prepare silver clusters for aminated surface coating (see procedures above), silver nitrate is dissolved in boiling double-distilled water, and sodium citrate in double-distilled water is added. The solution is kept boiling for 5 min.

A novel technique for coating with silver clusters might be employed [68]. In short: the reduction of Ag⁺ ions by *N,N*-dimethylformamide (DMF), both in the presence and

in the absence of a stabilizing agent, results in the formation of small cluster-type nanoparticles. The reduction can lead to the formation of either thin films of silver nanoparticles electrostatically attached to surfaces, or stable dispersions of silver nanoparticles if the silane (e.g., 3-aminopropyltrimethoxysilane) is present. Various parameters affect the reduction process and the reducing ability of DMF.

3.3. Surface-Enhanced Infrared Spectroscopy

Surface-enhanced infrared absorption (SEIRA) is a process that is highly dependent on the nanostructure of the matrix. The electromagnetic field effects as well as chemical effects contribute to the total enhancement process. The bands due to different vibration modes give rise to distinct enhancement processes, suggesting a “chemical” origin of this process.

In 1980 the first enhancement of chemisorbing molecules on Ag and Au surfaces was described. This phenomenon was later denoted as surface-enhanced infrared absorption. Of all the papers published on this topic, nearly half of them were printed within the last 3 years. SEIRA has several advantages over standard infrared spectroscopy and SERS, such as nondestructivity and a remarkable signal-to-noise ratio. A full understanding of SEIRA is nevertheless required before it can be widely applied [69–71].

Samples used for SEIRA are prepared by methods similar to those used for SERS. A thin film of metal clusters is deposited on the chip. The effect is highly dependent on the appropriate nanostructure of the cluster film. In contrast to UV-vis techniques, silicon or germanium is the preferred substrate. The organic material to be analyzed is dispersed on the chip. Most studies point out that the effect is very short-range and applicable only to the first monolayer adsorbed to the surface. Some of the molecular vibrations are dramatically enhanced, whereas others remain unamplified. The models indicate that the molecule must be bound chemically with an appropriate orientation to the metal surface.

First applications of this concept were set up to detect *Salmonella* species. Antibodies to the organism are bound to the chip surface. The spectrum is recorded and the chip is placed in a solution with *Salmonellae* for a few minutes. A further spectrum is obtained and compared with the former. A band is observed at 1085 and 990 cm⁻¹, which after interaction with the analyte is shifted to 1045 cm⁻¹. The experimenters assigned this vibration to a phospholipid in the cell wall of the captured cell. Furthermore, the contour of the spectrum changes significantly.

3.4. Scattered Evanescent Waves

The setup first described and patented by Schutt et al. relies upon the detection of back-scattered light from an evanescent wave disturbed by the presence of a colloidal gold label brought to the interface by an immunological reaction [72]. The evanescent wave at the interface is the result of a totally internally reflected incident light wave. Placement of the

detector at a back angle above the critical angle ensures a superior signal-to-noise ratio.

The SEW assay relies upon the identification of the critical angle associated with total internal reflectance. The angle is largely a function of the refractive index of the material through which an incident light wave is directed (e.g., plastic) and the relatively lower refractive index of the material in which the immunoassay is being conducted (e.g., an aqueous solution). It is measured from a line perpendicular to the interface between the two materials ($90^\circ =$ plane of the interface).

Light directed through the chip toward the interface formed by the aqueous sample and chip surface layer at the critical angle will result in total internal reflectance of the light within the layer. Note that materials in the real world are perfect, and, accordingly, it is preferred that the incident light be directed toward the interface at an angle several degrees greater than the critical angle. At such an angle, the incident light, preferably from a laser, is totally internally reflected within the chip layer. Unlike conventional fluorescent techniques, this assay is flexible with respect to light wavelength, since particle size may be readily adjusted to match the available light source.

A light source such as a He-Ne laser is used, and still other sources suggest themselves, including light-emitting diodes and other non-laser-light sources.

The system is based on conventional immunoassay techniques. The system employs a cluster label (with a refractive index higher than that of the solution, and most preferably higher than that of the first light transmissive material, e.g., plastic). Such clusters (most preferably, colloidal gold) are used as a label for the solution-phase immunologically active component. Because of the interaction of the colloidal gold particles with the evanescent wave, light is decoupled from the evanescent field. Particles with an increasingly higher index of refraction than that of the underlying solid generally increasingly scatter light.

The detector is placed at an angle greater than the critical angle and in a location whereby only light scattered backward toward the light source is detected. This location thereby avoids the detection of scattered light within the bulk liquid medium.

3.5. Surface-Enhanced Raman Scattering

The extremely small cross sections of Raman scattering would preclude its use at the single-molecule level. However, this situation is dramatically altered for surface-enhanced Raman scattering. Molecules in close proximity to metal-cluster-coated surfaces exhibit large (typically 10^6 -fold) enhancements in vibration spectral intensities. Even larger enhancement factors on the order of 10^{14} corresponding to effective Raman cross sections of $\sim 10^{-16}$ cm²/molecule have been reported. These Raman cross sections are comparable to or even higher than fluorescence cross sections.

When a laser used to excite SERS is in resonance with an electronic transition of the substances (surface-enhanced resonance Raman scattering or "resonant SERS"), an additional 10^3 -fold enhancement is obtained. SERS has been utilized in a wide variety of applications, including detection of molecules, elaboration of structure and function of

large biomolecules, and elucidation of chemical processes at interfaces.

This assay format is particularly suitable for sandwich-type immunoassays and hybridization assays. The readout can only be done with standard instrumentation.

A wide variety of approaches were published for the setup, fabrication, and assembly of structures with the required nanostructure. These include evaporated metal films, cured metal films, aggregated colloidal metal sols, and electrochemically roughened electrodes. In all of these approaches, the substance studied by SERS is placed in direct contact with or close proximity to the surface.

At metal SERS substrates most biomolecules adsorb and denature. In contrast, biomolecules conjugated to colloidal gold often retain their biological activity.

The SERS intensities for standard colloids are often quite weak. To observe SERS signals from chromophores within proteins, it is necessary to drive them via the electromagnetic field of the SERS active surface. Thus, for proteins an additional step is required.

Placing a strong chromophore near the surface of a metal cluster generates a more suitable SERS active particle. The metal clusters are adsorbed to a metal chip surface, preferably in a sandwich-type assay. Thus, it is important to bind the protein to the surface of a colloidal particle and to bind the particle to the SERS active surface. Ideally the analyte is sandwiched between two SERS active clusters.

From theoretical modeling of SERS processes it clearly turned out that the enhancement process has to be divided into two categories:

- The short-range or molecular or chemical enhancement seems to rely on adsorption-induced changes in Raman susceptibility.
- The long-range electromagnetic enhancement is a manifestation of the strongly enhanced fields present at clusters and rough metal surfaces.

At present, the electromagnetic part seems to dominate the overall effect in most situations. Optical detection of single molecules on single clusters has been done with rhodamine 6G, and an overall amplification of the Raman signal of 10^{14} to 10^{15} has been obtained. This enormous enhancement leads to vibration signals that are more pronounced and stable than single-molecule fluorescence. SERS enhancement is at least a factor of 10 higher with gold-coated silver particles.

Proteins are perfectly suited for adsorption to particles with gold at their outside surfaces. The SERS active surface is coated with the first antibody. The SERS active particle is created by coating gold colloids first with the second antibody and, if necessary, with a Hem protein. The analyte is sandwiched between the cluster and the surface. Devices providing two-dimensional resolution of the signal-generating surface can be used to apply the principle to array-type assays.

Standard performance of a SERS metal surface is highly dependent on the nanostructure. Whereas smooth metal films give only very small enhancement, the nanostructure of the surface has to be very defined to obtain reproducible results. Variation in the coating process may change the effect by orders of magnitude. In particular the particle size

and shape and, moreover, the grain boundaries within the particles contribute to the effect. Grain boundaries are sufficiently different from the bulk material to support local plasmons. Most pronounced effects are found at larger grain sizes of 30–200 nm. This might be explained by an increase in volume plasmon damping of around 10 times observed in Al if the grain size is small.

Recently it has been shown that the tip of an atomic force microscope can be used to selectively excite surface-enhanced Raman scattering. A conventional AFM tip can provide spatially selective enhancement of a Raman signal by SERS. The AFM tip is acting as a locally introduced nanometer-sized cluster from which enhancement mechanisms operate.

3.6. Cluster-Quenched Fluorescence

A molecular assembly setup of a small gold nanocluster, a fluorescent dye, and a ssDNA molecule is called a molecular beacon. The beacon is a nucleic acid probe with a hairpin-shaped structure in which the ends are self-complementary, bringing a fluorophore and a quencher into close nanometric proximity. The metal particle quenches the fluorescence of the organic molecule because of near-field deexcitation. The fluorescence is restored when the probe binds to a complementary nucleic acid and refolds.

Beacons or molecular beacons exhibit one main advantage: easy direct detection of unlabeled oligonucleotides. Nevertheless, a limiting factor is the fluorescence quenching efficiency due to the background generated by nonquenched fluorescence. An organic quencher such as 4-((4'(dimethylamino)phenyl)azo) benzoic acid quenches down to 1% or residual fluorescence of the dye placed in its proximity. The quenching efficiency decreases for dyes emitting at longer wavelengths. A better quencher would greatly increase the dynamic range and, moreover, the sensitivity of molecular beacons. Small metal nanoclusters can replace organic molecules as a quencher of fluorescence. Because of strong near-field effects they quench fluorescence as much as 100 times better. The extremely high quenching efficiency opens new perspectives for beacon probes in fluorescence-based assays [73] (dynamic range (DABCYL/gold cluster): fluorescein (71/172), rhodamine 6G (43/1000), Cy5 (27/68), Texas red (27/64).

Covalent linkage of a gold cluster and a fluorophore to ssDNA is done using a 25–30-base synthetic oligonucleotide modified with a primary amine at its 3' end and a sulfide at its 5' end. The oligonucleotide sequence is chosen to create a hairpin-loop structure because the five nucleotides at its extremities are complementary. The design of the sequence provides a hairpin structure at room temperature. Often a poly-TTTTTTTT tail is used in the middle of the sequence to allow the proper back-folding of the DNA molecule.

Such a beacon opens easily on hybridization of the loop to the analyte DNA. A fluorophore (e.g., rhodamine 6G or cyanine dye) is attached with an amine-reactive dye to the 3' end of the oligo. The protection group from the 5' end is removed, and the free sulfhydryl is covalently attached to small 1–3-nm gold clusters. Either direct interaction with metal gold or *N*-propylmaleimide-coated cluster ("Nanogold") is used. An excess of gold clusters is necessary

to avoid multiple attachment. A high concentration of salt ensures that the ssDNA forms a hairpin.

The beacon is tested in a standard microcuvette. As the target hybridizes to the hairpin-DNA loop, the fluorescence rises considerably. The ratio of the fluorescence intensity is measured in the cuvette before and after the addition of the analyte DNA. Rhodamine 6G is the best quenched dye, with an average quenching efficiency of ~99.5%. Some probes exhibit quenching efficiencies of >99.9%. High quenching efficiencies extend the dynamic range of molecular beacons from 50 to around 1000.

DNA hybridization technology is applied at a temperature at which the hybridization can discriminate between a perfectly matched probe and a mismatched one. The standard temperature is around 55 °C. This is not optimal for the quenching of the dye, because its average distance from the quencher increases with temperature because gold nanoparticles are unstable above 50 °C.

To overcome this problem and to be able to work at room temperature, buffers with low salt concentrations are used. A buffer containing 90 mM KCl and 10 mM Tris (pH 8.0) gives the best sensitivity.

Quenching of fluorescence by metal clusters results primarily from nonradiative energy transfer from the molecule to the metal. The surface provides an alternative nonradiative relaxation mechanism, resulting in the production of electron-hole pairs or surface plasmons. These mechanisms increase the nonradiative decay rate of the fluorophore. The nonradiative deexcitation involves dipole-dipole interactions, which are described by a Foerster-phenomenon. Thus, the nonradiative relaxation depends on the distance of the fluorophore from the surface of the cluster and on the overlap of the energy profile of the fluorophore and the cluster. The cluster relaxes radiatively or nonradiatively. Resistive heating as a result of fluctuating electric fields within the metal cluster is significant. With undecagold no quenching is observed. Small 1–2-nm-diameter gold particles show no sign of surface plasmon resonance, in contrast to larger particles, which exhibit a strong plasmon resonance at 520 nm. If necessary, the surface plasmon resonance of a metal cluster might be tuned precisely by changing the shape, the size, or the composition of the cluster.

In short: The amino-reactive dye is bound to the terminal 3' amino group, the product is purified with a Sephadex column and fractionated on a C18 reverse-phase HPLC, fluorescent DNA fractions are collected and dried in a SpeedVac, the powder is resuspended to a final oligonucleotide concentration of 15 μM, the disulfide bond is cleaved, the oligonucleotide solution is purified by reverse-phase chromatography, and the elution product is suspended in water and immediately reacted with monomaleimido-gold clusters. The cluster-modified DNA is analyzed by gel electrophoresis.

3.7. Cluster Emission Devices

For detection of biorecognitive interactions, usually fluorophores are bound to the target molecule. However, fluorophores have a limited lifetime of <10⁷ absorption-emission processes, resulting in a declining signal for consecutive measurements. A cluster emission device (CED)

provides a novel method for detecting biomolecules with far-field optics at single-molecule resolution [74].

Figure 30 shows a crosssection of a microchannel in which a protein (ligand) is labeled with a nanoparticle (cluster, nanofiber, etc.). Figure 31 shows a 30-nm gold cluster that has been bound at a microdotted receptor molecule on a biochip. When after evacuation a high voltage is applied to the bottom chromium electrode, the cluster will emit electrons toward the extractor (a 20-nm aluminum thin film on glass), making use of electric breakdown in the protein complex (Fig. 32). The thin film thus locally heats up and evaporates within milliseconds, clearing an area of about $1 \mu\text{m}^2$. A microscope monitors the process by shining light from below through the thin ($\sim 20 \text{ nm}$) chromium electrode, displaying each cluster as a bright spot. The voltage should be pulsed to allow the device to cool down between evaporation cycles, and the polymer distance layer should have a high breakdown strength ($>1 \text{ kV/mm}$).

The field-dependent transmission coefficient was calculated for the vacuum potential barrier in the right figure with the Wentzel-Kramers-Brillouin approximation. Integrating over all energies in a nearly free electron gas at room temperature resulted in an exponentially increasing I-V curve that reaches 1 nA at 0.7 kV. As proteins are insulators (band gap of $>2 \text{ eV}$), electric breakdown is proposed as a conduction mechanism. As no reliable data are available on the intrinsic breakdown strength of single surface-bound proteins, an average of $\sim 0.5 \text{ kV}/\mu\text{m}$ for insulating polymers seems reasonable. Taking into account the enhanced electric field line density under the cluster at zero current, breakdown occurs at a voltage of about 200 V. Use of nanofibers further decreases the potential necessary for tip emission to less than 100 V. As an alternative to ablation, thermal oxidation in air may be used to create transparent areas within seconds; the required extraction potential may then be lowered because of plasma formation.

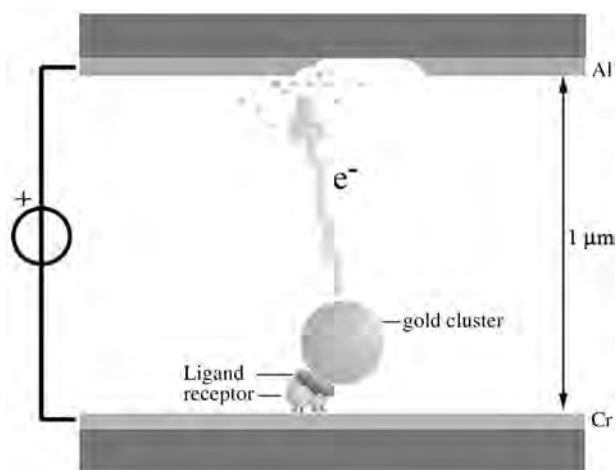


Figure 31. Cluster emission device. Proteins are insulators: band gap of $\sim 2 \text{ eV}$, electric breakdown at $\sim 500 \text{ V}/\mu\text{m}$, nanocluster-enhanced breakdown at about 3–200 V.

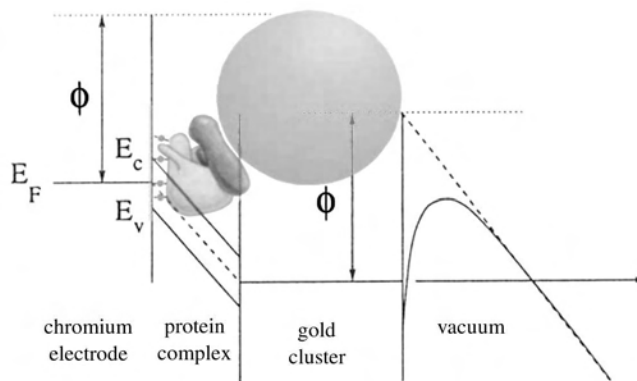


Figure 32. Cluster emission.

GLOSSARY

Cantilever sensor A multi-micro-AFM measures the tiny forces acting on the sharp tips of a cantilever chip. By shrinking the cantilever structure to a microscopic size one obtains a low spring constant (high sensitivity), a high resonant frequency, fast response, and high immunity to external mechanical noise.

Electron beam-induced deposition (EBD) Repeated line scan induces the polymerization of amorphous carbonaceous material along the path of the electron beam on the substrate, which appears as a black line in the SEM contrast. The lines are used for nanobonding of molecular devices.

Gold conjugates Gold (sometimes silver or platinum) colloids are coated with protein or DNA in a 2–3-fold excess (for several hours). Excess of the ligand is removed by washing. Bioreactive clusters are used, for example, as detection agents or as nano-building blocks.

MCB junction A mechanically controllable break device set up by breaking a small metal strip deposited on a chip via bending of the substrate and then attaching a single molecule to the nanotips formed.

Molecular beacon The beacon is a nucleic acid probe with a hairpin-shaped structure in which the ends are self-complementary, bringing a fluorophore and a quencher into close nanometric proximity. The metal particle quenches the fluorescence of the organic molecule because of near-field deexcitation. The fluorescence is restored when the probe binds to a complementary nucleic acid and refolds.

Molecular motors Nanoscale motor based on proteins (rotary and linear) as ideal tools for nanoactuation and fabrication.

Nanocluster (nano-island, precipitate, colloid particle) A number of atoms bound or arranged together, forming an assembly of nanoscale size. Metal nanoclusters exhibit tunable resonant behavior; semiconductor clusters show quantum-dot behavior.

Nanotweezer Nanoactuators to pick nano-objects or move tiny structures. Tweezers consist, for example, of two carbon nanotubes. With the application of a potential, these tubes bend and thus the ends of the nanotubes open or close (compare optical tweezer using a laser beam).

Resonance-enhanced fluorescence (REF) Nanoresonant multilayer films have the potential to amplify the local field and thus to enhance the fluorescence signal of labeled (bio)molecules on biochip surfaces. Fluorophores are bound at a well-defined distance within the field of the resonant structure, resulting in enhanced absorption and emission of the fluorophore driven by the resonant field.

Resonant cavities Nanostructures with a high degree of symmetry are resonant in a way similar to that of, for example, micrometer-sized glass structures for light waves. Optimized design allows wavelength tuning via defined band-gap materials.

S-layer These layers are regular protein crystals that form the outermost cell envelope component of many prokaryotes exhibiting different kinds of lattice symmetry. S-layers are used for nanocluster arrays and biotemplating.

Scattered evanescent waves (SEWs) The setup relies upon the detection of back-scattered light from an evanescent wave disturbed by the presence of gold colloids brought to the interface by an immunological reaction. The evanescent wave at the interface is the result of a totally internally reflected incident light wave. Placement of the detector at a back angle above the critical angle ensures a superior signal-to-noise ratio.

Surface-enhanced infrared spectroscopy (SEIRA) Surface-enhanced infrared absorption is a process highly dependent on the nanostructure of the matrix. The electromagnetic field effects as well as chemical effects contribute to the total enhancement process. The bands due to different vibration modes give rise to distinct enhancement processes, suggesting a "chemical" origin of this process.

Surface-enhanced optical absorption (SEA) An absorbing cluster positioned at a defined distance from a metal mirror represents a special kind of reflection interference system. At a certain distance of the cluster from the mirror the electromagnetic field reflected by the mirror has the same phase at the position of the absorbing layer as the incident fields, and thus by this feedback mechanism the effective absorption coefficient of the absorbing layer is strongly enhanced.

Surface-enhanced Raman scattering (SERS) The extremely small cross sections of Raman scattering would preclude its use at the single-molecule level. However, this situation is altered for surface-enhanced Raman scattering. Molecules in close proximity to metal-cluster-coated surfaces exhibit large (typically 10^6 -fold) enhancements in vibration spectral intensities. Even larger enhancement factors on the order of 10^{14} have been reported. These Raman cross sections are comparable to or even higher than fluorescence cross sections.

ACKNOWLEDGMENTS

Part of this work was supported by the LifeTech program at TUDELFT/the Netherlands. The author Dr. Mayer, TUDELFT, the Netherlands; Dr. Bauer, November AG-Erlangen, Germany; and Prof. Aussenegg and Prof. Leitner from the University of Graz, Austria, for helpful discussions and support.

REFERENCES

1. U. Kreibig and M. Vollmer, in "Optical Properties of Metal Clusters." Springer-Verlag, Heidelberg, 1995.
2. H. Dörrfler, in "Grenzflächen und Kolloidchemie." VCH, Weinheim, 1994.
3. H. Adair, in "Applied Colloid & Surface Chemistry." 1999.
4. E. Garbowski, in "A Short Textbook of Colloid Chemistry." Pergamon, Oxford, 1954.
5. R. D. Piner, J. Zhu, F. Xu, S. H. Hong, and C. A. Mirkin, *Science* 283, 661 (1999).
6. P. Kim and C. M. Lieber, *Science* 286, 2148 (1999).
7. L. A. Bumm, J. J. Arnold, M. T. Cygan, T. D. Dunbar, T. P. Burgin, L. Jones II, D. L. Allara, J. M. Tour, and P. S. Weiss, *Science* 271, 1705 (1996).
8. H. W. Fink and C. Schonenberger, *Nature* 398, 407 (1999).
9. P. J. de Pablo, F. Moreno-Herrero, J. Colchero, J. Gomez Herrero, P. Herrero, A. M. Baro, P. Ordejon, J. M. Soler, and E. Artacho, *PRL* 85, 4992 (2000).
10. M. A. Reed, C. Zhou, C. J. Muller, T. P. Burgin, and J. M. Tour, *Science* 278, 252 (1997).
11. C. Kergueris, J.-P. Bourgoin, S. Palacin, D. Esteve, C. Urbina, M. Magoga, and C. Joachim, *Phys. Rev. B: Solid State* 59, 12505 (1999).
12. R. Kirsch, M. Mertig, W. Pompe, R. Wahl, G. Sadowski, and E. Unger, *Thin Solid Films* 305, 248 (1997).
13. R. Guckenberger, M. Heim, G. Cevc, H. F. Knapp, W. Wiegräbe, and A. Hillebrand, *Science* 266, 1538 (1994).
14. M. Yanagida, Y. Hiraoka, and I. Katsura, *Cold Spring Harbor Symp. Quant. Biol.* 47, 177 (1983).
15. S. Wennmalm, L. Edman, and R. Rigler, *Proc. Natl. Acad. Sci. U.S.A.* 94, 10641 (1997).
16. S. B. Smith, Y. Cui, and C. Bustamante, *Science* 271, 795 (1996).
17. D. W. Wang, H. Yin, R. Landick, J. Gelles, and S. M. Block, *Biophys. J.* 71, 1335 (1997).
18. T. R. Strick, J. F. Allemand, D. Bensimon, A. Bensimon, and V. Croquette, *Science* 271, 1835 (1996).
19. S. B. Smith, L. Finzi, and C. Bustamante, *Science* 258, 1122 (1992).
20. Ph. Cluzel, A. Lebrun, Ch. Heller, R. Lavery, J.-L. Viovy, D. Chatenay, and F. Caron, *Science* 271, 792 (1996).
21. H.-W. Fink and Ch. Schönenberger, *Science* 398, 407 (1999).
22. H. G. Hansma, R. L. Sinsheimer, M.-Q. Li, and P. K. Hansma, *Nucleic Acids Res.* 20, 3585 (1991).
23. K. Brown and M. Natan, *Langmuir* 14, 726 (1998).
24. G. Frens, *Nat. Phys. Sci.* 241, 20 (1973).
25. J. Slot and H. Geuze, *Eur. J. Cell Biol.* 38, 87 (1985).
26. F. Caruso, *Nanoeng. Particle Surf. Adv. Mater.* 13, 11 (2001).
27. M. Valina-Saba, G. Bauer, N. Stich, F. Pittner, and Th. Schalkhammer, *Supramol. Sci. Mater. Sci. Eng. C* 8-9, 205 (1999).
28. J. Leuvering, B. Goverde, P. Thal, and A. Schuurs, *J. Immunol. Methods* 60, 9 (1983).
29. J. Leuvering, P. Thal, M. Van der Waart, and A. Schuurs, *J. Immunol. Methods* 45, 183 (1981).
30. R. Elghanian, J. Storhoff, R. Mucic, R. Letsinger, and C. Mirkin, *Science* 277, 1078 (1997).
31. C. Mirkin, R. Letsinger, R. Mucic, and J. Storhoff, *Nature* 382, 607 (1996).
32. C. Mirkin, *MRS Bull.* 25, 43 (2000).
33. C. Mirkin, *Inorg. Chem.* 39, 2258 (2000).
34. J. Storhoff and C. Mirkin, *Chem. Rev.* 99, 1849 (1999).
35. M. Mertig, R. Kirsch, W. Pompe, and H. Engelhardt, *Eur. Phys. J. D* 9, 45 (1999).
36. K. Bromann, M. Giovannini, H. Brune, and K. Kern, *Eur. Phys. J. D* 9, 25 (1999).
37. D. Pum, A. Neubauer, E. Györvary, M. Sara, and U. Sleytr, *Nanotechnology* 11, 100 (2000).

38. U. B. Sleytr, P. Messner, D. Pum, and M. Sara, "Crystalline Bacterial Cell Surface Proteins." Academic Press, San Diego, 1996.
39. O. D. Velev and E. W. Kaler, *Langmuir* 15, 3693 (1999).
40. M. Natan, "IBC Conference on Biosensor Technology," Boston, 1998.
41. H. Takei, "Technical Digest of the 16th Sensor Symposium," 123, 1998.
42. H. Takei, *SPIE* 5515, 278 (1998).
43. A. Leitner, Z. Zhao, H. Brunner, F. Aussenegg, and A. Wokaun *Appl. Opt.* 32, 102 (1993).
44. Th. Schalkhammer, *Chem. Monthly* 129, 1067 (1998).
45. Th. Schalkhammer, G. Bauer, F. Pittner, A. Leitner, and F. Aussenegg, *SPIE* 3253, 12 (1998).
46. G. Bauer, F. Pittner, and Th. Schalkhammer, *Mikrochim. Acta* 131, 107 (1999).
47. G. Bauer, N. Stich, and Th. Schalkhammer, *SPIE* 3602, 62 (1999).
48. C. Mayer, N. Stich, R. Palkovits, G. Bauer, F. Pittner, and T. Schalkhammer, *J. Pharm. Biomed. Anal.* 24, 773 (2001).
49. C. Mayer, R. Verheijen, and Th. Schalkhammer, *SPIE* 4265, 134 (2001).
50. C. Mayer, N. Stich, T. Schalkhammer, and G. Bauer, *Fresenius' J. Anal. Chem.* 371, 238 (2001).
51. F. Aussenegg, H. Brunner, A. Leitner, F. Pittner, G. Bauer, T. Schalkhammer, European Patent EP00677738B1, 2000; U.S. Patent US05611998, 1997.
52. Th. Schalkhammer, Ch. Lobmaier, F. Pittner, A. Leitner, H. Brunner, and F. R. Aussenegg, *Sens. Actuators, B* 24, 166 (1995).
53. F. R. Aussenegg, H. Brunner, A. Leitner, Ch. Lobmaier, Th. Schalkhammer, and F. Pittner, *Sens. Actuators, B* 29, 204 (1995).
54. Th. Schalkhammer, Ch. Lobmaier, F. Pittner, A. Leitner, H. Brunner, and F. R. Aussenegg, *Mikrochim. Acta* 121, 259 (1995).
55. G. Bauer, S. Voinov, G. Sontag, A. Leitner, F. Aussenegg, F. Pittner, and Th. Schalkhammer, *SPIE* 3606, 40 (1999).
56. M. Lepek, R. Palkovits, G. Bauer, T. Schalkhammer, and F. Pittner, *Recent Res. Dev. Anal. Biochem.* 1, 1 (2001).
57. Th. Schalkhammer, Ch. Lobmaier, F. Pittner, F. Aussenegg, A. Leitner, and H. Brunner, *SPIE* 2508, 102 (1995).
58. C. Mayer, R. Palkovits, G. Bauer, and T. Schalkhammer, *J. Nanoparticle Res.* 3, 361 (2001).
59. F. Aussenegg, H. Brunner, A. Leitner, F. Pittner, G. Bauer, and T. Schalkhammer, U.S. Patent US05866433, 1999.
60. K. Sokolov, G. Chumanov, and T. Cotton, *Anal. Chem.* 70, 3898 (1998).
61. N. Strekal, A. Maskevich, S. Maskevich, J. Jardillier, and I. Nabiev, *Biopolymers* 57, 325 (2000).
62. W. H. Weber and E. F. Eagan, *Opt. Lett.* 4, 236 (1979).
63. I. Pockrand, A. Brillante, and D. Mobius, *Chem. Phys. Lett.* 69, 499 (1980).
64. Th. Schalkhammer, F. Aussenegg, A. Leitner, H. Brunner, G. Hawa, Ch. Lobmaier, and F. Pittner, *SPIE* 2976, 129 (1997).
65. C. Mayer, N. Stich, G. Bauer, and T. Schalkhammer, *SPIE* 4252, 37 (2001).
66. N. Stich, C. Mayer, and Th. Schalkhammer, *SPIE* 4434, 128 (2001).
67. N. Stich, A. Gandhum, V. Matushin, C. Mayer, and Th. Schalkhammer, *J. Nanosci. Nanotechnol.* 1, 397 (2001).
68. I. Pastoriza-Santos and L. Liz-Marzán, *Pure Appl. Chem.* 72, 83 (2000).
69. Ch. Brown, Y. Li, J. Seelenbinder, A. Rand, St. Letcher, O. Gregory, and M. Platek, *Anal. Chem.* 10, 2991 (1998).
70. J. Seelenbinder, Ch. Brown, P. Pivarnik, and A. Rand, *Anal. Chem.* 71, 1963 (1999).
71. Z. Zhang and T. Imae, *Colloid Interface Sci.* 233, 99 (2001).
72. E. Schutt, S. Richard, P. William, B. George, E. Raymond, L. Karin, and L. David, U.S. Patent US05017009, 1991.
73. B. Dubertret, M. Calame, and A. Libchaber, *Nat. Biotechnol.* 19, 365 (2001).
74. M. Dorrestijn and Th. Schalkhammer, Biosensor with single molecule sensitivity using field emission from metal clusters, Lab-on-a-Chip and Microarrays. CHI, Zürich, 2001.

Bionanomotors

Dmitri Grigoriev, Dieter Moll, Jeremy Hall, Peixuan Guo

Purdue University, West Lafayette, Indiana, USA

CONTENTS

1. Introduction
 2. General Classification of Motors-Linear, Rotary, and Nucleic Acid Translocating or Sliding Motors
 3. Components of Molecular Motors-Mechanical Frame and Energy Supply
 4. Energy Source-ATP Hydrolysis and Proton Flow
 5. Specific Bionanomotors
 6. Conclusions
- Glossary
References

1. INTRODUCTION

The ability to perform active movement is one of the most prominent features that distinguish living organisms from inanimate matter. Nanobiomotors are nanoscale machines formed by macromolecular complexes that convert a primary energy source to mechanical motion between moving and framework components. They are responsible for most forms of active biological motion, including internal material transport. Motor complexes are vital to the sustenance of biological systems, and they support efficient, directional motility of cellular components within cells, adenosine triphosphate (ATP) synthesis, the packaging of viral DNA, rotation of bacterial filaments, and muscle contraction [1–3]. Thanks to progress in structural biology, single molecule methods [4], and molecular biology approaches, our understanding of the molecular basis of biological movement has improved to the point where we can start thinking about possible applications of biomolecular motors in nanotechnology [5].

On a macroscopic scale, we are all very familiar with motors, because we are surrounded by both combustion engines and electric motors. So the question arises: can we downscale the way we think of motors to the molecular range? The possible applications of molecular motors in nanotechnology will certainly be very different from the way we use traditional macromotors. However, when we look at

the basic mechanisms of these motors, there are many striking parallels: just like macroscopic motors, biological nanomotors are assembled from static components that form a framework for moving components, even though the moving parts are not always restricted to rotary motion but can instead, in some motors, perform linear motion. Also, both macroscopic and molecular motors work by repeating the same cycle of steps over and over.

Another parallel is that biomolecular motors also need a primary energy source from which to derive mechanical energy. There is even a strong equivalence with the two types of energy sources, fossil fuels and electrical energy, that we most often use in conventional motors; some biomolecular motors are powered by breaking down an energy-rich bond of nucleotide triphosphates, typically ATP, just as our combustion engines break down the molecules of oil products. Yet other molecular motors are driven by the flow of protons along a proton gradient (i.e., an electrochemical potential across a membrane) just as electric motors are powered by the flow of electrons along an applied voltage. In fact, these two types of energy supply can be readily interconverted in biology: by sharing a rotating axle between two biomolecular motors, F_1F_0 -ATP synthase [6–8] can convert the energy stored in the proton gradient to rotation and then to energy stored in ATP. The process is reversible and exhibits nearly 100% efficiency [1]. If we look at our macroscopic equivalent, an electric generator driven by a combustion engine, we must deal with efficiencies below 50% and an irreversible reaction: we cannot produce fossil fuel from electrical energy. These unique attributes of biomolecular nanomotors should be our focus as we contemplate possible applications. These features involve instances where molecular motors outperform conventional motors, or where molecular motors perform motions and tasks that have no conceptual equivalent in our macroscopic world. Such examples include the continuous specific translocation of single DNA molecules by the DNA packaging motor of bacteriophage phi29 [3, 9–12], the linear “walking” mechanism of the cytoskeletal motor protein kinesin [13–16], and the ability of the flagellar motor to switch between clockwise and counterclockwise motion [2, 17] (Table 1). There are many proteins and biomolecular machines (Table 2) that

Table 1. Well-characterized bionanomotors.

Name	Energy source	Functions
Linear motors		
kinesin	ATP	organelle transport, mitosis, microtubule dynamics
myosin	ATP	muscle contraction, organelle transport, cytokinesis
dynein	ATP	organelle transport, mitosis, cilia beating
Rotary motors		
F ₁ F ₀ complex	H ⁺ /ATP	ATP synthesis
bacterial flagellar	H ⁺ /Na ⁺	bacterial movement, rapidly reversible motor
Nucleic acid translocating motor		
helicases	ATP	DNA strand separating activity
RNA polymerase	ATP	RNA transcription
viral DNA packaging	ATP	packaging of viral DNA

perform functions similar to those of the biological nanomotors covered in this chapter: G-proteins undergo ATP-driven conformational changes as part of their function [18–21], and the 19S subunit of the proteasome moves and unfolds proteins actively [22]. These examples of active work performed by biomolecules are enabled by the P-loop structure [23], a protein fold that is also present in the ATP-driven motors described here. Ion pumps [24] and active transporters [25] are also capable of converting a primary energy source into active work. However, for this chapter, we have restricted the term “bionanomotor” to those biological complexes that (i) have active mechani-

Table 2. Potential bionanomotors.

Name	Functions	Ref.
AAA proteins	proteolysis, protein folding, membrane trafficking, cytoskeletal regulation, organelle biogenesis, DNA replication, intracellular motility	[34]
GroEl	protein folding	[35, 294]
SMC proteins	chromosome formation	[240, 241, 243, 246]
G proteins	signal transduction, movement of peptidyl-tRNA and mRNA in the ribosome	[18–21, 295]
Actin	cellular motility, cortical organization	[242, 296]
Microtubule	mitosis, cytoplasmic organization	[32, 37, 297]
Dynamain	endocytosis, vesicle budding	[298]
Spasmin/centrin	contraction	[299]
Cilia	diverse processes (left-right axis pattern formation, cerebrospinal fluid flow, sensory reception, mucociliary clearance etc.)	[300–302]
Ion pumps	ion gradient formation	[24, 38, 303]

cal work as their main function, (ii) derive their activity through utilization of a primary energy source, (iii) function via the relative motion between active and framework components, and (iv) perform tasks through repetition of the same cycle of steps. We analyze the most thoroughly characterized biomolecular motors: F₁F₀-ATP synthase, the bacterial flagellar motor, myosin, kinesin, the viral DNA-packaging motor, helicases, and RNA polymerase (Table 1).

2. GENERAL CLASSIFICATION OF MOTORS-LINEAR, ROTARY, AND NUCLEIC ACID TRANSLOCATING OR SLIDING MOTORS

Molecular motors can be divided into linear, rotary, and nucleic acid translocating/sliding motors (Table 1) [26–32]:

2.1. Linear Motors

The motor proteins kinesin and dynein are the most commonly cited and studied examples of this class. They move along microtubules to induce directional motility of membranous vesicles, organelles, chromosomes, proteins, and RNA [32–38]. Another important member of the class of linear motors is myosin. It is involved in cellular motility, cytokinesis, endocytosis, and vesicle transport. In muscle fibers, bundles of myosin act on actin filaments, thereby driving muscular contraction [39].

2.2. Rotary Motors

The F₁ ATPase and bacterial flagellar motors are common representatives of this class of motors. F₁F₀-ATP synthase is a double-rotary motor located in the mitochondrial, bacterial, and chloroplast membranes. This motor is responsible for ATP generation and is powered by a proton gradient [1]. Bacterial rotary motors drive the spinning of flagella and therefore make active swimming of bacteria possible [2].

2.3. Nucleic Acid Translocating or Sliding Motors

There is a group of nucleic acid-processing complexes that plays a similar role in DNA or RNA translocating, tracking, or sliding related to DNA replication, translocation, recombination, and RNA transcription [36, 40–42]. It can be categorized into two subsets, components that bind nucleic acid and components that act on nucleic acid. The common feature of these two subsets is that they interact with RNA or DNA in a polymer conformation with a ring-shaped morphology. Most members of this group are hexamers. This subset includes helicase [43, 44], viral DNA-packaging motors [45–48], DNA polymerase [49], RNA polymerase [50], the *E. coli* transcription termination protein Rho [51, 52], the yeast DNA polymerase processivity factor [53],

bovine papillomavirus E1 replication initiator [54], and the *E. coli* DNA polymerase III holoenzyme [55, 56], which exist as hexamers [43, 57–60]. Though the mechanisms of this kind of DNA–protein interaction remain to be elucidated, the finding of the common feature in the formation of hexameric ring indicates it might have something in common. The process of both viral DNA packaging, DNA replication, RNA transcription, or DNA/RNA riding involves the relative motion of two components, one of which is nucleic acid. In bacterial virus phi29, the motor involves a novel RNA that forms a ring with six subunits [42, 61, 62]. It would be intriguing to show how phi29 hexameric pRNA may play a role similar to that which protein enzymes, such as DNA-helicases or the termination factor Rho, play.

Some members of the subset that acts on nucleic acid require ATP to provide energy and play an active role in motion. These members will be placed in the category of nucleic acid translocating or sliding motors. Most motors contain members of the other subset, proteins that bind nucleic acid. This chapter will only cover the well-studied motors, such as DNA helicase, RNA polymerase, and the viral DNA-packaging motors. Some, if not all, of the motors in this group might rotate. Since the action of these motors has yet to be further characterized, they are tentatively classified into this special category.

3. COMPONENTS OF MOLECULAR MOTORS-MECHANICAL FRAME AND ENERGY SUPPLY

Molecular motors exhibit wide variability in structure. Most are quite complex, but in general the structures consist of the same essential components: a mechanical frame that consists of both moving and static parts, along with an energy supply. The mechanical frame is formed by proteins in most molecular motors. However, the DNA-packaging motor of bacteriophage phi29 also includes a hexamer of RNA molecules as an essential component [63]. F_1F_0 complex is located in a lipid membrane, and the flagellar motor is anchored to the cell envelope. The energy supply can be from energy-rich nucleotide triphosphates, typically ATP, or from a proton gradient. The linear-acting motor proteins need extended cytoskeletal macromolecules for their action. Even though we describe these features as static components when considered in terms of motor mechanism, they are not static at all within the cell: actin filaments, the substrate of myosin, continuously assemble and disassemble in the cell in a highly dynamic, ATP-driven manner. The continuous assembly and disassembly of microtubules, the substrate of kinesin and dynein, from protein monomers is also controlled by ATP [64, 65]. Furthermore, actin filaments and microtubules are being actively moved through the action of myosin and dynein, respectively.

The DNA helicases and RNA polymerase are track-laying motors. DNA and RNA can be considered components of these motors since they are required for the unwinding or polymerization process [43, 66–69].

4. ENERGY SOURCE-ATP HYDROLYSIS AND PROTON FLOW

Molecular motors, just like any other sort of motor, need energy in order to function. Most molecular motors use chemical energy derived from the hydrolysis of adenosine triphosphate. The active sites on motor proteins bind ATP and catalyze the decomposition to adenosine diphosphate (ADP) and inorganic phosphate (Pi), thereby releasing a significant quantity of energy, which in turn leads to conformational change in the motor protein and ultimately results in motor movement. This catalytic process then repeats with another ATP molecule, and the motor protein can continue further movement.

For instance, kinesin “walks” using 8 nm steps along the microtubule protofilament axis, and each of these steps expends one ATP molecule [15, 16, 70–73]. In the case of cytoskeletal motors such as myosin and kinesin, ATP circulation causes a motor to cycle between weak and strong binding states with their tracks. ATP binding and turnover deliver the energy to detach the motor from its track and indirectly give the opportunity to reattach to a new site in the step-forward direction. Both the pRNA and gp16 of phi29 bind ATP [73a, 239]. ATP hydrolysis also provides the driving force for viral DNA-packaging motors. Current estimates indicate that one ATP molecule is required for every two DNA base pairs that are packaged [45, 48].

The F_1F_0 complex is composed of two motors [1] which are connected by a common rotor axle and can exchange the energy of proton translocation and ATP synthesis/hydrolysis through mechanical rotation. The F_0 motor generates torque connected with proton flow across a membrane and the F_1 subcomplex rotates with discrete 120° steps, each driven by the hydrolysis of one ATP molecule. In the typical situation in a chloroplast, mitochondrion, or bacterial cell, a steep proton gradient is maintained by photosynthesis or substrate oxidation, and this allows for proton flow through the F_0 motor of F_1F_0 complex, thereby driving the synthesis of ATP. However, if the ATP concentration is high and the electrochemical potential is low, the F_1 motor is stronger and reverses the F_0 motor, creating a proton pump [74, 75].

The bacterial flagellar motor is another example of the use of proton flow (protonomotive force) as an energy source. This motor is powered by the flux of hydrogen (H^+) or sodium (Na^+) ions (depending on the organism) across the membrane [2]. The protonomotive force is supported by metabolic processes that pump protons out of the cell and drive the flagellar motor through reverse flow. Each proton that flows back into the cell can supply up to 2.4×10^{-20} J of free energy to drive the motor, and a flow of approximately 10^3 protons is associated with each rotation of the motor [2].

5. SPECIFIC BIONANOMOTORS

5.1. Linear Motion Motors

5.1.1. Kinesin

Kinesin is a filament-dependent motor protein and is part of the cytoskeletal motor family [65]. Kinesin was first discovered in neuronal tissue, and it has been found to move

microtubules in an ATP-dependent mode; that is, the movement of this motor along the surface of the microtubule is supported by chemical energy released from the hydrolysis of ATP. Kinesin is processive [76] and moves forward in discrete steps of 8 nm [4, 77, 78], which corresponds to the distance between tubulin dimers along the microtubule [79]. Like many polynucleotide motors (polymerases, helicases, nucleases, etc.), kinesin can translocate through many enzymatic cycles before dissociating from the substrate [66, 68, 79]. Individual molecules typically move about 800 nm before disengaging at a speed of 800 nm/s (100 steps/s) *in vitro*, and they are capable of continuing movement against loads of up to -6 pN. A number of significant characteristics of kinesin movement, including the unidirectionality of the motion, the force-velocity relationship, the time dependence of the movement, and the displacement variance have been demonstrated *in vitro* [15, 16, 70–73, 80, 81].

Native kinesin is a dimeric molecule with two well-separated globular ($\sim 9 \times 3 \times 3$ nm) heads (Fig. 1) that are rotated by about 120° and displaced from each other by 8 nm. Each of these heads is formed from a single polypeptide that is 345 amino acids long and is responsible for both enzymatic and motor activity. Kinesin also contains two identical “heavy” and two identical “light” chains that can be divided into four domains: the catalytic core, the neck, the stalk, and the tail [82–84]. It has been found that single-headed kinesin constructs do not support processive movement [85, 86]; instead, the two heads of kinesin have been found to work in a coordinated mode, such that the binding and hydrolysis of ATP by one head stimulates ADP release by the other head [68].

Also, it has been shown [87] that in the presence of ADP, the motor domain of kinesin, while still bound to the microtubule, adopts a highly mobile state. All of these support the conception that dimeric kinesin moves “hand-over-hand,” moving its heads forward alternately. In this way, at least one head stays bound to the substrate at any given time (Fig. 1).

Two basic classes of possible models for the stepping of kinesin have been proposed [88]. One is the “long-stride” model, in which during the stepping process the back head passes the bound front head and advances 16 nm. At this point, the heads change their roles and a new step may take place [89]. Another model has been examined which suggests a “two-step” process [90, 91]. These models provide an explanation for the experimentally measured low dislocation variance, suggesting two consistent subprocesses: for the duration of one cycle one of the two heads takes an 8 nm step first, and then the other head takes an 8 nm step in order to maintain the 8 nm distance.

5.1.2. Myosin

Myosin is not one particular protein motor but rather a large family of proteins that can be divided into at least 15 different classes by amino acid sequence similarity. These proteins are responsible for many of the tasks involved in cell motility, including muscle contraction, chemotaxis, cytokinesis, pinocytosis, and targeted vesicle transport [92].

In general, myosins consist of three functional subdomains: the motor (or catalytic) domain, the neck domain,

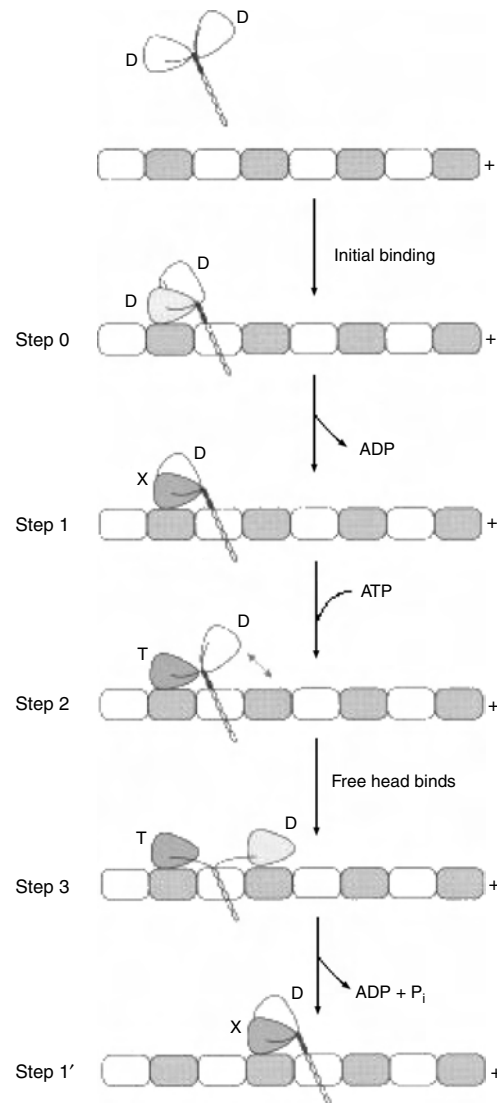


Figure 1. The schematic illustration of a kinesin movement along the microtubule. Dimeric kinesin moves “hand-over-hand,” moving its heads forward alternately. At least one head stays bound to the substrate at any given time. D and T—bound nucleotides ADP and ATP respectively. X—nucleotide free. Reprinted with permission from [247], F. J. Kull, *Essays in Biochem.* 35, 61 (2000). © 2000, Portland Press.

and the tail domain [92]. The most common example is muscle myosin, which was discovered over 60 years ago in the muscles and cytoplasm of animal cells; it is an asymmetric 470 kDa protein containing two 90 kDa globular *N*-terminal heads, subfragment-1, and an α -helical coiled-coil tail [27]. A catalytic domain is located in the globular head and contains the ATP and actin-binding sites. A neck region connects the catalytic domain to the tail and its cargo.

Class I of the myosin family is involved in both endocytic and exocytic membrane traffic. Myosin II is a component of the contractile ring in dividing cells and the sarcomere in muscle cells. Myosin III assists in signal transduction in retinal photoreceptor cells [93]. Class V myosins play an important role in organelle transport. It has been shown [94–96] that myosin V is a highly efficient, processive motor

like kinesin (Fig. 2). Myosin V and XI function as organelle motors in animal and plant cells, respectively. Myosin VI is a reverse motor that can move toward the “minus” end of actin filaments [64, 97, 98].

In order to help explain myosin’s role in the mechanism of muscle contraction, several models have been proposed. In the “swinging cross-bridge” model, myosin pulls an actin filament by swinging its head [99, 100]. However, direct evidence for the swinging cross-bridge model has not been obtained to this point. According to the “lever-arm” model, structural change in the catalytic domain of the myosin head is amplified by the pivoting of the light-chain binding domain, which acts as a lever arm [4, 101, 102].

Unlike kinesin and the polynucleotide motors, not all myosins are processive; classes I and II are prominent examples. Instead of the “Inchworm” model, the “hand-over-hand” model was confirmed by single fluorophore imaging [103].

5.2. Rotary Motors

5.2.1. $F_1 F_0$ ATPase

ATP synthesis is the basic method of cell energy production and one of the most frequently occurring enzymatic reactions in biology. This synthesis takes place on the $F_1 F_0$ -ATP synthase enzyme.

$F_1 F_0$ -ATP synthase consists of two motors, F_1 and F_0 , and is found in the inner membranes of mitochondria, the thylakoid membranes of chloroplasts, and the plasma membranes of bacteria [1]. These two motors are connected by a common rotor shaft (Fig. 3a). Such a connection allows for proton translocation energy to be converted and utilized in ATP synthesis through mechanical rotation [1].

The motors of ATP synthase have different functions and characteristics. F_1 subcomplex can be dissociated from F_0 . The resultant enzyme is termed F_1 -ATPase, and its catalyzed

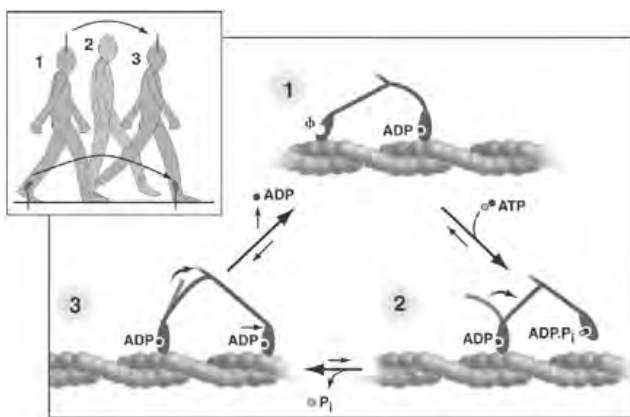


Figure 2. Myosin walks hand-over-hand using three steps. Model for movement of two myosins heads along actin filament. The “power stroke” of the leading head causes a transition from state 1 to state 2 with ATP hydrolysis and production of ADP and inorganic phosphate; trailing head becomes leading head. The leading head falls to state 2 as a result of biased diffusion, which induces extra movement and aids in the completion of the third step. Reprinted with permission from [310], J. Molloy and C. Veigel, *Science* 300, 2061 (2003). © 2003, American Association for the Advancement of Science.

reaction is the hydrolyzation of ATP. The energy of ATP hydrolysis is transferred to mechanical rotation (Fig. 3b). This complex consists of $\alpha_3\beta_3\gamma_1\delta_1\epsilon_1$ subunits and as has been shown [104] requires at least a $\alpha_3\beta_3\gamma$ to maintain ATPase-activity. Three α and three β subunits arranged into a hexameric ring with a central cavity [105] and half of the γ subunit is inserted in this cavity. F_1 subcomplex catalytic sites are located on the β subunit and $\gamma\epsilon$ subunits attached to the c subunits of F_0 subcomplex and form a rotor shaft [106, 107]. The rotation of γ is the result of the cooperative changing of nucleotide binding states of the three catalytic sites on the β subunits. These catalytic sites can adopt different binding states. The first binds with Mg-AMP-PNP [adenosine 5’-(β , γ -imino)-triphosphate], the second binds with Mg-ADP, and the third is empty [1].

Direct observation of F_1 motor rotation [6] has been accomplished with an optical microscope (Fig. 4). As has been shown, the motor rotates in discrete 120° steps [4], and each step requires the hydrolysis of one ATP molecule. An intermediate state [108] after ATP binding and before ADP

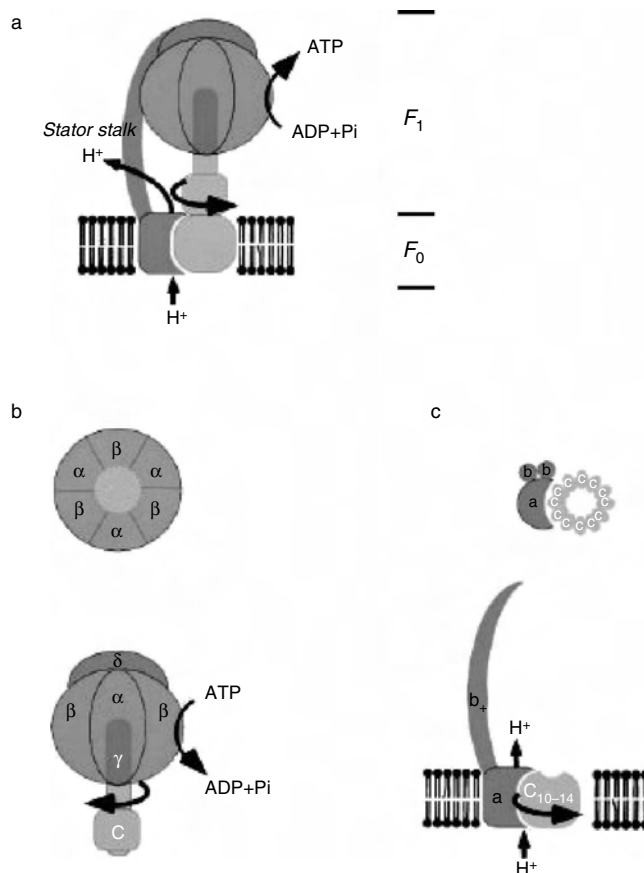


Figure 3. Schematic diagram of ATP synthase (a) $F_1 F_0$ -ATP synthase consists of two motors, F_1 and F_0 , which are connected by a common rotor shaft. The energy of ATP hydrolysis is transferred to mechanical rotation of the F_1 subcomplex (b) Structure of F_1 subcomplex. The $\gamma\epsilon$ subunits attached to the c subunits of F_0 subcomplex and form rotor shaft (c) Structure of F_0 subcomplex. This subcomplex generates torque associated with the movement of proton flow. Reprinted with permission from [1], H. Noji and M. Yoshida, *J. Biol. Chem.* 276, 1665 (2001). © 2001, American Society for Biochemistry and Molecular Biology.

(and Pi) release at 90° degree of the γ subunit was shown. So each 120° step can be dissolved into 90° and 30° substeps driven by ATP binding and ADP (and Pi) release respectively. A new crystal structure of an intermediate state was shown [109].

The F_0 complex does not use energy from ATP hydrolysis. The rotation of this motor is associated with the flow of protons (Fig. 2c). When protons flow through F_0 , the F_1 complex synthesizes ATP. This synthesis is reversible and when F_1 hydrolyzes ATP, the F_0 motor can pump reverse flow of protons through the membrane [1].

5.2.2. Bacterial Flagella

The bacterial flagellar motor is one of the most intriguing biological nanomotors. Many well-known bacterial species can swim using flagellar filaments [2, 110]. These filaments have a stiff, helical structure, are approximately 10 μm in length, and have a period of about 2 μm .

The flagellar motors of enteric bacteria *E. coli* and *S. typhimurium* have been the most often analyzed examples. All rotary motors can be divided into two parts: the rotor and the stator (the stationary section of the motor). Four rings (C, MS, L, and P) and the rod together form the rotor of the flagellar motor (Fig. 5). About 12–14 particles together form the stator. They are organized around the MS and C rings in the cytoplasmic membrane and are attached to the cell wall. The L and P rings (FlgI and FlgH) are located in the outer membrane and peptidoglycan, respectively. The MS (FliF) ring (~25 nm disk) crosses the cell inner membrane. The C ring (FliM and FliN) is attached to the MS ring and extends into the cytoplasm. The filament (FliC) is connected to the motor by a flexible hook (FlgE) and to the hook by hook-associated proteins (FlgK, FlgL, and FliD). Such a connection provides the filament

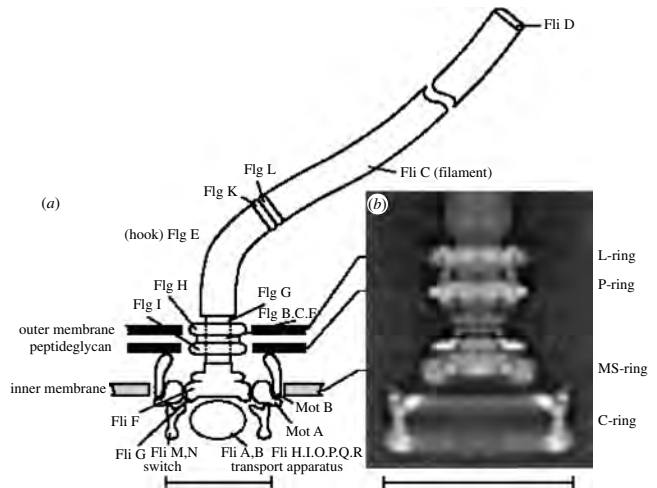


Figure 5. (a) A schematic diagram of the flagellar motor. (b) Reconstruction of electron microscope images of hook-basal bodies [309]. Reprinted with permission from [306], N. R. Francis et al., *J. Mol. Biol.* 235, 1261 (1994). © 1994, Elsevier Science.

and motor the freedom to rotate around different axes. FliG is bound to the inner face of the MS ring. MotA and MotB cross the inner membrane and are organized in a circular group around the MS and C rings [111]. These two Mot proteins bind to each other [112]. One possible method of torque generation is the alternating protonation and deprotonation of Asp32 of MotB, which modulates the interaction of a specific charged region in the cytoplasmic domain of MotA with a complementary charged region in the C-terminal domain of FliG.

The flagellar motor is powered by an ion flow through channels located in the plasma membrane. Ions utilizing this trough include hydrogen (H^+) and sodium (Na^+). Chemical energy derived from metabolic processes helps to support the ion flow. Such energy is required in order to pump ions out of the cell; reverse ion flow in cells drives various systems, including the flagellar motor [110, 113]. Flagellar motors can rotate both clockwise and counterclockwise and this rotation changing is regulated in such a manner as to allow the bacteria to perform chemotaxis.

A number of models have been proposed to explain the mechanism of flagellar motor function [114–123]. In the model proposed in [118] the rotation mechanism is based on the symmetry mismatch between the C and M rings. Other models (Fig. 6) are based on the geometric relation between the position of the rotor and the paths of ions flowing through the flagellar motor. The “electrostatic” model [120, 121, 123] is based on electrostatic interaction between proton flow and negatively charged areas of the rotor. Such interaction forces the rotor to rotate in order to keep negatively charged areas close to positively charged protons. Another model is based on the geometrical mismatch of in- and out-proton channels in the rotor [114, 115]. As a result, protons flowing through the outer channel can pass into the cell only through other channels in the stator, and they must be transferred to these channels by the rotation of the rotor.

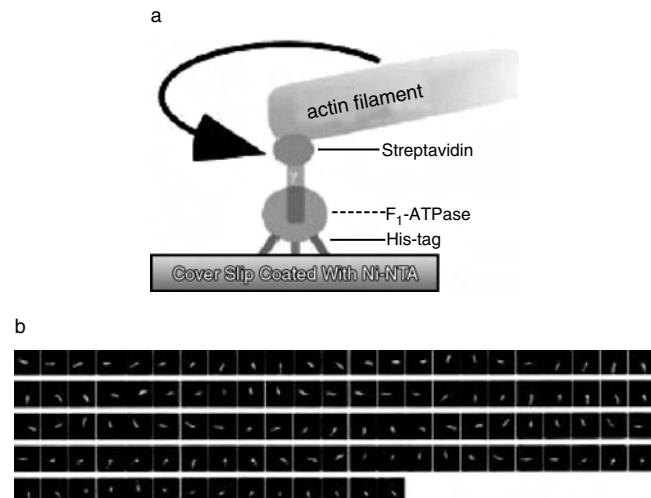


Figure 4. The direct observation of the γ subunit rotation in the F_1 motor [6]. (a) The scheme of experimental system for the observation of the γ rotation using an optical microscope. (b) Rotary movement of an actin filament observed with an epifluorescent microscope. Reprinted with permission from [1], H. Noji and M. Yoshida, *J. Biol. Chem.* 276, 1665 (2001). © 2001, American Society for Biochemistry and Molecular Biology.

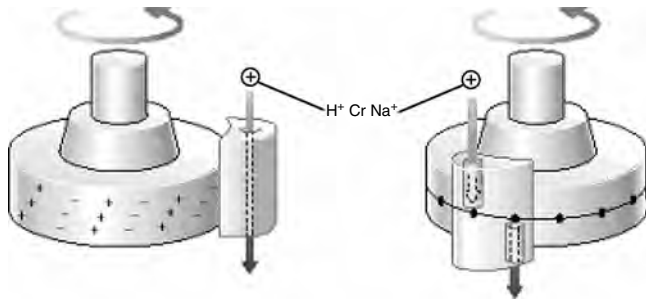


Figure 6. “Electrostatic proton turbine” (left) and “turnstile” (right) models of a flagellar motor. “Electrostatic proton turbine” model is based on electrostatic interaction of protons flow and charged rotor. “Turnstile” model is based on geometrical mismatch of in- and out-proton channels in the rotor. Reprinted with permission from [110], R. Berry, *Bacterial Flagella: Flagellar Motor*, in *Encyclopedia of Life Sciences*, 2, (2001). © 2001, Nature Publishing Group.

5.3. Nucleic Acid Translocating or Sliding Motors

5.3.1. Viral DNA-Packaging Motor

One striking feature in the assembly of many linear double-stranded DNA (dsDNA) viruses, including adenovirus [124–128], herpesvirus [129–131], poxvirus [132–134], and bacteriophages T1 [135], T3 [136], T4 [137], T5 [138], T7 [139, 140], P1 [141], P2 [142, 143], P22 [144–146], Mu [147], ϕ 21 [148], ϕ 29 [11, 149–151], SP01 [152, 153], SPP1 [154, 155], λ [156–159], and their relatives, is that the viral genome is inserted into a preformed shell called a procapsid during maturation [160–163]. This energetically unfavorable DNA-packaging reaction is accomplished by a viral nanomotor using ATP as energy.

One of the essential components of the motor is a connector complex that is a dodecameric structure with a central channel (30–60 Å) through which viral DNA is packaged into the capsid and exits during infection [143, 164–169]. Though the portal proteins from different viruses have little sequence homology and large variation in molecular weight, portal complexes show significant morphological similarity [160]. In the case of phi29, a bacterial virus that infects *Bacillus subtilis*, the structure of one phage portal protein has been determined at atomic resolution [164, 165]. The connector ring consists of a 12 α -helical subunit, with three long helices of each subunit forming the central channel. The ring is 138 Å across at its wide end and 66 Å at the narrow end. The internal channel is 60 Å at the top and 36 Å at the bottom. The wider end of the connector is located in the prohead and its narrow end partially protrudes out of the capsid. The connector is located at the fivefold vertex of the viral capsid, which leads to a symmetry mismatch between capsid and portal [160, 170]. As has been assumed, such a mismatch is required for the smooth rotation of the portal protein during DNA packaging [3, 170].

An examination of extensively studied dsDNA viruses, such as T3 [136], T4 [171, 172], P22 [146, 173, 174], P1 [175], psiM2 [176], Sfi21 [177], lambda [156, 178, 179], T7 [180, 181], phi29 [45, 61, 63, 182], and herpesvirus [167, 183], reveals that all DNA packaging motors involve two non-structural components typical of ATPase. Further examina-

tion has found that these two proteins can be classified into two categories according to their major role in DNA packaging [45]. One category is for procapsid binding, such as gpA of λ [156, 159], gp12 of phi21 [184], gp17 of T4 [185], gp19 of T3/T7 [48, 140, 186], and gp16 of phi29 [63, 187]. The second category is for interaction with DNA, such as gpNu1 of λ , gp1 of phi21, gp16 of T4; gp3 of phi29 and gp18 of T3/T7 [45]. Emerging information reveals that the mechanism of herpes virus DNA packaging is very similar to that of phages [167, 183, 188–191]. The DNA-packaging reaction is energy dependent and involves ATP hydrolysis. Estimates indicate that one ATP molecule is required for every two base pairs that are packaged [45]. Emerging information reveals that the mechanism of herpes virus DNA packaging is very similar to that of phages [167, 183, 188–191].

The translocation of double-stranded DNA into the phi29 procapsid requires a virus-encoded packaging RNA (pRNA) [36, 63, 187] (Fig. 7a). Mg^{2+} induces appropriate folding of pRNA for dimerization [192, 193]. pRNA dimers bind to the portal vertex (connector) and serve as the building blocks for hexamer assembly [192, 194] (Fig. 7b). The pRNA molecules interact intermolecularly via hand-in-hand interaction to form a hexameric complex that is a crucial part of the viral DNA translocation motor [36, 42, 62, 193, 195, 196]. pRNA appears to be directly involved in the DNA translocation process, and it leaves the procapsid when DNA packaging is completed [193, 197, 198].

pRNA contains two functional domains: the procapsid binding domain, located at the central region [194, 199–201] and comprising bases 23–97, and the DNA translocation domain, which is found at the 5'/3' paired ends [202]. This conclusion has resulted from several diagnostic studies, including (a) base deletion and mutation [202–205], (b) ribonuclease probing [193, 200, 203, 206], (c) oligo targeting [207, 208], (d) competition assays to inhibit phage assembly [195, 208, 209], (e) UV-cross-linking to portal protein [199], (f) psoralen cross-linking, and (g) primer extension [210].

In vitro virus assembly involves two steps: DNA packaging with the aid of the viral motor and virion maturation [161–163, 211, 212]. The defined *in vitro* DNA-packaging systems have been constructed for phi29 [61], T3 [213], T4 [214], and λ [215]. Infectious virions have been assembled *in vitro* by extract complementation [216–234], or by the use of synthetic nucleic acid and purified recombinant protein components [149, 235]. With the purified procapsid, gp16, pRNA, and ATP, upto 90% of the added DNA-gp3 can be packaged into the procapsid via the motor constructed with recombinant gene products. After DNA packaging, the *in vitro* assembly system can convert a DNA-filled capsid into infectious phi29 virions with the addition of the purified proteins gp9, gp11, gp12, and gp13 [149, 235]. With this system, up to 5×10^9 infectious virions per ml can be obtained in the presence of all the required components, yet not a single infectious virion is detected in the absence of even one essential component. This system, with a sensitivity of eight orders of magnitude, is used for the assay of the function of the DNA-packaging motor [12, 36, 198].

Several models for DNA translocation into the phi29 procapsid have been proposed [3, 154, 165, 196, 236]. It is generally believed that DNA is translocated through the axial

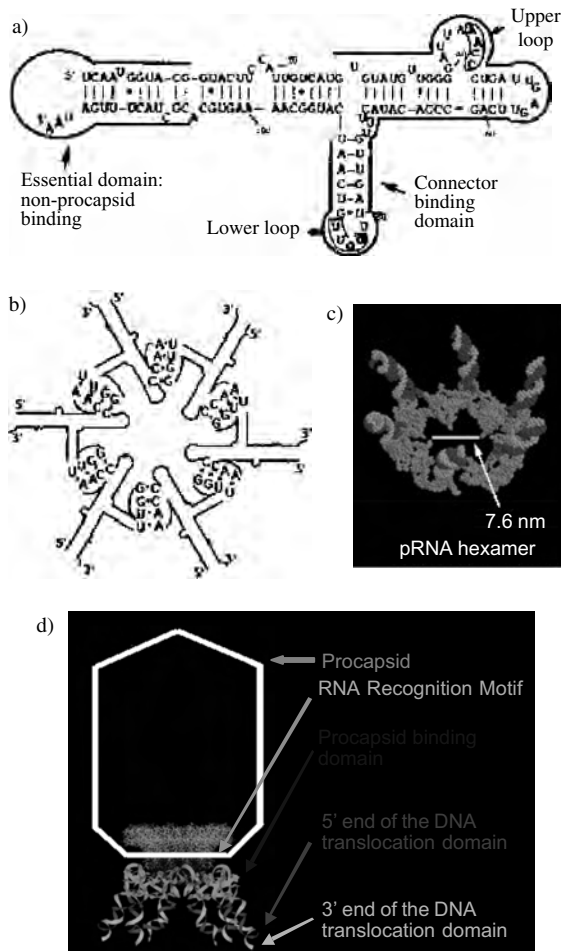


Figure 7. Bacterial virus phi29 DNA-packaging motor with six copies of a pRNA molecule (pRNA hexamer). (a) Sequence and secondary structure of phi29 DNA-packaging pRNA; (b) Formation of pRNA hexamer by hand-in-hand interaction. Reprinted with permission from [308], C. Chen et al., *RNA* 5, 805 (1999). © 1999, RNA Society (c) Tertiary structure of pRNA hexamer; (d) Sketch of phi29 viral particle with the motor tertiary structure. Reprinted with permission from [237], S. Hoeplich and P. Guo, *J. Biol. Chem.* 277, 20794 (2002). © 2002, American Society for Biochemistry and Molecular Biology.

hole of the portal vertex, much like a threaded rod moving along a nut. Another model hypothesizes that supercoiled DNA wraps around the portal vertex and that rotation of the portal vertex allows DNA to pass into the procapsid via the outside of the portal vertex [236]. In the model that was proposed in 1997 [3] (Fig. 8B), sequential action of multiple pRNAs, in conjunction with other components, is vital to DNA packaging. Six copies of pRNA form a hexamer that interacts with the capsid pentamer and moves in discrete 12° steps. Thirty ATPs are needed for each completed cycle of motor rotation. This model shows good agreement with three-dimensional (3D) structural data (Figs. 8A and 7C, D) that were obtained recently by crystallography [165], complementary modification, photoaffinity cross-linking, chemical modification, chemical modification interference, nuclease probing, AFM, and computer modeling [237] methods.

In the model proposed in [165], DNA located in the central channel interacts with one subunit of the portal. A 12°

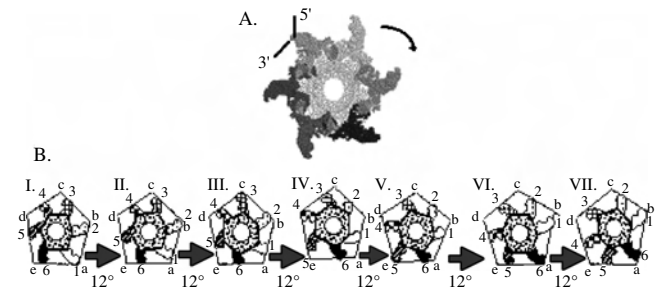


Figure 8. DNA-packaging model of bacterial virus phi29. (A) 3D model of the motor showing connector and pRNA hexamer. (B) Depicts the sequential action of pRNAs in the phi29 DNA-packaging motor. The left panel shows the 3D structure of the motor complex, including the connector and pRNA hexamer. A-G show the six steps of rotation; the hexagon represents the phi29 connector, and the surrounding pentagon represents the capsid. The six protrusions represent six pRNAs with variable pRNA patterns portraying the pRNA in serial energetic states. For example, pRNA 4 and 1, in panel A, represent contracted and relaxed conformations, respectively. Arrows mark the different transition states of pRNA 1. Each step, e.g., A to B, rotates 12°, since a five to six-fold symmetry mismatch generates 30 equivalent positions, and $360^\circ/30 = 12^\circ$. The portal vertex turns 72° after six steps of rotation. For example, pRNA 1 moves from vertex a in A to vertex b in G, and rotates 72°. Each step consumes one ATP to induce one conformational change in pRNA, and six ATPs are used for the transition from one vertex to another. The drawing is the view from inside the procapsid. Reprinted with permission from [3], C. Chen and P. Guo, *J. Virol.* 71, 3864 (1997). © 1997, American Society for Microbiology.

rotation of the narrow end of the connector leads to lengthwise expansion of the connector via a slight change in the angle of the long helices, and the wide end of the connector follows the narrow end. Such a “following” allows the structure to relax and contract while translating two base pairs of DNA into the capsid [165]. Also, the “motor-ratchet” hypothesis model of DNA packaging has been proposed and reviewed recently [211]. In this model, the connector rectifies DNA motion via either thermal, biased thermal, or oscillating processes. The motor-ratchet hypothesis has also been used to explain data in biochemistry, genetics, energetic, structure, and dynamics in packaging.

In recent times, the forces involved in phi29 DNA packaging were measured directly [238], using a defined *in vitro* DNA-packaging system [61]. In these experiments, a polystyrene bead was attached to biotinylated DNA of partially prepackaged complexes and captured in an optical trap. The capsid was fixed by binding with another bead coated with anticapsid antibodies. During the addition of ATP, the distance between the two beads decreased due to the packaging process. It was shown that the motor can drive DNA into the head with approximately 30% efficiency until the internal force builds to ~50 pico-Newtons. This indicates that the phi29 motor is one of the strongest known molecular motors, with a strength about two times that of RNA polymerase and eight times that of kinesin. All of this suggests that the viral DNA-packaging motor represents a powerful new class of motor worthy of further investigation.

One of the recent advances in the study of the phi29 nanomotor is the finding that its pRNA binds ATP [239]. This is the first demonstration of a natural RNA molecule that binds ATP, and the first case to report the presence of a

SELEX-derived RNA aptamer in living organisms. RNA is much easier to manipulate than proteins. Inclusion of RNA as essential components makes the phi29 motor a fascinating potential part for nanodevices.

5.3.2. Helicase

Helicases are motors that move along nucleic acid polymers by using energy derived from nucleoside triphosphate hydrolysis to facilitate both translocation and double-strand nucleic acid polymer unwinding [240–243]. Many cellular processes, such as nucleotide excision repair, homologous recombination, transcription, conjugation, and replication, require helicases [240, 244–246].

Because helicases are involved in important bimolecular processes such as recombination, replication, and DNA repair, helicase dysfunction can lead to a number of human pathologies, including cancer, premature aging, and immunodeficiency [247–253].

Helicases can be classified according to any of several characteristics: direction of movement ($5' \rightarrow 3'$ or $3' \rightarrow 5'$ polarity) [242], nucleic acid substrate type (DNA or RNA helicases) [240, 241], their primary sequences, and by their quaternary or oligomeric structures. For instance, helicases can be separated by structure into two different structural classes: hexameric helicases (assembled into ring-shaped hexamers) and nonhexameric helicases.

The presence of Mg^{2+} ions and binding with nucleotides are necessary for the formation of a hexameric structure. Also binding with NTP and the formation of hexameric structures are necessary for binding with DNA or RNA. Binding with DNA or RNA stabilizes hexamer structure and stimulates NTPase activity [254–257].

Helicase movement and DNA unwinding activity require energy derived from the hydrolysis of NTP. The NTP hydrolysis activity of helicases is from 10 to 100 times lower in the absence of DNA when compared with the presence of DNA [254, 258–260]. Though hexamer helicases can hydrolyze different ribonucleoside and deoxyribonucleoside triphosphates, not all nucleotides support DNA unwinding, and ATP is the preferred nucleotide for most hexameric helicases.

As has been shown, one strand of duplex DNA is bound in the central channel of the hexameric ring [69, 254, 261–264]. This binding is sequence-independent, and not all of the six DNA binding sites are involved in interaction simultaneously [257, 265–267]. Because helicases must not only bind DNA but also need to translocate along it, they may change between several DNA binding states (tight, weak, and no affinity) during translocation.

Several translocation models have been proposed [263, 266, 268, 269]. According to the three-site sequential translocation model, the three catalytic sites all participate in the NTPase reaction. They can adopt different conformational states such as: tight interaction with DNA, bound to NTP; weak interaction with DNA, bound to NDP; and empty state, not bound to DNA. These states undergo simultaneous change for each site in the order NTP-bound, NDP-bound, empty. Binding with NTP leads to conformational change and results in movement; the NDP-bound site loses its DNA connection and the empty site binds DNA in a different location. The cycle then repeats. Such a repetition

of cycles allows helicase to achieve processive and unidirectional movement. In the two-site model, the catalytic sites can adopt only two states: NTP-bound and NDP-bound. The NDP-bound subunit does not change to the empty state but starts to rebind DNA at a different location after release. The translocation model is based upon the notion of a fluctuating electrostatic field [67]. According to this model, the binding of NTP to a hydrolysis site induces conformational change that exposes one pair of negatively and positively charged regions per nucleotide hydrolysis site near the inner surface of the channel. These charged regions are not of equal size, are oriented at an angle to the circumferential meridian, and are not constant, appearing and disappearing with the binding and hydrolysis of NTP respectively. The field of these charged regions can sequentially interact with the closest negatively charged DNA phosphate that gives an “electrostatic push” in the direction of the charge pair axis. The combined effect of the charged pairs produces a sustained torsional and axial thrust.

The action of helicases includes not only unidirectional translocation along DNA but also base pair separation, and this process requires the disruption of the intermolecular forces that stabilize the duplex DNA. Several models have been proposed to help describe this unwinding mechanism. In the “wedge” model, only one of the separated DNA strands is tightly bound in the central channel; the other strand does not have tight interactions with the helicase. NTPase activity supports unidirectional movement of the helicases along the strand bound in the central channel and provides enough force for the destabilization of DNA base pairs by helicases through functioning like a wedge. Unlike in the “wedge” model, in the torsional model both separated DNA strands interact with helicase—the one bound in the central channel and the other with outside parts. Such interaction allows helicase to generate torque and rotate strands, leading to unwinding of the dsDNA. According to the helix-destabilization model, helicase interacts with both strands of DNA. But unlike the torsional model, in this model the outer part interacts with dsDNA. Such interactions and conformational changes caused by NTPase activity allow helicase to separate DNA and translocate along the separated strand [269, 270].

Not all helicases adopt a hexameric configuration; some of them can act as dimers or monomers [271–280]. Well-known representatives of such helicases include PcrA helicase [274, 275], RecBC helicase [242], *E. coli* DNA helicase II (UvrD) [271], and Rep helicase [277].

For describing translocation and the unwinding mechanism of RecBC helicase, the “inchworm” model has been proposed [242]. According to this model, the translocation and unwinding of DNA are two separate, consecutive events. First, translocation occurs in a 23-bp “step” and, second, unwinding occurs in several smaller events of 2–5 bp for each ATP molecule hydrolyzed. It was proposed that the RecBC enzyme possesses two nonequivalent DNA-binding sites: the first DNA-binding site is the leading domain of the enzyme that binds to one strand of double-stranded DNA and functions to anchor the enzyme during DNA unwinding. The second DNA-binding site is the trailing domain that functions as the helicase domain of the enzyme and is responsible for separating the strands

of DNA. One complete cycle of translocation and DNA unwinding is achieved by the expansion and contraction of the enzyme that includes the hydrolysis of at least 5 to 12 ATP molecules [242]. It has been shown that helicases such as PcrA DNA helicase [274, 275], *E. coli* DNA helicase II [271], *E. coli* RecG helicase [273], and P143 DNA helicase [281] also most likely utilize an “inchworm” mechanism.

A different, “rolling” model for DNA unwinding has also been proposed for Rep helicase. In this model, ATP binding, hydrolysis, and release cause a series of conformational changes of the Rep dimer. Each conformational state differs from the others with regard to the relative affinity of the second subunit of the Rep dimer for single stranded (ss) versus double stranded (ds) DNA. The Rep dimer is moved along the DNA and is driven by a subunit switching mechanism, and duplex DNA is actively unwound when one subunit of the Rep dimer is bound to the duplex region ahead of the ss/ds DNA junction [282].

5.3.3. RNA Polymerase

RNA polymerase is a molecular motor that processes along a DNA strand and transcribes the information coded in the DNA's base pair sequence into RNA [43, 66–69, 283–287].

Like the other biological nanomotors, RNA polymerase converts chemical energy to mechanical movement. In the case of polymerase, such chemical energy takes the form of free energy supplied by nucleotide polymerization and RNA folding. In order for the polymerization process to be initiated, RNA polymerase must bind to a promoter. During this first step, RNA polymerase binds to DNA and then randomly slides along the duplex until it meets a promoter. Protein initiation factors are necessary elements for establishing sequence-specific binding with promoter. After initiation of the RNA chain, this binding with the promoter is terminated and initiation factors are released. The chain elongation process will take place until polymerase reaches the termination DNA sequence. During transcription, ~35 bp fit into the major DNA groove and the DNA is separated into a template strand and a nontemplate strand, forming a “transcription bubble” that is ~17 bp long (Fig. 9). This domain contains the catalytic (active) site. The catalytic site normally consists of two binding sites—a substrate binding site and a product site. In the substrate binding site, NTP can weakly bind to a template base, and if they are complementary, they form a hydrogen bond. This can lead to

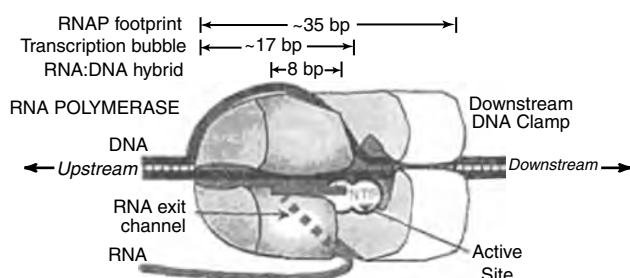


Figure 9. Schematic diagram of RNA polymerase (RNAP). Reprinted with permission from [66], J. Gelles and R. Landick, *Cell* 93, 13 (1998). © 1998, Cell Press.

hydrolysis of the pyrophosphate group and the formation of a phosphodiester link with the previous base [66].

To explain how RNA polymerase utilizes chemical energy for translocation, two main models, the “Brownian ratchet” model and the “power-stroke” model, were proposed [288, 66]. According to the “Brownian ratchet” model [288], the enzyme fluctuates between the two closest template positions under the influence of Brownian motion. When binding occurs, the polymerase in the next position undergoes a conformational change which prevents movement back to the previous position. The process then repeats [288, 289]. In the “power-stroke” model, movement of polymerase on 1 bp along DNA is powered by conformational change produced by the strong binding of an enzyme domain with the DNA template [66].

For obtaining information about the movement of RNA polymerase and for the determination of what mechanism is responsible for this process, single-molecule experimental techniques have been employed (Fig. 10). These techniques are all based upon isolating a single RNA polymerase molecule and immobilizing it on a surface. Such an approach allows for the observation of single DNA translocation by microscopy. Several different single-molecule methods, such as the tethered particle motion method, the laser tweezers method, and the surface force microscopy, method have been utilized in the study of RNA polymerase [287, 290–292]. These studies demonstrate both the high efficiency of chemical-to-mechanical energy conversion and the ability of RNA polymerase to translocate DNA against large opposing loads. It was also found that RNA polymerase rotates DNA by tracking its right-handed helix and that the polymerase does so over thousands of base pairs, thereby producing >5 pN nm of torque [293].

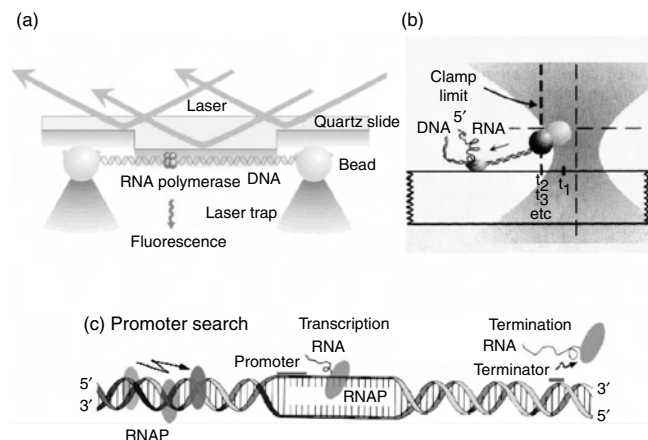


Figure 10. Schematic illustration of single-molecule experiments which were used for obtaining information about the movement of RNA polymerase. (a) Monitoring of a single RNA polymerase movement along DNA during promoter searching by fluorescence imaging [287]. (b) Transcription process is monitored by laser trap nanometry. (c) Illustration of the transcription process which can be completely visualized at the molecular level. Reprinted with permission from [307], Y. Ishii and T. Yanagida, *Trends Biotechnol.* 19, 6 (2001). © 2001, Elsevier.

6. CONCLUSIONS

Nanobiomotors are tiny machines that help convert a primary energy source into mechanical motion. They are crucial to the sustenance of living systems, since they allow for most forms of biological motion, helping to direct cellular components to their proper destinations, package DNA, contract muscles, and perform a variety of other functions. Biomotors exhibit a diversity of complex structures. Most have the same basic components, including a mechanical frame (usually composed of proteins) with both moving and static parts that is powered by an energy supply. This energy is typically derived from the hydrolysis of ATP, which leads to conformational change in the motor protein and results in movement; some motors use energy produced from ion gradients. These motors are typically divided into categories based on the type of motion displayed: the most well-studied motors are categorized tentatively into linear motors, rotary motors, and nucleic acid translocating/sliding motors.

GLOSSARY

Nanobiomotors Nanoscale machines formed by macromolecular complexes that convert a primary energy source to mechanical motion between active and framework components.

ACKNOWLEDGMENTS

The authors thank Dr. W. E. Moerner, Stanford University; Dr. Hiroyuki Noji, University of Tokyo; Dr. Imre Derenyi, Eötvös University; Dr. P. Satir, Yeshiva University; Dr. Konrad J. Böhm, Institute of Molecular Biotechnology; Dr. Yoshie Harada, The Tokyo Metropolitan Institute of Medical Science; Dr. Eckhard Jankowsky, Case Western Reserve University; Dr. Ron Vale, University of California; Dr. Nadrian Seeman, New York University; Dr. Peter Prevelige, Jr., Univ. of Alabama; Dr. Kazuhiko Kinoshita, Okazaki National Research Institutes; Dr. Christof Niemeyer, Dortmund University; Dr. Toshio Yanagida and Dr. E. Taniguchi, Osaka University for critical reading of the manuscript and helpful discussions. The work in the authors' lab was supported by current NIH grant GM59944 and also GM60529 to Dr. Guo.

REFERENCES

- H. Noji and M. Yoshida, *J. Biol. Chem.* 276, 1665 (2001).
- D. J. DeRosier, *Cell* 93, 17 (1998).
- C. Chen and P. Guo, *J. Virol.* 71, 3864 (1997).
- Y. Ishii, A. Ishijima, and T. Yanagida, *Trends Biotechnol.* 19, 211 (2001).
- H. Hess and V. Vogel, *Rev. Mol. Biotechnol.* 82, 67 (2001).
- H. Noji, R. Yasuda, M. Yoshida, and K. Kinoshita, Jr., *Nature* 386, 299 (1997).
- R. K. Nakamoto, C. J. Ketchum, and M. K. al Shawi, *Annu. Rev. Biophys. Biomol. Struct.* 28, 205 (1999).
- G. Oster and H. Wang, *Nature* 396, 279 (2003).
- M. Bjornsti, B. E. Reilly, and D. L. Anderson, *J. Virol.* 45, 383 (1983).
- P. Guo, S. Grimes, and D. Anderson, *Proc. Natl. Acad. Sci.* 83, 3505 (1986).
- L. Huang and P. Guo, *Virology* 312, 449 (2003).
- S. Grimes, P. J. Jardine, and D. Anderson, *Adv. Virus Res.* 58, 255 (2002).
- J. Howard, A. J. Hudspeth, and R. D. Vale, *Nature* 342, 154 (1989).
- K. Hall, D. G. Cole, Y. Yeh, J. M. Scholey, and R. J. Baskin, *Nature* 364, 457 (1993).
- K. Svoboda, C. F. Schmidt, B. J. Schnapp, and S. M. Block, *Nature* 365, 721 (1993).
- K. Svoboda and S. M. Block, *Cell* 77, 773 (1994).
- W. S. Ryu, R. M. Berry, and H. C. Berg, *Nature* 403, 444 (2000).
- J. Sonddek, D. G. Lambright, J. P. Noel, H. E. Hamm, and P. B. Sigler, *Nature* 372, 276 (1994).
- H. R. Bourne, D. A. Sanders, and F. McCormick, *Nature* 349, 117 (1991).
- E. P. Sablin and R. J. Fletterick, *Curr. Opin. Struct. Biol.* 11, 716 (2001).
- R. D. Vale, *J. Cell. Biol.* 135, 291 (1996).
- M. Bochtler, L. Ditzel, M. Groll, C. Hartmann, and R. Huber, *Annu. Rev. Biophys. Biomol. Struct.* 28, 295 (1999).
- J. E. Walker, M. Sarasate, M. J. Runswick, and N. J. Gray, *EMBO J.* 1, 945 (1982).
- C. Toyoshima, M. Nakasako, H. Nomura, and H. Ogawa, *Nature* 405, 647 (2000).
- J. Chen, S. Sharma, F. A. Quioco, and A. L. Davidson, *Proc. Natl. Acad. Sci. USA* 98, 1525 (2001).
- R. Vale, Motor proteins, in "Guidebook to the Cytoskeletal and Motor Proteins." Oxford Univ. Press, London, 1993.
- Y. E. Goldman, *Cell* 93, 1 (1998).
- P. I. Hanson, R. Roth, H. Morisaki, R. Jahn, and J. E. Heuser, *Cell* 90, 523 (1997).
- M. D. Wang, M. J. Schnitzer, H. Yin, R. Landick, J. Gelles, and S. M. Block, *Science* 282, 902 (1998).
- B. Bukau and A. L. Horwich, *Cell* 92, 351 (1998).
- T. Hirano, *Genes Dev.* 13, 11 (1999).
- L. Goldstein and R. Vale, *Nature* 352, 569 (1991).
- S. Leibler, *Nature* 370, 412 (1994).
- J. Darnell, H. Lodish, and D. Baltimore, in "Molecular Cell Biology." Scientific American Books, New York, 1990.
- R. Abeles, P. Frey, and W. Encks, in "Biochemistry." Jones and Bartlett, New York, 1992.
- P. Guo, *Progr. Nucl. Acid Res. Mol. Biol.* 72, 415 (2002).
- A. Kamal, A. Almenar-Queralt, J. LeBlanc, E. Roberts, and L. Goldstein, *Nature* 414, 643 (2001).
- R. Sakowicz, M. Berdelis, K. Ray, C. Blackburn, C. Hopmann, D. Faulkner, and L. Goldstein, *Science* 280, 292 (1998).
- R. C. Woledge, N. A. Curtin, and E. Homsher, *Monogr. Physiol. Soc.* 41, 1 (1985).
- V. Ellison and B. Stillman, *Cell* 106, 655 (2001).
- M. M. Hingorani and M. O'Donnell, *Curr. Biol.* 10, 25 (2000).
- P. Guo, C. Zhang, C. Chen, M. Trottier, and K. Garver, *Mol. Cell.* 2, 149 (1998).
- S. C. West, *Cell* 86, 177 (1996).
- T. Niedenzu, D. Roleke, G. Bains, E. Scherzinger, and W. Saenger, *J. Mol. Biol.* 306, 479 (2001).
- P. Guo, C. Peterson, and D. Anderson, *J. Mol. Biol.* 197, 229 (1987).
- H. Lin and L. W. Black, *Virology* 242, 118 (1998).
- Y. Hwang and M. Feiss, *J. Mol. Biol.* 261, 524 (1996).
- M. Morita, M. Tasaka, and H. Fujisawa, *Virology* 193, 748 (1993).
- D. Jeruzalmi, O. Yurieva, Y. Zhao, M. Young, J. Stewart, M. Hingorani, M. O'Donnell, and J. Kuriyan, *Cell* 106, 417 (2001).
- P. Cramer, D. A. Bushnell, and R. D. Kornberg, *Science* 292, 1863 (2001).
- E. P. Gogol, S. E. Seifried, and P. H. von Hippel, *J. Mol. Biol.* 221, 1127 (1991).
- B. R. Burgess and J. P. Richardson, *J. Biol. Chem.* 276, 4182 (2001).
- J. Bowers, P. T. Tran, A. Joshi, R. M. Liskay, and E. Alani, *J. Mol. Biol.* 306, 957 (2001).

54. J. Sedman and A. Stenlund, *J. Virol.* 72, 6893 (1998).
55. F. P. Leu and M. O'Donnell, *J. Biol. Chem.* (2001).
56. M. S. Song, H. G. Dallmann, and C. S. McHenry, *J. Biol. Chem.* 276, 40668 (2001).
57. E. P. Geiduschek, *Chem. Biol.* 2, 123 (1997).
58. M. C. Young, D. E. Schultz, D. Ring, and P. H. von Hippel, *J. Mol. Biol.* 235, 1447 (1994).
59. D. R. Herendeen, G. A. Kassavetis, and E. P. Geiduschek, *Science* 256, 1298 (1992).
60. J. Geiselmann, Y. Wang, S. E. Seifried, and P. H. von Hippel, *Proc. Natl. Acad. Sci. USA* 90, 7754 (1993).
61. P. Guo, S. Grimes, and D. Anderson, *Proc. Natl. Acad. Sci. USA* 83, 3505 (1986).
62. F. Zhang, S. Lemieux, X. Wu, S. St.-Arnaud, C. T. McMurray, F. Major, and D. Anderson, *Mol. Cell.* 2, 141 (1998).
63. P. Guo, S. Erickson, and D. Anderson, *Science* 236, 690 (1987).
64. A. L. Wells, A. W. Lin, L. Q. Chen, D. Safer, S. M. Cain, T. Hasson, B. O. Carragher, R. A. Milligan, and H. L. Sweeney, *Nature* 401, 505 (1999).
65. R. D. Vale and R. J. Fletterick, *Annu. Rev. Cell Dev. Biol.* 13, 745 (1997).
66. J. Gelles and R. Landick, *Cell* 93, 13 (1998).
67. C. Doering, B. Ermentrout, and G. Oster, *Biophys. J.* 69, 2256 (1995).
68. T. M. Lohman, K. Thorn, and R. D. Vale, *Cell* 93, 9 (1998).
69. X. Yu, M. M. Hingorani, S. S. Patel, and E. H. Egelman, *Nat. Struct. Biol.* 3, 740 (1996).
70. R. D. Vale, T. S. Reese, and M. P. Sheetz, *Cell* 42, 39 (1985).
71. S. Ray, E. Meyhofer, R. A. Milligan, and J. Howard, *J. Cell. Biol.* 121, 1083 (1993).
72. A. J. Hunt, F. Gittes, and J. Howard, *Biophys. J.* 67, 766 (1994).
73. K. Svoboda, P. P. Mitra, and S. M. Block, *Proc. Natl. Acad. Sci. USA* 91, 11782 (1994).
74. P. D. Boyer, *Nature* 402, 247, 249 (1999).
75. Y. Wada, Y. Sambongi, and M. Futai, *Biochim. Biophys. Acta* 1459, 499 (2000).
76. D. D. Hackney, *Nature* 377, 448 (1995).
77. M. J. Schnitzer and S. M. Block, *Nature* 388, 386 (1997).
78. W. Hua, E. C. Young, M. L. Fleming, and J. Gelles, *Nature* 388, 390 (1997).
79. S. M. Block, *Cell* 93, 5 (1998).
80. J. O. Stracke, A. J. Fosang, K. Last, F. A. Mercuri, A. M. Pendas, E. Llano, R. Perris, P. E. Di Cesare, G. Murphy, and V. Knauper, *FEBS Lett.* 478, 52 (2000).
81. K. J. Böhm, *Nanotechnology* 12, 238 (2001).
82. F. Kozielski, S. Sack, A. Marx, M. Thormahlen, E. Schonbrunn, V. Biou, A. Thompson, E. M. Mandelkow, and E. Mandelkow, *Cell* 91, 985 (1997).
83. E. P. Sablin, R. B. Case, S. C. Dai, C. L. Hart, A. Ruby, R. D. Vale, and R. J. Fletterick, *Nature* 395, 813 (1998).
84. F. J. Kull, E. P. Sablin, R. Lau, R. J. Fletterick, and R. D. Vale, *Nature* 380, 550 (1996).
85. R. D. Vale, T. Funatsu, D. W. Pierce, L. Romberg, Y. Harada, and T. Yanagida, *Nature* 380, 451 (1996).
86. E. Berliner, E. C. Young, K. Anderson, H. K. Mahtani, and J. Gelles, *Nature* 373, 718 (1995).
87. H. Sosa, E. J. Peterman, W. E. Moerner, and L. S. Goldstein, *Nat. Struct. Biol.* 8, 540 (2001).
88. S. M. Block and K. Svoboda, *Biophys. J.* 68, 2305S (1995).
89. C. S. Peskin and G. Oster, *Biophys. J.* 68, 202S (1995).
90. I. Derenyi and T. Vicsek, *Proc. Natl. Acad. Sci. USA* 93, 6775 (1996).
91. R. D. Astumian and I. Derenyi, *Biophys. J.* 77, 993 (1999).
92. J. R. Sellers, *Biochim. Biophys. Acta* 1496, 3 (2000).
93. C. Montell and G. M. Rubin, *Cell* 52, 757 (1988).
94. A. Mehta, *J. Cell Sci.* 114, 1981 (2001).
95. A. D. Mehta, R. S. Rock, M. Rief, J. A. Spudich, M. S. Mooseker, and R. E. Cheney, *Nature* 400, 590 (1999).
96. R. S. Rock, M. Rief, A. D. Mehta, and J. A. Spudich, *Methods* 22, 373 (2000).
97. V. Mermall and K. G. Miller, *J. Cell Biol.* 129, 1575 (1995).
98. R. F. Thompson and G. M. Langford, *Anat. Rec.* 268, 276 (2002).
99. H. E. Huxley, *Science* 164, 1356 (1969).
100. I. Rayment, W. R. Rypniewski, K. Schmidt-Base, R. Smith, D. R. Tomchick, M. M. Benning, D. A. Winkelmann, G. Wesenberg, and H. M. Holden, *Science* 261, 50 (1993).
101. R. Cooke, *Physiol. Rev.* 77, 671 (1997).
102. E. M. Ostap and T. D. Pollard, *J. Cell Biol.* 132, 1053 (1996).
103. A. Yildiz, J. N. Forkey, S. A. McKinney, T. Ha, Y. E. Goldman, and P. R. Selvin, *Science* 300, 2061 (2003).
104. T. Matsui and M. Yoshida, *Biochim. Biophys. Acta* 1231, 139 (1995).
105. J. P. Abrahams, A. G. Leslie, R. Lutter, and J. E. Walker, *Nature* 370, 621 (1994).
106. D. Stock, A. G. Leslie, and J. E. Walker, *Science* 286, 1700 (1999).
107. S. Wilkens, J. Zhou, R. Nakayama, S. D. Dunn, and R. A. Capaldi, *J. Mol. Biol.* 295, 387 (2000).
108. R. Yasuda, H. Noji, M. Yoshida, K. Kinoshita, Jr., and H. Itoh, *Nature* 410, 898 (2001).
109. R. I. Menz, J. E. Walker, and A. G. Leslie, *Cell* 106, 331 (2001).
110. R. M. Berry, *Encyclopedia Life Sci.* (2001).
111. M. L. DePamphilis and J. Adler, *J. Bacteriol.* 105, 396 (1971).
112. H. Tang, T. F. Braun, and D. F. Blair, *J. Mol. Biol.* 261, 209 (1996).
113. D. Fung and H. Berg, *Nature* 375, 809 (1995).
114. S. Khan and H. Berg, *Cell* 32, 913 (1983).
115. H. Berg and L. Turner, *Biophys. J.* 65, 2201 (1993).
116. T. Atsumi, *J. Theor. Biol.* 213, 31 (2001).
117. D. Walz and S. Caplan, *Biophys. J.* 78, 626 (2000).
118. D. Thomas, D. Morgan, and D. DeRosier, *Proc. Natl. Acad. Sci. USA* 96, 10134 (1999).
119. R. Berry and H. Berg, *Biophys. J.* 76, 580 (1999).
120. T. Elston and G. Oster, *Biophys. J.* 73, 703 (1997).
121. R. Berry, *Biophys. J.* 64, 961 (1993).
122. F. Oosawa and S. Hayashi, *Adv. Biophys.* 22, 151 (1986).
123. P. Lauger, *Biophys. J.* 53, 53 (1988).
124. K. E. Gustin and M. J. Imperiale, *J. Virol.* 72, 7860 (1998).
125. S. I. Schmid and P. Hearing, *J. Virol.* 71, 3375 (1997).
126. J. C. D'Halluin, M. Milleville, P. A. Boulanger, and G. R. Martin, *J. Virol.* 26, 344 (1978).
127. C. L. Cepko and P. A. Sharp, *Cell* 31, 407 (1982).
128. B. Edvardsson, E. Everitt, E. Joernvall, L. Prage, and L. Philipson, *J. Virol.* 19, 533 (1976).
129. F. J. Rixon and D. McNab, *J. Virol.* 73, 5714 (1999).
130. J. Y. Lee, A. Irmiere, and W. Gibson, *Virology* 167, 87 (1988).
131. A. Dasgupta and D. W. Wilson, *J. Virol.* 73, 2006 (1999).
132. B. Moss, Replication of poxviruses, in "Virology." Raven Press, New York, 1985.
133. A. M. DeLange, M. Reddy, D. Scraba, C. Upton, and G. McFadden, *J. Virol.* 59, 249 (1986).
134. B. L. Parsons and D. J. Pickup, *Virology* 175, 69 (1990).
135. H. Drexler, *J. Virol.* 49, 754 (1984).
136. H. Shibata, H. Fujisawa, and T. Minagawa, *Virology* 159, 250 (1987).
137. V. B. Rao and L. W. Black, *Cell* 42, 967 (1985).
138. R. D. Everett, *J. Gen. Virol.* 52, 25 (1981).
139. M. E. Cerritelli and F. W. Studier, *J. Mol. Biol.* 285, 299 (1996).
140. M. Sun, D. Louie, and P. Serwer, *Biophys. J.* 77, 1627 (1999).
141. K. Skorupski, B. Sauer, and N. Sternberg, *J. Mol. Biol.* 243, 268 (1994).
142. G. Pruss and R. Calendar, *Virology* 86, 454 (1978).
143. S. Rishovd, A. Holzenburg, B. V. Johansen, and B. H. Lindqvist, *Virology* 245, 11 (1998).
144. B. Greene and J. King, *J. Biol. Chem.* 274, 16135 (1999).
145. S. D. Moore and P. E. Prevelige, Jr., *J. Biol. Chem.* 276, 6779 (2001).

146. K. Eppler, E. Wyckoff, J. Goates, R. Parr, and S. Casjens, *Virology* 183, 519 (1991).
147. C. M. Burns, H. L. B. Chan, and M. S. DuBow, *Proc. Natl. Acad. Sci. USA* 87, 6092 (1990).
148. M. P. Smith and M. Feiss, *Gene* 126, 1 (1993).
149. C. S. Lee and P. Guo, *J. Virol.* 69, 5018 (1995).
150. C. Gutierrez, R. Freire, M. Salas, and J. M. Hermoso, *EMBO J.* 13, 269 (1994).
151. J. M. Valpuesta, J. J. Fernandez, J. M. Carazo, and J. L. Carrascosa, *Struct. Fold. Des.* 7, 289 (1999).
152. K. S. Jeng, A. Daniel, and M. M. Lai, *J. Virol.* 70, 2403 (1996).
153. K. S. Jeng, P. Y. Su, and M. M. Lai, *J. Virol.* 70, 4205 (1996).
154. P. Dubé, P. Tavares, R. Lurz, and M. van Heel, *EMBO J.* 12, 1303 (1993).
155. A. Gual, A. G. Camacho, and J. C. Alonso, *J. Biol. Chem.* 275, 35311 (2000).
156. A. Becker and M. Gold, *J. Mol. Biol.* 199, 219 (1988).
157. T. Dokland and H. Murialdo, *J. Mol. Biol.* 233, 682 (1993).
158. L. Woods and C. E. Catalano, *Biochemistry* 38, 14624 (1999).
159. J. Q. Hang, C. E. Catalano, and M. Feiss, *Biochemistry* 40, 13370 (2001).
160. C. Bazinet and J. King, *Annu. Rev. Microbiol.* 39, 109 (1985).
161. L. W. Black, *Ann. Rev. Microbiol.* 43, 267 (1989).
162. S. Casjens and R. Hendrix, Control mechanisms in dsDNA bacteriophage assembly, in "The Bacteriophages," Vol. 1. Plenum, New York, 1988.
163. P. Guo, *Sem. Virol.* 5, 1 (1994).
164. A. Guasch, J. Pous, B. Ibarra, F. X. Gomis-Ruth, J. M. Valpuesta, N. Sousa, J. L. Carrascosa, and M. Coll, *J. Mol. Biol.* 315, 663 (2002).
165. A. A. Simpson, Y. Tao, P. G. Leiman, M. O. Badasso, Y. He, P. J. Jardine, N. H. Olson, M. C. Morais, S. Grimes, D. L. Anderson, T. S. Baker, and M. G. Rossmann, *Nature* 408, 745 (2000).
166. J. M. Valpuesta, H. Fujisawa, S. Marco, J. M. Carazo, and J. Carrascosa, *J. Mol. Biol.* 224, 103 (1992).
167. W. W. Newcomb, R. M. Juhas, D. R. Thomsen, F. L. Homa, A. D. Burch, S. K. Weller, and J. C. Brown, *J. Virol.* 75, 10923 (2001).
168. J. Kochan, J. L. Carrascosa, and H. Murialdo, *J. Mol. Biol.* 174, 433 (1984).
169. L. E. Donate, L. Herranz, J. P. Secilla, J. M. Carazo, H. Fujisawa, and J. L. Carrascosa, *J. Mol. Biol.* 201, 91 (1988).
170. R. W. Hendrix, *Proc. Natl. Acad. Sci. USA* 75, 4779 (1978).
171. V. S. Manne, V. B. Rao, and L. W. Black, *J. Biol. Chem.* 257, 13223 (1982).
172. D. Powell, J. Franklin, F. Arisaka, and G. Mosig, *Nucleic Acids Res.* 18, 4005 (1990).
173. R. Gope and P. Serwer, *J. Virol.* 47, 96 (1983).
174. P. E. J. Prevelige, D. Thomas, J. King, S. A. Towse, and G. J. J. Thomas, *Biochemistry* 29, 5626 (1990).
175. K. Skorupski, J. C. Pierce, B. Sauer, and N. Sternberg, *J. Mol. Biol.* 223, 977 (1992).
176. P. Pfister, A. Wasserfallen, R. Stettler, and T. Leisinger, *Mol. Microbiol.* 30, 233 (1998).
177. F. Desiere, S. Lucchini, and H. Brussow, *Virology* 241, 345 (1998).
178. C. E. Catalano, D. Cue, and M. Feiss, *Mol. Microbiol.* 16, 1075 (1995).
179. F. Sanger, A. R. Coulson, G. F. Hong, D. F. Hill, and G. B. Petersen, *J. Mol. Biol.* 162, 729 (1982).
180. M. Son, S. J. Hayes, and P. Serwer, *Virology* 162, 38 (1988).
181. J. J. Dunn and F. W. Studier, *J. Mol. Biol.* 166, 477 (1983).
182. K. J. Garvey, M. S. Saedi, and J. Ito, *Gene* 40, 311 (1985).
183. H. Scheffczik, C. G. Savva, A. Holzenburg, L. Kolesnikova, and E. Bogner, *Nucleic Acids Res.* 30, 1695 (2002).
184. M. Feiss, S. Frackman, and J. Sippy, *J. Mol. Biol.* 183, 239 (1985).
185. L. W. Black, *BioEssays* 17, 1025 (1995).
186. D. Endy, D. Kong, and J. Yin, *Biotechnol. Bioeng.* 55, 375 (1997).
187. P. Guo, S. Bailey, J. W. Bodley, and D. Anderson, *Nucleic Acids Res.* 15, 7081 (1987).
188. A. K. Sheaffer, W. W. Newcomb, M. Gao, D. Yu, S. K. Weller, J. C. Brown, and D. J. Tenney, *J. Virol.* 75, 687 (2001).
189. D. Yu and S. K. Weller, *Virology* 243, 32–44 (1998).
190. D. Yu and S. K. Weller, *J. Virol.* 72, 7428 (1998).
191. J. S. Hwang and E. Bogner, *J. Biol. Chem.* 277, 6943 (2002).
192. M. Trottier, Y. Mat-Arip, C. Zhang, C. Chen, S. Sheng, Z. Shao, and P. Guo, *RNA* 6, 1257 (2000).
193. C. Chen and P. Guo, *J. Virol.* 71, 495 (1997).
194. C. Chen, S. Sheng, Z. Shao, and P. Guo, *J. Biol. Chem.* 275, 17510 (2000).
195. M. Trottier and P. Guo, *J. Virol.* 71, 487 (1997).
196. R. W. Hendrix, *Cell* 94, 147 (1998).
197. D. Shu and P. Guo, *Virology* 309, 108 (2003).
198. P. Guo, *Acta Biochim. Biophys. Sinica* 34, 533 (2002).
199. K. Garver and P. Guo, *RNA* 3, 1068 (1997).
200. R. J. D. Reid, J. W. Bodley, and D. Anderson, *J. Biol. Chem.* 269, 5157 (1994).
201. R. J. D. Reid, F. Zhang, S. Benson, and D. Anderson, *J. Biol. Chem.* 269, 18656 (1994).
202. C. L. Zhang, C.-S. Lee, and P. Guo, *Virology* 201, 77 (1994).
203. R. J. D. Reid, J. W. Bodley, and D. Anderson, *J. Biol. Chem.* 269, 9084 (1994).
204. J. Wichitwechkarn, D. Johnson, and D. Anderson, *Mol. Biol.* 223, 991 (1992).
205. C. L. Zhang, T. Tellinghuisen, and P. Guo, *RNA* 3, 315 (1997).
206. S. Bailey, J. Wichitwechkarn, D. Johnson, B. Reilly, D. Anderson, and J. W. Bodley, *J. Biol. Chem.* 265, 22365 (1990).
207. C. L. Zhang, K. Garver, and P. Guo, *Virology* 211, 568 (1995).
208. M. Trottier, K. Garver, C. Zhang, and P. Guo, *Nucleic Acids Symp. Ser.* 36, 187 (1997).
209. M. Trottier, C. L. Zhang, and P. Guo, *J. Virol.* 70, 55 (1996).
210. M. L. Perdue, J. C. Cohen, M. C. Kemp, C. C. Randall, and D. J. O'Callaghan, *Virology* 64, 187 (1975).
211. P. Serwer, *J. Struct. Biol.* 141, 179 (2003).
212. R. W. Hendrix and R. L. Garcea, *Sem. Virol.* 5, 15 (1994).
213. K. Hamada, H. Fujisawa, and T. Minagawa, *Virology* 151, 119 (1986).
214. V. B. Rao and L. W. Black, *J. Mol. Biol.* 200, 475 (1988).
215. Y. Hwang and M. Feiss, *Virology* 211, 367 (1997).
216. S. Tonegawa and M. Hayashi, *J. Mol. Biol.* 48, 219 (1970).
217. U. Laemmli, *Nature* 227, 680 (1970).
218. U. Laemmli, E. Molbert, M. Showe, and E. Kellenberger, *J. Mol. Biol.* 49, 99 (1970).
219. D. Kaiser and T. Masuda, *Proc. Natl. Acad. Sci. USA* 70, 260 (1973).
220. J. King and S. Casjens, *Nature* 251, 112 (1974).
221. A. D. Kaiser, M. Syvanen, and T. Masuda, *J. Mol. Biol.* 91, 175 (1975).
222. J. V. Israel, T. H. Anderson, and M. Levine, *Proc. Natl. Acad. Sci. USA* 57, 284 (1967).
223. C. Kerr and P. D. Sadowski, *Proc. Natl. Acad. Sci. USA* 71, 3545 (1974).
224. B. Hohn, *J. Mol. Biol.* 98, 93 (1975).
225. G. J. Pruss, J. C. Wang, and R. Calendar, *J. Mol. Biol.* 98, 465 (1975).
226. A. Becker, M. Marko, and M. Gold, *Virology* 78, 291 (1977).
227. J. Miyazaki, H. Fujisawa, and T. Minagawa, *Virology* 91, 283 (1978).
228. H. Murialdo and A. Becker, *J. Mol. Biol.* 125, 57 (1978).
229. A. R. Poteete, V. Jarvik, and D. Botstein, *Virology* 95, 550 (1979).
230. L. W. Black, *Virology* 113, 336 (1981).
231. M. A. Bjornsti, B. E. Reilly, and D. L. Anderson, *Proc. Natl. Acad. Sci. USA* 78, 5861 (1981).
232. M. Fuller and J. King, *J. Mol. Biol.* 156, 633 (1982).

233. A. Aoyama, R. K. Hamatake, and M. Hayashi, *Proc. Natl. Acad. Sci. USA* 80, 4195 (1983).
234. E. Strobel, W. Behnisch, and H. Schmieger, *Virology* 133, 158 (1984).
235. C. S. Lee and P. Guo, *Virology* 202, 1039 (1994).
236. S. Turnquist, M. Simon, E. Egelman, and D. Anderson, *Proc. Natl. Acad. Sci. USA* 89, 10479 (1992).
237. S. Hoepflich and P. Guo, *J. Biol. Chem.* 277, 20794 (2002).
238. D. E. Smith, S. J. Tans, S. B. Smith, S. Grimes, D. L. Anderson, and C. Bustamante, *Nature* 413, 748 (2001).
239. D. Shu and P. Guo, *J. Biol. Chem.* 278, 7119 (2003).
240. E. Jankowsky, C. Gross, S. Shuman, and A. Pyle, *Nature* 403, 447 (2000).
241. E. Jankowsky, C. Gross, S. Shuman, and A. Pyle, *Science* 291, 121 (2001).
242. P. Bianco and S. Kowalczykowski, *Nature* 405, 368 (2000).
243. T. Ha, I. Rasnik, W. Cheng, H. P. Babcock, G. H. Gaus, T. M. Lohman, and S. Chu, *Nature* 419, 638 (2002).
244. R. M. Twyman, in "Advanced Molecular Biology: A Concise Reference." BIOS Scientific, 1998.
245. P. S. Pang, E. Jankowsky, P. J. Planet, and A. M. Pyle, *EMBO J.* 21, 1168 (2002).
246. P. Bianco, L. Brewer, M. Corzett, R. Balhorn, Y. Yeh, S. Kowalczykowski, and R. Baskin, *Nature* 409, 374 (2001).
247. N. A. Ellis, J. Groden, T. Z. Ye, J. Straughen, D. J. Lennon, S. Ciocci, M. Proytcheva, and J. German, *Cell* 83, 655 (1995).
248. J. K. Karow, R. K. Chakraverty, and I. D. Hickson, *J. Biol. Chem.* 272, 30611 (1997).
249. C. E. Yu, J. Oshima, Y. H. Fu, E. M. Wijsman, F. Hisama, R. Alisch, S. Matthews, J. Nakura, T. Miki, S. Ouais, G. M. Martin, J. Mulligan, and G. D. Schellenberg, *Science* 272, 258 (1996).
250. J. C. Shen, M. D. Gray, J. Oshima, and L. A. Loeb, *Nucleic Acids Res.* 26, 2879 (1998).
251. M. D. Gray, J. C. Shen, A. S. Kamath-Loeb, A. Blank, B. L. Sopher, G. M. Martin, J. Oshima, and L. A. Loeb, *Nat. Genet.* 17, 100 (1997).
252. N. A. Ellis, *Curr. Opin. Genet. Dev.* 7, 354 (1997).
253. R. K. Chakraverty and I. D. Hickson, *BioEssays* 21, 286 (1999).
254. M. T. Washington, A. H. Rosenberg, K. Griffin, F. W. Studier, and S. S. Patel, *J. Biol. Chem.* 271, 26825 (1996).
255. M. M. Hingorani and S. S. Patel, *Biochemistry* 35, 2218 (1996).
256. S. Guo, S. Tabor, and C. C. Richardson, *J. Biol. Chem.* 274, 30303 (1999).
257. L. E. Bird, K. Hakansson, H. Pan, and D. B. Wigley, *Nucleic Acids Res.* 25, 2620 (1997).
258. S. S. Patel, A. H. Rosenberg, F. W. Studier, and K. A. Johnson, *J. Biol. Chem.* 267, 15013 (1992).
259. K. Arai and A. Kornberg, *J. Biol. Chem.* 256, 5253 (1981).
260. C. C. Liu and B. M. Alberts, *J. Biol. Chem.* 256, 2813 (1981).
261. E. H. Egelman, X. Yu, R. Wild, M. M. Hingorani, and S. S. Patel, *Proc. Natl. Acad. Sci. USA* 92, 3869 (1995).
262. P. D. Morris and K. D. Raney, *Biochemistry* 38, 5164 (1999).
263. W. Bujalowski and M. J. Jezewska, *Biochemistry* 34, 8513 (1995).
264. M. R. Sawaya, S. Guo, S. Tabor, C. C. Richardson, and T. Ellenberger, *Cell* 99, 167 (1999).
265. S. S. Patel, M. M. Hingorani, and W. M. Ng, *Biochemistry* 33, 7857 (1994).
266. X. Yu, M. J. Jezewska, W. Bujalowski, and E. H. Egelman, *J. Mol. Biol.* 259, 7 (1996).
267. M. J. Jezewska, U. S. Kim, and W. Bujalowski, *Biochemistry* 35, 2129 (1996).
268. Y. Yong and L. J. Romano, *J. Biol. Chem.* 270, 24509 (1995).
269. S. S. Patel and K. M. Picha, *Annu. Rev. Biochem.* 69, 651 (2000).
270. Y. Ishimi and K. Matsumoto, *Proc. Natl. Acad. Sci. USA* 90, 5399 (1993).
271. L. Mechanic, M. Hall, and S. Matson, *J. Biol. Chem.* 274, 12488 (1999).
272. M. Dillingham, D. Wigley, and M. Webb, *Biochemistry* 41, 643 (2002).
273. P. McGlynn, A. Mahdi, and R. Lloyd, *Nucleic Acids Res.* 28, 2324 (2000).
274. S. Velankar, P. Soutanas, M. Dillingham, H. Subramanya, and D. Wigley, *Cell* 97, 75 (1999).
275. L. Bird, J. Brannigan, H. Subramanya, and D. Wigley, *Nucleic Acids Res.* 26, 2686 (2003).
276. K. Chao and T. Lohman, *J. Mol. Biol.* 221, 1165 (1991).
277. I. Wong, K. Chao, W. Bujalowski, and T. Lohman, *J. Biol. Chem.* 267, 7596 (1992).
278. M. Amaratunga and T. Lohman, *Biochemistry* 32, 6815 (1993).
279. K. Bjornson, M. Amaratunga, K. Moore, and T. Lohman, *Biochemistry* 33, 14306 (1994).
280. K. Bjornson, I. Wong, and T. Lohman, *J. Mol. Biol.* 263, 411 (1996).
281. V. McDougal and L. Guarino, *J. Virol.* 75, 7206 (2001).
282. I. Wong and T. Lohman, *Science* 256, 350 (1992).
283. D. A. Erie, T. D. Yager, and P. H. von Hippel, *Annu. Rev. Biophys. Biomol. Struct.* 21, 379 (1992).
284. A. Polyakov, E. Severinova, and S. A. Darst, *Cell* 83, 365 (1995).
285. H. Y. Wang, T. Elston, A. Mogilner, and G. Oster, *Biophys. J.* 74, 1186 (1998).
286. T. D. a. v. H. P. Yager, American Society for Microbiology, Washington, DC, 1987.
287. Y. Harada, T. Funatsu, K. Murakami, Y. Nonoyama, A. Ishihama, and T. Yanagida, *Biophys. J.* 76, 709 (1999).
288. R. Guajardo and R. Sousa, *J. Mol. Biol.* 265, 8 (1997).
289. R. Landick, *Cell* 88, 741 (1997).
290. H. Yin, R. Landick, and J. Gelles, *Biophys. J.* 67, 2468 (1994).
291. H. Yin, M. D. Wang, K. Svoboda, R. Landick, S. M. Block, and J. Gelles, *Science* 270, 1653 (1995).
292. S. Kasas, N. H. Thomson, B. L. Smith, H. G. Hansma, X. Zhu, M. Guthold, C. Bustamante, E. T. Kool, M. Kashlev, and P. K. Hansma, *Biochemistry* 36, 461 (1997).
293. Y. Harada, O. Ohara, A. Takatsuki, H. Itoh, N. Shimamoto, and K. Kinoshita, Jr., *Nature* 409, 113 (2001).
294. F. J. Kull, *Essays Biochem.* 35, 61 (2000).
295. M. V. Rodnina, A. Savelsbergh, V. I. Katunin, and W. Wintermeyer, *Nature* 385, 37 (1997).
296. H. Miyata, S. Nishiyama, K. Akashi, and K. Kinoshita, Jr., *Proc. Natl. Acad. Sci. USA* 96, 2048 (1999).
297. T. Kaneko, T. J. Itoh, and H. Hotani, *J. Mol. Biol.* 284, 1671 (1998).
298. S. M. Sweitzer and J. E. Hinshaw, *Cell* 93, 1021 (1998).
299. W. B. Amos, L. M. Routledge, and F. F. Yew, *J. Cell. Sci.* 19, 203 (1975).
300. P. Satir, *FASEB J.* 13, S235 (1999).
301. P. Satir, *Environ. Health Perspect.* 35, 77 (1980).
302. I. Ibanez-Tallon, N. Heintz, and H. Omran, *Hum. Mol. Genet.* 12, R27 (2003).
303. W. Stoekenius, *Protein Sci.* 8, 447 (1999).
304. I. Rayment, H. M. Holden, M. Whittaker, C. B. Yohn, M. Lorenz, K. C. Holmes, and R. A. Milligan, *Science* 261, 58 (1993).
305. S. M. Block, *Cell* 87, 151 (1996).
306. N. R. Francis, G. E. Sosinsky, D. Thomas, and D. J. DeRosier, *J. Mol. Biol.* 235, 1261 (1994).
307. Y. Ishii and T. Yanagida, *Trends Biotechnol.* 19, 6 (2001).
308. C. Chen, C. Zhang, and P. Guo, *RNA* 5, 805 (1999).
309. C. H. Berg, *Philos. Trans. R. Soc. Lond. B Biol. Sci.* 355, 491 (2000).
310. J. Molloy and C. Veigal, *Science* 300, 2061 (2003).

Bismuth Nanostructured Materials

Joshua T. Moore, Charles M. Lukehart

Vanderbilt University, Nashville, Tennessee, USA

CONTENTS

1. Introduction and Scope
2. Zero-Dimensional Bismuth Nanostructured Materials
3. One-Dimensional Bismuth Nanostructured Materials
4. Two-Dimensional Bismuth Nanostructures
5. Summary
- Glossary
- References

1. INTRODUCTION AND SCOPE

For many years, bismuth (Bi) has found applications in various materials ranging from pigments, pharmaceuticals, and cosmetics to alloys, catalysts, and electronics. Most recently, there has been increased interest in the preparation of nanostructured bismuth, bismuth alloys, and bismuth intermetallic substances because of useful properties exhibited by these materials. The unique electronic structure of bismuth, specifically a small electron effective mass and a long electron mean-free path, make quantum confinement effects much more pronounced in nanoscale bismuth materials. Of particular interest is the application of nanoscale bismuth structures as thermoelectric materials.

The efficiencies of thermoelectric materials are determined through measurement of the dimensionless thermoelectric figure of merit, denoted ZT . The equation for this figure of merit is given as

$$ZT = S^2 \sigma T / \kappa$$

where S represents the Seebeck coefficient, σ represents the electrical conductivity of the material, κ represents the thermal conductivity of the material, and T is the absolute temperature of the measurement. Most state-of-the-art thermoelectric materials used for solid-state refrigeration have a value of $ZT \leq 1$. Bismuth and bismuth alloys exhibit favorable thermoelectric properties, and, as a result, many

state-of-the-art commercial thermoelectric devices contain elemental Bi, Bi_2Te_3 , or other Bi alloys as the thermoelectrically active components. Theoretical calculations indicate that nanostructured Bi or Bi alloy materials might exhibit greatly enhanced ZT values due to quantum effects. There is much current interest research in the preparation of nanostructured Bi materials to investigate how such quantum confinement effects could enhance desired thermoelectric properties.

A comprehensive review of the preparation of zero-, one-, and two-dimensional nanostructures of elemental bismuth and bismuth intermetallic substances or alloys is provided. Nanostructured materials described in this review have at least one dimension in the range of 1–100 nm, where the dimensionality of a nanostructure denotes the number of dimensions in which electron motion is not confined to the nanoscale. Two-dimensional nanostructures exhibit quantum confinement in one dimension as represented by very thin films, quantum wells, or superlattice structures. One-dimensional nanostructures, such as quantum wires, nano-rods, or nanofibers, are spatially confined in two dimensions, and zero-dimensional nanostructures have shapes confined in all three dimensions, as found with nanoparticles, nanocrystals, or quantum dots.

Bi nanostructures (n-Bi) have been prepared using a variety of physical, chemical, or electrochemical synthesis strategies, as summarized in Table 1. More detailed discussion of these various preparation methods and the types of nanostructured materials formed is presented below.

2. ZERO-DIMENSIONAL BISMUTH NANOSTRUCTURED MATERIALS

2.1. Elemental Bismuth Nanoparticles

Bismuth nanoparticles have been prepared as nanocomposite materials in metal, ceramic, or organic polymer matrices, and as nascent particles having various degrees of surface passivation. In general, chemical synthesis strategies give better control of average particle size.

Bi/metal nanocomposites are known for aluminum or Al-Cu-Fe matrices. Goswami and Chattopadhyay [1] have reported the formation of a 10 wt% Bi material in an

Table 1. Listing of bismuth nanostructured materials, including method of preparation and particulate size range classified according to order of dimension (D).

	Nanomaterial	Method	Size (nm)	Ref.		
0D	Bi/Al matrix	Induction melting	20–100	[1]		
	Bi/Al-Cu-Fe matrix	Melt spinning	50	[2]		
	Bi/SiO ₂ matrix	H ₂ reduction of Bi ³⁺ dopants	100–250	[3]		
	Bi/Mo-Ti oxide matrix	H ₂ reduction of Bi ³⁺ dopants	10	[4]		
	Bi/SiO ₂ (or TiO ₂) matrix	Sol-gel/H ₂ reduction of Bi ³⁺ dopants	5.3–10	[5]		
	Bi		Evaporation of Bi metal	4.5–9.5	[6]	
			Chemical reduction of Bi ³⁺ compounds	15	[7]	
			Inverse micelles/chemical reduction	3.2–8.0	[9]	
				20	[10]	
	Bi/polymer matrix		Microemulsion/polymerization	13.2	[11]	
			Metathesis between Bi ³⁺ and S ²⁻	5	[12]	
			Bi ₂ S ₃	N/A	[13]	
			Bi ₂ Se ₃	Dissolution in acetonitrile	10	[14]
			Bi ₂ Te ₃	Inverse micelles	10	[14]
Bi-E/SiO ₂ matrix (E = Te, Sb, Sn, Sb/Sn)			Sol-gel/H ₂ reduction of Bi ³⁺ dopants	11–15	[15]	
1D	Bi	Vacuum melting/pressure injection	4.3–56	[28, 29]		
		Vacuum deposition	7–200	[19, 30]		
		Electrodeposition	20–70	[31, 32]		
			50	[33]		
			3–100	[34]		
		95–400	[35]			
		Capillary filling of C nanotubes	Approx. 1	[36, 37]		
	Electrolysis of Bi powder in molten LiCl	N/A	[38]			
	Electron beam lithography	50	[39]			
	Bi ₂ S ₃		Solvothermal decomposition	130–200	[41]	
			Solvothermal reaction	20	[42]	
	Bi ₂ E ₃ (E=S, Se)		Electrodeposition	40	[43]	
				280	[44]	
2D	Bi	MBE	5–80	[45]		
			40–80	[46]		
	Bi/Sb	MBE	N/A	[47]		
			1–10	[48]		
	Bi _{0.88} Sb _{0.12}	MBE	75	[49]		
			7.5/6.5	[50]		
	Nanoporous Bi film	Spin coating/H ₂ reduction	5–10	[51]		
(channel width)						
Bi ₂ Te ₃ /Sb ₂ Te ₃	CVD	1–10	[52, 53]			

Note: MBE = molecular beam epitaxy, CVD = chemical vapor deposition.

aluminum matrix. The nanocomposite is prepared by induction melting of ultra high purity elemental Al (99.999%) and Bi in an Ar atmosphere. The as-cast alloy is rapidly cooled producing a large number of Bi nanoparticles in an Al matrix. Transmission electron microscopy (TEM) micrographs reveal Bi particles ranging in size from 20–100 nm. Similarly, Singh and Tsai [2] have reported the preparation and melting behavior of Bi nanoparticles embedded in an Al-Cu-Fe matrix. This nanocomposite is prepared by melting a mixture of highly pure metals under an Ar atmosphere in an electric arc furnace. Bi particles are embedded into the melt-by-melt spinning at a loading of 10 wt%. The Bi nanoparticles formed have an average size of 50 nm and display spheroidal morphology with little or no faceting of the particles.

Several n-Bi/ceramic nanocomposites are known. Czajka et al. [3] prepared n-Bi/silica composites by doping SiO₂ melts with Bi₂O₃. Reduction of Bi-doped silica glass by

hydrogen at temperatures ranging from 160–500 °C gives a uniform distribution of solid particles having diameters ranging from 100–250 nm within the glass matrix. The observation of a strong X-ray diffraction peak centered at 27.1°2θ is consistent with diffraction from the (012) lattice planes of Bi metal.

While investigating the redox chemistry of bismuth molybdate (Bi₂O₃ · 2MoO₃) catalysts embedded in TiO₂, Grunwaldt et al. [4] found that Bi³⁺ ions are easily reduced to Bi⁰ at room temperature under a reducing atmosphere. Bi-Mo-Ti mixed-metal oxides are prepared using sol-gel processing by adding a Bi precursor, such as BiCl₃ or Bi(NO₃)₃, along with a Mo precursor compound to a solution of Ti[OCH(CH₃)₂]₄ in isopropanol. Aqueous HNO₃ is used to initiate Ti-alkoxide hydrolysis and condensation. Reduction of the obtained mixed-metal oxide gel intermediate gives a Bi/Mo-Ti oxide composite containing Bi nanoparticles of ca. 10 nm average diameter.

Using a similar strategy, Moore and Lukehart [5] prepared n-Bi/SiO₂ or TiO₂ xerogel nanocomposites by the sol-gel processing of solely metal alkoxide reagents. Co-hydrolysis and heterocondensation of the Bi alkoxide, Bi(OCH₂CH₂OCH₃)₃, with either Si(OCH₃)₄ or Ti[OCH(CH₃)₂]₄ results in formation of mixed-metal oxide gels. Calcination of the gel intermediates to remove excess organic functionalities followed by reduction in flowing hydrogen at 250 °C affords n-Bi/SiO₂ or n-Bi/TiO₂ xerogel composites containing Bi nanoparticles of 10 nm or 5.3 nm average diameter, respectively. Powder X-ray diffraction (XRD) scans typical of n-Bi/SiO₂ and n-Bi/TiO₂ xerogel nanocomposites are shown in Figure 1. The principal peaks expected of crystalline Bi are observed. Peak broadening is an independent measure of nanoparticle size. Energy dispersive spectra (EDS) of these two nanocomposite materials are shown in Figure 2. X-ray emission from Bi and the matrix metals, Ti or Si, are observed. The relative intensities of these emission peaks can be correlated to the relative atomic fraction of each metal present within the sample.

Nascent Bi nanoparticles have been formed and stabilized with various degrees of intentional surface passivation. Wurl et al. [6] prepared unsupported Bi nanoparticles by high-temperature evaporation of Bi metal. Aggregation of Bi atoms within a flow of inert gas leads to the growth of Bi nanoparticles. Depending on evaporation temperature and the rate of gaseous flow, Bi particles are formed having particle diameters in the range of 4.5–9.5 nm.

Fang et al. [7] prepared self-assembled Bi nanoparticles using a high-temperature decomposition process similar to arrested precipitation methods known to form CdSe nanoparticles. Reduction of bismuth(III) 2-ethylhexanoate in dioctyl ether by Li[B(CH₂CH₃)₃H] precipitates nanocrystalline Bi. The Bi nanoparticles have near spherical morphology with an average diameter of 15 nm. These nanoparticles self-assemble into a two-dimensional monolayer exhibiting local hexagonal ordering.

Yu et al. [8] produced nearly monodisperse nanoparticles of Bi, as well as Sn and In, using a heterogeneous seeded-growth process. Bi nanoparticles form when Bi([N(Si(CH₃)₃)₂]₃) is thermally decomposed in a solution containing 1.5 nm Au seed crystals. The polymer, poly(styrene_{0.86}-co-vinyl-pyrrolidinone_{0.14}), is present to stabilize the Bi nanoparticles during particle formation. The

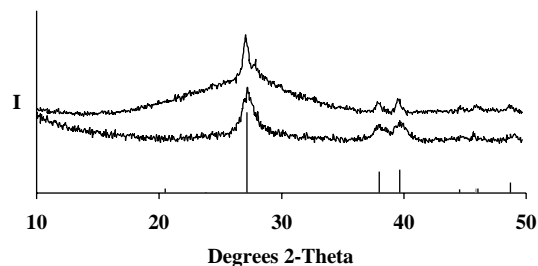


Figure 1. XRD scans (Cu K α radiation) of a typical Bi/silica xerogel nanocomposite (top) and Bi/titania xerogel nanocomposite (bottom) along with the standard line pattern for Bi metal. The top scan shows a diffraction peak near 29° in 2 θ corresponding to a small amount of unreduced Bi₂O₃ impurity.

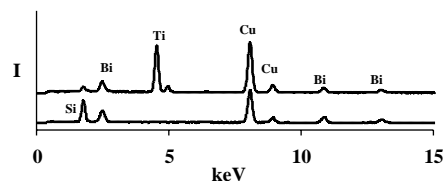


Figure 2. Energy dispersive/(EDS) spectra of a typical Bi/titania xerogel nanocomposite (top) and Bi/silica xerogel nanocomposite (bottom); Cu emission from the sample holder is also evident.

resulting Bi nanoparticles are then precipitated from solution as a black powder. Bi average particle sizes range from 8.6–12.4 nm depending on reaction conditions.

Nearly monodisperse Bi nanoparticles are obtained using inverse micelle, or microemulsion, synthesis methods. Foos et al. [9] prepared Bi nanoparticles having average diameters of 3.2–8.0 nm by adding an inverse-micelle solution containing aqueous BiOClO₄ to a second inverse-micelle solution containing aqueous NaBH₄ as a reducing agent. The as-prepared, surfactant-capped Bi nanoparticles are precipitated from solution and washed with methanol to remove excess surfactant molecules leaving an insoluble black powder of Bi nanoparticles. Similarly, Fang et al. [10] found that reaction of inverse micelles containing bismuth(III) citrate with inverse micelles containing NaBH₄ also affords Bi nanoparticles. When mixed surfactant systems are used, Bi particles having an average particle diameter of approximately 20 nm are formed.

Using a variation of the inverse micelle method, Fang et al. [7] obtain polymer-encapsulated Bi nanoparticles using an *in-situ* polymerization-microemulsion process. Addition of a microemulsion solution containing slightly acidic aqueous Bi(NO₃)₃ to a second microemulsion containing aqueous NaBH₄ results in the formation of surfactant-capped Bi nanoparticles. Dissolution of methyl methacrylate and hydroxyethyl methacrylate as comonomers in the oil phase along with ethylene glycol dimethacrylate as a cross-linking agent and 2,2-dimethoxy-1-phenylacetophenone as a (UV) polymerization initiator results in the formation of a polymeric network surrounding the nano-sized water pockets present in the microemulsions. Bi nanoparticles of average diameter 13.2 nm are formed in the initial emulsion. Annealing the polymer-stabilized nanocomposite in Ar at 160 °C, 200 °C, and 240 °C gives n-Bi/polymer composites containing Bi particles having average diameters of 15.3 nm, 22.6 nm, and 23.9 nm, respectively.

2.2. Bismuth Alloy and Intermetallic Nanoparticles

Bismuth alloy and intermetallic nanoparticles have been obtained as either unsupported or matrix-stabilized nanoclusters. Chalcogenide elements serve as the most common intermetallic component.

Suarez et al. [12] prepared nanocrystalline Bi₂S₃ colloids using two different methods. In the first method, acetonitrile solutions of BiI₃ are reacted with H₂S gas to precipitate colloidal Bi₂S₃. In the second method, addition of a solution of Na₂S to a solution of Bi₂I₃ in acetonitrile solvent initiates formation of a Bi₂S₃ colloid. A light brown solution quickly

forms during both procedures, thus indicating the formation of Bi_2S_3 colloidal material. Upon standing for approximately 15 min and then degassing the respective reaction suspensions, a brown colloidal suspension of Bi_2S_3 is obtained. In both cases, Bi_2S_3 is formed with an average particle size of ≤ 5 nm.

Comor et al. [13] have obtained Bi_2Se_3 quantum dots by slow precipitation of Bi_2Se_3 from acetonitrile solvent. A colloidal dispersion 6×10^{-6} M in Bi_2Se_3 is formed while heating a solution of high purity Bi_2Se_3 in acetonitrile at 60°C over a period of four days. Although the Bi_2Se_3 particle size was not determined, analysis of absorption spectral data is consistent with the formation of particles containing 150 Bi_2Se_3 formula units.

Foos et al. [14] formed nanoparticulate Bi_2Te_3 using an inverse micelle strategy. Reaction of an aqueous solution of $\text{Bi}(\text{OClO}_4)_3$ as an inverse micelle dissolved in hexane with a hexane solution of $[(\text{CH}_3)_3\text{Si}]_2\text{Te}$ yields a black suspension of Bi_2Te_3 . Removal of surfactant molecules present in the inverse micelle formulation by successive washing followed by drying in vacuo affords a dry black powder identified as Bi_2Te_3 by both elemental microanalysis and powder X-ray diffraction. The product contains Bi_2Te_3 nanoparticles having an average diameter below 10 nm.

Moore and Lukehart [15] prepared nanocrystals of Bi-Te, Bi-Sb, Bi-Sn, or Bi-Sb/Sn alloys widely dispersed throughout a SiO_2 xerogel matrix using elemental alkoxide reagents and a sol-gel processing synthesis strategy. Co-hydrolysis and heterocondensation of solutions of $\text{Bi}(\text{OCH}_2\text{CH}_2\text{OCH}_3)_3$ containing various amounts of $\text{Te}(\text{OCH}_2\text{CH}_3)_4$, $\text{Sb}(\text{OCH}_2\text{CH}_3)_3$, or $(\text{C}_4\text{H}_9)_2\text{Sn}(\text{OCH}_3)_2$ as a dopant reagent with $\text{Si}(\text{OCH}_3)_4$ results in the formation of mixed-metal oxide gels. Calcination of the mixed-metal gel to remove excess organic functionalities followed by reduction in hydrogen at 250°C affords Bi alloy nanoparticles having average diameters of 11 nm, 15 nm, 12 nm, and 14.5 nm for the Bi-Te, Bi-Sb, Bi-Sn, and Bi-Sb-Sn alloys, respectively. TEM micrographs reveal predominantly spheroidal particles for the Bi-Sb, Bi-Sn, and Bi-Sb-Sn alloy particles, while the Bi-Te particles exhibit nearly regular hexagonal particle morphology (see Fig. 3). Powder XRD

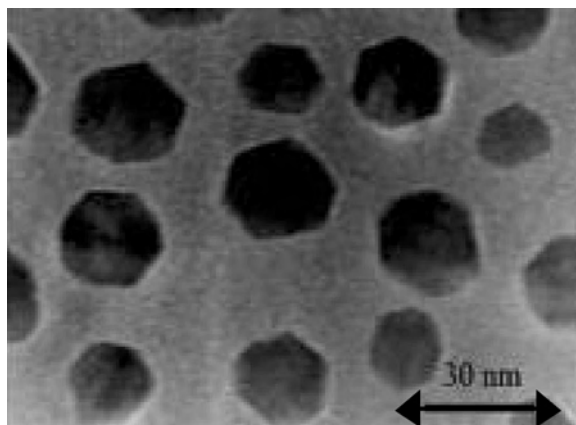


Figure 3. Transmission electron micrograph of a Bi-Te/silica xerogel nanocomposite showing Bi-Te alloy nanoparticles having nearly hexagonal shape (bar = 30 nm).

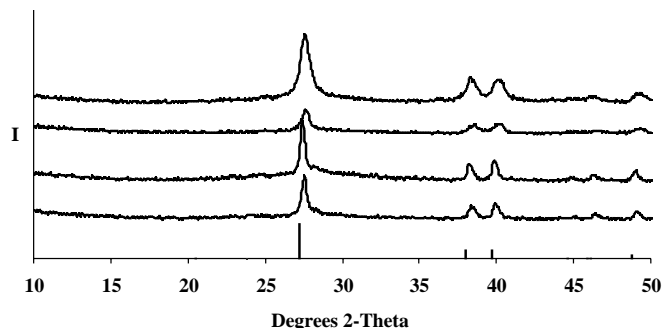


Figure 4. XRD scans ($\text{Cu K}\alpha$ radiation) of typical Bi-E/silica xerogel nanocomposites for alloying elements, $E = \text{Te, Sb, Sn, Sb/Sn}$ (top to bottom) along with the standard line pattern for Bi metal.

scans typical of these n-Bi-E alloy/ SiO_2 xerogel nanocomposites are shown in Figure 4. The principal peaks of crystalline Bi are observed with only slight displacement in the expected two-theta values due to the presence of the alloying metal, E. Peak broadening provides an independent measure of nanoparticle size. Energy dispersive spectra of these same four nanocomposite materials are shown in Figure 5. X-ray emission from Bi, the alloying element E, and the matrix metal, Si, are all observed. The relative intensities of these emission peaks can be correlated to the relative atomic fraction of each metal present within the sample.

3. ONE-DIMENSIONAL BISMUTH NANOSTRUCTURED MATERIALS

One-dimensional Bi nanostructured materials have been an area of intense research interest during the past 5 years due to the enhanced thermoelectric figure of merit expected of elemental Bi or its alloys as nanowire structures. As noted by several researchers, the very low electron effective mass and the semimetallic nature of Bi make it an ideal candidate for the study of quantum confinement effects in nanostructured “1D” structures. Although the physics and theory leading to these predictions is beyond the scope of this review, the findings relevant to the synthesis of 1D Bi materials will be summarized here.

Sun et al. [16] developed a theoretical model of the electronic band structure of Bi showing relationships between the band structure and the thermoelectric properties expected of Bi nanowires. Calculations reveal that Bi quantum wires

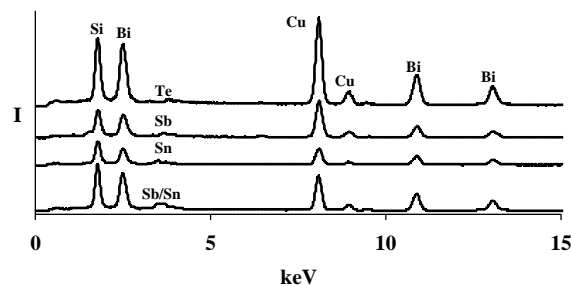


Figure 5. Energy dispersive/(EDS) spectra of typical Bi-E/silica xerogel nanocomposites for alloying elements, $E = \text{Te, Sb, Sn, Sb/Sn}$ (top to bottom); Cu emission from the sample holder is also evident.

grown along the trigonal axis of the rhombohedral unit cell of Bi would have a greatly enhanced thermoelectric figure of merit. Since that time, a significant amount of theoretical work has led to better predictions of the optimum nanowire diameter and appropriate doping conditions necessary to achieve enhancement of the thermoelectric figure of merit of 1D Bi structures.

Semimetallic Bi possesses an equal number of electrons and holes with electrons localized at the L points of the Brillouin zone and holes localized at a T point. Lin et al. [17] report that a semimetal to semiconductor transition should occur at a critical nanowire diameter between 39–55 nm. The one-dimensional thermoelectric figure of merit ($Z_{1D}T$) is predicted to be substantially increased for nanowires having diameters less than 10 nm when the Bi is properly doped. Suppression or removal of T points in Bi nanowires, such as by doping with antimony, can further enhance $Z_{1D}T$. Discussions of the thermoelectric figure of merit [18, 19], thermoelectric and electronic transport properties [20–24], conductance [25], and magnetoresistance [26, 27] of Bi or Bi alloy nanowire arrays are available.

3.1. Elemental Bismuth Nanowires

The most prevalent method for the production of Bi nanowires and arrays of nanowires is based on template-assisted or template-directed nanowire growth processes. Anodized alumina discs have been used extensively for this purpose. Alumina anodiscs contain a hexagonal array of open, parallel nanochannels with pore diameters ranging from 9–30 nm. Zhang et al. [28, 29] prepared Bi quantum-wire arrays using a vacuum-melting and pressure-injection process. Molten Bi is injected at high pressures (40 GPa of Ar gas) into evacuated porous alumina anodiscs forming an array of Bi nanowires of diameters ranging from 4.3–56 nm. Control of the Bi nanowire diameter is achieved by variation of the pore size of the open channels present within the alumina anodisc. Using the same template, Heremans and Thrush [19] prepared Bi nanowire arrays by vacuum deposition of Bi vapor into the pores of alumina anodiscs. Bi nanowire arrays having wire diameters ranging from 7–200 nm can be prepared using this technique. This method has also been extended to the preparation of Sb nanowire arrays [30].

Electrodeposition of Bi in the channels of either anodized alumina discs or polycarbonate membrane templates can produce Bi nanowire arrays. Using alumina anodiscs having highly ordered open channels as a template matrix, Wang et al. [31, 32] electrodeposited Bi in these open channels as single-crystalline nanowires having diameters of 20 nm, 50 nm, or 70 nm and high aspect ratios when using $\text{Bi}(\text{NO}_3)_3 \cdot 7\text{H}_2\text{O}$ as the source of Bi. Similarly, Yin et al. [33] prepared highly oriented hexagonal arrays of Bi nanowires of 50 nm diameter with lengths of up to 50 μm by electrodeposition of Bi in the open channels of alumina anodiscs using BiCl_3 dissolved in DMSO as an electrolyte solution.

Peng et al. [34] isolated unsupported Bi nanowires by first electrodepositing Bi in the pores of anodized alumina discs using an electrolyte solution containing BiCl_3 . Subsequent dissolution of the alumina matrix using 0.1 M $\text{NaOH}_{(\text{aq})}$ gives matrix-free Bi nanowires having diameters

ranging from 3–100 nm. Using a similar strategy, Piraux et al. [35] prepared arrays of Bi nanowires by electrodeposition of Bi from a Bi^{3+} electrolyte solution in the pores of a polycarbonate membrane containing parallel open channels formed by nuclear-track etching. Dissolution of the polycarbonate membrane by an organic solvent yields matrix-free Bi nanowires having diameters ranging from 95–400 nm.

Bi nanowires have also been obtained by capillary filling of single-walled carbon nanotubes in a template-directed synthesis. Kiang et al. [36, 37] first reported the preparation of single-walled carbon nanotubes synthesized from a graphite rod containing 2% cobalt catalyst and 5% bismuth as a cocatalyst. Approximately 1% of the large-diameter carbon nanotubes produced are filled with Bi metal. Heating a mixture of large-diameter single-walled carbon nanotubes with Bi nanoparticles to 400 °C for 30 min leads to capillary filling of the carbon nanotubes and increases the fraction of Bi-filled carbon nanotubes to approximately 10%. The Bi nanowires produced by this procedure have diameters of approximately 1 nm with lengths on the order of tens of nanometers. Demetallated single-walled carbon nanotube soot absorbs acidified 1 M $\text{Bi}(\text{NO}_3)_3$ solution, and reduction of these solution-filled carbon nanotubes under H_2 gas at 350 °C for 3 h gives carbon nanotubes filled with Bi. About 30% of the nanotubes contain Bi nanowires having lengths ranging from a few nanometers to a few hundred nanometers.

Hsu et al. [38] observed formation of Bi nanowires inside carbon nanotubes during the electrolysis of molten LiCl using graphite electrodes. Addition of small amounts (<1% by mass) of Bi powder to the molten LiCl electrolyte results in Bi incorporation inside the nanotubes.

Choi et al. [39] used low-energy electron beam lithography with silver nanocrystal shadowmasks for the preparation of Bi nanowires. A 40-nm thick Bi single-crystal film grown on a CdTe (111) substrate is generated by molecular beam epitaxy. The Bi/CdTe composite is then coated with 1% PMMA (polymethylmethacrylate). Silver nanowires of high aspect ratio are transferred as a Langmuir–Schaeffer film onto the Bi/CdTe substrate. This decorated substrate is exposed to a 50 $\mu\text{C}/\text{cm}^2$ dose of electrons and is subsequently developed with a 1:3 mixture of methyl isobutyl ketone and isopropanol. Following development, reactive chlorine etching produces Bi nanowire structures on the surface of the substrate that are 50 nm wide and have a height of 40 nm.

Li et al. [40] prepared Bi nanotubes using a low-temperature, controlled hydrothermal reduction method. Bismuth(III) nitrate reacts with aqueous hydrazine solution in distilled water to give a black precipitate. Following adjustment of the pH to ~12 and heating the reaction mixture to 120 °C for 12 h in an autoclave, Bi nanotubes are isolated. The Bi nanotubes are composed of α -Bi sheets and have uniform diameters of approximately 5 nm and lengths of 0.5–5.0 μm .

3.2. Bismuth Alloy and Intermetallic Nanowires

Yu et al. [41] obtained Bi_2S_3 nanowires using a solvothermal decomposition process. Ethanol solutions of BiCl_3 and thiourea (H_2NCSNH_2) react in an autoclave at 140 °C for

12 h to precipitate dark brown Bi_2S_3 nanowires. These nanowires have average diameters of 130–200 nm and lengths of 3.5 μm . Using a similar method, Su et al. [42] prepared Bi_2E_3 (E = Se, S) nanowires by solvothermal reaction of BiCl_3 , Se powder, and triphenyl phosphine sulfide in ethylenediamine. Heating this reaction solution at 120 °C for 20 h results in the formation of Bi intermetallic nanowires having diameters of 20 nm and lengths of 1.5 μm .

Nanowires of Bi_2Te_3 have also been obtained by electrodeposition within the pores of anodized alumina discs. Prieto et al. [43] formed high-density nanowire arrays of Bi_2Te_3 by electrodeposition of Bi_2Te_3 within the channels of alumina anodiscs using an electrolyte solution prepared by dissolving Bi^0 and Te^0 in 1 M HNO_3 . Etching away the alumina matrix using a solution of H_3PO_4 and CrO_3 affords matrix-free Bi_2Te_3 nanowires having average diameters of 40 nm. Sapp et al. [44] electrodeposited Bi_2Te_3 nanowires in the pores of anodized alumina from an electrolyte solution prepared by dissolving $\text{Bi}(\text{NO}_3)_3 \cdot 5\text{H}_2\text{O}$ and Te powder in 1 M HNO_3 . Bi_2Te_3 nanowires having an average diameter of 280 nm are obtained.

4. TWO-DIMENSIONAL BISMUTH NANOSTRUCTURES

4.1. Nanostructures Formed by Molecular Beam Epitaxy

Epitaxial growth of Bi and Bi alloy or intermetallic films is typically carried out using semi-insulating CdTe wafers as the substrate material. DiVenere et al. [45] first reported successful epitaxial growth of Bi layers on a CdTe substrate. The Bi layer thickness could be varied from 5–80 nm. Subsequent work demonstrated that epitaxial Bi films of 100 nm thickness show thermoelectric properties in good agreement with those of the bulk crystal [46]. However, when the thickness of Bi films is reduced to 40–80 nm, the thermoelectric properties are enhanced over those of bulk Bi.

Superlattice structures with alternating Bi and Sb layers grown by MBE have been reported by Takahashi and Miyagawa [47]. Epitaxial growth of a Bi/Sb superlattice containing a total of 60 layers has been achieved. Cho et al. [48] produced epitaxial Bi/Sb superlattices having individual layer thicknesses ranging from 1–10 nm with a periodicity ranging from 30–300.

Solid-solution Bi alloy superlattice structures have also been prepared by MBE. Takahashi et al. [49] produced a $\text{Bi}_{0.88}\text{Sb}_{0.12}$ thin film having a thickness of 75 nm. Yi et al. [50] prepared a bilayer structure comprised of a 7.5 nm layer of $\text{Bi}_{0.89}\text{Sb}_{0.11}$ and a 6.5 nm layer of Bi that was repeated 20 times to form a superlattice.

4.2. Nanostructures Formed by Chemical Methods and Chemical Vapor Deposition

Shen et al. [51] prepared nanoporous Bi thin films using a wet chemical deposition method. Solutions of either bismuth 2-ethylhexanoate or bismuth acetate in 2-methylpropanol containing 5% glycerol are spin-coated onto Si(100) wafers.

Subsequent reduction at 250–270 °C for 3–6 h under hydrogen gives a nanoporous Bi thin film containing porous channels 5–10 nm in width.

Chemical vapor deposition (CVD) and metal-organic chemical vapor deposition (MOCVD) have been used to prepare thin films containing Bi. Venkatasubramanian et al. [52, 53] used MOCVD methods to obtain Bi_2Te_3 and Sb_2Te_3 thin films and superlattice structures. Trimethyl bismuth, $[(\text{CH}_3)_3\text{Bi}]$, diisopropyl telluride, $[\text{((CH}_3)_2\text{CH)}_2\text{Te}]$, and tris dimethylamino antimony, $[\text{((CH}_3)_2\text{N)}_3\text{Sb}]$, are used as metal-organic precursor molecules. Deposition of Bi_2Te_3 thin films of 1–10 nm thickness on basal plane sapphire or GaAs (100) substrates occurs at 350 °C and 350 torr.

5. SUMMARY

A variety of chemical and physical synthesis methodologies have been used for the chemical preparation of Bi nanostructures. Inverse micelles, sol-gel processing, and controlled precipitation have been used to prepare Bi and Bi alloy nanoparticles or nanowires with dimensions as small as 1–2 nm or as large as 200 nm. Formation of the nano-Bi phase is typically carried out by the reduction of a Bi^{3+} source using solution or gas-phase chemical methods or electrochemical reduction. CVD, MOCVD, MBE, and high-pressure injection are useful techniques for preparing Bi and Bi alloy or intermetallic nanowires, thin films, or superlattices.

GLOSSARY

Energy dispersive spectroscopy (EDS) The spectrum of x-radiation emitted by a sample under high-energy bombardment by electrons.

Nanocomposite A solid mixture or two or more substances in which at least one component exists in a morphology having at least one dimension less than 100 nm in scale.

One-dimensional (1D) nanostructures Particle morphologies in which two dimensions are less than 100 nm in scale, such as rod-like nanoparticles.

Two-dimensional (2D) nanostructures Particle morphologies in which only one dimension is less than 100 nm in scale, such as nano-scale thin films.

Zero-dimensional (0D) nanostructures Particle morphologies in which all three dimensions are less than 100 nm in scale, such as nearly spherical nanoparticles.

ACKNOWLEDGMENT

C. M. L. gratefully acknowledges financial support provided by the National Science Foundation through grant number CTS-0210366.

REFERENCES

1. R. Goswami and K. Chattopadhyay, *Acta Mater.* 44, 2421 (1996).
2. A. Singh and A. P. Tsai, *Scr. Mater.* 44, 2005 (2001).
3. R. Czajka, K. Trzebiatowski, W. Polewska, B. Koscielska, S. Kaszczyszyn, and B. Susla, *Vacuum* 48, 213 (1997).

4. J.-D. Grunwaldt, M. D. Wildberger, T. Mallat, and A. Baiker, *J. Catal.* 177, 53 (1998).
5. J. T. Moore and C. M. Lukehart, *J. Mater. Chem.* 12, 288 (2002).
6. A. Wurl, M. Hyslop, S. A. Brown, B. D. Hall, and R. Monot, *Eur. Phys. J. D* 16, 205 (2001).
7. J. Fang, K. L. Stokes, J. Wiemann, and W. Zhou, *Mater. Lett.* 42, 113 (2000).
8. H. Yu, P. C. Gibbons, K. F. Kelton, and W. E. Buhro, *J. Am. Chem. Soc.* 123, 9198 (2001).
9. E. E. Foos, R. M. Stroud, A. D. Berry, A. W. Snow, and J. P. Armistead, *J. Am. Chem. Soc.* 122, 7114 (2000).
10. J. Fang, K. L. Stokes, J. A. Wiemann, W. L. Zhou, J. Dai, F. Chen, and C. J. O' Connor, *Mater. Sci. Eng., B* B83, 254 (2001).
11. J. Fang, K. L. Stokes, W. L. Zhou, W. Wang, and J. Lin, *Chem. Commun.* (Cambridge, U.K.) 1872 (2001).
12. R. Suarez, P. K. Nair, and P. V. Kamat, *Langmuir* 14, 3236 (1998).
13. M. I. Comor, M. D. Dramicanin, Z. Rakocevic, S. Zec, and J. M. Nedeljkovic, *J. Mater. Sci. Lett.* 17, 1401 (1998).
14. E. E. Foos, R. M. Stroud, and A. D. Berry, *Nano Lett.* 1, 693 (2001).
15. J. T. Moore and C. M. Lukehart, *J. Cluster Sci.* 14 (2003), (in press).
16. X. Sun, Z. Zhang, and M. S. Dresselhaus, *Appl. Phys. Lett.* 74, 4005 (1999).
17. Y.-M. Lin, X. Sun, and M. S. Dresselhaus, *Phys. Rev. B* 62, 4610 (2000).
18. O. Rabina, Y.-M. Lin, and M. S. Dresselhaus, *Appl. Phys. Lett.* 79, 81 (2001).
19. J. Heremans and C. M. Thrush, *Phys. Rev. B: Condens. Matter Mater. Phys.* 59, 12579 (1999).
20. K. Liu, C. L. Chien, P. C. Searson, and K. Yu-Zhang, *Appl. Phys. Lett.* 73, 2222 (1998).
21. Z. Zhang, X. Sun, M. S. Dresselhaus, J. Y. Ying, and J. P. Heremans, *Appl. Phys. Lett.* 73, 1589 (1998).
22. Z. Zhang, X. Sun, M. S. Dresselhaus, J. Y. Ying, and J. Heremans, *Phys. Rev. B* 61, 4850 (2000).
23. Y.-M. Lin, S. B. Cronin, J. Y. Ying, M. S. Dresselhaus, and J. P. Heremans, *Appl. Phys. Lett.* 76, 3944 (2000).
24. M. R. Black, M. Padi, S. B. Cronin, Y. M. Lin, O. Rabin, T. McClure, G. Dresselhaus, P. L. Hagelstein, and M. S. Dresselhaus, *Appl. Phys. Lett.* 77, 4142 (2000).
25. T. E. Huber, M. J. Graf, C. A. Foss, Jr., and P. Constant, *J. Mater. Res.* 15, 1816 (2000).
26. K. Hong, F. Y. Yang, K. Liu, D. H. Reich, P. C. Searson, C. L. Chien, F. F. Balakirev, and G. S. Boebinger, *J. Appl. Phys.* 85, 6184 (1999).
27. E. N. Bogachek, A. G. Scherbakov, and U. Landman, *Phys. Rev. B* 62, 10467 (2000).
28. Z. Zhang, D. Gekhtman, M. S. Dresselhaus, and J. Y. Ying, *Chem. Mater.* 11, 1659 (1999).
29. Z. Zhang, J. Y. Ying, and M. S. Dresselhaus, *J. Mater. Res.* 13, 1745 (1998).
30. J. Heremans, C. M. Thrush, Y.-M. Lin, S. B. Cronin, and M. S. Dresselhaus, *Phys. Rev. B* 63, 085406/1 (2001).
31. X. F. Wang, L. D. Zhang, J. Zhang, H. Z. Shi, X. S. Peng, M. J. Zheng, J. Fang, J. L. Chen, and B. J. Gao, *J. Phys. D: Appl. Phys.* 34, 418 (2001).
32. X. F. Wang, J. Zhang, H. Z. Shi, Y. W. Wang, G. W. Meng, X. S. Peng, L. D. Zhang, and J. Fang, *J. Appl. Phys.* 89, 3847 (2001).
33. A. J. Yin, J. Li, W. Jian, A. J. Bennett, and J. M. Xu, *Appl. Phys. Lett.* 79, 1039 (2001).
34. Y. Peng, D.-H. Qin, R.-J. Zhou, and H.-L. Li, *Mater. Sci. Eng.* B77, 246 (2000).
35. L. Piraux, S. Dubois, J. L. Duvail, A. Radulescu, S. Demoustier-Champagne, E. Ferain, and R. Legras, *J. Mater. Res.* 14, 3042 (1999).
36. C.-H. Kiang, J.-S. Choi, T. T. Tran, and A. D. Bacher, *J. Phys. Chem. B* 103, 7449 (1999).
37. C.-H. Kiang, *Carbon* 38, 1699 (2000).
38. W. K. Hsu, J. Li, H. Terrones, M. Terrones, N. Grobert, Y. Q. Zhu, S. Trasobares, J. P. Hare, C. J. Pickett, H. W. Kroto, and D. R. M. Walton, *Chem. Phys. Lett.* 301, 159 (1999).
39. S. H. Choi, K. L. Wang, M. S. Leung, G. W. Stupian, N. Presser, B. A. Morgan, R. E. Robertson, M. Abraham, E. E. King, M. B. Tueling, S. W. Chung, J. R. Heath, S. L. Cho, and J. B. Ketterson, *J. Vac. Sci. Technol., A* 18, 1326 (2000).
40. Y. Li, J. Wang, Z. Deng, Y. Wu, X. Sun, D. Yu, and P. Yang, *J. Am. Chem. Soc.* 123, 9904 (2001).
41. S.-H. Yu, L. Shu, J. Yang, Z.-H. Han, Y.-T. Qian, and Y.-H. Zhang, *J. Mater. Res.* 14, 4157 (1999).
42. H. Su, Y. Xie, P. Gao, H. Lu, Y. Xiong, and Y. Qian, *Chem. Lett.* 790 (2000).
43. A. L. Prieto, M. S. Sander, M. S. Martin-Gonzalez, R. Gronsky, T. Sands, and A. M. Stacy, *J. Am. Chem. Soc.* 123, 7160 (2001).
44. S. A. Sapp, B. B. Lakshmi, and C. R. Martin, *Adv. Mater.* 11, 402 (1999).
45. A. DiVenere, X. J. Yi, C. L. Hou, H. C. Wang, J. Chen, J. B. Ketterson, G. K. Wong, J. R. Meyer, C. A. Hoffman, and F. J. Bartoli, *J. Vac. Sci. Technol., B* 12, 1136 (1994).
46. S. Cho, A. DiVenere, G. K. Wong, J. B. Ketterson, J. R. Meyer, and C. A. Hoffman, *Solid State Commun.* 102, 673 (1997).
47. J. Takahashi and T. Miyagawa, *Jpn. J. Appl. Phys.* 31, L1114 (1992).
48. S. Cho, Y. Kim, A. DiVenere, G. K. Wong, J. B. Ketterson, and J.-I. Hong, *J. Vac. Sci. Technol., A* 17, 2987 (1999).
49. J. Takahashi, T. Miyagawa, M. Araki, and T. Obata, *Jpn. J. Appl. Phys.* 31, L1110 (1992).
50. X. J. Yi, H. C. Wang, A. DiVenere, C. L. Hou, J. Chen, J. B. Ketterson, and G. K. Wong, *Appl. Phys. Lett.* 64, 1283 (1994).
51. W. N. Shen, B. Dunn, C. D. Moore, M. S. Goorsky, T. Radetic, and R. Gronsky, *J. Mater. Chem.* 10, 657 (2000).
52. R. Venkatasubramanian, T. Colpitts, E. Watko, M. Lamvik, and N. El-Masry, *J. Cryst. Growth* 170, 817 (1997).
53. R. Venkatasubramanian, T. Colpitts, B. O' Quinn, S. Liu, N. El-Masry, and M. Lamvik, *Appl. Phys. Lett.* 75, 1104 (1999).

Boron-Carbon Nitride Nanohybrids

Yoke Khin Yap

Michigan Technological University, Houghton, Michigan, USA

CONTENTS

1. Introduction
 2. Precursors of $B_xC_yN_z$ Hybrids
 3. $B_xC_yN_z$ Hybrids
 4. Prospect of $B_xC_yN_z$ Hybrids
- Glossary
References

1. INTRODUCTION

Tremendous research interest on nanotubular structures was stimulated after the evidence of carbon nanotubes (CNTs) was found in 1991 [1–6]. Structural similarity between pure carbon and boron nitride (BN) solids has motivated the investigations on the boron nitride nanotubes (BNNTs) [7–9], and the hybrid of CNTs and BNNTs: boron-carbon nitride ($B_xC_yN_z$) nanotubes [10–12]. CNTs are either semiconductor or metallic, while BNNTs are predicted to have wide energy bandgap of 5.5 eV [8]. The $B_xC_yN_z$ nanotubes/nanohybrids are expected to have physical properties between those of CNTs and BNNTs. Thus, $B_xC_yN_z$ nanohybrids are prospective semiconducting nanomaterials [10].

In fact, research interest on $B_xC_yN_z$ hybrids was initiated more than three decades ago. The first claim of hybridized $B_xC_yN_z$ compound was a solid solution of graphite and hexagonal phase BN (h-BN) [13]. The possible atomic arrangement for hexagonal phase hybrid (h- BC_2N) was then reported [14]. This hybrid is expected to be a new semiconductor. Another motivation on $B_xC_yN_z$ materials is to combine properties of diamond and cubic phase BN (c-BN) [15–20]. Such a cubic phase hybrid (c- BC_2N) is expected to be harder than c-BN and chemically more stable than diamond. Many experiments have been conducted on preparing these $B_xC_yN_z$ compounds. However, a common difficulty in the synthesis of BCN hybrids is phase separation [21, 22]. Atoms inside the $B_xC_yN_z$ compounds have the tendency to segregate as pure carbon and BN materials. That is, carbon atoms tend to bond among each other, while B and N atoms prefer to form pure BN grains. Competition between phases like pure carbon, BN, boron carbides, and carbon

nitrides is possible during the formation of $B_xC_yN_z$ hybrids and nanotubes.

Recent results indicate that $B_xC_yN_z$ hybrids can be grown as fibrous nanostructures [23, 24]. The increase of film thickness or physical dimensions of these nanostructures leads to phase separation. In fact, the first report on hybridized $B_xC_yN_z$ compound had grain dimension below 20 nm [13]. These results suggest that h- BC_2N and c- BC_2N should be considered as nanostructures or nanocrystals instead of macroscopic single crystals. The research interest on BCN hybrids appears to move towards $B_xC_yN_z$ nanohybrids including the $B_xC_yN_z$ nanotubes/nanofibers, h- $B_xC_yN_z$, and cubic (c- $B_xC_yN_z$) nanocrystals. All these aspects will be reviewed in this chapter.

2. PRECURSORS OF $B_xC_yN_z$ HYBRIDS

The research on $B_xC_yN_z$ hybrids was initiated for combining structural and physical properties of pure carbon and BN materials. Thus the properties of $B_xC_yN_z$ hybrids are related with the bonding configurations of their precursors. In order to understand $B_xC_yN_z$ hybrids, it is important to review the bonding configurations of phases in pure carbon and BN materials. The bond lengths of various carbon and BN bonds are summarized in Tables 1 and 2.

2.1. Phases of Pure Carbon Solids

Carbon is the sixth atom in the periodic table and has six electrons, which occupy $1s^2$, $2s^2$, and $2p^2$ atomic orbitals. The valence electrons in $2s$, $2p_x$, $2p_y$, and $2p_z$ orbitals are involved in various bonding configurations in carbon solids. Since the energy differences between these orbitals are small compared to the binding energy, the electronic wave functions for these four electrons can readily mix with each other to maximize the binding energy of C atom with its neighboring atoms. The mixing of a single $2s$ electron with one to three $2p$ electrons is called sp^n hybridization ($n = 1, 2, 3$). Thus carbon can be bonded in sp , sp^2 , and sp^3 hybridizations. That is, each C can be bonded to one to four carbon atoms in various carbon polymorphs [4, 5].

In diamond, each carbon is sp^3 -hybridized to form four covalent sigma (σ) bonds in a tetrahedral structure using all

Table 1. Bond lengths for various carbon and BN bonds [4, 5, 27, 35–39].

Bonds	Bond lengths/nm		
	sp^3	sp^2	π bond between two hexagonal planes
C-to-C	0.142	0.154	0.355
B-to-N	0.145	0.157	0.334

the $2s$, $2p_x$, $2p_y$, and $2p_z$ orbitals. These sp^3 bonds can be arranged in either cubic or hexagonal (würtzite) polymorphs [25, 26]. The cubic diamond is stable in ambient conditions and will be referred hereafter. The bond length for sp^3 C—C bonds in diamond is 0.154 nm [27]. Likewise, all carbon atoms in graphite are sp^2 -hybridized for three covalent σ bonds ($2s$, $2p_x$, and $2p_y$) in a planar trigonal structure and thus form a hexagonal network with sp^2 C=C bond length of 0.142 nm. The $2p_z$ orbital of each of the carbon atoms will form the π -bonding between hexagonal networks/sheets that are stacked in an ABAB ... sequence, with a separation of 0.355 nm between sheets. The sp -bonded carbon was known as “carbyne” for many years and remained a subject of research [28–31]. Little is known about the properties of carbynes [4]. Likewise, graphite is soft, semi-metallic, and has a zero energy bandgap while diamond is superhard with a bandgap of 5.4 eV. Beside these carbon materials, fullerenes [32–34] and CNTs [1–6] are both sp^2 -hybridized carbon solids realized in the past two decades. These two materials have different bond angles and molecular packing as compared to graphite and thus have very distinguishable physical properties. Articles for further reading on diamond [35, 36] and graphite [4, 37] are available.

2.2. Phases of Pure BN Solids

BN solids are structurally similar to those in the pure carbon system. We have h-BN, c-BN, and BNNTs polymorphs, which are analogous to the graphite, diamond, and CNTs, respectively. Despite the structural similarity, these carbon and BN materials have very different physical properties. For instance, h-BN has a layered structure that is similar to graphite with the exception that hexagonal rings of the basal planes in h-BN are positioned directly above each other and rotated by 180° between alternative layers [38–40]. The h-BN sheets are stacked in an eclipsed ABAB ... sequence with B eclipsed by N and vice versa. As a result, graphite is a semimetal with a slight energy overlap (0.04 eV) [41, 42] of the valence and conduction band, while h-BN is an insulator with a bandgap >3.8 eV [43]. Experimental result indicates that h-BN thin films and single crystals could have a bandgap of 5.8 eV [44] and 5.6 eV [45], respectively. The

Table 2. Bond lengths of various types of bonds in h-BC₂N hybrids [10, 14, 57].^a

Bonds	Bond lengths/nm
C-to-C	0.142
B-to-C	0.155
B-to-N	0.145
C-to-N	0.132

^aThese are also applicable for BC₂N nanotubes.

sp^2 B=N bond length is 0.145 nm, while the distance between hexagonal BN planes is 0.334 nm [40].

Like the sp^3 bonded carbon solids, there are cubic and würtzite BN phases that have tetrahedral bond configuration [40, 46]. Again, the cubic phase (c-BN) is stable in ambient condition and will be considered hereafter. The sp^3 B-N bond length is 0.157 nm, slightly longer than that of diamond [17], and the density of c-BN is thus 3.48 g/cm³, lower than that of diamond (3.52 g/cm³). This cubic phase has a Vickers hardness of about 4500 kg/mm², second in hardness only to diamond (9000 kg/mm²) [17, 47, 48]. The fact that c-BN does not react with ferrous metals [47] (as does diamond [49]) makes c-BN a better material for hard coatings. Recent reviews on c-BN thin films are available in various articles [46, 50–52].

The BNNTs are sp^2 -bonded like CNTs. BNNTs are expected to have a bandgap of 5.5 eV, lower than that of h-BN [8]. This bandgap is nearly independent of the tube diameter, number of walls, and chirality (the way the h-BN sheet rolls up as a seamless hollow cylinder). This means the electronic properties of BNNTs are stable and uniform. This is the advantage of BNNTs compared to CNTs. The bandgap of CNTs could exist only for single-wall nanotubes, which depend on the chirality and tube diameter. Further reading on BNNTs are available elsewhere [5, 6].

3. B_xC_yN_z HYBRIDS

The attempts to synthesize B_xC_yN_z hybrids are motivated by the possibility to merge the physical properties of their pure carbon and BN precursors. To date, there are three themes on preparing BCN hybrids: (1) hybrid of graphite and h-BN; (2) hybrid of diamond and c-BN; and (3) hybrid of CNTs and BNNTs. Hereafter, discussion will be separated into these subsections on their bond configuration, properties, and synthesis approaches.

3.1. Hexagonal Phase Hybrid: h-B_xC_yN_z

There seems to be little doubt that h-B_xC_yN_z hybrid has been made by chemical vapor deposition (CVD) processes [13, 17, 53]. However, there is evidence that co-deposition of carbon and BN materials leads to a two-phase compound composed of pure BN and boron doped graphitic domains [21]. Such a condition is usually called phase separation. As quoted in [21], deposition of BCN compounds by CVD using the mixtures of BCl₃, NH₃, and C₂H₂ at 1700 °C also resulted in phase separation [54, 55].

Formation of crystalline h-B_xC_yN_z hybrid seems to occur at a very narrow experimental window [13]. Polycrystalline h-B_xC_yN_z films were deposited by CVD from mixtures of BCl₃, CCl₄, nitrogen, and hydrogen at 1900 °C. Below this temperature, crystalline B₄C films were formed, and above 1900 °C, the h-B_xC_yN_z films were contaminated by Si from the quartz tube. The composition of the crystalline hybrid was (BN)_xC_{1-x}, $0 < x < 1$, and its lattice constant a changed from 0.246 nm at $x = 0$ (graphite) to 0.250 nm at $x = 1$ (BN). It is noteworthy that the grain dimension along the a -axis of the hybrid was 20 nm and that along the c -axis was 8 nm. This means that the crystalline h-B_xC_yN_z hybrid was nanostructure: B_xC_yN_z nanohybrids.

In fact, there is another evidence that crystalline $h\text{-B}_x\text{C}_y\text{N}_z$ hybrid has the tendency to form nanostructures [56]. In that report, $\text{B}_x\text{C}_y\text{N}_z$ compounds were prepared from the interaction of BCl_3 , acetylene (carbon black), and ammonia at 400–700 °C. The compositions of the products ranged from $\text{B}_{0.485}\text{C}_{0.03}\text{N}_{0.485}$ to $\text{B}_{0.35}\text{C}_{0.3}\text{N}_{0.35}$ when prepared at 400 °C and 700 °C, respectively. The $\text{B}_{0.35}\text{C}_{0.3}\text{N}_{0.35}$ compounds were crystallized in the hexagonal phase with lattice constants $a = 0.249$ nm and $c = 0.335$ nm. According to high-resolution transmission electron micrographs, these $h\text{-B}_x\text{C}_y\text{N}_z$ hybrids had grain diameter of 10 nm. These hybrids had a room temperature conductivity = $6(1) \times 10^{-4}$ S cm^{-1} and showed a linear relation to the inverse of the absolute temperature. These results implied that $h\text{-B}_x\text{C}_y\text{N}_z$ hybrids are semiconducting with a thermal bandgap of 0.2 eV [56].

Although many experimental results on the $h\text{-B}_x\text{C}_y\text{N}_z$ hybrids have been reported, the actual atomic configuration is not easy to determine. In general, a truly hybridized BC_2N compound must consist of all the C–C, C–N, B–C, and B–N bonds. Theoretically, three types of atomic configuration of $h\text{-BC}_2\text{N}$ hybrid were calculated [14]. Two of these configurations were found to have the lowest total energy and the highest chemical bond energy. These configurations are shown in Figure 1a and b and are predicted to be metallic and semiconducting, respectively [10]. In the first configuration (type-I sheet), each C atom has a C, B, and N nearest neighbor, while each B (N) has two C's and one N (B) as the nearest neighbors. This arrangement is likely to have zero structural stress and a chemical bond energy of 23.7 eV/molecule. In the second configuration (type-II sheet), each C atom is bonded to two other C's and either one B or one N. Every B (N) atom has two N (B) and one C nearest neighbors. This atomic arrangement has some structural stress but has a higher chemical bond energy (24.7 eV/molecule) than the type-I sheet. Thus the type-II configuration is expected to have higher stability [10]. The local-density-approximation (LDA) gap of the type-II configuration is approximately 1.6 eV, and was quoted as an *indirect* bandgap [14]. However, the type-II sheet was stated as a direct bandgap of 1.76 eV in a later literature [10]. The bond lengths chosen for these calculations are: $d_{\text{C-C}} = 0.142$ nm, $d_{\text{B-C}} = 0.155$ nm, $d_{\text{B-N}} = 0.145$ nm, and $d_{\text{C-N}} = 0.132$ nm [10, 14, 57]. All bond angles are 120°, and $120^\circ \pm 2^\circ$ for the arrangements in Figure 1a and b, respectively. Several theoretical investigations of $h\text{-BC}_2\text{N}$ hybrid were reported on the equivalent structure [58] and the vibrational properties [59, 60].

Many experimental works have been devoted to preparing $\text{B}_x\text{C}_y\text{N}_z$ thin films [21, 61–76]. There are uncertainties regarding the homogeneity of some of these compounds and the actual atomic configurations. Some of these works claimed that BC_2N films are semiconducting with an indirect bandgap of ~ 1.8 eV [77]. These BCN films were prepared by CVD method using BCl_3 and acetonitrile (CH_3CN) at 850 °C [61, 74–76]. These BC_2N films were previously reported to emit photoluminescence (PL) with a peak at 2.1 eV (~ 590 nm), and a bandgap of ~ 1.4 eV as estimated by scanning tunneling microscopy (STM) [78]. Previous results indicate that these films were p-type semiconductor [75, 76].

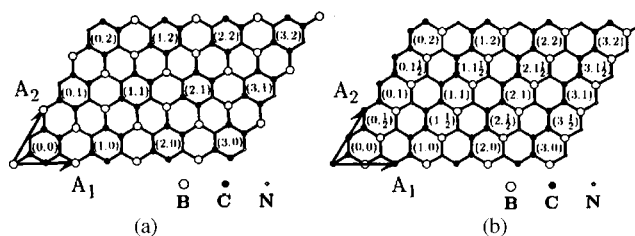


Figure 1. Atomic configuration of (a) type-I sheet and (b) type-II sheet of $h\text{-BC}_2\text{N}$ hybrids. Reprinted with permission from [10], Y. Miyamoto et al., *Phys. Rev. B*, 50, 4976 (1994). © 1994, American Physical Society.

3.2. Cubic Phase Hybrid: $c\text{-B}_x\text{C}_y\text{N}_z$

One of the motivations for preparing a cubic phase $\text{B}_x\text{C}_y\text{N}_z$ hybrid ($c\text{-B}_x\text{C}_y\text{N}_{1-x-y}$) is to realize superhard materials that are harder than $c\text{-BN}$. The hardness of $c\text{-BN}$ is just half of that of diamond. However, $c\text{-BN}$ is chemically inert to ferrous metals and more stable than diamond at high temperatures in the presence of oxygen. It is believed that $c\text{-BC}_2\text{N}$ hybrid could be harder than $c\text{-BN}$ and chemically stable like $c\text{-BN}$. The possible atomic configuration of $c\text{-BC}_2\text{N}$ is shown in Figure 2b, as compared to those of diamond (Fig. 2a) and $c\text{-BN}$ (Fig. 2c) [18]. The cubic phase hybrid is also expected to be a new wide bandgap semiconductor. Like $c\text{-BN}$ and diamond, the $c\text{-B}_x\text{C}_y\text{N}_z$ hybrids are expected to be a high-pressure phase. Thus, experiments on preparing such a cubic phase hybrid were concentrated at high-pressure, high-temperature (HPHT) procedures [79–86]. Besides, reactive vapor phase deposition employed for preparing $c\text{-BN}$ films [22], and ball milling [87, 88], were also attempted to prepare the $c\text{-B}_x\text{C}_y\text{N}_z$ hybrids. Unfortunately, results reported by different authors differ considerably. Some reported on achieving solid solution of $c\text{-B}_x\text{C}_y\text{N}_z$ hybrids, but other reports describe phase separation into other phases. A promising synthesis route for preparing such a cubic phase has not been identified.

Badzian showed that $c\text{-B}_x\text{C}_y\text{N}_z$ hybrids can be obtained by using HPHT technique at static pressure of 14 GPa and temperature of 3000 °C [79]. Polycrystals of $h\text{-B}_x\text{C}_y\text{N}_{1-x-y}$ produced by CVD were used as the starting materials [13], without using any catalyst as required to form diamond and $c\text{-BN}$. The composition of these starting materials was $(\text{BN})_{0.26}\text{C}_{0.74}$. The $c\text{-}(\text{BN})_{0.26}\text{C}_{0.74}$ hybrids had lattice constant of 0.3582 ± 0.0002 nm, in between that of diamond

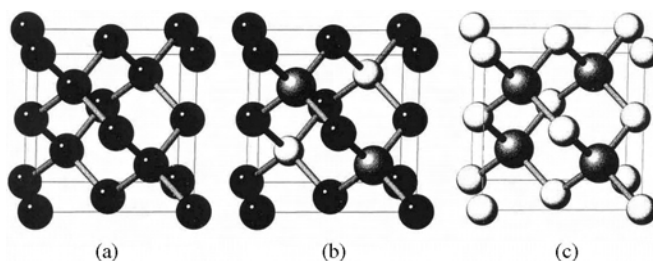


Figure 2. Graphical representations of several cubic phase materials including (a) diamond, (b) $c\text{-BC}_2\text{N}$, and (c) $c\text{-BN}$ structures with the black, white, and gray spheres as C, B, and N atoms, respectively. Reprinted with permission from [18], D. M. Teter, *MRS Bull.* 23, 22 (1998). © 1998, Materials Research Society.

(0.3570 ± 0.0001 nm) and c-BN (0.3615 ± 0.0001 nm). Electron microscopes showed that these hybrids were polycrystals, with a dimension of several micrometers. However, according to the data of transmission electron microscopy (TEM), the grain size of c-(BN)_{0.26}C_{0.74} crystals is on the order of nanometers. A similar experiment was also carried out using a laser-heated diamond cell [86]. Again, c-B_xC_yN_z hybrids were obtained at static pressures >30 GPa and temperatures >1500 K. Starting materials were polycrystals of h-B_{x0.35}C_{0.3}N_{0.35} and h-B_{x0.2}C_{0.6}N_{0.2} [56]. The lattice constants for the c-B_{x0.35}C_{0.3}N_{0.35} and c-B_{x0.2}C_{0.6}N_{0.2} obtained were 0.3613 ± 0.0003 nm and 0.3596 ± 0.0003 nm, respectively, as estimated using the lattice constants of diamond (0.3567 ± 0.0001 nm) and c-BN (0.3617 ± 0.0001 nm). A reststrahlen band ranging from 1000 to 1120 cm⁻¹ and a Raman longitudinal optic mode at 1323 (±2) cm⁻¹ were detected from these samples. The bulk modulus of c-B_{x0.33}C_{0.33}N_{0.33} was determined as 355 (±19) GPa, lower than those of diamond (442 GPa) and c-BN (369 GPa). Theoretical effort was attempted to simulate the bulk modulus of c-B_xC_yN_z [89]. On the other hand, direct transformation of h-B_xC_yN_z to c-B_xC_yN_z was also demonstrated using a shock-wave compression technique at 30–40 GPa [80–82]. Possible physical properties of c-B_xC_yN_z are summarized in Table 3.

Direct transformation of h-B_xC_yN_z to c-B_xC_yN_z hybrids at HPHT conditions appeared to be promising. However, these crystals are generally poor in crystallinity and their diffraction patterns are substantially difficult to identify a genuine BCN hybrid [83]. A catalytic HPHT technique was attempted at a pressure of 5.5 GPa and temperatures of 1400–1600 °C using Co metals as the catalyst [83]. Such an attempt failed to produce c-B_xC_yN_z hybrids from h-B_xC_yN_z. A mixed crystal of diamond and c-BN was obtained with some graphite and h-BN. Such kind of phase separation was also observed in a later attempt using the direct transformation technique without catalyst at 7.7 GPa and 2000–2400 °C [84, 85]. Again, h-B_xC_yN_z was used as the starting material and subjected to static pressure of 7.7 GPa for 15–60 minutes. The *sp*² to *sp*³ transformation started at temperatures above 2150 °C and completed at 2400 °C. The products consisted of three components, c-BN, diamond with minor B and N, and c-B_xC_yN_z. With the increase of temperature, the B and N impurities inside the diamond were reduced, and the c-B_xC_yN_z was decomposed into c-BN and pure diamond. These results suggest a phase separation of c-B_xC_yN_z to c-BN and diamond. The cubic phase crystals (c-BN, diamond, and c-B_xC_yN_z) obtained at 2300 °C were 20–30 nm in diameter. Again, c-B_xC_yN_z hybrids obtained so far were nanocrystals.

Table 3. Physical properties of c-B_xC_yN_z hybrids [79, 86].

Properties	Cubic phase materials		
	Diamond	c-B _x C _y N _z hybrids	c-BN
Lattice constant (nm)	~0.3570	0.3570–0.3615	~0.3615
IR absorption band (cm ⁻¹)	N/A	1000–1120	1367–1390
Raman vibrational mode (cm ⁻¹)	~1333	~1323	~1304
Bulk modulus (GPa)	~442	~355	~369

Attempts to prepare c-B_xC_yN_z hybrids by using other techniques were reported. Annealing of amorphous BCN compounds was reported to form c-B_xC_yN_z nanocrystals [87]. The starting materials were prepared by ball-milling of graphite and h-BN powders with a mole ratio of 1:1. The mixture-to-ball-weight ratio was 1:20. After a milling duration of 120 h, all h-BN and graphite crystals converted into an amorphous BC₂N compound. Subsequent annealing of this compound in atmosphere at temperatures of 800–900 K results in the formation of B₂O₃ and c-B_xC_yN_z crystals. The hybrids were notated as c-(BN)_{0.35}C_{0.65} with grain dimension of 10–50 nm. The lattice constant of this cubic phase was determined as 0.3587 nm, in between those of diamond and c-BN. However, these results could not be repeated in a later experiment [88]. In this case, ball-milling results in an amorphous BCN phase (a-BCN) in a nanometer scale. Such an a-BCN phase is a mechanical mixture rather than a chemical mixture. This a-BCN phase undergoes a phase separation after annealing at ambient pressure. Phase separation also occurred after annealing at 7.7 GPa and 2300 °C. The resultant phases are c-BN, amorphous carbon, and turbostratic graphite. In another report, annealing of similar a-BCN plate prepared by ball-milling was reported to produce a new structure comprising alternate arrangement of h-BN and hexagonal graphite layers [90]. However, similar result could not be repeated in a recent experiment [88].

Phase separation of BCN compounds was also detected in the attempts to prepare BCN compounds by using other techniques. By using reactive magnetron sputtering, BCN films were found to consist of c-BN, amorphous carbon, and amorphous boron grains [22]. In fact, recent calculation using *ab initio* linear-muffin-tin orbital (LMTO) in the atomic-sphere approximation (ASA) have shown that the cubic phase β-BC₂N structure energetically favors segregation into superlattices of alternate diamond and c-BN layers [91].

3.3. B_xC_yN_z Nanotubes and Nanofibers

CNTs are promising building blocks for future nanoelectronic devices. Single-wall carbon nanotubes (SWNTs) can be metallic or semiconducting depending on the tube diameter and chirality (the way the graphene sheet rolls up as a seamless hollow cylinder) [92–94]. Semiconducting SWNTs have been used as the building blocks of advanced electronic devices for single electron transport [95, 96], spin transport [97], rectification [98, 99], and switching [100]. Recent research also points to the need for nanotube-based wide bandgap semiconductors. Boron nitride nanotubes (BNNTs) are predicted to have uniform bandgap of 5.5 eV, making them an intrinsic wide bandgap semiconductor for future nanoscale electronic devices [8].

Like the motivation of preparing cubic and hexagonal B_xC_yN_z hybrids in the past three decades, there are interests to merge the properties of CNTs and BNNTs: B_xC_yN_z nanotubes with tunable energy bandgap between those of SWNTs and BNNTs. According to theoretical calculation, hybridized BC₂N nanotubes have a direct bandgap of ~1.26 eV [10]. The corresponding atomic configurations of these BC₂N nanotubes were investigated based on those of h-BC₂N hybrid [14] as shown in Figure 1b, that is, type-II

h-BC₂N sheet. This bandgap is smaller than that of type-II h-BC₂N sheet. Thus, B_xC_yN_z nanohybrids are expected to have a direct bandgap ranging from 1.26 eV (BC₂N nanotubes) to 5.5 eV (BN nanotubes), tunable by the atomic composition. Potentially, B_xC_yN_z nanotubes are applicable for high-power electronic and photonic nanodevices which are not achievable by using CNTs. Potential applications of B_xC_yN_z nanotubes include nanoscale laser and light emitting devices (LED) with tunable wavelengths that cover the whole visible range and extend to the ultraviolet.

The approach of growing B_xC_yN_z nanotubes is similar to the techniques employed for growing CNTs: substitution of carbon in CNTs by boron and nitrogen species. The growth of CNTs requires specific metal nanoparticles. These nanoparticles are commonly called catalysts and their dimensions determine the diameter of nanotubes. The well-accepted mechanism involves the diffusion of growth species into the catalyst until saturation, and then segregation as nanotubes from the catalyst [6, 101, 102].

Like the growth of CNTs, B_xC_yN_z nanotubes were grown by using arc discharge [103–106] and laser ablation [107]. These techniques involve physical evaporation of electrodes by either dc arc discharge or laser ablation. The actual temperatures involved are higher than 3000 °C within the arc and laser plasmas. In the first report, arc discharge is performed in nitrogen atmosphere between a pure graphite cathode and a graphite anode with a central hole filled with a mixture of boron and graphite powders [103]. The products are a mixture of thin graphite sheets, CNTs, boron doped CNTs, B_xC_yN_z nanotubes, and other amorphous products. According to the data of electron energy-loss spectroscopy (EELS), the composition is not uniform along the length or cross section of the tubes. Concentration profiles of B and N in some tubes resemble outer carbonated BN coating shells for the inner BN-substituted carbon tubes. This result indicates the formation of BN-rich/C-rich/BN-rich sandwich-like structures, a tendency of phase separation toward a BN/C/BN structure. Concentration profiles of B and N acquired along a BCN sheet indicate the formation of pure BN and C islands within a same graphitic shell [103, 105]. Nanoscale domains of pure carbon and pure BN networks are formed within a same tubular shell. This result coincides with the total energy calculation that a two-dimensional BC₂N sheet tends to form islands of pure BN and C [58]. In a later experiment, a BC₄N electrode is used to replace the B/C composite electrode [105]. Boron doped CNTs are the dominant product instead of the B_xC_yN_z nanotubes. The tendency of forming B_xC_yN_z nanotubes with a higher concentration of B and N is small, as compared to the yield of boron doped CNTs. Again, the detected B_xC_yN_z nanotubes are constructed of BN-rich/C-rich/BN-rich sandwich-like structures. Synthesis of B_xC_yN_z nanotubes is also attempted by arc discharge in a helium environment between a graphite cathode and a graphite anode filled with a solid BN rod at the center [104]. The elemental concentration profiles of these nanotubes were not reported.

In another report, a graphite cathode is used to arc with an HfB₂ anode in a nitrogen atmosphere [106]. In this case, nanoparticles and nanotubes with well-separated layers of

BN and C are detected. The dominant product is metallic hafnium boride nanoparticles (5 to 20 nm), encapsulated in polyhedral concentric graphitic shells with 10 to 50 layers. The outer shells of these particles are pure carbon layers and the inner shells are BN-rich or pure BN layers. Besides, pure BNNTs are detected. Two types of B_xC_yN_z nanotubes are detected: one where the inner BN layers are coated by carbon layers, and another, which is dominant with a C-rich/BN-rich/C-rich sandwich-like structure. Again the tendency of phase separation is observed. In fact, phase separation was reported on so-called BN:C nanoboxes [108]. In this case, square-like nanotubes were grown on NaCl substrates by dc magnetron sputtering. These tubes appeared like nanoboxes when observed along the tubular axis under the transmission electron microscope. These tubes are in a sandwich-like pattern of C/BN/C shell structure. All these nanofibers are structurally different from the theoretically predicted BC₂N nanotubes [10].

The BN-rich/C-rich/BN-rich sandwich-like structures are also detected from B_xC_yN_z nanotubes produced by laser ablation with a Nd:YAG laser in a nitrogen atmosphere [107]. The target is a pressed pellet made of mixed powder of BN, carbon, nickel, and cobalt with an atomic ratio of 100:100:0.6:0.6. The products from this attempt consist of micrometer-sized h-BN crystals in addition to the usual soot of laser ablation. Multiwall CNTs, nanoparticles, and amorphous B_xC_yN_z phase are found in the soot with no evidence of SWNTs. The multiwall CNTs usually have an inner diameter of 2–3 nm and an outer diameter of 4–10 nm. The B_xC_yN_z nanotubes, on the contrary, have a larger outer diameter. These B_xC_yN_z nanotubes have uneven diameters from one end to another end of a tubular structure. They consist of segments with different number of tubular shells. The radial distributions of boron and carbon atoms of these nanotubes are investigated by EELS line scan technique. Figure 3 shows the concentration of boron and carbon scanned across a B_xC_yN_z nanotube with 13 tubular shells. As shown, the peak positions of boron and carbon concentration profiles do not coincide. This nanotube is interpreted as constructed of six inner layers of pure carbon tubes and seven outer layers of BC₇N tubes. This is a carbon-rich/pure carbon/carbon-rich sandwich-like structure. Again, it is difficult to introduce higher B and N atoms into the CNT structure.

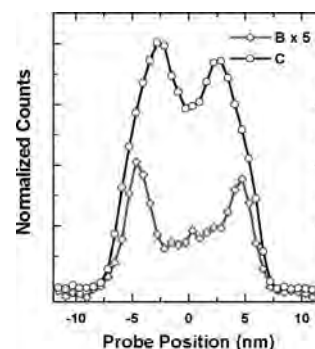


Figure 3. Elemental concentration profiles of B and C scanned across a B_xC_yN_z nanotube. The as-shown concentration of B was multiplied by a factor of 5. Reprinted with permission from [107], Y. Zhang et al., *Chem. Phys. Lett.* 279, 264 (1997). © 1997, Elsevier Science.

The schematic growth models of such heterogeneous structures are shown in Figure 4. The first step of the growth involves the nucleation of multiwall CNTs, which determines the inner diameters of the nanotubes. The second step is the partial coating of $B_xC_yN_z$ layers, which may originate from a defect, or attached particles on the CNT surface. These heterogeneous nanotubes are structurally different from the theoretically predicted BC_2N nanotubes [10].

Besides the physical evaporation techniques discussed so far, $B_xC_yN_z$ nanofibers were also prepared by catalytic pyrolysis of CH_3CN and BCl_3 over Co powder at 900–1000 °C [109], as well as BH_3 and $N(CH_3)_3$ over Co powder at 1000 °C [110]. All these $B_xC_yN_z$ nanofibers have the bamboo-like structures with the internal graphitic walls of the fibers linked across the fiber axis. Similar structure is detected from $B_xC_yN_z$ nanofibers that were grown by hot-filament CVD on CNT templates [111]. In such a CVD approach, N_2 , H_2 , and CH_4 were first introduced for the growth of the multiwall CNTs on nickel wafers. Then, an addition of B_2H_4 gas was filled into the growth chamber for the formation of $B_xC_yN_z$ nanofibers on top of the multiwall CNTs. The growth temperatures for the whole process were maintained at 600–650 °C, significantly lower than other techniques discussed so far. The bamboo-like structures of these $B_xC_yN_z$ nanofibers are shown in Figure 5 [112]. In fact, this figure indicates the structural difference between multiwall CNTs and $B_xC_yN_z$ nanofibers. Figure 5a is the typical multiwall CNT. These CNTs are in the tubular structure with a hollow core along the tube axis. When $B_xC_yN_z$ nanofibers are grown on top of these CNTs, the bamboo-like structures of the nanofibers are formed as shown in Figure 5b and c, regardless of the composition. By comparing these two images, the number of cross-links and compartments are observed to increase with the increase of B and N compositions. A magnified structure of such $B_xC_yN_z$ nanofibers is shown in Figure 6 [113]. As shown, these $B_xC_yN_z$ nanofibers contain significant structural defects. In fact, similar defects are typically observed on $B_xC_yN_z$ nanofibers obtained so far by various pyrolysis processes [109–117]. The actual mechanism involved is still unknown. Again, these $B_xC_yN_z$ nanofibers are different from the theoretically predicted BC_2N nanotubes [10]. Some of the $B_xC_yN_z$ nanofibers were demonstrated to emit photoluminescence [113–116].

There have been attempts to grow $B_xC_yN_z$ nanotubes by substitution reaction of carbon nanotubes, which were carried out at 1600 °C [118, 119]. This technique was also used to prepare BN nanotubes ($y = 0$) [120, 121]. In this technique, CNTs were reacted with B_2O_3 powder in the presence of N_2 gas. It was shown that subsequent heating of these

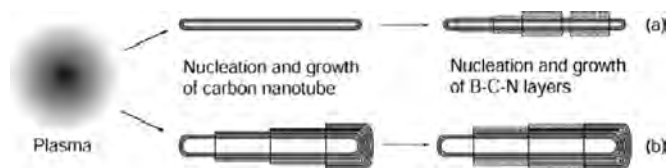


Figure 4. Schematic growth model of $B_xC_yN_z$ nanotubes. The solid and dotted lines represent carbon and $B_xC_yN_z$ layers, respectively. Reprinted with permission from [107], Y. Zhang et al., *Chem. Phys. Lett.* 279, 264 (1997). © 1997, Elsevier Science.

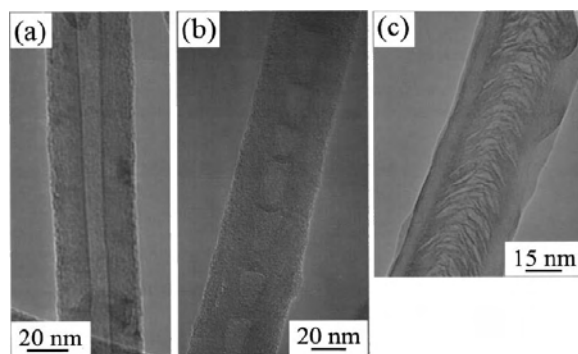


Figure 5. Images of (a) multiwall CNTs, (b) $B_{0.08}C_{0.76}N_{0.16}$ nanofibers, and (c) $B_{0.45}C_{0.29}N_{0.26}$ nanofibers. Reprinted with permission from [112], J. D. Guo et al. *Appl. Phys. Lett.* 80, 124 (2002). © 2002, American Institute of Physics.

$B_xC_yN_z$ nanotubes in air at 700 °C converts the $B_xC_yN_z$ nanotubes into BN nanotubes with an efficiency of 60%. This result is explained by the oxidation of pure carbon shell of the C/BN/C sandwich-like $B_xC_yN_z$ nanotubes. Oxidation could remove the outer pure carbon shells and leave the pure BN shells remaining as BN nanotubes. This means 60% of these $B_xC_yN_z$ nanotubes are in C/BN/C sandwich-like structures. The remaining 40% could be in the BN/C/BN sandwich-like structure where the oxidation of pure carbon shells was prevented by the protection of pure BN shells. Again, $B_xC_yN_z$ nanotubes produced by the substitution reaction are phase separated into pure carbon and pure BN shells, different from that predicted theoretically [10].

Recently, careful elemental profile analysis was carried out on some of the $B_xC_yN_z$ nanofibers that were prepared by pyrolysis [122, 123]. Line scan across the tubular axis using high-resolution EELS indicates that these nanofibers are constructed of sandwich-like pattern of C/BN/C shell structures. As discussed earlier, similar structures were detected on $B_xC_yN_z$ nanofibers that were prepared by arc discharge [103, 105, 106], laser ablation [107], BN:C nanoboxes [108], and substitutional reaction of carbon nanotubes [119]. Such a phase separation in $B_xC_yN_z$ nanofibers seems to be a universal phenomenon regardless of the synthesis technique. The elemental concentration profiles of most $B_xC_yN_z$ nanotubes/nanofibers are still not clear [110–118, 124–126].

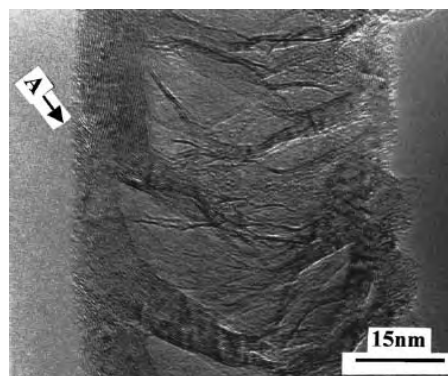


Figure 6. Magnified images of a $B_xC_yN_z$ nanofiber. Reprinted with permission from [113], X. D. Bai et al., *Appl. Phys. Lett.* 77, 67 (2000). © 2000, American Institute of Physics.

4. PROSPECT OF $B_xC_yN_z$ HYBRIDS

As a summary, the present research status of $B_xC_yN_z$ hybrids has been reviewed. There is strong evidence that both the h- $B_xC_yN_z$ and c- $B_xC_yN_z$ that have been synthesized so far are nanostructures. Together with recent interest on $B_xC_yN_z$ nanotubes, the research interest on $B_xC_yN_z$ hybrids is converting into the investigation of $B_xC_yN_z$ nanohybrids. This trend will be continued because of the motivation of nanoscale materials for novel devices in future nanotechnology and nanoscience.

However, a clear deviation between theoretical and experimental works is observed. Phase separation appeared to be the main obstacle to realize the theoretically predicted $B_xC_yN_z$ materials. It seems to be a thermodynamic tendency that pure carbon and pure BN will separate into nanoscale domains. Ability to control the bonding between B, C, and N atoms is still challenging—a true nanoscience that needs to be emphasized in the future. Recent attempt with extremely low deposition rate in a superlattice manner (BN/C/BN/C atomic layers) has indicated the possibility to hybridize $B_xC_yN_z$ materials on nickel substrates at high synthesis temperature [23, 24]. Such a manner could allow mutual bonding between B, C, and N atoms at suppressed tendency of phase separation. Novel fibrous nanostructures were revealed as shown in Figure 7a. It was shown that such hybridized nanostructures are stable only in nanoscale dimension. Phase separation occurred at thicker deposition and/or at higher carbon content. At thicker deposition, the morphology of the nanostructures changed toward continuous films as shown in Figure 7b. These results indicate that formation of macroscopic-scale $B_xC_yN_z$ materials is challenging. Alternatively, one should consider $B_xC_yN_z$ hybrids as nanostructures. Further, it is not easy to maintain the hybridized bonding at elemental composition approaching the theoretically predicted BC_2N configurations. According to a correlated characterization technique involving IR absorption, Raman spectroscopy, and X-ray photoelectron spectroscopy (XPS) [23, 24], the fibrous nanostructures are constructed of various bondings (BN, CN, BC, and CC bonds) required for the hybridized BCN ternary phase. In Figure 8a, the IR absorptions of h-BN are detected from phase-separated BCN films deposited on Si substrates. In Figure 8b, the IR absorption bands of BN, CN, and BC bonds from the hybridized $B_xC_yN_z$ nanostructures are indicated. The IR absorption spectra seem to be a convenient technique to identify hybridized $B_xC_yN_z$ materials.

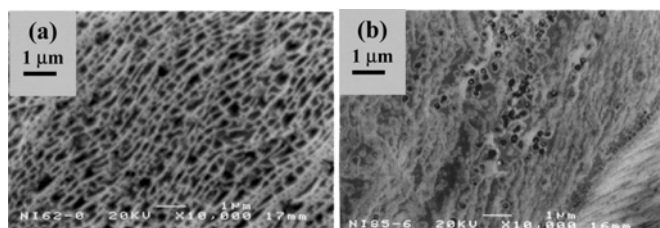


Figure 7. Surface morphologies of (a) $B_xC_yN_z$ fibrous nanostructures deposited for 6 h, and (b) $B_xC_yN_z$ films deposited for 10 h under the same deposition condition. Reprinted with permission from [24], Y. K. Yap et al., *Appl. Phys. Lett.* 80, 2559 (2002). © 2002, American Institute of Physics.

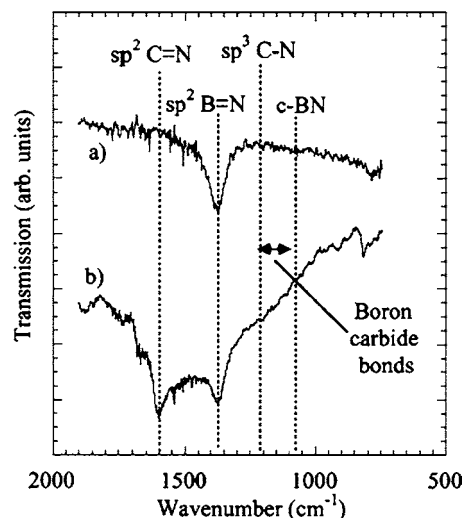


Figure 8. IR spectra for $B_xC_yN_z$ films deposited on (a) Si substrates, and (b) Ni substrates. Reprinted with permission from [23], Y. K. Yap et al., *Diamond Relat. Mater.* 10, 1137 (2001). © 2001, Elsevier Science.

IR spectra were used to identify hybridized and/or crystalline $B_xC_yN_z$ materials [127–131]. Recently, crystalline or hybridized $B_xC_yN_z$ films were also synthesized by using nickel substrates [132], pulsed laser deposition [133], laser-assisted CVD [134], and other reactive deposition techniques [135, 136].

On the other hand, $B_xC_yN_z$ nanotubes were recently reported to display semiconducting behavior with an estimated bandgap of ~ 1 eV [137]. This result seems to have overcome the phase-separation issue of the tubular nanohybrids discussed so far. The nanotubes were prepared by a technique similar to the substitutional reaction [118–121] with the addition of metal oxide promoters [138, 139]. A graphite crucible with mounted layers of B_2O_3 , Au_2O_3 , and CVD-grown CNTs was heated in a furnace under a constant N_2 flow of 3.2 l/min. The heating proceeded gradually to 1950 K, held at 1950 K for 30 minutes, before cooling down to room temperature over 2 hours. The growth mechanism is not yet well understood, although $B_xC_yN_z$ nanotubes are frequently observed on the CNT templates. Energy-filtered transmission electron microscopy (TEM) was used to determine the elemental profile of B, C, and N. Figure 9 shows the zero-loss and energy-filtered TEM images of (a) a four-walled and (b) a double-walled $B_xC_yN_z$ nanotube. The mapping of B, C, and N atoms seems to match with the tubular structure of the four-walled nanotube. This is also indicated by the (c) intensity profiles of B and C atoms across the tube. As shown, the peak positions of B and C intensity profiles are spatially coincident. These results imply that the nanotube consists of homogeneous B, C, and N atoms. Mapping of nitrogen on the double-walled tube failed due to the low signal intensity and tube damage due to the electron beam irradiation. The B and C mapping contrast intensity profiles along the double-walled tube (from top to bottom) are shown in (d). The authors suggest that high-resolution EELS alone, routinely used in most previous work [103, 105–107, 122, 123], could not conclude that

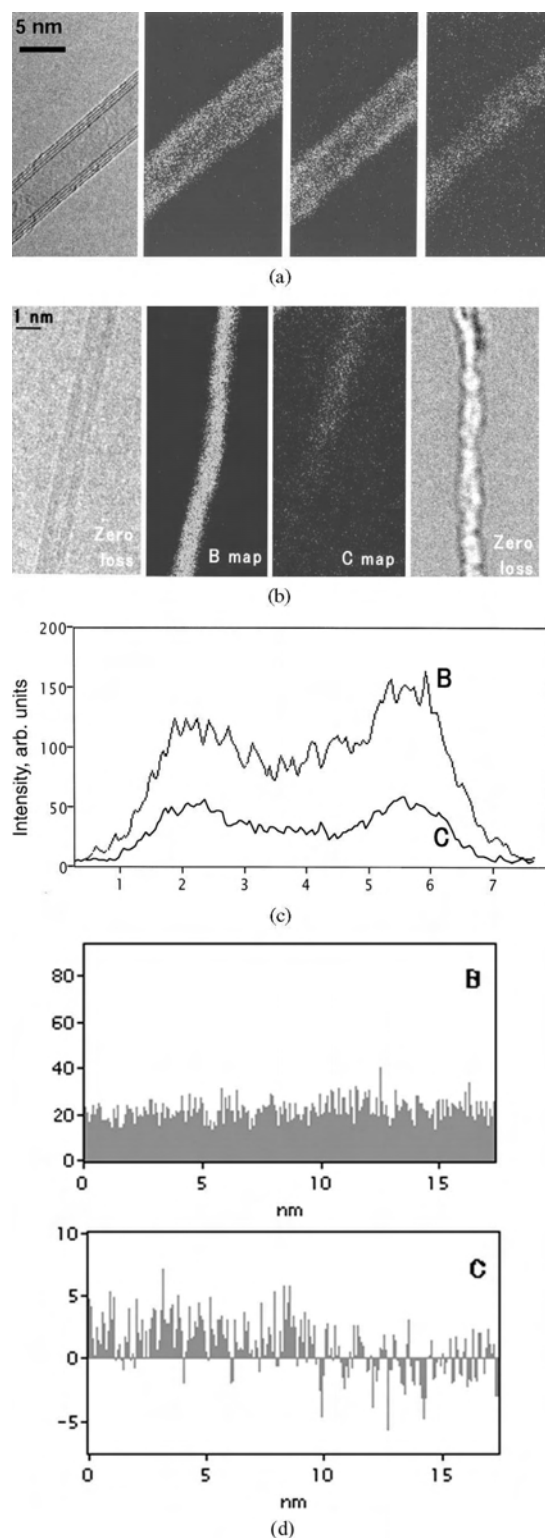


Figure 9. Zero-loss and energy-filtered TEM images of (a) a four-walled, and (b) a double-walled $B_xC_yN_z$ nanotube. Mappings of B, C, and N are recorded for the four-walled tube. Tube damage due to electron irradiation causes the N-mapping of the double-walled tube to be unattainable. The B- and C- elemental profiles scanned (c) across the four-walled, and (d) along the double-walled nanotubes are shown. Reprinted with permission from [137], D. Golberg et al., *Chem. Phys. Lett.* 359, 220 (2002). © 2002, Elsevier Science.

$B_xC_yN_z$ nanotubes are composed of phase-separated BN and C shells and/or domains.

Clearly, another challenge that needs more emphasis in the near future is techniques that enable reliable characterization of atomic bonds, and atomic configuration between the B, C, and N atoms. This is critical for the analysis of nanoscale materials. The issue of imaging and characterizing nanostructures has gained increasing attention [140, 141]. As discussed so far, high-resolution EELS and energy-filtered TEM have been used for atomic-scale characterization. Many other techniques have been examined for characterizing $B_xC_yN_z$ materials, including secondary ion mass spectroscopy (SIMS) [142], X-ray absorption near edge spectroscopy (XANES) [143–145], and X-ray emission spectra [146]. However, it is difficult to identify the actual atomic configuration of $B_xC_yN_z$ materials by a single characterization technique. Recently, interesting approaches have been demonstrated by using a combination of various techniques including IR absorption, X-ray photoelectron spectroscopy (XPS), Raman spectroscopy [23, 24, 147] or IR absorption, and XANES [145]. These approaches require careful comparison and correlation of different information acquired from various techniques. Most of these techniques involve macroscopic area analysis, which could not provide detailed structural information of $B_xC_yN_z$ nanohybrids. The addition of high-resolution EELS and/or energy-filtered TEM is required.

Various properties of $B_xC_yN_z$ materials have been examined despite the uncertainty of phase separation, and the lack of information on the actual atomic configuration of many $B_xC_yN_z$ materials. Field electron emission has been tested on some $B_xC_yN_z$ thin films [148–152] and $B_xC_yN_z$ nanofibers [113, 125, 153]. Mechanical properties like stress [154–157] and hardness [158–166] have attracted significant attention. Some of these films were found to have higher hardness and lower friction coefficient than the diamond-like carbon (DLC) films [163]. Besides, other physical properties of $B_xC_yN_z$ thin films like thermal diffusivity [167–169], magnetoresistance [170], refractive index [171], and low dielectric constant (as the insulator for ultra-large-scale integrated semiconductor devices) [172–175] have been reported. Efforts on exploring properties of $B_xC_yN_z$ materials are important. However, structural properties of the tested materials are not well established in some cases. The relation between the structural and physical properties of $B_xC_yN_z$ materials needs more emphasis in the future. In any case, physical properties are the driving force that promotes the research on $B_xC_yN_z$ materials. The efforts on growing $B_xC_yN_z$ materials have remained very active in the past few years. Various synthesis techniques have been attempted including CVD [176–184], physical vapor deposition [185–193], pyrolysis [194], and physical evaporation techniques like arc discharge [195]. This trend is expected to continue with the additional interest in $B_xC_yN_z$ nanohybrids like the nanotubes and nanofibers.

In fact, superhard c- BC_2N was recently synthesized at pressures up to 30 GPa and temperatures up to 3500 K by static and dynamic compression of graphite-like BN-C solid solution [196]. These materials are harder than c-BN single crystals and have grain sizes ranging from 10 to 30 nm

[196–198]. The detected lattice constant ($a = 0.3642$) is larger than those of both diamond and c-BN [198].

Theoretical calculation is very important to assist the experimental investigation on $B_xC_yN_z$ materials. Future calculations are required to predict novel structures, physical properties, and the growth dynamic of $B_xC_yN_z$ materials. For instance, calculations on the sandwich-like BN/C/BN or C/BN/C heterostructures should also be initiated for both the nanotubular and thin-film materials. Novel physical properties could be realized from such a configuration [199]. Theoretical prediction can always inspire new research on $B_xC_yN_z$ materials. However, the issue of deviation between theoretical prediction and experimental evidence should be emphasized in the near future. In fact, the ultimate goal for the research of $B_xC_yN_z$ materials is to prove that mankind can predict, design, and synthesize materials with desirable structural and physical properties.

GLOSSARY

$B_xC_yN_z$ Boron-carbon nitride ternary phase constructed of boron, carbon, and nitrogen. It is also represented by abbreviations like BCN, B-C-N, or B/C/N in literature.

$B_xC_yN_z$ nanotubes Boron-carbon nitride ternary phase in a tubular structure. Theoretically referred to as the h- $B_xC_yN_z$ network(s) that roll up to make seamless hollow cylinder(s) about a common axis.

c- $B_xC_yN_z$ Boron-carbon nitride ternary phase in a face-centered cubic crystal structure.

Fibrous nanostructures Nanomaterials in a fiberlike appearance.

h- $B_xC_yN_z$ Boron-carbon nitride ternary phase in a hexagonal crystal structure.

Nanofibers Nanomaterials in an elongated appearance.

Nanohybrids Nanomaterials that hybridize or combine from two or more types of substances.

Nanomaterials Materials with physical dimension below 100 nm.

Phase separation Inhomogeneous mixing of a compound with grains/sections of different phases/types of materials.

Wide bandgap semiconductors Semiconductor materials with bandgap larger than 2 eV. Bandgap is the difference in energy between the lowest point in the conduction band and the highest point of the valence band.

REFERENCES

1. S. Iijima, *Nature* 354, 56 (1991).
2. S. Iijima and T. Ichihashi, *Nature* 363, 603 (1993).
3. D. S. Bethune, C. H. Kiang, M. S. de Vries, G. Gorman, R. Savoy, J. Vazquez, and R. Beyers, *Nature* 363, 605 (1993).
4. R. Saito, G. Dresselhaus, and M. S. Dresselhaus, "Physical Properties of Carbon Nanotubes." Imperial College Press, London, 1998.
5. M. S. Dresselhaus and G. Dresselhaus, Eds., "Carbon Nanotubes: Synthesis, Structure, Properties and Applications." Springer-Verlag, Berlin, 2001.
6. P. J. F. Harris, "Carbon Nanotubes and Related Structures—New Materials for the Twenty-first Century." Cambridge Univ. Press Cambridge, 2001.
7. A. Rubio, J. L. Corkill, and M. L. Cohen, *Phys. Rev. B* 49, 5081 (1994).
8. X. Blasé, A. Rubio, S. G. Louie, and M. L. Cohen, *Europhys. Lett.* 28, 335 (1994).
9. N. G. Chopra, R. J. Luyken, K. Cherry, V. H. Crespi, M. L. Cohen, S. G. Louie, and A. Zettl, *Science* 269, 966 (1995).
10. Y. Miyamoto, A. Rubio, M. L. Cohen, and S. Louie, *Phys. Rev. B* 50, 4976 (1994).
11. O. Stephan, P. M. Ajayan, C. Colliex, Ph. Redlich, J. M. Lambert, P. Bernier, and P. Lefin, *Science* 266, 1683 (1994).
12. Z. Weng-Sieh, A. Zettl, and R. Gronsky, *Phys. Rev. B* 51, 11229 (1995).
13. A. R. Badzian, T. Niemyski, S. Appenheimer, and E. Olkušnik, in "Proceeding of the 3rd International Conference on Chemical Vapor Deposition" (F. A. Claski, Ed.), pp. 747–753. American Nuclear Society, Hinsdale, IL, 1972.
14. A. Y. Liu, R. M. Wentzcovitch, and M. L. Cohen, *Phys. Rev. B* 39, 1760 (1989).
15. W. R. L. Lambrecht and B. Segall, *Phys. Rev. B* 40, 9909 (1989).
16. W. R. L. Lambrecht and B. Segall, *Phys. Rev. B* 47, 9289 (1993).
17. R. C. DeVries, in "Diamond and Diamond-like Films and Coatings" (R. E. Clausing, L. L. Horton, J. C. Agus, and P. Koidl, Eds.), NATO ASI Series B: Physics, Vol. 266, p. 151. Kluwer, Dordrecht, 1991.
18. D. M. Teter, *MRS Bull.* 23, 22 (1998).
19. E. Knittle, R. B. Kaner, R. Jeanloz, and M. L. Cohen, *Phys. Rev. B* 51, 12149 (1995).
20. Y. Tateyama, T. Ogitsu, K. Kusakabe, S. Tsuneyuki, and S. Itoh, *Phys. Rev. B* 55, R10161, (1997).
21. A. W. Moore, S. L. Strong, G. L. Doll, M. S. Dreeselhaus, I. L. Spain, C. W. Bowers, J. P. Issi, and L. Piraux, *J. Appl. Phys.* 65, 5109 (1989).
22. S. Ulrich, H. Ehrhardt, T. Theel, J. Schwan, S. Westermeyr, M. Scheib, P. Becker, H. Oechsner, G. Dollinger, and A. Bergmaier, *Diamond Relat. Mater.* 7, 839 (1998).
23. Y. K. Yap, Y. Wada, M. Yamaoka, M. Yoshimura, Y. Mori, and T. Sasaki, *Diamond Relat. Mater.* 10, 1137 (2001).
24. Y. K. Yap, M. Yoshimura, Y. Mori, and T. Sasaki, *Appl. Phys. Lett.* 80, 2559 (2002).
25. F. P. Bundy and J. S. Kasper, *J. Chem. Phys.* 46, 3437 (1967).
26. T. Yagi, W. Utsumi, M. Yamakata, T. Kikegawa, and O. Shimomura, *Phys. Rev. B* 46, 6031 (1992).
27. T. W. Capehart, T. A. Perry, C. B. Beetz, D. N. Belton, G. B. Fisher, C. E. Beall, B. N. Yates, and J. W. Taylor, *Appl. Phys. Lett.* 55, 957 (1989).
28. R. J. Lagow, J. J. Kampa, H. C. Wei, S. L. Battle, J. W. Genge, D. A. Laude, C. J. Harper, R. Bau, R. C. Stevens, J. F. Haw, and E. Munson, *Science* 267, 362 (1995).
29. V. I. Kasatochkin, V. V. Korshak, Y. P. Kudryavtsev, A. M. Sladkov, and I. E. Sterenberg, *Carbon* 11, 70 (1973).
30. A. G. Whittaker, *Science* 200, 763 (1978).
31. R. B. Heimann, J. Kleiman, and N. M. Slansky, *Nature* 306, 164 (1983).
32. H. W. Kroto, J. R. Heath, S. C. O'Brien, R. F. Curl, and R. E. Smalley, *Nature* 318, 162 (1985).
33. H. W. Kroto, *Rev. Mod. Phys.* 69, 703 (1997).
34. R. E. Smalley, *Rev. Mod. Phys.* 69, 723 (1997).
35. M. W. Geis and M. A. Tamor, in "Encyclopedia of Applied Physics" (G. L. Trigg, Ed.), Vol. 5, pp. 1–24. VCH Publishers, Weinheim, West Germany, 1993.
36. O. J. Vohler, F. von Sturm, and E. Wege, in "Encyclopedia of Applied Physics" (G. L. Trigg, Ed.), Vol. 3, pp. 21–40. VCH Publishers, Weinheim, West Germany, 1993.
37. M. S. Dresselhaus and G. Dresselhaus, in "Encyclopedia of Applied Physics" (G. L. Trigg, Ed.), Vol. 7, pp. 289–301. VCH Publishers, Weinheim, West Germany, 1993.
38. S. Larach and R. E. Shrader, *Phys. Rev.* 104, 68 (1956).

39. R. Greick, C. H. Perry, and G. Rupprecht, *Phys. Rev.* 146, 543 (1966).
40. R. M. Wentzcovitch, S. Fahy, M. L. Cohen, and S. G. Louie, *Phys. Rev. B* 38, 6191 (1988).
41. J. W. McClure, *Phys. Rev.* 108, 612 (1957).
42. N. Barlett and B. W. McQuillan, in "Intercalation Chemistry" (M. S. Whittingham and A. J. Jacobson, Eds.), p. 24. Academic Press, New York, 1982.
43. M. B. Khusidman, *Sov. Phys. Solid State* 14, 2791 (1973).
44. A. Zunger, A. Katzir, and A. Halperin, *Phys. Rev. B* 13, 5560 (1974).
45. M. Yano, Y. K. Yap, M. Okamoto, M. Onda, M. Yoshimura, Y. Mori, and T. Sasaki, *Jpn. J. Appl. Phys.* 39, L300 (2000).
46. P. B. Mirkarimi, K. F. McCarty, and D. L. Medlin, *Mater. Sci. Eng. R* 21, 47 (1997).
47. L. Vel, G. Demanzeau and J. Etourneau, *Mater. Sci. Eng. B* 10, 149 (1991).
48. H. Holleck, *J. Vac. Sci. Technol. A* 4, 2661 (1986).
49. R. Haubner and B. Lux, *Diamond Relat. Mater.* 2, 1277 (1993).
50. S. P. S. Arya and A. D'Amico, *Thin Solid Films* 157, 267 (1988).
51. W. Kulish and S. Reinke, *Diamond Film Technol.* 7, 105 (1997).
52. T. Yoshida, *Diamond Relat. Mater.* 5, 501 (1996).
53. M. Kawaguchi, *Adv. Mater.* 9, 615 (1997).
54. R. J. Diefendorf, U.S. Patent 3, 432, 330, 1969.
55. S. H. Chen and R. J. Diefendorf, "Proceeding of 3rd International Carbon Conference," 1980, p. 44.
56. R. B. Kaner, J. Kouvetakis, C. E. Warble, M. L. Sattler, and N. Bartlett, *Mater. Res. Bull.* 22, 399 (1987).
57. D. Tománek, R. M. Wentzcovitch, S. G. Louie, and M. L. Cohen, *Phys. Rev. B* 37, 3134 (1988).
58. H. Nozaki and S. Itoh, *J. Phys. Chem. Solids* 57, 41 (1996).
59. H. Nozaki and S. Itoh, *Phys. Rev. B* 53, 14161 (1996).
60. Y. Miyamoto, M. L. Cohen, and S. G. Louie, *Phys. Rev. B* 52, 14971 (1995).
61. J. Kouvetakis, T. Sasaki, C. Shen, R. Hagiwara, M. Lerner, K. M. Krishnan, and N. Bartlett, *Synth. Metals* 34, 1 (1989).
62. L. Maya, *J. Am. Ceram. Soc.* 71, 1104 (1988).
63. L. Maya, *J. Electrochem. Soc.* 135, 1278 (1988).
64. L. Maya and L. A. Harris, *J. Am. Ceram. Soc.* 73, 1912 (1990).
65. T. M. Besmann, *J. Am. Ceram. Soc.* 73, 2498 (1990).
66. M. Morita, T. Hanada, H. Tsutsumi, Y. Matsuda, and W. Kawaguchi, *J. Electrochem. Soc.* 139, 1227 (1992).
67. J. Bill, M. Friess, and R. Riedel, *Eur. J. Solid State Inorg. Chem.* 29, 195 (1992).
68. A. Derré, L. Filipozzi, F. Bouyer, and A. Marchand, *J. Mater. Sci.* 29, 1589 (1994).
69. F. Sagnac, F. Teyssandiev, and A. Marchand, *J. Am. Ceram. Soc.* 75, 161 (1992).
70. M. Yamada, M. Nakaishi, and K. Sugisshima, *J. Electrochem. Soc.* 137, 2242 (1990).
71. K. Montasser and S. Hattori, *Thin Solid Films* 117, 311 (1984).
72. N. Kawaguchi and T. Kawashima, *J. Chem. Soc. Chem. Commun.* 14, 1133 (1993).
73. M. Hubacek and T. Sato, *J. Solid State Chem.* 114, 258 (1995).
74. M. O. Watanabe, S. Itoh, K. Mizushima, and T. Sasaki, *Appl. Phys. Lett.* 68, 2962 (1996).
75. M. O. Watanabe, S. Itoh, K. Mizushima, and T. Sasaki, *J. Appl. Phys. Lett.* 78, 2880 (1995).
76. M. O. Watanabe, T. Sasaki, S. Itoh, and K. Mizushima, *Thin Solid Films* 281, 334 (1996).
77. Y. Chen, J. C. Barnard, R. E. Palmer, M. O. Watanabe, and T. Sasaki, *Phys. Rev. Lett.* 83, 2406 (1999).
78. M. O. Watanabe, S. Itoh, T. Sasaki, and K. Mizushima, *Phys. Rev. Lett.* 77, 187 (1996).
79. A. R. Badzian, *Mat. Res. Bull.* 16, 1385 (1981).
80. Y. Kakudate, M. Yoshida, S. Usuba, H. Yokoi, S. Fujiwara, M. Kawaguchi, K. Sako, and T. Sawai, *Trans. Mater. Res. Soc. Jpn. B* 14, 1447 (1994).
81. T. Komatsu, M. Nomura, Y. Kakudate, and S. Fujiwara, *J. Mater. Chem.* 6, 1799 (1996).
82. T. Komatsu, Y. Kakudate, and S. Fujiwara, *Faraday Trans.* 92, 5067 (1996).
83. T. Sasaki, M. Akaishi, S. Yamaoka, Y. Fujiki, and T. Oikawa, *Chem. Mater.* 5, 695 (1993).
84. S. Nakano, M. Akaishi, T. Sasaki, and S. Yamaoka, *Chem. Mater.* 6, 2246 (1994).
85. S. Nakano, T. Sasaki, M. Akaishi, and S. Yamaoka, *Mater. Sci. Eng. A* 209, 26 (1996).
86. E. Knittle, R. B. Kaner, R. Jeanloz, and M. L. Cohen, *Phys. Rev. B* 51, 12149 (1995).
87. B. Yao, L. Liu, and W. H. Su, *J. Mater. Res.* 13, 1753 (1998).
88. J. Huang, Y. Zhu, and H. Mori, *J. Mater. Res.* 16, 1178 (2001).
89. K. Matsunaga, C. Fisher, and H. Matsubara, *Jpn. J. Appl. Phys.* 39, L48 (2000).
90. Y. F. Zhang, Y. H. Tang, C. S. Lee, I. Bello, and S. T. Lee, *Diamond Relat. Mater.* 8, 610 (1999).
91. R. Q. Zhang, K. S. Chan, H. F. Cheung, and S. T. Lee, *Appl. Phys. Lett.* 75, 2259 (1999).
92. M. S. Dresselhaus, G. Dresselhaus, and R. Saito, *Phys. Rev. B* 45, 6234 (1992).
93. J. W. Mintmire, B. I. Dunlap, and C. T. White, *Phys. Rev. Lett.* 68, 631 (1992).
94. N. Hamada, S. Sawada, and A. Oshiyama, *Phys. Rev. Lett.* 68, 1579 (1992).
95. S. J. Tans, M. H. Devoret, H. Dai, A. Thess, R. E. Smalley, L. J. Geerlings, and C. Dekker, *Nature* 386, 474 (1997).
96. M. Bockrath, D. H. Cobden, P. L. McEuen, N. G. Nasreen, G. Chopra, A. Zettl, A. Thess, and R. E. Smalley, *Science* 275, 1992 (1997).
97. K. Tsukagoshi, B. W. Alphenaar, and H. Ago, *Nature* 401, 572 (1999).
98. Z. Yao, H. W. Ch. Postma, L. Balents, and C. Dekker, *Nature* 402, 273 (1999).
99. R. D. Antonov and A. T. Johnson, *Phys. Rev. Lett.* 83, 3274 (1999).
100. S. J. Tan, A. R. M. Verschueren, and C. Dekker, *Nature* 393, 49 (1998).
101. J. C. Charlier and S. Iijima, in "Carbon Nanotubes: Synthesis, Structure, Properties and Applications," M. S. Dresselhaus and G. Dresselhaus, Eds., pp. 55–80. Springer-Verlag, Berlin, 2001.
102. S. Amelinckx, X. B. Zhang, D. Bernaerts, X. F. Zhang, V. Ivanov, and J. B. Nagy, *Science* 265, 635 (1994).
103. O. Stephan, P. M. Ajayan, C. Colliex, Ph. Redlich, J. M. Lambert, P. Bernier, and P. Lefin, *Science* 266, 1683 (1994).
104. Z. Weng-Sieh, A. Zettl, and R. Gronsky, *Phys. Rev. B* 51, 11229 (1995).
105. Ph. Redlich, J. Loeffler, P. M. Ajayan, J. Bill, F. Aldinger, and M. Rühle, *Chem. Phys. Lett.* 260, 465 (1996).
106. K. Suenaga, C. Colliex, N. Demoncey, A. Loiseau, H. Pascard, and F. Willaime, *Science* 278, 653 (1997).
107. Y. Zhang, H. Gu, K. Suenaga, and S. Iijima, *Chem. Phys. Lett.* 279, 264 (1997).
108. M. P. Johansson, K. Suenaga, N. Hellgren, C. Colliex, J. E. Sundgren, and L. Hultman, *Appl. Phys. Lett.* 76, 825 (2000).
109. M. Terrones, A. M. Benito, C. Manteca-Diego, W. K. Hsu, O. I. Osman, J. P. Hare, D. G. Reid, H. Terrones, A. K. Cheetham, K. Prassides, H. W. Kroto, and D. R. M. Walton, *Chem. Phys. Lett.* 257, 576 (1996).
110. R. Sen, B. C. Satishkumar, A. Govindaraj, K. R. Harikumar, G. Raina, J. P. Zhang, A. K. Cheetham, and C. N. R. Rao, *Chem. Phys. Lett.* 287, 671 (1998).
111. X. D. Bai, J. D. Guo, J. Yu, E. G. Wang, J. Yuan, and W. Zhou, *Appl. Phys. Lett.* 76, 2624 (2000).

112. J. D. Guo, C. Y. Zhi, X. D. Bai, and E. G. Wang, *Appl. Phys. Lett.* 80, 124 (2002).
113. X. D. Bai, E. G. Wang, J. Yu, and H. Yang, *Appl. Phys. Lett.* 77, 67 (2000).
114. J. Yu, J. Ahn, S. F. Yoon, Q. Zhang, B. Rusli, K. Gan, M. Chew, B. Yu, X. D. Bai, and E. G. Wang, *Appl. Phys. Lett.* 77, 1949 (2000).
115. J. Yu, X. D. Bai, J. Ahn, S. F. Yoon, and E. G. Wang, *Chem. Phys. Lett.* 323, 529 (2000).
116. X. D. Bai, C. Y. Zhi, and E. G. Wang, *J. Nanosci. Nanotechnol.* 1, 55 (2000).
117. X. D. Bai, J. Yu, S. Liu, and E. G. Wang, *Chem. Phys. Lett.* 325, 485 (2000).
118. W. Han, J. Cumings, X. Huang, K. Bradley, and A. Zettl, *Chem. Phys. Lett.* 346, 368 (2001).
119. W. Han, W. Mickelson, J. Cuming, and A. Zettl, *Appl. Phys. Lett.* 81, 1110 (2002).
120. W. Han, Y. Bando, K. Kurashima, and T. Sato, *Appl. Phys. Lett.* 73, 3085 (1998).
121. W. Han, Y. Bando, K. Kurashima, and T. Sato, *Jpn. J. Appl. Phys.* 38, L755 (1999).
122. Ph. Kohler-Redlich, M. Terrones, C. Manteca-Diego, W. K. Hsu, H. Terrones, M. Rühle, H. W. Kroto, and D. R. W. Walton, *Chem. Phys. Lett.* 310, 459 (1999).
123. M. Terrones, N. Grobert, and H. Terrones, *Carbon* 40, 1665 (2002).
124. C. Y. Zhi, X. D. Bai, and E. G. Wang, *Appl. Phys. Lett.* 80, 3590 (2002).
125. C. Y. Zhi, J. D. Guo, X. D. Bai, and E. G. Wang, *J. Appl. Phys. Lett.* 91, 5325 (2002).
126. Y. Moriyoshi, Y. Shimizu, and T. Watanabe, *Thin Solid Films* 390, 26 (2001).
127. Z. X. Cao and H. Oechsner, *J. Appl. Phys.* 93, 1186 (2003).
128. Z. X. Cao, L. M. Liu, and H. Oechsner, *J. Vac. Sci. Technol. B* 20, 2275 (2002).
129. J. L. He, Y. J. Tian, D. L. Yu, T. S. Wang, S. M. Liu, L. C. Guo, D. C. Li, X. P. Jia, L. X. Chen, G. T. Zou, and O. Yanagisawa, *Chem. Phys. Lett.* 340, 431 (2001).
130. B. Yao, L. Liu, and W. H. Su, *J. Appl. Phys.* 86, 2464 (1999).
131. Z. F. Zhou, I. Bello, M. K. Lei, K. Y. Li, C. S. Lee, and S. T. Lee, *Surf. Sci. Coat Technol.* 128–129, 334 (2000).
132. T. Kawano, M. Kawaguchi, Y. Okamoto, H. Enomoto, and H. Bando, *Solid State Sci.* 4, 1521 (2002).
133. M. Dinescu, A. Perrone, A. P. Caricato, L. Mirengchi, C. Gerardi, C. Ghica, and L. Frunza, *Appl. Surf. Sci.* 127–129, 692 (1998).
134. I. Morjan, O. Conde, M. Oliveira, and F. Vasiliu, *Thin Solid Films* 340, 95 (1999).
135. J. Loeffler, I. Konyashin, J. Bill, H. Uhlig, and F. Aldinger, *Diamond Relat. Mater.* 6, 608 (1997).
136. J. Yue, W. Cheng, X. Zhang, D. He, and G. Chen, *Thin Solid Films* 375, 247 (2000).
137. D. Golberg, P. Dorozhkin, Y. Bando, M. Hasegawa, and Z. C. Dong, *Chem. Phys. Lett.* 359, 220 (2002).
138. D. Golberg, Y. Bando, K. Kurashima, and T. Sato, *Solid State Commun.* 116, 1 (2000).
139. D. Golberg, Y. Bando, L. Bourgeois, K. Kurashima, and T. Sato, *Appl. Phys. Lett.* 77, 1979 (2000).
140. Ph. Redlich, D. L. Carroll, and P. M. Ajayan, *Curr. Opin. in Solid State Mater. Sci.* 4, 325 (1999).
141. W. Zhou and J. M. Thomas, *Curr. Opin. in Solid State Mater. Sci.* 5, 75 (2001).
142. T. Kolber, K. Piplits, S. Dreer, E. Mersdorf, R. Haubner, and H. Hutter, *Appl. Surf. Sci.* 167, 79 (2000).
143. R. Gago, I. Jiménez, J. M. Albella, and L. J. Terminello, *Appl. Phys. Lett.* 78, 3430 (1997).
144. R. Gago, I. Jiménez, T. Sajavaara, E. Rauhala, and J. M. Albella, *Diamond Relat. Mater.* 10, 1165 (2001).
145. R. Gago, I. Jiménez, F. Agulló-Rueda, J. M. Albella, Zs. Czigány, and L. Hultman, *J. Appl. Phys.* 92, 5177 (2002).
146. E. Z. Kurmaev, A. V. Ezhov, S. N. Shamin, V. M. Cherkashenko, Y. G. Andrew, and T. Lundstrom, *J. Alloys Comp.* 248, 86 (1997).
147. Y. Wada, Y. K. Yap, M. Yoshimura, Y. Mori, and T. Sasaki, *Diamond Relat. Mater.* 9, 620 (2000).
148. R. W. Pryor, *Appl. Phys. Lett.* 68, 1802 (1996).
149. M. V. Ugarov, V. P. Ageev, A. V. Karabutov, E. N. Loubnin, S. M. Pimenov, V. I. Konov, and A. Bensaoula, *J. Appl. Phys.* 85, 8436 (1999).
150. J. Yu and E. G. Wang, *Appl. Phys. Lett.* 74, 2948 (1999).
151. J. Yu, E. G. Wang, J. Ahn, S. F. Yoon, Q. Zhang, J. Cui, and M. B. Yu, *J. Appl. Phys. Lett.* 87, 4022 (1999).
152. T. Sugino and H. Hieda, *Diamond Relat. Mater.* 9, 1233 (2000).
153. P. Dorozhkin, D. Golberg, Y. Bando, and Z.-C. Dong, *Appl. Phys. Lett.* 81, 1083 (2002).
154. A. Lousa, J. Esteve, S. Muhl, and E. Martínez, *Diamond Relat. Mater.* 9, 502 (2000).
155. D. He, W. Cheng, J. Qin, J. Yue, E. Xie, and G. Chen, *Appl. Surf. Sci.* 191, 338 (2002).
156. A. Kratzsch, S. Ulrich, H. Leiste, M. Stüber, and H. Holleck, *Surf. Coat. Technol.* 116–119, 253 (1999).
157. D. Kurapov, D. Neuschütz, R. Cremer, T. Pedersen, M. Wuttig, D. Dietrich, G. Marx, and J. M. Schneider, *Vacuum* 68, 335 (2002).
158. N. Badi, A. Tempez, D. Starikov, V. Zomorrodian, N. Medelci, A. Bensaoula, J. Kulik, S. Lee, S. S. Perry, V. P. Ageev, S. V. Garnov, M. V. Ugarov, S. M. Klimentov, V. N. Tokarev, K. Waters, and A. Shultz, *AIP Conf. Proc.* 420, 666 (1998).
159. E. Martínez, A. Lousa, and J. Esteve, *Diamond Relat. Mater.* 10, 1892 (2001).
160. M. N. Oliveira and O. Conde, *J. Mater. Res.* 16, 734 (2001).
161. V. Linss, I. Hermann, N. Schwarzer, U. Kreissig, and F. Richter, *Surf. Coat. Technol.* 163–164, 220 (2003).
162. S. Stöckel, K. Weise, D. Dietrich, T. Thamm, M. Braun, R. Cremer, D. Neuschütz, and G. Marx, *Thin Solid Films* 420–421, 465 (2002).
163. H. Yasui, Y. Hirose, K. Awazu, and M. Iwaki, *Colloids Surf. B: Biointerfaces* 19, 291 (2000).
164. D. C. Reigada and F. L. Freire, *Surf. Coat. Technol.* 142–144, 894 (2001).
165. A. Perrone, A. P. Caricato, A. Luches, M. Dinescu, C. Ghica, V. Sandu, and A. Andrei, *Appl. Surf. Sci.* 133, 239 (1998).
166. E. Martínez, J. Esteve, J. L. Andújar, and M. C. Polo, *Diamond Relat. Mater.* 7, 376 (1998).
167. S. Chattopadhyay, L. C. Chen, S. C. Chien, S. T. Lin, C. T. Wu, and K. H. Chen, *Thin Solid Films* 420–421, 205 (2002).
168. S. Chattopadhyay, S. C. Chien, L. C. Chen, K. H. Chen, and H. Y. Lee, *Diamond Relat. Mater.* 11, 708 (2002).
169. S. Chattopadhyay, L. C. Chen, S. C. Chien, S. T. Lin, and K. H. Chen, *J. Appl. Phys.* 92, 5150 (2002).
170. L. Filipozzi, A. Marchand, A. Derré, A. Adouard, and M. Kinany-Alaoui, *J. Mater. Res.* 12, 1711 (1997).
171. M. K. Lei, Q. Li, Z. F. Zhou, I. Bello, C. S. Lee, and S. T. Lee, *Thin Solid Films* 389, 194 (2001).
172. T. Sugiyama, T. Tai, and T. Sugino, *Appl. Phys. Lett.* 80, 4214 (2002).
173. T. Sugino, Y. Etou, and T. Tai, *Appl. Phys. Lett.* 80, 649 (2002).
174. T. Sugino, T. Tai, and Y. Etou, *Diamond Relat. Mater.* 10, 1375 (2001).
175. Y. Etou, T. Tai, T. Sugiyama, and T. Sugino, *Diamond Relat. Mater.* 11, 985 (2002).
176. M. C. Polo, E. Martínez, J. Esteve, and J. L. Andújar, *Diamond Relat. Mater.* 8, 423 (1999).
177. B. Maquin, A. Derré, C. Labrugère, M. Trinquescoste, P. Chadeyron, and P. Delhaès, *Carbon* 38, 145 (2000).
178. H. S. Kim, I. H. Choi, and Y.-J. Baik, *Surf. Coat. Technol.* 133–134, 473 (2000).

179. J. Wöhle, H. Ahn, and K.-T. Rie, *Surf. Coat. Technol.* 116–119, 1166 (1999).
180. K. Gammer, T. Kolber, K. Piplits, K. Nowikow, X. Tang, R. Haubner, and H. Hutter, *Thin Solid Films* 406, 98 (2002).
181. R. Weissenbacher, R. Haubner, K. Aigner, and B. Lux, *Diamond Relat. Mater.* 11, 191 (2002).
182. Z. Y. Xie, J. H. Edgar, T. L. McCormick, and M. V. Sidorov, *Diamond Relat. Mater.* 7, 1357 (1998).
183. R. Brydson, H. Daniels, M. A. Fox, R. Greatrex, and C. Workman, *Chem. Commun.* 2002, 718 (2002).
184. M. N. Oliveira, A. M. Botelho do Rego, and O. Conde, *Surf. Coat. Technol.* 100–101, 398 (1998).
185. H. Ling, J. D. Wu, J. Sun, W. Shi, Z. F. Ying, and F. M. Li, *Diamond Relat. Mater.* 11, 1623 (2002).
186. R. Gago, I. Jiménez, and J. M. Albella, *Thin Solid Films* 373, 277 (2000).
187. R. Gago, I. Jiménez, I. García, and J. M. Albella, *Vacuum* 64, 199 (2002).
188. R. Gago, I. Jiménez, U. Kreissig, and J. M. Albella, *Diamond Relat. Mater.* 11, 1295 (2002).
189. T. Kolber, K. Piplits, S. Dreer, E. Mersdorf, R. Haubner, and H. Hutter, *Appl. Surf. Sci.* 167, 79 (2000).
190. S. Ulrich, A. Kratzsch, H. Leiste, M. Stüber, P. Schloßmacher, H. Holleck, J. Binder, D. Schild, S. Westermeyer, P. Becker, and H. Oechsner, *Surf. Coat. Technol.* 116–119, 742 (1999).
191. H. Yokomichi, T. Funakawa, and A. Masuda, *Vacuum* 66, 245 (2002).
192. N. P. Barradas, C. Jaynes, Y. Kusano, J. E. Evetts, and I. M. Hutchings, *AIP Conf. Proc.* 475, 504 (1999).
193. A. Tempez, N. Badi, A. Bensaoula, and J. Kulik, *J. Vac. Sci. Technol. A* 16, 2896 (1998).
194. A. V. K. Westwood, R. Brydson, R. Coult, M. A. Fox, B. Rand, and K. Wade, *Carbon* 40, 2157 (2002).
195. T. Nakajima, M. Koh, and T. Katsube, *Solid State Sci.* 2, 17 (1998).
196. V. L. Solozhenko, *High Pressure Research* 22, 519 (2002).
197. V. L. Solozhenko, S. N. Dub, and N. V. Novikov, *Diamond Relat. Mater.* 10, 2228 (2001).
198. V. L. Solozhenko, D. Andrault, G. Fiquet, M. Mezouar, and D. C. Rubie, *Appl. Phys. Lett.* 78, 1385 (2001).
199. X. Blasé, J. C. Charlier, A. De Vita, and R. Car, *Appl. Phys. Lett.* 70, 197 (1997).

Boron Nitride Nanotubes

Dmitri Golberg, Yoshio Bando

National Institute for Materials Science, Tsukuba, Ibaraki, Japan

CONTENTS

1. Introduction
 2. Boron Nitride (BN) Nanotube Synthesis
 3. Structure of BN Nanotubes
 4. Chemical Composition and Bonding in Pure and C-Doped BN Nanotubes
 5. Irradiation Stability of BN Nanotubes
 6. Metal-Filled BN Nanotubes
 7. Physical Properties
 8. Applications
 9. Concluding Remarks
- Glossary
References

1. INTRODUCTION

A boron nitride (BN) nanotube (NT) [1] is a carbon (C) nanotube [2] analog: alternating B and N atoms may partially or entirely substitute for C atoms in a graphitic sheet without significant changes in atom spacing. BNNTs were first foretold theoretically [3, 4] and then were successfully synthesized in 1995 [1]. Primarily, the interest to the BNNTs is due to the undisputed fact that in contrast to the metallic or semiconducting CNT [5] the BNNT is insulating with a ~ 5.5 eV bandgap independent of its chirality and morphology (i.e., diameter and number of layers) [4]. In addition, layered BN is known to be much more thermally and chemically stable than graphitic C [6]. Therefore, there have been intuitive expectations that the BNNTs should inherit these advantageous properties. Therefore the main interest in BNNTs is related to specific applications in nanotubular protective shields for various nanomaterials embedded within (i.e., nanowires, nanorods, and/or clusters). Surprisingly, the amount of successful research work performed to date on BNNTs has been negligibly low compared to that on CNTs [7–22].

It is worth noting that the lack of research performed on BNNTs is solely due to the significant difficulties involved in

their preparation as compared to the relative ease in making conventional CNTs.

The present contribution, along with a comprehensive state-of-the-art review in the field, is additionally enhanced by the original authors' data on high-temperature chemical syntheses and structural analysis of BNNTs over last several years using thorough high-resolution transmission electron microscopy (HRTEM) paired with electron diffraction analysis and energy-filtered TEM, and pioneering thermal and electrical property measurements.

2. BORON NITRIDE (BN) NANOTUBE SYNTHESIS

Initially, we note that reliable and well-established techniques of NT growth developed for C systems, for example, arc discharge [2], laser ablation [23], and chemical vapor deposition (CVD) [24], do not effectively work for the BN system. Resultantly, a number of new techniques including continuous laser heating at superhigh [25–27] or ambient pressure [28, 29], oven heating of milled B powders [30] or B-containing reagent mixtures [31, 32], a plasma-jet method [33], direct recombination of spraying B and N atoms on a clean tungsten substrate in an ultrahigh vacuum [34], metal-boride-catalyzed CVD [35], La-catalyzed arc discharge [36], and high-temperature chemical syntheses [37–49] have been developed, although with limited success as described in the following sections.

2.1. Arc Discharge

First BNNTs were discovered in an arc-discharged material by Chopra et al. [1]. Many BN nanotubes were found to contain metallic nanoparticles attached to the tips. The particles presumably originated from a tungsten hollow electrode used for encapsulating a starting BN powder. Later on, arc-discharge syntheses of BNNTs were performed by Loiseau et al. [16] and Terrones et al. [50]. In [16] the electrodes made of graphite and HfB_2 were used as a cathode and an anode, respectively. An arc was created in a N_2 atmosphere. The setup presumes that a C source is separated from that

of B and N; this was thought to be the reason for BN-rich nanotube compositions. NTs with definite phase separation of BN and C layers were observed in a deposit on the anode. The purity of a BN nanomaterial was not high enough with respect to C contamination. In [50] a tantalum tube press-filled with a BN powder and a water-cooled Cu disk were used as electrodes. As the anode rod was consumed a product containing BN nanoparticles and NTs was collected. In both methods (i.e., [16, 50]) the yield of NTs, as compared to that of bulk BN particles, was not claimed to be high.

Saito and Maida [51] used ZrB_2 rods as electrodes and high purity nitrogen gas (99.999%) during their arc-discharge runs. BNNTs were found in the products crystallized on the anode, albeit at limited yields.

2.2. Laser Ablation

Pioneering experiments on laser ablation of a hexagonal or cubic BN target were carried out by Golberg et al. [25]. A continuous CO_2 laser was focused on a target placed into a diamond anvil cell filled with liquid nitrogen. After reducing a spacing between diamond anvils, superhigh nitrogen pressure was generated inside the chamber. A temperature of approximately 5000 K was estimated on the BN target surface, where dozens of short pure BNNTs were found to protrude from an amorphous-like melted BN residue. The drawback of the synthesis was a relatively small number of BNNTs as compared to standard amorphous-like, cubic, or hexagonal BN.

Later on, catalyst-assisted excimer laser ablation experiments at high temperature were carried out during which some BNNTs were also observed [28]. Lee et al. [52] reported on catalyst-free continuous CO_2 laser ablation of BN targets leading to BNNT formation. Most of nanotubes were reported to have only a single layer and form long bundles. Boron nanoparticles, frequently observed as a by-product, were frequently encapsulated into the tip-ends of NTs. They were thought to play a key role for the growth mechanism. By contrast, Laude et al. [29], though applying a similar setup and also continuous CO_2 laser vaporization, did not find single-layered BNNTs; rather the NTs, assembled in bundles, frequently had a few layers. The results bring a significant controversy to the reproducibility of single-layered BN nanotube synthesis.

2.3. Chemical Vapor Deposition

Lourie et al. [35] reported on first CVD synthesis of BNNTs on nickel boride catalyst particles at 1273–1373 K using the borazine as a precursor. A characteristic feature of the process was the fact that the precursor was generated *in-situ* from a molten salt which formed mixtures of $(NH_4)_2SO_4$, $NaBH_4$, and Co_3O_4 at 573–673 K. The BNNTs exhibited lengths of up to 5 micrometers and often possessed bulbous, flaglike and/or clublike tips.

In another CVD run, Ma et al. [53] used a $B_4N_3O_2H$ precursor during synthesis of BNNTs. It was suggested that the tips encapsulating boron oxynitride nanoclusters doped with silicon, aluminum, and calcium served as the effective promoters for BN tube CVD growth. Recently, somewhat controlled preparation of BNNTs and related nanostructures—BN nanobamboos and nanorods—has been achieved by the

same authors [54]. To date, the method has allowed to researchers prepare only milligram quantities of a product containing BNNTs.

2.4. Other Chemical Syntheses

Terauchi et al. [55] used simple oven heating at ~ 1473 K of B and Li powders in a BN crucible in a N_2 atmosphere and observed a few short pure BNNTs of less than 30 nm in diameter in the resultant powders. Chen et al. [30] produced BNNTs by thermal annealing at 1273 K of elemental B powders which were previously ball-milled in ammonia gas for 150 h at room temperature. It was suggested that high-energy ball-milling induced nitriding reaction between the boron powder and the ammonia gas; thus a metastable material is formed consisting of disordered BN and nanocrystalline boron. BNNTs then grew out from this metastable and chemically activated structure during heat treatment in the presence of nitrogen gas. However, the yield and structural perfection of BNNTs were not high enough, as revealed by transmission electron microscopy observation.

An efficient route to synthesize tens of milligram quantities of BN and B–C–N NTs was invented by Han et al. [37]. During the synthesis pure CVD CNTs served as templates. They were chemically modifying by highly reactive boron oxide vapor and flowing nitrogen gas at 1300–1900 K. The diameters of the resultant tubes perfectly matched those of the starting templates; this lead the authors to suggest that C to BN substitution took place. The major drawback of the synthesis was a significant fraction of ternary B–C–N NTs with significant amounts of the remaining C at the expense of pure BN nanotubes. A dramatic increase in pure BNNT fraction was later achieved by Golberg et al. [40] using the same method through careful selection of synthesis promoters. Metal oxides (i.e., MoO_3 , CuO , and/or PbO) were found to be most useful. The oxide vapors caused the CNT template to begin to open at the initial reaction stages at moderate temperatures (600–900 K) via intense oxidation. This promotes an effective substitution BN to C on both sides of the C templates and crystallization of BN domains from inside-out and outside-in of the tubes. In addition, the substitution reaction route was utilized by the same authors [38, 39] to produce B-doped, B–C–N, and BNNTs from the bundles of pure C single-walled nanotubes, albeit with limited success. Marginal B-doping of the C-based nanostructures was found to occur easily; by contrast, large-scale preparation of pure BN single-layered NTs was not successful; the latter were only rarely found.

2.5. Atom Deposition Technique

Bengu and Marks [34] first described *in-situ* synthesis of BN nanostructures using electron–cyclotron resonance nitrogen and electron beam boron source onto polycrystalline tungsten substrates. The nanostructures of 0.5–3.0 nm in diameter were prepared in an ultrahigh vacuum of 2×10^{-9} Pa. Characterization of the resultant structures was performed without their exposure to air; thus all possible artificial structures due to chemisorption were entirely excluded. The crystallinity of the BN nanostructures was not perfect; rather

they frequently revealed undulating, wavy BN layers. However, the method was claimed to be useful for production of different BN-based coatings with well-controlled structure.

2.6. Plasma-Jet Method

Shimizu et al. [33] reported on a flash evaporation method using a direct current plasma. Porous BC_4N sintered bodies were used as a raw material. The plasma was operated under conditions of 25 V and 300 A by using Ar and $\text{N}_2\text{-H}_2$ for plasma gas and sheath gas, respectively. The porous BC_4N was evaporated by irradiation of the plasma flame. Nanotubes were formed in a high temperature zone (~ 3000 K). Significant amounts of the remaining C were determined in the structures, decreasing its purity, whereas the product was clearly divided into three morphology types such as CNTs, BNNTs, and CNTs surrounded with BNNTs.

Based on Sections 2.1–2.6 it is obvious that the presently achievable yield of BNNTs still remains negligibly low compared to that of CNTs. Moreover, even if the BNNTs are successfully produced and ready to be analyzed, their structural identification and/or analysis are prone to many almost insurmountable difficulties arising from the electrically insulating nature of BN and consequent charging phenomena during electron microscopy, which, in turn, lead to image blurring. As a result, the number of research groups successfully overcoming all of the above-mentioned complications is very small, as described in the following sections.

3. STRUCTURE OF BN NANOTUBES

3.1. Morphology as Revealed by Transmission Electron Microscopy

Similarly to CNTs [2, 7], BNNTs crystallize in multiwalled (MWNT) and single-walled (SWNT) morphologies, albeit notable yields of SWNTs were observed only in a single recent work by Lee et al. [52] as was mentioned previously. All other research groups very accidentally found BN SWNTs [16, 34, 38, 39], a double-layered NT morphology being preferred [17, 29, 44]. In fact, in an early paper on BNNT synthesis by Chopra et al. [1] only BN MWNTs were observed. Later Loiseau et al. [16] presented a few HRTEM pictures of BNNTs with a varying number of layers (including SWNT). However, it was noted that BN SWNTs always had undulating, wavy, and poorly structured wall fringes. Theoreticians assigned this to the fact that in a BN hexagonal sheet the B and N atomic planes are slightly shifted in a direction perpendicular to the tube axis [56]. In addition, it is thought that the high ionicity of BNNTs (i.e., strong B–N bonds) may stabilize MWNT morphologies due to the strong so-called “lip–lip” interactions between adjacent layers [56]. In a homogeneous C graphene sheet, where chemical bonds of only one type are present (i.e. C–C), the interactions between layers are weaker and not important for NT growth. Thus, in contrast to C, where high yields of SWNTs are routinely obtained nowadays [57], the single-layer morphology is supposed not to be natural for the BN system by many researchers.

Figure 1a and b depicts representative HRTEM micrographs of a BN MWNT and SWNT [19, 38]. The BN tubular

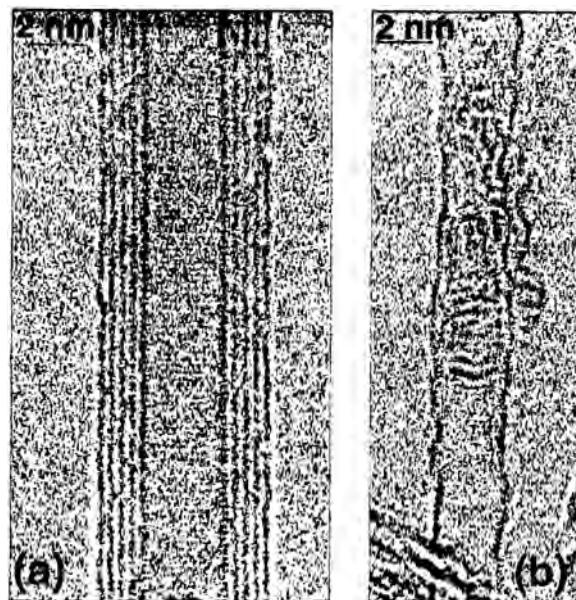


Figure 1. (a) Representative HRTEM image of a BN MWNT. The typical intershell distance is 0.33–0.34 nm. (b) HRTEM image of an isolated BN SWNT exhibiting a nested four-shelled BN fullerene encapsulated within. The fullerene lattice image does not resemble a circle typical for a standard C_{60} -based molecule. By contrast, the image would be consistent with a nanocage of the octahedral symmetry. Note also a wavy, undulating contrast for the BN SWNT wall fringes in (b). Figure 1a reprinted with permission from [19], D. Golberg et al., *J. Appl. Phys.* 86, 2364 (1999). © 1999, American Institute of Physics. Figure 1b reprinted with permission from [38], D. Golberg et al., *Chem. Phys. Lett.* 308, 337 (1999). © 1999, Elsevier Science.

shells are imaged as dark contrast fringes separated by an average intershell distance of $\sim 0.33\text{--}0.34$ nm (in the case of MWNTs), characteristic of the d_{0002} spacing in hexagonal BN [6]. Figure 1b particularly highlights that a nested BN fullerene is embedded in the channel of a SWNT. The unique feature of the fullerene is a nonspherical HRTEM image, contradicting the characteristic spherical shape of the well-known C_{60} molecule. Obviously, this is due to a striking difference in topological defects (leading to graphitic-like sheet curling) in the C and BN systems, as described below.

It is established that the energetically favorable defect in C is a five-membered ring defect (i.e., a pentagon), leading to a 60° inclination of a graphene sheet made of hexagons. By contrast, in BN, the presence of a five-membered ring defect requires the existence of B–B and/or N–N bonds, which are less energetically stable than the B–N bond [56]. Thus, in the BN system an even-membered ring defect (i.e., square and/or octagon) normally forms, leading to a nearly 90° inclination in a graphitic-like sheet [16, 58]. As a result a fully closed structure in BN (i.e., the fullerene-like molecule) accumulates only 6 squares instead of 12 pentagons (Euler rule), as in C. It, therefore, exhibits octahedral symmetry rather than icosahedral symmetry typical for all C sealed nanocages. In terms of crystallography, it turns out that a BN curled and closed nanocage should have very differing HRTEM projections in various crystallographic orientations: square-like [zone axis $\langle 100 \rangle$], rectangle-like [zone axis $\langle 211 \rangle$]; hexagon-like [zone axis $\langle 111 \rangle$], as in Figure 1b, and rhomb-like images

[zone axis $\langle 100 \rangle$] are visible depending on the orientation of a nanocage with respect to an incident electron beam [58]. Therefore, a BNNT cap, which requires a semiclosed fullerene, might frequently exhibit flat motifs like the one shown in Figure 2a. The existence of the flat cap, absent in CNTs, was initially prescribed as a distinguishing feature of a BNNT [16], although later some conical caps were also observed [51, 59]. In addition, BN tube caps may be open (Fig. 2b). This type of capping was frequently observed in the case of high-temperature NT chemical syntheses [20, 40–45], when the nonhexagonal defects are effectively annealed out due to the high atom mobility and/or aging effect resulting from the presence of metallic catalysts [44].

In practice, the particular type of BNNT topological defect is determined by the interplay between structural and energetic factors. Clearly, a 90° inclination (an even-membered ring defect) requires larger internal stress introduced into a graphite-like sheet than that of a 60° inclination (an odd-membered defect). For instance, Bourgeois et al. [60] demonstrated that basically both types of defects exist in a BN nanocone apex, depending on the particular growth kinetics and stress distribution. This is also applicable to BNNTs: Saito and Maida [51] have considered square, pentagon, and heptagon rings in BNNTs, as revealed by experimentally observed tube cap TEM images.

Frequently, the BNNTs tend to assemble in bundles/ropes made of dozens of individual tubes, as shown in Figure 2b [17, 20, 29, 38–45]. These ropes were seen for both MWNTs [41] and SWNTs [38, 39]. It was proposed that the individual tubes within the ropes interact through weak Van der Waals interactions and are packed in a honeycomb-like array (in cross-section view). Splitting of the diffraction spots on the equatorial line in the electron diffraction patterns makes possible calculation of the intertube spacing, $d = 0.34$ nm, between individual tubes in a rope [41, 43], the characteristic value of the d_{0002} distance in many graphitic materials, including CNTs [57].

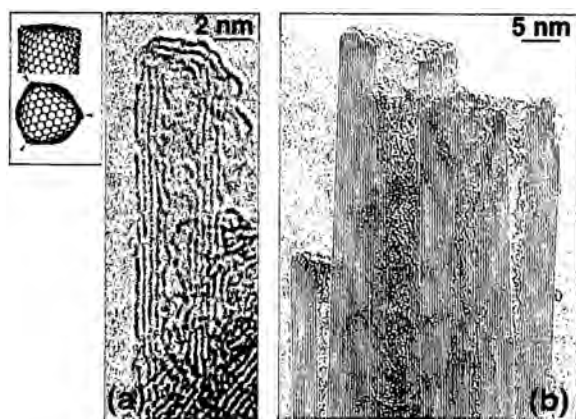


Figure 2. (a) HRTEM image of a typical BNNT flat tip-end termination with a possible arrangement of three four-member ring defects in the cap [50], shown on the inset with arrows, explaining the experimentally observed flat tip. (b) HRTEM image of solely open BN MWNTs. Figure 2a reprinted with permission from [19], D. Golberg et al., *J. Appl. Phys.* 86, 2364 (1999). © 1999, American Institute of Physics. Figure 2b reprinted with permission from [44], D. Golberg and Y. Bando, *Appl. Phys. Lett.* 79, 415 (2001). © 2001, American Institute of Physics.

3.2. Atomic Order as Revealed by Electron Diffraction

The theory of nanotube electron diffraction was developed by Iijima [2] and later extended by Zhang et al. [11]. This theory is fully applicable to BNNTs. For instance, Figure 3a depicts a typical nanobeam diffraction pattern (NBD, electron probe size was 1.6 nm) taken from an individual BNNT [19]. The NBD displays a row of $(000l)$ reflections originating from the NT walls oriented edge-on to an incident electron beam and a hexagon-like pattern originating from the front and back NT fragments oriented perpendicular to the beam. The pattern is a characteristic of the so-called “zigzag” nanotube (the $[10\text{--}10]$ direction of the graphitic sheet is parallel to the tube axis) [5].

Figure 3b displays the NBD taken with a larger electron probe size (~ 50 nm) from a whole rope composed of dozens of BN MWNTs [41]. An exciting feature of the pattern is fairly uniform shell chirality. Diffraction spots are clustering around those typical for the “zigzag” arrangement (compared with Fig. 3a). The marginal deviations from the ideal “zigzag” orientation are just within $\alpha = 10^\circ$ (semiangle, α , between marked diffraction spots in the vicinity of the $[01\text{--}10]$ reflection in Fig. 3b).

The preferential “zigzag” orientation was further verified through taking NBDs from a plenty of individual BN MWNTs, as shown on the histogram in Figure 4 [41]. Although “armchair” (tube axis is parallel to the $[11\text{--}20]$ orientation of the graphitic-like sheet) and helical tubes with varying chiral angle were also observed, the majority of tubes, namely, $\sim 82\%$, displayed “zigzag” or near “zigzag” atomic arrangements, as revealed by a statistical analysis of NBDs from 45 individual tubes (Fig. 4).

Importantly, the preferential BNNT “zigzag” atomic configuration has been observed in various BN tubular products by many researchers. For instance, Golberg et al. [25–27] showed that such assembly is natural for BNNTs produced

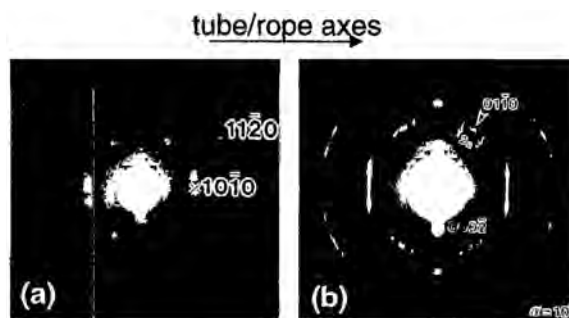


Figure 3. Representative diffraction patterns (DPs) taken from an individual five-layered BNNT (a) and from a BN MWNT rope containing dozens of nanotubes (b). Both DPs exhibit diffraction spots that are clustered around characteristic of the so-called “zigzag” atomic arrangement of a graphitic-like sheet. The deviations from the ideal “zigzag” orientation (the $[10\text{--}10]$ direction is strictly parallel to the tube/rope axis) are represented by the semiangle $\alpha = 10^\circ$ in (b) between a couple of the marked diffraction spots in the vicinity of the $[10\text{--}10]$ reflection. Figure 3a reprinted with permission from [19], D. Golberg et al., *J. Appl. Phys.* 86, 2364 (1999). © 1999, American Institute of Physics. Figure 3b reprinted with permission from [41], D. Golberg et al., *Solid State Comm.* 116, 1 (2000). © 2000, Elsevier Science.

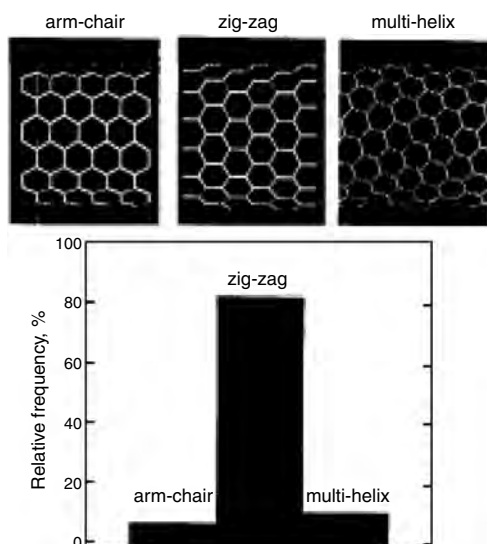


Figure 4. A histogram showing BNNT shell helicity distribution in MWNTs based on the statistical analysis of 45 individual BNNT DPs (taken with an electron probe of 1.6 nm in diameter). The corresponding three-dimensional structural models of the representative “armchair” {10,10}, “zigzag” {20,0}, and helical {14.5} tubes are shown for clarity above the histogram. Reprinted with permission from [41], D. Golberg et al., *Solid State Comm.* 116, 1 (2000). © 2000, Elsevier Science.

by BN target laser heating under superhigh N_2 pressure and for those obtained via simple high-temperature chemical syntheses [19, 40–45]. A preferential “zigzag” arrangement of BNNTs was later observed by Bourgeois et al. [59] in BN tubular fibers synthesized through heating of BN powders. It is noted that these experimental results are opposed to the theoretical predictions based on the molecular dynamics calculations performed by Blase et al. [56]; those favor the growth of “armchair” BN tubes rather than “zigzag” ones. However, the significant difference between experimental synthesis temperatures, 5000 K [25–27] and 1773–1973 K [19, 40–45], and those used for calculations, 3000 K [56], may be of prime importance for this disagreement. By contrast, later Menon and Srivastava [61] calculated that for the most frequently observed flat BN tube caps [16, 19] the “zigzag” morphology is energetically preferable. This latter phenomenon is in line with the experimental HRTEM data by different research groups. It is worth noting that the “zigzag” atomic arrangement in B-doped CNTs was also found to be dominating [62]. Most recently, “zigzag” BNNTs were repeatedly observed by Terauchi et al. [55], Ma et al. [53, 63], Demczyk et al. [64], and Lee et al. [52] in BNNTs prepared via different synthetic routes.

It is noteworthy that conventional CNTs do not show any preferential helicity and display a wide variety of chiralities [2, 5, 65], which are statistically equally probable. Thus, preferential crystallization of the “zigzag” BN tubular shells is related to the definite kinetic characteristics of the BNNT growth yet to be clarified by energy calculations.

Existence of preferential helical angles in BNNT shells leads to a number of the unique features in BNNTs compared to CNTs, as far as the MWNT layer stacking is concerned. HRTEM images of two BN MWNTs are shown in Figure 5a and b [42]. Lattice fringes with an average distance of ~ 0.22 nm which correspond to the (10–10) lattice spacing

in BN are clearly resolved for wall fragments. The difference in HRTEM dotlike contrast in the tube walls is apparent between Figure 5a and b. Vertical atomic columns (hexagonal *h*BN-stacking) are visible for the wall fringes in Figure 5a, whereas those in Figure 5b have an angle of 12.5° with respect to the tube axis (rhombohedral *r*BN-stacking) [6], as highlighted in the enlarged atomically resolved wall segments (insets). Both tubes in Figure 5a and b have a similar BN hexagon arrangement along the tube axis; that is, the tube axes are parallel to the [10–10] graphene-like sheet orientation (“zigzag” type). The computer simulations of hexagonally and rhombohedrally packed tubular segments for the “zigzag” oriented BNNTs, revealing a perfect fit with the optical contrast on the HRTEM micrographs, are finally shown on the right-hand sides of the HRTEM images.

Existence of definite stacking in BNNT shells reflects the particular importance of the intershell interactions in BNNTs compared to the C system where turbostratic stacking between shells typically dominates. Thus it is suggested that the driving force behind the particular shell stacking in BNNTs is due to the alternating B and N sites in the neighboring shells in the direction normal to the tube axis in line with bulk BN ordering.

For many of BNNT HRTEM images experimentally observed so far, no visible changes between the fringe contrast intensity in NT wall and core regions, which are common characteristics of cylindrical tubes, were detected [42]. In the view of the authors this may imply that the cross-section of the BNNT is flattened (i.e., elliptical), with the longer ellipse axis in the image plane. In fact, in such

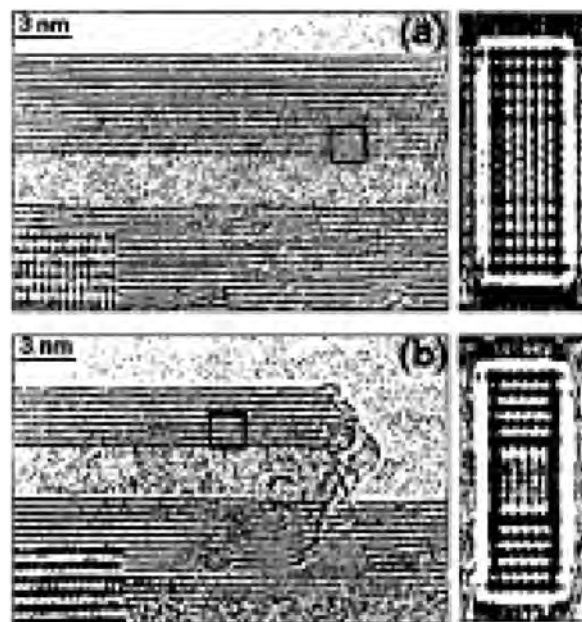


Figure 5. (a), (b) HRTEM images of “zigzag” BN MWNTs. Definite but different stacking order is apparent in marked areas in (a) and (b) as highlighted in the insets. Hexagonal type stacking in (a) and rhombohedral-type stacking in (b) are confirmed by corresponding computer-simulated HRTEM images (right-hand side images) for BN MWNTs having the axes parallel to the [10–10] orientation (“zigzag” NTs). Reprinted with permission from [42], D. Golberg et al., *Appl. Phys. Lett.* 77, 1979 (2000). © 2000, American Institute of Physics.

a case one should expect nearly similar atomic densities for the wall and core domains for the HRTEM micrographs. The flattened CNTs have been indeed reported [66]. Mazzoni and Chacham [67] have recently calculated that flattening causes a reduction of the bandgap in a CNT from 0.92 to 0 eV. Similar results were obtained in the case of a flattened “zigzag” BNNT by Kim et al. [68]. In the latter case, the bandgap reduces from ~ 5 eV (cylindrical pure BNNT) to ~ 2 eV (collapsed or flattened BNNT). Interestingly, this phenomenon was not seen for an “armchair” BNNT. Thus, the BNNT flattening phenomena may open the exciting possibility of smooth tuning BNNT semiconducting properties.

4. CHEMICAL COMPOSITION AND BONDING IN PURE AND C-DOPED BN NANOTUBES

4.1. Electron Energy Loss Spectroscopy

The typical electron energy loss (EEL) spectrum taken on an individual isolated BNNT is depicted in Figure 6 [20]. It displays clear core-loss *K*-edges of B and N at 188 and 401 eV, respectively. They correspondingly show that the $1s \rightarrow \pi^*$ (left-hand side peak of the edge) and $1s \rightarrow \sigma^*$ (right-hand side band of the edge) transition features are similar to those of layered BN (hexagonal or rhombohedral) [6], implying the existence of a generally sp^2 -hybridized structure. On the other hand, Terauchi et al. [69] reported that the valence electron excitation spectra (so-called plasmon loss) of BNNTs has a considerable difference from that of layered BN due to the fact that the bandgap energy of BNNTs decreases with respect to layered BN by an amount of 0.6–0.7 eV due to the curving of a sheet into a nanotube.

4.2. Energy-Filtered Transmission Electron Microscopy

Spatially resolved EELS and energy-filtered electron microscopy becomes the most useful experimental technique as far as atom distribution in C-doped BN and/or ternary B-C-NNTs is concerned [70–76].

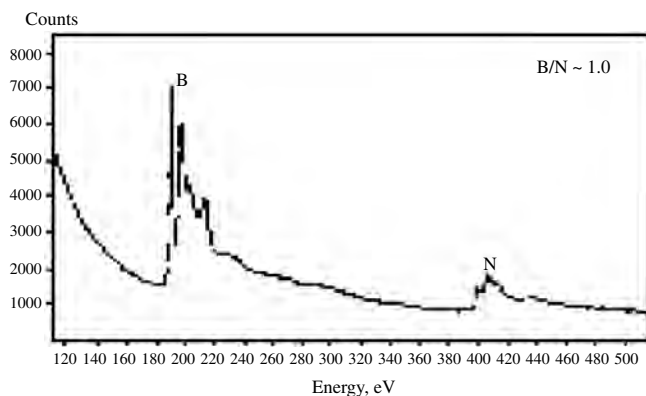


Figure 6. Representative EEL spectrum taken from an individual isolated 10-shelled BNNT. The B and N *K* edges at 188 and 401 eV are visible. The fine structure of the edges corresponds to sp^2 -hybridized nanostructure. The calculated atomic B/N ratio is ~ 1.0 .

For instance, Figure 7 depicts the HRTEM micrograph of a straight, well-ordered four-shelled C-doped BNNT [47]. The wall fringes exhibit bright contrast in the B and N elemental maps and barely visible contrast for the C map. By contrast, inside the tube, an encapsulated C-rich amorphous-like residue is visible. The residue contains fullerene-like molecules, as shown in the inset. Such molecules, whose diameter roughly corresponds to the theoretical diameter of a C_{60} molecule, ~ 0.7 nm, were often seen embedded in the B–C–N and BNNTs [47]. So-called peapod structures made of NTs and encapsulated fullerenes have often been observed in pure CNTs [77]. The data presented in Figure 7 serve as solid experimental evidence that encapsulation of fullerene-like molecules may also take place in BN-rich NTs. It is suggested that the present BN-rich NT/fullerene assembly may create a nanostructural molecular device with intriguing and unique electronic properties, especially if one keeps in mind the insulating nature of BNNTs and an exciting possibility of shuffling/moving of C_{60} molecules inside the NT channel.

TEM intensity profile analysis on the B, C, and N maps in the C-doped BN nanotubes [78] led the authors to the assumption that all three species may actually reside in the B–C–N tube walls. This is in striking contrast to the common beliefs on the dominant trend for BN and C shell separation via organization into so-called sandwich-like structures across the NTs [71–75, 79, 80] and/or domains along the NTs of B–C–N. However, the mentioned experimental results remarkably verify several theoretical predictions of homogeneous B–C–N layer stability [70, 74, 81, 82].

The fairly close values of the B and N atomic ratios measured in many EEL spectra [78] taken on B–C–N NTs led the researchers to the assumption that nearly stoichiometric

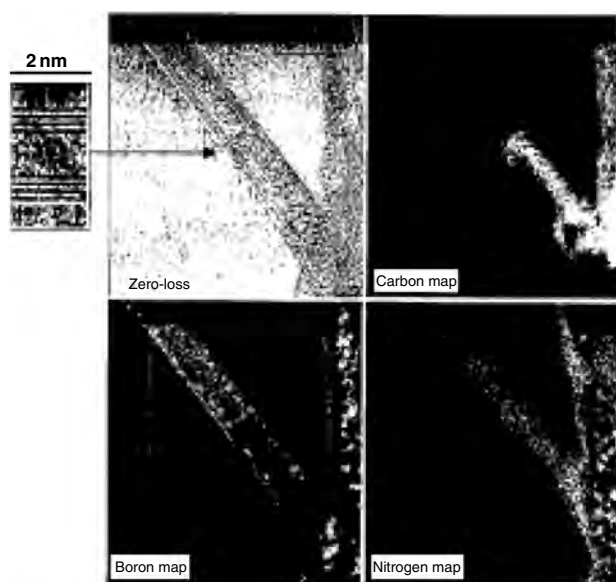


Figure 7. Zero-loss (HRTEM) and corresponding energy-filtered images of BN-rich MWNT with an encapsulated C-rich amorphous-like residue. The residue contains irregularly shaped and randomly stacked C_{60} -fullerene-like molecules as highlighted in the inset to the zero-loss image. Reprinted with permission from [47], Y. Bando et al., *Chem. Phys. Lett.* 346, 29 (2001). © 2001, Elsevier Science.

BN islands may occasionally form within a given C sheet, but the size of these islands should be well below the resolving power of the Omega filter TEM instrument used (~ 0.5 nm) [83]. On the other hand, it is noted that in most EELS runs on B–C–N NTs the N contents prevailed over those of B or vice versa. This implies that the random spatial distribution of B and N atoms in the C sheets via assemblage of complex B–C–N, B–C, and/or C–N containing six-membered rings should also be presumed to exist.

It is considered now that the peculiarities and kinetics (rather than thermodynamics) of a given BN/B–C–N NT synthesis are most important as far as the final elemental distribution is concerned.

For instance, Figure 8a depicts a HRTEM image (zero-energy loss) and B-, C-, and N-elemental maps of a rope synthesized via high-temperature chemical synthesis from aligned CN_x NTs [46, 48]. The B and N contents are seen as dominant ones. A key feature of the Figure 8 is the obvious BN/C domain segregation not visible for the shells of the individual B–C–N NT in Figure 7. The segregation is particularly documented in Figure 8b where intensity profiles of the B, C, and N species across the rope (the cross-section of interest is depicted in the zero-loss image in Fig. 8a) are thoroughly shown. The digits (shown in nm) on the horizontal axis correspond to the distance along the marked line (Fig. 8) starting from its left-hand side. One may immediately note that while the B and N profiles appear to correlate, that of C may either correlate or anticorrelate with the former two. Most importantly, the BN layers are frequently shielded with the C-rich layers (right-hand part of Fig. 8b, ~ 60 – 80 nm range), verifying the appearance of the “sandwich”-like structures. In addition, the B–C–N layers with variable elemental ratios might also present, as the left-hand part of Figure 8b displays (~ 40 – 60 nm range).

Thus, in the latter case, the rope is composed of conducting/semiconducting C-rich and/or B–C–N NTs shielded with insulating BN-rich tubular shells [46, 48] in contrast to the individual B–C–N NTs with homogeneous B, C, and N

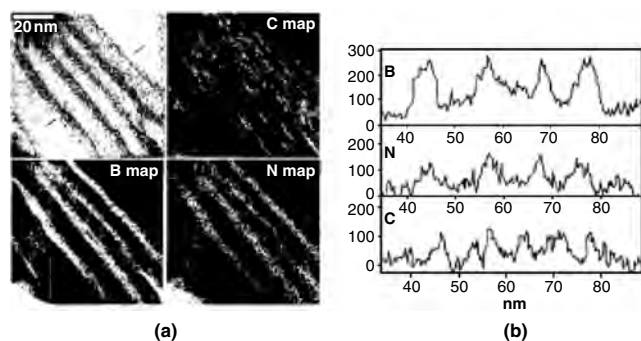


Figure 8. (a) HRTEM (zero-loss) and elemental maps taken on a BN-rich B–C–N NT rope synthesized at 2046 K from aligned CN_x nanotube mats, B_2O_3 and N_2 . The cross-section of interest is marked with the black bars on the zero-loss image. (b) The elemental map intensity profiles across the BN-rich B–C–N rope [along the line shown in the HRTEM image in (a); from left to right], displaying complex assembly of BN-rich, C-rich, and B–C–N layers. See text for details. Reprinted with permission from [48], D. Golberg et al., *Chem Phys. Lett.* 360, 1 (2002). © 2002, Elsevier Science.

distributions across and along the layers, as discussed earlier (Fig. 7).

5. IRRADIATION STABILITY OF BN NANOTUBES

The stability of a given nanotubular structure against various environments is of prime importance as far as its real practical applications are concerned.

The BNNT shells were found to be rather sensitive to the electron beam irradiation. At low dose irradiation the annealing-out of NT growth defects effectively occurs [26]. Figure 9a–d depicts consecutive HRTEM images of a BN MWNT irradiated under normal TEM imaging conditions (10 – 20 A/cm²). The time interval between consecutive micrographs is ~ 2 min. The initial NT lattice image in Figure 9a exhibits numerous undulating, dangling BN

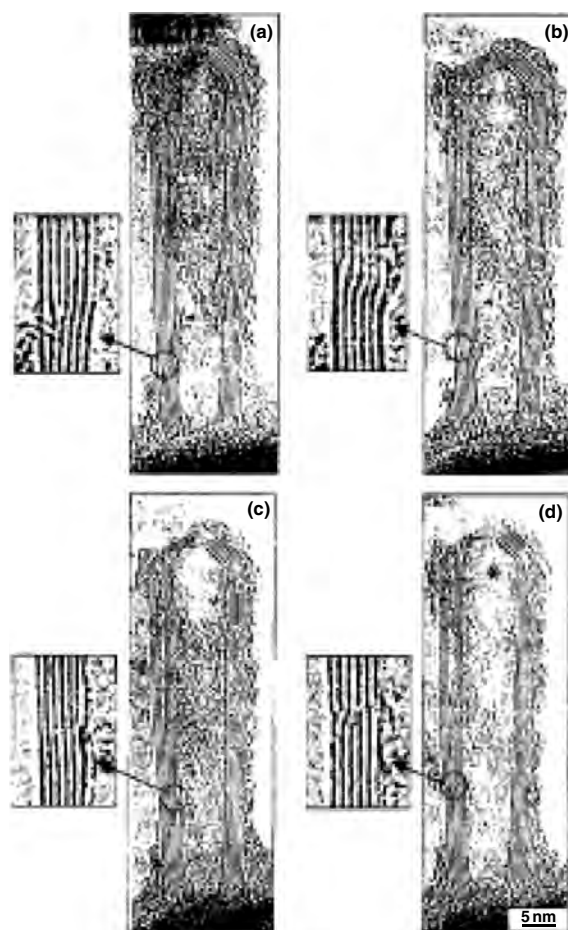


Figure 9. (a)–(d) Consecutive HRTEM images of a BN MWNT found in a material laser heated at superhigh nitrogen pressure (11 GPa), taken at intervals of ~ 2 min under normal TEM imaging conditions (flux density ~ 10 – 20 A/cm²). Dangling, undulating BN sheets—a commonly observed growth defect—are indicated by arrows. The MWNT section viewed edge-on contains irregularities in shell spacing, which are marked with a circle and enlarged separately in the insets. Annealing-out of the growth defects occurs under irradiation. Reprinted with permission from [26], D. Golberg et al., *Chem. Phys. Lett.* 279, 191 (1997). © 1997, Elsevier Science.

sheets viewed edge-on in the areas indicated by the arrows, in particular for the innermost NT sheet. The spacing between BN layers in the NT wall is extremely irregular, showing a very poor degree of crystallinity in the direction perpendicular to the NT axis. The observed irregularities caused by an extra atomic plane (i.e., dislocation edge), Figure 9a–c, or transverse shift of upper and lower internal sheet parts, Figure 9d, are marked with a circle and subsequently enlarged in the insets.

With increasing time of irradiation striking changes in the NT morphology take place. BN sheets become straight and align in the direction of the initial growth, while almost complete ordering of the NT shells occurs. The only defect remaining in the NT structure is an irregularity between the third and fourth lattice fringes on the left-hand side of the image. The observed movement of the dislocation edge apparently suggests virtual temporary sp^3 -character bonding between shells and a changeable stress gradient in the walls under electron beam irradiation.

An electron beam heats the specimen by energy absorption [84]. A temperature of several hundreds Kelvin can be reached on the thin specimen area. In order to distinguish growth defects from those resulting from electron beam irradiation, the BNNTs were irradiated for longer times, as shown in Figure 10 [85]. The results were similar to those for CNTs: longer irradiation of the entire illuminated NT region (Fig. 10) at an irradiation dose of $\sim 30 \text{ A/cm}^2$ over 90 min leads first to a decrease in the (0002) fringe contrast sharpness and, then, to the complete destruction of the nanotubular morphology, leaving the material with the consecutive appearance of a near-amorphous BN rod and near-amorphous BN rectangle-“onion”-like nanoparticle, a shape which is characteristic in the BN system (see Section 3).

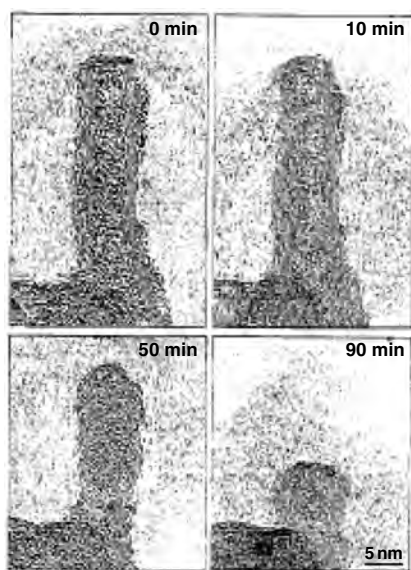


Figure 10. Consecutive HRTEM images demonstrating structural changes of a BN MWMT into a nested, highly defective octahedral-like BN “onion” under electron irradiation with a $\sim 30 \text{ A/cm}^2$ flux density. The irradiation time is shown on the figures. Reprinted with permission from [85], D. Golberg et al., *Mater. Res. Soc. Symp. Proc.* 593, 27 (2000). © 2000, Materials Research Society.

6. METAL-FILLED BN NANOTUBES

In spite of the existing intriguing possibility of making insulating “nanocables” composed of a conducting metal core and an insulating BN shield, a BNNT can hardly be filled with any metal due to its relatively poor wetting properties [6], as opposed to the relative ease in encapsulation of different metals and alloys into conventional CNTs.

The filling of CNTs with metal, metal oxides, or metal chlorides by capillarity or wet chemistry methods has been known for a decade [86]. However, all well-established techniques for CNT filling do not effectively work for BNNTs. As a result, to date the research on capillarity-induced filling of BNNTs with metals has not been actively carried out. During conventional laser vaporization or arc discharge accidentally formed metal-based nanoparticles originating from electrode and/or crucible materials have so far been observed at the BNNT tip-ends [1, 16, 50]. Undulating BN tubular fibers with a continuous ceramic core made of SiC were produced using a thermochemical C template method [87]. There have been also recent results on electrochemical deposition of Cu into submicrometer thick BN tubular fibers [88].

The present authors invented the simple, low-cost, and original way of continuous filling BNNTs with 3d-transition metal via capillarity using a two-step high-temperature synthesis involving (i) preliminary filling of C-based NTs with the metallic nanoparticles during the standard CVD process, followed by (ii) a high-temperature $\text{C} \rightarrow \text{BN}$ conversion within NT layers through consecutive chemical reactions [18]. Figure 11a and b depicts TEM micrographs of the resultant BNNTs continuously filled with the Invar Fe–Ni alloy (Fig. 11a) and pure Co (Fig. 11b) nanorods using this innovative technique.

The yield of filled NTs in the resultant products reached $\sim 5 \text{ vol}\%$. The diameter of metal-filled NTs ranged between 30 and 300 nm, whereas the filled length reached several micrometers [18]. A “nanocable” shown in Figure 11a exhibits an outer diameter of $\sim 40 \text{ nm}$ and contains a nanorod of alloy with a diameter of $\sim 20 \text{ nm}$. That shown in Figure 11b displays an external diameter of $\sim 45 \text{ nm}$ and displays a Co nanorod with diameter $\sim 30 \text{ nm}$. The chemical compositions of BN tubular layers and metallic fillings and their orientation relationship were thoroughly verified by EELS, EDX, and electron diffraction [18]. Depending on

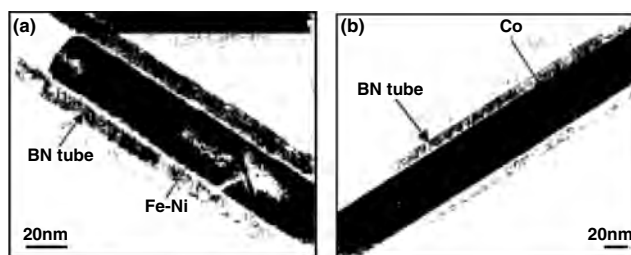


Figure 11. (a), (b) TEM images of BN MWNTs with embedded 3d-transition metal nanorods through high-temperature chemical syntheses: (a) a Fe–Ni filling and (b) a pure Co filling. Reprinted with permission from [18], Y. Bando et al., *Chem. Phys. Lett.* 347, 349 (2001). © 2001, Elsevier Science.

synthetic route used, composite structures may also be prepared: in the latter case the external BN layers may cover the innermost C layers, which together wrap the innermost conducting metallic nanowire, as was reported by Zhang et al. [79] and Ma et al. [80].

The unique features of the filled BNNT are the insulating properties of the BN tubular shields and conductive properties of the metallic cores (Fe–Ni, Co), which together made the first naturally insulated “nanocable.” The unmatched electrical, magnetic, and mechanical properties of the novel nanostructures should find appropriate applications in nano-electronics, nanoscale thermostats, and/or magnetic storage devices.

In the case of using metallic oxides as a filling medium, discrete metal clusters were also successfully encapsulated into BNNT channels. Golberg et al. [45] for the first time embedded pure discrete Mo clusters into BNNTs (Fig. 12). The clusters were just $\sim 1\text{--}2$ nm in size and spread over the whole nanotube length of ~ 0.5 μm . The inset in Figure 12 displays a cluster exhibiting lattice fringes with a separation of ~ 0.223 nm, which perfectly matches the (110) lattice spacing of a pure crystalline Mo, 0.222(5) nm. Since the clusters do not wet the internal BN shells they freely levitate within the tubular channel which thus may serve as a natural “pipeline” for tiny metallic cluster delivery and/or thermochemical protection.

7. PHYSICAL PROPERTIES

7.1. Thermal Stability

Figure 13a–c shows a comparison between thermal stability in air of the CNTs (grown either by a CVD process or arc discharge) and ropes consisting of BN MWNTs [20]. Differential thermal analysis (DTA) and thermogravimetry (TG) curves are shown. While oxidation of the CVD CNTs and the arc-discharge CNTs start respectively at ~ 844 and ~ 1013 K (as revealed by the corresponding DTA peaks and dramatic weight losses for the TG curves in Fig. 13), the reaction temperature of the BNNT ropes with air shifts to a

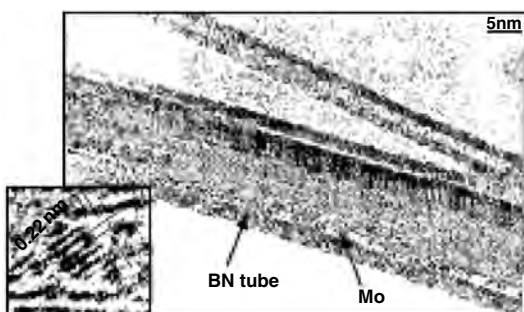


Figure 12. TEM image of a BN MWNT assembled within a rope and filled with Mo clusters of just 1–2 nm in size over the whole NT length. HRTEM image of a representative cluster is shown in the inset. The cluster displays lattice fringes separated by ~ 0.22 nm which fairly well match the (100) lattice spacing [0.220(8) nm] of a body-centered cubic Mo cluster. Reprinted with permission from [45], D. Golberg et al., *J. Nanosci. Nanotech.* 1, 49 (2001). © 2001, American Scientific Publishers.

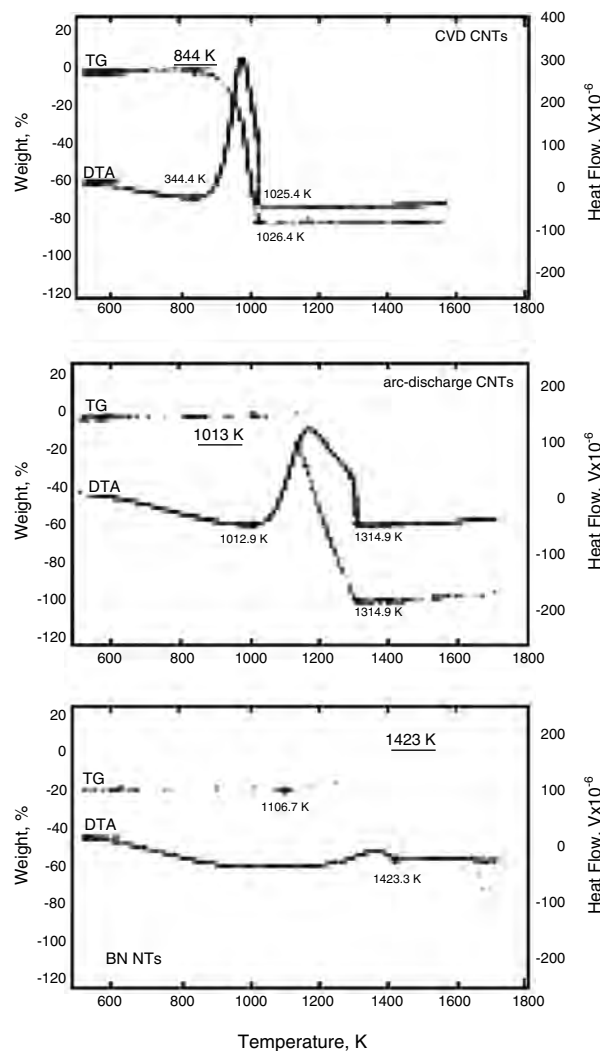


Figure 13. Comparative DTA and TG curves of BN and C MWNTs. Characteristic temperatures discussed in the text are particularly highlighted. Reprinted with permission from [20], D. Golberg et al., *Scripta Mater.* 44, 1561 (2001). © 2001, Elsevier Science.

much higher temperature range. Thorough modelling of the oxidation process shows that during BN tube oxidation, first, B_2O_3 starts to form above ~ 1107 K and, then, it vaporizes above 1423 K. To sum up, the BNNTs display much better thermal and chemical stability than their C counterparts. Thus, BN is preferred as far as NT-based device application is expected at high temperature and in chemically active and/or hazard environments. Thermal stability and chemical toughness of BNNTs are also of high importance in performing NT-based field emitters in flat panel displays and in field emission (FE) tips for scanning tunnelling (STM) and atom force (AFM) electron microscopes.

7.2. Transport I – V Characteristics

Recent striking theoretical predictions with respect to the unique mechanical and electrical properties of BNNTs pave the way to the real property measurements [89–103]. For

instance, Bettinger et al. [101] calculated that a BNNT should have greater yield resistance compared to a CNT, suggesting the promising use of the BNNT in environmentally stable reinforcing nanofibers for various composites. Kral et al. [92] calculated that an electrical current should appear when a BNNT is exposed to the polarized light (i.e., ultrafast optoelectronic and optomechanical devices may be expected). Moreover, thermal conductivity of a given nanotubular structure was calculated to approach the record value among of all materials existing on the Earth [93]; thus efficient use may be found for cooling computer chips performing at ultrahigh frequency (>1 THz) in modern computers. The insulating character of pure BNNTs also made possible electrical insulation of encapsulated metallic nanowires in complex electrical circuits.

The first experiment on practical evaluation of FE for an individual pure BNNT has been reported by Cumings and Zettl [22] during which an electrically insulating (expected *a priori*) BNNT surprisingly demonstrated notable FE currents at relatively low voltages. In order to further evaluate the transport and FE prospects of BN-based NT devices, Golberg et al. [78] performed marginal doping of BNNTs with C (in order to smoothly tune a bandgap) and analyzed the resultant I - V and FE characteristics of an individual C-doped BNNT rope in a Fresnel projection electron microscope [so-called low energy electron source microscope (LEEPS)] [78, 107].

The LEEPS images of a representative BN-rich CNT bundle [before (a) and after (b) I - V measurements] together with the detected I - V characteristics are shown in Figure 14a-c [78]. The shape of the I - V curves in Figure 14c is characteristic of a semiconductor with ~ 1 eV bandgap. Three consecutive I - V curves from [78] (sweeps 1, 2, and 3) that display fairly good reproducibility are shown in Figure 14c.

To date, there have been a few theoretical predictions that layered B-C-N materials may display semiconducting properties intermediate between metallic CNTs and dielectric BNNTs. For instance, Liu et al. [105] calculated a 2.0 eV

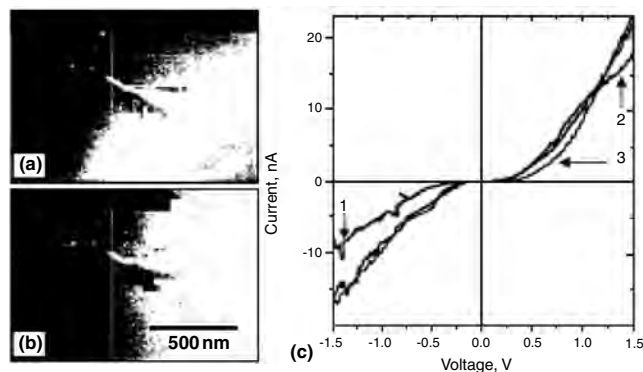


Figure 14. Fresnel projection microscope images. (a) Before transport measurements, (b) after transport measurements, and (c) consecutive I - V curves of an individual C-doped BNNT rope: first sweep; second sweep; and third sweep. All curves are characteristic of a semiconductor with an estimated bandgap of ~ 1 eV. Reprinted with permission from [78], D. Golberg et al., *Chem. Phys. Lett.* 359, 220 (2002). © 2002, Elsevier Science.

bandgap for a BC_2N stoichiometric sheet, while Zhu et al. [106] obtained a 0.2 eV gap for a BCN layered network. There has been an experimental estimate of the bandgap in a mat of ternary $B_{0.34}C_{0.42}N_{0.24}$ undulating highly defective CVD tubular fibers using photoluminescence, stated to be around 1.0 eV [28]. The value of the bandgap experimentally determined for an individual straight perfectly ordered BN-rich B-C-N NT rope was close to ~ 1 eV [78]. The small value of the bandgap is due to the global reduction of the ionicity of the C-doped BNNT network compared to pure BNNTs (bandgap of ~ 5.5 eV [4]) in the earlier experiments of Cumings and Zettl [22].

7.3. Field Emission Parameters

FE properties of aligned NT mats composed of B, C, and N atoms were found to be mostly governed by the chemical composition [104]. For instance, Figure 15a displays a LEEPS image of a representative individual C-doped BNNT rope, utilized for FE measurements [107]. The image of the same rope after the FE event is also given in Figure 15b. Figure 15c shows consecutively recorded I - V FE curves.

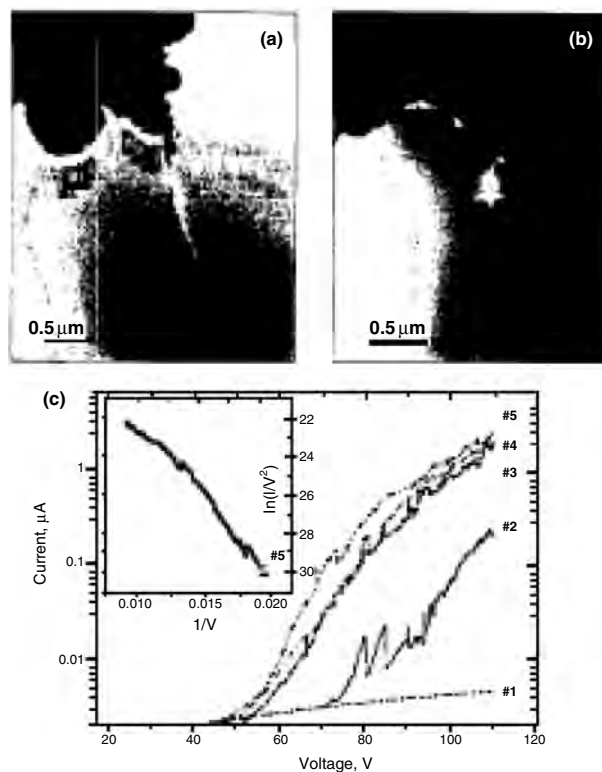


Figure 15. LEEPS images of a C-doped BN MWNT rope before (a) and after (b) FE measurements; and (c) consecutive I - V curves taken at three distances between the tungsten tip of the LEEPS microscope and the rope: curve 1—infinitely large distance; curve 2—when notable FE current was first recorded; curves 3–5—consecutive runs taken at a shorter distance. FE current gradually increases while the rope is presumably “sharpened” (3–5). Inset in (c) shows a representative Fowler–Nordheim plot for curve 5. Reprinted with permission from [107], P. Dorozhkin et al., *Appl. Phys. Lett.* 81, 1083 (2002). © 2002, American Institute of Physics.

Curve 1 was taken at a large distance, d , between the microscope tip and the rope and shows only a small leakage current. The tip was then moved closer to the rope until a notable FE current was first detected (curve 2). Then, the tip-rope distance was finally decreased and three consecutive I - V curves (3–5) were recorded at fixed d .

Remarkably, the last recorded curve 5 demonstrated stable FE current up to at least $2.5 \mu\text{A}$, which is fairly close to the maximum stable FE current ($\sim 2 \mu\text{A}$) reported for an individual CNT [108]. When plotted in Fowler–Nordheim [109] coordinates (inset to Fig. 15c) curve 5 fits a line at low voltages proving that a conventional FE process is taking place.

To summarize, a C-doped BNNT rope is a good field emitter with emission characteristics comparable to those of CNTs. While its ability to produce high FE currents is similar to that of CNTs, the BN-based NT rope exhibits better environmental stability for FE, opening the new horizon in a wide application of C-doped BNNTs in flat panel displays and/or FE tips for the STM and AFM microscopes of the new generation.

8. APPLICATIONS

8.1. Gas Adsorption

It is noted that investigations aiming to probe gas adsorption properties of BNNTs for potential applications are becoming more and more important. For instance, hydrogen—the cleanest source of energy—holds promise for solving current environment pollution problems with zero-emission vehicles. The research on hydrogen uptake in BN nanotubes was initially promoted by that in counterpart CNTs. Single-walled CNTs were intensively studied and revealed strong interactions between hydrogen molecules and tube walls [110]. However, quite different uptake values were reported by various groups [110–112]. This may be caused by the difference in electronic interactions between hydrogen and CNTs exhibiting various atomic structure; in fact, CNT electrical properties are highly sensitive to its morphology and atomic order which are yet not under control [5]. By contrast, BN nanotubes are quite electrically uniform offering stable insulating properties independent of the atomic structure, diameter, and number of layers. Recently Ma et al. [113] has demonstrated that BN nanostructures may absorb hydrogen at the level equal or even exceeding that for C nanotubes. Multiwalled BNNTs could adsorb 1.8–2.6 wt% of nitrogen under ~ 10 MPa at room temperature. Innovative nanostructures in BN may also be of great importance in the field [114–120]. For instance, Tang et al. [120] has demonstrated that significant hydrogen uptake increase (up to 4.8 wt%) may occur in collapsed BNNTs having highly developed surface area due to breaking of straight tubular shells into hairlike fragments attached to the tubular-like core. High thermal and chemical stability of BNNTs which is superior to that of CNTs [20, 121] may be also an advantageous factor for applications in hydrogen storage NT capacitors, since the latter presumes long-time thermal cycling in nonvacuum conditions.

8.2. Electrical Nanoinsulators

The insulating nature of BNNTs opens up a new horizon in producing electrically insulated embedded nanowires in downsized electrical devices and complex nanocircuits. The problem of poor wetting properties of BN material could be effectively overcome through conducting two-stage filling processes [18, 45], simultaneous growth of a nanowire and BN shells, or substitution of BN coating for the filling procedure [115–122]. Another possible route is production of BNNT insulated C or B–C–N NTs through sandwich-like tubular structure formation [48, 79, 80]. Recently perfect insulating performance of mechanically tough BN tubular shields and excellent conductive properties of the internal tubular B–C–N layers were verified for such eagerly awaited nanostructures during *in-situ* transport and field emission experiments in a LEEPS microscope [123].

8.3. Field-Emitting Devices

Due to the insulating nature of BN material field emission from pure BNNTs may doubtfully be of interest due to naturally high turn-on fields, low current densities, possible arcing, and resistance heating [6, 124]. In fact, high turn-on fields of 15.2 to 8.3 $\text{V}/\mu\text{m}$ [125] were measured on microcrystalline BN thin films. For comparison, the best field emitters made of aligned CNTs typically have turn-on fields in the range of 1–3 $\text{V}/\mu\text{m}$. Doping of BNNTs with C seems preferable for lowering turn-on fields and increasing current densities of BNNTs [106]. In fact, turn-on fields of 2–3 $\text{V}/\mu\text{m}$ and current densities of $\sim 3 \text{ mA}/\text{cm}^2$ have recently been achieved on C-doped BNNT films at 5.5 $\text{V}/\mu\text{m}$ macroscopic fields [126]. For comparison the best field emitters made of CNTs may reach 10 mA/cm^2 below 4.5 $\text{V}/\mu\text{m}$ —thus the better parameters. Particular selection of C or BN–C NT field emitters for a given application thus should be governed by the interplay between the importance of the environmental stability (better for BN–C NTs) and absolute field emission characteristics (better for CNTs).

9. CONCLUDING REMARKS

We conclude that in spite of the significant difficulties in BNNT preparation, structural analysis, and property measurements, the notable breakthroughs in their synthesis and atomic structure determination have been achieved within a few experimental and theoretical research groups, among those Y. Bando's group at NIMS (Japan), A. Zettl's group at the University of California, Berkeley (USA), A. Loiseau's group at CNRS (France), C. N. R. Rao's group at the Bangalore CSIR Centre (India), Y. Saito's group at the Mie University (Japan), M. Terauchi's group at Tohoku University (Japan), A. Rubio's group at the University of Pais Vasco (Spain), D. Tomanek's group at Michigan State University (USA), M. Terrones's group at IPICYT (Mexico), R. Ruoff's group at Northwestern University (USA), and Y. Chen's group at Australian National University may be mentioned.

The main challenge is now to significantly increase the yield of BNNTs to promote their advantageous applications as compared to conventional CNTs and to exploit novel BNNT structures [127–129].

GLOSSARY

Armchair nanotubes Nanotubes having their axes in parallel with the [11–20] orientation of a graphitic sheet.

Energy filtered elemental maps Images of nanostructures using electron loss energies characteristic of a band transition of a particular element.

Field emission Extracting electrons from a substance placed at a particular distance from a positively biased electrode.

Multiwalled nanotube A nanotube having more than two layers.

Nanotube A cylinder made of a wrapped graphitic sheet exhibiting diameters down to 4 Angstroms.

Single-walled nanotube A nanotube having a single atomic shell.

Zigzag nanotubes Nanotubes having their axes in parallel with the [10–10] orientation of a graphitic sheet.

ACKNOWLEDGMENTS

The authors are indebted to Dr. T. Sato, Dr. L. Bourgeois, Dr. M. Mitome, Dr. W. Han, Dr. M. Eremets, Dr. A. Louchev, Dr. O. Stephan, Dr. M. Terrones, Dr. J. Sloan, Dr. S. Saito, Professor Z.-L. Wang, Professor A. Zettl, Professor M. Cohen, Professor S. G. Louie, Professor D. Tomanek, and Dr. A. Loiseau for valuable discussions in the course of this work. Thanks are also due to Dr. P. Dorozhkin and Dr. Z.-C. Dong for collaborative work on BNNT electrical property measurements using a Fresnel projection microscope, and to Mr. M. Hasegawa and Mr. T. Ogawa for participation in BN tube filling project. We are also grateful to Mr. K. Kurashima for the continuous technical support of the JEOL-3000F microscope and to JEOL engineers Dr. E. Okunishi, Dr. T. Kaneyama, Dr. Y. Okura, and Dr. M. Naruse for the maintenance of the Omega filter JEOL3100FEF electron microscope.

REFERENCES

- N. G. Chopra, R. J. Luyken, K. Cherrey, V. H. Crespi, M. L. Cohen, S. G. Louie, and A. Zettl, *Science* 269, 966 (1995).
- S. Iijima, *Nature (London)* 354, 56 (1991).
- A. Rubio, J. L. Corkill, and M. L. Cohen, *Phys. Rev. B* 49, 5081 (1994).
- X. Blase, A. Rubio, S. G. Louie, and M. L. Cohen, *Europhys. Lett.* 28, 335 (1994).
- J. W. G. Wildöer, L. C. Venema, A. G. Rinzler, R. E. Smalley, and C. Dekker, *Nature (London)* 391, 59 (1998).
- J. J. Pouch and A. Alterovitz, "Synthesis and Properties of Boron Nitride," *Mater. Sci. Forum*, Vol. 54–55. Trans. Tech., Switzerland, 1990.
- S. Iijima and T. Ichihashi, *Nature (London)* 363, 603 (1993).
- T. W. Ebbesen and P. M. Ajayan, *Nature (London)* 358, 220 (1992).
- S. C. Tsang, Y. K. Chen, P. J. F. Harris, and M. L. H. Green, *Nature* 372, 159 (1994).
- S. Iijima, T. Ichihashi, and Y. Ando, *Nature (London)* 356, 776 (1992).
- X. F. Zhang, X. B. Zhang, G. Van Tendeloo, S. Amelinckx, M. Op de Beeck, and J. Van Landuyt, *J. Cryst. Growth* 130, 368 (1993).
- P. M. Ajayan, T. W. Ebbesen, T. Ichihashi, S. Iijima, K. Tanigaki, and H. Hiura, *Nature (London)* 362, 522 (1993).
- M. M. J. Treacy, T. W. Ebbesen, and J. M. Gibson, *Nature (London)* 381, 678 (1996).
- T. W. Ebbesen, H. J. Lezec, H. Hiura, J. W. Bennett, H. F. Ghaemi, and T. Thio, *Nature (London)* 382, 54 (1996).
- J. Hone, M. Whitney, C. Piscoti, and A. Zettl, *Phys. Rev. B* 59, R2514 (1999).
- A. Loiseau, F. Willaime, N. Demoncey, G. Hug, and H. Pascard, *Phys. Rev. Lett.* 76, 4737 (1996).
- J. Cumings and A. Zettl, *Chem. Phys. Lett.* 316, 211 (2000).
- Y. Bando, K. Ogawa, and D. Golberg, *Chem. Phys. Lett.* 347, 349 (2001).
- D. Golberg, W. Han, Y. Bando, K. Kurashima, and T. Sato, *J. Appl. Phys.* 86, 2364 (1999).
- D. Golberg, Y. Bando, K. Kurashima, and T. Sato, *Scripta Mater.* 44, 1561 (2001).
- N. G. Chopra and A. Zettl, *Solid State Comm.* 105, 297 (1998).
- J. Cumings and A. Zettl, in "Electronic Properties of Molecular Nanostructures" (H. Kuzmany et al., Eds.), AIP Conf. Proc. Ser., p. 577. Am. Inst. of Phys., New York, 2001.
- T. Guo, P. Nikolaev, A. G. Rinzler, D. Tomanek, D. T. Colbert, and R. E. Smalley, *J. Phys. Chem. B* 99, 694 (1995).
- M. Endo, K. Takeuchi, S. Igarashi, K. Kobori, M. Shiraiishi, and H. W. Kroto, *J. Phys. Chem. Solids* 54, 1841 (1993).
- D. Golberg, Y. Bando, M. Eremets, K. Takemura, K. Kurashima, and H. Yusa, *Appl. Phys. Lett.* 69, 2045 (1996).
- D. Golberg, Y. Bando, M. Eremets, K. Takemura, K. Kurashima, T. Tamiya, and H. Yusa, *Chem. Phys. Lett.* 279, 191 (1997).
- D. Golberg, Y. Bando, M. Eremets, K. Takemura, K. Kurashima, T. Tamiya, and H. Yusa, *J. Elec. Microsc.* 46, 281 (1997).
- D. P. Yu, X. S. Sun, C. S. Lee, I. Bello, S. T. Lee, H. D. Gu, K. M. Leung, G. W. Zhou, Z. F. Dong, and Z. Zhang, *Appl. Phys. Lett.* 72, 1966 (1998).
- T. Laude, Y. Matsui, A. Marraud, and B. Jouffrey, *Appl. Phys. Lett.* 76, 3239 (2000).
- Y. Chen, L. T. Chadderton, J. Fitz Gerald, J. S. Williams, and S. Bulcock, *Appl. Phys. Lett.* 74, 2960 (1999).
- P. Gleize, M. C. Schouler, P. Gadelle, and M. Caillet, *J. Mater. Sci.* 29, 1575 (1994).
- C. C. Tang, M. Lamy de la Chapelle, P. Li, Y. M. Liu, H. Y. Dang, and S. S. Fan, *Chem. Phys. Lett.* 342, 492 (2001).
- Y. Shimizu, Y. Morioishi, H. Tanaka, and S. Komatsu, *Appl. Phys. Lett.* 75, 929 (1999).
- E. Bengu and L. D. Marks, *Phys. Rev. Lett.* 86, 2385 (2000).
- O. R. Lourie, C. R. Jones, B. M. Bartlett, P. C. Gibbons, R. S. Ruoff, and W. E. Buhro, *Chem. Mater.* 12, 1808 (2001).
- M. Kuno, T. Oku, and K. Sukanuma, *Diam. Rel. Mater.* 10, 1231 (2001).
- W. Han, Y. Bando, K. Kurashima, and T. Sato, *Appl. Phys. Lett.* 73, 3085 (1998).
- D. Golberg, Y. Bando, W. Han, K. Kurashima, and T. Sato, *Chem. Phys. Lett.* 308, 337 (1999).
- D. Golberg, Y. Bando, L. Bourgeois, K. Kurashima, and T. Sato, *J. Carbon* 38, 2017 (2000).
- D. Golberg, Y. Bando, K. Kurashima, and T. Sato, *Chem. Phys. Lett.* 323, 181 (2000).
- D. Golberg, Y. Bando, K. Kurashima, and T. Sato, *Solid State Comm.* 116, 1 (2000).
- D. Golberg, Y. Bando, L. Bourgeois, K. Kurashima, and T. Sato, *Appl. Phys. Lett.* 77, 1979 (2000).
- D. Golberg, Y. Bando, K. Kurashima, and T. Sato, *Diam. Rel. Mater.* 10, 63 (2001).
- D. Golberg and Y. Bando, *Appl. Phys. Lett.* 79, 415 (2001).
- D. Golberg, Y. Bando, K. Kurashima, and T. Sato, *J. Nanosci. Nanotech.* 1, 49 (2001).
- D. Golberg, Y. Bando, M. Mitome, K. Kurashima, N. Grobert, M. Reyes-Reyes, H. Terrones, and M. Terrones, *Physica B* 323, 60 (2002).

47. Y. Bando, D. Golberg, M. Mitome, K. Kurashima, and T. Sato, *Chem. Phys. Lett.* 346, 29 (2001).
48. D. Golberg, Y. Bando, M. Mitome, K. Kurashima, N. Grobert, M. Reyes-Reyes, H. Terrones, and M. Terrones, *Chem. Phys. Lett.* 360, 1 (2002).
49. C. N. R. Rao, B. C. Satishkumar, A. Govindaraj, and M. Nath, *Chem. Phys. Chem.* 2, 78 (2001).
50. M. Terrones, W. K. Hsu, H. Terrones, J. P. Zhang, S. Ramos, J. P. Hare, R. Castillo, K. Prassides, A. K. Cheetham, H. W. Kroto, and D. R. M. Walton, *Chem. Phys. Lett.* 259, 568 (1996).
51. Y. Saito and M. Maida, *J. Phys. Chem. A* 103, 1291 (1999).
52. R. S. Lee, J. Cavillet, M. L. de la Chapelle, A. Loiseau, J. L. Cochon, D. Pigache, J. Thibault, and F. Willaime, *Phys. Rev. B* 64, 1405 (2001).
53. R. Z. Ma, Y. Bando, T. Sato, and K. Kurashima, *Chem. Mater.* 13, 2965 (2001).
54. R. Z. Ma, Y. Bando, and T. Sato, *Adv. Mater.* 14, 366 (2002).
55. M. Terauchi, M. Tanaka, K. Suzuki, A. Ogino, and K. Kimura, *Chem. Phys. Lett.* 324, 359 (2000).
56. X. Blase, A. de Vita, J. C. Charlie, and R. Car, *Phys. Rev. Lett.* 80, 1666 (1998).
57. A. Thess, P. Nikolaev, H. J. Dai, P. Petit, J. Robert, C. H. Xu, Y. H. Lee, S. G. Kim, A. G. Rinzler, D. T. Colbert, G. E. Scuseria, D. Tomanek, J. E. Fisher, and R. E. Smalley, *Science* 273, 483 (1996).
58. D. Golberg, Y. Bando, O. Stéphan, and Kurashima, *Appl. Phys. Lett.* 73, 2441 (1998).
59. L. Bourgeois, Y. Bando, and T. Sato, *J. Phys. D* 33, 1902 (2000).
60. L. Bourgeois, Y. Bando, K. Kurashima, and T. Sato, *Philos. Mag. A* 80, 129 (2000).
61. M. Menon and D. Srivastava, *Chem. Phys. Lett.* 307, 407 (1999).
62. X. Blase, J.-C. Charlie, A. De Vita, R. Car, Ph. Redlich, M. Terrones, W. S. Hsu, H. Terrones, D. L. Carroll, and P. M. Ajayan, *Phys. Rev. Lett.* 83, 5078 (1999).
63. R. Z. Ma, Y. Bando, and T. Sato, *Chem. Phys. Lett.* 337, 61 (2001).
64. B. G. Demczyk, J. Cumings, A. Zettl, and R. O. Ritchie, *Appl. Phys. Lett.* 78, 2772 (2001).
65. M. Terrones, W. K. Hsu, H. W. Kroto, and D. R. M. Walton, "Nanotubes: A Revolution in Materials Science and Electronics," p. 227. Springer, Berlin, 1999.
66. N. G. Chopra, L. X. Benedict, V. H. Grespi, M. L. Cohen, S. G. Louie, and A. Zettl, *Nature (London)* 377, 135 (1995).
67. M. S. C. Mazzoni and H. Chatham, *Appl. Phys. Lett.* 76, 1561 (2000).
68. Y.-H. Kim, K. J. Chang, and S. G. Louie, *Phys. Rev. B* 63, 205408 (2001).
69. M. Terauchi, M. Tanaka, M. Matsumoto, and Y. Saito, *J. Electr. Microsc.* 47, 319 (1998).
70. O. Stéphan, P. M. Ajayan, C. Colliex, Ph. Redlich, J. M. Lambert, P. Bernier, and P. Lefin, *Science* 266, 1683 (1994).
71. X. Blase, J.-C. Charlier, A. De Vita, and R. Car, *Appl. Phys. Lett.* 70, 197 (1997).
72. K. Suenaga, C. Colliex, N. Demoncey, A. Loiseau, H. Pascard, and F. Willaime, *Science* 278, 653 (1997).
73. Y. Zhang, H. Gu, K. Suenaga, and S. Iijima, *Chem. Phys. Lett.* 279, 264 (1997).
74. Ph. Kohler-Redlich, M. Terrones, C. Manteca-Diego, W. K. Hsu, H. Terrones, M. Rühle, H. W. Kroto, and D. R. M. Walton, *Chem. Phys. Lett.* 310, 459 (1999).
75. O. A. Louchev, Y. Sato, H. Kanda, and Y. Bando, *Appl. Phys. Lett.* 77, 1446 (2000).
76. W. Q. Han, J. Cumings, and A. Zettl, *Appl. Phys. Lett.* 78, 2769 (2001).
77. B. W. Smith, M. Monthieux, and D. Luzzi, *Nature (London)* 396, 323 (1998).
78. D. Golberg, P. Dorozhkin, Y. Bando, M. Hasegawa, and Z.-C. Dong, *Chem. Phys. Lett.* 359, 220 (2002).
79. Y. Zhang, K. Suenaga, C. Colliex, and S. Iijima, *Science* 281, 973 (1998).
80. R. Z. Ma, Y. Bando, and T. Sato, *Chem. Phys. Lett.* 350, 1 (2001).
81. Y. Miyamoto, A. Rubio, S. G. Louie, and M. L. Cohen, *Phys. Rev. B* 50, 18360 (1994).
82. T. Kar, M. Cuma, and S. Scheiner, *J. Phys. Chem. A* 102, 10134 (1998).
83. Y. Bando, M. Mitome, D. Golberg, Y. Kitami, and K. Kurashima, *Jpn. J. Appl. Phys.* 40, L1193 (2001).
84. F. Banhart, N. Grobert, M. Terrones, J.-C. Charlier, and P. M. Ajayan, *Int. J. Mod. Phys.* 15, 4037 (2001).
85. D. Golberg, Y. Bando, W. Han, L. Bourgeois, K. Kurashima, and T. Sato, *Mater. Res. Soc. Symp. Proc.* 593, 27 (2000).
86. E. Dujardin, T. W. Ebbesen, H. Hiura, and K. Tanigaki, *Science* 265, 1850 (1994).
87. W. Han, P. Redlich, F. Ernst, and M. Rühle, *Appl. Phys. Lett.* 75, 1875 (1999).
88. K. B. Shelimov and M. Mockovits, *Chem. Mater.* 12, 250 (2000).
89. L. A. Chernozatonskii, E. G. Gal'perin, I. V. Stankevich, and Ya. K. Shimkus, *Carbon* 37, 117 (1999).
90. Y.-K. Kwon, D. Tomanek, and S. Iijima, *Phys. Rev. Lett.* 82, 1470 (1999).
91. L. Vaccarini, C. Goze, L. Henrard, E. Hernandez, P. Bernier, and A. Rubio, *Carbon* 38, 1681 (2000).
92. P. Kral, E. J. Mele, and D. Tomanek, *Phys. Rev. Lett.* 85, 1512 (2000).
93. S. Berber, Y.-K. Kwon, and D. Tomanek, *Phys. Rev. Lett.* 84, 4613 (2000).
94. P. Zhang and V. Crespi, *Phys. Rev. B* 62, 11050 (2000).
95. P. E. Lammert, V. H. Crespi, and A. Rubio, *Phys. Rev. Lett.* 87, 6402 (2001).
96. D. Srivastava, M. Menon, and K. Cho, *Phys. Rev. B* 63, 195413-1 (2001).
97. O. E. Alon, *Phys. Rev. B* 64, 3408 (2001).
98. S. Erkoç, *J. Mol. Struct-Theochem.* 542, 89 (2001).
99. K. N. Kudin, G. E. Scuseria, and B. I. Yakobson, *Phys. Rev. B* 64, 235406 (2001).
100. J. Kongsted, A. Osted, L. Jensen, P. O. Astrand, and K. V. Mikkelsen, *J. Phys. Chem.* 105, 10243 (2001).
101. H. F. Bettinger, T. Dumitrica, G. E. Scuseria, and B. I. Yakobson, *Phys. Rev. B* 65, 041406 (2002).
102. V. Meunier, C. Roland, J. Bernholc, and M. B. Nardelli, *Appl. Phys. Lett.* 81, 46 (2002).
103. S. Okada, S. Saito, and A. Oshiyama, *Phys. Rev. B* 65, 165410 (2002).
104. C. Y. Zhi, J. D. Guo, X. D. Bai, and E. G. Wang, *J. Appl. Phys.* 91, 5325 (2002).
105. A. Y. Liu, R. M. Wetzcvitch, and M. L. Cohen, *Phys. Rev. B* 39, 1760 (1988).
106. H.-Y. Zhu, D. J. Klein, N. H. March, and A. Rubio, *J. Phys. Chem. Sol.* 59, 1303 (1998).
107. P. Dorozhkin, D. Golberg, Y. Bando, and Z.-C. Dong, *Appl. Phys. Lett.* 81, 1083 (2002).
108. K. A. Dean and B. R. Chalamala, *Appl. Phys. Lett.* 76, 375 (2000).
109. R. Gomer, "Field Emission and Field Ionization." Harvard Univ. Press, Cambridge, MA, 1961.
110. A. C. Dillon, K. M. Jones, T. A. Bekkedahl, C. H. Kiang, D. S. Bethune, and M. J. Heben, *Nature* 386, 377 (1997).
111. A. Chambers, C. Park, R. T. K. Baker, and N. M. Rodriguez, *J. Phys. Chem. B* 102, 4253 (1998).
112. C. Liu, Y. Y. Fan, M. Liu, H. T. Cong, H. M. Cheng, and M. S. Dresselhaus, *Science* 286, 1127 (1999).
113. R. Z. Ma, Y. Bando, H. W. Zhu, T. Sato, C. L. Xu, and D. H. Wu, *J. Am. Chem. Soc.* 124, 7672 (2002).

114. R. Ma, Y. Bando, T. Sato, and L. Bourgeois, *Diam. Rel. Mater.* 11, 1397 (2002).
115. C. C. Tang, Y. Bando, T. Sato, K. Kurashima, X. X. Ding, Z. W. Gan, and S. R. Qi, *Appl. Phys. Lett.* 80, 4641 (2002).
116. I. Narita and T. Oku, *Diam. Rel. Mater.* 11, 949 (2002).
117. C. C. Tang, Y. Bando, T. Sato, and K. Kurashima, *J. Mater. Chem.* 12, 2002 (2002).
118. F. L. Deepak, C. P. Vinod, K. Mukhopadhyay, A. Govindaraj, and C. N. R. Rao, *Chem. Phys. Lett.* 353, 345 (2002).
119. C. C. Tang, Y. Bando, and D. Golberg, *Chem. Comm.* 2826 (2002).
120. C. C. Tang, Y. Bando, X. X. Ding, S. R. Qi, and D. Golberg, *J. Am. Chem. Soc.* 124, 14550 (2002).
121. W. Q. Han, W. Mickelson, J. Cumings, and A. Zettl, *Appl. Phys. Lett.* 81, 1110 (2002).
122. C. C. Tang, Y. Bando, T. Sato, and K. Kurashima, *Adv. Mater.* 14, 1290 (2002).
123. D. Golberg, P. S. Dorozhkin, Y. Bando, Z.-C. Dong, N. Grobert, M. Reyes-Reyes, H. Terrones, and M. Terrones, *Appl. Phys. Lett.* 82, 1275 (2003).
124. J.-M. Bonard, M. Croci, C. Klinke, R. Kurt, O. Noury, and N. Weiss, *Carbon* 40, 1715 (2002).
125. T. Sugino, C. Kimura, and T. Yamamoto, *Appl. Phys. Lett.* 80, 3602 (2002).
126. D. Golberg, P. S. Dorozhkin, Y. Bando, Z.-C. Dong, C. C. Tang, Y. Uemura, N. Grobert, M. Reyes-Reyes, H. Terrones, and M. Terrones, *Appl. Phys. A.* 76, 499 (2003).
127. W. Mickelson, S. Aloni, W. Q. Han, J. Cumings, and A. Zettl, *Science* 300, 467 (2003).
128. F. F. Xu, Y. Bando, R. Ma, D. Golberg, Y. B. Li, and M. Mitome, *J. Am. Chem. Soc.* 125, 8032 (2003).
129. F. F. Xu, Y. Bando, D. Golberg, R. Ma, Y. B. Li, and C. C. Tang, *J. Chem. Phys.* 119, 6 (2003).

C₆₀-Based Materials

J. G. Hou, A. D. Zhao, Tian Huang, Shan Lu

University of Science and Technology of China, Hefei, Anhui, People's Republic of China

CONTENTS

1. Introduction
2. C₆₀ Molecule
3. C₆₀ Crystal
4. C₆₀-Based Materials
5. Low-Dimensional Structures
 - Appendix A
 - Appendix B
 - Glossary
 - References

1. INTRODUCTION

Since the discovery of Buckminsterfullerene C₆₀ by Kroto et al. [1] in 1985 and the discovery of large quantity synthesis by Krätschmer et al. [2] in 1990, this molecular allotrope of carbon has attracted intense interest because of its unique physical and chemical properties. Varied novel materials based on C₆₀ have been synthesized successfully showing fantastic properties.

C₆₀ is a beautiful spherical hollow molecule with a diameter of ~1 nm possessing the highest degree of symmetry of all known molecules. Remarkable potential applications in future nanoscale molecular electronic devices were proposed [3] for C₆₀ molecules based on their fantastic properties and structural and chemical stabilities. Moreover, the molecule shows a strong ability to form derivative structures, such as substituted heterofullerenes, encapsulated endohedrals fullerenes, metal-adsorbed exohedral fullerenes, and so on. These novel structures broaden the field of nanostructured carbon materials and stimulated the research on fullerene-based nanotechnology.

Crystalline C₆₀, as a new third form of crystalline carbon, along with diamond and graphite, has also exhibited many interesting properties. Solid C₆₀ is a typical molecular crystal, it can be intercalated by metal atoms and molecules, polymerized, or composited to form complex solid-state structures. Many novel properties have been discovered such

as high temperature superconductivity in alkali metal intercalated C₆₀ compounds, ultrahigh hardness even exceeding diamond in three-dimensional (3D) polymerized C₆₀, and high temperature organic ferromagnetism in 2D rhombohedral polymerized C₆₀.

In this chapter, we summarize the structure and properties of the single C₆₀ molecule and C₆₀ based materials, including metal-intercalated, polymerized, doped, composite, and other derivative compounds. Moreover, recent progress in the search for some novel low-dimensional C₆₀ derivative structures, such as heterofullerenes, endohedral fullerenes, exohedral fullerene complexes, C₆₀ in carbon nanotubes, and (C₆₀)_n clusters, is also summarized.

2. C₆₀ MOLECULE

2.1. Synthesis

Fullerenes can be extracted from the soot made by either combustion [4–7] or pyrolysis of aromatic hydrocarbons [8–13] or by an arc-discharge process [1]; the latter is now the most commonly adopted and convenient method. It is usually achieved by heating resistively and evaporating carbon (usually graphite) electrodes with a small gap controlled as a constant in a helium or an argon atmosphere by passing a high electric arc-discharge current between them (see Fig. 1). For the carbon arc-discharge method, the best inert gas atmosphere is high-purity helium with preferred quenching-gas pressure in the range 100–200 Torr. Rods of smaller diameter of about 5 mm are most suitable for currents of 100 ampere; larger reactor volumes and high purity rods give higher yields and lower impurity content soot. Since the fullerene containing soot is better able to diffuse away from the hot discharging zone and the intense ultraviolet (UV) light of the arc, it is better that the inert gas is flowed through the arc zone. Either ac or dc discharge may be available and the latter results in consumption of the anode only which gives facilities for the use of anode rod autoloading and continuous operation. The common yield of fullerenes in soot through this method is about 10%, of which the yields of C₆₀ and higher fullerenes (mainly C₇₀) are about 75 and 25%, respectively.

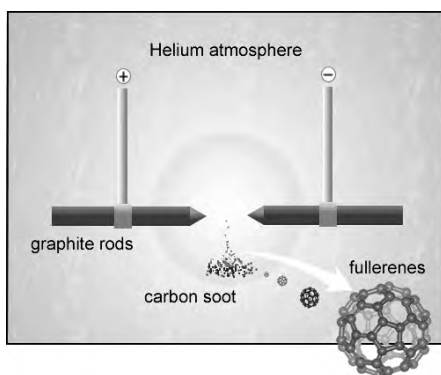


Figure 1. Schematic view of the generation process of fullerenes.

During the fullerene formation process, insoluble nanoscale carbon soot is formed together with soluble fullerenes and other soluble impurity molecules. Extraction can now most conveniently be performed with chloroform or toluene. The latter is more rapid but risks reaction brought about by the toluene (or xylene, mesitylene, etc.) solvent due to their susceptibility to electrophilic substitution reaction and degradation. The efficiency of this solvent method for the extraction is tied to the solubility of the fullerene molecules in solvents.

Liquid column chromatography is the main technique used for fullerene purification. Here purification means the separation of the fullerenes to distinguish C₆₀, C₇₀, etc. Earlier experiments used alumina [14] or mixtures of alumina/charcoal with toluene/hexane elution [15, 16]. The simpler and less expensive method employs Norit Elorit carbon granules as the stationary phase with toluene elution for C₆₀ and following 1,2-dichlorobenzene for C₇₀, in this way C₆₀ can be obtained at a fairly high rate of 10 gram per hour [17]. It is also necessary to wash the samples after purification with acetone to remove traces of hydrocarbons and other impurities.

A recent experiment showed that C₆₀ can be synthesized in 12 steps from commercially available starting materials by rational chemical methods [18]. A molecular polycyclic aromatic precursor bearing chlorine substituents at key positions forms C₆₀ when subjected to flash vacuum pyrolysis at 1100 °C and no other fullerenes are formed as by-products.

2.2. Structure

For C₆₀ there are 1812 possible structures [19], but the most stable isomer and the only one in which all the pentagons are nonadjacent is depicted as a truncated icosahedron cage structure with 90 edges, 60 vertices, and 32 surfaces, 12 of which are pentagonal and 20 are hexagonal (see Fig. 2 [20]). This building principle obeys Euler's theorem predicting that exactly 12 pentagons and an arbitrary number n of hexagons are required for the closure of a carbon closed cage. Otherwise C₆₀ is the most stable fullerene because it is the smallest possible to obey the isolated pentagon rule (IPR) [21, 22] which predicts fullerene structures with all the pentagons isolated by hexagons to be stabilized against structures with adjacent pentagons. The mean diameter of a C₆₀ molecule is

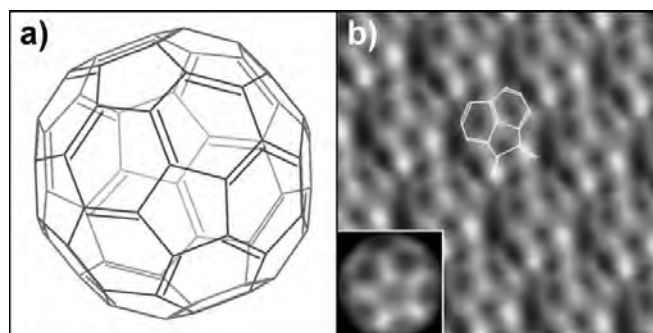


Figure 2. (a) Schematic 3D structural diagram for a C₆₀ molecule. (b) Scanning tunneling microscopy images of a C₆₀ molecular array which shows clearly the cage structure and double and single bonds. Inset is a theoretical simulation image. Adapted with permission from [20], J. G. Hou et al. *Nature* 409, 304 (2001). © 2001, Macmillan Magazines Ltd.

about 7.10 Å [23], or considering the thickness of the electron cloud shell the outer and inner diameters are approximately 10 and 4 Å, respectively.

The point group of C₆₀ is icosahedral I_h which comprises 120 symmetry operations consist of identity operation, 12 fivefold axes through the centers of the 12 pentagons, 20 threefold axes through the centers of the 20 hexagons, and 30 twofold axes through the centers of the 30 edges joining 2 hexagons combined with their inversion operations. Thus the C₆₀ molecule has the highest degree of symmetry of any known molecule.

The 2D representation of the 3D structure of C₆₀ is shown in Figure 3 [24]. It is created by shrinking the polygons of the nearest face and expanding those of the far face to fit all 60 carbon atoms within one plane. Obviously the Schlegel diagrams for C₆₀ may have either a pentagon or hexagon at the center, and a pentagon in Figure 3.

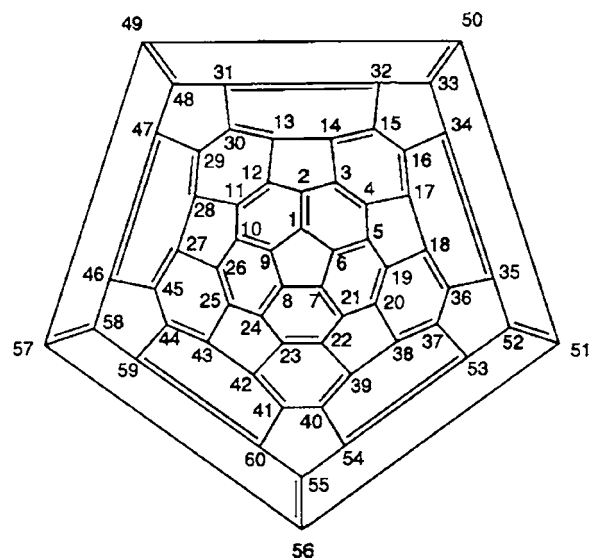


Figure 3. 2D Schlegel diagram for a C₆₀ molecule. Adapted with permission from [24], A. Hirsch, in "Fullerenes and Related Structures, Topics in Current Chemistry" (A. Hirsch, Ed.), Vol. 199, p. 13. Springer-Verlag, Berlin/Heidelberg, (1999). © 1999, Springer-Verlag.

2.3. Electronic Structure

A neutral C₆₀ molecule has 240 valence electrons; 180 are involved in σ -bonding energy levels lying well below the Fermi level. They brace and stabilize the cage structure. The remaining 60 electrons are involved in π -bonds, contributing to the conduction.

Since C₆₀ forms a near-sphere cage structure, the deviation from planarity leads to an admixture of s orbitals character into the p_z orbitals, where z is perpendicular to the (local) surface of the buckyball sphere. An average σ bond hybridization of $sp^{2.278}$ with a fractional s (about 9%) character into the p_z orbitals was estimated [25–29], compared to graphite with pure bond hybridization of sp^2 . Geometrically the p_z orbitals extend further outside the cage than inside the cage.

The bonds at the junctions of two hexagons ([6,6] bonds) (~ 1.40 Å) are somewhat shorter than the bonds at the junctions of a hexagon and a pentagon ([5,6] bonds) (~ 1.45 Å); thus the [6,6] bonds are usually considered to be double bonds and the [5,6] single. The shortening of bonds is caused by the partial localization of the π -orbitals into localized bonds and thus is directly related to the symmetry of C₆₀. This nonuniformity of bond lengths has been demonstrated by a series of theoretical [30, 31] and experimental investigations [32–34]. As a consequence, the double bonds in C₆₀ only lie at the junctions of the hexagons ([6,6] double bonds) and do not lie in the pentagonal rings.

Due to the near-spherical shape of the C₆₀ molecules, the fullerene electronic eigenstates can be considered by spherical harmonics and classified by their angular momentum quantum numbers l (see Fig. 4). Due to the Pauli exclusive principle, 50 π -electrons fully occupy the angular momentum states up through $l = 4$, leaving 10 π -electrons in the $l = 5$ state which can accommodate 22 electrons in full spherical symmetry, assuming that all the $l = 5$ states are filled before any $l = 6$ level becomes occupied. For C₆₀¹⁰⁺ with $l = 4$ filled, no significant bond length alternation is

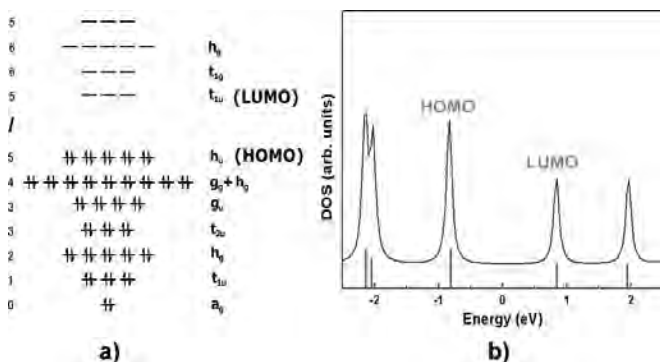


Figure 4. (a) Schematic diagram of the electronic structure for the 60 π -electrons in C₆₀ by Hückel theory calculation of the molecular energy spectrum of neutral C₆₀. The number l is the orbital angular quantum of the spherical harmonic from which a molecular orbital is derived. (b) Density of states (DOS) for the isolated C₆₀ molecule calculated using the discrete variational local density approximation method. Vertical lines denote energy levels of the molecule. The DOS is obtained by broadening the discrete levels with a Lorentz function for better comparison with experimental data.

expected. But in the case of neutral C₆₀ with the symmetry lowered from ideal spherical symmetry to icosahedral symmetry, the $l = 5$ state split into the ($h_u + t_{1u} + t_{2u}$) irreducible representations and the fivefold-degenerate h_u level (the lowest energy level) is completely filled by the remaining 10 electrons (see Fig. 4). This level forms the highest occupied molecular orbital (HOMO) in C₆₀. The threefold-degenerate t_{1u} level of $l = 5$ state forms the lowest unoccupied molecular orbital (LUMO) and this low-lying LUMO suggests that the C₆₀ is a fairly electronegative molecule. The HOMO–LUMO gap is calculated to be about 1.7 eV.

2.4. Properties of Single C₆₀ Molecule

2.4.1. Main Description

The main properties of C₆₀ molecule are summarized in Table 1 [23, 30–39]. The comparison of properties of C₆₀ with other fullerenes (from C₂₀, C₃₆, ... to C₁₀₆) is listed in Appendix A [23, 36, 40–55].

2.4.2. Electronic Transport Properties

Electronic transport properties of individual C₆₀ molecules have been investigated using a scanning tunneling microscope (STM) which enables controlled two-terminal measurements or a three-terminal transistor configuration which enables gate-voltage controlled current amplifications.

The resistance of a C₆₀ molecule was determined by the study of electrical contact with an individual C₆₀ introduced between a STM tip and a clean Au(110)-(1 × 2) surface at 300 K in ultrahigh vacuum [56]. It was revealed that at low applied bias voltages of ± 200 mV this system exhibited linear current–voltage (I – V) characteristics at all fixed tip displacement, indicating that the system behaves similarly to a metal–vacuum–metal tunnel junction at low bias voltage within the C₆₀ HOMO–LUMO gap. In this sense, the linearity allows us to define the intrinsic electrical resistance of an individual C₆₀ molecule. It was observed in

Table 1. Properties of C₆₀ molecules.

Property	Quantity	Ref.
IPR isomers	1	
Symmetry (point group)	I_h	
Double bond length	~ 1.40 Å	[30–34]
Single bond length	~ 1.45 Å	[30–34]
Average C–C distance	1.44 Å	[33]
Diameter	7.10 Å (mean)	[23]
Volume per molecule (πabc)	$1.87 \times 10^{-22}/\text{cm}^3$	
Number of distinct C sites	1	
Number of distinct C–C bonds	2	
Binding energy per atom	7.40 eV	[35]
Electron affinity	2.65 ± 0.05 eV	[36]
Cohesive energy per C atom	1.4 eV/atom	[37]
Ionization potential	7.95 ± 0.02 eV	[38]
HOMO–LUMO gap	1.7 eV (Dmol3 cal.)	
Heat of formation	$(41.8 \pm 0.3$ kJ per C atom) (at 298 k)	[39]

the current–distance (I – s) characteristics that the tunneling current increases approximately exponentially with tip displacement in the tunnel regime, but this behavior changes significantly as contact is established. A theoretical calculation using the elastic scattering quantum chemistry technique configured for STM (STM-ESQC) [57] considering the full atomic structure and valence orbitals of the tip, the C₆₀ molecule, and the Au(110) surface agreed very well with the experimental I – s curve. The deformation of C₆₀ was also included in STM-ESQC using the molecular mechanics (MM2) routine with a standard sp^2 carbon parametrization [58], and the C₆₀ conformation was optimized for each tip displacement s . The current I through the molecule was then calculated for each conformation. The point of electrical contact was found to be $s = 12.3$ Å, where the van der Waals expansion induced by tip attraction is compensated by tip compression, and the C₆₀ molecule may be considered approximately as its original shape. An apparent electrical resistance of 54.80 MΩ for the total junction with C₆₀ was determined at this point. In the Landauer formalism [59] of $T = (h/2e^2)R^{-1}$, this value corresponds to the C₆₀ electronic transparency (ease of transmission) of $T = 2.3 \times 10^{-4}$.

This experiment of “squeezing” a C₆₀ molecule by applying a small force in the nanonewton range with a metallic STM tip also results in a shift of the molecular orbital levels [56]. The mechanically induced shift provides a means to modulate tunnelling through a single C₆₀ molecule, even in a nonresonant tunnelling regime, and to change its resistance up to a limiting value approaching the quantum of resistance, $h/2e^2$ (~ 12.9 kΩ) [56]. The phenomenon, mechanically modulated virtual-resonant tunnelling, has also been used to design an single-molecule electromechanical amplifier, by making use of the ability to mechanically reduce molecular level degeneracy [60].

Electronic transport properties of C₆₀ molecules have also been studied in some other systems: The scanning tunneling spectroscopy (STS) investigation of an isolated C₆₀ molecule considered as a quantum dot in a double barrier tunnel junction (DBTJ) configuration [61] was carried out showing clear discrete molecular-level spectrum and obvious interplay with single-electron charging effects.

A novel negative differential resistance (NDR) molecular device is realized involving two C₆₀ molecules; one is adsorbed on a STM tip and the other is on the surface of the hexanethiol self-assembled monolayer [62]. It was demonstrated that it is the narrow local density of states features near the Fermi energy of the C₆₀ molecules that lead to the obvious stable and reproducible NDR effect.

In a single-C₆₀ nanomechanical transistor configuration based on an individual C₆₀ molecule connected to gold electrodes [63], the transport measurements provided obvious evidence for a coupling between the center-of-mass motion of the C₆₀ molecules and a single-electron hopping—a novel conduction mechanism. The coupling is manifest as quantized nanomechanical oscillations of the C₆₀ molecule against the gold surface with a frequency of about 1.2 THz which agreed well with a simple theoretical estimate based on van der Waals and electrostatic interactions between C₆₀ molecules and gold electrodes [63].

2.4.3. Scanning Tunneling Spectroscopy

Scanning Tunneling Spectroscopy of Isolated C₆₀ Molecule The scanning tunneling microscope is a powerful tool for measuring the local density states of surfaces and molecules. STS of an isolated C₆₀ molecule can be obtained in a DBTJ system (see Fig. 5a) where the individual C₆₀ molecule is coupled via two tunnel junctions to the metal substrate and an STM tip of vacuum and insulating layer, respectively, in order to eliminate the interaction between the metal substrate and C₆₀ molecule. Figure 5 shows a schematic view and equivalent circuit of the experimental setup and a typical spectroscopy of C₆₀ in this system.

Zeng et al. [62] measured the STS with such a system at a low temperature of 78 K by employing a hexanethiol self-assembled monolayer as the insulating barrier between C₆₀ and a gold substrate. Their results exhibited a noticeably larger HOMO–LUMO gap of ~ 2.8 eV (see Fig. 5), which is about 1 eV larger than the intrinsic HOMO–LUMO gap of ~ 1.7 eV. Because the size of a C₆₀ molecule is about 7 Å, much smaller than other metal or semiconductor quantum dots so far, the charging energy E_C of such a nanojunction, about 1 eV, is significant enough to be comparable with the molecular HOMO–LUMO bandgap (E_g) of a neutral C₆₀ molecule. So they attributed the larger gap width they observed to the sum of E_g and E_C . It was also noted that their differential tunneling spectra showed clearly fine peaks at the position of HOMO and LUMO energy regions. The three peaks in the negative bias region and five peaks in the positive bias region were well attributed to the degenerate splitting of threefold degenerated LUMO (t_{1u}) and fivefold degenerate HOMO (h_{1u}) level. The reason for the orbital degeneracy was considered to be the strong local electrical field and the Jahn–Teller effect.

Porath et al. [61] performed similar experiments at a low temperature of 4.2 K by using a polymethyl-methacrylate layer (less than 40 Å thick, determined by X-ray measurements) as the insulating barrier. The tunneling current–voltage spectra they observed also showed both Coulomb blockade and Coulomb staircase behavior and rich fine structures resulting from the discrete levels of a single C₆₀ molecule and the splitting of the degenerate energy levels. But the HOMO–LUMO gap in their spectra observed was about 0.8 eV (generally less than 1.5 eV), which is much less than that of a free neutral C₆₀ molecule. They attributed the

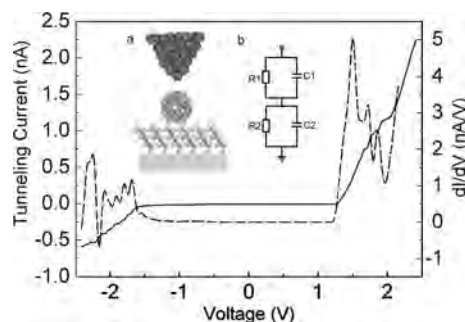


Figure 5. Scanning tunneling spectroscopy of a single C₆₀ molecule in a double barrier tunneling junction system. Dashed line is the dI/dV curve; solid line is the I – V characteristic curve.

origin of the smaller gap mainly to the level space between LUMO(C₆₀⁻) and HOMO(C₆₀⁺).

Inelastic Electron Tunneling Spectroscopy of Single C₆₀ Molecule Inelastic electron tunneling spectroscopy (IETS) is a powerful technique to obtain average vibrational information on condensed molecule species [64]. Combined IETS–STM can provide vibrational information resolved on single molecules [65–72]. It has been demonstrated that when C₆₀ is adsorbed on a surface, the structure of the free molecule remains fairly unaltered [73]. Pascual et al. [64] extend the inelastic STS (ISTS) studies to single C₆₀ molecules adsorbed on Ag(110) surface; they observed peaks at ±54 mV in the d^2I/d^2V curves in ISTS spectra on those C₆₀ molecules which oriented along one of their symmetry axes upon adsorption (see Fig. 6). In strong coincidence, those fullerenes maintain a resonance structure at the Fermi level that resembles the first unoccupied molecular orbital distribution of a free molecule. The enhanced signal was attributed to the excitation of a fullerene-cage vibrational mode by inelastic tunneling electrons. The vibration was assigned to the $H_g(\omega_2)$ mode (431 cm⁻¹), a fivefold degenerated mode of a free C₆₀ molecule corresponding to a “gerade” breathing of the molecular cage with larger radial component along the C_{5v} symmetry axis. Only in those cases where some molecular symmetry survives upon adsorption does some mode degeneracy remain, leading to a detectable contribution in the inelastic signal; for molecules in a non-symmetric orientation, degeneracy splitting, and subsequent mode mixing, may be so extensive that the observation of clear vibrational features in the ISTS spectra is suppressed. They concluded that the nature of the electronic molecular resonances around the Fermi level E_F , which determines the vibrational mode primarily, and the existence of a surviving symmetry on the adsorbed species, which determines the magnitude, were the two principal detection selection rules.

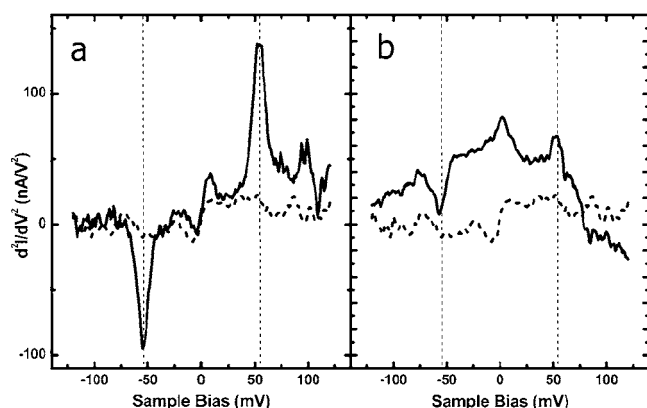


Figure 6. Comparison of ISTS spectra measured consecutively on two neighboring C₆₀ molecules. The dashed plot corresponds to the spectrum acquired on the bare silver surface. Each spectrum is the average of six bias voltage scans (25 sec/scan). In (a), the peak at 54 mV (–54 mV) represents a normalized change in conductance of 9% (8%). ($I = 1.6$ nA, $V_s = 0.5$ V, $V_{ac} = 5$ mV rms at $f_{ac} = 341$ Hz.) Adapted with permission from [64], J. I. Pascual et al., *J. Chem. Phys.* 117, 9531 (2002). © 2002, American Institute of Physics.

2.4.4. ¹³C Nuclear Magnetic Resonance Spectroscopy

By using room temperature ¹³C nuclear magnetic resonance (NMR) spectroscopy, Taylor et al. [14] and several research groups [74–76] obtained the first structure data for C₆₀ molecules in solution. In the spectrum, there is only one peak, showing extremely simple character, at a chemical shift of 143.2 ppm relative to tetramethyl silane (the standard reference molecule for ¹³C NMR spectroscopy). This only-one-peak character confirms that each carbon atom in the C₆₀ molecule is equivalent in the solution environment. In comparison with C₆₀, the C₇₀ molecule has five inequivalent carbon sites out of total atoms in geometry, corresponding to a richer NMR spectrum character of five peaks at 130.9, 145.4, 147.4, 148.1, and 150.7 ppm in a ratio of 10:20:10:20:10. Figure 7 shows typical ¹³C NMR spectra for the C₆₀ and C₇₀/C₆₀ mixture in benzene solution showing clear peak features [74].

2.4.5. Optical Properties

In gas phase or in organic solutions, optically excited fullerene molecules are influenced relatively weakly by their environments, thus the photophysical properties can be considered as those for near free molecules. The molecular energy level and photophysical behavior of electronically energized states for an individual C₆₀ molecule can be well described by using a Jablonski diagram, as shown in Figure 8. In this type of diagram, photoexcited electronic states of molecules include spin triplets ($S = 1$) and spin singlets ($S = 0$). The energy state definitions and transitions between these states are interpreted in Table 2.

The low-lying electronic transitions in C₆₀ are only weakly allowed because of the high degree of symmetry in the

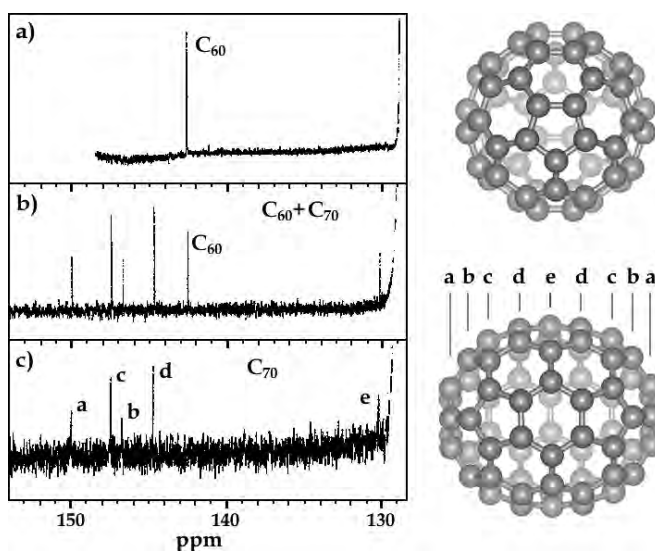


Figure 7. ¹³C NMR spectra for C₆₀, C₇₀, and C₇₀/C₆₀ mixture in benzene solution at 298 K. (a) C₆₀ sample; (b) C₆₀/C₇₀ mixture sample; (c) C₇₀ sample, peaks labeled a, b, c, d, and e are assigned to C₇₀ and correspond to the distinct five carbon atoms in a C₇₀ molecule in the right panel. Adapted with permission from [14], R. Taylor et al., *Chem. Commun.* 1423 (1990). © 1990, Royal Society of Chemistry.

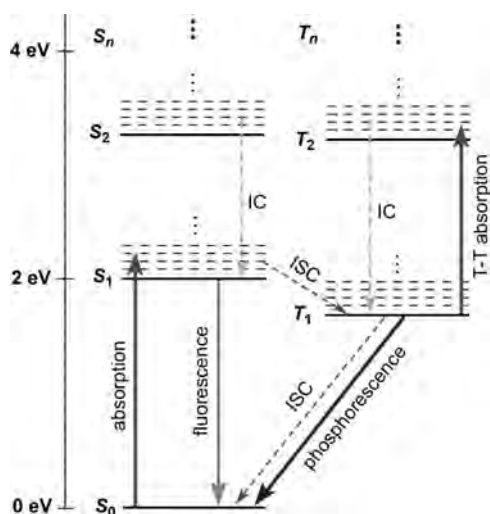


Figure 8. Diagram of electronic energy levels of C₆₀ molecule.

closed-shell electronic configuration. The absorption band of C₆₀ in the visible is very weak, with the molar absorptivity at the band maximum of only $\sim 950 \text{ M}^{-1} \text{ cm}^{-1}$ [14, 74, 77, 78]. Only a small fraction of the broad visible absorption band in the 430–670 nm region is due to the contribution of the transition to the lowest excited singlet state S₁ [79].

With extensive experimental investigations [79–95], it was well known that both C₆₀ and C₇₀ are only weakly fluorescent from the lowest singlet S₁ to the ground state, with C₇₀ having a slightly higher fluorescence quantum yield. Due to the weak interaction with each other, fluorescence lifetimes and fluorescence quantum yields of the fullerene molecules in solution under ambient conditions are essentially solvent independent.

In fact, upon photoexcitation, the excited singlet state S₁ decays are mainly dominated by nonradiative intersystem crossing to the excited triplet state T₁, with a very large quantum yield of nearly 100% [77, 96–99]. The extremely efficient intersystem crossing produces a high population of the excited triplet state T₁. Phosphorescence emission from the T₁ state to the ground state S₀ is so weak that it could not be detected initially even in a cryogenic sample [100]. The weak

phosphorescence reflects a low radiative rate for T₁ → S₀ emission, which is both spin and orbitally forbidden, plus comparatively rapid T₁ → S₀ nonradiative decay of intersystem crossing; see Figure 8. Previous results for the triplet T₁ lifetime of C₆₀ in room-temperature solutions range from 37 to 285 μs and even longer [77, 96, 98, 99, 101–105]. Recently Weisman [106] concluded that the wide discrepancies among these values likely reflect the presence of bimolecular decay channels such as self-quenching or unrecognized triplet–triplet annihilation, the effects of impurities in solution, or uncertainties in the kinetic data. He obtained an intrinsic T₁ triplet lifetime of 143 μs by eliminating the self-quenching component of this decay of 0.21%/μM.

Fullerenes and their derivatives were found to be excellent optical limiters in room-temperature solution [107–111]. The first report of the optical limiting (OL) of C₆₀ was that C₆₀ in toluene possesses the strongest OL response toward a laser at 532 nm. Optical power limiting occurs when the optical transmission of a material decreases with increasing laser fluence [112] which is now attributed to strong triplet absorption [112–115]. C₆₀ is an excellent broadband nonlinear absorber for potential optical limiting and optical switching applications [108, 112, 116–119], because of higher triplet–triplet transient absorption cross sections than the ground-state absorption cross sections [101, 108, 120]. However, a recent study suggested that in addition to the strongly absorptive excited singlet and triplet state, other transient species that are most likely associated with photoexcited state bimolecular processes may also be responsible for the observed strong optical limiting responses of fullerene in solution [119, 121]. There have been several mechanisms suggested to account for the optical limiting behavior of C₆₀, including reverse saturable absorption (RSA) [107], nonlinear scattering [122], thermal blooming [108, 123], and multiphonon absorption [108]. RSA was proved by transient absorption spectra to be the dominant mechanism, whereas other processes become important at high input influences [108, 122].

Photoexcited fullerenes are also excellent electron acceptors, exhibiting strong interactions with a variety of electron donors [89, 124, 125]. The unique properties of fullerenes with respect to photoinduced electron transfers include the small solvent reorganization energy [126] and the ability of a single fullerene cage to accept multiple electrons [127]. Photochemical reactions of fullerenes through an electron transfer mechanism often yield products that are different from those expected on the basis of known reactions of typical aromatic systems [128, 129], and in these reactions fullerenes often behave quite differently from polyaromatic compounds and other electron acceptors such as porphyrins. The recent development of cage functionalization methods [118, 130–133] has made it possible to prepare redox active fullerene derivatives for fundamental studies of photoinduced electron transfers and charge separations and for potential technological applications such as solar energy conservation. Fullerene molecules and their derivatives have also been used as charge generators in photoconductive polymer thin films [134–136].

The photophysical quantities for C₆₀ molecules in solution are listed in Table 3, corresponding to the physical properties illustrated in Figure 8.

Table 2. Energy states and transitions in a C₆₀ molecule.

Energy states	
S ₀	ground (singlet) state
S ₁ (T ₁)	first excited singlet (triplet) state
S _n (T _n)	higher excited singlet (triplet) state
Transitions or decays	
Absorption	including ground state absorption S ₀ → S _n and excited state absorption T _n → T _m (n, m ≥ 1)
Fluorescence	S ₁ → S ₀ (usually)
Phosphorescence	T ₁ → S ₀ (usually)
Internal conversion	S _n → S _{n-1} and T _n → T _{n-1} , radiationless transitions
Intersystem crossing (ISC)	S _n → T _m for n > 0, or T _m → S _n for m > 0, radiationless transitions

Table 3. Photophysical quantities for C₆₀ molecules in solution.

Property	Quantity	Ref.
S ₁ energy	2.0 eV	[77]
T ₁ energy	1.62–1.69 eV	[77, 137]
S ₂ energy	3.4 eV	[120]
T ₂ energy	3.3 eV	[120]
Φ _T , ISC quantum yield (S ₁ → T ₁)	0.88–0.98 (near 100%)	[77, 96–99]
Φ _F , fluorescence quantum yield	3.2 × 10 ⁻⁴	[79]
τ _F , singlet (S ₁) lifetime (fluorescence lifetime)	1.2 ns	[138, 111]
Φ _P , phosphorescence quantum yield	8.5 × 10 ⁻⁴	[77]
τ _P , triplet (T ₁) lifetime (phosphorescence lifetime)	143 μs	[106]

2.4.6. Solubility Properties of C₆₀

Solubility of C₆₀ in Various Solvents The solubility of C₆₀ in various solvents has been measured extensively in the past 10 years [139–153]. These experimental studies were mainly motivated to improve the efficiency of the separation process of fullerenes. Studying the organic solvents of C₆₀ is important for the separation of fullerenes, investigation of their chemical properties, and the synthetic reaction to functionalize fullerene in organic solvents. Moreover, the globular molecule provides a near-ideal model for the theoretical studies of solubility. Full coverage of the solubility properties of C₆₀ in various solvents from various literature is given in Table 4. In general, C₆₀ has poor solubility in most common solvents. These results include: C₆₀ is slightly soluble in alkanes with the solubility increasing with the number of carbons; the solubility in halogen-containing alkanes is generally higher than in alkanes and it is essentially insoluble in polar and H-bonding solvents such as alcohol and water; the solubility in aromatic solvents is generally higher than in other solvents, so increasing the size of the aromatic system (benzene to naphthalene) will increase the solubility. The highest solubilities of C₆₀ of about 50 mg ml⁻¹ are found to be in naphthalene derivatives.

In recent years, there have also been a number of theoretical studies focused on the decision of the relationship between possible influential factors and solubility parameters [140, 143, 154–158].

No single solvent parameter or property can uniformly predict the solubility. Early studies indicated the composite picture of solvents with high solubility for C₆₀: large index of refraction *n*, dielectric constant ϵ around 4, large molecular volume, and Hildebrand solubility parameter δ around 19 MPa^{-1/2} [140, 143]. Recently, several theoretical studies were performed in order to develop applicable and suitable influencing factor relationships. Marcus et al. [154, 155] analyzed a comprehensive set of solubility data of C₆₀ in various solvents at 298 and 303 K by multivariate stepwise linear regression applied as the linear solvation energy relationships (LSER) approach. Considering the formation of crystalline solvates in a few solvents, they used the calculated “hypothetical solubility” of unsolvated C₆₀ instead of the solubility of the solvate in the statistical procedure. Their results showed that increasing molar

Table 4. Room temperature solubility of fullerene C₆₀.

Solvent	Solubility (mg ml ⁻¹)
Nonaromatic hydrocarbons	
Noncyclic:	
<i>n</i> -pentane	0.005, 0.004 (303 K)
<i>n</i> -hexane	0.043, 0.052, 0.040 (303 K)
octane	0.025 (303 K)
isooctane	0.026 (303 K)
<i>n</i> -decane	0.071, 0.070 (303 K)
dodecane	0.091 (303 K)
tetradecane	0.126 (303 K)
Cyclic and derivatives:	
cyclopentane	0.002
cyclohexane	0.036, 0.035, 0.051 (303 K)
decalin (3:7 <i>cis</i> and <i>trans</i> mixture)	4.60
<i>cis</i> -decalin	2.20
<i>trans</i> -decalin	1.30
1,5,9-cyclododecatrien	7.14
cyclopentyl bromide	0.41
cyclohexyl chloride	0.53
cyclohexyl bromide	2.20
cyclohexyl iodide	8.06
(+ -)- <i>trans</i> -1,2-dibromocyclohexane	14.28
cyclohexane	1.21
1-methyl-1-cyclohexane	1.03
methylcyclohexane	0.17
1,2-dimethylcyclohexane (<i>cis</i> and <i>trans</i> mixture)	0.13
ethylcyclohexane	0.25
Halogen-containing alkanes and alkyne:	
dichloromethane	0.26, 0.23, 0.25 (303 K)
tetrachloromethane	0.32, 0.45
chloroform	0.16, 0.17, 0.25
carbon tetrachloride	0.32, 0.45 (303 K)
dichloroethane	0.36
bromoform	5.64
iodomethane	0.13
bromochloromethane	0.75
bromoethane	0.07
iodoethane	0.28
freon TF (dichlorodifluoroethane)	0.02
1,1,2-trichlorotrifluoroethane	0.01
1,1,2,2-tetrachloroethane	5.30
1,2-dichloroethane	0.08
1,2-dichloromethane	0.50
1,1,1-trichloroethane	0.15
1-chloropropane	0.02
1-bromopropane	0.05
1-iodopropane	0.17
2-chloropropane	0.01
2-bromopropane	0.03
2-iodopropane	0.11
1,2-dichloropropane	0.10
1,3-dichloropropane	0.12
(+ -) 1,2-dibromopropane	0.35
1,3-dibromopropane	0.40
1,3-diiodopropane	2.77
1,2,3-trichloropropane	0.64
1,2,3-tribromopropane	8.31
1-chloro-2-methylpropane	0.03
1-bromo-2-methylpropane	0.09
1-iodo-2-methylpropane	0.34

continued

Table 4. Continued

Solvent	Solubility (mg ml ⁻¹)
2-chloro-2-methylpropane	0.01
2-bromo-2-methylpropane	0.06
2-iodo-2-methylpropane	0.23
1,2-dibromoethylene	1.84
trichloroethylene	1.40
tetrachloroethylene	1.20
1-chloro-2-methylpropane	0.21
bromopropin	0.22
Aromatic hydrocarbons	
Benzene and derivatives:	
benzene	1.70, 1.50, 0.88, 0.89, 1.44 (303 K)
toluene	2.80, 2.90, 0.54 2.15 (303 K)
1,2-dimethylbenzene	8.70, 7.35, 9.30
1,3-dimethylbenzene	1.40, 2.83
1,4-dimethylbenzene	5.90, 3.14
1,2,3-trimethylbenzene	4.70
1,2,4-trimethylbenzene	17.90
1,3,5-trimethylbenzene	1.50, 1.70, 1.00 (303 K)
1,2,3,4-tetramethylbenzene	5.80
1,2,3,5-tetramethylbenzene	20.80
ethylbenzene	2.60, 2.16
<i>n</i> -propylbenzene	1.50
isopropylbenzene	1.20
<i>n</i> -butylbenzene	1.90
hexabutylbenzene	1.10
tributylbenzene	0.90
tetrahydronaphthalene	16.00
fluorobenzene	0.59, 1.20
chlorobenzene	7.00, 5.70
bromobenzene	3.30, 2.80
iodobenzene	2.10
1,2-dichlorobenzene	27.00, 24.60, 7.11
1,2-dibromobenzene	13.80
1,3-dichlorobenzene	2.40
1,3-dibromobenzene	13.80
1,2,4-trichlorobenzene	8.50, 10.40, 4.85
<i>o</i> -creosol	0.01
benzotrile	0.41
nitrobenzene	0.80
methoxybenzene	5.60
benzaldehyde	0.42
pentylisooctane	2.44
2-nitrotoluene	2.43
3-nitrotoluene	2.36
thiophenol	6.91
benzylchloride	2.46
benzylbromide	4.94
α,α,α -trichlorotoluene	4.80
Naphthalene derivatives:	
1-methylnaphthalene	33.00, 33.20
dimethylnaphthalene	36.00
1-phenylnaphthalene	50.00
1-chloronaphthalene	51.00
1-bromo-2-methylnaphthalene	34.80

continued

volume and solvent polarity (as measured by the Dimroth-Reichardt "general polarity" parameter, E_T [30, 158]) will decrease the solubility of C₆₀, but electron pair donation ability and polarizability will enhance solubility. Natarajan

Table 4. Continued

Solvent	Solubility (mg ml ⁻¹)
Polar solvents:	
methanol	0.000, 0.000035
ethanol	0.001, 0.0008
1-propanol	0.0041
1-butanol	0.094
1-pentanol	0.030
1-hexanol	0.042
1-octanol	0.047
nitromethane	0.000
nitroethane	0.002
acetone	0.001
acetonitrile	0.000
acrylonitrile	0.0040
<i>n</i> -butylamine	3.688
monomethylglycol ether	0.032
<i>N,N</i> -dimethylformamide	0.027
dioxane	0.041 (303 K)
Miscellaneous	
carbon disulfide (CS ₂)	7.90, 7.70, 5.16 (303 K)
tetrahydrofuran	0.00, 0.06
thiophene	0.40, 0.24
tetrahydrothiophene	0.03, 0.11
2-methylthiophene	6.80
<i>N</i> -methyl-2-pyrrolidone	0.89
pyridine	0.89, 0.30
methithiol	1.5, 1.0
quinoline	7.20
Inorganic solvents	
water	1.3×10^{-11}
silicon (IV) chloride	0.09

et al. [156] examined the solubility of C₆₀ in 75 organic solvents and succeeded in developing a solubility model of quantitative structure–solubility relationships by using the quantitative structure–property relationships (QSPR) approach. They used topological indices and polarizability parameters computed from refractive indexes to form the regression models. Kiss et al. [157] utilized a multiparameter artificial neural network (ANN) approach to model the solubility of C₆₀ in 126 solvents. The trend of nonlinear fit of the ANN suggested the same results as in the LSER studies: the solubility in a large number of solvents decreases with increasing molar volumes of the solvent and increases with increasing polarizability parameters, saturated surface areas, and average polarizability.

One of the most striking peculiarities of fullerenes in solutions is the extraordinary nonmonotonic behavior of the temperature dependence of the solubility of fullerene C₆₀. Experimental results of temperature dependence of the solubility of C₆₀ in hexane, toluene, CS₂ [139], and xylene [153] in the temperature range 200–400 K showed that, whereas the absolute values of the solubility of C₆₀ for different solvents differ over two orders of magnitude, the nonmonotonic behavior of the temperature dependence of the solubility is almost independent of the type of solvent over a wide range of temperature variation. This dependence reaches its maximum magnitude near 280 K and notably decreases at further enhancement of temperature. It is of

interest to note that the nonmonotonic temperature dependence of solubility is inherent only to C₆₀ and is not observed for other fullerenes, such as C₇₀. The temperature dependences of the solubility of fullerene C₇₀ in toluene, xylene, and CS₂ [153] are monotonically rising, which is inherent to the majority of solvent–solute pairs. The experimentally found distinctions in the temperature dependence of solubility of different fullerenes may be explained by a cluster mechanism of solubility based on the possibility of formation in solution of clusters consisting of a number of fullerene molecules [159, 160]. This aggregation phenomenon influences the thermodynamic parameters of fullerenes in solutions as well as the solubility; thus the observed lowering in the solubility of C₆₀ with rising temperature can be treated as a result of the thermal decomposition of clusters.

C₆₀ in Water Fullerene is not soluble in water. But it can be dispersed in water with the C₆₀ concentration >2 mM (1.4 mg/ml) and forms two types of fullerene–water colloidal systems: molecular-colloidal C₆₀ solution in water (also called C₆₀FWS; here FWS is the abbreviation of “fullerene–water system”) [161–164] and typical monodisperse C₆₀ hydrosol (also called ChH) [165].

C₆₀FWS can be produced by transferring fullerene from organic solution into the aqueous phase with the help of ultrasonic treatment [162], without using any stabilizers and chemical modification. It has been characterized as an aqueous molecular-colloidal solution having properties of both true solutions and colloidal systems simultaneously, which consists of both single hydrated fullerene molecules, C₆₀@{H₂O}_n, and their fractal spherical clusters [161–164]. Tests of C₆₀FWS biological activity showed that these hydrated fullerenes appeared to be very promising in the context of their biological and therapeutical applications [166]. ChH is another monodisperse aqueous colloidal system with a particle size of 10 nm [165], it can be obtained by oxidation of the C₆₀ anion with oxygen in “tetrahydrofuran–water” solutions. Both C₆₀FWS and ChH have the following similar characteristics: (i) high concentration (1 mg/ml and more); (ii) high stability, that is, preservation of their properties within a number of months even more under ambient conditions; (iii) almost identical color of solutions (from pale red to dark brown–red) that depends on C₆₀ concentration; (iv) negative charge of colloidal particles; (v) preservation of the same properties in the case of dilution or concentration of both colloidal solutions; (vi) a similar ability to coagulate under the inorganic cation influence [166, 167].

In contrast to well-known reasons of stabilization of typical colloidal systems [168], the main mechanism of FWS stabilization is the hydration of fullerene molecules with formation of the supramolecular complex of C₆₀@{H₂O}_n type [164] (see Fig. 9). The C₆₀@{H₂O}_n clusters are stabilized by the weak donor–acceptor interactions of unpaired electrons of H₂O oxygen atoms with fullerene molecule to form -OH•••π hydrogen bonds (such -OH•••π hydrogen bonds have been found to possess about half the binding energy of -OH•••O hydrogen bonds with, optimally, the -OH atoms centrally and vertically placed and the distances from the oxygen atom to the aromatic centroid of about 3.1–3.7 Å [169]) and by the formation of the ordered, H-bounded,

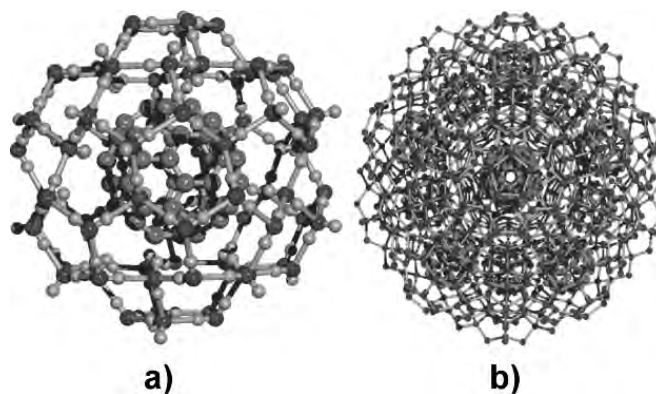


Figure 9. (a) A model of C₆₀{H₂O}₈₀ cluster, obtained from an icosahedral water cluster with a C₆₀ molecule taking the place of its inner water dodecahedron. (b) C₆₀ molecules in aqueous solution form colloidal clusters based on 3.4-nm-sized icosahedral arrangements of 13 C₆₀ molecules, where the C₆₀ molecules are separated by water molecules [164]. The water network is formed by fully tessellated tetrahedral tricyclo decamer (H₂O)₁₀ structures.

and spherulike H₂O molecular shells around the fullerene’s surface.

2.5. C₆₀ on Surfaces

2.5.1. On Metal Surfaces

C₆₀ adsorbed on a noble-metal surface usually form strong ionic bonding via charge transfer [170–179] from the metal near-Fermi-level surface states to the fullerene 5t_{1u}-derived LUMO. Quantities of charge transfer can be estimated indirectly from the following experimental results: (i) the shift of C₆₀ vibrational energies in high-resolution electron-energy-loss spectroscopy (HREELS) (Au(110) [171], Ni(110) [180], and Cu(111) [181]); (ii) the shift of carbon C_{1s} core-level absorption spectra using electron-energy-loss spectroscopy (EELS) (Au(110) [171]); (iii) using near-edge x-ray-absorption spectroscopy (NEXAFS) (Cu(111) [179]) compared to the known shift of alkali-doped compounds [182]; (iv) the angular dependence in angle-resolved valence-band photoemission spectroscopy (PES) (Au(111) [183]); and (v) direct comparison of relative photoemission intensities (Ag(111) [175] and Cu(111) [179]). But for Al [184, 185] and Pt(111) [186] surfaces, experimental results by NEXAFS, HREELS, or PES show no charge transfer evidence and suggest the interaction of a covalent bonding.

At the initial state the individual C₆₀ molecules are readily mobile on most metal surfaces at room temperature, stabilized at the step edges on Au(110) [172], Au(111) [187], Ag(111) [188], and Cu(111) [189], and form two-dimensional islands on Ag(110) [190].

On many low-index metal surfaces, C₆₀ forms commensurate monolayers, such as Au(111) (23 × √3) [187, 191], Ag(111) [188], Ag(110) [190], Cu(111)-c(1 × 1) [192], and Au (100)-c(5 × 20), with uniaxial stress along the <110> direction [193]. But C₆₀ adsorption on Au(110) [172] and Ni(110) [178] surfaces causes strong substrate reconstructions due to the strong interaction between the substrates and the C₆₀ adsorbates. In the case of a high anisotropic Au(110)-p(1 × 2) surface, C₆₀ molecules adsorbed on this

surface induce the Au surface atoms to form a (1×5) missing row reconstruction as a precursor for the $p(6 \times 5)$ adsorbate structure and form a hexagonal close-packed corrugated layer [172]. Recent in-plane X-ray diffraction data suggested that a large fraction of Au surface atoms are displaced from their original positions producing microscopic pits to accommodate the C₆₀ molecules [194]. In the case of Ni(110) surface, strong interaction between C₆₀ and the surface causes a formation of added/missing Ni [001] rows which creates a corrugated structure resulting in formation of (100) microfacets and maximizing the C₆₀-Ni coordination [178]. It is suggested that the small separation between the LUMO of C₆₀ and Ni Fermi level located in the *d* band leads to a strong hybridization interaction (i.e., covalent in character). Generally, the interaction between C₆₀ and transition metal surfaces is stronger than that between C₆₀ and noble metal surfaces [170, 178].

Images of the intramolecular features of adsorbed C₆₀ molecules which are bias dependent have been studied by STM in C₆₀/Cu(111)- $c(4 \times 4)$ [195] and C₆₀/Au(110) [196] systems. X-ray photoelectron diffraction has also been used to determine the molecular orientation of adsorbed C₆₀ molecules [196–200].

For C₆₀ monolayers on several common metal surfaces, the adsorptive structures as well as their interactions are summarized in Table 5, and a typical $(2\sqrt{3} \times 2\sqrt{3})R30^\circ$ model of the adsorptive structure on M(111) (M = Au, Ag, Al) surfaces is shown in Figure 10 [185].

2.5.2. On Semiconductor Surfaces

The initial state of adsorption of C₆₀ on most common semiconductor surfaces shows individual isolated molecules, no island or specific interaction with step edge or defects on the surface. At room temperature the C₆₀ molecules are generally immobile, showing strong interactions with the surface.

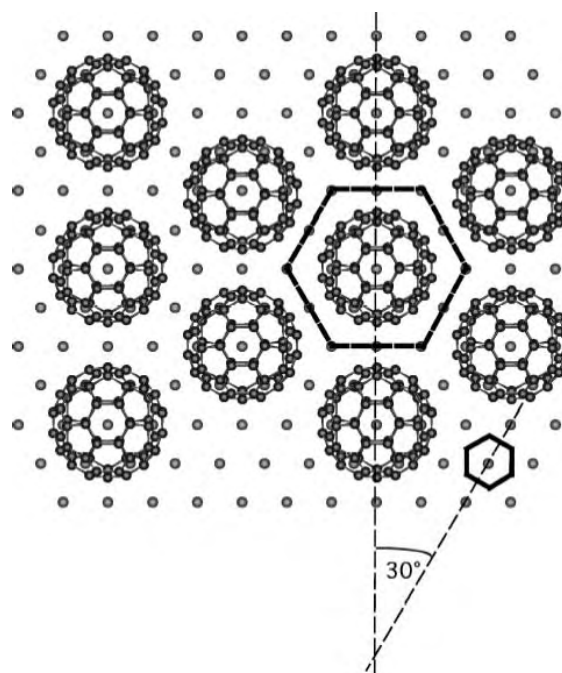


Figure 10. A model of the $(2\sqrt{3} \times 2\sqrt{3})R30^\circ$ phase. The dashed hexagon encloses an overlayer-induced unit cell, while the solid hexagon encloses a unit cell of the M(111) surface (M = Au, Ag, Al). Adapted with permission from [185], A. J. Maxwell et al., *Phys. Rev. B* 57, 7312 (1998). © 1998, American Physical Society.

Si(111)-(7 × 7) The interaction of adsorbed C₆₀ molecules with the Si surface is still not very clear. The Si(111)-(7 × 7) surface is (weakly) metallic due to the surface dangling bonds. Initially, it was suggested [205, 206] that the C₆₀-Si(111) interaction was ionic in character and similar to the C₆₀-noble metal interactions. HREELS data supported this

Table 5. Summary of C₆₀ adsorption structures and interactions for several common metal surfaces.

Surface	Structure	NDD (Å)	Interaction	CT (eV)	DT (K)	WF of clean sample (eV)	WF with 1 ML C ₆₀ (eV)
Au (111)	$38 \times 38^\circ$ in phase' $R14^\circ (2\sqrt{3} \times 2\sqrt{3})$ $R30^\circ$ [188, 191]	~10 [188]	intermediate chemisorption, ionic	0.8 [183]	770 [188]	5.3 [183]	4.7 [183]
Au (110)	$p(6 \times 5)$ [194, 172] reconstruction	10.04 [201]			800 [202]	5.37 [185]	4.82 ± 0.05 [185]
Ag (111)	$(2\sqrt{3} \times 2\sqrt{3})$ $R30^\circ$ [188]	~10 [188]	intermediate chemisorption, ionic	0.75 [175]	770 [188]		
Ag (110)	$c(4 \times 4)$ [190]	10.07, 10.23 [190]				4.52 [203]	4.9 [203]
Cu (111)	$c(4 \times 4)$ [192]	10.2 [192, 179]	intermediate chemisorption, ionic	1.6 [183] 1.5–2.0 [179]		4.94 [179]	4.86 [179]
Cu (110)	$\begin{pmatrix} 10 & 0 \\ 1 & 3 \end{pmatrix}$ [178]	9.7–11.1 [178]			730 [178]	4.48 [178]	
Ni (110)	Reconstruction [178]	10.5, 10.0 [178]	strong mainly covalent	2 ± 1 [180]	690 [204]	5.04 [203]	5.61 [203]
Al (111)	(6×6) , $(2\sqrt{3} \times 2\sqrt{3})$ $R30^\circ$ [185]	9.91, ~10.04 [185]	intermediate mainly covalent [185]		730 [185]	4.25 [185]	5.15 [185]
Al (110)	Pseudo- $c(4 \times 4)$ [185]	9.91, 11.44, 12.13 [185]			730 [185]	4.35 [185]	5.25 [185]
Pt (111)	$(\sqrt{13} \times \sqrt{13})$ $R(\pm 13.9)^\circ$ [186]	10.0 ± 0.3 [186]	mainly covalent [186]	<0.8 [186]	560 [204]	5.7 [186]	

Note: NDD—nearest neighbor distance, WF—work function, CT—charge transfer, DT—decomposition temperature.

charge-transfer model well with quantitative estimates of the amount of electron transfer to the fullerene LUMO being as high as (3 ± 1) electrons per molecule at the coverage lower than 0.25 monolayer (ML) and (0.7 ± 1) electrons at an average of about 1 ML [207]. But photoemission measurements [208–210] showed that the charge transfer to the fullerene LUMO is negligible, suggesting that the bonding is strongly covalent in character with a clear Si–C-related peak observed in both the C_{1s} core level and valence-band photoemission spectra.

Individual isolated C₆₀ molecule adsorption on Si(111)-(7 × 7) surface is strongly site dependent due to the different surface atom arrangements and dangling bond configurations caused by surface (7 × 7) reconstruction [205, 211, 212]. STM experiment reveals that about 80% C₆₀ molecules are adsorbed on faulted half and unfaulted half sites (sites A and A'), about 13% molecules on corner holes (site B), and only 7% on dimer lines (site C) [212]. Figure 11 gives high resolution STM images of single C₆₀ molecules adsorbed on different surface sites showing clear and rich intramolecular features which agree well with the theoretical calculation using the local density approximation with C₆₀Si_mH_l cluster models [212].

A STS study was also carried out to probe the local electronic structure of individual C₆₀ molecules on Si(111)-(7 × 7) surfaces (see Fig. 12). It was found that the HOMO–LUMO gaps of C₆₀ adsorbed at sites A, B, and C are 1.4, 0.8, and 1.3 eV, respectively, much smaller than that of free C₆₀ molecules (~1.8 eV). Thus it was confirmed that the mixing states of the C₆₀ orbitals with the local density of states (LDOS) of Si(111)-(7 × 7) are site dependent due to the strong interaction between the C₆₀ and the dangling bonds of the surface and the different surface structures at different sites [213].

As the submonolayer coverage increases to about 1 ML, the adsorbate–adsorbate interaction becomes large enough that two kinds of local ordered structural domains registered with those pinned on the substrate corner holes will form [214]. After the completion of monolayer C₆₀ coverage, a R-19° double-domain structure forms in which the

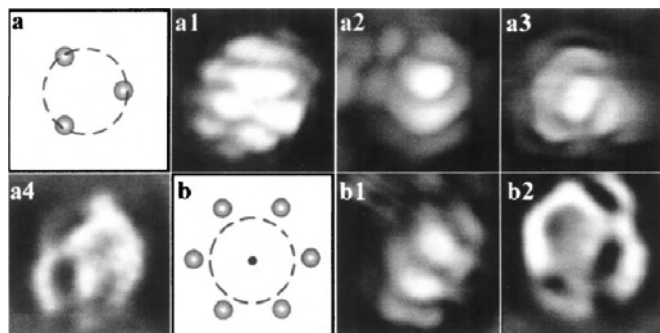


Figure 11. High resolution STM images of single C₆₀ molecule recorded with different bias voltages on a faulted half site: (a1) $V_s = -1.8$ V, (a2) $V_s = 1.5$ V, (a3) $V_s = 1.8$ V, and (a4) $V_s = 2.5$ V; and on corner holes: (b1) $V_s = -1.8$ V and (b2) $V_s = 2.3$ V. The tunneling current is 0.15 nA for positive bias images and 0.1 nA for negative bias images. Adapted with permission from [212], J. G. Hou et al., *Phys. Rev. Lett.* 83, 3001 (1999). © 1999, American Physical Society.

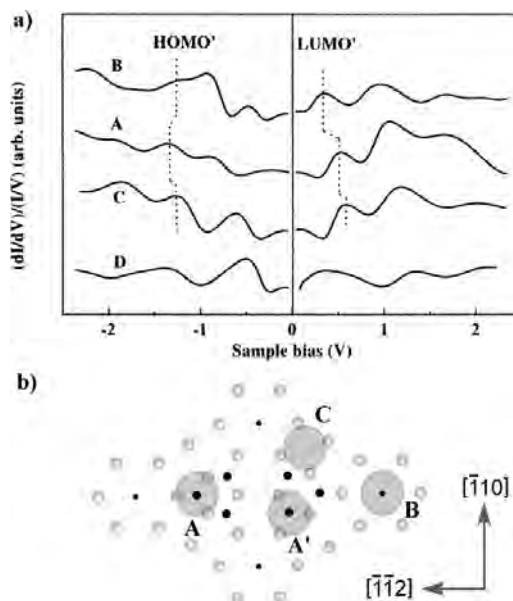


Figure 12. Curves A, B, and C are typical STS results corresponding to C₆₀ adsorbed at sites A, B, C (see Fig. 11b), respectively, on a Si(111)-(7 × 7) surface. Curve D is the average STS result on the bare Si surface. These STS results are represented in a graph of $(dI/dV)/(I/V)$ vs V . Adapted with permission from [213], H. Wang et al., *Surf. Sci.* 442, L1024 (1999). © 1999, Elsevier Science.

two domains exhibit interfacial structures with the C₆₀ $[\bar{1}10]$ directions $\pm 11^\circ$ off the $[\bar{2}11]$ axis of a Si substrate [215, 216].

Si(100)-(2 × 1) The interaction of C₆₀ with Si(100)-(2 × 1) surfaces is suggested to be weak and van der Waals force like [217, 218] without charge transfer [207]. Annealing the surface at an elevated temperature will cause a rearrangement of surface Si atoms and change the interaction from physical adsorption to a chemical one [90] and cause a hybridization of C₆₀ molecular orbitals with the surface states [219].

At room temperature, individual isolated adsorbed C₆₀ molecules on the Si(100)-(2 × 1) surface reside in the valleys between the (2 × 1) reconstruction dimer rows randomly at the initial state [220]. For monolayers on Si(100)-(2 × 1) surfaces, C₆₀ form two short-range local order structures of $c(4 \times 4)$, and $c(4 \times 3)$, with nearest-neighbor distances of 10.9 and 9.6 Å [217], respectively.

In the case of chemical adsorption of C₆₀ on Si(100)-(2 × 1) surfaces after annealing, the scanning tunneling spectroscopy of individual C₆₀ molecules on two different adsorption sites of the Si(100) surface was investigated [221, 222] (see Fig. 13). It was found that the HOMO–LUMO gap of C₆₀ molecules at the top of a single dimer (type A molecules) is about 1.8 eV, which is about the same as that of free C₆₀ molecules; the HOMO–LUMO gap of these molecules which is usually located at a missing dimer defect (type B molecules) is about 2.2 eV, which is close to the bandgap of SiC [223, 224]. STS results indicated that the interaction between a type B molecule and the Si surface is much stronger than that for a type A molecule; type B molecules form covalent bonds not only with second layer Si atoms but also with the surrounding Si atoms in the first layer.

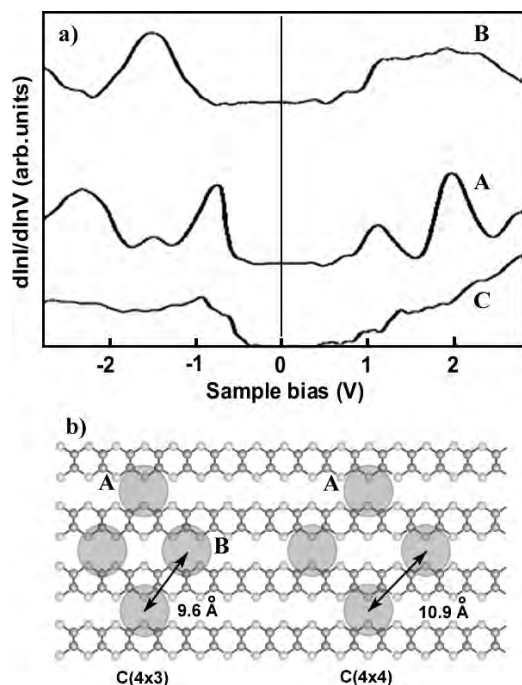


Figure 13. Curves A, B, and C are typical STS results corresponding to C₆₀ adsorbed at sites A, B (see Fig. x2b), respectively, on an Si(100)-(2 × 1) surface. Curve C is the average STS result on the bare Si surface. These STS results are represented in a graph of $(d \ln I/d \ln V)$ vs V . Adapted with permission from [221], X. Yao et al., *Surf. Sci.* 366, L743 (1996). © 1996, Elsevier Science.

Ge(100)-(2 × 1) and Ge(111)-(2 × 8) The C₆₀ monolayer adsorbed on Ge(100)-(2 × 1) exhibits uniaxial incommensurate near-ordered lattice close to a structure of $c(3 \times 4)$ in the direction of the dimer rows of the Ge(100)-(2 × 1) surface [218, 225–227] and preserves the Ge(100)-(2 × 1) reconstruction [227].

In contrast to Ge(100) and Si(111), the Ge(111) surface undergoes a structural rearrangement upon the adsorption of C₆₀ molecules [228]. The C₆₀ monolayer on a Ge(111) system exhibits several ordered structures as a function of the annealing temperature [228]. Two stable surface phases, $(3\sqrt{3} \times 3\sqrt{3})R30^\circ$ and $(\sqrt{13} \times \sqrt{13})R14^\circ$, form upon annealing at 450–500 and above 500 °C, respectively, as well as a localized metastable 5×5 phase by suddenly quenching the $(3\sqrt{3} \times 3\sqrt{3})R30^\circ$ phase heated at 500 °C. The interaction of C₆₀ with the Ge(111) surface is prevalently covalent and strong [229].

GaAs(110) and GaAs(001) The interaction of C₆₀ molecules on the GaAs(110)-(1 × 1) surface is weak (dominantly via van der Waals force), resulting in well-ordered C₆₀ thin film growth and rotating C₆₀ molecules. The C₆₀ layer on GaAs(110)-(1 × 1) is stressed due to the competition between the intermolecular interaction and the adsorbate–substrate interaction and the fact that the lattice parameter of the GaAs(110) substrate does not match with those of C₆₀ [230, 231].

The interaction of C₆₀ molecules on the GaAs(001) surface is weak too and the C₆₀ molecules are mobile at room temperature on the surface [232, 233]. Particularly in the case of C₆₀ on the As-rich 2 × 4 substrate, the epitaxial

growth is found to be unique and quite different from other GaAs(001) phases: C₆₀ film takes its (110) crystalline axis which cannot be obtained on other substrate. The C₆₀ overlayer is highly strained with a lattice expansion of ~13% due to a charge transfer from the As-dangling bonds to C₆₀ and a site-specific C₆₀–substrate interaction, and this structure is very stable at least up to 10 ML [233].

3. C₆₀ CRYSTAL

3.1. Structure

3.1.1. Main Description

At room temperature (RT), solid C₆₀ usually forms black or brownish powder or crystals. C₆₀ single crystal forms a molecular crystal through weak van der Waals force C₆₀–C₆₀ bonding and adopts a closed-packed face-centered cubic (fcc) structure with a lattice constant of 14.17 Å [234, 235] and a nearest neighbor C₆₀–C₆₀ distance of 10.02 Å [236]. It is chemically active but stable in air or at temperatures well above RT. A pure C₆₀ single crystal and a schematic view of the fcc structure is shown in Figure 14 [237]. The more physical constant for crystalline C₆₀ in the solid state is shown in Table 6. The comparison of properties of solid C₆₀ with other fullerene solids (C₃₆, C₇₀, C₇₆, C₇₈, C₈₄) is listed in Appendix B.

3.1.2. Symmetry and Space Group

The symmetry of the space group for fcc C₆₀ crystal at RT has been identified by X-ray and neutron diffraction [235, 238, 272, 273] to be O_h^5 or $Fm\bar{3}m$, using the Schoenflies and International Crystallographic nomenclature, respectively.

Solid state ¹³C NMR [32, 274–276], quasi-elastic neutron scattering [277], and muon spin resonance (μ SR) [278, 279] studies showed that the C₆₀ molecules in the crystal are rotating rapidly with three degrees of rotational freedom and reorienting rapidly. The rotational reorientation time at RT is about 9–12 ps which is 50% faster than molecular reorientation in solution (about 15.5 ps) [280], so that solid C₆₀ may be considered as a nearly ideal close-packed configuration of spheres at room temperature. The rapid reorienting and rotating mechanism is consistent with RT NMR results that all carbon atoms are equivalent although

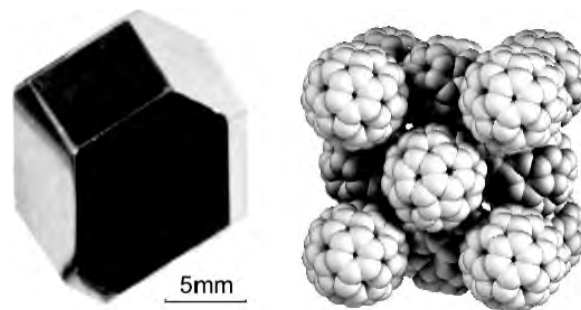


Figure 14. Pure C₆₀ crystal (left) and schematic view of the fcc structure of the solid (right). Adapted with permission from [110], L. Forró and L. Mihály, *Rep. Progr. Phys.* 64, 649 (2001). © 2001, Institute of Physics Publishing.

Table 6. Physical constant for crystalline C₆₀ in the solid state.

Property	Quantity
Fcc lattice constant	14.17 Å [234, 235]
C ₆₀ -C ₆₀ distance	10.02 Å [236]
Tetrahedral interstitial site radius	1.12 Å [236]
Octahedral interstitial site radius	2.07 Å [236]
Mass density	1.72 g/cm ³ [236]
Volume thermal-expansion coefficient	6.2 × 10 ⁻⁵ /K [238]
Molecular density	1.44 × 10 ²¹ cm ³ [236]
Compressibility (-d ln V/dP)	6.9 × 10 ⁻¹² cm ² /dyn [239] (compared with: graphite 2.7, diamond 0.18)
Bulk Modulus	6.8 GPa [240] ~12 GPa [241]
Young's modulus	15.9 GPa [242]
Phase transition temperature (T ₀₁)	260–261 K [243]
dT ₀₁ /dP	~11–16K/kbar [244, 245] ^a
Sublimation temperature	~434 °C [246]
Heat of sublimation	38 kJ mol ⁻¹ [247]
Cohesive energy	~1.7 eV [248, 249]

^a The value varies with different pressure medium.

the point group I_h of C₆₀ molecule is incompatible with any crystal space group [14].

Figure 15 shows an X-ray powder-diffraction pattern of crystalline C₆₀ compared to that of gold. In these two kinds of materials, both the C₆₀ molecules and the gold atoms present a close-packed fcc structure, but in the pattern of C₆₀ crystals the (200) and (400) diffraction peaks are missing. The reason for the missing peaks can be attributed to the unique intrinsic properties of C₆₀ molecules. Because C₆₀ molecules are rotating rapidly at room temperature, all molecules in the fcc lattice can be well approximated by hollow spherical shells filled by electrons. This “hollow-sphere”

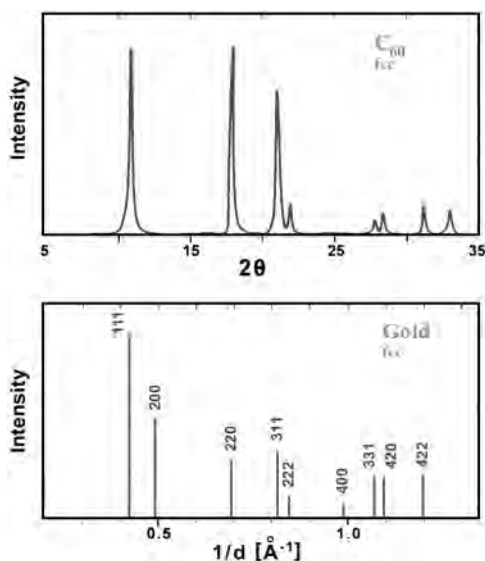


Figure 15. X-ray powder-diffraction pattern of crystalline C₆₀ compared to that of gold. In both kinds of materials, the molecules (i.e., atoms in case of gold) crystallize in a face-centered-cubic arrangement, corresponding to a closest packing of spheres. Notice the absence of the (200) and (400) diffraction peaks in crystalline C₆₀.

scattering introduces additional interference which happens to extinguish just those fcc diffraction peaks [235].

For the RT fcc structure, subsequent studies in very close detail by X-ray [281, 282] and neutron diffraction [282–285] reveal that the molecular rotation is not, in fact, completely free, and provide evidence for pronounced local orientational order with a correlation length ~40 Å [282] which is four times the shortest intermolecular distance and consists of several dozen molecules. The local order seems to be driven by the same nearest neighbor interaction which leads to long range order below the phase transition temperature T_{01} but does not possess the symmetry of the low temperature structure [282].

3.2. Vibrational Modes

3.2.1. Overview

The vibrations of C₆₀ molecules can be very well classed into two distinct groups: intermolecular and intramolecular vibrations. For intermolecular molecular vibrations, C₆₀ molecules translate or rotate as nearly rigid entities, and the highest measured intermolecular phonon frequency at room temperature is only ~50 cm⁻¹, well below that of the lowest intramolecular frequency, namely 272 cm⁻¹ for the $H_g(1)$ “squashing” mode [286, 287].

The intramolecular vibrations of an isolated C₆₀ molecule involve changes of the bond distances or bond angles of the carbon atoms on the C₆₀ molecule. Starting with 60 × 3 = 180 total degrees for an isolated C₆₀ molecule and subtracting the 6 degrees of freedom corresponding to 3 translations and 3 rotations results in 174 vibrational degrees of freedom. However, there are only 46 distinct mode frequencies corresponding to the 174 degrees of freedom due to the high symmetry of C₆₀ (point group I_h). According to the symmetry of the displacement patterns, the 46 distinct intramolecular vibrations can be classed into several groups as follows:

$$2A_g + 1A_u + 3T_{1g} + 4T_{1u} + 4T_{2g} + 5T_{2u} + 6G_g + 6G_u \\ + 8H_g + 7H_u$$

Here, the subscripts g (gerade or even) and u (ungerade or odd) refer to the symmetry of the eigenvector under the action of the inversion operator. The T -modes are triply, the G -modes are fourfold, and the H -modes are fivefold degenerate. These degeneracies are a consequence of the high symmetry of the C₆₀ molecule and lead to the fact that the number of distinct modes (46) is much lower than 174 (the vibrational degrees of freedom). Group theory indicates that only 10 of the 46 distinct mode frequencies are Raman-active ($2A_g + 8H_g$) in first order and 4 (T_{1u}) are infrared (IR)-active in first order. These activated frequencies have been assigned with certainty. The remaining 32 modes ($1A_u + 3T_{1g} + 4T_{2g} + 5T_{2u} + 6G_g + 6G_u + 7H_u$) are optically inactive (“silent”) so that the identification of these modes has been difficult. Early calculations of the vibrational frequencies of C₆₀ used mainly classical force constant treatments [288–293] or relied on quantum chemistry calculations [294–300]. However, they did not display the accuracy required to use them as a reliable guide for a clear identification of the silent modes. Analysis of the second-order

Raman and infrared spectra for C₆₀ provides a good determination of assignments of the 32 silent mode frequencies [301–303]. The results of density functional theory (DFT) calculations can provide a more reliable complete assignment of the C₆₀ modes [304–308]. Since Raman and infrared spectra can only provide 14 active mode frequencies, a number of other experimental techniques were developed to probe silent modes, such as inelastic neutron scattering, EELS, and single oxygen photoluminescence (PL). Table 7 gives recommended values for the 46 distinct vibrational frequencies of an isolated C₆₀ molecule and their assignments [309]. Several alternative assignments of vibrational frequencies in C₆₀ can be found in the literature [301, 303, 310–315].

3.2.2. Raman and Infrared Spectra

First-Order Active Raman and Infrared Modes Raman and IR spectra provide the most quantitative methods for determining the vibrational mode frequencies. Since C₆₀ is very nearly an ideal molecular solid, so the Raman and infrared spectra are sensitive for distinguishing C₆₀ from higher-molecular-weight fullerenes with lower symmetry (e.g., C₇₀ has *D*_{5h} symmetry). Because most of the higher molecular weight fullerenes have lower symmetry as well as more degrees of freedom, they have many more infrared- and Raman-active modes [316, 317].

Table 7. Recommended values for the 46 distinct normal mode frequencies of an isolated C₆₀ molecule [309].

Even modes			Odd modes		
Frequency (cm ⁻¹)	Assignment	Activated modes	Frequency (cm ⁻¹)	Assignment	Activated modes
496	A _g (1)	R	984	A _u (1)	
1470	A _g (2)	R			
			526	T _{1u} (1)	IR
568	T _{1g} (1)		575	T _{1u} (2)	IR
831	T _{1g} (2)		1182	T _{1u} (3)	IR
1289	T _{1g} (3)		1429	T _{1u} (4)	IR
553	T _{2g} (1)		342	T _{2u} (1)	
756	T _{2g} (2)		753	T _{2u} (2)	
796	T _{2g} (3)		973	T _{2u} (3)	
1345	T _{2g} (4)		1205	T _{2u} (4)	
			1525	T _{2u} (5)	
485	G _g (1)			G _u (1)	
567	G _g (2)		353	G _u (2)	
736	G _g (3)		764	G _u (3)	
1079	G _g (4)		776	G _u (4)	
1310	G _g (5)		961	G _u (5)	
1482	G _g (6)		1309	G _u (6)	
			1422	G _u (7)	
272	H _g (1)	R		H _u (1)	
433	H _g (2)	R	403	H _u (2)	
709	H _g (3)	R	534	H _u (3)	
772	H _g (4)	R	668	H _u (4)	
1099	H _g (5)	R	743	H _u (5)	
1252	H _g (6)	R	1223	H _u (6)	
1425	H _g (7)	R	1344	H _u (7)	
1575	H _g (8)	R	1567	H _u (8)	

Note: “R” represents Raman activated mode; “IR” represent infrared activated mode.

The Raman and IR spectra of the pristine monomeric fcc phase of C₆₀ are shown in Figures 16 and 17, together with the spectra of the orthorhombic (*O*), tetragonal (*T*), and rhombohedral pressure-polymerized (*R*) phase of C₆₀ as well as the pressure-dimerized state for comparison (for comprehensive knowledge on the polymerized C₆₀, please refer to Section 4.2). Raman and IR spectra of solid C₆₀ remain almost unchanged relative to the isolated C₆₀ molecule. Raman scattering spectra in Figure 16 for solid C₆₀ show 10 strong Raman lines, including two “breathing” A_g-modes related to symmetric oscillations of the entire molecule (496 cm⁻¹) and of pentagons (1468 cm⁻¹), and eight H_g-modes: 272, 432, 710, 772, 1100, 1248, 1422, and 1574 cm⁻¹ [301, 318–323]. The first-order infrared spectrum for C₆₀ contains only four strong lines (see Fig. 17) at 526, 576, 1184, and 1428 cm⁻¹, each identified with an intramolecular T_{1u} mode [303, 318, 324].

Isotopic Effects in the Raman Spectra The natural abundance of ¹³C isotopes is about 1.1%, with the result that approximately half of the molecules in ordinary C₆₀ samples produced from natural graphite contain one or more ¹³C isotopes. The isotopic distribution within the molecule is random [325]. The truncated icosohedral structure of C₆₀ molecule belongs to icosohedral point group (*I*_h). The ¹²C₆₀ molecule shows the highest degree of symmetry and most stringent selection rules and there are 4 infrared-active and 10 Raman-active modes for the molecule. The remaining 32 distinct modes, silent modes, are IR and Raman forbidden. However, the addition of ¹³C isotopes lowers the symmetry of the molecule. Since the symmetry restrictions against first-order Raman or IR activity for the silent modes have been removed, it is expected that all of the previous silent modes become active. The lowering of the icosohedral symmetry by the presence of ¹³C isotope has been used to investigate the silent modes in the isotopically pure molecule [310, 326–329].

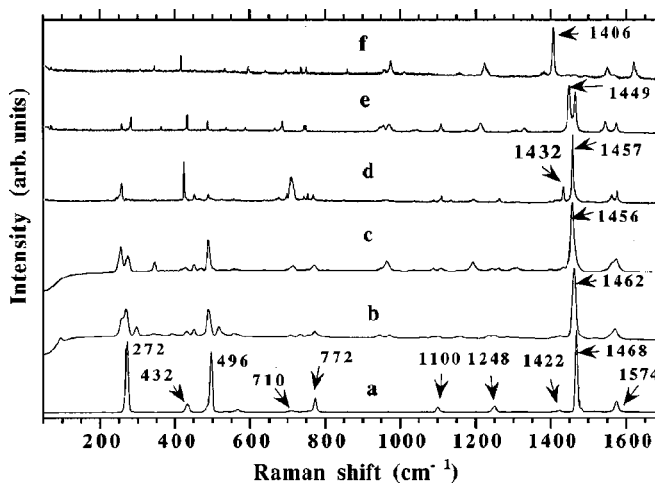


Figure 16. Raman spectra of the pristine C₆₀ (a), polymerized DS (b), and *O* phase (c), excited by a 1064-nm line; those of the *O* (d), *T* (e), and *R* (f) phases, excited by a 568.2-nm line. Adapted with permission from [318], V. A. Davydov et al., *Phys. Rev. B* 61, 11936 (2000). © 2000, American Physical Society.

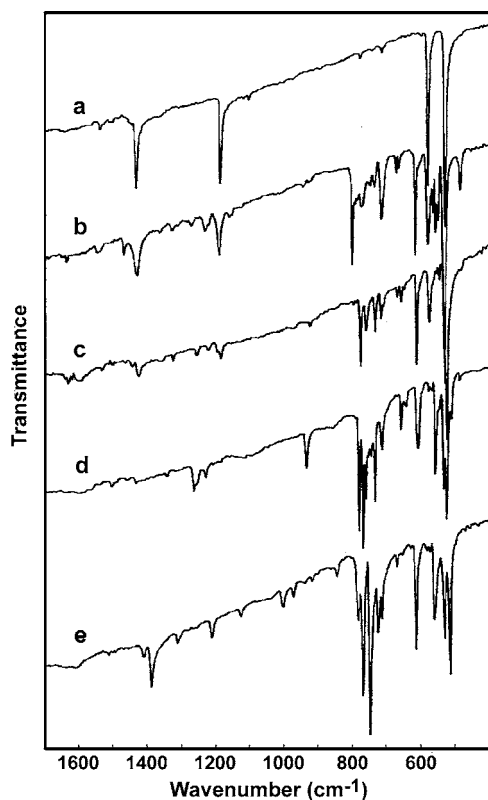


Figure 17. IR spectra of the pristine C₆₀ (a), and polymerized O (c), T (d), R (e) phases, and DS (b). Adapted with permission from [318], V. A. Davydov et al., *Phys. Rev. B* 61, 11936 (2000). © 2000, American Physical Society.

Besides the symmetry-lowering phenomena due to the presence of ¹³C, the isotopes can also cause the shifts and splittings of the active modes [330, 331]. This isotope effect on the mode frequencies is due to their dependence on $(\kappa/M)^{1/2}$, where κ and M are the force constants and atomic mass, respectively. Thus in a C₆₀ molecule with n ¹³C isotopes, at first order, the vibrational frequency is expected to be lowered proportional to the mass difference between ¹²C₆₀ and ¹³C_{*n*}¹²C_{60-*n*}, which can be simply written as

$$\frac{\omega(n)^2}{\omega(0)^2} = 1 - \frac{n}{720}$$

where $\omega(0)$ is an eigenmode frequency of ¹²C₆₀ and 720 a.u. is its atomic mass.

A high-resolution Raman spectrum for a C₆₀ sample with the natural isotopic abundance is shown in Figure 18. To reduce the natural Raman linewidth, the C₆₀ was dissolved in CS₂ solution, and the spectrum was taken at 30 K. A fine structure of the high-energy pentagonal-pinch A_g(2) mode near 1470 cm⁻¹ was observed. Three peaks in the fine structure could be resolved, associated with ¹²C₆₀, ¹³C₁¹²C₅₉, and ¹³C₂¹²C₅₈, respectively. The measured separation between the first and second peaks is 0.98 ± 0.01 cm⁻¹, while for the second and third peaks it is 1.02 ± 0.02 cm⁻¹. Spectra taken at higher temperatures are shown in the inset [330]. Figure 19 shows Raman and mass spectra for a ¹³C enriched C₆₀ sample, which is produced by enriching the graphite nod

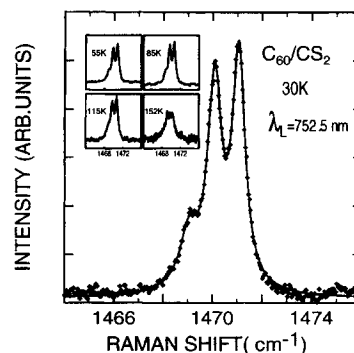


Figure 18. Unpolarized Raman spectrum of a frozen solution of C₆₀ in CS₂ at 30 K. The solid line is a 3-Lorentzian fit to the experimental data. The highest frequency peak is assigned to the totally symmetric pentagonal-pinch A_g mode in ¹²C₆₀. The other two lines are assigned to the pentagonal-pinch mode in molecules containing one and two ¹³C isotopes, respectively. The inset shows the evolution of these peaks as the solution is heated. They are no longer resolved as the solution melts above 150 K. Adapted with permission from [330], S. Suha et al., *Phys. Rev. Lett.* 72, 3359 (1994). © 1994, American Physical Society.

with ¹³C. Comparison between the Raman and mass spectra shows that the two line shapes have a remarkable correlation [330]. The simple correlation was further confirmed by using a variety of first-principle and phenomenological dynamical models [332]. Within the framework of a first-principle calculation, normal modes of vibration of the C₆₀ isotopomers ³C₁¹²C₅₉ and ¹³C₂¹²C₅₈ have been calculated [333].

3.2.3. Inelastic Neutron Scattering Spectrum

Inelastic neutron scattering (INS) offers the potential to detect all 46 intramolecular distinct modes of C₆₀, including those silent for first-order Raman and infrared spectroscopies, because the technique is sensitive to modes of all symmetries. The scattering intensity is proportional to the mode degeneracy, which can be used to identify the vibrations. Although, in principle, inelastic neutron scattering allows one to unambiguously assign all the modes, it has so far not been so ideal. In fact this technique has two main disadvantages, which make it difficult to individually assign all of the modes. First, the determination of eigenvectors is traditionally based on single-crystal samples, but the available C₆₀ crystals were too small for inelastic neutron-scattering experiments. Second, the poor spectral resolution

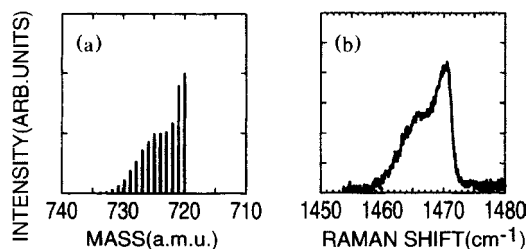


Figure 19. Comparison of the mass spectra and the Raman spectra for a ¹³C-enriched C₆₀ sample. Adapted with permission from [330], S. Suha et al., *Phys. Rev. Lett.* 72, 3359 (1994). © 1994, American Physical Society.

of INS makes it difficult if not impossible to achieve assignments of many of the C₆₀ modes, especially those whose frequencies are clustered within a narrow range. A number of workers have measured the intramolecular mode frequencies for C₆₀ by INS, and the results are summarized in Table 8. For more experimental and theoretical details and the principal INS technique, one can read several review and original research papers [285, 334–340].

3.2.4. High-Resolution Electron Energy Loss Spectrum

Infrared-active modes can be observed in HREELS measurements because the electric dipole associated with infrared-active vibrations can scatter the incident monoenergetic electrons. An ultrahigh vacuum environment is necessary for HREELS experiments and the resolution of HREELS experiments can not match that of optical measurements. Although HREELS has no obvious advantage in the determination of the infrared mode frequencies, it is very useful for the assignment of vibrational frequencies in C₆₀. This is because all modes in C₆₀ can induce inelastic scattering of electrons due to the impact scattering mechanism [341, 342]. In the impact scattering mode, the electron

Table 8. Assignment and comparative list of peak positions (in meV) of neutron inelastic scattering, HREELS, and photoluminescence (PL).

Assignment	Neutron [336]	HREELS [343]	PL [346]
<i>H_g</i>	33	34	33
<i>T_{2u}, G_u</i>	43,44	43,43	43
<i>H_u</i>	50		50
<i>H_g</i>	54	54,53	53
<i>G_g, A_g</i>	60		60
<i>T_{1u}</i>	66	66,66	66
<i>T_{1u}</i>	71	72	72
	77		
	83		82
<i>H_g</i>	88		88
	92	94,94	94
<i>H_g</i>	96		96
	104		103
	109		
	114		
	119	119,119	119
	124		
	132	133	134
<i>H_g</i>	136	136	136
	139		
<i>T_{1u}</i>	147	147	146
	149		150
<i>H_g</i>	156	156,161	158
	168		166
<i>H_g, T_{1u}</i>	176	179,178	177
<i>A_g</i>	184		
<i>H_g</i>	196	194,192	195

Note: The HREELS peak positions observed in an ordered C₆₀ film on GaSe(0001) and a crystalline C₆₀ film on GeS(001) are italic. The other numbers correspond to the peaks detected in the spectra of an amorphous C₆₀ films on Si(100).

scattering is by short-range components of the electron-molecule interaction.

A few experimental works have performed HREELS experiments on C₆₀ films, using a variety of substrates [343–345]. Depending on the substrate used, the films are crystalline or disordered. This has a significant effect on the relative intensity of the different spectral features (see Table 8).

3.2.5. Optical Spectroscopy

Some optical spectra, including singlet oxygen PL [346], fluorescence, and phosphorescence spectra, can also be powerful tools for the identification of intramolecular vibrational modes of C₆₀. The applicability of the photoluminescence technique to probe fundamental vibrational excitations of C₆₀ is based on the weak vibronic coupling of O₂ molecules intercalated into the C₆₀ lattice. Thirty-two of the 46 distinct vibrational modes of C₆₀ can be observed in the PL spectra, some of which are not Raman and IR first-order active modes. Mode energies determined from this technique show good agreement with those determined from INS, IR, and Raman spectroscopies. At high energies (>700 cm⁻¹), the technique has a significant advantage over INS, since the much sharper peaks can provide very accurate data for mode frequencies [346]. By investigating the vibrational fine structure in the fluorescence [347] and phosphorescence [348] spectra of C₆₀ molecules isolated in neon and argon matrices, the unambiguous identification of several vibrational modes of *T_{3u}*, *H_u*, and *G_u* symmetry were obtained.

3.3. Phase Transition

3.3.1. Orientational Phase Transition

On cooling below a temperature of about *T*₀₁ ~ 260 K, the nearly free rotation of C₆₀ molecules in solid C₆₀ will be frozen by losing two of their three degrees of rotational freedom; the four neighboring molecules in an fcc unit cell remain in their positions but become orientationally inequivalent. Their rotation motions are constrained along two standard favorite orientations and become hindered, resulting in an orientational ordering [235, 243, 249, 273, 349], but the random reorientation between the two possible standard orientations for each molecule in the solid still lead to a residue disorder (a so-called “merohedral disorder”) [32, 243, 274, 275, 349–352]. The two favorite orientations are corresponding to electron-rich double bonds on one molecule facing the electron deficient centers of hexagons (HF) and pentagons (PF) respectively on its adjacent molecules, obtained by rotating the molecules around the four <111> axes of the C₆₀ molecules through about 38° and 98° (60° jumps) respectively [243, 284, 349, 353–355]. Recently, elastic diffuse neutron-scattering study, considering the optimization of nearest-neighbor orientations rather than long-range orientational order, showed that the actual angles may be closer to 42° and 102° [356]. The PF structure has been indicated to be an idealized ordered structure and the HF structure a “defect structure,” because the HF structure has a slightly higher energy than the PF structure. The lower energy configuration is about only 11.4 meV [352, 357] below the higher energy configuration, and the two are

separated by a potential barrier of ~ 235 – 295 meV [243, 274, 280, 284, 349, 352, 357–361] which has been confirmed by various experiments.

A schematic 3D model of a close-packed (111) plane of C₆₀ molecules exhibiting uniaxial reorientation about $\langle 111 \rangle$ directions (low temperature phase, 90–260 K) is shown in Figure 20 [243]. The molecules reorientate between a number of different sites but principally perform 60° jumps about $[111]$ residing in the two configurations corresponding to 38° and 98° (or 42° and 102°, using latest data) rotations.

Although the centers of the C₆₀ molecules remain in the same places, the four molecules of the conventional fcc unit cell become orientationally nonequivalent. The incompatibility of the icosahedral molecular symmetry of the different molecular orientations and the cubic lattice symmetry lowers the crystal symmetry from fcc into a simple cubic (sc) structure (space group T_h^6 or $Pa\bar{3}$, which is a subgroup of the space group $Fm\bar{3}m$ of an fcc structure) [235, 273, 362]. Thus the C₆₀ crystal undergoes a so-called orientational ordering phase transition.

The orientational ordering transition is first order [111]. The occurrence of this transition has been confirmed by various experimental methods such as differential scanning calorimetry (DSC) [235, 273, 363], X-ray diffraction [235, 273], NMR [14, 23, 274–276, 363–366], neutron diffraction [243], dielectric spectroscopy [359]; μ SR [279]; specific heat measurements [352, 361, 367, 368], inelastic neutron scattering [33, 277, 369, 370], electron diffraction [371], sound velocity and ultrasonic attenuation [242, 372], and Raman spectroscopy [326, 373–375].

Figure 21 shows a comparative electron diffraction patterns of crystalline C₆₀ at room temperature and at 100 K [371]. Additional spots appear at positions which are extinct in an fcc lattice on cooling below T_{01} and correspond to a primitive cubic lattice. The appearance of these spots reveals the low temperature structure in which the molecules are still situated on an fcc lattice but orientationally ordered and also shows that the space group $Pa\bar{3}$ is a subgroup of the space group $Fm\bar{3}m$ of the high temperature fcc phase.

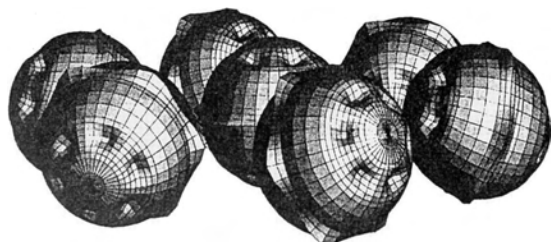


Figure 20. Close-packed (111) plane of C₆₀ molecules depicting uniaxial reorientation about $\langle 111 \rangle$ directions (low temperature phase, 90–260 K). The “dimples” correspond to the centers of electron-poor hexagonal/pentagonal faces; the equatorial protrusions depict electron-rich 6:6 bonds. The constraints demanded by $Pa\bar{3}$ symmetry imply that the electron-rich and electron-poor regions have well-defined loci corresponding to constant latitudes relative to $[111]$. These electrostatic considerations are consistent with the assumption that the preferred easy reorientation direction is $[111]$. Adapted with permission from [243], W. I. F. David et al., *Europhys. Lett.* 18, 219 (1992). © 1992, EDP Science.

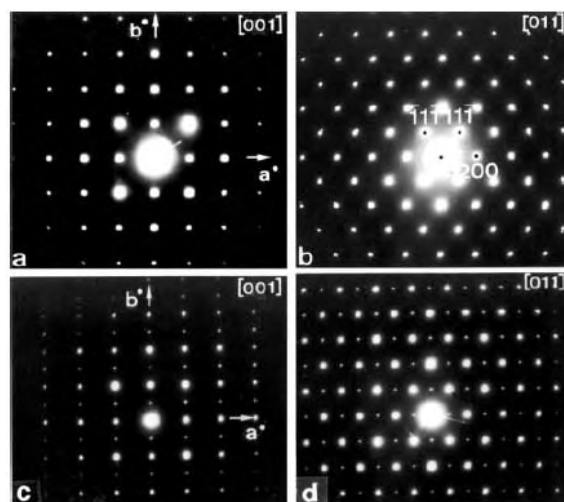


Figure 21. Electron diffraction patterns of C₆₀ crystallite along $[001]$ (a, c) and along $[011]$ (b, d) at room temperature (a, b) and at 100 K (c, d). Note the appearance of extra reflections at low temperature related to a lowering of symmetry due to orientation ordering. Adapted with permission from [371], G. Van Tendeloo and S. Amelinckx, in “Electron Microscopy of Fullerenes and Related Materials, Characterization of Nanophase Materials” (Z. L. Wang, Ed.), Wiley-VCH, 2000. © 2000, Wiley-VCH.

Figure 22 shows the ¹³C NMR spectra of solid C₆₀ at temperatures from 295 down to 77 K [275]. The low-temperature NMR line shape for the C₆₀ solid is quite different from that of C₆₀ in solution. From RT to low temperature below T_g , the spectra changes from a single line peak at 298 K to a line shape at 77 K. The symmetry of the molecule and the equivalence of all C₆₀ carbon atoms in C₆₀ crystals are broken by two factors: the presence of the crystal lattice and the applied magnetic field. As the temperature is reduced, the “motionally narrowed” NMR line at 295 K (143 ppm from tetramethyl silane) in the ¹³C NMR spectrum of C₆₀, which proves that C₆₀ molecules are rotating rapidly with respect to the NMR time scale at RT, is broadened and the C₆₀ molecule’s orientation become static on the NMR time scale. At 77 K there is little evidence of the narrow line at 143 ppm, and a fit to this line shape yields an asymmetric chemical-shift tensor with components of 220, 186, and 25 ppm, reflecting the chemical-shift anisotropy of the ¹³C nuclei averaged over the crystallite orientations.

The phase transition affects various physical properties; the changes of some of these properties at the transition temperature T_{01} are listed in Table 9.

It has also been indicated that both the transition temperature and the size and shape of the transition anomalies are strongly influenced by deformation, impurities, and solvent [354, 378].

3.3.2. Glass Transition

Below about 90 K the molecules in C₆₀ crystal are entirely frozen but never order perfectly; the C₆₀ crystal undergoes a so-called glass transition. The glass transition of C₆₀ crystal is second order [243].

The fraction of molecules in the more stable PF orientation is only about 60% near 260 K but increases to

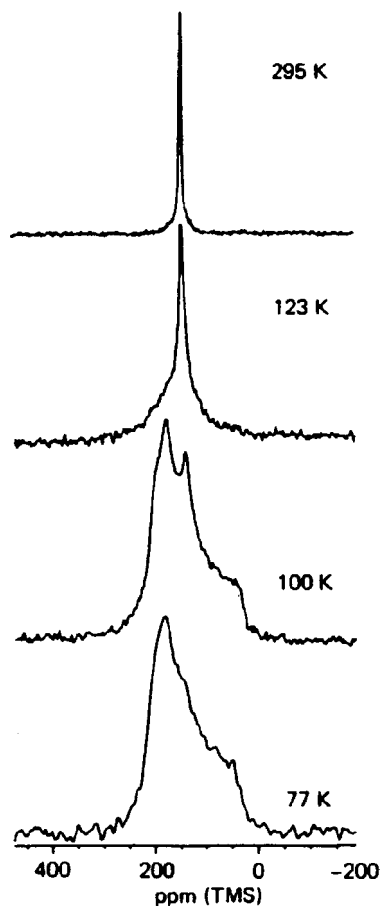


Figure 22. ¹³C NMR spectra of solid C₆₀ obtained at ambient temperatures of 123, 100, and 77 K. The ¹³C NMR spectrum of C₆₀ is expected to be a broad “powder pattern” resonance (width greater than ~200 ppm) reflecting the chemical-shift anisotropy of the ¹³C nuclei averaged over the crystallite orientations. The “motionally narrowed” NMR line at 295 K (143 ppm from tetramethyl silane) proves that C₆₀ molecules are rotating rapidly with respect to the NMR time scale, which is defined by the inverse of the spectral spread (~10⁻⁴ s). As the temperature is reduced, the powder pattern is recovered as the molecular motion decreases. At 77 K there is little evidence of the narrow line at 143 ppm, and a fit to this line shape yields an asymmetric chemical-shift tensor with components of 220, 186, and 25 ppm. Adapted with permission from [275], C. S. Yannoni et al., *J. Phys. Chem.* 95, 9 (1991). © 1991, American Chemical Society.

about 84% near $T_g \sim 90$ K, the glass transition temperature [243]. Below T_g , the thermal energy becomes too small compared with the energy barrier between the two states for further reorientation to occur; therefore the C₆₀ molecules are frozen in their orientation and the fraction of PF orientation (~84%) or HF orientation (~16%) becomes invariable. The remaining orientational disorder causes an orientational glass phase. Because the nearest-neighbor distance of HF oriented C₆₀ molecules is slightly smaller than that of the PF oriented molecules, there is an anomalous increase of volume thermal expansion coefficient in the transition temperature [243].

Evidence for this glass transition at low temperature has been provided by a number of experimental techniques, including velocity of sound and ultrasonic attenuation

Table 9. Physical properties at orientational phase transition temperature T_{01} .

Quantity	Under T_{01}	Above T_{01}	Jump
Structure	sc	fcc	—
Space group	$Pa\bar{3} (T_h^6)$	$Fm\bar{3}m (O_h^5)$	—
Lattice constant	14.11 Å	14.15 Å	0.04 Å [238, 243]
Reorientational correlation time of C ₆₀ molecules	2×10^{-9} s	9.2×10^{-12} s	~200 times [274]
Volume	small	large	~1% [243]
Thermal conductivity	0.5 W/m K	0.4 W/m K	25% [352]
Enthalpy change	low	high	9000 J/kg (6500 J/mol) [368] 12,500 J/kg (9000 J/mol) [376]
Young's modulus	high	low	8% [242]
Magnetic susceptibility	small	large	1.2% [377]
	~4.56 (10 ⁻⁹ in cgs)	~4.61 (10 ⁻⁹ in cgs)	

studies [242, 372], specific heat measurements [361, 379], thermal conductivity [352, 380], elasticity [242, 358, 372], high resolution capacitance dilatometry [357], dielectric relaxation studies [359], electron microscopy observations [381], and neutron scattering measurements [243, 349]. It has been demonstrated that the measured values of transition temperature T_g varying in a wide range (~90–165 K) rely strongly on the time scale of the measurements [358]. The temperature dependence of the relaxation time may be described by the relation $\tau_t = \tau_{t0} \exp(E_{At}/k_B T)$, where E_{At} is the activation energy for the transition and τ_{t0} is a characteristic relaxation time with values of $\tau_{t0} = 4 \pm 2 \times 10^{-14}$ s and $E_{At} = 300 \pm 10$ meV [358]. For high-frequency measurement probes, the molecules cannot reorient quickly enough to follow the probe frequency, so that the molecules seem to be frozen at a higher transition temperature and a lower transition temperature for low-frequency measurement probes. It is concluded that below T_g a quenched disorder occurs rather than an equilibrium glass phase [358].

3.3.3. Phase Transition in Low-Dimensional Structures

At room temperature, the molecules on C₆₀ (111) surfaces are hexagonal close-packed and rotating and reorientating freely corresponding to a (1 × 1) structure. Below a temperature of surface orientational ordering transition temperature T_{s01} about 230 K [382–386] (about 30 K lower than that of C₆₀ bulk), the C₆₀ (111) surface exhibits a (2 × 2) reconstruction [382, 387] due to the four inequivalent frozen molecules in a (2 × 2) unit cell holding four different orientations. STM study clearly revealed the surface structure and indicated that the orientational configurations of the C₆₀ molecules on the surface are similar to those in the bulk, except for some complex details. This similarity indicates that it is the

interaction of the neighboring C₆₀ molecules that drives the molecules to an orientational ordered state [387]. Recently, a two-stage rotational disordering mechanism, with a new intermediate regime between a low-temperature ordered (2 × 2) state and a high-temperature (1 × 1) disordered phase, has been proposed for this surface phase transition based on Monte Carlo simulations [388].

C₆₀ submonolayers adsorbed on a self-assembled monolayer of an alkylthiol can be considered as ideal two-dimensional hexagonal arrays with a nearest-neighbor distance of ~10 Å [20] due to the weak van der Waals force between C₆₀ and the organic monolayer surface. At room temperature the C₆₀ molecules at this surface are mobile and rotating freely. At 77 K, the C₆₀ molecule appears as a hemisphere, a tilted doughnut, or an asymmetric dumb-bell, each being consistent with a rotating pattern around a fixed axis. That is, unlike in the case of bulk C₆₀, the two-dimensional rotationally ordered phase persists down to 77 K (already 13 K below the bulk freezing temperature) [20].

Unlike the orientation-related glass phase in bulk C₆₀ and the bulk C₆₀ (111) surface, the two-dimensional C₆₀ array forms orientationally ordered domains at 5 K although the C₆₀ molecules are not commensurate with alkylthiol monolayer [20]. The molecular rotation is frozen and the internal fine pattern of C₆₀ with a well-known native cage structure can be clearly revealed by STM, because of the fairly weak interaction between C₆₀ and the organic monolayer surface with a negligible influence on the C₆₀ molecule by the substrate.

3.3.4. Phase Diagram

Figure 23 gives an equilibrium phase diagram of C₆₀ crystal covering a wide range of temperatures and pressures, drawn on logarithmic scales to bring out clearly the low-pressure behavior [389].

The solid lines are derived from experiment, and dashed lines are theoretical or reflect extrapolations from experiment. The solid–vapor coexistence line $P(T)$ is given by plotting the equilibrium vapor pressure against temperature. The thermal gravimetric analysis data (shown by solid circles) [247] are fitted to $P(T) = P_0 \exp(-\Delta H/kT)$, which can be derived from the Clausius–Clapeyron equation assuming ideal gas behavior [390]; the low pressure experimental data (shown by a bar and an open diamond) [389, 391] are in good agreement with extrapolation of the solid–vapor coexistence line using the ideal gas relationship. It can be indicated from the diagram that solid fcc C₆₀ sublimates on heating without forming a liquid phase at normal pressures.

The fcc–sc coexistence line at the left of the phase diagram defines the pressure-dependent temperature of the solid-state orientational ordering phase transition; the data shown by filled squares are measured using DSC [244].

At high temperature or under ultrahigh pressure, the C₆₀ molecules will collapse into amorphous carbon. Under higher pressure (>1 GPa) and high temperature, which is not shown in the phase diagram, crystal C₆₀ will polymerize, induced by pressure. The pressure-induced polymerization will be introduced in Section 4.2.

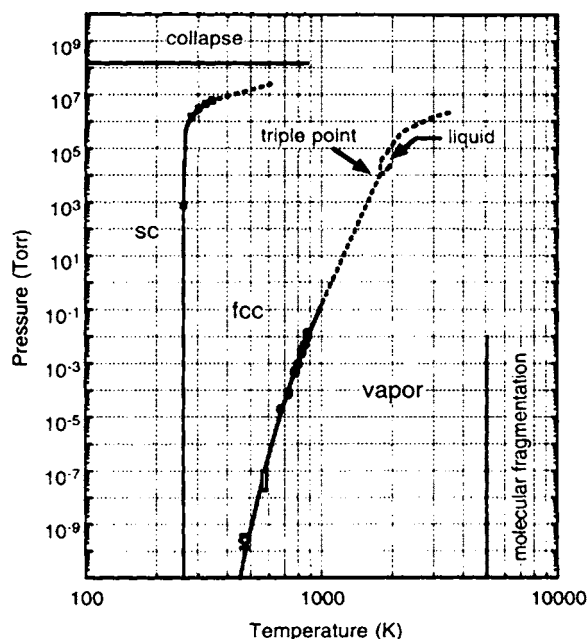


Figure 23. Phase diagram of C₆₀ drawn on a logarithmic pressure scale to show the low pressure range: (—), data from experiment; (---), theoretical curves or extrapolations from experiment. Adapted with permission from [389], D. M. Poirier et al., *Phys. Rev. B* 51, 1830 (1995). © 1995, American Physical Society.

3.4. Crystal Growth

3.4.1. Single Crystal

Solvent grown C₆₀ crystals may form various structures due to the intercalation of solvent molecules or small atmospheric molecules into C₆₀ crystal lattices [392–395], such as hexagonal close packed (hcp) structure [2, 396], fcc structure [397], orthorhombic or monoclinic structure [398, 399], and so on, and various shapes, even decagonal crystals with pseudo tenfold symmetry, can be formed [392, 400, 401].

C₆₀ has an extraordinarily high vapor pressure of strong temperature dependence [246] (at 500 °C, the vapor pressure of C₆₀ is about 10³⁵ times greater than that of the graphite [247]) and solid C₆₀ sublimates at relatively low temperature (see Table 4) [247]. A vapor transport method is used to grow pure C₆₀ single crystal free of solvent or gas in a large quantity and a perfect quality conveniently by slow condensation or deposition of the molecules from vapor [402]. See Table 10.

The vapor growth technique for synthesizing single-crystal fullerenes usually uses a carefully cleaned, dynamically

Table 10. Available rate of weight loss and vapor pressure of C₆₀ at selected temperatures [247].

Temperature (°C)	dw/dt (μg/s)	Vapor pressure (mTorr)
400	0.004	0.019
450	0.014	0.069
500	0.085	0.446
550	0.43	2.32
600	1.75	9.67

pumped, horizontal quartz tube (usually about 50 cm long by 1 cm in diameter) placed in a furnace with a temperature gradient [403–405] (see Fig. 24). The initial C₆₀ powder is filled in a gold boat and heated in the vacuum furnace at about 250 °C under dynamic vacuum for 6–72 hours in order to remove the solvent intercalated in the powder. Subsequently the Au boat is heated above the C₆₀ sublimation temperature to about 590–620 °C, and high-purity, dry helium flow kept at a flow rate below 5 cc/min is employed to carry the C₆₀ vapor to the colder part of the quartz tube. Crystallization starts at the part where the temperature is below 520 °C. The growth rate in this method is expected to be about 15 mg per day. The vapor transport procedure is always kept for several days to yield larger C₆₀ crystals.

Several modified techniques based on the vapor transport growth method have been developed to grow larger and more perfect C₆₀ crystals such as the vibrating temperature method [406], the double temperature gradient method [407], optimization of temperature distribution [408], use of a vertical furnace with a pulling technique [409], the Pizzarello method [410, 411], very small temperature gradient control [412], and so on.

3.4.2. Thin Films

High-quality crystalline C₆₀ thin films have been grown successfully on many substrates and studied extensively for the understanding of growth mechanisms and properties. The potential applications of C₆₀ thin films in electronic devices have been explored, such as rectifying electronic diodes [413], photodiodes and solar cells [413], and thin-film field-effect transistors [414–416]. The results showed those fullerene electronic devices have stable, reproducible performances and excellent device characteristics.

Most of the C₆₀ thin films are grown under ultrahigh vacuum (UHV) environment using a sublimation-deposition method, such as a simple or enhanced vapor deposition technique [417–419], organic molecular beam epitaxy [420], the hot-wall diffusion method, or the ionized cluster beam deposition technique [421–425]. A schematic sketch of a universal hot-wall diffusion method setup is shown in Figure 25. The diffusion oven (lower part of Fig. 25) employed is composed of three parts. The temperature of each part can be controlled independently to get three different temperature zones (upper part of Fig. 25). The source C₆₀ powder and substrate are placed in zone I and zone III in a quartz tube, respectively. The C₆₀ molecules are evaporated from zone I, through zone II, then deposited on the substrate in zone III. The temperature of zone II (hot wall) is higher than the other two zones, which can generate a very low growth rate. As an example, the temperatures of zone I and zone II are

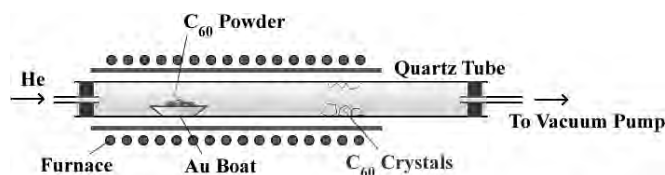


Figure 24. Schematic view of a horizontal quartz tube furnace apparatus for the vapor transport growth of C₆₀ single crystals.

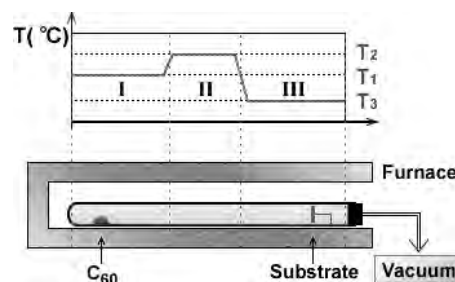


Figure 25. A sketch of diffusion oven composed of three independently temperature-controlled zones; T_1 , T_2 , and T_3 are the temperatures of the C₆₀ source: “hot wall” and substrate, respectively. Adapted with permission from [426], J. G. Hou et al., *Thin Solid Films* 320, 179 (1998). © 1998, Elsevier Science.

set to $T_1 = 420$ °C and $T_2 = 440$ °C, respectively [426]. The substrate temperature (T_3) is usually set from 100 to 200 °C.

Most of well-ordered C₆₀ thin films or multilayers were grown on substrates including layered substrates, alkali halides surfaces, semiconductor surfaces, and metal surfaces.

But studies showed that crystalline films can grow relatively easily on layered substrates like mica [417, 427–439], graphite [386, 440, 441], MoS₂ [437–439, 442, 443], fluorophlogopite [444], and lamellar substrates such as GeS(001) [445–448], GaSe(0001) [341, 343], and Sb [449]. Because of the natural passivation of these substrate surfaces, the C₆₀–substrate interactions are dominated by van der Waals force which can relax the stringent lattice match condition and result in the formation of fcc (111) oriented C₆₀ crystal grains.

Well-ordered crystal C₆₀ monolayers and thin films can also be grown on alkali halides and other ion crystals such as NaCl [417, 418, 437, 438, 450, 451], KCl [418, 438, 450, 451], KBr [418, 438, 450–453], KI [245, 246], and CaF₂ [247, 248], due to the very weak surface bonding dominated by the electrostatic force that restricts the diffusion of C₆₀ ad-species.

But C₆₀ thin films grown on metal substrates are much different from the weak-bonding substrates mentioned. It has been shown that there exist very strong interfacial interactions and charge transfer from the metal substrate to the LUMO of C₆₀ [172, 191]. Compared with the nonmetal substrates, the metal substrates are usually less smooth and contain much higher densities of steps, so it is more difficult to grow high-quality single crystal films on metal surfaces. There have been reported high-quality C₆₀ (111) oriented films successfully grown on Au [191, 419, 458], Ag [191, 419, 459, 460], Cu(111) [191, 461, 462], as well as Ni₃Fe(111), Ni₃Co(111), and Ni₃Fe(110) [426, 463] using a hot-wall diffusion method.

Several techniques have been attempted to improve the crystallization and quality of C₆₀ thin films. Using a self-mediated process [451] or using Sb as the surfactant or buffer layer [464, 465] and the multistep growth method [418], higher quality and larger grain-sized C₆₀ can be obtained. Figure 26 shows a transmission electron microscopy (TEM) image as well as diffraction pattern of a high-quality single crystal C₆₀ fcc (111) oriented film with a thickness of about 60 nm prepared by using Sb as the surfactant on a freshly cleaved (001) NaCl single crystal surface [465].

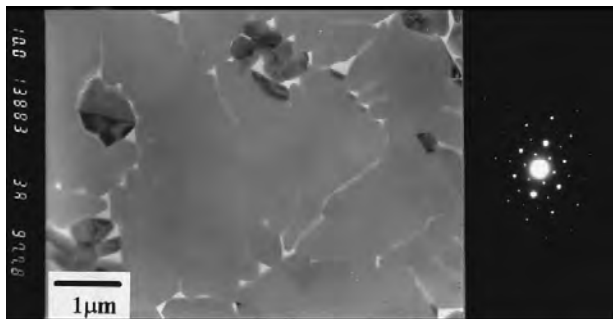


Figure 26. TEM image and diffraction pattern of a C₆₀ film with nominal thickness of 60 nm. Large (111) orientated C₆₀ grains with average size of about a few micrometers were formed. Adapted with permission from [465], J. G. Hou et al., *J. Appl. Phys.* 84, 2906 (1998). © 1998, American Institute of Physics.

3.5. Properties

3.5.1. Electronic Structure

C₆₀ solid is a semiconductor with a minimum of the energy gap at the *X* point of the Brillouin zone. The value of the energy gap is still under debate, which is in the range of 1.43–2.35 eV. In early studies, a typical and widely referenced band calculation for solid C₆₀ is based upon the local density approximation (LDA) in density functional theory, in which all many-body effects are collected into the exchange-correlation energy, which is evaluated within a free-electron model. The LDA calculations obtained a bandgap of ~1.5 eV for fcc C₆₀ crystals [466] and a value of 1.18 eV for the bandgap at the *X* point [467]. The band structure of C₆₀ crystals is derived from the energy level distribution of an isolated C₆₀ molecule. Figure 27 shows the electronic structure of the HOMO- and LUMO-derived bands of C₆₀ in the solid state obtained from LDA calculations.

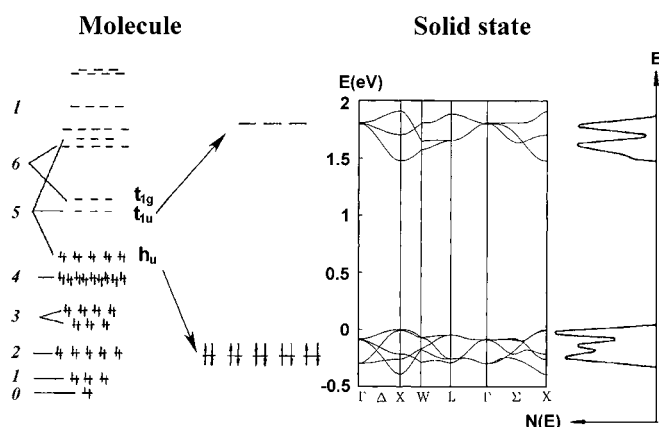


Figure 27. Left-hand panel; a schematic diagram of the C₆₀ π -molecular orbit energy scheme. The HOMO (h_{1u}) and LUMO (t_{1u}) are shown in the expanded region. Central panel; the band structure of the HOMO- and LUMO-derived bands of C₆₀ in the solid state. Right-hand panel; the density of states of the HOMO- and LUMO-derived bands of solid C₆₀ predicted from LDA calculations [466]. Adapted with permission from [468], M. Knupfer, *Surf. Sci. Rep.* 42, 1 (2001). © 2001, Elsevier Science.

By properly treating the electron excitations with an *ab initio* quasiparticle approach, a GW (G represents Green's function and W is a dynamically screened Coulomb interaction) approach was developed. In the GW approach, the Dyson equation is solved within a Green's function formalism using a dynamically screened Coulomb interaction W to obtain the quasiparticle energy spectrum. Because the method includes a treatment of the electron self-energy (in terms of a dynamically screened Coulomb interaction), it predicted a larger value of 2.15 eV [469] for the HOMO–LUMO gap, with bandwidths of 0.9, 0.7, and 0.8 eV for the HOMO-, LUMO-, and (LUMO + 1)-derived bands, respectively. This result is very close to the gap value of ~2.3 eV given by high-energy spectroscopy experiments like PES and inverse photoemission spectroscopy (IPES) [470–472]. There are also many other experiments carried out by different methods showing different results [473]. A scheme in Figure 28 shows the difference of the gap values given by different methods.

A detailed electronic structure of C₆₀ thin films was studied by surface photovoltage spectroscopy [474, 483, 484]. It is illustrated in Figure 29, which includes a mobility gap of 2.25 eV and exponential Urbach tails of states determining the optical gap of 1.65 eV [481, 485]. In addition, there exist two deep gap states: one donor and one acceptor. The acceptor level lies 0.8 eV below the conduction band tail, and the donor level is 1.25 eV higher than the valence band tail. The exponential Urbach tails in the density of gap states may be due to thermal disorder rather than from static structure, topological, or compositional disorder. The donor level arises from the unbound intercalated oxygen and the acceptor level is considered to be the result of chemical reaction of oxygen with fullerene. This detailed electronic structure shows that the optical absorption edge [481] is not simply connected to the HOMO–LUMO gap.

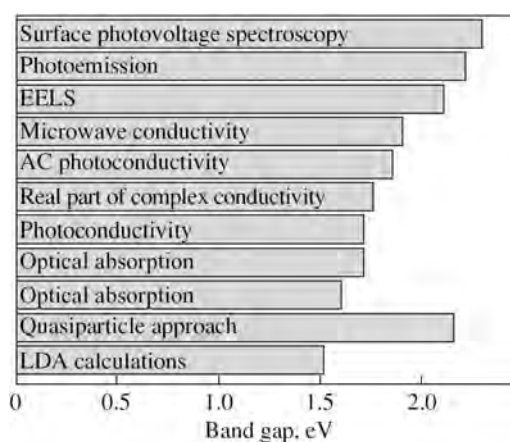


Figure 28. Energy gap of C₆₀ fullerene, obtained in various studies, including: surface photovoltage spectroscopy [474], photoemission [471], EELS [475], microwave conductivity [476], ac photoconductivity [477], real part of complex conductivity [478], photoconductivity [479], optical absorption [480] (the upper one), optical absorption [481] (the lower one), quasiparticle approach [482], and LDA calculations [466]. Adapted with permission from [473], T. L. Makarova, *Semiconductors* 35, 243 (2001). © 2001, MAIK Nauka/Interperiodika.

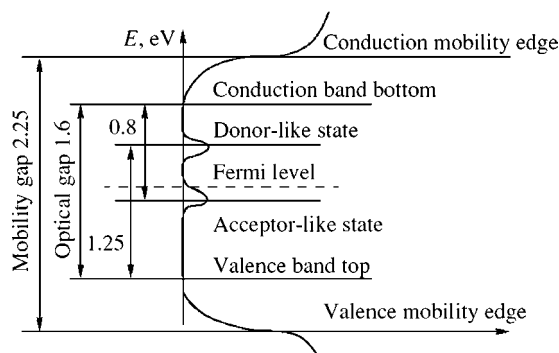


Figure 29. Electronic structure of C₆₀ thin films, from which we can see exponential tails of states between conduction mobility edge and conduction band bottom, as well as tails between valence band top and valence mobility edge. Adapted with permission from [474], B. Mishori et al., *Solid State Commun.* 102, 489 (1997). © 1997, Elsevier Science.

To get a complete description of the electronic structure of C₆₀ solids, a number of many-body calculations have focused on calculations of quantities of electron correlation effects. Direct *in-situ* comparison of C 1s absorption spectra taken in the gas phase with those from solid C₆₀ reveals a close similarity [486]. It can be concluded that solid-state interactions are not important in this new material, and the electron correlation effects are mainly intramolecular. So the Coulomb repulsion (U) of two holes on the same molecule in solid C₆₀ is an important quantity, which is nearly independent of the molecular orbital of the hole with a value of 1.6 eV [471]. This value of U leads to Frenkel-type molecular excitons with energy of about 1.5–2 eV corresponding to h_u-t_{1u} intramolecular excitations which correspond to the lowest-energy-observed optical transitions of electronic origin. The calculated values of such Frenkel excitons are 1.58 and 1.30, with experimentally measured values of 1.83 and 1.55 eV [487, 488].

3.5.2. Electrical Transport Properties

At room temperature, pristine C₆₀ solids are n -type semiconductors with a high resistivity [415, 489]. The electron mobility is considerably larger than the hole mobility. The electron and hole drift mobilities are 1.3 and 2×10^{-4} cm²/V s, respectively, and the recombination lifetime is 1.7×10^{-6} s [490]. The dc conductivities in C₆₀ follow a purely thermally activated behavior. The conductivity of the crystalline C₆₀ is obviously higher than that of the amorphous films. The dc conductivity of C₆₀ single crystal is 1.7×10^{-8} (Ω cm)⁻¹ and the activation energy is 0.581 eV [491]. But for polycrystalline films, the conductivity and activation energy are reported to be 10^{-6} – 10^{-8} (Ω cm)⁻¹ and 0.3–0.6 eV [492–496], respectively. For amorphous films, these values are within the intervals 10^{-7} – 10^{-14} (Ω cm)⁻¹ and 0.5–1.1 eV [479, 497–499]. With improving crystallinity of C₆₀ films, their conductivity increases, and the activation energy falls [500, 501].

The thermally activated conductivity in fullerene systems [493, 502] obeys the Meyer–Neldel (MN) rule [503]. The MN rule describes an exponential relation between the activation energy E_a and the pre-exponential factor σ_0 . The expression of the MN rule for the dc conductivity can be

written as $\sigma = \sigma_0 \exp(-E_a/kT)$, and the prefactor σ_0 correlates with the activation energy E_a as $\sigma_0 = \sigma_{00} \exp(-E_a/kT)$, where σ_{00} and T_0 are the Meyer–Neldel parameters. For example, the relationship between the conductivity prefactor σ_0 and activation energy E_a in C₆₀ films under different O₂ exposure can be described by the MN rule. The obtained σ_{00} and kT_0 are 15.6 (Ω cm)⁻¹ and 0.11 eV, respectively [493]. The relationship between the conductivity prefactor and activation energy in C₆₀ films at different stages of the growth process also obeys the MN rule with the MN parameters of $\sigma_{00} = 7.7 \times 10^{-19}$ (Ω cm)⁻¹ and $kT_0 = 0.012$ eV [493].

High pressure has a strong effect on the conductivity, as well as the width of the gap between LUMO- and HOMO-derived bands of C₆₀ solids [504, 505]. The electric conductivity changes four orders of magnitude from 2×10^{-6} (Ω cm)⁻¹ (below 8 GPa) to 3×10^{-2} (Ω cm)⁻¹ (around 20 GPa). The bandgap is as follows: 1.6 ± 0.1 eV at 3 and 6 GPa, and 1.2 ± 0.1 eV at 10 GPa. Exposed to air, upon the interaction with oxygen, the conductivity of C₆₀ single crystals [506] and films falls [493, 507] by 3–6 orders of magnitude. Such an effect may be caused by trap levels for carriers and neutralizes defects forming localized electronic states, which are created by the intercalated oxygen.

The conduction mechanism at different temperatures has been studied by measuring the ac ($1 < f < 50$ kHz) conductance of C₆₀ polycrystals [508]. In the temperature range of 100–150 K, the ac conductance linearly depends on the temperature and nearly has a power law of $\omega^{0.8}$ dependence on the frequency, which is characteristic of the model of the variable range hopping between midgap localized states around the Fermi level [509]. In this model, the ac conductance can be described as $\sigma(\omega, T) \sim \pi e^2 kT [N(E_F)]^2 \alpha^{-5} \omega [\ln(\nu_{ph})/\omega]^4$. Here, $N(E_F)$ is the density of states at the Fermi level, ν_{ph} is the phonon frequency, and α is a constant. In the temperature range of 200–350 K, the frequency dependence of conductance at a fixed temperature can also be roughly described as a power law $\sigma \sim \omega^s$ ($s = 0.8$). However, in this temperature range (as the frequency varied from 1 to 10 kHz), the ac conductance increases rapidly with temperature and shows a thermal activated behavior with an activation energy E_a of 0.389 eV below 265 K and 0.104 eV above it. This is proposed to be caused by the hopping process among the tails of localized states, which can be described as $\sigma(T) \propto \exp(-E_a/kT)$. The two activation energies can be ascribed to the coexistence of the crystalline and amorphous phase of C₆₀. At very high temperatures approaching the sublimation temperature of about 430 °C, experiments suggest that the mechanism of conductivity of C₆₀ changes from hopping conductivity to band conductivity (charge transfer over delocalized states) [510–512]. From these results, it can be concluded that the C₆₀ solid conductivity can be described in terms of the conduction mechanism of disordered semiconductors.

3.5.3. Optical Properties

Optical Absorption and Photoluminescence Spectroscopies The optical properties of solid C₆₀ in the visible-UV range were investigated by a variable angle spectroscopic ellipsometry (VASE) technique [513–515] and

near-normal-incidence reflection and transmission experiments [516]. UV data above ~ 7 eV were obtained using EELS [475] by Kramers–Kronig analysis of the EELS loss function. The observed optical properties of C₆₀ solids are usually expressed in terms of the complex optical dielectric function $\varepsilon(\omega) = \varepsilon_1(\omega) + i\varepsilon_2(\omega)$. Figure 30 shows the results for $\varepsilon_1(\omega)$ and $\varepsilon_2(\omega)$, obtained from VASE and transmission-FTIR (Fourier transform infrared) studies on thin solid films of C₆₀ on KBr substrate at $T = 300$ K [316]. The strong, sharp structure at low energy (below 0.5 eV) is identified with infrared-active optic phonons. The imaginary part of the dielectric constants of C₆₀ begins to rise at 1.7 eV, which can be considered the absorption edge. At higher energies in the visible and UV ranges, the spectrum structure is due to allowed optical transitions at 3.5–5.6 eV and to excitons at energies below 3 eV. There are four prominent absorption peaks at ~ 2.7 , 3.6, 4.7, and 5.6 eV for the pristine C₆₀ with dipole-allowed electronic transition [480, 481, 517–519]. Optical transitions between the HOMO and LUMO bands are forbidden by symmetry [520].

Luminescence spectra appear to be more sensitive to sample quality and to show wider sample to sample variation than absorption spectra [521]. The temperature dependence of the photoluminescence spectra is given in [522]. At a temperature of 7 K, the absorption curve intersects the photoluminescence curve at the point 1.8 eV, which may be the optical gap at this temperature [523].

Transition Assignment An accurate study of optical transition in C₆₀ was carried out by comparing the optical spectra of C₆₀ films on mica with the transmission of toluene, hexane, and heptane solutions [480]. Experimental spectra were fitted with Gauss–Lorentz (GL) line shapes to determine the energy positions of individual transitions.

The assignment of the electronic transitions given in Table 11 is based on the calculated transition energies of [524–526]. The best agreement of the calculated gap positions with experimental results is provided by the tight-binding models [525, 526]. An overview of the energy levels and optical transitions discussed is shown in Figure 31.

The three leading GL bands *D*, *E* + *F*, and *G* are assigned to the transitions $h_g, g_g \rightarrow t_{1u}$, $h_u \rightarrow h_g$, and $h_g, g_g \rightarrow t_{2u}$,

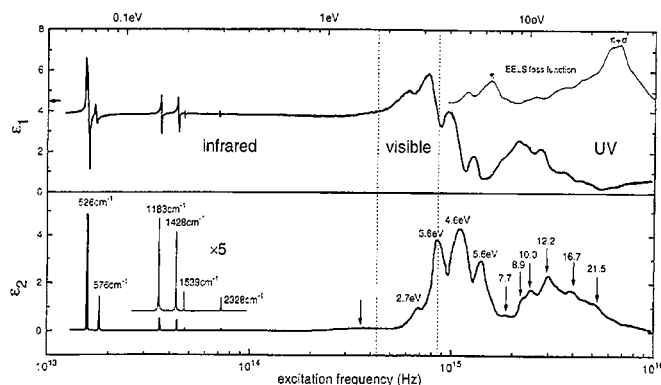


Figure 30. Real and imaginary parts of the dielectric function $\varepsilon(\omega)$ determined from VASE and FTIR measurements for C₆₀. Adapted with permission from [520], M. S. Dresselhaus et al., *Synthetic Metals* 78, 313 (1996). © 1996, Elsevier Science.

Table 11. Spectral features for solid C₆₀ and C₆₀ molecules. All energies are given in eV [480].

Band code	Solid C ₆₀	C ₆₀ molecules	Transition assignment
γ_0	1.918	1.995	$h_u \rightarrow t_{1u} + T_{1u}, H_u, G_u$ (+ H_g, A_g)
γ_1		2.035	
γ_2	1.992	2.070	
γ_3	2.028	2.105	
γ_5	2.097	2.180	
A	2.41		$h_u \rightarrow t_{1g}$
B	2.70		
C	3.2		
D1	3.489	3.58	$h_g, g_g \rightarrow t_{1u}$
D2	3.541	3.732	
E	3.99	4.21	$h_u \rightarrow h_g$
F1	4.36		
F2	4.546	4.6	
G1	5.500	5.437	$h_g, g_g \rightarrow t_{2u}$
G2	5.77	5.73	

respectively [480, 513]. The oscillator strengths of these dipole-allowed transitions are in reasonable agreement with the calculations of [525]. The *D* band assigned to $h_g, g_g \rightarrow t_{1u}$ transitions is strongly reduced in doped films due to the filling of the lowest state in the conduction band derived from the t_{1u} molecular states [527]. The molecular $F_{1,2}$ band, which originates from the $h_u \rightarrow h_g$ transition, split into *F1* and *F2* bands in the solid due to the splitting of the fivefold-degenerate $h_u(h_g)$ levels to the threefold- and twofold-degenerate $t_u(t_g)$ and $e_u(e_g)$ levels, respectively [467]. The weak *E* band possibly also originates from the $h_u \rightarrow h_g$ transition.

The assignment of the two lowest transitions, $h_u \rightarrow t_{1u}$ and $h_u \rightarrow t_{1g}$, is more delicate. The $t_{1g}h_u^{-1}$ molecular state consists of electron–hole excited states with T_{1u}, T_{2u}, H_u , and G_u symmetry [528]. According to several calculations, the lowest allowed transition $h_u \rightarrow t_{1g}$ to the T_{1u} excited state should be located near 3 eV with an oscillator strength of about 3% of that of the $h_g, g_g \rightarrow t_{1u}$ band at 3.5 eV

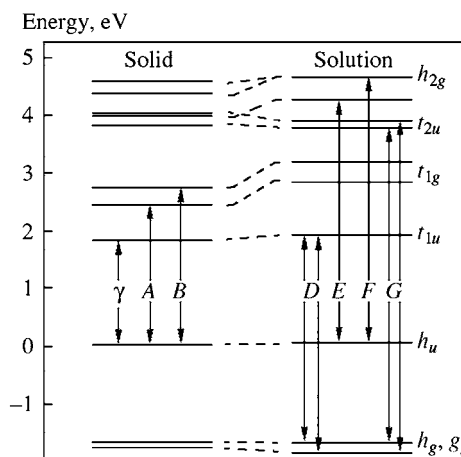


Figure 31. Electronic energy levels in solid C₆₀ and in C₆₀ solution in *n*-hexane. Adapted with permission from [480], J. Hora et al., *Phys. Rev. B* 54, 5106 (1996). © 1996, American Physical Society.

[524, 525, 529]; the very small oscillator strength has been attributed to plasmon screening [525]. In addition to this allowed transition, phononinduced transitions of comparable strengths [529] to the T_{2u} , H_u , and G_u excited states [528] should appear in the same energy region. The comparison of the energies and oscillator strengths of the B and D bands is essential for the following assignment of γ , B , B' , and D subbands to the electronic transitions (see Table 11).

The A-group is attributed to the $t_{1g}h_u^{-1}$ electron-hole state parity forbidden in an isolated molecule, but becoming partially allowed because of level splitting.

The γ -group results from the forbidden molecular transition $h_u \rightarrow t_{1u}$. These transitions gain nonzero strength through the excitation of an appropriate odd-parity vibrational mode [530] (Hertzberg-Teller coupling) and their upper electronic states can be influenced by Jahn-Teller dynamic distortions [518].

Photoconductivity Experiments confirmed the existence of the photoconductivity in fullerene solids [531, 532]. Photoconductivity spectra of C₆₀ are, on the whole, similar to the absorption spectra, apart from the conduction dip at about 350 nm of wavelength. Such a photoconduction dip appears frequently in intense absorption regions in many photoconductors. The photoconduction edge is at about 730 nm (1.7 eV) [523]. The main spectra features are related to excitons rather than to interband transitions. The photoconduction spectra measured at various light-intensity modulation frequencies, light intensities, and applied voltages shows that the photocurrent is proportional to light intensity and applied voltage. Moreover, the photocurrent increases with decreasing light-intensity modulation frequency, which may arise from some deep carrier traps in the energy gap.

3.5.4. Dielectric Properties

Solid C₆₀ is a soft dielectric material [533]. The complex dielectric function $\varepsilon(\omega) = \varepsilon_1(\omega) + i\varepsilon_2(\omega)$ of solid C₆₀ was studied over a broad frequency range using a wide variety of techniques including ac impedance measurements at low frequencies and optical measurements at high frequencies [259, 391, 475, 516, 517, 534].

The complex optical dielectric function $\varepsilon(\omega) = \varepsilon_1(\omega) + i\varepsilon_2(\omega)$ can be expressed in the terms of the complex refractive index $N(\omega) = [n(\omega) + ik(\omega)]$. Here, n is the refractive index and k is the extinction coefficient. Both n and k are frequency-dependent optical constants. The expression is $\varepsilon(\omega) = [N(\omega)]^2 = [n(\omega) + ik(\omega)]^2$. The optical dielectric function $\varepsilon(\omega)$ of C₆₀ was studied over a wide frequency range of 10^{13} – 10^{16} Hz (corresponding to 0.05–40 eV, 1 eV = 8066 cm⁻¹). Below 7 eV, it was studied using infrared (between 0.05 and 0.5 eV) [534] and visible-UV (1.5–5.5 eV) [516, 525] spectroscopies. UV data above 7 eV were obtained using EELS by Kramers-Kronig analysis of the EELS loss function [475]. The features of the $\varepsilon_2(\omega)$ dielectric loss spectrum in the infrared range include four strong lines at 526, 576, 1182, and 1428 cm⁻¹ due to molecular vibrations. At higher energies in the visible and UV ranges, the imaginary $\varepsilon_2(\omega)$ part of the dielectric constants begins to rise at 1.65 eV and there are four prominent peaks at ~2.75, 3.55, 4.50, and 5.50 eV in the $\varepsilon_2(\omega)$ spectrum, corresponding to four absorption peaks [269]. An absolute

value of the real $\varepsilon_1(\omega)$ part at 1.5 eV is 4.1. The whole trend of the optical dielectric function of C₆₀ is as below. Where there is a loss process represented by a peak in the $\varepsilon_2(\omega)$ dielectric loss spectrum, there is a rise or a resonant oscillation in the $\varepsilon_1(\omega)$ spectrum. This result is consistent with Kramers-Kronig relations. With frequency decreasing to 10^{13} Hz, $\varepsilon_1(\omega)$ is approaching its dc value. The small difference between $\varepsilon_1(10^{13} \text{ Hz}) \approx 3.9$ [517] and $\varepsilon_1(10^5 \text{ Hz}) \approx 4.4$ [391] might be due to the losses associated with C₆₀ molecules rapidly rotating (at the rate of $\sim 10^9$ Hz) at room temperature ($T > T_{01}$, $T_{01} = 260$ K is the structure transition temperature).

In the low frequency regime (below 10^5 Hz), polarization mechanisms come into play. The dielectric properties in this regime were investigated by ac impedance measurements, which are usually performed on a sample between closely spaced parallel conducting plates. These M-C₆₀-M (M = metal) “sandwich” structures consist of 200- μm -wide aluminum down stripes as base electrodes, a known thickness of C₆₀, and 200- μm -wide aluminum cross stripes as counterelectrode [535]. The ac equivalent capacitance $C(\omega)$ and the dissipation factor $D(\omega)$ of the resulting capacitor can be obtained. The real part of the relative dielectric function $\varepsilon_1(\omega)$ can be calculated since the relation between the capacitance and $\varepsilon_1(\omega)$ is known to be $C(\omega) = \varepsilon_1(\omega)\varepsilon_0 A/d$. Here, A is the cross-sectional area of the capacitor, d is the separation distance between the plates, and ε_0 is the absolute permittivity of free space (8.85×10^{-12} F/m). The imaginary part of the dielectric function $\varepsilon_2(\omega)$ can be extracted from measurement of the dissipation factor $D(\omega) = \varepsilon_2(\omega)/\varepsilon_1(\omega)$. To ascertain the intrinsic dc $\varepsilon_1(0)$ of C₆₀, the dielectric measurement needs to be performed at frequencies low enough to include the intrinsic relaxation processes of the material, but high enough to escape the effects of impurities (e.g., molecular oxygen). The effects of oxygen and other impurities occupying the interstitial sites of solid C₆₀ on the dielectric relaxation of C₆₀ films can be ignored only above ~ 5 kHz. So the intrinsic dielectric constant was obtained by performing a series of capacitance measurements at 100 kHz. By this method, a value of 4.4 ± 0.2 was obtained for the relative permittivity $\varepsilon_1(0)$ [391].

The plate spacing d of the C₆₀ capacitor may change due to the thermal expansion or to phase transition at $T_{01} \approx 260$ K. The interaction of oxygen or other species into the interstitial spaces of C₆₀ solid can also lead to such problems. To avoid these problems, a microdielectrometry technique [536, 537] has been employed at low frequencies (from 10^{-2} to 10^5 Hz). In this technique, a coplanar electrode configuration was used as an alternative to the “sandwich” configuration. Both electrodes in the microdielectric measurement are placed on the same surface of an integrated circuit, and C₆₀ film is placed over the electrodes by thermal sublimation in vacuum [391]. In comparison with the “sandwich” geometry, this geometry has the advantages as follows. First, the comb electrodes of a coplanar sensor, in contrast to parallel plates, ensure proper calibration of the device even if the material being measured undergoes structure transformations. Moreover, the open-face layout facilitates studies of diffusion of foreign species into the bulk of the material.

By means of capacitance and dissipation factor measurements discussed previously, the temperature dependence of

the dielectric properties of C₆₀ single crystals, polycrystalline C₆₀, and microcrystalline C₆₀ films were studied [359, 538, 539]. On cooling below the first-order structural phase transition at 260 K, a Debye-like relaxational contribution to the dielectric response was observed. From the Debye-like relaxation, the presence of permanent electric dipoles was found, which are unexpected in the centrosymmetric structure of the pure ordered cubic phase C₆₀. It is suggested that the high degree of frozen orientational disorder of the C₆₀ molecules is responsible for the existence of electric dipolar activity. In addition to the structure phase transition at 260 K, a signature of the glass transition was detected at ~90 K. Studies on the dielectric properties of C₆₀ films in the high-temperature region discovered that both the capacitance and dissipation factor curves as a function of temperature have a pronounced feature at 435 K, which confirms the fact that above 400 K a phase transition does occur in the crystal [539].

A small charge transfer between the C₆₀ and O₂ molecules, which occupy interstitial space of solid C₆₀ exposed to oxygen (or ambient air), creates large electrical dipole moments due to the large size of the C₆₀ molecules [535]. The dipole moments can be coupled to the applied ac electric field via a diffusion-controlled relaxation mechanism. This leads to a significant increase in the permittivity ϵ_1 accompanied by a broad dielectric loss peak ϵ_2 at ~10–100 Hz. For instance, the dielectric function $\epsilon_1(\omega)$ increases dramatically from 4.4 at 10⁵ Hz to 18.4 at 100 Hz due to the polarization caused by the interstitial oxygen [535]. With increasing oxygenation, the interstitial sites are nearly fully occupied. As a result, interstitial hopping is inhibited, and the loss peaks disappear.

3.5.5. Magnetic Properties

Pristine C₆₀ solids are diamagnetic materials due to the presence of ring currents in the C₆₀ molecule [1]. In comparison with other carbon-based materials [540–543], such as graphite and diamond, C₆₀ has an unusually small diamagnetic susceptibility of about -0.35×10^{-6} emu/g [544, 545]. This is because there is an unusual cancellation of ring currents in the C₆₀ molecule. There are two kinds of rings in the C₆₀ molecule: the aromatic rings and the pentagonal rings. The aromatic rings in C₆₀ set up shielding screening currents in a magnetic field [546, 547] which contribute a diamagnetic term to susceptibility χ , while the pentagonal rings contribute a paramagnetic term of almost equal magnitude. Table 12 presents the diamagnetic susceptibility for C₆₀ and related materials.

Table 12. The diamagnetic susceptibility for C₆₀ and related materials at $T = 300$ K.

Material	χ (10^{-6} emu/g)	Ref.
C ₆₀	-0.35	[544, 545]
C ₇₀	-0.59	[544, 545]
Graphite	-21.1 (<i>c</i> -axis) ^a	[548]
Carbon nanotubes	-10.2	[549, 550]
Diamond	-0.49	[551]

^a The value refers to *c*-axis susceptibility of graphite. The *H* in-plane susceptibility of graphite is 0.4×10^{-6} emu/g.

The measurement performed on a C₆₀ powder sample shows the temperature dependence of the magnetic susceptibility [544]. At temperatures greater than 180 K the susceptibility is temperature independent with a mass value of $\chi_g = -0.35 \times 10^{-6}$ emu/g, where the subscript *g* refers to the susceptibility per gram of sample. At low temperatures, due to a relatively small number of electron spins, χ_g increases and becomes paramagnetic, yielding a molar Curie constant $C_M = \chi_M T = 0.75 \times 10^{-4}$ (χ_M is a molar susceptibility), which gives an electron spin value of 1.5×10^{-4} per carbon atom. It is believed that the Curie constant here is caused by a foreign paramagnetic impurity in the C₆₀ sample.

Magnetization of a large single C₆₀ crystal was measured as functions of applied field and temperature [377]. The sample was carefully prepared and handled to avoid oxygen contamination. The result shows no low-temperature Curie term, from which it is concluded that the low-temperature Curie contribution is likely due to oxygen contamination. In addition, near $T_{01} = 260$ K, a discontinuity with a 1.2% change in susceptibility was observed, with $\chi(T_{01}^-)$ more negative than $\chi(T_{01}^+)$ for the susceptibility at either side of the phase transition. The discontinuity is attributed to the change in the intramolecular geometry at the orientational order–disorder transition. The susceptibility can be considered to be independent of the temperature below and above the structural transition temperature, $T_{01} = 260$ K. The experiment demonstrated that the cooperative phase transition affects the magnetic susceptibility of a single molecule.

Whereas the unpolymerized C₆₀ is diamagnetic, a few fullerene-based materials were found to be ferromagnetic. Ferromagnetism has previously been observed in [TDAE]C₆₀ [TDAE = tetrakis(dimethylamino)ethylene] below 17 K [552]. It has been reported that hydrogenated fullerene [553], C₆₀H₂₄, and some palladium fullerenes [554], C₆₀Pd_{*n*}, may be ferromagnetic. Recently, the finding of ferromagnetism in pure Rh-C₆₀ (rhombohedral phase 2D C₆₀ polymer) samples by Makarova et al. [555] appears to be the first report on magnetic ordering in a pure molecular carbon material up to temperatures above 300 K (see Section 4.2.4).

3.5.6. Thermal Properties

Specific Heat Measurement of the temperature dependence of the heat capacity at constant pressure $C_p(T)$ provides the most direct method for the study of the temperature evolution of the degrees of freedom, phase transitions, and the enthalpy change.

The temperature dependence of the specific heat of C₆₀ solids is studied mainly by DSC. The overall shape of the C₆₀ specific-heat curve in the temperature range of 0.2–400 K is as follows. At very low temperature (below 1 K), the specific heat shows a $C_p(T) = C_1 T + C_3 T^3$ behavior. The T^3 dependence component of $C_p(T)$ yields a Debye temperature $\Theta_D = 80$ K [556–558]. The linear T contribution arises from the tunneling modes in the glassy systems [559]. The contribution saturates above ~5 K and contributes little at high temperatures. In the temperature range $2 \leq T \leq 80$ K, there is an initial rise in the specific heat, followed by a plateau near 80 K [560]. The intermolecular modes of C₆₀ contribute

significantly in this range. The plateau is due to the saturation of these low-energy excitations. The low-energy excitations in this range consist of both acoustic (translational) modes and rotations (also called librations) involving the entire C₆₀ cage. Because the bonds between cages are weak van der Waals bonds, these low-energy modes saturate below 80 K. With six modes (three translational and three librational) and a molecular number density ($N/60$), the Dulong–Petit limit for the C₆₀ molecules is $6(N/60)k_B = 69.3$ mJ/g K, which matches the level of the plateau. Here, N is the number density (per unit mass) of carbon atoms.

Above 100 K, there is a nearly linear rise in $C_p(T)$ curve, and this rise in C_p is caused by the higher energy intramolecular excitations on the ball, which start to be activated and contribute to the specific heat. The Dulong–Petit limit for the carbon atoms is equal to $3Nk_B = 2.08$ J/g K. Based on the highest energy on-ball mode (196 meV), the saturation temperature is expected to be above 2500 K. Since C₆₀ sublimes around 300 °C, it could not be observed anyway. It is the large difference in bond strength between the covalent bonds on the cage and the molecular bonds between the cages that leads to the energy separation between the intra- and intermolecular modes [560].

A remarkable feature in the temperature dependence of the specific heat for C₆₀ is the large specific heat anomaly near $T_{01} = 261$ K orientational order–disorder transition [368, 561]. The structure of the $C_p(T)$ curve near the phase transition temperature T_{01} is strongly impurity concentration dependent. Moreover, the specific heat of C₆₀ depends dramatically on the cooling or heating rate. Extremely slow heating and cooling runs (at rates of the order of 100 mK/h) showed that even at such low scanning rates the results are rate dependent [368]. The material is not in a thermodynamic equilibrium state and behaves as a system with a very long internal relaxation time (order of 10 h) in completing the first-order transition. The lower the scanning rate, the more the ordering transition temperature shifts to lower (higher) temperatures for the heating (cooling) runs. Measurements [368] on high-purity sublimed C₆₀ show that for the orientational transformation occurring at 262.4 K during the heating run, the associated $C_p(T)$ peak is remarkably sharp and attains a value of 12,360 J/kg K. The corresponding heat of transition is about 9000 J/kg (6500 J/mol), a value considerably smaller than reported for single crystal of 12,500 J/kg (9000 J/mol) [376]. For the slow cooling run an even larger peak value of 16,730 J/kg K at a transition temperature of 260.6 K is observed.

If the specific heat anomalies associated with phase transitions are removed from the experimental $C_p(T)$ data for C₆₀, then the temperature dependence of the residual specific heat contribution for C₆₀ is in good agreement with that of graphite [367, 562] for $T \geq T_{01}$ (261 K).

Thermal Expansion The temperature dependence of the lattice constant a_0 for C₆₀ shows a large discontinuity at the structure phase transition temperature $T_{01} = 261$ K, where the lattice parameter a_0 jumps by $+0.044 \pm 0.004$ Å on heating [238]. The fractional jump of the unit cell volume of $\Delta v = (\Delta V)/V$ is $(9.3 \pm 0.8) \times 10^{-3}$. The average isobaric volume coefficient of thermal expansion α both above and below the transition is $(6.2 \pm 0.2) \times 10^{-5}$ K⁻¹ [238, 349]. It is

surprising that measurements of α taken to high temperature (1180 K) show a lower value of $4.7 \times 10^{-5}/\text{K}$ than for the lower temperature range [563]. The thermal expansion coefficient of C₆₀ films with thickness t were investigated. As t decreases α increases and is described well by the relation $\alpha = 17 \times 10^{-6} \text{ K}^{-1} + 8.3 \times 10^{-5} \text{ nm K}^{-1} t^{-1}$ [564].

Thermal Conductivity Because C₆₀ is a van der Waals-bonded molecular solid, its Debye temperature θ_D due to the intermolecular phonon modes is low with a value of about 70–80 K [350, 556]. Above the Debye temperature the specific heat due to propagating modes is independent of temperature. Consequently, the thermal conductivity κ is an ideal probe of the phonon mean free path through the kinetic expression $\kappa = C v_s \lambda / 3$, where C is the specific heat, v_s is the sound velocity, and λ is the phonon mean free path. Experiments showed that $\kappa \sim 0.4$ W/mK at room temperature and is approximately temperature independent down to 260 K [380, 352]. At 260 K, κ takes a sharp jump from 0.4 to 0.5 W/mK with a transition width of ~ 2 K. Because the heat capacity due to intermolecular modes is constant at 260 K, the 25% jump in κ must be due to a sudden increase in the phonon mean free path. Upon further cooling, the thermal conductivity increases. At about 85 K, the thermal conductivity shows a shoulderlike structure. The temperature and time dependence of the thermal conductivity below 260 K can be described by a phenomenological model that involves thermally activated jumping motion between two nearly degenerate orientations, separated by an energy barrier of ~ 260 meV.

3.5.7. Mechanical Properties

Primary C₆₀ is fcc molecular crystal formed by Van der Waals interaction between rigid C₆₀ molecules. It is a soft and friable material showing low strength and high-elastic compliance. Information on the temperature dependence of the elastic moduli is incomplete and partially contradictory [242, 358, 372, 565–567]. The elastic constants of single-crystal C₆₀ at room temperature have been established [568, 569]. Since solid C₆₀ at room temperature is cubic, the matrix of the elastic constants has three independent components: C_{11} , C_{12} , and C_{44} . The elastic moduli C_{11} , C_{12} , and C_{44} were obtained experimentally on the basis of sound velocity and the density ρ by using the well-known relations between the elastic moduli and sound velocity in cubic crystal: $\rho v_T^2 = C_{44}$, where v_T is the velocity of transverse ultrasonic waves in the [100]-direction, $\rho v_T^2 = (C_{11} - C_{12} + C_{44})/3$, where v_T is the velocity of transverse ultrasonic waves in the [111]-direction, and $\rho v_L^2 = C_{11}$, where v_L is the velocity of longitudinal waves in the [100]-direction. These values of the elastic moduli determined by the experiments are presented in Table 13.

Table 13. Experimental and theoretical values of the elastic moduli C_{ij} (GPa) of the fcc phase of solid C₆₀ (300 K).

C_{11}	C_{12}	C_{44}	$C_{11}-C_{12}$	Ref.
14.9 ± 0.9	8.8 ± 1.0	6.6 ± 0.18	6.1 ± 0.45	Experiment [571]
13.8	6.6	7.0	7.2	Theory [570]

For comparison, the theoretical values of the elastic stiffness constants obtained in terms of the model intermolecular interaction are also given in Table 7 [570]. In the theory approach, the interatomic Buckingham potential was used for calculating the intermolecular interaction and the electrostatic interaction was taken into account.

To compare the previous results of a single crystal with the measurements of the elastic properties performed on compact samples and polycrystalline films of C₆₀, the isotropic moduli of polycrystalline C₆₀ were estimated by averaging the elastic constants C_{ij} of a single crystal. By regarding the anisotropy in polycrystalline C₆₀ as a result of the disordered orientation of individual single-crystal grains, the bulk modulus K is determined from the equation $K = (C_{11} + 2C_{12})/3$ and the shear modulus G from the relation $G = [(C_{11} - C_{12})/2C_{44}]^{2/5}$. All other elastic constants of the polycrystal material (Young's modulus E , the longitudinal modulus C_L , and the Poisson's ratio ν) can be estimated from G and K using the well-known relations between the elastic moduli of an isotropic medium. Isotropic moduli obtained from single-crystal, compacted samples and polycrystal films are presented in Table 14.

4. C₆₀-BASED MATERIALS

4.1. Intercalated Compounds

4.1.1. Alkali Metal Doped C₆₀

M₃C₆₀ (M = K, Rb, and Cs) When the alkali metals (M = K, Rb, and Cs) are doped in C₆₀, stable crystalline phases M₁C₆₀, M₃C₆₀, M₄C₆₀, and M₆C₆₀ are formed. The M₃C₆₀ system is the most widely studied of the doped C₆₀ compounds because of the discovery of superconductivity [574].

K₃C₆₀ and Rb₃C₆₀

(i) **Synthesis** The usual way to produce M₃C₆₀ compounds is the vapor transport technique which is most suitable for intercalation of heavy alkali metals into C₆₀ lattice. A wide variety of methods based on this technique have been employed to prepare the samples with different crystalline forms (thin film [575], powder [576, 577], and single crystal [578, 579]).

For preparing powder samples, the alkali metals are measured out using precision inner-diameter capillary tubes. The quantity of the metal is controlled by cutting an alkali metal-filled capillary tube to the required length in a dry box. The capillary tube is then placed in a 5–10 mm Pyrex (or quartz) tube along with the C₆₀ powders. Then the Pyrex (or quartz) tube is sealed under high vacuum and heated to a temperature of 200 to 450 °C for several days. The alkali metals

appear to be completely absorbed by the C₆₀. After that, the sample tube is held at 200–300 °C for a period between 24 and 72 hours to ensure complete diffusion of the metal into the C₆₀ sample.

For preparing single-crystalline samples, the intercalation process can be controlled by measuring the conductivity of the samples *in-situ*. Electrical contacts to the pristine C₆₀ samples are made prior. Then the conductivity apparatus is sealed together with fresh alkali metal in a Pyrex glass apparatus under high vacuum. Uniform doping is accomplished using a repeating high-temperature dope–anneal cycle. Both the sample and dopant are heated uniformly from room temperature to ~200 °C in a furnace first while the sample resistance is continuously monitored. At the point where the resistance of the sample reaches a minimum, the alkali-metal end of the tube is cooled to room temperature and the sample alone is annealed for several hours. Then the metal end is reheated and the sample was further doped until a new resistivity minimum point is reached. The sample alone is then again annealed for several hours. This doping and annealing process is repeated until the resistance reaches an equilibrium state. A method similar to this is also applied to obtain thin film M₃C₆₀ samples [575].

In order to obtain M₃C₆₀ samples with more certain chemical compositions, two methods based on vapor transport are used. One is the azide technique, in which the metal azides (i.e., MN₃, M = K, Rb) are used as the metal sources [580–582]. A mixture of C₆₀ powders and stoichiometric amounts of azides is loaded into a quartz tube and heated slowly under dynamical vacuum. At 550 °C for a couple of hours, the azide of any alkali metal decomposed into free alkali metal and N₂, during which C₆₀ is doped. After completion of the reaction, the sample is cooled to room temperature and sealed to avoid exposure to air. In the other method, stoichiometric control is markedly improved by reacting pristine C₆₀ with the saturation-doped product [577]. Two aliquots of C₆₀ are weighed outside the drybox first. A weighed amount of C₆₀ is treated with a large excess of alkali metal at 225 °C under vacuum to produce M₆C₆₀. The air-sensitive product is then diluted with the C₆₀ in the dry box. After heating and annealing under vacuum, the single-phase K₃C₆₀ and Rb₃C₆₀ are prepared.

Metal fullerides can also be prepared in solution at low temperatures [583]. The solvents usually used are THF, liquid ammonia, or CS₂. The compounds are obtained by dissolving proportional molar amounts of the metal and the C₆₀ powder in the solvent and then heating at ~300 °C to remove the solvents.

(ii) **Crystal structure** In K₃C₆₀ and Rb₃C₆₀ compounds, the structure of K₃C₆₀ and Rb₃C₆₀ is still fcc although the lattice constants become larger than that of pristine C₆₀. Table 15 summarizes some of the structural parameters of K₃C₆₀ and Rb₃C₆₀.

M₃C₆₀ have a merohedral disorder which means the individual C₆₀ molecules have two different possible orientations in the fcc lattice. Except this disorder, the symmetry of the C₆₀ molecule is not further reduced by the doping from C₆₀ to M₃C₆₀. Vibrational properties have been studied by Raman scattering [586–590] and IR spectroscopy in the mid-IR and the far-IR spectral range [324, 591].

Table 14. Isotropic moduli obtained from different samples.

K (GPa)	G (GPa)	E (GPa)	C_L (GPa)	ν	Sample
10.8 ± 0.75	4.85 ± 0.18	12.6 ± 0.45	17.2 ± 0.45	0.306 ± 0.012	a
8.4 ± 0.5	3.75 ± 0.1	9.8 ± 0.4	13.4 ± 0.4	0.305 ± 0.02	b
6.4 ± 0.5	4.1 ± 0.2	12 ± 1	13.3 ± 0.8	0.18 ± 0.04	c

Note: Sample a—Isotropic moduli of polycrystalline C₆₀, calculated from the values of the moduli C_{ij} of a single crystal [568]; b—compacted samples powder [572]; c—polycrystalline films [573].

Table 15. Crystal structure and lattice constants of M₃C₆₀.

Compounds	K ₃ C ₆₀	Rb ₃ C ₆₀
Cation position	occupy all the available tetrahedral and octahedral interstitial sites of the host lattice	
Lattice constant (Å)	14.24	14.43
Distance of C ₆₀ -C ₆₀ (Å)	10.06	10.20
Distance of C-M (Å)	3.27	3.33
ρ (g/cm ³)	1.93	2.16
Ref.	[236]	[584, 585]

(iii) Normal state properties

Electronic structure In M₃C₆₀, the alkali metal is expected to donate its electron to the t_{1u} -derived conduction band. Hence M₃C₆₀ is expected to be a metal, with a half-filled t_{1u} band. In the solid, molecular orbitals on neighboring molecular sites mix to form bands. The band structure and density of states for K₃C₆₀ using the LDA in DFT are shown in Figure 32 [592, 593]; the electronic structure of C₆₀ is also shown in the figure for comparison.

In the M₃C₆₀ solids (M = K, Rb), the C₆₀ molecules have binary (merohedral) orientational disorder, and the statistical occupancy of the two molecular orientations remains disordered even at low temperatures [236]. This disorder was predicted to have significant effects on the band structure of the materials [594], with a smearing out of the fine structure in the t_{1u} -derived conduction band density of states (DOS), whose width remains unaffected by the disorder [595]. However, despite the disorder, the electronic states near E_F are best described using an effective Bloch wave vector, and the states localized due to disorder lie only at the bottom or top of the band [596].

The calculated t_{1u} -derived bandwidth is ~ 0.5 eV for K₃C₆₀ [597]. The LDA-DOS clearly supports a rigid-band picture. In this rigid band model, the band structure of M₃C₆₀ (M = alkali) remains roughly the same as that of pure C₆₀, expect that the Fermi level is shifted due to the filling of electrons donated by the alkali atoms [598]. Many other calculations of the electronic properties of M₃C₆₀ were performed at different levels of accuracy [594, 599–606]. Whereas the

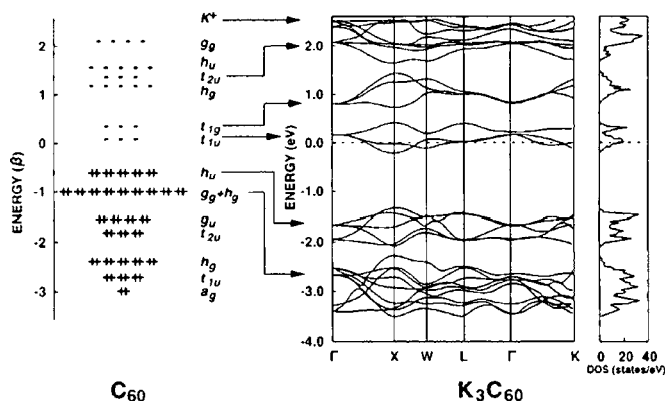


Figure 32. Left: Hückel theory calculation of the molecular energy spectrum of neutral C₆₀. Right: Band structure and density of states using the LDA formalism [592]. Adapted with permission from [593], C. H. Pennington and V. A. Stenger, *Rev. Mod. Phys.* 68, 855 (1996). © 1996, American Physical Society.

effect of the intermolecular binding on the molecular geometry itself can be represented reasonably within LDA at any level, the band structure depends more significantly on the level of accuracy of the calculations. The band dispersion is also determined by the weak interaction between the chains, which cannot be expected to be correctly described within the LDA.

PES and EELS were widely used to investigate the electronic structure of the C₆₀ compounds [382, 607–618]. The metallic nature of M₃C₆₀ has been reported from PES studies [182, 610, 611, 619] as well as from conductivity measurements [620, 621]. The PES result indicated the metallic ground state for K₃C₆₀ through a considerable density of states at the Fermi level and a clear Fermi cutoff in the spectra [608, 609]. The C_{1s} excitation spectrum results of K₃C₆₀ and C₆₀ implied the half-filling of the t_{1u} -derived band [622, 623]. The bandwidth observed for the half-filled t_{1u} -derived conduction band is about 1.2 eV and is much larger than the band structure calculations [624]. A clue to the explanation of this observation can be gained from high resolution PES studies of Rb₃C₆₀ and K₃C₆₀ [609, 610] at low temperature. PES profiles of M₃C₆₀ calculated within a model [609, 625] showed that good agreement can be obtained by taking into account relatively strong coupling of the electronic system to the molecular A_g and H_g vibrational modes, together with an additional coupling to the charge carrier plasmon observed at about 0.5 eV in the loss function.

Electrical resistivity The electrical resistivity (ρ) of M₃C₆₀ was measured on various samples using different methods such as dc four-point measurement [578, 579, 626–632] and other contactless techniques [627, 633–635]. Temperature dependences of the $\rho(T)$ of single crystal K₃C₆₀ and Rb₃C₆₀ have been measured under conditions of constant sample pressure [578, 579]. The measurement results are typically metallic as the sharp drop of resistivity at T_c and $\rho(T)$ varies as $(a + bT^2)$. Results on pellets (pressed from polycrystalline powders and subsequently annealed) obtained with a contactless technique such as optical excitation spectrum and microwave techniques also showed that $\rho(T)$ varies as $(a + bT^2)$ [627, 635]. Early $\rho(T)$ measurement for underdoped granular film showed that $\rho(T)$ increases with decreasing temperature [626]. However, it has been confirmed with new measurements on crystalline films that the transport properties of both K₃C₆₀ and Rb₃C₆₀ exhibit metallic behavior up to 500 K and a T^2 -like dependence at temperatures from 50 to 250 K [631]. The granularity of the thin films is most probably the reason for the discrepancy. Although the electron–phonon (el–ph) scattering mechanism is expected to result in a linear temperature dependence of the resistivity, however, the T^2 -like dependence behavior cannot be the evidence for other scattering mechanism because the volume of sample varies along with the temperature during the constant pressure measurements and this change will affect the temperature dependence of ρ significantly. The measurement of ρ vs T under conditions of constant sample volume can help to find the real scattering mechanism. A linear temperature dependence $\rho(T) \sim T$ on Rb₃C₆₀ was reported [630] and this linearity is consistent with the picture that the scattering mechanism is simply of the electron–phonon type with a coupling constant $\lambda_{tr} \sim 0.65$ – 0.80 . Table 16 lists some values of ρ .

Table 16. Electrical resistivity of M₃C₆₀.

Property	K ₃ C ₆₀	Rb ₃ C ₆₀	Ref.
ρ (transport, crystalline paraconductivity)	0.12 m Ω cm	0.23 m Ω cm	[579]
ρ (optical)	0.77 m Ω cm	0.8 m Ω cm	[633, 634]
ρ (microwave)	0.41 m Ω cm	—	[627]
ρ (room-temperature, ambient pressure)	—	2.5 m Ω cm	[630]

(iv) Superconductivity

T_c and superconductivity gap It is widely believed that M₃C₆₀ (M = K, Rb) are *s*-wave BCS-like superconductors, driven by the coupling to the intramolecular H_g phonons and probably with some strong-coupling effects [636]. Transition temperature (T_c) as a function of the lattice constant a has been widely studied for M₃C₆₀ superconductors [272, 637–639]. In these studies the constant a was changed either by chemical substitution or by applied pressure. It was found that T_c is increased by substituting Rb for K and the authors speculated that an elastic response of the lattice to the large ionic size of Rb would lead to a narrowing of the conduction band and a subsequent increase in $N(E_F)$ which has the general effect of raising T_c [640].

A linear relationship between T_c and pressure P was observed with $dT_c/dP = -6.3 \pm 0.8$ K GPa⁻¹ performed up to 0.6 GPa [641] and with $dT_c/dP = 7.8$ K GPa⁻¹ performed up to 2 GPa respectively for K₃C₆₀ [637]. A similar result has also been obtained in Rb₃C₆₀ with $dT_c/dP = -9.7$ K GPa⁻¹ [642]. The authors considered that applied pressure causes band broadening, which leads to both a smaller $N(E_F)$ and a smaller T_c .

In the BCS theory for a system with only one type of ion with mass M , the transition temperature behaves as $T_c \sim M^{-\alpha}$, where $\alpha = 0.5$. The isotope effect when ¹²C is substituted by ¹³C in M₃C₆₀ has been investigated in order to establish the mechanism of superconductivity. Various values of α were obtained by different groups [643–646] and it was indicated that $\alpha = 0.3$ should be the best available experimental result [645, 646].

The superconductivity energy gap (Δ) was first measured by point-contact tunneling spectroscopy using a scanning tunneling microscope [647], which gave a reduced energy gap $2\Delta/k_B T_c = 5.3$ for Rb₃C₆₀. NMR measurements were also performed to obtain $2\Delta/k_B T_c$ and were found to be in good agreement with the BCS value of 3.53 for the gap [648]. Moreover, the data has been obtained using other methods such as muon spin relaxation [649], optical methods, [634, 650], and photoemission [651]. It is noted that the data obtained from different experiments show substantial variation ranging from the BCS value of 3.53 up to about 4.2 (see Table 17). The value of the reduced gap that is substantially larger than the BCS value indicates that strong coupling effects are important.

Upper critical field and coherence length A large number of experiments was performed to determine the upper critical field for crystal [184, 578, 651, 655–657], powder [642, 658–663], and thin film [626] samples of M₃C₆₀ using different techniques such as magnetization [642, 659],

Table 17. T_c and reduction gap of M₃C₆₀.

Property	K ₃ C ₆₀	Rb ₃ C ₆₀	Ref.
T_c	19.5 K	29.5 K	[636]
$2\Delta/k_B T_c$ (tunneling)	5.3 ± 0.2	5.2 ± 0.3	[647, 652]
$2\Delta/k_B T_c$ (tunneling)	—	2.0–4.0	[653]
$2\Delta/k_B T_c$ (NMR)	3.0	4.1	[654]
$2\Delta/k_B T_c$ (optical)	3.44	3.45	[634]
$2\Delta/k_B T_c$ (tunneling and optical)	—	4.2 ± 0.2	[650]
$2\Delta/k_B T_c$ (μ SR)	—	3.6 ± 0.3	[649]
$2\Delta/k_B T_c$ (photoemission)	—	4.1	[651]

ac susceptibility [660, 661], transport [626, 663], and radio frequency (rf) absorption [662].

Early measurements were usually carried on powder samples. Field-cooled curves from dc magnetization are first used to obtain the temperature dependence of the upper critical field [$H_{c2}(T)$]. Measurements on powder K₃C₆₀ [659] and Rb₃C₆₀ [642] samples in this way both showed that the temperature dependence of H_{c2} is linear at temperatures not far below T_c . Due to the experimental limitations of the magnetic field window (5–8 T in superconductivity quantum interference device (SQUID) magnetometers), measurements of H_{c2} by this method are usually performed at temperatures close to the transition temperature. Therefore a large uncertainty will occur in the extrapolations of $H_{c2}(T)$ to $T = 0$ K which depend on the fitting scheme significantly. Using the standard theory of Werthamer–Helfand–Hohenberg (WHH) [664], the critical field extrapolated to $T = 0$ K is $H_{c2}(0) = 49$ T for K₃C₆₀ [659] and $H_{c2}(0) = 78$ K for Rb₃C₆₀ [642], respectively.

Ac susceptibility [660, 661] and rf absorption [662] technique measurements also show linear temperature dependence of H_{c2} near T_c . These two measurements can obtain the data under high fields (the ac susceptibility technique can be performed up to 30 T [660, 661] and the rf absorption technique can be performed up to 60 T [662]). Therefore the $H_{c2}(T)$ curves can extend near 0 K and this will reduce the uncertainty in the extrapolations of $H_{c2}(T)$ to 0 K. More accurate values of $H_{c2}(0)$ are obtained in these experiments (28 T for K₃C₆₀ and 40 T for Rb₃C₆₀ [660], 30–38 T for K₃C₆₀ [661], 38 T for K₃C₆₀, and 76 T for Rb₃C₆₀ [662]). Good agreements of the experimental $H_{c2}(T)$ curves with the WHH predictions are obtained [660, 662], demonstrating that this theory is successful in describing fullerene superconductors. However, a result of an enhancement of $H_{c2}(T)$ compared to theory has also been found [661]. A likely mechanism proposed by the authors is the dirty-limit effect which showed that the high upper critical fields might partly result from a reduction of the mean free path by different types of defects and the limitation of the mean free path could be the reason for the strong scatter of the experimental data for $H_{c2}(0)$ [661]. The magnetoresistance of K₃C₆₀ samples with different granularity has been measured in fields up to 7.5 T and showed that $H_{c2}(T)$ is dependent on the grain size of the K₃C₆₀ regions within the sample. $dH_{c2}(T)/dT$ varies from -2.18 to -2.8 T/K near the superconducting transition temperature [663].

Upper critical fields in single-crystalline samples have been obtained using various methods. All of these results

showed a linear temperature dependence of H_{c2} near T_c [655, 656, 665, 666]. The $H_{c2}(0)$ has first been estimated from transport measurements, with the results 17.5 T for K_3C_{60} [655] and 62 T for Rb_3C_{60} [656], and later from dc magnetization measurements, with the results 28.5 T for K_3C_{60} [665] and 43 T for Rb_3C_{60} [666].

A upturn of $H_{c2}(T)$ at temperatures very close to T_c has been observed in almost all experiments on all superconducting compounds. Different authors suggested different explanations for this effect and the best possible explanation [657] is that the upturn is a consequence of the anisotropy of the Fermi surface of fullerene superconductors [599].

From $H_{c2}(0)$, the coherence length ξ can be calculated using Ginzburg–Landau relations. Despite a large scatter (see Table 18) arising from the large scatter of $H_{c2}(0)$, it is clearly seen that the coherence length of M_3C_{60} is very small (a few tens of nanometers) and comparable to the short ξ of high- T_c superconductors.

Lower critical field and penetration depth A large number of experiments were performed to determine the lower critical field using various methods [642, 659, 665, 667–671].

Results on H_{c1} for powder K_3C_{60} [659] and Rb_3C_{60} [642] samples were first obtained from a dc magnetization method. In this method H_{c1} was defined as the field at which a deviation from linearity in $M(H)$ first appeared. The result show that the values of $H_{c1}(0)$ lies in the range 10–16 mT and $H_{c1}(T)$ follows the simple empirical formula $H_{c1}(T)/H_{c1}(0) = 1 - (T/T_c)^2$ [642, 659].

However, different from the ideal superconductor, the measurements of $M(H)$ in K_3C_{60} and Rb_3C_{60} usually do not exhibit ideal linearity and only have a smooth positive (even a negative) curvature. The deviation is so small that it is very hard to get the point of first deviation from such a curve. Therefore this method may not provide the “intrinsic” values of the H_{c1} . Politis et al. [667] measured the reversible magnetization at high external fields and calculated H_{c1} from Ginzburg–Landau relations. The value of H_{c1} obtained by this method is slightly smaller (9–11.4 mT at zero temperature) than the data obtained by the first method.

Table 18. Experimentally obtained $H_{c2}(0)$ and ξ of M_3C_{60} .

Samples	Measurements	K_3C_{60}		Rb_3C_{60}		Ref.
		$H_{c2}(0)$	ξ (nm)	$H_{c2}(0)$	ξ (nm)	
Powder	dc magnetization	49 T	2.6	—	—	[659]
Powder	dc magnetization	—	—	78 T	2	[642]
Powder	ac susceptibility	28 T	3.4	40 T	3	[660]
Powder	ac susceptibility	30–38 T	2.9–3.3	—	—	[661]
Powder	rf absorption	38 T	3.1	76 T	2.4	[662]
Single crystal	transport	17.5 T	4.5	—	—	[655]
Single crystal	dc magnetization	28.5 T	3.40	—	—	[665]
Single crystal	transport	—	—	62 T	2.4	[656]
Single crystal	dc magnetization	—	—	43.0 T	2.77	[666]
Film	transport	47 T	—	—	—	[626]

In the second method based on direct measurements of the reversible magnetization, the quantitative calculation is uncertain, especially in case of powder sample with a large distribution of grain sizes. Therefore a method based on measurement of the trapped magnetization was used to evaluate H_{c1} [668]. This measurement was performed on powder and single crystalline K_3C_{60} and Rb_3C_{60} samples [665, 668]. Much smaller values of H_{c1} , which are about 1 mT at zero temperature, were obtained in these studies. It is considered that wave functions between adjacent C_{60}^{3-} ions overlap relatively weakly leading to the smallness of H_{c1} [668].

Using Ginzburg–Landau relations, the penetration depth λ has been calculated and the value of the coherence length used in the calculations was obtained from independent measurements. These values of λ are listed in Table 19.

Moreover, the penetration depth has also been estimated from muon spin resonance, with the results 480 nm for K_3C_{60} and 420 nm for Rb_3C_{60} [672, 673], from optical conductivity, with the result 800 nm for both K_3C_{60} and Rb_3C_{60} [674], and from NMR data, which give 600 nm for K_3C_{60} and 460 nm for Rb_3C_{60} [654].

Critical current density The critical current density (J_c) in the M_3C_{60} system has been obtained from magnetization measurements by using Bean’s critical state model [675]. Based on this model, J_c is determined simply from the dc magnetization curve by the equation $J_c = A(M_+ - M_-)/R$. In the equation, A is a coefficient which is dependent on the sample geometry, M_+ and M_- denote the magnetization measured in increasing and decreasing fields at a certain magnetic field, and R is the sample radius [675, 676].

In the case of powders which can be approximated as a collection of spheres, R is set by the average grain size which can be measured in various ways. Different values of J_c for M_3C_{60} powders are obtained from magnetization measurements which showed substantial hysteresis up to high enough fields (higher than 5 T) [642, 659, 677–679]. However, the values of J_c in the order of 10^{10} A m⁻² indicate substantial flux pinning and high values of the critical current density.

For single crystalline samples, certain assumptions about the internal microstructure must be made to obtain R . J_c of single crystal K_3C_{60} and Rb_3C_{60} obtained from magnetization measurements by using Bean’s critical state model [670] was of the order of 10^7 A m⁻², that is, much smaller than the value of J_c for powdered samples ($\sim 10^{10}$ A m⁻²).

The qualitative character of the temperature and magnetic field dependence of J_c has been acquired. J_c shows a near logarithmic dependence on H and does not correspond

Table 19. Experimentally obtained $H_{c1}(0)$ and λ of M_3C_{60} .

Samples	K_3C_{60}		Rb_3C_{60}		Ref.
	$H_{c1}(0)$	λ (nm)	$H_{c1}(0)$	λ (nm)	
Powder	13.2 mT	240	—	—	[659]
Powder	—	—	12 ± 3 mT	247	[642]
Powder	—	—	16.2 mT	215	[669]
Powder	—	—	9–11.4 mT	240–280	[667]
Single crystal	4.2 mT	—	3.2 mT	—	[670]
Single crystal and powder	1.2 mT	890	1.3 mT	850	[665, 668]

to a simple analytic functional form [670] in single crystalline K₃C₆₀ and Rb₃C₆₀ samples. The temperature dependence of J_c was first found to follow the empirical equation $J_c \sim J_c(0)[1 - (T/T_c)^2]^n$, with $n = 3-5$ [680] in Rb₃C₆₀ powders. Subsequently, similar results for K₃C₆₀ [681, 682] and Rb₃C₆₀ powders [681] were obtained with $n = 1.3-5$. This temperature dependence was confirmed by measurements on single-crystalline K₃C₆₀ [657] and Rb₃C₆₀ [670]. The higher the magnetic field, the more rapidly J_c decreases with increasing temperature.

Cs₃C₆₀ Cs₃C₆₀ cannot be synthesized by vapor transport reaction because of its thermodynamic instability above ~200 °C which will cause the phase to segregate into the more stable CsC₆₀ and Cs₄C₆₀. Stable Cs₃C₆₀ was synthesized in solution using liquid ammonia as solvent [683]. Raman measurement showed the Cs₃C₆₀ has a single sharp Ag mode centered at 1447 cm⁻¹ with a linewidth of 11 cm⁻¹ [683]. This indicated that all the fullerene molecules are in the 3⁻ state. X-ray diffraction data showed that the compound consists of two phases: a body-center tetragonal (bct) Cs₃C₆₀ and an A15 cubic Cs₃C₆₀. The lattice parameters are $a = 12.057$ and $c = 11.432$ Å for the bct phase, and $a = 11.77$ Å for the A15 phase. It was reported that the Cs₃C₆₀ had a T_c of 40 K under high pressure [683], but this result has not yet been reproduced.

M_{3-x}M'_xC₆₀ Structures (M, M' = K, Rb, Cs) A series of ternary alkali doped C₆₀ have been synthesized with the general formulae of M_{3-x}M'_xC₆₀ [272, 684, 685]. All of these compounds are fcc structures. Most of these M_{3-x}M'_xC₆₀ compounds are superconductors. Table 20 lists some of these compounds as well as their structural parameters and T_c 's.

M_{3-x}M'_xC₆₀ has merohedral orientational disorder like M₃C₆₀. The relations of T_c and lattice constants in these compounds are similar to M₃C₆₀ (see Fig. 34). The overall trend is an increase in T_c with increasing lattice constant, which is interpreted in terms of a decrease in the LUMO-derived bandwidth and hence an enhancement of the Fermi energy density of states $N(E_F)$ at constant band filling [272, 639, 684-687].

M_xC₆₀ (M = K, Rb, and Cs, x = 1, 4, 6)

MC₆₀ MC₆₀ can be synthesized by reacting an appropriate amount of pristine C₆₀ with the saturation-doped product (M₆C₆₀) using the vapor transport technique [688-690]. The existence of a crystal phase with stoichiometric MC₆₀ was first indicated by Raman [688], photoemission [691, 692], and X-ray diffraction (XRD) [690] studies.

Table 20. Structural parameters and T_c of M_{3-x}M'_xC₆₀.

M _{3-x} M' _x C ₆₀	Dopant location ^a	a (Å)	T_c (K)	Ref.
KRb ₂ C ₆₀	K(t)Rb(t)Rb(o)	14.243	23.0	[686]
K _{1.5} Rb _{1.5} C ₆₀	K(t)K(o)Rb(t)Rb(o)	14.253	22.2	[272]
K ₂ RbC ₆₀	K(t)K(t)Rb(o)	14.243	23.0	[686]
K ₂ CsC ₆₀	K(t)K(t)Cs(o)	14.292	24.0	
RbCs ₂ C ₆₀	Rb(t)Cs(t)Cs(o)	14.555	33.0	
Rb ₂ KC ₆₀	Rb(t)K(t)Rb(o)	14.323	27.0	
Rb ₂ CsC ₆₀	Rb(t)Rb(t)Cs(o)	14.431	31.3	[272]

^a (o) = Octahedral site, (t) = tetrahedral site.

(i) **High temperature MC₆₀** Above 400 K the XRD pattern showed that MC₆₀ has a fcc rocksalt structure in which C₆₀ molecules are orientationally disordered [690]. M ion occupies an octahedral site in the fcc lattice (shown in Fig. 33). This phase is nonmetallic. The lattice parameters of MC₆₀ are listed in Table 21. This phase is nonmetallic.

(ii) **(MC₆₀)_n** When the fcc MC₆₀ is gradually cooled, new metallic polymeric phase forms [692-694]. Covalent bonding is formed between neighboring C₆₀ ions and results in the short interfullerene distance along the distorted orthorhombic a -axis (also shown in Fig. 33). The linkage is through a [2 + 2] cycloaddition [695]. Therefore MC₆₀ phase exhibits a quasi-one-dimensional polymer character as in the case in pristine C₆₀ [693-697]. The (MC₆₀)_n is used to denote this phase. These polymer phases are stable in air, in contrast to the vast majority of fulleride salts which are extremely sensitive in air [696]. Polymerization is reversible; heating the sample recovers the monomer fcc phase. XRD studies indicated that (MC₆₀)_n phase has a body-centred orthorhombic (bco) lattice with space group $Pnmm$. The lattice parameters of (MC₆₀)_n are listed in Table 21.

¹³C NMR spectroscopy gave the direct evidence for the presence of sp^3 hybridized carbon atoms in (MC₆₀)_n [698, 699]. Another piece of direct spectroscopic identification of the intermolecular bridging C-C modes in (MC₆₀)_n (M = Rb, Cs) has been achieved by neutron inelastic scattering measurements [700, 701]. A first-principles quantum molecular dynamics model was developed [702] to describe the vibrational properties of polymerized fullerenes. Rigid ball-chain modes are predicted to occur in the energy range 10-20 meV in good agreement with the measured low-temperature neutron spectra.

Only few DFT-based calculations have been performed on the (MC₆₀)_n to obtain the band structures [703, 704].

(iii) **Metastable structure MC₆₀** Moreover, depending on the cooling rate from the high temperature rocksalt fcc phase, a variety of other metastable phases are encountered. A medium quenching rate to just below room temperature leads to the stabilization of a low-symmetry insulating structure which has been characterized by synchrotron XRD studies to comprise (C₆₀⁻)₂ dimers, bridged by single C-C bonds [705, 706]. The RbC₆₀ dimer phase crystallizes in the monoclinic space group $P2_1/a$ with lattice parameters $a = 17.141$ Å, $b = 9.929$ Å, $c = 19.277$ Å, and $\beta = 124.4^\circ$ at 220 K [706] and transforms back to the polymer phase on heating. Another metastable conducting phase of RbC₆₀ and CsC₆₀ was reported with very rapid quenching by immersing the high- T sample in liquid nitrogen [707]. In this case,

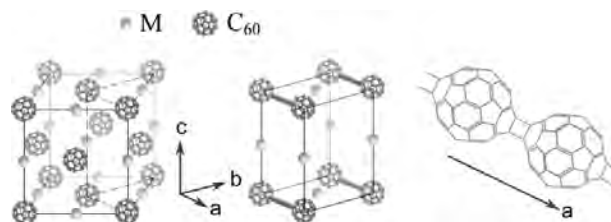


Figure 33. The left: high- T fcc phase of MC₆₀; the middle: bco polymer phase stabilized by slow cooling from the fcc phase. The thick lines represent polymer chains; right: the linkage of C₆₀ in (MC₆₀)_n.

Table 21. Crystal structure and parameters for M_xC₆₀ (x = 1, 4, 6).

M _x C ₆₀	Crystal structure	Lattice constants (Å)	Ref.
KC ₆₀	fcc (rock salt)	a = 14.07	[690]
RbC ₆₀	fcc (rock salt)	a = 14.08	
CsC ₆₀	fcc (rock salt)	a = 14.12	
(KC ₆₀) _n	bco	a = 9.11, b = 9.95, c = 14.32	[693, 694]
(RbC ₆₀) _n	bco	a = 9.11, b = 10.10, c = 14.21	
(CsC ₆₀) _n	bco	a = 9.10, b = 10.21, c = 14.17	
K ₄ C ₆₀	bct	a = 11.867, c = 10.765	[711]
Rb ₄ C ₆₀	bct	a = 11.969, c = 11.017	
Cs ₄ C ₆₀	bct (orthorhombic distorted)	a = 12.15, b = 11.90, c = 11.45	[710]
K ₆ C ₆₀	bcc	a = 11.38	[724, 725]
Rb ₆ C ₆₀	bcc	a = 11.54	
Cs ₆ C ₆₀	bcc	a = 11.79	

the 3D isotropic character of the structure is retained while orientational ordering of the C₆₀⁻ ions leads to a simple cubic structure with a = 13.9671 Å at 4.5 K. Upon heating, it returns to the most stable polymer phase.

M₄C₆₀ K₄C₆₀ and Rb₄C₆₀ were synthesized by a vapor transport technique [584, 585, 708, 709]. XRD results showed that they have a bct structure with a space group *I4/mmm* [709]. The early experiments suggested that Cs₄C₆₀ is isostructural with K₄C₆₀ [584, 708]. Single phase Cs₄C₆₀, which has an orthorhombic distortion of the ideal bct structure, was later synthesized by the low-temperature liquid ammonia route [710]. Cs₄C₆₀ is not as well studied as K₄C₆₀ and Rb₄C₆₀ due to problems in stabilizing single phase samples. The structure parameters for M₄C₆₀ are listed in Table 21.

M₄C₆₀ compounds have an insulating, nonmagnetic ground state [620, 712] although their t_{1u}-derived bands are only partly (2/3) filled, which would lead one to expect a metallic behavior within a one-electron description. Detailed LDA calculations predict that M₄C₆₀ is a metal [713]; this indicated that the insulativity does not come from the gap created by tetragonal symmetry split of the conduction band. Furthermore, electron paramagnetic resonance (EPR) [714], NMR [715] and EELS [716] measurements imply that orientational disorder is not a key ingredient in the insulating behavior of the M₄C₆₀ phases. The scenarios proposed to explain this insulativity have included the suggestion of a Mott–Hubbard ground state for M₄C₆₀ [471, 717, 718] and a description of these compounds as Jahn–Teller insulators [719, 720].

A systematic study of the optical conductivities of M₄C₆₀ has provided strong evidence for a Mott–Hubbard ground state of these compounds [716]. Low-temperature NMR showed the development of a Koringa-like term under pressure, indicating that a metal–insulator transition occurs above 8 kPa [721]. Either a Mott insulator or a Jahn–Teller distortion is consistent with this NMR observation. It seems that a complete understanding of the electronic properties of M₄C₆₀ requires a unique combination of both electron

correlation and Jahn–Teller effects which may lead to a Mott insulator without a magnetic ground state.

No superconductivity has been observed in M₄C₆₀ down to 2 K.

M₆C₆₀ The alkali metal-saturated compounds M₆C₆₀ were synthesized by a vapor transport technique [709]. Synchrotron XRD data indicated that the M₆C₆₀ compound has a bcc structure and corresponds to the space group *T_h⁵* or *Im $\bar{3}$* [722]. In the M₆C₆₀ structure, the alkali metal ions all occupy equivalent distorted tetrahedral sites, which are surrounded by four C₆₀ anions, two with adjacent pentagonal faces and two with adjacent hexagonal faces. NMR spectra of M₆C₆₀ are quite similar and in good agreement with the X-ray studies [723]. From the result it is apparent that the C₆₀ molecules are ordered at all temperatures. The structural parameters for M₆C₆₀ are given in Table 21.

M₆C₆₀ has completely filled electronic levels which results in its observed insulating nature. No superconductivity was observed in M₆C₆₀.

Na and Li Doped C₆₀

Na Doped C₆₀

(i) **Na_xC₆₀** The Na_xC₆₀ compounds were synthesized by a vapor transport technique [684]. All of the Na_xC₆₀ phases except Na₄C₆₀ have intercalated fcc structures. In Na₂C₆₀, the dopants fill the tetrahedral sites, leaving the octahedral sites unoccupied [726]. In Na₆C₆₀, two Na ions occupy tetrahedral sites and four Na atoms (not ions) go into octahedral sites [684]. It was reported that Na₃C₆₀ tends to phase separate (disproportionate) into Na₂C₆₀ and Na₆C₆₀ [684, 727, 728]. The small size of the Na atom also allows the intercalation of Na to high concentrations. The saturated phase is Na₁₀C₆₀ in which Na atoms are located at the tetrahedral and octahedral sites, and at the general point with fractional occupancies [728]. Later a new Na₄C₆₀ polymer phase which has a body-centered monoclinic unit cell was identified [729, 730]. Superconductivity has not been observed in any Na–C₆₀ binary compounds. The structural parameters for Na_xC₆₀ are listed in Table 22.

(ii) **Na₂MC₆₀** (M = Alkali, Cs_{1-x}Rb_x, Hg_x) The vacant octahedral site in Na₂C₆₀ allows this unique phase to act as a host lattice for further intercalation of dopants into the vacant octahedral site. The crystal structure and lattice parameters of Na₂MC₆₀ are listed in Table 23.

Superconductivity was observed in Na₂MC₆₀ with M = K, Rb, Cs and Cs_{1-x}Rb_x. The T_c-lattice parameter correlation

Table 22. Crystal structure and parameters of Na_xC₆₀.

Compound	Lattice constant	Group	Ref.
Na ₂ C ₆₀	a = 14.19 Å	<i>Pa$\bar{3}$</i>	[726]
Na ₃ C ₆₀	T ≥ 250 K, a = 14.183 Å T < 250 K, unknown low-symmetry structure	<i>Fm$\bar{3}m$</i>	[684]
Na ₄ C ₆₀	T < 500 K, a = 11.235 Å, b = 11.719 Å, c = 10.276 Å, β = 96.16° T > 500 K, a = 11.731 Å, c = 11.438 Å	<i>I2/m</i> <i>I4/mmm</i>	[729] [730]
Na ₆ C ₆₀	a = 14.38 Å	<i>Fm$\bar{3}m$</i>	[684]
Na ₁₀ C ₆₀	a = 14.59 Å	<i>Fm$\bar{3}m$</i>	[728]

Table 23. Structural properties and T_c 's of Na₂MC₆₀.

Na ₂ MC ₆₀	Structural properties	Ref.
Na ₂ KC ₆₀	$Pa\bar{3}$, $a = 14.025 \text{ \AA}$, $T_c = 2 \text{ K}$	[731]
Na ₂ RbC ₆₀	fast cooling $\rightarrow Pa\bar{3}$, $a = 14.095 \text{ \AA}$, $T_c = 3.5 \text{ K}$	[732]
	slow cooling $\rightarrow P2_1/a$, $a = 13.711 \text{ \AA}$, $b = 14.544 \text{ \AA}$, $c = 9.373 \text{ \AA}$, $\beta = 133.53^\circ$, no T_c	[733]
Na ₂ CsC ₆₀	$Pa\bar{3}$, $a = 14.19 \text{ \AA}$, $T_c = 12 \text{ K}$	[726]
Na ₂ Rb _x Cs _{1-x} C ₆₀	$Pa\bar{3}$ for $0 < x < 1$ with $T_m \approx 300 \text{ K}$ $x = 0.50 \rightarrow a = 14.110 \text{ \AA}$, $T_c = 10.5 \text{ K}$ $x = 0.75 \rightarrow a = 14.103 \text{ \AA}$, $T_c = 8.0 \text{ K}$	[726]
Na ₂ Hg _y C ₆₀	$y = 0.618$, $Pa\bar{3}$, $a = 14.194 \text{ \AA}$, no T_c	[734]
Na ₂ Cs _x C ₆₀	$Pa\bar{3}$, no T_c for $x < 2.75$ $x = 2.75 \rightarrow a = 14.145 \text{ \AA}$, $T_c = 10.5 \text{ K}$ $x = 2.85 \rightarrow a = 14.139 \text{ \AA}$, $T_c = 8.0 \text{ K}$	[735]

in this class of fulleride superconductors is different from the case in M₃C₆₀ (see Fig. 34) [735].

Li Doped C₆₀

(i) Li_xC_{60} The Li-C₆₀ system is the least investigated among all alkali doped C₆₀ because of the difficulties in synthesis of single-phase samples. Li_xC₆₀ compounds can be synthesized by thermal decomposition of alkali metal azides or reaction of Li metal and C₆₀ powder in liquid ammonia or by electrochemical doping [736–738]. Structural parameters for some of the Li_xC₆₀ compounds are listed in Table 24. No superconductivity was observed in Li fullerides.

(ii) Li_xMC_{60} ($M = Cs$ and Rb) For smaller alkali metal K and Na, Li₂MC₆₀ phase is not stable and phase separates [739]. The crystal structure and lattice parameters of Li₂MC₆₀ ($M = Cs$ and Rb) are listed in Table 25.

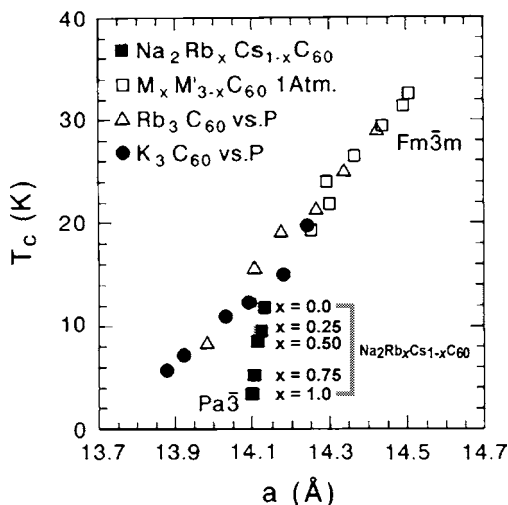


Figure 34. T_c as a function of the lattice parameter a for the $Fm\bar{3}m$ (triangles, circles, and open squares) and $Pa\bar{3}$ (filled squares) superconductors. For K_3C_{60} and Rb_3C_{60} the lattice parameter was varied by changing the pressure, while for $M_xM'_{3-x}C_{60}$ (with $M, M' = K, Rb, Cs$) the lattice parameter was varied by changing the composition. Adapted with permission from [735], T. Yildirim et al., *Solid State Commun.* 93, 269 (1995). © 1995, Elsevier Science.

Table 24. Structural parameters of Li_xC₆₀.

Compound	Structural parameters	Ref.
Li ₃ C ₆₀	hexagonal, $a = 9.840 \text{ \AA}$, $c = 16.10 \text{ \AA}$	[737]
Li ₄ C ₆₀	hexagonal, $a = 9.835 \text{ \AA}$, $c = 16.16 \text{ \AA}$	
Li ₆ C ₆₀	hexagonal, $a = 9.918 \text{ \AA}$, $c = 16.26 \text{ \AA}$	
Li ₁₂ C ₆₀	$Fm\bar{3}m$ ($T > 553 \text{ K}$), $a = 14.09 \text{ \AA}$, no T_c $I4/mmm$ ($T < 553 \text{ K}$), $a = 14.21 \text{ \AA}$, $c = 13.98 \text{ \AA}$ (at $T = 293 \text{ K}$)	[738]

Ammoniated M_xC₆₀ The ammoniated alkali metal fullerides have been prepared by either exposing preformed metal fullerides to ammonia vapor or reaction of metal and C₆₀ in liquid NH₃. Ammoniation induces structure expansion and often changes the symmetry. Table 26 lists some of these compounds and their structural parameters. Some of these ammoniated M_xC₆₀ are superconductors under pressure. Table 26 also lists the T_c of them.

4.1.2. Alkaline–Earth Metal Doped C₆₀

Alkaline–earth fullerides show complicated structures and interesting properties [234, 746–751]. They are more difficult to synthesize and are less understood compared to the alkali–metal fullerides. Their electronic properties show a departure from the simple band-filling picture of the fulleride bands [750–754].

Ca_xC₆₀ The Ca_xC₆₀ compounds were synthesized by solid phase reaction. The mixture of high-purity Ca and C₆₀ powder was heated at 550 °C under a vacuum of 10^{−6} Torr for several hours to obtain Ca_xC₆₀ [234].

Ca₅C₆₀ X-ray diffraction studies indicated the formation of a simple cubic phase at $x = 5$. The proposed structural model involves multiple occupancy of the octahedral sites by Ca²⁺ ions [234]. The lattice constant of Ca₅C₆₀ is 14.01 Å [234, 755, 756].

Calcium intercalation into single-crystal C₆₀ thin films was studied with scanning tunneling microscopy and their real-space images were obtained [757]. A model of the Ca₅C₆₀ structure was deduced in which octahedral sites of the fcc lattice are occupied by four Ca ions while one of the tetrahedral sites is filled. The other tetrahedral site is filled at higher concentration, but these later-filled sites are arranged in rectangular or triangular lattices so that their distances are maximized.

Measurements of microwave loss, magnetic susceptibility, and Meissner effect first showed that Ca₅C₆₀ becomes superconducting below 8.4 K [234]. The T_c for Ca₅C₆₀ follows the same relation between T_c and the C₆₀–C₆₀ separation found in the alkali–metal compounds. However, the

Table 25. Structural properties and T_c 's of Li_xMC₆₀.

Li _x MC ₆₀	Structural and electronic properties	Ref.
Li ₂ RbC ₆₀	Li(t)Li(t)Rb(o), $a = 13.896 \text{ \AA}$, no T_c	[739]
Li ₂ CsC ₆₀	Li(t)Li(t)Cs(o), $a = 14.120 \text{ \AA}$, $T_c = 12 \text{ K}$	[685, 740]
Li _x CsC ₆₀	X-ray, no T_c for $x < 2.5$ and $x > 4.5$ $x = 3 \rightarrow Fm\bar{3}m$, $T_c = 10.5 \text{ K}$ $x = 4 \rightarrow Fm\bar{3}m$, $T_c = 8.0 \text{ K}$	[741]

Table 26. Structural parameters and T_c of ammoniated M_xC_{60} .

Compounds	Synthesis method	Structure	Lattice parameter (Å)	T_c (K)	Ref.	
$(NH_3)_3K_3C_{60}$	vapor	fcc	$14.971 \times 14.895 \times 13.687$	No T_c	[742, 743]	
$(NH_3)_8K_3C_{60}$		bct	12.15×15.7		[743]	
$NH_3NaK_2C_{60}$	liquid NH_3	fcc	4.36	8		
$NH_3NaRb_2C_{60}$		fcc	14.52	8.5		
$(NH_3)_xNaK_2C_{60}$		fcc	14.500	17		
		$x = 0.55$		14.520	12	[744]
		$x = 0.60$		14.531	8.5	
		$x = 1.01$		14.531	8.5	
$(NH_3)_xNaRb_2C_{60}$			14.350	13		
	$x = 0.67$		14.369	11		
	$x = 0.71$		14.400	8		
	$x = 1.06$		14.400	8		
$(NH_3)_4Na_2CsC_{60}$	vapor	fcc	14.473	29.6	[745]	

Note: Although $(NH_3)_3K_3C_{60}$ exhibits no superconductivity at ambient pressure, superconductivity can be induced by hydrostatic pressure with an onset at 28 K.

pressure dependence of T_c of Ca_5C_{60} is quite different. Schirber et al. [758] found that opposite to that observed in the alkali fullerenes, the T_c of Ca_5C_{60} increases with increasing pressure.

Band calculations using the local density approximation [752–754] showed that the t_{1u} level is totally filled, while the t_{1g} level of C_{60} is half-filled. These half-filled t_{1g} -hybridized levels are the ones responsible for the conductivity and superconductivity in Ca_5C_{60} . Experimental evidence for the partial filling of the t_{1g} level comes from both photoemission spectra [755] and transport measurements [759, 760]. Electron energy loss [761] and inverse photoemission [755] studies showed that the completely filled t_{1u} band for $x < 3$ is below E_F , giving nonmetallic character.

$Ca_{2.75}C_{60}$ Studies by Ozdas et al. showed that $Ca_{2.75}C_{60}$ is the only stable phase for $1.8 < x < 2.8$ [737]. X-ray patterns and calculated results showed that the structure is a $2 \times 2 \times 2$ supercell with space group $Pcab$, a direct subgroup of $Pa\bar{3}$, and the lattice parameters are $27.93 \times 28.03 \times 27.95$ Å (at 298 K). Ca cations are located in both the tetrahedral (T) and octahedral (O) interstitial sites of the cubic close-packed C_{60} lattice. All of the O-sites are occupied by single Ca cations, which are displaced off-center. By contrast, one out of every eight T-sites in the subcell is vacant.

The $Ca_{2.75}C_{60}$ phase is not superconducting down to 2 K under ambient pressure. Electron energy loss [761] and inverse photoemission [755] studies showed that the completely filled t_{1u} band for $x < 3$ is below E_F , giving nonmetallic character.

AE_xC_{60} ($AE = Ba, Sr$) In contrast to calcium fullerenes which are fcc at all compositions, Ba_xC_{60} and Sr_xC_{60} only exist in bcc-based structures at $x = 3$, $x = 4$, and $x = 6$ [746–749]. All of these compounds have been synthesized by solid phase reaction [746]. Their crystal structure and lattice constant are listed in Table 27.

No superconducting transition is observed down to 1.5 K in Ba_3C_{60} and Sr_3C_{60} [763, 762]. Early investigations show that both of the Ba_6C_{60} and Sr_6C_{60} are superconductors, with transition temperatures of 7 and 4 K, respectively [746, 762]. However, later studies indicate that AE_4C_{60} ($AE = Ba, Sr$) is the actual superconducting phase rather than AE_6C_{60} ($AE = Ba, Sr$) as originally proposed [747–749]. In contrast to Ca_5C_{60} , T_c of Ba_4C_{60} decreased with increasing pressure. High magnetic susceptibility measurements show that AE_6C_{60} phases are metallic, even though they are not superconducting [749]. Moreover, these magnetic susceptibility measurements and calculated [752] results combined with the different lattice constants dependence of T_c for Ba_4C_{60} [764] and Ca_5C_{60} [758] indicate that there is no clear relation between T_c and $N(E_F)$ in AE_xC_{60} compounds.

Alkali–Earth Substituted M_xC_{60}

$M_{3-x}Ba_xC_{60}$ ($0 < x < 2$) Direct synthesis of alkali–alkaline earth fullerenes by vapor transport is impractical due to huge differences in vapor pressures. This can be avoided by using azides BaN_6 and MN_3 ($M =$ alkali metal) as metal source. Direct reactions with BaN_6 and MN_3 yielded complicated mixed phases [763]. Stable compounds were eventually synthesized by reacting BaN_6 powder with the fcc M_1C_{60} phase

Table 27. Structural parameters of AE_xC_{60} ($AE = Ba$ and Sr , $x = 3, 4, 6$).

AE_xC_{60} ($AE = Ba$ and Sr)	Synthesis	Crystal structure	Lattice constant	Ref.
AE_3C_{60}	solid phase reaction	simple cubic A15	11.34 Å	[763]
Ba_3C_{60} Sr_3C_{60}		fcc and A15 coexistence	14.144 Å (fcc) 11.140 Å (A15)	[762]
AE_6C_{60}	Ba_6C_{60} Sr_6C_{60}	body-centered cubic	11.171 Å	[746]
			10.975 Å	[762]
AE_4C_{60}	Ba_4C_{60} Sr_4C_{60}	orthorhombic (bco)	$11.25 \times 11.69 \times 10.90$ Å	[747, 748]
			—	[749]

prepared by the azide decomposition method [582, 624, 765–767]. This process worked well for all MBa₂C₆₀ with M = K, Rb, or Cs. But the M₂BaC₆₀ cannot be obtained following the same process. However, starting from CsC₆₀ ensuring octahedral Cs and then adding BaN₆ and AN₃ together in the second step yielded single-phase products MBaCsC₆₀ for M = Na or K, while phase separation occurred for M = Rb or Cs. X-ray diffraction and Raman scattering showed that these compounds are fcc with pentavalent and quadrivalent C₆₀'s, respectively [768]. Table 28 lists the structural parameters of these compounds.

No superconductivity was observed in these compounds down to 0.5 K [624]. Electron spin resonance (ESR) indicated weakly metallic behavior [769]. ¹³C NMR indicated strong dynamical disorder above room temperature, which may be related to the anisotropic crystal field induced by cations of different valence [624, 770].

M_{3-y}M'_yBa₃C₆₀ (M, M' = K, Rb, Cs) Samples of M_{3-y}M'_yBa₃C₆₀ were typically synthesized by intercalation of alkali metals into preformed Ba₃C₆₀ [765–767]. XRD for the samples show single phase bcc patterns with space group *Im-3*. Simulation of diffraction patterns indicates the random occupation of the interstitial sites by M and Ba. The lattice parameter in M₃Ba₃C₆₀ is controllable by changing linearly with the alkali ionic radii. Moreover, by changing the y in K_yRb_{3-y}Ba₃C₆₀, the lattice parameter can be tuned quasi-continuously between K₃Ba₃C₆₀ and Rb₃Ba₃C₆₀ [765]. The structural parameters of these compounds are listed in Table 29.

M₃Ba₃C₆₀ is a half-filled metal in which the Fermi energy exists at the center of the next lowest unoccupied molecular orbital with the t_{1g} symmetry [767]. Superconductivity was observed in all compounds except for Cs₃Ba₃C₆₀ in which superconductivity was absent down to 0.5 K [765]. T_c decreased with increasing lattice parameter in M₃Ba₃C₆₀ [765]. This T_c-lattice parameter correlation is in striking contrast with the positive correlation between T_c and the fcc cell parameter in M₃C₆₀ superconductors.

4.1.3. Rare-Earth and Lanthanide Metal Doped C₆₀

Yb_{2.75}C₆₀ Yb_{2.75}C₆₀ was successfully synthesized by solid phase reaction [771]. X-ray diffraction studies showed that Yb_{2.75}C₆₀ has an orthorhombic unit cell with *Pcab* symmetry and lattice constants of a = 27.87 Å, b = 27.98 Å, and

c = 27.87 Å [771]. Near-edge X-ray absorption measurements show that all of the Yb cations are divalent, meaning that the average negative charge of the C₆₀ anions is 5.5 [772, 773]. EXAFS and Raman measurements also reveal that the C₆₀ anions are distorted in shape, despite their well-ordered local structure around the Yb cations [773]. Yb_{2.75}C₆₀ becomes superconducting below 6 K.

Sm Doped C₆₀ The Sm_xC₆₀ compounds have been synthesized by solid phase reactions [774]. The unit cell structure of the nominal Sm₃C₆₀ phase is identified as orthorhombic (a = 28.17 Å, b = 28.07 Å, and c = 28.27 Å) derived from the fcc M₃C₆₀ (M = Alkali metal) cell by doubling the cell dimension in each direction, analogous to that of Yb_{2.75}C₆₀ [774]. However, the exact structure of the Sm₃C₆₀ phase is still an open question. The quality of the diffraction data has prevented a full structure determination. Sm₃C₆₀ is superconducting at T_c = 8 K [774].

Temperature dependent resistivity measurements of Sm_xC₆₀ samples have been reported. The results show that the resistivity decreases with increasing Sm concentration x [775, 776]. The temperature coefficient of resistivity is negative for all compositions and the absolute value decreases with increasing x.

Eu Doped C₆₀ Eu_xC₆₀ compounds can be synthesized by either high-temperature solid state reaction [777, 778] or through the liquid ammonia route [779].

The Eu_xC₆₀ prepared by ammonia route was found to be amorphous by XRD [779]. Crystalline phases prepared by solid state reaction with the compositions of x ~ 3 and 6 are stabilized [777, 778]. The structure of the x ~ 3 phase is complicated. Experimental data show the coexistence of a minor A15 phase and a majority phase that has the same structure as Yb_{2.75}C₆₀.

The Eu₆C₆₀ phase has the same bcc structure of the saturation M₆C₆₀ (M = alkali metal) compounds [777, 778]. The experiments reveal the presence of both Eu²⁺ and Eu³⁺ ions. Furthermore, it is found that at T = 65 K ferromagnetic Eu pairs form through a superexchange mechanism via the C₆₀ molecules [777].

4.1.4. Halogen Intercalated C₆₀

I₂ Intercalated C₆₀ Iodine-doped C₆₀ C₆₀I₄ was synthesized by vapor phase reaction of iodine with pure C₆₀ under helium gas of 10 Torr at 250 °C for several days in evacuated Pyrex tubes [780]. XRD results show that C₆₀I₄ has a simple hexagonal cell with a = 9.962 and c = 9.984 Å. In this structure the C₆₀ host material exhibits a sequence of (AAA...) layers, interleaved with guest iodine layers

Table 28. Structural parameters and T_c of M_{3-x}Ba_xC₆₀ (0 < x < 2) compounds.

M _{3-x} Ba _x C ₆₀	Crystal structure	Lattice constant	Atom position	T _c	Ref.
KBa ₂ C ₆₀	fcc	14.173 Å	K(o)Ba(t)	no T _c	[624]
RbBa ₂ C ₆₀	fcc	14.185 Å	Rb(o)Ba(t)		
CsBa ₂ C ₆₀	fcc	14.206 Å	Cs(o)Ba(t)		
KbaCsC ₆₀	fcc	14.215 Å	Cs(o), K and Ba randomly occupy (t)		

Note: (o) = Octahedral site, (t) = tetrahedral site.

Table 29. Structural parameters and T_c of M_{3-y}M'_yBa₃C₆₀ (M, M' = K, Rb, Cs) compounds.

M _{3-y} M' _y Ba ₃ C ₆₀	Crystal structure	Lattice constant	Atom position	T _c	Ref.
K ₃ Ba ₃ C ₆₀	bcc	11.24 Å	Randomly	5.6 K	[765]
Rb ₃ Ba ₃ C ₆₀	bcc	11.34 Å	occupy	1.9 K	
Cs ₃ Ba ₃ C ₆₀	bcc	11.47 Å		no T _c	

between the host layers, as in a graphite intercalation compound. The {111} planes of the fcc C₆₀ become the {001} planes in the compound by relative shear motions which transform the layer stacking sequence from ABCABC... in fcc C₆₀ to A/A/A/... in C₆₀I₄, where “/” denotes an iodine guest layer in the C₆₀I₄ compound. The shortest I–I (in-plane) distance is 2.53 Å, which is close to the value of 2.72 Å for the molecular solid I₂ [780].

Another intercalation compound of C₆₀ with iodine was also prepared under fairly similar conditions [781] with a final composition of C₆₀I_{1.6} [782]. The XRD pattern was interpreted in terms of a C-centered orthorhombic cell with $a = 17.33$, $b = 9.99$, $c = 9.97$ Å, containing two formula units. Iodine atoms were placed in sites slightly shifted from the centers of the trigonal prisms, with near-neighbor and next-near-neighbor distances of 3.9 and 7.21 Å, respectively [781, 782].

Iodine intercalated C₆₀ is nonmetallic and has a resistivity at 300 K of 10⁹ Ω cm. In addition, no superconductivity is observed down to 4 K. Photoemission [783], X-ray absorption [784], and ¹³C NMR [785] results confirm the insulating (clathrate) nature (i.e., the absence of guest–host charge transfer).

Halogenation of C₆₀ Halogenation reactions of C₆₀X_{*n*} (X = Br, Cl, F) have been reported for various *n* values. In these reactions the halogen is attached to a carbon atom on the fullerene shell through a single radial covalent bond that is formed by using one electron provided by the fullerene and the other by the halogen.

The species C₆₀F₃₆ have been reported by several groups [786, 787]. Complete fluorination of C₆₀ (C₆₀F₆₀) has also been reported [788]. A very high chlorine content has been found in a photochlorinated fullerene sample which was found to fit the average formula C₆₀Cl₄₀ [789]. Bromination of C₆₀ has also been observed in chemical reactions carried out in the 25–55 °C range. X-ray crystallographic evidence indicates the existence of C₆₀Br₆, C₆₀Br₈, and C₆₀Br₂₄ [790, 791]. These X-ray studies showed that the attachment of Br is accomplished by placing Br at symmetrically bonding vertices of the C₆₀ molecule. These Halogenated fullerenes can be used in substitution reactions to attach aromatic groups sequentially to the fullerene shell.

4.1.5. Molecules Intercalated C₆₀

Intercalation of Gases into Solid C₆₀ Various gases such as H₂, N₂, H₂O, CH₄, CO, and O₂ can be intercalated into solid C₆₀. These neutral gas molecules can be intercalated into the interstitial sites of the C₆₀ lattice without drastically altering the host structure. The intercalants occupy octahedral sites of the C₆₀ lattice and depress the C₆₀'s fcc–sc transition temperature (*T_m*). These compounds have possible potential applications such as gas separation, sensors, hydrogen storage, etc. Table 30 lists some of these compounds along with a few structural properties.

Intercalation of Larger Species into Solid C₆₀ When the guest species are larger than the voids in the C₆₀ solids, a change in stacking of the fullerene molecules from cubic to hexagonal usually occurs. Structures of these compounds are different from C₆₀. In most of these phases, C₆₀ molecules

Table 30. Synthesis and structural properties of gas intercalated C₆₀.

Compound	Synthesis	Structural properties	Ref.
(N ₂) _{<i>x</i>} C ₆₀	Powder and pellets samples of pure C ₆₀ were	0 < <i>x</i> < 1, <i>T_m</i> ~ 255 K	[792]
(O ₂) _{<i>x</i>} C ₆₀	separately subjected to nitrogen and oxygen, at 0.15 kbar for 7 days at room temperature.	0 < <i>x</i> < 1, <i>T_m</i> ~ 240 K	[792] [793]
(H ₂) _{<i>x</i>} C ₆₀	Pellet samples of pure C ₆₀ were separately subjected to hydrogen gas, at 750 atm for 5 h at 323 K and soon was cooled below 150 K, thereby “freezing” the interstitial H ₂ inside the C ₆₀ lattice.	0 < <i>x</i> < 1, out gas at <i>T</i> ~ 260 K, nearly free quantum rotor at all <i>T</i>	[794] [795]
(CH ₄) _{<i>x</i>} C ₆₀	The powdered C ₆₀ was loaded into a high-pressure gas cell filled with CH ₄ and heated to ~400 °C up to 70 h. The cell was quenched in running cold water. The pressure at temperature in the cell is estimated to be between 1 and 2 kbar.	0 < <i>x</i> < 1, <i>T_m</i> ~ 241 K	[796]

form triangular planes as in the case of graphite sheets and the intercalants go between them. This is the case in simple systems such as C₆₀(P₄)₂, C₆₀(S₈)₂. Larger organic and organometallic molecules, like benzene and ferrocene, can also be intercalated to give C₆₀(C₆H₆)₄ and C₆₀(ferrocene)₂, respectively. In addition, reacting C₆₀ with protonic acids, Lewis acids SbCl₅, AsF₅, InCl₃ [797–799] also produce different compounds. Table 31 lists some of these compounds and their structural parameters.

Table 31. Structural parameters of larger species intercalated C₆₀.

Compound	Structural properties	Ref.
C ₆₀ (P ₄) ₂	hexagonal, $a = 10.084$ Å, $c = 10.105$ Å	[800, 801]
C ₆₀ (S ₈) ₂	monoclinic, $a = 20.867$ Å, $b = 21.062$ Å, $c = 10.508$ Å, $\beta = 111.25^\circ$, four formula per cell.	[802]
C ₆₀ (ferrocene) ₂	triclinic, $a = 9.899$ Å, $b = 10.366$ Å, $c = 11.342$ Å, $\alpha = 90.96^\circ$, $\beta = 90.96^\circ$, $\gamma = 118.33^\circ$ (at 143 K)	[803]
C ₆₀ (AsF ₅) _{1.88}	tetragonal (bct), $a = 12.794$ Å, $c = 12.426$ Å	[797, 798]
C ₆₀ (C ₆ H ₆) ₄	triclinic, $a = 9.938$ Å, $b = 15.031$ Å, $c = 17.425$ Å, $\alpha = 65.38^\circ$, $\beta = 88.30^\circ$, $\gamma = 74.83^\circ$ (at 104 K)	[804, 805]

The TDAE intercalated C₆₀ organic molecular system raised much interest owing to its ferromagnetic-like phase transition at $T_c = 16$ K [552]. Furthermore, the TDAE-C₆₀ material has the highest T_c of any molecular organic ferromagnet [552]. An X-ray diffraction study first established that TDAE-C₆₀ is a stoichiometric material with a TDAE:C₆₀ ratio of 1:1 [806]. The diffraction data were interpreted in terms of a centered monoclinic unit cell, $a = 15.807$ Å, $b = 12.785$ Å, $c = 9.859$ Å, and $\beta = 94.02^\circ$ [806].

4.2. Polymerized C₆₀

4.2.1. Synthesis and Preparation

Photopolymerization of C₆₀ First evidence for polymerization [534] showed that oxygen-free thin films of C₆₀ can be polymerized by the irradiation of intense visible or ultraviolet light with photon energies greater than the optical absorption edge (~ 1.7 eV) [534, 807]. Because of the strong light absorption of C₆₀, only films thinner than $0.1 \mu\text{m}$ can be photopolymerized efficiently. The photopolymerized C₆₀ no longer dissolves in many common organic solvents compared to pristine C₆₀. Dioxygen diffused into C₆₀ films seem to be inhibitors during the photopolymerization process [534, 808] and CCl₄ can promote the process [809]. The photopolymerization process found to occur only in the fcc phase above 260 K, the orientational transition temperature of pristine C₆₀ crystals [808], goes by the [2 + 2] cycloaddition mechanism [534] with the double intramolecular bonds broken and a four-atom ring formed by covalent C–C bonds (i.e., accompanied with rehybridizations from sp^2 to sp^3). Direct evidence for the covalent intermolecular bonds confirms the photopolymerization from laser desorption mass spectroscopy measurements [534, 810]. On heating above ~ 400 K polymerized C₆₀ reverts to normal monomeric C₆₀ by breaking up the intermolecular bonds and reforming the intramolecular bonds. Recent Raman [811] and atomic force microscopy studies [812] also suggested that two different photopolymerized states might exist. Photopolymerization at temperatures above 350 K seems to produce mainly dimers, while material polymerized at 320 K and below contains larger oligomers. The photopolymerization of C₆₀ usually forms one-dimensional linear-chain structured polymers.

Pressure-Induced Polymerization of C₆₀ Pressure-induced polymerization has been studied extensively under various temperatures and pressures in recent years [813]. Several polymerized fullerenes have been synthesized from the fcc C₆₀ by applying moderate pressures at elevated temperatures [814–816]. Three different phases possessing one- or two-dimensional C₆₀–C₆₀ networks have been identified: one-dimensional orthorhombic phase (O-phase) [816], two-dimensional tetragonal phase (T-phase) [816], and two-dimensional rhombohedral phases (3R-phase, also called Rh-C₆₀) [814–816]. Recently single crystals of these three structures have been successfully synthesized (O-phase [817, 818], T-phase [819–823], and 3R-phase [824, 825]). The one-dimensional and two-dimensional pressure-induced polymerization of C₆₀ goes by the same cycloaddition mechanism of the photopolymerization.

Under ultrahigh pressure and a higher temperature (~ 13 GPa, 820 K), evidence for the existence of 3D

polymers has been observed [826]. But high purity 3D polymers with uniform structure have not been synthesized efficiently.

Other Polymerization Methods Polymerization of C₆₀ can also be accomplished by plasma treatments [827, 828], ion bombardments at a low dose [829], a low-energy electron injection from STM probe tips to C₆₀ films [830], or electron-beam bombardments from an electron gun [560]. The latter process has been successfully used for chlorine-based reactive ion beam etching in electron beam lithography where a C₆₀ film acts as a negative-type electron beam resist mask [831].

4.2.2. Structures and Phase Diagram Structures

1D Orthorhombic Phase The orthorhombic phase forms a one-dimensional linear molecular-chain structure along the $\langle 110 \rangle$ direction of the original fcc phase (see Fig. 16a) [813, 833]. The smaller value (~ 9.1 – 9.2 Å, compared to the value of 10.02 Å of pristine C₆₀) of the nearest-neighbor distance observed by XRD experiment provides the evidence for a covalent bonding between the C₆₀ cages. The space group has been identified as *Pmnn*, corrected from the earlier proposed *Immm* space group [818, 834].

2D Tetragonal Phase The tetragonal phase forms a two-dimensional tetragonal molecular-network layered structure via [2+2] cycloaddition in the (001) plane of the original fcc phase (see Fig. 16b) [813, 833]. The most recent study identified the “tetragonal” phase representing a pseudo-tetragonal packing model with an orthorhombic space group *Immm* [823] although with a very small higher energy (4 kJ mol^{-1}) [835] than another possible packing model with a truly tetragonal space group *P4₂/mmc*.

2D Rhombohedral Phase The rhombohedral phase forms a two-dimensional hexagonal molecular-network layered structure via [2 + 2] cycloaddition in the (111) plane of the original fcc phase (see Fig. 16c) [813, 833]. The hexagonal layers are proposed to be stacked in a close-packed arrangement of the type ABCABC with space group *R3m* [816]. There are three possible packing modes of the hexagonal layers proposed [835]; recent XRD studies confirmed most stable modes, which suggest a trigonal symmetry in individual layers but not a hexagonal one [818, 825].

3D Polymers and Superhard Phase The structure of 3D C₆₀ polymers is still ambiguous due to the complex structure and bonding mechanism. There are several theoretically and experimentally suggested structures under nonhydrostatic or hydrostatic compression and high temperature treatment [836–839]. Recently one superhard phase of 3D polymer treated under 13 GPa, 820 K has been characterized to be a body-centered orthorhombic structure (space group *Immm*), with [3 + 3] cycloaddition bonding between the [2 + 2] cycloaddition bonded tetragonal layers from a 2D polymer [826, 840].

Figure 35 gives the geometric structural diagrams of C₆₀ polymers. The crystallographic data from different authors for the 1D and 2D C₆₀ polymers are listed in Table 32.

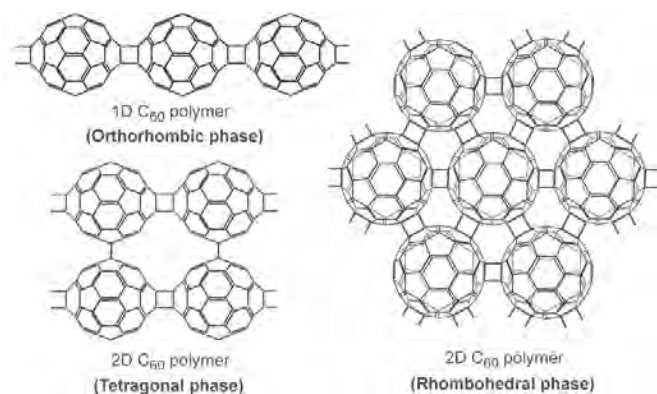


Figure 35. Geometric structures of C₆₀ polymers: (a) 1D C₆₀ polymer (orthorhombic phase), (b) 2D C₆₀ polymer (tetragonal phase), (c) 2D C₆₀ polymer (rhomboidal phase).

Phase Diagram There have been several tentative phase diagrams under pressure–temperature treatments of C₆₀ presented in some of the literature [318, 813]. Since the phase formation and purity of polymerized C₆₀ depend strongly on the temperature and pressure as well as the time of the treatment, those phase diagrams are still under discussion. The typical detailed conditions for the formation of pressure-polymerized C₆₀ have been reported as follows: 1D orthorhombic phase 1–2 GPa, 550–585 K, about 5 hours [318, 818]; 2D tetragonal phase: 2–2.5 GPa, 700–873 K 0.5–4 hours [318, 822, 823]; 2D rhombohedral phase 5–6 GPa, 773–873 K, 0.5–1 hours [318, 825]. It has also been reported that after a 1000 s treatment under conditions of temperature of ~1.5 GPa and pressure of ~423 K, most of the pristine C₆₀ will form dimer phase with a (C₆₀)₂ content of about 80 mol% [318] (to learn more about C₆₀ donors. See Section 5.2).

4.2.3. Electronic Structures and Energetics

Electronic Structures Polymerization of fullerene C₆₀ results in the narrowing of the HOMO–LUMO gap that is caused by the splitting of the degenerated molecular orbitals

of the icosahedral C₆₀ due to its distortion and the formation of intermolecular bonds. The electronic structures of 1D and 2D C₆₀ polymers have been studied theoretically using tight-binding calculation and LDA in the framework of the DFT.

From tight-binding calculation, a linear C₆₀ chain has been found to be semiconductive with a finite band gap of 1.148 eV and almost pure *s*-type intermolecular bonding [843]. Assuming the weak van der Waals interlayer interaction in the rhombohedral and tetragonal polymers, a theoretical prediction on stability and conducting properties has been made according to the tight-binding calculation of a single layer [844]. Different numbers of intermolecular covalent bonds in the tetragonal and rhombohedral structures were found to cause the distinction of bandgap values, which were estimated to be 1.2 and 1.0 eV, respectively. The investigation of the electronic structure of the rhombohedral and tetragonal 2D C₆₀ polymers has been carried out using the LDA [845, 846]. These phases were found to be elemental semiconductors having indirect gaps of 0.35 and 0.72 eV and three-dimensional electronic structures due to the short interlayer distance. Although the LDA generally underestimates the energy gap, its value is consecutively reduced from the C₆₀ to the rhombohedral phase, which correlates well with the result of tight-binding calculations [844].

Recently, empirical tight-binding calculations showed that all 1D and 2D polymers are semiconductors with the smallest energy gap for the rhombohedral phase, and the greatest energy stability for the 1D polymer [847].

Energetics and Stabilities DSC study [848] showed that all polymers are more stable than monomers because the stabilization energy decreases with increasing number of intermolecular bonds per molecule. Formation of polymer bonds lowers the total energy [844]. The stability sequence of a distinct polymerized phase of C₆₀ is dimer (C₁₂₀) > 1D polymer > 2D polymer > Pristine C₆₀ (monomer). All polymers depolymerize into pristine C₆₀ on heating to 300 °C and the depolymerization reaction is endothermic, indicating that the monomer form is the least stable phase [848].

Table 32. Crystallographic data for C₆₀ polymers.

Polymer phase	Space group	<i>a</i> (Å)	<i>b</i> (Å)	<i>c</i> (Å)	<i>V</i> (Å ³), <i>Z</i>	<i>d</i> (g/cm ³)	Ref.
Orthorhombic phase	<i>Immm</i>	9.26	9.88	14.22	650		[816]
	<i>Immm</i>	9.29	9.81	14.08	641		[841]
	<i>Pmnn</i>	9.098	9.831	14.72	658		[834, 841, 842]
	<i>Pmnn</i>	9.14	9.90	14.66	663		[818]
Tetragonal phase	<i>Immm</i>	9.09	9.09	14.95	618, 1		[816]
	<i>P4₂/mmc</i>	9.097	9.097	15.04	1245, 2	1.92 (cal.) 1.88 (exp.)	[819]
	<i>P4₂/mmc</i>	9.097	9.097	15.02	622, 1		[834]
	<i>P4₂/mmc</i>	9.02	9.02	14.93			[822]
	<i>Immm</i>	9.026	9.083	15.077	1236, 2	1.936 (calcd.)	[823]
	Rhombohedral phase	<i>R$\bar{3}$m</i>	9.19	—	24.50	597	
	<i>R$\bar{3}$m</i> (60°)	9.204	—	24.61	602		[834]
	<i>R$\bar{3}$m</i> (60°)	9.175	—	24.568	1791.1,3	2.004	[825]
3D polymer	<i>Immm</i>	8.67	8.81	12.60		2.48 (X-ray) 2.5 (exp.)	[840]
	<i>Immm</i>	8.69	8.74	12.71		2.43 (X-ray) 2.5 (exp.)	

Compared to the most stable phase, graphite, the energies of diamond and C₆₀, reckoned from the graphite level, are, respectively, 0.020 and 0.42 eV per carbon atom. The total energy of distinct phases of C₆₀ occur within a very narrow energy range of about 0.01 eV per carbon atom and the difference between the polymer and monomer forms of C₆₀ is rather small [848].

4.2.4. Physical Properties

Electrical Properties Generally, the conductivity of polymerized C₆₀ increases with the polymerization degree and depends on their structure and the ratio of the number of sp^2 to sp^3 .

Field effect transistor investigations indicate that the 1D plasma-polymerized C₆₀ acts as a *p*-type semiconductor in contradiction to the *n*-type semiconductor behavior of pristine C₆₀ [849]. The gas and photosensitivity of transport properties of a C₆₀ polymer thin film are promising for a sensing device [849]. In addition, it is known that the alkali-metal doped (AC₆₀)_{*n*} 1D polymer will formed spontaneously below 400 K from the monomer AC₆₀ salts. It was found that (KC₆₀)_{*n*} has metallic conductivity; (RbC₆₀)_{*n*} and (CsC₆₀)_{*n*} are also conducting at high temperatures but have a metal-insulator transition at 50 and 40 K, respectively [850].

2D C₆₀ high-oriented C₆₀ polymer shows a gigantic conductivity anisotropy. Conductivity in the polymerized planes exhibits a metallic-like behavior and the out-of-plane one is semiconductor-like [851]. The anisotropy is temperature dependent and lies in the range of 10³–10⁶. A randomly oriented polymer shows a semiconductor behavior and obeys the Arrhenius law [852]. The observed in-plane conductivity has been explained by a theoretical calculation which considered the formation of distinguishable intermolecular bondings of 66/66, 56/66, and 56/65 models. The calculated results indicated that the occurrence of regions containing 65/56 bonded molecules within a 66/66 connected hexagonal layer may cause variations of in-plane conductivity from a semiconducting behavior to a metallic behavior [853]. If a 2D polymer is formed at a temperature above the collapse temperature of the C₆₀ molecular cages (about 800 °C), the conductivity increases intensively by four orders of magnitude [824].

Both semimetallic, variable range hopping (VRH) and semiconducting behaviors have been observed in the electrical resistivity measurement on samples with disordered structures synthesized from pure C₆₀ at pressures in the range 8–12.5 GPa and temperatures of 900–1500 K [854]. Particularly, the temperature dependence of resistivity in a disordered crystalline 3D-polymerized C₆₀ obtained after 9.5 GPa and 900 K treatment fits Mott's VRH law $\rho = 0.07[\exp(1/T)^{1/4} - 1]$ Ω cm in the range 270 K down to 5 K for hopping conductivity [854].

Optical Properties Optical absorption and PL spectra of polymerized fullerenes have noticeably broader bands than those in pristine C₆₀ [855], and the optical absorption ranges and PL peaks are shifted to the lower energies [522]. Oxygen-containing polymerized fullerene films show strong photoluminescence in the near-IR and visible ranges (1.50–2.36 eV) at room temperature, and the photoluminescence

decrease in intensity after being annealed at different high temperatures [856].

The inverse transmission spectra for 1D and 2D polymers indicate that raising the polymerization temperature shifts the absorption edge to lower energies [857], showing that the polymers are semiconductors with energy gaps $E_g \sim 1.4$ and 1.1 eV which agree well with the theoretical calculations for the orthorhombic and rhombohedral phases ($E_g \sim 1.2$ and 1.0 eV, respectively) [844].

The Raman and infrared spectroscopies of polymerized has also been studied; the spectra are given as comparisons with those of pristine C₆₀ crystals in Section 2.2.2.

Magnetic Properties Among all the 1D and 2D C₆₀ polymers, the 2D rhombohedral polymer is the only phase known that shows ferromagnetic features such as saturation magnetization, large hysteresis, and attachment to a small samarium–cobalt magnet at room temperature (shown in Figure 36) [555]. The temperature dependences of the saturation and remanent magnetization indicate a remarkably high Curie temperature about 500 K higher than that of the other known organic ferromagnets [555, 858]. The discovery of ferromagnetism in Rh-C₆₀ has opened up the possibility of a whole new family of magnetic fullerenes.

Elastic Properties Ultrasonic measurements have revealed that the elastic module of C₆₀ polymer increases with the polymerization degree which depends on the polymerization pressure and temperature [859]. Table 33 gives the elastic properties of C₆₀ polymers compared to pristine C₆₀ and polycrystalline diamond [859]. Remarkably, the disordered 3D polymer and amorphous C₆₀ synthesized at a temperature higher than the collapse temperature of C₆₀ cages shows comparable and exceeding bulk moduli with diamond, respectively.

It has been shown that amorphous C₆₀ synthesized at very high pressure and temperature (~13 GPa, 1850 K) can scratch the diamond surface easily [860, 861], with hardness exceeding that of diamond making the ultrahard C₆₀ among the hardest known materials.

4.3. Metal/C₆₀ Composites

For metals other than alkali or alkali earth ones, which have much higher cohesive energy, it is energetically unfavorable for them to diffuse into the interstitial sites of the C₆₀

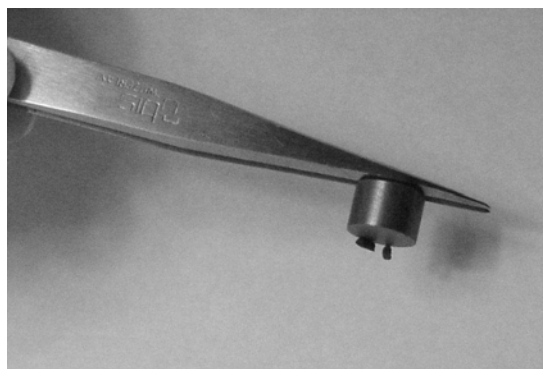


Figure 36. 2D rhombohedral polymerized C₆₀ attached to a small samarium–cobalt magnet at room temperature.

Table 33. Measured values of sound velocities and elastic moduli in 1D and 2D polymerized C₆₀ samples.

Material	$p(\text{GPa})/T$ (K)	ρ (g/cm ³)	c_L (km/s)	c_T (km/s)	K (GPa)	G (GPa)	σ	Structure (X-ray results)
Pristine C ₆₀		1.68			10.8	4.85	0.31	polycrystalline
1D polymer	8/500	1.75	6.0	3.70	30	24	0.19	orthorhombic
			7.4	4.8	42	40	0.14	
2D polymer	8/900	1.9	6.8	4.1	45	30	0.20	rhombohedral
			7.4	4.2	50	40		
3D polymer	9.5/970	2.62	18.5	11.4	450	340	0.20	disordered (fcc + bcc)
Amorphous C ₆₀	13/1770	3.30	18.4	8.7	790	250	0.29	one halo
Diamond		3.74			490	350		polycrystalline

Note: c_L and c_T are longitudinal and transverse sound velocities. K and G are bulk and shear elastic moduli; σ is Poisson ratio. Accuracy of ultrasonic measurements is ~5% [859].

lattice and form a M_xC₆₀ compound similar to M_xC₆₀ alkali fullerenes [170, 862]. Therefore M/C₆₀ composites (phase-separated solids of M/C₆₀) were obtained and investigated to study the metal–C₆₀ interaction. The most common composites are multilayer films [863–865] and the nanodispersion films [865–871]. Both of them can be easily obtained by the co-deposition method using metals and pure C₆₀ (>99.9%) under high vacuum [865, 869].

In the M/C₆₀ nanodispersion films, metal nanocrystallites are well dispersed in the C₆₀ polycrystalline matrix and the grains of M are very small [866–869]. The volume fraction of the metal and the grain size of the metal particles can be controlled by adjusting the deposition rates of C₆₀ and the metal, and the temperature of the substrate, respectively [869].

4.3.1. Al, Cu, Ag/C₆₀ Composites

Al/C₆₀ Al–C₆₀ interaction was first studied in multilayers [863]. *In-situ* resistivity measurements showed that the presence of underlying layers of C₆₀ reduced the critical thickness at which Al became conducting from ~35 to ~20 Å and there was a sudden increase in resistance that occurs when each Al layer was covered by a monolayer of C₆₀. A downward shift of 40 cm⁻¹ in frequency of a considerably broadened Raman-active A_g(2) pentagonal-pinch mode was observed. A charge transfer model in which up to six electrons per C₆₀ were transferred from the Al to the C₆₀ layer across the planar Al–C₆₀ interface was proposed to explain these experimental results [863].

However, the PES and C 1s X-ray-absorption spectra of C₆₀ monolayers on Al(111) surfaces indicated that Al–C₆₀ bonding is covalent [184]. Therefore Raman spectra were measured on Al/C₆₀ nanodispersion films in order to get some insight into the Al–C₆₀ interfacial interactions [868, 872]. The A_g(2) pentagon-pinch mode of C₆₀ splits into two peaks, one pristine mode which still remains at 1468 cm⁻¹, and one softened mode with a shift of ~6 to 9 cm⁻¹. The presence of the pristine mode of C₆₀ demonstrates that Al–C₆₀ interaction is a localized interface effect. In addition, the shifts of the softened A_g(2) mode depend weakly on the Al/C₆₀ ratio and the microstructures of the films. The distinct relative increase in intensity of the H_g(7) and H_g(8) modes compared to A_g(2) mode has also been observed. This result as well as the local effect of Al–C₆₀ interaction

suggest that covalent bonding may play a major role in the interaction between Al/C₆₀ as that reported by Maxwell et al. [184].

Cu/C₆₀ Hebard et al. found that C₆₀ covered on the surface of a Cu layer showed a metallic characteristic [863] and a similar result was also observed by STM research on a C₆₀ layer covered upon the surface of a Cu substrate [14]. Moreover, it was reported that the cover of C₆₀ on a layer of metal can effectively affect the conductivity of metal films [3, 15]. Cu/C₆₀ nanodispersion films grown by a co-deposition method were obtained and the structures were observed by TEM [869, 870, 874, 875]. The uniformly granular microstructure and the small clusters or grains in Cu–C₆₀ films might form a kind of doped fullerene nanostructure so that electrons could be transferred from metal atoms to the surface layers of C₆₀ at the interface [869].

The temperature dependence of the conductivities has been measured *in-situ* [874]. The linear relationship $\ln(\sigma/\sigma_{\text{RT}}) \propto (1/T)$ was observed when the temperature was lower than 250 K, and the relation $\ln(\sigma/\sigma_{\text{RT}}) \propto (1/T^{1/4})$ was observed for temperatures higher than 260 K. The values of conductivity of these films (typically in the range of 10⁻²–10² S cm⁻¹) are much higher than that of the pristine C₆₀ solid (~10⁻⁷ S cm⁻¹). The conduction of Cu/C₆₀ interface compounds is dominated by the electrons hopping between the localized states [874].

A Raman backscattering spectra method was performed on Cu/C₆₀ as-grown films [869, 875]. The peak width of the pentagon-pinch mode [A_g(2)] becomes wider and the peak position shifts to the lower frequency as the atomic ratio of Cu/C₆₀ increases. The vibrational frequencies of the softened modes are about 6 cm⁻¹ lower than that of the pristine mode so it can be inferred that about one electron is transferred to C₆₀.

Ag/C₆₀ Ag/C₆₀ nanodispersion films have been prepared by the co-deposition method [866]. Linear relationships of $\ln \sigma$ versus $1/T$ were observed in electrical conductivity measurement from ~200 to ~300 °C and the conductivities are in a range similar to those in Cu/C₆₀ films [869]. The shift of the soft A_g(2) mode in Raman spectra indicated that about 1–1.5 electrons are transferred from Ag to C₆₀. Moreover, Although the peak positions of the H_g(7) and H_g(8) modes are about the same as that of C₆₀, the relative intensities of them increase significantly in the Ag–C₆₀ film and

this increase is difficult to interpret with the charge transfer model. A plausible explanation is that Ag atoms may diffuse into the C₆₀ lattice to form a limited dilute interstitial solid solution under high temperatures similar to the result observed in the Al-C₆₀ system [863]. The conductance of discontinuous granular Ag films covered by C₆₀ was measured *in-situ* during C₆₀ covering [876]. An anomalous peak of conductivity was observed when the thickness of the C₆₀ overlayer was around 1.6 nm. This result indicates that 1–2 monolayer(s) of C₆₀ covered upon the granular Ag films are “metallic,” which is attributed to the charge transfer between Ag and C₆₀ [876].

Charge transfer has also been observed in Ag deposited C₆₀ films grown on the Si(111)-(7 × 7) surface by using scanning tunneling microscopy [877]. It is found that for individual Ag atoms and very small Ag clusters, the charge transfer is inhibited or less effective, and there is no chemical bonding between Ag and C₆₀. Only after the Ag atoms aggregated to form Ag clusters larger than a critical size will the charge transfer will become effective. From the lateral size distribution of the Ag/C₆₀ clusters, the critical size is concluded to be no more than 4 nm. Furthermore, the results indicate that the growth of the Ag/C₆₀ clusters should be limited to sizes smaller than 10 nm. This self-limiting growth process and the critical size effects provide a possible method to control the growth of metal clusters with a narrow distribution size.

4.3.2. Magnetic-Metal/C₆₀ Composites

Ni/C₆₀ Ni/C₆₀ granular films were also prepared by the co-deposition method [878]. High-resolution transmission electron microscopy (HRTEM) results show that Ni nanoparticles are well isolated and embedded in an amorphous C₆₀ matrix in the films. Raman spectra indicated that the charge transferred to each C₆₀ molecule in an N(Ni):N(C₆₀) = 30 film is ~4 electrons, and that in N(Ni):N(C₆₀) = 1.5 and 6 films are ~2 electrons. The charges transferred from Ni to C₆₀ reduce when the Ni nanoparticles become smaller (the average sizes of Ni particles in N(Ni):N(C₆₀) = 1.5, 6, and 30 films are 2.6, 3.3, and 6.6 nm, respectively). This is attributed to the quantum size effects of Ni nanoparticles [878].

Measurements of the surface magneto-optical Kerr effect show that the coercivities (H_c) of Ni/C₆₀ films are enhanced significantly. In other words, the critical size of superparamagnetic transition (3.3 nm) is much smaller compared to Ni nanoparticles embedded in graphite (13.6 nm) [879] or SiO₂ matrix [880]. It was suggested that the enhancement of H_c may be attributed to surface spin disorder of Ni particles induced by the strong interfacial interaction between Ni and C₆₀.

Fe, Co/C₆₀ Unlike the C₆₀ based materials we discussed, Fe, Co/C₆₀ composite films obtained by adding C₆₀ as a minor component into Fe, Co matrix have also been investigated [881]. The concentrations of the as-deposited thin films were expressed in a formula of B_xC₆₀ (M = Fe, Co). TEM images showed that the grains are extremely uniform in the film. Raman spectroscopy shows that most of the fullerenes are stable in the films and the electronic diffraction shows no

graphite phase; the carbon interfacial phase is mainly composed of fullerenes.

Out-of-plane hysteresis loops for the Co₁₆₂C₆₀ films show that both the remanence and the coercivity increase significantly in the films. These values are comparable to the promising perpendicular recording media, Co-Cr and Co-CrTa [882]. These C₆₀ comprising media have the potential to achieve ultrahigh storage density because the C₆₀ molecules limit grain growth, reside at grain boundaries, and reduce the magnetic coupling between grains which can lower media noise [883].

The in-plane major hysteresis loops and the virgin magnetization curve of the Fe₇₃C₆₀ film display a fast switching property, which suggests this material had the potential to be used in magnetic memory, magnetic switches, spin valves, magnetic springs, and other magnetic devices. The uniformity of the grains and distribution of C₆₀ may contribute to this fast switching ability.

5. LOW-DIMENSIONAL STRUCTURES

5.1. Heterofullerenes

5.1.1. Introduction

Heterofullerenes (“dopeyballs,” “heterohedral” fullerenes) are fullerenes in which one or more carbon atoms in the cage structure are substituted by a noncarbon atom (i.e., a heteroatom). In this case, heterofullerene formation is a kind of “on-ball” or “in-cage” doping of the fullerene cage. First spectroscopic evidence for heterofullerenes was observed in gas phase of heterofullerene ions produced by laser vaporization of a graphite pellet containing boron nitride powder [884].

Through modification of the cage structure of heterofullerene, significant modification of geometry, chemical functionality, and electronic character of the fullerenes would occur. So it was anticipated that these heterofullerenes should exhibit a variety of properties and lead to formations of various derivatives due to the in-cage introduction of guest atoms.

5.1.2. C₅₉N/(C₅₉N)₂

The aza[60]fullerene C₅₉N is formed by substituting a nitrogen atom for a carbon atom in the C₆₀ cage structure. Neutral C₅₉N is an open shell molecule due to the trivalency of nitrogen leaving a “dangling bond” on an adjacent carbon atom in the cage (see Fig. 37a). Aza[60]fullerene in the first oxidized state is sometimes called aza[60]fullerocation, for which one resonance structure is shown in Figure 37b. C₅₉N radical is highly reactive and it easily bonds to form (C₅₉N)₂ dimer, the most stable form of azafullerene (see Figure 38), or is hydrogenized to form hydroazafullerene C₅₉NH.

Synthesis Up to now, the azafullerenes are the only known heterofullerenes which can be isolated as pure substances.

Nitrogen-doped fullerenes can be synthesized basically by vaporization of graphite in nitrogen containing atmosphere [885, 886] or by laser ablation of fullerene derivatives which possess organic ligands bound to the carbon cage through

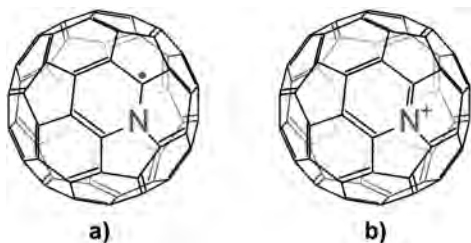


Figure 37. Important resonance structures of (a) aza[60]fullerene radical and (b) aza[60]fullerene cation.

a nitrogen atom [887], or by condensed-phase organic synthesis. But the latter which yields aza[60]fullerene dimer is proved to be the only efficient method leading to the isolation of macroscopic quantities of azafullerenes so far. There are two different methods succeeding organic synthesis.

In 1995 it was found to occur by the effective formation of azafullerene C₅₉N⁺ in the gas phase during fast atom bombardment mass spectrometry of a cluster opened *N*-methoxyethoxy methyl ketolactam, so Hummelen et al. applied this process in solution in the presence of strong acid and isolated C₅₉N as its dimer (C₅₉N)₂ [888]. In 1996, Grösser et al. succeeded in converting a bisazahomofullerene [889] to the aza[60]fullerene dimer (C₅₉N)₂ in a different way [890]. By both these methods high-purity (C₅₉N)₂ samples can be obtained after high performance liquid chromatography (HPLC) purification.

Properties

Structure Properties It was found that the C₅₉ dimer is formed by linking two cages in a *trans*-configuration by one single bond to minimize the repulsion of the nitrogen atoms and to optimize the whole structure (see Fig. 38). The link is made by the two carbon atoms (C, C') each of which joins two hexagons together with the N atom in a C₅₉N molecule. The molecule has C_{2h} symmetry. The C–C' dimer bond was calculated to be 1.609 Å, (i.e., 0.05 Å longer than that between two average sp³ carbon atoms) [891]. The binding energy was calculated to be ~18 kcal mol⁻¹ [891].

The bonding energy is relatively low and the dimer can be cleaved both thermally and photochemically into two C₅₉N[•] radicals [892]. Light-induced ESR measurement of a solution of (C₅₉N)₂ in 1-chloronaphthalene, using 532 nm laser pulses, yielded a spectrum with three equidistant lines of equal intensity, indicative of ¹⁴N hyperfine interaction [893]. The hyperfine coupling constant is 3.73 G. The reported values for the *g* factor of C₅₉N[•] are 2.0011(1) and 2.0013(2), higher than that of C₆₀ radical anion, 1.9991 [894]. This

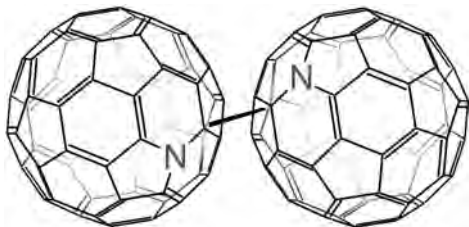


Figure 38. Schematic 3D structure for a (C₅₉N)₂ molecule.

unusually low *g* value of C₆₀^{•-} can be explained in terms of Jahn–Teller distortion that splits the triply degenerate t_{1u} states, thus leading to quenching of angular momentum.

Electronic Properties Based upon the extended SSH model for C₅₉N, the calculated results are very consistent with those from the SCF-MO method. The lattice structure of C₅₉N is different from that of pure C₆₀ due to effects of the dopant ion, but the deformations of the substituted fullerene cage for the C₅₉N are mainly limited in the vicinity of the dopant ions [895]. As one electron is doped into the LUMO of C₆₀ in C₅₉N, it was changed so significantly that the energy level near the Fermi level and the corresponding smaller bandgap between HOMO and LUMO was about 0.3 eV [895, 896]. The calculated gap was much smaller than that for C₆₀. The HOMO states are mainly localized on the N–C double bonds and the excessive electron density is concentrated on the impurity sites. The excessive electron density of the N atom is 0.27, which implies that electronic charge accumulates on the doped N site and the N atom exists as an acceptor [895].

The electronic properties of (C₅₉N)₂ in thin films have been studied by using PES and EELS [897, 898]. It was found that the HOMO of (C₅₉N)₂ is located mainly on N atoms and the intermolecular C–C' bond. In contrast, the LUMO has mainly a C-character. The optical gap of the dimer is ~1.4 eV, some 0.4 eV smaller than that of C₆₀ (1.7–1.8 eV). It was obtained from the energy-loss functions that the static dielectric constant ε₁(0) of (C₅₉N)₂ is about 5.6, which is larger than that of C₆₀ [ε₁(0) ~ 4], reflecting the smaller energy gap of the heterofullerene dimer.

Properties of (C₅₉N)₂ Solid Solid structural investigation of (C₅₉N)₂ using X-ray powder diffraction techniques showed that samples of (C₅₉N)₂ obtained by recrystallization from CS₂ exhibit a hexagonal structure (space group P6₃/mmc or a subgroup). The hexagonal phase remains stable under hydrostatic compression to 22 GPa, signifying it is somewhat less compressible than pristine C₆₀ [899]. The diffraction patterns point to a CS₂ content of about 1/2 molecule per formula unit. The CS₂ can be removed by sublimation of the material *in vacuo* at temperatures of 500–600 °C. This leads to a monoclinic structure with the space group of at most probably C2/m, where the C₅₉N dimers sit on the sites of a monoclinic *c*-centered Bravais lattice with lattice parameters *a* = 17.25 Å, *b* = 9.96 Å, *c* = 19.45 Å, and β = 124.32°, *T* = 295 K [900]. (C₅₉N)₂ are observed to be unstable at temperatures higher than 200 °C in UHV.

5.1.3. Other Heterofullerenes

Borafullerenes Borafullerenes were the first reported heterofullerenes observed in 1991 [884]. In 1996, the macroscopic preparation of borafullerenes was realized by using the arc-evaporation method on graphite rods doped with either boron nitride, boron carbide, or boron [901]. Extraction and enrichment were used for the heterofullerene content of the soot, involving pyridine extraction and subsequent treatments of the extract with CS₂ and pyridine. XPS spectra of the extract showed a peak at 188.8 eV that was assigned to boron (1s level) in borafullerene (C₅₉B mainly). The extracted materials appeared to be moisture sensitive, leading to the formation of boron oxide or boric acid [901].

There is another method to synthesize borafullerene by high-temperature laser ablation of a B₄C-graphite composite rod under an argon atmosphere. The product was analyzed with a laser desorption/ionization mass spectrometer, revealing that C₅₉B ($m/z = 719$) was formed together with the C₆₀ molecule [902].

Azafullerenes with Multinitrogen Atoms The synthesis of C₅₈N₂ is possibly complicated if the formations of the two N sites are not simultaneous, which may cause an open shell intermediate as found in the synthesis of (C₅₉N)₂, giving rise to an undesired reaction route. Synthetic route toward C₅₈N₂ starting from C₆₀ [903] has been proposed; recently, (1,3,5)pyridinophanes having [4.3.2]propellatriene units were synthesized as precursors to macrocyclic polyene C₅₈H₄N₂ and diazafullerene anion C₅₈N₂⁻ was detected in the laser desorption mass spectrum of the pyridinophanes [904].

A new fullerene-like material, consisting of cross-linked nano-onions of C and N, was reported [905]. Growth of the onion shells takes place atom by atom on a substrate surface and yields thin solid films during magnetron sputter deposition. The N content in the onions, up to 20%, is the highest measured for an azafullerene in the solid phase. Total energy calculations of C_{60-2n}N_{2n} molecules suggest the existence of a novel C₄₈N₁₂ molecule.

Azaborafullerenes Recently, it was reported that C₅₈BN can be produced by a BN substitution reaction of fullerene C₆₀ upon irradiation by a KrF excimer laser at room temperature [906] and isolated by HPLC. Mass spectra and X-ray photoelectron spectroscopy analysis confirmed the substituted formation of C₅₈BN ($m/z = 721$).

Heterofullerenes with Heteroatoms Other than N, B Early theoretical calculation of Si in-cage doped heterofullerenes (C₅₉Si, 1,2-, 1,6-, and 1,60-C₅₈Si₂) predicted that these structures are stable and show a steady decrease of the bandgaps with an increasing number of Si atoms [907]. First evidence for the possible existence of silicon heterofullerenes is provided by analyzing the products from pulsed-laser vaporization of silicon-carbon composite rods by time-of-flight mass spectrometry (TOF-MS) [908], which showed small peaks that would match the masses of SiC_n⁺ clusters ($61 \geq n \geq 56$). Recently, silicon heterofullerenes have been synthesized in a laser vaporization source from targets processed as mixtures of graphite and silicon powders [909] or Si_xC_{1-x} mixed composition targets [910, 911]. Another method to generate silicon in-cage doped fullerenes is laser-induced photofragmentation of parent clusters of composition C₆₀Si_x which are produced in a low pressure condensation cell, through the mixing of silicon vapor with a vapor containing C₆₀ molecules [912]. It was indicated from the analysis of photofragmentation mass spectra that at least three Si atoms can be incorporated in fullerenes, the Si atoms are located close to each other in fullerenes, and Si doping was also predicted to increase the fullerene chemical reactivity [911]. *Ab initio* calculation of optimized geometrical structures of C₅₉Si and C₅₈Si₂ isomers showed that the geometrical modifications of the heterofullerenes occur in the vicinity of the Si dopant atom [913].

In the case of oxygen, there is some possible evidence for the existence of O heterofullerenes in the form of

C₅₉O⁺ ions in gas-phase experiments [914] or C₅₉O⁻¹ anions produced via collision-induced dissociation of oxy-fullerene anions C₆₀O₂₋₄⁻ [915].

Evidence for the existence of C₅₉P has been identified in mass spectroscopy. The formation of these heterofullerenes was achieved by evaporating phosphorus and carbon simultaneously but at different positions in a radio frequency furnace (i.e., at different temperatures) [916].

Existence of substitutionally doped fullerenes C₅₉M has also been identified by mass-spectrometric evidence, where M represents the atom of the transition metals such as Fe, Co, Ni, Rh, and Ir. These in-cage doped fullerenes were produced by the photofragmentation of precursor metal-fullerene clusters C₆₀M_x [917].

5.2. C₁₂₀ (C₆₀ Dimer)

Since the discovery of the photopolymerization of C₆₀ via [2 + 2] cycloaddition [534, 807], there have been a lot of theoretical studies [918–924] on the smallest subunit of a C₆₀ polymer: C₁₂₀ (C₆₀ dimer), a dumb-bell-shaped all-carbon molecule polymerized from two individual C₆₀ molecules (see Fig. 39). The most stable isomer of C₁₂₀ is confirmed to be polymerized via the same [2 + 2] cycloaddition mechanism of C₆₀ polymers (i.e., the double intramolecular bonds broken and a four-atom ring formed by covalent C–C bonds, accompanied with rehybridizations from *sp*² to *sp*³).

5.2.1. Synthesis

C₁₂₀ can be synthesized by many methods, such as photopolymerization [534, 808], solid-state mechanochemical reaction [925–927], quasi-hydrostatic compression of C₆₀ [928], and squeezing of a C₆₀ compound [929].

The photopolymerization method gave the first evidence for the existences of C₆₀ dimer and polymer [534, 808]. It was observed that solid C₆₀ exposed to visible or ultraviolet light forms a polymerized phase which is no longer soluble in toluene.

The solid state mechanochemical reaction of C₆₀ with KCN by the use of a high-speed vibration milling (HSVM) technique is the first efficient method to synthesize bulk C₁₂₀ [925, 926]. In a standard procedure, a mixture of C₆₀ and 20 molar equivalents is placed in a capsule and vigorously vibrated under HSVM conditions for 30 min in a glovebox filled with nitrogen. Separation of the reaction mixture by flash chromatography on silica gel, eluted with hexane/toluene and then with toluene/*o*-dichlorobenzene (ODCB), gives 70% of recovered C₆₀ and 18% of C₁₂₀ [925, 926]. It was found that this reaction can take place efficiently also by the use of potassium salts such as K₂CO₃

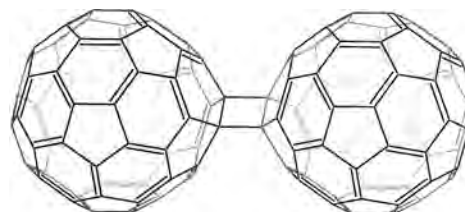


Figure 39. Schematic 3D structure for a C₁₂₀ (C₆₀ dimer) molecule.

and CH₃CO₂K which contain nucleophilic anions, metals such as Li, Na, K, Mg, Al, and Zn (while Ni and Cu are not effective), and organic bases such as 4-(dimethylamino)- and 4-aminopyridine [925, 927]. Single crystals of C₁₂₀ can grow in an ODCB solution since it is hardly soluble in most common organic solvents but has a reasonable solubility in ODCB [925, 926].

The quasi-hydrostatic compression method for the dimerization of C₆₀ is achieved under a high-pressure, high-temperature treatment [928, 930, 931]. It was shown that the dimerization occurs even at room temperature in the entire pressure range above ~1.0 GPa. However, the formation of a dimer phase as a stable modification is at least at temperatures above 400 K. No condition was found that may yield pure C₆₀ dimers so far. A typical condition with the pressure, temperature, and treatment time of 1.5 GPa, 423 K, and 1000 s yields about 80% C₆₀ dimers [930].

Squeezing of a C₆₀ compound was reported to be a high yield selective synthesis method of C₆₀ dimers [929]. Squeezing the organic molecular compound crystal (ET)₂C₆₀ [ET = bis(ethylenedithio)tetrathiafulvalene] at 5 GPa and 200 °C followed by removing unreacted ET molecules by sonication in CH₂Cl₂ produces C₆₀ dimers, with a yield of about 80%. Most of the product is soluble in *o*-dichlorobenzene, while there remains a small amount of insoluble material, which may be one-dimensional oligomers or ladder polymers.

5.2.2. Structure

The isolated C₁₂₀ forms a dark brown powder. The ¹³C NMR spectrum exhibited 15 signals (including one overlapped signal) in the *sp*² region and one signal at 76.22 ppm in the *sp*³ region, which are fully consistent with the assigned structure with *D*_{2h} symmetry [925]. It was also indicated that C₁₂₀ is indeed the essential subunit of these polymers by comparing the data with the ¹³C NMR spectra of C₆₀ polymers.

The single crystal structure was determined by X-ray crystallography; it was found that there is no obvious difference in the length of the four bonds in the [2 + 2] cycloaddition four-atom ring. The intracage bond length was determined to be 1.575(7) Å, and intercage bond length was found to be 1.581(7) Å [925]. In single crystals grown in an ODCB solution, the C₁₂₀ molecules are arrayed in highly order layers, which is different from the face-centered cubic structure of C₆₀ [925].

5.2.3. Electronic Structure

The lowered symmetry of the C₁₂₀ as a consequence of dimerization molecule will result in an increased splitting of energy levels and a narrowing of the optical bandgap [920]. The presence of *sp*³ intermolecular bonds and the caused distortion of the C₁₂₀ molecule also change its electronic structure.

The electronic DOS confirms universal expectations about the electronic and vibrational energy levels. Due to the dimerization of C₆₀, the LUMO *t*_{1u} states split into a quasi-doublet and singlet state but the HOMO *h*_u state mixes strongly with the lower *g*_g and *h*_g levels leading to a generally broader DOS [932].

5.2.4. Properties

Far-infrared vibrational property investigation of the C₆₀ dimer showed that all the modes are nondegenerate. *H*_g(1)-derived modes are allowed in the dimer and appear as a weak quadruplet near 250 cm⁻¹ [933]. The number of *T*_{3u}(1)-derived modes is three, in agreement with group-theory predictions for the *D*_{2h} symmetry of the dimer.

In room-temperature solution, a systematic study of the photophysical properties and nonlinear absorptive optical limiting responses of the C₆₀ dimer was given [934]. It was found that the absorption, fluorescence (spectrum, quantum yield, lifetime), and photoinduced electron-transfer properties of the C₆₀ dimer are somewhat different from those of C₆₀ but qualitatively similar to those of other C₆₀ derivatives, indicating that the dimer may be considered as a pair of 1,2-functionalized C₆₀ derivatives. The triplet-triplet absorption of the C₆₀ dimer is noticeably weaker than those of C₆₀ and other C₆₀ derivatives, corresponding to lower optical limiting responses of the C₆₀ dimer at 532 nm. It was also concluded that the C₆₀ dimer is photochemically stable since there is no meaningful change in both absorption and fluorescence spectra of the dimer solution after 10 h of continuous photoirradiation.

The thermal behavior of the C₆₀ dimer was investigated in the range 80–220 °C at a rate of 1 °C min⁻¹ using differential scanning calorimetry [925]. An endothermic peak from 150 to 175 °C and centered at 162 °C was found in the heating process, while no such peak was observed in the cooling scan. It was also found that the C₆₀ dimer could dissociate quantitatively into C₆₀ by heating its ODCB solution at 175 °C for 15 min. C₁₂₀ should have equal chemical reactivity to C₆₀ considering their close reduction potentials.

5.3. Endohedral C₆₀

Endohedral fullerenes are novel forms of fullerene-based materials in which the fullerenes are encapsulated by atom(s) (even some small molecules) in their inner hollow space (see Fig. 40). These new fullerene derivatives are usually described using the symbol “@” conventionally and conveniently with the encaged atom(s) listed to the left of the “@” symbol. For example, a C₆₀-encaged metal species (M) is written as M@C₆₀ [935]. In recent years endohedral fullerenes have attracted a lot of interest due to their fascinating properties and novel electronic structures.

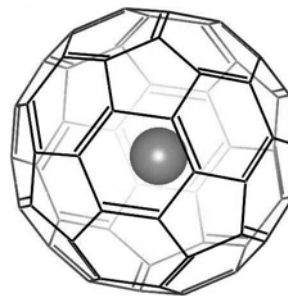


Figure 40. Schematic 3D structure for an endohedral fullerene molecule.

5.3.1. M@C₆₀, M = Metal

The first evidence for endohedral metallofullerenes based on C₆₀ (M@C₆₀) was proposed from a magic number due to LaC₆₀ in a mass spectrum prepared by laser vaporization of a LaCl₂-impregnated graphite rod [936]. Further evidence showing that the La C₆₀⁺ ions did not react with H₂, O₂, NO, and NH₃ confirmed that the active metal atoms are indeed encapsulated inside the C₆₀ cage [937].

Original soot containing M@C₆₀ (M = Y, Ba, La, Ce, Pr, Nd, Gd, Er, Eu, and Dy) is usually produced by arc-discharge-heating of an M_xO_y/graphite (M_xO_y = Y₂O₃, BaO, La₂O₃, CeO₂, Pr₆O₁₁, Nd₂O₃, Gd₂O₃, Er, and Eu₂O₃) composite rod under a 50–100 Torr He atmosphere [938–941]. But the extraction of M@C₆₀ from the soot is difficult because of almost all known M@C₆₀ so far showing high reactivity and they are insoluble and unstable in normal fullerene solvents such as toluene and carbon disulfide (CS₂). Ca@C₆₀ has been extracted by pyridine or aniline [942], M@C₆₀ (M = Y, Ba, La, Ce, Pr, Nd, Gd, and Sr) can be extracted by aniline [943], and Li@C₆₀ prepared by an ion implantation technique can be extracted by CS₂ [942, 943].

Pure samples of Eu@C₆₀, Er@C₆₀, and Dy@C₆₀ have obtained by combining sublimation and HPLC with aniline as an eluent [939–941]. The X-ray-absorption near edge structure spectrum showed that the valence of Eu atom in Eu@C₆₀ was +2 [939], while the Raman spectrum indicated that the valence of Dy atom in Dy@C₆₀ is +3 [941] with 3 electrons transferring from the Dy atom to the C₆₀ cage. It has also been indicated that the Dy in Dy@C₆₀ is located at an off-center position 1.25–1.30 Å from the center of the C₆₀ cage, and the UV-visible–IR spectrum suggested that the HOMO–LUMO gaps of Dy@C₆₀, Er@C₆₀, and Eu@C₆₀ molecules are small [939–941].

5.3.2. R@C₆₀, R = N, P

Endohedrals of group-V elements N@C₆₀ and P@C₆₀ can be prepared by an ion implantation method [944, 945]. The C₆₀ fullerene is continuously evaporated onto a substrate and simultaneously bombarded with low-energy (40 eV) nitrogen or phosphorous ions. The resulting film is subsequently scratched from the substrate and dissolved in toluene and filtered. The soluble part contains only intact fullerenes, with the ratio of encapsulated to empty fullerenes typically on the order of 10⁻⁴. HPLC techniques are used to obtain pure endohedral fullerenes. These two systems are soluble in organic solvents and stable at room temperature while As@C₆₀ is calculated to be unstable [946]. Experimentally, ESR studies [944, 945, 947–950] revealed that the encapsulated nitrogen and phosphorus are located at the center of the cage, the N or P atom is in quartet electronic spin ground state $S = 3/2(^4S_{3/2})$, and the highly reactive ⁴S spin states of N and P do not interact with the C₆₀ cage. The fact of well-isolated electron spin of group-V atoms encapsulated in fullerenes and the easy positioning of endohedral C₆₀ offer a very flexible possible implementation of quantum-information bits for a promising spin quantum computer [951].

5.3.3. X@C₆₀, X = Noble Gases

Noble gas atoms can also be trapped in C₆₀ cages. In fact, the C₆₀ molecule cage is large enough to enclose all of the noble gases including helium, neon (Ne), argon (Ar), krypton (Kr), and xenon (Xe) [952, 953].

The noble-gas endohedral fullerenes are usually prepared by treating the fullerene with the gas under high temperature and pressure [952, 953]. Treatment at ~650 °C and ~3000 atm yields a C₆₀/X@C₆₀ (X = He, Ne, Ar, Kr, Xe) mixture with the ratio of encapsulated to empty fullerenes only on the order of 10⁻³. Recently, remarkable enrichment of Ar@C₆₀ (with a purity of 40%) [954], Xe@C₆₀ (with a purity of 31%) [955], and Kr@C₆₀ samples [956] with a purity as high as 90% has been realized by HPLC using a semipreparative PYE[2-(1-pyrenyl)ethylsilyl] column (10 × 250 mm) with toluene as the eluent [957].

The fact that noble gases with smaller masses do not interact significantly [952, 953] (the interaction is suggested to be van der Waals force mainly) with the inner parts of π-orbitals of the C₆₀ cage implies that the chemical and physical properties of these compounds will not differ much from those of empty C₆₀ molecules. But ¹²⁹Xe NMR spectroscopy study shows that in the case of Xe, the 5*p* electrons of the Xe are much closer to and interact much more strongly with the π-electrons of the C₆₀ [955].

5.4. C₆₀M_n

The exohedral metal complexes of C₆₀, usually written as C₆₀M_n, where M is the metal species, can be categorized as the third type of C₆₀ complex compared to the hetero- and endohedral fullerenes (see Fig. 41). The study of gas phase C₆₀M_n compounds has been stimulated by the discovery of the superconductivity of alkali doped fullerenes. C₆₀M_n complexes are suitable model systems for studying the electronic properties of nanostructures and understanding the fundamental interactions between two nanosystems, particularly metal–covalent interfaces.

5.4.1. Alkali Metals and Alkaline Earth Metals

In a pioneering experimental work, Wang and co-workers first studied the photoelectron spectra of C₆₀K_n⁻ clusters, *n* = 0–3, and they found evidence for charge transfer from the alkali atoms to the C₆₀ molecules [958]. The electron affinities of the species were found to have a linear relationship

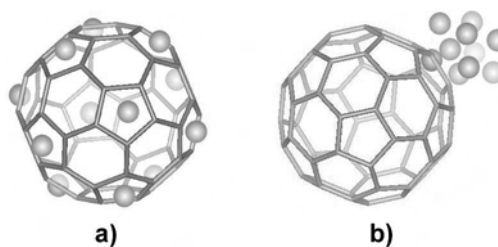


Figure 41. Schematic 3D structures for two types of exohedral metal–fullerene clusters (C₆₀M_n). (a) A “wet” structure where metal atoms spread over the fullerene cage. Here a C₆₀M₁₂ molecule with one metal atom on each 12 pentagon facet. (b) A “dry” structure where metal atoms form an adsorbed droplet on C₆₀.

with the number of K atoms. This indicated that C₆₀K_{*n*} are quite ionic because each K atom donates its outer 4*s* electron to the *t*_{1*u*} LUMO of C₆₀. A dipole-supported state is found in KC₆₀⁻, yielding an inter-K-C₆₀ stretching vibration of 140 cm⁻¹.

Zimmermann et al. have given a systematic study on alkali metal–fullerene clusters by using photoionization time-of-flight mass spectrometry [959]. The C₆₀M_{*n*} clusters were produced by coevaporation of fullerenes and metal in a gas aggregation cell. It was suggested that the stability of the alkali metal–fullerene clusters seems to be determined primarily by the electronic rather than the geometric configuration. The C₆₀M₆ clusters are found to be particularly stable formations for any alkali metal. Coating a fullerene with more than seven alkali metal atoms led to an even–odd alternation in the mass spectra, which signals the beginning of metal–metal bonding [959]. But C₆₀Li₁₂ was found to be an exception to the electronically determined cluster stability. It retains the icosahedral symmetry of the C₆₀ molecule because each Li atom was found to be stable when above one of the pentagonal faces. C₆₀Li₁₂ is very stable both in the singly and the doubly ionized state. The origin of the enhanced stability might be interpreted to be of geometric origin [959, 960]. Alkaline earth metal covered fullerenes C₆₀M_{*n*} (*n* = 0–500; M = Ca, Sr, Ba) were also studied in these works [959, 961]. It was suggested that these clusters are formed by the completion of metal layers around a central C₆₀ molecule; the first layer is complete when one metal atom is situated above each of the 32 facets of the C₆₀ cage.

Recently, the electronic and geometric properties of C₆₀Na_{*n*}⁻ and C₆₀Au_{*n*}⁻ cluster anions were investigated by TOF-MS and PES [962]. The C₆₀-Na and C₆₀-Au clusters were produced in a double-rod laser vaporization source. Both the adiabatic electron affinity and the vertical detachment energy, extracted from the PES spectra, exhibit even–odd alteration with the successive addition of Au atoms on C₆₀. So odd-*n* species have high relative stability. C₆₀Au_{*n*} takes a “dry” structure where Au atoms aggregate as a cluster (see Fig. 41a). In contrast, C₆₀Na_{*n*} adopts the direct binding of the Na atoms into stable trimers, each sodium atom lying above a pentagonal ring; thus C₆₀Na_{*n*} takes a “wet” structure where the Na atoms spread over the fullerene cage (see Fig. 41b). For C₆₀Na_{*n*} clusters, strong periodical oscillations are observed with a high cluster stability at smaller sizes (*n* = 3, 6, 9, and 12). When *n* > 12, the sodium atoms begin to exhibit a metallic layer behavior considering the much smoother adiabatic electron affinity (AEA) and vertical detachment energy (VDE) variations [963]. Additional PES experiments, performed with a 5.83 eV photodetachment energy, have shown that for *n* = 1 to 3 the charge transfer from the valence orbital of the Na atoms to the fullerene LUMO is approximately complete, whereas at *n* = 4 this charge transfer is only partial. This result not only points out the specificity of Na compared with the larger alkali elements but also suggests a full rearrangement of the cluster geometric configuration at the intermediate sizes.

In contrast to the previous work, another individual study based on the measurement of the polarizability and dipole of isolated C₆₀Na_{*n*} (*n* = 1–34) molecules in a static electric field showed the existence of a permanent electric dipole for every size with increasing *n* from 1 to 34; these results

cannot be explained by a metal shell around the C₆₀ with a regular distribution but are in agreement with a sodium cluster bound to the C₆₀ molecule (i.e., a sodium droplet on C₆₀) [964]. For clusters with more than one sodium atom (*n* > 2), it was suggested that there is a strong decrease in ionization potential as the sodium cluster size increases, and a full electron transfer from sodium atoms to the C₆₀ molecule is expected.

The electric dipole moment of isolated single-alkali-atom-C₆₀ molecules (C₆₀Li, C₆₀Na, C₆₀K, C₆₀Rb, and C₆₀Cs) has been measured by molecular beam deflection experiments [965]. It was shown that the dipole increases from 12.4 D for C₆₀Li to 21.5 D for C₆₀Cs. These results indicated a strong electron transfer from the alkali atom to the C₆₀ cage, which is partial for Na and almost complete for K and Cs. It was also found that the C₆₀K molecules have a giant polarizability at room temperature, equal to 2506 ± 250 Å³, but no permanent dipole by using the molecular beam deflection technique [966]. The addition of a potassium atom enhances by more than a factor of 20 the polarizability of a pure C₆₀ molecule. This giant polarizability is caused by the free skating of the K atom on the C₆₀ surface. C₆₀K behaves like a paraelectric system with an electric dipole of 17.7 ± 0.9 D.

5.4.2. Transition Metals

In the case of transition metals, the compound clusters C₆₀M_{*x*} (*x* = 0, . . . , 150; M = Ti, Zr, V, Y, Ta, Nb, Fe, Co, Ni, Rh) have been produced using modified laser vaporization of a transition metal target in a low-pressure inert gas condensation cell [917, 967, 968]. It was found that the metals form complete layers around the central fullerene molecule (i.e., forming transition metal coated fullerenes). Mass spectrometric studies on these free metal–fullerene clusters showed that upon heating with an intensive laser pulse, these metal–fullerene clusters transform into metal carbides (M = V, Ti) and bulklike metallo-carbohedrene clusters (M = Nb, Ta where *x* < 2) [967]. Photofragmentation mass spectra of metal–fullerene clusters C₆₀M_{*x*} (M = Fe, Co, Ni, Rh; *x* = 0, . . . , 30) reveal the existence of a reaction channel which yields clusters having the composition of metal in-cage doped heterofullerenes C_{59–2*n*}M (*n* = 0, . . . , 10) [917]. Additional tandem TOF experiments on mass selected C₅₉M indicated that the initial fragmentation step of this new kind of substitutionally doped fullerene is the loss of a neutral MC molecule [917]. Recently, evidence for the existence of C₆₀M_{*x*} (M = Sm, Pt) has also been observed in photofragmentation study by excimer laser ablation-TOF mass spectrometry [969].

5.5. C₆₀@Carbon Nanotubes

C₆₀ can be encapsulated into carbon nanotubes in the form of self-assembled one-dimensional chains and form a new type of self-assembled hybrid structure called “bucky-peapods” (see Fig. 42). The novel structure may give potential applications in data storage [970] and promising high-temperature superconductors [971].

Pulsed laser vaporization of graphite with certain metallic catalysts can produce both carbon nanotubes and C₆₀ molecules [972]. To obtain nanotube production, most of

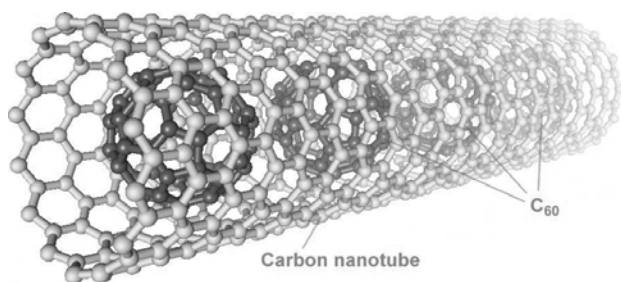


Figure 42. Schematic 3D view for C₆₀@carbon nanotubes.

the C₆₀ is removed by purification and annealing. Nevertheless, HRTEM observation showed that C₆₀ encapsulated in single-wall carbon nanotubes (SWCNTs), usually written as C₆₀@SWCNTs, can also be obtained via the same method. The encapsulated fullerenes can coalesce into longer capsules under the action of the electron beam [973] or under a high temperature treatment [974, 975].

The encapsulated C₆₀ molecules are positioned in a way that a preferred van der Waals separation (0.3 nm) was maintained between the cages and the nanotubes. The presence or absence of encapsulated cages was strongly correlated with the tubes' diameters, mostly observed to be 1.3–1.4 nm [976]. In a row of encapsulated C₆₀ molecules concentric with a tube axis, the center-to-center distance between two C₆₀ molecules was observed to be 1.0 nm [973], whereas for paired C₆₀ molecules, this distance was 0.9 nm [976]. In another study using electron diffraction, it was found that the intermolecular spacing of adjacent fullerenes in SWNTs is 0.97 nm, smaller than that of the three-dimensional bulk C₆₀ crystal but larger than that of polymerized C₆₀ crystal [977].

Yields of almost 100% C₆₀@SWCNTs have been obtained by heating SWCNTs in dry air for 50 hours at 400 °C [978]. Another individual work which yielded ~90% C₆₀@SWCNTs in abundance by a vapor phase method was confirmed by HRTEM observation indicating a simple lattice of 1.0 nm of the encapsulated one-dimensional C₆₀ molecules [979]. Both experimental results based on HRTEM observation [974] and theoretical results using molecular dynamical calculation [980] suggested an optimum temperature range from 350 to 450 °C and that the filling mechanism is most likely through the defect on the surface of SWCNTs but not through the ends of them.

EELS experiments study on C₆₀@SWCNTs showed that the electronic and optical properties of the encapsulated C₆₀ molecules are very similar to fcc C₆₀ with only small changes suggesting a weak van der Waals interaction between the SWCNTs and the C₆₀ molecules [981].

Refined measurements of electrical resistivity, thermopower, and thermal conductivity of highly C₆₀-filled SWCNTs and unfilled controls from 1.5 to 300 K have been performed recently [982]. It was shown that additional

conductive paths form via the filling of interior C₆₀ chains, which can effectively bridge defects on the tube walls, reduce the electrical resistivity, and also reduce the effects of charge carrier localization at low temperature [982]. It can also be indicated from the measurements that the filling of C₆₀ also increases the photon scattering, enhances the thermal conductivity in some sense, and effectively prevents other molecules (such as oxygen molecules) from doping into SWCNTs [982]. Another direct-current electric resistance measurement carried out by the four-probe method using the matlike films of C₆₀@SWCNTs showed somewhat different results in that, for the temperature range $5 < T < 300$ K, the resistances in logarithmic scale exhibit linear temperature dependence when the abscissa is represented by $T^{-1/4}$, suggesting an electron transport associated with three-dimensional VRH [978]. Hongo et al. measured the transport properties and their temperature dependences of C₆₀@SWCNTs bundles on a membrane structure consisting of a 50–100 nm thick silicon nitride on a Si wafer and Pt/Ti(30/30 nm) gap electrodes [983]. Their results showing high resistances of the peapod bundles, with two kinds of temperature dependence characters: one exhibits linear temperature dependence with respect to $T^{-1/4}$; the resistance increases as temperature decreases, which agrees with the VRH aforementioned mechanism. The other shows resistance saturation at low temperature, which suggested the existence of weak localization or disorder [984].

A variety of fullerenes were found to exist inside SWCNTs, including C₆₀ molecules and 0.7 nm diameter fullerene capsules of various lengths [976]. Many of the hybrid structures spontaneously jump during observation. Under the present experimental conditions, chains containing 2–5 C₆₀ molecules are most often seen to jump and each jump is typically 1–10 nm. This dynamic behavior could be driven by beam–specimen interactions.

5.6. (C₆₀)_n

In a (C₆₀)_n cluster, C₆₀ molecules interact with each other by weak van der Waals forces. Because the interaction has a very short range, investigations of C₆₀ clusters are focused on structure behavior. Experimental studies of fullerene clusters indicate they probably have icosahedral structure, similar to inert gas clusters [985]. Systematic optimization of the lowest energy structures of the (C₆₀)_n ($n \leq 57$) clusters has been carried out with a genetic algorithm and database conjugate-gradient method [986]. These structures show transitions at $n = 17$ from icosahedral to decahedral and at $n = 38$ from decahedral to fcc. The second energy difference curve indicates that $n = 13, 38, 55$ (C₆₀)_n clusters are especially stable. However, taking account of the thermal effect, the icosahedral structure instead of decahedral and close-packed ones is the most stable structure when the cluster is cooled from a high-temperature state by a molecular dynamics simulation.

Appendix A. Inserting Properties on horizontal axis and Fullerenes on Vertical axis.

Fullerenes	Non-IPR isomers [40]	IPR isomers [41]	Chiral isomers [41]	Point group ^a	Diameter or length of the 3 principal axes (Å)	Distinct carbon atoms	Electron affinity (eV)	Ionization energy (eV)	Heat of formation (kcal/mol)
C ₂₀	1	0	0	<i>I_h</i>		1	2.25 [48]		723 [53]
C ₃₆	15	0	0	<i>D_{6h}</i> , <i>D_{2d}</i> [42]	~5 [42]	3 (<i>D_{6h}</i>)	2.5 [49]		840.8 [54]
C ₆₀	1812 [19]	1	0	<i>I_h</i>	7.10 [23]	1 [41]	2.65 [50]	7.95 [38] 7.57 [52]	618.1 [55]
C ₇₀	1	1	0	<i>D_{5h}</i>	7.76 [43]	5 [41]	2.666 [36] 2.73 [50]	7.48 [38] 7.36 [52]	657.7 [55]
C ₇₂	1	1	0	<i>D_{6h}</i>		4 [41]	3.09 [50]	7.31 [52]	704.8 [55]
C ₇₄	1	1	0	<i>D_{3h}</i>			3.28 [50]	7.13 [52]	694.6 [55]
C ₇₆	2	2	1	<i>D₂</i> , <i>T_d</i>	8.75 × 7.50 × 6.54 [44]	19 (<i>D₂</i>) [41]	2.89 [50]	7.10 [38] 7.34 [52]	699.1 [55]
C ₇₈	5	5	1	<i>D₃</i> , <i>C_{3v}</i> , <i>C_{2v}</i> , <i>D_{3h}</i> , <i>D_{3d}</i>	8.20 [43]	21 (<i>C_{2v}</i>), 22 (<i>C_{3v}</i>) 8 (<i>D_{3h}</i>), 8 (<i>D_{3d}</i>) 13 (<i>D₃</i>) [41]	3.10 [50]	7.05 [38] 7.26 [52]	694.3 (<i>C_{2v}</i>) 697.8 (<i>D₃</i>) 697.8 (<i>D_{3d}</i>) 702.3 (<i>D_{3h}</i>) [41] 702.6 (<i>C_{2v}</i>) 727.2 (<i>D_{3h}</i>) [55] 724.6 (<i>D_{5d}</i>) 733.6 (<i>D₃</i>) [55] 720.1 (<i>C₂</i>)
C ₈₀	7	7	0	<i>D_{5d}</i> , <i>D₂</i> , <i>C_{2v}</i> , <i>C_{2v}</i> , <i>D₂</i> (<i>I_h</i>), <i>D₃</i> , <i>D_{5h}</i>			3.17 [50]	7.30 [52]	
C ₈₂	9	9	0	<i>C₂</i> , <i>C₃</i> , <i>C₂</i> , <i>C₃</i> , <i>C₂</i> , <i>C₃</i> , <i>C_{3v}</i> , <i>C_{3v}</i> , <i>C_{2v}</i>			3.14 [50]	7.25 [52]	
C ₈₄	24	24	10	<i>D₂</i> , <i>D_{2d}</i> (two major isomers)	8.70 [43] 7.79 × 8.45 × 8.16 (<i>D₂</i>), 7.90 × 8.30 × 8.50 (<i>D_{2d}</i>) [45, 46]		3.14 (first [50, 51]) 2.3 (second) [51]	7.15 [38] 7.17 [52]	750.8 (<i>C_{3v}</i>) [55] 716.4 (<i>D_{2d}</i>) 768.1 (<i>D₂</i>) [55]
C ₈₆	19	19	0				3.23 [50]	7.16 [52]	776.2 (<i>C_{2v}</i>) 735.4 (<i>C₃</i>) [55]
C ₈₈	35	35	0				3.20 [50]	7.09 [52]	745.2 (<i>C₂</i>) 804.6 (<i>D₂</i>) [55]
C ₉₀	46	46	0		9.542 (max.)(<i>C₁</i>), 6.918 (min.)(<i>C₁</i>) [47]		3.27 [50]	7.09 [52]	784.0 (<i>C_{2v}</i>) 763.7 (<i>D_{5h}</i>) [55]
C ₉₂	86	86	0				3.20 [50]	7.03 [52]	826.7 (<i>C_{2v}</i>) 757.5 (<i>D₂</i>) [55]
C ₉₄	134	134	0				3.21 [50]	6.96 [52]	813.0 (<i>C_{2v}</i>) 839.3 (<i>C₃</i>) [55]
C ₉₆	187	187	0				3.28 [50]	6.92 [52]	820.1 (<i>C_{2v}</i>) 878.3 (<i>D_{3h}</i>) [55]
C ₉₈	259	259	0				3.26 [50]	6.95 [52]	822.0 (<i>C₃</i>) 836.7 (<i>C₃</i>) [55]
C ₁₀₀	450	450	0				3.32 [50]	6.95 [52]	794.8 (<i>C₁</i>) [55] 793.9 (<i>C₁</i>) [55]
C ₁₀₂	616	616	0				3.38 [50]	6.89 [52]	806.1 (<i>D₃</i>) 852.2 (<i>C_{2v}</i>) [55]
C ₁₀₄							3.42 [50]	6.96 [52]	
C ₁₀₆							3.39 [50]	6.92 [52]	

^a Some higher fullerenes have too many isomers, structures, point groups therefore all are not listed here.

Appendix B. Properties of solid fullerenes from C₃₆ to C₈₄.

Property	C ₃₆	C ₆₀	C ₇₀	C ₇₆	C ₇₈	C ₈₄
Structure	hcp [42] fcc [250] (polymerized)	fcc	fcc/hcp	fcc/hcp [43]	fcc/hcp [43]	fcc/hcp [43, 251, 252]
Unit-cell parameter	6.68 Å [42]	(hcp) 10.02 Å [43] (fcc) 14.17 Å [236]	(hcp) 10.70 Å [43] (fcc) 15.01 Å [253]	(hcp) 11.00 Å [43] (fcc) 15.3 Å [254]	(hcp) 11.12 Å (fcc) 15.6 Å [43]	(hcp) 15.92 Å [255], 15.935 Å [250] (fcc) 11.34 [43]
Mass density (g/cm ³)	1.05 (cal.) [250]	1.72 [109]		1.64 (estim.) [254]		
Color of solution/solid	yellow-brown (pyridine)/black [42]	magenta/black brown [14]	port-wine red/ reddish brown [14]	bright yellow-green color both in solution and crystalline state [41]	C _{2v} -chestnut brown D _{3h} -golden-yellow [41]	greenish yellow (mix of two major isomers of D _{2d} ' and D ₂) [256] D _{2d} '-green D ₂ -yellow brown [257]
Resistivity [(Ω cm) ⁻¹]	>10 ⁻⁷ [42]	~10 ⁻⁸				
Transition temperature		260 K, 90 K [116]	280 K, 340 K [253, 258]	170–135 K, glass [259]		181 K, 235 K [260]
Bulk modulus (GPa)	70 (cal.) [250]	6.8 [113] ~12 [114] 18 [252]	25 [252]			20 GPa [252]
Bandgap (eV)	0.9 [261]	1.7 [262]	1.8 [262]	1.3 [262]	0.7 (C _{2v}) 0.85 (C _{2h}) [263] 47 ± 18 [264]	1.2 [262] 59 ± 6 [264]
Heat of sublimation (kJ mol ⁻¹)		38 [120] 39 ± 5 [264]	43 ± 5 [264]			
Sublimation standard enthalpy (kJ mol ⁻¹)		181 ± 2 (at 298 K) [39]	200 ± 6 (at 298 K) [265]	190 ± 7 (at 764 K), 202 ± 18 (at 803 K) [266] 206 ± 4 [267]		210 ± 6 (at 950 K) [268]
Dielectric constant		~4 [262]	~4.6 [269]	4–5 [262]		5–6 [270]
Static magnetic susceptibility (cgs ppm per mole of carbon)		-4.33 ± 0.33 [271] -4.38 ± 0.10 [259]	-7.85 ± 0.71 [271] -8.82 ± 0.11 [259]	-7.16 ± 0.10 [259]		

EQUATIONS

$$T = (h/2e^2)R^{-1} \quad (1)$$

$$\frac{\omega(n)^2}{\omega(0)^2} = 1 - \frac{n}{720} \quad (2)$$

$$\tau_i = \tau_{i0} \exp(E_{Ai}/k_B T) \quad (3)$$

$$P(T) = P_0 \exp(-\Delta H/kT) \quad (4)$$

$$\sigma = \sigma_0 \exp(-E_\alpha/kT) \quad (5)$$

$$\sigma_0 = \sigma_{00} \exp(-E_\alpha/kT_0) \quad (6)$$

$$\sigma(\omega, T) \sim \pi e^2 kT [N(E_F)]^2 \alpha^{-5} \omega [\ln(\nu_{ph})/\omega]^4 \quad (7)$$

$$\varepsilon(\omega) = \varepsilon_1(\omega) + i\varepsilon_2(\omega) \quad (8)$$

$$\varepsilon(\omega) = \varepsilon_1(\omega) + i\varepsilon_2(\omega) \quad (9)$$

$$N(\omega) = [n(\omega) + ik(\omega)] \quad (10)$$

$$\varepsilon(\omega) = [N(\omega)]^2 = [n(\omega) + ik(\omega)]^2 \quad (11)$$

$$C(\omega) = \varepsilon_1(\omega)\varepsilon_0 A/d \quad (12)$$

$$D(\omega) = \varepsilon_2(\omega)/\varepsilon_1(\omega) \quad (13)$$

$$C_p(T) = C_1 T + C_3 T^3 \quad (14)$$

$$k = C v_s \lambda / 3 \quad (15)$$

$$\rho v_T^2 = C_{44} \quad (16)$$

$$\rho v_T^2 = (C_{11} - C_{12} + C_{44})/3 \quad (17)$$

$$\rho v_L^2 = C_{11} \quad (18)$$

$$K = (C_{11} + 2C_{12})/3 \quad (19)$$

$$G = [(C_{11} - C_{12})/2C_{44}]^{2/5} \quad (20)$$

$$H_{c1}(T)/H_{c1}(0) = 1 - (T/T_c)^2 \quad (21)$$

$$J_c = A(M_+ - M_-)/R \quad (22)$$

$$J_c \sim J_c(0)[1 - (T/T_c)^2]^n \quad (23)$$

$$\rho = 0.07[\exp(1/T)^{1/4} - 1] \quad (24)$$

GLOSSARY

Buckminsterfullerene Or buckyball, C₆₀, hollow cage carbon molecule consisting 60 carbon atoms named for R. Buckminster Fuller because of the resemblance of its molecular structure to his geodesic domes. Buckminsterfullerene (C₆₀) was originally detected in soot in 1985; isolation was first reported in 1990.

C₁₂₀ Also called C₆₀ dimer. A dumb-bell-shaped all-carbon molecule consisting of two C₆₀ molecules connected by two single C–C bonds via cycloaddition.

Endohedral C₆₀ Novel C₆₀-based complex in which the fullerene molecule (C₆₀) is encapsulated by atom(s) or some small molecules in the inner hollow space of its carbon cage. These kinds of molecules are usually written as M@C₆₀; M is the endohedral species.

Exohedral C₆₀ Novel C₆₀-based complex in which the fullerene molecule (C₆₀) is adsorbed by exohedral atoms (usually metal atoms, including alkali metals, alkaline earth

metals, and transition metals), forming gas-phase stable compounds.

Fullerene superconductivity Some kinds of metal doped C₆₀ compounds have superconductivity. The M₃C₆₀ (M = alkali metal) system is the most widely studied of them. The highest T_c found in M₃C₆₀ is about 30 K (Rb₃C₆₀). It is widely believed that M₃C₆₀ are s-wave BCS-like superconductors, driven by the coupling to the intramolecular H_g phonons and probably with some strong-coupling effects.

Fullerene Any of a class of carbon molecules in which the carbon atoms are arranged into 12 pentagonal faces and 2 or more hexagonal faces to form a hollow sphere, cylinder, or similar figure. The smallest possible fullerene molecule may have as few as 32 atoms of carbon, and fullerene-like molecules as few as 20 carbon atoms. The most common and stable fullerene is buckminsterfullerene (C₆₀).

Fullerite Solid state form of fullerene; usually means solid state C₆₀. It usually forms black powders or black-brownish crystals.

Heterofullerene Fullerenes in which one or more carbon atoms in the carbon cage structure is substituted by a noncarbon atom (heteroatom), also called “dopeyballs” or heterohedral fullerene, including borafullerenes (C₅₉B, ...), azafullerenes (C₅₉N, C₅₈N₂, C₆₉N, ...), and heterofullerenes with heteroatoms other than N, B.

Metal doped C₆₀ compound Or metal doped fullerite. A kind of material formed by intercalating metal atom into the interstitial sites of C₆₀ host lattice. The metal usually used includes alkali metal, alkaline earth metal, and some lanthanide metals. Some kinds of these materials have superconductivity.

Metal/C₆₀ composite A kind of phase-separated solid of M/C₆₀. These metals (such as Al, Cu, Ag, etc.) usually have high cohesive energy and cannot be intercalated C₆₀ lattice. The most common composites are multilayer films and the nanodispersion films.

Polymerized C₆₀ Solid C₆₀ can be polymerized by irradiation of intense visible or ultraviolet light, or under high-temperature, high-pressure treatment. During polymerization, some of the internal C–C bonds of C₆₀ molecules are broken and connected via intermolecular cycloaddition.

REFERENCES

1. H. W. Kroto, J. R. Heath, S. C. O'Brien, R. F. Curl, and R. E. Smalley, *Nature* 318, 162 (1985).
2. W. Krätschmer, L. D. Lamb, K. Fostiropoulos, and D. R. Huffman, *Nature* 347, 354 (1990).
3. C. Joachim, J. K. Gimzewski, and A. Aviram, *Nature* 408, 541 (2000).
4. J. B. Howard, J. T. McKinnon, Y. Makarovskiy, A. L. Lafleur, and M. E. Johnson, *Nature* 352, 139 (1991).
5. D. S. Bethune, C. H. Kiang, and M. S. Devries, *Nature* 363, 605 (1993).
6. M. Bachman, J. Griesheimer, and K. H. Homann, *Chem. Phys. Lett.* 223, 506 (1994).
7. W. J. Grieco, A. L. Lafleur, K. C. Swallow, H. Richter, K. Taghizadeh, and J. B. Howard, in “27th Symposium (International) on Combustion,” p. 1669. The Combustion Institute, Pittsburgh, PA, 1998.

8. R. F. Curl, *Carbon* 30, 1149 (1992).
9. R. Taylor, G. J. Langley, H. W. Kroto, and D. R. M. Walton, *Nature* 366, 728 (1993).
10. M. C. Zumwalt and D. R. Huffman, in *Proc. Electrochem. Soc.* 94-24, 360 (1994).
11. C. Crowley, R. Taylor, H. W. Kroto, D. R. M. Walton, P.-C. Cheng, and L. T. Scott, *Synth. Met.* 77, 17 (1996).
12. J. Osterodt, A. Zettl, and F. Vögtle, *Tetrahedron* 52, 4949 (1996).
13. N. R. Conley and J. J. Lagowski, *Carbon* 40, 949 (2002).
14. R. Taylor, J. P. Hare, A. K. Abdul-Sada, and H. W. Kroto, *Chem. Commun.* 1423 (1990).
15. W. A. Scrivens, P. V. Bedworth, and J. M. Tour, *J. Am. Chem. Soc.* 114, 7917 (1992).
16. W. A. Scrivens and J. M. Tour, *J. Org. Chem.* 57, 6922 (1992).
17. A. D. Darwish, H. W. Kroto, R. Taylor, and D. R. M. Walton, *Chem. Commun.* 15 (1994).
18. L. T. Scott, M. M. Boorum, B. J. McMahon, S. Hagen, J. Mack, J. Blank, H. Wegner, and A. Meijere, *Science* 295, 1500 (2002).
19. D. E. Manolopolous, *Chem. Phys. Lett.* 192, 330 (1992).
20. J. G. Hou, J. Yang, H. Wang, Q. Li, C. Zeng, L. Yuan, B. Wang, D. M. Chen, and Q. Zhu, *Nature* 409, 304 (2001).
21. H. W. Kroto, *Nature* 329, 529 (1987).
22. S. T. G. Chmaltz, W. A. Seitz, D. J. Klein, and G. E. Hite, *J. Am. Chem. Soc.* 110, 1113 (1988).
23. R. D. Johnson, D. S. Bethune, and C. S. Yannoni, *Acc. Chem. Res.* 25, 169 (1992).
24. A. Hirsch, in "Fullerenes and Related Structures, Topics in Current Chemistry" (A. Hirsch, Ed.), Vol. 199, p. 13. Springer-Verlag, Berlin, 1999.
25. R. C. Haddon, *J. Am. Chem. Soc.* 108, 2837 (1986).
26. R. C. Haddon, *J. Am. Chem. Soc.* 109, 1676 (1987).
27. R. C. Haddon, *Acc. Chem. Res.* 21, 243 (1988).
28. R. C. Haddon, *J. Am. Chem. Soc.* 112, 3385 (1990).
29. R. C. Haddon, *Acc. Chem. Res.* 25, 127 (1992).
30. M. Schulman, R. L. Disch, M. A. Miller, and R. C. Peck, *Chem. Phys. Lett.* 141, 45 (1987).
31. M. Häser, J. Almhöf, and G. E. Scuseria, *Chem. Phys. Lett.* 181, 497 (1991).
32. C. S. Yannoni, P. P. Bernier, D. S. Bethune, G. Meijer, and J. R. Salem, *J. Am. Chem. Soc.* 113, 3190 (1991).
33. W. I. F. David, R. M. Ibberson, J. C. Matthewman, K. Prassides, T. J. S. Dennis, J. P. Hare, H. W. Kroto, R. Taylor, and D. R. M. Walton, *Nature* 353, 147 (1991).
34. S. Liu, Y. J. Lu, M. M. Kappes, and J. A. Ibers, *Nature* 254, 408 (1991).
35. S. Saito and A. Oshiyama, *Phys. Rev. B* 44, 11532 (1991).
36. L. S. Wang, J. Conceicao, C. Changming, and R. E. Smalley, *Chem. Phys. Lett.* 182, 5 (1991).
37. A. Tokmakoff, D. R. Haynes, and S. M. George, *Chem. Phys. Lett.* 186, 450 (1991).
38. H. Steger, J. Holzapfel, A. Hielscher, W. Kamke, and I. V. Hertel, *Chem. Phys. Lett.* 234, 455 (1995).
39. V. Piacente, G. Gigli, P. Scardala, A. Giustini, and D. Ferro, *J. Phys. Chem.* 99, 14052 (1995).
40. P. W. Fowler and D. E. Manolopoulos, "An Atlas of Fullerenes," p. 254. Clarendon Press, Oxford, 1995.
41. F. Diederich and R. L. Whetten, *Acc. Chem. Res.* 25, 119 (1992).
42. C. Piskoti, J. Yarger, and A. Zettl, *Nature* 393, 771 (1998).
43. D. L. Dorset and J. R. Fryer, *J. Phys. Chem. B* 105, 2356 (2001).
44. S. Saito, S. Sawada, N. Hamada, and A. Oshiyama, *Mater. Sci. Eng. B* 19, 105 (1993).
45. X. Q. Wang, C. Z. Wang, B. L. Zhang, and K. M. Ho, *Chem. Phys. Lett.* 207, 349 (1993).
46. S. Saito, S. Sawada, and N. Hamada, *Phys. Rev. B* 45, 13845 (1992).
47. S. Okada and S. Saito, *Chem. Phys. Lett.* 247, 69 (1995).
48. H. Prinzbach, A. Weller, P. Landenberger, F. Wahl, J. Worth, L. Scot, M. Gelmont, D. Olevano, and B. V. Issendorff, *Nature* 407, 60 (2000).
49. A. Ito, T. Monobe, T. Yoshii, and T. Tanaka, *Chem. Phys. Lett.* 328, 32 (2000).
50. O. V. Boltalina, E. V. Dashkova, and L. N. Sidorov, *Chem. Phys. Lett.* 256, 253 (1996).
51. O. V. Boltalina, D. B. Ponomarev, and L. N. Sidorov, *Mass Spectrom. Rev.* 16, 333 (1997).
52. O. V. Boltalina, I. N. Ioffe, L. N. Sidorov, G. Seifert, and K. Vietze, *J. Am. Chem. Soc.* 122, 9745 (2000).
53. A. Ito, T. Monobe, T. Yoshii, and K. Tanaka, *Chem. Phys. Lett.* 330, 281 (2000).
54. E. G. Gal'pern, A. R. Sabirov, I. V. Stankevich, A. L. Chistyakov, and L. A. Chernozatonskii, *JETP Lett.* 73, 556 (2001).
55. J. Cioslowski, N. Rao, and D. Moncrieff, *J. Am. Chem. Soc.* 122, 34 (2000).
56. C. Joachim, J. K. Gimzewski, R. R. Schlittler, and C. Chavy, *Phys. Rev. Lett.* 74, 2102 (1995).
57. C. Chavy, C. Joachim, and A. Altibelli, *Chem. Phys. Lett.* 214, 569 (1993).
58. N. L. Allinger, R. A. Kok, and M. R. Iman, *J. Comp. Chem.* 9, 591 (1988).
59. R. Landauer, *Z. Phys. B* 64, 217 (1987).
60. C. Joachim and J. K. Gimzewski, *Chem. Phys. Lett.* 265, 353 (1997).
61. D. Porath, Y. Levi, M. Tarabiah, and O. Millo, *Phys. Rev. B* 56, 9829 (1997).
62. C. Zeng, H. Wang, B. Wang, J. Yang, and J. G. Hou, *Appl. Phys. Lett.* 77, 3595 (2000).
63. H. Park, J. Park, A. K. L. Lim, E. H. Anderson, A. P. Alivisatos, and P. L. McEuen, *Nature* 407, 57 (2000).
64. J. I. Pascual, J. Gomez-Herrero, D. Sanchez-Portal, and H.-P. Rust, *J. Chem. Phys.* 117, 9531 (2002).
65. G. Binnig, N. Garcia, and H. Rohrer, *Phys. Rev. B* 32, 1336 (1985).
66. B. N. J. Persson and A. Baratoff, *Phys. Rev. Lett.* 59, 339 (1987).
67. B. C. Stipe, M. A. Rezaei, and W. Ho, *Science* 280, 1732 (1998).
68. J. R. Hahn, H. J. Lee, and W. Ho, *Phys. Rev. Lett.* 85, 1914 (2000).
69. J. I. Pascual, J. J. Jackiw, Z. Song, P. S. Weiss, H. Conrad, and H.-P. Rust, *Phys. Rev. Lett.* 86, 1050 (2001).
70. J. Gaudio, L. J. Lauhon, and W. Ho, *Phys. Rev. Lett.* 85, 1918 (2000).
71. L. J. Lauhon and W. Ho, *J. Phys. Chem. A* 104, 2463 (2000).
72. N. Lorente, M. Persson, L. J. Lauhon, and W. Ho, *Phys. Rev. Lett.* 86, 2593 (2001).
73. J. I. Pascual, J. Gomez-Herrero, C. Rogero, A. M. Baro, D. Sanchez-Portal, E. Artacho, P. Ordejon, and J. M. Soler, *Chem. Phys. Lett.* 321, 78 (2001).
74. H. Ajje, M. M. Alvarez, S. J. Anz, R. D. Beck, F. Diederich, K. Fostiropoulos, D. R. Huffman, W. Krätschmer, Y. Rubin, K. E. Schriver, D. Sensharma, and R. L. Whetten, *J. Phys. Chem.* 94, 8630 (1990).
75. R. D. Johnson, G. Meijer, J. R. Salem, and D. S. Bethune, *J. Am. Chem. Soc.* 113, 3619 (1991).
76. R. D. Johnson, D. S. Bethune, and C. S. Yannoni, *Acc. Chem. Res.* 25, 169 (1992).
77. J. W. Arbogast, A. P. Darmanyan, C. S. Foote, Y. Rubin, F. N. Diederich, M. M. Alvarez, and R. L. Whetten, *J. Phys. Chem.* 95, 11 (1991).
78. Y.-P. Sun, P. Wang, and N. B. Hamilton, *J. Am. Chem. Soc.* 115, 6378 (1993).
79. B. Ma and Y.-P. Sun, *J. Chem. Soc., Perkin Trans. 2*, 2157 (1996).
80. C. S. Foote, in "Physics and Chemistry of the Fullerenes" (K. Prassides, Ed.), p. 79. Kluwer Academic, Dordrecht, 1994.
81. S. K. Leach, in "Physics and Chemistry of the Fullerenes" (K. Prassides, Ed.), p. 117. Kluwer Academic, Dordrecht, 1994.
82. A. T. Werner, H. J. Byrne, and S. Roth, *Fullerene Sci. Technol.* 4, 757 (1996).

83. D. K. Palit and J. P. Mittal, *Fullerene Sci. Technol.* 3, 643 (1996).
84. J. S. Ahn, K. Suzuki, Y. Iwasa, and T. Mitani, *J. Lumin.* 72, 464 (1997).
85. D. Wang, J. Zuo, Q. Zhang, Y. Luo, Y. Ruan, and Z. Wang, *J. Appl. Phys.* 81, 1413 (1997).
86. M. Ichida, M. Sakai, T. Yajima, and A. Nakamura, *J. Lumin.* 72, 499 (1997).
87. S. M. Argentine, K. T. Kotz, T. Rudalevige, D. Zaziski, A. H. Francis, R. Zand, and J. A. Schleuter, *Res. Chem. Intermed.* 23, 601 (1997).
88. A. Fedorov, M. N. Berberan-Snatos, J.-P. Lefevre, and B. Valeur, *Chem. Phys. Lett.* 267, 467 (1997).
89. Y.-P. Sun, in "Molecular and Supramolecular Photochemistry" (V. Ramamurthy and K. S. Shanze, Eds.), Vol. 1, p. 325. Dekker, New York, 1997.
90. C. S. Foote, in "Topics in Current Chemistry: Electron Transfer I" (J. Mattay, Ed.), p. 347, Springer-Verlag, Berlin, 1994.
91. S. Nath, H. Pal, D. K. Palit, A. V. Sapre, and J. P. Mittal, *J. Phys. Chem. B* 102, 10158 (1998).
92. F. Negri and G. Orlandi, *J. Chem. Phys.* 108, 9675 (1998).
93. A. Sassara, G. Zerza, F. Negri, and G. Orlandi, *J. Chem. Phys.* 107, 8731 (1997).
94. A. Sassara, G. Zerza, and M. Chergui, *J. Phys. Chem. A* 102, 3072 (1998).
95. J. S. Ahn, K. Suzuki, Y. Iwasa, N. Otsuka, and T. Mitani, *J. Lumin.* 76, 201 (1998).
96. M. Terazima, N. Hirota, H. Shinohara, and Y. Saito, *J. Phys. Chem.* 95, 9080 (1991).
97. L. Biczok, H. Linschitz, and R. I. Walter, *Chem. Phys. Lett.* 195, 339 (1992).
98. R. V. Bensasson, T. Hill, C. Lambert, E. J. Land, S. Leach, and T. G. Truscott, *Chem. Phys. Lett.* 201, 326 (1993).
99. C. Luo, M. Fujitsuka, A. Watanabe, O. Ito, L. Gan, Y. Huang, and C.-H. Huang, *J. Chem. Soc. Faraday Trans.* 94, 527 (1998).
100. M. R. Wasielewski, M. P. O'Neil, K. R. Lykke, M. J. Pelin, and D. M. Gruen, *J. Am. Chem. Soc.* 113, 2774 (1991).
101. T. W. Ebbesen, K. Tanigaki, and S. Kuroshima, *Chem. Phys. Lett.* 181, 501 (1991).
102. Y. Kajii, T. Nakagawa, S. Suzuki, Y. Achiba, K. Obi, and K. Shibuya, *Chem. Phys. Lett.* 181, 100 (1991).
103. G. L. Closs, P. Gautam, D. Zhang, P. J. Krusic, S. A. Hill, and E. Wasserman, *J. Phys. Chem.* 96, 5228 (1992).
104. D. K. Palit, A. V. Sapre, J. P. Mittal, and C. N. Rao, *Chem. Phys. Lett.* 195, 1 (1992).
105. N. M. Dimitrijevic and P. V. Kamat, *J. Phys. Chem.* 96, 4811 (1992).
106. R. B. Weisman, in "Optical and Electronic Properties of Fullerenes and Fullerene-Based Materials" (J. Shinar, Z. V. Vardeny, and Z. H. Kafafi, Eds.), p. 83. Dekker, New York, 2000.
107. L. Tutt and A. Kost, *Nature* 356, 225 (1992).
108. D. Mclean, R. Sutherland, M. Brant, D. Brandelik, P. Fleitz, and T. Pottenger, *Opt. Lett.* 18, 858 (1993).
109. L. Smilowitz, D. McBranch, V. Klimov, J. Robinson, A. Koskelo, M. Grigorova, B. Mattes, H. Wang, and F. Widl, *Opt. Lett.* 21, 922 (1996).
110. J. E. Riggs and Y.-P. Sun, *J. Chem. Phys.* 112, 4221 (2000).
111. Y.-P. Sun, G. E. Lawson, J. E. Riggs, B. Ma, N. Wang, and D. K. Moton, *J. Phys. Chem. A* 102, 5520 (1998).
112. L. Tutt and T. Boggess, *Progr. Quant. Electron.* 17, 299 (1993).
113. J. Perry, K. Mansour, S. Marder, K. Perry, J. D. Alvarez, and I. Choong, *Opt. Lett.* 19, 625 (1994).
114. J. Shirk, R. Pong, F. Bartoli, and A. Snow, *Appl. Phys. Lett.* 63, 1880 (1993).
115. T. Xia, D. J. Hagan, A. Dogariu, A. A. Said, and E. W. V. Stryland, *Appl. Opt.* 36, 4110 (1997).
116. J. W. Perry, in "Nonlinear Optics of Organic Molecules and Polymers" (H. S. Nalwa and S. Miyata, Eds.), p. 813. CRC Press, New York, 1997.
117. M. Prato and M. Maggini, *Acc. Chem. Res.* 31, 519 (1998).
118. N. Martin, L. Sanchez, B. Illescas, and I. Perez, *Chem. Rev.* 98, 2527 (1998).
119. Y.-P. Sun and J. E. Riggs, *Int. Rev. Phys. Chem.* 18, 43 (1999).
120. M. Lee, O.-K. Song, J.-C. Seo, and D. Kim, *Chem. Phys. Lett.* 196, 325 (1992).
121. J. E. Riggs and Y.-P. Sun, *J. Phys. Chem. A* 103, 485 (1999).
122. S. Mishra, H. Rawat, M. P. Joshi, and S. Mehendale, *J. Phys. B* 27, L157 (1994).
123. B. Justus, Z. Kafafi, and A. Huston, *Opt. Lett.* 18, 19, 1603 (1993).
124. D. Gust, T. A. Moore, and A. L. Moore, *Res. Chem. Intermed.* 23, 621 (1997).
125. H. Imahori and Y. Sakata, *Adv. Mater.* 9, 537 (1997).
126. H. Imahori, K. Hagiwara, T. Akiyama, M. Aoki, S. Taniguchi, T. Okada, M. Shirakawa, and Y. Sakata, *Chem. Phys. Lett.* 263, 545 (1996).
127. Q. Xie, E. Perez-Cordero, and L. Echegoyen, *J. Am. Chem. Soc.* 114, 3978 (1992).
128. G. E. Lawson, A. Kitaygorodskiy, B. Ma, C. E. Bunker, and Y.-P. Sun, *Chem. Commun.* 2225 (1995).
129. K. F. Liou and C. H. Cheng, *Chem. Commun.* 15 (1996).
130. A. Hirsch, "The Chemistry of the Fullerenes," Thieme, Stuttgart, 1994.
131. F. Diederich and C. Thilgen, *Science* 271, 31 (1996).
132. M. Prato, *J. Mater. Chem.* 7, 1097 (1997).
133. M. Prato and M. Maggini, *Acc. Chem. Res.* 31, 519 (1998).
134. E. K. Miller, K. Lee, K. Hasharoni, J. C. Hummelen, F. Wudl, and A. J. Heeger, *J. Chem. Phys.* 108, 1390 (1998).
135. K. Yoshino, K. Tada, A. Fujii, K. Hosoda, S. Kawabe, H. Kajii, M. Hirohata, R. Hidayat, H. Araki, A. A. Zakhidov, R. Sugimoto, M. Iyoda, M. Ishikawa, and T. Masuda, *Fullerene Sci. Technol.* 5, 1359 (1997).
136. K. Y. T. Akashi, S. Morita, M. Yoshida, M. Hamaguchi, K. Tada, A. Fujii, T. Kawai, S. Uto, M. Ozaki, M. Onoda, and A. A. Zakhidov, *Synth. Met.* 70, 1317 (1995).
137. R. E. Haufler, L.-S. Wang, L. P. F. Chibante, C.-M. Jin, and S. K. Kim, *Chem. Phys. Lett.* 179, 449 (1991).
138. D. Kim, M. Lee, Y. D. Suh, and S. K. Kim, *J. Am. Chem. Soc.* 114, 4429 (1992).
139. R. S. Ruoff, R. Malhotra, and D. L. Huestis, *Nature* 361, 140 (1993).
140. N. Sivaraman, R. Dhamodaran, I. Kaliappan, T. G. Srinivasan, P. R. V. Rao, and C. K. Mathews, *J. Org. Chem.* 57, 6077 (1992).
141. N. Sivaraman, R. Dhamodaran, I. Kaliappan, T. G. Srinivasan, P. R. V. Rao, and C. K. Mathews, *Fullerene Sci. Technol.* 2, 233 (1994).
142. N. Sivaraman, R. Dhamodaran, I. Kaliappan, T. G. Srinivasan, P. R. V. Rao, and C. K. Mathews, in "Recent Advances in the Chemistry and Physics of Fullerenes and Related Materials" (K. M. Kadish and R. S. Ruoff, Eds.), 1994, Rep. 1211.
143. R. S. Ruoff, D. S. Tse, R. Malhotra, and D. C. Lorents, *J. Phys. Chem.* 97, 3379 (1993).
144. W. A. Scrivens and J. M. Tour, *J. Chem. Soc. Chem. Commun.* 1207 (1993).
145. W. A. Scrivens, A. M. Cassell, K. E. Kinsey, and J. M. Tour, in "Recent Advances in the Chemistry and Physics of Fullerenes and Related Materials" (K. M. Kadish and R. S. Ruoff, Eds.), 1994.
146. M. T. Beck, G. Mandi, and S. Keki, *Fullerene Sci. Technol.* 2, 1510 (1995).
147. M. T. Beck and G. Mandi, *Fullerene Sci. Technol.* 3, 32 (1996).
148. M. T. Beck and G. Mandi, *Fullerene Sci. Technol.* 5, 291 (1997).
149. M. T. Beck, G. Mandi, and S. Keki, in "Fullerenes" (R. S. Ruoff and K. S. Kadish, Eds.), Vol. 2. The Electrochem. Soc., Pennington, NJ, 1995.
150. M. T. Beck and G. Mandi, in "Fullerenes" (R. S. Ruoff and K. S. Kadish, Eds.), Vol. 3. The Electrochem. Soc., Pennington, NJ, 1996.

151. M. T. Beck and G. Mandi, *Fullerene Sci. Technol.* 5, 291 (1997).
152. D. Heyman, *Fullerene Sci. Technol.* 4, 509 (1996).
153. X. H. Zhou, J. B. Liu, Z. X. Jin, Z. N. Gu, Y. Q. Wu, and Y. L. Sun, *Fullerene Sci. Technol.* 5, 285 (1997).
154. Y. Marcus, *J. Phys. Chem. B* 101, 8617 (1997).
155. Y. Marcus, A. L. Smith, M. V. Korobov, A. L. Mirakyan, N. Avramenko, and E. B. Stukalin, *J. Phys. Chem. B* 105, 2499 (2001).
156. N. Sivaraman, T. G. Srinivasan, P. R. V. Rao, and R. Natarajan, *J. Chem. Inf. Comput. Sci.* 41, 1067 (2001).
157. I. Z. Kiss, G. Mandi, and M. T. Beck, *J. Phys. Chem. A* 104, 8081 (2000).
158. C. Reichardt, "Solvents and Solvent Effects in Organic Chemistry," 2nd ed., p. 534. VCH, Weinheim, 1998.
159. V. N. Bezmelnitsyn, A. V. Eletsii, and E. V. Stepanov, in "Progress in Fullerene Research" (H. Kuzmany et al., Eds.), p. 45. World Scientific, Singapore, 1994.
160. V. N. Bezmelnitsyn, A. V. Eletsii, and E. V. Stepanov, *J. Phys. Chem.* 98, 6665 (1994).
161. G. V. Andrievsky, M. V. Kosevich, O. M. Vovk, V. S. Shelkovsky, and L. A. Vashenko, *J. Chem. Soc., Chem. Commun.* 1281 (1995).
162. G. V. Andrievsky, M. V. Kosevich, O. M. Vovk, V. S. Shelkovsky, and L. A. Vashchenko, in "Chemistry and Physics of Fullerenes and Related Materials" (R. S. Ruoff and K. M. Kadish, Eds.), *Electrochem. Soc. Proc. Series*, PV 95-10, p. 1591. Electrochem. Soc., Pennington, NJ, 1995.
163. G. V. Andrievsky, V. K. Klochkov, E. L. Karyakina, and N. O. Mchedlov-Petrosyan, *Chem. Phys. Lett.* 300, 392 (1999).
164. G. V. Andrievsky, V. K. Klochkov, A. Bordyuh, and G. I. Dovbeshko, *Chem. Phys. Lett.* 364, 8 (2002).
165. X. Wei, M. Wu, L. Qi, and Z. Xu, *J. Chem. Soc., Perkin Trans. 2*, 1389 (1997).
166. A. D. Roslyakov, G. V. Andrievsky, A. Yu. Petrenko, and L. T. Malaya, *Zh. Akad. Med. Nauk. Ukrainy* 5, 338 (1999) [in Russian].
167. N. O. Mchedlov-Petrosyan, V. K. Klochkov, , and G. V. Andrievsky, *J. Chem. Soc., Faraday Trans.* 93, 4343 (1997).
168. B. V. Derjaguin, "The Theory of Stability of Colloids and Thin Films." Nauka, Moscow, 1986 [in Russian].
169. T. Steiner, *Biophys. Chem.* 95, 195 (2002).
170. T. R. Ohno, Y. Chen, S. E. Harvey, G. H. Kroll, J. H. Weaver, R. E. Haufler, and R. E. Smalley, *Phys. Rev. B* 44, 13747 (1991).
171. S. Modesti, S. Cerasari, and P. Rudolf, *Phys. Rev. Lett.* 71, 2469 (1993).
172. J. K. Gimzewski, S. Modesti, and R. R. Schlittler, *Phys. Rev. Lett.* 72, 1036 (1994).
173. G. K. Wertheim and D. N. E. Buchanan, *Phys. Rev. B* 50, 11070 (1994).
174. B. W. Hoogenboom, R. Hesper, L. H. Tjeng, and G. A. Sawatzky, *Phys. Rev. B* 57, 11939 (1998).
175. L. H. Tjeng, R. Hesper, A. C. L. Heessels, A. Heeres, H. T. Jonkman, and G. A. Sawatzky, *Solid State Commun.* 103, 31 (1997).
176. R. Hesper, L. H. Tjeng, and G. A. Sawatzky, *Europhys. Lett.* 40, 177 (1997).
177. S. J. Chase, W. S. Basca, M. G. Mitch, L. J. Pilione, and J. S. Lannin, *Phys. Rev. B* 46, 7873 (1992).
178. P. W. Murray, M. Ø. Pedersen, E. Laegsgaard, I. Stensgaard, and F. Besenbacher, *Phys. Rev. B* 55, 9360 (1997).
179. K.-D. Tsuei, J.-Y. Yuh, C.-T. Zeng, R.-Y. Chu, S.-C. Chung, and K.-L. Tsang, *Phys. Rev. B* 56, 15412 (1997).
180. M. R. C. Hunt, S. Modesti, P. Rudolf, and R. E. Palmer, *Phys. Rev. B* 51, 10039 (1995).
181. T. Kobayashi, C. Tindall, O. Takaoka, Y. Hasegawa, and T. Sakurai, *J. Korean Phys. Soc.* 31, S5 (1997).
182. C. T. Chen, L. H. Tjeng, P. Rudolf, G. Meigs, J. E. Rowe, J. Chen, J. P. McCauley, Jr., A. B. Smith III, A. R. McGhie, W. J. Romanow, and E. W. Plummer, *Nature* 352, 603 (1991).
183. C.-T. Zeng, W.-S. Lo, J.-Y. Yuh, R.-Y. Chu, and K.-D. Tsuei, *Phys. Rev. B* 61, 2263 (2000).
184. A. J. Maxwell, P. A. Brühwiler, S. Andersson, D. Arvanitis, B. Hernnäs, O. Karis, D. C. Mancini, N. Mårtensson, S. M. Gray, M. K.-J. Johansson, and L. S. O. Johansson, *Phys. Rev. B* 52, R5546 (1995).
185. A. J. Maxwell, P. A. Bruhwiler, D. Arvantis, J. Hasselstrom, M. K.-J. Johansson, and N. Martensson, *Phys. Rev. B* 57, 7312 (1998).
186. C. Cepek, A. Goldoni, and S. Modesti, *Phys. Rev. B* 53, 7466 (1996).
187. E. I. Altman and R. J. Colton, *Surf. Sci.* 279, 49 (1992).
188. E. I. Altman and R. J. Colton, *Surf. Sci.* 295, 13 (1993).
189. T. Hashizume and T. Sakurai, *J. Vac. Sci. Technol. B* 12, 1992 (1994).
190. T. David, J. K. Gimzewski, D. Purdie, B. Reihl, and R. R. Schlittler, *Phys. Rev. B* 50, 5810 (1994).
191. E. I. Altman and R. J. Colton, *Phys. Rev. B* 48, 18244 (1993).
192. K. Motai, T. Hashizume, H. Shinohara, Y. Saito, H. W. Pickering, Y. Nishina, and T. Sakurai, *Jpn. J. Appl. Phys.* 32, L450 (1993).
193. Y. Kuk, D. K. Kim, Y. D. Suh, K. H. Park, H. P. Noh, S. J. Oh, and S. K. Kim, *Phys. Rev. Lett.* 70, 1948 (1993).
194. M. Pedio, R. Felici, X. Torrelles, P. Rudolf, M. Capozzi, J. Rius, and S. Ferrer, *Phys. Rev. Lett.* 85, 1040 (2000).
195. T. Hashizume, K. Motai, X. D. Wang, H. Shinohara, Y. Maruyama, K. Ohno, Y. Nishina, H. W. Pickering, Y. Kuk, and T. Sakurai, *Phys. Rev. Lett.* 71, 2959 (1993).
196. R. Gaisch, R. Berndt, J. K. Gimzewski, B. Reihl, R. R. Schlittler, W. D. Schneider, and M. Tschudy, *J. Vac. Sci. Technol. B* 12, 2153 (1994).
197. R. Fasel, P. Aebi, R. G. Agostino, D. Naumovic, J. Osterwalder, A. Santaniello, and L. Schlapbach, *Phys. Rev. Lett.* 76, 4733 (1996).
198. R. Fasel, R. G. Agostino, P. Aebi, and L. Schlapbach, *Phys. Rev. B* 60, 4517 (1999).
199. C. Cepek, R. Fasel, M. Sancrotti, T. Greber, and J. Osterwalder, *Phys. Rev. B* 63, 125406 (2001).
200. J. Weckesser, C. Cepek, R. Fasel, J. V. Barth, F. Baumberger, T. Greber, and K. Kern, *J. Chem. Phys.* 115, 9001 (2001).
201. J. K. Gimzewski, S. Modesti, T. David, and R. R. Schlittler, *J. Vac. Sci. Technol. B* 12, 1942 (1994).
202. S. Modesti, R. R. Schlittler, and J. K. Gimzewski, *Surf. Sci.* 331–333, 1129 (1995).
203. V. Saltas and C. A. Papageorgopoulos, *Surf. Sci.* 488, 23 (2001).
204. M. Pedio, K. Hevesi, N. Zema, M. Capozzi, P. Perfetti, R. Gouttebaron, J.-J. Pireaux, R. Caudano, and P. Rudolf, *Surf. Sci.* 437, 249 (1999).
205. X. D. Wang, T. Hashizume, H. Shinohara, Y. Saito, Y. Nishina, and T. Sakurai, *Japan. J. Appl. Phys.* 31, L983 (1992).
206. D. Chen and D. Sarid, *Phys. Rev. B* 49, 7612 (1994).
207. S. Suto, K. Sakamoto, T. Wakita, C. W. Hu, and A. Kasuya, *Phys. Rev. B* 56, 7439 (1997).
208. P. Moriarty, M. D. Upward, A. W. Dunn, Y.-R. Ma, P. H. Beton, and D. Teehan, *Phys. Rev. B* 57, 362 (1998).
209. K. Sakamoto, M. Harada, D. Kondo, A. Kimura, A. Kakizaki, and S. Suto, *Phys. Rev. B* 58, 13951 (1998).
210. C. Cepek, P. Schiavuta, M. Sancrotti, and M. Pedio, *Phys. Rev. B* 60, 2068 (1999).
211. Y. Z. Li, M. Chander, J. C. Partin, J. H. Weaver, L. P. F. Chibante, and R. E. Smalley, *Phys. Rev. B* 45, 13837 (1992).
212. J. G. Hou, J. Yang, H. Wang, Q. Li, C. Zeng, H. Lin, B. Wang, D. M. Chen, and Q. Zhu, *Phys. Rev. Lett.* 83, 3001 (1999).
213. H. Wang, C. Zeng, Q. Li, B. Wang, J. Yang, J. G. Hou, and Q. Zhu, *Surf. Sci.* 442, L1024 (1999).
214. D. Chen, J. Chen, and D. Sarid, *Phys. Rev. B* 50, 10905 (1994).
215. H. Xu, D. M. Chen, and W. N. Creager, *Phys. Rev. Lett.* 70, 1850 (1993).
216. Y. Fujikawa, K. Saiki, and A. Koma, *Phys. Rev. B* 56, 12124 (1997).
217. D. Chen and D. Sarid, *Surf. Sci.* 329, 206 (1995).
218. D. Klyachko and D. M. Chen, *Phys. Rev. Lett.* 75, 3693 (1995).

219. S. Suto, K. Sakamoto, D. Kondo, T. Wakita, A. Kimura, A. Kakizaki, C.-W. Hu, and A. Kasuya, *Surf. Sci.* 438, 242 (1999).
220. D. Chen, M. J. Gallagher, and D. Sarid, *J. Vac. Sci. Technol. B* 12, 1947 (1994).
221. X. Yao, T. G. Ruskell, R. K. Workman, D. Sarid, and D. Chen, *Surf. Sci.* 366, L743 (1996).
222. X. Yao, R. K. Workman, C. A. Peterson, D. Chen, and D. Sarid, *Appl. Phys. A* 66, S107 (1998).
223. A. V. Hamza, M. Balooch, and M. Moalem, *Surf. Sci.* 317, L1129 (1994).
224. D. Chen, R. Workman, and D. Sarid, *Surf. Sci.* 344, 23 (1995).
225. D. Klyachko and D. Chen, *J. Vac. Sci. Technol. B* 14, 974 (1996).
226. D. V. Klyachko, J.-M. Lopez-Castillo, J.-P. Jay-Gerin, and D. M. Chen, *Phys. Rev. B* 60, 9026 (1998).
227. R. D. Aburano, H. Hong, K.-S. Chung, M. C. Nelson, P. Zschack, H. Chen, and T.-C. Chiang, *Phys. Rev. B* 57, 6636 (1999).
228. H. Xu, D. M. Chen, and W. N. Creager, *Phys. Rev. B* 50, 8454 (1994).
229. A. Goldoni, C. Cepek, M. De Seta, J. Avila, M. C. Asensio, and M. Sancrotti, *Phys. Rev. B* 61, 10411 (2000).
230. Y. Z. Li, J. C. Patrin, M. Chander, J. H. Weaver, L. P. F. Chibante, and R. E. Smalley, *Science* 252, 547 (1991).
231. Y. Z. Li, J. C. Patrin, M. Chander, J. H. Weaver, L. P. F. Chibante, and R. E. Smalley, *Science* 253, 429 (1991).
232. Q. Xue, T. Ogino, Y. Hasegawa, H. Shinohara, and T. Sakurai, *Phys. Rev. B* 53, 1985 (1996).
233. T. Sakurai, Qikun Xue, T. Hashizume, and Y. Hasegawa, *J. Vac. Sci. Technol. B* 15, 1628 (1997).
234. A. R. Kortan, N. Kopylov, S. H. Glarum, E. M. Gyorgy, A. P. Ramirez, R. M. Fleming, F. A. Thiel, and R. C. Haddon, *Nature* 355, 529 (1992).
235. P. A. Heiney, J. E. Fischer, A. R. McGhie, W. J. Romanow, A. M. Denenstien, J. P. McCauley, Jr., A. B. Smith, and D. E. Cox, *Phys. Rev. Lett.* 66, 2911 (1991).
236. P. W. Stephens, L. Mihaly, P. L. Lee, R. L. Whetten, S.-M. Huang, R. B. Kaner, F. Diederich, and K. Holczer, *Nature* 351, 632 (1991).
237. L. Forró and L. Mihaly, *Rep. Progr. Phys.* 64, 649 (2001).
238. P. A. Heiney, G. B. M. Vaughan, J. E. Fischer, N. Coustel, D. E. Cox, J. R. D. Copley, D. A. Neumann, W. A. Kamitakahara, K. M. Creegan, D. M. Cox, J. P. McCauley, Jr., and A. B. Smith III, *Phys. Rev. B* 45, 4544 (1992).
239. J. E. Fischer, P. A. Heiney, A. R. McGhie, W. J. Romanow, A. M. Denenstien, J. P. McCauley, Jr., and A. B. Smith III, *Science* 252, 1288 (1991).
240. A. Lundin and B. Sundqvist, *Phys. Rev. B* 53, 8329 (1996).
241. J. E. Schirber, G. H. Kwei, D. Jorgensen, R. L. Hitterman, and B. Morosin, *Phys. Rev. B* 51, 12014 (1995).
242. X. D. Shi, A. R. Kortan, J. M. Williams, A. M. Kini, B. M. Saval, and P. M. Chaikin, *Phys. Rev. Lett.* 68, 827 (1992).
243. W. I. F. David, R. M. Ibberson, T. J. S. Dennis, J. P. Hare, and K. Prassides, *Europhys. Lett.* 18, 219 (1992).
244. G. A. Samara, J. E. Schirber, B. Morosin, L. V. Hansen, D. Loy, and A. P. Sylwester, *Phys. Rev. Lett.* 67, 3136 (1991).
245. G. A. Samara, L. V. Hansen, R. A. Assink, B. Morosin, J. E. Schirber, and D. Loy, *Phys. Rev. B* 47, 4756 (1993).
246. C. Pan, M. P. Sampson, Y. Chai, R. H. Hauge, and J. L. Margrave, *J. Phys. Chem.* 95, 2944 (1991).
247. J. Abrefah, D. R. Olander, M. Balooch, and W. J. Siekhaus, *Appl. Phys. Lett.* 60, 1313 (1992).
248. H. Kataura, N. Irie, N. Kobayashi, Y. Achiba, K. Kikuchi, T. Hanyu, and S. Yamaguchi, *Jpn. J. Appl. Phys.* 32, L1667 (1993).
249. M. B. Jost, N. Troullier, D. M. Poirier, J. L. Martins, J. H. Weaver, L. P. F. Chibante, and R. E. Smalley, *Phys. Rev. B* 44, 1966 (1991).
250. V. Rosato, M. Celino, G. Bvenedek, and S. Gaito, *Phys. Rev. B* 60, 16928 (1999).
251. S. Margadonna, C. M. Brown, T. J. S. Dennis, A. Lappas, P. Pattison, K. Prassides, and H. Shinohara, *Chem. Mater.* 10, 1742 (1998).
252. I. Margiolaki, S. Margadonna, K. Prassides, S. Assimopoulos, K. P. Meletov, G. A. Kourouklis, T. J. S. Dennis, and H. Shinohara, *Physica B* 318, 372 (2002).
253. G. B. M. Vaughan, P. A. Heiney, J. E. Fischer, D. E. Luzzi, D. A. Ricketts-Foot, A. R. McGhie, Y. W. Hui, A. L. Smith, D. E. Cox, W. J. Romanow, B. H. Allen, N. Coustel, J. P. McCauley, and A. B. Smith III, *Science* 254, 1350 (1991).
254. Y. Saito, N. Fujimoto, K. Kikuchi, and Y. Achiba, *Phys. Rev. B* 49, 14794 (1994).
255. S. Margadonna, C. M. Brown, T. J. S. Dennis, A. Lappas, P. Pattison, K. Prassides, and H. Shinohara, *Chem. Mater.* 10, 1742 (1998).
256. F. Diederich, R. Ettl, Y. Rubin, R. L. Whetten, R. Beck, M. Alvarez, S. Anz, D. Sensharma, F. Wudl, K. C. Khemani, and A. Koch, *Science* 252, 548 (1992).
257. T. John, S. Dennis, T. Kai, T. Tomiyama, and H. Shinohara, *Chem. Commun.* 619 (1998).
258. Y. Maniwa, A. Ohi, K. Mizoguchi, K. Kume, K. Kikuchi, K. Saito, I. Ikemoto, S. Suzuki, and Y. Achiba, *J. Phys. Soc. Jpn.* 62, 1131 (1993).
259. Y. Maniwa, K. Kume, K. Kikuchi, K. Saito, I. Ikemoto, S. Suzuki, and Y. Achiba, *Phys. Rev. B* 53, 14196 (1996).
260. R. Almairac, D. Tranqui, J. P. Lauriat, J. Lapasset, and J. Moret, *Solid State Commun.* 106, 437 (1998).
261. P. G. Collins, J. C. Grossman, M. Cote, M. Ishigami, C. Piskoti, S. G. Louie, M. L. Cohen, and A. Zettl, *Phys. Rev. Lett.* 82, 165 (1998).
262. R. Kuzuo, M. Terauchi, and M. Tanaka, *Phys. Rev. B* 51, 11018 (1995).
263. M. Knapfer, O. Knauff, M. S. Golden, J. Fink, M. Burk, D. Fuchs, S. Schuppler, R. H. Michel, and M. M. Kappes, *Chem. Phys. Lett.* 258, 513 (1996).
264. M. Moalem, M. Balooch, A. V. Hamza, and R. S. Ruoff, *J. Phys. Chem.* 99, 16736 (1995).
265. V. Piacente, G. Gigli, P. Scardala, A. Giustini, and G. Bardi, *J. Phys. Chem.* 100, 9815 (1996).
266. O. V. Boltalina, V. Yu. Markov, A. Ya. Borschevskii, L. N. Sidorov, V. N. Bezmelnitsin, A. V. Eletsii, and R. Taylor, *Rapid Commun. Mass Spectrom.* 12, 1028 (1998).
267. B. Brunetti, G. Gigli, E. Giglio, V. Piacente, and P. Scardala, *J. Phys. Chem. B* 101, 10715 (1997).
268. V. Piacente, C. Palchetti, G. Gigli, and P. Scardala, *J. Phys. Chem. A* 101, 24, 4303 (1997).
269. H. Kataura, H. Y. Endo, T. Hanyu, S. Yamaguchi, Y. Achiba, and K. Kikuchi, *J. Phys. Chem. Solid* 58, 1913 (1997).
270. J. F. Armbruster, M. Roth, H. A. Romberg, M. Sing, M. Schmidt, P. Schweiss, P. Adelman, M. S. Golden, J. Fink, R. H. Michel, J. Rockenberger, F. Hennrich, and M. M. Kappes, *Phys. Rev. B* 50, 4933 (1994).
271. R. C. Haddon, L. F. Schneemeyer, J. V. Waszczak, S. H. Glarum, R. Tycko, G. Dabbagh, A. R. Kortan, A. J. Muller, A. M. Muijsce, M. J. Rosseinsky, S. M. Zahurak, A. V. Makhija, F. A. Thiel, K. Raghavachari, E. Cockayne, and V. Elser, *Nature* 350, 46 (1991).
272. R. M. Fleming, A. P. Ramirez, M. J. Rosseinsky, D. W. Murphy, R. C. Haddon, S. M. Zahurak, and A. V. Makhija, *Nature* 352, 787 (1991).
273. P. A. Heiney, J. E. Fischer, A. R. McGhie, W. J. Romanow, A. M. Denenstien, J. P. McCauley, Jr., A. B. Smith III, and D. E. Cox, *Phys. Rev. Lett.* 67, 1468 (1991).
274. R. Tycko, G. Dabbagh, R. M. Flemming, R. C. Haddon, A. V. Makhija, and S. M. Zahurak, *Phys. Rev. Lett.* 67, 1886 (1991).
275. C. S. Yannoni, R. D. Johnson, G. Meijer, D. S. Bethune, and J. R. Salem, *J. Phys. Chem.* 95, 9 (1991).
276. R. Tycko, R. C. Haddon, G. Dabbagh, S. H. Glarum, D. C. Douglass, and A. M. Muijsce, *J. Phys. Chem.* 95, 518 (1991).
277. D. A. Neumann, J. R. D. Copley, R. L. Cappelletti, W. A. Kamitakahara, R. M. Lindstrom, K. M. Creegan, D. M. Cox, W. J.

- Romanow, N. Coustel, J. P. McCauley, Jr., N. C. Maliszewskij, J. E. Fischer, and A. B. Smith III, *Phys. Rev. Lett.* 67, 3808 (1991).
278. R. F. Kiefl, J. W. Schneider, A. MacFarlane, K. Chow, T. L. Duty, T. L. Wstle, B. Hitti, R. L. Lichti, E. J. Ansaldo, C. Schwab, P. W. Percival, G. Wei, S. Wlodek, K. Kojima, W. J. Romanow, J. P. McCauley, Jr., N. Coustel, J. E. Fischer, and A. B. Smith III, *Phys. Rev. Lett.* 68, 1347 (1992).
279. R. F. Kiefl, J. W. Schneider, A. MacFarlane, K. Chow, T. L. Duty, T. L. Wstle, B. Hitti, R. L. Lichti, E. J. Ansaldo, C. Schwab, P. W. Percival, G. Wei, S. Wlodek, K. Kojima, W. J. Romanow, J. P. McCauley, Jr., N. Coustel, J. E. Fischer, and A. B. Smith III, *Phys. Rev. Lett.* 68, 2708 (1992).
280. R. D. Johnson, C. S. Yannoni, H. C. Dorn, J. R. Salem, and D. S. Bethume, *Science* 255, 1235 (1992).
281. P. C. Chow, X. Jiang, G. Reiter, P. Wochner, S. C. Moss, J. D. Axe, J. C. Hanson, R. K. McMullan, R. L. Meng, and C. W. Chu, *Phys. Rev. Lett.* 69, 2943 (1992).
282. L. Pintschovius, S. L. Chaplot, G. Roth, and G. Heger, *Phys. Rev. Lett.* 75, 2843 (1995).
283. R. J. Papoular, G. Roth, G. Heger, M. Haluska, and H. Kuzmany, in "Electronic Properties of Fullerenes" (H. Kuzmany, J. Fink, M. Mehring, and S. Roth, Eds.), Springer Series in Solid State Sciences, Vol. 117, p. 189. Springer, Berlin/Heidelberg, 1993.
284. W. I. F. David, R. M. Ibberson, and T. Matsuo, *Proc. Roy. Soc. London Ser. A* 442, 129 (1993).
285. L. Pintschovius, *Rep. Progr. Phys.* 57, 473 (1996).
286. J. D. Axe, S. C. Moss, and D. A. Neumann, in "Solid State Physics" (H. Ehrenreich and F. Spaepen, Eds.), Vol. 48, p. 149. Academic, New York, 1994.
287. J. Yu, R. K. Kalia, and P. Vashishta, *Appl. Phys. Lett.* 63, 3152 (1993).
288. R. A. Jishi, R. M. Mirie, and M. S. Dresselhaus, *Phys. Rev. B* 45, 13685 (1992).
289. J. L. Feldman, J. Q. Broughton, L. L. Boyer, D. E. Reich, and M. D. Kluge, *Phys. Rev. B* 46, 12731 (1992).
290. D. E. Weeks and W. G. Harter, *Chem. Phys. Lett.* 144, 366 (1988).
291. E. Brendsdal, B. N. Cyvin, J. Brunvoll, and S. J. Cyvin, *Spectrosc. Lett.* 21, 313 (1988).
292. S. J. Cyvin, E. Brendsdal, B. N. Cyvin, and J. Brunvoll, *Chem. Phys. Lett.* 143, 377 (1988).
293. R. S. Ruoff and A. L. Ruoff, *Appl. Phys. Lett.* 59, 1553 (1991).
294. Z. C. Wu, D. A. Jelski, and T. F. George, *Chem. Phys. Lett.* 137, 291 (1987).
295. R. E. Stanton and M. D. Newton, *J. Phys. Chem.* 92, 2141 (1988).
296. Z. Slanina, J. M. Rudzinski, M. Togasi, and E. Osawa, *J. Mol. Struct.* 202, 169 (1989).
297. F. Negri, G. Orlandi, and F. Zerbetto, *Chem. Phys. Lett.* 144, 31 (1988).
298. G. B. Adams, J. B. Page, O. F. Sankey, K. Sinha, J. Menendez, and D. R. Huffman, *Phys. Rev. B* 44, 4052 (1991).
299. R. Jones, C. D. Latham, M. I. Heggie, V. J. B. Torres, S. Öberg, and S. K. Estreicher, *Philos. Mag. Lett.* 65, 291 (1992).
300. J. Kohanoff, W. Andreoni, and M. Parrinello, *Phys. Rev. B* 46, 4371 (1992).
301. Z. H. Dong, P. Zhou, J. M. Holden, P. C. Eklund, M. S. Dresselhaus, and G. Dresselhaus, *Phys. Rev. B* 48, 2862 (1993).
302. M. Martin, J. Fabian, J. Godard, P. Bernier, J. M. Lambert, and L. Mihaly, *Phys. Rev. B* 51, 2844 (1995).
303. K. A. Wang, A. M. Rao, P. C. Eklund, M. S. Dresselhaus, and G. Dresselhaus, *Phys. Rev. B* 48, 11375 (1993).
304. V. Schettino, M. Pagliai, and G. Cardini, *J. Phys. Chem. A* 106, 1815 (2002).
305. V. Schettino, M. Pagliai, L. Ciabini, and G. Cardini, *J. Phys. Chem. A* 105, 11192 (2001).
306. C. H. Choi, M. Kertesz, and L. Mihaly, *J. Phys. Chem. A* 104, 102 (2000).
307. P. Giannozzi and S. Baroni, *J. Chem. Phys.* 100, 8537 (1994).
308. G. B. Adams, J. B. Page, O. F. Sankey, and M. O' Keeffe, *Phys. Rev. B* 50, 17471 (1994).
309. J. Menéndez and J. B. Page, Light scattering in solids VIII, in "Topics in Applied Physics" (M. Cardona and G. Güntherodt, Eds.), Vol. 76, p. 27. Springer-Verlag, Berlin/Heidelberg, 2000.
310. M. C. Martin, X. Q. Du, J. Kwon, and L. Mihaly, *Phys. Rev. B* 50, 173 (1994).
311. V. Schettino, P. R. Salvi, R. Bini, and G. Cardini, *J. Chem. Phys.* 101, 11079 (1994).
312. P. Bowmar, W. Hayes, M. Kurmoo, P. A. Pattenden, M. A. Green, P. Day, and K. Kikuchi, *J. Phys.: Condens. Matter* 6, 3161 (1994).
313. L. Akselrod, H. J. Byrne, S. Donovan, and S. Roth, *Chem. Phys.* 192, 307 (1995).
314. W. Brockner and F. Menzel, *J. Mol. Struct.* 378, 147 (1996).
315. A. Graja, A. Lapinski, and S. Król, *J. Mol. Struct.* 404, 147 (1997).
316. M. S. Dresselhaus, G. Dresselhaus, and P. C. Eklund, "Science of Fullerenes and Carbon Nanotubes." Academic, San Diego, 1995.
317. M. S. Dresselhaus, G. Dresselhaus, P. C. Eklund, and R. Saito, in "Optical and Electronic Properties of Fullerenes and Fullerene-Based Materials" (J. Shinar, Z. V. Vardeny, and Z. H. Kafafi, Eds.), Vol. 8, p. 217. Dekker, New York, 1999.
318. V. A. Davydov, L. S. Kashevarova, A. V. Rakhmanina, V. M. Senyavin, R. Ceolin, H. Szwarc, H. Allouchi, and V. Agafonov, *Phys. Rev. B* 61, 11936 (2000).
319. K. A. Wang, Y. Wang, P. Zhou, J. M. Holden, S. L. Ren, G. T. Hager, H. F. Ni, P. C. Eklund, G. Dresselhaus, and M. S. Dresselhaus, *Phys. Rev. B* 45, 1955 (1992).
320. D. S. Bethune, G. Meijer, W. C. Tang, and H. J. Rosen, *Chem. Phys. Lett.* 174, 219 (1990).
321. P. Zhou, K. A. Wang, Y. Wang, P. C. Eklund, M. S. Dresselhaus, G. Dresselhaus, and R. A. Jishi, *Phys. Rev. B* 46, 2595 (1992).
322. P. Zhou, A. M. Rao, K. A. Wang, J. D. Robertson, C. Eloi, M. S. Meier, S. L. Ren, X. X. Bi, P. C. Eklund, and M. S. Dresselhaus, *Appl. Phys. Lett.* 60, 2871 (1992).
323. S. J. Duclos, R. C. Haddon, S. H. Glarum, A. F. Hebard, and K. B. Lyons, *Science* 254, 1625 (1991).
324. H. Kuzmany, R. Winkler, and T. Pichler, *J. Phys.: Condens. Matter* 7, 6601 (1995).
325. J. M. Hawkins, A. Mayer, S. Loren, and R. Nunlist, *J. Am. Chem. Soc.* 113, 9394 (1991).
326. S. P. Love, D. McBranch, M. I. Salkola, N. V. Coppa, J. M. Robinson, B. I. Swanson, and A. R. Bishop, *Chem. Phys. Lett.* 225, 170 (1994).
327. A. Rosenberg and C. Kendziora, *Phys. Rev. B* 51, 9321 (1995).
328. M. C. Martin, J. Fabian, J. Godard, P. Bernier, J. M. Lambert, and L. Mihaly, *Phys. Rev. B* 51, 2844 (1995).
329. P. J. Horovsky, M. L. W. Thewalt, and T. R. Anthony, *Phys. Rev. Lett.* 74, 194 (1995).
330. S. Suha, J. Menendez, J. B. Page, G. B. Adams, G. S. Spencer, J. P. Lehman, P. Giannozzi, and S. Baroni, *Phys. Rev. Lett.* 72, 3359 (1994).
331. J. Menendez, J. B. Page, and S. Guha, *Philos. Mag. B* 70, 651 (1994).
332. S. Guha, J. Menendez, J. B. Page, and G. M. Adams, *Phys. Rev. B* 56, 15431 (1997).
333. J. R. Soto, A. Calles, and J. L. Moran-Lopez, *J. Chem. Phys.* 113, 1055 (2000).
334. R. Heid, L. Pintschovius, and J. M. Godard, *Phys. Rev. B* 56, 5925 (1997).
335. R. L. Cappelletti, J. R. D. Copley, W. A. Kamitakahara, F. Li, J. S. Lannin, and D. Ramage, *Phys. Rev. Lett.* 66, 3261 (1991).
336. K. Prassides, T. J. S. Dennis, J. P. Hare, J. Tomkinson, H. W. Kroto, R. Taylor, and D. R. M. Walton, *Chem. Phys. Lett.* 187, 455 (1991).
337. C. Coulombeau, H. Jobic, P. Bernier, C. Fabre, D. Schultz, and A. Rassat, *J. Phys. Chem.* 96, 22 (1992).
338. C. Coulombeau, H. Jobic, C. J. Carlile, S. M. Bennington, C. Fabre, and A. Rassat, *Fullerene Sci. Technol.* 2, 247 (1994).

339. F. Gompf, B. Renker, W. Schober, P. Adelman, and R. Heid, *J. Supercond.* 7, 643 (1994).
340. J. R. D. Copley, D. A. Neumann, and W. A. Kamitakahara, *Can. J. Phys.* 73, 763 (1995).
341. G. Gensterblum, L.-M. Yu, J. J. Pireaux, P. A. Thiry, R. Caudano, P. Lambin, A. A. Lucas, W. Kratschmer, and J. E. Fischer, *J. Phys. Chem. Solids* 53, 1427 (1992).
342. A. A. Lucas, *J. Phys. Chem. Solids* 53, 1415 (1992).
343. G. Gensterblum, L. M. Yu, J. J. Pireaux, P. A. Thiry, R. Caudano, J. M. Themlin, S. Bouzidi, F. Coletti, and J. M. Debever, *Appl. Phys. A* 56, 175 (1993).
344. G. Gensterblum, J. J. Pireaux, P. A. Thiry, R. Caudano, J. P. Vigneron, P. Lambin, A. A. Lucas, and W. Kratschmer, *Phys. Rev. Lett.* 67, 2171 (1991).
345. A. Lucas, G. Gensterblum, J. J. Pireaux, P. A. Thiry, R. Taylor, and P. Lambin, *Phys. Rev. B* 45, 13692 (1991).
346. M. K. Nissen, S. M. Wilson, and M. L. W. Thewalt, *Phys. Rev. Lett.* 69, 2423 (1992).
347. A. Sassara, G. Zerza, and M. Chergui, *J. Phys. B* 29, 4997 (1996).
348. A. Sassara, G. Zerza, and M. Chergui, *Chem. Phys. Lett.* 261, 213 (1996).
349. W. I. F. David, R. M. Ibberson, T. J. S. Dennis, J. P. Hare, and K. Prassides, *Europhys. Lett.* 18, 735 (1992).
350. T. Atake, T. Tanaka, R. Kawaji, K. Kikuchi, K. Saito, S. Suzuki, I. Ikemoto, and Y. Achiba, *Physica C* 185–189, 427 (1991).
351. W. P. Beyermann, M. F. Hundley, J. D. Thompson, F. N. Diederich, and G. Gruner, *Phys. Rev. Lett.* 68, 2046 (1992).
352. R. C. Yu, N. Tea, M. B. Salamon, D. Lorens, and R. Malhotra, *Phys. Rev. Lett.* 68, 2050 (1992).
353. H.-B. Bürgi, E. Blanc, D. Schwarzenbach, S. Liu, Y. Lu, M. M. Kappes, and J. A. Ibers, *Angew. Chem. Int. Ed. Engl.* 31, 640 (1992).
354. P. Heiney, *J. Phys. Chem. Solids* 53, 1333 (1992).
355. J. D. Axe, S. C. Moss, and D. A. Neumann, *Solid State Phys.* 48, 149 (1994).
356. O. Blaschko, G. Krexner, Ch. Maier, and R. Karawatzki, *Phys. Rev. B* 56, 2288 (1997).
357. F. Gugenberger, R. Heid, C. Meingast, P. Adelman, M. Braun, H. Wuhl, M. Haluska, and H. Kuzmany, *Phys. Rev. Lett.* 69, 3774 (1992).
358. W. Schranz, A. Fuith, P. Dolinar, H. Warhanek, M. Haluska, and H. Kuzmany, *Phys. Rev. Lett.* 71, 1561 (1993).
359. G. B. Alers, B. Golding, A. R. Kortan, R. C. Haddon, and F. A. Theil, *Science* 257, 511 (1992).
360. D. A. Neumann, J. R. D. Copley, W. A. Kamitakahara, J. J. Rush, R. L. Paul, and R. M. Lindstrom, *J. Phys. Chem. Solids* 54, 1699 (1993).
361. T. Matsuo, H. Suga, W. I. F. David, R. M. Ibberson, P. Bernier, A. Zahba, C. Fabre, A. Rassat, and A. Dworkin, *Solid State Commun.* 83, 711 (1992).
362. R. Sachidanandam and A. B. Harris, *Phys. Rev. Lett.* 66, 1467 (1991).
363. A. Dworkin, H. Szwarc, S. Leach, J. P. Hare, T. J. Dennis, H. W. Kroto, R. Taylor, and D. R. M. Walton, *C. R. Acad. Sci., Paris Ser. II* 312, 979 (1991).
364. R. D. Johnson, G. Meijer, and D. S. J. Bethune, *J. Am. Chem. Soc.* 112, 8983 (1990).
365. R. Blinc, J. Seliger, Dolinsek, and D. Arcon, *Eur. Phys. Lett.* 23, 355 (1993).
366. A. Dworkin, C. Fabre, D. Schutz, G. Kriza, R. Ceolin, H. Szwarc, P. Bernier, D. Jerome, S. Leach, A. Rassat, J. P. Hare, T. J. Dennis, H. W. Kroto, R. Taylor, and D. R. M. Walton, *C. R. Acad. Sci., Paris Ser. II* 313, 1017 (1991).
367. E. Grivei, B. Nysten, M. Cassart, A. Demain, and J. P. Issi, *Solid State Commun.* 85, 73 (1993).
368. G. Pitsi, J. Caerels, and J. Thoen, *Phys. Rev. B* 55, 915 (1997).
369. L. Pintschovius, B. Renker, F. Gompf, R. Heid, S. L. Chaplot, M. Haluska, and H. Kuzmany, *Phys. Res. Lett.* 69, 2662 (1992).
370. D. A. Neumann, J. R. D. Copley, W. A. Kamitakahara, J. J. Rush, R. L. Cappelletti, N. Coustel, J. E. Fischer, J. P. McCauley, Jr., A. B. Smith III, K. M. Creegan, and D. M. Cox, *J. Chem. Phys.* 96, 8631 (1992).
371. G. Van Tendeloo and S. Amelinckx, in “Electron Microscopy of Fullerenes and Related Materials, Characterization of Nanophase Materials” (Z. L. Wang, Ed.), Ch. 12. Wiley-VCH, Weinheim, 2000.
372. S. Hoen, N. G. Chopra, X. D. Xiang, R. Mostovoy, J. Hou, W. A. Vareka, and A. Zettl, *Phys. Rev. B* 46, 12737 (1992).
373. P. H. M. van Loosdrecht, P. J. M. van Bentum, and G. Meijer, *Phys. Rev. Lett.* 68, 1176 (1992).
374. P. H. M. van Loosdrecht, P. J. M. van Bentum, M. A. Verheijen, and J. Meijer, *Chem. Phys. Lett.* 198, 587 (1992).
375. M. Matus and H. Kuzmany, *Appl. Phys. A* 56, 241 (1993).
376. J. De Bruyn, A. Dworkin, H. Szwarc, J. Godard, R. Céolin, C. Fabre, and A. Rassart, *Europhys. Lett.* 24, 551 (1993).
377. W. Luo, H. Wang, R. S. Ruoff, J. Cioslowski, and S. Phelps, *Phys. Rev. Lett.* 73, 186 (1994).
378. P. Byszewski, F. L. Diduszko, E. Kowalska, J. Fink-Finowicki, and A. Witowski, *Appl. Phys. Lett.* 61, 2981 (1992).
379. E. Grivei, B. Nysten, M. Cassart, J. P. Issi, L. Langer, B. Nysten, J. P. Michenaud, C. Fabre, and A. Rassat, *Phys. Rev. B* 48, 8514 (1993).
380. N. H. Tea, R. C. Yu, M. B. Salamon, D. C. Lorents, R. Malhotra, and R. S. Ruoff, *Appl. Phys. A* 56, 219 (1993).
381. G. Van Tendeloo, S. Amelinckx, M. A. Verheijen, P. H. M. van Loosdrecht, and G. Meijer, *Phys. Rev. Lett.* 69, 1065 (1992).
382. P. J. Benning, F. Stepniak, and J. H. Weaver, *Phys. Rev. B* 48, 9086 (1993).
383. C. Cepek and S. Modesti, *Phys. Rev. B* 54, 2890 (1996).
384. A. Glebov, V. Senz, J. P. Toennies, and G. Gensterblum, *J. Appl. Phys.* 82, 2329 (1997).
385. D. Passerone and E. Tosatti, *Surf. Rev. Lett.* 4, 859 (1997).
386. Z. Y. Li, *Surf. Sci.* 441, 366 (1999).
387. H. Wang, C. Zeng, B. Wang, J. G. Hou, Q. Li, and J. Yang, *Phys. Rev. B* 63, 85417 (2001).
388. C. Laforge, D. Passerone, A. B. Harris, P. Lambin, and E. Tosatti, *Phys. Rev. Lett.* 87, 85503 (2001).
389. D. M. Poirier, D. W. Owens, and J. H. Weaver, *Phys. Rev. B* 51, 1830 (1995).
390. R. Glang, in “Handbook of Thin Film Technology” (L. I. Maissel and R. Glang, Eds.), Ch. 1. McGraw-Hill, New York, 1970.
391. A. F. Hebard, R. C. Haddon, R. M. Fleming, and A. R. Kortan, *Appl. Phys. Lett.* 59, 2109 (1991).
392. R. M. Fleming, A. R. Kortan, B. Hessen, T. Siegrist, F. A. Thiel, R. C. Haddon, R. Tycho, G. Dabbaagh, M. L. Kaplan, and A. M. Mujsc, *Phys. Rev. B* 44, 888 (1991).
393. B. Morosin, P. P. Newcomer, R. J. Baughman, E. L. Venturini, D. Loy, and J. E. Schirber, *Physica C* 184, 21 (1991).
394. N. A. Fortune, K. Murata, F. Iga, Y. Nishihara, K. Kikuchi, S. Suzuki, I. Ikemoto, and Y. Achiba, *Physica C* 185–189, 425 (1991).
395. H. Ogata, T. Inable, H. Hoshi, Y. Maruyama, Y. Achiba, S. Suzuki, K. Kikuchi, and I. Ikemoto, *Jpn. J. Appl. Phys.* 31, L166 (1992).
396. D. L. Dorset, *J. Phys. Chem.* 99, 16748 (1995).
397. R. A. Assink, J. E. Schirber, D. A. Loy, B. Morosin, and G. A. Carlson, *J. Mater. Res.* 7, 2136 (1992).
398. K. Kikyuchi, S. Suzuki, K. Saito, H. Shiromaru, I. Ikeromoto, and Y. Achiba, *Physica C* 185–189, 415 (1991).
399. S. Pekker, G. Faigel, K. Fodorcorba, L. Granasy, E. Jakab, and M. Tegze, *Solid State Commun.* 83, 423 (1992).
400. F. Michaud, M. Barrio, S. Toscani, D. O. Lopez, J. Ll. Tamatit, V. Agafonov, H. Szwarc, and R. Ceolin, *Phys. Rev. B* 57, 10351 (1998).

401. S. Toscani, H. Allouchi, J. Ll. Tamarit, D. O. López, M. Barrio, V. Agafonov, A. Rassat, H. Szwarc, and R. Céolin, *Chem. Phys. Lett.* 330, 491 (2000).
402. R. L. Meng, D. Ramirez, X. Jiang, P. C. Chow, C. Diaz, K. Matsushishi, S. C. Moss, P. H. Hor, and C. W. Chu, *Appl. Phys. Lett.* 59, 3402 (1991).
403. J. Z. Liu, J. W. Dykes, M. D. Lan, P. Klavins, R. N. Shelton, and M. M. Olmstead, *Appl. Phys. Lett.* 62, 531 (1992).
404. J.-B. Shi, W.-Y. Chang, S.-R. Su, and M.-W. Lee, *Jpn. J. Appl. Phys.* 35, L45 (1996).
405. X. D. Xiang, J. G. Hou, G. Briceno, W. A. Vareka, R. Mostovoy, A. Zettl, V. H. Crespi, and M. L. Cohen, *Science* 256, 1190 (1992).
406. J. Li, S. Komiyama, T. Tamura, C. Nagasaki, J. Kihara, K. Kishio, and K. Kitazawa, *Physica C* 195, 205 (1992).
407. M. Haluska, H. Kuzmany, M. Vybornov, P. Rogl, and P. Fejdi, *Appl. Phys. A* 56, 161 (1993).
408. M. Tan, B. Xu, H. Li, Z. Qi, and Y. Xu, *J. Crystal Growth* 182, 375 (1992).
409. K.-C. Chiu, J.-S. Wang, C.-Y. Lin, T.-Y. Lin, and C.-S. Ro, *Mater. Res. Bull.* 30, 883 (1995).
410. K. Matsumoto, E. Schonherr, and M. Wojnowski, *J. Crystal Growth* 135, 154 (1994).
411. K. Murakami, K. Matsumoto, H. Nagatomo, E. Schönherr, and M. Wojnowski, *Ultramicroscopy* 73, 191 (1998).
412. H. Li, Y. Xu, J. Zhang, P. He, H. Li, T. Wu, and S. Bao, *Progr. Natural Sci.* 11, 427 (2001).
413. A. Al-Mohamad and A. W. Allaf, *Synth. Metals* 104, 39 (1999).
414. R. C. Haddon, A. S. Perel, R. C. Morris, T. T. M. Palstra, A. F. Hebard, and R. M. Fleming, *Appl. Phys. Lett.* 67, 121 (1995).
415. C. P. Jarret, K. Pichler, R. Newbould, and R. H. Friend, *Synth. Metals* 77, 35 (1996).
416. K. Horiuchi, K. Nakada, S. Uchino, S. Hashii, A. Hashimoto, N. Aoki, and Y. Ochiai, *Appl. Phys. Lett.* 81, 1911 (2002).
417. W. Krakow, N. M. Rivera, R. A. Roy, R. S. Ruoff, and J. J. Cuomo, *Appl. Phys. A* 56, 185 (1993).
418. Z. Dai, H. Naramoto, K. Narumi, S. Yamamoto, and A. Miyashita, *Thin Solid Films* 360, 28 (2000).
419. E. A. Katz, D. Faiman, S. Shtutina, and A. Isakina, *Thin Solid Film* 368, 49 (2000).
420. W. M. Tong, D. A. A. Ohlberg, H. K. You, R. S. Williams, S. J. Anz, M. M. Alvarez, R. L. Whetten, Y. Rubin, and F. N. Diederich, *J. Phys. Chem.* 95, 4709 (1991).
421. Z.-M. Ren, Z.-F. Ying, X.-X. Xiong, M.-Q. He, Y.-F. Li, F.-M. Li, and Y.-C. Du, *J. Phys. D* 27, 1499 (1994).
422. S. Isoda, H. Kawakubo, S. Nishikawa, and O. Wada, *Nucl. Instrum. Methods B* 112, 94 (1996).
423. H. Gao, Z. Xue, and Sh. Pang, *J. Phys. D* 29, 1870 (1996).
424. X. Shi, X. J. Fan, H. X. Guo, and Q. Fu, *Solid State Commun.* 99, 445 (1996).
425. X. Zou, S. Zhu, J. Xie, and J. Feng, *J. Crystal Growth* 200, 441 (1999).
426. J. G. Hou, J. Zeng, Y. Li, and Z. Q. Wu, *Thin Solid Films* 320, 179 (1998).
427. D. Schmicker, S. Schmidt, J. G. Skofronick, J. P. Toennies, and R. Vollmer, *Phys. Rev. B* 44, 10995 (1991).
428. J. E. Fischer, E. Werva, and P. A. Heincy, *Appl. Phys. A* 56, 193 (1993).
429. T. Thundat, R. J. Warmack, D. Ding, and F. L. N. Compton, *Appl. Phys. Lett.* 63, 891 (1993).
430. A. Fatash, *Appl. Phys. Lett.* 64, 1877 (1994).
431. S. Henke, K. M. Thürer, and S. Geier, *Appl. Phys. A* 60, 383 (1995).
432. G. Ma, Y. Yang, and G. Chen, *Mater. Lett.* 31, 297 (1997).
433. D. Stifter and H. Sitter, *Appl. Phys. Lett.* 66, 679 (1995).
434. D. Stifter and H. Sitter, *J. Cryst. Growth* 156, 79 (1995).
435. D. Stifter and H. Sitter, *Thin Solid Films* 280, 83 (1996).
436. J. K. N. Linder, S. Henke, B. Rauschenbach, and B. Stritzker, *Thin Solid Films* 279, 106 (1996).
437. K. Tanigaki, S. Kuroshima, J. Fujita, and T. W. Ebbesen, *Appl. Phys. Lett.* 63, 2351 (1993).
438. K. Tanigaki, S. Kuroshima, and T. W. Ebbesen, *Thin Solid Films* 257, 154 (1995).
439. H. Gaber, *Appl. Phys. Lett.* 65, 378 (1994).
440. J. Fujita, S. Kuroshima, T. Satoh, J. S. Tsai, T. W. Ebbesen, and K. Tanigaki, *Appl. Phys. Lett.* 63, 1008 (1993).
441. D. J. Kenny and R. E. Palmer, *Surf. Sci.* 447, 126 (2000).
442. M. Sakurai, H. Tada, K. Saiki, and A. Koma, *Jpn. J. Appl. Phys.* 30, L1892 (1991).
443. M. Sakurai, H. Tada, K. Saiki, A. Koma, H. Funasaka, and Y. Kishimoto, *Chem. Phys. Lett.* 208, 425 (1993).
444. G. Chen and G. Ma, *Thin Solid Films* 323, 309 (1998).
445. D. Bernaerts, G. Van Tendeloo, S. Amelinckx, K. Hevesi, G. Gensterblum, L. M. Yu, J.-J. Pireaux, F. Grey, and J. Bohr, *J. Appl. Phys.* 80, 3310 (1996).
446. U. D. Schwarz, W. Allers, G. Gensterblum, J.-J. Pireaux, and R. Wiesendanger, *Phys. Rev. B* 52, 5967 (1995).
447. J.-M. Themlin, S. Bouzidi, F. Coletti, J.-M. Debever, G. Gensterblum, L.-M. Yu, J.-J. Pireaux, and P. A. Thiry, *Phys. Rev. B* 46, 15 602 (1992).
448. G. Gensterblum, L. M. Yu, J.-J. Pireaux, P. A. Thiry, R. Caudano, Ph. Lambin, A. A. Lucas, W. Kräschmer, and J. E. Fischer, *J. Phys. Chem. Solids* 53, 1427 (1992).
449. J. Dura, P. M. Pippenger, N. J. Halas, X. Z. Xiong, P. C. Chow, and S. C. Moss, *Appl. Phys. Lett.* 63, 3443 (1993).
450. T. Ichihashi, K. Tanigaki, T. W. Ebbesen, S. Kuroshima, and S. Iijima, *Chem. Phys. Lett.* 190, 179 (1992).
451. Z. Dai, H. Naramoto, K. Narumi, S. Yamamoto, and A. Miyashita, *Appl. Phys. Lett.* 74, 1686 (1999).
452. Y. Kim, L. Jiang, T. Iyoda, K. Hashimoto, and A. Fujishima, *Appl. Phys. Lett.* 71, 3489 (1997).
453. Y. Kim, L. Jiang, T. Iyoda, K. Hashimoto, and A. Fujishima, *Appl. Surf. Sci.* 130–132, 602 (1998).
454. H. Yanagi and T. Sasaki, *Appl. Phys. Lett.* 65, 1222 (1994).
455. H. Yanagi, S. Doumi, T. Sasaki, and H. Tada, *J. Appl. Phys.* 80, 4990 (1996).
456. E. J. Snyder, M. S. Anderson, W. M. Tong, R. S. Williams, S. J. Anz, M. M. Alvarez, Y. Rubin, F. N. Diederich, and R. L. Whetten, *Science* 253, 171 (1991).
457. S. Fölsch, T. Maruno, A. Yamashita, and T. Hayashi, *Appl. Phys. Lett.* 62, 2643 (1993).
458. A. Fartash, *Appl. Phys. Lett.* 67, 3901 (1995).
459. A. Fartash, *Phys. Rev. B* 52, 7883 (1995).
460. G. Costantini, S. Rusponi, E. Giudice, C. Boragno, and U. Valbusa, *Carbon* 37, 727 (1999).
461. T. Hashizume, K. Motai, X. D. Wang, H. Shinohara, Y. Saito, Y. Maruyama, K. Ohno, Y. Kawazoe, Y. Nishina, H. W. Pickering, Y. Kuk, and T. Sakurai, *Phys. Rev. Lett.* 71, 2959 (1993).
462. A. Fartash, *J. Appl. Phys.* 79, 742 (1996).
463. J. Zeng, Y. Wang, Y. Li, and J. G. Hou, *Physica C* 282–287, 739 (1997).
464. W. Xu and J. G. Hou, *J. Appl. Phys.* 86, 4660 (1999).
465. J. G. Hou, W. Xu, H. Wang, and Y. Li, *J. Appl. Phys.* 84, 2906 (1998).
466. S. Saito and A. Oshiyama, *Phys. Rev. Lett.* 66, 2637 (1991).
467. N. Troullier and J. L. Martins, *Phys. Rev. B* 46, 1754 (1992).
468. M. Knupfer, *Surf. Sci. Rep.* 42, 1 (2001).
469. E. L. Shirley and S. G. Louie, *Phys. Rev. Lett.* 71, 133 (1993).
470. J. H. Weaver, *J. Phys. Chem. Solids* 53, 1433 (1992).
471. R. W. Lof, M. A. van Veenendaal, B. Koopmans, H. T. Jonkman, and G. A. Sawatzky, *Phys. Rev. Lett.* 68, 3924 (1992).
472. M. Skibowski and L. Kipp, *J. Electron Spectrosc. Relat. Phenom.* 68, 77 (1994).
473. T. L. Makarova, *Semiconductors* 35, 243 (2001).
474. B. Mishori, E. A. Katz, D. Faiman, and Y. Shapira, *Solid State Commun.* 102, 489 (1997).

475. E. Sohmen, J. Fink, and W. Krätschmer, *Z. Phys. B* 86, 87 (1992).
476. T. Rabenau, A. Simon, R. K. Kremer, and E. Sohmen, *Z. Phys. B* 90, 69 (1993).
477. T. Ohgami, Y. Shimada, H. Kubota, H. Tanaka, S. Matsuzaki, and M. Nagata, *Physica B* 239, 32 (1997).
478. P. Mondal, P. Lunkenheimer, and A. Loidl, *Z. Phys. B* 99, 527 (1996).
479. M. Hosoya, K. Ichimura, Z. H. Wang, G. Dresselhaus, M. S. Dresselhaus, and P. C. Eklund, *Phys. Rev. B* 49, 4981 (1994).
480. J. Hora, P. Pánek, K. Navrátil, B. Handlířová, J. Humlíček, H. Sitter, and D. Stifer, *Phys. Rev. B* 54, 5106 (1996).
481. A. Skumanich, *Chem. Phys. Lett.* 182, 486 (1991).
482. R. Schwedhelm, L. Kipp, A. Dallmeyer, and M. Skibowski, *Phys. Rev. B* 58, 13176 (1998).
483. B. Mishori, E. A. Katz, D. Faiman, A. Belu-Marian, and Y. Shapira, *Fullerene Sci. Technol.* 6, 113 (1998).
484. E. A. Katz, D. Faiman, B. Mishori, Y. Shapira, A. I. Shames, S. Shtutina, and S. Goren, *J. Appl. Phys.* 84, 3333 (1998).
485. M. Kaiser, W. K. Maser, H. J. Byrne, J. Beichenbach, J. Anders, A. Mittelbach, and S. Roth, in "Electronic Properties of Fullerenes" (H. Kuzmany, J. Fink, M. Mehring, and S. Roth, Eds.), Vol. 117, p. 418. Springer-Verlag, Berlin/Heidelberg, 1993.
486. S. Krummacher, M. Biermann, M. Neeb, A. Liebsch, and W. Eberhardt, *Phys. Rev. B* 48, 8424 (1993).
487. E. L. Shirley, L. X. Benedict, and S. G. Louie, *Phys. Rev. B* 54, 10970 (1996).
488. M. Knupfer and J. Fink, *Phys. Rev. B* 60, 10731 (1999).
489. K. Kaneto, K. Yamanaka, K. Rikitake, T. Akiyama, and W. Takashima, *Jpn. J. Appl. Phys.* 35, 1802 (1996).
490. G. Priebe, B. Pietzak, and R. Könenkamp, *Appl. Phys. Lett.* 71, 2160 (1997).
491. C. Wen, J. Li, K. Kitazawa, T. Aida, I. Honma, H. Komiyama, and K. Yamada, *Appl. Phys. Lett.* 61, 2162 (1992).
492. H. Habuchi, S. Nitta, D. Han, and S. Nonomura, *J. Appl. Phys.* 87, 8580 (2000).
493. A. Hamed, Y. Y. Sun, Y. K. Tao, R. L. Meng, and P. H. Hor, *Phys. Rev. B* 47, 10873 (1993).
494. A. Zahab and L. Firlej, *Solid State Commun.* 87, 893 (1993).
495. He Peimo, Xu Yabo, Z. Xuanjia, and Li Wenzhou, *Solid State Commun.* 89, 373 (1994).
496. J. Mort, R. Ziolo, M. Machonkin, D. R. Huffman, and M. I. Ferguson, *Chem. Phys. Lett.* 186, 284 (1991).
497. K. Hoshimono, S. Fujimori, and S. Fujita, *Jpn. J. Appl. Phys.* 2 32, L1070 (1993).
498. T. Takahashi, S. Suzuki, T. Morikawa, H. Katayama-Yoshida, S. Hasegawa, H. Inokuchi, K. Seki, K. Kikuchi, S. Suzuki, K. Ike-moto, and Y. Achiba, *Phys. Rev. Lett.* 68, 1232 (1992).
499. S. Fujimori, K. Hoshimono, and S. Fujita, *Solid State Commun.* 89, 437 (1994).
500. S. Gonda, M. Kawasaki, T. Arakane, and H. Koinuma, *Mater. Res. Soc. Symp. Proc.* 349, 25 (1994).
501. K. Rikitake, T. Akiyama, W. Takashima, and K. Kaneto, *Synth. Met.* 86, 2357 (1997).
502. J. Paloheimo and H. Isotalo, *Synth. Met.* 55, 3185 (1993).
503. J. C. Wang and Y. F. Chen, *Appl. Phys. Lett.* 73, 948 (1998).
504. Y. Saito, H. Shinohara, M. Kato, H. Nagashima, M. Ohkohchi, and Y. Ando, *Chem. Phys. Lett.* 189, 236 (1992).
505. S. Matsuura and T. Ishiguro, *Fullerene Sci. Technol.* 3, 437 (1995).
506. T. Arai, Y. Murakami, H. Suematsu, K. Kikuchi, Y. Achiba, and I. Ike-moto, *Solid State Commun.* 84, 827 (1992).
507. M. Kaiser, W. K. Maser, H. J. Byrne, A. Mittelbach, and S. Roth, *Solid State Commun.* 87, 281 (1993).
508. F. Yan, Y. N. Wang, Y. N. Huang, M. Gu, Q. M. Zhang, and H. M. Shen, *Phys. Lett. A* 201, 443 (1995).
509. I. G. Austin and N. F. Mott, *Adv. Phys.* 18, 41 (1969).
510. N. I. Nemchuk, T. L. Makarova, O. I. Konkov, Y. F. Biriulin, and A. Y. Vul, *Mol. Cryst. Liq. Cryst. C* 7, 183 (1996).
511. T. Rabenau, S. Roth, and R. K. Kremer, *Acta Phys. Pol. A* 87, 881 (1995).
512. R. K. Kremer, T. Rabenau, W. K. Maser, M. Kaiser, A. Simon, M. Haluska, and H. Kuzmany, *Appl. Phys. A* 56, 211 (1993).
513. M. K. Kelly, P. Etchegoin, D. Fuchs, W. Krätschmer, and K. Fostiropoulos, *Phys. Rev. B* 46, 4963 (1992).
514. T. L. Makarova, *Mol. Cryst. Liq. Cryst. C* 7, 199 (1996).
515. P. Milani, M. Manfredini, G. Guizzetti, F. Marabelli, and M. Patrini, *Solid State Commun.* 90, 639 (1994).
516. S. L. Ren, Y. Wang, A. M. Rao, E. McRae, G. T. Hager, K. A. Wang, W. T. Lee, H. F. Ni, J. Selegue, and P. C. Eklund, *Appl. Phys. Lett.* 59, 2678 (1991).
517. Y. Wang, J. M. Holden, A. M. Rao, W. T. Lee, X. X. Bi, S. L. Ren, G. W. Lehman, G. T. Hager, and P. C. Eklund, *Phys. Rev. B* 45, 14396 (1992).
518. S. Leach, M. Vervloet, A. Despres, A. Despres, E. Breheret, J. P. Hare, T. J. Dennis, H. W. Kroto, R. Taylor, and D. R. M. Walton, *Chem. Phys.* 160, 451 (1992).
519. T. Gotoh, S. Nonomura, S. Hirata, and S. Nitta, *Appl. Surf. Sci.* 114, 278 (1997).
520. M. S. Dresselhaus, G. Dresselhaus, A. M. Rao, and P. C. Eklund, *Synth. Met.* 78, 313 (1996).
521. T. N. Thomas, J. F. Ryan, R. A. Taylor, D. Mihaiovic, and R. Zamboni, *Int. J. Mod. Phys. B* 6, 3931 (1992).
522. U. D. Venkateswaran, D. Sanzi, A. M. Rao, P. C. Eklund, L. Marques, J.-L. Hodeau, and M. Núñez-Regueiro, *Phys. Rev. B* 57, R3193 (1998).
523. S. Mochizuki, M. Sasaki, and R. Rupp, *J. Phys.: Condens. Matter* 10, 2347 (1998).
524. M. Braga, S. Larsson, A. Rosen, and A. Volosov, *Astron. Astrophys.* 245, 232 (1991).
525. G. F. Bertsch, A. Bulgac, D. Tománek, and Y. Wang, *Phys. Rev. Lett.* 67, 2690 (1991).
526. K. Harigaya and S. Abe, *Phys. Rev. B* 49, 16746 (1994).
527. T. Pichler, M. Matus, J. Kürti, and H. Kuzmany, *Solid State Commun.* 81, 859 (1992).
528. K. Yabana and G. F. Bertsch, *Chem. Phys. Lett.* 197, 32 (1992).
529. M. I. Salkola, *Phys. Rev. B* 49, 4407 (1994).
530. M. S. Dresselhaus, G. Dresselhaus, and P. C. Eklund, *J. Mater. Res.* 8, 2054 (1993).
531. J. Mort, K. Okumura, M. Machonkin, R. Ziolo, D. R. Huffman, and M. I. Ferguson, *Chem. Phys. Lett.* 186, 281 (1991).
532. M. Kaiser, J. Reichenbach, H. J. Byrne, J. Anders, W. Maser, S. Roth, A. Zahab, and P. Bernier, *Solid State Commun.* 81, 261 (1992).
533. A. Fartash, *Phys. Rev. B* 54, 17215 (1996).
534. A. M. Rao, P. Zhou, K.-A. Wang, G. T. Hager, J. M. Holden, Y. Wang, W.-T. Lee, X.-X. Bi, P. C. Eklund, D. S. Cornett, M. A. Duncan, and I. J. Amster, *Science* 259, 955 (1993).
535. B. Pevzner, A. F. Hebard, and M. S. Dresselhaus, *Phys. Rev. B* 55, 16439 (1997).
536. S. D. Senturia, J. N. F. Sheppard, H. L. Lee, and D. R. Day, *J. Adhesion* 15, 69 (1982).
537. N. F. Sheppard, D. R. Day, H. L. Lee, and S. D. Senturia, *Sensors Actuators* 2, 263 (1982).
538. F. Yan and Y. N. Wang, *Appl. Phys. Lett.* 72, 3446 (1998).
539. J. S. Su, Y. F. Chen, and K. C. Chiu, *Appl. Phys. Lett.* 75, 1607 (1999).
540. V. Elser and R. C. Haddon, *Nature* 325, 792 (1987).
541. V. Elser and R. C. Haddon, *Phys. Rev. A* 36, 4579 (1990).
542. A. Pasquarello, M. Schlüter, and R. C. Haddon, *Science* 257 (1992).
543. B. T. Kelly, "Physics of Graphite." Applied Science, London, 1981.
544. R. S. Ruoff, D. Beach, J. Cuomo, T. Mcguire, R. L. Whetten, and F. Diederich, *J. Phys. Chem.* 95, 3457 (1991).
545. R. C. Haddon, L. F. Schneemeyer, J. V. Waszczak, S. H. Glarum, R. Tycko, G. Dabbagh, A. R. Kortan, A. J. Muller, A. M. Mujsce,

- M. J. Rosseinsky, S. M. Zahurak, A. V. Makhija, F. A. Thiel, K. Raghavachari, E. Cockayne, and V. Elser, *Nature (London)* 350, 46 (1991).
546. P. W. Fowler, P. Lasseretti, and R. Zanasi, *Chem. Phys. Lett.* 165, 79 (1990).
547. R. C. Haddon and V. Elser, *Chem. Phys. Lett.* 169, 362 (1990).
548. N. Ganguli and K. S. Krishnan, *Proc. Roy. Soc. London Ser. A* 177, 168 (1941).
549. X. K. Wang, R. P. H. Chang, A. Patashinski, and J. B. Ketterson, *J. Mater. Res.* 9, 1578 (1994).
550. J. Heremans, C. H. Olk, and D. T. Morelli, *Phys. Rev. B* 49, 15122 (1994).
551. Y. G. Dorfman, "Diamagnetism and the Chemical Bond." Elsevier, New York, 1966.
552. P. M. Allemand, K. C. Khemani, A. Koch, F. Wudl, K. Holczer, S. Donovan, G. Grüner, and J. D. Thompson, *Science* 253, 301 (1991).
553. V. E. Antonov, I. O. Bashkin, S. S. Khasanov, A. P. Moravsky, Yu. G. Morozov, Yu. M. Shul'ga, Yu. A. Ossipyan, and E. G. Ponyatovsky, *J. Alloys Compd.* 330, 365 (2002).
554. Y. M. Shul'ga, A. S. Lobach, I. N. Ivleva, Y. G. Morozov, and V. N. Spector, *Mol. Cryst. Liq. Cryst.* 10, 201 (1998).
555. T. L. Makarova, B. Sundqvist, R. Höhne, P. Esquinazi, Y. Kopelevich, P. Scharff, V. A. Davydov, L. S. Kasherova, and A. V. Rakhmanina, *Nature* 413, 716 (2001).
556. J. R. Olson, K. A. Topp, and R. O. Pohl, *Science* 259, 1145 (1993).
557. S. P. Tewari, P. Silotia, and K. Bera, *Solid State Commun.* 107, 129 (1998).
558. W. P. Beyermann, M. F. Hundley, and J. D. Thompson, *Phys. Rev. Lett.* 68, 2046 (1992).
559. P. W. Anderson, B. I. Halperin, and C. M. Varma, *Philos. Mag.* 25, 1 (1972).
560. K. Allen and F. Hellman, *Phys. Rev. B* 60, 11765 (1999).
561. J. E. Fischer, A. R. McGhie, J. K. Estrada, M. Haluška, H. Kuzmany, and H.-U. ter Meer, *Phys. Rev. B* 53, 11418 (1996).
562. W. DeSorbo and W. W. Tyler, *J. Chem. Phys.* 21, 1660 (1953).
563. G. B. M. Vaughan, P. A. Heiney, D. E. Cox, J. E. Fischer, A. R. McGhie, A. L. Smith, R. M. Strongin, M. A. Cichy, and A. B. Smith III, *Chem. Phys.* 178, 599 (1993).
564. A. T. Pugachev, N. P. Churakova, N. I. Gorbenko, Kh. Saadli, and E. S. Syrkin, *J. Exp. Theor. Phys.* 87, 1014 (1998).
565. Ya. M. Soifer and N. P. Kobelev, *Mol. Mater.* 7, 267 (1996).
566. F. Yan, M. Gu, and Y. N. Wang, *J. Phys. IV* 6, C8 (1996).
567. N. P. Kobelev, R. K. Nikolaev, N. S. Sidorov, and Ya. M. Soifer, *Phys. Solid State* 44, 429 (2002).
568. N. P. Kobelev, R. K. Nikolaev, Ya. M. Soifer, and S. S. Khasanov, *Phys. Solid State* 40, 154 (1998).
569. N. P. Kobelev, Ya. M. Soifer, R. K. Nikolaev, and V. M. Levin, *Phys. Status Solidi B* 214, 303 (1999).
570. E. Burgos, E. Halac, and H. Bonadeo, *Phys. Rev. B* 49, 15544 (1994).
571. N. P. Kobelev, R. K. Nikolaev, Ya. M. Soifer, and S. S. Khasanov, *Chem. Phys. Lett.* 276, 263 (1997).
572. N. P. Kobelev, A. P. Moravski, Ya. M. Soifer, I. O. Bashkin, and O. G. Rybchenko, *Phys. Solid State* 36, 1491 (1994).
573. H. Coufal, K. Meyer, R. K. Grygier, M. de Vries, D. Jenrich, and P. Hess, *Appl. Phys. A* 59, 83 (1994).
574. A. F. Hebard, M. J. Rosseinsky, R. C. Haddon, D. W. Murphy, S. H. Glarum, T. T. M. Palstra, A. P. Ramirez, and A. R. Kortan, *Nature* 350, 600 (1991).
575. R. C. Haddon, A. F. Hebard, M. J. Rosseinsky, D. W. Murphy, S. J. Duclos, K. B. Lyons, B. Miller, J. M. Rosamilia, R. M. Fleming, A. R. Kortan, S. H. Glarum, A. V. Makhija, A. J. Muller, R. H. Eick, S. M. Zahurak, R. Tycko, G. Dabbagh, and F. A. Thiel, *Nature* 350, 320 (1991).
576. L. Holczer, O. Klein, S. M. Huang, R. B. Kaner, K. J. Fu, R. L. Whetten, and F. Diederich, *Science* 252, 1154 (1991).
577. J. P. McCauley, Jr., Q. Zhu, N. Coustel, O. Zhou, G. Vaughan, S. H. J. Idziak, J. E. Fischer, S. W. Tozer, D. M. Froski, N. Bykovetz, C. L. Lin, A. R. McGhie, B. H. Allen, W. J. Romanow, A. M. Denenstein, and A. B. Smith III, *J. Am. Chem. Soc.* 113, 8537 (1991).
578. X. D. Xiang, J. G. Hou, G. Briceno, W. A. Vareka, R. Mostovoy, A. Zettl, V. H. Crespi, and M. L. Cohen, *Science* 256, 1190 (1992).
579. X. D. Xiang, J. G. Hou, V. H. Crespi, A. Zettl, and M. L. Cohen, *Nature* 361, 54 (1993).
580. F. Bensedat, B. Xiang, and L. Kevan, *J. Phys. Chem.* 96, 6118 (1992).
581. M. Tokumoto, Y. Tanaka, N. Kinoshita, and T. Kinoshita, *J. Phys. Chem. Solids* 54, 1667 (1993).
582. T. Yildirim, L. Barbedette, J. E. Fischer, G. M. Bendele, P. W. Stephens, C. Lin, C. Goze, F. Rachdi, J. Robert, P. Petit, and T. T. M. Palstra, *Phys. Rev. B* 54, 981 (1996).
583. T. Inabe, H. Ogata, Y. Maruyama, Y. Achiba, S. Suzuki, K. Kikuchi, and I. Ikemoto, *Phys. Rev. Lett.* 69, 3797 (1992).
584. Q. Zhu, O. Zhou, N. Coustel, G. B. M. Vaughan, J. P. McCauley, Jr., W. J. Romanow, J. E. Fischer, and A. B. Smith III, *Science* 254, 545 (1991).
585. P. W. Stephens, L. Mihaly, J. B. Wiley, S. M. Huang, R. B. Kaner, F. Diederich, R. L. Whetten, and K. Holczer, *Phys. Rev. B* 45, 543 (1992).
586. P. Zhou, K. A. Wang, Y. Wang, and P. C. Eklund, *Phys. Rev. B* 46, 2595 (1992).
587. M. K. Kelly and C. Thomsen, *Phys. Rev. B* 50, 18572 (1994).
588. J. Winter and H. Kuzmany, *Phys. Rev. B* 54, 655 (1996).
589. X. H. Chen, T. Takenobu, T. Muro, H. Fudo, and Y. Iwasa, *Phys. Rev. B* 60, 12462 (1999).
590. I. D. Hands, J. L. Dunn, and C. A. Bates, *Phys. Rev. B* 63, 245414 (2001).
591. K. J. Fu, W. L. Karney, O. L. Chapman, S. M. Huang, R. B. Kaner, F. Diederich, K. Holczer, and R. L. Whetten, *Phys. Rev. B* 46, 1937 (1992).
592. A. F. Hebard, *Phys. Today* 45, 26 (1992).
593. C. H. Pennington and V. A. Stenger, *Rev. Mod. Phys.* 68, 855 (1996).
594. S. Satpathy, V. P. Antropov, O. K. Andersen, O. Jepsen, O. Gunnarsson, and A. I. Lichtenstein, *Phys. Rev. B* 46, 1773 (1992).
595. M. P. Gelfand and J. P. Lu, *Phys. Rev. Lett.* 68, 1050 (1992).
596. E. J. Mele and S. C. Erwin, *Phys. Rev. B* 50, 2150 (1994).
597. S. Satpathy, V. P. Antropov, O. K. Andersen, O. Jepsen, O. Gunnarsson, and A. I. Lichtenstein, *Phys. Rev. B* 46, 1773 (1992).
598. S. C. Erwin, "Buckminsterfullerenes" (W. E. Billups, and M. A. Ciufolini, Eds.), pp. 217-255. VCH, New York.
599. S. E. Erwin and W. E. Pickett, *Science* 254, 842 (1992).
600. M. Z. Huang, Y. N. Xu, and W. Y. Ching, *Phys. Rev. B* 46, 6572 (1992).
601. D. L. Novikov, V. A. Gubanov, and A. J. Freeman, *Physica C* 191, 399 (1992).
602. J. L. Martins and N. Troullier, *Phys. Rev. B* 46, 1776 (1992).
603. A. Oshiyama, S. Saito, N. Hamada, and Y. Miyamoto, *J. Phys. Chem. Solids* 53, 1457 (1992).
604. W. Andreoni, P. Giannozzi, and M. Parrinello, *Phys. Rev. B* 51, 2087 (1995).
605. K. P. Bohnen, R. Heid, K. M. Ho, and C. T. Chan, *Phys. Rev. B* 51, 5805 (1995).
606. O. Gunnarsson, S. C. Erwin, E. Koch, and R. M. Martin, *Phys. Rev. B* 57, 2159 (1998).
607. P. J. Benning, D. M. Poirier, T. R. Ohno, Y. Chen, M. B. Jost, F. Stepniak, G. H. Kroll, J. H. Weaver, J. Fure, and R. E. Smalley, *Phys. Rev. B* 45, 6899 (1992).
608. M. Merkel, M. Knupfer, M. S. Golden, and J. Fink, *Phys. Rev. B* 47, 11740 (1993).
609. M. Knupfer, M. Merkel, M. S. Golden, and J. Fink, *Phys. Rev. B* 47, 13944 (1993).

610. P. J. Benning, F. Stepniak, D. M. Poirier, J. L. Martins, J. H. Weaver, L. P. F. Chibante, and R. E. Smalley, *Phys. Rev. B* 47, 13843 (1993).
611. M. De Seta and F. Evangelisti, *Phys. Rev. Lett.* 71, 2477 (1993).
612. O. Gunnarsson, H. Handschuh, P. S. Bechthold, B. Kessler, G. Gantefor, and W. Eberhardt, *Phys. Rev. Lett.* 74, 1875 (1995).
613. M. S. Golder, M. Knupfer, J. Fink, J. F. Armbruster, T. R. Cummins, H. A. Romberg, M. Roth, M. Sing, M. Schmidt, and E. Sohmen, *J. Phys.: Condens. Matter* 7, 8219 (1995).
614. O. Gunnarsson, A. I. Liechtenstein, V. Eyert, M. Knupfer, J. Fink, and J. F. Armbruster, *Phys. Rev. B* 53, 3455 (1996).
615. O. Gunnarsson, V. Eyert, M. Knupfer, J. Fink, and J. F. Armbruster, *J. Phys.: Condens. Matter* 8, 2557 (1996).
616. A. I. Liechtenstein, O. Gunnarsson, M. Knupfer, J. Fink, and J. F. Armbruster, *J. Phys.: Condens. Matter* 8, 4001 (1996).
617. H. Li, Y. Xu, S. Bao, H. Li, P. He, J. Zhang, J. Wang, H. Qian, F. Liu, and Y. Kuirisi, *Phys. Rev. B* 61, 13256 (2000).
618. R. Hesper, L. H. Tjeng, A. Heeres, and G. A. Sawatzky, *Phys. Rev. Lett.* 85, 1970 (2000).
619. J. H. Weaver and D. M. Poirier, in "Solid State Physics 48" (H. Ehrenreich and F. Saepen, Eds.), p. 225. Academic, New York, 1994.
620. F. Stepniak, P. J. Benning, D. M. Poirier, and J. H. Weaver, *Phys. Rev. B* 48, 1899 (1993).
621. R. C. Haddon, A. S. Perel, R. C. Morris, S. H. Chang, A. T. Fiory, A. F. Hebard, T. T. M. Palstra, and G. P. Kochanski, *Chem. Phys. Lett.* 218, 100 (1994).
622. M. Knupfer, J. F. Armbruster, H. A. Romberg, and J. Fink, *Synth. Met.* 70, 1321 (1995).
623. E. Sohmen, J. Fink, and W. Kratschmer, *Europhys. Lett.* 17, 51 (1992).
624. T. Yildirim, L. Barbette, J. E. Fischer, C. L. Lin, J. Robert, P. Petit, and T. T. M. Palstra, *Phys. Rev. Lett.* 77, 167 (1996).
625. V. P. Antropov, O. Gunnarsson, and A. I. Liechtenstein, *Phys. Rev. B* 46, 7651 (1993).
626. T. T. M. Palstra, R. C. Haddon, A. F. Hebard, and J. Zaanen, *Phys. Rev. Lett.* 68, 1054 (1991).
627. O. Klein, G. Gruner, S. M. Huang, J. B. Wiley, and R. B. Kaner, *Phys. Rev. B* 46, 11247 (1992).
628. A. F. Hebard, T. T. M. Palstra, R. C. Haddon, and R. M. Fleming, *Phys. Rev. B* 48, 9945 (1993).
629. A. Zettl, L. Lu, X. D. Xiang, J. G. Hou, W. A. Vareka, and M. S. Fuhrer, *J. Supercond.* 7, 639 (1994).
630. W. A. Vareka and A. Zettl, *Phys. Rev. Lett.* 72, 4121 (1994).
631. T. T. M. Palstra, A. F. Hebard, R. C. Haddon, and P. B. Littlewood, *Phys. Rev. B* 50, 3462 (1994).
632. J. G. Hou, L. Lu, V. H. Crespi, X. D. Xiang, A. Zettl, and M. L. Cohen, *Solid State Commun.* 93, 973 (1995).
633. L. Degiorgi, G. Gruener, P. Wachter, S. M. Huang, J. Wiley, R. L. Whetten, R. B. Kaner, K. Holczer, and F. Diederich, *Phys. Rev. B* 46, 11250 (1992).
634. L. Degiorgi, G. Briceno, M. S. Fuhrer, A. Zettl, and P. Wachter, *Nature* 359, 541 (1994).
635. L. Degiorgi, E. J. Nicol, O. Klein, G. Gruner, P. Wachter, S. M. Huang, J. B. Wiley, and R. B. Kaner, *Phys. Rev. B* 49, 7012 (1994).
636. O. Gunnarsson, *Rev. Mod. Phys.* 69, 575 (1997).
637. G. Sparn, J. D. Thompson, S. M. Huang, R. B. Kaner, F. Diederich, R. L. Whetten, G. Gruner, and K. Holczer, *Science* 252, 1829 (1991).
638. K. Tanigaki, T. W. Ebbesen, S. Saito, J. Mizuki, J. S. Tsai, Y. Kubo, and S. Kuroshima, *Nature* 352, 222 (1991).
639. O. Zhou, G. B. M. Vaughan, Q. Zhu, J. E. Fischer, P. A. Heiney, N. Coustel, J. P. McCauley, Jr., and A. B. Smith III, *Science* 255, 833 (1992).
640. R. J. Rosseinsky, A. P. Ramirez, S. H. Glarum, D. W. Murphy, R. C. Haddon, A. F. Hebard, T. T. M. Palstra, A. R. Kortan, S. M. Zahurak, and A. V. Makhija, *Phys. Rev. Lett.* 66, 2830 (1991).
641. J. E. Schirber, D. L. Overmeyer, H. H. Wang, J. M. Williams, K. D. Carlson, A. M. Kini, U. Welp, and W. K. Kwok, *Physica C* 178, 137 (1991).
642. G. Sparn, J. D. Thompson, R. L. Whetten, S. M. Huang, R. B. Kaner, F. Diederich, G. Gruner, and K. Holczer, *Phys. Rev. Lett.* 68, 1228 (1992).
643. T. W. Ebbesen, J. S. Tsai, K. Tanigaki, J. Tabuchi, Y. Shimakawa, Y. Kubo, I. Hirosawa, and J. Mizuki, *Nature* 355, 620 (1992).
644. A. P. Ramirez, A. R. Kortan, M. J. Rosseinsky, S. J. Duclos, A. M. Mujsce, R. C. Haddon, D. W. Murphy, A. V. Makhija, S. M. Zahurak, and K. B. Lyons, *Phys. Rev. Lett.* 68, 1058 (1992).
645. C. C. Chen and C. M. Lieber, *J. Am. Chem. Soc.* 114, 3141 (1992).
646. C. C. Chen and C. M. Lieber, *Science* 259, 655 (1993).
647. Z. Zhang, C. C. Chen, S. P. Kelty, H. Dai, and C. M. Lieber, *Nature* 353, 333 (1991).
648. V. A. Stenger, C. H. Pennington, D. R. Buffinger, and R. P. Ziebarth, *Phys. Rev. Lett.* 74, 1649 (1995).
649. R. F. Kiefl, W. A. MacFarlane, K. H. Chow, S. Dunsiger, T. L. Duty, T. M. S. Johnston, J. W. Schneider, J. Sonier, L. Brard, R. M. Strongin, J. E. Fischer, and A. B. Smith III, *Phys. Rev. Lett.* 70, 3987 (1993).
650. D. Koller, M. C. Martin, and L. Mihaly, *Phys. Rev. Lett.* 77, 4082 (1996).
651. C. Gu, B. W. Veal, R. Liu, A. P. Paulikas, P. Kostic, H. Ding, K. Gofron, J. C. Campuzano, J. A. Schlueter, H. H. Wang, U. Geiser, and J. M. Williams, *Phys. Rev. B* 50, 16566 (1994).
652. Z. Zhang, C. C. Chen, and C. M. Lieber, *Science* 254, 1619 (1991).
653. P. Jess, U. Hubler, S. Behler, V. Thommen-Geiser, H. P. Lang, and H. J. Güntherodt, *Synth. Met.* 77, 201 (1996).
654. R. Tycko, G. Dabbagh, M. J. Rosseinsky, D. W. Murphy, A. P. Ramirez, and R. M. Fleming, *Phys. Rev. Lett.* 68, 1912 (1992).
655. J. G. Hou, V. H. Crespi, X. D. Xiang, W. A. Vareka, G. Briceno, A. Zettl, and M. L. Cohen, *Solid State Commun.* 86, 643 (1993).
656. J. G. Hou, X. D. Xiang, V. H. Crespi, M. L. Cohen, and A. Zettl, *Physica C* 228, 175 (1994).
657. V. Buntar and H. W. Weber, *Supercond. Sci. Technol.* 9, 599 (1996).
658. R. Tycko, G. Dabbagh, M. J. Rosseinsky, D. W. Murphy, R. M. Fleming, A. P. Ramirez, J. C. Tully, *Science* 253, 884 (1991).
659. K. Holczer, O. Klein, G. Gruner, J. D. Thompson, F. Diederich, and R. L. Whetten, *Phys. Rev. Lett.* 67, 271 (1991).
660. C. E. Johnson, H. W. Jiang, K. Holczer, R. B. Kaner, R. L. Whetten, and F. Diederich, *Phys. Rev. B* 46, 5880 (1992).
661. G. S. Boebinger, T. T. M. Palstra, A. Passner, M. J. Rosseinsky, and D. W. Murphy, *Phys. Rev. B* 46, 5676 (1992).
662. S. Foner, E. J. McNiff, D. Heiman, S. M. Huang, and R. B. Kaner, *Phys. Rev. B* 46, 14936 (1992).
663. J. G. Hou, X. D. Xiang, M. L. Cohen, and A. Zettl, *Physica C* 232, 22 (1994).
664. N. R. Werthamer, E. Helfand, and P. C. Hohenberg, *Phys. Rev.* 147, 295 (1966).
665. V. Buntar, F. M. Sauerzopf, and H. W. Weber, *Phys. Rev. B* 56, 14128 (1997).
666. S. Chu and M. E. McHenry, *Phys. Rev. B* 55, 11722 (1997).
667. C. Politis, A. I. Sokolov, and V. Buntar, *Mod. Phys. Lett. B* 6, 351 (1992).
668. V. Buntar, F. M. Sauerzopf, and H. W. Weber, *Phys. Rev. B* 54, R9651 (1996).
669. V. Buntar, U. Eckern, and C. Politis, *Mod. Phys. Lett. B* 6, 1037 (1992).
670. S. H. Irons, J. Z. Liu, P. Klavins, and R. N. Shelton, *Phys. Rev. B* 52, 15517 (1995).
671. M. Dressel, L. Degiorgi, O. Klein, and G. Gruner, *J. Phys. Chem. Solids* 54, 1411 (1993).
672. Y. J. Uemura, A. Keren, L. P. Le, G. M. Luke, B. J. Sternlieb, W. D. Wu, J. H. Brewer, R. L. Whetten, S. M. Huang, S. Lin, R. B. Kaner, F. Diederich, S. Donovan, G. Gruner, and K. Holczer, *Nature* 352, 605 (1991).

673. Y. J. Uemura, L. P. Le, and G. M. Luke, *Synth. Met.* 56, 2845 (1993).
674. L. Degiorgi, P. Wachter, G. Grüner, S. M. Huang, J. Wiley, and R. B. Kaner, *Phys. Rev. Lett.* 69, 2987 (1992).
675. C. P. Bean, *Phys. Rev. Lett.* 8, 250 (1962).
676. W. A. Fietz and W. W. Webb, *Phys. Rev.* 178, 657 (1969).
677. C. Politis, V. Buntar, W. Krauss, and A. Gurevich, *Europhys. Lett.* 17, 175 (1992).
678. M. Baenitz, M. Heinze, E. Straube, H. Werner, R. Schlögl, V. Thommen, H. J. Güntherodt, and K. Lüders, *Physica C* 228, 181 (1994).
679. J. D. Thompson, G. Sparn, K. Holczer, O. Klein, G. Grüner, R. B. Kaner, F. Diederich, and R. L. Whetten, in "Physical and Material Properties of High Temperature Superconductors" (S. K. Malic, and S. S. Shah, Eds.), p. 139. Nova, Commack, NJ, 1994.
680. C. Politis, V. Buntar, and V. P. Seminozhenko, *Int. J. Mod. Phys. B* 7, 2163 (1993).
681. M. W. Lee, M. F. Tai, S. C. Luo, and J. B. Shi, *Physica C* 245, 6 (1995).
682. M. F. Tai, G. F. Chang, and M. W. Lee, *Phys. Rev. B* 52, 1176 (1995).
683. T. T. M. Palstra, O. Zhou, Y. Iwasa, P. E. Sulewski, R. M. Fleming, and B. R. Zegarski, *Solid State Commun.* 93, 327 (1995).
684. M. J. Rosseinsky, D. W. Murphy, R. M. Fleming, R. Tycko, A. P. Ramirez, T. Siegrist, G. Dabbagh, and S. E. Barrett, *Nature* 356, 416 (1992).
685. K. Tanigaki, I. Hirosawa, T. W. Ebbesen, J. Mizuki, Y. Shimakawa, Y. Kubo, J. S. Tsai, and S. Kuroshima, *Nature* 356, 419 (1992).
686. K. Tanigaki and K. Prassides, *J. Mater. Chem.* 5, 1515 (1995).
687. I. Hirosawa, K. Tanigaki, J. Mizuki, T. W. Ebbesen, Y. Shimakawa, Y. Kubo, and S. Kuroshima, *Solid State Commun.* 82, 979 (1992).
688. J. Winter and H. Kuzmany, *Solid State Commun.* 84, 935 (1992).
689. P. W. Stephens, *Nature* 356, 383 (1992).
690. Q. Zhu, O. Zhou, J. E. Fischer, A. R. McGhie, W. J. Romanow, R. M. Strongin, M. A. Cichy, and A. B. Smith, III, *Phys. Rev. B* 47, 13948 (1993).
691. D. M. Poirier, T. R. Ohno, G. H. Kroll, P. J. Benning, F. Stepniak, J. H. Weaver, L. P. F. Chibante, and R. E. Smalley, *Phys. Rev. B* 47, 9870 (1993).
692. D. M. Poirier and J. H. Weaver, *Phys. Rev. B* 47, 10959 (1993).
693. P. W. Stephens, G. Bortel, G. Faigel, M. Tegze, A. Janossy, S. Pekker, G. Oszlanyi, and L. Forro, *Nature* 370, 636 (1994).
694. O. Chauvet, G. Oszlanyi, L. Forro, P. W. Stephens, M. Tegze, G. Faigel, and A. Janossy, *Phys. Rev. Lett.* 72, 2721 (1994).
695. S. Pekker, L. Forro, L. Mihaly, and A. Janossy, *Solid State Commun.* 90, 349 (1996).
696. S. Pekker, A. Janossy, L. Mihaly, O. Chauvet, M. Carrard, and L. Forro, *Science* 265, 1077 (1994).
697. G. Faigel, G. Bortel, M. Tegze, L. Granasy, S. Pekker, G. Oszlanyi, O. Chauvet, G. Baumgartner, L. Forro, P. W. Stephens, L. Mihaly, and A. Janossy, *Phys. Rev. B* 52, 3199 (1995).
698. T. Kalber, G. Zimmer, and M. Mehring, *Z. Phys. B* 97, 1 (1995).
699. H. Alloul, V. Brouet, E. Lafontaine, L. Malier, and L. Forro, *Phys. Rev. Lett.* 76, 2922 (1996).
700. B. Renker, H. Schober, F. Gompf, R. Heid, and E. Ressouche, *Phys. Rev. B* 53, R14701 (1996).
701. L. Cristofolini, C. M. Brown, A. J. Dianoux, M. Kosaka, K. Prassides, K. Tanigaki, and K. Vavakis, *Chem. Commun.* 2465 (1996).
702. G. B. Adams, J. B. Page, O. F. Sankey, and M. O'Keeffe, *Phys. Rev. B* 50, 17471 (1994).
703. S. C. Erwin, G. V. Krishna, and E. J. Mele, *Phys. Rev. B* 51, 7345 (1995).
704. T. Ogitsu, T. M. Briere, K. Kusakabe, S. Tsuneyuki, and Y. Kateyama, *Phys. Rev. B* 58, 13925 (1998).
705. Q. Zhu, D. E. Cox, and J. E. Fischer, *Phys. Rev. B* 51, 3966 (1995).
706. G. Oszlanyi, G. Bortel, G. Faigel, L. Granasy, G. Bendele, P. W. Stephens, and L. Forro, *Phys. Rev. B* 54, 11849 (1996).
707. M. Kosaka, K. Tanigaki, T. Tanaka, T. Take, A. Lappas, and K. Prassides, *Phys. Rev. B* 51, 12018 (1995).
708. R. M. Fleming, M. J. Rosseinsky, A. P. Ramirez, D. W. Murphy, J. C. Tully, R. C. Haddon, T. Siegrist, R. Tycko, S. H. Glarum, P. Marsh, G. Dabbagh, S. M. Zahurak, A. V. Makhija, and C. Hampton, *Nature* 352, 701 (1991); Erratum; *Nature* 353, 868 (1991).
709. O. Zhou, J. E. Fisher, N. Coustel, S. Kycia, Q. Zhu, A. R. McGhie, W. J. Romanow, J. P. McCauley, Jr., A. B. Smith III, and D. E. Cox, *Nature* 351, 462 (1991).
710. P. Dahlke, P. F. Henry, and M. J. Rosseinsky, *J. Mater. Chem.* 8, 1571 (1998).
711. A. K. Christine, G. M. Bendele, and P. W. Stephens, *Phys. Rev. B* 55, R3366 (1997).
712. R. F. Kiefl, T. L. Duty, J. W. Schneider, A. MacFarlane, K. Chow, J. W. Elzey, P. Mendels, G. D. Morris, J. H. Brewer, E. J. Ansaldo, C. Niedermayer, D. R. Noakes, C. E. Stronach, B. Hitti, and J. E. Fischer, *Phys. Rev. Lett.* 69, 2005 (1992).
713. S. C. Erwin and C. Bruder, *Physica B* 199–200, 600 (1994).
714. H. Suematsu, Y. Murakami, T. Arai, K. Kikuchi, Y. Achiba, and I. Ikemoto, *Mater. Sci. Eng. B* 19, 141 (1993).
715. C. Goze, F. Rachdi, and M. Mehring, *Phys. Rev. B* 54, 5164 (1996).
716. M. Knupfer and J. Fink, *Phys. Rev. Lett.* 79, 2714 (1997).
717. G. A. Sawatzky, "Physics and Chemistry of Fullerenes and Derivatives" (H. Kuzmany, J. Fink, M. Mehring, and S. Roth, Eds.), 1995. World Scientific, Singapore, p. 373.
718. J. P. Lu, *Phys. Rev. B* 49, 5687 (1994).
719. Y. Iwasa, T. Kaneyasu, M. Nagata, and N. Mizutani, *Synth. Met.* 70, 1361 (1995).
720. R. Kerkoud, P. Auban-Senzier, D. Jerome, S. Brazovskii, N. Kirova, I. Lukyanchuk, F. Rachdi, and C. Goze, *Synth. Met.* 77, 205 (1996).
721. R. Kerkoud, P. Auban-Senzier, D. Jerome, S. Brazovskii, I. Kukyanchuk, N. Kirova, F. Rachdi, and C. Goze, *J. Phys. Chem. Solids* 57, 143 (1996).
722. D. W. Murphy, M. J. Rosseinsky, R. M. Fleming, R. Tycko, A. P. Ramirez, R. C. Haddon, T. Siegrist, G. Dabbagh, J. C. Tully, and R. E. Walstedt, *J. Phys. Chem. Solids* 53, 1321 (1992).
723. L. Hajji, F. Rachdi, C. Goze, M. Mehring, and J. E. Fischer, *Solid State Commun.* 100, 493 (1996).
724. O. Zhou and D. E. Cox, *J. Phys. Chem. Solids* 53, 1373 (1992).
725. W. Andreoni, F. Gygi, and M. Parrinello, *Phys. Rev. Lett.* 68, 823 (1992).
726. T. Yildirim, J. E. Fischer, A. B. Harris, P. W. Stephens, D. Liu, L. Brard, R. M. Strongin, and A. B. Smith III, *Phys. Rev. Lett.* 71, 1383 (1993).
727. K. Tanigaki, I. Hirosawa, T. W. Ebbesen, J. I. Mizuki, and J. S. Tsai, *J. Phys. Chem. Solids* 54, 1645 (1993).
728. T. Yildirim, O. Zhou, J. E. Fischer, R. A. Strongin, M. A. Cichy, A. B. Smith III, C. L. Lin, and R. Jelinek, *Nature* 369, 568 (1992).
729. G. Oszlanyi, G. Baumgartner, G. Faigel, and L. Forro, *Phys. Rev. Lett.* 78, 4438 (1997).
730. G. Oszlanyi, G. Baumgartner, G. Faigel, L. Granasy, and L. Forro, *Phys. Rev. B* 58, 5 (1998).
731. K. Tanigaki, I. Hirosawa, T. W. Ebbesen, J. Mizuki, and S. Kuroshima, *Chem. Phys. Lett.* 203, 33 (1993).
732. K. Prassides, K. Vavakis, K. Kordatos, K. Tanigaki, G. M. Bendele, and P. W. Stephens, *J. Am. Chem. Soc.* 119, 834 (1997).
733. G. M. Bendele, P. W. Stephens, K. Prassides, K. Vavakis, K. Kordatos, and K. Tanigaki, *Phys. Rev. Lett.* 80, 736 (1998).
734. J. M. Fox, P. F. Henry, and J. M. Rosseinsky, *Chem. Commun.* 2299 (1996).
735. T. Yildirim, J. E. Fischer, R. Dinnebier, P. W. Stephens, and C. L. Lin, *Solid State Commun.* 93, 269 (1995).
736. Y. Chabre, D. Djurado, M. Armand, W. J. Romanow, N. Coustel, J. P. McCauley, Jr., J. E. Fischer, and A. B. Smith III, *J. Am. Chem. Soc.* 114, 764 (1992).

737. E. Ozdas, A. R. Kortan, N. Kopylov, A. P. Ramirez, T. Siegrist, and P. H. Citrin, in "Fullerenes: Recent Advances in the Physics and Chemistry of Fullerenes and Related Materials" (K. M. Kadish and R. S. Ruoff, Eds.), The Electrochemical Society Proceedings, Vol. 3. pp. 1176–1185. Electrochem Soc., Pennington, NJ, 1996.
738. L. Cristofolini, M. Riccò, and R. D. Renzi, *Phys. Rev. B* 59, 8343 (1999).
739. K. Tanigaki, T. W. Ebbesen, J.-S. Tsai, I. Hirosawa, and J. Mizuki, *Europhys. Lett.* 23, 57 (1993).
740. I. Hirosawa, K. Prassides, J. Mizuki, K. Tanigaki, M. Gevaert, A. Lappas, and J. K. Cockcroft, *Science* 264, 1294 (1994).
741. M. Kosaka, K. Tanigaki, K. Prasside, S. Margadonna, A. Lappas, C. M. Brown, and A. N. Fitch, *Phys. Rev. B* 59, R6628 (1999).
742. M. J. Rosseinsky, D. W. Murphy, R. M. Fleming, and O. Zhou, *Nature* 364, 425 (1993).
743. O. Zhou, T. T. M. Palstra, Y. Iwasa, R. M. Fleming, A. F. Hebard, P. E. Sulewski, D. W. Murephy, and B. R. Zegarski, *Phys. Rev. B* 52, 483 (1995).
744. H. Shimoda, Y. Iwasa, Y. Miyamoto, Y. Maniwa, and T. Mitani, *Phys. Rev. B* 54, R15653 (1996).
745. O. Zhou, R. M. Fleming, D. M. Murphy, M. J. Rosseinsky, A. P. Ramirez, R. B. van Dover, and R. C. Haddon, *Nature* 362, 433 (1993).
746. A. R. Kortan, N. Kopylov, S. Glarum, E. M. Gyorgy, A. P. Ramirez, R. M. Fleming, O. Zhou, F. A. Thiel, P. L. Trevor, and R. C. Haddon, *Nature* 360, 566 (1992).
747. M. Baenitz, M. Heinze, K. Luders, H. Werner, R. Schlogl, M. Weiden, G. Sparn, and F. Steglich, *Solid State Commun.* 96, 539 (1995).
748. Th. Schedel-Niedrig, M. C. Böhm, H. Werner, J. Schulte, and R. Schlögl, *Phys. Rev. B* 55, 13542 (1997).
749. B. Gogia, K. Kordatos, H. Suematsu, K. Tanigaki, and K. Prassides, *Phys. Rev. B* 58, 1077 (1998).
750. Th. Schedel-Niedrig, M. C. Böhm, H. Werner, J. Schulte, and R. Schlögl, *Solid State Commun.* 98, 463 (1996).
751. D. M. Deaven, P. E. Lammert, and D. S. Rokhsar, *Phys. Rev. B* 52, 16377 (1995).
752. S. Saito and A. Oshiyama, *Phys. Rev. Lett.* 71, 121 (1993).
753. S. Saito and A. Oshiyama, *Solid State Commun.* 83, 107 (1992).
754. S. Saito and A. Oshiyama, *J. Phys. Chem. Solids* 54, 1759 (1993).
755. Y. Chen, D. M. Porier, M. B. Jost, C. Gu, T. R. Ohno, J. L. Martins, J. H. Weaver, L. P. F. Chibante, and R. E. Smalley, *Phys. Rev. B* 46, 7961 (1992).
756. X. H. Chen, X. J. Zhou, and S. Roth, *Phys. Rev. B* 54, 3971 (1996).
757. Y. Z. Li, J. C. Patrin, M. Chander, J. H. Weaver, L. P. F. Chibante, and R. E. Smalley, *Phys. Rev. B* 46, 12914 (1992).
758. J. E. Schirber, W. R. Bayless, A. R. Kortan, and N. Kopylov, *Physica C* 213, 190 (1993).
759. R. C. Haddon, G. P. Kochanski, A. F. Hebard, A. T. Fiory, and R. C. Morris, *Science* 258, 1636 (1992).
760. R. C. Haddon, G. P. Kochanski, A. F. Hebard, A. T. Fiory, R. C. Morris, and A. S. Perel, *Chem. Phys. Lett.* 203, 433 (1993).
761. H. Romberg, M. Roth, and J. Fink, *Phys. Rev. B* 49, 1427 (1994).
762. A. R. Kortan, N. Kopylov, E. Ozdas, A. P. Ramirez, R. M. Fleming, and R. C. Haddon, *Chem. Phys. Lett.* 223, 501 (1994).
763. A. R. Kortan, N. Kopylov, R. M. Fleming, O. Zhou, F. A. Thiel, and R. C. Haddon, *Phys. Rev. B* 47, 13070 (1993).
764. G. Sparn, A. Link, F. Steglich, M. Baenitz, K. Luders, H. Werner, and R. Schlogl, *J. Low. Temp. Phys.* 105, 1703 (1996).
765. Y. Iwasa, M. Kawaguchi, H. Iwasaki, T. Mitani, N. Wada, and T. Hasegawa, *Phys. Rev. B* 57, 13395 (1998).
766. Y. Iwasa, H. Hayashi, T. Furudate, and T. Mitani, *Phys. Rev. B* 54, 14960 (1996).
767. Y. Iwasa, H. Hayashi, T. Furudate, M. Kawaguchi, and T. Mitani, *Synth. Met.* 86, 2309 (1997).
768. T. Yildirim, L. Barbedette, J. E. Fischer, G. M. Bendele, P. W. Stephens, C. L. Lin, C. Goze, F. Rachdi, J. Robert, P. Petit, and T. T. M. Palstra, *Phys. Rev. B* 54, 11981 (1996).
769. Y. Errammach, A. Rezzouk, and F. Rachdi, *Synth. Met.* 129, 147 (2002).
770. H. Tou, Y. Manjwa, S. Taga, Y. Iwasa, T. Mitani, K. Tanigaki, B. Gogia, and H. Suematsu, *Synth. Met.* 102, 1463 (1999).
771. E. Özdas, A. R. Kortan, N. Kopylov, A. P. Ramirez, T. Siegrist, K. M. Rabe, H. E. Bair, S. Schuppler, and P. H. Citrin, *Nature* 375, 126 (1995).
772. P. H. Citrin, E. Ozdas, S. Schuppler, A. R. Kortan, and K. B. Lyons, *Phys. Rev. B* 56, 5213 (1997).
773. K. M. Rabe and P. H. Citrin, *Phys. Rev. B* 58, R551 (1998).
774. X. H. Chen and G. Roth, *Phys. Rev. B* 52, 15534 (1995).
775. X. H. Chen, S. Y. Li, G. G. Qian, K. Q. Ruan, and L. Z. Cao, *Phys. Rev. B* 57, 10770 (1998).
776. D. Claves, Y. Ksari, G. Chouteau, A. Collomb, and Ph. Touzain, *Solid State Commun.* 99, 359 (1996).
777. Y. Ksari-Habiles, D. Claves, G. Chouteau, P. Touzain, C. Jeandey, J. L. Oddou, and A. Stepanov, *J. Phys. Chem. Solids* 58, 1771 (1997).
778. D. Claves, Y. Ksari-Habiles, G. Chouteau, and P. Touzain, *Solid State Commun.* 106, 431 (1998).
779. A. S. Ginwalla, A. L. Balch, S. M. Kauzlarich, S. H. Irons, P. Klavins, and R. N. Shelton, *Chem. Mater.* 9, 278 (1997).
780. Q. Zhu, D. E. Cox, J. E. Fischer, K. Kniaz, A. R. McGhie, and O. Zhou, *Nature* 366, 712 (1992).
781. M. Kobayashi, Y. Akahama, H. Kawamura, H. Shinohara, H. Sato, and Y. Saito, *Solid State Commun.* 81, 93 (1992).
782. Y. Akahama, M. Kobayashi, H. Kawamura, H. Shinohara, H. Sato, and Y. Saito, *Mater. Sci. Eng.* 19, 100 (1993).
783. H. Werner, M. Wesemann, and R. Schlögl, *Europhys. Lett.* 20, 107 (1992).
784. N. G. Park, S. W. Cho, S. J. Kim, and J. H. Choy, *Chem. Mater.* 8, 324 (1996).
785. Y. Maniwa, T. Shibata, K. Mizoguchi, K. Kume, K. Kikuchi, I. Ike-moto, S. Suzuki, and Y. Achiba, *J. Phys. Soc. Jpn.* 61, 2212 (1992).
786. R. E. Haufler, J. J. Conceicao, L. P. F. Chibante, Y. Chai, N. E. Byrne, S. Flanagan, M. M. Haley, S. C. O'Brien, C. Pan, Z. Xiao, W. E. Billups, M. A. Ciufolini, R. H. Hauge, J. L. Margrave, L. J. Wilson, R. F. Curl, and R. E. Smalley, *J. Phys. Chem.* 94, 8634 (1990).
787. H. Selig, C. Lifshitz, T. Peres, J. E. Fischer, A. R. McGhie, W. J. Romanow, J. P. McCauley, Jr., and A. B. Smith III, *J. Am. Chem. Soc.* 113, 5475 (1997).
788. J. H. Holloway, E. G. Hope, R. Taylor, G. J. Langley, A. G. Avent, T. J. Dennis, J. P. Hare, H. W. Kroto, and D. R. M. Walton, *Chem. Commun.* 966 (1991).
789. F. Cataldo, *Carbon* 32, 437 (1994).
790. P. R. Birkett, P. B. Hitchcock, H. W. Kroto, R. Taylor, and D. R. M. Walton, *Nature* 357, 479 (1992).
791. F. N. Tebbe, R. L. Halow, D. B. Chase, D. L. Thorn, G. C. Campbell, Jr., J. C. Calabrese, N. Herron, R. J. Young, Jr., and E. Wasserman, *Science* 256, 822 (1992).
792. M. Gu, T. B. Tang, C. Hu, and D. Feng, *Phys. Rev. B* 58, 659 (1998).
793. J. E. Schirber, R. A. Assink, G. A. Samra, B. Morosin, and D. Loy, *Phys. Rev. B* 51, 15552 (1995).
794. S. A. FitzGerald, T. Yildirim, L. J. Santodonato, D. A. Neumann, J. R. D. Copley, J. J. Rush, and F. Trouw, *Phys. Rev. B* 60, 6439 (1999).
795. S. A. FitzGerald, S. Forth, and M. Rinkoski, *Phys. Rev. B* 65, 140302 (2002).
796. B. Morosin, R. A. Assink, R. G. Dunn, T. M. Massis, J. E. Schirber, and G. H. Kwei, *Phys. Rev. B* 56, 13611 (1997).
797. W. R. Datars, T. R. Chien, R. K. Nkum, and P. K. Ummat, *Phys. Rev. B* 50, 4937 (1994).
798. W. R. Datars, J. D. Palidwar, and P. K. Ummat, *J. Phys. Chem. Solids* 57, 977 (1996).
799. R. Francis, P. K. Ummat, and W. R. Datarsi, *J. Phys. Condens. Matter* 9, 7223 (1997).

800. I. W. Locke, A. D. Darwish, H. W. Kroto, K. Prassides, R. Taylor, and D. R. M. Walton, *Chem. Phys. Lett.* 225, 186 (1994).
801. R. E. Douthwaite, M. L. H. Green, S. J. Heyes, M. J. Rosseinsky, and J. F. C. Turner, *Chem. Commun.* 1367 (1994).
802. G. Roth and P. Adelmann, *Appl. Phys. A* 56, 169 (1993).
803. J. D. Crane, P. B. Hitchcock, H. W. Kroto, R. Taylor, and D. R. M. Walton, *Chem. Commun.* 1764 (1992).
804. A. L. Balch, J. W. Lee, B. C. Noll, and M. M. Olmstead, *J. Chem. Soc., Chem. Commun.* 56 (1993).
805. M. F. Meidine, P. B. Hitchcock, H. W. Kroto, R. Taylor, and D. R. M. Walton, *Chem. Commun.* 1534 (1992).
806. P. W. Stephens, D. Cox, J. W. Lauher, L. Mihaly, J. B. Wiley, P. M. Allemand, A. Hirsch, K. Holczer, Q. Li, J. D. Thompson, and F. Wudl, *Nature* 355, 311 (1992).
807. P. Zhou, A. M. Rao, K. A. Wang, J. D. Robertson, C. Eloi, M. S. Meier, S. L. Ren, X. X. Bi, P. C. Eklund, and M. S. Dresselhaus, *Appl. Phys. Lett.* 60, 2871 (1992).
808. P. Zhou, Z.-H. Dong, A. M. Rao, and P. C. Eklund, *Chem. Phys. Lett.* 211, 337 (1993).
809. F. Cataldo, *Polym. Int.* 48, 143 (1999).
810. D. S. Cornett, I. J. Amster, M. A. Duncan, A. M. Rao, and P. C. Eklund, *J. Phys. Chem.* 97, 5036 (1993).
811. B. Burger, J. Winter, and H. Kuzmany, *Synth. Met.* 86, 2329 (1997).
812. A. Hassanien, J. Gasperic, J. Demsar, I. Muševic, and D. Mihailovic, *Appl. Phys. Lett.* 70, 417 (1997).
813. B. Sundqvist, *Adv. Phys.* 48, 1 (1999).
814. Y. Iwasa, T. Arima, R. M. Fleming, T. Siegrist, O. Zhou, R. C. Haddon, L. J. Rothberg, K. B. Lyons, H. L. Carter, Jr., A. F. Hebard, R. Tycko, G. Dabbagh, J. J. Krajewski, G. A. Thomas, and T. Yagi, *Science* 264, 1570 (1994).
815. G. Oszlanyi and L. Forro, *Solid State Commun.* 93, 265 (1995).
816. M. Núñez-Regueiro, L. Marques, J.-L. Hodeau, O. Béthoux, and M. Perroux, *Phys. Rev. Lett.* 74, 278 (1995).
817. B. Sundqvist, O. Andersson, U. Edlund, A. Fransson, A. Inaba, P. Jacobsson, D. Jhnels, P. Launois, C. Meingast, R. Moret, T. Moritz, P.-A. Persson, A. Soldatov, and T. Wågberg, in "Fullerenes: Recent Advances in the Chemistry and Physics of Fullerenes and Related Materials" (K. M. Kadish and R. S. Ruoff, Eds.), ECS Proceedings, Vol. 3, p. 1014. The Electrochemical Society, Pennington, NJ, 1996.
818. R. Moret, P. Launois, P.-A. Persson, and B. Sundqvist, *Europhys. Lett.* 40, 55 (1997).
819. V. A. Davydov, L. S. Kashevarova, A. V. Rakhmanina, V. Agafonov, H. Allouchi, R. Ceolin, A. V. Dzyabchenko, V. M. Senyavin, and H. Szwarc, *Phys. Rev. B* 58, 14786 (1998).
820. V. A. Davydov, V. Agafonov, H. Allouchi, R. Ceolin, A. V. Dzyabchenko, and H. Szwarc, *Synth. Met.* 103, 2415 (1999).
821. V. A. Davydov, L. S. Kashevarova, A. V. Rakhmanina, V. Agafonov, H. Allouchi, R. Ceolin, A. V. Dzyabchenko, V. M. Senyavin, H. Szwarc, T. Tanaka, and K. Komatsu, *J. Phys. Chem. B* 103, 1800 (1999).
822. R. Moret, P. Launois, T. Wågberg, and B. Sundqvist, *Eur. Phys. J. B* 15, 253 (2000).
823. X. Chen and S. Yamanaka, *Chem. Phys. Lett.* 360, 501 (2002).
824. T. L. Makarova, T. Wågberg, B. Sundqvist, Xiao-Mei Zhu, E. B. Nyeanchi, M. E. Gaevski, E. Olsson, V. Agafonov, V. A. Davydov, A. V. Rakhmanina, and L. S. Kashevarova, *Mol. Mater.* 13, 151 (2000).
825. X. Chen, S. Yamanaka, K. Sako, Y. Inoue, and M. Yasukawa, *Chem. Phys. Lett.* 356, 291 (2002).
826. L. A. Chernozatonskii, N. R. Serebryanaya, and B. N. Mavrin, *Chem. Phys. Lett.* 316, 199 (2000).
827. M. Ata, N. Takahashi, and K. Nojima, *J. Phys. Chem.* 98, 9960 (1994).
828. N. Takahashi, H. Dock, N. Matsuzawa, and M. Ata, *J. Appl. Phys.* 74, 5790 (1993).
829. J. Kastner, H. Kuzmany, and L. Palmetshofer, *Appl. Phys. Lett.* 65, 543 (1994).
830. Y. Nakamura, Y. Mera, and K. Maeda, *Appl. Phys. Lett.* 77, 2834 (2000).
831. Y. B. Zhao, D. M. Poirier, R. J. Pechman, and J. H. Weaver, *Appl. Phys. Lett.* 64, 577 (1994).
832. A. Matsutani, F. Koyama, and K. Iga, *Jpn. J. Appl. Phys.* 37, 4211 (1998).
833. L. Marques, J.-L. Hodeau, and M. Núñez-Regueiro, *Mol. Mater.* 8, 49 (1996).
834. V. A. Davydov, L. S. Kashevarova, A. V. Rakhmanina, V. M. Senyavin, R. Céolin, H. Szwarc, H. Allouchi, and V. Agafonov, *Phys. Rev. B* 61, 11936 (2000).
835. V. A. Davydov, V. Agafonov, A. V. Dzyabchenko, R. Céolin, and H. Szwarc, *J. Solid State Chem.* 141, 164 (1998).
836. S. Okada, S. Saito, and A. Oshiyama, *Phys. Rev. Lett.* 83, 1986 (1999).
837. V. V. Brazhkin and A. G. Lyapin, *Phys. Rev. Lett.* 85, 5671 (2000).
838. S. Okada, S. Saito, and A. Oshiyama, *Phys. Rev. Lett.* 85, 5672 (2000).
839. L. Marques, M. Mezouar, J.-L. Hodeau, M. Núñez-Regueiro, N. R. Serebryanaya, V. A. Ivdenko, V. D. Blank, and G. A. Dubitsky, *Science* 283, 1720 (1999).
840. N. R. Serebryanaya and L. A. Chernozatonskii, *Solid State Commun.* 114, 537 (2000).
841. V. Agafonov, V. A. Davydov, L. S. Kashevarova, A. V. Rakhmanina, A. Kahn-Harari, P. Dubois, R. Céolin, and H. Szwarc, *Chem. Phys. Lett.* 267, 193 (1997).
842. V. A. Davydov, L. S. Kashevarova, A. V. Rakhmanina, A. V. Dzyabchenko, V. N. Agafonov, P. Dubois, R. Céolin, and H. Szwarc, *JETP Lett.* 66, 120 (1997).
843. K. Tanaka, Yu. Matsuura, Y. Oshima, T. Yamabe, Y. Asai, and M. Tokumoto, *Solid State Commun.* 93, 163 (1995).
844. C. H. Xu and G. E. Scuseria, *Phys. Rev. Lett.* 74, 274 (1995).
845. S. Okada and S. Saito, *Phys. Rev. B* 55, 4039 (1997).
846. S. Okada and S. Saito, *Phys. Rev. B* 59, 1930 (1999).
847. V. V. Belavin, L. G. Bulusheva, A. V. Okotrub, D. Tománek, *J. Phys. Chem. Solids* 61, 1901 (2000).
848. Y. Iwasa, K. Tanoue, T. Mitani, and T. Yagi, *Phys. Rev. B* 58, 16374 (1998).
849. M. Shiraiishi, M. Ramm, and M. Ata, *Appl. Phys. A* 74, 613 (2002).
850. F. Bommeli, L. Degiorgi, P. Wachter, Ö. Legeza, A. Jánosy G. Oszlanyi, O. Chauvet, and L. Forro, *Phys. Rev. B* 51, 14794 (1995).
851. T. L. Makarova, P. Scharff, B. Sundqvist, B. narymbetov, H. Kobayashi, M. Tokumoto, V. A. Davydov, A. V. Rakhmanina, and L. S. Kashevarova, *Synth. Met.* 121, 1099 (2001).
852. T. L. Makarova, B. Sundqvist, P. Scharff, M. E. Gaevski, E. Olsson, V. A. Davydov, A. V. Rakhmanina, and L. S. Kashevarova, *Carbon* 39, 2203 (2001).
853. A. V. Okotrub, V. V. Belavin, L. G. Bulusheva, V. A. Davydov, T. L. Makarova, and D. Tománek, *J. Chem. Phys.* 115, 5637 (2001).
854. S. G. Buga, V. D. Blank, G. A. Dubitsky, L. Edman, X.-M. Zhu, E. B. Nyeanchi, and B. Sundqvist, *J. Phys. Chem. Solids* 61, 1009 (2000).
855. Y. Wang, J. M. Holden, A. M. Rao, P. C. Eklund, U. D. Venkateswaran, D. Eastwood, R. L. Lidberg, G. Dresselhaus, and M. S. Dresselhaus, *Phys. Rev. B* 51, 4547 (1995).
856. C. Xu, G. Chen, E. Xie, and J. Gong, *Appl. Phys. Lett.* 70, 2641 (1997).
857. G. Lyapin, V. V. Brazhkin, S. G. Lyapin, S. V. Popova, T. D. Varfolomeeva, R. A. Voloshin, A. A. Pronin, N. E. Sluchanko, A. G. Gavrilyuk, and I. A. Trojan, *Phys. Status Solidi B* 211, 401 (1999).
858. R. A. Wood, M. H. Lewis, M. R. Lees, S. M. Bennington, M. G. Cain, and N. Kitamura, *J. Phys.: Condens. Matter* 14 L385 (2002).
859. V. M. Levin, V. D. Blank, V. M. Prokhorov, Ja. M. Soifer, and N. P. Kobelev, *J. Phys. Chem. Solids* 61, 1017 (2000).

860. V. D. Blank, S. G. Buga, N. R. Serebryanaya, G. A. Sulyanov, M. Yu. Popov, V. N. Denisov, A. N. Ivlev, and B. N. Mavrin, *Phys. Lett. A* 220, 149 (1996).
861. V. Blank, M. Popov, G. Pivovarov, N. Lvova, K. Gogolinsky, and V. Reshetov, *Diamond Relat. Mater.* 7, 427 (1998).
862. G. K. Wertheir and D. N. E. Buchanam, *Solid State Commun.* 88, 97 (1993).
863. A. F. Hebard, C. B. Eom, Y. Iwasa, K. B. Lyons, G. A. Thomas, D. H. Rapkine, R. M. Fleming, R. C. Haddon, J. M. Phillips, J. H. Marshall, and R. H. Eick, *Phys. Rev. B* 50, 17740 (1994).
864. B. Wang, H. Wang, Y. Li, B. Xie, and J. G. Hou, *Physica C* 282, 735 (1997).
865. L. Xiang, H. Wang, W. N. Wang, Y. J. Tang, H. W. Zhao, W. S. Zhan, and J. G. Hou, *J. Phys.: Condens. Matter* 13, 3987 (2001).
866. J. G. Hou, Y. Wang, W. Xu, Li Yang, and Y. H. Zhang, *Appl. Phys. Lett.* 70, 3100 (1997).
867. J. G. Hou, Y. Wang, W. Xu, L. Yang, and Y. H. Zhang, *Mater. Lett.* 34, 36 (1998).
868. J. G. Hou, Y. Li, Y. Wang, W. Xu, J. Zuo, and Y. H. Zhang, *Phys. Status Solidi A* 163, 403 (1997).
869. J. G. Hou, X. Li, and H. Wang, *Adv. Mater.* 11, 1124 (2000).
870. R. Popescu, D. Macovei, A. Devenyi, R. Manaila, P. B. Barna, A. Kovacs, and J. L. Lábár, *Eur. Phys. J. B* 13, 737 (2000).
871. B. Wang, H. Q. Wang, Y. Q. Li, S. Y. Zhang, and J. G. Hou, *Mater. Res. Bull.* 35, 511 (2000).
872. Y. Li, Y. Wang, W. Xu, J. G. Hou, and Y. H. Zhang, *Physica C* 282, 737 (1997).
873. X. D. Zhang, W. B. Zhao, K. Wu, J. L. Zhang, C. Y. Li, D. L. Yin, Z. N. Gu, X. H. Zhou, and Z. X. Jin, *Chem. Phys. Lett.* 228, 100 (1994).
874. J. G. Hou, X. Li, H. Wang, and B. Wang, *J. Phys. Chem. Solids* 61, 995 (2000).
875. X. Li, Y. J. Tang, H. W. Zhao, and W. S. Zhan, *Appl. Phys. Lett.* 77, 984 (2000).
876. X. Li, Y. J. Tang, H. Wang, H. W. Zhao, W. S. Zhan, and J. G. Hou, *Phys. Status Solidi A* 186, 57 (2001).
877. H. Q. Wang, J. G. Hou, O. Takeuchi, Y. Fujisaku, and A. Kawazu, *Phys. Rev. B* 61, 2199 (2000).
878. Z. Zhao, H. Q. Wang, B. Wang, J. G. Hou, G. L. Liu, and X. F. Jin, *Phys. Rev. B* 65, 235413 (2002).
879. J. A. Block, K. Parvin, J. L. Alpers, T. Sezen, and R. LaDuca, *IEEE Trans. Magn.* 34, 982 (1998).
880. B. Zhao, J. Y. Chow, and X. Yan, *J. Appl. Phys.* 79, 6022 (1996).
881. L. A. Zheng, B. M. Lairson, E. V. Barrera, and R. D. Shull, *Appl. Phys. Lett.* 77, 3242 (2000).
882. T. C. Arnolduseen, in "Magnetic Recording Technology" (C. D. Mee and E. D. Daniel, Eds.), pp. 4–36. McGraw-Hill, New York, 1995.
883. K. E. Johnson, J. B. Mahlke, K. J. Schultz, and A. C. Wall, *IEEE Trans. Magn.* 29, 215 (1993).
884. T. Guo, C. Jin, and R. E. Smalley, *J. Phys. Chem.* 95, 4948 (1991).
885. Z. C. Ying, R. L. Hettich, R. N. Compton, and R. E. Haufler, *J. Phys. B* 29, 4935 (1996).
886. Y. F. Jia, Q. Zhu, and K. M. Thomas, *Chem. Phys. Lett.* 364, 171 (2002).
887. N. L. Clipston, T. Brown, Y. Y. Vasil'ev, M. P. Barrow, R. Herzschuh, U. Reuther, A. Hirsch, and T. Drewello, *J. Phys. Chem. A* 104, 9171 (2000).
888. J. C. Hummelen, B. Knight, J. Pavlovich, R. González, and F. Wudl, *Science* 269, 1554 (1995).
889. T. Grösser, M. Prato, V. Lucchini, A. Hirsch, and F. Wudl, *Angew. Chem. Int. Ed.* 34, 1341 (1995).
890. B. Nuber and A. Hirsch, *Chem. Commun.* 1421 (1996).
891. W. Andreoni, A. Curioni, K. Holczer, K. Prassides, M. Keshavarz-K, J. C. Hummelen, and F. Wudl, *J. Am. Chem. Soc.* 118, 11335 (1996).
892. C. Bellavia-Lund, R. González, J. C. Hummelen, R. G. Hicks, A. Sastre, and F. Wudl, *J. Am. Chem. Soc.* 119, 2946 (1997).
893. A. Gruss, K.-P. Dinse, A. Hirsch, B. Nuber, and U. Reuther, *J. Am. Chem. Soc.* 119, 8728 (1997).
894. P.-M. Allemand, G. Srdanov, A. Koch, K. Khemani, F. Wudl, Y. Rubin, M. Diederich, M. M. Alvarez, S. J. Anz, and R. L. Whetten, *J. Am. Chem. Soc.* 113, 2780 (1991).
895. J. Dong, J. Jiang, Z. D. Wang, and D. Y. Xing, *Phys. Rev. B* 51, 1977 (1995).
896. W. Andreoni, F. Gygi, and M. Parrinello, *Chem. Phys. Lett.* 190, 159 (1992).
897. T. Pichler, M. Knupfer, R. Friedlein, S. Haffner, B. Umlauf, M. Golden, O. Knauff, H.-D. Bauer, J. Fink, M. Keshavarz-K, C. Bellavia-Lund, A. Sastre, J. C. Hummelen, and F. Wudl, *Synth. Met.* 86, 2313 (1997).
898. S. Haffner, T. Pichler, M. Knupfer, B. Umlauf, R. Friedlein, M. Golden, J. Fink, M. Keshavarz-K, C. Bellavia-Lund, A. Sastre, J. C. Hummelen, and F. Wudl, *Eur. Phys. J. B* 1, 11 (1998).
899. C. M. Brown, E. Beer, C. Bellavia, L. Cristofolini, R. Gonzalez, M. Hanfland, D. Häusermann, M. Keshavarz-K, K. Kordatos, K. Prassides, and F. Wudl, *J. Am. Chem. Soc.* 118, 8715 (1996).
900. C. M. Brown, L. Cristofolini, K. Kordatos, K. Prassides, C. Bellavia-Lund, R. Gonzalez, M. Keshavarz-K., F. Wudl, A. K. Cheetham, J. P. Zhang, W. Andreoni, A. Curioni, A. N. Fitch, and P. Pattison, *Chem. Mater.* 8, 2548 (1996).
901. H.-J. Muhr, R. Nesper, B. Schnyder, and R. Kötz, *Chem. Phys. Lett.* 249, 399 (1996).
902. T. Nakamura, K. Ishikawa, K. Yamamoto, T. Ohana, S. Fujiwara, and Y. Koga, *Phys. Chem. Chem. Phys.* 1, 2631 (1999).
903. U. Reuther and A. Hirsch, *Chem. Commun.* 1401 (1998).
904. Y. Tobe, H. Nakanishi, M. Sonoda, T. Wakabayashi, and Y. Achiba, *Chem. Commun.* 1625 (1999).
905. L. Hultman, S. Stafström, Z. Czizgany, J. Neidhardt, N. Hellgren, I. F. Brunell, K. Suenaga, and C. Colliex, *Phys. Rev. Lett.* 87, 225503 (2001).
906. T. Nakamura, K. Ishikawa, A. Goto, M. Ishihara, T. Ohana, and Y. Koga, *Diamond Relat. Mater.* 10, 1228 (2001).
907. D. A. Jelski, J. R. Bowser, R. James, X. Xia, G. Xinfu, J. Gao, and T. F. George, *J. Cluster. Sci.* 4, 173 (1993).
908. T. Kimura, T. Sugai, and H. Shinohara, *Chem. Phys. Lett.* 256, 269 (1996).
909. M. Pellarin, C. Ray, J. Lermé, J. L. Vialle, M. Broyer, X. Blase, P. Kéghélian, P. Mélinon, and A. Perez, *Eur. Phys. J. D* 9, 49 (1999).
910. M. Pellarin, C. Ray, P. Mélinon, J. Lermé, J. L. Vialle, P. Kéghélian, A. Perez, and M. Broyer, *Chem. Phys. Lett.* 277, 96 (1997).
911. C. Ray, M. Pellarin, J. L. Lermé, J. L. Vialle, M. Broyer, X. Blase, P. Kéghélian, P. Mélinon, and A. Perez, *Phys. Rev. Lett.* 80, 5365 (1998).
912. I. M. L. Billas, F. Tast, W. Branz, N. Malinowski, M. Heinebrodt, T. P. Martin, M. Boero, C. Massobrio, and M. Parrinello, *Eur. Phys. J. D* 9, 337 (1999).
913. I. M. L. Billas, C. Massobrio, M. Boero, M. Parrinello, W. Branz, F. Tast, N. Malinowski, M. Heinebrodt, and T. P. Martin, *J. Chem. Phys.* 111, 6787 (1999).
914. J. F. Christian, Z. Wan, and S. L. Anderson, *Chem. Phys. Lett.* 199, 373 (1992).
915. J. J. Stry and J. F. Garvey, *Chem. Phys. Lett.* 243, 199 (1995).
916. C. Moschel and M. Jansen, *Z. Anorg. Allg. Chem.* 625, 175 (1999).
917. W. Branz, I. M. L. Billas, N. Malinowski, F. Tast, M. Heinebrodt, and T. P. Martin, *J. Chem. Phys.* 109, 3425 (1998).
918. L. D. Strout, R. L. Murry, C. H. Xu, W. C. Eckhoff, G. F. Odom, and G. E. Scuseria, *Chem. Phys. Lett.* 214, 576 (1993).
919. N. Matsuzawa, M. Ata, D. A. Dixon, and G. Fitzgerald, *J. Phys. Chem.* 98, 2555 (1994).

920. M. Menon, K. R. Subbaswamy, and M. Sawtarie, *Phys. Rev. B* 49, 13966 (1994).
921. D. Porezag, M. R. Pederson, T. Frauenheim, and T. K. Köhler, *Phys. Rev. B* 52, 14963 (1995).
922. J. Kürti and K. Németh, *Chem. Phys. Lett.* 256, 119 (1996).
923. G. E. Scuseria, *Chem. Phys. Lett.* 257, 583 (1996).
924. S. Osawa, M. Sakai, and E. Osawa, *J. Phys. Chem. A* 101, 1378 (1997).
925. G.-W. Wang, K. Komatsu, Y. Murata, and M. Shiro, *Nature* 387, 583 (1997).
926. K. Komatsu, G.-W. Wang, Y. Murata, T. Tanaka, and K. Fujiwara, *J. Org. Chem.* 63, 9358 (1998).
927. S. Lebedkin, A. Gromov, S. Giesa, R. Gleiter, B. Renker, H. Rietschel, and W. Krätschmer, *Chem. Phys. Lett.* 285, 210 (1998).
928. V. A. Davydov, L. S. Kashevarova, A. V. Rakhmanina, V. M. Senyavin, V. Agafonov, R. Ceolin, and H. Szwarc, *JETP Lett.* 68, 928 (1998).
929. Y. Iwasa, K. Tanoue, T. Mitani, A. Izuoka, T. Sugawara, and Yagi, *Chem. Commun.* 1411 (1998).
930. V. A. Davydov, L. S. Kashevarova, A. V. Rakhmanina, V. M. Senyavin, R. Céolin, H. Szwarc, H. Allouchi, and V. Agafonov, *Phys. Rev. B* 61, 11936 (2000).
931. A. V. Dzyabchenko, V. Agafonov, and V. A. Davydov, *J. Phys. Chem. A* 103, 2812 (1999).
932. M. R. Pederson and A. A. Quong, *Phys. Rev. Lett.* 74, 2319 (1995).
933. V. C. Long, J. L. Musfeldt, K. Kamarás, G. B. Adams, J. B. Page, Y. Iwasa, and W. E. Mayo, *Phys. Rev. B* 61, 13191 (2000).
934. B. Ma, J. E. Riggs, and Y.-P. Sun, *J. Phys. Chem. B* 102, 5999 (1998).
935. Y. Chai, T. Guo, C. Jin, R. E. Haufler, L. P. F. Chibante, J. Fure, L. Wang, J. M. Alford, and R. E. Smalley, *J. Phys. Chem.* 95, 7564 (1991).
936. J. Heath, S. C. O'Brien, Q. Zhang, Y. Liu, R. F. Curl, H. W. Kroto, F. K. Tittel, and R. E. Smalley, *J. Am. Chem. Soc.* 107, 7779 (1985).
937. F. D. Weiss, J. L. Elkind, S. C. O'Brien, R. F. Curl, and R. E. Smalley, *J. Am. Chem. Soc.* 110, 4464 (1988).
938. Y. Kubozono, H. Maeda, Y. Takabayashi, K. Hiraoka, T. Nakai, S. Kashino, S. Emura, S. Ukita, and T. Sogabe, *J. Am. Chem. Soc.* 118, 6998 (1996).
939. T. Inoue, Y. Kubozono, S. Kashino, Y. Takabayashi, K. Fujitaka, M. Hida, M. Inoue, T. Kanbara, S. Emura, and T. Uruga, *Chem. Phys. Lett.* 316, 381 (2000).
940. T. Ogawa, T. Sugai, and H. Shinohara, *J. Am. Chem. Soc.* 122, 3538 (2000).
941. T. Kanbara, Y. Kubozono, Y. Takabayashi, S. Fujiki, S. Iida, Y. Haruyama, S. Kashino, S. Emura, and T. Akasaka, *Phys. Rev. B* 64, 113403 (2001).
942. A. Gromov, W. Krätschmer, N. Krawez, R. Tellgmann, and E. E. B. Campbell, *Chem. Commun.* 2003 (1997).
943. Ch. Kusch, N. Krawez, R. Tellgmann, B. Winter, and E. E. B. Campbell, *Appl. Phys. A* 66, 293 (1998).
944. T. Almeida Murphy, T. Pawlik, A. Weidinger, M. Höhne, R. Alcalá, and J.-M. Spaeth, *Phys. Rev. Lett.* 77, 1075 (1996).
945. J. A. Larsson, J. C. Greer, W. Harneit, and A. Weidinger, *J. Phys. Chem.* 116, 7849 (2002).
946. M. Waiblinger, K. Lips, W. Harneit, and A. Weidinger, *Phys. Rev. B* 64, 159901 (2001).
947. B. Pietzak, M. Waiblinger, T. Almeida Murphy, A. Weidinger, M. Höhne, E. Dietel, and A. Hirsch, *Chem. Phys. Lett.* 279, 259 (1997).
948. C. Knapp, N. Weiden, H. Käss, K.-P. Dinse, B. Pietzak, M. Waiblinger, and A. Weidinger, *Mol. Phys.* 95, 999 (1998).
949. A. Weidinger, M. Waiblinger, B. Pietzak, and T. A. Murphy, *Appl. Phys. A* 66, 287 (1998).
950. E. Dietel, A. Hirsch, B. Pietzak, M. Waiblinger, K. Lips, A. Weidinger, A. Gruss, and P. Dinse, *J. Am. Chem. Soc.* 121, 2432 (1999).
951. W. Harneit, *Phys. Rev. A* 65, 32322 (2002).
952. M. Saunders, H. A. Jiménez-Vázquez, R. J. Cross, and R. J. Poreda, *Science* 259, 1428 (1993).
953. M. Saunders, R. J. Cross, H. A. Jiménez-Vázquez, R. Shimshi, and A. Khong, *Science* 271, 1693 (1996).
954. B. A. Diccamillo, R. L. Hettich, G. Guiochon, R. N. Compton, M. Saunders, H. A. Jiménez-Vázquez, A. Khong, and R. J. Cross, *J. Phys. Chem.* 100, 9197 (1996).
955. M. S. Syamala, R. J. Cross, and M. Saunders, *J. Am. Chem. Soc.* 124, 6216 (2002).
956. K. Yamamoto, M. Saunders, A. Khong, R. J. Cross, Jr., M. Grayson, M. L. Gross, A. F. Benedetto, and R. B. Weisman, *J. Am. Chem. Soc.* 121, 1591 (1999).
957. K. Kimata, K. Hosoya, T. Areki, and N. Tanaka, *J. Org. Chem.* 58, 282 (1993).
958. L.-S. Wang, O. Cheshnovsky, R. E. Smalley, J. P. Carpenter, and S. J. Hwu, *J. Chem. Phys.* 96, 4028 (1992).
959. U. Zimmermann, N. Malinowski, A. Burkhardt, and T. P. Martin, *Carbon* 33, 995 (1995).
960. U. Zimmermann, A. Burkhardt, N. Malinowski, U. Näher, and T. P. Martin, *J. Chem. Phys.* 101, 2244 (1994).
961. U. Zimmermann, N. Malinowski, U. Näher, S. Frank, and T. P. Martin, *Phys. Rev. Lett.* 72, 3542 (1994).
962. B. Palpant, Y. Negishi, M. Sanekata, K. Miyajima, S. Nagao, K. Judai, D. M. Rayner, B. Simard, P. A. Hackett, A. Nakajima, and K. Kaya, *J. Chem. Phys.* 114, 8459 (2001).
963. B. Palpant, A. Otake, F. Hayakawa, Y. Negishi, G. H. Lee, A. Nakajima, and K. Kaya, *Phys. Rev. B* 60, 4509 (1999).
964. Ph. Dugourd, R. Antoine, D. Rayane, I. Compagnon, and M. Broyer, *J. Chem. Phys.* 114, 1970 (2001).
965. R. Antoine, D. Rayane, E. Benichou, Ph. Dugourd, and M. Broyer, *Eur. Phys. J. D* 12, 147 (2000).
966. D. Rayane, R. Antoine, Ph. Dugourd, E. Benichou, A. R. Allouche, M. Aubert-Frécon, and M. Broyer, *Phys. Rev. Lett.* 84, 1962 (2000).
967. F. Tast, N. Malinowski, S. Frank, M. Heinebrodt, I. M. L. Billas, and T. P. Martin, *Phys. Rev. Lett.* 77, 3529 (1996).
968. F. Tast, N. Malinowski, S. Frank, M. Heinebrodt, I. M. L. Billas, and T. P. Martin, *Z. Phys. D* 40, 351 (1997).
969. Q. Kong, Y. Shen, L. Zhao, J. Zhuang, S. Qian, Y. Li, Y. Lin, and R. Cai, *J. Chem. Phys.* 116, 128 (2002).
970. Y.-K. Kwon, D. Tománek, and S. Iijima, *Phys. Rev. Lett.* 82, 1470 (1999).
971. R. F. Service, *Science* 292, 45 (2001).
972. A. G. Rinzler, J. Liu, H. Dai, P. Nikolaev, C. B. Huffman, F. J. Rodríguez-Macías, P. J. Boul, A. H. Lu, D. Heymann, D. T. Colbert, R. S. Lee, J. E. Fischer, A. M. Rao, P. C. Eklund, and R. E. Smalley, *Appl. Phys. A* 67, 29 (1998).
973. B. W. Smith, M. Monthieux, and D. E. Luzzi, *Nature* 396, 323 (1998).
974. B. W. Smith and D. E. Luzzi, *Chem. Phys. Lett.* 321, 169 (2000).
975. S. Bandow, M. Takizawa, K. Hirahara, M. Yudasaka, and S. Iijima, *Chem. Phys. Lett.* 337, 48 (2001).
976. B. W. Smith, M. Monthieux, and D. E. Luzzi, *Chem. Phys. Lett.* 315, 31 (1999).
977. K. Hirahara, S. Bandow, K. Suenaga, H. Kato, T. Okazaki, H. Shinohara, and S. Iijima, *Phys. Rev. B* 64, 115420 (2001).
978. K. Hirahara, K. Suenaga, S. Bandow, H. Kato, T. Okazaki, H. Shinohara, and S. Iijima, *Phys. Rev. Lett.* 85, 5384 (2000).
979. B. W. Smith, R. M. Russo, S. B. Chikkannanavar, and D. E. Luzzi, *J. Appl. Phys.* 91, 9333 (2002).
980. S. Berber, Y.-K. Kwon, and D. Tománek, *Phys. Rev. Lett.* 88, 85502 (2002).

981. K. Hirahara, S. Bandow, K. Suenaga, H. Kato, T. Okazaki, H. Shinohara, and S. Iijima, *Phys. Rev. B* 65, 45419 (2001).
982. J. Varo, M. C. Llaguno, B. C. Satishkumar, D. E. Luzzi, and J. E. Fischer, *Appl. Phys. Lett.* 80, 1450 (2002).
983. H. Hongo, F. Nihey, M. Yudasaka, T. Ichihashi, and S. Iijima, *Physica B* 323, 244 (2002).
984. L. Langer, V. Bayot, E. Grivei, J.-P. Issi, J. P. Heremans, C. H. Olk, L. Stockman, C. Van Haesendonck, and Y. Bruynseraede, *Phys. Rev. Lett.* 76, 479 (1996).
985. T. P. Martin, U. Näher, H. Schaber, and U. Zimmermann, *Phys. Rev. Lett.* 70, 3079 (1993).
986. W. Zhang, L. Liu, J. Zhuang, and Y. Li, *Phys. Rev. B* 62, 8276 (2000).

Calixarenes

Chebrolu P. Rao, Mishtu Dey

Indian Institute of Technology, Mumbai, India

CONTENTS

1. Introduction
2. Calixarene Conformations
3. Organic Functionalization
4. Metallocalixarenes
5. Physical Properties of Calixarenes
6. Spectral Properties of Calixarenes
7. Structures by X-Ray Crystallography
8. Applications
9. Conclusions
- Glossary
- References

1. INTRODUCTION

1.1. Genesis of Calixarenes

About 150 years ago, Adolph von Baeyer demonstrated the formation of a hard, resinous, and noncrystalline product from the reaction of aqueous formaldehyde with phenol that remained essentially uncharacterized for almost 70 years. However, three decades later, Leo Baekeland smartly designed a process for this product, which he marketed under the name “bakelite,” with tremendous commercial success [1]. In 1942 Zinke and Ziegler researched the products of the reaction of phenol and its substitutes with formaldehyde.

Phenol itself reacts with formaldehyde in acid or base at the *ortho*- and *para*-positions to form a highly cross-linked three-dimensional polymer in which each phenolic residue is attached to three other neighbors as shown in Figure 1. On the other hand, *para*-alkylphenol can react only at its two *ortho*-positions and thereby forms a linear one-dimensional polymer (Fig. 2) by reducing the cross-linking possibilities, in addition to the formation of several macrocyclic oligomers. However, the same reaction in the presence of base at high temperatures yielded high melting and high

molecular weight substance to which Zinke assigned a cyclic tetrameric structure [2], where the product was proven to be a mixture later on as shown in Figure 3. This problem was not overcome until late 1970s when Gutsche became intrigued by the emerging area of enzyme mimics where he explored the Zinke cyclic tetramers as cavity-containing substances appropriate for enzyme mimic building blocks. He later showed that a careful control of reaction conditions could provide good yields of pure compounds of various ring sizes, calix[*n*]arenes.

1.2. Scope of the Chapter

The main aim of this chapter is to bring into focus the newer developments of calixarenes and its derivatives and the many applications exhibited by these systems. In order to fulfill such a focus, the authors take the approach of showing the developments that took place since the realization of simple calixarenes and their putative applications in biology and materials leading to the nanoscience of such supramolecular systems. Since the work carried out as well as the understanding of calix[6 & 8]arenes is rather limited in the literature, we confine our discussions mostly to calix[4]arenes.

1.3. Nomenclature

The name calixarene is of Greek origin (Greek calix, a chalice or cup; arene referring to the aromatic ring), having recognized the cyclic tetramer in the conformation in which all of its four aryl groups are oriented in the same direction of a chalice or cuplike shape [3–7] similar to that of a Greek crater vase (Fig. 4). The substitution at the *para*-position precedes calix[*n*]arene in order to accommodate the number of aryl groups present by giving a numerical value to [*n*]. For example, the cyclic tetramer derived from *p*-*tert*-butylphenol is written as *p*-*tert*-butylcalix[4]arene. For a more systematic application of the calixarene nomenclature, the basic name calix[*n*]arene is retained, and identities of all substituents are indicated and their positions are specified by a number (e.g., calixarene is derived from *p*-*tert*-butylphenol and formaldehyde is named as 5,11,17,23-tetra-*tert*-butyl-25,26,27,28-tetrahydroxycalix[4]arene as shown in Fig. 5).

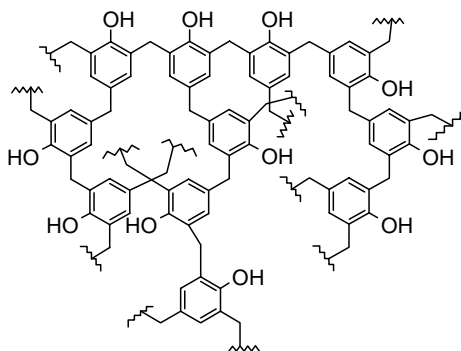


Figure 1. Schematic view of a highly cross-linked three-dimensional polymer, *bakelite*, obtained from the condensation of phenol with formaldehyde.

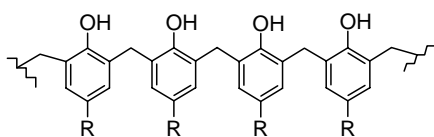


Figure 2. Schematic view of one-dimensional polymer formed from the linear condensation of *para*-substituted phenol with formaldehyde. R = any alkyl group.

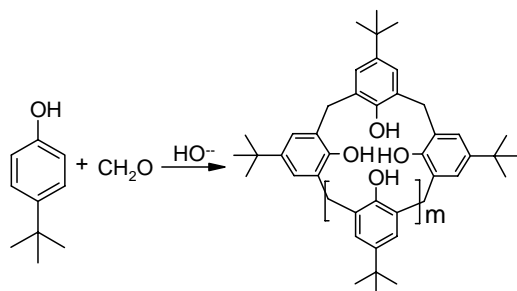


Figure 3. Cyclic condensation of *p*-*tert*-butyl phenol with formaldehyde resulting in the formation of highly ordered structures referred to as calixarenes. Ring size can be controlled based on the reaction conditions, leading to *p*-*tert*-butyl calix[4, 6, 8]arenes [$m = 1, 3, 5$].

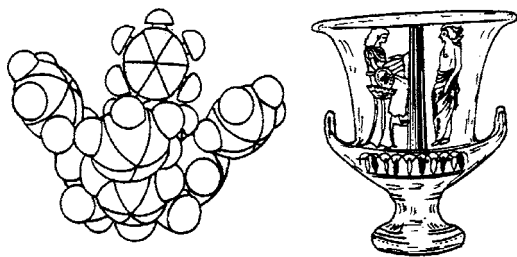


Figure 4. Structure of calix[4]arene resembling Greek crater vase. Adapted from [3], V. Bohmer and J. Vicens, "Calixarenes: A Versatile Class of Macrocyclic Compounds." Kluwer Academic, Dordrecht, 1991. © 1991, Kluwer Academic Publishers.

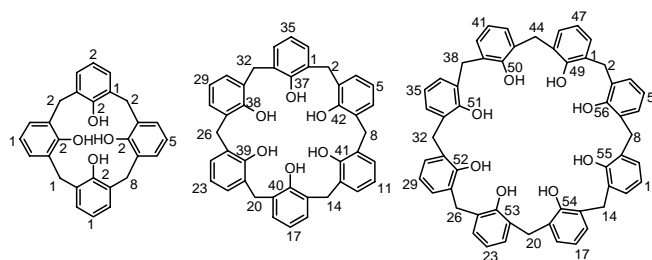


Figure 5. Structure and numbering scheme for calix[n]arenes, where $n = 4, 6, \text{ and } 8$.

As this nomenclature is very inconvenient, in this chapter we have also used the appropriate short form as used by others in the literature.

2. CALIXARENE CONFORMATIONS

Calixarenes generally show conformational mobility in solution and are frozen into a particular conformation only upon crystallization. X-ray crystallographic structures have been established for simple and functionally modified calixarenes. Simple calixarenes have many conformational isomers because of two possible rotational modes of phenol units, the *para*-substituent and the oxygen through the annulus rotation (Fig. 6), and hence shows fluxional behavior [8]. Functionalized calixarenes, at either the lower or upper rim, would have further influence on the conformational mobility and in some derivatives such mobility is frozen. Calix[4]arene shows four conformers and these are designated by Gutsche and co-workers as the "cone" (C_{2v} , C_{4v}), "partial-cone" (C_s), "1,2-alternate" (C_{2h}), and "1,3-alternate" (D_{2d}) forms [9] as shown in Figure 7. All the four conformations are accessible by rotation about the bridging methylene groups. In the cone conformation all four phenolic OH groups are involved in circular hydrogen bonding.

On the other hand, calix[6]arene can assume 8 up-down conformational isomers, designated as cone, partial-cone, 1,2-alternate, 1,3-alternate, 1,4-alternate, 1,2,3-alternate, 1,2,4-alternate, and 1,3,5-alternate. Because of the increased flexibility of this system, additional conformations are possible in which one or more aryl rings assumes a position approximately in the average plane of the molecule designated as an out alignment and named a winged conformation by Gutsche. In *p*-*tert*-butylcalix[8]arene, the molecule

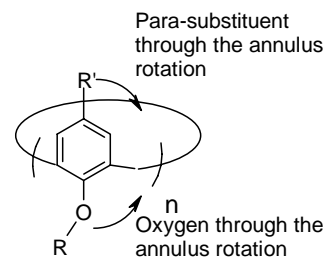


Figure 6. Annulus rotation in calixarenes. R = any substituent including *tert*-butyl group.

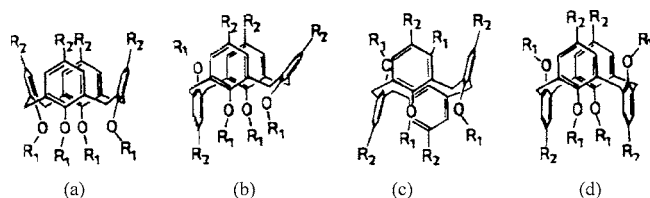


Figure 7. Conformations exhibited by calix[4]arene: (a), (b), (c), and (d) represent cone, partial-cone, 1,2-alternate, and 1,3-alternate conformations respectively. R_1 = any group and R_2 = any group including the *tert*-butyl group.

exists in a pleated loop form. For calix[8]arene, there are 16 up-down forms, as well as many others in which one or more aryl groups assume the out alignment [10].

3. ORGANIC FUNCTIONALIZATION

Since the pathway for conformational inversion in the calix[4]arene involves rotation of the aryl groups in a direction that brings the OH groups through the annulus of the macrocyclic ring, the most obvious way to curtail this motion is by derivatization. Thus, functionalization of calixarenes at the lower rim (phenolic OH groups) or at the upper rim (*para*-position of the aromatic moiety) often produces derivatives with reduced conformational mobility (Fig. 8). It is indeed possible to selectively introduce organic functionalities both on the lower rim as well as on the upper rim of calix[4]arenes. Due to chemical modifications, calixarenes and their derivatives can act as useful receptors or baskets for a range of guests including neutral, cationic, and anionic species. In these modifications the calix[4]arene acts as a platform to which an array of functional groups is attached resulting in the cone conformation and hence is capable of acting as the primary binding site.

3.1. Lower Rim Functionalization

The lower rims of the calixarenes are already functionalized with hydroxyl groups which provide excellent sites for the introduction of other functional groups, by either direct acylation or alkylation (Williamson method) by bringing in groups such as $-\text{CH}_2\text{C}(\text{O})\text{R}$ (R = alkyl [11, 12], or aryl [13], or $\text{N}(\text{alkyl})_2$ [14, 15], or $-\text{NHCH}(\text{R}')\text{COOH}$ (gly, ala, asp, glu) [16] or $-\text{NH}-\text{CH}_2\text{Py}$ [16], $-\text{CH}_2\text{CH}_2\text{OR}$ [17, 18], $-\text{CH}_2\text{P}(\text{O})\text{Ph}_2$ [19, 20], CH_2 -pyridyl [21, 22], CH_2CN [12, 23], $-\text{CH}_2\text{C}\equiv\text{CH}$ [23]. Further, selective alkylation in terms of the degree as well as the site specificity can be achieved by appropriately manipulating the

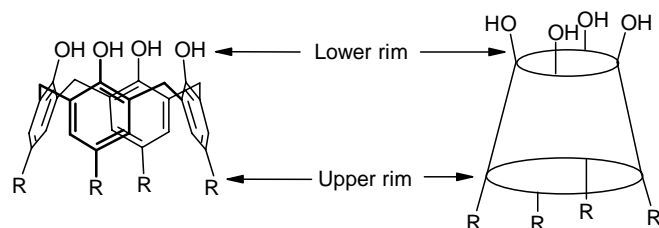


Figure 8. “Lower rim” and “upper rim” in calix[4]arene where R = *tert*-butyl.

experimental conditions [24, 25]. In the literature, strategies are reported for di-functionalization of distal (1,3) and proximal (1,2) positions in *p*- R -calix[4]arenes [26]. We have recently obtained 1,3-di-derivatives built through amide linkages originating from amino acids, heterocyclic amines, and saccharide amines and further derivatized so that 2,4-OH groups are methylated [27, 28]. The conformational freezing can also be achieved by bridging between transannular oxygens at the lower rim resulting in crown etherlike structures [29, 30].

3.2. Upper Rim Functionalization

The *p-tert*-butyl group attached to the phenyl ring is removed by de-alkylation using AlCl_3 -phenol as catalyst [31, 32]. A variety of methods are available to selectively or totally introduce functional groups into the *p*-position of the phenyl ring, which includes electrophilic substitution, such as halogenation (Cl, Br, and I) [33, 34], nitration [35], sulphonation [36, 37], acylation [31], and formylation [38–40]; *para*-Claisen rearrangement [41]; chloromethylation [42] and subsequent replacement of chloride, resulting in the formation of a variety of potential ligands; and Mannich reaction with dialkylamines followed by conversion of nitrogen into quaternary structure and then treatment with nucleophiles [43].

4. METALLOCALIXARENES

Calixarenes and their functionalized derivatives provide the basic structural framework for developing coordination chemistry, and when properly tuned with appropriate functional groups to provide biomimetic model systems. Both simple (parent) and functionalized calixarenes possessing O, S, N donor groups either at the upper rim or at the lower rim have been used as ligands to complex the transition metal ions.

4.1. Metal Ion Complexes of Simple Calixarenes

Simple calixarenes can bind to metal ions via deprotonated phenolate moieties at the lower rim. Neutral complexes of *p-tert*-butyl-calix[4]arene (metal to ligand ratio) using Ti(IV) (2:2), Fe(III) (2:2), Co(III) (3:2), Nb(V) (1:1 with Nb=O), Ta(V) (1:1 with Ta=O), Mo(VI) (1:1 with $\text{M}=\text{NR}$), and W(VI) (1:1 with $\text{W}=\text{O}$ or $\text{W}(\text{Cl})_2$) were reported in the literature as shown in Figure 9a–f [44–49]. Harrowfield et al. [50–54] have reported a series of lanthanide metal ion complexes of europium, terbium, and cerium with *p-tert*-butyl-calix[4]arene. The two europium ions were coordinated to the calixarene either as a 2:2 metal/calix[4]arene complex (Fig. 9g) or as a 2:1 metal/calix[8]arene complex.

4.2. Calixarenes Possessing Pendant Binding Sites

Introduction of appropriate functional groups on either the upper or lower rim leads to the derivatives of a versatile nature and would be of great use in a variety of applications. Calixarenes possessing different donor groups (N, P, S)

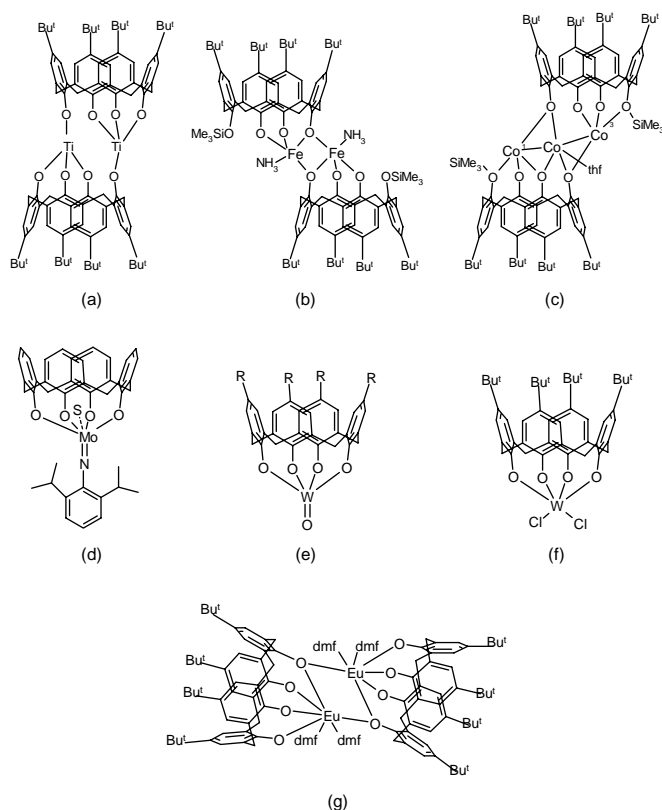


Figure 9. (a)–(f) Transition and (g) lanthanide metal ion complexes of *p*-*tert*-butyl calix[4]arene, where dmf = *N,N*-dimethylformamide; thf = tetrahydrofuran; R = *t*-Bu, H; S = CH₃CN.

including pendant acids have been synthesized [16]. Some of these molecules and their coordination chemistry aspects are summarized in this section.

4.3. Coordination Chemistry Aspects of Calixarenes with Pendant Nitrogen Donors

Nitrogen containing donor groups have been introduced at either the lower or upper rim of the calix[4]arene as shown in Figure 10 [55, 56]. Interaction of ligand (a) with Ni(II), Cu(II), Pd(II), Co(II), and Fe(II) metal salts yields no complexes attributable to the presence of four mobile ethylamine arms that prevented the formation of rigid and/or closed cavities. However, when ligand (b) is reacted with Ni(ClO₄)₂·6H₂O and NaN₃, it yields a binuclear complex (d) and when ligand (c) is reacted with Ru(bipy)₂ complex, it results in the formation of a (bipy)₂Ru(bipy-calixarene) complex.

4.4. Coordination Chemistry Aspects of Calixarenes with Pendant Sulphur Donors

A limited number of thio-derivatives of calixarenes, viz., tetra mercaptocalix[4]arene and dihydroxy-di mercaptocalix[4]arene, were reported in the literature [57–61]. The former exists in 1,3-alternate conformation both in the free

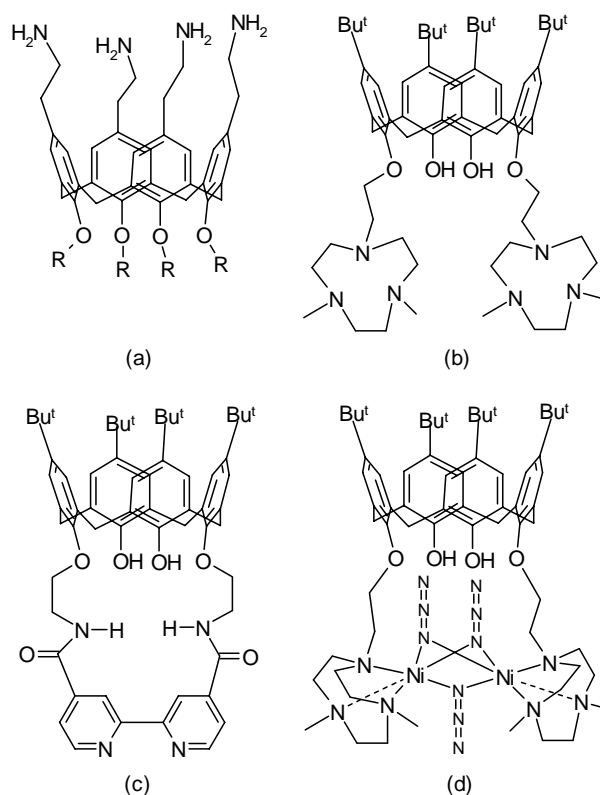


Figure 10. (a)–(c) Calix[4]arene derivatives with pendant nitrogen donors; (d) dinuclear nickel complex of (b); R = *p*-O₂SC₆H₄Br.

state as well as in its complexed state. The complex with Hg(acetate)₂ yielded 2:1 with tetra-mercaptocalix[4]arene and 1:1 with dihydroxy-dimercaptocalix[4]arene, and in both cases the calixarene exists in 1,3-alternate conformation as shown in Figure 11.

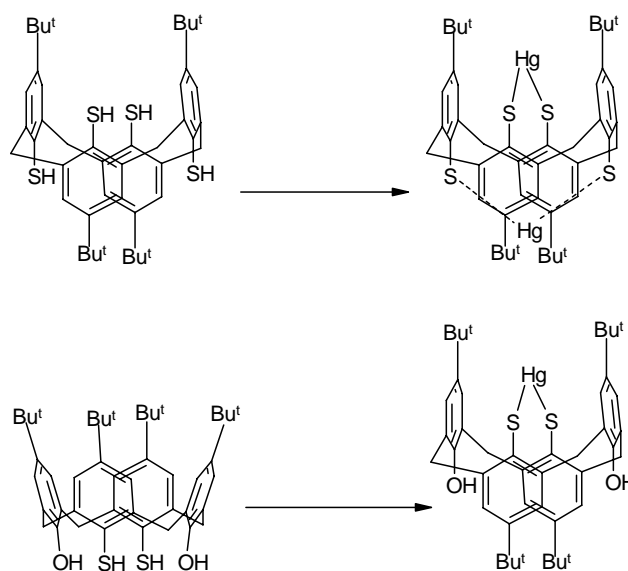


Figure 11. Two thio-calix[4]arene derivatives and their mercury complexes.

5. PHYSICAL PROPERTIES OF CALIXARENES

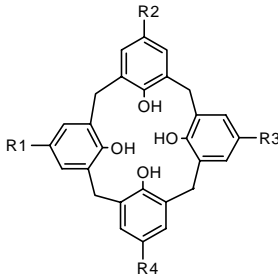
A few physical properties, such as melting point, solubility, and pKa's, are discussed in this section both for the organic derivatives as well as for their inorganic ones.

5.1. Melting Temperatures of Calixarenes

Melting point is a characteristic property of many calixarenes. The parent calixarenes containing the free hydroxyl groups melt at high temperatures and increase progressively going from calix[4]arene to calix[6]arene to calix[8]arene and the melting points are generally in the range 340–450 °C. It has been noticed that even the nature of the substituent present in the *p*-position affects the melting point (Table 1, compounds 1, 4, 6). It is understood from the literature that [62] calix[6]arenes produced from *p*-*n*-alkyl-phenols exhibit melting points as low as 110 °C when the substituent is *p*-*n*-octadecyl. The melting point is also known to be affected by the position of the substituents on

the “upper rim” of the calix[4]arene (Table 1, compounds 7a–7c). The effect of substituents on the melting points has been observed in the case of isomeric compounds that differ only in the arrangement of identical groups around the “upper rim” of the calixarene. Thus Bohmer's compounds [63] 7a, 7b, and 7c in Table 1 have melting points 185–190, 270, and 368 °C respectively. Hence derivatization of the calixarenes greatly affects the melting point. Lower rim calixarene derivatives of esters and ethers generally melt at temperatures lower than the parent compound (Table 1). For example, 8 and 9 melt at 226–228 and 230–231 °C, respectively (Table 1). However, there are exceptions where the trimethylsilyl ether of *p*-*tert*-butylcalix[4]arene at the lower rim melts at 411–412 °C and the tetraacetate melts at 383–386 °C. Among the calix[4]arene derivatives 12–17 (Table 1), the esters melt at lower temperatures than their carboxylic acid counterparts indicating a decrease in the hydrogen-bond interactions. Generally the decrease in the melting point upon derivatization at the lower rim is consistent with a decrease in hydrogen bonding interactions and a similar trend observed with the derivatives at the upper rim is consistent with an increase in the hydrophobic nature.

Table 1. Melting points and solubilities of calixarene derivatives.

Codes	Compounds	Melting point (°C)	Solubility
1	<i>p</i> - <i>tert</i> -butylcalix[4]arene	342–344	less soluble in CHCl ₃
2	<i>p</i> - <i>tert</i> -butylcalix[6]arene	380–381	
3	<i>p</i> - <i>tert</i> -butylcalix[8]arene	411–412	
4	<i>p</i> -phenylcalix[4]arene	407–409	
5	<i>p</i> -phenylcalix[8]arene	>450	
6	<i>p</i> - <i>n</i> -octadecylcalix[4]arene	110	more soluble in CHCl ₃
7	 R1 R2 R3 R4 a Ph t-Bu CO ₂ Et Me b Ph t-Bu Me CO ₂ Et c Me t-Bu CO ₂ Et Ph	185–190, 270 368	
8	tetramethyl ether of <i>p</i> - <i>tert</i> -butylcalix[4]arene	226–228	
9	tetrabenzyl ether of <i>p</i> - <i>tert</i> -butylcalix[4]arene	230–231	
10	trimethylsilyl ether of <i>p</i> - <i>tert</i> -butylcalix[4]arene	411–412	
11	tetraacetate of <i>p</i> - <i>tert</i> -butylcalix[4]arene	383–386	
12	gly-ester of <i>p</i> - <i>tert</i> -butylcalix[4]arene	182	CHCl ₃
13	gly-dev of <i>p</i> - <i>tert</i> -butylcalix[4]arene	210	DMSO
14	ala-ester of <i>p</i> - <i>tert</i> -butylcalix[4]arene	176–178	CHCl ₃
15	ala-dev of <i>p</i> - <i>tert</i> -butylcalix[4]arene	196–198	DMSO
16	glu-ester of <i>p</i> - <i>tert</i> -butylcalix[4]arene	168–170	CHCl ₃
17	glu-dev of <i>p</i> - <i>tert</i> -butylcalix[4]arene	172	DMSO
18	<i>p</i> -acetylcalix[4]arene		Hot benzene
19	calix[4]arene tetraacetate		Insoluble in benzene
20	tetracarboxymethyl ether of <i>p</i> - <i>tert</i> -butylcalix[4]arene		Water

5.2. Solubility

Simple calixarenes are insoluble in water and aqueous base and are only slightly soluble in organic solvents; however, they are sufficiently soluble in chloroform, pyridine, or carbon disulfide [64]. It is this feature that makes some of the calixarenes difficult to isolate, purify, and characterize. Alkyl groups in the *para*-position of a calix[4]arene affect the solubility in organic solvent and the solubility increases as the chain length increases (Table 1, compounds 1 and 6) [65]. Lower rim derivatives of esters and ethers of calix[4]arenes show increased solubility and the difference in solubility may be used to separate the components from a mixture. For example, No et al. [66] separated the product, *p*-acetylcalix[4]arene, from its reactant, calix[4]arene tetraacetate, which is soluble in hot benzene.

Water soluble calixarenes were developed due to their ability to interact with ions and molecules and also due to their catalytic properties. A first water soluble calixarene, tetracarboxymethyl ether of *p*-*tert*-butylcalix[4]arene, was synthesized by Ungaro et al. [67] whose solubility was found to be in the range 5×10^{-3} to 5×10^{-4} M depending upon the accompanying cation. *p*-Carboxy-calix[4-8]arenes were found to be soluble in 10^{-3} M aqueous base as reported by Gutsche et al. [33, 42, 43]. However, *p*-sulphonato calix[4-8]arenes were much more soluble than the counter-carboxy-derivatives and the former is soluble up to an extent of 0.1 M as reported by Shinkai et al. [36, 37]. However, the upper rim aminocalixarenes are moderately soluble in dilute aqueous acid [42, 43, 55].

5.3. pK_a

Due to their low solubility it was difficult to obtain the dissociation constants for the OH groups of the *p*-*tert*-butylcalixarenes. The pK₁ values were found to be 6.0 and 4.3 for the mono-nitrocalixarenes (Figure 12a and b) in 1:1 water:methanol by measuring their ultraviolet absorption as a function of pH as reported by Bohmer et al. [68]. Thus these nitro-calixarenes are somewhat more acidic than *p*-nitrophenol. The pK difference of 1.7 units between the

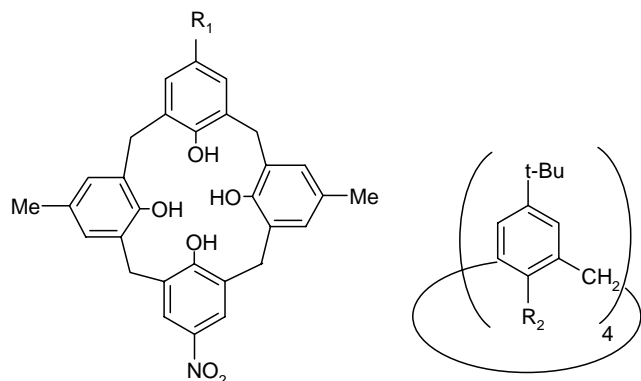


Figure 12. (i) Mono-nitro calix[4]arenes: R₁ = Me, 1a; R₁ = *t*-Bu, 1b. (ii) Tetraesters and ethers of *p*-*tert*-butylcalix[4]arene: R₂ = OCOCH₃, 2a; R₂ = OCO₂Et, 2b; R₂ = OCH₂CO₂Et, 2c; R₂ = OCH₂CO₂Bu, 2d; R₂ = OCH₂CONEt₂, 2e; R₂ = OCH₂COCH₃, 2f.

two compounds that differ only in a single *p*-alkyl substituent is attributed to the conformational effects arising from the relative sizes of the methyl and *tert*-butyl groups.

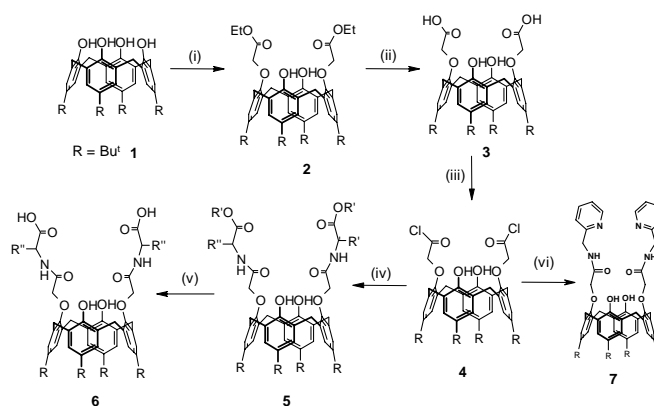
6. SPECTRAL PROPERTIES OF CALIXARENES

Spectral properties, such as vibrational, electronic, nuclear magnetic resonance (NMR), and mass, of both organic and inorganic derivatives of calixarenes are discussed in this section by taking several examples. Luminescence spectral studies are presented in Sections 8.5 and 8.6.

6.1. Vibrational Spectroscopy

One of the most distinct features in the infrared spectra of the calixarenes is the observation of very low frequency for ν_{OH} , viz., 3150 cm^{-1} in the case of calix[4]arene and 3300 cm^{-1} in case of calix[5]arene, which is attributed to the strength of intramolecular hydrogen bond interaction involving the -OH groups at the lower rim in these calixarenes [69, 70]. In the fingerprint region between 1500 and 900 cm^{-1} , the spectra look almost similar in all the calixarenes. However, in the 900 – 500 cm^{-1} region, the patterns vary to some extent depending upon the derivative.

As shown in Scheme 1, the parent, *p*-*tert*-butylcalix[4]arene **1**, shows a band at 3186 cm^{-1} for ν_{OH} . Esterification of **1** resulted in **2** and in the spectrum of **2** the ν_{OH} and $\nu_{\text{C=O}}$ appear at 3425 and 1757 cm^{-1} indicating the disruption of the circular hydrogen bond to some extent upon derivatization. The base hydrolysis of **2** resulted in the corresponding diacid **3**, where ν_{OH} and $\nu_{\text{C=O}}$ appear at 3424 and 1747 cm^{-1} respectively. In case of **3**, $\nu_{\text{Phe-OH}}$ overlaps with the carboxylic ν_{OH} and thereby exhibits a broad band as compared to its precursor, **2**. Upon treating with SOCl_2 , the acid is converted to acid-chloride, **4**, where both peaks have shifted to



Scheme 1. Stepwise syntheses of *p*-*tert*-butylcalix[4]arene derivatives. (i) $\text{BrCH}_2\text{CO}_2\text{Et}$, K_2CO_3 , acetone, reflux; (ii) 15% aq. NaOH, EtOH, reflux; (iii) SOCl_2 , benzene, reflux; (iv) amino acid ester.HCl, Et_3N , THF, RT; (v) LiOH, THF/ H_2O ; (vi) 2-(2-amino methyl)pyridine, Et_3N , RT. R' = CH₃, R'' = Gly, **5a**; R' = CH₃, R'' = Ala, **5b**; R' = CH₂Ph, R'' = Asp, **5c**; R' = CH₂CH₃, R'' = Glu, **5d**; R' = Gly, **6a**; R' = Ala, **6b**; R'' = Asp, **6c**; R'' = Glu, **6d**.

higher frequencies (Fig. 13). The reaction of acid-chloride, **4**, with the amino acid esters [71] yields the corresponding amides (**5a–5d**) that exhibit characteristic ester and amide bands in the ranges 1741–1754, 1679–1685 (amide I), and 1531–1539 cm^{-1} (amide II, δ_{NH}). Thus the data are indicative of the formation of the pendants with peptide linkages. Conversion of these by base hydrolysis to the corresponding carboxylic acids (**6a–6d**) resulted in a frequency shift of amide bands to lower values shown in Figure 14.

6.2. Ultraviolet Spectroscopy

The linear and cyclic oligomers show two absorption bands at 280 and 288 nm in the ultraviolet spectra. The ratio of the absorptions at these two wavelengths is a function of the size of the ring. Conforth and co-workers [2] carried out the lower rim alkylation of calixarenes by monitoring the disappearance of the absorption at 300 nm (characteristic of the free phenol) and the growth of absorption at 270–280 nm arising from the ether.

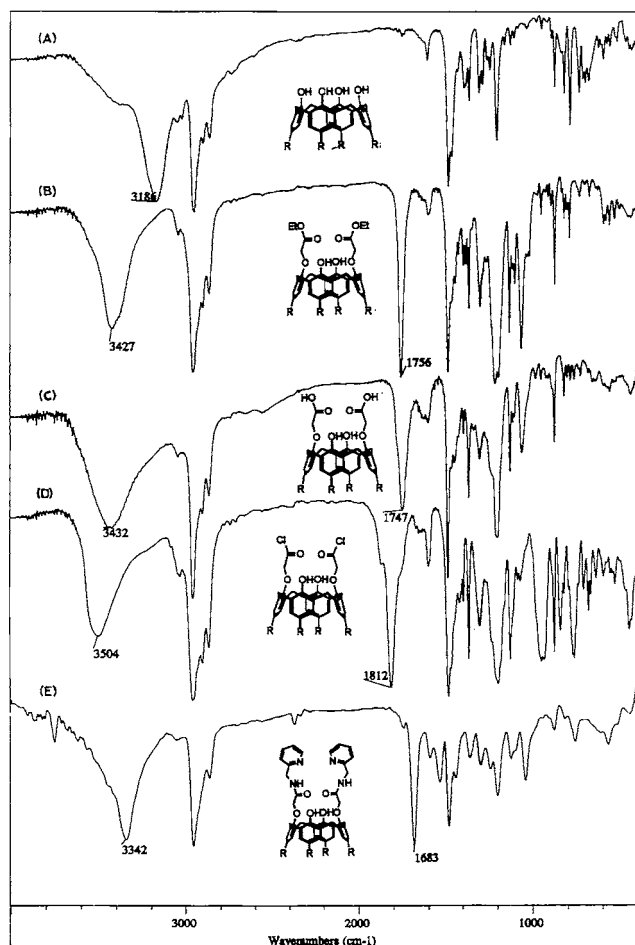


Figure 13. Fourier transform infrared (FTIR) spectra corresponding to the structures showed under each spectrum. (A), (B), (C), (D), and (E) respectively correspond to the compounds **1**, **2**, **3**, **4**, and **7** which were given in Scheme 1.

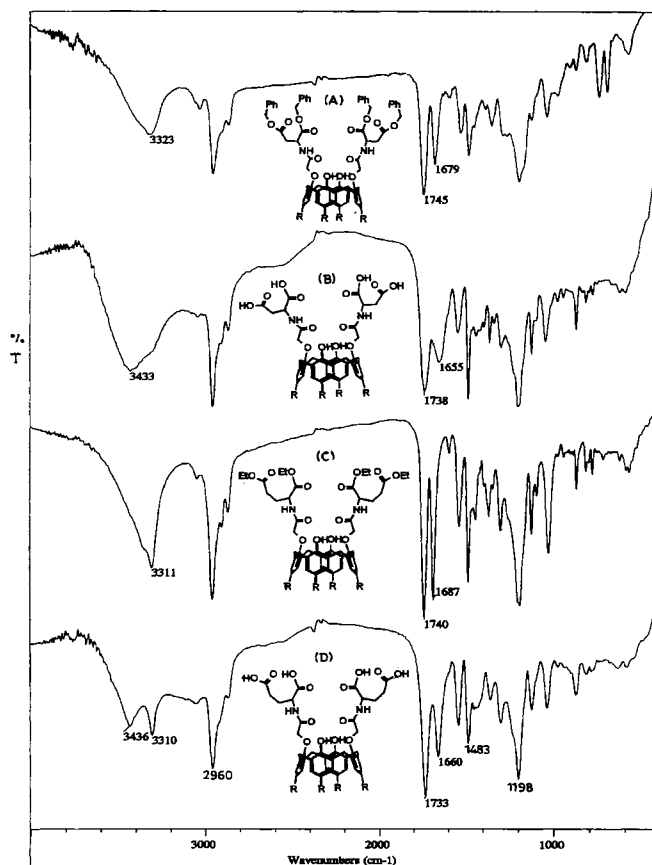


Figure 14. FTIR spectra corresponding to the structures shown under each spectrum. (A), (B), (C), and (D) respectively correspond to the compounds **5c**, **6c**, **5d**, and **6d** which were given in Scheme 1.

6.3. Nuclear Magnetic Resonance Spectroscopy

In the ^1H NMR spectrum of *p*-*tert*-butylcalix[4]arene at room temperature, resonances from the aromatic protons, the *tert*-butyl protons, and the hydroxyl protons are observed as singlets, and those from the CH_2 protons are observed as a pair of doublets. However, these doublets collapse to a singlet when the temperature is raised from 20 to 60 $^\circ\text{C}$ in chloroform [72]. On the basis of nuclear Overhauser effect experiments, Ungaro et al. [67] assigned the higher field doublet to the equatorial protons (closer to the aromatic rings) and the lower field doublet to the axial protons (closer to the hydroxyl groups). Gutsche et al. [73, 74] have shown that calix[8]arenes behave in a similar manner but calix[6]arenes show only a singlet resonance even at room temperature and split at lower temperature. Calix[4]arene and calix[8]arene can be differentiated [75] by the fact that in pyridine the former retains the pair of doublets at 0 $^\circ\text{C}$ whereas the latter shows only a singlet at temperatures as low as -90 $^\circ\text{C}$.

Rao et al. [16] reported that the ^1H NMR spectra of **1** (Scheme 1) shows a single *tert*-butyl signal at 1.26 and an AB quartet for bridged methylene group at 3.50 and 4.30 ppm and a singlet for aromatic protons at 7.05 ppm. The phenolic proton appeared as a singlet at 10.30 ppm that disappears upon D_2O exchange. The ^1H NMR spectra of

1,3-di-derivatives (**2**, **3**, and **4**) exhibited doubling of peaks for *tert*-butyl groups (0.93–1.05 and 1.26–1.27 ppm) and aromatic protons (6.78–6.93 and 7.06–7.08 ppm), one each corresponding to the substituted part and the unsubstituted one. Spectra of these also exhibited an AB quartet for the bridged methylene group in the ranges 3.32–3.41 and 4.13–4.45 ppm. A singlet for the methylene group arising from O–CH₂–CO was observed in the range 4.66–5.03 ppm. The spectrum of **2** shows signals corresponding to the ethyl ester group which is absent in **3** and **4**. Thus the data suggest that the substitution in the di-derivatives is of 1,3-alternate type and the calix[4]arene exists in the cone conformation. The splitting pattern observed for the bridged –CH₂ group in ¹H NMR spectra provides a signature for the type of conformation present.

In case of the 1,3-di-derivatives built using peptide linkages, **5** and **6**, the protons and/or carbon (in ¹³C NMR) as well as that of calixarene resonances were assigned by correlation spectroscopy (COSY) and hetero multiple quantum coherence experiments. The ¹H NMR data corresponding to these derivatives are given in Table 2. In the ¹H NMR spectra, the amide N–H proton signals appeared in the range 9.27 to 9.63 (CDCl₃) and 8.97 to 9.20 ppm (DMSO-*d*₆) for **5a–5d** and 8.72 to 9.14 ppm for **6a–6d** (DMSO-*d*₆). These chemical shifts were comparable with those observed in case of the tetra-substituted amino acid ester derivatives [76]. The positions of amide proton signals were confirmed through the cross-coupling peaks of C^αH in COSY experiments. While the amide –NH protons were not exchanged upon addition of D₂O in the case of **5**, these were found to be exchanged in the case of **6** due to the changes in the confirmation of the pendant groups. From these results it can be concluded that there exists strong intramolecular hydrogen bonding in **5** in CDCl₃. However, **5** when measured in DMSO-*d*₆ showed upfield shifts of amide proton signals indicating the disruption of intramolecular hydrogen bond interactions present in the molecule. However, the phenolic –OH proton signals disappear upon D₂O exchange. The aromatic protons (Ar–H) in **5a** (gly- derivative) appeared as two singlets whereas **5b–5d** (ala-, asp-, and glu- derivatives) showed two doublets due to the presence of pendant chiral amino acid units. For the same reason, the axial and equatorial calixarene bridged CH₂ protons showed two pairs of doublets in **5b–5d**. This chiral effect is also seen in the signals of OCH₂CO protons as two doublets. In case of **6a–6d**, a similar splitting pattern was observed. All the spectra were

indicative of the presence of cone conformations of these 1,3-di-derivatives.

6.4. Mass Spectrometry

Rao and co-workers [16] have reported mass spectral data for the calixarene 1,3-diderivatives of amino acid and their esters formed through peptide linkage. The molecular weights were confirmed by the presence of molecular ion peaks in the mass spectra obtained by the FAB mass method or the EI method.

7. STRUCTURES BY X-RAY CRYSTALLOGRAPHY

Single crystal X-ray diffraction provides a powerful means of determining the molecular and crystal structures. The lower rim derivatives of the calix[4]arenes can exist in any one or more of the possible four conformations as given in Section 2. Undoubtedly, X-ray crystallography is the most confirmative way to ascertain the conformations exhibited by the calixarenes and their derivatives. In several cases the solid state structural studies were further augmented by NMR conformational analysis in solution.

7.1. Crystal Structures of Calixarenes and Their Derivatives

The earliest example was reported by Rizzoli et al. [77], wherein the tetraacetate of *p-tert*-butylcalix[4]arene was shown to exist in partial-cone conformation as shown in Figure 15. Ester and ether derivatives, such as **1b–1f** (Fig. 12), exist in cone conformation [14, 29, 78, 79] for which X-ray structures have been obtained. The synthesis of 25, 27-dimethoxy-26, 28-dimethylester-*p-tert*-butylcalix[4]arene was reported and its structure was established wherein it is observed that the calixarene assumes a partial-cone conformation [80]. The corresponding potassium salt of this ester exists in 1,3-alternate conformation whereas in the sodium salt the calixarene is in a distorted cone or flattened partial-cone conformation (Fig. 16). The crystal structure of a tetra(benzyl)amide of calix[4]arene exhibits a distorted cone conformation [81]. Syntheses of lower rim substituted aryl ethers of *p-tert*-butylcalix[4]arene were reported [82] where the crystal structure of one of the 1,2-disubstituted compounds exists in a partial-cone conformation. One of the aryl ether pendants is sandwiched

Table 2. ¹H NMR data of 1,3-diderivatives of *p-tert*-butylcalix[4]arene with aminoacids and their corresponding esters.

Compound ^a	NH	OH	Ar-H	C ^α H	OCH ₂ CO	ArCH ₂ Ar	C ^β H	C ^γ H	C(CH ₃) ₃
5a	9.27	7.83	7.25, 6.92	4.14	4.63	4.23, 3.43			1.27, 1.03
5b	9.42	7.85	7.08, 6.93	4.74–4.69	4.53, 4.69–4.74	4.31, 3.40, 4.18, 3.46	1.47		1.28, 0.97
5c	9.63	7.92		5.03	4.77, 4.37	4.29, 4.14, 3.42, 3.24	2.97		1.24, 1.04
5d	9.37	7.78	6.99, 6.83	4.65	4.85, 4.31	4.24, 4.13, 3.40, 3.26	2.29	3.97	1.19, 0.96
6a	8.89	8.41	7.17	4.03	4.53	4.23, 3.47			1.20, 1.13
6b	9.09	8.30	7.22–7.17	4.41–4.36	4.77, 4.31	4.41–4.36, 4.15, 3.54, 3.45	1.40		1.20, 1.12
6c	8.88	8.20	7.14	4.76	4.61	4.26, 3.43	2.81–2.78		1.20, 1.17
6d	8.87	8.17	7.20–7.12	4.40–4.33	4.75, 4.40–4.33	4.40–4.33, 4.21, 3.51, 3.44	2.08–1.99	2.36–2.32	1.20, 1.11

^a Refer to Scheme 1 for compound names.

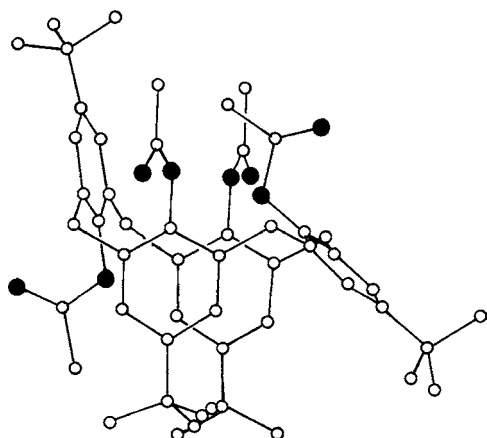


Figure 15. Lower rim tetraacetate derivative of *p*-*tert*-butylcalix[4]arene. Open circles denote carbons and filled circles denote oxygens. Adapted from [77], C. Rizzoli et al., *J. Mol. Struct.* 82, 133 (1982). © 1982, Elsevier Science.

between two neighboring O-unsubstituted phenyl rings within the calixarene cavity. Synthesis and structure determinations of thiacalix[4]arenes bearing four keto-groups and four amido-groups on the lower rim have been reported. All three derivatives have been found to adopt 1,3-alternate conformation [83]. A calix tube is formed when two thia-bridged calix[4]arenes were connected at their lower rim phenolic oxygens through four ethylene linkers [84]. This is shown to adopt a flexible C_{2v} flattened cone arrangement as shown in Figure 17. Zinic et al. [85] reported the synthesis of chiral calix[4]arene derivatives with four O-(*N*-acetylphenylgly-OMe) or O-(*N*-acetyl-Leu-OMe) strands. X-ray structure analysis of the glycine derivative revealed distorted cone conformation with C_2 symmetry and the structure is organized into infinite chains by intra- and intermolecular hydrogen bonds. The solid and solution structures of the corresponding sodium complex were identical with cone conformation having C_4 symmetry.

A number of lower rim O-alkylated derivatives of mono-, di-, tri-, and tetra-substituted picolyl ones with or without *p*-*tert*-butyl groups were synthesized and their conformations

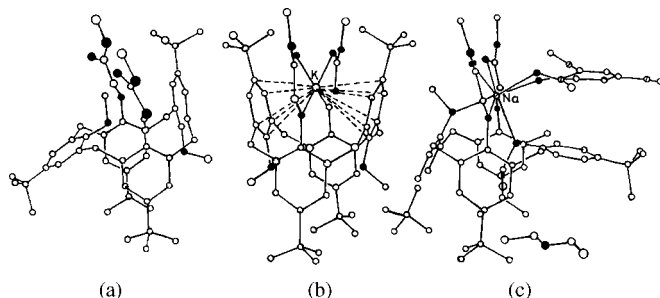


Figure 16. Crystal structures of (a) 25,27-dimethoxy-26,28-dimethyl-ester-*p*-*tert*-butylcalix[4]arene (partial-cone conformation); (b) its potassium ion complex (1,3-alternate conformation), and (c) its sodium ion complex (flattened partial-cone conformation). Open circles denote carbons, filled circles denote oxygens, and circles with a line denote nitrogens. Sodium and potassium ion centers are labeled in the figure. Adapted from [80], I. Oueslati et al., *Tetrahedron Lett.* 41, 8439 (2001). © 2001, Elsevier Science.

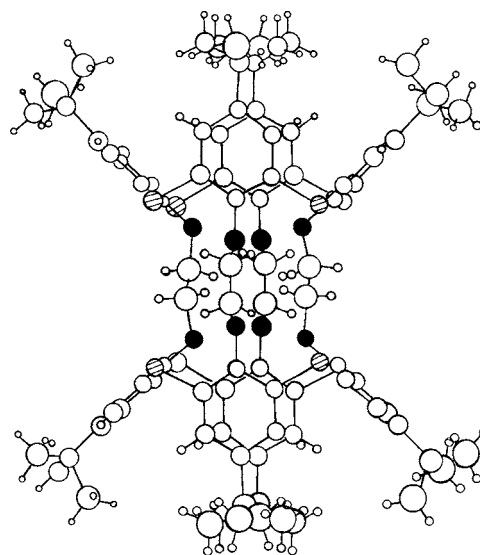


Figure 17. Crystal structure of thiacalix[4]arene tube. Big and small open circles denote carbons and hydrogens respectively; filled circles denote oxygens and circles with lines denote sulphurs. Adapted from [84], S. E. Matthews et al., *New J. Chem.* 25, 1355 (2001). © 2001, Royal Society of Chemistry.

were established [21]. It has been found that the type of base used during the synthesis [20 equivalents of the picolylchloride (HCl), NaH (70–80% cone), K_2CO_3 (36% of partial cone, 55% of 1,3-alternate, and 9% of cone), or Cs_2CO_3 (54% of partial cone, 18% of 1,3-alternate, and 9% of cone)] influences the conformation of the tetra-substituted picolyl derivative of calix[4]arene obtained. Such influence of the base used in the reaction on the conformation of the tetraalkylated calix[4]arenes was also reported by Reinholdt and co-workers [86]. This group also reported that the tetraethyl ether of *p*-*tert*-butylcalix[4]arene exists in a fixed 1,2-alternate conformation [87] for which the X-ray structure was determined as shown in Figure 18.

The reaction of *p*-*tert*-butyl calix[4]arene with a flexible and reactive sebacoil chloride yielded the singly intrabridged calix[4]arene derivative [88]. The crystal structure of this compound showed a distorted cone conformation (Fig. 19). Selective functionalization of calix[4]arenes at the

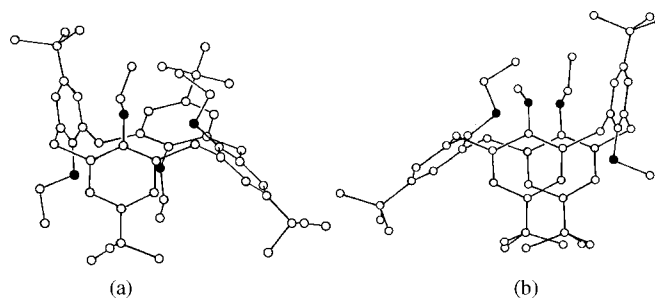


Figure 18. Molecular structures of (a) tetraethyl ether of *p*-*tert*-butylcalix[4]arene in a fixed 1,2-alternate conformation; (b) 1,4-dimethyl-2,3-diethyl ether of *p*-*tert*-butylcalix[4]arene in partial-cone conformation. Open circles denote carbons and filled circles denote oxygens. Adapted from [87], L. C. Groenen et al., *J. Am. Chem. Soc.* 113, 2385 (1991). © 1991, American Chemical Society.

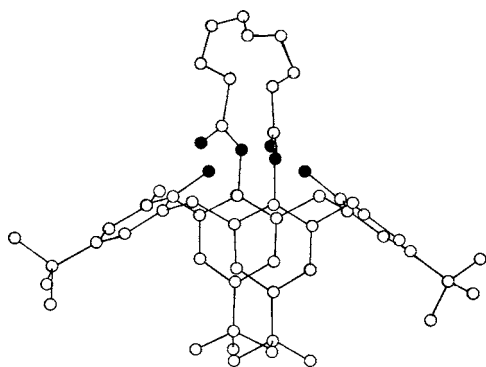


Figure 19. Singly intrabridged structure (using sebacoyl chloride) connecting 1,3-phenolic moieties in *p-tert*-butylcalix[4]arene in a distorted cone conformation. Open circles denote carbons and filled circles denote oxygens. Adapted from [88], J.-D. Van Loon et al., *J. Org. Chem.* 55, 5176 (1990). © 1990, American Chemical Society.

upper rim led to the formation of 26,28-dimethoxy-11,23-dinitrocalix[4]arene, the crystal structure of which (shown in Fig. 20) reveals that the macrocycle is in a flattened cone conformation [89]. A series of bridged calix[4]arenes with two opposite phenolic units connected by an aliphatic chain were synthesized [90]. The length of the chain was varied from 5 and 16 carbon atoms. ^1H NMR spectra support that the cone conformation is fixed in these compounds. X-ray analysis also revealed a distortion of the ideal cone conformation with shorter connecting chains, which is attributed to the weaker intramolecular hydrogen bonds.

7.2. Structures of the Metal Ion Complexes of Calixarenes and Its Derivatives

The treatment of calixarenes and its derivatives with inorganic salts and/or compounds results in the formation of the complexes, whose three-dimensional structures can be established by X-ray crystallography. Power and co-workers established the first crystal structure of a calix[4]arene-transition metal ion complex by the reaction of *p-tert*-

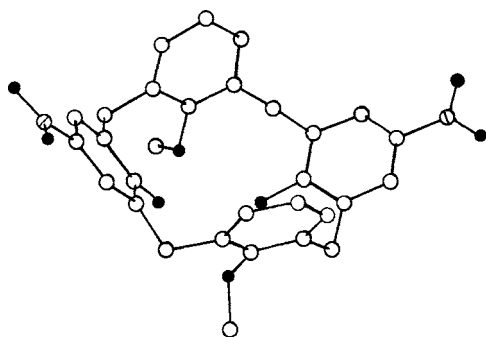


Figure 20. Structure of 26,28-dimethoxy (lower rim)-11,23-dinitro (upper rim) calix[4]arene in a flattened cone conformation. Open circles denote carbons, filled circles denote oxygens, and circles with a line denote nitrogens. Adapted from [89], J.-D. Van Loon et al., *Tetrahedron Lett.* 30, 2681 (1989). © 1989, Elsevier Science.

butylcalix[4]arene with $\text{Ti}(\text{NMe}_2)_4$ [44]. The structure shows two titanium ions sandwiched between two calixarene units and the calixarene exists in a partial-cone conformation with the titanium centers in tetrahedral coordination geometry. Similarly, iron and cobalt complexes of calix[4]arene were synthesized and their structures were determined by X-ray crystallography. The iron assumes a distorted trigonal pyramidal geometry and that of cobalt is irregular (Fig. 9).

Andreeti and co-workers [91] treated *p-tert*-butylcalix[6]arene with $\text{Ti}(\text{OPr})_4$ and the resultant product exhibited a structure consisting of two calixarene units in a cone conformation coordinated with two titanium centers as a Ti–O–Ti unit, with distorted trigonal bipyramidal geometry around each titanium center.

Harrowfield et al. [92] have synthesized an europium complex of *p-tert*-butylcalix[8]arene whose crystal structure was found to contain two europium atoms in a pinched conformer of the cyclic octamer. Ripmeester and co-workers have reported [93] that xenon is encapsulated in the *p-tert*-butylcalix[4]arene cavity and behaves both as a guest and as a cavity probe. ^{129}Xe NMR and X-ray diffraction data show that the Xe occupies two cavity sites (Fig. 21). Oxomolybdenum (VI) binds four oxygen atoms from a calix[4]arene with cone conformation, and in the lattice this unit is co-crystallized with a free calix[4]arene by trapping a nitrobenzene between these two units [47]. Reaction of mercury(II)acetate with *p-tert*-butyl-1,3-dihydroxy-2,4-disulfanylcalix[4]arene yielded a mononuclear complex in which the Hg(II) ion is coordinated linearly to two arenethiolate groups [61] and the calixarene adopts a 1,3-alternate conformation (Fig. 22). Calix[4]arene–W(VI)–(OAr) $_2$ complex is exhibited in the lattice self-assembly of these, resulting in a columnar structure as reported by Floriani's group [94].

Reaction of a 10-fold excess of NaH and LiH with *p-tert*-butylcalix[4]arene in THF results in the formation of the corresponding salts of mono-oxyanion and di-oxyanion calixarenes respectively [95], where the additional metal coordination sites are filled by MeOH and H $_2$ O to result in tetra-coordination around Li $^+$ and penta-coordination around Na $^+$ as shown in Figure 23a and b. Reaction of the hexamethyl ether of *p-tert*-butylcalix[6]arene with TiCl_4 in toluene [96] resulted in crystals of [(calix[6]arene)–(Cl $_3$ TiOTiCl $_2$) $_2$] (Fig. 24).

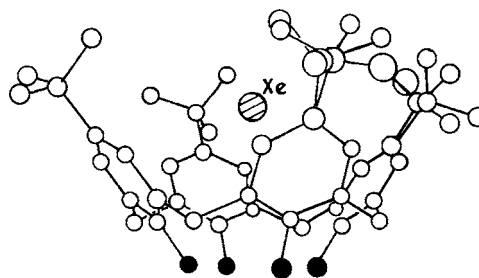


Figure 21. Clathration of Xe (labeled in the figure) into the *p-tert*-butylcalix[4]arene cavity as a guest. Open circles denote carbons and filled circles denote oxygens. Adapted from [93], E. B. Brouwer et al., *J. Chem. Soc., Chem. Commun.* 939 (1997). © 1997, Royal Society of Chemistry.

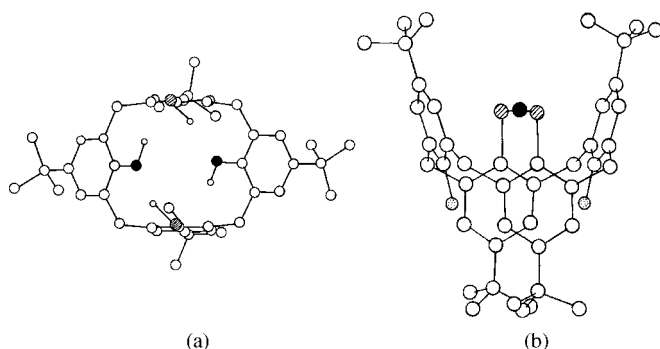


Figure 22. (a) Cone conformation of *p*-*tert*-butyl-1,3-dihydroxy-2,4-disulfanylcalix[4]-arene (top view) and (b) its Hg complex (linear) in 1,3-alternate conformation (lateral view). Open circles denote carbons, circles with lines represent sulphurs; filled circles denote oxygens in (a); circles with dots represent oxygens in (b); and filled circles in (b) denote Hg. Adapted from [61], X. Delaguiue et al., *J. Chem. Soc., Chem. Commun.* 609 (1995). © 1995, Royal Society of Chemistry.

Reactions of aluminium alkyls with a number of calixarene methyl ethers have been established [97, 98]. The reaction of tetramethyl ether of *p*-*tert*-butylcalix[4]arene with Me_3Al in benzene–toluene solution resulted in crystals, the structure of which shows that the calixarene is in 1,2-alternate conformation with two molecules of Me_3Al per calixarene. On the other hand the reaction with MeAlCl_2 or EtAlCl_2 resulted in a complex having the same composition but the calix[4]arene takes up an 1,3-alternate rather than the 1,2- conformation observed in the previous case. The 1,3-bis(trimethylsilyl)ether of *p*-*tert*-butylcalix[4]arene has been synthesized and used as a dianionic ligand for complexing Ge and Sn [99]. The crystal structure of the Ge complex exhibits *exo/endo* isomerism (Fig. 25a and b).

Transition metals can be used for shaping and electronically enriching the calix[4]arene cavity so that the π -basic cavities can be adapted to alkali–metal cation complexation in the hydrophobic zone [100]. Thus the structure of the calixarene–alkali metal cation was determined by X-ray diffraction (XRD) wherein the calixarene assumes

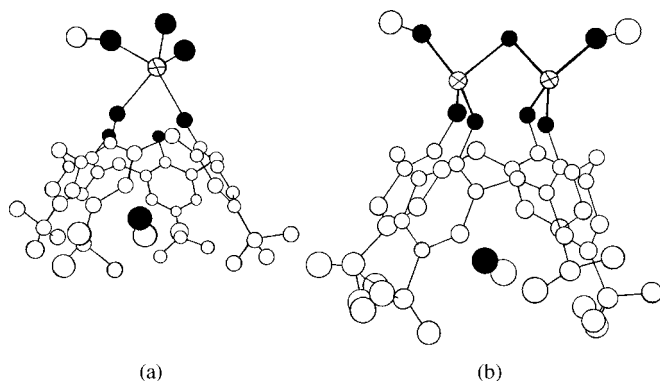


Figure 23. Structures of (a) $[\text{Na}(\text{MeOH})(\text{H}_2\text{O})_2][p\text{-tert-butylcalix[4]arene}] \cdot \text{MeOH}$ and (b) $[\text{Li}(\text{MeOH})_2(\mu\text{-H}_2\text{O})][p\text{-tert-butylcalix[4]arene}] \cdot \text{MeOH}$. Open circles denote carbons, filled circles denote oxygens, and circles with crosses denote metal ions. Adapted from [95], F. Hamada et al., *Supramol. Chem.* 2, 19 (1993). © 1993, Taylor & Francis, Ltd.

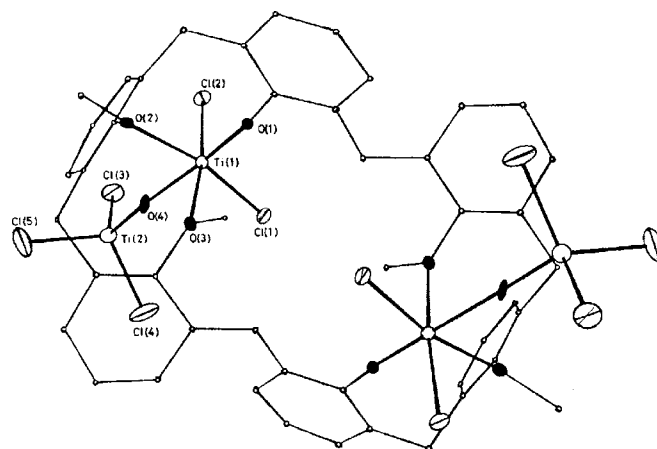


Figure 24. Structure of calix[6]arene $[\text{TiCl}_2(\mu\text{-O})\text{TiCl}_3]_2$. Adapted from [96], S. G. Bott et al., *J. Chem. Soc., Chem. Commun.* 610 (1986). © 1986, Royal Society of Chemistry.

a flattened cone conformation. Complexes of Fe(III) and Er(III) of a calix[4]arene diamide were reported [101] to form 1:1 complexes where the calix[4]arene is found to be in cone conformation.

Two extended-array metallocalixarenes derived from the ring opening of imido-molybdenum precursors have been synthesized and their structures were determined [102]. It is observed that the metallocalixarenes are organized in a “cup-to-cup” arrangement that gives rise to a calixarene “socket” and this potentially hosts guest molecules.

A calix[4]arene derivative, 1-carboxylic acid-3-diethyl amide, exhibited efficient extraction properties toward rare-earth ions and the crystal structure of a neutral 1:1 uranyl complex of dinuclear nature was determined [103]. Syntheses and X-ray crystal structures of neutral dimeric europium (Fig. 26), samarium, and monomeric lutetium complexes and the selective extraction properties of the 1,3-acid-diethyl amide substituted calix[4]arene ligand have been determined [104]. While the monomeric lutetium complex is seven-coordinated (Fig. 27), both the dimeric complexes exhibit eight-coordination around each metal ion. The structures show that the substituted calix[4]arene exists in cone conformation.

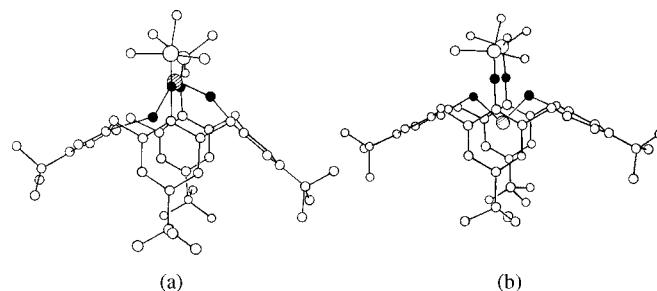


Figure 25. Molecular structures of $[p\text{-tert-butylcalix}(\text{trimethylsilyl})_2]\text{Ge}$: (a) *exo*-form and (b) *endo*-form. Open circles denote carbons, filled circles denote oxygens, and circles with lines denote Ge. The big open circles represent Si. Adapted from [99], T. Hascall et al., *J. Chem. Soc., Chem. Commun.* 101 (1998). © 1998, Royal Society of Chemistry.

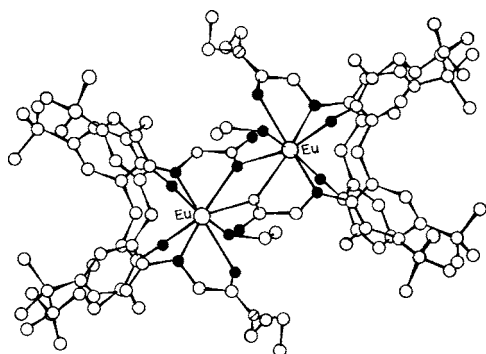


Figure 26. Crystal structure of $[\text{Eu}(\text{1,3-diacid-diethylamide substituted calix[4]arene})(\text{EtOH})_2]$. Open circles denote carbons, filled circles denote oxygens, and circles with a line denote nitrogens. Adapted from [104], P. D. Beer et al., *J. Chem. Soc., Chem. Commun.* 1117 (1996). © 1996, Royal Society of Chemistry.

Complexes of La(III), Eu(III), Gd(III), Tb(III), and Lu(III) with the lower rim functionalized tetrakis[2-(diethylcarbamoyl-methoxy)ethoxy]calix[4]arene have been synthesized and the crystal structure of the Lu complex was established where Lu(III) is 9-coordinated in which the calixarene is in the cone conformation [105]. Calixarene derivatives of phosphine oxide moieties [calix-($\text{OCH}_2\text{CH}_2\text{POPh}_2$) $_n$, where $n = 4, 6, 8$] attached to the lower rim have been reported to exist in distorted cone conformation [106]. These act as receptors for the extraction of Eu(III), Th(IV), Pu(IV), and Am(IV) in nuclear waste treatment.

The reaction of 5,11,17,23-tetra-*tert*-butyl-25,27-dihydroxy-26,28-bis[*N*-(2-diphenyl phosphino)phenyl] carboxyamidemethoxy]calix[4]arene with $[\text{Cu}(\text{CH}_3\text{CN})_4]\text{ClO}_4$ and $\text{Pt}(\text{COD})\text{Cl}_2$ formed complexes whose structures were determined by X-ray analysis. The copper complex has two seven-membered metallocycles, the platinum complex

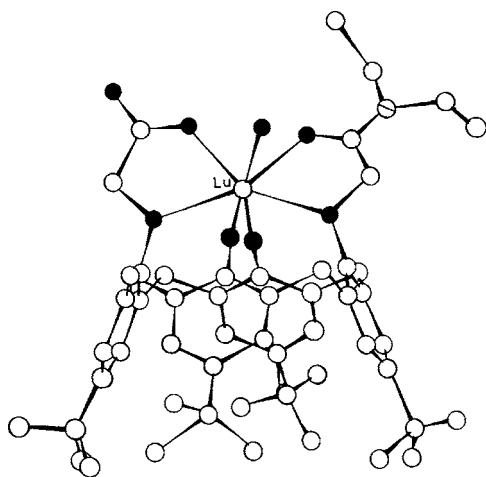


Figure 27. Crystal structure of $[\text{Lu}(\text{1,3-diacid-diethylamide substituted calix[4]arene})(\text{H}_2\text{O})]$ monomer. Open circles denote carbons, filled circles denote oxygens, and circles with a line denote nitrogens. Adapted from [104], P. D. Beer et al., *J. Chem. Soc., Chem. Commun.* 1117 (1996). © 1996, Royal Society of Chemistry.

has one five-membered metallocycle, and both complexes assume the cone conformation [107].

X-ray studies reveal that the dimeric supramolecular assemblies of water-soluble calix[4]arenes are formed by a combination of hydrophobic effects and either hydrogen bonding or secondary bonding [108]. It is observed that for copper complex, the dimeric association is based on a secondary bonding interaction between the copper(II) ion and a sulfonato oxygen atom combined with hydrophobic interactions.

The coordination form and hence the cavity of the calix[4]arene ligands can be controlled by other ligands in transition-metal calix[4]arene complexes, if strong directing co-ligands such as oxo groups are used. Radius [109] described the synthesis and structure of Ti(IV) and Mo(VI) complexes of 1,3-dimethoxy-calix[4]arene where TiCl_2 and MoO_2 moieties arising from TiCl_4 and MoO_2Cl_2 control the coordination form and hence the cavity. While the ligand adopts an elliptically distorted cone conformation in TiCl_2 complex as shown in Figure 28, the same adopts a partial-cone conformation in the molybdenum complex (Fig. 29).

Transition-metal complexes of 5,11,17,23-tetra-*tert*-butyl-25,26,27,28-tetrakis(diethyl-carbamoylmethoxy)calix[4]arene in the cone conformation have been synthesized and the crystal structures of Fe(II), Ni(II), Cu(II), Zn(II), and Pb(II) complexes have been established by Ogden and co-workers [110]. The structures of the complexes of Fe(II), Zn(II), and Pb(II) are almost similar with the metal ions coordinated to all eight oxygen atoms of the ligand as can be seen in Figure 30. The copper complex is somewhat different with four bonds slightly shorter than the remaining four. On the other hand, the nickel structure is completely different where the ligand has undergone rearrangement to accommodate the metal cation in a distorted octahedral environment (Fig. 31). The same group also reported Fe(III) complexes of 5,11,17,23-tetra-*tert*-butyl-25-hydroxy, 26,27,28 tris(diethylcarbamoylmethoxy)-calix[4]-arene whose structure was determined by XRD [111]. The structure shows that Fe(III) is bound to all seven oxygen atoms of calix[4]arene with $\text{Fe}-\text{O}_{\text{phenolic}}$ distance being the shortest (Fig. 32).

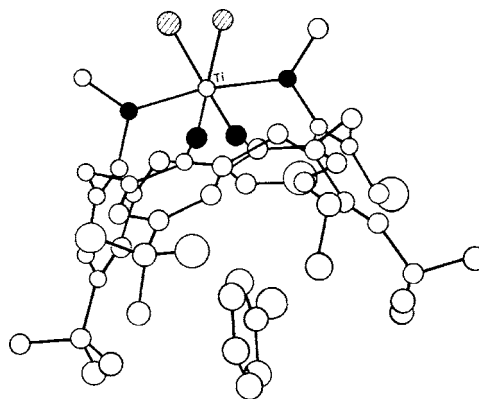


Figure 28. Molecular structure of $[p\text{-tert-butylcalix[4]arene}(\text{OMe})_2\text{-O}_2\text{TiCl}_2]$ in elliptical distorted cone conformation. Open circles denote carbons, filled circles denote oxygens, and circles with lines denote chlorines. Adapted from [109], U. Radius, *Inorg. Chem.* 40, 6637 (2001). © 2001, American Chemical Society.

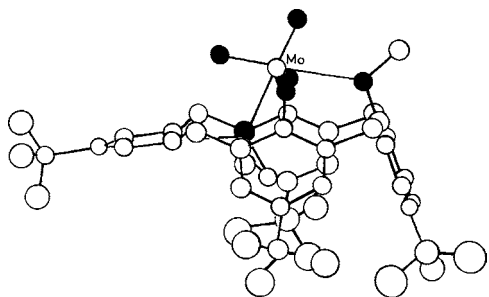


Figure 29. Molecular structure of $[p\text{-tert-butylcalix[4]arene(OMe)}_2\text{-O}_2\text{MoO}_2]$ in partial conelike mode. Open circles denote carbons and filled circles denote oxygens. Adapted from [109], U. Radius, *Inorg. Chem.* 40, 6637 (2001). © 2001, American Chemical Society.

8. APPLICATIONS

Parent calixarenes are insoluble in water, have generally low solubility in most organic solvents, and are characterized by their high melting points. However, through appropriate derivatization these exhibit good solubility in either medium [112]. Aqueous solutions (0.1 M) can be prepared with *p*-sulphonato-calix[4]arene. The acylated calixarenes possess antioxidant and heat stabilizing properties that are useful for the plastics. Thus simple calixarenes, their functionalized

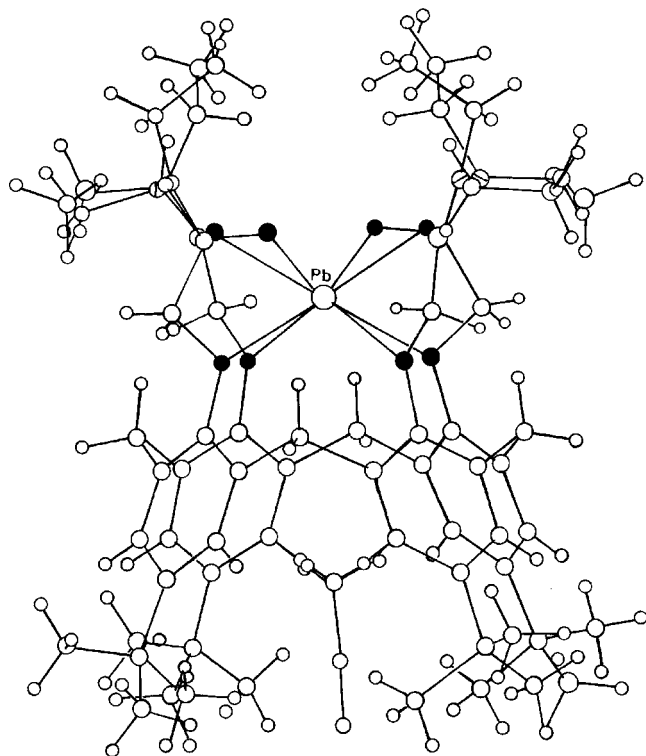


Figure 30. Structure of lead(II) complex of *p*-tert-butylcalix[4]arene tetraamide together with the included MeCN. Open circles denote carbons, filled circles denote oxygens, and circles with a line denote nitrogens. Adapted from [110], P. D. Beer et al., *J. Chem. Soc., Dalton Trans.* 1273 (1995). © 1995, Royal Society of Chemistry.

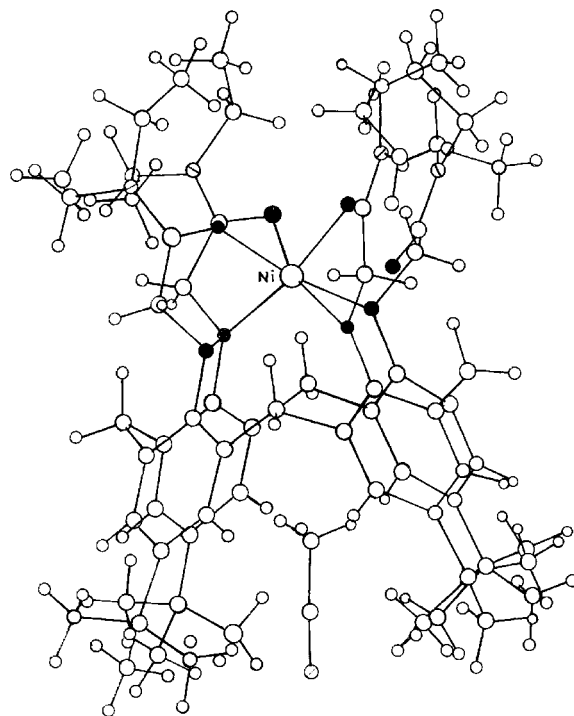


Figure 31. Structure of the nickel(II) complex of *p*-tert-butylcalix[4]arene tetraamide with included acetonitrile molecule. Open circles denote carbons, filled circles denote oxygens, and circles with a line denote nitrogens. Adapted from [110], P. D. Beer et al., *J. Chem. Soc., Dalton Trans.* 1273 (1995). © 1995, Royal Society of Chemistry.

derivatives, and the metal ion complexes of all these offer a number of applications having impacts in chemistry, biology, and materials. Details of some such applications are presented in this section.

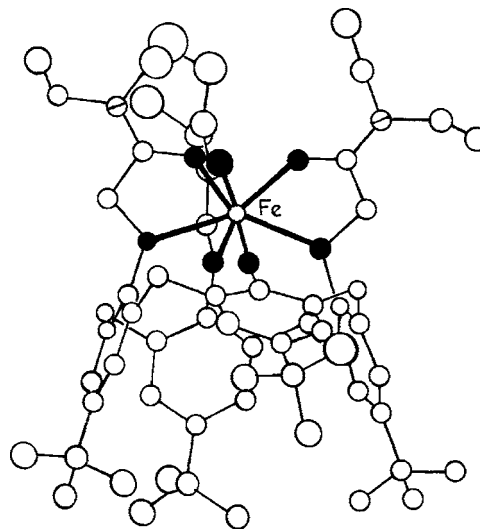


Figure 32. Molecular structure of $[\text{Fe}(p\text{-tert-butylcalix[4]arenetriamide-H})](\text{FeCl}_4)_2$. Open circles denote carbons, filled circles denote oxygens, and circles with a line denote nitrogens. Adapted from [111], M. I. Ogden et al., *J. Chem. Soc., Dalton Trans.* 3073 (2001). © 2001, Royal Society of Chemistry.

8.1. Supramolecular Formation

Undoubtedly the most useful property of calixarenes and its derivatives is their ability to function as molecular baskets and bind neutral and/or ionic guests resulting in supramolecular arrays. Rapid and extensive developments have taken place through exploration of the receptor property of the simple calix[4]arene and its functionally modified derivatives, thereby contributing to the area of analytical devices. Inclusion complexes of neutral guest molecules, such as toluene, benzene, xylene, anisole, and pyridine, in the chalice-like molecular cavity of calix[4]arene have been reported [113]. Attractive $\text{CH}_3 \cdots \pi$ interactions may contribute to the binding. Based on the X-ray diffraction studies, Atwood [114] and co-workers demonstrated a water inclusion complex of an upper rim sulphonated calix[4]arene (Fig. 33). The water molecule occupies a distorted conical cavity with its two hydrogen atoms directed toward the two nearest juxtaposed benzene rings. Structures of this type may provide important clues about how water molecules interact with aromatic moieties in biological systems. A 1:1 clathrate complex of calix[4]arene-tetracarbonate and acetonitrile is reported to have C_{4v} symmetry. In this clathrate, the acetonitrile resides in the hydrophobic cavity with nitrogen atom protruding from the lower rim.

8.2. Calixarenes as Receptors

Calixarenes can function as ion receptors by selective transport of alkali cations from one aqueous phase to another through a chloroform membrane containing the *p-tert*-butyl-tetramer, -hexamer, or -octamer [115]. When the source phase was neutral, practically no transport was observed, but when the source phase was made basic to allow ionization of the hydroxyl groups ion transport takes place, the octamer showing the fastest rate with cation selectivity order $\text{Cs}^+ > \text{Rb}^+ \gg \text{K}^+ > \text{Na}^+ > \text{Li}^+$. The presumption that neutral alkali phenoxides contain the cation in or near the cavity has received support from a recent X-ray analysis of neutral cesium salt of the tetramer [116]. Here the cation is found in the center of the cavity. The four phenolic C–O bonds are completely equivalent, indicating a rapidly exchanging network of hydrogen bonds around the four oxygen atoms. It is reported that the calix[4]arene was selective for sodium as compared to the other group I and II metal ions [117]. The studies also showed that there was a size selective effect manifested by a peak extraction of

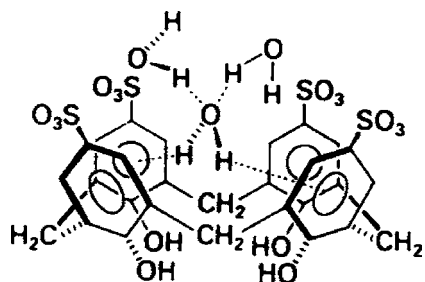


Figure 33. Inclusion complex of a calix[4]arene sulphonate with water as guest. Adapted from [51], J. M. Harrowfield et al., *J. Chem. Soc., Chem. Commun.* 1159 (1991). © 1991, Royal Society of Chemistry.

cesium by the ester derivative of calix[6]arene. Thus, among the alkali cations, calix[4]arene derivatives have the highest affinity for Na^+ .

Some advantages of calixarene as receptors are evident from the complexation of UO_2^{2+} species because the uranyl ion requires hexagonal coordination unlike many competing heavy metal ions that have an octahedral coordination sphere. Shinkai and co-workers [118] have found stability constants for UO_2^{2+} with sulphonic and carboxylic acid derivatives of calix[6]arene, up to 10^{19} mol^{-1} and selectivity factors of 10^{11} – 10^{19} when compared to the divalent cations, viz., Mg^{2+} , Zn^{2+} , Ni^{2+} . Though most of the complexation studies with calixarenes deal with alkali and alkali earth cations, the derivatives containing soft donor atoms like N and S act as effective receptors for a range of transition-metal ions. Therefore, changing the nature of the substituents/pendants at the lower rim can produce dramatic changes in the selectivity. For instance, if the ester moiety at the lower rim of *p-tert*-butyl calix[4]arene is substituted by soft donors, like thio and thioamide groups, the selectivity is shifted from Na^+ to Ag^+ . Similarly, phosphine derivatives have been synthesized to study their complexation with lanthanide and actinide ions for the selective extraction of radioactive elements from nuclear waste.

8.3. Calixarenes as Ion-Selective Electrodes

Calixarenes containing cation complexing groups at the lower rim possess the molecular requirements for the type of ionophores used in ion-selective electrodes. This is so, because calixarenes possess rigid cavities that are predisposed to selectively complex with cations and the high lipophilicity associated with the *t*-butyl groups prevents the organic derivative and its cation-complexed product from leaching nonpolar membrane into aqueous solution. Ion selective electrodes for K^+ and Cs^+ have been successfully developed using dioxacalix[4]arene [119] and calix[6]arene [120] respectively. Calix[4]arene derivatives containing S and N donor groups have been developed as ion selective electrodes as well as used to make chemically modified electrodes suitable to determine Hg^{2+} , Pb^{2+} , Ag^+ , and Cu^{2+} [121]. Ion selective field effect transistors containing a calixpherand as the ionophore enable the quantitative determination of K^+ in the presence of even a large excess of Na^+ [122].

8.4. Calixarenes as Biosensors

A tetra-ester derivative of calix[4]arene, **1** (Fig. 34), has been used to make bench and miniaturized Na^+ selective electrodes [123] and for Na^+ detection in flow injection analysis [124]. These devices have been used to determine Na^+ in human blood plasma [125]. This sensor has also been used along with several other sensors in an array giving accurate assays of ions in blood [126] and mineral water [127].

8.5. Calixarenes as Optical Sensors

The signal in potentiometric sensors is generated by selective exchange of cations into the membrane phase, which is mediated by a calixarene ligand. However, for optical

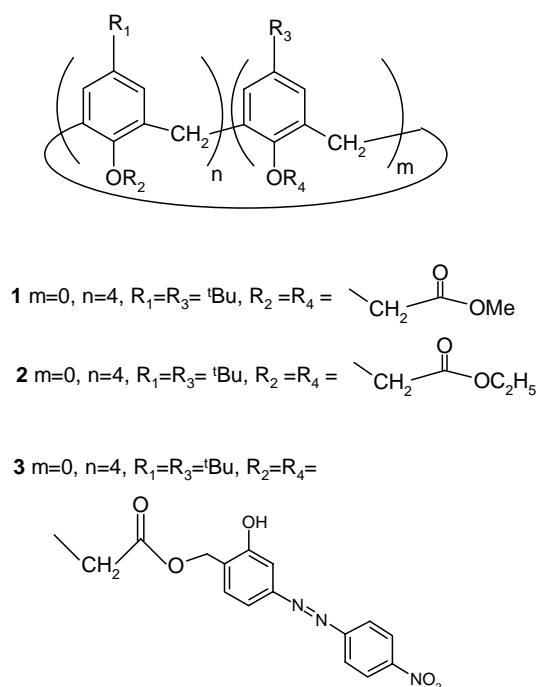


Figure 34. Schematic representation of the structure of calix[4]arene derivatives used as optical sensors (suitable for absorption studies) in their “cone” conformation.

transduction, an optically responsive mechanism must be coupled with the ion–ligand complexation process. This can be achieved by co-immobilizing a lipophilic, acido-chromic dye in the membrane with the ligand. The complexation of the metal ion by the ligand results in the expulsion of a proton from the dye to the sample phase, which maintains overall charge neutrality [128]. This approach has been used to design a series of ion-selective optical sensors (optodes), based on the same type of calixarene ligands (Fig. 34) that is used for ion-selective electrodes. The dyes, such as acridine derivatives, can produce optodes with longer lifetimes [129]. It is also possible to attach acido-chromic groups directly on the upper or lower rim of the calixarene [130]. A calix[4]arene derivative [131] containing the nitrophenol-azaphenol chromophore, **3** (Fig. 34), in chloroform changes color upon addition of Li^+ in the presence of tri-*n*-dodecylamine (TDDA). On complexation of Li^+ , the labile proton of the dye is transferred to TDDA, and the color changes from a pale yellow to deep brownish red by shifting the absorption maximum from ~ 380 to ~ 530 nm. A mixture of tetraester of calix[4]arene, **2** (Fig. 34), Girard’s reagent P derivative of butyraldehyde, and chromoionophore ETH5294 has been used to detect low molecular weight aldehydes. 1,1’-Binaphthyl (at the lower rim) as well as the bis(indolphenol) (at the upper rim)-derived calix[4]arene crown ether derivative (Fig. 35) was developed as a sensor to differentiate the enantiomers of host amines and amino acids through color change. While one of the enantiomers respond through change in visual coloration, the other does not when these are interacted with this calix[4]arene derivative [132].

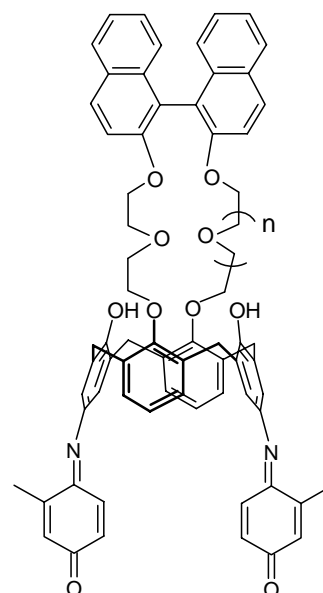


Figure 35. Schematic structure of 1,1’-binaphthyl (on lower rim) as well as bis(indolphenol) (on upper rim)-derived calix[4]arene as molecular sensor for chiral recognition ($n = 0, 1$).

Some of these chromogenic calixarene derivatives reported are novel and have important analytical applications, such as light-switching properties, where the derivative possesses a fluorescent pyrene group in the 1-position and a *p*-nitrobenzyl quencher in the 3-position as shown in Figure 36 [133]. Fluorescence is absent in the cation-free form of the calixarene, but the presence of a cation guest in the cavity forces the lower rim into a more open conformation, with quencher and fluorophore spatially separated, thus allowing fluorescence to occur. Thus, these receptors are of use in fluorescence-based ion sensors. Also, calixarenes functionalized on their lower rim to contain luminescent ruthenium(II) trisbipyridal complex [134] are found to act as potential amine sensors.

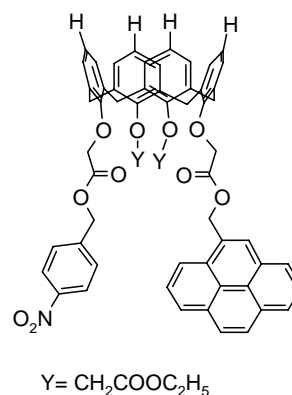


Figure 36. Schematic representation of the structure of calix[4]arene derivative possessing pyrene group on the lower rim as sensor that is suitable for fluorescence studies.

8.6. Electrochemiluminescence of Calixarenes

Upper rim carboxylic acid derivatives of calixarenes shown in Figure 37, when coated on a porous silicon electrode surface, exhibited interesting luminescence properties [135, 136] in 1.0 M H_2SO_4 electrolyte solution through anodic oxidation of the calixarene derivative. It was found that both the duration as well as efficiency of the light emission are affected depending upon the nature of the calixarene derivative used. Electrochemiluminescence can be generated for longer periods of time for these coated porous Si junctions relative to the untreated porous Si ranging from up to 3 h for calix[4]arene-coated porous Si to about 30 min for the calix[n]arene ($n = 5, 7, 8$) derivatives. These observations are attributed to packing differences between different calixarene carboxylic acid derivatives as thin films and subsequent bias-induced Si nanoparticle oxidation in the porous matrix. The studies also focused on the effect of electrochemiluminescence on the size of the calixarene as well as on the chain length of the carboxylic tether to the rim.

8.7. Calixarenes as Catalysts

Shinkai and co-workers [137, 138] have studied kinetics with a series of sulfonato-calixarene derivatives shown in Figure 38 as catalysts for the reaction of addition of water to 1-benzyl-1,4-dihydronicotinamide to form 1-benzyl-6-hydroxy-1,4,5,6-tetrahydronicotinamide. The results showed that the calixarenes having a protic lower rim (a and b) are better catalysts than those lacking this feature (c and d). The same reaction was carried out using *p*-(carboxyethyl)calixarenes [43] (Fig. 37, with $n = 6$), and it was found that *p*-sulphonato calix[6]arene is about four times more effective as a catalyst than *p*-(carboxyethyl)calix[6]arene. This is attributed to the greater concentration of negative charge at the upper rim of the calixarene, the six sulfonato groups being held more rigidly in place than the more flexible carboxyethyl moieties.

8.8. Biomimetic Catalysis

Although calix[4]arene-based molecular receptors have been reported [139, 140], calix[4]arene-based enzyme models have hardly been developed [141–146]. A Ba(II) complex of crown ether attached to the lower rim of calix[4]arene was

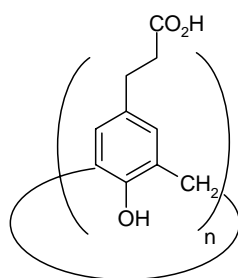


Figure 37. Schematic representation of the structure of calixarene carboxylic acid derivatives ($n = 5-8$) at the upper rim used in electrochemiluminescence.

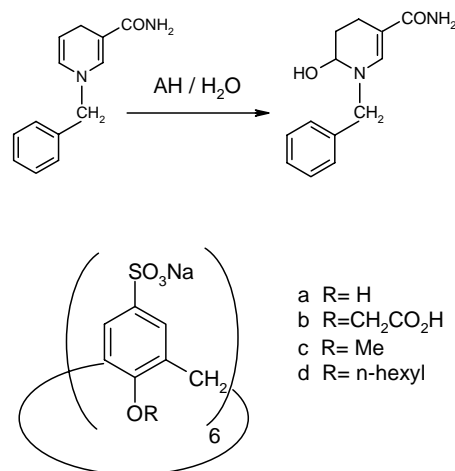


Figure 38. Addition of water to 1-benzyl-1,4-dihydronicotinamide catalyzed by sulphonato calix[6]arenes in the presence of acid (AH).

reported to exhibit *trans*-acylase activity in the methanolysis of *p*-nitro phenyl acetate [147].

Calix[4]arene-based binuclear complexes (Fig. 39) have been shown to efficiently catalyze phosphate diester cleavage with a high degree of cooperation between the two Zn^{II} or the two Cu^{II} centers [139–143]. It has been observed that the binuclear zinc complex 3- Zn_2 having calixarene moiety exhibits a very high activity in the *trans*-esterification of the RNA model substrate HPNP (2-hydroxypropyl *p*-nitrophenyl phosphate). The catalytic activity of mononuclear calix[4]arene 2-Zn and the reference complex 1-Zn, lacking the flexible calix[4]arene backbone, are low by a factor of 50 and 300 respectively [144, 145]. The binuclear Zn^{II} complex of the bis(aminomethyl)pyridine ligand 3 shows a higher catalytic rate than its Cu^{II} analog 3- Cu_2 . This is in

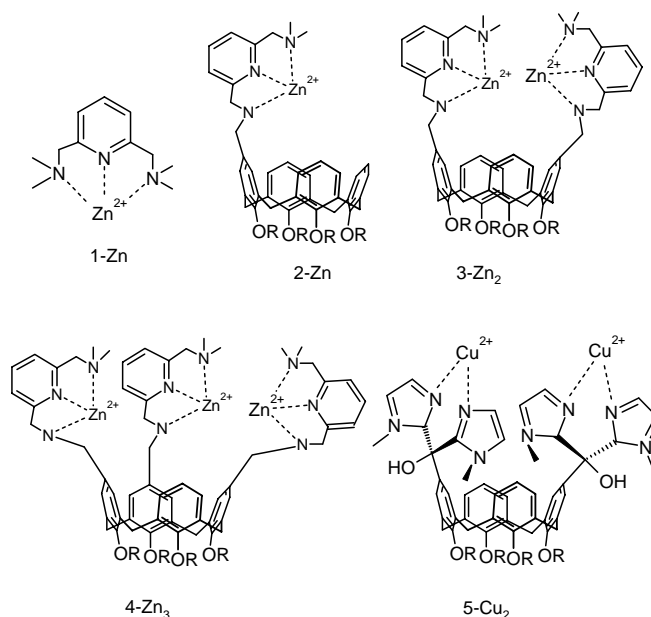


Figure 39. Calix[4]arene based model systems for metallophosphodiesterases [$\text{R} = -\text{CH}_2\text{CH}_2\text{OCH}_2\text{CH}_3$].

contrast to the dinucleating bisimidazolyl ligand **5**, which forms a highly active Cu^{II} complex, **5-Cu₂**, and a weakly active Zn^{II} complex, **5-Zn₂**. Comparison of dinuclear Cu^{II} -calix[4]arene **5-Cu₂** with binuclear Zn^{II} shows that the high catalytic activity of **5-Cu₂** in HPNP *trans*-esterification is mainly a result of a high turnover rate (k_{cat}) combined with a moderate substrate-catalyst binding constant (K_{ass}). However, the observed low activity of **3-Zn₂** is mainly due to strong substrate-catalyst affinity along with a relatively moderate turnover rate. This agrees well with the reported higher phosphate affinity of Zn^{II} . The differences observed in the reactivity between the Zn^{II} complexes (**3-Zn₂** and **5-Zn₂**) and the Cu^{II} complexes (**3-Cu₂** and **5-Cu₂**) are reflective of their preferential coordination geometries [142, 143]. It was therefore concluded that the tether length and the geometry of the binding arms of the ligands determine the catalytic activity and the mechanism of catalysis. Proposed mechanisms for HPNP cleavage by calix[4]arene complexes of **3-Zn₂** and **5-Cu₂** are shown in Figure 40. Hence these calix[4]arene based binuclear complexes can be used as models for binuclear metallo-phosphodiesterases [141–145]. Extension to systems with a third metal ion binding site afforded a trinuclear Zn^{II} complex **4-Zn₃** (Fig. 39) that mimics trinuclear Zn^{II} phosphodiesterases [142, 146] due to the cooperative action of three Zn^{II} centers resulting in an enhanced reactivity.

8.9. Calixarenes as Liquid Crystals

Tungsten complexes with 8 and 12 dodecyloxy side chains on lower rim were found to exhibit liquid crystalline phase [148]. Swager et al. reported a new type of columnar liquid crystal with a rigid bowl-like core based on tungsten-oxo calix[4]arene complexes which is stable over a very wide temperature range. These complexes display mesophases of unusually high stability and novel host-guest effects, which suggests that head-to-tail organization occurs in the mesomorphic state.

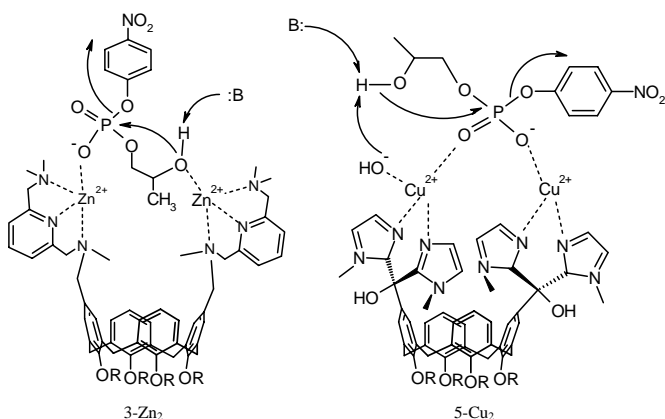


Figure 40. Proposed mechanism for 2-hydroxypropyl *para*-nitrophenyl phosphate cleavage by calix[4]arene based model complexes, **3-Zn₂** (left) and **5-Cu₂** (right) [R = $-\text{CH}_2-\text{CH}_2-\text{O}-\text{CH}_2-\text{CH}_3$].

8.10. Calixarenes in Nonlinear Optics

Organic molecules with π electron systems and unsymmetrical charge distributions are useful in nonlinear optics, for frequency-doubling of laser light and electro-optic switching [149, 150]. Reinhoudt and co-workers [151] reported that the tetranitrocalix[4]arene, shown in Figure 41, contains four nonconjugated D- π -A dipoles within a single molecule and it can be present in four idealized conformations with different relative orientations of the intramolecular nonlinear optic-phores. The high μ value of the tetranitrocalix[4]arene enables a high degree of orientation upon poling in a polymeric matrix [152]. It is reported that calix[4]arene based chromophore, calix[4]stilbazole, forms densely packed, highly ordered monolayers on silica surfaces [153]. The second order nonlinear optical properties of calix[4]arene for its different conformations have been investigated theoretically [154]. For further details on this subject, one may refer a recent textbook [155], *Nonlinear Optics of Organic Molecules and Polymers*.

8.11. Nanocavities

The design and synthesis of nanoscale molecular containers such as cavitands [156–158], hemicarcerands [159], and capsules [160–162] result in the selective binding, separation, and sensing of smaller molecules and ions, molecular transport and delivery, stabilization of reactive intermediates, and catalysis through encapsulation [163]. They also mimic the hydrophobic pockets of enzymes [164]. Synthetic calixarene derivatives having cavities of 15–20 Å contribute to molecular recognition thus giving new directions into nanotechnology, microfabrication, and molecular biology [165, 166]. The nanocavities can be used for the encapsulation of drugs and their active transport/delivery through cell membranes. In calix[4]arenes, the aromatic rings were fixed in the perfect cone conformation through the covalent bridging of proximal phenol oxygens with diethylene glycolic chains [167]. Thus the calix-cavitands formed are more rigid and show better affinity toward guest molecules. The crystal structures of calixarenes and the smaller cavitands derived from them showed that the guest molecule is positioned above the plane of the four carbon atoms of the cyclic polyaromatic skeleton [165, 166, 168–170]. The cavity's depth is generally less than 4 Å and this space is just sufficient for one methyl-sized fragment to be included. Several approaches have been developed to enlarge the cavity and achieve better guest entrapment. For example, triethylene glycol footed deep cavitands are functionalized with four *m*-amidinium groups

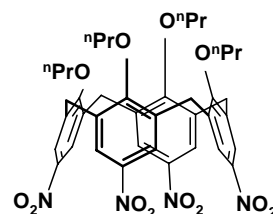


Figure 41. *para*-Nitro-calix[4]arene where phenolic oxygens are alkylated with *n*-propyl group.

at the upper rim in order to effectively bind mono- and dinucleotides in buffered aqueous and methanol solutions [171]. In addition to charged interactions and hydrogen bonding, the cavity also contributes to the overall binding process. A proposed adenosine monophosphate complex of this cavitand is shown in Figure 42. ^1H NMR and molecular modeling studies suggest that the adenine part is located deep inside the host cavity [172].

The cavitand shown in Figure 43 is a much deeper and open ended container molecule with a nanoscale cavity ~ 14 Å deep and 12 Å wide reported to date [173]. According to molecular modelling, such a cavity is able to accommodate up to three benzene or chloroform sized molecules. However, its complexing ability toward small organic guests in nonpolar solutions appeared to be poor. The electron-rich interior resulted in considerable interactions with electron deficient fullerene C_{60} in toluene as shown in Figure 43. The open-ended nature of the cavitand is responsible for its host-guest properties.

An alternative strategy to make deep cavitands is to employ self-assembly through intermolecular hydrogen bonding. Multicomponent cavitands have been constructed by MacGillivray in the solid state by co-crystallization of resorcinarene ($\text{R} = \text{Me}$) and 4,4'-bipyridine from ethanol in the presence of an aromatic or polycyclic guest. This resulted in an one-dimensional wavelike polymer structure (guest = ferrocene, 1,1'-diacetyl ferrocene, *p*-chlorotoluene, adamantanon, and [2.2]paracyclophane), where the guest molecules interact with the aromatic walls through multiple $\text{C}-\text{H} \cdots \pi$ contacts as shown in Figure 44 [174–176].

8.12. Clamshell-Shaped Molecular Containers

Geometrically, clamshell-shaped hosts impose more constrictive binding than cavitands and their inner cavities are still exposed to the bulk exterior. Unlike self-assembling

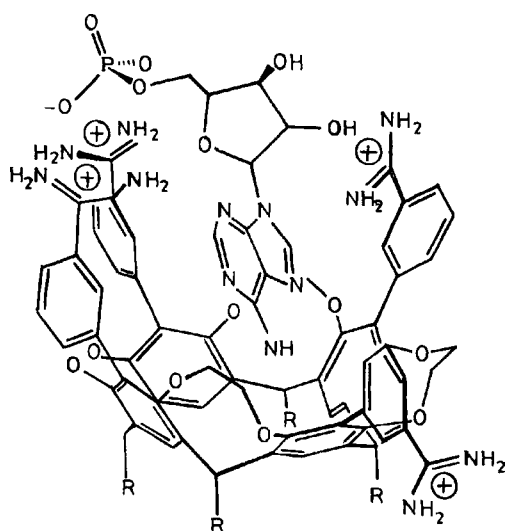


Figure 42. Proposed complex of cavitand with adenosine monophosphate as molecular recognition unit [$\text{R} = -(\text{CH}_2)_3(\text{OCH}_2\text{CH}_2)_3\text{OCH}_3$]. Adapted from [171], K. T. Chapman and W. C. Still, *J. Am. Chem. Soc.* 111, 3075 (1989). © 1989, American Chemical Society.

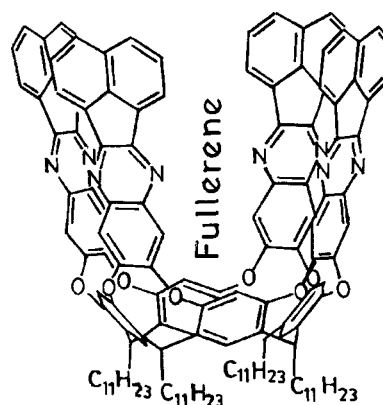


Figure 43. Deep cavitand with nanoscale cavity having electron rich interior provides considerable interaction for filling with fullerene, C_{60} . Adapted from [173], F. C. Tucci et al., *J. Org. Chem.* 64, 4555 (1999). © 1999, American Chemical Society.

capsules, their cavities are constructed through covalent bonding. Reinhoudt et al. reported the synthesis of large clamshell-shaped hydrophobic surfaces by linking two calix[4]arenes with one resorcinarene or one calix[4]arene with two resorcinarenes as shown in Figure 45 [177]. Four strong intramolecular hydrogen bonds between the bridging acetamide $\text{CH}_2\text{C}(\text{O})-\text{NH}$ and the oxygens of the cavitand acetal bridges were found to significantly rigidify the structure of these extended surfaces. The resultant hosts (Fig. 45) bind corticosteroids, carbohydrates, nucleosides, and alkaloids in CDCl_3 solutions.

8.13. Self-Assembling Nanocapsules

Self-assembly represents an alternative way to construct nanocavities and their host-guest complexes [160, 161]. With appropriate curvature and carefully designed positioning of interacting sites, calixarene-based self-assembling systems generate capsules. Capsules have been organized through hydrogen bonding and metal-ligand interactions. An example of self-assembling cavities is the calix[4]arene tetraurea dimer shown in Figure 46 [178, 179]. This has an internal volume of only $50\text{--}250$ Å³ and can entrap a single guest molecule of moderate dimensions [180, 181].

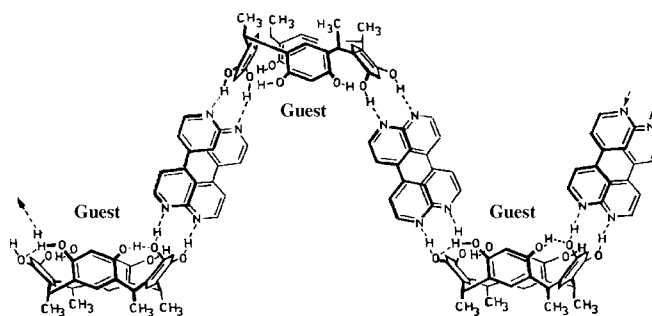


Figure 44. Self-assembling cavitand formed between resorcinarene and 4,4'-bipyridine through intermolecular hydrogen bonds. The cavities are filled with guest molecules, such as ferrocene, *p*-chlorotoluene, adamantanon, and [2.2]paracyclophane. Adapted from [174], L. R. MacGillivray and J. L. Atwood, *J. Am. Chem. Soc.* 119, 6931 (1997). © 1997, American Chemical Society.

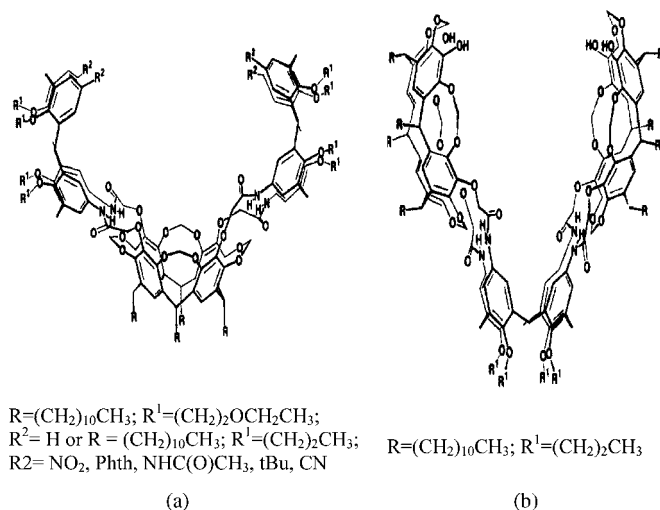


Figure 45. Clamshell-shaped molecular containers formed by linking calix[4]arene and resorcinarene (either in 1:2 or in 2:1 ratio) through hydrogen bonds, possessing hydrophobic interiors to bind corticosteroids, carbohydrates, nucleosides, or alkaloids. Adapted from [177], I. Higler et al., *J. Org. Chem.* 61, 5920 (1996). © 1996, American Chemical Society.

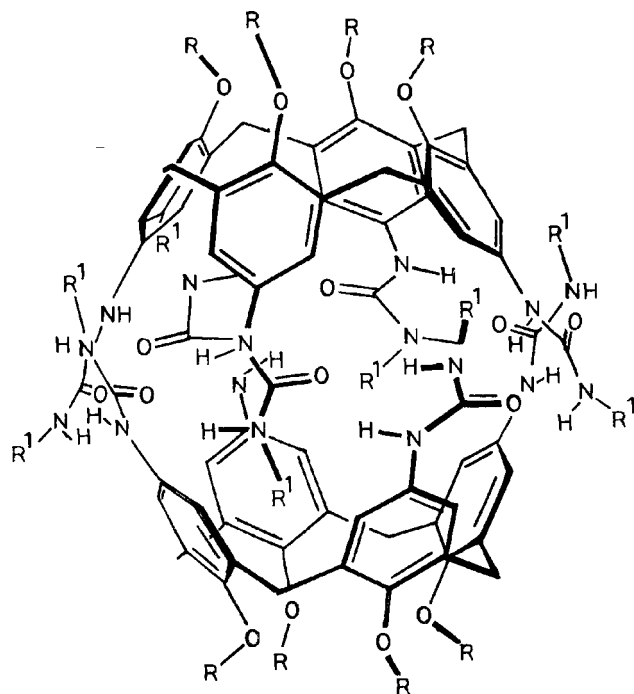


Figure 46. Self-assembling calixarene capsule formed from calix[4]arene tetraurea dimer through intermolecular hydrogen bonds. $R = \text{Alk}$, $R^1 = \text{Alk}$, Ar, Ts. Adapted from [178], K. D. Shimizu and J. Rebek, Jr., *Proc. Natl. Acad. Sci. USA* 92, 12403 (1995). © 1995, National Academy of Sciences.

8.14. Spheres and Tubular Structures

The *p*-sulfonatocalix[4]arene has been reported to assemble in an up-up fashion to result in curved structures by Atwood and co-workers [182], using a reaction system consisting of $Na_5[p\text{-sulfonatocalix[4]arene}$, pyridine *N*-oxide, and $La(NO_3)_3 \cdot 6H_2O$ in 2:2:1 ratio. The hydrophobic regions of the calixarenes are assembled in an up-up radial symmetric fashion along the surface of a sphere, where they constitute an organic shell around an aqueous polar core. This spherical assembly measures $\sim 28 \text{ \AA}$ across and has a volume of $\sim 11,000 \text{ \AA}^3$. The interior of the sphere consists of two $Na(H_2O)_6$ ions surrounded by an additional 24 water molecules. The cavities of the calixarenes are situated just below the polar surface of the sphere and constitute a series of hydrophobic pockets. Twelve pyridine *N*-oxide molecules penetrate the polar surface of the sphere and are bound within the hydrophobic pockets via π -stacking interactions. Their oxygen atoms extend outward and coordinate to La^{3+} ions above the surface of the sphere. The hydrophilic interstitial regions between the spheres contain, in addition to La^{3+} ions, an array of water molecules and hydrated Na^+ ions. The core of each sphere has a diameter of $\sim 15 \text{ \AA}$ and a volume of $\sim 1700 \text{ \AA}^3$. Adjacent spheres are tethered to one another by coordination of sulfonate oxygen atoms to interstitial lanthanum ions. Thus these $La(III)$ ion centers are both first- and second-sphere coordinated to the calixarene molecules.

When the three components are taken in a molar ratio of 2:8:1, crystals obtained revealed a tubular assembly of $\sim 28 \text{ \AA}$ in diameter. The calixarene molecules are arranged along the surface of a cylinder that is analogous to the spherical assembly in that there is a polar core, a hydrophobic midregion constituting the tube, and a polar outer shell. However, the organic shell is not composed of purely calixarene molecules but contains pyridine *N*-oxide molecules intercalated between the aromatic rings of adjacent macrocycles. The calixarene and the pyridine *N*-oxide molecules form a chiral helical assembly along the length of the tube. The helix consists of a single strand of alternating calixarene and pyridine *N*-oxide molecules and there are 4.5 such units per turn. Both the hydrophilic core and the hydrophilic interstices between the tubules contain complex arrays of sodium, lanthanum, and water molecules.

8.15. Synthetic Nanotubes

Calix[4]arenes in 1,3-alternate conformations have a π -basic benzene hole or interlayers through which metal ions can easily pass with the help of cation- π interaction [183]. This plays a crucial role in metal ion transport across ion channels, metal ion inclusion in fullerenes, and intercalation of metal cations into graphite layers [184]. Nanotubes of 1,3-alternate calix[4]arenes having a well-defined inner diameter for the metal tunneling have been reported (Fig. 47) [185].

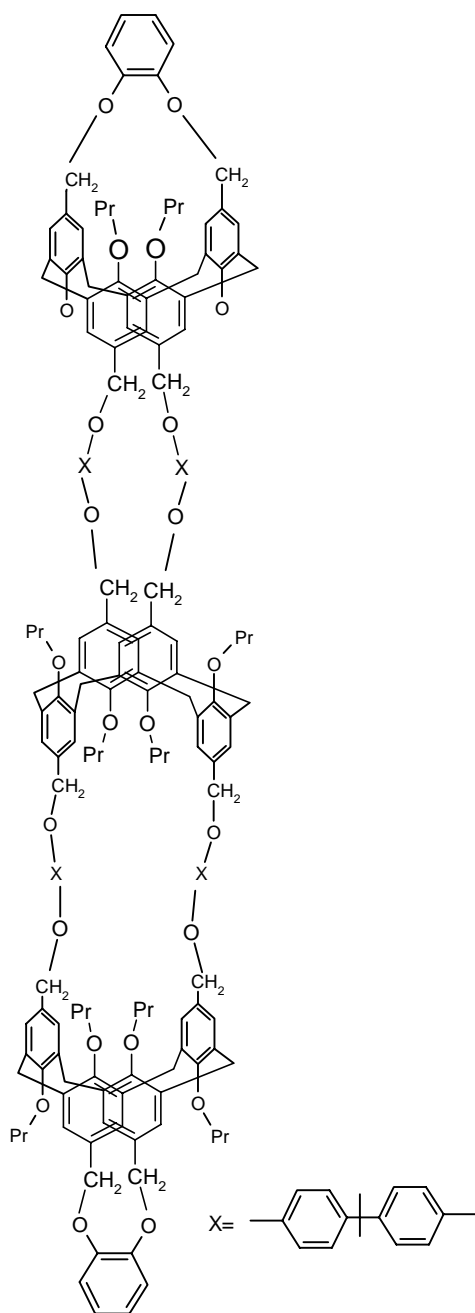


Figure 47. Synthetic nanotubes of 1,3-alternate-calix[4]arene having a π -basic hole for metal tunneling.

9. CONCLUSIONS

It is evident from the literature that the field of calixarenes has been going through rapid phase changes during the past two decades ever since these were synthesized in pure and in large quantities. During the initial period, the literature was primarily focused on developing methods for organic derivatization, particularly of calix[4]arenes, at both its lower and upper rims. As a result of this, the literature of calix[4]arenes on one hand became very rich with a spectrum of organic derivatives; on the other hand, such an outcome led to the rational design of calix[4]arene derivatives

to suit special applications of these based on their intrinsic properties. Properties such as metal ion binding and the capacity to hold and/or recognize molecules or species of calix[4]arenes have been guided and thoroughly refined by the rational design followed by the development. The metal ion complexation chemistry of calix[4]arene derivatives is still going on at a very slow pace. While the biomimetic chemistry of calix[4]arene derivatives is in its early phase, their ability to host organic and/or inorganic species in their neutral, cationic, or anionic form seems to have grown very rapidly during the past few years. Characterization of both the organic and the corresponding inorganic derivatives of calixarenes by different spectral and crystallographic methods has become an important feature in the current literature on calixarenes. Very recent studies have shown the putative utility of carefully designed calix[4]arene derivatives to act as catalysts, hosts, receptors, sensors, cavitands, and nanomaterials as reported in this review chapter. Based on the rate at which the studies are going on with the calixarenes in the literature, it is logical to draw a conclusion that the smartly designed derivatives of calix[4]arene would be occupying a pivotal role in molecular recognition, analytical devices, and materials science and technology that leads to the enrichment of the knowledge of nanoscience in order to eventually get into nanotechnology of calixarenes in the very near future.

GLOSSARY

Arene cavity The cavity formed by the enclosure of the aromatic rings in a calixarene.

Calix[*n*]arenes A group of phenolic macrocyclic molecules resulting from the condensation of *para*-substituted phenol and formaldehyde (*n* refers to the number of phenolic units).

Crystal structure Three-dimensional arrangement of atoms derived from single crystal X-ray diffraction that provides information about the structure, conformation, and geometry of the molecule.

Functionalization Chemical modification on the lower or upper rim leading to the formation of derivatives containing appropriate functional groups.

Lower rim The rim containing the phenolic -OH groups in a *para*-substituted calixarene.

Metalloenzymes Those enzymes that exhibit their function as a result of the presence of a specific metal ion.

Receptor A molecule that possesses the ability to bind to neutral or ionic species through recognition.

Upper rim The rim containing the groups present at the *para*-position in a calixarene.

ACKNOWLEDGMENTS

C. P. R. expresses his appreciation to his former student, Dr. P. Venkateswara Rao, who has ventured into this exciting field of calixarene chemistry and acknowledges the help rendered by the groups of Professor E. Kolehmainen and Professor K. Rissanen, Finland. We thank Amjad Ali for help

during the preparation of this review chapter. C. P. R. gratefully acknowledges the financial support extended by the Department of Science and Technology, BRNS of Department of Atomic Energy, and Council for Scientific and Industrial Research (CSIR), New Delhi. M. D. acknowledges CSIR for the award of a senior research fellowship.

REFERENCES

1. C. D. Gutsche, Calixarenes, in "Monographs in Supramolecular Chemistry" (J. F. Stoddart, Ed.). Royal Society of Chemistry, London, 1989.
2. J. W. Cornforth, E. D. Morgan, K. T. Potts, and R. J. W. Rees, *Tetrahedron* 29, 1659 (1973).
3. V. Bohmer and J. Vicens, "Calixarenes: A Versatile Class of Macrocyclic Compounds." Kluwer Academic, Dordrecht, 1991.
4. C. D. Gutsche and R. Muthukrishnan, *J. Org. Chem.* 43, 4905 (1978).
5. C. D. Gutsche and M. Iqbal, *Org. Syn.* 68, 234 (1989).
6. C. D. Gutsche, B. Dhawan, M. Leonis, and D. Stewart, *Org. Syn.* 68, 238 (1989).
7. J. H. Munch and C. D. Gutsche, *Org. Syn.* 68, 243 (1989).
8. A. Ikeda and S. Shinkai, *Chem. Rev.* 97, 1713 (1997).
9. V. Bocchi, D. Foina, R. Ungaro, and G. D. Andreetti, *Tetrahedron* 38, 373 (1982).
10. C. D. Gutsche, A. E. Gutsche, and A. I. Karaulov, *J. Incl. Phenom.* 3, 447 (1985).
11. G. Ferguson, B. Kaitner, M. A. McKerverey, and E. M. Seward, *J. Chem. Soc., Chem. Commun.* 584 (1987).
12. E. M. Collins, M. A. McKerverey, and S. J. Harris, *J. Chem. Soc., Perkin Trans. 1* 372 (1989).
13. F. Arnaud-Neu, E. M. Collins, M. Deasy, G. Ferguson, S. J. Harris, B. Kaitner, A. J. Lough, M. A. McKerverey, E. Marques, B. L. Ruhl, M.-J. Schwing-Weill, and E. M. Seward, *J. Am. Chem. Soc.* 111, 8681 (1989).
14. G. Calestani, F. Ugozzoli, A. Arduini, E. Ghidini, and R. Ungaro, *J. Chem. Soc., Chem. Commun.* 344 (1987).
15. A. Arduini, E. Ghidini, A. Pochini, R. Ungaro, G. D. Andreetti, G. Calestani, and F. Ugozzoli, *J. Incl. Phenom.* 6, 119 (1988).
16. P. V. Rao, C. P. Rao, E. Kolehmainen, E. K. Wegelius, and K. Rissanen, *Chem. Lett.* 1176 (2001).
17. S.-K. Chang and I. Cho, *J. Chem. Soc., Perkin Trans. 1* 211 (1986).
18. K. Araki, A. Yangi, and S. Shinkai, *Tetrahedron* 49, 6763 (1993).
19. C. Loeber, D. Matt, A. De Cian, and J. Fischer, *J. Organomet. Chem.* 475, 297 (1994).
20. C. Dieleman, C. Loeber, D. Matt, A. De Cian, and J. Fischer, *J. Chem. Soc., Dalton Trans.* 3097 (1995).
21. S. Pappalardo, L. Giunta, M. Foti, G. Ferguson, J. F. Gallagher, and B. Kaitner, *J. Org. Chem.* 57, 2611 (1992).
22. S. Pappalardo, G. Ferguson, P. Neri, and C. Rocco, *J. Org. Chem.* 60, 4576 (1995).
23. E. M. Collins, M. A. McKerverey, E. Madigan, M. B. Moran, M. Owens, G. Ferguson, and S. J. Harris, *J. Chem. Soc., Perkin Trans. 1* 3137 (1991).
24. H. Yamamoto, T. Skaki, and S. Shinkai, *Chem. Lett.* 469 (1994).
25. L. C. Groenen, B. H. M. Ruel, A. Casnati, W. Verboom, A. Pochini, R. Ungaro, and D. N. Reinhoudt, *Tetrahedron* 47, 8379 (1991).
26. J.-D. Van Loon, W. Verboom, and D. N. Reinhoudt, *Organic Preparations Procedures Int.* 24, 437 (1992).
27. M. Dey, C. P. Rao, E. Kolehmainen, and P. Guionneau, to be published.
28. A. Ali, C. P. Rao, and E. Kolehmainen, to be published.
29. G. Alfieri, E. Dradi, A. Pochini, R. Ungaro, and G. D. Andreetti, *J. Chem. Soc., Chem. Commun.* 1075 (1983).
30. R. Ungaro, A. Pochini, and G. D. Andreetti, *J. Inclusion Phenom.* 2, 199 (1984).
31. C. D. Gutsche and I.-G. Lin, *Tetrahedron* 42, 1633 (1986).
32. C. D. Gutsche and J. A. Levine, *J. Am. Chem. Soc.* 104, 2652 (1982).
33. C. D. Gutsche and P. F. Pagoria, *J. Org. Chem.* 50, 5795 (1985).
34. P. Timmerman, W. Verboom, D. N. Reinhoudt, A. Arduini, S. Grandi, A. R. Sicuri, A. Pochini, and R. Ungaro, *Synthesis* 2, 185 (1994).
35. Z. Asfari and J. Vicens, *J. Incl. Phenom.* 19, 85 (1994).
36. S. Shinkai, S. Mori, T. Tsubaki, T. Sone, and O. Manabe, *Tetrahedron Lett.* 25, 5315 (1984).
37. S. Shinkai, K. Araki, T. Tsubaki, T. Arimura, and O. Manabe, *J. Chem. Soc., Perkin Trans. 1* 2297 (1987).
38. A. Arduini, G. Manfredi, A. Pochini, A. R. Sicuri, and R. Ungaro, *J. Chem. Soc., Chem. Commun.* 936 (1991).
39. A. Arduini, S. Fanni, G. Manfredi, A. Pochini, R. Ungaro, A. Sicuri, and F. Ugozzoli, *J. Org. Chem.* 60, 1448 (1995).
40. A. Arduini, M. Fabbi, M. Mantovani, L. Mirone, A. Pochini, A. Secchi, and R. Ungaro, *J. Org. Chem.* 60, 1454 (1995).
41. C. D. Gutsche, J. A. Levine, and P. K. Sujeeth, *J. Org. Chem.* 50, 5802 (1985).
42. M. Almi, A. Arduini, A. Casnati, A. Pochini, and R. Ungaro, *Tetrahedron* 45, 2177 (1989).
43. C. D. Gutsche and I. Alam, *Tetrahedron* 44, 4689 (1988).
44. M. M. Olmstead, G. Sigel, H. Hope, X. Xu, and P. P. Power, *J. Am. Chem. Soc.* 107, 8087 (1985).
45. F. Corazza, C. Floriani, A. Chiesi-Villa, and C. Guastini, *J. Chem. Soc., Chem. Commun.* 1083 (1990).
46. J. A. Acho, L. H. Doerrer, and S. J. Lippard, *Inorg. Chem.* 34, 2542 (1995).
47. F. Corazza, C. Floriani, A. Chiesi-Villa, and C. Guastini, *J. Chem. Soc., Chem. Commun.* 640 (1990).
48. V. C. Gibson, C. Redshaw, W. Clegg, and M. J. R. Elsegood, *J. Chem. Soc., Chem. Commun.* 2371 (1995).
49. F. Corazza, C. Floriani, A. Chiesi-Villa, and C. Rizzoli, *Inorg. Chem.* 30, 4465 (1991).
50. J. M. Harrowfield, M. I. Ogden, and A. H. White, *Aust. J. Chem.* 44, 1249 (1991).
51. J. M. Harrowfield, M. I. Ogden, W. R. Richmond, and A. H. White, *J. Chem. Soc., Chem. Commun.* 1159 (1991).
52. J. M. Harrowfield, M. Mocerino, B. W. Skelton, C. R. Whitaker, and A. H. White, *Aust. J. Chem.* 47, 1185 (1994).
53. B. M. Furphy, J. M. Harrowfield, M. I. Ogden, B. W. Skelton, A. H. White, and F. R. Wilner, *J. Chem. Soc., Dalton Trans.* 2217 (1989).
54. J. M. Harrowfield, M. I. Ogden, A. H. White, and F. R. Wilner, *J. Chem. Soc., Dalton Trans.* 2153 (1991).
55. C. D. Gutsche and K. C. Nam, *J. Am. Chem. Soc.* 110, 6153 (1988).
56. P. D. Beer, M. G. B. Drew, P. B. Leeson, K. Lyssenko, and M. I. Ogden, *J. Chem. Soc., Chem. Commun.* 929 (1995).
57. C. G. Gibbs and C. D. Gutsche, *J. Am. Chem. Soc.* 115, 5338 (1993).
58. H. Kwart and E. R. Evans, *J. Org. Chem.* 31, 410 (1966).
59. M. S. Newman and H. A. Karnes, *J. Org. Chem.* 31, 3980 (1966).
60. X. Delagie, J. M. Harrowfield, M. W. Hosseini, A. De Cain, J. Fischer, and N. Kyritsakas, *J. Chem. Soc., Chem. Commun.* 1579 (1994).
61. X. Delagie, M. W. Hosseini, N. Kyritsakas, A. De Cain, and J. Fischer, *J. Chem. Soc., Chem. Commun.* 609 (1995).
62. Z. Asfari and J. Vicens, *Tetrahedron Lett.* 29, 2659 (1988).
63. V. Bohmer, F. Marscholke, and L. Zetta, *J. Org. Chem.* 52, 3200 (1987).
64. S.-I. Chen, Ph.D. Thesis, Washington University, St. Louis, 1985, pp. 46-47.
65. J. H. Munch, *Makromol. Chem.* 178, 69 (1985).
66. K. No, Y. Noh, and Y. Kim, *Bull. Korean Chem. Soc.* 7, 442 (1986).

67. A. Arduini, A. Pochini, S. Reverberi, and R. Ungaro, *J. Chem. Soc., Chem. Commun.* 981 (1984).
68. V. Bohmer, E. Schade, and W. Vogt, *Makromol. Chem., Rapid Commun.* 5, 221 (1984).
69. W. Saenger, C. Betzel, B. Hingerty, and G. M. Brown, *Angew. Chem. Int. Ed. Engl.* 22, 883 (1983).
70. S. W. Keller, G. M. Schuster, and F. L. Tobiason, *Polym. Mater. Sci. Eng.* 57, 906 (1987).
71. P. V. Rao, Ph.D. Thesis, Indian Institute of Technology Bombay, India, 2000, Chaps. 5 and 6.
72. H. Kammerer, G. Happel, and F. Caesar, *Makromol. Chem.* 162, 179 (1972).
73. C. D. Gutsche, B. Dhawan, K. H. No, and R. Muthukrishnan, *J. Am. Chem. Soc.* 103, 3782 (1981).
74. C. D. Gutsche, B. Dhawan, K. H. No, and R. Muthukrishnan, *J. Am. Chem. Soc.* 106, 1891 (1984).
75. C. D. Gutsche and L. J. Bauer, *Tetrahedron Lett.* 22, 4763 (1981).
76. F. Sansone, S. Barbosa, A. Casnati, M. Fabbi, A. Pochini, F. Ugozzoli, and R. Ungaro, *Eur. J. Org. Chem.* 897 (1998).
77. C. Rizzoli, G. D. Andreetti, R. Ungaro, and A. Pochini, *J. Mol. Struct.* 82, 133 (1982).
78. M. A. McKerver, E. M. Seward, G. Ferguson, and B. L. Ruhl, *J. Org. Chem.* 51, 3581 (1986).
79. M. A. McKerver, E. M. Seward, G. Ferguson, B. Ruhl, and S. J. Harris, *J. Chem. Soc., Chem. Commun.* 388 (1985).
80. I. Oueslati, R. Abidi, H. Amri, P. Thuery, M. Nierlich, Z. Asfari, J. Harrowfield, and J. Vicens, *Tetrahedron Lett.* 41, 8439 (2000).
81. A. Hamdi, R. Abidi, M. T. Ayadi, P. Thuery, M. Nierlich, Z. Asfari, and J. Vicens, *Tetrahedron Lett.* 42, 3595 (2001).
82. S. Chowdhury and P. E. Georghiou, *J. Org. Chem.* 66, 6257 (2001).
83. R. Lamartine, C. Bavoux, F. Vocanson, A. Martin, G. Senlis, and M. Perrin, *Tetrahedron Lett.* 42, 1021 (2001).
84. S. E. Matthews, V. Felix, M. G. B. Drew, and P. D. Beer, *New J. Chem.* 25, 1355 (2001).
85. L. Frkanec, A. Visnjevac, B. Kojic-Prodic, and M. Zinic, *Chem. Eur. J.* 6, 442 (2000).
86. L. C. Groenen, B. H. M. Ruel, A. Casnati, P. Timmerman, W. Verboom, S. Harkema, A. Pochini, R. Ungaro, and D. N. Reinhoudt, *Tetrahedron Lett.* 32, 2675 (1991).
87. L. C. Groenen, J.-D. Van Loon, W. Verboom, S. Harkema, A. Casnati, R. Ungaro, A. Pochini, F. Ugozzoli, and D. N. Reinhoudt, *J. Am. Chem. Soc.* 113, 2385 (1991).
88. J.-D. Van Loon, D. Kraft, M. J. K. Ankone, W. Verboom, S. Harkema, W. Vogt, V. Bohmer, and D. N. Reinhoudt, *J. Org. Chem.* 55, 5176 (1990).
89. J.-D. Van Loon, A. Arduini, W. Verboom, R. Ungaro, G. J. Van Hummel, S. Harkema, and D. N. Reinhoudt, *Tetrahedron Lett.* 30, 2681 (1989).
90. H. Goldmann, W. Vogt, E. Paulus, and V. Bohmer, *J. Am. Chem. Soc.* 110, 6811 (1988).
91. G. D. Andreetti, G. Calestani, F. Ugozzoli, A. Arduini, E. Ghidini, A. Pochini, and R. Ungaro, *J. Inclusion Phenom.* 5, 123 (1987).
92. B. M. Furphy, J. M. Harrowfield, D. L. Kepert, B. W. Skelton, A. H. White, and F. R. Wilner, *Inorg. Chem.* 26, 4231 (1987).
93. E. B. Brouwer, G. D. Enright, and J. A. Ripmeester, *J. Chem. Soc., Chem. Commun.* 939 (1997).
94. A. Zanotti-Gerosa, E. Solari, L. Giannini, C. Floriani, A. Chiesi-Villa, and C. Rizzoli, *J. Chem. Soc., Chem. Commun.* 119 (1996).
95. F. Hamada, K. D. Robinson, G. W. Orr, and J. L. Atwood, *Supramol. Chem.* 2, 19 (1993).
96. S. G. Bott, A. W. Coleman, and J. L. Atwood, *J. Chem. Soc., Chem. Commun.* 610 (1986).
97. S. W. Bott, A. W. Coleman, and J. L. Atwood, *J. Inclusion Phenom.* 5, 747 (1987).
98. S. W. Bott, A. W. Coleman, and J. L. Atwood, *J. Am. Chem. Soc.* 108, 1709 (1986).
99. T. Hascall, A. L. Rheingold, I. Guzei, and G. Parkin, *J. Chem. Soc., Chem. Commun.* 101 (1998).
100. A. Zanotti-Gerosa, E. Solari, L. Giannini, C. Floriani, A. Chiesi-Villa, and C. Rizzoli, *J. Chem. Soc., Chem. Commun.* 183 (1997).
101. P. D. Beer, M. G. B. Drew, P. B. Leeson, and M. I. Ogden, *Inorg. Chim. Acta* 246, 133 (1996).
102. V. C. Gibson, C. Redshaw, W. Clegg, and M. R. J. Elsegood, *J. Chem. Soc., Chem. Commun.* 1969 (1998).
103. P. D. Beer, M. G. B. Drew, D. Heseck, M. Kan, G. Nicholson, P. Schmitt, P. D. Sheen, and G. Williams, *J. Chem. Soc., Dalton Trans.* 2783 (1998).
104. P. D. Beer, M. G. B. Drew, A. Grieve, M. Kan, P. B. Leeson, G. Nicholson, M. I. Ogden, and G. Williams, *J. Chem. Soc., Chem. Commun.* 1117 (1996).
105. F. De M. Ramirez, L. Charbonniere, G. Miller, R. Scopelliti, and J.-C. G. Bunzil, *J. Chem. Soc., Dalton Trans.* 3205 (2001).
106. J. F. Malone, D. B. Marrs, M. A. McKerver, P. O'Hagan, N. Thompson, A. Walker, F. Arnaud-Neu, O. Mauprivez, M.-J. Schwing-Weill, J.-F. Dozol, H. Rouquette, and N. Simon, *J. Chem. Soc., Chem. Commun.* 2151 (1995).
107. X.-X. Han, L.-H. Weng, X.-B. Leng, and Z.-Z. Zhang, *Polyhedron* 20, 1881 (2001).
108. J. L. Atwood, G. W. Orr, F. Hamada, S. G. Bott, and K. D. Robinson, *Supramol. Chem.* 1, 15 (1992).
109. U. Radius, *Inorg. Chem.* 40, 6637 (2001).
110. P. D. Beer, M. G. B. Drew, P. B. Leeson, and M. I. Ogden, *J. Chem. Soc., Dalton Trans.* 1273 (1995).
111. M. I. Ogden, B. W. Skelton, and A. H. White, *J. Chem. Soc., Dalton Trans.* 3073 (2001).
112. J. L. Atwood and S. G. Bott, "Calixarenes, a Versatile Class of Macrocyclic Compounds" (J. Vicens and V. Bohmer, Eds.), p. 199. Kluwer, Dordrecht, 1991.
113. G. D. Andreetti and F. Ugozzoli, "Calixarenes, a Versatile Class of Macrocyclic Compounds" (J. Vicens and V. Bohmer, Eds.), p. 87. Kluwer, Dordrecht, 1991.
114. J. L. Atwood, F. Hamad, K. D. Robinson, G. W. Orr, and R. L. Vincent, *Nature (London)* 349, 683 (1991).
115. S. R. Izatt, R. T. Hawkins, J. J. Christensen, and R. M. Izatt, *J. Am. Chem. Soc.* 107, 63 (1985).
116. J. M. Harrowfield, M. I. Ogden, W. R. Richmond, and A. H. White, *J. Chem. Soc., Chem. Commun.* 1159 (1991).
117. M. J. Schwing-Weill and M. A. McKerver, "Calixarenes, a Versatile Class of Macrocyclic Compounds" (J. Vicens and V. Bohmer, Eds.), p. 149. Kluwer, Dordrecht, 1991.
118. S. Shinkai, in "Calixarenes, a Versatile Class of Macrocyclic Compounds" (J. Vicens and V. Bohmer, Eds.), p. 173. Kluwer, Dordrecht, 1991.
119. A. Cadogan, D. Diamond, S. Cremin, A. M. McKerver, and S. J. Harris, *Anal. Proc.* 28, 13 (1991).
120. A. Cadogan, D. Diamond, M. R. Smyth, G. Svehla, M. A. McKerver, E. M. Seward, and S. J. Harris, *Analyst* 115, 1207 (1990).
121. F. Cadogan, P. Kane, M. A. McKerver, and D. Diamond, *Anal. Chem.* 71, 5544 (1999).
122. J. A. Brunink, J. R. Haak, J. G. Bomer, D. N. Reinhoudt, M. A. McKerver, and S. J. Harris, *Anal. Chim. Acta* 254, 75 (1991).
123. D. Diamond, G. Svehla, E. Seward, and M. A. McKerver, *Anal. Chim. Acta* 204, 223 (1988).
124. M. Telting-Diaz, D. Diamond, and M. R. Smyth, *Anal. Chim. Acta* 251, 149 (1991).
125. M. Telting-Diaz, F. Regan, D. Diamond, and M. R. Smyth, *J. Pharm. Biomed. Anal.* 8, 695 (1990).
126. R. J. Forster, F. Regan, and D. Diamond, *Anal. Chem.* 63, 876 (1991).
127. R. J. Forster and D. Diamond, *Anal. Chem.* 64, 1721 (1992).
128. D. Diamond and K. Nolan, *Anal. Chem.* 73, 22A (2001).
129. S. O'Neill, S. Conway, J. Twellmeyer, O. Egan, K. Nolan, and D. Diamond, *Anal. Chim. Acta* 398, 1 (1999).

130. W. H. Chan and X. J. Wu, *Analyst* 123, 2851 (1998).
131. M. McCarrick, B. Wu, S. J. Harris, D. Diamond, G. Barrett, and M. A. McKervey, *J. Chem. Soc., Chem. Commun.* 1287 (1992).
132. Y. Kubo, S. Maeda, S. Tokita, and M. Kubo, *Nature* 382, 522 (1996).
133. I. Aoki, T. Sakaki, S. Tsutsui, and S. Shinkai, *Tetrahedron Lett.* 33, 89 (1992).
134. R. Grigg, J. M. Holmes, S. K. Jones, and W. D. J. A. Norbert, *J. Chem. Soc., Chem. Commun.* 185 (1994).
135. L. Zhang and J. L. Coffey, *J. Phys. Chem. B* 101, 6874 (1997).
136. L. Zhang, J. L. Coffey, J. Wang, C. D. Gutsche, J.-J. Chen, and O. Chyan, *J. Am. Chem. Soc.* 118, 12840 (1996).
137. S. Shinkai, H. Koreishi, S. Mori, T. Sone, and O. Manabe, *Chem. Lett.* 1033 (1985).
138. S. Shinkai, S. Mori, H. Koreishi, T. Tsubaki, and O. Manabe, *J. Am. Chem. Soc.* 108, 2409 (1986).
139. V. Bohmer, *Angew. Chem. Int. Ed. Engl.* 34, 713 (1995).
140. J. Scheerder, J. P. M. Van Duynhoven, J. F. J. Engbersen, and D. N. Reinhoudt, *Angew. Chem. Int. Ed.* 35, 1090 (1996).
141. P. Molenveld, S. Kapsabelis, J. F. J. Engbersen, and D. N. Reinhoudt, *J. Am. Chem. Soc.* 119, 2948 (1997).
142. P. Molenveld, W. M. G. Stikvoort, H. Kooijman, A. L. Spek, J. F. J. Engbersen, and D. N. Reinhoudt, *J. Org. Chem.* 64, 3896 (1999).
143. P. Molenveld, J. F. J. Engbersen, H. Kooijman, A. L. Spek, and D. N. Reinhoudt, *J. Am. Chem. Soc.* 120, 6726 (1998).
144. P. Molenveld, J. F. J. Engbersen, and D. N. Reinhoudt, *J. Org. Chem.* 64, 6337 (1999).
145. P. Molenveld, J. F. J. Engbersen, and D. N. Reinhoudt, *Eur. J. Org. Chem.* 3269 (1999).
146. P. Molenveld, J. F. J. Engbersen, and D. N. Reinhoudt, *Angew. Chem. Int. Ed.* 38, 3189 (1999).
147. R. Cacciapaglia, A. Casnati, L. Mandolini, and R. Ungaro, *J. Am. Chem. Soc.* 114, 10956 (1992).
148. B. Xu and T. M. Swager, *J. Am. Chem. Soc.* 115, 1159 (1993).
149. D. J. Williams, *Angew. Chem. Int. Ed. Engl.* 23, 6 (1984).
150. "Nonlinear Optical Properties of Organic Molecules and Crystals" (D. S. Chemla and J. Zyss, Eds.), Vols. 1 and 2. Academic Press, Orlando, 1987.
151. E. Kelderman, L. Derhaeg, G. J. T. Heesink, W. Verboom, J. F. J. Engbersen, N. F. Van Hulst, A. Persoons, and D. N. Reinhoudt, *Angew. Chem. Int. Ed. Engl.* 31, 1075 (1992).
152. S. Nijhuis, G. L. J. A. Rikken, E. E. Havinga, W. Ten Hoeve, H. Wynberg, and E. W. Meijer, *J. Chem. Soc., Chem. Commun.* 1093 (1990).
153. D. Q. Li, X. Yang, and D. McBranch, *Synthetic Metals* 86, 1849 (1997).
154. E. Brouyere and J. L. Bredas, *Synthetic Metals* 71, 1699 (1995).
155. "Nonlinear Optics of Organic Molecules and Polymers" (H. S. Nalwa and S. Miyata, Eds.), p. 885. CRC Press, Boca Raton, FL, 1997.
156. J. R. Moran, S. Karbach, and D. J. Cram, *J. Am. Chem. Soc.* 104, 5826 (1982).
157. R. C. Helgeson, M. Lauer, and D. J. Cram, *J. Chem. Soc., Chem. Commun.* 101 (1983).
158. Cavitands: D. M. Rudkevich and J. Rebek, Jr., *Eur. J. Org. Chem.* 1991 (1999).
159. A. Jasat and J. C. Sherman, *Chem. Rev.* 99, 931 (1999).
160. M. M. Conn and J. Rebek, Jr., *Chem. Rev.* 97, 1647 (1997).
161. D. Philp and J. F. Stoddart, *Angew. Chem. Int. Ed. Engl.* 35, 1155 (1996).
162. Self-assembling capsules: (a) J. de Mendoza, *Chem.-Eur. J.* 4, 1373 (1998); (b) J. Rebek, Jr., *Acc. Chem. Res.* 32, 278 (1999).
163. Reactions inside cavities: R. Warmuth, *Eur. J. Org. Chem.* 423 (2001).
164. C. D. Gutsche, *Acc. Chem. Res.* 16, 161 (1983).
165. D. J. Cram and J. M. Cram, "Container Molecules and their Guests." Royal Society of Chemistry, Cambridge, UK, 1997.
166. C. D. Gutsche, "Calixarenes Revisited." Royal Society of Chemistry, Cambridge, UK, 1998.
167. A. Arduini, W. M. McGregor, D. Paganuzzi, A. Pochini, A. Sechi, F. Ugozelli, and R. Ungaro, *J. Chem. Soc., Perkin Trans. 2* 839 (1996).
168. D. J. Cram, S. Karbach, H.-E. Kim, C. B. Knobler, E. F. Maverick, J. L. Ericson, and R. C. Helgeson, *J. Am. Chem. Soc.* 110, 2229 (1988).
169. D. J. Cram, K. D. Stewart, I. Goldberg, and K. N. Trueblood, *J. Am. Chem. Soc.* 107, 2574 (1985).
170. J. A. Tucker, C. B. Knobler, K. N. Trueblood, and D. J. Cram, *J. Am. Chem. Soc.* 111, 3688 (1989).
171. K. T. Chapman and W. C. Still, *J. Am. Chem. Soc.* 111, 3075 (1989).
172. L. Sebo, F. Diedrich, and V. Gramlich, *Helv. Chim. Acta* 83, 93 (2000).
173. F. C. Tucci, D. M. Rudkevich, and J. Rebek, Jr., *J. Org. Chem.* 64, 4555 (1999).
174. L. R. MacGillivray and J. L. Atwood, *J. Am. Chem. Soc.* 119, 6931 (1997).
175. L. R. MacGillivray and J. L. Atwood, *J. Chem. Soc., Chem. Commun.* 181 (1999).
176. L. R. MacGillivray, H. A. Spinney, J. L. Reid, and J. A. Ripmeester, *J. Chem. Soc., Chem. Commun.* 517 (2000).
177. I. Higler, P. Timmerman, W. Verboom, and D. N. Reinhoudt, *J. Org. Chem.* 61, 5920 (1996).
178. K. D. Shimizu and J. Rebek, Jr., *Proc. Natl. Acad. Sci. USA* 92, 12403 (1995).
179. O. Mogeck, V. Bohmer, and W. Vogt, *Tetrahedron* 52, 8489 (1996).
180. S. Mecozzi and J. Rebek, Jr., *Chem. Eur. J.* 4, 1016 (1998).
181. R. Meissner, X. Garcias, S. Mecozzi, and J. Rebek, Jr., *J. Am. Chem. Soc.* 119, 77 (1997).
182. G. W. Orr, L. J. Barbour, and J. L. Atwood, *Science* 285, 1049 (1999).
183. A. Ikeda and S. Shinkai, *J. Am. Chem. Soc.* 116, 3102 (1994).
184. R. A. Kumpf and D. A. Dougherty, *Science* 261, 1708 (1993).
185. A. Ikeda and S. Shinkai, *J. Chem. Soc., Chem. Commun.* 2375 (1994).

Cantilever-Based Sensors

D. Then, C. Ziegler

University of Kaiserslautern, Kaiserslautern, Germany

CONTENTS

1. Introduction
2. Sensors and Biosensors
3. Transduction Principles
4. Sensor Applications in the Gas Phase
5. Sensor Applications in the Liquid Phase
6. Summary and Future Trends
in Microcantilever Sensors
- Glossary
- References

1. INTRODUCTION

The invention of scanning force microscopy (SFM) by Binnig et al. in 1986 [1] was a first bridge between microscopy and micromechanics. SFM measures the interaction forces between two surfaces from the micrometer level down to the atomic scale. Intermolecular forces are not the only forces that can be detected by this technique. A wide variety of different signal domains such as magnetic [2], electrical [3], electrochemical [4], elastic [5], thermal [6], biological [7], and chemical [8] signals can be detected with high sensitivity and (moderate) speed through transduction into a mechanical motion of a cantilever beam. SFM measures the small forces acting on a sharp tip at the apex of a thin beam clamped at one side, the cantilever. The force on the tip bends the cantilever, which acts as a force transducer. The support of the cantilever is mounted into a holder and the motion of the beam is measured via the tunneling effect, with an interferometer, or via the optical lever deflection technique, the latter being the most commonly used method in commercially available SFMs due to its high resolution and its low costs. Newly developed smart force sensors use micromachined devices with integrated piezoresistive, integrated piezoelectric, and integrated capacitance detection of the cantilever deflection.

It is possible to produce inexpensive force sensors in a reproducible way by taking advantage of the batch silicon micromachining techniques developed for integrated circuit (IC) process technology. Miniaturization and mass

production are the main reasons for the success of SFM in research laboratories and industrial applications. These lead to cantilevers with low spring constants for a high sensitivity to the applied forces or high resonance frequencies for faster response times and insensitivity to external disturbances. The commercial cantilevers are typically made of silicon, silicon nitride, or silicon oxide and are available in a great variety of different shapes, dimensions, and force sensitivities [9–14]. Recent developments combine the newest IC and complementary metal oxide semiconductor (CMOS) technologies to get intelligent cantilevers [15–23], extremely small cantilevers [24–31], or large arrays [32–39].

In the last few years a second evolution in the world of nanoscience was seen, and cantilevers were applied in scenarios other than detecting surfaces. Because of their above-mentioned benefits of high sensitivity, small dimensions, short response times, and low price they were used to detect changes in temperature, surface stress, and mass in picogram amounts of analyte without touching the surface any more. Cantilevers were used in sensor systems to get a completely new type of miniaturized transducer based on fundamental principles of physics such as the bimetallic effect, surface stress, or the harmonic oscillator. With cantilever sensors it is possible to push “the powers of 10” into a region in which otherwise only time-consuming and expensive analytical tools can be applied or which is completely inaccessible by means of macroscopic techniques.

In this chapter the fundamental physics of microcantilever sensors will be described as well as recent methods, experiments, and prospective directions of the newest sensing systems. The discussion is limited to chemical and/or biological sensors as well as radiation sensors. Physical sensing devices such as accelerometers [40, 41], gyroscopes [42], or flow sensors [43, 44] with beam architecture will be excluded, but micromachined cantilevers show interesting abilities to enhance the power of these devices, too.

2. SENSORS AND BIOSENSORS

(Bio-)chemical sensors are miniaturized devices that convert a chemical state into an electrical signal. The chemical state is determined by different concentrations, partial pressures, or activities of particles such as atoms, molecules,

ions, or biologically relevant compounds to be detected in the gas, liquid, or solid phase [45]. A sensor can be divided into three main components. The first is the *recognition site* with a sensitive or selective layer that recognizes the signal of interest. In some cases there is also a preprocessing element (e.g., filter, temperature, catalyst, or preconcentration) that can add further selectivity or sensitivity. The second part of a sensor system is the signal *transducer*. It converts the chemical or biological information into the physical signal (e.g., mass change into frequency change of a quartz crystal microbalance [46]) which then can be detected, filtered, amplified, and displayed by a *readout system* as the third part (Fig. 1). There are a huge variety of transducer principles, but in the present context only acoustic (often called mass-sensitive) transducers are of importance. The advantage of using acoustic sensors compared with classical analytical techniques or most optical sensors is the possibility of working label-free.

An optimal sensor system should be highly selective, stable, and sensitive to the analyte (“sss”). It should be able to work continuously and time-resolved to allow for on-line or in-line detection of changes in concentrations. This is only possible if the sensor response is completely reversible. By the combination of several different sensors into arrays with pattern recognition and multicomponent analysis of the complex data pattern the challenge to analyze complex mixtures could be met successfully. Such arrays are often called “electronic nose” [47] or “electronic tongue” [48] although there are only a few similarities to the functions of a human nose and tongue. In an ideal electronic nose or tongue, each single sensor should respond to only one analyte with a signal proportional to the analyte concentration, ensuring complete reversibility. The vector space spanned by such sensor signals would consist of orthogonal basis vectors, which would make the required data processing easy and the sensor response unique. In reality, sensor signals are never unique and cross-sensitivities occur. The scientist or user has to select the best sensors with respect to the application, that is, sensitive layers that cover the range of possible interactions.

A biosensor is often defined as a compact analytical device incorporating a biological or biologically derived sensing element either integrated within or intimately associated with a physicochemical transducer [49]. Its recognition layer therefore consists of an enzyme, antibody, nucleic acid, microorganism, cell, or tissue. However, biological molecules can also be detected unspecifically on a nonbiological sensor surface, which will also be covered in this review.

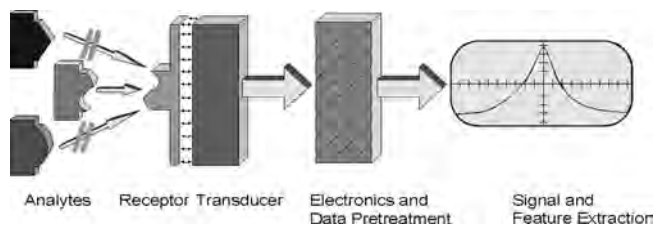


Figure 1. Schematic drawing of a sensor system. The information about the chemical nature and concentration of the analyte will be transduced into an electrical signal that can be displayed and stored.

The detection elements may be divided into three groups: In catalytic biosensors enzymes catalyze a reaction. In affinity sensors a specific recognition reaction between a receptor and a ligand, that is, a key–lock interaction, is detected. This includes antibody–antigen, nucleic acid–nucleic acid, enzyme–enzyme inhibitor, and other receptor systems. The third class includes all other principles, for example, membrane transport through specific pores or whole-cell sensors, in which one or more of the above-mentioned interactions can occur.

In this chapter only those systems in which mass changes take place are relevant. Therefore, mainly affinity sensors will be stressed in the following. One problem in the definition of an affinity biosensor is the antagonism of specificity and reversibility. A rule of thumb is that with increasing strength of the chemical interaction between sensitive layer and target analyte, sensitivity and selectivity are enhanced whereas the reversibility of the sensor decreases. Reversibility can be achieved either by selecting an appropriate chemical interaction (e.g., solubility interactions) or by refreshing cycles of the system (e.g., purging with reference/neutralizing gas/solution, adsorbing/desorbing steps) [50]. This reversibility is in strong contrast to the highly specific binding process of, for example, antibodies and antigens with high-affinity constants. Therefore, most affinity biosensors are not sensors according to the definition given above but can be better described as dosimeters because the biomolecules pile up on the surface with exposure time.

3. TRANSDUCTION PRINCIPLES

In general there are three different methods to transduce the recognition event into a micromechanical motion. First, the frequency change due to additional mass loading or a change in the force constant can be measured; that is, the cantilever is used as a microbalance. Second, the bending of a bimetallic cantilever can be used as temperature sensor. In addition, cantilevers can work as stress sensors by measuring the bending due to changes in the surface stress at one side of the cantilever. The transduction principles are shown in Figure 2.

3.1. Resonant Behavior of Cantilever Beams

A basic understanding of the mechanical behavior of cantilever beams is crucial to develop cantilever sensors with optimized sensitivity and geometry. (However, those readers only interested in the general subject may skip this section.) The spring constant, resonance frequency, and corresponding quality factor will be derived in this section using the one-dimensional Euler–Bernoulli differential equation of an initially flat, thin, homogenous cantilever beam [51]:

$$\hat{E}I \frac{\partial^4 w(x,t)}{\partial x^4} + (\rho A + \chi) \frac{\partial^2 w(x,t)}{\partial t^2} + \xi \frac{\partial w(x,t)}{\partial t} = q(x,t) \quad (1)$$

\hat{E} and ρ denote the apparent Young’s modulus [see Eq. (2)] and specific mass density of the beam material, $A = hb$, the cross-sectional area, and I is the moment of inertia. ξ is the damping coefficient per unit length per unit velocity,

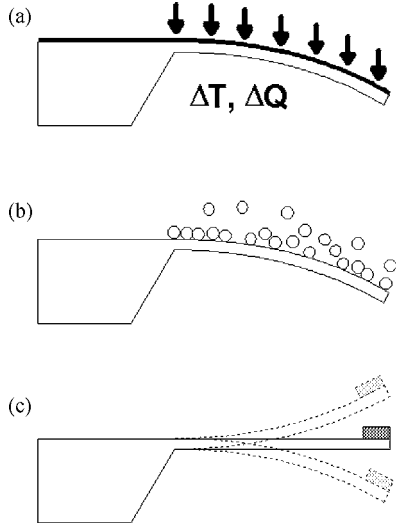


Figure 2. Schematic drawings of the possible cantilever transduction principles: (a) bimetallic temperature and heat sensor; (b) surface stress sensor; (c) microbalance due to additional mass loading.

and χ is an additional mass per unit length. $q(x, t)$ represents the driving load in N/m. The additional mass χ can either exist due to adsorbing molecules on the surface or describe the mass of molecules of the surrounding media that are accelerated by the vibration of the beam. This leads to dependence of the resonance frequency, respectively, the resonance behavior, in general from the surrounding media. Effects of rotary inertia and shear deformations are not included in Eq. (1) nor are nonlinear terms due to a large vibration amplitude. Under the assumption of a beam structure with $b \gg h$, the apparent Young's modulus is given by

$$\widehat{E} = \frac{E}{1 - \nu^2} \quad (2)$$

where ν is the Poisson's ratio and E is the Young's modulus of the beam material. The moment of inertia for a rectangular beam can be calculated as

$$I = \int_0^b \int_{-h/2}^{h/2} z^2 dz dy = \frac{1}{12} bh^3 \quad (3)$$

By assuming a harmonic time dependence a variable separation with $w(x, t) = W(x)T(t)$ can be performed. For the case without an additional driving load this leads to [52]

$$\frac{\widehat{E}I}{\rho A + \chi} \frac{\partial^4 W(x)}{\partial x^4} = -\frac{\xi}{\rho A + \chi} \frac{\partial T(t)}{\partial t} - \frac{\partial^2 T(t)}{\partial t^2} \equiv \omega_0^2 = \text{const} \quad (4)$$

The time variable can be written as

$$\frac{d^2 T(t)}{dt^2} + \frac{\xi}{\rho A + \chi} \frac{dT(t)}{dt} + \omega_0^2 T(t) = 0 \quad (5)$$

The solution is a function of time which is equal to that of the model of the one-dimensional harmonic oscillator with $T(t) = Be^{-\gamma t} \sin(\omega_0 t + \varphi)$.

The variable of position can be written as

$$\frac{\widehat{E}I}{\rho A + \chi} \frac{d^4 W(x)}{dx^4} - \omega_0^2 W(x) = 0 \quad (6)$$

The solution of a homogenous fourth-order differential equation is the sum of four linear independent solutions,

$$W(x) = c_1 \cos\left(\frac{\lambda}{L}x\right) + c_2 \sin\left(\frac{\lambda}{L}x\right) + c_3 \sinh\left(\frac{\lambda}{L}x\right) + c_4 \cosh\left(\frac{\lambda}{L}x\right) \quad (7)$$

with the constants c_1 , c_2 , c_3 , and c_4 assuming the boundary conditions

$$W(0) = 0 \quad \left. \frac{dW(x)}{dx} \right|_{x=0} = 0 \quad \left. \frac{d^2 W(x)}{dx^2} \right|_{x=L} = 0 \quad \left. \frac{d^3 W(x)}{dx^3} \right|_{x=L} = 0 \quad (8)$$

with L as the length of the cantilever and the nondimensional parameter, λ , defined by

$$\left(\frac{\lambda}{L}\right)^4 := \frac{\rho A \omega_0^2}{\widehat{E}I} \quad (9)$$

The first two boundary conditions are due to the fact that one end of the beam is clamped. The third excludes any bending moment at the free end of the cantilever and the fourth excludes any torsion [53]. By assuming the boundary conditions, a characteristic equation can be calculated:

$$\cos \lambda \cosh \lambda = -1 \quad (10)$$

with discrete values λ_a for λ for the first four modes [54]

$$\lambda_0 = 1.875, \quad \lambda_1 = 4.69, \quad \lambda_2 = 7.86, \quad \lambda_3 = 11.00 \quad (11)$$

By inserting these parameters into Eq. (9) the resonance frequency of a clamped beam with rectangular cross-section can be calculated as

$$\omega_{a,0} = 2\pi f_{a,0} = \frac{\lambda_a^2 h}{\sqrt{12} L^2} \sqrt{\frac{E}{\rho(1 - \nu^2) + \chi}} = \frac{\lambda_a^2}{L^2} \sqrt{\frac{\widehat{E}I}{\rho A + \chi}} \quad (12)$$

with $a = 0, 1, 2, \dots$

With the introduction of the quality factor

$$Q = \frac{\omega(\rho A + \chi)}{\xi} \quad (13)$$

the resonance frequency of a cantilever beam can then be expressed as

$$\omega_a = \omega_{a,0} \cdot \left[1 + \frac{1}{4Q^2}\right]^{-1/2} \quad (14)$$

$\omega_{a,0}$ is the resonance frequency in the undamped case $\xi = 0$. From Eq. (13) one can expect the quality factor to increase linearly with the resonance frequency of the cantilever beam.

Looking at Eq. (12) one can use the model of the one-dimensional harmonic oscillator

$$f = \frac{1}{2\pi} \sqrt{\frac{k}{m \cdot n}} \quad (15)$$

with $n = 0.24$ as a geometrical parameter for the fundamental mode of a rectangular cantilever beam and k as the force constant:

$$k = \widehat{E} \left(\frac{h}{L} \right)^3 \frac{b}{4} \quad (16)$$

An additional mass uniformly distributed over the surface can be correlated with a frequency change by

$$\Delta m = -\frac{k}{4\pi^2 n} \left(\frac{1}{f_0^2} - \frac{1}{f_m^2} \right) \quad (17)$$

where f_m is the frequency of the loaded beam

$$f_m = \frac{1}{2\pi} \sqrt{\frac{k}{m^* + n\Delta m}} = \frac{f_0}{\sqrt{1 + \frac{\Delta m}{m}}} \quad (18)$$

A Taylor series taking into account only the first order and $f_m = f_0 + \Delta f$ results in

$$f_m \approx f_0 \left(1 - \frac{1}{2} \frac{\Delta m}{m} \right) \Rightarrow \frac{\Delta f}{f_0} \approx -\frac{1}{2} \frac{\Delta m}{m} \quad (19)$$

By using the material parameters the sensitivity per unit area can be written as

$$\frac{\Delta m}{A} \approx -4\pi\sqrt{n} \cdot L^2 \cdot \sqrt{\frac{\rho^3(1-\nu^2)}{E}} \cdot 2\Delta f \quad (20)$$

The minimum detectable mass is given if one takes the minimum measurable frequency change. By considering that all material parameters are constant, the only variable parameter is the length of the cantilever. To achieve a better mass resolution and therefore a higher mass sensitivity the length of the cantilever has to be reduced. However, the length reduction is usually accompanied by a reduction of area also. The second possibility for getting a higher frequency change for a given mass change is to operate the system at higher modes.

Besides the frequency characteristics, the force constant is another important parameter. According to Eq. (17) the force constant has to be known if a quantitative calculation of the mass change due to the frequency change is performed. In the literature the mechanical behavior and the determination of spring constants is well described for various methods [55–61]. In Eq. (16) the force constant can be calculated from the material parameters. In reality the material parameters are unknown variables because of the production process of the cantilevers. The length and the width of the cantilever can be controlled quite well during the etching process, but the thickness of the cantilever is the critical parameter. In addition, the Young's modulus of the bulk material can change due to reflective coatings on one side of the cantilever. This could be calculated, too, but there are more elegant possibilities to calculate the force constant.

One possibility is to measure the static deflection of the cantilever because of the influence of defined forces [62, 63] or pressing with a reference spring [64, 65]. Dynamic methods will use the mean square amplitude of the thermal noise [53, 66] or the frequency shift due to adding a known mass at the apex [67] of the cantilever. For the thermal noise method especially, an easy and fast method for determination of the spring constant of soft cantilevers, the sensitivity of the optical detection system has to be known. The most common method for the determination of this lever sensitivity is that the cantilever is brought into contact with a hard surface and then moved a known distance. The slope of the resulting cantilever deflection versus distance yields the sensitivity, assuming that the piezo scanner driving the cantilever is calibrated. A method without touching the surface by using the drag forces of a moving cantilever is presented in [68].

The third important parameter to characterize the movement of a cantilever is the quality factor Q . The quality factor of a resonator is defined as

$$Q = 2\pi \frac{W_0}{\Delta W} \quad (21)$$

where W_0 is the stored vibrational energy and ΔW is the total energy lost per cycle [compare Eq. (13) for Q described by material parameters]. The frequency stability of a resonator depends on different parameters. One is the noise acting on the resonator as well as the ability to store the energy that is applied to it. The minimum detectable frequency shift $\delta\omega$ of a cantilever with resonance frequency ω_0 under the influence of a thermal noise $k_B T$ can be estimated to be [69]

$$\delta\omega = \sqrt{\frac{\omega_0 k_B T B}{k Q \langle A^2 \rangle}} \quad (22)$$

where B , k , k_B , and T denote the bandwidth, spring constant of the cantilever, Boltzmann constant, and absolute temperature respectively. $\langle A^2 \rangle$ is the mean square vibrational amplitude. From Eq. (22) it becomes obvious that an improved frequency resolution of the resonator is associated with an improved quality factor. The dissipation mechanisms that contribute to ΔW can be distinguished as internal damping due to the physical structure of the resonator and external damping caused by viscous and turbulent flow of the surrounding media. The inverse quality factor can then be written as [70]

$$\frac{1}{Q} = \sum_i \frac{1}{Q_i} = \frac{1}{Q_{\text{int}}} + \frac{1}{Q_{\text{ext}}} \quad (23)$$

Q_{int} represents all dissipation effects due to the internal structure of the cantilever, whereas Q_{ext} includes all external effects (like viscous media) that act on the cantilever.

The gas damping in microstructures can be accessed by a finite-element simulation and is described in [71]. Another approach uses the model of a moving string of beads [72] instead of a beam-shaped geometry. The resulting drag force is the sum of the drag forces of the individual spheres. By assuming that the motion of the cantilever is in a viscous medium (e.g., liquids) the Reynolds numbers are not small

and the drag force becomes not only proportional to the speed but also to the acceleration. The damping can then be expressed as

$$\xi = 6\pi\eta R \left(1 + \frac{R}{\delta_L}\right) \quad (24)$$

The additional or induced mass can be expressed as [73]

$$\chi = \left(\frac{2}{3}\right)\pi R^3 \rho_L \left(1 + \frac{9}{2} \frac{\delta_L}{R}\right) \quad (25)$$

whereas R is the radius of the sphere, η is the viscosity of the medium, and ρ_L is the density. $\delta_L = \sqrt{(2\eta/\rho_L\omega)}$ can be derived from the Navier–Stokes equation and equals the thickness of an additional layer of molecules sticking at the sphere that have to be moved during the oscillation. The mass of the cantilever can therefore be described by a virtual mass $m' = m^* + m_I$ (m_I describes the additional mass of the accelerated molecules) [74].

The relative frequency change due to damping can be approximated by

$$\frac{\Delta\omega}{\omega_0} = -\frac{\pi R^3 \rho_L}{3\rho L b} \left(1 + \frac{9}{2} \frac{\delta_L}{R}\right) \quad (26)$$

The change in resonance characteristics leads to a change in the quality factor [75]

$$Q = \frac{\lambda_a b h^2 \sqrt{\rho E/12}}{6\pi\eta R L (1 + R/\delta_L)} \quad (27)$$

where ρ and E denote the mass density and the Young's modulus of the beam material and δ_L is again the width of the boundary layer perpendicular to the direction of motion around the sphere. This result indicates an increasing quality factor with decreasing length or increasing resonance frequency. For more information on this complex theme, see, for example, [74, 76–78].

It can be seen from Eq. (22) and the above derivations that the quality factor is an important parameter in the resonance characteristics of a cantilever. An increased quality factor indicates a decreasing minimum detectable frequency change and therefore a better resolution (and sensitivity) of the sensor system. To increase the quality factor the method of active feedback can be used (Fig. 3). This was first introduced in [79] and is normally used for increasing speed and resolution in tapping-mode atomic force microscopy [80, 81].

The active feedback electronic consists of a variable phase shifter ϕ and a gain amplifier G . The equation of motion of a damped feedback system can be written as

$$\ddot{z}(t) + \gamma\dot{z}(t) + \omega^2 z(t) = F_0 e^{i\omega t} + F_2 \quad (28)$$

where k is the force constant, γ is the damping constant, and F_2 is a second periodic force generated by the feedback circuit. The original signal of the oscillator $z(t) = A e^{i\omega t}$ is amplified with G and phase shifted with $\frac{\pi}{2}$ and fed back into the original system:

$$F_2 = G \cdot A e^{i(\omega t + \pi/2)} = G e^{i\pi/2} z(t) \quad (29)$$

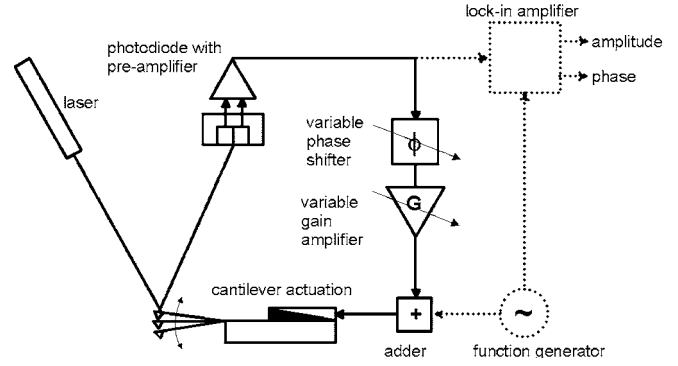


Figure 3. Schematic drawing of an active feedback circuit with a variable phase shifter and gain amplifier (black and dotted lines) first presented by [79] and a self-oscillating system (only black lines).

The first-time derivative

$$\frac{dz}{dt} = i\omega e^{i\omega t} = \omega z e^{i\pi/2} \Rightarrow F_2 = \left(\frac{G}{\omega}\right) \frac{dz}{dt} \quad (30)$$

leads to an effective reduced damping constant by inserting Eq. (30) into Eq. (28):

$$\gamma_{\text{eff}} = \gamma - \left(\frac{G}{\omega}\right) \quad (10)$$

The reduced damping leads to a reduced full width at half-peak maximum and therefore to a smaller minimum detectable frequency shift.

Besides the actively driven system the electronic feedback circuit can be designed in a way that the system is self-oscillating and no further actuation has to be done. The electronic circuit has to be designed in a way that only the resonance frequencies of the cantilever are amplified and fed back and that the environmental noise is high enough to start the oscillation; that is, it has to contain the resonance frequency. This principle is well known from quartz crystals driven by an oscillation circuit to build a microbalance [82, 83]. Examples of cantilever sensors driven by a self-oscillating system will be discussed later.

3.2. Bending Behavior of Cantilever Beams

A uniform surface stress acting on an isotropic material increases (compressive stress) or decreases (tensile stress) the surface area. If this stress is not compensated for at the opposite side of a thin plate or beam, the whole structure will bend (Fig. 4). Between the areas of compressive stress and tensile stress there is a neutral plane that is not deformed. Because of the bending, a force F is acting at the distance x and in the neutral plane results in a bending moment $M = F \cdot x$. Therefore the radius of curvature R is given by

$$\frac{1}{R} = \frac{d^2 z}{dx^2} = \frac{M}{EI} \quad (31)$$

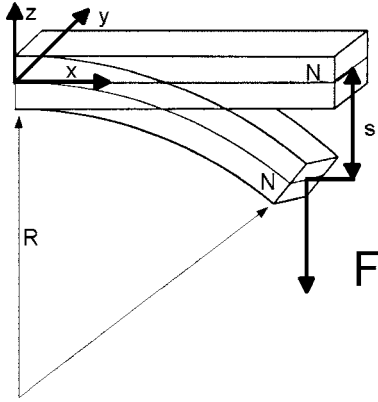


Figure 4. Side view of a thin beam. The beam bends around a neutral plane N with a curvature R due to a force F . The origin of the bending can be also be a change in the surface stress (see text).

where \hat{E} is the apparent Young's modulus and I is the moment of inertia, which is given by Eq. (3) for rectangular beams.

The change in the surface stress at one side of the beam will cause a static bending and the bending moment can be calculated [84] by

$$M = \frac{\Delta\sigma bh}{2} \quad (32)$$

$\Delta\sigma = \sigma_1 - \sigma_2$ is the differential surface stress with σ_1 and σ_2 as surface stress at the upper and lower sides of the cantilever, respectively. Inserting this into Eq. (31) yields Stoney's formula [85]

$$\frac{1}{R} = \frac{6(1-\nu)}{Eh^2} \Delta\sigma \quad (33)$$

By taking into account the boundary conditions of a cantilever ($R \gg L$) [86], Eq. (33) can be solved and the displacement of the cantilever s can be written as

$$s = \frac{3L^2(1-\nu)}{Eh^2} \Delta\sigma \quad (34)$$

Changes in surface stress can be the result of an adsorption process or electrostatic interactions between charged molecules on the surface as well as changes in the surface hydrophobicity and conformational changes of the adsorbed molecules.

In addition to surface stress-induced bending, the volume expansion of bimaterial cantilevers can result in a static bending. A bimaterial cantilever undergoes bending due to gas adsorption if the volume expansion coefficients of the two materials are different [87].

3.3. Thermal Effects on Cantilevers

By assuming a beam with a constant cross-section consisting of only one material, a change in the surrounding temperature will change the physical dimensions of the beam due to thermal expansion and the elastic properties of the beam material. In considering Eq. (12) the length L , width b , height h , and the Young's modulus \hat{E} show a temperature

dependence. With the assumption of a constant Poisson's ratio the relative change of the resonance frequency with temperature can be written as

$$\frac{1}{f_0} \frac{\partial f}{\partial T} = \frac{1}{2} \left(3 \frac{1}{h_0} \frac{\partial h}{\partial T} - 3 \frac{1}{L_0} \frac{\partial L}{\partial T} + \frac{1}{b_0} \frac{\partial b}{\partial T} + \frac{1}{E_0} \frac{\partial E}{\partial T} \right) \quad (35)$$

The subscript zero indicates the variable to be at the starting temperature T_0 . The isotropic thermal expansion coefficient is given by

$$\alpha = \frac{1}{h_0} \frac{\partial h}{\partial T} = \frac{1}{L_0} \frac{\partial L}{\partial T} = \frac{1}{b_0} \frac{\partial b}{\partial T} \quad (36)$$

and the temperature coefficient of the Young's modulus by

$$\beta = \frac{1}{E_0} \frac{\partial E}{\partial T} \quad (37)$$

If these equations are inserted into Eq. (35), the temperature-dependent relative frequency change will be

$$\frac{1}{f_0} \frac{\partial f}{\partial T} = \frac{1}{2} (\alpha + \beta) \quad (38)$$

These considerations do not take into account different beam materials in a sandwich structure cantilever. A composite beam of two materials with two different thermal expansion coefficients undergoes a static bending if the temperature changes. For uniform heating the bending z is proportional to the adsorbed heating power and is expressed by the differential equation [88]

$$\frac{d^2z}{dx^2} = 6(\alpha_1 - \alpha_2) \frac{h_1 + h_2}{h_2^2 K} (T - T_0) L^2 \quad (39)$$

with

$$K = 4 + 6 \left(\frac{h_1}{h_2} \right) + 4 \left(\frac{h_1}{h_2} \right)^2 + \frac{E_1}{E_2} \left(\frac{h_1}{h_2} \right)^3 + \frac{E_2}{E_1} \left(\frac{h_2}{h_1} \right) \quad (40)$$

By assuming λ as the thermal conductivities of layers 1 and 2 and P as the total power on the sensor, the bending is derived as

$$z = \frac{5}{4} (\alpha_1 - \alpha_2) \frac{t_1 + t_2}{t_2^2 K} \frac{L^3}{(\lambda_1 T_1 + \lambda_2 T_2) b} P \quad (41)$$

Devices can be calibrated *in-situ* by following the bending of the sensor for a known power transduced into heat at the sensor [89].

Because of the above explanations, on the one side the cantilever can be used as a highly sensitive temperature sensor, but on the other side every temperature change will cause trouble if another parameter like the frequency change is the measured quantity.

3.4. Cantilever Deflection Detection Techniques

The most common method to measure the deflection of a cantilever is the optical lever technique [90]. This technique works with a focused laser diode beam at the free end of the cantilever, which is reflected into a split photodiode or a position-sensitive detector. When the cantilever bends, the reflected light moves on the photodetector surface. This movement is proportional to the cantilever deflection.

Another optical detection method is based on the interference effect [91–93]. The interference occurs between a reference laser beam and the reflection from the cantilever. This can be realized with a cleaved end of an optical fiber brought close to the cantilever [94]. One part of the light is reflected at the interface fiber/surrounding media and the other part is reflected at the cantilever back into the fiber. These two beams interfere inside the fiber and the interference signal can be measured with a photodiode. Interferometry is very sensitive and provides a direct and absolute measurement of the displacement, but it is limited by the wavelength of the laser light and therefore works only for small deflections.

If the distance between two parallel plates is changed, the capacitance between these plates is changing, too. This is used in capacitive sensors to measure the distance between the plates. If one of the plates is a cantilever, small changes in distance can be measured [95–97]. This technique is highly sensitive and provides absolute displacements, but it is unable to measure large displacements and does not work in electrolyte solutions because of the Faradaic currents between the capacitor plates [98]. It is therefore only of limited use in biosensor applications.

Alternative approaches use interdigital cantilevers as an optical diffraction grating. The reflected laser light forms a diffraction pattern, where the intensity is proportional to the cantilever deflection [99, 100]. This can be used for atomic force microscopy and infrared detection [101, 102] and is proposed for chemical sensing [103].

An alternative method uses piezoresistive cantilevers. If a piezoresistive material is set under stress, it changes its electrical conductivity. Implemented into cantilevers this effect can be used to monitor stress and therefore the bending of the cantilever. Such stress sensors can be integrated on a cantilever structure with a Wheatstone bridge measuring the resistivity [104–107]. A lot of developments are under way in the field of piezoresistive cantilevers to gain better resolution and error-free measurements. The advantage compared to standard optical techniques is that neither additional optical components nor laser alignment is needed. Also the readout electronics can be integrated on the same chip using CMOS fabrication [16, 17], and they are unaffected by optical artifacts arising from distributions of the surrounding medium. The disadvantage of most piezoresistive cantilevers is that they only can be used in nonliquid environments because of Faradaic currents that will result in a short circuit. Recent improvements allow the fabrication of thin, passivated resistors on cantilevers that can be used in electrolyte solutions [108]. Drift compensation is possible due to the development of a symmetrical configuration where the output signal is the difference between a sensing and a reference cantilever [23]. Piezoresistive cantilevers can also vary

their surface temperature by increasing the electrical current flow through the resistor layer. This is proposed to be implemented as a tool for breaking ligand–receptor bindings for the regeneration process of the sensing layer in biosensor applications [98].

3.5. Cantilever Actuation Methods

For cantilever sensors based on the measurement of the frequency change it is necessary to drive the cantilever. Without any external actuation the cantilever is only driven by the thermal noise $k_B T$. At room temperature the thermal energy is very low, and long measurement times are the consequence. A better way to drive the cantilever is to apply an external force. In the most commercially available scanning probe microscopes this is done by an external driving piezo mounted near the cantilever. The excitation takes part through mechanical stimulation by shaking the cantilever as well as the complete measurement setup. In a liquid environment the disadvantage of this method is that a lot of standing waves are generated through the acoustic stimulation of the medium. This can be avoided by direct driving of the cantilever using a piezoresistive layer similar to the piezoresistive readout [22, 106, 109–112]. Lorentz forces can be used for the actuation of a cantilever either by evaporating a magnetic layer on the cantilever and applying an external magnetic field [113–117] or by a conductive pathway on the cantilever with an alternating current and the application of a constant external field [118–121]. Instead of magnetic actuation it is also possible to drive the cantilever with electrostatic forces [118, 122–125] or by an additional heater at the bottom of the cantilever [16, 18, 126].

4. SENSOR APPLICATIONS IN THE GAS PHASE

As is described above two basic operation principles are possible for micromachined beams: measurement of the frequency change or measurement of the static bending. In this section an overview from the first experiments to recent developments in the field of sensor applications in the gas phase is given.

First, experiments with the deflection detection will be introduced. The bending of a cantilever is very sensitive to changes in the environment of the cantilever and, more interesting, is very sensitive to changes at the surface of the cantilever. Even the smallest changes of the material properties due to adsorbing molecules will cause a static bending. One problem is that the changes have to occur only on one side of the cantilever and that the processes are very complicated and often not completely understood. Often a bending that occurs cannot be explained in full detail and therefore it is nearly impossible to make quantitative measurements. The other problem of the bending measurements compared to frequency measurements is that they are very prone to disturbances in the environment such as temperature changes (if one does not want to measure them) or vibrations.

Measuring the frequency changes seems to be better because one can easily quantify mass changes and the operation is a lot more stable. But there are other problems to

deal with: First of all the measurement setup is more complicated because of the active driving of the cantilever and one needs a complicated electronic device for the frequency feedback. In addition, the frequency change can arise from temperature changes and/or changes in the force constant.

This shows that each method has advantages and disadvantages and one has to decide upon the nature of the task that one has chosen. It is best to measure both the bending and the frequency change at one time. In this case the surface effects can be separated from mass effects. Most modern sensor systems measure the bending and the frequency change simultaneously.

4.1. Deflection Detection

The first experiments with microcantilevers beams published in 1994 dealt with temperature measurements and surface stress-induced deflections. Tiny heat fluxes were detected with bimetallic cantilevers by measuring the static deflection of the apex of a cantilever due to temperature changes. In [127] the observation of a chemical reaction with a sensitivity of 1 pJ and a temperature limit of $\sim 10^{-5}$ K was published, whereas in [128] thermal and ambient temperature-induced deflections were described. Then calorimeters and photothermal spectroscopy were presented with bending cantilevers as sensors. The use as a calorimeter for investigating surface catalytic reactions was achieved by coating the sensor with a thin Pt layer, which catalyzes the exothermic conversion of H_2 and O_2 to form water [88]. The thermal analysis of picoliter volumes was shown with the enthalpy change detection during the phase transition of *n*-alkanes [129–131]. The measurement of heat transfer during a chemical reaction was also described in [132].

By coating the sensor with a specific photon-absorbing material, it was possible to monitor heat effects as a function of wavelength [133]. With a multilayer architecture cantilevers could be used for photothermal spectroscopy as well [134]. In [135] a radiation dosimeter was presented with ultraviolet cross-linking polymers coated at one side of a cantilever as optical detectors. The exposure to radiation causes a bending in the cantilever. Sensing infrared radiation with high sensitivity and resolution was already shown in [136–139]. In [140] cantilevers were introduced as vibration sensors to control the power between two optical fibers.

The capability of micromachined cantilevers as stress sensors was shown with the adsorption of molecules to a freshly cleaved gold surface. The unspecific adsorption of ambient molecules like water or hydrocarbons [128] could be seen as well as the forming of self-assembled monolayers of thiols on the gold surfaces [141–144]. The alkanthiols formed a monolayer producing a compressive stress, which can be time-resolved, monitored, and fitted with a Langmuir kinetic. Cantilevers can be used to monitor thin film growth processes [84, 145] too. Good overviews of early cantilever sensor achievements are given in [89] and [146]. By measuring the electric field emanating from a charged-particle collecting sphere, cantilevers can be used as charged-particle flux detectors [147].

Bending microcantilevers can be used as chemical sensors by coating one side with a sensitive layer. This layer will amplify the bending effect compared with an uncoated

cantilever. This was shown for the water adsorption of an uncoated and a gelatine-coated cantilever [148].

For (specific) chemical sensing a sensitive or selective layer is necessary to get any kind of signal, because without coating there will not be any interaction between the cantilever and the analyte. Polymer-coated cantilevers can be used to monitor concentration changes of different volatile organic compounds [149, 150]. It is easy to apply the polymers to the sensor surface with spray coating, a polymer solution with an airbrush pistol, or the use of a patch-clamp pipette and a micromanipulator. The polymer sticks due to physisorption at the surface and no further modification is necessary.

By using array architectures with sensitively coated cantilevers and uncoated reference cantilevers, it is possible to distinguish between a real signal and an error signal and to improve the signal-to-noise ratio. Cantilever arrays with differently coated cantilevers have been realized by a number of different groups. In [151–156] a system with a sequential optical readout was described for an array of eight cantilevers. Through coating with different polymers a great variety of organic compounds could be analyzed using multivariate data analysis techniques. The qualitative and quantitative analysis of mixtures of different organic solvents, perfume oils, flavors, and whiskies was performed. A multiple input chemical sensing unit with coated cantilevers, which are produced by including microelectromechanical system (MEMS) processes, was presented in [157, 158]. In [159] a complete microcantilever system with coated cantilevers was described. In [103] chemical sensing using optical diffraction from an array of microcantilevers was proposed. The micromachined cantilevers contained embedded deformable diffraction gratings and are functionalized with polymer coatings.

The latest inventions use array techniques combined with the high resolution of bending cantilevers for radiation detection arrays such as quantum well photon detectors [160] or electromagnetic and nuclear radiation [161]. A new field of investigation and invention for microcantilevers is array infrared detectors for building uncooled infrared devices [37, 102, 162–165] or thermal nanoprobe [33, 166]. Another approach in chemical sensing combines the adsorption-induced stress and the photoinduced stress of target molecules in one device. Microcantilevers that have adsorbed molecules will undergo photoinduced bending that depends on the number of adsorbed molecules on the surface. Also, when microcantilevers undergo photoinduced bending, molecules will adsorb on their surface differently. Depending on the wavelength and cantilever material used, the bending direction can be altered. By combining this with a chemically sensitive coating, a tunable selectivity is achieved [167–170].

A last approach of a microcantilever sensing device brings an array of piezoresistive cantilevers in contact with a sensitive layer. The swelling of the sensitive layer due to analyte exposure is measured directly by measuring the bending of the cantilever [171].

4.2. Frequency Detection

Mass-sensitive devices are well established in the wide field of sensors. One of the most popular representatives is the quartz crystal microbalance (QCM) device. They are well

described in the literature, work in gaseous and liquid environments, and are relatively cheap and easy to handle. They are driven by an oscillation circuit and are therefore very insensitive against external disturbances, providing very good mass sensitivity [172–174]. The reason for new mass-sensitive devices based on microcantilevers is the low mass of cantilevers compared with that of quartz crystal systems. If one calculates the mass sensitivity of a commercially available QCM with 10 MHz compared with that of a cantilever made of single crystal silicon with a fundamental frequency of 100 kHz, one gets a 1000 times higher mass resolution for the cantilever [175]. The mechanical properties together with the low price and fast response times make vibrating beams ideal candidates for new sensor systems. The first use of a coated beam structure as a chemical sensor was reported in [176], and it was first shown in practice with scanning probe microscopy cantilevers in [128], probing the resonance frequency shift due to water adsorption on the cantilever surface. The first CMOS processed beams for sensor purpose were presented in [177]. With these early devices a mass resolution ranging from nanograms to picograms was predicted. The sensitivity of the humidity sensing device could be enhanced by coating with gelatine or phosphorous acid [148, 178]. An early experiment for testing cantilevers as mass-sensing devices was the adsorption of mercury vapors to gold-coated cantilevers [146, 148, 179]. The first interactions between adsorption, force constant change, and frequency change were described in [84]. If the evaporated mercury layer is too thick, the change in the elastic properties of the beam material will completely compensate for the mass effects due to adsorption. A way to enhance the sensitivity of microdevices to mass loading is the use of materials with a high surface-to-mass ratio as a coating material. This was shown for humidity sensing with a few zeolite single crystals attached to a cantilever sensor [180–182]. Good overviews of the first experiments with cantilever sensors are given in [89] and [146]. A micromechanical sensor for charged-particle flux detection is demonstrated in [147] with α particles. Frequency and damping rate variation due to electrostatic force gradients were measured. In [30] cantilevers are used as a low-cost detector in molecular beam experiments to measure the ratio of neutral to ionized clusters and the molecular beam profile with an array architecture of cantilevers.

In all these experiments no additional electronic circuit for active feedback was integrated. They were all driven either by the thermal energy or with an additional piezoelectric crystal as is used in scanning probe microscopes for the tapping mode.

A typical application of cantilever sensors is the detection of volatile organic compounds with an array of differently coated cantilevers. The selective coating consists of polymers that have shown their versatility in QCM systems [183]. The effect is based on a solubility interaction between an adsorbed analyte and the polymer. The closer the chemical properties of the analyte and the polymer, the more analyte is solved in the polymer matrix. This effect increases the density and the polymer gets heavier and starts to swell. With these effects and the chemical selectivity of different polymers it is possible to build a sensor array for analyzing mixtures of organic solvents.

A chemical sensor based on a micromechanical cantilever array consisting of eight differently coated cantilevers with a sequential readout system using a time multiplexing scheme was introduced in [154, 184]. In this setup the cantilever motion is detected via beam deflection with an array of vertical cavity surface-emitting lasers and a position-sensitive detector. The time-multiplexing scheme allows only one cantilever at a time to be monitored. In the dynamic mode the cantilever is driven by a piezoelectric actuator and the frequency change is controlled with a phase locked loop (PLL) controller. This system enables the simultaneous detection of the frequency change and the static bending.

A different approach uses an array of piezoresistive cantilevers with an integrated microheater for calorimetry and mass detection [33]. For microbalance purposes the frequency change during the outgassing process of photoresist due to ultraviolet exposure was monitored.

In [185–188] the parallel frequency readout of an array of polymer-coated mass-sensitive transducers for sensor applications is described. The coated cantilevers were exposed to vaporized organic solvents. Parallel detection of the thermal noise of the cantilevers was possible with an optical beam deflection technique. By adding a cylindrical lens in front of the laser diode a line focus is formed, which can be used to illuminate a whole array of cantilevers. The light is reflected from the beams and collected in a split photodiode. The Fourier spectrum of the detector signal represents the response of the cantilever array to thermal excitation and reveals the resonance frequencies of each individual cantilever. The advantage is the simultaneous detection of several cantilevers and the improvement of the sensitivity by measuring higher eigenmodes. However, this method is very time consuming (the Fourier analysis requires long recording times), and it is impossible to monitor the bending of the cantilever at the same time. The data were evaluated with principal component regression (partial least squares, one method of the multivariate data analysis) for quantitative and qualitative analysis. Therefore, the prediction of unknown concentrations in a binary mixture was possible.

A new way to enhance sensitivity is the use of bridge structures, which are both-ends-supported beams. In [189] the fabrication of a micromechanical mass-sensitive resonator using silicon-on-insulator substrates was presented. Bridge structures have a 6.3 times higher fundamental frequency compared with one-end-supported beam structures and therefore have a higher mass sensitivity. The resonators are driven electrostatically and read out optically by means of the beam deflection method.

In all these experiments no additional electronic circuits for active feedback have been integrated. They were all driven either by the thermal energy or with an additional driving system (piezoelectric crystal or electrostatic) as is used in scanning probe microscopes for the tapping mode. As described in Section 3.1 the sensitivity can be enhanced by enhancing the quality factor. The quality factor is related to damping and an active feedback loop reduces damping. This was realized in the latest cantilever sensor systems where one can find stable self-oscillating cantilevers with extremely enhanced sensitivity.

In [190] a feedback driven system was developed. In this approach an additional feedback circuit is added and PLL device actively drives the frequency. Due to the magnetic actuation this system can be used in a liquid environment as well (see Section 5.3).

A promising approach for microcantilever applications is the combination of the sensitivity of micromachined beams with CMOS technology. By including the CMOS process in cantilever fabrication, it is possible to integrate the electronics on the substrate and to get extremely compact devices. A CMOS resonant beam gas-sensing system with on-chip self-excitation was presented in [38, 50, 121, 191–194]. In these devices the cantilever is thermally excited with two heating resistors in the cantilever base that are heated periodically. The temperature increase on the cantilever generates a bending moment due to the difference in thermal expansion coefficients. The cantilever motion is detected with a piezoresistive Wheatstone bridge at the base of the cantilever. The active feedback circuit is integrated on-chip. The output signal of the Wheatstone bridge is filtered and amplified, and the phase shift is controlled by a Schmitt trigger that can be adjusted externally. The phase is shifted to ensure positive feedback. The result is an integrated oscillator operating at the cantilever resonance frequency with short-term stability of better than 0.1 Hz [38, 195]. The cantilever has an on-chip thermal actuation and a closed feedback loop preamplifier circuitry (Fig. 5). For sensor test purposes the cantilevers were coated with different polymers for the identification of organic vapors. With multivariate data analysis it is possible to analyze quantitatively and qualitatively a binary mixture of two different organic solvents. Advantages of this system are the high sensitivity, its compact design, the array architecture, and the integrated electronics. The disadvantages are the limitations with a gaseous environment (the CMOS circuits have not been stable in liquids so far) and the fact that the simultaneous detection of static bending is not possible.

Another approach for the use of scanning probe microscopy cantilevers as transducers in gas sensor systems

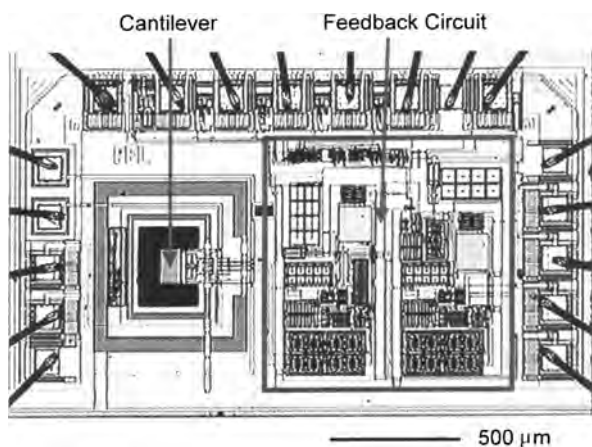


Figure 5. Micrograph of a 150 μm long resonant cantilever with an on-chip feedback circuit, piezoresistive Wheatstone bridge, and thermal actuation. Reprinted with permission from [38], D. Lange et al., *Anal. Chem.* 74, 3084 (2002). © 2002, American Chemical Society.

was described in [175]. The cantilevers were either actuated electrostatically or magnetically and read out optically with the beam deflection technique. For the electrostatic actuation they were integrated in a capacitor-like circuit in which either the cantilever or the counter electrode was supplied with alternating current voltage and the other electrode with direct current voltage or vice versa. For magnetic actuation the cantilevers were coated with a magnetic material like iron or cobalt and premagnetized normal to the cantilever axis. An array was built up of two times three cantilevers at each substrate with different polymer coatings. The measurement chamber was integrated in a gas-mixing station to provide different gases and gas mixtures to the measurement system. The readout can only be done sequentially so far. The cantilever system was integrated in a closed-loop feedback system in which the signal from the cantilever is filtered, amplified, and fed back. The closed loop setup provides stable self-oscillation at the resonance frequency of the cantilever with a short-term stability of 0.005 Hz for the electrostatic and 0.01 Hz for the magnetic actuation [196]. The quality factor can be enhanced for a cantilever with 100 kHz from ~ 200 with vibrating in air driven by the thermal energy up to 400,000 driven actively. This enhancement provides a 1000 times higher frequency stability compared with the systems actuated with thermal energy (Fig. 6). With this measurement electronics it is possible to measure frequency changes and the static bending of the cantilever simultaneously.

For gas-sensing purposes different polymers were chosen so that with multivariate data analysis it was possible to analyze quantitatively and qualitatively a ternary mixture of three different organic solvents. A qualitative principal component analysis of the mixture after normalizing the data set is shown in Figure 7. In a principal component analysis (PCA), a high dimensional vector space (one dimension from each cantilever sensor if only one variable like maximum frequency change is evaluated) can be projected to two (or at least less than the original) dimensions, which nonetheless contain nearly the whole information. In the so-called scores plot of a PCA, data points which reflect similar properties cluster in a certain region. The more similar the properties, the closer two points are together.

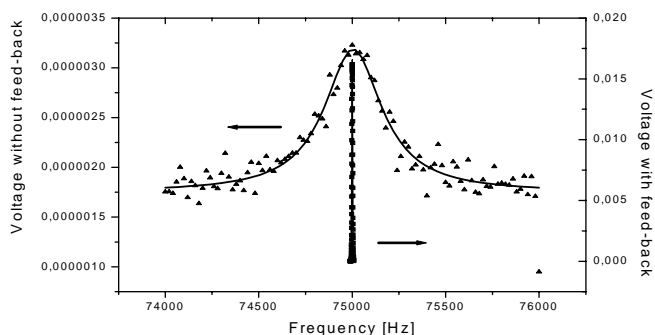


Figure 6. Frequency spectrum of a cantilever driven by thermal noise (upper curve, triangles) and of the same cantilever driven with a closed feedback loop and magnetic actuation (lower curve, squares), measured with the spectrum analyzer function of a hp4195A [175].

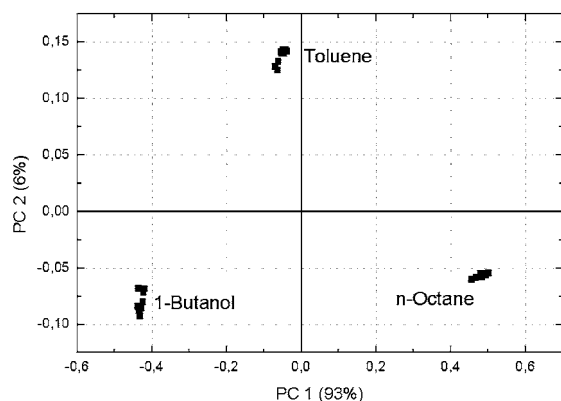


Figure 7. PCA scores plot for the calibration of an array of six polymer-coated cantilevers showing the first two principal components for qualitative and quantitative analysis of a ternary mixture of organic solvents (before calculation of the PCA the data were normalized).

Which property leads to the clustering depends on the particular system. Here, data points cluster if interactions with the sensors and hence their chemical natures are similar. As can be seen in Figure 7 the data points rearrange in clusters. The larger the distance between two clusters the better the sensor array is able to separate the two analytes. After the system was calibrated with a training set of different ternary mixtures, a linear regression model with the partial least squares (PLS) method was applied and a prediction of unknown concentrations could be done. In Figure 8 the predicted values are plotted against the true concentration values of an organic solvent. The concentration is given in parts per million of the carrier gas (synthetic air). Obviously, an acceptable prediction is achieved.

Advantages of this system are the high short-term stability, the easy setup, and the possible use in liquid environments. The disadvantage is that so far a parallel readout is not possible.

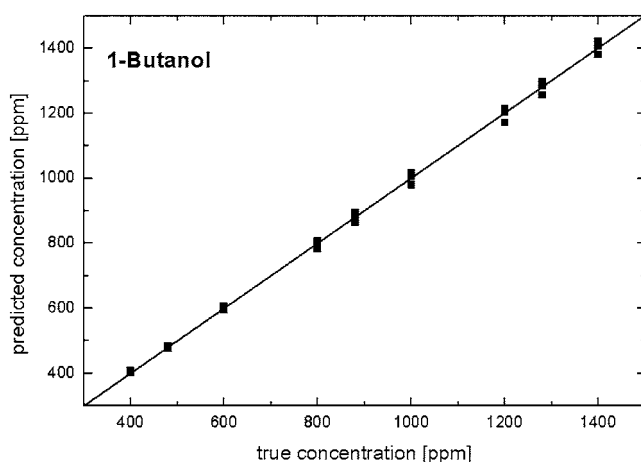


Figure 8. Predicted concentrations vs. true concentrations for 1-butanol. The model used for this prediction was a linear regression model (PLS2). The ternary mixture was evaluated for only one unknown concentration after training the model with the data from Figure 7.

5. SENSOR APPLICATIONS IN THE LIQUID PHASE

In biosensing applications there is a need for fast, easy to use, cheap, and highly sensitive methods for the recognition of biomolecules. A high grade of parallelization is a must because of the demand of the pharmaceutical industry for high throughput screening. All these points can be fulfilled by micromachined cantilever sensors, and therefore they are the ideal candidates for biosensing applications.

5.1. Surface Modification

As defined in Section 2 a liquid sensor or, more specifically, a biosensor has as its main part a transducer combined with a recognition unit. The recognition element is in most cases a single-strand DNA, a protein, or an antibody. These molecules usually will not stick at the surface themselves. Their long-term stability on the surface is in most cases not given. Therefore, a chemical surface functionalization has to be applied to deposit a receptor layer on a cantilever surface. The ideal case of a surface functionalization is a closed, uniform monolayer of the receptor that is covalently anchored to the surface with enough space to interact with the specific ligand. The receptor activity should be maintained over time and resist several regeneration cycles.

To anchor a molecule covalently to a surface the sensor has to be modified and functionalized. Most cantilevers are made of silicon, silicon nitride, or silicon dioxide. Such a surface can be activated and functionalized with silanes [197]. The silanes form a dense polymer covalently linked to the surface with free functional side groups. These groups can react with other side groups of the target molecule. Another popular method for surface functionalization is the evaporation of thin layers of noble metals like gold. Alkane chain molecules with thiol side groups form ordered self-assembled monolayers (SAM) on gold substrates [198]. These uniform, densely packed, and covalently linked monolayers can be synthesized with different chain lengths and end groups. The end groups are used to link other molecules to the functionalized surface. With the chain length one can vary the spacer length between the surface and the active site in the recognition layer and therefore guarantee the best possible activity. Because of their variability SAMs are one of the most popular methods used for biosensor applications.

From the application point of view, one has to decide which surface modification technique is required. Among others, the following parameters are involved in the choice of the chemical surface modification protocol: type of substrate (e.g., plastic, glass, silicon, gold, or ceramics), the functional unit that has to be attached (e.g., polymers, antibodies, or other proteins or lipids), the type of sample (e.g., DNA, DNA-protein mixtures, pure proteins, or cells), and the type of liquid transport (e.g., pressure driven or electroosmotic). Additional introductions to surface coating techniques and reviews can be found in [199, 200].

If one wants to use the deflection detection method for cantilevers, only one side has to be functionalized. Using thiol monolayers this can be done by evaporating gold only on one side of the cantilever or incubating only one side

of a double-sided gold-coated cantilever in the thiol solution. Incubating only one side always causes stress that has to be taken into account [143]. In [201] a procedure is described for coating each side of the cantilever with a different thiol. Nevertheless, surface functionalization is as easy as it sounds, but if deflection detection is used the experimenter has to ensure that the specific interaction occurs only at one side of the cantilever and, even more important, unspecific interaction is blocked. One easy way to block surfaces against unspecific adsorptions is treatment with bovine serum albumin (BSA), a protein with the ability to adsorb on nearly every surface and to be very resistant to a wide variety of chemical and physical conditions such as changes in salt concentration, weak acids and alkaline solutions, and temperature changes. Besides the property of blocking surfaces, the unspecific protein adsorption can be used for surface modification too. By using functionalized BSA a surface can easily be modified biologically with a close, uniform, and compact layer. One example is the modification with biotinylated BSA to get a biotin surface coverage [202]. Another way to modify surfaces with adsorbing proteins is protein A. Protein A has nearly the same adsorbing characteristics as BSA, and it is able to bind the F_c fragment of most immunoglobulin G antibodies [203], which comprise the largest class of antibodies. With this method an antibody-coated surface can be prepared. Besides blocking the surface against unspecific adsorption with BSA or other proteins, the surface can be covered with a monolayer of nonreactive macromolecules or polymers. Polyethyleneglycols have proven their suitability for protecting surfaces against the unspecific absorption of proteins [204, 205].

Organic layers can be created on solid substrates without the need for reactive surface sites with Langmuir–Blodgett (LB) film transfer. The LB deposition transfers ordered layers of amphiphilic molecules from the water/air to the solid/air interface and allows the precise control of multilayer formation [206]. Sol–gels can be used for surface functionalization too [207]. They allow the creation of layers of porous materials with controlled pore size [98]. An increase in the active area can act as a catalyst with the pores serving as a mechanical filter to improve the specificity of the interaction [208].

5.2. Deflection Detection

With the deflection detection method in liquids it is possible to use cantilevers as stress sensors by performing electrocapillary curves with gold- or platinum-coated cantilevers as working electrodes [209]. The change in voltage causes a static bending and enables the study of the thermodynamics of the electrode–electrolyte interface. Similar electrocapillary curves were reported in [89, 210]. In [211] the bending of a cantilever due to the electrochemical deposition of polyaniline to one side of the cantilever is reported. By cyclic oxidation and reduction of the polymer the cantilever is reversibly deflected and restored to its original position.

Changes in surface energy can also be measured with bending microcantilevers. In [212] a cantilever deflects due to changes in the pH value or salt concentration of the surrounding liquid. This effect could also be shown for thiol-modified cantilevers [201]. Differences in the

pH dependence of a mercaptohexadecanoic acid-coated cantilever and a hexadecanethiol-covered reference cantilever were reported in [213]. Additional experiments have been presented with metal-modified and aminosilane-modified surfaces. Only the change in the pH value influences the bending; negligible bending was found for variations in salt concentrations [214]. Trace amounts of Hg^{2+} can be detected by using a gold-coated microcantilever [215]. The bending occurs due to accumulation of the Hg^{2+} on the gold surface. Coating the surface with a SAM of a long-chain thiol compound could improve the sensitivity. The detection of cesium and calcium ions was possible with the modification of the surface with an ion-selective SAM. A method for *in-situ* monitoring of ions in the range 10^{-7} – 10^{-11} M was developed in [216, 217]. In addition, the use as a temperature sensor in liquid environment was shown in [89]. A polymer-coated cantilever can be used for the detection of different amounts of ethanol in water. It was proposed in [150] that the bending of the cantilever due to a change in ethanol concentration is caused by a swelling of the polymer matrix. In addition, the adsorption-induced variation in the spring constant of microcantilevers due to Na^+ ions was proposed in [218].

All of these experiments based on the measurement of the bending of the cantilever and a wide range of signal domains such as pH value, salt concentration, temperature, and electrochemical activity can and will be transduced by a static deflection of the cantilever. During the measurement of a biological affinity reaction all these parameters have to be kept constant or the result is ambiguous. This problem and the difficulties in the quantification of the results are always present during the experiments.

It is possible to build a chemical sensor based on polymer-coated microcantilevers in a liquid environment. In [219] thiolated β -cyclodextrins form a SAM on the cantilever surface, which enables an unspecific interaction with analyte molecules such as a naphthalene derivative. Similar results could be obtained for other cyclodextrin layers on smooth and nanostructured gold surfaces.

Since the introduction of microcantilevers many biological experiments using static deflection have been presented. In [220–222] a so-called force-amplified biological sensor was used to take advantage of the high sensitivity of scanning probe microscope cantilevers to detect the presence of small magnetic particles bound to a cantilever by a sandwich immunoassay technique. The magnetic particles were functionalized with a specific biological species whose counterpart is on the cantilever surface. To detect the binding event the deflection of the cantilever is measured while the magnetic particles amplify the deflection through magnetization of a strong permanent magnet and a modulated additional magnetic field. With this technique concentrations down to 10^{-18} M were proposed to be detectable.

An important field of investigation is the unspecific adsorption of proteins and cells. In [223] the interrogation of living cells grown directly on the cantilever surface to external chemical stimuli was proposed. The unspecific adsorption of proteins such as BSA on one side of the cantilever causes stress and therefore a static bending of the cantilever [153, 212, 224]. The differentiation between the adsorption of a low-density lipoprotein and its oxidized form on heparin

was monitored in [225] as well as the surface stress induced by slow conformational changes of proteins in [226].

Besides the field of unspecific adsorption, the field of specific binding events is very promising. In [146] the variation in an antibody-coated microcantilever deflection as a function of time due to interactions with antigens was reported. The adsorption kinetics and mechanical properties of thiol-modified DNA oligonucleotides on gold were investigated with microcantilever sensors [227, 228]. The sensor used had an integrated piezoresistive readout and is integrated in a microfluidic handling system. The specific detection of two forms of prostate-specific antigen over a wide range of concentrations in a background of different proteins was reported in [229]. The antigen–antibody interaction of biotin and streptavidin or the binding of a herbicide to its monoclonal antibody with a bending cantilever as transducer is described in [201, 230]. This enables the label-free detection of an antigen–antibody interaction with a miniaturized micromechanical system.

With cantilever sensors one can also enter the field of genomics. A first example of an array of cantilevers detecting DNA hybridization was presented in [231]. The hybridization of complementary oligonucleotides showed that a single mismatch between two 12-mer oligonucleotides is clearly detectable. The principle of this hybridization reaction is shown in Figure 9. These promising results were obtained in

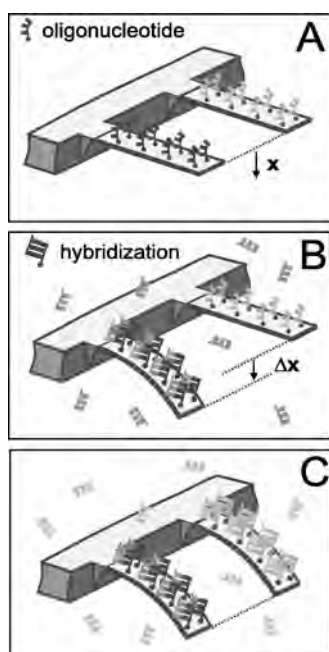


Figure 9. Schematic illustration of a hybridization experiment. Each cantilever is functionalized on one side with a different 12-mer oligonucleotide base (red or blue) differing in only one base. (a) The differential deflection signal is set to zero. (b) After injection of the first complementary oligonucleotide (green), hybridization occurs on the cantilever providing the matching sequence (red) and increasing the differential signal Δx . (c) Injection of the second complementary oligonucleotide (yellow) causes the cantilever functionalized with the second oligonucleotide (blue) to bend. Reprinted with permission from [231], J. Fritz et al., *Science* 288, 316 (2000). © 2000, American Association for the Advancement of Science.

[232] with a 10-mer oligonucleotide. It is possible to measure with cantilever sensors single nucleotide polymorphisms fast and easily.

5.3. Frequency Detection

All of the previously mentioned examples of cantilever liquid sensors are based on the bending of the micromachined beam. The most important problem that has to be solved if the frequency change in liquids should be the measured value is the damping in liquids. As described in Section 3.1, in liquids high damping occurs with a decreasing resonance frequency and, even more important, a decreasing quality factor. Generally the quality factor decreases by 2 orders of magnitude if the surrounding medium is changed from air to water. Because of these effects it is nearly impossible to measure frequency changes below 10–20 Hz.

The damping is caused by changes in the density and the viscosity in the surrounding medium and can be explained by an increase of the effective mass due to an added mass of the liquid being dragged with the cantilever. The resulting frequency change can be used for quantitative measurements of the density/viscosity of different liquids [74, 233].

In [146] the hybridization of an 8-mer DNA oligonucleotide is proposed to be measured with the frequency change of a resonating cantilever, but no data have been published. With a cantilever operated in the resonating mode in [234] the adsorption of bacteria was investigated. The number of bacteria adsorbed onto an antibody-coated surface could be weighed and counted. The measurements were not only measurements in the liquid phase, they were also performed on a dry cantilever in air to get a higher frequency resolution. In [235] cells were been immobilized, but measurement of the frequency change was not reported.

The main problem in all these measurements is the high damping, not the biological preparation. A solution to this problem is to take advantage of the closed feedback loop described earlier. If it is possible to design a closed feedback loop that will work in liquids in an appropriate manner, the damping could be reduced and the quality factor enhanced. This was done in [190] to measure ethanol in water with a polymer-coated cantilever and the antigen–antibody interaction STAR71-BRAC30. In this measurement setup the cantilever is driven with a PLL-controlled oscillator connected to a feedback loop with a variable phase shifter and gain amplifier. The results obtained are a first step in the direction of measuring biological interactions in the liquid phase with resonating microcantilevers. Another promising result is described in [175]. In this setup a self-oscillating system is designed that needs no further actuation. This easy design enables the stable oscillation of cantilevers in the liquid environment. The versatile use of this system was proven with the quantitative measurement of the viscosity and density changes in different ethanol/water mixtures. The short-term frequency stability obtained is approximately 0.3 Hz and therefore an enhancement of the quality factor of 2 orders of magnitude was possible.

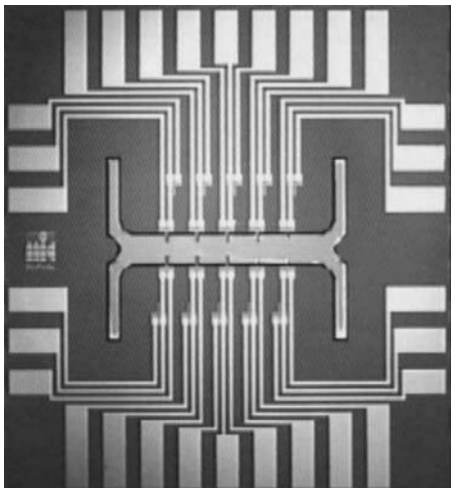


Figure 10. Optical microscope images of a sensor chip which consists of 10 piezoresistive cantilevers in a channel and 4 inlets/outlets. The piezoresistor, which serves as a readout mechanism to detect the bending of the cantilever, is fully encapsulated and can be used in liquids. Reprinted with permission from [227], J. Thaysen et al. "International Conference of Microelectromechanical Systems," pp. 401–404, 2001. © 2001, IEEE.

6. SUMMARY AND FUTURE TRENDS IN MICROCANTILEVER SENSORS

In this chapter it was shown that most of the fundamental problems in cantilever sensor technology are solved in the laboratory state. It is possible to fabricate small cantilevers with low force constants that are very sensitive to bending moments. On the other hand, stiff cantilevers can be produced with high frequencies that are very sensitive to mass changes or changes in the force constant. There are a large variety of different methods for measuring the movement of the cantilever, starting with optical techniques and ending with CMOS-manufactured piezoresistive cantilevers. A few different methods for coating the surface with different polymers for gas sensing purposes and with biological layers for biosensing purposes were introduced. First approaches to work with arrays of cantilevers for reference measurements and pattern recognition to improve signal quality were presented. In addition, some methods based on closed feedback loop operations for the enhancement of the quality factor in gaseous and liquid environment were shown.

Most of these measurements are promising approaches to a completely new class of miniaturized sensor systems. However, under real conditions sensors have to be stable long-term with low power consumption in an extremely small housing for low cost. Ease of use and reproducibility are additional factors for an industrial sensor system. In biomedicine and biotechnology only small amounts of reagents are available and high sensitivity and high throughput screening are requirements. Furthermore, the preparation of high amounts of reproducible biofunctionalized surface modifications in an easy-to-use liquid handling system is necessary for biosensing applications.

At present there are several approaches to solving these problems. In Figure 5 CMOS-processed cantilevers combined with subsequent CMOS-compatible micromachining

were presented with the complete electronic circuitry for cantilever driving and signal conditioning [38, 195]. With this industrial technique it is easy to mass produce large and compact arrays of integrated cantilevers for the detection of gaseous analytes.

Besides an integrated readout and driving system it is necessary to combine sensing systems with the requirements of biotechnology. One approach is an array of 10 cantilevers with a piezoresistive readout for deflection detection integrated into a microfluidic handling system onto a silicon chip as shown in Figure 10. These cantilevers are completely encapsulated and can be operated stably in liquid environments.

Another development focuses on larger arrays. At the moment an array of 2 to 10 cantilevers is state of the art, but this is not enough for the requirements of the industry for extremely high parallelization. Large sensor arrays with 1024 cantilevers combined with MEMS technology are used in [34, 236, 237] as ultra-high density storage devices. Besides the piezoresistive readout of these large arrays, new optical readout techniques are being explored [37, 103, 165, 238] for parallel optical detection.

One next step will be to go to smaller cantilevers with higher frequencies and therefore better mass resolution in the dynamic mode of operation. These approaches are presented in [24–31] for an optical detection system. Nanometer-sized cantilevers with frequencies in the megahertz range and integrated CMOS circuitry are the newest steps in the future direction of high resolution mass sensitivity [239, 240].

GLOSSARY

Biosensor Often defined as a compact analytical device incorporating a biological or biologically derived sensing element either integrated within or intimately associated with a physicochemical transducer.

Complementary metal oxide semiconductor (CMOS) Special semiconductor technology, standard process for most integrated circuits.

Integrated circuit (IC) Semiconductor device (e.g., amplifier, oscillator, or microprocessor), in which all resistors, capacitors, and transistors which perform the desired function of the circuit are processed together.

Multivariate data analysis Methods for dealing with large tables of data by displaying the data in a few meaningful plots that contain the most important information. Methods for displaying are, for example, principal component analysis for an overview over groups and trends, the classification or discriminant analysis for analyzing the groups, and the multiple regression analysis or partial least squares projection to build quantitative models for prediction of unknown analytes.

Scanning force microscopy (SFM) A method to measure the interaction forces between two surfaces for getting a three-dimensional picture of the surface.

Sensor A miniaturized device that converts a chemical state into an electrical signal. It mainly consists of three parts: the recognition site, the transducer, and the readout system.

REFERENCES

1. G. Binnig, C. F. Quate, and C. Gerber, *Phys. Rev. Lett.* 56, 930 (1986).
2. H. Hosoi, M. Kimura, K. Hayakawa, K. Sueoka, and K. Mukasa, *Appl. Phys. A* 72, S23 (2001).
3. W. F. Heinz and J. H. Hoh, *Biophys. J.* 76, 528 (1999).
4. S. M. Smith and J. L. Gilbert, in "Compatibility of Biomedical Implants, Proceedings of the Electrochemical Society," 1994, pp. 229–240.
5. A. L. Weisenhorn, M. Khorsandi, S. Kasas, V. Gotzos, and H.-J. Butt, *Nanotechnology* 4, 106 (1993).
6. M. Maywald, R. J. Pylkki, and L. J. Balk, *Scanning Microsc.* 8, 181 (1994).
7. R. Ros, F. Schwesinger, C. Padeste, A. Plückthun, D. Anselmetti, H.-J. Güntherodt, and L. Tiefenauer, *Proc. SPIE-Int. Soc. Opt. Eng.* 3607, 84 (1999).
8. G. Haehner, A. Marti, and N. D. Spencer, *Tribol. Lett.* 3, 359 (1997).
9. Olympus Optical Co., Ltd., <http://www.olympus.co.jp/probe/index.html> (2002).
10. Nanosensors GmbH & Co. KG, <http://www.nanosensors.com/products.htm> (2002).
11. NT-MDT Co., <http://www.ntmdt.ru/> (2002).
12. MikroMasch, <http://www.spmtips.com/> (2002).
13. NanoDevices Inc., <http://www.nanodevices.com> (2002).
14. TM Microscopes, <http://www.spmprobes.com/> (2002).
15. M. Ono, D. Lange, O. Brand, C. Hagleitner, and H. Baltes, *Ultramicroscopy* 91, 9 (2002).
16. D. Lange, T. Akiyama, C. Hagleitner, A. Tonin, H. R. Hidber, P. Niedermann, U. Staufer, N. F. De Rooij, O. Brand, and H. Baltes, "Technical Digest of the 12th, IEEE International Conference on Micro Electro Mechanical Systems," 1999, pp. 447–452.
17. C. Hagleitner, D. Lange, T. Akiyama, A. Tonin, R. Vogt, and H. Baltes, *Proc. SPIE-Int. Soc. Opt. Eng.* 3673, 240 (1999).
18. W. Franks, D. Lange, S. Lee, A. Hierlemann, N. Spencer, and H. Baltes, *Ultramicroscopy* 91, 21 (2002).
19. H. Takahashi, K. Ando, and Y. Shirakawabe, *Ultramicroscopy* 91, 63 (2002).
20. N. Satoh, K. Kobayashi, S. Watanabe, T. Fujii, T. Horiuchi, H. Yamada, and K. Matsushige, *Appl. Surf. Sci.* 188, 425 (2002).
21. I. W. Rangelow, P. Grabiec, T. Gotszalk, and K. Edinger, *Surf. Interface Anal.* 33, 59 (2002).
22. Y. Miyahara, M. Deschler, T. Fujii, S. Watanabe, and H. Bleuler, *Appl. Surf. Sci.* 188, 450 (2002).
23. J. Thaysen, A. Boisen, O. Hansen, and S. Bouwstra, *Sens Actuators* 83, 47 (2000).
24. T. E. Schaffer, *J. Appl. Phys.* 91, 4739 (2002).
25. A. Chand, M. B. Viani, T. E. Schaffer, and P. K. Hansma, *J. Microelectromech. Syst.* 9, 112 (2000).
26. T. E. Schäffer, M. Viani, D. A. Walters, B. Drake, E. K. Runge, J. P. Cleveland, M. A. Wendman, and P. K. Hansma, *Proc. SPIE-Int. Soc. Opt. Eng.* 3009, 48 (1997).
27. M. B. Viani, T. E. Schäffer, A. Chand, M. Rief, H. E. Gaub, and P. K. Hansma, *J. Appl. Phys.* 86, 2258 (1999).
28. M. B. Viani, T. E. Schäffer, G. T. Paloczi, L. I. Pietrasanta, B. L. Smith, J. B. Thompson, M. Richter, M. Rief, H. E. Gaub, K. W. Plaxco, A. N. Cleland, H. G. Hansma, and P. K. Hansma, *Rev. Sci. Instrum.* 70, 4300 (1999).
29. D. A. Walters, M. Viani, G. T. Paloczi, T. E. Schäffer, J. P. Cleveland, M. A. Wendman, G. Gurley, V. Ellings, and P. K. Hansma, *Proc. SPIE-Int. Soc. Opt. Eng.* 3009, 43 (1998).
30. T. Bachelis and R. Schäfer, *Rev. Sci. Instrum.* 69, 3794 (1998).
31. M. Hoummady and H. Fujita, *Nanotechnology* 10, 29 (1999).
32. E. M. Chow, G. G. Yaralioglu, C. F. Quate, and T. W. Kenny, *Appl. Phys. Lett.* 80, 664 (2002).
33. N. Abedinov, P. Grabiec, T. Gotszalk, T. Ivanov, J. Voigt, and I. W. Rangelow, *J. Vac. Sci. Technol. A* 19, 2884 (2001).
34. P. Vettiger, M. Despont, U. Drechsler, U. Dürig, W. Häberle, M. I. Lutwyche, H. E. Rothuizen, R. Sturz, R. Widmaier, and G. K. Binnig, *IBM J. Res. Dev.* 44, 323 (2000).
35. U. Dürig, G. Cross, M. Despont, U. Drechsler, W. Häberle, M. I. Lutwyche, H. Rothuizen, R. Stutz, R. Widmer, P. Vettiger, G. K. Binnig, W. P. King, and K. E. Goodson, *Tribol. Lett.* 9, 25 (2000).
36. P. Vettiger, J. Brugger, M. Despont, U. Drechsler, U. Dürig, W. Häberle, M. Lutwyche, H. Rothuizen, R. Stutz, R. Widmer, and G. Binnig, *Microelectron. Eng.* 46, 11 (1999).
37. Y. Zhao, M. Mao, R. Horowitz, A. Majumdar, J. Varesi, P. Norton, and J. Kitching, *J. Microelectromech. Syst.* 11, 136 (2002).
38. D. Lange, C. Hagleitner, A. Hierlemann, O. Brand, and H. Baltes, *Anal. Chem.* 74, 3084 (2002).
39. R. McKendry, J. Zhang, Y. Arntz, T. Strunz, M. Hegner, H. P. Lang, M. K. Baller, U. Certa, E. Meyer, H.-J. Güntherodt, and C. Gerber, *Proc. Nat. Acad. Sci. USA* 99, 9783 (2002).
40. K. Nilsson and E. Nilsson, U.S. Patent, 6252335, 2001.
41. D. L. Polla, R. S. Muller, and R. M. White, *IEEE Electron Device Lett.* EDL-7, 254 (1986).
42. X. Li, M. Bao, H. Yang, S. Shen, and D. Lu, *Sens. Actuators, A* 72, 217 (1999).
43. Y. Su, A. G. R. Evans, A. Brunnschweiler, and G. Ensell, "ESS-DERC '96, Proceedings of the 26th European Solid State Device Research Conference," 1996, pp. 717–720.
44. T. Matsuura, M. Taguchi, K. Kawata, and K. Tsutsumi, *Sens. Actuators, A* 60, 197 (1997).
45. W. Göpel and K. Schierbaum, in "Sensors: A Comprehensive Survey" (W. Göpel, J. Hesse, and J. N. Zemel, Eds.), Vol. 2, pp. 1–27. VCH, Weinheim, 1991.
46. M. Kaspar, H. Stadler, T. Weiss, and C. Ziegler, *Fresenius J. Anal. Chem.* 366, 602 (2000).
47. T. C. Pearce, J. W. Gardener, and W. Göpel, in "Sensors Update" (W. Göpel, J. Hesse, and H. Baltes, Eds.), Vol. 3, pp. 61–130. Wiley-VCH, Weinheim, 1998.
48. Cardiff University, Electronic 'tongue' for environmental monitoring, <http://www.cardiff.ac.uk/news/releases/0204/020404.html> (2002).
49. A. P. F. Turner, I. Karube, and G. S. Wilson, "Biosensors: Fundamentals and Application" p. 770, Oxford University Press, Oxford, 1987.
50. H. Baltes, A. Koll, and D. Lange, "Proceedings of the IEEE, ISIE '97," 1997, pp. SS152–SS157.
51. W. Weaver, S. P. Timoshenko, and D. H. Young, "Vibration Problems in Engineering, Wiley, New York, 1990.
52. O. Brand and H. Baltes, in "Sensors Update" (H. Baltes, W. Göpel, and J. Hesse, Eds.), Vol. 4, pp. 3–51. VCH, Weinheim, 1998.
53. H.-J. Butt and M. Jaschke, *Nanotechnology* 6, 1 (1995).
54. R. D. Blevin, "Formulas for Natural Frequencies and Mode Shapes," Van Nostrand Reinhold, New York, 1979.
55. J. M. Neumeister and W. A. Ducker, *Rev. Sci. Instrum.* 65, 2527 (1994).
56. J. E. Sader, *Rev. Sci. Instrum.* 66, 4583 (1995).
57. J. E. Sader, I. Larson, P. Mulvaney, and L. R. White, *Rev. Sci. Instrum.* 66, 3789 (1995).
58. J. E. Sader, J. W. M. Chon, and P. Mulvaney, *Rev. Sci. Instrum.* 70, 3967 (1999).
59. J. E. Sader and L. White, *J. Appl. Phys.* 74, 1 (1994).
60. R. Lévy and M. Maaloum, *Nanotechnology* 13, 33 (2002).
61. J. D. Holbery, V. L. Eden, M. Sarikaya, and R. M. Fisher, *Rev. Sci. Instrum.* 71, 3769 (2000).
62. H.-J. Butt, P. Siedle, K. Seifert, K. Fendler, T. Seeger, A. Bamberg, A. L. Weisenhorn, K. Goldie, and A. Engel, *J. Microsc.* 169, 75 (1993).
63. T. J. Senden and W. A. Ducker, *Langmuir* 10, 1003 (1994).
64. E.-L. Florin, V. T. Moy, and H. E. Gaub, *Science (Washington, DC)* 264, 415 (1994).

65. Y. Q. Li, N. J. Tao, J. Pan, A. A. Garcia, and S. M. Lindsay, *Langmuir* 9, 637 (1993).
66. J. L. Hutter and J. Bechhoefer, *Rev. Sci. Instrum.* 64, 1868 (1993).
67. J. P. Cleveland, S. Manne, D. Bocek, and P. K. Hansma, *Rev. Sci. Instrum.* 64, 403 (1993).
68. Asylum Research, <http://www.asylumresearch.com/QuantMolecForcesAbstract.pdf> (2002).
69. T. R. Albrecht, P. Grütter, D. Horne, and D. Rugar, *J. Appl. Phys.* 69, 668 (1991).
70. D. Lange, "Cantilever-Based Microsystems for Gas Sensing and Atomic Force Microscopy," Dissertation, Swiss Federal Institute of Technology, Zurich, 2000.
71. J. Mehner, S. Kurth, D. Billep, C. Kaufmann, K. Kehr, and W. Dötzel, "Proceedings of IEEE Micro Electro Mechanical Systems (MEMS)," 1998, pp. 240–245.
72. K. Kokobun, M. Hirata, M. Ono, H. Murakami, and Y. Toda, *J. Vac. Sci. Technol.* A5, 2450 (1987).
73. L. D. Landau and E. M. Lifshitz, "Fluid Mechanics," New York, Pergamon Press, 1959.
74. G. Y. Chen, R. J. Warmack, T. Thundat, D. P. Allison, and A. Huang, *Rev. Sci. Instrum.* 65, 2532 (1994).
75. F. R. Blom, S. Bouwstra, M. Elwenspoek, and J. H. J. Fluitman, *J. Vac. Sci. Technol. B* 10, 19 (1992).
76. J. E. Sader, *J. Appl. Phys.* 84, 64 (1998).
77. W. Y. Shih, X. Li, H. Gu, W.-H. Shih, and I. A. Aksay, *J. Appl. Phys.* 89, 1497 (2001).
78. S. Rast, C. Wattering, U. Gysin, and E. Meyer, *Rev. Sci. Instrum.* 71, 2772 (2000).
79. B. Anczykowski, J. P. Cleveland, D. Krüger, V. Ellings, and H. Fuchs, *Appl. Phys. A* 66, S885 (1998).
80. T. Sulchek, R. Hsieh, J. D. Adams, G. G. Yaralioglu, S. C. Minne, C. F. Quate, J. P. Cleveland, A. Atalar, and D. M. Adderton, *Appl. Phys. Lett.* 76, 14731 (2000).
81. J. Tamayo, A. D. L. Humphris, and M. J. Miles, *Appl. Phys. Lett.* 77, 582 (2000).
82. G. Sauerbrey, *Z. Phys.* 155, 206 (1959).
83. F. Eichelbaum, R. Borngräber, R. Lucklum, P. Hauptmann, and S. Rösler, *Technisches Messen* 65, 434 (1998).
84. G. Y. Chen, T. Thundat, E. A. Wachter, and R. J. Warmack, *J. Appl. Phys.* 77, 3618 (1995).
85. G. G. Stoney. "Proceedings of the Royal Society of London A82," 1909, p. 172.
86. T. Honda, K. I. Arai, and M. Yamaguchi, *J. Appl. Phys.* 76, 6994 (1994).
87. Z. Hu, T. Thundat, and R. J. Warmack, *J. Appl. Phys.* 90, 427 (2001).
88. J. R. Barnes, R. J. Stephenson, C. N. Woodburn, S. J. O'Shea, M. E. Welland, T. Rayment, J. K. Gimzewski, and C. Geber, *Rev. Sci. Instrum.* 65, 3793 (1994).
89. R. Berger, C. Gerber, H. P. Lang, and J. K. Gimzewski, *Microelectron. Eng.* 35, 373 (1997).
90. G. Meyer and N. M. Amer, *Appl. Phys. Lett.* 53, 1045 (1988).
91. R. Erlandsson, G. M. McClelland, C. M. Mate, and S. Chiang, *J. Vac. Sci. Technol., A* 6, 266 (1988).
92. C. A. J. Putman, B. G. D. Grooth, N. F. V. Hulst, and J. Greve, *J. Appl. Phys.* 72, 6 (1992).
93. Y. Martin, C. C. Williams, and H. K. Wickramasinghe, *J. Appl. Phys.* 61, 4723 (1987).
94. D. Rugar, H. J. Mamin, and P. Guethner, *Appl. Phys. Lett.* 55, 2588 (1989).
95. N. Blanc, J. Brugger, N. F. d. Rooij, and U. Dürig, *J. Vac. Sci. Technol., B* 14, 901 (1996).
96. Y. Shiba, T. Ono, K. Minami, and M. Esashi, *Trans. Ins. Electr. Eng. Jpn.* 118-E, 647 (1998).
97. J. Brugger, N. Blanc, P. Renaud, and N. F. d. Rooij, *Sens. Actuators, A* 43, 339 (1994).
98. R. Raiteri, M. Grattarola, and R. Berger, *Mater. Today* 22 (2002).
99. G. G. Yaralioglu, A. Atalar, S. R. Manalis, and C. F. Quate, *J. Appl. Phys.* 83, 7405 (1998).
100. S. R. Manalis, S. C. Minne, and A. Atalar, *Appl. Phys. Lett.* 69, 3944 (1996).
101. T. Perazzo, M. Mao, O. Kwon, A. Majumdar, J. B. Varesi, and P. Norton, *Appl. Phys. Lett.* 74, 3567 (1999).
102. S. R. Manalis, S. C. Minne, C. F. Quate, G. G. Yaralioglu, and A. Atalar, *Appl. Phys. Lett.* 70, 3311 (1997).
103. T. Thundat, E. Finot, Z. Hu, R. H. Ritchie, G. Wu, and A. Majumdar, *Appl. Phys. Lett.* 77, 4061 (2000).
104. M. Tortonese, R. C. Barrett, and C. F. Quate, *Appl. Phys. Lett.* 62, 834 (1993).
105. R. Linnemann, T. Gotszalk, L. Hadjiiski, and I. W. Rangelow, *Thin Solid Films* 264, 159 (1995).
106. S. C. Minne, S. R. Manalis, and C. F. Quate, *Appl. Phys. Lett.* 67, 3918 (1995).
107. B. W. Chui, T. D. Stone, T. W. Kenny, H. J. Mamin, B. D. Terris, and D. Rugar, *Appl. Phys. Lett.* 69, 2767 (1996).
108. O. Hansen and A. Boisen, *Nanotechnology* 10, 51 (1999).
109. S. S. Lee and R. M. White, *Sens. Actuators, A* 52, 41 (1996).
110. S. R. Manalis, S. C. Minne, A. Atalar, and C. F. Quate, *Rev. Sci. Instrum.* 67, 3294 (1996).
111. P.-F. Indermühle, G. Schürmann, G.-A. Racine, and N. F. d. Rooij, *J. Micromech. Microeng.* 7, 218 (1997).
112. C. Lee, T. Itoh, T. Ohashi, R. Maeda, and T. Suga, *J. Vac. Sci. Technol., B* 15, 1559 (1997).
113. W. Han, S. M. Lindsay, and T. Jing, *Appl. Phys. Lett.* 69, 4111 (1996).
114. M. A. Lantz, S. J. O'Shea, and M. E. Welland, *Appl. Phys. Lett.* 65, 409 (1994).
115. E.-L. Florin, M. Radmacher, B. Fleck, and H. E. Gaub, *Rev. Sci. Instrum.* 65, 639 (1994).
116. A. Schemmel and H. E. Gaub, *Rev. Sci. Instrum.* 70, 1313 (1999).
117. I. Revenko and R. Proksch, *J. Appl. Phys.* 87, 526 (2000).
118. E. Sarraute and I. Dufour, "Proceedings of the 1999 International Conference on Modeling and Simulation of Microsystems," 1999, pp. 266–269.
119. M. Dufour, M. T. Delaye, F. Michel, J. S. Danel, B. Diem, and G. Delapierre, *Sens. Actuators, A* 34, 201 (1992).
120. A. Buguin, O. D. Roure, and P. Silberzan, *Appl. Phys. Lett.* 78, 2982 (2001).
121. D. Lange and O. Brand, European Patent 1197726, 2002.
122. S. Tsuchitani and R. Kaneko, *Trans. Inst. Electr. Eng. Jpn.* 118-E, 6 (1998).
123. D. F. Cunningham, L. Jenkins, and M. A. H. Khalid, *Sens. Actuators, A* 63, 125 (1997).
124. P. Attia, M. Boutry, A. Bosseboeuf, and P. Hesto, *Microelectronics J.* 29, 641 (1998).
125. G. Abadal, Z. J. Davis, B. Helbo, X. Borriase, R. Ruiz, A. Boisen, F. Campabadal, J. Esteve, E. Figueras, F. Perez-Murano, and N. Barniol, *Nanotechnology* 12, 100 (2001).
126. T. Akiyama, U. Staufer, N. F. de Rooij, D. Lange, C. Hagleitner, O. Brand, H. Baltes, A. Tonin, and H. R. Hidber, *J. Vac. Sci. Technol., B* 18, 2669 (2000).
127. J. K. Gimzewski, C. Gerber, E. Meyer, and R. R. Schlittler, *Chem. Phys. Lett.* 217, 589 (1994).
128. T. Thundat, R. J. Warmack, G. Y. Chen, and D. P. Allison, *Appl. Phys. Lett.* 64, 2894 (1994).
129. R. Berger, C. Gerber, J. K. Gimzewski, E. Meyer, and H.-J. Güntherodt, *Appl. Phys. Lett.* 69, 40 (1996).
130. R. Berger, C. Gerber, and J. K. Gimzewski, "Symposium on Microscale Thermal Phenomena in Electronic Systems," 1996.
131. R. Berger, C. Gerber, and J. K. Gimzewski, "2nd International Symposium on Micro Total Analysis Systems," 1996.
132. T. G. Thundat and M. J. Doktycz, World Patent 9947911, 1999.
133. J. R. Barnes, R. J. Stephenson, M. E. Welland, C. Gerber, and J. K. Gimzewski, *Nature (London)* 372, 79 (1994).

134. G. Li, L. W. Burggraf, and W. P. Baker, *Appl. Phys. Lett.* 76, 1122 (2000).
135. T. Thundat, S. L. Sharp, W. G. Fisher, R. J. Warmack, and E. A. Wachter, *Appl. Phys. Lett.* 66, 1563 (1995).
136. E. A. Wachter, T. Thundat, P. I. Oden, R. J. Warmack, P. G. Datskos, and S. L. Sharp, *Rev. Sci. Instrum.* 67, 3434 (1996).
137. J. Varesi, J. Lai, T. Perazzo, Z. Shi, and A. Majumdar, *Appl. Phys. Lett.* 71, 306 (1997).
138. P. I. Oden, P. G. Datskos, T. Thundat, and R. J. Warmack, *Appl. Phys. Lett.* 69, 3277 (1996).
139. P. G. Datskos, P. I. Oden, T. Thundat, E. A. Wachter, R. J. Warmack, and S. R. Hunter, *Appl. Phys. Lett.* 69, 2986 (1996).
140. E. Peiner, D. Scholz, A. Schlachetzki, and P. Hauptmann, *Sens. Actuators, A* A65, 23 (1998).
141. R. Berger, E. Delamarche, H. P. Lang, C. Gerber, J. K. Gimzewski, E. Meyer, and H.-J. Güntherodt, *Appl. Phys. A* 66, S55 (1998).
142. R. Berger, H. P. Lang, E. Delamarche, C. Gerber, J. K. Gimzewski, C. Andreoli, J. Brugger, M. Despont, and P. Vettiger, in "8th International Conference on Sensors and Their Applications," 1997.
143. R. Berger, E. Delamarche, H. P. Lang, C. Gerber, and J. K. Gimzewski, *Science (Washington, DC)* 276, 2021 (1997).
144. P. G. Datskos and I. Sauers, *Sens. Actuators, B* B61, 75 (1999).
145. D. Sander, A. Enders, and J. Kirschner, *Rev. Sci. Instrum.* 66, 4734 (1995).
146. T. Thundat, P. I. Oden, and R. J. Warmack, *Microscale Thermophys. Eng.* 1, 185 (1997).
147. A. C. Stephan, T. Gaudlen, A. D. Brown, M. Smith, L. F. Miller, and T. Thundat, *Rev. Sci. Instrum.* 73, 36 (2002).
148. E. A. Wachter and T. Thundat, *Rev. Sci. Instrum.* 66, 3662 (1995).
149. H. Jensenius, J. Thaysen, A. A. Rasmussen, L. H. Veje, O. Hansen, and A. Boisen, *Appl. Phys. Lett.* 76, 2615 (2000).
150. A. Boisen, J. Thaysen, H. Jensenius, and O. Hansen, *Ultramicroscopy* 82, 11 (2000).
151. R. Berger, H. P. Lang, J. P. Ramseyer, F. Battiston, J. H. Fabian, L. Scandella, C. Andreoli, J. Brugger, M. Despont, P. Vettiger, E. Meyer, H.-J. Güntherodt, C. Gerber, and J. K. Gimzewski, Research Report IBM Research Division RZ 2986, 1997, pp. 1–9.
152. H. P. Lang, R. Berger, F. Battiston, J.-P. Ramseyer, E. Meyer, C. Andreoli, J. Brugger, P. Vettiger, M. Despont, T. Mezzacasa, L. Sandella, H.-J. Güntherodt, C. Gerber, and J. K. Gimzewski, *Appl. Phys. A* 66, S61 (1998).
153. M. K. Baller, H. P. Lang, J. Fritz, C. Gerber, J. K. Gimzewski, U. Drechsler, H. Rothuizen, M. Despont, P. Vettiger, F. M. Battiston, J. P. Ramseyer, P. Fornaro, E. Meyer, and H.-J. Güntherodt, *Ultramicroscopy* 82, 1 (2000).
154. F. M. Battiston, J.-P. Ramseyer, H. P. Lang, M. K. Baller, C. Gerber, J. K. Gimzewski, E. Meyer, and H.-J. Güntherodt, *Sens. Actuators, B* B77, 122 (2001).
155. H. P. Lang, M. K. Baller, R. Berger, C. Gerber, J. K. Gimzewski, F. M. Battiston, P. Fornaro, J. P. Ramseyer, E. Meyer, and H.-J. Güntherodt, Research Report IBM Research Division, 1998, pp. 1–7.
156. H. P. Lang, R. Berger, C. Andreoli, J. Brugger, M. Despont, P. Vettiger, C. Gerber, J. K. Gimzewski, J. P. Ramseyer, E. Meyer, and H.-J. Güntherodt, *Appl. Phys. Lett.* 72, 383 (1998).
157. C. L. Britton, R. L. Jones, P. I. Oden, Z. Hu, R. J. Warmack, S. F. Smith, W. L. Bryan, and J. M. Rochelle, *Ultramicroscopy* 82, 17 (2000).
158. C. L. Britton, Jr., R. J. Warmack, W. L. Bryan, R. L. Jones, P. I. Oden, and T. Thundat, U.S. Patent 6167748, 2001.
159. T. G. Thundat and E. A. Wachter, U.S. Patent 5719324, 1998.
160. P. G. Datskos, S. Rajic, L. R. Senesac, and I. Datskou, *Ultramicroscopy* 86, 191 (2001).
161. T. G. Thundat, R. J. Warmack, and E. A. Wachter, World Patent 9726556, 1997.
162. Y. Zhao, J. Yamaguchi, J. Choi, S. Morales, R. Horowitz, A. Majumdar, P. Norton, J. Kitching, H. Li, and M. Athavale, in 369-1, "Proceedings of the ASME Heat Transfer Division—2001," Vol. 1, 2001, pp. 367–370.
163. M. Mao, T. Perazzo, O. Kwon, Y. Zhao, A. Majumdar, J. Varesi, and P. Norton, *Microelectromech. Syst.* 1, 309 (1999).
164. M. Mao, T. Perazzo, O. Kwon, A. Majumdar, J. Varesi, and P. Norton, "Technical Digest of the 12th IEEE International Conference on Micro Electro Mechanical Systems," 1999, pp. 100–105.
165. T. Perazzo, M. Mao, O. Kwon, A. Majumdar, J. B. Varesi, and P. Norton, *Appl. Phys. Lett.* 74, 3567 (1999).
166. I. W. Rangelow, T. Gotszalk, N. Abedinov, P. Grabiec, and K. Edinger, *Microelectron. Eng.* 57–58, 737 (2001).
167. P. G. Datskos, S. Rajic, M. J. Sepaniak, N. Lavrik, C. A. Tipple, L. R. Senesac, and I. Datskou, *J. Vac. Sci. Technol., B* 19, 1173 (2001).
168. P. G. Datskos, World Patent 0058688, 2000.
169. P. G. Datskos, M. J. Sepaniak, C. A. Tipple, and N. Lavrik, *Sens. Actuators, B* 76, 393 (2001).
170. T. G. Thundat, U.S. Patent 6212939, 2001.
171. T. L. Porter, M. P. Eastman, D. L. Pace, and M. Bradley, *Sens. Actuators, A* 88, 47 (2001).
172. J. Rickert, G. L. Hayward, B. A. Ravi, M. Thompson, and W. Göpel, "Sensors Update," VCH, Weinheim, 1998.
173. K. Bodenhöfer, A. Hierlemann, G. Noetzel, U. Weimar, and W. Göpel, "Proceedings of Transducers '95," 1995, pp. 728–731.
174. M. Haug, K. D. Schierbaum, G. Gauglitz, and W. Göpel, *Sens. Actuators, B* 11, 383 (1993).
175. A. Vidic, D. Then, and C. Ziegler, Ultramicroscopy, accepted, 2002.
176. J. M. O'Connor and J. C. Patton, European Patent 72744, 1983.
177. S. Prescesky, M. Parameswaran, A. Rawicz, R. F. B. Turner, and U. Reichl, *Can. J. Phys.* 70, 1178 (1992).
178. T. Thundat, G. Y. Chen, R. J. Warmack, D. P. Allison, and E. A. Wachter, *Anal. Chem.* 67, 519 (1995).
179. T. Thundat, E. A. Wachter, S. L. Sharp, and R. J. Warmack, *Appl. Phys. Lett.* 66, 1695 (1995).
180. L. Scandella, G. Binder, T. Mezzacasa, J. Gobracht, R. Berger, H. P. Lang, C. Gerber, J. K. Gimzewski, J. H. Koegler, and J. C. Jansen, Research Report IBM Research Division, 1997, pp. 1–8.
181. J.-H. Fabian, J. Gobrecht, L. Scandella, R. Berger, H. P. Lang, C. Gerber, J. K. Gimzewski, and E. Meyer, Research Report IBM Research Division, 1998, pp. 1–4.
182. L. Scandella, G. Binder, T. Mezzacasa, J. Gobrecht, R. Berger, H. P. Lang, C. Gerber, J. K. Gimzewski, J. H. Koegler, and J. C. Jansen, *Microporous Mesoporous Mater.* 21, 403 (1998).
183. K. Bodenhöfer, Medien Verlag Köhler, Tübingen, 1997.
184. H. P. Lang, F. M. Battiston, M. K. Baller, R. Berger, J.-P. Ramseyer, P. Fornaro, E. Meyer, H.-J. Güntherodt, C. Andreoli, J. Brugger, M. Despont, P. Vettiger, J. H. Fabian, T. Mezzacasa, L. Scandella, C. Gerber, and J. K. Gimzewski, Research Report, p. 4.
185. M. Maute, S. Raible, F. E. Prins, D. P. Kern, H. Ulmer, U. Weimar, and W. Göpel, *Sens. Actuators, B* 58, 505 (1999).
186. M. Maute, S. Raible, F. E. Prins, D. P. Kern, U. Weimar, and W. Göpel, *Microelectron. Eng.* 46, 439 (1999).
187. B. H. Kim, M. Maute, F. E. Prins, D. P. Kern, M. Croitoru, S. Raible, U. Weimar, and W. Göpel, *Microelectron. Eng.* 53, 229 (2000).
188. B. H. Kim, F. E. Prins, D. P. Kern, S. Raible, and U. Weimar, *Sens. Actuators, B* 3944, 1 (2001).
189. B. H. Kim, D. P. Kern, S. Raible, and U. Weimar, *Microelectron. Eng.* 61–62, 947 (2002).
190. J. Tamayo, A. D. L. Humphris, A. M. Malloy, and M. J. Miles, *Ultramicroscopy* 86, 167 (2001).
191. D. Lange, C. Hagleitner, O. Brand, and H. Baltes, "IEEE Micro Electro Mechanical Systems 14th International Conference," 2001, pp. 547–552.

192. C. Hagleitner, A. Hierlemann, D. Lange, A. Kummer, N. Kerness, O. Brand, and H. Baltes, *Nature (London)* 414, 293 (2001).
193. A. Hierlemann, D. Lange, C. Hagleitner, N. Kerness, A. Koll, O. Brand, and H. Baltes, *Sens. Actuators, B* 70, 2 (2000).
194. A. Roncaglia, L. Colalongo, D. Lange, and M. Rudan, *Sens. Actuators, B* 69, 320 (2000).
195. C. Hagleitner, A. Hierlemann, D. Lange, A. Kummer, N. Kerness, O. Brand, and H. Baltes, *Nature (London)* 414, 293 (2001).
196. D. Then, Miniaturisierte massensensitive Sensoren und deren Anwendung in der Gas- und Flüssigkeitsanalytik, Dissertation 2002.
197. J. Piehler, A. Brecht, K. E. Geckeler, and G. Gauglitz, *Bios. Bioelectron.* 11, 579 (1996).
198. M. Mrksich and G. Whitesides, *Biosens. Bioelectron.* 14, 247 (1996).
199. B. Ratner, *Biosens. Bioelectron.* 10, 797 (1995).
200. N. Alcantar, E. Aydil, and J. Israelachvili, *J. Biomed. Mater. Res.* 51, 343 (2000).
201. R. Raiteri, M. Gratturolo, H.-J. Butt, and P. Skládal, *Sens. Actuators, B* 79, 115 (2001).
202. V. T. Moy, E.-L. Florin, and H. E. Gaub, *Science (Washington, DC)* 266, 257 (1994).
203. R. Krapf, Dissertation, Universität Tübingen, 2001.
204. K. Feldman, G. Hähner, N. D. Spencer, P. Harder, and M. Grunze, *J. Am. Chem. Soc.* 121, 10134 (1999).
205. K. L. Prime and G. M. Whitesides, *J. Am. Chem. Soc.* 115, 10714 (1993).
206. M. C. Pretty, Langmuir-Blodgett Films. Cambridge University Press, Cambridge, UK, 1996.
207. B. C. Fagan, C. A. Tipple, Z. Xue, M. J. Sepaniak, and P. G. Datskos, *Talanta* 53, 599 (2000).
208. C. J. Brinker and G. W. Scherer, Sol-Gel Science: The Physics and Chemistry of Sol-Gel Processing. Academic Press, San Diego, 1990.
209. R. Raiteri and H.-J. Butt, *J. Phys. Chem.* 99, 15728 (1995).
210. S. J. O'Shea, M. E. Welland, T. A. Brunt, A. R. Ramadan, and T. Rayment, *J. Vac. Sci. Technol., B* 14, 1383 (1996).
211. M. Lahav, C. Durkan, R. Gabai, E. Katz, I. Willner, and M. E. Welland, *Angew. Chem.* 113, 4219 (2001).
212. H.-J. Butt, *J. Colloid Interface Sci.* 180, 251 (1996).
213. J. Fritz, M. K. Baller, H. P. Lang, T. Strunz, E. Meyer, H.-J. Güntherodt, E. Delamarche, C. Gerber, and J. K. Gimzewski, *Langmuir* 16, 9694 (2000).
214. H.-F. Ji, K. M. Hansen, Z. Hu, and T. Thundat, *Sens. Actuators, B* 72, 233 (2001).
215. X. Xu, T. G. Thundat, G. M. Brown, and H.-F. Ji, *Anal. Chem.* 74, 3611 (2002).
216. H.-F. Ji, E. Finot, R. Dabestani, T. Thundat, G. M. Brown, and P. F. Britt, *Chem. Commun.* 457 (2000).
217. H.-F. Ji and T. Thundat, *Biosens. Bioelectron.* 17, 337 (2002).
218. S. Cherian and T. Thundat, *Appl. Phys. Lett.* 80, 2219 (2002).
219. C. A. Tipple, N. V. Lavrik, M. Culha, J. Headrick, P. Datskos, and M. J. Sepaniak, *Anal. Chem.* 74, 3118 (2002).
220. D. R. Baselt, G. U. Lee, and R. J. Colton, *J. Vac. Sci. Technol., B* 14, 789 (1996).
221. D. R. Baselt, G. U. Lee, K. M. Hansen, L. A. Chrisey, and R. J. Colton, *Proc. IEEE* 85, 672 (1997).
222. D. R. Baselt, G. U. Lee, M. Natesan, S. W. Metzger, P. E. Sheenhan, and R. J. Colton, *Biosens. Bioelectron.* 13, 731 (1998).
223. M. D. Antonik, N. P. D'Costa, and J. H. Hoh, *IEEE Eng. Med. Biol.* 16, 66 (1997).
224. J. Fritz, M. K. Baller, H. P. Lang, T. Strunz, E. Meyer, H.-J. Güntherodt, E. Delamarche, C. Gerber, and J. K. Gimzewski, *Langmuir* 16, 9694 (2000).
225. A. M. Moulin, S. J. O'Shea, and M. E. Welland, *Ultramicroscopy* 82, 23 (2000).
226. A. M. Moulin, S. J. O'Shea, R. A. Badley, P. Doyle, and M. E. Welland, *Langmuir* 15, 8776 (1999).
227. J. Thaysen, R. Marie, and A. Boisen, "International Conference of Microelectromechanical Systems," 2001, pp. 401-404.
228. R. Marie, H. Jensenius, J. Thaysen, C. B. Christensen, and A. Boisen, *Ultramicroscopy* 91, 29 (2002).
229. G. Wu, R. H. Datar, K. M. Hansen, T. Thundat, R. J. Cote, and A. Majumdar, *Nat. Biotechnol.* 19, 856 (2001).
230. R. Raiteri, G. Nelles, H.-J. Butt, W. Knoll, and P. Skládal, *Sens. Actuators, B* 61, 213 (1999).
231. J. Fritz, M. K. Baller, H. P. Lang, H. Rothuizen, P. Vettiger, E. Meyer, H.-J. Güntherodt, C. Gerber, and J. K. Gimzewski, *Science (Washington, DC)* 288, 316 (2000).
232. K. M. Hansen, H.-F. Ji, G. Wu, R. Datar, R. Cote, A. Majumdar, and T. Thundat, *Anal. Chem.* 73, 1567 (2001).
233. S. Weigert, M. Dreier, and M. Hegner, *Appl. Phys. Lett.* 69, 2834 (1996).
234. B. Ilic, D. Czaplowski, H. G. Craighead, P. Neuzil, C. Campagnolo, and C. Batt, *Appl. Phys. Lett.* 77, 450 (2000).
235. S. Prescesky, M. Parameswaran, A. Rawicz, R. F. B. Turner, and U. Reichl, *Can. J. Phys.* 70, 1178 (1992).
236. M. Lutwyche, C. Andreoli, G. Binnig, J. Brugger, U. Drechsler, W. Haberle, H. Rohrer, H. Rothuizen, P. Vettiger, G. Yaralioglu, and C. Quate, *Sens. Actuators, A* 73, 89 (1999).
237. G. Binnig, M. Despont, U. Drechsler, W. Haberle, M. Lutwyche, P. Vettiger, H. J. Mamin, B. W. Chui, and T. W. Kenny, *Appl. Phys. Lett.* 74, 1329 (1999).
238. J. P. Roger, A. C. Boccara, M.-C. Potier, M. Guirardel, and C. Bergaud, *Proc. SPIE* 4434, 138 (2001).
239. G. Abadal, Z. J. Davis, B. Helbo, X. Borriose, R. Ruiz, A. Boisen, F. Campabadal, J. Esteve, E. Figueras, F. Perez-Murano, and N. Barniol, *Nanotechnology* 12, 1 (2001).
240. Z. J. Davis, G. Abadal, O. Kuhn, O. Hansen, F. Grey, and A. Boisen, *J. Vac. Sci. Technol., B* 17, 612 (2000).

Carbon Nanomaterials

Maheshwar Sharon

Indian Institute of Technology, Mumbai, India

CONTENTS

1. Introduction
 2. Classification of Carbon
 3. Diamond-Type Carbon with Pure sp^3 Configured Carbon Atoms
 4. Graphite-Type Carbon with Pure sp^2 Carbon Configured Atoms
 5. Intermediate Forms of Carbon Containing Mixture of sp^2 and sp^3 Configured Carbon Atoms
 6. Need for Precursors not Derived from Fossil Fuels
 7. Summary
- Glossary
References

1. INTRODUCTION

The element carbon occupies a special place in nature. The whole living world is built of carbon, which makes a huge number of (organic) compounds. This is possible because of the electronic structure of the carbon atom, resulting in different chemical bonds. Though carbon belongs to the same group as silicon, thanks to the carbon bonding degeneracy, unlike silicon, carbon can exist in various allotropic forms, starting from sp^2 bonded graphite, across a whole variety of carbon materials including glassy carbon, amorphous sp^2 bonded carbon, polymeric materials, fullerenes, nanotubes, amorphous diamond-like carbon with majority of sp^3 bonded atoms, to diamond with strong sp^3 tetrahedral bonds.

Carbon has been accepted by the power source industry because of its unique properties of good electronic conductivity, good intercalation capability, chemical inertness, low cost, wide availability, ease of fabrication, and availability in many different forms. One of the earliest uses of carbon in a commercial battery was in 1841, when Robert Bunsen proposed replacing the expensive platinum current collector of a Grove cell with a more cost-effective carbon one.

Nowadays the unique properties of carbon make it a preferred constituent of virtually all power source technologies. Better performance of carbon in lithium battery is achieved using Chevron acetylene black, which has a surface area of $40 \text{ m}^2 \text{ g}^{-1}$, instead of graphite ($5 \text{ m}^2 \text{ g}^{-1}$). High-surface-area carbons, such as Ketjenblack ($1000 \text{ m}^2 \text{ g}^{-1}$) or Black pearl 2000 ($2000 \text{ m}^2 \text{ g}^{-1}$), could further improve its performance. Various forms of carbon have been considered as hydrogen storage media, such as carbon nanotubes or carbon nanofibers [1]. If the high storage capacity of nanofibers can be realized in a practical system, it could revolutionize hydrogen storage for fuel cell application. Carbon in supercapacitors is also being developed as a rechargeable power source for electric vehicles and consumer electronics. Carbon is one of the most common electrode materials, either in powdered form or as woven cloths with surface areas in the range of 1000 to $2000 \text{ m}^2 \text{ g}^{-1}$ and pore size from $<2 \text{ nm}$ to $>5 \text{ nm}$. Intense research is being conducted worldwide into development of carbon nanomaterials for lithium battery technology, hydrogen storage, and fuel cells.

Carbon has also been gaining importance for its ability to induce different properties and to form composite materials. The term composite materials is often taken to mean continuous fiber-reinforced polymer-matrix composites. This family includes glass fiber-reinforced polyester resins, used for boats and large tanks, and carbon fiber-reinforced epoxy resins, used on many aircraft. They offer a very good combination of high stiffness and low density. Another form of commercial carbon is "whiskers," which are fibrous single crystal and which have been produced commercially since 1962. Relatively inexpensive silicon carbide whiskers can be formed by the pyrolysis of rice husk. The husk of rice is rich in silica. During pyrolysis the cellulose dehydrates to carbon; this reduces the silica to silica monoxide. Silicon carbide whiskers are apparently formed by the interaction of silicon monoxide vapor with carbon [2].

Prior to 1985, it was known that two allotropic forms of carbon exist: diamond and graphite. However, after the discovery of the fullerene family by Kroto et al. [3], and their microscopic preparation by Kratchmer et al. [4], it has become well known that carbon has three allotropic forms, namely diamond, graphite, and the fullerene family. But is it really so? In addition to these forms, we have many other

forms of carbon such as active carbon, black carbon, carbon beads, nanobeads, nanotubes, fibers, etc. Which class of carbon should these materials therefore be considered as? For example, has the classification of carbon as diamond and graphite led us to think of the existence of the fullerene family? Certainly not. Moreover, does the classical classification give us any impetus to think of the possibility of developing any new forms of carbon? The answer is No.

Thus, there is a need to evolve a new classification of carbon which on one hand, can give us an insight for developing new forms of carbon, and on the other, should be able to classify all the existing forms of carbon. For this purpose, perhaps it would be advisable to examine some of the properties of carbon, which are distinctly different from other forms of carbon. We shall discuss this aspect here in more detail.

However, it would be a difficult task to cover all aspects of carbon in this small review, since each aspect of carbon can form a book in itself. Hence, in this review, an inquiry is made into the suitability of the conventional classification of various allotropes of carbon and whether classification gives an insight into developing newer forms of carbon. This is followed by a brief description of conventional types of synthesis, properties, and applications of carbon, which have been discovered lately. In order to keep the list of references to a minimum number, references appearing within a given paper are, as far as possible, not included in the list of references.

2. CLASSIFICATION OF CARBON

Conventionally carbon has been classified in two forms: diamond and graphite. Has this type of classification given us any help in searching for newer allotropes of carbon? After the discovery of the fullerenes family, a third allotrope of carbon, “fullerenes,” was adopted. Hence there is a need to reconsider the classification procedure for carbon to evolve a classification which can help to discover newer carbon materials. A classification of carbon based on the nature of carbon atoms present in the carbonaceous material perhaps may be more appropriate and may open a Pandora’s box for developing many new varieties of carbon than what we have been able to even think of. For example, diamond has atoms with 100% sp^3 type of carbon, while graphite has 100% sp^2 carbon atoms. The former is an insulator due to its very large bandgap (5.5 eV) while the latter is a conductor (bandgap being in vicinity of 0.25 eV or low). These two examples immediately give us a clue that there is a possibility of millions of permutations and combinations of sp^3 and sp^2 , giving an innumerable variety of carbon with varied bandgaps in the range of 0.25 to 5.5 eV. Diamond-like carbon (DLC) and glassy carbon are two examples of such combinations. Neither of them can be classified as diamond or graphite. Therefore, a classification of carbon on the basis of ratio of sp^3 and sp^2 carbon atoms present in the material may be more appropriate than the conventional classification. We can thus classify carbon again in three forms: (i) diamond (100% sp^3), (ii) intermediate carbon (with different ratios of sp^3/sp^2 carbon atoms), and (iii) graphite (100% sp^2). All forms of carbons will fall in one of these three categories. This classification also gives us an opportunity

to understand the reasons for carbon showing its novelty. Carbon nanobeads, carbon nanotubes, carbon fibers, active carbon, charcoal, and fullerenes all fall in the intermediate group of carbon because they contain different ratios of sp^3/sp^2 . Perhaps it may be a good idea to devote some time to discuss structural aspects, applications, and properties of carbon belonging to these three new groups of carbon.

3. DIAMOND-TYPE CARBON WITH PURE sp^3 CONFIGURED CARBON ATOMS

3.1. Structural Aspect

Material containing 100% sp^3 bonded carbon is classified as “diamond.” Carbon in the form of diamond belongs to the cubic system and is the hardest material known. It has the same space lattice as zinc blend (Fig. 1a) except that alternate tetrahedral sites and all octahedral sites are filled with carbon atoms instead of sulfur and zinc, respectively.

The essential point of this structure is that every carbon atom is surrounded by four other carbon atoms situated at the corners of a regular tetrahedron. Thus, all carbon in diamond has the sp^3 configuration. The distance between the centers of two adjoining atoms is 1.54 Å which, strangely, corresponds very closely to the distance between two carbon atoms attached to each other by a single covalent bond in aliphatic organic compounds. This agreement, together with the fact that each carbon atom in diamond has four others situated around it at the corners of a rectangular tetrahedron, suggests that every atom is joined to four others by covalent linkages. It will be noticed from Figure 1b that the carbon atoms form a series of hexagonal “puckered” rings similar to those in cyclohexane, where the carbon atoms

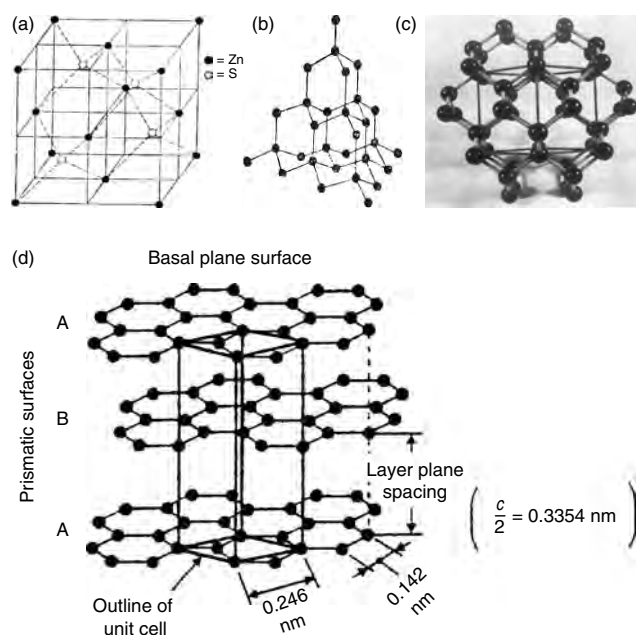


Figure 1. (a) Zinc sulfide (zinc blend) lattice and (b) space lattice of diamond forming hexagonal “puckered” ring like cyclohexane. (c) Carbon atom surrounded by four other carbon atoms forming channels in diamond structure.

are joined by single linkages. This figure, however, clearly shows the possibility of the existence of many interlocked hexagonal nanochannels, and the diameter of the channel would have a dimension similar to the hexagonal cyclohexane ring (Fig. 1c). Hence diamond can also exist in hexagonal form (lonsdaleite) with a wurtzite crystal structure where the C—C bond length is 1.52 Å. The crystal density of both types of diamond is 3.52 g cm^{-3} .

3.2. Synthesis of Diamond and Diamond Films

Until the 1950s, nature was the only source of diamond, because of the extreme conditions required for its formation. Since at room temperature and atmospheric pressure the trigonal bond is more stable, a very high temperature (greater than 2500 K) and high pressure (around 100,000 atm) are required to induce the formation of tetrahedral bond. In the 1950s, scientists simulated these conditions in the laboratory to produce synthetic diamond.

Two decades later, in the 1970s, scientists showed that diamond could be produced at lower temperature (1000 K) and subatmospheric pressure by thermal dissociation of hydrocarbon gases, for example, methane, ethane, acetylene, etc. This process involves dissociation of hydrocarbon, typically methane-hydrogen mixture, with the addition of small amount of oxygen. Techniques such as hot filament, flame (acetylene torch), or microwave excitation are used for the dissociation process. The growth process consists of a competition between the tetrahedral and trigonal bonds where the former are promoted and the latter suppressed by their etching generated by atomic hydrogen and oxygen or internal rearrangement of carbon atoms [5]. It was believed earlier that the substrate's temperature in excess of 1000 K was necessary to get a diamond film, but now it has been shown that diamond film can be grown at 700 K or less also. Sharon and co-workers [6] have been able to prepare diamond by chemical vapor deposition of soot of camphor (Fig. 2).

The standard free energy changes for the process $\text{C}_{\text{gas}} \rightarrow \text{graphite}$ and $\text{C}_{\text{gas}} \rightarrow \text{diamond}$ are -671.26 and $-668.36 \text{ kJ mol}^{-1}$ at 298 K, respectively. This comparison suggests that the thermodynamic driving forces for forming graphite and diamond from vapor phase are similar. Hence large numbers of chemical vapor deposition (CVD) diamond deposition techniques have been developed. The following are the essential requirements for deposition of diamond film by CVD process:

- (i) A carbon source gas that is rich in hydrogen but dilute (typically $\sim 1.0 \text{ vol}\%$) in the carbon-containing gas. The gas mixture may contain oxygen in form of CO.
- (ii) A process to activate the gas to produce free radicals, excited molecular species, or plasma.
- (iii) A temperature-controlled substrate (typically at 500–900 °C).

CVD processes can be classified as thermal methods (e.g., hot filament methods) and plasma methods (direct current, radio frequency, and microwave). Film deposition rates range from less than $0.1 \mu\text{m h}^{-1}$ to $\sim 1 \text{ mm h}^{-1}$ depending upon the method used, although over a small area,

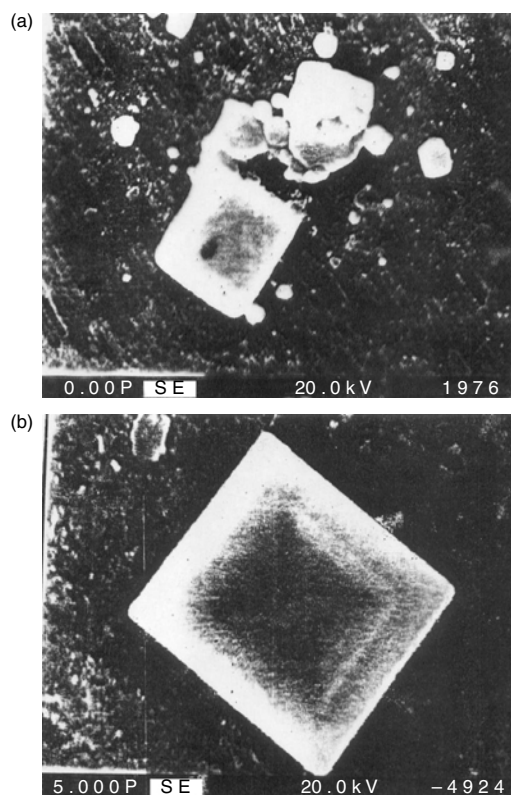


Figure 2. (a) Diamond thin film deposited over quartz glass from the soot of camphor. (b) Magnified SEM view of the diamond film. Reprinted with permission from [6], K. Mukhopadhyay et al., *Mater. Chem. Phys.* 49, 252 (1997). © 1997, Elsevier Science.

high deposition rates of 100 mm h^{-1} or more have been reported. Thinner films with good adhesion to substrates (e.g., silicon wafer) have been achieved, but in thicker films spalling or delamination occurs because of built-in-stress [7].

CVD diamond films can be deposited on a wide range of substrates (metals, semiconductors, insulators, single crystals and polycrystalline solids, glassy and amorphous solids). Most of the CVD diamond films reported to date have been grown on single-crystal Si wafers, mainly due to availability, low cost, and favorable properties of Si wafers. However, one could use any other substrate for deposition of diamond provided it meets the following requirements [8]:

1. Substrate must have melting point higher than the temperature required for diamond growth. This precludes the use of plastic, aluminum, and glasses, GaAs, etc.
2. Thermal expansion of substrate material must be comparable to that of diamond. Otherwise, diamond film will experience compressive stresses from the shrinking substrate, leading to bowing of the sample and/or cracking, flaking, or even delamination of the entire film.
3. In order to form adherent films, it is a requirement that substrate material be capable of forming a carbide layer to a certain extent. The carbide layer can be pictured as the “glue” which promotes the growth of diamond and aids the adhesion. Therefore, material which does not have many tendencies to form carbide (e.g., Cu, Sn, Pb, Ag, Au, and Ge, sapphire, alumina) forms only few

layers of carbide. This layer of carbide helps the growth of the subsequent layer of diamond as well as helps to form a strong adhesion with the substrate. But those materials which have greater ability to form carbide (e.g., Pt, Pd, Rh, Ni, Ti, and Fe) promote the growth of a thicker layer of carbide over the substrate. These materials, in addition to helping the growth of diamond, also modify the property of deposited diamond. There are some materials which form carbide easily (e.g., metals like Ti, Zr, Hf, V, Nb, Ta, Cr, Mo, W, Co, Ni, Fe, Y, Al, etc., and nonmetals like B), and when these materials are used as substrate, most of the layers of the diamond are in form of carbide; thus the property of diamond is completely changed.

It is believed that mechanical polishing with diamond grit ranging from 10 nm to 10 μm aids nucleation by creating appropriately shaped scratches in the surface, which act as growth templates, or by embedding nanometer-sized fragments of diamond into the surface, which then act as seed crystals, or a combination of both [9].

Diamond thin films have been grown from a diluted mixture of a hydrocarbon gas (e.g., methane) in hydrogen. For example, a gas mixture consisting of methanol and hydrogen introduced at pressure of 10 Torr gives a deposition of diamond on the substrate maintained at 800 °C. Atomic hydrogen prevents the surface reconstruction from a saturated sp^3 diamond to sp^2 graphite microstructure. Hydrogen also helps in abstracting hydrogen from hydrocarbon surface sites and gas-phase hydrocarbon species to form reactive radicals. Sharon and Chatterjee [10] have been able to get diamond film by pyrolysis of turpentine oil with iron catalyst at 650 °C under argon gas (Fig. 3).

The purity and the property of the film are strongly controlled by the graphitic carbon content in diamond film. Doping by phosphorus gives n-type diamond. This was achieved by carrying vapor of phosphorus/methanol mixture into the reactor from a solution of P_2O_5 in methanol [11]. Microwave plasma-assisted CVD from a mixture of H_2S in 1% CH_4/H_2 on a Si substrate [12] has also given n-type diamond. Diamond has also been doped with nitrogen by allowing vapor of urea into the reactive chamber where n-type diamond is being formed [13]. For this purpose a saturated solution of urea and methanol in acetone is vaporized and

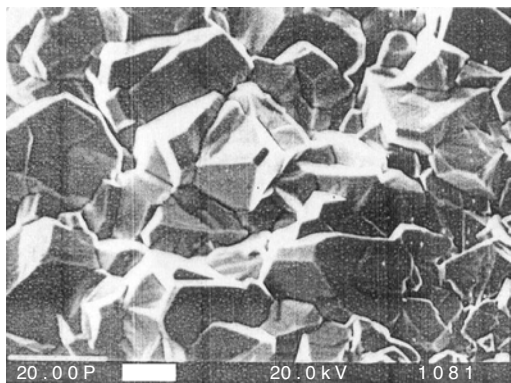


Figure 3. SEM micrograph of diamond film obtained at 650 °C from pyrolysis of turpentine oil in presence of ferrocene catalysts.

carried into the hot-filament chemical vapor deposition unit along with acetone and hydrogen. Nitrogen could be doped to $\sim 3.5 \times 10^{20}$ N atoms per cubic centimeter into the diamond. Such a high concentration of N is usually difficult to incorporate in diamond when using nitrogen or ammonia as the dopants. Boron doping of diamond has been achieved by dissolving B_2O_3 in methanol [14]. This process gives volatile trimethylborate $(\text{CH}_3\text{O})_3\text{B}$. Ferreira et al. [15] prepared boron doped diamond by hot-filament technique. CH_4 flow (0.5 s cm^{-3}) was maintained along with flow of hydrogen through a solution of B_2O_3 in methanol. Boron could be carried by hydrogen from this mixture. Furnace temperature was maintained at 800 °C.

3.3. Properties of Diamond Thin Films

Although the standard enthalpies of diamond and graphite only differ by 2.9 kJ mol^{-1} , a large activation barrier separates the two phases, preventing interconversion between them at room temperature and pressure. Ironically, this large energy barrier, which makes diamond so rare, is also responsible for its existence, since diamond, once formed, cannot spontaneously be converted to the more stable graphite phase. Thus diamond is said to be metastable, that is, kinetically stable but thermodynamically unstable.

Diamond possesses several technologically important properties, including extreme hardness, high electrical resistance, chemical inertness, high thermal conductivity, high electron and hole mobility, and optical transparency (Table 1).

As per the solid-state concept of vacuum scale, electrons present in or above the vacuum scale are expected to be free electrons. Since the conduction band of diamond lies above the vacuum scale, this means that if electrons of diamond are excited from valence band to conduction band, they will behave like free electrons. This condition is different from a state of any other material whose conduction band lies below the vacuum scale. With such material, although electrons excited from its valence band to conduction band are free, they still belong to the same material, whereas with diamond, they become nonbound free electrons. This also suggests that if diamond were heavily doped such that its Fermi level shifted to about 0.1 eV below the conduction band, diamond would become a free electron emitter. Unfortunately, it has not been possible to dope diamond with donor atoms to this extent so far.

It is interesting to observe that naturally occurring diamond, though in pure form (intrinsic diamond), is p-type. The reasons for intrinsic diamond being the p-form are not very well understood, though many explanations have been given. The author of this chapter would like to propose the following arguments to explain this behavior. Conversion of material into either n- or p-type depends upon the nature of dopant added into the materials. If dopant has a greater number of electrons than the host atom, the material becomes n-type, and if the dopant has a smaller number of valence electrons than the host, the material becomes p-type. This behavior is quite reasonably understood. Why diamond in pure form should exist in p-form is not very well understood. Perhaps, this strange behavior of diamond can be explained by considering the electronic configuration of carbon atoms bonded into the structure.

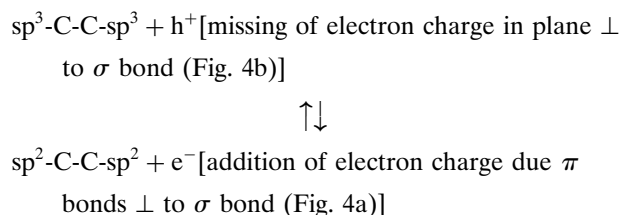
Table 1. Some outstanding properties of diamond.

Property	Value
Atomic mass	12.01
Crystalline structure	fcc
Symmetry	Fd3m
Chemical bond	covalent sp^3
Lattice parameter	3.56
Density	3.51 g cm^{-3}
Melting temperature	$4000 \text{ }^\circ\text{C}$
Highest bulk modulus	$1.2 \times 10^{12} \text{ N m}^{-2}$
Hardness	6000–10000 kg mm^{-2}
Linear expansion coefficient at 300 K	$1.18 \times 10^{-6} \text{ deg}^{-1}$
Lowest compressibility	$18.3 \times 10^{-13} \text{ m}^2 \text{ N}^{-1}$
Highest room temperature thermal conductivity	$2.0 \times 10^3 \text{ W m}^{-1} \text{ K}^{-1}$
Thermal expansion coefficient at room temperature	$1.0 \times 10^{-6} \text{ K}$
Highest sound propagation velocity	17.5 km s^{-1}
Room temperature resistivity (undoped)	$8.3 \times 10^{-13} \text{ m}^2 \text{ N}^{-1}$
Bandgap	1.5 eV (indirect)
Breakdown voltage	$10 \times 10^7 \text{ V cm}^{-1}$
Biological compatibility	yes
Mobility (electron) at 300 K [27]	$1000\text{--}2200 \text{ cm}^2 \text{ V}^{-1} \text{ s}^{-1}$
Mobility (hole) at 300 K	$1400\text{--}1600 \text{ cm}^2 \text{ V}^{-1} \text{ s}^{-1}$
Raman shift	1332 cm^{-1}
Work function	4.7 eV (close to graphite)
Dangling bond	$\sim 1.4 \text{ eV}$ above valence band
Boron doping	acceptor level at 0.38 eV above E_v
Phosphorus doping [28]	donor level 0.46 eV below E_c
Nitrogen doping	creates two levels, one at 1.7 eV below E_c and the other one doubly occupied just above E_v due to quasi-N lone pair
Electron affinity of the bare surface of diamond [29]	+0.37 eV
EA for hydrogenated C (111):H surface [30]	–1.27 eV. Thus E_v lies between 5.9 eV and 4.2 eV below vacuum level

The combination of one s orbital with two p orbitals leads to the formation of three sp^2 hybridized orbitals. Each of these orbitals has one large and one small lobe. All these hybridized orbitals lie in the same plane (the plane containing the two p orbitals from which they were formed) and point toward the corners of an equilateral triangle. Each sp^2 hybridized carbon atom has one electron in a p valence orbital that is perpendicular to the plane of the σ bonds. These p orbitals can overlap to form π bonds. This type of bond places electron density above and below the line joining the bonded atoms (i.e., above or below the plane in which σ bond lies). In contrast to this, the mixing of the s and all three p orbitals yields four sp^3 hybridized orbitals. Again, each of these orbitals has a large and a small lobe. The large lobes point at the corners of the tetrahedron. Unlike sp^2 hybridized carbon atoms, due to absence of π bonds, the charge density in sp^3 carbon atoms can be

assumed to be zero; that is, the plane perpendicular to the plane containing σ bonds will have no charge (Fig. 4).

Therefore, in contrast to diamond, graphite should have some charge density in space, perpendicular to the σ bonds of diamond. In other words, removal of this charge from π bond by addition of hole should lead to a structure of diamond. If we assume the existence of some kind of equilibrium between the graphite and diamond (based on the charge density), then the following equilibrium between sp^2 and sp^3 carbon atom can be conceived:



If this concept is accepted, then diamond should intrinsically exist as p-type material and graphite should exist as n-type material. This is what is normally observed with these materials. The conversion of graphite to diamond can therefore be viewed as substitution of sp^3 configured into sp^2 configured carbon atoms. This explanation also suggests that while pure diamond and pure graphite should exhibit p- and n-type character, respectively, materials containing carbon-bonded atoms of some suitable ratio of sp^3 and sp^2 should exhibit a true intrinsic character. Sharon et al. [16] observed that pyrolyzing camphor under inert atmosphere and sintering it under inert atmosphere for different time, changes the ratio of sp^2/sp^3 carbon. They also observed that if this ratio is 33%, the resulting carbon behaves like true intrinsic material. If this ratio is greater than 33%, pyrolyzed carbon shows n-type character, and if it is less than this value, pyrolyzed carbon shows p-type character. This change in behavior is observed only due to change in the ratio of sp^2 and sp^3 and not due to any external doping (Fig. 5).

This result has suggested that in carbonaceous materials, the meaning of n- and p-type needs to be addressed differently and should not perhaps be treated as we normally do with inorganic materials. Thus, naturally occurring p-type diamond need not be due to presence of dopant. It may be due to presence of larger concentration of sp^3 carbon atom. In other words, p-character is due to the absence of electron in π bond. Perhaps this may be the reason why it is difficult to either make or naturally obtain n-type diamond.

However, substitution with impurity atoms like nitrogen of some of the carbon atoms during the diamond film growth makes the film n-type. Nitrogen atoms in the diamond make bonds to both carbon and hydrogen. Therefore, the total bonding configuration changes by nitrogen addition. It forms a distorted substitutional site with one long bond forming a

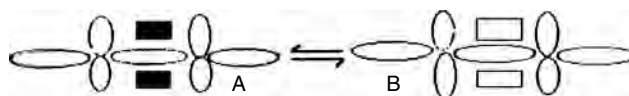


Figure 4. (a) sp^2 carbon with π bond (shown in black square) exchanges with (b) sp^3 carbon, creating empty π bond (shown in empty square).

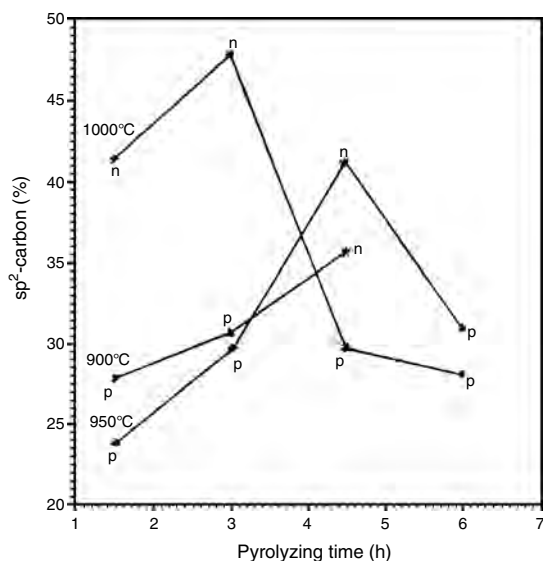


Figure 5. Variation in the sp^2 carbon content in the camphor pyrolyzed carbon films as a function of pyrolyzing time. Reprinted with permission from [16], M. Sharon et al., *Mater. Chem. Phys.* 56, 284 (1998). © 1998, Elsevier Science.

deep singly occupied donor level, 1.7 eV below the conduction band E_c , and also a doubly occupied state just above E_v due to quasi-N lone pair of this C—N bond [17]. The decrease of hydrogen bonded to carbon atoms can cause the increase of sp^2 bonding fraction, hence the decrease of the optical bandgap [18]. Doping diamond [19] with boron produces a shallow substitutional acceptor with a level at 0.38 eV above E_v . Phosphorus also acts like a substitutional donor, with a level about 0.46 eV below E_c . Replacement of one CH group by one phosphorus atom causes diamond to become n-type.

Typical Raman spectra for high-quality diamond and boron-doped diamond thin films feature one intense band at 1332 cm^{-1} with a line width of 5 to 8 cm^{-1} . The significantly broadened and shifted diamond line for the noncrystalline films results from decreasing grain size to the nanometer scale. To a first approximation, the linewidth is a measure of the phonon lifetime. The more defects (e.g., grain boundaries) and impurities (e.g., nitrogen) there are, the shorter the phonon lifetime and the broader the linewidth. Weak scattering intensity in the region of 1520 cm^{-1} is observed due to nondiamond sp^2 bonded carbon peak resulting from the π -bonded carbon atoms in the grain boundaries [20, 21] impurities in the film. Graphite, however, gives rise to a broader peak at 1580 cm^{-1} . The ratio of the intensities of these two peaks indicates how much of each phase is present. It is also dependent on the wavelength of excitation (normally excitation is done with 532 nm).

It can be seen that the ratio of the diamond to the non-diamond band intensities, I_{1339}/I_{1560} , is largest for the film deposited without any added N_2 and decreases for the film deposited with the gas. However, the ratio is independent of the N_2 level [22]. Raman spectra of boron-doped diamond films were studied by Ferreira et al. [15]. It is interesting to note that the intensity of the peak at 1332 cm^{-1} decreased as the concentration of boron was increased. Moreover, a new

peak started to appear at around 1200 cm^{-1} , whose intensity also increased with increase in doping concentration. This suggests that one may be able to establish a relationship between boron concentration and the intensity of either the 1332 cm^{-1} or the 1200 cm^{-1} peak.

Some of the CVD grown diamond film exhibits photoconductive signal if it contains absorption bands between 1.3 eV and 1.5 eV. This photoconductive response in the visible region can impair the performance of diamond detectors made for ultraviolet application [23]. Photoconductivity studies, therefore, are a useful technique to characterize diamond. It is interesting to note that Hall mobility in boron doped diamond decreases as the concentration of dopant is increased [24]. While at hole concentration of $5 \times 10^{14}\text{ cm}^{-3}$, Hall mobility is in the vicinity of $1500\text{ cm}^2/\text{Vs}$, for $5 \times 10^{15}\text{ cm}^{-3}$ hole concentration it falls down to $250\text{ cm}^2/\text{Vs}$.

Three low-index morphologies are usually obtained during growth of diamond film: (100), (110), and (111), the latter being the most abundant. It is observed that while the morphology of the (111) and (110) surface is rough, (100) crystallites grow as platelets or tiles with partial overlap between neighboring ones. Most electrochemical studies are carried out with surfaces preponderant with (111) crystallites [25]. Robertson and co-workers [26] have suggested that chemical termination of (111) diamond surfaces shifts the electron affinity from +0.35 eV for clean surface to -1.3 eV for H terminated ones and about +2 eV for oxygen terminated ones. The shift occurs because the terminating groups are slightly polar and introduce a surface dipole layer. In the case of C—H groups, the H atoms are positive and the dipole reduces the electron affinity, while oxygen has a negative charge and the C—O bond dipole makes the affinity more positive. As these effects are localized on the chemical bond, similar affinity changes may be expected on $ta\text{-C}$ surfaces.

In Table 1, various properties of diamond are enumerated.

3.4. Electrochemical Properties of Diamond Film

In electrochemical work, there is a need to use an electrode which is inert and does not need larger additional potential (known as overpotential) than the equilibrium potential for carrying out electrochemical reactions. Moreover, one also needs a large potential difference between oxidation and reduction potential of water so that the electrode can be used safely for electrochemical reaction within the so-called window of the potential (i.e., within the range of potential in which water does not get electrolyzed) in aqueous solution. For this purpose, platinum or mercury has been used by electrochemists. Conducting diamond, being inert to alkali and acid, has been used as an electrode. Since doping of diamond has been possible, lately, boron-doped diamond films are getting more popularity in electrochemical studies than carbon electrodes (glassy carbon). Diamond thin-film electrode shows a very small background current and low double-layer capacitance. With 0.1M KCl solution between -1000 to $+1000\text{ mV}$, current is observed in the range of $50\text{ mA}/\text{cm}^2$ and is highly stable. Sometimes a small oxidation peak is observed on the forward sweep at $\sim 1200\text{ mV}$ just prior to the onset of chlorine evolution [31]. Boron-doped

diamond thin film shows a wide working potential window for solvent-electrolyte electrolysis in aqueous media. This means that diamond has large overpotentials for both hydrogen evolution and oxygen evolution. In 0.1M KCl as well as in 0.5M H₂SO₄, the working potential window is 3.5 V (i.e., from -1.25 to 2.3 V vs standard hydrogen electrode) as compared to 2.5 V for glassy carbon. These ranges greatly exceed the theoretical range of stability of water under ambient conditions (1.23 V). Diamond film is reported to show an increase in background current by less than 5% even after constant use for 15 hr, whereas in glassy carbon it increases to a value greater than 30.0%. Another application of diamond film is anodic stripping voltammetry of heavy-metal ions in aqueous media. It has been possible to electrodeposit Pt, Hg, and Pb on boron-doped diamond thin films [32]. Ferro et al. [33] have observed chlorine evolution at highly boron-doped diamond electrodes. They reported the chlorine evolution below 1 V versus SCE with NaCl solution. Since this electrode is stable in perchlorate solution, one can think of making a fuel cell operating with chlorine/hydrogen gas.

3.4.1. Electron Field Emission Effect

The field emission display (FED) is a new type of flat panel display which overcomes many limitations of liquid crystal display, because of its superior brightness, viewing angle, color rendition, response time, and operating temperature range. The activity in field emission display, sometimes called cold emission devices, is concentrated now mainly in vacuum microelectronic devices based on broad area multiple arrays, for example, flat panel displays, microwave devices, vacuum electron sources for electron guns for electron microscopes [34], etc.

For a perfectly flat metal surface with a typical work function of 5 eV, the electric field necessary to get measurable emission current is in the range of 2.5 V nm⁻¹, or in more appropriate units, 2500 V μm⁻¹. To generate such high electric fields, one has to use the effect of field enhancement at tip-like structures. For such purpose, silicon or metal micro-tips are generally used. Nevertheless, these materials suffer emission degradation due to sputter erosion and chemical contamination and therefore require a high vacuum environment for operation. On the other hand, carbon and especially diamond is found to emit at a very low electric field. The chemical inertness of carbon field emitters especially is one of the most important advantages over silicon or metal micro-tips.

Field emission from semiconductors in general can originate from the valence band or the conduction band, from an accumulation layer at the surface [35]. The great interest in electron emission from diamond was kindled by the work of Himpfel et al. [36], who reported high quantum yield for photon-electron emission from the (111) hydrogen terminated surface of diamond. Later it was determined [37] that the (111) hydrogen terminated diamond surface exhibits a negative electron affinity. The electron affinity of a semiconductor describes the energy barrier between the vacuum level outside the surface and the conduction band minimum inside the sample. Given this definition, the electron affinity of these prepared surfaces of diamond would exhibit a negative value, because the energy of electrons at the conduction

band minimum for diamond would be above the vacuum level, and this condition is termed negative electron affinity. The presence of a negative electron affinity means that electrons in the conduction band can be freely emitted into vacuum.

Field emission from high-quality diamond is actually quite difficult, largely because of its high resistivity. Field emission from polycrystalline diamond is easier and is found to vary inversely with the grain size. Development of conducting diamond thin films thus has led to new areas of cold electron emission from diamond. Recent results from diamond cold cathode demonstrate high emission current, good current stability, uniform emission, from an array of emitters, and emissivity even under poor vacuum conditions. Two approaches using ungated field emission cathodes with diamond coating have been proposed: (i) flat-film display, where patterned diamond film is used as addressable cathodes (lines) [38], and (ii) arrays of silicon tips with diamond coating, where addressing occurs by switching of p-n junctions formed in the Si substrate [39]. The turn-on fields of diamond films have been in the range of 1–30 V mm⁻¹; that is, the electric field needed to inject electrons from diamond film is in the range of 1–30 V mm⁻¹. A schematic of a test circuit of the field emission [40] is shown in Figure 6.

Sometimes, a series resistance of 5 MΩ is also connected to the sample to protect the equipment. The emitting area could be of the size 15 mm × 5 mm separated by a distance in the order of a few hundred micrometers. The system is kept in vacuum (~10⁻⁷ torr or sometimes even lower than this). When potential is applied across anode and cathode, current will appear after certain threshold voltage is applied. To show the nature of CV characteristics, a typical current density (A cm⁻²) versus applied electric field obtained with kerosene-pyrolyzed carbon film deposited over alumina plate at 1000 °C is shown in Figure 7 [40].

It will be noticed that there is a threshold voltage of 2.20 V μm⁻¹ before which no emission occurs. It is also necessary to confirm that this emission is not due to electric discharge of gas present in the system. In order to confirm, normally polarity of electrode is altered and current density (μA cm⁻²) versus applied electric field (V μm⁻¹) is measured. If current characteristic as shown in Figure 7 were not obtained, this would suggest the absence of any current due

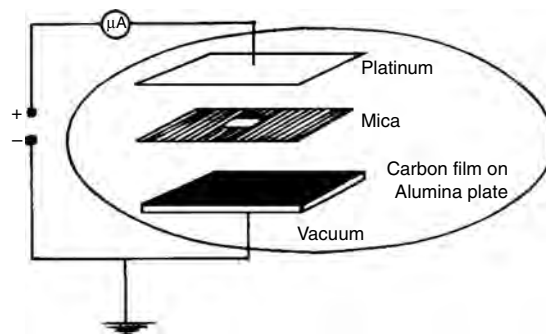


Figure 6. Schematic diagram of the field emission device. Reprinted with permission from [40], M. Kumar et al., *Diamond Related Mater.* 10, 883 (2001). © 2001, Elsevier Science.

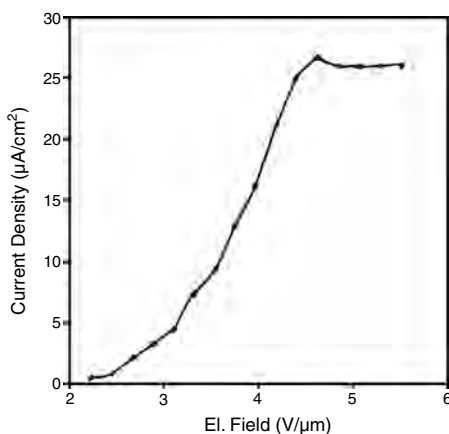


Figure 7. Current density ($\mu\text{A cm}^{-2}$) vs applied electric field ($\text{V } \mu\text{m}^{-1}$) obtained from kerosene-pyrolyzed thin film of carbon deposited over alumina plate utilizing configuration as shown in Figure 6. Reprinted with permission from [40], M. Kumar et al., *Diamond Related Mater.* 10, 883 (2001). © 2001, Elsevier Science.

to electric discharge process. It has been reported that some fluctuation of field emission occurs. It is believed that the fluctuation of field emission current is caused by migration of adsorbed gas molecules over the emitter surface, and ion bombardment to the emitter surface [41–43]. So the fluctuation can be increased as the impinging rates of the gas molecules and ions are increased. In order to reduce this effect, high vacuum is necessary. However, before a reliable emitter structure can be developed, the electron transport properties of the material must be well understood, especially regarding limitations on the current density and energy spread of the transmitted beam. Furthermore, an understanding of the emission process is necessary to accurately interpret emission [44]. There is ambiguity in explaining the actual phenomena which are responsible for the electron emission from diamond or materials like diamond. A simplified mechanism is discussed here so that this process can be qualitatively understood.

A basic process for injection of electrons into diamond is the tunneling of electrons from the cathode substrate through a potential barrier at the interface (i.e., a forbidden energy region) into the conduction band of diamond film [45]. It is expected that the cathode or metal over which diamond is deposited forms a metal/Schottky type of contact. An energy barrier is formed at the interface of the metal/diamond contact. When a negative bias is applied to the metal electrode (cathode), electrons are injected into the diamond film from the metal. The number of injected electrons depends on the barrier height and thickness. Therefore, the electron emission characteristics are improved by forming a low barrier height and by enhancing the electric field at the barrier of the diamond. In the case of the ideal Schottky junction, choosing the metal work function can change the barrier height. In order to enhance the electric field at the metal/diamond contact, on the other hand, it is desirable to use diamond films doped with shallow donor impurities because of the formation of a space charge layer due to ionized impurities. Incidentally, Geis et al. [46] have

found that phosphorus doping improves the emission in diamond. The process of electron emission can be summarized as follows:

1. Tunneling from the substrate (e.g., metal or semiconductor) into the conduction band (CB) of diamond. This is designated as electron injection process into the CB.
2. Transportation of the electrons to the diamond surface.
3. Escape of the electrons from the diamond surface to a vacuum.

The electrode of the behind diamond film, such as Si, Mo, etc. (i.e., substrate), forms a Schottky barrier. The electrons are injected from the electrode to the conduction band of the behind diamond film through the Schottky barrier by applying the electric field (step 1). The electrons at the diamond surface, on the other hand, can easily be emitted to a vacuum even by applying low electric field, because the diamond surface has negative electron affinity (step 3). However, it is difficult to transport electrons from the behind diamond film to the surface (step 2) because there is no effective means for n-type doping in the case of diamond. The emission current density strongly depends on the electron-transportation mechanism in the diamond film.

In addition to these, there is a possibility that the following process may also work to facilitate the electron injection [47].

1. Tunneling from the valence band (VB) of the semiconductor substrate into the CB of diamond. This is designated as hole injection from the diamond into the semiconductor substrate.
2. Zener tunneling, which is transition across the energy gap from the VB to the CB of a semiconductor or insulator under the internal applied field. This process is negligible for a wide-bandgap material such as diamond, except for extremely high fields ($\sim 10^4 \text{ V } \mu\text{m}^{-1}$).
3. Transition to the CB from the local impurity or imperfection level. This is field ionization process.

Druz et al. [48] have reported that reversibility of emission current versus applied potential (I-E cycles) depends upon the magnitude of emission current. It is also interesting to study whether electron field emission can be sustained by diamond films for a long period. In this context, they also have studied the time stability of the emission current of the DLC films. They observed the I-E curves to be reproducible after many measuring cycles, or after many hours without field applied; emission current was found to be constant at different fixed fields during at least one hour [49]. Sugino et al. [45] reported that emission property of polycrystalline diamond film depends upon the work function of the metal (e.g., Cu/diamond, Al/diamond, and Si/diamond) used for making the back contact with diamond. The reduction in the threshold voltage for these metals as compared to silicon is believed due to formation of a low energy barrier to electrons at the metal/diamond contact. On the contrary, Robertson and co-workers [50] have suggested that threshold field, instead of depending on the work function of substrate, depends upon the extent of nitrogen doping.

The field at which emission begins is also found to depend on sp^3 content [45]. Sugino et al. [45] and Robertson and co-workers [50] have reported that variation in threshold energy depends upon the nitrogen content in the diamond film: as the concentration increases, the threshold field decreases to a minimum value at 0.4% N in the film, and thereafter it increases again with increase in nitrogen content in the film. It is concluded that the reduction in emission at higher N content suggests that bulk sp^2 bonding in diamond does not favor emission.

3.4.1.1. Fowler–Nordheim Theory Electron field emission for metal has been known for many years, and among the various theories put forward to explain this process, Fowler–Nordheim theory is used most for explaining the process in diamond or diamond-like carbon. It would be difficult to deal here in detail with this theory. However, Forbes [51] has given an extremely good review on the Fowler–Nordheim theory and its limitations. The theory of cold field emission of electrons from metal into vacuum is often called *Fowler–Nordheim (FN) theory*, after the first author to treat this effect as wave-mechanical tunneling through a triangular barrier. The standard physical assumptions of FN theory are that:

- (i) the metal has a free-electron band structure;
- (ii) electrons are in thermodynamic equilibrium and obey Fermi–Dirac statistics;
- (iii) the surface is smooth and flat;
- (iv) local work function is uniform across the emitting surface and is independent of external field;
- (v) there is a uniform electric field above the emitting surface.

Considering these assumptions, the magnitude of emission current (J) may be written as

$$J = Aa\phi^{-1}E^2 \exp\{-b\phi^{3/2}/E\} \equiv Aa\phi^{-1}E^2 \exp\{-b\phi^{3/2}/E\}$$

Or

$$\ln J/E^2 = \ln(Aa\phi^{-1}) - b\phi^{3/2}/E$$

where $a \equiv e^3/8\pi h = 1.541434 \times 10^{-6} \text{ A eV V}^{-2}$ (in SI unit), $b \equiv \{(4/3)(2m_e)^{1/2}\}/e\hbar = 6.830888 \times 10^9 \text{ eV}^{-3/2} \text{ V m}^{-1}$ (in SI Unit), ϕ = the local work function of the emitting surface, E = external electric field (taken as a positive quantity), and A = area of emission.

Thus a plot of $\ln J/E^2$ versus $1/E$ would give a linear plot with a slope equal to $b\phi^{3/2}$. Since value of constant “ b ” is known, local work function of the emitting surface (ϕ) can be calculated from this analysis.

It has been also observed that when current-voltage characteristics of the electron emission are plotted in the Fowler–Nordheim coordinates of $\log(1/E^2)$ versus $1/E$, broken lines are observed, and near the break, plots have a more or less extended “shelf” segment where emission current is only weakly dependent on voltage. This behavior of getting broken line is in contrast to expected continuous line.

4. GRAPHITE-TYPE CARBON WITH PURE sp^2 CARBON CONFIGURED ATOMS

4.1. Structure of Graphite

Graphitic carbon is carbonaceous material with a layered structure but with a number of structural defects. Its density is 2.36 g cm^{-3} . It consists of layers in which each carbon atom is linked to three other carbon atoms by strong interplanar, covalent bonds which are stronger than those in diamond, with a C—C bond length of 1.42 \AA (Fig. 8). However, a weak carbon-carbon bond exists between widely separated layers (interlayer distance of 3.354 \AA). These widely separated layers account for the ease with which the layers glide over each other and cause the familiar softness of graphite.

Graphite, thus, has a structure in which trigonal planar carbon atoms are present in horizontal planes and each plane is separated by a distance of 3.354 \AA . XRD of graphite is shown in Figure 9 [52]. For comparison, XRD of graphite, graphene sheet, hard-shell carbon, and multiwall carbon nanotubes are also shown. The most intense peak corresponds to (002).

From a crystallographic point of view, the term “graphite” is applicable only to carbon materials having a layered lattice structure with a perfect stacking order of graphene layers, either the more prevalent ABABAB... (hexagonal graphite) or the less common ABCABCABC... (rhombohedral graphite). Due to the small energy required for the transformation of an AB- into an ABC-stacking (and vice versa), perfectly stacked graphite crystals are practically not available. Therefore, the term “graphite” is commonly used regardless of the stacking order. In some carbons, the aggregates are large and relatively free of defects, for example, in highly oriented pyrolytic graphite (HOPG). For both forms of graphite, the in-plane C—C distance is 142 pm . This length is in between the bond length of $C_{sp^3}-C_{sp^3}$ (i.e., 153 pm) and $C_{sp^2}=C_{sp^2}$ (132 pm). There is a large difference between in-plane C—C distance, 142 pm , and the interlayer distance, 335.4 pm , in graphite (Fig. 8) that results from the different types of chemical bonding. Within planes

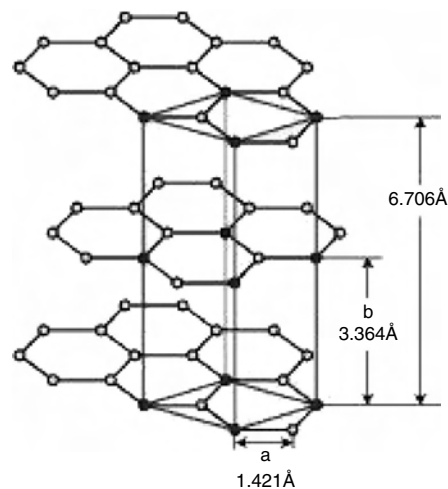


Figure 8. Schematic drawing of the crystal structure of hexagonal graphite showing AB-layer stacking sequence and unit cell.

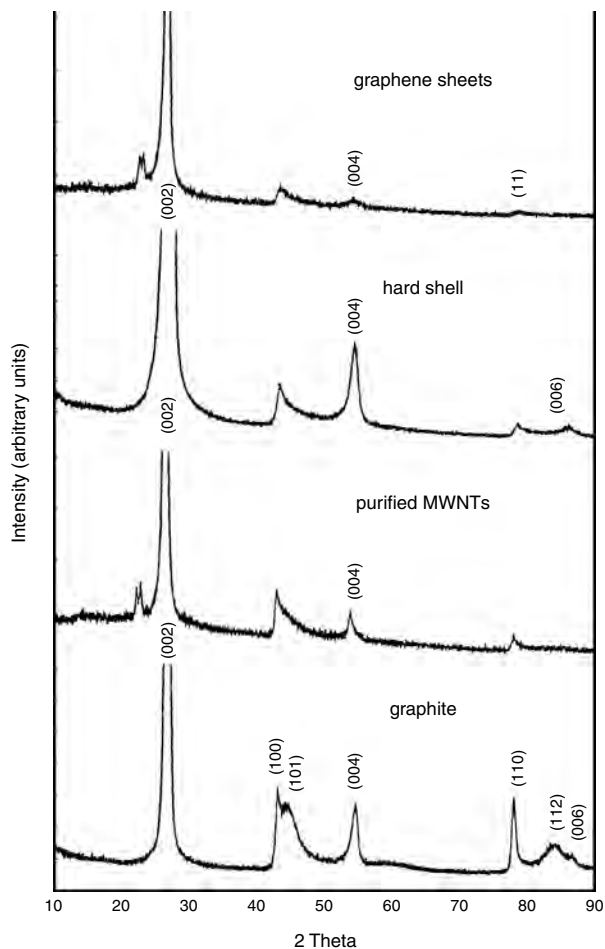


Figure 9. XRD of graphene sheet, hard shell, purified MWNT, and graphite. Reprinted with permission from [52], X. Zhao et al., *J. Cryst. Growth* 198/199, 934 (1999). © 1999, Elsevier Science.

the C—C bonds are trigonal sp^2 hybrid σ bonds with delocalized π bonds. The large interlayer spacing suggests that the contribution to interlayer bonding from π -bond overlap is negligible.

When the turbostratically disordered structure becomes more distinct and dominates among the crystallites, the carbonaceous material is no longer graphitic and can be considered as a nongraphitic carbon. Nongraphitic carbonaceous materials consist of carbon atoms with most of them arranged in a planar hexagonal network but without the crystallographic order in the c -direction of the graphite structure. The ability for graphitization is higher (i) if the precursor material comprises highly condensed aromatic hydrocarbons, and (ii) if neighboring graphene layers or graphitic crystallites are suitably oriented to each other.

Unlike diamond, in which all the orbitals of the four valent electrons of carbon atom (one s and three p 's) are hybridized (sp^3 hybridization) to make four equivalent, strong strictly directed bonds, in graphite only three of the four orbitals are combined (sp^2 hybridization), making three equivalent, strong, coplanar bonds with an angle of 60° between three σ bonds. The remaining fourth electron is quasi-free, that is, free to move within its layer, and it makes very weak bonds (π bonds) directed perpendicular to the

hexagon layers, thus bonding these layers to each other. The atoms within the layer are strongly bound and therefore the layers are compact and difficult to break. On the other hand, neighboring layers are hardly bound to each other, so that they can be easily moved with respect to each other, or even separated. Since it is very difficult to break the layers (i.e., by stretching them), graphite's strength is very large parallel to the layers, but since the layers can be easily separated from each other, strength is nearly zero across them. Along the layers, electrons can move easily and therefore graphite is a good conductor of electricity parallel to the layers, but an insulator across them.

Traditional graphite is made of a very large number of tiny crystals randomly oriented; that is, they point to different directions. Therefore, if one crystal is a good conductor in one direction, its neighbor may be an insulator in that direction, so that the net result is no bulk anisotropy at all. On the other hand, it is clear that if we could make all crystals to point in the same direction, we would have an anisotropic material. This is what we have in a pyrolytic carbon. Pyrolytic carbon is a monolithic polycrystalline graphitizable carbon material obtained by pyrolysis of a hydrocarbon vapor and deposition of carbon on a solid substrate heated to high temperature. The structure of pyrolyzed carbon is characterized by a strong preferred orientation of the constituent crystallites with their basal planes mostly parallel to the substrate surface. Properties of such carbon depend upon preparation conditions and are mostly determined by the deposition temperature.

Graphitization of carbon by metal is one of the processes to prepare graphite at lower temperature. It is observed that temperature at which graphitization occurs depends upon the initial state of the carbon. The lowest temperature of graphitization by Ni occurs for diamond or diamond-like carbon at 700°C and 500°C , respectively [53].

There has been considerable interest in the doping of graphite with elements such as boron, nitrogen, and silicon in order to modify the electronic, mechanical, and oxidative properties of this material. In recent years, a number of carbon-boron, carbon-nitrogen, and carbon-boron-nitrogen alloy structures have been proposed from the results of theoretical calculations, notably BC_3 , C_3N_4 , and BC_2N [54–57]. In terms of boron doping within the graphitic structure, it has been shown that the thermodynamic solubility of B in the C lattice [58] is around 2.35 at.%. Introduction of boron in graphite-like lattice induces the presence of disordered phases. These domains occur when boron content level is higher than a few percent. The exact nature of the boron sites in the higher-boron-content material still remains unclear.

The perfectly conjugated polyne ($(-C\equiv C-)_n$), called “carbyne,” is known as one of the carbon allotropes. Though many attempts have been made to synthesize it, synthesis is still under investigation [59, 60]. Carbyne has been considered to be a transition phase between graphite and diamond and a carbynoid material was experimentally observed to form diamond [61]. On the other hand, polyne was suggested to be a precursor for fullerene [62].

4.2. Application of Graphite

Graphite has been used for many industrial applications. It has been used as an electrode in electrochemical works, an inert crucible for high-temperature application, a solid lubricant, a precursor for synthesis of fullerenes, in carbon nanotubes, etc. It would be impossible to discuss applications of graphite in this chapter because of space limitations; also, they are well known and documented nicely at many places. However, recently graphite has found an application in an area related to environmental problems, for example, leakage of oil during transportation; its large absorbent capacity and easy manipulation are expected to avoid serious pollution problem. So far, some porous polymers, such as poly(propylene) and poly(ethylene terephthalate), have been used for the absorption of spilled oil, of which maximum absorption capacity is ~ 10 – 20 g of heavy oil per 1 g of polymer [63]. Moreover, most of the polymers absorb water, as well as heavy oil. They do not have special selectivity for heavy oils. On the other hand, exfoliated graphite was found to absorb selectively a large amount of heavy oil. It is reported that about 80 g of heavy oil floating on water can be removed from 1 g of exfoliated graphite [64].

5. INTERMEDIATE FORMS OF CARBON CONTAINING MIXTURE OF sp^2 AND sp^3 CONFIGURED CARBON ATOMS

In previous discussions we dealt with carbon with 100% either sp^2 carbon (graphite) or sp^3 (diamond). Now we shall discuss carbon material possessing both forms of carbons. It will be noticed that the variation in the percentage composition of sp^3 and sp^2 carbon yields different forms of carbon. Therefore, a new method of classification has been suggested here, where the structure and properties of carbon materials are mainly governed by the ratio of these two forms of carbon. Under a suitable condition of preparation, it is possible to create different forms of carbon having different ratio of sp^3 and sp^2 carbon atoms. Diamond-like carbon and glassy carbon are two examples of such configurations, because they have different structures from graphite and possess both types of carbons (i.e., carbon with sp^3 and sp^2 configuration). We shall now try to discuss this class of carbon materials in brief.

5.1. Diamond-Like Carbon

5.1.1. Structural Aspects of DLC Film

Elemental carbon has six electrons, with configuration $1s^2 2s^2 2p^2$. Thus when carbon atoms combine, there is flexibility in terms of allocation (hybridization) of the electrons in the 2s and 2p orbitals, giving rise to graphite (sp^2), diamond (sp^3), or a third allotrope of carbon, diamond-like carbon containing a mixture of sp^2 and sp^3 carbon atoms. When the diamond structure is incorporated with both tetrahedral (sp^3) and trigonal planar (sp^2) carbon-bonded atoms, the resulting film takes the form of diamond-like structure. In other words, in DLC, the clusters of three coordinated sp^2 carbon atoms are embedded in a sp^3 bonded matrix. The sp^2 regions of the DLC film are found to control electronic

properties such as bandgap, while the sp^3 regions control mechanical properties such as rigidity and hardness. Because of this, diamond-like structure shows almost all properties of diamond and the conductance properties of graphite. DLC films, depending upon the ratio of sp^2 and sp^3 carbon atoms, can also be stable, hard, and chemically inert like diamond.

Depending upon the ratio of sp^2 and sp^3 nature of carbon, various types of DLC films can be obtained [65]. Furthermore, there are two types of semiconducting amorphous carbon: (a) with hydrogen (a-C:H); and (b) pure carbon without hydrogen (a-C). In a-C:H, commonly obtained when a hydrogen gas is used as the plasma source, the rigidity of the amorphous network, and hence the “diamond-like” content, is influenced by the fraction of polymeric C—H bonds in different configurations. In a-C, it is the relative amounts of sp^2 and sp^3 C—C bonds in the network which determines the macroscopic electronic, optical, and mechanical properties of the materials. Thus, DLC covers a wide range of materials, from the a-C:H containing sp^3 content in the range of 20 to 50%, to the tetrahedral amorphous carbon (ta-C) containing essentially no hydrogen and sp^3 contents up to 70–85%.

A systematic classification of amorphous carbon films has been given by Biswas et al. [66]. According to them, classification of amorphous carbon films can be shown graphically in form of a triangle. The corners at the base of the triangle correspond to graphite (100% sp^2) and diamond (100% sp^3 carbon). The apex represents 100% H, but the upper limit for formation of solid films is defined by the tie line between the compositions of polyethylene, $-(CH_2)_n-$, and polyethylene, $-(CH)_n-$. The majority of a-C films contain mainly sp^2 carbon, but the sp^3 carbon content can be varied over the range 5–55%; the hardness of the films increases with sp^3 content. The H content of a-C:H films can be varied over a wide range and the hardness of a-C:H film is inversely related to the hydrogen content. Films with very high sp^3 content (~ 80 – 90%) and correspondingly high hardness have been called tetrahedrally bonded amorphous carbon films (ta-C films). Hard a-C:H films are called “diamond-like carbon” (DLC). Thus, in general, hardness increases with sp^3 carbon content, as the proportion of DLC increases. Conversely, the films become softer as the sp^2 carbon content and/or hydrogen content increases [67, 68].

5.1.2. Synthesis of DLC Films

There is a good review on the DLC films by Zhang et al. [69]. Generally, two basic ways have been used to synthesize a DLC film: one is through the vapor phase via hydrocarbon gases, and the other is by sputtering of a solid carbon source. The latter process usually gives nonhydrogenated or a-C films. In this process, classified as plasma vapor deposition (PVD), plasma of argon is allowed to hit the carbon target to sputter carbon, which in turn is deposited at the substrate to give a DLC film. In other processes, like chemical vapor deposition (CVD), hydrocarbon gas or mixture of hydrogen and a hydrocarbon such as methane (CH_4), n-butane (C_4H_{10}), acetylene (C_2H_2), camphor, etc., are used as the carbon source. These gases are activated by direct-current glow discharge, rf discharge, microwave discharge, ion beam, pyrolysis, etc. Sharon and co-workers [6] have

been able to get DLC film by pyrolysis of various naturally occurring precursor camphors.

5.1.3. Properties of DLC Films

5.1.3.1. Electrical Properties In DLC, the clusters of three coordinated sp^2 carbon atoms are embedded in a sp^3 -bonded matrix. Consequently, the bandgap of DLC film can be varied from 1 to nearly 4 eV according to the fraction of sp^3 bonding. Heat treatment of amorphous carbon films leads to the evolution of hydrogen and causes a structural change. Gradual release of hydrogen at the temperature range from 400 °C to 600 °C converts tetrahedral sp^3 into trigonal sp^2 structure. If this happens, then the bandgap of DLC film will decrease as ratio of sp^2/sp^3 increases. Sharon et al. [16] have shown that pyrolysis of camphor can give DLC films with various bandgaps depending upon the concentration of sp^2 present in the film. In addition to this, Sharon et al. [70] also studied the electrical conductivity of DLC film prepared by pyrolysis of camphor vapor and observed that if films are thermally heated below 600 °C, values of electrical conductivity are reproducible. This suggested that up to this temperature, there seems to be not much change in the ratio of sp^3 and sp^2 carbon and activation energy for conduction remains 1–1.3 eV. However, when the film is heated above this temperature, electrical value takes an altogether different reproducible path and the activation energy for conduction becomes much lower than 0.1 eV. This suggested that concentration of sp^2 carbon must have increased to make it highly conducting. These observations suggest that while ratio of sp^2/sp^3 controls the bandgap, pyrolyzing below 650 °C or sintering at temperature below 600 °C does not alter the ratio of sp^2/sp^3 carbon present in the DLC film. This property of DLC is useful if we wish to make semiconducting carbon of a specific bandgap and to know the temperature up to which the ratio of sp^2/sp^3 carbon present in the film does not alter.

It has been suggested that in a-C:H and a-C, it is the π bonding and π^* antibonding electronic states resulting from p -orbital bonding at sp^2 sites which determine the optical bandgap [71, 72]. The electronic properties of a-C are also determined by the π and π^* states as they in effect form the valence band and the conduction band edge states, respectively. In ta-C with very low sp^2 content, the π and π^* electronic states are highly localized within the much-wider-gap (~ 5 eV) σ - σ^* states arising mainly from the sp^3 hybridized diamond-like bonds. Does this mean that any carbon material with sp^3 configuration will always result in bandgap of ~ 5 eV? This cannot be true. Earlier we discussed the reasons why natural diamond is p-type (Fig. 4), which has 100% sp^3 carbon, and why graphite with 100% sp^2 carbon is an electronic conductor. When carbon system contains both sp^3 and sp^2 carbon, a complex interaction of π bonding and π^* antibonding with σ bonding and σ^* antibonding should be considered in the formation of bandgap of a DLC film rather than only interaction of π bonding and π^* antibonding, because presence of σ bonding coming out of sp^3 carbon in DLC film neither can be neglected nor can be assumed to be ~ 5 eV. It is therefore necessary to take a fresh look into the exact mechanism of the formation of bandgap in carbon films containing both sp^2 and sp^3 carbon. This is more

important because bandgap of DLC film can be varied from 1 to nearly 4 eV according to the fraction of sp^3 bonding.

In an amorphous network, however, the orientation of the π orbitals is randomized, so that two π bonds which are next to each other will not interact electronically if their orientations are orthogonal to each other. Therefore, in amorphous carbon even when there are a significant number of π - π^* states, conduction is through a hopping related process and consequently electronic properties such as mobility will remain very low compared to other amorphous semiconductors such as a-S:H [73].

Robertson and co-workers [74] have observed that ta-C changes its bandgap as per the doping level of nitrogen and so does the conductivity of the film. At nitrogen content above about 2%, the bandgap begins to close and bonding reverts towards sp^2 . Like diamond, pure DLC films and those containing Cu exhibit p-type conduction, and those containing Ti and Si have n-type conduction [75]. However, they also reported that Cu concentration does not exceed 3.0 at.%. Incorporation of Cu into DLC films decreases the resistivity significantly.

Sharon et al. [76] have studied electrochemical properties of DLC film deposited on an alumina plate by pyrolysis of kerosene at 1000 °C in argon atmosphere. The electrochemical potential window of this film in contact with H_2SO_4 solution was investigated in potential range 2.5 V to -1.5 V vs SCE. The same experiment was repeated with platinum and glassy electrodes using a Pt electrode as a counter-electrode. The kerosene DLC film has the widest potential window (2.91 V) as compared to Pt (2.02 V) and glassy carbon (2.79 V). This result has suggested that kerosene-pyrolyzed carbon electrode can be used as an oxygen electrode more efficiently. They have suggested that DLC film prepared from kerosene is as good as platinum electrode.

5.1.3.2. Spectroscopic Properties Since DLC film is a mixture of sp^3 and sp^2 carbon atoms, there is no crystallinity in the film. It is quite amorphous in nature and hence XRD cannot be taken as a confirmation for DLC film. Raman spectroscopy has been found very handy to characterize DLC film or to differentiate it from either graphite or diamond. If films contain amorphous sp^2 -bonded (graphitic) carbon and sp^3 -bonded (diamond-like) carbon (DLC), one gets broad ill-defined bands with high-frequency cut-off near 1332 cm^{-1} (in the range of 1350 – 1372 cm^{-1} , known as D-band or Raman active E_{2g2} mode of graphite) for the sp^3 -bonded carbon, and around 1580 cm^{-1} (usually in the range of 1519 – 1580 cm^{-1} , known as G-band, also referred to as the A_{1g} mode frequency) for the sp^2 -bonded carbon [77, 78]. Schwan et al. [79] have suggested that the G peak is not necessarily composed only of the E_{2g2} mode of graphite, but also of sp^2 C=C stretch vibrations because single benzene rings exhibit a Raman peak at 1588 cm^{-1} . This feature is valid for all aromatic rings and condensed benzene rings. Therefore, it is suggested that possible contribution to the G peak may arise from the C=C sp^2 stretch vibrations of olefinic or conjugated carbon chains at about 1620 cm^{-1} . Thus, the existence of a G peak in the Raman spectrum does not necessarily prove that the a-C film consists only of graphite or fused benzene rings. The G peak might as well have its origin in olefinic chains in the carbon films. The existence of

a peak centered at about 1350 cm^{-1} proves the existence of aromatic or benzene clusters incorporated in the amorphous (hydrogenated) carbon films.

G-band is normally observed to be very broad. In principle, there may be four significant reasons for line-broadening feature in a-C:H films, namely, the cluster size, the cluster distribution, the influence of the stress in the films, and broadening due to chemical bonding. For graphite, Sakata et al. [80] found that the half-width of line- 1580 cm^{-1} peaks increases linearly with increasing stress.

In hydrogenated DLC (a-C:H) films or unhydrogenated DLC (a-C) films, D-band is broad as compared to G-band. Nevertheless, intensity of D-band is greater with a-C type films as compared to a-C:H films [81]. The presence of the D-band and G-band peaks, therefore, can also indicate the co-existence of sp^2 bonds with sp^3 bonds. The shifting of the G-band resonance peak towards 1580 cm^{-1} infers the decrease in the sp^3 to sp^2 bond ratio. This is supported by the observations made by Cheng et al. [82]. They have shown that as the temperature of the substrate (gold coated silicon) over which DLC films was grown increases, the intensity of D-band (an indication of increase of sp^3 constituent of the film) increases.

It is reported that in a DLC film prepared below $400\text{ }^\circ\text{C}$, no Raman signal is observed unless it is annealed above $400\text{ }^\circ\text{C}$ [83]. It is observed that with increase of the annealing temperature, the intensity ratio of I_D/I_G increased slightly. Shifting of G-line position from 1580 to about 1606 cm^{-1} and D-line position from 1380 to about 1345 cm^{-1} , and change in the intensity, are the most sensitive indications that the film is changing from one with bond-angle disorder to one containing three fold-coordinated crystallites, that is, the film is undergoing a graphitization process.

In principle, these reasons may also be true for the linewidth of D-band. It is possible to get some useful information about the cluster size in amorphous carbon from ratio of intensity of D-peak and G-peak (i.e., I_D/I_G) and the G linewidth [79]. In pure graphite, D peak is expected to be absent [84]. But if graphite is assumed to be disturbed by presence of sp^3 bonded carbon, the D peak will develop and rise in magnitude in the Raman spectrum. When material is composed entirely of sp^3 bonded carbon (and/or olefinic chains connected by sp^3 bonded carbon), the D peak should not be detected, because there exist no benzene clusters that give rise to disorder regions, which are responsible for the D peak. In other words, in a completely sp^3 network the I_D/I_G ratio will be zero. Schwan [79] thus suggested that the I_D/I_G ratio would go through a maximum if it is plotted versus G linewidth. Moreover, Tuinstra and Koenig [84] found that the Raman intensity of I_D/I_G is inversely proportional to the graphite crystallite size (L_a) as determined by XRD:

$$1/L_a \propto I_{1355}/I_{1575} = I_D/I_G$$

It has been suggested that when G linewidth increases beyond 50 cm^{-1} , the resulting decrease in the I_D/I_G ratio would be indicative of a cluster size smaller than 10 \AA . Raman spectra of graphite rod, graphene, sheet and multiwall nanotube are shown in Figure 10 to illustrate these behaviors.

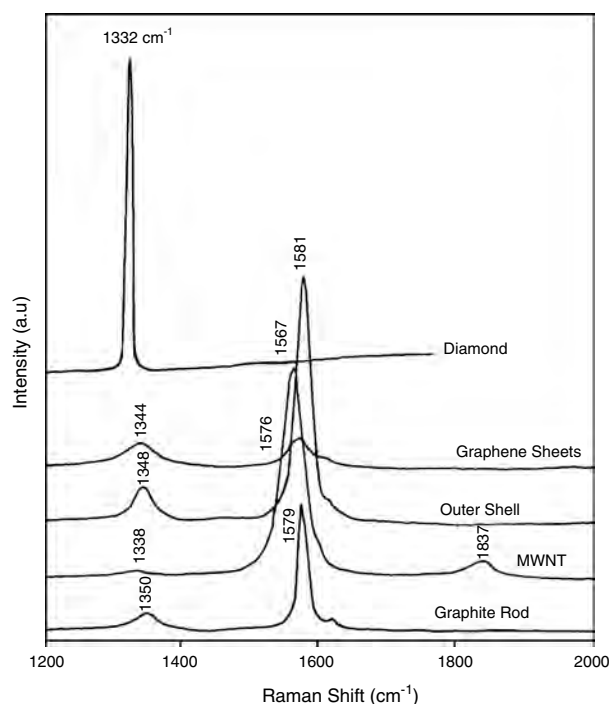


Figure 10. Raman spectra in the frequency range $1200\text{--}2000\text{ cm}^{-1}$ for graphene sheets, outer shell, purified MWNTs, and graphite rod. Reprinted with permission from [85], Y. Ando et al., *J. Inorg. Mater.* 1, 77 (1999). © 1999, Elsevier Science.

Ager [86] has suggested that hydrogen incorporation into DLC films saturates double bonds, thus forming smaller sp^2 domains and helping sp^3 to cross-link; this increases both the optical gap to higher energy and the hardness of the film. Veerasamy et al. [87] have shown two prominent IR absorption peaks at 2920 cm^{-1} and 2840 cm^{-1} . They have assigned these peaks to stretching mode of C—H bond in sp^3 configuration in C—H₃ and C—H sites, respectively. Optical absorption coefficient [88] of a typical DLC film is reported to be 10^4 to 10^5 cm^{-1} . ^{13}C NMR spectrum of a-C:H film shows two peaks, one at around $30\text{--}40\text{ ppm}$ due to sp^3 bonding configuration and the other at about 150 ppm due to sp^2 configuration [89]. DLC can thus be amorphous carbon (a-C) or hydrogenated amorphous carbon (a-C:H) with a bandgap in the range of 1 to 4 eV according to the fraction of sp^3 bonding. Sharon et al. [16] have shown the dependence of bandgap with ratio of sp^2/sp^3 of DLC film (Fig. 11) prepared from pyrolysis of camphor.

5.1.3.3. Photovoltaic Effect Because DLC is known to possess a bandgap in the range of 1.0 to 4.1 eV , there have been some efforts to make a photovoltaic cell from semiconducting carbon like DLC. One of the constituents of most photovoltaic cells developed is inorganic semiconducting material such as Si, GaAs, etc. This has raised a question whether photocurrent obtained from such cell is due to inorganic semiconductor (e.g., due to Si or GaAs) or due to carbon as well. It is also questioned whether in these cells, carbon is acting as a metal, thus forming a metal-Schottky-type cell. In addition, none of these photovoltaic cells could be more economical than the silicon photovoltaic cell. Nevertheless, following are a few examples of

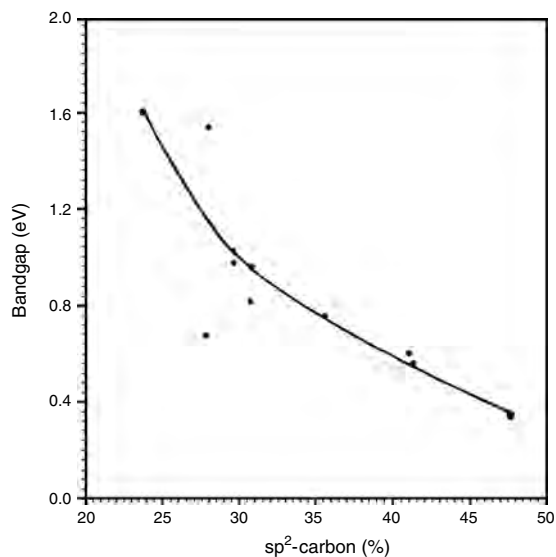


Figure 11. Variation of the bandgap of camphor pyrolyzed carbon as a function of the sp^2 carbon contents in the grown films. Reprinted with permission from [16], M. Sharon et al., *Mater. Chem. Phys.* 56, 284 (1998). © 1998, Elsevier Science.

the attempts made in developing a photovoltaic cell utilizing carbon as one of the constituents of the cell. A photovoltaic cell of configuration “C/n-Si” fabricated from the carbonaceous amorphous thin film prepared from the pyrolysis of 2,5-dimethyl-p-benzoquinone in argon atmosphere at 500 °C has been studied exhaustively by Hong-an et al. [90]. They have also given the band diagram of the junction. Since the optical bandgap of carbon was observed to be 0.25 eV and the nature of carbon (n- or p-type) is not known, this photovoltaic cell may be considered as metal-Schottky-type cell, where carbon behaves like a metal. Recently, Romero et al. [91] have fabricated a carbon nanotube/BCHA-PPV. This shows a rectifying behavior as well as photocurrent. A semiconducting polymer, commercially available, soluble di-cholestanol derivative of poly(p-phenylenevinylene), poly(2,5-bis(cholestanoxo)-1,4-phenylenevinylene) (BCHA-PPV), was used as one component of the cell. The surface of a carbon nanotube was covered with a solution of BCHA-PPV in xylene under an overpressure of 2 atmospheres of argon in order to allow the polymer to penetrate the space between the tubes. A final layer of the polymer was subsequently spin cast onto the carbon nanotube. A second metallic contact of aluminum or gold thermally evaporated onto the polymer completed the device. Sharon et al. have developed a photoelectrochemical cell with DLC, carbon prepared from camphor [92]. They also developed a homojunction [93–94] carbon solar cell from semiconducting carbon obtained by pyrolysis of camphor of configuration p-C (100 nm)/n-C(100 nm)/n-Si(380 nm) giving an efficiency of 1.2%. Soga et al. [95] have fabricated homo- and heterojunction carbon solar cells of configuration “n-C/p-Si,” “p-C/n-Si,” and “n-C/p-C/p-Si” using amorphous carbon (a-C and a-C:H). The efficiency of these cells is about 2.1%. A p-n junction has been formed by bonding n-GaAs with p-diamond epitaxial layer [96]. A photoelectrochemical behavior of semiconducting boron-doped diamond

thin films has also been studied exhaustively, principally by Pleskov and his co-workers [97–101] and by Fujishima and his co-workers [102]. Ago et al. [103] have made a photovoltaic cell of configuration “Al(transparent)/PPV(poly(p-phenylene vinylene)/MWNT/ITO (glass substrate).” They studied its current-voltage characteristics as well as its quantum efficiency (1.8%). A heterojunction carbon solar cell of configuration “Al/n-C₆₀/p-Si/Al” has been reported by Katz et al. [104]. Under natural sunlight conditions the short-circuit current density was found to be 42 $\mu\text{A cm}^{-2}$ and the open-circuit voltage was 322 mV. A significant rectification property is obtained in the I-V characteristic of the junction.

In spite of this work, there is a need to make efforts to develop a homojunction carbon photovoltaic cell which is cheaper than the silicon photovoltaic cell, giving efficiency at least 10% so that it can be commercially viable.

5.1.3.4. Electron Field Emission Effect Details of theory and techniques to study electron field emission have been discussed in the diamond section. Here we shall discuss this behavior in relation to DLC films only.

Field emission from DLC is generally found more easily than from diamond. It is observed that the substrate over which diamond-like film is deposited has an essential impact upon the electron emission characteristics of the film. Either the electron properties of the interface itself or the growth morphology and structure of the film influence the electron field emission properties. When a diamond-like film is deposited on a flat substrate through a mask, the emission sites are most abundant at the edges of the film. It is likely that the most favorable conditions for emission will always be attained somewhere at the film edge [105]. Xu et al. [106] have proposed that, in the DLC films consisting of a mixture of sp^3 and sp^2 bonds, the sp^3 bonds in the clusters are the electron emission sites, whereas the sp^2 bonds in the clusters play the role of a transport path for supplying electrons. Cheng et al. [107] have studied the electron emission behavior of DLC film deposited over Cr/Si tip by laser ablation process (600 mJ laser energy). They reported that as the temperature of substrate increases, Raman shift at around 1550 cm^{-1} increases, which in turn increases, the current density of 340–436 $\mu\text{A cm}^{-2}$. This suggests that as the sp^2 content in film increases, emission current also increases. This observation also implies that emission current may increase with increase in sp^2 concentration up to some optimum concentration of sp^2 ; otherwise graphite should have given the maximum emission current. There has been considerable discussion about whether field emission from diamond and DLC is intrinsic or due to surface damage caused during its formation. There is a need to examine this behavior in detail. Sharon et al. [16] have suggested that carbon with 33.3% sp^2 behaves like an intrinsic material, and while higher concentration makes it n-type, lower concentration of sp^2 makes it p-type carbon. It would be interesting to study the electron field emission with carbon possessing different concentration of sp^2 carbon to establish any possible relationship with intrinsic character of carbon.

Threshold emission field for DLC is 20–40 $\text{V } \mu\text{m}^{-1}$ which can be lowered to about 10 $\text{V } \mu\text{m}^{-1}$ for optimized films, and to 5 $\text{V } \mu\text{m}^{-1}$ for nitrogen-doped films [108, 109]. On the contrary, Kuo et al. [110] have observed that hydrogenated

DLC film grown in presence of NH_3 needs higher threshold voltage than film grown in presence of nitrogen for the electron field emission. They suggested that nitrogen doping is more effective with NH_3 than with nitrogen. It appears from the discussions that exact reasons for field emission with DLC films need more rigorous studies to arrive at some definite conclusion.

5.2. Fullerenes

5.2.1. Structural Aspect

The discovery of C_{60} , one of the family members of fullerene, was first reported in 1985 when Kroto et al. [3] measured a carbon cluster containing 60 atoms arising from their laser vaporization apparatus. The C_{60} molecules contain 12 pentagons and 20 hexagons. In the C_{60} molecules each carbon atom is bonded to three others by two longer bonds (length ~ 145 pm) and one shorter bond (bond length ~ 140 pm). This stable pure carbon molecule was found to have geodesic properties of a truncated icosahedral hollow cage and was named Buckminsterfullerene (C_{60}). An excellent and informative review on the growth of carbon nanostructure and fullerenes is given by Popov and co-workers [111]. Fullerene family are the most ordered structures among the known carbon clusters. They are said to be ordered structures because other forms of carbon are believed to be amorphous (e.g., carbon black, charcoal, active carbon, etc.). Crystals of C_{60} formed by vacuum sublimation have a face-centered cubic (fcc), crystal structure at room temperature $a_0 = 141.7$ pm. Those grown from solution have a variety of crystal structures depending upon the solvent used, for example, fcc, hexagonal close-packed (hcp), or orthorhombic structures. Since there are many good reviews, in-depth discussions on this material will not be made.

5.2.2. Properties

The discovery of Buckminsterfullerene has created a torrent of activity spanning the scientific disciplines. It has been speculated that the fullerenes should be excellent lubricants due to their low intermolecular shear strength and high volume compressibility. The optical and electrical properties and the electronic structure of C_{60} are still a matter of dispute. For example, the bandgap of C_{60} has been reported in the range of 1.5–2.15 eV by various authors [112]. Interestingly, Faiman et al. [113] have shown that the optical bandgap of C_{60} thin film can be shifted at will by controlling the deposition conditions leading to effective optical bandgap in the range of 1.5–2.5 eV. Kuzmany et al. [114] have shown a heterojunction photovoltaic solar cell (Al/ C_{60} /p-Si/Al) giving an open-circuit voltage (under the sunlight illumination) of 322 mV. Licht et al. [115] fabricated a photoelectrochemical solar cell with C_{60} with various redox electrolytes (aqueous and nonaqueous) and have shown that such type of cell may be feasible with this material provided this material is cheaply available. Some of the properties of crystalline forms of carbon are shown in Table 2.

More information is becoming available about the biological properties of C_{60} and its derivatives. For example, C_{60} inhibits the replication of simian immunodeficiency virus

Table 2. Properties of diamond, graphite, and C_{60} .

Property	Diamond [116] (cubic)	Graphite [117] (hexagonal)	C_{60} [118] fcc
Bond length (pm)	154	142,335	146,144
Density (g cm^{-3})	3.52	2.26	1.72
Bulk modulus (Gpa)	442	286	6.8
Young's modulus (Gpa)	1054	102,036.3	16
Melting point (K)	4500	4450	1180
Thermal conductivity ($\text{W m}^{-1} \text{K}^{-1}$)	15,000	2800	0.4

(SIV) *in vitro* and the activity of Moloney murine leukemia virus (M-MuLV) reverse transcriptase [119]. A polyfullerenol has been found to suppress the levels of the microsomal enzymes *in vivo* and decrease the activities of P450-dependent monooxygenase and mitochondrial oxidative phosphorylation *in vitro* [120]. Water-soluble polyethylene modified C_{60} accumulated at the site of tumors during testing, and after light irradiation the volume of the tumor was significantly reduced [121].

5.2.3. Synthesis

Much evidence suggests that fullerenes are a by-product of soot formation; on the other hand, there are observations pointing out that soot produced in fullerene processes is somewhat special compared to other soots. Small carbon clusters (less than 12 atoms) have been observed in sooting flames, in acetylene pyrolysis, and in carbon plasma produced by different methods. It is suggested that fullerenes and soot have the same precursors [122]. C_{60} has been produced from carbon materials other than graphite, such as coals, polymers, benzene soot, glassy carbons, kerosene, corongite camphor [123, 124], etc. Unique fullerene-related materials to be synthesized include metallofullerenes and nanotubes and polyhedra. Many metals like cesium, potassium, barium, etc. have been successfully encapsulated into a fullerene cage. Laser vaporization [125] of graphite disk impregnated with lanthanum oxide gives a soot containing La_2C_{82} .

5.3. Carbon Nanomaterials

5.3.1. Structural Aspects

There are many mechanisms proposed to elucidate the formation of carbon nanotubes. One of the most accepted mechanisms is formation of carbon nanotube over a molten catalyst. A nucleation of metal and hydrocarbons takes place on the particle surface, it diffuses, and dissociates at the contact angle of the particle with the reactor wall. A carbon shell is produced which develops by lateral growth into a carbon nanotube.

A good description of nanotubes and various aspects related to carbon nanotubes are nicely dealt with in an article published by Kroto and co-workers [126]. Carbon nanotubes consist of graphene sheets wrapped to a cylinder. In other words, nanotubes consist of concentric hexagon-rich cylinders, made up of sp^2 hybridized carbons, as in graphite, and terminated by end-caps arising from the presence of

12 pentagons (six per end). It is possible to construct a cylinder by rolling up a hexagonal graphite sheet in different ways. There exist three forms of nanotubes (NTs): achiral NTs of the “armchair type,” achiral “zigzag” NTs, and chiral or helical NTs (each pair of the hexagon sides is arranged at an angle other than 0° and 90° relative to the NT axis). First two of these are “nonhelical” in the sense that graphite lattices at the top and the bottom of the tube are parallel. In the armchair structure, two C—C bonds on opposite sides of each hexagon are perpendicular to the tube axis, whereas in the zigzag arrangement, these bonds are parallel to the tube axis. The structures of these NTs are usually described by means of two indices, n and m , which are related unambiguously to the NT diameter (d) and the chiral angle (θ), characterizing the deviation from the “zigzag” configuration and ranging from 0 to 30°):

$$d = a\sqrt{3(n^2 + m^2 + mn)}/\pi$$

$$\theta = \arctan\{(-\sqrt{3}m)/(2n + m)\}$$

where a is the interatomic distance in the planar network. (n, m) nanotubes can be characterized by the chiral vector $\mathbf{C}_h = n\mathbf{a}_1 + m\mathbf{a}_2$ on the honeycomb lattice of a flat graphene sheet, where \mathbf{a}_1 and \mathbf{a}_2 denote the lattice vectors of graphite. The cylinders are formed by rolling up graphene sheet so that sites defined by lattice vector \mathbf{R} fall on top of sites given by the lattice vector $\mathbf{R} + \mathbf{C}_h$. The chiral angle θ is given with respect to the $(\mathbf{a}_1 + \mathbf{a}_2)$ direction. Thus achiral NT of the “armchair” type are characterized by indices (n, m) , those of the “zigzag” type have indices $(n, 0)$ and chiral ones are described by (n, m) . Because of the sixfold symmetry of the honeycomb lattice, several different integer pairs (n, m) describe equivalent tubes. Dresselhaus and co-workers [127] observed that the intershell spacing (d_{002}) between the two graphene sheets of the nanotubes ranges from 0.34 to 0.39 nm and d_{002} increases as the tube diameter decreases. The empirical equation for the best fit to the data is found to be

$$d_{002} = 0.344 + 0.1 e^{-D/2} \text{ (nm) for } D \geq 0$$

where D is the inner tube diameter. The intershell spacing decreases exponentially and approaches 0.344 nm for tube of diameter greater than ~ 10 nm.

Apart from these classifications, two kinds of carbon nanotubes are now available: multiwalled nanotubes (MWNTs) and single-walled nanotubes (SWNTs). The diameter of MWNTs is typically in a range from 10 to 50 nm, and length is more than 10 μm . On the other hand, SWNTs are much thinner, being only 1.0 to 1.4 nm in diameter, while the length is on the order of 100 μm . The number of walls in MWNTs is theoretically unlimited but normally it does not exceed a few dozen. The distances between the neighboring shells are close to the interlayer spacing in graphite (0.34 nm); thus, the smallest diameter of carbon NT is ~ 0.7 nm. The diameter of the second and subsequent coaxial atomic layers is stipulated by the diameter for the innermost layer. In this connection, the structure of NT resembles that of onion fullerenes; if the inner shell is C_{60} , the second shell is C_{240} , the third one is C_{540} , etc. In most cases, the tips of NT are covered by hemispherical or conical caps, which

contain not only hexagons but also pentagons, in which the configuration of the carbon atoms is less stable. These caps are somewhat more chemically reactive than the lateral surfaces.

Raman-scattering spectra [128] of single-walled nanotubes measured with incident laser wavelength from 488 to 783 nm shows two peaks, one at 1590.9 cm^{-1} and the other at 1567.5 cm^{-1} , with broad peak at 1549.2 cm^{-1} as compared to graphite peak at 1580 cm^{-1} . Their measurements suggest that as the diameter of the nanotubes increases, the resolution of Raman-scattering peaks, especially of 1567.5 cm^{-1} and 1549.2 cm^{-1} , diminishes and finally becomes one broad peak around 1580 cm^{-1} . When the diameter becomes about 5 nm, it is exhibited by multiwall nanotubes, polyhedral graphitic nanoparticles, or even graphitic layers.

The XRD patterns of graphene sheets, hard shell, purified MWNTs, and graphite rod are shown in Figure 9. In the XRD pattern of MWNTs, the (002) and (004) peaks shift to a lower angle as compared to those from raw graphite, indicating the wide d_{002} spacing of MWNTs.

One of the useful aspects of carbon nanometer tubes is their size-dependent physical and chemical properties. Theoretically, nanotubes are expected to be either an insulator or metal depending upon their diameter [129]. There have been some efforts to establish experimentally as well as theoretically a relationship between the diameter of the semiconducting carbon nanotubes and the bandgap. Smalley and others [130, 131] have reported a relationship between the bandgap and the diameter of the CNT which has been found to be in good agreement with the theoretical estimation [132].

Amaratunga et al. [133] have measured the activation energy (~ 0.6 eV for high-temperature range) for the electrical conductivity as well as the Hall mobilities ($2.75 \times 10^{-5} \text{ cm}^2 \text{ V}^{-1} \text{ s}^{-1}$) and optical bandgap (in the range of 1.5–2.0 eV) of carbon nanotube prepared under different conditions. It is interesting to note that Hall mobility is very low compared to diamond ($1000\text{--}2200 \text{ cm}^2 \text{ V}^{-1} \text{ s}^{-1}$). Moreover, there seems to be a large difference between activation energy for electrical conduction and optical bandgap, suggesting that CNTs may possess many defect states promoting electrical conduction.

5.3.2. Preparation of Nanotubes

5.3.2.1. Carbon Arc Process

Iijima and co-workers were the first to discover carbon nanotubes in the deposit on the cathode of carbon arc [134, 135]. Since then, there have been various approaches adopted to prepare carbon nanotubes. Rakov [136] has given a very exhaustive review on methods for preparation of carbon nanotubes. Nowadays, carbon nanotubes are produced by diverse techniques such as arc-discharge, pyrolysis of hydrocarbons over catalysts, laser evaporation of graphite, condensed phase electrolysis, for example, electrolysis of metal salts using graphite electrode, etc. All these techniques would be difficult to discuss in detail here. Hence, only a few of them are highlighted here.

The arc-discharge method is similar to that used for the synthesis of fullerenes. An inert gas atmosphere (preferably He) is flowed through a reaction vessel [137] at a controlled pressure. Two graphite rods constitute the electrodes,

between which a potential difference is applied. As the rods are brought closer, a discharge occurs resulting in formation of plasma. A deposit, which may contain carbon nanotubes under certain conditions, forms on the large negative electrode (cathode) while the smaller positive electrode (anode) is consumed. When a metal catalyst is to be used along with graphite, a hole is drilled in the carbon anode and it is filled with a mixture of metal and graphite powder. In this case, most nanotubes are found in the soot deposited on the arc-chamber wall. It has been found that vaporization of an anode containing Co, Co-Ni, Co-Y, Co-Fe, Ni, Ni-Y, Ni-Lu, and Ni-Fe gives deposits looking like a lace collar or a soft belt being formed around the cathode deposit. They contain SWNTs mixed with amorphous carbon and metal particles. Some catalysts (Cu, Cu with Ni, Pt, Y, or Fe; Ni, Ni with Y, Lu, or Fe) cause the formation of a “web.” The addition of sulfur to Co catalysts also results in a greater amount of the web-like products. Higher yields of SWNTs with diameter ranging from 0.55 to 6 nm have been obtained with the positive graphite electrode mixed with different metals (Ni, Fe, Co, La) [138]. Since sulfur itself does not catalyze the formation of nanotube, its role seems to reduce to the stabilization of dangling bonds. The addition of Bi and Pb also causes increase in the NT diameter.

5.3.2.2. Catalytic-Assisted Pyrolysis (Chemical Vapor Deposition)

Pyrolysis of hydrocarbon (chemical vapor deposition) has also been extensively used for this purpose. Catalytic pyrolysis of hydrocarbons had been used to prepare carbon fibers even before the discovery of NT and fullerenes [139]. In this method, chemical precursor along with inert carrier gas is allowed to pass through a quartz tube maintained at some specific temperature. Organic precursor decomposes and the products are deposited on alumina plate. This method has given large quantity of nanotubes. Under this method one could use one furnace [140] and allow the vapor of precursor to enter the furnace for the pyrolysis. Alternatively, two furnaces could be used [141], one for pyrolysis and the other for vaporization of the precursor. Metal nanoparticles employed in the CVD synthesis of carbon nanotubes have been prepared by varieties of methods. Catalysts have also been used for this purpose. Catalyst powder of nanoparticles size could be kept in the furnace over which vapor of hydrocarbon is catalytically decomposed to form carbon nanotubes. Catalysts could also be mixed with precursor and vaporized to enter the furnace along with the vapor of precursor. Alternatively, catalysts could be in form of thin film deposited over some ceramic materials. One method is to use nanoporous or mesoporous substrates, such as zeolites [142], porous Si [143], and anodized Al_2O_3 [144], in which metal nanoparticles are confined through evaporation or impregnation. Another method is to etch a metal substrate or a metal-coated substrate by laser ablation [145] or plasma treatment [146]. The physical etching generates metallic nanoparticles, which play a role as catalysts for nanotubes growth. Many parameters, including the temperature and duration of the treatment, the gas composition and flow rate, and catalyst nature and size affect the nature of carbon species in the resulting materials [147]. For each type of precursor, one has to establish the best conditions to get the desired type

of carbon nanotubes. One of the best and easiest methods is to follow Taguchi Analysis [148].

It has been observed that nickel-catalyzed decomposition of CH_4 (99.99%) and H_2 (in 9:1) helps the growth of carbon nanotubes at 600 °C better than either 500 °C or 700 °C. In general, admixtures of Li, Cu, Ag, Zn, Cd, B, Al, In, Y, La, lanthanides, Si, Ge, Sn, Ti, Hf, Pb, Bi, S, Se, Cr, W, Mn, Ru, Pd, Pt, mixtures of two metals or of a metal with a nonmetal, and several carbides and oxides have been tested as catalyst for such purpose [149–153].

Huang et al. [154] have synthesized large-area highly oriented carbon nanotubes at temperature below 666 °C by plasma-enhanced hot-filament chemical vapor deposition. Acetylene gas is used to provide carbon and ammonia gas is used for dilution and catalyst. Pyrolytic methods have been used to generate helical nanotubes [155], hemitoroidal nanotube caps [156, 157], and bent nanotubes [158].

Pyrolysis of metallocene such as ferrocene, cobaltocene, and nickelocene yields carbon nanotubes and metal-filled onion-like structure [159, 160]. Decomposition of Fe and Co phthalocyanines is also accompanied by the formation of nanotube, whereas Cu phthalocyanine gives neither nanotube nor graphitized particles. Ferrocene has been used as the floating catalyst in the pyrolysis of thiophene giving relatively thick “ropes” and ribbons colored silvery black. The longest ropes were 3–4 cm long and have a diameter of 0.1 mm. Lee et al. [161] observed that nickel deposited over SiO_2 substrate dipped in dilute solution of HF for 100–200 s, or etched by NH_3 , results in Ni particles acting as the nucleation seeds for the growth of carbon nanotubes. They could get vertically well-aligned CNTs of length 50 μm . Cao et al. [162] have been able to get bundles of aligned MWNTs by pyrolysis of xylene containing ferrocene. In a horizontal furnace maintained at 800 °C, mixture of hydrogen (150 sccm) and argon (900 sccm) has allowed to carry drop by drop a solution of ferrocene in xylene (0.12 g/ml) at an interval of 2 min. This arrangement gave bundles of MWNTs of average length 60 μm . Cheng et al. [163] have developed a high yield, low cost, and continuous nanotube growth process. Benzene or methane is transported to the furnace maintained at 1100–1200 °C with carrier gas hydrogen along with ferrocene as a catalyst. To enhance the growth of SWNTs a sulfur-containing additive (thiophene) was employed.

Helically coiled nanotubes [164] have been prepared by catalytic decomposition of benzene on Co/ SiO_2 catalyst at 873 K. They have a 10 nm coil diameter, 50 nm coil pitch, and around 1 m length.

Carbon nanotubes have been synthesized by chemical vapor deposition at 700 °C and 800 °C using Ni-phthalocyanine as starting material. The tubes grew perpendicularly on the quartz surface. This precursor was preferred because Ni-phthalocyanine ($\text{NiC}_{32}\text{N}_8\text{H}_{16}$) can supply Ni, C, N, and H at the atomic ratio of 1:32:8:16 to preparation system [165].

Zhao et al. [166] have developed a simple technique to grow aligned MWNTs. Al sheet is electropolished in phosphoric/glycerol solution at 13–15 V for 10 min at 70–80 °C until a mirror finished is obtained. This Al sheet is anodized in 0.3 M oxalic acid solution for about 1 hr under 40 V at 25 °C. This sheet is immersed in 5% H_3PO_4 for some time

to remove partial alumina template, and then it is anodized again under the same condition. This gives a regular pore structure. Over this sheet cobalt metal was deposited in the pores by an ac current source of 50 Hz. Alumina membrane is removed from substrate by immersing in saturated HgCl_2 solution. By this process, a deposition of Co in the pores was achieved. This system was used for depositing carbon nanotubes by keeping it in a furnace at 650 °C and passing acetylene vapor. In this way, carbon nanotubes were deposited in the pores of the membrane. Advantage of this method is that carbon nanotubes are deposited as aligned nanotubes over metallic aluminum plate. Recently Maruyama et al. [167] have demonstrated a simple catalytic vapor deposition technique to synthesize high-purity SWNTs at low temperature (550 °C) by using methanol as the carbon source. It is suggested that the etching effect of decomposed OH radical attacking carbon atoms with a dangling bond, impurities such as amorphous carbon, MWNT, metal particles, and carbon nanoparticles are completely suppressed even at relatively low reaction temperature. Alcohol was sucked into the furnace rather than pushing through a carrier gas.

Sharon and his group [168] have been trying to synthesize carbon nanotubes by pyrolysis of natural precursors. Their group has been able to synthesize various forms of carbon nanotubes from natural precursor like turpentine and camphor (Fig. 12).

5.3.2.3. Laser Technique Laser technique has been successfully used for the growth of carbon nanotubes. Single-walled carbon nanotube yield depends upon the power of laser beam (532 nm) used to ablate carbon target, irradiation time, the composition of the target, the pressure and flow rate of inert gas, and the target temperature. Kroto and co-workers [169, 170] pyrolyzed 2-amino-4,6-dichloro-s-triazine over cobalt thin films (deposited on an inverted silica substrate) and etched using laser technique. A bundle of aligned nanotubes of uniform length of around 100 nm and diameter of 30–50 nm grown perpendicularly over the substrate were observed. Guo et al. [171] have proposed an original method for the synthesis of SWNTs in which mixture of carbon and transition-metal are vaporized by a laser impinging on a metal-graphite composite target. They pointed out that in contrast to the arc method, direct vaporization allows far greater control over growth condition permitting continuous operation, and produces nanotubes in higher yield and better quality. Rinzler et al. [172] have been able to develop laser ablation technique to produce SWNTs yielding in the range of 60–90 vol.% of the carbonaceous soot material and at a production rate of about 1 g day⁻¹. There is a good review on the production of carbon nanotubes by Wolfgang et al. [173]. Some standard conditions for synthesis of nanotubes (SWNT and MWNT) using laser are given in Table 3. A self-explanatory schematic diagram of the laser evaporation technique is shown in Figures 13 and 14.

5.3.2.4. Electrochemical Method Electrochemical method has lately been tried for the growth of carbon nanotubes. Matveev et al. [174] have been able to get MWNTs from acetylene at room temperature for the first time. Gaseous acetylene was purified by passing it through iron chloride solution. Gas was then dried by passing it through

a layer of freshly melted KOH flakes. Purified acetylene was dissolved in liquid ammonia to get 15–20 mol% acetylene solution. This solution was electrolyzed at 233 K using n-Si (100) electrodes (separated by 4 cm) at 150 V for 5–10 h. Carbon curled nanotubes were found on the electrodes and exhibited a high aspect ratio (length/diameter) >1000. Liquid ammonia helps to dissolve hydrocarbon as well as to initiate chain radical reactions in the solution of hydrocarbon to facilitate growth of carbon nanotubes. Windle and co-workers [175] as well as Kroto and co-workers [176] have synthesized carbon nanotubes and nanoparticles electrolytically from normal graphite in molten alkali chlorides such as LiCl, NaCl, and KCl. Carbon nanotubes as well as nanoparticles and onion-like structures have been generated. The nature of products depends upon several factors including the electrolysis voltage and current, depth of electrode immersion in the electrolyte, the length of time the current is maintained, and the electrolyte. It is reported that carbon consumption for nanotube formation occurs at the graphite cathode where alkali metals form during the electrolysis. However, the major hurdle is the nonconducting nature of most organic precursors and insolubility of the organic materials in polar solvents or in solvents with high dielectric constant. Hence, though this technique is very suitable, these limitations have to be overcome before it can be used for large-scale synthesis of carbon nanostructures.

5.3.2.5. Effect of Particle Size of Catalyst It has been observed that the particle size of the catalyst plays a role in the growth of MWNTs as well as SWNTs. For multi-walled nanotubes, the particle size needs to be larger than the nanotube diameter since catalytic process requires carbon species to diffuse through catalyst like Ni in order to grow multiwall nanotubes. For the growth of single-walled carbon nanotubes, the particle, which is attached to one end of the nanotubes, has to have the same size as the nanotube diameter where the carbon shell on the particles grows and transforms to a carbon nanotube. These relationships agree with the experiential evidences [177–179].

5.3.2.6. Opening and Insertion of Metal into Carbon Nanotubes Carbon nanotubes prepared by any of these methods would be normally closed from one end of the tube. Hence, efforts have also been made to open one of the ends so that some chemistry could be done with these carbon nanotubes. One simple method is by a chemical route for opening multiwalled carbon nanotubes. This is achieved by boiling suspensions of nanotubes in aqueous nitric acid for several hours (~24 h) at 150 °C [180]. Several efforts have been made to encapsulate metallic particles like iron into carbon nanoparticles [181]. After opening the closed end of carbon nanotubes, filling *in-situ* with metal oxides such as NiO [182] or even metal like palladium has been achieved [183]. Ajayan and co-workers have been able to coat carbon nanotube with a single layer of metal oxide (V_2O_5) [184]. A novel electrolytic technique has been discovered by Kroto and co-workers [185] which yields fully filled metallic Sn nanowires. They also succeeded in coating carbon nanotubes with Sn nanowires by electrolyzing graphite electrode in molten mixture of LiCl and SnCl_2 under argon atmosphere.

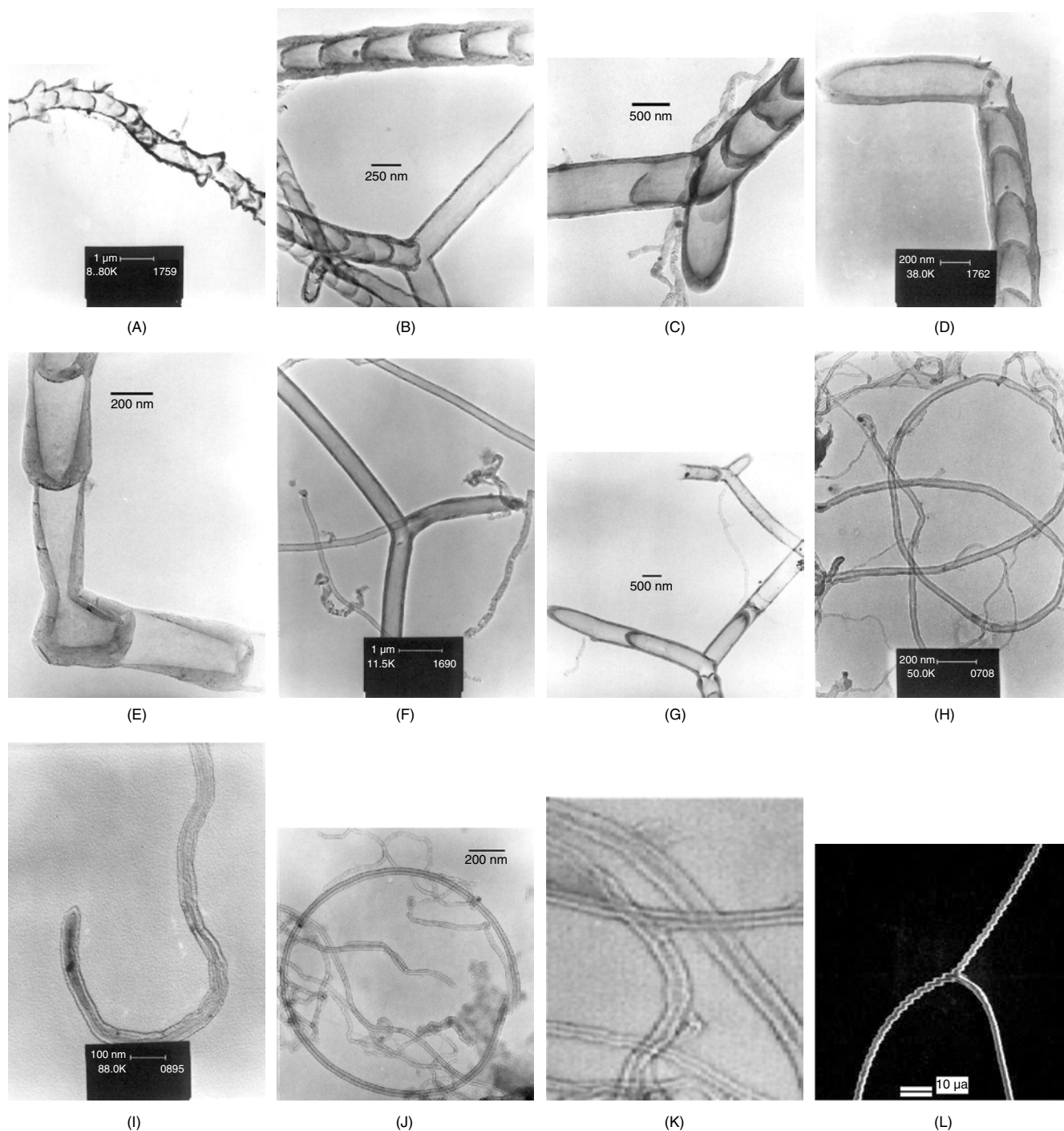


Figure 12. Various types of carbon nanomaterials synthesized from turpentine and camphor. Bamboo-shaped branched CNT (A, B, C, F); Y-junction CNT (D, E); coiled double-walled CNT (G, I, J); enlarged portion of (G) to show double-walled CNT (H); formation of branching in CNT (K); Yofork type CNT (L) [168].

In this fashion many types of elements such as Pb, Bi, Cs, S, Se, etc. have been introduced into the carbon nanotubes easily. It has also been possible to dope potassium into single-walled nanotube. Due to donation of electron by potassium, its doping causes generation of electron carriers in the carbon nanotube. The Hall mobility for the electron is found to be $20\text{--}60\text{ cm}^2\text{ V}^{-1}\text{ s}^{-1}$, a value which is similar to hole effective mobility in nanotubes [186].

5.3.3. Purification of Carbon Nanotubes

When one measures the physical properties of MWNTs or SWNTs and plans their practical application, impurities like carbon nanoparticles are not desirable. There is a good review on the purification of SWNTs by Chiang et al. [187]. Many attempts have been made for purification of MWNTs [188]. Carbon single-walled nanotubes or multiwalled carbon

Table 3. Some favorable standard laser ablation conditions for synthesis of nanotubes.

Source	Source conditions	Target	Temperature	Gas	Results
Single pulsed Nd:YAG	λ 532 nm	Graphite (G)	Furnace 1200 °C	Argon	MWNTs
Double pulsed Nd:YAG	λ 1064 nm	G (98)/Ni (0.6)Co (0.6) at. %	Furnace 1200 °C	Argon	SWNTs 60–90 vol.%, 1 g/day
Cw-CO ₂	λ 1064 nm	G (95)/Ni (4)/Y (1) at. %	No furnace	Argon	SWNTs 80 vol.%, 130 mg/h
Solar light	Sunlight	G (96)/Ni (2)Co (2) at. %	No furnace	Argon	MWNTs and few SWNTs

Source: Reprinted with permission from [173], K. Wolfgang et al., *Carbon* 40, 1685 (2002). © 2002, Elsevier Science.

nanotubes are typically accompanied by other carbonaceous materials when synthesized. A number of purification methods have been developed. They can be categorized into four major methods: (i) acid oxidation, (ii) gas oxidation, (iii) filtration, and (iv) chromatography. In the acid reflux procedure raw nanotubes are refluxed in nitric acid to oxidize the metals and impurity carbon. Sharon and co-workers [189] have purified carbon nanotube by refluxing it with concentrated HNO₃ for 24 h. TEM images of CNT films are shown in Figure 15. While Figure 15a shows the CNT before purification, Figure 15b shows CNT after purification. Globular particles at the end of the CNT (Fig. 15a) are the Co catalyst, which are absent in the purified material (Fig. 15b).

Unfortunately, acid-treated nanotubes are thought to have carboxylic acid groups at the tube ends, possibly, at defects on the sidewalls. Hence, acid-purified tubes must be checked before its application. Gas phase oxidation is used for the purification of MWNT [190]. This process suffers from the disadvantage of destroying SWNT. Combination of acid wash and gas oxidation process has also been applied for purification. Oxidation of acid-treated products at 550 °C for 30 min has given a good result to purify SWNT. TGA studies indicate that these purified tubes can withstand temperature up to 600 °C in air. Microfiltration and chromatography methods have also been found suitable, but are not so popular. Purification of multiwalled carbon nanotubes containing necessary carbon particles has been also achieved by heating the sample with infrared radiation in air [191, 192]. Unfortunately, more than 95% of the nanotubes are also destroyed in this process and the remaining nanotubes lose their protective end-caps. Recently, it has been suggested to

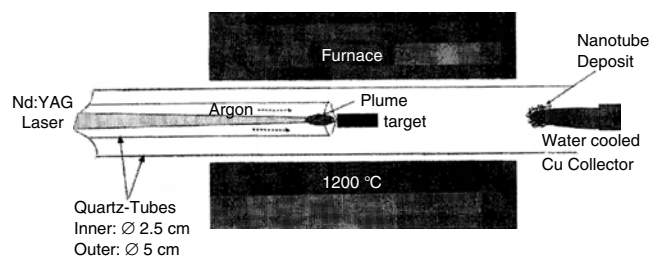


Figure 13. Sketch of the up-scales Nd:YAG laser evaporation experimental setup. Reprinted with permission from [173], K. Wolfgang et al., *Carbon* 40, 1685 (2002). © 2002, Elsevier Science.

treat carbon nanomaterials (impure) with HCl and then with HNO₃.

5.3.4. Properties of Carbon Nanotubes

Before discussing various applications of carbon nanotubes, perhaps it would be appropriate to spend some time discussing the general properties of carbon nanotubes. Measurements of Young's modulus show that single nanotubes are stiffer than commercial carbon fibers. MWNTs can pass a very high current density of the order of 10^8 A cm⁻² without adverse effect [193]. Properties of nanotubes depend on atomic arrangement (how the sheets of graphite are rolled), the diameter and length of the tubes, and the morphology or nanostructure. Work functions of MWNTs and graphite have been evaluated from the secondary electron in UPS HeI spectra by Ago et al. [194]. These values are given in Table 4. X-ray profile of purified and annealed SWNT has been given by Smalley and co-workers [196], showing well-defined reflections at 2θ corresponding to 6.3, 10.5, 16.5, and 22°.

An essential problem in understanding conduction in nanotubes is a crossover from metallic to nonmetallic behavior as the temperature is lowered [197]. Recent electrical transport measurements on bulk nanotubes, individual

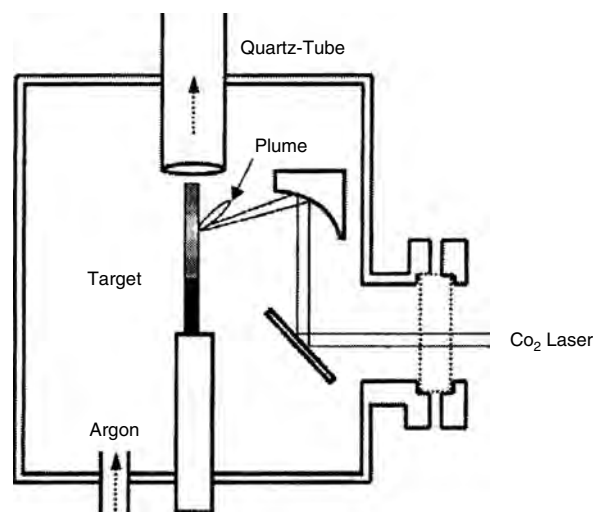


Figure 14. Drawing of cw-CO₂ laser evaporation system. Reprinted with permission from [173], K. Wolfgang et al., *Carbon* 40, 1685 (2002). © 2002, Elsevier Science.

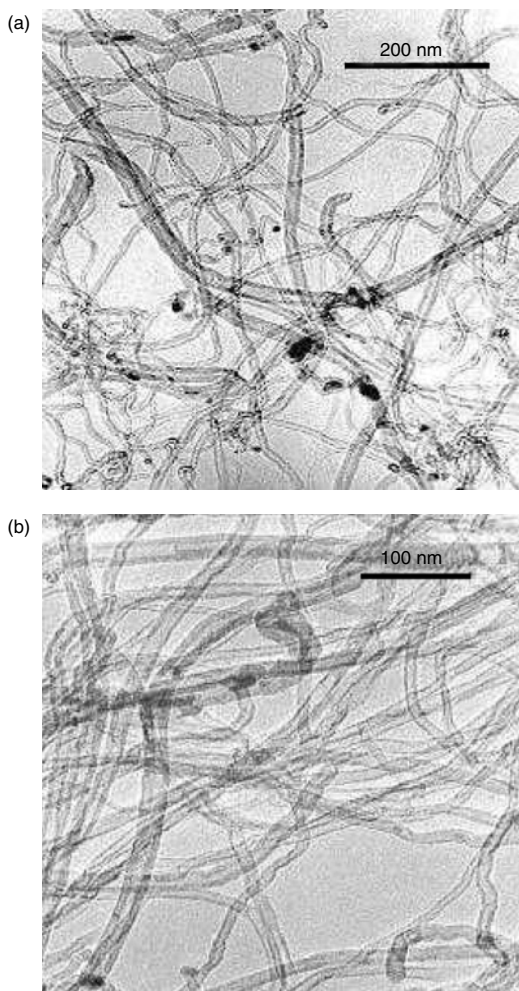


Figure 15. TEM image of the CNT (a) before purification and (b) after purification. Reprinted with permission from [189], A. K. Chatterjee et al. *Electrochim. Acta.* 48, 3439 (2003). © 2003, Elsevier Science.

multilayered tubes, and single-walled tubules have revealed that their conducting properties depend markedly on the degree of graphitization, helicity, and diameter. Carbon nanotubes are found to behave like metal, insulator, or semiconductor, depending upon the method of production—which controls the degree of graphitization, the helicity, and the diameter.

Collins et al. [198] have recently found that the thermopower of SWNT thin films changes from a large positive

value to approximately $20 \mu\text{V K}^{-1}$ (at a temperature of 350 K) in air to negative values of approximately $-12 \mu\text{V K}^{-1}$ in vacuum, and so ascribed the positive thermopowers observed to the adsorption of oxygen. However, the negative thermopower magnitude seen in vacuum is still larger than typical metallic values instead of being close to zero. Grigorian et al. [199] found a negative thermopower for SWNT mats doped with Cs, again reaching a rather large magnitude of $-15 \mu\text{V K}^{-1}$ near 150 K before decreasing in magnitude at higher temperature.

Carbon nanostructured materials are also considered for some electrochemical applications such as membrane support of catalyst for the electrocatalytic reduction of oxygen and the oxidation of methanol [200, 201], storage of lithium [202, 203], and supercapacitors [204, 205]. These properties are discussed later in detail.

5.3.5. Applications of Carbon Nanotubes

5.3.5.1. Biochemical Applications SWNTs can be cut into smaller sections using sonication in a mixture of concentrated sulfuric acid and nitric acid. This process makes the tube open. Once opened, tubes can be filled with a variety of materials, for example, enzymes, protein [206], and DNA [207]. The biomolecules appear to be encapsulated within an environment which offers some protection, and subsequent analysis of the catalytic activity of the immobilized enzymes showed that a significant amount of the enzyme retains its activity. Opening of tube tips has enabled the resultant OH and COOH groups to be functionalized using the standard chemical reaction conditions. For example, SWNTs have been functionalized at the opened tips by reaction with thionyl chloride and octadecylamine: the derivatized tubes are more soluble in organic solvents than their parent compounds and can subsequently be reacted further along the waists of the molecules [208]. This type of research is expected to help in drug delivery to infected human organs. A suitable drug can be inserted into the hollow space of the nanotubes and can be injected into body (with functionalized soluble carbon nanotubes). Drug will start operating slowly at the site, which is infected.

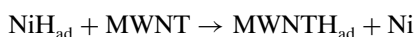
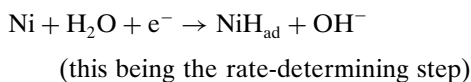
5.3.5.2. Hydrogen Storage by Carbon Nanotubes

Good reviews on hydrogen storage by adsorption in carbon nanotubes are given by Darkrim et al. [209] and Simonyan et al. [209, 210]. There are conflicting reports about the magnitude of hydrogen adsorbed by carbon nanotubes. However, soon we shall arrive at some results, which are reproducible. Dillon et al. [211] have reported that crystalline SWNTs have hydrogen capacity of 5–10 wt% at pressure less than 1 bar near room temperature. It has also been observed that some nanotubes can electrochemically store relatively large amount of (110 mA h g^{-1}) hydrogen, corresponding to a hydrogen storage capacity of 0.39 wt%. The reaction is reversible, indicating that the nanotubes can be used to produce electrodes for rechargeable batteries. Considering these properties, Rajalakshmi et al. [212] have made electrodes of purified and open single-walled carbon nanotubes and found them to behave like metal hydride electrodes in Ni-MH batteries, showing high electrochemical reversible charging capacity up to 800 mA h g^{-1} corresponding to hydrogen storage capacity of 2.9% compared

Table 4. Work function of MWNTs.

Sample	Work function (eV)	
	Ago [194]	Shiraishi [195]
Purified MWNTs	4.3	4.95
Air-oxidized MWNTs	4.4	—
Plasma-oxidized MWNTs	4.8	—
Acid-oxidized MWNTs	5.1	—
Highly oriented pyrolytic graphite (HOPG)	4.4	4.80
Single-walled nanotube (SWNTs)	—	5.05
C ₆₀	—	6.5

to known AB_5 , AB_2 metal hydride electrodes. The charging and discharging potential was around -0.8 and -0.6 V versus SCE, respectively. In a separate attempt, Qin et al. [213] reported that MWNTs are promising candidates for hydrogen storage. The electrochemical capacity of MWNTs-Ni electrode can reach over 200 mA h g^{-1} at a current density of 200 mA g^{-1} . MWNT-Ni electrode showed a high rate of discharge capacity and long charge-discharge cycle life. The electrochemical reaction of MWNTs-Ni was controlled by the step of the hydrogen adsorption and the hydrogen oxidation, that is,



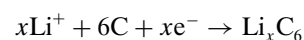
If this could be improved, then low-weight, high-power density Ni-carbon hydrogen battery could become a reality. Zuttel et al. [214] have tried to study the hydrogen storage capacity of carbon samples at room temperature by means of electrochemical galvanostatic measurement in a 6M KOH electrolyte. During the charge process, the water in the electrolyte dissociates at the working electrode (sample, negative electrode) into the adsorbed atomic hydrogen and OH^- ions remaining in the electrolyte. The adsorbed atomic hydrogen may intercalate in the electrode or recombine at the surface to molecular hydrogen and diffuse into the electrode or form gas bubbles at the surface of the electrode. During discharge process, the hydrogen in the electrode recombines with OH^- ions in the electrolyte to form water. This reaction is accompanied with a charge transfer and therefore, the amount of hydrogen desorbed from the electrode can be measured by measuring the electric charge, which is equal to the product of current and time in galvanostatic setup. In Zuttel's experiment, there is no evidence that discharged hydrogen has been completely adsorbed in the carbon. Hence, the experiment has to be designed such that one can be sure beyond any doubt discharge current is proportional to quantity of hydrogen gas adsorbed in the carbon matrix. This hydrogen storage is very attractive from the viewpoint of fuel cell technology, which requires a very high density of hydrogen molecules for clean combustion. The temperature programmed desorption (TPD) profiles of closed- and open-tip SWNTs with diameters of around 1.2 nm are compared with the results of activated carbon, which has micropores with diameter of around 3.0 nm. The peak at 133 K is seen to originate due to hydrogen molecules adsorbed inside the contamination amorphous carbon. This hydrogen is not useful because it cannot be used at room temperature. A peak at 288 K found only in the open-tip CNTs suggests that the hydrogen molecules are incorporated inside the hollow spaces of CNTs. The high-temperature desorption (288 K) of a large number of hydrogen molecules is a fascinating property for this application. The heat of adsorption for this site (19.6 kJ mol^{-1}) is larger than those for graphite ($\sim 4 \text{ kJ mol}^{-1}$) and activated carbons (12 kJ mol^{-1} for low coverage and 4 kJ mol^{-1} for high coverage). The well-aligned SWNTs with the diameter of 2.0 nm were predicted to be good candidates for use in vehicles, much better than metal hydrides [215]. It is reported that 4 wt% or higher of hydrogen can be stored in SWNT.

5.3.5.3. Lithium Secondary Battery One of the biggest advantages of lithium battery is that one can get operating voltage in the range of 4.7–5.0 V. The theoretical capacity of lithium metal is considerably high 3862 mA h g^{-1} . Since lithium reacts vigorously with water, it is difficult to get this power in aqueous solution. Alternative method is to use nonaqueous solution and some device such that lithium could be transported into the solution. Herold [216] reported the first synthesis of Li-intercalated graphite. Later Besenhard [217, 218] observed electrochemical intercalation of alkali metal in graphite that is immersed in a nonaqueous electrolyte. Cyclic voltammetry of graphite in dimethylsulfoxide (DMSO), 1,2-dimethoxyethane (DME), or PC indicated reversible electrochemical reduction at potential more positive than that for Li deposition. This was attributed to an intercalation reaction involving lithium. General formula for intercalated lithium can be Li_xC_y ; for $x = 1$, y is equal to 6 and for $x = 0.5$, y is equal to 12. For LiC_6 , the electrochemical capacity is equivalent to 372 mA h g^{-1} C, and 186 mA h g^{-1} for LiC_{12} . In some special cases, it has been possible to get 1600 mA h g^{-1} capacity but soon after first cycle of operation, the capacity falls down to 460 mA h g^{-1} . Introducing defect by ball-milling is found to improve the capacity to 1000 mA h g^{-1} .

This observation attracted scientists to develop lithium battery using graphite as an electrode. The overall charge (Li intercalation in carbon, de-intercalation of metal oxide) reaction in a Li-ion battery that contains graphitic carbon and a lithiated metal oxide (MO_2 , $M = \text{Co, Ni, or Mn}$) is



The electrochemical synthesis of Li-intercalated graphite in a nonaqueous electrolyte containing a lithium salt can be represented by



During charging, Li from the metal oxide is transferred to the carbon to form the negative electrode. Correspondingly, discharge (de-intercalation of Li from carbon) of Li-ion cell involves the reverse reaction. Lithiated carbon, in which the Li species are intercalated between the layer planes (i.e., in graphite) or associated with other sites (i.e., in disordered carbons), are produced by both chemical and electrochemical process. This transport of lithium back and forth during the charge and discharge process has led to the use of terminology such as “rocking chair,” “shuttlecock,” “SWING,” etc., to describe Li-ion cell. After the discovery of carbon nanotube, this idea has been extended to carbon nanotubes.

The electrochemical intercalation of lithium in MWNT was achieved by placing lithium metal foil, a polypropylene porous separator soaked with the electrolyte solution, and a cathode prepared by mixing nanotubes with 5% of black carbon and 5% of polytetrafluoroethylene (PTFE) as a binder. Electrolytes are normally prepared with LiPF_6 (1M) in carbonate mixture (EC:PC:3DMC) [219]. Shinoda et al. [220], however, has suggested that lithium intercalation is possible with open SWNT.

Sharon and co-workers [221–223] have studied the application of carbon nanotubes and carbon nanobeads prepared

from pyrolyzed camphor and observed that capacity of battery is as good as that obtained with graphitic carbon. Slurry of camphoric carbon nanotubes was made with acetylene black and ethylene propylene diene monomer as a binder in a proportion of 86:10:4. This slurry was spread evenly onto a finally polished copper sheet. Lithium metal was used as counterelectrode. A Celgard 2500 microporous polypropylene, wetted with dimethyl carbonate, served as a separator. 1M LiPF₆ solution, prepared in 1:1 mixture of dimethyl carbonate and ethylene carbonate, was used as the electrolyte.

Typically, the potential of the carbon is >1 V before Li intercalation takes place. In the case of highly graphitized carbon, when current is applied to intercalate Li, the potential initially drops rapidly to near 0.8 V (vs Li/Li⁺) where electrolyte decomposition and the formation of a surface film occur. When these reactions are taking place, the potential remains close to a constant value. Following electrolyte decomposition, the potential declines and the majority of Li intercalation occurs at <0.25 V. In the extreme case, electrolyte decomposition and gas evolution can occur with little or no lithium intercalation. In addition, the difference between the charge and discharge half cycles is attributed to the irreversible capacity loss, which represents the charge (coulomb) associated with electrolyte decomposition. Unfortunately, irreversible capacity is of the order of 120 mA h g⁻¹. Because the cell is manufactured in the discharged state, that is, no lithium present in the carbon structure, it is advantageous to minimize the irreversible capacity loss which reduces the amount of lithium that is available for the intercalation or insertion reactions.

Studies on various carbons indicate that the irreversible capacity loss increases with increase in the surface area. Nevertheless, some of the important properties that affect the electrochemical behavior of carbon in Li-ion cells are crystallinity, surface area, type and amount of surface groups, and particle size and shape. These parameters influence the capacity, cycle life, charge/discharge rate, and energy efficiency.

Recently, Fukutsuka et al. [224] have used sp² type carbonaceous thin film for insertion and extraction of lithium ion in a lithium secondary battery. However, the current density of only 26 mA g⁻¹ could be obtained with such films.

In commercial cells, LiCoO₂ is the dominant lithiated metal oxide in the positive electrode (i.e., for the cathode). Spinel structure oxides [225, 226] like LiNi_xMn_{2-x}O₄, LiNiVO₄ [227], LiCr_xMn_{2-x}O₄ [228], LiCu_xMn_{2-x}O₄ [229, 230], and less toxic spinel cathode Li₂FeMn₃O₈ [231] have also been used as cathode materials.

It is important to realize that though we can get the highest voltage with lithium battery, because lithium is scarcely available, in the long run, its cost can become very high for common man to use. On the other hand, other alkali metal like potassium, which is available in plenty, may prove to make a more cost-effective battery than lithium battery. Claye et al. [232] have been able to dope potassium into a SWNT. Since potassium is able to intercalate with SWNT, why not try to make a potassium battery?

5.3.5.4. Carbon Nanotubes as Supercapacitor Supercapacitors are intermediate systems between electrochemical batteries, which can store high energy associated with

low power values, and dielectric capacitors, which can deliver very high power during few milliseconds. There is a good review on this topic by Burke [233]. Supercapacitors are also called electrochemical capacitors, electric double layer capacitors, or ultracapacitors. They are classified into three types: (i) electrostatic capacitor, (ii) electrolytic capacitor, and (iii) electrochemical capacitor. The electrostatic capacitor has a small capacitance. However, it can be charged/discharged at high voltage. Examples are ceramic capacitor, glass capacitor, mica capacitor, etc. The electrolytic capacitor has been used most generally up to now, because it has a large specific capacitance. The electrochemical capacitor is a new type of capacitor offering new features. The electrical energy storage system utilizing charge-discharge process of electric double layer on porous electrode is called "electric double layer capacitor (EDLC)." The specific capacitance of electrochemical capacitor is much larger (over 10–1000 times) than that of conventional capacitors. They have many advantages compared to the secondary battery; for instance, long cycle life (>100,000 cycles), simple principle and mode of construction, short charging time, safety, and high power density. The energy density of supercapacitors, however, is smaller than that of secondary batteries.

The most common applications of double layer capacitor are as button cell, memory backup for electronic equipment. They are also used as auxiliary power sources in small appliances like laptop computers, alarms, VCR, telephones, etc. They are well suited as a backup source because of their energy storage density, low cost, and maintenance-free long life operation. They have been used as a memory backup device because of their high cycle efficiency and the long cycle life. Moreover, recently EDLC is expected as the subpower source for hybrid electric vehicle (HEV) because EDLC can provide high power density (from 0.5 to 20 kW kg⁻¹) during few seconds or more, which leads to specific energy densities ranging from 0.5 to 10 Wh kg⁻¹. The electrochemical capacitor can use either nonaqueous electrolyte system or aqueous electrolyte system. Nonaqueous system can work at high working voltage, but internal resistance is high and needs hermetic seal to avoid moisture absorption. Absorption of moisture spoils the performance of the capacitor. On the other hand, aqueous solvent system has high ion mobility and high dielectric constant, making the internal resistance very small. However, this works at low voltage (around 1.3 V).

There are three different types of EDLC supercapacitors: (i) carbon/carbon, (ii) metal oxide, and (iii) electronically conducting polymers. In carbon supercapacitors, the electric charge is stored between a high surface area of carbon electrode/electrolyte interface. In these systems, the use of organic electrolytes allows the increase of the working voltage as compared to aqueous electrolyte. The electrode is composed of a current collector (e.g., nickel foam) in contact with an activated carbon. The current collector has to be electrochemically inactive in the potential window in which the system works. The active material is an activated carbon. Under a powder form, activated carbon (approximately 95%) is mixed with a binder (about 5% mixture of binder like carboxymethylcellulose and PTFE) and sometimes with an electronic conductor in order to reach good mechanical

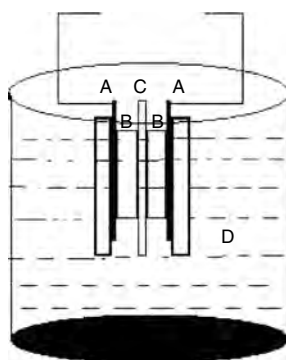
and electronic properties to the electrode. After drying, the active material is laminated on each side of the current collector, to make about 600- μm -thick electrode. A basic typical design of the electrochemical capacitor of configuration $\text{CNT}|\text{H}_2\text{SO}_4||\text{H}_2\text{SO}_4|\text{CNT}$ sandwiched between two pieces of carbon paper assembled between Perspex plates is shown in Figure 16.

Pellet of CNT (B) is charged with external potential and when needed the same charge can be discharged externally to get the power. In order to increase the capacitance, carbon nanotube needs to be activated. Activated carbon used in supercapacitors must possess the following characteristics: (i) a high specific surface area to ensure high specific capacitance value, (ii) a low resistivity, and (iii) a microstructure well adapted in order to allow good electrolyte accessibility into inner surface of the electrode. The practical electrode material for EDLC is porous carbon such as activated carbons. The high capacitance (100–200 F g^{-1}) is due to high specific area (1000 $\text{m}^2 \text{g}^{-1}$) produced by many micropores (2 nm > pore width). In general, it is believed that there is a proportional relationship between the specific surface area and the electric double layer capacitance of the activated carbon. The electric double layer capacitance can be calculated by the amount of electricity passed during the charge or discharge process by using the following equation [234]:

$$c = it/w\Delta V$$

where c = electric double layer capacitance (F g^{-1}), i = current (A), t = charge or discharge time (s), w = weight of activated carbon in the electrode (g), and ΔV = potential change during charge or discharge process.

The surface area of activated carbons results from a complicated porous structure which involves pores of different size: macropores (>500 Å wide), mesopores (20–500 Å), and micropores (<20 Å). The smaller the pore size, the more difficult it is for the electrolyte to get in and, hence, the



- A Pt electrode
- B CNT pellets
- C Filter paper soaked with 0.1M Sulphuric Acid
- D 0.1M Sulphuric Acid

Figure 16. Schematic diagram of a CNT based double layer capacitor. (A) Carbon paper, (B) CNT, (C) separator (filter paper soaked with electrolyte), (D) electrolyte. The assembly is held together by two Perspex plates.

capacitance of these materials depends not only on the surface area but also on the pore size distribution. At present, the best performing commercial activated carbons in organic electrolytes display capacitance values of about 120 F g^{-1} . These values are significantly lower than those in aqueous solutions.

Niju et al. [235] and Liu et al. [236] have suggested that carbon nanotubes can be used effectively as an electrode for supercapacitors. Barisci et al. [237] have found that electrode made out of nanotubes discharges faster in 1.0M NaCl solution at negative potential due to influence of dissolved oxygen. However, with 7.0M H_2SO_4 or 5.0M KOH, a different pattern is observed. A positive charge appeared to be better kept in acid while negative charge was more lasting in base, despite the influence of oxygen. Charges could be retained for more than 800 s.

Carbon aerogels, that is, a monolithic three-dimensional mesoporous network of carbon nanoparticles, are considered as promising materials for electrochemical capacitors [238]. The pyrolysis of organic aerogels based on resorcinol-formaldehyde (RF) or phenol-furfural (PF) precursors via a sol-gel process obtains carbon aerogels. The advantages of carbon aerogels for capacitor application are their high surface area, low density, good electrical conductivity, and the possibility of their usage without binding substances. The special porosity of aerogels is based on the interconnection with a specific surface area between 500 and 900 $\text{m}^2 \text{g}^{-1}$ and a high pore volume (0.4–2.6 $\text{cm}^3 \text{g}^{-1}$). It has been proved that carbon aerogels with a diameter of pores in the range from 3 to 13 nm pointed out the best voltammetry characteristics and the highest capacitance values (70–150 F g^{-1}).

5.3.5.5. Electron Field Emission In this section, we shall devote our efforts to discuss the electron field emission studies made with carbon nanomaterials only. Detailed theory and other experimental details have been discussed in earlier section dealing with diamond. One of the striking properties of carbon nanotube films is that they are exceptionally good field emitters. Sometimes it has been assumed, wrongly, that nanotubes behave like metallic needle to describe the field emission properties. This is clearly an overly simplified picture of the situation, because we have to deal with a covalently bonded nanoscaled system. Thus, in contrast to the emission mechanism of DLC and CVD diamond films, where the emission mechanism is disputed, the field emission from nanotubes is clearly governed by their geometrical field enhancing properties. The electron field emission phenomenon with carbon nanotubes has been explained by tunneling of electrons from localized states at a tip with energies close to the Fermi energy, stimulated by the enhancement of the electric field from their structure [239].

Recently, Bonard et al. [240] developed a field emission diode in a cylindrical geometry with MWNTs deposited on the metallic cathode as the electron source. [Kanthal (Fe-Al-Cr) wire on which a liquid Fe catalyst is applied by dipping the rod in an ethanolic solution of 40 mM $\text{Fe}(\text{NO})_3 \cdot 9\text{H}_2\text{O}$ and dried.] This rod is heated to 720 °C and acetylene vapor is pyrolyzed to get a deposition of MWNTs over the rod. This coaxial rod coated with carbon nanotube is

found to give electron field emission. Most interesting part of this report is in observing electron emission even when anode and cathode are separated by a distance of 20 mm. They could show even illumination of tube by this method. A cylindrical assembly of luminescent tube containing carbon nanotube coated wire at its axis showed emission of light intensity like conventional mercury tube giving intensity to $10,000 \text{ cd cm}^{-2}$. It is suggested that this assembly may have applications in vacuum gauges of magnetic field sensors.

Bonard et al. [241] observed that maximum current that could be drawn from one MWNT was $\sim 0.2 \text{ mA}$. The emission current was stable for few seconds before a catastrophic failure of the emission. Mostly large diameter tubes remained on the film after emission. It is very probable that the small diameter tubes were destroyed, through the ion bombardment (by gas phase electron ionization or by ion desorption from the anode or the isolator, both induced by the emitted electrons). On single nanotube tip, stable emission was observed for more than 100 hr at $\sim 2 \mu\text{A}$ emission current (with 300 V).

Based on the Fowler–Nordheim model, it was calculated that electric field at the tip of SWNT is enhanced to about 1300 times what is observed with DLC, but there is some discussion on the validity of this model to SWNT. The model that electrons are emitted from single atomic wires protruding from the tip of CNTs is still hypothetical and has not been confirmed. It is very interesting to note that the opening of tips by oxidation with either oxygen-plasma treatment or by heating in oxygen gas makes the CNTs more highly emissive [242–244]. For this purpose, they produced aligned carbon nanotube films. An ethanol dispersion of the arc-produced carbon nanotubes is allowed to pass through an aluminum oxide micropore filter. In the filtration process, the nanotubes get stuck in the pores of the filter, causing them to stand perpendicular to the filter surface. The nanotubes-covered filter is placed face down on a teflon sheet and the nanotubes are printed onto the sheet under pressure, producing a layer of more or less vertically aligned nanotubes. This sheet is then covered with a perforated mica sheet of thickness 30 μm . A current was observed when a potential was applied between the carbon nanotubes (cathode) and the anode kept over the mica sheet. The I-V curve followed Fowler–Nordheim behavior. Carbon nanotubes/organic semiconducting polymer heterojunction has been found to show a rectifying behavior [245]. Over a teflon sheet, first carbon nanotubes are deposited, followed by deposition of a semiconductor polymer (commercially available di-cholestanol derivative of poly(p-phenylenevinylene), poly(2,5-bis(cholestanoxyl)-1,4-phenylenevinylene), and then finally a thin film of aluminum or gold is deposited to give the ohmic contact. Threshold field for electron emission can be as low as $1 \text{ V } \mu\text{m}^{-1}$. It is argued that the emission results from sharp tips, as their work function is that of graphite, 4.7 eV.

5.4. Activated Carbon

Among the different forms of carbon materials, activated carbons are especially attractive as electrodes for capacitors from an economical point of view. In this case, a very developed surface area of the order of $2000 \text{ m}^2 \text{ g}^{-1}$, with a controlled distribution of pores during the activation process,

can be reached. Theoretically, the higher the specific surface area of an activated carbon, the higher the specific capacitance should be expected. The relationships between the BET surface area, the total pore volume, the average pore size, and the pore size distribution of activated carbon and its electrochemical performance as electrodes for supercapacitors have been discussed in detail by Shi and co-worker [246, 247].

Activated carbon has been extensively used as adsorbents, catalysts, and catalyst supports for the removal of pollutant species from gases or liquids and for purification or recovery of chemicals. Porosity of activated carbon is dependent not only on the starting materials (like coal, wood, coconut shell, etc), but also on the activation methods and processes. The processes for the preparation of activated carbons can be classified into two categories: physical and chemical activation. Physical activation involves carbonization of the raw materials followed by gasification of the resulting char in the presence of some oxidizing agents, such as steam or CO_2 . The chemical activation is performed by the thermal decomposition of the precursor materials impregnated with chemical agents, such as KOH, ZnCl_2 , and H_3PO_4 . In the chemical activation, all chemicals act as dehydrating agents, promoting the formation of cross-link, resulting in the formation of rigid matrix. Surface functional group of activated carbon fibers can be improved by treatment with sulfuric acid, H_3PO_4 , and HNO_3 . Such activated carbon fibers are found to show increase in the absorption capacity of NH_3 [248] and chromium [249].

Other form of carbon, which has been known for ages, is carbon fiber. The basic structural unit of a carbon fiber is a planar network of connected benzene rings. These graphene planes are stacked on top of each other like the pages of a newspaper.

Hollow fibers are produced since carbon cannot reach the back of the particle. The growth will continue as long as the metal particle is covered by carbon and no clean surface is available. Therefore, from many points of view, nanotube can be considered as an extension of carbon fibers on a nanometer scale. Hollow coaxial tubes of graphitic sheets, ranging in number from 2 to 50, are typically observed in fullerene soot. The separation between concentric sheets is approximately 3.5 \AA corresponding to (002) plane of graphite. The inner diameter varies between 1 and 3 nm.

6. NEED FOR PRECURSORS NOT DERIVED FROM FOSSIL FUELS

From these discussions, it is amply clear that though new forms of carbons like fullerenes, carbon nanotube, diamond films, and DLC films, are extremely useful forms of carbon and have many industrial applications, these materials have not been synthesized economically to be commercially attractive.

The sophistication needed by the conventional methods to get these materials in large quantity is the major reason for synthesis being uneconomical. This is primarily because most of the processes used for the synthesis of these materials include precursors containing either 100% sp^3 carbon

bonded materials or 100% sp^2 carbon bonded materials. The new carbon materials like nanomaterials belong to the intermediate class of carbon (as suggested in this chapter); their structures need the presence of a mixture of sp^3 and sp^2 carbon bonded materials. Hence, it becomes essential to convert one of the pure forms of carbon, either sp^3 to sp^2 carbon bonded materials or vice versa, as the case may be, so that the resulting material has the required proportion of sp^3 and sp^2 carbon bonded atoms.

In addition, earlier discussions also revealed that all these nanomaterials need a combination of hexagonal and pentagonal structures. Most of the conventional precursors have only the hexagonal structures. For the formation of pentagonal structure, carbon of the precursor must break into elemental carbon to build the requisite number of pentagonal structures as and when needed during the synthesis. Therefore, there is a need to investigate some new type of precursor which meets above requirements as well as not being derived from fossil fuels like petroleum products. Sharon and his group have been exploring possible uses of precursors which are plant based, like camphor, turpentine oil, cashew nut oil, coconut shell oil, mustard oil, linseed oil, etc. With these precursors, their group has been able to synthesize almost all forms of carbon nanomaterials which are synthesized from petroleum based precursors like acetylene, benzene, etc. The advantage of plant based precursors is that when technology of carbon nanotechnology is established, it would have no fear of nonavailability of source materials, because one can cultivate them as and when needed, within few months period, whereas fossil fuels are destined to deplete one day and cannot be synthesized in such short span of time.

7. SUMMARY

Emphasis is made to classify carbon materials based on percentage of carbon atoms of sp^3 type present in the samples rather than conventional classification. This type of classification opens a Pandora's box to prepare varieties of novel carbon materials. Various types of novel carbon materials, which have been synthesized by various techniques using various precursors, are discussed. Efforts have also been made to discuss the various newer applications of the novel carbon materials. Finally, a point has been brought to suggest that there is a need to discover nonconventional precursors which can be grown by cultivation and which are not related to fossil fuels.

GLOSSARY

Camphor A white crystalline substance, obtained from the tree *Cinnamomum camphora*, but the name has been given to various concrete odorous volatile products, found in different aromatic plants. The commercial Camphor comes only from *C. camphora* and *Dryobalanops camphora* (fam. *Dipterocarpaceae*). *C. camphora* is an evergreen tree; it grows to a great size. While the tree grows in China, etc., it can be cultivated successfully in sub-tropical countries, such as India and Ceylon, and it will thrive in Egypt, Formosa, Madagascar, Canary Islands and southern parts of Europe, California, Florida, and also in Argentina. The odor is peculiar, like

sassafras and distinctly camphoraceous; this oil is said to be used in Japan for burning, making varnish, and for Chinese inks, as a diluent for artists' colors; it has a capacity for dissolving resins that oil of Turps has not. There is an erroneous idea that camphor acts as a preventive to infectious diseases. It is a well-known preventive of moths and other insects, such as worms in wood.

Chemical vapor deposition (CVD) One of the efficient ways of implementing vapor phase deposition in a manufacturing environment. Unlike physical deposition, CVD involves chemical reactions on the surface.

cw-CO₂ This laser is capable of continuously generating high power as much as 10 kW at a relatively ~40% efficiency. The active medium of the laser is a gas mixture of CO₂ and nitrogen with additive like He and water vapour.

Dangling bond At the interface of any solid material, for example, diamond, some of the bonds of carbon present at the interface is broken due to absence of carbon (i.e., at the interface), leaving carbon with an additional single unpaired electron. This unpaired electron can form bond with other material present at the interface. This type of bond is often referred as dangling bond to differentiate from normal covalent bond. Dangling bond is not of permanent type as covalent.

Electron affinity The energy difference between the energy state of a neutral atom and the energy state of a negative ion of the same atom is called electron affinity.

Fermi-Dirac statistics After the development of quantum mechanics, Sommerfeld modified the free electron theory by replacing the classical statistics of Boltzmann by the quantum statistics of Fermi and Dirac. The free electron theory suggests that all electron of the metal can have same energy so that, at the absolute zero of temperature, they all occupy the lowest available energy levels.

Fullerene A class of cage-like carbon compounds composed of fused, pentagonal and/or hexagonal sp^2 carbon rings. Fullerenes were first discovered in 1985 when the soccer ball shaped C₆₀ (Buckminsterfullerene) was synthesized. The carbon atoms in C₆₀ are arranged in a geometric shape consisting of 12 pentagons and 20 hexagons.

Hall Mobility The conductivity σ can be defined in terms of the number of conduction electrons (or holes) by $\sigma = n e \mu$, where μ is the mobility and is equal to the drift velocity per unit field. It has been shown by Hall that both the mobility and the mean free path of the electrons (or holes) can be determined experimentally. Thus conventionally mobility is also referred as Hall mobility.

Laser An acronym of light amplification by stimulated emission of radiation. They are monochromatic in nature and can be generated from various systems, like cw-CO₂, Nd-YAG etc.

Nd-YAG The neodymium doped yttrium aluminium garnet laser is a solid-state laser.

Pyrolysis Formally defined as chemical decomposition induced in organic materials by heat in the absence of oxygen. In practice, it is not possible to achieve a completely oxygen-free atmosphere; actual pyrolytic systems are operated with less than stoichiometric quantities of oxygen.

Because some oxygen will be present in any pyrolytic system, nominal oxidation will occur. If volatile or semivolatile materials are present in the waste, thermal desorption will also occur.

Work function The work that must be done to remove an electron, which is inside the material at a distance far removed from the material, is called as the work function.

REFERENCES

- J. S. Noh, R. K. Agrawal, and J. A. Schwarz, *Int. Hydrogen Energy* 12, 693 (1987).
- N. K. Sharma, W. S. Williams, and A. Zangvil, *J. Am. Ceram. Soc.* 67, 715 (1984).
- H. W. Kroto, J. R. Heath, S. C. O'Brien, R. F. Curl, and R. E. Smalley, *Nature* 318, 162 (1985).
- W. Kratchmer, D. L. Lamb, K. Fostiropoulos, and D. R. Huffman, *Nature* 347, 345 (1990).
- L. S. Pan, S. Han, D. R. Kania, and K. Okano, *Diamond Films Technol.* 2, 99 (1992).
- K. Mukhopadhyay, K. M. Krishna, and M. Sharon, *Mater. Chem. Phys.* 49, 252 (1997).
- M. N. R. Ashfold, P. W. May, C. A. Rego, and M. Everitt, *Chem. Soc. Rev.* 23, 21 (1994).
- W. P. May, *Philos. Trans. R. Soc. London Ser. A* 358, 473 (2000).
- N. Slobodan and J. S. Marinkovic, *Chem. Soc.* 62, 81 (1997).
- M. Sharon and A. Chatterjee, *J. Power Sources* (submitted) (2003).
- T. Sugino, K. Kuriyama, C. Kimura, and S. Kawasaki, *Appl. Phys. Lett.* 73, 268 (1998).
- G. Fuge, Investigation of Sulfur Doped Diamond Films Grown by Microwave Plasma Enhanced Chemical Vapour Deposition, B.Sc. Thesis, University of Bristol, 2001. <http://www.chm.bris.ac.uk/~gf8856/BScThesis.htm>.
- K. Okano, S. Koizumi, S. Ravi, P. Silva, and A. J. G. Amarantunga, *Nature* 381, 140 (1996).
- M. W. Geis, *Mater. Res. Soc. Symp. Proc.* 62, 15 (1990).
- N. G. Ferreira, L. L. G. Silva, E. J. Corat, V. J. Trava-Airoldi, and K. Iha, *Brazilian J. Phys.* 29, 760 (1999).
- M. Sharon, S. Jain, P. D. Kichambre, and M. Kumar, *Mater. Chem. Phys.* 56, 284 (1998).
- P. Briddon and R. Jones, *Phys. B* 179, 185 (1993).
- E. J. Chi, J. Y. Shim, and H. K. Baik, *J. Vac. Sci. Technol. B* 17, 728 (1999).
- S. Koizumi, H. Ozaki, M. Kamo, Y. Sato, and T. Inuzuka, *Appl. Phys. Lett.* 71, 1065 (1997).
- D. Zhou, D. M. Gruen, L. C. Qin, T. G. McCauley, and A. R. Krauss, *J. Appl. Phys.* 84, 1981 (1998).
- W. A. Yarbrough and R. Messier, *Science* 247, 688 (1990).
- Q. Chen, D. M. Gruen, A. R. Krauss, T. D. Corrigan, M. Witek, and G. M. Swain, *J. Electrochem. Soc.* 148, E44 (2001).
- L. Allers and A. T. Collins, *J. Appl. Phys.* 77, 3879 (1995).
- H. Okushi, *Diamond Related Mater.* 10, 281 (2001).
- R. Tenne and C. Levy-Clement, *Israel J. Chem.* 38, 57 (1998).
- W. I. Milne, J. Robertson, B. S. Satyanarayana, and A. Hart, *Appl. Phys. Lett.* 71, 1430 (1997).
- D. Takeuchi, S. Yamanaka, H. Wantanabe, and H. Okushi, *Phys. Stat. Sol. (a)* 186, 269 (2001).
- S. A. Kajihara, A. Antonelli, and J. Bernholc, *Phys. Rev. Lett.* 66, 2010 (1991).
- J. Robertson, *Mat. Res. Soc.* 471, 217 (1997).
- J. B. Cui, J. Ristein, and L. Ley, *Phys. Rev. Lett.* 81, 429 (1998).
- F. Beck, W. Kaiser, and H. Krohn, *Electrochim. Acta* 45, 4691 (2000).
- J. Xu, C. M. Ganger, Q. Chen, W. Jerzy, S. Tedd, E. Lister, M. Greg, and M. Swain, *Anal. Chem.* 69, 591A (1997).
- A. Ferro, I. De Battisti, Ch. Duo, W. Comninellis, A. Haenni, and J. Perret, *Electrochem. Soc.* 147, 2614 (2000).
- E. I. Givargizov, V. V. Zhirnov, N. N. Chubun, and A. N. Stepanova, *J. Vac. Sci. Technol. B* 15, 442 (1997).
- A. Modinos, *Surf. Sci.* 42, 205 (1975).
- F. J. Himpsel, J. A. Knapp, J. A. Van Vechten, and D. A. Eastman, *Phys. Rev. B* 20, 624 (1979).
- B. B. Pate, *Surf. Sci.* 120, 83 (1986).
- C. Xie, C. N. Potter, R. L. Fink, C. Hilbert, A. Krishnan, D. Eichenman, N. Kumar, H. K. Schmidt, M. H. Klark, A. Ross, B. Lin, L. Fredin, B. Baker, D. Patterson, and W. Brookover, *Rev. Vide Couches Mines Suppl.* 271, 229 (1994).
- E. I. Givargizov, V. V. Zhirnov, N. N. Chubun, and A. N. Stepanova, *J. Vac. Sci. Technol. B* 15, 450 (1997).
- M. Kumar, M. Sharon, Y. Ando, and X. Zhao, *Diamond Related Mater.* 10, 883 (2001).
- H. Todokoro, N. Saitou, and S. Yamamoto, *J. Appl. Phys.* 10, 1513 (1982).
- Ch. Klient, *Surf. Sci.* 25, 394 (1971).
- R. Gomer, *Surf. Sci.* 38, 373 (1973).
- J. E. Yater, A. Shih, and R. Abrams, *J. Vac. Sci. Technol. A* 16, 913 (1998).
- T. Sugino, Y. Iwasaki, S. Kawasaki, R. Hattori, and J. Shirafuji, *Diamond Related Mater.* 6, 889 (1997).
- M. W. Geis, J. C. Twichell, N. N. Efremov, K. Krohn, and T. M. Lyszczarz, *Appl. Phys. Lett.* 68, 2294 (1996).
- P. H. Cutler, N. M. Miskovsky, P. B. Lerner, and M. S. Chung, *Appl. Surf. Sci.* 146, 126 (1999).
- B. L. Druz, V. I. Polyakov, A. V. Karabutov, N. M. Rossukanyi, A. I. Rukovichnicov, E. Ostan, A. Hayes, V. D. Frolov, and V. I. Konov, *Diamond Related Mater.* 7, 695 (1998).
- A. V. Karabutov, V. I. Konov, V. G. Ralchenko, E. D. Obratsova, V. D. Frolov, S. A. Ugllov, and M. S. Nunuparov, *J. Chemical Vapor Deposition* 5, 348 (1997).
- B. S. Satyanarayana, A. Hart, W. I. Milne, and J. Robertson, *Appl. Phys. Lett.* 71, 1430 (1997).
- R. G. Forbes, *Ultramicroscopy* 79, 11 (1999).
- X. Zhao, M. Ohkohchi, H. Shimoyama, and Y. Ando, *J. Cryst. Growth* 198/199, 934 (1999).
- M. Yudasak, K. Tasaka, R. Kikuchi, Y. Ohki, and S. Yoshimura, *J. Appl. Phys.* 81, 7623 (1997).
- D. Tomanek, R. M. Wentzcovitch, S. G. Louie, and M. L. Cohen, *Phys. Rev. B* 37, 3134 (1988).
- A. Y. Liu, R. M. Wentzcovitch, and M. L. Cohen, *Phys. Rev. B* 39, 1760 (1989).
- K. M. Krishan, *Appl. Phys. Lett.* 58, 1857 (1991).
- A. Y. Liu and R. M. Wentzcovitch, *Phys. Rev. B* 50, 10362 (1994).
- C. E. Lowell, *J. Am. Ceram. Soc.* 7, 175 (1967).
- A. G. Whittaker and P. L. Kintner, *Science* 165, 589 (1969).
- L. Kavan and F. P. Dousek, *Synth. Met.* 58, 63 (1993).
- Y. P. Kudryavtsev and S. E. Evsyukov, *Diamond Relat. Mater.* 6, 1743 (1997).
- H. W. Kroto and D. R. M. Walton, *Philos. Trans. R. Soc. London Ser. A* 343, 103 (1993).
- T. Fukuoka, *Fushokufu-Iyoho* 6-8, 1999 (1999).
- M. Inagaki, M. Toyoda, N. Iwashita, Y. Nishi, and H. Konno, *Carbon Sci.* 2, 1 (2001).
- R. E. Clausing, "Diamond and Diamond Like Films and Coatings," p. 173. Plenum, New York, 1990.
- R. Biswas, R. M. Martin, R. J. Needs, and O. H. Nielson, *Phys. Rev. B* 35, 9559 (1987).
- D. R. McKenzie, *Rep. Prog. Phys.* 59, 1611 (1996).
- F. Xiong, Y. Y. Wang, and R. P. H. Chang, *Phys. Rev. B* 48, 8016 (1993).
- S. Zhang, B. Wang, and J. Y. Tang, *Surf. Eng.* 13, 303 (1997).
- M. Sharon, D. Pradhan, Y. Ando, and X. Zhao, *Current Appl. Phys.* 2, 445 (2002).

71. G. Jungnickel, T. Frauenheim, D. Povezag, P. Blandeck, and U. Stephan, *Phys. Rev. B* 50, 6709 (1994).
72. G. Jungnickel, T. Frauenheim, D. Povezag, P. Blandeck, and U. Stephan, *Phys. Rev. B* 49, 1489 (1994).
73. G. A. J. Amaratunga, M. Chhowalla, K. G. Lim, D. A. L. Munindradasa, S. D. Pringle, M. Baxendale, I. Alexandrou, C. J. Kiely, and B. Keyse, *Carbon* 36, 575 (1998).
74. B. S. Satyanarayana, A. Hart, W. I. Milne, and J. Robertson, *Appl. Phys. Lett.* 71, 1430 (1997).
75. Q. Wei, J. Shankar, A. K. Sharma, S. Oktyabrsky, J. Narayan, and R. J. Narayan, *J. Mater. Res.* 15, 633 (2000).
76. M. Sharon, M. Kumar, P. D. Kichambre, and M. Neumann-Spallart, *J. Appl. Electrochem.* 28, 1399 (1998).
77. J. Nemanich, J. T. Glass, G. Lucovsky, and R. E. Schroder, *J. Vac. Sci. Technol. A* 6, 1783 (1988).
78. F. Tuinstra and J. Koenig, *J. Chem. Phys.* 53, 1126 (1970).
79. J. Schwan, S. Ulrich, V. Batori, H. Ehrhardt, and S. R. P. Silva, *J. Appl. Phys.* 80, 440 (1996).
80. H. Sakata, G. Dresselhaus, M. S. Dresselhaus, and M. Endo, *J. Appl. Phys.* 63, 2769 (1988).
81. S. Zhang, B. Wang, and J. Y. Tang, *Surf. Eng.* 13, 303 (1997).
82. H.-F. Cheng, F. Y. Chung, C.-H. Tsai, W.-C. Wang, C.-M. Huang, and I.-N. Lin, *Appl. Surf. Sci.* 142, 504 (1999).
83. D. Guo, K. Cai, L.-T. Li, Y. Huang, Z.-L. Gui, and H.-S. Zhu, *Chem. Phys. Lett.* 329, 346 (2000).
84. F. Tuinstra and J. Koenig, *J. Chem. Phys.* 53, 1126 (1970).
85. Y. Ando, X. Zhao, H. Shimoyama, G. Sakai, and K. Kaneto, *J. Inorg. Mater.* 1, 77 (1999).
86. J. W. Ager, III, *IEEE Trans. Magn.* 29, 259 (1993).
87. V. S. Veerasamy, G. A. J. Amaratunga, W. L. Milne, P. Hewitt, P. J. Fallon, D. R. McKenzie, and C. A. Davis, *Diamond Related Mater.* 2, 782 (1993).
88. J. J. Hauser, *J. Non-Cryst. Solids* 23, 21 (1977).
89. M. A. Petrich, *Mater. Sci. Forum* 52/53, 387 (1989).
90. Y. U. Hong-an, T. Kaneko, S. Otani, Y. Sasaki, Y. Suhng, and S. Yohimura, *Jpn. J. Appl. Phys.* 37, 59 (1998).
91. D. B. Romero, M. Carrard, W. De Heer, and L. Zuppiroli, *Adv. Mater.* 8, 899 (1996).
92. M. Sharon, I. Mukhopadhyay, and K. Mukhopadhyay, *Solar Energy Mater. Solar Cells* 45, 35 (1997).
93. K. M. Krishna, T. Soga, K. Mukhopadhyay, M. Sharon, and M. Umeno, *Solar Energy Mater. Solar Cells* 48, 25 (1997).
94. K. Mukhopadhyay, I. Mukhopadhyay, M. Sharon, T. Soga, and M. Umeno, *Carbon* 35, 863 (1997).
95. T. Soga, T. Jimbo, K. M. Krishna, and U. Umeno, *Int. J. Mod. Phys. B* 14, 206 (2000).
96. T. Sugino, T. Itagaki, and J. Shirafuji, *Diamond Relat. Mater.* 5, 714 (1996).
97. Y. V. Plescov, A. Y. Sakharova, M. D. Krotova, L. L. Bouilov, and B. V. Sitsyn, *J. Electroanal. Chem.* 228, 19 (1987).
98. Y. V. Plescov, A. Y. Sakharova, E. V. Kasatkin, and V. A. Shepelin, *J. Electroanal. Chem.* 344, 401 (1993).
99. Y. V. Plescov, A. Y. Sakharova, F. D. Quarto, S. Piazza, C. Sunseri, I. G. Teremetskaya, and V. P. Varnin, *Russ. J. Electrochem.* 31, 169 (1995).
100. Y. V. Plescov, A. Y. Sakharova, F. D. Quarto, S. Piazza, C. Sunseri, I. G. Teremetskaya, V. P. Varnin, and V. Y. Mishuk, *J. Electrochem. Soc.* 142, 2704 (1995).
101. Y. V. Plescov, A. Y. Sakharova, I. G. Teremetskaya, V. P. Varnin, and I. G. Churikov, *Russ. J. Electrochem.* 32, 1075 (1996).
102. L. Boonma, T. Yano, D. A. Tryk, K. Hashimoto, and A. Fujishima, *J. Electrochem. Soc.* 144, L142 (1997).
103. H. Ago, K. Petritsch, M. S. P. Shaffer, A. H. Windle, and R. H. Friend, *Adv. Mater.* 11, 1281 (1999).
104. E. A. Katz, D. Faiman, S. Goren, S. Shtutina, B. Mishori, and Yoram Shapira, "Proceedings of the 14th European Photovoltaic Solar Energy Conference and Exhibition," 1997.
105. A. A. Dadykin, A. G. Naumovets, N. V. Novikov, V. D. Andreev, T. A. Nachalnaya, and V. A. Semenovich, "Proceedings of the 3rd International Symposium on Diamond Films," 1998, p. 38.
106. N. S. Xu, Y. Tzeng, and R. V. Latham, *J. Phys. D* 26, 1776 (1993).
107. H.-F. Cheng, J.-G. Kao, and T.-S. Lai, *Appl. Surf. Sci.* 142, 490 (1999).
108. G. A. Amaratunga and S. R. P. Silva, *Appl. Phys. Lett.* 68, 2529 (1996).
109. B. S. Satyanarayana, A. Hart, W. I. Milne, and J. Robertson, *Appl. Phys. Lett.* 71, 1430 (1970).
110. M. T. Kuo, P. W. May, A. Gunn, J. C. Marshall, M. N. R. Ashfold, and K. N. Rosser, *Int. J. Mod. Phys. B* 14, 295 (2000).
111. Y. E. Lozovik and A. M. Popov, *Phys. Usp.* 40, 717 (1997).
112. B. Mishori, E. A. Katz, D. Faiman, and Y. Shapira, *Solid State Commun.* 102, 489 (1997).
113. D. Faiman, S. Goren, E. A. Katz, M. Koltun, N. Melnik, A. Shames, and S. Shtutina, *Thin Solid Films* 295, 283 (1997).
114. H. Kuzmany, J. Fink, M. Mehring, and S. Roth, "Proceedings of the International Winter School on Electronic Properties of Novel Materials," 1996, p. 618.
115. S. Licht, O. Khaselev, P. A. Ramakrishnam, D. Faiman, E. A. Katz, A. Shames, and S. Goren, *Solar Energy Mater. Solar Cells* 51, 9 (1998).
116. J. E. Field, Ed., "The Properties of Natural and Synthetic Diamond." Academic Press, London, 1992.
117. B. T. Kelly, "Physics of Graphite." Applied Science Publishers, London, 1981.
118. X. D. Wang, T. Hashizume, H. Shinohara, Y. Saito, Y. Nishina, and T. Sakurai, *Phys. Rev. B* 47, 15923 (1993).
119. J. Nasca, J. Segesdi, A. Gyuris, T. Braun, H. Rausch, A. Buvari-Barcza, L. Barcza, J. Minarovits, and J. Molnar, *Fullerene Sci. Technol.* 5, 969 (1997).
120. T. H. Ueng, J. J. Kang, H. W. Wang, Y. W. Cheng, and L. Y. Chiang, *Toxicol. Lett.* 93, 29 (1997).
121. Y. Tabata, Y. Murakami, and Y. Ikada, *Fullerene Sci. Technol.* 5, 989 (1997).
122. P. Milani, *Riv. Nuovo Cimento* 19, 1 (1996).
123. F. G. Hopwood, K. J. Fisher, P. Greenhill, G. D. Willett, and R. Zhang, *J. Phys. Chem. B* 101, 1070 (1997).
124. K. Mukhopadhyay, K. M. Krishna, and M. Sharon, *Phys. Rev. Lett.* 72, 3182 (1994).
125. Y. Chia, T. Guo, C. Jin, R. E. Haufler, L. P. F. Chibante, J. Fure, L. Wang, J. M. Alford, and R. E. Smalley, *J. Phys. Chem.* 95, 239 (1991).
126. M. Terrones, W. K. Hsu, H. W. Kroto, and D. R. M. Walton, *Top. Curr. Chem.* 199, 190 (1999).
127. C.-H. King, M. Endo, P. M. Ajayan, G. Dresselhaus, and M. S. Dresselhaus, *Phys. Rev. Lett.* 81, 1869 (1998).
128. A. Kasuya, M. Sugano, T. Maeda, Y. Saito, K. Tohji, H. Takahashi, Y. Sasaki, M. Fukushima, C. Horie, and Y. Nishina, *Phys. Rev. B* 57, 57 (1998).
129. A. Kasuya, Y. Sasaki, Y. Saito, K. Tohji, and Y. Nishina, *Phys. Rev. Lett.* 78, 4434 (1997).
130. T. W. Odom, J.-L. Huang, P. Kim, and C. M. Lieber, *Nature* 391, 62 (1998).
131. T. Pichler, M. Knapfer, M. S. Golden, J. Fink, A. Rinzler, and R. E. Smalley, *Phys. Rev. Lett.* 80, 4729 (1998).
132. M. S. Dresselhaus, G. Dresselhaus, and P. C. Eklund, "Science of Fullerenes and Carbon Nanotubes." Academic Press, San Diego, 1996.
133. G. A. J. Amaratunga, M. Chhowalla, K. G. Lim, D. A. I. Munindradasa, S. D. Pringle, M. Baxendale, I. Alexandrou, C. J. Kiely, and B. Keyse, *Carbon* 36, 575 (1998).
134. S. Iijima, *Nature* 354, 56 (1991).
135. S. Iijima, T. Ichihashi, and Y. Ando, *Appl. Phys.* 32, L107 (1993).
136. E. G. Rakov, *Russ. Chem. Rev.* 69, 35 (2000).
137. Y. Ando and X. Zhao, *Mol. Cryst. Liq. Cryst.* 340, 707 (2000).

138. C.-H. Kiang and W. A. Goddard III, *Phys. Rev. Lett.* 76, 2515 (1996).
139. C. J. Lee, S. C. Lyu, H.-W. Kim, C.-Y. Park, and C.-W. Yang, *Chem. Phys. Lett.* 359, 109 (2002).
140. K. Mukhopadhyay and M. Sharon, *Mater. Chem. Phys.* 49, 105 (1997).
141. D. Pradhan and M. Sharon, *Mater. Sci. Eng. B* 96, 24 (1996).
142. K. Mukhopadhyay, A. Koshio, T. Sugai, N. Tanaka, H. Shinohara, Z. Konya, and J. B. Negy, *Chem. Phys. Lett.* 303, 117 (1999).
143. S. Fan, M. G. Chapline, N. R. Franlin, T. W. Tombler, A. M. Cassell, and H. Dai, *Science* 283, 512 (1999).
144. J. Li, C. Papadopoulos, J. M. Xu, and M. Moskovits, *Appl. Phys. Lett.* 75, 367 (1999).
145. M. Terrones, N. Grobert, J. P. Zhang, H. Terrones, K. Kordatos, W. K. Hsu, J. P. Hare, P. D. Townsend, K. Prassides, A. K. Cheetham, H. W. Kroto, and D. R. M. Walton, *Nature (London)* 388, 52 (1997).
146. Z. F. Ren, Z. P. Huang, J. W. Xu, J. H. Wang, P. Bush, M. P. Siegal, and P. N. Provencio, *Science* 282, 1105 (1998).
147. M. Sharon, R. Zacharia, P. R. Apte, and S. C. Purandare, *J. Appl. Phys.* (submitted).
148. P. J. Ross, "Taguchi Techniques for Quality Engineering." McGraw-Hill, New York, 1988.
149. J.-C. Charlier, A. De Vita, X. Blasé, and R. Car, *Science* 275, 646 (1997).
150. S. Seraphin and D. Zhou, *Appl. Phys. Lett.* 64, 2087 (1994).
151. S. Seraphin, *J. Electrochem. Soc.* 142, 290 (1995).
152. A. Loiseau and H. Pascard, *Chem. Phys. Lett.* 256, 246 (1996).
153. C. Journet, W. K. Maser, P. Berner, A. Loiseau, M. L. de la Chapelle, S. Lefrant, P. Deniard, R. Lee, and J. E. Fischer, *Nature (London)* 388, 756 (1997).
154. Z. P. Huang, J. W. Xu, Z. F. Ren, J. H. Wang, M. P. Siegal, and P. N. Provencio, *Appl. Phys. Lett.* 73, 3845 (1998).
155. H. Terrones, M. Terrones, and W. K. Tsu, *Chem. Soc. Rev.* 24, 341 (1995).
156. M. Endo, K. Takeuchi, H. W. Kroto, and A. Sarkar, *Carbon* 33, 873 (1995).
157. A. Sarkar, H. W. Kroto, and M. Endo, *Carbon* 33, 51 (1995).
158. D. Bernaerts, X. B. Zhang, S. Amelinckx, G. Van Tendeloo, J. Van Landuyt, V. Ivanov, and J. B. Nagy, *Philos. Mag. A* 71, 605 (1995).
159. R. Sen, A. Govindaraj, and C. N. R. Rao, *Chem. Phys. Lett.* 267, 276 (1997).
160. H. M. Cheng, F. Li, X. Sun, S. D. M. Brown, M. A. Pimenta, A. Marucci, G. Dresselhaus, and M. S. Dresselhaus, *Chem. Phys. Lett.* 289, 602 (1998).
161. C. J. Lee, J. Park, S. Y. Kang, and J. H. Lee, *Chem. Phys. Lett.* 326, 175 (2000).
162. A. Cao, Ci. Lijie, G. Wu, B. Wei, C. Xu, J. Ling, and D. Wu, *Carbon* 39, 137 (2001).
163. H. M. Cheng, C. Liu, Y. Y. Fan, F. Li, G. Su, H. T. Cong, L. L. He, and M. Liu, *Z. Metallkund* 91, 306 (2000).
164. G. Diaz, M. Benaissa, J. G. Santiesteban, and M. J. Yacaman, *Fullerene Sci. Technol.* 6, 853 (1998).
165. M. Yudasaka, R. Kikuchi, Y. Ohki, and S. Yoshimura, *Carbon* 35, 195 (1997).
166. J. Zhao, Q. Y. Gao, C. Gu, and Y. Yang, *Chem. Phys. Lett.* 358, 77 (2002).
167. S. Maruyama, R. Kojima, Y. Miyauchi, S. Chiashi, and M. Kohno, *Chem. Phys. Lett.* 360, 229 (2002).
168. M. Sharon, A. Chatterjee, and R. Zhazaria, unpublished.
169. M. Terrones, N. Grobert, J. P. Zhang, H. Terrones, J. Olivares, W. K. Hsu, J. P. Hare, A. K. Cheetham, H. W. Kroto, and D. R. M. Walton, *Chem. Phys. Lett.* 285, 46, 299 (1998).
170. M. Terrones, N. Grobert, J. Olivares, J. P. Zhang, H. Terrones, K. Kordatos, W. K. Hsu, J. P. Hare, P. D. Townsend, K. Prassides, A. K. Cheetham, H. W. Kroto, and D. R. Walton, *Nature* 388, 52 (1997).
171. T. Guo, P. Nikolaev, A. Thess, D. T. Colbert, and R. E. Smalley, *Chem. Phys. Lett.* 260, 471 (1996).
172. A. G. Rinzler, J. Liu, H. Dai, P. Nikolaev, C. B. Huffman, and F. J. Rodriguez-Macias, *Appl. Phys. A* 69, 29 (1998).
173. K. Wolfgang, M. Ana, M. Benito, and T. Martinez, *Carbon* 40, 1685 (2002).
174. A. T. Matveev, D. Golberg, V. P. Novikov, L. L. Klimkovich, and Y. Bando, *Carbon* 39, 155 (2001).
175. G. Z. Chen, X. Fan, A. Luget, M. S. P. Shaffer, D. J. Fray, and A. H. Windle, *J. Electroanal. Chem.* 446, 1 (1998).
176. W. K. Hsu, M. Terrones, J. P. Hare, H. Terrones, H. W. Kroto, and D. R. M. Walton, *Chem. Phys. Lett.* 262, 161 (1996).
177. N. M. Rodriguez, *J. Mater. Res.* 8, 3233 (1993).
178. H. J. Dai, A. G. Rinzler, P. A. Thess, D. T. Colbert, and R. E. Smalley, *Chem. Phys. Lett.* 260, 471 (1996).
179. F. A. Govindaraj, A. Peigney, Ch. Laurent, A. Rousset, and C. N. R. Rao, *Chem. Phys. Lett.* 300, 236 (1999).
180. M. Terrones, N. Grobert, W. K. Hsu, Y. Q. Zhu, W. B. Hu, H. Terrones, J. P. Hare, H. W. Kroto, and D. R. M. Walton, *MRS Bull.* 43 (1999).
181. B. K. Pradhan, T. Toba, T. Kyotani, and A. Tomita, *Chem. Mater.* 10, 2510 (1998).
182. S. C. Tsang, Y. K. Chen, P. J. F. Harris, and M. L. H. Green, *Nature (London)* 372, 159 (1994).
183. R. M. Lago, S. C. Tsang, K. L. Lu, Y. K. Chen, and M. L. H. Green, *J. Chem. Soc. Chem. Commun.* 1355 (1994).
184. P. M. Ajayan, O. Stephan, Ph. Redlich, and C. Colliex, *Nature (London)* 375, 564 (1995).
185. M. Terrones, W. K. Hsu, A. Schilder, H. Terrones, N. Grobert, J. P. Hare, Y. Q. Zhu, M. Schwoerer, K. Prassides, H. W. Kroto, and D. R. M. Walton, *Appl. Phys. A* 66, 307 (1998).
186. R. Martel, T. Schmidt, H. R. Shea, T. Hertel, and P. Avouris, *Appl. Phys. Lett.* 73, 24447 (1998).
187. I. W. Chiang, B. E. Brinson, R. E. Smalley, J. L. Margrave, and R. H. Hauge, *J. Phys. Chem.* 105, 157 (2001).
188. A. G. Rinzler, J. Liu, H. Dai, P. Nikolaev, C. B. Huffman, F. J. Rodriguez-Macias, P. J. Boul, A. H. Lu, D. Heymann, D. T. Colbert, R. S. Lee, J. E. Fischer, A. M. Rao, P. C. Eklund, and R. E. Smalley, *Appl. Phys. A* 67, 29 (1998).
189. A. K. Chatterjee, M. Sharon, R. Banerjee, and M. Neumann-Spallart, *Electrochim. Acta* 48, 3439 (2003).
190. T. W. Ebbesen, P. M. Ajayan, H. Hiura, and T. Tanigaki, *Nature* 367, 519 (1994).
191. Y. Ando, X. Zhao, and M. Ohkohch, *Jpn. J. Appl. Phys.* 37, L61 (1998).
192. Y. Ando, X. Zhao, H. Kataura, Y. Achiba, K. Kaneto, M. Tsuruta, S. Uemura, and S. Iijima, *Diamond Related Mater.* 9, 847 (2000).
193. B. Q. Wei, R. Vajai, and P. M. Ajayan, *Appl. Phys. Lett.* 79, 1172 (2001).
194. H. Ago, T. Kugler, F. Cacialli, W. R. Salaneck, M. S. P. Shaffer, A. H. Windle, and R. H. Friend, *J. Phys. Chem. B* 103, 8116 (1999).
195. M. Shiraiishi, *Carbon* 39, 1913 (2001).
196. S. Agnès, J. E. Fischer, C. B. Huffman, A. G. Rinzler, and R. E. Smalley, *J. Electrochem. Soc.* 147, 2845 (2000).
197. A. B. Kaiser, G. C. McIntosh, K. Edgar, J. L. Spencer, H. Y. Yu, and Y. W. Park, *Curr. Appl. Phys.* 1, 50 (2001).
198. P. G. Collins, K. Bradley, M. Ishigama, and A. Zettl, *Science* 287, 1801 (2000).
199. L. Grigorian, G. U. Sumanasekera, A. L. Loper, S. Fang, J. L. Allen, and P. C. Eklund, *Phys. Rev. B* 58, R4195 (1998).
200. G. Che, B. B. Laxmi, E. R. Fischer, and C. R. Martin, *Nature* 393, 346 (1998).
201. G. Che, B. B. Laxmi, E. R. Fischer, and C. R. Martin, *Langmuir* 15, 750 (1999).
202. C. Nutzenadel, A. Zuttel, D. Chartouni, and L. Schlapbach, *Electrochem. Solid-State Lett.* 2, 30 (1999).

203. M. Kumar, P. D. Kichambre, M. Sharon, N. R. Avery, and K. J. Black, *Mater. Chem. Phys.* 66, 83 (2000).
204. E. Frackowiak, S. Gautier, H. Gaucher, S. Bonnamy, and F. Bèguin, *Carbon* 27, 61 (1999).
205. F. Leroux, K. Mètènier, S. Gautier, E. Frackowiak, S. Bonnamy, and F. Bèguin, *J. Power Sources* 81–82, 317 (1999).
206. J. J. Davis, M. L. H. Green, H. A. O. Hill, Y. C. Leung, P. J. Sadler, J. Sloan, A. V. Xavier, and S. C. Tsang, *Inorg. Chim. Acta* 272, 261 (1998).
207. Z. J. Guo, P. J. Sadler, and S. C. Tsang, *Adv. Mater.* 10, 701 (1998).
208. J. Chen, M. A. Hamon, H. Hu, Y. S. Chen, A. M. Rao, P. C. Eklund, and R. C. Haddon, *Science* 282, 95 (1998).
209. F. Lamari Darkrim, P. Malbrunot, and G. P. Tartaglia, *Int. Hydrogen Energy* 27, 193 (2002).
210. V. V. Simonyan and J. K. Johnson, *J. Alloy Compounds* 330–332, 659 (2002).
211. A. C. Dillon, K. M. Jones, T. A. Bekkedahl, C. H. Kiang, D. S. Bethune, and M. J. Heben, *Nature* 386, 377 (1997).
212. N. Rajalakshmi, K. S. Dhathathreyan, A. Govindaraj, and B. C. Satishkumar, *Electrochim. Acta* 45, 2000 (2003).
213. X. Qin, X. P. Gao, H. Liu, H. T. Yuan, D. Y. Yan, W. L. Gong, and D. Y. Song, *Electrochem. Solid-State Lett.* 3, 532 (2000).
214. A. Zuttel, P. Sudan, Ph. Mauron, T. Kiyobayashi, Ch. Emmenegger, and L. Schlapbach, *Int. J. Hydrogen Energy* 27, 203 (2002).
215. H. Ago, K. Nagata, K. Yoshizawa, K. Tanaka, and T. Yamabe, *Bull. Chem. Soc. Jpn.* 70, 1717 (1997).
216. A. Herold, *Bull. Soc. Chim. Fr.* 187, 999 (1955).
217. J. Besenhard and H. Fritz, *J. Electroanal. Chem.* 53, 329 (1974).
218. J. Besenhard, *Carbon* 14, 111 (1976).
219. G. Maurin, Ch. Bousquet, F. Henn, P. Bernier, R. Almairac, and B. Simon, *Chem. Phys. Lett.* 312, 14 (1999).
220. H. Shinoda, B. Gao, X. P. Tang, A. Kleinhammes, I. Flemming, Y. Wu, and O. Zhou, *Phys. Rev. Lett.* 88, 7 (2002).
221. M. Sharon, M. Kumar, P. D. Kichambre, N. R. Avery, and K. J. Black, *Mol. Cryst. Liq. Cryst.* 340, 523 (2000).
222. M. Kumar, P. D. Kichambre, M. Sharon, N. R. Avery, and K. J. Black, *Mater. Chem. Phys.* 66, 83 (2000).
223. M. Sharon, W. K. Hsu, H. W. Kroto, D. R. M. Walton, A. Kawahara, T. Ishihara, and Y. Takita, *J. Power Sources* 104, 148 (2002).
224. T. Fukutsuka, T. Abe, M. Inaba, Z. Ogumi, Y. Matsuo, and Y. Sugie, *Carbon Sci.* 1, 129 (2001).
225. Q. Zhong, A. Bonakdarpour, M. Zhang, Y. Gao, and J. R. Dahn, *J. Electrochem. Soc.* 144, 205 (1997).
226. K. Amine, H. Tukamoto, H. Yasuda, and Y. Fujita, *J. Power Sources* 68, 604 (1997).
227. G. T.-K. Fey, W. Li, and J. R. Dahn, *J. Electrochem. Soc.* 141, 2279 (1994).
228. C. Sigala, D. Guyomard, A. Verbaere, Y. Piffard, and M. Tournoux, *Solid State Ionics* 81, 167 (1995).
229. Y. Ein-Eli and W. F. Howard, Jr., *J. Electrochem. Soc.* 144, L205 (1997).
230. Y. Ein-Eli, W. F. Howard, Jr., S. H. Lu, S. Mukherjee, J. McBreen, J. T. Vaughey, and M. M. Thackeray, *J. Electrochem. Soc.* 145, 1238 (1998).
231. H. Kawai, M. Nagata, H. Tukamoto, and A. R. West, *J. Power Sources* 81–82, 67 (1999).
232. A. S. Claye, N. M. Nemes, A. Jánossy, and J. E. Fischer, *Phys. Rev. B* 62, R4845 (2000).
233. A. Burke, *J. Power Sources* 91, 37 (2000).
234. S. Shiraiishi, H. Kurihara, and A. Oya, *Carbon Sci.* 1, 133 (2001).
235. C. Niju, E. K. Sichel, R. Hoch, D. Moy, and H. Tennent, *Appl. Phys. Lett.* 1480, 70 (1997).
236. C. Liu, A. J. Bard, F. Wudl, I. Weitz, and J. R. Heath, *Electrochem. Solid-State Lett.* 2, 577 (1999).
237. J. N. Barisci, G. G. Wallace, and R. H. Baughman, *J. Electroanal. Chem.* 488, 92 (2000).
238. E. Frackowiak and F. Bèguin, *Carbon* 39, 937 (2001).
239. W. A. De Heer, J.-M. Bonard, K. Fauth, A. Chatelain, L. Forro, and D. Ugarte, *Adv. Mater.* 9, 87 (1997).
240. J.-M. Bonard, T. Stöckli, O. Noury, and A. Châtelain, *Appl. Phys. Lett.* 78, 2775 (2001).
241. J.-M. Bonard, F. Maier, T. Stöckli, A. Châtelain, W. A. de Heer, J.-p. Salvetat, and L. Forró, *Ultramicroscopy* 73, 7 (1998).
242. A. G. Rinzler, J. H. Hafner, P. Nikolaev, L. Lou, S. G. Kim, D. Tomanek, P. Nordlander, D. T. Colbert, and R. E. Smalley, *Science* 269, 1550 (1995).
243. P. G. Collins and A. Zettl, *Phys. Rev. B* 55, 9391 (1997).
244. Q. H. Wang, T. D. Corrigan, J. Y. Dai, R. P. H. Chang, and A. R. Krauss, *Appl. Phys. Lett.* 70, 3308 (1997).
245. D. B. Romero, M. Carrad, W. De Heer, and L. Zuppiroli, *Adv. Mater.* 8, 899 (1996).
246. H. Shi, *Electrochim. Acta* 41, 1633 (1996).
247. D. Qu and H. Shi, *J. Power Source* 74, 99 (1998).
248. K. H. Kim and C. S. Shin, *Carbon Sci.* 2, 109 (2001).
249. S.-J. Park and W.-Y. Jung, *Carbon Sci.* 2, 15 (2001).

Carbon Nanostructures for Cold Electron Sources

P. Gröning

University of Fribourg, Fribourg, Switzerland

L. Nilsson

COMET AG, Liebefeld-Bern, Switzerland

P. Ruffieux, R. Clergereaux

University of Fribourg, Fribourg, Switzerland

O. Gröning

*Swiss Federal Laboratory for Materials Testing and Research,
Dübendorf, Switzerland*

CONTENTS

1. Introduction
 2. Characterization of the Field Emission Behavior
 3. Carbon Based Electron Emitters
 4. Microscopic Characterization of Thin Film Emitters
 5. Conclusions
- Glossary
References

1. INTRODUCTION

Electron sources are used today in a wide range of applications such as microwave traveling wave tubes, e-beam evaporators, mass spectrometers, etc. Most applications rely on thermionic electron emitters operating in a temperature range of 950–2000 °C. Due to the high operating temperatures, the potential of miniaturization of thermionic emitters is strongly limited. Field electron emitters operating at room temperature, in contrast, hold great potential for miniaturization. The miniaturization of electron sources opens the

field for new applications such as parallel e-beam lithography, flat panel displays, or data storage devices. However, the development of field emission electron sources has been hampered for half a century by the fact that tip-like field enhancing structures are needed to create locally high electric fields for field electron emission to take place. Today there is only one mature technology to produce field emitter arrays. This technology is the so-called Spindt type metal microtip process. The drawbacks of this technology are the expensive production, the critical lifetime in technical vacuum conditions, and the high operating voltage. Carbon nanostructures can be regarded as the potential second-generation technology to the Spindt type metal microtips. The advantages of carbon nanostructures are above all a potentially larger lifetime due to chemical inertness and lower operating voltage due to higher local field enhancement.

1.1. Electron Emission Sources in Vacuum Microelectronic Devices

In contrast to the well established solid state microelectronics, which relies on the scattering dominated drift of electrons (or holes) in the conduction band (valence band) of a semiconductor such as silicon, vacuum microelectronics makes use of the collision-free, ballistic motion of electrons in vacuum. The advantage of using a semiconductor as

transport medium for electrons resides in the fact that the energy required to promote an electron from the valence band into the conduction band is in the order of 1 eV and therefore much lower than the work function ϕ , the energy required to put an electron from solid into vacuum, which is usually in the order of 4–5 eV. Using doped semiconductors, the activation energy to produce carriers in the conduction band can be reduced further to a few meV, which makes it possible to have a saturated carrier concentration even at room temperature. Yet the motion of electrons in a solid has also some important disadvantages. Due to the collision dominated motion of the electrons in the conduction band, the drift velocities are considerably smaller than for ballistic motion in vacuum at comparable electric fields. Furthermore, power is dissipated due to the interaction of the electrons with the lattice. Especially for high power, high frequency applications, this power dissipation becomes a problem. It is this way in the field of high power radio frequency and microwave amplifiers that vacuum electronic devices such as electron tubes, magnetrons, or klystrons are still being used. In these devices the free electrons are usually generated by thermionic electron sources. Albeit rather inexpensive and delivering high current densities, thermionic electron sources have a number of significant drawbacks: The large heat dissipation causes rather large energy consumption, and most important of all, the thermionic electron sources cannot be made very small and cannot be turned on and off at high frequencies. The term “small” here refers to length scales in the order of micrometers. Field electron emission from solids may open the door for the miniaturization of electron sources. However, it was not until two decades ago that improvements in microfabrication techniques triggered much progress in manufacturing of devices with miniaturized electron sources. These devices are commonly called vacuum microelectronic devices and make use of a large number of micrometer-sized field emitting electron sources (Fig. 1).

A device design based on a large number of parallel operating micrometer-sized electron sources can offer interesting technological applications, such as high power radio frequency amplifiers, electron guns for klystrons or travel-

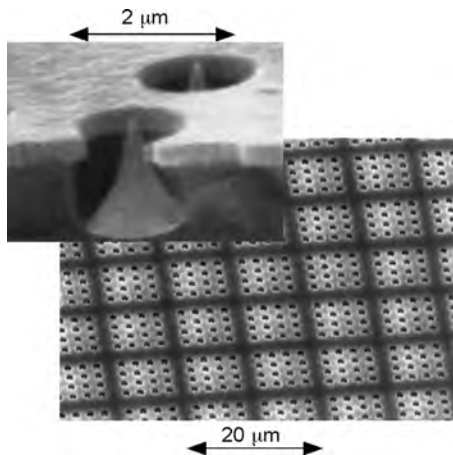


Figure 1. Field emitter array of evaporated metal tips, so-called Spindt tips [1].

ing wave tubes, parallel e-beam lithography, or data storage [2] where field emitted electron beams are used to read and write bits of data into a storing medium. However, the first large scale commercial application of microfield emission sources is likely to be for arrays of miniature, cold cathodes, which are required for thin matrix addressable cathodoluminescent display devices, called field emission flat panel displays (FED). It has become evident during the last decade that the fabrication process for Spindt type field emitter arrays using micrometer-sized metal tips (Fig. 1) is highly critical and cost intense. Therefore less expensive and less critical fabrication techniques of the electron emitting cathode must be sought.

An ideal electron source in a micrometer-sized device has to meet several important requirements [3]:

- The electron source must be capable of being fabricated to submicrometer tolerances so that the emitting area is precisely defined and geometrically and chemically stable during its operation lifetime.
- The emission current should be voltage controllable, preferably with drive voltages in a range obtained from “off the shelf” integrated circuits (<100 V).
- The source must be capable of emitting very high current densities so that the total current emitted from the small available area is sufficient for device operation. Even a current of one microampere from one square micrometer area requires a current density of 100 A cm^{-2} . Ten A cm^{-2} current density may be regarded as a lower limit for a source to reach wide applications in vacuum microelectronic devices.
- The energy spread of the emitted electrons should be comparable to conventional thermionic cathodes (i.e., <0.5 eV), or within tolerable limits for the particular device being considered.
- The emission characteristics should be reproducible from one source to another and should be stable over very long periods of time (ten thousands of hours) for acceptable device lifetimes.
- The cathode must be resistant to unwanted occurrences in the vacuum device environment, such as ion bombardment, reaction with the residual gases, temperature extremes, and arcing.
- Cathode manufacturing should be inexpensive, without highly critical processes, and adaptable to a wide variety of applications

With regard to these requirements field emission electron sources are regarded as a good choice, because they can satisfy many of the aforementioned requirements. They can deliver very high emission current densities in the order of several thousand A cm^{-2} with a very steep current–field characteristic. In order to generate the necessary electric field of $>2500 \text{ V } \mu\text{m}^{-1}$ to get sufficiently high field emission currents, classical field emission sources rely on field enhancing microtip structures. These microtips suffer from some inherent problems such as tip degradation due to sputtering effects, altering of the field emission properties due to tip contamination, and inhomogeneous emission properties in the tip array due to varying geometries. The development of new field emitters should focus on solving some of the aforementioned problems that microtips have. Namely, the

emitter should be rather insensitive to sputter erosion and contamination, so that the emission properties remain stable over the entire lifetime of the device.

1.2. Electron Emission

Electron emission is defined as liberation of free electrons from the surface of a material caused by external energy in the form of light, heat, high electric fields, or collisions transferred to the electrons. The amount of energy required by the electron to emit from the solid surface is known as work function ϕ . According to the energy sources, the following four electron emission processes can be distinguished:

1. photoemission
2. thermionic emission
3. field emission
4. secondary emission

1.2.1. Photoemission

Photoemission is the emission of electrons from solids, liquids, or gases by the action of electromagnetic radiation. When radiation is absorbed by a solid, some of the electrons in the material gain sufficient energy to overcome the work function ϕ and escape into vacuum. The photoemission process could not be explained by classical physics until Einstein applied Planck's quantum theory to the photoelectric effect [4]. He postulated that light is absorbed by the solid in quantified manner so that the energy of an absorbed photon is completely transformed into the kinetic energy of an electron. The number of photoelectrons released is therefore proportional to the number of incident photons. The Einstein relation [See Eg. (1)] relates the kinetic energy E_{kin} of the photoemitted electron with its binding energy E_B in the solid and the energy of the incident photon $h\nu$

$$E_{\text{kin}} = h\nu - E_B - \phi \quad (1)$$

1.2.2. Secondary Emission

Secondary electron emission occurs from solid surfaces bombarded by high-speed electrons or other particles. When high-speed electrons suddenly strike a solid surface, they may give some or all of their kinetic energy to electrons in the solid. The secondary electron yield depends on many factors and is generally higher for high atomic number elements and at higher angles of incidence.

1.2.3. Thermionic Emission

Thermionic emission is the emission of electrons from hot solids. If an anode is placed near a heated solid (cathode) in vacuum, a current of electrons passes from the hot cathode to the anode. The current density depends only on the nature of the cathode material and the temperature of the cathode. The current is nearly independent of the electric field provided it is not too large, but still large enough to overcome the space charge limitation. The subject was first investigated by Richardson in 1902 quantitatively. He suggested empirically the following formula for the emission current density [5]

$$j = AT^{0.5} \exp\left(-\frac{b}{T}\right) \quad (2)$$

In 1914 Willson considered the thermionic emission to thermal evaporation of electrons and applied the Clausius–Clapeyron equation to the system. Richardson accordingly changed his original equation and suggested instead

$$j = AT^2 \exp\left(-\frac{\phi}{k_B T}\right) \quad (3)$$

Dushman in 1923 derived this formula theoretically using the Clausius–Clapeyron equation and assuming that the electrons obey Maxwell–Boltzmann statistics. The introduction of quantum mechanics and the recognition that electrons obey the Fermi–Dirac statistic led to a new treatment of the thermionic emission by Nordheim in 1928 who determined A to be $120 \text{ A cm}^{-2} \text{ K}^{-2}$ [6]. This value was twice as large as the one determined by Dushman due to the two spin states of the electrons.

1.2.4. Field Emission

The emission of electrons from the surface of a solid caused by a high electric field is called field emission. This phenomenon was first reported by Wood in 1897 and occurs at electric fields in the order of $5 \times 10^9 \text{ V m}^{-1}$ [7]. Such high fields are extremely difficult to realize on flat surfaces but can be generated by the field enhancing properties of tiplike structures.

Qualitatively, the field enhancement of a needle shaped tip with a spherical cap can be understood as follows. Let us assume a metallic sphere with radius r floating in a homogeneous electric field F_0 at a height h above a metal plate to which the sphere is electrically connected. For $h \gg r$ the electric potential of the sphere with respect to the surrounding space is $\phi = F_0 \cdot h$. The electric potential φ at the surface of the sphere can be written as

$$\varphi = \frac{1}{4\pi\epsilon_0} \frac{Q}{r} = F_0 \cdot h \quad (4)$$

with Q being the charge on the sphere. The electric field F on the surface of the sphere is

$$F = \frac{1}{4\pi\epsilon_0} \frac{Q}{r^2} \quad (5)$$

With the substitution of (4) into (5) we get for the local electric field F

$$F = \frac{\varphi}{r} = \frac{h}{r} F_0 \quad (6)$$

Equation (6) shows that the electric field at the surface of the sphere is enhanced by a factor equal to the ratio of the height h (above the metal plate) and the radius r of the sphere. This factor is called the field enhancement factor and is usually labeled by β , which is why it is sometimes called the beta factor.

In 1928 Fowler and Nordheim delivered the first generally accepted explanation of field emission in terms of the newly developed theory of quantum mechanics [8]. Fowler and Nordheim treated the conduction electrons in the metal as a gas of free particles obeying the Fermi–Dirac statistic. The electrons are confined to the metal by the surface

potential barrier, the shape of which is considered to be determined by the potential inside the metal (work function ϕ), the image charge potential, and the applied external potential.

In Figure 2 the situation of an electron with kinetic energy E near the Fermi energy E_F tunneling through the surface barrier is depicted. Assuming that inside the metal ($x < 0$) the electron experiences a constant potential ($V = 0$) and that at the surface ($x = 0$) there is a potential step to E_{vac} (vacuum energy), the electron potential $V(x)$ outside the metal ($x > 0$) and under the action of an electric field can be written by

$$V(x) = E_{\text{vac}} - eFx \quad (7)$$

Taking the influence of the image charge potential into account $V(x)$ is

$$V(x) = E_{\text{vac}} - eFx - \frac{1}{4\pi\epsilon_0} \frac{e^2}{4x} \quad (8)$$

The transmission probability $D(E)$ for an electron with the energy E to tunnel a potential barrier $V(x)$ is given in the Wenzel, Kramers, Brillouin approximation [9] by

$$D(E) = \exp\left(-2\frac{\sqrt{2m_e}}{\hbar} \int_{x_1}^{x_2} \sqrt{V(x) - E_x} dx\right) \quad (9)$$

with $E_x = \hbar^2 k_x^2 / 2m_e$ the kinetic energy component perpendicular to the surface.

With the integration limits $V(x_1) = V(x_2) = E_x$ the transmission probability $D(E)$ for a given potential $V(x)$ only depends on E_x . For a triangular surface potential barrier (7) $x_1 = 0$ and $x_2 = (E_{\text{vac}} - E_x)/eF$. Substitution of (7) in (9) will lead to

$$D(E) = \exp\left(-2\frac{\sqrt{2m_e}}{\hbar} \int_0^{(E_{\text{vac}} - E_x)/eF} \sqrt{E_{\text{vac}} - eFx - E_x} dx\right) \quad (10)$$

By solving the elementary integral we find

$$D(E) = \exp\left(-\frac{4\sqrt{2m_e}}{3eF\hbar} (E_{\text{vac}} - E_x)^{1.5}\right) \quad (11)$$

The formula shows that the transmission probability $D(E)$ rapidly decreases with E_x so that only the highest occupied electron states near the Fermi energy E_F contribute

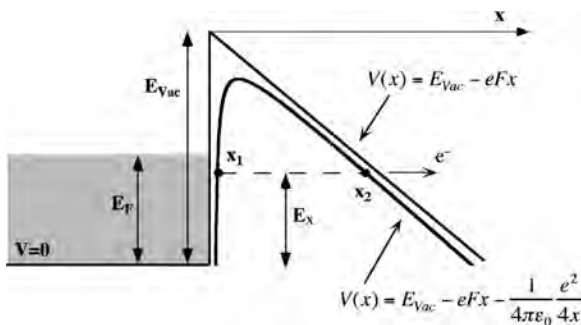


Figure 2. Schematic illustration of the surface potential barrier under the action of an external electric field.

to the emission current. With a first order development of $(E_{\text{vac}} - E_x)^{1.5}$ at E_F

$$(E_{\text{vac}} - E_x)^{1.5} \approx (E_{\text{vac}} - E_F)^{1.5} - \frac{3}{2}(E_{\text{vac}} - E_F)^{0.5}(E_x - E_F) \quad (12)$$

and the substitution of (12) into (11) and with $E_{\text{vac}} - E_F = \phi$, we find

$$D(E) = \exp\left(-\frac{4\sqrt{2m_e}}{3\hbar} \frac{\phi^{1.5}}{eF}\right) \exp\left(\frac{2\sqrt{2m_e}}{\hbar} \frac{\phi^{0.5}}{eF} (E_x - E_F)\right) \quad (13)$$

The emission current j density can be obtained by integrating the product of the occupation probability $f(E, E_F, T)$ (Fermi–Dirac statistic), the transmission probability $D(E)$, and the velocity component perpendicular to the surface v_x over all electron states in k -space:

$$j = 2e \int_k f(E, E_F, T) D(E) v_x \frac{d^3k}{(2\pi)^3} \quad (14)$$

For $T = 0$ K the Fermi–Dirac distribution is a step function and the integration has only to be carried out over states with $k < k_F$ with k_F being the Fermi wave vector. Therefore (14) transforms into

$$j = \frac{2e}{(2\pi)^3} \int_{k_x^2 + k_y^2 + k_z^2 < \frac{2m_e E_F}{\hbar^2}} D(E) \frac{\hbar k_x}{m_e} dk_x dk_y dk_z \quad (15)$$

By substituting (13) into (15) and solving the integral, we obtain the well known Fowler–Nordheim relation for the emission current density j ,

$$j = \frac{e^3}{4(2\pi)^2 \hbar \phi} F^2 \exp\left(-\frac{4\sqrt{2m_e}}{3\hbar} \frac{\phi^{1.5}}{eF}\right) \quad (16)$$

where j is in A m^{-2} , F is the electric field in V m^{-1} , and ϕ is the work function in Joules. Usually the Fowler–Nordheim relation is expressed with numerical constants and with j in A cm^{-2} , F in V cm^{-1} and the work function ϕ in electronvolts:

$$j = 1.56 \times 10^{-6} \frac{F^2}{\phi} \exp\left(-6.83 \times 10^7 \frac{\phi^{1.5}}{F}\right) \quad (17)$$

1.3. Work Function and Negative Electron Affinity

1.3.1. Work Function

As can be seen from the Fowler–Nordheim relation (16) the work function ϕ is the relevant physical parameter for the electron emission behavior of a conducting material. Therefore we will discuss here some important implications of the work function related to the field emission behavior of carbon thin films.

A possible definition of the work function ϕ is the amount of energy required to remove one electron at the Fermi energy from the solid and bring it to rest at an infinite distance from the solid. This definition leads to the situation that all metal surfaces electrically connected to each

other have the same work function. This is in contradiction to the observation. In order to get a sensible definition of the work function, the final state of the electron has to be chosen differently. A more precise definition of the work function is therefore: “The work function ϕ is the energy difference between two states of the whole crystal.” In the initial state the neutral crystal containing N electrons is in the ground state with energy E_N . In the final state one electron is removed from the crystal to a region having only electrostatic energy denoted by ϕ_V . The crystal with the remaining $N - 1$ electrons is assumed to be in its ground state with the energy E_{N-1} . This leads to

$$E_N + \phi = E_{N-1} + \phi_V \Rightarrow \phi = (E_{N-1} - E_N) + \phi_V \quad (18)$$

At nonzero temperatures, removal of an electron from the solid can be considered a thermodynamic change of states of the crystal. The energy difference $E_N - E_{N-1}$ can be replaced by the derivative of the Helmholtz free energy F with respect to the electron number with constant crystal volume and temperature

$$E_N - E_{N-1} \rightarrow \left(\frac{\partial F}{\partial N} \right)_{T,V} = \mu \Rightarrow \phi = \phi_V - \mu \quad (19)$$

The chemical potential μ can be considered as the bulk part and the electrostatic potential ϕ_V as the surface depending part of the work function ϕ . The concept of surface and bulk depending part of the work function ϕ is depicted in Figure 3.

Figure 3a shows schematically the situation at the surface of a finite crystal without distortion of the charge density. The centers of gravity of the positive and negative charges in the Wigner–Seitz cell are the same (crystal with inversion symmetry) and therefore no electrostatic dipole moment occurs. The work function ϕ in this case depends on the chemical potential μ only. Yet this is not the real situation at a crystal surface as the electrons at the surface have the tendency to “spill” out into vacuum. Due to this the charge the Wigner–Seitz cell at the surface is different than inside the crystal. Also the position of the atoms at the surface can differ considerably due to relaxation and reconstruction effects as depicted in Figure 3b. The changed charge distribution results in a surface dipole moment. The direction of the surface dipole due to electron spill put is such that energy is needed to move the electron from inside the solid into vacuum. This energy has to be added to the chemical potential in order to obtain the work function. A further dipole due to spill-out of electrons occurs leading to a dipole moment which tends to decrease the work function. This contribution to the work function observed on rough (or highly stepped) surfaces is called the Smoluchowski effect. It explains also the tendency of body centered cubic crystal to show a decrease work function in the sequence of the (100) \rightarrow (110) \rightarrow (111) planes and an increasing work function for face centered cubic crystals in the same sequence. A good parameter to characterize the work function ϕ of an element is the electronegativity χ . The electronegativity is defined as the arithmetic mean of the first ionization potential and the electron affinity of the neutral atom. The correlation between these two parameters

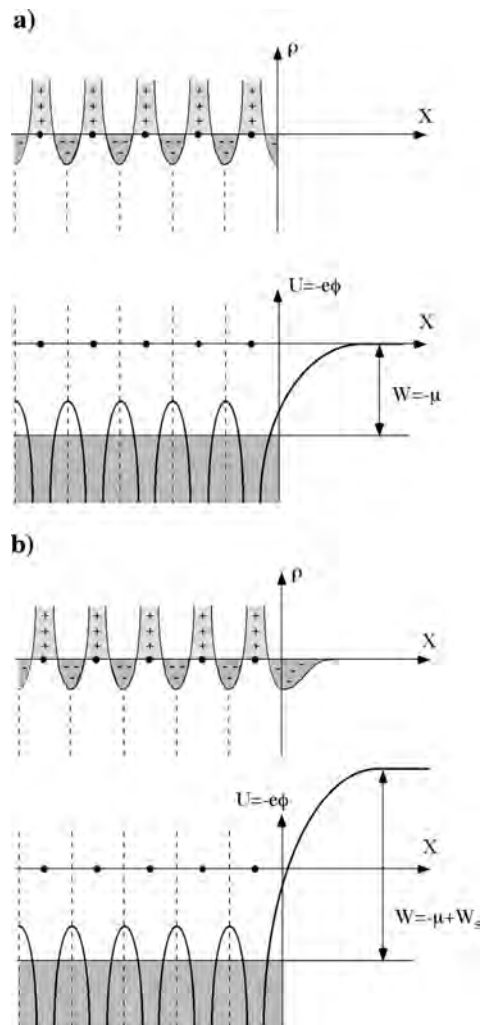


Figure 3. Schematic illustration of the electrostatic potential at the crystal surface. (a) Without distortion of the charge density (bulk density). (b) With modified charge density due to relaxation and reconstruction effects at the surface.

illustrates that the work function of an element still strongly reflects the property of the atom. The experimental data can be fitted to a straight line giving

$$\phi = 0.34 + 0.72\chi \quad [\text{eV}] \quad (20)$$

Another interesting relation between the work function and the cohesion energy can be established. Solids with large cohesive energy have high work functions. This can be qualitatively understood as work function and cohesive energy are coupled via the chemical potential μ . Using relation (20) we obtain for carbon with an electronegativity of $\chi_C = 6.2$ eV a work function $\phi_C = 4.8$ eV which is very close the 4.7 eV measured value on graphite [10]. With regard to the work function ϕ , carbon seems not to be the material of choice for cathodes of electron emitters. To give a comparison LaB₆ has a work function of 2.66 eV and YB₆ of 2.2 eV.

Adsorption or deposition of an element with a low electronegativity onto a solid with higher electronegativity will result in an electron transfer from the adsorbate to the solid

and therefore in the creation of a surface dipole moment. This dipole moment is opposed to the intrinsic surface dipole moment and thus reduces the work function. The work function lowering of thin layers of alkaline and earth alkaline metals has been known for a long time and is used in thermionic emitters [11, 12]. In order to lower the work function of thermionic emitters monolayer coverages of ThO, Sc₂O₃, or BaO are used. The world record of emission current density is currently held by a W/Re + Sc₂O₃ dispenser cathode with 400 A cm⁻² at 965 °C [13]. The work function of this cathode was determined to be 1.16 eV. Here the combination of scandium and oxygen results in the drastic work function lowering due to electron transfer from scandium to oxygen. This creates a strong surface dipole moment reducing the work function of the W/Re of about 4.7 eV by 3.5 eV.

1.3.2. Work Function of Carbon Species and the Role of Hydrogen

On carbon materials hydrogen can take the role of the work function, lowering adsorbate. The influence of hydrogen and oxygen at the surface of tetrahedral amorphous carbon (*ta*-C) is illustrated in Figure 4. The samples produced by laser ablation of graphite are hydrogen free and with a high *sp*³/*sp*² ratio, and we measured consistently work function values of 5.0 ± 0.2 eV. Between a *sp*³/*sp*² ratio of 65% and 90% no significant variation of the work function value ϕ was observed. The termination of the surface with hydrogen or oxygen was performed by electron cyclotron resonance plasma treatment. The ultraviolet photoemission spectra (UPS) displayed in Figure 4 show the low energy region of the photoemission which is dominated by the emission of scattered electrons. The cutoff in these spectra denotes the minimum energy required for an electron to be emitted and therefore shows the energetic position of the vacuum level. For the hydrogen terminated *ta*-C surface (60 s H₂ plasma) the work function is reduced from

5 to 3.5 eV. Careful investigations of the corresponding X-ray photoemission spectrum reveal that hydrogen is incorporated into the first three monolayers (9 Å). The work function change induced by hydrogen has not only to be understood in terms of the surface dipole moment. In fact localization of electrons in the C–H bonds can also reduce the work function [14].

Exposing the same sample after hydrogen termination to an O₂ plasma increases the work function again to 6.6 ± 0.2 eV. The oxygen plasma strongly etches the superficial C–H groups forming C–O groups at the surface. Obviously oxygen, being a strong electron acceptor, leads to a surface dipole moment which increases the work function. As one can see the work function of the carbon surface can be varied between 3.5 and 6.6 eV depending on the surface termination.

1.3.3. Negative Electron Affinity

In the case of diamond the surface termination by hydrogen leads to a new aspect. Due to the wide bandgap and the lowering of the work function on a hydrogen terminated surface, the vacuum level can be lower than the conduction band minimum. This situation where the lowest unoccupied electron state (at the bottom of the conduction band) is higher than the lowest state in vacuum is called negative electron affinity (NEA). It means that an electron excited into the conduction band at the surface of a NEA diamond can be emitted into vacuum without any surface potential barrier. The NEA influences strongly the photoelectron as well as the secondary electron emission. Figure 5 displays schematically the photoemission process on a NEA diamond surface. On the left hand side a schematic band diagram is depicted and on the right side the UPS spectrum of a nanocrystalline chemical vapor deposition (CVD) diamond film after H₂ plasma treatment is depicted. The film was grown on Si(100) at 950 °C substrate temperature and with a 5% CH₄ in H₂ gas mixture at 40 mbar. Films grown under

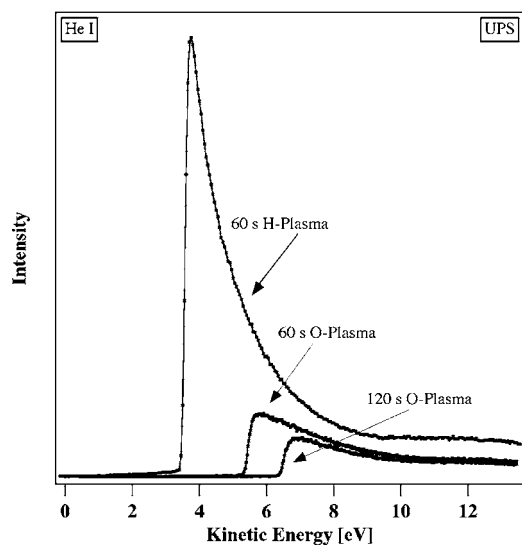


Figure 4. UPS spectra of hydrogen and oxygen plasma treated *ta*-C. Reprinted with permission from [46], O. Gröning, Ph.D. Thesis No. 1258, University of Fribourg, Switzerland, 1999.

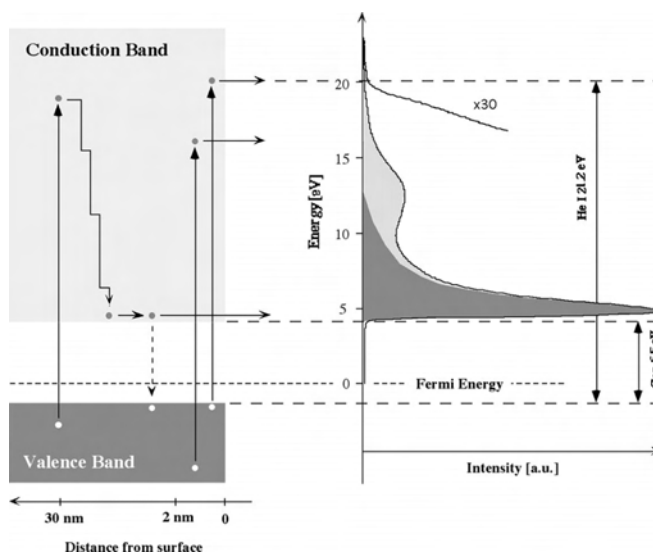


Figure 5. UPS spectrum of NEA nanocrystalline CVD diamond surface. Reprinted with permission from [46], O. Gröning, Ph.D. Thesis No. 1258, University of Fribourg, Switzerland, 1999.

these conditions exhibit good field emission properties (see Section 1.5.2). By irradiating the sample with ultraviolet (UV) (He: $h\nu = 21.2$ eV), electrons from the valence band are excited into the conduction band leaving a hole behind. Near the surface the surface (2 nm) the excited electrons have a good probability to escape the solid before losing energy due to inelastic scattering (light gray region in the spectrum of Fig. 5). At a larger distance from the surface the excited electrons lose energy due to inelastic scattering on their way to the surface. The typical scattering length is in the order of 1 nm for low energy electrons. Eventually the electrons will thermalize to the conduction band minimum (CBM), where the electrons can only lose further energy by recombination with holes in the valence band or by being trapped in defect states. As the lifetime (typically 1 ns) of an electron at the CBM is much larger than the scattering time during thermalization (typically 1 ps) there will be an accumulation of electrons at the CBM. In k -space the CBM is close to the X -point of the Brillouin zone and therefore the emission is preferred in the crystallographic (100) direction. This leads to a very intense and sharp peak in the UPS of (100) single crystalline diamond at the energetic position of the CBM [15, 16]. In the presented case of nanocrystalline diamond with crystallite size of a few nanometers, the peak is not as sharp; yet the low energy cutoff in the spectrum is at the position of the CBM indicating the NEA of this surface. By O_2 plasma treatment the work function of the diamond surface rises above the CBM and we have the situation of a positive electron affinity surface with measured work function values up to 6.3 ± 0.2 eV.

1.3.4. Local Aspect of Work Function Changes

As discussed in Section 1.3.1 the work function ϕ depends on the surface dipole moment, which can be influenced by adsorbates. In the case of carbon films hydrogen chemisorption at the surface can lead to a reduced work function. It has been suggested that the low threshold field for electron emission on carbon films is in fact connected with low local fields and that the emission takes place due to the extremely low work function in the range of 0.1 eV [17, 18]. Yet such low work functions are macroscopically not observed. Therefore it was proposed that the low work function regions are of atomic dimensions (e.g., due to the quantization of electron states in thin grain boundaries or due to electronically active defects) [19]. This model has some attractive properties as it would explain that the field emission is not homogenous but originates from some spots on the surface and that a high density of grain boundaries or defects (as in nanocrystalline CVD diamond) would lead to high density of emission spots.

Yet taking the small size of the low work function region into account one can observe that the relation between low work function and low field electron emission is not as straightforward as the Fowler–Nordheim relation might suggest. Changes in the work function on a surface have to be regarded as changes in the vacuum potential, with the occurrence of external electric fields. This situation is depicted in Figure 6a where the changed vacuum potential over a low work function (0.1 eV) spot of 2 nm diameter on a surface

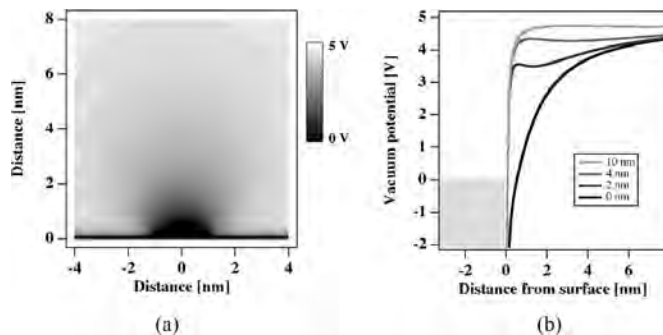


Figure 6. Change in the vacuum potential over a low work function (0.1 eV) spot ($\phi = 2$ nm) on a high work function (5 eV) surface without external electric field applied. Reprinted with permission from [46], O. Gröning, Ph.D. Thesis No. 1258, University of Fribourg, Switzerland, 1999.

with 5 eV work function is shown. What the possible origins of such a very low work function could be we do not want to discuss here, but we want to focus on the effects on electron emission. As one can see from Figure 6a the low work function spot creates a kind of potential pocket over the surface, where the vacuum potential rises quickly to a value close to 5 V at some distance from the spot. In Figure 6b the shape of the vacuum potential perpendicular to the surface is depicted for four different lateral distances from the center of the spot. Here again one can observe that the work function is not effectively lowered. In case of thermionic emission the introduction of small low work function spots on the cathode surface would not affect the emission behavior unless their density becomes so important that they cover a non-neglecting part of the surface ($>10\%$). With regard to thermionic emission only the average work function $\langle\phi\rangle$ is given by

$$\langle\phi\rangle = \frac{1}{A_S} \int_{A_S} \phi(\vec{r}) dA \quad (21)$$

where A_S is the surface area and $\phi(\vec{r})$ denotes the local work function.

The situation for field emission with an external electric field applied is depicted in Figure 7. The parameters for the calculation are the same as used before: low work function spot of 2 nm in diameter and 0.1 eV work function value on a surface with 5 eV work function. The applied external electric field is of $1000 \text{ V } \mu\text{m}^{-1}$. If we just apply the Fowler–Nordheim relation (16) we would expect for a work function of 0.1 eV detectable field emission currents in the pA range for electric fields around $5 \text{ V } \mu\text{m}^{-1}$. In Figure 7b we can see the tunneling barrier an electron would encounter for four different lateral distances from the center of the spot. The strongest effect of the low work function is of course at the center of the spot where the tunneling barrier is lowered considerably. Still in order to get a sufficient high transmission through the barrier the electric field has to be in the order of 1000 and not $5 \text{ V } \mu\text{m}^{-1}$. As can be seen the triangular barrier approximation (7) in this case is not valid anymore and therefore considerable deviation from Fowler–Nordheim behavior should be observed. The effect of a low work function spot on field emission is of course size dependent. One can make the estimation that in order to get

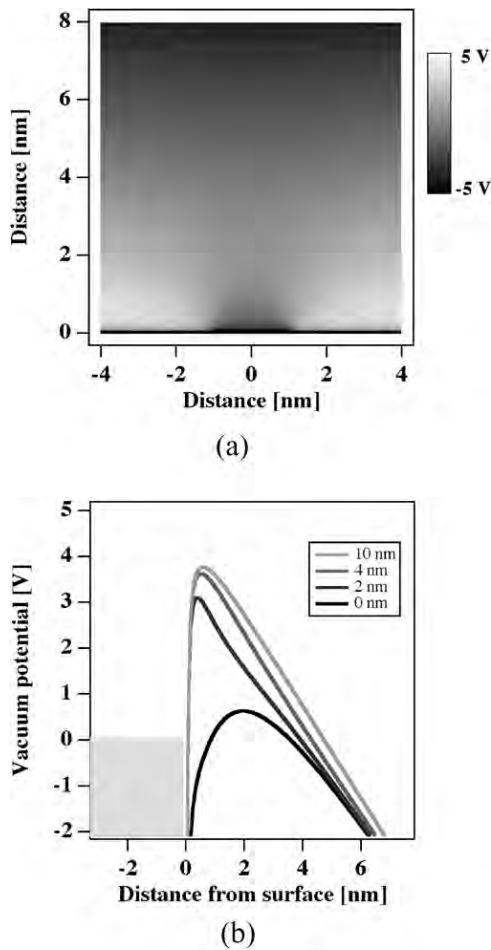


Figure 7. Change in the vacuum potential over a low work function (0.1 eV) spot ($\phi = 2$ nm) on a high work function (5 eV) surface with an external electric field of $1000 \text{ V } \mu\text{m}^{-1}$. Reprinted with permission from [46], O. Gröning, Ph.D. Thesis No. 1258, University of Fribourg, Switzerland, 1999.

detectable field emission from a 0.1 eV work function spot at $5 \text{ V } \mu\text{m}^{-1}$, the spot size should have a diameter of about $1 \mu\text{m}$ and more. To our knowledge such a low work function area was never observed. Modifications of the work function cause changes in the vacuum potential; thus large electric fields can be generated at the border between two regions of different work functions. As the work function changes can be in the range of 1–2 eV and the distances over which these changes occur are in the order of nm, the fields associated with the work function change can be in the order of $1000 \text{ V } \mu\text{m}^{-1}$. Figure 8 depicts the situation occurring at a surface with 3 eV work function (e.g., H-terminated amorphous carbon) where a spot of 10 nm in diameter has a higher work function of 5 eV (e.g., amorphous carbon without H-termination).

Robertson [20, 21] suggested that the low threshold field electron emission of carbon films occurs due to high electric fields present at the transition zones from high to low work function regions. Figure 8a depicts the vacuum potential over the high work function spot. The inset in Figure 8a shows the equipotential lines and the electric field strength at the border of the low and high work function region. One

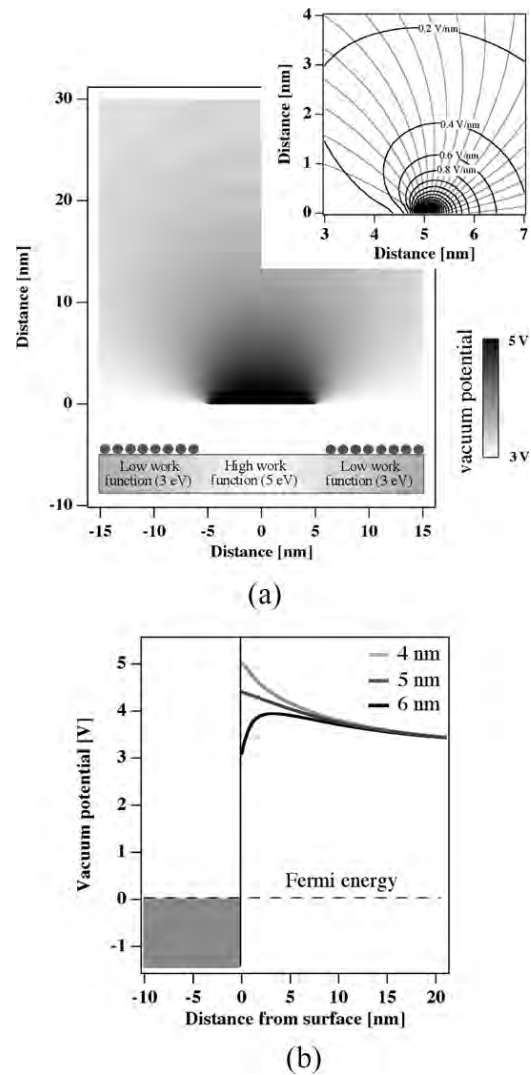


Figure 8. Vacuum potential change and occurrence of surface fields due to work function changes at an external electric field of $500 \text{ V } \mu\text{m}^{-1}$. Reprinted with permission from [46], O. Gröning, Ph.D. Thesis No. 1258, University of Fribourg, Switzerland, 1999.

can see that the electric fields in this transition region can easily exceed $1000 \text{ V } \mu\text{m}^{-1}$. Figure 8b shows that the surface potential barrier even at a quite elevated electric field is not strongly affected by the transition from a high (4 nm) to low (6 nm) work function region. The external fields required to get detectable field emission currents are not lower in the transition region than in the low work function region. In order to understand why the high local fields occurring from a change of work function do not influence significantly the field emission behavior we have to look at the conditions which lead to field emission at surfaces. These conditions can be expressed in a very simple manner: “There must be states available in the vacuum into which electrons from the Fermi energy or below can tunnel with sufficient high probability. This means that the vacuum potential has to be lowered below the Fermi energy within 2 nm from the surface (2 nm being roughly the tunneling distance for low energy electrons). This leads to a very simple relation between the work

function ϕ and the applied field F as $eF > \phi/2$ nm. In the model we are discussing the work function is always higher than or equal to 3 eV and therefore an external electric field at least of $1500 \text{ V } \mu\text{m}^{-1}$ is needed in order to get the conditions for field emission.

1.4. Carbon and Its Allotropes

Carbon is a group IV element with the atomic number 6 and has the electronic configuration $1s^2 2s^2 2p^2$. Carbon materials span an enormous range of mechanical and electronic properties that is larger than that of any other element. The large range of physical properties for carbon materials is mainly due to the fact that the energies of the $2s$ and $2p$ states are very close in carbon, allowing different bonding configurations by rearranging its outer electrons. The reconfiguration of the $2s$ and $2p$ electrons is called hybridization.

1.4.1. Diamond

One possible hybridization consists of the linear combination of one s -state and three p -states resulting in a tetrahedral arrangement of the bonds, each at an angle of 109.5° to the other. The configuration is called sp^3 and results in a coordination number of four. Diamond is one example of the sp^3 configuration. The band structure of diamond is characterized by a large energy gap of 5.5 eV between the valence band maximum and the conduction band minimum. This makes it, in the undoped case, an insulator with a resistivity of $\sim 10^{20} \text{ } \Omega \text{ cm}$ at room temperature. The large carrier mobility and the thermal properties make diamond an interesting material for electronic applications. The p -type doping has been realized with boron, resulting in an acceptor level at 0.37 eV above the valence band maximum [22]. However, n -type doping on the other hand has proven to be very difficult. Although substitutional doping can be achieved using the group V element nitrogen, the donor level at 1.7 eV below the conduction band minimum is far too low to be excited to the conduction band at room temperature [23]. Current investigations try to substitutionally dope diamond with phosphorus, another group V element, and with lithium and sodium, two group I elements, which are expected to be incorporated on interstitial lattice positions.

1.4.2. Graphite

Another possible configuration for the bonding electrons occurs for carbon atoms that are arranged in a honeycomb network. In this geometry, bonding orbitals composed of one s and two p orbitals (sp^2) are formed 120° to each other in one plane. These form the strong covalent bonds between the carbon atoms in graphene layers of graphite called σ -bonds. The resulting atom lattice consists of a hexagonal atom arrangement with a nearest-neighbor distance of $1.421 \text{ } \text{Å}$, which is about 7% shorter than in the diamond lattice. The one remaining orbital is delocalized and has a p_z configuration, called the π -orbital. Near the Fermi level, the density of states (DOS) consists exclusively of the delocalized π -electrons. These states are directly related to the presence of sp^2 -bonded carbon and their spectral weight

in a photoemission spectrum allows, for example, the determination of the fraction of sp^2 -bonded carbon in amorphous carbon [24]. The two-dimensional dispersion relation for the π -electron system can be calculated within the tight-binding approximation [25] and is displayed in Figure 9. If the interaction between the graphene sheets is neglected the DOS at the Fermi level E_F drops to zero. This is due to the fact that the occupied π -bands and the unoccupied π^* -bands just touch at the corners of the first Brillouin zone, called K points, making graphene a zero bandgap semiconductor. The Fermi surface consists in this case the six K points. The occupied and the unoccupied π -bands are symmetric with respect to the Fermi energy E_F . The displayed hexagon shows the two-dimensional Brillouin zone and defines the plane with $E = E_F$. The bottom of the occupied band is related to the nearest neighbor C–C overlap integral γ_0 and is, for the honeycomb structure, equal $3\gamma_0$. For graphite, γ_0 can be estimated to be $2.8 \pm 0.2 \text{ eV}$ [26]. The overlap of the π -orbitals on adjacent atoms of the same layer is the reason for the delocalization of the π -states and is responsible for the high charge carrier mobility in graphite. The description of graphene, however, is not sufficient to understand the properties of three-dimensional graphite, in particular regarding the π -states near the Fermi level. The weak inter-layer bonding of graphite, which is often incorrectly referred to as van der Waals bonding, originates from the small overlap of the π -orbitals between the atoms of adjacent layers. This creates two types of atoms, since in the ABA stacked graphite, only one-half of the atoms, called α -atoms, are positioned above an atom of the adjacent layer. The consequence on the electronic structure is that the degeneracy of the π -bands is lifted. See Figure 10.

1.4.3. Fullerenes and Nanotubes

Fullerenes can be viewed as closed networks of sp^2 -bonded carbon. The local curvature needed for the closure is induced by the incorporation of pentagons in the atomic arrangement. The experimental discovery of fullerenes occurred in the investigation of unusual infrared emission from large carbon clusters streaming out of red giant carbon stars [27] and the development of a laser vaporization cluster technique to produce such kinds of carbon clusters [28].

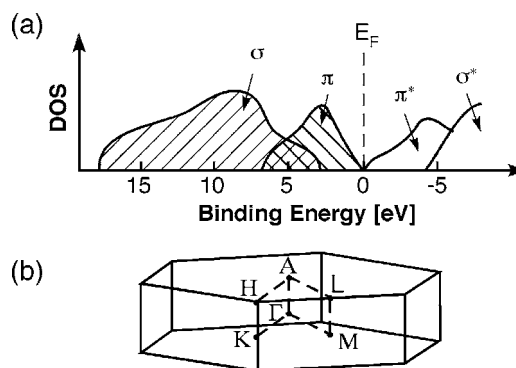


Figure 9. Schematic representation of the DOS of graphite showing the energy position of the π - and σ -derived states relative to the Fermi level E_F . Reprinted with permission from [129], P. Ruffieux, Ph.D. Thesis No. 1387, University of Fribourg, Switzerland, 2002.

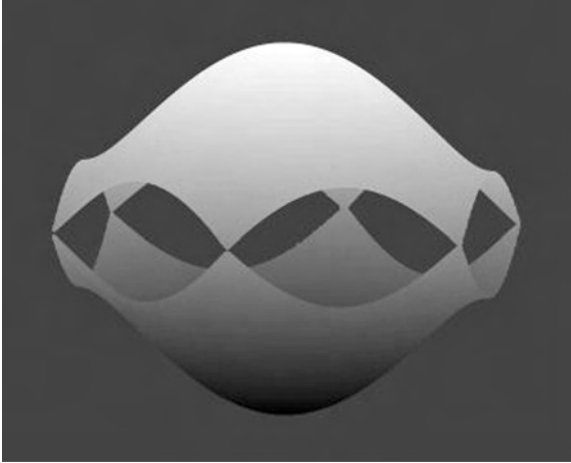


Figure 10. Band dispersion of the occupied and unoccupied π -bands in the first Brillouin zone of graphene. The gray scales indicate the energy relative to the Fermi level E_F : Black corresponds to -8.4 eV and white to $+8.4$ eV. The white lines show the two-dimensional Brillouin zone. Reprinted with permission from [129], P. Ruffieux, Ph.D. Thesis No. 1387, University of Fribourg, Switzerland, 2002.

According to Euler's theorem, 12 pentagons are required to close a structure. The most stable molecule is C_{60} , where all 60 carbon atoms have identical positions located at the corners of a truncated icosahedron. See Figure 11.

Another class of carbon nanostructures related to fullerenes was discovered in 1991 by Iijima [29] and consists of rolled-up graphene sheets, so-called carbon nanotubes (CNT). Depending on the number of shells present in the tube, one refers to single-walled nanotubes (SWNT) or multiwalled nanotubes (MWNT). Typical dimensions of the tubes are one to several nanometers in diameter with lengths of several micrometers.

The band structure of SWNTs can basically be explained by the dispersion relation calculated for graphene (Fig. 12b). However, one important restriction on the allowed states originates from the periodic boundary conditions in the circumferential direction of the tube. This reduces drastically the number of allowed wave vectors in this direction and leads to the one-dimensionality of the bands, which expresses itself in the appearance of van Hove singularities in the density of states. Figure 12b shows the band dispersion of graphene as a gray-level plot and the allowed states for a (5, 5) SWNT (black lines). This representation

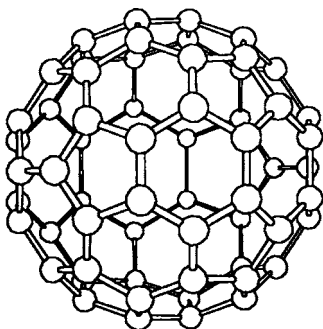


Figure 11. Buckminster (C_{60}) fullerene.

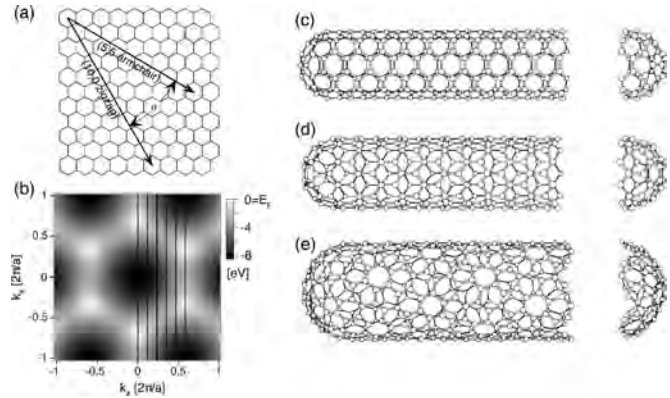


Figure 12. (a) Wrapping vectors (n, m) for two SWNTs. (b) Two-dimensional band dispersion for graphene [25] with allowed wave vectors for a (5, 5) SWNT (black lines). (c)–(e) Armchair tube, zigzag tube, and chiral tube. Reprinted with permission from [30], M. S. Dresselhaus et al., “Science of Fullerenes and Carbon Nanotubes.” Academic Press, San Diego, 1996. © 1996, Academic Press.

of the allowed states shows that the electronic properties of a SWNT are directly related to the chirality of the tube. The tubes are metallic if the allowed wave vectors cross the K point of the Brillouin zone or are otherwise semiconducting. Using the description with the wrapping vector (n, m) , the tubes are metallic if $n - m = 3i$, i being an integer, or are semiconducting if $n - m \neq 3i$. The energy bandgap E_g of semiconducting tubes decreases with increasing tube diameter according to $E_g = (\gamma_0 \cdot a_{C-C})/d_T$ [30]. Here, a_{C-C} denotes nearest-neighbor distance and d_T denotes the tube diameter which is given by $d_T = \sqrt{3}a_{C-C}\sqrt{m^2 + mn + n^2}/\pi$. This leads to a bandgap of 0.34 eV for a typical tube diameter of 1.2 nm.

1.5. Carbon Thin Films

As mentioned, due to its three possible hybridization states (sp , sp^2 , sp^3), carbon can exist in various stable allotropic forms. The thermodynamically stable form of carbon at normal conditions is graphite. The free energy difference between the different allotropic phases is relatively small, for instance 0.03 eV/atom between diamond and graphite, which is slightly higher than $k_B T$ at room temperature (0.025 eV). However, there is always a large energy barrier between the different allotropic phases, which makes them all very stable at normal conditions. Therefore all stable allotropic as well as amorphous carbon phases can be synthesized or deposited as thin films by plasma processes or pyrolysis.

1.5.1. Diamond Films

In 1971 Deryagin and Fedoseev reported successful continuous growth of diamond at low pressures by methods which they later described [31]. The outstanding properties of diamond, including its hardness, chemical inertness, good optical transparency, and high thermal conductivity, triggered enormous research activity in diamond thin film deposition during the past 15 years. The book *Low-Pressure Synthetic Diamond* edited by Dischler and Wild [32] gives a nice and complete overview on the manufacturing and applications of diamond thin films.

Diamond thin films can be deposited by various low-pressure techniques such as hot-filament, MW plasma, dc plasma, or plasma jet methods [33]. The low-pressure diamond deposition process is fundamentally different from those of diamondlike carbon (DLC). Characteristic for the DLC deposition process is the physical effect of the impinging energetic ions with the hydrocarbons physisorbed on the surface of the growing film. In opposition to that the diamond deposition process is the result of various chemical reactions on the surface of the growing film. The difference between the DLC and the diamond deposition processes clearly finds expression by the precursor gas needed. While for diamond deposition the hydrocarbon precursor must be strongly diluted with hydrogen (typically $\text{CH}_4/\text{H}_2 = 1/99$), the DLC deposition process does not need hydrogen. The hydrogen chemistry is essential for diamond growth at low pressures. The ternary C, H, O Bachmann diagram (Fig. 13) shows with which gas composition CVD diamond can be grown. The growth surface of diamond can be represented schematically by a layer of carbon atoms terminated with atomic hydrogen. Individual hydrogen atoms are removed and provide a chemically active site for addition of carbon. Hydrogen abstraction has been estimated to occur every $70 \mu\text{s}$ on average, with each such site being refilled after $15 \mu\text{s}$ [35, 36]. Growth occurs when a hydrocarbon radical is attached at an active site of the lattice and loses its hydrogen atoms through hydrogen abstraction. Among the different radicals (acetylene, acetyl [37], methane and methyl [38]), methyl radicals are usually accepted as the main growth species, especially for the (100) surface [38]. Harris [39] proposed a five-step methyl based growth model as shown in Figure 14. First, the abstraction of a surface hydrogen atom by atomic hydrogen of the plasma produces a H_2 molecule and a radical site on the growing surface (Fig. 14b). This site can receive a hydrogen atom (Fig. 14a) or a methyl radical (Fig. 14c). The next step is the abstraction by atomic hydrogen from the plasma of a hydrogen atom of the methyl group or of another surface hydrogen atom (Fig. 14d). Finally, another hydrogen atom is abstracted to leave two adjacent radical carbon atoms. They react to form a carbon-carbon

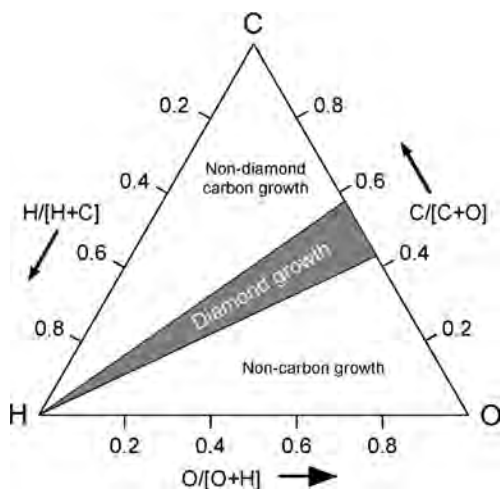


Figure 13. Ternary diagram for CVD diamond film growth according to Bachmann et al. [34].

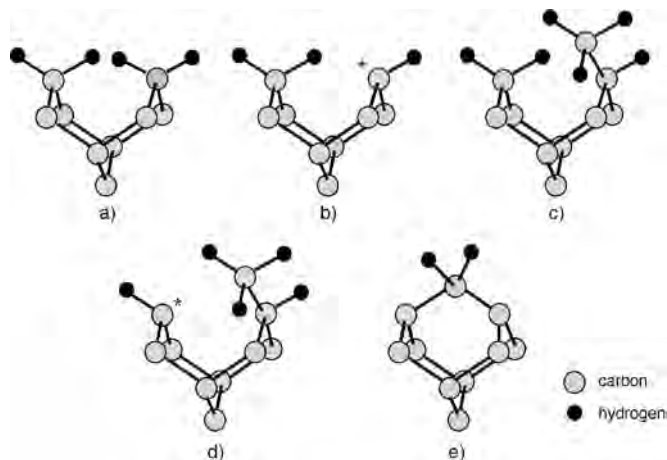


Figure 14. Methyl based diamond growth according to Harris [39].

bond (Fig. 14e). The so-formed molecule is called adamantane. In parallel, a methyl group can be added to the CH_2 radical site to form an ethyl group (C_2H_5), diversifying the growth mechanisms [39]. Frenklach and Spear [40] proposed a growth mechanism based on addition of acetylene to radical site. Characteristic for CVD diamond deposition is the need for nucleation centers on the substrate surface. On commercial silicon wafer without any treatment the CVD diamond process leads to the deposition of individual nanocrystallites with a very low density, lower than 10^5 nuclei per cm^2 . The main reason for this extremely low nucleation density is the high surface energy of diamond. Surface nucleation enhancement is necessary in order to get continuous polycrystalline films. Three main mechanisms are known for diamond nucleation:

- nucleation on dislocation ledges, kinks, or intentional scratches
- diffusion barrier enhanced nucleation
- nucleation on a molecular precursor

The corresponding techniques are:

- Scratching the substrate with diamond or ceramic powders creates defects which act as nucleation centers [41]. The nucleation density is between 10^5 and 10^{10} cm^{-2} .
- Enhanced nucleation on a precursor such as thin metal films, graphite fibers, C_{60} , or others [41, 42] can also be used. The nucleation density is between 10^6 and 10^{10} cm^{-2} depending on the precursor.
- A further technique is the bias enhanced nucleation by applying a dc or radio frequency potential during the first few minutes of the deposition [43–45]. The nucleation density obtained with this technique is between 10^8 and 10^{11} cm^{-2} . This technique is the only one which allows oriented growth relative to the substrate as shown in Figure 15.

The quality of the diamond films depends strongly on the deposition conditions and can be indicated by the full width at half maximum (FWHM) of the Raman line at 1332 cm^{-1} . Films with high crystalline quality are typically grown at $T = 850 \text{ }^\circ\text{C}$ and carbon precursor concentration of about 1%

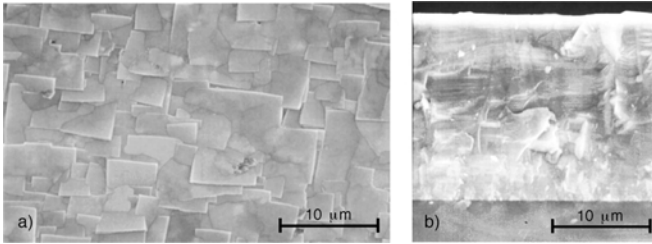


Figure 15. SEM pictures of (100)-oriented polycrystalline diamond film grown by PACVD on silicon (100): (a) top view, (b) side view. Reprinted with permission from [130], E. Maillard-Schaller, Ph.D. Thesis No. 1145, University of Fribourg, Switzerland, 1996.

(e.g., CH_4) in hydrogen. These films exhibit a strong and sharp Raman line 1332 cm^{-1} (Fig. 16a). For higher substrate temperatures $T > 950\text{ }^\circ\text{C}$, and higher carbon precursor concentration the diamond films become nanocrystalline or ballast like as shown in Figure 16b. Zhu et al. [47] were the first to point out a relation between the quality of the diamond films measured by the FWHM of the Raman 1332 cm^{-1} line and the field emission properties. By decreasing the crystalline quality, monitoring it with the FWHM of the 1332 cm^{-1} Raman line, the threshold field to get an emission current of 1 nA decreases. The film they have investigated showed threshold fields above $20\text{ V } \mu\text{m}^{-1}$. Today CVD diamond films exhibiting threshold fields below $5\text{ V } \mu\text{m}^{-1}$ can be grown with reasonably good reproducibility.

1.5.2. Amorphous and Diamondlike Carbon Films

Apart from crystalline graphite and diamond, carbon films consisting of a disordered network of sp^2 and sp^3 bonded carbon can be deposited. Due to their disordered nature these films are referred to as being amorphous carbon. Amorphous carbon thin films may be broadly classified as:

- Amorphous carbon ($a\text{-C}$), usually deposited by physical vapor deposition processes.
- Hydrogenated carbon, ($a\text{-C:H}$), usually deposited by plasma-assisted chemical vapor deposition (PACVD) [48–51].

In general amorphous carbon films are well characterized by two parameters, the ratio of sp^3 to sp^2 bonded carbon and the amount of hydrogen in the films. According to that, the classification of amorphous carbon can be represented in a ternary phase diagram as shown in Figure 17. The corners at the base of the triangle correspond to diamond ($100\% sp^3$) and graphite ($100\% sp^2$). The upper limit for formation of solid films is defined by the tie line between the compositions of polyethylene $-(\text{CH}_2)_n-$ and polyethyne $-(\text{CH})_n-$.

The tetrahedral amorphous carbon ($ta\text{-C}$) and the hydrogenated tetrahedral amorphous carbon ($ta\text{-C:H}$) are often called diamondlike carbon as they can exhibit hardnesses close to that of diamond. DLC films can be synthesized at room temperature by PACVD or other ion assisted processes. Any hydrocarbon precursor with sufficient vapor pressure can in principle be used for PACVD of DLC films. Commonly used process gases are acetylene (C_2H_2) and methane (CH_4). The DLC deposition is a nonequilibrium

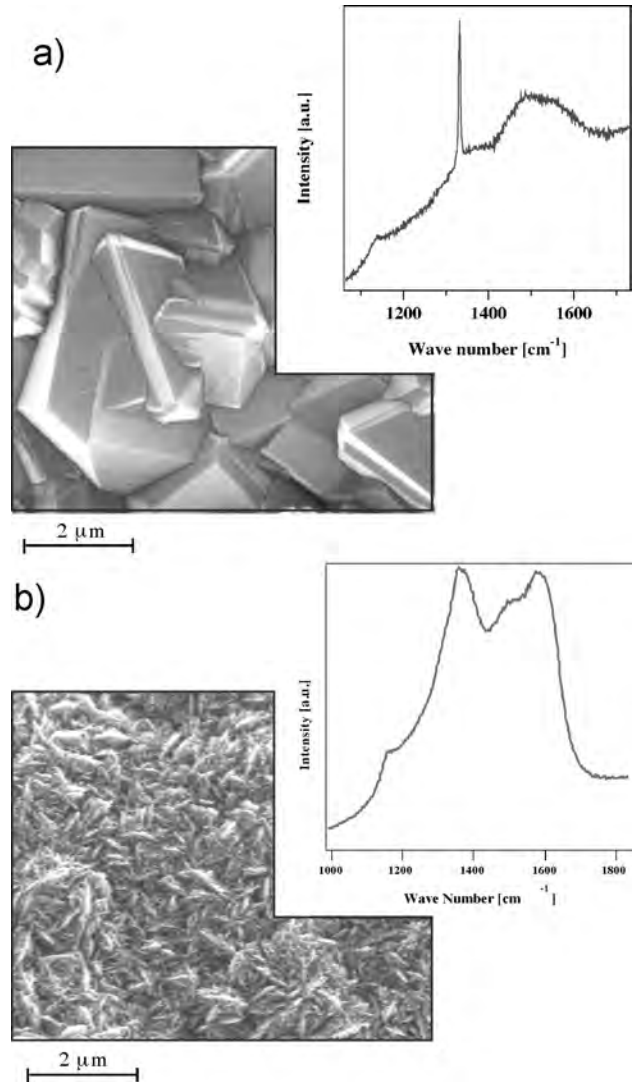


Figure 16. SEM images and Raman spectra. (a) Good crystalline diamond film grown @ $850\text{ }^\circ\text{C}$ and 1% CH_4 in H_2 . (b) Nanocrystalline diamond film grown @ $950\text{ }^\circ\text{C}$ and 5% CH_4 in H_2 . Reprinted with permission from [107], O. Gröning et al., *J. Vac. Sci. Technol. B* 17, 1064 (1999). © 1999, American Institute of Physics.

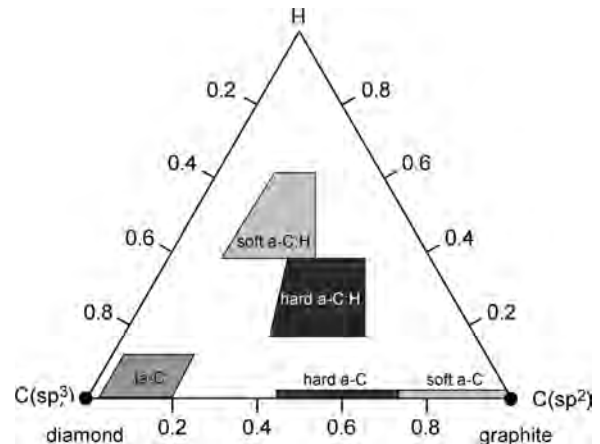


Figure 17. Phase diagram for amorphous carbon thin films according to Bachmann [52].

process characterized by the interaction of energetic ions with the surface of the growing film. The deposition of DLC by PACVD has to be done on negatively biased substrates to actuate reactions like thermal and pressure spikes at the growth surface by energetic ions. Tsai and Bogy [53] calculated for 100 eV ions thermal spikes of 3300 K and pressures of 1.3×10^{10} Pa for a period of 10^{-10} seconds. The lifetime of these spikes is much longer than the vibrational period ($\sim 10^{-14}$ s) for diamond and thus well beyond what is required to allow bonding. The DLC process forms a metastable amorphous material whose structure is conserved due to extremely high quenching rates of the thermal spikes. The hardness of the DLC film can be varied adjusting the substrate bias [54]. An excellent overview on the growth, physical properties, and applications of amorphous carbon thin films has been given by Silva et al. [55].

With regard to the electronic properties the ratio of the π and σ states plays an important role. Where the π states originate from sp^2 and sp^1 bonded carbon, σ states are contributed from all carbon atoms. As a consequence the σ states always form two extended bands as illustrated in Figure 18a. Depending on the amount of sp^2 and sp^1 bonded carbon, π bands of a more or less extended character are formed at the edges of the σ bands [56]. Therefore it is clear that the amount of the π states in the amorphous carbon will strongly influence the bandgap of the material. Due to the disordered nature of the material the band edges are not sharp but there are tail states extending into the gap. The semiconducting properties of amorphous carbon arise from the differences in the carrier mobility of extended and localized states and lead to the formation of a mobility gap as shown in Figure 18b. Due to the presence of localized states around the Fermi level and the band tails, electronic transport properties are associated with four different regions of the DOS [47].

- (a) transport by carrier excitation beyond the mobility edges into extended states at E_C and E_V

$$\sigma = \sigma_0 \exp\left(-\frac{E_C - E_V}{k_B T}\right) \quad (22)$$

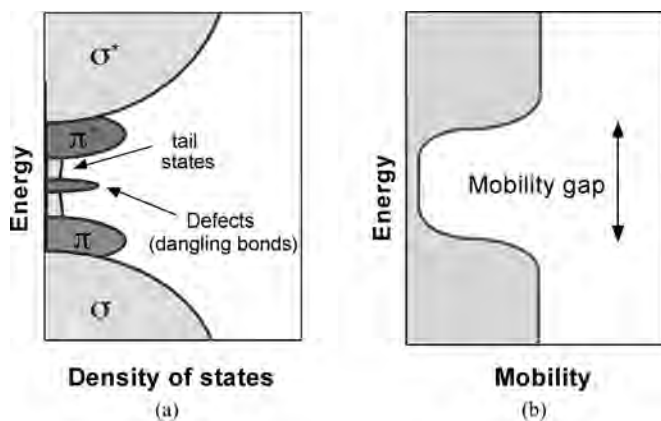


Figure 18. (a) Sketch of the DOS and (b) the mobility gap of a-C as a function of energy.

where $\sigma_0 = \mu_{\text{ext}} \cdot e \cdot N(E_C) \cdot k_B T$, μ_{ext} is the extended state mobility, and $N(E_C)$ is the density of states at the conduction band edge

- (b) transport by carrier excitation to localized states at the band edges and hopping at the band tail

$$\sigma = \sigma_1 \exp\left(-\frac{E_C^* - E_F + \omega_1}{k_B T}\right) \quad (23)$$

where $\sigma_1 \ll \sigma_0$, ω_1 is the hopping activation energy, and E_C^* is the tail states energy of the conduction band

- (c) transport by hopping of carriers in the tail states around the Fermi energy E_F

$$\sigma = \sigma_2 \exp\left(-\frac{\omega_2}{k_B T}\right) \quad (24)$$

where ω_2 is the hopping activation energy

- (d) variable-range hopping, dominant for most material at lower temperatures

$$\sigma = \sigma'_2 \exp(-BT^{-1/4}) \quad (25)$$

where $B = 2(\alpha^3/k_B N(E_F))^{1/4} = \text{const}$, α is a measure of the decay of the wave function on a single potential well, $\sigma'_2 = v_{\text{ph}} e^2 N(E_F) \langle R \rangle^2$, $\langle R \rangle$ is the average hopping distance, and v_{ph} depends on the phonon frequency

Hydrogen being monovalent can saturate dangling bonds in the amorphous carbon and therefore reduce the defect states in the gap as in the case of amorphous silicon [58].

1.5.3. Nanotube Films

Carbon nanotubes are ultrathin carbon fibers with nanometer-size diameter and micrometer-size length and were discovered by Iijima in 1991 [29] in the carbon cathode used for arc-discharge processing of fullerenes (C_{60}). The structure of CNTs may be viewed as enrolled cylindrical graphene sheets and closed by fullerene end caps. There exist SWNTs and MWNTs, consisting of several nested coaxial single wall tubules. Typical dimensions of MWNTs are: outer diameter 2–30 nm, inner diameter 1–3 nm, length 1–100 μm . The intertubular distance in MWNTs is 0.340 nm, slightly larger than the interplanar distance in graphite, which is equal to half of the unit-cell parameter c ($0.5c = 0.3455$ nm). SWNTs tend to agglomerate and form bundles of several tens of nanotubes. The SWNTs in bundles are in two dimensions and closed-packed, and the intertube distance is 0.334 nm [59].

Several methods have been developed to synthesize CNTs. All of them, arc evaporation [60], laser ablation [61], CVD [62], and plasma enhanced chemical vapor deposition (PECVD) [63], work at elevated temperatures (>600 $^\circ\text{C}$) and metal particles (e.g., Fe, Co, Ni) are involved in the reaction. The CNT growth by CVD or PECVD requires a metallic catalyst. The catalytic methods for CNT growth have their origin in the corresponding works on carbon fibers [64, 65]. Baker and Harris [65] proposed a model for the catalytic carbon filament growth in which the hydrocarbon precursor is decomposed on the surface of the catalytic

metal particle, producing hydrogen and carbon, which then dissolves into the metal. Then the dissolved carbon diffuses through the particle, to be precipitated on the trailing face, forming the filament. This model seems also be applicable for the general CNT growth (Fig. 19). Figure 20 shows scanning electron microscope (SEM) pictures of a CNT brush grown perpendicularly on the substrate. The backscattered electron image (Fig. 20b) reveals small metal clusters (white spots) on top of the CNT brush. This picture supports that the catalytic growth model for carbon fibers proposed by Baker and Harris [65] is also valid for CNTs. Figure 21b shows a transmission electron microscope (TEM) picture of a nanotube with the encapsulated metal catalyst. However the growth mechanisms responsible for the structure type of the growing CNT (SWNT, MWNT, chirality) are still unknown.

Using the CVD process dense CNT films with preferential orientation normal to the substrate surface can be grown [66–68]. The orientation of the individual nanotubes in the film is forced by the tube density. Above a critical density the direction of the growing nanotube is confined by the surrounding growing tubes resulting in a growth orientation normal to the surface. Remarkable for the growth of dense CNT films by CVD is that all individual nanotubes have exactly the same height. The SEM picture in Figure 21a reveals that the CNT film consists straight as well as twisted CNTs suggesting that the individual CNTs have different growth rates. The straight nanotubes in the film may have the lowest growth rate and may limit the growth rate of the entire film by anchoring the “cap” of the film. We observed that the “cap,” the top of the CNT film, is a thin layer composed of clusters from the metal catalyst and amorphous carbon. It seems that the individual nanotubes cannot pass through this thin film. Nanotubes with higher growth rates are therefore confined within in the growing film and are forced to twist which may explain the film structure shown in Figure 21. Because the CNT growth is a catalytic process it is relatively easy to prepare patterned films. For this two strategies can be followed, one by patterning the catalyst material, from solutions or by evaporation onto the substrate using classical lithography techniques [69, 70]. We, for example, used microcontact printing to pattern the catalyst onto the substrate [71]. For this a polydimethylsiloxane stamp was first hydrophilized to considerably increase the affinity between stamp and the metal catalyst–ethanol

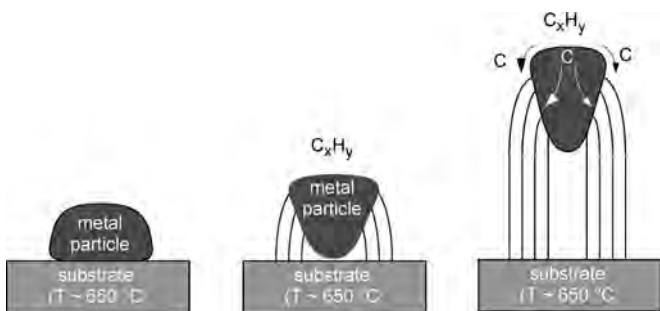


Figure 19. Model for the catalytic growth of CNT according to the model of Baker and Harris [65] proposed for the growth of carbon filaments.

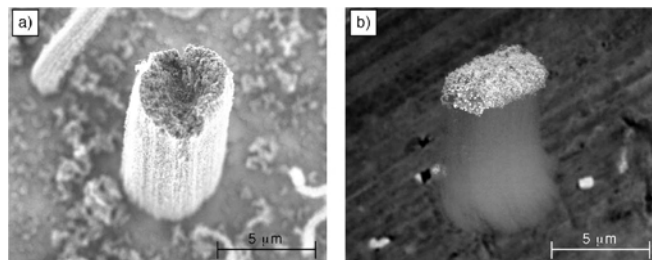


Figure 20. SEM pictures of a CNT brush produced by CVD: (a) secondary electron image, (b) backscattered electron image.

solution. The stamp was subsequently inked and after drying the catalyst was printed on a silicon wafer. Wei et al. [72] showed another route to produce patterned CNT films. Instead of patterning the catalyst onto the substrate they stimulated CVD growth of a CNT by exposing SiO_2 patterned Si-wafers to a xylene/ferrocene [$\text{C}_8\text{H}_{10}/\text{Fe}(\text{C}_5\text{H}_5)_2$] vapor mixture. They used substrate consisting of Si(100) wafers capped with 100 nm thick thermal oxide. Patterning of Si/ SiO_2 was generated by photolithography followed by a combination of wet and/or dry etching (i.e., standard microfabrication technology). The precursor mixture used gives rise to selective growth of MWNTs of diameters 20–30 nm on silica surfaces [73]. There is no CNT growth on Si, but the aligned CNTs grow readily on SiO_2 in a direction normal to the substrate surface.

Recently several research groups have shown that well-aligned CNTs with controlled site density can be grown by PECVD [74–77]. Bower et al. [78] used microwave CH_4/H_2 plasma to show that PECVD enables a vertically oriented growth of MWNTs. In elegant experiments, the growth was first started with the plasma on and after a certain period, the plasma was turned off and the growth was continued with the same deposition parameters. While the nanotubes in the first period under PECVD conditions exhibited a high degree of alignment, the continued growth under CVD conditions showed randomly oriented curly tubes. The authors claimed that the electric self-bias imposed on the substrate surface appears to be the primary mechanism responsible for the conformal alignment. The advantage of the PECVD process compared to the CVD process is that the alignment

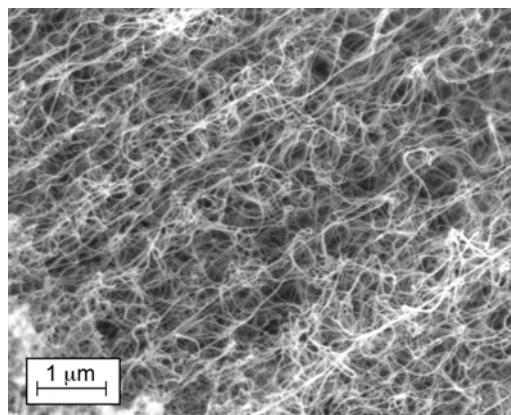


Figure 21. SEM picture from the side view of the CNT brush shown in Figure 20.

of the CNT can be achieved by the influence of the electric field and not by steric repulsion, which allows the growth of aligned CNTs with controlled site densities as shown in Figure 22.

1.6. Hope for the Flat Thin Film Electron Emitter

In the early 1990s several publications [80–82] were given showing highly efficient electron emission at low electric fields from carbon based materials like diamond and DLC thin films. These cathode films are referred to as flat thin film electron emitters and were thought to provide the solution to several of the technological difficulties associated with the cathode design in FEDs. The reason for this stems from the fact that a surface which emits electrons more or less homogeneously at fields as low as some few volts per micrometer due to a low work function ϕ or NEA requires less expensive patterning processes, much simpler device design, and much cheaper driving electronic circuitry. Probably the most influential paper was that of Geis et al. [82]. They built an array of diodes (Fig. 23), known as a hot-electron device, described in 1966 [83]. These diodes apparently work by adiabatic heating the electrons by passage across a p - n junction and hot electrons escape from the lateral surfaces. It is suggested that electron emission efficiency be improved by having low electron affinity emitting surface. Geis and his co-workers suggested for their diamond devices that the NEA of certain crystal planes is responsible for the electron emission, which leads peoples to dream about a flat electron emitter. In contrast to the micrometer-sized design of field emitter array (FEA) tips, the ideal flat electron emitter could be homogeneously deposited by, for example, chemical vapor deposition over rather large areas

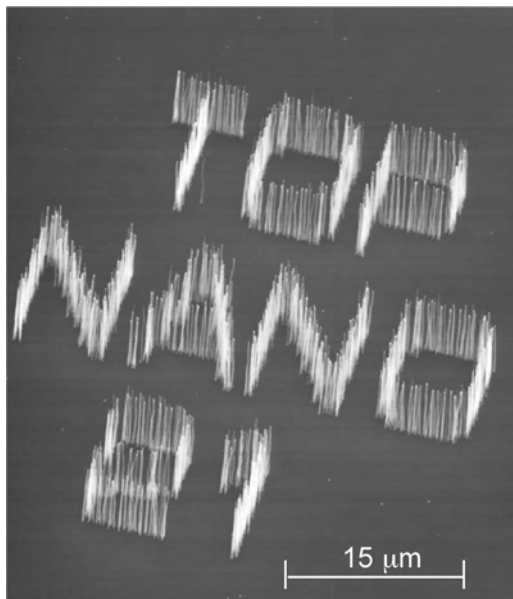


Figure 22. SEM image of deterministically grown carbon nanofibers using PECVD showing the name of the Swiss CTI program Top Nano 21 (in collaboration with K. Teo and W. Mine from the University of Cambridge [79]).

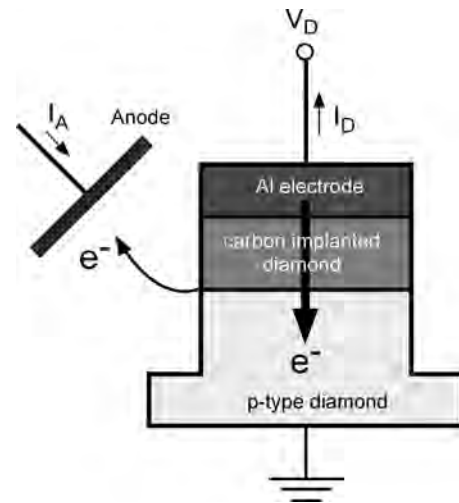


Figure 23. Drawing of the cathode design used by Geis et al. [82].

with much lower spatial tolerance and hence lower cost. Instead of defining hundreds of FEA microtips as electron sources for one pixel of an FED, the whole FEA subelement could be replaced by an electron emitting flat thin film as illustrated in Figure 24, where, however, the gate not has been sketched around the flat thin film emitter.

2. CHARACTERIZATION OF THE FIELD EMISSION BEHAVIOR

In the 1990s carbon thin films received great interest as electron emitting cathodes. In 1991 the Russian scientists Djubua and Chubun [80] investigated the electron field emission from different materials in Spindt tip geometry and found DLC emitters show the lowest turn-on voltages. In the same year Wang and co-workers [81] presented electron field emission measurements on polycrystalline CVD diamond films. They suggested that emission comes from areas between crystallites and not from sharp pointed crystallites as might be expected. They speculated that graphite inclusions or NEA might be responsible for the low turn-on voltages. Afterward, for a wide range of different carbon

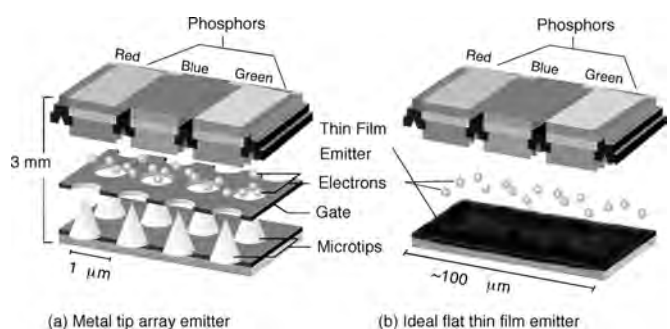


Figure 24. The principal design of a flat field emission display in the case of (a) a metal tip array [84] and (b) an ideal flat thin film emitter without surface asperities or tips. Reprinted with permission from [121], L. O. Nilsson, Ph.D. Thesis No. 1337, University of Fribourg, Switzerland, 2001.

based materials unusual field emission properties have been demonstrated [85–91]. Certain DLC and CVD diamond films show emission currents in the mA range at applied electric fields as low as $2 \text{ V } \mu\text{m}^{-1}$. Despite the promising experimental results little was known about the mechanism which accounts for the observed currents. Several theoretical approaches have been forwarded suggesting emission from energy bands in the gap [92]. However, all models fail when explaining the outstanding role of carbon material for field emission. Investigations on CVD diamond film have shown that emission does not occur homogeneously over the surface but is rather concentrated in μm and sub- μm sized spots [93].

2.1. Emission Models and Energy Distribution of the Emitted Electrons

As mentioned, many models to explain the field emission from CVD diamond and also from single crystalline diamond have been presented. Figure 25 schematically shows different emission models. Since the measurement of the field emitted electron energy distribution (FEED) will be important within the context in this chapter, implications of the different models on the peak shape and position of the electron distribution are discussed here. The models presented cannot give a complete overview of all proposed models for the origin of the low field electron emission from diamond and related materials. An excellent overview on hypotheses about emission mechanism from carbon films has been given by Forbes [94].

2.1.1. Classical Fowler–Nordheim Model

In Figure 25a the classical situation of field emission from metals is depicted. On the left hand side the density of occupied electron states of the emitter near the Fermi energy is assumed to be the Fermi–Dirac distribution for $T = 300 \text{ K}$. An electric field of $2700 \text{ V } \mu\text{m}^{-1}$ and an emitter work function of 5.3 eV are assumed. Under the action of the intense field the surface potential step, confining the electrons to the solid, becomes a triangular barrier. If the width of the barrier at the Fermi energy decreases below about 2 nm the tunneling probability for the electrons is not neglectable anymore and an emission current can be observed. On the right hand side of Figure 25a the resulting FEED is shown. The energy distribution shows a peak centered at the Fermi energy E_F of the emitter. The low energy side of the peak shows the exponentially decreasing tunneling probability with decreasing energy due to the increasing width of the tunneling barrier. The position of the FEED peak in energy is located at the potential of the emitting surface. Usually the reference energy is the Fermi level position of the back contact to the emitter. This means that if there is a potential difference between the emitter surface and the contact, the position of the FEED peak will shift to lower energies. Such potential drops always occur due to the electron emission which charges the emitter surface positively. The amount of emitter charging is such that it brings emission current and supply current through the emitter in equilibrium. The current–field characteristic of the emission is described by the Fowler–Nordheim relation (16).

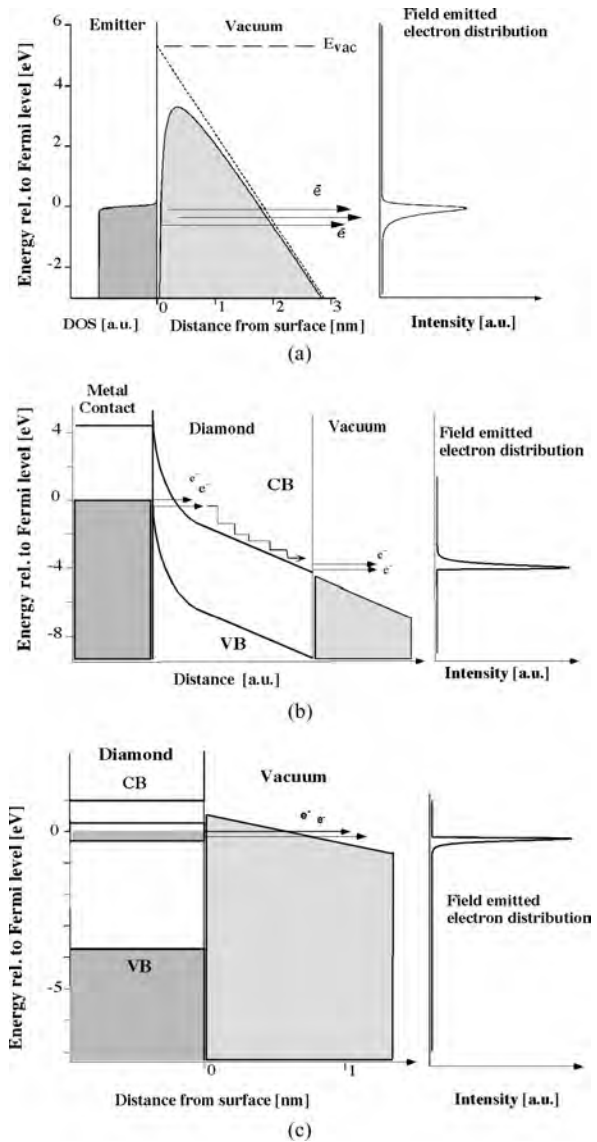


Figure 25. Different electron emission models proposed for diamond and the resulting electron energy distributions. (a) Classical Fowler–Nordheim tunnelling, (b) conduction band emission due to electron injection, (c) defect band emission. Reprinted with permission from [111], O. Gröning et al., *J. Vac. Sci. Technol. B* 17, 1970 (1999). © 1999, American Institute of Physics.

2.1.2. Conduction Band Emission Model

Figure 25b displays the emission model proposed by Geis et al. [95] to explain the low field electron emission from nitrogen containing single crystalline diamond and polycrystalline CVD diamond having NEA. The EA of a solid is defined as the energy difference between the lowest unoccupied electron state in the solid and the energy of an electron at rest outside the solid (vacuum level). In case of metals the work function ϕ and the electron affinity χ are equivalent, since there is no energy difference between the highest occupied and the lowest unoccupied states ($T = 0 \text{ K}$). In case of semiconductors and insulators the situation is different due to separation of the occupied and unoccupied states by the energy gap. Semiconductors and insulators show NEA, if the

vacuum level is below the conduction band minimum. This means that electron in the conduction band will experience no surface potential barrier for the emission. In case of diamond surfaces it was demonstrated that hydrogen termination of the (111) and (100) of *p*-type diamond surfaces leads to NEA [96, 97]. It is obvious that NEA related electron emission will crucially depend on an efficient mechanism to populate the empty conduction band with electrons. In the case of boron doped single crystalline diamond such population of the conduction band during field emission seems not to occur and it was found that the field emission originates from the valence band at local fields above $2000 \text{ V } \mu\text{m}^{-1}$ [98]. Substitutional nitrogen in diamond is known to produce a deep donor state 1.7 eV below the conduction band [99]. But the activation energy of 1.7 eV is too large to give an efficient thermal excitation of electrons into the conduction band at room temperature. Nevertheless, Geis proposed the ionization of this donor state can lead to a space charge layer at the metal diamond interface, causing downward band bending in the diamond. In the case of an ionized donor density of more than $2 \times 10^{19} \text{ cm}^{-3}$, the depletion region is thinner than 20 nm, which allows electrons to be injected from the metal contact into the conduction band of the diamond, when a relatively low potential drop of a few volts over the depletion layer is present. The injected electrons will thermalize quickly (typically in 10^{-12} s) to the conduction band minimum, where they are transported in a diffusion dominated process, with typical lifetimes of 10^{-9} s [100], to the surface and are emitted into vacuum due to NEA. In the case of nitrogen containing diamond a CsO monolayer seems to be necessary to create a sufficiently large dipole moment to produce the NEA.

Diederich et al. [16] have shown by UPS that hydrogen termination can generate an efficient NEA surface for the *B*-doped diamond (100) surface but not for the *N*-doped diamond (100) surface due to the high upward band bending. In the NEA model the field emission current will be limited by the tunneling of electrons through the interfacial potential barrier and not by the surface potential barrier. The FEED will reflect the energy distribution of the indicating position of the conduction band minimum. In the ideal case of flat band conditions at the surface the width of the FEED peak should be of the order of $k_B T$ although strong band bending at the surface can lead to a significantly larger width of the FEED peak. Furthermore, the position of the FEED peak should be shifted to lower energies, reflecting the potential drop between the diamond surface and the metal contact, which is necessary for electron injection.

2.1.3. Defect Band Emission

Figure 25c displays the emission model proposed first proposed by Zhu et al. [47]. This model accounts for the experimental observation that the field emission properties of CVD diamond films correlate with the film quality measured by the FWHM of the Raman 1332 cm^{-1} line, indicating a decreasing threshold field with increasing linewidth. In order to explain this behavior Zhu et al. proposed the presence of defects bands in the energy gap of the diamond. The formation of these defects bands is supposed to raise the Fermi level close to the vacuum level and is

therefore responsible for a strong reduction of the work function of the defective diamond film. This could only occur if no Fermi level pinning at the surface states is assumed. Furthermore, the defects bands would provide a steady current flow to the surface and sustain a continuous current. The reduced work function will then give rise to the observed field emission. A threshold field of $20 \text{ V } \mu\text{m}^{-1}$ for 1 nA emission current corresponds to a work function $\phi \cong 0.2 \text{ eV}$ and a threshold field of $3 \text{ V } \mu\text{m}^{-1}$ would correspond to $\phi \cong 0.05 \text{ eV}$ (assuming Fowler–Nordheim-like emission with no field enhancement). These work function values are extremely low and highly questionable. Yet, if a moderate local field enhancement, which could also explain the spotty local emission characteristic of diamond films, of 10–30 is taken into account, the work function values would increase to a more reasonable range around 1 eV. There are materials showing work function values around 1.2 eV, like ScO [101]. In this model the electrons are emitted due to the tunneling through the surface potential barrier, like the classical Fowler–Nordheim tunneling (Fig. 25a). Yet due to the reduced work function the local fields involved in the emission process can be considerably low. The resulting FEED would be characterized by very narrow peaks due to the low local field at the emission site. The width of the surface potential barrier would rapidly increase with decreasing energy, leading to a narrow energy range, where the tunneling probability is large enough to give measurable electron emission.

2.2. Measurement of the Field Emission Properties

2.2.1. Current–Voltage Measurements

Usually current–voltage (I – V) measurements are used to characterize the electron emission behavior according to the Fowler–Nordheim relation (16). From these measurements technologically important parameters such as threshold field F_{th} or the current density j can be determined, but not the work function ϕ as the physically relevant parameter. The reason for this is that experimentally one does not measure current–field characteristics but current–voltage characteristics, where one relates the applied voltage to some applied field for example by dividing the applied voltage with the anode cathode distance. The problem is that this applied field may not correspond to the local field present at the emission site due to some field enhancement effects. Assuming that F_0 ($F = F_0\beta$) denotes the applied electric field in a field emission measurement, the Fowler–Nordheim relation (16) will change to

$$j = \frac{e^3}{4(2\pi)^2 \hbar \phi} F_0^2 \beta^2 \exp\left(-\frac{4\sqrt{2m_e}}{3\hbar} \frac{\phi^{1.5}}{eF_0\beta}\right) \quad (26)$$

with

$$B_v = \frac{e^3}{4(2\pi)^2 \hbar \phi} \quad \text{and} \quad A_v = \frac{4\sqrt{2m_e}}{3\hbar e}$$

The Fowler–Nordheim relation can be written by

$$j = B_v F_0^2 \beta^2 \exp\left(-A_v \frac{\phi^{1.5}}{F_0\beta}\right) \quad (27)$$

By replacing the local field F at the emission site by the applied field F_0 , the electron emission will yield a straight line in the Fowler–Nordheim (FN) plot [$\ln(j/F_0^2)$ vs $1/F_0$], as can be seen from the Fowler–Nordheim relation (27). The slope of this straight line will be equal to

$$\text{FN}_{\text{Slope}} = -A_v \frac{\phi^{1.5}}{\beta} \quad (28)$$

F_0 is a function of the applied voltage, whereas β generally is unknown. In the case of well defined emitter geometry (e.g., a tip with aspect ratio $h/r = \beta$), the work function ϕ can be calculated within a certain accuracy. In the case of thin film emitters this is generally not possible. This means that the work function ϕ of the emitter cannot be determined from the measurement of the I – F_0 (resp. I – V) characteristics alone.

2.2.2. Field Emission Spectroscopy

The situation is different when one has additional information such as the energy distribution of the field-emitted electrons [46]. Figure 26 shows schematically the situation at a metal surface under field emission conditions ($\phi = 5.3$ eV and $F = 2700$ V/ μm), and the resulting energy distribution of the emitted electrons.

In section 1.2.4, Eq. (13), it was shown that the transmission probability for an electron with energy $E(k_x, k_y, k_z)$ close to the Fermi energy E_F can be expressed by

$$D(E) = \exp\left(-\frac{4\sqrt{2m_e} \phi^{1.5}}{3\hbar} \frac{eF}{eF}\right) \exp\left(\frac{2\sqrt{2m_e} \phi^{0.5}}{\hbar} \frac{eF}{eF} (E_x - E_F)\right)$$

with $E_x = \hbar^2 k_x^2 / 2m_e$ (the kinetic energy component perpendicular to the emitter surface).

The total energy distribution $P(E)$ of the field emitted electrons can be derived from (13) by

$$P(E) = \frac{2e}{(2\pi)^3} f(E, E_F, T) \int_{k_x^2 + k_y^2 + k_z^2 = E} D(E) \frac{\hbar k_x}{m_e} dk_x dk_y dk_z \quad (29)$$

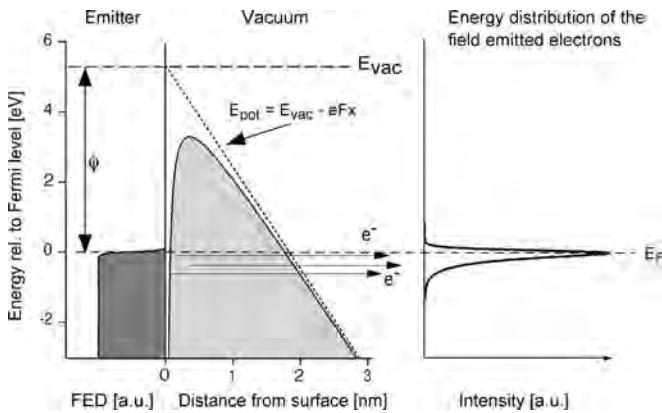


Figure 26. Schematic illustration of the situation at a surface under field emission conditions and the resulting energy distribution of the field emitted electrons (calculated for $F = 2700$ V/mm and $\phi = 5.3$ eV).

Substituting of (13) into (29) and solving the integral, one finds

$$P(E) = f(E, E_F, T) \frac{\sqrt{2m_e}}{2(2\pi)^2 \hbar^2} \frac{eF}{\phi^{0.5}} \exp\left(-\frac{4\sqrt{2m_e} \phi^{1.5}}{3\hbar} \frac{eF}{eF}\right) \times \exp\left(2 \frac{\sqrt{2m_e} \phi^{0.5}}{\hbar} \frac{eF}{eF} (E - E_F)\right) \quad (30)$$

This relation for the total energy distribution of the emitted electrons can be divided in an energy dependent and a field dependent intensity term, denoted as $B(F, \phi)$. The relation (30) can then simplified to

$$P(E) = f(E, E_F, T) \cdot B(F, \phi) \exp\left(2 \frac{\sqrt{2m_e} \phi^{0.5}}{\hbar} \frac{eF}{eF} (E - E_F)\right) \quad (31)$$

Stratton [102] modified relations (30), (31) in order to describe the total field emitted energy distribution of electrons originating from the valence band and obtained

$$P_V(E) = f(E, E_F, T) \cdot B(F, \phi) \times \exp\left(\frac{2\sqrt{2m_e} (\chi + E_G)}{\hbar} \frac{eF}{eF} (E - E_V)\right) \times \left(1 - \exp\left(-\frac{2r\sqrt{2m_e} (\chi + E_G)}{\hbar} \frac{eF}{eF} (E - E_V)\right)\right) \quad (32)$$

where χ is the electron affinity of the semiconductor, E_G is the energy gap, E_V is the energy of the valence band maximum, and $r = m_e/m^*$ is the ration of the electron mass and the band electron mass. To fit the field emission spectra (FES) of carbon materials the relation (32) with $E_V = E_F$, $E_G = 0$, $\chi = 0$, and $r = 1$ can be used due to the zero bandgap semiconductor character of graphite. It has to stressed that relation (31) assuming emission from a free electron gas and relation (32) assuming emission from the valence band edge are extreme cases for carbon materials; the true character can be somewhere in between.

With

$$C_v := 2 \frac{\sqrt{2m_e}}{e\hbar} \quad (33)$$

one can easily see from relations (26) and (31) that

$$\frac{A_v}{C_v} = \frac{2}{3} \phi U_0 \Rightarrow \phi = \frac{3}{2U_0} \frac{A_v}{C_v} \quad (34)$$

where A_v is the slope of the Fowler–Nordheim plot (28) with respect to the applied voltage U_0 and C_v is the exponential factor of the low energy part of the field emission energy distribution measured at the applied voltage. By determining A_v and C_v the work function ϕ at the emission site can be determined without the need to know the field enhancement factor β . Knowing the work function the local field present at the emission site can be determined from

$$F = 2 \frac{\sqrt{2m_e} \phi^{0.5}}{e\hbar} \frac{eF}{C_v} \quad (35)$$

In these considerations and derivations a triangular emission barrier as described by relation (7) is assumed.

A significant improvement of the emission model results from the influence of the image charge potential on the derivation of the Fowler–Nordheim law and the total energy distribution. The Fowler–Nordheim relation (16) becomes

$$j = \frac{e^3}{4(2\pi)^2 \hbar \phi} \frac{1}{t^2(y)} F^2 \exp\left(-\frac{4\sqrt{2m_e} \phi^{1.5}}{3\hbar} \frac{\phi^{1.5}}{eF} v(y)\right) \quad (36)$$

with

$$y = \frac{\Delta\phi(F)}{\phi} = \frac{\sqrt{\frac{e^3 F}{4\pi\epsilon_0}}}{\phi} \quad (37)$$

where $t(y)$ and $v(y)$ are the so-called elliptical functions which are tabulated [103]. The parameter y is the ratio if the field dependent work function lowering $\Delta\phi(F)$, due to the influence of the image charge potential (Schottky effect) and the work function ϕ of the emitter. The total energy distribution transforms into

$$P(E) = f(E, E_F, T) \frac{\sqrt{2m_e}}{2(2\pi)^2 \hbar^2} \frac{eF}{\phi^{0.5}} \frac{1}{t(y)} \times \exp\left(-\frac{4\sqrt{2m_e} \phi^{1.5}}{3\hbar} \frac{\phi^{1.5}}{eF} v(y)\right) \times \exp\left(\frac{2\sqrt{2m_e} \phi^{0.5}}{\hbar} \frac{\phi^{0.5}}{eF} t(y)(E - E_F)\right) \quad (38)$$

Figure 27 displays the values of the elliptical functions $t(y)$ and $v(y)$. In the field and work function range for carbon field emitters the parameter y varies between 0.3 and 0.4. In this regime the following approximations for $t(y)$ and $v(y)$ can be made:

$$t(y) \approx 1.02 \quad (39)$$

$$v(y) \approx 0.98 - 1.1y^2 \quad (40)$$

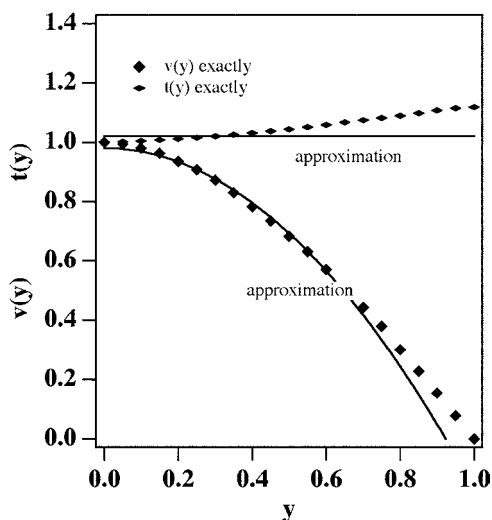


Figure 27. Plot of the elliptical functions $t(y)$ and $v(y)$. The markers represent the tabulated values [103] and the solid lines are approximations to $t(y)$ and $v(y)$.

Substituting (39) and (40) into (37) the Fowler–Nordheim relation becomes

$$j = \frac{1}{1.04} \frac{e^3}{4(2\pi)^2 \hbar} \frac{F^2}{\phi} \exp\left(\frac{e^2 \sqrt{2m_e}}{3\pi \hbar \epsilon_0 \phi^{0.5}}\right) \times \exp\left(-0.98 \frac{4\sqrt{2m_e} \phi^{1.5}}{3\hbar} \frac{\phi^{1.5}}{eF}\right) \quad (41)$$

From relations (41) and (38) one can see that the estimation of the work function ϕ taking into account the image charge potential, using the slope of the Fowler–Nordheim plot A_v and the exponential factor C_v , will lead to

$$\phi = \frac{1.02}{0.98} \frac{3}{2} \frac{A_v}{C_v U_0} = 1.04 \frac{3}{2} \frac{A_v}{U_0 C_v} \quad (42)$$

This is about 4% larger than without taking the image charge potential into account (34).

2.2.3. Example: Determination of the Work Function ϕ of MWNT

Experimental Setup The energy resolved field emission measurements were carried out in an OMICRON surface analysis system (base pressure $p < 10^{-10}$ mbar) equipped with a VSW EA 125 HR electron energy analyzer. The measurements were carried out in the constant analyzer energy mode with pass energy of 5 eV which corresponds to an energy resolution of 40 meV between 100 and 1000 eV kinetic energy. The high voltage was set to the sample by a Keithly 237 instrument with a ripple voltage less than 5 mV. The field emission spectra were measured between 1 pA and 1 nA total emission current, with count rates of 100 to 10^6 cps. Figure 28 shows the cut through the sample holder used for the measurements. Details of the experiment can be found in [104].

Results Figure 29 displays a series of FES measured from a sample of MWNTs recorded at room temperature at different applied voltages and therefore different electric fields. The applied voltage U_0 was subtracted from the kinetic energy scale of all spectra giving the energy relative to the

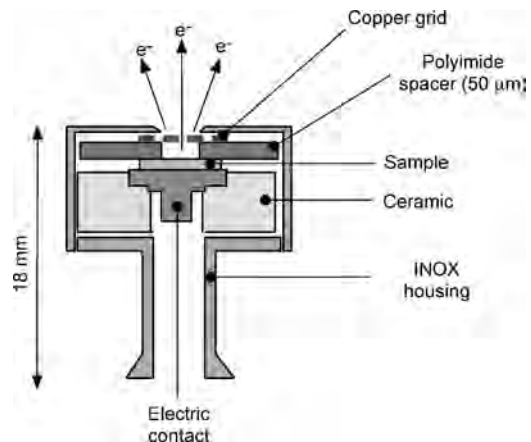


Figure 28. Schematic cross-sectional view of the sample holder used for the FES measurements.

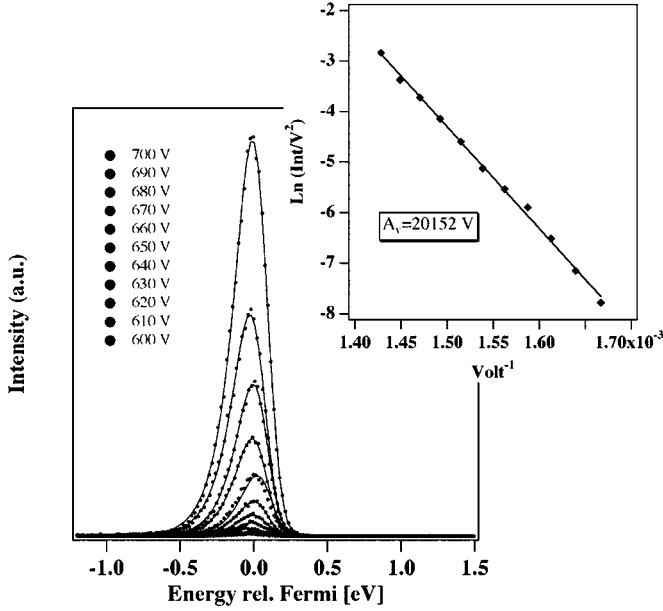


Figure 29. Series of FES of a MWNT field emitter recorded at different applied voltages. The inset shows the FN plot derived from the FE spectra. A_v is the slope of the FN plot. Reprinted with permission from [46], O. Gröning, Ph.D. Thesis No. 1258, University of Fribourg, Switzerland, 1999.

Fermi energy E_F . The solid lines are fits to the data using relation (32) assuming $T = 0$ K and taking the spectrometer resolution into account. By integrating the spectra over the energy we obtain a value which is proportional to the emission current density. Therefore we obtain a current-voltage characteristic that can be displayed in a FN plot (inset Fig. 29).

The FES in Figure 29 show a very narrow, asymmetric shaped energy distribution (FWHM = 375 meV) of the emitted electrons located at the Fermi energy E_F . As discussed in Section 2.1 such an energy distribution is characteristic for Fowler–Nordheim tunneling (Fig. 25a). The straight line in the FN plot (inset Fig. 29) over five orders of magnitude in the emission current proves the Fowler–Nordheim emission for the MWNT field emitter.

As the slope of the FN plot with respect to the field F at the emission site depends on the work function alone by $\phi^{1.5}$, the work function ϕ of the emitter can be determined. Yet we have to realize that in a field emission experiment current-voltage characteristics are measured. In the case of two parallel plates acting as anode and cathode separated by a distance d , the applied field is given by $F_0 = U_0/d$. The local field F at the emission site is then $F = F_0 \cdot \beta$. As discussed β is generally not known and the FN plot is plotted with coordinates $\ln(j/F_0)$ vs F_0^{-1} . Hence the slope of the FN plot is proportional to $\phi^{1.5}\beta^{-1}$. The FN plot depicted in the inset of Figure 29 is given with respect to the applied voltage and the slope $\text{FN}_{\text{slope}} = -A_v\phi^{1.5}\beta^{-1}$ (28) equals 20,152 V. The local field F at the emission site can be expressed by $F = U_0 \cdot \beta$, where β is the field enhancement factor, this time not with respect to the applied field F_0 but to the applied voltage U_0 . Therefore β has in this case the dimension $[\text{m}^{-1}]$.

Figure 30 shows the field emission spectrum from the series in Figure 29 recorded at an applied voltage of $U_0 = 680$ V. The dashed line is a Gaussian curve fitted to the high energy side of the peak, whereas the solid line is a fit according to relation (32). One can see the asymmetric shape of the field emission distribution, where the low energy side of the peak shows the exponential decrease with decreasing energy as expected. Using the definition (33) for C_v the relation for the total energy distribution $P(E)$ (31) can be simplified to

$$P(E) = f(E, E_F, T)B(F, \phi) \exp\left(C_v \frac{\phi^{0.5}}{F}(E - E_F)\right) \quad (43)$$

Using this relation the low energy side of the FES can be fitted and we can obtain a value of

$$C_v\phi^{0.5}F^{-1} = C_v\phi^{0.5}U_0^{-1}\beta^{-1} = 9.09 [\text{eV}]^{-1}$$

With this value, the value for FN_{slope} , and relation (34) the work function ϕ at the emission site can be determined:

$$\begin{aligned} \frac{A_v\phi^{1.5}\beta^{-1}}{C_v\phi^{0.5}U_0^{-1}\beta^{-1}} &= \frac{A_v}{C_v}\phi U_0 = \frac{2}{3}\phi U_0 \\ \Rightarrow \phi &= \frac{3}{2U_0} \frac{A_v\phi^{1.5}\beta^{-1}}{C_v\phi^{0.5}U_0^{-1}\beta^{-1}} \\ \phi &= \frac{3}{2 \cdot 680 [\text{V}]} \cdot \frac{20156 [\text{V}]}{9.09 [\text{eV}]} = 4.89 \text{ eV} \end{aligned}$$

As can be seen the unknown field enhancement factor β is cancelled out in this calculation. The obtained work function value $\phi = 4.89 \pm 0.3$ eV is a bit higher than for highly oriented pyrolytic graphite with a work function of 4.55 ± 0.1 eV but is in very good agreement with the work function of sputtered graphite (highly disordered) of 4.9 ± 0.2 eV.

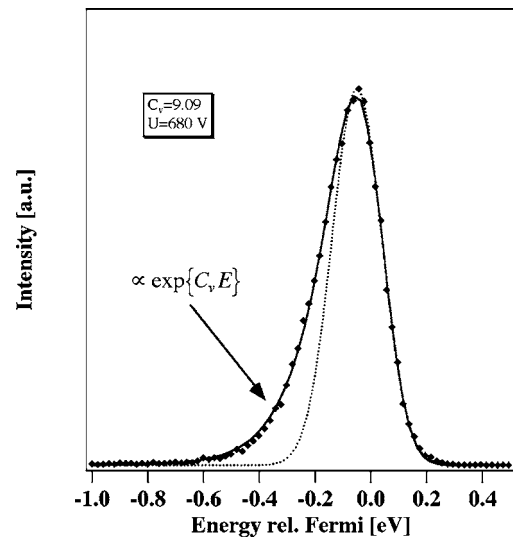


Figure 30. FES spectrum recorded at an applied voltage $U_0 = 680$ V from the FES series depicted in Figure 29. Reprinted with permission from [46], O. Gröning, Ph.D. Thesis No. 1258, University of Fribourg, Switzerland, 1999.

This example shows that the work function ϕ at the emission site can be determined accurately by measuring the I - V characteristic and the energy distribution of the emitted electrons. Knowing the emitter work function ϕ , the local electric field F present at the emission site can be determined from definition (33) using

$$\begin{aligned} C_v \phi^{0.5} F^{-1} &= 9.09 \text{ [eV]}^{-1} = 5.68 \times 10^{19} \text{ [J}^{-1}\text{]} \\ \Rightarrow F &= C_v \frac{\phi}{5.68 \times 10^{19} \text{ [J}^{-1}\text{]}} \\ &= 2 \frac{\sqrt{2m_e}}{e\hbar} \cdot \frac{8.93 \times 10^{-10} \text{ [J}^{0.5}\text{]}}{5.68 \times 10^{19} \text{ [J}^{-1}\text{]}} \\ &= 2.5 \times 10^9 \text{ [Vm}^{-1}\text{]} \end{aligned}$$

This value for the electric field at the emission site corresponds very well to the electric field of $2700 \text{ V}/\mu\text{m}$ predicted by the Fowler–Nordheim relation (16).

3. CARBON BASED ELECTRON EMITTERS

Since the first observation and investigations of the low field electron emission properties of natural and chemical vapor deposited diamond in the early 1990s [20, 21], the interest in this field has steadily increased until the present day. This interest is not of a scientific nature only (over 150 patents [105] were issued on the subject of diamond field emitters alone) although the physical nature of the low field electron emission from diamond is still under dispute.

Our works on carbon thin films show clearly that one has to distinguish strictly between the applied electric field (defined as the applied voltage divided by the anode–cathode distance) and the local field present at the emission site. From the technological point of view the applied field is the relevant parameter to characterize the field emission, as it determines what voltage has to be applied for a given anode–cathode distance. Yet, with regard to the physical nature of the emission, only the local field present at the emission site is relevant. In a field emission experiment in general only the applied electric field can be determined directly and it is very difficult to estimate the local fields on a real cathode surface. The combined measurement of the current–field characteristic and the field emitted electron energy distribution of an emitter allows one to determine independently the local field F and the work function ϕ of the emitter. In all cases we have investigated (CVD diamond, DLC films, and CNTs) we found that the local fields present at the emission site are always in the order of $2500 \text{ V}/\mu\text{m}$ and higher, although the applied field ranges between 1 and $50 \text{ V}/\mu\text{m}$. The emission process is in all cases ordinary Fowler–Nordheim tunneling with emitter work functions around 5 eV.

3.1. CVD Diamond Thin Film Emitter

On CVD diamond films exhibiting a good crystalline quality, with a low defect density and large ($>1 \text{ mm}$) crystallites (Fig. 16a), we found in most cases that the field emission showed very distinct, nonreversible activation characteristics

[106–109]. Figure 31 shows a typical current–field characteristic of the activation of boron doped good crystalline CVD diamond film. In the first voltage sweep from zero upward, the measured current remained below 1 pA up to a critical field E_C . At this field, a sudden and persistent increase of the current occurs. The value of E_C can vary significantly with the film under investigation because the occurrence of vacuum discharge depends on many parameters such as residual gas pressure, surface roughness, surface contamination, and anode–cathode geometry [110]. In our setup, typical values for E_C ranged between 100 and $400 \text{ V}/\mu\text{m}$. When the voltage is lowered, a reversible field emission characteristic can be observed at a turn-on field E_{on} . The values for E_{on} can range between 2 and $50 \text{ V}/\mu\text{m}$.

Typically the arc formed a small crater in the diamond film. By means of atomic force microscopy and Raman spectroscopy a graphitization of the diamond film around the crater can be observed. This results in an increased local conductivity and an increased roughness in the submicrometer range in this zone. Field emission spectroscopy showed that after the activation process the field emitted electrons originated from the states at the Fermi energy E_F indicating the metallic nature of the emission site. The local field F at the emission sites is in the order of $3000 \text{ V}/\mu\text{m}$ and the work function ϕ of the emitter is around 5 eV.

CVD diamond films exhibiting bad crystalline quality, nanocrystalline films (Fig. 16b), do not require an activation step. Usually these films are characterized by a Raman spectrum showing a very weak or even absent 1332 cm^{-1} diamond line but strong features of sp^2 bonded carbon. These films exhibit turn-on fields below $5 \text{ V}/\mu\text{m}$ [111, 112]. The current–field characteristics of these films are Fowler–Nordheim-like in the low current regime. In the high current regime deviations from the Fowler–Nordheim law can be observed depending on the resistivity of the deposited

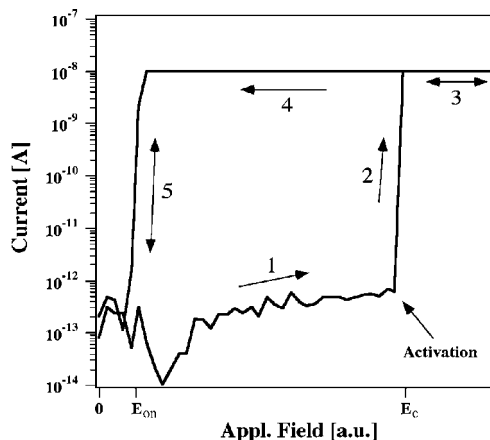


Figure 31. Typical current–field characteristic of the activation of a weakly emitting CVD diamond film. At a critical field E_C the discharge activation takes place and leads to a drastically and persistently increased current (1–2). If the field is subsequently lowered (4–5), a reversible field emission characteristic around E_{on} can be observed (5–4–3). (The constant current observed for higher fields is due to the current limitation of the voltage source.) Reprinted with permission from [107], O. Gröning et al., *J. Vac. Sci. Technol. B* 17, 1064 (1999). © 1999, American Institute of Physics.

film. From FES an average work function ϕ of 5.7 eV for nanocrystalline diamond can be determined. The local field F present at emission sites is around $2500 \text{ V } \mu\text{m}^{-1}$, whereas the applied fields range between 2 and $10 \text{ V } \mu\text{m}^{-1}$. This implies that strong field enhancement effects are the basis for the low field emission property of this material. Internal field emission and injection of electrons into the conduction band of the diamond and subsequent emission due to negative electron affinity could be ruled out as a possible emission model. This is due to the absence of internal electric fields in the diamond film under field emission conditions. The strong field enhancement effect is most probably due to the surface morphology of the films with a large peak to peak roughness of up to several micrometers and sharp local features on the nanometer scale.

3.2. Diamondlike Carbon Thin Film Emitter

Diamondlike carbon films show field emission properties very similar to those of CVD diamond films. On smooth, structureless (with regard to the surface morphology) DLC films, we only could observe discharge activated field emission [113]. This activation can be observed on polymer films as well as on carbon films with high sp^3 content. This shows that in the activation step the film acts mainly as a carbon source whereas the chemical nature of the carbon film we start is not of major importance.

Nonactivated low field electron emission from DLC films with applied field range of $10\text{--}30 \text{ V } \mu\text{m}^{-1}$ can be observed when graphitic clusters are present in or on the film. Compared to the smooth parts of the DLC films these clusters show an enhanced conductivity. As in the case of the nanocrystalline CVD diamond the current–field characteristic of the emission is Fowler–Nordheim-like in the low current regime and the FES exhibit the typical shape of Fowler–Nordheim tunneling. Local fields F of $2500\text{--}3000 \text{ V } \mu\text{m}^{-1}$ and emitter work functions ϕ around 5 eV have been determined. The investigation of the graphitic clusters on the DLC films by high resolution scanning electron microscopy revealed nanotubelike structures, with diameters down to 7 nm and lengths up to several hundred nanometers (Fig. 32). Laser ablation and filtered cathodic arc deposition seem to be the methods of choice to deposit good emitting DLC films. Both methods are used in the production of nanotubes as well.

3.3. Carbon Nanotube Field Emitter

3.3.1. Work Function of Carbon Nanotubes

The investigations on the field emission properties of CVD diamond and DLC emitters show clearly that the electron emission of carbon based materials is ordinary Fowler–Nordheim tunneling and field enhancement structures on the surface are required for low field electron emission. Nanotubes (CNTs) have the ideal shape to act as field enhancing structures and they can be produced relatively simply in large quantities.

We have investigated the field emission properties of MWNTs and SWNTs. On thin films we measured emission site densities of $10,000 \text{ cm}^{-2}$ at applied fields below

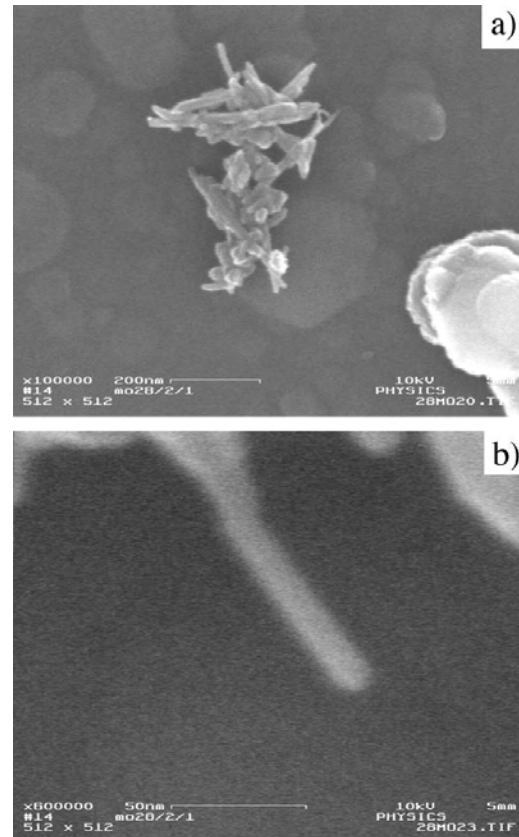


Figure 32. SEM pictures of graphitic structures present on good emitting DLC films.

$5 \text{ V } \mu\text{m}^{-1}$ [104, 114, 115]. Simultaneous field and photoemission electron spectroscopy (XPS) allowed us to compare the work function at the emission site with the average work function of the CNT films. In the case of the MWNTs we determined an emitter work function $\phi = 4.9 \pm 0.3 \text{ eV}$ by FES. By XPS we measured an average function of $4.8 \pm 0.1 \text{ eV}$. In the case of SWNTs we determined a lower work function of $3.7 \pm 0.3 \text{ eV}$ by FES.

The reduced work function for SWNTs can be attributed to an electrostatic effect, due to the small radius of curvature of the SWNTs at their ends. One of the constituents to the work function is the work an electron has to perform against the image force. In the case of nanostructures, it is important to notice that the image potential for a plane and a small sphere (radius $<10 \text{ nm}$) differs considerably. In the planar and the spherical case the image potential can be written as [116]

$$\varphi_{\text{plane}}(x) = -\frac{1}{4\pi\epsilon_0} \frac{e^2}{4x} \quad (44)$$

$$\varphi_{\text{sphere}}(r) = -\frac{1}{4\pi\epsilon_0} \frac{e^2 R^3}{2r^2(r^2 - R^2)} \quad (r > R) \quad (45)$$

where R is the radius of the sphere. It can be easily seen that for $r/R = 1 + d$ ($d \ll 1$) φ_{sphere} coincides with φ_{plane}

with $x = R \cdot d$. The difference in work function between the planar and the spherical case equals [117]

$$\phi_{\text{sphere}} = \phi_{\text{plane}} - \frac{5}{8R^{-1}} \frac{e^2}{4\pi\epsilon_0} \quad (46)$$

This effect was demonstrated by the observation that the ionization potential of small clusters depends on their size. An increase of the ionization potential with decreasing size was observed [118, 119]. According to (46) in SWNTs with diameter around 1.4 nm the work function is reduced by 1.3 eV. Compared to MWNTs with work function values around 5 eV SWNTs with 1.4 nm diameter would have work function values of 3.7 eV which corresponds well with the values we determined by FES.

3.3.2. Environmental Stability

The term environmental stability is used to describe the interaction of electron emitters with the gaseous environment in which they are operated. Such interactions typically lead to emission current fluctuations on a time scale of seconds to minutes. If the current fluctuations are large they may negatively affect the device performance. In addition the device long-term stability is dependent on the emitter interactions with its environment, wherefore investigations on environmental stability are important. Such investigations have been done in the past on etched metal tips using field emission microscopy. The field emission microscope (FEM) invented by Müller [120] in 1937 has for a long time been the state of the art to investigate adsorption and diffusion phenomena at surfaces with almost atomic resolution.

Figure 33 shows FEM patterns commonly observed from SWNTs and MWNTs. These emission patterns are not stable in time but show switching from one configuration to another. The switching frequency increases with increasing currents and is in the order of 1 Hz. Associated with this instability of the emission spot are fluctuations in the emission current as indicated by the different intensities of the emission patterns in Figure 33b. Each emission pattern has

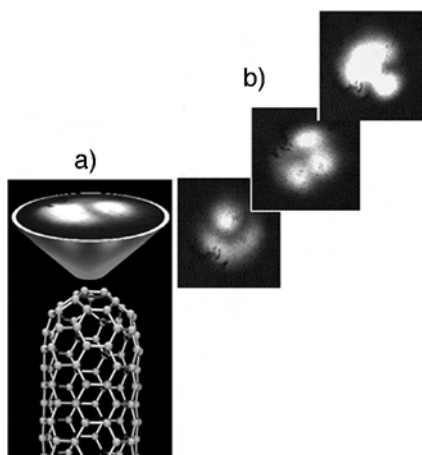


Figure 33. (a) The lobed FEM pattern of a MWNT at 300 K. (b) Some examples of a large variety of such patterns commonly observed from SWNTs and MWNTs. Reprinted with permission from [121], L. O. Nilsson, Ph.D. Thesis No. 1337, University of Fribourg, Switzerland, 2001.

a well defined emission current for a given applied voltage. Therefore the emission current fluctuates between different current levels associated to the different emission patterns. The difference between the highest and lowest current level can be up to a factor of 10. Such kind of random telegraphic noise was observed by different groups [46, 121, 122]. It is recognized that the FEM patterns on the screen reflect the electronic structure, the anisotropy of the work function, local variation of the microscopic field, and electron transmission probability of a CNT cap. This means that atomically sized areas on the CNT cap, where the work function is lower or the local electric field is higher than the surrounding regions, are reproduced with higher intensity on the phosphor screen. Therefore the different emission patterns of CNTs can be understood in terms of switching between different states with relatively small energy differences in levels close to the Fermi energy. In order to illustrate how these states are formed and what they may look like one can take the π -states of a benzene molecule (C_6H_6) as an example (Fig. 34).

In analogy to the C_6H_6 molecule the π -states of CNT cap can be thought as linear combinations of p_x orbitals which protrude out perpendicular to the carbon lattice on the tube apex. The limited variety in shape, style, and energy of such π -states can only partly explain the large number of emission patterns observed by the FEM. It therefore seems plausible to think that the energy levels of the CNT at the apex are modified through adsorbed molecules coming from the gas phase during field emission. Sometimes the sticking is very firm and may result in a resonant tunneling state which can lead to increased tunneling probability and anisotropy in the field emission current [123]. We observed that the field emission fluctuations are not sensitive to H_2 and H_2O , the two the main components of residual gases in vacuum systems, up to 10^{-4} mbar gas pressure. Increased partial pressure of O_2 causes degradation of the field emission due to

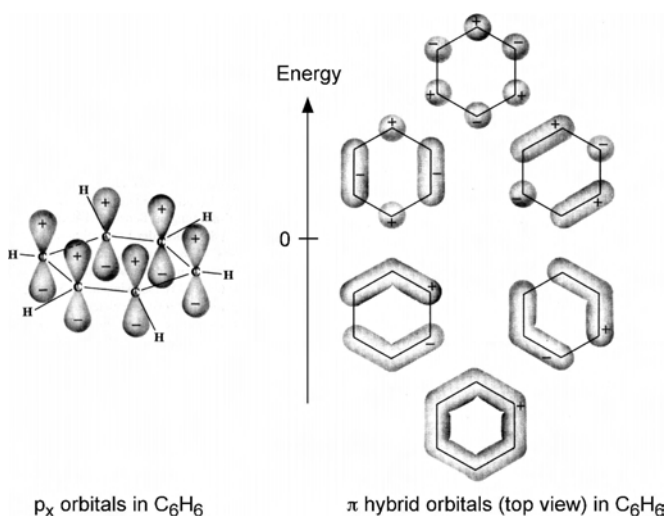


Figure 34. The p_x orbitals (a) of benzene C_6H_6 can form six π hybrid orbitals of delocalized electrons (b), of which three are in binding stabilized state and three are in an antibinding state. Reprinted with permission from [121], L. O. Nilsson, Ph.D. Thesis No. 1337, University of Fribourg, Switzerland, 2001.

reactive ion etching. The suggestion of Rinzler et al. [122] that the emission fluctuations are due to individual desorption processes induced by ion bombardment seems very convincing.

4. MICROSCOPIC CHARACTERIZATION OF THIN FILM EMITTERS

The development of field emission electron sources has been hampered for half a century by the fact that tiplike field enhancing structures are needed to create locally high fields for field electron emission to take place. Usually the higher the field enhancement, the smaller the effective emission area of the tips gets, as the radius of curvature gets increasingly small. Although the field emission current density can easily exceed 1000 A cm^{-2} , the total emission current per single tip remains small as the emitting surface, being the apex of the field enhancing tip, is small. The total current per single tip in field emission rarely surpasses 0.1 mA . In contrast, thermionic emitters can deliver electron emission currents of up to 400 A cm^{-2} . This situation resulted in the fact that field emitters are only used where high brightness rather than high currents are requested, for example, in the case of high resolution electron microscopy (SEM, TEM). The key to reaching planar field emitters of high current density approaching 1 A cm^{-2} resides in the integration of a large number of field enhancing tips on a surface.

4.1. Field Enhancement Distribution Function

Whereas a single field electron emitter can be said to be completely characterized in terms of its work function ϕ at the emission site, the field enhancement factor β , and the resistance R , the description of the overall emission behavior from a thin film emitter with a large number of emission sites requires a statistical approach [121]. The number of degrees of freedom with regard to geometrical alignment, orientation, length, diameter, and interemitter distances within the thin film emitter ensemble is much larger than for a single emitter. It can also be expected that ϕ and R exhibit some variation. Electrostatic screening has to be taken into account for thin film emitters, since the presence of a large number of emitters may affect the local electric field F at the emission sites. The emission properties can therefore vary considerably from one position to another within the thin film emitter.

An example of a thin film emitter with a large scatter in the spatial emission current $I(x, y)$ is shown in Figure 35a, where parts of the surface show no emission at all. The spatial scatter in the electron emission $I(x, y)$ is highly undesirable, because the device performance with regard to brightness homogeneity is largely reduced. In order to understand and improve the electron emission homogeneity of thin film emitters with a large number emitter sites a quantitative description of the $I(x, y)$ map in terms of field enhancement factor β , work function ϕ , emission area A , and resistance R is needed.

Thin film electron emitters are often characterized in terms of a "threshold" field F_{thr} required to obtain a given

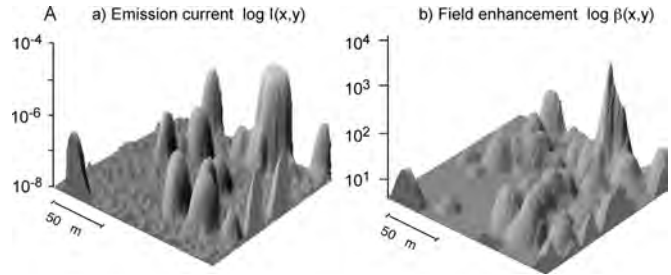


Figure 35. (a) Variation of the emission current $I(x, y)$ under a constant applied voltage $U_0 = 320 \text{ V}$ (tip–cathode distance $d \sim 7 \mu\text{m}$). (b) Corresponding local variation of the field enhancement factor $\beta(x, y)$. Reprinted with permission from [121], L. O. Nilsson, Ph.D. Thesis No. 1337, University of Fribourg, Switzerland, 2001.

field emission current density in a typical large anode diode type field emission experiment. Such characterization can be misleading since a cathode with a spatial extension in the mm^2 range may contain a small number (sometimes only one) of strong emitters and thus can have a low threshold field F_{thr} which obviously will not guarantee a high emission current density, because the emitter ensemble shows a certain distribution of the field enhancement factor β and therefore in the emission current density. In this picture the field emission properties of a thin film must be represented by a function $f(\beta)$, where the number of emitters dN on a surface area A with field enhancement factors in the interval $[\beta, \beta + d\beta]$ is given by

$$dN(\beta) = A \cdot f(\beta) \cdot d\beta \quad (47)$$

The field enhancement distribution function $f(\beta)$ is then defined as

$$f(\beta) = \frac{1}{A} \frac{dN}{d\beta} \quad [\text{emitter}/\text{cm}^2] \quad (48)$$

According to the definition, $f(\beta)$ is proportional to the probability of the field enhancing structures in the interval $[\beta, \beta + d\beta]$ per unit area. Consequently one may view $f(\beta)$ as a probability distribution. Assuming the same relation for the emission current as a function of the local field F at the emission site for all emitters of the thin film, the field emission properties are completely determined by the field emission distribution function $f(\beta)$.

In terms of the Fowler–Nordheim relation (16) the assumption of a general relation for the current–field dependence of the electron emission means that all emitters have the same emitting area and the same work function ϕ . The assumption that the work function ϕ is constant for all emitters can partially be justified by the fact that the emitters consist of the same material. Actually, we have found in FES that the work function at the emission site of carbon based materials is always in the range of $4.7\text{--}5.1 \text{ eV}$. The argument that the emission area should be constant can for CNTs be partially justified by the fact that all the emitters are of the same dimensions.

In order to describe the emission current as a function of the local field F the simplified Fowler–Nordheim relation

as proposed by Brodie and Spindt [3], where the elliptic functions are approximated, can be used

$$I = A \cdot \frac{1.5 \times 10^{-6}}{\phi} \cdot F^2 \exp\left(\frac{10.4}{\phi^{0.5}}\right) \exp\left(-6.44 \times 10^7 \frac{\phi^{1.5}}{F}\right) \quad (49)$$

I is the emission current in amperes per single emitter, A is the emission area of the emitter in cm^2 , ϕ is the work function in eV, and F is the local electric field [V/cm] present at the emission site.

In a field emission device, the external electric field F_0 is generated by a voltage U_0 applied between the cathode with the emitting structures and an anode. In configurations where anode and cathode are represented by two parallel plates separated by a vacuum gap d the applied field is $F_0 = U_0/d$. The local field at the emission site is then defined as $F = F_0 \cdot \beta$. Relation (49) becomes

$$I = A \cdot \frac{1.5 \times 10^{-6}}{\phi} \cdot F_0^2 \cdot \beta^2 \exp\left(\frac{10.4}{\phi^{0.5}}\right) \times \exp\left(-6.44 \times 10^7 \frac{\phi^{1.5}}{F_0 \cdot \beta}\right) \quad (50)$$

This is now the relation for the emission current I of a single emitter for a given applied field F_0 which depends only on the field enhancement factor β . The field emission behavior of an ensemble of field emitters is therefore completely determined by the field enhancement distribution function $f(\beta)$. Important parameters such as the threshold field F_{thr} and the emission site density can be immediately derived from the field enhancement distribution function $f(\beta)$. Using relation (50) for the emission current the threshold field F_{thr} can be determined from the following relation

$$I_{\text{thr}} = A \int_0^\infty f(\beta) \cdot I(\beta, F_{\text{thr}}) d\beta \\ = A \cdot \frac{1.5 \times 10^{-6}}{\phi} \exp\left(\frac{10.4}{\phi^{0.5}}\right) \cdot \int_0^\infty d\beta \cdot f(\beta) \cdot F_{\text{thr}}^2 \cdot \beta^2 \\ \times \exp\left(-6.44 \cdot 10^7 \frac{\phi^{1.5}}{F_{\text{thr}} \cdot \beta}\right) \quad (51)$$

Here A denotes the surface of the cathode under investigation. It is worth noting that the threshold field F_{thr} will depend on the cathode area which is measured, so that it is only sensible to define the threshold field F_{thr} with regard to a given emission current density j_{thr} . In other words, the measured threshold field F_{thr} decreases with increasing surface area measured. The characterization of the emission properties of a thin film emitter just by stating the threshold field F_{thr} is therefore very questionable.

4.2. Emission Site Density

The emission site density (ESD), which gives the number of active emitters per unit area at a given applied field or voltage, is one of the key parameters in characterizing the field emission performance or quality of a planar field emission cathode. An active emitter is an emitter giving an emission

current larger than some threshold current (e.g., 10 nA). Therefore the ESD as function of the applied field F_0 can be calculated from $f(\beta)$ by

$$\text{ESD}(F_0) = \int_{\beta_{\text{min}}=F_{\text{min}}/F_0}^\infty f(\beta) d\beta \quad [\text{cm}^{-2}] \quad (52)$$

F_{min} is the local field at the emission site required to produce a minimum detectable emission current I_{min} . In an experimental setup using a phosphorous screen I_{min} corresponds to the minimum emission site current, required to observe the emission spot by eye.

The emission current density is calculated in a similar manner

$$j(F_0) = \int_0^\infty f(\beta) \cdot j(\beta, F_0) d\beta \quad [\text{A cm}^{-2}] \quad (53)$$

Unfortunately in many publications the performance of planar field emission cathodes is still characterized by I - V measurements alone. Figure 36 displays the field emission spots on a phosphorous screen of two carbon thin film emitters at the same applied field and emitting roughly the same emission current density of about 0.1 mA cm^{-2} , so that from the I - V characteristic both thin film emitters would yield a comparable behavior and one would judge them to have the same field emission performance. It is, however, obvious that the ESD is considerably higher for sample B. Whereas on sample B the emission current originates from a relative high density of emission sites the emission current of sample A is delivered from only a few but quite strong emitters. Therefore the emission performance of sample B should be judged considerably higher than for sample A because emitter degradation will more easily occur on sample A at higher fields.

In conclusion, any standards of characterization of thin film electron emitters must include the field enhancement distribution function $f(\beta)$ and knowledge of the spatial emitting properties $\beta(x, y)$. With these two parameters the collective emitting behavior of thin film electron emitters is completely characterized.

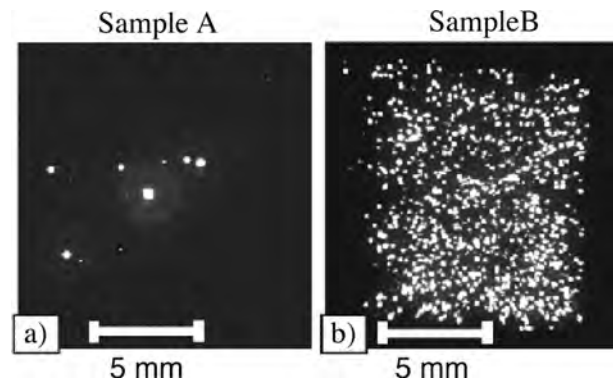


Figure 36. Optical micrographs of field emission spots collected on a phosphorous screen of two different diamond thin film emitters at the same applied electric field of $4.5 \text{ V } \mu\text{m}^{-1}$.

4.3. Characterization by Scanning Anode Field Emission Microscopy

The scanning anode field emission microscope (SAFEM) allows the investigation of the field emission properties of thin film emitters with lateral resolution in the submicrometer range [124]. The SAFEM is based on a micrometer-sized tip which serves as an anode. By recording the emission as a function of the spatial position of the tip above the thin film emitter, field emission maps with submicrometer resolution can be obtained. Such maps can be extended up to $5000 \times 5000 \mu\text{m}^2$. The SAFEM can operate in two different modes. In the first mode the emission current is recorded for a constant applied voltage U_0 . This mode is called the constant voltage mode (CVM). The $I(x, y)$ map obtained in the CVM is the analog to the electron emission on a phosphor screen, albeit with higher resolution. In the second mode of operation the emission current is maintained on a constant level for every tip position along the field emission scan and the voltage applied to the tip must therefore be adjusted according to the individual emitter efficiency. Since the spatially recorded emission voltage $V(x, y)$ is determined for a constant emission current this mode is called the constant current mode (CCM).

As shown in the previous section, the knowledge of the field enhancement distribution function $f(\beta)$ gives an almost complete characterization of field emission behavior of thin film emitters. Therefore the experimental characterization of thin film emitters should include the determination of $f(\beta)$. The field enhancement distribution function $f(\beta)$ can be obtained from the spatial distribution of field enhancement factors β , the so-called field enhancement map $\beta(x, y)$. In theory $\beta(x, y)$ can be calculated from the topography of the surface $h(x, y)$, for example, by solving the Poission equation at the surface. However, in general the Poission equation cannot be solved because it is extremely difficult to measure $h(x, y)$ with nanometer resolution. Therefore another method is used to derive $\beta(x, y)$. Through relation (50), the emission current I is directly related to field enhancement factor β ; therefore the local emission current $I(x, y)$ on thin film emitter is given by

$$I(x, y) = A \cdot \frac{1.5 \times 10^{-6}}{\phi} \cdot F_0^2 \cdot (\beta(x, y))^2 \exp\left(\frac{10.4}{\phi^{0.5}}\right) \times \exp\left(-6.44 \times 10^7 \frac{\phi^{1.5}}{F_0 \cdot \beta(x, y)}\right) \quad (54)$$

Hence, the measurement of $I(x, y)$ could theoretically be used to calculate $\beta(x, y)$.

Scanning anode field emission measurements operating in the CVM can be principally used to obtain spatially resolved emission current $I(x, y)$. Since the anode is located very close to the emitting surface, the surface topography and the local field enhancement cause the applied electric field to fluctuate several times from one site to another. Such variation in the applied electric field causes emission current fluctuations of many orders of magnitude into the regime of resistor limited emission and emitter degradation [125]. Since expression (54) describes pure Fowler–Nordheim emission, field emission measurements (CVM) which may

go into the resistor limited emission regime cannot be used as the basis to calculate $\beta(x, y)$.

In order to derive $\beta(x, y)$ and avoid current saturation effects, not to say emitter destruction, the scanned electron emission measurement has to be performed in the CCM. In the CCM the voltage applied to the anode varies as a function of the anode position over the thin film emitter, in order to maintain the same emission current for every point. If the current is reasonably low ($\sim 50 \text{ nA}$), one will obtain a spatially resolved field emission image of the extraction voltage $V(x, y)$, without current saturation effects or emitter destruction. This is both experimentally and conceptually beautiful since $V(x, y)$ is actually an inverted image of the field enhancement landscape $\beta(x, y)$ according to

$$\beta(x, y) = \frac{d \cdot F}{V(x, y)} \quad (55)$$

where d is the tip–sample distance and F is the local field at the emission site required for a fixed emission current I predicted by the Fowler–Nordheim relation (54) (see Fig. 37).

4.4. Carbon Nanotube Thin Film Emitters

As discussed, the key for reaching planar field emitters of high current density approaching 1 A cm^{-2} resides in the integration of a large number of field enhancing tips on a surface. Depending on the required emission current density, the density of the emitting tips has to be in the range of 10^6 – 10^8 cm^{-2} . This limits their size to micrometer or even submicrometer dimensions. CNTs have proven to be ideally suited to serve as field enhancing structures for field emission applications due to their exceptionally high aspect ratio with lengths in the micrometer range and diameters ultimately down to one nanometer. Furthermore, they can be readily produced in large numbers by relatively simple and cost effective techniques. One has to acknowledge that when it comes down to creating free electrons in vacuum the method most widely employed to produce these electrons is thermionic emission. The advantage of thermionic electron

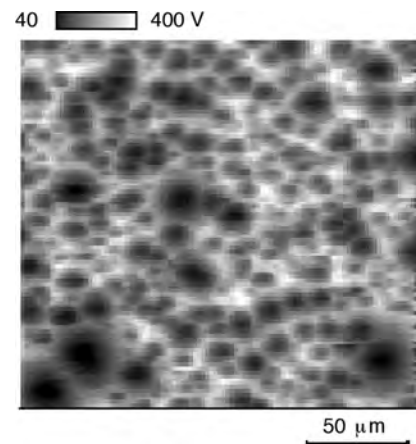


Figure 37. SAFEM measurement from a CNT thin film in the CCM. Extraction voltage map $V(x, y)$ for 10 nA emission recorded with an tip–cathode distance of $7 \mu\text{m}$.

sources is their simple operation. However, thermionic electron sources have some major drawbacks. They are power controlled, via the temperature, and therefore direct modulation of the emission is rather slow. Further, due to operation at high temperatures (~ 2000 K) the realization of micrometer sized emitters is practically impossible due to insufficient heat dissipation. Micro- and nanosized field electron emitters hold the possibility of miniaturizing vacuum electronic devices. In this context CNT thin film emitters offer an attractive possibility to produce the key component of an electron source, namely the field emitting tip, in large numbers using inexpensive processes.

In CNT thin films as they are produced by CVD over supported catalysts the growth yields to nanotubes with rather ill defined diameter, length, orientation, and spatial distribution. All these properties, however, influence the field enhancement and therefore the field emission properties. The field enhancement of a metallic needle shaped structure perpendicular in a homogeneous electric field is in first approximation h/r . From this it is clear that the length, diameter, and orientation of the CNT with respect to the electric field will immediately influence the field enhancement. In addition, the tube density will influence the field enhancement due to electrostatic shielding [126]. As discussed in the previous section, the ensemble of field emitters represented by a CNT thin film is therefore difficult to be characterized a single parameter such as threshold electric field F_{thr} to obtain a given field emission current density. Because the CNT emitter ensemble shows a certain distribution in the field enhancement the emission properties have to be described statistically by the field enhancement function $f(\beta)$ according definition (48). It was shown that under the assumption that all emitters have the same work function ϕ , the local emission current $I(x, y)$ on thin film emitter can be written as

$$I(x, y) = A \cdot \frac{1.5 \times 10^{-6}}{\phi} \cdot F_0^2 \cdot (\beta(x, y))^2 \exp\left(\frac{10.4}{\phi^{0.5}}\right) \times \exp\left(-6.44 \times 10^7 \frac{\phi^{1.5}}{F_0 \cdot \beta(x, y)}\right)$$

In order to account for experimental observed emission currents and field emission spectra of MWNTs, $A = 10^{-9}$ cm² is a reasonable value for the emission area of a MWNT. This value might seem too large for a MWNT with a typical diameter of 30 nm. Yet one has to consider that though the pre-exponential factor A_v [see (27)] has the dimension of a surface, it not only takes account of the emitting area but also depends on the band structure of the emitter. Assuming a mean value of 4.9 eV for the work function and using the emission area A mentioned previously the emission current I for a MWNT is given by

$$I(x, y) = 3.36 \times 10^{-14} \cdot F_0^2 \cdot (\beta(x, y))^2 \exp\left(-\frac{6.99 \times 10^8}{F_0 \cdot \beta(x, y)}\right) \quad (56)$$

and the threshold field F_{thr} for a MWNT thin film emitter can be determined from the following relation according to

relation (51)

$$I_{\text{thr}} = A \int_0^{\infty} f(\beta) \cdot I(\beta, F_{\text{thr}}) d\beta \\ = A \int_0^{\infty} d\beta \cdot f(\beta) \cdot 3.36 \\ \times 10^{-14} \cdot F_{\text{thr}}^2 \cdot \beta^2 \exp\left(-\frac{6.99 \times 10^8}{F_{\text{thr}} \cdot \beta}\right) \quad (57)$$

A calculated $\beta(x, y)$ landscape compiled from a extraction voltage map $V(x, y)$ is presented in Figure 38a. By counting the field enhancement values ΔN in the interval $[\beta, \beta + d\beta]$ one can get a histogram with the distribution of the field enhancement factors β , as shown in Figure 38b. It is worth noting that the amplitude of the histogram is, however, dependent on the choice of the bin with $d\beta$. The normalized distribution $dN/d\beta$ equals the scanned area A times a functional dependence $f(\beta)$. At first glance the shape of the normalized distribution $dN/d\beta \propto f(\beta)$ appears to be asymmetric with a maximum located at the β value of 50. This apparent asymmetric behavior is, however, due to a measurement artifact. β values below 50 are “screened” due to neighboring field emitters with large β values. The probability to detect field emitters is thus a monotonic increasing function of β according to

$$A_E \propto \left(1 - A_0 \int_{\beta}^{\infty} f(\beta) d\beta\right) \rightarrow 1 \quad \text{when } \beta \rightarrow \infty \quad (58)$$

The integral can be understood as the area A_E occupied by emitters with field enhancement factors larger than β . The effective β distribution $\phi(\beta) = A_E(\beta)f(\beta)$, as calculated from the true β distribution $f(\beta)$, can be fitted to the experimental values as shown in Figure 38b. It can be shown that $f(\beta)$ can be fitted to experimental data over five orders of magnitudes using scanning and integral (screen) field emission measuring techniques according to

$$f(\beta) = k_1 \exp(-k_2\beta) \quad (59)$$

where k_1 is the measured macroscopic emission site density and k_2 is connected with the structural order/disorder of the field enhancing structures. By changing k_1 , k_2 the field emission properties of any surface can thus be tuned. Engineering technological relevant field emission cathodes is

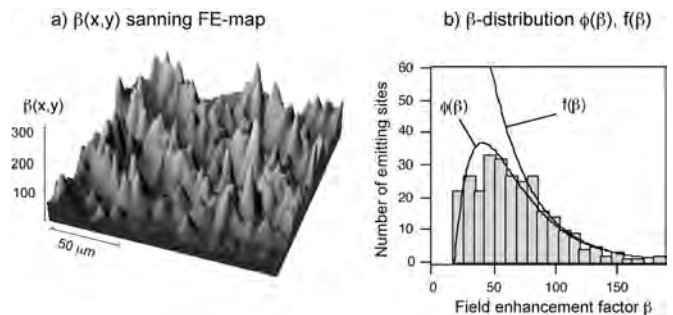


Figure 38. (a) Field enhancement $\beta(x, y)$ landscape calculated from an extraction voltage map $V(x, y)$ which is an analog of the one presented in Figure 37. (b) Histogram of the field enhancement factors β in (a).

thus the story of how to change/manipulate the fundamental relation (59).

The question as to what a technologically relevant and useful ESD for a CNT thin film emitter will be has to be answered in view of the application the emitter should be used in and of course in view of the competing technologies. Comparison with silicon or metal microtip arrays indicates that an ESD of the order of 10^6 up to 10^8 cm^{-2} at applied electric fields below 50 $\text{V } \mu\text{m}^{-1}$ should be aimed at. The characterization of EDSs above 10^4 cm^{-2} using a phosphorous screen setup is challenging due to the overlap of the emission spots. As in the phosphorous screen the anode–cathode distance gives the resolution of the SAFEM. Figure 39 displays three field enhancement maps of the same region of a randomly oriented MWNT thin film at different tip–sample distances evidencing the increasing resolution with decreasing tip–sample distance. As can be seen in Figure 39c a resolution is given in first approximation as twice the tip–sample distance. This means that in order to resolve 10^7 emitters per cm^2 the tip–sample distance should be of the order of $2\text{--}3$ μm . Such a tip–sample distance is of the same order as the typical height of the CNTs and therefore is about the limit of what can be achieved.

Figure 40 displays a high resolution field enhancement map derived from a SAFEM voltage map $V(x, y)$ recorded at a tip–sample distance of $2\text{--}3$ μm on a randomly oriented CNT thin film. The black diamond dots indicate the position of emission sites with field enhancement factors larger than 130. On the investigated area of 2.4×10^{-5} cm^{-2} 164 such emitters could be detected resulting in an ESD of 6.8×10^6 cm^{-2} . The field enhancement was determined under the assumption that the local field present at the CNT apex is 3800 $\text{V } \mu\text{m}^{-1}$ in order to emit 11 nA, which is the current at which the SAFEM $V(x, y)$ map was recorded. A field enhancement factor larger than 130 therefore means that the applied field is lower than 30 $\text{V } \mu\text{m}^{-1}$. This measure-

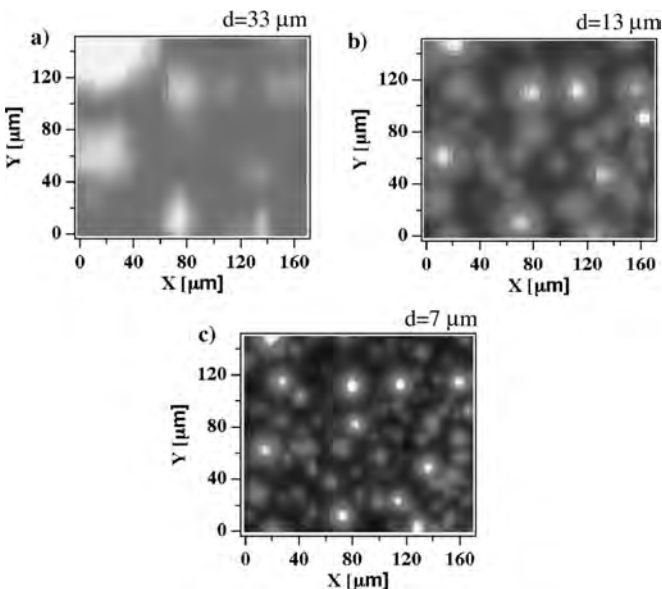


Figure 39. SAFEM field enhancement maps recorded at 11 nA emission current of the same region of a randomly oriented CNT thin film emitter with different tip–sample distances ($d = 33, 13, 7$ μm).

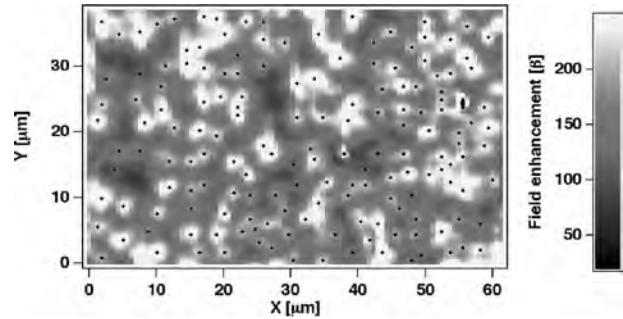


Figure 40. High resolution SAFEM field enhancement map $\beta(x, y)$ of a randomly oriented CNT thin film recorded at 11 nA emission current and a tip–sample distance of ~ 3 μm .

ment demonstrates that relatively crude, as-deposited CNT thin films exhibit already the potential to achieve technologically relevant ESDs at moderate applied fields. However, it is important to point out that the high ESD indicated of a few million per cm^{-2} is to a certain extent academic as it cannot be exploited on large cathode surfaces. The reason for this is the large spread in the field enhancement factor β the individual emitters exhibit. For the randomly oriented CNT thin films we discuss here the field enhancement distribution $f(\beta)$ follows an exponential law as described in (57). This kind of field enhancement results in the situation that on a large cathode area (e.g., 1 cm^{-2}) there are a few very strong emitters of very high field enhancement (~ 1500) resulting in a threshold field of $1\text{--}2$ $\text{V } \mu\text{m}^{-1}$. However the ESD is very low, only $1\text{--}10$ cm^{-2} . Upon an increase in the applied field the ESD increases rapidly, but at the same time the emission current from the first few emitters increases exponentially. With further increase of the applied field the point is reached where the emission current of the first strong emitters is so large that they get destroyed. From this point the ESD hardly increases anymore as a situation is reached where the appearance of a new emitter is balanced by the disappearance of old strong emitters upon increase of the applied field. For as-deposited MWNT thin film emitters this point is reached typically at about 10 $\text{V } \mu\text{m}^{-1}$ with an ESD of $\sim 10,000$ cm^{-2} and an emission current density of ~ 10 $\text{mA } \text{cm}^{-2}$ over the whole thin film emitter. It is clear that under such circumstances the cathode suffers irreversible degradation and that the operation of a cathode in such conditions is highly critical from the point of view of stability and lifetime. The values for the field, the ESD, and the emission current density given are not of a general nature as they depend on numerous parameters. However, it is important to notice that the emitter degradation at low applied fields is the limiting factor for the performance of such cathodes. In order to enhance the field emission performance of such cathodes a detailed understanding of the degradation of the degradation mechanism and subsequently the improvement of the degradation behavior is required.

Figure 41 shows the SAFEM field enhancement map $\beta(x, y)$ of a randomly oriented MWNT thin film emitter, with regions which have suffered high emission current degradation previously. The region from $x = 0$ μm to $x = 55$ μm has been strained with 1.5 μA and the region from

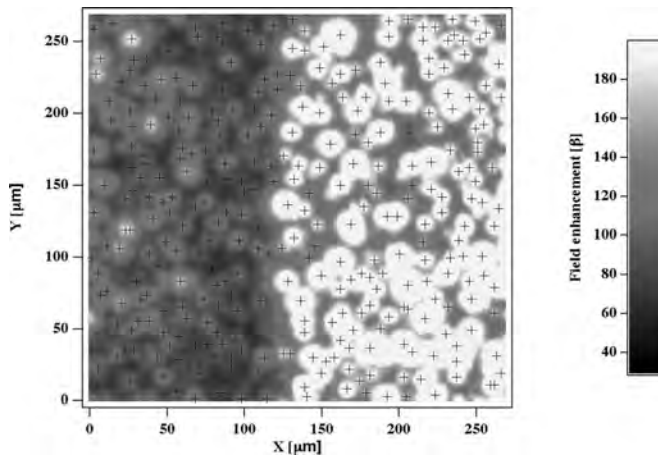


Figure 41. SAFEM field enhancement map $\beta(x, y)$ of a randomly oriented MWNT thin film with two high emission current strained regions on the left hand side. Region I ($0 < x < 55 \mu\text{m}$) has been strained previously with $1.5 \mu\text{A}$ and region II ($55 < x < 110 \mu\text{m}$) with $2 \mu\text{A}$.

$x = 55 \mu\text{m}$ to $x = 110 \mu\text{m}$ has been strained with $2 \mu\text{A}$ emission current by the SAFEM. The region $x > 110 \mu\text{m}$ has not been current strained. After current straining a field enhancement map $\beta(x, y)$ was recorded at 11 nA and a tip-sample distance of $4\text{--}5 \mu\text{m}$. One can observe that in the current strained regions the emitters with a high field enhancement factor β have been removed, whereas they are still present in the unstrained region. The values at which the current degradation occurs can vary from 500 nA up to a few μA , which is more than 100 times lower than for a single CNT welded on a metal tip. $I\text{--}V$ measurements on two point contacted CNTs have shown that straight and probably defect-free CNTs, repeatably can conduct currents up to 3 mA ballistically without heat dissipation [127, 128].

The emitters which are then left over with a lower field enhancement factor β are typically very stable and robust, which means that they can sustain emission currents well above $1 \mu\text{A}$ even up to $100 \mu\text{A}$ for short periods of time. A closer inspection of the regions strained by 1.5 and $2 \mu\text{A}$ shows that the average field enhancement is higher in the region strained with the lower current. This behavior indicates that the high current degradation is linked to the enhancement, where the critical current for degradation decreases with increasing field enhancement and therefore increasing aspect ratio.

Figure 42 illustrates the degradation of a single emitter as opposed to the collective current degradation behavior displayed in Figure 41. Figure 42a and b shows field enhancement maps $\beta(x, y)$ (@ 11 nA emission current) before and after the central emitter has been subjected to high current degradation. The $I\text{--}V$ characteristic displayed in Figure 42c shows that the irreversible degradation occurs abruptly at an applied voltage of 290 V , which corresponds to an applied electric field of $14.5 \text{ V } \mu\text{m}^{-1}$, and at a current level of $2.2 \mu\text{A}$. The degradation manifests itself by a current drop of almost three orders of magnitude. As can be evaluated from the field enhancement maps the value of the field enhancement at this position has decreased from 630 to 250 . It has to be pointed out that most probably the

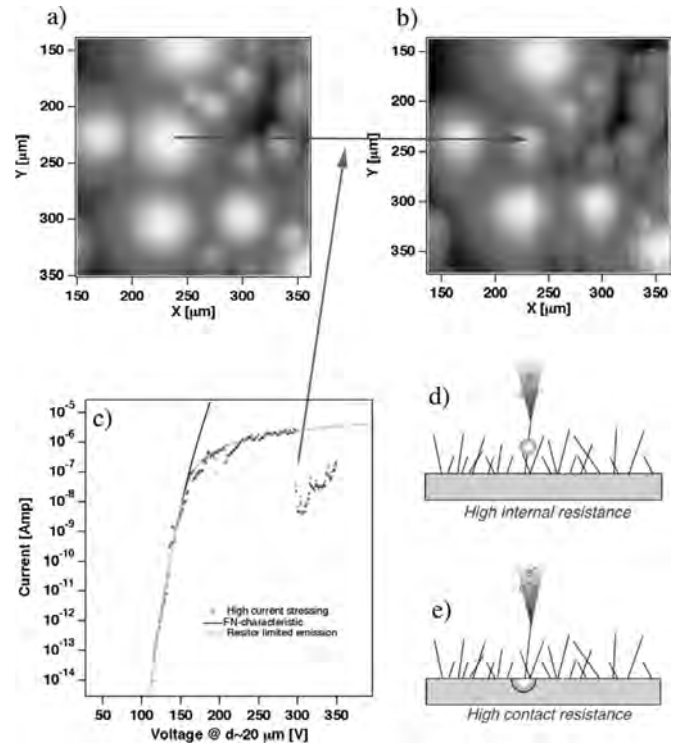


Figure 42. Single emitter high current degradation measured on a MWNT cathode. The field enhancement maps (a) and (b) show the reduction in the field enhancement factor for the emitter indicated by the arrow (a) before and (b) after the degradation event. In the maps white corresponds to high and black to low field enhancement. Diagram (c) displays the $I\text{--}V$ characteristic of the degradation where the crosses indicate the experimental data, the black solid line the theoretical Fowler–Nordheim behavior, and the gray solid line the resistor limited $I\text{--}V$ behavior. The schematic drawings (d) and (e) represent emitter degradation due to large power dissipation due to either high intratube resistance or high contact resistance.

emission after degradation does not originate from the same CNT as before but from a tube nearby, which was concealed by the original emitter.

The black curve in Figure 42c indicates the theoretical Fowler–Nordheim emission behavior. One can observe that in the low current regime the measured $I\text{--}V$ characteristic is well described by the Fowler–Nordheim law. However, above 100 nA emission current a pronounced deviation from the Fowler–Nordheim behavior can be observed. This current saturation continues to a voltage of about 290 V and an emission current of $2.2 \mu\text{A}$, where a sudden and irreversible decrease of the emission current to a value of 7 nA occurs. The emission behavior in the non-Fowler–Nordheim regime can be modeled using a resistor limitation approach, where it is assumed that there is a voltage drop between the emission site (being the CNT apex) and the electron reservoir (being the electrical contact of the CNT on the substrate). This results in the situation that the full applied voltage does not generate the extraction field F for the electron emission, but this voltage is reduced by the product of the emission current and the resistance in the current path. Assuming an ohmic resistor the high voltage behavior in Figure 42c can

be modeled reasonably well with the following relation:

$$I = C_1 \cdot (V - \Delta V)^2 \exp\left(-\frac{C_2}{V - \Delta V}\right) \\ = C_1 \cdot (V - R \cdot I)^2 \exp\left(-\frac{C_2}{V - R \cdot I}\right) \quad (60)$$

C_1 and C_2 are positive constants in Eq. (60) which is equivalent to the Fowler–Nordheim relation (16) taking into account the proportionality between the voltage and the field. Relation (60) is of course recursive and has to be evaluated numerically. From the emission current and the voltage drop one can estimate the amount of power dissipated in the resistor. In principle the voltage drop could be determined from the model; it has to be stressed, however, that in order to do so the influence of the voltage drop on the local field at the apex of the tube should be known. This in turn requires information on the exact location of the voltage drop in the current path and the amount of electrostatic shielding the emitter experiences. Both are generally unknown. The draws in Figure 42d and e illustrate the possible origins of the voltage drop due to either a high internal resistance in the CNT (e.g., due to defects) or a high contact resistance. It can be estimated that the voltage drop in the saturation regime has to be of the order of 10 V at 2 μ A emission current which gives a power of 20 μ W dissipated. Taking into account the very small volume of the contact $V_c \cong (d_{\text{tube}})^3 \approx 5 \times 10^{-17} \text{ cm}^3$ one estimates a power density in the range of 10^{12} W/cm^3 dissipated in the contact. This can easily explain the emission degradation and the observed local substrate melting due to high emission currents [125].

From this consideration it becomes obvious that the operating the emitter in the current saturation regime is always risky as the current saturation is a sign of power dissipation and therefore of possible degradation. From the I - V curve in Figure 42c it becomes apparent that the voltage window where the emitter can be operated usefully with an emission current between 10 nA and 2 μ A is rather small. This finding can be related generally to CNT emitters by realizing that the window of operation for an emitter corresponds to about twice the threshold field. Together with the large spread in the field enhancement distribution function $f(\beta)$, this leads to the limitation in the emission performance of randomly oriented CNT thin film emitters. The threshold field of macroscopic CNT thin film emitters of 1 cm^2 area is generally around 2 $\text{V } \mu\text{m}^{-1}$. SAFEM investigations, however, show that an interesting ESD of the order of 10^6 cm^{-2} is reached only for applied fields higher than 25 $\text{V } \mu\text{m}^{-1}$. According to the previous consideration emitter degradation has to be expected for applied fields around 5 $\text{V } \mu\text{m}^{-1}$. It is therefore not possible to reach that required for the high ESD without very severe emitter degradation.

4.5. Optimal Structure for Carbon Nanotube Based Electron Field Emitters

As shown in the previous sections the field emission properties of a thin film emitter can be fully characterized by the field enhancement distribution function $f(\beta)$, which depends on the geometry of the emitting structure and the

electrostatic shielding between the emitting structures. To quantify the negative influence of electrostatic shielding on the emission properties we have carried out computer simulations, calculating the field emission current density for CNT arrays of tube different densities. Figure 43 illustrates the effect of the electrostatic shielding in CNT films with different tube densities. A quantitative analysis of the computer simulation shows that optimum field emission properties for a CNT film can be expected, if the mean distance between the tubes is about twice their height. The simulations show further that the field enhancement factor β of the tubes in a film shows a wide distribution, as it is influenced by the orientation of the tube with respect to the applied electric field and by the degree of electrostatic shielding a tube receives from its neighboring tubes. In real CNT films the differences of length and diameter of the individual tubes will further contribute to the distribution of the field enhancement factor β among the CNTs. This distribution gives rise to inhomogeneous field emission properties of CNT thin film emitters. The simulations shown demonstrate clearly why a homogenous emitting CNT film must be formed by identically ordered CNTs. The ideal case of such a CNT film is displayed in Figure 44, where all tubes have the same length, diameter, orientation, and distance from each other. As shown in Section 1.5.3, it is possible to grow films with well-oriented CNTs. The problem of all these films for field emission is that the spacing between the individual tubes is not large enough to prevent electrostatic shielding. It is a big challenge for the nanotechnology to develop processes required for the deposition of CNT films, optimal for field emission. In the case of a flat panel display a CNT based field emission technology will ultimately need to fulfill the following requirements to be competitive with the current metal tip technology:

- growth of individual CNTs at well-defined positions, tolerance $\sim 100 \text{ nm}$
- growth of individual CNTs with well-defined orientation
- growth of individual CNTs with a well-defined aspect ratio ($\beta = h/r$), tolerance $d\beta/\beta \sim 5\%$

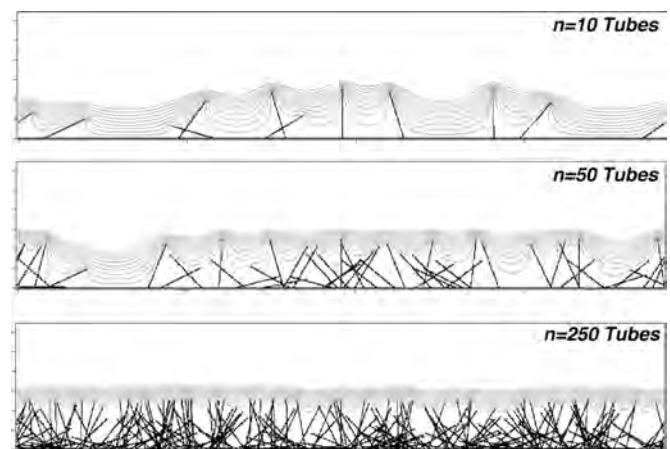


Figure 43. Two-dimensional simulation of the electrostatic potential in films with random distributed and oriented CNTs and different tube densities. (All tubes have the same length and diameter.)

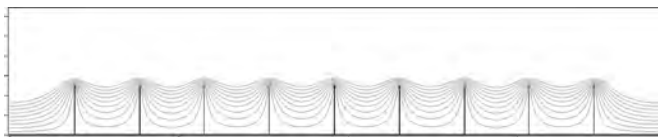


Figure 44. Two-dimensional simulation of the electrostatic potential in an ordered CNT array.

- massively parallel processing (10^8 tubes per cm^2)
- large area deposition ($\sim\text{m}^2$)
- low cost processes

5. CONCLUSIONS

Significant progress in the understanding of the electron emission has been achieved since the first reports on the low threshold field electron emission from carbon thin film emitters in the early 1990s. It seems certain that the low threshold field electron emission from carbon thin film electron emitters can be accurately described by Fowler–Nordheim tunneling. Fowler–Nordheim tunneling requires high electric fields in the order of $3000\text{ V}/\mu\text{m}$ generated by field enhancing structures.

Contrary to a single emitter, the emission properties of a thin film emitter require a statistical treatment, since the field enhancing structures exhibit a distribution with regard to the field enhancement β . Therefore the electron emission properties of thin film emitter with an ensemble of field enhancement structures have to be characterized in terms of the spatial field enhancement, the field enhancement map $\beta(x, y)$. The variation in β for different field enhancement structures leads to a β distribution, the field enhancement distribution function $f(\beta)$, which can be seen as a probability function of the field enhancing structures. The field enhancement distribution function $f(\beta)$ can be said to give an almost complete characterization of the field emission properties, contrary to the threshold field F_{th} of thin film emitters. The field enhancement distribution function $f(\beta)$ has been shown to be exponential for randomly oriented CNT thin films. In order to obtain a field emission device with uniform brightness and high emission site density from thin films, stringent requirements must be placed on the permitted spatial variation of the emitting sites and therefore the variation of the field enhancement β . Homogeneous electron emission from an ensemble of field emitting structures, defined as $dI/I < 50$, requires a relative variation of the field enhancement $d\beta/\beta$ smaller than 4%. Therefore it is desirable to optimize the density of sites close to the highest field enhancement of the ensemble to the limit of electrostatic screening effect. The example of CNT based field electron emission technology demonstrates clearly the difficult path from *nanoscience* to *nanotechnology*. The development of devices based on nanostructures needs, in addition to the process technology, characterization methods and knowledge which cover all aspects, from the fundamental physical phenomena of the individual nanostructure up to the integral behavior of the large number of nanostructures forming the macroscopic device.

GLOSSARY

Carbon nanotube (CNT) A carbon allotrope consisting of rolled-up graphene sheets.

Emission site density (ESD) The number of emitters per unit area, which delivers for a given applied electric field an emission current larger than a given threshold current.

Field emission spectroscopy (FES) Measurement of the energy distribution of the field emitted electrons.

Scanning anode field emission microscope (SAFEM) A scanning probe microscope working with a micrometer-sized tip scanned at constant distance over the cathode surface and with applied fields high enough for field electron emission.

ACKNOWLEDGMENTS

The authors acknowledge the immense contributions of Dr. O. M. Küttel, Dr. E. Maillard-Schaller, and Dr. R. Clergereaux to this work. The results of some of the work reported in this chapter were partly supported by the Swiss TOP Nano 21 Initiative on Nanotechnology and Motorola Inc. Res., Tempe, AZ (USA).

REFERENCES

1. P. R. Schwoebel and I. Brodie, *J. Vac. Sci. Technol. B* 13, 1391 (1995).
2. Hewlett Packard, *Sci. Ame.* May 2000, p. 50.
3. I. Brodie and C. Spindt, *Adv. Electron. Electron Phys.* 83, 6 (1992).
4. A. Einstein, *Ann. Phys.* 17, 132 (1905).
5. O. W. Richardson, *Philos. Trans. Roy. Soc. London* 201, 497 (1903).
6. L. W. Nordheim, *Proc. Roy. Soc. London Ser. A* 121, 626 (1928).
7. R. W. Wood, *Phys. Rev. Ser. I* 5, 1 (1897).
8. R. H. Fowler and L. W. Nordheim, *Proc. Roy. Soc. London Ser. A* 119, 173 (1928).
9. The WKB method was published in 1926 independently by three authors: G. Wentzel, *Z. Phys.* 38, 518 (1926); H. A. Kramers, *Z. Phys.* 39, 828 (1926); L. Brillouin, *C. R. Acad. Sci. Paris* 183, 24 (1926).
10. H. F. Ivey, *Phys. Rev.* 76, 567 (1949).
11. F. Rohrbach, CERN Report 71-5/TC-L, 1971.
12. I. Langmuir, *J. Am. Chem. Soc.* 54, 2798 (1932).
13. G. Gärtner, P. Geittner, H. Lydtin, and A. Ritz, *Appl. Surf. Sci.* 111, 11 (1997).
14. P. Ruffieux, O. Gröning, M. Biemann, P. Mauron, L. Schlapbach, and P. Gröning, *Phys. Rev. B*, in press.
15. J. van der Weide, Z. Zhang, P. K. Baumann, M. G. Wensell, J. Bernholc, and R. J. Nemanich, *Phys. Rev. B* 50, 5803 (1994).
16. L. Diederich, O. M. Küttel, P. Aebi, and L. Schlapbach, *Surf. Sci.* 418, 219 (1998).
17. S. P. Bozeman, P. K. Baumann, B. L. Ward, M. J. Cuomo, R. J. Nemanich, and D. L. Dreifuss, *Diamond Relat. Mater.* 5, 802 (1996).
18. J. Robertson, *Mater. Res. Soc. Symp. Proc.* 509, 83 (1998).
19. J. E. Jaskie, U.S. Patent 5, 619, 092.
20. J. Robertson, *Mater. Res. Soc. Symp. Proc.* 498, 197 (1998).
21. J. Robertson, *J. Vac. Sci. Technol. B* 17, 659 (1999).
22. L. S. Pan and D. R. Kania, "Diamond: Electronic Properties and Applications." Kluwer Academic, Boston, 1995.
23. G. Davis, "Properties and Growth of Diamond." Inspec, London, 1994.
24. S. R. P. Silva, J. Robertson, W. I. Mine, and G. A. J. Amaratunga, "Amorphous Carbon: State of the Art." World Scientific, Singapore, 1997.

25. P. R. Wallace, *Phys. Rev.* 71, 622 (1947).
26. A. Santoni, L. J. Terminello, F. J. Himpsel, and T. Takahashi, *Appl. Phys. A* 52, 299 (1991).
27. E. Herbig, *Astrophys. J.* 196, 129 (1975).
28. T. G. Dietz, M. A. Duncan, D. E. Powers, and R. E. Smalley, *J. Chem. Phys.* 74, 6511 (1981).
29. S. Iijima, *Nature* 354, 56 (1991).
30. M. S. Dresselhaus, G. Dresselhaus, and P. C. Eklund, "Science of Fullerenes and Carbon Nanotubes." Academic Press, San Diego, 1996.
31. B. V. Deryagin and D. V. Fedoseev, *Science* 233, 102 (1975).
32. B. Dischler and C. Wild, "Low-Pressure Synthetic Diamond." Springer-Verlag, Berlin, 1998.
33. P. K. Bachmann, in "Properties and Growth of Diamond" (G. Davis, Ed.), EMIS Datareviews Series, p. 349. Short Run Press Ltd., Exeter, 1994.
34. P. K. Bachmann, D. Leers, and H. Lydt, *Diamond Relat. Mater.* 1, 1 (1991).
35. L. S. Plano, Growth of CVD diamond for electronic applications, in "Electronic Properties and Applications" (L. S. Pan and D. R. Kania, Eds.). Kluwer, Boston, 1995.
36. J. E. Butler and R. L. Woodlin, *Philos. Trans. Roy. Soc. London Ser. A* 342, 209 (1993).
37. S. Skotov, B. Weimer, and M. Franklach, *J. Phys. Chem.* 99, 5616 (1995).
38. C. J. Chu, R. H. Hauge, J. L. Margrave, and M. P. D'Evelyn, *Appl. Phys. Lett.* 61, 1393 (1992).
39. S. J. Harris, *Appl. Phys. Lett.* 56, 2298 (1990).
40. M. Frenklach and K. E. Spear, *J. Mater. Res.* 3, 133 (1988).
41. H. Lui and D. S. Dandy, *Diamond Relat. Mater.* 4, 535 (1995).
42. M. Ece, B. Oral, J. Patscheider, and K.-H. Ernst, *Diamond Relat. Mater.* 4, 720 (1995).
43. B. R. Stoner, G. H. M. Ma, S. D. Wolter, and J. T. Glass, *Phys. Rev. B* 45, 11067 (1992).
44. C. Wild, P. Koidl, W. Müller-Seibert, H. Walcher, R. Kohl, N. Herres, R. Locher, and R. Brenn, *Diamond Relat. Mater.* 2, 158 (1993).
45. E. Maillard-Schaller, O. M. Küttel, P. Gröning, O. Gröning, R. G. Agostino, P. Aebi, L. Schlapbach, P. Würzinger, and P. Pongartz, *Phys. Rev. B* 55, 15895 (1997).
46. O. Gröning, Field Emission Properties of Carbon Thin Films and Carbon Nanotubes, Ph.D. Thesis No. 1258, University of Fribourg, Switzerland, 1999.
47. W. Zhu, G. P. Kochanski, S. Jin, and L. Seibles, *J. Appl. Phys.* 78, 2707 (1995).
48. S. Aisenberg and R. Chabot, *J. Appl. Phys.* 42, 2953 (1971).
49. J. Robertson, *Progr. Solid State Chem.* 21, 199 (1991).
50. D. R. McKenzie, *Rep. Progr. Phys.* 59, 1611 (1996).
51. J. Robertson, in "Amorphous Carbon: State of the Art." World Scientific, Singapore, 1998.
52. P. K. Bachmann, *Ullman's Encyclopaedia Ind. Chem. A* 26, 720 (1996).
53. H. Tsai and D. B. Bogy, *J. Vac. Sci. Technol. A* 5, 3287 (1987).
54. R. Hauert, J. Patscheider, L. Knoblauch, and M. Diserens, *Adv. Mater.* 11, 175 (1999).
55. S. R. P. Silva, J. D. Carey, R. U. A. Kahn, E. G. Gerstner, and J. V. Anguita, in "Handbook of Thin Film Materials" (H. S. Nalwa, Ed.), Vol. 4, p. 403. Academic Press, San Diego, 2002.
56. J. Robertson and E. P. O'Reilly, *Phys. Rev. B* 35, 2946 (1987).
57. N. F. Mott and E. A. Davis, in "Electronic Processes in Non-Crystalline Materials," Ch. 1. Oxford Univ. Press, Oxford, 1971.
58. R. A. Street, "Hydrogenated Amorphous Silicon." Cambridge Univ. Press, Cambridge, UK, 1991.
59. F. Darkrim and D. Levesque, *J. Chem. Phys.* 109, 4981 (1998).
60. T. W. Ebbesen, *Annu. Rev. Mater. Sci.* 24, 235 (1994).
61. T. Guo, P. Nikolaev, A. Thess, D. T. Colbert, and R. E. Smalley, *J. Phys. Chem.* 55, 10694 (1995).
62. M. Endo, K. Takeuchi, S. Igarashi, K. Kobori, M. Shiraiishi, and H. W. Kroto, *J. Phys. Chem. Solids* 54, 1841 (1993).
63. S. Iijima, T. W. Ebbesen, and P. M. Ajayan, *Nature* 358, 229 (1992).
64. "Graphite Fibres and Filaments" (M. S. Dresselhaus, G. Dresselhaus, I. L. Spain, and H. A. Goldberg, Eds.). Springer-Verlag, New York, 1998.
65. R. T. K. Baker and P. S. Harris, *Chem. Phys. Carbon* 14, 83 (1978).
66. S. H. Tsai, C. W. Chao, C. L. Lee, and H. C. Shih, *Appl. Phys. Lett.* 74, 3462 (1999).
67. J. Li, C. Papadopoulos, J. M. Xu, and M. Moskivits, *Appl. Phys. Lett.* 75, 367 (1999).
68. C. Bower, *Appl. Phys. Lett.* 77, 830 (2000).
69. J. Kong, H. T. Soh, A. M. Cassell, C. F. Quate, and H. Dai, *Nature* 385, 878 (1998).
70. S. Fan, M. G. Chapline, N. R. Franklin, T. W. Tombler, A. M. Cassell, and H. Dai, *Science* 283, 512 (1999).
71. H. Kind, J.-M. Bonard, Ch. Emmenegger, L.-O. Nilsson, K. Her-nadi, E. Maillard Schaller, L. Schlapbach, L. Forro, and K. Kern, *Adv. Mater.* 11, 1285 (1999).
72. B. Q. Wei, R. Vajtai, Y. Jung, J. Ward, R. Zhang, G. Ramanath, and P. M. Ajayan, *Nature* 416, 495 (2002).
73. Z. J. Zhang, B. Q. Weis, G. Ramanath, and P. M. Ajayan, *Appl. Phys. Lett.* 77, 3764 (2000).
74. Y. Tu, Z. P. Huang, D. Z. Wang, J. G. Wen, and Z. F. Ren, *Appl. Phys. Lett.* 80, 4018 (2002).
75. L. Delzeit, I. MacAninch, B. Cruden, D. Hash, B. Chen, J. Han, and M. Meyyappan, *J. Appl. Phys.* 91, 6027 (2002).
76. M. Tanemura, K. Iwata, K. Takahashi, Y. Fujimoto, and F. Okuyama, *J. Appl. Phys.* 90, 1529 (2001).
77. Y. S. Woo, D. Y. Jeon, I. T. Han, N. S. Lee, J. E. Jung, and J. M. Kim, *Diamond Relat. Mater.* 11, 59 (2002).
78. Ch. Bower, W. Zhu, S. Jin, and O. Zhou, *Appl. Phys. Lett.* 77, 830 (2000).
79. K. B. K. Teo, M. Chowalla, G. A. J. Amaratunga, W. I. Milne, D. G. Hasko, G. Pirio, P. Legagneux, F. Wyczisk, and D. Pribat, *Appl. Phys. Lett.* 79, 79 (2001).
80. B. C. Djubua and N. N. Chubun, *IEEE Trans. Electron Devices* 38, 2314 (1991).
81. C. Wang, A. Garcia, D. C. Ingram, M. Lake, and M. E. Kordesch, *Electron. Lett.* 27, 1459 (1991).
82. M. W. Geis, N. M. Elfremov, J. D. Woodhouse, M. D. McAleese, M. Marchywka, D. G. Socker, and J. F. Hochedez, *IEEE Electron Device Lett.* 12, 456 (1991).
83. L. N. Dobretsov and M. V. Gomoyunova, "Emission Electronics." (Izdatel'stvo Nauka, Moscow, 1966); Israel Programme for Scientific Translations, Jerusalem, 1971.
84. See www.pixtech.com
85. K. Okano, K. Hoshina, and M. Iida, *Appl. Phys. Lett.* 64, 2742 (1994).
86. Yu. V. Gulyaev, L. A. Chernozatonskii, Z. Ya. Kosakovskaya, N. I. Sinitzyn, G. V. Torgashov, and Yu. F. Zakharchenko, in "Proc. 7th Int. Vac. Microelectronics Conf.," Grenoble, France, 1994, p. 322.
87. A. Y. Tcherepanov, A. G. Chakhovskoi, and V. V. Sharov, in "Proc. 7th Int. Vac. Microelectronics Conf.," Grenoble, France, 1994, p. 76.
88. D. Hong and M. Aslam, *J. Vac. Sci. Technol. B* 12, 427 (1995).
89. V. V. Zirnov, E. I. Givargizov, and P. S. Plekhanov, *J. Vac. Sci. Technol. B* 13, 418 (1995).
90. G. A. J. Amaratunga and S. R. P. Silva, *Appl. Phys. Lett.* 68, 2529 (1996).
91. K. Okano, S. Koizumi, S. Ravi, P. Silva, and G. A. J. Amaratunga, *Nature* 381, 140 (1996).
92. Z.-H. Huang, P. H. Cutler, N. M. Miskovsky, and T. E. Sullivan, in "Proc. 7th Int. Vac. Microelectronics Conf.," Grenoble, France, 1994, p. 92.
93. N. S. Xu, Y. Tzeng, and R. V. Latham, *J. Phys. D* 27, 1988 (1994).
94. R. G. Forbes, *Solid-State Electron.* 45, 779 (2001).

95. M. W. Geis, J. C. Twichell, and T. M. Lyszczarz, *J. Vac. Sci. Technol. B* 14, 2060 (1996).
96. F. J. Himpsel, J. A. Knapp, J. A. Van Vechte, and D. E. Eastman, *Phys. Rev. B* 20, 624 (1979).
97. J. van der Weide, Z. Zang, P. K. Baumann, M. G. Wensell, J. Bernholz, and R. J. Nemanich, *Phys. Rev. B* 50, 5803 (1994).
98. C. Bradis and B. B. Pate, *Appl. Phys. Lett.* 69, 4123 (1996).
99. R. G. Farrer, *Solid State Comm.* 7, 685 (1969).
100. E. Aluker, St. Chernov, and V. Garilov, *Phys. Status Solidi K* 25, 172 (1992).
101. G. Gärtner, P. Geittner, H. Lydtin, and A. Ritz, *Appl. Surf. Sci.* 111, 11 (1997).
102. R. Stratton, *Phys. Rev. A* 135, 794 (1964).
103. R. E. Burges, H. Kroemer, and J. M. Houston, *Phys. Rev.* 90, 515 (1953).
104. O. Gröning, O. M. Küttel, Ch. Emmenegger, P. Gröning, and L. Schlapbach, *J. Vac. Sci. Technol. B* 18, 665 (2000).
105. IBM Patent Server, www.patents.ibm.com.
106. O. Gröning, O. M. Küttel, E. Schaller, P. Gröning, and L. Schlapbach, *Appl. Phys. Lett.* 68, 476 (1996).
107. O. Gröning, O. M. Küttel, P. Gröning, and L. Schlapbach, *J. Vac. Sci. Technol. B* 17, 1064 (1999).
108. O. Gröning, O. M. Küttel, P. Gröning, and L. Schlapbach, *Appl. Phys. Lett.* 71, 2253 (1997).
109. O. M. Küttel, O. Gröning, Ch. Emmenegger, L. O. Nilsson, E. Maillard, L. Diederich, and L. Schlapbach, *Carbon* 37, 745 (1999).
110. R. Latham, "High Voltage Vacuum Insulation." Academic Press, San Diego, 1995.
111. O. Gröning, O. M. Küttel, P. Gröning, and L. Schlapbach, *J. Vac. Sci. Technol. B* 17, 1970 (1999).
112. O. Gröning, L. O. Nilsson, P. Gröning, and L. Schlapbach, *Solid State Electron.* 45, 929 (2001).
113. O. Gröning, O. M. Küttel, P. Gröning, and L. Schlapbach, *Appl. Surf. Sci.* 111, 135 (1997).
114. O. M. Küttel, O. Gröning, Ch. Emmenegger, and L. Schlapbach, *Appl. Phys. Lett.* 73, 2113 (1998).
115. K. A. Dean, O. Gröning, O. M. Küttel, and L. Schlapbach, *Appl. Phys. Lett.* 75, 2773 (1999).
116. L. D. Landau and E. M. Lifshitz, "Electrodynamics of Continuous Media," Pergamon, New York, 1960.
117. D. M. Wood, *Phys. Rev. Lett.* 46, 749 (1981).
118. G. Markov, A. Nitzan, and L. E. Brus, *J. Chem. Phys.* 88, 5076 (1988).
119. V. Bonacic-Koutecky, P. Fantucci, and J. Koutecky, *Chem. Rev.* 91, 1035 (1991).
120. E. W. Müller, *Z. Phys.* 106, 541 (1937).
121. L. O. Nilsson, Microscopic Characterisation of Electron Field Emission from Carbon Nanotubes and Carbon Thin Film Emitters, Ph.D. Thesis No. 1337, University of Fribourg, Switzerland, 2001.
122. A. G. Rinzler, J. H. Hafner, P. Nikolaev, L. Lou, S. G. Kim, D. Tomanek, P. Nordlander, D. T. Colbert, and R. E. Smalley, *Science* 269, 1550 (1995).
123. K. Dean and B. R. Chalamala, *Appl. Phys.* 85, 3822 (1999).
124. L. O. Nilsson, O. Gröning, O. Küttel, P. Gröning, and L. Schlapbach, *J. Vac. Sci. Technol. B* 20, 326 (2002).
125. L. O. Nilsson, O. Gröning, P. Gröning, and L. Schlapbach, *Appl. Phys. Lett.* 79, 1036 (2001).
126. L. O. Nilsson, O. Gröning, Ch. Emmenegger, O. M. Küttel, E. Schaller, and L. Schlapbach, *Appl. Phys. Lett.* 76, 2071 (2000).
127. S. Frank, P. Poncharal, Z. L. Wang, and W. A. de Heer, *Science* 280, 1744 (1998).
128. A. Zettel and J. Cumings, in "Proc. XIV Inter. Winterschool on Electr. Prop. of Novel Materials," Kirchberg, Tirol, Austria, 2000, p. 526.
129. P. Ruffieux, Ph.D. Thesis No. 1387, University of Fribourg, Switzerland, 1999.
130. E. Maillard-Schaller, Ph.D. Thesis No. 1145, University of Fribourg, Switzerland, 1996.

Carbon Nanotube Growth by Chemical Vapor Deposition

M. Meyyappan

NASA Ames Research Center, Moffett Field, California, USA

CONTENTS

1. Introduction
2. Growth Apparatus
3. Catalyst Preparation
4. Growth Results
5. Growth Mechanisms
6. Applications for CVD/PECVD
Grown Nanotubes
- Glossary
- References

1. INTRODUCTION

The interest in carbon nanotubes (CNTs) and the level of research activities across the world have been extraordinary in the last decade. CNTs were first discovered by Sumio Iijima of the NEC Corporation in 1991 [1] in the soot of an arc-discharge apparatus. These are elongated fullerenes with diameters as small as 0.7 nm and lengths of up to several microns. Single-walled carbon nanotubes (SWNTs) exhibit unique electronic properties in that they can be metallic or semiconducting, depending on their helicity. This allows the formation of semiconductor–semiconductor and semiconductor–metal junctions useful in device fabrication. SWNTs also possess extraordinary mechanical properties. The Young's modulus of individual SWNTs has been estimated to be around 1 TPa, and the yield strength can be as large as 120 GPa [2].

The interesting combination of electronic and mechanical properties of CNTs has led to wide-ranging investigations of their potential in future electronics and computing, field-emitter devices, sensors, electrodes, high-strength composites, and storage of hydrogen, lithium, and other metals. For a detailed discussion on the properties and applications, the reader is referred to several volumes edited by Saito et al. [2], Meyyappan and Srivastava [3], and other review articles [4]. This chapter focuses on CNT growth and large-scale production by chemical vapor deposition (CVD) and related techniques such as plasma-enhanced

CVD (PECVD). The early processes used for CNT production were laser ablation and an arc-discharge approach. Both are able to produce single- and multiwalled nanotubes, and continue to be popular among researchers. Details on these processes can be found in [4–6]. CVD is amenable for nanotube growth on patterned surfaces, suitable for the fabrication of electronic devices, sensors, field emitters, and other applications where controlled growth over masked areas is needed for further processing.

A variety of different CNT structures is possible by CVD and related techniques. A SWNT is a rolled-up tubular shell of graphene sheet which is composed of benzene-type hexagonal rings of carbon atoms. A multiwalled carbon nanotube (MWNT) is a rolled-up stack of graphene sheets into concentric cylinders. The walls of each layer of the MWNT or the graphite basal planes are parallel to the central axis ($\theta = 0$). In contrast, a stacked-cone arrangement (also known as a Chevron structure, ice-cream-cone structure, or piled-cone structure) is also seen, where the angle between the graphite basal planes and the tube axis is nonzero [7]. Nolan et al. [7] suggest that hydrogen satisfies the valences at cone edges in such structures. (An MWNT has no graphite edges, and therefore there is no need for valence-satisfying species such as hydrogen.) Since the stacked-cone structures exhibit only small θ values, and are not solid cylinders but are mostly hollow, they can be called multiwalled carbon nanofibers (MWNFs) [8]. Note that the terminologies graphitic carbon fibers (GCFs) and vapor-grown carbon fibers (VGCFs) have long been used to denote solid cylinders.

The CNT growth literature has grown rapidly in recent years. A reasonably complete (but not exhaustive) list of references in areas discussed in this chapter is given below:

- early works on carbon fibers/filaments [9–15]
- thermal CVD of SWNTs [16–27, 59]
- thermal CVD of MWNTs [7, 28–55]
- CNT growth on atomic force microscope (AFM) cantilevers [56–59]
- electric-field assistance in thermal CVD [60–62]
- floating catalyst CVD of SWNTs [63–69] and MWNTs [70, 71]

- PECVD of MWNTs and MWNFs [8, 59, 72–92]
 - dc plasma [83–85, 87–91]
 - plasma-assisted hot filament [72, 73, 75]
 - microwave plasma [74, 76–82]
 - RF capacitive and inductive [8, 59, 86, 92]
- theoretical analysis of CNT growth [93–95]
- computational model and simulation of CNT growth [96–98].

This chapter is organized as follows: Section 2 presents an overview of the growth apparatus used in thermal CVD and PECVD; catalyst preparation techniques are outlined in Section 3; growth results from thermal CVD of SWNTs and MWNTs, the effect of the electric field on alignment, and plasma-grown nanotubes are presented in Section 4. Growth mechanism is the subject of Section 5, and a brief overview of applications for the thermal CVD- and PECVD-grown material is presented in Section 6.

2. GROWTH APPARATUS

As markets for CNTs are not developed, there is no commercial equipment industry now, unlike the case with the semiconductor equipment industry. So, the equipment is mostly homemade, low-throughput batch reactors. When the market changes to large-scale product-oriented (devices, sensors, nanoelectromechanical systems, etc.) from the current academic-research-dominated scenerio, the worldwide equipment vendors (currently catering to the semiconductor and MEMs market) will undoubtedly move in to meet the demands since the growth hardware is very much similar, as will be seen below.

2.1. Thermal CVD

The thermal CVD apparatus for CNT growth is very simple [18, 24, 59]. It consists of a quartz tube (diameter of 1–2 in) inserted into a tubular furnace capable of maintaining ± 1 °C over a 25 cm zone. Thus, it is a hot-wall system, and primarily atmospheric pressure CVD. Cold-wall reactors, common in the semiconductor industry, where the substrate holder is directly heated from below (resistance, inductance, or other heaters), have not been reported in the literature. Since the growth is catalyst promoted at temperatures of 500–1000 °C and does not depend on precursor dissociation at these temperatures, either a hot- or a cold-wall system could be designed to be effective for CNT growth. The substrate, typically about or smaller than 1 in now, is placed inside the quartz tube. In thermal CVD, either CO or some hydrocarbon such as methane, ethane, ethylene, acetylene, or other higher hydrocarbons is used without any dilution. The feedstock is metered through a mass flow controller. A typical growth run would involve purging the reactor first with argon or some other inert gas until the reactor reaches the desired growth temperature. Then the gas flow is switched to the feedstock for the specified growth period. At the end, the gas flow is switched back to the inert gas while the reactor cools down to 300 °C or lower before exposing the nanotubes to air. Exposure to air at elevated temperatures can cause damage to the CNTs.

Typical growth rates range from a few nm/min to 2–5 $\mu\text{m}/\text{min}$. CNT growth is largely empirical at present, and

diagnostics and modeling studies are rare. For example, the effects of reactor length and diameter, flow rate, and so on, on growth characteristics are completely unknown. One study using a mass spectrometer [99] and another involving a computational fluid dynamics modeling [98] confirm that the precursor dissociation (in the case of methane at 900 °C) indeed is very small, and the growth proceeds due to the catalytic activity of methane on particle surfaces.

For growth on substrates, the catalyst mixture needs to be applied to the substrate (see Section 3) prior to loading it inside the reactor. This is the so-called supported catalyst approach. In contrast, CVD can also be used to grow large quantities of nanotubes using a “floating-catalyst” approach [63–71]. In this case, a nozzle system [64, 65] may be used to inject the vaporized catalyst precursor into the flowing CO or hydrocarbon. A second furnace may be required to heat up the catalyst precursor system to its dissociation temperature [63, 70]. The floating-catalyst approach is amenable to scale up for large-scale production to meet the “commodity market” demands of nanotubes in a variety of structural applications.

2.2. PECVD

The plasma enhancement in CVD first emerged in microelectronics because certain processes cannot tolerate the high wafer temperatures of the thermal CVD. For example, charring of photoresists on patterned wafers could be a problem. The plasma CVD allowed an alternative at substantially lower wafer temperatures (room temperature to 100 °C), and hence, has become a key step in integrated-circuit manufacturing. The low-temperature operation is possible since the precursor dissociation (necessary for the deposition of all common semiconductor, metallic, and insulating films) is enabled by the high-energy electrons in an otherwise cold plasma. In contrast to this familiar scenerio, CNT growth does not need precursor dissociation, and as such, the well-known efficiency of a plasma to tear apart the precursor gas for reactive radical generation should not be a factor. What is known to date about the catalytic activity of the transition metal particles for CNT growth tells us that growth does not occur below 550 °C. Hence, the cold wafer scenerio is out of the question, at least for now, until new knowledge emerges. It is not clear, then, what the true role of the plasma in CNT growth is, despite a large number of articles in this field [8, 59, 72–92]. However, there is enough empirical evidence that the cold plasma enables more vertically aligned CNTs than thermal CVD [59, 75, 81, 85, 92]. Whereas any marginal alignment seen in thermal CVD samples is due to a crowding effect (nanotubes supporting each other by van der Waals attraction), individual, free-standing, and vertically oriented CNTs are possible with PECVD, as will be seen in Section 4.

As in the case of earlier technology waves such as microelectronics materials and diamond deposition, researchers have attempted dc [83–85, 87–91], RF [86], hot-filament aided with dc [72, 73, 75], microwave [74, 76–82], electron cyclotron resonance, and inductively coupled plasma reactors [8, 59, 92]. An overview of plasma fundamentals and plasma equipment can be found in [100, 101]. A dc plasma reactor consists of a pair of electrodes in a grounded chamber, with one electrode grounded and the second connected

to a power supply. The negative dc bias applied to the cathode leads to a breakdown of the feedgas. The wafer with the catalyst layer may be placed either on the anode or cathode for CNT deposition. The electrode holding the wafer may need an independent heating source to raise the wafer temperature to the desired growth temperature. Instead of a resistive heater underneath the electrode, a tungsten wire suspended in the plasma stream may serve as the heating source. This is the so-called hot-filament system with plasma assistance. These two systems have successfully yielded MWNTs and MWNFs, as evidenced from [72, 73, 75, 83–85, 87–91]. However, the bias on the wafer in these systems appears to be very high (>300 V). It is well known that ions gain substantial energy in the sheath from high electric fields, and the high-energy ion bombardment of the wafer often leads to damage, which is well known from silicon and III–V semiconductor literature. It is for this reason and the poor efficiency of the dc systems that the semiconductor industry abandoned these sources a few decades ago.

Since the plasma can dissociate the hydrocarbon, creating many reactive radicals, pure hydrocarbon feedstock in plasma reactors may lead to substantial amorphous carbon deposition. Therefore, it is desirable to dilute the hydrocarbon with argon [8], hydrogen [8, 59], or ammonia [75, 81]. The pressure in the reactor typically ranges from 1–20 torr, with a hydrocarbon fraction of up to 20%. Atmospheric pressure operation of plasma systems is uncommon due to power coupling problems. Low-pressure operation in the tens of millitorrs would result in very slow growth rates. So, PECVD reactors are typically operated at 1–20 torr pressure levels for CNT growth. At these pressure levels, inductive coupling to hydrocarbon/ H_2 systems appears to be difficult; the coupling appears to have a large capacitive component [8, 92]. The capacitive component decreases with an increasing fraction of argon. Microwave sources are very popular at these pressures and power levels of up to 2 KW, and have been widely used for diamond deposition. Following this success, CNT literature also consists of several successful demonstrations of MWNT growth using microwave sources [79–82].

In addition to the source, matching network, and other power-coupling components, the equipment consists of mass flow controllers and one or more vacuum pumps. The growth chamber itself is grounded. All plasma reactors are cold-wall systems, with the substrate directly heated using some form of heat source from below the substrate holder. First, the wafer is loaded in the reactor, and the system is pumped down to 10^{-5} torr or below to minimize impurities and water vapor. The substrate holder is heated to the desired temperature. Then the feedstock is admitted, and the flow rate and chamber pressure can be set to desired levels independent of each other with the aid of a throttle valve. Next, the power from the power source is coupled to the plasma. At the end of the run, the heater, power source, and gas flow are turned off, and the system is purged with argon flow. The wafer is removed after the reactor cools down below 300 °C.

3. CATALYST PREPARATION

Although there have been some studies reporting CNT growth without catalysts in arc discharge processes, it is widely acknowledged that transition metal catalysts are needed for SWNT, MWNT, and MWNF growth by CVD. It is also believed that the catalyst on the substrate must be in the form of particles instead of smooth, continuous films. There have been several studies indeed correlating the catalyst particle size and the diameter of the resulting nanotubes [26, 41, 53, 55, 79, 86, 88, 102]. The metals used to date as catalysts include Fe, Ni, Co, and Mo. It is possible to apply these onto the substrate from solutions containing them or they can be directly deposited using some physical techniques. These two approaches are different in terms of needed resources, time and cost, and the nature of the resulting products. A brief overview is provided on the two routes to supported-catalyst preparation, and also the floating-catalyst approach for large-scale production.

3.1. Solution-Based Catalyst Preparation

The literature contains numerous recipes for preparing catalysts from solutions, and one such recipe is given below [44]. First, 0.5 g (0.09 mmol) of Pluronic P-123 triblock copolymer is dissolved in 15 cm^3 of a 2:1 mixture of ethanol and methanol. Next, SiCl_4 (0.85 cm^3 , 7.5 mmol) is slowly added using a syringe into the triblock copolymer/alcohol solution, and stirred for 30 min at room temperature. Stock solutions of $\text{AlCl}_3 \cdot 6\text{H}_2\text{O}$, $\text{CoCl}_2 \cdot 6\text{H}_2\text{O}$, and $\text{Fe}(\text{NO}_3)_3 \cdot 6\text{H}_2\text{O}$ are prepared at the concentration of the structure directing agent (SDA) and inorganic salts. The catalyst solutions are filtered through $0.45\text{ }\mu\text{m}$ polytetrafluoroethylene membranes before applying onto the substrate. The substrate with the catalyst formulation is loaded into a furnace, and heated at 700 °C for 4 h in air to render the catalyst active by the decomposition of the inorganic salts and removal of the SDA. Admission of hydrocarbon feedstock into the reactor at this point would initiate nanotube growth.

It is noted that a mixture of transition-metal-containing compounds along with structure-directing agents is used in the above recipe. It is difficult to find optimum concentrations of each constituent in a trial-and-error approach as the number of trials is large. Cassell and coauthors pioneered a combinatorial optimization process for catalyst discovery for the growth of SWNTs [25] and MWNTs [44]. This rapid throughput approach, coupled with characterization techniques, allows the development of catalyst libraries with a minimal number of growth experiments.

In general, even with the right formulation known *a priori*, solution-based approaches are time consuming. A typical preparation includes such steps as dissolution, stirring, precipitation, refluxing, separation, cooling, gel formation, reduction, drying/annealing/calcinations, and so on. The overall process is cumbersome and time consuming; some recipes even call for overnight annealing. Another problem is the difficulty in confining the catalyst within small patterns.

3.2. Physical Techniques for Catalyst Preparation

Physical techniques, such as electron gun evaporation [83–85, 102], thermal evaporation [88], pulsed laser deposition [46], ion beam sputtering [8, 24, 55, 59, 92], and magnetron sputtering [75, 78, 79, 86, 91], have been successfully used in catalyst preparation. These techniques are quick, easy, and amenable to produce small patterns, in contrast to the solution-based approaches discussed in the previous section. Typically, a thin catalyst film (<20 nm) is applied by these techniques. The eventual particle size and the resultant nanotube diameter seem to correlate to film thickness. Thinner films in general lead to smaller particles and tube diameters [88, 102]. While a small grain size is not guaranteed in as-prepared films, further insurance steps appear to help in breaking the films into desired particles. For example, in PECVD techniques, an inert gas plasma or hydrogen plasma is run first prior to admitting the feedgas and initiating growth [76, 80]. The plasma ion bombardment will create particles. In thermal CVD, the substrate with the catalyst often first faces a “preparation step,” where an inert gas at the growth temperature flows through the reactor for about 10 min, prior to admitting the feedgas. This influences the size of the particles. In some cases, particularly with Ni films, a pretreatment with NH_3 has been used, where Ni is etched into small particles [75, 83, 91]. Delzeit et al. [24, 55] have shown that the introduction of a metal underlayer (such as Al) can be used instead of any chemical pretreatment steps. Thermodynamics and kinetic studies [7] indicate that alloying a catalyst with a noncatalytic metal increases the number of reactive sites through surface clusters. In addition, an underlayer such as Al allows tuning of the final conductivity of the substrate plus CNTs. The metal underlayer may also play the role of a barrier layer between an incompatible catalyst metal and substrate, which is the case with Fe and a highly oriented pyrolytic graphite substrate.

3.3. Floating-Catalyst Approach

If a stream of catalyst particles can be injected into the flowing feedstock, it is possible to produce nanotubes in the gas phase. This approach is amenable for scale up to large-scale production. Sen et al. [70] first reported such a possibility when they used ferrocene or nickelocene as a source of the transition metal and benzene as carbon source. Nikolaev et al. [64] used CO disproportionation aided by Fe clusters created from $\text{Fe}(\text{CO})_5$. The transition metal sources vaporize at temperatures much lower than that for the gas phase pyrolysis of the carbon sources. In using ferrocene or $\text{Fe}(\text{CO})_5$, the iron particles condense together and form clusters. An iron cluster of 40–50 atoms (~ 0.7 nm diameter) is about the size of the smallest SWNT. Smaller clusters tend to evaporate, and are unstable. Very large clusters are also not ideal for nanotube growth as they favor graphitic overcoating. Declustering or break up of large clusters also happens in the reactor. It is the competition between various processes (clustering, evaporation) that creates favorable-size clusters [96]. Tuning of various parameters such as temperature, flow rates of various gases, injection velocity of the $\text{Fe}(\text{CO})_5$, residence time, and so on is done to obtain

reasonable quantities of nanotubes. The kinetics of cluster formation and nanotube growth reactions is not well understood, and a preliminary model is presented by Dateo et al. [96]. The availability of reliable kinetics data would lead to reactor and process design simulations, based on traditional chemically reacting flow models, as attempted by Gokcen et al. [97].

4. GROWTH RESULTS

This section presents sample results from the literature to give an indication of the current possibilities. In Section 3.1, a solution-based catalyst recipe was discussed, along with optimization procedures using a combinatorial approach. Figure 1 shows results from such an optimization run. The top image shows a 5×5 array, with each spot having different compositions of Si, Fe, Co, and Al-containing compounds. The wafer with 25 different formulations was loaded in a CVD reactor, and the growth was carried out at 850 °C for 20 min. Scanning electron microscopy (SEM) and confocal Raman spectroscopy were used to characterize SWNTs from each spot to identify the most active catalyst compositions. An SEM image of SWNTs from one such location is given in Figure 1.

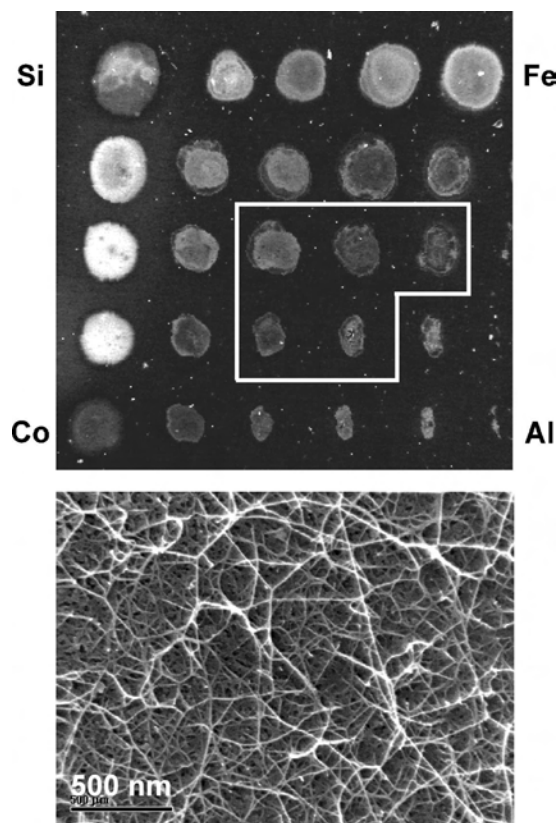


Figure 1. SWNT growth by thermal CVD. Top panel shows a low-magnification SEM image of a discovery library of candidate SWNT catalysts. The most active region is outlined in white. A representative high-magnification image of a composition within the active region shows (bottom panel) a predominance of SWNTs. (Image courtesy of A. M. Cassell.)

Figure 2 shows results for SWNT growth by thermal CVD on a 400 mesh TEM grid used as a substrate. First, an underlayer of Al (10 nm thick) and an active catalyst layer of Fe (1 nm) were deposited inside the open areas of the grid using ion beam sputtering [24]. The results are for 1000 sccm of methane flow at 900 °C for a period of 10 min in a thermal CVD reactor. SWNTs are seen in each of the open areas; a larger magnitude SEM image in Figure 2b clearly indicates a mat of nanotubes. Figure 3 provides a TEM image of this sample indicating SWNTs.

Raman spectroscopy is a valuable tool to characterize CNTs, identify if they are semiconductor or metallic, and determine impurities present. Figure 4 shows an example of Raman spectra obtained with 514 and 633 nm excitation lasers. The laser power is 2 mW focused on a 1 μm spot. The sample shows the characteristic narrow G band at 1590 cm^{-1} . A signature band at 1730 cm^{-1} for SWNTs is also seen. From the radial breathing mode, the sample is estimated to have a broad SWNT diameter distribution from 1.14 to 2.0 nm.

Ion-beam-sputtered catalyst layers such as Fe or Ni along with the Al underlayer can also be used to grow MWNTs. MWNT growth is facilitated by using ethylene at 700 °C (lower than for SWNTs), as seen in Figure 5. A theoretical

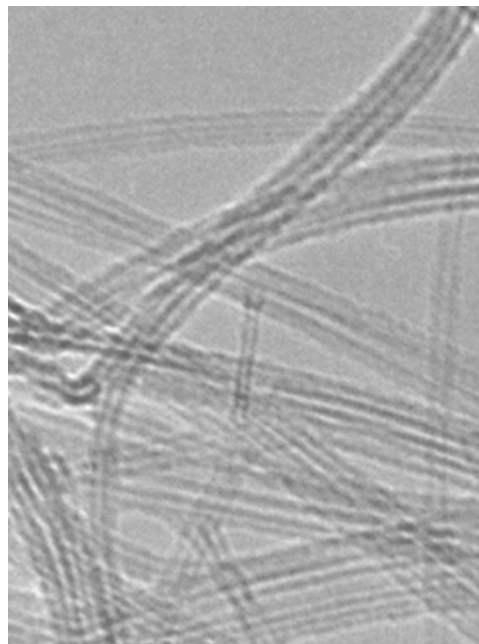
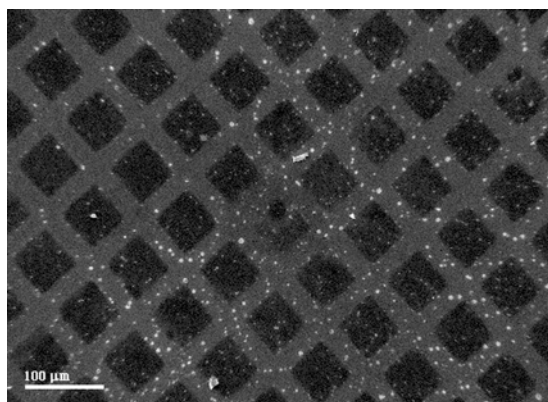
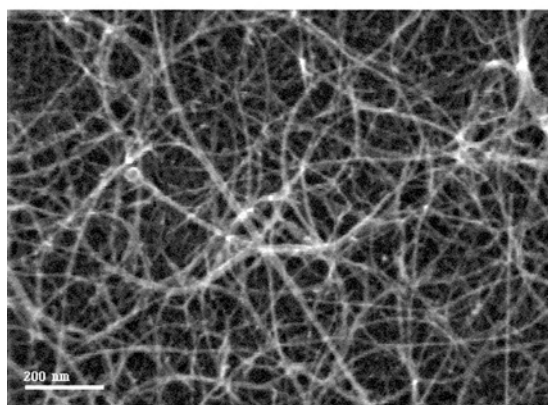


Figure 3. TEM image of the sample in Figure 2.



(a)



(b)

Figure 2. SWNT growth on a 400 mesh TEM grid. Prior to growth, 10 nm Al and 1 nm Fe are deposited into open areas. Growth conditions: 1000 sccm methane at 900 °C for 10 min. (a) Low-magnification image of SWNTs. (b) High-resolution SEM of one of the squares. (Image courtesy of L. Delzeit.)

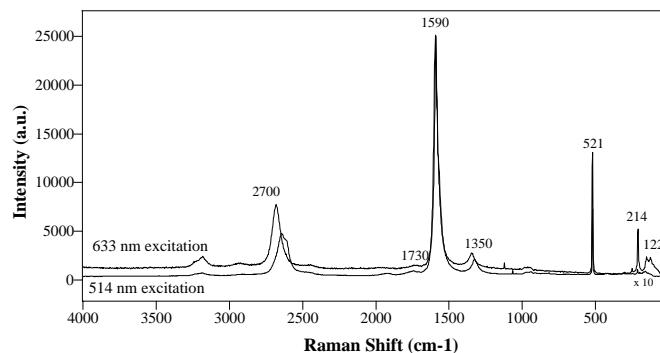


Figure 4. Raman spectra results for SWNT samples from Figure 2.

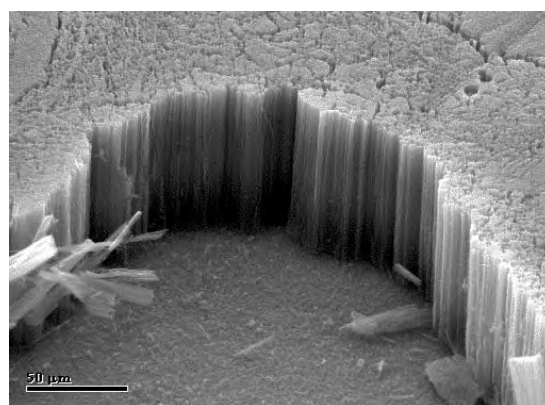


Figure 5. MWNT tower grown by thermal CVD. (Image courtesy of L. Delzeit.)

analysis by Karzow and Ding [93] indicates that production of MWNTs is favored over SWNTs when the growth temperature is kept below 900 °C and the carbon supply at the catalyst particle surface is relatively high (note that this does not imply carbon supply from gas phase pyrolysis, which leads to unwanted amorphous carbon). The MWNT tower seen in Figure 5 can be obtained on a variety of substrates such as silicon, quartz, mica, and highly oriented pyrolytic graphite.

Most SWNT and MWNT growth on substrates tends to result in either a mat of nanotubes (as in Fig. 1b or Fig. 2b) or towers as in Figure 5. However, in some applications, such as in transistor fabrication, it is desirable to have a single nanotube (preferably SWNT) bridging two electrodes. While one can always transplant a nanotube from bulk samples, *in-situ* growth is preferable. This can be accomplished by using an electric field to direct the growth [61, 62]. The electric-field effect in thermal CVD has been demonstrated by Delzeit et al. [62], in which directed growth of an SWNT spans across two electrodes 25 μm apart.

Figure 6 shows vertically aligned, individual, freestanding MWNFs grown in a high-density plasma reactor. The reactor consists of an inductive coil, as well as a separate RF capacitive power supply at the bottom electrode supporting the wafer. The nominal pressure in the reactor is 3 torr. At this pressure, the power coupling to the plasma is not entirely inductive, but there is a capacitive component. The gas flow consists of 100 sccm of a 20:80 methane/ H_2 mixture. Vertical MWNFs as in Figure 6 are suitable for the development of electrodes needed in biosensors and other applications [103, 104]. The MWNFs contain the catalyst particles at the tip, as shown in the TEM image in Figure 7. The metal particles can be easily removed using a two-step procedure of thermal oxidation in air (200–400°), followed by a dilute acid (12% HCl) treatment [105]. The production of MWNFs seems to correlate with the high percentage of H_2 in the feedgas mixture and high RF powers to the substrate; this correlation was verified using atomic hydrogen emission lines in an emission spectroscopy analysis of the plasma [8]. In contrast, when the hydrogen dilution is low, for example, by adding a large fraction of argon or at low substrate power levels, MWNTs result instead of MWNFs. A TEM image of these MWNTs is shown in Figure 8.

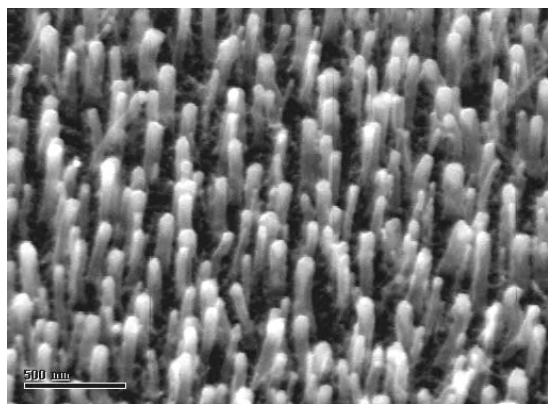


Figure 6. MWNFs grown in a plasma reactor. (Image courtesy of L. Delzeit.)

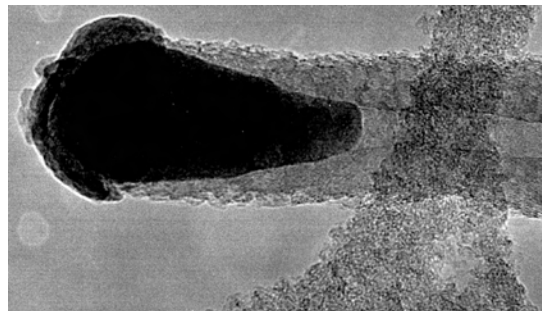


Figure 7. TEM image of one of the fibers in Figure 5 showing an Fe particle at the tip.

It was mentioned in Section 2.2 that a variety of plasma sources is used by the nanotube community. Figure 9 shows well-aligned, individual, freestanding MWNFs using a dc plasma-assisted hot-filament CVD. The SEM image shows that catalyst particles remain at the top of the MWNFs. In this case, the silicon substrate contains a 100 nm Cr barrier layer and a 20 nm nickel catalyst layer. The catalyst layer is pretreated with 80 sccm of NH_3 at 4 torr for about 10 min with filament heating. For MWNF deposition, 35 sccm of C_2H_2 is used. The dc bias on the substrate is 550 V. The height of MWNFs in Figure 9 is about 10 μm for a growth time of 20 min. In order to obtain the type of vertical structures shown in Figures 6 and 9 with thermal CVD, one needs to use porous templates to hold the catalysts. For example, Li et al. [36] grew vertical MWNTs by using a porous alumina template in which the pore spacing can be controlled.

5. GROWTH MECHANISMS

Nanotube growth on catalyst particles has similarities to traditional gas–solid interaction processes such as thin-film deposition on substrates. The process proceeds according to the following sequence of steps, and one or more of these steps may be rate controlling, which varies from case to case and requires careful experimental analysis:

1. diffusion of precursor(s) through a thin boundary layer to the substrate
2. adsorption of species onto the surface
3. surface reactions
4. desorption of product species
5. diffusion of species through the boundary layer into the bulk stream.

In low-temperature plasmas, the bombardment of positive ions on the substrate may provide the energy needed in step 3 or aid in the desorption in step 4.

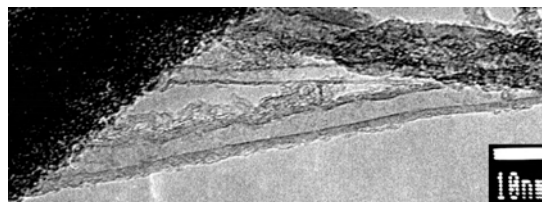


Figure 8. TEM image of an MWNT.

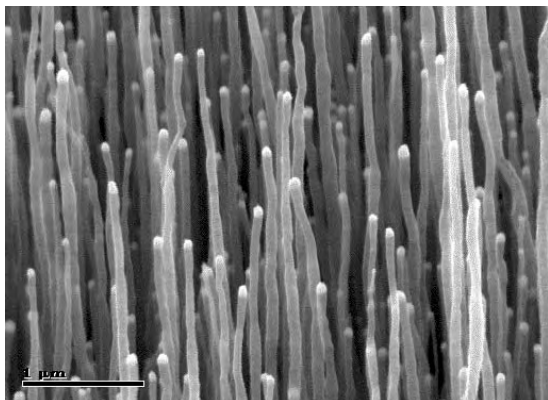


Figure 9. MWNFs grown by dc plasma-assisted hot-filament CVD. (Image courtesy of A. M. Cassell.)

In common processes in microelectronics such as the deposition of silicon, aluminum, silicon nitride, and so on, extensive studies have been performed to identify rate-controlling steps and to understand surface processes. The diamond literature also features numerous such studies. Unfortunately, in CNT growth, there have been no careful experimental investigations to date on this subject. However, earlier studies on carbon filaments in the 1970s discussed the process sequence described above [9–11]. A hydrocarbon such as methane adsorbed onto the catalytic particle surface releases carbon upon decomposition, which dissolves and diffuses into the particle. When a supersaturated state is reached, carbon precipitates in a crystalline tubular form. At this juncture, two different scenarios are envisioned. If the particle adherence to the surface is strong, then carbon precipitates from the top surface of the particle, and the filament continues to grow with the particle anchored to the substrate. This is called the base growth model. In cases where the particle attachment to the surface is weak, then carbon precipitation occurs at the bottom surface of the particle, and the filament lifts the particle as it grows. In this case, the top end of the filament is decorated with the catalyst particle. This scenario is aptly called the tip growth model.

Baker and coworkers [9–11] arrived at the above mechanisms for carbon filament growth based on temperature-dependent growth rates, activation energy for various steps, and electron microscopy observations. It is commonly believed in the CNT community now that the mechanisms for the filament growth apply, by extension, to nanotube growth as well [18, 95]. The most common reason is the visual observation of catalyst particles on the top or bottom ends, as was the case with filament studies.

In CNT literature, the term “vertical alignment” is the most misused. In most cases, any alignment seen is due to the crowding effect, and in SEM images with large-scale bars, crowded CNTs about $0.5\ \mu\text{m}$ and above in height would look well aligned. But individual CNTs within the ensemble grow almost like vines, although the ensemble looks nicely aligned. This is the case with both thermal and plasma CVD. However, individual, free-standing, vertical carbon nanostructures are also enabled by PECVD [8, 75, 84, 85, 88, 89]. Invariably, these are MWNFs, and coinciden-

tally, they all follow the tip growth mechanism. In plasma CVD, it is entirely likely that ion bombardment not only creates particles from thin catalyst films, but also makes their attachment to the surface weak. Hence, the observed tip growth mechanism is not surprising. Merkulov et al. [85] assert that the presence of the catalyst particle at the tip is essential for the vertical alignment of MWNFs. Combining the effects of electric field and the compressive or tensile stress at the particle interface, they argue that the particle at the tip provides a stable negative feedback mechanism assuring vertically aligned growth.

The development of reliable, reproducible, large-scale processes requires an understanding of growth mechanisms, the effect of process parameters on growth characteristics, and gas phase and surface kinetics. Such knowledge is possible only with careful diagnostics and modeling studies. While the CNT literature is full of recipes, growth results, and early application demonstrations, diagnostics and modeling articles are almost nonexistent. A fundamental question in CNT growth relates to the identification of precursor species responsible for growth. In thermal CVD, it is almost unambiguous that the feedstock hydrocarbon reacts at particle surfaces to produce carbon for diffusion into the particles; the temperatures are kept at a level to minimize gas phase pyrolysis of the hydrocarbons [98, 99]. In contrast, the cold plasma in PECVD dissociates the feedstock hydrocarbon, and produces other stable hydrocarbons and very active (high sticking coefficient) radicals in the bulk phase [8, 98]. All of these species, not just the feedstock from the supply tank, reach the catalyst particle surface. This will make the PECVD results different from thermal CVD CNT structures. The situation in PECVD is more complex, and not well understood.

6. APPLICATIONS FOR CVD/PECVD GROWN NANOTUBES

A SWNT grown directly on an AFM cantilever has been shown to be a robust, high-resolution tip for atomic scale imaging [57]. Whereas conventional silicon probes either wear out quickly or even break, SWNT tips wear only slowly. Imaging of metallic, semiconductor, and dielectric surfaces [57], DNAs [59], and proteins with atomic scale resolution has been demonstrated. The use of MWNT tips has allowed us to perform profilometry [58] in integrated-circuit manufacturing, where the need exists to map the depth and shape of holes and trenches. These demonstrations have led to the active development of scale-up techniques to produce hundreds of CNT tip cantilevers on a wafer compared to the current one-at-a-time production.

The ability to grow nanotubes on patterned substrates has potential applications in field emitters, which are being considered for flat panel displays for TV and computer screens and large outdoor displays. CNT-based nanoelectronics is not a near-term technology. Although CNT-based diodes and transistors have been demonstrated, it is not clear what the eventual device, circuit, or architecture will look like, but CVD and related techniques are expected to play a significant role.

Vertically aligned multiwalled nanotubes and fibers, which are free standing, appear to be suitable as electrodes. An

array of such MWNTs reinforced with SiO₂ (in the space between individual tubes) for isolation and mechanical stability has been demonstrated [103]; such gap-filled arrays can be used in biosensor development, where DNA is attached to individual fiber ends [104]. This type of array has also been considered for the development of infrared detectors [106]. When scale-up efforts become successful and the price goes down, SWNTs are expected to play a significant role in structural applications through high-strength, low-weight composites. The field of CNTs is still very young, and it will take another decade or so to see matured technologies and successful commercial applications.

GLOSSARY

Carbon nanotube A cylindrical form of carbon, configurationally equivalent to a two-dimensional graphene sheet rolled into a tube.

Chemical vapor deposition Thin-film preparation technique which relies on source gases or vapor of chemicals which react on a substrate to produce the desirable product film.

Plasma-enhanced chemical vapor deposition Similar to CVD, where gas dissociation is by energetic electrons instead of by thermal heating.

ACKNOWLEDGMENTS

The author thanks Alan Cassell, Bin Chen, and Lance Delzeit for their work covered here, and for providing unpublished figures.

REFERENCES

1. S. Iijima, *Nature* 354, 56 (1991).
2. R. Saito, G. Dresselhaus, and M. S. Dresselhaus, "Physical Properties of Carbon Nanotubes." Imperial College Press, London, 1998.
3. M. Meyyappan and D. Srivastava, Carbon nanotubes, in "Handbook of Nanoscience, Engineering, and Technology." CRC Press LLC, Boca Raton, FL, 2003.
4. M. S. Dresselhaus, G. Dresselhaus, and Ph. Avouris, Eds., "Carbon Nanotubes." Springer, Berlin, 2001.
5. T. Guo, P. Nikolev, A. Thess, D. T. Colbert, and R. E. Smalley, *Chem. Phys. Lett.* 243, 49 (1995).
6. C. H. Kiang, W. A. Goddard, R. Beyers, and D. Bethune, *Carbon* 33, 903 (1995).
7. D. Nolan, D. C. Lynch, and A. H. Cutler, *J. Phys. Chem. B* 102, 4165 (1998).
8. L. Delzeit, I. McAninch, B. A. Cruden, D. Hash, B. Chen, J. Han, and M. Meyyappan, *J. Appl. Phys.* 91, 6027 (2002).
9. R. T. K. Baker, M. A. Barber, P. S. Harris, F. S. Feates, and R. J. Waite, *J. Catal.* 26, 51 (1972).
10. R. T. K. Baker, P. S. Harris, R. B. Thomas, and R. J. Waite, *J. Catal.* 30, 86 (1973).
11. R. T. K. Baker, *Carbon* 27, 315 (1989).
12. H. P. Boehm, *Carbon* 11, 583 (1973).
13. G. G. Tibbetts, *J. Cryst. Growth* 66, 632 (1984).
14. G. G. Tibbetts, M. G. Devour, and E. J. Rodda, *Carbon* 25, 367 (1987).
15. G. G. Tibbetts, *Appl. Phys. Lett.* 42, 666 (1983).
16. H. Dai, A. G. Rinzler, P. Nikolaev, A. Thess, D. T. Colbert, and R. E. Smalley, *Chem. Phys. Lett.* 260, 471 (1996).
17. J. H. Hafner, M. J. Bronikowski, B. R. Azamian, P. Nikolaev, A. G. Rinzler, D. T. Colbert, K. A. Smith, and R. E. Smalley, *Chem. Phys. Lett.* 296, 195 (1998).
18. J. Kong, H. T. Soh, A. M. Cassell, C. F. Quate, and H. Dai, *Nature* 395, 878 (1998).
19. A. M. Cassell, N. R. Franklin, T. W. Tombler, E. M. Chan, J. Han, and H. Dai, *J. Am. Chem. Soc.* 121, 7975 (1999).
20. A. M. Cassell, J. A. Raymakers, J. King, and H. Dai, *J. Phys. Chem. B* 103, 6484 (1999).
21. W. Kim, H. Choi, M. Shim, Y. Li, D. Wang, and H. Dai, *Nanolett.* 2, 703 (2002).
22. B. Kitiyanan, W. E. Alvarez, J. H. Harwell, and D. E. Resasco, *Chem. Phys. Lett.* 317, 497 (2000).
23. M. Su, B. Zheng, and J. Liu, *Chem. Phys. Lett.* 322, 321 (2000).
24. L. Delzeit, B. Chen, A. M. Cassell, R. Stevens, C. Nguyen, and M. Meyyappan, *Chem. Phys. Lett.* 348, 368 (2001).
25. B. Chen, G. Parker, III, J. Han, M. Meyyappan, and A. Cassell, *Chem. Mater.* 14, 1891 (2002).
26. Y. Homma, T. Yamashita, P. Finnie, M. Tomita, and T. Ogino, *Jpn. J. Appl. Phys.* 41, 89 (2002).
27. E. Joselevich and C. M. Lieber, *Nanolett.* 2, 1137 (2002).
28. P. E. Nolan, M. J. Schabel, D. C. Lynch, and A. H. Cutler, *Carbon* 33, 79 (1995).
29. J. Jiao, P. E. Nolan, S. Seraphin, A. H. Cutler, and D. C. Lynch, *J. Electrochem. Soc.* 143, 932 (1996).
30. V. Ivanov, J. B. Nagy, Ph. Lambin, A. Lucas, X. B. Zhang, X. F. Zhang, D. Bernaerts, G. Van Tendeloo, S. Amelinckx, and J. Van Landuyt, *Chem. Phys. Lett.* 223, 329 (1994).
31. M. Yudasaka, R. Kikuchi, T. Matsui, Y. Ohki, S. Yoshimura, and E. Ota, *Appl. Phys. Lett.* 67, 2477 (1995).
32. M. Yudasaka, R. Kikuchi, Y. Ohki, E. Ota, and S. Yoshimura, *Appl. Phys. Lett.* 70, 1817 (1997).
33. P. Chen, H. B. Zhang, G. D. Lin, Q. Hong, and K. R. Tsai, *Carbon* 35, 1495 (1997).
34. Z. W. Pan, S. S. Xie, B. H. Chang, C. Y. Wang, L. Lu, W. Liu, W. Y. Zhou, W. Z. Li, and L. X. Qian, *Nature* 394, 631 (1998).
35. S. Fan, M. G. Chapline, N. R. Franklin, T. W. Tombler, A. M. Cassell, and H. Dai, *Science* 283, 512 (1999).
36. J. Li, C. Papadopoulos, J. M. Xu, and M. Moskovits, *Appl. Phys. Lett.* 75, 367 (1999).
37. R. R. Bacsa, Ch. Laurent, A. Peigney, W. S. Bacsa, Th. Vaugien, and A. Rousset, *Chem. Phys. Lett.* 323, 566 (2000).
38. K. Hernadi, A. Fonseca, J. B. Nagy, A. Siska, and I. Kiricsi, *Appl. Catal. A* 199, 245 (2000).
39. C. J. Lee, D. W. Kim, T. J. Lee, Y. C. Choi, Y. S. Park, Y. H. Lee, W. B. Choi, N. S. Lee, G. S. Park, and J. M. Kim, *Chem. Phys. Lett.* 312, 461 (1999).
40. C. J. Lee, J. H. Park, and J. Park, *Chem. Phys. Lett.* 323, 560 (2000).
41. C. L. Lee, S. C. Lyu, Y. R. Cho, J. H. Lee, and K. I. Cho, *Chem. Phys. Lett.* 341, 245 (2001).
42. H. Kind, J. M. Bonard, L. Forro, K. Kern, K. Hernadi, L. Nilsson, and L. Schlapbach, *Langmuir* 16, 6877 (2000).
43. A. M. Cassell, M. Meyyappan, and J. Han, *J. Nanoparticle Res.* 2, 387 (2000).
44. A. M. Cassell, S. Verma, L. Delzeit, and M. Meyyappan, *Langmuir* 17, 266 (2001).
45. C. Klinke, J. M. Bonard, and K. Kern, *Surf. Sci.* 492, 195 (2001).
46. J. I. Sohn, C. J. Choi, S. Lee, and T. Y. Seong, *Appl. Phys. Lett.* 78, 3130 (2001).
47. Y. S. Han, J. Shin, and S. T. Kim, *J. Appl. Phys.* 90, 5731 (2001).
48. J. M. Ting and C. C. Chang, *Appl. Phys. Lett.* 80, 324 (2002).
49. G. S. Choi, Y. S. Cho, S. Y. Hong, J. B. Park, K. H. Son, and D. J. Kim, *J. Appl. Phys.* 91, 3847 (2002).
50. Y. H. Lee, Y. T. Jang, C. H. Choi, E. K. Kim, B. K. Ju, D. H. Kim, C. W. Lee, and S. S. Yoon, *J. Appl. Phys.* 91, 6044 (2002).

51. C. F. Chen, C. L. Lin, and C. M. Wang, *Jpn. J. Appl. Phys.* 41, 67 (2002).
52. F. Zheng, L. Liang, Y. Gao, J. H. Sukamoto, and C. L. Aardahl, *Nanolett.* 2, 729 (2002).
53. N. Chopra, P. D. Kichambare, R. Andrews, and B. J. Hinds, *Nanolett.* 2, 1177 (2002).
54. A. Cassell, L. Delzeit, C. Nguyen, R. Stevens, J. Han, and M. Meyyappan, *J. Physique IV* 11, 401 (2001).
55. L. Delzeit, C. V. Nguyen, B. Chen, R. Stevens, A. Cassell, J. Han, and M. Meyyappan, *J. Phys. Chem. B* 106, 5629 (2002).
56. J. H. Hafner, C. L. Cheung, and C. M. Lieber, *J. Am. Chem. Soc.* 121, 9750 (1999).
57. C. V. Nguyen, K.-J. Chao, R. Stevens, L. Delzeit, A. M. Cassell, J. Han, and M. Meyyappan, *Nanotechnol.* 12, 363 (2001).
58. C. V. Nguyen, R. Stevens, J. Barber, J. Han, and M. Meyyappan, *Appl. Phys. Lett.* 81, 901 (2002).
59. L. Delzeit, C. V. Nguyen, R. M. Stevens, J. Han, and M. Meyyappan, *Nanotechnol.* 13, 280 (2002).
60. Y. Avigal and R. Kalish, *Appl. Phys. Lett.* 78, 2291 (2001).
61. Y. Zhang, A. Chang, J. Cao, Q. Wang, W. Kim, Y. Li, N. Morris, E. Yenlomez, J. Kong, and H. Dai, *Appl. Phys. Lett.* 79, 3155 (2001).
62. L. Delzeit, R. Stevens, C. Nguyen, and M. Meyyappan, *Int. J. Nanotech.* (2002).
63. B. C. Sathishkumar, A. Govindraj, R. Sen, and C. N. R. Rao, *Chem. Phys. Lett.* 293, 47 (1998).
64. P. Nikolaev, M. J. Bronikowsky, R. K. Bradley, F. Rohmund, D. T. Colbert, K. A. Smith, and R. E. Smalley, *Chem. Phys. Lett.* 313, 91 (1999).
65. M. J. Bronikowski, P. A. Willis, D. T. Colbert, K. A. Smith, and R. E. Smalley, *J. Vac. Sci. Technol. A* 19, 1800 (2001).
66. H. M. Cheng, F. Li, X. Sun, S. D. M. Brown, M. A. Pimenta, A. Marucci, G. Dresselhaus, and M. S. Dresselhaus, *Chem. Phys. Lett.* 289, 602 (1998).
67. H. M. Cheng, F. Li, G. Su, H. Y. Pan, L. L. He, X. Sun, and M. S. Dresselhaus, *Appl. Phys. Lett.* 72, 3282 (1998).
68. L. Ci, S. Xie, D. Tang, X. Yan, Y. Li, Z. Liu, X. Zou, W. Zhou, and G. Wang, *Chem. Phys. Lett.* 349, 191 (2001).
69. H. W. Zhu, C. L. Xu, D. H. Wu, B. Q. Wei, R. Vajtai, and P. M. Ajayan, *Science* 296, 884 (2002).
70. R. Sen, A. Govindaraj, and C. N. R. Rao, *Chem. Phys. Lett.* 267, 276 (1997).
71. R. Andrews, D. Jacques, A. M. Rao, F. Derbyshire, D. Qian, X. Fan, E. C. Dickey, and J. Chen, *Chem. Phys. Lett.* 303, 467 (1999).
72. Y. Chen, Z. L. Wang, J. S. Yin, D. J. Johnson, and R. H. Prince, *Chem. Phys. Lett.* 272, 178 (1997).
73. Y. Chen, L. P. Guo, D. J. Johnson, and R. H. Prince, *J. Cryst. Growth* 193, 342 (1998).
74. L. C. Qin, D. Zhou, A. R. Krauss, and D. M. Gruen, *Appl. Phys. Lett.* 72, 3437 (1998).
75. Z. F. Ren, Z. P. Huang, J. W. Xu, J. H. Wang, P. Bush, M. P. Siegel, and P. N. Provencio, *Science* 282, 1105 (1998).
76. S. H. Tsai, C. W. Chao, C. L. Lee, and H. C. Shin, *Appl. Phys. Lett.* 74, 3462 (1999).
77. Q. Zhang, S. F. Yoon, J. Ahn, B. Gan, Rusli, and M. B. Yu, *J. Phys. Chem. Solids* 61, 1179 (2000).
78. Y. C. Choi, Y. H. Lee, B. S. Lee, G. Park, W. B. Choi, N. S. Lee, and J. M. Kim, *J. Vac. Sci. Technol. A* 18, 1864 (2000).
79. Y. C. Choi, Y. M. Shin, S. C. Lim, D. J. Bae, Y. H. Lee, B. S. Lee, and D. Chung, *J. Appl. Phys.* 88, 4898 (2000).
80. M. Okai, T. Muneyoshi, T. Yaguchi, and S. Sasaki, *Appl. Phys. Lett.* 77, 3465 (2000).
81. C. Bower, W. Zhu, S. Jin, and O. Zhou, *Appl. Phys. Lett.* 77, 830 (2000).
82. H. Cui, O. Zhou, and B. R. Stoner, *J. Appl. Phys.* 88, 6072 (2000).
83. V. I. Merkulov, D. H. Lowndes, Y. Y. Wei, G. Eres, and E. Voelkl, *Appl. Phys. Lett.* 76, 3555 (2000).
84. V. I. Merkulov, M. A. Guillorn, D. H. Lowndes, M. L. Simpson, and E. Voelkl, *Appl. Phys. Lett.* 79, 1178 (2001).
85. V. I. Merkulov, A. V. Melechko, M. A. Guillorn, D. H. Lowndes, and M. L. Simpson, *Appl. Phys. Lett.* 79, 2970 (2001).
86. G. W. Ho, A. T. S. Wee, J. Lin, and W. C. Tjui, *Thin Solid Films* 388, 73 (2001).
87. K. B. K. Teo, M. Chhowalla, G. A. J. Amaratunga, W. I. Milne, D. G. Hasko, G. Pirio, P. Legagneux, F. Wyczisk, and D. Pribat, *Appl. Phys. Lett.* 79, 1534 (2001).
88. M. Chhowalla, K. B. K. Teo, C. Ducati, N. L. Rupersinghe, G. A. J. Amaratunga, A. C. Ferrari, D. Roy, J. Robertson, and W. I. Milne, *J. Appl. Phys.* 90, 5308 (2001).
89. K. B. K. Teo, M. Chhowalla, G. A. J. Amaratunga, W. I. Milne, G. Pirio, P. Legagneux, F. Wyczisk, J. Olivier, and D. Pribat, *J. Vac. Sci. Technol. B* 20, 116 (2002).
90. M. Tanemura, K. Iwata, K. Takahashi, Y. Fujimoto, F. Okuyama, H. Sugie, and V. Filip, *J. Appl. Phys.* 90, 1529 (2001).
91. J. Han, J. B. Yoo, C. Y. Park, H. J. Kim, G. S. Park, M. Yang, I. T. Han, N. Lee, W. Yi, S. G. Yu, and J. M. Kim, *J. Appl. Phys.* 91, 483 (2002).
92. K. Matthews, B. Cruden, B. Chen, M. Meyyappan, and L. Delzeit, *J. Nanosci. Nanotech.* 2, 475 (2002).
93. H. Karczow and A. Ding, *Phys. Rev. B* 60, 11180 (1999).
94. H. Karczow, C. Lenski, and A. Ding, *Phys. Rev. B* 63, 125402 (2001).
95. S. B. Sinnott, R. Andrews, D. Qian, A. M. Rao, Z. Mao, E. C. Dickey, and F. Derbyshire, *Chem. Phys. Lett.* 315, 25 (1999).
96. C. Dateo, T. Gokcen, and M. Meyyappan, *J. Nanosci. Nanotech.* 2, 523 (2002).
97. T. Gokcen, C. Dateo, and M. Meyyappan, *J. Nanosci. Nanotech.* 2, 535 (2002).
98. D. Hash and M. Meyyappan, *J. Appl. Phys.* 92 (2003).
99. N. R. Franklin and H. Dai, *Adv. Mater.* 12, 890 (2002).
100. M. A. Lieberman and A. J. Lichtenberg, "Principles of Plasma Discharges and Materials Processing." Wiley, New York, 1994.
101. O. A. Popov, Ed., "High Density Plasma Sources." Noyes Publications, 1995.
102. Y. Y. Wei, G. Eres, V. I. Merkulov, and D. H. Lowndes, *Appl. Phys. Lett.* 78, 1394 (2001).
103. J. Li, R. Stevens, L. Delzeit, H. T. Ng, A. Cassell, J. Han, and M. Meyyappan, *Appl. Phys. Lett.* 81, 910 (2002).
104. C. V. Nguyen, L. Delzeit, A. M. Cassell, J. Li, J. Han, and M. Meyyappan, *Nanolett.* 2, 1079 (2002).
105. C. V. Nguyen, L. Delzeit, K. Matthews, B. Chin, and M. Meyyappan, *J. Nanosci. Nanotech.* (2003).
106. J. M. Xu, *Infrared Phys. Tech.* 42, 455 (2001).

Carbon Nanotube Sensors

Jun Li, Hou Tee Ng

NASA Ames Research Center, Moffett Field, California, USA

CONTENTS

1. Introduction
 2. Fabrication of Carbon Nanotube Sensing Devices
 3. Applications and Mechanisms of Carbon Nanotube Sensors
 4. Discussions and Future Developments
- Glossary
References

1. INTRODUCTION

Carbon nanotubes (CNTs) belong to a family of materials consisting of seamless graphitic cylinders with extremely high aspect ratios [1–4]. The typical diameters vary from about one to hundreds of nm and the length spreads from tens of nanometers to hundreds of micrometer or even centimeters. The cylindrical structure of CNTs was originally discovered by scientists at NEC in 1993 [5]. Due to their intriguing nanometer scale structures and unique properties, CNTs have quickly attracted intensive attention in the past few years in many fields such as nanoelectronic devices [6–13], composite materials [14], field-emission devices [15, 16], atomic force microscope probes [17–20], and hydrogen/lithium ion storage [21, 22]. Many studies have also reported ultrahigh sensitivity of CNT-based sensors [13, 23–25]. The extremely high surface-to-volume ratio of a carbon nanotube is naturally ideal for efficient gas/chemical adsorption. The one-dimensional quantum wire nature makes their electronic properties very sensitive to gas or chemical adsorption. Both of these factors are essential for achieving high sensitivity of the sensors. In the past few years, CNT sensors have been demonstrated in many applications involving gas molecules, liquid phase chemicals, and biomolecules. CNTs have shown improved performance compared to conventional sensors utilizing materials such as semiconducting metal oxides [26], silicon [27], organic/polymeric materials [28], and carbon black–polymer composites [29]. In this chapter, we intend to summarize the

most recent progress in CNT sensors and discuss the common materials properties and sensing mechanisms behind the different applications.

2. FABRICATION OF CARBON NANOTUBE SENSING DEVICES

2.1. Growth of Carbon Nanotubes

The methods to grow CNTs with desired quantities and qualities for sensor applications were only established in the past few years. A host of experimental approaches have been explored, improved, and modified to successfully synthesize CNTs, both single- and multi-walled, for sensor applications. Commonly used techniques include electrical arc-discharge, laser ablation, and chemical vapor deposition. In most growth processes, a catalyst which is either a metal or a mixed alloy is used.

The growth of single-walled CNTs (SWCNTs), though in small quantities, was first demonstrated by Iijima and Ichihashi [30] and Bethune et al. [31] using the electrical arc-discharge techniques. The SWCNTs were typically accompanied by a substantial amount of amorphous carbon, carbon nanoparticles, and other carbon-based materials. By using the laser ablation method, Smalley et al. [32] have further improved the purity and synthesized amount of SWCNTs on the grams level. The as-synthesized SWCNTs are presented mostly in the form of ropes with individual nanotubes aggregating into hexagonal crystals due to the van der Waals interaction. An example of a SWCNT rope is shown in Figure 1. Subsequent studies by other groups have improved on either the designs or experimental formulations to obtain better quality and larger quantity products. For example, Kajiura et al. [33] have used a newly designed chamber which was equipped with a filtering zone to produce high content of SWCNT ropes under controlled gas flow conditions. Journet et al. [34] have optimized the SWCNT growth by incorporating yttrium and nickel into a carbon anode. Both techniques as mentioned above have also been successfully used to synthesize multiwalled CNTs (MWCNTs).

Recently, chemical vapor deposition (CVD) has gained popularity in synthesizing both SWCNTs and MWCNTs with good yields. A typical growth process involves passing a

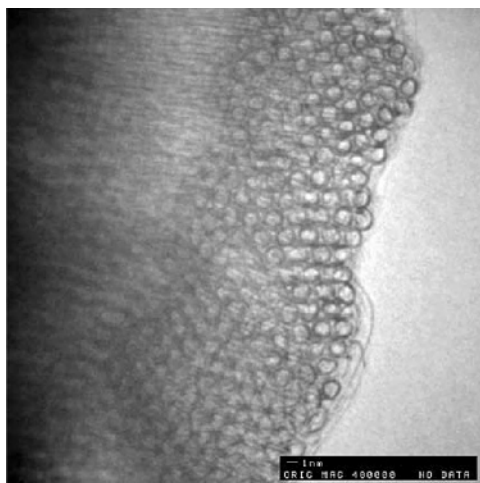


Figure 1. Transmission electron microscopy images of the cross-section of the end of a SWCNT rope made of hundreds of SWCNTs. The scale bar is about 1 nm. Reprinted with permission from [43], A. G. Rinzler et al., *Appl. Phys. A* 67, 29 (1998). © 2002, Springer-Verlag.

hydrocarbon gas over a heated catalyst at high temperature for a period of time. Dai et al. [35] have demonstrated using the techniques to synthesize SWCNTs with high quality by passing methane over alumina supported catalyst in the temperature range of 850–1000 °C. By optimizing the catalyst preparation and growth conditions, the quality and yields of the nanotubes could be further improved as demonstrated, for instance, by the work of Liu et al. [36], Colomer et al. [37], Rao et al. [38], and Smalley et al. [39]. More recently, Smalley et al. [40] have demonstrated large-scale production (10 g/day) of high purity SWCNTs using a gas phase CVD process, termed the HiPco process. By using iron catalytic clusters, formed *in-situ* from $\text{Fe}(\text{CO})_5$, with a high pressure (30–50 atm) and a high temperature (900–1000 °C) process, they have reported that SWCNT material of up to 97 mol% purity could be produced at a rate of 450 mg/h.

With continual effort in the development of growth techniques and methodology, it is expected that CNTs with the desired properties, qualities, and quantities could be obtained in the near future.

2.2. Preparation of Carbon Nanotube Films

The active component of a carbon nanotube sensor (see Section 3) is presented either in the form of a thin film or a single nanotube configuration. In the former, it is usually fabricated separately and integrated subsequently in the device fabrication route, unlike the latter. The fabrication of the thin film CNTs usually starts from the raw CNT materials. Because of the use of catalytic materials, for example, transition metals and metallic species, in the synthesis of nanotubes, the as-synthesized CNTs usually contain certain amounts of these metallic nanoparticles, coexisting with various forms of carbon. In order for the CNTs to be useful in various sensor applications, it is important that they should be free of the impurities and made into the right geometrical configurations. Indeed, various efforts have been demonstrated by researchers to purify CNTs.

Bandow et al. [41] have demonstrated a purification procedure for SWCNTs, which were prepared by pulse laser ablation, that separates coexisting carbon nanospheres (CNS), metallic nanoparticles (MN), polyaromatic carbon, and fullerenes from the SWCNT fraction. According to the reported procedure whereby no oxidation treatment was used, the process involved first the suspension of CNS, MN, and SWCNTs in nonaqueous solution using a cationic surfactant and then subsequent trapping of SWCNTs on a membrane filter. Approximately 84 and 6 wt% of purified SWCNTs and CNS can be separated respectively from the as-prepared samples. Using an alternative method which incorporates hydrothermal treatment along with Soxhlet extraction of fullerenes, oxidation, and strong acid dissolution of metallic particles, Tohji et al. [42] have shown a purification approach to obtain arc-discharge SWCNTs with purity ~ 95 wt%. For large-scale purification of CNTs, Rinzler et al. [43] have demonstrated a readily scalable process capable of handling SWCNTs in large batches. The typical purification process begins with refluxing the as-synthesized samples in strong nitric acid, followed by repetitive washing/centrifugation and filtration cycles. The finished product could then be readily peeled off the filter membrane to produce a freestanding mat, the so-called “bucky paper.” Another treatment approach, which involved air oxidation at elevated temperature as the first step and subsequent micro-filtration, was reported by Shi et al. [44] to obtain more than 90% purity SWCNTs. Cinke et al. recently reported SWCNTs with purity up to 99.6% after a two-step purification process [45].

To quantify the effectiveness of the purification process, microscopic techniques such as scanning (Fig. 2) or transmission electron microscopy have been used to investigate the microstructures of the treated samples. Alternatively, spectroscopic techniques including Raman spectroscopy and analytical techniques such as thermogravimetric analysis have been used to determine the quality of the treated samples.

2.3. Fabrication of Sensing Devices

Depending on the sensing applications, different device architectures and fabrication routes are required to successfully achieve their desired functions. Common to all, carbon nanotubes as the critical components of the sensing devices are integrated either directly or indirectly during the fabrication routes. A variety of different methods, ranging from advanced micro- or nano-lithographic techniques to hand-made processes, have been demonstrated by various researchers to build functional devices.

In the arena of gas sensing devices, both single and thin film CNTs have been utilized. To fabricate single SWCNT field-effect gas sensors, Soh et al. [46] and Kong et al. [13] have combined a synthesis method and microfabrication techniques to obtain CNT-based electrical circuits on a silicon substrate with controllable positions and length (ranging from 300 nm to 10 μm). The electrical circuits could then be connected to macroscopic electrodes leading to external monitoring devices. In a typical fabrication process, three steps of electron beam lithography using polymethylmethacrylate as the resist were involved. As depicted

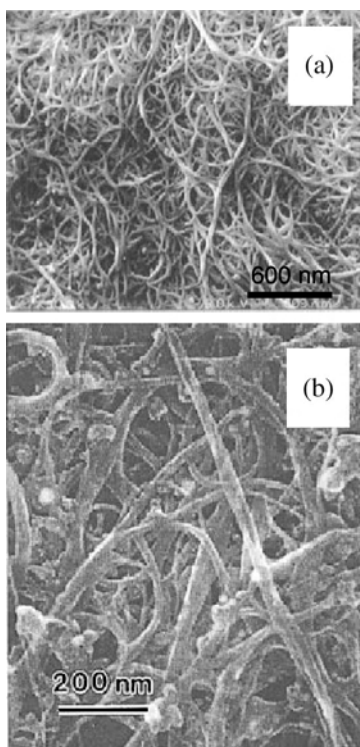


Figure 2. Scanning electron microscopy images of purified SWCNTs prepared by (a) dc arc-discharge and (b) laser pulse ablation. (a) Reprinted with permission from [42], K. Tohji et al., *J. Phys. Chem. B* 101, 1974 (1997). (b) Reprinted with permission from [41], S. Bandow et al., *J. Phys. Chem. B* 101, 8839 (1997). © 1997, American Chemical Society.

in Figure 3, the first step involves patterning of the Ti/Au alignment marks on the Si substrate. In the second step, regular windows ($5\ \mu\text{m} \times 5\ \mu\text{m}$) were formed in the resist followed by deposition of the catalyst. Next, the resist was removed, leaving behind the patterned catalyst islands. Carbon nanotubes were then synthesized via methane CVD to bridge between the islands. A final step involving patterning of the electrical contact pads over the catalyst islands was performed to complete the devices. The as-described approach has been reported to allow a large number of integrated CNT sensors to be built in an array although various issues including the interface between the nanotube and catalyst metal as well as metal contact electrodes remain to be investigated.

A simpler fabrication route which involved deposition of dichloroethane-dispersed SWCNT thin film onto silicon dioxide substrates with prepatterned gold electrodes was adopted by Collins et al. [23] to realize gas sensing. The approach was adapted by Sumanasekera et al. [24], without the underlying gold electrodes, to fabricate gas sensors for detection of hydrocarbons. Using a different fabrication route, Ng et al. [25] have used freestanding MWCNT thin films grown from soft-lithography-mediated selective CVD approach to successfully integrate a flexible polydimethylsiloxane (PDMS) framework into microsensing devices. As shown in Figure 4A, a PDMS substrate with integrated ultra-sharp polymeric probes was first fabricated by a micromolding technique [21]. This was then followed by an imprint

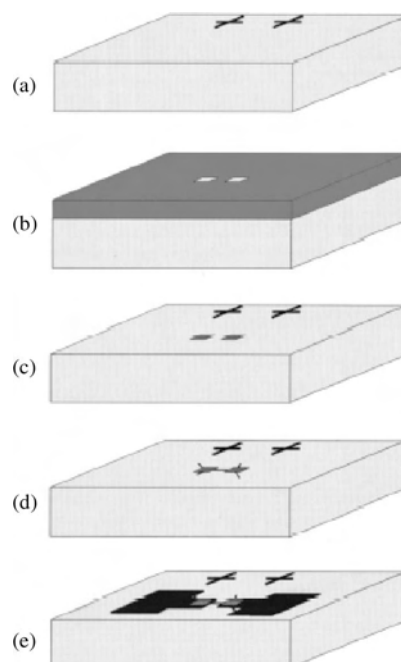


Figure 3. Schematic of processing steps to fabricate SWCNT FET sensors. Reprinted with permission from [46], H. T. Soh et al., *Appl. Phys. Lett.* 75, 627 (1999). © 1999, American Institute of Physics.

process and Au evaporation to lay down the contact pads. The MWCNT membrane was then anchored by spreading onto the polymeric probes' region, which simultaneously overlaid onto the Au contact pads (Fig. 4C). Another PDMS slab with an opening was then bonded permanently onto the framework. Using a different platform, Chopra et al. [47] have demonstrated that either SWCNTs or MWCNTs could be casted as a thin film on an etched copper conductor circuit sitting on a Duroid board to achieve resonator based remote gas sensing.

The aforementioned gas sensors are typically solid-state devices. However, with simple adaptation and modification, liquid-phase chemical sensors could be fabricated as well. As demonstrated by Nugent et al. [48], a MWCNT microbundle was picked out from a boule produced by electrical arc-discharge and physically attached to the end of a copper wire electrode using a conductive silver paint. The electrode assembly was then placed in a typical electrochemical setup such that only the nanotube bundle came into contact with the solution. Alternatively, it has been shown by Britto et al. [49] and Li et al. [50] that random CNTs (mixed thoroughly with bromoform) and bulky paper strips respectively could be packed inside a glass tube to serve as a working electrode for the detection of electrochemical active species.

While using a bottom-up integrated approach, Li et al. [51] have demonstrated uniquely the fabrication of vertical arrays of CNTs on a silicon substrate which could serve as a chemical and biosensor upon attachment of biomolecular or chemically active species as shown in Figure 5. The vertically aligned MWCNTs were first grown using dc biased hot-filament plasma CVD on a metal film covered silicon substrate. They were then subjected to tetraethyloxysilicate (TEOS) CVD for gap-filling of SiO_2 . SiO_2 dielectrics was found conformally filled in the gap between individual

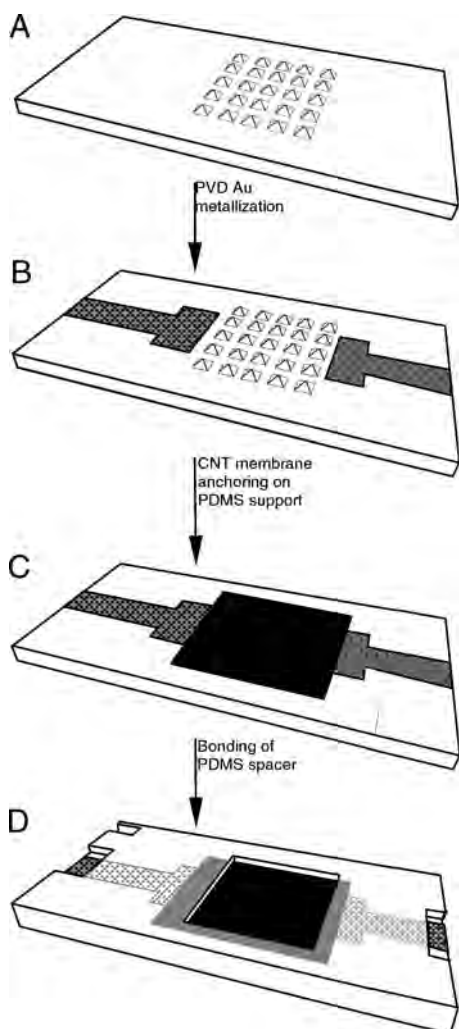


Figure 4. Schematic of processing steps to fabricate a MWCNT film sensor.

MWCNTs and hence reinforced the MWCNT array. The excess SiO_2 was subsequently removed and allowed the exposure of MWCNT tips via a mechanical polishing step. The fabrication route is reported to be suitable for fabricating various nanoelectronic devices besides sensor applications.

3. APPLICATIONS AND MECHANISMS OF CARBON NANOTUBE SENSORS

3.1. Gas Sensors

As we mentioned earlier, CNTs have a common property in their large surface-to-volume ratio. This makes them potentially very useful adsorbent materials. In particular, extensive work has been focused on their potential as ultrahigh H_2 storage medium [21, 52–54]. Rich literature including both theoretical and experimental efforts can be found on the gas adsorption phenomena on various CNTs prepared and treated with different methods. For the interests of applications in gas sensors, we address only the work relevant to electronic properties of CNTs, the change of which, upon

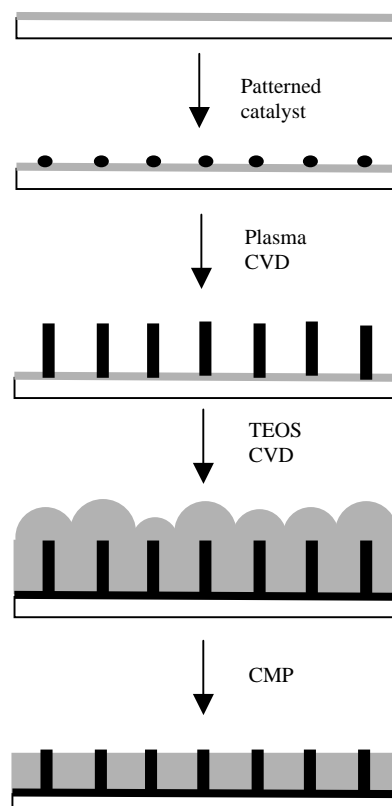


Figure 5. Schematic of processing steps to fabricate vertical carbon nanotube nanoelectrode arrays by a bottom-up method. Reprinted with permission from [51], J. Li et al., *Appl. Phys. Lett.* 81, 910 (2002). © American Institute of Physics.

gas adsorption, can be readily transduced into measurable sensing signals. By far, most reported CNT gas sensors are based on these transduction mechanisms.

3.1.1. Adsorption of Gas Molecules on Carbon Nanotubes

In the last section, we described the structures of SWCNTs, MWCNTs, SWCNT bundles/ropes, and SWCNT/MWCNT films. Obviously, each type of CNT has quite different absorbing properties for different gases. Even in the simplest case of a single SWCNT, the gas adsorption and its effects on CNT properties depend strongly on the chirality of the CNT, which is generally assumed to be randomly distributed with two-thirds of it semiconducting and the remaining one-third of it metallic. On the other hand, most of the transport studies of CNTs were carried out under ambient conditions, which are inevitably affected by the oxygen adsorption [55]. It is important to understand the fundamental issues of gas adsorption on CNTs.

The dependence of electronic properties on chemical environment was first reported by Kong et al. [13] based on the study of a single SWCNT field-effect transistor (FET). Collins et al. [23] and Sumannasekera et al. [24] later reported that both electrical resistance R and thermoelectric power (TEP) S of SWNT bundles and thin films are sensitive to gas adsorption. Upon exposure to O_2 , NO_2 , or NH_3 gases, the conductance of semiconducting tubes is changed dramatically, presumably due to the charge transfer from

the adsorbates [13, 23]. The TEP of SWNT bundles was also found to be sensitive to inert gases such as N_2 and He due to the collision with CNT walls [24]. Theoretically, it has been shown that O_2 adsorption has a significant effect on the electronic properties of small semiconducting nanotubes [55]. Zhao et al. studied the electronic properties of three types of SWCNTs, that is, semiconducting zigzag (10,0) and (17,0) tubes and metallic armchair (5,5) tubes upon the adsorption of O_2 , NO_2 , NH_3 , CO_2 , CO , H_2O , N_2 , H_2 , and He with first principles methods [56]. It was found that O_2 and NO_2 are electron acceptors (-0.06 to -0.14 electron per molecule) with relatively larger adsorption energy (~ 0.30 to 1.0 eV) while all other gas molecules are electron donors with negligible charge transfer (~ 0.01 to 0.035 electron per molecule) and weak binding (< 0.15 eV). Generally, all the gas molecules studied are weakly physisorbed on CNT surfaces. Charge fluctuation of even the weakly bonded molecules was found to have a pronounced effect on the transport properties of metallic SWCNT, consistent with previous experimental studies [24].

Most as-prepared SWCNTs, particularly those by high temperature techniques such as arc-discharge and laser ablation methods, are long and capped (i.e., sealed at the ends). Only the exterior surfaces are considered accessible by gas molecules. However, the long SWCNTs can be uncapped or cut into short open tubes by acid treatment [45, 57, 58]. The open tubes expose the internal channels to gas molecules resulting in a much larger adsorption. A study using CH_4 adsorbate shows a large hysteresis loop after nitric acid treatment, indicating the capillary condensation inside the nanotube [59]. The diameter of a carbon nanotube is expected to be important in defining the adsorption of gases inside the internal pores of CNTs. A grand canonical Monte Carlo simulation work found that the preferential adsorption of gas molecules with different size in a binary mixture can be switched by controlling the internal diameter of the tube and the temperature [60].

Commonly, SWCNTs pack together into bundles (or ropes) due to van der Waals interaction as revealed by Thess et al. [32]. As a result, there are at least four distinct sites in which gas molecules can adsorb (see Fig. 6) [61]. The interior *pore* of an individual tube, as we mentioned earlier, is only one of them. The other three sites are all related to the exterior surfaces of individual tubes, including: (1) the external bundle *surface*, (2) the *groove* formed at the contact between adjacent tubes on the bundle outer surface, and (3) inside an interstitial *channel* at the contact of three tubes in the bundle interior [60]. Depending on the size and wettability, some of these sites might be excluded for specific gas molecules. For hydrogen adsorption, it has reported that the binding energy (E_B) at these sites following the order $E_B(\text{channels}) > E_B(\text{grooves}) > E_B(\text{pores}) > E_B(\text{surface})$ [61, 62]. Williams et al. calculated the binding energy and specific surface area contributions (σ) of these sites to be (1) channels: $E_B = 0.119$ eV, $\sigma = 45$ m²/g, (2) grooves: $E_B = 0.089$ eV, $\sigma = 22$ m²/g, (3) pores: $E_B = 0.062$ eV, $\sigma = 783$ m²/g, and (4) surfaces: $E_B = 0.049$ eV, $\sigma = 483$ m²/g [61, 62]. Clearly, the channels and grooves have much larger binding energy but less available surface area. The outer surface has only weak adsorption consistent with the

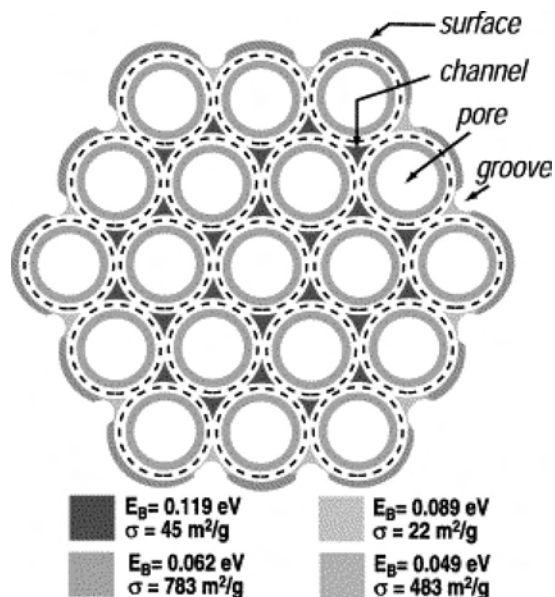


Figure 6. Schematic structure of a SWCNT bundle showing different sites for gas adsorption. Reprinted with permission from [65], C. K. W. Adu et al., *Chem. Phys. Lett.* 337, 31 (2001). © 2001, Elsevier Science.

study of a single SWCNT surface [56]. These studies provide a good fundamental understanding of the gas adsorption on SWCNTs. For individual MWCNTs and MWCNT films, much less work has been done due to the complexity in tube structure. However, both the external and internal surfaces are expected to contribute to the gas adsorption. The defects, in particular, could play a more important role in changing the electrical properties of MWCNTs upon gas adsorption.

3.1.2. Gas Sensors Based on Single Carbon Nanotube FETs

The Si-based field-effect transistors are sensitive to the electron transfer induced by gas adsorption and therefore could be used as gas sensors for certain applications [27]. SWCNTs are known to be semiconducting if their chirality (m, n) satisfies $m - n \neq 3 \times \text{integer}$. It was demonstrated that a semiconducting SWCNT (S-SWCNT) connected to two metal electrodes exhibits *p*-type transistor characteristics with the conductance tunable over several orders of magnitude by changing the gate voltage applied on the Si substrate [13]. Such a phenomenon was attributed to the adsorption of O_2 as electron acceptor in ambient environment. The theoretical work mentioned above predicts about 0.1 electron transfer per O_2 molecule [56]. With the typical diameter (~ 2 nm) and length (~ 3 μm) of the S-SWCNT in the FET device (see Fig. 3), the adsorption/desorption of even a single O_2 molecule can produce about a 1×10^{16} e/mm³ charge density in the SWCNT if simply calculated from the volume. This is about the level of the charge density in a moderately doped Si device. In reality, the quantum wire nature of SWCNT makes the conductance of the tube even more sensitive to any local charge along the one-dimensional

wire. Therefore, the sensitivity of single molecule adsorption/desorption could, in principle, be achieved with such miniaturized S-SWCNT FETs.

Kong et al. [13] demonstrated that the conductance of a single S-SWCNT sample decreased by about 100-fold after exposure to NH_3 (0.1 to 1% in Ar or air) for about 10 minutes. On the other hand, exposure to NO_2 molecules [2 to 200 parts per million (ppm) in Ar] increased the conductance of the S-SWCNT sample by about 1000 times when it was initially depleted by a back-gate voltage (V_g) of +4 V. The sensitivity, that is, the ratio between the resistance after and before gas exposure ($R_{\text{after}}/R_{\text{before}}$), was found to be significantly better than other room-temperature operated gas sensors based on conventional materials. Since the SWCNT is a hole-doped semiconductor, the adsorption of electron donating NH_3 molecules causes the hole depletion and reduced conductance while NO_2 exposure results in enriched hole carriers and enhanced conductance. The chemical nature of the gas molecules is indicated in the I - V_g curve which is characteristically shifted by -4 V after exposure to NH_3 and shifted by $+4$ V after exposure to NO_2 . It is possible to fabricate arrays of such miniaturized sensing devices with ultrahigh sensitivity as well as chemical characteristics. A significant drawback is the slow recovery time (~ 12 hr) after exposure to NO_2 , which is likely due to the slow desorption of strong adsorbates. The influence of O_2 in the ambient environment to the initial sample is also worth further investigation. Much more systematic study is still needed to develop this system for practical applications.

3.1.3. Electrical Resistance Based Gas Sensors

Molecular interactions were found not only to affect the conductance of a single S-SWCNT but also to change that of bulk samples consisting of SWCNT bundles/ropes. Br and I intercalations were reported to enhance the conductance of bulk film consisting of SWCNT ropes [62, 63]. Kong et al. demonstrated that the resistance of a SWNT mat decreased to about a half of the original value after exposure to a 200 ppm NO_2 flow for ~ 10 min while it increased to about 1.5 times of the original value in a 1% NH_3 flow [13]. Apparently, both metallic and semiconducting SWCNTs in the bulk sample are affected by the gas adsorption. The effect of different gas molecules such as NH_3 and NO_2 on the bulk sample is very consistent with that of the single S-SWCNT transistors.

Collins et al. also found that the electrical resistance R measured with a thin film of SWCNT bundles is particularly sensitive to O_2 in the environment [23]. An experiment measuring the electrical resistance switched by 10 to 15% as the chamber was alternately flooded with air or evacuated to $\sim 10^{-6}$ Torr. Measurable changes in R were found at oxygen partial pressure as low as 10^{-10} Torr. However, other major gas constituents of air such as N_2 , CO_2 , H_2O , etc. and inert gas molecules such as Ar and He have little effect on the electrical properties of the SWCNT film. Further transport experiments indicate that once SWCNTs have been exposed to oxygen, it is not possible to fully deoxygenate them at room temperature even under high-vacuum conditions. This irreversibility is similar to that of

NO_2 adsorption on a S-SWCNT transistor gas sensor, which limits the application of CNTs in gas sensors.

Apparently, electron acceptors such as O_2 and NO_2 have dramatic effects on the electrical properties of SWCNTs. Many previously reported electronic properties of CNTs are dominated by preadsorbed O_2 from ambient environment. The slow recovery time or irreversibility is likely due to the strong adsorption or capillary effects, particularly when using open-ended SWCNT bundles. MWCNTs with much larger tube diameter, on the other hand, can change from microporous (such as SWCNT bundles) to mesoporous or even macroporous materials. MWCNTs could potentially have much less interaction with the gas molecules. The sensitivity of electrical resistance R to the gas environment may drop but the reversibility could be improved.

Ng et al. reported a study of gas sensing using a $1.5 \text{ mm} \times 1.5 \text{ mm} \times 25 \mu\text{m}$ freestanding MWCNT membrane grown on a polymer template by thermal CVD (as shown in Fig. 4) [25]. Due to the decomposition and shrinkage of the polymer material, the MWCNT-catalyst composite membrane peeled off from the substrate while still maintaining the desired pattern from the substrate. Thus formed membrane contains loosely entangled MWCNTs mixed with catalyst and carbon particles. As shown in Figure 7, simple electrical resistance measurements following cycling the chamber pressure between ambient atmosphere and high vacuum

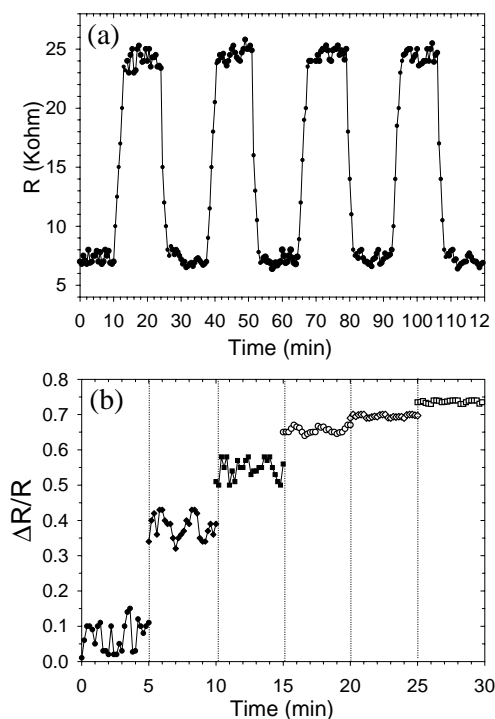


Figure 7. Variations in the electrical resistance (R) of the MWCNT membrane with the surrounding medium, (a) spontaneous changes in R while cycling the environment between vacuum and ambient atmosphere, and (b) the ratio of the electrical resistance drop from the value at the base pressure vs different oxygen dosing pressure: ●, 6.4×10^{-7} Torr; ◆, 3.1×10^{-4} Torr; ■, 9.0×10^{-4} Torr; ○, 1.4×10^{-3} Torr; ◇, 2.7×10^{-3} Torr. Reprinted with permission from [25], H. Ng et al., *J. Nanosci. Nanotech.* 1, 375 (2001). © 2001, American Scientific Publishers.

show a very reversible response. R drops by a factor of three (from about 24 to about 7 kOhm) when venting the vacuum with air. Similar to Collins et al. [23], Ar or N_2 did not show any effect. The recovery time is about 2 to 3 minutes which is likely limited by the pumping and venting speed. Stepwise increase of the oxygen base pressure indicates that R is most sensitive to O_2 in the range from 10^{-6} to 10^{-3} Torr. About 80% of the changes in R occurred at oxygen base pressure less than 10^{-3} Torr. Over about 3×10^{-3} Torr, the change in R is saturated likely because all the surface sites have already been occupied.

It is worth noting that most studies [13, 23, 25] were carried out at room temperature, at which oxygen is difficult to remove once they adsorbed onto the CNTs. As a result, the measured electrical resistance R was dominated by the preadsorbed O_2 molecules and little change was observed when exposing the sample to inert gases such as N_2 and Ar. However, Sumanasekera et al. found that the four-probe electrical resistance $R(T)$ of a mat of SWNT bundles showed easily measurable change even upon exposure to 1 atm of N_2 or He after being degassed in high vacuum at elevated temperature (~ 500 K) [24]. The change in R is small (~ 2 – 3% increase from vacuum to 1 atm N_2 and $\sim 10\%$ increase from vacuum to 1 atm He). The recovery time is slow (>2 hr) but quite reversible. The increase in R upon exposure to inert gas was attributed to the gas collisions with the nanotube wall.

3.1.4. Thermoelectric “Nanonoses”

The thermoelectric power (TEP) S , defined as

$$S = \Delta V / \Delta T \quad (1)$$

where ΔV and ΔT are voltage difference and temperature difference between two spots in the sample, is another parameter strongly correlated with the electronic properties of the materials. Collins et al. studied the change in TEP upon cycling the environment between vacuum and pure atmospheric pressure oxygen [23]. The response was found to be in good consistency with the change of R . The oxygen exposed SWCNT film has a positive TEP of about $+20 \mu\text{V/K}$. The value quickly decreases and reaches about $-10 \mu\text{V/K}$ a few minutes after oxygen was removed from the chamber. This phenomenon was attributed to the change in the carrier (hole) density upon the adsorption/desorption of O_2 as electron acceptors.

Eklund et al. did a series of careful work at elevated temperature (~ 500 K) at which the adsorption/desorption of both strong adsorbates and inert gas molecules is completely reversible [24, 65, 66]. They attributed the strongly negative TEP after degassing to the change of metallic tubes to n -type semiconductors. As we mentioned earlier, at 500 K, easily measurable electrical resistance change was obtained even upon exposure to inert gases. Both TEP and the SWNT bundle resistivity ρ can be measured at different wt% of gas adsorption. Eklund et al. [65] attributed the total bundle resistivity to two things: (1) the scattering mechanisms preexisting in the bundle before gas adsorption (ρ_0), for example, from phonons and wall defects, and (2) the extra impurity scattering due to the adsorbed gas (ρ_a) with

$$\rho = \rho_0 + \rho_a \quad (2)$$

Approximately, the TEP and resistivity have the Nordheim–Gorter (NG) relation as

$$S = S_0 + (\rho_a / \rho_0)(S_a - S_0) \quad (3)$$

where S_0 and S_a are the contributions to the thermoelectric power from the host resistivity ρ_0 and additional impurity resistivity ρ_a from the adsorbed gas, respectively. If the gas molecules are physisorbed on the tube walls by van der Waals interaction, E_F will be unaffected and $(S_a - S_0)$ is a constant, resulting in linear NG curves as shown in Figure 8 for N_2 , He, and H_2 . On the other hand, strong chemisorption has a much more profound effect on the host band structure and E_F . Thus, $(S_a - S_0)$ must depend on the gas coverage, resulting in nonlinear NG plots as shown in Figure 8 for O_2 and NH_3 . It is noteworthy that the NG plots for even inert gases such as N_2 , He, and H_2 are significantly distinct from each other. Potentially, the NG plots at elevated temperature can differentiate different molecules and find applications in thermoelectric “nanonose” as proposed by Eklund et al. [65].

3.1.5. Remote Gas Sensors

The above-mentioned gas sensors based on single CNT FET, electrical resistance, and TEP all rely on direct electrical connections to the sensing elements exposed in the sampling environments. For some applications such as detection of corrosive gases and samples in sealed environments, remote or non-direct-contact sensors are required. Recently, Chopra et al. reported a carbon-nanotube-based resonant-circuit sensor for ammonia [47]. Similar to the electrical resistance and TEP sensors, tens of micrometer thick CNT film was used as the adsorbent material due to the large uptake capability defined by its huge surface area. Both

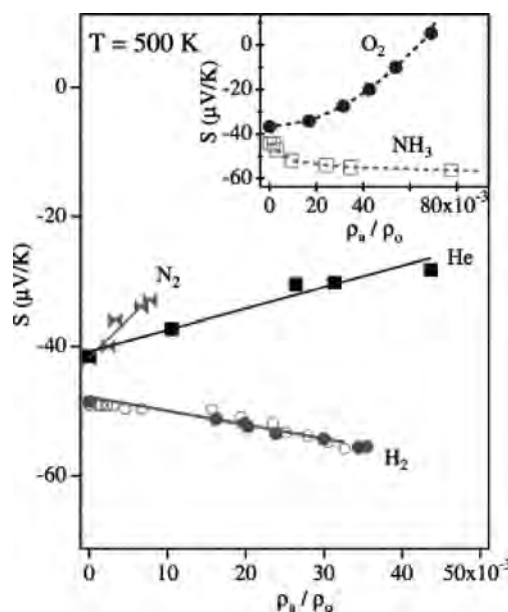


Figure 8. NG plots (S vs ρ) showing the effect of gas adsorption on the electrical properties of the SWCNT mat. Reprinted with permission from [65], C. K. W. Adu et al., *Chem. Phys. Lett.* 337, 31 (2001). © 2001, Elsevier Science.

SWCNTs and MWCNTs were used. The CNT films were simply deposited on a disk shaped Cu resonator on a Duroid board. A radio frequency transmitter sends a microwave signal to the interrogation region of the Cu resonator, producing a strong signal at its resonant frequency (~ 4 GHz). The resonant frequency was found shift downward by a few MHz after exposure to NH_3 gas over ~ 100 ppm. The response and recovery time were found to be about 10 min, a reasonable short time. The resonant frequency shift was attributed to the change in the effective dielectric constant of the CNT film upon exposure to NH_3 . In principle, other strong adsorbates may affect the downshift of the resonant frequency differently and the chemical nature of the gas may be derived. Even though the sensitivity is low, the remote sensor may find applications in certain corrosive or toxic environments as well as those that require nondestructive testing.

3.2. Liquid-Phase Chemical Sensors

From the structural point of view, the main body of CNTs, particularly MWNTs, can be considered as graphitic layers rolled into cylinders. The sidewall of CNTs is expected to present similar physical and electronic properties to the graphite basal plane. The studies discussed in previous sections on the gas adsorption on the sidewall of CNTs is, in many aspects, consistent with previous studies on graphite surfaces [67–69] except for the difference in the surface area. Along the tube axis, it is expected to present high conductivity similar to graphite in-plane properties. For SWCNTs, the large curvature and small tube dimension are likely to cause interesting quantum effects to deviate from graphite properties. The electronic properties of SWCNTs are also easily affected by adsorbates since almost every carbon atom is exposed at the surface. MWCNTs, on the other hand, have essentially only the outmost and innermost shells exposed to other molecules and thus are less sensitive to the perturbation from adsorbates. Their larger size also makes them more similar to graphite cylinders. In liquid solutions, the sidewall of MWCNTs is expected to present an anomalously small effective capacitance and a slow electron transfer rate similar to graphite basal plane electrodes. However, the open end is a very active electrode similar to the graphite edge plane. Electron transfer along the tube axis is expected to be fast similar to that within a graphite plane. These properties made CNTs, particularly MWCNTs, very interesting electrode materials. Electrons could be caught at the active end and transported along the tube to the other end without much interference from the solution. For this purpose, the interest is in the nanostructure of CNTs which improves the performance over conventional materials rather than the influence of their electronic properties by other molecules. In this section, we summarize some of the studies using CNTs as electrodes, which may potentially lead to dramatic improvements in the performance of current chemical and biological sensors by incorporating unique properties of CNTs.

Nugent et al. demonstrated an ideal Nerstain behavior of the $\text{K}_4\text{Fe}(\text{CN})_6$ reaction using an open end WCNT bundle produced by electric arc-discharge [70]. The fast electron transfer rate from the tube ends along the tube axis agrees well with the cylindrical graphite model. Ideal reversible

cyclic voltammeteries were also obtained in measuring the oxidation of neurotransmitter dopamine [48] and redox proteins such as cytochrome *c* and a “blue” copper protein azurin [71]. Efficient electrocatalytic reduction of dissolved O_2 was also demonstrated [72]. However, all these studies use compact CNT paste or big bundles in which CNTs mixed with each other as well as organic binders in an uncontrolled way. Even though the specific capacitance of the graphitic sidewall is relatively small, they still contribute a huge capacitive background due to the enormous surface area [49, 73, 74]. For chemical sensor applications, the exposed surface area needs to be minimized. It was demonstrated that a loosely packed MWCNT membrane is able to detect neurotransmitter catechols at concentrations down to a few μMs [25]. A series of CNTs with different densities was carefully studied by Li et al. to explore these issues [50].

Much work is desired to develop well-defined CNT electrodes from both the fundamental and application points of view. Campbell et al. demonstrated that single MWCNTs ~ 80 – 200 nm in diameter and 15 – 50 μm in length show reversible characteristic steady-state radial diffusion behavior consistent with fast electron transfer [75]. The sidewall of the CNT can be insulated with polymer and only the very end of the tube is exposed. This can find unique applications in the analysis of redox biospecies such as neurotransmitters and proteins in a live single cell [76].

Another effort in the development of well-defined CNT electrodes was demonstrated by NASA scientists using vertically aligned MWCNTs [50]. Li et al. used vertically aligned CNTs with an average diameter of ~ 50 – 100 nm and nearest-neighbor distance of ~ 200 – 500 nm on metal coated Si substrates. SiO_2 was deposited by TEOS CVD to insulate both CNTs and substrate metal layers. A mechanical polishing process followed to planarize the sample to remove excess materials which results in an array of nanoelectrodes with only the open ends of MWCNTs exposed. This method provides a unique bottom-up scheme to fabricate nanoelectrode ensembles (NEEs) similar to those demonstrated by Menon and Martin [77] by filling metals into the one-dimensional pores in the filtration membranes. The sensitivity is expected to be improved by orders of magnitude for measuring small redox species using such NEEs compared to conventional electrodes. Ordered nanoelectrode arrays with precisely controlled size and density could be achieved by employing appropriate lithographic techniques. The nanoelectrode array approach is very promising since it takes full advantage of CNTs via miniaturization to achieve ultimate sensitivity and may be incorporated into microfluidic devices, microelectromechanical systems (MEMS) chromatography instruments, and biomedical/environmental monitoring devices.

3.3. Biosensors

As we described in the discussion of S-SWCNT FET gas sensors [13], even small electron transfer between S-SWCNT and adsorbates can cause a significant change in the conductance of the device. Biomolecules such as DNA, RNA, and proteins are all heavily charged molecules in most conditions. The adsorption of such molecules onto the CNT

surface is expected to change its electronic properties similar to gas molecules. Therefore, the FET devices could be employed as biosensors. Particularly, recognition of specific biomolecules could be realized through the specific interaction with preimmobilized molecules. For this purpose, the functionalization of biomolecules such as DNA and proteins was intensively pursued in the past few years.

Dai et al. have reported a series of work for sidewall functionalization of single SWCNTs for protein immobilization [78, 79]. The SWNT is intended to be used as the sensing element based on its electronic properties. As a result, the graphitic sp^2 sidewall structure has to be preserved. Noncovalent bonding of some precursor molecules on the CNT sidewall was demonstrated for this purpose, either by the π -stacking of the conjugate pyrenyl group of 1-pyrenebutanoic, succinimidyl ester, or coating with a surfactant (Triton) mixed with amine-terminated poly(ethylene glycol). Both methods efficiently modified the CNT surface and incorporated functional groups so that further covalent bonding of protein molecules such as biotin can be followed. The functionalized CNTs were then demonstrated with specific recognition of ferritin and streptavidin. These methods can be extended to the recognition of other biomolecules based on specific interactions of antibody-antigen and complementary DNA strands. However, the response in electrical conductance has not been reported so far.

The very end of the CNT, particularly the open end, is chemically much more active due to the dangling sp^2 bonds similar to the graphite edge plane. The chemistry to functionalize these sites is more mature. Wong et al. demonstrated that the open end of the CNT is rich in $-\text{COOH}$ group and thus can be used for selective covalent bonding of primary amine molecules by carbodiimide chemistry [18, 80]. NASA scientists further demonstrated that DNA oligoprobes can be covalently functionalized, by the same chemistry, to an array of vertically aligned MWNTs embedded in SiO_2 matrix with only the open ends exposed [81]. Similar to other DNA microarrays, the covalently bonded DNA probes can sustain more stringent control such as washing at elevated temperatures so that only specifically binded target DNA molecules can be hybridized with the probes. A NASA-NCI joint work has demonstrated an electrochemical DNA sensor based on an array of DNA functionalized nanotube electrodes [51, 81, 82]. The nano-bioelectronics platform is expected to provide unsurpassed electrochemical sensitivity, a high degree of miniaturization, great ease, and low cost operation.

4. DISCUSSIONS AND FUTURE DEVELOPMENTS

In summary, CNTs are attractive materials for various sensor applications. Their small dimension and large surface-to-volume ratio make them very sensitive to adsorbates from the environment. The electronic properties such as resistance/conductance, thermoelectric power, and dielectric constant can directly indicate the adsorption of target species. For applications which do not involve direct measurements of the inherent electrical properties of CNTs, the finite size and unique graphitic properties of CNTs can

still dramatically improve the performance, as demonstrated in electrochemical applications. It has been reported that CNTs can be used in sensing gases, liquid-phase chemicals, and biomolecules. The work summarized here only covers the CNT which is only one of the doors leading us to the nanotechnology world. Other nanomaterials such as semiconducting or metallic nanowires [83], nanoparticles [84, 85], quantum dots [86–88], and dendrimers [89] have all shown great potential in sensor applications. These nanomaterials allow bridging of the gap between microdevices and biomolecules to achieve an integrated micro-nano-bio heterogeneous system. We should expect great progress in this field in the near future.

A few papers reported the most recent progress on gas adsorption on CNTs during the period in which manuscript was written. A Ricca et al. [90] studied the physisorption and chemisorption of O_2 on the inner and outer walls of a (9, 0) CNT using ONIOM method and the MP2 correlation treatment which includes long-range dispersion interactions. In contrast to previous theoretical work using density functional theory [55, 56], only physisorption of triplet O_2 occurs both inside and outside the tube with very weak binding energy and little charge transfer. Chemisorption likely occurs with singlet O_2 which has a very high barrier and is not popular under normal conditions. The CNT FETs were also proposed to operate as unconventional “Schottky barrier transistors”, in which transistor action occurs primarily by varying the contact resistance rather than channel conductance [91]. Therefore, the mechanism of the CNT FET sensor for gas adsorption needs further investigation.

GLOSSARY

Carbon nanotube Seamless graphitic cylindrical fibers made of carbon atoms. It could be single walled if there is only one graphitic sheet in the cylindrical structure or multi-walled if there is more than one sheets rolled into the tube.

Chemical mechanical polishing (CMP) A process typically used in the semiconductor industries to planarize the surfaces of a wafer to achieve optically flat topography. A slurry which consists of small spherical particulates and additives is used during the polishing process. The compositions of the slurry could be tailored to selectively polish the material of interest.

Chemical vapor deposition (CVD) A process which involves deposition of a thin film using a selected choice of chemical precursors at elevated temperature.

Deoxyribonucleic acid (DNA) A macromolecule consisting of one or two strands of linked deoxyribonucleotides.

DNA hybridization Formation of a duplex structure by two complementary single strands of DNA.

Polydimethylsiloxane (PDMS) A network of polymer chains with Si-O backbones and methyl (CH_3) side group.

Single-walled carbon nanotube ropes/bundles Multiple single-walled carbon nanotubes aggregated into hexagonally packed ropes/bundles side by side due to the strong van der Waals interactions between them.

Soft lithography A lithographic technique which involves non-optical components to achieve patterning of features with dimensions ranging from the millimeter to nanometer length scale.

ACKNOWLEDGMENTS

We acknowledge helpful discussions with Jie Han, Jing Kong, Jing Li, and M. Meyyappan during preparation of this manuscript.

REFERENCES

- M. S. Dresselhaus, G. Dresselhaus, and P. C. Eklund, "Science of Fullerenes and Carbon Nanotubes." Academic Press, New York, 1996.
- T. W. Ebbesen, "Carbon Nanotubes: Preparation and Properties." CRC Press, Boca Raton, FL, 1997.
- R. Saito, M. S. Dresselhaus, and G. Dresselhaus, "Physical Properties of Carbon Nanotubes." World Scientific, New York, 1998.
- D. Tománek and R. Enbody, "Science and Application of Nanotubes." Kluwer Academic, New York, 2000.
- S. Iijima, *Nature* 354, 56 (1991).
- S. J. Tans, A. R. M. Verschueren, and C. Dekker, *Nature* 393, 49 (1998).
- M. S. Fuhrer, J. Nygard, L. Shih, M. Forero, Y.-G. Yoon, M. S. C. Mazzoni, H. J. Choi, J. Ihm, S. G. Louie, A. Zettl, and P. L. McEuen, *Science* 288, 494 (2000).
- C. W. Zhou, J. Kong, E. Yenilmez, and H. Dai, *Science* 290, 1552 (2000).
- T. Rueckes, K. Kim, E. Joselevich, G. Y. Tseng, C. L. Cheung, and C. M. Lieber, *Science* 289, 94 (2000).
- V. Derycke, R. Martel, J. Appenzeller, and Ph. Avouris, *Nano Letters* 1, 453 (2001).
- A. Bachtold, P. Hadley, T. Nakanishi, and C. Dekker, *Science* 294, 1317 (2001).
- X. L. Liu, C. Lee, C. W. Zhou, and J. Han, *Appl. Phys. Lett.* 79, 3329 (2001).
- J. Kong, N. R. Franklin, C. W. Zhou, M. G. Chapline, S. Peng, K. Cho, and H. Dai, *Science* 287, 622 (2000).
- B. Vigolo, A. Penicaud, C. Coulon, C. Sauder, R. Paillet, C. Journet, P. Bernier, and P. Poulin, *Science* 290, 1331 (2000).
- W. A. de Heer, A. Chatelain, and D. Ugarte, *Science* 270, 1179 (1995).
- A. G. Rinzler, J. H. Hafner, P. Nikolaev, L. Lou, S. G. Kim, D. Tomanek, P. Nordlander, D. T. Colbert, and R. E. Smalley, *Science* 269, 1550 (1995).
- H. Dai, J. H. Hafner, A. G. Rinzler, D. T. Colbert, and R. E. Smalley, *Nature* 384, 147 (1996).
- S. Wong, E. Joselevich, A. Woolley, C. Cheung, and C. Lieber, *Nature* 394, 52 (1998).
- J. Li, A. Cassell, and H. Dai, *Surf. Interface Anal.* 28, 8 (1999).
- C. V. Nguyen, K. J. Chao, R. M. D. Stevens, L. Delzeit, A. Cassell, J. Han, and M. Meyyappan, *Nanotechnology* 12, 363 (2001).
- C. F. Liu, Y. Y. Fan, M. Liu, H. T. Cong, H. M. Chen, and M. S. Dresselhaus, *Science* 286, 1127 (1999).
- G. Che, B. B. Lakshmi, E. R. Fisher, and C. R. Martin, *Nature* 393, 346 (1998).
- P. G. Collins, K. Bradley, M. Ishigami, and A. Zettl, *Science* 287, 1801 (2000).
- G. U. Sumanasekera, C. K. W. Adu, S. Fang, and P. C. Eklund, *Phys. Rev. Lett.* 85, 1096 (2000).
- H. T. Ng, A. Fang, J. Li, and S. F. Y. Li, *J. Nanosci. Nanotech.* 1, 375 (2001).
- G. Heiland, *Sensors Actuators* 2, 343 (1982).
- A. Mandelis and C. Christofides, "Physics, Chemistry, and Technology of Solid State Gas Sensor Devices." Wiley, New York, 1993.
- M. S. Wrighton, *Science* 231, 32 (1986).
- M. C. Longergan, E. J. Severin, B. J. Doleman, S. A. Beaber, R. H. Grubbs, and N. S. Lewis, *Chem. Mater.* 8, 2298 (1996).
- S. Iijima and T. Ichihashi, *Nature* 363, 603 (1993).
- D. S. Bethune, C. H. Kiang, M. S. de Vries, G. Gorman, R. Savoy, J. Vazquez, and R. Beyers, *Nature* 363, 605 (1993).
- A. Thess, R. Lee, P. Nikolaev, H. Dai, P. Petit, J. Robert, C. Xu, Y. H. Lee, S. G. Kim, A. G. Rinzler, D. T. Colbert, G. E. Scuseria, D. Tománek, J. E. Fischer, and R. E. Smalley, *Science* 273, 483 (1996).
- H. Kajiura, S. Tsutsui, H. Huang, M. Miyakoshi, Y. Hirano, A. Yamada, and M. Ata, *Chem. Phys. Lett.* 346, 356 (2001).
- C. Journet, W. Maser, P. Bernier, A. Loiseau, M. Delachapelle, S. Lefrant, P. Deniard, R. Lee, and J. Fischer, *Nature* 388, 756 (1997).
- J. Kong, A. M. Cassell, and H. Dai, *Chem. Phys. Lett.* 292, 567 (1998).
- M. Su, B. Zheng, and J. Liu, *J. Chem. Phys. Lett.* 322, 321 (2000).
- J.-F. Colomer, C. Stephan, S. Lefrant, G. Tendeloo, I. Willems, Z. Kónya, A. Fonseca, C. Laurent, and J. Nagy, *J. Chem. Phys. Lett.* 317, 83 (2000).
- E. Flahaut, A. Govindaraj, A. Peigney, C. Laurent, and C. N. Rao, *Chem. Phys. Lett.* 300, 236 (1999).
- J. Hafner, M. Bronikowski, B. Azamian, P. Nikolaev, D. Colbert, and R. E. Smalley, *Chem. Phys. Lett.* 296, 195 (1998).
- M. J. Bronikowski, P. A. Willis, D. T. Colbert, K. A. Smith, and R. E. Smalley, *J. Vac. Sci. Technol. A* 19, 1800 (2001).
- S. Bandow, A. M. Rao, K. A. Williams, A. Thess, R. E. Smalley, and P. C. Eklund, *J. Phys. Chem. B* 101, 8839 (1997).
- K. Tohji, H. Takahashi, Y. Shinoda, N. Shimizu, B. Jeyadevan, I. Matsuoka, *J. Phys. Chem. B* 101, 1974 (1997).
- A. G. Rinzler, J. Liu, H. Dai, P. Nikolaev, C. B. Huffman, F. J. Rodríguez-Macías, P. J. Boul, A. H. Lu, D. Heymann, D. T. Colbert, R. S. Lee, J. E. Fischer, A. M. Rao, P. C. Eklund, and R. E. Smalley, *Appl. Phys. A* 67, 29 (1998).
- Z. Shi, Y. Lian, F. Liao, X. Zhou, Z. Gu, Y. Zhang, and S. Iijima, *Solid State Comm.* 112, 35 (1999).
- M. Cinke, J. Li, B. Chen, A. Cassell, L. Delzeit, J. Han, and M. Meyyappan, *Chem. Phys. Lett.* 365, 69 (2002).
- H. T. Soh, C. F. Quate, A. F. Morpurgo, C. M. Marcus, J. Kong, and H. Dai, *Appl. Phys. Lett.* 75, 627 (1999).
- S. Chopra, A. Pham, J. Gaillard, A. Parker, A. M. Rao, *Appl. Phys. Lett.* 80, 4632 (2002).
- J. M. Nugent, K. S. V. Santhanam, A. Rubio, and P. M. Ajayan, *Nano Letters* 1, 87 (2001).
- P. J. Britto, K. S. V. Santhanam, and P. M. Ajayan, *Bioelectrochem. Bioenergetics* 41, 121 (1996).
- J. Li, A. Cassell, L. Delzeit, J. Han, and M. Meyyappan, *J. Phys. Chem. B* 106, 9299 (2002).
- J. Li, R. Stevens, L. Delzeit, H. T. Ng, A. M. Cassell, J. Han, and M. Meyyappan, *Appl. Phys. Lett.* 81, 910 (2002).
- A. C. Dillon, K. M. Jones, T. A. Bekkedahl, C. H. Kiang, D. S. Bethune, and M. J. Heben, *Nature* 386, 377 (1997).
- Y. A. Ye, C. C. Ahn, C. Witham, B. Fultz, J. Liu, A. G. Rinzler, D. Colbert, K. A. Smith, and R. E. Smalley, *Appl. Phys. Lett.* 74, 2307 (1999).
- S. M. Lee and Y. H. Lee, *Appl. Phys. Lett.* 76, 2877 (2000).
- S.-H. Jhi, S. G. Louie, and M. L. Cohen, *Phys. Rev. Lett.* 85, 1710 (2000).
- J. Zhao, A. Buldum, J. Han, and J. P. Lu, *Nanotechnology* 13, 195 (2002).
- J. Liu, A. G. Rinzler, H. Dai, J. H. Hafner, R. K. Bradley, P. J. Boul, A. Lu, T. Invernson, K. Shelimov, C. B. Huffman, F. Rodríguez-Macías, Y.-S. Shon, T. R. Lee, D. T. Colbert, and R. E. Smalley, *Science* 280, 1253 (1998).

58. A. Kuznetsova, D. B. Mawhinney, V. Naumenko, J. T. Yates Jr., J. Liu, and R. E. Smalley, *Chem. Phys. Lett.* 321, 292 (2000).
59. E. B. Mackie, R. A. Wolfson, L. M. Arnold, K. Lafdi, and A. D. Migone, *Langmuir* 13, 7197 (1997).
60. K. G. Ayappa, *Langmuir* 14, 880 (1998).
61. K. A. Williams and P. C. Eklund, *Chem. Phys. Lett.* 320, 352 (2000).
62. G. Stan, V. H. Crespi, M. W. Cole, and M. Boninsegni, *J. Low Temp. Phys.* 113, 447 (1998).
63. R. S. Lee, H. J. Kim, J. E. Fischer, A. Thess, and R. E. Smalley, *Nature* 388, 255 (1997).
64. L. Grigorian, K. A. Williams, S. Fang, G. U. Sumanasekera, A. L. Loper, E. C. Dickey, S. J. Pennycook, and P. C. Eklund, *Phys. Rev. Lett.* 80, 5560 (1998).
65. C. K. W. Adu, G. U. Sumanasekera, B. K. Pradhan, H. E. Romero, and P. C. Eklund, *Chem. Phys. Lett.* 337, 31 (2001).
66. H. E. Romero, G. U. Sumanasekera, G. D. Mahan, and P. C. Eklund, *Phys. Rev. B* 65, 205410 (2002).
67. K. Lenghaus, and D. H. Solomon, in "Encyclopedia of Surface and Colloidal Science" (A. Hubbard, Ed.), p. 609. Dekker, Santa Barbara, 2002.
68. L. S. Singer, in "Proceedings of the 5th Carbon Conference," Vol. 2, p. 37. Pergamon, New York, 1961.
69. S. M. Lee, Y. H. Lee, Y. G. Hwang, J. R. Hahn, and H. Kang, *Phys. Rev. Lett.* 82, 217 (1999).
70. J. M. Nugent, K. S. V. Santhanam, A. Rubio, and P. M. Ajayan, *Nano Letters* 1, 87 (2001).
71. J. J. Davis, R. J. Coles, and H. A. O. Hill, *J. Electroanal. Chem.* 440, 279 (1997).
72. P. J. Britto, K. S. V. Santhanam, A. Rubio, J. A. Alonso, and P. M. Ajayan, *Adv. Mater.* 11, 154 (1999).
73. C.-Y. Liu, A. J. Bard, F. Wudl, I. Weitz, and J. R. Heath, *Electrochem. Solid-State Lett.* 2, 577 (1999).
74. J. N. Barisci, G. G. Wallace, and R. H. Baughman, *J. Electrochem. Soc.* 147, 4580 (2000).
75. J. K. Campbell, L. Sun, and R. M. Crooks, *J. Am. Chem. Soc.* 121, 3779 (2000).
76. T. Vo-Dinh, J.-P. Alarie, B. M. Cullum, and G. D. Griffin, *Nature Biotechnol.* 18, 764 (2000).
77. V. P. Menon and C. R. Martin, *Anal. Chem.* 67, 1920 (1995).
78. R. J. Chen, Y. Zhang, D. Wang, and H. Dai, *J. Am. Chem. Soc.* 123, 3838 (2001).
79. M. Shim, N. W. S. Kam, R. J. Chen, Y. Li, and H. Dai, *Nano Letters* 2, 285 (2002).
80. S. S. Wong, A. T. Woolley, E. Joselevich, C. L. Cheung, and C. M. Lieber, *J. Am. Chem. Soc.* 120, 8557 (1998).
81. C. V. Nguyen, L. Delzeit, A. M. Cassell, J. Li, J. Han, and M. Meyyappan, *Nano Letters* 2, 1079 (2002).
82. J. Li, H. Chen, A. M. Cassell, W. Fan, J. E. Koehne, C. V. Nguyen, H. Ng, R. Stevens, J. Han, and M. Meyyappan, in preparation.
83. Y. Cui, Q. Wei, H. Park, and C. M. Lieber, *Science* 293, 1289 (2001).
84. R. Elghanian, J. J. Storhoff, R. C. Mucic, R. L. Letsinger, and C. A. Mirkin, *Science* 277, 1078 (1997).
85. S.-J. Park, T. A. Taton, and C. A. Mirkin, *Science* 295, 1503 (2002).
86. M. Bruchez Jr., M. Moronne, P. Jin, S. Wiess, and A. P. Alivisatos, *Science* 281, 2031 (1998).
87. W. C. W. Chan and S. Nie, *Science* 281, 2016 (1998).
88. M. Han, X. Gao, J. Z. Su, and S. Nie, *Nature Biotechnol.* 19, 631 (2001).
89. S. Uppuluri, D. R. Swanson, L. T. Piehler, J. Li, G. L. Hagnauer, and D. A. Tomalia, *Adv. Mater.* 12, 796 (2000).
90. A. Ricca, and J. A. Drocco, *Chem. Phys. Lett.* 362, 217 (2002).
91. S. Heinze, J. Tersoff, R. Martel, V. Derycke, J. Appenzeller, and Ph. Avouris, *Phys. Rev. Lett.* 89 (10), 106801 (2002).

Carbon Nanotubes: Synthesis by Arc Discharge Technique

Yoshinori Ando

Meijo University, Tenpaku-ku, Nagoya, Japan

CONTENTS

1. Introduction
 2. Preparation of Multiwalled Carbon Nanotubes (MWNTs) by Carbon Arc
 3. Preparation of Single-walled Carbon Nanotubes (SWNTs) by Carbon Arc
 4. Properties of SWNTs and MWNTs
 5. Applications of MWNTs and SWNTs
- Glossary
References

1. INTRODUCTION

Carbon nanotubes were serendipitously discovered by Iijima [1] in 1991 in a specimen of the present author [2]. Arc discharge between two graphite rods was carried out to make fullerenes [3], and the nanotubes were observed in the residual of the cathode deposit. The method was similar to Krätschmer's ac contact arc [4], with the difference that the two graphite rods were 1–2 mm apart and a dc arc was used. It was done by replacing the silicon block of one electrode by a graphite rod in the apparatus used for making ultrafine powder of SiC [5]. On the other hand, Iijima had been interested in observing various kinds of carbon [6, 7] by using high-resolution transmission electron microscopy (HRTEM), since before the discovery of fullerenes [8]. The observation of a fullerene byproduct, the cathode deposit of the dc arc discharge, was also one of them. As a result, he found one-dimensional fibers having quite a new morphology of carbon [1]. They are made of rolled graphene sheets classified into two categories depending on the number of concentric shells: single-walled carbon nanotubes (SWNTs) or multiwalled carbon nanotubes (MWNTs). After the discovery of MWNTs in the cathode deposit of the carbon arc [1], two years later SWNTs were found [9, 10] in sootlike deposits formed in the carbon arc chamber.

It should be noticed that both MWNTs and SWNTs were first prepared by dc arc discharge of graphite, though there is a difference in the catalyst requirement [9, 10]. Later on,

in order to prepare MWNTs, the chemical vapor deposition (CVD) method for large-scale synthesis [11] and thermal decomposition of SiC for aligned MWNT synthesis [12] were applied. However, highly crystallized MWNTs could be produced only by the arc method, because of the high power density under the growth condition. A high yield of SWNTs could be produced by laser ablation [13], whereas the arc discharge [14] and CVD [15] methods were found suitable for their large-scale production. This review focuses only on the arc-discharge method for producing MWNTs and SWNTs.

In the case of the arc method, apart from dc/ac, arc current, gas pressure, and so on, the nature of the ambient gas also plays an important role [16, 17]. Especially, the crystallinity of the MWNTs is highly elaborated when evaporating in pure hydrogen gas [18]. The characteristic features of H₂ arc MWNTs are high crystallinity and a very thin innermost tube. The physical properties and Raman spectra of H₂ arc MWNTs are extremely intrinsic [19–23], and H₂ arc MWNTs really resemble quantum fibers. Electrical and mechanical applications of these H₂ arc MWNTs are expected.

2. PREPARATION OF MULTIWALLED CARBON NANOTUBES BY CARBON ARC

2.1. The Method

To prepare MWNTs, dc arc discharge between two pure graphite rods has been carried out [2, 16, 24, 25] using a vacuum chamber, as shown in Figure 1. Of course, the alignment of the two graphite rods can be vertical [16, 24, 25] or horizontal [17, 26]. After the chamber is evacuated to a vacuum higher than 10⁻⁵ torr by using an oil diffusion pump, an inert gas (or appropriate active gas) is introduced into the chamber. Then a dc arc voltage of approximately 25 V is applied between the two graphite rods which are 1–2 mm apart. Within a few minutes, the anode is consumed and carbon soot is formed in the chamber. When an inert gas is used as the ambient gas, fullerenes are included in the soot [3].

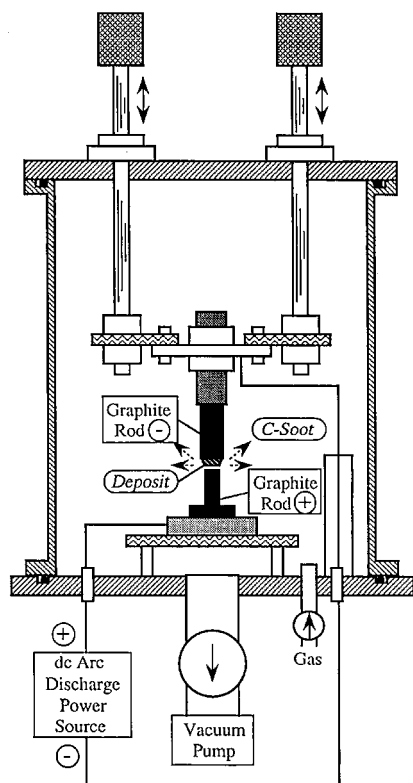


Figure 1. Schematic diagram of arc apparatus producing MWNTs. Reprinted with permission from [25], X. Zhao et al., *Bull. Res. Inst. Meijo Univ.* 1, 7 (1996). © 1996, Research Institute of Meijo University.

Another part of the evaporated carbon is deposited on the top of the cathode. In the cathode deposit [2, 24] and on the top of the cathode deposit [27], MWNTs and coexisting carbon nanoparticles are observed by using scanning electron microscopy (SEM).

HRTEM observation of the cathode deposit dispersed on a TEM microgrid has been carried out. There is a concentric Russian doll structure of rolled graphene sheets with some helical arrangement [1], as shown in Figure 2. The distance between each layer is the same as the {002} lattice spacing of graphite, namely, 0.34 nm. A schematic atomic model of a four-wall MWNT is shown in Figure 3, which has a helical arrangement and the edge is zigzag type [28]. When the cathode deposit is observed by using SEM, the MWNTs are seen as fibers, as shown in Figure 4. Usually, not only fibrous MWNTs but also a number of coexisting carbon nanoparticles are observed [2, 27], as shown in Figure 4. The evaporation of graphite rods has been carried out in He ambient gas, and fibrous MWNTs are observed in the cathode deposit and on the top surface of the cathode deposit as well [27].

2.2. Effect of Ambient Gas

The first specimen of MWNTs was prepared by dc arc discharge evaporation in the ambient gas of He [3], although Iijima erroneously wrote Ar in his first report [1]. Since then, not only inert gas such as He or Ar but also active CH₄ gas has been tried as the ambient gas of arc discharge [2, 16, 17, 24]. As a result, MWNTs are formed in all gases of He,

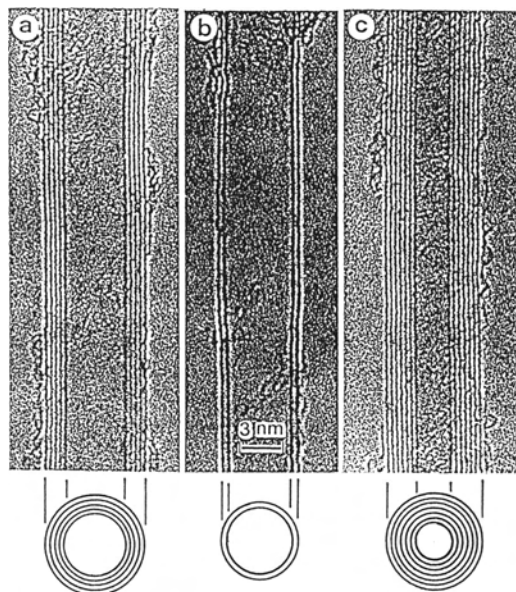


Figure 2. HRTEM micrographs of MWNTs: (a) five-wall, diameter 6.7 nm; (b) two-wall, diameter 5.5 nm; (c) seven-wall, diameter 6.5 nm and the smallest hollow diameter 2.2 nm. Reprinted with permission from [1], S. Iijima, *Nature* 354, 56 (1991). © 1991, Macmillan Magazines Ltd.

Ar, and CH₄ within a pressure range of 20–200 torr. At an intermediate pressure of 100 torr, the quantity of prepared MWNTs is found as follows: Ar < He < CH₄ [24]. It is known that fullerenes such as C₆₀ cannot be produced in an ambient gas containing hydrogen atoms. On the contrary, thin and long MWNTs with few coexisting nanoparticles can be prepared in CH₄ gas more than in an inert gas; as an example, see the SEM micrograph [16] shown in Figure 5. From the mass spectra of the chamber gas before and after evaporation [17], it was confirmed that methane undergoes a thermal decomposition as follows:

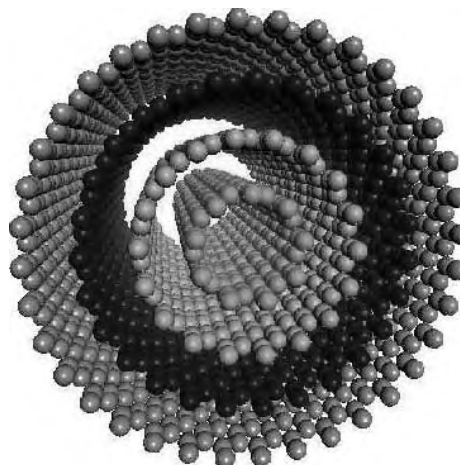


Figure 3. Atomic model of four-walled carbon nanotube.

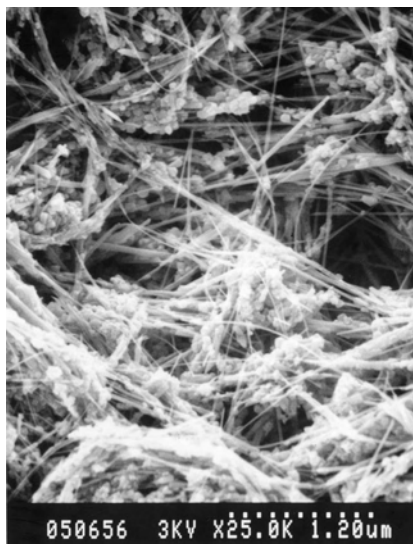


Figure 4. SEM micrograph of MWNTs prepared at dc arc current of 70 A in He 200 torr.

In this reaction, the calculated mole ratio of the gas before and after evaporation was 1:2. This led to the necessity to carry out the arc evaporation of the graphite rod in pure C_2H_2 or pure H_2 ambient gas. In the case of pure C_2H_2 gas, a similar result as in CH_4 gas is obtained. On the contrary, arc discharge in pure H_2 gas shows quite remarkable improvement [18].

A typical optical photograph of the top of the cathode [18, 29] after H_2 arc evaporation is shown in Figure 6, which is obtained after 3 min evaporation by a dc arc current of 50 A in H_2 gas at 60 torr. The top surface is composed of three regions: a central black region *A*, a surrounding silver-gray region *B*, and a very thin outer region *C*. When the outer region *C* is observed using SEM, “carbon roses” are seen [18, 29, 30], as shown in Figure 7. Each petal of a carbon rose is made of very thin graphene sheets [30], that is, nanopetals. In fact, they are composed of several lay-

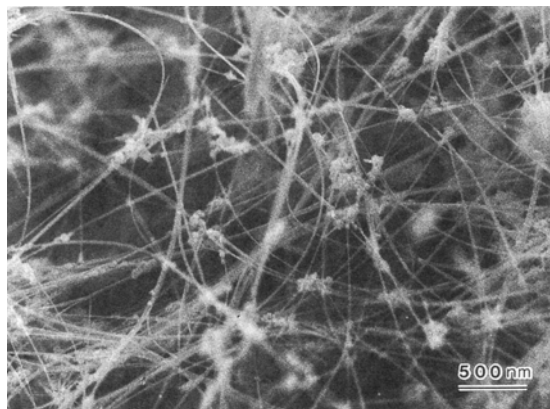


Figure 5. SEM micrograph of thin, long MWNTs on the top surface. The original specimen was prepared at CH_4 20 torr and dc arc current of 30 A. Reprinted with permission from [16], X. Zhao et al., *Jpn. J. Appl. Phys.* 35, 4451 (1996). © 1996, Institute of Pure and Applied Physics, Japan.

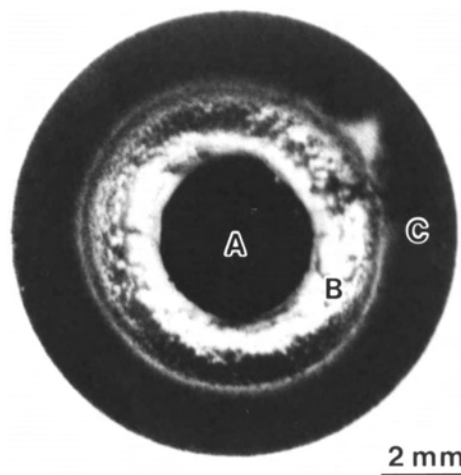


Figure 6. Top-view photograph of the deposited cathode after H_2 arc discharge. Reprinted with permission from [29], X. Zhao et al., *J. Cryst. Growth* 198/199, 934 (1999). © 1999, Elsevier Science.

ers of parallel graphene sheets, the thinnest one consisting of only two graphene sheets. The region *B* is a hard, thick deposit which is observed to be a graphitic layered structure. MWNTs are observed in the central thick black deposit *A*, as shown in Figure 8a. There are fewer nanoparticles coexisting with the pristine MWNTs in H_2 (Fig. 8a) than in He or Ar gas. Therefore, purification is very easily achieved by infrared radiation in air at 500 °C for 30 min [20, 31], as shown in Figure 8b. Such purified MWNTs look like a sponge (Fig. 9) [31], which is easy to manipulate with tweezers for various measurements. The size of the sponge is 10 mm^2 area \times 0.1 mm thickness, and the mass is about 1 mg.

2.3. Structure of H_2 Arc MWNTs

The structural features of MWNTs produced by H_2 arc discharge can be elucidated by HRTEM [18, 21]. As shown in Figure 10a, as-grown MWNTs are highly crystallized with perfect coaxial tube layers [21]. The diameter of the innermost tube *A* is about 1.2 nm and the outer diameter of

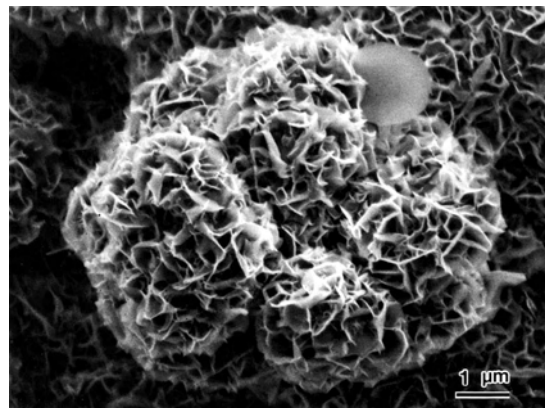


Figure 7. SEM micrograph of “carbon rose.” Reprinted with permission from [18], X. Zhao et al., *Carbon* 35, 775 (1997). © 1997, Elsevier Science.

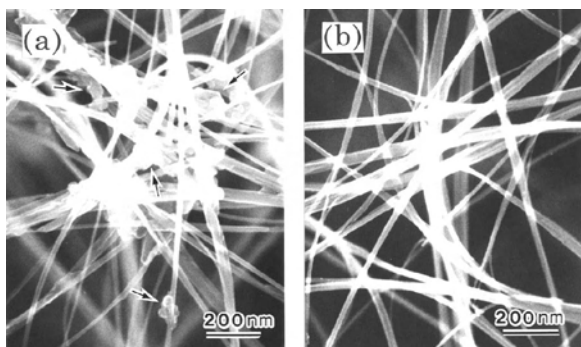


Figure 8. SEM micrographs of MWNTs produced by hydrogen arc discharge: (a) as grown, (b) after purification. Reprinted with permission from [20], Y. Ando et al., *Trans. Mater. Res. Soc. Jpn.* 25, 817 (2000). © 2000, Materials Research Society of Japan.

the MWNT is 13 nm. There are 16 graphene sheets on both sides with a regular spacing of 0.34 nm. The arrow *B* points out amorphous carbon seen in pristine MWNTs. A cross-sectional view of an MWNT (but not of the same one as in Fig. 10a) is shown in Figure 10b. Concentric circles are seen, but with half-fringe discrepancy at each arrowed position.

Based on HRTEM observation, the innermost diameter distribution can be obtained [22]. The mean value of the innermost tube is 1.0 nm, whereas that for He arc MWNTs is usually more than 3 nm. The innermost tube observed in H₂ arc MWNTs is 0.4 nm (Fig. 11) [32]. The innermost tube is supposed to possess an armchair (3,3) structure.

3. PREPARATION OF SINGLE-WALLED CARBON NANOTUBES BY CARBON ARC

3.1. Lab-Scale Production

Two years after the discovery of MWNTs, SWNTs were found by Iijima and Ichihashi [9] and by Bethune et al. [10], independently. An HRTEM micrograph of the single-shell tube with diameter 1.37 nm [9] is shown in Figure 12.

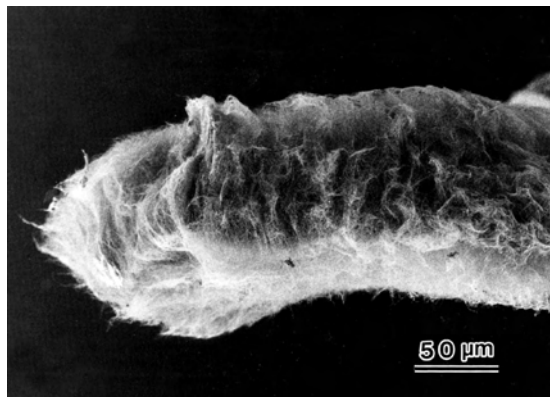


Figure 9. SEM micrograph of purified MWNTs sponge. Reprinted with permission from [31], Y. Ando et al., *Jpn. J. Appl. Phys.* 37, L61 (1998). © 1998, Institute of Pure and Applied Physics, Japan.

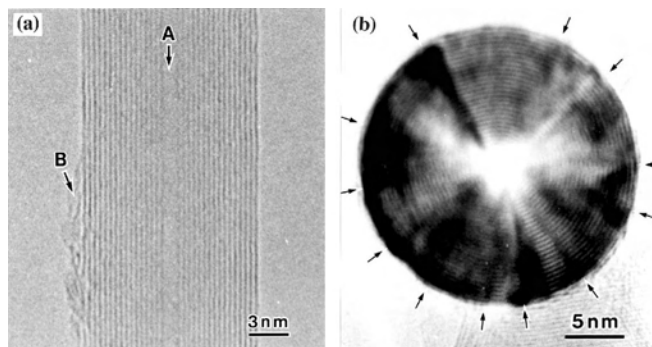


Figure 10. HRTEM micrographs of MWNT prepared by hydrogen arc discharge: (a) side view, (b) edge-on view. Reprinted with permission from [21], Y. Ando et al., *Carbon* 39, 569 (2001). © 2001, Elsevier Science.

SWNTs were found in the specimen produced by arc discharge using a graphite rod including a metal catalyst (Fe), not in the cathode deposit but in the carbon soot. Incorporation of the metal catalyst is essential to produce SWNTs. In Iijima's case, a mixture of methane (10 torr) and argon (40 torr) was used as the ambient gas [9]. Bethune et al. prepared SWNTs under slightly different conditions using a Co catalyst in helium gas [10]. However, in both cases, the yield of SWNTs was very small.

3.2. Mass-Scale Production

High-yield SWNTs were first obtained by laser ablation [13], in which unwanted nanoparticles were negligible as compared to SWNTs. However, the overall quantity of SWNTs

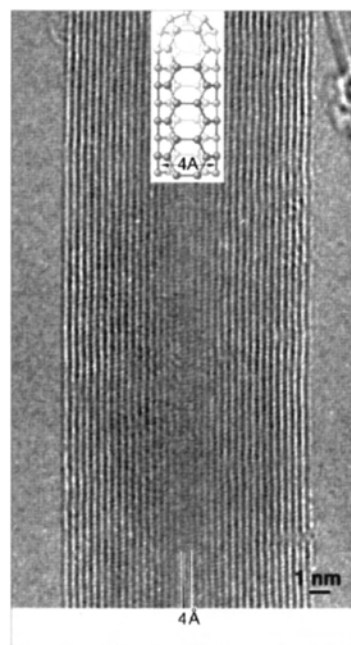


Figure 11. HRTEM micrograph of a 4-Å tubule. Reprinted with permission from [32], L.-C. Qin et al., *Nature* 408, 50 (2000). © 2000, Macmillan Magazines Ltd.

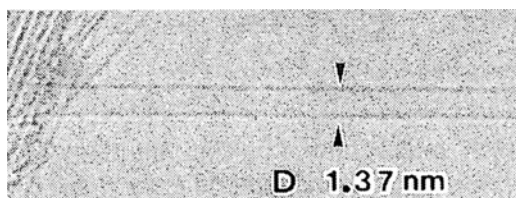


Figure 12. HRTEM micrograph of SWNT. Reprinted with permission from [9], S. Iijima and T. Ichihashi, *Nature* 363, 603 (1993). © 1993, Macmillan Magazines Ltd.

obtained was still very small. Later on, Journet et al. succeeded in obtaining a large quantity of SWNTs by the arc discharge method [14]. They used a bimetallic catalyst; the best results were obtained with 1 at% Y and 4.2 at% Ni. An SEM micrograph of SWNTs as high density of entangled carbon filaments is shown in Figure 13, which is formed as a collar around the cathode deposit and is not the cathode deposit itself. Such SWNTs are also obtained in other places, that is, rubbery soot condensed on the chamber walls, web-like structures between the cathode and the reactor walls, and a cylindrical deposit at the cathode end.

3.3. Arc Plasma Jet Method

Unlike the case of MWNTs, the cathode deposit of arc discharge using a metal-doped anode does not include SWNTs [14]. Hence, an attempt was made to reduce the cathode deposit and increase the quantity of soot generated that contains SWNTs [33]. A pure graphite cathode and metal-doped anode were set at an angle of 30°, and discharge was carried out with the arc flame occurring along the inclined cathode. This new method to produce SWNTs is known as the arc plasma jet (APJ) method [33].

The evaporation rate of the anode and the production rates of the carbon soot and cathode deposit measured in SWNT production experiments under He gas at 500 torr [33] are shown in Figure 14a and b. In the case of APJ, more than 80% of the evaporated anode yields cotton-like soot containing SWNTs and less than 20% appears as cathode deposit. On the contrary, the quantity of deposit in the conventional arc method is larger than the soot at a dc

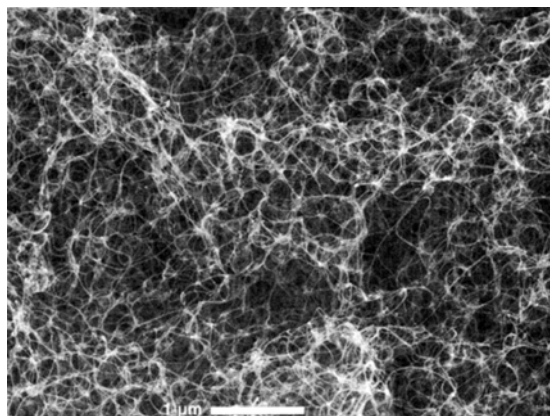


Figure 13. SEM micrograph of large-scale production of SWNTs by arc discharge. Reprinted with permission from [14], C. Journet et al., *Nature* 388, 756 (1997). © 1997, Macmillan Magazines Ltd.

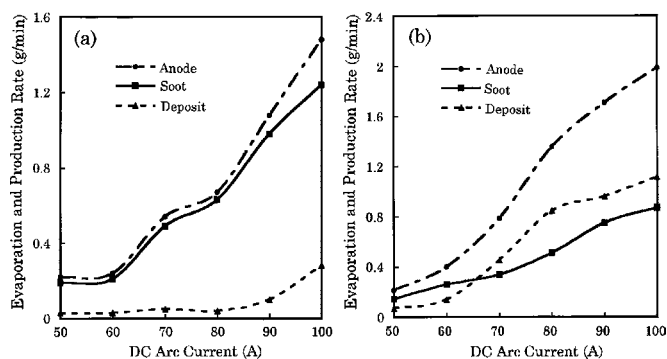


Figure 14. Evaporation rate of the anode, production rate of carbon soot, and production rate of deposit measured in SWNT production experiments under He gas of 500 torr: (a) APJ method, (b) conventional arc method. Reprinted with permission from [33], Y. Ando et al., *Chem. Phys. Lett.* 323, 580 (2000). © 2000, Elsevier Science.

arc current higher than 70 A. Figure 15 shows a characteristic SEM micrograph of cotton-like carbon soot produced by the APJ method [33]. A large number of entangled SWNT bundles and nanoparticles of Ni are seen. The catalyst metal particles are usually covered by thick amorphous carbon, which is hard to remove. Nevertheless efforts to purify as-grown SWNTs are in progress.

4. PROPERTIES OF SWNTS AND MWNTS

4.1. Structures

The helical structures of MWNTs and SWNTs are elucidated from their electron diffraction patterns observed by TEM [1, 9]. The atomic structure of individual SWNTs can be determined by scanning tunneling microscopy (STM) [34, 35]. All three types of possible structures predicted theoretically—chiral, zigzag, and armchair—were confirmed experimentally by STM images [34–36].

X-ray diffraction (XRD) measurement of H₂ arc MWNTs is performed using a synchrotron radiation source [37]. The

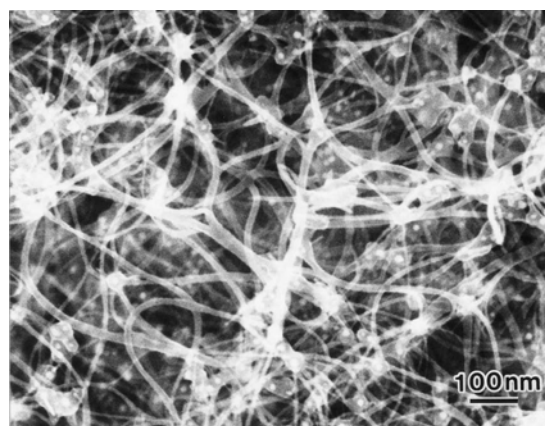


Figure 15. SEM micrograph of carbon soot containing SWNTs which were prepared by the APJ method. Reprinted with permission from [33], Y. Ando et al., *Chem. Phys. Lett.* 323, 580 (2000). © 2000, Elsevier Science.

powder XRD patterns (wavelength 0.9942 Å) are collected using a powder X-ray diffractometer equipped with an imaging plate. H₂ arc MWNT samples are sealed in a quartz capillary and the temperature is controlled in a range from room temperature (RT) to 900 K. XRD profiles are taken as a function of temperature. The XRD profiles of the (002) peak at RT and 873 K are analyzed by Gaussian line shape as shown in Figure 16. Thus, each peak is decomposed into three kinds of peaks: A, B, and C. The first two peaks, A and B, are due to defective MWNTs, while peak C is most probably due to a perfect Russian-doll-type structure.

4.2. Electric Properties

Not only the helical structure of SWNTs but also the electronic density of states can be measured by STM [34, 35]. It has been confirmed that SWNTs are metallic or semiconducting depending on the wrapping angle and the tube diameter. The electrical transport measurements of individual SWNTs [38] also coincide with the theoretical predictions [39].

On the other hand, the electric resistance of individual MWNTs has been measured by a micro-manipulator system [40]. Individual H₂ arc MWNTs can conduct high electric current [19], 1.0×10^7 A/cm². The temperature dependence of their electric resistance in curve *a* (Fig. 17) shows that the resistance decreases with increasing temperature. This

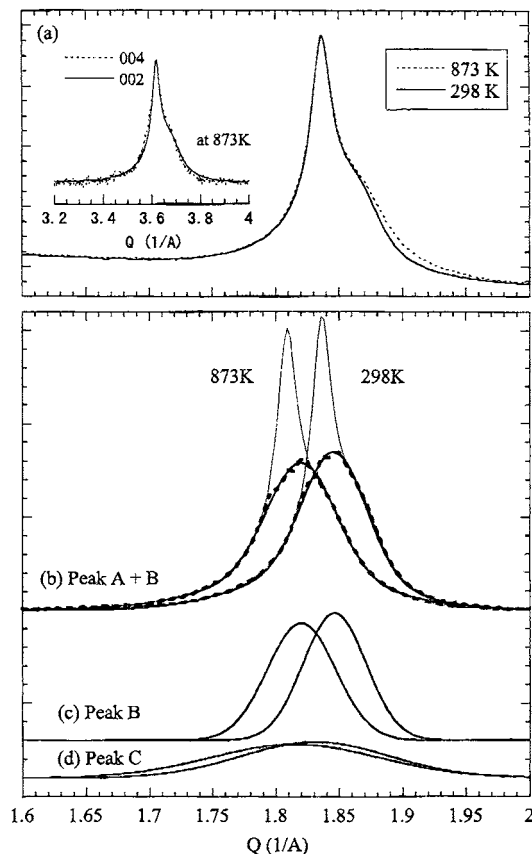


Figure 16. X-ray diffraction profile of H₂ arc MWNTs. Reprinted with permission from [37], Y. Maniwa et al., *Phys. Rev. B* 64, 073105 (2001). © 2001, American Institute of Physics.

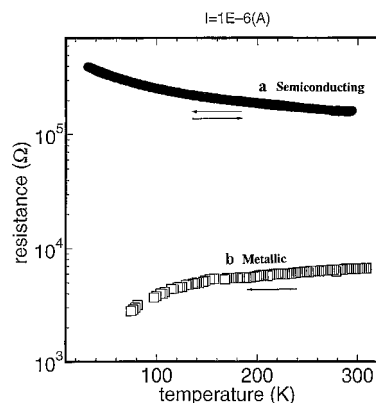


Figure 17. Temperature dependence of electric resistance of MWNT. Curve *a* is obtained from a single MWNT and curve *b* is obtained from a bundle of MWNTs. The arrows show the direction of the temperature change. Curve *a* is semiconducting and curve *b* is metallic. Reprinted with permission from [19], Y. Ando et al., *Diamond Relat. Mater.* 9, 847 (2000). © 2000, Elsevier Science.

temperature dependence corresponds to the semiconducting character of MWNTs. In curve *b*, the resistance increases with increasing temperature, namely, metallic character.

Field emission measurements of the spongy bulk of H₂ arc MWNTs have also been carried out [19]. A practically desirable field emission current density of 1 mA/cm² is achieved only at an anode voltage of 580 V. The value of the applied voltage is reduced to a field (applied voltage/gap distance) of 1.2 V/μm. A light source device, which emits primary color of super-high luminance and fast switching, has been developed by using the spongy bulk of the H₂ arc MWNTs [41]. High current density is obtained and enough electron emission is maintained for a long time. A super-high green luminance of 1.0×10^6 cd/m² is achieved by the light source device.

4.3. Raman Spectra

The Raman spectra of SWNTs show their characteristic features [42, 43]. In the low-frequency region, radial breathing modes (RBMs) are observed at frequency values inversely proportional to the diameter of the SWNTs [42, 43]. The observation of RBM peaks is necessary to confirm the presence of SWNTs. In the high-frequency region, the splitting of G-band modes and its splitting due to the cylindrical structure of SWNTs are observed.

In the past decade, extensive Raman experiments have been performed on MWNTs synthesized by arc discharge evaporation in helium gas and by CVD. However, the reported Raman spectra closely resemble that of graphite, and no RBMs have yet been found [44–46] except by Jantoljak et al. [47]. On the other hand, many Raman-active modes [22, 48] are observed for H₂ arc MWNTs in the low-frequency region. The resonance effect of each mode [49] is similar to that of the RBM in an SWNT. It is known that RBMs are expected to have an A_{1g} symmetry, and the wave number of the RBM is proportional to the inverse of the diameter of the SWNT [42, 43].

Figure 18 shows the micro-Raman spectra [22] in the low-frequency region (100–600 cm⁻¹) for three specimens of

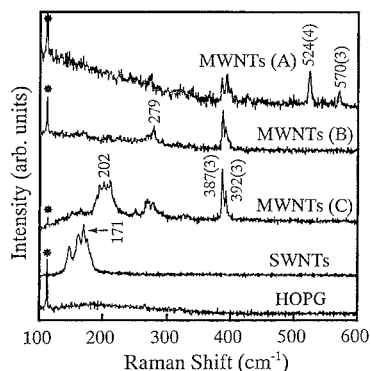


Figure 18. Raman spectra of MWNT mat in low-frequency region. Reprinted with permission from [22], X. Zhao et al., *Chem. Phys. Lett.* 361, 169 (2002). © 2002, Elsevier Science.

H_2 arc MWNT mats, (A)–(C). For comparison, the Raman spectra of SWNTs produced by the APJ method [33] and highly oriented pyrolytic graphite (HOPG) are also displayed in Figure 18. In contrast to HOPG, many sharp Raman-active peaks are observed in the Raman spectra of the MWNT mats. The highest frequency peak is observed at $570(3) \text{ cm}^{-1}$ in MWNTs (A), where the full width at half-maximum (FWHM) is given in parentheses. By observing the polarized Raman spectra from single straight bundles of MWNTs, each Raman-active peak in Figure 18 is assigned an RBM [22]. In the case of MWNTs, the RBM comes from the thin innermost diameter. From the RBM frequency the diameter of the innermost tube can be determined. Thus, the highest frequency peak 570 cm^{-1} is due to the smallest innermost tube of 0.4 nm [32].

The characteristic features of the Raman spectra are also observed in the high-frequency region for individual H_2 arc MWNTs dispersed onto a silver substrate [23]. Surface-enhanced Raman scattering (SERS) spectra are taken from a single H_2 arc MWNT. Three examples of Raman spectra are shown in Figure 19a and b for the low- ($100\text{--}600 \text{ cm}^{-1}$) and high- ($1450\text{--}1650 \text{ cm}^{-1}$) frequency regions, respectively. In Figure 19a, single RBM peaks of different frequencies with sharp FWHM can be seen for each H_2 arc MWNT, A, B, and C. The RBM frequencies of 216 , 403 , and 192 cm^{-1}

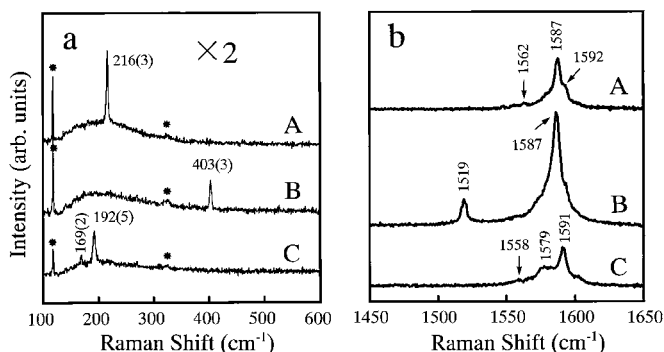


Figure 19. Surface-enhanced Raman spectra from individual MWNT: (a) low-frequency region, (b) high-frequency region. Reprinted with permission from [23], X. Zhao et al., *Appl. Phys. Lett.* 81, 2550 (2002). © 2002, American Institute of Physics.

correspond to the innermost diameters of H_2 arc MWNTs: 1.09 , 0.58 and 1.23 nm , respectively. SERS spectra A, B, and C in Figure 19b show multiple splitting of the G-band modes in H_2 arc MWNTs. These peaks are analyzed by Lorentz fit [23] and decomposed into a broad graphite-like line at approximately $1580(20) \text{ cm}^{-1}$ and sharp lines with FWHM of about 4 cm^{-1} . The latter originate from the thin innermost tubes of H_2 arc MWNTs [23].

4.4. Nanocomposite Structure

By removing the cap of the MWNT or SWNT, other materials such as some metals or fullerenes can be inserted into the tube [50–52]. Nanotubes act as molds for the fabrication of metallic wires, some of which are less than 2 nm in diameter [50]. From these viewpoints, new composite materials have been made. As an interesting phenomenon, heat treatment of SWNTs filled with C_{60} [52] leads to the formation of double-wall carbon nanotubes (DWNTs) [53]. This is a new method for making DWNTs.

5. APPLICATIONS OF MWNTS AND SWNTS

Potential applications of carbon nanotubes are predicted for electrical, electronic, mechanical, and chemical applications, such as field emission [54], flat-panel display source, quantum wires [38], X-ray source [54], contact needle of atomic force microscopy, hydrogen storage, gas sensors, capillarity-induced filling of metal [50], and fullerene peapods [52]. Highly crystallized MWNTs and SWNTs produced by arc discharge should have more potential for electronic and mechanical applications. Application-based research of SWNTs and MWNTs is continuously increasing worldwide.

GLOSSARY

Arc discharge Evaporation method of graphite electrode using arc discharge. Usually carried out in inert gas.

Arc plasma jet (APJ) Method to prepare SWNTs by a special kind of arc discharge.

Carbon nanoparticles Nanometer-sized particles made of carbon, which usually has onion-type layered structure.

Carbon nanotube Tube composed of carbon atoms only, having a diameter on the order of nanometers. Each tube is made of a rolled graphene sheet.

Carbon roses Petal-like carbon made of graphene sheets, which resemble a rose.

Chemical vapor deposition (CVD) An alternative method to make fibers or carbon nanotubes.

Field emission Electron emission from metal just by applying electric field without heating the metal.

Fullerenes Represented by C_{60} , which is a macromolecule having a cage structure consisting of hexagonal and pentagonal carbon rings.

G band Typical Raman peak of graphite observed at 1582 cm^{-1} , which has E_2 symmetry.

H₂ arc MWNTs MWNTs prepared by dc arc discharge in H₂ gas.

Multiwalled carbon nanotubes (MWNTs) Consisting of many rolled graphene sheets.

Radial breathing mode (RBM) Observed in low-frequency region of Raman spectra of thin tube. The frequency is proportional to the inverse of the tube diameter.

Raman spectra Spectra of Raman shift measured by laser acquisition.

Single-walled carbon nanotubes (SWNTs) Consisting of only one rolled graphene sheet.

X-ray diffraction (XRD) Pattern to clarify crystal structures.

REFERENCES

1. S. Iijima, *Nature* 354, 56 (1991).
2. Y. Ando and S. Iijima, *Jpn. J. Appl. Phys.* 32, L107 (1993).
3. Y. Saito, M. Inagaki, H. Shinohara, H. Nagashima, M. Ohkohchi, and Y. Ando, *Chem. Phys. Lett.* 200, 643 (1992).
4. W. Krätschmer, L. D. Lamb, K. Fostiropoulos, and D. R. Huffman, *Nature* 347, 354 (1990).
5. Y. Ando and M. Ohkohchi, *J. Cryst. Growth* 60, 147 (1982).
6. S. Iijima, *J. Cryst. Growth* 50, 675 (1980).
7. S. Iijima, *J. Phys. Chem.* 91, 3466 (1987).
8. H. W. Kroto, J. R. Heath, S. C. O'Brien, R. F. Curl, and R. E. Smalley, *Nature* 318, 162 (1985).
9. S. Iijima and T. Ichihashi, *Nature* 363, 603 (1993).
10. D. S. Bethune, C. H. Kiang, M. S. de Vries, G. Gorman, R. Savoy, J. Vazquez, and R. Beyers, *Nature* 363, 605 (1993).
11. M. José-Yacamán, M. Miki-Yoshida, L. Rendón, and J. G. Santi-esteban, *Appl. Phys. Lett.* 62, 202 (1993).
12. M. Kusunoki, T. Suzuki, K. Kaneko, and M. Ito, *Philos. Mag. Lett.* 79, 153 (1999).
13. A. Thess, R. Lee, P. Nikolaev, H. Dai, P. Petit, J. Robert, C. Xu, Y. H. Lee, S. G. Kim, A. G. Rinzler, D. T. Colbert, G. E. Scuseria, D. Tománek, J. E. Fischer, and R. E. Smalley, *Science* 273, 483 (1996).
14. C. Journet, W. K. Maser, P. Bernier, A. Loiseau, M. Lamy de la Chapelle, S. Lefrant, P. Deniard, R. Lee, and J. E. Fischer, *Nature* 388, 756 (1997).
15. H. M. Cheng, F. Li, G. Su, H. Y. Pan, L. L. He, X. Sun, and M. S. Dresselhaus, *Appl. Phys. Lett.* 72, 3282 (1998).
16. X. Zhao, M. Wang, M. Ohkohchi, and Y. Ando, *Jpn. J. Appl. Phys.* 35, 4451 (1996).
17. M. Wang, X. Zhao, M. Ohkohchi, and Y. Ando, *Fullerene Sci. Technol.* 4, 1027 (1996).
18. X. Zhao, M. Ohkohchi, M. Wang, S. Iijima, T. Ichihashi, and Y. Ando, *Carbon* 35, 775 (1997).
19. Y. Ando, X. Zhao, H. Kataura, Y. Achiba, K. Kaneto, M. Tsuruta, S. Uemura, and S. Iijima, *Diamond Relat. Mater.* 9, 847 (2000).
20. Y. Ando, X. Zhao, H. Kataura, Y. Achiba, K. Kaneto, S. Uemura, and S. Iijima, *Trans. Mater. Res. Soc. Jpn.* 25, 817 (2000).
21. Y. Ando, X. Zhao, and H. Shimoyama, *Carbon* 39, 569 (2001).
22. X. Zhao, Y. Ando, L.-C. Qin, H. Kataura, Y. Maniwa, and R. Saito, *Chem. Phys. Lett.* 361, 169 (2002).
23. X. Zhao, Y. Ando, L.-C. Qin, H. Kataura, Y. Maniwa, and R. Saito, *Appl. Phys. Lett.* 81, 2550 (2002).
24. Y. Ando, *Fullerene Sci. Technol.* 2, 173 (1994).
25. X. Zhao, M. Wang, M. Ohkohchi, and Y. Ando, *Bull. Res. Inst. Meijo Univ.* 1, 7 (1996).
26. T. W. Ebbesen and P. M. Ajayan, *Nature* 358, 220 (1992).
27. Y. Ando, *Jpn. J. Appl. Phys.* 32, L1342 (1993).
28. R. Saito, G. Dresselhaus, and M. S. Dresselhaus, "Physical Properties of Carbon Nanotubes." Imperial College Press, 1998.
29. X. Zhao, M. Ohkohchi, and Y. Ando, *J. Cryst. Growth* 198/199, 934 (1999).
30. Y. Ando, X. Zhao, and M. Ohkohchi, *Carbon* 35, 153 (1997).
31. Y. Ando, X. Zhao, and M. Ohkohchi, *Jpn. J. Appl. Phys.* 37, L61 (1998).
32. L.-C. Qin, X. Zhao, K. Hirahara, Y. Miyamoto, Y. Ando, and S. Iijima, *Nature* 408, 50 (2000).
33. Y. Ando, X. Zhao, K. Hirahara, K. Suenaga, S. Bandow, and S. Iijima, *Chem. Phys. Lett.* 323, 580 (2000).
34. J. W. G. Wildöer, L. C. Venema, A. G. Rinzler, R. E. Smalley, and C. Dekker, *Nature* 391, 59 (1998).
35. T. W. Odom, J.-L. Huang, P. Kim, and C. M. Lieber, *Nature* 391, 62 (1998).
36. S. G. Lemay, J. W. Janssen, M. van den Hout, M. Mooij, M. J. Bronikowski, P. A. Willis, R. E. Smalley, L. P. Kouwenhoven, and C. Dekker, *Nature* 412, 617 (2001).
37. Y. Maniwa, R. Fujiwara, H. Kira, H. Tou, E. Nishibori, M. Takata, M. Sakata, A. Fujiwara, X. Zhao, S. Iijima, and Y. Ando, *Phys. Rev. B* 64, 073105 (2001).
38. S. J. Tans, M. H. Devoret, H. Dai, A. Thess, R. E. Smalley, L. J. Geerligs, and C. Dekker, *Nature* 386, 474 (1997).
39. N. Hamada, A. Sawada, and A. Oshiyama, *Phys. Rev. Lett.* 68, 1579 (1992).
40. Y. Ando, X. Zhao, H. Shimoyama, G. Sakai, and K. Kaneto, *Inorg. Mater.* 1, 77 (1999).
41. J. Yotani, S. Uemura, T. Nagasako, H. Kurachi, H. Yamada, T. Esaki, Y. Saito, Y. Ando, X. Zhao, and M. Yumura, *J. Vac. Soc. Jpn.* 44, 956 (2001) (in Japanese).
42. A. M. Rao, E. Richter, S. Bandow, B. Chase, P. C. Eklund, K. A. Williams, S. Fang, K. R. Subbaswamy, M. Menon, A. Thess, R. E. Smalley, G. Dresselhaus, and M. S. Dresselhaus, *Science* 275, 187 (1997).
43. S. Bandow, S. Asaka, Y. Saito, A. M. Rao, L. Grigorian, E. Richter, and P. C. Eklund, *Phys. Rev. Lett.* 80, 3779 (1998).
44. P. C. Eklund, J. M. Holden, and R. A. Jishi, *Carbon* 33, 959 (1995).
45. W. Li, H. Zhang, C. Wang, Y. Zhang, L. Xu, K. Zhu, and S. Xie, *Appl. Phys. Lett.* 70, 2684 (1997).
46. A. M. Rao, A. Jorio, M. A. Pimenta, M. S. S. Dantas, R. Saito, G. Dresselhaus, and M. S. Dresselhaus, *Phys. Rev. Lett.* 84, 1820 (2000).
47. H. Jantoljak, J.-P. Salvetat, L. Forró, and C. Thomsen, *Appl. Phys. A* 67, 113 (1998).
48. X. Zhao and Y. Ando, *Jpn. J. Appl. Phys.* 37, 4846 (1998).
49. H. Kataura, Y. Achiba, X. Zhao, and Y. Ando, *Mater. Res. Soc. Symp. Proc.* 593, 113 (2000).
50. P. M. Ajayan and S. Iijima, *Nature* 361, 333 (1993).
51. S. C. Tsang, Y. K. Chen, P. J. F. Harris, and M. L. H. Green, *Nature* 372, 160 (1994).
52. B. W. Smith, M. Monthieux, and D. E. Luzzi, *Nature* 396, 323 (1998).
53. S. Bandow, M. Takizawa, K. Hirahara, M. Yudasaka, and S. Iijima, *Chem. Phys. Lett.* 337, 48 (2001).
54. H. Sugie, M. Tanemura, V. Filip, K. Iwata, K. Takahashi, and F. Okuyama, *Appl. Phys. Lett.* 78, 2578 (2001).

Carbon Nanotube-Based Field Emitters

Seong Chu Lim, Hee Jin Jeong, Kay Hyeok An,
Dong Jae Bae, Young Hee Lee

Sungkyunkwan University, Suwon, Republic of Korea

Young Min Shin

Samsung Advanced Institute of Technology, Suwon, Republic of Korea

Young Chul Choi

Samsung SDI, Gongse-ri, Kiheung-eup, Youngin, Republic of Korea

CONTENTS

1. Introduction
 2. Advantages of Carbon Nanotubes
 3. Field Emission Properties of Carbon Nanotubes
 4. Applications
 5. Conclusions
- Glossary
References

1. INTRODUCTION

The source of the most commonly used cathode ray tube (CRT) is an electron, which is thermally ejected from a hot cathode surface. To facilitate the electron ejection, a material with low work function such as a barium oxide compound has been used [1]. The ejected electrons are accelerated through the electric field for rastering and exciting the phosphor screen to display images. The electron emission and acceleration process lead the CRT to consume a lot of power, to operate at high voltage, and to be very bulky. Even though there are some advantages to conventional CRTs such as wide viewing angle, fast response time, unlimited colors, and low price, these CRTs are losing the competition in the display market these days. One major reason is that, in nature, the large dimension and high operational voltage do not allow the CRT to be portable. Portability, however,

is one of the essential features that a display must satisfy in the information age to permit accessibility to the intellectual resources at any time and any place. Therefore, the demand for a flat-panel display, which is slim, light, and operating at low voltage and at low power consumption, has become even stronger.

The annual revenue of the fast-growing global market of flat-panel displays (FPDs) is supposed to reach 80 billion dollars in 2010 [2]. Such tremendous growth of the FPD market has been empowered by the wide distribution of the laptop computer and technical developments in the area of FPDs. In the FPD market, there are several types of displays: liquid crystal display (LCD), plasma display panel (PDP), organic electroluminescence display (OELD), and field emission display (FED). At present, the LCD, dominating about 80% of the market, is very light and slim and operates at low voltage, but contains problems such as limited colors, narrow viewing angle, narrow operation voltage, and high power consumption. LCDs should overcome these problems in order to maintain their position in the market. At the same time, other types of FPDs have to show technical superiority to survive in the market. For instance, PDPs can be readily scaled up to over 60 in., but consume heavy power for plasma generation and still do not show the wide color range that CRTs can display. The OELD, which is flexible and can be fit into almost any shape, operates successfully only for a few hundred hours and degrades fast and furthermore shows low thermal stability.

Among these displays, the FED has captured only a small portion of the market. The CRT and FED have many internal structural features in common, except for the electron

ejection gun. In FEDs, the electrons are ejected by the strong local electric field from many sharp tips. The electric field can be switched on and off swiftly, contributing to the fast response time. FEDs can also provide unlimited colors, a wide viewing angle, and a wide operating temperature, but with low power consumption and low applied voltage. In addition to the above advantages, there are millions of tips in a pixel. Therefore, if one of the emitters stops functioning, another emitter contributes to the field emission. All these properties of the FED make it an almost perfect display. However, many technical issues have yet to be resolved to meet the requirements for commercialization.

The field emission phenomenon was not clearly understood until the adoption of quantum mechanics, because field emission is different from thermionic emission, where sufficient kinetic energy should be given to the electrons in order to surmount the potential barrier at the interface between the vacuum and the surface of the emitter [3–5]. Field emission is a tunneling phenomenon, which cannot be described by classical mechanics. In the presence of a strong electric field, electrons can tunnel through the potential barrier since the barrier becomes dramatically narrow under such a strong field, as shown in Figure 1. Therefore, the field emission is expected to vary with the strength of the applied field and the work function of the emitter materials. Some efforts neglecting this tunneling effect were made in the 20th century, but turned out to be unsuccessful for characterizing the relationship among the above parameters [6], until Fowler and Nordheim formulated the relationship based on quantum mechanics. In their formula, the emission currents can be described as follows:

$$J = A(\beta V)^2 \exp(-B\phi^{3/2}/\beta V) \quad (1)$$

where ϕ is the work function of the tip, A and B are constants, and β is a field enhancement factor depending on the geometrical structure [7].

Metal tips were used to study the field emission in the early days. The metal tips are prepared by electrochemical etching [8, 9] and lead to an intensification of the electric field. Among various metals, refractory metals, such as tungsten, and molybdenum are utilized for field emitters

because of their high melting temperature and mechanical robustness to high electrical stress [10, 11]. An emitter coated with a thin film of low work function, such as Cs, can render lower operation voltage, but the chemically reactive Cs becomes easily oxidized, decreasing the current density [12]. However, the high work function and low field enhancement factor of metal emitters of about 10 require an ultrahigh vacuum environment and appreciable emission voltage in the range of $3\text{--}7 \times 10^9$ V/m, which would eventually result in the ionization of the residual gases, physical sputtering of the emitter tip, and fluctuation of the emission currents. For these reasons, coating the emitter tips with wide bandgap materials (WBGs) exhibiting negative electron affinity (NEA) such as diamond, SiC, *c*-BN, LiF, and CaF have been attempted [13–16]. Even though the high mechanical hardness and chemical inertness of the WBG are very beneficial for field emitters, concurrently a wide bandgap becomes a prime obstacle that hinders large electron emission and lowers electrical conductivity unless the coating thickness is controlled with high precision.

Another attempt to circumvent the high turn-on voltage of the metal emitters is miniaturization of the device by microfabrication techniques from the semiconductor industry. The pioneering achievement was first made by Spindt in 1968 [17]. He fabricated a gate-structured cathode consisting of a cathode and a gate electrode. For the cathode, thermal evaporation of molybdenum was conducted through the microcavity, which had been preformed on a layered structure of gate/insulator/cathode. The gap between the gate and the conical-shaped emitter is only about $0.5 \mu\text{m}$ and the cathode is a matrix-addressed Mo emitter array. The proximity of the gate electrode and the high population of emitters, 2.5×10^7 emitters/cm², contribute to the large available emission current of 1000 A/cm² at a bias voltage of 100 V [18]. Despite the fact that such prominent advancements enable us to operate FEDs at low voltage with large emission current, the operation voltage is still too high to be met by the current integrated circuit (IC) chip driving circuit and furthermore thin-film deposition for making the emitter array is not an effective approach for lowering the manufacturing cost and scale-up of the display.

2. ADVANTAGES OF CARBON NANOTUBES

As briefly mentioned in the previous section, field emitters should be robust in order to sustain a high electric field and large emission current. Therefore, the emitter material should have a high melting point, high thermal and electrical conductivity, and high physical stiffness. In addition, low work function is one of the important factors in making a field emission device operable at low voltage. High mechanical stiffness would help emitters to minimize the geometric deformation from ion bombardments; chemical inertness must be a significant advantage making emitters immune to the residual gases. However, it is not easy to find a material satisfying all these requirements. Nonetheless, carbon nanotubes (CNTs) are a potential material for field emitters in many aspects. The CNT first reported by Iijima et al. is a seamless tubular structure formed by rolling

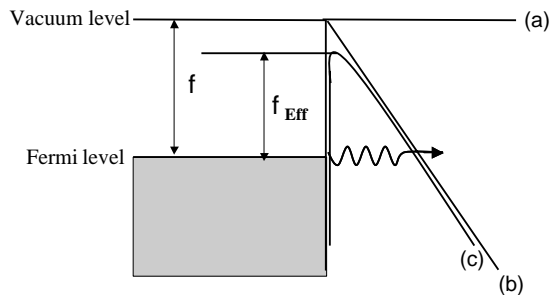


Figure 1. Schematic diagram of potential barrier (a) on the emitter surface, (b) under an applied electric field, and (c) with the effect of image potential. ϕ and ϕ_{eff} are the work functions on the emitter surface without and with the combination of the applied field and image charge, respectively.

up and matching a graphene sheet [19]. The cylindrical CNT is composed of single layers or concentric multilayers of the graphene sheet. The geometric structure of the CNTs makes them very effective field emitters when they are placed inside the electric field due to the large aspect ratio coming from a small diameter ranging from one to several nanometers for single-walled CNTs (SWCNTs) and a few tens of nanometers for multiwalled CNTs (MWCNTs) and a length of several micrometers. CNTs, sp^2 -bonded carbon networks, are supposed to have a high Young's modulus with low mass density. However, the technical difficulties involved in the manipulation of the nanotubes mainly come from the small diameter and the tendency of the CNTs to form bundles, which makes direct measurement of the mechanical properties a challenging subject. As a consequence, only a few measurements on the Young's modulus have been reported. The studies have been carried out under or inside a microscope. One approach is to correlate it with the amplitude of a standalone oscillating CNT whose bottom is fixed at the substrate [20, 21]. The detailed characteristics of the CNT motions observed inside a transmission electron microscope (TEM) are analytically studied after printing the micrographs. Measurements made on many SWCNTs reveal that the Young's modulus is 1.25 TPa, which is greater than the modulus along the basal plane of the graphite. Another approach is to use atomic force microscopy (AFM) to bend an SWCNT bridging a pore of an ultrafiltration alumina membrane using an AFM tip [22, 23]. But, regardless of the experimental methods, the Young's modulus of the SWCNT is about 1 TPa. Also, in the case of the multiwalled CNT with a diameter larger than 2 nm, the Young's modulus is on the same order as that of the graphite. This suggests that a large diameter does not induce stiffening [22].

CNTs, quasi-one-dimensional structures with the unique electronic structure of a graphene sheet [24], exhibit very high electric and thermal conductivity [25]. The electronic properties are highly responsible for the geometric structures [26]. Although graphite is a semimetal, the CNT can be a metal or a semiconductor, depending on the diameter and chirality of the tube, with various energy bandgaps usually below 1 eV [26–29]. The influence of these versatile electronic properties on the geometrical structures originates from the unique mirror-image band structure of the graphene sheet and the quantization of wave vectors along the circumferential direction. The periodic boundary condition along the circumference allows only a certain set of k states of the planar graphite sheet to be available, depending on the tube diameter and chiral angle. In general, the chiral angle of each single-walled CNT can be designated by an integer pair (n, m) , where n and m are indices of two basis vectors of the graphene sheet. Any choice of (n, m) classifies CNTs into two categories, depending on the metallicity. All (n, n) tubes have a band degeneracy, which is induced by crossing π and π^* states at $k = 2/3(\pi/a_0)$. Therefore, these tubes should be metallic. The (n, m) tubes satisfying $n - m = 3i$, where i is a nonzero integer, should also be metallic. All others are large-gap semiconductors. For semiconducting tubes, the bandgap decreases inversely proportional to the diameter. The above band-folding scheme is valid for tubes with a large diameter. However, for the

$(n, 0)$ tube with a small diameter, this scheme is not adequate because the strain energy dramatically increases as the degree of curvature becomes larger. This curvature effect or strain opens up the small bandgap, whereas the tube is practically metallic at room temperature due to the small bandgap. The curvature effects become more prominent, at which point the tube is under mechanical stress because of an enhanced mixing of the σ and π states [30].

To construct the closure of the graphene sheet, the incorporation of topological defects, pentagons, is essential. It results that, many different structures can exist at the cap. The variety in cap structures stems from the variable number of pentagons involved and their relative positions with respect to the hexagons [31]. Due to this property, it is possible that there exist several different cap structures at the same tube diameter and the consequence is remarkable differences in the electronic structures at the cap.

The electronic structures in correlation with the chirality and the diameter of the tube have been examined by scanning tunneling spectroscopy (STS) [32–34]. Raman spectroscopy has proved to be an easily accessible, reliable, and nondestructive method to probe the chirality and diameter of the individual tube [35]. However, these approaches are not applicable for the investigation of the cap geometry. The structure of the cap has been investigated using field emission microscopy (FEM) [36–38]. A pentagon ring of carbon is clearly seen. In addition, since the pentagon is a defect, the electronic structure at the cap should be different from that on the wall. As mentioned previously, the diversity in structure results in various local electronic structures at the cap [39]. Understanding the local density of states (LDOS) originating from these defects has huge significance for discovering the field emission properties since, in some topological configurations, the localized states can emerge very near the Fermi level at which the field emission takes place [40]. At pentagonal sites, the field emission is observed to be stronger and gas adsorption is more active than at other hexagonal areas [36]. Dean et al. have proposed that the nonmetallic behavior observed at the high voltage region might be related to the defect states [41]. Unfortunately, complete comprehension of the emission behavior correlated with the cap geometry is not well established. This will require systematic studies in the near future.

When the carbon nanotube was first discovered in 1991, it was a soot synthesized by arc discharge [19]. Usually, this growth method together with laser ablation is known to produce highly crystalline single-walled and multiwalled nanotubes [42]. The generated CNTs are entangled in bundles, with amorphous carbon, graphitic particles, and other forms of carbons as by-products [43, 44].

The entanglement of the CNTs with amorphous carbon layer and catalyst particles along the tube leads to the laborious purification process consisting of sonication, air oxidation, and acid treatments [44]. After the purification process, only a small amount of CNT with high quality is obtained. However, in the two growth methods, since the synthesis takes place over a very local area at extremely high temperature, the scale-up of the growth system is practically impossible. Also, without the removal of amorphous carbon, metal particles, and graphitic particles, the application of pristine

CNTs as field emitters causes the emission properties to be uncontrollable. However, if we understand the growth mechanism, where catalytic decomposition of hydrocarbon is involved, the control of diameter, length, directional growth, and scale-up of growth system, which are impossible in arc discharge and laser ablation, would be achieved in a chemical vapor deposition (CVD) system.

In CVD, all the growth parameters from arc discharge and laser ablation are precisely controlled and slowed down over a prolonged growth period. First, in CVD, the heating of catalyst metals is carried out after the CVD chamber is filled with carrier gases and hydrocarbon sources up to a certain pressure. Usually, catalyst metals such as Fe, Ni, and Co are deposited on a Si substrate or porous support such as alumina and zeolite to hold the nanoparticles inside the channels [45–47]. During the temperature elevation, the control of diffusion and agglomeration of metal particles due to thermal energy is very critical to monitor the tube diameter and density [48]. The growth temperature varies with the gas species and catalyst metals, but ranges between 600 and 1000 °C. As carbon sources, C₂H₂, CH₄, CO, ethylene, and even alcohol are used [48–51]. Recently, the growth of CNTs aligned in the perpendicular direction to the substrates has successfully been accomplished by many groups [52–55]. CVD tubes grown for 20–30 min are, on average, about 10–50 μm long and 50 nm wide. The huge progress in CNT growth using the CVD method has led to a reduction in the purification steps and resulted in vertically aligned tubes. Still, the growth of CNTs below 550 °C over a large area in an economic way requires further investigation for their practical application.

3. FIELD EMISSION PROPERTIES OF CARBON NANOTUBES

Before de Heer and his group studied the field emission using highly oriented CNTs [56], the growth of the CNTs using the CVD method had been demonstrated [57, 58]. Although CVD growth promises several advantages for applications as field emitters compared to arc discharge and laser ablation synthesis, the realization of the field emitter was postponed due to poor alignment of the CVD-grown tubes. However, later, more adaptable CNTs with better orientation were grown on mesoporous media by the CVD method by Li et al. [59]. The above pioneering research has ignited worldwide research on CNTs as field emitters. MWCNTs can be grown in a preferential direction using catalyst particles deposited on Si substrates using a magnetron sputter. However, the complexity of the growth parameters such as temperature, flow rate, catalyst metal, gas species, pressure, and grain size of catalyst metal results in wide diversities in tube structure, diameter, density, length, and crystal quality.

Characterizations of electron field emission from CNTs, which are placed inside a strong electric field, have been carried out in many different ways. We know from (1) that the emission currents are a function of work function and field enhancement factor. However, the work function, in particular, at the emitting site, is not the same as that at the bulk and is very sensitive to local electronic structures. Many groups have demonstrated from FEM studies

that field emission occurred through the cap, and the cap structures observed on the phosphor screen are different from tube to tube. This implies that emission currents might change dramatically depending on the cap geometry, but systematic studies have not been carried out due to the various geometries. Some theoretical calculations on the effects of cap structures have been conducted only on certain types of tubes [39, 60]. Kim et al. proposed that the localized states of the pentagon defect contribute to the field emission only at strong electric field and the degree of charge accumulation at the cap shows stronger dependence on the tip sharpness rather than the local atomic geometry [61].

From the aspect of electronic structures, CNTs are different from previous metal emitters. Nevertheless, the Fowler–Nordheim (F–N) characteristic curve obtained from CNTs resembles that of metal emitters. Due to the advantage of the tip geometry, the CNT has a lower turn-on voltage, between 1 and 2 V/μm. The SWCNT has a lower turn-on voltage than the MWCNT. The evaluated field enhancement factor from the F–N plot based on a work function of 5.0 eV is about 1000–3000 and 2500–10,000 for MWCNTs and SWCNTs, respectively [62]. The higher field enhancement factor for SWCNTs is attributed to the smaller diameter. Bonard et al. have also tested the emission stability of both tubes for long-term operation. The emission currents from the SWCNTs degrade about 10 times faster than those from the MWCNTs. This degradation could be explained possibly by the structural weakness of the SWCNT edge to the ion bombardment of residual gases [62]. The higher stability of the MWCNTs could also be explained by the tube edge interactions, where the tube edges are stabilized by lip–lip interactions via spot-welded adatoms [63].

The directional dependence of the emission properties was also studied. The field emission has been examined as a function of the angle of CNTs with respect to the substrate [64]. Contrary to the general belief that the low turn-on voltage of CNTs is attributed to the high aspect ratio, where the aspect ratio is presumed to be even greater with the CNTs aligned in parallel with the electric field, the CNTs parallel to the substrate eject electrons at a lower turn-on voltage. It has been proposed that numerous defect sites along the tube wall contribute to easier electron emission. Another possible explanation is the catalyst existing at the end of the tube, which degrades the field emission currents.

With regard to the fabrication of flat-panel displays based on the CNTs, depositing the emitters with an optimum number of CNTs per unit area is crucial, since the poor emission properties observed from the CNT films grown by CVD are speculated to originate from high tube density due to the shielding effect of the electric fields. Several approaches have been attempted to regulate the CNT emitter density on the substrates. One approach is to regulate the grain size and density of the catalytic particles during thin-film deposition using typically RF (radio frequency) magnetron sputter, which enables one to control the grain size and density by the plasma power, substrate temperature, and deposition time [65].

Another way to deposit catalyst particles is to print using a stamp. This is called micro-contact printing (μCP), which uses a patterned elastomeric stamp to transfer a self-assembling material (SAM)–forming ink. The stamp is

made by casting a polydimethylsiloxane (PDMS) elastomer on a master with a designed pattern prepared by MEMS (microelectromechanic system) techniques. A catalyst-containing solution is used for the ink. [66–68]. The transfer of catalyst particles is made by compressing a stamp against the substrate after dipping the stamp into the ink or placing a droplet on the stamp. The primary advantages of μ CP are its simplicity and scalability. One can readily change the concentration of the catalyst ink and generate reproducibly the same pattern over a large area. Bonard et al. have examined the correlation of concentration of catalyst ink to CNT growth. In their study, up to a certain concentration, the alignment of CVD-grown CNT becomes better along the vertical direction and then CNTs do not grow above the optimum concentration [69].

Another way to control the emitter density is to use a template, which arranges the metal particles along geometric channels. The template is composed of arrays of pores, whose diameter and pore–pore distance are well defined through the anodizing process [70]. During the anodization of high-purity aluminum, we can change the pore diameter, pore–pore distance, and pore depth by varying the voltage, temperature, reaction time, and proper choice of chemicals. Using an anodized aluminum oxide (AAO) template, monodispersed pores with a high regularity over a large area have been obtained by several groups [71–74]. One of the benefits of using the AAO template is that we can precisely control the ratio of height to diameter, which is an essential factor for regulating field emission and minimizing screening effects, as shown in Figure 2a and b. The detailed significance of screening effects due to the neighboring tubes is well documented in the literature [75]. The most efficient ratio of tube height to tube–tube distance is known to be

about unity. The field enhancement factor at this configuration ranges from 2500 to 3500, as shown in Figure 2c and d.

All the approaches mentioned above manage the as-grown tube density by arranging catalyst particles before the tube growth. The following screen-printing method is used to handle the ready-grown nanotubes. In the screen-printing approach, the as-grown or purified SWCNTs are dispersed in isopropyl alcohol and mixed with an organic binder such as nitrocellulose and ethylcellulose. The mixture with homogeneously dispersed CNTs is pasted on the prepatterned cathode electrodes [76, 77]. However, the number of emitters per unit area is also very sensitive to the pasting techniques.

Another parameter as significant as the tube density in achieving emission uniformity is the film roughness. Initially, the emission pattern of the CVD-grown tube is very poor. The reason is that tubes protruding out from their neighborhood dominate the emission currents. Improvement in the uniformity of the emission pattern requires removal of those protruded tubes. The removal process is known as high-voltage annealing, since the tube is gradually burned away by resistive heating at large emission currents. While the duration of the annealing process is strongly dependent on the applied voltage and emission currents, it usually lasts longer than 24 h.

The field emission characteristics of CNTs at room temperature exhibit current suppression at a high-field region, that is, a decrease in the slope of the F–N curve, which is different from those of the typical metal tips [18, 78]. The turn-on voltage of the CNTs is as low as a few volts per micrometer, lower than that of the typical metal tips by a factor of 100 [79]. Several mechanisms such as space charge, screening effects, metal particles at the cap, and gas adsorbates have been proposed in order to explain the current suppression at high field.

Lim et al. have checked various possible causes and have concluded from a slope change during only rise sweep, not fall sweep, in their I – V curves that the release of gas adsorbates at large emission currents are the origin of current suppression [80]. Several groups have observed thermal motions of the gas adsorbates at the cap using FEM [36, 37, 81, 82]. The cause of thermal fluctuation in FEM images is local heating for large emission currents. At the stage that gas adsorbates initially reside on the surface of cap, the emission currents are stable and the FEM image is motionless. As the increasing emission currents start to heat up the cap resistively, local heating, the emission currents fluctuate as do the FEM images. At even higher bias voltage, a complete desorption of gas adsorbates on the cap is observed with a significant current decrease. At desorption, the temperature is reported to be around 1000 K [41, 82]. The cyclic repetition of voltage sweep generates consistent I – V characteristics and FEM micrographs. As a consequence, local resonant states present on the surface of the cap temporarily disappear and reappear in parallel with an increase and decrease in the emission currents. Field emission enhanced through the resonant states becomes suppressed in the absence of adsorbates.

For the purpose of clarifying the effects of each gas species, Dean et al. intentionally exposed CNTs to different gases and studied the variation of the emission properties.

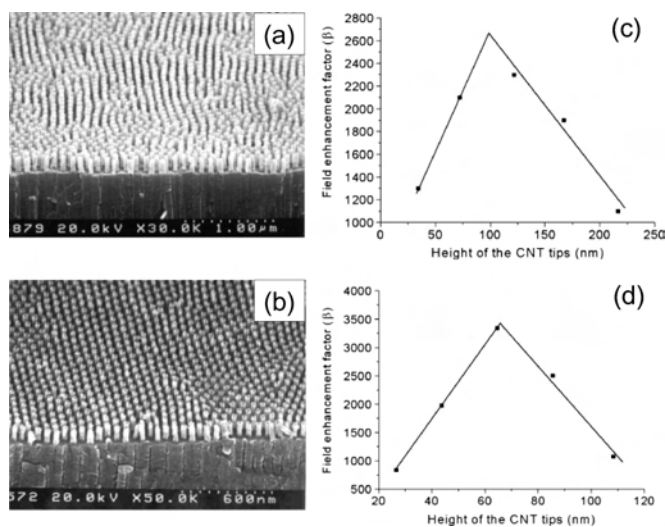


Figure 2. SEM images of CVD-grown CNTs using AAO template. The average tube diameter and tube–tube distance are (a) 38 and 104 nm and (b) 19 and 65 nm, respectively. The variation of field enhancement factors in the function of tube height. The intertube distance is (a) 104 nm and (b) 65 nm. Reprinted with permission from [75], J. S. Suh et al., *Appl. Phys. Lett.* 80, 2392 (2002). © 2002, American Institute of Physics.

Saito et al. have investigated the variation of the emission properties upon adsorption and desorption of gas adsorbates [36]. They observed the migration of gas adsorbates on the cap of the CNT and found that the pentagon site is favorable for electron emission because of not only geometrical protrusion but also the presence of strongly localized states. It is also found that the gas adsorbates preferred to reside on the pentagon sites. To remove the gas adsorbates, heating to about 1300 K is required. This temperature is somewhat higher than the desorption temperature witnessed by Dean et al. After heating, the stepwise decrease in emission currents was observed as the gas adsorbates came off the cap, as shown in Figure 3.

Among the species introduced into a vacuum system, water vapor is the only species enhancing emission currents. Water molecules are removed from the surface of the CNT at about 900 K and degrade the emission. Lim et al. studied the effects of different gases on the field emission properties as a function of exposure times. In their experiment, oxygen gas reduces the emission currents significantly through the oxidative etching process. The erosive etching of oxygen gases destroys the sp^2 network and depletes the $2p-\pi$ electron states, which contribute to the field emission currents [83, 84]. The destruction of tube structure and reduction in electronic states near the Fermi level result in high turn-on voltage and low emission currents. After oxidation, the contents of the sp^3 -bonded structures increase. The reverse transition from sp^3 to sp^2 is partially achieved as the MWCNTs were annealed above 750 °C.

Theoretical calculations on the electronic structures in the presence of gas adsorbates and an adsorption mechanism have provided a clearer understanding of the effects of field emission upon gas species [85–87]. The influence of water molecules on field emission has been studied. Water molecules, whether they maintain the molecular structure or break into ions on the cap, always increase the emission currents. Maiti and his colleagues have assessed the influence

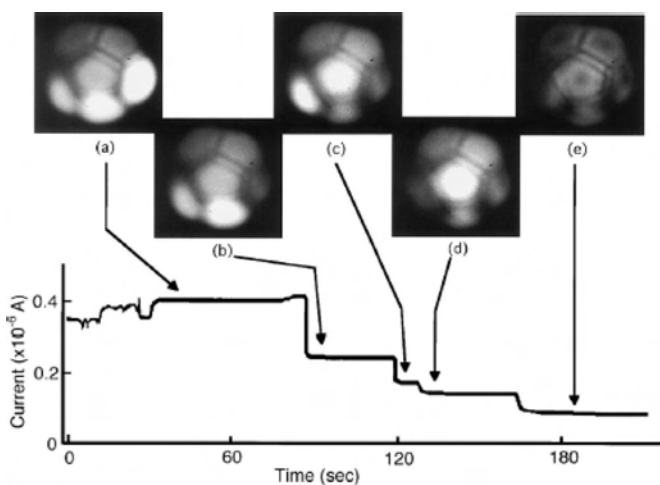


Figure 3. FEM images showing progressive desorption of gas adsorbates with the change of emission currents. The first pattern was taken 60 s after the beginning of heating. The following patterns were taken (b) 90 s, (c) 120 s, and (d) 130 s after heating, respectively. (e) Heating was turned off. Reprinted with permission from [36], K. Hata et al., *Surf. Sci.* 490, 296 (2001). © 2001, Elsevier Science.

of water molecules that exist on the cap. In their study, they chose a closed tube and water molecules to be physisorbed on the cap. Polar water molecules construct complexes stable up to several hundred degrees, with a corresponding decrease in the ionization potential and stability of the highest occupied molecular orbital (HOMO). The resulting electronic structure becomes more favorable to field emission. The preservation of the molecular structure of water neglects the possibility that water molecules can break into H and OH ions. The residence of water fragments such as H and OH ions on the open edge of armchair and zigzag tubes is theoretically well simulated by Hwang and Lee [88]. The resulting electronic states with the Fermi level shifted toward the conduction band by 0.14–0.17 eV enhance the field emission for both armchair and zigzag tubes, where the effect is more pronounced in the zigzag tube edge because of the introduction of additional states near the Fermi level.

Kim et al. have explored the adsorption of hydrogen, nitrogen, and oxygen molecules at the open edge of CNTs. The shift of the Fermi level upon each gas is presented in Table 1. In their study, oxygen gases with stronger electronegativity suppress the emission currents by creating a dipole layer toward the inner tube at the edge of the tip. In the case of hydrogen gases, the weaker electronegativity in the hydrogen atom than in the carbon atom is supposed to promote the emission currents. However, experimental results show that the hydrogen gases do not affect the field emission appreciably. Such a result may be attributed to the absence of resonant states, even though adsorption of hydrogen gases shifts the Fermi level toward the conduction band. Nitrogen gases are supposed to be less effective than other gases, since the binding state to the edge is relatively weak and the dipole strength is weak due to a negligible charge transfer [85].

As CNTs are exposed to oxygen gases, the situation becomes more complicated due to the progressive change in the cap geometry. The etching process must be more active around the cap area than the wall due to the pentagonal defect sites. Park et al. have pointed out that at the stage of molecular adsorption emission currents are enhanced by the electronic structures and local field intensification at the adsorption sites. In the case of atomic adsorption, the latter effect is more dominating, whereas molecular oxygen generates more currents from the new energy states. However, for prolonged exposure, the cap structure becomes open and the edge can be terminated with atomic oxygen, resulting in a decline in the emission currents [87].

Strengthening of the electric field due to sharp geometry occurs at the cap. The amplified field narrows the potential barrier so that electrons tunnel more easily into a vacuum. Therefore, the field emission electron strongly reflects the

Table 1. Change in the Fermi level due to gas adsorption at various sites.

	Armchair, top	Armchair, seat	Zigzag, top
O ₂	−0.31	−0.50 [®]	−0.12 [®]
H ₂	0.08		0.15
N ₂			0.04

Note: [®] indicates the resonant states. Units are in eV.

local density of states (DOS) at the emitting site. As mentioned earlier, the integration of pentagon rings into the hexagon network creates significant modification in the local DOS. In addition, it is shown by scanning tunneling spectroscopy (STS) that the number of pentagon rings and their relative positions to the hexagon generate a wide variation in electronic structures [39]. The theoretical evaluation of a (5, 5) metallic nanotube, whose cap is a hemisphere of C_{60} , reveals the existence of localized states about 0.8 eV above the Fermi level. Therefore, this means that the local DOSs at the cap strongly influence the field emission behavior. The energy distribution of electrons emitted from the MWCNT was measured by Fransen et al. [37]. A distinguishable difference between the metal tip and the MWCNT tip is the shift in the peak position upon extraction voltage. This opens up two possibilities. One is that the nanotube is semiconducting and the other is that the insulation layer between the W tip and the nanotube induces a voltage drop. It is not clear yet which mechanism dominates.

The reason that we have studied various emitter materials and examined the environmental stabilities is to securely preserve the tip from degradation. The degradation process either breaks out abruptly or progressively develops over a long period. The degradation of the tips can be divided into two types: chemical contamination and physical destruction of the tip geometry. Since current suppression, triggered by the chemical adsorption of gas molecules, was addressed previously, here, the cause of the geometrical damage due to large emission currents and ion bombardments will be discussed. Usually, in metal emitters, vacuum breakdown results from the abrupt increase in pressure between the electrodes, which is responsible for the introduction of materials from the cathode and anode. When the tip is involved in the vacuum breakdown, the sudden increase in pressure between the two electrodes is attributed to large emission currents, which melt and evaporate the tips. This catastrophic vacuum breakdown forms a conducting path between the electrodes, leaving the devices malfunctional. Another deformation of the tip is triggered by the bombardment of ionized residual gases. The gases existing between the gap become ionized by the emitted electrons and the ionized gas molecules are accelerated toward the tip. The sputtering process continues progressively during the operation of the FED and can end up with a vacuum breakdown in the long run. Although CNTs show exceptional conductivity and physical stiffness, they develop slow variations in their structures unless the driving voltage is less than the sputtering threshold. The circumstance in which CNTs are exposed to energetic ion particles has been well simulated inside a field ion microscope (FIM) by Hata et al., who found that CNTs are damaged at an electric field above 10 V/nm [89]. The study also reports that the field evaporation of MWCNTs and SWCNTs produces carbon clusters. The major product constituting the cluster is C_{20} , which is the smallest cage structure composed of hexagons and pentagons. For the field-induced unraveling process, it was shown by Lee et al. from theoretical simulation that the zigzag tube is more favorable for the unraveling of carbon atoms and the field strength is similar to the result from the previous experiment [90]. Dean et al. also witnessed a slow disintegration of carbons from the tip [91]. In their field

emission microscopy (FEM) studies, an individual SWCNT is able to withstand emission currents up to 1–2 μA , corresponding to 10^9 A/cm². Above this current level, CNTs begin to show local heating evidenced by blurred ring images spinning continuously, as shown in Figure 4. The rotating ring on an FEM image is evidence that the CNT is being eroded away from thermal evaporation at about 1600 K.

To enhance environmental stability and durability to ion bombardment, chemical contamination, and local heating, various materials have been used as coatings at the apex of the metal tip [92–94]. However, in the case of CNTs, only a couple of studies have been carried out. The criteria for the choice of coating material include chemical inertness, mechanical hardness, and thermal conductivity. Diamond-like carbons (DLCs), which consist of sp^2 and sp^3 carbon, are good electric and thermal conductors and are physically hard as well due to the tetrahedral sp^3 bond. It is reported that deposition of 20-nm-thick DLC reduces the turn-on voltage from 2.6 to 1.5 V/ μm [95]. However, such advantageous effects disappear as the coating thickness increases to 50 nm. Another material studied is MgO deposited on CVD-grown vertically aligned MWCNTs. The role of the MgO layer is to lower the turn-on voltage by resonantly enhancing tunneling inside the MgO layer [96].

Doping is another way to enhance the field emission properties by altering the electronic structure. The most commonly used doping materials are boron and nitrogen. Several studies report remarkable changes in the structure and growth behavior. However, the correlation of those changes with field emission effects has not been reported. Only one group has reported that Cs-doped SWCNT film shows a remarkable decrease in work function and turn-on voltage, which is similar to the metal tip [97]. Although the encouraging reduction in work function of the CNT has been achieved, Cs deposition is not applicable to the usual vacuum environment of FED due to degradation [98].

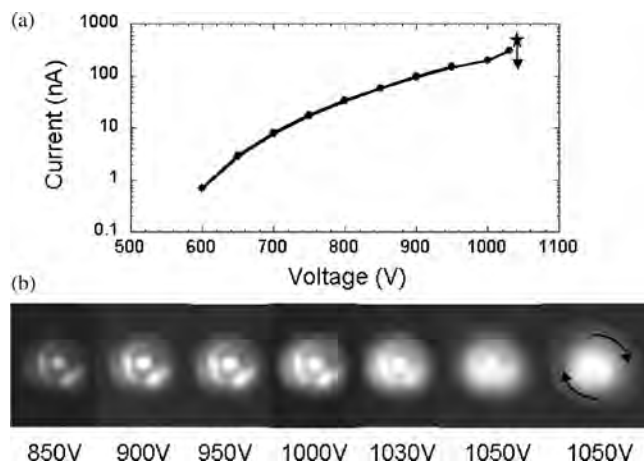


Figure 4. (a) I - V behavior of SWCNT beyond F-N region. (b) Evolution of the FEM image with an increase in emission currents. The image at 1050 V rotates with a frequency over 5 Hz. Reprinted with permission from [81], K. A. Dean and B. R. Chalamala, *Appl. Phys. Lett.* 76, 375 (2000). © 2000, American Institute of Physics.

4. APPLICATIONS

Several applications such as FED, electron multiplier, and X-ray gun have been demonstrated. Among these applications, the FED will have the largest impact on our society by revolutionizing the display. The fast-growing FPD market and the superior properties of FED have led companies such as Motorola and Candescant to invest in research and development of microtip FEDs. In spite of well-established fabrication technologies, the high production expense, tip degradation, and difficulty in scale-up make Mo tip-based FED uncompetitive with other types of FPDs in the market. The array of the microtip, called the Spindt cathode, was made by evaporating an emitter material through the gate holes. As the size of the cathode becomes larger, the nonuniformity and production cost go up rapidly.

To overcome the problems arising from scalability and fabrication cost, several concepts for low-cost and scalable cathodes were proposed by different industries such as Canon, Matsushita, Hitachi, Samsung, and ISE Electronics. Among these enterprises, Samsung and ISE Electronics are using CNTs as field emitters.

The first FED taking advantage of CNTs, demonstrated by Wang et al., has a different form of cathode array [99]. For this cathode construction, a composite of nanotube and epoxy is squeezed into microchannels on a glass substrate since selectively CVD-grown CNT emitters are not accessible to a large area and sodalime glass substrate. The growth temperature inside the CVD chamber is between 650 and 1000 °C. The emitter density of the as-prepared cathode in the FED is about two tubes/ μm^2 . A panel, $1 \times 1 \text{ cm}^2$ in diode structure, successfully operates inside a vacuum system at an applied voltage of 300 V.

A fully sealed FED, 4.5 in. in diagonal, with a high brightness of 1800 cd/cm² has been demonstrated by Choi et al. [76]. To achieve an operable pressure, a nonevaporable getter was used. In the display, purified SWCNT was mixed with an organic binder. This composite was squeezed into a premade substrate through the metal mesh. In this method, the uniform dispersion and vertical alignment of the CNTs must be satisfied in order to meet the practical performance requirements. To meet the requirements, after pasting the composite, a pretreatment such as rubbing and electric field conditioning was carried out to align the embedded CNTs in the vertical direction, followed by burning of the organic binder [100]. This fully sealed diode-type display (200- μm glass spacer) turns on at less than 1 V/ μm and emits 1.5 mA at 3 V/ μm .

The matrix-addressed CNT-FED proves that the cathode array produced by mechanical printing of the mixture of the CNT and epoxy/organic binder on the electrode-patterned sodalime glass is scalable, enabling one to enlarge the panel without limitation in size and with low production cost.

The above two prototype FEDs are configured in a diode structure, consisting of a cathode and anode. Under this configuration, the ejection of electrons from the emitter surface is achieved at high voltage since the vacuum gap is about 200 μm . The diode structure is not able to tune the colors and brightness once the electrons leave the surface of the emitter. Imposing an additional gate electrode at a typical distance of about 1 μm above the emitter makes for

low-voltage operation and a full range of colors. A few gate structures and fabrication processes have been suggested [99, 101–103]. The common aim of all these different structures is to efficiently tune the emission currents, simplify the fabrication process, and collimate the electron beam to the corresponding phosphor cells with a finer color tuning.

The most common triode structure is a normal gate. The gate electrode is placed between the emitter and the anode. Samsung developed a fully sealed normal-gated FED with an active area of 5 in. [101]. The CNT emitters inside the microcavity are electrically isolated from the gate electrode and sit on a resistive amorphous Si layer. The gate hole and the emitter diameter are 30 μm and 20 μm , respectively. The applied voltage over the 1.5- μm insulator gap between the gate and the cathode turns on the display panel at 65–70 V. The emitted electrons are accelerated through a 1.1-mm vacuum gap at 1.0–1.5 kV. Researchers at Samsung observed that at a higher anode voltage the anode current increased, since the transmittance of the ejected electrons became higher. The device renders 256 gray scales. Since Samsung prepared the emitter array using the printing method, the whole process can be carried out below 400 °C.

The organic binder degrades the vacuum inside the FED, even after combustion of the organic binder. Therefore, depositing CNT emitters in the microcavity using the thermal/MPE-CVD method might be effective to avoid the current fluctuation due to outgassing [104, 105]. Current fluctuation due to outgassing is observed to be larger than 7% in a fully sealed FED [76]. In the CVD approach, the critical issue is how to control the tube number and vertical alignment inside the microcavity. Precise control of these parameters requires monitoring the grain shape, the size of the Ni particles, and the morphology of the TiN sublayer. Pribat et al. implanted a single CNT in each cavity with a diameter of 200 nm by controlling the size of the catalyst particles.

The normal-gated FED fabricated by Samsung has displayed promising picture quality. However, one of the problems observed with the normal-gated FED is crosstalk. The circular shape of the cathode in the microcavity enhances the electric field at the edge of the cathode, leading to a strong widening of the electron trajectory [106]. Therefore, the emission pattern is brighter at the edge rather than at the center due to crosstalk with neighboring pixels. Another disadvantage of the normal-gate structure arises from the cathode fabrication. Since the gate electrode is formed at the final fabrication step, the contamination of the CNT with gate materials is unavoidable.

In the under-gate structure, the gate electrode is located below or at the same height as the cathode so that the trajectory of electrons is tilted with respect to the normal direction. The schematic view of an under-gate structure is shown in Figure 5a. The CNT film is pasted at the edge of the cathode electrode. This geometry, which concentrates the electric field at the edge, contributes to a narrowing of the electron trajectory, resulting in a uniform emission pattern and better color separation. A benefit of the under-gate configuration in terms of fabrication is that the manufacturing process becomes greatly simplified. A prototype monochromatic FED, 15 in. in diagonal, designed with the under-gate structure is shown in Figure 5b.

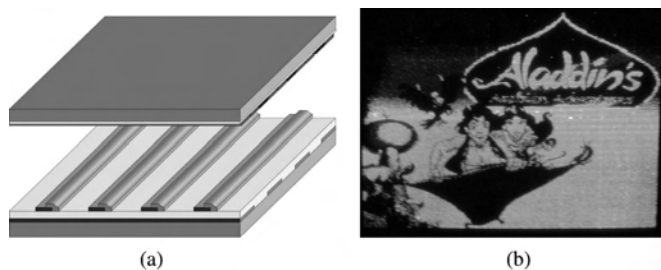


Figure 5. (a) Schematic view of an under-gate structure. (b) Monochromatic 15-in. FED fabricated with an under-gate structure.

ISE Electronics also demonstrated a CNT-based FED, which is shown in Figure 6a. This FED has many different features compared to the FED made by Samsung. In the display from ISE Electronics, the emitters are prepared using the thermal CVD method. The benefit of the CVD-grown tubes is good uniformity in the emission pattern, resulting from the smooth surface and round edges of the CNT electrodes [107]. However, the problems found during operation of the display are thermal distortion and vibration of the gate electrode. Deformation of the gate electrode is not a result of the growth temperature. The gate electrode is made of metal and is formed like a long metal wire [108]. The gate electrode shows local thermal expansion by emission currents. The inhomogeneous emission pattern contributed by the thermal distortion was circumvented by introducing a gate–insulator composite between the ribs of the anode

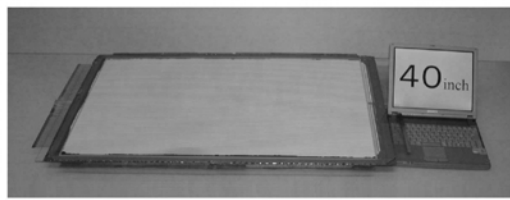
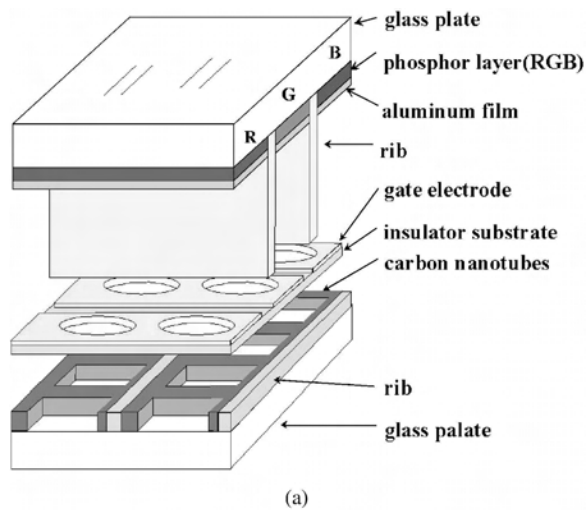


Figure 6. (a) Schematic of a triode structure with gate–insulator composite having through holes. (b) CNT-FED panel in 40 in. diagonal. Reprinted with permission from [110], S. Uemura et al., “SID’02 Digest,” 2002, p. 1132. © 2002, Society of Information Display.

and cathode electrodes. The composite is compressed by an atmospheric pressure during the evacuation process, which enables the gate–insulator composite to compensate for the thermal distortion. In addition, the combination of metal and insulator is also advantageous in preventing thermal vibration due to the insulator. All these new features in the display enhance the emission pattern tremendously by maintaining the exact distance between the gate and the cathode electrodes over the whole area. ISE Electronics demonstrated a 40-in. CNT-FED panel with the benefits of all the above features, as shown in Figure 6b. The pixel size of the panel is 2.54 mm × 7.62 mm [3 (RGB) × 2.54 mm] [109, 110].

The application of a CNT as an electron multiplier does not seem to be attractive because of the metallic characteristics of the sp^2 bond. Therefore, the secondary electron emission (SEE) is not expected to be high. Usually, a large amount of SEE has been observed on the surface of an insulator such as MgO, SiO₂, and diamond. The common property among these materials is that they are insulators with sparse free electrons. Therefore, once the valence electrons are released by energetic incident electrons, the valence electrons do not lose energy by an inelastic collision with conduction electrons. Consequently, those electrons arriving at the surface can escape into the vacuum as long as their kinetic energy is larger than the work function. From all these aspects, the electronic structures of the CNT are not good for the SEE. Nevertheless, what makes the nanotube attractive as an electron multiplier is its geometric structure. The possible application of CNTs to electron multipliers was demonstrated for the first time by Yi et al. [111]. In their experiment, catalytically CVD-grown MWCNTs on a silica glass were coated with a MgO layer, which is one of the SEE materials. As they bombarded the surface of the MgO, a huge electron emission was detected with this geometry. The SEE yield in this case is measured to be 22,000 and is very sensitive to the backbias, a voltage applied to the MWCNTs [112]. This value is promisingly large compared to the MgO by itself, whose SEE yield is about 800. Kim et al. proposed that Townsend avalanche effects due to field amplification at the tip of the MWCNT is responsible for the generation of the huge number of secondary electrons in the MgO film. The large field enhancement factor of CNTs, however, highly exaggerates the electric field at the tip and triggers the secondary electron emission. The field enhancement factor of the MWCNTs is about 1000–2000. The thickness of the MgO layer is also one of the critical parameters determining the SEE yield. The amplification phenomenon is most prominent in a MgO layer with a nominal thickness of about 500–2000 Å.

Luminescent lighting elements equipped with carbon nanotube emitters have been successfully exhibited [113, 114]. The lighting elements shown so far are, in principle, working on field emission. In particular, the flashlight designed by Saito et al. is similar to a gated-structured FED. The technical advancements accomplished by CNTs, compared to conventional thermionic filaments, include superior environmental and emission stability together with low power consumption. This device can operate in a high vacuum range

and sustain stable emission currents over 4000 h. In addition, the intensity of luminance is twice that of conventional devices [115, 116].

Another application of the lighting element was accomplished by Bonard and his colleagues [114]. A luminescent tube was constructed in a cylindrical shape to take advantage of the stronger electric field than diode structure at the same gap distance. Inside the tube, tungsten wire, which was coated with catalyst particles, was used for the growth of MWCNTs and placed at the center of the tube for electron emission. The I - V characteristics of the tube show a good agreement with the Fowler–Nordheim equation. The brightness obtained from a tube 50 mm long and 21 mm wide is reported to be 10,000 cd/cm².

Most X-ray tubes currently on the market produce electrons by resistively heating a tungsten filament above 2000 °C. Some of the problems naturally inherent in thermionic electron emission have been mentioned before. In addition, the thermionic cathode intrinsically has low response time and the chemical reaction with residual gases shortens the lifetime, which leads to failure of the cathode as well. To liberate the current X-ray tube from the above-mentioned problems, the hot cathode has been replaced by a CNT-based cold cathode [117]. In this setup, tungsten wire, on which MWCNTs were grown after deposition of cobalt as a catalyst, was used as the electron source. The MWCNT-covered W cathode contributes to a better X-ray image compared to the thermionic cathode due to the narrower energy distribution of the emitted electrons. It also shows a high operating vacuum pressure of 10⁻⁷ torr. However, low emission currents and short lifetime at this pressure prove that the tube is still far from the marketable stage. Yue et al. resolved the problems of coating SWCNTs on a flat metal disk by electrophoresis [118]. In this case, the solid attachment of the CNT to a metal disk is very crucial, particularly under a strong electric field. To enhance the adhesion between the tube and the metal disk, an iron interlayer was evaporated onto the substrate. The as-prepared cathode easily yields a current density of 30 mA/cm² with negligible fluctuation during operation for 18 h. The above results show that CNT-based X-ray tubes seem to overcome the technical difficulties in present X-ray tubes such as lifetime, environmental stability, and portability.

5. CONCLUSIONS

The availability of CNT-based vacuum microelectronics on the market is dependent on technical advancements and a profound understanding of the fundamental field emission mechanism. All the studies carried out on individual or multiple tubes have shown that the field emission properties are well explained by the Fowler–Nordheim formula. Nevertheless, there exist many scientific issues that are not clearly answered. For instance, the effects of defect states existing at the cap, at which field emission actively takes places, have not been studied well. In addition to this defect effect, comprehension of the difference between an open and a closed tube under intensive electric field is also important. The deposition of CNTs over a large area and at a temperature below 500 °C is another issue to be solved. The cause of

field penetration observed from FEM studies is still ambiguous whether it is due to the existence of a semiconducting tube or an insulating layer between the CNT emitter and the metal support.

The effective work function at the cap of the clean CNT is one of the intrinsic parameters to be clarified. Several groups have measured the work function of the CNT and reached the conclusion that the work function is slightly less than that of graphite. However, field emission preferentially takes place at the pentagon defects, in which strong localized states are observed near the Fermi level. Therefore, the work function at the emitting site is expected to be different from the previously known values. Comprehension of the work function at the emitting sites can elucidate the real field enhancement factor appearing in the F–N plots, since these two parameters are strongly correlated.

There are unique properties originating from low dimensionality. The ballistic movement and Luttinger liquid behavior of conduction electrons have been observed. The details of these properties are well described in the literature [119, 120]. How these low-dimensional properties influence the field emission currents are to be explored in the future.

Regardless of the lack of understanding of the intrinsic field emission properties of CNTs, various realizations of CNT-based applications have shown that the CNT is very efficient for field emitters. However, these applications are just prototypes. To meet commercializable performance, the existing technical obstacles should be resolved.

One of the key parameters that significantly influences the performance of the FED is phosphor. Even though phosphor has a long history of use, the FED has demanded a new phosphor suitable for low voltage operation. In the cathode ray tube, the electrons are sufficiently accelerated to excite the phosphor screen, which is protected by a thin metal film. The phosphor used in CRTs can generate a full range of colors with acceptable efficiency. In addition, conventional high-voltage phosphors are well characterized, commercially acceptable, and widely used. The most widely used phosphors for color display are P22 red, green, and blue triplets. Among these, green has the most significant effect on brightness.

The use of high-voltage phosphor for FED turned out to be unsuitable due to the degradation in lifetime and luminance efficiency. Large emission currents can be supplied to compensate for the low brightness, but this leads to shorter lifetime due to significant chemical degradation. In addition, the larger emission currents will end up increasing the manufacturing cost for high-power circuits.

Numerous materials have been tried and their luminescence properties have been examined. Following are most the promising luminescent materials for low-voltage full-color FED applications: for red, SrTiO₃:Pr, Y₂O₃:Eu, Y₂O₂S:Eu; for blue, ZnGa₂O₄, Y₂SiO₅:Ce, ZnS:Ag, Cl; for green, Zn(Ga,Al)₂O₄:Mn, Y₃(Al,Ga)₅O₁₂:Tb, Y₂SiO₅:Tb, ZnS:Cu,Al [121]. Among the above phosphors, only the ZnO:Zn phosphor shows a lifetime longer than 10,000 h and stable emission and is comparable in performance to monochromatic FEDs [122]. To improve the current phosphor, various modifications have been made and the modifications can be classified into three categories: formation of conducting films, improvement

of chemical and radiation stability, and increase in the luminance efficiency [123]. Modification of the luminescent materials has consisted of the formation of the corresponding salt and solution with subsequent annealing in air. The reduction process results in an insulating layer such as SiO_2 , MgO , TiO_2 , and SnO_2 . These layers are resistant to electron bombardment, are chemically stable, and are known to increase the luminescence efficiency and conductivity as well. With all the above properties, new low-voltage phosphor is supposed to have a fast decay time, thermal stability during the panel manufacturing process, no evaporable substances contaminating the emitters, and acceptable grain size for precise coating [124].

The cathode arrays can be prepared using thermal evaporation through a gate hole. This approach, however, is not easy for scale-up and the production cost may be high. Screen printing is a new approach to overcome the scalability problem with an easy manufacturing process. Regarding the size of the cathode, this approach has no limitations. Printing the mixture of CNT and organic binder requires a firing step to burn out the organic binder at about 350 °C. After removing the binder, the solid attachment of the CNT to the electrode is very important. Therefore, an appropriate choice of electrode material can reduce the firing temperature [125].

The width of the pasted CNTs is about 120 μm on the 390- μm -wide cathode electrodes [106]. The large space between the cathode electrodes fabricated by the screen-printing method provides only 240×576 lines in a 9-in. FED. The smallest pixel size that one can obtain from the current screen-printing method is about 70 μm . Therefore, the finer pitch pattern could define pictures more precisely. A new patterning process permitting a higher resolution FED with finer pitches such as the liftoff method and photolithography has been shown [77, 125]. Using the photolithography approach, the pixel was downsized to 30 μm .

The solid insulation between the cathode and the anode should be obtained for field emission. To insulate between two electrodes, a thin insulating layer, called a spacer, is used. The choice of spacer materials brings many important issues into consideration. For instance, the spacer must be thin, mechanically strong, vacuum compatible, exhibiting low leakage current, and withstanding a strong electric field [126]. Since the spacer is supporting the voltage difference between the cathode and the anode and being exposed to emitted electrons, the resistance of the spacer should be high enough to prevent leakage current and, simultaneously, low enough to dissipate accumulated charges. Electron bombardment can charge the spacer negatively or positively, depending on the energy of the emitted electrons. Induced charges on the surface of the spacer will significantly change the trajectory of the electrons, resulting in image distortion. Choi et al. have simulated the trajectory of electrons in the presence of the charged spacer. Their results show that the image of the dot arrays near the charged spacer appears less luminescent and the dot size looks smaller than one near the uncharged spacer [127].

In certain cases generation of the secondary electron emission along the spacer surface can lead to disastrous failure of the device. This voltage breakdown along the

spacer, called surface flashover, is initiated in the triple-junction region, where spacer, vacuum, and electrode join [128]. Although the detailed mechanism of how the electron ejection at the triple-junction area develops into surface flashover is not clearly understood, the most widely accepted mechanism is secondary electron emission avalanche (SEEA), which is initiated at the triple junction.

Since the surface flashover is ignited by electrons emitted from the triple junction, the introduction of a void at the junction area lowers the electric field. In addition to the void, the insertion of metal strips into the spacer can be advantageous in two ways. First, the metal strips reduce the flashover since it is strongly correlated with charging of the spacer. Second, the image distortion due to charge accumulation on the spacer could be minimized by the conducting strips. However, besides the above two parameters, other parameters also have significant effects on the surface flashover. For instance, the length of the spacer, the spacer surface roughness, the sharpness of the electrodes at the edge, the surface condition of the spacer, and the spacer material itself can all trigger a catastrophic vacuum breakdown.

Physical sputtering of the CNT emitters shortens the lifetime of the FED rapidly. The prototype CNT-FEDs introduced in the literature degrade significantly in a few hours. While an effort to extend the lifetime has been made using double-wall nanotubes (DWNTs), the FED cannot survive long enough to meet the commercial requirement, about 20,000 h.

In this review, we have discussed many important aspects of carbon nanotube-based field emitters that are still under intensive research and development. Because of their short history, some of the phenomena observed during field emission are not well identified. Nevertheless, it has been proven that CNTs are a great applicant for field emitters and tremendous progress has been made. Also, various types of applications have been exhibited. Bringing the prototype devices to the point of acceptable performance and marketable manufacturing cost requires overcoming many of the challenging problems described previously.

GLOSSARY

Adsorbate A substance that adheres on the surface of the material under investigation.

Anodization Method of plating metal for corrosion resistance, electrical insulation, thermal control, abrasion resistance, sealing, improving paint adhesion, and decorative finishing. Anodizing consists of electrically depositing an oxide film from an aqueous solution onto the surface of a metal, often aluminum, which serves as the anode in an electrolytic cell. Plate properties such as porosity, abrasion resistance, color, and flexibility depend on the type, concentration, and temperature of the electrolyte, the strength of the electrical current and the processing time, and the type of metal being plated.

Electronegativity In chemistry, the tendency of an atom to attract an electron pair shared with another atom in a chemical bond.

Electrophoresis The electrostatic attractive movement of charged particles in a colloidal solution that is under the influence of an electric field.

Fermi level A measure of the energy of the least tightly bound electrons within a solid. The value of the Fermi level at absolute zero is called the Fermi energy and is a constant for each solid. The Fermi level changes as the temperature increases and as electrons are added to or withdrawn from the solid. According to quantum mechanics, each energy level can accommodate only two electrons. The Fermi level is the energy level having the probability that it is exactly half filled with electrons. Levels of lower energy than the Fermi level tend to be entirely filled with electrons, whereas energy levels higher than the Fermi level are unoccupied.

Field enhancement Amplification of the applied electric field at the edge of the emitter.

Getter A material with a high sticking coefficient. Therefore, residual gases physically colliding with the surface of getter materials are permanently removed from a vacuum system. After the saturation of the getter surface, the getter is reactivated and adsorbed gas molecules sink into the bulk of the getter. Th, V, Ti, and Zr are used for pumping a vacuum system.

Microcavity A cavity is about 1 μm deep and a few micrometers wide in Spindt structure. This cavity is fabricated by MEMS techniques to form metal emitters through the thermal evaporator.

Shielding effect Weakening of the applied electric field at the tip of the emitters due to the high density of the emitters.

Thermionic emission Emission of electrons that has high enough energy to overcome the surface potential from thermal excitation.

Work function Required energy for electrons to overcome the surface potential barrier.

ACKNOWLEDGMENTS

The authors extend their appreciation to those who allowed their prestigious work to be presented in this review. We also thank Hyun Jin Kim and Im Bok Lee for their valuable support. This work was supported by the Ministry of Science and Technology through the National Research Laboratory program and the KOSEF through the Center for Nanotubes and Nanostructured Composites at Sungkyunkwan University.

REFERENCES

- S. H. Magnus, D. N. Hill, and W. L. Ohlinger, *Appl. Surf. Sci.* 111, 42 (1997).
- H. D. Park, "Field Emission Workshop '02," 2002, p. 143.
- E. L. Murphy and R. H. Good, Jr., *Phys. Rev.* 102, 1461 (1962).
- P. A. Redhead, *J. Vac. Sci. Technol., A* 16, 1394 (1998).
- E. Guth and C. J. Mullin, *Phys. Rev.* 61, 339 (1942).
- W. Schottky, *Phys. Z.* 15, 872 (1914).
- R. H. Fowler and L. W. Nordheim, *Proc. R. Soc. London* 119, 173 (1928).
- W. P. Dyke, J. K. Trolan, E. E. Martin, and J. P. Barbour, *Phys. Rev.* 91, 1043 (1953).
- J. P. Barbour, W. W. Dolan, J. K. Trolan, E. E. Martin, and W. P. Dyke, *Phys. Rev.* 92, 45 (1953).
- E. W. Muller and T. T. Tsong, "Field Ion Microscopy." Elsevier, New York, 1969.
- C. A. Spindt, I. Brodie, L. Humphrey, and E. R. Westerberg, *J. Appl. Phys.* 47, 5248 (1976).
- J. M. Macaulay, I. Brodie, C. A. Spindt, and C. E. Holland, *Appl. Phys. Lett.* 61, 997 (1992).
- V. V. Zhirnov, G. J. Wojak, W. B. Choi, J. J. Cuomo, and J. J. Hren, *J. Vac. Sci. Technol., A* 15, 1733 (1997).
- M. C. Benjamin, C. Wang, R. F. Davis, and R. J. Nemanich, *Appl. Phys. Lett.* 64, 3288 (1994).
- D. A. Lapiano-Smith, E. A. Eklund, F. J. Himpsel, and L. J. Terminello, *Appl. Phys. Lett.* 59, 2174 (1991).
- S. C. Lim, R. E. Stallcup II, I. A. Akwani, and J. M. Perez, *Appl. Phys. Lett.* 75, 1179 (1999).
- C. A. Spindt, *J. Appl. Phys.* 39, 3504 (1968).
- C. A. Spindt, *Surf. Sci.* 266, 145 (1992).
- S. Iijima, *Nature (London)* 354, 56 (1991).
- M. M. J. Treacy, T. W. Ebbesen, and J. M. Gibson, *Nature* 381, 678 (1996).
- A. Krishnan, E. Dujardin, T. W. Ebbesen, P. N. Yianilos, and M. M. J. Treacy, *Phys. Rev. B* 58, 14013 (1998).
- J.-P. Salvetat, A. J. Kulik, J.-M. Bonard, G. Andrew, D. Briggs, T. Stöckli, K. Méténier, S. Bonnamy, F. Béguin, N. A. Burnham, and L. Forró, *Adv. Mater.* 11, 161 (1999).
- E. W. Wong, P. E. Sheehan, and C. M. Lieber, *Science* 277, 1971 (1997).
- P. Chen, X. Wu, X. Sun, J. Lin, W. Ji, and K. L. Tan, *Phys. Rev. Lett.* 82, 2548 (1999).
- S. Berber, Y.-K. Kwon, and D. Tománek, *Phys. Rev. Lett.* 84, 4613 (2000).
- J. W. Mintmire, B. I. Dunlap, and C. T. White, *Phys. Rev. Lett.* 68, 631 (1992).
- R. Saito, M. Fujita, G. Dresselhaus, and M. S. Dresselhaus, *Phys. Rev. B* 46, 1804 (1992).
- C. T. White, D. H. Robertson, and J. W. Mintmire, *Phys. Rev. B* 47, 5485 (1993).
- R. Saito, G. Dresselhaus, and M. S. Dresselhaus, *J. Appl. Phys.* 73, 494 (1993).
- A. Rochefort, D. R. Salahub, and Ph. Avouris, *Chem. Phys. Lett.* 297, 45 (1998).
- R. Tamura and M. Tsukada, *Phys. Rev. B* 49, 7697 (1994).
- W. Rivera, J. M. Perez, R. S. Ruoff, D. C. Lorents, R. Malhotra, S. Lim, Y. G. Rho, E. G. Jacobs, and R. F. Pinizzotto, *J. Vac. Sci. Technol., B* 13, 327 (1995).
- K. Sattler, *Carbon* 33, 915 (1995).
- C. H. Olk and J. P. Heremans, *J. Mater. Res.* 9, 259 (1994).
- A. M. Rao, E. Richter, S. Bandow, B. Chase, P. C. Eklund, K. A. Williams, S. Fang, K. R. Subbaswamy, M. Menon, A. Thess, R. E. Smalley, G. Dresselhaus, and M. S. Dresselhaus, *Science* 275, 187 (1997).
- K. Hata, A. Takakura, and Y. Saito, *Surf. Sci.* 490, 296 (2001).
- M. J. Fransen, Th. L. van Rooy, and P. Kruit, *Appl. Surf. Sci.* 146, 312 (1999).
- Y. Saito and S. Uemura, *Carbon* 38, 169 (2000).
- D. L. Carroll, P. Redlich, P. M. Ajayan, J. C. Charlier, X. Blase, A. De Vita, and R. Car, *Phys. Rev. Lett.* 78, 2811 (1997).
- R. Tamura and M. Tsukada, *Phys. Rev. B* 52, 6015 (1995).
- K. A. Dean, P. von Allmen, and B. R. Chalamalab, *J. Vac. Sci. Technol., B* 17, 1959 (1999).
- T. Guo, P. Nikolaev, A. Thess, D. T. Colbert, and R. E. Smalley, *Chem. Phys. Lett.* 243, 49 (1995).
- Y. S. Park, K. S. Kim, H. J. Jeong, W. S. Kim, J. M. Moon, K. H. An, D. J. Bae, Y. S. Lee, G.-S. Park, and Y. H. Lee, *Synth. Met.* 126, 245 (2002).

44. J.-M. Moon, K. H. An, Y. H. Lee, Y. S. Park, D. J. Bae, and G.-S. Park, *J. Phys. Chem. B* 105, 5677 (2001).
45. H. J. Jeong, S. Y. Jeong, Y. M. Shin, J. H. Han, S. C. Lim, S. J. Eum, C. W. Yang, N. G. Kim, C. Y. Park, and Y. H. Lee, *Chem. Phys. Lett.* 361, 189 (2002).
46. G. Che, B. B. Lakshmi, C. R. Martin, E. R. Fisher, and R. S. Rouff, *Chem. Mater.* 10, 260 (1998).
47. J. Kong, H. T. Soh, A. M. Cassell, C. F. Quate, and H. Dai, *Nature* 395, 878 (1998).
48. H. J. Jeong, Y. M. Shin, S. Y. Jeong, Y. C. Choi, Y. S. Park, S. C. Lim, G.-S. Park, I.-T. Han, J. M. Kim, and Y. H. Lee, *Chemical Vapor Deposition* 8, 11 (2001).
49. O. Groning, O. M. Kuttel, Ch. Emmenegger, P. Groning, and L. Schlappbach, *J. Vac. Sci. Technol., B* 18, 665 (2000).
50. S. Maruyama, R. Kojima, Y. Miyauchi, S. Chiashi, and M. Kohno, *Chem. Phys. Lett.* 360, 229 (2002).
51. Y. Zhang, A. Chang, J. Cao, Q. Wang, W. Kim, Y. Li, N. Morris, E. Yenilmez, J. Kong, and H. Daia, *Appl. Phys. Lett.* 79, 3155 (2001).
52. Y. C. Choi, D. J. Bae, Y. H. Lee, B. S. Lee, I. T. Han, W. B. Choi, N. S. Lee, and J. M. Kim, *Synth. Met.* 108, 159 (2000).
53. C. J. Lee, D. W. Kim, T. J. Lee, Y. C. Choi, Y. S. Park, W. S. Kim, Y. H. Lee, W. B. Choi, N. S. Lee, J. M. Kim, Y. G. Choi, and S. C. Yu, *Appl. Phys. Lett.* 75, 1721 (1999).
54. Y. C. Choi, D. J. Bae, Y. H. Lee, B. S. Lee, G.-S. Park, W. B. Choi, N. S. Lee, and J. M. Kim, *J. Vac. Sci. Technol., A* 18, 1864 (2000).
55. A. Cao, X. Zhang, C. Xu, J. Liang, and D. Wu, *Appl. Phys. Lett.* 79, 1252 (2001).
56. D. Ugarte, A. Châtelain, and W. A. de Heer, *Science* 268, 845 (1995).
57. M. Endo, K. Takeuchi, S. Igarashi, K. Kobori, M. Shiraishi, and H. W. Kroto, *J. Phys. Chem. Solids* 54, 1841 (1993).
58. V. Ivanov, J. B. Nagy, Ph. Lambin, A. Lucas, X. B. Zhang, X. F. Zhang, D. Bernaerts, G. Van Tendeloo, S. Amelinckx, and J. Van Landuyt, *Chem. Phys. Lett.* 223, 329 (1994).
59. W. Z. Li, S. S. Xie, L. X. Qian, B. H. Chang, B. S. Zou, W. Y. Zhou, R. A. Zhao, and G. Wang, *Science* 274, 1701 (1996).
60. S. Suzuki, Y. Watanabe, T. Kiyokura, K. G. Nath, T. Ogino, S. Heun, W. Zhu, C. Bower, and O. Zhou, *Phys. Rev. B* 63, 245418 (2001).
61. C. Kim, B. Kim, S. M. Lee, C. Jo, and Y. H. Lee, *Phys. Rev. B* 65, 165418 (2001).
62. J.-M. Bonard, J.-P. Salvetat, T. Stöckli, W. A. de Heer, L. Forró, and A. Châtelain, *Appl. Phys. Lett.* 73, 918 (1991).
63. Y. K. Kwon, Y. H. Lee, S. G. Kim, Ph. Jund, R. E. Smalley, and D. Tomaneck, *Phys. Rev. Lett.* 79, 2065 (1997).
64. A. L. C. Triques, C. M. B. Cordeiro, V. Balestrieri, B. Lesche, W. Margulis, and I. C. S. Carvalho, *Appl. Phys. Lett.* 76, 2469 (2000).
65. Y. C. Choi, Y. M. Shin, S. C. Lim, D. J. Bae, Y. H. Lee, and B. S. Lee, *J. Appl. Phys.* 88, 4898 (2000).
66. G. Gu, G. Philipp, X. Wu, M. Burghard, A. M. Bittner, and S. Roth, *Adv. Funct. Mater.* 11, 295 (2001).
67. R. Kurt, J.-M. Bonard, and A. Karimi, *Thin Solid Films* 398, 193 (2001).
68. A. M. Cassell, N. R. Franklin, T. W. Tomblor, E. M. Chan, J. Han, and H. Dai, *J. Am. Chem. Soc.* 121, 7975 (1999).
69. J.-M. Bonard, H. Kind, T. Stöckli, and L.-O. Nilsson, *Solid-State Electron.* 45, 893 (2001).
70. D. N. Davydov, P. A. Sattari, D. AlMawlawi, A. Osika, T. L. Haslett, and M. Moskovits, *J. Appl. Phys.* 86, 3983 (1999).
71. J. Li, C. Papadopoulos, and J. M. Xu, *Appl. Phys. Lett.* 75, 367 (1999).
72. J. S. Suh and J. S. Lee, *Appl. Phys. Lett.* 75, 2047 (1999).
73. S. H. Jeong, H. Y. Hwang, K. H. Lee, and Y. Jeong, *Appl. Phys. Lett.* 78, 2052 (2001).
74. Z. H. Yuan, H. Huang, H. Y. Dang, J. E. Cao, B. H. Hu, and S. S. Fan, *Appl. Phys. Lett.* 78, 3127 (2001).
75. J. S. Suh, K. S. Jeong, and J. S. Lee, *Appl. Phys. Lett.* 80, 2392 (2002).
76. W. B. Choi, D. S. Chung, J. H. Kang, H. Y. Kim, Y. W. Jin, I. T. Han, Y. H. Lee, J. E. Jung, N. S. Lee, G. S. Park, and J. M. Kim, *Appl. Phys. Lett.* 75, 3129 (1999).
77. Y. R. Cho, J. H. Lee, C. S. Hwang, Y. H. Song, H. S. Uhm, D. H. Kim, S. D. Ahn, C. H. Chung, B. C. Kim, and K. I. Cho, *Jpn. J. Appl. Phys., Part 1* 41, 1532 (2002).
78. C. A. Spindt, *J. Appl. Phys.* 33, 2917 (1962).
79. V. T. Binh and Ch. Adessi, *Phys. Rev. Lett.* 85, 864 (2000).
80. S. C. Lim, H. J. Jeong, Y. M. Shin, K. H. An, D. J. Bae, Y. H. Lee, N. S. Lee, and J. M. Kim, *Adv. Mater.* 13, 1536 (2001).
81. K. A. Dean and B. R. Chalamala, *Appl. Phys. Lett.* 76, 375 (2000).
82. L. Nilsson, O. Groning, P. Groning, O. Kuttel, and L. Schlappbach, *Thin Solid Films* 383, 78 (2001).
83. H. Ago, T. Kugler, F. Cacialli, W. R. Salaneck, A. H. Windle, and R. H. Friend, *J. Phys. Chem. B* 103, 8116 (1999).
84. S. C. Lim, C. Jo, H. J. Jeong, Y. M. Shin, Y. H. Lee, I. A. Samayoa, and J. Choi, *Jpn. J. Appl. Phys., Part 1* 41, 5635 (2002).
85. C. Kim, Y. S. Choi, S. M. Lee, J. T. Park, B. Kim, and Y. H. Lee, *J. Am. Chem. Soc.* 124, 9906 (2002).
86. A. Maiti, J. Andzelm, N. Tanpipat, and Ph. von Allmen, *Phys. Rev. Lett.* 87, 155502 (2001).
87. N. Park, S. Han, and J. Ihm, *Phys. Rev. B* 64, 125401 (2001).
88. Y. G. Hwang and Y. H. Lee, unpublished.
89. K. Hata, M. Ariff, K. Tohji, and Y. Saito, *Chem. Phys. Lett.* 308, 343 (1999).
90. Y. H. Lee, G. K. Seong, and D. Tománek, *Chem. Phys. Lett.* 265, 667 (1997).
91. K. A. Dean, T. P. Burgin, and B. R. Chalamala, *Appl. Phys. Lett.* 79, 1873 (2001).
92. V. V. Zhirnov, A. N. Alimova, and J. J. Hren, *Appl. Surf. Sci.* 191, 20 (2002).
93. J. H. Jung, B. K. Ja, Y. H. Lee, J. Jang, and M. H. Oh, *IEEE Electron Device Lett.* 18, 197 (1997).
94. C. Kimura, T. Yamamoto, T. Hori, and T. Sugino, *Appl. Phys. Lett.* 79, 4533 (2001).
95. S. Dimitrijevic, J. C. Withers, V. P. Mammana, O. R. Monteiro, J. W. Ager III, and I. G. Brown, *Appl. Phys. Lett.* 75, 2680 (1999).
96. S. Yu, W. Yi, T. Jeong, W. S. Kim, J. Lee, H. Heo, C. S. Lee, J.-B. Yoo, Y. H. Lee, and J. M. Kim, *Physica B* 323, 177 (2002).
97. A. Wadhawan, R. E. Stallcup II, and J. M. Perez, *Appl. Phys. Lett.* 78, 108 (2001).
98. J. M. Macaulay, I. Brodie, C. A. Spindt, and C. E. Holland, *Appl. Phys. Lett.* 61, 997 (1994).
99. Q. H. Wang, A. A. Setlur, J. M. Lauerhaas, J. Y. Dai, E. W. Seelig, and R. P. H. Chang, *Appl. Phys. Lett.* 72, 2912 (1998).
100. J. M. Kim, W. B. Choi, N. S. Lee, and J. E. Jung, *Diamond Relat. Mater.* 9, 1184 (2000).
101. D.-S. Chung, S. H. Park, H. W. Lee, J. H. Choi, S. N. Cha, J. W. Kim, J. E. Jang, K. W. Min, S. H. Cho, M. J. Yoon, J. S. Lee, C. K. Lee, J. H. Yoo, J.-M. Kim, J. E. Jung, Y. W. Jin, Y. J. Park, and J. B. You, *Appl. Phys. Lett.* 80, 4045 (2002).
102. C. G. Lee, S. H. Jo, E. J. Chi, J. S. Lee, S. J. Lee, S. H. Cho, J. W. Kim, B. G. Lee, J. C. Cha, H. S. Han, S. H. Ahn, K. W. Jung, K. S. Ryu, S. Y. Park, S. H. Jin, Y. S. Choi, J. W. Nam, H. Y. Kim, Y. S. Han, H. J. Lee, S. J. Lee, J. H. You, and J. M. Kim, "IDMC '02," 2002.
103. Q. H. Wang, M. Yan, and R. P. H. Chang, *Appl. Phys. Lett.* 78, 1294 (2001).
104. D. Pribat, G. Pirio, P. Legagneux, K. B. K. Teo, M. Chhowalla, G. A. J. Amaratunga, W. I. Milne, and D. G. Hasko, "IDMC '02," 2002.
105. Y.-H. Lee, Y.-T. Jang, D.-H. Kim, J.-H. Ahn, and B.-K. Ju, *Adv. Mater.* 13, 479 (2001).

106. N. S. Lee, D. S. Chung, I. T. Han, J. H. Kang, Y. S. Choi, H. Y. Kim, S. H. Park, Y. W. Jin, W. K. Yi, M. J. Yun, J. E. Jung, C. J. Lee, J. H. You, S. H. Jo, C. G. Lee, and J. M. Kim, *Diamond Relat. Mater.* 10, 265 (2001).
107. S. Uemura, "IDRC '00," 2000, p. 398.
108. J. Yotani and S. Uemura, "IDRC '01," 2001, p. 1209.
109. S. Uemura, J. Yotani, T. Nagasako, H. Kurachi, H. Yamada, T. Ezaki, T. Maesoba, Y. Saito, and M. Yumura, "IDMC '02," 2002.
110. S. Uemura, J. Yotani, T. Nagasako, H. Kurachi, H. Yamada, T. Ezaki, T. Maesoba, and T. Nakao, "SID '02 Digest," 2002, p. 1132.
111. W. Yi, S. Yu, W. Lee, I. T. Han, T. Jeong, Y. Woo, J. Lee, S. Jin, W. Choi, J. Heo, D. Jeon, and J. M. Kim, *J. Appl. Phys.* 89, 4091 (2001).
112. W. S. Kim, W. Yi, S. Yu, J. Heo, T. Jeong, J. H. Lee, C. S. Lee, J. M. Kim, H. J. Jeong, Y. M. Shin, and Y. H. Lee, *Appl. Phys. Lett.* 81, 1098 (2002).
113. Y. Saito, S. Uemura, and K. Hamaguchi, *Jpn. J. Appl. Phys.* 37, L346 (1998).
114. J.-M. Bonard, T. Stöckli, O. Noury, and A. Châtelain, *Appl. Phys. Lett.* 78, 2775 (2001).
115. S. Uemura, Y. Seko, H. Kamogawa, M. Morikawa, and T. Shimojo, *ITE Tech. Rep.* 17, 31 (1999).
116. M. Morikawa, Y. Seko, H. Kamogawa, M. Morikawa, S. Uemura, and T. Shimojo, "Japan Display '92," 1992, p. 385.
117. H. Sugie, M. Tanemura, V. Filip, K. Iwata, K. Takahashi, and F. Okuyama, *Appl. Phys. Lett.* 78, 2578 (2001).
118. G. Z. Yue, Q. Qiu, B. Gao, Y. Cheng, J. Zhang, H. Shimoda, S. Chang, J. P. Lu, and O. Zhou, *Appl. Phys. Lett.* 81, 355 (2002).
119. S. Frank, Ph. Poncharal, Z. L. Wang, and W. A. de Heer, *Science* 280, 1744 (1998).
120. Z. Yao, H. W. Ch. Postma, L. Balents, and C. Dekker, *Nature* 402, 273 (1999).
121. S. Itoh, H. Toki, F. Kataoka, Y. Sato, K. Tamura, and Y. Kagawa, *IEICE Trans. Electron.* E82-C, 1808 (1999).
122. S. Itoh, T. Watanabe, T. Yamaura, and K. Yano, "Technical Digest of Asia Display '95," 1995, p. 617.
123. S. A. Bukesov, "Proceedings of SPIE Advanced Display Technologies: Basic Studies of Problems in Information Display (FLOWERS 2000)," 2000, p. 43.
124. S. Itoh, Y. Yonezawa, H. Toki, F. Kataoka, K. Tamura, and Y. Sato, "Extended Abstracts of the Third International Conference on Science and Technology of Display Phosphor," 1997, p. 275.
125. Y.-R. Cho, J. H. Lee, Y.-H. Song, S.-Y. Kang, M.-Y. Jung, C.-S. Hwang, and K. I. Cho, *J. Vac. Sci. Technol.* 19, 1012 (2001).
126. X. Ma and T. S. Sudarshan, *IEEE Trans. Dielectric Electric Insul.* 7, 277 (2000).
127. Y. S. Choi, S. N. Cha, S. Y. Jung, J. W. Kim, J. E. Jung, and J. M. Kim, *IEEE Trans. Electron Devices* 47, 1673 (2000).
128. H. C. Miller, *IEEE Trans. Electric Insul.* 28, 512 (1993).

Carbon Nanotube-Based Supercapacitors

Young Hee Lee, Kay Hyeok An, Ji Young Lee, Seong Chu Lim

Sungkyunkwan University, Suwon, Korea

CONTENTS

1. Introduction
 2. Principles of Operation
 3. Differences Between a Supercapacitor and a Battery
 4. Electrode Materials for Supercapacitors
 5. Carbon Nanotube-Based Supercapacitors
 6. Conclusions
- Glossary
References

1. INTRODUCTION

Recently, there have been considerable attempts to use carbon nanotubes (CNTs) for the electrodes of electrochemical energy storage systems, such as Li-ion secondary batteries [1–6], electrochemical hydrogen storage [7–9], fuel cells [10, 11], and supercapacitors [12–21]. Carbon nanotubes are attractive materials for the electrodes of electrochemical energy storage devices due to their superb characteristics of chemical stability, low mass density, low resistivity, and large surface area. Recent developments in massive synthesis of carbon nanotubes [22–24] have accelerated new applications of these materials to the area of electrical energy storage systems.

In particular, applications of CNTs as the electrode materials for supercapacitors have ignited significant worldwide investigations on their microscopic and macroscopic porous structures and electrochemical behaviors [12–14, 20–21, 25–30]. The CNT electrodes exhibit a unique pore structure and high usage efficiency of specific surface areas [12, 15, 17, 19–21]. The CNT electrodes for the electric double-layer type of supercapacitor have excellent absorption characteristics due to the accessible mesopores formed by the entangled individual CNTs [12, 13, 19–21].

Supercapacitors [31–36] (also called electrochemical capacitors, electric double-layer capacitors, or ultracapacitors) have several advantages compared to the secondary

battery, for instance, long cycle life (>100,000 cycles), simple principle and mode of construction, short charging time, safety, and high power density. Among them, the power density of supercapacitors is the most remarkable property. The power density of supercapacitors is larger than that of the secondary battery by about 10 times [31, 35, 36], although the energy density of supercapacitors is smaller than that of the secondary battery, which is a serious drawback to be applied for practical devices. Supercapacitors have been used as small-scale energy storage devices in electronic stationary, such as memory backup devices and solar batteries with semipermanent charge–discharge cycle life. Now the capability of supercapacitors with high power density extends its application to various other novel devices of load leveling, hybrid capacitor–battery system, cold-starting assistance, and catalytic converter preheating [31]. To apply the supercapacitors to various practical devices—even to electric vehicles—the development of supercapacitors with both high power density and high energy density is prerequisite.

The principle of electric energy storage by an electric double layer in a charged capacitor has been known since 1745. The idea of utilizing this principle to store the electrochemical energy for practical purposes of battery cells had been first proposed in the patent granted to Becker in 1957 [37]. The patent proposed electrical energy storage by means of the charges held at the interfacial double layer of a porous carbon material in aqueous electrolytes. After Becker, the SOHIO Corporation in Cleveland commercialized the electric double-layer capacitor (EDLC) with high surface area of carbon materials in a nonaqueous solvent (organic solvent) containing a dissolved tetraalkylammonium salt electrolyte [38]. Such organic electrolyte systems provided higher operating voltages (2.3–3.0 V) owing to the higher decomposition voltages of organic electrolytes than those of aqueous ones. Therefore, they can accommodate higher charge densities and provide larger specific energy storage increase by the square of the operating voltage attainable on charge.

A different principle of the capacitor using metal oxide electrodes, originating from the redox reaction as in a battery, was developed between 1975 and 1981 by the Conway group [39–42]. Although these systems have some problems

for commercial applications in that the electrode materials are expensive and have a limiting nominal voltage of 1 V, useful military applications have been developed [31].

After the discovery of conducting polymers in the 1980s, the possibility of employing electroactive conducting polymers, such as polypyrrole or polyaniline, for electrochemical pseudocapacitor materials was suggested by the Gottesfeld group [43–45]. These conducting polymer systems offer opportunities for storing electrochemical energy through the redox capacitance, the so called pseudocapacitance.

The large capacitance compared to conventional capacitors (on the order of several or more farads per gram) that can be developed with metal oxides and conducting polymer–pseudocapacitor systems and also with carbon double-layer capacitors led to the terms “supercapacitor” and “ultracapacitors” for these two types of high-specific-capacitance devices [31, 35]. Recently, it has been suggested that the more general term “electrochemical capacitors” be used to refer to these systems [31, 35]. The operating principles of electric double-layer capacitors and electrochemical pseudocapacitors, the differences between these two types of capacitors, the different types of electrode materials, and the differences between a supercapacitor and a battery are discussed in Sections 2–4.

2. PRINCIPLES OF OPERATION

In a conventional capacitor (condenser), the charge accumulation is achieved electrostatically by positive and negative charges residing on two interfaces separated by a vacuum or a molecular dielectric (a film of mica, a space of air, or an oxide film). Supercapacitors store the electric energy in an electrochemical double layer formed at the interfaces between the polarizable electrodes and the electrolyte solution. Positive and negative ionic charges within the electrolyte accumulate at the surface of the polarizable electrodes and compensate for the electronic charges at the electrode surface, as shown in Figure 1. This charge distribution layer is called the electric double layer (or electrochemical double layer). Figure 1 presents the principle of an electrochemical capacitor. The thickness of the double layer depends on the concentration of the electrolyte and on

the size of the ionic clusters and is typically on the order of 5–10 Å for concentrated electrolytes [46]. The capacitance, C , accumulated in the electric double layer formed at the interface between the polarizable electrodes and the electrolyte solution is defined by

$$C = \epsilon/4\pi\delta \int dS \quad (1)$$

where ϵ is the dielectric constant of the electrolyte, δ is the distance from the electrode interface to the center of the ion, and S is the surface area of the electrode interface. The corresponding electric field in the electrochemical double layer is very high and assumed to be up to 10^6 V/cm easily [31, 35]. Compared to conventional capacitors where a total capacitance is typically on the order of picofarads and microfarads, the capacitance and the energy density stored in the supercapacitor by the electrochemical double layer is much higher. To achieve a higher capacitance, the surface area of the electrode is additionally enlarged by using porous electrodes, where an extremely large internal surface area is expected.

There are several techniques for determining the specific capacitance, such as a unit-cell test (two-electrode system), a half-cell test (three-electrode system), and an impedance test. The unit-cell and half-cell tests are mainly used to determine the specific capacitance of the supercapacitor. The specific capacitances reported in the literature are not consistent, mainly due to the experimental methods used to determine them. For the sake of consistency, it is worth specifying the electrochemical technique for intercalculating the specific capacitance between the two-electrode and three-electrode systems. Figure 2a shows the double layer of electrodes used in the two-electrode system (2E), which represents a real double-layer supercapacitor device and its equivalent circuit. Figure 2b shows the double layer of electrodes used in the three-electrode system (3E), which is used in the lab cell with a reference electrode and its equivalent circuit. Assuming that the weight of each individual electrode is m , then $C_1 = C_2 = C$. The capacitance measured for

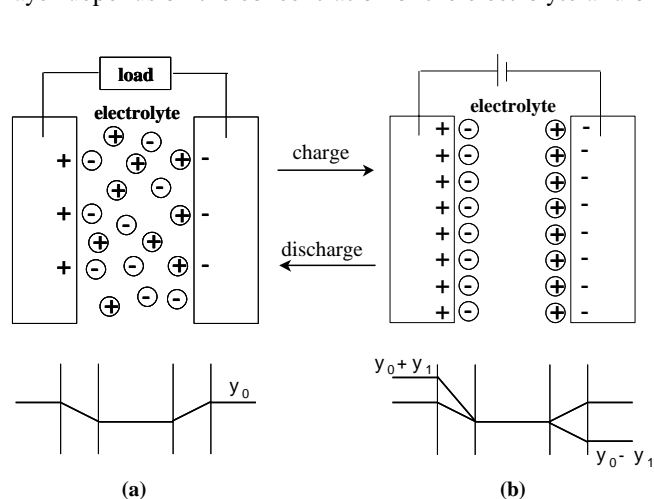


Figure 1. Principle of an electric double-layer capacitor.

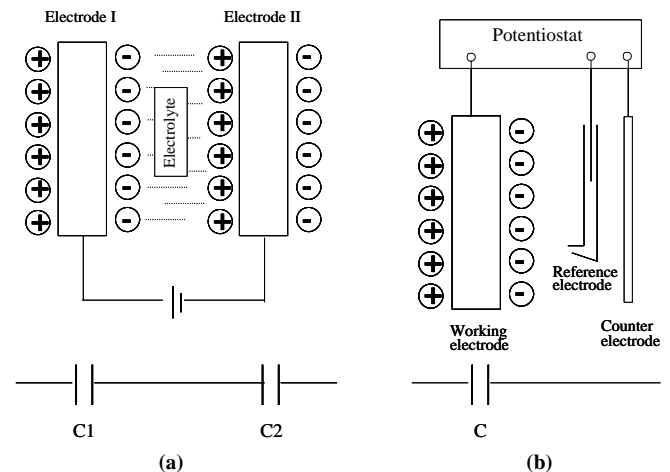


Figure 2. Electric double layer and its equivalent circuit in (a) two-electrode system and (b) three-electrode system.

the two-electrode system is $C_{2E} = \frac{1}{2}C$. The specific capacitance turns out be $C_{\text{spec-2E}} = C_{2E}/(2m) = \frac{1}{4}(C/m)$. However, for the three-electrode system, the double-layer capacitance measured is $C_{3E} = C$ and the specific capacitance is $C_{\text{spec-3E}} = C_{3E}/m = (C/m)$. Thus, the relationship between the specific capacitance measured with the two-electrode and three-electrode techniques is $C_{\text{spec-3E}} = 4C_{\text{spec-2E}}$.

In the double layer at plane electrodes, charge densities of about 16–50 $\mu\text{F}/\text{cm}^2$ are commonly realized [31]. Taking an average value of 30 $\mu\text{F}/\text{cm}^2$, the capacitance of a single polarizable electrode with a typical surface area of 1000 m^2/g for porous materials leads to a specific capacitance of 300 F/g. At 1 V in an aqueous electrolyte, the maximum storage energy, E , is $E = CV_i^2/2 = (300 \times 1^2)/2 = 150 \text{ W-s/g}$, 150 kJ/kg, or 42 W-h/kg, theoretically. This value is considerably lower than that obtained for available batteries but much higher than that for conventional capacitors. It should be mentioned that the above value depends on the double-layer capacitance, the specific surface area of the respective electrode material, the wetting behavior of the pores, and the nominal cell voltage.

The maximum power density of a supercapacitor is given by $P_{\text{max}} = V_i^2/4R$ [V_i = initial voltage, R = equivalent series resistance (ESR)] [31]. Therefore, the key factors determining the power of supercapacitors are the resistivity of the electrode itself, the resistivity of the electrolyte within the porous layer of electrode, and the contact resistance between the electrode and the current collector, as shown in Figure 3. In evaluating the performance of supercapacitors, the characterization of their energy density and power

density is one of the most important factors of rating electrochemical power devices. In addition, from practical and fundamental points of view, there is a question of how the energy density and power density are related for various types of electrochemical power sources, including fuel cells and rechargeable batteries.

3. DIFFERENCES BETWEEN A SUPERCAPACITOR AND A BATTERY

The most important difference between a supercapacitor and a battery is the principle of electrochemical energy storage. Electrochemical energy can be stored in two fundamentally different ways. In a battery, the potentially available chemical energy storage requires Faradic oxidation and reduction of electrochemically active reagents to release charges that can perform electric work when they flow between two electrodes having different potentials; that is, the charge storage is achieved by an electron transfer that produces a redox reaction in the electroactive materials according to Faraday’s law [31, 47, 48].

With an electric double-layer capacitor (EDLC), the charge storage process is non-Faradic; that is, ideally, no electron transfer takes place across the electrode interface and the storage of electric charge and energy is electrostatic. Actual electron charges are accumulated on the electrode surfaces with lateral repulsion and involvement of redox chemical changes. Table 1 summarizes the perceived advantages and disadvantages of EDLC energy storage. Because the charging and discharging of such EDLCs involve no chemical phase and composition changes, such capacitors have a high degree of cyclability on the order of 10^6 times and a high specific power density, although the specific energy density is rather small [31]. However, in some cases of the supercapacitor based on pseudocapacitance (redox type of supercapacitor), the essential process is Faradic; that is, the charge storage is achieved by an electron transfer that produces a redox reaction (Faradic reaction) in the electroactive materials according to Faraday’s law. The supercapacitors based on pseudocapacitance have higher specific capacitance than the EDLCs, due to the redox reaction as in a battery, although the redox reaction gives rise to

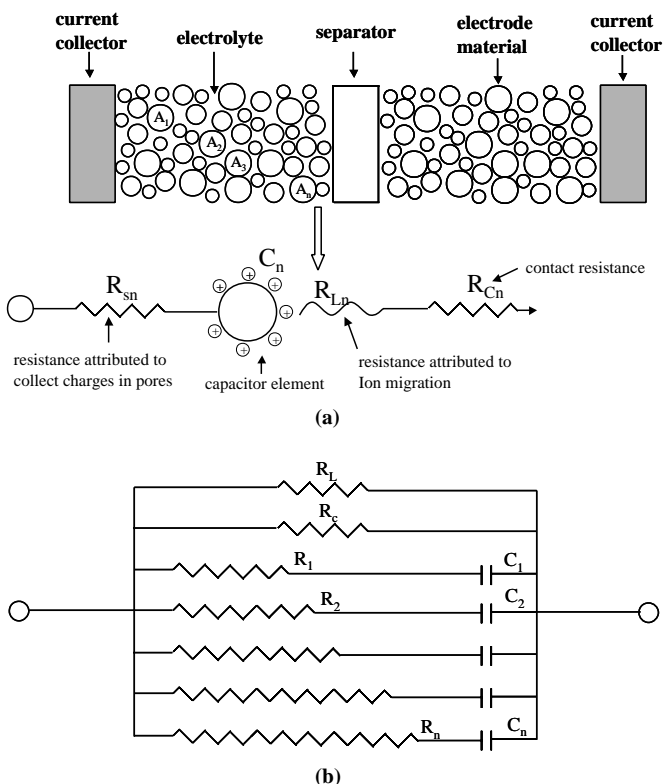


Figure 3. Equivalent circuit of an electrochemical capacitor.

Table 1. Advantages and disadvantages of supercapacitor energy storage.

Advantages
Long cycle life, >100,000 cycles
Excellent power density, >10 ⁶ W/kg
Simple principle and mode of construction
Combines state of charge indication
Can be combined with secondary battery for hybrid applications (electric vehicles)
Disadvantages
Limited energy density
Poor volume energy density
Low working voltage
Requires stacking for high potential operation (electric vehicles)

high internal resistance in supercapacitors, resulting in a decrease in specific power density. The typical electrodes of the supercapacitors based on pseudocapacitance are metal oxides (i.e., RuO_2 , IrO_2 , Co_3O_4) and conducting polymers (i.e., polypyrrole, polyaniline, polythiophene) [39–45].

A supercapacitor requires two equivalent electrodes, one of which is charged negatively with respect to the other, the charge storage and separation being electrostatic. At each electrode, the charge storage and separations are established across the electrode interface. Usually, the electrodes of supercapacitors have high surface area and porous matrices. However, batteries have bipolar electrode configurations for higher voltage series combinations [31].

For a battery, the maximum Gibbs energy is the product of charge Q and the difference of potential, ΔE , between the Nernstian reversible potentials of the two electrodes, that is, $G = Q \cdot \Delta E$. In the capacitor case, for a given charge Q , G is $\frac{1}{2}QV$. For a given electrode potential difference, $\Delta E = V$, it is then evident that the energy stored by a two-electrode cell accommodating a given Faradic charge Q at voltage $\Delta E = V$, is twice that stored in a capacitor charged with the same Q at the same voltage. In the process of charging a pure electric double-layer capacitor, every additional element of charge has to do electrical work (Gibbs energy) against the charge density already accumulated on the electrodes, progressively increasing the interelectrode potential difference [31, 47–50].

In a battery cell being charged, a thermodynamic potential (ideally) exists independent of the extent of charge Q added, as long as two components (reduced and oxidized forms) of the electroactive material remain coexisting. Thus, the potential difference (electromotive force) of the battery cell is ideally constant throughout the discharge or recharge half-cycles, so that $G = Q \cdot \Delta E$ rather than $Q \cdot \frac{1}{2}\Delta E$ (or $\frac{1}{2}V$) [31, 47–50]. This difference can be illustrated by the discharge curves shown schematically in Figure 4, where the voltage in the capacitor declines linearly with the extent of charge, while that for an ideal battery remains constant as long as two phases remain in equilibrium. The decline in the supercapacitor voltage arises formally since $C = Q/V$ or $V = Q/C$; therefore, $dV/dQ = 1/C$ [31, 47–50]. The ideal battery cell voltages on discharge and recharge, as a function of state of charge, are shown as parallel lines of zero slope in Figure 4. In the slope of the discharge and recharge

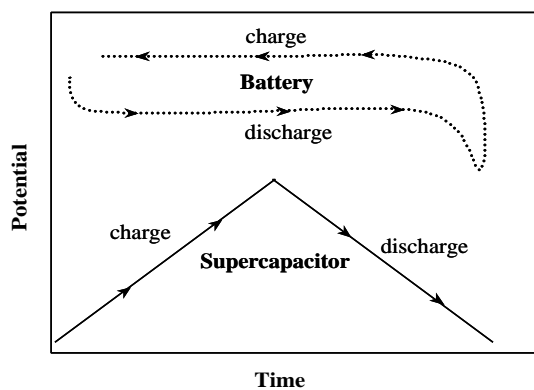


Figure 4. Difference in discharge and recharge relationships for a supercapacitor and a battery.

Table 2. Overall comparison of supercapacitor and battery characteristics.

Item	Supercapacitor	Battery
Slope of charge and discharge curve	Declining slope	Constant slope
Intrinsic stage of charge indication	Good	Bad
Energy density	Poor	Good
Power density	Good	Poor
Cyclability and cycle life	Excellent	Bad
Origin of internal IR	High area matrix + electrolyte	Active electrode materials + electrolyte
Activation polarization	Little or none	Significant (Faradic resistance)
Lifetime	Long	Poor
Cell stacking by bipolar system	Possible	Impossible

lines for the supercapacitor in Figure 4, there is a significant IR drop, depending on the discharging and recharging rates. An overall comparison of electrochemical capacitor and battery characteristics is given in Table 2.

4. ELECTRODE MATERIALS FOR SUPERCAPACITORS

4.1. Metal Oxides

The concept and use of metal oxide as an electrode material in electrochemical capacitors can be traced back to the paper by Trasatti and Buzzanca [41] on ruthenium dioxide (RuO_2) as a new interesting electrode material. Some other oxides, such as IrO_2 , Co_3O_4 , MoO_3 , WO_3 , and TiO_2 , as electrode materials in electrochemical capacitors have been discovered [51–54].

The cyclic voltammogram of the metal oxide electrodes has an almost rectangular shape and exhibits good capacitor behavior [31, 35, 55, 56]. However, the shape of the cyclic voltammogram is not a consequence of pure double-layer charging, but a consequence of the redox reactions occurring in the metallic oxide, giving rise to the redox pseudocapacitance [31, 35, 55, 56].

A very high specific capacitance of up to 750 F/g was reported for RuO_2 prepared at relatively low temperatures [57]. Conducting metal oxides such as RuO_2 or IrO_2 were the favored electrode materials in early electrochemical capacitors used for space or military applications [31, 35]. The high specific capacitance in combination with the low resistance resulted in very high specific powers. An energy density of 8.3 W-h/kg and a power density of 30 kW/kg was achieved in a prototype 25-V electrochemical capacitor built only with $\text{RuO}_2 \cdot x\text{H}_2\text{O}$ material and electrolyte [31]. These capacitors, however, turned out to be too expensive. A rough calculation of the capacitor cost showed that 90% of the cost resides in the electrode material [31, 35]. In addition, these capacitor materials are only suitable for aqueous electrolytes, thus limiting the nominal cell voltage to 1 V [31, 35].

Several studies have attempted to take advantage of the material properties of such metal oxides at a reduced cost.

The dilution of the costly noble metal by the formation of perovskites was investigated by Guther et al. [58]. Other forms of metal compounds such as nitrides were investigated by Liu et al. [59]. However, these materials are not yet commercially available in the electrochemical capacitor market.

4.2. Conducting Polymers

The discovery of conducting polymers has given rise to a rapidly developing field of electrochemical polymer science. Conducting polymers, such as polyacetylene, polyaniline, polythiophene, and polypyrrole, have been suggested by several authors for electrochemical capacitors [43–45, 49]. The conducting polymers have fairly high electronic conductivities, typically of magnitudes of 1–100 S/cm [31, 35, 49].

The electrochemical processes of conducting polymers are electrochemical redox reactions associated with sequential Lewis acid or Lewis base production steps so that the polymer molecules are converted to multiply charged structures through electrochemical Lewis-type reactions involving electron withdrawal or electron donation [31, 35, 49]. Therefore, the pseudocapacitance by Faradic redox processes in conducting polymer-based electrochemical capacitors is dominant, although about 2–5% of double-layer capacitance is included in the total specific capacitance [31, 35].

Such polymer electrode materials are much cheaper than RuO₂ or IrO₂ and can generate comparably large specific capacitance. However, the polymer electrode materials do not have the long-term stability and cycle life during cycling, which may be a fatal problem in applications. Swelling and shrinking of electroactive conducting polymers is well known and may lead to degradation during cycling [31, 35, 49]. Therefore, these electroactive conducting polymers are also far from being commercially used in electrochemical capacitors.

4.3. Carbons

Carbon materials for electrochemical energy devices, such as secondary batteries [60–62], fuel cells [63–65], and supercapacitors [66–69], have been extensively studied. However, each type of electrochemical energy device requires different physical properties and morphology. For supercapacitors, the carbon material for the EDLC type must have (i) high specific surface area, (ii) good intra- and interparticle conductivity in porous matrices, (iii) good electrolyte accessibility to intrapore surface area, and (iv) the available electrode production technologies [31, 35, 36]. Carbons for supercapacitors are available with a specific surface area of up to 2500 m²/g as powders, woven cloths, felts, or fibers [31, 35]. The surface conditioning of these carbon materials for supercapacitor fabrication is of substantial importance for achieving the best performance, such as good specific surface area, conductivity, and minimum self-discharge rates.

Carbons with high specific surface area have many oxygen functional groups, such as ketone, phenolic, carbonyl, carboxylic, hydroquinoid, and lactone groups, introduced during the activation procedure for enlarging the surface area [31, 35]. These oxygen functional groups on activated carbons or activated carbon fibers give rise to one kind of electrochemical reactivity, oxidation or reduction. Oxidation or

reduction of the redox functional groups shows pseudocapacitance, which amounts to about 5–10% of the total realizable capacitance [31]. However, the various surface functionalities in activated carbons are one of the factors that increase the internal resistance (equivalent series resistance; ESR) due to the redox reaction [31].

Activated carbons are much cheaper than metal oxides and conducting polymers and they have much larger specific surface area than the others. Activated carbon-based supercapacitors have been commercialized for small memory backup devices. However, activated carbons show lower conductivity than metal oxides and conducting polymers, resulting in a large ESR, which gives smaller power density. In addition, the observed specific capacitances of the carbon-based supercapacitors are about one-fourth the theoretical capacitance in spite of their high specific surface area (2000–3000 m²/g), which is attributed to the existence of micropores [31, 35]. This is a weak point of active carbons as electrode materials in supercapacitors with high energy density and power density.

5. CARBON NANOTUBE-BASED SUPERCAPACITORS

During the last decades, the application of activated carbons as the electrode materials in supercapacitors has been intensively investigated because of their high specific surface area and relatively low cost [31, 35, 36, 66–69]. Since the specific capacitance of a supercapacitor is proportional to the specific surface area, the effective surface area of the electrode materials is important [31, 35, 36]. Theoretically, the higher the specific surface area of an activated carbon, the higher the specific capacitance should be. Unfortunately, the theoretical capacitance of the activated carbons is not in good agreement with the observed value, because a significant part of the surface area remains in the micropores (<20 Å), which are not accessible to the electrolyte ions [31, 35]. Therefore, the pore size distribution together with the surface area is important for the determination of the electric double-layer capacitance. From this point of view, carbon nanotubes have several advantages as the electrode materials of supercapacitors. CNTs have a narrow distribution of mesopore sizes, highly accessible surface area, low resistivity, and high stability, attracting great interest worldwide for building supercapacitors using CNTs [12–14, 20, 21, 25–30].

5.1. Carbon Nanotube Electrodes

A supercapacitor can be classified into two types by the type of electrolyte: organic electrolytes and aqueous electrolytes. The advantage of organic electrolytes is the higher achievable voltage. According to the equation of maximum storage energy, $E = CV^2/2$, the square of the unit-cell operating voltage determines the maximum stored energy. Organic electrolytes allow for a unit-cell voltage above 2 V. Typically the cell operating voltage is 2.3 V with a possibility to increase the voltage for a short time to 2.7 V. On the other hand, organic electrolytes have a significantly higher specific resistance, compared to concentrated aqueous electrolytes

[31, 35]. The higher electrolyte resistance also affects the equivalent distributed resistance of the porous layer and, consequently, reduces the maximum usable power [31, 35].

Aqueous electrolytes limit the unit-cell voltage of the supercapacitors to typically 1 V, thus reducing the available energy density significantly compared to organic electrolytes [31, 35]. However, the advantages of aqueous electrolytes include higher conductance, resulting in a diminished ESR. Therefore, in aiming for high power density, the capacitors using aqueous electrolytes are more appropriate. In addition, the cost of aqueous electrolytes is usually much lower than that of suitable organic electrolytes.

In recent years, high-power supercapacitors based on CNT electrodes using aqueous electrolytes have been reported. Niu et al. [12] realized that supercapacitor electrodes, prepared from catalytically grown multiwalled CNTs whose surface area is 430 m²/g, show a maximum specific capacitance of 113 F/g and a power density of 8 kW/kg at an energy density of 0.56 W-h/kg in an aqueous electrolyte of 38 wt% H₂SO₄. The sample preparation procedure seems to be a key factor in achieving high capacitance. The CNT surface was chemically functionalized by nitric acid treatment and the individually dispersed CNTs in water were further reassembled into an interconnected, entangled, freestanding structure. This freestanding sheet of the entangled CNTs shows an open porous structure, which cannot be obtained typically with activated carbon or carbon fibers. The nitric acid treatment increases the Brunauer-Emmett-Teller (BET) surface area from 250 to 430 m²/g with narrow pore diameter distribution. The surface area of the CNT electrode resides in volumes and crevices larger than 20 Å, which are easily accessible to the electrolyte. These properties are highly desirable for high power and long cycle life of the supercapacitor.

Ma et al. [14] also used CNT electrodes, where the CNTs were prepared similarly to the previous works but in this case they introduced a binder to form solid electrodes. A mixture of CNTs and phenolic resin powders serving as a binder was molded and then carbonized at 850 °C for 2–4 h in a nitrogen gas ambient. The carbonized electrode was finally immersed in a hot mixture of concentrated sulfuric acid and nitric acid for 15 min. The electrode has a bulk density of around 1.0 g/cm³ and the BET surface area is about 120 m²/g, which is lower than that of Liu's CNT electrode. They obtained specific capacitances of 15–25 F/g in an aqueous solution of 38 wt% H₂SO₄. They discussed the effect of functional groups induced by the acid treatment. Functional groups, such as —COOH, —OH, and >C=O, enhance the capacitance of the CNT electrode. However, the IR drop at the initial stage of discharging is large due to the Faradic reactions of the functional groups, giving rise to a large ESR. The discharge profile is also different from the typical profile of electric double-layer capacitors. The discharging slope of $\Delta V/\Delta t$ is not linear due to the Faradic reaction by the functional groups.

Frackowiak et al. [15] investigated the electrochemical characteristics of supercapacitors built from multiwalled CNT electrodes with a specific surface area of 430 m²/g in 1 M KOH aqueous solution and the correlation of the microtexture and elemental composition of materials. They argued that the presence of mesopores due to the central

canal and/or entanglement of CNTs is the origin of an easy accessibility of the ions to the electrode/electrolyte interface for charging the electrical double layer. They detected pure electrostatic attraction of ions as well as quick pseudo-Faradic reactions upon varying surface functionality, which was induced during acidic oxidation. The values of the specific capacitance varied from 4 to 135 F/g, depending on the type of nanotubes or/and their posttreatments (acidic oxidation). They demonstrated that even with a moderate specific surface area below 470 m²/g, due to their accessible mesopores, the multiwalled CNT electrodes represent attractive materials for supercapacitors as compared to the best activated carbons.

Zhang et al. [17] studied a supercapacitor using multiwalled CNT electrodes in an organic electrolyte system. The multiwalled CNT electrodes showed a specific surface area of approximately 100 m²/g and a measured specific capacitance up to 18.2 F/g (16.6 F/cm³) with 1 M LiClO₄ in a mixture of ethylene carbonate and propylene carbonate (1:1 in volume ratio) as an organic electrolyte solution. The measured specific capacitance is relatively lower than that of other groups using aqueous electrolytes, due to the low specific surface area of the multiwalled CNT electrodes and the organic electrolyte solution system. However, the energy density of the supercapacitor can reach up to 20 W-h/kg with a 10-mA discharge current density, due to the high operation voltage in the organic electrolyte solution. The relative volume of mesopores and macropores of the used electrodes exceeds about 92%, and the micropores are nearly negligible. For organic electrolytes, because of their larger molecular structure, only the mesopores and macropores of their electrode pores are accessible and are much larger than those of activated carbons.

Raymundo-Piñero et al. [70] also studied supercapacitors using multiwalled CNTs with a high surface area prepared by KOH activation. Micropores of pure multiwalled CNTs have been highly developed using chemical KOH activation. Depending on the nanotubular material, the burn-off ranged from 20 to 45% after the activation process. The surface area was at least doubled with maximum values of 1050 m²/g for a treatment condition of KOH:CNT in a ratio of 4:1. The activated multiwalled CNTs still possess a nanotubular morphology with many defects on the outer walls, giving a significant increase in the micropore volume, while keeping a noticeable mesoporosity. The high efficiency of KOH activation in the development of the surface area is attributed to the redox reactions between carbon nanotubes and KOH followed by potassium intercalation and separation of the graphitic layers. This process is very efficient for the formation of pores, especially for the multiwalled CNTs with well-graphitized walls, while preserving nanotubular morphology. The creation of defects on the nanotube walls developed microporosity, which is responsible for excellent capacitance behavior. Such activated multiwalled CNTs have been used for the electrode materials of supercapacitors in alkaline, acidic, and aprotic medium. Enhanced values of capacitance are always observed after activation: In some cases, the capacitance increased almost 7 times from 15 F/g (for non-activated nanotubes) to 90 F/g (after chemical activation) in alkaline medium (6 M KOH). In an organic electrolyte, the capacitance of activated multiwalled CNTs reached 65 F/g

with a boxlike shape characteristic of cyclic voltammetric behavior. Such a significant modification of surface micro- porosity for essentially mesoporous nanotubular materials is of great interest for many electrochemical applications.

Frackowiak et al. [19] also studied supercapacitors comparatively for multiwalled and single-walled CNT electrodes. They obtained a maximum specific capacitance of 40 F/g using single-walled CNTs. This value is twice as small as that for multiwalled CNTs, which have a maximum specific capacitance of 80 F/g. They argued that the low specific capacitance of the single-walled CNT electrodes is attributed to the perfect bundle structure of the single-walled CNTs.

An et al. [20, 21, 27] reported on the key factors determining the performance of supercapacitors using single-walled CNT electrodes, which were synthesized by direct-current (dc) arc discharge. The single-walled CNTs consisted of bundles with diameters of 10–20 nm. The sample purity was roughly estimated to be about 30% [71]. A mixture of the single-walled CNTs and poly-vinylidene chloride or poly-vinyl alcohol used as a binder was molded and then carbonized at 500–1000 °C for 30 min in an argon gas ambient. The thickness of the electrode is about 150 μm . The measured apparent mass density of the electrode is 0.75 g/cm^3 . They obtained a maximum specific capacitance of 180 F/g and a measured power density of 20 kW/kg at an energy density of 7 $\text{W}\cdot\text{h}/\text{kg}$ in a solution of 7.5 N KOH. They demonstrated that heat treatment at high temperature is necessary to increase the capacitance and reduce the CNT electrode resistance. The increased capacitance is due to the enhancement of the specific surface area and the abundant pore distribution at lower pore sizes of 30–50 Å estimated from the BET(N_2) measurements. They also found that most of the BET surface area of the electrode contributes to the theoretically estimated specific capacitance, unlike activated carbons. They also claimed that minimization of the contact resistance is independent of the specific capacitance but directly related to maximization of the power density.

The performance of several types of supercapacitors using various carbon nanotubes reported in recent years is summarized in Table 3. Table 3 shows that the types of CNTs, the CNT morphologies, and the electrode preparation conditions are critically important in determining the specific

capacitance, the specific power density, and the specific energy density of supercapacitors. Although many of them are still to be determined in order to obtain the best performance for real applications, there is plenty of room to improve the performance of supercapacitors using CNT electrodes.

5.2. Carbon Nanotube–Composite Electrodes

Even if the CNT electrodes exhibit a unique pore structure and high usage efficiency of specific surface areas and some processes for disintegrating the bundle structure of the CNTs may enhance the utilization efficiency of their surface area, there is a limitation to widening the effective surface area of the CNTs. The specific capacitance of supercapacitors using CNT electrodes is still smaller than that of supercapacitors using activated carbons and activated carbon fibers (~ 250 F/g), which are commonly used as electrode materials for supercapacitors. Therefore, it is necessary to improve the SWNTs for applications that require a high capacitance. The small specific energy density of supercapacitors is a serious drawback to their application in practical devices, and, consequently, the main interest in supercapacitors is their ability to deliver high specific capacitance and energy density.

In the energy storage by supercapacitors, there are two fundamentally different approaches, as discussed in the previous section. A hybrid of an electric double-layer system and a pseudo-Faradic system could be a candidate for a supercapacitor with high specific capacitance and energy density. Currently, there is considerable interest in studying a new type of nanocomposite using CNTs and conducting polymers to improve the conductivity, electronic transport, and electromagnetic properties of organic conducting polymers [72–79]. These nanocomposites are regarded as one of the fascinating candidates for applications in nanoelectronic element and electro-optical devices.

Recently, Jurewicz et al. [18] demonstrated that the composite electrode based on multiwalled carbon nanotubes (MWNTs) coated with polypyrrole (Ppy) can be used in supercapacitors. They realized that a homogeneous layer of Ppy could be deposited on the nanotubular materials by

Table 3. Summary of the performance of many types supercapacitors using various carbon nanotubes reported in recent years.

Type of CNT	Treatment of CNT	Surface area of CNT (m^2/g)	Type of binder	Type of electrolyte	Maximum capacitance (F/g)	Power density (kW/kg)	Energy density ($\text{W}\cdot\text{h}/\text{kg}$)	Ref.
MWNT	Nitric acid	430	—	38wt% H_2SO_4	102	>8	—	[12]
MWNT	Sulfuric/nitric acid carbonization	120	Phenolic resin	38 wt% H_2SO_4	27	—	—	[14]
MWNT	Nitric acid	475	PVDF	1 M KOH	135	—	—	[15]
MWNT	Nitric acid	~ 100	PTFE	1M $\text{LiClO}_4/\text{EC} + \text{PC}$	18	—	20	[17]
SWNT	—	—	PVDF	6 M KOH	40	—	—	[19]
MWNT	KOH activation	1050	PVDF	6 M KOH	95	—	—	[70]
SWNT	Carbonization	360	PVdC	7.5 M KOH	180	>20	7	[20]

Note: MWNT, multiwalled carbon nanotube; SWNT, single-walled carbon nanotube; PVDF, polyvinylidene fluoride; PTFE, polytetrafluoroethylene; PVdC, polyvinylidene chloride; EC, ethylene carbonate; PC, propylene carbonate.

electrochemical polymerization of pyrrole. The composite electrodes in all cases enhanced the specific capacitance. They obtained a maximum value of 163 F/g for MWNTs prepared at 600 °C and modified by a Ppy layer of 5 nm, whereas it is only 50 F/g for the pristine nanotubes. It has been proposed that the nanocomposite electrode favors the formation of a three-dimensional electrical double layer, allowing a more effective contribution to the pseudo-Faradic properties of Ppy.

Frackowiak et al. [19] also reported on composite electrodes based on MWNTs deposited with Ppy for supercapacitors, although they prepared the nanocomposite electrodes of MWNTs and Ppy by chemical polymerization of pyrrole using an oxidant in an acidic solution. The value of the specific capacitance obtained from MWNT electrodes modified by Ppy has reached 172 F/g, about twice that given either by pristine MWNTs (ca. 80 F/g) or by pure Ppy (ca. 90 F/g). They also observed pseudocapacitance and speculated the origin of pseudocapacitance as the surface functionalities, metallic particles, or conducting polymers.

Lee and co-workers [80, 81] introduced SWNT-Ppy nanocomposite electrodes to improve the specific capacitance of the supercapacitor by combining the electric double layer and the redox reaction. The individual nanotubes and nanoparticles are uniformly coated with Ppy by *in-situ* chemical polymerization of pyrrole. In comparison to the pure Ppy and the SWNTs, the SWNT-Ppy nanocomposite electrodes exhibit a specific capacitance that is 5–10 times higher. They show that this large specific capacitance of the SWNT-Ppy nanocomposite is due to the uniformly coated Ppy on the SWNTs, increasing the active sites on Ppy chains. Lee and co-workers emphasized that the pseudocapacitance by the redox reaction and the capacitance by the electric double layer are simultaneously enhanced by the enlarged surface area of Ppy. They also studied the effects of the conducting agent added in the nanocomposite electrodes on the specific capacitance and the internal resistance of supercapacitors. They obtained a maximum specific capacitance of 265 F/g from the SWNT-Ppy nanocomposite electrodes containing 15 wt% of the conducting agent. They argued that the addition of a conducting agent into the SWNT-Ppy nanocomposite electrodes gives rise to the increase in the specific capacitance by reducing the internal resistance of the supercapacitor.

6. CONCLUSIONS

Some of the important challenges in this world are the conversion, storage, and distribution of energy. These are clearly connected with the development of several key technologies such as transportation communications, and electronics. The environmental problems and economical aspects related to the development and use of electrochemical energy storage devices are of significance. Air pollution and abusive use of the earth's natural resources are of major concern. If only 10% of vehicles are electrically powered, petroleum consumption will be cut by 700 million barrels per year, the reduction in expenses would be 14 billion at \$20 per barrel, and air pollution would be reduced by 1011 kg of CO₂ [82]. Therefore, new applications and development of supercapacitors are directly related to technologies of an

electric vehicle (EV) or a hybrid electric vehicle (HEV). The supercapacitor in an EV or an HEV will serve as a short-term energy storage device with high power capability and will allow us to store the energy obtained from regenerative braking. This energy will be reused in the next acceleration and boost. It also allow us to reduce the size of the primary power sources [batteries (EV), internal combustion engine (HEV), fuel cell] and keep them running at an optimized operation point [31, 35]. High-power supercapacitors for an EV or an HEV will require a high working voltage of 100–300 V with low resistance and high energy density by the series and parallel connections of elemental capacitors. Note also that homogeneous performance in each supercapacitor unit is essential in such a system [31, 35].

The remaining problems in the technology of supercapacitors are connected with the engineering of high-rate production lines for the fabrication of very well matched units for stacking in multicell and high-voltage devices and the production of reliably sealed, low-ESR, bipolar, stacked devices. The lowered ESR for high-power supercapacitors strongly depends on the manufacturing technology. However, the energy density of the supercapacitors is mainly governed by the properties of the electrode materials. Therefore, the development of novel electrode materials will accelerate the supercapacitor having an energy density as high as a secondary battery.

Another future application is the microsupercapacitor for the power source of micro (or nano) electromechanical systems (MEMS or NEMS). In recent years, MEMS (or NEMS) technologies have attracted attention worldwide for many applications, including medical devices, communications equipment, sensors, and actuators. There are many technical problems with the development of these types of microdevices. One of the most important challenges is to develop the optimal micropower source to operate these devices. In many cases, the MEMS (or NEMS) requires extremely low current and power. This may be possible by using microsupercapacitors as the power sources for these devices.

GLOSSARY

Battery A device that stores electrical energy using electrochemical cells. Chemical reactions occur spontaneously at the electrodes when they are connected through an external circuit, producing an electrical current.

Capacitor An electrical device that stores electricity or electrical energy. It has three essential parts: two electrical conductors, which are usually metal plates, separated and insulated by the third part, called the dielectric. The plates are charged with equal amounts of positive and negative electrical charges, respectively.

Carbon nanotubes Graphitic layers rolled into the form of a hollow cylinder whose diameter is an order of nanometer scale.

Cell A device that converts chemical energy into electrical energy or vice versa when a chemical reaction occurs in the cell. Typically, it consists of two metal electrodes immersed into an electrolyte with electrode reactions at the electrode-solution surfaces.

Electric double layer Development of a net charge at the particle surface affects the distribution of ions in the surrounding interfacial region, resulting in an increased concentration of counterions (ions of opposite charge to that of the particle) close to the surface.

Electrodes The two electronically conducting parts of an electrochemical cell.

Electrolyte A chemical compound (salt, acid, or base) that dissociates into electrically charged ions when dissolved in a solvent. The resulting electrolyte solution is an ionic conductor of electricity.

Equivalent series resistance The single resistor that draws the same current as the combination of constituent resistors.

Faradic redox process An oxidation–reduction reaction that occurs in an electrochemical cell. The essential feature is that the simultaneous oxidation–reduction reactions are spatially separated.

Polarizable electrode An electrode that is easily polarizable. That is, the potential of the electrode will change significantly from its equilibrium potential with the application of even a small current density.

Pseudocapacitance The capacitance due to the Faradic redox process in a supercapacitor.

Separator A thin structural material (usually a sheet) used to separate the electrodes of a divided electrochemical cell into two or more compartments.

Supercapacitor A high-energy version of a conventional electrolytic capacitor holding hundreds of times more energy per unit volume or mass than a normal capacitor.

REFERENCES

1. F. Leroux, K. Metenier, S. Gautier, E. Frackowiak, S. Bonnamy, and F. Beguin, *J. Power Sources* 81–82, 317 (1999).
2. G. T. Wu, C. S. Wang, X. B. Zhang, H. S. Yang, Z. F. Qi, P. M. He, and W. Z. Li, *J. Electrochem. Soc.* 146, 1696 (1999).
3. E. Frackowiak, S. Gautier, H. Gaucher, S. Bonnamy, and F. Beguin, *Carbon* 37, 61 (1999).
4. E. Jouguelet, C. Mathis, and P. Petit, *Chem. Phys. Lett.* 318, 561 (2000).
5. B. Gao, A. Kleinhammes, X. P. Tang, C. Bower, L. Fleming, Y. Wu, and O. Zhou, *Chem. Phys. Lett.* 307, 153 (1999).
6. B. Gao, C. Bower, J. D. Lorentzen, L. Fleming, A. Kleinhammes, X. P. Tang, L. E. McNeil, Y. Wu, and O. Zhou, *Chem. Phys. Lett.* 327, 69 (2000).
7. C. Nutzenadel, A. Zuttel, D. Chartouni, and L. Schlapbach, *Electrochem. Solid-State Lett.* 2, 30 (1999).
8. S. M. Lee, K. S. Park, Y. C. Choi, Y. S. Park, J. M. Bok, D. J. Bae, K. S. Nahm, Y. G. Choi, S. C. Yu, N. G. Kim, T. Frauenheim, and Y. H. Lee, *Synth. Met.* 113, 209 (2000).
9. A. K. M. Fazle Kibria, Y. H. Mo, K. S. Park, K. S. Nahm, and M. H. Yun, *Int. J. Hydrogen Energy* 26, 823 (2001).
10. B. Rohland, K. Eberle, J. Scholta, and J. Garche, *Electrochim. Acta* 43, 3841 (1998).
11. N. Muradov, *Catal. Commun.* 2, 89 (2001).
12. C. Niu, E. K. Sichel, R. Hoch, D. Moy, and H. Tennent, *Appl. Phys. Lett.* 70, (1997) 1480.
13. L. Diederich, E. Barborini, P. Piseri, A. Podesta, P. Milani, A. Schneuwly, and R. Gallay, *Appl. Phys. Lett.* 75, 2662 (1999).
14. R. Z. Ma, J. Liang, B. Q. Wei, B. Zhang, C. L. Xu, and D. H. Wu, *J. Power Sources* 84, 126 (1999).
15. E. Frackowiak, K. Metenier, V. Bertagna, and F. Beguin, *Appl. Phys. Lett.* 77, 2421 (2000).
16. E. Frackowiak and F. Beguin, *Carbon* 39, 937 (2001).
17. B. Zhang, J. Liang, C. L. Xu, B. Q. Wei, D. B. Ruan, and D. H. Wu, *Mater. Lett.* 51, 539 (2001).
18. K. Jurewicz, S. Delpeux, V. Bertagna, F. Beguin, and E. Frackowiak, *Chem. Phys. Lett.* 347, 36 (2001).
19. E. Frackowiak, K. Jurewicz, S. Delpeux, and F. Beguin, *J. Power Sources* 97–98, 822 (2001).
20. K. H. An, W. S. Kim, Y. S. Park, Y. C. Choi, S. M. Lee, D. C. Chung, D. J. Bae, S. C. Lim, and Y. H. Lee, *Adv. Mater.* 13, 497 (2001).
21. K. H. An, W. S. Kim, Y. S. Park, J.-M. Moon, D. J. Bae, S. C. Lim, Y. S. Lee, and Y. H. Lee, *Adv. Funct. Mater.* 11, 387 (2001).
22. C. Journet, W. K. Maser, P. Bernier, A. Loiseau, M. L. de la Chapelle, S. Lefrant, P. Deniard, R. Lee, and J. E. Fischer, *Nature (London)* 388, 756 (1997).
23. A. Thess, R. Lee, P. Nikolaev, H. Dai, P. Petit, J. Robert, C. Xu, Y. H. Lee, S. G. Kim, A. G. Rinzler, D. T. Colbert, G. E. Scuseria, D. Tomanek, J. E. Fisher, and R. E. Smalley, *Science* 273, 483 (1996).
24. H. M. Cheng, F. Li, G. Su, H. Y. Pan, L. L. He, X. Sun, and M. S. Dresselhaus, *Appl. Phys. Lett.* 72, 3282 (1998).
25. J. N. Barisci, G. G. Wallace, and R. H. Baughman, *J. Electrochem. Soc.* 147, 4580 (2000).
26. C.-Y. Liu, A. J. Bard, F. Wudl, I. Weitz, and J. R. Heath, *Electrochem. Solid-State Lett.* 2, 577 (1999).
27. K. H. An, K. K. Jeon, W. S. Kim, Y. S. Park, D. J. Bae, S. C. Lim, and Y. H. Lee, *J. Korean Phys. Soc.* 39, S511 (2001).
28. A. Peigney, Ch. Laurent, E. Flahaut, R. R. Bacsca, and A. Rousset, *Carbon* 39, 507 (2001).
29. R. R. Bacsca, Ch. Laurent, A. Peigney, W. S. Bacsca, Th. Vaugien, and A. Rousset, *Chem. Phys. Lett.* 323, 566 (2000).
30. M. Eswaramoorthy, R. Sen, and C. N. R. Rao, *Chem. Phys. Lett.* 304, 207 (1999).
31. B. E. Conway, “Electrochemical Supercapacitors: Scientific Fundamentals and Technological Applications.” Kluwer Academic/Plenum, New York, 1999.
32. S. T. Mayer, R. W. Pekala, and J. L. Kaschmitter, *J. Electrochem. Soc.* 140, 446 (1993).
33. A. Yoshida, S. Nonaka, I. Aoki, and A. Nishino, *J. Power Sources* 60, 213 (1996).
34. Y. Kibi, T. Saito, M. Kurata, J. Tabuchi, and A. Ochi, *J. Power Sources* 60, 225 (1996).
35. R. Kotz and M. Carlen, *Electrochim. Acta* 45, 2483 (2000).
36. M. Endo, T. Takeda, Y. J. Kim, K. Koshiba, and K. Ishii, *Carbon Sci.* 1, 117 (2001).
37. H. E. Becker, U.S. Patent 2,800,616 (to General Electric), 1957.
38. D. I. Boos, U.S. Patent 3,536,963 (to Standard Oil, SOHIO), 1970.
39. B. E. Conway and H. A. Kozłowska, *Acc. Chem. Res.* 14, 49 (1981).
40. S. Hadzi-Jordanov, H. A. Kozłowska, M. Vukovic, and B. E. Conway, *J. Electrochem. Soc.* 60, 1471 (1978).
41. S. Trasatti and G. Buzzanca, *J. Electroanal.* 29, 1 (1971).
42. R. Galizzoli, F. Tantardini, and S. Trasatti, *J. Appl. Electrochem.* 4, 57 (1974).
43. S. Gottesfeld, A. Redondo, and S. W. Feldberg, *J. Electrochem. Soc.* 134, 271 (1987).
44. A. Rudge, I. Raistrick, S. Gottesfeld, and J. P. Ferraris, *Electrochem. Soc.* 39, 273 (1994).
45. A. Rudge, J. Davey, I. Raistrick, and S. Gottesfeld, *J. Power Sources* 47, 89 (1994).
46. B. E. Conway, J. O’M. Bockris, and I. A. Ammar, *Trans. Faraday Soc.* 47, 756 (1951).
47. G. Hambitzer, K. Pinkwart, C. Ripp, and C. Schiller, in “Handbook of Barrey Materials” (M. Wakihara and O. Yamamoto, Eds.), Chap. 1. Wiley–VCH, Weinheim, 1999.
48. G. W. Vinal, “Storage Battery.” Wiley, New York, 1955.

49. A. Burke, *J. Power Sources* 91, 37 (2000).
50. B. E. Conway, V. Birss, and J. Wojtowicz, *J. Power Sources* 66, 1 (1997).
51. J. B. Goodenough, in "Progress in Solid-State Chemistry" (N. Reiss, Ed.), Vol. 5. Pergamon, New York, 1971.
52. W. D. Ryden, A. W. Lawson, and C. C. Sartain, *Phys. Lett. A* 26, 209 (1968).
53. H. Schafer, G. Schneiderei, and W. Gerhardt, *Z. Anorg. Allg. Chem.* 319, 372 (1963).
54. S. Trasatti and G. Lodi, in "Conductive Metal Oxides" (S. Trasatti, Ed.), Vol. A, p. 338. Elsevier, Amsterdam, 1980.
55. S. Ardizzzone, G. Fregonara, and S. Trasatti, *Electrochim. Acta* 35, 263 (1990).
56. R. Kotz and S. Stucki, *Electrochim. Acta* 31, 1311 (1986).
57. J. P. Zheng, P. J. Cygan, and T. R. Jow, *J. Electrochem. Soc.* 142, 2699 (1995).
58. T. J. Guther, R. Oesten, J. Garche, F. M. Delnick, D. Ingersoll, X. Andrieu, and K. Naoi, "Electrochemical Capacitors II, Proceedings of the Electrochemical Society," 1997, Vol. 96-25, p. 16.
59. T.-C. Liu, W. G. Pell, B. E. Conway, and S. L. Roberson, *J. Electrochem. Soc.* 145, 1882 (1998).
60. Y. Sato, K. Tanuma, T. Takayama, K. Kobayakawa, T. Kawai, and A. Yokoyama, *J. Power Sources* 97-98, 165 (2001).
61. W. Lu and D. D. L. Chung, *Carbon* 39, 493 (2001).
62. Y. Kida, K. Yanagida, A. Funahashi, T. Nohma, and I. Yonezu, *J. Power Sources* 94, 74 (2001).
63. S. Lj. Gojkovic and T. R. Vidakovic, *Electrochim. Acta* 47, 633 (2001).
64. A. L. Sauvet and J. Foulletier, *J. Power Sources* 101, 259 (2001).
65. X. Wang, I.-M. Hsing, and P. L. Yue, *J. Power Sources* 96, 282 (2001).
66. J. Gamby, P. L. Taberna, P. Simon, J. F. Fauvarque, and M. Chesneau, *J. Power Sources* 101, 109 (2001).
67. D. Qu and H. Shi, *J. Power Sources* 74, 99 (1998).
68. Y. Kibi, T. Saito, M. Kurata, J. Tabuchi, and A. Ochi, *J. Power Sources* 60, 219 (1996).
69. H. Shi, *Electrochim. Acta* 41, 1633 (1996).
70. E. Raymundo-Piñero, D. Carzorla-Amorós, A. Linares-Solano, S. Delpeuk, E. Frackowiak, K. Szostak, and F. Béguin, *Carbon* 40, 1597 (2002).
71. J.-M. Moon, K. H. An, Y. H. Lee, Y. S. Park, D. J. Bae, and G.-S. Park, *J. Phys. Chem. B* 105, 5677 (2001).
72. A. B. Kaiser, G. U. Flanagan, D. M. Stewart, and D. Beaglehole, *Synth. Met.* 117, 67 (2001).
73. B. H. Chang, Z. Q. Liu, L. F. Sun, D. S. Tang, W. Y. Zhou, G. Wang, L. X. Qian, S. S. Xie, J. H. Fen, and M. X. Wan, *J. Low Temp. Phys.* 119, 41 (2000).
74. S. Lefrant, I. Baltog, M. Lamy de la Chapelle, M. Baibarac, G. Louarn, C. Journet, and P. Bernier, *Synth. Met.* 100, 13 (1999).
75. K. Yoshino, H. Kajii, H. Araki, T. Sonoda, H. Take, and S. Lee, *Fullerene Sci. Technol.* 7, 695 (1999).
76. H. S. Woo, R. Czerw, S. Webster, D. L. Carroll, J. W. Park, and J. H. Lee, *Synth. Met.* 116, 369 (2001).
77. G. Z. Chen, M. S. P. Shaffer, D. Coleby, G. Dixon, W. Zhou, D. J. Fray, and A. H. Windle, *Adv. Mater.* 12, 522 (2000).
78. J. Fan, M. Wan, D. Zhu, B. Chang, Z. Pan, and S. Xie, *Synth. Met.* 102, 1266 (1999).
79. J. Fan, M. Wan, D. Zhu, B. Chang, Z. Pan, and S. Xie, *J. Appl. Polym. Sci.* 74, 2605 (1999).
80. K. H. An, K. K. Jeon, J. K. Heo, S. C. Lim, D. J. Bae, and Y. H. Lee, *J. Electrochem. Soc.* 149, A1058 (2002).
81. Y. H. Lee, K. H. An, S. C. Lim, W. S. Kim, H. J. Jeong, W. Lee, and J. M. Kim, *New Diamond Frontier Carbon Technol.* 14, 209 (2002).
82. R. M. Dell and D. A. J. Rand, *J. Power Sources* 100, 2 (2001).

Carbon Nanotubes in Composite Materials

Ch. Laurent, A. Peigney

Université Paul-Sabatier, Toulouse, France

CONTENTS

1. Introduction
 2. Carbon Nanotube–Metal–Matrix Composites
 3. Carbon Nanotube–Ceramic–Matrix Composites
 4. Carbon Nanotube–Polymer–Matrix Composites
 5. Conclusions
- Glossary
References

1. INTRODUCTION

1.1. Carbon Nanotube Discovery and Description

Although hollow carbon fibers have been prepared for several decades, it is the report by Iijima [1] in 1991 on obtaining of carbon tubes with a diameter in the nanometer range, the so-called carbon nanotubes (CNTs), and on their relations to the recently discovered fullerenes that initiated a worldwide research effort devoted to improving their synthesis, determining their structure, and calculating and measuring their physical properties.

Rolling a graphene sheet onto itself so that the open edges match exactly produces a hollow cylinder which is termed a single-walled CNT (SWNT). Two such concentric cylinders form a double-walled CNT (DWNT). A CNT with more walls is named a multiwalled CNT (MWNT). To close the tips, half fullerenes or more complex structures that include pentagons are required. However, the cylindrical part of the CNT, which contains only hexagons, is considered infinite in most studies. There are several ways to roll the graphene sheet, which can be described by a helical vector (or chiral vector, or roll-up vector) represented by a pair of integers (n, m) [2, 3] as described in Figure 1 [4]. The limiting cases are referred to as zigzag $(n, 0)$ and armchair (n, n) SWNTs, with a helical (or chiral) angle equal to 0 and 30°, respectively. Other SWNTs have a helical (often termed chiral) structure. As mentioned in a later section, the helicity has significant implications on the electronic properties of CNTs. For MWNTs, the measured interlayer distance (about

0.34 nm) is close to that measured between graphene sheets in graphite and no particular correlation appears between the helicity of concentric layers.

SWNTs have a diameter in the range 0.4–6 nm and a length reaching several tens or even hundreds of micrometers, resulting in a very high aspect ratio: indeed, the length/diameter ratio could be in the range 1000–100,000, although the upper limit is difficult to evaluate because the length is difficult or impossible to measure. Another notable characteristic of CNTs is the high specific surface area (1315 m²/g considering the outer surface of infinite SWNTs) which is mostly dependent on the number of walls and, in a lesser way, on the diameter [5]. The hollow structure of the CNTs is of course also interesting because it offers a nanometric cavity which can be filled with various materials.

More on the fundamental relations governing the geometry of CNTs can be found in the early review by Dresselhaus et al. [6] which also highlights the implications of symmetry on the vibrational and electronic structure of one-dimensional carbon. The following sections will very briefly describe the synthesis and the general properties of the CNTs.

1.2. Synthesis

The first report on the preparation of filamentous carbon by the decomposition of carbonaceous gases dates back to the 19th century [7]. Rodriguez [8] reviewed the considerable amount of work done on the topic since then. Although very small hollow nanofilaments were prepared by catalytic chemical vapor deposition (CCVD) in the 1970s [9], Iijima's report [1] and the subsequent development of the field triggered an enormous amount of research aiming at the synthesis of CNTs. We will only briefly describe here the formation mechanisms of the CNTs, the main synthesis methods (arc discharge, laser vaporization, and CCVD), and the characteristics of the so-prepared CNTs. Rakov [10] published a review, with 282 references, on the topic. It is important to note something which was not fully appreciated at the beginning of the development of the “nanotube” field, that is, that each method produces different CNTs samples, that differences subsist depending on the experimental conditions for

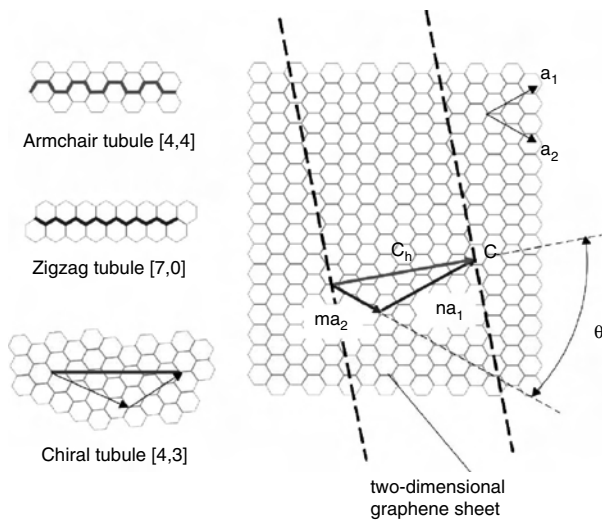


Figure 1. The helical (chiral) vector OC or $C_h = na_1 + ma_2$ is defined on the hexagonal lattice of carbon atoms by unit vectors a_1 and a_2 and the helical (chiral) angle θ with respect to the zigzag axis. Reprinted with permission from [4], K. T. Lau and D. Hui, *Composites B* 33, 263 (2002). © 2002, Elsevier Science.

a given method, and that even different batches from a single source may not be exactly identical. However, the field is evolving extremely quickly.

The formation mechanisms of the SWNTs (and DWNTs) and that of the MWNTs are basically different (see [11] for an early review). Arc-discharge MWNTs are prepared without the use of a metal catalyst, so mechanisms involving the incorporation of carbon atoms (C1, C2, C3) and thickening by lateral growth of graphene planes on existing surfaces were proposed [12–16]. Typically, the outer diameter of arc-discharge MWNTs ranges between 2 and 20 nm and the inner diameter ranges between 1 and 3 nm [3, 15, 17, 18]. The length is of the order of one to several micrometers. MWNTs form regularly organized bundles, which may contain tens or hundreds of individual tubes. The bundles in turn are combined into fibers with a diameter of about 50 μm , which themselves form threads with a diameter of about 1 mm. It was noted that the arc-discharge MWNTs contain many defects [19–21]. When using CCVD, relatively large metal particles (about 10–30 nm) can produce MWNTs with a matching diameter by mechanisms established long ago for hollow filaments [9, 22, 23], resembling the vapor-liquid-solid (VLS) mechanism [24].

For SWNTs, two cases are observed: one particle produces either one CNT or many CNTs, depending on its size and other factors. Accordingly, two formation mechanisms, also bearing a certain relation with VLS, were proposed. The “one particle–many CNTs” mechanism [25] is dominant when using arc discharge or laser vaporization. A large number of SWNTs bundles originate from the surface of a metal particle several tens of nm in diameter [25–27]. All observed SWNTs are narrow (0.8–2 nm). A narrow catalyst particle distribution centered on 15 nm appears to give the highest SWNT yields [28]. The diameter distribution of arc-discharge SWNTs is very narrow, generally in the range 0.7–1.6 nm [14, 29, 30]. However, various carbon species

are found in the deposits including SWNTs, MWNTs, amorphous carbon, spherical metallic nanoparticles, empty or filled graphitic nanoparticles, a few graphitic sheets, as well as round spherical metallic particles. The SWNTs are mostly organized in bundles consisting of a few to a few tens of individual tubes forming a triangular lattice and more or less covered with some carbon soot. Lengths reach up to several micrometers. It is claimed that laser vaporization [31] allows far greater control over growth conditions and produces SWNTs in higher yield (70–90%) and of better quality. The SWNTs are about 1–1.6 nm in diameter, with a very narrow distribution, and are arranged in large bundles that may be 100 μm long. No amorphous coating is observed. The diameter distribution can be slightly changed and SWNTs close to 6 nm in diameter were reported [32, 33].

In the “one particle–one CNT” case, observed when using CCVD, the diameter of the SWNTs is in the range 0.5–5 nm and is directly related to that of the catalyst particle. Hafner et al. [34] calculated a critical diameter of 3 nm above which the formation of concentric carbon layers around the particle is favored, in good agreement with experimental results [34, 35]. The so-called “yarmulke” mechanism [36] allows for a second cap (and thus a second CNT) to form underneath the first one. This is also observed experimentally [34]. CCVD specimens may contain several species in addition to Iijima-type CNTs, including amorphous carbon, carbon particles, and carbidic carbon particles, but tremendous progress on the selectivity has been made in recent years. Several groups have reported progresses in the yield, control of the diameter, and the number of walls [34–49]. The CCVD SWNTs are quite flexible and in general contain more defects than those produced by arc discharge and laser vaporization. Note that CCVD methods are becoming increasingly attractive due to their great potential for the production of large quantities of CNTs at a low cost. Length is in the range between ca. 100 nm and several micrometers (or tens of micrometers) and the surface is free of the amorphous carbon coating typically observed in CCVD MWNTs, which generally are even longer.

Purification procedures are required to eliminate the residual metal catalyst and the nontubular carbon species. Several techniques, usually involving thermal and acidic treatments, have been proposed. The sensitivity of SWNTs to chemical processing was investigated by transmission electron microscopy (TEM) [50]. The chemistry of CNTs, which encompasses the aspects of purification and functionalization, is a very important field for the development of future applications. Rakov [51] published a review with 573 references on the topic. Chemical functionalization was also reviewed by Sinnott [52]. Several methods for attachment of oxygen-containing groups to the CNT surfaces have been developed [53, 54]. Carboxylic, carbonyl, and hydroxyl groups were found covering the CNT walls [55]. The concentration of acid groups on the surfaces of HNO_3 treated CNTs was higher than that found for graphite treated under the same conditions [56]. Sonication of CNTs prior to the functionalization in acids increases the concentration of acid groups. Oxidation of CNTs with a H_2SO_4 – HNO_3 mixture also leads to a higher concentration of functional groups on the surface [57]. Long-term acid treatment of CNTs also induces modifications. Functional groups can be removed

from the surface of CNTs by heating. It should be noted that SWNTs obtained by different methods exhibit different behavior in the course of acid treatment and subsequent oxidation.

1.3. General Properties

This section will very briefly highlight some general properties of CNTs which are treated in detail in several books [58–60]. A complete coverage of the electrical, thermal, and mechanical characteristics of the different kinds of CNTs (SWNTs, DWNTs, MWNTs, and bundles) is indeed far beyond the scope of this chapter.

The electrical characteristics of CNTs have been investigated by theoretical and experimental works [2, 3, 61–65] which have brought to light some remarkable features related to the unique one-dimensional nature of the CNTs. A review on the electronic properties of CNTs is published in this Encyclopedia [66]. The most important characteristic to note for use of the CNTs in composites is that either metallic or semiconducting behavior may be observed depending on the helicity. The electrical conductivity of a metallic CNT could reach 10,000 S/cm and that of a semiconducting CNT is in the range 0.1–100 S/cm.

The thermal conductivity of CNTs was addressed both theoretically [67–69] and experimentally [70–72]. Calculations showed that the thermal conductivity exhibits a peaking behavior as a function of temperature and that it strongly depends on CNT diameter but does not or weakly depends on helicity. The extrapolation of measurements on compressed mats of CNTs bundles gave values of thermal conductivity ranging from 1750 to 5850 Wm⁻¹ K⁻¹, to be compared with the highest known thermal conductivity, that of the in-plane value of graphite (3000 Wm⁻¹ K⁻¹).

Reviews on the mechanical properties of CNTs were published by several authors [73–75]. A low density of defects confers excellent mechanical properties to CNTs. Furthermore, the intrinsic strength of the carbon–carbon *sp*² bond is expected to give CNTs the highest strength and modulus among all existing whiskers.

Theoretical [76–78] and experimental studies have shown that CNTs have excellent elastic properties. Treacy et al. [79] first investigated the elastic modulus (Young's modulus) of MWNTs using thermal vibration experiments performed in a transmission electron microscope. The average value, obtained over 11 isolated MWNTs, was 1.8 TPa. Atomic force microscopy (AFM) was used to perform a direct measurement of the stiffness and strength of individual MWNTs [80]. An elastic modulus of 1.26 TPa was obtained and the average bending strength measured was 14.2 ± 8 GPa. Salvetat et al. [81] measured the properties of SWNT bundles with the AFM. The axial and shear moduli decrease significantly upon an increase of the bundle diameter, suggesting slipping of the SWNTs within the bundle. A yield strength of 45 ± 7 GPa was calculated for SWNT bundles from experimental strain measurements on the AFM, with an elastic modulus taken at 1.25 TPa [82]. The Poisson ratio is defined by the variation of the radius of the SWNT resulting from longitudinal deformations along the axis. *Ab initio* calculations indicate that it retains graphitic value (0.17) except for a possible slight reduction for small radii and shows a helicity dependence [74].

The deformation behavior of CNTs under stress is also remarkable. Several studies [83–86] have shown that both thin- and thick-walled CNTs exhibit compressive strengths one order of magnitude higher than any other known fiber. Moreover, the flexibility of CNTs is remarkable [87, 88] and the bending may be fully reversible up to a critical angle value as large as 110° for SWNTs [89]. However, this leads to the formation of kinks and highly strained regions. The flexibility arises from the ability of the *sp*² C–C bonds to reversibly change hybridization when deformed out of plane. Tensile-load experiments on MWNTs ropes found a tensile strength and modulus of 3.6 and 450 GPa, respectively [90]. Other tension tests performed on MWNT [91] and SWNT ropes [92] reported tensile strengths in the range of 11–63 GPa, in reasonable agreement with the theoretical value of about 100 GPa and no apparent dependence on the outer wall diameter. Thostensson et al. [73] noted that 63 GPa is a value 50 to 60 times greater than that of high-quality steels. In the case of MWNTs, the failure of the outermost tube occurred followed by pullout of the inner CNTs. The effectiveness of load transfer to the inner walls or within a bundle and its influence on stiffness is still under debate and was notably studied on DWNTs [67, 93, 94].

A study of the radial compressibility of CNTs by AFM [95] showed that at low pressure, the modulus is similar to that of graphite along the *c*-axis (ca. 10 GPa), while at higher pressure, repulsion forces from the more deformed sides increase the elastic modulus. The collapse of CNTs into nanoribbons has been observed [96], which could account for the competition between the van der Waals attraction and elastic energy.

Regarding the use of CNTs in composites, it is important to note [74] that strengthening but also toughening are major concerns in structural elements involving a brittle matrix. For example, fibers longer than the critical length and a strong interfacial bond are required for fiber–polymer composites with a high fracture strength, whereas a weaker interface will promote a high toughness through fiber–matrix debonding and pullout.

With so many unique or exceptional characteristics, the potential applications of CNTs are plentiful, notably as a component of composite materials. Applications in car body panels [97], car and truck bumpers, bullet-proof jackets, the construction of earthquake-proof buildings, support of a human Martian mission, electromagnetic shielding, waveguides, etc., have already been envisioned [51]. In the following sections, the works reported on composite materials containing CNTs will be addressed, successively reviewing materials with metal, ceramic, and polymer matrix. Earlier reviews on CNT composites were published by Thostenson et al. [73] and Lau and Hui [4]. Note that materials consisting of “simply” filled or coated CNTs will not be considered here. A review on CNT filling was published by Monthioux [98].

2. CARBON NANOTUBE–METAL–MATRIX COMPOSITES

A few papers report the fabrication of CNT–metal composites by powder metallurgy techniques and some results on the stability of CNTs toward the solid metal matrix at high

temperatures or on the influence of CNTs on the electrical and mechanical properties of the materials.

Xu et al. [99] studied the electrical properties of MWNT–Al composites. The MWNTs (CCVD, diameter 30 nm) were ground with an aluminum powder and the resulting mixtures were hot-pressed at 793 K. In the obtained material, MWNTs are located mainly at Al grain boundaries and some aluminum carbides were formed, which was attributed to a reaction between amorphous carbon and Al. The electrical resistivity at room temperature increases slightly (3.4–5.5 $\mu\Omega$ cm) with increasing MWNT volume fraction. From room temperature down to 80 K all the composites show the typical metallic decrease of the electrical resistivity. At about 80 K their resistivity abruptly drops by more than 90%. Kuzumaki et al. [100] also investigated MWNT–Al composites using unpurified arc-discharge MWNTs. The composites (5 or 10 vol% MWNTs) were produced by hot-pressing at 873 K and hot-extrusion at 773 K. The MWNTs were found undamaged and, on the contrary to conventional carbon fiber/systems, no aluminum carbides were detected at the interface with the matrix, even after a heat treatment at 983 K. The tensile strength and elongation of the composites are only slightly affected by annealing at 873 K in contrast to those of aluminum.

The same group [101] also studied MWNT–Ti composites using similar samples of MWNTs (diameter 5–50 nm), containing graphitic particles and amorphous carbon. The powders were mixed and hot-pressed at 1208 K. The relative density of a pure Ti specimen prepared as a 13 reference was 98.6% and that of the composite was 95.8%. The formation of TiC was observed but TEM observations showed that the MWNTs themselves did not react with the titanium matrix. Probably, TiC comes from the reaction between amorphous carbon and the matrix. The Young's modulus of the composite is about 1.7 times that of pure Ti. This result may be caused by both TiC formation and the addition of MWNTs. The composite has about 5.5 times the Vickers' hardness of pure Ti. This is associated with the suppression of coarsening of the Ti grains, TiC formation, and addition of MWNTs with an extremely high Young's modulus. It is proposed that the MWNTs play an important role in blocking migration of dislocations.

Dong et al. [102] prepared CCVD MWNT–Cu composites by similar techniques. The hardness of the composites increases while the coefficient of friction and wear loss both decrease with the increase in the MWNT fraction (0–25 vol%). Rolling tests reveal that the composites can reach a deformation of 50–60% and have a good isotropy of the mechanical properties.

The structure and superconductivity of CCVD MWNT–MgB₂ prepared by mixing and heat treatment (950 °C, 2 h, Ar) were reported by Wei et al. [103]. Carbon atoms coming from the MWNTs do substitute for boron in the MgB₂ lattice. Depending on the MWNT content and on the extent of substitution, the composites are either semiconductive or metallic.

Thus, these first works have shown the stability of MWNTs in some solid metal environments during the hot-pressing or hot-extrusion processes. But the homogeneity of the dispersion of CNTs has to be improved and the use of

SWNTs has to be tested. The study of more optimized materials will probably confirm the beneficial influence of CNTs on some mechanical properties of metal–matrix composites.

Li et al. [104] prepared a MWNT–metallic glass Fe₈₂P₁₈ composite by rapid solidification of a pressed and melted mixture of MWNTs (CCVD, 3 wt%), Fe–P, and Fe powders. The MWNTs, some of which are filled with an iron alloy, are well dispersed in the so-obtained composite ribbons (40 μ m thick). Thus, it seems that techniques involving molten metals can also be considered to fabricate CNT–metal composites.

Coatings with CNTs are also studied with the aim to obtain excellent tribological properties. Chen et al. [105] reported the electrodeposition of CCVD MWNTs and nickel on a carbon steel substrate. The MWNT content in the deposit was increased upon the increase to a maximum value of a number of factors including the concentration of the MWNTs in the solution, the current density, and the agitation rate. Ball-milling the MWNTs to decrease their length was found to be beneficial to increase the maximum concentration in the solution. Observation of fracture surfaces shows that the MWNTs appear well dispersed in the nickel matrix, with one end embedded into it and the other end protruding from the surface. CCVD MWNT–Ni–P composite coatings were prepared by electroless deposition [106–108]. These coatings exhibit a high wear resistance and a low friction coefficient compared to SiC–Ni–P and graphite–Ni–P coatings.

3. CARBON NANOTUBE– CERAMIC–MATRIX COMPOSITES

Studies on CNT–ceramic composites using oxide, carbide, and carbon matrices have been reported and usually involve mixing raw or purified CNT samples with the matrix or a corresponding precursor before a densification step. An alternative route involves composite powders with *in-situ* grown CNTs which are very homogeneously dispersed.

Ma et al. [109] prepared MWNT–SiC composites (10 wt% MWNTs) by hot-pressing mixtures of CCVD MWNTs (diameter 30–40 nm) and nano-SiC powders. A densification of 94.7% was achieved of by hot-pressing at 2000 °C and using 1 wt% B₄C as a sintering aid. It is claimed that the presence of the MWNTs provides an increase of about 10% of both the bending strength and fracture toughness, notably by crack deflection and MWNT debonding.

The application of SWNTs for thermal management in ceramics was reported [110]. Purified laser SWNTs were mixed into a slurry containing partially stabilized zirconia. Samples (1% SWNTs) with thickness over 200 μ m were prepared by tape casting. Thermal treatments were performed for binder burnout and sintering. Although the SWNTs do not survive the final treatment, they remain intact long enough to serve as templates to create a SWNT-based microstructure. However, the thermal conductivity of these composites is higher than that of the pure matrix, which is opposed to what was aimed for. This could be a consequence of the presence of residual metal catalyst particles. In contrast, the dispersion of 1 wt% vapor-grown carbon fibers (VGCF), which withstand the sintering, provokes a decrease of about 30% of the thermal conductivity.

MWNTs were included in a TiO_2 matrix by a sol-gel method [111]. CCVD MWNTs (diameter 15 nm) covered by a thin layer of amorphous carbon were dispersed by various methods into a TiO_2 -precursor sol. Films were prepared by dip coating and were annealed in air at different temperatures. The MWNTs are preserved for treatments at or below 400 °C and TEM observation reveals that they appear to act as preferential sites for the crystallization of rutile- TiO_2 nanocrystals. The porosity of the films is about 20%.

The effect of CNT addition on the tribological behavior of carbon/carbon composites was reported [112]. Slurries of MWNTs (CCVD, 12–15 walls) were infiltrated into the composites (0–20 wt% CNTs) which were then carbonized in N_2 . The surface of the final composite is covered with a CNT/carbon layer. The friction coefficient increases and the wear loss decreases upon the increase in CNT loading, so that the wear resistance is doubled with 20 wt% CNTs compared to the 0 wt% material. Andrews et al. [113] reported the dispersion of purified laser-ablation SWNTs in isotropic petroleum pitch matrices to form composite carbon fibers with a diameter of about 18 μm . SWNTs loadings of 8 and 10 wt% were found to be too high to form a fiber. The tensile strength, elastic modulus, and electrical conductivity of a composite fiber (5 wt% SWNTs) are increased by about 90%, 150%, and 340% respectively, as compared to the corresponding values for unmodified isotropic pitch fibers.

Hwang and Hwang [114] prepared SiO_2 glass rods of micrometer size by using surfactant-MWNT (arc-discharge) co-micelles as templates. The rods were mixed with SiO_2 and dense composites (6 wt%) MWNTs were prepared. It is claimed that the Vickers hardness of the MWNTs/ SiO_2 rods- SiO_2 materials is twice that of SiO_2 rods- SiO_2 composites but it is unclear whether this is due to the MWNTs themselves or to the change in rod morphology they provide. Arc-discharge SWNT- SiO_2 glass composites were prepared using a sol-gel technique [115]. The purified and shortened (300–500 nm) SWNTs were functionalized with dendron methyl 3,5-di(methyltriglycoloxy)benzyl alcohol prior to ultrasonic blending in the sol phase and gelification. Heating the glasses to 600 °C produced materials with 80% densification and a good optical transparency, revealing the homogenous dispersion of the SWNTs (0.1–1.0 wt%). Non-linear optical transmission was observed.

The synthesis of MWNT/sol-gel composites [116] was also performed by adding various silane precursor sols (methyl-, ethyl-, and propyltrimethoxysilane) to CCVD MWNTs and mechanically mixing to ensure a uniform composition. The mixture was packed and allowed to dry for 24–48 h depending on the amount of sol. The final composites contained 34, 44, or 61 wt% of MWNTs. However, the composition of the matrix at this stage is unclear. The authors note that negatively charged silanol groups may be present. SEM observations reveal that the composites are quite porous. The development of electrochemical devices was investigated. It was found that varying the sol and the amount of MWNTs allowed one to obtain a double-layer capacitance on a wide range (0.2–100 mF/cm^2). A high capacitance is required for energy-storage applications while a low capacitance is required for electrochemical sensors. Fast electron-transfer kinetics are observed and it is proposed that the so-called

selectivity of the composite (followed by the shift of the oxidation peak of ascorbic acid on cyclic voltammograms) could be controlled.

The present authors have reported a novel catalytic route for the *in-situ* formation of SWNTs and thin MWNTs in a composite powder by reduction in H_2 - CH_4 of an alumina-based solid solution [42]. From the beginning, one of the aims was to further use such composite powders to produce dense composites. Incidentally, to the best of our knowledge, this was the first time that the formation of SWNTs by CCVD of a hydrocarbon was reported. With the aim to favor the formation of tubular carbon (notably SWNTs and DWNTs) with respect to other carbon species (fibers, hollow or filled particles, disordered carbon), several parameters related to the material were studied: allotropic form of the solid solution [117], iron content [118], specific surface area [119]. Parameters related to the reduction treatment such as the composition of the H_2 - CH_4 atmosphere [49, 120] and the temperature [35] were also studied in detail. The method was expanded to MgAl_2O_4 -based solid solutions in order to be able to use divalent cations and therefore compare the catalytic efficiency of Fe, Co, and Ni [121, 122] and their binary alloys [123]. Solid solutions in the form of foams rather than powders were prepared and the formation of SWNTs from such foams was reported for the first time [124]. The method was further expanded to MgO -based solid solutions [43, 44, 125–127]. The CNTs can be extracted without damage from the CNT-metal-MgO composite powders by a mild treatment (soaking in dilute HCl at room temperature). They thus can be used for dispersion in other matrices such as epoxy as mentioned in a following section. The specific surface area of the so-obtained CNTs specimens is very high (over 800 m^2/g) [44], in good agreement [5] with the distributions of the number of walls and diameter.

The CNTs being grown *in-situ* in the powders are thus very homogeneously dispersed between the metal-oxide grains (Fig. 2) in a way that seems very difficult to achieve by methods involving mechanical mixing. The CNTs gather in extensively branched bundles, forming a weblike network between the matrix agglomerates. The bundles are always smaller than 100 nm in diameter, they appear to be very flexible, and some have been traced for 100 μm .

Several studies have dealt with the preparation of dense CNT-Fe- Al_2O_3 , CNT-Co-MgO, and CNT-FeCo-Mg Al_2O_4 composites by hot-pressing [128–131] and hot-extrusion [132] and on the determination of some of their mechanical and electrical characteristics. The precise CNT content in the dense materials is difficult to determine, so the carbon content in the starting composite powders (2–10 wt%) and a unique parameter derived from specific surface area measurements [5, 42, 128] representing the quantity of CNTs were used to compare the different specimens. The early studies [128–130] showed that in comparison to similar carbon-free nanocomposites, the relative densities of the CNT-Fe- Al_2O_3 composites are lower, the matrix grains are smaller, and the fracture strength and fracture toughness are generally markedly lower. Nevertheless, scanning electron microscopy (SEM) observations of composite fractures indicated that the CNT bundles locally act to dissipate some of the fracture energy. The too-low volume fraction of CNTs

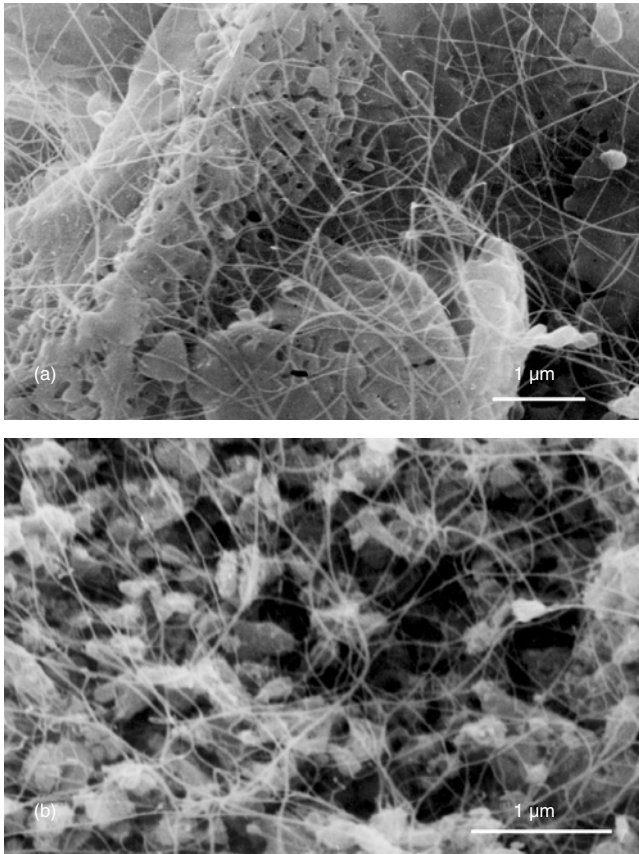


Figure 2. Scanning electron micrographs of CNT-Fe- Al_2O_3 composite powders with micronic (a) and submicronic (b) matrix grains. Long bundles of CNTs are observed.

and the presence of others species, notably large diameter (>15 nm) filamentous carbon, could explain the lack of mechanical reinforcement at the macroscopic scale.

As mentioned, works on the powder synthesis allowed one to increase both the quantity of CNTs and the quality of carbon (much less nanofibers) in the CNT-Fe- Al_2O_3 powders and to prepare novel composite powders, CNT-Fe/Co- MgAl_2O_4 and CNT-Co- MgO . Hot-pressed composites were investigated [131]. For the sake of comparison, ceramics (MgAl_2O_4 and MgO) and metal-oxide composites

(i.e., without CNTs) were prepared in the same conditions. With the Al_2O_3 matrix, the increase of the quantity of CNTs in the powder leads to a refinement of the microstructure of the hot-pressed specimen. With both the Al_2O_3 and the MgAl_2O_4 matrix, a fraction of the CNTs seems to be destroyed during hot-pressing at 1500°C (in a vacuum). When using the MgO matrix, most CNTs are destroyed during a hot-pressing at 1600°C , but the CNTs are not damaged if the treatment is limited to 1200°C . It seems that the quantity of CNTs retained in the massive composite is more dependent on the treatment temperature than the nature of the oxide matrix. CNT damage produces disordered graphene layers which gather at matrix grain junctions. Probably due to a too-low relative density (87–93%), the fracture strength (measured by three-point bending) and the fracture toughness (measure by the single-etched notched beam technique) of the CNT-containing composites (Tables 1 and 2) are generally lower than those of the carbon-free metal-oxide composites and only marginally higher than those of the ceramics.

SEM observations (Fig. 3) showed that some CNTs are trapped inside the matrix grains or at grain boundaries and seem to be wetted by the matrix in the case of alumina. Most of these CNTs are cut near the fracture surface after some pull-out (Fig. 4) and could contribute to a mechanical reinforcement. However, this is not demonstrated at a macroscopic scale.

It was shown that CNTs confer an electrical conductivity to ceramic-matrix composites. Indeed, whereas the corresponding ceramics and metal-oxide nanocomposites are insulators, the CNT-metal-oxide composites are electrical conductors (electrical conductivity in the range $0.2\text{--}4.0\text{ S cm}^{-1}$) due to the percolation of the CNTs. The values of the electrical conductivity are fairly well correlated to the relative quantity of CNTs, the specimens becoming insulators when the CNTs are destroyed. Recently [133], it was found that the percolation threshold is below 1 vol% of CNT and that controlling the CNT quantity in the starting powders allows one to control the electrical conductivity in the range $0.01\text{--}10\text{ S cm}^{-1}$.

Peigney et al. [132] reported that extrusion at high temperatures (in a vacuum) allows one to align CNTs in ceramic-matrix bulk nanocomposites, as opposed to fibers or thin films. The superplastic forming is made easier by the CNTs, which inhibit the matrix grain growth and also

Table 1. Relative density and microstructural characteristics of the hot-pressed ceramics and nanocomposites.

Ceramic or composite	Label	d (%)	G_m (μm)	d_{metal} (μm)	d_{ZrO_2} (μm)
CNT-Fe- Al_2O_3	CMA1	88.7	0.3	≤ 0.5	—
CNT-Fe- Al_2O_3^*	CMA2	87.5	0.3	≤ 0.5	≤ 1
MgO	B	90.1	5	—	—
Co- MgO	MB	96.6	7	≤ 2	—
CNT-Co- MgO	CMB	92.9	3	≤ 1.5	—
MgAl_2O_4	D	99.7	13	—	≤ 1
Fe/Co- MgAl_2O_4	MD	98.2	0.8	≤ 0.5	≤ 1
CNT-Fe/Co- MgAl_2O_4	CMD	90.6	0.5	≤ 0.5	≤ 1

Note: d : relative density calculated by assuming that all carbon has the density of graphite, with $d_{\text{graphite}} = 2.25\text{ g/cm}^3$; G_m : average grain size of the oxide; d_{metal} : diameter of the larger metal particles; d_{ZrO_2} : diameter of the larger ZrO_2 particles in specimens prepared from powders attrition-milled before reduction (*).

Source: Reprinted with permission from [131], E. Flahaut et al., *Acta Mater.* 48, 3803 (2000). © 2000, Elsevier Science.

Table 2. Electrical conductivity (σ), fracture strength (σ_f), fracture toughness (K_{Ic}), and fracture mode of the hot-pressed ceramics and nanocomposites.

Ceramic or composite	Label or reference	σ (S cm ⁻¹)	σ_f (MPa)	K_{Ic} (MPa m ^{1/2})	Fracture mode
Al ₂ O ₃	[34]	—	335	4.4	intergranular
Fe–Al ₂ O ₃	[34]	—	630	7.2	mixed
CNT–Fe–Al ₂ O ₃	[17]	—	540	3.6	mixed
CNT–Fe–Al ₂ O ₃ ^a	[18]	—	295	2.7	intergranular
CNT–Fe–Al ₂ O ₃	CMA1	0.4–0.8	400	5.0	mixed
CNT–Fe–Al ₂ O ₃ ^a	CMA2	2.8–4.0	296	3.1	intergranular
MgO	B	n.m.	202	—	intergranular
Co–MgO	MB	n.m.	283	—	mixed
CNT–Co–MgO	CMB	0.2	254	—	intergranular
MgAl ₂ O ₄ ^a	D	n.m.	308	—	transgranular
Fe/Co–MgAl ₂ O ₄ ^a	MD	n.m.	212	2.94	mixed
CNT–Fe/Co–MgAl ₂ O ₄ ^a	CMD	1.5–1.8	221	1.71	mixed

Note: n.m.: not measurable; mixed: the fracture presents both the inter- and transgranular characters.

Source: Reprinted with permission from [131], E. Flahaut et al., *Acta Mater.* 48, 3803 (2000). © 2000, Elsevier Science.

^a Specimens prepared from powders attrition-milled before reduction.

act as a lubricating agent. The CNTs withstand the extreme shear stresses occurring during the extrusion up to 1500 °C. In addition to electron microscopy revealing the alignment, the composites show an anisotropy of the electrical conductivity [about 30 times larger in the longitudinal direction (20 S cm⁻¹) than in the transverse direction], which could be adjusted by controlling the amount of CNTs (carbon content in the range 0.6–8 wt%).

Siegel et al. [134] mixed arc-discharge MWNTs with a nanometric alumina powder in ethanol dispersion using an ultrasonic probe. The mixture was dried in two steps, first in an ultrasonic bath and then in an oven. Hot-pressing was performed in argon at 1300 °C. A single composite was prepared (10 vol% MWNTs). It is claimed that the fracture toughness (derived from Vickers microhardness

measurements) is increased by 24% (to 4.2 MPa m^{1/2}). However, basic materials characteristics such as the density and grain size are not given, making it difficult to consider this result as evidence for the beneficial role of the MWNTs themselves.

Zhan et al. [135] prepared SWNT–alumina composites using small-diameter SWNT bundles obtained by the HIPCo technique and a nanometric alumina powder (50 nm). The two components were mixed by ball-milling, which produced a reasonably homogeneous dispersion without damaging the SWNTs. Fully dense composites were obtained by the spark plasma sintering (SPS) technique, in which the specimen is annealed at lower temperatures (1150 °C) and during much lower times (3 min) than using other sintering processes. SPS does not damage the SWNTs. The bundles can be seen to be located mainly at the boundaries of the alumina grains and have good contact with the alumina matrix. The authors report a very large gain in fracture toughness (derived from Vickers indentation) in alumina composites containing 10 vol% SWNT (from 3.7 MPa m^{1/2} for pure Al₂O₃ to 9.7 MPa m^{1/2}). Moreover, one of these SWNT–Al₂O₃ composites which was not fully densified (about 14% of residual porosity) presented a quite remarkable fracture toughness—about twice that of the fully densified but unreinforced alumina matrix. Sun et al. [136] reported the development of a colloidal process to coat CNTs with alumina prior to another mixing step with a concentrated alumina suspension, so that the final material contains only 0.1 wt% CNTs. SPS was used to fully densify (at 1300 °C) the composite. The Vickers hardness is slightly higher than that of pure alumina (17.6 versus 16.9 GPa) and the Vickers indentation-derived toughness is increased from 3.7 to 4.9 MPa m^{1/2} upon the addition of 0.1 wt% CNTs. It is proposed that coating the CNTs before sintering results in an improved bonding with the matrix. Crack bridging and CNT pullout could also lead to the increase in fracture toughness. These studies [135, 136] have thus demonstrated that CNT–ceramic composites warrant further investigation with respect to the mechanical properties [137]. For example, the preparation of larger specimens to test the fracture strength would be of interest [137].

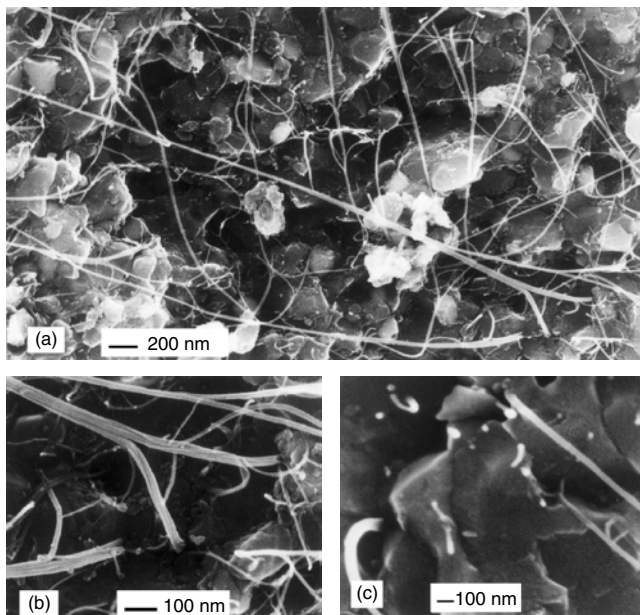


Figure 3. Scanning electron micrographs of the fractures of CNT–Fe–Al₂O₃ composites. Reprinted with permission from [130], A. Peigney et al., *Ceram. Int.* 26, 677 (2000). © 2000, Elsevier Science.

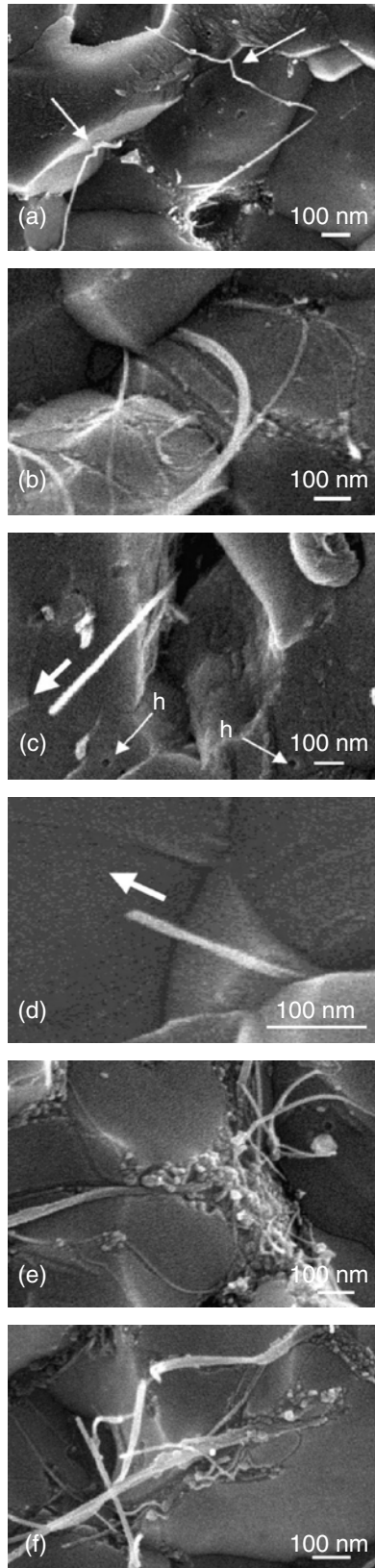


Figure 4. FEG-SEM images of the fracture of the CNT-Fe-Al₂O₃ composite showing some aspects of the CNT-matrix interactions. Reprinted with permission from [131], E. Flahaut et al., *Acta Mater.* 48, 3803 (2000) © 2000, Elsevier Science.

MWNT-lanthanum cobaltate composites were tested for a possible application as an oxygen electrode in rechargeable zinc/air batteries [138]. La_{1-x}M_xCoO₃ (M = Ca, Sr) particles were coated with a citrate precursor containing more cobaltate with a slight excess of cobalt oxide. The mixture was treated in acetylene (700 °C) to produce MWNTs (diameter 20–30 nm, length about 20 μm) grown on the oxide surface. An electrode was manufactured and promising results were obtained. The CNTs formed directly at the oxide surface could improve the electrical junction between the oxide and the carbon-containing substrate.

MWNTs (arc discharge, 3 wt%) were embedded into Bi₂Sr₂CaCu₂O_{8+δ} (a Bi-2212 superconductor) in order to improve pinning properties [139]. The insulator-supraconductor transition is slightly lower in the composite than in the Bi-2212 material (87 vs 95 K). The increase in current densities shows that the MWNTs function like columnar defects produced by heavy-ion irradiation.

4. CARBON NANOTUBE–POLYMER–MATRIX COMPOSITES

CNT-polymer composites are by far the most studied. In the following sections, we will successively review composites with epoxy, polymethylmethacrylate, and other matrices. Lordi and Yao [140] noted that three key issues affect the performance of a fiber-polymer composite: the strength of the fiber phase, the toughness of the fiber phase, and good interfacial bonding which is crucial for load transfer to occur and fiber orientation. These authors [140] performed calculations related to the interfacial adhesion in CNT-polymer composites. It is shown that interfacial binding energies are only slightly correlated with adhesion in actual composites, as determined by comparison with experimental observations of fiber pullout by various authors. It is also reported that hydroxy side-groups, and to a lesser extent phenyl side-groups, on the polymer seem advantageous for strong interfaces. The key factor in forming a strong bond the CNTs and the matrix lies in the polymer's ability to form large-diameter helices around individual CNTs. The strength of the interface may result from molecular-level entanglement of the two phases and forced long-range ordering of the polymer. In addition, it is proposed that weak frictional interactions between layers of MWNTs and between SWNTs in bundles indicate that isolated SWNTs are desired for dispersion in a matrix. Schadler et al. [141] noted that a high interfacial shear stress between the fiber and the matrix will transfer the applied load to the fiber over a short distance, whereas a low interfacial shear stress will require a long distance. The first main mechanism of load transfer is micromechanical interlocking, which could be difficult with CNTs due to their atomically smooth surface. Other mechanisms include chemical bonding and van der Waals bonding between the CNTs and the matrix.

4.1. Epoxy–Matrix Composites

The first work on a CNT-polymer composite was reported by Ajayan et al. in 1994 [142]. Purified arc-discharge MWNTs were dispersed in a liquid-epoxy base resin by mechanical stirring. After evacuation to remove trapped air

bubbles, pastes of the material were hardened by heating above 6 °C for 2 hours. Thin slices were cut and observed by TEM. It was demonstrated that, during cutting, the majority of MWNTs were straightened in the strain direction rather than broken. These results suggested, first, that MWNTs have excellent mechanical properties and second that anisotropy can be induced by a flow in such a material. Only several years later, in 1998, were other works published on CNT-polymer composites.

Schadler et al. [141] reported the dispersion of 5 wt% MWNTs in an epoxy resin by an ultrasonic treatment. Although the MWNTs were well separated, they remain poorly distributed. Mechanical tests and associated Raman spectroscopy revealed that the load transfers to the MWNTs were much higher in compression than in tension. It was inferred that, under loading, only the outer layers of the MWNTs are stressed in tension because all the inner tubes are sliding within the outer, whereas all the layers are stressed in compression.

Further investigations on the load transfer in such materials were reported. Both laser-ablation SWNTs and arc-discharge MWNTs were used. It was found [85] that the compressive strength of thin- and thick-walled CNTs is more than two orders of magnitude higher than the compressive strength of any known material, which is close to 0.05 GPa. Compressive stresses were induced in composite films, 200 μm thick, from the shrinkage of the matrix due to polymerization and by further quenching from room temperature to low temperatures (223–81 K) [143, 144]. The frequency of some Raman bands being stress-sensitive, it has been demonstrated that this spectroscopy can be used to study the strain distribution in fiber composites and to calculate the Young's modulus [145]. The obtained values were close to those previously reported for SWNTs and MWNTs, about 5 and 1.8 TPa, respectively [79, 146]. The fracture of a SWNT-epoxy composite, observed in real time by TEM, revealed a good polymer-CNT wetting and significant CNT-polymer adhesion [147]. Raman spectroscopy investigations of SWNT-epoxy and MWNT-epoxy composites [148] allowed one to determine the effective modulus of the CNTs (about 1 TPa and 0.3 MPa for the SWNTs and MWNTs, respectively). Stress transfer between the different phases was demonstrated.

The formation of damage doublets in adjacent MWNTs was reported in microtomed thin slices of arc-discharge MWNT-epoxy composite films [149] (Fig. 5). It was concluded that despite the enormous difference in scale, fundamental concepts pertaining to continuum mechanics of fiber composites such as "stress concentration factor" and "effective matrix radius" could be valid at the nanometric level, at least to some degree. Interactions between CNTs should also be taken into account.

Mechanical tests conducted on 5 wt% SWNT-epoxy composites [150] showed that SWNT bundles were pulled out of the matrix during the deformation of the material. In some areas, the SWNTs appeared broken and relaxed but in other regions, they were fully stretched and bridging a crack (Fig. 6).

On the basis of Raman spectroscopy results and SEM observations, the authors inferred that the load transfer is limited because the SWNTs are slipping, under tension

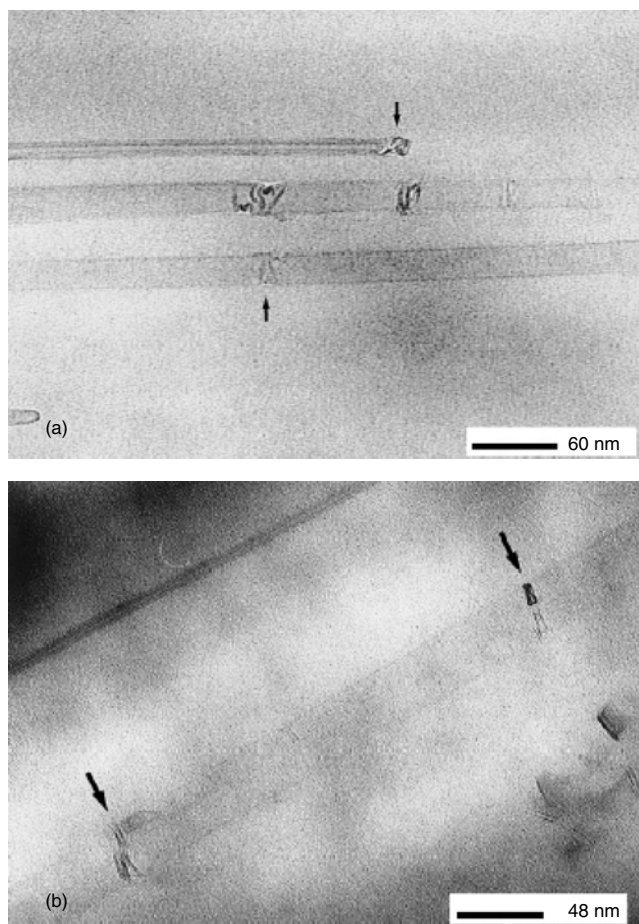


Figure 5. (a) TEM image of aligned MWNTs close to the film surface, revealing CNT fragmentation and the formation of a doublet of adjacent breaks (bottom arrow). A doublet consisting of a CNT end and a nanotube break is also shown (top arrow). (b) TEM picture of two aligned MWNTs in close contact, revealing the formation of two doublets of adjacent breaks (arrows). Reprinted with permission from [149], O. Lourie and H. D. Wagner, *Comp. Sci. Tech.* 59, 975 (1999) © 1999, Elsevier Science.

strain, within the bundles. It was also reported [151] that the combination of standard mechanical tests and Raman scattering tests allows the determination of residual strains due to matrix shrinkage, the elastic properties of embedded SWNTs/bundles, their dispersion, and load transfer effectiveness.

The influence of the interfacial interaction between CNTs and the epoxy matrix was evidenced by Gong et al. [152]. Dynamic mechanical measurements and SEM observations were performed on 1 wt% CNT-epoxy composites, prepared either with or without a nonionic surfactant addition (polyoxyethylene 8 lauryl). For the former composite, the glass transition temperature was increased from 63 to 88 °C and the elastic modulus was also increased by more than 30% in comparison with the matrix. In contrast, the latter composite, prepared without surfactant addition, presents only moderated improvements of these properties. SEM observations confirmed that the surfactant addition improved the dispersion of the CNTs, thus allowing the dramatic effects of CNTs on the properties of the material.

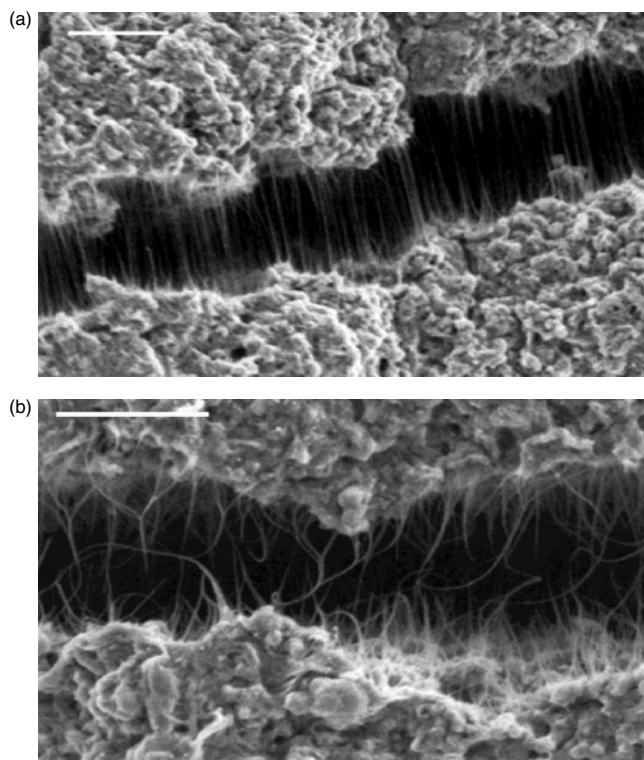


Figure 6. (a) SEM image of SWNT bundles stretched across cracks observed in a CNT-carbon composite pellet for certain critical crack widths. (b) Curved bundles of SWNTs that are no longer under load, as observed in a SEM image. The scale bars in the images correspond to 1 μm . Reprinted with permission from [150], P. M. Ajayan et al., *Adv. Mater.* 12, 750 (2000). © 2000, Wiley-VCH.

Allaoui et al. [153] claimed to have quadrupled the elastic modulus and the yield strength (measured through tensile test) of an epoxy matrix by the incorporation of 4 wt% of both very large CCVD MWNTs and VGCFs (15–400 nm in diameter). Conductivity measurements revealed that the insulator-conductor transition occurred for MWNT contents in the range 0.5–1 wt%.

CCVD MWNTs (inner diameter 5 nm, outer diameter 10 nm, length a few micrometers) were dispersed in an epoxy matrix (0.0225–0.15 wt% MWNTs) [154]. The exposure to ultrasound early in the process and the subsequent intense stirring of the resin dramatically improved the dispersion of the MWNTs in the matrix. The percolation threshold was found to be between 0.0225 and 0.04 wt% MWNTs. An electrical conductivity of about 10^{-2} S/m, sufficient for antistatic applications, was achieved with 0.04 wt% MWNTs, that is, using a loading about one-tenth of that needed using carbon black (Fig. 7). It is noted that at these low filler fractions, neither the processing behavior of the matrix nor the surface finish of the samples is adversely affected and that the mechanical properties of the epoxy matrix should not be compromised.

Using CCVD CNTs (80% SWNTs or DWNTs) prepared by the solid solution route as mentioned in a previous section, Barrau et al. [155] prepared CNT-epoxy composites,

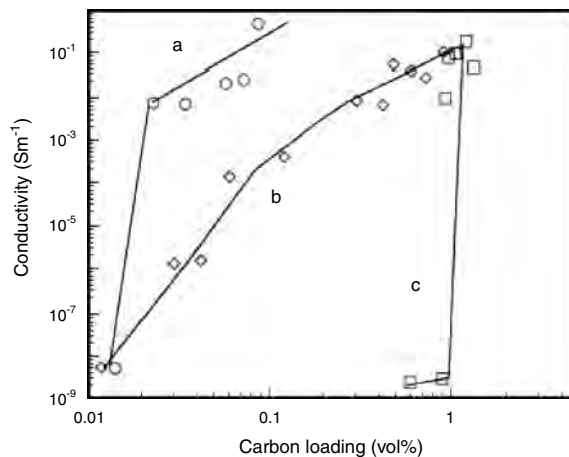


Figure 7. Comparative log-log plot of the conductivity of nanocomposites containing: (a) CCVD CNTs, (b) carbon black with copper-chloride, and (c) carbon black only, as a function of the filler volume content. Lines are included as visual aids. Reprinted with permission from [154], J. Sandler et al., *Polymer* 40, 5967 (1999). © 1999, Elsevier Science.

with CNT fractions in the range 0.04–2.5 wt%. An analysis of the dc and ac electrical conductivity in the temperature range 20–110 °C and frequency range 10^{-2} Hz–1 MHz was reported. There is an increase in dc conductivity of 10 orders of magnitude between 0.2 and 0.6 wt% CNTs, the highest conductivity being 10^{-4} S/cm for 2.5 wt%. A percolation threshold was found at 0.3 wt% CNTs independent of the temperature. The critical exponent β of the scaling law of the percolation theory $\sigma \propto (f - f_c)^\beta$ increases with the temperature (1.71 ± 0.20 at 100 °C) and tends toward the value (1.94) predicted by the tridimensional percolation theory of randomly distributed objects. Indications that tunneling conduction may be the main conduction mechanism are presented. The frequency dependence of the conductivity obeys the universal dynamic response. The behavior of the frequency exponent with the temperature is consistent with the correlated barrier hopping mechanism.

CCVD SWNTs were used to augment the thermal transport properties of industrial epoxy [156]. Samples loaded with 1 wt% unpurified SWNTs (containing 15–25 wt% residual Fe catalyst) showed an increase in thermal conductivity of 70% and 125% at 40 K and at room temperature, respectively. Electrical conductivity data showed a percolation threshold in the range 0.1–0.2 wt% SWNTs. The Vickers hardness rose monotonically with SWNT loading up to a factor of 3.5 at 2 wt%. It is noted that these results suggest that the thermal and mechanical properties of SWNT-epoxy composites are improved without the need to chemically functionalize the SWNTs.

Thostenson et al. [157] reported the direct growth of MWNTs on carbon fibers by CCVD. Embedding the coated fibers in an epoxy matrix produces a multiscale composite. Single-fiber composites were prepared. It is reported that the MWNT coating improves the interfacial load transfer, possibly by local stiffening of the polymer matrix near the fiber/matrix interface.

4.2. Polymethylmethacrylate–Matrix Composites

Unpurified and purified laser-ablation SWNTs were dispersed and aligned in polymethylmethacrylate (PMMA) using a combination of solvent mixing and melt mixing, a method expected to be applicable to most thermoplastic polymers [158]. Composite films (1–8 wt% SWNTs) showed a higher electrical conductivity along the flow direction than perpendicular to it. The conductivity increases with SWNTs loading. In addition, composite fibers with well aligned SWNTs were prepared by melt spinning. The highest draw ratio was achieved for pure PMMA and specimens with 1% SWNTs. However, the fiber diameter is not uniform along the axis and specimens with the higher SWNT contents tend to fracture during the melt-spinning process, revealing a much increased viscosity of the melt. The weight fraction of SWNTs necessary for percolation increases as the SWNTs are aligned.

Unpurified arc-discharge MWNTs (diameter 30 nm) melt-blended with PMMA were compressed (8–9 MPa, 210 °C, 5 min) to produce transparent films [159]. Different contents (4–30 wt%) of MWNTs were used and it is claimed that they are well dispersed in the matrix with no apparent damage. Thermogravimetric analysis (TGA) shows that, compared to pure PMMA, the thermal degradation occurs at a slightly higher temperature when 26 wt% MWNTs are added. The dynamic mechanical behavior was investigated, showing that the storage modulus (E') is increased upon the incorporation of MWNTs, particularly at high temperatures (120–140 °C) (Fig. 8). It was, however, thought necessary to improve the wetting between the MWNTs and the PMMA, so the MWNTs were mixed and therefore coated with poly(vinylidene fluoride) prior to melt blending with PMMA [160]. The presence of a small amount of poly(vinylidene fluoride) indeed results in an increased storage modulus, but this effect diminishes at higher temperatures.

Jia et al. [161] mixed purified CCVD MWNTs with a free radical initiator (2,2'-azobisisobutyronitrile) and the

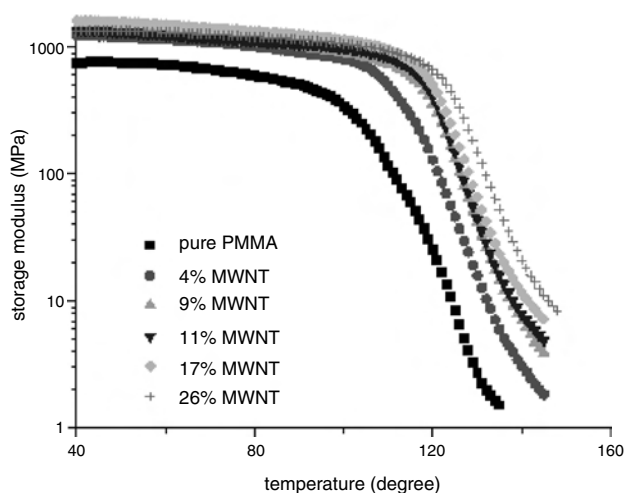


Figure 8. Storage moduli of PMMA and various composites. Reprinted with permission from [159], Z. Jin et al., *Chem. Phys. Lett.* 337, 43 (2001). © 2001, Elsevier Science.

monomer MMA to obtain MWNT–PMMA composites by an *in-situ* process. Two kinds of MWNTs were used: as-purified specimens and ball-milled purified samples. The ball-milling treatment produces much shorter and better separated MWNTs. It is claimed that the MWNTs take part in the polymerization reaction, obstructing the growth of PMMA. C–C bonds are formed between the MWNTs and PMMA results in a strong interface. The tensile strength, toughness, hardness, and deflection temperature of the ball-milled MWNT–PMMA composites are improved compared to pure PMMA up to 7 wt% MWNTs. A higher loading is reported to generate residual stresses in the matrix which causes the composite to become very brittle. In contrast the as-purified MWNT–PMMA composites show weaker mechanical properties because of a poor dispersion of the MWNTs.

MWNT–PMMA (arc-discharge MWNTs, diameter 10–15 nm, length 2–3 μm) and SWNT–PMMA composites (laser-ablation SWNTs, diameter 1.4–2 nm, length 200–400 μm , in bundles) were prepared using a dry powder mixing method [162]. The final step of the preparation was to extrude the materials in order to align the CNTs. The efficiency of the method is demonstrated by SEM, TEM, and Knoop hardness analyses. In particular, the Knoop hardness is at a maximum when the long diagonal of the indenter is perpendicular to the orientation of the CNTs. The tensile modulus was almost insensitive to the presence of the CNTs while the impact strength was significantly increased with only 0.1 wt% of SWNTs. It is proposed that this apparent increase in toughness is due to a weak interfacial adhesion, to the high flexibility of the SWNTs, and to the pullout and sliding of individual SWNTs within a bundle.

The characterization by Raman spectroscopy of SWNT–PMMA composite films (2.5–20 wt% SWNTs) prepared by spin casting was reported [163, 164]. The SWNTs, prepared by different methods (arc discharge, laser ablation, and solar energy), are organized in bundles. In the case of arc discharge, composites were prepared with SWNT samples from different parts of the so-called collaret. Comparing the Raman spectra allowed one to get a diameter distribution of the SWNTs and to confirm the presence of armchair SWNTs. It was shown that the diameter distribution slightly changes from one collaret sample to the other, whereas spectra from composites with laser ablation or solar energy SWNTs are rather similar. Furthermore, for low SWNT loadings, the amorphous carbon formed during the synthesis of the SWNTs was found to be dispersed in the PMMA and the bundles appeared to be undone. It is expected that such composite films could be used in multilayer diodes. The transport properties of SWNT–PMMA composite films (10 μm thick) were studied in great detail [165, 166]. The SWNTs (diameter 1.3–1.5 nm) are produced by arc discharge with a typical purity of about 70–90%. Most SWNTs form bundles with a typical size of 7–12 nm. The electrical conductivity strongly depends on the SWNTs content. It increases by nine orders of magnitude from 0.1 to 8 wt% (Fig. 9). The room-temperature conductivity is well described with the standard percolation theory. Transport is due to localized carriers originating from the metallic SWNTs. The critical behavior $\sigma \propto (f - f_c)^\beta$ is observed

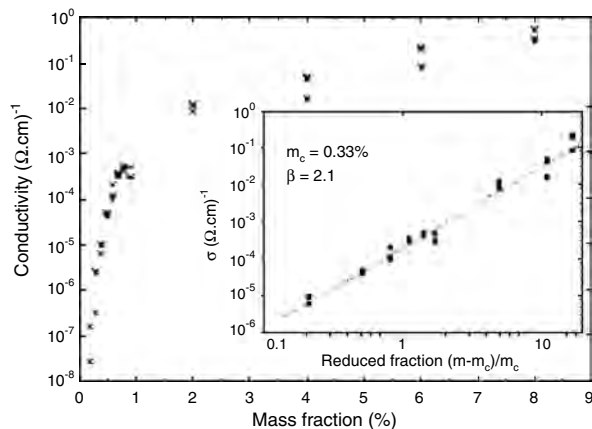


Figure 9. Dependence of the room-temperature (RT) composite conductivity with the SWNT content. Inset: RT power law dependence of σ versus the reduced mass fraction of SWNTs. Reprinted with permission from [165], J. M. Benoit et al., *Synth. Met.* 121, 1215 (2001). © 2001, Elsevier Science.

with a percolation threshold $f_c = 0.33 \pm 0.03\%$ and a critical exponent $\beta = 2.1 \pm 0.1$. The low value of f_c arises from the very high aspect ratio of the SWNTs, estimated at about 850. The critical exponent β is in good agreement with the conventional 1.94 exponent found for random tridimensional connectivity. This quasi-ideal percolation behavior confirms the good dispersion of the SWNTs in the matrix. The temperature (4–300 K) dependence of the resistivity of some composites was studied, revealing a behavior usually ascribed to hopping in the presence of Coulomb interactions opening a soft Coulomb gap. This suggests that a distribution of intertube/interbundle barriers is superposed to the topological percolation network. It is proposed that the Coulomb gap is due to the Coulomb charging energy involved in the transport process from one bundle (or one SWNT) to the neighboring one. It is further suggested that using composites close to the percolation threshold may be a way to access intrinsic SWNT properties at a macroscopical level and that this approach may be developed for the thermal conductivity as well.

Grimes et al. [167] investigated SWNT-PMMA composite films (thickness about 500 μm) with much higher SWNT loading. Indeed 0–23 wt% of arc-discharge SWNTs (diameter 10 nm, length 1 μm) were dispersed. The electrical conductivity varied over nine orders of magnitude and the percolation threshold was found to be close to 3 wt%. Addition of the SWNTs has a dramatic effect on the measured permittivity spectra (for example at 500 MHz, the real permittivity increases by a factor of 35 and the complex permittivity increases by over three orders of magnitude upon increasing the SWNT loading from 0 to 23 wt%). Both sets of data (electrical conductivity and complex permittivity) fall on a reasonably smooth curve indicating a good dispersion of the SWNTs in the matrix. It is, however, noted that no percolation threshold is observed in the 500 MHz data. Comparison of the permittivity measurements (500–5500 MHz) with theoretical predictions using an effective medium theory were found to be in reasonable agreement.

4.3. Polymer Composites with Other Matrices

Shaffer and Windle [168] prepared CCVD MWNT-polyvinyl alcohol (PVA) composite films with a wide range of MWNT loadings (5–60 wt%). The dry film thickness varied from 53 to 44 μm , with increased loading. SEM images revealed an even dispersion of the MWNTs and pullout lengths of about 100 nm were observed on fracture surfaces. TGA showed that although there is a retardation of the onset of PVA decomposition, resulting possibly from the absorption of the decomposition-generated free radicals by activated carbon surfaces, the subsequent progress of the degradation of PVA is not affected. Below the glass transition of the matrix, the tensile elastic modulus increases due to the presence of the MWNTs. The stiffness of the MWNTs was evaluated at about 150 MPa, well below values reported for isolated tubes. This low experimental value could reflect defects in the MWNTs or the difficulty of shear stress transfer between the walls. Above the glass transition, a large proportion of the stiffness observed below is retained, denoting a much more significant effect of the MWNTs. The onset of the glass transition was not affected by the MWNTs but the high-temperature side was broadened, because polymer molecules near the MWNT surface would have a reduced mobility. The percolation threshold was found to be in the range 5–10 wt%. It is noted that the electrical conductivity is rather lower compared to that of MWNT-epoxy composites containing very low MWNTs loadings [154], possibly because the adsorbed layer of polymer on each MWNT reduces the quantity and quality of electrical contacts between the MWNTs.

Vigolo et al. [169] proposed an original method for the fabrication of macroscopic composite fibers and ribbons incorporating flow-aligned SWNTs. The elastic modulus was found to be equal to 15 GPa, lower than that of individual CNTs or conventional carbon fibers, but nevertheless giving hope for future improvements. It was shown that such fibers can be netted and even knotted.

Starting with arc-discharge MWNTs randomly dispersed in a thermoplastic polymer (polyhydroxyaminoether) prepared by solution casting, Jin et al. [170] prepared composites with aligned MWNTs by mechanical stretching above the glass transition temperature of the polymer. X-ray diffraction (XRD) analysis showed that the fraction of aligned MWNTs increased with increasing stretching ratio. Decreasing the MWNT content also favored alignment, due to a higher mobility. Interestingly, no alignment was achieved with SWNTs using similar stretching ratios. A further study [171] revealed that buckling was observed in bent MWNTs of large curvature, some being completely collapsed. Buckling is thought to be caused by the shrinkage of the polymer during cooling down to room temperature in the final stage of preparation. In some cases, heating by electron irradiation in the TEM restored the cylindrical shape, showing that buckling is an elastic deformation, at least at moderate strain. The onset buckling strain was estimated at about 5%, in good agreement with results from AFM lateral force measurements [80]. The observation of fractured surfaces revealed that failure occurred from MWNT pullout and fracture of the matrix but that the load transfer was not

sufficient to fracture the MWNTs. The fracture strain was found to be greater than 18%.

Wagner et al. [172] prepared arc-discharge MWNT-polyurethane acrylate films 200 μm thick. Tensile test were performed and subsequently thin slices (70 nm) cut in a direction parallel to the film surface were observed by TEM. A progressive fragmentation process was detected which was thought to originate in the large stresses induced in the MWNTs during the tensile tests. The MWNT-matrix stress transfer efficiency was estimated to be at least one order of magnitude larger than in fiber-based composites. This could arise from a strong reactivity of MWNTs toward double bonds in the polymeric chains upon ultraviolet (UV) curing of the specimen. The macrofragmentation and microfragmentation phenomena were studied in detail in a further work [173].

Wood et al. [174] prepared 0.1 wt% SWNT-polyurethane acrylate films 150 μm thick using a flow orientation technique to align the SWNTs. Micro-Raman spectra for specimens cut both parallel and perpendicular to the flow direction were significantly different, as a function of mechanical strains, allowing one to probe the alignment. It is proposed that the adhesion between the SWNTs and the polymer exceeds the shear yield strength of the matrix. A further work [175] showed that using polarized resonance Raman spectroscopy allows one to use unoriented SWNTs as strain sensors. The Raman spectral shifts of the SWNTs were also used to study the glass transition and secondary transitions in the polyurethane acrylate and polycarbonate polymers [176].

The rheological behavior of MWNT-polycarbonate composites was reported by Pötschke et al. [177]. CCVD MWNTs (diameter 10–15 nm, length 1–10 μm) were used. One-kilogram mixtures of polycarbonate with the MWNTs were extruded at 240 °C using a twin-screw extruder. Composites with MWNTs loadings of 0.5, 1, 2, and 5 wt% (corresponding to about 0.34, 0.68, 1.37, and 3.40 vol%, respectively) were formed into bars by compression molding. SEM observations showed that the MWNTs are randomly dispersed in the matrix and that a layer of polycarbonate covers the MWNTs, indicating some wetting and phase adherence. MWNT-polyamide-6 prepared for the sake of comparison did not exhibit the same MWNT-covering features. Electrical resistivity measurements revealed that the percolation threshold is between 1 and 2 wt%. The rheological behavior was investigated by oscillatory rheometry at 260 °C. The viscosity of composites with less than 2 wt% MWNTs had similar frequency dependency than pure polycarbonate and reached a Newtonian plateau at low frequencies. Above 2 wt%, the viscosity decreases to a greater extent with frequency and a non-Newtonian behavior is obtained to much lower frequencies. The coincidence between the electrical and rheological thresholds indicates that the rheology of the material is sensitive to the interconnectivity of the MWNTs. The increase in viscosity with MWNT content is much higher than that reported for nanofibers and carbon black, because of the higher aspect ratio of the MWNTs. The viscosity increase appears along an increase of the elastic melt properties, the increase of the storage modulus being much more important than that of the loss modulus.

MWNT-polycarbonate and MWNT-polybutylene terephthalate (CCVD MWNTs, 8–15 walls, loading 3.5 and 5.0 wt%) were reported [178] to have improved mechanical and electrical properties compared to the corresponding pure polymer. It is noted that the MWNTs must be untangled for optimized performance, which can be done by high shear in a compounding operation.

The synthesis of MWNT-polyaniline composites by *in-situ* polymerization was reported [179]. Arc-discharge MWNTs (10, 20, 30, and 50 wt% with respect to aniline monomer) were used. A composite of 30 wt% MWNTs and *ex situ* polymerized polyaniline was also prepared for comparison. In this process, polyaniline exists in its primary doped form called emeraldine salt. X-ray diffraction analysis showed that no additional order had been introduced. Comparison of the different Raman spectra revealed that a site-selective interaction between the quinoid ring of the doped polymer and the MWNTs occurs as a consequence of the *in-situ* polymerization. This interaction may influence charge-transfer processes. The transport properties of MWNTs, polyaniline and the different composites were studied between 300 and 1.25 K. At the higher temperatures, the electrical conductivity is dominated by the polyaniline. At low temperatures, the MWNT network which shows a very weak temperature dependence becomes more conductive than the matrix. Interestingly, it is shown that the conductivity of both the polyaniline and the MWNTs has increased during the *in-situ* polymerization, indicating improved electrical contacts between the MWNTs and the polyaniline grains. Thus the composite material is more conductive than the starting components. Studies using arc-discharge SWNTs [180] revealed that the dispersion in polyaniline is poor for all SWNT contents (2, 5, 10, 20, 30, 50 wt% with respect to aniline monomer), probably because the SWNTs contain residual catalyst particles and amorphous carbon, as well as form entangled bundles.

Qian et al. [181] reported the preparation of MWNT-polystyrene films about 400 μm thick by a solution-evaporation method. One wt% of MWNTs 30 nm in diameter and either 15 or 50 μm long were used. Tensile tests revealed a 25% increase in break stress and a 36–42% increase in elastic modulus. A higher elastic modulus being achieved with longer MWNTs reveals that the external tensile loads are successfully transmitted to the MWNTs through the interface with polystyrene. It is claimed that the MWNTs are superior to VGCF and high-modulus carbon fibers due to their very large length-to-diameter ratio. *In-situ* TEM observations showed that cracks tend to nucleate at low MWNTs density areas then propagate along weak interfaces or relatively low MWNT density areas. The MWNTs align perpendicular to the crack direction and bridge the crack faces. They break and/or pull out from the matrix when the crack opening displacement exceeds 800 nm.

A theoretical study on the interfacial characteristics of SWNT- and DWNT-polystyrene composites using molecular mechanics simulations and elasticity calculations was reported by Liao and Li [182]. It is found that in the absence of atomic bonding between the CNTs and the matrix, the nonbond interactions (electrostatic and van der Waals interactions), the deformation induced by these forces, and the stress/deformation arising from the thermal expansion

coefficient mismatch all contribute to the interfacial stress transfer ability, which is the critical parameter controlling material performance. The interfacial shear stress derived from a CNT pullout simulation is about 160 MPa, significantly higher than for most carbon fiber reinforced polymer composites. Fisher et al. [183] showed by a combined finite element and micromechanical approach that curved CNTs significantly reduce the effective reinforcement when compared to straight CNTs. The model that is developed suggests that the so-called CNT waviness limits the modulus enhancement of CNT-polymer composites.

Watts et al. studied the electrical behavior of polystyrene-matrix composites loaded with boron-doped MWNTs [184] and Fe-filled MWNTs [185]. In the first report [184], arc-discharge MWNTs (diameter 5–40 nm, length 4–10 μm) and B-MWNTs (1–5% boron, diameter 5–40 nm, length over 20 μm) were mixed with a solution of polystyrene in toluene (2.5, 5, 7.5, 10, 12.5 wt% carbon-to-polymer). The solutions were sonicated and evacuated to remove toluene, resulting in the formation of composite films ca. 300 μm thick. The electrical conducting path is established via bundling or tube-tube crossing. Polymer-coated CNTs were also observed. Impedance measurements were carried out under compression or bending. The composites exhibited relatively low resistance, being essentially ohmic conductors at frequencies 1–10⁴ Hz. The B-MWNTs showed a lower resistivity because boron doping results in an increase in charge density on MWNTs. In the second work [185], Fe-filled MWNTs are prepared by CCVD. Encapsulated Fe nanowires over 1 μm long were frequently found inside the MWNTs. Current-voltage measurements showed that the film resistivity decreased with increasing MWNT content. Impedance measurements (1 MHz–0.1 Hz) revealed that the composites exhibit inductive, capacitive, and resistive phases. The extent of inductive phase increases with the increase of Fe content, while the extent of the capacitive phase increases with the decrease of MWNT content. It is proposed that electromagnetic induction arises from the encapsulation of long Fe crystals in helical MWNTs that form a solenoid-like structure.

Frankland et al. [186] reported simulations on load transfer in (10, 10) SWNT-polyethylene composites. It is predicted that in the case of nonbonded SWNT-matrix interactions, SWNTs longer than 10–100 μm are needed for significant load-bearing ability. In contrast, SWNTs cross-linked to the matrix should increase the shear yield by one or two orders of magnitude, the critical SWNT length thus being reduced to 1 μm . A further study [187] showed that the introduction of a relatively low density (<1%) of chemical bonds between the SWNTs and the matrix can increase the shear strength at the interface by over an order of magnitude. The change in tensile modulus of a (10, 10) nanotube is then predicted to be negligible. Interestingly, it is noted that inadvertent chemical bonding between CNTs and polymer matrices during processing may in part account for the enhanced stress transfer observed in some systems. Another study on the topic of load transfer in SWNT-polymer composites was reported by Wagner [188]. It is notably shown that for SWNT diameters above 2–3 nm, the interfacial shear strength loses its sensitivity to the diameter. Below this diameter a strong effect is predicted. Also, for a given

diameter, the SWNT strength variability leads to strong interfacial shear strength variability. Minute defects in the otherwise perfect hexagonal structure of the SWNT should considerably lower the SWNT tensile strength. It is likely that defects are limiting the working length of SWNTs. Thus, it is predicted that a large variability will therefore exist and should be experimentally observed in the interfacial strength of apparently identical SWNTs. Large values compared to those in current advanced fiber-polymer composites should be attainable.

The thermostructural behavior of SWNT-polyethylene composites was investigated theoretically [181]. Classical molecular dynamics simulations employing the Brenner potential for intra-SWNT interactions and van der Waals forces for the SWNT-polyethylene interface were used to investigate the thermal expansion and diffusion characteristics of the composites, below and above the glass transition temperature (T_g). However, it is to be noted that most simulations use (10, 0) SWNTs only 2 nm long (204 atoms) embedded in the polymer matrix with a volume fraction of about 8%. The addition of SWNTs is found to increase T_g , thermal expansion, and diffusion coefficients in the composite above T_g . Simulations on a larger system using (10, 0) SWNTs 20 nm long (1804 atoms) have verified the increase of the thermal expansion coefficient.

Pirlot et al. [189] reported the preparation of CCVD MWNT-polyacrylonitrile composites films. The method involved three steps: (i) dissolving the polyacrylonitrile in dimethylformamide, (ii) adding the purified MWNTs and mixing using either an ultrasonic bath or ultrasonic finger, and (iii) evaporating the dimethylformamide to produce a film 50 μm thick (4 and 25 wt% MWNTs). A better dispersion of the MWNTs is achieved when the ultrasonic finger is used. XRD and X-ray photoelectron spectroscopy studies demonstrated the nonalteration of the structures of the MWNTs and the polyacrylonitrile.

The photoconductivity of MWNT-oxotitanium phthalocyanine (TiOPc) films was investigated by Cao et al. [190]. Purified and cut CCVD MWNTs were used. Some samples were chemically modified to graft dodecylamine groups at the surface of the MWNTs, which enhanced the solubility and miscibility in the polymer matrix. The charge-generation layer of photoreceptor devices consisted of 1 μm thick composite films. The photosensitivity of the photoreceptor with modified MWNTs/TiOPc was higher than that with pristine TiOPc and increased with increasing the content of modified MWNTs in the composites. By contrast, the photosensitivity of unmodified MWNTs/TiOPc was lower than that of pure TiOPc. It is proposed that the intramolecular charge transfer occurred in the modified MWNT/TiOPc composite, which favored charge-carrier generation.

Curran et al. [191] worked on CNT-polymer composites for applications as materials for molecular optoelectronics. The conjugated polymer used is poly(*m*-phenylenevinylene-*co*-2,5-dioctoxy-*p*-phenylenevinylene) (PmPV), whose structure is a variation of that of polyphenylenevinylene (PPV).

The polymer tends to coil, forming a helical structure. Arc-discharge MWNTs (diameter 20 nm, length 500 nm–1.5 μm) and PmPV were mixed together in toluene and sonicated briefly. A TEM image revealing the pullout of coated CNTs is shown in Figure 10. It was thought probable

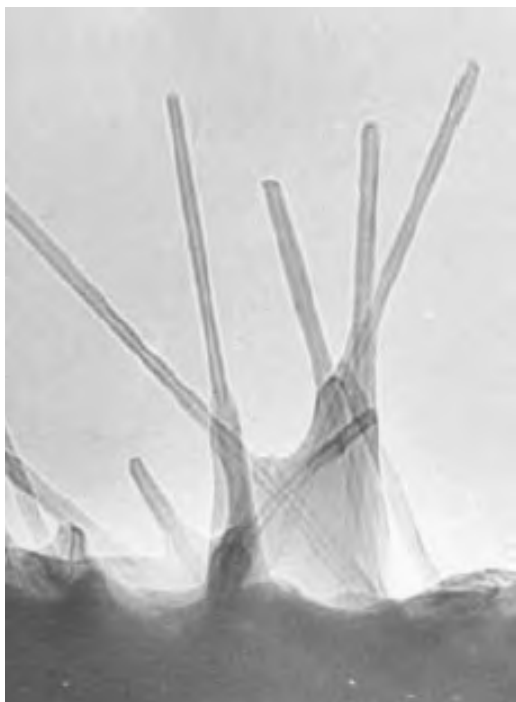


Figure 10. TEM image showing the edge of the CNT-polymer composite film and the pullout of CNTs. Notice that a thin membrane of polymer has enveloped the CNTs, suggesting good wetting and hence mechanical strengthening of the composite film. The diameter of the protruding nanotubes is approximately 15 nm. Reprinted with permission from [191], S. A. Curran et al., *Adv. Mater.* 10, 1091 (1998). © 1998, Wiley-VCH.

that the coiled polymer conformation allows it to surround the MWNTs, favoring π - π interactions. This kind of physical doping is thought to be desirable compared to chemical doping.

The wrapping by the polymer was evidenced by further spectroscopic investigation [192] and was also observed for arc-discharge SWNT-PmPV and CCVD MWNT-PmPV composites [193]. The electrical conductivity of the composite films (4–36 wt% MWNTs) prepared by spin-casting is increased by eight orders of magnitude compared to that of PmPV, reaching 10^{-2} S/m for the 36 wt% MWNT-PmPV specimen [191]. Light-emitting diodes were prepared by casting the composite onto indium tin oxide and then sputtering an aluminum electrode on top. Electroluminescence was achieved in such diodes which use the composite as the emissive layer. It is reported that the MWNTs act as a heat sink, preventing the buildup of large thermal effects which would degrade the conjugated polymer. Using the MWNT-PmPV composites as the electron-transport layer in light-emitting diodes allows for a significant increase in brightness, but with the undesirable increase in the operating voltage [194]. A further work [195] on the electrical conductivity of 0.5–36 wt% MWNT-PmPV films revealed a percolation threshold at 8.4 wt%.

Below this value, a mixed conduction process is probable, with both carrier doping and partial conductive parts. Results obtained from absorption and luminescence spectra of 0–12 wt% MWNT-PmPV films [196] revealed a drop

in quantum efficiency for a low MWNT fraction (1 wt%) compared to the undoped PmPV, then an increase in quantum efficiency upon the increase in MWNT content. However, the opposite effect was reported [197] for 0–7 wt% SWNT-PmPV films. More work [198] on SWNT-PmPV films incorporated in light-emitting diodes with various device structures notably showed that the SWNTs act as a hole-trapping material blocking the holes in the composites, the traps probably being induced through long-range interactions within the matrix. Woo et al. [199] reported the photoluminescence and current-voltage characteristics of light-emitting-diode devices using arc-discharge SWNT-polyethylene dioxythiophene (PEDOT) composite layers (thickness 80 nm). PEDOT is a hole-conducting buffer polymer. Notably, there is a significant decrease of the electroluminescence compared to devices using pure PEDOT. It is proposed that electronic interaction originates from the hole-trapping nature of the SWNTs dispersed in the hole-conducting PEDOT.

Photovoltaic devices using a MWNT-PPV composite were investigated by Ago et al. [200]. MWNTs films were prepared by spin-coating using thin or thick CCVD MWNTs that were submitted to prior chemical oxidation to improve their dispersion in water. It is noted that MWNTs are advantageous over SWNTs since the inner walls remain unreacted and thus retain their electronic characteristics. The composite films were prepared by addition and subsequent conversion of a layer of pure PPV. This procedure is reported to produce composites with highly interpenetrating networks. The external quantum efficiency was found to be about twice as high compared to the standard indium-tin-oxide-based devices. It was found that the MWNT layer acts as a hole-collecting electrode. The enhanced efficiency was explained in terms of the high surface area of the MWNT film and a stronger built-in field. Further studies [201] led to the conclusion that the predominant electronic interaction is a nonradiative energy transfer of singlet excitons from the polymer to the MWNTs, in contrast to other results [198].

A preliminary study [202] of arc-discharge MWNT-poly(3-octylthiophene) composite films revealed an increase of the electrical conductivity by five orders of magnitude compared to the undoped polymer. A higher hardness, determined only qualitatively, and an increased stability under the electron beam were also reported. SWNT-poly(3-octylthiophene) composite films were also studied [203]. Several loadings (0–35 wt%) of arc-discharge SWNTs (purity of about 60 wt%) were used. Composite films of 100 nm were prepared by drop-casting for UV-infrared transmission and reflection studies and measurement of the electrical conductivity. There is no change in the absorption spectra in the loading range 0–8 wt% showing that there is no charge transfer between the SWNTs and the polymer. The electrical conductivity is increased by five orders of magnitude from 0 to 35 wt% SWNTs. The maximum value is close to 10^{-3} S/m for the 35 wt% composite, approaching that measured for a mat of SWNTs (0.05 S/m). The percolation threshold was found at 11 wt%, a much higher value than those reported for other systems. The critical exponent β of the scaling law of the percolation theory is approximately close to the value (1.94) predicted for tridimensional percolation theory.

This group also tested such composite films as field emitters [204]. The materials were formed on n^+ -Si by mixing the SWNTs and the polymer after they had been dissolved in chloroform. Three different structures were tested: a SWNT mat, a SWNT mat on a 30 wt% SWNT-polymer composite, and a SWNT mat on pure polymer. The electrical conductivity of the SWNT-polymer composite is very much lower than that of the SWNT mat but the field emission threshold is lower and the emission current higher. Comparing the field enhancement factors and the expected aspect ratios shows that enhancement due to an additional field enhancement mechanism other than that due to the geometrical shape of the SWNTs must exist. It is proposed that the field due to the surface potential modification at the triple junction between SWNTs, polymer, and vacuum is adequate to create additional field emission from such sites.

Yoshino et al. [205] dispersed large CCVD MWNTs (diameter 40–200 nm, length 20–40 μm) in poly(3-hexylthiophene). The mixture (1–20 vol% MWNTs) was sonicated and films several micrometers thick were cast on a quartz plate. The electrical conductivity increases over about six orders of magnitude. A relatively high value was reported for the critical exponent of percolation ($\beta = 2.6$). An analysis according to a model based on a Fermi-Dirac distribution gave a percolation threshold at about 5.9 vol%.

5. CONCLUSIONS

CNTs combine some very particular electrical, thermal, and mechanical characteristics with a low density and a very high aspect ratio. Composite materials with CNTs are increasingly studied due to the many interesting applications that are envisioned in some key areas such as the aerospace, automotive, building, and electronics industries. Metal (notably Al, Cu, Ti)-matrix and ceramic (mostly oxides and SiC)-matrix composites containing CNTs have so far been much less studied than polymer (chiefly epoxy and PMMA)-matrix composites. Powders, thin and thick films, as well as bulk materials have been prepared and tested.

Key issues to overcome include:

- achieving the homogeneous dispersion of the CNTs, especially at the relatively high loadings that may be required for applications as structural materials,
- achieving a total (or very high) densification of the composite,
- achieving a certain degree of bonding between the CNTs and the matrix,
- understanding and/or controlling the reactivity between the CNTs and the surrounding materials, both during the processing and during in-service conditions.

It is to be remembered that basic CNT characteristics such as the diameter, number of walls, extent of bundling, length, and defect density depend very strongly on the synthesis method. Thus choosing the appropriate CNTs for a particular application will be of the utmost importance. The development of CNTs composites is still hampered by the unavailability of large quantities of CNTs, and also by the price of high-quality specimens. The emergence of industrial production methods is expected to drastically cut

the price from ca. 500 US\$/g down to 20 US\$/kg. It is anticipated that nanocomposites with CNTs, combining several unusual or exceptional properties, will find technological applications in the near future.

GLOSSARY

Carbon nanotube (CNT) Made up of one or several concentric cylinders (rolled graphene sheets).

Catalytic chemical vapor deposition (CCVD) A CVD technique using a catalyst to activate the decomposition of the appropriate gas.

Chemical vapor deposition (CVD) A technique to deposit a solid by the thermal or chemical decomposition of a gas (or mixture of gases) containing the desired element(s).

Double-walled carbon nanotube (DWNT) Made up of two concentric cylinders.

Multiwalled carbon nanotube (MWNT) Made up of several concentric cylinders.

PmPV (*m*-Phenylenevinylene-*co*-2,5-dioctoxy-*p*-phenylenevinylene), a polymer whose structure is a variation of that of polyphenylenevinylene.

Single-walled carbon nanotube (SWNT) Made up of only one cylinder.

Vapor-grown carbon fiber (VGCF) A filament of carbon that is not necessarily hollow nor nanometric in diameter.

Vapor-liquid-solid (VLS) A mechanism to explain the formation of long, hollow filaments.

Yarmulke Yiddish word meaning skull-cap, used to describe a monolayer of carbon (graphene) covering a fraction of the surface of a catalyst particle; the formation of a yarmulke is a key step in a proposed mechanism for the formation of carbon nanotubes.

REFERENCES

1. S. Iijima, *Nature* 354, 56 (1991).
2. J. W. Mintmire, B. I. Dunlap, and C. T. White, *Phys. Rev. Lett.* 68, 631 (1992).
3. N. Hamada, S. Sawada, and A. Oshiyama, *Phys. Rev. Lett.* 68, 1579 (1992).
4. K. T. Lau and D. Hui, *Composites B* 33, 263 (2002).
5. A. Peigney, Ch. Laurent, E. Flahaut, R. R. Bacsá, and A. Rousset, *Carbon* 39, 507 (2001).
6. M. S. Dresselhaus, G. Dresselhaus, and R. Saito, *Carbon* 33, 883 (1995).
7. P. Schützenberger and L. Schützenberger, *C. R. Acad. Sci. Paris* 111, 774 (1890).
8. N. M. Rodriguez, *J. Mater. Res.* 8, 3233 (1993).
9. A. Oberlin, M. Endo, and T. Koyama, *J. Cryst. Growth* 32, 335 (1976).
10. E. G. Rakov, *Russ. Chem. Rev.* 69, 35 (2000).
11. Ch. Laurent, E. Flahaut, A. Peigney, and A. Rousset, *New J. Chem.* 22, 1229 (1998).
12. S. Iijima, P. M. Ajayan, and T. Ichihashi, *Phys. Rev. Lett.* 69, 3100 (1992).
13. R. E. Smalley, *Mater. Sci. Eng. B* 19, 1 (1993).
14. S. Iijima and T. Ichihashi, *Nature (London)* 363, 603 (1993).
15. R. Saito, G. Dresselhaus, and M. S. Dresselhaus, *Appl. Phys. Lett.* 60, 2204 (1992).
16. M. Endo and H. W. Kroto, *J. Phys. Chem.* 96, 6941 (1992).

17. T. W. Ebbesen, H. Hiura, J. Fujita, Y. Ochiai, S. Matsui, and K. Tanigaki, *Chem. Phys. Lett.* 209, 83 (1993).
18. K. Tanaka, K. Okahara, M. Okada, and Y. Yamabe, *Chem. Phys. Lett.* 191, 469 (1992).
19. S. Q. Feng, D. P. Yu, G. Hu, X. F. Zhang, and Z. Zhang, *J. Phys. Chem. Solids* 58, 1887 (1997).
20. O. Zhou, R. M. Fleming, D. W. Murphy, C. H. Chen, R. C. Haddon, A. P. Ramirez, and S. H. Glarum, *Science* 263, 1744 (1994).
21. V. Z. Mordkovich, M. Baxendale, S. Yoshimura, and R. P. H. Chang, *Carbon* 34, 1301 (1996).
22. W. B. Downs and R. T. K. Baker, *J. Mater. Res.* 10, 625 (1995).
23. G. G. Tibbetts, *J. Cryst. Growth* 66, 632 (1984).
24. R. S. Wagner and W. C. Ellis, *Appl. Phys. Lett.* 4, 89 (1964).
25. Y. Saito, *Carbon* 33, 979 (1995).
26. Y. Saito, M. Okuda, N. Fujimoto, T. Yoshikawa, M. Tomita, and T. Hayashi, *Jpn. J. Appl. Phys.* 2 33, L526 (1994).
27. D. Zhou, S. Seraphin, and S. Wang, *Appl. Phys. Lett.* 65, 1593 (1994).
28. J. Gavillet, A. Loiseau, F. Ducastelle, S. Thair, P. Bernier, O. Stephan, J. Thibault, and J.-C. Charlier, *Carbon* 40, 1649 (2002).
29. D. S. Bethune, C. H. Kiang, M. S. de Vries, G. Gorman, R. Savoy, J. Vazquez, and R. Beyers, *Nature (London)* 363, 605 (1993).
30. C. Journet, W. K. Maser, P. Bernier, A. Loiseau, M. Lamy de la Chapelle, S. Lefrant, P. Deniard, R. Lee, and J. E. Fischer, *Nature (London)* 388, 756 (1997).
31. T. Guo, P. Nikolaev, A. Thess, D. T. Colbert, and R. E. Smalley, *Chem. Phys. Lett.* 243, 49 (1995).
32. F. Kokai, K. Takahashi, M. Yudasaka, R. Yamada, T. Ichihashi, and S. Iijima, *J. Phys. Chem. B* 103, 4346 (1999).
33. H. Kataura, Y. Kumazawa, Y. Maniwa, Y. Ohtsuka, R. Sen, S. Suzuki, and Y. Achiba, *Carbon* 38, 1691 (2000).
34. J. H. Hafner, M. J. Bronikowski, B. R. Azamian, P. Nikolaev, A. G. Rinzler, D. T. Colbert, K. A. Smith, and R. E. Smalley, *Chem. Phys. Lett.* 296, 195 (1998).
35. A. Peigney, P. Coquay, E. Flahaut, R. E. Vandenberghe, E. De Grave, and Ch. Laurent, *J. Phys. Chem. B* 105, 9699 (2001).
36. H. Dai, A. G. Rinzler, P. Nikolaev, A. Thess, D. T. Colbert, and R. E. Smalley, *Chem. Phys. Lett.* 260, 471 (1996).
37. Y. M. Li, W. Kim, Y. G. Zhang, M. Rolandi, D. W. Wang, and H. J. Dai, *J. Phys. Chem. B* 105, 11424 (2001).
38. A. M. Cassell, J. A. Raymakers, J. Kong, and H. Dai, *J. Phys. Chem. B* 103, 6484 (1999).
39. J. F. Colomer, G. Bister, I. Willems, Z. Konya, A. Fonseca, J. B. Nagy, and G. Van Tendeloo, *Chem. Commun. (Cambridge)* 1343 (1999).
40. H. M. Cheng, F. Li, X. Sun, S. D. M. Brown, M. A. Pimenta, A. Marucci, G. Dresselhaus, and M. S. Dresselhaus, *Chem. Phys. Lett.* 289, 602 (1998).
41. B. C. Satishkumar, A. Govindaraj, R. Sen, and C. N. R. Rao, *Chem. Phys. Lett.* 293, 47 (1998).
42. A. Peigney, Ch. Laurent, F. Dobigeon, and A. Rousset, *J. Mater. Res.* 12, 613 (1997).
43. E. Flahaut, A. Peigney, Ch. Laurent, and A. Rousset, *J. Mater. Chem.* 10, 249 (2000).
44. R. R. Bacsa, Ch. Laurent, A. Peigney, W. S. Bacsa, T. Vaugien, and A. Rousset, *Chem. Phys. Lett.* 323, 566 (2000).
45. B. Kitiyanan, W. E. Alvarez, J. H. Harwell, and D. E. Resasco, *Chem. Phys. Lett.* 317, 497 (2000).
46. J. E. Herrera, L. Balzano, A. Borgna, W. E. Alvarez, and D. E. Resasco, *J. Catal.* 204, 129 (2001).
47. M. Su, B. Zheng, and J. Liu, *Chem. Phys. Lett.* 322, 321 (2000).
48. C. L. Cheung, A. Kurtz, H. Park, and C. M. Lieber, *J. Phys. Chem. B* 106, 2429 (2002).
49. E. Flahaut, A. Peigney, and Ch. Laurent, *J. Nanosci. Nanotech.* 3, 151 (2003).
50. M. Monthieux, B. W. Smith, B. Bouteaux, A. Claye, J. E. Fischer, and D. E. Luzzi, *Carbon* 39, 1251 (2001).
51. E. G. Rakov, *Russ. Chem. Rev.* 70, 827 (2001).
52. S. B. Sinnott, *J. Nanosci. Nanotech.* 2, 113 (2002).
53. K. Esumi, M. Ishigami, A. Nakajima, K. Sawada, and H. Honda, *Carbon* 34, 279 (1996).
54. H. P. Boehm, *Carbon* 759 (1994).
55. P. A. Cahill and C. M. Rohlffing, *Tetrahedron* 52, 5247 (1996).
56. R. M. Lago, S. C. Tsang, K. L. Lu, Y. K. Chen, and M. L. H. Green, *J. Chem. Soc., Chem. Commun.* 1355 (1995).
57. R. Yu, L. Chen, Q. Liu, J. Lin, K.-L. Tan, S. C. Ng, H. S. O. Chan, G.-Q. Xu, and T. S. A. Hor, *Chem. Mater.* 10, 718 (1998).
58. "Science of Fullerenes and Carbon Nanotubes" (M. S. Dresselhaus, G. Dresselhaus, and P. C. Eklund, Eds.). Academic Press, San Diego, 1996.
59. M. S. Dresselhaus, G. Dresselhaus, and P. Avouris, "Carbon Nanotube Synthesis, Structure, Properties, and Applications," *Top. Appl. Phys.*, Vol. 80. Springer-Verlag, Berlin, 2001.
60. P. J. F. Harris, "Carbon Nanotubes and Related Structures—New Materials for the Twenty-First Century." Cambridge Univ. Press, Cambridge, UK, 1999.
61. L. Langer, L. Stockman, J. P. Heremans, V. Bayot, C. H. Olk, C. Van Haesendonck, Y. Bruynseraede, and J. P. Issi, *J. Mater. Res.* 9, 927 (1994).
62. Y. Nakayama, S. Akita, and Y. Shimada, *Jpn. J. Appl. Phys.* 2 34, L10 (1995).
63. H. Dai, E. W. Wong, and C. M. Lieber, *Science* 272, 523 (1996).
64. T. W. Ebbesen, H. J. Lezec, H. Hiura, J. W. Bennett, H. F. Ghaemi, and T. Thio, *Nature (London)* 382, 54 (1996).
65. S. J. Tans, M. H. Devoret, H. Dai, A. Thess, R. E. Smalley, L. J. Geerligs, and C. Dekker, *Nature (London)* 386, 474 (1997).
66. M. Ahlskog, M. Baxendale, and Ch. Laurent, this Encyclopedia.
67. R. S. Ruoff and D. C. Lorents, *Carbon* 33, 925 (1995).
68. J. Che, T. Cagin, and W. A. Goddard III, *Nanotechnology* 11, 65 (2000).
69. M. A. Osman and D. Srivastava, *Nanotechnology* 12, 21 (2001).
70. W. Yi, L. Lu, Z. Dian-lin, Z. W. Pan, and S. S. Xie, *Phys. Rev. B* 59, R9015 (1999).
71. J. Hone, M. Whitney, C. Piskoti, and A. Zettl, *Phys. Rev. B* 59, R2514 (1999).
72. J. Hone, M. C. Llaguno, N. M. Nemes, A. T. Johnson, J. E. Fischer, D. A. Walters, M. J. Casavant, J. Schmidt, and R. E. Smalley, *Appl. Phys. Lett.* 77, 666 (2000).
73. E. T. Thostenson, Z. Ren, and T. W. Chou, *Compos. Sci. Technol.* 61, 1899 (2001).
74. J.-P. Salvetat-Delmotte and A. Rubio, *Carbon* 40, 1729 (2002).
75. B. I. Yakobson and A. Rubio, "Nanotubular Structures: Characterization and Simulation on the Atomic Scale." Gordon & Breach, New York, 2001.
76. J. P. Lu, *Phys. Rev. Lett.* 79, 1297 (1997).
77. J. P. Lu, *J. Phys. Chem. Solids* 58, 1649 (1997).
78. E. Hernandez, C. Goze, P. Bernier, and A. Rubio, *Phys. Rev. Lett.* 80, 4502 (1998).
79. M. M. J. Treacy, T. W. Ebbesen, and J. M. Gibson, *Nature (London)* 381, 678 (1996).
80. E. W. Wong, P. E. Sheehan, and C. M. Lieber, *Science* 277, 1971 (1997).
81. J.-P. Salvetat, G. A. D. Briggs, J.-M. Bonard, R. R. Bacsa, A. J. Kulik, T. Stockli, N. A. Burnham, and L. Forro, *Phys. Rev. Lett.* 82, 944 (1999).
82. D. A. Walters, L. M. Ericson, M. J. Casavant, J. Liu, D. T. Colbert, K. A. Smith, and R. E. Smalley, *Appl. Phys. Lett.* 74, 3803 (1999).
83. M. B. Nardelli, B. I. Yakobson, and J. Bernholc, *Phys. Rev. A* 57, R4277 (1998).
84. M. B. Nardelli, B. I. Yakobson, and J. Bernholc, *Phys. Rev. Lett.* 81, 4656 (1998).

85. O. Lourie, D. M. Cox, and H. D. Wagner, *Phys. Rev. Lett.* 81, 1638 (1998).
86. D. Srivastava, M. Menon, and K. Cho, *Phys. Rev. Lett.* 83, 2973 (1999).
87. J. F. Després, E. Daguette, and K. Lafdi, *Carbon* 33, 87 (1995).
88. M. R. Falvo, G. J. Clary, R. M. Taylor, II, V. Chi, F. P. Brooks, Jr., S. Washburn, and R. Superfine, *Nature (London)* 389, 581 (1997).
89. S. Iijima, C. Brabec, A. Maiti, and J. Bernholc, *J. Chem. Phys.* 104, 2089 (1996).
90. S. Xie, W. Li, Z. Pan, B. Chang, and L. Sun, *J. Phys. Chem. Solids* 61, 1153 (2000).
91. M.-F. Yu, O. Lourie, M. J. Dyer, K. Moloni, T. F. Kelly, and R. S. Ruoff, *Science* 287, 637 (2000).
92. M.-F. Yu, B. S. Files, S. Arepalli, and R. S. Ruoff, *Phys. Rev. Lett.* 84, 5552 (2000).
93. C. Q. Ru, *J. Appl. Phys.* 87, 7227 (2000).
94. A. N. Kolmogorov and V. H. Crespi, *Phys. Rev. Lett.* 85, 4727 (2000).
95. W. Shen, B. Jiang, B. S. Han, and S.-S. Xie, *Phys. Rev. Lett.* 84, 3634 (2000).
96. N. G. Chopra, L. X. Benedict, V. H. Crespi, M. L. Cohen, S. G. Louie, and A. Zettl, *Nature (London)* 377, 135 (1995).
97. P. Calvert, *Nature (London)* 399, 210 (1999).
98. M. Monthieux, *Carbon* 40, 1809 (2002).
99. C. L. Xu, B. Q. Wei, R. Z. Ma, J. Liang, X. K. Ma, and D. H. Wu, *Carbon* 37, 855 (1999).
100. T. Kuzumaki, K. Miyazawa, H. Ichinose, and K. Ito, *J. Mater. Res.* 13, 2445 (1998).
101. T. Kuzumaki, O. Ujiie, H. Ichinose, and K. Ito, *Adv. Eng. Mater.* 2, 416 (2000).
102. S. R. Dong, J. P. Tu, and X. B. Zhang, *Mater. Sci. Eng. A* 313, 83 (2001).
103. J. Wei, Y. Li, C. Xu, B. Wei, and D. Wu, *Mater. Chem. Phys.* 78, 785 (2003).
104. Y. B. Li, Q. Ya, B. Q. Wei, J. Liang, and D. H. Wu, *J. Mater. Sci. Lett.* 17, 607 (1998).
105. X. H. Chen, F. Q. Cheng, S. L. Li, L. P. Zhou, and D. Y. Li, *Surface Coatings Technol.* 155, 274 (2002).
106. W. X. Chen, J. P. Tu, H. Y. Gan, Z. D. Xu, Q. G. Wang, J. Y. Lee, Z. L. Liu, and X. B. Zhang, *Surface Coatings Technol.* 160, 68 (2002).
107. W. X. Chen, J. P. Tu, Z. D. Xu, W. L. Chen, X. B. Zhang, and D. H. Cheng, *Mater. Lett.* 57, 1256 (2003).
108. W. X. Chen, J. P. Tu, L. Y. Wang, H. Y. Gan, Z. D. Xu, and X. B. Zhang, *Carbon* 41, 215 (2003).
109. R. Z. Ma, J. Wu, B. Q. Wei, J. Liang, and D. H. Wu, *J. Mater. Sci.* 33, 5243 (1998).
110. L. Yowell, B. M. Mayeux, H. Wang, and E. V. Barrera, *Mater. Res. Soc. Symp. Proc.* 633, A17.4.1 (2001).
111. P. Vincent, A. Brioude, C. Journet, S. Rabaste, S. T. Purcell, J. L. Brusq, and J. C. Plenet, *J. Non. Cryst. Solids* 311, 130 (2002).
112. D.-S. Lim, J.-W. An, and H. J. Lee, *Wear* 252, 512 (2002).
113. R. Andrews, D. Jacques, A. M. Rao, T. Rantell, F. Derbyshire, Y. Chen, J. Chen, and R. C. Haddon, *Appl. Phys. Lett.* 75, 1329 (1999).
114. G. L. Hwang and K. C. Hwang, *J. Mater. Chem.* 11, 1722 (2001).
115. J. DiMaio, S. Rhyne, Z. Yang, K. Fu, R. Czerw, J. Xu, S. Webster, Y. P. Sun, D. L. Carroll, and J. Ballato, *Inf. Sci.* 149, 69 (2003).
116. V. G. Gavalas, R. Andrews, D. Bhattacharyya, and L. G. Bachas, *Nano Lett.* 1, 719 (2001).
117. Ch. Laurent, A. Peigney, and A. Rousset, *J. Mater. Chem.* 8, 1263 (1998).
118. A. Peigney, Ch. Laurent, O. Dumortier, and A. Rousset, *J. Eur. Ceram. Soc.* 18, 1995 (1998).
119. Ch. Laurent, A. Peigney, E. Flahaut, and A. Rousset, *Mater. Res. Bull.* 35, 661 (2000).
120. A. Peigney, Ch. Laurent, and A. Rousset, *J. Mater. Chem.* 9, 1167 (1999).
121. A. Govindaraj, E. Flahaut, Ch. Laurent, A. Peigney, A. Rousset, and C. N. R. Rao, *J. Mater. Res.* 14, 2567 (1999).
122. P. Coquay, E. De Grave, R. E. Vandenberghe, C. Dauwe, E. Flahaut, Ch. Laurent, A. Peigney, and A. Rousset, *Acta Mater.* 48, 3015 (2000).
123. E. Flahaut, A. Govindaraj, A. Peigney, Ch. Laurent, A. Rousset, and C. N. R. Rao, *Chem. Phys. Lett.* 300, 236 (1999).
124. S. Rul, Ch. Laurent, A. Peigney, and A. Rousset, *J. Eur. Ceram. Soc.* 23, 1233 (2003).
125. P. Coquay, E. De Grave, A. Peigney, R. E. Vandenberghe, and Ch. Laurent, *J. Phys. Chem. B* 106, 13186 (2002).
126. P. Coquay, A. Peigney, E. De Grave, R. E. Vandenberghe, and Ch. Laurent, *J. Phys. Chem. B* 106, 13199 (2002).
127. R. R. Bacsá, Ch. Laurent, A. Peigney, T. Vaugien, E. Flahaut, W. S. Bacsá, and A. Rousset, *J. Am. Ceram. Soc.* 85, 2666 (2002).
128. A. Peigney, Ch. Laurent, and A. Rousset, *Key Eng. Mater.* 132–136, 743 (1997).
129. Ch. Laurent, A. Peigney, O. Dumortier, and A. Rousset, *J. Eur. Ceram. Soc.* 18, 2005 (1998).
130. A. Peigney, Ch. Laurent, E. Flahaut, and A. Rousset, *Ceram. Int.* 26, 677 (2000).
131. E. Flahaut, A. Peigney, Ch. Laurent, C. Marliere, F. Chastel, and A. Rousset, *Acta Mater.* 48, 3803 (2000).
132. A. Peigney, E. Flahaut, Ch. Laurent, F. Chastel, and A. Rousset, *Chem. Phys. Lett.* 352, 20 (2002).
133. S. Rul, Thesis, Paul Sabatier University, Toulouse, France, 2002.
134. R. W. Siegel, S. K. Chang, B. J. Ash, J. Stone, P. M. Ajayan, R. W. Doremus, and L. S. Schadler, *Scr. Mater.* 44, 2061 (2001).
135. G. D. Zhan, J. D. Kuntz, J. Wan, and A. K. Mukherjee, *Nature Mater.* 2, 38 (2003).
136. J. Sun, L. Gao, and W. Li, *Chem. Mater.* 14, 5169 (2002).
137. A. Peigney, *Nature Mater.* 2, 15 (2003).
138. A. Weidenkaff, S. G. Ebbinghaus, and T. Lippert, *Chem. Mater.* 14, 1797 (2002).
139. S. L. Huang, M. R. Koblischka, K. Fossheim, T. W. Ebbesen, and T. H. Johansen, *Physica C* 311, 172 (1999).
140. V. Lordi and N. Yao, *J. Mater. Res.* 15, 2770 (2000).
141. L. S. Schadler, S. C. Giannaris, and P. M. Ajayan, *Appl. Phys. Lett.* 73, 3842 (1998).
142. P. M. Ajayan, O. Stephan, C. Colliex, and D. Trauth, *Science* 265, 1212 (1994).
143. O. Lourie and H. D. Wagner, *J. Mater. Res.* 13, 2418 (1998).
144. O. Lourie, H. D. Wagner, Y. Zhang, and S. Iijima, *Adv. Mater.* 11, 931 (1999).
145. C. Galiotis and D. N. Batchelder, *J. Mater. Sci. Lett.* 7, 545 (1988).
146. G. Overney, W. Zhong, and D. Z. Tomaneck, *Z. Phys. D* 27, 93 (1993).
147. O. Lourie and H. D. Wagner, *Appl. Phys. Lett.* 73, 3527 (1998).
148. C. A. Cooper, R. J. Young, and M. Halsall, *Composites A* 32, 401 (2001).
149. O. Lourie and H. D. Wagner, *Comp. Sci. Technol.* 59, 975 (1999).
150. P. M. Ajayan, L. S. Schadler, C. Giannaris, and A. Rubio, *Adv. Mater.* 12, 750 (2000).
151. V. G. Hadjiev, M. N. Iliiev, S. Arepalli, P. Nikolaev, and B. S. Files, *Appl. Phys. Lett.* 78, 3193 (2001).
152. X. Gong, J. Liu, S. Baskaran, R. D. Voise, and J. S. Young, *Chem. Mater.* 12, 1049 (2000).
153. A. Allaoui, S. Bai, H. M. Cheng, and J. B. Bai, *Comp. Sci. Technol.* 62, 1993 (2002).
154. J. Sandler, M. S. P. Shaffer, T. Prasse, W. Bauhofer, K. Schulte, and A. H. Windle, *Polymer* 40, 5967 (1999).
155. S. Barrau, P. Demont, A. Peigney, Ch. Laurent, and C. Lacabanne, *Macromolec.* 36, 5187 (2003).
156. M. J. Biercuk, M. C. Llaguno, M. Radosavljevic, J. K. Hyun, A. T. Johnson, and J. E. Fischer, *Appl. Phys. Lett.* 80, 2767 (2002).

157. E. T. Thostenson, W. Z. Li, D. Z. Wang, Z. F. Ren, and T. W. Chou, *J. Appl. Phys.* 91, 6034 (2002).
158. R. Hagenmueller, H. H. Gommans, A. G. Rinzler, J. E. Fischer, and K. I. Winey, *Chem. Phys. Lett.* 330, 219 (2000).
159. Z. Jin, K. P. Pramoda, G. Xu, and S. H. Goh, *Chem. Phys. Lett.* 337, 43 (2001).
160. Z. Jin, K. P. Pramoda, S. H. Goh, and G. Xu, *Mater. Res. Bull.* 37, 271 (2002).
161. Z. Jia, Z. Wang, C. Xu, J. Liang, B. Wei, D. Wu, and S. Zhu, *Mater. Sci. Eng. A* 271, 395 (1999).
162. C. A. Cooper, D. Ravich, D. Lips, J. Mayer, and H. D. Wagner, *Comp. Sci. Technol.* 62, 1105 (2002).
163. C. Stephan, T. P. Nguyen, M. Lamy de la Chapelle, S. Lefrant, C. Journet, and P. Bernier, *Synth. Met.* 108, 139 (2000).
164. M. Lamy de la Chapelle, C. Stéphan, T. P. Nguyen, S. Lefrant, C. Journet, P. Bernier, L. Alvarez, D. Laplaze, E. Munoz, A. Benito, W. K. Maser, M. T. Martinez, G. F. de la Fuente, T. Guillard, G. Flamant, L. Alvarez, and D. Laplaze, *Synth. Met.* 103, 2510 (1999).
165. J. M. Benoit, B. Corraze, S. Lefrant, W. J. Blau, P. Bernier, and O. Chauvet, *Synth. Met.* 121, 1215 (2001).
166. J. M. Benoit, B. Corraze, and O. Chauvet, *Phys. Rev. A* 65, 241405/1 (2002).
167. C. A. Grimes, C. Mungle, D. Kouzoudis, S. Fang, and P. C. Eklund, *Chem. Phys. Lett.* 319, 460 (2000).
168. M. S. P. Shaffer and A. H. Windle, *Adv. Mater.* 11, 937 (1999).
169. B. Vigolo, A. Penicaud, C. Coulon, C. Sauder, R. Paillet, C. Journet, P. Bernier, and P. Poulin, *Science* 290, 1331 (2000).
170. L. Jin, C. Bower, and O. Zhou, *Appl. Phys. Lett.* 73, 1197 (1998).
171. C. Bower, R. Rosen, L. Jin, J. Han, and O. Zhou, *Appl. Phys. Lett.* 74, 3317 (1999).
172. H. D. Wagner, O. Lourie, Y. Feldman, and R. Tenne, *Appl. Phys. Lett.* 72, 188 (1998).
173. H. D. Wagner, O. Lourie, and X. F. Zhou, *Composites A* 30, 59 (1998).
174. J. R. Wood, Q. Zhao, and H. D. Wagner, *Composites A* 32, 391 (2001).
175. M. D. Frogley, Q. Zhao, and H. D. Wagner, *Phys. Rev. A* 65, 113413/1 (2002).
176. Q. Zhao, J. R. Wood, and H. D. Wagner, *J. Polym. Sci.* 39, 1492 (2001).
177. P. Potschke, T. D. Fornes, and D. R. Paul, *Polymer* 43, 3247 (2002).
178. *Plastic Additives Compound.* 22 (2001).
179. M. Cochet, W. K. Maser, A. M. Benito, M. A. Callejas, M. T. Martinez, J.-M. Benoit, J. Schreiber, and O. Chauvet, *Chem. Commun.* 1450 (2001).
180. W. K. Maser, A. M. Benito, M. A. Calleja, T. Seeger, M. T. Martinez, J. Schreiber, J. Muszynski, O. Chauvet, Z. Osvath, A. A. Koos, and L. P. Biro, *Mater. Sci. Eng. C* 23 (2003).
181. D. Qian, E. C. Dickey, R. Andrews, and T. Rantell, *Appl. Phys. Lett.* 76, 2868 (2000).
182. K. Liao and S. Li, *Appl. Phys. Lett.* 79, 4225 (2001).
183. F. T. Fisher, R. D. Bradshaw, and L. C. Brinson, *Appl. Phys. Lett.* 80, 4647 (2002).
184. P. C. P. Watts, W. K. Hsu, G. Z. Chen, D. J. Fray, H. W. Kroto, and D. R. M. Walton, *J. Mater. Chem.* 11, 2482 (2001).
185. P. C. P. Watts, W. K. Hsu, V. Kotzeva, and G. Z. Chen, *Chem. Phys. Lett.* 366, 42 (2002).
186. S. J. V. Frankland, A. Caglar, D. W. Brenner, and M. Griebel, *Mater. Res. Soc. Symp. Proc.* 633, A14.17.1 (2001).
187. S. J. V. Frankland, A. Caglar, D. W. Brenner, and M. Griebel, *J. Phys. Chem. B* 106, 3046 (2002).
188. H. D. Wagner, *Chem. Phys. Lett.* 361, 57 (2002).
189. C. Pirlot, I. Willems, A. Fonseca, J. B. Nagy, and J. Delhalle, *Adv. Eng. Mater.* 4, 109 (2002).
190. L. Cao, H. Chen, M. Wang, J. Sun, X. Zhang, and F. Kong, *J. Phys. Chem. B* 106, 8971 (2002).
191. S. A. Curran, P. M. Ajayan, W. J. Blau, D. L. Carroll, J. N. Coleman, A. B. Dalton, A. P. Davey, A. Drury, B. McCarthy, S. Maier, and A. Strevens, *Adv. Mater.* 10, 1091 (1998).
192. B. McCarthy, A. B. Dalton, J. N. Coleman, H. J. Byrne, P. Bernier, and W. J. Blau, *Chem. Phys. Lett.* 350, 27 (2001).
193. B. McCarthy, J. N. Coleman, R. Czerw, A. B. Dalton, M. Panhuis, A. Maiti, A. Drury, P. Bernier, J. B. Nagy, B. Lahr, H. J. Byrne, D. L. Carroll, and W. J. Blau, *J. Phys. Chem. B* 106, 2210 (2002).
194. P. Fournet, D. F. O'Brien, J. N. Coleman, H. H. Horhold, and W. J. Blau, *Synth. Met.* 121, 1683 (2001).
195. J. N. Coleman, S. Curran, A. B. Dalton, A. P. Davey, B. McCarthy, W. Blau, and R. C. Barklie, *Phys. Rev. B* 58, R7492 (1998).
196. A. B. Dalton, H. J. Byrne, J. N. Coleman, S. Curran, A. P. Davey, B. McCarthy, and W. Blau, *Synth. Met.* 102, 1176 (1999).
197. S. Curran, A. P. Davey, J. Coleman, A. Dalton, B. McCarthy, S. Maier, A. Drury, D. Gray, M. Brennan, K. Ryder, M. Lamy de la Chapelle, C. Journet, P. Bernier, H. J. Byrne, D. Carroll, P. M. Ajayan, S. Lefrant, and W. Blau, *Synth. Met.* 103, 2559 (1999).
198. H. S. Woo, R. Czerw, S. Webster, D. L. Carroll, J. Ballato, A. E. Strevens, and W. J. Blau, *Appl. Phys. Lett.* 77, 1393 (2000).
199. H. S. Woo, R. Czerw, S. Webster, D. L. Carroll, J. W. Park, and J. H. Lee, *Synth. Met.* 116, 369 (2001).
200. H. Ago, K. Petritsch, M. S. P. Shaffer, A. H. Windle, and R. H. Friend, *Adv. Mater.* 11, 1281 (1999).
201. H. Ago, M. S. P. Shaffer, D. S. Ginger, A. H. Windle, and R. H. Friend, *Phys. Rev. B* 61, 2286 (2000).
202. I. Musa, M. Baxendale, G. A. J. Amaratunga, and W. Eccleston, *Synth. Met.* 102, 1250 (1999).
203. E. Kymakis, I. Alexandrou, and G. A. J. Amaratunga, *Synth. Met.* 127, 59 (2002).
204. I. Alexandrou, E. Kymakis, and G. A. J. Amaratunga, *Appl. Phys. Lett.* 80, 1435 (2002).
205. K. Yoshino, H. Kajii, H. Araki, T. Sonoda, H. Take, and S. Lee, *Fullerene Sci. Technol.* 7, 695 (1999).

Catalysis by Gold Nanoparticles

Masatake Haruta

National Institute of Advanced Industrial Science and Technology, Tsukuba, Japan

CONTENTS

1. Introduction
 2. Preparation of Gold Nanoparticles
 3. Catalytic Properties of Gold Nanoparticles
 4. Mechanism for Low-Temperature CO Oxidation
 5. Catalytic Capabilities and Applications of Supported Gold Nanoparticles
 6. Conclusions
- Glossary
References

1. INTRODUCTION

Since iron-based heterogeneous catalysts were commercially used for ammonia production, a variety of metal oxides, metal sulfides, and metals have been used in inorganic chemical syntheses, petroleum refinery and other chemical processes, and in environmental protection. Metal catalysts are most widely used for a variety of reactions [1] including hydrogenation, complete and partial oxidation, and reduction of NO_x with hydrocarbons [2]. They are usually dispersed in the form of small particles on stable metal oxides such as Al_2O_3 and SiO_2 . Elements used as metallic catalysts are actually limited to 12, which belong to the groups VIII and Ib of the periodic table. Most widely used are the 3d metals of Fe, Co, Ni, and Cu, the 4d metals of Rh, Pd, and Ag, and a 5d metal of Pt. Ruthenium (4d) and Ir (5d) have only limited applications. Osmium is usually excluded as a catalyst component because its oxide is toxic. Gold (5d) is the only exception and has been regarded to be poorly active as a catalyst.

The intrinsic catalytic capabilities of group VIII metals can be ascribed to the optimum degree of d-band vacancy. The elements of group Ib, so-called coinage metals, Cu, Ag, and Au have fully occupied d-bands. Owing to relatively low ionization potentials, Cu and Ag readily lose electrons to yield d-band vacancies. In fact, in the chemical industry, Cu is used for the hydrogenation of carbon oxides to produce methanol, and Ag is used for the reaction of ethylene

with molecular oxygen to produce ethylene oxide. On the other hand, Au has a high ionization potential and accordingly has poor affinity towards molecules such as H_2 and O_2 .

Surface science investigation [3–6] and density functional theory calculations [7] have proved that no dissociative adsorption of H_2 and O_2 takes place over the smooth surfaces of Au at temperatures below 473 K, indicating that Au should be catalytically inactive for hydrogenation and oxidation reactions. Indeed, the conventional supported Au catalysts were much less active than supported Pt group metal catalysts. But it should be noted that Au particles were usually larger than 30 nm when prepared by the impregnation method, while Pt particles were distributed at around 3 nm in diameter [8]. This is partly because the melting point of Au is much lower than those of Pd and Pt (Au: 1336 K, Pd: 1823 K, Pt: 2042 K). Due to the quantum-size effect, the melting point of Au particles with a diameter of 2 nm is estimated to be lowered to 600 K [9], so that these small Au nanoparticles tend to coagulate with each other to form much larger Au particles during calcination of catalyst precursors. Therefore, no answer has yet been given to the question whether the rough surfaces or nanoparticles of Au, having substantial number of steps, edges, and corners, are catalytically inactive or not.

An indication that Au might not always be poorly active when dispersed as small particles was presented in the 1970's by Bond and Sermon for the hydrogenation of alkenes and alkynes at temperatures below 473 K over Au/ SiO_2 [10, 11] and by Cha, Paravano, and Galvano for oxygen and hydrogen transfer reactions over Au/MgO and Au/ Al_2O_3 catalysts [12, 13]. These landmarks concerning the catalysis by Au until 1981 were reviewed by Schwank [14]. On the other hand, pioneering attempts were made on the reactivities of Au clusters and atoms. Ozin et al. reported that atomic Au species reacted with a solid matrix of CO and O_2 at 10 K to form a complex, which was subsequently decomposed at temperatures above 30 K to produce CO_2 [15]. Cox et al. reported Au clusters were reactive with O_2 , H_2 , and CH_4 depending on the number of atoms [16].

We reported in 1987 that some composite oxides of Au with three-dimensional transition metals prepared by co-precipitation exhibited surprisingly high catalytic activity

for CO oxidation even at 200 K [17]. Later, it was revealed that these active gold catalysts were composed of Au nanoparticles homogeneously dispersed on metal oxide supports such as Fe_2O_3 , Co_3O_4 , and NiO [18–20]. This finding, followed by the first commercial application to an odor eater for toilette in 1992, has gradually evoked renewed interests in Au catalysts [21–26].

This article deals with preparation methods for Au nanoparticles deposited on metal oxides, the correlation between nano structure and catalytic properties, a probable reaction mechanism, and ongoing and future applications.

2. PREPARATION OF GOLD NANOPARTICLES

A variety of methods have been developed to deposit Au nanoparticles on metal oxides and activated carbon. They are classified into three categories [27]. The first category is characterized by the preparation of well-mixed precursors, for example, hydroxide, oxide, or metal mixtures of Au with the metal component of the support by co-precipitation [17, 18], co-sputtering [28], or amorphous alloying [29], respectively. These precursor mixtures are then transformed during calcination in air at temperatures above 550 K into metallic Au particles strongly attached to the crystalline metal oxides such as $\alpha\text{-Fe}_2\text{O}_3$, Co_3O_4 , or ZrO_2 . Gold catalysts are advantageous over other noble metal catalysts in that reduction treatment by H_2 is, in principle, not necessary.

The second category is based on the deposition or adsorption of Au compounds, for example, Au hydroxide by deposition-precipitation (DP) [30], or organogold complexes by gas-phase grafting (GG) [31, 32] and liquid-phase grafting (LG) [33, 34]. The last category is to use monodispersed Au colloids stabilized by organic ligands or polymer compounds [35, 36]. Although none of the former six techniques of the first and second categories are effective for depositing Au nanoparticles on activated carbon, this can be realized by dipping activated carbon in Au sols stabilized with polyvinyl pyrrolidone or tetrakis (hydroxymethyl) phosphonium chloride [36].

In the preparation of well-defined model catalysts for surface science studies, size-selected Au anion clusters can be deposited with homogeneous dispersion on single crystals of TiO_2 (rutile) and MgO [37, 38]. Surface defect sites or specific surface cages are suggested to be the sites for stabilizing Au clusters on metal oxides or Si support [38, 39].

The DP method is of the easiest handling and, therefore, is used for producing commercial Au catalysts. Due to the amphoteric properties of $\text{Au}(\text{OH})_3$, the pH of aqueous HAuCl_4 solution is adjusted at a fixed point in the range of 6 to 10, which is selected by taking into account of the isoelectric points (IEP) of the metal oxide supports. Careful control of the concentration (around 10^{-3} M), pH (6 ~10), and temperatures (323 K~363 K) of the aqueous HAuCl_4 solution enables the selective deposition of $\text{Au}(\text{OH})_3$ only on the surfaces of support metal oxides without precipitation in the liquid phase. Because the precursor can be thoroughly washed before drying, Na and Cl ions are removed to a level of a few

tens ppm. The removal of Cl ions is indispensable because Cl ions markedly promote the coagulation of Au nanoparticles. The only constraint of DP is that it is not applicable to metal oxides, the IEPs of which are below 5 and to activated carbon. Gold hydroxide cannot be deposited on SiO_2 (IEP = 2), $\text{SiO}_2\text{-Al}_2\text{O}_3$ (IEP = 1), and WO_3 (IEP = 1). In contrast, GG using dimethyl-goldacetylacetonate is unique because it can deposit Au nanoparticles even on SiO_2 and $\text{SiO}_2\text{-Al}_2\text{O}_3$ [32].

A catalyst sample of $\text{Au}/\alpha\text{-Fe}_2\text{O}_3$ prepared by co-precipitation and by calcination at 673 K had relatively narrow size distribution of Au particles, giving mean diameters in the range of 3 to 5 nm with standard deviation of about 30% [18]. A major reason why Au particles remain as nanoparticles even after calcination at 673 K is the epitaxial contact of Au nanoparticles with the metal oxide supports, as typically shown by Figure 1 [18]. Gold particles always exposed its most densely packed plane, (111) plane, in contact with $\alpha\text{-Fe}_2\text{O}_3$ (110), Co_3O_4 (111), NiO (111) [20], anatase TiO_2 (112), and rutile TiO_2 (110) [40].

In the case of Au/TiO_2 (anatase), the surface atomic configuration is better matched for Au (111) plane sitting on the oxygen layer of anatase TiO_2 than on the Ti layer. Three-dimensional nanostructure analyses by electron holography together with high-resolution transmission-electron microscopy (TEM) revealed that smaller hemispherical Au particles with diameters below 2 nm had contact angles with the support below 90° (wet interface), whereas larger Au particles with a diameter of 5 nm had that angle above 90° (dry interface) [41]. This difference in the wettability of Au particles may come out of the change in the electronic state of the contact interfaces with the particle size. With an increase in the calcination temperature above 573 K, Au particles coagulated with each other forming larger particles mostly gathered at the valleys of junction between the TiO_2 particles [42].

3. CATALYTIC PROPERTIES OF GOLD NANOPARTICLES

Except for H_2 oxidation and hydrocarbon hydrogenations, most reactions are remarkably structure-sensitive over supported Au catalysts. Two typical reactions are CO oxidation

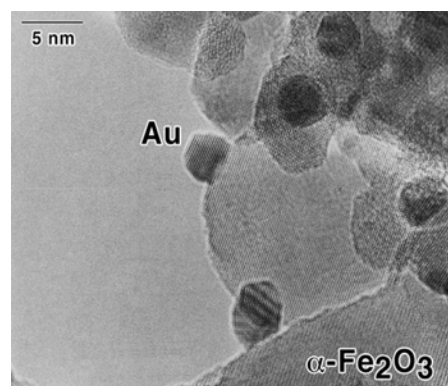


Figure 1. TEM for $\text{Au}/\alpha\text{-Fe}_2\text{O}_3$ prepared by co-precipitation and calcination at 673 K.

and propylene epoxidation. The oxidation of CO is the simplest reaction and has been most intensively studied [43]. This reaction is practically important in the purification of engine exhaust gases and of hydrogen produced by steam reforming of methanol and hydrocarbons for polymer electrolyte fuel cells [44]. The direct epoxidation of propylene to produce propylene oxide is regarded as a Holy Grail of sorts because current industrial processes require two-stage reactions [45]. These two reactions over Au catalysts are remarkably sensitive to the contact structure of Au particles with the support, the type of metal oxide support, and the size of Au particles.

3.1. Effect of the Contact Structure of Gold Particles

Figure 2 shows turnover frequencies (TOFs), the reaction rate over one single surface metal atom per second, of CO oxidation at 300 K over Au/TiO₂ and Pt/TiO₂ catalysts prepared by DP, photocatalytic deposition, and impregnation (IMP) methods [8]. The DP method yields hemispherical metal particles with their flat planes strongly attached to the TiO₂ support, while photocatalytic deposition and IMP methods yield spherical particles simply loaded on the TiO₂ support and, therefore, much larger particles particularly in the case of Au. Over Pt/TiO₂, the reaction of CO with O₂ takes place preferentially on the Pt surfaces and the metal oxide support is not directly involved in the reaction. This can account for why different preparation methods do not make any appreciable difference in the TOF of Pt catalysts. On the other hand, the TOF of Au/TiO₂ markedly depends on preparation methods and changes by four orders of magnitude. The TOF of strongly attached hemispherical Au particles exceeds that of Pt by one order of magnitude. The dramatic difference suggests that the contact structure is the most critical factor in supported Au catalysts.

The strong contact of Au particles is also indispensable for the epoxidation of propylene in the gas phase containing O₂ and H₂ [46]. Figure 3 shows that spherical Au particles loaded on TiO₂ (prepared by IMP) need higher temperatures for reactions to occur, and causes complete oxidation to produce only CO₂ and H₂O with the yield of H₂O much larger than that of CO₂. These facts indicate that H₂ oxidation and the complete oxidation of propylene take

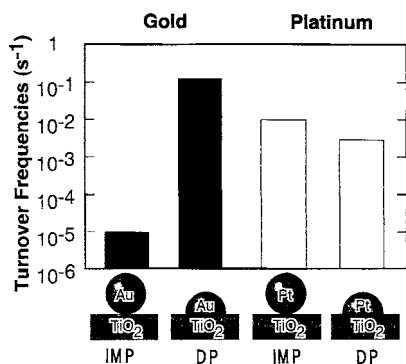


Figure 2. Turnover frequencies for CO oxidation at 300 K over Au/TiO₂ and Pt/TiO₂ prepared by different methods [8].

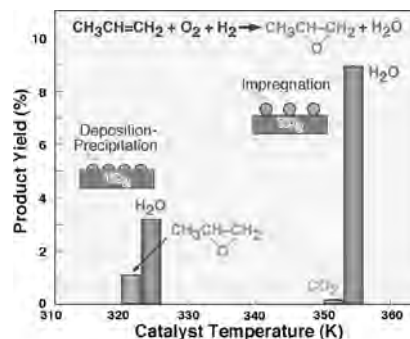


Figure 3. Product yields as a function of catalyst temperature in the reaction of propylene with O₂ and H₂ over Au/TiO₂ prepared by different methods. Reactant gas: C₃H₆/O₂/H₂/Ar = 10/10/10/70; space velocity: 4000 h⁻¹ · ml/g-cat.

place separately and the former proceeds much faster. On the other hand, hemispherical Au particles strongly attached to the TiO₂ support (prepared by DP) produce propylene oxide with almost 100% selectivity at a lower temperature—323 K. The H₂ consumption is only about three times that of propylene conversion and appreciably smaller than that over spherical Au partial catalysts. Because epoxidation of propylene does not proceed without H₂, the simultaneous reaction among C₃H₆, O₂, and H₂ takes place, probably at the periphery of Au particles with adsorption at the surfaces of Au particles and the TiO₂ surfaces.

The sharp contrast between spherical and hemispherical Au nanoparticle catalysts in CO oxidation and propylene epoxidation suggests that the reactions may take place at the perimeter interfaces around Au particles. To confirm this hypothesis, Liu and Vannice prepared an inversely supported catalyst, namely, TiO₂ layers deposited on Au substrate, and observed appreciable catalytic activity [47]. A catalyst sample of Au/TiO₂ was also prepared by mechanically mixing a colloidal solution of Au particles of 5 nm in diameter with TiO₂ powder and by calcination in the air at different temperatures [48]. Calcination at 873 K promoted the coagulation of Au particles to form larger particles with diameters above 10 nm, but at the same time with stronger contact (observed by TEM), leading to much higher catalytic activity than calcination at 573 K.

3.2. Support Effect

For CO oxidation, many oxides, except for strongly acidic materials such as Al₂O₃-SiO₂ and activated carbon, can be used as a support and bring about activity even below 300 K. In the case of Pd and Pt, semiconductive metal oxides lead to enhanced catalytic activities but at temperatures above 300 K. Semiconductive metal oxides such as TiO₂, Fe₂O₃, and NiO provide more stable Au catalysts than insulating metal oxides such as Al₂O₃ and SiO₂. Among Au supported on Al₂O₃, SiO₂, and TiO₂, TOFs at room temperature are nearly equal, indicating that the contribution of metal oxide supports is more or less similar in intensities [49]. The difference appears in the moisture effect: Al₂O₃ and SiO₂ needs higher H₂O concentration above 10 ppm than TiO₂ for CO oxidation to proceed at room temperature [50]. Alkaline earth-metal hydroxides, such as Be(OH)₂ and Mg(OH)₂, are

the best in exhibiting the highest activity at a temperature as low as 196 K [20, 51]. In contrast, when acidic materials, such as $\text{Al}_2\text{O}_3\text{-SiO}_2$, WO_3 , activated carbon, are used as a support, gold exhibits poor activity and even at temperatures above 473 K the conversions are far below 100% [49].

For the selective oxidation of hydrocarbons in the co-presence of O_2 and H_2 , only TiO_2 and Ti-silicates act as effective supports [46, 52–58]. Other metal oxide supports result in producing acetone and CO_2 . The requirements to the crystalline structure of support are very strict. Only anatase TiO_2 , neither rutile nor amorphous TiO_2 , makes Au selective to epoxidation at temperatures below 373 K [52]. Transmission electron microscopy observations showed that Au particles were more often epitaxially contacted on anatase than on rutile, indicating that the location of Ti cations around Au particles is more regular on the anatase surfaces [40]. When Ti cations are isolated from each other on the surfaces or in the bulk network of SiO_2 , namely, the atomic ratio of Ti/Si is below 3/100 in Ti-MCM-41, Ti-MCM-48, Ti- β -zeolite, and TS-1, Au is also selective to epoxidation up to 473 K, giving propylene conversions higher than 3%. The distance between Ti cations may be important; on the surfaces of anatase and Ti silicate, Ti cations are separated from each other at a distance of the diameter of oxygen anion or much far, while on the rutile surface, they are located closer.

3.3. Size Effect of Gold Particles

Figure 4 shows that the main product in the reaction of propylene with O_2 and H_2 switches from propylene oxide to propane at a critical diameter of 2 nm [46]. Over Pd and Pt catalysts, the major product is only propane, irrespective of the size of metal particles and of the presence or absence of O_2 , while propane is formed over Au catalysts only when Au particles are smaller than 2 nm in diameter and O_2 is present. This implies that a change in the surface property of Au clusters must be induced by donating an electron to O_2 to form negatively charged oxygen species. The critical diameter, 2 nm, corresponds to a layer of three atoms thick when the Au clusters are hemispherical in shape. The bandgap measured with scanning tunneling spectroscopy shows that the electronic state of Au clusters deviates from that of bulk at two or three atoms in thickness [59, 60].

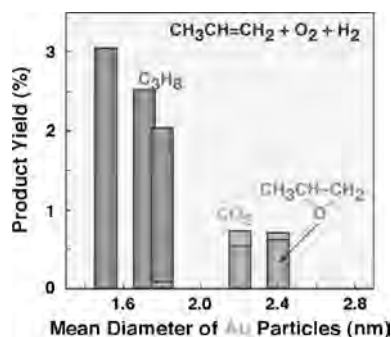


Figure 4. Product yields as a function of mean diameter of Au particles in the reaction of propylene with O_2 and H_2 over Au/ TiO_2 catalysts at 353 K. Reactant gas: $\text{C}_3\text{H}_6/\text{O}_2/\text{H}_2/\text{Ar} = 10/10/10/70$; space velocity: $4000 \text{ h}^{-1} \cdot \text{ml/g-cat}$.

Figure 5 plots the TOFs of CO oxidation over Au/ TiO_2 , Au/ Fe_2O_3 , and Au/ Co_3O_4 as a function of mean diameter of Au particles [19]. The TOFs sharply increase with a decrease in the diameter of Au particles from 4 nm, indicating that minimizing the size of Au particles is very rewarding owing to the increases in both TOF and specific surface area. In contrast, Pt group metals usually show decreasing or steady TOF; thus smaller particles are not always beneficial [61]. The increased TOFs of smaller Au particles can be explained by assuming that the adsorption sites for CO on the Au surfaces are edge, corner, or step sites and the reaction zone is the periphery around Au particles, because the fractions of these sites on and around hemispherical Au particles increase with a decrease in the size of Au particles [62].

Among supported noble metal catalysts, Au supported on $\text{Mg}(\text{OH})_2$ is the most active for CO oxidation at a temperature as low as 196 K; however, it suddenly dies after 3 to 4 months, losing activity even at 473 K [63]. Estimation of the most probable size distribution of Au particles by using Debye functional analyses of X-rays scattered by Au particles for fresh and aged catalysts suggested that the active Au species were 13-atom Au clusters. When they grew to 55-atom clusters with truncated decahedral structure, the catalytic activity was completely lost. Among the two structures of 13-atom clusters, it is likely that the icosahedron is active, whereas the cubo-octahedron is inactive [51]. The active Au/ $\text{Mg}(\text{OH})_2$ catalyst, which was assumed to be mainly composed of icosahedral Au clusters of 13 atoms, showed negative apparent activation energy in the temperature range from 196 K to 273 K [64]. This can be explained by the enhanced transformation of the icosahedron into the cubo-octahedron with a rise in reaction temperature.

Heiz and Abbet et al. prepared model catalysts by depositing size-selected Au anion clusters onto a single crystal of MgO. Although the size and structures of Au clusters deposited were not confirmed by STM, appreciable size dependency of CO adsorption was reported with a maximum for 11 atoms [65]. The higher activity of Au clusters on defect-rich MgO than on defect-poor MgO was observed and *ab initio* simulations indicate that partial electron transfer from the surface of the Au clusters to oxygen-vacancy defects in the support play an essential role for the genesis of catalytic activity [66, 67].

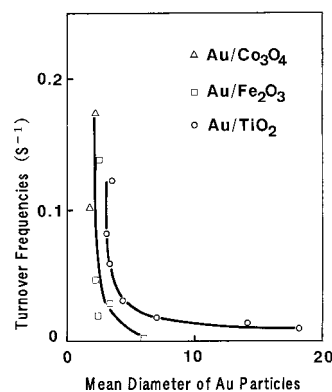


Figure 5. Turnover frequencies for CO oxidation over Au/ TiO_2 , Au/ Fe_2O_3 , and Au/ Co_3O_4 at 273 K [19].

4. MECHANISM FOR LOW-TEMPERATURE CO OXIDATION

Figure 6 shows Arrhenius plots for CO oxidation over noble metal catalysts. A unique feature of Au catalysts is that apparent activation energies (E_a) are very low. At temperatures below 300 K, E_a is 20~40 kJ/mol and is nearly zero at temperatures above 300 K. In contrast, Pt group metals have E_a ranging from 80 to 170 kJ/mol [68] and are more active than Au only at temperatures above 500 K. At room temperature, Au is more active by more than four orders of magnitude.

The rate of CO oxidation over Au/TiO₂, Au/Fe₂O₃, Au/Co₃O₄ is independent of the concentration of CO and is slightly dependant on the concentration of O₂ (0~0.25 order) [19]. This feature is beneficial for the removal of dilute CO from air, because the conversion of CO increased with a decrease in the concentration of CO. Over unsupported Au powder with mean diameters of primary Au particles of 17 nm, the rate is almost independent of the concentrations of CO and O₂ [69]. These independencies suggest that both CO and O₂ are adsorbed on the catalyst surfaces nearly to saturation and the reaction of the two adsorbed species is the rate-determining step.

Figure 7 shows FT-IR spectra for CO adsorption at 90 K over Au/TiO₂ calcined in air at different temperatures [70]. The most active sample (calcined at 573 K, mean diameter of Au particles 2.4 nm) has the largest intensity of the peak at 2110~2120 cm⁻¹, which is assigned to CO linearly adsorbed on the metallic Au sites. When Au particles become larger than 10 nm in diameter (sample calcined at 873 K), the intensity of this peak is markedly reduced, indicating that CO adsorption takes place only on steps, edges, and corners of Au particles, not on the smooth surfaces. This is in agreement with what has been discussed based on self-consistent density functional theory calculations by Mavrikakis et al. [62].

No direct experimental evidence has yet been presented where oxygen is activated for reacting with CO adsorbed on the Au surfaces, and whether oxygen molecules are dissociatively or nondissociatively adsorbed. A temporal analysis of products (TAP) study of O₂ adsorption and the reaction of O₂ with CO [71, 72], ¹⁸O₂ isotope experiments [71–73], and ESR measurements [73, 74] indicates that molecularly

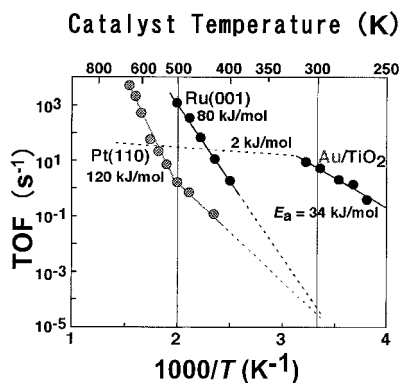


Figure 6. Arrhenius plots for CO oxidation over noble metal catalysts. The data for Pt group metals are taken from [68].

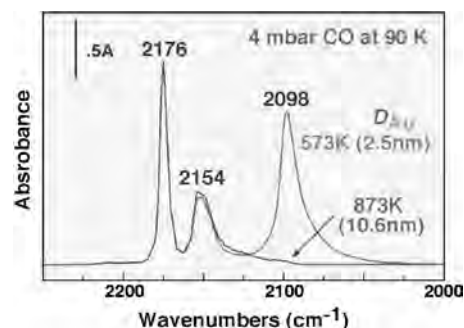


Figure 7. FT-IR spectra for CO adsorption at 90 K over Au/TiO₂ calcined in air at 573 K and 873 K [70].

adsorbed O₂, most likely O₂⁻ at the perimeter interface, is involved in the oxidation of CO. When C¹⁶O was introduced to Au/TiO₂ at 300 K after preadsorption of ¹⁸O₂ [70], C¹⁶O₂ is formed with quantity comparable to that of C¹⁶O¹⁸O, indicating that oxygen species (¹⁶O) contained in the surface layer of the TiO₂ support are also involved in CO oxidation at room temperature.

There are still other arguments about the active species of Au, especially in the case of Au/Fe₂O₃: oxidized Au species, either Au⁺ [75] or Au^{δ+} [76], or metal-oxide support surfaces with modified reducibility by the interaction with Au nanoparticles [77, 78]. It is unlikely that oxidic Au species are major catalytically active phases, because the most active supported Au catalysts are usually prepared by calcination in the air at 573 K, where Au precursors (hydroxides or organo complexes) can be transformed mostly into metallic particles. A certain fraction of Au species remain as atomically dispersed species in the matrix of the support, which was proved by EXAFS [24, 76, 79, 80], XPS [77], Mössbauer [78, 81], IR for adsorbed CO species [70, 75]; however, no correlation between the amount of oxidic Au species and catalytic activity has yet been presented. It is speculated that the samples that mainly consisted of oxidic Au could exhibit high catalytic activity probably because oxidic Au species are transformed into metallic particles during reaction or storage of the sample after preparation.

Even though metallic Au particles are indispensable, a question arises why the periphery of Au particles can activate O₂ molecules at low temperatures. As proposed by Bond and Thompson [82], it is probable that the perimeter interfaces contain oxidic Au species, most probably Au(OH)₃ or Au(OH) under usual conditions where H₂O is present at concentrations above 1 ppm. These hydroxides may be stabilized and reversibly formed and decomposed by the aid of the metal-oxide supports.

Another argument proposed by Goodman et al. is that the nonmetallic nature of Au clusters leads to the enhanced catalytic activity [37, 59]. This mechanism is questionable because the transition of the electronic state was measured for one specific Au cluster of a defined diameter by scanning tunneling spectroscopy, whereas the catalytic activity was measured for a whole specimen of Au/TiO₂ model catalyst with a mean diameter of all Au clusters. A maximum in catalytic activity with respect to the mean diameter of hemispherical Au clusters was observed at 3.5 nm (this might not be reproducible), which corresponded to two or three atoms

thick, where the transition of the electronic state of the specific Au cluster occurred from a metallic to nonmetallic one. This result can be more reasonably explained by assuming that metallic Au surfaces are necessary for CO adsorption and the peripheries act as reaction zones with O₂. A maximum in the perimeter sites and the number of step sites of metallic Au clusters is obtained at a thickness of two atoms [62], where the transition to a nonmetallic state begins.

Based on the above arguments, a most probable pathway for CO oxidation over supported Au catalysts can be depicted as shown in Figure 8. The rates over Au/TiO₂ were about one order of magnitude larger when measured by lowering the temperature from 353 K than when measured by raising the temperature from 203 K [26, 69]. This difference is assumed to arise from the accumulation of carbonate species on the surfaces of the support at low temperatures resulting in the loss of the activating power of the perimeter interfaces for O₂. Therefore, the rate over Au/TiO₂ that was deactivated during experiments at lower temperatures is regarded to be close to the rate of CO reaction with O₂ over the surfaces of Au particles without the contribution of O₂ activation at the perimeter interfaces. The one order of magnitude difference in the rate between fresh (obtained by high-temperature measurements) and deactivated (after low-temperature measurements) Au/TiO₂ can be ascribed to the contribution of the TiO₂ support.

5. CATALYTIC CAPABILITIES AND APPLICATIONS OF SUPPORTED GOLD NANOPARTICLES

Gold catalysts can also promote many reactions other than CO oxidation and propylene epoxidation when suitable support materials are selected. Table 1 lists such reactions catalyzed by Au at much lower temperatures or with much higher selectivities than by other metals.

The complete oxidation (combustion) of hydrocarbons, CO₃O₄, which is the most active catalyst among base metal oxides, brings about the highest catalytic activity to Au as a support [83, 84]. In the oxidative decomposition of nitrogen-containing hydrocarbons, ferric oxides and nickel ferrites lead to the highest catalytic activities owing to their strong affinities to nitrogen [85]. The oxidative decomposition of trimethylamine, which is a typical odor compound, proceeds

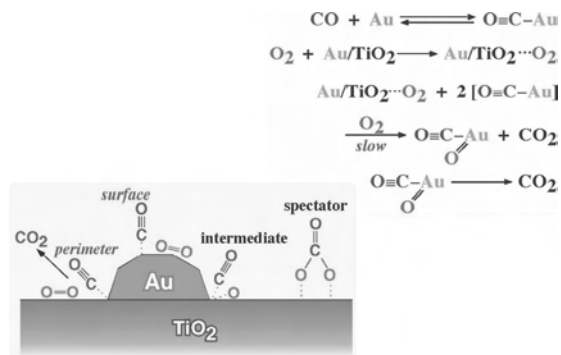


Figure 8. Schematic representation for a probable pathway of CO oxidation over supported Au catalysts.

over Au/NiFe₂O₄ at temperatures below 373 K, yielding mainly N₂ and CO₂, while N₂O is mainly produced over Pd and Pt catalysts even at higher temperatures. Gold deposited on Fe₂O₃, which was supported on a zeolite wash-coated honeycomb, has been commercially used as an odor eater in modern Japanese toilets since 1992.

A characteristic feature of Au catalysts for the hydrogenation of unsaturated hydrocarbons is that partial hydrogenation takes place very selectively—butadiene to butene, acetylene to ethylene [10, 11, 86, 87]. Hydrocarbon hydrogenations are known to be structure-insensitive, proceeding at approximately the same TOF on metal particles of various sizes [88]. It was also the case of the hydrogenation of butadiene over Au catalysts as far as Al₂O₃, SiO₂, and TiO₂ were concerned as a support [86], because TOF only differed by a factor of three among Au particles with mean diameters ranging from 3.5 to 7 nm. In the hydrogenation of α, β unsaturated aldehyde, selectivity to the hydrogenation of C=O against that of C=C can reach 80% when Au particles are deposited on ZnO [89]. For methanol synthesis by the hydrogenation of CO and CO₂, ZnO, which has been used as a support for commercial Cu catalysts, also works as the best support [90, 91].

Gold supported on activated carbon, γ -Al₂O₃, or TiO₂, is more active and selective than other noble metal catalysts for the oxidation in a MeOH-H₂O (6:4) solvent of diols to α -hydroxy acids, which are used in the cosmetics and food industries [36, 92, 93].

The reduction of NO with hydrocarbons to N₂ in the co-presence of excess O₂ and H₂O is an important reaction for the exhaust gas treatments of gasoline and diesel engines. This reaction takes place over some supported Au catalysts [94, 95]. Alkenes (C₂H₄, C₃H₆) are more effective as a reductant than alkanes (CH₄, C₂H₆, C₃H₈) because the formers can adsorb on the Au surfaces more strongly. The optimum temperature and maximum efficiency for NO reduction depends on the kind of metal-oxide supports and increase in the order of α -Fe₂O₃ (523 K, 12%), ZrO₂ (523 K, 32%), ZnO (523 K, 49%), TiO₂ (623 K, 30%), MgO (623 K, 42%), Al₂O₃ (673 K, 80%). The NO conversion to N₂ obtained over Au/Al₂O₃ in the presence of 5 vol% O₂ and 10 vol% H₂O is comparatively higher than the other catalysts reported so far [2]. The reaction passes through NO oxidation with O₂ to form NO₂, which then reacts with propylene. Therefore, enhanced activity is obtained with a mechanical mixture of Au/Al₂O₃ with Mn₂O₃, which is active for NO oxidation to NO₂ [96]. Gold wire [97] and film [98] were known to be active for N₂O decomposition to N₂ and O₂. Recently, Au/Co₃O₄ has been reported to be active for this reaction even at 523 K in the co-presence of 10 vol% O₂ and 5 vol% H₂O [99].

Owing to ongoing applications of polymer electrolyte fuel cells to automobiles and to residential co-delivery systems for electricity and heat, low-temperature, water-gas shift reaction is attracting renewed interest. In comparison to commercial catalysts based on Ni or Cu, which is operated at 900 K or at 600 K, respectively, Au supported on TiO₂, Fe₂O₃, or ZrO₂ appear to be advantageous in operating at a temperature as low as 473 K [100–102]. For selective CO removal in H₂ stream, Au supported on Al₂O₃, TiO₂, Mn₂O₃, and Fe₂O₃ [44, 103, 104] are stable and potentially

Table 1. Reactions Catalyzed by Gold.

Type of Reaction	Reactant	Temperature (K)	Support	Comments	Ref.
Complete oxidation	CO	200~400	Be(OH) ₂ , Mg(OH) ₂ , Mn ₂ O ₃ , Fe ₂ O ₃ , etc.	acidic metal oxides are excluded as a support	[51] [18, 19, 44, 103]
	HCHO	300~450	TiO ₂	regenerable by sunlight	[119]
	CH ₃ OH	300~450	TiO ₂	regenerable by sunlight	[119]
	CH ₄ , C ₃ H ₈	450~650	Co ₃ O ₄	as active as Pd, Pt catalysts	[83, 84]
	trimethylamine	330~500	Fe ₂ O ₃ , NiFe ₂ O ₄	commercialized for odor eater	[85]
Oxidative decomposition	chlorofluorocarbon o-chlorophenol	450~550	Co ₃ O ₄ , Al ₂ O ₃ , LaF ₃ Fe ₂ O ₃	integrated with Pt/SnO ₂ + Ir/La ₂ O ₃	[106, 107] [108]
	dioxin	400~500	Fe ₂ O ₃	integrated with Pt/SnO ₂ + Ir/La ₂ O ₃	[108]
Reduction or decomposition of NO _x	NO + C ₃ H ₆	450~800	Al ₂ O ₃	to N ₂ , mixed with Mn ₂ O ₃	[94–96]
	N ₂ O (+O ₂ + H ₂ O)	500~	Co ₃ O ₄	to N ₂	[99]
Reduction or oxidation of CO _x	CO + H ₂ O	400~500	TiO ₂ , ZrO ₂ , CeO ₂	to CO ₂ + H ₂	[100–102]
	CO + 2H ₂	400~500	ZnO	to methanol	[90]
	CO ₂ + 3H ₂	400~500	ZnO	to methanol	[90, 91]
	CO ₂ + 3H ₂	400~500	TiO ₂	to CO	[90]
Selective oxidation	C ₃ H ₆ + H ₂ + O ₂	300~500	TiO ₂ (anatase), Ti-SiO ₂	to propylene oxide	[46, 52–58]
	C ₃ H ₈ + O ₂ + H ₂	300~400	TiO ₂ (anatase)	to acetone	[46]
	C ₄ H ₁₀ + O ₂ + H ₂	300~400	TiO ₂ (anatase)	to butanol	[46]
	glycols	room temp.	activated carbon	to α-hydroxy acids, liquid phase	[36, 92, 93]
Selective hydrogenation	CH≡CH	400~500	Al ₂ O ₃	to ethylene	[86]
	CH ₂ =CH-CH=CH ₂	400~500	Al ₂ O ₃ , SiO ₂ , TiO ₂	to butenes	[10, 11, 86]
	crotonaldehyde	500~550	ZnO	to crotyl alcohol	[89]
	acrolein	513~593	ZrO ₂	to allyl alcohol	[120]
Hydrochlorination	CH≡CH	373~393	AuCl ₃ /activated carbon	to vinyl chloride	[105]

advantageous over other noble metal catalysts because only supported Au catalysts are much more active for CO oxidation than for H₂ oxidation.

Because of the stability of Au against halogens, some supported Au catalysts have been reported to be more active and stable for reactions involving halogens such as oxidative decomposition of chlorofluorocarbons and dioxins than other noble metal catalysts [105–108]. It should be noted that AuCl₃ supported on activated carbon is the most active among metal chloride catalysts for the hydrochlorination of acetylene to produce vinylchloride [105].

The characteristic features of supported gold catalysts are: remarkable structure sensitivity of reactions, low apparent activation energies (active at low temperatures), and activation by moisture. By taking advantage of these properties, the first direction of future approaches is the discovery of new capabilities for Au particles larger than 2 nm which are stable up to 673 K. The combination with other metal catalysts can expand the capabilities of Au catalysts. Gold supported on Fe₂O₃ or La₂O₃ is the most active among noble metal catalysts for the oxidative decomposition of dioxin at temperatures below 473 K. As shown in Figure 9, the integration of Ir, Pt, and Au catalysts supported on La₂O₃, SnO₂, and TiO₂, respectively, resulted in 95% decomposition of dioxin from the outlet gases of an incinerator even at 423 K, at an hourly space velocity of 12,000 h⁻¹. ml/g-cat. It is interesting that the least active Ir catalyst exhibits an excellent booster effect [108].

The second direction is the extension of the catalytic mechanism and the preparation techniques for Au catalysts to other noble metals. The genesis of the catalysis by Au is, in most cases, ascribed to the perimeter interfaces around Au particles. This presents a new guiding principle to create a wide range of new catalytic systems, because combination of catalytic metals with a variety of support materials should present a great deal of novel catalysts. Good examples are Pd/CeO₂ and Pt/ZrO₂ prepared by co-precipitation for the low-temperature decomposition and synthesis of methanol [109] and for the low-temperature oxidation of CO and reduction of NO [110].

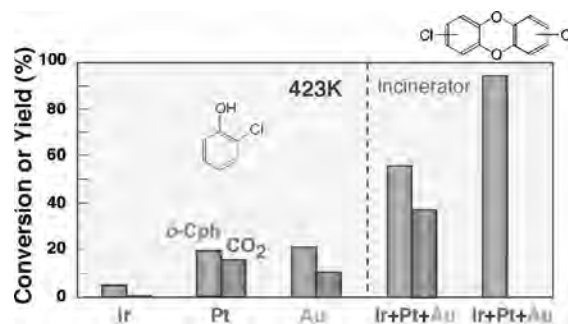


Figure 9. Oxidative decomposition of ortho-chlorophenol over supported, noble metal catalysts at 423 K [108]. The integration of different noble metal catalysts led to improved performance in the conversion of dioxin in a small incinerator at 423 K.

The third direction is the fundamental study of cluster physics and chemistry for Au particles smaller than 2 nm. Significant work has recently been emerging to understand the unique catalysis of Au and its size- and structure-dependency. By means of surface science techniques using well-defined catalytic materials (most often size-selected Au clusters deposited on single crystalline metal oxides such as MgO [65] and TiO₂ [37, 59, 111–115]) an atomic scale understanding is being accumulated in combination with theoretical calculations [7, 62, 66]. It is also instructive that the catalytic activity may change dramatically depending on the three-dimensional structure of 13 atoms Au clusters [51]. In this approach, Au may be the best target of research because Au itself is poorly active and the detectable activity is obtained only when the specific structure and size of Au particles are given. It is also advantageous in Au model catalyst studies that the activity is usually detectable at lower temperatures where designed structures can be maintained.

In order to combine experimental work using both real catalysts and model catalysts with theoretical calculations more effectively [116], the effect of moisture should be taken into account. Most surface science work is carried out in ultra-high vacuum, while catalytic activity measurements for real catalysts are carried out in a fixed bed flow reactor using reactant gas containing moisture at least 1 ppm, usually in the order of 10 ppm. It is reasonable to assume that the catalyst surfaces are covered with OH groups and water molecules at room temperature. For CO oxidation, which does not produce H₂O and proceeds at temperatures below 373 K, moisture markedly changes the catalytic activity of metal oxides and Au catalysts. Under a dry condition with H₂O concentration of 80 ppb, CO oxidation can take place even at 210 K over Co₃O₄ without Au [117, 118], while supported Au catalysts prefers moisture [50].

6. CONCLUSIONS

Three factors define the catalytic properties of gold—strong contact between Au particles and the support, selection of the support, and the size of Au particles. Perimeter interfaces provide the sites for reaction, while metallic Au surfaces are still necessary as a reservoir for one of the reactants. Gold catalysts are advantageous in environmental applications because of very low apparent activation energies and enhancement by moisture. Gold is the best sample for fundamental studies on the size effect below 2 nm through model catalysts and theoretical calculations.

GLOSSARY

Au clusters When the number of Au atoms is smaller than 300 with a diameter below 2 nm, physicochemical properties often differ markedly from those of Au nanoparticles with a diameter above 2 nm.

Epitaxial contact The contact interface where the atomic configuration of the two phases fits well two dimensionally with each other, leading to the growth of crystallite in a specific direction.

Isoelectric point (IEP) The pH where the surfaces of solid in an aqueous solution are charged equally with positive ions

and negative ions. Acidic materials have low IEP, whereas basic ones have high IEP.

Structure sensitive reaction Reactions whose rates per active site (TOFs) are dependent on the crystal planes, size, and shape of catalytic materials. In the case of supported metal catalysts, TOF is usually expressed by rate divided by the number of surface-exposed metal atoms.

Turnover frequency (TOF) Reaction rate per one single active site, TOF, is a common parameter to compare the catalytic activity among a variety of catalysts, for example, single crystal, metal oxide particles, and supported metal catalysts.

REFERENCES

1. V. Ponec and G. C. Bond, "Catalysis by Metals and Alloys," Elsevier, Amsterdam, 1996.
2. M. Iwamoto, *Studies Surf. Sci. Catal.* 130, 23 (2000).
3. A. G. Sault, R. J. Madix, and C. T. Campbell, *Surf. Sci.* 169, 347 (1986).
4. L. Stobiński and R. Duś, *Vacuum* 45, 299 (1994).
5. N. Saliba, D. H. Parker, and B. E. Koel, *Surf. Sci.* 410, 270 (1998).
6. J. Wang and B. E. Koel, *J. Phys. Chem. A* 102, 8573 (1998).
7. B. Hammer and J. K. Nørskov, *Nature* 376, 238 (1995).
8. C. R. Bamwenda, S. Tsubota, T. Nakamura, and M. Haruta, *Catal. Lett.* 44, 83 (1997).
9. Ph. Buffet and J.-P. Borel, *Phys. Rev. A* 13, 2287 (1976).
10. G. C. Bond and P. A. Sermon, *Gold Bull.* 6, 102 (1973).
11. G. C. Bond and P. A. Sermon, *JCS Chem. Comm.* 444 (1973).
12. D. Y. Cha and G. Parravano, *J. Catal.* 18, 200 (1970).
13. S. Galvano and G. Parravano, *J. Catal.* 55, 178 (1978).
14. J. Schwank, *Gold Bull.* 16 (4), 103 (1983).
15. H. Huber, D. McIntosh, and G. A. Ozin, *Inorg. Chem.* 16, 975 (1977).
16. D. M. Cox, R. Brickman, K. Creegan, and A. Kaldor, *Z. Phys. D-Atoms, Molecules and Clusters* 19, 353 (1991).
17. M. Haruta, T. Kobayashi, H. Sano, and N. Yamada, *Chem. Lett.* 405 (1987).
18. M. Haruta, N. Yamada, T. Kobayashi, and S. Iijima, *J. Catal.* 115, 301 (1989).
19. M. Haruta, S. Tsubota, T. Kobayashi, H. Kageyama, M. J. Genet, and B. Delmon, *J. Catal.* 144, 175 (1993).
20. M. Haruta, T. Kobayashi, S. Iijima, and F. Delannay, "Proc. 9th Intern. Congr. Catal.," Calgary, Canada, 1988, p. 1206.
21. M. Haruta, *Catal. Today* 36, 153 (1997).
22. M. Haruta, *Catal Surveys from Japan* 1, 61 (1997).
23. G. C. Bond and D. T. Thompson, *Catal. Rev.-Sci. Eng.* 41, 319 (1999).
24. Osaka National Research Institute, Activity Report No. 393, 1999.
25. M. Haruta and M. Daté, *Appl. Catal. A: General* 222, 427 (2001).
26. M. Haruta, *CATTECH* 6 (3), 102 (2002).
27. M. Haruta, S. Tsubota, and M. Okumura, "Advances in Catalyst Preparation," p. 39 (Japanese) (Y. Ono et al., Eds.), Association for the Promotion of Catalyst Preparation Chemistry, Tokyo, 2000.
28. T. Kobayashi, M. Haruta, S. Tsubota, and H. Sano, *Sensors and Actuators B* 1, 222 (1990).
29. M. Shibata, N. Kuwata, T. Matsumoto, and H. Kimura, *Chem. Lett.*, 1605 (1985).
30. S. Tsubota, M. Haruta, T. Kobayashi, A. Ueda, and Y. Nakahara, *Studies Surf. Sci. Catal.* 63, 695 (1991).
31. M. Okumura, K. Tanaka, A. Ueda, and M. Haruta, *Solid State Ionics* 95, 143 (1997).
32. M. Okumura, S. Tsubota, M. Iwamoto, and M. Haruta, *Chem. Lett.*, 315 (1998).

33. Y. Yuan, A. P. Kozlova, K. Asakura, H. Wan, K. Tsai, and Y. Iwasawa, *J. Catal.* 170, 191 (1997).
34. M. Okumura and M. Haruta, *Chem. Lett.*, 396 (2000).
35. J.-D. Grunwaldt, C. Kiener, C. Wögerbauer, and A. Baiker, *J. Catal.* 181, 223 (1999).
36. L. Prati and M. Rossi, "Green Chemistry: Challenging Perspectives," p. 183 (P. Tundo, P. Anastas, Eds.), Oxford, 2000.
37. M. Valden, S. Pak, X. Lai, and D. W. Goodman, *Catal. Lett.* 56, 7 (1998).
38. W. T. Wallace and R. L. Whetten, *J. Phys. Chem. B* 104, 10964 (2000).
39. K. Kishi, M. Daté, and M. Haruta, *Surf. Sci.* 486, L475 (2001).
40. T. Akita, K. Tanaka, S. Tsubota, and M. Haruta, *J. Electron. Microscopy* 49, 657 (2000).
41. M. Ichikawa, T. Akita, M. Okumura, K. Tanaka, and M. Haruta, "Proc. 7th Intern. Symp. Advanced Physical Fields," p. 369 (Noda, Ed.), National Institute of Materials Science, Tsukuba, Japan, 2001.
42. T. Akita, P. Lu, S. Ichikawa, K. Tanaka, and M. Haruta, *Surf. Interface Anal.* 31, 73 (2001).
43. G. Ertl, *Chem. Record* 1, 33 (2001).
44. R. M. Torres Sanchez, A. Ueda, K. Tanaka, and M. Haruta, *J. Catal.* 168, 125 (1997).
45. *Chem. Eng. News*, July 5, 1999, p. 33.
46. T. Hayashi, K. Tanaka, and M. Haruta, *J. Catal.* 178, 566 (1998).
47. Z. M. Liu and M. A. Vannice, *Catal. Lett.* 43, 51 (1997).
48. S. Tsubota, T. Nakamura, K. Tanaka, and M. Haruta, *Catal. Lett.* 56, 131 (1998).
49. M. Okumura, S. Nakamura, S. Tsubota, T. Nakamura, M. Azuma, and M. Haruta, *Catal. Lett.* 51, 53 (1998).
50. M. Daté and M. Haruta, *J. Catal.* 201, 221 (2001).
51. D. A. H. Cunningham, W. Vogel, H. Kageyama, S. Tsubota, and M. Haruta, *J. Catal.* 177, 1 (1998).
52. M. Haruta, B. S. Uphade, S. Tsubota, and A. Miyamoto, *Res. Chem. Intermed.* 24, 329 (1998).
53. Y. A. Kalvachev, T. Hayashi, S. Tsubota, and M. Haruta, *J. Catal.* 186, 228 (1999).
54. B. S. Uphade, Y. Yamada, T. Nakamura, and M. Haruta, *Appl. Catal. A: General* 215, 137 (2001).
55. E. E. Stangland, K. B. Stavens, R. P. Andres, and W. N. Delgass, *J. Catal.* 191, 332 (2000).
56. G. Mul, A. Zwiijnenburg, B. Linden, M. Makkee, and J. A. Moulijn, *J. Catal.* 201, 128 (2001).
57. C. Qi, T. Akita, M. Okumura, and M. Haruta, *Appl. Catal. A: General* 218, 81 (2001).
58. A. K. Sinha, S. Seelan, T. Akita, S. Tsubota, and M. Haruta, *Appl. Catal. A: Gen.*, in press.
59. M. Valden, X. Lai, and D. W. Goodman, *Science* 281, 1647 (1998).
60. Y. Maeda, M. Okumura, S. Tsubota, M. Kohyama, and M. Haruta, to be submitted.
61. M. Haruta, "Catalysis and Electrocatalysis on Nanoparticles," (A. Wieckowski, E. R. Savinova, and C. G. Vayenas, Eds.), Marcel Dekker, New York, in press.
62. M. Mavrikakis, P. Stolze, and J. K. Nørskov, *Catal. Lett.* 64, 101 (2000).
63. W. Vogel, D. A. H. Cunningham, K. Tanaka, and M. Haruta, *Catal. Lett.* 40, 175 (1996).
64. D. A. H. Cunningham, W. Vogel, and M. Haruta, *Catal. Lett.* 63, 43 (1999).
65. U. Heiz and W.-D. Schneider, *J. Phys. D: Appl. Phys.* 33, R85 (2000).
66. S. Abbet, U. Heiz, H. Häkkinen, and U. Landman, *Phys. Rev. Lett.* 86, 5950 (2001).
67. U. Heiz, A. Sanchez, S. Abbet, and W.-D. Schneider, *J. Am. Chem. Soc.* 121, 3214 (1999).
68. C. H. F. Peden, "Surface Science of Catalysis-In Situ Probes and Reaction Kinetics," p. 143 (D. J. Dwyer and F. M. Hoffmann, Eds.), *ACS Symp. Ser.* 482, American Chemical Society, Washington, DC, 1992.
69. Y. Iizuka, T. Tode, T. Takao, K. Yatsu, T. Takeuchi, S. Tsubota, and M. Haruta, *J. Catal.* 187, 50 (1999).
70. F. Boccuzzi, A. Chiorino, M. Manzoli, P. Lu, T. Akita, S. Ichikawa, and M. Haruta, *J. Catal.* 202, 256 (2001).
71. M. Olea, M. Kunitake, T. Shido, and Y. Iwasawa, *Phys. Chem. Chem. Phys.* 3, 627 (2001).
72. M. M. Schubert, S. Hackenberg, A. C. van Veen, M. Muhler, V. Plzak, and R. J. Behm, *J. Catal.* 197, 113 (2001).
73. H. Liu, A. I. Kozlov, A. P. Kozlova, T. Shido, K. Asakura, and Y. Iwasawa, *J. Catal.* 185, 252 (1999).
74. M. Okumura, J. M. Coronado, J. Soria, M. Haruta, and J. C. Conesa, *J. Catal.* 203, 168 (2001).
75. S. Minicò, S. Scirè, C. Crisafulli, A. M. Visco, and S. Galvagno, *Catal. Lett.* 47, 273 (1997).
76. Z. Hao, L. An, H. Wang, and T. Hu, *React. Kinet. Catal. Lett.* 70, 153 (2000).
77. D. Horváth, L. Toth, and L. Guzzi, *Catal. Lett.* 67, 117 (2000).
78. F. E. Wagner, S. Galvagno, C. Milone, A. M. Visco, L. Stievano, and S. Calogero, *J. Chem. Soc. Faraday Trans.* 93, 3403 (1997).
79. H. Kageyama, N. Kamijo, T. Kobayashi, and M. Haruta, *Physica B* 158, 183 (1989).
80. S. Tsubota, D. A. H. Cunningham, and M. Haruta, *Studies Surf. Sci. Catal.* 91, 227 (1995).
81. Y. Kobayashi, S. Nasu, S. Tsubota, and M. Haruta, *Hyperfine Interactions* 126, 95 (2000).
82. G. C. Bond and D. T. Thompson, *Gold Bull.* 33, 41 (2000).
83. M. Haruta, *Now and Future* 7, 13 (1992).
84. R. D. Walters, J. J. Weimer, and J. E. Smith, *Catal. Lett.* 30, 181 (1995).
85. A. Ueda and M. Haruta, *Shigen Kankyou Taisaku* (Resources and the Environmental Technology) 28, 1035 (1992).
86. M. Okumura, T. Akita, and M. Haruta, *Catal. Today* 74, 265 (2002).
87. J. Jia, K. Haraki, J. N. Kondo, K. Domen, and K. Tamaru, *J. Phys. Chem. B* 104, 11153 (2000).
88. Z. Xu, F.-S. Xiao, S. K. Purnell, O. Alexeev, S. Kawi, S. E. Deutsh, and B. C. Gates, *Nature* 372, 346 (1994).
89. J. E. Bailie, H. A. Abdullah, J. A. Anderson, C. H. Roehchester, N. V. Richardson, N. Hodge, J.-G. Zhang, A. Burrows, C. J. Kiely, and G. Hutchings, *J. Phys. Chem. Chem. Phys.* 3, 4113 (2001).
90. H. Sakurai and M. Haruta, *Appl. Catal. A: General* 127, 93 (1995).
91. A. Baiker, M. Kilo, M. Maciejewski, S. Menzi, and A. Wokaun, "Proc. 10th Intern. Congr. Catal.," p. 1257 (L. Guzzi, et al. Eds.), Elsevier, Amsterdam, 1993.
92. C. Bianchi, F. Porta, L. Prati, and M. Rossi, *Topics in Catal.* 13, 231 (2000).
93. F. Porta, L. Prati, M. Rossi, S. Coluccia, and G. Martra, *Catal. Today* 61, 165 (2000).
94. A. Ueda and M. Haruta, *Appl. Catal. B: Environmental* 285, 81 (1996).
95. A. Ueda and M. Haruta, *Gold Bull.* 32, 3 (1999).
96. A. Ueda and M. Haruta, *Appl. Catal. B: Environmental* 18, 115 (1998).
97. C. N. Hinshelwood and C. R. Prichard, *Proc. Roy. Soc. London* 108A, 211 (1925).
98. V. M. Stepanov, V. D. Yagodovskii, and H. Agilar, *Russian J. Phys. Chem.* 49, 1335 (1975).
99. L. Yan, X. Zhang, T. Ren, H. Zhang, X. Wang, and J. Suo, *J. Chem. Soc. Chem. Comm.*, 860 (2002).
100. H. Sakurai, A. Ueda, T. Kobayashi, and M. Haruta, *J. Chem. Soc. Chem. Commun.* 271 (1997).
101. D. Andreeva, I. V. Idakiev, T. Tabakov, and A. Andreev, *J. Catal.* 158, 354 (1996).
102. T. Tabakova, V. Idakiev, D. Andreeva, and I. Mitov, *Appl. Catal. A: General* 202, 336 (2000).

103. M. J. Kahlich, H. A. Gasteiger, and R. J. Behm, *J. Catal.* 182, 430 (1999).
104. M. M. Schubert, S. Hachenberg, A. C. van Veen, M. Muhler, V. Plzak, and R. J. Behm, *J. Catal.* 187, 113 (2001).
105. B. Nkosi, M. D. Adams, N. J. Coville, and G. J. Hutchings, *J. Catal.* 128, 333, and 378 (1991).
106. T. Aida, R. Higuchi, and H. Niiyama, *Chem. Lett.* 2247 (1990).
107. Y. Takita, T. Imamura, Y. Mizuhara, Y. Abe, and T. Ishihara, *Appl. Catal. B: Environmental* 1, 79 (1992).
108. M. Okumura, M. Haruta, X. Wang, O. Kajikawa, and O. Okada, "Third Intern. Conf. Environmental Catal." (abstract) p. 15, Tokyo, 2001.
109. Y. Usami, K. Kagawa, M. Kawazoe, Y. Matsumura, H. Sakurai, and M. Haruta, *Appl. Catal. A: General* 171, 123 (1998).
110. S. Golunsky, R. Rajaram, N. Hodge, G. Hutchings, and C. Kiely, *J. Catal. Today* 72, 107 (2002).
111. F. Cosandey and T. E. Madey, *Surf. Rev. Lett.* 8, 73 (2001).
112. V. A. Bondzie, S. C. Parker, and C. T. Campbell, *Catal. Lett.* 63, 143 (1999).
113. C. T. Campbell, S. C. Parker, and D. E. Starr, *Science* 298, 811 (2002).
114. A. Kolmakov and D. W. Goodman, *Surf. Sci.* 490, L597 (2001).
115. C. E. J. Mitchell, A. Howard, M. Carney, and R. G. Egdell, *Surf. Sci.* 490, 196 (2001).
116. R. Schlögel, *CATTECH* 5, 146 (2001).
117. D. A. H. Cunningham, T. Kobayashi, N. Kamijo, and M. Haruta, *Catal. Lett.* 25, 257 (1994).
118. M. Haruta, M. Yoshizaki, D. A. H. Cunningham, and T. Iwasaki, *Ultraclean Technology* (in Japanese) 8, 1 (1996).
119. M. Daté, Y. Ichihashi, and M. Haruta, Japan Patent Appl. 2000, 158422.
120. C. Mohr, H. Hofmeister, M. Lucas, and P. Claus, *Chemie. Ingenieur. Techn.* 71, 869 (1999).

Catalytic Synthesis of Carbon Nanotubes and Nanofibers

Kenneth B. K. Teo

University of Cambridge, Cambridge, United Kingdom

Charanjeet Singh

University of Cambridge, Cambridge, United Kingdom

Manish Chhowalla

Rutgers University, Piscataway, New Jersey, USA

William I. Milne

University of Cambridge, Cambridge, United Kingdom

CONTENTS

1. Introduction
 2. Growth Mechanism of Carbon Nanotubes and Nanofibers
 3. Catalyst Preparation
 4. Chemical Vapor Deposition Configurations and Considerations
 5. Summary
- Glossary
References

1. INTRODUCTION

Carbon nanotubes and nanofibers are graphitic filaments/whiskers with diameters ranging from 0.4 to 500 nm and lengths in the range of several micrometers to millimeters. Carbon nanofibers and nanotubes are grown by the diffusion of carbon (via catalytic decomposition of carbon containing gases or vaporized carbon from arc discharge or laser ablation) through a metal catalyst and its subsequent precipitation as graphitic filaments [1–6]. Three distinct structural types of filaments have been identified based on the angle of the graphene layers with respect to the filament axis [5, 7], namely *stacked*, *herringbone* (or *cup-stacked* [8]), and *nanotubular* [9] as shown in Figure 1.

It can be seen that the graphite platelets are perpendicular to the fiber axis in the stacked form, the graphene platelets are at an angle to the fiber axis in the herringbone form, and tubular graphene walls are parallel to the fiber axis in the nanotube. In the literature today, the common practice is to classify the stacked and herringbone forms of graphitic filaments under the general nomenclature of “nanofibers” whereas “nanotube” is used to describe the case where tubular graphene walls are parallel to the filament axis. In some instances, large diameter (>20 nm) nanotubular structures or structures containing defects/amorphous carbon have also been classified as nanofibers. In this work, we prefer to use the term nanotube to describe carbon filaments with tubular graphene walls parallel to the axis and use the term nanofiber for carbon filaments with graphene layers at other angles. This is because special physical properties arise from the “nanotube” structure which distinguish it from the “nanofiber” structure, which itself has other advantageous properties, as will be described later.

Carbon nanofibers and nanotubes have been synthesized since the 1960s, but why has one particular form (i.e. the nanotube) received so much attention recently? In 1991, Iijima reported that highly graphitized carbon nanotubes, formed from the arc discharge of graphite electrodes, contained several coaxial tubes and a hollow core [9]. This important discovery led to the realization that with graphene tubes parallel to the filament axis, these highly crystallized tubular carbon structures would inherit several

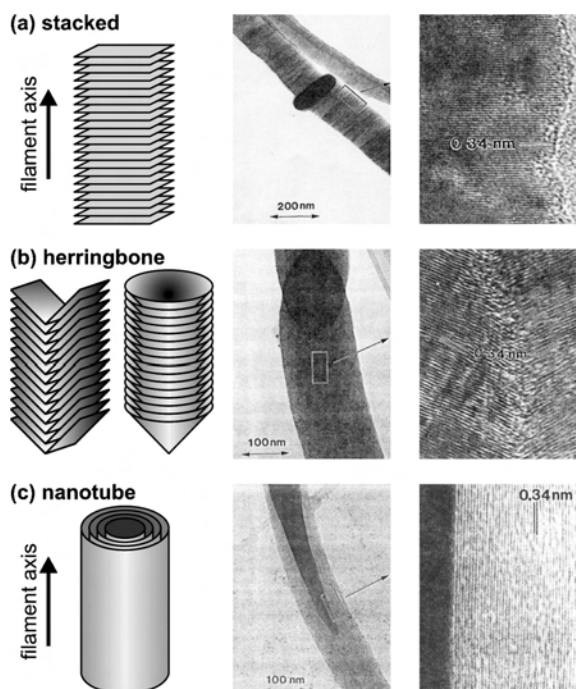


Figure 1. The three structural forms of carbon nanofibers, classified by the angle of the graphene layers/platelets with respect to the filament axis. Adapted with permission from [5], N. M. Rodriguez et al., *Langmuir* 11, 3862 (1995). © 1995, American Chemical Society.

important properties of “intraplane” graphite. In particular, a nanotube exhibits high electrical conductivity, thermal conductivity, and mechanical strength along its axis. As there are very few open edges and dangling bonds in the structure, nanotubes are also very inert and species tend to be physically adsorbed onto graphene walls rather than chemically react with them. Note that carbon nanotubes are completely covalently bonded which implies that as electrical conductors, they would not suffer from electromigration or atomic diffusion like metals. These properties make carbon nanotubes a technologically important material for various electronic and mechanical applications as will be listed later. The stacked and herringbone nanofibers tend to be investigated solely for energy storage applications such as electrodes for lithium batteries or fuel cells as small

ions/molecules can enter via open edges and intercalate between the graphene layers. Already, large amounts of nanofibers can be purchased commercially from companies such as Hyperion Catalysis International, Applied Sciences Incorporated, Catalytic Materials, Showa Denko, and Nanomirae [10]. Nanotubes are also available commercially from companies such as Carbon Nanotechnologies Inc., Iljin Nanotech, and NanoLab among many others listed in [11].

Nanotubes are further classified into two types, namely multiwall and single wall [9, 12, 13]. The multiwall carbon nanotube contains several concentric, coaxial graphene cylinders with interlayer spacings of ~ 0.34 nm [14]. Note that this spacing is larger than single crystal graphite (0.335 nm). Recent studies have shown that the intershell spacing can actually range from 0.34 to 0.39 nm, where the intershell spacing decreases with increasing carbon nanotube diameter, and this effect is more pronounced in small diameter nanotubes (<15 nm) due to the high curvature [15, 16]. The geometrical constraints in forming the seamless “honeycomb” graphene cylinders cause the layers to be uncorrelated with respect to one another, which is in contrast to crystalline graphite that exhibits perfect “ABAB” layer stacking [17]. Thus, multiwall carbon nanotubes tend to exhibit the properties of turbostratic graphite whose layers are essentially uncorrelated. For example, in highly crystallized multiwall carbon nanotubes (such as those obtained by arc discharge), it has been shown that if contacted on the outside, the electric current is conducted through its outermost shell only [18].

In the case of single wall carbon nanotubes, the structure consists of a single graphene cylinder and special properties emerge from the strong one-dimensionality and crystalline perfection of the structure. Single wall carbon nanotubes can be metallic (0 eV bandgap) or semiconducting (typically 0.4–0.7 eV bandgap) depending on the geometrical characteristics of their structure, namely the orientation of the hexagons with respect to the nanotube axis (i.e., chirality) and inversely proportional to the diameter [19–21]. Reviews on the electronic properties of carbon nanotubes are presented in [22–24]. In the case of a multiwall carbon nanotube where conduction occurs through the outermost shell, the large diameter of the outer nanotube causes the gap to approach 0 eV and the nanotube is essentially

Table 1. Properties of carbon nanotubes; see also [34].

Mechanical properties		Thermal properties at room temperature	
Young's modulus of multiwall nanotubes	$\sim 1\text{--}1.2$ TPa [25, 26]	Thermal conductivity of single wall nanotube	1750–5800 W mK [28]
Young's modulus of single wall nanotube ropes	~ 1 TPa [27]	Thermal conductivity of multiwall nanotube	>3000 W mK [29]
Tensile strength of single wall nanotube ropes	~ 60 GPa [25]		
Electrical properties		Electronic properties	
Typical resistivity of single and multiwall nanotube	10^{-6} Ω m [22, 30]	Single wall nanotube bandgap— whose $n\text{--}m$ is divisible by 3	0 eV [22] (metallic)
Typical maximum current density	$10^7\text{--}10^9$ A cm $^{-2}$ [31, 32]	whose $n\text{--}m$ is nondivisible by 3	0.4–0.7 eV [20, 21] (semiconducting)
Quantized conductance, theoretical/measured	$(6.5 \text{ k}\Omega)^{-1}/(12.9 \text{ k}\Omega)^{-1}$ [22, 33]	Multiwall nanotube bandgap	~ 0 eV [22] (nonsemiconducting)

nonsemiconducting. Table 1 lists several reported properties of carbon nanotubes.

Carbon nanotubes and nanofibers are being investigated for a wide range of applications today. Reviews of carbon nanotube applications are presented in [24, 35–42], and only an overview is presented in this chapter. Let us first consider the nanotube as a high aspect ratio, electrically conductive wire with diameter in the nanometer range. These structures are highly desirable as field emission tips for applications such as field emission displays [43–48], X-ray tubes [49], electron sources for microscopy and lithography [50], gas discharge tubes [51], and vacuum microwave amplifiers. The use of nanotubes as a field emission electron source has recently been commercialized in a portable X-ray source by Oxford Instruments [52]. Nanofibers have also been investigated as electron sources [53, 54]. The high aspect ratio and small diameter of the nanotube is also desirable for scanning probe tips [55–57]. In fact, nanotube-based scanning probe tips (“Probemax”) are commercially available today from nPoint (also known as Piezomax) [58].

Single wall carbon nanotubes, which can be electronically semiconducting, are also being investigated as transistors or logic elements [59–62]. Containing only one carbon tube, the electronic properties of the carbon nanotubes are highly sensitive to adsorbed molecules/species [63, 64]. Although this implies that in logic circuits, the nanotubes must be suitably encapsulated, the high sensitivity of the nanotubes can be advantageously utilized in chemical or biological sensors to detect poisonous or dangerous gases in the environment. In addition, the coherent nature of electron transport in well-crystallized nanotubes would find these structures applicable in spin–electronic devices [65]. Carbon nanotubes could also be used as electromechanical sensors as their electrical characteristics respond to mechanical deformation of their structure [66].

Another interesting application for these structures is as electrodes in electrochemical supercapacitors [35, 67–71]. When nanotubes/fibers are produced en masse (i.e., woollike or forestlike), they have large surface areas which could lead to higher charge storage capabilities than standard capacitors and batteries [35, 72]. The cycle characteristics of lead acid and lithium ion batteries can also be improved when carbon nanofibers are used as fillers in the battery electrodes [73]. The high electrical conductivity and relative inertness of nanotubes make them potential candidates as electrodes in electrochemical reactions too [74, 75]. The large surface area of nanotubes, both inside and outside, can be usefully employed to support reactant particles in catalytic conversion reactions [76, 77]. It was also proposed that hydrogen could also be stored among and inside nanotubes/nanofibers for fuel cell applications [7, 76–81], although recent results show that the amount of hydrogen stored is not as high as originally anticipated [82]. Nanotubes can also mechanically deflect under electric stimulation (e.g., due to charge induced on the nanotubes) and this opens up applications such as cantilevers or actuators [35, 83–85]. The use of nanotubes and nanofibers as filters or membranes for molecular transport has been recently proposed [86].

The exceptional mechanical properties and low weight of nanotubes and nanofibers make them potential filling materials in polymer composites. Nanotubes and nanofibers

can improve the strength and stiffness of a polymer, as well as add multifunctionality (such as electrical conductivity) to polymer based composite systems [87–95]. Carbon nanotubes should be ideal reinforcing fibers for composites due to their high aspect ratio and high in-axis strength [96]. Furthermore, carbon nanotubes, unlike macroscopic carbon fibers, are short enough to flow through conventional polymer processing equipment so that complicated shapes or small parts could be molded from their composites [96, 97]. As fillers for composites, single wall carbon nanotubes are preferred to multiwall nanotubes because the inner layers of the multiwall nanotubes contribute little under structural loading and thus would reduce the stiffness for a given volume fraction of tubes [26, 96].

It is evident that for the various different applications, nanotubes or nanofibers of different morphologies are required. For instance, scanning probe applications require a single high aspect ratio nanotube whereas polymer strengthening requires “masses” of nanotubes/nanofibers. Field emission applications ideally require vertically aligned nanotubes which are spaced about twice their height apart [98–100], whereas horizontally aligned nanotubes are more suited for electrical transport or electronic (transistor/spin) applications. The great flexibility of catalytic chemical vapor deposition (CVD) is that this technique can be adapted to producing nanotubes and nanofibers for *virtually all* these applications.

In the case of nanotubes, chemical vapor deposition is very different from the other two common methods used for nanotube production, namely arc discharge [101, 102] and laser ablation [30]. Arc discharge and laser ablation can be classified as high temperature (>3000 K) and short time reactions (μs – ms), whereas catalytic chemical vapor deposition is a medium temperature (700–1400 K) and long time reaction (typically minutes to hours). Although carbon filament/nanofiber growth by catalytic chemical vapor deposition was established in the 1960s–1980s [3, 4, 103–105], much of the fundamental work on the properties of nanotubes in the early 1990s was performed on nanotubes produced by arc discharge and laser ablation because of their superior straightness and crystallinity due to the high temperature deposition. The main technological drawbacks with arc discharge and laser ablation were that the nanotubes had to be produced separately (i.e., not directly on substrates), purified [106, 107], and then manipulated onto substrates before use. At that time, most CVD-grown nanotubes were “spaghetti-like” and largely defective, but the potential of the technique to satisfy technological requirements was recognized. From 1998 onward, substantial and rapid progress was made in the development of CVD to establish it as a highly controlled technology for the production of carbon nanotubes and nanofibers: today, it is possible to fabricate high quality single wall carbon nanotubes [108, 109] or multiwall carbon nanotubes [110], horizontally [111, 112] or vertically aligned [113–115], as an individual nanotube [116–118] or “en masse” [110, 119], with controlled diameter [120, 121] and length [122, 123], structurally as a tube or stacked layered nanofiber form [5, 124], directly onto substrates or in bulk as a raw material [4, 125]. A major advantage of CVD is that the nanotubes/nanofibers can be used directly without

further purification unless the catalyst particle is required to be removed, methods for which will be discussed later.

The rest of this chapter discusses the growth mechanism of carbon nanotubes and nanofibers, the various methods of catalyst preparation, and variations in the chemical vapor deposition technique. This provides the technologist with a repertoire of techniques from which he/she can choose the most suitable one for his/her specific application.

2. GROWTH MECHANISM OF CARBON NANOTUBES AND NANOFIBERS

2.1. General Mechanisms

In general, carbon nanotube and nanofiber growth by the catalytic CVD method require catalyst nanoparticles (usually Fe, Co, or Ni), a carbon feedstock (e.g., hydrocarbon or CO), and heat. The diameter of the filament produced is often closely related to the physical dimension of the metal catalyst. The peculiar ability of these transition metals to form graphitic carbon is thought to be related to a combination of factors that include their catalytic activity for the decomposition of volatile carbon compounds, the formation of metastable carbides, and the diffusion of carbon through the metal particles [126]. We present some of the growth models that have been proposed both for nanotubes and nanofibers which are widely accepted by the research community.

The most commonly accepted mechanism was postulated by Baker et al. in the early 1970s, who explained the growth of carbon filaments by catalytic decomposition of the carbon feedstock and bulk diffusion of carbon [1]. According to this mechanism (Fig. 2a), the hydrocarbon gas decomposes on the front-exposed surfaces of the metal particle to release hydrogen and carbon, which dissolve in the particle. The dissolved carbon diffuses through the particle and is precipitated at the trailing end to form the body of the carbon filament. Due to the exothermic decomposition of hydrocarbons, it is believed that a temperature gradient exists across the catalyst particle. Since the solubility of carbon in a metal is temperature dependent, precipitation of excess carbon will

occur at the colder zone behind the particle, thus allowing the solid filament to grow with the same diameter as the width of the catalyst particle. Such a process will continue until the leading tip of the catalyst particle is “poisoned” or deactivated. A common cause of catalyst poisoning is the formation of carbon around it, thus preventing the gas from reaching the catalyst particle. Support for this bulk diffusion model comes from experiments on the kinetics of growth of carbon filaments from acetylene (C_2H_2) catalyzed by Ni particles, which yielded an activation energy of (eV) 140 kJ mole^{-1} [2]. This value is similar to the activation energy for bulk diffusion of carbon through solid Ni (i.e., 133 kJ mole^{-1}) [127]. Similarly, the enthalpies for the growth of filaments with α -Fe, γ -Fe, Ni, Co, Fe–Ni, and Cu catalyst were found to be similar to the enthalpy of diffusion. Thus, the rate limiting step in the growth is believed to be the diffusion of carbon through the catalyst. In general, the filament length depends on the duration of the catalytic process, where longer durations result in longer filaments [128, 129]. This general bulk diffusion mechanism accounts for the formation of both nanofibers and nanotubes.

However, two irregularities of this growth mechanism should be noted. First, not all hydrocarbon dehydrogenation reactions are exothermic (e.g., methane), and yet growth has been observed from these hydrocarbons. Moreover, it is unlikely that there is a temperature gradient across such a small metal particle. This is because the metal particle has a high thermal conductivity and thus a small temperature gradient implies that a massive heat flow is occurring through the particle, which is physically intangible. The exothermic decomposition of the hydrocarbon probably raises the temperature of the entire filament, and the growth of the carbon filament is also probably driven by a concentration gradient of carbon across the particle.

One common question asked is whether the catalyst is a liquid or solid during nanotube/nanofiber growth. If we assume Fe as the metal catalyst, most of the growth experiments are typically well below the melting temperature of iron ($1534 \text{ }^\circ\text{C}$) and also below the iron–carbon eutectic temperature ($1147 \text{ }^\circ\text{C}$). The formation of graphite platelets from certain crystallographic faces of the catalyst particle (see Section 2.2) suggests that the catalyst is in a solid form. The agreement between the enthalpy for the growth of filaments and the enthalpy of diffusion for the bulk catalyst metals as discussed earlier also suggests that the catalyst is in the solid phase. Although growth is performed below the eutectic temperature and metal melting point (N.B. usually these temperatures are quoted at 1 atm and will change with operating pressure), one should note that the catalyst metal nanoparticles will behave completely differently than their bulk metal form because these small particles will have exceptionally high surface energy, area, and mobility. For example, Hou et al. reported that annealing iron encapsulated carbon particles in argon between 1000 to $1100 \text{ }^\circ\text{C}$ completely removes the iron, indicating that these small iron particles were highly mobile at these temperatures [130]. Because of the high mobility and reactivity of the metal atoms, the catalyst nanoparticles are often in the shape of metallic clusters or have been observed to undergo certain surface reconstruction. If temperatures above the metal–carbon eutectic are used, the growth would be similar to the

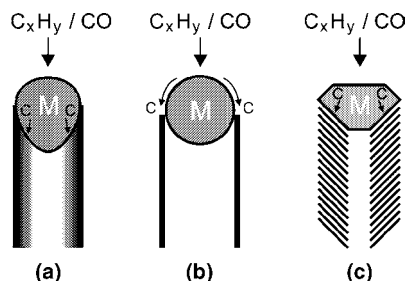


Figure 2. The growth of carbon nanotubes and nanofibers involves the catalytic decomposition of a carbon feedstock (hydrocarbon or CO), carbon diffusion, and its precipitation as a filament. In (a), the carbon diffuses through the bulk of the metal catalyst “M” as proposed by the Baker model [3]. In (b), the carbon diffuses over the surface of the metal catalyst and forms a tubular structure from the circumference of the catalyst as proposed by the Oberlin model [134]. In (c), angled graphene layers are precipitated from a faceted catalyst particle to form a nanofiber as proposed by Rodriguez and Terrones [5, 147].

general vapor–liquid–solid mechanism proposed by Wagner [131, 132] where diffusion through a liquid-phase particle is responsible for the synthesis of filaments.

Instead of bulk diffusion, another common growth model is a catalytic process involving the surface diffusion of carbon around the metal particle [133–135] as shown in Figure 2b. The carbon atoms diffuse over the catalyst surface to form a tubular structure which emanates from the circumference of the catalyst. Note that the tubular structure is favored for carbon filaments with nanometric diameters. A single graphene layer of finite size has many dangling bonds which correspond to high energy states, and for such a small structure, there would be an enormous percentage of dangling bonds if a stacked planar graphite was formed [17, 136]. By the formation of closed tubular carbon shells, the total energy of the system is reduced [136].

An alternative model based on the minimization of surface energy of nanoparticles was suggested by Dai et al. [137]. Nanoparticles contain a very high percentage of surface atoms; as a result a large amount of surface energy exists. Excess carbon can help solve this problem by assembling a graphene cap on the particle surface, called a “yarmulke,” with its edges strongly chemisorbed to the metal. Since the basal plane of graphite has an extremely low surface energy (10–20 times smaller than most metals), the total surface energy diminishes. A crucial feature of the yarmulke mechanism was its avoidance at all stages of growth of any open graphene edges, which would expose energetically costly dangling bonds. It also provides an automatic solution to forming caps and resulting structures are tubes which have no seams. Carbon can add to the cylindrical section of a growing layer. Once the smallest yarmulke has formed, insertion of new carbon between the tube edge and the catalytic particle is the best solution, as long as complete overcoating of the particle (i.e., encapsulation) is avoided which would deactivate it.

The actual composition of the active catalyst particle is a widely debated issue, and further research could be performed in this area. High carbon content carbides were determined to be a prerequisite for carbon fiber growth [138–140]. However, there are many conflicting reports concerning the actual composition of the catalyst particle; for example, in the case of an iron catalyst, a hexagonal form with composition $\text{Fe}_{2.2}\text{C}$ or Fe_2C was postulated, rather than Fe_3C [134]. There are also arguments as to whether a carbide particle is indeed the active catalyst [103]. These are based on the findings that the loss of catalytic activity of iron was accompanied by a gradual conversion of the catalyst to a stable carbide. The catalyst could be reactivated by treatment with hydrogen, reducing the carbide back to iron.

2.2. Nanofiber Growth

Let us now focus our discussion on catalysts used for nanofiber growth and why nanofibers form. The ability to control and tailor the structure of nanofibers (stacked or herringbone) has been demonstrated by Rodriguez et al. [5, 124]. The general concept used here is the creation of a faceted catalyst particle [5, 124, 141] so that carbon feedstock decomposition occurs at certain faces whereas carbon precipitation (in the form of graphite layers) occurs at other

faces as shown in Figure 2c. The graphitic platelets are precipitated parallel to the surface of the faceted catalyst particle, and hence the angle between the planes and the fiber axis is determined by the shape of the catalyst particle, as proposed by Boellard et al. [138]. Under certain conditions of gas composition, temperature, and catalyst composition, the catalyst particles undergo surface reconstruction to form unique geometrical shapes which drive the formation of nanofibers [5, 124, 142, 143]. For example, the herringbone structure was found to grow from Fe–Cu (7:3) particles in a C_2H_4 – H_2 (4:1) gas mixture at 600 °C, whereas the stacked structure formed from Fe-based catalyst in a CO – H_2 (4:1) gas mixture at 600 °C [5]. The formation of herringbone structures is favored when the catalyst particle is an alloy [124, 144–146], although Pd has also been used alone under certain growth conditions to yield similar structures [147]. Nolan et al. [148] have suggested that hydrogen plays a significant role in the formation of nanofibers. This is because the presence of hydrogen in abundance can terminate the large number of dangling bonds at the edges of the stacked graphite platelets, whereas without hydrogen termination, the more stable form of the carbon filament would be closed tubular graphene shells where there are no dangling bonds. In plasma enhanced CVD, the carbon filaments formed are often nanofibers rather than nanotubes. This is thought to be due to the large amount of atomic hydrogen formed in the gas phase due to plasma decomposition of the hydrocarbon gas or the use of hydrogen as a dilution gas. Delzeit et al. showed that by controlling the relative amount of hydrogen in the gas phase via altering the plasma parameters, one could change the structure from nanotubes to herringbone nanofibers, with high hydrogen content favoring the latter [149].

2.3. Multiwall and Single Wall Nanotube Growth

Let us now concentrate on the formation of nanotubes. Without an abundance of dangling bond terminating species (e.g., H) in the gas phase, carbon nanotubes will tend to form when the diameter of the filaments is ~50 nm or less. This is because a single graphene layer of finite size has many dangling bonds, and these dangling bonds correspond to high energy states [17, 136]. The total energy of a small number of carbon atoms is reduced by eliminating these dangling bonds, even at the expense of increasing the strain energy, thereby promoting the formation of the closed tubular structure [17, 136, 150]. The catalytic activity of the metal catalyst in the formation of nanotubes has also been studied in considerable detail. Besides the commonly used Fe, Co, and Ni catalysts, other metals (such as Mo, Cu) or metal mixtures (Fe–Ni, Fe–Mo, Fe–Co, Co–Ni, and Co–Mo) have been used for nanotube synthesis [109, 113, 122, 128, 137, 151–162]. Using thermal CVD, Co and Fe catalysts generally tend to form hollow and well-graphitized nanotubes, whereas Ni and Cu produced structures which were not as well graphitized [158, 163]. One should note that different metal catalysts would have their optimum catalytic activity at different temperatures [128, 129, 163]. The yield and crystallinity of nanotubes can be improved by the use of metal

catalyst mixtures such as Co–Fe or Co–Ni [158, 164]. Furthermore, it has also been reported that the addition of Mo to Fe or Co [109, 122, 151–157] increases the yield of single wall nanotubes compared to when a single metal catalyst is used [161]. A Co to Mo ratio of 1:2 is reported to be optimal for a high synthesis yield of single wall carbon nanotubes.

Figure 3 shows various forms of nanotubes. Here, the nanotubes are examined using transmission electron microscopy and hence we are looking at a cross section of the nanotubes. The solid black lines in the micrographs represent the hexagonal sheets of carbon atoms which make up the walls of the nanotubes. Under ideal growth conditions, the nanotubes produced should be straight (e.g., Fig. 3a) and contain graphene walls parallel to the tube axis without

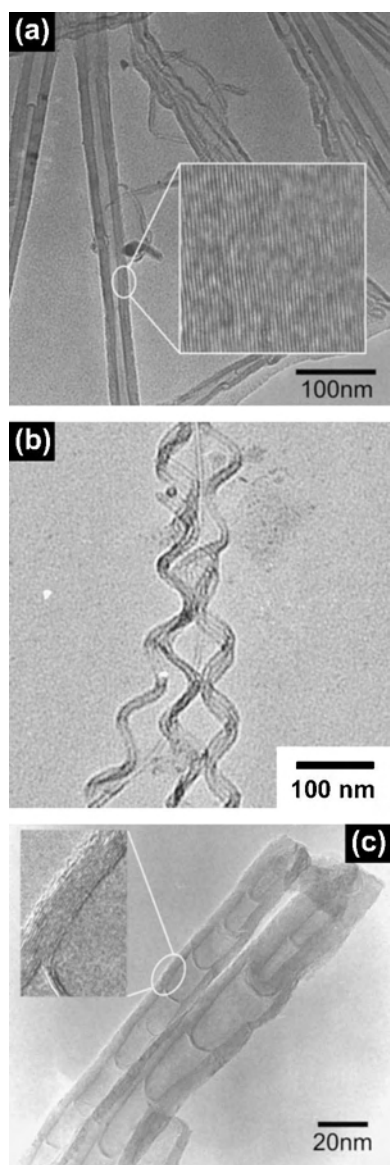


Figure 3. (a) TEM of straight nanotubes grown from the floating catalyst method using ferrocene–toluene at 760 °C. (b) Helical nanotubes grown from CVD of C_2H_2/Ar at 700 °C with Ni catalyst. (c) Straight nanotube with bamboo compartments grown by plasma enhanced CVD of C_2H_2/NH_3 at 700 °C with Fe catalyst.

any defects. Dai proposed that a high growth temperature is required to anneal out defects so that well-crystallized and straight nanotubes could be obtained [165]. The occurrence of defects (e.g., pentagons or heptagons) would cause the nanotube to bend during growth. When carbon nanotubes are formed by the electric arc or laser ablation, temperatures of ~ 3000 K are obtained and this possibly explains why mostly straight and well-crystallized nanotubes are obtained from these processes. In lower temperature CVD processes (~ 700 – 1400 K), “curly” and “coiled” nanotubes (Fig. 3b) are common variations to the perfectly linear nanotube. The growth of various shapes of nanotubes, especially wavy and helical tubes, was investigated by Amelinckx et al. [166]. The concept of a spatial velocity was introduced to describe the extrusion of carbon from the catalyst particle to form the nanotube. Essentially, when the extruded carbon material was uniform, straight nanotubes are obtained, whereas nonuniform extrusion caused the nanotube to deform elastically into complicated patterns such as the helix shape. Nanotubes containing bamboo compartments are also commonly observed, as shown in Figure 3c. A growth model for bamboo-shaped carbon nanotubes was proposed by Lee and Park [167]. Their transmission electron microscopy (TEM) evidence showed that the bamboo-shaped compartment layers were due to the surface geometry of the catalyst particle and the precipitation of carbon sheets from the bulk of the catalyst particle. Li et al. found that when using a higher deposition pressure of carbon feedstock, the nanotubes became bamboo in structure [168]. They argued that at high pressures, the carbon concentration was sufficiently high to cause bulk diffusion of carbon through the catalyst, forming the bamboo compartments behind the catalyst particle. In the literature, bamboo structures are sometimes called “nanofibers.” However, note from Figure 3c that the bamboo structure actually contains graphene walls parallel to the filament axis, which suggest that these structures would inherit the physical properties of the “nanotube.” It is possible to obtain the growth of straight nanotubes by close-packed growth, use of porous templates, electric field directed growth, or plasma-induced alignment as will be discussed later.

Under what conditions is the growth single wall carbon nanotubes preferred? The size of the catalyst is probably the most important parameter for the nucleation of single wall carbon nanotubes. Conclusive evidence on the dependence of catalyst size on the formation of single wall carbon nanotubes has been reported in [159, 160, 169]. Li et al. (Duke University) prepared catalyst nanoparticles of uniform diameters (between 3 to 14 nm) by thermal decomposition of metal carbonyl complexes using a mixture of long-chain carboxylic acid and long-chain amine as protective agents [169]. Their results indicate that the upper limit for single wall nanotube growth occurred at catalyst sizes between 4 and 8 nm. Above 8.5 nm, no more single wall structures were observed [169]. Li et al. (Stanford University) also grew single wall carbon nanotubes from discrete catalytic nanoparticles of various sizes [159]. Discrete nanoparticles were prepared by placing a controllable number of metal atoms into the cores of apoferritin. Their TEM studies indicated that the nanotube diameters were closely correlated to the size of the catalytic nanoparticles.

Furthermore, the nanotubes grew by a base-growth mechanism with the nanoparticles seen to be anchored to the support material. Smaller nanoparticles ($< \sim 1.8$ nm) were more active in producing single wall nanotubes, while nanoparticles with diameters of ~ 7 nm did not show single wall nanotube growth, consistent with the group at Duke University [169]. Cheung et al. prepared monodispersed nanoclusters of iron with diameters of 3, 9, and 13 nm [160]. After growth using C_2H_4 , single wall and double wall nanotubes were nucleated from the 3 and 9 nm diameter nanoclusters, whereas only multiwall nanotubes were observed from the 13 nm nanoclusters. These works clearly suggest that single wall nanotubes are favored when the catalyst particle is ~ 5 nm or less. However, it is worth mentioning that there are reports which suggest that single wall carbon nanotubes can be grown from larger catalyst particles. One hypothesis put forward was that bundles of nanotubes could be precipitated from a single larger metal particle and that the bundle formation would be linked to the nature of the metal surface [161]. Note that when arc discharge and laser ablation are used to synthesize nanotubes, bundles of single wall nanotubes are commonly observed to emerge from a large catalyst particle [6]. There is a report of single wall nanotubes grown from ~ 10 nm diameter colloids, suggesting that the size of the metal nanoparticles may not need to be the same as the diameter of the nanotube [170]. Such reports, however, are rare for the case of CVD and in general, the diameters of the nanotubes and nanofibers grown are often correlated with the size of the catalyst particle.

As mentioned earlier, binary catalyst mixtures have also been reported to increase the yield of single wall carbon nanotubes. A mixture of Co and Mo gives a higher yield of single wall nanotubes than if a single metal catalyst is used [154, 155]. Using X-ray absorption spectroscopy, it was found that Co, originally in an oxide state, is gradually reduced to a metal whereas Mo transformed to its carbide after growth. The role of Mo in the catalyst is to stabilize the small particles of oxidized cobalt species (Co^{2+}), which are highly active for the production of single wall carbon nanotubes [155, 156]. Adding a small amount of Mo to Fe catalyst also increases the yield of single wall nanotubes [152, 153, 171].

Another common observation is that single wall nanotubes are produced via the base-growth mechanism [108, 151, 159] (except for the floating catalyst technique discussed later where there is no base support material). The base growth model is based on TEM evidence which shows that the nanotube tip ends are particle free. Multiwall nanotubes are commonly deposited by both the tip-growth and base-growth mechanisms (see later).

The choice of the carbon feedstock also affects the growth of carbon nanotubes. Baker and Harris [104] reported that unsaturated hydrocarbons such as C_2H_2 had much higher yields and higher deposition rates than more saturated gases (e.g., 100 times that of C_2H_4). They also observed that saturated carbon gases tended to produce highly graphitized filaments with fewer walls compared with unsaturated gases. Thus, hydrocarbons such as methane and carbon monoxide are commonly used for single wall carbon nanotube growth [108, 137, 154–156, 172] whereas hydrocarbons such as

acetylene, ethylene, and benzene, which are unsaturated and thus have high carbon content, are typically used for multiwall carbon nanotube growth [122, 129, 158, 164, 173–175].

Hafner et al. further suggested that the growth rate of single wall nanotubes is limited by the carbon supply to the catalyst particles, whereas for multiwall nanotubes, the growth is limited by the diffusion of carbon through the catalyst particle [109]. The authors demonstrated that single wall carbon nanotubes could in fact be grown from a highly diluted gas mixture of C_2H_4 . A limited carbon supply will likely allow the structures to form more slowly, giving each carbon atom more time to anneal to its lowest energetic configuration as shown by energetics calculations. Cheung et al. reported that the partial pressure of C_2H_4 had to be increased accordingly in order to nucleate nanotubes from larger nanoclusters [160].

Methane is commonly used as the carbon source for single wall carbon nanotube growth because it is a kinetically stable hydrocarbon and undergoes the least pyrolytic decomposition at high temperatures, typically $900^\circ C$ [108, 137]. A small amount of hydrogen or benzene present in the methane flow can enhance the growth yield, as discussed in [176, 177], but too much of these additives impede nanotube growth. Recall that high temperatures are favored for less defective and well crystallized nanotubes, and hence it is important to select a hydrocarbon which does not thermally decompose to form unwanted amorphous carbon (i.e., lower the purity of nanotubes) at high temperatures. Similarly, CO has been used to grow single wall nanotubes at elevated temperatures [172].

Lastly, although it is possible to control the filament structure to obtain nanofibers, multiwall nanotubes, or single wall nanotubes, at the writing of this chapter it is not possible to control the chirality (i.e., electronic properties, either metallic or semiconducting) of the single wall nanotubes through synthesis.

In some applications, the catalyst which was used for growth is not desired. This can be removed by oxidation (to remove carbon layers which may have encapsulated the catalyst particle after growth) followed by acid treatment, similar to what is usually done to purify arc discharge or laser ablated nanotubes [106]. For nanotubes or nanofibers which are tip grown (i.e., catalyst on top), plasma etching could also be used to remove the catalyst particle [178]. It is also possible to run the catalyst back down the nanotube and hence open it by exposing it to hydrogen after growth [3].

Now that we have discussed the growth of carbon nanofibers, multiwall nanotubes, and single wall nanotubes, we shall describe the practical processes for preparing the catalyst and the techniques used for growth.

3. CATALYST PREPARATION

3.1. Growth of Nanotubes/Nanofibers on Substrates

The first step is to prepare the catalyst nanoparticles—it is worthwhile to remember that it is the size of the nanoparticle which approximately determines the final diameter of the nanofiber/nanotube (in some cases also whether a single wall or multiwall nanotube is formed). Hence,

for some applications, it will be necessary to control this parameter. There are several routes for catalyst preparation depending on the final application of the nanotubes. Let us first examine substrate growth or “supported catalyst” growth. There are essentially two reasons to use substrate growth. First, for some applications, it is desirable to coat nanofibers/nanotubes directly onto a particular surface. For example, when carbon nanotubes or nanofibers are used as field emission electron sources for vacuum microelectronic applications, it is desirable to deposit the nanotubes/nanofibers directly within gated apertures to ensure that the structures are as close as possible to the gate so that low operating voltages may be obtained [45, 46, 54, 179–181]. Second, for the large-scale production of nanotubes, it is desirable to anchor the metal catalyst firmly to a support to impede the formation of larger catalyst clusters. Large catalyst clusters are the result of the sintering/coalescence of the metal catalyst particles due to the high surface mobility of the metal atoms and their strong cohesive forces. At the growth temperature, typically 500 to 900 °C, these metal catalyst particles have sufficient mobility to coalesce into larger particles. This effect is especially unwanted if structures of a particular diameter or small diameter (e.g., single wall nanotubes) are required.

Two different growth modes (Fig. 4a and b) can result based on the interaction of the catalyst with its support as described by Baker [3] and Rodriguez [124]. The interaction of the catalyst with the support can be characterized by its contact angle at the growth temperature, analogous to “hydrophobic” (weak interaction) and “hydrophilic” (strong interaction) surfaces. For example, Ni on silica (SiO_2) has a large contact angle (i.e., weak interaction) at 700 °C and thus tip growth is favored in this system [182] as shown schematically in Figure 4a. On the other hand, it is reported that Co or Fe on silicon [110, 183, 184] favors base growth (Fig. 4b), indicating that a strong interaction exists between Co or Fe and Si. Thus, the surface interaction between the catalyst and its support is an important consideration which dictates the growth mode.

Furthermore, one should consider the chemical interaction between the catalyst and its support material which can vary for different temperature ranges. The support/substrate

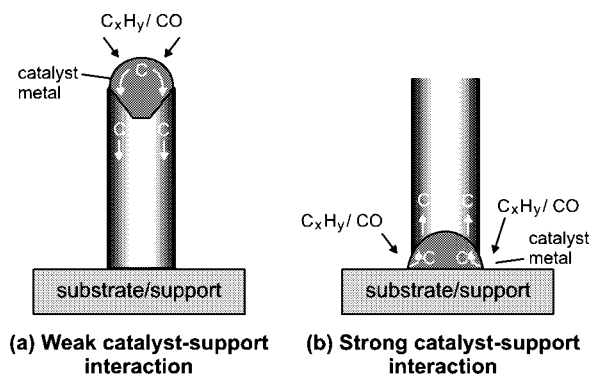


Figure 4. Two types of growth, namely tip or base growth, resulting from different catalyst–support interactions. Adapted with permission from [3], R. T. K. Baker, *Carbon* 27, 315 (1989). © 1989, Elsevier Science.

should not react or alloy with the catalyst at the growth temperature. This is because the catalyst can be “consumed” by the support/substrate if such a reaction occurs. Typical support materials are alumina and silica, which are stable at the range of temperatures used for nanotube growth [152, 153, 155]. Recently, however, much work has focused on the use of silicon substrates in order to reap the benefits of silicon processing to create nanotube electronic devices. Co, Fe, and Ni are known to diffuse into silicon at temperatures near those used for nanotube growth. For example, poor growth yield (or no growth) occurs when Ni catalyst is deposited directly on cleaned Si and reacted with acetylene at 700 °C. This is because Ni diffuses into the Si to form NiSi_x at temperatures above 450 °C [185]. To achieve high yield and uniform growth on Si substrates using Ni catalyst, a diffusion barrier (sometimes called a buffer layer) such as a thin insulating SiO_2 layer (~8 nm) or a conductive titanium nitride (TiN) layer (~20 nm) is used to support the Ni on the Si substrate [186, 187]. On the other hand, Co and Fe are known to have higher diffusion temperatures with silicon [185] and so they can be directly used on silicon substrates at ~700 °C [110, 183, 184]; however, the use of a diffusion barrier (e.g., TiN or SiO_2) is still recommended with these catalysts as it can significantly improve the nanotube yield [188]. This example illustrates the need for careful selection of the catalyst and its support, given the constraints of growth temperature and the particular application of the nanotubes (e.g., on a particular substrate material). Note that a similar problem may arise when Fe/Co/Ni are used directly on metal substrates because the metals may form an alloy at high temperatures. The solution is again to use a diffusion barrier (e.g., conductive metal nitrides or more stable metals) or lower the growth temperature.

Interestingly, for some applications, it is advantageous to use a support layer which does react with the catalyst so that the yield and density of the resultant nanofibers/nanotubes can be controlled. For example, for field emission applications, a densely packed forest of nanotubes/fibers is undesirable because the screening of the applied electric field from the adjacent nanotubes/fibers reduces the overall geometric field enhancement obtained from the high aspect ratio of the nanotube/nanofiber. Instead, sparsely spread structures, roughly spaced twice their height apart [98–100], overcome field screening problems. The growth of sparsely spread nanotubes/nanofibers is achieved by using an “imperfect” barrier layer which only consumes some of the catalyst, as described in [186].

There are several routes to the production of catalyst nanoparticles, and the most commonly used methods are described in the following sections.

3.2. Wet Catalyst

In the wet catalyst method, a liquid solution containing the catalyst in salt form is applied to the substrate via dipping the substrate, spray coating [189], spin coating [190], or microcontact printing [191]. Soluble salts are typically used, such as acetates or nitrates (e.g., in [191] iron, nickel, or cobalt nitrates [$\text{Fe}(\text{NO}_3)_3 \cdot 9\text{H}_2\text{O}$, $\text{Ni}(\text{NO}_3)_2 \cdot 6\text{H}_2\text{O}$, $\text{Co}(\text{NO}_3)_2 \cdot 6\text{H}_2\text{O}$]). After application to the substrate, the salt solution is often reduced to oxide nanoparticles by calcination (i.e., heating in air) [192].

Metal oxides are stable and improve the catalyst–support interaction at growth temperature—in some cases, metal oxides are used directly as the catalyst [108]. During growth, these oxides are reduced to metal nanoparticles (e.g., using hydrogen) which catalyze the subsequent growth of carbon nanotubes or nanofibers. Note that catalyst decomposition and reduction can occur as part of the deposition process because the nanotube growth is usually performed at elevated temperatures. The density of the nanotubes/nanofibers is simply controlled by the concentration of the catalyst solution, which is typically in the range of 1 to 500 mM [98]. Selective growth on substrates with wet catalysts often involves the use of inked stamps/molds, inkjet printing onto desired areas, or wet coating of a resist-masked substrate [151].

Mixtures of different metal salts have also been used as catalysts for nanotube growth. The combination of different metal catalysts can enhance the yield of nanotubes as described in the previous section. However, with different combinations of metal salts, it becomes increasingly difficult to find an optimum “recipe.” One method to overcome this challenge is to use high-throughput inkjet printing or microarray printing to transfer different catalyst mixtures onto a substrate [193–195]. Microarray printing has the advantage of being relatively low cost when applied over large areas, and it can provide relatively high spot density ($>10^3$ spots per cm^2) and experimental flexibility with different mixtures of catalyst solutions. For example, this method was used to study the effectiveness of different metal salts to determine the optimal catalyst composition for the growth of multiwall and single wall carbon nanotubes [194, 195].

It is also possible to deposit catalyst nanoparticles onto a substrate by electrochemical deposition with a metal salt solution. Tu et al. used a solution of 0.01 M of $\text{Ni}(\text{SO}_4)$ and 0.01 M of H_3BO_3 to electroplate Ni nanoparticles onto a Si substrate which was metallized with Cr [196]. By changing both the current density and time during electrochemical deposition, it is possible to control the density of the particles and hence the density of the carbon nanotubes on the substrate.

The catalyst support for nanotubes/nanofibers could also be in the form of a powder/nanoparticles (typically alumina, silica, or graphite). In the wet catalyst method, these powders are impregnated with the catalyst [163, 173]. For example, graphite can be impregnated with a 40 vol% ethanol/60 vol% water of iron (III) oxalate to form a 2.5 wt% Fe/graphite sample as described in [173]. This sample was next dried in nitrogen at 250 °C and reduced in hydrogen to form metallic iron which was then used to catalyze the growth of multiwall nanotubes using acetylene at 700 °C. The impregnation method has also been used to prepare catalyst for single wall nanotubes as well [161, 197]. The most promising catalyst that has been reported by such a method is a Co–Mo metal supported on silica as described previously [155, 157]. The impregnation technique is often used for the bulk production of nanotubes and nanofibers. At the end of the reaction, the support can be removed by dissolution in strong acid or alkali to yield the carbon structures.

Another wet catalyst preparation route is co-precipitation which involves the reaction of metal salt solutions with

ammonium bicarbonate to form metal carbonates. The metal carbonates can be reduced to metal oxides by calcination [5] and further reduced to the metal catalyst during growth using hydrogen.

Wet catalysts are especially useful for coating nonplanar geometries such as wires or tips [198–201]. These surfaces can either be dipped in the catalyst solution or the solution can be spin-coated onto the substrate.

3.3. Thin Film Metals

Another common technique of depositing the metal catalyst is by physical vapor deposition. A very thin film of Fe, Co, or Ni is carefully deposited on a substrate using sputtering or evaporation. The film thickness is usually in the few nanometer range and is monitored during deposition using a quartz oscillator-type film thickness monitor for accuracy. When this thin film is heated up to a high temperature (such as the growth temperature), the thin film breaks up and coalesces to form nanoclusters due to increased surface mobility and strong cohesive forces of the metal atoms [117, 183]. These nanoclusters then catalyze the growth of the carbon nanotubes or nanofibers. In general, the size of the nanoclusters formed can be controlled by the thickness of the catalyst film [182, 183, 202], by the temperature [203, 204], or by the annealing time. Thicker films, higher temperatures, and lengthy annealing times lead to the formation of larger metal clusters due to increased surface migration of the metal atoms. Although these parameters may be used to control the average size of the nanoclusters (i.e., diameter of resultant nanofibers/nanotubes), one should note that the formation of nanoclusters from the metal film is a random process and thus there will still be a distribution in the diameters of the structures [183, 202].

Multilayer metal films have also been used to catalyze nanotube growth. A noncatalyst metallic underlayer can be used to control the surface properties of the catalyst or the deposition yield as discussed earlier. Single wall nanotubes have been grown using a three layer metal film containing 0.2 nm Mo on 1 nm Fe on 10 nm Al on a silicon substrate [171]. These authors showed that the metal films formed Fe/Mo catalyst particles of ~ 2 nm diameter which seeded the single wall nanotubes.

The advantage of using catalyst thin films is that they can easily and accurately be patterned by using masking or etching techniques based around photolithography or electron beam lithography. In fact, individual freestanding nanotubes and nanofibers have been deposited using this process [116–118]. Figure 5 shows some examples where a 7 nm thin Ni film was patterned with lines and dots, which were then used to nucleate nanotubes. To obtain single freestanding structures, the Ni film must be patterned into dots of ~ 300 – 350 nm or less [117, 205]. When the Ni film dots are heated up to the growth temperature (700 °C), the film forms a single catalyst cluster of equal volume and catalyzes the growth of the nanotube. The vertically standing nanotubes of Figure 5 were deposited by plasma enhanced chemical vapor deposition which will be discussed later.

Note that when the metal film thickness exceeds a few tens of nanometers, nanoclusters are no longer formed and the film forms islands a few micrometers in size. These large

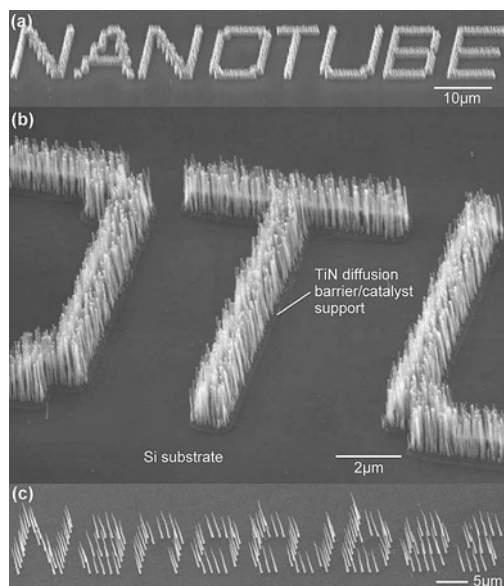


Figure 5. A 7 nm film of Ni catalyst, prepared by sputtering, was patterned using lithography into lines (a,b) and dots (c). The substrate used was Si, and hence a TiN diffusion barrier (also prepared by sputtering) was used to support the catalyst as Ni reacts with Si at the growth temperature. The growth was performed by plasma enhanced CVD of $C_2H_2:NH_3$ at 700 °C. The nanotubes formed are straight, vertically aligned, and typically bamboo in structure (like the TEM shown in Fig. 3c). Using plasma enhanced CVD, it is also possible to attain slightly conical shaped structures by altering the synthesis conditions which is described in [268].

micrometer-size islands/particles usually do not catalyze filament growth but instead absorb carbon into their bulk. Nanotube/nanofiber growth is usually found around the grain boundaries of metal islands. This is because smaller (submicrometer) catalyst particles are often present around the grain boundaries. Baker et al. also observed that carbon filament growth occurred only from the edges of macroscopic Fe foil [192]. In this case, the catalyst material probably easily detached at the metal foil edges to form small catalyst particles which nucleated the carbon filaments. Note that large (micrometer-sized) catalyst grains or thick continuous catalyst films do not nucleate nanotubes. The uniform growth of nanotubes inside large metal grains or catalyst metal substrates is only possible if nanoparticles are present on the surface of the metal as described in the next section.

3.4. Thick Metal Catalyst Films or Metal Catalyst Substrates

Nanotubes or nanofibers can be grown with high yield on thick catalyst metal films or catalyst metal substrates when surface treatment techniques are first used to roughen the substrate surfaces. Mechanical roughening (e.g., by using sandpaper) or electrochemical etching may be used to generate a coarse surface. Plasma etching or ion bombardment has also been used to increase the roughness of the metal surface and to generate submicrometer metal islands/particles [113, 206–208]. These surface roughening

techniques generate the small catalyst particles needed to grow carbon filaments. An alternative technique is to oxidize the metal surface through heating in oxygen or by rusting [192]. During growth, the metal catalyst nanoparticles are formed from the rusty, porous oxide surface by decomposing it with a reducing gas (e.g., H_2).

3.5. Colloids

Colloidal metal (or oxide) particles have also been used to catalyze the growth of nanotubes. Colloids are usually synthesized (or bought) in liquid suspensions where the colloids are separated by adsorbed charged species or organic molecules. The advantage of using colloids is that these can be highly homogenous in size and can be synthesized in diameters down to 2 nm. Thus, the use of colloidal catalysts allows the growth of nanotubes with well defined diameters, in contrast to the other techniques mentioned above which tend to produce nanotubes with a significant variation in diameter (except for the growth of single nanotubes from a small catalyst patterned dot where the catalyst is essentially fixed in size/volume). Cheung et al. describes the preparation of monodisperse Fe clusters with different diameters and uses these to catalyze the growth of single wall nanotubes supported on an oxidized Si substrate [160]. Li et al. have also synthesized colloids of diameters varying from 3 to 14 nm to catalyze nanotube growth [169]. Colloidal metal suspensions can in general be applied to the substrate using similar techniques as for the wet catalyst. Additionally, colloidal solutions in which the particles are separated by charge can be easily applied/adhered to substrates which have been functionalized with oppositely charged surface layers [209].

3.6. Sol–Gel Technique

The sol–gel technique has also been used to prepare catalyst for both multiwall and single wall carbon nanotube synthesis [153, 158]. Sol–gels impregnated with metal catalysts have very high surface area, high porosity, and ultralow density—these characteristics lead to a high yield of nanotubes during growth. For example, a Fe–Mo catalyst was prepared by the sol–gel technique based on supercritical CO_2 drying and then used for single wall carbon nanotube synthesis, as described in [153]. This catalyst was reported to be capable of deposition yield of over 200% compared with the original weight of the catalyst for a 1 hour deposition. The catalyst was active for 6.5 hours of growth, yielding 600% weight gain in total. The high yields were the result of the aerogel having a high surface area, high porosity, and good metal–support interaction. As yet, no other research group has been able to exceed the yields of single wall carbon nanotubes on a supported substrate by sol–gel [153].

3.7. Unsupported/Floating Catalyst Method

The floating catalyst method is commonly used for the bulk/mass production of nanotubes/nanofibers by CVD. The main advantage of using this technique is that purification is not required to recover nanotubes from the substrate. The simplest method is to inject catalyst nanoparticles (e.g., in the form of a colloidal/particle suspension or organometallic precursors with a carbon feedstock) directly into the CVD

chamber. In this case, a vertical CVD chamber is usually used so that the nanotubes/nanofibers grow as the catalyst particles fall from top to the bottom of the chamber. This technique has been used to prepare vapor grown carbon fibers for over 20 years [4, 105, 210–212].

Organometallic compounds are often used as precursors for the catalyst. Examples of organometallic compounds that have been commonly used are metallocenes, iron pentacarbonyl, and iron (II) phthalocyanine [4, 172, 211–219]. These precursors are usually sublimed and catalyst nanoparticles are formed *in-situ* when the compound is decomposed/reduced by heat or hydrogen. A double stage furnace is typically needed because of the different temperatures needed for organometallic sublimation and nanotube growth. In general, the sublimation of metallocenes offers little control over the structural parameters of the nanotubes such as length and diameter, although it has been shown that by varying the relative concentration of the metallocene to carbon in the gas phase the average diameter of the structures may be changed [219, 220]. An improvement over the double stage furnace is to use a syringe pump and atomizer to continuously feed a metallocene–liquid carbon feedstock solution into a single stage furnace where nanotube growth occurs [219, 221–223]. Aligned, high yield and pure multiwall carbon nanotubes can be obtained with conversion rates of 25% of the carbon input using this method. Very often, the floating catalyst technique leads to highly dense/close-packed nanotube deposition where essentially only upward (i.e., “aligned”) growth of the nanotubes is possible.

Interestingly, the floating catalyst method can also be used to selectively grow nanotubes on substrates [224, 225]. It was observed that multiwall carbon nanotubes grown by CVD of ferrocene and xylene at 800 °C only occurred on silica (SiO₂) surfaces and not on Si surfaces. Thus, by using lithographic means to pattern SiO₂ on a Si substrate, selective growth of nanotubes was obtained [225]. The multiwall nanotubes were aligned and grew perpendicularly from the SiO₂ surfaces. In this case, it was suggested that it was the good catalyst–support interaction between SiO₂ and Fe that led to the growth of nanotubes. If metal layers of nickel (Ni) were patterned onto Si, the nanotubes were seen to lift these metal patterns during growth [226]. Such aligned nanotubes have also been grown on gold and MgO substrates and palladium seeds [227–229].

Typically, metallocene assisted chemical vapor deposition of hydrocarbons (e.g., benzene, xylene) produces multiwall carbon nanotubes at lower temperatures (~700 °C) whereas a combination of multiwall and single wall nanotubes are produced at much higher (>900 °C) temperatures. For example, pyrolysis of iron pentacarbonyl with benzene at 900 °C leads to single wall nanotube formation [220]. Nickelocene and cobaltocene were reported to be more favorable for single wall nanotube synthesis than ferrocene, although no differences in single wall nanotube yields were observed when binary mixtures of metallocenes were used, except that the nanotubes appeared to be “cleaner” when mixtures were used [230].

The addition of trace amounts of thiophene (sulfur containing compound) to liquid hydrocarbons has also been reported to promote the growth of single wall carbon

nanotubes [170, 231, 232], although higher concentrations of thiophene were reported to revert the growth back to multiwall in structure (>5 wt%) [170, 231]. Recently, extremely long ropes (several centimeters in length) of high purity single wall nanotubes have been synthesized with the vertical floating catalyst method using a ferrocene, *n*-hexane, and thiophene mixture with hydrogen as the carrier gas [232–234]. These macroscopic ropes will definitely enable the use of single wall nanotubes in mechanical applications.

“HiPCO,” developed at Rice University, is also a process involving a high pressure gas phase catalytic process for single wall nanotube growth [172, 235]. The catalyst is formed *in-situ* by the thermal decomposition of iron pentacarbonyl in a heated flow of CO, and growth is performed at pressures ranging from 1 to 10 atmospheres (atm) and temperatures ranging from 800 and 1200 °C. The optimum condition for maximum yield was at 1200 °C and 10 atm. The rate at which the reactant gases were heated also had substantial effects on the amount and quality of nanotubes produced. The addition of small amounts of methane (0.7% by volume) produced clean nanotubes and increased the yield as well. Although milligram quantities were obtained, such a process is continuous and is being currently scaled up to produce larger quantities of single wall nanotubes (marketed as HiPCO™ single wall carbon nanotubes by Carbon Nanotechnologies Inc.).

4. CHEMICAL VAPOR DEPOSITION CONFIGURATIONS AND CONSIDERATIONS

4.1. Horizontal Furnace

The horizontal furnace is the most popular configuration for the production of carbon nanofibers and nanotubes [4, 124, 137, 173]. In its simplest form, it is a heated quartz tube in which the substrates/catalyst are placed. The reactant gases are flowed over the substrates/catalyst which sit in a removable ceramic boat/holder in the center of the quartz tube (see Fig. 6a). The horizontal furnace is advantageous because there is no (or small) temperature gradient within the heated zone. In most cases, the length of the nanotubes/nanofibers can be simply controlled by the length of the deposition time.

When samples are first put into the chamber, the quartz tube is first flushed with a “carrier” gas. The most popular carrier gases are argon, hydrogen, and nitrogen [4, 115, 158, 161, 221, 232]. Argon is mostly used as it easily displaces air and therefore easily forms an inert atmosphere in the chamber. The furnace is then heated up to the growth temperature in the inert atmosphere. Hydrogen is often added to the gas flow to reduce the catalyst particles (e.g., oxides) during heating. Even if the chamber is evacuated by a pump, it is important to maintain a forward flow of inert/reducing gases during heating as it is possible that nanotubes may undesirably grow from the catalytic cracking of pump oil (e.g., from back streaming). When the growth temperature is reached, the carbon feedstock is introduced. As discussed in the growth mechanism section, the choice of carbon feedstock and other additives is based on whether nanofibers, multiwall nanotubes,

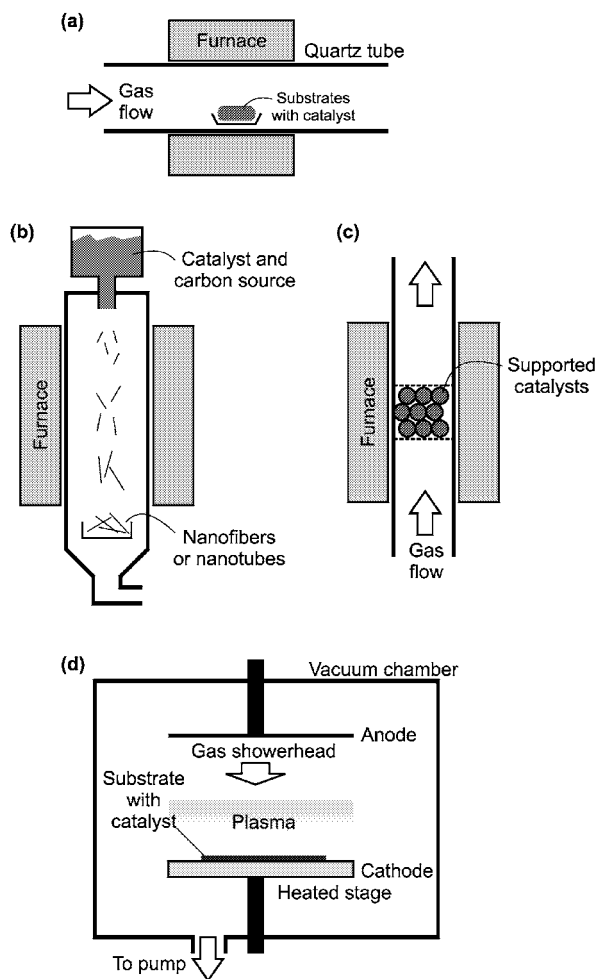


Figure 6. Types of chambers used for catalytic CVD of nanofibers and nanotubes. The most commonly used is the horizontal furnace (a). For mass production, the vertical furnace (b) has been employed. (c) The fluidized bed reactor and (d) a basic plasma enhanced CVD system based around a vacuum chamber.

or single wall nanotubes are desired. Reactions are usually conducted at temperatures below 1000 °C to reduce the formation of undesirable carbon deposits such as amorphous carbon [151]. The amorphous carbon is deposited from the thermal decomposition (pyrolysis) of the carbon feedstock gas, whereas the carbon nanotubes/nanofibers are grown from the catalytic decomposition of the carbon feedstock gas. In most cases, “clean” (i.e., amorphous carbon-free) growth of highly crystallized structures is desired and hence the highest deposition temperature without significant self-decomposition of the carbon feedstock is preferred.

In order to determine the highest growth temperature possible using a particular carbon feedstock, it is necessary to consider the thermodynamic stability of the compound depending on temperature. The driving force for the pyrolytic reactions involving gaseous components can be derived from plots of the free enthalpy of formation versus temperature (generated using [236]) as shown in Figure 7. The term pyrolytic is defined as converting the carbon feedstock to solid carbon as the main product and to different

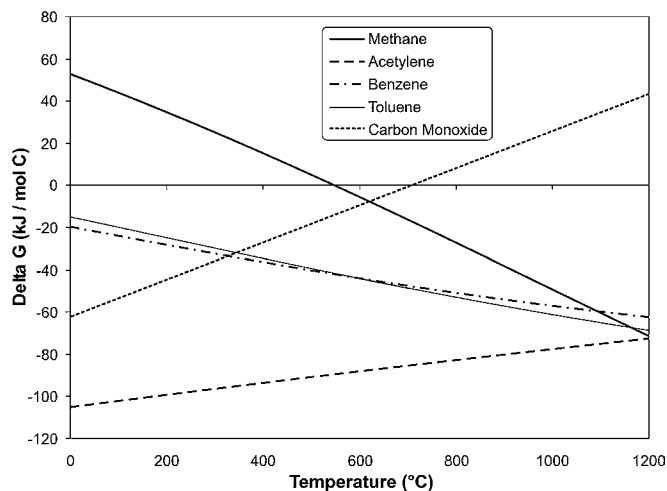


Figure 7. The free enthalpy of formation of some carbon compounds, calculated from [236, 237].

volatile compounds as by-products [237]. The stability of the compound increases with the free enthalpy, whereas the driving force for breaking the compound into its elements decreases. For example, the forward reaction producing elementary carbon from carbon monoxide is favored at temperatures below 700 °C.

In general, there is a compromise between obtaining high purity carbon nanotubes/fibers and high crystallinity. The growth temperature affects the crystallinity of the structure produced, but too high a temperature leads to the formation of pyrolytic amorphous carbon. Furthermore, the diffusion of carbon through the catalyst is a thermally activated process, and hence, in general, higher temperatures lead to higher growth rates which may be desirable for mass-production processes.

One strategy to reduce the formation of amorphous carbon is to decrease the contact time between the carbon feedstock and the substrates. This is achieved by using very high gas flow rates (in cases where only carbon feedstock is used in the flow) or high dilution [129, 163, 175, 238]. Thus, the carbon feedstock is often diluted by the carrier gases. Normally there is an optimum ratio of carbon feedstock to carrier gas; for example, using acetylene and nitrogen, the optimized combination was 9% by volume of the total gas flow. If the acetylene combination is increased, amorphous carbon begins to form due to the self-pyrolysis carbon feedstock and the increased exposure of the sample to the carbon feedstock [129].

A small amount of hydrogen in the gas flow is useful in keeping the catalyst particle active by reducing it. It is well known that the growth of nanofibers is enhanced in a hydrogen atmosphere [4, 148, 189, 239]. Hydrogen also reduces the formation of undesirable carbon deposits from the pyrolysis of carbon feedstock [159]. This is because hydrogen rehydrogenates the reactive carbon species in the gas phase. Franklin et al. found that for clean single wall carbon nanotube growth at 900 °C, the optimum flow of hydrogen was between 100 and 150 ml/min in a predominantly CH₄ flow (CH₄ = 1500 ml/min) [176]. The flow of hydrogen had to be increased to 200 ml/min to maintain

“clean” growth when a temperature of 950 °C was used. In the absence of hydrogen flow, the CH₄ was found to pyrolyze and form amorphous carbon deposits all over the substrate.

Alternatively, the floating catalyst method can also be used in the horizontal furnace configuration for carbon nanofiber or nanotube growth [4, 212]. As discussed before, the catalyst can be sublimed in a preceding furnace stage and flowed into the main furnace for growth or injected directly into the growth furnace using a syringe pump or atomizer spray [4, 213–219, 221–223, 240]. The growth of nanotubes would then occur all over the walls of the quartz tube and also on any substrates placed inside the furnace. This technique is very useful for bulk production since the material can simply be removed from the walls of the chamber or from the substrates after growth. Note that selective area growth is also possible with the floating catalyst technique by using different substrate materials; for example, SiO₂ supports nanotube growth whereas Si does not [224, 225].

Finally, note that a furnace is not necessarily required to generate the heat needed for nanotube growth. It is possible to grow nanotubes on wires through direct heating with electrical current [241]. Furthermore, plasma or radio-frequency (rf)-induced heating of the catalyst particle can also generate sufficient temperature locally for carbon nanofiber/nanotube growth at lower process temperatures [242].

4.2. Vertical Furnace

The vertical furnace configuration, as shown in Figure 6b, is usually employed for the continuous production of carbon fibers, nanofibers, and nanotubes [4, 125, 211, 232, 243]. The catalyst and carbon source is injected at the top of the furnace and the resultant filaments grow during flight and are collected at the bottom of the chamber. The vertical furnace can be run continuously for the mass production of carbon nanotubes and nanofibers. Ultrafine metal catalyst particles are either introduced into the reactor directly or formed *in-situ* using precursors such as metallocenes as discussed previously. Note that the residence time of the catalyst particle in the vertical furnace is relatively short compared to the horizontal furnace.

As discussed earlier, the growth of multiwall or single wall nanotubes is dependent on the temperature and gases used, with higher temperatures and the addition of a sulfur containing compound (e.g., thiophene) favoring single wall nanotube production [170, 231, 232]. The main advantage with the vertical furnace configuration is the continuous nature of nanofiber/nanotube production and high purity product eliminating the need for purification or removal from the substrate. The vertical furnace technique has been commercialized for the production of multiwall nanotubes and nanofibers, in quantities of tons per year. Most of this material is used in the electrodes of lithium-ion batteries [73] and as fillers in conductive polymers [35].

The fluidized bed reactor (Fig. 6c) is a variation of the vertical furnace. Fluidization is defined as the transformation of solid particles into a fluidlike state through suspension in a gas or liquid. As seen in Figure 6c, supported catalysts are usually placed in the center of the furnace and an upward flow of carbon feedstock gases is used.

The fluidization process involves the supported catalysts to remain much longer in the furnace than in the vertical floating technique. The fluidization method is relatively new for the bulk production of carbon nanotubes [244–246], and thus far, production rates up to tens of kilograms of multi-wall carbon nanotubes a day have been achieved [244].

4.3. Aligned and Directed Nanotube Growth

In some applications, the deposition of well aligned carbon nanotubes or nanofibers on substrates is desired. In this area, chemical vapor deposition is uniquely superior to the other nanotube production techniques (i.e., electric arc discharge and laser ablation) in that nanotube/nanofiber alignment on substrates is readily achievable during growth. Whenever very dense and closely packed nanotubes are deposited (see Fig. 8a), they are forced to grow in an upward ensemble (i.e., perpendicularly) from the substrate—this is sometimes referred to as “self-oriented” or “self-assembled” growth. It is generally believed that the nanotube ensemble is held together by van der Waals interaction and that the nanotubes are so closely packed that the only possible

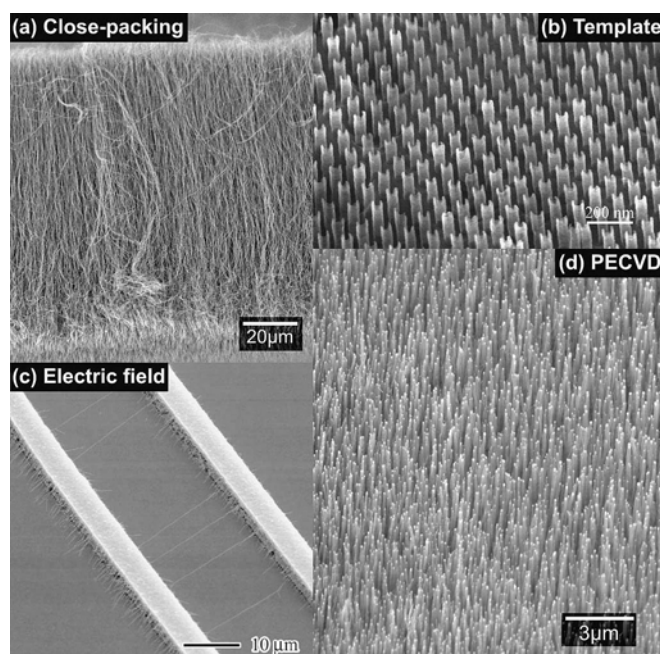


Figure 8. Methods of aligning nanotubes during growth. In (a), densely packed nanotubes grow approximately vertically aligned, as shown in this peeled section of a nanotube “film.” This was deposited using the floating catalyst technique employing a ferrocene–toluene solution injected into a heated furnace (750 °C). In (b), perfectly straight, same diameter, and same length nanotubes are grown in the pores of a nanochannel alumina template. In (c), a lateral electric field of 0.5 V/μm is used to guide these single wall nanotubes horizontally between electrodes during growth. In (d), straight, vertically aligned carbon nanotubes were grown using plasma enhanced CVD. It is believed that the electric field in the plasma sheath which forms over the substrate aligns the structures during growth. (b) Reprinted with permission from [250], J. Li et al., *Appl. Phys. Lett.* 75, 367 (1999). © 1999, American Institute of Physics. (c) Reprinted with permission from [111], Y. G. Zhang et al., *Appl. Phys. Lett.* 79, 3155 (2001). © 2001, American Institute of Physics.

growth direction is upward. Thus, the key factor in achieving this type of dense, aligned growth is the preparation of dense and active catalyst particles on the substrate surface. One of the most spectacular examples of this was reported by a Chinese research group [114, 119]. The authors prepared iron oxide nanoparticles in the pores of mesoporous silica, which was then reduced to iron particles by H_2/N_2 flow at 550 °C, followed by reaction with C_2H_2 at 700 °C for nanotube growth. Dense arrays of nanotubes grew perpendicularly outward from the mesoporous silica, and bundles of nanotubes up to 2 mm in length were synthesized [119].

Fan et al. also synthesized “towers” of densely packed nanotubes by using a 5 nm thin film of evaporated iron on electrochemically etched porous silicon [110]. The authors explained that during growth, the walls of the nanotubes interact with their neighbors via van der Waals to form a rigid bundle during growth. In fact, close examination of these nanotube “towers” revealed that there were no nanotubes which “branched out” from the main tower. As the catalyst was rooted at the base of the structure (i.e., base growth), the porous substrate played a key role in the growth as it allowed the deposition gas to continuously feed the catalyst. The strong interaction between the substrate and the catalyst also meant that the catalyst was well rooted and did not sinter to form larger catalyst particles at the growth temperature. Dense and aligned nanotube growth on substrates has also been observed with evaporated iron on oxidized Si [167], from laser-ablated Co catalyst on silica substrates [115], and from substrates coated by nanotubes from the floating catalyst method as discussed earlier [218, 220, 221, 225]. In general, the close-packed nanotubes are not perfectly straight and exhibit some degree of waviness as seen in Figure 8a.

Another common means of achieving aligned growth is through the use of templates, the most popular of which are vertical nanopores created by the electrochemical processing (anodization) of aluminum. Porous alumina membranes typically contain vertical nanopores which are a few to hundreds of nanometers in diameter and lengths which can range from a few micrometers to hundreds of micrometers. The electrochemical parameters can be varied to control the pore diameter, length, and density—a review of the template preparation and growth of nanomaterials in templates is given in [247]. The intent is to grow nanotubes within the alumina pores so that the diameter, length, density, and alignment of the structures reflect that of the original template. The use of porous alumina in the synthesis of carbon nanotubes was first reported in 1995 [248]. In general, two types of template grown structures are possible, namely catalyzed and pyrolytic (no catalyst). The latter usually requires higher temperatures in order to decompose the carbon feedstock gas. Che et al. prepared carbon nanotubes with diameters ~ 20 nm using an alumina template in ethylene/pyrene with a Ni catalyst at 545 °C or without catalyst at 900 °C [249]. After growth, the alumina template can be removed by dipping in HF or NaOH solution to reveal an array of well-ordered carbon tubules standing perpendicular on the substrate. Figure 8b shows what is possible with this technique—a well-aligned, hexagonally packed nanotube ensemble with highly homogenous diameter and lengths. This was prepared by Li et al. using an alumina

template together with Co/Ni catalysis of acetylene at 650 °C [250]. The smallest nanotubes, 4 Å (0.4 nm) in diameter, have been fabricated using zeolite templates [251].

Another strategy of obtaining vertical nanotube/nanofiber growth is through the use of electric fields. Avigal et al. used a vertical electric field during growth to achieve vertical alignment of nanotubes [252]. A similar effect arises during plasma enhanced chemical vapor deposition (see Fig. 8d) which is discussed in the next section.

The above techniques yield the growth of vertically aligned structures—but what about horizontally aligned ones? Horizontally aligned nanotubes are necessary for the mass production of nanotube electronic and spintronic devices. The group led by Dai, at Stanford University, is a pioneer in this area. In their early work, straight, single wall nanotubes were grown from patterned catalyst but in random directions [151]. In some cases, the nanotubes grew in the correct direction (e.g., between electrical contacts) which allowed the fabrication of nanotube electronic devices [63, 253, 254]. Clearly there was a need to control the growth direction in order to achieve a higher fabrication yield of nanotube devices. In [177], they fabricated silicon pillars and contact printed the catalyst for single wall nanotubes on top of the pillars. A suspended network of nanotubes was observed from the pillars after growth. Fascinatingly, the direction of the suspended nanotubes followed the pattern of the pillars—for example, when the pillars were lined up in rows, nanotubes would be found to be suspended from the pillar tops resembling a power line. Using this technique, 100–150 μm long single wall nanotubes were grown. If four pillars were arranged in a square, a square arrangement of suspended nanotubes would join the tops of the pillars. The authors reasoned that the nanotubes growing toward a pillar would adhere to the pillar and become suspended, whereas nanotubes growing in other directions do not meet a pillar and would fall down toward the substrate. Thus, the arrangement of pillars essentially defined the growth direction of the nanotubes.

Lateral electric fields can also be used to guide nanotubes during growth. Zhang et al. prepared electrode and catalyst “fingers” on a quartz substrate which were biased during chemical vapor deposition in order to create a lateral electric field [111, 112]. The authors found that electric fields of 0.13–0.5 V/ μm were needed to guide and align the single wall nanotubes during growth, as shown in Figure 8c. The mechanism of alignment was due to the electric dipole polarization of the nanotubes which made them align in the applied electric field.

Lee et al. also presented a technique for the directed growth of lateral nanotubes. These authors made a sandwich structure comprised of SiO_2 –Ni–Nb on silicon [255]. Using microfabrication, only one face of the sandwich was left exposed to the gases and it was from this face that the Ni catalyzed the outward/lateral growth of multiwall nanotubes in C_2H_2/N_2 at 650 °C.

4.4. Plasma Enhanced Chemical Vapor Deposition

Plasma enhanced chemical vapor deposition (PECVD) is a relatively new technique of producing vertically aligned carbon nanotubes and nanofibers, and it is considerably

different from the horizontal and vertical furnace techniques. A plasma is an excited/ionized gas, and the processing plasmas, usually known as “cold” plasmas, are generated using dc, rf, or microwave excitation. The simplest plasma system to implement is the dc plasma which is shown in Figure 6d. The dc glow discharge plasma is generated by grounding the anode and applying a negative dc bias of a few hundred volts to the cathode (note that the substrate for nanotube/nanofiber growth is on the cathode in this case such that the plasma would form a sheath over it with a large voltage drop). Plasma systems are commonly used in semiconductor processing for etching or low temperature deposition of thin films. A review presenting the different configurations of plasma systems is presented in [256]. Today, carbon nanotube/nanofiber growth has been demonstrated with hot filament assisted PECVD [113, 206–208], microwave PECVD [257–262], dc glow discharge PECVD [117, 182], inductively coupled plasma PECVD [74, 149], and rf PECVD [242, 263]. Plasma depositions are very stable—this leads to highly controllable and reproducible growth conditions. PECVD is usually used to produce vertically aligned carbon nanotubes/nanofibers or grow nanofibers at low temperatures.

Chen et al. used a combination of hot filament and dc PECVD (via negative bias on the substrate) to grow aligned carbon nanofibers using a single crystal Ni(100) surface with CH₄ and N₂ gases [206]. This process was later refined using 3% C₂H₂ in N₂ and a polycrystalline Ni substrate to grow nanofibers of 60–70 nm average diameter and few micrometers in length [207]. The structures produced by Chen et al. were classed as nanofibers because their TEM showed that the graphene planes were slightly tilted/herringbone, although the nanofiber was hollow in the center. These films showed excellent field emission characteristics with low turn-on electric fields and high emission currents.

A major application for carbon nanotubes is the electron source in field emission displays (a flat panel display technology). The major drawback, however, is that nanotube growth typically requires temperatures of 700 °C or higher which exceeds the strain point of the best “display” glass (by Corning) of 666 °C. Hence, there was great excitement in 1998 when Ren et al. demonstrated that vertically aligned carbon nanotubes could indeed be deposited below that temperature on glass, using hot filament assisted dc-PECVD of C₂H₂ and NH₃ [113]. The aligned nanotubes produced were uniform and very straight and stood “individually” as shown in Figure 8d, in contrast to the aligned nanotubes produced by dense growth in which nanotubes were bundled together and wavy. The authors used a thin film Ni catalyst which was sputtered onto the glass substrates and also showed that plasma bombardment could be used to break up the thin film into islands. Furthermore, this work also demonstrated that the initial film thickness of the film could be used to control the diameter of the resultant nanotubes. Huang et al. later used this process to grow nanotubes uniformly on a polycrystalline Ni substrate which was pre-etched to create Ni islands [208]. Ren et al. [116] later used electron beam lithography to pattern submicrometer Ni dots directly on a silicon substrate and achieved the growth of single, freestanding vertical nanotubes. These nanotubes, however, were not very uniform in terms of height and yield which

could be due to the absence of a diffusion barrier between the Ni catalyst and Si substrate. Huang et al. [264] next studied thin film Co, Fe, and Ni catalysts on a Ti substrate using the hot filament dc-PECVD process and found that the nanotubes produced with Ni were structurally the best in terms of graphitization, straightness, lack of amorphous carbon overcoating, and structural defects such as openings in the walls. The nanotubes nucleated from Ni also had the fastest growth rate (in terms of length). The authors noted that the diameters of the Ni catalyzed nanotubes were larger than the nanotubes catalyzed by Co and Fe, indicating that Ni had the weakest interaction with the Ti substrate and hence formed the largest catalytic clusters. Huang et al. studied the growth of individual nanotubes from patterned Ni dots and forests of nanotubes from a larger area Ni film [265]. They found that the Ni catalyst particle attained a particular orientation after growth, namely with the <220> orientated in the direction of the plasma. The individual nanotubes were also better crystallized with tubular walls, compared with the forests of nanotubes which had herringbone-like structures (i.e., nanofibers). They suggested that plasma focusing and heating of the catalyst particle in the case of the individual nanotube were responsible for its different structure.

Bower et al. devised an elegant set of experiments to investigate the alignment mechanism of the nanotubes [257]. A microwave PECVD system was used to grow carbon nanotubes catalyzed from a Co thin film on a Si substrate. Carbon nanotubes were deposited using PECVD and then the plasma was stopped for conventional thermal CVD to continue. The resultant nanotubes were thus straight for the plasma-grown section and curly for the thermally grown section. Additionally, when nonplanar or angled substrates were introduced into the plasma, the nanotubes still grew perpendicularly from the substrate surfaces because the microwave plasma formed a sheath around these objects. The authors concluded that the alignment was indeed a plasma induced effect and that it was probably the electric field in the plasma sheath formed around objects which guided the growth of the nanotubes perpendicularly from the objects. The electric field in the plasma sheath was estimated to be 0.1 V/μm, which is of the same order of magnitude as the electric field used to align single wall carbon nanotubes laterally during growth discussed previously.

Chen et al. [266], who used a hot filament dc-PECVD system, showed that by placing a substrate at an angle to the biased cathode electrode, nanotubes also grew at an angle which followed the direction of the electric field in the plasma sheath. Tsai et al., who used a microwave plasma to synthesize aligned nanotubes, proposed a model based on anisotropic etching in order to explain the vertical alignment of the nanotubes [267]. They suggested that nanotubes which grew in random orientations were unprotected by their metal catalyst particle and were hence anisotropically etched away in the plasma [267].

Merkulov et al. developed a simple dc-PECVD system to grow vertically aligned carbon nanofibers [117]. The system used a resistively heated cathode which was biased at –550 V to generate a dc glow discharge. The gases used were C₂H₂ and NH₃, and Ni, deposited on top of a Ti

barrier layer on silicon substrates, was used as the catalyst. They investigated the lithographic conditions necessary to nucleate single, freestanding nanofibers as well as single-file lines of nanofibers. The maximum catalyst dimensions were determined to be 350 nm for a catalyst dot and 200 nm for the width of a catalyst line (i.e., for a single file line of nanofibers). Above these dimensions, the catalyst was observed to break into multiple nanoclusters at the growth temperature which nucleated more than one nanofiber. Merkulov et al. named their filaments nanofibers because they were highly disordered and bamboolike. In further studies, these authors found that the thickness of the catalyst layer controlled the average diameter of the nanofibers grown by PECVD [202], the ratio of C_2H_2 in the gas flow caused the nanofibers to attain a conical shape due to amorphous carbon buildup on walls of the nanofiber as it grew upward [268], and the direction of the nanofiber growth was determined by the local electric field in the plasma sheath [269]. The authors studied the field emission properties of their nanofibers and also fabricated gated microelectronic field emitters and electrochemical electrodes based on single nanofibers [54, 75, 270–272].

Chhowalla et al. performed a parametric study of the dc-PECVD growth of carbon nanotubes using C_2H_2 and NH_3 gases with Ni catalyst [182]. The structures were termed nanotubes because the filaments had well-crystallized graphene walls parallel to the filament axis (see Fig. 3c for a typical TEM), with bamboo compartments along their axis. They studied the effect of the initial catalyst thickness (with thicker films leading to larger diameter nanotubes which were shorter and of lower areal density), the effect of the C_2H_2 ratio in the gas flow (with higher ratios leading to conical structures), the effect of pressure and deposition time (with higher pressures and longer times leading to longer nanotubes), and the effect of the dc bias on the substrate (with higher biases leading to straighter, aligned nanotubes). By examining the plasma characteristics, it was determined that $0.15 \text{ V}/\mu\text{m}$ was the minimum electric field in the plasma sheath necessary for vertical alignment of the nanotubes. Clearly, to obtain a high degree of vertical alignment, one should thus maximize the electric field in the plasma sheath by increasing the substrate bias or by increasing the gas pressure (which increases ionization, leading to a higher field in the sheath). By investigating the effect of the growth temperature, it was found that the activation energy for PECVD growth was less (i.e., 0.76 eV) than that for thermal CVD (i.e., 1.21 eV), the latter being close to the bulk diffusion of carbon through Ni [204]. This indicates that the plasma plays a role in lowering the activation barrier necessary for nanotube growth. Teo et al. used the dc PECVD process to demonstrate the high yield and uniform growth of patterned areas of nanotubes and individual nanotubes [118, 273], examples of which are shown in Figure 5. In patterned growth especially, the C_2H_2 to NH_3 ratio was found to be important in achieving amorphous carbon free growth. During growth, the C_2H_2 is continuously being decomposed by the plasma (at a rate much faster than thermal pyrolysis) to form amorphous carbon on the substrate surface, and the role of NH_3 in the plasma is to etch away this unwanted amorphous carbon. The N and H species in the NH_3 plasma react with the amorphous carbon to form

volatile C–N and C–H species. Hence, there exists an optimum condition, which was determined to be a flow ratio of 40:200 sccm of $C_2H_2:NH_3$ at 700°C , where the production and etching of amorphous carbon is balanced, thus yielding substrates which are free of amorphous carbon. Teo et al. also found that individual vertical nanotubes, nucleated from Ni clusters of controlled size/volume, could be grown with a high degree of uniformity in terms of tip radius and height. The standard deviations in the tip diameter and height were found to be 4.1 and 6.3% of the average respectively [205]. This high degree of structural uniformity leads to good uniformity in terms of field emission characteristics from adjacent nanotubes in an array [205, 274].

Delzeit et al. performed a parametric study of vertically aligned carbon nanotube and nanofiber growth in an inductively coupled plasma [149]. The authors used thin film Fe catalyst which was deposited on an aluminum layer on Si substrates, and the nanofibers/nanotubes were grown using CH_4 , H_2 , and Ar gases. By varying the process conditions, the authors found a clear transition between two structural forms of carbon filaments grown (i.e., the nanotube with parallel graphene walls and nanofiber with walls which were inclined to the filament axis). Until then, it was known that some plasma processes produced nanotubes (which were mostly bamboo), but other plasma processes produced nanofibers (with angled graphene layers but mostly hollow inside). The authors conclusively found that it was the relative amount of hydrogen species in the gas phase which determined whether nanotube or nanofiber growth was favored. Nanofiber growth was favored under process conditions which contained a large amount of hydrogen because the hydrogen could terminate the large number of dangling bonds protruding from angled graphene layers. The lack of hydrogen (e.g., achieved by Ar dilution) in the gas phase produced nanotubes which have closed, tubular graphene shells with few dangling bonds.

One of the most significant results recently is the demonstration of room temperature growth of nanofibers using rf-PECVD [242]. The authors used a CH_4 and H_2 plasma with Ni powder catalyst to grow nonaligned nanofibers at room temperature and at 100 and 250°C . The authors claimed that instead of thermal energy, the energy of the plasma and induced rf heating of the catalyst particle allowed the formation of the carbon nanofibers at ambient temperature.

4.5. Growth of Branched Structures

The growth of branched filaments allows direct “wiring” of nanotube/nanofiber structures. Y-branched nanotubes would also allow switching and rectification behavior over a network of wires, similar to neural networks in biological systems. The growth of Y-branched nanotubes and nanofibers has been reported by several groups using the catalytic CVD [275–280]. Using the catalytic methods, the Y-junctions are generally formed at high temperatures ($1000\text{--}1100^\circ\text{C}$) [277, 279] or by using mixed metal or Cu catalysts [275, 276, 280–282]. For example, Chambers et al. found that branching is promoted when Co catalyst is alloyed with 2% Cu [275, 276] while Li et al. [280] observed branching when the catalyst is doped with Si or Ca. Another method for fabricating Y-junctions is to use a nanochannel

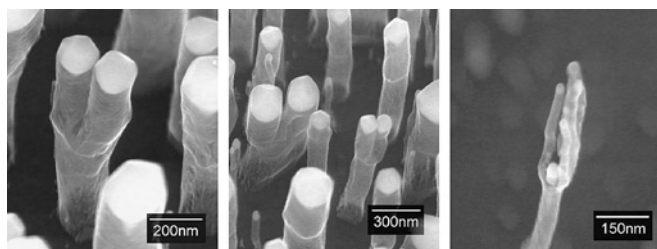


Figure 9. Branched structures as a result of a rapid drop in temperature from 700 to 550 °C during growth. The drop in temperature caused the Ni catalyst here (bright dot at the tip of the structure) to break up. After the temperature perturbation, the temperature was brought back to 700 °C for normal growth.

alumina template that has been prepared such that the pores are Y-shaped [283, 284]. The electrical measurements on these Y-junction nanotubes showed nonlinear conductance and reproducible rectification [284].

It is also possible to grow branched structures without catalyst additives, templates, or high temperatures. In fact, all that is required is a simple perturbation during deposition in order to promote the formation of smaller catalyst particles (to catalyze branches) from a single, larger catalyst (which forms the main “stem”). In Figure 9, the branched nanofiber structures were formed by growth using dc-PECVD of $C_2H_2:NH_3$ with Ni catalyst at 700 °C for 3 minutes, then rapidly decreasing the growth temperature from 700 to 550 °C and then normal deposition at 700 °C again for 3 minutes. As the solubility of carbon in the catalyst decreases at lower temperatures, the rapid drop in temperature causes the catalyst to become oversaturated and to split up to form more surface area to expel the carbon. After the catalyst has been broken up by the rapid drop in temperature, further growth at the normal temperature (700 °C) is used to extend the length of the nanofiber branches.

5. SUMMARY

Catalytic chemical vapor deposition is an extremely versatile technique for the production of carbon nanofibers and nanotubes. This chapter has shown that by controlling the catalyst and synthesis conditions, one can control many aspects of the growth, such as the structure (nanofiber vs nanotube), diameter, length, and alignment. The catalytic CVD technique can be adapted for mass production purposes or for the controlled growth of nanotubes/fibers at particular sites on a substrate for various applications.

GLOSSARY

Carbon nanofiber The carbon nanofiber is a generic term used to describe filaments/whiskers of carbon which have diameters less than 500 nm. The term fiber usually implies that the structures have a high aspect ratio, and hence the lengths of nanofibers are usually in the range of few micrometers or more. Although the carbon nanotube (see next) can be classed as a form of nanofiber, the carbon nanotube is typically used to describe structures which are comprised of tubular graphene walls parallel to the fiber axis. Hence,

recently, the term carbon nanofiber is used to imply filaments which are comprised of graphene layers which are stacked at an angle to the fiber axis (such as the herringbone, cup-stacked, or stacked type filaments). Also, carbon nanofibers can be used to describe filaments of disordered/amorphous carbon.

Carbon nanotube The carbon nanotube is comprised of graphene sheets (containing hexagonally arranged, sp^2 bonded carbon atoms) which have been rolled up to form a seamless tubular structure. The simplest form is known as the single wall carbon nanotube in which the structure consists of a single graphene shell/tube. Multiwall carbon nanotubes consist of multiple, concentric tubular graphene shells.

ACKNOWLEDGMENTS

The authors thank M. Castignolles for the TEM image in Figure 3c, D. G. Hasko for use of electron beam lithography equipment to prepare Figure 5, and R. Lacerda for sample preparation. We also thank G. A. J. Amaratunga for invaluable discussions and help. K.B.K.T. acknowledges the support of Christ’s College Cambridge. C.S. acknowledges the financial support of SIRIM Berhad (Malaysia), the Cambridge Commonwealth Trust, Selwyn College, and the Lundgren Fund.

REFERENCES

1. R. T. K. Baker, M. A. Barber, P. S. Harris, F. S. Feates, and R. J. Waite, *J. Catal.* 26, 51 (1972).
2. R. T. K. Baker, P. S. Harris, R. B. Thomas, and R. J. Waite, *J. Catal.* 30, 86 (1973).
3. R. T. K. Baker, *Carbon* 27, 315 (1989).
4. M. Endo, *Chemtech* 18, 568 (1988).
5. N. M. Rodriguez, A. Chambers, and R. T. K. Baker, *Langmuir* 11, 3862 (1995).
6. J. Gavillet, A. Loiseau, C. Journet, F. Willaime, F. Ducastelle, and J. C. Charlier, *Phys. Rev. Lett.* 87, 275504 (2001).
7. C. A. Bessel, K. Laubernds, N. M. Rodriguez, and R. T. K. Baker, *J. Phys. Chem. B* 105, 1115 (2001).
8. M. Endo, Y. A. Kim, T. Hayashi, Y. Fukai, K. Oshida, M. Terrones, T. Yanagisawa, S. Higaki, and M. S. Dresselhaus, *Appl. Phys. Lett.* 80, 1267 (2002).
9. S. Iijima, *Nature* 354, 56 (1991).
10. <http://www.fibrils.com>, <http://www.apsci.com/home.html>, <http://www.nanomirae.com/eng/main.htm>, <http://www.sdk.co.jp>.
11. <http://www.personal.rdg.ac.uk/~scscharip/tubes.htm>.
12. D. S. Bethune, C. H. Kiang, M. S. Devries, G. Gorman, R. Savoy, J. Vazquez, and R. Beyers, *Nature* 363, 605 (1993).
13. S. Iijima and T. Ichihashi, *Nature* 363, 603 (1993).
14. Y. Saito, T. Yoshikawa, S. Bandow, M. Tomita, and T. Hayashi, *Phys. Rev. B* 48, 1907 (1993).
15. M. Endo, K. Takeuchi, T. Hiraoka, T. Furuta, T. Kasai, X. Sun, C. H. Kiang, and M. S. Dresselhaus, *J. Phys. Chem. Solids* 58, 1707 (1997).
16. C. H. Kiang, M. Endo, P. M. Ajayan, G. Dresselhaus, and M. S. Dresselhaus, *Phys. Rev. Lett.* 81, 1869 (1998).
17. M. S. Dresselhaus and M. Endo, in “Carbon Nanotubes Synthesis, Structure, Properties and Applications” (M. S. Dresselhaus, G. Dresselhaus, and P. Avouris, Eds.), p. 11. Springer-Verlag, New York, 2001.

18. A. Bachtold, C. Strunk, J. P. Salvetat, J. M. Bonard, L. Forro, T. Nussbaumer, and C. Schonenberger, *Nature* 397, 673 (1999).
19. M. Endo, S. Iijima, and M. S. Dresselhaus, "Carbon Nanotubes." Elsevier Science, Oxford, 1996.
20. T. W. Odom, J. L. Huang, P. Kim, and C. M. Lieber, *Nature* 391, 62 (1998).
21. J. W. G. Wildoer, L. C. Venema, A. G. Rinzler, R. E. Smalley, and C. Dekker, *Nature* 391, 59 (1998).
22. L. Forro and C. Schonenberger, in "Carbon Nanotubes Synthesis, Structure, Properties and Applications" (M. S. Dresselhaus, G. Dresselhaus, and P. Avouris, Eds.), p. 329. Springer-Verlag, New York, 2001.
23. R. Saito, G. Dresselhaus, and M. S. Dresselhaus, "Physical Properties of Carbon Nanotubes." Imperial College Press, London, 1998.
24. P. G. Collins and P. Avouris, *Sci. Am.* 283, 62 (2000).
25. E. W. Wong, P. E. Sheehan, and C. M. Lieber, *Science* 277, 1971 (1997).
26. M. F. Yu, O. Lourie, M. J. Dyer, K. Moloni, T. F. Kelly, and R. S. Ruoff, *Science* 287, 637 (2000).
27. M. F. Yu, B. S. Files, S. Arepalli, and R. S. Ruoff, *Phys. Rev. Lett.* 84, 5552 (2000).
28. J. Hone, M. Whitney, C. Piskoti, and A. Zettl, *Phys. Rev. B* 59, R2514 (1999).
29. P. Kim, L. Shi, A. Majumdar, and P. L. McEuen, *Phys. Rev. Lett.* 8721, 215502 (2001).
30. A. Thess, R. Lee, P. Nikolaev, H. J. Dai, P. Petit, J. Robert, C. H. Xu, Y. H. Lee, S. G. Kim, A. G. Rinzler, D. T. Colbert, G. E. Scuseria, D. Tomanek, J. E. Fischer, and R. E. Smalley, *Science* 273, 483 (1996).
31. C. Schonenberger, A. Bachtold, C. Strunk, J. P. Salvetat, and L. Forro, *Appl. Phys. A* 69, 283 (1999).
32. W. A. de Heer and R. Martel, *Phys. World* 13, 49 (2000).
33. S. Frank, P. Poncharal, Z. L. Wang, and W. A. de Heer, *Science* 280, 1744 (1998).
34. <http://www.pa.msu.edu/cmp/csc/ntproperties/>, compiled by T. A. Adams II.
35. R. H. Baughman, A. A. Zakhidov, and W. A. de Heer, *Science* 297, 787 (2002).
36. P. J. F. Harris, "Carbon Nanotubes and Related Structures. New Materials for the Twenty-first Century." Cambridge Univ. Press, Cambridge, UK, 1999.
37. T. W. Ebbesen, *Phys. Today* 49, 26 (1996).
38. H. J. Dai, *Surf. Sci.* 500, 218 (2002).
39. P. M. Ajayan, *Chem. Rev.* 99, 1787 (1999).
40. P. M. Ajayan and O. Z. Zhou, *Carbon Nanotubes Topics Appl. Phys.* 80, 391 (2001).
41. C. N. R. Rao, B. C. Satishkumar, A. Govindaraj, and M. Nath, *Chem. Phys. Chem.* 2, 78 (2001).
42. L. M. Dai and A. W. H. Mau, *Adv. Mater.* 13, 899 (2001).
43. W. B. Choi, D. S. Chung, J. H. Kang, H. Y. Kim, Y. W. Jin, I. T. Han, Y. H. Lee, J. E. Jung, N. S. Lee, G. S. Park, and J. M. Kim, *Appl. Phys. Lett.* 75, 3129 (1999).
44. A. G. Rinzler, J. H. Hafner, P. Nikolaev, L. Lou, S. G. Kim, D. Tomanek, P. Nordlander, D. T. Colbert, and R. E. Smalley, *Science* 269, 1550 (1995).
45. I. T. Han, H. J. Kim, Y. J. Park, N. Lee, J. E. Jang, J. W. Kim, J. E. Jung, and J. M. Kim, *Appl. Phys. Lett.* 81, 2070 (2002).
46. Y. H. Lee, Y. T. Jang, D. H. Kim, J. H. Ahn, and B. K. Ju, *Adv. Mater.* 13, 479 (2001).
47. D. S. Chung, S. H. Park, H. W. Lee, J. H. Choi, S. N. Cha, J. W. Kim, J. E. Jang, K. W. Min, S. H. Cho, M. J. Yoon, J. S. Lee, C. K. Lee, J. H. Yoo, J. M. Kim, J. E. Jung, Y. W. Jin, Y. J. Park, and J. B. You, *Appl. Phys. Lett.* 80, 4045 (2002).
48. W. B. Choi, Y. W. Jin, H. Y. Kim, S. J. Lee, M. J. Yun, J. H. Kang, Y. S. Choi, N. S. Park, N. S. Lee, and J. M. Kim, *Appl. Phys. Lett.* 78, 1547 (2001).
49. G. Z. Yue, Q. Qiu, B. Gao, Y. Cheng, J. Zhang, H. Shimoda, S. Chang, J. P. Lu, and O. Zhou, *Appl. Phys. Lett.* 81, 355 (2002).
50. N. deJonge, Y. Lanny, K. Schoots, and T. H. Oosterkamp, *Nature* 420, 393 (2002).
51. R. Rosen, W. Simendinger, C. Debbault, H. Shimoda, L. Fleming, B. Stoner, and O. Zhou, *Appl. Phys. Lett.* 76, 1668 (2000).
52. <http://www.oxfordxtg.com/products/coldcath.htm>, Oxford Instruments plc., 2002.
53. C. J. Lee, T. J. Lee, and J. Park, *Chem. Phys. Lett.* 340, 413 (2001).
54. M. A. Guillorn, A. V. Melechko, V. I. Merkulov, E. D. Ellis, C. L. Britton, M. L. Simpson, D. H. Lowndes, and L. R. Baylor, *Appl. Phys. Lett.* 79, 3506 (2001).
55. H. J. Dai, J. H. Hafner, A. G. Rinzler, D. T. Colbert, and R. E. Smalley, *Nature* 384, 147 (1996).
56. H. Nishijima, S. Kamo, S. Akita, Y. Nakayama, K. I. Hohmura, S. H. Yoshimura, and K. Takeyasu, *Appl. Phys. Lett.* 74, 4061 (1999).
57. C. V. Nguyen, K. J. Chao, R. M. D. Stevens, L. Delzeit, A. Cassell, J. Han, and M. Meyyappan, *Nanotechnology* 12, 363 (2001).
58. <http://www.piezomax.com>, nPoint, 2002.
59. S. J. Tans, A. R. M. Verschueren, and C. Dekker, *Nature* 393, 49 (1998).
60. R. Martel, T. Schmidt, H. R. Shea, T. Hertel, and P. Avouris, *Appl. Phys. Lett.* 73, 2447 (1998).
61. V. Derycke, R. Martel, J. Appenzeller, and P. Avouris, *Nano Lett.* 1, 453 (2001).
62. A. Bachtold, P. Hadley, T. Nakanishi, and C. Dekker, *Science* 294, 1317 (2001).
63. J. Kong, N. R. Franklin, C. W. Zhou, M. G. Chapline, S. Peng, K. J. Cho, and H. J. Dai, *Science* 287, 622 (2000).
64. P. G. Collins, K. Bradley, M. Ishigami, and A. Zettl, *Science* 287, 1801 (2000).
65. K. Tsukagoshi, B. W. Alphenaar, and H. Ago, *Nature* 401, 572 (1999).
66. T. W. Tomblor, C. W. Zhou, L. Alexseyev, J. Kong, H. J. Dai, L. Lei, C. S. Jayanthi, M. J. Tang, and S. Y. Wu, *Nature* 405, 769 (2000).
67. K. H. An, W. S. Kim, Y. S. Park, Y. C. Choi, S. M. Lee, D. C. Chung, D. J. Bae, S. C. Lim, and Y. H. Lee, *Adv. Mater.* 13, 497 (2001).
68. E. Frackowiak, K. Metenier, V. Bertagna, and F. Beguin, *Appl. Phys. Lett.* 77, 2421 (2000).
69. C. M. Niu, E. K. Sichel, R. Hoch, D. Moy, and H. Tennent, *Appl. Phys. Lett.* 70, 1480 (1997).
70. M. Hughes, M. S. P. Shaffer, A. C. Renouf, C. Singh, G. Z. Chen, J. Fray, and A. H. Windle, *Adv. Mater.* 14, 382 (2002).
71. M. Hughes, G. Z. Chen, M. S. P. Shaffer, D. J. Fray, and A. H. Windle, *Chem. Mater.* 14, 1610 (2002).
72. E. Frackowiak and F. Beguin, *Carbon* 40, 1775 (2002).
73. M. Endo, Y. A. Kim, T. Hayashi, K. Nishimura, T. Matusita, K. Miyashita, and M. S. Dresselhaus, *Carbon* 39, 1287 (2001).
74. J. Li, R. Stevens, L. Delzeit, H. T. Ng, A. Cassell, J. Han, and M. Meyyappan, *Appl. Phys. Lett.* 81, 910 (2002).
75. M. A. Guillorn, T. E. McKnight, A. Melechko, V. I. Merkulov, P. F. Britt, D. W. Austin, D. H. Lowndes, and M. L. Simpson, *J. Appl. Phys.* 91, 3824 (2002).
76. G. L. Che, B. B. Lakshmi, E. R. Fisher, and C. R. Martin, *Nature* 393, 346 (1998).
77. E. S. Steigerwalt, G. A. Deluga, D. E. Cliffel, and C. M. Lukehart, *J. Phys. Chem. B* 105, 8097 (2001).
78. A. Chambers, C. Park, R. T. K. Baker, and N. M. Rodriguez, *J. Phys. Chem. B* 102, 4253 (1998).
79. C. Park, P. E. Anderson, A. Chambers, C. D. Tan, R. Hidalgo, and N. M. Rodriguez, *J. Phys. Chem. B* 103, 10572 (1999).
80. A. C. Dillon, K. M. Jones, T. A. Bekkedahl, C. H. Kiang, D. S. Bethune, and M. J. Heben, *Nature* 386, 377 (1997).

81. B. Gao, A. Kleinhammes, X. P. Tang, C. Bower, L. Fleming, Y. Wu, and O. Zhou, *Chem. Phys. Lett.* 307, 153 (1999).
82. M. Hirscher, M. Becher, M. Haluska, U. Dettlaff-Weglikowska, A. Quintel, G. S. Duesberg, Y. M. Choi, P. Downes, M. Hulman, S. Roth, I. Stepanek, and P. Bernier, *Appl. Phys. A* 72, 129 (2001).
83. P. Kim and C. M. Lieber, *Science* 286, 2148 (1999).
84. R. H. Baughman, C. X. Cui, A. A. Zakhidov, Z. Iqbal, J. N. Barisci, G. M. Spinks, G. G. Wallace, A. Mazzoldi, D. De Rossi, A. G. Rinzler, O. Jaschinski, S. Roth, and M. Kertesz, *Science* 284, 1340 (1999).
85. J. Cumings and A. Zettl, *Science* 289, 602 (2000).
86. L. Zhang, A. V. Melechko, V. I. Merkulov, M. A. Guillorn, M. L. Simpson, D. H. Lowndes, and M. J. Doktycz, *Appl. Phys. Lett.* 81, 135 (2002).
87. J. Sandler, P. Werner, M. S. P. Shaffer, V. Demchuk, V. Altstadt, and A. H. Windle, *Compos. A* 33, 1033 (2002).
88. W. B. Downs and R. T. K. Baker, *J. Mater. Res.* 10, 625 (1995).
89. D. D. L. Chung, *Carbon* 39, 1119 (2001).
90. D. D. L. Chung, *Carbon* 39, 279 (2001).
91. J. Sandler, M. S. P. Shaffer, T. Prasse, W. Bauhofer, K. Schulte, and A. H. Windle, *Polymer* 40, 5967 (1999).
92. E. Kymakis and G. A. J. Amaratunga, *Appl. Phys. Lett.* 80, 112 (2002).
93. B. Vigolo, A. Penicaud, C. Coulon, C. Sauder, R. Pailler, C. Journet, P. Bernier, and P. Poulin, *Science* 290, 1331 (2000).
94. R. Andrews, D. Jacques, A. M. Rao, T. Rantell, F. Derbyshire, Y. Chen, J. Chen, and R. C. Haddon, *Appl. Phys. Lett.* 75, 1329 (1999).
95. P. A. O. Muisener, L. Clayton, J. D'Angelo, J. P. Harmon, A. K. Sikder, A. Kumar, A. M. Cassell, and M. Meyyappan, *J. Mater. Res.* 17, 2507 (2002).
96. P. Calvert, *Nature* 399, 210 (1999).
97. L. S. Schadler, S. C. Giannaris, and P. M. Ajayan, *Appl. Phys. Lett.* 73, 3842 (1998).
98. J. M. Bonard, N. Weiss, H. Kind, T. Stockli, L. Forro, K. Kern, and A. Chatelain, *Adv. Mater.* 13, 184 (2001).
99. L. Nilsson, O. Groening, C. Emmenegger, O. Kuettel, E. Schaller, L. Schlapbach, H. Kind, J. M. Bonard, and K. Kern, *Appl. Phys. Lett.* 76, 2071 (2000).
100. O. Groning, O. M. Kuttel, C. Emmenegger, P. Groning, and L. Schlapbach, *J. Vac. Sci. Technol. B* 18, 665 (2000).
101. T. W. Ebbesen and P. M. Ajayan, *Nature* 358, 220 (1992).
102. C. Journet, W. K. Maser, P. Bernier, A. Loiseau, M. L. delaChapelle, S. Lefrant, P. Deniard, R. Lee, and J. E. Fischer, *Nature* 388, 756 (1997).
103. "Chemistry and Physics of Carbon" (J. Philip, L. Walker, and P. A. Thrower, Eds.), Vol. 14. Dekker, New York/Basel, 1978.
104. R. T. K. Baker and P. S. Harris, in "Chemistry and Physics of Carbon" (J. P. L. Walker and P. A. Thrower, Eds.), Vol. 14, p. 83. Dekker, New York/Basel, 1978.
105. M. S. Dresselhaus, G. Dresselhaus, K. Sugihara, I. L. Spain, and H. A. Goldberg, "Graphite Fibers and Filaments," Vol. 5. Springer-Verlag, Berlin, 1988.
106. G. S. Duesberg, J. Muster, H. J. Byrne, S. Roth, and M. Burghard, *Appl. Phys. A* 69, 269 (1999).
107. A. G. Rinzler, J. Liu, H. Dai, P. Nikolaev, C. B. Huffman, F. J. Rodriguez-Macias, P. J. Boul, A. H. Lu, D. Heymann, D. T. Colbert, R. S. Lee, J. E. Fischer, A. M. Rao, P. C. Eklund, and R. E. Smalley, *Appl. Phys. A* 67, 29 (1998).
108. J. Kong, A. M. Cassell, and H. J. Dai, *Chem. Phys. Lett.* 292, 567 (1998).
109. J. H. Hafner, M. J. Bronikowski, B. R. Azamian, P. Nikolaev, A. G. Rinzler, D. T. Colbert, K. A. Smith, and R. E. Smalley, *Chem. Phys. Lett.* 296, 195 (1998).
110. S. S. Fan, M. G. Chapline, N. R. Franklin, T. W. Tomblor, A. M. Cassell, and H. J. Dai, *Science* 283, 512 (1999).
111. Y. G. Zhang, A. L. Chang, J. Cao, Q. Wang, W. Kim, Y. M. Li, N. Morris, E. Yenilmez, J. Kong, and H. J. Dai, *Appl. Phys. Lett.* 79, 3155 (2001).
112. A. Ural, Y. Li, and H. Dai, *Appl. Phys. Lett.* 81, 3464 (2002).
113. Z. F. Ren, Z. P. Huang, J. W. Xu, J. H. Wang, P. Bush, M. P. Siegal, and P. N. Provencio, *Science* 282, 1105 (1998).
114. W. Z. Li, S. S. Xie, L. X. Qian, B. H. Chang, B. S. Zou, W. Y. Zhou, R. A. Zhao, and G. Wang, *Science* 274, 1701 (1996).
115. M. Terrones, N. Grobert, J. Olivares, J. P. Zhang, H. Terrones, K. Kordatos, W. K. Hsu, J. P. Hare, P. D. Townsend, K. Prassides, A. K. Cheetham, H. W. Kroto, and D. R. M. Walton, *Nature* 388, 52 (1997).
116. Z. F. Ren, Z. P. Huang, D. Z. Wang, J. G. Wen, J. W. Xu, J. H. Wang, L. E. Calvet, J. Chen, J. F. Klemic, and M. A. Reed, *Appl. Phys. Lett.* 75, 1086 (1999).
117. V. I. Merkulov, D. H. Lowndes, Y. Y. Wei, G. Eres, and E. Voelkl, *Appl. Phys. Lett.* 76, 3555 (2000).
118. K. B. K. Teo, M. Chhowalla, G. A. J. Amaratunga, W. I. Milne, D. G. Hasko, G. Pirio, P. Legagneux, F. Wycisk, and D. Pribat, *Appl. Phys. Lett.* 79, 1534 (2001).
119. Z. W. Pan, S. S. Xie, B. H. Chang, C. Y. Wang, L. Lu, W. Liu, M. Y. Zhou, and W. Z. Li, *Nature* 394, 631 (1998).
120. L. An, J. M. Owens, L. E. McNeil, and J. Liu, *J. Am. Chem. Soc.* 124, 13688 (2002).
121. C. H. Choi, W. Kim, D. Wang, and H. Dai, *J. Phys. Chem. B*, in press.
122. H. J. Dai, J. Kong, C. W. Zhou, N. Franklin, T. Tomblor, A. Cassell, S. S. Fan, and M. Chapline, *J. Phys. Chem. B* 103, 11246 (1999).
123. Y. C. Choi, Y. M. Shin, Y. H. Lee, B. S. Lee, G. S. Park, W. B. Choi, N. S. Lee, and J. M. Kim, *Appl. Phys. Lett.* 76, 2367 (2000).
124. N. M. Rodriguez, *J. Mater. Res.* 8, 3233 (1993).
125. H. G. Tennent, J. J. Barber, and R. Hoch, Hyperion Catalysis, Cambridge, MA, 1996.
126. S. B. Sinnott, R. Andrews, D. Qian, A. M. Rao, Z. Mao, E. C. Dickey, and F. Derbyshire, *Chem. Phys. Lett.* 315, 25 (1999).
127. G. G. Tibbetts, *Appl. Phys. Lett.* 42, 666 (1983).
128. A. Fonseca, K. Hernadi, P. Piedigrosso, J. F. Colomer, K. Mukhopadhyay, R. Doome, S. Lazarescu, L. P. Biro, P. Lambin, P. A. Thiry, D. Bernaerts, and J. B. Nagy, *Appl. Phys. A* 67, 11 (1998).
129. P. Piedigrosso, Z. Konya, J. F. Colomer, A. Fonseca, G. Van Tendeloo, and J. B. Nagy, *Phys. Chem. Chem. Phys.* 2, 163 (2000).
130. H. Q. Hou, A. K. Schaper, F. Weller, and A. Greiner, *Chem. Mater.* 14, 3990 (2002).
131. R. S. Wagner and W. C. Ellis, *Appl. Phys. Lett.* 4, 89 (1964).
132. R. S. Wagner, in "Whiskers Technology" (A. P. Levitt, Ed.), p. 47. Wiley, New York, 1970.
133. T. Baird, J. R. Fryer, and B. Grant, *Carbon* 12, 591 (1974).
134. A. Oberlin, M. Endo, and T. Koyama, *J. Crystal Growth* 32, 335 (1976).
135. A. Oberlin, M. Endo, and T. Koyama, *Carbon* 14, 133 (1976).
136. G. G. Tibbetts, *J. Crystal Growth* 66, 632 (1984).
137. H. J. Dai, A. G. Rinzler, P. Nikolaev, A. Thess, D. T. Colbert, and R. E. Smalley, *Chem. Phys. Lett.* 260, 471 (1996).
138. E. Boellaard, P. K. Debokx, A. Kock, and J. W. Geus, *J. Catal.* 96, 481 (1985).
139. P. K. Debokx, A. Kock, E. Boellaard, W. Klop, and J. W. Geus, *J. Catal.* 96, 454 (1985).
140. A. Kock, P. K. Debokx, E. Boellaard, W. Klop, and J. W. Geus, *J. Catal.* 96, 468 (1985).
141. E. Tracz, R. Scholz, and T. Borowiecki, *Appl. Catal.* 66, 133 (1990).
142. N. Krishnakutty, N. M. Rodriguez, and R. T. K. Baker, *J. Catal.* 158, 217 (1996).
143. A. Chambers and R. T. K. Baker, *J. Phys. Chem. B* 101, 1621 (1997).
144. M. S. Kim, N. M. Rodriguez, and R. T. K. Baker, *J. Catal.* 134, 253 (1992).

145. C. Park, E. S. Engel, A. Crowe, T. R. Gilbert, and N. M. Rodriguez, *Langmuir* 16, 8050 (2000).
146. C. Singh, T. Qusted, C. B. Boothroyd, P. Thomas, I. A. Kinloch, A. I. Abou-Kandil, and A. H. Windle, *J. Phys. Chem. B* 106, 10915 (2002).
147. H. Terrones, T. Hayashi, M. Munoz-Navia, M. Terrones, Y. A. Kim, N. Grobert, R. Kamalakaran, J. Dorantes-Davila, R. Escudero, M. S. Dresselhaus, and M. Endo, *Chem. Phys. Lett.* 343, 241 (2001).
148. P. E. Nolan, D. C. Lynch, and A. H. Cutler, *J. Phys. Chem. B* 102, 4165 (1998).
149. L. Delzeit, I. McAninch, B. A. Cruden, D. Hash, B. Chen, J. Han, and M. Meyyappan, *J. Appl. Phys.* 91, 6027 (2002).
150. H. W. Kroto, J. R. Heath, S. C. O'Brien, R. F. Curl, and R. E. Smalley, *Nature* 318, 162 (1985).
151. J. Kong, H. T. Soh, A. M. Cassell, C. F. Quate, and H. J. Dai, *Nature* 395, 878 (1998).
152. A. M. Cassell, J. A. Raymakers, J. Kong, and H. J. Dai, *J. Phys. Chem. B* 103, 6484 (1999).
153. M. Su, B. Zheng, and J. Liu, *Chem. Phys. Lett.* 322, 321 (2000).
154. B. Kitiyanan, W. E. Alvarez, J. H. Harwell, and D. E. Resasco, *Chem. Phys. Lett.* 317, 497 (2000).
155. W. E. Alvarez, B. Kitiyanan, A. Borgna, and D. E. Resasco, *Carbon* 39, 547 (2001).
156. J. E. Herrera, L. Balzano, A. Borgna, W. E. Alvarez, and D. E. Resasco, *J. Catal.* 204, 129 (2001).
157. W. E. Alvarez, F. Pompeo, J. E. Herrera, L. Balzano, and D. E. Resasco, *Chem. Mater.* 14, 1853 (2002).
158. A. Kukovecz, Z. Konya, N. Nagaraju, I. Willems, A. Tamasi, A. Fonseca, J. B. Nagy, and I. Kiricsi, *Phys. Chem. Chem. Phys.* 2, 3071 (2000).
159. Y. M. Li, W. Kim, Y. G. Zhang, M. Rolandi, D. W. Wang, and H. J. Dai, *J. Phys. Chem. B* 105, 11424 (2001).
160. C. L. Cheung, A. Kurtz, H. Park, and C. M. Lieber, *J. Phys. Chem. B* 106, 2429 (2002).
161. J. F. Colomer, G. Bister, I. Willems, Z. Konya, A. Fonseca, G. Van Tendeloo, and J. B. Nagy, *Chem. Commun.* 1343 (1999).
162. J. Geng, C. Singh, D. Shephard, M. Shaffer, B. F. G. Johnson, and A. H. Windle, *Chem. Commun.* 2666 (2002).
163. V. Ivanov, J. B. Nagy, P. Lambin, A. Lucas, X. B. Zhang, X. F. Zhang, D. Bernaerts, G. Vantendeloo, S. Amelinckx, and J. Vanlanduyt, *Chem. Phys. Lett.* 223, 329 (1994).
164. L. F. Sun, J. M. Mao, Z. W. Pan, B. H. Chang, W. Y. Zhou, G. Wang, L. X. Qian, and S. S. Xie, *Appl. Phys. Lett.* 74, 644 (1999).
165. H. J. Dai, *Phys. World* 13, 43 (2000).
166. S. Amelinckx, X. B. Zhang, D. Bernaerts, X. F. Zhang, V. Ivanov, and J. B. Nagy, *Science* 265, 635 (1994).
167. C. J. Lee and J. Park, *Appl. Phys. Lett.* 77, 3397 (2000).
168. W. Z. Li, J. G. Wen, Y. Tu, and Z. F. Ren, *Appl. Phys. A* 73, 259 (2001).
169. Y. Li, J. Liu, Y. Q. Wang, and Z. L. Wang, *Chem. Mater.* 13, 1008 (2001).
170. H. Ago, S. Ohshima, K. Uchida, and M. Yumura, *J. Phys. Chem. B* 105, 10453 (2001).
171. L. Delzeit, B. Chen, A. Cassell, R. Stevens, C. Nguyen, and M. Meyyappan, *Chem. Phys. Lett.* 348, 368 (2001).
172. P. Nikolaev, M. J. Bronikowski, R. K. Bradley, F. Rohmund, D. T. Colbert, K. A. Smith, and R. E. Smalley, *Chem. Phys. Lett.* 313, 91 (1999).
173. M. Joseyacaman, M. Mikiyoshida, L. Rendon, and J. G. Santiesteban, *Appl. Phys. Lett.* 62, 657 (1993).
174. M. Endo, K. Takeuchi, S. Igarashi, K. Kobori, M. Shiraishi, and H. W. Kroto, *J. Phys. Chem. Solids* 54, 1841 (1993).
175. A. M. Benito, Y. Maniette, E. Munoz, and M. T. Martinez, *Carbon* 36, 681 (1998).
176. N. R. Franklin, Y. M. Li, R. J. Chen, A. Javey, and H. J. Dai, *Appl. Phys. Lett.* 79, 4571 (2001).
177. N. R. Franklin and H. J. Dai, *Adv. Mater.* 12, 890 (2000).
178. V. I. Merkulov, A. V. Melechko, M. A. Guillorn, D. H. Lowndes, and M. L. Simpson, *Chem. Phys. Lett.* 350, 381 (2001).
179. D. S. Y. Hsu, *Appl. Phys. Lett.* 80, 2988 (2002).
180. C. Bower, W. Zhu, D. Shalom, D. Lopez, L. H. Chen, P. L. Gamme, and S. Jin, *Appl. Phys. Lett.* 80, 3820 (2002).
181. G. Pirio, P. Legagneux, D. Pribat, K. B. K. Teo, M. Chhowalla, G. A. J. Amaratunga, and W. I. Milne, *Nanotechnology* 13, 1 (2002).
182. M. Chhowalla, K. B. K. Teo, C. Ducati, N. L. Rupesinghe, G. A. J. Amaratunga, A. C. Ferrari, D. Roy, J. Robertson, and W. I. Milne, *J. Appl. Phys.* 90, 5308 (2001).
183. C. Bower, O. Zhou, W. Zhu, D. J. Werder, and S. H. Jin, *Appl. Phys. Lett.* 77, 2767 (2000).
184. J. I. Sohn, S. Lee, Y. H. Song, S. Y. Choi, K. I. Cho, and K. S. Nam, *Appl. Phys. Lett.* 78, 901 (2001).
185. S. M. Sze, "VLSI Technology," 2nd ed., p. 309. McGraw-Hill, New York, 1988.
186. K. B. K. Teo, M. Chhowalla, G. A. J. Amaratunga, W. I. Milne, G. Pirio, P. Legagneux, F. Wyczisk, D. Pribat, and D. G. Hasko, *Appl. Phys. Lett.* 80, 2011 (2002).
187. A. M. Rao, D. Jacques, R. C. Haddon, W. Zhu, C. Bower, and S. Jin, *Appl. Phys. Lett.* 76, 3813 (2000).
188. T. de los Arcos, F. Vonau, M. G. Garnier, V. Thommen, H. G. Boyen, P. Oelhafen, M. Duggelin, D. Mathis, and R. Guggenheim, *Appl. Phys. Lett.* 80, 2383 (2002).
189. M. S. Dresselhaus, G. Dresselhaus, K. Sugihara, I. L. Spain, and H. A. Goldberg, "Graphite Fibers and Filaments" Vol. 5, Springer-Verlag, Berlin, 1988.
190. C. Emmenegger, P. Mauron, A. Zuttel, C. Nutzenadel, A. Schneuwly, R. Gallay, and L. Schlapbach, *Appl. Surf. Sci.* 162, 452 (2000).
191. H. Kind, J. M. Bonard, C. Emmenegger, L. O. Nilsson, K. Hernadi, E. Maillard-Schaller, L. Schlapbach, L. Forro, and K. Kern, *Adv. Mater.* 11, 1285 (1999).
192. R. T. K. Baker, J. R. Alonzo, J. A. Dumesic, and D. J. C. Yates, *J. Catal.* 77, 74 (1982).
193. S. K. Hwang, K. D. Lee, and K. H. Lee, *Jpn. J. Appl. Phys. 2 Lett.* 40, L580 (2001).
194. A. M. Cassell, S. Verma, L. Delzeit, M. Meyyappan, and J. Han, *Langmuir* 17, 260 (2001).
195. B. Chen, G. Parker, J. Han, M. Meyyappan, and A. M. Cassell, *Chem. Mater.* 14, 1891 (2002).
196. Y. Tu, Z. P. Huang, D. Z. Wang, J. G. Wen, and Z. F. Ren, *Appl. Phys. Lett.* 80, 4018 (2002).
197. J. F. Colomer, C. Stephan, S. Lefrant, G. Van Tendeloo, I. Willems, Z. Konya, A. Fonseca, C. Laurent, and J. B. Nagy, *Chem. Phys. Lett.* 317, 83 (2000).
198. J. M. Bonard, T. Stockli, O. Noury, and A. Chatelain, *Appl. Phys. Lett.* 78, 2775 (2001).
199. K. Matsumoto, S. Kinoshita, Y. Gotoh, T. Uchiyama, S. Manalis, and C. Quate, *Appl. Phys. Lett.* 78, 539 (2001).
200. J. H. Hafner, C. L. Cheung, and C. M. Lieber, *Nature* 398, 761 (1999).
201. E. B. Cooper, S. R. Manalis, H. Fang, H. Dai, K. Matsumoto, S. C. Minne, T. Hunt, and C. F. Quate, *Appl. Phys. Lett.* 75, 3566 (1999).
202. Y. Y. Wei, G. Eres, V. I. Merkulov, and D. H. Lowndes, *Appl. Phys. Lett.* 78, 1394 (2001).
203. M. P. Siegal, D. L. Overmyer, and P. P. Provencio, *Appl. Phys. Lett.* 80, 2171 (2002).
204. C. Ducati, I. Alexandrou, M. Chhowalla, G. A. J. Amaratunga, and J. Robertson, *J. Appl. Phys.* 92, 3299 (2002).
205. K. B. K. Teo, S. B. Lee, M. Chhowalla, D. G. Hasko, H. Ahmed, G. A. J. Amaratunga, W. I. Milne, V. Semet, V. T. Binh, O. Groening, M. Castignolles, A. Loiseau, P. Legagneux, G. Pirio, and D. Pribat, *Nanotechnology*, 14, 204 (2003).

206. Y. Chen, Z. L. Wang, J. S. Yin, D. J. Johnson, and R. H. Prince, *Chem. Phys. Lett.* 272, 178 (1997).
207. Y. Chen, S. Patel, Y. G. Ye, S. T. Shaw, and L. P. Luo, *Appl. Phys. Lett.* 73, 2119 (1998).
208. Z. P. Huang, J. W. Wu, Z. F. Ren, J. H. Wang, M. P. Siegal, and P. N. Provencio, *Appl. Phys. Lett.* 73, 3845 (1998).
209. T. Sato, D. G. Hasko, and H. Ahmed, *J. Vac. Sci. Technol. B* 15, 45 (1997).
210. T. Koyama, *Carbon* 10, 757 (1972).
211. T. Kato, K. Kusakabe, and S. Morooka, *J. Mater. Sci. Lett.* 11, 674 (1992).
212. L. J. Ci, Y. H. Li, B. Q. Wei, J. Liang, C. L. Xu, and D. H. Wu, *Carbon* 38, 1933 (2000).
213. M. Endo, K. Takeuchi, K. Kobori, K. Takahashi, H. W. Kroto, and A. Sarkar, *Carbon* 33, 873 (1995).
214. B. C. Satishkumar, A. Govindaraj, and C. N. R. Rao, *Chem. Phys. Lett.* 307, 158 (1999).
215. R. Sen, A. Govindaraj, and C. N. R. Rao, *Chem. Phys. Lett.* 267, 276 (1997).
216. S. M. Huang, L. M. Dai, and A. W. H. Mau, *J. Phys. Chem. B* 103, 4223 (1999).
217. Y. Y. Yang, S. M. Huang, H. Z. He, A. W. H. Mau, and L. M. Dai, *J. Am. Chem. Soc.* 121, 10832 (1999).
218. D. C. Li, L. M. Dai, S. M. Huang, A. W. H. Mau, and Z. L. Wang, *Chem. Phys. Lett.* 316, 349 (2000).
219. C. Singh, M. S. P. Shaffer, and A. H. Windle, *Carbon* 41, 363 (2003).
220. R. Sen, A. Govindaraj, and C. N. R. Rao, *Chem. Mater.* 9, 2078 (1997).
221. R. Andrews, D. Jacques, A. M. Rao, F. Derbyshire, D. Qian, X. Fan, E. C. Dickey, and J. Chen, *Chem. Phys. Lett.* 303, 467 (1999).
222. R. Kamalakaran, M. Terrones, T. Seeger, P. Kohler-Redlich, M. Ruhle, Y. A. Kim, T. Hayashi, and M. Endo, *Appl. Phys. Lett.* 77, 3385 (2000).
223. M. Mayne, N. Grobert, M. Terrones, R. Kamalakaran, M. Ruhle, H. W. Kroto, and D. R. M. Walton, *Chem. Phys. Lett.* 338, 101 (2001).
224. Z. J. Zhang, B. Q. Wei, G. Ramanath, and P. M. Ajayan, *Appl. Phys. Lett.* 77, 3764 (2000).
225. B. Q. Wei, R. Vajtai, Y. Jung, J. Ward, R. Zhang, G. Ramanath, and P. M. Ajayan, *Nature* 416, 495 (2002).
226. B. Q. Wei, Z. J. Zhang, G. Ramanath, and P. M. Ajayan, *Appl. Phys. Lett.* 77, 2985 (2000).
227. A. Y. Cao, L. J. Ci, D. J. Li, B. Q. Wei, C. L. Xu, J. Liang, and D. H. Wu, *Chem. Phys. Lett.* 335, 150 (2001).
228. R. Vajtai, K. Kordas, B. Q. Wei, J. Bekesi, S. Leppavuori, T. F. George, and P. M. Ajayan, *Mater. Sci. Eng. C* 19, 271 (2002).
229. B. Q. Wei, R. Vajtai, Z. J. Zhang, G. Ramanath, and P. M. Ajayan, *J. Nanosci. Nanotechnol.* 1, 35 (2001).
230. C. N. R. Rao, A. Govindaraj, R. Sen, and B. C. Satishkumar, *Mater. Res. Innov.* 2, 128 (1998).
231. H. M. Cheng, F. Li, G. Su, H. Y. Pan, L. L. He, X. Sun, and M. S. Dresselhaus, *Appl. Phys. Lett.* 72, 3282 (1998).
232. H. W. Zhu, C. L. Xu, D. H. Wu, B. Q. Wei, R. Vajtai, and P. M. Ajayan, *Science* 296, 884 (2002).
233. H. W. Zhu, B. Jiang, C. L. Xu, and D. H. Wu, *Chem. Commun.* 1858 (2002).
234. B. Q. Wei, R. Vajtai, Y. Y. Choi, P. M. Ajayan, H. W. Zhu, C. L. Xu, and D. H. Wu, *Nano Lett.* 2, 1105 (2002).
235. M. J. Bronikowski, P. A. Willis, D. T. Colbert, K. A. Smith, and R. E. Smalley, *J. Vac. Sci. Technol. A* 19, 1800 (2001).
236. HSC Chemistry Version 4.1, Outokumpu Research Oy, 2002.
237. "Chemistry and Physics of Carbon" (J. Philip, L. Walker, and P. A. Throver, Eds.), Vol. 7. Dekker, New York, 1971.
238. V. Ivanov, A. Fonseca, J. B. Nagy, A. Lucas, P. Lambin, D. Bernaerts, and X. B. Zhang, *Carbon* 33, 1727 (1995).
239. J.-B. Donnet and R. C. Bansal, "Carbon Fibers," 2nd ed., Vol. 10. Dekker, New York, 1990.
240. C. Singh, M. S. P. Shaffer, I. Kinloch, and A. H. Windle, *Physica B* 323, 339 (2002).
241. J. M. Bonard, M. Croci, F. Conus, T. Stockli, and A. Chatelain, *Appl. Phys. Lett.* 81, 2836 (2002).
242. B. O. Boskovic, V. Stolojan, R. U. A. Khan, S. Haq, and S. R. P. Silva, *Nature Mater.* 1, 165 (2002).
243. S. Ohshima, H. Ago, H. Inoue, and M. Yumura, *New Diam. Front. Carbon Technol.* 11, 437 (2001).
244. Y. Wang, F. Wei, G. Luo, H. Yu, and G. Gu, *Chem. Phys. Lett.* 364, 568 (2002).
245. Y. Wang, F. Wei, G. Gu, and H. Yu, *Physica B* 322, 327 (2002).
246. A. Weidenkaff, S. G. Ebbinghaus, P. Mauron, A. Reller, Y. Zhang, and A. Zuttel, *Mater. Sci. Eng. C* 15, 119 (2002).
247. A. Huczko, *Appl. Phys. A* 70, 365 (2000).
248. T. Kyotani, L. F. Tsai, and A. Tomita, *Chem. Mater.* 7, 1427 (1995).
249. G. Che, B. B. Lakshmi, C. R. Martin, E. R. Fisher, and R. S. Ruoff, *Chem. Mater.* 10, 260 (1998).
250. J. Li, C. Papadopoulos, J. M. Xu, and M. Moskovits, *Appl. Phys. Lett.* 75, 367 (1999).
251. N. Wang, Z. K. Tang, G. D. Li, and J. S. Chen, *Nature* 408, 50 (2000).
252. Y. Avigal and R. Kalish, *Appl. Phys. Lett.* 78, 2291 (2001).
253. H. T. Soh, C. F. Quate, A. F. Morpurgo, C. M. Marcus, J. Kong, and H. J. Dai, *Appl. Phys. Lett.* 75, 627 (1999).
254. J. Kong, C. Zhou, A. Morpurgo, H. T. Soh, C. F. Quate, C. Marcus, and H. Dai, *Appl. Phys. A* 69, 305 (1999).
255. Y. H. Lee, Y. T. Jang, C. H. Choi, D. H. Kim, C. W. Lee, J. E. Lee, Y. S. Han, S. S. Yoon, J. K. Shin, S. T. Kim, E. K. Kim, and B. K. Ju, *Adv. Mater.* 13, 1371 (2001).
256. H. Conrads and M. Schmidt, *Plasma Sources Sci. Technol.* 9, 441 (2000).
257. C. Bower, W. Zhu, S. H. Jin, and O. Zhou, *Appl. Phys. Lett.* 77, 830 (2000).
258. L. C. Qin, D. Zhou, A. R. Krauss, and D. M. Gruen, *Appl. Phys. Lett.* 72, 3437 (1998).
259. N. Wang and B. D. Yao, *Appl. Phys. Lett.* 78, 4028 (2001).
260. M. Okai, T. Muneyoshi, T. Yaguchi, and S. Sasaki, *Appl. Phys. Lett.* 77, 3468 (2000).
261. Y. C. Choi, Y. M. Shin, S. C. Lim, D. J. Bae, Y. H. Lee, B. S. Lee, and D. C. Chung, *J. Appl. Phys.* 88, 4898 (2000).
262. H. Murakami, M. Hirakawa, C. Tanaka, and H. Yamakawa, *Appl. Phys. Lett.* 76, 1776 (2000).
263. K.-Y. Lee, K. Fujimoto, S. Ohkura, S. Honda, M. Katayama, T. Hirao, and K. Oura, *Mater. Res. Soc. Symp. Proc.* 675, W3.1 (2001).
264. Z. P. Huang, D. Z. Wang, J. G. Wen, M. Sennett, H. Gibson, and Z. F. Ren, *Appl. Phys. A* 74, 387 (2002).
265. J. G. Wen, Z. P. Huang, D. Z. Wang, J. H. Chen, S. X. Yang, Z. F. Ren, J. H. Wang, L. E. Calvet, J. Chen, J. F. Klemic, and M. A. Reed, *J. Mater. Res.* 16, 3246 (2001).
266. Y. Chen, D. T. Shaw, and L. P. Guo, *Appl. Phys. Lett.* 76, 2469 (2000).
267. S. H. Tsai, C. W. Chao, C. L. Lee, and H. C. Shih, *Appl. Phys. Lett.* 74, 3462 (1999).
268. V. I. Merkulov, M. A. Guillorn, D. H. Lowndes, M. L. Simpson, and E. Voelkl, *Appl. Phys. Lett.* 79, 1178 (2001).
269. V. I. Merkulov, A. V. Melechko, M. A. Guillorn, M. L. Simpson, D. H. Lowndes, J. H. Whealton, and R. J. Raridon, *Appl. Phys. Lett.* 80, 4816 (2002).
270. L. R. Baylor, V. I. Merkulov, E. D. Ellis, M. A. Guillorn, D. H. Lowndes, A. V. Melechko, M. L. Simpson, and J. H. Whealton, *J. Appl. Phys.* 91, 4602 (2002).
271. M. A. Guillorn, M. D. Hale, V. I. Merkulov, M. L. Simpson, G. Y. Eres, H. Cui, A. A. Puzos, and D. B. Geohegan, *Appl. Phys. Lett.* 81, 2860 (2002).

272. V. I. Merkulov, D. H. Lowndes, and L. R. Baylor, *J. Appl. Phys.* 89, 1933 (2001).
273. K. B. K. Teo, M. Chhowalla, G. A. J. Amaratunga, W. I. Milne, G. Pirio, P. Legagneux, F. Wyczisk, J. Olivier, and D. Pribat, *J. Vac. Sci. Technol. B* 20, 116 (2002).
274. V. Semet, V. T. Binh, P. Vincent, D. Guillot, K. B. K. Teo, M. Chhowalla, G. A. J. Amaratunga, W. I. Milne, P. Legagneux, and D. Pribat, *Appl. Phys. Lett.* 81, 343 (2002).
275. A. Chambers, N. M. Rodriguez, and R. T. K. Baker, *J. Phys. Chem.* 99, 10581 (1995).
276. A. Chambers, N. M. Rodriguez, and R. T. K. Baker, *J. Mater. Res.* 11, 430 (1996).
277. B. C. Satishkumar, P. J. Thomas, A. Govindaraj, and C. N. R. Rao, *Appl. Phys. Lett.* 77, 2530 (2000).
278. F. L. Deepak, A. Govindaraj, and C. N. R. Rao, *Chem. Phys. Lett.* 345, 5 (2001).
279. J. M. Ting and C. C. Chang, *Appl. Phys. Lett.* 80, 324 (2002).
280. W. Z. Li, J. G. Wen, and Z. F. Ren, *Appl. Phys. Lett.* 79, 1879 (2001).
281. B. Gan, J. Ahn, Q. Zhang, S. F. Yoon, Rusli, Q. F. Huang, H. Yang, M. B. Yu, and W. Z. Li, *Diam. Relat. Mater.* 9, 897 (2000).
282. B. Gan, J. Ahn, Q. Zhang, Rusli, S. F. Yoon, J. Yu, Q. F. Huang, K. Chew, V. A. Ligatchev, X. B. Zhang, and W. Z. Li, *Chem. Phys. Lett.* 333, 23 (2001).
283. J. Li, C. Papadopoulos, and J. Xu, *Nature* 402, 253 (1999).
284. C. Papadopoulos, A. Rikitin, J. Li, A. S. Vedenev, and J. M. Xu, *Phys. Rev. Lett.* 85, 3476 (2000).

Ceramic Nanoparticle Synthesis

Xiangdong Feng

Ferro Corporation, Ohio, USA

Michael Z. Hu

Oak Ridge National Laboratory, Oak Ridge, Tennessee, USA

CONTENTS

1. Introduction
2. Methods for Categorizing Nanoparticle Synthesis
3. Descriptions of Major Synthesis Methods by Media
4. Summary
Glossary
References

1. INTRODUCTION

Nanotechnology has been viewed as the “little big science” [1], which is considered the impetus for the next industrial revolution. The ability to work at the molecular level, atom by atom, to create large structures with fundamentally new properties and functions is the core of nanoscale science, engineering, and technology [2]. One of the building blocks of nanotechnology is nanostructured materials such as nanoparticles [3].

Nanoparticles may be defined according to their physical dimensions as *particles with a size range of 1 to 100 nm* [3, 4]. A typical nanoparticle most often consists of several small “primary particles” [5]. The size of nanoparticles usually refers to the “secondary” particle size. Primary particles agglomerate into these “secondary” particles [5]. The primary particles have a very high surface-to-volume ratio. The proportion of atoms on the surface and at the grain boundaries of a nanoparticle is significant. Nanoparticles have about 98, 40, and 10% of their atoms on the surfaces or at the grain boundaries if their primary particles are 1, 5, and 20 nm, respectively. The high proportion of surface and grain boundary atoms is responsible for the different properties (electronic, optical, electrical, magnetic, chemical, and mechanical) of nanoparticles with respect to the

bulk materials [6, 7]. This represents new opportunities in science, such as the change of properties and laws as the dimensions of the nanomaterials become comparable to, or smaller than, relevant length scales, such as the mean-free path or the coherence length. New material properties result when the surface and the grain boundary atoms represent a large proportion of the total number of atoms, or when processes become dominated by quantum effects, or—in general—by the transition from atomic and molecular behavior to condensed matter behavior [8].

The size range for nanoparticles may be more accurately defined as the size range from 1 nm to the largest nanometer dimension, where the ratio of the number of atoms on surfaces and at grain boundaries to those at the center is such that new physical, chemical, and biological properties occur, compared to bulk materials [9]. The upper limit of the nanoparticle size may be different from 100 nm, depending upon the sizes of the atoms and molecules in question.

Nanoparticles have large surface areas [7] and high reactivity due to the unsaturated bonds on their pristine surfaces. Nanoparticles tend to react among themselves to form necking, and hence agglomerate into large secondary particles. This imposes extreme challenges for industry to produce large quantities of nanoparticles with identical properties inexpensively and reliably. Selecting the proper manufacturing methods for a specific application requires a thorough understanding of the fundamental aspects of nanoparticle formation.

There are numerous reported synthetic methods for the production of nanoparticles [10]. The challenge is to control the nanoparticle size, size distribution, morphology, crystallinity, shape, and properties, to assemble the nanoparticles for a given purpose, and to make them from a variety of materials. The synthetic methods reported can be classified according to synthesis strategies, the branches of science involved in the process, sources of energy input, and the media in which nanoparticles are formed.

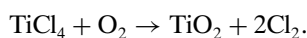
2. METHODS FOR CATEGORIZING NANOPARTICLE SYNTHESIS

2.1. By Synthesis Strategy

Strategies are important for the synthesis of nanoparticles. There are two basic strategies used in the syntheses of nanoparticles: bottom up and top down [9, 11].

2.1.1. Bottom-Up Strategy

This strategy is more in line with the basic strategy of nanoscience and technology. Here, nanoparticles are built up atom by atom, or molecule by molecule, at the will of their creators. Most nanoparticle syntheses belong to this category. A simple example of this approach is the flame synthesis of TiO_2 from gaseous TiCl_4 and oxygen according to



It has been shown that nucleation and surface growth determine the primary particle size of titania [12–14]. Other studies [15, 16] show that coagulation of the primary particles of titania could also dominate particle growth during flame synthesis of TiO_2 . The molecular TiO_2 formed in the flame can grow into particles through nucleation and surface oxidation of TiCl_4 , aggregation, or the combination of both mechanisms. Under certain processing conditions, either one of the mechanisms could dominate the overall particle growth.

2.1.2. Top-Down Strategy

This strategy is most applied in the traditional particle-making process. Here, nanoparticles are synthesized by breaking down bulk materials gradually into smaller sizes until they are nanosized. The end results could also be achieved by leaching out one type of molecule in a bulky homogeneous molecular solid mixture.

Mechanical breakdown, such as high-energy ball milling, is a simple case of the top-down strategy. $\gamma\text{-Al}_2\text{O}_3$ powders have been ball milled into nanocrystalline alumina powders with different surface areas of up to $100 \text{ m}^2/\text{g}$, depending on the milling atmosphere of air or inert gases [17]. High-energy ball milling is useful for deriving nanocrystalline materials of high-temperature phases without going to extreme heat treatment, which would promote significant grain growth and surface area loss. For example, nanocrystalline $\alpha\text{-Al}_2\text{O}_3$ with a high surface area was obtained through ball milling [18].

Another example of the top-down strategy is illustrated by the synthesis of nanosize yttrium-stabilized zirconia by leaching bulky yttrium-doped BaZrO_3 or bulky yttrium-doped Na_2ZrO_3 [19]. In this approach, yttrium-doped BaZrO_3 or yttrium-doped Na_2ZrO_3 is first synthesized from BaCO_3 , ZrO_2 , and Y_2O_3 , and from Na_2CO_3 , ZrO_2 , and Y_2O_3 by a conventional solid-state reaction method. The synthesized yttrium-doped BaZrO_3 or yttrium-doped Na_2ZrO_3 is then boiled to leach away the unwanted species, BaO or Na_2O , either in a diluted HNO_3 solution for BaZrO_3 or in water for Na_2ZrO_3 . The residues of the skeleton form fine, nanosize yttrium-stabilized zirconia of 3–15 nm.

2.2. By Nature of the Process

Different nanoparticle-making techniques may involve different scientific processes, such as physical, chemical or biological, or some combination of these processes.

2.2.1. Physical Methods

A physical process involves only changes in physical state, such as size, shape, and phase of the matter. Mechanical size reduction is a physical process. Condensing gaseous metal vapor into nanoparticles is another example. The formation of nanoparticles in the gas phase is accomplished by a rapid quenching of supersaturated metal vapors with room-temperature or cold inert gas [20].

2.2.2. Chemical Methods

Most nanoparticle syntheses involve chemical changes. For instance, a sol-gel process converts metal alkoxides into oxide particles [21]. A hydrothermal process converts titanium isopropoxide and barium hydroxide into BaTiO_3 [22]. Other chemical methods will be described in more detail in following discussions.

2.2.3. Biological Methods

Nanostructured materials are synthesized in nature by a process known as biomineralization (the *in vivo* formation of inorganic crystals and/or amorphous particles in biological systems [23, 24]). In nearly all cases, the growth of the inorganic phases is controlled by biologically produced membranes or templates, which are usually composed of proteins and/or polysaccharides [25]. In some cases, the phase of the inorganic element is dictated by the organic template, by molecular complementarities, or by epitaxial matching of the organic and inorganic surfaces. In some cases, the biological membrane may act to limit the size and morphology of the resulting crystal by providing a defined space and chemical environment within which precipitation can occur. Fendler [26, 27] has shown that a mimetic approach in nanoparticle synthesis addresses the essential requirement of biomineralization. It is to have compartments capable of providing structural, spatial, and chemical controls for nanoparticle generation and stabilization. The mimetic approach using aqueous micelles, reverse micelles, microemulsions, vesicles, polymerized vesicles, monolayers, self-organized multilayers, and bilayer lipid membranes has successfully generated nanocrystalline Ag_2O [28], and less than 10 nm monodispersed Pt, Pd, Rh, and Ir particles [29, 30]. Pierre et al. have also demonstrated the synthesis of nanoscale (<10 nm) iron oxide using protein cages and polysaccharide networks [31].

2.2.4. Combination Methods

Most of the synthetic methods for nanoparticles are a combination of both physical and chemical processes. The biological method discussed above is more often a combination of chemical and physical (structural and spatial) control. Many of the synthetic methods to be discussed in detail below are combinations of chemical and physical processes.

2.3. By Energy Sources

Energy is always involved in the synthesis of nanoparticles. Nanoparticle synthesis methods can then be classified based on the types of energy input used in the synthetic processes. Laser synthesis, for example, refers to lasers being used as the energy source in the production of nanoparticles. Lasers could be used for evaporating materials into gas phases, promoting chemical reactions among gas molecules, and decomposing molecules. The following are examples of synthetic methods that are named after energy sources:

- laser
- plasma
- joule heating
- sputtering
- electron beam
- microwave
- hydrothermal
- freeze drying
- high-energy ball milling
- combustion
- flame
- supercritical

2.4. By Media in which Nanoparticles are Formed

Nanoparticles are always formed in a medium of either gas phase, liquid phase, or solid phase. The classifications based on the media where nanoparticles are formed are perhaps the most important and most widely used classification [32, 33]. By focusing on the media in which nanoparticles are formed, many issues common to all of the techniques within each specific medium arise. By summarizing the very different techniques used for synthesis in any one medium, one may perhaps learn and incorporate the best attributes of the different techniques to develop a nanoparticle synthesis method most suitable for one's own applications. The media for nanoparticle syntheses are usually classified as

- gas phases
- liquid phases
- solid phases

The detailed discussion in this chapter is arranged according to this medium classification.

3. DESCRIPTIONS OF MAJOR SYNTHESIS METHODS BY MEDIA

3.1. Gas-Phase Synthesis

Gas-phase syntheses described here are those methods where particles are formed as a result of reactions among gaseous molecules, gas molecule condensation and/or decomposition, nucleation, growth, and possibly agglomeration. In general, gas-phase syntheses using gases as reactants involve low concentration because of the low density of gases. This has an advantage for producing nanoparticles because nucleating particles in such low concentrations tend to be less agglomerated [34]. It is also generally true that

gas-phase methods are not as convenient for multiple components as are solution methods. This is because of the difference in saturated gas vapor pressures and the difficulty of controlling the reaction rates among different gases.

Gas-phase syntheses can be further divided into two broad types: vapor condensation and vapor reaction (the latter includes vapor decomposition).

3.1.1. Vapor Condensation Synthesis

This technique involves the physical conversion of gaseous vapor into solid clusters and particles. Research on the vapor condensation method for nanoparticles started in the 1960s [35–37]. Siegel [38] has summarized the early development of this type of synthesis, and Kimura has provided a review of its more recent development [20]. Two growth mechanisms have been proposed: the absorption growth process, where particle nuclei grow with the absorption of metal atoms; and the coalescence growth process, where particles grow by collision of particle nuclei and clusters. The advantages of these methods have been noted as having

1. ultrafine sizes
2. particle surface cleanness
3. applicability to metals, alloys, intermetallic compounds, ceramics, and semiconductors
4. flexibility in controlling crystallinity.

Inert-gas condensation has been suggested as the best method for making ultrafine metal particles [36]. Fuchs and Sutugin [39] have pointed out the difficulties of such methods, which arise from the presence of the more highly volatile impurity oxides that become the first particles formed, and also from impurities from the evaporation of the chamber materials. Brock [40] has raised further concern that the condensation method has not been shown to preserve stoichiometry. It is reasonable to suppose that the more volatile species will evaporate first, but condense last.

Vapor condensation synthesis includes many different methodologies:

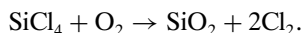
1. inert gas evaporation technique [35], in which the target material is heated in a vacuum chamber with an atmosphere of several torr inert gas
2. matrix isolation method, where a cold substance instead of a room-temperature wall is used to control particle agglomeration [38, 41, 42]
3. gas flow/cold trap method, where a vapor of organic liquid is introduced into a particle carrier gas, and then trapped on a liquid-nitrogen-cooled wall [20]
4. gas flow/solution trap method, where nanoparticles in a carrying gas are bubbled through a precooled solvent, such as ethanol, at -30 to 140 °C, depending on the organic solvent(s) [43].

Much of the vapor condensation work has used resistance heating [38]. More and more work has been done with laser [44, 45], plasma discharging [46, 47], sputtering [48, 49], and electron beam [50].

3.1.2. Vapor Reaction Synthesis

This is perhaps the most important technology in gas-phase synthesis. It usually involves the reaction of two or more gaseous molecules to generate ceramic nanoparticles. Even

the simple decomposition of gaseous molecules, such as the chlorides and nitrates, usually involves the reaction of the salt with oxygen molecules, as in the following example:



This technique can be further divided into flame synthesis and chemical vapor reaction.

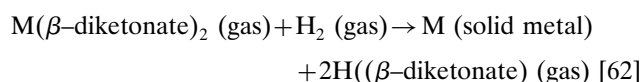
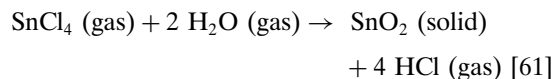
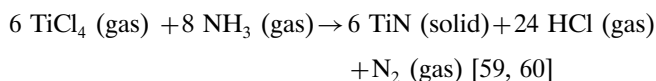
Flame Synthesis Flame synthesis refers to a synthesis in which gaseous reactants react in a flame to produce particles. The flame contains fuel molecules and oxidizing molecules. Flames are exothermal systems, which provide the energy for particle formation. Flame technology is an established industrial process for the manufacture of carbon blacks and ceramic commodities, such as fumed silica, pigment titania, zinc oxides, and alumina powders. The current production volume using this technology is on the order of several million metric tons per year [51]. Pratsinis [52] provided a detailed review of this technology. Fumed silica is synthesized by feeding gaseous SiCl_4 together with air and hydrogen into the burner to form a silica aerosol [53]. The silica is separated from the HCl-containing gases by cyclone separators or filters. The specific surface area of fumed silica is 50–380 m^2/g . The particles consist of aggregates of amorphous spherical primary particles up to a few nanometers [54]. Amorphous and $\delta\text{-Al}_2\text{O}_3$ powders of size 10–200 nm were obtained by reacting AlCl_3 vapor in an oxygen–hydrogen diffusion flame [55]. Pratsinis [52] has pointed out that: (1) the role of gas or surface reaction on particle formation and growth in flame synthesis is very important since surface growth favors a much narrower size distribution compared to pure coagulation; (2) the competition between collision and coalescence is responsible for aggregation, and aggregates collide much faster than equivalent spheres; (3) reactant mixing is a critical variable in controlling flame temperature and, subsequently, the chemistry, size, and composition of aggregate and primary particles over a wide spectrum in diffusion flame reactors, which are widely used in industry; and (4) it appears that electric fields across the flame provide one of the best means for precise control of primary particle size and crystallinity—and even aggregate size [56].

Janzen and Roth [57] prepared 4–20 nm single-crystal $\gamma\text{-Fe}_2\text{O}_3$ nanoparticles via a gas-phase route using an $\text{H}_2/\text{O}_2/\text{Ar}$ low-pressure flame. The burner-stabilized flame was doped with different amounts of Fe–pentacarbonyl ($\text{Fe}(\text{CO})_5$), with concentrations in the range of 262–2096 ppm. The particles were analyzed *in-situ* according to their mass and charge by a particle mass spectrometer.

The advantages of flame synthesis include: simple oxides easily produced in short residence time; scale up demonstrated for SiO_2 , TiO_2 , Al_2O_3 , and other oxides; and high purity. The disadvantages may include: formation of hard agglomerates under most of the conditions; broad particle size distribution; nonuniform temperature and residence time profiles; and difficulties in producing other particles such as nitrides, borides, and so on.

Kleinwechter et al. [58] have synthesized 4–8 nm ZnO in a low-pressure flame reactor and a microwave reactor in $\text{Zn}(\text{CH}_3)_2$ -doped $\text{H}_2/\text{O}_2/\text{Ar}$ flames and $\text{Zn}(\text{CH}_3)_2$ -doped Ar/O_2 plasmas, respectively.

Chemical Vapor Reactions Chemical vapor reactions for gas-phase nanoparticle syntheses usually involve a mixture of gas reactants in a reaction chamber, and the chemical reactions among the gas molecules are induced by an input of energy such as resistant heating, laser, and plasma. Chlorides are popular reactants for the formation of both nonoxides and oxides because of their generally low vaporization temperature and low cost. Some of the typical reactions include



Di Lello et al. [64] synthesized 30 nm AlN nanoscale particles from the vapor phase using ammonia and aluminum chloride vapor as reactants. van der Waals forces and the tendency for surface energy minimization cause the particles to hold together, and what the SEM, in fact, revealed are small particle aggregates. TEM observations, however, confirm the nanoscale nature of such particles, with an average particle size of 30 nm of single crystals.

Jiang et al. [65] prepared Si-based nanopowders from $((\text{CH}_3)_3\text{Si})_2\text{NH}$ by chemical vapor decomposition (CVD). The powders synthesized at 1000–1500 °C were all amorphous. The particles synthesized were near spherical, with sizes of 8–10 nm. After annealing at high temperatures, the powders synthesized at low temperatures formed whiskers of mainly SiC with a small amount of Si_3N_4 , while the powders synthesized at high temperatures formed 20–40 nm particles of mainly $\beta\text{-SiC}$, with a small amount of $\alpha\text{-SiC}$.

The energy input can be thermal plasma [66, 67], laser [63, 68], or furnace heating [69]. Furnace-heated tubular flow reactors have the advantages of simplicity, easy scale up, and the ability to produce oxides, nonoxides, semiconductors, and metals. The disadvantages include hard agglomeration at high aerosol loading. The primary advantage of a laser-driven process is the production of high-purity products, and its disadvantage is the requirement for complex and expensive systems. The plasma process is unique in its use of high melting point materials and rapid cooling, with the disadvantages of broad particle size distribution and high-energy input.

3.1.3. Aerosol Synthesis

In general, *gas-phase synthesis* refers to those methods where gaseous molecules and atoms are directly converted into nanoparticles through gas-phase reaction [14, 52], condensation, and/or decomposition, nucleation, growth, and possibly agglomeration. However, in an aerosol process, a homogeneous liquid starting material is converted into an aerosol

(i.e., small liquid droplets suspended in gas phase) [70–72]. This aerosol is then converted into solid particles suspended in a gas stream by heating. The aerosol syntheses discussed here are only pseudogas-phase syntheses. These pseudogas-phase syntheses can be further classified into the following two broad types: aerosol pyrolysis and flame–aerosol pyrolysis.

Aerosol Pyrolysis An aerosol pyrolysis process is also called spray pyrolysis [73] or vapor pyrolysis. It consists of three parts: aerosol generation, particle formation inside a furnace, and particle collection, as shown in Figure 1. A homogeneous liquid solution (organic, aqueous, or a mixture) containing the reactants is converted into an aerosol using air, nitrogen gas, or a mixture of gases. The sizes of the droplets formed in the aerosol depend on the types of aerosol generators used, the carrying gas volume, and the nature of the liquid [20, 74]. An ultrasonic generator usually gives very fine droplets that may be suitable for making nanoparticles [73]. The aerosol is then carried by the gas into a preheated furnace, where the liquid droplets go through solvent evaporation, solute precipitation, solute decomposition, and oxide sintering to final particles, as shown in Figure 1. Eventually, the particles are carried out by the gases into a particle collection section, where the particles may be quenched with cold gases and collected by filters or bags (Fig.1).

In order to generate uniform and small droplets of aerosol, the first step of the process is to prepare a uniform solution. In the case of making nano-BaTiO₃, the solution contains barium and titanium. This solution can be made from simple inorganic salts such as TiCl₄ and BaCl₂ [75], or TiCl₄ and Ba(NO₃)₂ [76], in a mixture of water and ethanol. The starting materials can also be a mixture of Ti alkoxides and barium salts such as Ba(NO₃)₂ in a mixture of water and alcohols [77, 78]. The sources of titanium and barium have also been tried with both organometallic compounds such as titanium alkoxides with barium acetate [78] and titanium lactate and barium acetate [79].

The different starting materials affect the BaTiO₃ formation mechanism and the characteristics of the BaTiO₃ formed. TiCl₄ has a strong tendency to dissociate and hydrolyze according to the following solution reaction, in a bulky solution or in aerosol droplets [75]:

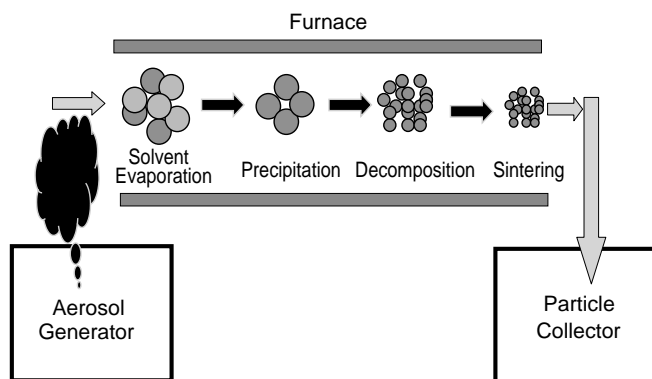
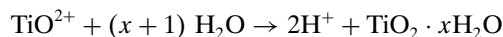
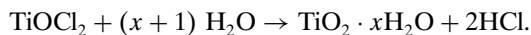


Figure 1. Schematic representation of an aerosol pyrolysis process.

When the droplets are carried into the furnace, the solvent begins to evaporate, and further hydrolysis occurs according to



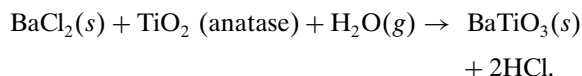
or



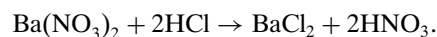
Upon further heating [77],



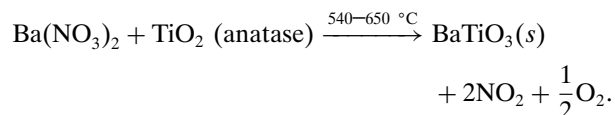
If BaCl₂ is involved,



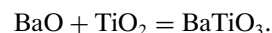
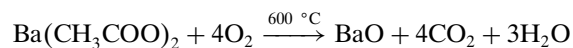
If Ba(NO₃)₂ is used, the above reaction may also be involved due to the formation of BaCl₂:



The following reaction has also been reported:



On the other hand, BaO is formed if organic barium sources are used [78]:



Ogihara et al. [78] obtained dense spherical BaTiO₃ of 930 nm using Ti(iso-OC₃H₇)₄ and Ba(CH₃COO)₂, while hollow spherical BaTiO₃ was produced using Ti(iso-OC₃H₇)₄ and Ba(NO₃)₂ using aerosol pyrolysis at 900 °C. They contributed such a difference in the BaTiO₃ due to the fact that reaction (9) occurs much more easily than reactions (5) and (7) at temperatures below 700 °C.

Milosevic and co-workers [75] produced 530 nm BaTiO₃ by aerosol pyrolysis of an ethanol/water solution of BaCl₂ and TiCl₄ using an ultrasonic atomizer. Cho et al. [76] prepared BaTiO₃ of size 300–900 nm by ultrasonic aerosol pyrolysis of solutions containing Ba(NO₃)₂ and TiCl₄.

BaTiO₃ particles were prepared in our laboratory using Ti isopropoxide and barium acetate in an aerosol pyrolysis process, as shown in Figure 2 [80], where particles of 50–600 nm were obtained. These particles are tetragonal in crystal structure, with a Ba/Ti ratio of 0.9999.

An issue in aerosol processes is the extent of agglomeration (particle adhesion) and aggregation (particle sintering), the latter referring to clusters of primary particles being cemented together by interparticle necks. While it is virtually impossible to eliminate the agglomeration of pristine nanopowders due to the strong van der Waals forces of attraction that keep the particles together, aggregation can

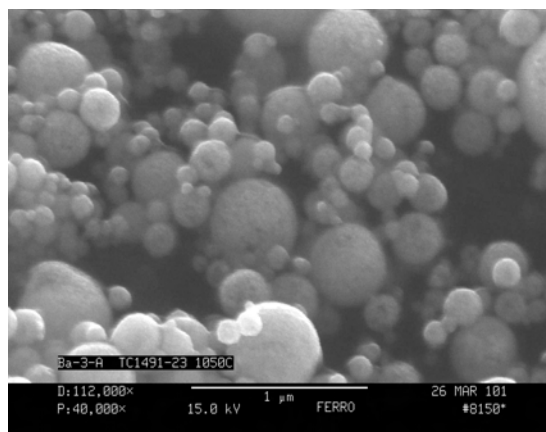


Figure 2. BaTiO₃ made from an aerosol pyrolysis process [80].

be restricted by controlled powder synthesis. Singhal et al. [81] developed a vapor-phase synthesis method, called combustion flame/chemical vapor condensation. It involves the pyrolysis of chemical precursors in a low-pressure flat flame, and is used to produce nanoparticles of TiO₂ and Al₂O₃. Nanoparticles of oxides that have an average secondary particle size of approximately 100 nm, and an average primary particle size less than 25 nm, were produced by controlling the time–temperature history of the particles in the hot zone of the flame.

In aerosol processes, it is important to analyze how the gas-phase molecules react, nucleate, agglomerate and sinter, and how these steps control the size distribution and morphology of particles. Nakaso et al. [82] studied the thermal decomposition of titanium tetraisopropoxide and oxidation of TiCl₄ by using a laminar-flow aerosol reactor. The effect of reaction temperature on the size and morphology of the generated particles was investigated under various conditions. The size distributions of agglomerates were measured using a differential mobility analyzer/condensation nuclear counter system. The growths of both agglomerates and primary particles were modeled simultaneously, using a two-dimensional discrete-sectional representation of the size distribution.

The advantages of aerosol pyrolysis for nanoparticle making include: (1) high purity, (2) spherical particles, (3) an easy and quick one-step process, and (4) minimal agglomeration. The disadvantages are: (1) a large size distribution, as shown in Figure 2, (2) the necessity of a large amount of carrying gas dilution in order to reduce agglomeration and aggregation, (3) low production rates, and (4) difficult scale up.

Flame–Aerosol Pyrolysis Flame–aerosol synthesis is a process in which an aerosol of starting materials is burned in a flame [73]. A flowchart of a flame–aerosol pyrolysis is shown in Figure 3 [83]. The chemistry in a flame–aerosol system is similar to that described for an aerosol pyrolysis process. The differences include the source of heating: flame–aerosol is heated by the burning of the fuel gases and organic solvents which are in direct contact with the precursor materials. The heating in an aerosol process is usually external and indirect by resistance heating or gas heating

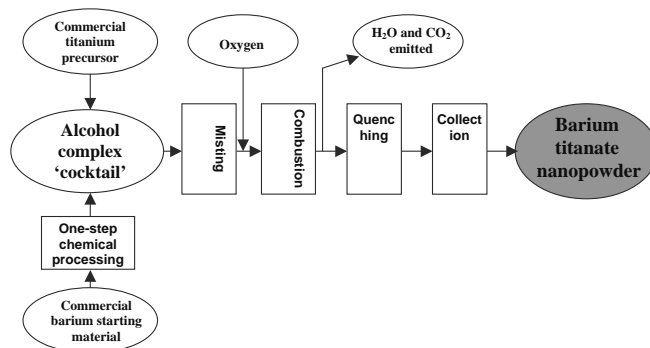


Figure 3. Flowchart of a flame–aerosol pyrolysis process [83].

through a heat-conducting wall. The burning of the fuels in a flame process directly affects the product's oxidation states and purity, while the heating source in an aerosol process does not introduce impurity into the final products, except that contamination may come from the heat-conducting walls.

Brewster and Kodas [84] have demonstrated the formation of chemically pure, crystalline (primarily tetragonal with hexagonal and cubic polymorphs), and unagglomerated dense BaTiO₃ particles of about 1400 nm by flame–aerosol of a 0.5 M solution of barium acetate titanium lactate and water at a flame temperature of >1500 °C (adiabatic).

These aerosol synthesis methods, aerosol pyrolysis and flame–aerosol pyrolysis, have produced BaTiO₃ particles less than 100 nm. The BaTiO₃ particles in Figure 2 also show broad particle size distributions. In general, these aerosol syntheses can produce spherical particles with clean surfaces, desired Ba/Ti ratio control, and good crystallinity via a continuous process. There are many reported studies in which nanoparticles of a few nanometers are produced [52, 74, 85–87]. In many cases, these are academic studies involving the collection of a few particles on a TEM grid. These nanoparticles are extremely reactive, and agglomerate quickly into large particles in an industrial collection system. The industrial process for producing large quantities of particles of nanosizes may require such a large dilution of the particle stream with the carrying gas as to make this process inefficient. The scale up to the production of tonnage quantity for the flame–aerosol process is much easier than for that of aerosol pyrolysis. In general, it is extremely challenging to make unagglomerated particles with a narrow size distribution.

3.2. Liquid-Phase Synthesis

Liquid-phase syntheses are the most common and diverse methods for nanoparticle synthesis. The critical particle formation step occurs in the liquid phase; however, under supercritical conditions, the particle formation phase is at both the liquid and gas phase since there is no distinction between gas and liquid under those conditions. The most common solvent is water, but more and more organic solvents are also used in an effort to reduce the agglomeration of nanoparticles. Common to all of the liquid-phase syntheses is that they begin with solution preparation. A true solution means homogeneity at the atomic or molecular scale.

The central goal for the diverse solution synthetic methods is to preserve as much of this homogeneity as possible in the particle formation process.

Liquid-phase syntheses are generally wet-chemical solution syntheses, sometimes called soft solution-processing routes. There is an increasing role that solution synthesis plays in the preparation of ceramic powders, particularly nanometer-sized particles with controlled size and morphology [88]. Wet-chemical processes have been widely recognized as an efficient approach to prepare nanocrystalline fine particles at low temperatures. In relation to other methods such as vapor-phase synthesis and physical methods (such as laser ablation and electron beam evaporation), major advantages of the liquid-phase synthesis include: (1) the process can be scaled up easily due to its bulk-processing nature; (2) the process is more controllable because chemical reactor technologies developed for chemical synthesis may be adapted and applied to the production of nanoparticles; (3) some processes require only mild conditions such as low temperature and atmospheric pressure; (4) the chemical composition of nanoparticles can be tailored in a liquid phase; (5) in the liquid phase, surface-controlling agents can be applied during and after nanoparticle formation to control the size and prevent unnecessary agglomeration; and (6) monodispersed nanoparticles can be made in the liquid phase via a homogeneous nucleation, growth, and aggregation mechanism. Uniform particle size is extremely important to nanoparticle self-assembly-based systems.

Wet-chemical syntheses are particularly suited to the synthesis of nanoparticles (solid, core-shell, or hollow) with tightly controlled parameters, such as: (1) the size and shape, (2) the monodispersity, (3) the chemical composition and purity, (4) the bulk substructure, (5) the crystallinity (polycrystalline, single crystalline, or amorphous), (6) the surface functional group (thus, the interfacial free energy and surface-charge density), (7) the shell-layer thickness in a core-shell nanoparticle, or even (8) the size and shell thickness of a hollow sphere particle. For ceramic processing, the above characteristics of nanoparticles will affect the processing behavior, as well as the properties of the final, casted, sintered ceramic materials.

The use of “nanoparticle(s)” as a popular technical term in the literature of wet-chemical synthesis of truly nanosized (i.e., <100 nm in particle size or crystallite size) ceramic particles did not appear until less than a decade ago. However, research on ultrafine, monodispersed colloid particles has been conducted as a major goal of colloidal science since the beginning of the 20th century. Some excellent review articles on monodispersed particles can be found [89, 90–94]. Colloids are typically defined as particles with a particle size ranging from 1 nm to 1 μm , which is more or less defined by the importance of Brownian motion. Colloidal particles, (hydrous) oxides in particular, have long been utilized as models or tools in scientific research; applied in fields such as drug delivery, biondiagnostics, and combinatorial synthesis; and used as the major components of industrial products such as paints, ink, foods, cosmetics, coatings, catalysts, pigments, papers, photographic films, recording materials, films, and rheological fluids. Some of these monodispersed

colloid studies have indeed produced nanosized monodispersed particles.

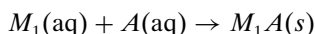
Major synthesis methods for ideal ceramic nanoparticle formation in the liquid phase depend on “controlled precipitation” or “homogeneous precipitation” reactions involving sequential nucleation and growth processes. As a general rule, a homogeneous solution system (consisting of ideally one phase where the monomer reservoir is normally built in the form of a solute) is necessary for generating uniform-size nanoparticles. Reactions belonging to this category include [94]: (1) the redox reaction, (2) precipitation by poor solvents, (3) direct reaction of ions, (4) reaction of chelates, (5) decomposition of compounds, (6) hydrolysis in organic media, and (7) hydrolysis in aqueous media. The particle growth process can be either by *molecular diffusion/addition* to the nuclei surface or by a *particle aggregation* mechanism, both of which have been demonstrated to generate monodispersed particles [95–99]. To obtain uniform particle size in a diffusional growth process, the nucleation stage must be separated from the particle growth stage. Seeding is one approach to achieve the separation of nucleation from growth.

In addition to the desirable goal of monodispersed particles, anisotropic particles are also strongly needed for important applications, such as the fabrication of composite materials and flat panel optical displays. Control of the size distribution, shape, and aspect ratio is a complex process requiring a fundamental understanding of the interactions among solid-state chemistry, interfacial reactions and kinetics, and solution chemistry [100].

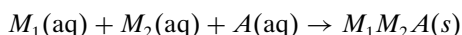
Regardless of the methods used, achieving homogeneous reaction or precipitation in homogeneous solutions is the key to producing uniform colloids or nanoparticles (either isotropic or anisotropic). Precipitation of alkoxide solutions and forced hydrolysis of some metal salt solutions surely satisfy the “homogeneous” criteria. Enough attention has been paid to the preparation of “ideal” sinterable ceramic nanopowders with improved densification properties compared with conventionally derived ceramic powders. In most literature studies of nanoparticle synthesis, particle size may not be monodispersed (due to the broad range of particle size distribution). The wet-chemical synthesis methods that have been reported so far in the recent literature to produce ceramic (oxide or hydrous oxide) nanoparticles or nanocrystalline powders can be mainly classified as chemical precipitation and coprecipitation, hydrothermal synthesis, forced hydrolysis, sol-gel synthesis, synthesis in microemulsion or reverse micelles, solvothermal synthesis and nonhydrolytic routes, microwave heating-assisted synthesis, sonochemical synthesis, electrochemical synthesis, and synthesis in supercritical fluids. Historically, the above-mentioned methods have been developed or studied for ultrafine ceramic particle synthesis. However, the majority of studies on these methods for the synthesis of truly nanosized particles appeared well within the last decade. In the following sections, each synthesis method will be reviewed and discussed, with a focus on its application in ceramic (oxide and hydrous oxide) nanoparticle or nanopowder production.

3.2.1. Chemical Precipitation and Coprecipitation

Chemical, or reactive, precipitation can be generally described by the solid phase formation from reactions of soluble reactive species (M_1 , M_2 , A) in a solution (aqueous or nonaqueous)



where M_1 is a metal cation species and A (aq) represents an anion species from a precipitating agent such as NH_4OH , NaOH , carbamate ($\text{NH}_2\text{CO}_2\text{NH}_4$), H_3PO_4 , etc. When more than one metal cation species is involved, for example, a second metal species, $M_2(\text{aq})$, could be coprecipitated



If $A(\text{aq})$ happens to be oxygen or a hydroxyl group, $M_1A(s)$ will be a single metal oxide or hydrous oxide, while $M_1M_2A(s)$ represents a mixed metal oxide.

A chemical precipitation process consists of three main steps: chemical reaction, nucleation, and crystal growth. Chemical precipitation is generally not a controlled process in terms of reaction kinetics and the solid phase nucleation and growth processes. Therefore, solids obtained by chemical precipitation have a wide particle size distribution plus uncontrolled particle morphology, along with agglomeration. In the preparation process of particles via reactive precipitation ($A + B \rightarrow P$), the chemical reaction is so fast that a high degree of supersaturation of the product solute P will be achieved in local sites in the reactor. This causes the nucleation to be dominated by homogeneous nucleation mechanisms, where the value of the power order in the nucleation rate expression equation can be in the range of 5–18 or so. Any tiny variation of the supersaturation of product P will lead to a significant change in the nucleation rate because of this high value of powder order. However, because of its simplicity, rapid solid formation kinetics, and bulk processing capability, chemical reaction is still a viable option for nanoparticle production as long as strategies are considered for controlling the kinetics (reactions between ions), reaction uniformity, and agglomeration. To obtain nanoparticles with a narrow size distribution, one should do as much as possible to meet the requirements of: (1) a high degree of supersaturation, (2) a uniform spatial concentration distribution inside a reactor, and (3) a uniform growth time for all particles or crystals [101].

Recently, chemical precipitation and coprecipitation have been reported in the active literature for nanoparticle synthesis. Table 1 summarizes some of the major research work on chemical precipitation of (hydrous) oxides, and Table 2 for chemical coprecipitation of mixed oxides. Most of the chemical precipitation processes are conducted in aqueous solutions, but a few are in nonaqueous solutions.

Zhou et al. [102] used NH_4OH to precipitate cerium nitrate at room temperature. They tried to obtain a high value for the supersaturation ratio (S), in order to establish an environmental condition that favors homogeneous nucleation, which typically results in the “burst” formation

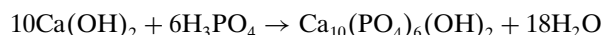
of uniform nuclei with a critical size which can be calculated from

$$r^* = 2\nu\gamma/[k_B T \ln(S)]$$

where ν = molecular volume of the precipitated embryo (m^3), γ = surface energy (J/m^2), k_B = Boltzmann's constant (J/K), T = temperature (K), and S = supersaturation value.

A three-stage process was developed to produce ZnO nanoparticles [103], involving: (1) the formation of metastable zinc complexes through a slow addition of ammonia; (2) the partial phase transformation of metastable zinc precursors to zinc oxide after washing the initial colloidal suspension with ethanol, $\text{Zn-OH}(s) + \text{C}_2\text{H}_5\text{OH}(l) \rightarrow \text{Zn-O-C}_2\text{H}_5(s) + \text{H}_2\text{O}(l)$; and (3) the complete transformation to ZnO by thermal treatment. The main strategy used is the *controlled release of cations* from a homogeneous suspension.

Water-soluble polymeric dispersants, such as poly (N-vinylpyrrolidone) (PVP), polyvinyl alcohol (PVA), and polyacrylic acid (PAA), have been utilized as stabilizers in chemical precipitation to prevent particle coagulation/agglomeration and to control size. Zhang and Guo [104] prepared antimony oxide nanoparticles by a refluxing reaction between SbCl_3 and NaOH in the presence of PVA: $\text{Sb}^3 + \text{OH}^- \rightarrow \text{Sb}_2\text{O}_3 + \text{H}_2\text{O}$. Rasmussen et al. [105] precipitated nanoscale aluminum hydroxide particles from sodium aluminate solutions by dilution and neutralization with water and oxalic acid in the presence of the surface-active polymers PVP and PVA. In the wet-chemical precipitation of needle-shaped hydroxyapatite nanocrystals, Bouyer et al. [106] used the following reaction



In precipitating europium oxide nanoparticles with NaOH , trioctyl phosphine oxide (TOPO) was used for the following three possible reasons [107]: (1) it prevents particle agglomeration (via steric passivation), (2) it achieves electrical passivation of surface dangling bonds (trap states); and (3) it controls particle size at the nanometer level. Chen and Chen [108] used PAA in the coprecipitation of strontium ferrite nanoparticles (34–41 nm for calcined powders). Pardoe et al. [109] used dextran and PVA in the coprecipitation of nanoscale iron oxide particles by ammonia.

Some chemical precipitation of nanoparticles was conducted in nonaqueous background solutions. Carnes et al. [110] attempted an “alkoxide-based” synthesis involving the NaOH precipitation of metal chloride in ethanol background solutions. Chemical precipitation produces metal hydroxide solids which are converted to oxides by heating. Wakefield et al. [107] precipitated europium oxide by NaOH in a methanol background solution. Meulenkamp [111] prepared ZnO nanoparticles by the dropwise addition of LiOH (dissolved in ethanol) into an ethanolic zinc acetate solution under vigorous stirring at 0°C . The presence of a small, but strictly limited, quantity of water (from the acetate salt) appeared necessary to warrant good particle growth. Manorama et al. [112] coprecipitated SnCl_4 and copper

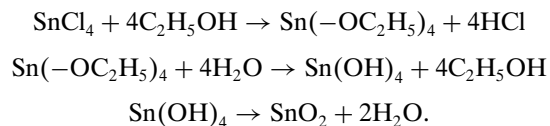
Table 1. Nanoparticle synthesis by chemical precipitation.

Nanoparticle materials	Characteristics of nanoparticle	Brief process description	Applications	Ref.
CeO ₂	4–5 nm, round-shaped, single crystals	Room-temperature homogeneous nucleation; cerium nitrate solution was added into aqueous NH ₄ OH precipitant	Raman-allowed modes shifting and broadening; pressure-induced phase transformation	[102]
CuO, NiO	7–9 nm CuO and 3–5 nm NiO crystallites, aggregate to form larger spherical particles	Precipitated by NaOH in ethanol background; “alkoxide-based” synthesis involving metal chlorides, ethanol, and water	CuO: in catalysis, metallurgy, high-temperature superconductors; NiO: electronic/magnetic properties, catalysis, <i>p</i> -type semiconductor	[155]
ZnO	~1 μm particle self-assembled with nanocrystals Microspheres consisting of aggregates of nanoscale (10–15 nm) rod-shaped primary particles 2–7 nm clean sol	Acidified zinc acetate aqueous solution titrated with NH ₄ OH solution to pH 9 Ammonium carbamate as a precipitating agent; flow injection synthesis Addition of LiOH (in ethanol) to an ethanolic zinc acetate solution	Pigments, rubber additives, gas sensors, varistors, transducers; used in photocells, as UV-absorbing material, in sunscreen lotions, as insulator, light-emitting diodes, ceramics, ion-insertion batteries, electrochromic devices	[103, 117, 111]
Sb ₂ O ₃	10–80 to 200 nm sizes, polyhedral-shaped, polycrystalline cubic phase	Reaction between SbCl ₃ and NaOH in the presence of polyvinyl alcohol in water solution	Flame retardants; optic materials; high proton conductivity; humidity-sensing materials	[104]
Fe ₂ O ₃	Spherical-shaped nanoparticles	Ammonium acetate as precipitating agent	Magnetic materials	[95]
Al(OH) ₃	80–300 nm in PVP; 200 nm–1.2 μm in PVA Nanofibrils (1–10 nm in diameter and 50–300 nm in length)	Oxalic acid as precipitating agent High-gravity reactive precipitation	Bayer process Nanocomposites, pharmaceuticals	[105, 101]
Hydroxyapatite	Needle-shaped, aspect ratio (= length/width) = 2–10	Ca(OH) ₂ precipitated by H ₃ PO ₄ , 25–85 °C	Bioceramic for biomedical applications such as bone substitute	[106]
Eu ₂ O ₃	2–40 nm, passivated with trioctyl phosphine oxide (TOPO)	At room temperature; precipitation of EuCl ₃ by NaOH in a methanol background solution in the presence of TOPO	Luminescent phosphors for flat-panel displays based on field-emitting arrays	[107]
In(OH) ₃	Multiple morphology precipitates which were peptized into 80–8000 nm powders (round-shaped) Uniform colloidal rod-like particles (aggregates of nanosize subunits)	Hydrolysis of indium chloride in EG/aqueous NaOH solutions, plus peptization Controlled double-jet precipitation	Semiconductor and optical properties	[114, 118]
CaCO ₃ or SrCO ₃	CaCO ₃ (17–36 nm particle size) SrCO ₃ (~40 nm particle size)	High-gravity reactive precipitation	In many industries such as electronics, opticals, pulp and paper, pharmaceuticals, etc.	[101]

Table 2. Nanoparticle synthesis by chemical coprecipitation.

Nanoparticle materials	Characteristics of nanoparticle	Brief process description	Applications	Ref.
Strontium ferrite (SrFe ₁₂ O ₁₉)	3.1 nm for mixed hydroxide precipitates; 34–41 nm for calcined powder	Polyacrylic acid (PAA) sodium salt used as protective agent; NaOH added to the mixed aqueous solution of PAA and corresponding nitrates salts Same as above	Magnetic material with high coercivity	[108]
Barium ferrite (BaFe ₁₂ O ₁₉)	4.5 nm for precipitate precursor; 23–82 nm for calcined powder	Mn and Li acetate salts dissolved in citric acid were precipitated by NH ₄ OH	Cathode material for lithium rechargeable batteries	[282]
LiMn ₂ O ₄	<100 nm crystal size, agglomerated for the calcined powder	Nonaqueous coprecipitation by cooling the mixed metal salt solution/sol (in stearic acid background) from 80–100 °C to ambient temperature to gel	Magnetic material with unique phenomena such as superparamagnetism and quantum tunneling of magnetization	[115]
Ba ₂ Co ₂ Fe ₂₈ O ₄₆	10–25 nm grain size	Iron source (Fe ²⁺ and Fe ³⁺) was added dropwise into alkali source (NaOH) under vigorous mechanical stirring; complete precipitation ~pH 7.5–14 while maintaining Fe ²⁺ /Fe ³⁺ = 1/2 under nonoxidizing environment		[116]
Fe ₃ O ₄	6–8 nm particle size and 1–6 nm crystal size, surfactant (Na oleate) coated	Coprecipitation of Fe(III) and Fe(II) by NH ₄ OH in the presence of polymer-dispersant PVA or dextran	Magnetic material, ferrofluids, biomedical and diagnostic applications, MRI contrast agents	[283]
	Cluster- and necklace-like chain aggregates (~100–200 nm length)	Coprecipitation of Fe(III) and Fe(II) by NH ₄ OH in the presence of polymer-dispersant PVA		[109]
	PVA coated (oxide core 5–10 nm, 108–155 nm outside PVA shell)	Precipitation of an aqueous solution of iron salts by tetramethylammonium hydroxide (TMAOH)		[284]
	5 nm stable uncoated nanoparticle	Using NaOH, NH ₃ , or N(CH ₃) ₄ OH to precipitate, adjusting pH and ionic strength to control particle size		[285]
	1.5–12.5 nm particle size, free from polymer, surfactant, or ligands	SnCl ₄ dissolved in HCl, SbCl ₃ , and SbCl ₅ was added, dropped into cold water, and precipitated by aqueous ammonia until pH 3–4 was reached	High <i>n</i> -type conductivity, high absorption coefficient in the NIR and IR regions (thus high reflective for IR radiation); applications in photovoltaic and optoelectronic devices; flat-panel displays	[286]
Sb-doped SnO ₂	4–9 nm particle size, spherical to ellipsoidal shaped, tend to form string-like agglomerates	“Alkoxide-like” hydrolysis: copper acetate added into mixture of equal molar solution of SnCl ₄ in water and ethanol, aged at 50 °C to precipitate	Catalyst for the oxidation of organics, solid-state sensors for reducing gases, transparent conductive thin-film coatings	[287]
	3–5 nm crystallite size	Aqueous solutions of FeCl ₃ and MgCl ₂ ·6H ₂ O precipitated by NaOH solution, digested in boiling water, washed until pH neutral		[112]
CuO-doped SnO ₂	A few nanometer to 20 nm grain size	(NH ₄) ₂ C ₂ O ₄ ·H ₂ O as coprecipitating agent	Superparamagnetism; magnetic resonance contrast agents, high-density information storage, ferrofluids, magnetocaloric refrigeration	[288]
Spinel ferrite MgFe ₂ O ₄	Powder with nanocrystallites	Heating of ZrOCl ₂ and Y(NO ₃) ₃ solution with an alcohol–water mixture, plus NH ₄ OH as precipitating agent and PEG as dispersant	High-proton conduction in atmosphere containing water at high temperature; as electrolyte in solid-state electrochemical devices	[289]
In-doped CaZrO ₃	Powder, 11–15 nm particle size, with weak agglomeration		High strength and toughness for structural ceramics	[290]
ZrO ₂ (3Y)				

acetate to obtain CuO-doped SnO₂ via “alkoxide-forming” reactions in the presence of ethanol:

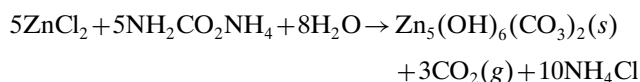


Sen et al. [113] prepared ferrite nanoparticles by a nonaqueous precipitation route: a homogeneous solution of stearic acid and iron (III) nitrate was treated with tetrahydrofuran to obtain precipitates.

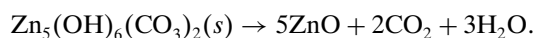
In some cases, chemical precipitation will generate large micrometer-size precipitates. Upon *peptization*, however, precipitates will be converted into nanosize particles. For example, Perez-Maqueda et al. [114] have prepared nanosize (as small as 80 nm) indium hydroxide by the peptization of colloidal precipitates. Precipitation was accomplished by the dropwise addition of an aqueous NaOH solution into indium chloride dissolved in ethylene glycol (EG) at 175 °C. For the peptization, the colloidal precipitate was washed to eliminate the EG, and then dispersed in distilled water (or isopropanol) in an ultrasonic bath. Organic solvents such as ethanol or EG have a significant effect on the shape and other properties of particles obtained by precipitation. Thus, mixed solutions of ethanol and water or EG and water have been utilized as a strategy to produce colloidal oxides of different morphologies. EG offers two useful advantages: (1) a high dielectric constant, which enhances the solubility of inorganic salts; and (2) a high boiling point (195 °C at atmospheric pressure), which makes it possible to carry out the preparation of inorganic compounds at relatively high temperatures using an open vessel.

For coprecipitation of multiple cations, the use of complexing or chelating agents seems important for controlling the chemical stoichiometry of the precipitated solid. Hwang et al. [115] used citric acid in the coprecipitation of Mn and Li by NH₄OH. Xiong and Mai [116] used stearic acid to dissolve mixed Ba, Co, and Fe salts at high temperature to prepare a sol, which precipitated to form a gel upon cooling.

In addition to chemical strategies, such as using dispersants and the controlled release of reactants, *engineering approaches* have been integrated into the chemical precipitation process to achieve bulk processing and homogeneous precipitation. Wang and Muhammed [117] used a flow injection synthesis (FIS) technique to prepare ZnO nanoparticles with rod-shaped morphology via precipitation by carbamate



The solid precipitate decomposes upon calcination to ZnO:



FIS borrowed the concept from the flow injection analysis (FIA) method in analytical chemistry. In an FIS process, a precise volume of reactant-containing solution is swept along by the carrier stream into the system. The main advantage of the FIS technique is that the precipitation process is only allowed to continue for a limited period of

1–2 min. The chemical reaction commences at the moment the solutions are mixed, and precipitation takes place and is complete in a confined zone. In this way, agglomeration is greatly limited since the short residence time allows only primary nucleation. The mixing of solutions *A* and *B* can be performed under reproducible conditions, and thus, powders with identical properties can be obtained. Chen et al. [101] have demonstrated a high-gravity reactive precipitation (HGRP) technology to produce nanoparticles of CaCO₃, Al(OH)₃, and SrCO₃ with a very narrow size distribution and a controlled morphology. Per chemical engineering analysis, micromixing (mixing on the molecular scale) and macromixing (mixing on the macro scale) have a significant effect on particle size distribution (PSD) in a reactive precipitation process. Micromixing is a key factor determining the degree of the supersaturation concentration of the solute and its local spatial distribution. The reaction rate and subsequent nucleation in precipitation will be controlled by the intrinsic kinetics without the influence of micromixing in the region of $t_m < \tau$, where t_m is the micromixing time and τ is the induction time, defined as the time from the first creation of the conditions for homogeneous nucleation to that of the establishment of a steady-state nucleation rate. The region $t_m < \tau$ should be chosen such that the rates of nucleation at different locations in a precipitator will be nearly the same, and so the PSD can be controlled at a uniform level. On the other hand, micromixing has little effect on crystal growth. Therefore, a rule for selecting a precipitation reactor is: a combination of a well-micromixed plug flow reactor (to separate the reaction and nucleation zones from the crystal growth zone) and a well-macromixed reactor (to locate crystal growth in a well-macromixed region). High-gravity technology in the form of a rotating packed bed of the earth is ideal to satisfy the above rule because it is effective in intensifying mass transfer, and is helpful in the generation of higher supersaturated concentrations of the product in the gas–liquid-phase reaction and precipitation process. Another engineering process, controlled double-jet precipitation (CDJP), has also been successfully utilized to produce uniform colloidal rod-like In(OH)₃ particles (aggregates of nanosize subunits) from relatively concentrated solutions [118]. Her and co-workers [119–123] have used CDJP to prepare colloidal spherical particles of SiO₂, Al(OH)₃, CuO, and BaTiO₃ of narrow size distributions. They [123] mixed TiCl₄ directly with 6 M NaOH/KOH to form BaTiO₃ at 85 °C within 3 min with the ability to control particle size between 70 and 400 nm. The optimum condition identified was pH 14, 85 °C, and with 0.1% cyclodextrin. The BaTiO₃ had a cubic structure with dielectric constants up to 18,000. They also established a growth mechanism for the uniform colloid formation under the CDJP condition [121]: nanosized primary particles formed immediately after mixing the reactants, followed by aggregation into larger uniform particles.

3.2.2. Hydrothermal Synthesis

“Hydrothermal process” (also called thermal hydrolysis or hydrothermal hydrolysis process) generally refers to processing aqueous solutions of metal salt(s) (metal and/or metal-organic) or autoclaving of precursor materials such as gels

at elevated temperatures (typically 100–300 °C) and pressures above 1 atm. In this method, ceramic sols are produced by chemical reactions in an aqueous or organoaqueous solution under the simultaneous application of heat and pressure in the presence of an alkali or acid that has a pseudocatalytic effect upon the reaction [124]. The reaction equilibrium of a metal salt aqueous solution changes with temperature, which results in the formation of metal hydroxide or metal oxides. Mineralization in nature, which has resulted in deposits and rocks, could have occurred by a hydrothermal process. In the laboratory, hydrothermal synthesis is typically used with a batch-type autoclave, in which an aqueous solution is heated up slowly to the target temperature, and then aged for several hours or days.

Hydrothermal synthesis has been considered a cost-effective and less complicated synthesis technique, suitable for large-scale production. There has been a trend to develop “mild hydrothermal processes” ($100\text{ °C} \leq T \leq 200\text{ °C}$, under autogenous pressure) for the synthesis of advanced ceramic powders, extending from zeolites and metal phosphates to binary and ternary transition metal oxides [125]. The low-temperature technique is critical to the formation of metastable phases not obtainable using traditional high-temperature methods. Process parameters, such as the pH of the reaction medium, temperature, and the cations in solution, determine what solid phases are formed. Cations such as medium-size spherical organic cations (e.g., tetramethyl ammonium) and large surfactants may act as the structure-directing species or template for the synthesis of nanoporous or mesoporous (2–50 nm) materials.

By changing the conditions of the solutions (pH, ionic strength, surfactant concentrations, cation concentrations, anion concentrations, and solvents) and processing conditions (temperature, duration, and stirring), one can effectively control the nanoparticle size and shape, and the extent of agglomeration. Nanoparticle CeO_2 can be made in different sizes and shapes by changing these reaction conditions [126], as shown in Figure 4.

Synthesis under hydrothermal conditions offers some significant advantages over other chemical synthesis techniques [124]: (1) it is easy to control particle size and morphology by varying synthesis conditions; (2) many materials can be synthesized directly in the desired crystalline phase at low temperature (hydrothermal synthesis offers a low-temperature, direct route to ultrafine oxide powders with a narrow size distribution, avoiding the calcination step required in sol–gel processing); and (3) the resulting sols can be used directly in the production of green bodies via pressure filtration or extrusion.

There is an enormous amount of literature on the hydrothermal processing of inorganic materials such as ceramic powders. Zeolite nanoparticles are a classic example of hydrothermal synthesis [127]. Here, we only focus on a review of the most recent work on the synthesis of true nanosize oxide particles (see Table 3).

Hydrothermal synthesis can also be conducted in the presence of other nonaqueous additives or solvents. Dong and Zhu [128] prepared $\alpha\text{-Fe}_2\text{O}_3$ nanoparticles by dropping a mixture of ethylene oxide (EO) and ethanol into an aqueous

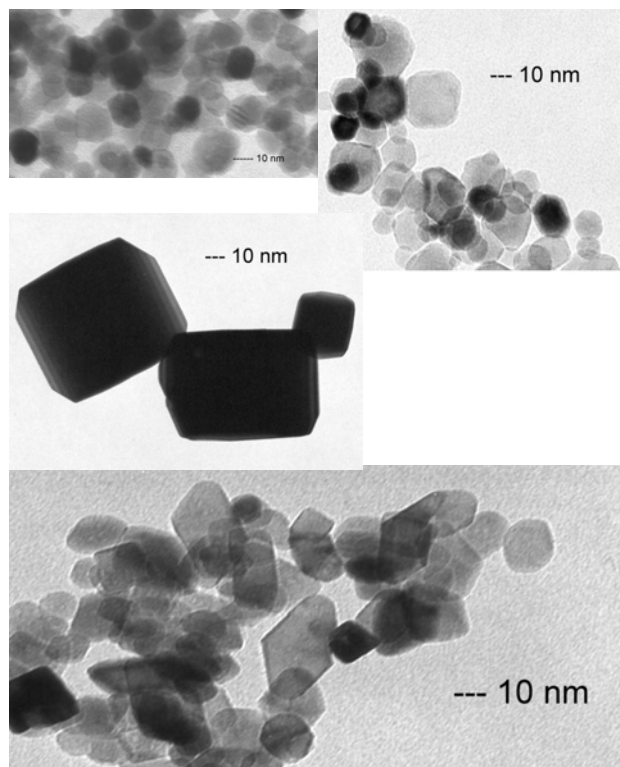
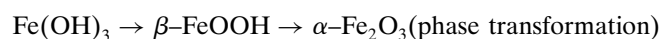
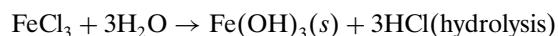


Figure 4. CeO_2 nanoparticles made from hydrothermal process [126].

solution of FeCl_3 , followed by aging and heating at 200 °C and the completion of phase transformation at 300 °C



In this process, ring-opening polymerization of EO may take place with FeCl_3 as a catalyst or with iron alkoxide as an intermediate, which can be formed by the reaction of ethylene glycol with FeCl_3 or of EO with FeCl_3 . Also, the possible byproduct of ethylene glycol may effect the prevention of $\text{Fe}(\text{OH})_3$ nanoparticle agglomeration.

In contrast to “mild hydrothermal synthesis,” synthesis under high temperature and pressure, as found in supercritical water conditions, also shows promise for the continuous and rapid production of nanocrystals [129].

3.2.3. Forced Hydrolysis

This method can be essentially considered a subcategory of the hydrothermal synthesis process at a relatively low-temperature range and using inorganic salt solutions, which are usually diluted (10^{-4} – 10^{-2} M). In this method, aqueous metal salt solutions are aged (hydrolyzed) at elevated temperatures (usually over the range 80–100 °C per Matijevic [92] and 50–150 °C per Sugimoto [94]) for different periods of time, depending on the hydrolysability of the cation in question. Forced hydrolysis takes advantage of the ability of many metals ions (especially of polyvalent cations) to readily hydrolyze in aqueous solutions at elevated temperatures.

Table 3. Nanoparticle synthesis by hydrothermal synthesis.

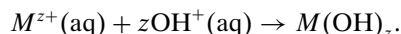
Nanoparticle materials	Characteristics of nanoparticle	Brief process description	Applications	Ref.
Mullite ($3\text{Al}_2\text{O}_3 \cdot 2\text{SiO}_2$)	55 nm–7.1 μm particle size, irregular shaped	Mixture of TEOS and Al tri-sec-butoxide, 170 °C 2 h	Monolithic or fiber-reinforced mullite components for high-temperature applications	[124]
Boehmite ($\gamma\text{-Al(OH)}$)	Needle-like particles from low-pH acid solution; platelet-shaped particles (40 nm diameter and 5 nm thickness) from high-pH alkaline conditions	Sols prepared from dispersion Al acetate, then autoclaved at 200–300 °C	Precursor for preparing high-purity and high-strength monolithic α -alumina ceramics by sol-gel technology, applications as substrate for electronic circuits, abrasive grains, high-temperature refractory materials, fibers and thin films; fillers in plastics and polymers, adsorbents and catalysts	[124]
ZrO_2	≤ 100 nm nearly monodispersed microcrystals of boehmite with a parallelogram shape 20–60 nm particle sizes, near spherical shape	Prepared from amorphous hydrated alumina gels at 255 °C for 24 h Zr acetate solution heated to 220 °C to produce a sol	Structural and functional ceramics; application as pump parts, engine parts, pressing dies, refractories, oxygen sensor in molten steel, for ceramic fiber coating, solid electrolyte	[124]
Yttria-doped zirconia	~ 45 nm tetragonal 3mol% Y_2O_3 -doped ZrO_2 powder (uniform aggregates) ~ 95 nm grain after sintering	Sol from ammonia-precipitated gel (containing both Zr and Y) + urea, heated at 150 °C, followed by a washing-drying and calcination	[292]	
TiO_2 doped with ZrO_2	9–13 nm crystallite size	Direct precipitation by cohydrolysis of acidic precursor solutions of TiOSO_4 and $\text{Zr(SO}_4)_2$ at 200–240 °C	Catalyst for photodecomposition and solar energy conversion, white pigment materials, UV protection	[293]
TiO_2	< 20 nm anatase particle size (round shaped); rod-like rutile nanocrystallites (9–32 nm diameter, 26–73 nm length) < 50 nm round shaped	Using amorphous titania as starting material and various acids (HF, HCl, HNO_3 , citric acids) as catalysts Hydrothermally treating the titania sols after peptization with tetraalkylammonium hydroxide at 240 °C	Photocatalysis, sensors	[294]
				[295]

continued

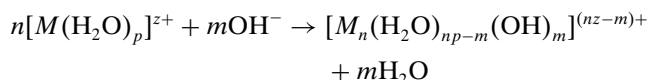
Table 3. Continued

Nanoparticle materials	Characteristics of nanoparticle	Brief process description	Applications	Ref.
Cerium oxide (CeO ₂)	<5 nm particle size, well dispersed ~6 nm cubic primary particle, <10 nm uniform size agglomerate of indefinite shape or large spherical agglomerate particle (~150–180 nm) 10–25 nm, cubic or octahedral	Citric acid as protective agent against particle growth Thermal hydrolysis of cerium ammonium nitrate solutions at 150–240 °C Sulfate ions cause spherical agglomeration of nanoparticles Heating solutions of cerium salts + urea (120–180 °C)	Polishing agents, sunscreens, solid electrolytes in solid oxide fuel cells, automotive exhaust catalysts (supports), additives for glass, stabilizers for ZrO ₂	[296] [297] [298]
Mg(OH) ₂ and MgO	Nanocrystallines with rod-, tube-, needle-, or lamella-like morphologies, maintained during decomposition	Using different magnesium precursors and solvents as the reactants Decomposition: Mg(OH) ₂ → MgO	Use in catalysis, toxic waste remediation, or as additives in refractory, paint, and semiconductor products	[299]
Maghemite (γ-Fe ₂ O ₃)	Highly crystalline, monodispersed nanoparticles (4–16 nm)	High-temperature (300 °C) aging of iron-oleic acid metal complex that was prepared by the thermal decomposition of iron pentacarbonyl in the presence of oleic acid at 100 °C, or direct oxidation of iron pentacarbonyl in the presence of oleic acid with trimethylamine oxide as an oxidant	Magnetic memory devices, ferrofluids, refrigeration systems, medical imaging, drug targeting, catalysis	[300]
Hematite (α-Fe ₂ O ₃)	20–50 nm particle size	Mixture (FeCl ₃ + EO + ethanol) heated at 200 and 300 °C		[128]
ZnGa ₂ O ₄	Needle or rod-like particles plus 10–20 nm nanoparticles	>180 °C treatment of mixed metal sulfate salt solutions +NH ₃	Transparent and conductive materials, phosphors	[297]
BaTiO ₃	Nanocrystalline powders	Amorphous Ti gel or anatase precursor in Ba(OH) ₂ solution	Dielectric or ferroelectric materials	[301]

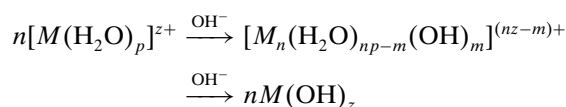
A commonly written equation for the hydroxylation of metal ions (M^{z+}) is



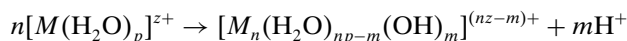
It only represents the mass balance of a precipitation process. In fact, metal complexes (also called solutes) $\{[M_n(\text{H}_2\text{O})_{np-m}(\text{OH})_m]^{(nz-m)+}\}$ act as precursors to nucleation and affect particle growth. In other words, the hydrolyzed species are intermediates to the precipitation of the corresponding hydroxides [130, 131]



or



During forced hydrolysis, the hydroxide ions are formed *in-situ* by the deprotonation of water molecules coordinated by the metal ions [131–133] according to

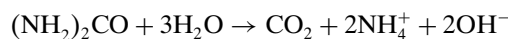


At elevated temperatures, the above forced hydrolysis can occur in the absence of base. Raising the temperature and adjusting the initial pH of the solution affects the hydroxylation of metal ions and the generation of complexes responsible for particle nucleation and diffusional growth. Typically, the pH decreases in the course of the reaction due to deprotonation of the hydrated cations, eventually leading to the formation of solid hydrous oxides. The low pH used in these systems is particularly important in order to keep a relatively low supersaturation with hydroxide ions that are constantly furnished by dissociation of water as their reservoir. Coagulation is prevented mainly by the repulsive force of the electric double layer exerted from the positively charged surfaces of each particle in the low pH range, which is effective at low ionic strength [94]. To consistently obtain particles with controlled characteristics, it is necessary to control the pH, the concentration of reactants, the temperature, the anions or counterions of a given metal salt solution, the method of mixing, etc. Anions could be highly responsible for the particle morphology. Forced hydrolysis can yield particles of different shapes (spherical, cubic, ellipsoidal, etc.), either of the same or different chemical composition.

In summary, the forced hydrolysis method requires an acidic solution containing a metal salt at a given concentration to be heated in order to produce hydroxide ligands *in-situ* by the deprotonation of bound water.

With less strongly hydrolysable cations, it is necessary to raise the pH somewhat by the addition of a weak base in order to promote or accelerate hydroxylation, and thus precipitation. For example, the hydrolysis of cations can be achieved by the *controlled release of anions (hydroxide ions)* into a metal salt solution [92] by gradual decomposition of certain organic compounds such as urea, formamide, or hexamethylenetetramine (HMTA). When urea is heated in

a solution, carbonate ions are produced, accompanied by a simultaneous increase in the pH homogeneously throughout the whole solution, leading to the precipitation of metal basic carbonates.



The gradual and uniform rise in pH can result in the nucleation and growth of uniformly nanosized particles. Calcination is usually required to transform the carbonates to metal oxides. Rojas and Ocana [134] used HMTA to enhance the forced hydrolysis of ceria (Pr doped). Song and Kang [135] have taken advantage of the gradual urea decomposition in aqueous solutions of SnCl_4 to prepare nanosized tin oxide particles. Similarly, uniform colloids can be obtained by the *controlled release of cations* approach—the slow release of cations from organometallic complexes, which then react with hydroxide ions in solution [133].

Another entirely different approach is the thermal decomposition of complex solutes in solution. Metal chelates or similar organometallic compounds can be decomposed in strongly alkaline solutions to yield uniform metal (hydrous) oxides. Complexing agents, such as triethanolamine (TEA), nitrilotriacetic acid (NTA), and (ethylenedinitrilo) tetraacetic acid (EDTA), appear to prevent both nucleation and coagulation during particle growth by shielding the metal ions. Meanwhile, complexes may liberate metal ions by degrees with the progress of precipitation. The decomposition of metal chelates typically requires much higher temperatures (i.e., similar to hydrothermal conditions) due to the stability of metal complexes. Particles obtained by this method show a relatively large size and a different crystal shape, other than spheres.

Some examples of using forced hydrolysis in (hydrous) oxide nanoparticle synthesis are shown in Table 4.

Most of the forced hydrolysis processes use aqueous solutions of inorganic salts. However, hydrolysis and inorganic polymerization can be carried out on salts dissolved in a nonaqueous medium such as a polyol medium. For example, Ammar et al. [136] have used this polyol approach to prepare monodispersed cobalt ferrite nanoparticles.

Instead of using a pure aqueous solution, the addition of alcohol to the solution could significantly affect the solid nucleation and growth kinetics, as well as the particle morphology. Hu et al. [137] have demonstrated that the addition of alcohol to an aqueous solution of metal salts can dramatically enhance the solid phase nucleation and growth rate, although the solid phase and morphology of the particles may be different from those obtained from forced hydrolysis of alcohol-free aqueous solutions. Li and Gao [138] prepared nanocrystalline zirconia in a water–ethanol mixture solution.

A forced hydrolysis process has been coupled with microwave heating (using a particularly fast heating rate) to enhance the process kinetics and uniformity of the nanoparticles. For example, Bellon et al. [139] prepared zirconia sols (i.e., colloidally stable suspensions) and powders by the microwave heating of ZrCl_4 solutions at 180 °C. Zhu et al. [140] prepared tin oxide nanoparticles, and Liao et al. [141] prepared amorphous hematite nanoparticles via this method.

Table 4. Nanoparticle synthesis by forced hydrolysis.

Nanoparticle materials	Characteristics of nanoparticle	Brief process description	Applications	Ref.
SnO ₂	~4 nm particle size 3–4 nm in diameter ~3 nm particle size, 4–60 nm crystallite size in annealed powder (200–800 °C)	Forced hydrolysis (160 °C) of aqueous SnCl ₄ solutions for 2–24 h Homogeneous precipitation, aqueous SnCl ₄ + urea, 90 °C Microwave heating (refluxing) of aqueous solution of SnCl ₄ and urea for 15 min	Gas sensors (H ₂ , CO, hydr4ocarbon, alcohol), catalysts, electrode materials (transparent electrode, glass-melting electrode), applications in solar energy conversion (dye-based solar cells), photocatalysis, electrochromic devices, and in optoelectronics	[302] [135] [140]
Pr-doped ceria	~12 nm uniform, nonagglomerated nanoparticles	Aging at 100 °C for 2 h aqueous solutions of cerium (III) nitrate, praseodymium (III) chloride, and hexamethylenetetramine (HMTA). HMTA is the precipitating agent	Three-way automotive catalysts, red ceramic pigments, high-conducting solid electrolytes used in high-temperature fuel cells and oxygen sensors	[134]
CeO ₂ (20–100mol%)-ZrO ₂	2–3 nm particle size, cubic and/or tetragonal fluorite-type structure	Forced cohydrolysis of acidic aqueous solutions of ZrOCl ₂ and (NH ₄) ₂ Ce(NO ₃) ₆ at 100 °C	Catalytic supports for automotive exhaust	[303]
CoFe ₂ O ₄	5.5 nm particle size, monodispersed, almost equiaxial	In a polyol medium by forced hydrolysis of ionic Co(II) and Fe(III) salts at 160 °C	Ferro fluids, magnetic drug delivery, magnetic high-density information storage	[136]
ZrO ₂	10–200 nm particle size, near monodispersed, monoclinic phase	Heating (95–120 °C) of aqueous ZrOCl ₂ solution without and with addition of isopropanol	Nanophas ceramics for high refractriness and corrosion resistance, mechanical strength and fracture toughness, and ion conduction	[137] [139]
ZrO ₂ (3%Y ₂ O ₃)	randomly shaped 30 nm particle (aggregates of 3–4 nm tetragonal and monoclinic crystallites) nanocrystalline, tetragonal phase, 300–500 nm particle size	Flash synthesis by microwave-forced hydrolysis of ZrCl ₄ and HCl for 2–10 min Zr and Y salts dissolved in water-ethanol mixture, PEG added as dispersant, heated to high temperature, followed by ammonia precipitation		[138]

continued

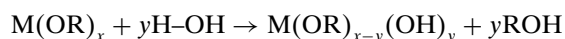
Table 4. Continued

Nanoparticle materials	Characteristics of nanoparticle	Brief process description	Applications	Ref.
ZrO ₂ (3%, 12% Y ₂ O ₃)	8–10 nm crystallite size	Hydrolyzing ZrOCl ₂ aqueous solution, then the resulting acidic sol was neutralized and coagulated with ammonia solution		[304]
Mn ₃ O ₄ , α-MnOOH, Mn ₂ O ₃	~20 nm colloid (equiaxial) or elongated (length <2 μm and width <0.4 μm)	Forced hydrolysis (80 °C) of aqueous Mn(II) acetate solutions In the presence of HCl, particle is elongated. Mn ₃ O ₄ → Mn ₂ O ₃ (800 °C) α-MnOOH → MnO ₂ (250–450 °C) → Mn ₂ O ₃ (800 °C)	Catalysts in environmental reactions and in synthesis of organic compounds, electrodes in alkaline batteries	[305]
TiO ₂	40–400 nm monodispersed particles (aggregates with primary particle size 3–10 nm) Nanosized (70–100 nm), near monodispersed spherical powder	Forced hydrolysis of TiOCl ₂ (from dilution of TiCl ₄) at 17–230 °C Forced hydrolysis of Ti(SO ₄) ₂ at boiling reflux for 5 h	Titania (rutile phase) as white pigments, coating materials for optical and electronic devices, photocatalysts	[306] [307]
Fe ₂ O ₃	3–5 nm primary particle size (amorphous), 12 nm crystallite in sintered powder (400 °C)	Microwave refluxing (10 min) of mixture solution containing PEG, FeCl ₃ , and urea	Solar energy transformation, magnetic storage media, catalysts	[308]

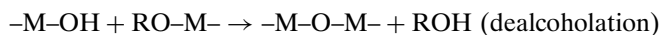
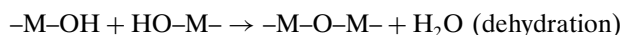
3.2.4. Sol–Gel Synthesis

Metal alkoxides dissolved in homogeneous alcohol–water solutions are typically used in a sol–gel process, which is so named because it usually involves a stage of sol (solids suspended in a continuous liquid phase) formation, and then a stage of gellation (liquid particles/pockets suspended in a continuous solid phase) process. Sol–gel also refers to processing in a liquid medium to obtain solid matter (such as particles) which does not settle under the effects of gravity [142]. Water and alkoxides are immiscible, and thus a mutual solvent such as alcohol is utilized. Catalysts such as mineral acids (such as HCl) or bases (such as ammonia) are mostly used, as well as many others (acetic acid, KOH, amines, KF, and HF). Acid-catalyzed processes tend to yield primarily linear or randomly branched polymers for use as coatings, while base-catalyzed processes yield highly branched clusters for making particles.

The sol–gel process typically involves alkoxide hydrolysis and a condensation reaction [143]



where R represents an alkyl group. The partially hydrolyzed species are then linked to form $M-O-M$ bonds by condensation via dehydration or dealcoholation



True metal alkoxides are highly sensitive to hydrolysis. Condensation reactions can be controlled via the chemical modification of metal alkoxides with complexing/chelating ligands such as acetyl acetone (acacH) [144, 145] and others (polyols, organic acids, β -diketones, and allied derivatives). The M -acac bond, stabilized by chelation, and β -diketonates, is much more difficult to hydrolyze than alkoxy groups. This process, involving hydrolysis \rightarrow polymerization \rightarrow nucleation \rightarrow growth, condenses the molecular units together into small clusters (the “sol”), eventually leading to the formation of an insoluble three-dimensional network (the “gel”), which can be further condensed into a solid.

Sol–gel processes, based on the hydrolysis and condensation of molecular precursors, have historically played a significant role in glass and ceramic coating applications. Through these processes, homogeneous oxide materials with desirable properties like hardness, optical transparency, chemical durability, tailored porosity and thermal resistance can be produced at room (or low) temperatures. This process contrasts to the much higher melting temperatures required in the production of conventional inorganic glasses. Factors that affect the rate of hydrolysis and condensation reactions (and thus the microstructure of the solid sol–gel-derived materials) include the pH, temperature, and time of reaction, reagent concentrations, catalyst nature and concentration, water/metal molar ratio, aging temperature and time, and drying. In addition, the chemical design of the molecular precursors provides an interesting tool to control condensation reactions and tailor the nanostructure of the oxide materials [145].

Sol–gel chemistry presents many advantages for the powderless processing of ceramics, the molecular design of advanced materials, or the synthesis of hybrid organic–inorganic compounds. The sol–gel process has also been reported for making nanophase ceramics (ceramic layers containing individual <10 nm nanoparticles) by using inverse micelle reaction media or acacH-modified alkoxides [144]. Pierre [142] has specifically discussed the principles for achieving monodispersity during the sol–gel processing of ceramic powders.

Some recent efforts in the sol–gel synthesis of nanosized oxide particles or nanocrystalline powders are summarized in Tables 5 and 6. A classic example of sol–gel processes for making ultrafine particles is the one developed by Stöber and Fink [146] for the production of monodispersed silica using an alkoxide (tetraethoxy silane, TEOS) and ammonia catalysis. The sizes of these so-called “Stöber spheres” range from a few nanometers to a few micrometers, depending on the conditions (concentrations of reactants such as TEOS, ammonia, and water; reaction temperature and time; method of mixing, etc.). Livage et al. [145] used acacH to tailor the alkoxide condensation reaction kinetics, and thus the zirconia nanoparticle size. The mean diameter increases when the ratio of $[H_2O]/[Zr]$ increases and the ratio of $[acac]/[Zr]$ decreases.

Some sol–gel processes do not have to use alkoxides as starting precursors. Chen and He [147] used all inorganic metal salts (with PAA as a complexing agent to couple the two metal species together) to achieve sol and gel formation, and thus produced nickel ferrite nanoparticles. In some other cases, transient alkoxide-like species were formed from reactions of inorganic metal salts and alcohol. Dong and Zhu [128] and Manorama et al. [112] prepared nanoparticles with transient alkoxide formation processes. Metallorganic compounds such as metal formates have also been used as precursors in the sol–gel synthesis of multi-component nanosize ceramic powders [148–151].

For mixed metal oxide powder synthesis, the use of single molecular multimetallic alkoxide precursors has certain advantages, such as precise control of chemical stoichiometry and composition homogeneity. Narayanan and Laine [152] developed the use of a trimetallic double alkoxide precursor to prepare phase-pure potassium aluminosilicate. O’Brien et al. [153] used a bimetallic alkoxide to synthesize monodispersed barium titanate nanoparticles in the 4–12 nm particle size range.

In addition to chemistry, other process strategies were taken into account to tailor the sol–gel synthesis of nanoparticles. Kim and Kim [154] developed a “semibatch–batch two-stage reaction” to decrease the size of titania nanoparticles. The particle size was reduced to 132 nm in the first stage, and decreased to 42 nm in the second stage. Better uniformity was another benefit.

Sol–gel processes at low temperatures generate mostly amorphous nanoparticles or gels, which require further high-temperature treatment such as calcination to obtain nanocrystalline powders. Some sol–gel processes are coupled with hydrothermal processing (in an autoclave reactor) to produce some as-prepared particles with the desired crystalline phases [155–157].

Table 5. Synthesis of single metal–oxide nanoparticles by sol–gel processes.

Nanoparticle materials	Characteristics of nanoparticle	Brief process description	Ref.
SiO ₂	Amorphous monodispersed nanoapheres	Ammonia-catalyzed hydrolysis and condensation of TEOS–ethanol–water homogeneous solutions	[146]
	13.7 nm monodispersed nanoparticles	Semibatch method using TEOS, ammonia, ethanol, HPC, and water	[309]
ZrO ₂	Sol of amorphous, monodispersed nanoparticles (~3 nm hydrodynamic dia.) <10 nm	Acetylacetonone (CH ₃ –CO–CH ₂ –CO–CH ₃) added to the Zr(OPr ⁱ) ₄ solution prior to hydrolysis to decrease reactivity: Zr(OPr ⁱ) ₄ + x acacH → Zr(OPr ⁱ) _{3–x} (acac) _x + x Pr ⁱ OH	[145] [144]
	Gel calcined into nanocrystalline phase (10–32 nm crystallite size)	Zr n–butoxide in terbutylic alcohol, with hydrolysis catalyst HCl, C ₂ H ₄ O ₂ , or NH ₄ OH, dried and annealed, then sulfated with H ₂ SO ₄	[310]
SnO ₂	2–12 nm particle sizes, 2.4–5.5 nm crystallite sizes	Hydrolysis of Sn (IV)–isopropoxide dissolved in ethanol	[302]
TiO ₂	Porous anatase nanoparticles, 9–15 nm particle size · crystallite size	Heating (348 K) of ethanol solution of Ti tetra isopropoxide and H ₂ O ₂ → Ti–peroxy compounds → Ti–peroxy gel, which was treated at 348 K for 6–48 h	[311]
	42 nm particle size	Semibatch reaction (Ti(OC ₂ H ₅) ₄ /HPC/ethanol feed into H ₂ O/ethanol, stir for 60 min), followed by batch reaction (add additional Ti(OC ₂ H ₅) ₄ /HPC/ethanol and H ₂ O/ethanol, stir 60 min), then drying at 70 °C for 12 h	[154]
	10.7 nm particle size	Semibatch method	
	1–5 nm core sizes (anatase), particle surface coated	Hydrolysis at 60 °C of Ti butoxide in the presence of acetylacetonone and paratoluenesulfonic acid; particle surface protection through: (1) complexation by acetylacetonato ligands, and (2) adsorbed organic–inorganic layer made with acetylacetonone, paratoluenesulfonic acid, and water.	[309]
	5–12 nm crystallite sizes	Hydrolysis of Ti(IV) isopropoxide; stabilized by hydroxylpropyl cellulose (HPC)	[312]
ZnO	3–5 nm zincite crystallites, which aggregate into larger spherical particles	Alkoxide-based synthesis involving diethylzinc, tert-butyl alcohol, ethanol, and water: Zn(CH ₂ CH ₃) ₂ + 2(CH ₃) ₃ COH → Zn[OC(CH ₃) ₃] ₂ + 2CH ₃ –CH ₃ Zn[OC(CH ₃) ₃] ₂ + 2H ₂ O (in ethanol) → Zn(OH) ₂ + 2(CH ₃) ₃ COH Zn(OH) ₂ → ZnO + H ₂ O (heating: RT → 90 °C 15 min → 250 °C 15 min)	[313] [314]
∇–Fe ₂ O ₃	Nanosized	Sol–gel process using ethylene oxide and FeCl ₃ as starting materials in ethanol	[315]
Sc ₂ O ₃ , ScOOH	<80 nm, lozenge-shaped platelets (66 × 37 × 4.5 nm)	Sc(acac) ₃ dissolved in 2–methoxyethanol, in which water/methoxyethanol was added, refluxed until yellow color vanished, and a light bluish aspect appeared.	[316]

Table 6. Synthesis of mixed metal-oxide nanoparticles by sol-gel processes.

Nanoparticle materials	Characteristics of nanoparticle	Brief process description	Ref.
NiFe ₂ O ₄	5–30 nm crystallite sizes	Aqueous solution of Ni nitrate and Fe (III) nitrate, mixed with aqueous solution of PAA (as a chelating agent), then add nitric acid → transparent green solution, evaporation at 50 °C → transparent sol, 50 °C 10 h → viscous brown gel, calcined → spinel nickel ferrite nanopowders	[147]
BaTiO ₃	Monodispersed nanoparticles (4–12 nm particle sizes)	Single bimetallic alkoxide molecular precursor method: barium titanium ethyl hexano-isopropoxide is injected into a mixture of diphenyl ether at 140 °C under argon or nitrogen. The mixture is cooled to 100 °C and 30% H ₂ O ₂ is injected, stirred over 48 h to promote further hydrolysis and crystallization of the product in an inverse micelle condition.	[153]
	Crystalline fine powders	Dissolve Ba metal in 2-methoxyethanol → add Ti isopropoxide → reflux under nitrogen at 135 °C → hydrolyze with water (water/alkoxide = 3/1) → amorphous gel powder → dry → calcine → powder	[317]
PbZr _x Ti _{1-x} O ₃ (PZT)	~17 nm nanocrystal size, free standing	Sol-gel synthesis using lead acetate, Ti(IV) ethoxide and Zr(IV) butoxide	[318]
Al ₂ O ₃ -TiO ₂	Nanocrystalline powder (1–150 nm grain sizes), spherical or cubic shaped	Poly(ethylene glycol) (PEG) sol-gel method	[319]
Binary and ternary oxide nanopowders	Calcined nanocrystalline powders of BaO-SiO ₂ (60–150 nm), mullite (85–15 nm), eucryptitite (140–205 nm), spodumene (150–200 nm)	Aqueous sol-gel method with formates and TEOS as precursors	[148, 150, 151]
IrO ₂ -Ta ₂ O ₅	Ultrafine, irregular shaped	IrCl ₃ dissolved in ethanol under nitrogen → Ir ethoxide → mixed with Ta(OC ₂ H ₅) ₅ → add ammonia → slow addition of H ₂ O ₂ (to oxidize Ir precipitates) → dried, calcined	[320]
RuO ₂ -SnO ₂	Ultrafine, irregular shaped	Hydrolysis and condensation of metal alkoxides in ethanol	[321]
Al ₂ O ₃ and Al ₂ O ₃ /MgO	<2 nm crystallites in powders	Sol-gel + autoclaving thermal conversion: modified aerogel synthesis involving Al and Mg alkoxides, toluene, methanol, ethanol, and water → gel → autoclave at 265 °C	[155]
TiO ₂	Dispersed colloids of tightly aggregated secondary particles (10 nm primary particle size, 100 nm secondary particle size) <10 nm particle size	Hydrothermal sol-gel	[157]
		Sol-gel synthesis → peptization → growth under hydrothermal treatment in a basic environment at 190–270 °C	[156]

3.2.5. Solvothermal Synthesis and Nonhydrolytic Route

While water is used for the hydrothermal synthesis of hydrated oxides, other nonaqueous solvents have also been utilized for liquid-phase thermal processing. Nonaqueous solvothermal processes and some nonhydrolytic approaches have been proven to play a significant role in the synthesis of advanced nonoxide ceramic materials by using reactions in nonaqueous solutions [158–160].

Parala et al. [161] have described a nonhydrolytic sol-gel approach to the preparation of uniform, quantum-confined titania nanocrystals using an intramolecular adduct-stabilized alkoxide precursor. The organic passivating ligand TOPO was used as the reaction medium for the

nucleation and growth of nanocrystals, and as a capping agent. Titanium alkoxide was modified by replacing one or more isopropoxide groups with donor functionalized alkoxide ligands such as dimethylaminoethoxide (dmae) or diethyl aminoethoxide (deae), leading to the formation of more fully saturated compounds that have reduced air/moisture sensitivity compared to the parent alkoxides. In a typical synthesis, TOPO was heated to 200 °C, degassed (flushed with argon), and heated to 325 °C. Then the modified alkoxide precursor was injected rapidly into the reaction flask under an argon atmosphere, and the reaction was maintained at 300 °C for 15 min. The resulting nanocrystals (3–5 nm, spherical shape) can be readily dispersed in polar solvents like toluene or hexane. In contrast to aqueous sol-gel

processes, the nonhydrolytic sol-gel technique in hydrocarbon solvents at high temperatures allows access to very small free-standing crystallites, and opens up new possibilities for control over size distribution, surface chemistry, and particle agglomeration.

Nonaqueous solvothermal processes can be defined as chemical reactions or transformations in an organic solvent under elevated temperature and pressure conditions, such as supercritical conditions or near such a pressure-temperature domain. The specific physicochemical properties of solvents in supercritical conditions in particular can markedly improve the diffusion of chemical species [160]. The chemical composition of the solvent must be adapted to the material to be prepared. Solvothermal processes have been developed for: (1) the shaping of materials (crystal growth or the preparation of fine microcrystallites), (2) the synthesis of new materials with interesting properties, and (3) the development of new processes for preparing functional materials. In particular, the solvothermal technique provides an alternative approach that allows the economical synthesis of fundamentally important well-defined nanometer-sized materials under mild conditions [162]. On the other hand, the direct precipitation of metal oxides from high-boiling-point organic solvents, as in "glycothermal synthesis," presents an alternative to wholly aqueous hydrothermal material synthesis routes [160, 163, 164]. These processes have used nonaqueous solvothermal processes to synthesize phyllosilicate-like oxides without the OH groups and stabilized nitrides (such as Mo₂N and/or MoN fine particles and C₃N₄) in nitriding solvents (NH₃ or NH₂NH₂). Yin and Wang [165] prepared cobalt and cobalt oxide (CoO) nanocrystals by the chemical decomposition of Co₂(CO)₈ in toluene (at 130 °C), in the presence of sodium bis(2-ethylhexyl) sulfosuccinate as a surface active agent. Adair et al. [163] synthesized alpha-alumina of controlled particle size and shape in 1,4-butanediol solutions (with a high boiling point). The glycothermal synthesis technique allows for the production of anisometrically shaped particles with controlled morphology and size distribution [164].

Hong et al. [162] developed a so-called "alcohol-thermal" route under mild conditions (110 °C) to prepare CuO nanoparticles (~3–9 nm, depending on reaction temperature) using copper acetate as the starting material. Hai et al. [166] prepared SnS₂ nanoparticles (~150 nm average particle size, laminar shape) by a solvent-thermal synthesis method using the precursor salts SnCl₂ and CS₂ dissolved in absolute alcohol autoclaved at 200 °C for 16 h. Qiu et al. [167] synthesized nanosized Y-TZP powders (~15 nm crystallite size) by a coprecipitation, followed by the distillation of the resulting gel in n-butanol. In some cases, a small quantity of water may be involved. For example, Kominami et al. [168] synthesized nanocrystalline tantalum (V) oxide powders by a solvothermal reaction of Ta pentabutoxide in toluene at 473–573 K in the presence of water.

Organic solution-phase decomposition of iron precursors at high temperatures has been widely used in iron oxide nanoparticle synthesis. Recent advances have demonstrated the synthesis of high-quality, monodispersed γ -Fe₂O₃ and Fe₃O₄ nanoparticles (<20 nm in diameter); one such method uses the high-temperature (265 °C) reaction of Fe(III) acetylacetonate in phenyl ether in the presence

of alcohol, oleic acid, and oleylamine [169]. By performing the reaction in propylene glycol under reflux, Rajamathi et al. [170] were able to hydrolyze FeCl₃ in the presence of n-octylamine to obtain soluble, monodispersed γ -Fe₂O₃ (~5 nm).

3.2.6. Microwave Heating Synthesis

Microwave-assisted synthesis for the production of inorganic compounds has been studied since 1986. As compared to conventional oven heating (with a slow heating rate and heat transfer), microwave "volumetric" heating of liquids is an alternative heating approach with specific advantages. Microwave heating of the hydrothermal reactor was found in some cases to cut the reaction time significantly, to generate remarkable size uniformity, and to produce some new phases as well as known ones [171].

Recently, there have been some reports on microwave dielectric heating for the liquid-phase synthesis of nanoparticles [172]. This literature is summarized in Table 7.

3.2.7. Synthesis in Microemulsions or Reverse Micelles

Microemulsions are thermodynamically stable, fluid, and optically clear dispersions (10–100 nm subphases) of two immiscible liquids such as water and oil. Microemulsions form when a surfactant, or more commonly a mixture of surfactants and cosurfactants, lowers the oil/water interfacial tension to ultralow values, allowing thermal motions to spontaneously disperse the two immiscible phases. Unlike conventional emulsions, however, microemulsion domains fluctuate in size and shape, and undergo spontaneous coalescence and break up [173]. *Miniemulsions* are systems where small droplets with high stability are created in a continuous phase by using high shear [174]. Reverse micelles are molecular self-assemblies from surfactants or block copolymers, which have a spherical shape with a hydrophilic (water-loving) core and a hydrophobic tail on the sphere surface.

Microemulsion synthesis is probably the most popularly reported method, in recent literature, for the synthesis of nanosized inorganic particles (oxides, mixed oxides, semiconductor nanocrystals, metal nanocrystals or nanoclusters, coated nanoparticles, etc.). It is still an active research topic. We, however, will mainly focus on the review of work on ceramic (oxide) nanoparticles. Self-assembly systems such as water-in-oil microemulsions (or reverse micelles), or other self-assembled structures of surfactants and block copolymers, have been utilized as "nanoreactors" that confine a solid phase formation [175–177]. The application of a microemulsion as a precipitation medium yields much smaller particles (with narrower size distribution) than can be obtained from homogeneous solutions [178, 179]. In addition, reverse micelles or water-in-oil (W/O) microemulsion methods have been utilized for the growth of anisotropic nanoparticles (such as plate-like oxides) and core-shell nanoparticles (via arrested precipitation) [180].

In a typical process for nanoparticle synthesis by a microemulsion technique, the organometallic and/or metal salt precursors are dissolved inside the water pools of the reverse spherical micelles, and are allowed to react via droplet collision and rapid intermicellar exchange of their

Table 7. Microwave heating liquid-phase synthesis of nanoparticles and nanocrystalline powders.

Nanoparticle materials	Characteristics of nanoparticle	Brief process description	Ref.
ZrO ₂	Polymer stabilized ZrO ₂ nanopowders with average crystallite size of 2.0 nm Randomly shaped particles of roughly 30 nm, which are aggregates of 3–4 nm crystallites of tetragonal and monoclinic phases	Microwave heating in an aqueous solution containing Zr(NO ₃) ₄ , PVA, and NaOH	[322]
		Flash synthesis by microwave-forced hydrolysis	[139]
SnO ₂	~3 nm particle (or crystallite) size in as-prepared powders; 4, 12, 18, and 60 nm avg. particle sizes for powders annealed at 200, 400, 600, and 800 °C	Microwave irradiation heating-forced hydrolysis of an aqueous solution in the presence of SnCl ₄ and urea	[140]
CeO ₂	Nanocrystalline powder (2.6 nm crystallite)	Microwave-assisted heating routes from aqueous solutions containing (NH ₄) ₂ Ce(NO ₃) ₆ , hexamethylenetetramine, and poly(ethylene glycol)-19000 (PEG)	[323]
γ-Fe ₂ O ₃	Monodispersed nanocrystalline powders (2.0 nm crystallite size)	Microwave irradiation of aqueous solution containing (NH ₄) ₂ Ce(NO ₃) ₆ , PEG, and NaAc	[308]
	Monodispersed red hematite spherical particles (30–66 nm in diameters)	Microwave hydrothermal treatment of solution containing FeCl ₃ and HCl at 100–160 °C 2–8 h	[324]
	Monodispersed hematite nanoparticles	Microwave thermohydrolysis of nitrate iron (III) solutions	[325]
	Uniform nanoparticles (coarse ~70 nm particle size, tetragonal shape 80 nm diagonal length, or ellipsoidal 50–100 nm particle sizes)	Microwave refluxing of mixed solutions of Fe(NO ₃) ₃ and HNO ₃ , Fe(NO ₃) ₃ and NaOH, or Fe(NO ₃) ₃ and NaH ₂ PO ₄	[326]
Amorphous Fe ₂ O ₃	~3–5 nm particle sizes in amorphous powder (agglomerate); sintered γ-Fe ₂ O ₃ riziiform particles (10 nm diameter × 30 nm length)	Microwave irradiation heating of an aqueous solution containing ferric chloride, polyethylene glycol-2000 and urea	[308]
Binary oxides BaTiO ₃ , Ba ₆ Ti ₁₇ O ₄₀ , BaZrO ₃ , PbTiO ₃	Particle sizes for as-prepared (heated) powders (nm): 10 (20–30), 15 (40–50), ~200 × 600 (same), and 5–7 (20–30), respectively. Crystallite sizes in as-prepared (heated) powders (nm): 9 (19), 11 (26), 1.8 (24), and 1.2 (17), respectively	Microwave-assisted soft-chemical route: using precursor salts BaCl ₂ hydrate, Pb(Ac) ₂ , Ti(OPr ⁱ) ₄ , and ZrOCl ₂	[327]
γ-Al ₂ O ₃	Crystalline powders (60–990 nm particle sizes)	Microwave-assisted “combustion” of redox solution mixtures containing the desired metal ions (from Al nitrate), urea as oxidizing reactant and fuel	[328]
BaTiO ₃	Ultrafine tetragonal-phase powders	Microwave heating of solutions containing BaCl ₂ , TiO ₂ , NaOH, and deionized water	[329]

water content [181]. The nanoparticle formation in the microemulsion process is controlled mainly by diffusion, and is also dependent on the nature of the surfactant. Two major procedures have been reported: (1) the catalyst is already contained in the water phase, and the precursor (such as an alkoxide), dissolved in the continuous medium, progressively enters the water pools of the reverse microemulsion; and (2) the precursor and the catalyst are prepared as two separate microemulsions, and are mixed together to allow the reaction to proceed via micellar exchange of two microemulsions.

Instead of water, an ethanol-in-oil microemulsion has been prepared for the synthesis of zinc oxide nanoparticles [182]. Some nanoparticle synthesis work has also been done with oil-in-water microemulsions (or normal micelles) involving ionic surfactants, in which counter ions are replaced by ions participating in the chemical reactions [175, 181]. This technique demonstrated the use of triblock

copolymer spherical micelles in tetrahydrofuran/hexanes as templates for the preparation of inorganic nanoparticles (iron oxide, ~4–16 nm particle sizes).

Tables 8 and 9 summarize some major microemulsion synthesis work from recent years, with a focus on the nanoparticles of oxides and mixed oxides.

3.2.8. Sonochemical Synthesis

Ultrasound has been applied to enhance chemical reactivity, particularly in synthetic materials chemistry. The chemical effects of ultrasound are derived primarily from acoustic cavitation. Bubble collapse in liquids results in an enormous concentration of energy from the conversion of the kinetic energy of the liquid motion into heating of the contents of the bubble. The high local temperatures and pressures, combined with extraordinarily rapid cooling, provide a unique means for driving chemical reactions under extreme conditions [183].

Table 8. Single-(hydrous)oxide nanoparticle synthesis in microemulsions (or reversed micelles).

Nanoparticle	Characteristics of nanoparticle	Brief process description	Ref.
SiO ₂	30–70 nm diameters, monodispersed spheres	Hydrolysis of TEOS in water-in-oil microemulsion consisting of polyoxyethylene (5) monylphenyl ether (NP5)/cyclohexane/ammonium hydroxide	[330]
	Monodispersed, 0.1–1.5 μm avg. sizes	Mix W/O catalyst(NH ₃)-containing microemulsion with TEOS containing microemulsion	[331]
	Particle sizes: 70–640 nm	Microemulsion using block copolymers and nonionic surfactant	[332]
ZrO ₂	Amorphous as-prepared particles	Reverse microemulsion: water–cyclohexane–hexanol–Triton X-100	[333]
	Crystallized (tetragonal) at 450 °C~4 nm 5–50 nm particle size (by TEM)	Two-emulsion precipitation technique: two solutions of reverse emulsion, one containing Zr ⁴⁺ aqueous droplets, and the other aqueous ammonia (or HMTA) droplets, with the same water/oil ratio are prepared separately and mixed together to form a slurry of ZrO ₂ precursors	[334]
Al oxide–hydroxide	5–8 nm spherical nonagglomerated particles Zn oxalate precursor nanoparticles (5–13 nm)	Ethanol-in-oil microemulsion: Zn-AOT/ethanol/isooctane, Na–DEHSS (diethylhexyl) sulfosuccinate as surfactant, Zn nitrate as salt precursor dissolved in ethanol	[335, 182]
	Amorphous, mean particle sizes of 1.0–2.4 nm	Hydrolysis of Al isopropoxide in the L-2 phase of amphiphilic (PDMS–POE) polydimethylsiloxanepolyoxyethylene Silwet L-7607–octanol/acetylacetone–water mixtures	[336]
TiO ₂	Nanoparticles (both anatase and rutile phase)	Hydrolysis of tetrabutyl titanate in water core of a water-in-oil microemulsion, provided by a functionalized surfactant Span-Tween 80 (mixture of sorbitol monooleate and polysorbate 80)	[337]
	20–50 nm particle sizes in agglomerated powders	Mix of microemulsions. Precipitation of Ti hydroxide by NH ₄ OH in microemulsion (water/Triton X-100/hexanol/cyclohexane).	[338]
Sb ₂ O ₄	Nanorods (50–175 nm diameter and several micrometer length)	Aqueous solution of SbCl ₃ and HCl → mixed with toluene containing AOT → ultrasonication → add NaOH slowly → take upper layer transparent yellow-colored solution and reflux → organosol → evaporation to get zerogel → drying to get powder	[339]
Fe ₃ O ₄	<10 nm particle size, equiaxial morphology	O/w microemulsion using cyclohexane as the oil phase, NP5 + NP9 as the surfactant phase, and a Fe(II)/Fe(III) salt solution as the aqueous phase	[340]
	~4 to ~16 nm sphere	Use of triblock copolymer micelles with hydrophilic cores as templates	[175]
	2–8 nm particle size range	Use cyclohexylamine to precipitate Fe(II) and Fe(III) by mixing two microemulsions (inverse micelles), a ternary system cyclohexane/Brij-97/water	[341]
–Fe ₂ O ₃	~10 nm spherical particle, coated with DBS and CTAB (cetyltrimethyl ammonium bromide)	Precipitation of FeCl ₃ by NaOH in microemulsion water sodium dodecyl benzene sulphonate (DBS)/toluene: Fe ³⁺ + OH [–] → 3–FeOOH → –FeOOH → –Fe ₂ O ₃	[342]
TiO ₂	As small as 2 nm, amorphous powder	Sol–gel reaction with Ti tetraisopropoxide in miw/o microemulsion containing water, cyclohexane, or octane, and surfactant such as polyoxyethylene (10) octylphenyl ether (TX-100), polyoxyethylene lauryl ether, or bis (2-ethylhexyl) sodium sulfosuccinate	[343]
Er ₂ O ₃	5–30 nm in diameters	Inverse microemulsion technique: cyclohexane as the oil phase, NP5 + NP9 as the surfactant phase, and a Er(III) nitrate salt solution as the aqueous phase	[344]

continued

Table 8. Continued

Nanoparticle	Characteristics of nanoparticle	Brief process description	Ref.
BiOCl	Monodispersed 250 nm long arrowhead-shaped particles (from hexagonal phase) or roughly spherical 5 nm particles (from lamellar phase)	Lyotropic liquid crystal nanoreactors: 3-D percolated hexagonal liquid crystal and 2-D percolated lamellar liquid crystal	[345]
SnO ₂	30–70 nm particle sizes for precursor hydroxide particles, dried powder is agglomerated	Water-in-oil microemulsion: water, AOT (surfactant), and n-heptane (oil) SnCl ₄ containing microemulsion was mixed with ammonia-containing microemulsion	[346, 347]
GeO ₂	Polyhedron (43–342 nm particle sizes), Spindle (445–838 nm), Cube (612–947 nm)	Hydrolyzing Ge tetraethoxide in a 2,2,4-trimethylpentane solution of sodium bis(2-ethylhexyl) sulfosuccinate (AOT) as a function of water content	[348]
CeO ₂	8–48 nm mean particle sizes	Precipitation of Ce(NO ₃) ₃ by ammonia in Titron N-101/ n-pentanol/n-octane/water microemulsion	[349]

The sonochemical decomposition of volatile organometallic precursors in low-volatility solvents has been a major technique in producing various nanostructured materials (such as metals/alloys, oxides, carbides, sulfides, nanosize colloids, etc.). Examples of decomposition include: (1) the decomposition of W(CO)₆ and Fe(CO)₅, and (2) the decomposition of urea to precipitate metal ions in solution.

Table 10 summarizes some of the most recent efforts in the sonochemical synthesis of inorganic nanoparticles (mainly oxides) from liquid-phase reactions.

3.2.9. Electrochemical Synthesis

Electrochemical processes take advantage of not only solution chemistry, but also of electrical current-enhanced phenomena through electrode(s) and electrochemical reactions at the electrode–solution interface.

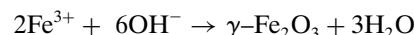
There are some recent reports on the synthesis of oxide ceramic nanoparticles using electrochemical routes. Borgohain et al. [184] prepared cuprous oxide (Cu₂O) quantum particles as small as 2 nm by a novel electrochemical route. A Cu anode and a Pt cathode were used in an electrolytic bath consisting of a mixture of acetonitrile (CH₃CN) and tetrahydrofuran (TMF) bubbled with nitrogen. The supporting electrolyte, tetra-n-octyl ammonium bromide (TOAB), also served as a stabilizer. On application of an electric current, the anode slowly dissolves, leading to the formation of Cu ions, which get oxidized immediately after formation by the residual oxygen in the bath, and subsequently get passivated by the active TOAB species. The cluster size of Cu₂O was found to decrease with an increase in current density. Pascal et al. [185] performed electrochemical synthesis in an organic medium for nanoparticles of maghemite α -Fe₂O₃ (with narrow size distribution, average sizes varying from 3 to 8 nm).

Electrochemical routes were also reported for the synthesis of nanostructured mixed oxides. Amigo et al. [186] synthesized magnetic nanoparticles of Sr–Fe oxides (average sizes from 2 to ~50 nm) in the shape of inverse cubic spinels. The nanoparticles were precipitated from nitrate media in the pH range of 1–3, and from chloride media within the pH range of 1–12, by electrolysis of nitrate and

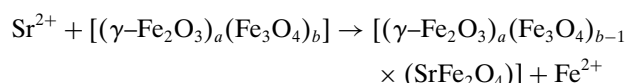
chloride solutions with Sr²⁺ and Fe³⁺ salts, using commercial Fe electrodes. This electrochemical procedure is based on the coprecipitation of oxides of Sr²⁺, Fe³⁺, and Fe²⁺ (supplied from the Fe anode) in the solution and electrodes under the action of the applied electrical field



Maghemite and magnetite are assumed to be produced in the alkaline region near the cathode



The resulting mixture of these oxides is further doped by Sr²⁺, which partially substitutes the Fe²⁺ in the magnetite to yield the final insoluble Sr–Fe oxide



Similarly, Torres et al. [187] prepared Mn–Zn–Fe mixed oxides (<50 nm nanoparticle size) as precipitates from chloride and nitrate solutions of pH 1.5 with Mn²⁺, Zn²⁺, and Fe²⁺ or Fe³⁺ at temperatures between 40 and 80 °C using electrodes of commercial iron.

In addition to oxides, the electrochemical route also has been utilized for the synthesis of nonoxides. Griffiths et al. [188] recently reported that the electrochemical oxidation of a titanium electrode in a solution of potassium amide in liquid ammonia resulted in the deposition of titanium nitride as nanoparticles or as a thin film.

Nyffenegger et al. [189] reported a hybrid “electrochemical/chemical (or E/C) method,” which is a relatively new wet-chemical method, for the synthesis of zinc oxide (ZnO) nanoparticles (with mean diameters of nanocrystallites in the range of 1.5–10 nm) and films (10–40 nm thickness, polycrystalline). The E/C procedure involves two steps: (1) zinc metal is first electrochemically deposited at basal-plane-oriented graphite electrode surfaces from dilute aqueous

Table 9. Mixed-oxide nanoparticle synthesis in microemulsions (or reversed micelles).

Nanoparticle materials	Characteristics of nanoparticle	Brief process description	Ref.
CoFe ₂ O ₄	Oval-shaped, avg. radius of 4.8 nm	Templating synthesis: self-assembly of mixed-metal oxides in block copolymers	[350]
	1–15 nm particle sizes	AOT reverse micelles: adding aqueous solutions of Fe(II) and Co(II) salts to AOT dissolved in isooctane	[351]
MFe ₂ O ₄ (M = Mn, Fe, Co)	5.5 nm uniform size particle	Two portions of solution of AOT in isooctane were mixed with aqueous solutions of the reactants, one containing metal salts and another one containing the precipitating agent NH ₄ OH	[352]
	10–20 nm particle sizes, spherical shape	Two portions of solution of AOT in isooctane were mixed with aqueous solutions of the reactants, one containing metal salts and another one containing the precipitating agent NH ₄ OH	[353]
CoLn _{0.12} Fe _{1.88} O ₄ (Ln = Ce, Sm, Eu, Gd, or Er)	~20 nm particle size	O/w micelles using sodium dodecyl sulfate as the surfactant	[354]
	uniform ~10 nm particle size	AOT (bis(2-ethylhexyl) sodium sulfosuccinate) in isooctane reverse micelle solutions containing the reactants FeSO ₄ , MnSO ₄ , NH ₄ OH (precipitant), and H ₂ O ₂ (oxidant)	[355]
Eu _x Y ₂ O ₃	10–100 nm particle sizes, red-emitting nanophosphor	Microemulsion containing petroleum ether (60–80 °C), nonionic surfactants NP ₅ /NP ₉ , aqueous yttrium nitrate/europium nitrate and ammonium hydroxide solution	[356]
	Spherical shape, narrow size distribution, high crystallinity, strong photoluminescence	Precipitation of aqueous yttrium nitrate/europium nitrate solution using ammonium hydroxide in the reverse microemulsions based on polyoxyethylene (5) nonylphenyl ether/polyoxyethylene (9) nonylphenyl ether, cyclohexane, and water	[357]
Ba-stabilized alumina	High thermal stability, high surface area, uniform, long-shaped particles (~20 nm length and ~8 nm width)	Microemulsion + hydrothermal techniques	[358]
PbBi ₂ Ta ₂ O ₉	Precursor powders are soft agglomerates with nanosized primary particles (near spherical, 40 nm primary particle size after calcinations)	Colloid emulsion process	[359]
Strontium ferrite	3.8 nm precursor particle sizes and 50–100 nm calcined particle sizes	Coprecipitation of Sr ²⁺ and Fe ³⁺ in a water-in-oil microemulsion of water/CTAB/n-butanol/isooctane → mixed hydroxide precursor → calcinations at 700 °C 5 h → pure strontium ferrite	[360]
PbCrO ₄	3–100 nm uniform particles (spherical) 240 × 140 nm (rectangular shaped)	W/o microemulsion: water/sodium bis(2-ethylhexyl)sulfosuccinate (AOT)/n-heptane Dropwise addition of Pb(NO ₃) ₂ containing microemulsion (colorless) into orange-colored K ₂ CrO ₄ -containing microemulsion	[361]
Barium hexaaluminate	~10–30 nm (calcined at 500–1300 °C)	Sol-gel processing (controlled hydrolysis and condensation of B and Al alkoxides) in reverse microemulsion media	[362, 363]
	3–10 nm precursor particle sizes		[364]

continued

Table 9. Continued

Nanoparticle materials	Characteristics of nanoparticle	Brief process description	Ref.
Barium ferrite (BaFe ₁₂ O ₁₉)	Nanosized	Mix two microemulsions: coprecipitation of ferri/barium salts by ammonium carbonate in microemulsion containing an aqueous phase, CTAB surfactant, n-butanol cosurfactant, and octane (oil).	[365]
SiO ₂ -coated iron oxide	As small as 1–2 nm iron oxide uniform particle size, coating as thin as 1 nm	W/O microemulsion using nonionic surfactants (Triton X-100, Igepal CO-520, and Brij-97), by coprecipitation of Fe(II)/ Fe(III) salts by NaOH or ammonia. Coating was with TEOS sol-gel reaction in microemulsion	[366]
Titania-coated silica	~60 nm monodispersed spheres	Controlled hydrolysis of TEOS and Ti n-butoxide in Triton X-45/cyclohexane/water reverse (w/o) microemulsions	[367]
Silica-copper oxide composite	20–50 nm with uniform elemental distribution, narrow distribution of mesopores (3–6 nm), 320–379 m ² /g	Controlled hydrolysis/polymerization of Na ₂ SiO ₃ and Cu(NO ₃) ₂ · 3H ₂ O via partial-microemulsion and double-microemulsion processes at 28 °C, consisting of sodium 1,4-bis(2-ethylhexyl) sulfosuccinate and sodium dodecyl sulfate, cyclohexane, and water.	[368]
Indium-tin oxide (ITO)	Monodispersed, 9–12 nm as-prepared particle size	Two emulsion mixing: ammonium hydroxide coprecipitation of aqueous solution of indium nitrate and tin chloride in AOT-based reverse microemulsions	[369]
Cu ₂ L ₂ O ₅ (L = Ho, Er)	25 nm crystalline agglomerates after calcinations at 700 °C Spherical calcined nanoparticle (15–25 nm in size)	Mixing (NH ₄) ₂ CO ₃ -containing microemulsion with microemulsion containing both Cu(NO ₃) ₂ and L(NO ₃) ₃ for coprecipitation. W/O microemulsion: water/CTAB/n-octane/1-butanol	[370]
BaTiO ₃	Precipitated Cu ₂ Ho ₂ (CO ₃) ₄ (OH) ₂ (25–30 nm) and Cu ₂ Er ₂ (CO ₃) ₄ (OH) ₂ (10–40 nm) Near-monodispersed, 6–17 nm sizes, nonagglomerated, cube-shaped crystals	Sol-gel reactions in W/O microemulsion without any sintering process (cyclohexane + 1-octanol + Tergitol™ + water) + (Ti isopropoxide + Ba isopropoxide)	[371]
Binary and ternary metal oxides	8–19 nm crystallite sizes in nanopowders Binary: TiO ₂ , ZrO ₂ Ternary: BaTiO ₃ , BaZrO ₃ , SrTiO ₃ , SrZrO ₃	Sol-gel chemistry plus W/O microemulsion technique	[372]
Perovskite-type metal oxides	~20 nm diameter metal oxalate particles, calcined into single phase into LaNiO ₃ , La ₂ CuO ₄ , and BaPbO ₃	Oxalate precipitation in inverse microemulsion	[373]

solutions; and (2) this deposit is then permitted to spontaneously oxidize and dehydrate at an open circuit in the pH = 1.0 plating solution. Most recently, Penner [190] utilized the hybrid electrochemical/chemical (or E/C) method for synthesizing oxide and semiconductor nanoparticles or quantum dots on graphite surfaces. This E/C method for the synthesis of quantum dots of the generic semiconducting salt MX typically involves three steps:

1. electrochemical deposition of size-monodispersed nanoparticles of the metal M^0 from a solution of metal ions M^{n+}

2. electrochemical oxidation of these metal particles to $MO_{n/2}$
3. displacement of the oxygen from $MO_{n/2}$ using HX (for example) to yield nanoparticles of semiconductor MX.

The conversion from metal to metal oxide to metal salt occurs on a particle-by-particle basis. The quantum dots thus prepared by the E/C method possess many of the attributes of quantum dots synthesized using molecular beam epitaxy, including epitaxial orientation on a substrate surface, a narrow size distribution, and strong, particle size-tunable photoluminescence.

Table 10. Liquid-phase sonochemical synthesis of metal–oxide nanoparticles.

Nanoparticle materials	Characteristics of nanoparticle	Brief process description	Ref.
Tungsten oxide	Amorphous as-prepared particles (100–200 nm sizes), globular agglomerates composed of <5 nm dense primary particles)	Sonochemical decomposition: ultrasound irradiation of a solution of tungsten hexacarbonyl $W(CO)_6$ in diphenylmethane in the presence of an $Ar(80\%)-O_2(20\%)$ gaseous mixture at 90 °C	[374]
Ceria	Nanocrystalline powder (2.6 nm crystallite)	Sonochemical-assisted heating routes from aqueous solutions containing $(NH_4)_2Ce(NO_3)_6$, hexamethylenetetramine, and poly(ethylene glycol)-19000 (PEG)	[323]
	Monodispersed, mean particle size of ca. 3.3 nm	Sonochemical synthesis using cerium nitrate and azodicarbonamide as starting materials, and ethylenediamine or tetraalkylammonium hydroxide as additives	[375]
Nickel aluminate spinel	Nanosized $NiAl_2O_4$ particles with a size of ~13 nm (crystallite size)	Sonicating an aqueous solution of nickel nitrate, aluminum nitrate, and urea yields and precursor, which on heating at 950 °C for 14 h yields nanosized particles	[376]
Yttria-stabilized zirconia (YSZ)	Monodispersed, 4.7 nm nanocrystal size, on the surface of $SrCO_3$ nanoparticles	Sonochemical treatment to induce crystallization of self-assembled hydrous YSZ on the surface of $SrCO_3$ nanoparticles	[377]
V–nickel hydroxide	Scaly particles with a length of ca. 120–200 nm and a width of ca. 10–15 nm	Ultrasound radiation of an aqueous solution of Ni nitrate and urea (purged with Ar, 80 °C)	[378]
CuO in PVA	~5–10 nm particle sizes	Ultrasonication of poly(vinyl alcohol) (PVA) and copper(II) acetate dissolved in water–dimethylformamide (DMF) under Ar at room temperature for 3 h	[379]
Amorphous iron oxide Fe_2O_3	Stable colloids of undecenoate, dodecyl sulfonate, and octyl phosphonate coated Fe_2O_3 nanoparticles of 5–16 nm in diameters	Sonochemical decomposition of volatile precursor $Fe(CO)_5$ solution in decane, in the presence of different surfactants, under air atmosphere at 273 K for 3 h	[380]
	Particle size of ~25 nm	Neat $Fe(CO)_5$ or a solution in decalin was irradiated ultrasonically under air atmosphere at 0 °C for 3 h	[381]
Co_3O_4 , ZnO	20–30 nm cobalt oxide particle sizes, 250–340 nm zinc oxide particle sizes	Sonochemical irradiation of metal acetate solutions in doubly distilled deoxygenated water or 10% water–DMF, under 1.5 atm of argon at room temperature for 3 h	[382]
Fe_3O_4	Pure nanocrystalline phase, particle size of ca. 10 nm, minimal agglomeration	Sonication of iron (II) acetate in water under an argon atmosphere at 25 °C for 3 h	[383]
$RuS_{1.7}$	Particle sizes of ca. 25 nm, nanocrystalline powders with certain aggregation	Sonication of an aqueous solution of ruthenium chloride and thiourea → X-ray amorphous product → heating at 650 °C → nanocrystalline ruthenium sulfide	[384]

3.2.10. Synthesis in Supercritical Fluids

Supercritical fluid (SCF) processing has been considered for particle design [191] and as a new route for materials synthesis, such as for the formation of novel inorganic nanoparticles, and for the preparation of different open-structure oxy(hydroxy)fluorides [192]. There are certain advantageous features of using SCF processes for materials processing [129]: (1) the ability to form nanoparticles, (2) the ability to control particle morphology to some extent with pressure

and temperature, and (3) the ability to provide homogeneous reducing or oxidizing atmospheres by introducing gases or additional components (O_2 , H_2 , H_2O_2).

When the fluid is water, the technique is called supercritical hydrothermal processing. The fluid could also be another solvent, such as CO_2 . Some solvothermal processing is, in fact, a subcategory of supercritical or subcritical fluid (solvent) processing. In particular, supercritical CO_2 and supercritical water (SCW) are chemically stable and

environmentally benign. SCF exhibits the combined characteristics of both gas and liquid solvents to provide a medium with densities characteristic of liquids, and with gas-like viscosities and diffusivities. Thus, mass-transfer rates approach those of gases, while solvation properties resemble those of conventional liquid solvents. Furthermore, supercritical fluids exhibit unique tunable solvation characteristics, as subtle changes in pressure and temperature in SCFs alter the solvent density. This property might be utilized to improve many aspects of nanocrystal processing, such as size-selective separations, synthesis, and self-assembly [193].

Hydrothermal synthesis under supercritical conditions has been studied for the synthesis of nanosize crystals of metal oxides such as CeO_2 and $\text{AlO}(\text{OH})$ [129]. In water, the dielectric constant dramatically decreases when heated and pressurized above the critical point ($T_c = 374^\circ\text{C}$, $P_c = 221$ bar). The solubility of salts decreases, and the solubility of organics increases [193]. The lower dielectric constant at supercritical conditions possibly results in enhancement of the hydrothermal reaction. There are two reasons why nanoparticles are formed at supercritical conditions: (1) larger particles are produced at subcritical conditions due to Ostwald ripening, that could not be observed in supercritical water because of the extremely low solubility; and (2) the nucleation rate is faster in supercritical water because of the lower solubility and the extremely fast reaction rate [129]. The use of stabilizing ligands to bind nanocrystal surfaces, or using compartmentalized heterogeneous media (such as micellar solutions) to control growth have recently been extended to SCFs with general success. When water is heated and pressurized above the critical point, it becomes a suitable solvent to employ organic capping ligands (such as alkanediols) to control and stabilize the synthesis of nanocrystals. Ziegler et al. [193] have prepared monolayer-stabilized copper nanocrystals (~ 7 nm in diameter) in the presence of 1-hexanediol and $\text{Cu}(\text{NO}_3)_2$. It is also reported that metal oxides can be prepared in SCW using metal nitrate salts, which decompose via a two-step mechanism of hydrolysis and dehydration [194]. The high temperature of SCW promotes crystallization, which eliminates the need for postprocess annealing. Oxidizers/reducers can be added to the reaction mixture to influence the product chemistry.

Water-in-sc- CO_2 microemulsions have been used as “microreactors” to produce nanocrystals of cadmium sulfide and silver [195, 196], while water-in-sc-ethane and water-in-sc-propane microemulsions have been similarly used to produce copper nanocrystals [197, 198]. Arrested precipitation methods have also recently been utilized in SCFs to produce sterically stabilized silicon nanocrystals (in sc-octanol and sc-hexane) [199] and silver, copper, palladium, platinum, and iridium nanocrystals (in sc- CO_2) [200].

Supercritical antisolvent precipitation (SAS), based on the fast dissolution of a liquid solution in a supercritical fluid, has been tested to produce nanoparticles of yttrium, samarium, europium, gadolinium, and neodymium acetates to be used as precursors for high-temperature superconductors [201, 202] and as a zinc oxide precursor (zinc acetate) [203]. Rapid expansion of supercritical solution (RESS) is another technique that has been tested for the preparation of nanoscale PbS particles. In this technique, one: (1) expands the supercritical solution into a liquid solution instead of a gas,

and (2) uses a reacting system in which one reactant is dissolved in the supercritical solution and one in the liquid receiving solution [204]. Supercritical ammonia, methanol, and acetone solutions have also been used for RESS. Most recently, a supercritical-assisted atomization (SAA) technique was also proposed and demonstrated for producing nanoparticles of different kinds of compounds (superconductor and catalyst precursors, ceramics, and pharmaceutical compounds) using different liquid solvents such as water, methanol, and acetone [205]. The chemical transformation of metallic precursors in a supercritical fluid (a mixture of $\text{CO}_2/\text{C}_2\text{H}_5\text{OH}$ or NH_3) has been developed as a new route for obtaining ultrafine homogeneous ceramic powders (oxides [Cu_2O , Fe_3O_4 , Ga_2O_3] and nitrides [Cu_3N , Fe_4N] [206]). This process consists of the solubilization and subsequent thermal decomposition of acetylacetonates of metals in SCF.

3.3. Solid-Phase Synthesis

Solid-phase syntheses are those methods in which nanoparticles are formed directly from solids or semisolids (such as viscous liquids). Most of these types of syntheses belong to the top-down approach, which includes traditional mechanical grinding and solid-state reactions. In the effort to produce nanoparticles, some new innovations have been added to these traditional methods, such as introducing reactive materials into the milling process, as shown in Figure 5, and combining milling with solid-state synthesis. Some new approaches include the extraction of soluble molecules from a uniform molecular solid mixture by acid/base leaching or evaporation to leave molecular skeleton residues that become nanoparticles.

3.3.1. Mechanical Milling

Mechanical forces, such as those involved in high-energy ball milling, are used to break bulk materials down. Plastic deformation and dislocation of cell structures are responsible for producing highly strained amorphous particulate materials. Crystalline nanoparticles can be produced when the dislocation of cells disappears. High-energy ball milling is already commercialized for generating magnetic [207], catalytic [208], and structural [209] nanoparticles.

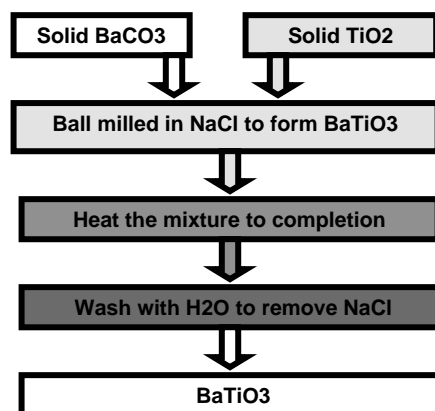


Figure 5. Flowchart for a mechanochemical synthesis.

Bohwik et al. [210] have obtained 16 nm nanoparticles of antiferromagnetic spinel CoRh_2O_4 by the mechanical milling of bulk materials for up to 60 h. Magnetic measurements suggest that the antiferromagnetic ordering at TN at 27 K exists in bulk as well as in nanoparticle samples. Nanoparticle $\text{Co}_{0.2}\text{Zn}_{0.8}\text{Fe}_2\text{O}_4$ spinel oxide was also synthesized by room-temperature mechanical milling [211]. The system is stabilized mainly in the spinel oxide phase after 78 h of milling time, and no other phases have been observed.

The simplicity of mechanical milling has shown its potential in nanoparticle synthesis without complex capital equipment. The development of new technologies such as bead mills with very small beads, and their use in combination with classification/filtration, make this technology applicable to nanoparticle synthesis. A drawback in this technology is contamination from media.

3.3.2. Mechanochemical Processing

Mechanochemical processing is considered the natural extension of mechanical processing. Here, the process not only involves physical reduction in a material's size, but it also uses the milling energy to initiate chemical reactions between the materials that are being milled. It usually involves two or more solid reactants. Sometimes, the starting materials are milled together in the presence of a large amount of sacrificial salt, such as NaCl, which prevents the agglomeration of the resulting nanoparticles, as shown in Figure 5 [212]. More and more mechanical milling processes are incorporating chemical reactions to make the process more amenable to nanoparticle syntheses [213]. Table 11 shows examples of nanoparticles of ferrites, CaTiO_3 , SnO_2 , Ag, Fe_2O_3 , CaCO_3 , Cu, Al_2O_3 , PbTiO_3 , ZnO, CeO_2 , Cr_2O_3 , Gd_2O_3 , ZrO_2 , and Group II–VI semiconductors that were made using mechanochemical methods.

Mechanochemical synthesis uses mechanical energy to activate chemical reactions, and to cause surface and structural change of the materials [214]. As a consequence, chemical reactions which otherwise require high temperatures can occur at low temperatures in a ball mill without external heating or with low external annealing.

Abe and co-workers [215, 216] made submicron BaTiO_3 by ball milling TiO_2 with $\text{Ba}(\text{OH})_2 \cdot 8\text{H}_2\text{O}$ in acetone for 6 h without external heating. A boundary–reaction-controlled interface contracting kinetics, and contraction kinetics with a crystallinity gradient inside the TiO_2 particles, have been proposed for the formation of BaTiO_3 .

van Hal et al. [217] showed the feasibility of making submicron BaTiO_3 by ball milling BaO_2 with TiO_2 for 256 h. The products are BaTiO_3 agglomerates consisting of 50% particles with a crystallite size of 12 nm, 30% particles with a crystallite size of 2 nm, and 20% amorphous particles. Heating of these agglomerates at 800 °C did not significantly improve the crystallinity.

McCormick and Tzuzuki [218] made truly nanosized BaTiO_3 by milling BaCO_3 and solid TiO_2 with a large amount (three times the mass of BaCO_3 plus TiO_2) of sacrificial salts, such as NaCl, for a few hours. Such milling induces reactions between BaCO_3 and TiO_2 , as well as mixing of BaCO_3 and TiO_2 . The diluent phase NaCl may have

two roles. The major role is to dilute or coat the BaTiO_3 particles formed so that the nanosized BaTiO_3 will not agglomerate together. The second role may be to promote the chemical reaction between BaCO_3 and TiO_2 . To complete the reaction, the milled products were subjected to external heating for 30 min at 700 °C. A final washing to remove NaCl with large amounts of water is needed to recover BaTiO_3 . BaTiO_3 of 50–100 nm was produced. However, there are still issues regarding the ability to achieve phase-pure materials with the proper Ba/Ti ratio, the need to prevent contamination from milling media and NaCl, and the desire to reduce the amount of waste water from extensive water washing. Furthermore, it is difficult to keep the nanosized BaTiO_3 from agglomerating again during washing, filtering, and drying after the BaCl_2 is dissolved away.

Mechanochemical processing has been demonstrated to be very versatile in making a broad range of nanoparticles (as shown in Table 11), including metals, oxides, carbonates, and sulfides. The chemical reactions for particle synthesis could happen during milling, but it is not necessary that they happen during this phase of the process. It is only necessary for the crystal size to be refined to the nanometer level during milling, after which the chemical reactions can be induced with a low-temperature heat treatment. Particle size control in this process is achieved via the milling conditions, and also by the addition of diluents, and this process has been shown to produce a range of sizes from 4 to 500 nm. It is cost effective in that it uses simple starting materials and simple milling equipment. The disadvantages of this process include contamination from milling vessels and media. The washing of the byproducts after heat treatment also presents challenges because a large volume of water is consumed, and because agglomeration of the particles may occur during washing and drying.

3.3.3. Cryochemical Processing

Cryochemical processing is a low-temperature process in which rapid cooling is applied to preserve the homogeneity of atomic-level mixtures. The cooling is usually very fast in order to prevent separate crystallization of solutions such as soluble nitrates. This is usually achieved by spraying the solution into liquid nitrogen. Removal of frozen water is usually accomplished by physical (freeze drying) or chemical means. Many cryochemical techniques have been developed for powder processing [219–222]. The process can be described by the following diagram:

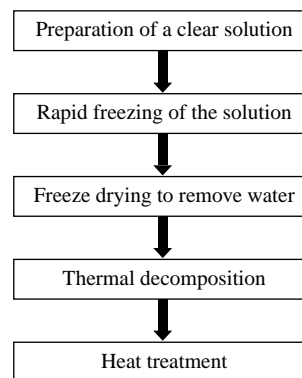


Table 11. Nanoparticle synthesis by mechanochemical process.

Nanoparticle materials	Characteristics of nanoparticle	Brief process description	Applications	Ref.
Ferrites ($\text{Fe}_3\text{O}_4/\text{Fe}_2\text{O}_3$, CoFe_2O_4 , $\text{Ni}_{0.5}\text{Zn}_{0.5}\text{Fe}_2\text{O}_4$)	20–30 nm, spinel structure	Mechanochemical reaction in aqueous solution of various corresponding chlorites and NaOH in a horizontal mill	Wide field of technological applications	[385]
CaTiO_3	20–30 nm crystallite	Mixture of CaO and TiO_2 was milled in a planetary mill at 200–300 rotations/min for 2–10 h	Dielectric materials and other applications	[386]
SnO_2	5–30 nm, tetragonal and orthorhombic SnO_2 formed after heat treatment	Mechanochemical milling of SnCl_2 and Na_2CO_3 followed by heat treatment in air	Various applications	[387]
Ag	50–1000 nm metallic silver with minor quantity of Ag_2Na	A solid-state displacement reaction between AgCl and Na by ball milling in a planetary-type ball mill. The byproduct NaCl was washed out	Electrode material, pigment, etc.	[388]
Fe_2O_3		Ammonium acetate as precipitating agent	Magnetic materials	[95]
CaCO_3	80–140 nm, crystalline	Milling of a CaCl_2 – Na_2CO_3 powder mixture, followed by heat treatment of the as-milled powder at 350 °C. NaCl was washed away	Various applications	[389]
Cu	Cu crystallite size of 28 nm with 3vol% $\text{CuO} \cdot \text{Al}_2\text{O}_3$	Milling CuO – $\text{CuO} \cdot \text{Al}_2\text{O}_3$ mixture for 8 h	Electronic materials, pigments, etc.	[390]
Al_2O_3	10–50 nm amorphous alumina	Milling ZnO and Al powder	Coating, paints, and various applications	[391]
PbTiO_3	10 nm grain size	High-energy ball mill of lead oxide and titanium oxide for 20 h without any posttreatment	Electric applications	[392]
ZnO , CeO_2 , SnO_2	28, 10, 40 nm crystalline nanoparticles, respectively	Milling of chlorides and carbonates, followed by water washing	In many industries	[393]
Cr_2O_3	10–80 nm crystalline	Milling of NaCr_2O_7 with S powder to form amorphous Cr_2O_3 ; crystalline Cr_2O_3 was formed after annealing under vacuum at 520 °C. Water washing to remove Na_2SO_4 formed	Various applications	[394]
II–VI semiconductor	<10 nm	Milling of chloride salts and alkali or alkaline earth chalcogenides, postheat treatment, and washing	Various applications	[395]
Gd_2O_3	20 nm cubic structure	Milling GsCl_3 with NaOH in the presence of NaCl, followed by calcinations at 500 °C	Various applications	[396]
ZrO_2	15–18 nm crystallite size stabilized zirconium in c- ZrO_2 polymorph with 5 mol% Cr^{3+} and Cr^{4+}	Milling $(\text{NH}_4)_2\text{Cr}_2\text{O}_7$ with amorphous precipitation of Zr(=4) oxyhydroxide, followed by heating at 500 °C	Coatings and other applications	[397, 398]

Tretyakov and Shlyakhtin [222] have provided an excellent review of recent progress in the cryochemical synthesis of oxide materials. A broad range of materials has been synthesized using cryochemical methods. These materials include ferrites, catalysts, resistive materials, high-temperature superconductors, magnetic semiconductors, superionics, and phosphors. One unique feature of this synthesis is that there is a large difference between the specific molar volumes of the frozen precursor salt and the oxide product formed after thermal decomposition of the precursor salt. Thermal decomposition transforms the salt crystallites into a porous oxide framework of almost the same size and shape as the initial salt crystallites. Subsequent heat treatment causes the rearrangement and sintering of framework elements of 10–40 nm in size into larger aggregated particles of 50–300 nm.

McHale et al. [223] recently demonstrated the synthesis of nanocrystalline BaTiO₃ using cryochemical methods. They first prepared a titanyl nitrate solution of pH 1.2 by dissolving hydrolyzed titanium isopropoxide with a diluted nitric acid. BaCO₃ was added to this acidic solution to achieve a molecular mixture solution of Ba:Ti = 1:1. This nitrate solution was then atomized using an ultrasonic spray nozzle, and was rapidly frozen by allowing the aerosol to fall into stirred liquid nitrogen. The fine white-to-pale-yellow particles (“snow”) were then dried in a freeze dryer at about –30 °C. The highly reactive precursor powder obtained from this freeze drying could be completely converted into 10–15 nm nanocrystalline BaTiO₃ of cubic structure by heating at 600 °C for 10 min. Prolonged heat treatment at 600 °C for up to 24 h resulted in little grain size growth. Higher temperature calcination and annealing, however, significantly grew the grain size (500 nm at 1000 °C), and resulted in the appearance of the tetragonal form of BaTiO₃.

Kirchnerova and Klvana [224] synthesized submicron lanthanum–strontium transition metal-based perovskites based on cryochemical methods. They used a reactive aqueous slurry of lanthanum (or another rare earth metal) hydroxides and of metal nitrate solution as a starting material. This well-homogenized suspension was then spray frozen, freeze dried, and calcined at as low as 627 °C to form the perovskite phase.

Thierauf et al. [225] produced superconducting YBCO powders of less than 300 nm via a freeze-drying process using the dissolved acetates as precursors. A crystallization temperature as low as 720 °C in air was realized due to the short diffusion lengths in the freeze-dried precursor materials.

The cryochemical method has broad applications; however, freeze drying itself cannot form the final products directly. A final calcination and annealing are always needed. This thermal treatment always aggregates, agglomerates the particles, and grows large crystals, which makes it difficult to synthesize monodispersed nanoparticles.

3.3.4. Self-Combustion Method

The self-combustion method has been widely used in the synthesis of oxides/ceramic particles. It is known by different names, such as self-sustaining/propagating high-temperature synthesis (SHS) [226], the combustion method

[227] and autoignition process [228], or is sometimes more specifically called glycine–nitrate synthesis [229, 230], and the organometallic polymer precursor method [231]. This method utilizes rapid exothermic reactions to form solid fine particles directly. It involves a molecular mixture of oxidizers (e.g., metal nitrates, ammonia nitrates, or ammonia perchlorate) and reducers (e.g., carbonaceous materials such as urea, carbonylhydrazide, glycine, PVA, sucrose, and EDTA), which can be ignited at relatively low temperatures. The ratio of oxidizer to reducer is usually calculated according to Jain and Adiga’s methods [232]. The combustion reaction can be initiated in a lab muffle furnace or even on a hot plate at temperatures of lower than 500 °C. The process can be illustrated by the following diagram:

In the above diagram, the route ending on the right side usually involves polymers such as polyvinyl alcohol (PVA), carboxylated starch (PAA) or sucrose, or complexing agents such as organic acids or organic amines and metal nitrates [227, 233, 234]. The route ending on the left side usually involves an unstable system such as metal nitrates and glycine, which could initiate self-combustion at temperatures as low as 200 °C [235–237].

Pathak and Pramanik [227, 238] have synthesized over 50 different ceramic oxides using combustion methods. These oxide systems include

- metal oxides: Fe₂O₃·NiO, Fe₂O₃·CuO, Fe₂O₃·TiO₂
- metal phosphates: Co₃(PO₄)₂, Ni₃(PO₄)₂, Cu₃(PO₄)₂, Ba₃(PO₄)₂, AlPO₃, CrPO₄, FePO₄
- metal vanadates: Ca₃(VO₄)₂, Co₃(VO₄)₂, Ni₃(VO₄)₂, Cu₃(VO₄)₂, CrVO₄, FeVO₄, MnVO₄
- metal molybdates: CaMoO₄, NiMoO₄, CoMoO₄, MgMoO₄, Sm₃(MoO₄)₃, Gd₃(MoO₄)₃
- metal tungstates: CaWO₄, MgWO₄, NiWO₄, CoWO₄
- rare-earth aluminates: LaAlO₃, SmAlO₃, NdAlO₃
- PZT and PLZT.

Their methods involve the combustion of a polymer (PVA or sucrose) and/or complex-based (EDTA/TEA/DEA) nitrate solution(s). The polymer plays a dual role in the process: it acts as a dispersing agent for the cations in the solution, and it also serves as a fuel that provides heat through combustion during calcination of the precursor powders. The principle of their methods is to atomistically disperse the metal ions in a matrix provided by a polymeric reagent or through complexation with various chelating agents that possess good coordination properties with metal ions. Evaporation of the precursor solutions results in a fluffy, voluminous carbonaceous mass that constitutes the precursor materials. The resulting particles from combustion of the precursor powders are 10–90 nm in diameter, have a narrow size distribution of high purity, and are obtained at relatively lower pyrolysis temperatures than those obtained from direct calcinations.

Chick and co-workers [229, 230, 235, 236, 239–242] have prepared nanosized metal powders such as Ni, Cu, and Fe, or the two-metal system containing Ni and Cu, using a glycine–nitrate combustion method. Their method consists of two steps. First, metal nitrates and a low molecular weight amino acid are dissolved in water. Second, the solution is boiled until it thickens and autoignites, undergoing self-sustaining combustion. The ash from the combustion is

composed of the oxide products. The glycine molecule has a carboxylic acid group at one end, with an amine group at the other, and serves two purposes: it prevents selective precipitation as water is evaporated, and it serves as fuel for the combustion, being oxidized by nitrate ions. The fuel-rich mixtures produce 10 nm spherical Ni (with 15% NiO), 30–40 nm Cu. The disadvantage of this method is that, in general, the glycine–nitrate combustion tends to produce agglomerated particles.

McKittrick et al. [243] prepared yttrium aluminum garnet ($Y_3Al_5O_{12}$, YAG) using a combustion process. They dissolved the metal nitrates with carbohydrazide in water, and placed the container in a muffle furnace preheated to 560 °C. The reaction proceeds as the precursor solution first boils, dehydrates, decomposes, and ruptures into a flame after 5–10 min, with the flame being sustained for about 15 s. The gaseous products that exist in greatest abundance are N_2 , CO_2 , and H_2O if the ratio of fuel to oxidizer is stoichiometric. The powders produced are single phase and well crystallized. The combustion-synthesized powders have an unusual morphology, forming a porous, foamy network in the as-synthesized state, due to the rapid release of gaseous products. The porous powders were easily reduced to a small particle size with light mixing. Combustion synthesis produces powders that are luminescent in the as-synthesized state, an attribute unattainable by conventional methods.

Another modification of combustion synthesis has been explored by Salze et al. [231] for synthesizing ZrO_2 , La_2NiO_4 , and $BaTiO_3$. The initial organometallic solution is obtained by first making an organic solvent solution (dissolution of 400 g citric acid in 500 mL of ethylene glycol). The solution is mechanically stirred until it becomes clear. To prepare tetragonal zirconia, zirconium n-propoxide and yttrium carbonate are dissolved in this organic solvent solution. To prepare pure $SrTiO_3$ or $BaTiO_3$, the corresponding titanium isopropoxide and $SrCO_3$ or $BaCO_3$ (dissolved in formic acid) are dissolved in the above-mentioned organic solvent solution. To prepare doped $SrTiO_3$ or $BaTiO_3$, niobium ethoxide is also added to the solutions cited for preparation of pure $SrTiO_3$ or $BaTiO_3$. To prepare lanthanum nickelate, lanthanum and nickel hydroxides freshly precipitated from nitrate solutions are dissolved. After polymerization at 110 °C in an Al_2O_3 crucible, a translucent resin having a homogenous chemical composition is obtained. This resin is then combusted in air or pure oxygen to obtain the desired powders. The mean diameters of individual particles observed by TEM are 10–60 nm for ZrO_2 combusted in oxygen at 400–950 °C, 10 nm for $SrTiO_3$ in air at 600 °C, 10 nm for $BaTiO_3$ in air at 800 °C, and 35 nm for La_2NiO_4 in air at 600 °C.

Zhou et al. [228] have synthesized 10 nm ZrO_2 containing up to 20mol% CeO_2 using the autoignition method. Zirconyl nitrate, cerous nitrate, and urea powders with stoichiometric composition are dissolved in water, and are then converted to tetragonal ZrO_2 by evaporation and combustion in a 600 °C furnace. The result is a foamy yellow powder with the characteristic color of ZrO_2 (CeO_2) powders.

Rajan et al. [244] recently synthesized 4–16 nm barium holmium zirconate, a new complex perovskite ceramic oxide, using a modified self-propagating combustion process. XRD

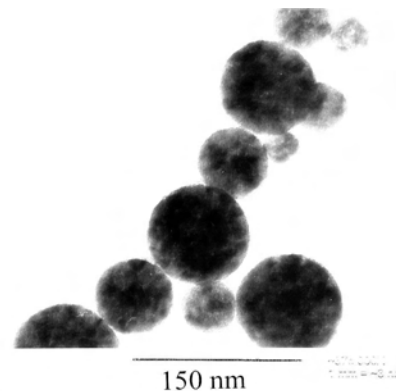


Figure 6. CeO_2 nanoparticles prepared from a combustion method [246].

and electron diffraction studies have shown that the as-prepared powder is phase-pure $Ba_2HoZrO_{5.5}$, and has a complex cubic perovskite ($A_2BB'O_6$) structure with a lattice constant $a = 8.428$ Å. The nanoparticles of $Ba_2HoZrO_{5.5}$ could be sintered to 98% theoretical density at 1500 °C.

Yu et al. [245] prepared nanosized $PbTiO_3$ powders using the self-combustion technique. $Pb(CH_3CHOHCOO)_2$ was used as the Pb precursor, and was formed from the reaction between PbO and $CH_3CHOHCOOH$, with viscous lactic acid as the solvent. The system lead lactate–lactic acid–ethanol–titanium butoxide was selected as the precursor for processing of $PbTiO_3$.

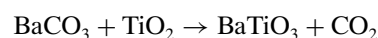
Feng [246] synthesized spherical CeO_2 using a combustion method, as shown in Figure 6. He prepared an $(NH_4)_2Ce(NO_3)_4$ aqueous solution, and added acetyl acetone and isopropanol as fuel and as complexing agents. This clear solution was turned into a viscous liquid by evaporation, and further heating on a hot plate induced vigorous self-combustion to form 15–80 nm crystalline CeO_2 particles directly.

Self-combustion synthesis has been widely demonstrated as effective for synthesizing ceramic powders [228, 237, 240, 247–256]. The technique may need more development to prevent agglomeration and aggregation of the powders during synthesis. Safe scale up to a commercial process demands further optimization studies.

3.3.5. Solid-State Synthesis

This is the most traditional approach for making many ceramic powders such as $BaTiO_3$. It involves milling $BaCO_3$ with TiO_2 to achieve comminution and mixing. This mixture is then calcined at 900–1200 °C to generate $BaTiO_3$. The reaction mechanism has been described in the literature to have the following steps [257–259]:

1. interface reaction by diffusion of Ba into TiO_2 to form a $BaTiO_3$ shell (layer) around TiO_2 ; the shell also limits Ba diffusion into TiO_2 :



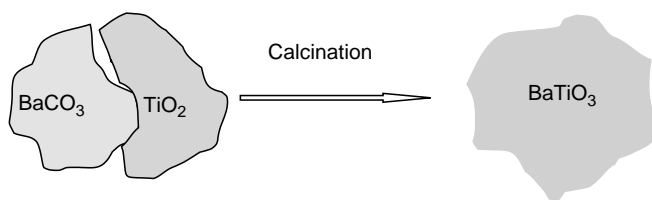
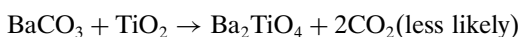
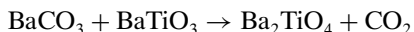
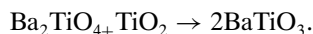


Figure 7. Solid-state reaction through interdiffusion to form BaTiO₃ during calcination.

2. formation of the orthotitanate phase:



3. final formation of BaTiO₃:



The high calcination temperature is needed to promote the interdiffusion of barium and titanium, which results in the solid-state reaction to form barium titanate, as shown in Figure 7. The distance of the interdiffusion depends on the sizes of the raw materials BaCO₃ and TiO₂ used for synthesis. After milling, these particles are usually in the range of 0.5 μm, and the interdiffusion distance is usually larger than 1 μm in the traditional solid-state synthesis. The reaction rate is controlled by this diffusion [260]. The interdiffusion is usually incomplete during calcination due to the large diffusion length, and therefore the final products usually contain titanium-rich and barium-rich intermediate particles [257, 261].

It has also been well known that BaTiO₃ is formed through a sequence of reactions and intermediate phases [258], and that prolonged calcinations at high temperature are usually needed to reduce the heterogeneities in the final products. This usually results in large and agglomerated particles which need extensive milling before BaTiO₃ can be used in the various forming processes. Milling introduces high levels of impurities from the milling equipment and media, such as alumina, silica, zirconia, and phosphorus. These impurities are known to have a deleterious effect on the electrical and mechanical properties of barium titanate-based products [262].

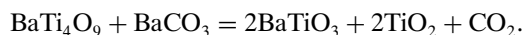
Current efforts in solid-state methods for synthesizing ultrafine particles of BaTiO₃ have been aimed at reducing the interdiffusion distance by utilizing finer starting materials or through intensive milling or utilization of precipitation to produce the solid starting materials *in-situ*.

High-energy ball milling of BaCO₃ and TiO₂ (rutile) has reduced BaTiO₃ formation temperatures down to 730 °C, and the resulting BaTiO₃ has a crystallite size of 40 nm [263]. The detrimental phases, like Ba₂TiO₄ (orthotitanate), have only been revealed as an intermediate minor phase that disappears by annealing at temperatures as low as 750 °C.

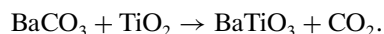
It has also been shown that milling does change the reaction sequence between BaCO₃ and TiO₂ [264]. However, milling reduces the formation temperature and accelerates the formation rate of BaTiO₃.

Instead of using solid TiO₂ particles, Han and Koo [265] precipitated titanium hydroxide/oxide particles directly onto the surface of BaCO₃. TiCl₄ or Ti alkoxide solutions were added directly to an aqueous slurry containing fine particles of BaCO₃ and ammonia at pH 9.5–10.3. The nanoparticles of titanium hydroxides/oxides were deposited or coated on the surface of BaTiO₃, which effectively reduced the interdiffusion distance. The filtered slurry was then calcined at 950 °C for 2 h to produce 180 nm BaTiO₃.

In a similar study, coprecipitation of a mixture of BaCl₂ and TiCl₄ with a solution of ammonium carbonate has also been studied [266]. It was found that crystallization of amorphous barium tetratitanate was observed when the precipitates were heated above 600 °C. At the same time, the following reaction is also suggested:



The newly formed TiO₂ begins to react with BaCO₃ directly at 800 °C:



The above reactions approached completion at 1100 °C.

Li et al. [267] used a solid-state reaction process to prepare perovskite-type LaCoO₃ nanocrystals with grain diameters of 15–40 nm. In the first step of the process, 5 nm composite hydroxide nanoparticles were prepared by the solid-state reaction of La(NO₃)₃·nH₂O and Co(NO₃)₂·6H₂O with KOH at ambient temperature. A perovskite-type rhombohedral LaCoO₃ phase appeared at 550 °C after the hydroxide was calcined at various temperatures. The phase transformation process was complete at about 800 °C, yielding a single-phase binary oxide.

Wang et al. [268] developed a one-step solid-state reaction in the presence of a nonionic surfactant, PEG 400, to synthesize CuO nanowhiskers with diameters of approximately 2–10 nm and lengths of more than 100 nm.

Zhuang et al. [269] prepared a precursor Co₂(OH)₂CO₂ by the solid-state reaction of Co(NO₃)₂·6H₂O with NH₄HCO₃ at ambient temperature. Nanophase Co₃O₄ with an average particle size of 13 nm was obtained by decomposition of the precursor at 250 °C for 3 h.

Yu et al. [270] prepared CeO₂ ultrafine particles by solid-state reactions at room temperature. These particles were found to have very fine particle sizes (~3 nm) with a fluorite structure ($a = 5.42 \text{ \AA}$). BET measurements showed that the surface area of the particles was 96.2 m²/g.

All of these current efforts in solid-state synthesis focus on minimizing the interdiffusion distances of solid-state reactions through intensive milling, coating particles with nanoparticles, and coprecipitations. The reduced interdiffusion effectively lowered the BaTiO₃ formation temperature, but the completion of the formation reaction still requires calcination temperatures from 750 to 1100 °C. This high-temperature calcination will inevitably promote particle agglomeration and particle size growth. The improvement in the solid-state reaction technique may be able to produce solid-state BaTiO₃ down to 300 nm at industrial quantity, but it is extremely difficult, if not impossible, to produce BaTiO₃ at about a 100 nm range via this method.

3.3.6. Colloidal Assembly Method

Colloidal assembly is a process by which nanometer-sized colloids (nanoparticles) are organized into structures by mixing two or more particle types (differences in sizes and/or chemical nature [271]). Assembly is controlled by either specific or nonspecific interactions between particles. The assembly process is usually performed such that smaller particles assemble around larger ones. Examples include chemical bonding, biological interactions, electrostatic interactions, capillary action, and physical adsorption.

Pileni [272] has reviewed syntheses of nanosized particles that used colloidal assemblies as templates. The chemical mechanisms in nanoparticle production using colloidal assemblies can differ from those usually observed in homogeneous solutions. The colloidal systems mimic nature to control the size and shape of nanomaterials. It is possible to select the size and markedly reduce the particle size distribution by using a surface treatment of the nanoparticles. This favors the formation of mono- and multilayers made of nanoparticles. These particles form crystals organized in a 3-D face-centered cubic superlattice.

An unusual phase diagram is presented by Pileni et al. [273]. It is composed of copper(II) bis(2-ethylhexyl) sulfosuccinate Cu(AOT)₂-isooctane-water. Syntheses performed in the various parts of the phase diagram show that the use of colloidal assemblies as templates favors control of the shape of nanoparticles. Cylindrical metallic copper particles having the same size can be obtained in various parts of the phase diagram when the template is made of interconnected cylinders. A small number of cylinders (13% of the amount that could be formed) are formed when the synthesis is performed in cylindrical reverse micelles. When the colloidal self-assembly is a mixture of several phases, various types of shapes can be obtained. In some cases, the polydispersity in size is so low that metallic particles are able to self-assemble in a hexagonal network. Multilayers can be observed, and are arranged in an FCC structure.

Monolayers of nanoparticles have been physically adsorbed onto highly oriented pyrolytic graphite, first by self-assembly, and second by assembly as Langmuir films and subsequent deposition. Nanoparticles have been self-assembled on gold, and immobilized by chemical absorption, using decanedithiol during assembly as a linking molecule. Rolandi et al. [274] have obtained scanning tunneling microscope images of the monolayers of gold nanocrystals, with mean diameter 2.8 nm, coated with an insulating chemically stable self-assembled monolayer of dodecanethiol.

Kurth et al. [275] have demonstrated that self-assembly of CdTe nanoparticles and alkylammonium surfactants gives stable, hydrophobic surfactant-encapsulated CdTe clusters that can be isolated as solid materials which dissolve in common organic solvents, spread at the air-water interface, and show enhanced photochemical stability.

Christophe and Pileni [276] have used colloidal assemblies to synthesize FCC cobalt nanoparticles. The nanocrystals are coated and extracted from micelles. These cobalt metal particles are stable in air, and have a narrow size distribution. After deposition on a graphite support, these nanocrystals form a 2-D hexagonal network. The magnetic properties are compared when they are dispersed in a solvent

and organized in 2-D superlattices. Changes in the hysteresis loop and in the blocking temperature are observed, and are attributed to a collective flip of the magnetization of adjacent particles.

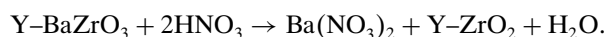
Self-assembly of solid colloids into nanoparticles with the assistance of organic molecules, surfactants, and polymerized vesicles has also been inspired by Mother Nature's organizational ability [26, 27, 234, 271, 277-279]. This method could provide a unique way to synthesize stable and unagglomerated nanoparticles at low temperature and in an environmentally friendly way [280, 281].

3.3.7. Selective Leaching of a Single-Phase Solid-Solution Method

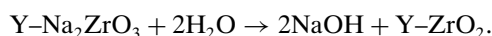
This is a top-down approach, but at a molecular scale. In this approach, a precursor powder of normal size (micro or macro) containing the desired elements is synthesized by any conventional method, such as a solid-state method. The unwanted species are then chemically leached away in a suitable liquid, which could be either water or an acid solution. The concomitant change in volume and crystal evolution during leaching leads to the formation of molecular-level fragments, resulting in nanoparticles. Jiang et al. [19] have demonstrated the synthesis of nanosized yttrium-stabilized zirconium by using this method. They have demonstrated this approach using two different precursors, Na₂ZrO₃ and BaZrO₃.

For the preparation of yttrium-stabilized BaZrO₃, the starting materials BaCO₃, ZrO₂, and Y₂O₃ were mixed in the requisite proportion, wet ball milled in alcohol for 24 h, and then dried. For the preparation of Y-Na₂ZrO₃, Na₂CO₃ and commercial yttrium-stabilized zirconium (YSZ) powders were mixed, wet milled, and then dried. The ball-milled and dried powders were calcined at various temperatures, and the resulting powders were examined to ensure that completely converted single-phase precursor powders (i.e., Y-BaZrO₃ or Y-Na₂ZrO₃) had been formed.

Chemical leaching of BaO from Y-BaZrO₃ was achieved in dilute aqueous HNO₃ solution. The Y-BaZrO₃ was boiled in a dilute HNO₃ solution, filtered, and washed repeatedly until the solution pH no longer changed. The washing process leached Ba²⁺ and left Y-ZrO₂ behind:



For the Y-Na₂ZrO₃ precursor, repeated boiling in water is sufficient to remove sodium according to



Chemical analysis of the boiled and washed powders showed only ZrO₂ and Y₂O₃.

XRD patterns of leached and washed powders from both precursors were identical, even though they showed very different XRD patterns before leaching. Both end products showed an XRD pattern similar to commercial Y-ZrO₂. The particle size was a few nanometers, and increased to tens of nanometers after thermal treatment at a temperature of 1000 °C.

4. SUMMARY

Here brief review of ceramic nanoparticle syntheses is provided. Nanoparticles can be defined as particles with a size range from 1 nm to a size whose ratio of the number of atoms on the surfaces and at the grain boundaries to the atoms at the center is such that new physical, chemical, and biological properties occur when compared with their corresponding bulk materials. The challenges in manufacturing nanoparticles are: controlling their size, morphology, crystallinity, shape, and properties, and making them with a variety of materials at large volumes and at a reasonable cost. The synthetic methods can be classified by the strategy of the synthesis (top down or bottom up), by the nature of the synthetic process (physical, chemical, or biological), by energy sources (laser, plasma, sputtering, microwave, electron beam, heating, freeze drying, hydrothermal, mechanical milling, combustion, flame, supercritical, etc.), and by the media in which nanoparticles are formed (gas, liquid, and solid). Gas-phase syntheses are actively coupled with liquid dispersion to achieve better deagglomeration. There is an increasing trend of using nonaqueous solvents in liquid-phase syntheses for preparing nanoparticles with less agglomeration. Solid-phase syntheses such as mechanical milling have been increasingly coupled with chemical reactions to broaden their applications in nanoparticle synthesis. The most viable methods for the production of nanoparticles are those that utilize low temperatures since high-temperature treatment always means aggregation and agglomeration. Biomineralization could be one of the future means for synthesizing nanoparticles if the synthesis can be carried out quickly and on a large scale. Selection of the most suitable synthetic methods is usually based on

- the desired attributes of the product, such as particle size and its distribution, crystallinity (amorphous or crystalline), morphology (single particle or agglomerates), and composition (single component versus multiple components)
- media for delivery (in solvents, dry powders, or other deposited forms)
- quantity and cost tolerance (how much is to be produced, and what kind of cost the product can bear)
- production facility considerations (cost, complexity, and operating parameters such as temperature, pressure, and toxicity).

GLOSSARY

Gel Liquid particles/pockets suspended in a continuous solid phase.

Nanoparticles Particles with a size range from 1 nm to the largest nanometer dimension, where the ratio of the number of atoms on surfaces and at grain boundaries to those at the center is such that new physical, chemical, and biological properties occur, compared to bulk materials. A typical nanoparticle most often consists of several small “primary particles.” The size of nanoparticles usually refers to the “secondary” particle size. Primary particles agglomerate into these “secondary” particles.

Sol Solid particles suspended in a continuous liquid phase.

Sol-gel process Refers to processing in a liquid medium to obtain solid matter at low temperature, and involves, first, the formation of sol, and then gel.

ACKNOWLEDGMENTS

Xiangdong Feng thanks the management (especially Brian Foster, Steve Florio, Bob Her, Jack Prendergast, Steve Jolly, Ron Harris, Carl Lentz, and Robert Rieger) of Ferro Corporation for supporting this work, Vicky Bryg and Dave Gnizak for the SEM and TEM work, Paul Seman, Anna Andrews, Bob Opalko, Tony Dean, and Mary Fedorcio for reviewing the manuscript, and Janice Ruf and Brook McGilvray for entering references. Michael Hu thanks the sponsorship by the Materials Chemistry Program, Materials Sciences and Engineering Division, Office of Basic Energy Sciences, U.S. Department of Energy. Oak Ridge National Laboratory is managed by UT-Battelle, LLC, for the U.S. Department of Energy under contract DE-AC05-00OR22725.

REFERENCES

1. G. Stix, *Sci. Amer.* 32 (2001).
2. M. C. Roco, Vol. 2002. National Science Foundation, 2002.
3. R. W. Siegel, WTEC Panel Report on: Nanostructure Science and Technology. R&D Status and Trends in Nanoparticles, Nanostructured Materials, and Nanodevices, (R. W. Siegel, E. Hu, and M. C. Roco, Eds.), Kluwer Academic, Boston, 1999, p. 5.
4. R. P. Andres, R. S. Averback, W. L. Brown, L. E. Brus, I. W. A. Goddard, A. Kaldor, S. G. Louie, M. Moscovits, P. S. Peercy, S. J. Riley, R. W. Siegel, S. F., and Y. Wang, *J. Mater. Res.* 4, 704 (1989).
5. G. M. Chow and K. E. Gonsalves (A. S. Edelstein, Ed.), p. 55. 1996.
6. H. Gräter, *Nanostruct. Mater.* 1 (1992).
7. K. J. Klabunde and C. Mohs, *J. Chem. Adv. Mater.* 271 (1998).
8. H. Rohrer, *Microelectron. Eng.* 32 (1996).
9. M. C. Roco, in “Nanostructured Materials; Vol. 3” (G. M. Chow and N. J. Noskova, Eds.), 3rd ed., pp. 71–92. Kluwer Academic, Boston, 1998.
10. T. Sugimoto (Ed.), “Fine Particles, Synthesis, Characterization, and Mechanisms of Growth.” Marcel Dekker, New York, 2000.
11. E. L. Hu and D. T. Shaw, in “Nanostructure Science and Technology” (R. W. Siegel, E. Hu, and M. C. Roco, Eds.), pp. 16–47. Kluwer Academic, Boston, 1999.
12. Y. Suyama and A. Kato, *J. Am. Ceram. Soc.* 59, 146 (1976).
13. S. Morooka, T. Tasutake, A. Kobata, K. Ikemizu, and Y. Kato, *Int. Chem. Eng.* 29 (1989).
14. H. D. Jang and J. Jeong, *J. Aerosol Sci. Technol.* 23, 553 (1995).
15. G. D. Ulrich, 4, 47 (1971).
16. A. P. M. George and E. R. Place, “Faraday Symposia of the Chemical Society,” Vol. 7. 1973.
17. P. A. Zielinski, R. Shulz, S. Kaliaguine, and A. Van Neste, *J. Mater. Res.* 8 (1993).
18. M. L. Panchula and J. Y. Ying, *Nanostruct. Mater.* 9, 161 (1997).
19. Y. Jiang, S. V. Bhide, and A. V. Virkar, *J. Solid State Chem.* 157, 149 (2001).
20. K. Kimura, in “Fine Particles: Synthesis, Characterization, and Mechanisms of Growth,” 92nd ed., pp. 513–550. 2000.
21. H. Schmidt, C. Lesniak, and T. Schlestel, in “Fine Particles and Technology” (E. Pelizzetti, Ed.), 3rd ed., pp. 623–642. Kluwer Academic, Boston, 1996.
22. S. A. Bruno, E. I. Du Pont de Nemours and Company, USA, 1992.
23. S. Mann, *Nature* 365, 499 (1993).

24. L. Addadi and S. Weiner, *Angew. Chem., Int. Ed. Engl.* 153, 31 (1992).
25. R. J. P. Williams, *Trans. R. Soc. Lond. B* 304, 411 (1984).
26. J. H. Fendler, *Chem. Rev.* 87, 877 (1987).
27. J. H. Fendler, *Chem. Mater.* 8, 1616 (1996).
28. J. L. Hutchinson, S. Mann, A. J. Skarnulis, A. J. Skaenulis, and R. J. P. Williams, *J. Chem. Soc., Chem. Commun.* 634 (1980).
29. M. Boutonnet, J. Kizling, P. Stenius, and G. Maire, *Colloids and Surf.* 5, 209 (1982).
30. M. Boutonnet, J. Kizling, R. Touroude, G. Maire, and P. Stenius, *Appl. Catal.* 20, 163 (1986).
31. T. G. S. Pierre, P. Sipos, P. Chan, W. Chua-Anusorn, K. R. Bauchspiess, and J. Webb, *Nanophase Mater.: Synthesis, Properties, Appl.* 260, 49 (1994).
32. D. W. Johnson, Jr., in "Advances in Ceramics: Ceramic Powder Science; Vol. 21," pp. 3-19. American Ceramic Society, 1987.
33. F. E. Kruis and H. Fissan, *KONA* 17, 130 (1999).
34. A. Goossens and J. Schoonman, *Eur. J. Solid State Inorg. Chem.* 32, 779 (1995).
35. K. Kimoto, Y. Kamiya, M. Nonoyama, and R. Uyeda, *Jpn. J. Appl. Phys.* 2, 702 (1963).
36. C. G. Granqvist and R. A. Buhrman, *J. Appl. Phys.* 47, 2200 (1976).
37. A. R. Tholen, *Acta Metall.* 27, 1765 (1979).
38. R. W. Siegel, *Annu. Rev. Mater. Sci.* 21, 559 (1991).
39. N. A. Fuchs and A. G. Sutugin, in "International Reviews of Aerosol Physics and Chemistry; Vol. 2" (G. M. Hidy and J. R. Brock, Eds.), p. 10. Pergamon, Oxford, 1971.
40. J. R. Brock, in "Nanostructured Materials: Science and Technology" (G. M. Chow and N. J. Noskova, Eds.), pp. 1-14. Kluwer Academic, Boston, 1998.
41. N. Wada, *J. Phys.* C2, 219 (1976).
42. E. C. Honea, J. S. Kraus, J. E. Bower, and M. F. Jarrold, *Z. Phys.* D26, 141 (1993).
43. K. Kimura and S. Bandow, *Bull. Chem. Soc. Jpn.* 56, 550 (1983).
44. M. Samy El-Shall, S. Li, D. Graiver, and U. Pernisz, "Nanotechnology: Molecularly Designed Materials" (ACS Symp. Ser.), 1996, Vol. 622, p. 79.
45. A. Matsunawa and S. Katayama, (C. Albright, Ed.). IFS Publ., 1985.
46. K. Baba, N. Shohata, and M. Yonezawa, *Appl. Phys. Lett.* 54, 2309 (1989).
47. H. Ohya, T. Ichihashi, and N. Wada, *Jpn. J. Appl. Phys.* 21, 554 (1982).
48. S. Bandow, K. Kimura, and A. K. Kaishi, *Nippon Kagaku Kaishi* 1957 (1984) (in Japanese).
49. H. Hahn and R. S. Averbach, *J. Appl. Phys.* 67, 1113 (1990).
50. S. Iwama, K. Hayakawa, and T. Arizumi, *J. Cryst. Growth* 56, 265 (1982).
51. P. L. Layman, *Chem. Eng. News*, 12 (1995).
52. S. Pratsinis, *Prog. Energy Combust. Sci.* 24, 197 (1998).
53. "Silicon Compounds, Inorganic to Stains, Microscopic; Vol. A24" (B. Elvers, Ed.). VCH, New York, 1993.
54. W. Hartmann, A. T. Liu, D. Peuckert, and P. Kieinschmit, *Mater. Sci. Eng.* A109, 243 (1989).
55. M. Formenti, F. Juillet, P. Meriaudeau, S. J. Teichner, and P. Vergnon, *J. Colloid Interface Sci.* 39, 79 (1972).
56. J. Hyeon-Lee, G. Beaucage, S. Vermury, and S. E. Pratsinis, "Proceedings of the 1997 Annual Meeting, AICE Particle Technology Forum," Los Angeles, CA, 1997, AICHE, New York, p. 267.
57. C. R. Janzen and P. Roth, *Combust. Flame* 125, 1150 (2001).
58. C. H. J. Kleinwechter, J. Knipping, H. Wiggers, and P. Roth, *J. Mater. Sci.* 37, 4349 (2002).
59. L. H. Dubois, *Polyhedron* 13, 24 (1994).
60. R. Fix, R. G. Gordon, and D. M. Hoffmann, *Chem. Mater.* 5, 614 (1993).
61. M. Nagasawa, S. Shionoya, and S. Makishima, *Jpn. J. Appl. Phys.* 4, 4 (1965).
62. R. C. Mehrotra, R. Bohra, and D. P. Gaur, "Metal B-Diketonate and Allied Derivatives." Academic, New York, 1978.
63. W. R. Cannon, S. C. Danforth, J. H. Flint, J. S. Haggerty, and R. A. Marra, *J. Am. Ceram. Soc.* 65, 324 (1982).
64. F. J. B. C. M. Di Lello and I. G. Solorzano, *Mater. Sci. Eng. C: Biomimetic and Supramolecular Syst.* C15, 67 (2001).
65. Z. D. L. Jiang, Z. Huang, and D. Yan, *Wuji Cailiao Xuebao* 12, 356 (1997).
66. C. M. Hollabaugh, D. E. Hull, L. R. Newkirk, and J. J. Petrovic, *J. Mater. Sci.* 11, 18 (1983).
67. J. V. R. Heberlein, *Mater. Res. Soc. Symp. Proc.* 30, 101 (1984).
68. E. Borsella, S. Botti, R. Giorgi, S. Martelli, S. Turta, and G. Zappa, *Appl. Phys. Lett.* 63, 1345 (1993).
69. A. Gurav, T. Kodas, T. Pluym, and Y. Xiaong, *Aerosol Sci. Technol.* 19, 411 (1993).
70. T. T. Kodas and M. J. Hampden-Smith, "Aerosol Processing of Materials." Wiley-VCH, New York, 1999.
71. G. L. Messing, S.-C. Zhang, and G. V. Jayanthi, *J. Am. Ceram. Soc.* 76, 2707 (1993).
72. K. N. Okuyama, *Koichi., Funtai Kagaku Kaishi* 39, 670 (2002).
73. T. T. Kodas and M. J. Hampden-Smith, "Aerosol Processing of Materials." Wiley-VCH, New York, 1999.
74. H. Muhlenweg, A. Schild, A. Gutsch, C. Klasen, and S. Pratsinis, *J. Metastable Nanocryst. Mater.* 8, 941 (2000).
75. O. B. Milosevic, M. K. Mirkovic, and D. P. Uskokovic, *J. Am. Ceram. Soc.* 79, 1720 (1996).
76. H.-J. Cho, J.-H. Lee, and S.-J. Park, *Ceram. Trans.* 22, 51 (1991).
77. K. Nonaka, S. Hayashi, K. Okada, N. Otsuka, and T. Yano, *J. Mater. Res.* 6, 1750 (1991).
78. T. Ogihara, H. Aikiyo, N. Ogata, and N. Mizutani, *Adv. Powder Technol.* 10, 37 (1999).
79. J. Ortega, Thesis, University of New Mexico, 1992.
80. X. Feng, unpublished results on BaTiO₃ made in an aerosol pyrolysis process; the author retains the right to republish the work in more detail (2002).
81. G. A. S. Singhal, A. Wang, N. Glumac, B. H. Kear, and R. D. Hunt, *Nanostruct. Mater.* 11, 545 (1999).
82. K. F. Nakaso, S. Toshiyuki, Takafuimi, M. Shimada, K. Okuyama, and M. M. Lunden, *Aerosol Sci. Technol.* 35, 929 (2001).
83. R. Baranwal, M. P. Villar, R. Garcia, and R. M. Laine, *J. Am. Ceram. Soc.* 84, 951 (2001).
84. J. H. Brewster and T. T. Kodas, *AICHE J.* 43, 2665 (1997).
85. H. K. Kammler and S. Pratsinis, *J. Nanopart. Res.* 1, 467 (1999).
86. S. Pratsinis, O. Arabi-Katbi, C. M. Megaridis, P. W. J. Morrison, S. Tsantilis, and H. K. Kammler, *Mater. Sci. Forum* 343-346, 511 (2000).
87. H. K. Kammler and S. Pratsinis, *Chem. Eng. Processing* 39, 219 (2000).
88. J. H. Adair, J. A. Kerchner, N. S. Bell, and M. L. Carasso, *ACS Symp. Ser.* 681, 82 (1998).
89. J. Y. Park, S. G. Oh, and B. H. Ma, *Korean J. Chem. Eng.* 18, 215 (2001).
90. Y. Xia, B. Gates, Y. Yin, and Y. Lu, *Adv. Mater.* 12, 693 (2000).
91. E. Matijevic, *Langmuir* 10, 8 (1994).
92. E. Matijevic, *Chem. Mater.* 5, 412 (1993).
93. E. Matijevic, *Pure Appl. Chem.* 60, 1479 (1988).
94. T. Sugimoto, *Adv. Colloid Interface Sci.* 28, 65 (1987).
95. J. Park, V. Privman, and E. Matijevic, *J. Phys. Chem. B* 105, 11630 (2001).
96. V. Privman, D. V. Goia, J. Park, and E. Matijevic, *J. Colloid Interface Sci.* 213, 36 (1999).
97. M. Ocana, Rodriguez-Clemente, and C. J. Serna, *Adv. Mater.* 7, 212 (1995).
98. C. F. Zukoski, D. F. Rosenbaum, and P. C. Zamora, *J. Chem. Eng.* 47, 723 (1996).
99. G. H. Bogush, M. A. Tracy, and C. F. Zukoski, IV, *J. Non-Cryst. Solids* 104, 95 (1988).

100. J. H. Adair and E. Suvaci, *Current Opinion in Colloid & Interface Sci.* 5, 160 (2000).
101. J. F. Chen, Y.-H. Wang, F. Guo, X.-M. Wang, and C. Zheng, *Ind. Eng. Chem. Res.* 39, 948 (2000).
102. X. D. Zhou, W. Huebner, and H. U. Anderson, *Appl. Phys. Lett.* 80, 3814 (2002).
103. J. E. Rodriguez-Paez, A. C. Caballero, M. Villegas, C. Moure, P. Duran, and J. F. Fernandez, *J. Eur. Ceram. Soc.* 21, 925 (2001).
104. Z. J. Zhang and L. Guo, *J. Mater. Res.* 16, 803 (2001).
105. D. H. Rasmussen, C. Brancewicz, B. Das, M. Graeffe, J. Rosenholm, and A. Toscano, *J. Dispersion Sci. Technol.* 22, 491 (2001).
106. E. Bouyer, F. Gitzhofer, and M. I. Boulos, *J. Mater. Sci.: Mater. Med.* 11, 523 (2000).
107. G. Wakefield, H. A. Keron, P. J. Dobson, and J. L. Hutchinson, *J. Colloid Interface Sci.* 215, 179 (1999).
108. D. H. Chen and Y. Y. Chen, *Mater. Res. Bull.* 37, 801 (2002).
109. H. Pardoe, W. Chua-Anusorn, T. G. St. Pierre, and J. Dobson, *J. Magnetism Magn. Mater.* 225, 41 (2001).
110. C. L. Carnes, J. Stipp, and K. J. Klabunde, *Langmuir* 18, 1352 (2002).
111. E. A. Meulenkaamp, *J. Phys. Chem. B* 102, 5566 (1998).
112. S. V. Manorama, C. V. Gopal Reddy, and V. J. Rao, *Nanostruct. Mater.* 11, 643 (1999).
113. D. Sen, P. Deb, S. Mazumder, and A. Basumallick, *Mater. Res. Bull.* 35, 1243 (2000).
114. L. A. Perez-Maqueda, L. Wang, and E. Matijevic, *Langmuir* 14, 4397 (1998).
115. B. J. Hwang, R. Santhanam, and D. G. Liu, *J. Power Sources* 97–98, 443 (2001).
116. G. Xiong and Z. H. Mai, *J. Appl. Phys.* 88, 519 (2000).
117. L. Wang and M. Muhammed, *J. Mater. Chem.* 9, 2817 (1999).
118. L. Wang, L. A. Perez-Maqueda, and E. Matijevic, *Colloid Polym. Sci.* 276, 847 (1998).
119. Y.-S. Her, E. Matijevic, and M. C. Chon, *J. Mater. Res.* 11, 3121 (1996).
120. Y.-S. Her, S.-H. Lee, and E. Matijevic, *J. Mater. Res.* 11, 156 (1996).
121. S.-H. Lee, Y.-S. Her, and E. Matijevic, *J. Colloid Interface Sci.* 186, 193–202 (1997).
122. Y.-S. Her, E. Matijevic, and M. C. Chon, *J. Mater. Res.* 10, 3106 (1995).
123. E. Matijevic and Y.-S. Her, Chon International Co., Ltd., Europe, 1998.
124. C. Kaya, J. Y. He, X. Gu, and E. G. Butler, *Microporous Mesoporous Mater.* 54, 37 (2002).
125. M. S. Whittingham, *Current Opinion in Solid & Mater. Sci.* 1, 227 (1996).
126. X. Feng, unpublished data on CeO₂ made in hydrothermal processes.
127. R. M. Barrer, "Hydrothermal Chemistry of Zeolites." Academic Press, London, 1982.
128. W. Dong and C. Zhu, *J. Mater. Chem.* 12, 1676 (2002).
129. T. Adschiri, Y. Hakuta, K. Sue, and K. Arai, *J. Nanopart. Res.* 3, 227 (2001).
130. D. Segal, *Sci. Eng.* A109, 261 (1989).
131. E. Matijevic, *Acc. Chem. Res.* 14, 22 (1981).
132. E. Matijevic, *Langmuir* 2, 12 (1986).
133. E. Matijevic, *High Tech Ceram.* (1987).
134. T. C. Rojas and M. Ocana, *Scripta Mater.* 46, 655 (2002).
135. K. C. Song and Y. Kang, *Mater. Lett.* 42, 239 (2000).
136. S. Ammar, A. Helfen, N. Jouini, F. Fievet, I. Rosenman, F. Villain, P. Molinie, and M. Danot, *J. Mater. Chem.* 11, 186 (2001).
137. M. Z. C. Hu, M. T. Harris, and C. H. Byers, *J. Colloid Interface Sci.* 198, 87 (1998).
138. W. Li and L. Gao, *Ceram. Int.* 27, 543 (2001).
139. K. Bellon, D. Chaumont, and D. Stuerger, *J. Mater. Chem.* 16, 2619 (2001).
140. J.-J. Zhu, J.-M. Zhu, X.-H. Liao, J.-L. Fang, M.-G. Zhou, and H.-Y. Chen, *Mater. Lett.* 53, 12 (2002).
141. X. Liao, J. S. Zhu, W. L. Zhong, and H.-Y. Chen, *Mater. Lett.* 50, 341 (2001).
142. A. C. Pierre, *Ceram. Bull.* 70, 1281 (1991).
143. M. B. Mooiman and K. C. Sole, *JOM* (June 18, 1994).
144. C. Guizard, C. Mouchet, J. C. Achddou, S. Durand, J. Rouviere, and L. Lot, *Mater. Sci. Forum* 152–153, 149 (1994).
145. J. Livage, F. Beteille, C. Roux, M. Chatry, and P. Davidson, *Acta Mater.* 46, 743 (1998).
146. W. Stöber and A. Fink, *J. Colloid Interface Sci.* 26, 62 (1968).
147. D. H. Chen and X. R. He, *Mater. Res. Bull.* 36, 1369 (2001).
148. N. N. Ghosh and P. Pramanik, *Nanostruct. Mater.* 8, 1041 (1997).
149. N. N. Ghosh and P. Pramanik, *Bull. Mater. Sci.* 20, 283 (1997).
150. N. N. Ghosh and P. Pramanik, *Brit. Ceram. Trans.* 95, 267 (1996).
151. N. N. Ghosh, S. K. Saha, and P. Pramanik, *Brit. Ceram. Trans.* 97, 180 (1998).
152. R. Narayanan and R. M. Laine, *ACS Symp. Ser.* 681, 134 (1996).
153. S. O'Brien, L. E. Brus, and C. B. Murray, *J. Am. Chem. Soc.* 123, 12085 (2001).
154. K. D. Kim and H. T. Kim, *Powder Technol.* 119, 164 (2001).
155. C. L. Carnes, P. N. Kapoor, and K. J. Klabunde, *Chem. Mater.* 14, 2922 (2002).
156. S. D. Burnside, V. Shklover, C. Barbe, and P. Comte, *Chem. Mater.* 10, 2419 (1998).
157. S. Ito, S. Yoshida, and T. Watanabe, *Chem. Lett.* 1, 70 (2000).
158. R. I. Walton, *Chem. Soc. Rev.* 31, 230 (2002).
159. S. H. Yu, *J. Ceram. Soc. Jpn.* 109, S65 (2001).
160. Demazeau, *J. Mater. Chem.* 9, 15 (1999).
161. H. Parala, A. Devi, R. Bhakta, and R. A. Fischer, *J. Mater. Chem.* 12, 1625 (2002).
162. Z. Hong, Y. Cao, and J. Deng, *Mater. Lett.* 52, 34 (2002).
163. J. H. Adair, S. B. Cho, N. S. Bell, and A. J. Perrotta, *J. Dispersion Sci. Technol.* 22, 143 (2001).
164. N. S. Bell, S. B. Cho, and J. H. Adair, *ACS Symp. Ser.* 681, 120 (1996).
165. J. S. Yin and Z. L. Wang, *J. Mater. Res.* 14, 503 (1999).
166. B. Hai, K. Tang, C. C. Wang, C. An, Q. Yang, G. Shen, and Y. Qian, *J. Cryst. Growth* 225, 92 (2001).
167. H. B. Qiu, L. Gao, H. Qiao, J. K. Guo, and D. S. Yan, *Nanostruct. Mater.* 6, 373 (1995).
168. H. Kominami, M. Miyakawa, Y. Murakami, T. Yasuda, M. Kohno, S. Onoue, Y. Kera, and B. Ohtani, *Phys. Chem. Chem. Phys.* 3, 2697 (2001).
169. S. Sun and H. Zheng, *J. Am. Chem. Soc.* 124, 8204 (2002).
170. M. Rajamathi, M. Ghosh, and R. Seshadri, *Chem. Commun.* 10, 1152 (2002).
171. S. Komarneni, Q. H. Li, and R. Roy, *J. Mater. Chem.* 4, 1903 (1994).
172. H. Wang and J. J. Zhu, *J. Inorg. Chem.* 18, 329 (2002).
173. J. Kilier, C. J. Tucker, T. H. Kalantar, and D. P. Green, *Adv. Mater.* 12, 1751 (2000).
174. K. Landfester, *Adv. Mater.* 13, 765 (2001).
175. R. S. Underhill and G. Liu, *Chem. Mater.* 12, 2082 (2000).
176. W. Meier, *Current Opinion in Colloid Interface Sci.* 4, 6 (1999).
177. W. F. C. Sager, *Current Opinion in Colloid Interface Sci.* 3, 276 (1998).
178. M. Lade, H. Mays, J. Schmidt, R. Willumeit, and R. Schomacker, *Colloids Sur. A: Physicochem. Eng. Aspects* 163, 3 (2000).
179. P. Ayyub, *Ind. J. Pure Appl. Phys.* 32, 611 (1994).
180. J. H. Adair, T. Li, T. Kido, K. Havey, J. Moon, J. Mecholsky, A. Morrone, D. R. Talham, M. H. Ludwig, and L. Wang, *Mater. Sci. Eng.* R23, 139 (1998).
181. E. Bourgeat-Lami, *J. Nanosci. Nanotechnol.* 2, 1 (2002).
182. M. Singhal, V. Chhabra, P. Kang, and D. O. Shah, *Mater. Res. Bull.* 32, 239 (1997).
183. K. S. Suslick and G. J. Price, *Ann. Rev. Mater.* 29, 295 (1999).

184. K. Borgohain, N. Murase, and S. Mahamuni, *J. Appl. Phys.* 92, 1292 (2002).
185. C. Pascal, J. L. Pascal, F. Favier, M. L. Elidrissi Moubtassim, and C. Payen, *Chem. Mater.* 11, 141 (1999).
186. R. Amigo, J. Asenjo, E. Krotenko, F. Torres, and J. Tejada, *Chem. Mater.* 12, 573 (2000).
187. F. Torres, R. Amigo, J. Asenjo, E. Krotenko, and J. Tejada, *Chem. Mater.* 12, 3060 (2000).
188. L. E. Griffiths, A. R. Mount, C. R. Pulham, M. R. Lee, H. Kondoh, and T. Ohta, *Chem. Commun.* 6, 579 (2001).
189. R. M. Nyffenegger, B. Craft, M. Shaaban, S. Gorer, G. Erley, and R. M. Penner, *Chem. Mater.* 10, 1120 (1998).
190. R. M. Penner, *Acc. Chem. Res.* 33, 78 (2000).
191. J. Jung and M. Perrut, *J. Supercrit. Fluids* 20, 179 (2001).
192. F. Cansell, B. Chevalier, A. Demourgues, J. Etourneau, C. Even, Y. Garrabos, V. Pessey, S. Petit, A. Tressaud, and F. Weill, *J. Mater. Chem.* 9, 67 (1999).
193. K. J. Ziegler, R. C. Doty, K. P. Johnston, and B. A. Korgel, *J. Am. Chem. Soc.* 123, 7797 (2001).
194. T. Adschiri, Y. Hakuta, and K. Arai, *Ind. Eng. Chem. Res.* 29, 4901 (2000).
195. J. D. Holmes, P. A. Bhargava, B. A. Korgel, and K. P. Johnston, *Langmuir* 15, 6613 (1999).
196. M. Ji, X. Chen, C. M. Wai, and J. L. Fulton, *J. Am. Chem. Soc.* 121, 2631 (1999).
197. J. Cason and C. Roberts, *J. Phys. Chem. B* 104, 1217 (2000).
198. J. Cason and Khambaswadkar, *Ind. Eng. Chem. Res.* 39, 4749 (2000).
199. J. D. Holmes, K. J. Ziegler, R. C. Doty, L. E. Pell, K. P. Johnston, and B. A. Korgel, *J. Am. Chem. Soc.* 123, 3743 (2001).
200. C. M. Wai and H. Ohde, *J. Chinese Inst. Chem. Eng.* 32, 253 (2001).
201. E. Reverchon, I. De Marco, and G. Della Porta, *J. Supercrit. Fluids* 23, 81 (2002).
202. E. Reverchon, G. Della Porta, A. Di Trolino, and S. Pace, *Ind. Eng. Chem. Res.* 37, 952 (1998).
203. E. Reverchon, G. Della Porta, D. Sannino, and P. Ciambelli, *Powder Technol.* 102, 127 (1999).
204. Y.-P. Sun, R. Guduru, F. Lin, and T. Whiteside, *Ind. Eng. Chem. Res.* 39, 4663 (2000).
205. E. Reverchon, *Ind. Eng. Chem. Res.* 41, 2405 (2002).
206. V. Pessey, R. Garriga, B. Chevalier, J. Etourneau, and F. Cansell, *High Pressure Res.* 20, 289 (2001).
207. D. L. Leslie-Pelecky, *Chem. Mater.* 8, 1770 (1996).
208. J. Y. Ying and T. Sun, *J. Electroceram.* 1, 219 (1997).
209. C. C. Koch, (S. a. al., Ed.), 1998.
210. R. N. N. Bohwmik and R. Ranganathan, *Condensed Matter*, 1 (2002).
211. R. N. R. Bhowmik, *J. Mater. Sci.* 37 (2002).
212. P. McCormick, "Fine, Ultrafine and Nano Powders '99 Conference Proceedings," 2000, p. 64.
213. S. Q. Z. Wu and J. Liu, *Guisuanyan Tongbao* 21, 32 (2002).
214. P. McCormick, in "Mechanochemical Processing—A Versatile, Low Cost Technology for the Manufacture of Nano Powders." 1999.
215. O. Abe and Y. Suzuki, *Mater. Sci. Forum* 225–227, 563 (1996).
216. O. Abe, Q. K. Dinh, and D.-S. Itoh, *Trans. Mater. Res. Soc. Jpn.* 25, 131 (2000).
217. H. A. M. van Hal, W. A. Groen, S. Maassen, and W. C. Keur, *J. Eur. Ceram. Soc.* 21, 1689 (2001).
218. P. McCormick and T. Tzuzuki, World, 1999.
219. A. Landsberg and T. T. Campbell, *J. Metals*, 856 (1965).
220. D. W. Johnson, Jr. and F. J. Schnettler, *J. Am. Ceram. Soc.* 53, 440 (1970).
221. P. K. Gallagher and F. Schrey, *Thermochimica Acta* 1, 465 (1970).
222. Y. D. Tretyakov and O. A. Shlyakhtin, *J. Mater. Chem.* 9, 19 (1999).
223. J. M. McHale, P. C. McIntyre, K. E. Sickafus, and N. V. Colla, *J. Mater. Res.* 11, 1199 (1996).
224. J. Kirchnerova and D. Klvana, *Solid State Ionics* 123, 307 (1999).
225. A. Thierauf, C. Egger, D. Sporn, and K. Keck, *Supercond. Sci. Technol.* 5, 123 (1992).
226. A. G. Merzhanov, *J. Self-Propag. High Temp. Synth.* 113 (1993).
227. A. Pathak and P. Pramanik, "Proceedings of the Indian National Science Academy, Part A: Physical Sciences," Vol. 67, 2001, pp. 47–70.
228. E. Zhou, S. Bhaduri, and S. B. Bhaduri, *Processing and Properties of Nanocryst. Mater.* 123 (1996).
229. L. A. Chick, G. D. Maupin, and L. R. Pederson, *Nanostruct. Mater.* 4, 603 (1994).
230. L. A. Chick, L. R. Pederson, G. D. Maupin, J. L. Bates, L. E. Thomas, and G. J. Exarhos, *Mater. Lett.* 10, 6 (1990).
231. H. Salze, R. Odier, and B. Cales, *J. Non-Cryst. Solids* 82, 314 (1986).
232. S. R. Jain and K. C. Adiga, *Combust. Flame* 40, 71 (1981).
233. V. Sankaren, J. Yue, R. E. Cahen, R. R. Schrock, and R. J. Silbey, *Chem. Mater.* 5, 1133 (1993).
234. Y. Yuan, J. Fendler, and I. Cabasso, *Chem. Mater.* 4, 312 (1992).
235. J. J. Kingsley, L. A. Chick, G. W. Coffery, D. E. McCready, and L. R. Pederson, *Mater. Res. Soc. Symp. Proc.* 271, 113 (1992).
236. L. A. Chick, L. R. Pederson, G. D. Maupin, and J. L. Bates, "Proceedings of the 5th Annual Conference on Fossil Energy Material," 1991, p. 117.
237. J. J. Moore, D. W. Readey, H. J. Feng, K. Monroe, and B. Mishra, *JOM* 72 (1994).
238. P. Pramanik, *Bull. Mater. Sci.* 19, 951 (1996).
239. L. R. Pederson, L. A. Chick, and G. J. Exarhos, Battelle Memorial Institute, USA, 1989.
240. L. A. Chick, L. R. Pederson, J. L. Bates, and G. D. Maupin, "Proceedings of the 5th Annual Conference on Fossil Energy Materials," 1991.
241. L. A. Chick, L. R. Pederson, G. D. Maupin, and J. Bates, "Proceedings of the 5th Annual Conference on Fossil Energy Material," 1991, p. 117.
242. L. A. Chick, G. D. Maupin, G. L. Graff, L. R. Pederson, D. E. McCready, and J. L. Bates, *Mater. Res. Soc. Symp. Proc.* 249, 159 (1992).
243. J. McKittrick, E. J. Bosze, C. F. Bacalski, and L. E. Shea, "Powder Materials: Current Research and Industrial Practices: Proceedings of a Symposium held during the 1999 TMS Fall Meeting" (F. D. S. Marquis, Ed.), 1999, pp. 139–157.
244. R. J. Jose, M. Asha, R. Divakar, and J. Koshy, *J. Am. Ceram. Soc.* 85, 2395 (2002).
245. J. C. D. S. H. Yu and L. Ba, *Amer. Ceram. Soc. Bull.* 81, 38 (2002).
246. X. Feng, unpublished data on CeO₂ made in a combustion process; the author retains the right to republish the work in more detail (2002).
247. Z. A. Munir, F. Charlot, F. Bernard, and E. Gaffet, Centre National de la Recherche Scientifique and The Regents of the University of California, USA, 2001.
248. M. Koizumi and Y. Miyamoto, "Combustion Plasma Synthesis of High-Temperature Materials Conference," 1990, pp. 54–60.
249. H. J. Feng, J. J. Moore, and D. G. Wirth, *Metall. Trans. A* 23A, 2373 (1992).
250. Y. Borilov and A. Borisova, "Proceedings of the 1993 National Spray Conference," 1993, pp. 139–144.
251. S. Govindarajan, K. Monroe, J. J. Moore, B. Mishra, D. L. Olson, and J. Disam, *Processing and Fabrication of Adv. Mater. III* 161 (1994).
252. W. J. Asher, D. L. Roberts, J. L. Jones, and D. E. Gottschlich, SRI International, USA, 1996.
253. C. H. Jung, J. Y. Park, M. Y. Lee, S.-J. Oh, H. Y. Kim, and G. W. Hong, *Korean J. Ceram.* 6, 47 (2000).
254. M. A. Sekar, G. Dhanaraj, H. L. Bhat, and K. C. Patil, *J. Mater. Sci.: Mater. Electron.* 3, 237 (1992).
255. M. M. A. Sekar and A. Halliyal, *J. Am. Ceram. Soc.* 81, 380 (1998).

256. M. A. Sekar and K. C. Patil, *J. Mater. Chem.* 2, 739 (1992).
257. P. P. Phule and S. H. Risbud, *J. Mater. Sci.* 25, 1169 (1990).
258. J. C. Mutin and J. C. Niepce, *J. Mater. Sci. Lett.* 18, 304 (1983).
259. H. Tagwa and J. Ohashi, *Denki Kagaku Ky Okao* 52, 485 (1984).
260. A. Bouger, J. C. Mutin, and J. C. Niepce, *J. Mater. Sci.* 18, 3543 (1983).
261. A. D. Hilton and R. Frost, *Key Eng. Mater.* 66–67, 145 (1992).
262. P. F. Bongers and P. E. C. Franken, *Adv. Ceram.* 1, 38 (1981).
263. V. Berbenni, A. Marini, and G. Bruni, *Thermochimica Acta* 374, 151 (2001).
264. C. Gomez-Yanez, C. Benitez, and H. Balmori-Ramirez, *Ceram. Int.* 26, 271 (2000).
265. K. R. Han and H. J. Koo, Korea Institute of Science and Technology, International, 2001.
266. T. F. Limar, A. I. Savos'kina, and N. G. Kisel, *Inorgan. Mater.* 12, 950 (1976).
267. X. F. Y. Li, L. Chen, H. Pan, and X. Xin, *J. Am. Ceram. Soc.* 85, 2177 (2002).
268. Y. W. Z. Wang, X. Wang, Y. Liu, C. Zheng, and G. Wang, *Mater. Res. Bull.* 37, 1093 (2002).
269. Y.-H. J. C. Zhuang, X. Wang, Q.-C. Wang, D.-M. Yang, and D.-Z. Jia, *Wuji Cailiao Xuebao* 16, 1203 (2001) (in Chinese).
270. F. X. L. Yu, X. Ye, X. Xin, and Z. Xue, *J. Am. Ceram. Soc.* 83, 964 (2000).
271. J. H. Fendler, *Korean J. Chem. Eng.* 18, 1 (2001).
272. M. P. Pileni, *Cryst. Res. Technol.* 33, 1155 (1998).
273. J. M. P. T. Pileni and A. Filankembo, *Colloids and Surf., A: Physicochem. Eng. Aspects* 123–124, 561 (1997).
274. K. M. S. Rolandi, E. G. Wilson, and F. C. Meldrum, *J. Appl. Phys.* 89, 1588 (2001).
275. D. G. L. Kurth, Pit, and C. Lesser, *Chem. Commun. (Cambridge)* 11, 949 (2000).
276. P. P. Christophe and M.-P. Pileni, "Cobalt Nanosized Particles Organized in a 2-D Superlattice: Synthesis, Characterization, and Magnetic Properties," New Orleans, LA, 1999 (American Chemical Society), p. PHYS-152.
277. J. H. Fendler, *Chem. Rev.* 87, 877 (1987).
278. J. H. Fendler, *Chem. Mater.* 8, 1616 (1996).
279. G. M. Chow, M. Markowitz, and A. Singh, "Synthesis and Processing of Nanocrystalline Powder: Proceedings of a Symposium Cosponsored by the Materials Design of Manufacturing Division (MDMD), Powder Metallurgy Committee, 125th TMS Meeting," 1996, pp. 47–56.
280. E. S. Ahn, N. J. Gleason, A. Nakahira, and J. Y. Ying, *Nano Lett.* 1, 149 (2001).
281. K. Kakegawa and J.-I. Mohri, *J. Amer. Ceram. Soc.* 67, C2 (1984).
282. D. H. Chen and Y. Y. Chen, *J. Colloid Interface Sci.* 235, 9 (2001).
283. D. K. Kim, Y. Zhang, W. Voit, K. V. Rao, and M. Muhammed, *J. Magnetism Magn. Mater.* 225, 30 (2001).
284. X. P. Qiu and F. Winnik, *Chinese J. Polymer Sci.* 18, 535 (200).
285. L. Babes, B. Denizot, G. Tanguy, J. J. Le Juune, and P. Jallet, *J. Colloid Interface Sci.* 212, 474 (1999).
286. L. Vayssieres, C. Chaneac, E. Tronc, and J. P. Jolivet, *J. Colloid Interface Sci.* 205 (1998).
287. T. Nutz and M. Haase, *J. Phys. Chem. B* 104, 8430 (200).
288. Q. Chen, A. J. Rondinone, B. C. Chakoumakos, and Z. J. Zhang, *J. Magnetism Magn. Mater.* 194, 1 (1999).
289. J. Le, L. N. van Rij, R. C. van Landschoot, and J. Schoonman, *J. Eur. Ceram. Soc.* 19, 2589 (1999).
290. W. Li, L. Gao, and J. K. Guo, *Nanostruct. Mater.* 10, 1043 (1998).
291. T. Tsuchida, *J. Eur. Ceram. Soc.* 20, 1759 (2000).
292. O. Vasylykiv and Y. Sakka, *J. Am. Ceram. Soc.* 84, 2489 (2001).
293. M. Hirano, C. Nakahara, K. Ota, and M. Inagaki, *J. Am. Ceram. Soc.* 85, 1333 (2002).
294. H. Yin, Y. Wada, T. Kitamura, S. Kambe, S. Murasawa, H. Mori, T. Sakata, and H. Yanagida, *J. Mater. Chem.* 11, 1694 (2001).
295. H. Yang, S. Mei, and J. M. F. Ferreira, *Mater. Sci. Eng. C* 15, 183 (2001).
296. T. Masui, H. Hirai, N. Imanaka, G. Adachi, T. Sakata, and H. Mori, *J. Mater. Sci. Lett.* 21, 489 (2002).
297. M. Hirano, Y. Fukuda, H. Iwata, Y. Hotta, and M. Inagaki, *J. Am. Ceram. Soc.* 83, 1287 (2000).
298. M. Hirano and E. Kato, *J. Am. Ceram. Soc.* 82, 786 (1999).
299. Y. Ding, G. Zhang, H. Wu, B. Hai, L. Wang, and Y. Qian, *Chem. Mater.* 13, 435 (2001).
300. T. Hyeon, S. S. Lee, J. Park, Y. Chung, and H. B. Na, *J. Am. Chem. Soc.* 123, 12798 (2001).
301. J. A. Kerchner, J. Moon, R. E. Chodelka, A. A. Morrone, and J. H. Adair, *ACS Symp. Ser. 681*, 106 (1998).
302. M. Ristic, M. Ivanda, S. Popovic, and S. Music, *J. Non-Cryst. Solids* 303, 270 (2002).
303. M. Hirano, T. Miwa, and M. Inagaki, *J. Solid State Chem.* 158, 112 (2001).
304. R. Ramamoorthy, R. N. Viswanath, and S. Ramasamy, *Nanostruct. Mater.* 6, 337 (1995).
305. M. Ocana, *Colloid Polym. Sci.* 278, 443 (2000).
306. S. D. Park, Y. H. Cho, W. W. Kim, and S.-J. Kim, *J. Solid State Chem.* 146, 230 (1999).
307. Y. Wei, R. Wu, and Y. Zhang, *Mater. Lett.* 41, 101 (1999).
308. X. H. Liao, J. M. Zhu, J. J. Zhu, J. Z. Xu, and H. Y. Chen, *Chem. Commun.* 10, 937 (2001).
309. S. K. Park and H. T. Kim, *J. Colloid Interface Sci.* 6, 365 (2000).
310. Bokhimi, A. Morales, O. Novaro, M. Portilla, T. Lopez, F. Tzompantzi, and R. Gomez, *Mater. Res. Soc. Symp. Proc.* 457, 51 (1997).
311. N. Uekawa, J. Kajiwara, K. Kakegawa, and Y. Sasaki, *J. Colloid Interface Sci.* 250, 285 (2002).
312. E. Scolan and C. Sanchez, *Chem. Mater.* 10, 3217 (1998).
313. M. Gotic, M. Ivanda, A. Sekulic, S. Music, S. Popovic, A. Turkovic, and K. Furic, *Mater. Lett.* 28, 225 (1996).
314. C. L. Carnes and K. J. Klabunde, *Langmuir* 16, 3764 (2000).
315. W. T. Dong, S. X. Wu, C. P. Chen, X. W. Jiang, and C. S. Zhu, *Chem. Lett.* 5, 496 (2000).
316. D. Grosso and P. A. Sermon, *J. Mater. Chem.* 10, 359 (2000).
317. S. Komarneni, I. R. Abothu, and A. V. Prasada Rao, *J. Sol-Gel Technol.* 15, 263 (1999).
318. C. Liu, B. Zou, A. J. Rondinone, and Z. J. Zhang, *J. Am. Chem. Soc.* 123, 4344 (2001).
319. G. Xiong, X.-M. Wang, L. D. Lu, X. J. T. Yang, and Y. F. Xu, *J. Solid State Chem.* 141, 70 (1998).
320. Y. Murakami, S. Tsuchiya, K. Yahikozawa, and Y. Takasu, *Electrochimica Acta* 39, 651 (1994).
321. M. Ito, Y. Murakami, H. Kaji, H. Ohkawauchi, K. Yahikozawa, and Y. Takasu, *J. Electrochem. Soc.* 141, 1243 (1994).
322. J. Liang, Z. Deng, X. W. Jiang, F. Li, and Y. Li, *Inorg. Chem.* 41, 3602 (2002).
323. H. Wang, J.-J. Zhu, J.-M. Zhu, X.-H. Liao, S. Xu, T. Ding, and H.-Y. Chen, *Phys. Chem. Chem. Phys.* 4, 3794 (2002).
324. H. Katsuki and S. Komarneni, *J. Am. Ceram. Soc.* 84, 2313 (2001).
325. P. Rigneau, K. Bellon, I. Zahreddine, and D. Stuerge, *Eur. Phys. J., Appl. Phys.* 7, 41 (1999).
326. Q. H. Li and Y. Wei, *Mater. Res. Bull.* 33, 779 (1998).
327. O. Palchik, J. J. Zhu, and A. Gedanken, *J. Mater. Chem.* 10, 1251 (2000).
328. R. H. G. A. Kiminami, M. R. Morelli, D. C. Folz, and D. E. Clark, *Am. Ceram. Bull.* 63 (2000).
329. Y. Ma, E. Vilen, S. L. Suib, and P. K. Dutta, *Chem. Mater.* 9, 3023 (1997).
330. F. J. Arriagada and K. Osseo-Asare, *J. Colloid Interface Sci.* 211, 210 (1999).
331. J. Esquena, T. F. Tadros, K. Kostarelos, and C. Solans, *Langmuir* 13, 6400 (1997).
332. R. Lindberg, J. Sjoblom, and G. Sundholm, *Colloids Surf. A: Physicochem. Eng. Aspects* 99, 79 (1995).

333. X. F. Yang and W. B. Li, *Acta Physico-Chimica Sinica* 18, 5 (2002).
334. C. Y. Tai, M.-H. Lee, and Y.-C. Wu, *Chem. Eng. Sci.* 56, 2389 (2001).
335. X. Li, C.-K. Loong, P. Thiagarajan, G. A. Lager, and R. Miranda, *J. Appl. Cryst.* 33, 628 (2000).
336. Y. Berkovich, A. Aserin, E. Wachtel, and N. Garti, *J. Colloid Interface Sci.* 245, 58 (2002).
337. R. B. Zhang and L. Gao, *Key Eng. Mater.* 224–222, 573 (2002).
338. V. Chhabra, V. Pillai, B. K. Mishra, A. Morrone, and D. O. Shah, *Langmuir* 11, 3307 (1995).
339. Z. J. Zhang, *J. Mater. Res.* 17, 1698 (2002).
340. Z. H. Zhou, J. E. Wang, X. Liu, and H. S. O. Chan, *J. Mater. Chem.* 11, 1704 (2001).
341. J. A. Lopez Perez, M. A. Lopez Quintela, J. Mira, J. Rivas, and S. W. Charles, *J. Phys. Chem. B* 101, 8045 (1997).
342. T. Liu, L. Guo, Y. Gao, Y. B. Wang, and W. D. Wang, *Nanostruct. Mater.* 11, 487 (1999).
343. Y. Mori, Y. Okastu, and Y. Tsujimoto, *J. Nanoparticle Res.* 3, 219 (2001).
344. W. Que, S. Buddhudu, Y. Zhou, Y. L. Lam, J. Zhou, Y. C. Chan, C. H. Kam, L. H. Gan, and G. Roshan Deen, *Mater. Sci. Eng. C* 16, 51 (2001).
345. T. M. Dellinger and P. V. Braun, *Scripta Mater.* 44, 1893 (2001).
346. K. C. Song and J. H. Kim, *Powder Technol.* 107, 268 (2000).
347. K. C. Song and J. H. Kim, *J. Colloid Interface Sci.* 212, 193 (1999).
348. T. Kawai, Y. Usui, and K. Kon-No, *Colloids Surf.* 149, 39 (1999).
349. S. Shi, R. H. Lu, T. T. Wang, H. Y. Sun, and H. Q. Wang, *J. Dispersion Sci. Technol.* 20, 1247 (1999).
350. S. R. Ahmed and P. Kofinas, *Macromol.* 35, 3338 (2002).
351. S. Li, L. Liu, V. T. John, C. J. O'Connor, and V. G. Harris, *IEEE Trans. Magn.* 37, 2350 (2001).
352. C. J. O'Connor, V. Kolesnichenko, E. Carpenter, C. Sangregorio, W. Zhou, A. Kumbhar, J. Sims, and F. Agnoli, *Synth. Metals* 122, 547 (2001).
353. C. J. O'Connor, C. T. Seip, E. E. Carpenter, S. Li, and V. T. John, *Nanostruct. Mater.* 12, 65 (1999).
354. M. L. Kahn and Z. J. Zhang, *Appl. Phys. Lett.* 78, 3651 (2001).
355. E. E. Carpenter and C. J. O'Connor, *J. Appl. Phys.* 85, 5175 (1999).
356. H. Huang, G. Q. Xu, W. S. Chin, L. M. Gan, and C. H. Chew, *Nanotechnol.* 13, 318 (2002).
357. M. H. Lee, S. G. Oh, and S. C. Yi, *J. Colloid Interface Sci.* 226, 65 (2000).
358. I. Balint, Z. You, and K. Aika, *Phys. Chem. Chem. Phys.* 4, 2501 (2002).
359. C. H. Lu and S. K. Saha, *Brit. Ceram. Trans.* 100, 120 (2001).
360. D. H. Chen and Y. Y. Chen, *J. Colloid Interface Sci.* 236, 41 (2001).
361. A. K. Panda, B. B. Bhowmik, A. R. Das, and S. P. Moulik, *Langmuir* 17, 1811 (2001).
362. A. J. Zarur, H. H. Hwu, and J. Y. Ying, *Langmuir* 16, 3042 (2000a).
363. A. J. Zarur, N. Z. Mehenti, A. T. Heibel, and J. Y. Ying, *Langmuir* 16, 9168 (2000b).
364. A. J. Zarur and J. Y. Ying, *Nature* 403, 65 (2000).
365. D. A. Rawlinson and P. A. Sermon, *J. De Physique IV* 7, 755 (1997).
366. S. Santra, R. Tapeç, N. Theodoropoulou, J. Dobson, A. Hebard, and W. Tan, *Langmuir* 17, 2900 (2001).
367. X. Fu and S. Qutubuddin, *Colloids Surf.* 179, 65 (2001).
368. K. Zhang, C. H. Chew, G. Q. Xu, J. Wang, and L. M. Gan, *Langmuir* 15, 3056 (1999).
369. D. W. Kim, S.-G. Oh, and J.-D. Lee, *Langmuir* 15, 1599 (1999).
370. F. Porta, C. Bifulco, P. Fermo, C. L. Bianchi, M. Fadoni, and L. Prati, *Colloids Surf. A: Physicochem. Eng. Aspects* 160, 281 (1999).
371. C. Beck, W. Hartl, and R. Hempelmann, *J. Mater. Res.* 13, 3174 (1998).
372. H. Herrig and R. Hempelmann, *Mater. Lett.* 27, 287 (1996).
373. L. M. Gan, L. H. Zhang, H. S. O. Chan, C. H. Chew, and B. H. Loo, *J. Mater. Sci.* 31, 1071 (1996).
374. Y. Koltypin, S. I. Nikitenko, and A. Gedanken, *J. Mater. Chem.* 12, 1107 (2002).
375. L. X. Yin, Y. Q. Wang, G. S. Pang, Y. Koltypin, and A. Gedanken, *J. Colloid Interface Sci.* 246, 78 (2002).
376. P. Jeevanandam, Y. Koltypin, and A. Gedanken, *Mater. Sci. Eng. B* 90, 125 (2002).
377. G. Pang, S. Chen, Y. Zhu, O. Palchik, Y. Koltypin, A. Zaban, and A. Gedanken, *J. Phys. Chem. B* 105, 4647 (2001).
378. P. Jeevanandam, Y. Koltypin, and A. Gedanken, *Nano Lett.* 1, 263 (2001).
379. R. Vijaya Kumar, R. Elgamiel, Y. Diamant, A. Gedanken, and J. Norwig, *Langmuir* 17, 1406 (2001).
380. K. V. P. M. Shafi, A. Ulman, X. Yan, N.-L. Yang, C. Estournes, H. White, and M. Rafailovich, *Langmuir* 17, 5093 (2001).
381. X. Cao, Y. Koltypin, R. Prozorov, G. Kataby, and A. Gedanken, *J. Mater. Chem.* 7, 2447 (1997).
382. T. Fujimoto, Y. Mizukoshi, Y. Nagata, Y. Maeda, and R. Oshima, *Scripta Mater.* 44, 2183 (2001).
383. R. Vijaya Kumar, Y. Koltypin, I. Felner, and A. Gedanken, *Mater. Sci. Eng. A* 286, 101 (2000).
384. P. Jeevanandam, Y. Koltypin, Y. Gofer, Y. Diamant, and A. Gedanken, *J. Mater. Chem.* 10, 2769 (2000).
385. Y. N. Todaka, Masahide, S. Hattori, K. Tsuchiya, and M. Umemoto, *Nippon Kinzoku Gakkaishi* 66, 34 (2002) (in Japanese).
386. Q. Z. Wu and Shaoming, Yancheng Institute of Technology, Yancheng, *Guisuanyan Xuebao* 29, 479 (2001) (in Chinese).
387. T. L. M. T. Cukrov and P. G. McCormick, *Scripta Mater.* 44, 1787 (2001).
388. P. J. R. Keskinen, M. Karttunen, and S.-P. Hannula, *Appl. Organometall. Chem.* 15, 393 (2001).
389. K. T. P. Tsuzuki and P. G. McCormick, *J. Nanoparticle Res.* 2, 375 (2000).
390. J. K. D. Durisinova and M. Orolinova, *Kovove Materialy* 39, 11 (2001).
391. J. M. Wu, *Mater. Lett.* 48, 324 (2001).
392. W. L. B. Z. Kong and O. K. Tan, *J. Mater. Sci. Lett.* 19, 1963 (2000).
393. T. M. Tsuzuki and P. G. McCormick, *Mater. Sci. Forum* 343 (2000).
394. T. M. Tsuzuki and P. G. McCormick, *Acta Materialia* 48, 2795 (2000).
395. T. N. Tsuzuki, P. N. H., and P. G. McCormick, "Synthesis of II-VI Semiconductor Nanoparticles by Mechanochemical Processing," Perth, Australia, 1998 (Institute of Electrical and Electronics Engineers), pp. 403–406.
396. T. P. Tsuzuki, E., and P. G. McCormick, *Nanostruct. Mater.* 11, 125 (1999).
397. S. S. R. Rana and S. K. Roy, *Mater. Manufact. Processes* 17, 529 (2002).
398. P. N. Z. Kuznetsov, A. M., and L. I. Kuznetsova, *Russian J. Appl. Chem.* 75, 171 (2002).

Ceramic Nanopowders

Yong S. Cho, Howard D. Glicksman

E. I. du Pont de Nemours and Company, Inc., North Carolina, USA

Vasantha R. W. Amarakoon

Alfred University, Alfred, New York, USA

CONTENTS

1. Introduction
 2. Chemical Processing for Nanopowders
 3. Sintering of Nanopowders
 4. Nanoceramic Materials
 5. Summary
- Glossary
References

1. INTRODUCTION

Ceramic nanopowders have received considerable attention during the last two decades, since they are expected to demonstrate improved or unique characteristics as compared to conventional ceramic materials [1–20]. Ceramic nanopowders can be utilized for various applications concerning mechanical, electronic, ionic, thermal, optical, and catalytic properties. In particular, the combination of a relatively large portion of interfacial or grain boundary atoms along with the interactions of photons, electrons, or dislocations can lead to unusual mechanical and electrical behavior.

The terminology of nanopowders is generally defined as powders having an average particle size of less than 100 nm. The specific advantages of the nanopowders include superior phase homogeneity and lower densification temperature. Beyond achieving nanoscaled particles, the control of other powder characteristics such as particle distribution, phase purity, and morphology are equally important in obtaining promising performance. For example, narrow size distribution and less agglomeration result in reduced microstructural defects in the sintered body by improving powder flow and packing efficiency during pressing. Figure 1 shows a typical example of ceramic nanopowders. The microstructure corresponds to the nanocrystalline powder (~20 nm of average particle size) of a LiZn ferrite composition, which was prepared by a combustion synthesis method.

The value of achieving nanosized particles is believed to be strongly associated with crystal structure of the given ceramic material, its formation energy, and chemical reaction route if multiple phases are involved. Simple oxide systems that can be synthesized at relatively low temperatures by solid-state reactions have a great potential of producing nanocrystalline powders by chemical processing. The formation of nanocrystalline powder is often difficult when intermediate phases are involved or structural ordering is required prior to the formation of phase-pure ceramics. Intensive energy sources generated by nonconventional techniques such as plasma, laser, and microwave processing have been successfully utilized to suppress unnecessary particle growth but provide sufficient activation energies for nucleation within a relatively short period.

Nanoscaled particles agglomerate easily due to the very strong van der Waals attraction force between small particles. Particle agglomeration leads to nonuniform packing density and inhomogeneous densification over the sample during firing. It can be minimized by additional processing treatments including chemical modification of particle surface, redispersion in a liquid medium, ultrasonication, or breaking-up in the dry state. Particle aggregation can also be a problem and often occurs after synthesis or subsequent calcination. Particle aggregation refers to a strong agglomeration state where particles form a neck between them by the recrystallization process during powder processing or thermal treatment. The aggregate acts as a single particle and is difficult to be broken up due to its strong bonding force.

There are several potential issues concerning the commercial production of ceramic nanopowders. They include cost efficiency, powder handling and related safety concerns, productivity, and difficulty in control of powder quality. High-reliability methods for the inexpensive production of large quantities of high-quality, multicomponent-capable nanopowders must be preferred for commercial applications to be realized.

This chapter concerning ceramic nanopowders consists of three major sections. The first section deals with chemical

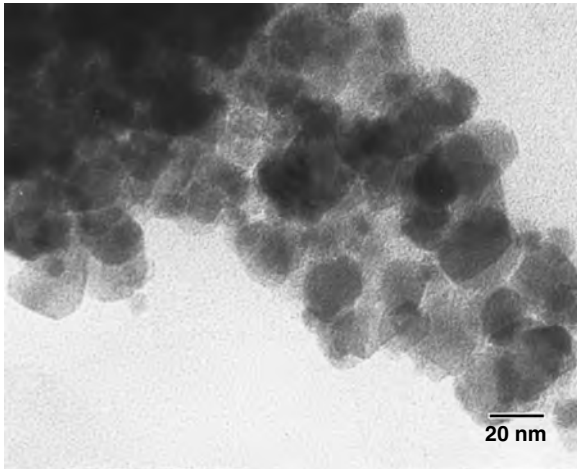


Figure 1. Typical nanocrystalline ceramic powder.

processing methods that have been successful in preparing ceramic nanopowders. The brief introduction and principle of each chemical method will be described based on the classification of two major categories: liquid phase precipitation and gas phase condensation. The second section covers the sintering behavior of ceramic nanopowders and additional processing techniques to improve packing density and homogeneous densification. Finally, various examples of ceramic materials including zirconia, alumina, silicon carbide, silicon nitride, titania, titanates, and ferrites will be described with obtainable powder characteristics and property benefits.

2. CHEMICAL PROCESSING FOR NANOPOWDERS

Production methods of ceramic nanopowders can be classified into two broad categories: liquid phase precipitation and gas phase condensation. Specific methods have evolved that differ only in the means by which thermal or mechanical energy is supplied to the precursor species. While it is virtually impossible to avoid agglomeration in pristine nanopowders, the extent of agglomeration depends on the synthesis technique [16].

In liquid phase synthesis, such as sol-gel or hydrothermal processes, nanopowders can be produced with relatively narrow size distributions. However, such processes often produce nanopowders that contain chemical residues. Gas phase condensation processes can avoid some of the contamination problems but have problems with agglomeration and coalescence associated with the high temperatures involved.

2.1. Liquid Phase Precipitation

The most common and widely used liquid phase chemistry process is sol-gel. Other wet chemistry methods include precipitation from solutions, hydrothermal processing, and microemulsion techniques.

2.1.1. Sol-Gel Processing

The sol-gel process is when chemical methods are used to turn solutions of metal compounds such as organometallics, into gels [42]. It is a low-temperature synthesis technique whereby ceramic particles are produced from a liquid solution or a colloidal suspension of metallic acids, metallic chlorides, colloidal metal oxides, and/or metal alkoxides (general formula of $M(OR)_n$ where R is an alkyl and M is a metal with a valence n).

The sol-gel process can be used to prepare metal oxides via the hydrolysis of reactive metal precursors, usually alkoxides in an alcoholic solution, resulting in the corresponding hydroxide. Usually a catalyst is necessary to make these reactions rapid. Condensation of the hydroxide molecules by elimination of water leads to the formation of a network of metal hydroxide. When all hydroxide species are linked in one network-like structure, gelation is achieved and a dense porous gel is obtained. Removal of the solvents and appropriate drying of the gel results in an ultrafine powder of the metal hydroxide. Mixed oxide nanoparticles are synthesized by combining sols or co-hydrolyzing or copolymerizing mixtures of alkoxides. Further heat treatment of the hydroxide leads to the corresponding ultrafine powder of the metal oxide. Since the process starts with nanosized units and undergoes reactions on the nanometer scale, it results in nanometer-sized materials [62, 66, 70].

Sol-gel processes have several advantages. These include the production of ultrafine porous powders and the homogeneity of the product as a result of the homogeneous mixing of the starting materials on the molecular level [27].

2.1.2. Hydrodynamic Cavitation

In hydrodynamic cavitation, nanoparticles are generated through creation and release of gas bubbles inside sol-gel solutions. By rapidly pressurizing in a supercritical drying chamber and exposing to cavitation disturbance and high-temperature heating, the sol-gel solution is intimately mixed. The erupted hydrodynamic bubbles are responsible for nucleation, growth, and quenching of the nanoparticles. Particle size can be controlled by adjusting the pressure and the solution retention time in the cavitation chamber [44].

2.1.3. Chemical Precipitation

Nanoscale particles can be synthesized by conventional chemical precipitation techniques. Although these systems can produce large amounts of nanosized powders, the rate of reaction is fast, difficult to control, and the powders tend to agglomerate and require post-treatment that will not produce nanocrystalline grain sizes. The use of homogeneous precipitation can help with these problems, producing <5-nm-size particles [61].

2.1.4. Hydrothermal Processing

Hydrothermal processes can be applied to most oxides. Most materials can be synthesized at temperatures <300 °C and at about 1250 psi. A water solution containing water soluble precursors is heated and pressurized to cause the metal ions to react with oxygen and hydroxide ions from the water. After treatment, the solution is brought back to ambient pressure and the ceramic nanoparticles collected [67].

2.1.5. Solvothermal Processing

Solvothermal synthesis is a similar process to hydrothermal except that the reaction is done in a solvent such as alcohol. Crystalline BaTiO₃ nanopowders were produced using a solvothermal process. This process had the advantages that stoichiometric powder can be obtained, the process was run under milder conditions than in an aqueous hydrothermal process, and the nanosized particles had a narrower size distribution and exhibited less agglomeration [35].

2.1.6. Microemulsion Technology

A microemulsion is a thermodynamically stable, optically isotropic, and transparent solution of two immiscible liquids (generally water and oil) stabilized by an interfacial film of surfactant. Water in oil microemulsion (or reverse micelles) can be used as microreactors to synthesize nanosized particles with a narrow particle size distribution. In a water in oil microemulsion, the aqueous phase is dispersed as microdroplets (typically 1–50 nm in size) surrounded by a monolayer of surfactant molecules in the continuous hydrocarbon phase. The key is controlling the growth inside the individual microdroplets. Since the microreactors are steric barriers for inhibiting the polymerization of reacting species among different droplets during the reaction period, the particles synthesized are smaller than 100 nm. It is possible to combine the microemulsion process with hydrothermal synthesis to produce nanoparticles of oxides such as titania. The hydrothermal treatment of the microemulsions enables crystalline nanoparticles to be formed under milder conditions than traditional post-treatment calcination processes [32, 33, 46, 68]. For silica particles, the size distribution correlates well with the size, connectivity, and stability of the microemulsion droplets. The final size distribution is predetermined in the particle's nucleation stage [34, 45].

2.2. Gas Phase Condensation

Gas phase synthesis is one of the best techniques with respect to size monodispersity. This can be achieved by using a combination of rigorous control of nucleation and growth with avoidance of coagulation by diffusion and turbulence. In addition, it is required to have effective collection of nanoparticles and their handling after the particles are formed. The stability of the collected nanoparticle powders against agglomeration, sintering, and composition changes can be ensured by collecting the nanoparticles in a liquid [48]. Gas phase synthesis offers easy control of process parameters including gas composition, pressure, temperature, and gas flows. Reactants can be gaseous, volatile liquids, or solids. Heating sources vary from conventional resistance furnaces, to lasers, plasma, and electron beams.

Advantages of gas condensation methods for preparing nanoparticles directly from supersaturated vapor include versatility, ease of performance and analysis, and generation of high-purity products. Disadvantages include high production cost because of lower yields, difficulty in scaling up, and potential reactions with the heating source [17].

Nanosized particles can be produced from the gas phase either by physical vapor deposition or by chemical vapor deposition. Physical vapor deposition involves vaporizing a

material and then quenching the vapor. No chemical reaction takes place. This can be used for some oxides and carbides, but is not suitable for most ceramics that have lower vapor pressures [23, 24].

2.2.1. Physical Vapor Deposition

Physical vapor deposition can be done on a ceramic where it is vaporized, condensed from the vapor, and then solidified into a new form. The process can start with a ceramic source material which is then heated to above its melting point so that a vapor is created. Nanoparticles are formed when supersaturation is achieved above the vapor source. Generally, a high pressure of inert gas is usually needed to achieve supersaturation. When the atoms encounter colder gas atoms, they cool and condense to form solid nanoparticles. These particles are transported to a cooled surface by a convection current or by a forced gas flow. By using a forced gas flow, the particle size can be controlled through coalescence [17].

In the gas evaporation methodology, individual nanosized particles can collide with each other while they are being transported by the flow of the gas. When the collisions occur at temperatures below the particle coalescence temperature, the particles form secondary particles in which multiple particles are sintered together. These particles can aggregate further during the collection process. To collect the nanosized particles, a process is needed that removes the nanosized particles from the generation area and dilutes their concentration such that collisions no longer occur [38].

2.2.2. Chemical Vapor Deposition

Chemical vapor deposition (CVD) is the process where a chemical reaction in the gas phase occurs to form the ceramic composition. The chemical vapor deposition process has the following advantages: agglomeration of the powders produced is suppressed, narrow size distributions can be obtained depending on the reaction conditions, and the atmosphere can be easily controlled thereby allowing the production of nitrides, carbides, and borides which are not easily made by other processes.

Metal chlorides are widely used as starting materials. Particle size can be controlled by the reaction temperature and the composition of the reacting gases. The simplest gas phase reaction process involves passing reactive gases through an externally heated reactor called a hot-walled reactor. Variations on this process include chemical flame processes, plasma processes, and laser processes. The properties of the particles synthesized are dependent on the physiochemical characteristics of the reaction system, the construction of the reactor, the heating method, the temperature gradient, and the method of introducing the gas reactants into the reactor [40].

Nanosized ceramic oxides can be prepared through the oxidation of hydrolysis of volatile metal chlorides or direct oxidation of metal vapor. Hydrolysis of metal chloride vapors proceeds faster than direct oxidation and therefore produces smaller sized particles. The reactions of metal chlorides with ammonia to produce nitrides have large equilibrium constants and nitride powders can be produced at relatively low temperatures. In general, high temperatures

are needed for the formation of carbides because the equilibrium constants are generally small at low temperatures where the reaction rates are also slow [40, 64, 71].

Direct oxidation synthesis of nanosized ceramic oxides is done by heating and evaporating metals and semi-metals in an oxygen-containing atmosphere. Resistance, induction, or arc-discharge heating can be used to heat the metal. Resistance heating and induction heating have difficulties due to potential reactions between the molten metal and the heating device. In the arc-discharge heating, the electrodes themselves are evaporated, alleviating the problem associated with resistance heating.

The arc-discharge process consists of a formation chamber, consumable positive and negative electrodes, DC power supply, a gas supply, and a vacuum pumping system. Evaporated metal atoms from the electrodes are collided with atmospheric gas and cooled and reacted, condensing into nanosized particles. The formed particles are deposited on an inner wall of the formation chamber. Generally the atmospheric gas pressure is controlled between 150 torr and 500 torr and the electric current is controlled between 50 A and 200 A. The nanoparticle size and properties are dependent on the kind of atmospheric gas, electric currents, and the pressures [26].

2.2.3. Flame Processes

Additional gas condensation techniques involve using flames in a combustion type process [19, 49–53, 57, 63]. Chemical precursors are vaporized and then oxidized in a combustion process using a flame powered by a fuel-oxidant mixture such as propane-oxygen or methane-air. The energy from a flame is used to drive chemical reactions that result in the formation of species with low vapor pressures, which then nucleate to form particles. A typical sequence of events occurs over a short distance as products and then clusters form. Figure 2 illustrates the formation of nanoparticles by flame processes. The cluster concentration is very high, leading to collisions among the clusters to form particles. At sufficiently high temperatures and sufficiently small particle sizes, the particles coalesce to form larger units that become the primary particles. Further collisions among these primary particles while the gas is cooling leads to the formation of hard aggregates (collections of primary particles that do not have sufficient time or energy to fuse together). The aggregates can range from a few up to many thousands of primary particles. The size range for primary particles is from a few nanometers to 500 nm. Maximum flame temperatures usually range from 1200 K to 2500 K. The temperatures in flame reactors are lower than in plasma reactors, but usually higher than those found in hot-wall, evaporation-condensation, or laser reactors.

Advantages of flame reactors include the ability to produce simple oxides easily using short residence times, simple and relatively inexpensive systems to build and operate, high purity, and ability to produce a large range of sizes (generally in aggregates). Disadvantages include the formation of hard aggregates under most conditions, broad particle size distribution, difficulty in maintaining a uniform temperature and velocity profile, difficulty in producing easily oxidized materials, and the fact that particle properties are

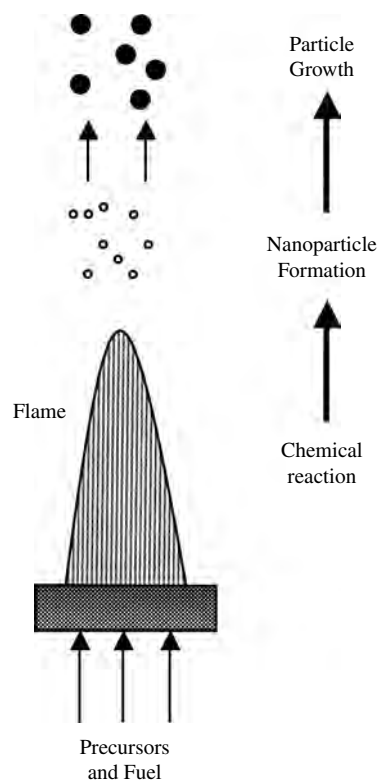


Figure 2. Typical sequence for flame processes.

affected by mixing of the precursors used [41]. Flame processes are used industrially to produce commercial quantities of ceramic powders because of the lower cost of production [17].

The controlled thermal decomposition of one or more precursors in an atmospheric pressure flame spray gave nanopowders of Al_2O_3 , SiO_2 , and yttria-stabilized zirconia with sizes ranging from 2 to 100 nm. These powders were collected in liquid to form a colloidal dispersion [18, 19].

The combustion flame-chemical vapor condensation process (CF-CVC) has been used to produce a variety of oxide nanopowders which include SiO_2 , TiO_2 , Al_2O_3 , SnO_2 , V_2O_5 , and ZrO_2 . This process can produce a high rate of production of nanopowders by making use of chemical precursors as the starting material and a low-pressure flat flame to provide the thermal energy required to pyrolyze the precursors. These powders have an average primary particle size in the range 15–25 nm and a secondary particle size of approximately 100 nm. The use of a low-pressure flat flame with a uniform temperature distribution has been shown to reduce the gas phase residence time and alleviate aggregation [17, 32, 60].

2.2.4. Laser Heating

Laser vaporization is achieved by focusing a high-energy pulsed laser onto a metal target. The temperature at the focusing spot is high enough to vaporize the material. The hot metal atoms are then allowed to react with the reactive gas inside the chamber and the nanosized particles of oxides, nitrides, or carbides are collected [17, 65].

Laser light can be used to drive chemical reactions that result in particle formation. There are two types of laser reactors. In the photothermal process, the laser light is absorbed by the reactor or other gaseous species and then energy is transferred to the carrier gas, resulting in the heating of the gas. After this, the reactions are thermally driven. The dynamics are similar to those found in flame reactors and hot-wall reactors. In the photochemical process, shorter wavelengths are used and the reactant molecules absorb the laser light at specific wavelengths, resulting in dissociation to form the condensable species. Temperatures can be near ambient in contrast to the photothermal case where temperatures are near 1000 °C or higher [41]. The advantages of using laser reactors include being able to produce simple oxides and non-oxide ceramics and high-purity powders, and the utilization of low gas temperatures (photochemical). The disadvantages include the need to use expensive reactants, formation of hard agglomerates under most conditions, the complexity of the system, and the generally high cost of the equipment [41].

2.2.5. Laser Ablation

The schematic of the laser ablation process is illustrated in Figure 3. Pulsed lasers with very high energy are used to ablate the precursor material and form nanoparticles. The laser beam is focused on the surface of a target where a large amount of energy is deposited into a small volume of material, causing the material to be vaporized and ionized. As the formed plume expands, it cools, and the species in the plume interact to generate the vapors that eventually condense to form particles. The chief advantage is the formation of nanophase materials [11, 41, 55].

2.2.6. Plasma Processes

Thermal plasma reactors use high-temperature plasmas to provide the energy required to drive the physical and chemical processes that lead to particle formation and growth.

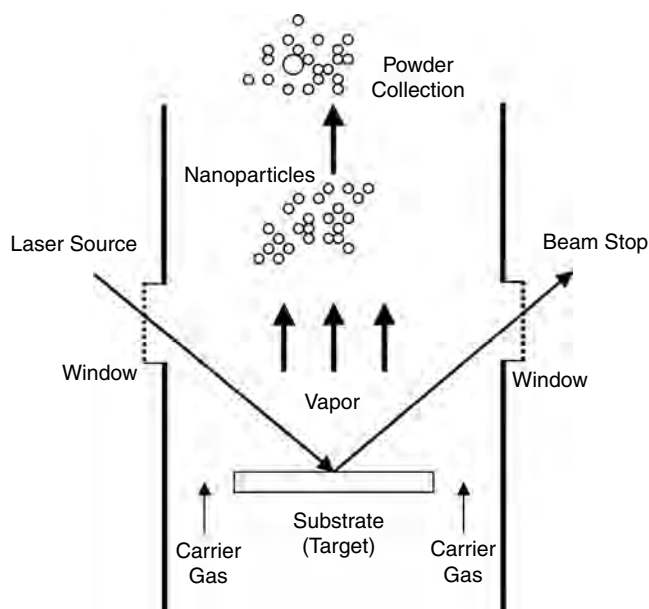


Figure 3. Particle formation by laser ablation.

A plasma is a system with a high energy content in which a significant fraction of the species are ionized and are conductors of electricity. In thermal plasmas, the temperatures of the electrons and ions are equal and the pressures are high. There are many variations dependent on how the reactants are introduced. The reactants can be introduced as powders, solutions, premixed gases, or gaseous reactants added downstream of the plasma. Temperatures are very high and complete vaporization and dissociation of the reactants into their atomic form is normal [41]. The advantages of this technology for preparation of various oxide powders include no hard agglomeration, availability of a wide range of precursors such as carbonates, alkoxides, hydrolytes, etc., ability to make single- or multicomponent powders, convenient and quick collection methods, and high-purity, uncontaminated powders. Figure 4 represents an example of nanoparticle formation by a plasma vaporization process.

The dissociation temperature of the starting elemental powder is an important factor in plasma synthesis. Carbides are much easier than nitrides and some materials may require addition of another material to decrease contamination. Carbides such as SiC, WC, and TaC can be formed with CH₄ whereas TiC and B₄C may need an addition of H₂ with the CH₄. Nitrides such as Si₃N₄ and AlN can be formed using NH₃ whereas TiN, ZrN, TaN, MgN, NbN, VN, and BN can be formed with N₂ with or without the addition of H₂. Oxides are generally formed in a plasma with the appropriate starting material and O₂.

Plasma pyrolysis technology was used to make nanometer-sized ZnO. Spherical, agglomerate-free 20-nm ZnO was produced using a plasma powder of 2500 W, a plasma gas flux of 10.0 m³/h, and a feed rate of about 7.0 kg/h [36].

In low-temperature plasmas such as glow discharges or microwave plasmas [12], the temperature of the electrons is much greater than that of the ions and the pressures are lower. The plasmas contain un-ionized atoms and molecules, ionized species, and electrons. The advantages of this process include being able to use materials with high melting points, use of inexpensive powder feeds, rapid cooling rates, and controlled production of non-oxide ceramics. The disadvantages include the difficulty in completely vaporizing the solid reactants, complicated and less understood mechanisms, broad particle size distributions, agglomerated and aggregated particles, and the requirement for high energy [41].

Plasma spray synthesis involves production of nanomaterial by spray pyrolysis in an open atmospheric plasma spray jet. Liquid precursors are atomized and injected into a plasma jet. Nanoparticles are collected as powder in an electrostatic precipitator or directly onto a substrate. Nanoparticles of zirconia powder with sizes varying between 3 and 80 nm were produced this way [56].

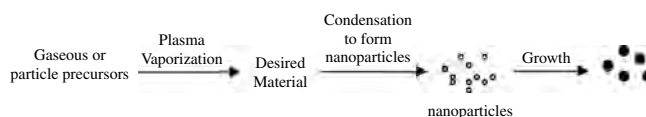


Figure 4. Nanoparticle formation by plasma vaporization.

There are a number of plasma torches that can be used. These include direct-current jet torch, radio frequency plasma torch, and hybrids of radio frequency–direct-current coupled plasma torches. Problem areas associated with using plasma torches include (1) lack of uniformity in the injection part of the plasma where there is a steep temperature gradient; (2) control of nucleation and growth processes associated with the quenching of the flow of material; (3) recovery of the materials without sintering and aggregation. Particle size can be controlled by adjusting the amount of injected reactants and by adjusting the cooling speed after reaction. Reactive quenching, in which the injected reactants are reacted and rapidly cooled simultaneously, can be used to effectively control the composition and particle size of the nanoparticles [39].

Carbide, nitride, and oxide powders can be formed in a vapor phase reaction under a high temperature generated by a plasma. Rapid quenching of these gases produces ultra-pure nanoparticles requiring no further milling or grinding. This can be achieved by having the plasma undergo a supersonic expansion into a deposition chamber with a large pressure drop across the nozzle. The nanoparticles are then deposited onto a temperature-controlled substrate [54].

2.3. Other Processes

2.3.1. Spray Pyrolysis

Spray pyrolysis describes all synthesis processes in which a solution is atomized and thermolyzed to attain the requisite phase. The following are all similar in their basic processing: solution aerosol thermolysis, evaporative decomposition of solutions, spray pyrolysis, ultrasonic spray pyrolysis, mist decomposition, spray roasting, chemical reactions with aerosols, aerosol decomposition, and high-temperature aerosol decomposition [14]. Starting materials in the spray pyrolysis process are chemical precursors dissolved in solution or as a colloidal suspension. Aqueous solutions are usually used because of their lower cost, safety, and a wide range of available precursors. The droplets are generated by nebulization or atomization of the starting solution or suspension. The droplets generated undergo evaporation with solute condensation within the droplet, drying, thermolysis of the precipitated particle at higher temperature to form a microporous particle, and finally sintering to form a dense particle. Figure 5 illustrates the process of nanoparticle formation by spray pyrolysis.

Nanoparticles can be directly synthesized from droplets or by liberating the individual crystallites comprising the produced particles after the thermolysis stage. To directly produce powders by spray pyrolysis requires control over droplet formation, coagulation, and evaporation processes as well as precipitation and decomposition processes. The final oxide particle size D_p after sintering can be approximated (assuming the solute concentration is uniform at C_s) by

$$D_p = D_o (C_o \rho_{\text{precursor}} W / C_s \rho_{\text{oxide}})^{1/3}$$

where D_o is the initial diameter of the solution droplet, C_o is the initial solution concentration, $\rho_{\text{precursor}}$ is the precursor theoretical density, ρ_{oxide} is the oxide theoretical density,

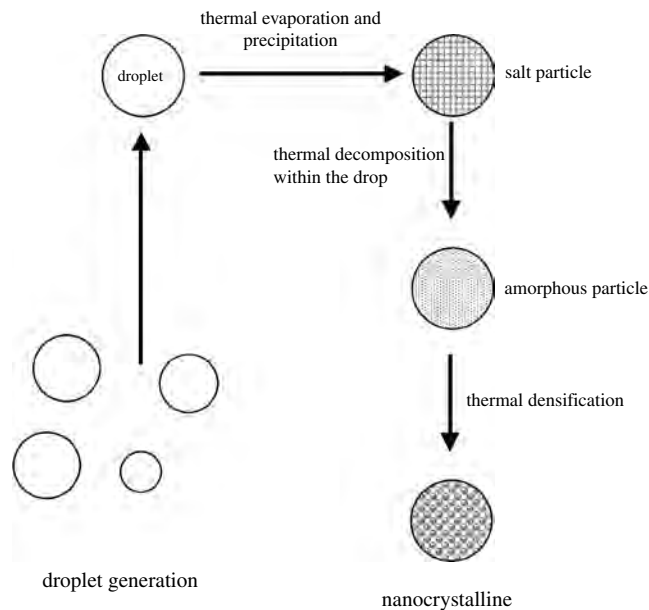


Figure 5. Spray pyrolysis nanoparticle formation stages.

and W is the oxide yield of the precursor. Direct production of nanoparticles by spray pyrolysis requires relatively dilute solutions (low C_o/C_s) and small initial droplet size (D_o) [14]. By way of an example, 50-nm ZnO and ZrO₂ particles were produced using a nebulizer and impactor [14]. Individual 14-nm MgO nanoparticles were produced by liberating individual crystallites of Mg(CH₃CHOO)₂ due to the oxidative disintegration of the initially formed particles [15].

Particles produced by spray pyrolysis are more uniform in size and composition than those produced by other techniques because of the microscale reaction within a droplet and the lack of a need for any type of milling. Each droplet contains precursors in the same stoichiometry as desired in the product. This process is very dependent on the aerosol generator. One variation on this process is the use of a filter expansion aerosol generator that was shown to produce ZnO particles less than 20 nm in size [19].

Advantages of spray pyrolysis include lower cost since it is a one step process, production of high-purity materials, the homogeneity of the particles as a result of the homogeneity of the original solution, the fact that each droplet/particle undergoes the same reaction conditions, and the fact that no subsequent milling is required [17]. The use of tubular flow reactors has the advantages of being simple, flexible, able to produce a wide range of sizes, and that they utilize well-understood mechanisms. The disadvantages include requiring precursors with significant vapor pressure, stable precursors below the reaction temperature, potentially expensive precursors, and aggregation at high loadings [41].

Less than 20-nm crystalline ZnO particles were produced using a filter expansion aerosol generator. This process involves spraying liquid through a pneumatic nozzle on to a glass filter surface using a carrier gas. A thin liquid film is formed which is pressed through the filter pores by the carrier gas and expanded into a low-pressure chamber.

2.3.2. Sonochemical and Sonothermal Processing

An acoustic cavitation process can generate a transient localized hot zone with extremely high temperature gradient and pressure. The sudden changes in temperature and pressure destroy the precursor material which enables the formation of nanoparticles [18, 43].

2.3.3. Mechanochemical Processing (High-Energy Ball Milling)

High-energy ball milling is a relatively simple, but normally acceptable method for making nanoparticles. Grinding particles for hours to achieve nanoparticles is considered a relatively dirty process where impurities are introduced through the grinding process, both from the media, from the equipment, and gaseous impurities from the atmosphere. However, the availability of tungsten carbide components and the use of inert atmosphere and/or high vacuum processes can reduce impurities to acceptable levels. Additional disadvantages include low surface area, highly polydispersed size distributions, and the partially amorphous state of the as-prepared powders thereby requiring post-treatment [48].

The intrinsic advantage of mechanochemical processing is that solid-state reactions are triggered by mechanical activation rather than high-temperature calcination. This has special advantages for lead-containing materials since the loss of lead can be avoided by operating at the low temperatures. Lead magnesium niobate particles of sizes ranging between 20 and 30 nm were produced using this method [60].

Nanosized particles can be prepared by starting with precursor powders (usually a salt and a metal oxide), milling the powder to form a nanoscale composite structure that reacts during the milling, and subsequent heating (if necessary) to form a mixture of dispersed nanocrystals of the desired oxide within a soluble salt matrix. The matrix can then be removed by washing or other suitable processes [17, 69]. For example, nanosized ZrO_2 powder was synthesized via the milling and subsequent heat treatment of a mixture of $ZrCl_4$ and CaO powders. The displacement reaction was induced in a steady-state manner forming ZrO_2 nanoparticles within a $CaCl_2$ matrix. Removal of the $CaCl_2$ by washing resulted in nonagglomerated 5-nm ZrO_2 particles [37].

2.3.4. Carbothermal Reduction

Carbothermal reduction is a high-temperature reaction with carbon or boron to produce borides and carbides. Generally, a colloid is mixed with a carbon or boron precursor which is then put into a high-temperature furnace. By adjusting atmosphere, reaction times, and then pressure reduction to vacuum, nanoparticles with sizes less than 100 nm can be obtained. Additional milling may be required [59].

3. SINTERING OF NANOPOWDERS

There have been numerous studies on the sintering behavior of ceramic nanopowders since the performance of ceramic materials depends strongly on their microstructural characteristics such as grain size, porosity, and grain boundary

nature [72–97]. Fine particles must possess a high driving force for sintering (or recrystallization) because sintering rate is inversely proportional to particle size. Usually, sintering temperature can be reduced by a few hundred degrees when nanosized particles are used. Figure 6 gives an example of the effect of nanopowders on densification in the case of nanocrystalline LiZn ferrite (~ 13 nm). It compares with powders having an average particle size of $\sim 0.3 \mu\text{m}$. The densification of nanocrystalline ferrites starts at much lower temperatures of ~ 400 °C compared to the sintering temperature of ~ 800 °C for the submicron powder. Generally, nanopowders exhibit much higher fired shrinkage values than conventional ceramic powders at saturated sintering temperatures.

It is very important to have a homogeneous packing density prior to sintering for uniform densification over the entire sample. In most cases, additional high-pressure processes such as hot-pressing, hot-forging, and very-high-pressure sintering have been used to provide better microstructural characteristics. The normal pressing of nanopowders is very difficult to prevent the occurrence of heterogeneously packed regions due mainly to the pre-existence of agglomeration or aggregation. The heterogeneously packed regions have wide variations in pore size and exert different driving forces during densification, leading to abnormal grain growth. Figure 7 shows a typical example of abnormal grain growth in the case of nanocrystalline LiZn ferrite sintered at two different temperatures of 1100 °C and 1200 °C after regular uniaxial pressing at ~ 80 MPa. Due to the nonuniform packing density resulting from the conventional pressing, highly packed regions (or agglomerated regions) tend to be densified earlier during firing compared to loosely packed regions. It leads to exaggeratedly grown grains with trapped large pores as shown in Figure 7. The grains tend to further grow through the coarsening process with small grains by increasing firing temperature. It is very difficult to eliminate the trapped pores even at very high temperatures.

Table 1 represents several examples of densification studies on the compacts of ceramic nanopowders. In many cases, the high-pressure processes during pressing or sintering were used to achieve a uniform packing density of ceramic nanopowders with a narrow distribution of

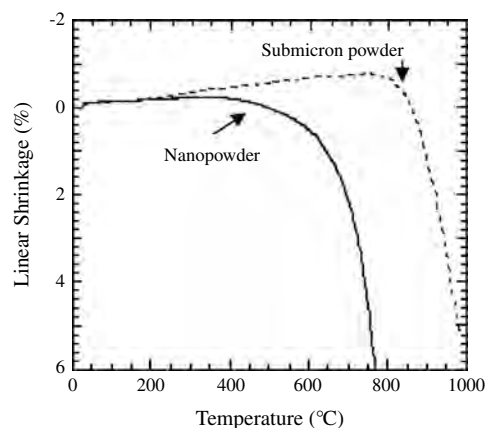


Figure 6. Densification behavior of nanocrystalline MnZn ferrite powder.

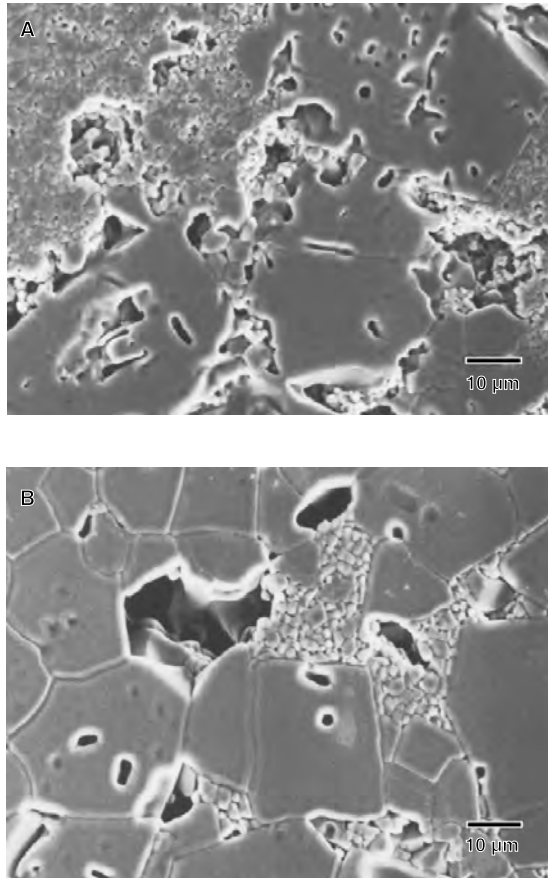


Figure 7. Microstructures of nanocrystalline LiZn ferrites showing abnormal grain growth. The samples were sintered at (A) 1100 °C for 3 hr and (B) 1200 °C for 3 hr after.

pores. Other sintering techniques such as fast-firing, plasma-assisted sintering, and microwave sintering, which do not require a high-pressure process, have been investigated to obtain nanograin structures. Chemical modification through proper dopants or surface treatment is also known to be effective in helping uniform densification without abnormal grain growth.

Sinter-forging is a processing technique to achieve the dieless compression of a powder compact at elevated temperatures [72, 94]. The compact undergoes simultaneous deformation and densification. It has been successfully documented that high-density materials were obtained without significant grain growth. Hague and Mayo [72] reported that plastic strain was largely responsible for the elimination of small pores in the sinter-forging study of nanocrystalline yttria-stabilized zirconia. They concluded that grain growth depended solely on porosity during the intermediate stage of sintering. Sintering at very high pressures (>1 GPa) can be another way to achieve dense nanocrystalline materials as evidenced in the sintering study of nanocrystalline alumina and titania powders [73, 74]. For example, bulk nanocrystalline titania samples with a grain size of <20 nm were produced when a high pressure (up to 8 GPa) was applied during sintering [74].

Plasma-assisted sintering was conducted to achieve the fast consolidation of nanocrystalline powders. Groza et al.

Table 1. Sintering studies of ceramic nanopowders with the assistance of non-conventional processing.

Nanocrystalline ceramics	Ceramic processing	Ref.
Y ₂ O ₃ -ZrO ₂ (15 nm)	Sinter-forging after cold isostatic pressing	[72]
γ-Al ₂ O ₃	High-pressure sintering at 1 GPa	[73]
TiO ₂ (20 nm)	High-pressure and low-temperature sintering	[74]
ZnO	Pressureless isothermal sintering after hot-pressing	[75]
TiN (70 nm)	Plasma-activated sintering with a pressure under vacuum	[76]
SiC (30 nm)	Fast-firing at >100 °C/min using pulse electric current sintering	[77]
MnZn ferrite (14 nm)	Fast firing at >100 °C/min with chemical dopants of Si and Ca	[78]
Y ₂ O ₃ -ZrO ₂ (10 nm)	Particle coating with a silicate glass	[79]

[76] reported that nanosized TiN powder of 150–200 nm was obtained at temperatures of 1150–1350 °C and a pressure of 66 MPa as a result of plasma-assisted sintering.

Fast-firing of nanocrystalline compacts can be used to obtain fine-grained microstructures by suppressing unnecessary grain growth [77, 78]. The process is assumed to skip some nondensifying mechanisms such as surface diffusion during firing, which are dominant at the initial sintering stage. Several nanocrystalline materials including Al₂O₃, SiC, BaTiO₃, MnZn ferrite were reported to produce better microstructures with fine grains when fast-firing was used with a heating rate of >100 °C/min.

On the other hand, chemical modification of particle surface or through dopants can largely contribute to homogeneous grain growth [78–80]. For example, the addition of Si and Ca to nanocrystalline ferrites via sol-gel processing was proven to be responsible for observed homogeneous grain growth. Figure 8 represents an improved microstructure prepared with the sol-gel additives in the case of nanocrystalline LiZn ferrite sample sintered at 1100 °C for 3 hr.

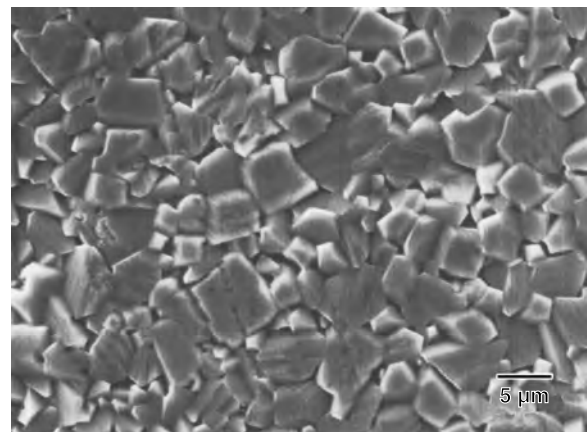


Figure 8. Microstructure of nanocrystalline LiZn ferrite sample with chemical additives of Si and Ca, sintered at 1100 °C for 3 hr.

The gel additives having a relatively low softening point are thought to penetrate into weak agglomeration and help rearranging nanoparticles at the initial stage of sintering. The additives are further found to inhibit grain growth by segregating at grain boundary and thus exerting a drag force against grain boundary movement. Oxide dopants having low softening points also can improve sintering behavior of nanopowders. Figure 9 demonstrates the effect of Bi_2O_3 addition on microstructure characteristics of nanocrystalline LiZn ferrite fired at 1100°C for 3 hr. The addition of Bi_2O_3 is believed to contribute significantly to the homogeneous grain growth via liquid phase sintering, but leads to relatively large grain sizes. Further control of heating profiles might be needed to suppress unnecessary grain growth and obtain nanostructured samples after sintering particularly when low softening additives are used.

4. NANOCERAMIC MATERIALS

4.1. ZrO_2

Zirconium oxide (ZrO_2) ceramics have been used for various thermal, mechanical, optical, and electrical applications [79, 98–100]. Their promising chemical and physical properties including excellent chemical resistance, high refractoriness, and ionic conductivity have created a lot of new applications and devices based on the zirconia materials.

ZrO_2 has four polymorphic forms depending on its transition temperature: monoclinic, tetragonal, orthorhombic, and cubic phases. Only the monoclinic form is stable at room temperature. The other polymorphic forms can be generated by quenching from certain high temperatures or by incorporating appropriate additives. Partially or fully stabilized zirconia obtained by adding various dopants such as CaO , Y_2O_3 , and CeO_2 is of particular interest for solid electrolytes, fuel cells, coatings, heating elements, and structural and wear components. The partially stabilized zirconia (PSZ) generally consists of two phases (cubic and tetragonal) or single phase (tetragonal).

The well-defined microstructure of dense zirconia determines its final properties and performance. For example, zirconia materials need to be pervious to gases and possess sufficiently high mechanical strength and toughness to

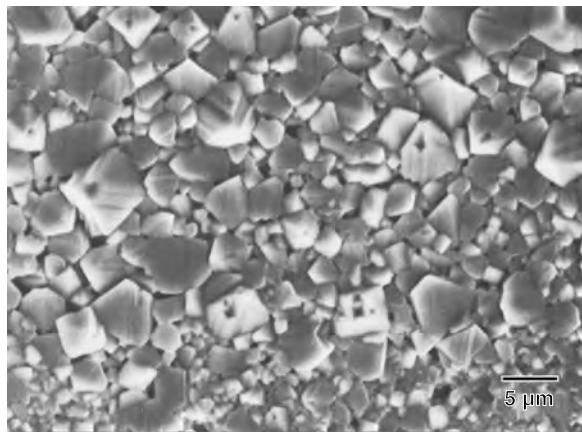


Figure 9. Microstructure of nanocrystalline LiZn ferrite sample with 3 wt% Bi_2O_3 , sintered at 1100°C for 3 hr.

avoid the breakdown of devices at elevated temperatures. To achieve optimal performance, a small grain size is often preferred with a narrow distribution of grain size. Small grain size gives superplastic deformation of ZrO_2 , where the deformation rate is proportional to the inverse or the inverse square of the grain size. Highly uniform packing of fine particles leads to low-temperature sintered zirconia with a uniform microstructure.

Many studies have been reported to synthesize nanoscale ZrO_2 -based powders and eventually obtain fine grain structures [79, 98–123]. Table 2 summarizes the results of nanocrystalline ZrO_2 obtained from various processing methods such as hydrothermal, combustion, sol-emulsion-gel method, vapor phase hydrolysis, and laser evaporation. Zirconium chloride or nitrate salt has been a popular choice as an inexpensive source for chemical processing of nanocrystalline ZrO_2 powders. Vasykiv and Sakka [98] reported that the nanosized tetragonal Y_2O_3 -doped ZrO_2 powder was produced by hydrothermal precipitation from metal chlorides and urea sol. Ultrasonication after the precipitation was proven to help deagglomerating nanocrystalline ZrO_2 powder. A microwave oven can be another way to improve continuous operation and processing effectiveness in the ZrO_2 hydrothermal synthesis as shown in the study by Bondioli et al. [99]. On the other hand, aqueous solutions of Y and Zr nitrates were used to synthesize nanocrystalline ZrO_2 powder by the combustion process utilizing oxalic dihydrazide as a fuel material [100]. The solution was spray-dried and then the resulting as-dried material was ignited onto a hot plate to produce nanocrystalline ZrO_2 powder.

4.2. Al_2O_3

Nanocrystalline α -alumina (corundum) powder has significant potentials for a wide range of applications including electronic devices and substrates, high-strength materials, and catalysts [124–131]. There have been various chemical processing routes for synthesizing fine corundum powders ranging from submicron to nanoscaled particle size. These chemical techniques include sol-gel process, precipitation, vapor phase reaction, flame-spray pyrolysis, and hydrothermal technique. However, many of the methods have difficulty in obtaining nanocrystalline α -alumina phase due to the stability of γ -alumina at low temperatures.

Janbey et al. [124] reported that nanocrystalline corundum phase (~ 20 nm average particle size) was successfully prepared by pyrolysis (or combustion) of a complex compound of aluminum with triethanolamine (TEA) and sucrose. The addition of TEA into an aqueous solution of aluminum nitrate forms metal-TEA compounds, while sucrose is used as a fuel for pyrolysis of the polymeric compounds. The amorphous precursor powder transformed into γ -alumina after subsequent firing and then became pure α -alumina with ~ 20 nm average size at 1150°C . They found that particle size depends on firing temperature and the amount of sucrose.

Glumac et al. [125] studied a modified chemical vapor condensation process that utilizes a low-pressure flame instead of hot-wall reactor. They used a carrier gas (helium, nitrogen, or ammonia) and aluminum butoxide as a liquid

Table 2. Chemical powder processing of nanocrystalline ZrO₂.

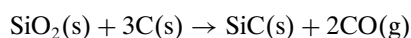
Materials	Powder processing	Precursor	Crystallite size	Comments	Ref.
3 mol% Y ₂ O ₃ -ZrO ₂	Hydrothermal precipitation	ZrOCl ₂ · 10H ₂ O	4–25 nm	Ultrasonication and calcination at 450–900 °C after washing precipitates	[98]
ZrO ₂	Microwave-hydrothermal synthesis	ZrOCl ₂ · 8H ₂ O	8–23 nm	Washing after microwave-hydrothermal treatment at 200 psi for 2 hr	[99]
4 mol% Y ₂ O ₃ -ZrO ₂	Combustion synthesis	zirconyl nitrate	8–31 nm	By using oxalic dihydrazide as a combustion source and spray-drying subsequent solution	[100]
ZrO ₂	Sol-emulsion-gel method	ZrO(NO ₃) ₂ · nH ₂ O	<30 nm	Ultrasonication and calcination at <900 °C	[101]
ZrO ₂	Alkoxide hydrolysis and condensation	Zr tetra- <i>n</i> -butoxide	<100 nm	Only tetragonal phase after heat treatment at <1000 °C	[101]
ZrO ₂	Vapor-phase hydrolysis	ZrCl ₄	6–70 nm	A vapor mixture of ZrCl ₄ and water reacts, forms nanocrystalline ZrO ₂	[103]
ZrO ₂	Laser evaporation and recondensation	ZrO ₂ rod or powder	10–50 nm	Use of a CO ₂ laser source and carrier gases for recondensation	[104]

precursor. The carrier gas accompanies precursor vapor, which is combined with premixed gas flames. The combustion of the precursors occurs in the preheat zone of the flame, and the particles condense as the flame gases cool upon approach to the substrate (acting as a collector). They reported that 3- to 50-nm-sized alumina (initially pure γ -Al₂O₃) was obtained with a high production rate (<50 g/hour).

On the other hand, a laser ablation technique utilizing a 1-kW Nd:YAG laser was reported to produce spherical nanocrystalline γ -alumina particles [126]. The nanopowder of ~14 nm median diameter was generated by ablation of solid corundum samples with the pulsed radiation of the laser and subsequent condensation of the resulting vapor in a controlled atmosphere.

4.3. SiC

Silicon carbide has been successfully used for thermomechanical, structural, and electronic applications because of its attractive properties such as high strength, stiffness, good wear and corrosion resistance, high thermal conductivity, and low thermal expansion coefficient [132–134]. Especially in electronic devices, SiC can be extensively utilized for various applications requiring high-power, high-frequency, and high-temperature operation. SiC has been generally produced by the well-known Acheson process, which includes a carbothermal reduction of sand by petrol coke at about 2400 °C. The carbothermal reaction of SiO₂ can be described by



The resultant SiC needs to be processed further for fine powders and purification. There are several chemical processing methods developed for nanocrystalline SiC powder because simple grinding of the SiC powder can not produce nanosized powders. Chemical vapor deposition (CVD)

process, sol–gel process, combustion synthesis using carbothermal reduction, and laser gas phase pyrolysis have been successfully reported in preparing nanocrystalline SiC powder.

Martin et al. [133] studied the synthesis of nanocrystalline SiC powder by the carbothermal reduction of nanosized SiO₂ precursor with the assistance of sugar. A solution of sugar in silica sol was frozen and freeze-dried before pretreatment at 800 °C in argon atmosphere. The pre-treated SiO₂/carbon mixture was converted to nanocrystalline SiC through the carbothermal reduction by heating it at reaction temperatures between 1500 °C and 1800 °C in controlled pressure and atmosphere conditions. The resulting SiC powder was less than 100 nm in average crystallite size with the oxygen content of <0.5 wt%.

CVD has been a useful technique in producing commercial nanocrystalline SiC powders [77, 134, 135]. There can be slightly different chemical vapor reactions to produce nanosized SiC powders depending on precursor and gas system and deposition condition. As an example of the CVD system, Yang and Ding [135] recently reported that the system of SiH₄-C₂H₄-H₂ could be successfully used to produce nanocrystalline SiC powder. A mixture of highly reactive gases such as SiH₄, C₂H₄, and H₂ was introduced into a reaction chamber by high-purity Ar carrier gas. The gas content was controlled by the gas partial pressure and the reaction pressure was adjusted by total flow rates. Resulting powders collected in a sealed flask by using a membrane separation technique showed average particle sizes of less than 30 nm depending on reaction temperature.

Some other efforts were made to improve the properties of nanocrystalline SiC by incorporating beneficial additives or making composites with SiC (e.g., Al₂O₃/SiC and Si₃N₄/SiC). For example, the effects of additives such as AlN, Al₄C₃, and B₄C have been investigated to improve particularly fracture strength, toughness, and electrical properties. Zhang et al. [132] reported that the incorporation of Al and N into SiC was successfully carried out

by making aerogels of SiO_2 and Al_2O_3 from the precursors of aluminum isopropoxide and tetraethylorthosilicate (TEOS), respectively. A carbothermal reaction was conducted at 1550 °C and in nitrogen atmosphere to form nanocrystalline SiC powders with an average crystallite size of <20 nm. On the other hand, Dong et al. [134] demonstrated that the nanocomposite of $\text{Si}_3\text{N}_4/\text{SiC}$ was fabricated by using nanocrystalline Si_3N_4 and SiC powder precursors and a HIP (hot isostatic press) process at 1750 °C and 150 MPa for 1 hr. The resultant microstructure appeared to be dense and homogeneous with an average grain size of 50 nm.

4.4. Si_3N_4

Silicon nitride has been considered as a promising candidate for high-temperature structural applications due to several excellent properties including high mechanical strength, good oxidation resistance, and good wear and thermal shock resistance [141–143]. Silicon nitride is known to have two polymorphic forms: low-temperature α phase and high-temperature β phase. The α to β transformation occurs at 1600–1700 °C, but the reverse transformation has not been observed. The ratio of the two phases is important in determining the final performance of sintered Si_3N_4 and usually influenced by the existence of liquid phases. Various sintering aids generating low melting phases, such as Y_2O_3 , Al_2O_3 , Yb_2O_3 , and ZrO_2 , have been added to achieve a high density at low sintering temperatures. In addition, ultrafine SiC powder with proper additives has been strongly motivated by the excellent potential of low-temperature densification and low-temperature superplastic behavior with accompanying favorable influences on the phase transformation.

Several chemical powder synthesis methods including laser-induced chemical vapor deposition, hybrid thermal plasma process, and RF plasma vapor method have been reported to prepare nanocrystalline Si_3N_4 powders [141–148]. The thermal plasma technique is one of the popular methods in producing high-quality Si_3N_4 powders. Gubicza et al. [141] reported that nanocrystalline Si_3N_4 powder (<100 nm) was successfully synthesized by the vapor reaction of silicon tetrachloride and ammonia in a radiofrequency thermal plasma reactor. The collected powder was heat-treated at 400 °C for 1 hr and then 1100 °C for 1 hr to achieve the complete decomposition of by-products. For subsequent crystallization, the powder was re-fired at temperatures of 1250 °C to 1500 °C in nitrogen atmosphere. Similar results on the synthesis of nanocrystalline Si_3N_4 by the RF plasma vapor method were also obtained by the study of Szepvolgyi and Mohai [143]. On the other hand, Li et al. [142] successfully demonstrated that nanocrystalline Si_3N_4 could be prepared by a laser-induced vapor phase induction in the study of crystallization and phase transformation of amorphous silicon nitride. The resulting particle diameter was in the range of 15–20 nm. They found that the crystallization and α/β phase transformation were greatly enhanced by applied high pressure during annealing.

4.5. TiO_2

Titania has been widely used for various commercial applications including pigment, enamels, catalytic support, ceramic membrane, gas sensor, and other electronic devices

[149–151]. Titania has three different natural crystalline structures, that is, rutile (tetragonal), anatase (tetragonal), and brookite (orthorhombic). Only rutile is thermodynamically stable, whereas the other two phases of anatase and brookite are metastable at all temperatures. Particularly, the transformation of anatase to rutile has been extensively studied due to its practical importance. The anatase to rutile transformation occurs between 400 and 1000 °C depending on impurity type and content, crystallite size, and reaction atmosphere. Reducing atmosphere or the addition of certain impurity such as CuO , MnO_2 , Fe_2O_3 , LiF, and Al was reported to promote the transformation rate. The existence of sulfate, chloride, fluoride, nickel, or silicon is known to retard the transformation. Very fine crystallite size was shown to enhance the transformation rate and initial transition temperature.

Commercial titania powders with controlled characteristics have been produced using various chemical methods such as the gas phase oxidation of titanium chloride or sulfate, hydrolysis of titanium chloride, precipitation of titanium hydroxide, sol-gel reactions of titanium alkoxide, and pyrolysis of titanium citrate [149–161]. Titania is a relatively easy material in forming nanosized particles less than 100 nm. Table 3 shows several examples of nanocrystalline titania powders resulting from various chemical routes including sol-gel, precipitation, laser ablation, hydrothermal synthesis, and vapor or aerosol pyrolysis.

Ahonen et al. [149] studied the synthesis of nanocrystalline titania powder by aerosol pyrolysis of titanium in butoxide with variations in synthesis temperature and atmosphere. They observed that subsequent firing after synthesis affected largely particle size distribution and morphology development. Anatase phase was found to start forming from amorphous phase at ~500 °C depending on synthesis and annealing temperature and firing atmosphere. Firing at nitrogen atmosphere was preferred to obtain pure anatase phase at lower pyrolysis temperatures presumably due to oxygen deficiency and subsequent Ti interstitials.

A laser pyrolysis method using CO_2 laser radiation was investigated in the synthesis of nanocrystalline TiO_2 powder doped with trivalent Al and Ga by Depero et al. [150]. Titanium isopropoxide and ethylene were used as a Ti source and a reaction sensitizer, respectively. Trimethyl-gallium and trimethyl-aluminum were used as dopant precursors. Very fine titania powders (<100 nm) were successfully prepared by the absorption of the CO_2 laser radiation. The incorporation of Ga or Al in the nanopowders was found to inhibit the formation of rutile by hindering the anatase to rutile phase transition.

4.6. Titanates

Various titanate materials that have perovskite structures and relatively high dielectric constants (k) have been extensively used for various electronic, piezoelectric, pyroelectric, and optoelectronic applications. BaTiO_3 , SrTiO_3 , PbTiO_3 , and $\text{Pb}(\text{Zr,Ti})\text{O}_3$ are representatives pertaining to the high- k ceramic material category. These materials have been important ingredients in manufacturing high capacitive chip devices including multilayer capacitors. Recent tendencies towards device miniaturization, volumetric efficiency, and

Table 3. Chemical powder processing of nanocrystalline TiO₂.

Materials	Powder processing	Precursor	Crystallite size	Comments	Ref.
TiO ₂	Aerosol pyrolysis	Ti <i>n</i> -butoxide	30–80 nm	Synthesis atmosphere and temperature affected phase transformation	[149]
TiO ₂ with Al and Ga	CO ₂ laser pyrolysis	Ti isopropoxide	<100 nm	Incorporation of Al and Ga inhibited the formation of rutile	[150]
TiO ₂	Hydrothermal synthesis	Ti <i>n</i> -butoxide	20–65 nm	Crystallite size and powder morphology depend on the type of peptizing agent	[151]
TiO ₂	Controlled precipitation	Ti tetra butoxide	<40 nm	Anhydrous acetone was used as solvent and acetic acid as catalyst for hydrolysis reaction	[152]
TiO ₂	Sol-gel method	TiCl ₄	4–12 nm	Ti(OH) ₄ inorganic gel forms after reactions with ethanol and water	[153]
TiO ₂ and TiN	Reactive ion beam evaporation	Ti target	4–45 nm	A high-power-density ion beam is focused on a Ti-target in an oxygen or nitrogen atmosphere (1–10 Torr)	[154]
TiO ₂	Vapor hydrolysis	Ti tetra-isopropoxide	5–65 nm	Vapor phase precursor reacts with steam to produce a supersaturated TiO ₂ vapor	[155]

cost reduction require thinner layers and the use of inexpensive electrode materials. Utilization of fine powders allows sintering to happen at lower temperatures with possible use of thinner layers and less expensive metallization. The conventional solid-state reaction had a tendency to produce coarse powders with particle agglomeration and compositional inhomogeneity. Therefore, various chemical processing methods such as combustion, sol-gel, co-precipitation, citrate route, and hydrothermal synthesis have been studied to prepare ultrafine, reactive titanate powders [162–178]. Most of earlier studies have focused on the fabrication of submicron-sized powders and control of powder characteristics such as particle distribution and agglomeration.

Table 4 demonstrates several examples of nanocrystalline titanate materials of BaTiO₃, SrTiO₃, PbTiO₃, and Pb(Zr,Ti)O₃ (PZT), which were prepared by chemical powder processing or mechanical activation. Chemical synthesis

techniques of perovskite BaTiO₃ ($k > 1000$) have been extensively studied because barium titanate and its solid solutions with other perovskite materials have been most popular in the capacitor application. The dielectric properties of BaTiO₃ depend strongly on Ba/Ti ratio, powder characteristics (i.e., purity, particle size and distribution, and agglomerates), and resultant microstructural characteristics (i.e., grain size and distribution, grain boundary nature, and porosity). Due to the sensitivity of electrical properties to its impurity level and microstructure, very tight control of chemical processing is necessary for reproducibility and consistent performance. Sol-gel, mechanical activation, and combustion processes have been among the successful methods for preparation of nanocrystalline BaTiO₃ powders [162–166].

SrTiO₃ ($k \sim 320$) has a few advantages over BaTiO₃, which include a lower dielectric loss, better temperature dependence of dielectric constant, and better high-frequency

Table 4. Chemical powder processing of nanocrystalline titanates.

Materials	Powder processing	Precursor	Crystallite size	Comments	Ref.
BaTiO ₃	Combustion synthesis	Ba and Ti nitrates	~70 nm	Common nitrate solution with alanine as a fuel was spray-dried and then heat-treated	[162]
BaTiO ₃	Mechanical activation	BaO and TiO ₂	10–30 nm	Mechanical activation at room temperature starts to generate nanopowder after 5 hr	[163]
BaTiO ₃	Sol-gel method	Ba oxyhydrate and Ti <i>n</i> -butoxide	13 nm	Precursor solution became a gel with the assistance of water-diluted ethylene glycol	[165]
BaTiO ₃	Sol-gel method	Ba alkoxide and Ti <i>n</i> -butoxide	<50 nm	Precursor solution was hydrolyzed via the addition of water and became a gel gradually after cooling	[166]
SrTiO ₃	Hydrothermal synthesis	Various precursors	<100 nm	Various Sr and Ti precursors were tested. KOH concentration affected particle size	[170]
SrTiO ₃	Combustion synthesis	Sr and Ti nitrates	<42 nm	Ethylene diamine tetra-acetic acid (EDTA) and NH ₄ NO ₃ were used as a reducing and an oxidizing agent, respectively	[171]
PbTiO ₃	Mechanochemical synthesis	Oxide mixture	<65 nm	Nanopowders were obtained by a shaker mill operating at 900 rpm for >5 hr	[173]
Pb(Zr _{0.7} Ti _{0.3})O ₃	Sol-gel synthesis	Pb acetate and Zr and Ti butoxides	~30 nm	Butyl alcohol was successfully used as a solvent	[175]
Pb(Zr _{0.5} Ti _{0.5})O ₃	High-energy ball-milling	Oxide mixture	~20 nm	Oxide mixture was ball-milled at 200 rpm in a tungsten carbide vial with tungsten carbide ball media up to 80 hr	[176]

performance. Solid solutions with BaTiO₃ or compositions containing various dopants have been technically important for bulk or thin-film capacitor applications. Several chemical processes including hydrothermal and combustion methods have been successfully used to prepare nanocrystalline SrTiO₃ powder [170–171].

4.7. Ferrites

Ferrites have been used mainly as magnetic core materials for inductors and transformers, microwave components, information storage devices, and permanent magnets [179, 180]. Various ferrite materials such as soft and hard ferrites and garnets have been developed to meet requirements depending on each application. For example, soft ferrites generally need to be designed to possess a maximum permeability, a minimum magnetic loss, an adequate saturation magnetization, and good response to temperature and frequency for inductors and transformers covering a wide range of operating frequency. On the other hand, microwave garnet devices have required polycrystalline single-phase materials with a high density and a high degree of chemical homogeneity for narrow line width and minimum low-field loss at microwave frequencies.

Ferrite materials are very sensitive to processing condition and impurity levels because small contents of non-magnetic impurities change significantly microstructures and resulting magnetic properties by diluting magnetic moments. For example, coercive force tends to increase as grain size decreases due to domain-wall pinning. It results in a higher energy required for switching. Especially for high-power applications, smaller grain size is required to minimize magnetic loss associated with the excitation of spin waves. Saturation magnetization is known to be less dependent on grain size.

Various soft ferrite materials having a spinel structure (e.g., NiZn and MnZn ferrites) have been a popular choice in the development of fine ferrite powders via chemical processing routes due to the ease of forming nano-scaled crystallite powders [78, 181–187]. Hard ferrite (e.g., Ba and Sr hexaferrites) and garnets (e.g., Y₃Fe₅O₁₂) are known to be difficult in preparing very fine powders from complex reaction routes involving intermediate phases and subsequent higher firing temperatures [189]. Table 5 demonstrates several examples of nanocrystalline soft ferrites prepared by chemical powder processing routes including hydrothermal,

sol-gel, co-precipitation, and combustion synthesis [181–186]. Inorganic salt-based chlorides, sulfates, and nitrates are usually selected as raw materials for chemical processing. In general, nanocrystalline phase-pure spinel ferrites with 5–50 nm are successfully produced after subsequent firing at less than 500 °C regardless of chemical processing method.

4.8. Other Ceramics

Many other ceramic materials including SiO₂ [190, 191], CeO₂ [192–195], Y₂O₃ [196–199], SnO₂ [200–203], ZnO [204, 205], AlN [206–209], TiN [210, 211], Pb(Mg_{1/3}Nb_{2/3})O₃ (PMN) [212, 213], Al₂TiO₅ [214, 215], LiMn₂O [216], Cordierite [217], and YAG [218] have been studied to produce nanopowders by various chemical processing methods. Although applications of each material are different, the concept and advantages of nanopowders are expected to lead to the enhancement of their actual performance. Most of the studies are focusing on the preparation of nanopowders via chemical processing, with less information on improved property characteristics.

Table 6 represents selected nanocrystalline ceramic materials prepared by chemical powder processing, which have been of considerable interest for their technical importance and commercial utilization. Ceria (CeO₂) is one of the important materials for applications of solid electrolytes in solid oxide fuel cells, chemical-mechanical polishing, and catalytic supports. Ceria has a prototypical fluorite structure that is stable from room temperature up to its melting temperature. In particular, hydrothermal synthesis using a cerium nitrate solution was reported to be successful in preparing nanocrystalline ceria powders less than 10 nm [192]. Yttria (Y₂O₃) is one of the traditional refractories and has a wide range of commercial applications including catalyst supports. Many chemical powder processes including combustion, sol-gel, and colloidal processing were found to be effective in preparing nanocrystalline yttria powders [196–199]. ZnO has been very useful in numerous chemical, electronic, cosmetic, and pigment applications [204, 205]. Nanocrystalline ZnO is expected to improve chemical reactivity, sensing performance, and light-absorbing capacity.

Aluminum nitride (AlN) has great potentials for several electronic applications due to its high thermal conductivity and excellent dielectric properties. Several studies on nanopowder processing and sintering behavior have been

Table 5. Chemical powder processing of nanocrystalline ferrites.

Materials	Powder processing	Precursor	Crystallite size	Comments	Ref.
LiZn ferrite	Combustion synthesis	Nitrates	<25 nm	Polyacrylic acid was used as a gelation agent and fuel for combustion	[181]
MnZn ferrite	Coprecipitation	Sulfates	~4 nm	HNO ₃ or NH ₄ OH was used to control pH	[182]
MnZn ferrite	Hydrothermal synthesis	Nitrates	<40 nm	Aqueous nitrate solution was hydrolyzed with diluted ammonia and reacted at 95 °C to 270 °C in a hydrothermal condition	[183]
Zn ferrite	Coprecipitation	Chlorides	~<10 nm	NaOH was used to control pH	[184]
Zn ferrite	Sol-gel method	Zn acetate and Fe acetylacetonone	<40 nm	Precursors were mixed in methanol and heated above 240 °C	[185]
NiZn ferrite	Coprecipitation	Nitrates	~27 nm	NH ₄ OH was used as a precipitant	[186]

Table 6. Chemical powder processing of various ceramic materials.

Materials	Powder processing	Precursor	Crystallite size	Comments	Ref.
CeO ₂	Hydrothermal synthesis	Ce diammonium nitrate	<10 nm	The effect of sulfate ions was investigated by adding (NH ₄) ₂ SO ₄ or H ₂ SO ₄	[192]
CeO ₂	Mechanochemical processing	CeCl ₃	10–30 nm	The mixture of CeCl ₃ and NaCl was milled with steel balls	[193]
Y ₂ O ₃	Gel combustion	Y nitrate	<50 nm	An aqueous solution of Y nitrate and citric acid was used for combustion reactions	[196]
SnO ₂	Sol–gel synthesis	SnCl ₄	~12 nm	A solution of SnCl ₄ in ethylene glycol was used to form gel at 120 °C	[200]
ZnO	Plasma pyrolysis	ZnSO ₄	~20 nm	Zn ₅ (CO ₃) ₂ (OH) ₆ precursor was synthesized from ZnSO ₄ and NH ₄ HCO ₃ for plasma pyrolysis	[204]
AlN	Plasma evaporation	Aluminum	<100 nm	A hot gas carrying aluminum vapor was reacted with ammonia to produce powders	[206]
TiN	Direct nitridation	Nanosized Ti oxide	<50 nm	Nanocrystalline TiO ₂ was reacted in a NH ₃ gas flow to form TiN nanopowders	[209]
Pb(Mg _{1/3} Nb _{2/3})O ₃	Mechanochemical synthesis	Oxides	20–30 nm	Powder mixture was milled using a shaker-mill at 900 rpm for 20 hr	[212]

reported with great success in achieving translucent, high-density AlN specimens [206–209]. The sintering of AlN often needs to be carried out with the use of rare-earth or alkaline-earth oxide additives to prevent the degradation of thermal conductivity from oxygen-related defects.

5. SUMMARY

The field of ceramic nanopowders (<100 nm) has great potentials for many advanced ceramic applications due to their unique characteristics particularly related to electrical, optical, mechanical, and thermal properties. Production methods of ceramic nanopowders can be classified into two major categories: liquid phase precipitation and gas phase condensation. Sol–gel, hydrothermal, co-precipitation, and microemulsion processes correspond to liquid phase precipitation. Powder processes based on gas phase condensation include physical vapor deposition, chemical vapor deposition, flame processing, laser ablation, and plasma processing. The choice of chemical processing generally depends on type of material, processing and firing condition, availability of raw materials, and safety concerns.

Agglomeration of nanoparticles happens easily due to the strong van der Waals force of attraction and has been responsible for poor microstructural characteristics after sintering. Several sintering techniques including high-pressure processing (e.g., hot-pressing and sinter-forging), high-energy processing (e.g., field-assisted sintering and microwave sintering), and controlled heating profiles have been suggested with successful evidence of improvement in microstructures. Ceramic nanopowders encompass a variety of materials such as oxides, carbides, nitrides, borides, and silicates. Zirconia, alumina, silicon carbide, silicon nitride, titania, titanates, and ferrite have been among the most popular materials for the nanopowder studies due to their scientific and technical significance. The nanopowder formation of the listed ceramic materials by various chemical processes has been successfully demonstrated with information on processing conditions and observed powder characteristics.

GLOSSARY

Agglomerate A Collection of particles where there has been no coalescence and that can be broken into individual particles.

Aggregates A collection of particles that can no longer be broken into individual particles.

Nanopowder Powder having an average particle size of less than 100 nm.

REFERENCES

1. M. N. Rittner, *Am. Ceram. Soc. Bull.* 81, 33 (2002).
2. N. Setter, *J. Eur. Ceram. Soc.* 21, 1279 (2001).
3. G. Skandan and A. Singhal, *Powder Metall.* 43, 313 (2000).
4. R. L. Axelbaum, *Powder Metall.* 43, 323 (2000).
5. T. Abraham, *Ceram. Ind.* 150, 28 (2000).
6. R. N. Das and P. Pramanik, *Br. Ceram. Trans.* 99, 153 (2000).
7. P. Pramanik and N. N. Ghosh, *Ceram. Trans.* 94, 195 (1998).
8. D. M. Liu, *Ceram. Int.* 25, 107 (1999).
9. R. Vassen, *Ceram. Forum Int.* 76, 19 (1999).
10. G. S. Tompa, G. Skandan, N. Glumac, and B. H. Kear, *Am. Ceram. Soc. Bull.* 78, 70 (1999).
11. K. Kugimiya, *Ceram. Jap.* 34, 857 (1999).
12. U. Popp, R. Herbig, G. Michel, E. Muller, and C. H. Oestreich, *J. Eur. Ceram. Soc.* 18, 1153 (1998).
13. G. Williams and G. S. V. Coles, *J. Mater. Chem.* 8, 1657 (1998).
14. G. L. Messing, S. Zhang, and G. V. Jayanthi, *J. Am. Ceram. Soc.* 76, 2707 (1993).
15. T. J. Gardner and G. L. Messing, *Am. Ceram. Soc. Bull.* 64, 1498 (1984).
16. A. Singhal and G. Skandan, *Int. J. Powder Metallurgy* 35, 45 (1998).
17. G. Skandan, N. Glumac, Y. Chen, and B. H. Kear, *Nanostructured Mater.* 11, 149 (1999).
18. Z. Wixin, W. Chang, Z. Xiaoming, and X. Yi, *Solid State Ionics* 117, 331 (1999).
19. Y. C. Kang and S. B. Park, *J. Mater. Sci.* 34, 2409 (1996).
20. B. H. Kear and L. E. McCandlish, *Nanostructured Mater.* 3, 19 (1993).
21. G. F. Gaertner and H. Lydtin, *Nanostructured Mater.* 4, 559 (1994).
22. D. Vollath and K. Sickafus, *Nanostructured Mater.* 1, 427 (1992).
23. Q. Ford, *Ceramic Industry* 31 (1998).

24. W. Chang, G. Skandam, H. Hahn, S. C. Danforth, and B. H. Kear, *Nanostructured Mater.* 4, 345 (1994).
25. Y. Zhu, Y. Qian, and M. Zhang, *Mater. Sci. and Eng.* B41, 294 (1996).
26. M. Oda, in "Characterization and Mechanisms of Growth" (T. Sugimoto, Ed.), p. 114. Xxxx, Xxxx, 2000.
27. A. Khaleel and R. M. Richards, in "Nanoscale Materials in Chemistry" (K. J. Klabunde, Ed.), p. 85. Xxxx, Xxxx, 2001.
28. A. T. Hunt, U.S. Patent 5,652,021, 1997.
29. M. Oljaca, Y. Xing, C. Lovelace, S. Shanmugham, and A. Hunt, *J. Mater. Sci. Lett.* 21, 621 (2002).
30. A. Singhal, G. Skandan, A. Wang, N. Glumac, B. H. Kear, and R. D. Hunt, *Nanostructured Mater.* 11, 545 (1999).
31. C. Kang and S. B. Park, *J. Mater. Sci.* 31, 2409 (1996).
32. M. Wu, J. Long, A. Huang, and Y. Luo, *Langmuir* 15, 8822 (1999).
33. K. C. Song and J. H. Kim, *J. Colloid Interface Sci.* 212, 193 (1999).
34. C. Chang and H. S. Fogler, *Langmuir* 13, 3295 (1997).
35. D. Chen and X. Jiao, *J. Am. Ceram. Soc.* 83, 2637 (2000).
36. Y. Lin, Z. Tank, and Z. Zhang, *J. Am. Ceram. Soc.* 83, 2869 (2000).
37. J. Ding, T. Tsuzuki, and P. G. McCormick, *Nanostructured Mater.* 8, 750 (1997).
38. M. Oda, in "Exploratory Science and Technology" (C. Hayashi, R. Uyeda, and A. Tasaki, Eds.), p. 133. Xxxx, Xxxx, 1997.
39. T. Yoshida, in "Ultra-Fine Particles, Exploratory Science and Technology" (C. Hayashi, R. Uyeda, and A. Tasaki, Eds.), p. 170. Xxxx, Xxxx, 1997.
40. A. Kato, in "Ultra-Fine Particles, Exploratory Science and Technology" (C. Hayashi, R. Uyeda, and A. Tasaki, Eds.), p. 197. Xxxx, Xxxx, 1997.
41. T. T. Kudas and M. Hampden-Smith, in "Aerosol Processing of Materials," p. 293. Xxxx, Xxxx, 1999.
42. J. W. Evans and L. C. De Jonghe, in "The Production of Inorganic Materials," p. 377. Xxxx, Xxxx, 1991.
43. K. S. Suslick, T. Hyeon, and F. Fang, *Chem. Mater.* 8, 2172 (1996).
44. J. E. Sunstrom, W. R. Moser, and B. Marshi-Guerts, *Chem. Mater.* 8, 2061 (1996).
45. F. J. Arriagada and K. Osseo-Asave, *J. Colloid Interface Sci.* 170 (1995).
46. R. J. Higgins, "Proceedings of the Joint NSF-NIST Conference on Nanoparticles," 1997.
47. D. L. Leslie-Pelecky and R. D. Reike, *Chem. Mater.* 8, 1770 (1996).
48. E. L. Ju and D. T. Shaw, "Nanostructure Science and Technology, R&D Status and Trends in Nanoparticles, Nanostructured Materials, and Nanodevices," National Science and Technology Council, 1999.
49. H. F. Calcote and D. G. Keil, "Proceedings of the Joint NSF-NIST Conference on Nanoparticles," 1997.
50. G. K. Gould and C. R. Dickson, U.S. Patent 5,021,221, 1991.
51. R. L. Axelbaum, "Proceedings of the Joint NSF-NIST Conference on Nanoparticles," 1997.
52. S. Vemury, S. E. Pratsinis, and L. Kibbey, *J. Mater. Res.* 12, 1031 (1997).
53. S. Vemury and S. E. Pratsinis, *J. Am. Ceram. Soc.* 78, 2984 (1995).
54. N. P. Rao, N. Tymiak, J. Blum, A. Newuman, H. J. Lee, S. L. Girshick, P. H. McMurry, and J. Heberlein, "Proceedings of the Joint NSF-NIST Conference on Nanoparticles," 1997.
55. M. F. Becker, J. R. Brock, and J. W. Keto, U.S. Patent 5, 585, 020, 1996.
56. C. C. Berndt, J. Karthikeyan, T. Chrask, and A. H. King, "Proceedings of the Joint NSF-NIST Conference on Nanoparticles," 1997.
57. J. Poth, R. Haberkorn, and H. P. Beck, *J. Eur. Ceram. Soc.* 20, 707 (2000).
58. N. G. Glumac, Y. Chen, G. Skandan, and B. Kear, *Mater. Lett.* 34, 148 (1998).
59. H. Martin, R. Ecke, and E. Muller, *J. Eur. Ceram. Soc.* 18, 1737 (1998).
60. J. Want, X. Junmin, W. Dongmei, and N. Weibeng, *J. Am. Ceram. Soc.* 82, 1358 (1999).
61. K. C. Song and Y. Kang, *Mater. Lett.* 42, 283 (2000).
62. W. Luan and L. Gao, *Ceram. Int.* 27, 645 (2001).
63. J. Grabis, I. Steins, D. Rasmene, and G. Heidemane, *J. Eur. Ceram. Soc.* 17, 1437 (1997).
64. B. Xia, W. Li, B. Zhang, and Y. Xie, *J. Mater. Sci.* 34, 3505 (1999).
65. U. Popp, R. Herbig, G. Michel, E. Muller, and C. Oestreich, *J. Eur. Ceram. Soc.* 18, 1153 (1998).
66. Y. Zhu, L. Zhang, C. Gao, and L. Cao, *J. Mater. Sci.* 35, 4049 (2000).
67. M. Hirano, Y. Fukuda, H. Iwata, Y. Hotta, and M. Inagaki, *J. Am. Ceram. Soc.* 83, 1287 (2000).
68. C. Lu and S. Saha, *J. Am. Ceram. Soc.* 83, 1320 (2000).
69. T. Tsuzuki and P. G. McCormick, *J. Am. Ceram. Soc.* 84, 1453 (2001).
70. B. Djuricic and S. Pickering, *J. Eur. Ceram. Soc.* 19, 1925 (1999).
71. X. Yang and Z. Ding, *J. Mater. Res.* 15, 2140 (2000).
72. D. C. Hague and M. J. Mayo, *J. Am. Ceram. Soc.* 80, 149 (1997).
73. R. S. Mishra, C. E. Lesher, and A. K. Mukherjee, *J. Am. Ceram. Soc.* 79, 2989 (1996).
74. S. Liao, J. Colaizzi, Y. Chen, B. H. Kear, and W. E. Mayo, *J. Am. Ceram. Soc.* 83, 2163 (2000).
75. A. P. Hynes, R. H. Doremus, and R. W. Siegel, *J. Am. Ceram. Soc.* 85, 1979 (2002).
76. J. R. Groza, J. D. Curtis, and M. Kramer, *J. Am. Ceram. Soc.* 83, 1281 (2000).
77. Y. Zhou, K. Hirao, M. Toriyama, and H. Tanaka, *J. Am. Ceram. Soc.* 83, 654 (2000).
78. Y. S. Cho, D. Schaffer, V. L. Burdick, and V. R. W. Amarakoon, *Mater. Res. Bull.* 34, 2361 (1999).
79. R. Ramamoorthy and R. Chaim, *J. Mater. Res.* 16, 296 (2001).
80. S. Kawano, J. Takahashi, and S. Shimada, *J. Am. Ceram. Soc.* 86, 701 (2003).
81. V. V. Srdic, M. Winterer, and H. Hahn, *J. Am. Ceram. Soc.* 83, 1853 (2000).
82. H. Ferkel and R. J. Hellmig, *Nanostruct. Mater.* 11, 617 (1999).
83. S. J. Wu, L. C. De Jonghe, and M. N. Rahaman, *J. Am. Ceram. Soc.* 79, 2207 (1996).
84. W. Zend, L. Gao, L. Gui, and J. Guo, *Ceram. Int.* 25, 723 (1999).
85. M. M. R. Boutz, L. Winnubst, A. J. Burggraaf, M. Nauer, and C. Carry, *J. Am. Ceram. Soc.* 78, 121 (1995).
86. A. J. Allen, S. Krueger, G. Skandan, G. G. Long, H. Hahn, H. M. Kerch, J. C. Parker, and M. N. Ali, *J. Am. Ceram. Soc.* 79, 1201 (1996).
87. J. Karch and R. Birringer, *Ceram. Int.* 16, 291 (1990).
88. H. Hahn and R. S. Averback, *J. Am. Ceram. Soc.* 74, 2918 (1991).
89. H. Hahn, J. Logas, and R. S. Averback, *J. Mater. Res.* 5, 609 (1990).
90. K. H. Ryu and J. M. Yang, *J. Mater. Res.* 13, 2588 (1998).
91. Y. L. Li, Y. Liang, F. Zheng, X. F. Ma, and S. J. Cui, *J. Mater. Res.* 15, 988 (2000).
92. J. Poth, R. Haberkorn, and H. P. Beck, *J. Eur. Ceram. Soc.* 20, 715 (2000).
93. P. Duran, F. Capel, J. Tartaj, and C. Moure, *J. Am. Ceram. Soc.* 84, 1661 (2001).
94. P. C. Panda, J. Wang, and R. Raj, *J. Am. Ceram. Soc.* 71, C-507 (1988).
95. L. Sangaletti, L. E. Depero, B. Allieri, F. Pioselli, R. Angelucci, A. Poggi, A. Tagliani, and S. Nocoletti, *J. Eur. Ceram. Soc.* 19, 2073 (1999).
96. L. Bergstrom, K. Shinozaki, H. Tomiyama, and N. Mizutani, *J. Am. Ceram. Soc.* 80, 291 (1997).
97. M. Rozman and M. Drogenik, *J. Am. Ceram. Soc.* 81, 1757 (1998).
98. O. Vasykiv and Y. Sakka, *J. Am. Ceram. Soc.* 84, 2489 (2001).
99. F. Bondioli, A. M. Ferrari, C. Leonelli, C. Siligardi, and G. C. Pellacani, *J. Am. Ceram. Soc.* 84, 2728 (2000).

100. K. R. Venkatachari, D. Huang, S. P. Ostrander, W. A. Schulze, and G. C. Stangle, *J. Mater. Res.* 10, 748 (1995).
101. S. D. Ramamurthi, Z. Xu, and D. A. Payne, *J. Am. Ceram. Soc.* 73, 2760 (1990).
102. M. Z. Hu, R. D. Hunt, E. A. Payzant, and C. R. Hubbard, *J. Am. Ceram. Soc.* 82, 2313 (1999).
103. B. Xia, L. Duan, and Y. Xie, *J. Am. Ceram. Soc.* 83, 1077 (2000).
104. U. Popp, R. Herbig, G. Michel, E. Muller, and C. Oestreich, *J. Eur. Ceram. Soc.* 18, 1153 (1998).
105. W. E. van Zyl, L. Winnubst, T. P. Raming, R. Schmuhl, and H. Verweij, *J. Mater. Chem.* 12, 708 (2002).
106. L. Gao, W. Li, H. Z. Wang, J. X. Zhou, Z. J. Chao, and Q. Z. Zai, *J. Eur. Ceram. Soc.* 21, 135 (2001).
107. A. Mukherjee, D. Harrison, and E. J. Podlaha, *Electrochem. Solid State Lett.* 4, D5 (2001).
108. F. Boulc'h, E. Djurado, L. Dessemond, and J. Fouletier, *J. Eur. Ceram. Soc.* 21, 1847 (2001).
109. O. Vasylykiv and Y. Sakka, *J. Ceram. Soc. Jap.* 109, 500 (2001).
110. O. Vasylykiv, Y. Sakka, and H. Borodians'ka, *J. Am. Ceram. Soc.* 84, 2484 (2001).
111. K. Moritz, R. Thauer, and E. Muller, *Ceram. Forum Int./Ber. DKG.* 77, E10 (2000).
112. O. L. Khasanov, E. S. Dvilis, and V. M. Sokolov, *Refract. Ind. Ceram.* 42, 37 (2001).
113. O. Vasylykiv and Y. Sakka, *J. Am. Ceram. Soc.* 83, 2196 (2000).
114. S. Maschio, B. Linda, S. Bruckner, and G. Pezzotti, *J. Ceram. Soc. Jap.* 108, 593 (2000).
115. D. G. Lamas and N. E. Walsoe de Reça, *J. Mater. Sci.* 35, 5563 (2000).
116. V. V. Srdic, M. Winterer, and H. Hahn, *J. Am. Ceram. Soc.* 83, 1853 (2000).
117. A. C. Dodd and P. G. McCormick, *J. Australas. Ceram. Soc.* 36, 15 (2000).
118. P. Duran, J. Tartaj, J. F. Fernandez, and C. Moure, *J. Mater. Res.* 14, 1686 (1999).
119. E. Djurado, E. Meunier, and M. Vaujany, "Third European Solid Oxide Fuel Cell Forum Proceedings," 1998, p. 81.
120. P. Duran, J. Tartaj, J. F. Fernandez, and C. Moure, *Mater. Lett.* 36, 174 (1998).
121. D. G. Lamas, G. E. Lascalea, and N. E. Walsoe de Reça, *J. Eur. Ceram. Soc.* 18, 1217 (1998).
122. H. Shan and Z. Zhang, *J. Eur. Ceram. Soc.* 17, 713 (1997).
123. J. C. Ray, A. B. Panda, C. R. Saha, and P. Pramanik, *J. Am. Ceram. Soc.* 86, 514 (2003).
124. A. Janbey, R. K. Pati, S. Tahir, and P. Pramanik, *J. Eur. Ceram. Soc.* 21, 2285 (2001).
125. N. G. Glumac, Y. J. Chen, G. Skandan, and B. Kear, *Mater. Lett.* 34, 148 (1998).
126. R. J. Hellmig, J. F. Castagnet, and H. Ferkel, *Nanostruct. Mater.* 12, 1041 (1999).
127. A. C. Sutorik, S. S. Neo, D. R. Treadwell, and R. M. Laine, *J. Am. Ceram. Soc.* 81, 1477 (1998).
128. W. Zeng, A. A. Rabelo, and R. Tomasi, "Advanced Powder Technology II. Proceedings of the 2nd International Latin-American Conference on Powder Technology," (1996), 168, 12.
129. J. M. Wu, *Mater. Lett.* 48, 324 (2001).
130. E. J. Gonzalez, G. White, and L. Wei, *J. Mater. Res.* 15, 744 (2000).
131. R. S. Mishra, S. H. Risbud, and A. K. Mukherjee, *J. Mater. Res.* 13, 86 (1998).
132. B. Zhang, J. Li, and J. Sun, *Mater. Lett.* 51, 219 (2001).
133. H. Martin, R. Ecke, and E. Muller, *J. Eur. Ceram. Soc.* 18, 1737 (1998).
134. S. Dong, D. Jiang, S. Tan, and J. Guo, *J. Mater. Sci. Lett.* 16, 1080 (1997).
135. X. Yang and Z. Ding, *J. Mater. Res.* 15, 2140 (2000).
136. Y. Chen, Y. Liang, F. Zheng, R. Zhou, and Z. Feng, *Ceram. Int.* 27, 73 (2001).
137. D. Bahloul-Hourlier, B. Doucey, E. Laborde, and P. Goursat, *J. Mater. Chem.* 11, 2028 (2001).
138. D. Liu, *Naihuo Cailiao* 35, 187 (2001).
139. R. Ren, Z. Yang, and L. L. Shaw, *Ceram. Eng. Sci. Proc.* 19, 461 (1998).
140. J. Zhang, Y. Hou, L. Gao, and F. Li, *J. Chin. Ceram. Soc.* 26, 762 (1998).
141. J. Gubicza, J. Szepevolgyi, I. Mohai, G. Ribarik, and T. Ungar, *J. Mater. Sci.* 35, 3711 (2000).
142. Y. L. Li, Y. Liang, F. Zheng, X-F. Ma, S-J. Cui, and L. Sun, *J. Mater. Res.* 16, 67 (2001).
143. J. Szepevolgyi and I. Mohai, *Ceram. Int.* 25, 717 (1999).
144. V. A. Hackley, *J. Am. Ceram. Soc.* 80, 2315 (1997).
145. A. Pechenik, G. J. Peirmarini, and S. C. Danforth, *Nanostruct. Mater.* 2, 479 (1993).
146. T. Wang, L. Zhang, and C. Mo, *Nanostruct. Mater.* 4, 207 (1994).
147. Y. Mroiyoishi and S. Futaki, Proceedings International Institute for the Science of Sintering Symposium, 1987, p. 992.
148. K. H. Ryu and J. M. Yang, *J. Mater. Res.* 13, 2580 (1998).
149. P. P. Ahonen, E. I. Kauppinen, J. C. Joubert, J. L. Deschanvres, and G. Van Tendeloo, *J. Mater. Res.* 14, 3938 (1999).
150. L. E. Depero, A. Marino, B. Allieri, E. Bontempi, L. Sangaletti, C. Casale, and M. Notaro, *J. Mater. Res.* 15, 2080 (2000).
151. J. Yang, S. Mei, and J. M. F. Ferreira, *J. Am. Ceram. Soc.* 84, 1696 (2001).
152. S. Mayadevi, S. S. Kulkarni, A. J. Patil, M. H. Shinde, H. S. Potdar, S. B. Deshpande, and S. K. Date, *J. Mater. Sci.* 35, 3943 (2000).
153. Y. Zhu, L. Zhang, C. Gao, and L. Cao, *J. Mater. Sci.* 35, 4049 (2000).
154. Y. Nakagawa, C. Grigoriu, K. Masugata, W. Jiang, and K. Yatsui, *J. Mater. Sci.* 33, 529 (1998).
155. Y-H. Zhang, C. K. Chan, J. F. Porter, and W. Guo, *J. Mater. Res.* 13, 2602 (1998).
156. K. R. Lee, S. J. Kim, J. S. Song, J. H. Lee, Y. J. Chung, and S. Park, *J. Am. Ceram. Soc.* 85, 341 (2002).
157. S. C. Liao, J. Colaizzi, Y. Chen, B. H. Kear, and W. E. Mayo, *J. Am. Ceram. Soc.* 83, 2163 (2000).
158. Q. Zhang, L. Gao, and J. Guo, *J. Eur. Ceram. Soc.* 20, 2153 (2000).
159. B. Xia, W. Li, B. Zhang, and Y. Xie, *J. Mater. Sci.* 34, 3505 (1999).
160. P. D. Moran, J. R. Bartlett, G. A. Bowmaker, J. L. Woolfrey, and R. P. Cooney, *J. Sol-Gel Sci. Technol.* 15, 251 (1999).
161. L. E. Depero, L. Sangaletti, B. Allieri, E. Bontempi, R. Salari, M. Zocchi, C. Casale, and M. Notaro, *J. Mater. Res.* 13, 1644 (1998).
162. Z. Zhong and P. K. Gallagher, *J. Mater. Res.* 10, 945 (1995).
163. J. Xue, J. Wang, and D. Wan, *J. Am. Ceram. Soc.* 83, 232 (2000).
164. P. Duran, F. Capel, J. Tartaj, and C. Moure, *J. Mater. Res.* 16, 197 (2001).
165. W. Luan and L. Gao, *Ceram. Int.* 27, 645 (2001).
166. D. Chen and X. Jiao, *J. Am. Ceram. Soc.* 83, 2637 (2000).
167. H. P. Beck, W. P. Eiser, and R. Haberkorn, *J. Eur. Ceram. Soc.* 21, 687 (2001).
168. H. J. Glasel, E. Hartmann, D. Hirsch, R. Bottcher, C. Klimm, D. Michel, H. C. Semmelhack, J. Hormes, and H. Rumpf, *J. Mater. Sci.* 34, 2319 (1999).
169. L. Bergstrom, K. Shinozaki, H. Tomiyama, and N. Mizutani, *J. Am. Ceram. Soc.* 80, 291 (1997).
170. D. Chen, X. Jiao, and M. Zhang, *J. Eur. Ceram. Soc.* 20, 1261 (2000).
171. J. Poth, R. Haberkorn, and H. P. Beck, *J. Eur. Ceram. Soc.* 20, 707 (2000).
172. S. Zhang, Y. Han, B. Chen, and X. Song, *Mater. Lett.* 51, 368 (2001).
173. J. Xue, D. Wan, and J. Wang, *Mater. Lett.* 39, 364 (1999).
174. L. B. Kong, W. Zhu, and O. K. Tan, *J. Mater. Sci. Lett.* 19, 1963 (2000).

175. Z. Surowiak, M. F. Kupriyanov, and D. Czekaj, *J. Eur. Ceram. Soc.* 21, 1377 (2001).
176. L. B. Kong, J. Ma, W. Zhu, and O. K. Tan, *J. Mater. Sci. Lett.* 21, 25 (2001).
177. D. Liu, W. Cai, H. Zhang, X. Wu, and L. Zhao, *J. Chin. Ceram. Soc.* 26, 313 (1998).
178. H. Xu and L. Gao, *J. Am. Ceram. Soc.* 86, 203 (2003).
179. G. M. Argentina and P. D. Baba, *IEEE Trans. Microwave Theory Tech.* 22, 652 (1974).
180. J. W. Lee, Y. S. Cho, and V. R. W. Amarakoon, *J. Appl. Phys.* 85, 5696 (1999).
181. Y. S. Cho, V. L. Burdick, and V. R. W. Amarakoon, *J. Am. Ceram. Soc.* 82, 1416 (1999).
182. T. Y. Tseng and S. Y. Jou, *J. Mater. Sci. Lett.* 8, 777 (1989).
183. M. Rozman and M. Drogenik, *J. Am. Ceram. Soc.* 78, 2449 (1995).
184. M. Seki, T. Sato, and S. Usui, *J. Appl. Phys.* 63, 1424 (1988).
185. H. H. Hamdeh, R. J. Wiley, J. Kramer, Y. Y. Chen, S. H. Lin, Y. D. Yao, M. Daturi, and G. Busca, *IEEE Transaction Magn.* 31, 3808 (1995).
186. T. Y. Seng and J. C. Lin, *J. Mater. Sci. Lett.* 8, 261 (1989).
187. R. V. Mangalaraja, S. Ananthakumar, P. Manohar, and F. D. Gnanam, *Mater. Lett.* 57, 2666 (2003).
188. T. K. Kundu and D. Chakravorty, *J. Mater. Res.* 14, 3957 (1999).
189. Y. S. Cho, V. L. Burdick, and V. R. W. Amarakoon, *IEEE Transactions Magn.* 34, 1387 (1998).
190. S. Harrington, D. M. Zhu, A. Thirunavukkarasu, and A. Misra, *J. Mater. Sci.* 34, 2075 (1999).
191. W. Cai, Y. Zhang, and L. Zhang, *J. Mater. Res.* 14, 1922 (1999).
192. M. Hirano, Y. Fukuda, H. Iwata, Y. Hotta, and M. Inagaki, *J. Am. Ceram. Soc.* 83, 1287 (2000).
193. T. Tsuzuki and P. G. McCormick, *J. Am. Ceram. Soc.* 84, 1453 (2001).
194. S. Zha, Q. Fu, Y. Lang, C. Xia, and G. Meng, *Mater. Lett.* 47, 351 (2001).
195. B. Djuricic and S. Pickering, *J. Eur. Ceram. Soc.* 19, 1925 (1999).
196. S. Roy, W. Sigmund, and F. Aldinger, *J. Mater. Res.* 14, 1524 (1999).
197. S. Polizzi, G. Fagherazzi, M. Battagliarin, M. Bettinelli, and A. Speghini, *J. Mater. Res.* 16, 146 (2001).
198. G. Fagherazzi, S. Polizzi, M. Bettinelli, and A. Speghini, *J. Mater. Res.* 15, 586 (2000).
199. P. K. Sharma, M. H. Jilavi, R. Nass, and H. Schmidt, *J. Mater. Sci. Lett.* 17, 823 (1998).
200. G. Zhang and M. Liu, *J. Mater. Sci.* 34, 3213 (1999).
201. J. Cerda, A. Cirera, A. Vila, R. Diaz, A. Cornet, and J. R. Morante, *Bol. Soc. Esp. Ceram. Vidrio.* 39, 560 (2000).
202. K. C. Song and Y. Kang, *Mater. Lett.* 42, 283 (2000).
203. L. Sangaletti, L. E. Depero, B. Allieri, F. Pioselli, R. Angelucci, A. Poggi, A. Tagliani, and S. Nicoletti, *J. Eur. Ceram. Soc.* 19, 2073 (1999).
204. Y. Lin, Z. Tang, Z. Zhang, F. Yuan, Y. Ling, J. Lee, and S. Huang, *J. Am. Ceram. Soc.* 83, 2869 (2000).
205. P. Duran, F. Capel, J. Tartaj, and C. Moure, *J. Am. Ceram. Soc.* 84, 1661 (2001).
206. A. C. Da Cruz, R. J. Munz, and H. Vali, *J. Mater. Sci. Lett.* 17, 1255 (1998).
207. R. K. Kalyanaraman, S. H. Yoo, M. S. Krupashankara, T. S. Sudarshan, and R. J. Dowding, *Powder Metall.* 43, 380 (2000).
208. Y. Kinemuchi, K. Murai, C. Sangurai, C. Cho, H. Suematsu, W. Jiang, and K. Yatsui, *J. Am. Ceram. Soc.* 86, 420 (2003).
209. J. Li, L. Gao, J. Sun, Q. Zhang, J. Guo, and D. Yan, *J. Am. Ceram. Soc.* 84, 3045 (2001).
210. J. Hu, Q. Lu, K. Tang, S. Yu, Y. Qian, G. Zhou, and X. Liu, *J. Am. Ceram. Soc.* 83, 430 (2000).
211. N. J. Welham and D. J. Llewellyn, *J. Eur. Ceram. Soc.*, 19, 2833 (1999).
212. J. Wang, J. Xue, D. Wan, and W. Ng, *J. Am. Ceram. Soc.* 82, 1358 (1999).
213. L. B. Kong, J. Ma, W. Zhu, and O. K. Tan, *J. Mater. Sci. Lett.* 20, 1241 (2001).
214. L. A. Stanciu, J. R. Groza, V. Y. Kodash, M. Crisan, and M. Zaharescu, *J. Am. Ceram. Soc.* 84, 983 (2001).
215. A. M. Segadaes, M. R. Morelli, and R. G. A. Kiminami, *J. Eur. Ceram. Soc.* 18, 771 (1998).
216. Y. M. Hon, S. P. Lin, K. Z. Fung, and M. H. Hon, *J. Eur. Ceram. Soc.* 22, 653 (2002).
217. S. J. Lee and W. M. Kriven, *J. Am. Ceram. Soc.* 81, 2605 (1998).
218. S. Choudhury, A. S. Gandhi, and V. Jayaram, *J. Am. Ceram. Soc.* 86, 247 (2003).

Charge Carrier Dynamics in Nanoparticles

Christian D. Grant, Thaddeus J. Norman, Jr., Jin Z. Zhang

University of California, Santa Cruz, California, USA

CONTENTS

1. Introduction
 2. Charge Carrier Dynamics in Semiconductor Nanoparticles
 3. Charge Carrier Dynamics in Metal Nanoparticles
 4. Conclusion
- Glossary
References

1. INTRODUCTION

Nanoparticles (NPs) have properties that differ from their bulk or atomic counterparts in many different ways. Typically, their equilibrium as well as dynamic properties, such as electronic and optical characteristics and charge carrier recombination rates, vary as a function of size, surface, and shape. For example, spatial confinement and reduced dimensionality often lead to changes in the density of states (DOS) for both electrons and phonons that affect their optical spectroscopy and rates and mechanisms of electron-hole relaxation. Relatively speaking, equilibrium or static properties of nanomaterials have been better studied and understood when compared to dynamic properties. Understanding dynamic characteristics can provide complementary information to static properties that may or may not be studied easily using static experimental techniques.

One way to directly probe the charge carrier dynamics (e.g., rates and mechanisms of electron-hole recombination or relaxation) in nanomaterials is to use time resolved laser spectroscopic techniques, since many of the dynamic processes occur on ultrafast time scales. Direct ultrafast studies of charge carrier dynamics in nanoparticles have emerged as an active area of research in nanoscience in the last decade. These studies have helped gain important fundamental insight into charge carrier properties. For instance, electronic relaxation dynamics sensitively reflects interaction of electrons with phonons, surfaces, and other charge carriers, as well as interparticle interaction. The objective of this chapter is to review some recent advances in the studies of charge carrier dynamics in both semiconductor and

metal nanomaterials with examples derived from research from our own lab and others. The first part of this chapter will deal with charge carrier dynamics in semiconductor nanoparticles while the second part of the chapter will cover electronic relaxation in metal nanoparticles.

2. CHARGE CARRIER DYNAMICS IN SEMICONDUCTOR NANOPARTICLES

2.1. Charge Carrier Relaxation and Trapping

Above bandgap photoexcitation of a semiconductor creates an electron in the conduction band (CB) and a hole in the valence band (VB). This process is analogous to a highest occupied molecular orbital to lowest unoccupied molecular orbital transition upon light absorption in molecules. This light absorption in the semiconductor particle creates a nonequilibrium situation. To return to equilibrium, the photogenerated carriers have a myriad of pathways, as illustrated in Figure 1. The simplest is radiative electron-hole recombination, releasing a photon. With above bandgap excitation, the electron and hole usually lose some of their initially acquired energy before they recombine. The electron and hole typically relax energetically to the bottom of the CB and to the top of the VB respectively. Hence, the emitted photon has a lower energy (or is redshifted) than that of the incident photon. For single crystal semiconductors, radiative electron-hole recombination is the dominant mechanism of relaxation and thus the material is highly fluorescent, with quantum yields typically >50%.

If impurities or defects are present in the crystal, new additional electronic states can be introduced within the bandgap and can act to trap the charge carriers. Trapping, then, becomes a major pathway for semiconductors with a high density of trap states.

If surface effects are ignored for the moment, and to first order perturbation, the rate of carrier relaxation (τ) through the emission of phonons is given by Fermi's golden rule [1],

$$\frac{1}{\tau} = \sum_q |\langle f|W|i\rangle|^2 \delta(E_f - E_i + \hbar\omega_q)(n_B(\hbar\omega_q, T) + 1) \quad (1)$$

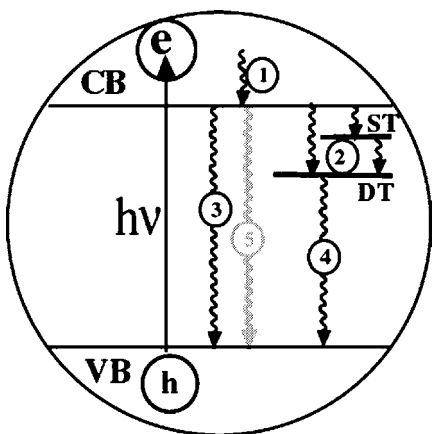


Figure 1. Schematic illustration of photoexcitation and photoluminescence. The curved lines with downward arrows indicate different relaxation processes: (1) electronic relaxation within the conduction band (CB), (2) trapping into shallow trap (ST) and deep trap (DT) states as well as further trapping from ST to DT, (3) bandedge electron-hole recombination, (4) trapped electron-hole recombination, and (5) exciton-exciton annihilation.

where $|i\rangle$ and $|f\rangle$ stand for the initial and final states of the exciton, respectively, \mathbf{q} is the wave vector of the emitted phonons, $\hbar\omega$ is the phonon energy, and n_B represents the Bose-Einstein distribution of phonons in the crystal lattice at temperature T ($n_B = 0$ when $T = 0$). The electron-phonon coupling operator, W , is characteristic of the semiconductor and depends on the relevant phonon frequencies and electronic band structure. Changes in phonon distribution and/or frequency or size dependent changes in the electron-phonon coupling will, therefore, affect the carrier relaxation time according to Eq. (1). Theoretical investigations of III-V semiconductor quantum dots indicate that the electron-phonon scattering rates decrease strongly with increasing spatial quantization [2].

The nature of the surface is an important factor that influences the relaxation. However, this is much more difficult to quantify at the first principles level. Qualitatively, the surface phonon frequencies and distributions are expected to change relative to bulk. This will affect the overall electron-phonon interaction [W in Eq. (1)] and thereby the relaxation time. In addition, the surface introduces a high density of electronic surface trap states within the bandgap that will act to trap the charge carriers. This often significantly shortens the carrier lifetime and is usually the dominant pathway of relaxation. Trapped carriers can then further relax radiatively or nonradiatively. Trapped electrons and holes significantly influence the nanoparticle optical properties and chemical reactivities. The trapping time scale is typically on the order of a few hundreds of fs to tens of ps, depending on the nature of the nanoparticles. Typically, a higher density of trap states leads to faster trapping. The energy difference between the trap states and the location of the bandedge (bottom of the CB for the electron and top of the VB for the hole) also affects the trapping time. The smaller the energy difference, the faster the trapping expected, provided that other factors are similar or the same.

Various trapping time constants have been measured for various semiconductor nanoparticles. Using transient

absorption techniques trapping times for CdS NPs of ~ 100 fs have been suggested [3, 4]. However, longer trapping times of 0.5–8 and 30 ps were yielded for CdSe [5] and CdS [6, 7] NPs using time resolved photon-echo and trap state emission experiments respectively. Another study reported a similar 30 ps electron trapping time for CdS based on the effects of adsorption of viologen derivatives on the nanoparticle surface [8]. A time resolved photoluminescence measurement on CdS reported a hole trapping time of 1 ps [6]. Sample differences or different data interpretations may be the reason for the discrepancies in the reported trapping times. However, it is not unreasonable to conclude that trapping time scales for electrons and holes occur on the subpicosecond (a few hundred fs) to tens of picoseconds time scales depending on the nature of the NP or quality of the sample. It should be noted that trapping times from bandedge to shallow traps or from shallow traps to deep traps might differ as well.

Recombination can be either radiative or nonradiative and can occur before or after electrons or holes have been trapped. Since the density of trap states is very large in nanoparticles, recombination usually takes place after trapping. Also due to the high density of traps in NPs, nonradiative recombination tends to be the dominant mechanism. A number of examples will be discussed next to illustrate the similarities and differences between different nanoparticle systems in terms of their electronic relaxation dynamics.

2.2. Metal Oxide Nanoparticles

Electronic relaxation dynamics have been studied for several metal oxide nanoparticle systems, for example, TiO_2 , ZnO , and Fe_2O_3 . For TiO_2 NPs with excitation at 310 nm, the photoinduced electrons were found to decay following second-order kinetics with a recombination rate constant of $1.8 \times 10^{-10} \text{ cm}^3 \text{ s}^{-1}$ [9]. The electron trapping was suggested to occur on the time scale of 180 fs [4]. Similar studies have been done on ZnO NPs for which the photoinduced electron decay was also found to follow second-order kinetics with 310 nm excitation [10]. It was also found that the initial electron trapping and subsequent recombination dynamics were size dependent. The trapping rate was found to increase with increasing particle size, which was explained with a trap-to-trap hopping mechanism. The electron-hole recombination is faster and occurs to a greater extent in larger particles because there are two different types of trap states. However, a different explanation, based on exciton-exciton annihilation upon trap state saturation, has been proposed for similar excitation intensity dependent and size dependent relaxation observed in CdS and CdSe NPs [11]. This explanation would also seem to be consistent with the results observed for TiO_2 [9] and ZnO [10].

A femtosecond electronic relaxation dynamics study was conducted for both γ and α phased Fe_2O_3 nanoparticles with 390 nm excitation [12]. The dynamics were found to be similar between the two types of particles, despite differences in both their magnetic properties and particle shape. γ -phased Fe_2O_3 is mostly spherical and paramagnetic, while the α -phase is spindlelike and diamagnetic [12]. The relaxation featured a multiexponential decay with time constants

of 0.36, 4.2, and 67 ps. The overall fast relaxation, in conjunction with very weak emission, indicates highly efficient nonradiative decay processes, most probably related to the intrinsic dense band structure or a large density of trap states. The fast relaxation of the photoinduced electrons is consistent with the low photocurrent efficiency of Fe_2O_3 electrodes. The short lifetime due to rapid electron–hole recombination does not favor charge transport that is necessary for photocurrent generation [12].

2.3. Metal Chalcogenide Nanoparticles

CdS is among the most extensively studied semiconductor nanoparticle systems. Earlier dynamics studies on the picosecond time scale identified a strong transient bleach feature near the excitonic absorption region of the spectrum [13–19]. It was observed that the peak of the bleach feature shifts with time. One explanation proposed was increased screening by charge carriers for the particles [20]. In addition, there was a redshift of the transient absorption features in CdSe, which was explained by some as a result of formation of biexcitons [21, 22]. Later, femtosecond measurements were carried out and a power dependence of the bleach recovery time was found for CdS [23]. The bleach recovery follows a double exponential rise with the fast component increasing with power faster than the slower component.

Work based on transient absorption measurements of CdS found a similar power dependence of the electronic relaxation dynamics featuring a double exponential decay behavior with a fast (2–3 ps) and slow (50 ps) component [3, 11, 24]. The amplitude of the fast decay component increases with excitation intensity faster than that of the slow component. The short component grows nonlinearly (Fig. 2), slightly subquadratically, with excitation intensity.

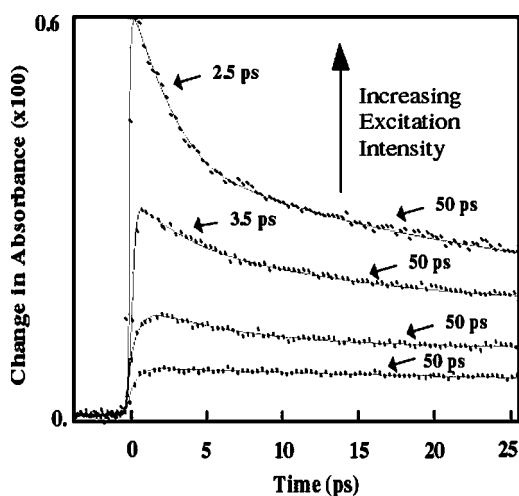


Figure 2. Excitation intensity dependence of CdS NPs photoinduced electronic relaxation dynamics probed at 780 nm following 390 nm excitation pulse. The 2.5–3.5 ps fast decay component increases nonlinearly with excitation intensity and is absent at low intensity. Reprinted with permission from [3], J. Z. Zhang et al., *J. Phys. Chem.* 98, 3859 (1994). © 1994, American Chemical Society.

This nonlinear fast decay was first attributed to nongeminate electron–hole recombination at high excitation intensities [3]. Subsequent studies using femtosecond transient absorption in conjunction with nanosecond time resolved fluorescence found that the bandedge fluorescence was also power dependent [11]. These results led to the proposal that the fast decay is due to exciton–exciton annihilation upon trap state saturation, as suggested previously [25], and the slow decay is due to trapped charge carrier recombination [11]. Therefore, the transient absorption signal observed has contributions from both bandedge electrons and trapped electrons. At early times, the bandedge electrons contribute significantly to the signal, especially when trap states are saturated at high excitation intensities, while as time progresses the contribution from trapped electrons becomes more dominant. On long time scales (hundreds of picoseconds to nanoseconds), the signal is essentially all from trapped charge carriers. It was believed that this is true of many other colloidal semiconductor nanoparticles [12, 26–29]. A more recent study of the emission lifetime of surface passivated and unpassivated CdS nanoparticles on the nanosecond time scale showed that the passivated sample with a lower density of surface trap states has a lower excitation threshold for observing exciton–exciton annihilation compared to the unpassivated sample [30]. This supports the model of exciton–exciton annihilation upon trap state saturation at high excitation intensities [11].

The charge carrier dynamics in CdSe nanocrystals ranging in size from 2.7 to 7 nm have recently been determined using femtosecond fluorescence upconversion spectroscopy [31]. It has been found that both the rise time and decay of the bandedge emission show a direct correlation to the particle size and the rise time depends on excitation intensity. The long lifetime of the bandedge emission was suggested to originate from a triplet state. The deep trap emission that appears within 2 ps was attributed to relaxation of a surface selenium dangling bond electron to the VB where it recombines radiatively with the initial photogenerated hole. This is also believed to be responsible for the large amplitude, fast (2–6 ps) decay of the bandedge emission. This work seems to indicate that the hole trapping is slower compared to electron trapping. Recent work by Burda et al. and Guyot-Sionnest et al. supports the assertion that hole trapping is slower than electron trapping [32–34].

CdTe has been widely used in optoelectronic devices [e.g., infrared (IR) detectors, solar energy conversion, and light-emitting devices]. In comparison to CdS and CdSe, CdTe has a smaller bandgap (~ 1.5 eV) and a larger exciton Bohr radius (~ 7.3 nm). Studies on CdTe nanoparticles have been limited due to its high susceptibility to tellurium anion oxidation. Recently, the ultrafast charge carrier dynamics have been measured in CdTe nanocrystals using femtosecond laser spectroscopy [35]. The charge carrier relaxation showed a fast decay (3.37 ps) that is strongly dependent on excitation intensity, followed by a slow decay (~ 230 ps) plus an offset of >600 ps. The offset and slow decay are assigned to surface or solvent trapped electron–hole recombination while the intensity dependent short decay is assigned to exciton–exciton annihilation (as discussed previously) or photoionization/Auger recombination.

Another recent study on thiol-capped CdTe showed an unusual power dependence of photoluminescence using nanosecond laser spectroscopy [36]. At high excitation intensities the photoluminescence of CdTe NPs showed an unexpected decrease in emission. Two possible mechanisms were proposed. Photoionization may be occurring during the nanosecond pulse (7 ns duration) that subjects the particles to a stronger repulsive Coulombic force than in the neutral particles. This has the effect of enhancing the Auger effect in the ionized particles. Electron-hole recombination then proceeds by mostly nonradiative pathways leading to the decrease in fluorescence. Alternatively, exciton-exciton annihilation, similar to the CdS case discussed previously, may be the reason for the abnormal excitation intensity dependence. Immediately after excitation, "hot" electrons quickly relax to the bottom of the CB. These bandedge electrons can then relax further by radiative or nonradiative pathways. At high excitation intensities, bandedge electrons can decay through nonradiative pathways such as exciton-exciton annihilation. This nonlinear process becomes increasingly dominant with increasing excitation intensity that in turn causes the unusual decrease in emission.

In comparison to bulk materials, nonlinear properties of nanomaterials are expected to be influenced by two major competing factors: quantum spatial confinement and surface effects. Quantum mechanical confinement, on the one hand, should lead to a lower threshold for nonlinear properties in nanomaterials due to, for example, more efficient exciton-exciton annihilation when compared to bulk materials. In contrast, fast and efficient trapping in nanoparticles due to a high density of trap states should increase the threshold for nonlinear processes. Hence, the higher the density of trap states, the higher the threshold for observing nonlinear properties, as exemplified in the study of passivated and unpassivated CdS samples [30]. Even though quantitative comparisons of nanomaterials and their corresponding bulk counterparts have not been made systematically in terms of nonlinear threshold, it is most likely that the surface effect is dominant in most systems due to the intrinsic high density of surface trap states in nanomaterials. If this conjecture is correct, nanomaterials will have a higher threshold for observing nonlinear properties. This can have important applications in areas such as radiation protection. Nanomaterials would be better than their corresponding bulk counterparts in absorbing high density radiation due to their higher threshold for nonlinearity or saturation.

PbTe nanoparticles of 1.5–3 nm embedded in a glass matrix revealed an interesting oscillatory behavior [37]. The oscillations in the femtosecond transient absorption experiment were assigned to coherent excitation of acoustic phonons similar to the case of PbS [38]. It was found that the oscillations had a damping time of 2.1 ps and a frequency of ~ 0.51 THz at a probe wavelength of 1.5 μm . A longer decay of 175 ps was also present along with an offset and was attributed to radiative/nonradiative recombination and long-lived thermal effects. A probe wavelength dependence (1.4–1.6 μm) of the frequency of oscillation indicated size selectivity since the absorption band is inhomogeneously broadened due to polydispersity in the sample. In addition, it was suggested that the damping mechanism was due to

energy loss to the surrounding medium, which is in contrast to colloidal gold nanoparticles where the damping mechanism of the oscillations was attributed to the polydispersity of the colloid [39]. Oscillations in metal nanoparticles will be discussed in more detail below.

Other metal sulfide nanoparticles such as Cu_xS ($x = 1$ or 2) and Ag_2S have also been studied in terms of their charge carrier dynamics. In the dynamics studies of CuS and Cu_2S [40], a dominant fast decay component followed by a slower decay observed for Cu_2S nanoparticles was found to be independent of excitation intensity, probe wavelength, and capping agent. The fast decay (1.1 ps) was assigned to charge carrier trapping at shallow trap sites, while the long decay (80 ps) component was assigned primarily to deep trapping. An interesting power dependence of the dynamics was observed for CuS. Low excitation intensities yielded a transient bleach at first due to ground state absorption followed by a fast recovery (430 fs) due to carrier trapping to shallow traps followed by a long time offset. The long time offset was attributed to relaxation from shallow to deep traps and further relaxation of charge carriers from deep traps. High excitation intensities, however, yielded only a transient absorption signal with a 1.1 ps decay and a slow rise with a lifetime >1 ns. The power dependence of the crystalline CuS could be attributed to trap state saturation [40]. A kinetic model developed to simulate the data for both Cu_2S and CuS led to the proposal of an alternative explanation for a middle-gap state. This was suggested to be either an electron-acceptor or unoccupied state, and the IR absorption band corresponds to a transition from the valance band to this state [40]. Cystine and glutathione capped Ag_2S NPs also displayed an interesting excitation dependence. The dynamics signal contains contributions from both transient absorption as well as transient bleach. At increasing excitation intensity, the transient absorption signal becomes more dominant over the bleach. A kinetic model developed suggested that the difference in dynamics observed between samples is due to different absorption cross sections of deep trap states. Similar to CuS NPs, the observed excitation intensity dependence is attributed to shallow trap state saturation at high intensities [41].

Au_2S is another metal chalcogenide nanoparticle system that has been synthesized and studied via femtosecond transient absorption spectroscopy [42, 43]. Au_2S has been used in photographic sensitization and suggested as a potential ion conductor [44–47]. The electronic relaxation dynamics have been measured with 390 nm excitation and probing at 790 and 850 nm. The transient decay profiles can be fit to a double exponential with time constants of 600 fs and 23 ps. The fast decay can be assigned to trapping of electrons from the conduction band to shallow trap states or from shallow traps to deep traps, while the long decay is assigned to recombination from shallow or deep trap states. Unlike Ag_2S [41] CuS [40], and CdS [11] already discussed, there is no power dependence indicating no trap state saturation and hence the overall fast relaxation can be attributed to a high density of intrinsic or surface trap states. In addition, this fast decay is nonradiative and consistent with a lack of observable luminescence at room temperature. EXAFS measurements were also performed and showed a 20% decrease in the first coordination shell for

nanoparticles relative to bulk, which supports a large number of surface dangling bonds that can contribute to a high density of surface trap states.

2.4. Effect of Nanoparticle Shape on Dynamics

A few studies have been made to study the shape dependence of electronic relaxation in semiconductor nanocrystals. In spherical particles, the bandgap increases as size decreases. However, as particles deviate from a spherical geometry (e.g., CdSe nanorods), it was found that the bandgap depends mainly on the width and, to a lesser degree, on the length of the rods [48]. Deviation from spherical geometry causes splitting of degenerate energy levels due to the lowering of particle symmetry. This effect may have potential consequences for electron–hole relaxation.

Electronic relaxation in CdSe nanorods has been found to be quite different from spherical CdSe particles [49]. Electron–hole kinetics for both CdSe nanodots and nanorods were monitored over the wavelength range of 480–585 nm using 400 nm excitation. In the wavelength range studied, the decay times for the nanorods increased as the energy decreased with ~ 300 fs for the 480–515 nm range, a few ps in the 530–575 nm range, and 50 ps for the bandgap state. The long decay for the bandgap state may be attributed to less effective surface trapping in the rods as will be discussed. This is in contrast to the nanodots that displayed a shorter lifetime in the bandgap state (2 and 36 ps) but longer, 2 ps, in the higher energy range (480–515 nm) than the nanorods. The fast carrier dynamics of the rods in the 480–515 nm region was explained by taking into consideration energy level splitting due to particle geometry. As the particles deviate from spherical geometry the energy states associated with the particles split [50, 51]. CdSe nanorods display more absorption bands in the early time bleach spectra than the corresponding nanodots due to the predicted splitting of the degenerate states in the dots. This is agreement with theoretical calculations [49–51]. Higher exciton states, introduced due to the splitting of degenerate states, are populated initially in the nanorods that then decay to lower lying states. Furthermore, nanoparticle geometry seems to play an important role in the formation of defects since surface states depend strongly on the surface curvature or strain. Along the long axis of the rods, charge carrier motion is relatively “free” leading to less effective trapping and thus a long lived bandgap state.

For PbS nanoparticles, attempts have been made to study the surface and shape dependence of electronic relaxation in differently shaped PbS NPs. In contrast to the CdSe nanorod case, when PbS particle shapes are changed from mostly spherical to needle and cube shaped by changing the surface capping polymers, the electronic relaxation dynamics remain about the same for the apparently differently shaped particles [27]. For all cases studied, the electronic relaxation was found to feature a double exponential decay with time constants of 1.2 and 45 ps that are independent of probe wavelength and excitation intensity. The shape independence was attributed to the dominance of the surface effects on the electronic relaxation. While the shapes are different, the different samples may have similar surface properties (e.g.,

high density of trap states). Therefore, if the dynamics are dominated by the surface, change in shape may not affect the electronic relaxation dynamics substantially.

2.5. Doped Nanoparticles

The dynamic properties of doped semiconductor nanoparticles are complex and intriguing, though most experimental results suggest that their optical properties are not significantly different from the corresponding bulk material. The most extensively studied doped nanoparticle system is Mn^{2+} doped ZnS. It was first reported by Bhargava et al. that the Mn emission lifetime in ZnS:Mn was on the ns time scale, significantly shorter than that of bulk [52–54]. They observed a double exponential decay with time constants of 3 and 20 ns. The bulk Mn^{2+} lifetime in ZnS:Mn is 1.8 ms, which is five times slower than in the corresponding nanoparticles. It was proposed that stronger coupling exists between donor (ZnS) and acceptor (Mn^{2+}) due to rehybridization, induced by quantum confinement, of the *s*–*p* conduction band in ZnS and the *3d* states in Mn^{2+} that enhances rapid energy transfer and hence fast radiative decay. A similar explanation was proposed for Mn^{2+} doped two-dimensional (2D) quantum well structures [55].

However, recent work has found that the Mn^{2+} emission lifetime in nanoparticles is essentially the same as that in bulk (1.8 ms). Bol and Meijerink observed nanosecond decay rates for the ZnS host lattice emission but for the Mn^{2+} emission a normal 1.9 ms decay time along with a small amplitude nanosecond decay was measured [56]. Furthermore, in their system the 420 nm host lattice emission band was observed to have a tail that extended into the orange Mn^{2+} region and could be observed with a 2 μs gate. Given this they stated that the fast nanosecond decay was due to ZnS trap state emission and not the Mn^{2+} emission. Unfortunately, the apparatus used in their experiment had limited time resolution. A subsequent study by Murase et al. [57] also suggested that the Mn^{2+} luminescence lifetime in ZnS: Mn^{2+} nanoparticles was similar to that of bulk.

Smith et al. [58] synthesized Mn^{2+} doped ZnS nanoparticles using reverse micelles and measured the emission kinetics on the picosecond, nanosecond, microsecond, and millisecond timescales with adequate time resolution in each time scale. The samples display Mn^{2+} emission in addition to some weak trap state emission from ZnS in the 585 nm region, and the Mn^{2+} emission lifetime in these ZnS nanoparticles is 1.8 ms, very similar to that of bulk. Faster nanosecond and microsecond decays are observed for both doped and undoped particles and attributed to ZnS trap state emission. The main difference between doped and undoped samples is on the millisecond time scales. These conclusions are consistent with those of Bol and Meijerink.

Similar conclusions have been reached in a more recent report by Chung et al. [59], who have further suggested that surface bound Mn^{2+} and lattice bound Mn^{2+} have different emission lifetimes, 0.18 and 2 ms, respectively. The particles were made via standard colloidal methods. An undoped sample was also prepared for reference. The transient absorption decay profile for the undoped sample had a 20 ns component, while the doped sample had no decay on the observed nanosecond time scale. This further confirms

the assignment of the 20 ns emission component observed by Bhargava et al. [52], Bol et al. [56], and Smith et al. [58] to ZnS trap state emission. The doped sample possessed a 700 ps rise component, which is attributed to energy transfer from the ZnS excited state to the $\text{Mn}^{2+} \ ^4T_1$ excited state.

The dynamics of Mn^{2+} doped ZnSe nanoparticles have also been studied [60]. The emission lifetime was on the order of 290 μs , which is an order of magnitude smaller than that of the corresponding lattice bound Mn^{2+} in ZnS. This shortened lifetime has been attributed to stronger spin-orbit coupling between the Mn^{2+} and Se^{2-} than Mn^{2+} and S^{2-} . The exchange interaction between Mn^{2+} centers in close proximity also has an effect on the luminescence lifetime. Higher Mn^{2+} concentrations have shorter lifetimes as a result of these interactions. It has been suggested that Mn^{2+} doping of ZnSe leads to faster electron-hole trapping in bulk and nanocrystalline material [60, 61]. Preliminary transient absorption measurements conducted by Norman et al. [62] support this assertion. They have found that the transient absorption decay profile of undoped ZnSe nanoparticles could be fit to a double exponential with lifetimes of 17 and 143 ps, while a Mn^{2+} doped ZnSe sample had shortened lifetimes of 1.7 and 33 ps.

Bol et al. [63] reported the luminescence lifetime of Pb^{2+} doped ZnS nanoparticles. Two excitation bands, red and white, were observed. The red band originated from 480 nm excitation, while the white band originated from 380 nm excitation. By measuring the temperature dependence of the lifetimes of the two bands the nature of the emission mechanism was determined. As the temperature increased from 4 to 50 K the emission lifetime for the red band decreased exponentially from 3 ms to 0.5 μs . This effect is the consequence of a charge transfer transition of Pb^{2+} on an interior Zn^{2+} lattice site. Above 40 K the white band emission lifetime displayed similar behavior except it possessed a double exponential decay whose components were of the same order of the red bands. Likewise the white band emission was also attributed to a charge transfer emission, but, because the emission peak shifted as a function of temperature, this emission band was assigned to that of Pb^{2+} at or near the surface or defect sites.

2.6. Layered Semiconductor Nanoparticles

Layered semiconductor nanoparticles are of importance due to potential use in photoelectronchemical cells because of high photostability [64]. They are also of interest due to their strong quantum confinement effect and weak electron-phonon coupling. However, only a few studies have been carried out on the dynamic properties of layered semiconductor nanoparticles. A picosecond transient absorption study of electronic relaxation in MoS_2 NPs has been reported [65] with the relaxation dominated by trap states. The relaxation from shallow trap states to deep traps is fast (40 ps) at room temperature. However, the relaxation slows down to 200 ps at 20 K. This is consistent with the suppression of nonradiative relaxation pathways at low temperatures, which should result in a longer lifetime of charge carriers. Recently, further studies have been performed on MoS_2 [66, 67]. The injection and trapping dynamics were compared between diethylthiocarbocyanine

iodide (DTDCI) sensitized MoS_2 and bare MoS_2 using a combination of time resolved emission and absorption spectroscopies [67]. Electron and hole trapping times were found to be 275 and 42 ps respectively in the unsensitized case. A hole injection time of 12 ps was found in DTDCI sensitized MoS_2 NPs. In addition, a decay constant of ~ 225 ps was observed and assigned to electron trapping and reverse electron transfer. By combining the 225 ps decay time in the sensitized case with the 275 ps decay in the unsensitized case, a reverse electron transfer time of 1.2 ns estimated. It was further found that following electron trapping to deep traps the reverse electron transfer to DTDCI is slow. The electron injection rate and subsequent back transfer may have implications for solar energy conversion in these layered systems.

One study of WS_2 particles using time resolved polarization emission spectroscopy found that electron trapping occurred on the time scale of ~ 300 – 500 ps while the hole trapping occurred more rapidly (~ 30 ps). It was also found that the hole traps were 3000 cm^{-1} above the valence band while the electron traps were only 270 cm^{-1} below the conduction band [68]. However, it was noted that the nature and depth of the trap states are sensitively dependent on nanocluster growth conditions and reagent quality. Another WS_2 nanoparticle study showed that trapping occurred on the 100 ps time scale and varied with trap state density, which is consistent with earlier work already presented. Synthetic conditions were found to dramatically control the density of trap states. For example, WS_2 particles synthesized in or extracted into acetonitrile showed little or no bandedge emission indicating a high density of trap states while those particles extracted or prepared in an octane phase had a lower trap state density and exhibited a long lived bandedge (~ 1.25 ns) emission [69].

Sengupta et al. have conducted a femtosecond study of charge carrier relaxation dynamics on the layered semiconductor PbI_2 nanoparticles and found the relaxation dominated by surface properties and independent of particle size in the size range (3–100 nm) studied [28]. The early time dynamics showed an interesting oscillation feature with a period varying with solvent (6 ps in acetonitrile and 1.6 ps in alcohol solvents). However, the period did not vary as a function of size. The origin of the oscillation is not clear and such features are rarely observed for colloidal semiconductor nanoparticles. In addition, the relaxation in aqueous PVA solution was found to be much faster than that observed in acetonitrile and alcohol. This was possibly due to aggregation of the nanoparticles as evidenced by a new absorption band in the electronic absorption spectrum and by transmission electron microscopy data [28].

Similar findings have been made for another layered semiconductor nanoparticle system, BiI_3 [70]. The electronic relaxation dynamics were found to be sensitive to solvent, yet insensitive to particle size. The relaxation was also independent of excitation intensity. Oscillations at early times were also observed, with periods changing with solvent (alcohol, 1.3 ps, and acetonitrile, 5 ps) but not with particle size, similar to those found in PbI_2 nanoparticles. The oscillation periods were slightly shorter with the overall relaxation somewhat faster than that in PbI_2 . However, the overall decay was much faster in aqueous PVA (9 ps) as

well as in inverse micelles (1.2 and 33 ps) with no oscillations observed. These results suggest that the surface plays a major role in the electronic relaxation process of BiI_3 nanoparticles, similar to PbI_2 nanoparticles. The independence on particle size implies that the relaxation is dominated by surface characteristics that do not vary significantly with size. In addition, the size is much larger than the exciton Bohr radius (0.61 nm for bulk BiI_3) [71] and thereby spatial confinement is not significant in affecting the relaxation process.

A similar study was conducted on another layered semiconductor, Bi_2S_3 [72], in order to test if the observed oscillation in PbI_2 and BiI_3 nanoparticles is unique only to iodide semiconductor particles. Most of the dynamic features observed in Bi_2S_3 are similar to those observed for PbI_2 and BiI_3 (e.g., solvent dependence and size independence). However, no oscillations were observed. One possibility is that the overall electronic relaxation is faster in Bi_2S_3 , which makes the observation of the oscillation difficult. On the other hand, the oscillation may simply be absent for Bi_2S_3 . If the latter is correct, the results may indicate that the oscillations observed for PbI_2 and BiI_3 are unique to layered, iodide semiconductor nanoparticles. Further study is clearly needed for a more complete explanation.

Recently, luminescent GaSe nanoparticles have been studied via transient emission and absorption spectroscopies by Chikan et al. [73–76]. After excitation by 400 nm light, a multicomponent emission decay was observed consisting of an 80 ps, 400 ps, and a 2.4 ns decay constant. A 270 cm^{-1} shift in the emission maximum was observed during the 80 ps decay and was assigned to a direct to indirect bandedge electron relaxation. The 400 ps decay exhibits a 170 cm^{-1} shift in the emission maximum. This decay was assigned to hole trapping to shallow traps. Finally, the 2.4 ns decay is assigned to further trapping of holes from shallow to deep traps. The assignments were made based on the energetics of bulk GaSe modified by large quantum confinement shifts found in the nanoparticles. Further studies of hole relaxation dynamics in GaSe via transient absorption spectroscopy and carrier quenching experiments were also carried out by Chikan et al. [75]. Following 387.5 nm excitation, a pulse width limited rise followed by a 20 ps rise was observed in the transient absorption with a subsequent decay of 400 ps and 2.4 ns similar to that of the transient emission studies discussed above [73, 76]. The lack of the 80 ps decay as well as the presence of the 400 ps and 2.4 ns decays indicate that the relaxation being probed is hole relaxation. The dynamics changed drastically when the known hole scavenger pyridine is added. The transient absorption is quenched confirming that the further relaxation on the longer time scale (400 ps and 2.4 ns) is due to hole relaxation. The 20 ps component wavelength maximum shifts over time to the blue as the relaxation proceeds indicating the presence of relaxed and unrelaxed hole intraband transition. This is on the same time scale, albeit faster, as electron relaxation in CdSe in the absence of the Auger mechanism.

2.7. Other Semiconductor Nanoparticles

The ultrafast charge carrier dynamics in AgI and core/shell structured AgI/Ag₂S and AgBr/Ag₂S NPs have been studied

[26]. The electronic relaxation of AgI was found to follow a double exponential decay with time constants of 2.5 ps and >0.5 ns, which are independent of excitation intensity at 390 nm. The fast decay was attributed to trapping and non-radiative electron–hole recombination dominated by a high density of trap states. The slow decay was assigned to reaction of deep trapped electrons with silver cations to form silver (Ag) atoms, which is the basis for latent image formation in photography. The slow decay agrees with early nanosecond studies [77]. When the two core/shell systems, AgI/Ag₂S and AgBr/Ag₂S, were compared, a new 4 ps rise component with AgBr/Ag₂S was observed which was taken as an indication of electron transfer from Ag₂S to AgBr [26]. However, subsequent experiments conducted on pure Ag₂S nanoparticles capped with cystine and glutathione found similar features to that of the core/shell structured AgBr/Ag₂S [41]. Therefore, the 4 ps rise feature is more likely due to transient bleach, since there is noticeable ground state absorption at the probe wavelength [41].

Copper chloride nanocrystals are interesting due to their promise as nonlinear materials; it has been observed that they show high optical gain when embedded in a NaCl matrix [78–80]. Dephasing time in CuCl nanocrystals has been measured using femtosecond transient degenerate four-wave mixing (DFWM). For nanocrystals less than 5 nm, a reservoir correlation time of 4.4–8.5 ps, which increases with increasing R , was found based on a stochastic model [81, 82]. This behavior is explained by an increase of exciton–acoustic phonon coupling strength and a change in the acoustic phonon DOS because of acoustic phonon quantum confinement. Exciton dephasing times have also been measured via DFWM and spectral hole burning on CuBr quantum dots embedded in borosilicate glass and were found to be 6.4 ps for the DFWM experiment and 2.3–2.7 ps from the spectral hole burning [83–85]. These represent upper and lower limits for the exciton dephasing times. (See Table 1.)

Carbon nanoparticles have recently been studied in terms of their ultrafast charge carrier properties [86]. Carbon NPs have attracted much interest because they are constituents of many systems including interstellar dust, arc generated soot, and vacuum deposited thin films. The particles ranged in size from 5 to 40 nm, and it was found that the size of the particles decreased with increasing sintering temperature. The ultrafast electronic relaxation followed a biexponential decay yielding a fast and slow component with both time constants varying according to particle size. Smaller C particles exhibited a faster overall decay than did larger particles. The fast decay was assigned to electron–phonon coupling as well as recombination of excited carriers while the long decay was assigned to trapped carriers. It was proposed that quantum size confinement and density of trap states accounted for the difference in dynamics between large and smaller particles [86].

A dynamics study on ion-implanted Si nanocrystals using femtosecond transient absorption identified two photoinduced absorption features. One was attributed to charge carriers in nanocrystal quantized states with higher energy and faster relaxation. The other was assigned to Si/SiO₂ interface states with lower energy and slower relaxation [87]. The observed red emission was shown to be from surface trap

Table 1.

Nanoparticle	Dimension	Decay times	Measurement method	Ref.
Ag ₂ S	9 nm	750 fs; 4.5 ps; >1 ns	TA/TB	[41]
AgBr/Ag ₂ S	not reported	800 fs; 4 ps rise; >1 ns	TA	
AgI	7 nm	2.5 ps; >0.5 ns	TA	[26]
AgI/Ag ₂ S	not reported	800 fs; 2.5 ps; >1 ns	TA	
Au ₂ S	4 nm	600 fs; 23 ps	TA	[42]
Bi ₂ S ₃	20–200 nm	aqueous PVA: 1.4 ps; 18.8 ps aqueous PVP: 4.8 ps; 667 ps aqueous gelatin: 0.9 ps; 5.7 ps	TA	[72]
	1.5–2.5 nm	micelles: 3.3 ps; 87 ps	TA	
BiI ₃	2–100 nm	micelles: 1.3 ps; 33 ps alcohol: 9 ps; 50 ps; oscillation period 1.3 ps acetonitrile: 50 ps; 1.3 ns; oscillation period 5 ps PVA: 9 ps	TA	[70]
C	5–40 nm	151–536 fs; 7.5–35 ps	TA	[86]
CdS	various	ps–ns	TRE, TA, TB	[3, 4, 6–8, 11, 13–19, 23, 24]
CdSe	various	ps–ns	TRE, TA, TB, TRPE	[5, 31–34]
CdSe Nanorods	4.2 × 13.5 nm	~300 fs (480–515 nm); a few ps (530–575 nm); 50 ps (585 nm)	TB	[49]
CdTe	2–3 nm	3.37 ps; 230 ps; >600 ps	TA	[35–36]
CuBr	2.8–12 nm	6.4 ps and 2.3–2.7 ps (exciton dephasing)	SHB and DFWM	[83–85]
CuCl	<5 nm	4.4–8.5 ps (reservoir correlation time)	DFWM	[78–80, 81, 82]
Cu ₂ S	10 nm	1.1 ps; 80 ps	TA	[40]
CuS	10 nm	low excitation: 430 fs (bleach recovery) + long time offset (absorption) high excitation: 1.1 ps (absorption); >1 ns (absorption)	TA/TB	[40]
Fe ₂ O ₃	γ-phased 1–2 nm α-phased 1 × 5 nm	0.36 ps; 4.2 ps; 67 ps 0.36 ps; 4.2 ps; 67 ps	TA TA	[12]
GaSe	4 nm	80 ps; 400 ps; 2.4 ns	TA/TB/TRE	[73–76]
Ge	4 and 16 nm	230 fs; 1.5 ps	TA/TB	[88, 89]
InP	2.5 and 3.5 nm	300 fs; 200 ps	TB	[90–92]
	<5 nm	240 fs (exciton dephasing)	TRPE	
MoS ₂	3.0 and 4.5 nm	40 ps (298 K); 200 ps (20 K)	TRE	[65, 66]
MoS ₂ and MoS ₂ /DTDCl	3.0 nm	42 ps; 225 ps (bare particle); 12 ps (injection to DTDCl); 1.2 ns (reverse electron transfer)	TA/TRE	[67]
PbI ₂	~3–100 nm	alcohol: 6 ps; 75 ps; oscillation period 1.6 ps acetonitrile: 75 ps; oscillation period 6 ps PVA: 1 ps; 40 ps; no oscillations observed	TA TA TA	[28]
PbS	8–12 nm cubic, needle, and spherical	PVP: 1.2 ps; 45 ps	TA	[27]
	8–12 nm cubic, needle, and spherical	DNA: 1.2 ps; 45 ps	TA	
	4–6 nm spherical	PVA: 1.2 ps; 45 ps	TA	
PbTe	1.5–3 nm	2.1 ps damping; 2.0 ps oscillation period; 175 ps recombination	TA	[37]
Si	2.5–3 nm	1.5 ps; 8 ps	TA	[87]
TiO ₂	2 nm	180 fs; 1.8 × 10 ⁻¹⁰ cm ³ s ⁻¹	TA	[4, 9]
WS ₂	4–7 nm	30 ps; 300–500 ps 100 ps	TRE TRE	[68] [69]
ZnO	3.2 nm	70 fs (trapping)	TA	[10]
	6.2 nm	<30 fs (trapping)	TA	
ZnS:Mn ²⁺	2.7–7.5 nm	3 ns; 20 ns (Mn ²⁺ emission)	TRE	[52–54]
	4 nm	1.9 ms (Mn ²⁺ emission)	TRE	[56, 57]
	1.2 nm	1–2 ms (Mn ²⁺ emission)	TRE	[58]
	6 nm	0.18 ms; 2 ms (Mn ²⁺ emission)	TA/TRE	[59]
ZnS:Pb ²⁺	4.3 and 5.5 nm	red emission: 3 ms (4 K); 0.5 μs (50 K) white emission: several ms (<40 K); 0.5 μs (>40 K)	TRE	[63]
ZnSe	3.5 nm	17 ps; 143 ps	TA	[62]
ZnSe:Mn ²⁺	3–4 nm	290 μs (Mn ²⁺ emission)	TRE	[60]
	3.5 nm	1.7 ps; 33 ps	TA	[62]

Note: transient absorption = TA; transient bleach = TB; spectral hole burning = SHB; time resolved emission = TRE; time resolved photon echo = TRPE.

states and not from quantized states. The faster relaxation of the blue emission relative to that of the red emission is similar to that observed for CdS NPs [11].

Two ultrafast studies on carrier dynamics have been performed on Ge nanocrystals evaporated onto an alumina film [88, 89]. Excitation pulses of 1.59, 3.18, and 4.77 eV were used to probe the relaxation processes in 4 and 16 nm Ge particles over a large range of probe wavelengths (1.7–2.8 eV). Using a model based on the band structure of Ge, it was found that the photogenerated electrons scatter rapidly out of the Γ valley part of the Ge band structure and into the X valley with a time constant of 230 fs where they further relax into the L valley on a time scale of about 1.5 ps.

Several time resolved ultrafast studies have been performed on the InP nanoparticle system. Early work utilizing femtosecond transient bleach experiments yielded a rise time of 300 fs followed by a decay that persists longer than 200 ps for both 2.5 and 3.5 nm particles. This long bleaching lifetime was attributed to trapping of charge carriers [90]. Subsequent studies showed that higher energy excitations above the first exciton peak resulted in a loss of relaxation efficiency. It was proposed that the high energy charge carriers are diverted to another channel where they are prevented from relaxing to the bandedge and have the effect of increasing nonradiative recombination [91, 92]. In addition, InP nanocrystal ($R < 5$ nm) dephasing times have also been measured via time resolved photon echo experiments and revealed a dephasing time of ~ 240 fs. The linewidth in InP nanocrystals at low temperature was found to be smaller than similar sized CdSe due to poorer coupling to LO phonons in InP.

Charge carrier dynamics in semiconductor quantum wires have also been investigated in a few cases, including notably GaAs [93–96]. High luminescence efficiency was found in some cases and the luminescence was found to be completely dominated by radiative electron–hole recombination [93]. A more direct, systematic comparison of electronic relaxation among 2D, 1D, and 0D quantum confined systems should be interesting but is made difficult by practical issues such as sample quality (e.g., surface characteristics, experimental conditions, excitation, wavelength, and intensities) that can significantly influence the measurements. Such studies should be carried out in the future, both experimentally and theoretically.

2.8. Charge Transfer Systems

Photoinduced charge transfer is a very important fundamental process involved in liquid–semiconductor or liquid–metal interfaces. It plays a crucial role in photocatalysis, photodegradation of wastes, photoelectrochemistry, and solar energy conversion [97–102]. Relaxation processes such as trapping and recombination compete with charge transfer. The charge transfer process is desired in many applications. For instance, charge transfer has been extensively studied for dye-sensitized metal oxide nanoparticles (e.g., TiO₂ and ZnO) for photovoltaic applications. TiO₂ dye sensitization is the most notable example because of its potential use for solar energy conversion [103] and photocatalysis [104]. TiO₂ ($E_g = 3.2$ eV) alone does not absorb visible

light; dye sensitization helps to extend the absorption into the visible region.

In dye sensitization, upon absorption of light an electron is promoted to an excited electronic state in the dye. The electron can then undergo charge transfer from the dye molecule to the TiO₂ (or other suitable metal oxide) nanoparticle if the dye is attached directly to the surface. There are several requirements for this to work effectively. The excited state of the dye molecule needs to lie above the bottom of the conduction band of the TiO₂ nanoparticle in order to provide a driving force (enthalpic as well as entropic) for the electron transfer to occur. Strong binding of the dye onto the TiO₂ nanoparticle surface is desired for fast and efficient injection. Back electron transfer to the oxidized dye following injection should be minimal (i.e., electron transfer from the conduction band of the TiO₂ to the ground state of the dye molecule). For solar energy conversion applications, the dye molecule must have strong absorption in the visible region preferably closely matching that of the solar spectrum. Many dye molecules have been studied and tested for solar energy conversion applications over the years [105]. The dye molecule that shows the most promise for photovoltaic applications is the ruthenium N3 dye, which showed the highest reported light-to-electricity conversion efficiency of 10% [103, 106]. This work has stimulated strong interest in understanding the mechanism of charge injection and recombination in dye-sensitized nanocrystalline systems.

The rates of electron injection and subsequent back electron transfer in dye sensitization are expected to depend on the nature of the dye molecule and the NPs, most notably the surface characteristics of the NPs. The interaction between dye and NP surface will determine the rates and yields of forward and reverse electron transfer [97, 107]. The shape (facets) and size of the particles may also be important and tend to vary from sample to sample depending on the preparation methods used.

To describe the electron transfer (ET) process from an adsorbed molecule on a nanoparticle surface, one can adopt an approach similar to that of Marcus and co-workers for ET between a discrete electron donor and acceptor level in solution [108–110]. The total ET rate from an adsorbate with discrete states to a semiconductor with a nearly continuum of product states can be expressed as [111]

$$K_{\text{ET}} = \frac{2\pi}{\hbar} \int_0^\infty dE \rho(E) |\bar{H}(E)|^2 \frac{1}{\sqrt{4\pi\lambda k_B T}} \times \exp\left[-\frac{(\lambda + \Delta G_0 - E)^2}{4\pi\lambda k_B T}\right] \quad (2)$$

where $\Delta G_0 = E_{\text{CB}} - E_{\text{ox}}$ is the energy difference between conduction bandedge and the redox potential of adsorbate excited state, $\rho(E)$ is the density of states at energy E from the conduction bandedge, which can contain both the bulk states and surface states, $H(E)$ is the average electronic coupling between the adsorbate excited state and different k states in the semiconductor at the same energy E , and λ is the total reorganization energy. Furthermore, since a distribution of adsorbate/semiconductor interactions exists, there should be a distribution of electronic coupling matrix elements, H , and hence injection rates [111]. Ergo, the electron

transfer rate depends on the detailed energetics of both the semiconductor and the adsorbate. In general, a strong electronic coupling, $H(E)$, and large energy difference ($E_{\text{ox}} - E_{\text{CB}}$) between the adsorbate excited state and the conduction band lead to faster electron transfer. It is often challenging to independently examine experimentally the effects of the different factors since they are often interrelated. However, they can be evaluated separately under certain approximations or special circumstances.

Electron injection rates (forward electron transfer) in dye-sensitized semiconductor metal oxide nanoparticles have generally been found to be extremely fast, ~ 100 fs. For instance, for the coumarin 343 dye on TiO_2 , the electron injection rate was found to be around 200 fs [112]. The first direct femtosecond measurement, for the N3 dye on TiO_2 , reported a hot electron injection time of less than 25 fs [113]. However, there has been some debate over possible degradation of the dye sample used [114, 115]. A picosecond infrared study showed an upper limit of 20 ps for electron injection time [116]. Ellington et al., more recently, reported an injection time of < 50 fs based on transient infrared measurements for N3 on TiO_2 [111, 117]. An electron injection time of anthocyanin dye adsorbed on TiO_2 NPs has been measured and found to be < 100 fs [118]. The assignment is made particularly simple in this system since the anthocyanin dye alone has a stimulated emission signal (similar to a transient bleach), while the dye on TiO_2 has a transient absorption signal due to the electron transfer. By carefully performing several control experiments, the transient absorption signal was unambiguously assigned to electrons injected into TiO_2 , which has a rise time of < 100 fs.

While forward electron transfer has generally been found to be very fast, back electron transfer has been found to occur on a range of time scales, from about 10 ps to μs , depending on the nature of the dye and the nanoparticle [118–120]. For example, both forward and reverse electron transfer have been studied in the case of anthracenecarboxylic acids adsorbed on different types of TiO_2 NPs. The transfer rates were found to be dependent on the molecular structure of the dye and the TiO_2 synthesis method [120].

Electron transfer studies are not confined only to dye-sensitized nanoparticle systems. Recently, a comparison of the electron transfer rate from poly[2-methoxy-5-(2-ethylhexyloxy)-(phenylene-vinylene)], a well known conducting polymer, to SnO_2 and TiO_2 semiconductor nanoparticles has been performed [121, 122]. It was found that the electron transfer rate was faster to TiO_2 (< 100 fs) than to SnO_2 (~ 800 fs). This was explained by the differences in electronic structure of the conduction bands between the two metal oxides even though there is a larger driving force for the polymer SnO_2 system. The SnO_2 conduction band has significant “s” character while TiO_2 is more “d” like, which affects coupling [see Eq. (2)] between nanoparticle and the polymer. However, even though the electron injection is occurring higher in the conduction band for SnO_2 than for TiO_2 , the density of states at the injection energy is lower for SnO_2 than for TiO_2 . These two factors lead to a higher injection rate for TiO_2 over that of SnO_2 .

Electron transfer can also take place from the semiconductor nanoparticle to an electron acceptor near or on the

surface of the nanoparticle, otherwise known as photoreduction. This is less studied compared to electron transfer from an adsorbate to the NP. For instance, electron transfer dynamics from CdS and CdSe NPs to electron acceptors (e.g. viologen derivatives) adsorbed on the particle surface have been studied using transient absorption/bleach and time resolved fluorescence [8, 123]. Electron transfer was found to take place on the time scale of 200–300 fs, which competes efficiently with trapping and electron–hole recombination. These results are important to understanding interfacial charge transfer involved in photocatalysis and photoelectrochemistry applications.

3. CHARGE CARRIER DYNAMICS IN METAL NANOPARTICLES

Electronic relaxation in metal nanoparticles occurs on the very short time scale. Direct probe of this relaxation can be monitored via femtosecond laser spectroscopy. Gold [124] and silver [125] nanoparticle electronic relaxation dynamics were first studied by Zhang and co-workers with initial work on Cu [126] performed by Bigot et al. Following these initial studies, many investigations have been performed on a myriad of different metal systems. These include Au [127–133], Ag [133–135], Sn [136], Pt [128, 137], Cu [138, 139], and Ga [140] as representative examples.

An issue of fundamental importance is the size dependence of electronic relaxation. As the size (number of atoms) is reduced from bulk (10^{23}) to the nanoscale (100–1000s) and smaller, how is the relaxation affected? The majority of the relaxation on the very short time scale is dominated by electron–phonon interactions or coupling (i.e., transfer of energy from excited electrons into phonons or vibrational motion). The relaxation time reflects how strongly the excited electrons couple to the phonons. With decreasing size the electron and phonon spectral density of states is expected to decrease as well as the spectral overlap between electrons and phonons. At the same time, the influence of surface becomes more significant with decreasing size. The change in DOS and surface may have competing effects on the electronic relaxation dynamics.

Early work based on transient absorption spectroscopy indicated a possible size dependence of the electronic relaxation in the 1–40 nm range [128]. However, subsequent measurements by Hartland and co-workers, as well as by El-Sayed et al., found no size dependence of the relaxation down to a particle size of 2.5 nm [129, 131–133]. The relaxation time in Au nanoparticles was reported to be the same as that in bulk gold (~ 1 ps). One complication in the study of size dependent relaxation in metal nanoparticles is the strong excitation intensity dependence of the dynamics [131, 132]. Another complication is that the relaxation has been found to be solvent dependent [137]. In the early transient absorption work by Zhang et al., the excitation intensities used were likely to have been much higher due to the small signal than those used in the transient bleach measurements by El-Sayed and Hartland. This could be the cause for the difference between the measured lifetimes. Another explanation for the difference is surface or solvent environment.

Measurements by Zhang et al. yielded a 7 ps decay in water and 5 ps in cyclohexane [124, 137]. Surface and solvent influence on relaxation is worthy of further investigation.

However, as particle size becomes smaller than 1 nm the electronic relaxation becomes more molecule-like. Measurements on Au₁₃ clusters indicate a very long lifetime ~300 ps [128]. Recently, clusters of 28 gold atoms capped with glutathione molecules have been investigated by femtosecond laser spectroscopy [141]. It was found that the decay was biexponential with a subpicosecond component as well as a longer nanosecond component. The fast component was assigned to relaxation from a higher lying excited state populated by the 400 nm excitation pulse to a lower electronic state. The longer nanosecond component was attributed to the radiative lifetime of the Au₂₈ clusters [142]. More recently, preliminary data on electronic relaxation in Au₁₁ clusters [143] (~0.7 nm diameter) reveal a similar long lifetime to Au₁₃ and Au₂₈, supporting the possibility that for very small metal clusters (molecule-like) the electronic relaxation becomes much slower due to weak electron–vibration coupling.

The relaxation of hot electrons in a metal nanoparticle can be described by a two-temperature model for energy exchange between electrons and the lattice [144–146],

$$\begin{aligned} C_e(T_e) \frac{\partial T_e}{\partial t} &= -g(T_e - T_l) \\ C_l \frac{\partial T_l}{\partial t} &= g(T_e - T_l) \end{aligned} \quad (3)$$

where T_e and T_l are the temperatures of the electrons and lattice respectively, $C_e(T_e) = \gamma T_e$ is the temperature dependent electronic heat capacity ($\gamma = 66 \text{ J m}^{-3} \text{ K}^{-2}$ for Au), C_l is the lattice heat capacity, and g is the electron–phonon coupling constant. Since the electronic heat capacity depends on the temperature of the electron distribution, the effective rate constant for the decay is $g/\gamma T_e$ and decreases as the initial electronic temperature increases. Higher excitation intensities produce higher electronic temperatures, which then yield longer decay times. The coupled differential equations thus describe quite well that higher excitation energies yield longer relaxation times, consistent with experimental observations [147].

A recent interesting discovery was oscillations in the electronic relaxation dynamics of Au, Ag, and bimetallic core/shell particles made of Au, Ag, Pt, and Pb [147–152]. The oscillations have been attributed to a coherent excitation of the radial breathing vibrational modes of the particles. After the initial excitation, electrons transfer their energy into the lattice heating up the particle and causing a rapid expansion. This has the effect of changing the volume of the particle and hence the electron density. This behavior manifests itself as a modulation in the transient signal (see Fig. 3) as the particle vibrates around its new “hot” particle radius. The frequency of the oscillation was found to be strongly dependent on particle size with the frequency increasing linearly with decreasing particle size. Interestingly, this phenomenon can be well described by classical mechanics. In addition, the degree of damping of the vibrational motion depends on the polydispersity of the nanoparticle sample. In a monodisperse (i.e., single sized)

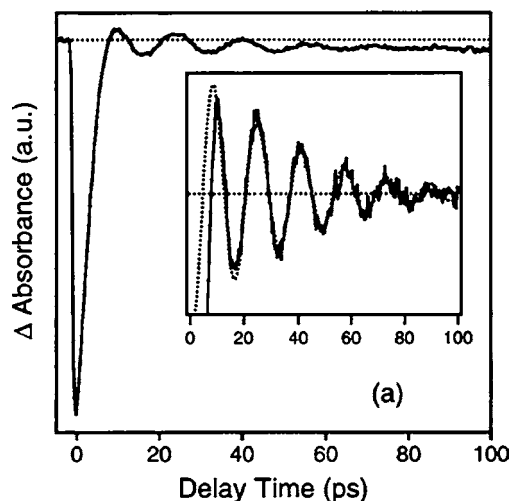


Figure 3. Transient bleach data for 60 nm isolated gold nanoparticles recorded with 400 nm excitation and 550 nm probe pulses. Modulations can be clearly seen due to the coherently excited radial breathing mode. Adapted with permission from [147], J. H. Hodak et al., *J. Phys. Chem. B* 104, 9954 (2000). © 2000, American Chemical Society.

sample of particles, upon excitation all the particles vibrate with the same frequency giving rise to the observed modulation. However, as the size distribution of the sample increases, the different sized particles vibrate with different frequencies that have the effect of washing out or damping the observable oscillations. Hence, the transient absorption/bleach technique can sensitively determine polydispersity of metal nanoparticle samples.

Similar vibrational motion has also been observed in gold nanorods [153], silver ellipsoids [154], and strongly coupled gold nanoparticle aggregates [155]. In the case of the silver ellipsoids embedded in a glass matrix, oscillations along both the long and short axes could be observed using transient optical spectroscopy. Somewhat surprisingly, gold nanorods exhibited an interesting probe wavelength dependence. Due to the polydispersity of the nanorod sample, the longitudinal band is inhomogeneously broadened [156]. Hence, at redder probe wavelengths, the observed period is longer than at bluer probe wavelengths. This is because the bluer probe pulses interrogate nanorods with a shorter length than the redder wavelengths. This technique provides homogeneous linewidth information of the longitudinal plasmon band of the rods. The period of the oscillations was determined to be $2L/c_l$, where L is the length of the rod and c_l is the transverse speed of sound of bulk gold. This is different from the silver ellipsoidal result, which depended on $2d/c_l$ where d is either the length or width of the ellipsoid and c_l longitudinal speed of sound in silver. The discrepancy might be explained as follows. First, the vibrational motion in gold nanorods may be fundamentally different from that of the Ag ellipsoid. Second, the use of bulk materials properties may be inappropriate for small crystallite rods. The elastic properties of a single crystal nanorod may be different from that of a polycrystalline rod.

Aggregates of metal nanoparticles are fundamentally interesting since they provide a means to study interparticle interactions. The interaction can be divided roughly

into the strongly and weak to moderately strong interacting regimes. Weak to moderately strong interactions are found in DNA-linked Au nanoparticles [157–159] and superlattice structures of Au nanoparticles [160] and manifest themselves as a substantial redshift of the transverse surface plasmon band. Strongly coupled gold nanoparticle aggregates, however, display a broad near-IR absorption band (700–950 nm) in addition to the visible plasmon resonance associated with isolated gold nanoparticles (see Fig. 4) [161–165]. This near-IR band is analogous to the longitudinal plasmon absorption seen in nanorods and arises from strongly interacting particles; it is termed the extended plasmon band (EPB). It is interesting to note that the transverse surface plasmon band in these aggregates does not redshift significantly (no redder than 540 nm) with respect to that of isolated particles.

In the dynamics studies of strongly interacting Au nanoparticle aggregates, the electronic relaxation time was found to be similar to that of isolated particles and bulk [155]. Surprisingly, periodic oscillations were observed despite the fact that aggregates tend to have very large polydispersity in size and shape, which could potentially dampen any possible oscillations [155]. The observation of oscillations in such aggregates strongly suggests that the broad EPB consisted of subbands from different sized and/or structured aggregates. In other words, the EPB is inhomogeneously broadened by aggregates with different sizes and/or structures. This conjecture suggested that different oscillation periods should be observed for different probe wavelengths because each probe wavelength would interrogate a particular size and/or structured aggregate. As the probe wavelength was varied from red to blue (see Fig. 5), the period of the oscillations became longer (37 ps at 720 nm to 55 ps at 850 nm), which is consistent with the previous conjecture.

To further confirm the model, spectral hole burning experiments were conducted and a hole was clearly burned with 810 nm laser excitation clearly supporting the proposal that the EPB is inhomogeneously broadened by different sized and/or structured aggregates. Earlier experimental and theoretical studies of Au nanoparticle aggregates also suggested that the EPB consists of subbands due to different aggregate sizes and/or structures [166–168]. The significance of the observation of oscillations in Au nanoparticle

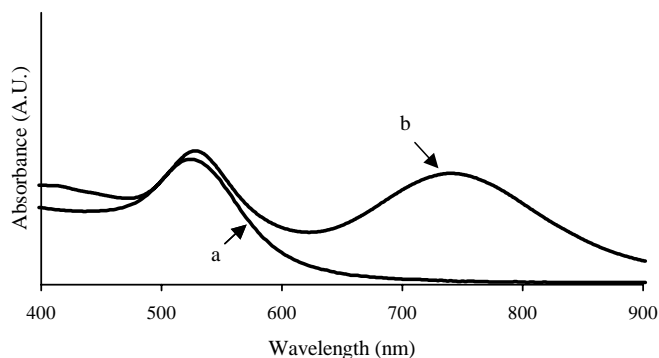


Figure 4. Comparative ultraviolet-visible between isolated Au nanoparticles (trace a) and strongly interacting gold nanoparticle aggregates (trace b). The appearance of the near-IR band is attributed to strong particle–particle interaction between gold NPs.

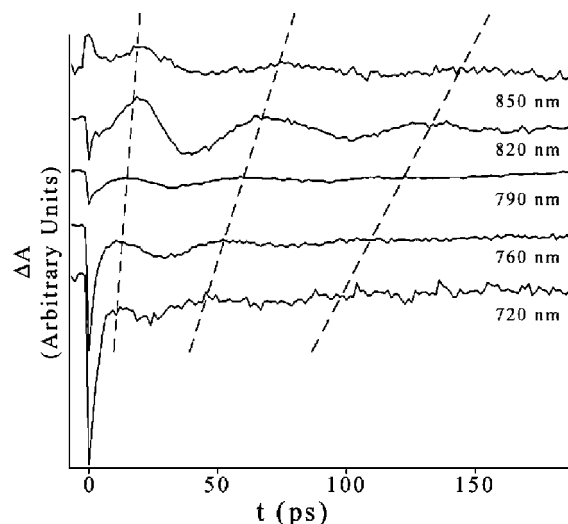


Figure 5. Ultrafast electronic relaxation dynamics of gold nanoparticle aggregates at varying probe wavelengths (shown at right) with excitation at 390 nm at 8 $\mu\text{J}/\text{pulse}$. Trend lines (dashed) demonstrate an increase in oscillation period and shift of the first peak toward longer time as probe wavelength is shifted to redder wavelengths. Reprinted with permission from [155], C. D. Grant et al., *J. Am. Chem. Soc.* 125, 549 (2002). © 2002, American Chemical Society.

aggregates is that it demonstrates that time resolved fs laser techniques can be used to determine very low frequency vibrational modes of such aggregates, in the $<1\text{ cm}^{-1}$ frequency range [155]. There is practically no other experimental means to determine such low vibrational frequencies for such condensed phase systems.

Similar to isolated gold NPs, the vibrational oscillations observed for Au nanoparticle aggregates were assigned to “radial” breathing modes. However, the vibrational behavior is somewhat different from that of purely isolated spherical particles. The Lamb equation predicts rather accurately the vibrational period of isolated spherical metal particles,

$$R = \frac{\eta\tau}{2\pi}c_l \quad (4)$$

where R is the radius of the aggregate or particle, η is the vibrational eigenvalue, τ is the period of the oscillations, and c_l is the longitudinal speed of sound in bulk gold. For the Au nanoparticle aggregates, the observed vibrational period from transient absorption is longer than that predicted based on Eq. (4) using the radius of the aggregates measured from dynamic light scattering. A possible explanation for the discrepancy is that the vibrational motion of the aggregates is “softer” than that of the isolated elastic spherical particles due to a lower speed of sound in the aggregates than in bulk gold. This seems plausible since the aggregates are not solid structures like the elastic nanoparticles [155].

4. CONCLUSION

In summary, charge carrier dynamics in both semiconductor and metal nanomaterials can be directly studied using powerful time resolved optical techniques. These dynamics studies provide complementary information to

static or equilibrium studies. The intimate interconnections between equilibrium and dynamic properties are illustrated with numerous examples. Dynamics studies are expected to continue to play an important and active role in the study and understanding of properties and functionalities of nanomaterials.

GLOSSARY

Band edge emission Fluorescent emission from electron-hole recombination from conduction band edge to valence band edge.

Exciton–exciton annihilation The process in which one exciton “collides” with another, transfers its energy, and undergoes non-radiative recombination.

Surface plasmon resonance Resonant interaction of conduction band electrons with incident light.

Trap state emission Fluorescent emission from electron-hole recombination from trap states. This emission is red shifted relative to band edge emission due to trap states lying inside the forbidden band-gap region.

Trap states Electronic states that lie energetic ally within the band-gap between the valence and conduction bands. These states act to trap charge-carriers and often affect their lifetimes significantly.

REFERENCES

- L. Jacak, A. Wójs, and P. Hawrylak, “Quantum Dots.” Springer, Berlin/New York, 1998.
- U. Bockelmann, *Semicond. Sci. Tech.* 9, 865 (1994).
- J. Z. Zhang, R. H. Oneil, and T. W. Roberti, *J. Phys. Chem.* 98, 3859 (1994).
- D. E. Skinner, D. P. Colombo, J. J. Cavaleri, and R. M. Bowman, *J. Phys. Chem.* 99, 7853 (1995).
- D. M. Mittleman, R. W. Schoenlein, J. J. Shiang, V. L. Colvin, A. P. Alivisatos, and C. V. Shank, *Phys. Rev. B* 49, 14435 (1994).
- V. Klimov, P. H. Bolivar, and H. Kurz, *Phys. Rev. B* 53, 1463 (1996).
- M. Oneil, J. Marohn, and G. McLendon, *Chem. Phys. Lett.* 168, 208 (1990).
- S. Logunov, T. Green, S. Marguet, and M. A. El-Sayed, *J. Phys. Chem. A* 102, 5652 (1998).
- D. P. Colombo, K. A. Roussel, J. Saeh, D. E. Skinner, J. J. Cavaleri, and R. M. Bowman, *Chem. Phys. Lett.* 232, 207 (1995).
- J. J. Cavaleri, D. E. Skinner, D. P. Colombo, and R. M. Bowman, *J. Chem. Phys.* 103, 5378 (1995).
- T. W. Roberti, N. J. Cherepy, and J. Z. Zhang, *J. Chem. Phys.* 108, 2143 (1998).
- N. J. Cherepy, D. B. Liston, J. A. Lovejoy, H. M. Deng, and J. Z. Zhang, *J. Phys. Chem. B* 102, 770 (1998).
- P. V. Kamat and N. M. Dimitrijevic, *J. Phys. Chem.* 93, 4259 (1989).
- N. M. Dimitrijevic and P. V. Kamat, *J. Phys. Chem.* 91, 2096 (1987).
- M. Haase, H. Weller, and A. Henglein, *J. Phys. Chem.* 92, 4706 (1988).
- E. F. Hilinski, P. A. Lucas, and W. Ying, *J. Chem. Phys.* 89, 3534 (1988).
- P. V. Kamat, N. M. Dimitrijevic, and A. J. Nozik, *J. Phys. Chem.* 93, 2873 (1989).
- Y. Wang, A. Suna, J. McHugh, E. F. Hilinski, P. A. Lucas, and R. D. Johnson, *J. Chem. Phys.* 92, 6927 (1990).
- T. Vossmeier, L. Katsikas, M. Giersig, I. G. Popovic, K. Diesner, A. Chemseddine, A. Eychmuller, and H. Weller, *J. Phys. Chem.* 98, 7665 (1994).
- A. Henglein, A. Kumar, E. Janata, and H. Weller, *Chem. Phys. Lett.* 132, 133 (1986).
- K. I. Kang, A. D. Kepner, S. V. Gaponenko, S. W. Koch, Y. Z. Hu, and N. Peyghambarian, *Phys. Rev. B* 48, 15449 (1993).
- V. Klimov, S. Hunsche, and H. Kurz, *Phys. Rev. B* 50, 8110 (1994).
- N. P. Ernstring, M. Kaschke, H. Weller, and L. Katsikas, *J. Opt. Soc. Am. B* 7, 1630 (1990).
- J. Z. Zhang, R. H. Oneil, T. W. Roberti, J. L. McGowen, and J. E. Evans, *Chem. Phys. Lett.* 218, 479 (1994).
- J. P. Zheng and H. S. Kwok, *Appl. Phys. Lett.* 65, 1151 (1994).
- M. C. Brelle and J. Z. Zhang, *J. Chem. Phys.* 108, 3119 (1998).
- A. A. Patel, F. X. Wu, J. Z. Zhang, C. L. Torres-Martinez, R. K. Mehra, Y. Yang, and S. H. Risbud, *J. Phys. Chem. B* 104, 11598 (2000).
- A. Sengupta, B. Jiang, K. C. Mandal, and J. Z. Zhang, *J. Phys. Chem. B* 103, 3128 (1999).
- J. Z. Zhang, *Acc. Chem. Res.* 30, 423 (1997).
- F. Wu, J. Z. Zhang, R. Kho, and R. K. Mehra, *Chem. Phys. Lett.* 330, 237 (2000).
- D. F. Underwood, T. Kippeny, and S. J. Rosenthal, *J. Phys. Chem. B* 105, 436 (2001).
- C. Burda, S. Link, M. Mohamed, and M. El-Sayed, *J. Phys. Chem. B* 105, 12286 (2001).
- C. Burda, S. Link, M. B. Mohamed, and M. El-Sayed, *J. Chem. Phys.* 116, 3828 (2002).
- P. Guyot-Sionnest, M. Shim, C. Matranga, and M. Hines, *Phys. Rev. B* 60, R2181 (1999).
- F. Wu and J. Z. Zhang, *Proc. SPIE* 4807, 189 (2002).
- F. Wu, J. Lewis, D. Kliger, and J. Z. Zhang, *J. Chem. Phys.*, in press.
- E. R. Thoen, G. Steinmeyer, P. Langlois, E. P. Ippen, G. E. Tudury, C. H. B. Cruz, L. C. Barbosa, and C. L. Cesar, *Appl. Phys. Lett.* 73, 2149 (1998).
- T. D. Krauss and F. W. Wise, *Phys. Rev. B* 55, 9860 (1997).
- J. H. Hodak, A. Henglein, and G. V. Hartland, *J. Chem. Phys.* 111, 8613 (1999).
- M. C. Brelle, C. L. Torres-Martinez, J. C. McNulty, R. K. Mehra, and J. Z. Zhang, *Pure Appl. Chem.* 72, 101 (2000).
- M. C. Brelle, J. Z. Zhang, L. Nguyen, and R. K. Mehra, *J. Phys. Chem. A* 103, 10194 (1999).
- C. D. Grant, T. J. Norman, T. Morris, G. Szulczewski, and J. Z. Zhang, *Proc. SPIE* 4807, 216 (2002).
- T. Morris, H. Copeland, and G. Szulczewski, *Langmuir* 18, 535 (2002).
- K. Ishikawa, T. Isonaga, S. Wakita, and Y. Suzuki, *Solid State Ion.* 79, 60 (1995).
- J. W. Mitchell, *Photogr. Sci. Eng.* 22, 249 (1978).
- J. W. Mitchell, *J. Photogr. Sci.* 31, 148 (1983).
- M. Christianson, *J. Imaging Sci. Technol.* 37, 576 (1993).
- L. S. Li, J. T. Hu, W. D. Yang, and A. P. Alivisatos, *Nano. Lett.* 1, 349 (2001).
- M. B. Mohamed, C. Burda, and M. A. El-Sayed, *Nano. Lett.* 1, 589 (2001).
- G. Cantele, D. Ninno, and G. Iadonisi, *J. Phys., Condens. Mater.* 12, 9019 (2000).
- G. Cantele, D. Ninno, and G. Iadonisi, *Nano. Lett.* 1, 121 (2001).
- R. N. Bhargava, D. Gallagher, X. Hong, and A. Nurmikko, *Phys. Rev. Lett.* 72, 416 (1994).
- R. N. Bhargava, D. Gallagher, and T. Welker, *J. Lumin.* 60–1, 275 (1994).
- R. N. Bhargava, *J. Lumin.* 70, 85 (1996).
- H. Ito, T. Takano, T. Kuroda, F. Minami, and H. Akinaga, *J. Lumin.* 72–4, 342 (1997).
- A. A. Bol and A. Meijerink, *J. Lumin.* 87–9, 315 (2000).
- N. Murase, R. Jagannathan, Y. Kanematsu, M. Watanabe, A. Kurita, K. Hirata, T. Yazawa, and T. Kushida, *J. Phys. Chem. B* 103, 754 (1999).

58. B. A. Smith, J. Z. Zhang, A. Joly, and J. Liu, *Phys. Rev. B* 62, 2021 (2000).
59. C. Jae Hun, A. Chil Seong, and J. Du-Jeon, *J. Phys. Chem. B* 105, 4128 (2001).
60. J. F. Suyver, S. F. Wuister, J. J. Kelly, and A. Meijerink, *Phys. Chem. Chem. Phys.* 2, 5445 (2000).
61. S. J. Weston, M. Oneill, J. E. Nicholls, J. Miao, W. E. Hagston, and T. Stirner, *Phys. Rev. B* 58, 7040 (1998).
62. T. J. Norman, Jr. and J. Z. Zhang, unpublished results (2002).
63. A. A. Bol and A. Meijerink, *Phys. Status Solidi B* 224, 173 (2001).
64. G. Gerischer, "Topics in Applied Physics" (B. O. Seraphim, Ed.), Vol. 31. Springer, Berlin, 1979.
65. R. Doolen, R. Laitinen, F. Parsapour, and D. F. Kelley, *J. Phys. Chem. B* 102, 3906 (1998).
66. V. Chikan and D. F. Kelley, *J. Phys. Chem. B* 106, 3794 (2002).
67. V. Chikan, M. R. Waterland, J. M. Huang, and D. F. Kelley, *J. Chem. Phys.* 113, 5448 (2000).
68. J. M. Huang and D. F. Kelley, *J. Chem. Phys.* 113, 793 (2000).
69. J. M. Huang, R. A. Laitinen, and D. F. Kelley, *Phys. Rev. B* 62, 10995 (2000).
70. A. Sengupta, K. C. Mandal, and J. Z. Zhang, *J. Phys. Chem. B* 104, 9396 (2000).
71. Z. K. Tang, Y. Nozue, and T. Goto, *J. Phys. Soc. Jpn.* 61, 2943 (1992).
72. A. Sengupta and J. Z. Zhang, in "First International Chinese Workshop on Nanoscience and Nanotechnology." Tsinghua Univ. Press, Beijing, 2001.
73. V. Chikan and D. F. Kelley, *J. Chem. Phys.* 117, 8944 (2002).
74. V. Chikan and D. F. Kelley, *Nano. Lett.* 2, 141 (2002).
75. V. Chikan and D. F. Kelley, *Nano. Lett.* 2, 1015 (2002).
76. V. Chikan and D. F. Kelley, *Proc. SPIE* 4807, 36 (2002).
77. O. I. Micic, M. Meglic, D. Lawless, D. K. Sharma, and N. Serpone, *Langmuir* 6, 487 (1990).
78. Y. Masumoto, T. Kawamura, and K. Era, *Appl. Phys. Lett.* 62, 225 (1993).
79. K. Edamatsu, S. Yano, S. Iwai, T. Itoh, T. Goto, and A. Ekimov, *J. Lumin.* 66-7, 406 (1995).
80. K. Edamatsu, S. Iwai, T. Itoh, S. Yano, and T. Goto, *Phys. Rev. B* 51, 11205 (1995).
81. A. Nakamura and H. Ohmura, *J. Lumin.* 83-4, 97 (1999).
82. H. Ohmura and A. Nakamura, *Phys. Rev. B* 59, 12216 (1999).
83. J. Valenta, J. Moniatte, P. Gilliot, B. Honerlage, J. B. Grun, R. Levy, and A. I. Ekimov, *Phys. Rev. B* 57, 1774 (1998).
84. J. Valenta, J. Dian, J. Hala, P. Gilliot, and R. Levy, *J. Chem. Phys.* 111, 9398 (1999).
85. J. Valenta, A. I. Ekimov, P. Gilliot, B. Honerlage, and R. Levy, *J. Lumin.* 72-4, 406 (1997).
86. D. Li, Y. Liu, H. Q. Yang, and S. X. Qian, *Appl. Phys. Lett.* 81, 2088 (2002).
87. V. I. Klimov, C. J. Schwarz, D. W. McBranch, and C. W. White, *Appl. Phys. Lett.* 73, 2603 (1998).
88. P. Tognini, A. Stella, S. De Silvestri, M. Nisoli, S. Stagira, P. Cheyssac, and R. Kofman, *Appl. Phys. Lett.* 75, 208 (1999).
89. S. Stagira, M. Nisoli, S. De Silvestri, P. Tognini, A. Stella, P. Cheyssac, and R. Kofman, *Phys. Rev. B* 62, 10318 (2000).
90. H. Giessen, B. Fluegel, G. Mohs, N. Peyghambarian, J. R. Sprague, O. I. Micic, and A. J. Nozik, *Appl. Phys. Lett.* 68, 304 (1996).
91. R. J. Ellingson, J. L. Blackburn, P. R. Yu, G. Rumbles, O. I. Micic, and A. J. Nozik, *J. Phys. Chem. B* 106, 7758 (2002).
92. G. Rumbles, D. C. Selmarten, R. J. Ellingson, J. L. Blackburn, P. R. Yu, B. B. Smith, O. I. Micic, and A. J. Nozik, *J. Photochem. Photobiol. A* 142, 187 (2001).
93. J. Christen, E. Kapon, M. Grundmann, D. M. Hwang, M. Joschko, and D. Bimberg, *Phys. Status Solidi B* 173, 307 (1992).
94. L. Rota, F. Rossi, P. Lugli, and E. Molinari, *Semicond. Sci. Tech.* 9, 871 (1994).
95. R. Cingolani, R. Rinaldi, M. Ferrara, G. C. Larocca, H. Lage, D. Heitmann, and H. Kalt, *Semicond. Sci. Tech.* 9, 875 (1994).
96. V. Dneprovskii, N. Gushina, O. Pavlov, V. Poborchii, I. Salamatina, and E. Zhukov, *Phys. Lett. A* 204, 59 (1995).
97. R. J. D. Miller, G. L. McLendon, A. J. Nozik, W. Schmickler, and F. Willig, Eds., "Surface Electron Transfer Processes." VCH, New York, 1995.
98. A. J. Nozik and R. Memming, *J. Phys. Chem.* 100, 13061 (1996).
99. P. V. Kamat and D. Meisel, "Semiconductor Nanoclusters—Physical, Chemical, and Catalytic Aspects" Elsevier, New York, 1997.
100. J. E. Moser, P. Bonnote, and M. Gratzel, *Coord. Chem. Rev.* 171, 245 (1998).
101. N. Serpone, *Res. Chem. Intermed.* 20, 953 (1994).
102. P. V. Kamat, *Progr. Reaction Kinetics* 19, 277 (1994).
103. B. Oregan and M. Gratzel, *Nature* 353, 737 (1991).
104. N. Serpone and E. Pelizzetti, "Photocatalysis: Fundamentals and Applications." Wiley, New York, 1989.
105. K. Kalyanasundaram and M. Gratzel, *Coord. Chem. Rev.* 177, 347 (1998).
106. M. K. Nazeeruddin, A. Kay, I. Rodicio, R. Humphrybaker, E. Muller, P. Liska, N. Vlachopoulos, and M. Gratzel, *J. Am. Chem. Soc.* 115, 6382 (1993).
107. M. Gratzel, "Heterogeneous Photochemical Electron Transfer." CRC Press, Boca Raton, 1989.
108. Y. Q. Gao and R. A. Marcus, *J. Chem. Phys.* 113, 6351 (2000).
109. S. Gosavi and R. A. Marcus, *J. Phys. Chem. B* 104, 2067 (2000).
110. Y. Q. Gao, Y. Georgievskii, and R. A. Marcus, *J. Chem. Phys.* 112, 3358 (2000).
111. J. B. Asbury, E. Hao, Y. Q. Wang, H. N. Ghosh, and T. Q. Lian, *J. Phys. Chem. B* 105, 4545 (2001).
112. J. M. Rehm, G. L. McLendon, Y. Nagasawa, K. Yoshihara, J. Moser, and M. Grätzel, *J. Phys. Chem.* 100, 9577 (1996).
113. T. Hannappel, B. Burfeindt, W. Storck, and F. Willig, *J. Phys. Chem. B* 101, 6799 (1997).
114. J. E. Moser, D. Noukakis, U. Bach, Y. Tachibana, D. R. Klug, J. R. Durrant, R. HumphryBaker, and M. Gratzel, *J. Phys. Chem. B* 102, 3649 (1998).
115. T. Hannappel, C. Zimmermann, B. Meissner, B. Burfeindt, W. Storck, and F. Willig, *J. Phys. Chem. B* 102, 3651 (1998).
116. T. A. Heimer and E. J. Heilweil, *J. Phys. Chem. B* 101, 10990 (1997).
117. R. J. Ellingson, J. B. Asbury, S. Ferrere, H. N. Ghosh, J. R. Sprague, T. Q. Lian, and A. J. Nozik, *J. Phys. Chem. B* 102, 6455 (1998).
118. N. J. Cherepy, G. P. Smestad, M. Gratzel, and J. Z. Zhang, *J. Phys. Chem. B* 101, 9342 (1997).
119. P. V. Kamat, *Progr. Inorg. Chem.* 44, 273 (1997).
120. I. Martini, J. H. Hodak, and G. V. Hartland, *J. Phys. Chem. B* 102, 9508 (1998).
121. N. A. Anderson, E. C. Hao, X. Ai, G. Hastings, and T. Q. Lian, *Physica E* 14, 215 (2002).
122. N. A. Anderson, E. C. Hao, X. Ai, G. Hastings, and T. Q. Lian, *Chem. Phys. Lett.* 347, 304 (2001).
123. C. Burda, T. C. Green, S. Link, and M. A. El-Sayed, *J. Phys. Chem. B* 103, 1783 (1999).
124. A. E. Faulhaber, B. A. Smith, J. K. Andersen, and J. Z. Zhang, *Mol. Cryst. Liq. Cryst. Sci.* 283, 25 (1996).
125. T. W. Roberti, B. A. Smith, and J. Z. Zhang, *J. Chem. Phys.* 102, 3860 (1995).
126. J. Y. Bigot, J. C. Merle, O. Cregut, and A. Daunois, *Phys. Rev. Lett.* 75, 4702 (1995).
127. T. S. Ahmadi, S. L. Logunov, and M. A. El-Sayed, *J. Phys. Chem.* 100, 8053 (1996).
128. B. A. Smith, J. Z. Zhang, U. Giebel, and G. Schmid, *Chem. Phys. Lett.* 270, 139 (1997).

129. S. L. Logunov, T. S. Ahmadi, M. A. El-Sayed, J. T. Khoury, and R. L. Whetten, *J. Phys. Chem. B* 101, 3713 (1997).
130. M. Perner, P. Bost, U. Lemmer, G. vonPlessen, J. Feldmann, U. Becker, M. Mennig, M. Schmitt, and H. Schmidt, *Phys. Rev. Lett.* 78, 2192 (1997).
131. J. Hodak, I. Martini, and G. V. Hartland, *Chem. Phys. Lett.* 284, 135 (1998).
132. J. H. Hodak, I. Martini, and G. V. Hartland, *J. Phys. Chem. B* 102, 6958 (1998).
133. S. Link and M. A. El-Sayed, *J. Phys. Chem. B* 103, 8410 (1999).
134. Q. F. Zhang, D. L. Wang, Q. H. Gong, and J. L. Wu, *J. Phys. D* 35, 1326 (2002).
135. D. L. Wang, H. Yang, H. B. Jiang, Q. H. Gong, Q. F. Zhang, and J. L. Wu, *Chin. Phys. Lett.* 19, 1115 (2002).
136. A. Stella, M. Nisoli, S. Desilvestri, O. Svelto, G. Lanzani, P. Cheyssac, and R. Kofman, *Phys. Rev. B* 53, 15497 (1996).
137. J. Z. Zhang, B. A. Smith, A. E. Faulhaber, J. K. Anderson, and T. J. Rosales, "Ultrafast Processes in Spectroscopy." Plenum Press, New York, 1996.
138. J. L. Wu, Q. F. Zhang, C. M. Wang, and Y. H. Zou, *Appl. Surf. Sci.* 183, 80 (2001).
139. Y. Takeda, J. P. Zhao, C. G. Lee, Gritsyna V. T., and K. N., *Nucl. Instrum. Methods B* 166, 877 (2000).
140. M. Nisoli, S. Stagira, S. DeSilvestri, A. Stella, P. Tognini, P. Cheyssac, and R. Kofman, *Phys. Rev. Lett.* 78, 3575 (1997).
141. S. Link, M. A. El-Sayed, T. G. Schaaff, and R. L. Whetten, *Chem. Phys. Lett.* 356, 240 (2002).
142. S. Link, A. Beeby, S. FitzGerald, M. A. El-Sayed, T. G. Schaaff, and R. L. Whetten, *J. Phys. Chem. B* 106, 3410 (2002).
143. C. D. Grant, A. M. Schwartzberg, Y. Yang, S. Chen, and J. Z. Zhang, *Chem. Phys. Lett.* submitted (2003).
144. H. E. Elsayed-Ali, T. B. Norris, M. A. Pessot, and G. A. Mourou, *Phys. Rev. Lett.* 58, 1212 (1987).
145. R. W. Schoenlein, W. Z. Lin, E. P. Ippen, and J. G. Fujimoto, *Appl. Phys. Lett.* 51, 1442 (1987).
146. C. K. Sun, F. Vallee, L. H. Acioli, E. P. Ippen, and J. G. Fujimoto, *Phys. Rev. B* 50, 15337 (1994).
147. J. H. Hodak, A. Henglein, and G. V. Hartland, *J. Phys. Chem. B* 104, 9954 (2000).
148. M. Nisoli, S. DeSilvestri, A. Cavalleri, A. M. Malvezzi, A. Stella, G. Lanzani, P. Cheyssac, and R. Kofman, *Phys. Rev. B* 55, 13424 (1997).
149. C. Voisin, N. Del Fatti, D. Christofilos, and F. Vallee, *J. Phys. Chem. B* 105, 2264 (2001).
150. C. Voisin, D. Christofilos, N. Del Fatti, and F. Vallee, *Physica B* 316, 89 (2002).
151. J. H. Hodak, I. Martini, and G. V. Hartland, *J. Chem. Phys.* 108, 9210 (1998).
152. Y. Hamanaka, J. Kuwabata, I. Tanahashi, S. Omi, and A. Nakamura, *Phys. Rev. B* 6310, 4302 (2001).
153. G. V. Hartland, M. Hu, O. Wilson, P. Mulvaney, and J. E. Sader, *J. Phys. Chem. B* 106, 743 (2002).
154. M. Perner, S. Gresillon, J. Marz, G. von Plessen, J. Feldmann, J. Porstendorfer, K. J. Berg, and G. Berg, *Phys. Rev. Lett.* 85, 792 (2000).
155. C. D. Grant, A. M. Schwartzberg, T. J. Norman, and J. Z. Zhang, *J. Am. Chem. Soc.* 125, 549 (2002).
156. S. Link, M. B. Mohamed, and M. A. El-Sayed, *J. Phys. Chem. B* 103, 3073 (1999).
157. A. A. Lazarides and G. C. Schatz, *J. Chem. Phys.* 112, 2987 (2000).
158. A. A. Lazarides and G. C. Schatz, *J. Phys. Chem. B* 104, 460 (2000).
159. J. J. Storhoff, A. A. Lazarides, R. C. Mucic, C. A. Mirkin, R. L. Letsinger, and G. C. Schatz, *J. Am. Chem. Soc.* 122 (2000).
160. J. R. Heath, C. M. Knobler, and D. V. Leff, *J. Phys. Chem. B* 101, 189 (1997).
161. A. N. Shipway, M. Lahav, R. Gabai, and I. Willner, *Langmuir* 16, 8789 (2000).
162. T. J. Norman, C. D. Grant, D. Magana, D. Cao, F. Bridges, J. Liu, A. van Buuren, and J. Z. Zhang, *J. Phys. Chem. B* 106, 7005 (2002).
163. K. S. Mayya, V. Patil, and M. Sastry, *Bull. Chem. Soc. Jpn.* 73, 1757 (2000).
164. P. Dimon, S. K. Sinha, D. A. Weitz, C. R. Safinya, G. S. Smith, W. A. Varady, and H. M. Lindsay, *Phys. Rev. Lett.* 57, 595 (1986).
165. J. P. Wilcoxon, J. E. Martin, and D. W. Schaefer, *Phys. Rev. A* 39, 2675 (1989).
166. M. Quinten, D. Schonauer, and U. Kreibig, *Z. Phys. D* 12, 521 (1989).
167. M. Quinten, *Appl. Phys. B* 73, 317 (2001).
168. D. Schonauer, M. Quinten, and U. Kreibig, *Z. Phys. D* 12, 527 (1989).

Chemical Derivatization of Carbon Nanotube Tips

Vladimir A. Basiuk, Elena V. Basiuk (Golovataya-Dzhymbeeva)

Universidad Nacional Autónoma de México, México D.F., Mexico

CONTENTS

1. Introduction
 2. Oxidized Nanotubes
 3. Derivatization
 4. Spectroscopic Characterization
 5. Properties
 6. Conclusions
- Glossary
References

1. INTRODUCTION

Despite the short history of carbon nanotubes (CNTs), comprising single-walled and multiwalled nanotubes (SWNTs and MWNTs, respectively), this class of materials gained unprecedented attention of scientists in different fields. The reason is that CNTs possess a number of chemical, structural, mechanical, and electronic properties that can hardly be found simultaneously in any other chemical compound or material. In particular, they are characterized by considerable chemical and thermal stability, extremely high tensile strength and elasticity, an extreme aspect ratio (especially for SWNTs), the ability to incorporate other molecules into their interior cavities, the possibility of chemical functionalization, and at the same time metallic and high thermal conductivity [1, 2]. Thus, the versatility of potential applications proposed for CNTs is not surprising. Some of them can be based on the as-grown nanotube materials, without an additional chemical treatment. For other applications, chemical modification might be necessary, such as grafting of moieties that allow assembly of modified SWNTs onto surfaces for electronic applications, moieties that allow reaction with host matrices in composites, and sensing applications that may require the presence of a variety of functional groups

bound to SWNTs [3]. Besides that, almost any technological application requires chemically pure and uniform nanotubes, which can be manipulated and investigated by analytical methods. Unfortunately, this remains a great challenge for chemists and material scientists. In this context, chemical derivatization is an especially attractive goal, since it can improve solubility and processibility of CNTs (SWNTs first of all) and allows their unique properties to be coupled to those of other types of materials [4].

A systematic development of the methods for CNT chemical functionalization started very recently: first results were published in 1998 [5–8]. The studies are focused primarily on SWNTs, which are much easier to handle and characterize due to their simpler, monomolecular structure, higher uniformity and solubility as compared to those of MWNTs. Two recent reviews [3, 4] summarized covalent chemistry of SWNTs (they comprised the data as of 2001; this area has been considerably enriched during the subsequent year). The authors considered all known types of the reactions, which can be divided into two main groups: (a) defect-group functionalization and (b) covalent sidewall functionalization. In this chapter we focus on the former group. Derivatization reactions of this kind are restricted mainly to the nanotube ends and thus are too localized to noticeably change main bulk properties of the materials (contrary to the sidewall functionalization). This is particularly true for their spectroscopic properties, which complicates extremely the product characterization. On the other hand, for some applications this kind of localized chemistry may be desirable and even the only acceptable one, since it does not alter appreciably electronic and mechanical properties of CNTs and generally (in some cases dramatically) improves solubility of SWNTs [3].

2. OXIDIZED NANOTUBES

Pristine CNTs produced by most methods are closed by all-carbon fullerene caps and thus cannot be qualified as functionalized materials. This situation changes if one subjects

the as-prepared nanotubes to an oxidative treatment with nitric acid, its mixture with a sulfuric acid, sulfuric acid–hydrogen peroxide mixture, etc., which are utilized for purification (removal of amorphous carbon, graphite, metals, and their oxides used as catalysts) and cutting of the CNTs [3, 4, 7–9]. The acid treatment methods were adopted from well-explored graphite chemistry [10, 11], where, for example, it is long known that $\text{HNO}_3\text{--H}_2\text{SO}_4$ mixtures intercalate and exfoliate graphite. The oxidation produces in CNTs terminations and wall defects with a number of oxygenated functionalities, the most important of them being carboxylic groups COOH. This was confirmed by analyzing the samples by vibrational (primarily infrared, IR) [8, 9, 12–14] and near-edge X-ray absorption fine structure (NEXAFS) [14] spectroscopy. In particular, IR spectra of the oxidized SWNTs were reported to exhibit a carboxylic band at 1720–1735 cm^{-1} ($\nu_{\text{C=O}}$) [8, 12–14], as well as quinone $\nu_{\text{C=O}}$ at 1660 cm^{-1} , a $\nu_{\text{C-O}}$ band at 1245 cm^{-1} , and $\nu_{\text{O-H}}$ absorption at 3644 cm^{-1} [13, 14]. In IR spectra of the oxidized MWNTs, the $\nu_{\text{C=O}}$ band at 1750 cm^{-1} was observed, along with $\nu_{\text{O-H}}$ absorption at 3500 cm^{-1} [9]. According to the NEXAFS results [14], both carbonyl (C=O) and ether (C–O–C) functionalities are present in the oxidized SWNTs. The conclusion on ether groups, however, seems rather confusing, since it is difficult to explain how they can survive strong hydrolytic media such as $\text{HNO}_3\text{--H}_2\text{SO}_4$ and $\text{H}_2\text{SO}_4\text{--H}_2\text{O}_2$ mixtures.

Titration of commercial acid-purified full-length SWNTs with NaOH and NaHCO_3 solutions was employed to estimate the total percentage of acidic sites and COOH groups, respectively [15]. Different samples gave fairly consistent results: the SWNT–COOH functionality was about 1–2%, and the total acid functionality was about 1–3%.

Another frequently employed way to oxidize CNTs is gas-phase ozone treatment [12, 16–18]. This process occurs at a room temperature, at a much lower rate as compared to fullerenes [16]. It is not used for the nanotube purification (as it is unable to remove metal impurities) but helps one to better understand the nature of oxygen-containing functionalities on the CNT tips and wall defects. Room temperature dry ozonation of open- and closed-ended SWNTs, preheated to 800 °C in a vacuum to remove most of the original oxygen-containing functional groups, gave rise to development of several IR bands [17]. The bands at 1739, 1200, and 1040 cm^{-1} are indicative of the production of ester groups. The band at 1650 cm^{-1} was assigned to $\nu_{\text{C=O}}$ of quinone groups, while the band at 1581 cm^{-1} was assigned to C=C bonds located near the newly formed oxygenated groups. The esters and quinones can be removed by heating in a vacuum to 600 °C. It is thought that the ozone oxidation is confined to the end caps and the dangling bonds created by the removal of these caps, whereas the structural integrity of the nanotube walls is maintained.

The same research group attempted to quantify the fraction of oxidized carbon sites present in closed-end SWNTs purified by acidic oxidation [12]. This was done by measuring the evolution of CO and CO_2 gases on heating to 1000 °C. Following the thermal treatment, the defect sites were titrated repeatedly with O_3 . According to the results, about 5% of the carbon atoms are localized at defective

sites, capable of facile oxidation by ozone. In turn, the high defect site density indicates that a significant number of these sites exist on the nanotube walls. At the same time, in neither of the two studies did the authors mention on the formation of COOH groups: the dry ozonation conditions employed are incapable to generate OH-containing moieties.

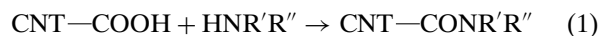
In view of the crucial importance of carboxylic groups for the defect-site covalent chemistry of CNTs, an important development was presented very recently by Cai et al. [18]. The authors modified the ozonation procedure by using simultaneously ultraviolet (UV) irradiation and allowing atmospheric moisture to be present in the reaction system. It was assumed that atmospheric moisture in the presence of UV radiation converts intermediate ozonides into carboxylic acids and other functionalities. The authors observed a $\nu_{\text{C=O}}$ peak at 1708 cm^{-1} and a broad hydrogen-bonded band $\nu_{\text{O-H}}$ at 3410 cm^{-1} , both suggestive of carboxylic acid groups present in the SWNT sample. At the initial oxidation stage, a 1630 cm^{-1} peak of quinone $\nu_{\text{C=O}}$ vibrations was observed as well but then became less distinguishable as a shoulder at the $\nu_{\text{C=C}}$ background band at 1580 cm^{-1} . The peaks at 1215 and 1055 cm^{-1} were attributed to the vibration modes $\nu_{\text{C-O-C}}$ of ester or $\nu_{\text{C-O}}$ of carboxylic acid.

The distribution of the oxygen-containing functionalities within CNTs has not yet been well characterized. As was mentioned above, they are believed to exist primarily at the nanotube ends and at sites along the sidewalls. By use of solution phase mid-IR spectroscopy, Hamon et al. [19] attempted to estimate the ratio of the carbon atoms in the SWNT backbone to the carbon atoms in the end-groups and at defect sites of the octadecylamido functionalized soluble SWNTs (see Section 3.1). Their analysis showed that the weight percentage of the octadecylamido functionality in the derivatized SWNTs is about 50%, which corresponds to a mole fraction of 6%. These high values (consistent with the value of ca. 5% for the oxidized carbon sites measured by the ozone titration [12]) suggested that a large proportion of the COOH-containing defect sites is located on the sidewalls, since the values of 5–6% are roughly one order of magnitude higher than would be indicated by models based solely on end-group functionalization. More detailed considerations on this subject will be presented in Section 4.

3. DERIVATIZATION

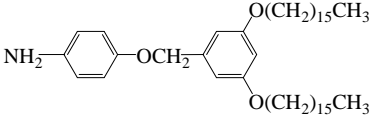
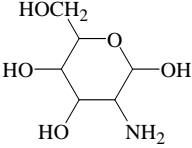
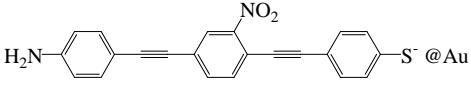
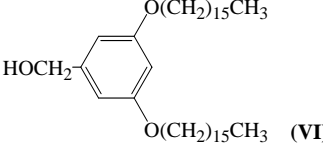
3.1. Amidation

Carboxylic groups can be readily derivatized by a variety of reactions. The easiest and most efficient way is to produce amide derivatives, by linking chemically activated COOH groups at the CNT terminations to amines, according to the general scheme



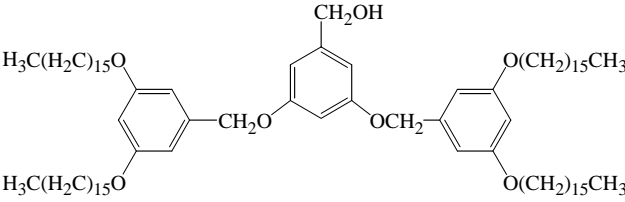
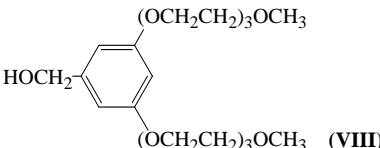
where R' and R'' are H, aliphatic, or aromatic substituents (Table 1).

Table 1. Amino components, alcohols, and activating agents used to derivatize CNT (SWNT and MWNT) tips through amidation reaction (1) and esterification (3).

Amino component/alcohol	Activating agent and reaction conditions	Nanotubes	Ref.
Amidation			
NH ₂ -(CH ₂) ₁₁ -SH	SOCl ₂ , RT, toluene	SWNT	[7]
NH ₂ -(CH ₂) ₁₇ -CH ₃	SOCl ₂ , amine melt, 90–100 °C, 96 h	SWNT	[8, 19, 21, 22, 24]
	amine vapor, 170 °C, 2 h	MWNT	[28]
NH ₂ -(CH ₂) ₈ -CH ₃	amine vapor, 160–170 °C, 1 h	SWNT	[40]
CH ₃ -(CH ₂) ₄ -NH-(CH ₂) ₄ -CH ₃	amine vapor, 160–170 °C, 1 h	SWNT	[38]
4-NH ₂ -C ₆ H ₄ -(CH ₂) ₁₃ -CH ₃	SOCl ₂ , amine melt, 100 °C, 96 h	SWNT	[21]
	SOCl ₂ , 75 °C, 48 h	SWNT, MWNT	[26]
 Glucosamine	SOCl ₂ , anhydrous THF, reflux, 48 h	SWNT	[34]
NH ₂ -[-(CH ₂) ₂ -O-] _n -H [-(CH ₂) ₂ -N(C(=O)C ₂ H ₅)-(CH ₂) ₂ -NH-] _n [poly(propionylethylenimine-co-ethylenimine), or PPEI-EI]	SOCl ₂ , DMF + aqueous NaOH, RT, 12 h	SWNT	[32]
	SOCl ₂ , polymer melt, 165 °C, 20 min to 2 h	SWNT, MWNT	[27–29, 31]
	EDC, KH ₂ PO ₄ buffer, RT, 2–6 h	MWNT	[30]
	polymer melt, 160–180 °C, 12 h	MWNT	[31]
NH ₂ -CH ₂ -C ₆ H ₅	EDC, buffer pH 6.0, RT, 2 h	MWNT	[5]
		SWNT	[6]
NH ₂ -(CH ₂) ₂ -NH ₂	EDC, buffer pH 6.0, RT, 2–48 h;	MWNT	[5]
	or EDC, DMF + aqueous buffer, RT, 48 h	SWNT	[6, 33]
NH ₂ -(CH ₂) ₁₁ -S ⁻ @ Au	DCC, DMF, 50–60, °C, 12 h	SWNT	[23]
NH ₂ -(CH ₂) ₂ -SH	DCC, ethanol, RT, 24 h	SWNT	[37]
	DCC (DMF), or EDC (aqueous solution)	SWNT	[18]
NH ₂ -(CH ₂) _{2n} -NH ₂ (n = 1–4)	DCC, DMF + THF, RT, 72 h	MWNT	[25]
Bovine serum albumin	EDC, KH ₂ PO ₄ buffer, RT, 24 h	SWNT, MWNT	[35]
DNA, H ₂ N-(CH ₂) ₆ -GCCGATGCACC	EDC + sulfo-NHS, aqueous solution, RT, 2 h	MWNT	[36]
NH ₂ -(CH ₂) ₁₀ -COO ⁻ @ TiO ₂	EDC, DMF + aqueous buffer, RT, 48 h	SWNT	[33]
NH ₂ -C(=O)-NH-NH ₂ (semicarbazide)	EDC, DMF + aqueous buffer, RT, 48 h	SWNT	[33]
Esterification			
CH ₃ -(CH ₂) ₁₇ -OH	SOCl ₂ , pyridine, 117 °C, 96 h	SWNT	[43]
[-CH ₂ -CH(OC(=O)CH ₃)-CH ₂ -CH(OH)-] _n [poly(vinyl acetate-co-vinyl alcohol), or PVA-VA]	SOCl ₂ , polymer melt, 165 °C, 20 min	MWNT	[27]
		SWNT	[29]
 (VI)	SOCl ₂ , 75 °C, 48 h	SWNT, MWNT	[26, 44, 45]

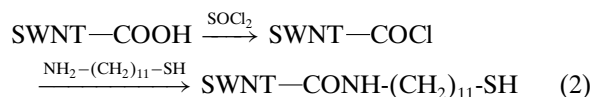
continued

Table 1. Continued

Amino component/alcohol	Activating agent and reaction conditions	Nanotubes	Ref.
 <p style="text-align: center;">(VII)</p>	SOCl ₂ , 75 °C, 48 h	SWNT, MWNT	[26]
 <p style="text-align: center;">(VIII)</p>	SOCl ₂ , THF, NaH, RT, 24 h	SWNT, MWNT	[26, 44]

Note: DCC, dicyclohexylcarbodiimide; EDC, 1-ethyl-3-(3-dimethylaminopropyl)carbodiimide; DMF, dimethylformamide; THF, tetrahydrofuran; sulfo-NHS, N-hydroxysulfo-succinimide; RT, room temperature; @, surface.

The broad applicability of this coupling reaction to aqueous and nonaqueous chemistry made it especially attractive and widely used for nanotube functionalization [5–8, 18–40]. In one of the very first reports on this subject [7], the derivatization was implemented by converting the carboxylic groups to the corresponding acid chloride by reaction with thionyl chloride SOCl₂ at room temperature, with subsequent exposure to an amino alkanethiol NH₂–(CH₂)₁₁–SH in toluene, also at room temperature, that is,



The nanotubes functionalized in this way were bound to 10-nm-diameter gold nanoparticles. Attachment of such strategically designed binding groups is thought to be very useful in directing assembly of CNTs into molecular devices [7].

Varying the structure of hydrocarbon moiety in the amine, one can afford an enhanced affinity to different media or substrates. In particular, the use of octadecylamine NH₂–(CH₂)₁₇–CH₃ [8, 19] (Table 1) gives rise to substantial solubility of the shortened (100–300 nm in length) SWNTs in chloroform, dichloromethane, aromatic solvents (benzene, toluene, chlorobenzene, 1,2-dichlorobenzene), tetrahydrofurane, pyridine, and CS₂, in sharp contrast to the starting nanotubes [8, 21, 22, 24]. If the reaction is carried out at elevated temperature for a few days, most of the SWNT bundles exfoliate to give individual SWNT macromolecules. SWNTs solubilized in this way can be purified by liquid-chromatographic techniques, offering functionalized material virtually free of contaminants. The nanotubes derivatized with 4-tetradecylaniline, 4-NH₂–C₆H₄–(CH₂)₁₃–CH₃, showed a similar solubility behavior [21] (the authors believed that the product exists primarily as imides, and not amides; in other words, one amine molecule covalently couples to two neighboring COOH groups).

Logically, the more extended the lipophilic moiety in the amino component, the higher the CNT solubility in nonpolar solvents is expected to be. Sun et al. [26] reported on

the functionalization of both SWNTs and MWNTs with a dendron-type derivative of 4-aminophenol (Table 1), via the same SOCl₂-activated reaction (2). An elevated temperature (typically 75 °C; stirring for 2 days under nitrogen atmosphere) was apparently a requirement for these reactions to proceed efficiently, since the use of lower temperatures (for example, 45 °C) resulted in a significantly less amount of the functionalized nanotubes (on the basis of solution color or visible absorption).

These studies on SWNT functionalization were aimed at solubilization in organic solvents. A much larger range of potential applications would open for water-soluble nanotubes. In particular, biochemical and biomedical applications would require SWNTs in aqueous media. Pompeo and Resasco [34] proposed a very efficient method to increase SWNT solubility in water, by choosing glucosamine as the amino component of high hydrophilicity, to react with the thionyl chloride-activated SWNTs. Aqueous solutions of the resulting functionalized nanotubes were very stable and remained translucent and without precipitation for weeks. When the pH of the solution was lowered to 2 at 80 °C by addition of hydrochloric acid, the SWNTs immediately dropped out of solution: this is apparently due to the hydrolysis of the amide bonds. The hydrolysis was much slower at room temperature.

High molecular weight compounds (polymers) can be used as the amino components as well. The reactive amino groups can be located either on the macromolecule termini, or within the polymer chain. Depending on that, two different types of nanotube–polymer assemblies can form, as is schematically explained in Figure 1. When reactive NH groups are located within the polymer chain, CNTs are bound as a side chain (Fig. 1a). If reactive NH (or NH₂) groups are terminal, then CNTs are incorporated into the main chain (Fig. 1b). An example of the latter is the grafting of SWNTs (whose carboxylic groups were activated with thionyl chloride) with monoamine-terminated poly(ethylene oxide) (PEO) [32]. Since amphiphilic PEO is soluble in water (as well as in many organic solvents), the PEO and SWNT segments take expanded and extended

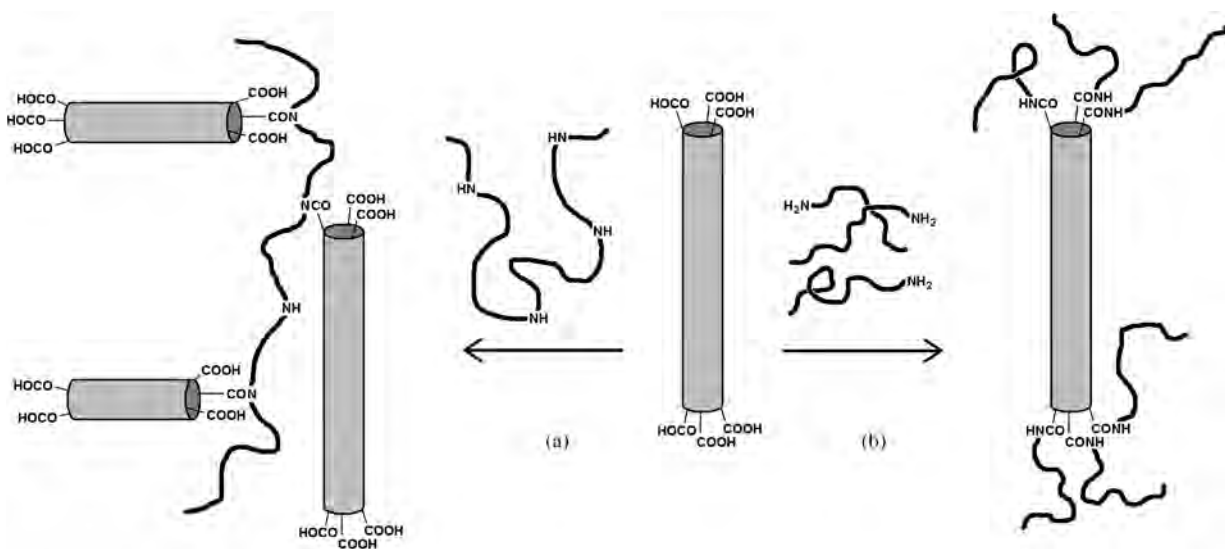


Figure 1. Two general ways of coupling carbon nanotubes with NH-containing polymers through amidation reaction (1): (a) reactive NH groups are located within the polymer chain, and CNTs are bound as a side chain; (b) reactive NH (or NH_2) groups are terminal, and CNTs are incorporated into the main chain.

conformations in aqueous medium. When the graft product is dispersed in chloroform, each SWNT segment collapses into a globular aggregate.

In a series of works by Sun et al. [27–29, 31] another possibility was explored (Fig. 1a), that is, to attach CNTs as a side chain to linear polymer poly(propionylethylenimine-co-ethylenimine) (PPEI-EI; Table 1). Both SWNTs and MWNTs were employed whose COOH groups were converted to acyl chlorides by treating with SOCl_2 . The amidation was performed by mixing the reactants and heating at 165°C for 20 min to 2 h. PPEI-PI is a highly soluble polymer, and the resulting polymer-bound nanotubes are soluble in both organic solvents and water, forming highly colored homogeneous solutions.

Thionyl chloride is not the only reagent which can be used to activate carboxylic groups in amide coupling reactions. Parallel to the works employing SOCl_2 to treat COOH groups of CNTs, a number of authors reported on the use of carbodiimide chemistry for the same purpose. Carbodiimides such as dicyclohexylcarbodiimide (commonly known as DCC) and 1-ethyl-3-(3-dimethylaminopropyl)carbodiimide (EDC) have some indisputable advantages as compared to thionyl chloride. The direct products of activation with carbodiimides (*O*-acylisoureas) are more stable to moisture (as compared to the acyl chloride intermediates), and the rate of their aminolysis is much higher than that of hydrolysis. This implies a high selectivity of the reaction, as well as allows some flexibility in choosing experimental conditions. Even more important is that some carbodiimides, for example EDC, are soluble in aqueous media (pure water and buffer solutions): this property is absolutely indispensable when working with biomolecules. And finally, they are not corrosive, contrary to SOCl_2 and HCl evolved upon the reaction; this property can be important when working with fine and sensitive devices such as atomic force microscopy (AFM) cantilevers.

It was the cantilever tip preparation where carbodiimide chemistry was for the first time employed to chemically modify CNT ends by Wong et al. [5]. They derivatized carboxylic MWNT tips with benzylamine and ethylenediamine (Table 1) through EDC-activated amidation in an aqueous buffer solution. The reaction does not require heating and is completed in 2 h. A little later, the same group implemented the above modification strategy with SWNTs [6], in order to achieve the highest lateral resolution in AFM to date. The experiment is schematically explained in Figure 2. The functionality at the SWNT tip ends was determined by measuring the adhesion force between the tip ends and hydroxyl-terminated self-assembled monolayer (SAM) surfaces; the fraction of proton dissociation can be readily monitored in this way. Force titrations made with carboxyl-terminated SWNTs on OH-terminated SAMs exhibited a well-defined drop in adhesion at ca. pH 4.5 (Fig. 2b), which is characteristic of COOH deprotonation. The absolute value of the adhesion force at low pH can vary between tips, and such differences are believed to reflect variations in the number of COOH groups at the ends of different tips. The similarity of the $\text{p}K_a$ determined from the SWNT force titrations (4.5) to the bulk solution value for benzoic acid (4.2) indicated that the COOH groups at the SWNT ends are well solvated and hence accessible for reactions. Then SWNT tips were amide-derivatized with benzylamine, which has non-ionizable, hydrophobic functionality, to yield the expected pH-independent adhesion forces on OH-terminated SAMs. This covalent modification eliminated the pH-dependent adhesion observed with the unmodified tips. The absolute values of the adhesion forces obtained in aqueous solutions using these phenyl-terminated tips were generally larger than for the COOH-terminated nanotubes and were consistent with the hydrophobic nature of such tips. Furthermore, force titrations with ethylenediamine-derivatized (amine-terminated) SWNT tips showed no measurable adhesion at low pH and finite adhesion above pH 8. This

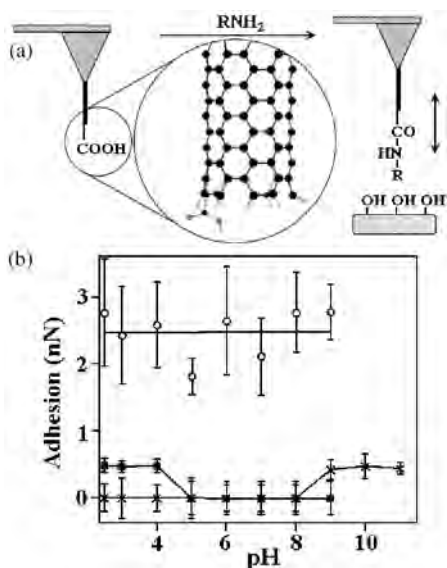


Figure 2. (a) Schematic illustrating the modification of a SWNT tip by coupling an amine (RNH_2) to a terminal COOH , and the application of this probe to sense specific interactions between the functional group (R) and surface OH groups. (b) Adhesion force as a function of pH between SWNT tips and an OH-terminated self-assembled monolayer: COOH /filled squares (unmodified); phenyl/open circles (modified with benzylamine); and amine/crosses (modified with ethylenediamine). Reprinted with permission from [6], S. S. Wong et al., *J. Am. Chem. Soc.* 120, 8557 (1998). © 1998, American Chemical Society.

pH-dependent behavior correlates with the authors' expectations for exposed amine groups that are neutral at high pH and protonated and charged at low pH. The modified SWNT tips were employed to produce chemically sensitive AFM images with the highest lateral resolution to date and can be used to study binding in biological and chemical systems.

In a similar study by Yang et al. [23], the amidation coupling was used to attach SWNTs to AFM tips, as shown in Figure 3. Commercial Si_3N_4 cantilever tips were coated with 100 nm gold by thermal evaporation onto a 10-nm adhesion layer of titanium. Then the gold-coated tips were immersed in ethanol solution of $\text{NH}_2-(\text{CH}_2)_{11}-\text{SH}$. Due to a high affinity to gold through S^--Au interactions, the amino alkanethiol formed a densely packed self-assembled monolayer, where the amino groups were available for further coupling with the DCC-activated carboxylic groups. Liu et al. [37] organized SWNTs on gold by linking them through a shorter amino alkanethiol, $\text{NH}_2-(\text{CH}_2)_2-\text{SH}$, by means of DCC-activated amidation.

For the fabrication of SWNT-based molecular devices, conjugated organic molecules with π -orbital overlap are required for charge transport and functional devices. Rigid-rod conjugated oligo(phenylene ethynylene)s, having an array of interesting electronic properties, were used as linking molecules to prepare rigid self-assembled monolayers of wet-ozonated SWNTs on gold [18]. The oligo(phenylene ethynylene)s contained a sulfhydryl group at one end, and one of them had an amino group at the opposite terminus (Table 1). The amidation was performed using either DCC or EDC.

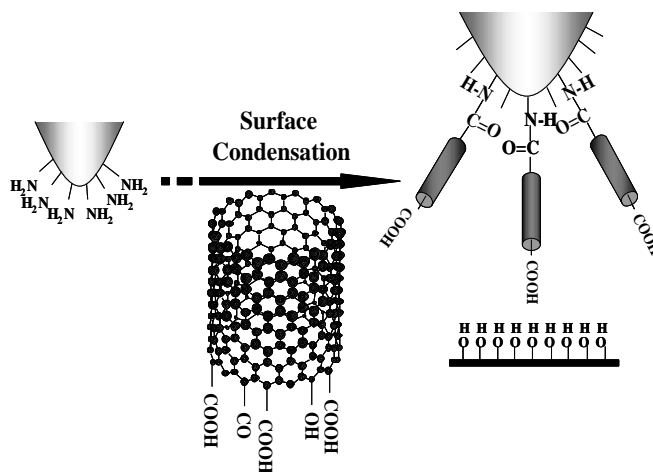


Figure 3. Schematic illustration of the preparation of single-walled carbon nanotube AFM tips and measurement of force titration. Reprinted with permission from [23], Y. Yang et al., *J. Phys. Chem. B* 106, 4139 (2002). © 2002, American Chemical Society.

There are several examples of coupling bi- or polyfunctional amino components to carboxylic groups of CNTs in the presence of carbodiimides. The simplest case is chemical modification of shortened MWNTs ($<1 \mu\text{m}$ length) with various straight-chain alkyldiamines, $\text{NH}_2-(\text{CH}_2)_{2n}-\text{NH}_2$ ($n = 1-4$), where DCC was used [25]. The derivatized nanotubes were dispersed in polar solvents such as ethanol, dimethyl sulfoxide (DMSO), and dimethylformamide (DMF) more easily than the starting material. The dispersions (at MWNT concentrations of more than 0.3 mg/ml) were stable without aggregation for more than one month.

EDC was used as an alternative to thionyl chloride in the amidation of MWNTs with high-molecular-weight PPEI-EI (Table 1) [30]. This reaction was found to be significantly improved in both efficiency and yield by sonication under ambient conditions. The enhancement in the reaction yield may be attributed to the sonication-induced activation of the carboxylic acids by EDC, as rationalized for the sonication enhancements in other diimide-activated reactions. It was also found that depending on the duration of sonication, the nanotubes were shortened to different lengths in the functionalization. The authors suggested that this method allows relatively efficient preparation of solubilized CNTs of a potentially selectable average length.

Similarly, SWNTs and MWNTs were functionalized by bovine serum albumin (BSA) via EDC-activated amidation under ambient conditions [35]. The nanotube-BSA conjugates thus obtained were highly water soluble, forming dark-colored aqueous solutions. Results from characterizations using AFM, thermal gravimetric analysis, Raman, and gel electrophoresis showed that the conjugate samples indeed contain both carbon nanotubes and BSA and that the protein species are intimately associated with the nanotubes. Bioactivities of the CNT-bound proteins were evaluated using the total protein microdetermination assay (the modified Lowry procedure). The results showed that the overwhelming majority ($\sim 90\%$) of the protein species in the nanotube-BSA conjugates remain bioactive.

In one of the most recent reports having implications for biosciences, vertically aligned MWNT arrays were fabricated as a nanoelectrode platform for biosensor development and then functionalized with nucleic acids [36]. Prior to chemical functionalization, metal catalyst particles at the nanotube ends were removed and the closed ends are opened, as usual. However, the author concluded that the oxidative treatment for generating COOH groups at the opened ends compromises the mechanical stability of the nanotubes, often leading to total collapse of the aligned MWNTs. To solve this problem, they developed a new approach for filling the gaps between the nanotubes with a spin-on glass (SOG). Nucleic acid attachment was accomplished using EDC along with *N*-hydroxysulfo-succinimide (sulfo-NHS). The EDC-derived ester intermediate rapidly undergoes hydrolysis; however, in the presence of excess sulfo-NHS a more water stable sulfo-succinimidyl intermediate is formed. Subsequently, the succinimidyl intermediate reacted with nucleic acid [DNA or $\text{H}_2\text{N}-(\text{CH}_2)_6-\text{GCCGATGCACC}$ oligonucleotide], resulting in the formation of desirable amide linkage. It appeared that the reaction was essentially completed after 2 h. Results from the coupling of nucleic acids to the MWNT arrays suggested that the SOG enhances the reactivity by providing structural support to the nanotubes. The SOG also covers the length of the sidewalls of CNTs, leading to a less hydrophobic interface, and thus may aid in improving the chemical reactivity.

Banerjee and Wong [33] synthesized SWNT-nanocrystal heterostructures of possible interest for molecular electronics, photocatalysis, and solar energy conversion and as probes for scanning force microscopy. Oxidized SWNTs were linked to cadmium selenide (CdSe) nanocrystals, capped with mercaptothiol derivatives (*para*-mercaptobenzoic, thioglycolic, and 3-mercaptopropionic acids), as well as to titanium dioxide (TiO_2) nanocrystals, functionalized with 11-aminoundecanoic acid (Table 1). The coupling with acid-terminated CdSe nanocrystals and acid-terminated tubes was facilitated with the aid of intermediary linking agents, such as ethylenediamine and semicarbazide $\text{NH}_2-\text{C}(=\text{O})-\text{NH}-\text{NH}_2$, in the EDC-activated amidation; this multistep procedure is schematically explained in Figure 4. Based on electronic absorption spectroscopy, charge transfer is thought to proceed from the nanocrystal to the nanotube in the CdSe-SWNT system, whereas in the TiO_2 -SWNT system, charge transfer is expected to occur from the nanotube to the nanocrystal.

From basic organic chemistry it is known that activation of carboxylic groups can be achieved by using not only chemical reagents like SOCl_2 and carbodiimides but also by simple heating. In one of the reports by Sun et al. on the functionalization of CNTs with aminopolymers (see above), the amide coupling was achieved by direct heating MWNTs with PPEI-EI at 160–180 °C, that is, in the polymer melt, under nitrogen protection for 12 h [31]. According to the authors' observations, this method seems less efficient in the MWNT dispersion as compared to the SOCl_2 activation, because the corresponding solution of the functionalized nanotubes exhibits more scattering in the UV-visible absorption measurements. But, on the other hand, the direct

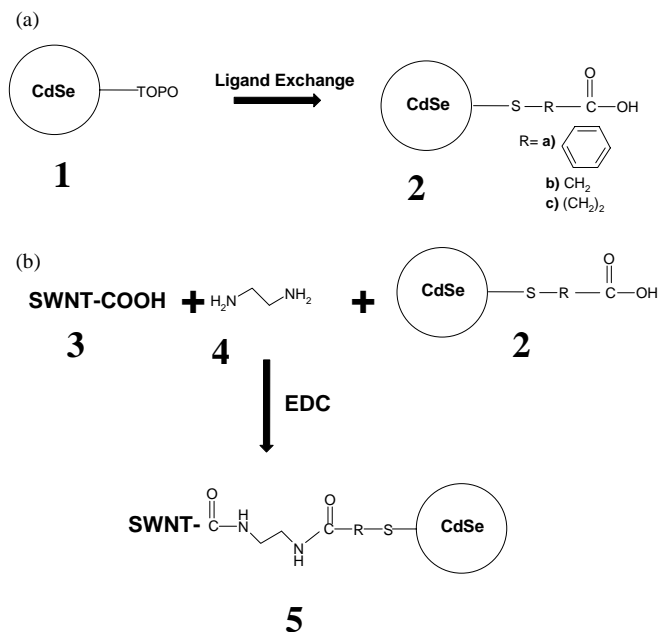


Figure 4. Schematic of the addition of CdSe nanocrystals to oxidized SWNTs. Trioctylphosphine oxide (TOPO) capped nanocrystals (1) were prepared by established methods using organometallic precursors. (a) TOPO capping was substituted by a thiol ligand to form an acid-terminated CdSe nanocrystal (2). Substituted thiocarboxylic acids used included *para*-mercaptobenzoic acid, thioglycolic acid, and 3-mercaptopropionic acid, as represented by different R groups shown. (b) (2) was linked to SWNTs (3) by an ethylenediamine linker (4) in the presence of EDC to form the adduct (5). The bonds at the interfaces are not drawn to scale. Reprinted with permission from [33], S. Banerjee and S. S. Wong, *Nano Lett.* 2, 195 (2002). © 2002, American Chemical Society.

heating apparently produces functionalized MWNT samples of a higher nanotube content.

We used the same strategy for the amidation of oxidized SWNTs with simple amines in the gas phase [38, 40]. This is an extension of the gas-phase derivatization technique originally developed for chemical modification of silica surfaces. Its attractive features are that the formation of amide linkages proceeds smoothly at 150–180 °C and is relatively fast (0.5–1 h), as well as providing high yields of the amide derivatives. Excess vaporous reagent can be removed from the reaction zone under moderate vacuum. In addition, there is no need to use a (organic) solvent medium; this feature is attractive not only from an ecological point of view but also in that it helps to avoid undesirable particle aggregation of the material derivatized. The amino components we employed were nonylamine, dipentylamine, and 1-octadecylamine (Table 1). The resulting SWNT products exhibit solubility properties similar to those of the SWNT derivatized with long-chain amines through thionyl chloride and carbodiimide activation.

An important aspect of CNT reactivity is the existence of different forms of the nanotubes by themselves: zigzag, armchair, and chiral forms [1, 2]. All of these species are apparently present in CNTs grown by most methods. For the particular case of direct (heating-induced) amidation reaction (1), one can expect that the reactivity of carboxylic

groups toward amines might be different depending on whether the nanotubes have an armchair or zigzag structure. Studying the specificity of such a sort can be considered as a possible pathway to selective derivatization of different forms of CNTs and to their further separation: for example, due to different solubility of derivatized and nonderivatized nanotubes. However, this goal seems to be very complicated from the experimental point of view and requires further sophistication of the methods of handling and observing individual CNTs. We tried to give some insight by using the two-level ONIOM (combined quantum mechanics/molecular mechanics) calculations [38, 39]. As model reaction systems, we considered monocarboxylated short fragments of (10, 0) zigzag and (5, 5) armchair SWNTs interacting with the simplest aliphatic amine, methylamine. The models are shown in Figure 5 along with the potential energy surfaces calculated at the B3LYP/6-31G(d) level of theory (energies relative to the level of separated reactants [39]). If one compares the energies of the transition states to those of the reactant level, their values do not differ significantly: 51.1 and 48.8 kcal mol⁻¹ for the armchair and zigzag SWNTs, respectively. Much bigger differences can be found for the reaction complexes and products. Energy for the armchair reaction complex (-2.9 kcal mol⁻¹) is 10.5 kcal mol⁻¹ higher than that for its zigzag counterpart (-13.4 kcal mol⁻¹). The situation is opposite for the amidation products: the armchair products (-9.0 kcal mol⁻¹) are lower by 7.5 kcal mol⁻¹ as compared to the zigzag products (-1.5 kcal mol⁻¹). This shows the direct formation of amides on armchair SWNT tips according to reaction (1) to be much more advantageous, as compared to that on zigzag SWNT tips. Moreover, since for the latter the

reaction complex appears to lie below the products, the amidation as a whole is energetically unfavorable (though it can be facilitated by pumping out water formed, as contemplated in the gas-phase derivatization technique [38]). Another strong argument supporting our conclusion is evident if one compares the transition state energies not to the reactant level but to the level of the reaction complexes. Barrier heights calculated in this way are 54.0 (armchair) and 62.2 kcal mol⁻¹ (zigzag), which is a significant difference, of 8.2 kcal mol⁻¹. It is too premature to discuss practical implications of the data obtained (and besides, as any theoretical results, they have to be taken with a certain precaution). Nevertheless, one can envision the use of this or other chemical reactions for selective derivatization of different forms of CNTs (armchair, zigzag, or chiral). In the case of amidation reaction (1) with long-chain amines, the derivatized nanotubes would acquire a higher solubility than underivatized CNTs, which would open a route to their facile separation.

3.2. Salts with Amines

When unactivated carboxylic groups are treated with amines, ammonium salts form. This type of interaction was employed as an alternative [to amidation reaction (1)] approach for the preparation of SWNTs soluble in organic solvents. The nanotubes were heated at 90–130 °C in molten long-chain amines octadecylamine and 4-tetradecylaniline for 4–8 days [21, 41]. Not only shortened but also uncut SWNTs (of lengths of over 1 μm [41]) acquired high solubility in common organic solvents. The authors give a strong preference to this method of CNT derivatization for the following reasons. (1) They found that the ionic functionalization approach generally gave a much higher yield of soluble SWNTs than the covalent functionalization approach. As they believe, the presence of zwitterions can significantly improve the solubility of SWNTs. (2) The acid–base reaction represents the simplest possible route to soluble SWNTs and can be readily scaled up at low cost. (3) Unlike the covalent amide bond, the amine cations formed on the nanotubes can be readily exchanged for other organic and inorganic cations. Thus it will be possible to adjust the solubility properties of the SWNTs and to use soluble SWNTs as versatile building blocks for advanced SWNT-based materials via supramolecular chemistry. Furthermore, such an ionic feature may allow electrostatic interactions between SWNTs and biological molecules and can serve as the basis for developing biocompatible SWNTs.

We would like to point, however, to the following circumstance. As was mentioned above, there are a few examples when the amide coupling was achieved by direct heating CNTs with amines. In particular, it was implemented for MWNTs, which were derivatized with molten PPEI-EI polymer by exposing their mixture at 160–180 °C for 12 h [31], as well as for SWNTs, treated with vaporous aliphatic amines at 160–170 °C for 1–2 h [38–40]. Of course, the temperature of 90–130 °C is substantially lower to cause that rapid amide condensation. Nevertheless, this temperature interval goes beyond the boiling point of water, and the equilibrium must be shifted to the amide formation, especially when the whole procedure extends to 4–8 days [21, 41]. Thus one can

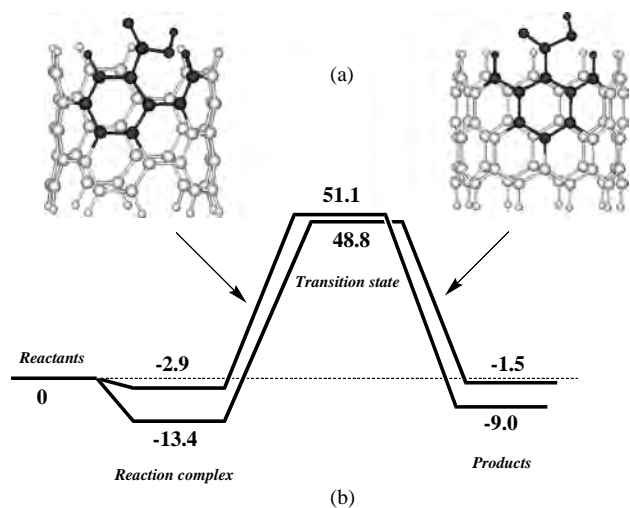


Figure 5. (a) Monocarboxyl-substituted fragments of (5, 5) armchair (left) and (10, 0) zigzag (right) SWNTs used for the two-level ONIOM calculations of the model gas-phase reaction with methylamine [39]. The highlighted (dark) atoms and the ones constituting methylamine molecules were treated at the B3LYP/6-31G(d) level of theory; the remaining SWNT atoms were treated with universal force field (UFF) molecular mechanics. (b) Calculated potential energy surfaces for the two SWNT models, including reaction complexes, transition states, and products (water molecules hydrogen-bound to the amide derivatives) with corresponding energies in kcal mol⁻¹.

suspect the presence of a large fraction of the amide derivatives in the SWNTs derivatized ionically.

The true ionic interactions of carboxylic acids with amines were employed to construct hollow spherical cages of nested SWNTs using self-assembly techniques [42]. The process (explained in Figure 6) consisted of the layer-by-layer adsorption of acid-oxidized SWNTs (diameter 1.2 nm) onto template silica gels (spherical particles of 6 μm in average diameter) and stabilization of adsorbed nanotubes. The SWNT dispersion in water was centrifuged at 3500 g, and only the supernatant solution was retained (I). Immediately afterward, amine-functionalized silica gel was added to adsorb SWNTs (II). After a typical immersion time of 30 min, SWNT-covered amine spheres were forced to sediment by centrifuging at 100 g, and the supernatant solution was decanted (III). SWNT spheres were collected on a Teflon filter and dried in oven (IV). Once dried, SWNT spheres were extremely stable: SWNTs did not desorb even when the dried SWNT spheres were redispersed in solution. For additional cycles of coating, the dried SWNT spheres were added to the freshly prepared SWNT dispersion, and processes II through IV were repeated. Silica at any cycle of coating can be etched away by hydrofluoric acid to give spherical cages made of only SWNTs (V). Thus, the initial amine-nanotube interactions determine the nested network, and nanotube-nanotube interactions thicken each arm of the nest.

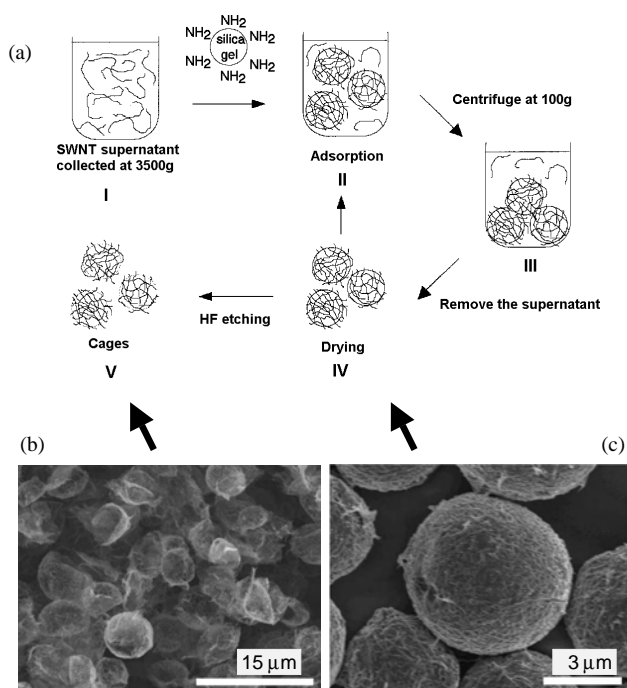
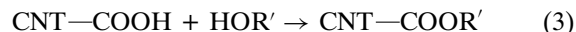


Figure 6. (a) Noncovalent self-assembly of oxidized SWNTs on spherical particles of amino-functionalized silica gel, employing ionic interactions of carboxylic groups with amines. Scanning electron microscopy (SEM) images of (b) amino-functionalized silica spheres after the first cycle of SWNT adsorption, and (c) SWNT cages obtained after three cycles of adsorption and HF etching. Reprinted with permission from [42], M. Sano et al., *Nano Lett.* 2, 531 (2002). © 2002, American Chemical Society.

3.3. Esterification

A close remnant of amidation reaction (1) is esterification according to the general scheme



where R' can be an aliphatic or aromatic substituent. Here one water molecule should be eliminated as well, and this can be done by preliminary activation of the carboxylic groups at CNT tips by thionyl chloride [the first step in reaction (2)]. The ester formation, however, is not as common in CNT chemistry as the amidation is, and there are a few reported examples only.

Hamon et al. [43] prepared soluble ester-functionalized SWNTs by reaction with linear octadecylalcohol (Table 1). SWNT-COCl and $\text{C}_{18}\text{H}_{37}\text{OH}$ were heated in pyridine at 117 $^{\circ}\text{C}$ for four days. The ester forms of SWNTs are soluble in common organic solvents (for example, in THF and chloroform) and were found to exist as both individual nanotubes and small bundles (2–5 nanotubes each).

Sun et al. [27, 29] attached CNTs as a side chain to poly(vinyl acetate-*co*-vinyl alcohol) (PVA-VA, a linear polymer with molecular weight $\approx 110,000$; Table 1). Both SWNTs and MWNTs whose COOH groups were converted to acyl chlorides by treating with SOCl_2 were derivatized. The esterification was performed by mixing the reactants and heating at 165 $^{\circ}\text{C}$ for 20 min. PVA-VA is a highly soluble polymer, and the resulting polymer-bound nanotubes were soluble in both organic solvents and water, forming intensely colored, stable homogeneous solutions.

Lipophilic (VI, VII; Table 1) and hydrophilic (VIII) dendron species were used to functionalize SWNTs and MWNTs in a similar way [26, 44, 45]. The ester-derivatized nanotubes, depending on the functionalities, were soluble in nonpolar and weakly polar solvents (for VI and VII), or both organic solvents and water (for VIII). When deuterated ethanol- d_6 was used as a co-reactant in the esterification reaction with VI, strong attachment of deuterium species (apparently as the corresponding ethanol- d_6 ester groups) was observed [45]. The CNTs prepared can be defunctionalized in homogeneous solutions under base- (sodium hydride in THF) and acid-catalyzed (trifluoroacetic acid) reaction conditions, recovering the starting nanotube materials as dark-colored precipitates [44].

Similarly to the heating-induced direct amidation [31, 38–40], esterification without the use of chemical activating reagents is possible as well. Although this process is not very efficient, there is a possibility to shift the equilibrium by eliminating water from the reaction zone. Unlike the former derivatization technique, the direct esterification of oxidized CNTs has not been reported so far. We attempted to explore this reaction theoretically by using the two-level ONIOM calculations [46]. The SWNT model species (reacting with the simplest alcohol, methanol) considered in this study were in many regards similar to those used for the amidation reaction with methylamine [38, 39]. In particular, the high (quantum mechanics) level included the atoms belonging to methanol molecule and the terminal carboxylic group, together with their adjacent C and H atoms, as shown in Figure 7a. In this way, an important parameter such as the number and nature of high level-treated atoms was kept the

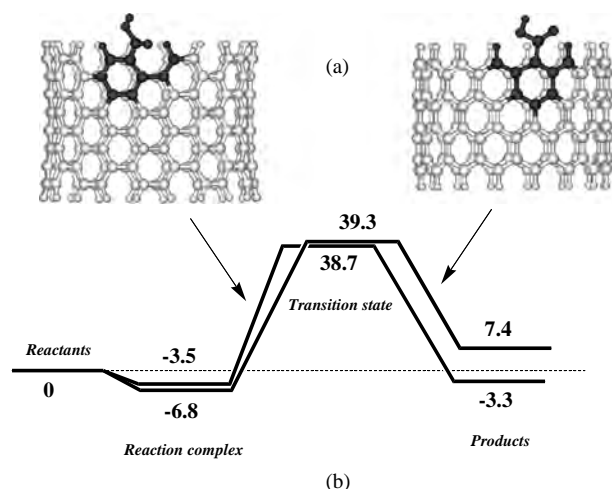


Figure 7. (a) Monocarboxyl-substituted fragments of (10, 10) armchair (left) and (16, 0) zigzag (right) SWNTs used for the two-level ONIOM calculations of the model gas-phase reaction with methanol [46]. The highlighted (dark) atoms and the ones constituting methanol molecules were treated at the B3LYP/6-31G(d) level of theory; the remaining SWNT atoms were treated with UFF molecular mechanics. (b) Calculated potential energy surfaces for the two SWNT models, including reaction complexes, transition states, and products (water molecules hydrogen-bound to the ester derivatives) with corresponding energies in kcal mol⁻¹.

same in the armchair and zigzag models. On the other hand, we rejected the nanotube diameter used previously, that is, (10, 0) for zigzag and (5, 5) for armchair SWNT models, since a detailed inspection revealed that within such narrow cavities, the opposite wall attracts methylamine molecules, making it equilibrate close to the nanotube axis. In turn, this can dramatically influence its position with respect to the carboxylic group, resulting in unrealistically long N–H···O separations, which are supposed to be hydrogen bonds, and apparently producing significant errors in energy estimates for the reaction complexes. To avoid this sort of undesirable effect, we chose armchair (10, 10) and zigzag (16, 0) nanotube models, with calculated diameters of ca. 1.3–1.4 nm approaching commonly observed SWNT diameters. The fragment length was also increased, to three complete rows of carbon hexagons (Fig. 7a; compare to Fig. 5a). The potential energy surfaces calculated at the B3LYP/6-31G(d) level of theory (energies relative to the level of separated reactants) are shown in Figure 7b. The energies of the transition states differ insignificantly: 38.7 and 39.3 kcal mol⁻¹ for the armchair and zigzag SWNTs, respectively. The differences for the reaction complexes and products are more substantial. Energy for the armchair reaction complex (–3.5 kcal mol⁻¹) is 3.3 kcal mol⁻¹ higher than that for its zigzag counterpart (–6.8 kcal mol⁻¹). The situation is quite opposite for the esterification products: the armchair products (–3.3 kcal mol⁻¹) lie lower by 10.7 kcal mol⁻¹ as compared to the zigzag products (7.4 kcal mol⁻¹). This has two implications. First, the direct ester formation on armchair SWNT tips according to reaction (3) is much more advantageous as compared to that on zigzag SWNT tips. Second and more important, since for the latter the products appear to lie above the level of separated reactants,

the esterification process is thermodynamically unfavorable at all. From the practical point of view, these results might imply that treating the oxidized CNTs with aliphatic alcohols under the gas-phase high-temperature conditions [38] would derivatize selectively COOH groups at the armchair nanotube tips. If a long-chain alcohol is used for the treatment, the resulting ester-derivatized armchair CNTs would acquire much better solubility in organic solvents than the underivatized zigzag nanotubes have, which in turn opens a facile route to their separation. For a final conclusion, our theoretical results need to be verified experimentally.

3.4. Metal Surfaces

Fabrication of dense arrays of SWNTs aligned normal to substrates is envisioned as an important step in the development of various technologically important devices such as sensors, field emitters, and organic light-emitting diodes, as well as for hydrogen and electrochemical energy storage. Wu et al. [47] proposed a simple technique for the assembly of oxidatively shortened SWNTs on silver surface. This technique is based on the salt formation between COOH groups at the open ends of carbon nanotubes and the surface silver cations. Silver-coated silicon wafers were dipped into colloidal SWNT suspensions in water, ethanol, and other polar solvents. Tapping mode AFM and transmission electron microscopy (TEM) observations of the assemblies formed showed that the SWNTs are perpendicular to the silver surface. TEM studies also revealed that most of the SWNTs (ca. 80%) assembled have a bundle size of 6.5 ± 0.5 nm, possibly suggesting the selective adsorption (chemisorption would be a more correct term) of SWNTs on silver.

The formation of dense arrays of oxidatively shortened SWNTs using Fe³⁺-assisted self-assembly from nonaqueous media was reported by Chattopadhyay et al. [48]. An additional feature is that this approach permits growth of successive stacks of SWNTs, one on top of each other, in a layer-by-layer (LBL) assembly format. To ensure a smooth and uniformly charged surface, the substrates [glass, (100) silicon wafers with native oxide and quartz crystal microbalance resonators] were modified with polyelectrolyte films via the LBL method. SWNTs/Fe³⁺ assemblies consisted of sequential dipping in an aqueous solution of FeCl₃ (pH 2.2, 15 min) followed by immersion in DMF-dispersed SWNTs (pH 8.5, typically 30 min) and separated by intermediate washing in DMF (pH 12.7). The elevated pH for both DMF wash and SWNTs dispersion causes the surface-immobilized Fe³⁺ layer to transform into its basic hydroxide form, providing the initial driving force (salt formation with the COOH groups of SWNTs) for this assembly to occur. A monolayer of densely packed, needlelike domains was obtained after the first 30-min immersion, with average domain width of 93 ± 22 nm. Its morphology was reminiscent of aggregated SWNTs, most likely tethered with only one of their ends to the substrate. This geometry is believed to be the result of (i) high concentration of COOH groups on the SWNT tips and hydroxy functionalization of Fe³⁺-decorated surfaces and (ii) strong hydrophobic interactions between adjacent SWNTs. Polarization Raman studies indicated significant orientation normal to the substrate. Subsequent adsorption of Fe³⁺ ions onto the carboxy-terminated SWNTs at the untethered ends

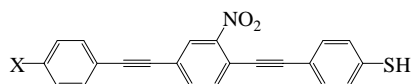
gave rise to the formation of multilayer Fe³⁺/SWNT assemblies. Both the average film thickness (measured by spectroscopic ellipsometry) and mass deposition (obtained via quartz crystal microbalance) were in good agreement with the formation of multilayered structures, readily observed by gradual substrate darkening. The linear increase in both average film thickness (ca. 37.7 nm) and mass (ca. 4.1 g/cm²) corresponded to an average density of 1.1 g/cm³ for the multilayer Fe³⁺/SWNTs assemblies.

Ionic interaction of carboxylic groups of oxidized SWNTs with metal ions at surfaces can also be used to improve resolution in scanning tunneling microscopy (STM). Nishino et al. [49] deposited acid-cut SWNTs onto the apexes of gold tips for STM. The affinity of COOH functionalities to gold is relatively weak, and the Au tips were first modified with self-assembled monolayers of 4-mercaptobenzoic acid, strongly adhering to gold surfaces due to the presence of thiol groups. Its carboxylic groups in *para*-position remained free for further derivatization steps and were used to anchor carboxylated SWNTs through Zn²⁺ ion-bridged coordination as follows:



The SWNTs deposited in this way were present on the gold tips as bundles of about 10 nm width. Since oxidatively shortened SWNTs have a broad distribution of their length, and the tunneling current flows only through the foremost part of the probe tip, a high STM resolution was achieved, even if not an individual SWNTs were present at the tip apex.

A very similar approach was employed by Cai et al. [18], who used rigid-rod conjugated oligo(phenylene ethynylenes) **X** and **XI**



X = COOH (**X**), SH (**XI**)

having an array of interesting electronic properties, as linking molecules to prepare rigid self-assembled monolayers of wet-ozonated SWNTs on gold [18]. As the first step, they were deposited onto gold surface, forming self-assembled monolayers. Then, in the case of the carboxylic derivative **X**, the COOH groups were chelated to Fe³⁺ ions; incubation in the oxidized SWNT dispersions produced ion bridges similar to the ones shown in the previous paragraph (**IX**). Likewise, the thiol derivative **XI** on gold was bridged to the SWNTs through Cu²⁺ ions, having high affinity to both COOH and SH functionalities. Aromatic and conjugated organic molecules of this sort, having π -orbital overlap capable of charge transport, are necessary for the fabrication of SWNT-based molecular devices.

3.5. Miscellaneous

CNT materials can be potentially utilized as effective reinforcements in advanced composites (although so far their cost remains prohibitive). In that case, a good chemical

bond to the matrix is highly desirable to efficiently transfer mechanical loads from the matrix to the nanotubes and thus take advantage of their outstanding mechanical properties. Organosilanes R-Si-R'₃ were proposed as coupling agents to chemically join CNTs and organic polymers [50]. The R group is chosen to be reactive depending on the organic matrix, and the R' group is usually methoxy radical (OCH₃), which is easily hydrolyzed to produce silanol Si-OH (in [50], 3-mercaptopropyl trimethoxysilane was used). In turn, the latter can be reacted with hydroxyl groups on the oxidized nanotubes, the authors suggested. One should remember, however, that phenoxy silanes with C-O-Si≡ bonds, and especially pseudo-esters with -C(=O)O-Si≡ linkage, are hydrolytically unstable and cannot serve to reliably join CNTs and the polymers.

Judging from the literature, there has not been much effort in treating carbon nanotubes as chemical reagents in their own right. Attempting to fill this gap, Banerjee and Wong [51, 52] studied complexation between oxidized SWNTs and platinum-metal coordination compounds: Vaska's compound, *trans*-IrCl(CO)(PPh₃)₂ [51], and Wilkinson's complex, RhCl(PPh₃)₃ [52]. Both reacted directly with SWNTs dispersed in DMF or DMSO, under inert atmosphere (nitrogen or argon) at 50–60 °C for a period of 0.5–3 days. According to the results of spectral measurements, the electronic structure of the nanotubes was preserved, suggestive of the fact that SWNTs are functionalized through coordinative attachment at the terminal carboxylic groups, as well as possibly hydroxylic (phenolic) and carbonyl groups. A more explicit characterization of the binding pattern was not achieved. The proposed functionalization process not only opens up the area of metal-organic chemistry to carbon nanotubes but also suggests potential applications in catalysis and molecular electronics. An increased solubility of the complex-derivatized SWNTs in DMF should facilitate their chemical manipulation and photophysical analyses.

4. SPECTROSCOPIC CHARACTERIZATION

Difficulties in characterizing the chemical structure of the derivatization products, "inability to declare success or failure in attempted functionalization reactions" [3], constantly hamper further developments in this area. A standard suite of techniques does not yet exist for adequate characterization of chemically modified nanotubes [3]. Solution phase absorption spectroscopy (UV/visible) is considered one of the most accessible techniques that offers some information on the electronic state of CNTs and hence functionalization. However, this can actually be fruitful for sidewall-functionalized but not defect-functionalized CNTs: obviously due to a low contribution of bands corresponding to the terminal derivatizing groups into the entire spectrum. What this technique allows in our case is to confirm the formation of true solutions (and not just dispersions), when the absorption phenomena are linearly dependent on the solution concentration (Lambert-Beer law) [26, 29–31, 35, 44]; to reveal unusual optical properties, such as strong luminescence of the polymer- and dendron-bound nanotubes [26, 27]; or to

conclude that the electronic structure of the CNTs, whose terminal groups were derivatized, is preserved [34, 52].

Raman [8, 21, 22, 24, 30, 41, 43] and near-IR spectra [22, 24, 41, 43, 52] very closely resemble those of the underivatized SWNTs. They are sensitive to changes in the electronic structure of CNTs and can detect chemical reactions along the sidewalls. But in our context these methods can only serve to estimate the diameter distribution of nanotubes, since the sidewalls do not undergo any detectable changes in the end-group derivatization.

^1H and ^{13}C nuclear magnetic resonance (NMR) spectroscopy can show the presence of long aliphatic [8, 21, 26, 44] or polymeric chains [30, 31] and the existence of magnetically different types nanotubes in the samples [8]. As a whole, the proton signals are broadened as compared to the spectra of individual starting organic reagents. For the dendron-derivatized CNTs [26, 44], this was explained in terms of two different mechanisms: the attachment of the monomeric dendrons VI–VIII to a “polymer-like” nanotube vs the effect of possible paramagnetic impurities in the solution. The latter is obviously relevant to the CNT-containing samples because of the possibility of residual metal catalysts. In their ^{13}C NMR spectra [26, 44], no signals due to carbons on the nanotubes themselves or the nanotube-bound carbonyl C atoms were detected. This is likely due to the fact that the CNT solution concentrations are too low even when saturated and that the relaxation times of the nanotube carbons are expected to be very long. When deuterated ethanol- d_6 was used as a co-reactant in the esterification reaction with VI, ^2H NMR measurements allowed one to detect strong attachment of deuterium species (apparently as the corresponding ethanol- d_6 ester groups) [45].

^{31}P NMR was employed to study the binding of Vaska's compound, *trans*- $\text{IrCl}(\text{CO})(\text{PPh}_3)_2$, to oxidized SWNTs [51]. The data were consistent with Ir coordination to oxygen atoms on the SWNTs; the presence of a multitude of peaks suggested the potential of several modes of coordination. Similar conclusions were made in the case of Wilkinson's complex, $\text{RhCl}(\text{PPh}_3)_3$ [52], from ^{31}P , ^1H , and ^{13}C NMR measurements.

As in the all modern organic chemistry, a “battle horse” for the characterization of chemically modified carbon nanotubes is mid-IR spectroscopy. This is especially true for CNTs reacted with organic amines [reactions (1) and (2)], whose IR spectra have been measured by many research groups [8, 19, 21, 24, 25, 33, 34, 37, 38, 41]. Unfortunately, the data reported so far do not allow an unambiguous interpretation of the spectral changes observed, since they turn out to be quite contradictory. In particular, after transforming oxidized SWNTs into their octadecylamide derivatives, Chen et al. [8] found two $\nu_{\text{C}=\text{O}}$ (amide I) bands at 1663 and 1642 cm^{-1} of almost equal intensity, and not one band as one normally expects. In the IR spectrum of octadecylamide SWNTs, presented later, only one $\nu_{\text{C}=\text{O}}$ band at 1660 cm^{-1} is seen [19]. Comparison of these two spectra makes one suspect that the band at about 1640 cm^{-1} corresponds to ν_{OH} vibrations in adsorbed water molecules (apparently the latter sample was dried better than the former). This feature is quite common for IR spectra of a vast variety of adsorbents, since water is ubiquitous. In the spectra of the amide-bound SWNT–nanocrystal heterostructures based on

titanium dioxide and cadmium selenide [33], whose surfaces are highly polar and always contain adsorbed water under ambient conditions, a band at 1638 cm^{-1} was observed systematically (interpreted by the authors as the amide I band). In the SWNTs amide-derivatized with 4-dodecylaniline [21] two bands at 1655 and 1598 cm^{-1} were assigned to $\nu_{\text{C}=\text{O}}$ (amide I) and δ_{NH} (amide II) vibrations, respectively. This is a reasonable assignment for the wavenumbers; however, the band intensities have to be taken into account equally. At the same time, in this spectrum the intensity of the δ_{NH} band is several times higher than that of the $\nu_{\text{C}=\text{O}}$ band [21], whereas in amides the carbonyl band is always more intense (usually by about a factor of two) than the amide II band. According to Liu et al. [37], SWNTs derivatized with cysteamine exhibit a band around 1600 cm^{-1} , which was assigned to amide I vibrations: this interpretation can hardly agree with all the preceding data.

One more alerting circumstance can be noticed in the case of octadecylamide and 4-dodecylanilide SWNTs [8, 19, 21], where the bands appearing after derivatization (Fig. 8) turn out to be much more intense than those typical for oxidized SWNTs (at 1200, 1590, and 1720 cm^{-1} ; Fig. 9a). This gives the impression that in the synthesized samples the amine content is higher than the SWNT content.

We monitored IR spectral changes during the gas phase amidation of oxidized SWNTs with nonylamine, dipentylamine, ethylenediamine, and propylenediamine [38]. Of four amines, only nonylamine treatment caused evident changes in the IR spectra (Fig. 9); for the others, the changes were at a noise level. If we admit that all the amines studied form amide bonds with carboxylic groups at SWNT tips (there are no logical reasons to expect otherwise), such spectral behavior is hard to explain: for smaller amine molecules, the efficiency of amide formation should be higher than for longer chain molecules (such as nonylamine), due to a better accessibility to the reacting carboxylic groups of SWNTs.

The IR spectrum of nonylamine-treated SWNTs (Fig. 9b) exhibited several new bands due to nonylamine: at 1358 (C–N stretch.), 1462 (C–H def.), 2856 (sym. C–H stretch.), 2927 (asym. C–H stretch.), and 1586 cm^{-1} . Assignment of the last band is the most important to characterize a

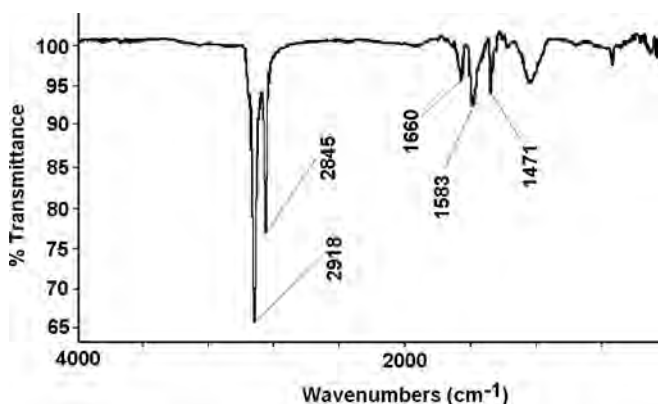


Figure 8. Mid-IR spectrum of SWNT-CONH(CH₂)₁₇CH₃ (thin film on quartz substrate). Reprinted with permission from [19], M. A. Hamon et al., *Chem. Phys. Lett.* 347, 8 (2001). © 2001, Elsevier Science.

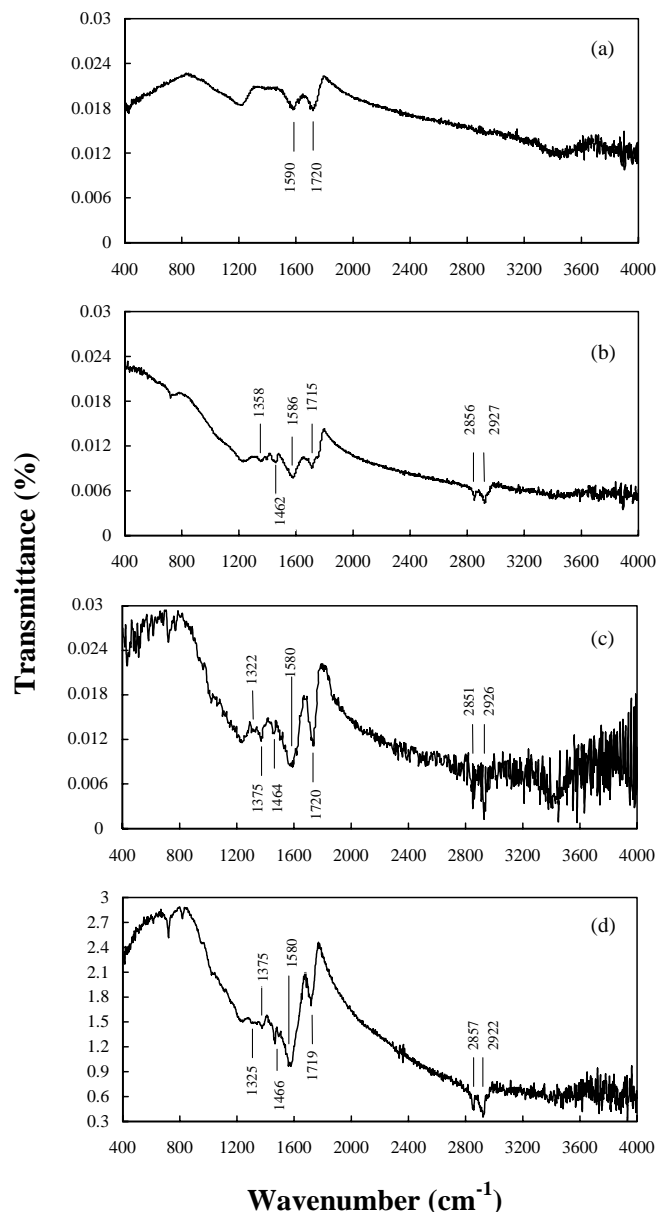


Figure 9. IR spectra of oxidized SWNTs (a), after gas-phase treatment with nonylamine (b), after liquid-phase impregnation with nonylamine from ethanol solution with SWNT–nonylamine mass ratio 3:1 (c) and 1:1 (d). 3% SWNT samples in KBr; spectra without baseline correction. Reprinted with permission from [38], E. V. Basiuk et al., *J. Phys. Chem. B* 106, 1588 (2002). © 2002, American Chemical Society.

chemical state of nonylamine, but obviously its frequency is too low to attribute this band to $\nu_{\text{C=O}}$ (amide I) vibrations: it should be assigned to δ_{NH} vibrations in NH_2 . Along with the above bands, there is one more at 1715 cm^{-1} , having a shoulder at about 1750 cm^{-1} . However, before attempting further interpretation, let us analyze in principle what kind of information on the terminal organic groups can be expected from IR spectra of typical SWNTs.

In some respect carbon nanotubes resemble chemically derivatized inorganic adsorbents (silica, alumina, amorphous carbon, graphite, etc.), where the contribution of surface organic groups to the whole IR spectrum is relatively low,

due to an overwhelming mass fraction of the adsorbent itself. For CNTs, the same effect should be expected due to their typically large aspect ratios and due to multishell structure in the case of MWNTs. Even SWNTs called “short,” prepared by oxidative cutting in strong acids, are on average 100–300 nm in length, at a diameter of $\approx 1.4\text{ nm}$. These parameters have crucial implications for band intensities in the IR spectra.

To evaluate the SWNT–nonylamine mass ratio in our gas-phase treated samples [38], we impregnated oxidized SWNTs with the amine from ethanol solution taking two different proportions SWNT:nonylamine of 3:1 and 1:1 by weight (Fig. 9). The gas-phase-treated sample had a closer resemblance to the first of them (3:1). What does it mean in terms of SWNT aspect ratios? Let us consider a (20, 0) zigzag SWNT backbone, containing 1920 carbon atoms (Fig. 10a), of $\approx 1.55\text{ nm}$ diameter and 10 nm length. Such a SWNT can have about 10 carboxylic groups at each tip (a higher density of COOH groups is unlikely for steric reasons). As a result, it can form amide bonds with 20 nonylamine molecules, and this stoichiometry would correspond to a SWNT:nonylamine mass ratio of 8.4:1. Thus, even if we suppose that oxidized SWNTs are on average 10 nm in length, to obtain the IR-band intensities shown in Figure 9b and c we would have to triplicate the nonylamine content. The sample would have to contain >60% nonylamine in a physically adsorbed form, and correspondingly >60% IR absorption would be due to the chemically unbound fraction. It should be obvious that for 100–300 nm long SWNTs, the amide contribution to the IR absorption will be even lower, by 10–30 times, and such bands are almost impossible to distinguish (especially given the generally poor quality of the CNT spectra). Consequently, the bands visible in most IR spectra of amide-derivatized CNTs correspond to the molecules, strongly physisorbed due to hydrophobic interactions between their hydrocarbon moieties and CNT sidewalls. Recent results afforded by temperature-programmed desorption mass spectrometry supported our conclusion by

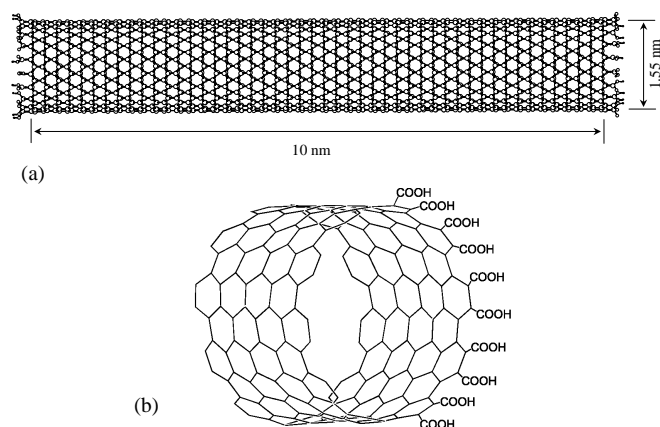


Figure 10. (a) Schematic representation of a (20, 0) zigzag SWNT, of $\approx 1.55\text{ nm}$ diameter and 10 nm length, containing 10 carboxylic groups at each tip. Reprinted with permission from [38], E. V. Basiuk et al., *J. Phys. Chem. B* 106, 1588 (2002). © 2002, American Chemical Society. (b) Schematic end section of (10, 10) SWNT–COOH. Reprinted with permission from [19], M. A. Hamon et al., *Chem. Phys. Lett.* 347, 8 (2001). © 2001, Elsevier Science.

revealing two different forms of nonylamine in the amide-derivatized SWNTs [38].

As we already mentioned, in the IR spectrum of the gas-phase-treated sample (Fig. 9b), one more band was detected at 1715 cm^{-1} with a shoulder at 1750 cm^{-1} . This band (reported in the $1700\text{--}1735\text{ cm}^{-1}$ range by different authors) is believed to correspond to the terminal COOH groups [8, 9, 12–14, 21, 37, 41]. A higher frequency absorption was reported as well: in particular, for SWNTs after oxidation with gaseous ozone (i.e., no liquid-phase treatment with strong acids), the band at 1739 cm^{-1} was assigned to ester $\nu_{\text{C=O}}$ vibrations [17]. A band at 1750 cm^{-1} was found also for CNTs after boiling in concentrated HNO_3 [9]; in this case, however, the existence of ester groups must be excluded: in strong acid media they are hydrolyzed into COOH groups. In our case the shoulder at 1750 cm^{-1} cannot be due to ester absorption for the same reason. One might suggest the formation of anhydrides through thermal condensation of neighboring carboxylic groups; however, carboxy anhydrides are extremely reactive, especially with amines. Besides that, we did not detect this absorption in IR spectra of oxidized SWNTs heated to $150\text{--}180\text{ }^\circ\text{C}$ in vacuum in the absence of amines.

The above considerations were presented in supposition that most reactive carboxylic groups are located at CNT tips. However, a considerable fraction of COOH functionalities are believed to exist at defect sites along the sidewalls. Can they account for the high IR band intensities? Hamon et al. [19] addressed this issue, determining the weight contribution of octadecylamine (ODA) in the amide-derivatized acid-cut SWNTs (Section 3.1). In their samples (for example, the IR spectrum in Fig. 8), the ODA corresponds to about 50% of the sample by weight. On a molar basis the ODA is incorporated to the extent of about 6%. If each ODA molecule reacts with a single COOH group in the SWNT, then this result corresponds to the number of reactive sites in the SWNTs. Other reported reactive site functionality determinations gave values of $\sim 5\%$ [12] and 3–4% [41] for the amount of carbon atoms at defect sites in purified SWNTs. While the results are consistent, they are far higher than would appear from the models based solely on end-group functionalization. The model employed for their estimates is shown in Figure 10b. It is an arm-chair (10, 10) SWNT, in which the ends are cut vertically to the nanotube axis. With these simplifications there are 20 carboxylic acid groups at each nanotube tip. Furthermore, the unit cell of a (10, 10) SWNT contains 40 carbon atoms and the translation repeat distance (a_0) of the unit cell along the one-dimensional lattice is $\sqrt{3}a$, where a is the length of the carbon–carbon bond, and thus $a_0 = 2.46\text{ \AA}$. A perfect 100-nm-long (10, 10) SWNT-COOH would contain $40 \times (1000/2.46) \approx 16,000$ carbon atoms (neglecting oxygen functionality) and 40 carboxylic acid groups. Thus the mole fraction of reactive end-group sites would be about 0.25% in such a perfect 100-nm-long SWNT-COOH. In order to match the experimental values of a few percent, the average length of perfect SWNT-COOH in the samples should be about 5 nm, whereas it is roughly two orders of magnitude longer (according to AFM). If the previous estimates of reactive sites are accepted (3–5% [12, 41]), this would suggest that there is a large concentration of SWNT

defect sites which are able to react with amines. At the same time, the Raman and near-IR spectra of the amide-derivatized SWNTs [8, 19, 21] provide convincing evidence for the preservation of the SWNT electronic band structure.

Thus, Hamon et al. [19] also came to the conclusion that there is a noncovalent interaction between the SWNTs and the ODA. In particular, the ODA molecules could occupy the interior gallery of the SWNTs, and the authors estimated the amount of material that could be accommodated inside the SWNTs. They took an interior van der Waals diameter of 1 nm for the SWNTs, and this allowed them to calculate an interior volume for a unit cell of a (10, 10) SWNT of $1.93 \times 10^{-22}\text{ cm}^3$. By using the density of ODA (0.862 g/cm^3), they obtained a mass of $1.66 \times 10^{-22}\text{ g}$ for the ODA that could occupy the interior of a unit cell of a (10, 10) SWNT. Using this value together with the weight of a unit cell of a (10, 10) SWNT ($7.98 \times 10^{-22}\text{ g}$), they obtained a weight percentage of the interior ODA of 17%—far less than the 50% they found experimentally. Similar results were obtained for the esterification [reaction (3)] of oxidized SWNTs with octadecylalcohol [43].

To summarize, we believe that some of the existing interpretations of mid-IR spectra of derivatized carbon nanotubes are premature and need further extensive studies. One of the most important points to take into account is that CNTs can behave as typical adsorbents, retaining large amounts of organic reagents (amines, alcohols, etc., and possibly solvents!) due to noncovalent interactions, both in their interiors (adsorption in nanopores) and on the outer walls (surface adsorption). Concentrations of such adsorbed molecules can be a few orders of magnitude higher than those of the covalently bound species: in this case IR spectroscopy is unable to provide information on the derivatization products.

5. PROPERTIES

Due to the large aspect ratios typical for carbon nanotubes (both SWNTs and MWNTs) and, in addition to that, due to multishell structure in the case of MWNTs, the derivatizing organic groups cannot cause visible morphological changes, unless they are high-molecular-weight polymers. Thus, the presence of relatively small functionalities cannot be seen by the commonly used microscopic techniques, such as SEM, TEM, AFM, and STM. On the other hand, when large polymeric chains (PPEI-EI and PVA-VA, molecular weight of 100,000–200,000) were attached to the CNTs, organization of the polymer at the tube tip and in many cases along the tube body was clearly visible by STM [29]. Similarly, the presence of poly(ethylene oxide) grafted to SWNTs was seen in AFM images [32].

The appearance of functional groups at CNT tips changes their affinity to solid surfaces and consequently can be used for the preparation of self-assembled monolayers. In some of them carboxylic groups of the oxidized CNTs are ionically bound to surface metal ions [47, 48], whereas in others the carboxylic groups are covalently linked through different organic groups [18, 23, 33, 37, 49]. In the case of nanotube cantilevers for AFM, the chemical alterations were characterized as changes in the adhesion force in a given pH range [5, 6]. Such chemically modified carbon nanotube tips are

suitable to produce chemically sensitive images with high lateral resolution, as well as to study binding in biological and chemical systems [5, 6, 49].

Increased solubility due to exfoliation of the nanotube bundles is the most important, common, and frequently reported property of the derivatized CNT materials. The amide and ester derivatization dramatically improves their solubility in organic solvents [8, 19, 21, 22, 24, 25, 40, 43–45]; similar solubility properties were obtained for amine zwitterion-functionalized SWNTs [21, 41]. SWNTs and MWNTs derivatized with highly soluble PPEI-EI, PVA-VA, and PEO polymers [27–32], as well as with PEO-derived dendron moieties [26], are soluble not only in organic solvents but also in water. Glucosamine [34] and protein conjugates with CNTs [35] are highly soluble in water as well; this can serve as the basis for developing biocompatible carbon nanotube materials. Attaching transition metal complexes to the nanotubes increases their solubility in dimethylformamide, dimethylsulfoxide, tetrahydrofuran, methanol, chloroform, toluene, etc. [51, 52], opening a new prospect for their applications not only in heterogeneous but also in homogeneous catalysis.

Strong luminescence was reported for the CNTs chemically bound to PPEI-EI, PVA-VA polymers, and PEO-derived dendron moieties [26, 27]. Luminescence quantum yields are substantial, for example 11% for MWNT–PPEI-EI in chloroform at 400 nm excitation [27].

6. CONCLUSIONS

The covalent chemistry at the carbon nanotube tips is not particularly rich. Unlike sidewall chemistry, which in many regards is similar to fullerene chemistry, it is limited to a few relatively simple reactions of terminal carboxylic groups. A very low mass contribution of the terminal functional groups causes only insignificant changes in spectral properties of the bulk material, which makes characterizing the chemical structure of the derivatization products a very complicated (sometimes unfeasible) task.

The present limitations in spectroscopic characterizations of the end-derivatized CNTs might create a pessimistic opinion on further prospects of this exciting and difficult area. Nevertheless, one should remember that the end goal here is not to obtain good-quality spectra, but the preparation of new nanomaterials with given properties, suitable for particular applications. And it is material science aspects where impressive results have been achieved. First, chemical derivatization of the carbon nanotube tips made possible the preparation of SWNTs and MWNTs soluble not only in organic but also in aqueous solvents. In turn, this allows facile purification and fractionation of the carbon nanotubes by liquid-chromatographic techniques, simplifies their handling, as well as solves the problem of their compatibility with biological systems. An especially important point is that this way of derivatization does not alter the sidewall structure and consequently preserves the unique electronic and mechanic properties of CNTs. Second, the chemical modification allows one to change CNT affinity to molecules, ions, and solid surfaces. This is especially important for the deposition of dense arrays of nanotubes aligned normal to substrates, considered as a crucial step in the

development of various technologically important devices such as sensors, field emitters, organic light-emitting diodes, etc. One of the goals already achieved is the preparation of carbon nanotube probe tips for atomic force microscopy and chemically sensitive imaging with high lateral resolution. Such probe tips have potential applications in many areas of chemistry and biology for titrating different surface functionalities, imaging patterned samples based on molecular interactions, and measuring the binding force between single protein–ligand pairs. Third, an array of hybrid carbon nanotube structures was prepared by combining them with organic polymers and inorganic microparticulate materials (silica gel, semiconductor nanocrystals of CdSe and TiO₂); these recent studies open new routes to CNT-based supramolecular chemistry and nanoscale assembly. And one more line suggesting potential applications in catalysis and molecular electronics is the combination of CNT materials with transition-metal complexes.

Coming back to the spectroscopic characterization of the end-derivatized carbon nanotubes, which is still very important to fully qualify the CNT chemistry as a branch of modern organic chemistry, a solution to this problem can, in principle, be found even with the typical sensitivity of the existing experimental techniques. Cutting the carbon nanotubes to short pieces of ca. 10 nm in length would substantially increase mass contribution of the end and wall-defect functionalities into the total sample mass, thus improving detectability of the species by 1–2 orders of magnitude. This turns to be an economical rather than a scientific issue, since the present high cost of purified CNTs (for example, more than USD 1000 for 1 g of 95% + SWNTs) and significant losses of the material during the acid cutting makes this approach prohibitive for many academic researchers. How fast the progress in this area will be relies upon the development of inexpensive and efficient methods of CNT production.

GLOSSARY

Carbon nanotubes Fullerene-related structures consisting of graphene cylinders. As-prepared carbon nanotubes are closed at either end with caps containing fused hexagonal and pentagonal rings. Oxidation with strong oxidants (nitric acid, ozone, hydrogen peroxide, etc.) destroys the caps, producing oxygen-containing functional groups at the nanotube tips.

Derivatization Converting functional groups into other groups, having different chemical properties.

Functionalization Chemical attachment of reactive (functional) groups to molecules.

MWNT Multiwalled (or multilayer) carbon nanotube, a carbon nanotube consisting of two or many coaxial graphene cylinders, maintained together by van der Waals forces.

Solubilization Enhancement of solubility of a chemical compound.

SWNT Single-walled (or single-layer) carbon nanotube, a carbon nanotube consisting of one graphene cylinder.

REFERENCES

1. R. Saito, G. Dresselhaus, and M. S. Dresselhaus, "Physical Properties of Carbon Nanotubes." Imperial College Press, London, 1998.
2. P. M. Ajayan, *Chem. Rev.* 99, 1787 (1999).
3. J. L. Bahr and J. M. Tour, *J. Mater. Chem.* 12, 1952 (2002).
4. A. Hirsch, *Angew. Chem. Int. Ed.* 41, 1853 (2002).
5. S. S. Wong, E. Joselevich, A. T. Woolley, C. L. Cheung, and C. M. Lieber, *Nature* 394, 52 (1998).
6. S. S. Wong, A. T. Woolley, E. Joselevich, C. L. Cheung, and C. M. Lieber, *J. Am. Chem. Soc.* 120, 8557 (1998).
7. J. Liu, A. G. Rinzler, H. Dai, J. H. Hafner, R. K. Bradley, P. J. Boul, A. Lu, T. Iverson, K. Shelimov, C. B. Huffman, F. Rodriguez-Macias, Y.-S. Shon, T. R. Lee, D. T. Colbert, and R. E. Smalley, *Science* 280, 1253 (1998).
8. J. Chen, M. A. Hamon, H. Hu, Y. Chen, A. M. Rao, P. C. Eklund, and R. C. Haddon, *Science* 282, 95 (1998).
9. Z. Jia, Z. Wang, J. Liang, B. Wei, and D. Wu, *Carbon* 37, 903 (1999).
10. K. Kinoshita, "Carbon Electrochemical and Physicochemical Properties." Wiley, New York, 1988.
11. S. F. McKay, *J. Appl. Phys.* 35, 1992 (1964).
12. D. B. Mawhinney, V. Naumenko, A. Kuznetsova, J. T. Yates, J. Liu, and R. E. Smalley, *Chem. Phys. Lett.* 324, 213 (2000).
13. A. Kuznetsova, D. B. Mawhinney, V. Naumenko, J. T. Yates, J. Liu, and R. E. Smalley, *Chem. Phys. Lett.* 321, 292 (2000).
14. A. Kuznetsova, I. Popova, J. T. Yates, M. J. Bronikowski, C. B. Huffman, J. Liu, R. E. Smalley, H. H. Hwu, and J. G. G. Chen, *J. Am. Chem. Soc.* 123, 10699 (2001).
15. H. Hu, P. Bhowmik, B. Zhao, M. A. Hamon, M. E. Itkis, and R. C. Haddon, *Chem. Phys. Lett.* 345, 25 (2001).
16. J. P. Deng, C. Y. Mou and C. C. Han, *Fullerene Sci. Technol.* 5, 1033 (1997).
17. D. B. Mawhinney, V. Naumenko, A. Kuznetsova, and J. T. Yates, *J. Am. Chem. Soc.* 122, 2383 (2000).
18. L. Cai, J. L. Bahr, Y. Yao, and J. M. Tour, *Chem. Mater.* 14, 4235 (2002).
19. M. A. Hamon, H. Hu, P. Bhowmik, S. Niyogi, B. Zhao, M. E. Itkis, and R. C. Haddon, *Chem. Phys. Lett.* 347, 8 (2001).
20. Y. Chen, R. C. Haddon, S. Fang, A. M. Rao, W. H. Lee, E. C. Dickey, E. A. Grulke, J. C. Pendergrass, A. Chavan, B. E. Haley, and R. E. Smalley, *J. Mater. Res.* 13, 2423 (1998).
21. M. A. Hamon, J. Chen, H. Hu, Y. Chen, M. E. Itkis, A. M. Rao, P. C. Eklund, and R. C. Haddon, *Adv. Mater.* 11, 834 (1999).
22. S. Niyogi, H. Hu, M. A. Hamon, P. Bhowmik, B. Zhao, S. M. Rozenzhak, J. Chen, M. E. Itkis, M. S. Meier, and R. C. Haddon, *J. Am. Chem. Soc.* 123, 733 (2001).
23. Y. Yang, J. Zhang, X. Nan, and Z. Liu, *J. Phys. Chem. B* 106, 4139 (2002).
24. B. Zhao, H. Hu, S. Niyogi, M. E. Itkis, M. A. Hamon, P. Bhowmik, M. S. Meier, and R. C. Haddon, *J. Am. Chem. Soc.* 123, 11673 (2001).
25. T. Saito, K. Matsushige, and K. Tanaka, *Physica B* 323, 280 (2002).
26. Y.-P. Sun, W. Huang, Y. Lin, K. Fu, A. Kitaygorodskiy, L. A. Riddle, Y. J. Yu, and D. L. Carroll, *Chem. Mater.* 13, 2864 (2001).
27. J. E. Riggs, Z. Guo, D. L. Carroll, and Y.-P. Sun, *J. Am. Chem. Soc.* 122, 5879 (2000).
28. J. E. Riggs, D. B. Walker, D. L. Carroll, and Y.-P. Sun, *J. Phys. Chem. B* 104, 7071 (2000).
29. R. Czerw, Z. Guo, P. M. Ajayan, Y.-P. Sun, and D. L. Carroll, *Nano Lett.* 1, 423 (2001).
30. W. Huang, Y. Lin, S. Taylor, J. Gaillard, A. M. Rao, and Y.-P. Sun, *Nano Lett.* 2, 231 (2002).
31. Y. Lin, A. M. Rao, B. Sadanadan, E. A. Kenik, and Y.-P. Sun, *J. Phys. Chem. B* 106, 1294 (2002).
32. M. Sano, A. Kamino, J. Okamura, and S. Shinkai, *Langmuir* 17, 5125 (2001).
33. S. Banerjee and S. S. Wong, *Nano Lett.* 2, 195 (2002).
34. F. Pompeo and D. E. Resasco, *Nano Lett.* 2, 369 (2002).
35. W. Huang, S. Taylor, K. Fu, Y. Lin, D. Zhang, T. W. Hanks, A. M. Rao, and Y.-P. Sun, *Nano Lett.* 2, 311 (2002).
36. C. V. Nguyen, L. Delzeit, A. M. Cassell, J. Li, J. Han, and M. Meyyappan, *Nano Lett.* 2, 1079 (2002).
37. Z. Liu, Z. Shen, T. Zhu, S. Hou, and L. Ying, *Langmuir* 16, 3569 (2000).
38. E. V. Basiuk, V. A. Basiuk, J.-G. Bañuelos, J.-M. Saniger-Blesa, V. A. Pokrovskiy, T. Yu. Gromovoy, A. V. Mischanchuk, and B. G. Mischanchuk, *J. Phys. Chem. B* 106, 1588 (2002).
39. V. A. Basiuk, E. V. Basiuk, and J.-M. Saniger-Blesa, *Nano Lett.* 1, 657 (2001).
40. V. A. Basiuk, K. Kobayashi, T. Kaneko, Y. Negishi, E. V. Basiuk, and J.-M. Saniger-Blesa, *Nano Lett.* 2, 789 (2002).
41. J. Chen, A. M. Rao, S. Lyuksyutov, M. E. Itkis, M. A. Hamon, H. Hu, R. W. Cohn, P. C. Eklund, D. T. Colbert, R. E. Smalley, and R. C. Haddon, *J. Phys. Chem. B* 105, 2525 (2001).
42. M. Sano, A. Kamino, J. Okamura, and S. Shinkai, *Nano Lett.* 2, 531 (2002).
43. M. A. Hamon, H. Hui, P. Bhowmik, H. M. E. Itkis, and R. C. Haddon, *Appl. Phys. A* 74, 333 (2002).
44. K. Fu, W. Huang, Y. Lin, L. A. Riddle, D. L. Carroll, and Y.-P. Sun, *Nano Lett.* 1, 439 (2001).
45. K. Fu, A. Kitaygorodskiy, A. M. Rao, and Y.-P. Sun, *Nano Lett.* 2, 1165 (2002).
46. V. A. Basiuk, *Nano Lett.* 2, 835 (2002).
47. B. Wu, J. Zhang, Z. Wei, S. Cai, and Z. Liu, *J. Phys. Chem. B* 105, 5075 (2001).
48. D. Chattopadhyay, I. Galeska, and F. Papadimitrakopoulos, *J. Am. Chem. Soc.* 123, 9451 (2001).
49. T. Nishino, T. Ito, and Y. Umezawa, *Anal. Chem.* 74, 4275 (2002).
50. C. Velasco-Santos, A. L. Martínez-Hernández, M. Lozada-Cassou, A. Alvarez-Castillo, and V. M. Castaño, *Nanotechnology* 13, 495 (2002).
51. S. Banerjee and S. S. Wong, *Nano Lett.* 2, 49 (2002).
52. S. Banerjee and S. S. Wong, *J. Am. Chem. Soc.* 124, 8940 (2002).

Chemical Synthesis of Nanoparticles

H. Bönemann, K. S. Nagabhushana

Max-Planck-Institut für Kohlenforschung, Mülheim, Germany

CONTENTS

1. Introduction
2. Wet Chemical Synthesis
3. Spectral Characterization of Nanoparticles
4. Physical Properties of Nanoparticles
5. Applications in Catalysis
6. Applications in Materials Science
7. Conclusion
- Glossary
- References

1. INTRODUCTION

The colloidal metals, particularly gold, generated considerable interest due to their intensive colors which enabled them to be used as pigments for glass or ceramics. Presently, with an increasing understanding of the unique electronic structure and extremely large surface areas of nanosized metal particles, there is a rapid growth in the number of potential technological applications. Generally, isolable particles between 1 and 50 nm size that are prevented from agglomeration by protecting shells are regarded as nanostructured metal colloids. Depending on the nature of the protecting shell, they can be redispersed either in water (“hydrosols”) or in organic solvents (“organosols”). As the size of the metal particle decreases to nanometer scale, the mechanical, electronic, optical, magnetic, as well as the thermodynamic properties are significantly altered from those of either the bulk or the single molecule. The object of this chapter is to provide a synopsis of the wet chemical method syntheses of colloidal nanoparticles exercised to date with a discussion on their potential applications. A brief discussion on their physical properties and some spectral characterizations are provided.

A wealth of knowledge has been acquired about these colloidal materials in the last few decades through the work of leading scientists in the field [1–12]. Mono- and bimetallic colloids in their dispersed forms can be used as precursors for a new type of catalyst that is applicable both in the homogeneous and heterogeneous phases [13–16]. Recent

studies show the potential of nanostructured metal colloids as fuel cell catalysts apart from the obvious applications in chemical catalysis [17–20]. Though presently there are no major industrial applications of nanostructured materials known, current developments are inching closer to it than ever before.

2. WET CHEMICAL SYNTHESIS

Production of nanostructured metal colloids is brought about by two methods. The “top-down method” involves chopping down the bulk metal by mechanical means, and the resulting colloidal particles are subsequently stabilized by colloidal protecting agents [21, 22]. Application of metal vapor techniques [23–26], which work on this principle, provides chemists with a very versatile route for the production of a wide range of nanostructured metal colloids on a preparative laboratory scale [27, 28]. However, this method has a few drawbacks in that it is difficult to obtain a narrow particle size distribution, and installation of metal vapor machines is highly demanding. On the other hand, “bottom-up methods” of wet chemical nanoparticle preparation basically rely on the chemical reduction of metal salts, electrochemical pathways, or the controlled decomposition of metastable organometallic compounds in solution. Control over the growth of the primarily formed nanoclusters and their agglomeration is effected by the use of a variety of stabilizers, in the form of donor ligands, polymers, and surfactants. Faraday, in 1857, was the first to report chemical reduction of transition-metal salts in the presence of stabilizing agents to generate zerovalent metal colloids in aqueous or organic media [29]. This reliable approach has become the most common and powerful synthetic method in this field [10, 11, 30]. Nearly a century later, Turkevich [1–3] established the first reproducible standard recipe for the preparation of 20-nm gold metal colloids by the reduction of $[\text{AuCl}_4]^-$ using sodium citrate. Additionally, he proposed a mechanism for the stepwise formation of nanoclusters based on nucleation, growth, and agglomeration [1] which in essence is still valid. With the help of better analytical techniques and data from more recent thermodynamic and kinetic results [31–41], this model has been refined as illustrated in Figure 1.

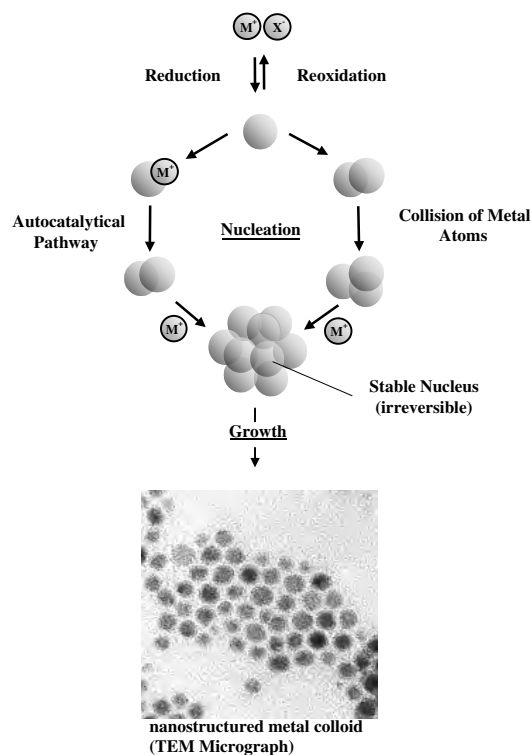


Figure 1. Formation of nanostructured metal colloids via the “salt reduction” method. Adapted with permission from [36], M. Maase, Ph.D. Thesis, Verlag Mainz, Aachen, 1999.

During the embryonic stage of nucleation [31], the metal salt is reduced to give zerovalent metal atoms. Collisions of these in solution with other metal ions, metal atoms, or clusters result in an irreversible “seed” of stable metal nuclei. The diameter of these seeds can be well below 1 nm depending on the strength of the metal-metal bonds and the difference in redox potentials of the metal salt and the reducing agent used.

The mechanism of colloidal metal formation has been carefully followed by a healthy combination of chemical reactions, NMR, ASAXS (anomalous small angle X-ray scattering), XAS (X-ray absorption spectroscopy), DFT (density functional theory) computations, and electron microscopy [37]. It has been exemplified in the reduction of $\text{Pt}(\text{acac})_2$ (acac = acetylacetonate) by trimethylaluminum yielding an intermediate having a four-membered ring containing alternate aluminum and platinum atoms with the remaining valencies of these atoms satisfied by methyl groups. From this complex (3), monodisperse platinum nanoparticles with a mean diameter of 1.2 nm are obtained. Formation of redispersible Pt-colloid of nearly 1.2 nm size from the reaction of the complex with excess of trialkylaluminum is an interesting observation. Figure 2 depicts the formation of the proposed platinum seed.

The central concept of seeds serving as nucleation centers has been evidenced by the wet chemical synthesis of gold nanoparticles via reduction of a gold salt. Examination of the effect of 12-nm gold seed concentration (obtained by citrate reduction of gold salt solution) in the solution phase preparation of gold nanoparticles for varied concentrations of different reducing agents and conditions [38, 39] led to

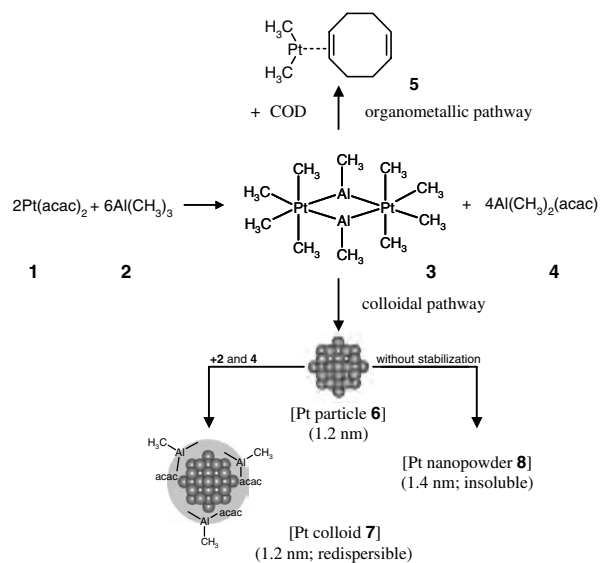


Figure 2. Schematic representation of the platinum seed formation through the intermediate complex (3). Adapted with permission from [37], K. Angermund et al., *Angew. Chem. Int. Ed.* 41, 4041 (2002). © 2002, VCH.

the observation that presence of seeds causes additional nucleation.

Size of nanoparticle products gets affected by two important parameters, namely, seed concentration and the rate of addition of the reducing agent. With increased addition rate of reducing agents, the presence of seeds promotes the formation of more seeds instead of growth of a particular seed. If the addition of the reducing agent is slow, there is growth of the seeds but this is compensated by uniform size distribution of the resulting colloids. On similar lines, Buhro and co-workers have reported results on a seeded growth mechanism in which 1.5-nm Au seeds are used to grow Bi, Sn, and In nanoparticles [40]. Seeding growth for size control of 5- to 40-nm diameter gold nanoparticles has also been studied [41].

For silver nanoparticle synthesis [31], it has been experimentally verified that stronger reducing agents produce smaller nuclei in the “seed.” During the “ripening” process, these nuclei grow to yield colloidal metal particles in the size range of 1–50 nm, having a narrow size distribution. It was assumed that the mechanism for the particle formation is an agglomeration of zerovalent nuclei in the “seed” or, alternately, collisions of already formed nuclei with reduced metal atoms. Stepwise reductive formation of Ag_3^+ and Ag_4^+ clusters by spectroscopic methods has been carefully followed by Henglein and co-workers [32]. An autocatalytic pathway was strongly suggested in which metal ions are adsorbed and successively reduced at the zerovalent cluster surface. In addition to the aforesaid results on nucleation, formation of colloidal Cu protected by cationic surfactants (NR_4^+) was investigated by *in-situ* X-ray absorption spectroscopy showing the formation of an intermediate Cu^+ state prior to the nucleation of the particles [35]. Although the processes during nucleation and particle growth cannot be analyzed separately, it is now generally accepted that the size of the resulting metal colloid is determined by the relative rates of nucleation and particle growth.

2.1. Particle Stabilization

Protective agents play a crucial role in stabilizing the nanostructured colloidal metals from agglomeration. Two basic modes of stabilization have been distinguished [30] though, in principle, a combination of these two effects, use of solvents or ligands for stabilization, can be regarded as a different mode of stabilization.

Electrostatic stabilization is caused by the Coulombic repulsion between particles, caused by the electrical double layer formed by ions adsorbed at the particle surface (e.g., sodium citrate) and the corresponding counter ions. The reduction of $[\text{AuCl}_4]^-$ with sodium citrate to produce gold sols is an example [1–3].

Steric stabilization is achieved because of the coordination of sterically demanding organic molecules that act as protective shields on the metallic surface. The nanometallic cores are separated from each other, preventing agglomeration. Polymers [42–46] and block copolymers; P, N, S-donors (e.g., phosphines, amines, thioethers) [6, 63–90]; solvents such as THF [6, 91], THF/MeOH [92], or propylene carbonate [93]; long chain alcohols [47–62, 94]; surfactants [6, 7, 9, 15, 16, 95–106], and organometallics [107–110] are the main classes of protective groups used. While lipophilic protective agents give metal colloids that are soluble in organic media (“organosols”), hydrophilic agents yield water soluble colloids (“hydrosols”). In Pd organosols stabilized by tetraalkylammonium halides, the metal core is protected by a surfactant monolayer [111]. A pictorial representation of tetraalkylammonium halide supporting a metal colloid is depicted (see Fig. 4). In contrast, metal hydrosols that are stabilized by zwitterionic surfactants capable of self-aggregation are enclosed in organic double layers. TEM micrographs (Fig. 3) show that the colloidal Pt particles (average size 2.8 nm) are surrounded by a double layer zone of the zwitterionic carboxybetaine (3–5 nm) after the application of contrasting agent in uranylacetate. The charged metal surface interacts with the hydrophilic head group of the betaine. The lipophilic tail is associated with the tail of a

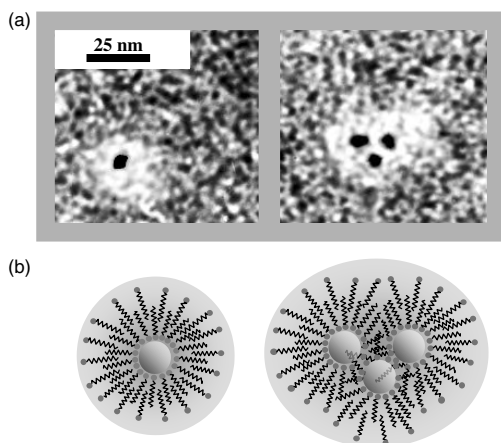


Figure 3. (a) TEM micrographs of colloidal Pt particles (single and aggregated, average core size = 2.8 nm) stabilized by carboxybetaine 12. (b) Schematic model of the hydrosol stabilization by a double layer of the zwitterionic carboxybetaine 12. Adapted with permission from [112], A. Schulze Tilling, Ph.D. Thesis, RWTH Aachen, 1996.

second surfactant molecule. As a result, a hydrophilic outer sphere is formed [112].

Pt or Pt/Au particles can be hosted in the hydrophobic holes of nonionic surfactants, for example, polyethylene monolaurate [113, 114]. High-resolution small-angle X-ray scattering and X-ray photon correlation spectroscopy have been used to find the structure and diffusive dynamics of a colloidal palladium aggregate sol under dilute and semidilute conditions. The sizes of the aggregates determined in the static structure and the one derived from diffusive dynamics at low concentration are found consistent with each other.

The aggregates tend to overlap at high concentration. While the system remains in a liquid-like state, the apparent diffusion constant decreases. The structural features obtained by comparison of static and dynamic data are not accessible solely by one technique [115].

2.2. Reducing Agents and Reduction Methods

2.2.1. Metal Salt Reduction

This is one of the most used wet chemical methods of nanoparticle synthesis. The major advantage of the salt reduction method is that it allows colloidal nanoparticles to be prepared with reproducibility in multigram amounts having a narrow size distribution. The classical Faraday route of reducing $[\text{AuCl}_4]^-$ by sodium citrate is still used to prepare standard 20-nm gold sols for histological staining applications [1, 116]. An array of chemical reducing agents and methods have successfully been applied to obtain nanostructured colloidal metals.

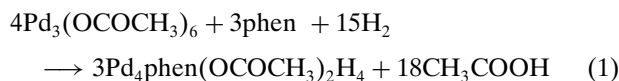
Diborane-as-reductant route was established by Schmid and co-workers for the synthesis of $\text{Au}_{55}(\text{PPh}_3)_{12}\text{Cl}_6$ (1.4 nm), a full shell (“magic number”) nanocluster stabilized by phosphine ligands [63–78]. Careful introduction of B_2H_6 into a Au^{III} ion solution essentially yielded uniform Au_{55} clusters. The “diborane route” for $\text{M}_{55}\text{L}_{12}\text{Cl}_n$ nanoclusters was reviewed by Aiken and Finke [11]. Bimetallic nanoclusters that were made accessible by this method [63–78] have been thoroughly characterized. The phosphine ligands may be exchanged in the Au_{55} nanoclusters quantitatively using silsesquioxanes which causes important changes in the physical and chemical behavior of the gold clusters [77, 78]. The synthesis and general chemistry of nano-sized silica coated metal particles have been elaborated by Mulvaney and co-workers [78].

The “alcohol reduction process” by Hirai and Toshima [10, 42–45, 117, 118] is widely applicable for the preparation of colloidal precious metals stabilized by organic polymers such as poly(vinylpyrrolidone) (PVP), poly(vinyl alcohol) (PVA), and poly(methylvinyl ether). During salt reduction, alcohols having α -hydrogen atoms are oxidized to the corresponding carbonyl compound. Thus methanol gets converted to formaldehyde. The method for preparing bimetallic nanoparticles via the co-reduction of mixed ions has been evaluated in a recent review [10]. Using ethylene glycol as a solvent and reducing agent, PVP stabilized Ag nanoprisms and nanorods [119], Au, Pt, Pd, Ir [120], Ru and Pt-Mn [120–122] are obtained by what is now termed as poly-ol synthesis. Nanometer-size platinum colloid, FePt nanoparticle

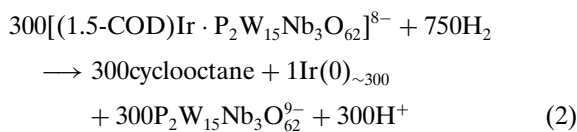
alloy, $(\text{Fe}_{49}\text{Pt}_{51})_{88}\text{Ag}_{12}$ nanoclusters are obtained by using ethylene glycol, glycerol, and other long chain polyols [88, 123–125]. While ethanol in aqueous medium has been used for generating Pd nanoparticles with varying particle sizes [126, 127], pure ethanol and in some instances methanol has been used to prepare Ag, Au, Pd, Cu, Ag-Pd, and Cu-Pd nanoparticles and alloys [128–130]. Reduction of a mixture of Pt and Ru salts on a support with atomic ratios of the metals in 1:1 and 7:3 respectively using a modified alcohol reduction procedure has been performed to good effect [131].

Hydrogen is an efficient reducing agent for the preparation of electrostatically stabilized metal sols and of polymer-stabilized hydrosols of Pd, Pt, Rh, and Ir [132–136]. Moiseev's giant palladium cluster [79–84] and Finke's polyoxoanion- and tetrabutylammonium-stabilized transition-metal nanoclusters [11, 34, 137–141] are all made by the hydrogen reduction method.

The characterization of Moiseev's "giant" cationic palladium clusters [79–84] [idealized formula $\text{Pd}_{\approx 561}\text{L}_{\approx 60} \cdot (\text{OAc})_{\approx 180}$ (L = phenanthroline, bipyridine)] and their catalytic properties have also been reviewed by Aiken and Finke [11]. The "giant Pd cluster" is synthesized in two steps: reduction of palladium(II) acetate in acetic acid by hydrogen gas in the presence of either 1,10-phenanthroline (phen) or 2,2'-bipyridine (bipy) yields an intermediate product $[\text{Pd}_4\text{phen}(\text{OAC})_2\text{H}_4]_{n \approx 100}$ of 2-nm size, Eq. (1):



In acetic acid solution, $[\text{Pd}_4\text{phen}(\text{OAC})_2\text{H}_4]_{n \approx 100}$ takes up to 5 Mol of O_2 per gram-atom of palladium over about 20 minutes to give air-stable and water-soluble "giant Pd cluster" in 85% yield. Finke's system [11, 34, 137–141] is synthesized via hydrogen reduction under completely air- and water-free conditions using a polyoxoanion-supported Ir(I) organometallic complex $[(n\text{-C}_4\text{H}_9)_4\text{N}]_5\text{Na}_3[(1.5\text{-COD})\text{Ir} \cdot \text{P}_2\text{W}_{15}\text{Nb}_3\text{O}_{62}]$ as the molecular precursor (Eq. (2)):



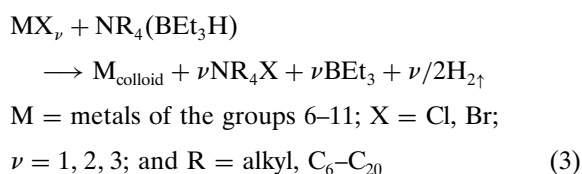
This represents a new subclass of transition-metal nanoclusters. A zerovalent transition-metal core, for example, Ir(0) [11, 34, 137, 138] or Rh(0) [139–141], is doubly stabilized by a cationic surfactant (e.g., NR_4^+) and by a polyoxoanion (e.g., $\text{P}_2\text{W}_{15}\text{Nb}_3\text{O}_{62}^{9-}$). Treatment of this precursor with H_2 in acetone and excess cyclohexene results in the formation of nearly monodisperse [i.e., $\pm 15\%$ size dispersion 2 ± 0.3 nm Ir(0) $_{\sim 300}$] nanoclusters. In the absence of cyclohexene, the same procedure yields larger Ir(0) $_{\sim 900}$ nanoclusters (3 ± 0.4 nm). The results of a combination of modern instrumental analysis methods applied to Finke's nanoclusters have been carefully discussed [11]. It was clear that the Ir(0) core is uncharged, and that the particles have an "extremely clean, exposed, chemically reactive surface." These experiments were done on a few milligram scales. Very recently, nearly a gram scale synthesis of polyoxoanion and tetrabutylammonium protected Ir(0) $_{\sim 2000}$ with a mean

particle size of 3.8 ± 0.6 nm and its activity before and after storage have been reported [142].

Shape-selective preparation of oxalate-stabilized Pt nanoparticles with a mean diameter of 6.5, 3.5, and 7.9 nm starting from $\text{K}_2[\text{Pt}(\text{C}_2\text{O}_4)]_2$, K_2PtCl_6 , and K_2PtCl_4 , respectively, using hydrogen as a reducing agent has been a recent development [143]. Production of Pt-Au bimetallic catalyst by surface redox reactions has been performed by direct redox reaction and refilling method [144], in which parent platinum metal adsorbed with hydrogen reduces the AuCl_4^- species by contact with the Pt-H interface at low temperatures. Using hydrogen as a reducing agent, platinum nanoparticles have been synthesized along with polyacrylic acid as capping material on alumina [145], or in the presence of N-propylacrylamide [146, 147].

Colloidal Pt in water [2, 148] is obtained using CO, formic acid, or sodium formate, formaldehyde, and benzaldehyde as reductants [149]. Silanes are found to be effective for the reductive preparation of Pt sols [150, 151]. Duff, Johnson, and Baiker and their co-workers have successfully introduced tetrakis(hydroxymethyl)phosphoniumchloride (THPC) as a reducing agent, which allows the size- and morphology-selective synthesis of Ag, Cu, Pt, and Au nanoparticles from the corresponding metal salts [152–157]. Further, hydrazine [158–160], hydroxylamine [41, 161, 162], and electrons trapped in, for example, $\text{K}^+[(\text{crown})_2\text{K}]^-$ [163], were applied as reductants. In spite of its disadvantage in the formation of transition-metal borides during the synthesis, BH_4^- is a powerful and valuable reagent for the salt reduction [46, 164–169]. Borate reduction followed by octa(3-aminopropyl)silsesquioxane (NSi_8) stabilization of silver nanoparticles on poly(styrenesulphonate)/silica has been prepared [170] and aqueous reduction using NaBH_4 is being used extensively [166, 167, 171–173]. Very recently, solvent-stabilized platinum and its alloy with Ru, Mo, W, and Ni with an average diameter of 1.7 nm has been reported. In an application oriented synthesis of platinum-based electrocatalysts, the reduction of platinum and the combining metal halides was performed using LiBH_4 as a reducing agent. The resulting nanoparticles were found dispersed in THF, being stabilized by the solvent. Evaporation of THF and further treatment with ethanol gave the desired product. This residue was then taken into benzene by sonication and then in water before checking their catalytic activity. Though this method gives relief to many synthetic chemists because of its simplicity and the quoted electrocatalytic activity, the redispersibility of the obtained nanoparticles and their solubility as naked metals in higher concentration in THF are questionable [188]. Cubic platinum nanoparticles are generated by NaBH_4 reduction of K_2PtCl_4 in an aqueous medium. Under the effect of phase transfer inducer HCl, Pt nanoparticles were transferred to a toluene solution containing dodecanethiol, forming a toluene organosol of cubic Pt nanoparticles protected by dodecanethiol which upon supporting on carbon resulted in a self-assembled nanoparticle [174]. Hydrotriorganoborates having tetraalkylammonium cations [6, 7, 9, 15, 95–97] offer a wide range of applications in the wet chemical reduction of transition-metal salts. In this case, the reductant $[\text{BEt}_3\text{H}^-]$ is combined with the stabilizing agent, NR_4^+ . The surface active NR_4^+ salts are formed

immediately at the reduction center in high local concentration and act as powerful protecting agents for the metal particles and prevent particle aggregation. This resulting colloid can be isolated in solid form and redissolved in various solvents. Another advantage is that trialkylboron is recovered unchanged from the reaction and no borides contaminate the products. It has been recently shown in the case of tetrabutylammonium- and tetraoctylammonium-stabilized Pd colloids [175] by various advanced physical methods that negatively charged chloride is present on the inner side of the protecting shell and is located between palladium core and $N(\text{alkyl})_4$ groups forming the protecting shell. Moreover, results also suggest a dependence of the equilibrium position of the chloride between the metal core and the alkyl chain length of the protecting shell. This picture (Fig. 4b) is in contrast to the previously presumed model as depicted (Fig. 4a):



From this method of colloidal synthesis, the NR_4^+ -stabilized metal "raw" colloids typically contain 6–12 wt % of metal. "Purified" transition-metal colloids containing ca. 70–85 wt % of metal are obtained by the workup with ethanol or ether and subsequent reprecipitation by a solvent of different polarity [6]. The pre-preparation of $[\text{NR}_4^+\text{BEt}_3\text{H}^-]$ can be avoided when NR_4X is coupled to the metal salt prior to the reduction step. NR_4^+ -stabilized transition-metal nanoparticles can also be obtained from NR_4X -transition-metal double salts. Since the local concentration of the protecting group is sufficiently high, a number of conventional reducing agents may be applied to get the protected colloidal metal (Eq. (4)) [7, 15]:

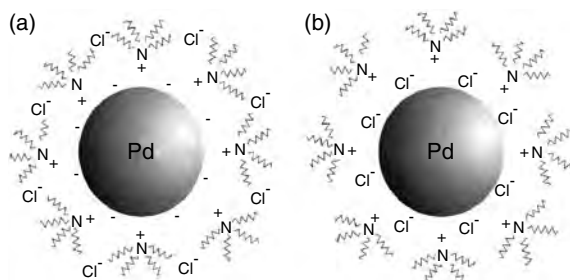
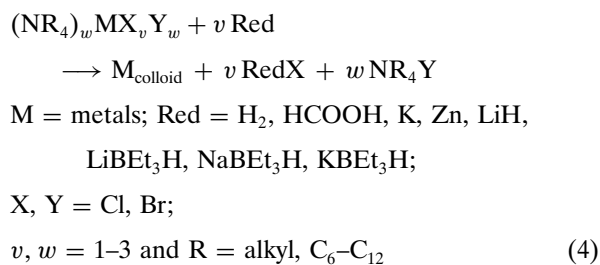
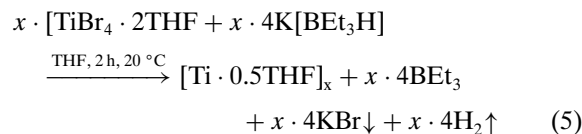


Figure 4. (a) Previously presumed model of NR_4Cl stabilized metal core. (b) Idealized model of NR_4Cl stabilized metal core. Adapted with permission from [175], B. J. Hormes et al., *Surf. Sci.* 497, 321 (2002). © 2002, Elsevier Science.

In a recent review [11], the scope and limitations of this method have been evaluated. Isolable colloids of the zerovalent early transition metals which are stabilized only with THF have been prepared via the $[\text{BEt}_3\text{H}^-]$ reduction of the preformed THF adducts of TiBr_4 (Eq. (5)), ZrBr_4 , VBr_3 , NbCl_4 , and MnBr_2 :



Detailed studies of $[\text{Ti} \cdot 0.5 \text{THF}]$ [91] show that it consists of Ti_{13} clusters in the zerovalent state, stabilized by six THF molecules (Fig. 5). By analogy, $[\text{Mn} \cdot 0.3 \text{THF}]$ particles (1–2.5 nm) were prepared [177] and the physical properties have been studied [108]. THF in Eq. (5) has been successfully replaced by tetrahydrothiophene (THT) in the case of Mn, Pd, and Pt organosols; but attempts to stabilize Ti and V this way led to decomposition [15] (Fig. 6).

Figure 7 gives a survey of the $[\text{BEt}_3\text{H}^-]$ method. The advantages of the method (Fig. 7) may be summarized as follows:

- The method is generally applicable to salts of metals in groups 4–11 in the periodic table.
- It yields extraordinary stable metal colloids that are easy to isolate as dry powders.
- The particle size distribution is nearly monodisperse.
- Bi- and plurimetallic colloids are easily accessible by co-reduction of different metal salts.
- The synthesis is suitable for multigram preparations and easy to scale up.
- The method is reproducible.

Although there is a drawback to this method in that the particle size of the resulting sols cannot be varied by altering the reaction conditions, this method has been conveniently used by other research groups in generating efficient electrocatalyst precursors [179–181]. Triethylhydroborate has also been used for the preparation of acicular iron particles and

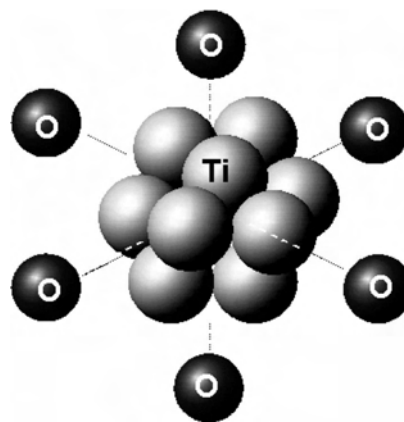


Figure 5. Ti_{13} cluster stabilized by six THF-O atoms in an octahedral configuration. Adapted with permission from [15], H. Bönemann and W. Brijoux, in "Advanced Catalysts and Nanostructured Materials" (W. Moser, Ed.), Chap. 7, p. 165. Academic Press, San Diego, 1996. © 1996, Elsevier Science.

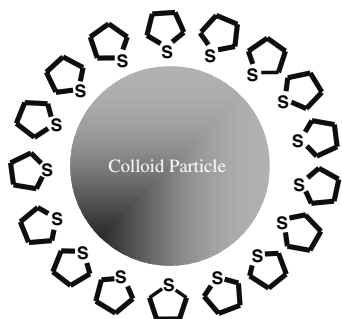
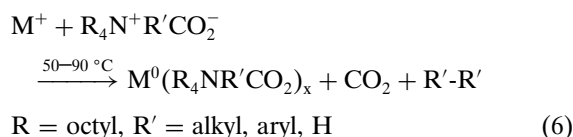


Figure 6. Organosols stabilized by tetrahydrothiophene. M = Ti, V (decomposition). M = Mn, Pd, Pt, stable colloids. Adapted with permission from [15], H. Bönemann and W. Brijoux, in "Advanced Catalysts and Nanostructured Materials" (W. Moser, Ed.), Chap. 7, p. 165. Academic Press, San Diego, 1996. © 1996, Elsevier Science.

granular particles, without using acicular starting materials during the reduction of FeCl_3 [176].

Highly water-soluble hydrosols, particularly those of zerovalent precious metals, were made accessible using betaines instead of NR_4^+ salts as the protecting group (Eq. (3)). As shown in Eq. (4), a broad variety of hydrophilic surfactants may be used [7, 15, 96]. A new method for the size- and morphology-selective preparation of metal colloids using tetraalkylammonium carboxylates of the type $\text{NR}_4^+\text{R}'\text{CO}_2^-$ (R = octyl, R' = alkyl, aryl, H) both as the reducing agent and the stabilizer (Eq. (6)) was reported by Reetz and Maase [36, 183, 184]:



The resulting particle sizes were found to correlate with the electronic nature of the R' group in the carboxylate. Electron donors produce small nanoclusters while electron-withdrawing substituents R', in contrast, yield larger particles. For example, Pd particles of 2.2 nm size are found when $\text{Pd}(\text{NO}_3)_2$ is treated with an excess of tetra(*n*-octyl)ammonium-carboxylate bearing R' = $(\text{CH}_3)_3\text{CCO}_2^-$

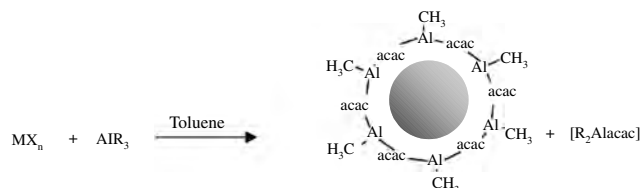
Ti 0.8	V	Cr 3.0	Mn 1-2.5	Fe 3.0	Co 2.8	Ni 2.8	Cu 8.3
Zr	Nb	Mo 2-3		Ru 1.3	Rh 2.1	Pd 2.5	Ag 2-13
		Re		Os	Ir 1.5	Pt 2.8	Au 10

- Nanometal powders
- THF-stabilized nanometals
- NR_4^+ -stabilized nanometals

Figure 7. Nanopowders and nanostructured metal colloids accessible via the $[\text{BEt}_3\text{H}^-]$ reduction method (Eqs. (3), (5)) (including the mean particle sizes obtained). Adapted with permission from [7], H. Bönemann et al., *J. Organomet. Chem.* 520, 143 (1996). © 1996, Elsevier Science.

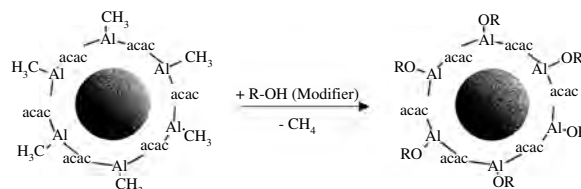
as the substituent. With R' = $\text{Cl}_2\text{CHCO}_2^-$ (an electron-withdrawing substituent) the particle size was found to be 5.4 nm. The following bimetallic colloids were obtained with tetra(*n*-octyl) ammonium formate as the reductant: Pd/Pt (2.2 nm), Pd/Sn (4.4 nm), Pd/Au (3.3 nm), Pd/Rh (1.8 nm), Pt/Ru (1.7 nm), and Pd/Cu (2.2 nm). The shape of the particles also depends on the reductant: With tetra(*n*-octyl) ammonium glycolate $\text{Pd}(\text{NO}_3)_2$ a significant amount of trigonal particles in the resulting Pd colloid was detected.

Organoaluminum compounds have been used for the reductive stabilization of mono- and bimetallic nanoparticles (see Eq. (7)) [107, 108]:



- M = metals of groups 6–11 PSE
 - X = halogene, acetylacetonate $n = 2-4$
 - R = C_1-C_8 -Alkyl
 - Particle sizes 1–12 nm
- (7)

From Eq. (7), it is clear that colloids of zerovalent elements of groups 6–11 of the periodic table (and also of tin) can be prepared in the form of stable, isolable organosols. This method is now shown to be a reliable approach for the production of a wide range of small zerovalent transition-metal particles that can be redispersed in organic solvents such as toluene or THF. The key feature of this synthesis is the formation of an organometallic colloidal protecting shell around the particles. In other words, highly reactive aluminum alkyl groups (e.g., $\text{Al-C}_2\text{H}_5$ or Al-CH_3) are present as protective agents for the colloids. Formation of alkyl aluminum protecting shell over platinum nanocluster was confirmed by quantitative protonolysis experiments, by using spacer molecules (bifunctional), and also modifiers (monofunctional). The mechanistic aspect has already been stated before. In the case of protonolytic reaction with diols, because of the presence of a second OH group in the molecule, an interconnection of particles is brought about. As the particles are statistically covered with reactive Al-CH_3 groups, this reaction leads to the formation of a three-dimensional (3D) cross-linked nanoparticle network having vitreous structure in contrast to modification that yields redispersible colloids (Eq. (8)):

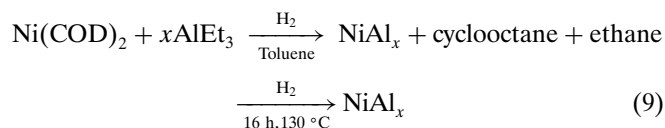


- Modifiers: alcohols, carbonic acids, silanols, sugars, polyalcohols, polyvinylpyrrolidone, surfactants, silica, alumina, etc.
- (8)

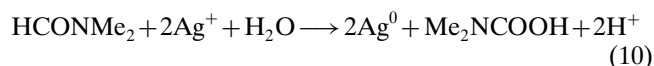
This “modification” (Eq. (8)) of the organoaluminum protecting shell can be used to tailor the dispersion characteristics of the original organosols. A vast spectrum of dissolubilities of the colloidal metals in hydrophobic and hydrophilic media (including water) has been achieved this way. Inorganic surfaces bearing -OH groups reacting with the active Al-C bonds in the colloidal protecting shell opens new ways in the heterogeneous catalyst preparation. The modification process does not alter the particle size of the metal core (see Fig. 8) [185].

Using a very similar route, a wet chemical method for the production of β -NiAl using alkylaluminum as a reducing agent has been developed [186]. The method involves reaction between $\text{Ni}(\text{COD})_2$ and trialkylaluminum in toluene. Hydrogen under high pressure is used to saturate the COD and ethylene. Through analysis and comparable literature data, an intermediate depicted in Figure 9 has been proposed.

The product is found in the form of a black powder which upon purification procedures is found in aggregates of 100–500 nm, comprising smaller particles (5–7 nm). In these reactions, aluminum organic acts not as a reducing agent but rather as a reaction partner for the $\text{Ni}(0)$ complex. The reaction can be summarized as shown in Eq. (9). Alloys of Ni and Al have been prepared in various stoichiometries by using appropriate ratios of the starting materials. The resulting product is then leached off aluminum in order to obtain skeletal nickel catalyst [187], to be compared with Raney nickel-type catalysts. The advent of this not only gives a versatile access to new bottom-up alloys between transition and main-group metals but also allows one to synthesize trimetallic or multimetal component nanoparticles:



Apart from these, a novel synthesis of anisotropic silver nanoparticles based on the use of N, N-dimethyl formamide as a solvent and as a reducing agent in the presence of polymer PVP has been performed recently [119]. The chemical reaction is presented in Eq. (10):



Particle size distribution: $(\text{CH}_3)_n$ -Al-acac Pt/Ru-colloid Particle size distribution: modified Pt/Ru-colloid

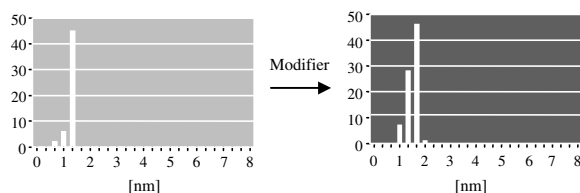


Figure 8. Size conservation of colloidal Pt/Ru particles under the hydrophilic modification of the $(\text{CH}_3)_n$ -Al-acac protecting shell using polyethylene glycol-dodecylether.

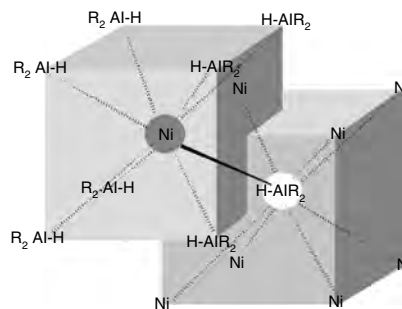


Figure 9. Proposed intermediate of the reaction of $\text{Ni}(\text{COD})_2$ with alkyl aluminum under hydrogen. Adapted with permission from [186], H. Bönemann et al., *Angew. Chem. Int. Ed.* 41, 599 (2002). © 2002, VCH.

This modification follows the preparation of silver nanoparticles by direct reduction using DMF [189]. Presence of different additives was shown to induce the formation of core-shell structures such as Ag on SiO_2 and Ag on TiO_2 [190, 191]. Preparation of PVP-protected gold and silver nanoparticles having low concentration of metal in the solution of DMF has been dealt with in great detail [192]. Another example of solvent acting as a reducing agent is the case of DMSO [193].

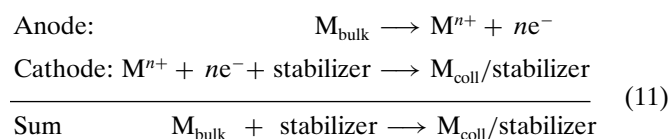
Preparation of gold nanoparticles protected by alkanethiol capping agents, performed by Brust et al., is probably the most popular preparation method for the synthesis of gold nanoparticles. This has been modified by other researchers and these methods are discussed later [182]. Alfalfa plants are shown to produce gold and silver nanoparticles when the plants are germinated in corresponding metal salt in either solid media or media solution. The analysis by extended X-ray absorption fine structure (EXAFS) clearly indicates the presence of zerovalent metal atoms [194, 195]. There are a few reports on biological systems producing nanoparticles. Magnetostatic bacteria have demonstrated the ability to synthesize magnetic nanoparticles and *verticillium* isolated from the *Taxus* plants have shown the capability of reducing silver ions from aqueous solutions intercellularly to corresponding nanoparticles [196, 197]. These have opened up new avenues of recovering precious metals from mining wastes and a new alternative to produce nanoparticles.

Digestive ripening process has been applied to obtain polydisperse colloidal gold in toluene using a series of alkyl thiols [198] and in generating monodisperse metal nanoparticles by the solvated metal atom dispersion method [199]. Other synthetic developments include production of thiol-stabilized CdTe nanocrystals via an alternate to organometallic synthetic route [200], core-shell nanoparticles of Au-Ag [201], and that of chalcogenides [202, 203]. Electroless deposition methods which describe three fundamentally different plating mechanisms including autocatalytic, substrate catalyzed, and galvanic displacements (immersion) processes, are on the rise in preparing metal on metal, metal on semiconductors, and metal on insulators [208–210]. Noble metal nanoparticle films on germanium surfaces have been done by controlled electroless deposition by the immersion of germanium substrate into dilute AuCl_4^- , PdCl_4^{2-} , and PtCl_4^{2-} aqueous solutions. Electroless

deposition of Cu on catalytically active Pd linked through a dendrimer to HOPG are also known [205].

2.2.2. Electrochemical Synthesis

Preparation route for nanostructured mono- and bimetallic colloids using this very versatile method has been further developed by Reetz and his group since 1994 [8, 98, 99]. The overall process of electrochemical synthesis (Eq. (11)) can be divided into six elemental steps:



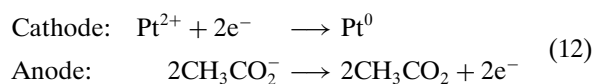
1. oxidative dissolution of the sacrificial Met_{bulk} anode
2. migration of Met^{n+} ions to the cathode
3. reductive formation of zerovalent metal atoms at the cathode
4. formation of metal particles by nucleation and growth
5. arrest of the growth process and stabilization of particles by colloidal protecting agents, for example, tetraalkylammonium ions
6. precipitation of the nanostructured metal colloids.

Advantages of the electrochemical pathway are that contamination with byproducts resulting from chemical reduction agents are avoided, and that the products are easy to isolate from the precipitate. A size-selective particle formation is an added advantage of the method. Experiments using Pd as the sacrificial anode in the electrochemical cell to give $(\text{C}_8\text{H}_{17})_4\text{N}^+\text{Br}^-$ -stabilized $\text{Pd}^{(0)}$ particles indicate that the particle size depends on the current density applied: While having high current densities produced small Pd particles (1.4 nm), low current densities, in contrast, gave larger particles (4.8 nm) [98]. As was seen in a careful analysis of tetraalkylammonium-stabilized Pd and Ni with a combination of TEM and SAX, the control of the particle size does not have a single cause. It can be brought about by adjusting the following parameters:

- distance between the electrodes
- reaction time and temperature
- polarity of the solvent.

The electrochemical synthesis yields almost monodisperse $\text{Pd}(0)$ particles with sizes between 1 and 6 nm according to the parameters above. It was also shown that the size of NR_4^+ -stabilized $\text{Ni}(0)$ particles [100] can be adjusted at will. The electrochemical method [98–105] (Eq. (11)) has been successfully applied to prepare a number of monometallic organosols and hydrosols, for example, of Pd, Ni, Co, Fe, Ti, Ag, and Au on a scale of several hundred milligrams (yields >95%). Solvent-stabilized (propylene carbonate) palladium particles (8–10 nm) have also been obtained using electrochemical pathway [93]. Bimetallic nanocolloids (Pd/Ni, Fe/Co, Fe/Ni) are accessible [103] if two sacrificial Met_{bulk} anodes are used in a single electrolysis cell. In case of Pt, Rh, Ru, and Mo, which are anodically less readily soluble, the corresponding metal salts were electrochemically reduced at the cathode.

In a Kolbe electrolysis at the anode, tetraalkylammonium acetate was used both as the supporting electrolyte and the stabilizer (see Eq. (12)) [104]:



Bimetallic nanocolloids can be prepared by combining the electrochemical methods described in Eqs. (11) and (12) [104].

In addition, the synthesis of layered bimetallic nanocolloids (e.g., Pt/Pd) has been achieved by modifying the electrochemical method [100, 105]. A preformed $(\text{Oct})_4\text{NBr}^-$ -stabilized Pt colloid core (size: 3.8 nm) was electrolyzed in 0.1 M $(\text{Oct})_4\text{NBr}/\text{THF}$ solution with Pd as sacrificial anode (Fig. 10). The preformed Pt core may be regarded as a “living-metal polymer” on which the Pd atoms are deposited to give “onion-type” bimetallic nanoparticles (5 nm). A combination of various analytical methods was used to elucidate the structure.

Layer-by-layer self-assembly of hexanethiol-stabilized gold nanoclusters has been synthesized by a series of alkanedithiol coupling agents $[\text{HS}(\text{CH}_2)_n\text{SH}]$, $n = 6, 8, 9, 12$ onto SiO_2/Si substrates with micron- and nanometer-scale. Gold clusters are initially generated by sodium borohydride reduction of the auric salt followed by stabilization through alkythiol. This stabilized gold cluster in combination with alkanedithiol coupling agents are used in self-assembling on silica using Au electrodes. (See Fig. 11.)

The chemistry of both single- and multiple-layer films of gold nanoclusters formed on insulating substrate has been nicely described [178]. Using anodic alumina membrane as masks, gold nanorods and nanowires are being synthesized by various groups [204, 205] and by template synthesis by Mallouk and co-workers [206].

Finely dispersed sandwich composite nanoparticles of Cu-Ni-Cu in the region of 31 nm and with an average length

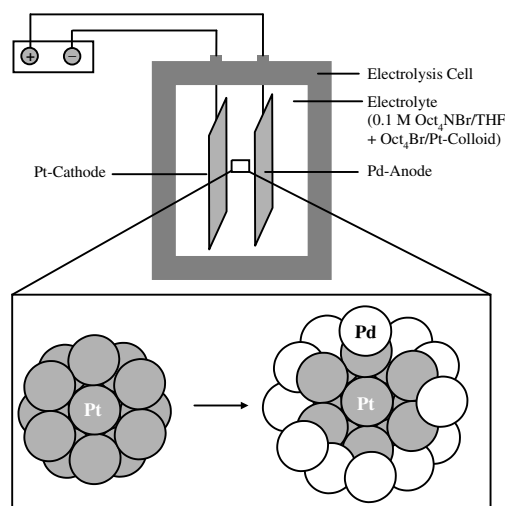


Figure 10. Modified electrolysis cell for the preparation of layered bimetallic Pt/Pd nanocolloids. Adapted with permission from [100], M. A. Winter, Ph.D. Thesis, Verlag Mainz, Aachen, 1998.

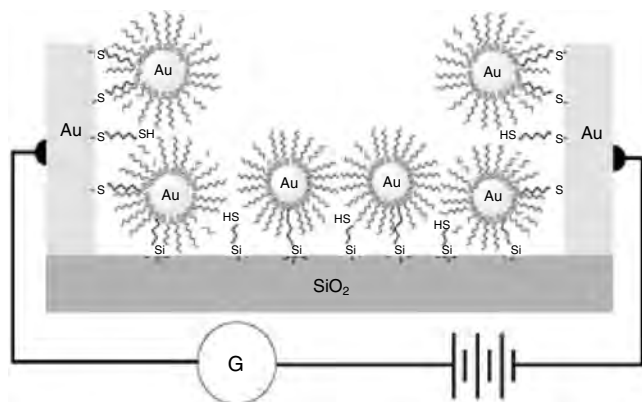


Figure 11. Representation of electrochemical formation of stabilized gold nanoparticles onto a gold electrode surface. Reprinted with permission from [178], A. A. Snow et al., *J. Mater. Chem.* 12, 1222 (2002). © 2002, Royal Society of Chemistry.

of 33 nm have been prepared by a novel method combining electrodeposition of Ni-Cu nanowires onto a template followed by template removal and ultrasonic treatment method [207].

2.2.3. Decomposition of Low-Valent Transition-Metal Complexes

Low-valent organometallic complexes and several organic derivatives of the transition metals decompose under the action of heat, light, or ultrasound to give short-lived nucleation particles of zerovalent metals in solution which may be stabilized by colloidal protecting agents. For example, thermolysis [211–216] leads to the rapid decomposition of cobalt carbonyls to give colloidal cobalt in organic solutions [212]. Colloidal Pd, Pt, and bimetallic Pd/Cu nanoparticles were obtained by thermolysis of labile precious metal salts in the absence of stabilizers [213]. The resulting particles showed a broad size distribution. These results were much improved when the thermolysis was performed in the presence of stabilizing polymers, such as PVP [214]. A review by Gonsalves et al. outlines the application of different methodologies for the production of nanostructured metals (Fe, Co, Ni) and metal alloys (Fe-Co, Pt-Pd, M50 steel) from their corresponding organometallics [217]. Recently, microwave heating in a simple household oven was chosen as a mode for preparing nanosized metal particles and colloids [215, 216, 218]. A modification to that is microwave assisted polyol reduction of PVP-supported platinum and silver salts to their corresponding nanoparticles [219]. The electromagnetic waves can heat the substrate uniformly, leading to a more homogeneous nucleation and a shorter aggregation time. It is instructive to compare the particle size of polymer-stabilized Pt colloids (spheres, 2–4 nm, narrow size distribution) prepared using dielectrical microwave heating with samples made by conventional heating under identical conditions.

The energy induced in the sonochemical decomposition of metal salts and organometallic complexes [220–225] is produced by the formation, growth, and implosive collapse of bubbles in a liquid. Suslick et al. [220] and Gedanken

and co-workers [221–223] have successfully developed this method. Fe, Mo₂C, Ni, Pd, and Ag nanoparticles in various stabilizing environments have been prepared. Within certain limits, the sonochemical decomposition also allows size control which has been observed in the case of Pd nanoparticles immobilized on alumina [224]. The growth of very clean colloidal metals has been achieved by the photolysis of organometallics and metal salts [113, 114, 225]. Henglein et al. [226–234, 236] and Belloni et al. [235] have studied the γ -radiolytic decomposition of metal ions to give nanostructured metal colloids. Short pulses of high-energy photons are applied to metal ions in solution. This allows the reduction process in the whole reaction medium to be “turned on” instantaneously. The process of nucleation and growth of the metal particles in solution can be monitored by spectroscopic methods. In the case of silver, the detailed mechanism of nucleation has been compared with the photographic process [227]. Nanostructured Cd colloids [231] and even bimetallic systems [230–232] have also been studied. In the case of gold, the particle size has been controlled at will. Bimetallic Au_{core}Pt_{shell} and Pt_{core}Au_{shell} colloids have also been obtained [236]. Using laser ablation, the size-selective formation of silver colloids has been reported [237, 238]. The limitation of photo-, γ -radiolysis, and laser irradiation methods lies in the restriction to low metal concentrations in solution. Consequently, they are not suitable to prepare nanostructured metal colloids on a preparative scale. Sonochemical process and conventional method reduction of [Pd(NH₃)₄]²⁺ complexes on Y-zeolite in an aqueous solution has been reported recently. The radicals formed from 2-propanol sonolysis reduces the Pd complex to yield zerovalent Pd [239].

Reduction of neutral molecular precursors of platinum and ruthenium with core composition of PtRu₅ and Pt₂Ru₄ yielding corresponding nanoparticles through reduction by hydrogen at elevated temperatures has been performed [240, 241]. Isolable yields of product in multigram amounts can be prepared by the controlled chemical decomposition of zerovalent transition-metal complexes on the addition of CO or H₂ in the presence of appropriate stabilizers [85–88, 242–250]. The growth of metallic Ru particles from Ru(COT)(COD) (COT = cyclooctatetraene, COD = cycloocta-1,5-diene) with low-pressure dihydrogen was initially reported by Pertuci and Vituli, and Ciardelli's group [242, 252]. Bradley and Chaudret and co-workers [85–88, 243–251, 253–255, 257–259] have demonstrated the use of low-valent transition-metal olefin complexes as a very clean source for the preparation of nanostructured mono- and bimetallic colloids. In one of their communications, they showed the decomposition of organometallic complexes of the type [M(dba)₂] (dba = dibenzylidene acetone, M = Pt, Pd) under low carbon monoxide pressure in the presence of polyvinylpyrrolidone (PVP) to give nanosized colloidal Pt or Pd particles having a fcc structure. Remarkably, the surface of the resulting particles undergoes no measurable interaction with the stabilizing polymer or with the solvent. Composition-induced structural changes in the bimetallic ruthenium platinum nanoparticles resulting from the relative concentration of the two complexes in the initial solution has been reported by the reaction of Pt(dba)₂

with Ru(COD)(COT) in various proportions under dihydrogen in the presence of PVP. The progressive incorporation of ruthenium into the platinum matrix leads to structural changes from face-centered cubic (fcc) for high platinum contents to hexagonal close packed (hcp) for high ruthenium contents. For the composition Pt_1Ru_3 , a contraction of the size of the particles (about 1.1 nm) and of the size distribution indicates the presence of a new phase consisting of monodisperse particles for which a model of truncated twinned octahedrons of 79 atoms was proposed [251].

Nanoparticles of Ru, Au, and Cu were obtained analogously from Ru(COT)(COD), (THT)AuCl (THT = tetrahydrothiophene), and $(\text{C}_5\text{H}_5)\text{Cu}(\text{Bu}'\text{NC})$. Colloidal molybdenum, silver, and bimetallic Cu/Pd colloids were also reported where a polymer matrix of PVP (polyvinylpyrrolidone), PPO (dimethylphenylene-oxide), or NC (nitrocellulose) was used as the stabilizing agent [85, 243–246]. Platinum and palladium nanoparticles stabilized by donor ligands such as carbonyl and phosphines have been described by Chaudret and Bradley. The structure of the particles is influenced by the ligands [86–88]. The cleavage of the complexed olefins from the coordination sphere of the metals and the simultaneous formation of nanosized colloidal particles occurs very smoothly and the hydrogenolysis of zerovalent organometallic olefin complexes has been established in the literature as a very clean and elegant method, for example, for the manufacture of monometallic colloids via the decomposition of $\text{Fe}(\text{COT})_2$, $\text{Ru}(\text{COT})(\text{COD})$, $\text{Co}(\text{C}_8\text{H}_{13})(\text{COD})$ ($\text{C}_8\text{H}_{13} = \eta^3\text{-cyclooctenyl}$), and $\text{Ni}(\text{COD})_2$ under H_2 . The hydrogenolysis method has been used to obtain a number of nanostructured Au, Pd, Pt colloids, and of bimetallic systems (Pt/Ru, Pt/Co, and Cu/Pd) in a polymer matrix [247–249]. Ultrafine cobalt particles have been obtained by the hydrogenolytic decomposition of $\text{Co}(\eta^3\text{-C}_8\text{H}_{13})(\eta^4\text{C}_8\text{H}_{12})$ in the presence of polyphenylphenyleneoxide to give particles of 4.2 nm size; when the same procedure was carried out with polyvinylpyrrolidone, the size of the resulting particles was 1.4 nm. It is clear from these results that a close relationship exists between the synthesis conditions and the structure of the resulting particles [250]. The reaction of $\text{Co}(\eta^3\text{-C}_8\text{H}_{13})(\eta^4\text{C}_8\text{H}_{12})$ and $\text{Pt}_2(\text{dba})_3$ (dba = bis-dibenzylidene acetone) under dihydrogen leads in the presence of poly(vinylpyrrolidone) to nanometric bimetallic particles $\text{Co}_x\text{Pt}_{1-x}$. The initial ratio of the two organometallic precursors determines the composition of the material [260]. Mo, W, Cu nanoparticles (5–50 nm) have been synthesized very recently from reactions employing metal complex and an organopolysilane oligomer either in hexane solution or in a sealed tube. The metal complexes are reduced due to the energetically favored reaction route by the oxo- and chlorophilicities of the silyl groups. Proper mixing of the reactants in vapor and solution phases allows the association and growth of molecules into small clusters, then into nanosized metal particles [261]. Recently it has been shown that Korantine peptized monodisperse Co nanoparticles with a particle size of 10 ± 1 nm can be prepared by thermal decomposition of $\text{Co}_2(\text{CO})_8$ in presence of trialkylaluminum. Another finding was that chain length in the aluminum organic has a direct influence on the particle size of the resulting nanoparticle [262–265]. Weakly ferromagnetic cobalt

nanoparticles were allowed to self-assemble into bracelet-like rings with discrete particle counts when dispersed by C-undecyl calix(4)resorcinarene. Herein, Co particles were prepared by the thermal decomposition of $\text{Co}_2(\text{CO})_8$ in hot toluene solutions containing resorcinarene tetraphosphonite. Another example of Co nanoparticle bracelet was the report by Alivisatos and co-workers [266, 267]. Redox transmetallation reactions between $\text{Co}_2(\text{CO})_8$ and $\text{Pt}(\text{hfac})_2$ (hfac = hexafluoroacetalacetate) is found to result in “solid solution” type alloy (e.g., CoPt_3) while addition of Co nanoparticles with $\text{Pt}(\text{hfac})_2$ in solution results in “ $\text{Co}_{\text{core}} \cdot \text{Pt}_{\text{shell}}$ ” type nanoalloys. The advantage of this method is the reaction does not need any additional reducing agents [268]. Using bis(hexyl(methyl)dithio-/diselenocarbamate)-cadmium(II)/zinc(II) compounds as a single source precursor, nanoparticles of CdSe/CdS, CdSe/ZnS, CdSe/ZnSe core/shell, and CdSe/CdS alloys have been prepared [207]. Similarly with block co-polymer of $\text{PS}_{25300}\text{-b-PMMA}_{25900}$ (poly(styrene-b-methyl methacrylate)), three-dimensional, patterned, anisotropic nanoparticulate self-assembly of cobalt has been evidenced [269]. Mixed metal clusters of ruthenium in association with either platinum or tin have been deposited onto multiwall carbon nanotubes (MWNTs) using metal complexes with dichloromethane-isopropanol (1:1 v/v). The size distribution of the resulting particles in the case of platinum ruthenium was found to be narrow with the average particle size of 1.8 ± 0.5 nm [270]. There are many such reports of nanoparticles decorating the exterior of a carbon nanotube [271–278] and an evidence for bimetallic particles formed inside nanotubes via a template method [279]. Thermal decomposition of manganese carbonyl on the polyol reduced platinum results in Mn-Pt nanoparticles which have ferromagnetic nanoparticles with a property totally different from its bulk. Thermal decomposition (673 K) of $\text{PtRu}_5\text{C}(\text{CO})_{16}$ under hydrogen resulting in Pt:Ru ratio of 1:5 with a mean particle size of 1.5 nm has been evidenced [280]. On the other hand, by subsequent reduction of platinum and iron, platinum-meghamite core-shell nanoparticles are obtained. Herein, platinum is initially reduced from its acetylacetonate precursor, yielding platinum nanoparticles. Iron oxide is then deposited on them by decomposing iron pentacarbonyl which undergoes oxidation under the reaction conditions to give Fe_2O_3 [281]. From a mixed metal acetate precursor, Ni and Ni-Co alloy nanoparticles have been generated [282].

2.2.4. Preparation in Micelles, Reverse Micelles, and Encapsulation

Colloidal assemblies have widely been used as templates in order to “preform” the size, shape, and polydispersity of nanosized metal particles [47–62]. Surfactant micelles may enclose metal ions to form amphiphilic “microreactors.” Water-in-oil reverse micelles or larger vesicles may function in similar ways. On the addition of reducing agents, nanosized metal particles are formed. The size and the shape of the products appear to be “imprinted” by the constrained environments in which they are grown. Surfactants play a crucial role in the compartmentalization of nanoparticles during their formation. A reverse micellar preparation of Cu_2S in aqueous micellar hosts reveals that different surfactants mediate the nanoparticle formation process and yield

different products, though it involves the same principle [283].

Tanori and Pileni [47] were first to grow cobalt rods with a length of 300–1500 nm and a diameter of between 10 and 30 nm in colloidal micelles. Cylindrical copper metal particles having identical sizes and shapes can be prepared in a template made of interconnected cylinders [49]. These form monolayers organized in a hexagonal network over very large domains of particles. Small or large aggregates can be produced at will, depending on the preformed template used. The particles are highly organized and form pseudo-crystals with a face-centered cubic structure. Colloidal metals have also been grown in reverse micelles. A series of articles by Pileni describes the micellar synthesis of metal nanoparticles, their fabrication into a three-dimensional array or domains and superlattices, followed by examination of their magnetic properties [284, 285]. These reports are apart from the micellar synthesis of copper nanoparticles [286–288] nanocrystal islands [289]. Micelles and inverse micelle synthesis techniques are used to prepare nanoparticles of platinum, palladium [290], Pt/Ru alloy [291], triangular CdS [292], and solid solution of $\text{Cd}_{1-y}\text{Mn}_y\text{S}$ [293].

Micellar formation of stable gold nanoparticles of different size and shape has been reported via UV photoactivation of HAuCl_4 in variable concentration of TX100 [TX100 = poly(oxyethylene) isooctylphenyl ether], which apparently acts as a reducing agent [294].

Platinum nanoparticles deposited on alumina support synthesized in water-in-oil microemulsions have been tested for the CO oxidation by oxygen. One of the two modes followed for the preparation and support involve platinum nanoparticles obtained by reducing the platinum complex PtCl_6^{2-} in a mixture of oil (cyclohexene or *n*-heptane) and 15 wt % surfactant (C_{12}E_4 or AOT) followed by reduction with hydrazine monohydrate. The other method involves addition of the alumina support to the particle suspension and the microemulsion subsequently destabilized by addition of tetrahydrofuran whereby the particles are deposited on alumina support. A detailed discussion on the particle size with the variation in surfactants and pH is depicted in detail [295]. Dodecanethiol-capped cadmium sulfide nanoparticles have been synthesized and characterized in a Winsor II microemulsion of diethyl ether/AOT/water [AOT = bis(2-ethyl-hexyl)-sulfosuccinate]. This follows a similar synthesis involving capped silver and gold nanoparticles [296–299]. Other important water-in-oil microemulsion syntheses include preparation of palladium nanoparticles [300], Pt-Ru [301], and Pd-Pt [302] nanoparticles.

Synthesis of silver and copper nanoparticles in water/ CO_2 microemulsions has been demonstrated. Sodium cyanoborohydride and N,N,N,N-tetramethyl-*p*-phenylenediamine were used as effective reducing agents for preparing the metal nanoparticles in the microemulsions [303]. In a similar environment, using hydrogen as reducing agent, metallic palladium was produced and *in-situ* hydrogenation of olefins was performed using this catalyst [304]. Dendrimers have been used to explore the method of immobilizing Pd nanoparticles on atomically flat surfaces. PAMAM dendrimers are the ones which are extensively used as templates for nanoparticle preparation. Cu, Pd, Pt, Au, Ag, and ceramic materials have

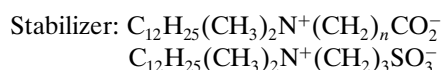
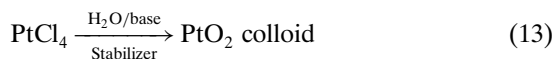
been successfully encapsulated inside these dendrimers [305–312]. These dendrimers are, however, pH sensitive. Recently, silver [313] and Pd nanoparticles [201] have been prepared by encapsulation methods using dendrimers.

Amphiphilic block copolymers for the “preformation” of the microreactors have been designed and used by Antonietti [52]. Micellar and ordered continuous topologies are adopted by self-assembly. The block lengths govern the size and topology of the resulting colloidal structures. The stability of these templates allows well-defined polymer/nanometal hybrid materials to be prepared. Noble metal colloids can be formed in block copolymer micro domains. Because of their enhanced stability, such colloids may be used directly as efficient catalysts. Besides controlling the particle growth, the self-assembly of the macromolecules allows the nanoparticles to take up well-defined arrangements on substrates, in thin films, or in bulk samples. Monodisperse noble metal particles, for example, gold, silver, palladium, have been applied to prepare thin polymer films. The strategies for the organization of nanoparticles into aggregate structures have been summarized in recent reviews in which the most successful approaches to form two- and three-dimensional arrays of nanoparticles having diameters between 1 and 20 nm are described [55, 56]. Additions to this synthetic method of using copolymer encapsulation are the preparation of aggregation stable gold nanoparticles using star-block copolymers [314] and addition-fragmentation chain transfer polymerization [315], reported recently. The encapsulation of small metal particles (Pd, Pd/Au) in solid organic [56] and inorganic matrices has also been achieved and used for applications in heterogeneous catalysis (discussed later). Gold nanoclusters have been encapsulated in a silica matrix, silica glass via a sol-gel procedure, and the optical properties of the product have been examined [59, 316]. Size-dependent silica-encapsulated gold nanoparticles with a special observation of having size-dependent melting points are also known [317]. In a silica sol-gel entrapment method, inclusion of metallic palladium and a rhodium(I) complex catalyst has been performed and its catalytic properties verified [318]. A novel two-step Pt nanoparticle encapsulation in mesoporous silica (SBA-15) has been done recently. In the first step, aqueous phase reduction of K_2PtCl_4 was carried out with the help of hydrogen and by using tri-block poly(ethyleneoxide)-poly(propyleneoxide)-poly(ethylene oxide) copolymer as capping material. In the next step, this supported nanoparticle was encapsulated into microporous silica synthesized using the same copolymer as template from tetraethyl orthosilicate by hydrolysis [319].

Nickel nanoparticles encapsulated in an amorphous carbon matrix have been synthesized by sonication of $\text{Ni}(\text{COD})_2$, and further heated at 773 K under an Ar atmosphere. Both as-prepared and heated samples have been fully characterized using high-resolution transmission electron microscopy (HRTEM), electron loss spectroscopy (EELS), and energy-filtered TEM (EFTEM). The EELS and EFTEM analyses show that the nickel nanocrystallites are surrounded by amorphous carbon which acts as a “protecting agent” and protects the nickel surface from oxidation [225].

2.2.5. Colloidal Nanostructured Metal Oxides

Preparation of nanometals is difficult in certain cases. Nano-sized (i.e., 3–5 nm) colloidal Fe⁽⁰⁾, Co⁽⁰⁾, and Ni⁽⁰⁾ particles cannot be redispersed after exposure to air because they are immediately oxidized both in solution and in powder form. When the addition of oxygen is precisely controlled, for example, by using stoichiometric amounts of O₂ diluted in large excess of argon, an organic solution of a 3-nm iron⁽⁰⁾-sol stabilized by N(octyl)₄⁺Br⁻ is transformed to a rusty-brown solution of colloidal Fe³⁺ oxide which is redispersible in THF [7]. N(octyl)₄⁺Br⁻-stabilized Co⁽⁰⁾ particles were oxidized in air to give colloidal CoO nanoparticles characterized by HRTEM [320]. The process was followed by UV-visible spectra and magnetic susceptibility measurements. The resulting CoO particles were supported on alumina. Small CoO and Co₃O₄ particles have been obtained in a polymer matrix dispersion by solid-state oxidation of 1.6-nm Co⁽⁰⁾ particles. The structural changes which occur during the oxidation process were monitored using physical analytic methods and it was shown that air oxidation at room temperature leads to surface passivation. The resulting particles have a metallic core which is surrounded by an oxide surface layer [321]. The particle size of nano-sized Pt dispersed on γ -Al₂O₃ is markedly influenced during the oxidation by O₂ [322]. A new process was recently reported for the manufacture of a water-soluble PtO₂ colloid which is applicable as a water-soluble “Adams catalyst” (see Eq. (13)) [323, 324]:



$$n = 1, 3$$

Using the simple hydrolysis/condensation of metal salts under basic aqueous conditions in the presence of carbo- or sulfobetaines, respectively, colloidal PtO₂ was obtained, the analytical data of which correspond to pure α -PtO₂ and to commercial samples of Adams catalyst. Bi- and trimetallic colloidal metal oxides as precursors for fuel cell catalysts, for example, colloidal Pt/RuO_x and Pt/Ru/WO_x, have also been prepared this way [325]. Magnetite particles below 20 nm size have been synthesized by high-temperature reaction of iron(III) acetylacetonate, in phenyl ether in the presence of alcohol, oleic acid, and oleylamine and the resulting particle was found to be monodisperse [326]. Organic soluble maghemite γ -Fe₂O₃ nanoparticles with monodispersity have been obtained by the reduction of FeCl₃ by glycol with *n*-octylamine serving as capping agent [327]. Another example of organic soluble titania is dodecylbenzenesulfonate capped nanoparticles [328]. A simple route for the synthesis of Ti, W, and V oxide nanoparticles using benzylalcohol under thermal conditions is a recent advancement [329].

2.2.6. Particle Size Control

Metal colloid sols where the particle size deviates less than 15% from the average value are generally addressed as “monodisperse.” Histograms with a standard deviation from

the mean particle size of approximately 20% are described as showing a “narrow size distribution.” The kinetics of the particle nucleation from atomic units and of the subsequent growth process cannot be observed directly by physical methods. The tools of the preparative chemist to control the particle size in practice are size-selective separation [49, 330, 331], and size-selective synthesis [36, 47–62, 98, 127, 183, 184, 332–348].

The so-called *size-selective precipitation* (SPP) was predominantly developed by Pileni [49, 349]. Monodisperse silver particles (2.3 nm, $\sigma = 15\%$) are precipitated from a polydisperse silver colloid solution in hexane by the addition of pyridine in three iterative steps. Followed by this, Schmid et al. [330] reported the two-dimensional “crystallization” of truly monodisperse Au₅₅ clusters. Schmid has also shown that the size of nanoparticles can be limited by steric restrictions imposed by a 3D polymer network [350]. Chromatographic separation methods proved unsuccessful because the colloid decomposed after the colloidal protecting shell had been stripped off [36]. The size-selective ultracentrifuge separation of Pt colloids has been developed by Cölfen and Pauck [331]. However, although this elegant separation method gives true monodisperse metal colloids, it still provides only milligram samples. The first size-selective colloid synthesis was described by Turkevich [1, 2]. Using the salt reduction method, he was able to vary the particle size of colloidal Pd between 0.55 and 4.5 nm. The crucial parameters were the amount of the reducing agent applied, and the pH value. According to the literature on the process of nucleation and particle growth, the essential factors which control the particle size are the strength of the metal-metal bond [45], the molar ratio of metal salt, colloidal stabilizer, and reduction agent [1, 118, 127, 149, 156, 256, 332–348, 351], the extent of conversion or the reaction time [149], temperature applied [1, 333, 345], and the pressure [333]. The preparation of near monodisperse nanostructured metal colloids using the salt reduction pathway is well documented in literature. In practice, however, the “control,” that is, the variation of particle sizes (and shapes), in wet chemical colloid synthesis is left to the intuition of the chemist. There are two kinds of methods used to control the morphology of the metal nanoparticles. The growth-directed preparation is performed by selecting a suitable metal precursor, protective agent, and the reduction method. On the other hand, template-directed preparation involves reducing metal ions or complexes that grow in a template. The shape and size of the resulting product is controlled by the template [352]. Pileni also has demonstrated that control of particle size and composition can be achieved using oil-in-water micelles [353].

At present, the electrochemical synthesis by Reetz and co-workers offers the most rational method for selecting the particle size (see Section 2.2.2). Using variable current densities and by suitable adjustment of further essential parameters, the authors have obtained at will, a monodisperse product in colloidal Pd and Ni between 1 and 6 nm [98–105]. In the thermal decomposition method, the resulting particle size depends on the heat source [216]. Size control has also been reported for the sonochemical decomposition method [237] and γ -radiolysis [238]. Size-dependent alloy formation of silver-coated gold nanoparticles (2.5–20 nm diameter) in

aqueous solution using radiolytic wet techniques at ambient temperature was observed [354]. Silver nanoparticles incorporated into SiO₂ matrix with a proper control over the particle size has been performed by the sol-gel method. The process involves complexation of the silicon alkoxide with AgNO₃ in an appropriate ratio, to be followed by hydrolysis, polycondensation, and subsequent thermal treatment of the resulting powder [355].

The control on shape of the metal particle via preformation of size and morphology of the products in nanoreaction chambers is the domain of preparation methods using constrained environments [47–62], such as the controlled temperature-induced size and shape manipulation of 2- to 6-nm gold particles which are encapsulated in alkanethiolate monolayers [60]. An enormous increase in the size of thiol-passivated gold particles up to ca. 200 nm has been induced by near-IR laser light [60]. A new medium-energy ion scattering (MEIS) simulation program has successfully been applied to the composition and average particle size analysis of Pt-Rh/ α -Al₂O₃ [61].

Synthesis of colloidal cobalt nanoparticles with controlled sizes and shapes has been performed. Rapid pyrolysis of cobalt carbonyl in an inert atmosphere was employed to produce monodispersed, stabilized, defect-free ϵ -cobalt nanocrystals with spherical shapes and sizes ranging from 3 to 17 nm [356]. Seeding growth was used for getting palladium nanoparticles [357], and with improved size control for polymer-stabilized Pd nanoparticles [358]. Laser light has been of great importance since it is possible to change the particles' size and shape after their preparation [359–370]. Schiffrin and co-workers' seminal work on the two-phase synthesis has led to the controlled particle size nanoparticles. The interesting part here is that by altering the ratio of the metal to octanethiol (capping agent), different particle size gold particles are obtained which show characteristically different colors. Octane thiol linked to gold atoms 1.6 (black), 2.1 (red), 2.8 (blue), 3.8 (dark violet), and 4.0 nm (cyan) are prepared and their properties studied [371].

Before going on to the further studies of these nanoparticles, it is appropriate to list the important methods available in literature on the synthesis of protected nanoparticles. Table 1 lists these.

3. SPECTRAL CHARACTERIZATION OF NANOPARTICLES

The whole exercise of characterization of nanoparticles lies in the determination of the particle size, overall composition, and seldom, the formidable, surface compositions. In case of stabilized particles, the interaction with the stabilizers, chelates, and adsorbates forms an interesting part of the characterization process. Various spectroscopic methods like ultraviolet-visible spectroscopy (UV-Vis), infrared (IR) and raman spectroscopy, nuclear magnetic resonance spectroscopy (NMR), and X-ray absorption spectroscopy (XAS, which includes EXAFS and XANES) have been adequately used in literature for the characterization purposes. However, for the understanding of the physical properties of the nanoparticles, the techniques of greatest utility are TEM and in instances where the particles are crystalline, X-ray

diffraction studies. Here, we highlight some of the spectroscopic methods which are conveniently used for the purpose of characterizing nanoparticles.

UV-Vis spectroscopy is very useful in characterizing semiconductor-type nanoparticles or metal particles whose plasmon resonance lies in the visible range as in the case of organic substrate linked Ag, Cu, and Au nanoparticles. UV-Vis spectra are also used for determining both particle size and the degree of cluster aggregation in the sample. With an increasing interest in the self-assembling of these semiconductor nanoparticles for varied applications, efforts on the characterization of such organized structures through this method are also on the rise (see also Section 6).

Tetraoctylammonium-stabilized transition-metal nanoparticles have been studied for their particle size determination by UV-Vis spectra. Characterization upon synthesis of Pd nanoparticles with diameters of 1.4, 2.3, and 4.1 nm is an example of this kind of a study [8]. Correlation between UV-Vis spectra on the nanoparticle size has been established by Chestnoy and co-workers in one of their premier works [372]. This was complemented by the study undertaken by Wilcoxon and co-workers on the shift in λ_{\max} depending on the size, shape, amount of aggregation, and the presence of adsorbates on the nanoparticles [373, 374]. In a recent development, gold nanorods with controlled aspect ratios dictated by the added silver ions in solution as seed have been studied. The gold nanorods formed in the absence of silver ions form gold nanoparticles and exhibit a characteristic absorption band at 530 nm, which is drastically changed upon addition of silver ions to a transversal surface plasma peak at 520 nm and an additional, longitudinal peak between 600 and 800 nm [375]. This study also describes how the presence of silver ions regulates the gold particle growth during the photochemical synthesis. Changes in the absorption maxima of programmed assembling in solution of mixed metal nanocrystal aggregates of silver and gold, forming new absorption bands corresponding to intercrystal plasmon resonance bands [376], synthesis of silver nanoparticles and nanorods in presence of PVP (polyvinyl pyrrolidone) [377, 378], BSA (bovine serum albumin) [377], interaction of gold nanoparticles with lithium ions [379], dendrimer protection of nanoparticles [305, 309, 380–382], their pH dependence [313], incorporation of TiO₂ as an additive to WO₃ nanoparticles [383], have all been studied.

In an application-directed study, interaction of pyrene methylamine (a fluorophore) onto gold nanoparticles has been examined. Interaction of this species is shown to alter the electron density of the gold nanoparticles on the metal surface, thereby directly affecting the absorption of the surface bound organic moiety as well as surface plasmon absorption band. Pyrene methylamine chromophore exhibits characteristic absorption bands at 313, 327.5, and 343.5 nm and upon addition of the gold nanoparticles, the absorption bands shift to 354, 361, 373, and 382 nm with a concomitant decrease in the absorption for the chromophore. This gives a direct measure of the alteration in the electronic properties of the chromophore as it binds to the gold nanoparticle. The presence of isobestic points at 319, 331, 338, and 347 nm for different concentrations of gold nanoparticles confirms the presence of both bound and free forms of pyrene methylamine [384]. There is a plethora of

Table 1. Major synthetic methods for the preparation of metal nanoparticles and nanoclusters.

Method/reducing agent	Nanoparticle metal/alloy systems	Metal stabilizers (protecting/capping/supporting)	Particle size (nm)	Ref.
diborane reduction	Au ₅₅ (PPh ₃) ₁₂ Cl ₆ and other M ₅₅ L ₁₆ Cl ₈ systems; also 'Pt ₃₀₉ Phen ₃₆ O _{30±10} ' and 'Pd ₅₆₁ Phen ₃₆ O ₁₉₀₋₂₀₀ '	phosphine ligands	1.4 nm	[4, 63-77, 416, 552, 555, 615, 617]
alcohol (polyol) reduction	A wide range of precious transition metals	PVP, PVA, PMVE	Variable (1-100 nm)	[10, 42-45, 117, 118]
	Ag, Pt, FePt, (Fe ₄₉ Pt ₅₁) ₈₈ Ag ₁₂ , Pd, Cu, Ag-Pd, Cu-Pd, Pt-Ru	PVP, ion conducting polymers, hydrophilic stabilizers	Variable particle size	[89, 123, 124-131]
	Pt	polymer	2-4 nm	[219]
hydrogen reduction	Pd, Pt, Rh, Ir	polymers	3-4 nm	[132-136]
	Pd giant clusters	acetate	—	[79-84]
	Various transition metals	tetrabutylammonium polymer	2-3 nm	[34, 137-141]
carboxylate reduction	Au	citrate	12-20 nm	[1-3, 38, 39, 116, 340]
	Au	ascorbate	>10 nm	[698]
	Pt	oxalate	6.5 nm	[143]
	Pd	—	2.2, 5.4 nm	—
	Pd/Pt	—	2.2 nm	—
	Pd/Sn	tetraalkylammonium	4.4 nm	[46, 183, 184]
	Pd/Au	carboxylates	3.3 nm	—
	Pd/Ru	—	1.8 nm	—
	Pd/Rh	—	1.7 nm	—
Pd/Cu	—	2.2 nm	—	
borate reduction	Au	alkanethiol	1-3 nm	[182]
	Au	other stabilizers	1-5 nm	[305, 188]
	Pt-Ru, Pt-Mo, Pt-W, Pt-Ni	THF solvent-stabilized	1.7 nm	[174]
	Pt	dodecanethiol	—	—
	Ni, Cu, Ru, Rh, Pd, Ag, Ir, Pt, Ru/Fe, Ru/Co, Ru/Ni, Pt/Co, Pt/Cu, Ru/Rh, Ru/Ir, Ru/Pt, Rh/Ir, Rh/Pt, Pd/Pt, Pd/Ag, Ir/Pt	SB12	All <10 nm	[7, 15, 96]
tetraalkylammoniumborohydride method (organosol)	Group 4-11 metals of the periodic table, also tin. Bi- and pluri-metallic combinations	tetraalkylammonium	See Figure 7 for particle size of monometal particles	[6, 7, 9, 15, 95-97, 175]
electrochemical method	Pd	tetraalkylammonium	1.4, 3.1, 4.8 nm	[98]
	Ni	—	1-6 nm	—
	Co, Fe, Ti, Ag and Au	tetraalkylammonium hydrosols and organosols	<10 nm	[100]
	—	organosols and hydrosols	8-10 nm	[100-105]
	Pd	propylene carbonate tetraoctylammonium	<10 nm	[93]
	Pd/Ni, Fe/Co, Fe/Ni, Pd/Pt	polymer	3.8 nm	[100, 105]
trialkylaluminum method	Pt-Pd onion-type colloid	organic template	5 nm	[207]
	Cu-Ni-Cu	—	31-33 nm	—
	Pt	organoaluminum	1.2 nm	[37]
	Co	organoaluminum	5-10 nm	[262-265]
	Pt/Ru	organoaluminum	1-3 nm	[594]
Bi and plurimetals from group 6-11 of periodic table	organoaluminum	<5 nm	—	
Ni-Al	aluminum organic	100-150 nm	[186, 187]	

continued

Table 1. Continued

Method/reducing agent	Nanoparticle metal/alloy systems	Metal stabilizers (protecting/capping/supporting)	Particle size (nm)	Ref.
oxoanion	Ir(0) ~ 300 and Rh Ir(0) ~ 900 and Rh	Polyoxoanion	2–3 nm 3.8–4.5 nm	[11, 34, 137–142]
decomposition of metal complexes	Mo, W, Cu	organopolysilane oligomer polyphenyloxide	5–50 nm	[261]
	Co	PVP	4.2 nm	[250]
	Co		1.4 nm	[250]

UV-Vis spectra for colloidal metals [384–386]. For colloidal particles which have an absorption band in the visible region, the absorption maxima are dependent on the size and shape of the particles, as well as how close the particles are relative to each other [386]. This implies, not only can a particle's size be determined by UV-Vis spectroscopy, but phenomena such as aggregation can also be verified [386]. The ability to tune the optical properties of a system by changing particle size, degree of aggregation, or surface composition holds potential for many applications [386–392]. Selective colorimetric detection of polynucleotides based on the distance-dependent optical properties of 13-nm-sized mercaptoalkyl derivatized gold nanoparticles studied by Mirkin and co-workers is an example of this [390]. The fascination of nanoparticles combined to biomolecules and their characterization, in part, by UV-Vis analysis can be obtained from the review of Niemeyer [393].

Infrared spectroscopy has been used as a surface probe in nanocluster systems, commonly done for surface adsorption of CO. The strong dipole associated with C-O makes this molecule a particularly easy one, but the metal-carbon bond which falls in frequency limits of 200 and 450 cm^{-1} is difficult to study. Carbon monoxide is an ideal ligand because it readily adsorbs to metal surfaces, and has characteristic vibrational frequencies around 1800–2100 cm^{-1} [5, 394]. The C-O stretch frequency is an excellent indicator for the way CO is bound to the substrate. Linearly adsorbed CO absorbs at frequencies between 2000 and 2130 cm^{-1} , twofold CO between 1880 and 2000 cm^{-1} , threefold CO between 1800 and 1880 cm^{-1} , and a fourfold bonded CO at wave numbers below 1800 cm^{-1} [395].

Some of the early studies on CO adsorption on metal include adsorption on silica-supported Pt-Ag alloys [396], Ni-Cu/SiO₂, Pd-Au/SiO₂, and the more interesting one, displacement of CO from a twofold adsorption site on palladium to a single adsorption site when NO was co-adsorbed [397]. Lewis and Lewis provided an early report of CO adsorbed to suspended metal particles, showing linear and doubly bridging CO on 2.3-nm Pt particles in methylene chloride [150]. Bradley's most comprehensive work in this area reports numerous IR studies of CO adsorbed onto colloidal and nanocluster metal surfaces [87, 214, 243, 244, 398–401]. The message here is that the infrared spectra of metal-bound CO change drastically as the size of the metal particle changes [87, 214, 243, 244, 398–401]. For instance, from a systematic IR study it was shown that as the Pd particle size increased, the ratio of terminal CO to bridging CO decreased for saturated CO adsorption of

poly(vinylpyrrolidone)-stabilized Pd clusters with diameters of 2.5, 4.0, and 6.0 nm in methanol [243]. Moreover, the largest particles showed only bridging CO on the metal surface [243]. Bradley has also used CO as a probe to study metal-surface enrichment in bimetallic Cu/Pd nanoclusters [214]; he finds that CO binds to both Cu and Pd, indicating that both metals are at the surface of the nanoparticles. Others have studied the effect of pH on nanocluster surface-bound CO [402], finding that increasing the pH leads to reduced CO coverage on Pt nanoparticles. Grazing-angle IR spectroscopy has been used to characterize the self-assembled monolayers on gold and further treatment of it in combination with cyclic voltammetry [403]. There are few other examples where infrared spectroscopy is used as a powerful tool in the characterization process [404–407].

To a lesser extent, surface enhanced raman spectroscopy (SERS) has been used to probe the surfaces of small metal particles, often involving metals like gold and silver [408, 409]. For example, the raman intensity of molecules adsorbed on electrochemically roughened silver electrodes is enhanced by factors of up to 10⁵ [410]. The magnitude of this enhancement is related to the roughness of the surface, that is to say, the state of division of the adsorbing surface. In the study of pyridine adsorbed on gold and silver hydrosols, Creighton and co-workers demonstrated that these same metals exhibit this effect. The initial yellow color of the sol, due to the plasma resonance at 380 nm, changed to red and then blue-gray as the particles agglomerated due to the presence of pyridine and thus showed enhanced raman scattering [411]. Multiplexed detection of oligonucleotide targets has been performed with gold nanoparticle probes labeled with oligonucleotides and raman-active dyes [408]. Raman spectroscopy has been recently used for the electrodeless addition of Pt to SnO₂ nanopowders, and CdS incorporation into MCM-41 and SBA 15 systems [412, 413]. For the reduction of silver(I) salt by Fe(II) using citrate, SERS has also been a very useful method of analysis to detect the adsorbates on the surface [414]. There is limited application of SERS because it should involve metals which have a well-defined plasmon band [5] needed to provide the required signal enhancement.

Mass spectrometry (also FAB-MS and TOF-MS) and Mössbauer spectroscopy are used in some cases.

Nuclear magnetic resonance (NMR) is a powerful method for characterizing the nanoparticulates associated with ligands and for probing the intermetallic interactions, the simplest one being ¹H NMR that could be conveniently used for characterizing organic ligands in the nanoparticle-bound

ligand complex [376]. Characterization of $\text{Rh}_{55}(\text{PPh}_3)_{12}\text{Cl}_6$ nanocluster by proton decoupled ^{31}P NMR was performed by Günter Schmid and co-workers. Spectral results obtained having a singlet with no ^{31}P - ^{103}Rh coupling under different solvents at room temperature, no appearance of additional peaks upon addition of phosphine, but rather resulting in an upfield shift of the signals, led to the conclusion that there is a fast exchange between the free and nanocluster-bound phosphine ligands with a calculated time of $3 \pm 0.5 \mu\text{s}$. In addition, the ^{31}P study in pyridine as solvent regenerates free phosphine displacing the ligated phosphine from the surface of the metal. However, this is one of the earlier studies which indicates the amount of information one can obtain by an NMR study [415, 416]. In one of the most important developments that took place in the recent past, EC NMR (electrochemical NMR), it is possible to investigate in detail metal/liquid interfaces by solid-state NMR under external potentiostatic control, in the presence of an electrolyte [417–419]. The multiple advantages of this are, it permits the determination of electronic properties of electrodes and of adsorbates as well as the study of the surface diffusion of adsorbates. This method also provides useful information on the dispersion of platinum-based fuel cell catalysts, on electrochemically generated sintering effects, and on the electronic effects caused by the presence of different surface adatoms. In general, EC NMR provides information on local frontier orbitals of the metal surface, adsorbate structure/bonding details, and even bond lengths, rates, and activation energies for surface diffusion and also, electrode potential effects on the electronic properties of the electrochemical interface, as seen by both metal and ligand NMR. A detailed review on this subject has been recently published by Wieckowski and co-workers based on their collective work performed on Pt-based fuel cell catalysts [417].

A classic example of using NMR for characterization of intermediates during nanoparticles synthesis is the one described very recently for preparation of platinum nanoparticles by trialkylaluminum reduction of platinum acetylacetonate. The most revealing finding was the information obtained from the *in-situ* ^1H NMR studies on the solution after 30 min from the addition of reactants to isolate the intermediate complex (compound **3** of Fig. 2). In this initial measurement, a signal was observed at $\delta = 0.51$ ppm that was assigned to methyl groups in an intermediate platinum complex on account of the coupling with ^{195}Pt ($I = 1/2$, 33.8% natural abundance), which increased in intensity over the next few hours. Through a series of convincing assignments, the methyl group not being located at the bridges between platinum atoms but instead as a terminal group was established. Additionally, long-range coupling (COSY; correlation spectroscopy) between the hydrogen atoms on the methyl carbons linked to platinum and aluminum established the bridging group of the complex, giving almost all the information needed for characterizing this intermediate. However, additional information from EXAFS (extended X-ray absorption fine structure), XANES (X-ray absorption near edge surfaces), and *in-situ* ASAXS (anomalous small-angle X-ray scattering) measurements helped in confirming the structure. From the EXAFS it was seen that Pt absorber atom is directly surrounded by a light backscatterer in either

C atom at a distance of $2.11 \pm 0.02 \text{ \AA}$ or O atom at a distance of $2.09 \pm 0.04 \text{ \AA}$ and an Al atom at a distance of $2.45 \pm 0.02 \text{ \AA}$, but surprisingly no backscattering from Pt, indicating no Pt-Pt bond in the complex [37]. EXAFS is a spectroscopic technique that probes the local coordination environment of an atom that corresponds well to the event of metal-metal interactions and the number of coordination shells that might be formed in a cluster of 1–2 nm range. The basis of this spectroscopic measurement involves the analysis of the absorption coefficient of a metal atom in a cluster from about 40 eV to about 1500 eV past the absorption edge. The oscillatory behavior of the absorption coefficient in this region can be thought of as being caused by an interference that occurs between the outgoing and incoming photoelectron waves, and given the formal scattering lengths associated with this effect, the interference signal contains information about the average atomic environment of an absorbing atom. There is a great deal of information on the use of EXAFS to investigate the geometric and electronic structures of supported metal particles [420–432]. Most of the recent structural elucidations involve one of these XAS measurements for the surface determination of metal nanoparticles. A recent review by Frenkel et al. describes the structural dynamics of supported Pt nanoscale particles [420]. For detailed information on the origin of X-ray absorption spectroscopy and the validity and use of these techniques for characterization of the nanoparticle colloids, see [433]. XAS study of Pt-Ru supported on carbon [240, 434] and giant Pd clusters [435] are some of the other recent major studies. There are mentions of the use of spectroscopic methods for characterization of nanoparticles in other sections of this chapter, where appropriate.

4. PHYSICAL PROPERTIES OF NANOPARTICLES

Physical properties of nanoparticles and nanoclusters are a subject of intense contemporary interest. As the size decreases to the nanometer scale, many of the mechanical, electronic, optical, magnetic, as well as the thermodynamic properties are significantly altered from those of either the bulk or the single molecule. An analogy in cyclohexane, benzene (C_6), and adamantane (C_{14}) which represent the molecular states, with C_{60} or C_{70} fullerenes (as clusters) with that of diamond and graphite (representing bulk) with differences in their chemical and physical properties is worth mentioning [5]. The properties of nanoparticles depend on the following, individually or in combination [217]:

- the grain size and size distribution,
- the chemical composition of the constituent phases,
- the presence of interfaces, more specifically grain boundaries, heterophase interfaces, or the free surface, and
- the interactions between the constituent atoms.

Production of inorganic clusters is a thermodynamically unfavorable condition for the energy that is stored in such high surface particles. The stability is also decided by the complicated interplay of surface energy, surface tension, and surface stress [436]. If two smaller-sized metal particles

are allowed to come together, they spontaneously club to become a single entity because of the exothermic coalescence, in order to have reduced total surface area. If two naked metal particles are separated by protecting shells or even have an impurity, then coalescence can be minimized, but the particles will then undergo aggregation wherein the two protected nanoparticles come together without a direct contact between the metal particles. The minimization of these two principles is possible if the nanoparticles are immediately stabilized by deposition on a support, a concept well known in literature as a “precursor method.” A detailed description of the properties related to particle aggregation and means of minimizing such effects are discussed [433].

Nanostructured materials bridge the gap between the molecular level and the solid (bulk) state and therefore display distinct physicochemical properties because of which many new technological applications can be found [437–440]. A simple case is Günter Schmid’s illustration (Fig. 1 of [69]) of the electronic states in a metal particle with bulk properties and its typical band structure (overlapped), a cluster of cubic close packing of atoms with small bandgap and a simple triatomic unit (representing a molecular status) with completely separated bonding and antibonding molecular orbitals [69]. Another important aspect of interest is that as the particle size gets lower and lower, there are more atoms at the surface that are coordinatively highly unsaturated. The electronic structures and thus properties of these metal atoms are different from those of the metals in the core of a cluster. Such effects are pronounced if the surface atoms are ligated. The other important issue is that a cluster of 1.5 nm was found to have some bulk metal characteristics and that the formation of metallic state is mainly determined by the cluster nucleus and not the surface atoms. This has been in some cases experimentally verified in that, a SQUID measurement on $\text{Pd}_{\sim 561}$ shows that the inner core has bulk metal-like magnetic susceptibility while the outer layer does not [69]. It is universally accepted now that as the cluster size increases, some physical properties converge to the crystalline value more rapidly than others. The changes in the melting points is one such. Initial attempts at theoretical understanding of the melting of small particles were made within a macroscopic framework [441–444]. Theoretical phenomenological considerations, based on the classical Kelvin equations, led to the development of a quantitative relationship between the melting temperature and the particle size [441]. When computational resources became available, the melting of specific clusters was treated microscopically using molecular dynamics simulations. Using this, of late, metal clusters of sodium [445], copper [446], gold [447, 448], beryllium [449], lead [450], and nickel [451] have been studied. These simulations reveal that some features of cluster melting are qualitatively different from bulk melting, such as a difference between the melting and freezing points and the coexistence of solid and liquid clusters.

Gold metal melts at 1064 °C whereas a 1.5-nm gold nanoparticle melts between 500 and 600 °C. This trend of depression in the melting point for nanosized materials is not only restricted to metals but encompasses semiconductors, and even molecular organic crystals. This led to the suspicion that the surface plays important roles [452–459], which has now been confirmed [460]. These include

structural demonstrations of liquid-skin formation on flat surfaces below the melting temperature of the interior crystal [461–463] and, in the case of some mono- and bimetallic nanoparticles [464–468], are readily studied by TEM. On the contrary, by exposing gold nanorods in solution to femtosecond and nanosecond laser irradiations, structural rearrangement of the gold atoms has been observed that starts at the interior of the rods by the creation of point and line defects which then evolve into planar defects on the spherical nanoparticles [468]. This is explained by the conversion of $\{110\}$ facets into the more stable $\{100\}$ and $\{111\}$ facets and hence minimization of their surface energy. These observations suggest that short laser pulsed photothermal melting begins with the creation of defects inside the nanorods followed by surface reconstruction and diffusion, in contrast with the thermal melting on the rods or the bulk material, where the melting starts on the surface. Similarly, using laser irradiation, induced interdiffusion of Au–Ag core-shell nanoparticles has been evidenced indicating a reduced temperature for the melting of bimetallic nanoparticles [206]. The size-dependent melting and surface melting of Pb nanocrystals is demonstrated by X-ray powder diffraction in ultra high vacuum. Measurements indicate that the melting temperature varies inversely with the crystallite size and quantitatively favors the liquid-skin melting model over the homogeneous melting model. Surface melting is also demonstrated via the reversible growth of a 0.5-nm liquid skin on 50-nm crystallites just below the size-dependent melting temperature [469]. Molecular-dynamics simulations using the Sutton–Chen body potential function, and the melting characteristics of nickel core and copper shell of $\text{Cu}_{0.25}\text{Ni}_{0.75}$ and $\text{Cu}_{0.5}\text{Ni}_{0.5}$ were examined. The melting characteristics determined on the basis of the variations of potential energy and heat capacity with temperature showed this bimetallic system to melt in two stages [470]. A similar study on the melting behavior of narrow-dispersity alkanethiol-functionalized Au and Pt nanoclusters in inverse micellar solutions has been performed [471].

There are, however, some anomalies to the observation that metal nanoparticles melt at a lower temperature than the bulk. A tin nanocluster melts at a higher melting point than that of the bulk, indicating a different structural arrangement in the nanocrystal than in the bulk. It is demonstrated that cluster ions of tin between 10 and 30 atoms remain solid at ~ 50 K above the melting point of bulk tin. A similar trend is expected of silicon and germanium owing to their heavily restructured geometries [472]. Investigations on the structural and dynamic properties of gold nanocrystallites with Au_{75} , Au_{146} , and Au_{459} were performed using molecular-dynamics simulations employing embedded-atom interactions. Diffusionless solid-to-solid structural transformations from the low-temperature optimal structures to icosahedral structures have been seen. These structural transformations were found to be precursors to the melting transition that occurs below the bulk melting temperature [473].

At the size of a few nanometers, metallic particles might become liquid, possibly labeled as droplets, even if their bulk metal temperatures are hundreds of degrees higher. This implies that even if composite particles are originally constructed as core-shell structures, they may spontaneously

alloy at relatively low temperatures and over relatively short periods of time. This has already been stated in the case of Au-Ag core-shell bimetallics [206]. The situation could be similar while considering the co-reduced bimetallics and their easy alloying at lower temperatures [317, 474].

Similar to melting, the changes in the structure upon incorporation of metals have been seen in the case of incorporation of ruthenium into platinum nanoparticles. The progressive incorporation of ruthenium into platinum matrix leads to structural changes from face-centered cubic (fcc) for high platinum contents to hexagonal close-packed (hcp) for high ruthenium contents [251]. Preparation of FePt monodisperse nanoparticles (3–10 nm) and further thermal annealing converts the internal particle structure from a chemically disordered face-centered cubic phase to the chemically ordered face-centered tetragonal phase and transforms the nanoparticles superlattices into ferromagnetic nanocrystal assemblies [89]. There have been some reports on the effect of additives on the thermal ordering of sputtered films of either CoPt or FePt alloys. Addition of Sn, Pb, Sb, Bi, or Ag into sputtered CoPt films is found to promote the disordered fcc to ordered tetragonal transformations, resulting in significant reductions in the temperature required for ordering [475, 476]. Similarly, reduction in the ordering temperature for FePt sputtered films by addition of Cu was seen [477]. Addition of Ag was found to promote the fcc to tetragonal phase transition, thereby reducing the temperature required for this transition by some 100 to 150 °C compared with pure FePt nanoparticles [125].

Nanoparticles, especially of the alkali metal and noble metals copper, silver, and gold, have a broad absorption band in the visible region of the electromagnetic spectrum. Solutions of these metal nanoparticles show very intense colors which are absent for the bulk material as well as for the atoms [467]. Their origin is attributed to the collective oscillation of the free conduction electrons induced by an interacting electromagnetic field. This has made them to be detected by spectral methods which have been discussed earlier. These resonances are also designated as surface plasmons. There have been many attempts to prepare Au-Ag systems using various reducing agents, obtaining different sized nanoparticles [478–483]. It is generally seen that when the reduced Au and Ag exist as separate entities, they possess two plasmon bands corresponding to each metal based on the Mie theory [484] which is widely applicable to explain the experimental results. These distinct bands get changed to a single absorption band upon alloying [478, 485, 486], which happens rapidly under reaction conditions.

An effective method for manipulating the semiconductor nanoparticles is impurity doping. Addition of, for example, Mn^{2+} to bulk semiconductors imparts unusual giant Zeeman, Faraday rotation, and magnetic polaron effects that characterize this class of materials [487]. Nanostructured magnetic materials also have received considerable attention for their fascinating applications in both mechanical and biomedical sciences. When magnetic nanoparticles are agglomerated in dense systems as granular films, the magnetic properties largely differ from those of both the individual particles and the bulk material. Thus, in order to understand the collective behavior of the two-dimensional and three-dimensional assemblies of magnetic nanocrystals,

models have been developed [285]. It has been quite clearly demonstrated that nanocrystals having a low size distribution are able to self-organize in a very-large-scale hexagonal network. On increasing these nanocrystal concentrations, 3D superlattices are obtained. Clarity over this issue can be had from the work which envisages control over the melting and optical properties of gold nanoparticle linked to DNA which has been studied in great detail by Mirkin, Schatz, and co-workers [488, 489].

Understanding the properties of protected colloids is not easy, as the protective groups change the electronic states of those metal atoms which are linked with the protective molecules. The protected nanoparticles will therefore not have the same properties as those without protection. This has been evidenced clearly in a few instances [65, 490–493]. The electronic behavior of Au_{55} clusters stabilized by $[P(C_6H_5)_3]_{12}Cl_6$ was analyzed by scanning tunneling microscopy. The arene rings of the ligand molecules could be imaged at 7 K. During spectral investigations, the discrete energy levels with an average spacing of 170 eV were attributed to Au_{55} core [494]. Aromaticity of Au_5Zn^+ clusters involving only σ orbitals has been demonstrated. The contention here is aromaticity is not restricted to organic compounds even M_2^- (Al, Ga, and In) has two delocalized π electrons satisfying the $4n + 2$ electron counting rule. Of the three low-energy conformers, a triangular structure with Zn atom located on a side of the triangle was the best fit. The formation of Au_5Zn^+ was evidenced by cationic photofragmentation mass spectroscopy [495]. The determination of particle size, and compositional studies by XRD for crystallites are the subject matter of all the scientific study done on nanoparticle synthesis and can be had from any of the references listed at the end of this chapter.

5. APPLICATIONS IN CATALYSIS

5.1. “Quasi-Homogeneous” Reactions

Lipophilic or hydrophilic nanostructured metal colloids dissolved in the form of organosols or hydrosols can serve as catalysts either in organic solution or in the aqueous phase. Schmid [70] has called these quasi-homogeneous catalytic reactions, which include solvated metal atom dispersions (SMAD) [26] “heterogeneous catalysis in solution.” Rhodium hydrosols dissolved in water were proved to be effective as hydrogenation catalysts in two-phase systems where the olefin is in the organic phase [496]. Solutions of Moiseev’s giant Pd colloids [79–84] were shown to catalyze a number of reactions in the “quasi-homogeneous” phase, namely oxidative acetoxylation reactions [79], the oxidative carbonylation of phenol to diphenyl carbonate [84], the hydrogen-transfer reduction of multiple bonds by formic acid [497], the reduction of nitriles and nitroarenes, and the acetal formation [498] with high turnover frequencies and significant lifetimes (see [11]). Anion ligands-preserved cationic giant Pd clusters were prepared and used for catalyzing oxidative acetoxylation of toluene in the presence of molecular oxygen [499]. Finke has reported remarkable catalytic lifetimes for the polyoxoanion- and tetrabutylammonium-stabilized transition-metal nanoclusters [137–141]. For example, in the

catalytic hydrogenation of cyclohexene, a common test for structure-insensitive reactions, the Ir(0) nanocluster [34] showed up to 18,000 total turnovers with turnover frequencies of 3200 h^{-1} [500]. As many as 190,000 turnovers were reported in the case of the Rh(0) analogue reported recently [501]. These results are quite unprecedented. Obviously, the polyoxoanion component prevents the precious metal nanoparticles from aggregating so that the active metals exhibit a high surface area [501]. A review [7] compares this new approach with the catalytic properties of other nanometallic systems active in “quasi-homogeneous” phase. The formation of olefins from aldehydes and ketones via McMurry-type coupling reactions were reported when nanostructured Ti colloids (3 nm) stabilized by Bu_4NBr were used [502]. THF-protected Ti_{13} nanoclusters [91] were found to hydrogenate Ti and Zr sponges in the “quasi-homogeneous” phase [503, 504]. The enantioselective hydrogenation of ethylpyruvate in HOAc/MeOH solution was performed using cinchonidine-stabilized Pt colloids [344]. Heck and Suzuki C–C–bond coupling reactions were catalyzed with NR_4^+X^- -stabilized Pd and Pd/Ni colloids in dimethylacetamide. The same reactions have been observed when solvent-stabilized Pd particles in propylene carbonate were applied as the catalyst [93, 505, 506]. Nanosized Pd colloids generated *in-situ* by reduction of Pd(II) to Pd(0) are involved in the catalysis of phosphine-free Heck and Suzuki reactions [507]. Hexagonal or quasi-two-dimensional Pd nanoparticles (hcp structure, 53 nm) encapsulated in graphite have also been tested as catalysts for the Heck reaction. Microphotographs confirmed that the nanoparticles are located between the spacing layers of graphite. The catalyst is very stable: Although no strong interaction is present between the nanoparticles and the carbon lattice, the particles cannot be washed out and they are still found inside the carbon lattice after the Heck reaction [508]. The [3 + 2] cycloaddition of methylenecyclopropane to methacrylate is effectively catalyzed by nanostructured nickel colloids (2.5 nm) in solution [509]. The liquid-phase hydrogenation of isomeric undecenoic acids has been demonstrated to be catalyzed selectively by Pt colloids encapsulated in polymerized micelles [510]. Metal colloids stabilized by amphiphilic block copolymers were used as efficient catalysts in the “quasi-homogeneous” phase [511–514]. A generally applicable synthesis of metal colloids in microemulsions, in particular, of nanostructured noble metals in amphiphilic block copolymers, has been worked out by Antonietti and co-workers [511, 512]. Micelles in which nanosized metals are incorporated are very stable; they undergo no significant change of the colloidal properties such as size and polydispersity and consequently are effective hydrogenation catalysts. The morphology of the metal core can be varied between a “cherry” type and a “raspberry” type architecture depending on the strength of the reducing agent. Block copolymer-stabilized Pd-“raspberry” colloids have an extraordinary high metal surface and no additional support is needed for catalytic applications in solution. This type of colloid catalyst combines the advantages of homogeneous and heterogeneous catalysis; that is, the high selectivity and reactivity of homogeneous hydrogenation catalysts are coupled with the long-term stability of the heterogeneous systems. Nanostructured metal colloids stabilized with

synthetic polymers [515–519] may be regarded as artificial enzyme models. The interaction between the “polymeric fields” and the reactive substrates determines the selectivity of the colloidal nanometal catalysts. Coordinating polymers such as poly(N-vinyl-2-pyrrolidone) have been shown to protect nanostructured metal particles that have an average diameter of ca. 1–3 nm and a narrow size distribution. The resulting materials are effective catalysts for olefin hydrogenation [516], nitrile hydration [517], photoinduced electron transfer [518], and Suzuki reactions [126]. The application of dendrimer-encapsulated Pd nanoparticles to fluorinated phase-soluble catalysts has been described recently [519]. The scope of ligand-stabilized transition-metal nanoparticles in catalysis was recently summarized by Schmid et al. [74, 520]. A very recent review on the catalytic activity of various soluble transition-metal nanoclusters as arene hydrogenation catalysts has been critically reviewed [521]. This work on the hydrogenation catalysts describes comprehensively 18 prominent catalyst systems from the literature, highlighting their synthesis and catalytic application.

5.2. Heterogeneous Reactions

Heterogeneous catalysts are readily obtained when pre-prepared nanometal colloids are deposited on supports [2]. The so-called “precursor concept” for manufacture of heterogeneous metal colloid catalyst was developed on this basis in the 1990s [6, 7, 9, 15, 95–97]. As a result, so-called *egg-shell* catalysts were obtained which contain the active metal particles as a thin layer (<250 nm) on the surface of the support. Metal colloid catalysts of this type have successfully been applied to hydrogenate C,C double bonds, organic carbonyl groups, unsaturated C,N bonds, and to reduce N,O bonds [522]. An obvious advantage of the precursor concept over the conventional salt-impregnation method is that both the size and the composition of the colloidal metal precursors may be tailored independently of the support. Further, the metal particle surface may be modified by lipophilic or hydrophilic protective shells and coated by intermediate layers, for example, of oxide. The modification of the precursor by dopants is also possible. The catalyst is manufactured by dipping the supports into organic or aqueous media containing the dispersed precursor at ambient temperature to adsorb the pre-prepared particles. This has been demonstrated for supports such as charcoal, various oxidic support materials, and even low-surface materials such as quartz, sapphire, and highly oriented pyrolytic graphite (HOPG). No subsequent calcination is required (see Fig. 12). The feasibility of preparing catalysts in this way for industrial purposes has been demonstrated by Degussa.

A combination of AFM, STM, and XPS [523, 524] has revealed the interaction of platinum hydrosols with oxide (sapphire, quartz) and graphite single-crystal substrates. The metal core is immediately adsorbed onto the support surface when dipped into aqueous Pt colloid solutions at 20 °C. The carpet-like coat formed over the particles by the protecting shell and the support surface cannot be removed from the particle surface even by intense washing with solvent. The organic protecting shell decomposes on annealing at 280 °C and above in UHV. The thermal degradation can be monitored by XPS up to 800 °C and by STM. It was shown

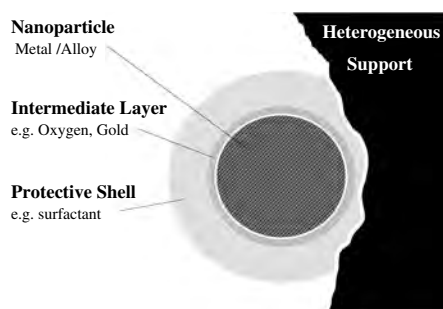


Figure 12. The precursor concept. Adapted with permission from [7], H. Bönemann et al., *J. Organomet. Chem.* 520, 143 (1996). © 1996, Elsevier Science.

that the Pt particles remain virtually unchanged at up to ca. 800 °C. Sintering processes are observed only above this temperature. Reetz et al. have used $N(\text{octyl})_4\text{Br}$ -stabilized Pd colloids (typical size, e.g., 3 nm) as precursors to form so-called “cortex catalyst,” where the active metal forms an extremely fine shell of less than 10 nm on the supports (e.g., Al_2O_3) [525]. Within the first 1–4 s, the impregnation of Al_2O_3 pellets by dispersed nanostructured metal colloids leads to the time-dependent penetration of the support which is complete after 10 s.

“Cortex catalysts” were reported to show a threefold higher activity in olefin hydrogenation than conventionally prepared catalysts of the same metal loading (5% Pd on Al_2O_3). Schmid [70] has described phosphine-stabilized Rh_{55} nanoclusters, namely $\text{Rh}_{55}[\text{P}(t\text{-Bu})_3]_{12}\text{Cl}_{20}$ and $\text{Rh}_{55}[\text{PPh}_3]_{12}\text{Cl}_{20}$, deposited on TiO_2 . These systems were used to catalyze the heterogeneous hydroformylation of propene with high turnover numbers giving equal amounts of *n*- and *i*-butanal. The observed turnover frequencies are higher than seen with homogeneous complex catalysts but the selectivity was found to be too low for practical applications. In the butyronitrile hydrogenation test, the activity of surfactant-stabilized colloidal rhodium (5 wt % on charcoal) was found to surpass that of conventional salt impregnation catalysts of the same metal loading. The addition of 0.2% of colloidal $\text{Ti}(0)$ to the supported noble metal [89] resulted in a significant enhancement in activity [7] (see Fig. 13).

The “dopants” are not restricted only to transition metals. The hydrogenation of acrylic acid can be promoted significantly by the addition of neodymium ions onto the palladium particles [526]. The selective transformation of 3,4-dichloronitrobenzene to the corresponding aniline has been selected to test pre-prepared Pt hydrosols as heterogeneous catalyst precursors (see Fig. 14) [527].

In batch and continuous tests, the performance of the colloidal catalyst system was evaluated and compared to conventional Pt/C systems. In summary, the potential of the colloidal heterogeneous catalyst lies in the possibility of tailoring the properties for specific applications by the addition of special dopants or “poisons” (such as sulfur). Further “fine tuning” of the complex process shown in Figure 14 has been achieved by using the synergistic effect of bimetallic precursors (e.g., Pt/Cu). The influence of metal ions on the hydrogenation of *o*-chloronitrobenzene

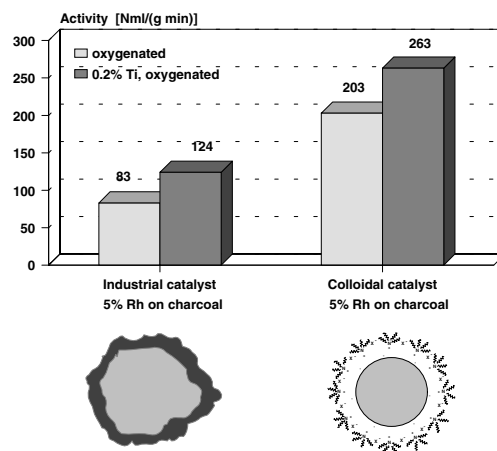


Figure 13. Activity of conventional and colloidal Rh/C catalysts, eventually doped with 2% colloidal $\text{Ti}(0)$, compared in the butyronitrile hydrogenation test (2d). Adapted with permission from [15], H. Bönemann and W. Brijoux, in “Advanced Catalysts and Nanostructured Materials” (W. Moser, Ed.), Chap. 7, p. 165. Academic Press, San Diego, 1996. © 1996, Elsevier Science.

over platinum colloids, and the effect of metal complexes on the catalytic performance of metal clusters have also been investigated [528–530]. It was found that the catalytic properties of platinum clusters for the hydrogenation of *o*-chloronitrobenzene to *o*-chloroaniline are very sensitive to the metallic cations added. When Ni^{2+} ions were used as the modifier, the activity and selectivity were enhanced. The selectivity for *o*-chloroaniline jumped from 44.7% to 66.3% while the activity of the catalyst was nearly doubled. The maximum activity and selectivity (82.9%) to *o*-chloroaniline was obtained at a molar ratio of Ni^{2+} to Pt of 8:1 [528]. The “doping effect” of additional metal complexes on the activity and selectivity of platinum clusters in the homogeneous liquid-phase hydrogenation of cinnamaldehyde was studied by the same authors [530]. The conversion was promoted from 65.5% to 78.0% using Na_3FeF_6 as the additive, while the selective formation of cinnamic alcohol increased from 17.7% to 75.0%. The addition of $\text{Ni}(\text{bipy})_3\text{Cl}_2$ to the

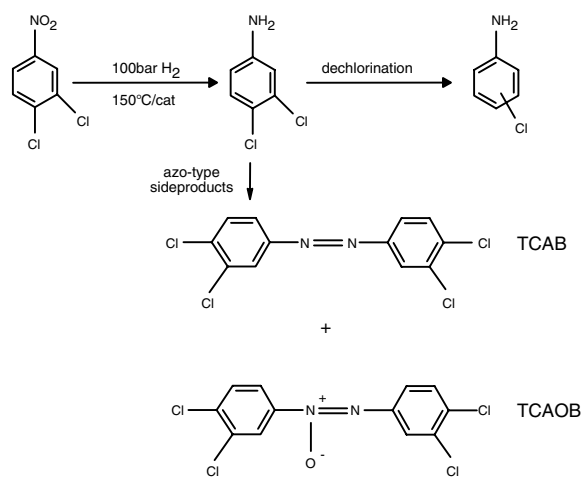


Figure 14. Reaction scheme for the hydrogenation of 3,4-dichloronitrobenzene.

colloidal platinum catalyst raised the conversion to 82.1%, while the selectivity towards hydrocinnamaldehyde was as high as 97.3%. In the hydrogenation of cinnamic acid to cinnamic alcohol, the selectivity can be varied by doping Rh colloid catalysts with Sn. A selectivity of 86% is achieved with a colloidal Rh/Sn (Rh:Sn = 1.5:1) catalyst on carbon [15]. Copper-catalyzed Suzuki cross-coupling reactions using mixed nanocluster catalysts have been studied recently. Copper-based catalysts were shown to be effective as reagents which can present an inexpensive and environmentally friendly alternate to noble metal catalysts. Remarkably, the stabilizing surfactant was shown to modify the colloidal metal surface and hence the catalytic properties [527]. Hanaoka et al. [531] have reported the selective photocatalytic transfer of hydrogen to 1,5-cyclooctadiene with a light transition-metal modified rhodium colloid catalyst. Bulk industrial processes often rely on alloy-like bimetallic catalysts [532–535]. Here, nanostructured bimetallic colloid catalysts have opened the possibility of differential studies on the mutual influence of two different metals on the catalytic properties. The controlled co-reduction of two different metal ions has made bimetallic colloids readily accessible [6, 7, 15, 42–45, 76, 98–105, 535]. The structural characterization and some catalytic aspects of bimetallic colloids have been reviewed recently [10]. The successive reduction of mixed metal ions allows the homogeneous structure of bimetallic particles to be altered to colloidal particles having composition gradients from the core to the shell [516, 536–539]. Truly layered particles consisting of, for example, a gold core plated by palladium or vice versa [76], have also been synthesized. Bimetallic particles having a gradient metal distribution or a layered structure are most interesting for catalytic applications. In the catalytic hydrogenation of crotonic acid to butanoic acid, a clear synergistic effect of Pt and Rh [6] was observed when bimetallic colloidal precursors ($\text{Pt}_{20}\text{Rh}_{80}$) have a gradient core/shell structure with an increase in the Rh concentration from the core towards the surface of the particle [536] (see Fig. 15). Toshima has discussed a similar effect in the partial hydrogenation of 1,3-cyclooctadiene with $\text{Pt}_{80}\text{Pd}_{20}$ and $\text{Pd}_{80}\text{Au}_{20}$ colloid catalysts [10].

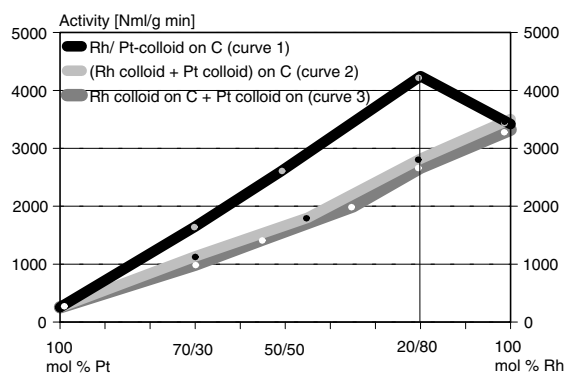


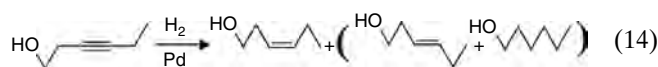
Figure 15. Activity plot of alloyed Rh/Pt/C and mixed Rh + Pt/C catalysts in the crotonic acid hydrogenation test (H_2 consumption). Adapted with permission from [15], H. Bönemann and W. Brijoux, in “Advanced Catalysts and Nanostructured Materials” (W. Moser, Ed.), Chap. 7, p. 165. Academic Press, San Diego, 1996. © 1996, Elsevier Science.

The difference between the electronegativities of Pd and Au together with the combination of the partially filled d band of Pd and the completely filled d band of Au result in a novel electronic structure. This may be the reason for the catalytic behavior of gold-palladium alloys [540–549]. Fascinating prospects for the design of new catalysts have been opened up using bimetallic particles with layered structures. First principles-based density functional methods and theoretical models have been used to investigate the reactivity of different RhCu alloys towards molecular hydrogen dissociation [550]. Schmid and Peschel [76] have applied the classical seed growth method [551] to synthesize layered bimetallic Au/Pd and Pd/Au colloids in the size range of 20 to 56 nm. The sequential reduction of gold salts and palladium salts with sodium citrate allows the gold core to be coated with Pd. The layered bimetallic colloid is stabilized by trisulfonated triphenylphosphane and sodium sulfanilate. More than 90% metal can be isolated in the solid state. The redispersion in water is possible in high concentration. Au/Pd and Pd/Au systems on a TiO_2 support have been used in stabilized and nonstabilized forms as heterogeneous catalysts for the hydrogenation of hex-2-yne to cis-hex-2-ene. Both the palladium-plated gold seeds and the gold-plated palladium particles showed considerably increased activities compared with the pure metals. The protecting ligand and shell enhances the lifetime of the ligand-stabilized colloid catalysts considerably. The influence of the electronegativity difference between Au and Pd on the activity and selectivity of the hydrosilylation reaction [552] on colloidal Pt surfaces [150, 151] was carefully investigated. In essence, the results demonstrate that the activity, selectivity, and the lifetime of metal colloid catalysts may be optimized by a defined variation of the core/shell composition in bimetallic precursor.

Residues of the stabilizing agents which are still present at the surface of the colloidal metal precursors (1 and 5 wt % metal loading on charcoal, glassy carbon, zeolites, TiO_2 , Al_2O_3 , CaCO_3 , SiO_2 , single-crystal oxides, or HOPG) may act as effective catalyst modifiers which control the selectivity and durability of heterogeneous colloid catalysts. Ligands such as phosphines or phenanthrolines [75], surfactants of various types [7, 15] or organic “envelopes” such as polymers [510, 553, 554] were found to control the regio- and enantioselectivity of heterogeneous metal colloid catalysts. In case of the semi-hydrogenation of hex-2-yne to cis-hex-2-ene, Schmid has found that even subtle changes in the chain length of the substituents of the alkyl-substituted phenanthrolines used as colloid stabilizers alter the regioselectivity significantly [555]. Seven- and eight-shell palladium clusters on TiO_2 , protected by phenanthroline, catalyze the semi-hydrogenation of hex-2-yne to cis-hex-2-ene with 93% cis-hex-2-ene selectivity. With the 3-*n*-decyl phenanthroline as the stabilizer, a similar selectivity resulted.

On substitution of the phenanthroline with *n*-butyl or *n*-heptyl groups, however, the activity drops dramatically and the consecutive isomerization or total hydrogenation of the cis-hex-2-ene is completely suppressed. Geometric, that is, steric, reasons were claimed to explain the strong influence on the selectivity and this has been illustrated by further

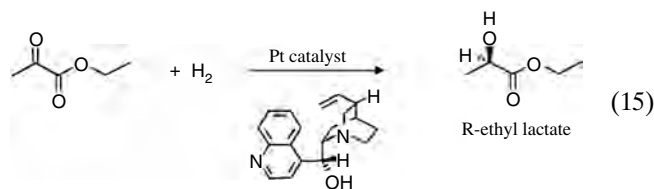
examples. A surfactant was found to control the selectivity in the cis-selective partial hydrogenation of 3-hexyn-1-ol, giving leaf alcohol, which is a valuable fragrance (Eq. (14)) [556]:



The performance in this reaction (Eq. (14)) of heterogeneous Pd colloid catalysts on CaCO_3 modified by a number of surfactants was compared with conventional Pd/C and Lindlar catalysts under optimized reaction conditions. The selectivity was found to depend on the support and various promoters. The highest activity and the best selectivity (98.1%) towards the desired cis-3-hexen-1-ol was found when employing a lead-acetate-promoted palladium colloid on CaCO_3 modified by the zwitterionic surfactant sulfobetaine-12 (N,N-dimethyldodecylammoniopropanesulfonate). Chemisorption measurements have shown that residual amounts of the surfactant are still present on the surface of the immobilized particles. This colloid catalyst was twice as active as a conventional Lindlar catalyst, and surpassed its selectivity by 0.5%. The contact of heterogenized metal colloid surfaces with substrates in aqueous media is improved when hydrophilic protecting shells are present. For example, a hydrophilic ruthenium colloid catalyst on lanthanum oxide was shown to convert benzene into cyclohexene with 59% selectivity at 50% benzene conversion when suspended in an aqueous solution of sodium hydroxide [557]. Chiral molecules on the surface of the metal colloid can induce enantioselectivity control. Following this concept, a new type of enantioselective platinum sol catalyst stabilized by the alkaloid dihydrocinchonidine was designed (see Fig. 16) [344, 558].

The colloidal catalysts have been prepared in different particle sizes by the reduction of platinum tetrachloride with formic acid in the presence of different amounts of alkaloid. Optical yields of 75–80% *ee* were obtained in the hydrogenation of ethyl pyruvate with chiral modified Pt sols (Eq. (15)). The catalysts were demonstrated to be

structure insensitive since turnover frequencies (ca. 1 sec^{-1}) and enantiomeric excess are independent of the particle size:



In order to evaluate the catalytic characteristics of colloidal platinum, the efficiency of Pt nanoparticles in the “quasi-homogeneous” reaction shown in Eq. (15) was compared with that of supported colloids of the same charge and of a conventional heterogeneous platinum catalyst. The “quasi-homogeneous” colloidal system surpassed the conventional catalyst in turnover frequency by a factor of 3 [558]. Köhler and Bradley [559, 560] and Liu and co-workers [561, 562] have studied the enantioselectivity of the reaction (Eq. (15)) in the presence of polyvinylpyrrolidone as the stabilizer. In addition, Köhler and Bradley [559] have observed that the presence of HCl in as-prepared Pt sols modified by cinchona alkaloids has a marked effect on rate and reproducibility. The performance of the catalysts was improved in both reproducibility and rate by the removal of HCl by dialysis. These “purified” colloidal catalysts can be used as reliable test systems to screen chiral modifiers alternative to cinchona alkaloids and for precise rate studies. In addition, a systematic variation of the reaction parameters relevant to the catalyst performance is possible without unwanted side effects. It was shown that an excess of polyvinylpyrrolidone present on the colloidal Pt catalyst is irrelevant to the access of modifier molecules to the colloidal metal surface. However, the polymer may adsorb at the metal surface, reducing the number of modified surface sites available for the enantioselective hydrogenation [560]. Nanostructured metal colloids can be used for the stereoselective and enantioselective transformation of specific prochiral substrates into valuable fine chemicals. The application of a rational ligand-control based on molecular modelling which has been successful in homogeneous metal complex catalysis promises similar results in heterogeneous metal colloid catalysis.

Superior lifetimes should be also achieved since it is reasonable to assume on the basis of the chemisorption results that the “coating” on catalytically active nanometal particles which is permeable for small molecules such as H_2 or O_2 effectively prevents the contact of the metal surface with poisons. In fact, the lifetime of the colloid catalysts is considerably longer than of conventional precipitation catalysts. For example, the activity of a conventional Pd/C catalyst expires completely in the hydrogenation of cyclooctene to cyclooctane after 38×10^3 catalytic cycles per Pd atom, but the Pd colloid/C catalyst still shows a residual activity after 96×10^3 catalytic turnovers [563] (Fig. 17).

Superior catalytic oxidation catalysts were obtained when surfactant-stabilized Pd-Pt precursors were supported on charcoal and promoted by bismuth. By comparison with industrial heterogeneous Pd/Pt catalysts, charcoal-supported $\text{Pd}_{88}/\text{Pt}_{12}\text{-(Oct)}_4\text{NCl}$ alloy particles (1.5 to 3 nm) show an

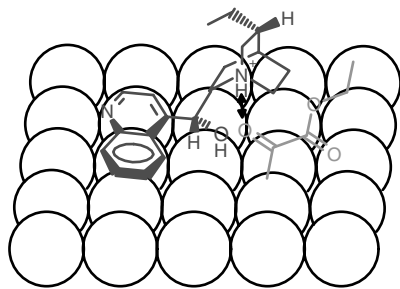


Figure 16. Enantioselective hydrogenation of ethyl pyruvate using dihydrocinchonidine-stabilized Pt colloids. Adapted with permission from [15], H. Bönemann and W. Brijoux, in “Advanced Catalysts and Nanostructured Materials” (W. Moser, Ed.), Chap. 7, p. 165. Academic Press, San Diego, 1996. © 1996, Elsevier Science.

it was found that the activity of the new systems is governed by the specific pore volume and the hydrophobic properties of the wall. The selectivity for cyclooctene was 93%. The most active of these sol-gel-entrapped Pd catalysts had a considerably higher activity than the commercially available Pd/Al₂O₃ samples. The preparation of a fully alloyed Pd-Au colloid of 3.0 nm particle size, by a modified sol-gel procedure using THF as the solvent, from the co-reduction of Pd and Au salts with tetraalkyl-ammonium-triethylhydroborate [6] and its embedding in a silica has been described [573]. The integrity of the incorporated Pd-Au alloy particles remained virtually untouched. After the removal of the protecting surfactant, a mesoporous texture with a comparatively narrow pore distribution remained. According to the physical characterization by a combination of techniques, the SiO₂-embedded Pd-Au colloid preserves the size and the structural characteristics of the colloidal metal precursor. Tetraalkyl-substituted Ru in either silica or zirconia sol-gel matrix has been used for hydrogenolysis [575]. In a similar fashion, colloidal palladium supported on silica gel has been conclusively proved to be involved in the direct reaction of H₂ and O₂ to give H₂O₂ [576]. The material exhibits excellent catalytic properties in selective hydrogenation test reactions. These few examples show that colloidal bimetallic precursors—embedded in matrices or deposited on various supports, and promoted by additives if necessary—may become of practical importance in heterogeneous catalysis. A recent review describes various synthetic strategies applied for the synthesis of metal nanoparticles which can be used as reusable catalysts with almost all kinds of reactions studied so far. They include hydrosilylation, oxidation, C-C coupling reactions such as carbonylation, Heck and Suzuki reactions, hydrogenation, chemoselective, regioselective, stereo-, and enantioselective reactions [577].

5.3. Fuel Cell Catalysts

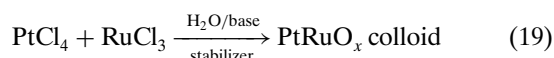
“Fuel cell technology” allows the direct conversion of chemical energy into electricity [578]. The fuel cell is an electrochemical reactor where the catalyst systems are an important component. Among the wide-ranging applications, fuel cells are best suited for low-emission transport systems, stationary power stations, and combined heat and power sources. The classical studies were carried out in the early 1900s and major innovations and improvements have been achieved over the last few years. The first “new electric cars” are expected to roll on the markets around the year 2010, but further developments are still needed, notably in the catalyst sector. Hydrogen fuel cell catalysts rely on pure Pt, whereas Pt-alloy electrocatalysts are applied for the conversion of reformer gas or methanol into electricity. The active components in the latter cases are small Pt-containing bi- or trimetallic particles of 1–3 nm size which scatter X-rays as nearly perfect “single crystals.” These systems offer improved efficiency and tolerance against certain contaminations, especially CO in the anode feed [579–584]. It was clear from patents filed in the early 1970s that finely particulated colloidal platinum sols should be the ideal precursors for the manufacture of fuel cell electrodes [579].

This survey focuses on recent developments in catalysts for phosphoric acid fuel cells (PAFC), proton exchange membrane fuel cells (PEMFC), and the direct methanol fuel cell (DMFC). There are six main types of fuel cell described in literature [585–589]. In PAFC, operating at 160–220 °C, orthophosphoric acid is used as the electrolyte, the anode catalyst is Pt, and the cathode can be, for example, Pt/Cr/Co [585–589]. For this application, a trimetallic colloidal precursor of the composition Pt₅₀Co₃₀Cr₂₀ (size 3.8 nm) was prepared by the co-reduction of the corresponding metal salts [590–592]. From XRD analysis, the trimetallic particles were found alloyed in an ordered fct structure. The electrocatalytic performance in a standard half-cell was compared with an industrial standard catalyst (trimetallic crystallites of 5.7 nm size) manufactured by co-precipitation and subsequent annealing to 900 °C. The advantage of the trimetallic colloid catalyst lies in its improved durability, which is essential for PAFC applications. After 22 h it was found that the potential had decayed by less than 10 mV [593].

PEM fuel cells use a solid proton-conducting polymer as the electrolyte at 50–125 °C. The cathode catalyst is based on Pt alone, but because of the required tolerance to CO, a combination of Pt and Ru is preferred for the anode [579–584]. Colloidal Pt/Ru catalysts are currently under widespread investigation for low-temperature (80 °C) polymer membrane fuel cells [593–595]. These have also been proposed for use in the DMFC or in PEMFC which are fed with CO-contaminated hydrogen produced in on-board methanol reformers. The ultimate dispersion state of the metals is essential for CO-tolerant PEMFC, and truly alloyed Pt/Ru colloid particles of less than 2 nm size seem to fulfill these requirements [17, 18, 20, 579, 581, 596–603]. Alternatively, bimetallic Pt/Ru PEM catalysts have been developed for the same purpose, where nonalloyed Pt nanoparticles <2 nm and Ru particles <1 nm are dispersed on the carbon support [581]. From the results it can be concluded that a Pt/Ru interface is essential for the CO tolerance of the catalyst regardless of whether the precious metals are alloyed. For the manufacture of DMFC catalysts, in contrast, Pt/Ru nanopowders of 3–5 nm size or thin films are used as the precursors [582–584]. For the electrocatalytic methanol oxidation, a Pt metal or a Pt metal alloy catalyst has been developed where a Ru phthalocyanine complex is added as a dopant to reinforce the catalytic effect substantially [592]. For comparison, the electrocatalytic activity was compared to that of a bimetallic Pt₅₀/Ru₅₀-N(Oct₄)Cl colloid prepared by the salt co-reduction method [6, 95–97] toward the oxidation of CO and a CO/H₂ gas mixture (simulated reformer gas) [17]. According to high-resolution transmission electron microscopy, the mean particle diameter was 1.7 nm. Alloyed state of the particles was verified by point-resolved energy-dispersive X-ray (EDX) analysis. CO tolerance and direct methanol oxidation on Pt₃Mo/C have been investigated in PEM fuel cell conditions. This catalyst has shown threefold enhancement for the CO tolerance, while for methanol oxidation no such enhancement was seen. It is also emphasized that the mechanism involved in CO oxidation is different from the conventional Pt-Ru catalysts. While ruthenium gets converted into its oxide that helps in the oxidation of CO, Mo oxide surface shows no

affinity for CO providing a pathway of easy oxidation at lower overpotentials [601].

Glassy carbon-supported Pt₅₀/Ru₅₀-N(Oct)₄Cl colloids were examined by CO-stripping voltammetry and the data were found to be essentially identical with those found in well-characterized bulk alloy electrodes. In a rotating disk electrode, the activity of the colloid toward the continuous oxidation of 2% CO in H₂ was determined at 25 °C in 0.5 M H₂SO₄, and the results led to the conclusion that these Pt/Ru colloids are very suitable precursors for high-surface-area fuel cell catalysts [20]. Structural information on the precursor was obtained by *in-situ* XRD via Debye function analysis. In addition, the XANES data support the bimetallic character of the particles. *In-situ* XRD has revealed the catalytic function of the alloyed Ru in the CO oxidation: surface oxide species are formed on the Ru surface at 280 °C which slowly coalesce to RuO₂ particles. After re-reduction the catalyst shows a pure hcp ruthenium phase and larger platinum-enriched alloy particles [604]. Scanning probe microscopy (SPM) has been applied in order to characterize the real-space morphology of the electrode surfaces of supported nanostructured metal colloids on the nanometer scale [605]. Colloidal Pt₅₀/Ru₅₀ precursors (<2 nm) raise the tolerance to CO, allowing higher CO concentrations in the H₂ feed of a PEMFC without a significant drop in performance [18–20]. A selective Pt/Mo oxidation catalyst for the oxidation of H₂ in the presence of CO in fuel cells comprises Pt_xMo_y particles, where *x* is 0.5–0.9 and *y* is 0.5–0.1 [606]. The colloid method was found to be a highly suitable exploratory approach to finding improved formulations for binary and ternary anode electrocatalysts. The metals used include Pt, Ru, W, Mo, and Sn [19]. The combinatorial screening method has successfully been applied to electrocatalysts [607], and it is an obvious step to include colloids in these experiments. As an alternative to the reductive metal colloid synthesis, the so-called “metal oxide concept” was developed which allows the fabrication of binary and ternary colloidal metal oxides as electrocatalyst precursors (Eq. (19)) [323–325]:



There are many recent reports of Pt-Ru being prepared by different methods and supported on different carbon supports to check their catalytic activity [608–613]. Colloidal Pt/RuO_x (1.5 ± 0.4 nm) stabilized by a surfactant was prepared by co-hydrolysis of PtCl₄ and RuCl₃ under basic conditions. The Pt:Ru ratio in the colloids can be varied between 1:4 and 4:1 by variation of the stoichiometry of the transition-metal salts. The corresponding zerovalent metal colloids are obtained by the subsequent application of H₂ to the colloidal Pt/Ru oxides (optionally in the immobilized form). Additional metals have been included in the “metal oxide concept” (Eq. (17)) in order to prepare binary and ternary mixed metal oxides in the colloidal form. Pt/Ru/WO_x is regarded as a good precatalyst especially for the application in DMFCs. Main group elements such as Al have been included in multimetallic alloy systems in order to improve the durability of fuel cell catalysts. Pt₃AlC_{0.5} alloyed with Cr, Mo, or W particles of 4–7 nm size has been prepared

by sequential precipitation on conductant carbon supports such as highly disperse Vulcan XC72® [614]. Alternatively, colloidal precursors composed of Pt/Ru/Al allow the manufacture of multimetallic fuel cell catalysts (1–2 nm) having a metal loading of >20%.

The colloidal Pt/Ru/Al precursor is pre-prepared via the organoaluminum route. In the absence of stabilizers, the co-reduction of organic Pt and Ru salts using Al(CH₃)₃ gives halogen-free, multimetallic Pt colloids, for example, Pt₅₀Ru₅₀/Al (size 1.2 ± 0.3 nm). When the stoichiometric ratio of the metal salts is changed, the ratio of Pt to the second metal in the colloid can be adjusted. The addition of alcohols or suitable surfactants allows the dispersivity of the colloidal precursor in organic media or water to be tailored without affecting the particle size. In the second step, the Pt/Ru/Al colloid is adsorbed on high-surface-area carbon by treatment at 40 °C for 24 h. In the third step (conditioning), the dried Pt/Ru/Al Vulcan catalyst powders are exposed to O₂ and H₂ for 30 minutes each at 250–300 °C to remove the surfactants completely. The particle size of the Pt/Ru/Al colloid adsorbed on the support was found to be virtually untouched (1.3 ± 0.4 nm) and after the thermal treatment only a moderate growth was determined (1.5 ± 0.4 nm). The aluminum was found to be present on the Pt/Ru surface in an oxidized form. This accounts for the size-stabilization observed in the Pt/Ru particles and for the improved durability of the resulting electrocatalysts. Recently, a fuel cell for generating electric power from a liquid organic fuel (“synfuel”) was described. It comprises a solid electrolyte membrane directly supporting the anode and cathode layers which contain 7–10% Pt and Ru, 70–80% of perfluorovinyl ether sulfonic acid, and 15–20% polytetrafluoroethylene [599]. In conclusion, nanostructured metal colloids are very promising precursors for manufacturing multimetallic fuel cell catalysts that are truly nanosized (i.e., <2 nm) and have high metal loadings (20 wt % of metal).

6. APPLICATIONS IN MATERIALS SCIENCE

Metal nanoparticles and their assemblies are expected to have numerous applications in materials science. They should exhibit a range of physical and chemical properties that are promising for potential application in a new generation of optical, electronic, chemical, and biological devices. Quantum size effects are related to the “dimensionality” of a system in the nanometer range. “Zero-dimensional” metal particles might still comprise hundreds of atoms. The differences between the material properties of nanosized particle structures and the bulk material stem from the loss of characteristic magnetic domain size, and from the particle sizes relative to the scattering length of conduction electrons and the de Broglie wavelength of the electron. Size reduction may even cause changes in the melting point. One-dimensional nanoparticle arrangements (cluster wires) are of potential practical interest as semiconducting nanopaths for applications in nanoelectronics. One-dimensional particle arrangements may be induced through host templates. Using vacuum or electrophoretic methods Schmid and co-workers [615–617] were able to fill the parallel channels of nanoporous alumina membranes with chains/rows

of 1.4-nm gold particles giving one-dimensional “quantum wires” consisting of insulated 20–100 Au₅₅ clusters in a helical array. The diameter of the nanowire could be controlled by varying the pore size. Interestingly, 1.4-nm Au particles were found to arrange themselves into a linear row when attached to single stranded DNA oligonucleotide [618]. Driven by the technological significance associated with such architectures, the fabrication of ordered two-dimensional nanoparticle arrays has successfully been achieved by several research groups. Their work was recently reviewed [619, 620]. Planar arrays of uniform metal nanoparticles would allow the design of new “supercomputers” having a superior data storage capacity. Langmuir–Blodgett films of nanometal systems have frequently been studied in this respect. Starting with nanoparticles of defined nuclearity, 2D lattices of thiolized Au₅₅, Pd₅₆₁, and Pd₁₄₁₅ have been made [619]. Recently, the first successful preparation of 2D hexagonal and cubic lattices of Au₅₅ nanoparticles by self-assembly on polymer films was reported. Simply dipping polyethylenimine-modified surfaces into aqueous solutions of acid-functionalized Au₅₅ cluster was shown to generate Au₅₅ monolayers [330]. A report on the molecular organization with special emphasis on the Langmuir–Blodgett and molecular self-assembly emphasizes the need for heterogenizing the homogeneous catalysts in achieving activity, selectivity, and recovery and recycling ability [621].

The interactions between the nanoparticles and the surface are obviously strong enough to prevent mechanical removal. Whereas the hexagonal form shown is normal for an ordered monolayer, the cubic orientation is unprecedented. Most of the work published on organized nanometal structures centers on gold particles and sulfur-containing groups in various ligands [622–627]. Water-soluble gold particles functionalized with a monolayer of 11-thioacetate-undecanol-derivatized neoglycoconjugates of two biologically significant oligosaccharides have been prepared [628], following a general method of *in-situ* functionalization synthesis of nanoparticles and monolayer-protected gold colloids [629].

Schiffirin and co-workers have achieved the self-organization of nanosized gold particles using NR₄⁺X⁻ surfactants [630]. Ramos et al. have recently reported surfactant-mediated two-dimensional crystallization of colloidal crystals [631]. The use of attractive Coulombic interaction between colloidal structures and surfactant structures offers a potential new route to self-assembly of ordered colloidal structures. Nanostructured palladium clusters, stabilized by a monomolecular coat of tetraalkylammonium halide surfactants, self-assemble on carbon surfaces in an ordered manner resulting in a hcp structure [632].

The self-organization of magnetic nanosized cobalt particles was studied by the group of Pileni [633, 634]. A comparison of the magnetic properties of deposited cobalt nanoparticles with those dispersed in a solvent indicates a collective flip of magnetization of adjacent particles when they are self-assembled. Additionally, Pileni and co-workers have recently published a number of articles concerning the self-assembly of nanoparticles and have developed numerous methods for the manipulation of these systems [635–637]. Marzan and Mulvaney have described in a recent review two-dimensional and three-dimensional assemblies of

metal-core-silica-shell nanoparticles [638]. A feature article by Balazs et al. [639] outlines how solid additives can be used to tailor the morphology of binary mixtures containing nanoscopic particles and thereby control the macroscopic properties (e.g., the mechanical integrity) of composites. In addition, computer-aided design has been employed to establish how self-assembled nanostructures can be induced to form arbitrary functional designs on surfaces [640]. Bifunctional spacer molecules such as diamines have been tried to link nanoparticles three-dimensionally [641]. The multilayer deposition of particle arrays on gold has been successfully achieved via the sequential adsorption of dithiol and near monodisperse nanometal or CdS particles [370].

Several monometal-, bimetal-, and plurimetal-semiconductor superlattices have been prepared by dipping a gold substrate into the respective solutions with intermediate steps involving washing and drying [642]. The stepwise three-dimensional assembly of layered gold nanoparticles in porous silica matrices has also been reported [643]. There are a few important developments in the self-assembly of gold and silver nanoparticles with varied applications foreseen [140, 644–658]. The Pileni description on the self-assemblies, their fabrication, and collective properties is one of the recent reviews in connection with Co nanoparticles [647]. In one of the most recent developments, an ambitious goal in the nanobiosciences has been realized in combining functionality and stability of inorganic nanostructured solids and the structural variety and self-organizing abilities of the biochemical molecules. Au nanoparticles with a mean diameter 2.2 nm was functionalized and built up to achieve a stable and specific conjugation with biotin linked to Avidin [659].

The ability of serotonin-labeled CdSe nanocrystals to interact with antidepressant-sensitive, human, and *Drosophila* serotonin transporters (hSERT, dSERT) expressed in HeLa and HEK-293 cells has been observed. These findings support further consideration of using ligand-conjugated nanocrystals as versatile probes for membrane proteins in living cells [660]. Refractive index sensors have been developed by the fabrication of a metal-coated three-dimensionally ordered macroporous film [661]. A different field of technological interest stems from the high spin density of nanostructured magnetic metals of the Fe, Co, Ni series [662, 663]. Magneto switchable bioelectrocatalysis has been performed by suitably derivatizing magnetite [664]. THF-stabilized Mn(0) particles which exhibit superparamagnetism below 20 K were described as the first example of an anti-ferromagnetic metal colloid [665]. The superparamagnetic properties of nanostructured Ni particles have also been investigated [666]. Cobalt nanoparticles stabilized in block copolymer micelles can be used as magnetic fluids [667]. Chaudret and co-workers have established the chemistry of ligand-free ultrafine cobalt particles in a polymer surrounding and studied their magnetic properties [668–670]. Magnetic cobalt nanoparticles—besides their potential applications in magneto-optical data storage and fluid magnetic lubricants—are of special interest in medicine. Three keywords here are “magnetic separation,” “magnetic drug carriers,” and “magnetic hyperthermia” [671–672]. The targeted transport of drugs by a magnetic field and the biological aspects of magnetic fluid technology have been reviewed

from the medical viewpoint [673, 674], and superparamagnetic nanoparticles have even been considered for the treatment of AIDS [675]. The growth of cobalt nanoparticles using wet chemical [6, 247] or electrochemical methods [676–678] is well established in the literature. An important prerequisite for all medical or biological applications, however, is the long-term protection of the nanosized magnetic material against water and air. In a first attempt to protect tetraalkylammonium-stabilized cobalt particles (3 nm) from corrosion by gold coating their surfaces, a toluene dispersion was treated with AuCl_3 which slowly dissolves and undergoes a redox reaction at the cobalt(0) surface according to Eq. (20):



Comparative magnetic susceptibility measurements with the naked and the gold-plated cobalt particles show that the magnetic stability of the naked cobalt (50 hr) is increased to 300 hr after the redox plating of the surface with gold. However, only an incomplete gold coverage of the cobalt surface is achieved by this simple method (Eq. (20)). Protection of the magnetic material is much improved by treating the cobalt particles with gold halides in the presence of excess borohydride and an enhanced magnetic stability of more than 1000 hr is observed. Similarly, using the aforementioned trialkylaluminum method of colloids, Co particles with considerable stability against oxidation is achieved. This property is going to be used in preparing magnetic fluids with special properties [263–265]. Information on the ferrofluids with their potential application has been elaborated [679].

New strategies utilizing DNA as a construction material for the generation of biometallic nanostructures have made it possible to develop larger “nanotechnology devices” (<100 nm) for microelectronic photolithographic applications. DNA is regarded as a promising construction material for the selective positioning of molecular devices because of its recognition capabilities, physicochemical stability, and mechanical rigidity. Seeman was the first to propose DNA for the precise spatial arrangement of 3D networks [680, 681]. Assemblies of DNA-derivatized gold colloids were recently prepared via the DNA hybridization-based self-organization pathway and the resulting defined arrangements of nanometal particles have actual applications in laser technology [682–692]. As already mentioned, Alivisatos et al. [618] have obtained defined monoadducts from commercially available 1.4-nm gold clusters where one reactive maleimido group is attached to every particle. These were coupled with thiolated 18-mer oligonucleotides in order to add an individual “codon” sequence. When a single-stranded DNA template containing complementary codons is added, a self-assembly of molecules is observed [683, 693] (Fig. 18). This work has been the subject of recent reviews [393, 693–695].

Niemeyer [393, 694] has reported the coupling of metal particles bearing a biotin substituent with the DNA-streptavidin hybrid. The growth of a 12 μm -long, 100-nm-wide conductive silver wire has been achieved using a DNA molecule stretched between two gold electrodes as

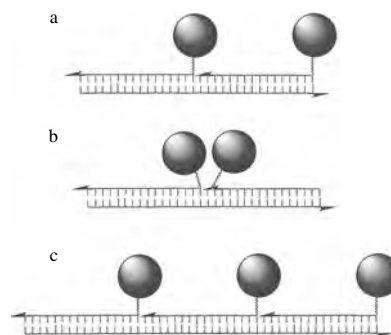


Figure 18. Self-organization of conjugates from gold particles (shaded spheres) and oligonucleotide codons to supramolecular assemblies by the addition of a template strand. The derivatization of the oligonucleotides in 3'- or 5'-position allows to control the mode of head-to-head (a) or head-to-tail (b) homodimers. The trimer (c) is formed using the complementary sequence in triplicate. Adapted with permission from [693], C. M. Niemeyer, *Angew. Chem. Int. Ed. Engl.* 36, 585 (1997). © 1997, VCH.

a template [696]. A recent inclusion in his study is deriving nanomechanical devices based on DNA [697]. See also [698].

7. CONCLUSION

We have reported the synthetic methods used for the synthesis of nanoparticles and highlighted their potential applications. It can now be said that during the last few decades an array of synthetic methodology for the wet chemical preparation of nanoparticles has been established. Powerful techniques for the detailed analysis of the geometrical and electronic structures of these materials have also been developed. It now remains to be seen how practical applications of these materials, namely, in the fields of catalysis and materials science, will grow from these seeds over the next few years.

GLOSSARY

Fuel cell An electrochemical cell that convert the chemical energy of a fuel and an oxidant to electrical energy.

Hydrosols and organosols Hydrosols are isolable, protected colloidal particles that can be readily redispersed in water. If the protecting shell is lipophilic (eg., tetraalkylammonium), such colloidal particles can be readily redispersible in organic solvents and are termed organosols.

Nanostructured metal colloids Isolable metal particles in the range of 1–50 nm that are prevented from agglomeration by protecting shells.

Precursor method A very efficient method for the preparation of active catalyst on a support in an *egg-shell* form via their precursor. The protected colloidal metal is loaded onto a support and the protecting shell is subsequently leached. Uniform coating of the metal catalyst on the support prevents its agglomeration.

Reductive stabilization A process in which the reductant is used in combination with the stabilizing agent. Protective shells for the reduced metals are formed immediately at the reduction centre in high local concentration and prevent their aggregation.

REFERENCES

- J. Turkevich, P. C. Stevenson, and J. Hillier, *Disc. Faraday Soc.* 11, 55 (1951).
- J. Turkevich and G. Kim, *Science* 169, 873 (1970).
- J. Turkevich, *Gold Bull.* 18, 86 (1985).
- G. Schmid, in "Aspects of Homogeneous Catalysis" (R. Ugo, Ed.), Vol. 7, p. 1. Kluwer, Dordrecht, 1990.
- G. Schmid, Ed., "Clusters and Colloids." VCH, Weinheim, 1994.
- H. Bönemann, W. Brijoux, R. Brinkmann, R. Fretzen, T. Jousen, R. Köppler, P. Neiteler, and J. Richter, *J. Mol. Catal.* 86, 129 (1994).
- H. Bönemann, G. Braun, W. Brijoux, R. Brinkmann, A. S. Tilling, K. Seevogel, and K. Siepen, *J. Organomet. Chem.* 520, 143 (1996).
- M. T. Reetz, W. Helbig, and S. A. Quaiser, in "Active Metals" (A. Fürstner, Ed.), p. 279. VCH, Weinheim, 1996.
- H. Bönemann and W. Brijoux, in "Active Metals" (A. Fürstner, Ed.), p. 339. VCH, Weinheim, 1996.
- N. Toshima and T. Yonezawa, *New J. Chem.* 1179 (1998).
- J. D. Aiken III and R. G. Finke, *J. Mol. Catal. A* 145, 1 (1999).
- B. F. G. Johnson, *Coord. Chem. Rev.* 190, 1269 (1999).
- G. Schmid, in "Applied Homogeneous Catalysis with Organometallic Compounds" (B. Cornils and W. A. Herrmann, Eds.), Vol. 2, p. 636. Wiley-VCH, Weinheim, 1996.
- W. A. Herrmann and B. Cornils, in "Applied Homogeneous Catalysis with Organometallic Compounds" (B. Cornils and W. A. Herrmann, Eds.), p. 1171. Wiley-VCH, Weinheim, 1996.
- H. Bönemann and W. Brijoux, in "Advanced Catalysts and Nanostructured Materials" (W. Moser, Ed.), Chap. 7, p. 165. Academic Press, San Diego, 1996.
- H. Bönemann and W. Brijoux, in "Metal Clusters in Chemistry" (P. Braunstein, L. A. Oro, and P. R. Raithby, Eds.), Vol. 2, p. 913. Wiley-VCH, Weinheim, 1999.
- T. J. Schmidt, M. Noeske, H. A. Gasteiger, R. J. Behm, P. Britz, W. Brijoux, and H. Bönemann, *Langmuir* 13, 2591 (1997).
- E. Auer, W. Behl, T. Lehmann, and U. Stenke, European Patent 09 24 784 A1, 1999.
- M. Götz and H. Wendt, *Electrochim. Acta* 43, 3637 (1998).
- T. J. Schmidt, M. Noeske, H. A. Gasteiger, R. J. Behm, P. Britz, and H. Bönemann, *J. Electrochem. Soc.* 145, 925 (1998).
- E. Gaffet, M. Tachikart, O. El Kedim, and R. Rahouadj, *Mater. Charact.* 36, 185 (1996).
- A. Amulyavichus, A. Daugvila, R. Davidonis, and C. Sipavichus, *Fizika Metallov I Metallovedenie* 85, 111 (1998).
- A. Schalnikoff and R. Roginsky, *Kolloid Z.* 43, 67 (1927).
- J. R. Blackborrow and D. Young, "Metal Vapor Synthesis." Springer-Verlag, New York, 1979.
- K. J. Klabunde, "Free Atoms and Particles." Academic Press, New York, 1980.
- K. J. Klabunde, Y. X. Li, and B. J. Tan, *Chem. Mater.* 3, 30 (1991).
- J. S. Bradley, in "Clusters and Colloids" (G. Schmid, Ed.), pp. 477f. VCH, Weinheim, 1994.
- K. J. Klabunde and G. C. C. Trivino, in "Active Metals" (A. Fürstner, Ed.), p. 237. VCH, Weinheim, 1996.
- M. Faraday, *Philos. Trans. R. Soc. London* 147, 145 (1857).
- J. S. Bradley, in "Clusters and Colloids" (G. Schmid, Ed.), p. 469. VCH, Weinheim, 1994.
- T. Leisner, C. Rosche, S. Wolf, F. Granzer, and L. Wöste, *Surf. Rev. Lett.* 3, 1105 (1996).
- R. Tausch Treml, A. Henglein, and J. Lilie, *Ber. Bunsen-Ges. Phys. Chem.* 82, 1335 (1978).
- M. Michaelis and A. Henglein, *J. Phys. Chem.* 96, 4719 (1992).
- M. A. Watzky and R. G. Finke, *J. Am. Chem. Soc.* 119, 10382 (1997).
- J. Rothe, J. Hormes, H. Bönemann, W. Brijoux, and K. Siepen, *J. Am. Chem. Soc.* 120, 6019 (1998).
- M. Maase, Ph.D. Thesis, Verlag Mainz, Aachen, 1999; also Ref. 182.
- K. Angermund, M. Bühl, U. Endruschat, F. T. Mauschick, R. Mörtel, R. Mynott, B. Tesche, N. Waldöfner, H. Bönemann, G. Köhl, H. Modrow, J. Hormes, E. Dinjus, F. Gassner, H. G. Haubold, and T. Vad, *Angew. Chem. Int. Ed.* 41, 4041 (2002).
- N. R. Jana, L. Gearheart, and C. J. Murphy, *Chem. Mater.* 13, 2313 (2002).
- K. R. Brown, D. G. Walter, and M. J. Natan, *Chem. Mater.* 12, 306 (2000).
- H. Heng, P. C. Gibbons, K. F. Kelton, and W. E. Buhro, *J. Am. Chem. Soc.* 123, 9198 (2001).
- N. R. Jana, L. Gearheart, and C. J. Murphy, *Langmuir* 17, 6782 (2001).
- H. Hirai, Y. Nakao, N. Toshima, and K. Adachi, *Chem. Lett.* 905 (1976).
- H. Hirai, Y. Nakao, and N. Toshima, *Chem. Lett.* 545 (1978).
- H. Hirai, Y. Nakao, and N. Toshima, *J. Macromol. Sci. Chem.* A12, 1117 (1978).
- H. Hirai, Y. Nakao, and N. Toshima, *J. Macromol. Sci. Chem.* A13, 727 (1979).
- Y. Liu, S. Z. D. Cheng, X. Wen, and J. Hu, *Langmuir* 18, 10500 (2002).
- J. Tanori and M. P. Pileni, *Langmuir* 13, 639 (1997).
- M. P. Pileni, *Langmuir* 13, 3266 (1997).
- M. Antonietti and C. Göltner, *Angew. Chem. Int. Ed. Engl.* 36, 910 (1997).
- M. P. Pileni, *Supramol. Sci.* 5, 321 (1998).
- M. P. Pileni, *Adv. Mater.* 10, 259 (1998).
- M. Antonietti, *Chem. Ing. Tech.* 68, 518 (1996).
- S. Förster, *Ber. Bunsen. Ges.* 101, 1671 (1997).
- J. J. Storhoff, R. C. Mucic, and C. A. Mirkin, *J. Cluster Sci.* 8, 179 (1997).
- M. Möller and J. P. Spatz, *Cur. Opin. Colloid Interface Sci.* 2, 177 (1997).
- G. B. Sergeev and M. A. Petrukhina, *Prog. Solid State Chem.* 24, 183 (1996).
- J. P. Wilcoxon and P. Provencio, *J. Phys. Chem. B* 103, 9809 (1999).
- T. Miyao, N. Toyozumi, S. Okuda, Y. Imai, K. Tyjima, and S. Naito, *Chem. Lett.* 1125 (1999).
- S. T. Selvan, M. Nogami, A. Nakamura, and Y. Hamanaka, *J. Noncryst. Solids* 255, 254 (1999).
- M. M. Maye, W. Theng, F. L. Leibowitz, N. K. Ly, and C. J. Zhong, *Langmuir* 16, 490 (2000).
- Y. Niidome, A. Hori, T. Sato, and S. Yamada, *Chem. Lett.* 310 (2000).
- I. Konomi, S. Hyodo, and T. Motohiro, *J. Catal.* 192, 11 (2000).
- G. Schmid, R. Pfeil, R. Boese, F. Bandermann, S. Meyer, G. H. M. Calis, and J. A. W. van der Velden, *Chem. Ber.* 114, 3634 (1981).
- G. Schmid, *Polyhedron* 7, 2321 (1988).
- L. J. de Jongh, J. A. O. de Aguiar, H. B. Brom, G. Longoni, J. M. van Ruitenbeek, G. Schmid, H. H. A. Smit, M. P. J. van Staveren, and R. C. Thiel, *Z. Phys. D: At. Mol. Clusters* 12, 445 (1989).
- G. Schmid, B. Morum, and J. Malm, *Angew. Chem. Int. Ed. Engl.* 28, 778 (1989).
- G. Schmid, N. Klein, and L. Korste, *Polyhedron* 7, 605 (1998).
- T. Tominaga, S. Tenma, H. Watanabe, U. Giebel, and G. Schmid, *Chem. Lett.* 1033 (1996).
- G. Schmid, *Chem. Rev.* 92, 1709 (1992).
- H. A. Wicrenga, L. Soethout, I. W. Gerritsen, B. E. C. van do Leemput, H. van Kempen, and G. Schmid, *Adv. Mater.* 2, 482 (1990).
- R. Houbertz, T. Feigenspan, F. Mielke, U. Memmert, U. Hartmann, U. Simon, G. Schön, and G. Schmid, *Europhys. Lett.* 28, 641 (1994).
- G. Schmid and A. Lehnert, *Angew. Chem. Int. Ed. Engl.* 28, 780 (1989).
- G. Schmid, V. Maihack, F. Lantermann, and S. Peschel, *J. Chem. Soc. Dalton Trans.* 589 (1996).

74. G. Schmid, H. West, J. O. Malm, J. O. Bovin, and C. Grenthe, *Chem. Eur. J.* 2, 1099 (1996).
75. U. Simon, R. Flesch, H. Wiggers, G. Schön, and G. Schmid, *J. Mater. Chem.* 8, 517 (1998).
76. G. Schmid and S. Peschel, *New J. Chem.* 22, 669 (1998).
77. G. Schmid, R. Pugin, J. O. Malm, and J. O. Bovin, *Eur. J. Inorg. Chem.* 813 (1998).
78. M. Giersig, L. M. L. Tarzan, T. Ung, D. Su, and P. Mulvaney, *Ber. Bunsen. Phys. Chem.* 101, 1617 (1997).
79. M. N. Vargaftik, V. P. Zargorodnikov, I. P. Stolarov, I. I. Moiseev, D. I. Kochubey, V. A. Likholobov, A. L. Chuvilin, and K. I. Zarnaraev, *J. Mol. Catal.* 53, 315 (1989).
80. M. N. Vargaftik, V. P. Zargorodnikov, I. P. Stolarov, I. I. Moiseev, V. A. Likholobov, D. I. Kochubey, A. L. Chuvilin, V. I. Zaikovskiy, K. I. Zamaraev, and G. I. Timofeeva, *J. Chem. Soc. Chem. Commun.* 937 (1985).
81. V. V. Volkov, G. V. Tendeloo, G. A. Tsirkov, N. V. Cherkashina, M. N. Vargaftik, I. I. Moiseev, V. M. Novotortsev, A. V. Kvit, and A. L. Chuvilin, *J. Cryst. Growth* 163, 377 (1996).
82. I. I. Moiseev, M. N. Vargaftik, V. V. Volkov, G. A. Tsirkov, N. V. Cherkashina, V. M. Novotortsev, O. G. Ellett, I. A. Petrunenka, A. L. Chuvilin, and A. V. Kvit, *Mend. Commun.* 87 (1995).
83. V. Oleshko, V. Volkov, W. Jacob, M. Vargaftik, I. I. Moiseev, and G. van Tendeloo, *Z. Phys. D* 34, 283 (1995).
84. I. I. Moiseev, M. N. Vargaftik, T. V. Chernysheva, T. A. Stromnova, A. E. Gekhman, G. A. Tsirkov, and A. M. Makhlina, *J. Mol. Catal. A: Chem.* 108, 77 (1996).
85. C. Amiens, D. de Caro, B. Chaudret, and J. S. Bradley, *J. Am. Chem. Soc.* 115, 11638 (1993).
86. D. deCaro, H. Wally, C. Amiens, and B. Chaudret, *J. Chem. Soc. Chem. Commun.* 1891 (1994).
87. A. Rodriguez, C. Amiens, B. Chaudret, M. J. Casanove, P. Lecante, and J. S. Bradley, *Chem. Mater.* 8, 1978 (1996).
88. M. Bardaji, O. Vidoni, A. Rodriguez, C. Amiens, B. Chaudret, M. J. Casanove, and P. Lecante, *New J. Chem.* 21, 1243 (1997).
89. S. Sun, C. B. Murray, D. Weller, L. Folks, and A. Moser, *Science* 287, 1989 (2000).
90. G. H. Moehrl, M. G. Warner, and J. E. Hutchison, *J. Phys. Chem. B* 106, 9979 (2002).
91. R. Franke, J. Rothe, J. Pollmann, J. Hormes, H. Bönemann, W. Brijoux, and Th. Hindenburg, *J. Am. Chem. Soc.* 118, 12090 (1996).
92. O. Vidoni, K. Philippot, C. Amiens, B. Chaudret, O. Balmes, J. O. Malm, J. O. Bovin, F. Senocq, and M. J. Casanove, *Angew. Chem. Int. Ed. Engl.* 38, 3736 (1999).
93. M. T. Reetz and G. Lohmer, *Chem. Commun.* 1921 (1996).
94. D. Mandler and I. Willner, *J. Phys. Chem.* 91, 3600 (1987).
95. H. Bönemann, W. Brijoux, and T. Joussen, U.S. Patent 5, 580, 492, 1993.
96. H. Bönemann, W. Brijoux, R. Brinkmann, E. Dinjus, T. Joussen, and B. Korall, *Angew. Chem. Int. Ed.* 30, 1344 (1991).
97. H. Bönemann, W. Brijoux, R. Brinkmann, and J. Richter, U.S. Patent 6, 090, 746, 1997.
98. M. T. Reetz and W. Helbig, *J. Am. Chem. Soc.* 116, 7401 (1994).
99. M. T. Reetz, W. Helbig, and S. Quaiser, U.S. Patents, 5, 620, 564, 1997, and 5, 925, 463, 1999.
100. M. A. Winter, Ph.D. Thesis, Verlag Mainz, Aachen, 1998.
101. J. A. Becker, R. Schäfer, W. Festag, W. Ruland, J. H. Wendorf, Pebler, S. A. Quaiser, W. Helbig, and M. T. Reetz, *J. Chem. Phys.* 103, 2520 (1995).
102. M. T. Reetz, S. A. Quaiser, and C. Merk, *Chem. Ber.* 129, 741 (1996).
103. M. T. Reetz, W. Helbig, and S. A. Quaiser, *Chem. Mater.* 7, 2227 (1995).
104. M. T. Reetz and S. A. Quaiser, *Angew. Chem.* 107, 2461 (1995); *Angew. Chem. Int. Ed. Engl.* 34, 2240 (1995).
105. U. Kolb, S. A. Quaiser, M. Winter, and M. T. Reetz, *Chem. Mater.* 8, 1889 (1996).
106. J. Kiwi and M. Grätzel, *J. Am. Chem. Soc.* 101, 7214 (1979).
107. H. Bönemann, W. Brijoux, R. Brinkmann, U. Endruschat, W. Hofstadt, and K. Angermund, *Rev. Roum. Chim.* 44, 1003 (1999).
108. J. Sinzig, L. J. de Jongh, H. Bönemann, W. Brijoux, and R. Köppler, *Appl. Organomet. Chem.* 12, 387 (1998).
109. H. Bönemann, W. Brijoux, and R. Brinkmann, WO 99/59713, 1999.
110. J. S. Bradley, E. W. Hill, M. E. Leonowicz, and H. Witzke, *J. Mol. Catal.* 41, 59 (1987).
111. M. T. Reetz, W. Helbig, S. A. Quaiser, U. Stimming, N. Breuer, and R. Vogel, *Science* 267, 367 (1995).
112. A. Schulze Tilling, Ph.D. Thesis, RWTH Aachen, 1996.
113. T. Yonezawa and N. Toshima, *J. Mol. Catal.* 83, 167 (1993).
114. N. Toshima, T. Takahashi, and H. Hirai, *Chem. Lett.* 1245 (1985).
115. T. T. Albrecht, G. Meier, P. M. Buschbaum, A. Patkowski, W. Steffen, G. Grubel, D. L. Abernathy, O. Diat, M. Winter, M. G. Koch, and M. T. Reetz, *Phys. Rev. E: Stat. Phys., Plasmas, Fluids, Relat. Interdiscip. Top.* 59, 642 (1999).
116. J. S. Bradley, in "Clusters and Colloids" (G. Schmid, Ed.), p. 471. VCH, Weinheim, 1994.
117. N. Toshima and K. Hirakawa, *Polym. J.* 31, 1127 (1999).
118. P. Lu, T. Teranishi, K. Asakura, M. Miyake, and N. Toshima, *J. Phys. Chem. B* 103, 9673 (1999).
119. I. P. Santos and L. M. L. Marzan, *Nano Lett.* 2, 903 (2002).
120. F. Bonet, V. Delmas, S. Grugeon, R. H. Urbina, P. Y. Silvert, and K. T. Elhsissen, *Nanostruct. Mater.* 8, 1277 (1999).
121. G. Viau, R. Brayner, L. Poul, N. Chakroune, E. Lacaze, F. F. Vincent, and F. Fievet, *Chem. Mater.* 15, 486 (2002).
122. K. Ono, R. Okuda, Y. Ishii, S. Kammimura, and M. Oshima, *J. Phys. Chem. B* 107, 1941 (2003).
123. A. Dalmia, C. L. Lineken, and R. F. Savinell, *J. Colloid Interface Sci.* 205, 535 (1998).
124. F. Fievet, J. P. Lagier, and M. Figlarz, *MRS Bull.* 14, 29 (1989).
125. S. Kang, J. W. Harell, and D. E. Nikles, *Nano Lett.* 2, 1033 (2002).
126. Y. Li, E. Boone, and M. A. El-Sayed, *Langmuir* 18, 4921 (2002).
127. T. Teranishi and M. Miyake, *Chem. Mater.* 11, 3414 (1999).
128. H. N. Vasani and C. N. R. Rao, *J. Mater. Chem.* 5, 1755 (1995).
129. S. Ayyappan, R. S. Gopalan, G. N. Subbana, and C. N. R. Rao, *J. Mater. Res.* 12, 398 (1997).
130. N. Malikova, I. P. Santos, M. Schierhorn, N. A. Kofor, and L. M. L. Marzan, *Langmuir* 18, 3694 (2002).
131. I. Wang and I. M. Hsing, *Electrochim. Acta* 47, 2981 (2002).
132. L. D. Rampino and F. F. Nord, *J. Am. Chem. Soc.* 63, 2745 (1941).
133. L. D. Rampino and F. F. Nord, *J. Am. Chem. Soc.* 63, 3268 (1941).
134. L. D. Rampino and F. F. Nord, *J. Am. Chem. Soc.* 65, 2121 (1943).
135. L. Hernandez and F. F. Nord, *J. Colloid. Sci.* 3, 363 (1948).
136. W. P. Dunsworth and F. F. Nord, *J. Am. Chem. Soc.* 72, 4197 (1950).
137. Y. Lin and R. G. Finke, *J. Am. Chem. Soc.* 116, 8335 (1994).
138. Y. Lin and R. G. Finke, *Inorg. Chem.* 33, 4891 (1994).
139. T. Nagata, M. Pohl, H. Weiner, and R. G. Finke, *Inorg. Chem.* 36, 1366 (1997).
140. J. D. Aiken III and R. G. Finke, *J. Am. Chem. Soc.* 120, 9545 (1998).
141. J. D. Aiken III and R. G. Finke, *Chem. Mater.* 11, 1035 (1999).
142. B. J. Hornstein and R. G. Finke, *Chem. Mater.* 15, 899 (2003).
143. X. Fu, Y. Wang, N. Wu, L. Gui, and Y. Tang, *Langmuir* 18, 4619 (2002).
144. D. Angel, J. M. Dominguez, G. D. Angel, J. A. Montoya, E. L. Pitara, S. Labruquere, and J. Barbier, *Langmuir* 16, 7210 (2000).
145. J. W. Yoo, D. Hathcock, and M. A. El-Sayed, *J. Phys. Chem. A* 106, 2049 (2002).
146. I. Balint, A. Miyazaki, and K. I. Aika, *Chem. Commun.* 1044 (2002).

147. L. A. Porter, J. H. C. Choi, A. E. Ribbe, and J. M. Buriak, *Nano Lett.* 2, 1067 (2002).
148. M. R. Mucalo and R. P. Cooney, *J. Chem. Soc. Chem. Commun.* 94 (1989).
149. K. Meguro, M. Torizuka, and K. Esumi, *Bull. Chem. Soc. Jpn.* 61, 341 (1988).
150. L. N. Lewis and N. Lewis, *J. Am. Chem. Soc.* 108, 7228 (1986).
151. L. N. Lewis and N. Lewis, *Chem. Mater.* 1, 106 (1989).
152. A. C. Curtis, D. G. Duff, P. P. Edwards, D. A. Jefferson, B. F. G. Johnson, A. I. Kirkland, and D. E. Logan, *Angew. Chem. Int. Ed. Engl.* 26, 676 (1987).
153. D. G. Duff, A. C. Curtis, P. P. Edwards, D. A. Jefferson, B. F. G. Johnson, and D. E. Logan, *J. Chem. Soc. Chem. Commun.* 1264 (1987).
154. A. C. Curtis, D. G. Duff, P. P. Edwards, D. A. Jefferson, B. F. G. Johnson, A. I. Kirkland, and A. S. Wallace, *Angew. Chem. Int. Ed. Engl.* 27, 1530 (1988).
155. D. G. Duff, P. P. Edwards, J. Evans, J. T. Gauntlett, D. A. Jefferson, B. F. G. Johnson, A. I. Kirkland, and D. J. Smith, *Angew. Chem. Int. Ed. Engl.* 28, 590 (1989).
156. D. G. Duff, A. Baiker, and P. P. Edwards, *Langmuir* 9, 2301 (1993).
157. W. Vogel, D. G. Duff, and A. Baiker, *Langmuir* 11, 401 (1995).
158. P. R. van Rheenen, M. J. McKelvey, and W. S. Glaunsinger, *J. Solid State Chem.* 67, 151 (1987).
159. J. Xiao, Y. Xie, and W. Luo, *Chem. Lett.* 462 (2002).
160. H. G. Zheng, J. H. Liang, J. H. Zeng, and Y. T. Qian, *Mater. Res. Bull.* 36, 947 (2001).
161. D. G. Duff and A. Baiker, in "Preparation of Catalysts VI" (G. Poncelet, J. Martens, B. Delmon, P. A. Jacobs, and P. Grange, Eds.), p. 505. Elsevier Science, New York, 1995.
162. H. C. Choi, S. Kundaria, D. Wang, A. Javey, Q. Wang, M. Rolandi, and H. Dai, *Nano Lett.* 3, 157 (2003).
163. K. L. Tsai and J. L. Dye, *Chem. Mater.* 5, 540 (1993).
164. J. van Wonerghem, S. Mørup, C. J. W. Koch, S. W. Charles, and S. Wells, *Nature* 322, 622 (1986).
165. G. N. Glavee, K. J. Klabunde, C. M. Sorensen, and G. C. Hadjipanayis, *Inorg. Chem.* 32, 474 (1993).
166. K. P. Velikov, G. E. Zegers, and A. van Blaaderen, *Langmuir* 19, 1384 (2003).
167. A. Yedra, L. F. Barquin, J. C. Gomez Sal, and Q. A. Pankhurst, *J. Mag. Mater.* 14, 254 (2003).
168. J. S. Jung, K. H. Choi, W. S. Chae, Y. R. Kim, J. H. Jun, L. Malkinski, T. Kodanandath, W. Zhou, J. B. Wiley, and C. J. O'Connor, *J. Phys. Chem. Solids* 64, 385 (2003).
169. Y. Song and R. W. Murray, *J. Am. Chem. Soc.* 124, 7096 (2001).
170. T. Cassagneau and F. Caruso, *Adv. Mater.* 14, 732 (2002).
171. K. W. Park, J. H. Choi, B. K. Kwon, S. A. Lee, Y. E. Sung, H. Y. Ha, S. A. Hong, H. Kim, and A. Wieckowski, *J. Phys. Chem. B* 106, 1869 (2002).
172. K. Kinoshita and P. Stonehart, "Modern Aspect of Electrochemistry," p. 12. Plenum, New York, 1996.
173. K. J. Klabunde and C. Mohs, in "Chemistry of Advanced Materials" (L. V. Interrante and L. V. H. Smith, Eds.), Chap. 3. Wiley-VCH, New York, 1998.
174. S. Y. Zhao, S. H. Chen, S. Y. Wang, D. G. Li, and H. Y. Ma, *Langmuir* 18, 3315 (2002).
175. B. J. Hormes, H. Modrow, R. Brinkmann, N. Waldöfner, H. Bönemann, L. Beuermann, S. Krischok, W. M. Friedrichs, and V. Kempter, *Surf. Sci.* 497, 321 (2002).
176. K. J. Takeuchi, A. C. Marschillok, C. A. Bessel, and N. R. Dollahon, *J. Catal.* 208, 150 (2002).
177. R. Franke, J. Rothe, R. Becker, J. Pollmann, J. Hormes, H. Bönemann, W. Brijoux, and R. Köppler, *Adv. Mater.* 10, 126 (1998).
178. A. W. Snow, M. G. Ancona, W. Kruppa, G. G. Jernigan, E. E. Foos, and D. Park, *J. Mater. Chem.* 12, 1222 (2002).
179. E. G. Franco, O. Neto, M. Linardi, and E. Arico, *J. Braz. Chem. Soc.* 13, 516 (2002).
180. A. O. Neto, E. G. Franco, E. Arico, M. Linardi, and E. R. Gonzalez, "International Workshop on Ceramic/Metal Interfaces Control at the Atomic Level," 2002.
181. C. Roth, N. Martz, and H. Fuess, *Phys. Chem. Chem. Phys.* 3, 315 (2001).
182. M. Brust, M. Walker, D. Bethell, D. Schiffrin, and R. Whyman, *J. Chem. Soc., Chem. Commun.* 801 (1994).
183. M. T. Reetz and M. Maase, *Adv. Mater.* 11, 773 (1999).
184. J. S. Bradley, B. Tesche, W. Busser, M. Maase, and M. T. Reetz, *J. Am. Chem. Soc.* 122, 4631 (2000).
185. H. Bönemann, N. Waldöfner, H. G. Haubold, and T. Vad, *Chem. Mater.* 14, 1115 (2002).
186. H. Bönemann, W. Brijoux, H. W. Hofstadt, T. O. Ely, W. Schmidt, B. Waßmuth, and C. Weidenthaler, *Angew. Chem. Int. Ed.* 41, 599 (2002).
187. R. Richards, G. Geibel, W. Hofstadt, and H. Bönemann, *Appl. Organometal Chem.* 16, 377 (2002).
188. S. A. Lee, K. W. Park, J. H. Choi, B. K. Kwon, and Y. E. Sung, *J. Elect. Chem. Soc.* 149, A1299 (2002).
189. I. P. Santos and L. M. L. Marzan, *Pure Appl. Chem.* 72, 83 (2000).
190. I. P. Santos and L. M. L. Marzan, *Langmuir* 15, 948 (1999).
191. I. P. Santos, D. Koktysh, A. A. Mamedov, M. Giersig, N. A. Kotov, and L. M. L. Marzan, *Langmuir* 16, 2731 (2000).
192. I. P. Santos and L. M. L. Marzan, *Langmuir* 18, 2888 (2002).
193. G. R. Gattorno, D. Diaz, L. Rendon, and G. O. H. Segura, *J. Phys. Chem. B* 106, 2482 (2002).
194. J. L. G. Torresdey, E. Gomez, J. R. P. Videia, J. G. Parsons, H. Troiani, and M. J. Yacaman, *Langmuir* 19, 1357 (2003).
195. J. L. G. Torresdey, J. G. Parsons, E. Gomez, J. P. Videia, H. E. Troiana, P. Santiago, and M. J. Yacaman, *Nano Lett.* 2, 397 (2002).
196. D. P. E. Dickson, *J. Mag. Mater.* 203, 46 (1999).
197. M. Priyabrata, A. Ahmad, D. Mandal, S. Senapati, S. R. Sainkar, M. I. Khan, R. Parishcha, P. V. Ajaykumar, M. Alam, R. Kumar, and M. Sastry, *Nano Lett.* 1, 515 (2001).
198. B. L. V. Prasad, S. I. Stoeva, C. M. Sorensen, and K. J. Klabunde, *Langmuir* 18, 7515 (2002).
199. S. Stoeva, K. J. Klabunde, C. M. Sorensen, and I. Dragieva, *J. Am. Chem. Soc.* 124, 2305 (2002).
200. N. Gaponik, D. V. Talapin, A. L. Rogach, K. Hoppe, E. V. Shevchenko, A. Kornowski, A. Eychmüller, and H. Weller, *J. Phys. Chem. B* 106, 7177 (2002).
201. J. H. Hodak, A. Henglein, M. Giersig, and G. V. Hartland, *J. Phys. Chem. B* 104, 11708 (2000).
202. M. A. Malik, P. O. Brien, and N. Revaprasadu, *Chem. Mater.* 14, 2004 (2002).
203. D. T. Tran, L. M. C. Beltran, C. M. Kowalchuk, N. R. Trefiak, N. J. Taylor, and J. F. Corrigan, *Inorg. Chem.* 41, 5693 (2002).
204. J. S. Yu, J. Y. Kim, S. Lee, J. K. N. Mbindyo, B. R. Martin, and T. E. Mallouk, *Chem. Commun.* 2445 (2000).
205. T. T. Albrecht, J. Schotter, G. A. Kastle, N. Emley, T. Shibauchi, L. K. Elbaum, K. Guarini, C. T. Black, M. T. Tuominen, and T. P. Russell, *Science* 290, 2126 (2000).
206. J. K. N. Mbindyo, T. E. Mallouk, J. B. Mattzela, I. Kratochvilova, B. Razavi, T. N. Jackson, and T. S. Mayer, *J. Am. Chem. Soc.* 124, 4020 (2002).
207. Y. G. Guo, L. J. Wan, J. R. Gong, and C. L. Bai, *Phys. Chem. Chem. Phys.* 4, 3422 (2002).
208. K. B. Jirage, J. C. Hulteen, and C. R. Martin, *Science* 278, 655 (1997).
209. L. Sun and R. M. Crooks, *Langmuir* 18, 8231 (2002).
210. T. C. Wang, M. F. Rubner, and R. E. Cohen, *Chem. Mater.* 15, 299 (2002).
211. P. H. Hess and P. H. Parker, *J. Appl. Polym. Sci.* 10, 1915 (1966).
212. J. R. Thomas, *J. Appl. Phys.* 37, 2914 (1966).

213. K. Esumi, T. Tano, K. Torigue, and K. Meguro, *Chem. Mater.* 2, 564 (1990).
214. J. S. Bradley, E. W. Hill, C. Klein, B. Chaudret, and A. Duteil, *Chem. Mater.* 5, 254 (1993).
215. Y. Wada, H. Kuramoto, T. Sakata, H. Mori, T. Sumida, T. Kitamura, and S. Yanagida, *Chem. Lett.* 607 (1999).
216. W. Yu, W. Tu, and H. Liu, *Langmuir* 15, 6 (1999).
217. K. E. Gonsalves, H. Li, R. Perez, P. Santiago, and M. J. Yacaman, *Coord. Chem. Rev.* 206–207, 607 (2000).
218. D. Boxall, G. Deluga, E. Kenik, W. King, and C. Lukehart, *Chem. Mater.* 13, 891 (2001).
219. S. Komarneni, D. Li, B. Newalkar, H. Katsuki, and A. S. Bhalla, *Langmuir* 18, 5959 (2002).
220. K. S. Suslick, T. Hyeon, M. Fang, and A. Cichowlas, in “Advanced Catalysts and Nanostructured Materials” (W. Moser, Ed.), Chap. 8, p. 197. Academic Press, San Diego, 1996.
221. A. Dhas and A. Gedanken, *J. Mater. Chem.* 8, 445 (1998).
222. Y. Koltypin, A. Fernandez, C. Rojas, J. Campora, P. Palma, R. Prozorov, and A. Gedanken, *Chem. Mater.* 11, 1331 (1999).
223. R. A. Salkar, P. Jeevanandam, S. T. Aruna, Y. Koltypin, and A. Gedanken, *J. Mater. Chem.* 9, 1333 (1999).
224. K. Okitsu, S. Nagaoka, S. Tanabe, H. Matsumoto, Y. Mizukoshi, and Y. Nagata, *Chem. Lett.* 271 (1999).
225. T. C. Rojas, M. J. Sayagues, A. Caballero, Y. Koltypin, A. Gedanken, L. Posonnet, B. Vacher, J. M. Martin, and A. Fernandez, *J. Mater. Chem.* 10, 715 (2000).
226. A. Henglein, in “Modern Trends in Colloid Science in Chemistry and Biology” (H. F. Bicke, Ed.), p. 126. Birkhauser Verlag, Stuttgart, 1985.
227. B. G. Ershov, E. Janata, A. Henglein, and A. Fojtik, *J. Phys. Chem.* 97, 4589 (1993).
228. A. Henglein, *J. Phys. Chem.* 97, 5457 (1993).
229. B. G. Ershov, E. Janata, and A. Henglein, *J. Phys. Chem.* 97, 339 (1993).
230. A. Henglein and M. Giersig, *J. Phys. Chem.* 98, 6931 (1994).
231. A. Henglein, M. Gutierrez, E. Janata, and B. Ershov, *J. Phys. Chem.* 96, 4598 (1992).
232. A. Henglein, P. Mulveney, A. Holzwarth, T. E. Sosebee, and A. Fojtik, *Ber. Bunsen. Phys. Chem.* 96, 2411 (1992).
233. P. Mulveney, M. Giersig, and A. Henglein, *J. Phys. Chem.* 96, 10419 (1992).
234. A. Henglein and D. Meisel, *Langmuir* 14, 7392 (1998).
235. J. Belloni, M. Mostafavi, H. Remita, J. L. Marignier, and M. O. Delcourt, *New J. Chem.* 22, 1239 (1998).
236. A. Henglein, *J. Phys. Chem. B.* 104, 2201 (2000).
237. J. S. Jeon, C. S. Yeh, and J. Chin, *Chem. Soc.* 45, 721 (1998).
238. F. Stietz and F. Träger, *Phys. Blätter* 55, 57 (1999).
239. K. Okitsu, A. Yue, S. Tanabe, and H. Matsumoto, *Bull. Chem. Soc. Jpn.* 75, 449 (2002).
240. C. W. Hills, M. S. Nashner, A. I. Frenkel, J. R. Shapley, and R. G. Nuzzo, *Langmuir* 15, 690 (1999).
241. R. D. Adams and W. J. Wu, *J. Cluster Sci.* 2, 271 (1991).
242. F. Ciardelli and P. Pertici, *Z. Naturforsch.* 40b, 133 (1985).
243. J. S. Bradley, E. W. Hill, S. Behal, C. Klein, B. Chaudret, and A. Duteil, *Chem. Mater.* 4, 1234 (1992).
244. A. Duteil, R. Quéau, B. Chaudret, R. Mazel, C. Roucau, and J. S. Bradley, *Chem. Mater.* 5, 341 (1993).
245. D. deCaro, V. Agelou, A. Duteil, B. Chaudret, R. Mazel, Ch. Roucau, and J. S. Bradley, *New J. Chem.* 19, 1265 (1995).
246. F. Dassenoy, K. Philippot, T. O. Ely, C. Amiens, P. Lecante, E. Snoeck, A. Mosset, M. J. Casanove, and B. Chaudret, *New J. Chem.* 19, 703 (1998).
247. J. Osuna, D. deCaro, C. Amiens, B. Chaudret, E. Snoeck, M. Respaud, J. M. Broto, and A. Fert, *J. Phys. Chem.* 100, 14571 (1996).
248. T. O. Ely, C. Amiens, B. Chaudret, E. Snoeck, M. Verelst, M. Respaud, and J. M. Broto, *Chem. Mater.* 11, 526 (1999).
249. J. S. Bradley, E. W. Hill, B. Chaudret, and A. Duteil, *Langmuir* 11, 693 (1995).
250. F. Dassenoy, M. Casanove, P. Lecante, M. Verelst, E. Snoeck, A. Mosset, T. O. Ely, C. Amiens, and B. Chaudret, *J. Chem. Phys.* 112, 8137 (2000).
251. C. Pan, F. Dassenoy, M. J. Casanove, K. Philippot, C. Amiens, P. Lecante, A. Mosset, and B. Chaudret, *J. Phys. Chem. B* 103, 10098 (1999).
252. P. Pertuci and G. Vituli, *Inorg. Synth.* 11, 178 (1983).
253. K. Soulantica, A. Maisonnat, M. Fromen, M. Casanove, P. Lecante, and B. Chaudret, *Angew. Chem. Int. Ed.* 40, 448 (2001).
254. C. Nayral, E. Viala, P. Fau, F. Senocq, J. Jumas, A. Maisonnat, and B. Chaudret, *Chem. Eur. J.* 6, 4082 (2000).
255. S. Gomez, K. Philippot, V. Colliere, B. Chaudret, F. Senocq, and P. Lecante, *Chem. Commun.* 19, 1945 (2000).
256. A. I. Kirkland, P. P. Edwards, D. A. Jefferson, and D. G. Duff, *Annual Reports on the Progress of Chemistry C*, Vol. 87, p. 247. Royal Society of Chemistry, Cambridge, 1990.
257. T. Ely, C. Pan, C. Amiens, B. Chaudret, F. Dassenoy, P. Lecante, M. Casanove, A. Mosset, M. Respaud, and J. Broto, *J. Phys. Chem. B* 104, 695 (2000).
258. C. Pan, F. Dassenoy, M. Casanove, K. Philippot, C. Amiens, P. Lecante, A. Mosset, and B. Chaudret, *J. Phys. Chem. B* 103, 10098 (1999).
259. M. Verelst, T. Ely, C. Amiens, E. Snoeck, P. Lecante, A. Mosset, M. Respaud, J. Broto, and B. Chaudret, *Chem. Mater.* 11, 2702 (1999).
260. T. O. Ely, C. Pan, C. Amiens, B. Chaudret, F. Dassenoy, P. Lecante, M. J. Casanove, A. Mosset, M. Respaud, and J. M. Broto, *J. Phys. Chem. B* 104, 695 (2000).
261. Y. H. Chang, H. W. Wang, C. W. Chiu, D. S. Cheng, M. Y. Yen, and H. T. Chiu, *Chem. Mater.* 14, 4334 (2002).
262. H. Bönemann, R. Brinkmann, N. Matoussevich, and N. Waldofner, “ECIS, XVIth Conference of the European Colloid and Interface Society,” 2002, p. 190.
263. H. Bönemann, W. Brijoux, R. Brinkmann, N. Matoussevich, and N. Waldofner, Patent Application Number, DE 10227779.6, 2002.
264. H. Bönemann, W. Brijoux, R. Brinkmann, N. Matoussevich, and N. Waldofner, *Mag. Hydrodynamics* 39, 29 (2003).
265. H. Bönemann, W. Brijoux, R. Brinkmann, N. Matoussevich, N. Waldofner, N. Palina, and H. Modrow, *Inorg. Chim. Acta* 350, 617 (2003).
266. S. L. Tripp, S. V. Pusztay, A. E. Ribbe, and A. Wei, *J. Am. Chem. Soc.* 124, 7914 (2002).
267. V. F. Puentes, K. Krishnan, and A. P. Alivisatos, *Science* 192, 2115 (2001).
268. J. I. Park and J. Cheon, *J. Am. Chem. Soc.* 123, 5743 (2001).
269. E. H. Tadd, J. S. Bradley, and R. Tannenbaum, *Langmuir* 18, 2378 (2002).
270. S. Hermans, J. Sloan, D. S. Shephard, B. F. G. Johnson, and L. H. Malcol, *Chem. Commun.* 276 (2002).
271. R. M. Lago, S. C. Tsang, K. L. Lu, Y. K. Chen, and M. L. H. Green, *J. Chem. Soc. Chem. Commun.* 1355 (1995).
272. A. Govindaraj, B. C. Satishkumar, M. Nath, and C. N. R. Rao, *Chem. Mater.* 12, 202 (2000).
273. A. Chu, J. Cook, R. J. R. Heesom, J. L. Hutchison, M. L. H. Green, and J. Sloan, *Chem. Mater.* 8, 2751 (1996).
274. T. Kyotani, L. Tsai, and A. Tomita, *Chem. Commun.* 701 (1997).
275. J. M. Planeix, N. Coustel, B. Coq, V. Brotons, P. S. Kumbhar, R. Dutartre, P. Geneste, P. Berneir, and P. M. Ajayan, *J. Am. Chem. Soc.* 116, 7935 (1994).
276. B. C. Satishkumar, E. M. Vogl, A. Govindaraj, and C. N. R. Rao, *J. Phys. D: Appl. Phys.* 29, 3173 (1996).
277. R. Yu, L. Chen, Q. Liu, J. Lin, K. L. Tan, S. C. Ng, H. S. O. Chan, G. Q. Xu, and T. S. A. Hor, *Chem. Mater.* 10, 718 (1998).
278. L. M. Ang, T. S. A. Hor, G. Q. Xu, C. H. Tung, S. P. Zhao, and J. L. S. Wang, *Carbon* 38, 363 (2000).

279. B. Rajesh, K. R. Thampi, J. M. Bonard, and B. Viswanathan, *J. Mater. Chem.* 10, 1757 (2000).
280. M. S. Nashner, A. I. Frenkel, D. L. Adler, J. R. Shapley, and R. G. Nuzzo, *J. Am. Chem. Soc.* 119, 7760 (1997).
281. X. Teng, D. Black, N. J. Watkins, Y. Gao, and H. Yang, *Nano Lett.* (2003).
282. A. Syukri, T. Ban, Y. Ohya, and Y. Takahashi, *Mat. Chem. Phys.* 78, 645 (2003).
283. S. G. Dixit, A. R. Muhadeshwar, and S. K. Haram, *Colloids Surfaces A: Physico-chem. Engg. Aspects* 133, 69 (1998).
284. J. Legrand, C. Petit, and M. P. Pileni, *J. Phys. Chem. B* 105, 5643 (2001).
285. C. Petit, J. Legrand, V. Russier, and M. P. Pileni, *J. Appl. Phys.* 91, 1502 (2002).
286. S. Qiu, J. Dong, and G. Chen, *J. Colloid Interface Sci.* 216, 230 (1999).
287. I. Lisiecki, F. Billoudet, and M. P. Pileni, *J. Mol. Liquids* 72, 251 (1997).
288. L. Qi, J. Ma, and J. Shen, *J. Colloid Interface Sci.* 186, 498 (1997).
289. P. Andre, F. Charra, P. A. Chollet, and M. P. Pileni, *Adv. Mater.* 14, 601 (2002).
290. J. E. Martin, J. P. Wilcoxon, J. Odinek, and P. Provencio, *J. Phys. Chem. B* 106, 971 (2002).
291. G. S. Attard, S. A. A. Leclerc, S. Maniguet, A. E. Russel, I. Nandhakumar, and P. N. Bartlett, *Chem. Mater.* 13, 1444 (2001).
292. N. Pinna, K. Weiss, H. S. Kongehl, W. Vogel, J. Urban, and M. P. Pileni, *Langmuir* 17, 7982 (2002).
293. L. Levy, D. Ingert, N. Feltn, V. Briois, and M. P. Pileni, *Langmuir* 18, 1490 (2002).
294. M. Mandal, S. K. Ghosh, S. Kundu, K. Esumi, and T. Pal, *Langmuir* 18, 7792 (2002).
295. H. H. Ingelsten, J. C. Beziat, P. Bergkvist, A. Palmqvist, M. Skoglundh, H. Qiahong, L. K. L. Falk, and K. Holmberg, *Langmuir* 18, 1811 (2002).
296. R. B. Khomane, A. Manna, A. B. Mandale, and B. D. Kulkarni, *Langmuir* 18, 8237 (2002).
297. A. Manna, B. D. Kulkarni, K. Bandyopadhyay, and A. Vijayamohan, *Chem. Mater.* 9, 3032 (1997).
298. A. Manna, T. Imae, T. Yogo, K. Aoi, and M. Okazaki, *J. Colloid Interface Sci.* 256, 297 (2002).
299. F. Porta, L. Prati, M. Rossi, and G. Scari, *Colloids Surfaces A: Physicochem. Engg. Aspects* 211, 43 (2002).
300. C. C. Wang, D. H. Chen, and T. C. Huang, *Colloids Surfaces A: Physicochemical Engg. Aspects* 189, 145 (2001).
301. X. Zhang and K. Y. Chan, *Chem. Mater.* 15, 451 (2003).
302. M. L. Wu, D. H. Chen, and T. C. Huang, *J. Colloid. Interface Sci.* 243, 102 (2001).
303. H. Ohde, F. Hunt, and C. M. Wai, *Chem. Mater.* 13, 4130 (2001).
304. H. Ohde, C. M. Wai, H. Kim, J. Kim, and M. Ohde, *J. Am. Chem. Soc.* 124, 4540 (2002).
305. M. Zhao, L. Sun, and R. M. Crooks, *J. Am. Chem. Soc.* 120, 4877 (1998).
306. M. Zhao and R. M. Crooks, *Angew. Chem. Int. Ed. Engl.* 38, 364 (1999).
307. B. I. Lemon and R. M. Crooks, *J. Am. Chem. Soc.* 122, 12 886 (2000).
308. L. Balogh and D. A. Tomalia, *J. Am. Chem. Soc.* 120, 7355 (1998).
309. L. Balogh, R. Valluzzi, K. S. Laverduer, S. P. Gido, G. L. Hagnauer, and D. A. Tomalia, *J. Nanoparticle Res.* 1, 353 (1999).
310. K. Sooklal, L. H. Hanus, H. J. Ploehn, and G. J. Murphy, *Adv. Mater.* 10, 1083 (1998).
311. J. Huang, K. Sooklal, and C. Murphy, *J. Chem. Mater.* 11, 3595 (1999).
312. E. Strable, J. W. M. Bulte, B. Moskowitz, K. Vivekanandan, M. Allen, and T. Douglas, *Chem. Mater.* 13, 2201 (2001).
313. J. Zheng, M. S. Stevenson, R. S. Hikida, and P. G. C. Patten, *J. Phys. Chem. B* 106, 1252 (2002).
314. J. H. Youk, M. K. Park, J. Locklin, R. Advincula, J. Yang, and J. Mays, *Langmuir* 18, 2455 (2002).
315. A. B. Lowe, B. S. Sumerlin, M. S. Donovan, and C. L. McCormick, *J. Am. Chem. Soc.* 124, 11562 (2002).
316. S. T. Selvan, T. Hayakawa, M. Nogami, Y. Kobayashi, L. M. L. Marzin, Y. Hamanaka, and A. Nakamura, *J. Phys. Chem. B* 106, 10157 (2002).
317. T. K. Dick, T. Dhanasekaran, Z. Zhang, and D. Meisel, *J. Am. Chem. Soc.* 124, 2312 (2002).
318. R. A. Reziq, D. Avnir, I. Miloslavski, H. Schumann, and J. Blum, *J. Mol. Catal. A: Chem.* 185, 179 (2002).
319. Z. Konya, V. F. Puentes, I. Kiricsi, J. Zhu, P. Alivisatos, and G. A. Somorjai, *Catal. Lett.* 81, 137 (2002).
320. M. T. Reetz, S. Quaiser, M. Winter, J. A. Becker, R. Schaefer, U. Stimming, A. Marmann, R. Vogel, and T. Konno, *Angew. Chem. Int. Ed.* 35, 2092 (1996).
321. M. Verelst, T. Ould Ely, C. Amiens, E. Snoeck, P. Lecante, A. Mosset, M. Respaud, J. M. Broto, and B. Chaudret, *Chem. Mater.* 11, 2702 (1999).
322. C. B. Wang and C. T. Yeh, *J. Catal.* 178, 450 (1998).
323. M. T. Reetz and M. Koch, PCT/EP 99/08594, 1999.
324. M. T. Reetz and M. Koch, *J. Am. Chem. Soc.* 121, 7933 (1999).
325. M. Koch, Ph.D. Thesis, Verlag Mainz, Aachen, 1999.
326. S. Sun and H. Zeng, *J. Am. Chem. Soc.* 124, 8204 (2002).
327. M. Rajamathi, M. Ghosh, and R. Sheshadri, *Chem. Commun.* 1152 (2002).
328. G. Ramakrishna and H. N. Ghosh, *Langmuir* 19, 505 (2002).
329. M. Niederberger, M. H. Bartl, and G. D. Stucky, *J. Am. Soc. Commun.* 124, 13642 (2002).
330. G. Schmid, M. Bäuml, and N. Beyer, *Angew. Chem. Int. Ed.* 39, 182 (2000).
331. H. Cölfen and T. Pauck, *Colloid Polym. Sci.* 275, 175 (1997).
332. T. Teranishi and M. Miyake, *Chem. Mater.* 10, 594 (1998).
333. E. Papirer, P. Horny, H. Balard, R. Anthore, C. Pepitas, and A. Martinet, *J. Colloid Interface Sci.* 94, 220 (1983).
334. T. Teranishi, M. Hosoe, and M. Miyake, *Adv. Mater.* 9, 65 (1997).
335. T. Teranishi, I. Kiyokawa, and M. Miyake, *Adv. Mater.* 10, 596 (1998).
336. K. Esumi, H. Ishizuka, S. Masayoshi, K. Meguro, T. Tano, and K. Torigoe, *Langmuir* 7, 457 (1991).
337. R. G. DiScipio, *Anal. Biochem.* 236, 168 (1996).
338. M. A. Watzky and R. G. Finke, *Chem. Mater.* 9, 3083 (1997).
339. T. Yonezawa, M. Sutoh, and T. Kunitake, *Chem. Lett.* 7, 619 (1997).
340. G. Frens, *Nature* 241, 20 (1997).
341. X. Zhai and E. Efrima, *Langmuir* 13, 420 (1997).
342. D. V. Leff, P. C. Ohara, J. R. Heath, and W. Gelbart, *J. Phys. Chem.* 99, 7036 (1995).
343. C. H. Chew, J. F. Deng, H. H. Huang, F. C. Loh, G. L. Loy, X. P. Ni, K. L. Tan, and G. Q. Xu, *Langmuir* 12, 909 (1996).
344. G. Braun and H. Bönemann, *Angew. Chem. Int. Ed. Engl.* 35, 1992 (1996).
345. M. B. Mohamed, Z. L. Wang, and M. A. E. Sayed, *J. Phys. Chem. A* 103, 10255 (1999).
346. T. Teranishi and M. Miyake, *Chem. Mater.* 11, 3414 (1999).
347. G. W. Busser, J. G. van Ommen, and J. A. Lercher, in "Advanced Catalysts and Nanostructured Materials" (W. Moser, Ed.), Chap. 7, p. 231. Academic Press, San Diego, 1996.
348. M. Antonietti, F. Gröhn, J. Hartmann, and L. Bronstein, *Angew. Chem. Int. Ed. Engl.* 36, 2080 (1997).
349. M. Pileni, *Pure Appl. Chem.* 72, 53 (2000).
350. A. Diffis, A. D'Archivio, K. Jerabek, G. Schmid, and B. Corain, *Adv. Mater.* 12, 1909 (2000).
351. K. Torigoe and K. Esumi, *Langmuir* 9, 1664 (1993).
352. A. Filankembo and M. P. Pileni, *Appl. Surf. Sci.* 164, 260 (2000).
353. J. Hochpied, P. Bonville, and M. Pileni, *J. Phys. Chem. B* 104, 905 (2000).

354. T. Shibata, B. A. Bunker, Z. Zhang, D. Meisel, C. F. Vardeman, and J. D. Gezelter, *J. Am. Chem. Soc.* 124, 11989 (2002).
355. M. Ohde, H. Ohde, and C. M. Wai, *Chem. Commun.* 2388 (2002).
356. V. F. Puentes, K. Krishnan, and A. P. Alivisatos, *Topics Catal.* 19, 145 (2002).
357. L. Lu, H. Wang, S. Xi, and H. Zhang, *J. Mater. Chem.* 12, 156 (2002).
358. H. P. Choo, K. Y. Liew, and H. Liu, *J. Mater. Chem.* 12, 934 (2002).
359. T. Wenzel, J. Bosbach, A. Goldmann, F. Stietz, and F. Traeger, *Appl. Phys. B* 69, 513 (1999).
360. J. Bosbach, D. Martin, F. Stietz, T. Wenzel, and F. Traeger, *Appl. Phys. Lett.* 74, 2605 (1999).
361. A. L. Stepanov, D. E. Hole, A. A. Bukharaev, P. D. Townsend, and N. I. Nurgazizov, *Appl. Surf. Sci.* 136, 298 (1998).
362. M. Kaempfe, T. Rainer, K. J. Berg, G. Seifert, and H. Graener, *Appl. Phys. Lett.* 74, 1200 (1999).
363. H. Kurita, A. Takami, and S. Koda, *Appl. Phys. Lett.* 72, 789 (1998).
364. A. Takami, H. Kurita, and S. Koda, *J. Phys. Chem. B* 103, 1226 (1999).
365. H. Fujiwara, S. Yanagida, and P. V. Kamat, *J. Phys. Chem. B* 103, 2589 (1999).
366. P. V. Kamat, M. Flumiani, and G. V. Hartland, *J. Phys. Chem. B* 102, 3123 (1998).
367. S. Chang, C. Shih, C. Chen, W. Lai, and C. R. C. Wang, *Langmuir* 15, 701 (1999).
368. S. Link, C. Burda, M. B. Mohamed, B. Nikoobakht, and M. A. E. Sayed, *J. Phys. Chem. A* 103, 1165 (1999).
369. S. Link, C. Burda, B. Nikoobakht, and M. A. E. Sayed, *J. Phys. Chem. B* 104, 6152 (2000).
370. S. Link, C. Burda, B. Nikoobakht, and M. A. E. Sayed, *Chem. Phys. Lett.* 315, 12 (1999).
371. B. S. Zelakiewicz, A. C. de Dios, and Y. Tong, *J. Am. Soc. Commun.* 125, 18 (2003).
372. N. Chestnoy, T. D. Harris, R. Hull, and L. E. Brus, *J. Phys. Chem.* 90, 3393 (1986).
373. J. P. Wilcoxon, R. L. Williamson, and R. Baughman, *J. Chem. Phys.* 98, 9933 (1993).
374. J. P. Wilcoxon, P. P. Newcomer, and G. A. Samara, *J. Appl. Phys.* 81, 7934 (1997).
375. F. Kim, J. H. Song, and P. Yang, *J. Am. Chem. Soc.* 124, 14316 (2002).
376. S. Fullam, H. Rensmo, S. N. Rao, and D. Fitzmaurice, *Chem. Mater.* 14, 3643 (2002).
377. M. J. Mezziani, H. W. Rollins, L. F. Allard, and Y. P. Sun, *J. Phys. Chem. B* 106, 11178 (2002).
378. Y. Sun, Y. Yin, B. T. Mayers, T. Herricks, and Y. Xia, *Chem. Mater.* 14, 4736 (2002).
379. S. O. Obare, R. E. Hollowell, and C. J. Murphy, *Langmuir* 18, 10407 (2002).
380. M. Zhao and R. M. Crooks, *Chem. Mater.* 11, 3379 (1999).
381. K. Esumi, A. Suzuki, A. Yamahira, and K. Torigoe, *Langmuir* 16, 2604 (2000).
382. S. Malynych, I. Luzinov, and G. Chumanov, *J. Phys. Chem. B* 106, 1280 (2002).
383. T. He, Y. Ma, Y. Cao, X. Hu, H. Liu, G. Zhang, W. Yang, and J. Yao, *J. Phys. Chem. B* 106, 12670 (2002).
384. P. V. Kamat, *J. Phys. Chem. B* 106, 7729 (2002).
385. J. A. Creighton and D. G. Eadon, *J. Chem. Soc. Faraday Trans.* 87, 3881 (1991).
386. G. Schmid, Ed., "Clusters and Colloids," p. 506. VCH, Weinheim, 1994.
387. P. G. Romero, *Adv. Mater.* 13, 163 (2001).
388. J. J. Hickmann, D. Ofer, P. E. Laibinis, G. M. Whitesides, and M. S. Wrighton, *Science* 252, 688 (1991).
389. S. Chen, R. S. Ingram, M. J. Hostetler, J. J. Pietron, R. W. Murray, T. G. Schaaff, J. T. Khoury, M. M. Alvarez, and R. L. Whetten, *Science* 280, 2098 (1998).
390. R. Elghanian, J. J. Storhoff, R. C. Mucic, R. L. Letsinger, and C. A. Mirkin, *Science* 277, 1078 (1977).
391. G. Markovich, C. P. Collier, S. E. Henrichs, F. Remacle, R. D. Levine, and J. R. Heath, *Acc. Chem. Res.* 32, 415 (1999).
392. I. Willner and B. Willner, *Pure Appl. Chem.* 73, 535 (2001).
393. C. M. Niemeyer, *Angew. Chem. Int. Ed. Engl.* 40, 4128 (2001).
394. J. W. Niemantsverdriet, "Spectroscopy in Catalysis, An introduction," p. 202. VCH, Weinheim, 1993.
395. N. Sheppard and T. T. Nguyen, in "Advances in Infrared and Raman Spectroscopy" (R. J. H. Clark and R. Hester, Eds.), Vol. 5, p. 67. Heyden, London, 1978.
396. Y. S. Noto and W. M. H. Sachtler, *J. Catal.* 32, 315 (1974).
397. R. Raval, G. Blyholder, S. Haq, and D. A. King, *J. Phys. Cond. Mat.* 1, SB165 (1989).
398. J. S. Bradley, J. M. Miller, and E. W. Hill, *J. Am. Chem. Soc.* 113, 4016 (1991).
399. J. S. Bradley, G. H. Via, L. Bonneviot, and E. W. Hill, *Chem. Mater.* 8, 1895 (1996).
400. D. de Caro and J. S. Bradley, *Langmuir* 13, 3067 (1997).
401. D. de Caro and J. S. Bradley, *Chem. Mater.* 14, 245 (1998).
402. M. R. Mucalo and R. P. Cooney, *J. Chem. Soc. Faraday Trans.* 87, 1221 (1991).
403. P. E. Colavita, M. S. Doescher, A. Molliet, U. Evans, J. Reddic, J. Zhou, D. Chen, P. G. Miney, and M. L. Myrick, *Langmuir* 18, 8503 (2002).
404. V. I. Parvulescu, H. Bonnemann, V. Parvulescu, U. Endruschat, A. Rufinska, C. W. Lehmann, B. Tesche, and G. Poncelet, *Appl. Catal. A* 214, 273 (2001).
405. S. Park, A. Wieckowski, and M. J. Weaver, *J. Am. Chem. Soc.* 125, 2282 (2003).
406. G. Vijayaraghavan, L. Gao, and C. Korzeniewski, *Langmuir* 19, 2333 (2003).
407. I. V. Yudanov, R. Sahnoun, K. M. Neyman, and N. Rösch, *J. Phys. Chem. B* 107, 255 (2002).
408. Y. C. Cao, R. Jin, and C. A. Mirkin, *Science* 297, 1536 (2002).
409. J. S. Bradley, in "Clusters and Colloids" (G. Schmid, Ed.), p. 467. VCH, Weinheim, 1994.
410. R. P. van Duyne, in "Chemical and Biological Applications of Lasers" (C. B. Moore, Ed.), p. 101. Academic Press, New York, 1978.
411. J. A. Creighton, C. G. Blatchford, and M. G. Albrecht, *J. Chem. Soc. Faraday II* 75, 790 (1979).
412. R. Díaz, J. Arbiol, F. Sanz, A. Cornet, and J. R. Morante, *Chem. Mater.* 14, 3277 (2002).
413. W. Xu, Y. Liao, and D. L. Akins, *J. Phys. Chem. B* 106, 11127 (2002).
414. M. Kerker, O. Siman, L. A. Bumm, and W. S. Wang, *Appl. Opt.* 19, 3253 (1980).
415. G. Schmid, *Struct. Bonding* 62, 51 (1985).
416. M. P. J. van Staveren, H. B. Brom, L. J. de Jongh, and G. Schmid, *Z. Phys. D: At. Mol. Clusters* 12, 451 (1989).
417. Y. Y. Tong, A. Wieckowski, and E. Oldfield, *J. Phys. Chem. B* 106, 2434 (2002).
418. Y. Y. Tong, H. S. Kim, P. K. Babu, P. Waszczuk, A. Wieckowski, and E. Oldfield, *J. Am. Chem. Soc.* 124, 468 (2002).
419. C. Rice, Y. Tong, E. Oldfield, and A. Wieckowski, *Electrochim. Acta.* 43, 2825 (1998).
420. A. I. Frenkel, C. W. Hills, and R. G. Nuzzo, *J. Phys. Chem. B* 105, 12689 (2001).
421. F. W. Lytle, G. H. Via, and J. H. Sinfelt, *J. Chem. Phys.* 67, 3831 (1977).
422. J. H. Sinfelt, G. H. Via, and F. W. Lytle, *J. Chem. Phys.* 68, 2009 (1977).
423. G. H. Via, J. H. Sinfelt, and F. W. Lytle, *J. Chem. Phys.* 71, 690 (1979).
424. J. H. Sinfelt, G. H. Via, and F. W. Lytle, *J. Chem. Phys.* 72, 4832 (1980).

425. J. H. Sinfelt, G. H. Via, F. W. Lytle, and R. B. Gregor, *J. Chem. Phys.* 75, 5527 (1981).
426. J. H. Sinfelt, G. H. Via, and F. W. Lytle, *J. Chem. Phys.* 76, 2779 (1982).
427. E. C. Marques, D. R. Sandstrom, F. W. Lytle, and R. B. Gregor, *J. Chem. Phys.* 77, 1027 (1982).
428. G. Meitzner, G. H. Via, F. W. Lytle, and J. H. Sinfelt, *J. Chem. Phys.* 78, 882 (1983).
429. G. Meitzner, G. H. Via, F. W. Lytle, and J. H. Sinfelt, *J. Chem. Phys.* 78, 2533 (1983).
430. G. Meitzner, G. H. Via, F. W. Lytle, and J. H. Sinfelt, *J. Chem. Phys.* 83, 353 (1985).
431. G. Meitzner, G. H. Via, F. W. Lytle, and J. H. Sinfelt, *J. Chem. Phys.* 83, 4793 (1985).
432. G. Meitzner, G. H. Via, F. W. Lytle, and J. H. Sinfelt, *J. Chem. Phys.* 87, 6354 (1987).
433. This chapter is a modified version of a section in: U. Kreibig, H. Bönnemann, and J. Hormes, in "Handbook of Surfaces and Interfaces of Materials" (H. S. Nalwa, Ed.), pp. 1–85. Academic Press, San Diego, 2001.
434. R. Vishwanathan, G. Hou, R. Liu, S. R. Bare, G. Modica, G. Mickelson, C. U. Segre, N. Keyarowska, and E. S. Smotkin, *J. Phys. Chem. B* 106, 3458 (2002).
435. K. Ebitani, K. M. Choi, T. Mizugaki, and K. Kaneda, *Langmuir* 18, 1849 (2002).
436. H. Ibach, *Surface Sci. Rep.* 29, 194 (1997).
437. R. W. Cahn, *Nature* 348, 389 (1990).
438. R. Dagani, *Chem. Eng. News* 72, 18 (1992).
439. H. Gleiter, *Nanostruct. Mater.* 6, 3 (1995).
440. D. Chakravorty and A. K. Giri, in "Chemistry for the 21st Century: Chemistry of Advanced Materials" (C. N. R. Rao, Ed.), p. 217. Blackwell Scientific, London, 1993.
441. P. Pawlow, *Z. Phys. Chem.* 65, 1 (1909).
442. D. J. Wales and R. S. Berry, *J. Chem. Phys.* 92, 4473 (1990).
443. K. Hoshino and S. A. Shimamura, *Philos. Mag. A* 40, 137 (1979).
444. J. Ross and R. P. Andres, *Surf. Sci.* 106, 11 (1981).
445. A. Maiti and L. M. Falicov, *Phys. Rev. A* 45, 6918 (1992).
446. S. Valkealahti and M. Manninen, *Z. Phys. D* 26, 255 (1993).
447. F. Ercolessi, W. Andreoni, and E. Tosatti, *Phys. Rev. Lett.* 66, 911 (1991).
448. I. L. Garzon and J. Jellinek, *Z. Phys. D* 20, 235 (1991).
449. Z. X. Cai, S. D. Mahanti, A. Antonelli, S. N. Khanna, and P. Jena, *Phys. Rev. B* 46, 7841 (1992).
450. H. S. Lim, C. K. Ong, and F. Ercolessi, *Z. Phys. D* 26, S45 (1993).
451. Z. B. Güvenc and J. Jellinek, *Z. Phys. D* 26, 304 (1993).
452. J. W. Christian, "The Theory of Transformations in Metals and Alloys." Pergamon, New York, 1975.
453. A. R. Ubbelohde, "The Molten State of Matter." Wiley, New York, 1978.
454. J. G. Dash, *Contemp. Phys.* 30, 89 (1989).
455. M. Faraday, *Faraday's Diary Bell, London* (1933).
456. I. N. Stranski, *Naturwissenschaften* 28, 425 (1942).
457. P. Z. Pawlow, *Z. Phys. Chem. Abt. A* 65, 545 (1909).
458. H. Reiss and I. B. Wilson, *J. Colloid Sci.* 3, 551 (1948).
459. P. R. Couchman and W. A. Jesser, *Nature (London)* 269, 481 (1977).
460. R. W. Cahn, *Nature (London)* 32, 3 (1986).
461. J. W. M. Frenken and J. F. van der Veen, *Phys. Rev. Lett.* 54, 134 (1985).
462. B. Pluis, A. W. D. van der Gon, J. W. M. Frenken, and J. F. van der Veen, *Phys. Rev. Lett.* 59, 2678 (1987).
463. B. Pluis, A. W. D. van der Gon, J. F. van der Veen, and A. J. Riemersma, *Surf. Sci.* 239, 265 (1990).
464. L. J. Lewis, P. Jensen, and J. L. Barrat, *Phys. Rev. B* 56, 2248 (1997).
465. F. Ercolessi, W. Andreoni, and E. Tosatti, *Phys. Rev. Lett.* 66, 911 (1991).
466. H. Fujiwara, S. Yanagida, and P. V. Kamat, *J. Phys. Chem. B* 103, 2589 (1999).
467. S. Link, Z. L. Wang, and M. A. El-Sayed, *J. Phys. Chem. B* 103, 3529 (1999).
468. S. Link, Z. L. Wang, and M. A. El-Sayed, *J. Phys. Chem. B* 104, 7867 (2000).
469. K. F. Peters, J. B. Cohen, and Y. W. Chung, *Phys. Rev. B* 57, 13430 (1998).
470. S. P. Huang and P. B. Balbuena, *J. Phys. Chem. B* 106, 7225 (2002).
471. J. E. Martin, J. Odinek, J. P. Wilcoxon, R. A. Anderson, and P. Provencio, *J. Am. Chem. Soc.* 107, 430 (2003).
472. A. A. Shvartsburg and M. F. Jarrold, *Phys. Rev. Lett.* 85, 2530 (2000).
473. C. L. Cleveland, W. D. Luedtke, and U. Landman, *Phys. Rev. B* 60, 5065 (1999).
474. T. Shibata, H. Tostmann, B. Bunker, A. Henglein, D. Meisel, S. Cheong, and M. Boyanov, *J. Synchrotron Radiat.* 8, 545 (2001).
475. C. Chen, O. Kitakami, S. Okamoto, and Y. Shimada, *Appl. Phys. Lett.* 76, 3218 (2000).
476. O. Kitakami, Y. Shimada, K. Oikawa, H. Daimon, and F. Fukamichi, *Appl. Phys. Lett.* 78, 1104 (2001).
477. T. Maeda, T. Kai, A. Kikitsu, T. Nagase, and Akiyama, *J. Appl. Phys. Lett.* 80, 2147 (2002).
478. G. C. Papavassiliou, *J. Phys. F: Metal Phys.* 6, L103 (1976).
479. J. Sinzig, U. Radtke, M. Quinten, and U. Kreibig, *Z. Phys. D* 26, 242 (1993).
480. L. M. Liz-Marzan and A. P. Philipse, *J. Phys. Chem.* 99, 15120 (1995).
481. B. K. Teo, K. Keating, and Y. H. Kao, *J. Am. Chem. Soc.* 109, 3494 (1987).
482. P. Mulvaney, M. Giersig, and A. Henglein, *J. Phys. Chem.* 97, 7061 (1993).
483. T. Sato, S. Kuroda, A. Takami, Y. Yonezawa, and H. Hada, *Appl. Organomet. Chem.* 5, 261 (1991).
484. G. Mie, *Ann. Phys.* 25, 377 (1908).
485. P. Mulvaney, *Langmuir* 12, 788 (1996).
486. K. Torigoe, Y. Nakajima, and K. Esumi, *J. Phys. Chem.* 97, 8304 (1993).
487. P. V. Radovanovic, N. S. Norberg, K. E. McNally, and D. R. Gamelin, *J. Am. Chem. Soc.* 124, 15192 (2002).
488. R. Jin, G. Wu, Z. Li, C. A. Mirkin, and G. C. Schatz, *J. Am. Chem. Soc.* 125, 1643 (2003).
489. J. J. Storhoff, A. A. Lazarides, R. C. Mucic, C. A. Mirkin, R. L. Letsinger, and G. C. Schatz, *J. Am. Chem. Soc.* 122, 4640 (2000).
490. D. Fenske and H. Krautscheid, *Angew. Chem. Int. Ed. Engl.* 29, 1452 (1990).
491. M. Kappes, *Chem. Rev.* 88, 369 (1998).
492. A. H. A. Smit, R. C. Thiel, L. J. de Jongh, G. Schmid, and N. Klein, *Solid State Commun.* 65, 915 (1988).
493. M. A. Marcus, M. P. Andrews, J. Zegenhagen, A. S. Bommanavar, and P. Montano, *Phys. Rev. B* 42, 3312 (1990).
494. H. Zhang, G. Schmid, and U. Hartmann, *Nano Lett.* 3, 305 (2003).
495. H. Tanaka, S. Neukermans, E. Janssens, R. E. Silverans, and P. Lievens, *J. Am. Chem. Soc.* (2003).
496. C. Larpent, F. Brisse-le-Menn, and H. Patin, *J. Mol. Catal.* 65, 35 (1991).
497. I. I. Moiseev, G. A. Tsirkov, A. E. Gekhman, and M. N. Vargaftik, *Mendelev Commun.* 1 (1997).
498. M. N. Vargaftik, N. Y. Kozitsyna, N. V. Cherkashina, R. I. Rudyi, D. I. Kochubei, B. N. Novgorodov, and I. I. Moiseev, *Kinetics Catal.* 39, 740 (1998).
499. K. Ebitani, K. M. Choi, T. Mizugaki, and K. Kaneda, *Langmuir* 18, 1849 (2002).
500. J. D. Aiken III, Y. Lin, and R. G. Finke, *J. Mol. Catal. A* 114, 29 (1996).
501. J. D. Aiken III and R. G. Finke, *J. Am. Chem. Soc.* 121, 8803 (1999).

502. M. T. Reetz, S. A. Quaiser, and C. Merk, *Chem. Ber.* 129, 741 (1996).
503. H. Bönemann and B. Korall, *Angew. Chem. Int. Ed. Engl.* 31, 1490 (1992).
504. H. Bönemann and W. Brijoux, *Nanostruct. Mater.* 5, 135 (1995).
505. M. T. Reetz, R. Breinbauer, and K. Wanninger, *Tetrahedron Lett.* 37, 4499 (1996).
506. M. Beller, H. Fischer, K. Kühlein, C. P. Reisinger, and W. A. Herrmann, *J. Organomet. Chem.* 520, 257 (1996).
507. M. T. Reetz and E. Westermann, *Angew. Chem. Int. Ed.* 39, 165 (2000).
508. J. Walter, J. Heiermann, G. Dyker, S. Hara, and H. Shioyama, *J. Catal.* 189, 449 (2000).
509. M. T. Reetz, R. Breinbauer, P. Wedemann, and P. Binger, *Tetrahedron* 54, 1233 (1998).
510. M. Ohtaki, N. Toshima, M. Komiyama, and H. Hirai, *Bull. Chem. Soc. Jpn.* 63, 1433 (1990).
511. M. Antonietti, E. Wenz, L. Bronstein, and M. Seregina, *Adv. Mater.* 7, 1000 (1995).
512. M. V. Seregina, L. M. Bronstein, O. A. Platonova, D. M. Chernyshov, P. M. Valetsky, J. Hartmann, E. Wenz, and M. Antonietti, *Chem. Mater.* 9, 923 (1997).
513. S. Förster, *Ber. Bunsen-Ges.* 101, 1671 (1997).
514. A. B. R. Mayer, *Mater. Sci. Eng. C* 6, 155 (1998).
515. N. Toshima, *Supramol. Sci.* 5, 395 (1998).
516. N. Toshima, T. Yonezawa, and K. Kushihashi, *J. Chem. Soc., Faraday Trans.* 89, 2537 (1993).
517. N. Toshima and Y. Wang, *Langmuir* 10, 4574 (1994).
518. N. Toshima and T. Yonezawa, *Makromol. Chem. Macromol. Symp.* 59, 281 (1992).
519. V. Chechik and R. M. Crooks, *J. Am. Chem. Soc.* 122, 1243 (2000).
520. G. Schmid, S. Emde, V. Maihack, W. M. Zaika, and S. Peschel, *J. Mol. Catal. A* 107, 95 (1996).
521. J. A. Widegren and R. G. Finke, *J. Mol. Catal. A: Chem.* 191, 187 (2003).
522. A. Freund and P. Panster, EP 715 889 A2, 1995.
523. G. Witek, M. Noeske, G. Mestl, S. Shaikhutdinov, and R. J. Behm, *Catal. Lett.* 37, 35 (1996).
524. S. K. Shaikhutdinov, F. A. Möller, G. Mestl, and R. J. Behm, *J. Catal.* 163, 492 (1996).
525. M. T. Reetz, S. A. Quaiser, R. Breinbauer, and B. Tesche, *Angew. Chem. Int. Ed. Engl.* 34, 2728 (1995).
526. T. Teranishi, K. Nakata, M. Miyake, and N. Toshima, *Chem. Lett.* 277 (1996).
527. H. Bönemann, W. Wittholt, J. D. Jentsch, and A. S. Tilling, *New J. Chem.* 22, 713 (1998).
528. X. Yang and H. Liu, *Appl. Catal. A: General* 164, 197 (1997).
529. W. Yu, H. Liu, X. An, X. Ma, Z. Liu, and L. Qiang, *J. Mol. Catal. A* 147, 73 (1999).
530. H. Feng and H. Liu, *J. Mol. Catal. A: Chem.* 126, L5 (1997).
531. T. Hanaoka, T. Matsuzaki, and Y. Sugi, *J. Mol. Catal. A* 149, 161 (1999).
532. J. H. Sinfelt, *Acc. Chem. Res.* 20, 134 (1987).
533. J. H. Sinfelt, G. H. Via, and F. W. Lytle, *J. Chem. Phys.* 72, 4832 (1980).
534. J. H. Sinfelt, G. H. Via, and F. W. Lytle, *J. Chem. Phys.* 75, 5527 (1981).
535. G. Schmid, A. Lehnert, J. O. Malm, and J. O. Bovin, *Angew. Int. Ed. Engl.* 30, 874 (1991).
536. H. Bönemann, W. Brijoux, J. Richter, R. Becker, J. Hormes, and J. Rothe, *Z. Naturforsch.* 50b, 333 (1995).
537. L. E. Aleandri, H. Bönemann, D. J. Jones, J. Richter, and J. Rozière, *J. Mater. Chem.* 5, 749 (1995).
538. N. Toshima, in "Fine Particles Science and Technology" (E. Pelizzetti, Ed.), p. 371. Kluwer Academic, Dordrecht, 1996.
539. M. Harada, K. Asakura, and N. Toshima, *J. Phys. Chem.* 98, 2653 (1994).
540. B. J. Joice, J. J. Rooney, P. B. Wells, and G. R. Wilson, *Disc. Faraday Soc.* 41, 223 (1966).
541. J. Schwank, *Gold Bull.* 18, 2 (1985).
542. W. Juszczak, Z. Karpinski, D. Lomot, J. Pielaszek, and J. W. Sobczak, *J. Catal.* 151, 67 (1995).
543. A. O. Cinneide and J. K. A. Clarke, *J. Catal.* 26, 233 (1972).
544. S. H. Inami and W. Wise, *J. Catal.* 26, 92 (1972).
545. C. Visser, I. G. P. Zuidwijk, and V. Ponc, *J. Catal.* 35, 407 (1974).
546. N. Toshima, *J. Macromol. Sci. A* 27, 1225 (1990).
547. A. O. Cinneide and F. G. Gault, *J. Catal.* 37, 311 (1975).
548. N. Toshima, H. Harada, Y. Yamazaki, and K. Asakura, *J. Phys. Chem.* 96, 927 (1992).
549. H. Liu, C. Mao, and S. Meng, *J. Mol. Catal.* 74, 275 (1992).
550. S. Gonzalez, C. Sousa, M. F. Garcia, V. Bertin, and F. Illas, *J. Phys. Chem. B.* 106, 7839 (2002).
551. J. B. Michel and J. T. Schwartz, in "Catalyst Preparation Science IV" (B. Delmon, P. Grange, P. A. Jacobs, and G. Poncelet, Eds.), p. 669. Elsevier, New York, 1987.
552. G. Schmid, H. West, H. Mehles, and A. Lehnert, *Inorg. Chem.* 36, 891 (1997).
553. N. Toshima, T. Takahashi, and H. Hirai, *J. Macromol. Sci. Chem. A* 25, 669 (1988).
554. M. Ohtati, M. Komiyama, H. Hirai, and N. Toshima, *Macromolecules* 24, 5567 (1991).
555. G. Schmid, V. Maihack, F. Lantermann, and S. Peschel, *J. Chem. Soc. Dalton Trans.* 591 (1996).
556. H. Bönemann, W. Brijoux, A. Schulze Tilling, and K. Siepen, *Topics Catal.* 4, 217 (1997).
557. H. Bönemann, P. Britz, and H. Ehwald, *Chem. Technik* 49, 189 (1997).
558. H. Bönemann and G. A. Braun, *Chem. Eur. J.* 3, 1200 (1997).
559. J. U. Köhler and J. S. Bradley, *Catal. Lett.* 45, 203 (1997).
560. J. U. Köhler and J. S. Bradley, *Langmuir* 14, 2730 (1998).
561. X. Zuo, H. Liu, and M. Liu, *Tetrahedron Lett.* 39, 1941 (1998).
562. X. Zuo, H. Liu, D. Guo, and X. Yang, *Tetrahedron* 55, 7787 (1999).
563. H. Bönemann, R. Brinkmann, and P. Neiteler, *Appl. Organomet. Chem.* 8, 361 (1994).
564. H. Bönemann, W. Brijoux, R. Brinkmann, A. Schulze Tilling, T. Schilling, B. Tesche, K. Seevogel, R. Franke, J. Hormes, G. Köhl, J. Pollmann, J. Rothe, and W. Vogel, *Inorg. Chim. Acta* 270, 95 (1998).
565. L. Djakovitch, M. Wagner, and K. Köhler, *J. Organomet. Chem.* 592, 225 (1999).
566. T. H. Galow, U. Drechsler, J. A. Hanson, and V. M. Rotello, *Chem. Commun.* 1076 (2002).
567. J. L. Bars, U. Specht, J. S. Bradley, and D. G. Blackmond, *Langmuir* 15, 7621 (1999).
568. S. W. Kim, M. Kim, W. Y. Lee, and T. Hyeon, *J. Am. Chem. Soc.* 124, 7642 (2002).
569. R. M. Crooks, M. Zhao, L. Sun, V. Chechik, and L. K. Yeung, *Acc. Chem. Res.* 34, 181 (2001).
570. Y. Li and M. A. El-Sayed, *J. Phys. Chem. B* 105, 8938 (2001).
571. G. Ihlein, B. Junges, U. Junges, F. Laeri, F. Schüth, and U. Vietze, *Appl. Organometallic Chem.* 12, 305 (1998).
572. M. T. Reetz and M. Dugal, *Catal. Lett.* 58, 207 (1999).
573. H. Bönemann, U. Endruschat, B. Tesche, A. Rufinska, C. W. Lehmann, F. E. Wagner, G. Filoti, V. Pärvulescu, and V. I. Pärvulescu, *Eur. J. Chem.* 819 (2000).
574. J. P. M. Niederer, A. B. J. Arnold, W. F. Hölderich, B. Spielthof, B. Tasche, M. Reetz, and H. Bönemann, *Topics Catal.* 18 (2002).
575. S. Oprescu, C. Parvulescu, A. Petride, M. D. Banciu, and V. I. Parvulescu, *J. Mol. Catal. A: Chem.* 186, 153 (2002).
576. P. D. Dissanayake and J. H. Lunsford, *J. Catal.* 206, 173 (2002).
577. A. Roucoux, J. Schulz, and H. Patin, *Chem. Rev.* 102, 3757 (2002).
578. K. Kordesch and G. Simader, "Fuel Cells and their Applications." VCH, Weinheim, 1996.
579. H. G. Petrow and R. J. Allen, U.S. Patent 4, 044, 193, 1977.

580. G. T. Burstein, C. J. Barnett, A. R. Kucernak, and K. R. Williams, *Catal. Today* 38, 425 (1997).
581. E. Auer, A. Freund, T. Lehmann, K. A. Starz, R. Schwarz, and U. Stenke, EP 0 880 188 A2, 1998.
582. M. S. Wilson and S. Gottesfeld, *J. Appl. Electrochem.* 22, 1 (1992).
583. M. S. Wilson, X. Ren, and S. Gottesfeld, *J. Electrochem. Soc.* 143, L12 (1996).
584. S. C. Thomas, X. Ren, and S. Gottesfeld, *J. Electrochem. Soc.* 146, 4354 (1999).
585. G. J. K. Acres, J. C. Frost, G. A. Hards, R. J. Potter, T. R. Ralph, D. Thompsett, G. T. Burstein, and G. J. Hutchings, *Catal. Today* 38, 393 (1997).
586. R. G. Cawthorn, *South Afr. J. Sci.* 95, 481 (1999).
587. Information available from "World Fuel Cell Council" e.V., Kroegerstrasse 5, D-60313 Frankfurt.
588. R. F. Service, *Science* 285, 682 (1999).
589. D. S. Cameron, *Platinum Metals Rev.* 43, 149 (1999).
590. F. J. Luczak and D. A. Landsman, U.S. Patent 4, 613, 582, 1986.
591. W. Wittholt, Ph.D. Thesis, RWTH Aachen, 1997.
592. H. Wendt and M. Götz, EP 0951 084 A2, 1999.
593. A. Freund, J. Lang, T. Lehmann, and K. A. Starz, *Catal. Today* 27, 279 (1996).
594. U. Paulus, U. Endruschat, G. Feldmeyer, T. Schmidt, H. Bönne-mann, and R. Behm, *J. Catal.* 195, 383 (2000).
595. L. Li, P. Cong, R. Vishwanathan, F. Qinbai, L. Renxuan, and E. S. Smotkin, *Electrochim. Acta* 43, 3657 (1998).
596. H. Bönne-mann, in "Extended Abstracts of the 3rd International Symposium on New Materials for Electrochemical Systems" (O. Savadogo, Ed.). École Polytechnique de Montréal, Canada, 1999.
597. H. Bönne-mann, R. Brinkmann, P. Britz, U. Endruschat, R. Mörtel, U. A. Paulus, G. J. Feldmeyer, T. J. Schmidt, H. A. Gasteiger, and R. J. Behm, *J. New Mat. Electrochem. Syst.* 3, 199 (2000).
598. T. Itoh and J. Sato, EP 0 952 241, 1999.
599. S. Narayanan, S. Surampudi, and G. Halpert, U.S. Patent 5, 945, 231, 1999.
600. T. J. Schmidt, H. A. Gasteiger, and R. J. Behm, *J. Electrochem. Soc.* 146, 1296 (1999).
601. S. Mukerjee and R. C. Urian, *Electrochim. Acta* 47, 3219 (2002).
602. A. Pozio, R. F. Silva, M. D. Francesco, F. Cardellini, and L. Giorgi, *Electrochim. Acta*, 48, 255 (2002).
603. L. Xiong, A. M. Kannan, and A. Manthiram, *Science* 4, 898 (2002).
604. W. Vogel, P. Britz, H. Bönne-mann, J. Rothe, and J. Hormes, *J. Phys. Chem. B* 101, 11029 (1997).
605. U. Stimming and R. Vogel, in "Electrochemical Nanotechnology" (W. J. Lorenz and W. Plieth, Eds.), p. 73. Wiley-VCH, Weinheim, 1998.
606. J. R. Giallombardo and E. S. De Castro, WO 99/53557, 1999.
607. E. Reddington, A. Sapienza, B. Gurau, R. Viswanathan, S. Sarangapani, E. S. Smotkin, and T. E. Mallouk, *Science* 280, 1735 (1998).
608. A. V. Tripkovic, K. D. Popovic, B. N. Grgur, B. Blizanac, P. N. Ross, and N. M. Markovic, *Electrochim. Acta* 47, 3707 (2002).
609. E. S. Steigerwalt, G. A. Deluga, and C. M. Lukehart, *J. Phys. Chem. B* 106, 760 (2002).
610. D. L. Boxall, G. A. Deluga, E. A. Kenik, W. D. King, and C. M. Lukehart, *Chem. Mater.* 13, 891 (2001).
611. P. Waszczuk, J. S. Gullon, H. S. Kim, Y. Y. Tong, V. Montiel, A. Aldaz, and A. Wieckowski, *J. Catal.* 203, 1 (2001).
612. S. Park, Y. Xie, and M. J. Weaver, *Langmuir* 18, 5792 (2002).
613. S. E. Steigerwalt, G. A. Deluga, D. E. Cliffel, and C. M. Lukehart, *J. Phys. Chem. B* 105, 8097 (2001).
614. A. Freund, T. Lehmann, K. A. Starz, G. Heinz, and R. Schwarz, EP 0 743 092 A1, 1996.
615. G. Hornyak, M. Kröll, R. Pugin, Th. Sawitowski, G. Schmid, J. O. Bovin, G. Karsson, H. Hofmeister, and S. Hopfe, *Chem. Eur. J.* 3, 1951 (1997).
616. T. Hanaoka, H. P. Kormann, M. Kröll, T. Sawitowski, and G. Schmid, *Eur. J. Inorg. Chem.* 807 (1998).
617. G. Schmid, *J. Chem. Soc. Dalton Trans.* 1077 (1998).
618. A. P. Alivisatos, K. P. Johnson, X. Peng, T. E. Wilson, C. J. Loweth, M. P. Burcher, Jr., and P. G. Schultz, *Nature* 382, 609 (1996).
619. C. N. R. Rao, G. U. Kulkarni, and P. J. Thomas, *Chem. Soc. Rev.* 29, 27 (2000).
620. S. Chen, *Adv. Mater.* 12, 186 (2000).
621. A. K. Kakkar, *Chem. Rev.* 102, 3579 (2002).
622. M. Sastry, A. Gole, and S. R. Sainkar, *Langmuir* 16, 3553 (2000).
623. T. Teranishi, M. Haga, Y. Shiozawa, and M. Miyake, *J. Am. Chem. Soc.* 122, 4237 (2000).
624. C. C. Hsueh, M. T. Lee, M. S. Freund, and G. S. Ferguson, *Angew. Chem. Int. Ed.* 39, 1228 (2000).
625. H. X. He, H. Zhang, Q. G. Li, and Z. F. Liu, *Langmuir* 16, 3846 (2000).
626. A. K. Boal, F. Illhan, J. E. DeRouche, T. Thurn-Albrecht, T. P. Russell, and V. M. Rotello, *Nature* 404, 746 (2000).
627. G. Schmid, W. M. Zaika, R. Pugin, T. Sawitowski, J. P. Majoral, A. M. Caminade, and C. O. Turrin, *Chem. Eur. J.* 6, 1693 (2000).
628. T. C. Rojas, J. M. de la Fuente, A. G. Barrientos, S. Penades, L. Ponsonnet, and A. Fernandez, *Adv. Mater.* 14, 585 (2002).
629. J. M. de la Fuente, A. G. Barrientos, T. C. Rojas, J. Rojo, J. Canada, A. Fernandez, and S. Penades, *Angew. Chem. Int. Ed.* 40, 2257 (2001).
630. J. Fink, C. J. Kiely, D. Bethell, and D. J. Schiffrin, *Chem. Mater.* 10, 922 (1998).
631. L. Rasmus, T. Lubensky, N. Dan, P. Nelson, and D. Weitz, *Science* 286, 235 (1988).
632. J. Eversole and H. P. Broida, *Phys. Rev. B* 15, 1644 (1977).
633. C. Petit, A. Taleb, and M. P. Pileni, *Adv. Mater.* 10, 259 (1998).
634. C. Petit, T. Cren, D. Roditchev, W. Sacks, J. Klein, and M. P. Pileni, *Adv. Mater.* 11, 1198 (1999).
635. J. Legrand, A. Ngo, C. Petit, and M. Pileni, *Adv. Mater.* 13, 58 (2001).
636. A. Ngo and M. Pileni, *J. Phys. Chem. B* 105, 53 (2001).
637. M. Maillard, L. Motte, A. Ngo, and M. Pileni, *J. Phys. Chem. B* 104, 11871 (2000).
638. L. Marzan and P. Mulvaney, *Recent Res. Dev. Phys. Chem.* 2, 1 (1998).
639. A. C. Balazs, V. V. Ginzburg, F. Qiu, G. Peng, and D. Jasnow, *J. Phys. Chem. B* 104, 3411 (2000).
640. H. Fan, Y. Lu, A. Stump, S. T. Reed, T. Baer, R. Schunk, V. P. Luna, G. P. Lopez, and C. J. Brinker, *Nature* 405, 56 (2000).
641. G. Schmid, M. Bäumle, M. Geerkens, I. Heim, C. Osemann, and T. Sawitowski, *Chem. Soc. Rev.* 28, 179 (1999).
642. K. V. Sarathy, P. J. Thomas, G. U. Kulkarni, and C. N. R. Rao, *J. Phys. Chem. B* 103, 399 (1999).
643. H. Fan, Y. Zhou, and G. P. Lopez, *Adv. Mater.* 9, 728 (1997).
644. S. Liu, R. Maoz, G. Schmid, and J. Sagiv, *Nano Lett.* 2, 1055 (2002).
645. K. C. Beverly, J. F. Sampaio, and J. R. Heath, *J. Phys. Chem. B* 106, 2131 (2002).
646. C. R. Mayer, S. Neveu, and V. Cabuil, *Adv. Mater.* 14, 595 (2002).
647. M. P. Pileni, *J. Phys. Chem. B* 105, 3358 (2001).
648. R. R. Bhat, D. A. Fischer, and J. Genzer, *Langmuir* 18, 5640 (2002).
649. R. Paulini, B. L. Frankamp, and V. M. Rotello, *Langmuir* 18, 2368 (2002).
650. Y. Jin and S. Dong, *Angew. Chem.* 114, 1082 (2002).
651. Y. Lu, Y. Yin, Z. Y. Li, and Y. Xia, *Nano Lett.* 2, 785 (2002).
652. A. Ivanisevic, K. V. McCumber, and C. A. Mirkin, *J. Am. Chem. Soc.* 124, 11997 (2002).
653. J. Won, K. J. Ihn, and Y. S. Kang, *Langmuir* 18, 8246 (2002).
654. K. A. Stevenson, G. Muralidharan, T. G. Thundat, and E. A. Kenik, *Langmuir* 18, 2392 (2002).
655. O. Vidoni, T. Reuter, V. Torma, W. M. Zaika, and G. Schmid, *J. Mater. Chem.* 11, 3188 (2001).

656. T. Wang, D. Zhang, W. Xu, S. Li, and D. Zhu, *Langmuir* 18, 8655 (2002).
657. S. Cobbe, S. Connolly, D. Ryan, L. Nagle, R. Eritja, and D. Fitzmaurice, *J. Phys. Chem. B* 107, 470 (2003).
658. B. L. Frankamp, A. K. Boal, and V. M. Rotello, *J. Am. Chem. Soc.* 124, 15146 (2002).
659. A. Schroedter and H. Weller, *Angew. Chem. Int. Ed.* 41, 3218 (2002).
660. S. J. Rosenthal, I. Tomlinson, E. M. Adkins, A. Schroeter, S. Adams, L. Swafford, J. McBride, Y. Wang, L. J. DeFelice, and R. D. Blakely, *J. Am. Chem. Soc.* 124, 4586 (2002).
661. Z. Z. Gu, R. Horje, S. Kubo, Y. Yamada, A. Fujishima, and O. Sato, *Angew. Chem.* 114, 1202 (2002).
662. J. L. Dormann and D. Fiorani, Eds., "Magnetic Properties of Fine Particles." North-Holland, Amsterdam, 1992.
663. L. J. deJongh, D. A. van Leeuwen, J. M. van Ruitenbeek, and J. Sinzig, *Nato Aso Ser. C* 484, 615 (1996).
664. R. Hirsch, E. Katz, and I. Willner, *J. Am. Chem. Soc.* 122, 12053 (2000).
665. L. J. de Jongh, J. Sinzig, H. Bönemann, W. Brijoux, and R. Köppler, *Appl. Organomet. Chem.* 12, 387 (1998).
666. Y. Volokitin, J. Sinzig, G. Schmid, H. Bönemann, and L. J. de Jongh, *J. Phys. D: At. Mol. Clusters* 40, 136 (1999).
667. O. A. Platonova, L. M. Bronstein, S. P. Solodovnikov, L. M. Yanovskaya, E. S. Obolonkova, P. M. Valetsky, E. Wenz, and M. Antonietti, *Colloid Polym. Sci.* 275, 426 (1997).
668. M. Respaud, J. M. Broto, H. Rakoto, A. R. Fert, L. Thomas, B. Barbara, M. Verelst, E. Snoeck, P. Lecante, A. Mosset, J. Osuna, T. Ould Ely, C. Amiens, and B. Chaudret, *Phys. Rev. B* 57, 2925 (1998).
669. M. Respaud, J. M. Broto, H. Rakoto, J. C. Ousset, J. Osuna, T. O. Ely, C. Amiens, B. Chaudret, and S. Askenazy, *Physica B* 246–247, 532 (1998).
670. M. Respaud, M. Goiram, J. M. Broto, F. H. Yang, T. O. Ely, C. Amiens, and B. Chaudret, *Phys. Rev. B* 59, R3934 (1999).
671. M. Meza, in "Scientific and Clinical Applications of Magnetic Carriers" (U. Häfeli, W. Schütt, J. Teller, and M. Zborowski, Eds.). Plenum, New York, 1997.
672. W. Andrä and H. Nowak, Eds., "Magnetism in Medicine." Wiley-VCH, Berlin, 1998.
673. E. K. Ruuge and A. N. Rusetski, *J. Mag. Mag. Mater.* 122, 335 (1993).
674. S. Roath, *J. Mag. Mag. Mater.* 122, 329 (1993).
675. D. M. Schulte, F. Füssl, H. Lueken, and M. D. Cuyper, *Alma Mater Aquensis* 31, 174 (1995).
676. J. A. Becker, R. Schaefer, R. Festag, W. Ruland, J. H. Wendorff, J. Pebler, S. A. Quaiser, W. Helbig, and M. T. Reetz, *J. Chem. Phys.* 103, 2520 (1995).
677. G. F. Hohl, S. D. Baranovski, J. A. Becker, F. Hensel, S. A. Quaiser, and M. T. Reetz, *J. Appl. Phys.* 78, 7130 (1996).
678. A. Becker, R. Schaefer, R. Festag, J. H. Wendorff, J. Pebler, S. A. Quaiser, W. Helbig, and M. T. Reetz, *Surf. Rev. Lett.* 3, 1121 (1996).
679. S. Odenbach, Ed., "Ferro Fluids: Magnetically Controllable Fluids and their Applications." Springer, Heidelberg, 2002.
680. N. C. Seeman, *J. Theor. Biol.* 99, 237 (1982).
681. B. H. Robinson, N. C. Seeman, R. C. Mucic, and J. J. Storhoff, *Nature* 382, 607 (1998).
682. C. A. Mirkin, R. L. Letsinger, R. C. Mucic, and J. J. Storhoff, *Nature* 382, 607 (1996).
683. W. J. Parak, T. Pellegrino, C. M. Micheel, D. Gerion, S. C. Williams, and A. P. Alivisatos, *Nano Lett.* 3, 33 (2003).
684. J. J. Storhoff, R. C. Mucic, and C. A. Mirkin, *Chem. Rev.* 99, 1849 (1999).
685. J. J. Storhoff, A. A. Lazarides, R. C. Mucic, C. A. Mirkin, R. L. Letsinger, and G. C. Schatz, *J. Am. Chem. Soc.* 122, 4640 (2000).
686. C. A. Mirkin, *Inorg. Chem.* 39, 2258 (2000).
687. S. Park, A. Lazarides, C. Mirkin, P. Brazis, C. Kannewurf, and R. Letsinger, *Angew. Chem. Int. Ed.* 39, 3845 (2000).
688. T. Taton, R. Mucic, C. Mirkin, and R. Letsinger, *J. Am. Chem. Soc.* 122, 6305 (2000).
689. R. Reynolds, C. Mirkin, and R. Letsinger, *Pure Appl. Chem.* 72, 229 (2000).
690. C. Mirkin and T. Taton, *Nature* 405, 626 (2000).
691. J. Storhoff, A. Lazarides, R. Mucic, C. Mirkin, R. Letsinger, and G. Schatz, *J. Am. Chem. Soc.* 122, 4640 (2000).
692. C. Mirkin, *Science* 286, 2095 (1999).
693. C. M. Niemeyer, *Angew. Chem. Int. Ed. Engl.* 36, 585 (1997).
694. C. M. Niemeyer, W. Bürger, and J. Peplies, *Angew. Chem. Int. Ed. Engl.* 37, 2265 (1998).
695. C. M. Niemeyer, *Appl. Phys. A* 68, 119 (1999).
696. E. Braun, Y. Eichen, U. Sivan, and G. B. Yoseph, *Nature* 391, 775 (1998).
697. C. M. Niemeyer and M. Adler, *Angew. Chemie Int. Ed. Engl.* 41, 3779 (2002).
698. J. W. Slot and H. J. Geuze, *J. Cell Biol.* 90, 533 (1981).

Chemically Prepared Magnetic Nanoparticles

M. A. Willard, L. K. Kurihara, E. E. Carpenter, S. Calvin, V. G. Harris

Naval Research Laboratory, Washington, DC, USA

CONTENTS

1. Introduction
 2. Applications
 3. Chemical Syntheses
 4. Structural Characterization
 5. Magnetic Properties of Nanoparticles
 6. Conclusions
- Glossary
References

1. INTRODUCTION

Interest in nanoparticle science and technology in the United States and abroad has experienced resurgence over the last 10 years largely spurred by the Presidential Nanoscience Initiative that was sponsored by both the Clinton and Bush administrations and their increased utility in a broad range of application.

Nanoparticles are typically defined as being less than 100 nm in all three dimensions. More often, they are particles made to be spherical having diameters on the order of 10 nm or less. At these length scales, a large fraction of the particle's atoms are at or near the surface providing them with unique properties. In the case of magnetic nanoparticles, crystal symmetry breaking at the surface has profound ramifications. For example, in metallic alloys the surface atoms oxidize quickly, forming oxides that are typically ferrimagnetic or in some cases antiferromagnetic. If the metallic alloy is not prone to oxidation, then there typically exists a magnetic "dead" layer at the surface of the particle. Atoms in the dead layer do not have enough magnetic neighbors in their first and second coordination sphere to support long-range ferromagnetism. Alternatively, the surfaces of magnetic oxide particles often experience bond bending through surface relaxation. The magnetism in oxide systems stems from double-exchange and/or superexchange interactions, both of which are very sensitive to the bond angles

that form between cation-anion-cation arrangements. Surface bond-bending in these cases leads to profound changes in the magnetic interactions, in some instances changing its behavior from ferromagnetism to antiferromagnetism or to a spin glass-like behavior. This surface relaxation has been linked to surface spin canting and spin disorder [1] which cause anomalously large magnetic anisotropy that requires very large fields to attain magnetic saturation.

In order to design magnetic nanoparticles for specific applications, one is challenged by the need to understand the atomic structure of the particle, surface structure, and its magnetic structure or spin dynamics. Specifically, for metallic nanoparticles, this includes understanding atomic symmetry and chemistry of the interior atoms and surface atoms, as well as the dynamics of both interior and surface spins. In addition, for the case of oxide nanoparticles, the surface energy and synthesis methodology may also lead to the stabilization of defects. All of these issues become more difficult to ascertain as the particle diameter is reduced, whereupon traditional characterization tools like X-ray diffraction and electron microscopy have only limited utility.

The goal of the present work is to provide a broad review of magnetic nanoparticle research that has been carried out during the past decade. We focus on chemical synthesis methods for producing magnetic nanoparticles, methods of effectively characterizing said particles, and finally a review of the magnetic nature of these nanoparticles.

2. APPLICATIONS

Magnetic nanoparticles have a wide range of uses in many diverse applications. These applications make use of magnetic nanoparticles in a variety of forms; for example, in solution as ferrofluids for audio speakers; as surface functionalized particles for biosensing applications [2]; as particle arrays in magnetic storage media [3]; as powder compacts for power generation, conditioning and conversion; in medical applications including magnetic-targeted drug delivery, contrasting agents in magnetic resonance imaging, and alternatives to radioactive materials as tracers.

2.1. Ferrofluids

A ferrofluid consists of surfactant-coated magnetic nanoparticles in a liquid host that forms a stable colloidal suspension. A typical ferrofluid has only 5 volume percent of magnetic particles, 10 volume percent surfactant, and the balance is the carrier liquid. The particles are coated with a surfactant that disperses the particles and prevents agglomeration by overcoming the local magnetic fields and van der Waals forces that exist between particles. As a result, when the ferrofluid is not in the presence of an external magnetic field it has no net magnetization. However, when a magnetic field is applied to the solution, the particles spontaneously orient with respect to and along the magnetic flux lines. When the field is removed, the particles again disperse randomizing their orientation and establishing a state of no net magnetization. Since the ferrofluid is sensitive to external fields, the particles can be positioned and controlled by fields with the forces holding the particles in place proportional to the applied field strength and the magnetization of the particles. These unique properties make ferrofluids useful in seals, bearings, dampers, stepping motors, loudspeakers, and sensors [4].

2.2. Magnetic Recording Media

It has recently been shown that surfactant-coated magnetic nanoparticles can self-assemble into periodic arrays. The equal spacing of the particles allow them to be considered for next generation magnetic storage materials as individually addressable bits. One example of this new material is the array of FePt nanoparticles created by researchers at IBM [3]. In this case, FePt monodispersed nanoparticles were processed by reduction of platinum acetylacetonate and decomposition of iron pentacarbonyl in the presence of oleic acid and oleyl amine stabilizers. The particles self-assemble into a disordered FCC particle lattice, whereas a heat treatment provides a chemically ordered tetragonal lattice of particles. The crucial properties for media applications is that the particles be monodispersed with a very tight size distribution of <10% and a high magnetocrystalline anisotropy. IBM is considering this form of media that may hold 100 times more data than today's products [5].

2.3. Power Generation, Conversion, and Conditioning

High frequency (*i.e.*, $f > 1\text{MHz}$) electronic components, including switch mode power supplies, filters for power conditioning, and power converters, typically use ferrite cores. Ferrites are desirable since they are insulating magnetic oxides with high electrical resistance that minimizes conduction-related losses. These cores are made by compaction of ferrite particles. Typically, these particles have diameters on the order of microns and are processed using chemical reduction methods followed by mixing, firing, compaction, and sintering. Recently, nanoparticle ferrites have been considered for these applications. Benefits of using nanoparticles include lower heat treatment temperatures, fewer processing steps, and in some instances, improved performance. Difficulties in the use of nanoparticle ferrites

include understanding cation disorder and the role of processing and surfaces. In addition, the compaction of nanoparticles to near their theoretical densities is very difficult and remains one of the major obstacles that are limiting the wide scale acceptance of nanoparticle ferrites.

2.4. Targeted Drug Delivery

It is well known that chemotherapy is an effective treatment to fight cancer cells, but since it is delivered as a full body dose, the side effects of its toxicity are often severe and devastating to the patient. One proposed use of magnetic nanoparticles that is particularly exciting is for targeted drug delivery. In this application, the magnetic particle is coated with activated carbon and serves to deliver pharmaceuticals to specific sites. In practice, the administered drug is absorbed to the particle and is localized to a specific site in the body by an external magnetic field. The physical force created by the external magnetic field acts to transport the particles through the vascular wall, thus positioning and retaining the drugs in close proximity to the cancer cells. This allows for more concentrated doses of the anti-cancer drugs to be delivered to the cancer and keep them on site for longer periods of time. This targeted drug therapy was in phase I and II trials as of June 2000 [6].

Magnetic nanoparticle for targeted drug delivery must be tailor-made for *in vivo* applications. In order to prevent dangerous agglomeration of the particles in the blood stream, the particles must be of a small size relative to dimensions of the capillaries, spherical in shape, and have a size distribution (*i.e.*, standard deviation) or less than 15%. In addition, the particles must have a high magnetic moment and switch their magnetization quickly and at low fields [7].

In this chapter, we discuss the chemical synthesis methods that are used in processing monodispersed magnetic nanoparticles (Section 3), characterization tools that allow one to determine the structure and phase of the nanoparticles (Section 4), and finally the magnetic nature of fine particles (Section 5). We limit our scope to 1990 to the present and make reference to other reviews predating this period where appropriate.

3. CHEMICAL SYNTHESSES

Three approaches are most often used to produce magnetic nanoparticles. These include physical vapor deposition, mechanical attrition, and chemical routes from solution. In both the vapor phase and solution routes, the particles are assembled from individual atoms to form nanoparticles. Alternatively, mechanical attrition involves the fracturing of larger coarse-grained materials to form nanostructures.

In this section, an overview of the chemical synthesis and processing of nanostructured particles is presented. Chemical routes often provide the best method for production of nanoparticles. Solution chemistry techniques offer the advantages of enhanced homogeneity due to molecular level design of the materials and, in many cases, cost-effective bulk quantity production. Solution chemical routes also allow control of particle size and size distribution, morphology, and agglomerate size through the manipulation of the

parameters that determine nucleation, growth, and coalescence. Surface modification of the particles during synthesis or post-synthesis is easily accomplished, providing additional functionality to the nanoparticles.

The synthesis of particles in a solution occurs by chemical reactions forming stable nuclei with subsequent particle growth. This phenomenon of precipitation of solids in solution has been well-studied [8, 9]. Upon the addition of precipitating, reducing, or oxidizing reagents to the solution containing the reactants, chemical reactions occur and the solution becomes supersaturated. Supersaturation drives the chemical system far past the minimum free-energy configuration for the precipitating species in solution. The thermodynamically equilibrated state is restored by condensation of nuclei of the reaction product.

Kinetic factors control the dynamics of approach to the thermodynamic equilibrium of the system in the growth process [10, 11]. These factors include reaction rates, transport rates of reactants, removal and redistribution of matter. The reaction and transport rates are affected by the temperature, pH, and mixing of the solution, as well as the concentration of reactants and the order in which the reagents are added to the solution. Reaction rates and impurities can influence the structure and crystallinity of the particle. The particle morphology is influenced by factors such as supersaturation, colloidal stability, nucleation and growth rates, recrystallization, and aging times. Generally, supersaturation has a dominant role in determining the morphology of precipitates. At low supersaturation, the particles are small with shape depending on crystal structure, composition, and surface energies. As the level of supersaturation is increased, larger, dendritic particles form. Finally, at high supersaturation levels, smaller but compacted, agglomerated particles form [10].

In a supersaturated solution when the nuclei form at nearly the same time, subsequent growth of these nuclei results in formation of particles with a very narrow size distribution [12]. This narrow size distribution can be maintained as long as agglomeration, Ostwald ripening, and secondary nucleation do not occur. The growth in solution is interface-controlled when the particle is small; after reaching a critical size, it becomes diffusion-controlled [12]. The formation of stable colloids and dispersion of agglomerated particles have been extensively investigated [13].

As a result of attractive van der Waals force, and the tendency of the system to minimize the total surface or interfacial energy, nanostructured particles often form agglomerates. Agglomeration of particles can occur during any of the following stages: synthesis, drying, handling, and/or post processing. For applications where dispersed particles or stabilized dispersions are required, agglomeration must be prevented at each processing step. To produce monodispersed particles without agglomeration, surfactants can be used to control the dispersion during chemical synthesis. Surfactants can also be used to disperse as-synthesized agglomerated fine particles.

A surfactant (an acronym for “surface-active agent”) is any substance that affects the surface or interfacial tension of the medium in which it is dissolved. As such, surfactants need not be completely soluble and may decrease or

increase surface tension by spreading over a surface or interface. Surfactants are used during nanoparticle synthesis in order to reduce interparticle interaction through an increase in repulsive forces. Surfactants are used to control particle size and distribution in most chemical synthesis routes.

In the following section, selected examples of various chemical routes used to prepare magnetic nanoparticles are given, highlighting some aspects of each route. Figure 1 gives an extensive overview of the types of nanoparticles that have been prepared using these methods.

3.1. Precipitation

One of the oldest techniques for the synthesis of nanoparticles is the precipitation of products from bulk solutions. In precipitation reactions, the metal precursors are dissolved in a common solvent (such as water) and a precipitating agent is added to form an insoluble solid. In most cases, a further reduction step is required, either in solution after synthesis (such as borohydride reduction) or to the collected precipitate (*i.e.*, heat treatment in hydrogen gas). Many magnetic nanoparticles can be synthesized using these classical aqueous precipitation reactions to yield nanoparticles that have broad size distribution and irregular morphology. These reactions can generate a wide range of magnetic materials including spinel ferrites, perovskites, metals, and alloys.

The major advantage of precipitation reactions is that large quantities of particles can be synthesized. However, it is difficult to tailor the particle size as only kinetic factors are available to control growth. Chelating agents (or ligands

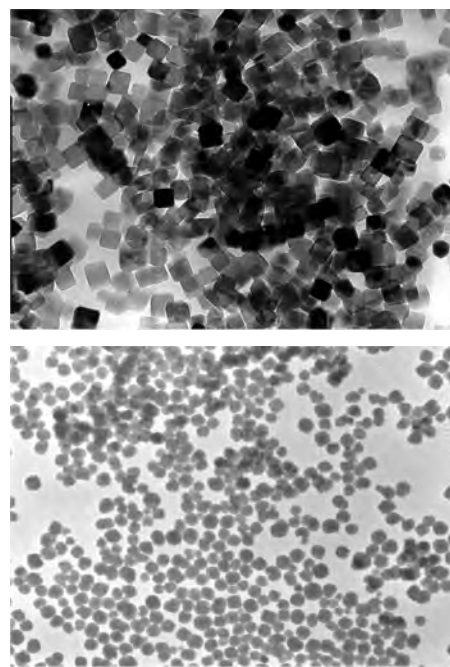


Figure 1. Transmission electron micrographs (TEMs) depicting anti-ferromagnetic KMnF_3 nanoparticles synthesized by reverse micelle reactions. (a) Polyhedral 13 nm average particle size synthesized by quenching the reaction after a short reaction time; (b) Spherical 39 nm particles formed after reacting for two hours [405, 406].

with multiple binding sites) may be used to help control the particle size, decomposing as the precursor is heated. The chelate-modified precipitation yields magnetic nanoparticles that often have very well-defined crystallinity but lack controlled morphologies. This method is used in precipitation of many ferrites such as barium and strontium hexaferrite.

The size and morphology of precipitated nanoparticles can be tailored with limited success through the tight control of synthesis parameters such as pH, metal cation concentration, and the type of the precipitating agent. These parameters allow for the formation of nanoparticles that have a large size distribution (greater than 30%) [14] and are roughly spherical. The concentration of the metal species present in the initial reaction mixture has the largest effect on the overall nanoparticle size [15]. Unfortunately, low concentrations result in limited particle growth, although the resultant particles are generally more uniform in size. As the metal concentration is increased, there is increased particle growth with a subsequent loss of size uniformity. The precipitating agent has a pronounced effect not only on the overall particle size but also on the phase purity of the particle formed. This is especially true in the case of mixed metal spinels. Numerous precipitating agents have been employed in the past including, citric acid [16–18], and oxalic acid [19]. In each case, there is a chelating effect that helps to facilitate complete precipitation. The precipitating agent is then evaporated through subsequent heating cycles. However, subjecting the metal solutions to alkaline media facilitates the precipitation of metal hydroxides that result in a product with less agglomeration.

The first controlled synthesis of magnetic nanoparticles utilizing this alkaline precipitation technique was performed by Massart [14]. In this synthesis, Fe_3O_4 nanoparticles were precipitated from FeCl_3 and FeCl_2 at a slightly basic pH of 8.2. These particles were roughly spherical, 10 nm in diameter with greater than 50% size distribution. Through size selection titration, the size distribution can be reduced to less than 5% [20]. Size selection titration is a technique that disperses nanoparticles in a solvent to form a stable colloidal suspension. The solution is then titrated with an electrolyte solution or a nonsolvent that disrupts the stable colloid causing larger nanoparticles to precipitate out, leaving the particles suspended in the supernatant nearly monodispersed. Temperature reduction has the same result. The precipitate can be collected using centrifugation or filtration. This can reduce the size distribution to less than 5%, generating a monodispersed colloidal solution [21]. Massart later expanded the synthesis of alkaline precipitation to include mixed ferrites (MFe_2O_4 , where $\text{M} = \text{Co}$ [22–24], Mn [22, 23], MnZn [25], and NiZn [26]). These mixed ferrites result in additional difficulties due to the varying solubilities of the metal hydroxides. In the case of $(\text{Mn,Zn})\text{Fe}_2\text{O}_4$, $\text{Fe}(\text{OH})_3$ starts to precipitate early at pH 2.6, while $\text{Mn}(\text{OH})_2$ precipitates at a much higher pH of 9.4. Zn^{2+} is amphoteric and precipitates as $\text{Zn}(\text{OH})_2$ at pH 7.6 but starts to redissolve at pH 9 forming $\text{Zn}(\text{OH})_4^{2-}$ [27]. Therefore, to create a uniform metal precipitate, the pH must be carefully controlled at a pH of 8.6. The synthesis is further complicated by the propensity of Fe to oxidize, forming the $\gamma\text{-Fe}_2\text{O}_3$. The Fe^{3+} cation undergoes oxidation at $\text{pH} > 9$, producing this common impurity phase resulting in poor magnetic properties.

Titration of the metal by the base increases pH to the target value more slowly than does a titration of the base by the metal. A slow titration tends to cause additional problems due to inhomogeneity. As the pH is slowly increased, the Fe^{3+} will be precipitated first and nearly completely before the Zn and finally the Mn. This results in a central core, which oxidizes to form $\gamma\text{-Fe}_2\text{O}_3$, coated by a shell of iron-deficient ferrite.

3.2. Borohydride Reduction

The reduction of metal salts using sodium borohydride can form very uniform spherical nanoparticles. Although the chemistry of the reduction can be very complex, the reduction of iron [28], cobalt [29], and nickel [30] have been explained in detail by Glave et al. Although boride formation is a side reaction, it can be eliminated with careful control of atmosphere and water content in the reaction. For this reason, the reactions are typically carried out in non-aqueous media (dimethylglyoxime, tetrahydrofuran, etc.) to obtain a pure phase material. Mixing metal salts to form one reaction before reduction can form alloys [31–33]. FeNiCu (Cu-Invar) is one example presented by Stolk and Manthiram [34]. In this case, the particles reduced by borohydride are spherical, 10–20 nm in diameter, and of predominantly Invar phase with some impurities of Cu_2O and $\text{Fe}(\text{BO}_2)_2$ present. This material can be heated where it undergoes a conversion to pure phase Cu-Invar, but the particle size increases to 200 nm.

3.3. Hydrothermal

Hydrothermal reactions are aqueous reactions carried out using autoclaves or high-pressure reactors where the pressure can be over 2000 psi at temperatures over 200 °C. At these supercritical conditions, water acts as a reactant, accelerating the kinetics of the hydrolysis reactions. At increased temperatures, the solubility of most ionic species increases and, with the lower viscosity of water, exhibits greater mobility. The increase mobility allows Ostwald ripening to continue at a faster rate increasing the uniformity of the precipitates.

Size and morphological control in hydrothermal reactions is achieved by controlling the conditions of time and temperature. The reactant conditions of precursor material and pH have an impact on phase purity of the nanoparticles. There are two main routes for the formation of ferrites via hydrothermal conditions: hydrolysis and oxidation, and neutralization of mixed metal hydroxides. Some lesser routes involve the hydrothermal treatment of mixed metal oxides [35, 36], or the use of other solvents such as ethylene glycol at supercritical conditions [37, 38]. Hydrolysis and oxidation reactions are very similar to neutralization reactions, except ferrous salts are used instead of ferric salts.

Rozman and Drogenik [39] gave a detailed account of the synthesis of MnZn ferrite nanoparticles using neutralization of the mixed metal hydroxides. The hydrothermal parameters of temperature and time were the first variables tested with 11 nm nanoparticles synthesized at both 95 °C for 50 h and 140 °C for 0.5 h. The shorter reaction time resulted in a nanoparticle surface with a greater amount

of hydroxide groups, while reduced temperatures allowed additional water to be incorporated in the crystal structure which caused increased lattice distortions. Differential thermal analysis showed that the water is actually incorporated into the lattice with final dehydration at temperatures in excess of 700 °C. This distortion and poor surface quality deteriorates magnetic properties. Rozman also noted that the spinel phase starts to crystallize at 90 °C and continues through to 200 °C. At temperatures greater than 200 °C, the spinel phase can recrystallize as γ -Fe₂O₃. The nanoparticle grains grow via Ostwald ripening to a maximum value. Longer times under hydrothermal conditions result in improved crystallinity but not larger grains.

Strontium [40] and barium [41] hexaferrites are more difficult to form due to the less thermodynamically favored magnetoplumbite structure. Initial reactants have a greater impact on the final size, morphology, and phase of the hexaferrites than in other mixed metal ferrites. As with other ferrite preparations, temperature and reaction time influence size, as does the ratio of Fe/Ba. The choice of precipitating reagent has a pronounced effect on nanoparticle crystallinity. The larger the spectator ion of the precipitating agent, the poorer the crystallinity. This phenomenon is presumably due to a change in the electrostatic potential of the metal hydroxides. The lower the electrostatic potential of the metal solution, the greater the likelihood that the metal sols coagulate. This coagulation tends to facilitate the formation of γ -Fe₂O₃ [42]. Since coagulation favors side reactions, stirring is often used. Stirring the hydrothermal solution has resulted in improved nanoparticle uniformity and phase purity.

3.4. Micelle Routes

Surfactant molecules may spontaneously form spherical aggregates called micelles or microemulsions. The difference between microemulsions and micelles is more than simple semantics, although recently, these terms have been used interchangeably. The difference lies in the size of the aggregate, with micelles being 1 to 10 nm in diameter, while microemulsions contain aggregates that are 10 to 100 nm in diameter [43].

Direct micelles have the hydrophilic portion of the surfactant on the outside of the aggregate, while reverse or inverse micelles have the hydrophobic portion on the outside. Micelles can form in the presence or absence of water. In the case of reverse micelles formed in hydrocarbon, water can be readily solubilized forming a “water pool,” where size is characterized by a water-to-surfactant ratio. In this fashion, the water pools within micelles impose kinetic and thermodynamic constraints on particle formation resulting in restricted “nano-reactors”.

Aerosol OT or AOT (sodium dioctylsulfosuccinate) was the first and most characterized surfactant system used in the synthesis of magnetic nanoparticles [44, 45]. Other systems, such as cetyltrimethylammonium bromide (CTAB) [46], sodium dodecylsulfate (SDS) [47], and polyethoxylates (Igepal, Brij, Tween, C₁₂E₅) [48] have been used, and more are being developed to optimize morphology and chemical parameters. Many of the reactions carried out in micelles

are very similar to those performed in bulk aqueous reactions but with the added morphological controls afforded by the surfactant system.

The first magnetic nanoparticles formed in micelles were from the oxidation of Fe²⁺ salts to form Fe₃O₄ and γ -Fe₂O₃ [49]. This reaction was carried out in an AOT/isoctane system and formed spherical nanoparticles with surprisingly tight size distributions of less than 10%. Later, other reactions, using hydrogen peroxide, were used to form MnFe₂O₄. The initial reaction conditions not only controlled the particle size, but also the cation occupancy [50].

An interesting phenomenon seen with iron reductions is the influence of the surfactant on the iron crystal structure. If anionic surfactants (such as AOT) are used α -Fe is formed with the expected body-centered cubic (BCC) crystal structure [51]. Conversely, if a nonionic surfactant is used (for instance, nonyl phenol polyethoxylate), a face-centered cubic (FCC) crystal structure forms [52]. The process for the formation of metals can be expanded to form metal alloys. Instead of using a single metal salt, mixed metal salts are used and reduced simultaneously [53]. It is essential that the reduction is carried out simultaneously or mixed phase products will be formed.

The precipitation of precursors that are subsequently fired to produce the end product is an important synthetic process. This has been used in the synthesis of many different ferrite materials: (Mn,Zn)Fe₂O₄, (Ni,Zn)Fe₂O₄, ZnFe₂O₄ [54], and BaFe₁₂O₁₉ [55]. In these cases, the particles were formed with sizes between 5 and 50 nm. The particles had spheroidal morphology with typical size variations of 10%, although higher conversion temperatures generally widen the size distribution to 10–20%.

Transmission electron microscopy (TEM) images of antiferromagnetic KMnF₃ nanoparticles synthesized using reverse micelles are shown in Figure 1. The reaction time of the metathesis reaction controlled the morphology and size of the particles for this reaction. Particles synthesized by quenching the reaction after short reaction times developed polyhedral morphology and 13 nm average particle size (Fig. 1a). Similar reactions carried out for 2 h resulted in particles with spherical morphology and 39 nm average grain diameters (Fig. 1b) [405, 406].

Although there are many examples of inverse micelles used as micro-reactors, there are only a few examples of the use of direct micelles. Sodium dodecylsulfate is the principle surfactant used in these reactions due to the morphology of the aggregate. The most striking example of direct micelle synthesis was presented by Liu et al. with the synthesis of CoFe₂O₄ [56]. In this example, Liu et al. created a chemometric model for predicting the size of a ferrite from the synthesis conditions of surfactant concentration, metal concentration, base concentration, and temperature. The synthesis was later expanded to include the mixed ferrites of MnFe₂O₄ and MgFe₂O₄ [57].

In order to control side reactions and precipitation common to aqueous systems, micelles are formed using alcohol as the polar phase. Fang et al. [58] utilized ethanol-based micelles to form SrFe₁₂O₁₉. In this case, Sr(OH)₂ has such a high solubility in water that inhomogeneous and Sr-deficient precipitates are formed. Although the particles formed

display a large size distribution, they also display a plate-like morphology with an average particle size of 100 nm.

Heating causes an increase in crystallinity, which in turn greatly affects the magnetic and electronic properties [59]. The heat treatment, however, can be carried too far resulting in increased grain growth. Excessive grain growth adversely affects the magnetic and electronic properties (e.g., magnetic domain formation). Microwave heating typically increases crystallinity with significant grain growth. The annealing temperature at which significant grain growth occurs has been shown to be half the melting point of the material [60]. It is important to note that nanoparticles generally possess reduced melting temperatures, primarily due to the large surface-to-volume ratio.

3.5. Thermolysis, Photolysis, and Sonolysis Methods

One of the simplest methods to prepare nanoparticles is the decomposition of organometallic precursors. This decomposition may be driven by heat (thermolysis), light (photolysis), or sound (sonolysis). Advantages of using organometallic compounds are that precursors can be decomposed at relatively low temperatures to form the final product. By controlling the decomposition temperature, the growth of the nanoparticles can be controlled. Since size and morphology have an effect on the properties of the nanoparticles, control of these properties is a primary goal. In many cases, polymers, organic capping agents, or structural hosts are used to limit the size of the nanoparticle growth [61–72]. If these restraints interact with the particle surface, then the magnetic properties may be altered. Polymers and capping agents are generally used to sterically protect the particles so that they do not coalesce. The biggest disadvantage of this approach is that most of the reactions involve air-sensitive reactants as well as the final precursor; therefore, glove box or schlenk line techniques must be used. Because of the air-sensitive nature of some of reactants, greater care must also be taken in preparation of solvents and the choice of atmospheres used. The particles synthesized are often agglomerated and have a large size distribution (<15%), and if they are stabilized with surfactants or other organics to prevent agglomeration, they can interact with the surface, changing the magnetic properties. It has been shown that the magnetic properties of nickel are effected by the presence of surface moieties [72–74].

There has been a renewed interest in the synthesis of magnetic nanoclusters with unique properties such as enhanced magnetization [75]. One polymer—polyvinylpyrrolidone (PVP)—has been shown to interact minimally with the surface of Co [61, 62]. It is suggested that the polymer matrix determines the cluster size and efficiently protects the particles. Cobalt nanoclusters were prepared by reduction of organometallic compounds of $\text{Co}(\eta^3\text{-C}_8\text{H}_{13})(\eta^4\text{-C}_8\text{H}_{12})$ in hydrogen and in the presence of PVP [61]. Dried colloids were noninteracting, superparamagnetic particles with enhanced magnetization relative to that of the bulk. By varying the decomposition temperature, the size of particles could be controlled. Organometallic precursors were also used to prepare other colloidal metal with a variation of size and structure.

In most cases, when carbonyls are decomposed in the presence of stabilizing polymers, spherical nanoparticles are formed. However, Dinega and Punttes et al. have shown that Co nanorods could be prepared by modifying the thermal decomposition of cobalt carbonyl in the presence of oleic acid and trioctylphospheneoxide (TOPO) [63–65]. They rapidly injected the organometallic precursor into a hot surfactant mixture. This rapid injection of the precursor allowed for a “size distribution focusing” [64–65] by separating nucleation from growth. The decomposition of the precursor and nucleation occurs immediately upon injection and metal nuclei are coated with the coordinating ligands. When a surfactant mixture is used, such as oleic acid and TOPO, and quenched shortly after injection, nanoparticles (4 nm × 25 nm) of hcp Co are formed. This indicates that the surfactants adsorb to different crystal faces with different strengths [64, 65]. If the reaction is allowed to proceed, the rods transform to monodispersed spherical ϵ -Co nanoparticles. This ϵ -Co crystal structure has been reported for Co nanoparticles prepared by a variety of solution techniques [63–66].

When the organometallic precursor, nickel bis-cycloocta-1,5-diene ($\text{Ni}(\text{COD})_2$) undergoes thermolysis in the presence of hexadecylamine (HAD) or TOPO, nanorods, spheres, or tear-shaped nanorods are formed, the shape being related to the concentration of the organic species [76]. Varying the organic stabilizing agents used could result in other shapes. Bracelet arrays of 27 nm Co are formed in the presence of resorcinarene tetraphosphonate [77] and tetrahedral structures [78] are found when cobalt nanoclusters are reacted with NaAOT/toluene at 130 °C.

CoPt alloys and Co with a Pt shell have been prepared using transmetallation and CO decomposition [79]. Alloys are prepared by the addition of $\text{Co}_2(\text{CO})_8$ to a hot solution of an organic solvent containing a platinum organometallic compound and oleic acid. As the carbonyl decomposes to form Co nuclei, it also undergoes a transmetallation reaction with the platinum organometallic compound. To prepare a core/shell material, cobalt colloids are first formed by the decomposition of the carbonyl and then they are refluxed with the platinum organometallic compound with dodecane isocyanide as a stabilizer. The decomposition process may also be applied to form magnetic oxides [80]. This can be done by either oxidizing the metal particles or through an oxidative decomposition. In the first case, an iron oleate precursor is formed from the decomposition of iron carbonyl in the presence of octyl ether and oleic acid at 100 °C. This solution is cooled to room temperature and the mild oxidizing agent, $(\text{CH}_3)_3\text{NO}$, is added and the solution refluxed. This results in 11 nm Fe_2O_3 particles that will also form a two-dimensional hexagonal, close-packed lattice. When the solution is refluxed, the iron oleate complex breaks down and iron particles are formed and then oxidized by $(\text{CH}_3)_3\text{NO}$. Changing the amount of reactants could vary the particle size and adding already prepared 11 nm nanoparticles into a fresh solution and reheating could form larger particles. Oxidative decomposition occurs when the oxidizing agent and surfactant are added to the original solution. If a bimetallic organometallic precursor is used, such as $(\eta^5\text{-C}_5\text{H}_5)\text{CoFe}_2(\text{CO})_9$, CoFe_2O_4 nanoparticles with sizes of 4–9 nm are formed [81].

In sonolysis or sonochemistry, ultrasound or acoustic waves are used to decompose the organometallic precursors. The formation, growth, and collapse of bubbles in a liquid drive high-energy, sonochemical reactions, without any molecular coupling of the ultrasound with the chemical species. This acoustic cavitation involves a localized hot spot of temperature of about 5000 K, a pressure of ~ 1800 atm and a subsequent cooling rate of about 10^9 K/sec, due to implosive collapse of a bubble in the liquid [82–92]. Generally, volatile precursors in low vapor pressure solvents are used to optimize the yield. Ultrasonic irradiation is carried out with an ultrasound probe, such as a titanium horn operating at 20 kHz.

Nanostructured particles are easily produced by sonochemically treating volatile organometallic precursors [82–100]. The powders formed are usually amorphous, agglomerated, and porous. To get the crystalline phases, these powders must be further annealed; however, this annealing temperature is lower than that needed to do the solid state conversion.

When organic solvents with high boiling points are used for sonolysis, highly porous amorphous powders are formed. For example, an amorphous iron powder was produced by the sonication of iron carbonyl in decalin [82–84]. This powder was comprised of small crystallites (5 \AA) and had a surface area of $120 \text{ m}^2\text{g}^{-1}$. Annealing this powder at $350 \text{ }^\circ\text{C}$ under nitrogen resulted in α -Fe that was 50 nm in diameter. FeCo [85, 86], FeNi [87], and CoNi [93] alloys have been prepared by this method. The as-synthesized powders are amorphous. Annealing these powders in argon at $450 \text{ }^\circ\text{C}$ for 5 h yields crystalline material. The FeCo is comprised of BCC Fe and a mixture of FCC and cobalt. The (Fe,Ni) and (Co,Ni) alloys possess a single set of FCC peaks.

If stabilizers or polymers are added postsonication or during sonication, then metal colloids result [84, 85, 88, 94]. These stabilizers could be alkyl thiols [86, 89, 94], PVP [84], oleic acid [84], octadecyltrichlorosilane (OTS) [94], sodium dodecylsulfate (SDS) [71]. Gedanken et al. [87, 88, 95] have also used sonochemical routes to prepare nanoparticles of Fe, Fe_3O_4 , Fe_2O_3 , cobalt ferrite and copper ferrite. If the sonication is done in the presence of oxygen, then oxides are formed [95, 96]. In the case of Fe_2O_3 , when the coating solution was present during sonolysis, amorphous powder resulted that was then converted to γ - Fe_2O_3 upon annealing at $300 \text{ }^\circ\text{C}$ for 3 h under an argon atmosphere. If the powder is first converted to γ - Fe_2O_3 , the OTS does not coat the powder. In general, nanoparticles with dimensions less than 10 nm will self-assemble to the lowest thermodynamically stable form. By pressing the nanoparticle solution on a substrate or interface, careful removal of the solvent will result in self-assembled monolayers (SAMs). The size of the SAM-coated nanoparticles is determined by the surfactant concentration in the coating solution. Oxide formation (Fe_3O_4 , Co_3O_4) was also seen if the sonication was done in aqueous conditions and with noncarbonyl precursors; however, the resulting powders are crystalline [96–99].

If the sonolysis is done in the presence of a support or porous host, then colloidal metal particles are formed. These powders have a surface area, over 100 times greater than powders commercially available. For example, 3–8 nm amorphous iron particles on silica support were synthesized at

$20 \text{ }^\circ\text{C}$ from iron pentacarbonyl ($\text{Fe}(\text{CO})_5$), decane, and silica gel [85]. These materials are generally considered for catalytic reactions and not for magnetic applications.

3.6. Sol–Gel Methods

Sol–gel processing can be used to prepare a variety of materials, including glass, powders, films, fibers, and monoliths. Traditionally, the sol–gel process generally involves hydrolysis and condensation of a metal alkoxides. Metal alkoxides are good precursors because they readily undergo hydrolysis; that is, the hydrolysis step replaces an alkoxide with a hydroxide group from water and free alcohol is formed. Once hydrolysis has occurred, the sol can react further and condensation (polymerization) occurs.

Factors that need to be considered in a sol–gel process are solvent, temperature, precursors, catalysts, pH, additives, and mechanical agitation. These factors can influence the kinetics, growth reactions, and hydrolysis and condensation reactions [101]. The solvent influences the kinetics and conformation of the precursors, and the pH affects the hydrolysis and condensation reactions. Acidic conditions favor hydrolysis, which means that fully or nearly full hydrolyzed species are formed before condensation begins. Under acidic conditions, there is a low cross-link density that yields a denser final product when the gel collapses. Basic conditions favor condensation reactions; therefore, condensation begins before hydrolysis is complete. The pH also affects the isoelectric point and the stability of the sol. These, in turn, affect the aggregation and particle size. By varying the factors that influence the reaction rates of hydrolysis and condensation, the structure and properties of the gel can be tailored. Because these reactions are done at room temperature, further heat treatments need to be done to get to the final crystalline state. Because the as-synthesized particles are amorphous or metastable, annealing and sintering can be done at lower temperatures rather than at conventional solid-state reactions.

Sol–gel routes can be used to prepare pure, stoichiometric, dense, equiaxed, and monodispersed particles of TiO_2 and SiO_2 [101]. But this control has not been extended to the metal ferrites. Generally, the particles produced are agglomerated. Ultrafine powders of CoFe_2O_4 (~ 30 nm) [102] and NiFe_2O_4 (5–30 nm) [103] after being fired at $450 \text{ }^\circ\text{C}$ and $400 \text{ }^\circ\text{C}$, respectively. Most of the ferrite sol–gel synthesis focus has been on cobalt ferrite doping studies with Mn [104], Cr [105], Bi [106], Y, La [107], Gd, Nd [108], and Zn [109].

Sol–gel routes have been attractive for the preparation of hexagonal ferrites. For example, the M-type hexagonal ferrite, $\text{Ba}_{1-x}\text{Sr}_x\text{Fe}_{12}\text{O}_{19}$, formed 80–85 nm hexagonal platelets after a $950 \text{ }^\circ\text{C}$ calcination for 6 h [110]. Nanospheres of the W-type ferrite, $\text{BaZn}_{2-x}\text{Co}_x\text{Fe}_{16}\text{O}_{27}$, resulted after calcination in air for 4 h at $650 \text{ }^\circ\text{C}$ [111]. The particle size ranged from 10 nm to 500 nm ($650 \text{ }^\circ\text{C}$ – $1250 \text{ }^\circ\text{C}$) and increased with increasing calcination temperatures. U-type hexagonal ferrite was also prepared, with 10–25 nm spherical particles formed at $750 \text{ }^\circ\text{C}$ [112]. The grain size could be changed by increasing the calcination temperature. These calcined powders had an amorphous layer on them. Yttrium iron garnets with particle sizes from 45–450 nm have also been prepared

[113]. Mathur and Shen [114] have prepared the manganite perovskite, $\text{La}_{0.67}\text{Ca}_{0.33}\text{MnO}_3$, by dissolving the metal precursors in an acidic ethanolic solution. Drying the solution at 120 °C and calcining at 300–400 °C leads to preceramic foam, which forms nanocrystalline $\text{La}_{0.67}\text{Ca}_{0.33}\text{MnO}_3$ (40 nm) after a heat treatment at 650 °C.

It should be noted that the sol-gel process is particularly attractive for the synthesis of multicomponent particles with binary or ternary compositions, using double alkoxides (two metals in one molecule) or mixed alkoxides (with mixed metal-oxane bonds between two metals). Atomic homogeneity is not easily achieved by coprecipitating colloidal hydroxides from a mixture of salt solutions, since it is difficult to construct double metal-oxane bonds from metal salt [101].

Hybrid materials such as metal oxide-organic nanocomposites can be prepared using the sol-gel approach. For example, controlled nanoheterogeneity can be achieved in metal/ceramic nanocomposites [101]. Reduction of metal oxide particles in hydrogen provided the metal-ceramic nanocomposite powders such as Fe in silica [115], Fe_2O_3 [116], and NiFe_2O_4 [117]. The metal particles, a few nanometers in size with a very narrow size distribution even for high metal loading, were statistically distributed in the oxide matrix without any agglomeration, as a result of anchoring the metal complexes to the oxide matrix. The narrow particle size distribution could not be achieved if the sol-gel processing was performed without complexation of metal ions.

3.7. Polyol

The polyol method, in which the polyol acts as a solvent as well as the reducing agent and a surfactant, is a suitable method for preparing nanophase- and micron-size particles with well-defined shapes and controlled particle sizes [118–151]. By this method, precursor compounds such as oxides, nitrates, and acetates are either dissolved or suspended in a diol, such as ethylene glycol or diethylene glycol. The reaction mixture is then heated to reflux between 180 °C and 199 °C. During the reaction, the metal precursors become solubilized in the diol, form an intermediate, and are then reduced to form metal nuclei that will then nucleate and form metal particles. Submicron-sized particles can be synthesized by increasing the reaction temperature or inducing heterogeneous nucleation via adding foreign nuclei or forming foreign nuclei *in-situ*. Nanocrystalline powders such as Fe, Co, Ni, Cu, Ru, Rh, Pd, Ag, Sn, Re, W, Pt, Au, Fe-Cu, Co-Cu, Co-Ni, and Ni-Cu were also synthesized using different salt precursors by this method [118–146]. In many cases, use of nucleating agents to assist formation of nanoparticles was not required. For example, nanostructured powders of $\text{Co}_x\text{Cu}_{100-x}$ ($4 \leq x \leq 49$ at. %) [118, 119] were synthesized by reacting cobalt acetate tetrahydrate and copper acetate hydrate in various proportions in ethylene glycol. The mixtures were refluxed at 180–190 °C for 2 h, the powders precipitated out of solution, and were subsequently collected and dried. Since Cu was more reducible than Co, nucleation of Cu occurred first, and Co subsequently nucleated on Cu crystallites. X-ray diffraction, often conventionally used to study alloy formation, showed some evidence to suggest that metastable alloy could have formed. Diffraction peaks due to FCC Cu were detected in all samples with different

copper concentrations, but Co diffraction peaks were not detected until $x = 19$ atomic percent. To confirm the structure of powders, studies of local atomic environment were performed using extended X-ray absorption fine structure (EXAFS) spectroscopy and solid-state nuclear magnetic resonance (NMR). The results from these investigations and vibrating sample magnetometry (VSM) ruled out the formation of metastable alloys, but confirmed the synthesis of nanocomposites of Co-Cu.

The polyol method has also been shown as a useful preparative technique for the synthesis of nanocrystalline alloys and bimetallic clusters. Fievet et al. have extensively studied the ferromagnetic system of Co-Ni, Fe-Co, Fe-Co-Ni [123–132]. The Co-Ni alloy particles had densities and saturation magnetization close to the bulk values, and showed a shift to higher resonance frequencies as the Co/Ni increased. This was also observed in the Fe-Co-Ni particles that were 50–150 nm in size. An example of the morphology of alloy nanoparticles formed by the polyol technique is shown in Figure 2. The particles depicted by the scanning electron microscope (SEM) image consist of $\text{Fe}_{48}\text{Co}_{52}$ [143].

Nanocrystalline $\text{Fe}_{10}\text{Co}_{90}$ powders with a grain size of 20 nm were prepared by reducing iron chloride and cobalt hydroxide in ethylene glycol without nucleating agents [133]. Nickel clusters were prepared using Pt or Pd as nucleation agents [134]. The nucleating agent was added 10 min after the nickel-hydroxide-PVP-ethylene glycol solution began refluxing. The Ni particle size was reduced from about 140 nm to 30 nm when nucleating agent was used. Reduction of particle size was also obtained by decreasing the nickel hydroxide concentration and by the use of PVP. Nickel prepared without nucleating agents had an oxidation temperature of 370 °C. Smaller nickel particles synthesized with nucleating aids oxidized at a lower temperature of 260 °C, as expected from the higher surface area of finer particles. Desorption studies showed the adsorbed surface species were CO moieties and H_2O , and nitrogen-containing species were not observed. This indicated that ethylene glycol, not the polymer, was adsorbed on the surface of particles. The ethylene glycol had only half monolayer coverage. When this protective glycol was completely removed from the surface, oxidation occurred. It was suggested that the Ni-Pd and Ni-Pt particles had a 7–9 nm Pd nucleus and a 6–8 nm Pt

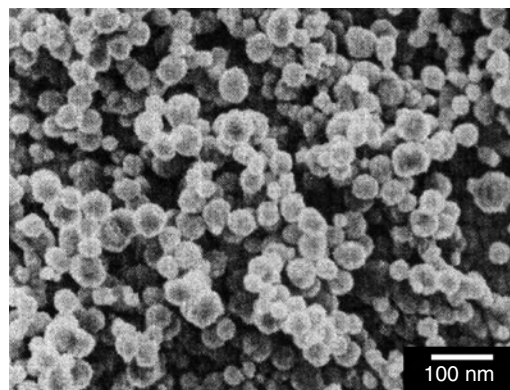


Figure 2. Scanning electron microscope (SEM) image of $\text{Fe}_{48}\text{Co}_{52}$ nanoparticles prepared by a polyol method [143].

nucleus, respectively. Oxidation studies showed that some alloying of Ni with Pt occurred. Cobalt nickel alloys of 210 to 260 nm particle sizes were also prepared using either Ag or Fe as nucleating agents [135].

Polymer-protected bimetallic clusters were also formed using a modified polyol process [135]. The modification included addition of other solvents and sodium hydroxide. In the synthesis of Co-Ni with average diameters between 150–500 nm, PVP and ethylene glycol were mixed with either cobalt or nickel acetate with PVP. The glycol and organic solvents were removed from the solution by acetone or filtration. The PVP-covered particles were stable in the air for extended periods of time (*i.e.*, months).

Compared to aqueous methods, the polyol approach resulted in the synthesis of metallic nanoparticles protected by surface-adsorbed glycol, thus minimizing the oxidation problem. The use of nonaqueous solvent, such as polyol, also further reduced the problem of hydrolysis of fine metal particles as did often occur in the aqueous case.

By modifying the polyol method with the addition of water to act more like a sol-gel reaction (forced hydrolysis), oxides can be prepared [136–139]. For example, 5.5 nm CoFe_2O_4 was prepared by the reaction of ferric chloride and cobalt acetate in 1,2-propanediol with the addition of water and sodium acetate.

Other heating sources for the polyol method have been reported [150–153] besides the conventional heating mantle. An alternative heating source includes a 2.45 GHz microwave gyrotron [150] and millimeter wave beam sources [151]. One technique, the laser-liquid method, uses a laser to heat the solution [152, 153]. This has been used to prepare submicron nickel particles.

3.8. Electrochemical/Electrodeposition

Electrochemical and electrodeposition routes are generally used to prepare nanocrystalline coatings, and are not the focus of this article. However, electrodeposition has been used to prepare wires of magnetic materials [154–164] and recently it has been used to prepare particles [165–173]. In electrodeposition, nucleation occurs by either the formation of new nuclei or the build-up of existing nuclei in solution. These two processes are in competition with each other. Grain growth is favored at low overpotentials and high surface diffusion rates, and nuclei formation is favored at high overpotentials and low diffusion rates. These conditions are experimentally achieved when using pulsed modes. Under pulsed conditions, the peak current density can be considerably higher than the limiting current density attained for the same electrolyte during direct current plating. It has been shown that nanostructured materials will result when the deposition variables (*i.e.*, bath composition, pH, temperature, current density, overpotential, and additives) are chosen so that nucleation is favored with reduced grain growth.

Recently, Penner et al. [165] has done a detailed study and modeling of the parameters that effect this nucleation and growth in electrodeposited nanoparticles and wires. He has tried to follow the LaMer [11] model to explain the formation of electrodeposited nanoparticles (Pt) on graphite electrodes, and found that when instantaneous nucleation and diffusion-controlled growth conditions were satisfied to

produce monodispersed particles, the particles formed were 7.2 nm with a standard deviation of 3.2 nm [174]. It was reasoned that there are two factors causing this particle size broadening. In electrodeposition, the nuclei are distributed on the electrode surface in a “pseudo-random” process. On the terraces, the nucleation process is random, yet while on the step edges, the nucleation process is aligned. The growth step is dependent on the number and proximity of the neighboring nuclei. Penner points out that these interparticle diffusion coupling (IDC) are the most important mechanisms for broadening of randomly nucleated particles. This condition also exists in solutions, but instead of being attached to a surface, the particles in solution collide and react and move on. Experimentally, to overcome IDC, the slow growth method [165, 166, 174, 175] or H_2 coevolution method were used. In the slow growth method, a high overpotential is applied to nucleate the electrode. A second low overpotential pulse is then applied to promote the growth step. Nickel nanoparticles were synthesized using this slow growth method [167]. In H_2 coevolution, convective mixing equalizes the growth rate of the nanoparticles. The formation of gas bubbles and their release and movement through the solution causes convective mixing. By varying the deposition time and potential, nickel nanoparticles from 2–250 nm were synthesized [165, 166].

Another electrochemical method that has been used to prepare nanoparticles involves the use of a sacrificial anode [167–169, 176]. Based on a method developed by Reetz [177], Pascal et al. [169] have prepared 3–8 nm maghemite from a sacrificial iron electrode in an aqueous solution of dimethylformamide (DMF) and cationic surfactants. Adjusting the current density controls the particle size. The as-prepared nanoparticles showed a broad scattering peak by X-ray diffraction consistent with an amorphous phase. Raman and selected area electron diffraction determined the magnetite phase. Hemplemann has used a similar strategy to prepare other metal oxides [167]. This technique is coined electrochemical deposition under oxidizing conditions (EDOCs). Here the anode is oxidized to produce Mn^+ species in solution, which are then reduced by electrons generated by the cathode in the presence of stabilizers. These stabilized metal species are then oxidized by oxygen that is bubbled into the system [167]. Electrochemical deposition under oxidizing conditions has been used to prepare nanoparticles Fe_2O_3 , Fe_3O_4 , Co_3O_4 , NiO, and CoFe_2O_4 [154]. The difference between Pascal's method and EDOC, is that in EDOC, oxygen is bubbled in, whereas in Pascal's synthesis, oxygen is produced from the electrochemical breakdown of water. Mixed oxides of Sr-Fe oxides [170] and Mn-Zn-Fe oxides [171] have also been prepared using sacrificial electrodes.

Nanowires are easily formed in porous templates by electrodeposition. In precipitation methods and chemical vapor deposition, care must be taken so as not to plug the pores during wire formation. In templated electrodeposition, material growth is from the base and there is not the problem of plugging the pores. This technique has been used to prepare nanowires of Co [155–159, 177], Ni [156–160, 168, 172], FePt [161], FeCo [162], FeNi [154], CoPt [161]. Common templates are polycarbonate [178], anodized alumina [155, 160], and mica [154].

3.9. Multi-Synthesis Processing Methods

The IBM nanoparticle synthesis route [3] is a combination and variation of the polyol method and the Alivisatos thermal decomposition routes [64, 66]. This synthesis involves a high temperature organic- or solution-phase synthesis followed by a size selective separation technique to get relatively monodispersed (<5%) nanoparticles. More specifically, by rapidly injecting the organometallic precursor into a hot solution containing the stabilizing agents, allows for the formation nuclei immediately upon injection. Because the capping agents/surfactants are present, the size and shape of the nanoparticles are controlled. By adjusting the reaction conditions such as time temperature, precursor concentration, and surfactant type and concentration, size and morphology can be controlled.

Sun and Murray et al. [3] have prepared monodispersed FePt nanoparticles and superlattices by the high temperature reduction of platinum acetylacetonate and the thermal decomposition of iron carbonyl in the presence of stabilizing agents. In the case of FePt, both reactions were carried out together in the presence of oleic acid and oleyl amine. The composition was controlled by the ratio of the iron precursor to that of the platinum precursor. The nanoparticles were produced with sizes tunable in the range of 3–10 nm. A colloidal solution of the nanoparticles was prepared by flocculating the particles and redispersing them in a non-polar solvent. This solution was put on a substrate and the solvent allowed to evaporate. This led to the self-assembly of the nanoparticles. A hcp three-dimensional superlattice was formed by the self-assembly of 6 nm Fe₅₀Pt₅₀ with the stabilizers oleic acid and oleyl amine. Changing the alkyl group on the stabilizers can change the interparticle distance. By changing the alkyl group from dodecyl to hexyl leads to a particle spacing of 1 nm, and a superlattice that is cubic close-packed. This hcp to cubic transition was also seen above with ϵ -Co. The superlattices show no aggregation at temperatures up to 600 °C.

The as-synthesized 4 nm Fe₅₂Pt₄₈ had a fcc structure and annealing at 560 °C for 30 min lead to particles with a fct internal structure. Superlattices of these particles exhibit a similar trend. The as-synthesized assembly has a chemically disordered fcc structure and annealing results in the Fe and Pt atom rearranging into the chemically ordered fct structure. The amount of ordering can be controlled by temperature and annealing time. Since the initial paper on FePt synthesis [3] there has been an explosion of research on FePt prepared by this method [179–186] or variations on this method [187, 188] or other magnetic materials (*i.e.*, CoPt [189], FePd [189], and SmCo [178]).

One of the greatest advantages of chemical routes is that they are done in solution. This allows for a great deal of versatility and compatibility. Since many of the chemical routes use similar or the same solvent systems, they may be interchanged for one another or done concurrently. Therefore, combining one or more techniques is relatively simple. Micellar techniques are often used to regulate the size of the nanoparticles in sol-gel synthesis. The versatility also comes from the fact that a broader spectrum of materials can be prepared by combining techniques. And because this is a solution technique, additives, capping agents, functionalities are easily added to the reaction. These additives can be

added presynthesis, *in-situ*, or post-synthesis. It is also possible to prepare nuclei or cores by one technique and injecting them into the solution of a second, and either forming particles or core/shell structures.

4. STRUCTURAL CHARACTERIZATION

The magnetic properties of nanoparticles are determined by their physical structure: the size and shape of the particles, their microstructure, the chemical phase or phases that are present, the defects, and differences between the crystal structure of nanoscale phases and their bulk counterparts. Although individual structural probes are sometimes capable of providing definitive information about some aspect of the particles, in many cases the results of a single probe are ambiguous, inconclusive, or difficult to interpret. This may be true even when the technique is reliable for bulk measurements. Consider, for example, an X-ray diffractogram of nanoparticles believed to consist of a single phase (see Fig. 3). Compared to a bulk standard, the peaks will be broadened. In the case of subnanometer particles, structural relaxation may change the lattice constant measurably. Surface effects, negligible in a bulk crystal, may play a significant role. These effects will result in differences between the nanoparticle diffractogram and the diffractogram of a standard bulk material, reducing the utility of diffraction as a “fingerprinting” technique.

Accordingly, a suite of complementary tools generally determines the physical characteristics of nanoparticles. Self-consistency between these techniques increases the certainty of a given characteristic’s accuracy. In some cases, the use of parameters from one technique can be used to refine

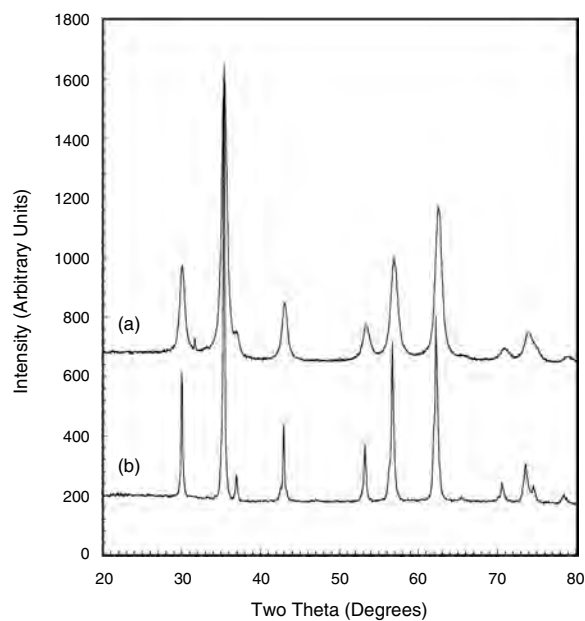


Figure 3. Diffraction patterns for a sample of (a) manganese zinc ferrite nanoparticles (12 nm in diameter) and (b) bulk manganese zinc ferrite sample. Although the diffraction patterns look similar, EXAFS analysis of these samples indicated that the particles were multi-phase. The broad peaks of the manganese zinc ferrite largely mask the iron oxide impurity phase.

parameters by another technique, thereby providing a better picture of the particle assembly. This is especially true of diffraction techniques (XRD and TEM) aiding Mössbauer effect or synchrotron radiation analyses.

The advent of increasingly sophisticated synchrotron radiation analyses have been important in this regard. Concurrent with the rapid increase in the intensity of ultraviolet and X-ray beamlines available to the scientific community has been the development of increasingly powerful experimental and analytical techniques for structural determinations.

The first portion of this section will discuss conventional tools for determining the structure of magnetic nanoparticles; a discussion of applying synchrotron radiation to the problem follows. A subjective summary of the relative applicability of the various probes discussed here is given in Table 1 [190].

4.1. Conventional Techniques

4.1.1. Size and Morphology Determinations

The defining characteristic of nanoparticles is, of course, their size. In principle, most structural probes are sensitive in one way or another to the size of the particles. In practice, however, nanoparticle “size” is an ambiguous concept. An assembly of nanoparticles generally consists of some distribution of sizes, approximating a log normal distribution. Often this distribution is significant. For magnetic nanoparticles, the superparamagnetic blocking temperature is strongly dependent on the size and size distribution of the particles. A different value will be obtained depending on whether a technique is sensitive to the median size or the mean size, and whether that median and mean is number-weighted or volume-weighted (the former case will yield smaller sizes than the latter). In addition, nanoparticles are not always single crystals. Many techniques yield a crystallite size; others give the size of the aggregate particles.

One of the most powerful tools for determining particle size and morphology is TEM. Transmission electron microscopy will generally report the total particle size (as well as crystallite size) and has the virtue of providing details of the size distribution. In many cases, aggregates of smaller particles can be discerned. If the nanoparticles consist of more than one phase and the phases provide enough contrast, then the individual phases may also be visible (Fig. 4). For further discussion of the capabilities of electron microscopy for investigating the physical and magnetic structure of nanostructured materials, see the review article by Thomas and Hütten [191]; imaging of small metallic nanoparticles is discussed by Ascencio et al. [192]. A few

representative examples of the application of TEM imaging to magnetic nanoparticles are given in the references [169, 193–199]. Dynamic light scattering [200] (DLS), also known as photon correlation spectroscopy (PCS) or quasi-elastic light scattering (QELS), is an important supplemental technique for determining the sizes of particles in solution, particularly when the size distribution is approximately log normal. Because of the ability to size particles in solution (including aerosols), DLS shows promise for *in-situ* studies of nanoparticle synthesis [201]. Dynamic light scattering is sensitive to total particle size, and yields information that is weighted by the square of the particle volume, although results are generally converted to volume- or number-weighting prior to publication.

For determinations of crystallite size, Scherrer analysis of XRD is commonly used [39, 202, 203]. This technique relies on the broadening of diffraction peaks due to the finite number of diffracting planes. Because other factors, such as strain, can broaden XRD peaks, Scherrer analysis generally provides a lower limit on mean crystallite size.

4.1.2. Phase Identification

Although XRD is often considered the gold standard for determination of crystal structure, it does possess significant limitations. As discussed in the introduction to this section, differences between nanoparticle and bulk crystal structures in combination with peak broadening and multiple phases may make XRD results less than conclusive. Sometimes, it yields almost no information: very small particles less than a nanometer across, core/shell structures with shells a few monolayers thick, and amorphous phases are all difficult to discern using conventional XRD. Certainly, XRD is still the method of choice for confirming the presence of a single expected phase with crystallite size greater than about 10 nanometers. But the nature of magnetic nanoparticles often yields samples that do not meet those criteria.

In some cases, the high intensities and small spot sizes of electron beams may make electron diffraction useful [195, 199, 204, 205]. Selected area electron diffraction (SAED or SAD) sometimes allows discrimination of phases as small as 1–2 nanometers in size, but at this scale, double diffraction, calibration issues, and the close proximity of diffraction spots arising from different phases often prevents an unambiguous identification [191].

4.1.3. Site Occupancy

Magnetic materials with the same nominal chemical composition, even when very high phase purity, often differ markedly from one another due to a different distribution of

Table 1. Applicability of structural probes to magnetic nanoparticles. One check indicates a technique which provides uncertain or incomplete information for a wide range of materials, or is only applicable in especially favorable situations. Three checks indicates a technique which is widely (but not universally) applicable and often gives fairly reliable information. Two checks is, of course, intermediate.

	TEM/SAD	DLS	XRD	ND	Mössbauer	XAS	XPS	EDXAS	DAFS
Size	✓✓✓	✓✓✓	✓✓	✓✓		✓		✓	✓
Morphology	✓✓✓								
Phase identification	✓✓✓		✓✓	✓✓	✓	✓✓	✓	✓✓	✓✓
Site occupancy			✓	✓✓	✓✓	✓✓	✓	✓✓	✓✓✓
Kinetics		✓✓	✓	✓	✓	✓	✓✓	✓✓✓	✓

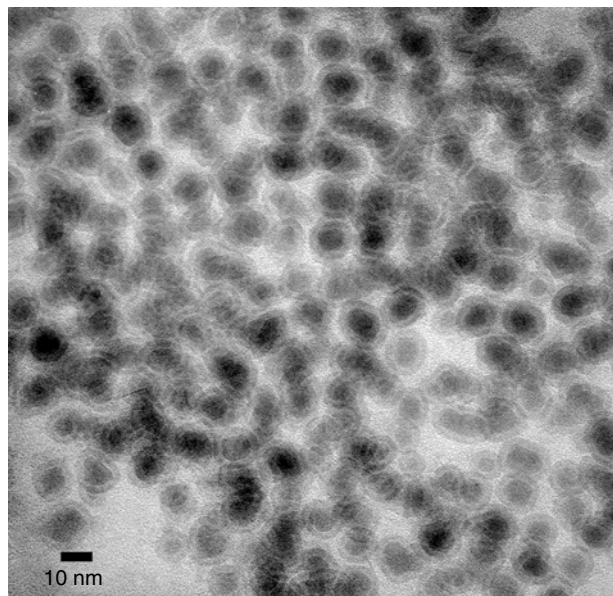


Figure 4. TEM of nanoparticles comprising an iron oxide shell on an iron core. The difference in contrast between the oxide and the metal allows the shells to be clearly visible.

species (atoms, ions, or vacancies) among the available crystallographic sites. This is especially true for ferrimagnetic materials containing multiple sublattices. Spinel ferrites, for example, have two sublattices with parallel coupling of the magnetic moments within each sublattice and antiparallel coupling between them. The result is that the magnetization of the material arises from the difference in magnetization of the sublattices. Often, different species reside on each sublattice. If vacancies are found preferentially on one sublattice, or if some of the atoms on one sublattice are switched with those on the other, the magnetization may be altered substantially [206]. It is thus very important to determine site occupancy in these materials.

If the material possesses atomic ordering, then diffraction techniques are often applicable. Even if the occupancy is random or quasi-random in nature, diffraction can often be used to obtain the average structure. For example, XRD can reveal the percentage of sites in the octahedral sublattice of a spinel compound that are vacant [207]. X-ray diffractograms cannot, however, conclusively reveal the local distortions caused by these vacancies, nor the tendency of vacancies to cluster or disperse. In the case of one atom substituting for another, however, XRD is only useful if the substituted atom differs substantially in its atomic scattering factor from the one being substituted for. The atomic scattering factor for a given scattering angle is, in turn, primarily a function of the number of electrons in the atom. Since in ferrimagnetic oxide materials, the substitution is often one first-row transition metal for another (particularly manganese, iron, cobalt, nickel, and zinc), this prevents XRD from being used to find average site occupancy in many cases. The same restrictions apply to electron diffraction.

Neutrons, on the other hand, are uncharged, and thus interact predominantly with the nucleus of atoms rather than the surrounding electrons. Since the coherent scattering

cross-section of nuclei is not correlated with atomic number, elements with very similar atomic scattering factors for X-rays may have very different scattering cross-sections for neutrons. For example, iron (with its isotopes present in their natural abundance) has about six times the cross-section for coherent scattering of thermal neutrons as does manganese, and more than 14 times that of cobalt. The atomic scattering factors for X-rays for these three elements, in contrast, are within a few percents of each other. In some cases, therefore, neutron diffraction (ND) can be useful for probing differences in site occupancy to which XRD is not sensitive [208, 209]. Since this is a diffraction technique, only the average structure can be obtained. In addition, neutrons possess a magnetic dipole moment, and thus are sensitive to magnetic ordering (for some examples of this use, see [210, 211]). Unfortunately, due to the small number of neutrons available for experimentation, relatively large sample sizes are necessary for this technique. This is sometimes difficult for nanoparticles synthesized by chemical means.

Mössbauer spectroscopy depends on the ability of Fe^{57} nuclei embedded in a crystal to emit “recoil-free” gamma radiation (*i.e.*, momentum is conserved by recoil of a macroscopic number of atoms, rather than an individual nucleus). Because essentially, no energy is lost to recoil, the energy distribution of the gamma rays is extremely narrow, and is dependent on the chemical and magnetic environment of the Fe^{57} nuclei. To create a spectrum, the source of the photons is vibrated, imparting a time-dependent Doppler shift to the photons. These photons can then undergo the inverse process in a sample, in which those of the appropriate energy are absorbed by Fe^{57} nuclei (“resonant absorption”). Thus, information is conveyed regarding the local environment of Fe^{57} in the sample, generally including coordination number and oxidation state. The dependence on the coordination number implies a dependence on *domain size* as well; it is possible to use this method to yield an estimate of domain size, even when the domain size cannot be extracted from magnetic parameters such as the superparamagnetic blocking temperature [212]. Because Mössbauer spectroscopy also depends on the magnetic environment, it is an important tool for investigating iron-containing nanoparticles [198, 203, 213–219].

Remarkably, thermal analysis techniques such as thermogravimetric analysis (TGA), differential thermal analysis (DTA), and differential scanning calorimetry (DSC) have been used to determine site occupancies. Each technique measures the value of a physical parameter as the temperature is changed in a controlled fashion. For TGA, the parameter is the mass of the sample (outgassing or oxidation accounts for the mass changes); for DSC, the parameter is the power required to keep the sample at the same temperature as a reference material; for DTA, the temperature of the sample relative to a reference material is measured. Some site occupancies in magnetic nanoparticles have been deduced from DSC and TGA [220], since the temperature at which ions oxidize (*e.g.*, Fe^{2+} going to Fe^{3+}) is dependent on the local environment of the ion [221]. Depending on the synthesis technique and particle size, however, this effect may be obscured by the effects of materials adsorbed onto the surface of the nanoparticles.

4.2. Synchrotron-Based Techniques

The suite of techniques discussed above can provide considerable structural information about many types of magnetic nanoparticles. There are, however, significant gaps. Diffraction, for example, can provide only very limited information about amorphous phases. Likewise, the structure of nanoparticle materials consisting of multiple chemical phases may resist solution via the above techniques. Fortunately, techniques that utilize synchrotron radiation are well suited to both of these scenarios.

About 40 dedicated “light-source” synchrotrons on four (soon to be five) continents are currently available to the scientific community. Although each facility has different capabilities, they generally provide broad-spectrum ultraviolet and X-ray radiation that is more than six orders of magnitude brighter than a conventional X-ray tube. These characteristics allow high-resolution spectroscopy to be conducted in a reasonably short time-frame, sometimes even allowing the kinetics of a synthesis to be observed *in-situ*. Although there are a variety of modes in which this spectroscopy can be conducted, many of which will be discussed later, the essential feature of these spectra is that they provide information about electronic structure and/or local environment that is completely element-specific. Because the information is inherently local, amorphous materials can be investigated; because the information is element-specific, the structures of materials consisting of multiple phases, or of those exhibiting point defects, can often be clarified.

4.2.1. Modes of Data Collection

X-ray absorption spectroscopy (XAS) experiments filter the photons emerging from the synchrotron with a monochromator so that only a narrow band of energies impinge on the sample at any given time; this energy is then varied to produce the spectrum. The intensity of transmitted photons, yield of fluorescent photons, total electron yield, may be measured independently. Total electron yield is surface-sensitive, with most of the signal coming from the first few nanometers of material (depending on the material and the energies involved). Fluorescence is less surface-sensitive, typically probing to a depth on the order of 10 microns, and is suitable for extremely dilute samples or those that are too thick for transmission. Transmission is sensitive to the entire thickness of the sample, but requires the sample to be on the order of several microns thick.

In emission techniques, a monochromator is still used, but the energy is left fixed. Instead, the distribution of kinetic energies produced by the emitted electrons is recorded, providing information about the electronic structure of the material. This is known as X-ray or ultraviolet photoelectron spectroscopy (XPS, UPS), or sometimes as electron spectroscopy for chemical analysis (ESCA).

Energy-dispersive X-ray absorption spectroscopy [222, 223] (EDXAS or DXAS) utilizes a curved polychromator to send photons through the sample with a range of energies corresponding to different diffracted angles, so that an entire spectrum can be collected simultaneously with a linear or areal detector. Energy-dispersive XAS holds promise for investigating the kinetic and mechanisms of reactions on the subsecond time scale [224–228]. The high intensity and

selectable energy of synchrotron radiation can also be used advantageously in XRD; this can be combined with XAS in a number of ways. For example, in diffraction anomalous fine structure [229–230] (DAFS) experiments, the angle of diffraction is varied simultaneously with the incident photon energy in such a way that the same Bragg peak is being sampled at different energies. The result is an element-specific spectrum that is sampling only atoms in sublattices that obey the Bragg condition for that peak. In this way, the local environment of an element in a particular phase, or under favorable conditions, a particular type of lattice site [231–234], can be probed. A comparison of DAFS and XAS analyses of nanoparticulate metals is given by Bazin et al. [235].

In DAFS, many energies are sampled at one Bragg peak. In anomalous diffraction, entire diffractograms are sampled at a small number of energies. This technique has recently been used to determine the site occupancy not only by element, but by valence as well [236].

4.2.2. Data Interpretation and Analysis

The interpretation of synchrotron-based X-ray absorption spectra is often not straightforward. For example, a portion of the X-ray absorption spectrum for iron is shown in Figure 5. The binding energy of the *K* electrons in iron is 7112 eV; therefore, the absorption shows a large jump (the “edge”) as the energy of the incident photon exceeds that energy. This binding energy will increase by a few eV if the iron is oxidized and the edge will shift accordingly; thus, the position of the edge can be used to estimate the oxidation state. The detailed structure within about 30 eV of the edge, known as X-ray absorption near-edge structure (XANES), is generally interpreted in terms of core electron transitions to available energy states (either above or below the Fermi level); XANES, therefore, yield information on bonding and the local symmetry of the atoms surrounding the absorber.

Extended X-ray absorption fine structure (EXAFS), the quasi-oscillatory features above 30 eV, are due to coherent scattering of atoms in the local environment up to a distance of several Ångströms from the absorbing atom.

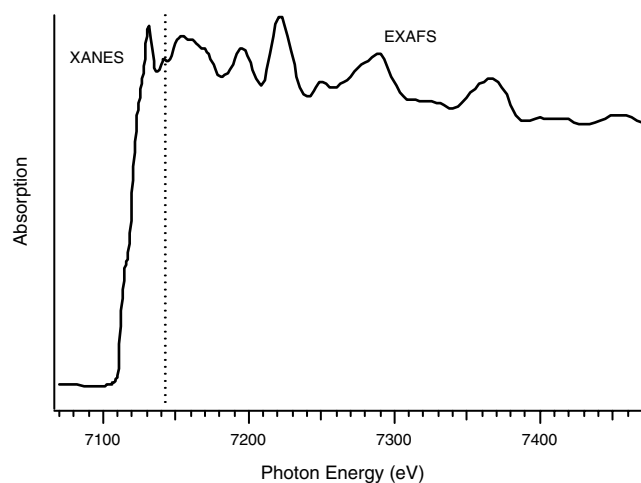


Figure 5. XAS of an iron foil near the *K* edge. Dotted line divides XANES from EXAFS region.

Depending on the sample, type, and region of spectrum, and desired information, several techniques are used to analyze this information (references immediately after the technique name are to applications of the technique to magnetic nanoparticles):

- (a) *Fingerprinting* [237]. The simplest method of analysis is to compare the spectrum with a known reference compound (the “empirical standard”). Of course, if the material is crystalline and sufficiently similar to the reference, XRD can perform this task without the need for a synchrotron. On the other hand, nanoparticle materials are often similar on a local scale to a bulk analogue, but lacking (or different) in long-range order. If the XANES (or the XPS) of the material is similar to the reference, it suggests that the immediate environment of the atoms is similar; if the EXAFS are similar, then the local environment may be similar out to several Ångströms.
- (b) *Comparison to theory* [219, 238, 239]. This may represent either qualitative assignments of particular spectral features to particular causes (*e.g.*, a particular electronic transition or backscattering from a particular coordination shell) or comparison to an *ab-initio* calculation [240, 241] of a spectrum (a “theoretical standard”).
- (c) *Curve-fitting to a theoretical standard* [242–243]. This technique is used most often to analyze EXAFS, including the oscillatory portion of DAFS [244]. In this technique, a model of the material, with several parameters left free, is hypothesized. For example, a sample may be hypothesized to consist of nanoparticles composed of bcc iron mixed with Fe_2O_3 . Free parameters might include the size of the particles and the fraction of each phase present. A theoretical standard is then calculated for reasonable values of the free parameters; theoretical expressions can be used to compute how the spectrum changes for different values of the parameters. Subsequently, the values of the free parameters are optimized by a least-squares fit of the modified theoretical standard to the data. A poor fit indicates that the model is poor; a good fit indicates that the model *may* be good. If the model is good, then the values of the free parameters that produce the fit are expected to reflect the actual structure of the material.

When used judiciously, this technique is among the most powerful and can be used profitably even when the material is made up of multiple phases. It is, however, prone to misinterpretation if used carelessly, partly because more than one model may correspond to the same spectrum or similar spectra (the model that does not correspond to the material is often termed a “false minimum”). For this reason, an EXAFS fit of a single coordination shell of a single sample under a single set of conditions is difficult to interpret uniquely. There are, however, several methods of reducing the likelihood of false minima. For example, the probability of a good fit being achieved with a poor model is considerably reduced if more than one absorption edge is

refined simultaneously. Likewise, fitting more than one coordination shell simultaneously is advisable, at least for crystalline phases, because this will reduce the correlation between parameters (a single-shell fit, for example, cannot distinguish the coordination number from the EXAFS quantum efficiency S_0^2) and because it will act as a powerful constraint on valid models. Of course, it is helpful if the number of free parameters can be reduced by using the results of other probes. Stoichiometry, for example, can be determined reliably by methods such as inductively coupled plasma-atomic emission spectroscopy (ICP-AES). The stoichiometry, in turn, can be used to constrain site occupancies of materials exhibiting substitutional disorder. It is also worth noting that analyses of EXAFS by the curve-fitting method are almost always dominated by systematic error; this error may stem from limitations of the *ab-initio* calculation, the choice of free parameters, the values chosen for fixed parameters, the method used to extract the EXAFS oscillations from the raw data, or the way in which the samples were prepared for measurement. Fortunately, these sources of systematic error do not vary much for a set of samples prepared and analyzed in the same way. Thus, if a series of measurements and fits are performed on a sample while varying some extrinsic parameters (*e.g.*, temperature, pressure) or measurements are performed on a series of samples differing in some way (*e.g.*, nanoparticle size, amount of dopant), the differences between the values of the parameters as determined by the fits are much more reliable than the values themselves. This is a particularly valuable strategy if one of the samples has been well-characterized by another method (*i.e.*, it is an empirical standard), since the degree of systematic error can then be ascertained.

- (d) *Principal component analysis* [245] (PCA): This technique requires a family of samples presumed to have differing (but unknown) proportions of chemical phases present, some (or all) of which may be unknown. For example, a sequence of core/shell nanoparticles could be prepared in such a way that the ratio of shell volume to core volume varies. As another example, an aging study could be performed on metallic nanoparticles: the ratio of oxide to metal could be expected to increase over time. If all the phases are unknown, PCA will yield only the number of phases present. If the identity of all of the phases are known and empirical or theoretical standards are available, then PCA reveals the fraction of each phase that is present. Finally, if the structures of some phases are known and others unknown, PCA may be combined with curve-fitting to a theoretical standard; this combination is sometimes called residual phase analysis (RPA). Principal component analysis has recently been used to analyze EXAFS [245–247], XANES [226, 228, 248, 249], and XPS [250, 251].

4.3. Future Trends

As the synthesis of magnetic nanoparticles has become more sophisticated, moving from ball-milling methods which generate a broad size distribution of disordered single-phase particles to wet chemical techniques which show promise for producing nearly monodisperse particles with a high degree of structural order, so have the techniques used to characterize them. Increasingly, synchrotron radiation has played a role, with both experimental and analytical techniques rapidly advancing and proliferating. High-intensity sources, for example, have stimulated the development of DAFS, enhancing the element-specificity of XAS with the ability, in many cases, to probe individual phases. Energy-dispersive XAS is now allowing the progress of synthesis reactions to be monitored at a scale of seconds or below; this technique as yet has been little-used with magnetic nanoparticles, but is likely to change as researchers broaden their focus from the end product of a synthesis to its mechanism and kinetics. Curve-fitting to theoretical standards is becoming increasingly sophisticated, with simultaneous multiedge refinements [243, 252] and models that account for the size and shape of nanoparticles [253–255] beginning to appear. Finally, PCA promises to yield significant structural information from materials that had previously resisted characterization.

5. MAGNETIC PROPERTIES OF NANOPARTICLES

This section emphasizes the magnetic characteristics important to nanoparticles. The following sections provide a general overview of the relevant parameters, behavior, and experimental tools used to examine magnetic properties. Additionally, select examples from recent literature have been included as examples of the types of research being conducted and to emphasize the strengths of the characterization techniques.

5.1. Magnetism of Fine Particles

The magnetic behavior of nanocrystals is largely dependent on the physical characteristics of individual particles (including particle morphology, intrinsic materials parameters, surfaces/interfaces, and size) and their environments (such as interparticle distance, temperature, and applied magnetic fields). When the particles are isolated and sufficiently small, magnetic responses similar to bulk magnetic materials fail to describe their conduct. However, their magnetic behavior is sufficiently similar to bulk materials as to warrant discussion in the following sections.

When the critical length scales for physical properties are similar in size to the structural length scales of the material, interesting physical phenomena arise. In the case of exchange-coupled magnetic materials, this length is called the exchange correlation length and is on the order of 1–100 nm. This naturally leads to the consideration of nanoparticulate materials for interesting magnetic phenomenon. Control of the processing of nanoparticle materials will yield a host of applications in the burgeoning fields

of nanoelectronics and bioelectronics. Size, shape, composition, and distributions of these qualities about the particle mean will determine the success of these materials for application.

In recent years, new processing techniques and novel use of proven characterization techniques have advanced our knowledge of magnetic nanoparticles. However, the recent technological attention simply adds to over half a century of basic research in this field. A number of excellent reviews have been published over the years that encompass many of the aspects of the topics contained herein [256–258].

5.1.1. Magnetism Terms and Units

Units of measurement for magnetic applications suffer from unusual definition conventions, making it difficult to easily convert between systems. This article will solely use SI magnetic units for clarity. This section provides definitions for some of the salient terms necessary for understanding the magnetism of nanoparticles. More in-depth descriptions of these terms and their uses are found elsewhere [259, 260].

Intrinsic magnetic characteristics of materials include Curie temperature, saturation magnetization, exchange stiffness, and magnetocrystalline anisotropy. These characteristics are generally invariant with respect to microstructure of the material. However, this is not necessarily the case for nanoparticles, where the large amount of surface area tends to affect these properties due to surface relaxation and truncation. As might be expected, the deviations from the bulk intrinsic properties grow as the particle size is reduced.

Each of the intrinsic magnetic properties mentioned above are described here as an introduction to their meaning. The phase transformation temperature from ferromagnetic (or ferrimagnetic) behavior to paramagnetic behavior occurs at the Curie temperature (T_c). The saturation magnetization (M_s) is the magnetic moment per unit volume of the material (amperes per meter) when a sufficiently large magnetic field is applied. The exchange stiffness (A) is a measure of the strength with which adjacent magnetic moments remain aligned with units of joules per meter. The magnetocrystalline anisotropy (K) is the internal energy density dependent on the direction of the magnetic moment, with respect to the crystalline lattice and has units of joules per cubic meter. Magnetic anisotropy will be discussed in more detail due to its strong influence on the magnetic properties of nanoparticles.

The extrinsic magnetic properties include coercivity, remanent magnetization, and magnetic susceptibility. These parameters depend upon the microstructure of the material and are naturally affected by the size of the particles. The coercivity (H_c) or coercive field is the applied magnetic field required for reduction of a saturated magnetic material to zero magnetization (amperes per meter). The remanent magnetization (M_r) is the magnetization that remains after an applied field has been removed (amperes per meter). The magnetic susceptibility (χ) is the magnetization normalized by the applied magnetic field (with proper normalization, it is unitless). The magnetic susceptibility acts as a technological figure of merit for magnetic nanoparticles, since it links the particles (through their magnetization) with a readily applied field.

5.1.2. Paramagnetism

Paramagnetic materials possess unfilled electronic shells giving them a permanent magnetic moment. This moment consists of contributions from the spin and orbital momentum of the atom's electrons. Paramagnets differ from the more technologically useful ferromagnetic materials due to the fact that their magnetic moments do not interact strongly with each other. The magnetic moments tend to align with an applied magnetic field in a stochastic manner, yielding a slightly positive magnetic susceptibility ($\sim 10^{-6}$). The temperature dependence of the susceptibility for many paramagnetic materials follows the well-known Curie law ($\chi = C/T$, where C is the Curie constant).

5.1.3. Ferromagnetism/Ferrimagnetism

More complex (and interesting) magnetic phenomena are found when the magnetic moments on adjacent atoms interact. Ferromagnetic materials have interactions causing the alignment of the magnetic moments. These materials have high susceptibility and net magnetic moments even in the absence of an applied field.

Still more complex, yet equally interesting from a technological standpoint, are ferrimagnetic materials. These materials consist of anti-parallel arrangements of the magnetic moments, yet the material maintains a net magnetization. This is due to either the numbers of moments being different in each direction, or the size of the magnetic moments in alternating directions being different (or both). Ferrimagnets have high susceptibility (up to 10^6) and net magnetic moments even in the absence of an applied field, much the same as ferromagnets. At sufficiently high temperatures, the magnetic ordering of both ferromagnetic and ferrimagnetic materials is disturbed causing a change to paramagnetic behavior (at the Curie temperature).

The most important technological materials in the bulk come from the classes of ferrimagnetic and ferromagnetic materials due to their high susceptibility and net magnetization. Common examples of technologically important ferromagnetic materials include Fe, Co, Ni, and their alloys and rare earth intermetallics (*i.e.*, $\text{Nd}_2\text{Fe}_{14}\text{B}$ and $\text{Sm}_2\text{Co}_{17}$). Prevalent ferrimagnetic materials include Fe-based oxide materials with the inverse spinel crystal structure (called ferrites) and rare earth/iron-based oxides (called garnets).

5.2. Ideal Particle Systems

The magnetic behavior of nanoparticles is diverse and complicated. The characteristics of particles and their environments will be discussed in the simplest manner in this section. This means a discussion of spherical, monodisperse particles without magnetic interactions between adjacent particles or agglomerations. Some complications of real nanoparticle systems will be discussed in the succeeding section.

5.2.1. Single-Domain Particles

As in the case of their bulk counterparts, a feature of primary interest for magnetic nanoparticles is magnetization reversal. In bulk magnetic materials, the nucleation and motion of domain walls through the material control the

reversal. The ease with which the domain walls move through the material when a magnetic field is applied determines the application for which the material is best suited. Pinning of domain walls on grain boundaries, voids, or non-magnetic inclusions cause an increase in the field necessary for magnetization reversal by hindering the motion of domain walls. The nucleation of magnetic domains arises to minimize the magnetostatic energy. As the size of a bulk ferromagnet is reduced, the nucleation of reverse domains becomes more difficult because of the large magnetostatic energy.

Bulk ferromagnetic materials are generally polycrystalline with each grain consisting of thousands of magnetic domains separated by boundaries called domain walls. In the simplest case, the magnetization in adjacent domains continuously changes direction by 180° over the width of the domain wall. The domain wall is a defect in the material that requires energy to form. As mentioned previously, the multiple domains form in a grain to alleviate the magnetostatic field exiting the grain. The first panel of Figure 6 shows a multidomain particle with 90° domain walls.

For a small ferromagnetic particle made up of a single spherical grain, the magnetostatic energy has the form $(\pi\mu_0 M_s^2 r^2 w)/9$ and the domain wall energy $(2\pi\rho^3\gamma)/w$, where r is the particle radius, γ is the domain wall energy per unit area, and w is the domain width. Minimizing the total energy with respect to the particle radius yields a relation for the critical radius under which a domain wall will not form in terms of materials parameters $((18AK)^{1/2}/(\mu_0 M_s^2))$ [261]. In a practical sense, particles below this limit consist of a single domain that thermodynamically cannot support the formation of a domain wall, and therefore have magnetization reversal by rotation of the spins into the applied field direction (as indicated by the second panel of Fig. 6).

The preferred direction of the magnetization for a ferromagnetic material is determined by magnetic anisotropies, which arise from many causes, including the shape of the magnet, the crystalline structure and chemistry of the material, and the strain in the material. Their origins are quite different and affect the characteristics of magnets of all sizes, particles and bulk alike. Generally, many types of anisotropy should be combined to fully describe the nanoparticles [262].

Shape anisotropy arises from the field formed by the magnetization of the material (a consequence of the Maxwell

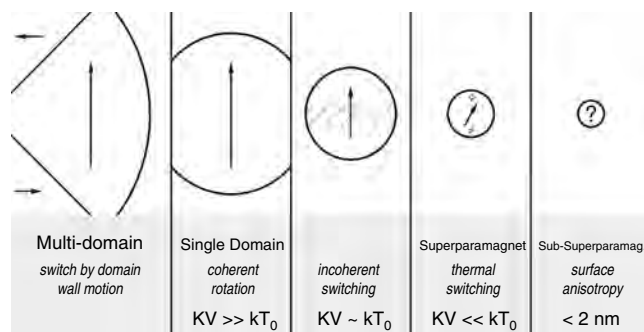


Figure 6. Noninteracting particles (compositionally invariant and single phase) as a function of the particle size, indicating the magnetization reversal mechanism regimes at an isothermal temperature, T_0 .

equations) [263, 264]. It is described analytically for ellipsoids of revolution, with a uniaxial form for prolate ellipsoids (*i.e.*, acicular particles): $E = 1/2M_s^2(N_b - N_a) \text{Sin}[\theta]^2$, where θ is the angle between the magnetization and the applied field, M_s is the saturation magnetization and N_b and N_a are the demagnetizing factors for the long and short axes of the spheroid, respectively. Slight aspheric distortions of near-spherical particles yield inconsequential differences in the shape anisotropy until the length of the aspheric axis exceeds approximately 30% of the sphere radius.

The magnetocrystalline anisotropy forms due to the spin-orbital coupling of the material and is linked with the symmetry of the crystal structure for the magnetic material. Uniaxial anisotropy for tetragonal, rhombohedral, and hexagonal crystal structured materials have the form: $E = K_1 \text{Sin}[\theta]^2 + K_2 \text{Sin}[\theta]^4$, while cubic materials follow: $E = K_1(\alpha_1^2\alpha_2^2 + \alpha_2^2\alpha_3^2 + \alpha_3^2\alpha_1^2) + K_2(\alpha_1^2\alpha_2^2\alpha_3^2)$, where α_i are the direction cosines for the magnetization. The strain derivative of the magnetocrystalline anisotropy provides additional anisotropic response through the magnetostriction coefficient (λ_s). For a single axis of stress, this term is uniaxial, with the form: $E = 3/2\lambda_s\sigma \text{Sin}[\theta]^2$, where σ is the stress on the material.

A simple, elegant model of the hysteretic behavior of single-domain particles was developed in the late 1940's. This Stoner–Wohlfarth (S-W) model [265, 266] considers the energy due to the magnetocrystalline anisotropy, shape anisotropy, and magnetostatic interactions of the particle as a function of a magnetic field applied at a fixed angle from the magnetic easy axis. As the applied field is increased, the magnetization is coherently rotated into the field direction.

Calculations based on the S-W model are presented in Figure 7. The ideal cases of isolated, monodisperse, noninteracting nanoparticles, both single domain and superparamagnetic, are shown. For an assembly of noninteracting particles with aligned magnetization, a square hysteresis loop with high coercivity and remanent magnetization is

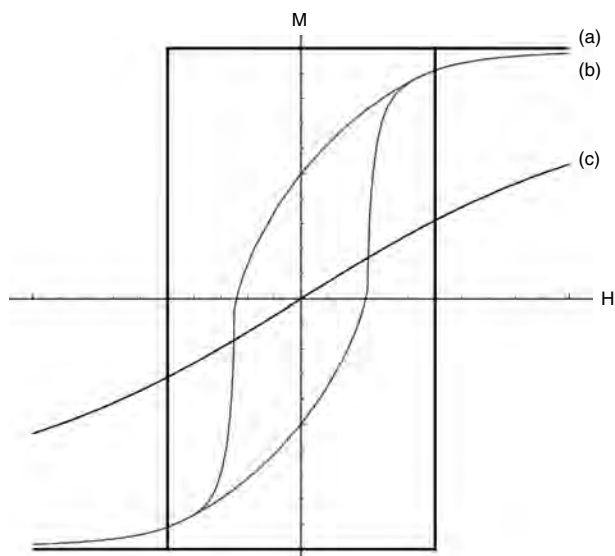


Figure 7. Hysteresis loops for an assembly of: (a) aligned single domain particles; (b) randomly oriented single domain particles; (c) superparamagnetic particles.

found (Fig. 7(a)). An assembly of randomly oriented particles, on the other hand, exhibits lower remanence and coercivity (Fig. 7(b)). The S-W model works well for single-domain particles; however, as the particle size is reduced further, the magnetostatic and anisotropic magnetic energies are no longer the only two of consequence—thermal energy plays an increasing role. As demonstrated in Figure 7(c) and discussed in the next subsection, this superparamagnetic behavior exhibits no remanent magnetization and no coercivity.

5.2.2. Superparamagnetism

Superparamagnetism is a magnetization reversal mechanism for fine particles driven by thermal energy [267]. At large particle sizes, the magnetization is confined to specific directions determined by the shape, crystal structure, lattice strain, etc. As the particle size is reduced, stochastic thermal fluctuations exceed the energy barrier, keeping the magnetization in its energy well. Similar to a ferromagnetic material, the magnetic moments of adjacent atoms remain aligned and acting as one large magnetic moment for the whole particle (*i.e.*, exchange coupled); however, their direction is not fixed. An assembly of these particles with “super moments” acts like a paramagnetic material—hence, the term superparamagnetism.

The thermal activation over the magnetic anisotropy energy barrier takes the form: $f = f_0 \text{Exp}[-E_b/kT]$ with E_b as the energy barrier (equal to KV for no applied field), f_0 is an attempt frequency on the order of 10^9 Hz, and kT is the Boltzmann energy term. When the time for activation over the energy barrier is long, the superparamagnetic particles are “blocked.” The blocking of superparamagnetic particles occurs below a temperature aptly named the blocking temperature. However, the blocking temperature is dependent on the time of measurement, applied magnetic field, and particle size distribution, making it an ill-defined parameter.

The size scale in-between superparamagnetism and single-domain particles is best described by its magnetization reversal behavior. The constant fluctuation of the superparamagnetic particles is not entirely present; however, magnetic relaxation does occur. The coherent rotation mechanism of the single-domain particles does not describe the particles, although they maintain hysteretic behavior. This size range for nanoparticles can best be described by incoherent rotation of the magnetization, one example of which is the magnetization curling mechanism (see the center panel of Fig. 6) [268].

5.2.3. Isolated Particles

The magnetization of an assembly of superparamagnetic particles has the same dependence on applied magnetic field as a paramagnetic material, with the replacement of the atomic magnetic moment of the paramagnet with the particle magnetic moment of the superparamagnet. The Langevin function describes this behavior $L[b] = \text{Coth}[b] - 1/b$, where $b = \mu H/kT$ and $\mu = M_s V$. This function reveals two of the characteristic features of the superparamagnet response to a magnetic field, namely, no coercivity and no remanent magnetization.

Since superparamagnetism is a stochastic phenomenon, the direction of the particle's magnetic moment fluctuates with time. Any specific particle will change its direction of magnetization during the time of magnetization measurement. Now the magnitude of the magnetic moment of an individual particle is a strong function of particle radius (or volume), and therefore, the magnetic properties of the nanoparticles will be dependent on the measurement time of the experiment. For example, measurement by SQUID magnetometry has a measurement time of roughly 10^2 s, yielding a blocking temperature defined by $25 = KV/kT_b$, whereas Mössbauer spectroscopy has a measurement time of 10^{-8} s, providing a blocking temperature of $2.7 = KV/kT_b$. In other words, when the measurement times are much greater than the relaxation time, thermal activation will provide a statistical average of the magnetization (for temperatures above a particle's blocking temperature).

As illustrated in the schematic Figure 8, the perceived blocking temperature can be manipulated by changing the measurement time (τ) or the applied field (H) for a given set of nanoparticles (possessing constant magnetic anisotropy, K). Increasing the measurement time increases the blocking temperature when the particle assembly and magnetic fields are kept constant. This is illustrated by the comparison in the previous paragraph between SQUID magnetometry and Mössbauer spectroscopy. When the magnetic field is increased (for a single measurement time and particle assembly), the blocking temperature is reduced. This is due to the stabilizing effect of the magnetic field on the particle assembly.

The smallest nanoparticle materials, with sizes below 1–2 nm, behave in manners that are difficult to relate to their bulk counterparts. Superparamagnetic materials have enough particle volume to remain bulk-like in the case of magnetocrystalline anisotropy and magnetization. However, when the fraction of surface atoms becomes too great, these intrinsic material properties are highly influenced by surface relaxation effects, thereby modifying their values. This, in turn, makes comparisons to the models for superparamagnetism difficult. This has been indicated in Figure 6 by the final panel with the title, "sub-superparamagnetic" particles for lack of a better term.

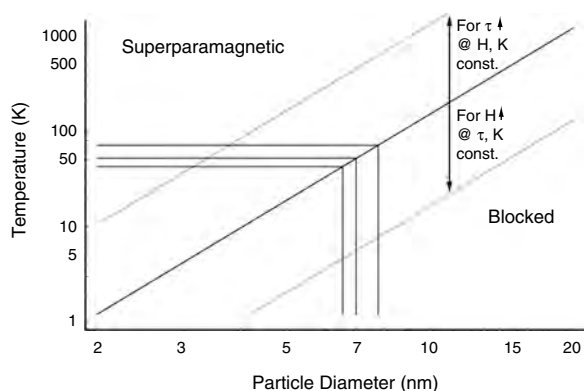


Figure 8. Diagram for the blocking temperature as a function of the particle diameter at constant measurement time, where up-arrows indicate the variation of τ or H .

5.3. Mechanisms for Complicating Magnetic Behavior

Up to this point, the magnetic properties have been simplified to a large degree to avoid confusing issues. These ideal particle systems have avoided the effects of oxidation, organic ligands bound to the particle surface, particle shape, agglomeration, multiphase materials, etc. All of these contribute to the difficulty of characterization and analysis of the magnetic characteristics of nanoparticles. The magnetic behavior of the nanoparticles is sensitive to the physical characteristics of individual particles (including morphology, intrinsic materials parameters, and size) and their environments (such as interparticle interactions, material at the particle surfaces, temperature, and applied magnetic fields). Therefore, a complete characterization of the particles and their surroundings should accompany any magnetic study. Failure to provide these prerequisites makes meaningful determination of the intrinsic magnetic properties of the nanoparticles difficult.

5.3.1. Interparticle Interactions

Interparticle interactions cause a host of complications in the magnetic properties of nanoparticle assemblies. The magnetostatic field generated by the particles can promote chaining of particles and agglomeration if the particles are free to move. As schematically shown in Figure 9, interparticle interactions play an increasing role as the distance between particles decreases. Particles are considered to be isolated when they have a sufficiently small interaction, as the magnetic field generated by adjacent particles is generally the longest range interaction; this limit is determined by some small arbitrary field generated by the particles in the assembly. The particles shown in Figure 6 are considered isolated; this is indicated on Figure 9 by a dashed line.

At large separation distances (d_{12}), the simple cases of superparamagnetic and single-domain particles are found. The hazy region between the two indicates the region where incoherent reversal modes make significant contributions to the magnetization reversal.

When the particles touch each other, short-range exchange interactions are possible. Depending on the amount of

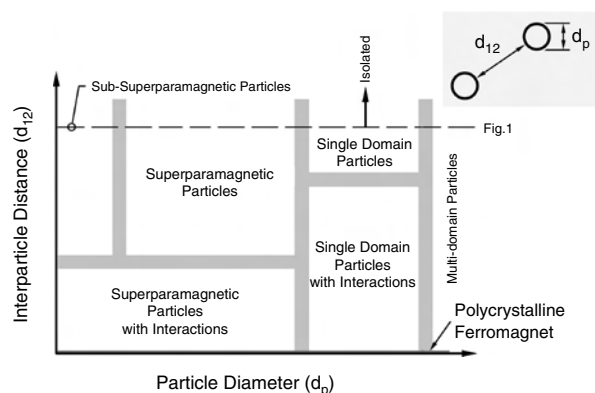


Figure 9. Schematic phase diagram for interparticle interactions as a function of the particle size.

interface, this might be considered a polycrystalline ferromagnetic material at this point (assuming a large fraction of particle surface is represented by interparticle interfaces). This is the desirable case for using nanoparticles as precursors for bulk compacted material, although the difficulties in achieving this goal are immense.

5.3.2. Intraparticle Effects

Other forms of anisotropy may form when a copious surface area is available. Anisotropy due to surface termination of the particle, exchange coupling to antiferromagnetic oxides, or bonding to surfactants alter the magnetic behavior and, in some cases, the anisotropy of the material directly.

In many cases, a desirable passivating coating has been applied to protect metallic nanoparticles, either from oxidation or as a means of making them compatible with specific environments (biological or chemical). The addition of shells to nanoparticles adds new dimensionality to the complexity of the magnetic response. As demonstrated in Figure 10, the simplest form of a core/shell nanoparticle is represented schematically. Six regions are enumerated for their potential to affect the magnetic properties of the composite material. It is noteworthy that the interface of some of these regions may be coherent and therefore difficult to ascertain. The shell surface has been shown to modify the “magnetic volume” of the particle, making it differ from that of the structural volume (as found by TEM, for instance). This might be due to the direct bonding of ligands to the surface or the missing bonds at the interface.

Depending upon the thickness of the shell, there may be a region with near bulk properties for the shell material. However, that region is sandwiched between a surface dominated region and an interphase, interfacial region near the

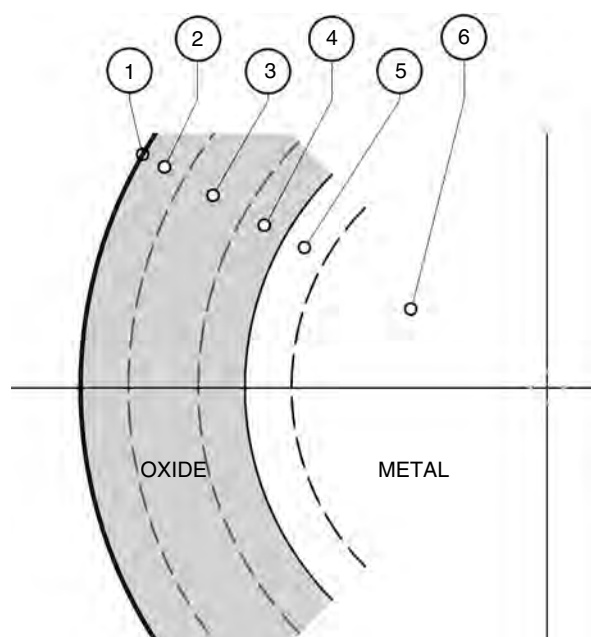


Figure 10. Schematic diagram of a metallic nanoparticle with oxidation at the surface, indicating various structural regions: 1) shell exterior surface; 2) shell relaxation region; 3) shell material; 4) shell interphase interface region; 5) core interphase interface; 6) core material.

core material. The shell material within a few unit cells of the surface of the particle presumably has a relaxation of the bonds due to the missing bonds at the surface, which can significantly change the magnetization, especially in magnetic oxides. The interdiffusion of material from the core into the shell material has significant feasibility, depending on how the particles were passivated. This region may also have significant strain produced during the formation of the shell and the interphase interface. Similarly, the diffusion of oxygen into the core material is possible with the same consequences as for the shell material. Finally, presuming that the particles do not fully oxidize, a metallic core with magnetic properties similar to the bulk resides at the center.

5.4. Measurement Techniques

Due to the stochastic nature of many magnetic nanoparticle effects, the magnetic properties obtained by different measurement techniques are dependent on the time scales of measurement, the measurement temperature, and the applied magnetic field strength. Complications arise when the effects of surface atoms, particle size distributions, and interparticle interactions are considered.

5.4.1. Direct Current Susceptibility

Direct current (DC) susceptibility measurement is a common method of determining the superparamagnetic blocking temperature. This is accomplished by examining a particle system assembly under zero-field cooled (ZFC) and field-cooled (FC) experimental conditions. The ZFC experiment requires cooling the sample to a low temperature with subsequent application of a small, applied magnetic field. The temperature is then raised at a constant rate and susceptibility data are collected. The susceptibility reaches a maximum at a temperature near the blocking temperature, with superparamagnetic decay of the susceptibility above the blocking temperature. The FC experiment provides more certainty in the temperature at which superparamagnetic behavior sets in. This experiment requires cooling the sample in a small magnetic field of the same strength as the ZFC experiment, again collecting susceptibility data as the temperature increased. The measurement time for these experiments is near 10 s.

Sun and Murray show that ZFC experiments on monodisperse self-assembled nanoparticles can be used for examination of interparticle interactions [269]. The magnetostatic fields generated by the nearby nanoparticles in the array shift the peak in the ZFC curve to lower temperatures in addition to sharpening the peak. It should be noted that these experiments were supported by evidence from X-ray diffraction, TEM, and inductively coupled plasma experiments, all of which added to the analysis of the magnetic properties.

The work of Pentes and Krishnan show interparticle dipolar interactions through the use of ZFC/FC experimentation [270]. The experiments on ϵ -Co self-assembled nanoparticles showed a broad peak in the ZFC susceptibility characteristic of dipolar interactions. They also observed a strong increase in the FC susceptibility at low temperatures, presumably due to Brownian motion of the particles

in the viscous oleic acid when the field was applied at high temperature.

5.4.2. Direct Current Hysteresis

Lack of coercivity in a particulate sample is a hallmark of superparamagnetic samples. The hysteretic behavior of a magnetic material can be probed by cycling a large magnetic field between opposite directions relative to the sample. The theoretical hysteresis curves shown in Figure 7 compare the ideal cases of isolated, monodisperse, noninteracting nanoparticles, either single domain, or superparamagnetic. More generally, a particle size distribution, where some of the particles are large enough to be blocked while others remain superparamagnetic, is necessary to describe a real material. As first demonstrated by Bean in 1955 [271], a weighted average of contributions from the superparamagnetic (Langevin function) and blocked particles (S-W model) describe the hysteretic behavior, barring interparticle interactions. Realistic models of this behavior have been developed in recent years to describe the variety of measured loop shapes [272, 273].

A basic type of hysteresis loop study for nanoparticle materials entails the measurement of loops above and below the blocking temperature of the material. This is illustrated by Chen and Zhang for MgFe_2O_4 spinel ferrites [274]. They show the increased susceptibility for large-sized superparamagnetic particles at high temperatures and the coercivity dependence on particle size for blocked particles.

Sun et al. used a SQUID magnetometer to examine the phase transformations via hysteresis loops of monodisperse self-assembled FePt nanoparticles [180]. Their hysteresis results identify annealing conditions and composition ranges that were optimized for large coercivity.

SQUID magnetometry studies of the surface effects on the magnetization of nanoparticles were performed by Toneguzzo et al. [130, 145]. These experiments showed a common effect in nanoparticle systems, namely, that the saturation magnetization is inversely proportional to the particle diameter (or proportional to the surface area divided by the volume). This has been explained by pinning of magnetization at the surface of the nanoparticles, the introduction of a “dead” layer at the surface [275], and the formation of surface oxides during various studies. Toneguzzo et al. use a metallo-organic and oxide phase shell model to analyze their data.

A similar study of yttrium-iron garnet ($\text{Y}_3\text{Fe}_5\text{O}_{12}$) by Sanchez et al. showed the saturation magnetization is inversely proportional to the particle diameter [113]. In this case, the oxide particles have a decreased magnetization presumably due to either a nonmagnetic surface layer or noncollinear spin arrangement. Shafi et al. have examined the surface effects of various surfactants on the surfaces of amorphous Fe_2O_3 nanoparticles [96]. They attribute low magnetization found in hysteresis loops for particles coated with octyl phosphonic acid as an indication of antiferromagnetic coupling to the nanoparticles.

5.4.3. Temporal Remanent Magnetization

The switching and relaxation behavior of nanoparticles can be examined by a number of different temporal remanent magnetization techniques. Thermoremanent magnetization

(TMR) studies provide relaxation information about particles that have been field cooled below the blocking temperature with ensuing removal of the magnetic field at the measurement temperature. Isothermal remanent magnetization (IMR) experiments require zero field cooling to the measurement temperature with subsequent application and removal of a magnetic field. Finally, similar to the IMR curves, DC demagnetization curves involve zero field cooling of the sample; however, a large magnetic field is applied to the sample and then a field is applied in the opposite direction from which it is finally removed. The combination of DC demagnetization and IMR experiments can provide interparticle interaction information through the calculation of the δM parameter [276, 277]. Since superparamagnetic particles do not have remanent magnetization, the magnetic remanence will come from the blocked magnetic particles at a given temperature.

The experiments of Zeng et al. have shown the interparticle interactions of FePt nanoparticles by use of δM curves [278]. The particles in this case are annealed, and thereby aggregate showing a trend of negative δM values indicating dipolar interactions for low annealing temperatures and large positive δM indicating exchange coupling at high annealing temperatures.

5.4.4. Alternating Current Susceptibility

Alternating current (AC) susceptibility measurements are a valuable source of magnetic characterization with measurement frequencies from 10 to 10 kHz. This technique gives information about the dynamic behavior of the nanoparticles with the capability for initial susceptibility measurements at very small fields. Experiments show the real part of the susceptibility (χ') is frequency independent at high temperatures due to thermal equilibrium of the superparamagnetic particles. When some of the superparamagnetic particles are blocked as the temperature is reduced, increased frequencies cause an increase in the temperature at which χ' peaks and a decrease in its magnitude.

These attributes are clearly shown by the work of Dormann et al. on $\gamma\text{-Fe}_2\text{O}_3$ nanoparticles [279]. Nanoparticles in varying sizes and degrees of interaction were examined by AC susceptibility. Particle samples (7.1 nm diameter) were examined as chains of particles and as entangled chain agglomerates. The particles with a chain-like environment possessed larger susceptibility for all measurement frequencies than the agglomerated sample. Additionally, the chained particle sample exhibited lower peak temperatures for χ' , indicating lower stability of the particles to thermal fluctuations than the agglomerated sample that possesses more near neighbors (thus higher magnetostatic interparticle interactions).

The effect of dilution on relaxation times of amorphous $\text{Fe}_{0.78}\text{C}_{0.22}$ particles as a function of temperature were examined by Djurberg et al. [280]. The more dilute sample showed much smaller relaxation times for a given temperature. This reflects the significance of interparticle interactions, where higher degrees of magnetostatic interaction provide stability to the system of particles.

5.4.5. Ferromagnetic Resonance

Ferromagnetic resonance (FMR) experiments provide information about the anisotropy, the distribution of particle easy axis orientations, and surface effects of magnetic nanoparticles. The experiment uses a strong magnetic field to align the magnetic moments of the particles and a transverse high frequency field to produce a precession of the magnetic moment about the strong applied field. These experiments are generally accomplished by fixing the high frequency field component and measuring the magnetic susceptibility as a function of the direction and magnitude of the large applied field. The many GHz frequency range of the high frequency field component gives a measurement time of greater than 10^{-9} s.

Studies carried out by Diehl et al. show the general trends of line sharpening for smaller particle size and higher measurement temperatures for ϵ -Co and twinned face centered cubic Co samples [281]. These effects are due to the thermal relaxation of the nanoparticles, yielding a single sharp resonance peak. The peak shape changes were accompanied by shifts in the resonance lines due to changes in the presence or magnitude of the particle anisotropy.

5.4.6. Mössbauer Spectroscopy

Mössbauer spectroscopic measurements use the absorption and emission of gamma rays to examine the local hyperfine fields at atomic nuclei. Generally, gamma rays with frequencies in the range 10^{18} to 10^{19} Hz are used for these experiments to excite the ^{57}Fe isotope within the sample. This technique can be used to reveal information about the crystal structure and magnetic characteristics of the nanoparticles with roughly a 10^{-8} s measurement time. Modeled Mössbauer spectra can be superimposed to incorporate many crystalline and amorphous phases, including separate contributions from surface atoms when relaxation effects are not significant. Due to thermal activation, superparamagnetic particles exhibit fluctuations in the hyperfine field parameters as a function of time. The effects of large surface area were examined by Bodker et al. by Mössbauer experiments on metallic Fe nanoparticles [282]. The anisotropy of the particles was determined *in-situ* as a function of grain size from the observed hyperfine field. The results indicated an increase in the anisotropy as the particle size

decreased, which was mainly attributed to magnetocrystalline anisotropy of the particles.

6. CONCLUSIONS

The goals of this chapter are to describe the chemical synthesis options available for the processing of magnetic nanoparticles, provide a review of useful and novel characterization methodologies to better understand the structure and chemistry of these particles, and to broadly review the magnetic properties of these particles in terms of their intrinsic magnetism as well as cooperative effects. We have limited our review to the time period beginning in 1990 and extending through 2002. Where appropriate, we direct the reader to other reviews and articles that provide the needed background to understand the outstanding issues addressing magnetic nanoparticles.

Table 2 summarizes different magnetic nanoparticles. Our scope has focused on the chemical methodologies that have been used to synthesize magnetic nanoparticles. Since these techniques use similar solvent systems, they offer the widest versatility and flexibility in processing. Combining one or more of these techniques is relatively simple and allows for the synthesis of many types of oxides and alloys. Of particular interest is the use of surfactant-mediated synthesis, including micellar, sol-gels, and polyol techniques. These techniques offer the ability to control particle size to less than 10% and allow for a wide range of materials and morphologies. Notwithstanding these powerful processing methods, gaining insight into the particles composition, phase, and structure remain elusive. To address this challenge, we propose the use of synchrotron radiation techniques to supplement the more routine laboratory characterization tools. Extended X-ray absorption fine structure has recently been used to analyze magnetic nanoparticles to determine element-specific phase purity, cation disorder, and particle size. This powerful tool can address many of the difficulties that exist in determining the nature of nanoparticles. Finally, we review the intrinsic and extrinsic magnetic properties of nanoparticles. Since the magnetism of these materials depend not only on particle chemistry and phase, but also on the particle size and environment, we explore the roles of interparticle interaction and surface functionalization in determining the magnetic properties of the system.

Table 2. Summary of Magnetic Nanoparticles.

Compound*	Method†	Size (nm)	Morphology	Characterization‡	Ref.
Fe	PPC	<200	Agglomerates	TEM, XRD, ICP, SQUID	[283]
α -Fe(β -FeOOH)	PPC and M	30–180	Needles	TEM, XRD, VSM	[284]
Fe(Fe ₃ O ₄)	PPC	20–200	Spheres	TEM, XRD, FTIR, VSM, ACSus	[285]
α -FeOOH	PPC	7–48	—	XRD, BET, MS	[286]
α -FeOOH	PPC	20–200	Needles	TEM, XRD, FTIR	[287]
α -FeOOH	PPC	10–150	Needles	SEM, XRD, SAXS, SQUID, magnetic birefringence	[288]
β -FeOOH	PPC	10–450	Needles	TEM, XRD, EXAFS, BET, ICP	[289]
γ -FeOOH	PPC	<400	Needles	TEM, XRD, ICP, FTIR	[290]
δ -FeOOH	PPC	10–100	Platelets	TEM, XRD, FTIR	[291]
MgFe ₂ O ₄	PPC	5–20	—	XRD, ND, ICP, MS, SQUID	[274, 292]
MnFe ₂ O ₄	PPC	~40	Spheres?	TEM, XRD, ND, EELS	[209]
MnFe ₂ O ₄	PPC	4–15	Spheres	TEM, XRD, BET, DSC, SQUID	[293]

continued

Table 2. Continued.

Compound*	Method†	Size (nm)	Morphology	Characterization‡	Ref.
MnFe ₂ O ₄	PPC	7–25	Spheres	TEM, XRD, magnetic fluxmeter	[22]
MnFe ₂ O ₄	PPC	5–15	Spheres	TEM, XRD, VSM	[23]
Fe ₃ O ₄	PPC	<80	Spheres	TEM, XRD, ICP, FTIR	[290]
Fe ₃ O ₄	PPC	<10	Spheres	TEM, XRD, SQUID, ACSus	[294]
Fe ₃ O ₄ /surfactant	PPC	<10	Spheres	TEM, XRD, SQUID, ACSus	[295]
CoFe ₂ O ₄	PPC	7–12	Spheres	TEM, VSM	[21]
CoFe ₂ O ₄	PPC	5–20	Spheres	TEM, XRD, magnetic fluxmeter	[22]
CoFe ₂ O ₄	PPC	5–130	Spheres, Needles	TEM, XRD, VSM	[23]
CoFe ₂ O ₄	PPC	600–1000	Spheres	TEM, XRD, XPS, FTIR, AA, magnetic susceptibility	[296]
NiFe ₂ O ₄	PPC	50–200	Spheres	SEM, XRD, TGA, BET	[297]
NiFe ₂ O ₄	PPC	4–6	—	XRD, SQUID	[298]
NiFe ₂ O ₄	PPC	3–5	Spheres	TEM, XRD, magnetic birefringence	[299]
NiFe ₂ O ₄	PPC	700–900	Spheres	TEM, UVvis, Zeta potential, VSM?	[300]
ZnFe ₂ O ₄	PPC	<100	Spheres	SEM, XRD, TGA	[301]
Mn _{1-x} Zn _x Fe ₂ O ₄	PPC	3–20	—	TEM, XRD, TGA, FTIR, ESR, SANS, VSM	[25, 302]
Mn _{0.66} Zn _{0.34} Fe ₂ O ₄	PPC	~9	—	TEM, XRD, AA, FMR, VSM	[303]
Ni _{1-x} Zn _x Fe ₂ O ₄	PPC	10–20	Spheres	TEM, XRD, AA, FTIR, VSM	[26]
Ni _{1-x} Zn _x Fe ₂ O ₄ /α-Fe/ α-Fe ₂ O ₃	PPC	~20	Spheres	TEM, SEM, XRD, MS, VSM	[304]
Ni _{0.8} Zn _{0.2} Fe ₂ O ₄	PPC	14–1000	Spheres, Agglomerates	SEM, XRD, VSM	[305]
Ni _{0.5} Zn _{0.5} Fe ₂ O ₄	PPC	~9	—	TEM, XRD, AA, FMR, VSM	[303]
α-Fe ₂ O ₃	PPC	20–50	Spheres	SEM, XRD	[306]
γ-Fe ₂ O ₃	PPC	4–12	—	XRD, ND, SANS, FMR	[307]
γ-Fe ₂ O ₃	PPC	2–9	Spheres	TEM, XRD	[308]
γ-Fe ₂ O ₃	PPC	6–12	Spheres	TEM, VSM	[21]
γ-Fe ₂ O ₃	PPC	2–15	Spheres	TEM, XRD, AA, DLS, SQUID	[309]
γ-Fe ₂ O ₃	PPC	<100	Platelets, Rods	TEM, XRD, XPS, MS	[310]
SrFe ₁₂ O ₁₉	PPC	35–40	Spheres	TEM, XRD, TGA, DTA, SQUID	[311]
BaFe ₁₂ O ₁₉	PPC	250–1000	—	SEM, XRD, TGA, DTA, XPS	[312]
BaFe ₁₂ O ₁₉	PPC	100–500	Hexagonal Platelets, Agglomerates	SEM, XRD, MS	[313]
BaFe ₁₂ O ₁₉	PPC	100–3000	Hexagonal Platelets, Agglomerates	SEM, XRD, DTA, VSM	[314]
BaFe ₁₂ O ₁₉	PPC	10–50	—	TEM, XRD, MS, VSM	[17]
BaFe ₁₂ O ₁₉	PPC	10–500	Hexagonal Platelets, Agglomerates	HRTEM, TEM, XRD, TGA, DTA, Raman, VSM	[315]
BaFe ₁₂ O ₁₉	PPC	400–3000	Hexagonal Platelets	SEM, XRD, TGA, DTA, VSM	[316]
BaFe ₁₂ O ₁₉	PPC	10–3000	Platelets	TEM, XRD, TGA, VSM	[317]
(Fe,Ni,Cu)	BH	10–200	Spheres	TEM, XRD, TMA	[34]
Co	BH	20–100	Spheres	TEM, XRD, ICP	[318]
Co	BH	<40	Agglomerates	TEM, XRD, ICP, DSC, BET, SQUID	[29]
Ni	BH	25–30	—	XRD, ICP	[30]
CoPt (L1 ₀)	BH	20–25	Spheres	TEM, XRD, ICP, EDX, VSM, SQUID	[319]
(Fe,Zr,B)(Fe ₃ B)(ZrO ₂)	BH	5–15	—	SEM, XRD, EDX, EXAFS, AA, FTIR, DSC, MS, SQUID	[320]
(M,B)M = Fe,Co,Ni,Mn	BH	7–12	—	XRD, MS, ACSus	[31]
(Fe,Ni,B)	BH	<50	Agglomerates	TEM, MS	[32]
(Fe,B) amorphous	BH	50–150	Spheres	TEM, DSC, BET, ICP, MS	[321]
Fe _{80-x} Cr _x B ₂₀	BH	20–200	Spheres	TEM, XRD, TGA, MS, SQUID	[322]
Fe _{80-x} Cr _x B ₂₀ amorphous	BH	3–200	Spheres, Agglomerates	TEM, XRD, MS, SQUID	[323, 324]
(Co,B) amorphous	BH	~40	Spheres	TEM, XRD, XPS, ICP, MS	[325]
MnFe ₂ O ₄	H	~25	—	XRD, FB	[326]
MnFe ₂ O ₄	H	~540	Spheres, Polyhedra	TEM, MS, SQUID	[327]
Fe ₃ O ₄	H	~340	Polyhedra	TEM, MS, SQUID	[327]
Fe ₃ O ₄	H	30–200	Polyhedra	TEM, XRD, AA	[328]
Fe ₃ O ₄	H	50–150	Spheres	SEM, XRD, BET	[38]
CoFe ₂ O ₄	H	~400	Spheres, Polyhedra	TEM, MS, SQUID	[327]

continued

Table 2. Continued.

Compound*	Method†	Size (nm)	Morphology	Characterization‡	Ref.
NiFe ₂ O ₄	H	20–100	Polyhedra	TEM, XRD, AA	[328]
NiFe ₂ O ₄	H	~680	Polyhedra	TEM, MS, SQUID	[327]
ZnFe ₂ O ₄	H	20–80	Polyhedra	TEM, XRD, AA	[328]
Mn _{1-x} Zn _x Fe ₂ O ₄	H	5–200	Spheres, Polyhedra	TEM, SEM, XRD, AA, DTA, TGA, AES, FB	[39]
Mn _{1-x} Zn _x Fe ₂ O ₄	H	10–17	—	XRD, ICP	[329]
Mn _{1-x} Zn _x Fe ₂ O ₄ / α-Fe ₂ O ₃	H	<12	Spheres, Large α Polyhedra	TEM, XRD, VSM	[330]
Ni _{1-x} Zn _x Fe ₂ O ₄	H	40–70	Spheres	SEM, XRD, VSM	[331]
SrFe ₁₂ O ₁₉	H	50–2000	Hexagonal platelets	SEM, XRD, AA, VSM	[40]
SrFe ₁₂ O ₁₉	H	8–30	Spheres	TEM, XRD, DTA, EPR	[332]
BaFe ₁₂ O ₁₉	H	100–1900	Hexagonal platelets	SEM, XRD	[333]
BaFe ₁₂ O ₁₉	H	50–800	Hexagonal platelets	SEM, XRD, VSM	[42]
BaFe ₁₂ O ₁₉	H	200–1000	Hexagonal platelets	SEM, XRD	[334]
BaFe ₁₂ O ₁₉	H	150–1500	Hexagonal platelets	SEM, XRD, BET, VSM	[335]
BaFe ₁₂ O ₁₉	H	150–10000	Hexagonal platelets, Needles	TEM, SEM, XRD, DLS, DTA, TGA, VSM	[41]
BaFe ₁₂ O ₁₉	H	40–700	Hexagonal platelets	TEM, XRD	[336–338]
BaFe ₁₂ O ₁₉	H	100–200	Hexagonal platelets	TEM, XRD	[339]
BaFe ₁₂ O ₁₉ /Ba ₅ Fe ₈ O ₁₇	H	<1000	Polyhedra, Spheres	TEM, XRD, VSM?	[36]
REFeO ₃ /RE ₃ Fe ₅ O ₁₂ RE = Er-Lu	H	<80	Spheres	TEM, XRD	[37]
α-Fe	M	10–100	Spheres	TEM, XRD, EELS, AGM, MS	[51]
Fe	M	2–15	Spheres	HRTEM, SAD	[52]
Fe	M	5–150	Needles	TEM, XRD, SAD, VSM	[283]
Fe	M	<5	Spheres	TEM, XRD, optical absorption, VSM, SQUID	[340]
α-Fe	M	50–150	Spheres	TEM, XRD, VSM?	[341]
α-Fe	M	20–1000	Spheres, Needles	TEM, XRD, VSM	[342, 343]
α-Fe(β-FeOOH)	M	10–200	Polyhedra, Spheres, Needles	TEM	[344]
Fe/FeB	M	<3	—	TEM, XPS, BET, MS	[345]
Co	M	<10	Spheres	TEM, XRD, SQUID	[75, 346]
Co	M	5–110	Spheres	TEM, Conductivity, AGM	[53]
Co	M	5–10	Spheres, SA	SEM, SQUID	[347, 348]
β-Co	M	2–10	Spheres	TEM, STM, XRD, SAXS, SQUID	[349–351]
Co	M	5–12	Spheres, SA	TEM, SEM, SQUID	[352]
β-Co	M	<5	Spheres	TEM, XRD, SQUID	[353]
Co/Au c/s	M	5–25	Spheres	TEM, AFM, UVvis	[354]
Ni	M	2–16	Spheres	TEM, XRD, SQUID	[204]
(Fe,Cu)	M	5–50	Spheres	TEM, XRD, EDS, Conductivity, EELS, AGM, MS, SQUID	[355]
FePt ₃	M	8–10	Spheres	TEM, XRD, SQUID	[356]
(Fe,Cu,B)	M	5–30	Spheres	TEM, SEM, XRD, EDS, EELS, MS, AGM, SQUID	[357, 358]
Co ₂ B	M	2–20	Spheres	TEM, SAD, UVvis, AGM	[359]
FeOOH	M	<80	Needles	SEM, XRD, UVvis, Conductivity	[49]
MnFe ₂ O ₄	M	5–10	Spheres	TEM, XRD, ND, ICP, MS, SQUID	[360]
MnFe ₂ O ₄	M	3–10	Spheres	TEM, XRD, SQUID	[361]
Fe ₃ O ₄	M	3–15	Spheres	TEM, DSC, TGA, SANS, SQUID	[360]
Fe ₃ O ₄	M	3–10	Spheres	TEM, XRD, SQUID	[361]
Fe ₃ O ₄	M	3–12	Spheres	TEM, XRD, AGM, MS, VSM	[362]
Fe ₃ O ₄	M	3–12	Spheres	TEM, XRD, VSM	[363]
Fe ₃ O ₄	M	5–20	—	TEM, XRD, AA, DLS, SQUID	[364]
Fe ₃ O ₄ (α-FeOOH)	M	8–100	Spheres, Needles	TEM, XRD, BET, DSC, VSM	[365]
CoFe ₂ O ₄	M	<15	—	TEM, XRD, ND, ICP, SQUID	[56]
CoFe ₂ O ₄	M	3–10	Spheres	TEM, XRD, SQUID	[361]
CoFe ₂ O ₄	M	10–18	Spheres	TEM, XRD, EXAFS, SQUID	[366]
CoFe ₂ O ₄	M	2–8	Spheres	TEM, XRD, XANES, SAXS, Conductivity, MS, AGM, SQUID	[367–370]
CoFe ₂ O ₄	M	2–15	Spheres	TEM, XRD, EDS, MS, SQUID	[371, 372]

continued

Table 2. Continued.

Compound*	Method†	Size (nm)	Morphology	Characterization‡	Ref.
CoFe ₂ O ₄	M	2–8	—	TEM, XRD, SAXS, EDS, SQUID	[373]
CoFe ₂ O ₄	M	5–35	Spheres	TEM, XRD, ND, ICP, MS, SQUID	[208, 374]
CoFe ₂ O ₄	M	5–20	Spheres	TEM, XRD, VSM	[375]
Co _{1-x} RE _x Fe ₂ O ₄ RE = Ce-Er	M	17–23	—	XRD, SQUID	[376]
Zn _{1-x} Fe _{2+x} O ₄	M	2–6	Spheres	TEM, EDS, MS, SQUID	[377]
Zn _{1-x} Fe _{2+x} O ₄	M	2–50	Spheres	TEM, XRD, DLS, BET, ICP, SQUID	[378]
Mn _{1-x} Zn _x Fe ₂ O ₄	M	25–130	Spheres	TEM, XRD, BET, PCS	[54]
Mn _{1-x} Zn _x Fe ₂ O ₄	M	3–1000	Agglomerates	SEM, XRD, BET, DTA, TGA	[379]
Co _{1-x} Zn _x Fe ₂ O ₄	M	<7	Spheres	TEM, SAD, EDS, AGM, FMR, SQUID	[380, 381]
Ni _{1-x} Zn _x Fe ₂ O ₄	M	20–150	Spheres	TEM, XRD, BET, PCS	[54]
γ-Fe ₂ O ₃	M	3–12	Spheres	TEM, XRD, AGM, MS, VSM	[362]
γ-Fe ₂ O ₃	M	4–20	Spheres	TEM, SEM, XRD, MS, SQUID	[382]
γ-Fe ₂ O ₃ /Fe ₃ O ₄	M	2–14	Spheres	TEM, XRD, VSM	[383]
SrFe ₁₂ O ₁₉	M	9–120	Hexagonal platelets	TEM, XRD, BET, DTA, TGA, VSM	[18]
SrFe ₁₂ O ₁₉	M	65–1000	Hexagonal platelets, Agglomerates	TEM, XRD, BET, DTA, TGA, FTIR, MS, VSM	[58]
SrFe ₁₂ O ₁₉	M	3–100	—	TEM, XRD, DTA, TGA, SQUID	[384]
BaFe ₁₂ O ₁₉	M	3–15	—	TEM, XRD, VSM	[55]
BaFe ₁₂ O ₁₉	M	5–100	Spheres	TEM, XRD, DTA, TGA, VSM	[385]
Co[Fe(CN) ₅ NO]	M	22–31	Polyhedra	TEM, FTIR	[386]
Cr ₃ [Cr(CN) ₆] ₂ ·H ₂ O	M	15–200	Polyhedra	TEM, FTIR	[386]
Co ₄ [Fe(CN) ₆] ₄	M	12–22	Polyhedra	TEM, FTIR	[386]
Co/PVP	T(OM)	<2	Spheres	TEM, HRTEM, SQUID	[61]
Ni/PVP	T(OM)	<5	Spheres, SA	TEM, EELS, FTIR, EDS	[387]
Ni/PVP	T(OM)	<5	Spheres, SA	HRTEM, WAXS, SQUID	[72]
Ni	T(OM)	4 × 15	Rods	TEM, SQUID	[76]
CoPt, CoPt ₃ , Co/Pt c/s	T(OM)	<10	Spheres	TEM, SQUID	[79]
CoO, Co ₃ O ₄ /PVP	T(OM)	5–12	Spheres	TEM, HRTEM, WAXS, SQUID	[62]
CoFe ₂ O ₄	T(OM)	4–9	Spheres, SA	TEM, XRD, SQUID	[81]
SrFe _{12-x} O _{19-1.5x}	T(OM)	200–500	—	XRD, DTA, TGA, FTIR, FB	[388]
Fe	T(CO)	5–8	Spheres	TEM, SQUID	[78]
Fe/TOPO	T(CO)	2–11	Needles	TEM, SQUID	[69]
Fe/polymer c/s	T(CO)	<100	Spheres	TEM, DSC, ICP, FTIR, NMR, SQUID	[389]
Fe, γ-Fe ₂ O ₃	T(CO)	10–15	Spheres	TEM, XRD	[80]
Co, CoO	T(CO)	4–5	Spheres	TEM, EELS	[67]
Co	T(CO)	50–100	Spheres	TEM, SQUID	[77]
Co	T(CO)	~12	Spheres	TEM, SQUID, FMR	[390]
Co, ε-Co	T(CO)	3–17	Spheres, Rods, Cubes, SA	TEM, XRD, EELS, HRTEM	[65, 66]
Co/PS	T(CO)	5–30	Agglomerates	TEM, FTIR	[70]
Co/HPS	T(CO)	2–15	Spheres	TEM, XRF, FMR	[68]
ε-Co/TOPO	T(CO)	4–25	Spheres, Rods, SA	TEM, XRD	[64]
ε-Co/TOPO	T(CO)	15–25	Spheres, Polyhedra	TEM, XRD	[63]
MnO	T(CO)	5–10	Spheres	TEM, XRD, SQUID	[391]
β-Fe ₂ O ₃ , γ-FeOOH	T(CO)	~30	Spheres	TEM, XRD, XPS, FTIR	[392]
Fe	UV	2–15	Chains	STM, ESR	[176]
Fe/PPO	S	1–12	Spheres	HRTEM, SQUID	[393]
Fe/SiO ₂ (Fe,Co)	S	3–8 10–20	Agglomerates	TEM, XRD, DSC, TPD, TPR-MS	[85]
Fe/Thiol	S	3–25	SA Monolayers	AES, XRD, XANES, XPS, DSC, TGA, FTIR, MS	[88, 89, 94]
Fe/PVP	S	3–8	Spheres	TEM, SQUID	[84]
Fe amorphous	S	<30	Spheres	TEM, XRD, TGA, DSC, SQUID	[82, 394]
Fe, Co, (Fe,Co)	S	2–20	Spheres	TEM, XRD, DSC	[83]
Co	S	30–200	Platelets	TEM, SAD, Lorentz microscopy	[91]

continued

Table 2. Continued.

Compound*	Method†	Size (nm)	Morphology	Characterization‡	Ref.
Ni	S	5–20	Spheres	TEM, XRD, TGA, DSC, SQUID	[92]
Ni/SiO ₂	S	10–50	Spheres	TEM, AFM	[90]
(Fe,Co)	S	<10	Spheres	TEM, SANS, DSC	[86]
(Fe,Ni)	S	<25	Agglomerates	TEM, XRD, TGA, DSC, BET, MS, SQUID	[87]
(Co,Ni)	S	<10	SA Monolayers	TEM, SEM, XRD, TGA, BET, VSM	[93]
Fe ₃ O ₄ /PVA	S	12–20	Spheres	TEM, AFM, XRD, DSC, TGA, MS, SQUID	[97]
Fe ₃ O ₄	S	<20	Spheres	TEM, XRD, TGA, MS, SQUID	[99]
Co ₃ O ₄ Fe ₃ O ₄	S	5–30	Polyhedra	TEM, XRD, DRS, BET	[98]
NiFe ₂ O ₄	S	<25	Agglomerates	TEM, XRD, BET, ESR, TGA, DSC	[95]
Fe ₂ O ₃ /UDA/OPA/ DSA/OTS	S	5–25	Spheres	TEM, XRD, FTIR, EPR, TGA, MS, SQUID, VSM	[96, 100]
M _{1-x} P _x M = Fe,Co,Ni	SG	2–10	Hexagonal platelets	TEM, XRD	[395]
Fe/SiO ₂	SG	<10	Agglomerates	TEM, XRD, MS, VSM	[115]
(Ni/Pd)/PVP	SG	1–5	Spheres	HRTEM, XRD, XPS, VSM	[149]
Fe ₂ O ₃ /SiO ₂	SG	5–15 c	Spheres	TEM, Fluorescent microscopy	[396]
Fe ₃ O ₄ /SiO ₂		2–100 s			
CoFe ₂ O ₄	SG	10–50	—	XRD, MS, VSM	[102]
Co _{0.9} Mn _{0.1} Fe ₂ O ₄	SG	10–50	—	TEM, XRD, MS, VSM	[104]
Co _{1-x} Cr _x Fe ₂ O ₄	SG	5–20	Spheres	TEM, XRD, ICP, VSM	[105]
CoBi _{0.1} Fe _{1.9} O ₄	SG	10–80	—	AFM, XRD, RBS, TGA, MS, VSM	[106]
CoGd _{0.1} Fe _{1.9} O ₄	SG	11–30	—	XRD, MS, VSM	[108]
CoNd _{0.1} Fe _{1.9} O ₄					
Co _{1-x} Zn _x Fe ₂ O ₄	SG	10–90	Agglomerates	SEM, XRD, MS, VSM	[109]
CoY _{0.1} Fe _{1.9} O ₄	SG	6–30	—	XRD, MS, VSM	[107]
CoLa _{0.1} Fe _{1.9} O ₄					
NiFe ₂ O ₄ /SiO ₂	SG	5–20	Agglomerates	XRD, TGA, FTIR, ESR, MS, VSM	[117]
NiFe ₂ O ₄	SG	5–30	Spheres?	TEM, XRD, DTA, BET, SQUID	[103]
Ni _{0.25} Cu _{0.25} Zn _{0.5} Fe ₂ O ₄	SG	40–50	Agglomerates	TEM, XRD, DTA, FTIR, ACPPerm	[397]
Ni _{0.5} Zn _{0.5} Fe ₂ O ₄ /Mg ₂ SiO ₄	SG	100–200	Agglomerates	SEM, XRD, ACPPerm	[398]
α-Fe ₂ O ₃	SG	20–60	Spindles, Spheres	TEM, XRD, SAXS	[399]
α-Fe ₂ O ₃	SG	50–3300	Spheres, Platelets	TEM, SEM, XRD, ICP, EDX, FTIR, UVvis	[400]
Fe ₂ O ₃ /SiO ₂	SG	9–50	Agglomerates	TEM, ESR, BET	[116]
BaFe ₁₂ O ₁₉	SG	100–250	Polyhedra	TEM, XRD, VSM	[401]
Ba ₄ Co ₂ Fe ₃₆ O ₆₀ (Co ₂ -U)	SG	10–100	Spheres, Cubes	TEM, XRD, XPS, BET, VSM	[112]
Ba _{1-x} Sr _x Fe ₁₂ O ₁₉	SG	80–85	Hexagonal Platelets	SEM, XRD, MS, VSM	[110]
BaZnCoFe ₁₆ O ₂	SG	5–500	Spheres	TEM, XRD, VSM	[111]
La _{0.67} Ca _{0.33} MnO ₃	SG	30–60	Agglomerates	TEM, XRD, TGA, XPS, FTIR, VSM	[114]
Y ₃ Fe ₂ O ₁₂	SG	30–4520	Agglomerates	TEM, SEM, XRD, VSM, SQUID	[113]
Fe, Ni, Co, (Fe,Co), (Fe,Cu), (Co,Cu)	P	5–50	Spheres	TEM, SEM, XRD	[122, 143]
Fe, (Fe,Co), (Fe,Ni), (Co,Ni,Fe)	P	5–250	Spheres	SEM, XRD, VSM	[125]
Co	P	~1200	Agglomerates	SEM, XRD, FMR	[147]
Co/Mica	P	1–500	Agglomerates	SEM, XRD, UVvis, IR	[144]
Co, Pt, CoPt, CoPt ₃	P	1–3	Spheres	TEM, XRD	[140]
Co/Ni/LDH	P	5–20	Turbostratic Aggregate	TEM, XRD, TGA, DTA, FTIR, UV-NRIR	[146]
Co, Ni, (Co,Ni)/PVP	P	100–600	Spheres	SEM, XRD, TGA, VSM	[135]
Co, (Co,Ni), (Co,Ni,Fe)	P	30–1000	Spheres	SEM, XRD, EDS, FMR, ACPPerm	[127]
Ni, Co	P	20–500	Spheres	TEM, XRD	[150]
Ni/montmorillonit e	P	8–45	Spheres	HRTEM, XRD, VSM	[141]
Ni/PVP	P	5–2000	Spheres	SEM, XRD, FTIR, TPD	[134]
(Fe,Co)	P	~20	Spheres	TEM, XRD, EELS, ACPPerm	[133]
(Ni,Co)	P	200–700	Spheres	SEM, XRD, TGA	[120]
(Ni,Co)	P	200–2000	Spheres	SEM, XRD, VSM, Permeability	[123, 124]
(Ni,Co)	P	150–700	Spheres	SEM, XRD, TGA	[121]
(Ni,Co)	P	210–260	Spheres	TEM, SEM, XRD, EDS, Microwave permeability	[128]

continued

Table 2. Continued.

Compound*	Method†	Size (nm)	Morphology	Characterization‡	Ref.
(Ni,Co)	P	60–500	Spheres	TEM, XRD	[132]
(Ni,Co)	P	25–600	Spheres	SEM, XRD, WAXS, VSM	[148]
(Ni,Co), (Fe,Ni)	P	200–500	Spheres	TEM, XRD	[126]
(Ni,Co), (Fe,Ni,Co)	P	25–2000	Spheres	TEM, SEM, ACPPerm	[129]
(Ni,Co), (Fe,Ni,Co)	P	20–40	Spheres	TEM, SEM, SQUID, ACPPerm	[130]
(Ni,Co), (Fe,Ni,Co)	P	25–250	Spheres	TEM, FMR, ACPPerm	[131]
(Ni,Co), (Fe,Ni,Co)	P	25–3000	Spheres	SEM, XRD, XRF, TGA, DSM, GPC, TPD/MS, SQUID, ACPPerm	[145]
(Co,Cu)	P	20–30	Spheres	TEM, XRD, NMR, EXAFS, VSM	[118, 119]
Co ₂ FeO ₄	P	4–8	Spheres	TEM, XRD, XANES, MS, DC Susceptibility	[139]
γ-Fe ₂ O ₃ , α-Fe ₂ O ₃	P	80–100	Spheres	SEM, XRD, DRS	[136, 138]
Fe ₂ O ₃ , CoO	P	30–300	Spheres	SEM, XRD	[137]
Co	ED	3–5	Templated Nanowires	TEM, HRTEM, VSM	[155]
Co	ED	~200	Templated Nanowires	SEM, XRD, CV, VSM	[156]
Co, (Co,Fe)	ED	18–78	Templated Nanowires	HRTEM, TEM, XRD, VSM	[162]
Ni	ED	~6	Templated Nanowires	TEM	[164]
Ni	ED	50–100	Spheres	SEM	[174]
Ni, Co	ED	18–500	Templated Nanowires	TEM, SEM, SQUID, VSM	[157, 163]
Ni, Co	ED	35–500	Templated Nanowires	MFM, SQUID	[160]
Ni	ED	<70	Templated Nanowires	TEM, Conductivity	[158]
Ni	ED	20–600	Spheres	SEM, TEM, CV	[172]
Ni, (Pd,Fe)	ED	<40	—	XRD, γγ angular spectroscopy	[168]
Fe ₂₆ Ni ₇₄	ED	~18	Templated Nanowires	TEM, Sem, XRD, VSM	[154]
CoPt, FePt	ED	25–100	Wires	TEM, XRD, VSM	[161]
Fe ₂ O ₃ , NiO, Co ₃ O ₄ , CoFe ₂ O ₄	ED	2–30	—	TEM, XRD, DLS, BET	[167]
SrFe _w O _z	ED	2–50	Agglomerates	SEM, XRD, ICP, SQUID	[170]
Fe, Ni, (Co,Ni)	EC	10–10000	Agglomerates	TEM, SEM, XRD, XRF, MS, SQUID	[173]
α-Fe, γ-Fe ₂ O ₃ , Fe ₃ O ₄	EC	9–55	—	XRD, MS	[204]
Mn _x Zn _y Fe _z O _w	EC	20–2000	—	SEM, XRD, ICP-MS, SQUID	[171]
γ-Fe ₂ O ₃	EC	1–25	Agglomerates	TEM, XRD, FTIR, BET, Raman, MS, SQUID	[169]
α-Fe, Co, Ni	MSP	6–10	Spheres, SA	HRTEM, WAXS, VSM, SQUID	[184]
ε-Co, hcp Co, mt-fcc Co	MSP	2–10	Spheres, SA	HREM, WAXS, SAXS, XRD, SQUID	[179]
(Fe,Pt)	MSP	2–5	Spheres, SA	TEM, PEELS, ICP, RBS, SQUID	[3, 180]
FePt	MSP	2–50	Spheres, Triangular Platelets	TEM, SEM, XRD	[188]
FePt (L1 ₀)	MSP	3–6	Spheres, SA	HRTEM, XRD, SQUID	[181, 186, 278]
FePt (L1 ₀)	MSP	1–4	Spheres, SA	TEM, VSM, SQUID	[182]
FePt (L1 ₀)	MSP	2–5	Spheres, SA	TEM	[183]
FePt (L1 ₀)	MSP	3–5	Spheres	TEM, XPS, MS, VSM	[185]
CoPt ₃ /ACA	MSP	1–50	Spheres, Wires	HRTEM, TEM, SEM, XRD, ICP, AES	[402]
FePd, CoPt, (Fe,Co)Pt (L1 ₀)	MSP	2–11	Spheres, SA	TEM, SEM, XRD, AGM, VSM	[187, 189]
(Fe ₄₉ Pt ₅₁) ₈₈ Ag ₁₂ (L1 ₀)	MSP	2–5	Spheres	TEM, XRD, VSM	[403]
(Sm,Co), (Nd,Fe)	MSP	~9	Clusters	TEM, SQUID	[178]
Fe ₃ O ₄	MSP	3–20	Spheres, SA	TEM, XRD	[404]

* c/s: Core/Shell; PVP: polyvinylpyrrolidone; TOPO: trioctylphosphineoxide; SDS: sodium dodecylsulfate; OTS: octadecyltrichlorosilane; UDA: 10-undecanoic acid; OPA: octylphosphonic acid; DSA: dodecylsulfonic acid; PPO: poly(dimethylphenylene oxide); ACA: 1-adamentanecarboxylic acid.

† PPC: precipitation; BH: borohydride; H: hydrothermal; M: micellar or microemulsion; T(OM): thermolysis-organometallic; T(CO): thermolysis-carbonyl decomposition; UV: photolysis; S: sonolysis; SG: sol-gel; P: polyol; EC: electrochemical; ED: electrodeposition; MSP: multi-synthesis processing.

‡ AA: atomic absorption spectroscopy; ACPPerm: alternating current permeametry; ACSus: alternating current susceptometry; AES: Auger electron spectroscopy; AFM: atomic force microscopy; BET: Brunauer-Emmett-Teller (a method of measuring surface area); CST: critical surface tension; CV: cyclic voltammetry; DRS: diffuse reflectance spectroscopy; DSC: differential scanning calorimetry; DTA: differential thermal analysis; EELS: electron energy loss spectroscopy; EM: electron microscopy; ESR: electron spin resonance; FB: Faraday balance; FMR: ferromagnetic resonance; FTIR: Fourier transform infrared spectroscopy; HRTEM: high resolution transmission electron microscopy; ICP: inductively coupled plasma; MFM: magnetic force microscopy; MS: Mössbauer effect spectroscopy; PCS: photon correlation spectroscopy; PEELS: parallel electron energy loss spectroscopy; RBS: Rutherford back-scattering spectroscopy; SAD: selected area electron diffraction; SANS: small angle neutron spectroscopy; SAXS: small angle X-ray spectroscopy; SEM: scanning electron microscopy; SQUID: superconducting quantum interference device magnetometry; STM: scanning tunneling microscopy; TEM: transmission electron microscopy; TGA: thermal gravimetric analysis; TPD: temperature programmed desorption; VSM: vibrating sample magnetometry; WAXS: wide-angle X-ray spectroscopy; XANES: X-ray absorption near edge spectroscopy; XRF: X-ray fluorescence; XPS: X-ray photoelectron spectroscopy; XRD: X-ray diffraction.

GLOSSARY

Absorption edge A large jump in X-ray absorption as a function of energy associated with the ejection of a core electron from a particular element (e.g. the “Fe K edge”).

Blocking temperature Time upon heating. Magnetic moment is frozen into place upon cooling. This parameter is sensitive to applied magnetic field strength, characteristic time of measurement, and particle volume.

Capping agent Anything that is added to a reaction solution to modify or control the chemical, physical and/or surface properties of nanoparticles. This agent is usually an organic moiety and help to prevent particle growth (e.g. polyvinylpyrrolidone (PVP)).

Chelating ligand A ligand that can form one or more bonds with a central metal ion (e.g. oxalic acid).

Coercivity The extrinsic magnetic property defined by the magnetic field required to reduce the magnetization of a ferromagnetic or ferrimagnetic material to zero. SI Units of A/m.

Condensation The combination of hydrolyzed or partially hydrolyzed reactants that lead to gel formation.

Curie temperature The phase transformation temperature at which a ferromagnetic material becomes paramagnetic thereby losing its spontaneous magnetization.

Differential scanning calorimetry (DSC) A thermal analysis technique in which the power required to keep the sample at the same temperature as a reference is the physical parameter.

Differential thermal analysis (DTA) A thermal analysis technique in which the temperature of the sample relative to the temperature of a reference material is measured.

Diffraction anomalous fine structure (DAFS) The variation in a Bragg X-ray diffraction peak as a function of energy near an absorption edge.

Disproportionation A reaction in which a species undergoes both oxidation and reduction simultaneously.

Dynamic light scattering (DLS) A technique for estimating nanoparticle sizes by measuring fluctuations in light scattered by the sample. Also known as photon correlation spectroscopy or quasi-elastic light scattering.

Electrodeposition The deposition of a metallic species from an electrolyte solution on a cathode where an external current is applied to the plating system.

Electron spectroscopy for chemical analysis (ESCA) A term encompassing X-ray photoelectron spectroscopy and ultraviolet photoelectron spectroscopy.

Energy dispersive X-ray absorption spectroscopy (EDXAS or DXAS) A fast variation of X-ray absorption spectroscopy, in which broad spectrum X-ray radiation is diffracted by the sample, allowing an entire energy spectrum to be collected simultaneously.

Exchange stiffness The strength of interaction between adjacent magnetic moments. The origin of exchange stiffness is a parameterization of the exchange interaction. The origin of exchange interaction, being quantum mechanical in nature, is the basis for ferromagnetic behavior. SI Units of J/m.

Extended X-ray absorption fine structure (EXAFS) The variation in X-ray absorption as a function of energy more than 30 eV above an absorption edge.

Ferrimagnetism The phenomenon exhibited by materials possessing spontaneous magnetization due to either unequal numbers of antiparallel atomic moments or antiparallel atomic moments of differing magnitudes (or both).

Ferromagnetic resonance (FMR) A magnetic characterization technique performed to examine the anisotropy and distribution of easy axes for assemblies of magnetic nanoparticles. This is accomplished by applying a large, saturating field simultaneously with a small oscillating magnetic field perpendicular to the saturating field, thereby producing a precession of the magnetic moments in the sample. Dynamic susceptibility as a function of field strength and orientation are generally measured.

Ferromagnetism The phenomenon exhibited by materials possessing spontaneous magnetization due to parallel alignment of atomic moments.

Hydrolysis The replacement of a ligand with a hydroxide group from water (i.e. alkoxide replacement in sol-gels).

Hydrophilic “Water attractive,” a molecule or compound that dissolves or is miscible in water. In a surfactant, the polar head group is hydrophilic.

Hydrophobic “Water repulsive,” a molecule or compound that does not mix or is immiscible in water (e.g. oil) the hydrophobic end of a surfactant is the hydrocarbon tail.

Hydrothermal reaction A reaction where an aqueous solution is heated above the boiling point of water in an autoclave or high pressure reactors (pressure can reach over 2000 psi and temperature over 200 °C).

Hysteresis loop A plot of the variation of the magnetization as an applied magnetic field is swept through a complete cycle (+/- H_{max}).

Inverse/reverse micelle A system in which the surfactant molecules entrap solubilized water pools in a hydrocarbon solvent (also known as water-in-oil microemulsions).

Isoelectric point The pH where the particle has no net surface charge.

Ligand A chemical molecule or anion that is directly bonded to a metal ion.

Magnetic domain A portion of a magnetically ordered material that possesses magnetic moments aligned in the same direction (region over which the spontaneous magnetization is aligned).

Magnetic susceptibility The ratio of magnetization to magnetic field, in general it is unitless, however it may be normalized by mass, volume, or moles for comparison between materials. The susceptibility may be determined by the application of alternating current or direct current magnetic fields.

Magnetocrystalline anisotropy The intrinsic magnetic property describing the strength of interaction between the crystalline lattice and magnetic moment. Generally, this is represented as a (low energy state) and any other axis (high energy state) in the material. It is described by materials constants (K_1 , K_2 , etc.), which in conjunction with angular dependent terms in reference to the easy axis, describe the

anisotropic energy for any other axis in the crystal. SI Units of J/m^3 .

Magnetostriction The strain dependent part of the magnetocrystalline anisotropy. Generally associated with a change in shape of a magnetic material as the magnetization is changed.

Micelle An aggregate of surfactant molecules in which the oil droplets are stabilized in an aqueous environment.

Mössbauer spectroscopy A spectroscopic technique utilizing the nearly recoilless emission of gamma rays, most often by ^{57}Fe nuclei, to probe the chemical and magnetic environment of the nuclei.

Multisynthesis processing The combination of two or more chemical reactions to produce the desired product, for example: FePt formed by the thermal decomposition of iron carbonyl and the reduction of platinum acetylacetonate in a polyol.

Number-weighted mean An average which counts each nanoparticle in a sample equally.

Organometallic compound A compound in which the organic species is directly bonded to the metal through a metal-carbon bond (e.g. nickel carbonyl ($\text{Ni}(\text{CO})_4$)).

Ostwald ripening The growth of large particles at the expense of smaller particles driven by the reduction of total surface energy for the assembly of particles as described by the Gibbs-Thomson effect.

Oxidation A reaction where the oxidation number increases or the oxidized species loses electrons.

Oxidation agent A reactant that accepts electrons from another reactant (e.g. hydrogen peroxide (H_2O_2)).

Paramagnetism The phenomenon exhibited by materials that are slightly attracted to magnetic fields however they possess no spontaneous magnetization. These materials have positive, low field, susceptibilities generally less than 10^{-3} in magnitude. The origin of the slightly positive susceptibility is thermal activation of atomic moments in materials with no exchange interaction.

Photolysis A chemical reaction in which the reaction is driven by light.

Photon correlation spectroscopy (PCS) See dynamic light scattering.

Polyol Any alcohol that contains 2 or more hydroxyl groups, commonly 2 hydroxide groups. Diols are a subgroup, which contain exactly 2 hydroxyl groups and are commonly used in polyol reactions (e.g. ethylene glycol).

Polyol reaction A chemical reaction in which the solvent and reducing agent is a polyol.

Precipitation A reaction where an insoluble solid is formed when two or more solutions are mixed.

Principle component analysis (PCA) An analysis technique which decomposes a series of related spectra into orthogonal "components."

Quasi-elastic light scattering (QELS) See dynamic light scattering.

Reducing agent A reactant that donates electrons to another reactant (e.g. borohydride (BH_4^-)).

Reduction A reaction where the oxidation number decreases or the reduced species gains electrons.

Remanent magnetization The remaining magnetization of a ferromagnetic or ferrimagnetic material after a saturating has been applied and removed. SI Units of A/m.

Saturation magnetization An intrinsic property of ferromagnetic and ferrimagnetic materials, indicating the magnetic moment per unit volume when sufficiently large magnetic fields are applied to align all magnetic moments in a specimen. SI Units of A/m.

Scherrer analysis A commonly used technique for estimating particle size from the broadening of peaks in an X-ray diffractogram.

Selected area electron diffraction (SAED or SAD) Diffraction of an electron beam focused on to a small area.

Self-assembly The spontaneous reorganization of molecules or particles to into an ordered arrangement. In the case of particles, this is generally accomplished by evaporation of the solvent from a mixture of particles suspended in that solvent.

Shape anisotropy A bias of the magnetization direction due to the magnetostatic self energy. The magnetostatic self energy is dependent on the shape of the sample and is a equations.

Sol-gel process Traditionally, the hydrolysis and condensation of metal alkoxides.

Sonolysis A chemical reaction in which the reaction is driven by sound, i.e. using ultasonics or acoustic waves (also known as sonochemistry).

Spontaneous magnetization The effect of the quantum mechanical exchange interaction whereby the magnetic moments in a ferromagnetic (or ferrimagnetic) material are aligned without the application of a magnetic field.

Superconducting quantum interference device (SQUID) magnetometer A magnetic measurement device that uses a Josephson junction to conduct very sensitive magnetic moment measurements (typically near 10^{-8} emu sensitivity).

Superparamagnetism The phenomenon where the magnetization reversal of an exchange coupled volume of magnetic material is changed by thermal activation (generally for finely divided ferromagnetic or ferrimagnetic materials). Characteristics of superparamagnetic materials include a lack of coercivity and the formation of a universal curve for the magnetization plotted against magnetic field normalized by temperature.

Surfactant An acronym for "surface active agent," is any substance that affects the surface or interfacial tension of the medium in which it is dissolved. A surfactant is composed of a hydrophilic head and a hydrophobic tail. A surfactant lowers the surface or interfacial tension of the medium in which it is dissolved.

Synchrotron radiation High-flux broad-spectrum radiation generated by high-speed electrons orbiting in storage rings.

Temporal remanent magnetization A set of techniques that examine the switching and relaxation behavior of nanoparticles, including thermoremanent magnetization (TMR) and isothermal remanent magnetization (IMR) measurements.

Thermogravimetric analysis (TGA) A thermal analysis technique with mass as the physical parameter.

Thermolysis A chemical reaction in which the reaction is driven by heat (e.g. the thermal decomposition of an organometallic precursor).

Ultraviolet photoelectron spectroscopy (UPS) A characterization technique in which ultraviolet photons of a fixed energy are absorbed by a sample, and the kinetic energy distribution of the resulting photoelectrons is measured.

Vibrating sample magnetometer (VSM) A magnetic measurement device used to measure magnetization of small samples which are vibrated in a magnetic field, inducing currents in sensing coils.

Volume-weighted mean An average which counts each atom in a sample equally.

ACKNOWLEDGMENTS

The authors gratefully acknowledge support for this work from the Office of Naval Research, DARPA, and the National Research Council.

REFERENCES

1. R. H. Kodama, A. E. Berkowitz, E. J. McNiff, and S. Foner, *Phys. Rev. Lett.* 77, 394 (1996).
2. M. M. Miller, G. A. Prinz, S. F. Cheng, and S. Bounnak, *Appl. Phys. Lett.* 81, 2211 (2002).
3. S. Sun, C. B. Murray, D. Weller, L. Folks, and A. Moser, *Science* 287, 1989 (2000).
4. http://www.fero.com/usa/ferrofluid_technology_overview.htm
5. <http://www.916.ibm.com/press/prnews.nsf/jan/c365d28cf5e8b9f5852568a50050bb42>
6. <http://www.cancernetwork.com/journals/oncology/o0006q.htm>
7. http://www.gatech.edu/news-room/archive/news_releases/zhang.html
8. A. E. Nielsen, in "Kinetics of Precipitation" Pergamon Press, New York, 1964.
9. A. G. Walton, in "The Formation and Properties of Precipitates" Robert Krieger Publishing Company, New York (reprint ed.), 1979.
10. M. G. Lagally, *Jap. J. Appl. Phys.* 32, 1493 (1993).
11. V. K. LaMer and R. H. Dinegar, *J. Am. Chem. Soc.* 72, 4847 (1950).
12. D. Turnbull, *Acta Metal.* 1, 684 (1953).
13. For example, see D. J. Shaneield, in "Organic Additives and Ceramic Processing, with Applications in Powder Metallurgy, Ink and Paint," Kluwer Academic Publishers, Boston, 1995.
14. R. Massart, *Compt. Rend. Series C* 291, 1 (1980).
15. R. Massart and V. Cabuil, *J. Chim. Phys.-Chim. Biol.* 84, 967 (1987).
16. W.-J. Lee and T.-T. Fang, *J. Mater. Sci.* 30, 4349 (1995).
17. V. K. Sankaranarayanan and D. C. Khan, *J. Magn. Magn. Mater.* 153, 337 (1996).
18. J. H. Choy, Y.-S. Han, and S.-W. Song, *Mater. Lett.* 19, 257 (1994).
19. C. A. Figueroa, E. E. Sileo, P. J. Morando, and M. A. Blesa, *J. Colloid Inter. Sci.* 225, 403 (2000).
20. R. Massart, E. Dubois, V. Cabuil, and E. Hasmonay, *J. Magn. Magn. Mater.* 149, 1 (1995).
21. S. Lefebure, E. Dubois, V. Cabuil, S. Neveu, and R. Massart, *J. Mater. Res.* 13, 2975 (1998).
22. F. A. Tourinho, R. Franck, and R. Massart, *J. Mater. Sci.* 25, 3249 (1990).
23. F. Tourinho, R. Franck, R. Massart, and R. Perzynski, *Prog. Colloid Polym. Sci.* 79, 128 (1989).
24. N. Moumen, I. Lisiecki, M. P. Pileni, and V. Briois, *Supermol. Sci.* 2, 161 (1995).
25. E. Auzans, D. Zins, E. Blums, and R. Massart, *J. Mater. Sci.* 34, 1253 (1999).
26. D. Zins, V. Cabuil, and R. Massart, *J. Mol. Liq.* 83, 217 (1999).
27. M. Pourbaix, in "Atlas of Electrochemical Equilibria in Aqueous Solutions." NACE International, Cebelcor, 1974, 640.
28. G. N. Glavee, K. J. Klabunde, C. M. Sorensen, and G. C. Hadjipanayis, *Inorg. Chem.* 34, 28 (1995).
29. G. N. Glavee, K. J. Klabunde, C. M. Sorensen, and G. C. Hadjipanayis, *Langmuir* 9, 162 (1993).
30. G. N. Glavee, K. J. Klabunde, C. M. Sorensen, and G. C. Hadjipanayis, *Langmuir* 10, 4726 (1994).
31. A. Yedra, L. F. Barquin, R. G. Calderon, Q. A. Pankhurst, and J. C. G. Sal, *J. Non-Cryst. Solids* 287, 20 (2001).
32. S. Morup, S. A. Sethi, S. Linderoth, C. Bender Koch, and M. D. Bentzon, *J. Mater. Sci.* 27, 3010 (1992).
33. S. Linderoth, S. Morup, and M. D. Bentzon, *J. Magn. Magn. Mater.* 83, 457 (1990).
34. J. Stolk and A. Manthiram, *Mater. Sci. Eng. B* 60, 112 (1999).
35. D. Makovec, M. Drogenik, and A. Znidarsic, *J. Am. Cer. Soc.* 82, 1113 (1999).
36. M.-L. Wang, Z.-W. Shih, and C.-H. Lin, *J. Cryst. Growth* 139, 47 (1994).
37. M. Inoue, T. Nishikawa, and T. Inui, *J. Mater. Res.* 13, 856 (1998).
38. D.-S. Bae, K.-S. Han, S.-B. Cho, and S.-H. Choi, *Mater. Lett.* 37, 255 (1998).
39. M. Rozman and M. Drogenik, *J. Am. Cer. Soc.* 78, 2449 (1995).
40. J. H. Lee, H. S. Kim, and C. W. Won, *J. Mater. Sci. Lett.* 15, 295 (1996).
41. A. Ataie, M. R. Piramoon, I. R. Harris, and C. B. Ponton, *J. Mater. Sci.* 30, 5600 (1995).
42. H. Kumazawa, Y. Maeda, and E. Sada, *J. Mater. Sci. Lett.* 14, 68 (1995).
43. M. P. Pileni and N. Duxin, *Chem. Innov.* 30, 25 (2000).
44. H. F. Eicke, in "Water-in-Oil Microemulsion Phenomenon" (K. L. Mittal et al., Eds.), 3, 1533-1549. Plenum Press, New York.
45. M. Zulauf and H.-F. Eicke, *J. Phys. Chem.* 83, 480 (1979).
46. P. Ayyub, A. Maitra, and D. O. Shah, *J. Chem. Soc. Faraday Trans.* 89, 3585 (1993).
47. M. M. Stecker and G. B. Benedek, *J. Phys. Chem.* 88, 6519 (1984).
48. G. T. Dimitrova, Th. F. Tadros, P. F. Luckham, and M. R. Kippes, *Langmuir* 12, 315 (1996).
49. K. Inouye, R. Endo, Y. Otsuka, K. Miyashiro, K. Kaneko, and T. Ishikawa, *J. Phys. Chem.* 86, 1465 (1982).
50. E. E. Carpenter, C. J. O'Connor, and V. G. Harris, *J. Appl. Phys.* 85, 5175 (1999).
51. N. Duxin, O. Stephan, C. Petit, P. Bonville, C. Colliex, and M. P. Pileni, *Chem. Mater.* 9, 2096 (1997).
52. J. P. Wilcoxon and P. P. Provencio, *J. Phys. Chem. B* 103, 9809 (1999).
53. J. Tanori, N. Duxin, C. Petit, I. Lisiecki, P. Veillet, and M. P. Pileni, *Colloid Polym. Sci.* 273, 886 (1995).
54. D. O. Yener and H. Giesche, *J. Am. Cer. Soc.* 84, 1987 (2001).
55. V. Pillai, P. Kumar, and D. O. Shah, *J. Magn. Magn. Mater.* 116, L299 (1992).
56. C. Liu, A. J. Rondinone, and Z. J. Zhang, *Pure Appl. Chem.* 72, 37 (2000).
57. C. Liu, B. S. Zou, A. J. Rondinone, and Z. J. Zhang, *J. Phys. Chem. B* 104, 1141 (2000).
58. J. Y. Fang, J. Wang, L.-M. Gan, S.-C. Ng, J. Ding, and X. Y. Liu, *J. Amer. Cer. Soc.* 83, 1049 (2000).
59. M. Rozman and M. Drogenik, *J. Am. Cer. Soc.* 81, 1757 (1998).
60. D. A. Porter and K. E. Easterling, "Phase Transformations in Metals and Alloys," 2nd ed., Chapman and Hall, New York, 1992.

61. J. Osuna, D. de Caro, C. Amiens, B. Chaudret, E. Snoeck, M. Respaud, J.-M. Broto, and A. Fert, *J. Phys. Chem.* 100, 14571 (1996).
62. M. Verelst, T. O. Ely, C. Amiens, E. Snoeck, P. Lecante, A. Mosset, M. Respaud, J. M. Broto, and B. Chaudret, *Chem. Mater.* 11, 2702 (1999).
63. D. P. Dinega and M. G. Bawendi, *Angew. Chem. Int. Ed.* 38, 1788 (1999).
64. V. F. Puntès, K. M. Krishnan, and A. P. Alivisatos, *Science* 291, 2115 (1999).
65. V. F. Puntès, K. Krishnan, and A. P. Alivisatos, *Top. Catal.* 19, 145 (2002).
66. V. F. Puntès, K. M. Krishnan, and A. P. Alivisatos, *Appl. Phys. Lett.* 78, 2187 (2001).
67. J. S. Yin and Z. L. Wang, *Phys. Rev. Lett.* 79, 2570 (1997).
68. S. N. Sidorov, L. M. Bronstein, V. A. Davankov, M. P. Tsyurupa, S. P. Solodovnikov, P. M. Valetsky, E. A. Wilder, and R. J. Spontak, *Chem. Mater.* 11, 3210 (1999).
69. S. J. Park, S. Kim, S. Lee, Z. G. Khim, K. Char, and T. Hyeon, *J. Am. Chem. Soc.* 122, 8581 (2000).
70. H. G. Rotstein and R. Tannenbaum, *J. Phys. Chem. B* 106, 146 (2002).
71. O. Rozenfeld, Y. Koltypin, H. Bamnolker, S. Margel, and A. Gedanken, *Langmuir* 10, 3919 (1994).
72. T. O. Ely, C. Amiens, B. Chaudret, E. Snoeck, M. Varelst, M. Respaud, and J. M. Broto, *Chem. Mater.* 11, 526 (1999).
73. D. A. van Leewen, J. M. van Ruitenbeek, L. J. de Jongh, A. Ceriotti, G. Pacchioni, O. D. Haberlen, and N. Rosch, *Phys. Rev. Lett.* 73, 1432 (1994).
74. N. Rosch, L. Ackermann, G. Pacchioni, and B. I. Dunlap, *J. Chem. Phys.* 95, 7004 (1991).
75. J. P. Chen, C. M. Sorensen, K. J. Klabunde, and G. C. Hadjipanayis, *Phys. Rev. B* 51, 11527 (1995).
76. N. Cordente, M. Respaud, F. Senocq, M. J. Casanove, C. Amiens, and B. Chaudret, *Nano Lett.* 1, 565 (2001).
77. S. L. Tripp, S. V. Puszta, A. E. Ribbe, and A. Wei, *J. Am. Chem. Soc.* 124, 7914 (2002).
78. R. V. Chamberlin, K. D. Humfeld, D. Farrell, S. Yamamuro, Y. Ijiri, and S. A. Majetich, *J. Appl. Phys.* 91, 6961 (2002).
79. J. I. Park and J. Cheon, *J. Am. Chem. Soc.* 123, 5743 (2001).
80. T. Hyeon, S. S. Lee, J. Park, Y. Chung, and H. B. Na, *J. Am. Chem. Soc.* 123, 12798 (2001).
81. T. Hyeon, Y. Chung, J. Park, S. S. Lee, Y. W. Kim, and B. H. Park, *J. Phys. Chem. B* 106, 6831 (2002).
82. K. S. Suslick, S. B. Choe, A. A. Cichowlas, and M. W. Grinstaff, *Nature* 353, 414 (1991).
83. K. S. Suslick, T. Hyeon, and M. Fang, *Chem. Mater.* 8, 2172 (1996).
84. K. S. Suslick, M. Fang, and T. Hyeon, *J. Am. Chem. Soc.* 118, 11960 (1996).
85. K. S. Suslick, T. Hyeon, M. Fang, and A. A. Cichowlas, *Mat. Sci. Eng. A* 204, 186 (1995).
86. R. Bellissent, G. Galli, T. Hyeon, P. Migliardo, G. Parette, and K. S. Suslick, *J. Non-Cryst. Solids* 205–207, 656 (1996).
87. K. V. P. M. Shafi, A. Gedanken, R. B. Goldfarb, and I. Felner, *J. Appl. Phys.* 81, 6901 (1997).
88. G. Katabi, Y. Koltypin, X. Cao, and A. Gedanken, *J. Cryst. Growth* 166, 760 (1996).
89. G. Katabi, T. Prozorov, Y. Koltypin, H. Cohen, C. N. Sukenik, A. Ulman, and A. Gedanken, *Langmuir* 13, 6151 (1997).
90. S. Ramesh, Y. Cohen, D. Aurbach, and A. Gedanken, *Chem. Phys. Lett.* 287, 461 (1998).
91. C. P. Gibson and K. J. Putzer, *Science* 267, 1338 (1995).
92. Y. Koltypin, G. Katabi, X. Cao, R. Prozorov, and A. Gedanken, *J. Non-Cryst. Solids* 201, 159 (1996).
93. K. V. P. M. Shafi, A. Gedanken, and R. Prozorov, *J. Mater. Chem.* 8, 769 (1998).
94. G. Katabi, Y. Koltypin, J. Rothe, J. Hormes, I. Felner, X. Cao, and A. Gedanken, *Thin Solid Films* 333, 41 (1998).
95. K. V. P. M. Shafi, Y. Koltypin, A. Gedanken, R. Prozorov, J. Balogh, J. Lendvai, and I. Felner, *J. Phys. Chem. B* 101, 6409 (1997).
96. K. V. P. M. Shafi, A. Ulman, X. Yan, N. L. Yang, C. Estournes, H. White, and M. Rafailovich, *Langmuir* 17, 5093 (2001).
97. R. V. Kumar, Y. Koltypin, Y. S. Cohen, Y. Cohen, D. Aurbach, O. Palchik, I. Felner, and A. Gedanken, *J. Mater. Chem.* 10, 1125 (2000).
98. R. V. Kumar, Y. Diamant, and A. Gedanken, *Chem. Mater.* 12, 2301 (2000).
99. R. V. Kumar, Y. Koltypin, I. Felner, and A. Gedanken, *Mater. Sci. Eng. A* 286, 101 (2000).
100. K. V. P. M. Shafi, A. Ulman, A. Dyal, X. Yan, N. L. Yang, C. Estournes, L. Fournes, A. Wattiaux, H. White, and M. Rafailovich, *Chem. Mater.* 14, 1778 (2002).
101. C. J. Brinker and G. W. Sherrer, in "Sol-Gel Science," Academic Press, New York, 1990.
102. J. G. Lee, H. M. Lee, C. S. Kim, and Y. J. Oh, *J. Mag. Mag. Mater.* 177–181, 900 (1998).
103. D. H. Chen and X. R. He, *Mater. Res. Bull.* 36, 1369 (2001).
104. C. S. Kim, Y. S. Yi, K. T. Park, H. Namgung, and J. G. Lee, *J. Appl. Phys.* 85, 5223 (1999).
105. G. Xiong, Z. H. Mai, C. Y. Wang, Y. M. Ni, Z. X. Zhao, M. Xu, C. X. Liu, and G. M. Luo, *Chin. Phys. Lett.* 18, 692 (2001).
106. W. C. Kim, C. W. Lee, and C. S. Kim, *Scripta Mater.* 44, 1451 (2001).
107. W. C. Kim, S. J. Kim, J. C. Sur, and C. S. Kim, *J. Mag. Mag. Mater.* 242–245, 197 (2002).
108. W. C. Kim, S. J. Kim, and C. S. Kim, *J. Appl. Phys.* 91, 7607 (2002).
109. S. W. Lee, Y. G. Ryu, K. J. Yang, K. D. Jung, S. Yan, and C. S. Kim, *J. Appl. Phys.* 91, 7610 (2002).
110. S. Y. An, S. W. Lee, S. W. Lee, and C. S. Kim, *J. Mag. Mag. Mater.* 242–245, 413 (2002).
111. X. H. Wang, T. L. Ren, L. Y. Li, and L. S. Zhang, *J. Mag. Mag. Mater.* 184, 95 (1998).
112. G. Xiong, M. Xu, and Z. Mai, *Solid State Comm.* 118, 53 (2001).
113. R. D. Sanchez, J. Rivas, P. Vaquero, M. A. Lopez-Quintela, and D. Caerio, *J. Magn. Magn. Mater.* 247, 92 (2002).
114. S. Mathur and H. Shen, *J. Sol-Gel Sci. Tech.* 25, 147 (2002).
115. J. P. Wang and H. L. Luo, *J. Appl. Phys.* 75, 7425 (1994).
116. A. Jitjanu, M. Crisan, M. Zaherescu, I. Rau, and A. Meghea, *IEEE Trans. Mag.* 267, 71 (2001).
117. L. Li, G. Li, R. L. Smith, Jr., and H. Inomata, *Chem. Mater.* 12, 3705 (2000).
118. G. M. Chow, L. K. Kurihara, K. M. Kemner, P. E. Schoen, W. T. Elam, A. Ervin, S. Keller, Y. D. Zhang, J. Budnick, and T. Ambrose, *J. Mater. Res.* 10, 1546 (1995).
119. G. M. Chow, L. K. Kurihara, and P. E. Schoen, U.S. Patent 6,436,167, August 20, 2002.
120. A. Bianco, G. Gusmano, R. Montanari, G. Montesperelli, and E. Traversa, *Mater. Lett.* 19, 263 (1994).
121. A. Bianco, G. Gusmano, R. Montanari, G. Montesperelli, and E. Traversa, *Thermochim. Acta* 269–270, 117 (1995).
122. L. K. Kurihara, G. M. Chow, and P. E. Schoen, *Nano Struct. Mater.* 5, 607 (1995).
123. G. Viau, F. Ravel, O. Acher, F. Fievet-Vincent, and F. Fievet, *J. Appl. Phys.* 76, 6570 (1994).
124. G. Viau, F. Ravel, O. Acher, F. Fievet-Vincent, and F. Fievet, *J. Mag. Mag. Mater.* 140–144, 377 (1995).
125. G. Viau, F. Fievet-Vincent, and F. Fievet, *J. Mater. Chem.* 6, 1047 (1996).
126. G. Viau, F. Fievet-Vincent, and F. Fievet, *Solid State Ionics* 84, 259 (1996).
127. G. Viau, F. Fievet-Vincent, F. Fievet, P. Toneguzzo, F. Ravel, and O. Acher, *J. Appl. Phys.* 81, 2749 (1997).

128. P. Toneguzzo, O. Acher, G. Viau, F. Fievet-Vincent, and F. Fievet, *J. App. Phys.* 81, 5546 (1997).
129. Ph. Toneguzzo, G. Viau, O. Acher, F. Fievet-Vincent, and F. Fievet, *Adv. Mater.* 10, 1032 (1998).
130. Ph. Toneguzzo, O. Acher, G. Viau, A. Pierrard, F. Fievet-Vincent, F. Fievet, and I. Rosenman, *IEEE Trans. Mag.* 35, 3469 (1999).
131. D. Mercier, J. C. S. Levy, G. Viau, F. Fievet-Vincent, F. Fievet, P. Toneguzzo, and O. Acher, *Phys. Rev. B* 62, 532 (2000).
132. G. Viau, P. Toneguzzo, A. Pierrard, O. Acher, F. Fievet-Vincent, and F. Fievet, *Scripta Mater.* 44, 2263 (2001).
133. A. K. Giri, K. M. Chowdary, and S. A. Majetich, *Mater. Phys. Mech.* 1, 1 (2000).
134. M. S. Hegde, D. Larcher, L. Dupont, B. Beaudoin, K. Tekaiia-Elhsissen, and J. M. Tarascon, *Solid State Ionics* 93, 33 (1997).
135. P. Saravanan, T. A. Jose, P. J. Thomas, and G. U. Kulkarni, *Bull. Mater. Sci.* 24, 515 (2001).
136. H. O. Jungk and C. Feldmann, *J. Mater. Res.* 15, 2244 (2000).
137. C. Feldmann and H. O. Jungk, *Angew. Chem. Int. Ed.* 40, 359 (2001).
138. C. Feldmann, *Adv. Mater.* 13, 1301 (2001).
139. S. Ammar, A. Heflen, N. Jouini, F. Fievet, I. Roseman, F. Villain, P. Molinie, and M. Danot, *J. Mater. Chem.* 11, 186 (2001).
140. W. Yu, Y. Wang, H. Liu, and W. Zheng, *J. Molec. Catal. A* 112, 105 (1996).
141. S. Aayyappan, G. N. Subbanna, R. Srinivasa Goplan, and C. N. R. Rao, *Solid State Ionics* 84, 271 (1996).
142. F. Kooli, V. Rives, and W. Jones, *Chem. Mater.* 9, 2231 (1997).
143. G. M. Chow, L. K. Kurihara, and P. E. Schoen, U.S. Patent 5,759,230, June 2, 1998.
144. T. Yamaguchi and K. Kitajima, *J. Mater. Sci.* 33, 653 (1998).
145. Ph. Toneguzzo, G. Viau, O. Acher, F. Guillet, E. Bruneton, F. Fievet-Vincent, and F. Fievet, *J. Mater. Sci.* 35, 3767 (2000).
146. L. Poul, N. Jouini, and F. Fievet, *Chem. Mater.* 12, 3123 (2000).
147. M. Wu, H. He, Z. Zhao, and X. Yao, *J. Phys. D* 33, 2927 (2000).
148. P. Elumalai, H. N. Vasam, M. Verelst, P. Lecante, V. Carles, and P. Tailhades, *Mater. Res. Bull.* 37, 353 (2002).
149. T. Teranishi and M. Miyake, *Chem. Mater.* 11, 3414 (1999).
150. L. K. Kurihara, D. Lewis, A. M. Jung, A. W. Fliflet, and R. W. Bruce, in "Structure and Mechanical Properties in Nanophase Materials" (M. J. Mayo and J. Weertman, Eds.), 2001, MRS, Pittsburgh, B6.15-6.21.
151. D. Lewis, A. Fliflet, S. H. Gold, R. W. Bruce, and L. K. Kurihara, U.S. Navy Case 83,975, application pending, 2002.
152. L. K. Kurihara and E. E. Carpenter, U.S. Navy Case 83,982, 2002, application pending.
153. D. Poondi, T. A. Dobbins, and J. Singh, *J. Mater. Sci.* 35, 6237 (2000).
154. H. R. Kahn and K. Petrikowski, *J. Mag. Mag. Mater.* 215-216, 526 (2000).
155. H. Zeng, M. Zheng, R. Skomski, D. J. Sellmyer, Y. Liu, L. Menon, and S. Bandyopadhyay, *J. Appl. Phys.* 87, 4718 (2000).
156. A. Kazadi Mukenga Bantu, J. Rivas, G. Zaragoza, M. A. Lopez-Quintela, and M. C. Blanco, *J. Non Cryst. Solids* 287, 5 (2001).
157. T. M. Whitney, J. S. Jiang, P. C. Searson, and C. L. Chien, *Science* 261, 1316 (1993).
158. C. R. Martin, *Science* 266, 1961 (1994).
159. J. Meier, B. Doudin, and J. Ph. Ansermet, *J. App. Phys.* 79, 6010 (1996).
160. R. Ferre, K. Ounadjela, J. M. George, L. Piraux, and S. Dubois, *Phys. Rev. B* 56, 14066 (1997).
161. Y. H. Huang, H. Okumura, G. C. Hadjipanayis, and D. Weller, *J. Appl. Phys.* 91, 6869 (2002).
162. H. R. Khan and K. Petrikowski, *Mater. Sci. Eng. C* 19, 345 (2002).
163. L. Sun, P. C. Searson, and C. L. Chien, *Phys. Rev. B* 61, 6463 (2000).
164. Z. Zhang, S. Dai, D. A. Blom, and J. Shen, *Chem. Mater.* 14, 965 (2002).
165. R. M. Penner, *J. Phys. Chem.* 106, 3339 (2002).
166. J. V. Zoval, J. Lee, S. Gorth, and R. M. Penner, *J. Phys. Chem.* 102, 1164 (1998).
167. A. Dierstein, H. Natter, F. Meyer, H. O. Stephan, C. Kropf, and R. Hempelmann, *Scripta Mater.* 44, 2209 (2001).
168. S. Lauer, Z. Guan, H. Wolf, H. Natter, M. Schmelzer, R. Hempelmann, and T. Wichert, *Nano Struct. Mater.* 12, 955 (1999).
169. C. Pascal, J. L. Pascal, F. Favier, M. L. Elidrissi Moubtassim, and C. Payen, *Chem. Mater.* 11, 141 (1999).
170. R. Amigo, J. Asenjo, E. Krotenko, F. Torres, J. Tejada, and E. Brillas, *Chem. Mater.* 12, 573 (2000).
171. F. Torres, R. Amigo, J. Asenjo, E. Krotenko, J. Tejada, and E. Brillas, *Chem. Mater.* 12, 3060 (2000).
172. M. P. Zach and R. M. Penner, *Adv. Mater.* 12, 878 (2000).
173. J. L. Delplancke, J. Dille, J. Reisse, G. J. Long, A. Mohan, and F. Grandjean, *Chem. Mater.* 12, 946 (2000).
174. H. Liu, F. Favier, K. Ng, M. P. Zach, and R. M. Penner, *Electrochim. Acta* 47, 671 (2001).
175. H. Liu and R. M. Penner, *J. Phys. Chem. B* 104, 9131 (2000).
176. G. B. Khomutov, A. Y. Obydenov, S. A. Yakovenko, E. S. Soldatov, A. S. Trifonov, V. V. Khanin, and S. P. Gubin, *Mat. Sci. Eng. C* 8-9, 309 (1999).
177. M. T. Reeb, W. Helbig, and S. A. Quasick, in "Active Metals, Preparation, Characterization, Applications" (A. Furster, Ed.), VCH, Weinheim, 1996.
178. K. Ono, Y. Kakefuda, R. Okuda, Y. Ishii, K. Kamimura, A. Kitamura, and M. Oshima, *J. App. Phys.* 91, 8480 (2002).
179. C. B. Murray, S. Sun, W. Gaschler, H. Doyle, T. A. Betley, and C. R. Kagan, *IBM J. Res. Dev.* 45, 451 (2001).
180. S. Sun, E. E. Fullerton, D. Weller, and C. B. Murray, *IEEE Trans. Mag.* 37, 1239 (2001).
181. Z. R. Dai, S. Sun, and Z. L. Wang, *Nano Lett.* 1, 443 (2001).
182. J. W. Harrell, S. Wang, D. E. Nikles, and M. Chen, *App. Phys. Lett.* 79, 4393 (2001).
183. S. Yamamuro, D. Farrell, K. D. Humfeld, and S. J. Majetich, *Mat. Res. Soc. Symp. Proc.* 636, D10.8.1 (2001).
184. C. B. Murray, S. Sun, H. Doyle, and T. Betley, *MRS Bull.* Dec, 985 (2001).
185. B. Stahl, N. S. Gajbhiye, G. Wilde, D. Kramer, J. Ellrich, M. Ghafari, H. Hahn, H. Gleiter, J. Weibmuller, R. Wurshum, and P. Schlossmacher, *Adv. Mater.* 14, 24 (2002).
186. Z. R. Dai, S. Sun, and Z. L. Wang, *Surf. Sci.* 505, 325 (2002).
187. M. Chen and D. E. Nikles, *Nano Lett.* 2, 211 (2002).
188. E. Shevchenko, D. Talapin, A. Kornowski, F. Wiekhorst, J. Kotzler, M. Haase, A. Rogach, and H. Weller, *Adv. Mater.* 14, 287 (2002).
189. M. Chen and D. E. Nikles, *J. Appl. Phys.* 91, 8477 (2002).
190. A similar table of structural probes, but without the emphasis on magnetic nanoparticles, can be found in A. R. West, "Solid State Chemistry and Applications," 48; 1984, Wiley, Chichester.
191. G. Thomas and A. Hütten, *Nanostruct. Mater.* 9, 271 (1997).
192. J. A. Ascencio, C. Gutiérrez-Wing, M. E. Espinosa, M. Marín, S. Tehuacanero, C. Zorrilla, and M. José-Yacamán, *Surf. Sci.* 396, 349 (1998).
193. T. Nakayama, T. A. Yamamoto, Y.-H. Choa, and K. Niihara, *J. Mater. Sci.* 35, 3857 (2000).
194. S. Tomita, M. Hikita, M. Fujii, S. Hayashi, and K. Yamamoto, *Chem. Phys. Lett.* 316, 361 (2000).
195. Y. S. Kwok, X. X. Zhang, B. Qin, and K. K. Fung, *Appl. Phys. Lett.* 77, 3971 (2000).
196. W. L. Zhou, E. E. Carpenter, J. Lin, A. Kumbhar, J. Sims, and C. J. O'Connor, *Eur. Phys. J. D* 16, 289 (2001).
197. W. Teunissen, F. M. F. de Groot, J. Geus, O. Stephan, M. Tence, and C. Colliex, *J. Catal.* 204, 169 (2001).
198. S. Santra, R. Tapeç, N. Theodoropoulou, J. Dobson, A. Hebard, and W. Tan, *Langmuir* 17, 2900 (2001).
199. X.-C. Sun and N. Nava, *Nano Lett.* 2, 765 (2002).
200. R. Pecora, *J. Nanopart. Res.* 2, 123 (2000).

201. R. Weber and G. Schwer, *J. Colloid Interface Sci.* 210, 86 (1999).
202. Z. Turgut, J. H. Scott, M. Q. Huang, S. A. Majetich, and M. E. McHenry, *J. Appl. Phys.* 83, 6468 (1998).
203. S. Giri, S. Ganguli, and M. Bhattacharya, *Appl. Surf. Sci.* 182, 345 (2001).
204. D. H. Chen and S. H. Wu, *Chem. Mater.* 12, 1354 (2000).
205. K. Sato, B. Bian, and Y. Hirotsu, *J. Appl. Phys.* 91, 8516 (2002).
206. J. Smit and H. P. J. Wijn, "Ferrites," 136–176, Wiley, New York, 1959.
207. G. Ennas, G. Marongiu, A. Musinu, A. Falqui, P. Ballirano, and R. Caminiti, *J. Mater. Res.* 14, 1570 (1999).
208. A. J. Rondinone, A. C. S. Samia, and Z. J. Zhang, *J. Phys. Chem. B* 103, 6876 (1999).
209. Z. J. Zhang, Z. L. Wang, B. C. Chakoumakos, and J. S. Yin, *J. Amer. Chem. Soc.* 120, 1800 (1998).
210. I. V. Golosovsky, I. Mirebeau, G. Andre, D. A. Kurdyukov, Y. A. Kumzerov, and S. B. Vakhruhev, *Phys. Rev. Lett.* 86, 5783 (2001).
211. S. N. Klausen, P. A. Lindgard, K. Lefmann, F. Bodker, and S. Morup, *Phys. Status Solidi A* 189, 1039 (2002).
212. V. I. Nikolaev, A. M. Shipilin, and I. N. Zakharova, *Phys. Solid State* 43, 1515 (2001).
213. X. X. Bi, B. Ganguly, G. P. Huffman, F. E. Huggins, M. Endo, and P. C. Eklund, *J. Mater. Res.* 8, 1666 (1993).
214. F. Bødker, S. Mørup, and S. Linderth, *Phys. Rev. Lett.* 72, 282 (1994).
215. G. Ennas, A. Musinu, G. Piccaluga, D. Zedda, D. Gatteschi, C. Sangregorio, J. L. Stanger, G. Concas, and G. Spano, *Chem. Mater.* 10, 495 (1998).
216. Z. W. Li, C. K. Ong, Z. Yang, F. L. Wei, X. Z. Zhou, J. H. Zhao, and A. H. Morrish, *Phys. Rev. B* 62, 6530 (2000).
217. H. H. Hamdeh, K. Barghout, J. C. Ho, R. J. Willey, M. J. O'Shea, and J. Chaudhuri, *J. Magn. Magn. Mater.* 212, 112 (2000).
218. A. S. Albuquerque, J. D. Ardisson, W. A. A. Macedo, and M. C. M. Alves, *J. Appl. Phys.* 87, 4352 (2000).
219. C. N. Chinnasamy, A. Narayanasamy, N. Ponpandian, K. Chatopadhyay, K. Shinoda, B. Jeyadevan, K. Tohji, K. Nakatsuka, T. Furubayashi, and I. Nakatani, *Phys. Rev. B* 63, Art. no. 184108 (2001).
220. B. Gillot, J. Lorimier, F. Bernard, V. Nivoix, S. Douard, and Ph. Tailhades, *Mat. Chem. Phys.* 61, 199 (1999).
221. B. Gillot, *J. Solid State Chem.* 113, 163 (1994).
222. J. W. Couves, J. M. Thomas, D. Waller, R. H. Jones, A. J. Dent, G. E. Derbyshire, and G. N. Greaves, *Nature* 354, 465 (1991).
223. S. Pascarelli, T. Neisius, S. De Panfilis, M. Bonfim, S. Pizzini, K. Mackay, S. David, A. Fontaine, A. San Miguel, J. P. Itie, M. Gauthier, and A. Polian, *J. Synch. Rad.* 6, 146 (1999).
224. T. Ressler, M. Hagelstein, U. Hatje, and W. Metz, *J. Phys. Chem. B* 101, 6680 (1997).
225. S. G. Fiddy, M. A. Newton, A. J. Dent, G. Salvini, J. M. Corker, S. Turin, T. Campbell, and J. Evans, *Chem. Comm.* 9, 851 (1999).
226. T. Ressler, O. Timpe, T. Neisius, J. Find, G. Mestl, M. Dieterle, and R. Schlogl, *J. Catal.* 191, 75 (2000).
227. A. Yamaguchi, T. Shido, Y. Inada, T. Kogure, K. Asakura, M. Nomura, and Y. Iwasawa, *Catal. Lett.* 68, 139 (2000).
228. H. Rumpf, J. Janssen, H. Modrow, K. Winkler, and J. Hormes, *J. Solid State Chem.* 163, 158 (2002).
229. H. Stragier, J. O. Cross, J. J. Rehr, L. B. Sorensen, C. E. Bouldin, and J. C. Woicik, *Phys. Rev. Lett.* 69, 3064 (1992).
230. I. J. Pickering, M. Sansone, J. Marsch, and G. N. George, *J. Amer. Chem. Soc.* 115, 6302 (1993).
231. K. Kobayashi, H. Kawata, and K. Mori, *J. Synch. Rad.* 5, 972–974, (1998).
232. A. I. Frenkel, J. O. Cross, D. M. Fanning, and I. K. Robinson, *J. Synch. Rad.* 6, 332 (1999).
233. H. Renevier, Y. Joly, J. Garcia, G. Subias, M. G. Proietti, J. L. Hodeau, and J. Blasco, *J. Synch. Rad.* 8, 390 (2001).
234. B. Ravel, S. Grenier, H. Renevier, and C. B. Eom, *J. Synch. Rad.* 8, 384 (2001).
235. D. C. Bazin, D. A. Sayers, and J. J. Rehr, *J. Phys. Chem. B* 101, 11040 (1997).
236. F. Bernard, J. Lorimier, V. Nivoix, N. Millot, P. Perriat, B. Gillot, J. F. Berar, and J. C. Niepce, *J. Solid State Chem.* 141, 105 (1998).
237. B. Ravel, E. E. Carpenter, and V. G. Harris, *J. Appl. Phys.* 91, 8195 (2002).
238. J. F. Hochepped, P. Sainctavit, and M. P. Pileni, *J. Magn. Magn. Mater.* 231, 315 (2001).
239. S. Li, L. Liu, V. T. John, C. J. O'Connor, and V. G. Harris, *IEEE Trans. Magn.* 37, 2350 (2001).
240. J. J. Rehr and R. C. Albers, *Rev. Mod. Phys.* 72, 621 (2000).
241. J. J. Rehr and A. L. Ankudinov, *J. Synch. Rad.* 8, 61 (2001).
242. B. Jeyadevan, K. Tohji, K. Nakatsuka, and A. Narayanasamy, *J. Magn. Magn. Mater.* 217, 99 (2000).
243. S. Calvin, E. E. Carpenter, B. Ravel, and V. G. Harris, *Phys. Rev. B*, to be published.
244. B. Ravel, M. Newville, J. O. Cross, and C. E. Bouldin, *Physica B* 209, 145 (1995).
245. A. I. Frenkel, O. Kleifeld, S. R. Wasserman, and I. Sagi, *J. Chem. Phys.* 116, 9449 (2002).
246. M. Ruitenbeek, A. J. van Dillen, F. M. F. de Groot, I. E. Wachs, J. W. Geus, and D. C. Koningsberger, *Top. Catal.* 10, 241 (2000).
247. M. J. Fay, A. Proctor, D. P. Hoffmann, M. Houalla, and D. M. Hercules, *Mikrochim. Acta* 109, 281 (1992).
248. S. R. Wasserman, *J. Phys. IV* 7, 203 (1997).
249. T. Ressler, J. Wong, J. Roos, and I. L. Smith, *Environ. Sci. Technol.* 34, 950 (2000).
250. M. A. Eberhardt, A. Proctor, M. Houalla, and D. M. Hercules, *J. Catal.* 160, 27 (1996).
251. G. Stakkestad, B. Grung, J. Sjoblom, and T. Sigvartsen, *Colloid Polym. Sci.* 277, 627 (1999).
252. B. Ravel, E. Cockayne, M. Newville, and K. M. Rabe, *Phys. Rev. B* 60, 14632 (1999).
253. A. I. Frenkel, C. W. Hills, and R. G. Nuzzo, *J. Phys. Chem. B* 105, 12689 (2001).
254. I. Arcon, A. Tuel, A. Kodre, G. Martin, and A. Barbier, *J. Synch. Rad.* 8, 575 (2001).
255. J. Riedel, S. Calvin, E. E. Carpenter, and V. G. Harris (unpublished).
256. R. W. Chantrell and K. O'Grady, in "NATO ASI Series E, Vol. 253, 113–164" (R. Gerber, C. D. Wright, and G. Asti, Eds.), Kluwer Academic Press, The Netherlands, 1994.
257. J. L. Dormann, D. Fiorani, and E. Tronc, *Adv. Chem. Phys.* 98, 283 (1997).
258. D. L. Leslie-Pelecky and R. D. Rieke, *Chem. Mater.* 8, 1770 (1996).
259. S. Chikazumi, "Physics of Ferromagnetism," Clarendon Press, Oxford, 1997.
260. R. C. O'Handley, "Modern Magnetic Materials," John Wiley & Sons, Inc., New York, 2000.
261. C. Kittel, *Rev. Mod. Phys.* 21, 541 (1949).
262. A. Aharoni, *J. Appl. Phys.* 75, 5891 (1994).
263. J. A. Osborn, *Phys. Rev.* 67, 351 (1945).
264. E. C. Stoner, *Phil. Mag. Ser. 7* 36, 803 (1945).
265. E. C. Stoner, F. R. S. Wohlfarth, and E. P. Wohlfarth, *Nature* 160, 650 (1947).
266. E. C. Stoner, F. R. S. Wohlfarth, and E. P. Wohlfarth, *Phil. Trans. Royal Soc. (London) A* 240, 599 (1948).
267. C. P. Bean and J. D. Livingston, *J. Appl. Phys.* 30, 120S (1959).
268. I. Eisenstein and A. Aharoni, *Phys. Rev. B* 14, 2078 (1976).
269. S. Sun and C. B. Murray, *J. Appl. Phys.* 85, 4325 (1999).
270. V. F. Puentes and K. M. Krishnan, *IEEE Trans. Mag.* 37, 2210 (2001).
271. C. P. Bean, *J. Appl. Phys.* 26, 1381 (1955).
272. M. Walker, P. I. Mayo, K. O'Grady, S. W. Charles, and R. W. Chantrell, *J. Phys. Cond. Matt.* 5, 2779 (1993).

273. L. Tauxe, T. A. T. Mullender, and T. Pick, *J. Geophys. Res.* 101, 571 (1996).
274. Q. Chen and Z. J. Zhang, *Appl. Phys. Lett.* 73, 3156 (1998).
275. A. E. Berkowitz, J. A. Lahut, I. S. Jacobs, L. M. Levinson, and D. W. Forester, *Phys. Rev. Lett.* 34, 594 (1975).
276. P. E. Kelly, K. O'Grady, and P. I. Mayo, *IEEE Trans. Mag.* 25, 3881 (1989).
277. P. I. Mayo, R. M. Erkkila, A. Bradbury, and R. W. Chantrell, *IEEE Trans. Mag.* 26, 1894 (1990).
278. H. Zeng, S. Sun, T. S. Vedantam, J. P. Liu, Z.-R. Dai, and Z.-L. Wang, *Appl. Phys. Lett.* 80, 2583 (2002).
279. J. L. Dormann, F. D'Orazio, F. Lucari, E. Tronc, P. Prene, J. P. Jolivet, D. Fiorani, R. Cherkaoui, and M. Nogues, *Phys. Rev. B* 53, 14291 (1996).
280. C. Djurberg, P. Svedlindh, P. Nordblad, M. F. Hansen, F. Bodker, and S. Morup, *Phys. Rev. Lett.* 79, 5154 (1997).
281. M. R. Diehl, J.-Y. Yu, J. R. Heath, G. A. Held, H. Doyle, S. Sun, and C. B. Murray, *J. Phys. Chem. B* 105, 7913 (2001).
282. F. Bodker, S. Morup, and S. Linderoth, *Phys. Rev. Lett.* 72, 282 (1994).
283. J. P. Chen and D. E. Nikles, *IEEE Trans. Magn.* 32, 4478 (1996).
284. M. Chen, B. Tang, and D. E. Nikles, *IEEE Trans. Magn.* 34, 1141 (1998).
285. L. Chen, W. J. Yang, and C. Z. Yang, *J. Mater. Sci.* 32, 3571 (1996).
286. A. Cabral-Prieto, A. A. Reyes-Felipe, and M. G. Siles-Dotor, *Nano Struct. Mater.* 10, 311 (1998).
287. S. Krehula, S. Popovic, and S. Music, *Mater. Lett.* 54, 108 (2002).
288. B. J. Lemaire, P. Davidson, J. Ferre, J. P. Jamet, P. Panine, I. Dozov, and J. P. Jolivet, *Phys. Rev. Lett.* 88, 125507 (2002).
289. T. Ishikawa, T. Motoki, R. Katoh, A. Yasukawa, K. Kandori, T. Nakayama, and F. Yuse, *J. Coll. Interface Sci.* 250, 74 (2002).
290. T. Ishikawa, M. Kumagai, A. Yasukawa, K. Kandori, T. Nakayama, and F. Yuse, *J. Corrosion Sci.* 44, 1073 (2002).
291. M. Gotic, S. Popovic, and S. Music, *Mater. Lett.* 21, 289 (1994).
292. Q. Chen, A. J. Rondinone, B. C. Chakoumakos, and Z. J. Zhang, *J. Magn. Magn. Mater.* 194, 1 (1999).
293. J. P. Chen, C. M. Sorensen, K. J. Klabunde, G. C. Hadjipanayis, E. Devlin, and A. Kostikas, *Phys. Rev. B* 54, 9288 (1996).
294. D. K. Kim, W. Voit, W. Zapka, B. Bjelke, M. Muhammed, and K. V. Rao, *Mat. Res. Soc. Symp. Proc.* 676, Y8.32 (2001).
295. W. Voit, D. K. Kim, W. Zapka, M. Muhammed, and K. V. Rao, *Mat. Res. Soc. Symp. Proc.* 676, Y7.8 (2001).
296. J. de Vicente, A. V. Delgado, J. D. G. Duran, and F. Gonzalez-Caballero, *Langmuir* 16, 7954 (2000).
297. H. J. Song, J. H. Oh, S. C. Choi, and J. C. Lee, *Phys. Stat. Sol. A* 189, 849 (2002).
298. M. H. Sousa, E. Hasmonay, J. Depeyrot, F. A. Tourinho, J.-C. Bacri, E. Dubois, R. Perzynski, and Yu. L. Raikher, *J. Magn. Magn. Mater.* 242–245, 572 (2002).
299. E. Hasmonay, J. Depeyrot, M. H. Sousa, F. A. Tourinho, J.-C. Bacri, and R. Perzynski, *J. Magn. Magn. Mater.* 201, 195 (1999).
300. R. C. Plaza, J. de Vincente, S. Gomez-Lopera, and A. V. Delgado, *J. Colloid Interface Sci.* 242, 306 (2001).
301. M. Ueda, S. Shimada, and M. Inagaki, *J. Mater. Chem.* 3, 1199 (1993).
302. R. Massart, D. Zins, F. Gendron, M. Rivoire, R. V. Mehta, R. V. Upadhyay, P. S. Goyal, and V. K. Aswal, *J. Magn. Magn. Mater.* 201, 73 (1999).
303. P. C. Fannin, S. W. Charles, and J. L. Dormann, *J. Magn. Magn. Mater.* 201, 98 (1999).
304. M. Pal, D. Das, S. N. Chinalapudi, and D. Chakravorty, *J. Mater. Res.* 15, 683 (2000).
305. P. S. Anil Kumar, J. J. Shrotri, S. D. Kulkarni, C. E. Deshpande, and S. K. Date, *Mater. Lett.* 27, 293 (1996).
306. X. L. Xu, J. D. Guo, and Y. Z. Wang, *Mat. Sci. Eng. B* 77, 207 (2000).
307. F. Gazeau, J. C. Bacri, F. Gendron, R. Perzynski, Yu. L. Raikher, V. I. Stepanov, and E. Dubois, *J. Magn. Magn. Mater.* 186, 175 (1998).
308. X. Xu, G. Friedman, K. D. Humfeld, S. A. Majetich, and S. A. Asher, *Chem. Mater.* 14, 1249 (2002).
309. A. Bee, R. Massart, and S. Neveu, *J. Magn. Magn. Mater.* 149, 6 (1995).
310. Y. Ni, X. Ge, Z. Zhang, and Q. Ye, *Chem. Mater.* 14, 1048 (2002).
311. D.-H. Chen and Y.-Y. Chen, *Mater. Res. Bull.* 37, 801 (2002).
312. T. Ogasawara and M. A. S. Oliveira, *J. Magn. Magn. Mater.* 217, 147 (2000).
313. S. E. Jacobo, C. Domingo-Pascual, R. Rodriguez-Clemente, and M. A. Blesa, *J. Mat. Sci.* 32, 1025 (1997).
314. S. R. Janasi, D. Rodrigues, M. Emura, and F. J. G. Landgraf, *Phys. Stat. Sol. A* 185, 479 (2001).
315. X. Liu, J. Wang, J. Ding, M. S. Chen, and Z. X. Shen, *J. Mater. Chem.* 10, 1745 (2000).
316. A. Ataie, S. Heshmati-Manesh, and H. Kazempour, *J. Mater. Sci.* 37, 2125 (2002).
317. S. R. Janasi, D. Rodrigues, F. J. G. Landgraf, and M. Emura, in "Advanced Powder Technology," 189–1, 661 (2001).
318. J. Lu, D. B. Dreisinger, and W. C. Cooper, *Hydromet.* 45, 305 (1997).
319. L. Yiping, Z. X. Tang, G. C. Hadjipanayis, C. M. Sorensen, and K. J. Klabunde, *IEEE Trans. Mag.* 29, 2646 (1993).
320. G. D. Forester, L. F. Barquin, R. L. Bilsborrow, Q. A. Pankhurst, I. P. Parkin, and W. A. Steer, *J. Mater. Chem.* 9, 2537 (1999).
321. J. Shen, Z. Li, Y. Fan, Z. Hu, and Y. Chen, *J. Sol. State Chem.* 106, 493 (1993).
322. L. Suber, H. Romero, D. Fiorani, A. M. Testa, A. Montone, M. V. Antisari, J. L. Dormann, J. Maknani, and N. Sparvieri, *Nano Struct. Mat.* 6, 949 (1995).
323. D. Fiorani, H. Romero, L. Suber, A. M. Testa, J. L. Dormann, J. Maknani, and N. Sparvieri, *J. Magn. Magn. Mater.* 140–144, 411 (1995).
324. D. Fiorani, H. Romero, L. Suber, A. M. Testa, M. Vittori, A. Montone, J. L. Dormann, and J. Maknani, *Mat. Sci. Eng. A* 204, 165 (1995).
325. J. Shen, Z. Li, Q. Yan, and Y. Chen, *J. Phys. Chem.* 97, 8504 (1993).
326. W. Wolski, E. Wolska, J. Kaczmarek, and P. Pizora, *Phys. Stat. Solidi* 152, K19 (1995).
327. M. Sorescu, D. Mihaila-Tarabasanu, and L. Diamandescu, *Appl. Phys. Lett.* 72, 2047 (1998).
328. X. Yi, Q. Yitai, L. Jing, C. Zuyao, and Y. Li, *Mat. Sci. Eng. B* 34, L1 (1995).
329. W.-H. Lin and C.-S. Hwang, *J. Mater. Sci.* 37, 1067 (2002).
330. C. Rath, K. K. Sahu, S. Anand, S. K. Date, N. C. Mishra, and R. P. Das, *J. Magn. Magn. Mater.* 202, 77 (1999).
331. L. Xiang, Y. P. Yin, and Y. Jin, *J. Mater. Sci.* 37, 349 (2002).
332. X. Y. Li, G. X. Lu, and S. B. Li, *J. Mater. Sci. Lett.* 15, 397 (1996).
333. S. Uchida, H. Kashiwagi, T. Sato, and A. Okuwaki, *J. Mat. Sci.* 31, 4625 (1996).
334. H. Kumazawa, H.-M. Cho, and E. Sada, *J. Mater. Sci.* 28, 5247 (1993).
335. X. Y. Liu, J. Wang, L.-M. Gan, and S.-C. Ng, *J. Magn. Magn. Mater.* 195, 452 (1999).
336. M.-L. Wang, Z.-W. Shih, and C.-H. Lin, *J. Cryst. Growth* 114, 435 (1991).
337. M.-L. Wang, Z.-W. Shih, and C.-H. Lin, *J. Cryst. Growth* 116, 483 (1992).
338. M.-L. Wang, Z.-W. Shih, and C.-H. Lin, *J. Cryst. Growth* 130, 153 (1993).
339. Y. Hakuta, T. Adschiri, T. Suzuki, T. Chida, K. Seino, and K. Arai, *J. Am. Cer. Soc.* 81, 2461 (1998).
340. M. C. Blanco, A. Meira, D. Baldomir, J. Rivas, and M. A. Lopez-Quintela, *IEEE Trans. Magn.* 30, 739 (1994).

341. J. L. Cain, S. R. Harrison, J. A. Nikles, and D. Nikles, *J. Magn. Magn. Mater.* 155, 67 (1996).
342. J. L. Cain and D. E. Nikles, *IEEE Trans. Magn.* 32, 4490 (1996).
343. J. L. Cain and D. E. Nikles, *J. Appl. Phys.* 79, 4860 (1996).
344. M. Chen and D. E. Nikles, *J. Appl. Phys.* 85, 5504 (1999).
345. A. Martino, M. Stoker, M. Hicks, C. H. Bartholomew, A. G. Sault, and J. S. Kawola, *Appl. Catal. A* 161, 235 (1997).
346. J. P. Chen, K. M. Lee, C. M. Sorensen, K. J. Klabunde, and G. C. Hadjipanayis, *J. Appl. Phys.* 75, 5876 (1994).
347. J. Legrand, C. Petit, and M. P. Pileni, *J. Phys. Chem. B* 105, 5643 (2001).
348. J. Legrand, A.-T. Ngo, C. Petit, and M. P. Pileni, *Adv. Mater.* 13, 58 (2001).
349. C. Petit, A. Taleb, and M. P. Pileni, *Adv. Mater.* 10, 259 (1998).
350. C. Petit, T. Cren, D. Roditchev, W. Sacks, J. Klein, and M. P. Pileni, *Adv. Mater.* 11, 1198 (1999).
351. C. Petit and M. P. Pileni, *Appl. Surf. Sci.* 162–163, 519 (2000).
352. C. Petit, J. Legrand, V. Russier, and M. P. Pileni, *J. Appl. Phys.* 91, 1502 (2002).
353. J. P. Chen, C. M. Sorensen, K. J. Klabunde, and G. C. Hadjipanayis, *J. Appl. Phys.* 76, 6316 (1994).
354. G. Salazar-Alvarez, M. Mikhailova, M. Toprak, Y. Zhang, and M. Muhammed, *Mat. Res. Soc. Symp. Proc.* 704, W7.1 (2002).
355. N. Duxin, N. Brun, C. Colliex, and M. P. Pileni, *Langmuir* 14, 1984 (1998).
356. E. E. Carpenter, J. A. Sims, J. A. Wienmann, W. L. Zhou, and C. J. O'Connor, *J. Appl. Phys.* 87, 5616 (2000).
357. N. Duxin, N. Brun, P. Bonville, C. Colliex, and M. P. Pileni, *J. Phys. Chem. B* 101, 8907 (1997).
358. N. Duxin, M. P. Pileni, W. Wernsdorfer, B. Barbara, A. Benoit, and D. Maillly, *Langmuir* 16, 11 (2000).
359. C. Petit and M. P. Pileni, *J. Magn. Magn. Mater.* 166, 82 (1997).
360. L. Shen, P. E. Laibinis, and T. A. Hatton, *J. Magn. Magn. Mater.* 194, 37 (1999).
361. C. T. Seip, E. E. Carpenter, C. J. O'Connor, V. T. John, and S. C. Li, *IEEE Trans. Magn.* 34, 1111 (1998).
362. N. Feltin and M. P. Pileni, *Langmuir* 13, 3927 (1997).
363. N. Feltin and M. P. Pileni, *J. de Phys. IV* 7, C1-609 (1997).
364. K. M. Lee, C. M. Sorensen, K. J. Klabunde, and G. C. Hadjipanayis, *IEEE Trans. Mag.* 28, 3180 (1992).
365. Z. H. Zhou, J. Wang, X. Liu, and H. S. O. Chan, *J. Mater. Chem.* 11, 1704 (2001).
366. S. C. Li, V. T. John, C. O'Connor, V. Harris, and E. Carpenter, *J. Appl. Phys.* 87, 6223 (2000).
367. N. Moumen, P. Veillet, and M. P. Pileni, *J. Magn. Magn. Mater.* 149, 67 (1995).
368. N. Moumen and M. P. Pileni, *J. Phys. Chem.* 100, 1867 (1996).
369. N. Moumen, P. Bonville, and M. P. Pileni, *J. Phys. Chem.* 100, 14410 (1996).
370. N. Moumen and M. P. Pileni, *Chem. Mater.* 8, 1128 (1996).
371. A. T. Ngo, P. Bonville, and M. P. Pileni, *Eur. Phys. J. B* 9, 583 (1999).
372. A. T. Ngo, P. Bonville, and M. P. Pileni, *J. Appl. Phys.* 89, 3370 (2001).
373. M. P. Pileni, N. Moumen, J. F. Hochepped, P. Bonville, and P. Veillet, *J. de Phys. IV* 7, C1-505 (1997).
374. A. J. Rondinone, A. C. S. Samia, and Z. J. Zhang, *J. Phys. Chem. B* 104, 7919 (2000).
375. V. Pillai and D. O. Shah, *J. Magn. Magn. Mater.* 163, 243 (1996).
376. M. L. Kahn and Z. J. Zhang, *Appl. Phys. Lett.* 78, 3651 (2001).
377. J. Hochepped, P. Bonville, and M. Pileni, *J. Phys. Chem. B* 104, 905 (2000).
378. F. Grasset, N. Labhsetwar, D. Li, D. C. Park, N. Saito, H. Haneda, O. Cadot, T. Roisnel, S. Mornet, E. Duguet, J. Portier, and J. Etourneau, *Langmuir* 18, 8209 (2002).
379. J. Wang, P. F. Chong, S. C. Ng, and L. M. Gan, *Mater. Lett.* 30, 217 (1997).
380. J. F. Hochepped and M. P. Pileni, *J. Appl. Phys.* 87, 2472 (2000).
381. J. F. Hochepped and M. P. Pileni, *J. Magn. Magn. Mater.* 231, 45 (2001).
382. A. T. Ngo and M. P. Pileni, *J. Phys. Chem. B* 105, 53 (2001).
383. J. A. Lopez-Perez, M. A. Lopez-Quintela, J. Mira, and J. Rivas, *IEEE Trans. Mag.* 33, 4359 (1997).
384. D. H. Chen and Y. Y. Chen, *J. Coll. Interface Sci.* 236, 41 (2001).
385. V. Pillai, P. Kumar, M. S. Multani, and D. O. Shah, *Colloids Surf. A* 80, 69 (1993).
386. S. Vaucher, J. Fielden, M. Li, E. Dujardin, and S. Mann, *Nano Lett.* 2, 225 (2002).
387. D. DeCaro and J. S. Bradley, *Langmuir* 13, 3067 (1997).
388. O. Carp, L. Patro, E. Segal, R. Barjega, and M. Brezeanu, *J. Therm. Anal. Calor.* 56, 513 (1999).
389. N. A. D. Burke, H. D. H. Stover, and F. P. Dawson, *Chem. Mater.* 14, 4752 (2002).
390. M. Spasova, U. Wiedwald, R. Ramchal, M. Farle, M. Hgendorff, and M. Giersig, *J. Mag. Mat.* 240, 40 (2002).
391. G. H. Lee, S. H. Huh, J. W. Jeong, B. J. Choi, S. H. Kim, and H.-C. Ri, *J. Am. Chem. Soc.* 124, 12094 (2002).
392. R. Alexandrescu, I. Morjan, A. Crunteanu, S. Cojocaru, S. Petcu, V. Teodorescu, F. Huiskn, D. Kohn, and M. Ehbrecht, *Mater. Chem. Phys.* 55, 115 (1998).
393. D. DeCaro, T. O. Ely, A. Mari, B. Chaudret, E. Snoeck, M. Respaud, J. M. Broto, and A. Fert, *Chem. Mater.* 8, 1987 (1996).
394. M. W. Grinstaff, M. B. Salamon, K. S. Suslick, *Phys. Rev. B* 48, 269 (1993).
395. J. P. Carpenter, C. M. Lukehart, S. B. Milne, S. R. Stock, J. E. Wittig, B. D. Jones, R. Glosser, and J. G. Zhu, *J. Organometal. Chem.* 557, 121 (1998).
396. Y. Lu, Y. Yin, B. T. Mayers, and Y. Xia, *Nano Lett.* 2, 183 (2002).
397. Z. Yue, J. Zhou, L. Li, H. Zhang, and Z. Gui, *J. Mag. Mag. Mater.* 208, 55 (2000).
398. H. Y. Luo, Z. X. Yue, and J. Zhou, *J. Mag. Mag. Mater.* 210, 104 (2000).
399. W. Dong and C. Zhu, *J. Mater. Chem.* 12, 1676 (2002).
400. T. Sugimoto and Y. Wang, *J. Colloid Interface Sci.* 207, 137 (1998).
401. W. Zhong, W. Ding, Y. Jiang, N. Zhang, J. Zhang, Y. Du, and Q. Yan, *J. Am. Cer. Soc.* 80, 3258 (1997).
402. E. V. Shevchenko, D. V. Talapin, A. L. Rogach, A. Kornowski, M. Haase, and H. Weller, *J. Am. Chem. Soc.* 124, 11480 (2002).
403. S. Kang, J. W. Harrell, and D. E. Nikles, *Nano Lett.* 2, 1033 (2002).
404. S. Sun and H. Zeng, *J. Am. Chem. Soc.* 124, 8204 (2001).
405. F. Agnoli, W. L. Zhou, and C. J. O'Connor, *Adv. Mater.* 13, 1697 (2001).
406. E. E. Carpenter, C. Sangregorio, and C. J. O'Connor, *Mol. Cryst. Liq. Cryst.* 334, 641 (1999).

Chemistry of Carbon Nanotubes

V. N. Khabashesku, J. L. Margrave

Rice University, Houston, Texas, USA

CONTENTS

1. Introduction
 2. Chemical Reactions of Pristine Carbon Nanotubes
 3. Chemical Modifications of Oxidized Carbon Nanotubes
 4. Reactions of Fluoronanotubes
 5. Summary
- Glossary
References

1. INTRODUCTION

Carbon nanotubes (tubular fullerenes or buckytubes) are structurally built from rolled graphene sheets closed at the ends by the fullerene caps. Single-walled nanotubes (SWNTs) consist of a single graphitic cylinder, while multiwalled nanotubes (MWNTs) are made of concentric graphitic layers surrounding the central tubule. The diameters of SWNTs can range from 0.4 to 4 nm and those of MWNTs from 1.4 to 100 nm. Since the discovery of MWNTs by Ijima in 1991 [1] and preparation of SWNTs in 1993 [2–4], the carbon nanotubes have become an area of intense research activity worldwide. The unique mechanical, optical, and electronic properties and other phenomena exhibited by carbon nanotubes offer many opportunities for their applications [5–9]. SWNTs, in particular, possess a remarkable tensile strength and, depending on their diameter and helicity, can be metallic, semiconducting, or insulating as well as chiral or achiral. The uses of SWNTs and MWNTs for fabrication of reinforced fibers and nanocomposites [10–12], electrochemical devices [9] and field-emission displays [13], nano-size scanning probe tips for atomic force microscopy [14], and their capability of hydrogen storage [15] are being investigated extensively.

Nanotubes tend to self-assemble into bundles in which up to several hundred tubes are held together by van der Waals bonding. For many applications, the separation of

individual nanotubes from their bundles is becoming essential. This would improve the dispersion and solubilization of the nanotubes in common organic solvents and/or water, which are needed for their processing and manipulation. To solve this problem, two main approaches based on noncovalent [16–21] and covalent [22, 23] modifications of nanotubes are being pursued. The covalent modifications involve chemical functionalization by the attachment of various functional groups to the ends or sidewalls of the nanotubes through covalent bonds. Besides improving the solubility and processibility, this functionalization also opens an opportunity for altering the structural and electronic properties of the nanotubes and for obtaining new types of nanotube-based materials with useful properties. However, the chemical functionalizations of the nanotube ends bring only a highly localized transformation of the nanotube electronic structure and do not change the bulk properties of these materials. These functionalizations have been most extensively explored through oxidation reactions, which are shown to form shortened nanotubes with carboxylic acid groups at the ends that can be further derivatized [23–26].

By comparison, the side-wall functionalization naturally results in a significant modification of the intrinsic properties of the nanotubes. The challenges faced in these types of chemical modifications are related to the fact that nanotubes are not very reactive due to a much lower curvature of nanotube walls (e.g., in [10,10] SWNTs) than in the fullerenes, which exhibit a rich chemistry [5], and to the necessity of preserving the tubular structure when attaching the functional groups to graphene walls. Therefore, the investigations of a variety of reagents and experimental conditions become important. Besides the technological demands, the research on functionalization chemistry of nanotubes is also fascinating from a fundamental point of view since it can provide an in-depth knowledge of chemical reactivity stemming from the nanoscale size and shape of materials. However, the number of documented results in this new field of chemistry is not yet great, mostly due to a high cost of the nanotubes, which has been limiting the research efforts to only a dozen or so chemical labs and centers. This Section provides a review of these results, which include the

chemical reactions of pristine carbon nanotubes as well as their chemical functionalizations using oxidized or fluorinated nanotubes as precursors for subsequent derivatization.

2. CHEMICAL REACTIONS OF PRISTINE CARBON NANOTUBES

2.1. Oxidation

Oxidation was the first reaction carried out on the carbon nanotubes [27–31]. It was shown that the caps on MWNTs can be opened by oxidation with oxygen, air, or carbon dioxide at temperatures above 700 °C. Carbon nanotubes show fairly high resistance to oxidation in air up to 700 °C, while C₆₀ burns in air at a much lower temperature (~500 °C). Oxidation in air or oxygen results in etching away of the tube caps and the thinning of tubes through layer-by-layer peeling of the outer layers, starting from cap regions. Carbon dioxide reacts as a milder oxidizing agent that erodes and strips the cap of the tube, exposing the terminated cylinder layers [27]. Heating MWNTs with an oxide Pb₃O₄ in an inert atmosphere facilitated opening at a lower temperature (~400 °C) [28].

The oxidation by boiling in concentrated HNO₃ or in aqueous solutions of other oxidants, such as KMnO₄, OsO₄, RuO₄, and their combinations, leads to an efficient cleavage (up to 91%) of the end-cap regions of carbon nanotubes. The mechanism of cap-opening by these oxidants most probably involves oxidative cleavage of the C=C double bonds and further conversion to vicinal diols followed by oxidative cleavage of diols to form a number of oxygen-containing end-functionalities, such as carboxylic acids, anhydrides, quinones, and esters, and is suggested to be controlled kinetically but not thermodynamically [30].

Treatments of SWNTs by sonication in HNO₃ or H₂SO₄/HNO₃, H₂SO₄/H₂O₂ mixtures [32–34] were found to cut the nanotubes by oxidizing/etching action to lengths ranging from 100 nm to 1 micron and generate carboxyl groups and other oxo-functionalities predominantly on nanotube open ends, according to IR and ¹³C NMR studies [35, 36]. It was shown that selective oxidation can occur for the thinner SWNTs when burning in oxygen or refluxing in nitric acid [37]. The acid oxidation chemistry has been successfully applied for enrichment of large-diameter nanotubes in the purified SWNT batches, which have been characterized by transmission electron microscopy (TEM) and Raman spectroscopy [38]. The detailed studies have clearly demonstrated that in air the smaller diameter SWNTs are oxidized more rapidly than the larger diameter nanotubes [39, 40]. The increased reactivity of smaller diameter SWNTs was also observed in experiments using room temperature oxidation by ozone [41]. This reaction was localized at the end caps, which have been removed by oxidation thus creating a dangling COOH and other groups, which in their turn could be removed by heating above 350 °C as CO and CO₂, leaving the nanotube sidewalls intact. Heating the acid-oxidized SWNTs to a higher temperature (1000 °C) was shown to produce up to ~5% defective sites both on the nanotube sidewalls and closed end-caps, capable of subsequent oxidation by ozone, which was used as a titration agent for estimation of the surface defect site density [42].

2.2. Fluorination

2.2.1. Preparation of Fluorinated Carbon Nanotubes

The direct fluorination of the SWNTs with elementary fluorine results in sidewall-fluorinated SWNTs (fluoronanotubes). They represent a new family of nanoscale fluorocarbon materials that have been prepared by fluorination of both laser ablation of graphite grown carbon nanotubes (L-SWNTs) [33, 43] and those produced by a high-pressure CO disproportionation process (HiPco-SWNTs) [44, 45] using the technology developed earlier for the fluorination of graphite [46]. Extensive fluorination studies [47–49] were carried out to establish optimal conditions (reaction temperatures, reaction times, addition of HF catalyst) to reach a saturation stoichiometry (nearly C₂F) without destruction of the tube structure. It was also found that the degree of fluorination depends on the residual metal content from catalysts used in the purified SWNTs and the conditions of preparation and treatment of the buckypaper samples (nature of solvent, annealing temperature) prior to fluorination.

The fluorination of L-SWNT buckypaper, pre-baked at 1100 °C in vacuum, was carried out at temperatures ranging from 150 to 600 °C. The IR spectroscopy (KBr pellet method) confirmed the presence of covalently bound fluorine (peaks of the C—F stretches in the 1220–1250 cm⁻¹ region) in the samples fluorinated in absence of HF catalyst at temperatures of 250 °C and higher, and not for those fluorinated at 150 °C. The TEM images indicated that the tube structures remained largely intact under treatment at temperatures as high as 325 °C, yielding approximately C₂F product bulk composition according to electron probe microanalysis (EPMA). The SWNTs are essentially all destroyed (i.e., “unzipped”) when fluorinated at 400 °C and above to form a fluorographite and some multiwall carbon nanotubelike material. As a result of the sidewall functionalization of the SWNTs by fluorine, the electrical properties of the fluoronanotubes differ dramatically from those of pristine SWNTs. The fluoronanotubes, prepared by fluorination at temperatures of 250 °C and above, are insulators (two-point resistance across the length of buckypaper sample > 20 MΩ), while the pristine nanotubes are good conductors (two-point resistance 10–15 Ω) [48].

With the addition of HF, which is a known catalyst for fluorination of graphite, the saturated C/F ratio (~2) for the L-SWNT tube structure was reached at a lower reaction temperature (250 °C) while maintaining the same reaction time (~5 hrs). The other observed effect of HF addition was a noticeable upshift of the C—F stretching frequency in the attenuated total reflectance (ATR) FTIR spectra of fluoronanotubes (Fig. 1A), which indicated the formation of more covalent and therefore stronger C—F bonds. The same upshifting effect and a higher relative intensity of the C—F band in the IR spectra were also seen when raising the fluorination temperature (Fig. 1B). These phenomena are in agreement with those observed earlier in fluorinated graphite [46].

The HiPco-SWNTs have a smaller average diameters (~1 nm for the [8,8] nanotubes) than L-SWNTs (~1.4 nm, corresponding to the [10,10] tubes) and, therefore, due to

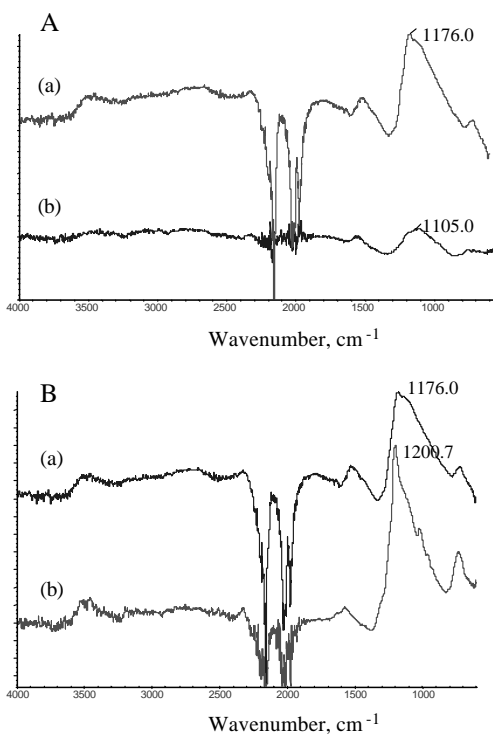


Figure 1. ATR-FTIR spectra of L-SWNTs: (A) Fluorinated at 200 °C with HF addition (a), and without HF addition (b); (B) Fluorinated at 200 °C (a), and at 250 °C (b). Negative absorptions at 2000 and 2200 cm^{-1} are due to the diamond crystal of the ATR accessory.

a higher curvature are more reactive. This is particularly indicated by the observation that under the same fluorination conditions more fluorine can be attached onto the side-walls of HiPco-SWNTs [49]. For instance, in the presence of HF, the near C_2F composition for the tubular structure of the HiPco-SWNTs has been produced at a fluorination temperature as low as 150 °C, while under the same conditions the L-SWNTs yielded fluoronanotubes with a significantly lower fluorine content (C/F ratio higher than 3).

Strong dependence of the fluorination on nanotube diameter was also observed for pyrolytically grown tubes with large diameters, ranging from 10 to over 100 nm [50]. After fluorination with the F_2 :HF gaseous mixtures for 19 h at 500 °C, these nanotubes revealed the presence of the C—F bonds in the electron energy loss spectra (EELS) only for tubes with diameters larger than 20 nm, which suggested that thin tubes are not or are minimally fluorinated (if fluorination occurred at all under conditions studied). Elemental mapping studies indicated that F is uniformly distributed within the nanotubes with diameters greater than 20 nm of approximately C_{12}F stoichiometry. EELS calculations using density functional theory confirmed the existence of ionic and covalent bonding of fluorine to carbon in these fluoronanotubes [50].

Multiwall carbon nanotubes, prepared by a template carbonization method and having open ends, reacted with elemental fluorine already at 50 °C and were shown to add more fluorine with increased reaction temperature [51]. When using a gaseous mixture of F_2 , HF, and IF_5 , the flu-

orination proceeded even at room temperature yielding the fluoronanotubes with $\text{CF}_{0.4}$ composition. The C—F bonds in these fluoronanotubes were suggested to possess a semi-ionic character, as indicated by a peak location of the C—F stretch at 1100 cm^{-1} in the FTIR spectra [52]. The fluorination of arc-discharge produced MWNTs has also been achieved at room temperature by using elemental fluorine on MWNT samples pretreated with a vapor over liquid Br_2 for 24 h and then with a vapor over a solution of BrF_3 in Br_2 for 7 days. This reaction resulted in fluoronanotubes with $\text{C}_1\text{F}_{0.3}\text{Br}_{0.02}$ composition, in which the presence of covalent C—F bonds has been concluded on the basis of X-ray diffraction (XRD), FTIR, and X-ray photoelectron spectroscopy (XPS) characterization data [53].

2.2.2. Solvation Properties of Fluoronanotubes

The fluoronanotubes prepared from SWNTs form metastable solutions in DMF, THF, and alcohols after sonication. They do not dissolve in perfluorinated solvents, water, diethylamine, or acetic acid. The solvation of individual (“unroped”) fluoronanotubes was verified by dispersing them on a mica substrate and examining with atomic force microscopy (AFM) [54]. The solutions in alcohols were stable for a few days to over a week. Among the series of alcohols studied, 2-propanol and 2-butanol were found to be the best solvents. Such solvation has been explained by hydrogen bonding between the hydroxyl hydrogen in alcohol and the nanotube-bound fluorine: $\text{R—O—H} \cdots \text{F—(C}_n\text{F)}$. This bonding is likely facilitated by an increased ionic nature of the C—F bond in fluoronanotubes in contrast with alkyl fluorides, in which, according to recent studies, the fluorine is suggested to be a poor hydrogen bond acceptor [55]. The XPS analysis of fluorinated SWNTs supports the concept of a more ionic fluorine bonded in fluoronanotubes by revealing an F 1s peak at a binding energy of 687 eV, located at a much lower binding energy than the F 1s peak in poly(tetrafluoroethylene) (691.5 eV).

2.2.3. Structure of Fluoronanotubes

Insights into the possible fluoronanotube structures have been provided by molecular modeling calculations and scanning tunneling microscopy (STM) imaging [56]. Based on the experimentally established C_2F stoichiometry at which fluorinated tubes can still maintain their tubular structure, two isomeric structures, resulting from fluorine addition to either (1,2) or (1,4) positions within a hexagonal ring on the graphene-like side wall of the nanotube, have been proposed (see Fig. 2). Due to the arrangement of the π -bonds, the 1,2-isomer can be conducting through an electron flow along the conjugated bonds parallel to tube axis, whereas the 1,4-isomer with its isolated double bonds will yield insulating fluoronanotubes. From the molecular mechanics (MM+) [49] and semi-empirical (AM1 and CNDO) [56] calculations, it was found that the 1,4-isomer is more stable, although the energy difference between the two isomers is quite small (only 1 kcal/mol per F atom). Higher level calculations on fluorinated armchair (10,10) SWNTs of C_2F stoichiometry using density functional theory (PBE/3 and LSDA/3-21G)

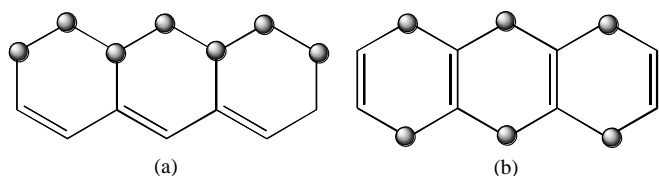


Figure 2. Proposed fluorine addition patterns on the fluoronanotubes: (a) 1,2-addition, (b) 1,4-addition.

and periodic boundary conditions revealed that, on the contrary, the 1,2-isomer is more stable than the 1,4-isomer; however, the total energy difference is again fairly small (about 4 kcal/mol per C_2F unit) [57]. Given such a small difference in the energies of these two isomers, calculated at various levels of theory, and the absence of separation procedures developed so far, it is reasonable to assume that they both coexist in the fluoronanotube material.

STM imaging (Fig. 3a) indicated that the fluorinated regions typically form bands around the circumference of the tube. This may imply that the addition of fluorine to the side wall of the pristine SWNT should occur more favorably around the circumference of the tube. Nevertheless, the AM calculations point out that the addition along the axis of the tube for the 1,2-isomer is about 30 kcal/mol more exothermic than circumferential 1,2-addition, while in the case of the 1,4-isomer the addition around the circumference of the tube is approximately 10 kcal/mol more energetically favorable than propagation along the tube axis [49, 56]. Based on that, the origination of the abrupt band boundaries, observed in the STM images of fluoronanotubes (even those having the saturated C_2F stoichiometry), could be explained by a circumferential addition mechanism proceeding via initiation of the 1,4-isomer at multiple sites along the tube and propagating on alternate pairs of rows (Fig. 3b). However, since the calculated energy difference between the 1,2- and 1,4-isomers is small, the possibility of having both types of fluorine addition occur simultaneously during the fluorination process and form discrete isomeric domains on the nanotube (Fig. 3c) also can be expected. Various defects in the sidewall graphene structure might also play an important role in either initiating or terminating such domains.

2.3. Hydrogenation

The preparation of hydrogenated carbon nanotubes (H-NTs) has been attempted by using the Birch reduction method [58, 59], which was applied previously for the hydrogenation of fullerenes [60]. The reaction of raw SWNTs produced by electric arc discharge with lithium in liquid ammonia did not yield the desirable H-NTs. When the unpurified L-SWNTs were reacted with lithium in ethylenediamine, the final product obtained was showing not only an added hydrogen (2.71%) but also a nitrogen (8.32%) by elemental analysis, meaning incorporation of some nitrogen into the samples. Although their Raman and IR spectra were consistent with the small structural changes in the SWNTs, implying chemical modification, no solid evidence for covalent attachment of hydrogen to the SWNT sidewalls

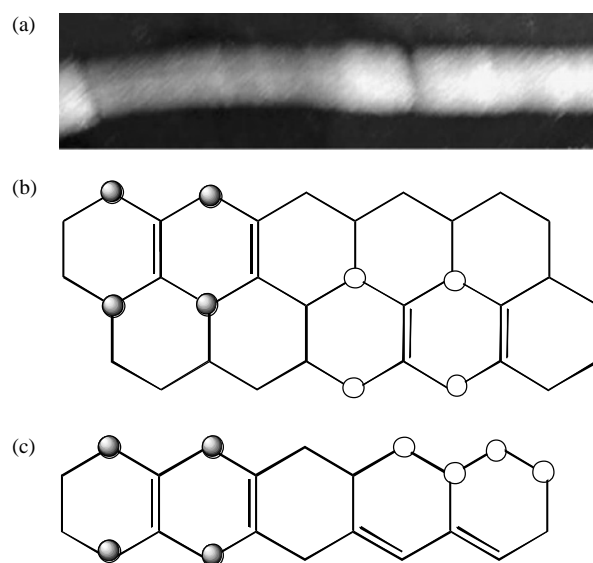


Figure 3. STM image of an individual fluoronanotube. Note gaps in fluorine decorations of the sidewall (a). Modeling of observed gap formation in STM images: (a) multiple fluorination initiation sites, (b) mixture of both 1,2- and 1,4-additions.

and not to the amorphous carbon present on the walls could be obtained [58].

Use of purified carbon nanotubes and a modified Birch reduction method, utilizing Li and methanol in liquid ammonia, has proven to be more successful in preparation of H-NTs [59]. Two types of nanotubes, L-SWNTs and MWNTs, have been hydrogenated to approximately $C_{11}H$ composition, determined from the yield of hydrogen evolved at elevated temperatures in the course of thermogravimetry-mass spectrometry (TG-MS) studies. Thus obtained H-NTs are thermally stable up to 400 °C. Above this temperature the evolution of hydrogen and a small amount of methane takes place, peaking at 500 °C, which provides firm evidence for covalent C—H bonds present in these hydrogenated samples. Based on these experimental data, it has been suggested that the C—H bonds in H-NTs are weaker than those in aliphatic and aromatic hydrocarbons, but can be compared with the thermal stability of C—H bonds in hydroaromatic compounds. This is supported by the density functional theory (DFT) calculations data, which show that the C—H bonding energy in SWNTs hydrogenated to their maximum capacity for hydrogen storage exceeding 14 wt. % is substantially lower than in methane [61].

2.4. Addition of Carbenes, Nitrenes, and Radicals

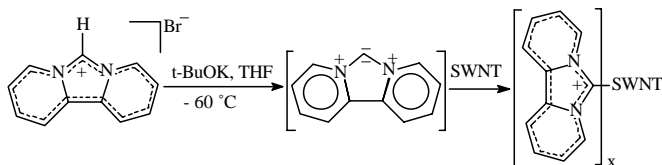
Dichlorocarbene was the first electrophilic carbene that was added to carbon nanotube double bonds in a similar reaction known for fullerenes [62]. The dichlorocarbene was generated either from chloroform by reaction with sodium hydroxide in the presence of phase transfer catalyst (PTC) [58] or from phenyl(bromodichloromethyl)mercury by thermal decomposition [23]. The analyses of the addition products to the purified SWNTs by FTIR spectroscopy showed

the C—Cl stretching modes at 798 cm^{-1} , while energy dispersive X-ray (EDX) spectroscopy revealed the presence of only about 2 at. % Cl, thus indicating a fairly low degree of functionalization [23]. See Scheme 1.

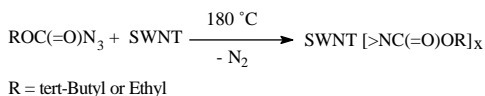


Scheme 1.

The addition of a nucleophilic carbene, generated by deprotonation of the dipyrindyl imidazolium cation, to the SWNTs has recently been reported [63]. The carbene adduct is soluble in DMSO, which permitted ^1H NMR analysis. However, it is thermally labile, as it loses the attached carbene as well as its dimer at $50\text{ }^\circ\text{C}$, as detected by mass spectrometry, and shows in the UV-Vis-NIR absorption spectra only slight changes with respect to pristine SWNTs. Therefore, at most these data point at a very modest functionalization achieved in this reaction (Scheme 2). The functionalizations of SWNTs also reported [63] by addition of nitrenes, generated by thermolysis of alkylazidoformates (Scheme 3), and by perfluorooctyl radical, produced photochemically from perfluorooctyl iodide, seem to be similarly questionable until a convincing evidence for covalent sidewall attachment of nitrenes and radicals is obtained from the TG-MS, Raman, and electron microscopy studies.



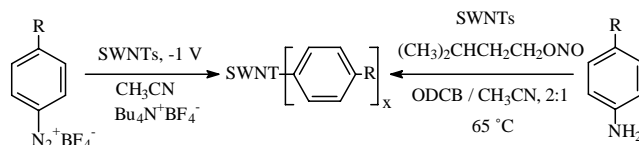
Scheme 2.



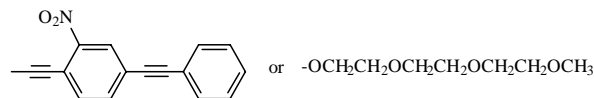
Scheme 3.

The addition reactions of several aryl radicals generated by electrochemical reduction of aryldiazonium salts [64, 65] or thermally from *in-situ* prepared diazonium compounds [66] to the HiPco-SWNTs have led to a more successful functionalization (Scheme 4). This was evidenced by a complete loss of band structure in the absorption spectra and changes in the Raman spectra showing a significant increase in the relative intensity of the disorder mode at about 1290 cm^{-1} due to the sp^3 carbons. The degree of functionalization by a number of substituted aryl diazonium salts has been estimated as 1 in 40 to 1 in 20 nanotube sidewall

carbons based on thermogravimetric and EDX elemental analyses [64, 66].

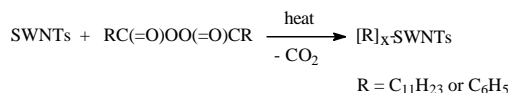


R = tert-Butyl, halogen, COOH, NO₂, COOH, CO₂CH₃ as well as



Scheme 4.

The idea of using the carbon nanotubes as a free radical “sponge” originates from the well-known ability of their fullerene relatives to add a variety of free radicals [5, 67]. In the recent studies [68, 69], HiPco-SWNTs have been reacted with a series of organic peroxides, such as lauroyl, benzoyl, *t*-butyl, and hydrogen peroxides, which are commonly used as radical precursors in polymerization processes, in attempts to functionalize the nanotube sidewalls. In case of acyl peroxides, such as lauroyl and benzoyl peroxide, their thermal decomposition in the presence of SWNTs, both in solution by refluxing at $80\text{--}100\text{ }^\circ\text{C}$ or in solid state by heating at $200\text{ }^\circ\text{C}$, resulted in undecyl and phenyl radical adducts to the sidewalls, respectively (Scheme 5), while other peroxides yielded mostly oxygen-containing products. Covalent functionalization of SWNTs by this fairly simple approach using the low-cost commercially available peroxides has been established by absorption UV-Vis-NIR and FTIR spectra, and Raman spectroscopy, and also TG-MS and TG-FTIR analyses indicating that approximately 1 in 20 sidewall carbons carries an attached group [69].

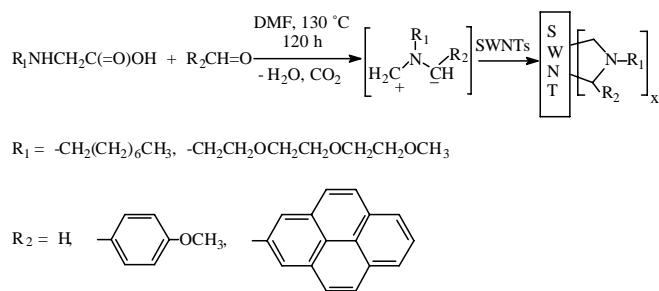


Scheme 5.

2.5. Cycloaddition

Covalent modification of carbon nanotubes by 1,3-dipolar cycloaddition of azomethine ylides, *in-situ* generated by condensation of an *N*-substituted α -amino acid and an aldehyde, has been performed by Georgakilas et al. [70] utilizing a reaction widely used in functionalization chemistry of fullerene C₆₀ [71]. The nanotubes were suspended in DMF

together with aldehyde and amino acid, and heated at 130 °C for 5 days (Scheme 6).

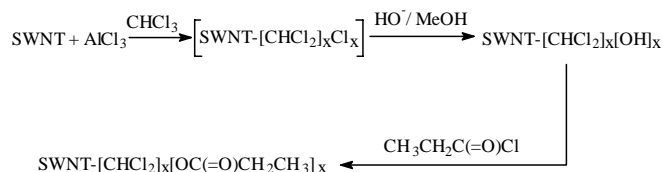


Scheme 6.

This method was reported to be successful in functionalization of both as-produced and purified SWNTs and also of MWNTs, yielding nanotube derivatives very soluble in polar solvents, such as $CHCl_3$, CH_2Cl_2 , acetone, alcohols, and water. For instance, solubility of some SWNT derivatives in $CHCl_3$ was claimed to be as high as 50 mg/ml, and no precipitation from solution was observed after two weeks. The main argument supporting the functionalization of SWNTs was based on NIR spectra, showing the loss of van Hove singularities due to altered electronic structure normally observed for sidewall derivatized nanotubes [22, 49].

2.6. Electrophilic Addition

The first electrophilic addition to carbon nanotubes has been reported by Tagmatarchis et al. [72]. This reaction utilized a commercially available HiPco-SWNTs (95 wt. % purity) for derivatization through electrophilic addition of $CHCl_3$ in the presence of $AlCl_3$ as a strong Lewis acid. The SWNTs were activated by solid state mechanical grinding with $AlCl_3$ and then refluxed in dry $CHCl_3$ for 48 h to produce a yellow colored intermediate adduct with the suggested $-CHCl_2$ and $-Cl$ groups attached to the SWNT sidewalls (Scheme 7).



Scheme 7.

Due to its labile nature, this material could not be isolated and characterized. Nevertheless, the isolable derivative was obtained after hydrolysis of this intermediate in a one-pot procedure with alkaline methanol to substitute the reactive Cl atoms with OH groups, which have been detected by FTIR spectroscopy using DRIFT accessory. Treatment of this derivative with propionyl chloride gave ester-functionalized SWNTs, showing characteristic bands of $C=O$, $C-O$, and CH stretches in IR spectrum and having a solubility in chloroform or acetone improved enough to allow characterization by 1H NMR spectroscopy.

3. CHEMICAL MODIFICATIONS OF OXIDIZED CARBON NANOTUBES

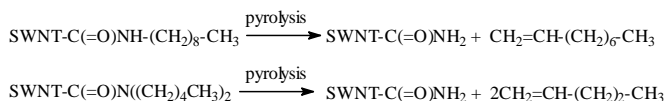
As discussed in Section 2.1., the oxidation of carbon nanotubes results predominantly in open-ended tubes terminated with carboxylic acid groups ($-COOH$). The reactivity of these groups has been utilized in further chemical modifications of nanotubes. The first derivatization of the open ends of the shortened SWNTs was done by Liu et al. [32] by converting the carboxylic groups to the corresponding acid chloride using $SOCl_2$. Subsequent treatment of the obtained SWNT-COCl with $NH_2-(CH_2)_{11}-SH$ yielded an amide linkage of the nanotube end to the alkanethiol. The formation of a free thiol moiety has been verified by tethering the end of the nanotube to 10 nm diameter colloidal gold particles and imaging by AFM. These thiol derivatized SWNTs have been assembled on gold substrates in orientation normal to the surface, providing an ordered array of SWNTs useful for various applications, for example, in field emission devices [73].

Chen et al. [23] and Hamon et al. [24] used a similar acyl chloride modification chemistry for producing the soluble nanotubes by attaching a long-chain octadecylamine $CH_3(CH_2)_{17}-NH_2$ and 4-dodecyl-aniline $4-CH_3(CH_2)_{13}C_6H_4NH_2$ to the open ends of the SWNTs via formation of the amide functionality. Both SWNT derivatives have shown similar solubility in chloroform, dichloromethane, aromatic solvents (benzene, toluene, chlorobenzene, 1,2-dichlorobenzene), and CS_2 . The solubilities in 1,2-dichlorobenzene and CS_2 , in particular, were found to be above 1 mg/ml. The IR spectra indicated that the amide derivatization took place, while the presence of long aliphatic chains at the ends of SWNTs was suggested based on solution 1H NMR spectra. In contrast to the sidewall functionalized SWNTs, no significant alteration of the band electronic structure as compared to pristine SWNTs has been observed in Raman and UV-Vis-NIR spectra of the end-derivatized nanotubes. The direct acid-base reaction of the oxidized nanotubes, SWNT-COOH, with octadecyl amine resulted in noncovalently bonded zwitterionic product $\{SWNT-COO^-, ^+NH_3(CH_2)_{17}CH_3\}$, soluble in THF and CH_2Cl_2 [24, 35]. The improved solubility of the amide end-functionalized SWNTs allowed their high purification by using gel-permeation chromatography [74].

The application of nanotubes, functionalized through modification of carboxyl groups by reactions with benzylamine or ethylenediamine, as nanosized probe tips in atomic force microscopy has been demonstrated by Wong et al. [14, 75]. End-to-end and end-to-side intermolecular nanotube junctions have been formed by reacting an open-end and sidewall acid chloride derivatized SWNTs with aliphatic diamine, $NH_2-(CH_2)_3NH(CH_2)_3NH(CH_2)_{23}-NH_2$, which served as a molecular linker [76]. These chemically created interconnections of nanotubes were imaged by AFM. The observed in Raman spectra (623.8 nm) downward shift (to 1578 cm^{-1}) of the tangential mode peak of the modified nanotubes versus that in pristine SWNTs (1583 cm^{-1}) can be explained by the NH_2 -terminal group of the sidewall functionality providing electron donation to the carbon π^* bond.

Basiuk et al. [77] have studied a chemical derivatization of the nanotube tips using a direct reaction of simple

aliphatic amines with oxidized SWNTs, which were treated by amine vapors under reduced pressure and temperatures of 160–170 °C. The amines studied included nonylamine, dipentylamine, ethylenediamine, and propylenediamine. It was concluded that the terminal amide functionalities formed on the SWNT tips can not be detected in the IR spectra because their concentrations are too low relative to the whole mass of the nanotube. Therefore, all IR bands observed for amine-treated samples in this and previous studies should be assigned only to corresponding amine molecules physisorbed on SWNT walls. Variable temperature pyrolysis-mass spectrometry (VTP-MS) analysis of the amine-treated samples heated above 200 °C indicated cleavage of alkenes, such as nonene and pentene, in case of nonylamine and dipentylamine-treated samples, respectively. These results were explained by thermal decomposition of the alkylamide groups on the SWNT tips (Scheme 8). DFT calculation data suggest that the direct formation of amides on armchair SWNTs should be more energetically favorable than in case of zigzag ends, although the activation energies are almost equal. This theoretical prediction could promote experimental studies aimed at selective end-functionalization, solubilization, and sorting of different types of SWNTs.



Scheme 8.

A series of soluble end-functionalized SWNTs and MWNTs has been prepared by Riggs et al. [25], Sun et al. [26], Czerw et al. [78], and Fu et al. [79] using amidation and esterification reactions of oxidized nanotubes. After conversion of their carboxylic acid groups into acyl chlorides, they were reacted with copolymers such as poly(propionylethylenimine-*co*-ethylenimine) and poly(vinyl acetate-*co*-vinyl alcohol) at 165 °C for 20 min [25, 78]. The resulting polymer-bound nanotubes are soluble both in organic solvents and water, forming highly colored solutions that show strong luminescence [25]. In a similar procedure, the lipophilic and hydrophilic dendron species terminated with long alkyl chains, and oligomeric poly(ethylene glycol) moieties have been attached to SWNTs and MWNTs [26, 79]. The lipophilic dendron-functionalized nanotubes are soluble in hydrocarbons and weakly polar organic solvents, while the nanotubes with attached poly(ethylene glycol) moieties dissolve in organic solvents and water. It was also shown that these nanotubes can be chemically defunctionalized under base and acid-catalyzed ester hydrolysis conditions, providing evidence for presence of ester linkages in the functionalized nanotubes [79].

4. REACTIONS OF FLUORONANOTUBES

4.1. Pyrolysis for Nanotube Cutting

Examination of the products of thermal decomposition of C₂F fluoronanotubes *in vacuo* at temperatures of up to 800 °C by VTP-MS revealed the following species: CF₃⁺

(*m/z* = 69), C₃F₅⁺ (*m/z* = 131), C₃F₇⁺ (*m/z* = 169), and C₄F₇⁺ (*m/z* = 181) [48]. These data indicate that the pyrolysis of fluoronanotubes is dominated by formation of volatile carbon-fluorine-containing molecules and not just the loss of elementary fluorine. Along with the observation of the extended dark bands in the STM images of the partially fluorinated SWNTs C_{*n*}F (*n* > 2) due to bare nanotube side walls, these results have led to the idea of using fluorination followed by pyrolysis as chemical “scissors” for cutting the nanotubes. Recently, Gu et al. [80, 81] have demonstrated a process that involves the fluorination of catalyst-free purified HiPco-SWNTs to a stoichiometry of C₅F followed by pyrolysis at temperatures up to 1000 °C in an argon atmosphere that results in cutting the nanotubes at the fluorinated sites to short lengths (20–200 nm). When the pyrolysis process was monitored *in-situ* with TGA-FTIR, the fluorine was shown to be driven from the fluoronanotube structure as CF₄ and COF₂ (due to oxygen covalently attached to the SWNT side-wall during the first steps of the purification procedure [82]). The cut SWNTs were characterized by Raman spectra, TGA data, and AFM images. The latter show their drastically shortened lengths in comparison with the pristine SWNTs. Studies of the cut SWNTs are now in progress for potential applications including chemically assisted assembly, gas adsorbants, drug delivery vehicles, and polymer composite reinforcements.

4.2. Chemical Derivatization of Fluoronanotubes

Recent DFT calculations of the electronic densities of states have shown that the Fermi energy of the fluoronanotubes is considerably shifted towards lower values compared to the pristine SWNTs. The conduction bands are energetically lowered as well [57]. This implies that the fluoronanotubes are better electron acceptors than the bare carbon nanotubes, and therefore they should more eagerly interact with strong nucleophilic reagents as well as undergo reduction to bare SWNTs by alkali metals. These chemical reactions are also facilitated by the fact that the C—F bonds in fluoronanotubes as in fluorinated fullerenes are weakened relative to the C—F bonds in alkyl fluorides owing to an eclipsing strain effect [83, 84], and thus fluorine could be more easily displaced. The unique electronic structure and improved solubility of fluoronanotubes and the weaker C—F bond have opened new opportunities for chemical syntheses of a wide variety of sidewall functionalized nanotubes with interesting properties using fluoronanotubes as precursors.

4.2.1. Reactions with Organolithium Reagents

Strong nucleophiles, such as alkyl lithium reagents, can be used to attach alkyl groups to the sidewalls of the nanotubes [49, 85]. The reactions have been carried out by adding the RLi (R = methyl, *n*-butyl, *t*-butyl, *n*-hexyl, phenyl) reagent to the fluoronanotubes, dispersed in THF, ether, or hexane, at –40 °C followed by sonication for 10 min and stirring at room temperature overnight under argon. After completion of the workup procedure [49], the final products were dried

in a vacuum oven and then characterized by ATR-FTIR, UV-Vis-NIR, TGA, and TGA-FTIR techniques.

The alkylated SWNTs have shown in the ATR-FTIR spectra the typical alkyl groups C—H stretching and deformation absorptions in the 2850–2970 cm^{-1} and 1000–1470 cm^{-1} regions, respectively, as well as a peak at about 1580 cm^{-1} due to an activated C=C stretching mode of the nanotubes (Fig. 4). The observed absence of the van Hove electronic transition features in the UV-Vis-NIR spectra supports the occurrence of sidewall functionalization, which dramatically alters the electronic structure of alkylated nanotubes with respect to the pristine SWNTs. As a result, these alkylated SWNTs are soluble in common organic solvents such as THF and chloroform.

Based on the weight loss at 200–450 °C during the TGA runs, the nanotube carbon-to-alkyl ratios were calculated for methyl, *n*-butyl, and *n*-hexyl SWNTs, which indicate that alkylation of the fluorinated HiPco-SWNTs results in a higher degree of functionalization in comparison with the L-SWNTs, in line with the expected enhanced reactivity due to the increased tube curvature. The obtained STM images of the sidewall butylated SWNTs show that for these derivatives the typical fluoronanotubes' banded morphology is no longer visible. Instead, relatively large (~ 10 Å) bright spots due to sidewall attached butyl groups with an average spacing of 50 Å are apparent while scanning along the nanotube [56].

The TGA-FTIR analysis has shown on the derivative plots a single maximum for the methylated and two maxima for the *n*-butylated and *n*-hexylated SWNTs, respectively. These maxima were synchronized by the same peaks on the chemigrams of the C—H stretching region in the FTIR spectra of volatile products, demonstrating the presence of corresponding alkyl groups in the nanotubes and also a likely two-step mechanism of the removal of the alkyl groups other than methyl. The VTP-MS studies of the methylated SWNTs have shown that under vacuum conditions the evolution of methyl groups ($m/z = 15$) is maximized at a temperature of

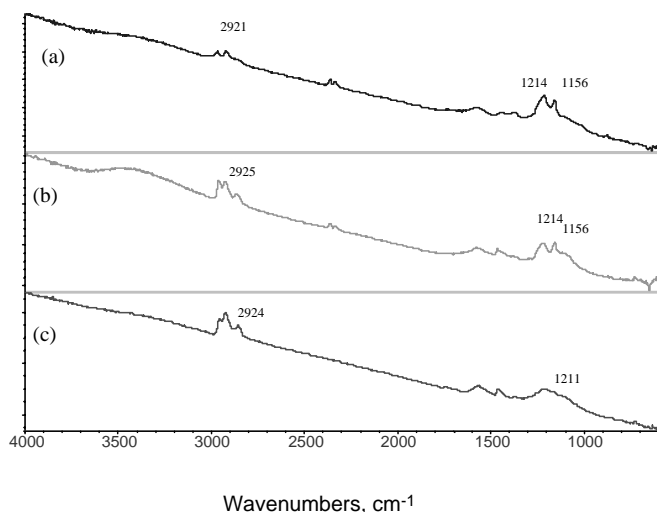


Figure 4. ATR-FTIR spectra of alkylated SWNTs: (a) $[\text{CH}_3]_x$ -SWNTs, (b) $[\text{CH}_3\text{CH}_2\text{CH}_2\text{CH}_2]_x$ -SWNTs, (c) $[\text{CH}_3\text{CH}_2\text{CH}_2\text{CH}_2\text{CH}_2\text{CH}_2]_x$ -SWNTs.

about 490 °C, which is far too high to be due to physisorbed species [48]. The alkylation of the SWNTs was found to be reversible, since after heating of these materials in Ar at 500 °C, a complete recovery of the pristine nanotubes has occurred.

Due to the steric effect, *t*-butyl lithium did not react effectively, resulting in a low alkylation and a predominant defluorination of the fluoronanotubes to yield a product showing the van Hove transition bands in the UV-Vis-NIR spectra. Steric effects can also account for more extensive alkylation observed in cases when less sterically demanding alkyl lithium reagents, such as methyl lithium, were used. These results are consistent with a multistep process that is initiated by a one-electron transfer to the fluoronanotube from the alkyl lithium reagent. Elimination of fluoride from the resulting radical-anion would lead to a radical site on the SWNT. Recombination of the alkyl radical with this radical site will result in the covalent attachment to the sidewall. This step is likely sterically controlled, suggesting that, due to crowding of the attaching groups, not every fluorine can be replaced by a new functionality, such as an alkyl group.

4.2.2. Reactions with Grignard Reagents

The sidewall alkylation of fluoronanotubes by the Grignard reagents (alkyl magnesium bromide) in THF has also been carried out [86]. These reactions were done simply by bath sonication of the fluoronanotube paper in excess Grignard reagent in THF for several hours. The solubility of the hexylated SWNTs prepared in a such way in chloroform was up to ~ 0.6 g/L, as compared to maximum concentration of 0.1 g/L of pristine nanotubes to form stable suspensions in DMF. By heating in air to 250 °C the pristine SWNTs were recovered from the hexylated derivative for which the attachment of a hexyl group to about 1 in every 10 sidewall carbon atoms has been calculated based on the weight loss monitored by TGA. The analyses of AFM images before and after air oxidation show that the recovered individual tubes are thinner by 2–5 Å after burning off the hexyl groups from side walls. The AFM data also indicate that unlike the partially fluorinated SWNTs, this procedure does not shorten the nanotubes. After removal of the hexyl groups, the two-point electrical resistance measurements across the bucky paper have shown a drop from 372.5 k Ω to 144.6 Ω , a value typical of pristine nanotube papers.

Longer alkyl chain substituents have been attached to the sidewalls of the SWNTs by first generating the Grignard reagents *in-situ*, and then adding the fluoronanotubes [87]. Thus, the *n*-decylated SWNTs were prepared by reacting 1-bromodecane with magnesium in ether and then quenching the decyl magnesium bromide with the fluoronanotube suspension in dry ether with stirring for 72 hours. The reaction with the di-Grignard reagent, prepared in a similar way from 1,10-dibromodecane, also resulted in sidewall functionalization and also in cross-linked nanotubes through alkane chains. The TGA and TGA-FTIR data indicate loss of attached alkyl groups at temperatures of 320–370 °C leading to a recovery of pristine SWNTs features in the Raman and UV-Vis-NIR spectra.

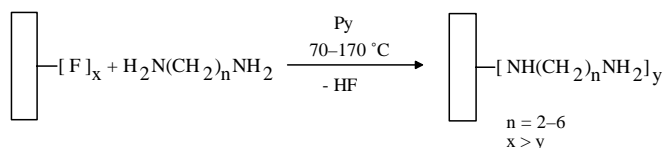
4.2.3. Reactions with Alkoxides

The solubility of fluoronanotubes in alcohols prompted their functionalization reactions with alkoxides. For instance, sonication of the fluoronanotubes ($\sim\text{C}_2\text{F}$) in methanol solution of sodium methoxide for 2 hrs resulted in the formation of methoxylated tubes with the stoichiometry of $\text{C}_{4.4}\text{F}(\text{OCH}_3)_{0.25}$ suggested from electron probe microanalysis (EPMA). Thermal degradation studies by VTP-MS show that under vacuum conditions this product loses significant quantities of methoxy groups ($m/z = 31$) at temperatures of 650–700 °C, indicating that these groups were originally strongly bonded to the nanotube. Based on these data and on elevated oxygen content from the EPMA, the conclusion was made that the methoxy groups are bonded to the nanotube sidewalls [48, 54]. Recently, the functionalizations of the fluorinated SWNTs by methoxy, ethoxy, and *iso*-propoxy groups were also done by sonication in lithium hydroxide solutions in methanol, ethanol, and *iso*-propanol, respectively [88].

4.2.4. Reactions with Hydrazine and Diamines

The SWNTs, once fluorinated, can be efficiently defluorinated with anhydrous hydrazine via the following reaction: $\text{C}_n\text{F} + 1/4\text{N}_2\text{H}_4 \rightarrow \text{C}_n + \text{HF} + 1/4\text{N}_2$, done by stirring at room temperature either in neat hydrazine for 1 hr or after addition of hydrazine to solutions of fluoronanotubes. The EPMA analysis of the solid precipitate yielded a very low fluorine content and no nitrogen, confirming that only defluorination and not the functionalization of the SWNTs by amino moiety has occurred [47, 48, 54]. Such an outcome of this highly exothermic reaction can be explained by the opportunity to produce (in addition to HF) the highly thermodynamically stable N_2 molecules. This defluorination process by hydrazine provides a useful tool for chemical modification of the side walls of the SWNTs, which can be applied for removal of residual fluorine from alkylated fluoronanotubes or for controlled partial defluorination of fluoronanotubes to produce SWNTs with various fluorine contents and, presumably, different properties.

Unlike the defluorinating action of hydrazine, the terminal diamines, $\text{H}_2\text{N}(\text{CH}_2)_n\text{NH}_2$ ($n = 2, 3, 4, 6$), can be used to functionalize the SWNTs by creating a direct C–N bonding attachments to the sidewalls. These reactions (Scheme 9) were performed by refluxing the fluoronanotubes in the corresponding diamine for 3 hrs in the presence of a catalytic amounts of pyridine [89, 90].



Scheme 9.

The elemental analysis of the washed and dried black precipitates by the EDX yielded a nitrogen content within 11–16 at. %, and only a very low fluorine content (1–2 at. %), suggesting its efficient displacement by the *N*-alkylamine functionalities. The TGA-FTIR and VTP-MS

studies have provided strong evidence for covalent functionalization by the diamines, showing a major loss of the corresponding attached groups at ~ 350 – 400 °C, which were detected, for example, in mass spectra by peak at $m/z = 59$ ($\text{HNCH}_2\text{CH}_2\text{NH}_2$) in case of ethylenediamino-SWNTs, and by peak at $m/z = 73$ ($\text{HNCH}_2\text{CH}_2\text{CH}_2\text{NH}_2$) in the case of propylenediamino-SWNTs. The TEM images of *N*-alkylaminated samples have revealed in addition to the individual sidewall functionalized SWNTs (Fig. 5a) also a number of the nanotubes cross-linked by the diamino chains, which are more abundant in the case of the larger chain derivatives, hexamethylenediamino-SWNTs (Fig. 5b). It is interesting that all *N*-alkylamine functionalized samples have been tested positively by the Kaiser testing procedure for the free NH_2 groups. Their availability makes these nanotubes soluble in dilute acids and water and allows them to react, for example, with the adipyl chloride to form new “nylon tube” materials, as well as to covalently bind to

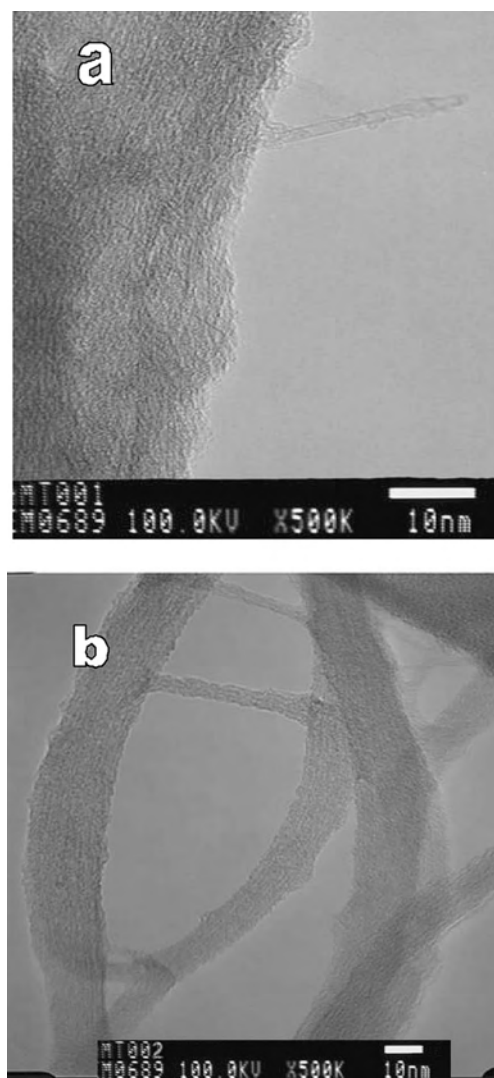


Figure 5. TEM images of aminoalkyl functionalized SWNTs: (a) ethylenediamino-SWNTs, (b) hexamethylenediamino-SWNTs.

polymer matrixes in nanocomposites or to attach the DNA base to the SWNTs.

4.2.5. Reactions with Peroxides

The fluorinated HiPco-SWNTs have been reacted with lauroyl and benzoyl peroxides under the same conditions as pristine nanotubes (see Section 2.4) in order to compare the reactivity of their corresponding polyaromatic and conjugated polyene π -systems toward radical addition [68, 69]. Both reactions resulted in successful attachment of undecyl and phenyl radicals to the sidewalls of fluoronanotubes along with the substantial removal of fluorine. The addition of undecyl radicals, $C_{11}H_{23}$, generated from lauroyl peroxide, was apparently proceeding more readily in case of fluoronanotubes than pristine SWNTs, as indicated by a much lower reaction time (3 hrs vs. 5 days) required for observation of prominent C—H stretch peaks in the ATR-FTIR spectra of undecylated fluoronanotubes (Fig. 6a). The covalent attachment of long-chain groups to the sidewalls in these derivatized nanotubes was imaged by the TEM (Fig. 6b) and confirmed by the TGA-FTIR and VTP-MS data, indicating the major loss of undecyl radicals and their dimer at temperature of about 350–400 °C (peaks in MS at $m/z = 155$ and 310, respectively).

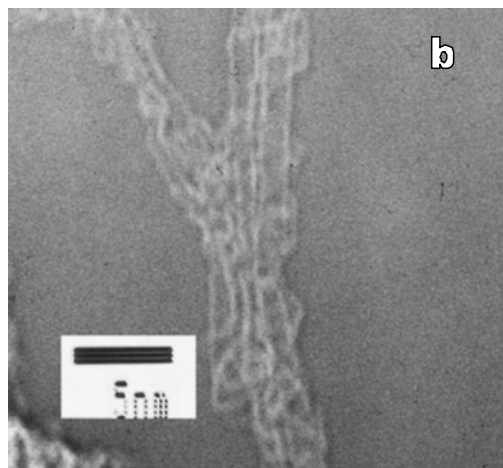
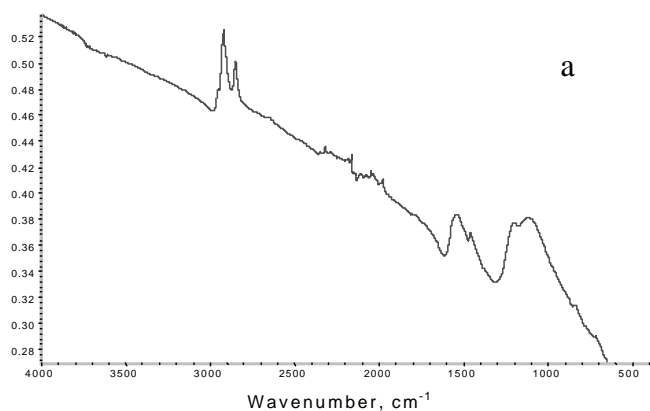
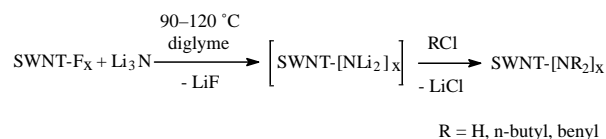


Figure 6. Characterization of undecyl radical ($C_{11}H_{23}$)-derivatized fluoronanotubes: (a) ATR-FTIR spectrum, (b) TEM image.

4.2.6. Solid State Inorganic Reactions

Studies of the solid state reactions of fluoronanotubes with the series of binary compounds of VA, VIA, and VIIA group elements were prompted by the initial observation of significant reduction of the intensity of the C—F stretch peak in the FTIR spectra of fluorinated SWNTs pressed into KBr pellets as compared to the ATR-FTIR spectra of neat samples [49]. When heating a mixture of fluoronanotubes, C_2F , with KBr at ~ 120 °C, the evolution of reddish gas was observed, and defluorinated SWNTs and KF were formed according to a reduction-oxidation reaction: $(C_2F)_n + nKBr \rightarrow 2C_n + n/2Br_2 + KF$, as established by the FTIR, Raman, and powder XRD analyses. The other halides, such as KI, LiI, LiBr, and LiCl, have undergone similar transformations, while NaCl and ZnI_2 produced minor changes of the fluoronanotubes [91]. For comparison, fluorinated C_{60} also reacts as an oxidant losing fluorine substantially when heated with KBr, while the fluorographite fluorine remains attached to graphite carbons under the same experimental conditions due to the much stronger C—F bonds [92]. Among the metal compounds of VA and VIA group elements studied, the sulfide anion in lithium sulfide has been easily oxidized to elemental sulfur by the fluoronanotubes already at room temperature, while in the case of zinc sulfide, prolonged heating (24 hrs) at 100 °C was required. The oxides, Li_2O , FeO, PbO, and MnO, did not react even at 200 °C, while lithium peroxide reacted at room temperature to form LiF, O_2 , and defluorinated SWNTs. The fluorination of aluminium phosphide by fluoronanotubes to form aluminium trifluoride also took place at room temperature, while the redox reaction with lithium nitride, Li_3N , yielding LiF and N_2 , proceeded at 200 °C. It should be noted that when the latter reaction was conducted in a diglyme solution at a lower temperature, no N_2 evolution was observed due to the apparent formation of a SWNT-(NLi_2) $_x$ intermediate, which after subsequent quenching with alkyl chlorides (RCl, R = H, *n*-butyl, benzyl) yielded sidewall amino- and alkylamino functionalized nanotubes [93] (Scheme 10).



Scheme 10.

In summary, the efficiency of solid state redox reactions of the fluoronanotubes studied are most likely influenced by a combination of two factors: (i) the electronegativity of VA, VIA, and VIIA group elements and (ii) the thermodynamic stability of metal fluoride products to be formed. This explains the mild conditions required for these reactions to proceed in case of lithium halides and a sulfide, and aluminium phosphide, containing the less electronegative elements and producing the very stable fluoride salts, AlF_3 and LiF.

In recent work [94], the fluoronanotubes, C_2F , were also used as cathodes in a lithium electrochemical cell, for which the discharging performance via a solid state redox reaction $C_2F + Li \rightarrow C_2 + LiF$ has been studied. This cell was

found to produce a higher cell potential than that of a commercially used fluorographite CF_x cell; however, it lasted a shorter time, consistent with the lower fluorine content and weaker C—F bonds in the fluoronanotubes.

5. SUMMARY

This review shows that although studies of the chemistry of carbon nanotubes have been in progress only for a few years, they already have led to the development of useful synthetic tools for chemical modification of single- and multi-wall carbon nanotubes. The chemical methods developed include oxidation; hydrogenation, fluorination; and addition of free radicals, carbenes, nitrenes, and 1,3-dipolar intermediates to pristine nanotubes. The oxidized nanotubes as well as fluoronanotubes are becoming in turn widely used as precursors for subsequent derivatizations, thus serving as chemical synthons for new nanoscale materials. The nanotube derivatives covalently functionalized at the open ends or at the sidewalls show improved solubility and processibility in common solvents, and electrical, optical, and spectroscopic properties different from pristine nanotubes. The “chemical scissor” method for chemical cutting of the single-wall carbon nanotubes 20–200 nanometer lengths, utilizing partial fluorination and pyrolysis of SWNTs, will open additional opportunities for the functionalization chemistry and studies of the length related properties of the cut nanotubes. As a result, various applications of chemically modified carbon nanotubes, e.g., in nanocomposites, nano-electronic devices, nanoengineered drug delivery systems, nanolubricants, etc., are expected to emerge from the continuing chemical research in the interdisciplinary field of nanotechnology.

GLOSSARY

Fluoronanotube Fluorinated nanotube. A macromolecule consisting of single-walled tubule surrounded by fluorine atoms chemically bonded to carbon atoms of the sidewall.

Functionalization A modification of the structure of material by attachment of the chemical functional groups bringing new physicochemical properties.

HiPco-SWNT A single-walled carbon nanotube produced by disproportionation reaction of carbon monoxide under high-pressure.

L-SWNT A single-walled carbon nanotube prepared by a process that utilizes laser vaporization of graphite.

Multiwalled nanotube (MWNT) A macromolecule made of concentric graphitic layers surrounding the central tubule.

Single-walled nanotube (SWNT) A macromolecule consisting of a single graphitic cylinder capped with fullerene-like halves.

ACKNOWLEDGMENT

The authors are pleased to acknowledge the support of the Robert A. Welch Foundation and the Texas Advanced Technology Program for research in nanoscience and nanotechnology.

REFERENCES

1. S. Iijima, *Nature* 354, 56 (1991).
2. S. Iijima and T. Ichihashi, *Nature* 363, 603 (1993).
3. D. S. Bethune, C. H. Kiang, M. S. deVries, G. Gorman, R. Savoy, J. Vazquez, and R. Bayers, *Nature* 363, 605 (1993).
4. M. Endo, K. Takeuchi, S. Igarashi, K. Kobori, M. Shiraishi, and H. W. Kroto, *Phys. Chem. Solids* 54, 1841 (1993).
5. M. S. Dresselhaus, G. Dresselhaus, and P. C. Eklund, “Science of Fullerenes and Carbon Nanotubes,” Vol. 1. Academic Press, San Diego, 1996.
6. R. Saito, M. S. Dresselhaus, and G. Dresselhaus, “Physical Properties of Carbon Nanotubes.” Imperial College Press, London, 1998.
7. T. W. Odom, J.-L. Huang, P. Kim, and C. M. Lieber, *J. Phys. Chem. B* 104, 2794 (2000).
8. C. N. R. Rao, B. C. Satishkumar, A. Govindaraj, and M. Nath, *CHEMPHYSICHEM* 2, 78 (2001).
9. R. Baughman, A. Zakhidov, and W. A. de Heer, *Science* 297, 787 (2002).
10. R. Haggemueller, H. H. Gommans, A. G. Rinzler, I. E. Fischer, and K. I. Winey, *Chem. Phys. Lett.* 330, 219 (2000).
11. D. Quian, E. C. Dickey, R. Andrews, and T. Rantell, *Appl. Phys. Lett.* 76, 2868 (2000).
12. M. J. Biercuk, M. C. Llaguno, M. Radosavljevic, J. K. Hyun, and A. T. Johnson, *Appl. Phys. Lett.* 80, 2767 (2002).
13. B. Gao, G. Z. Yue, Q. Qiu, Y. Cheng, H. Shimodu, L. Fleming, and O. Zhou, *Adv. Mater.* 13, 1770 (2001).
14. S. S. Wong, J. D. Harper, P. T. Lansbury, and C. M. Lieber, *J. Am. Chem. Soc.* 120, 603 (1998).
15. C. Liu, Y. Y. Fan, M. Liu, H. T. Cong, H. M. Cheng, and M. S. Dresselhaus, *Science* 286, 1127 (1999).
16. B. Vigolo, A. Penicaud, C. Coulon, C. Sauder, R. Paillet, C. Journet, P. Bernier, and P. Poulin, *Science* 290, 1331 (2000).
17. R. J. Chen, Y. Zhang, D. Wang, and H. Dai, *J. Am. Chem. Soc.* 123, 3838 (2001).
18. Z. Jin, L. Huang, S. H. Goh, G. Xu, and W. Ji, *Chem. Phys. Lett.* 332, 461 (2000).
19. M. J. O’Connell, P. J. Boul, L. M. Ericson, C. B. Huffman, Y. Huang, E. H. Haroz, K. D. Ausman, and R. E. Smalley, *Chem. Phys. Lett.* 342, 265 (2001).
20. A. Star, J. F. Stoddart, D. Steuerman, M. Diehl, A. Boukai, E. W. Wong, X. Yang, S.-W. Chung, H. Choi, and J. R. Heath, *Angew. Chem., Int. Ed. Engl.* 40, 1721 (2001).
21. A. B. Dalton, C. Stephan, J. N. Coleman, B. McCarthy, P. M. Ajayan, S. Lefrant, P. Bernier, W. J. Blau, and H. J. Byrne, *J. Phys. Chem. B* 104, 10012 (2000).
22. J. L. Bahr and J. M. Tour, *J. Mater. Chem.* 12, 1952 (2002).
23. J. Chen, M. A. Hamon, H. Hu, Y. Chen, A. M. Rao, P. C. Eklund, and R. C. Haddon, *Science* 282, 95 (1998).
24. M. A. Hamon, J. Chen, H. Hu, Y. S. Chen, M. E. Itkis, A. M. Rao, P. C. Eklund, and R. C. Haddon, *Adv. Mater.* 11, 834 (1999).
25. J. E. Riggs, Z. Guo, D. L. Carroll, and Y.-P. Sun, *J. Am. Chem. Soc.* 122, 5879 (2000).
26. Y.-P. Sun, W. Huang, Y. Lin, K. Fu, A. Kitaigorodsky, L. A. Riddle, Y. J. Yu, and D. L. Carroll, *Chem. Mater.* 13, 2864 (2001).
27. S. C. Tsang, P. J. F. Harris, and M. L. H. Green, *Nature* 362, 520 (1993).
28. P. M. Ajayan, T. M. Ebbesen, T. Ichihashi, S. Iijima, K. Tanigaki, and H. Hiura, *Nature* 362, 522 (1993).
29. R. M. Lago, S. C. Tsang, K. L. Lu, Y. K. Chen, and M. L. H. Green, *Chem. Commun.* 1355 (1995).
30. K. C. Hwang, *Chem. Commun.* 173 (1995).
31. H. Hiura, T. W. Ebbesen, and K. Tanigaki, *Adv. Mater.* 7, 275 (1995).
32. J. Liu, A. G. Rinzler, H. Dai, J. H. Hafner, R. K. Bradley, P. J. Boul, A. Lu, T. Iverson, K. Shelimov, C. B. Huffman, F. Macias-Rodriguez, Y.-S. Shon, T. R. Lee, D. T. Colbert, and R. R. Smalley, *Science* 280, 1253 (1998).

33. A. G. Rinzler, J. Liu, H. Dai, P. Nikolaev, C. B. Huffman, F. J. Rodriguez-Macias, P. J. Boul, A. H. Lu, D. Heymann, D. T. Colbert, R. S. Lee, J. E. Fischer, A. M. Rao, P. C. Eklund, and R. E. Smalley, *Appl. Phys. A* 67, 29 (1998).
34. I. W. Chiang, B. E. Brinson, R. E. Smalley, J. L. Margrave, and R. H. Hauge, *J. Phys. Chem. B* 105, 1157 (2001).
35. J. Chen, A. M. Rao, S. Lyuksyutov, M. E. Itkis, M. A. Hamon, H. Hu, R. W. Cohn, P. C. Eklund, D. T. Colbert, R. E. Smalley, and R. C. Haddon, *J. Phys. Chem. B* 105, 2525 (2001).
36. C. G. Bac, S. Latl, V. Jourdain, R. Aznar, F. Rachdi, P. Bernier, M. Holzinger, A. Hirsch, C. Mathis, P. Petit, and A. Rubio, "Proc. Int. Winterschool on Electronic Properties of Molecular Nanostructures," Kirchberg H. Kuzmany et al., Eds. AIP Conference Proceedings, Melville, NY, 2001.
37. S. Nagasawa, M. Yudasaka, K. Hirahara, T. Ichihashi, and S. Iijima, *Chem. Phys. Lett.* 328, 374 (2000).
38. Y. Yang, H. Zou, B. Wu, Q. Li, J. Zhang, Z. Liu, X. Guo, and Z. Du, *J. Phys. Chem. B* 106, 7160 (2002).
39. W. Zhou, Y. H. Ooi, R. Russo, P. Papanek, D. E. Luzzi, J. E. Fischer, M. J. Bronikowski, P. A. Willis, and R. E. Smalley, *Chem. Phys. Lett.* 350, 6 (2001).
40. A. M. Rao, J. Chen, E. Richter, U. Schlecht, P. C. Eklund, R. C. Haddon, U. D. Venkateswaran, Y. K. Kwon, and D. Tomanek, *Phys. Rev. Lett.* 86 (2001).
41. D. V. Mawhinney, V. Naumenko, A. Kuznetsova, J. T. Yates, J. Liu, and R. E. Smalley, *J. Am. Chem. Soc.* 122, 2382 (2000).
42. D. V. Mawhinney, V. Naumenko, A. Kuznetsova, J. T. Yates, J. Liu, and R. E. Smalley, *Chem. Phys. Lett.* 324, 213 (2000).
43. A. Thess, R. Lee, P. Nikolaev, H. Dai, P. Petit, J. Robert, C. Xu, Y. H. Lee, S. G. Kim, A. G. Rinzler, D. T. Colbert, G. E. Scuseria, D. Tomanek, J. E. Fischer, and R. E. Smalley, *Science* 273, 483 (1996).
44. P. Nikolaev, M. J. Bronikowski, R. K. Bradley, F. Rohmund, D. T. Colbert, K. A. Smith, and R. E. Smalley, *Chem. Phys. Lett.* 313, 91 (1999).
45. M. J. Bronikowski, P. A. Willis, D. T. Colbert, K. A. Smith, and R. E. Smalley, *J. Vac. Sci. Technol. A* 19, 1800 (2001).
46. R. J. Lagow, R. B. Badachape, J. L. Wood, and J. L. Margrave, *J. Chem. Soc., Dalton Trans.* 12, 1268 (1974).
47. E. T. Mickelson, C. B. Huffman, A. G. Rinzler, R. E. Smalley, R. H. Hauge, and J. L. Margrave, *Chem. Phys. Lett.* 296, 188 (1998).
48. E. T. Mickelson, Novel Chemistry of Elemental Carbon: Graphite, Fullerenes and Nanotubes, Ph.D. Thesis, Rice University, Houston, TX, 1999.
49. I. W. Chiang, Science of Single-Wall Carbon Nanotubes: Purification, Characterization and Chemistry, Ph.D. Thesis, Rice University, Houston, TX, 2001.
50. T. Hayashi, M. Terrones, C. Scheu, Y. A. Kim, M. Rühle, T. Nakajima, and M. Endo, *Nano Lett.* 2, 491 (2002).
51. Y. Hattori, Y. Watanabe, S. Kawasaki, F. Okino, H. Touhara, B. K. Pradhan, T. Kyotani, and A. Tomita, "Extended Abstracts of International Symposium on Carbon Science and Technology for New Carbons," Tokyo, p. 180, 1998.
52. A. Hamwi, H. Alvergnat, S. Bannamy, and F. Beguin, *Carbon* 35, 723 (1997).
53. A. V. Okotrub, N. F. Yudanov, A. L. Chuvilin, I. P. Asanov, Yu. V. Shubin, L. G. Bulusheva, A. V. Gusel'nikov, and I. S. Fyodorov, *Chem. Phys. Lett.* 322, 231 (2000).
54. E. T. Mickelson, I. W. Chiang, J. L. Zimmerman, P. J. Boul, J. Lozano, J. Liu, R. E. Smalley, R. H. Hauge, and J. L. Margrave, *J. Phys. Chem. B* 103, 4318 (1999).
55. J. D. Dunitz and R. Taylor, *Chem.—Eur. J.* 3, 89 (1997).
56. K. F. Kelly, I. W. Chiang, E. T. Mickelson, R. H. Hauge, J. L. Margrave, X. Wang, G. E. Scuseria, C. Radloff, and N. J. Halas, *Chem. Phys. Lett.* 313, 445 (1999).
57. K. N. Kudun, H. F. Bettinger, and G. E. Scuseria, *Phys. Rev. B* 63, 45413 (2001).
58. Y. Chen, R. C. Haddon, S. Fang, A. M. Rao, P. C. Eklund, W. H. Lee, E. C. Dickey, E. A. Grulke, J. C. Pendergrass, A. Chavan, B. E. Haley, and R. E. Smalley, *J. Mater. Res.* 13, 2423 (1998).
59. S. Pekker, J.-P. Salvelat, E. Jakab, J.-M. Bonard, and L. Forro, *J. Phys. Chem. B* 105, 7938 (2001).
60. R. E. Haufler, J. Conceicao, L. P. F. Chibante, Y. Chai, N. E. Byrne, S. Flanagan, M. M. Haley, S. C. O'Brien, C. Pan, Z. Xiao, W. E. Billups, M. A. Ciufolini, R. H. Hauge, J. L. Margrave, L. J. Wilson, R. F. Curl, and R. E. Smalley, *J. Phys. Chem.* 94, 8634 (1990).
61. S. M. Lee and Y. H. Lee, *Appl. Phys. Lett.* 76, 2877 (2000).
62. M. Tsuda, T. Ishida, T. Nogami, S. Kurono, and M. Ohashi, *Tetrahedron Lett.* 34, 6911 (1993).
63. M. Holzinger, O. Vostrowsky, A. Hirsch, F. Hennrich, M. Kappes, R. Weiss, and F. Jellen, *Angew. Chem.* 40, 4002 (2001).
64. J. L. Bahr, J. Yang, D. V. Kosynkin, M. J. Bronikowski, R. E. Smalley, and J. M. Tour, *J. Am. Chem. Soc.* 123, 6536 (2001).
65. S. E. Kooi, U. Schlecht, M. Burghard, and K. Kern, *Angew. Chem., Int. Ed. Engl.* 41, 1353 (2002).
66. J. L. Bahr and J. M. Tour, *Chem. Mater.* 13, 3823 (2001).
67. B. L. Tumanski, *Russ. Chem. Bull.* 45, 2267 (1996).
68. P. Reverdy, H. Peng, V. N. Khabashesku, and J. L. Margrave, Rice Quantum Institute Fifteenth Annual Summer Research Colloquium, Aug. 17, 2001, Abstr., p. 19.
69. H. Peng, P. Reverdy, V. N. Khabashesku, and J. L. Margrave, *Chem. Commun.* 362 (2003).
70. V. Georgakilas, K. Kordatos, M. Prato, D. M. Guldi, M. Holzinger, and A. Hirsch, *J. Am. Chem. Soc.* 124, 760 (2001).
71. M. Prato and M. Maggini, *Acc. Chem. Res.* 31, 519 (1998).
72. N. Tagmatarchis, V. Georgakilas, M. Prato, and H. Shinohara, *Chem. Commun.* 2010 (2002).
73. Z. Liu, Z. Shen, T. Zhu, S. Hou, and L. Ying, *Langmuir* 16, 3569 (2000).
74. B. Zhao, H. Hu, S. Niyogi, M. E. Itkis, M. A. Hamon, P. Bhowmik, M. S. Meier, and R. C. Haddon, *J. Am. Chem. Soc.* 123, 11673 (2001).
75. S. S. Wong, E. Joselevich, A. T. Woolley, C. L. Cheung, and C. M. Lieber, *Nature* 394, 52 (1998).
76. P. W. Chiu, G. S. Duesberg, U. Dettlaff-Weglikowska, and S. Roth, *Appl. Phys. Lett.* 80, 3811 (2002).
77. E. V. Basiuk, V. A. Basiuk, J.-G. Banuelos, J.-M. Saniger-Blesa, V. A. Pokrovskiy, T. Yu. Gromovoy, A. V. Mischanchuk, and B. G. Mischanchuk, *J. Phys. Chem. B* 106, 1588 (2002).
78. R. Czerw, Z. Guo, P. M. Ajayan, Y.-P. Sun, and D. Carroll, *Nano Lett.* 1, 423 (2001).
79. K. Fu, W. Huang, Y. Lin, L. A. Riddle, D. Carroll, and Y.-P. Sun, *Nano Lett.* 1, 439 (2001).
80. Z. Gu, H. Peng, J. L. Zimmerman, I. W. Chiang, V. N. Khabashesku, R. H. Hauge, and J. L. Margrave, 223rd ACS National Meeting, April 7–11, 2002, Orlando, FL, Abstracts and Papers, Division of Fluorine Chemistry, Abstr., p. 12.
81. Z. Gu, H. Peng, R. H. Hauge, R. E. Smalley, and J. L. Margrave, *Nano Lett.* 2, 1009 (2002).
82. I. W. Chiang, B. E. Brinson, A. Y. Huang, P. A. Willis, M. J. Bronikowski, J. L. Margrave, R. E. Smalley, and R. H. Hauge, *J. Phys. Chem. B* 105, 8297 (2001).
83. R. Taylor, *Russ. Chem. Bull.* 47, 823 (1998).
84. H. F. Bettinger, K. N. Kudun, and G. E. Scuseria, *J. Am. Chem. Soc.* 123, 12849 (2001).
85. V. N. Khabashesku, W. E. Billups, and J. L. Margrave, *Acc. Chem. Res.* 35, 1037 (2002).
86. P. J. Boul, J. Liu, E. T. Mickelson, C. B. Huffman, L. M. Ericson, I. W. Chiang, K. A. Smith, D. T. Colbert, R. H. Hauge, J. L. Margrave, and R. E. Smalley, *Chem. Phys. Lett.* 310, 367 (1999).
87. I. Tonks, B. McClain, Z. Gu, V. N. Khabashesku, and J. L. Margrave, Rice Quantum Institute Fifteenth Annual Summer Research Colloquium, August 17, 2001, Abstr., p. 19.

88. R. Lobo, V.N. Khabashesku, and J. L. Margrave, Unpublished results.
89. A. Y. Huang, I. W. Chiang, V. N. Khabashesku, and J. L. Margrave, Rice Quantum Institute Fifteenth Annual Summer Research Colloquium, Aug. 17, 2001, Abstr., p. 18.
90. J. L. Stevens, A. Y. Huang, I. W. Chiang, V. N. Khabashesku, and J. L. Margrave, *Nano Lett.* 2003 ASAP article.
91. H. Peng, Z. Gu, Y. Liu, I. W. Chiang, R. E. Smalley, R. H. Hauge, V. N. Khabashesku, and J. L. Margrave, *J. Nanosci. Nanotech.* 2003 (in press).
92. R. Shukla, B. McClain, I. W. Chiang, V. N. Khabashesku, and J. L. Margrave, Rice Quantum Institute Fifteenth Annual Summer Research Colloquium, Aug. 17, 2001, Abstr., p. 19.
93. G. A. Derrien, Z. Gu, H. Peng, V. N. Khabashesku, and J. L. Margrave, Rice Quantum Institute Sixteenth Annual Summer Research Colloquium, Aug. 9, 2002, Abstr., p. 3.
94. H. Peng, Z. Gu, J. Yang, J. L. Zimmerman, P. A. Willis, M. J. Bronikowski, R. E. Smalley, R. H. Hauge, and J. L. Margrave, *Nano Lett.* 1, 625 (2001).

Chiral Macrocycles

Suk Joong Lee, Wenbin Lin

University of North Carolina, Chapel Hill, North Carolina, USA

CONTENTS

1. Introduction
 2. Organic Macrocycles
 3. Chiral Macrocycles Containing Metals
 4. Concluding Remarks
- Glossary
References

1. INTRODUCTION

A contemporary topic of modern chemistry is concerned with expanding its ability to mimic forms and functions of Mother Nature [1, 2]. Synthetic chemists have strived to accomplish this via spontaneous self-assembly of well-defined, complex supramolecular assemblies from constituent subunits in solution [3]. Since the discovery of crown ethers in 1967 [4], numerous studies have been carried out on cyclic and cage compounds, and as a result, many interesting synthetic receptors are now available and have found important practical applications. Examples of practically useful macrocycles include naturally occurring antibiotic nonactin (**1**) which has been used as the receptor in commercial ion sensitive electrodes for NH_4^+ and a chiral crown ether (**2**) which has been used in commercial high performance liquid chromatography columns for the separation of α -amino acids (Scheme 1) [5]. In addition to their important practical applications, rational design of such nanoscopic supramolecular assemblies represents an important bottom-up approach toward the burgeoning field of nanoscience and nanotechnology [6].

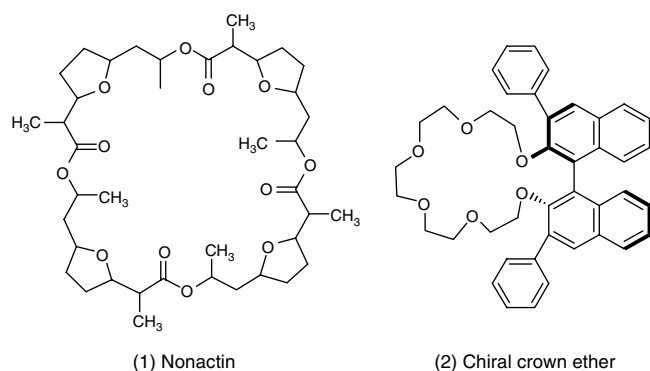
Typically low-yielding synthesis of macrocycles and cages have, however, impeded many more potentially practical applications. In order to avoid the formation of undesired linear oligomers, macrocycles and cages are normally synthesized under high-dilution conditions. Such synthetic conditions require the use of enormous amounts of solvents and present a major burden to the environments and are thus not suitable for their large-scale syntheses. Whereas macrocyclization under the aforementioned kinetic controls is a challenging process, macrocycles can sometimes be obtained in high yields under thermodynamic conditions.

Excellent examples of high yield formation of macrocycles under thermodynamic conditions are provided by phenol-formaldehyde or resorcinol-aldehyde cyclic oligomers (calixarenes) that are formed under equilibrium conditions. Facile synthesis of calixarenes suggests that thermodynamic control should be a good strategy for macrocycle (or cage) synthesis [7].

The concept of thermodynamic control has recently been applied to noncovalent syntheses. Spontaneous generation of well-defined supramolecular architectures has been achieved under thermodynamic conditions via self-assembly driven by noncovalent bonds such as hydrophobic interactions, π - π interactions, hydrogen bonding, and metal-ligand ligation [8, 9]. In particular, metal-ligand coordination bonding has been extensively used to construct such supramolecular structures as helices, rods, macrocycles, and cages [7]. These structures are spontaneously generated by simply mixing component ligands and metals in solution. Among defined structures, macrocycles and cages are particularly interesting because of their potential application as synthetic receptors. Several excellent reviews have appeared on the topic of coordination-driven self-assembly of metallosupramolecular systems over the past few years [10]. In this chapter, we will focus on recent developments in rational design of discrete chiral macrocycles, with a particular emphasis on chiral metal-containing self-assembled macrocyclic structures. Potential applications of these interesting chiral supramolecular systems will also be presented.

1.1. Rational Design of Macrocycles

A major advance in the design of macrocyclic structures lies in the ability to predict the structures of resulting supramolecular assemblies based on the information contained in their molecular building blocks. Well-defined supramolecular architectures can be rationally assembled via recognition-driven spontaneous assembly of presynthesized subunits. Such a "coden" approach is extremely important for the synthesis of macrocyclic species based on stronger interactions such as covalent and coordination bonds [11]. Unlike supramolecular structures found in Mother Nature which are built from relatively weak hydrogen bonds and van der Waals interactions, macrocycles and cages built from



Scheme 1.

stronger covalent or coordination bonds do not necessarily exhibit appreciable kinetics for reversible annealing of defects during the self-assembly processes. Therefore, properly designed building subunits with appropriate shapes and functionalities are needed for the assembly of discrete supramolecular assemblies.

Such a “coden”-based approach has been elaborated by Fujita and Ogura [12] and systematized by Stang et al. for the synthesis of metallomacrocycles and metallocages [13, 14]. By using rigid, highly directional multibranching ligands as donor units and unsaturated transition metal moieties with fixed bond angles as the acceptor units, well-defined metallocycles can be readily assembled via metal-ligand coordination [6]. Both angular and linear building subunits are needed for the construction of cyclic structures. While angular subunits contain two reactive sites that are oriented at an angle between 0° and 180° [13], linear subunits possess two reactive sites which are opposite to each other (i.e., $\sim 180^\circ$). The combination of these building subunits will lead to a metallosupramolecular system whose structure depends solely on the symmetry and the number of binding sites within each subunit. For example, the assembly of a planar triangle requires the combination of three linear building subunits blocks and three 60° angular ones. A molecular square can be assembled in several different ways, including a combination of four linear and four 90° angular building units and a combination of two different 90° angular subunits. Combining five linear subunits with five angular ones that possess a 108° angle between their binding sites will generate a molecular pentagon as illustrated in Figure 1 [6, 13, 14]. These principles assume total conformational rigidity of subunits, but some distortion of the binding angle can occur. Metallocycles of different shapes from those predicted by these simple geometrical relationships can sometimes result from the combination of building subunits.

1.2. Thermodynamic Factors in the Self-Assembly of Metallocycles

As mentioned earlier, the requirements for thermodynamic self-assembly of a metallocycle are that (i) coordination bonds must form between the donor and acceptor elements involved, (ii) the bonds must be kinetically labile to allow self-correction, and (iii) the desired assembly must be thermodynamically favorable over competing species [8].

Ditopic Subunit \ Ditopic Subunit	60°	90°	109.5°	120°	180°
60°					
90°					
109.5°					
120°					
180°					

Figure 1. Schematic depiction of routes for the self-assembly of cyclic structures. Reprinted with permission from [6], S. Leininger et al., *Chem. Rev.* 100, 853 (2000). © 2000, American Chemical Society.

Thermodynamic factors in the self-assembly of macrocyclic compounds have been widely examined [15, 16]. It is well established that cyclic structures are preferred over linear ones for enthalpic reasons, while small cycles are favored over large cycles (at low concentrations) for entropic reasons. The enthalpic preference arises from the fact that an increased number of bonds per subunit is possible in a cyclic arrangement relative to a linear one. For example, a square consisting of two angular units and two linear units contains four coordinate bonds, that is, one bond per building block (Fig. 2a). Its equivalent acyclic coordination oligomer is coordinatively unsaturated in one end and therefore contains only three bonds, that is, 0.75 bonds per building block (Fig. 2b).

Acyclic oligomers can polymerize to increase the number of bonds formed. However, the donor and acceptor sites at each end of the polymer will always remain uncoordinated. Thus, the ideal scenario of one bond per building block cannot be achieved unless cyclization occurs. If cyclization is unfavorable, it is likely that the oligomers will polymerize until higher oligomers precipitate as kinetic products.

The entropic preference referred to is a result of Le Chatelier's law, which states that a perturbation to a dynamic equilibrium results in a readjustment of the equilibrium to minimize its effect. Thus, dilution of a solution containing an equilibrium mixture of cyclic oligomers results in a shift of the equilibrium to increase the total number of species present. At low concentrations smaller cycles are consequently favored, with the reverse being the case

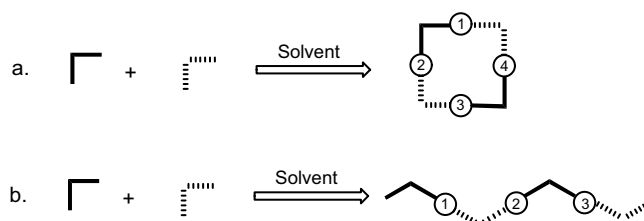


Figure 2. Different number of bonds in cyclic and acyclic structures.

at high concentrations. As most self-assembly reactions are performed in dilute solution, the smallest possible cycles are usually favored. In metallocycles, the enthalpic driving forces invariably dominate the entropic ones because of the large enthalpy of coordination bond formation.

2. ORGANIC MACROCYCLES

Molecular recognition is key to many biochemical processes such as antibody–antigen interactions, biocatalytic reactions, and signal transcriptions [17]. The use of single enantiomeric forms of amino acids and sugars in biological systems is largely responsible for these remarkable biochemical processes that make life possible. Synthetic chemists have devoted significant effort to the design and synthesis of chiral macrocycles for the stereoselective recognition of chiral substrates.

Cram and co-workers have carried out pioneering studies of enantiomeric recognition of organic ammonium salts by solvent extraction techniques [18–20], transport of amides through liquid membranes [21], and partial resolution of amino acids on silica gel or polystyrene that are grafted with chiral host materials [22]. Lehn and Sirlin have found that reactivity of the thiolization reaction of certain *p*-nitrophenyl esters increased drastically after the addition of chiral host molecules [23]. Many other chiral macrocycles have been designed and used as synthetic receptors for enantioselective recognition over the past few years. Exciting recent developments in nanoscopic cyclopeptides [24–27] and circular oligonucleotides [28, 29] will not be discussed here.

Zhao and Hua [17] reported α -amino acid derived chiral macrocycles for enantioselective recognition of D- and L-amino acid methyl ester hydrochloride. These chiral macrocycles were prepared by the acylation cyclization of 2,6-pyridinedicarbonyl dichloride and chiral diamine dihydrobromide intermediates which were obtained from condensation of chiral amino acids and 2,6-bis(hydroxymethyl)pyridine, in highly diluted solution at room temperature. When L-alanine and L-valine derived diamine intermediates were used as the chiral building blocks, both [1 + 1] and [2 + 2] cyclization products **1a–e** were obtained. In contrast, only [1 + 1] cyclization product was obtained when the L-proline derived diamine intermediate was used (Fig. 3). These chiral macrocycles exhibited interesting chiral recognition for the enantiomers of D- and L-amino acid methyl ester hydrochlorides, which have been characterized by fluorescence spectroscopy.

In a recent publication, Kohler and co-workers [30] reported a series of chiral macrocycles, **2a–b**, which consist of two angular chiral building units and two linear building units (Fig. 4). These novel semirigid, chiral cycles were synthesized by condensation of two rigid oligoarylene rods and two chiral spiroindane clips. With electronically interacting arylene chromophores and internal helicity resulting from chiral spiroindane clips, these macrocycles act as chiral dopants of polymeric nematic liquid crystals.

Helically arranged, electronically interacting chromophores are keys to the design of novel chiroptical materials, particularly light-emitting materials that provide intrinsically circularly polarized light. Chiral ensembles of electronically interacting chromophores in such materials will give rise to

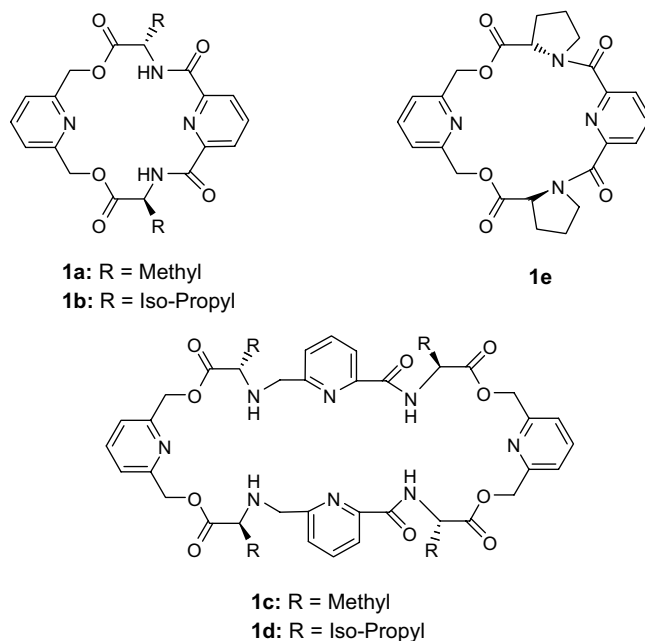


Figure 3. Chiral macrocycles for amino acid recognition. Reprinted with permission from [17], H. Zhao and W. Hua, *J. Org. Chem.* 65, 2933 (2000). © 2000, American Chemical Society.

the chiroptical effects which can be interpreted on the basis of the so-called exciton coupling model [31]. Such chiral interactions in a polymeric material can be experimentally studied on model dimers composed of two chromophores that are fixed at a chiral core unit [32], for example, a chiral 3,4-diaminodecaline core. However, this type of chiral model compound has a comparably high degree of remaining conformational freedom and thus does not adequately represent the chiroptical effects in a rigid, chiral conjugated polymer. The cyclic structure of **2a–b** with two rigid chromophores that are fixed by two chiral clips on both ends provides a better model for chiroptical effects in a rigid, chiral conjugated polymer.

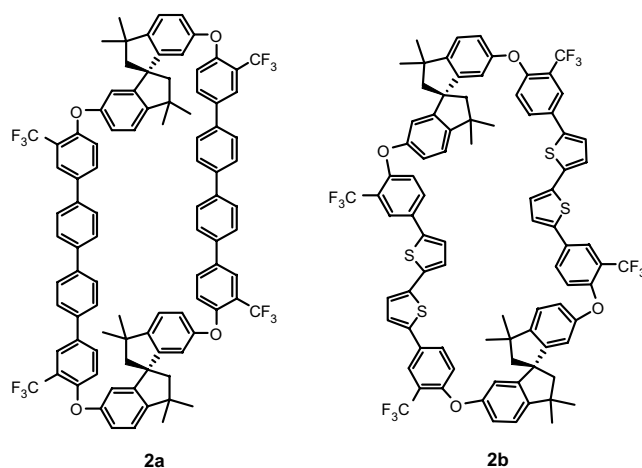


Figure 4. Chiral macrocycles containing two arylene chromophores. Reprinted with permission from [30], B. Kohler et al., *Chem. Eur. J.* 7, 3000 (2001). © 2001, Wiley–VCH.

Organic macrocyclic molecules with rings larger than 20 atoms are far less abundant than their smaller ring counterparts [33, 34]. An interesting class of organic macrocycles, polyazamacrocycles, are typically synthesized either by Schiff base condensation between aliphatic diamines and aromatic dialdehydes or by cyclic amide formation between aliphatic diamines and dicarboxylic acids dichlorides under high-dilution conditions [35–38]. These condensation techniques only allow the synthesis of small- to medium-sized rings. An alternative cation templating method is needed to form larger size rings in which multiple components are preorganized by the cation templates. For example, π -conjugated and partially reduced macrocyclic Schiff bases have been obtained by efficient proton-templated [2 + 2] cyclocondensation of 2,6-diformyl-4- R_1 -phenol ($R_1 = \text{Me}$, $t\text{-Bu}$) and 1,2-diamino-4,5- R_2 -benzene ($R_2 = \text{H}$, Me) [39].

Larger macrocycles can be obtained in high yields if the intermediates adopt a restricted conformation which favors the cyclization of large rings. The synthesis of hexamethylenetetramine from ammonia and formaldehyde provides an excellent example of an efficient assembly of a multicyclic compound. This reaction is believed to proceed through a diimine intermediate and is directed by the ability of the chair-like 6-membered rings to form an adamantane-like structure [40]. Preferential formation of a 12-membered heterocycle over the open-chain oligomers has also been achieved by taking advantage of conformational effect of the bulky N -tosyl substituents in the diamine component [41]. Recently, Gawroński et al. [42] demonstrated conformationally driven [3 + 3] cyclocondensations to give chiral macrocyclic triangular structures using (1*R*, 2*R*)-1,2-diaminocyclohexane as a chiral building unit (Fig. 5). Since this building unit contains a rigid structure and equatorial amino substituents, it would facilitate ring formation in the reaction with planar molecules. The two C–N bonds in angular units are projected at a 60° angle from the center of the cyclohexane ring and provide rigid and equatorial ditopic reaction sites, and hence macrocycle formation is anticipated to proceed through a [3 + 3] diamine–dialdehyde addition when 180° linear or planar ditopic building units are encountered, with molecules 60° angular unit placed at each vertex of a regular triangle in the final product (Fig. 5).

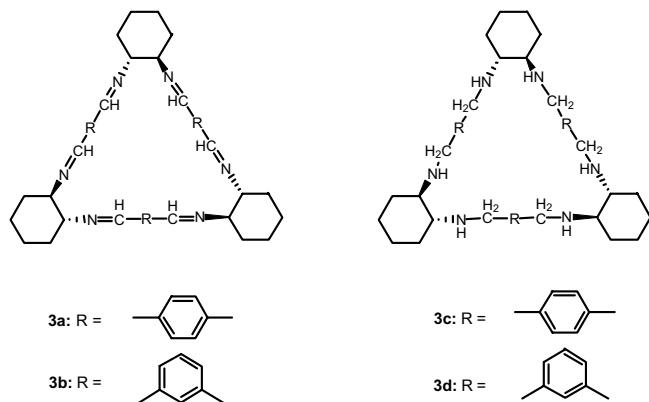


Figure 5. Triangular organic chiral macrocycles with 60° vertices. Reprinted with permission from [42], J. Gawroński et al., *J. Org. Chem.* 65, 5768 (2000). © 2000, American Chemical Society.

Remarkably, chiral macrocycles **3a–b** were indeed synthesized in very high yields (ca. 90%) even in high concentrations (ca. 0.4 M). **3a** and **3b** possess D_3 and C_3 point group symmetry, respectively, and they can be readily reduced by NaBH_4 to give chiral macrocycles **3c** and **3d**.

The major advantage of the introduction of a cage moiety into the chiral macrocyclic system is the generation of rigidity into the macrocycles which influences their overall conformational mobility [43]. Moreover, since the cage moiety can perform as a lipophilic component, the solubility of cage-containing crown ethers in nonpolar solvents can be improved compared to that of the non-cage-containing crown ethers. One of these examples has been demonstrated by Marchand and co-workers [43]. They reported the synthesis of a series of chiral cage-annulated crown ethers for the host–guest interaction study. These novel chiral macrocycles were synthesized by incorporating either an optically active monosaccharide derivative or a tartaric acid derivative into each cage-annulated crown ether to generate the chirality via a NaH promoted reaction in dried THF (Fig. 6).

An et al. [44] demonstrated very interesting enantiopure double-helical alkynyl cyclophanes **12** of both enantiopure forms (Fig. 7). As is shown in the crystal structure, the cyclophane backbone is twisted, resulting in the double-helical motif. The alkynyl groups are slightly bent from linearity. Interestingly, the dihedral angles of the two binaphthyl groups are significantly different by about 10 degrees (68° and 78°, respectively). Since the inside hydrogen atoms of the phenylene rings are located very close to each other, the ring strain generates unsymmetrical locations of the binaphthyl ends in the solid state. However, ^1H nuclear magnetic resonance (NMR) indicates no unsymmetrical patterns due to the strained structure as observed in solid state. This reflects the rapid fluctuation of the cyclophane framework in solution.

Anderson and co-workers [45] demonstrated a very interesting carbohydrate recognition with 1,1'-binaphthyl based chiral cyclic receptors (Fig. 8). These chiral macrocyclic receptors were derived from the 3,3'-diethynyl-1,1'-binaphthyl-2,2'-diol spacer using an oxidative Glaser–Hay coupling reaction. Since this series of chiral macrocycles contains 6, 8, and 10 OH groups that converge upon a central cavity, these receptors generate enough space

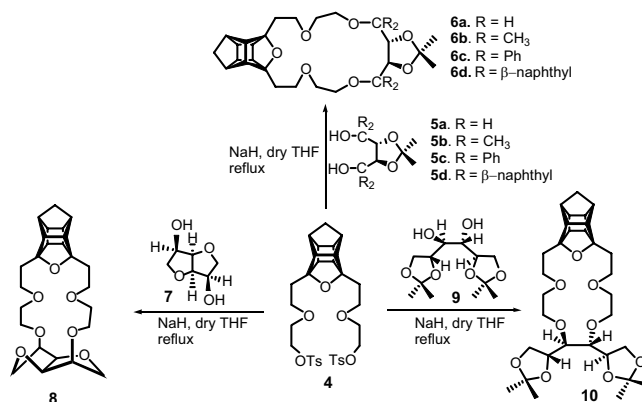


Figure 6. Synthesis of cage-annulated chiral macrocycles.

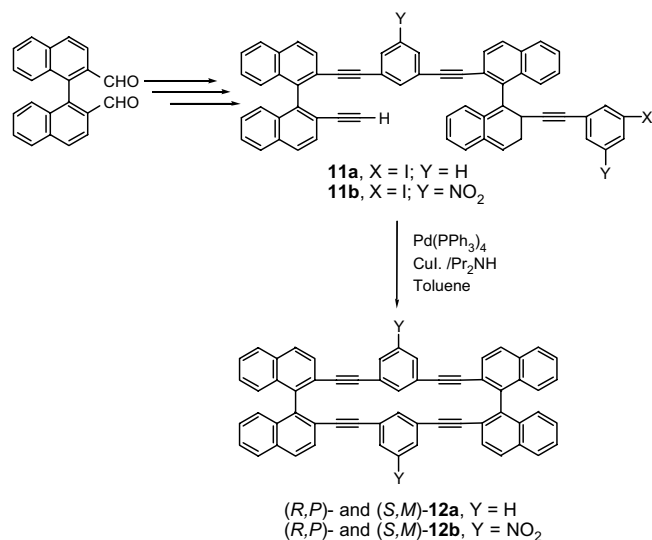


Figure 7. Synthesis and structure of double-helical alkynyl cyclophanes. Reprinted with permission from [44], D. L. An et al., *Angew. Chem., Int. Ed. Engl.* 41, 171 (2002). © 2002, Wiley-VCH.

for the guest molecules and hydrogen bonding sites for carbohydrates recognition. Specially, ¹H NMR titration studies with **14b** and 1-*O*-octyl pyranosides (**15a–c**) in dry CDCl₃, in which the change in chemical shift of the receptor OH protons was monitored as a function of the concentration of guest, showed the formation of stable 1:1 complexes with the association constants *K*_a of 90 (when the guest was **15b**), 195 (when the guest was **15a**), and 370 L mol⁻¹ (when the guest was **15c**) at 300 K. Interestingly, this type of recognition was not observed when the spacer only was used as a receptor. Therefore, more than one of the three binaphthyl spacers' OH groups in the macrocyclic cavity is required at the recognition event with the pyranosides.

Moreover, the incorporation of phosphodiester groups into 1,1'-binaphthyl-derived cyclophane receptors provides a better driving force for the complexation processes

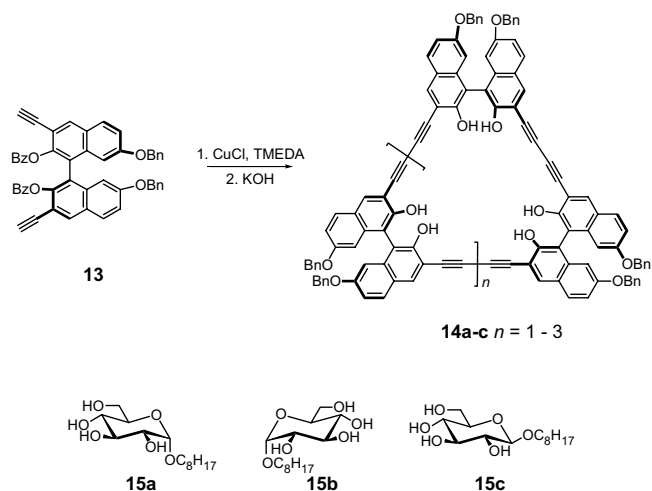


Figure 8. Synthesis of chiral macrocyclic receptors and their guests. Reprinted with permission from [45], S. Anderson et al., *Angew. Chem., Int. Ed. Engl.* 34, 1596 (1995). © 1995, Wiley-VCH.

between anionic phosphodiester groups and the hydroxyl groups of pyranosides in the presence of a protic co-solvent which competes for the hydrogen bonding sites [46]. Similarly, complexation of disaccharides **17a–c** was studied by ¹H NMR titration at 300 K in CD₃CN/CD₃OD (88:12 *v/v*) (Fig. 9). Compound **16** exhibited a high binding affinity (*K*_a ≈ 10⁴ dm³ mol⁻¹, -Δ*G*⁰ ≈ 5.5 kcal mol⁻¹) for all three disaccharides **17a–c**. While no selectivity among these substrates was observed, the selectivity over monosaccharides was very high. Interestingly, no evidence of the complexation was observed upon the addition of more than 2 equiv. of receptor to a 0.25 mmol dm⁻³ solution of glucoside **17d**; however, 60–80% saturation binding was observed with disaccharides **17a–c** under this condition. Apparently, the cavity size of the receptor is responsible for this high selectivity.

Lin et al. have successfully demonstrated chiral discrimination of α-hydroxycarboxylic acids via luminescence with binaphthyl-containing chiral macrocycles [47]. The fluorescence technique for enantioselective recognition is one of the most successful techniques because it provides a real-time method for the determination. Since successfully designed sensors have a tendency to screen or enhance the intensity of fluorescence, enantioselective recognition of chiral molecule is possible. The chiral bisbinaphthyl macrocycles (–)-**21** are synthesized by condensation of (*S*)-**18** with (*R,R*)-**19** followed by reduction of the macrocyclic salen **20** (Fig. 10). When α-hydroxycarboxylic acid coordinates to chiral macrocycle (–)-**21** through multiple hydrogen bonding, protonation of nitrogen atoms inhibits the photoinduced electron transfer (PIET) of the lone pair electrons of nitrogen atoms [48–50]. Specially, when the solution of (–)-**21** in benzene containing 2% of DME is treated with (*S*)-mandelic acid, the fluorescence intensity of (–)-**21** increases dramatically. However, fluorescence quenching is observed when the (–)-**21** solution is treated with (*R*)-mandelic acid (Fig. 11). The lone pair electrons of macrocycles is not available for the PIET process when the host and the guest molecules form a very strong bond. Therefore, the stronger bond formation between (–)-**21** and (*S*)-mandelic acid provides unusual fluorescence intensity for enantioselective recognition.

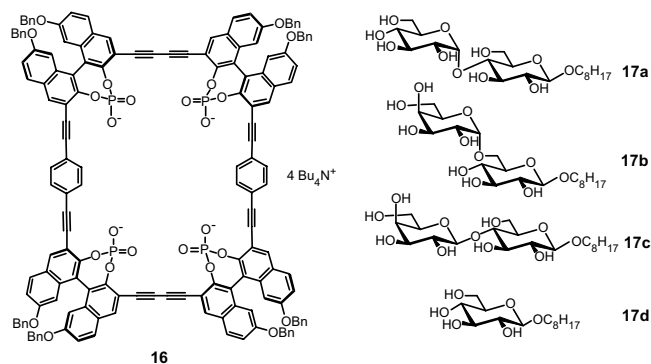


Figure 9. Phosphonodiester-containing chiral macrocyclic receptors and their guests. Reprinted with permission from [46], U. Neidlein and F. Diederich, *Chem. Commun.* 1493 (1996). © 1996, Royal Society of Chemistry.

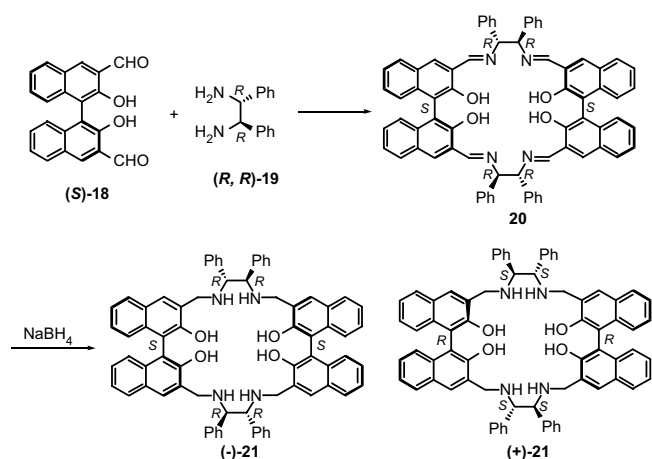


Figure 10. Synthesis of the bisbinaphthyl macrocycles (–)-**21** and (+)-**21**. Reprinted with permission from [47], J. Lin et al., *Org. Lett.* 4, 3297 (2002). © 2002, American Chemical Society.

Botta and co-workers have reported a chiral resorcin[4]arene **22_L** cavity for enantioselective recognition under solvent-free condition [51]. Since the solvent plays an important role in host/guest complexation in solution and complicates the understanding of the implicit principles, the enantioselective recognition study in the gas phase is often considered. In this work, a synthetic macrocycle, resorcin[4]arene **22_L**, with a cavity-shaped very flexible architecture, is considered as an artificial enzyme. The chirality of this macrocycle comes from four axial pendants containing the chiral L-valine group (Fig. 12). The inherent enantioselectivity of the **22_L** host is checked by generating proton-bonded complexes with representative amino acids in the gas phase and by monitoring the exchange rate of amino acids with (S)-(+)- and (R)-(–)-2-butylamine. In case of alanine as an amino acid, the exchange rate constants happen to be $k_D = 7.7$ and $k_L = 5.0$ for D-ala and L-ala, respectively, with (R)-(–)-2-butylamine. When (S)-(+)-2-butylamine is used, the exchange rate constants are $k_D = 7.1$ and $k_L = 5.9$ for D-ala and L-ala, respectively. Therefore, these results represent that the chiral resorcin[4]arene is a very promising system for chiral discrimination studies in the gas phase.

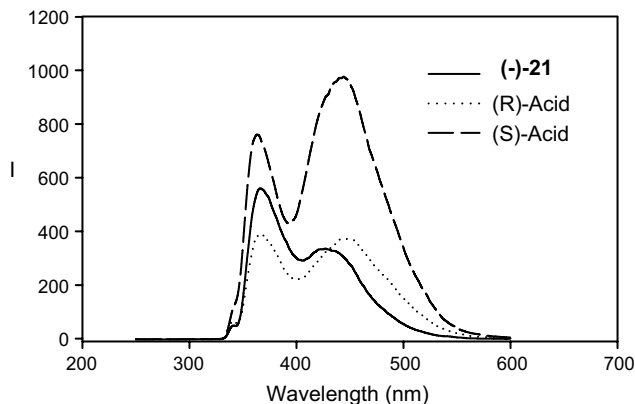


Figure 11. Fluorescence spectra of (–)-**21** both with and without (R)- and (S)-mandelic acid. Reprinted with permission from [47], J. Lin et al., *Org. Lett.* 4, 3297 (2002). © 2002, American Chemical Society.

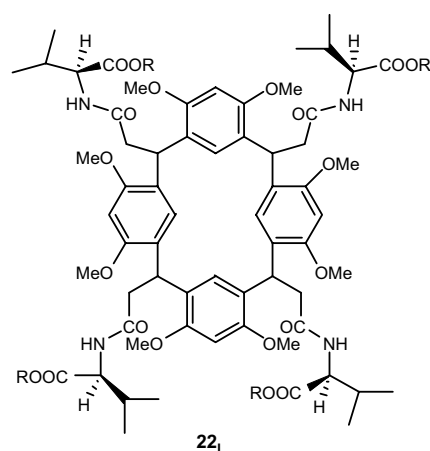


Figure 12. Formular and top view ($R = \text{ethyl}$) of a local minimum geometry for resorcin[4]arene. Reprinted with permission from [51], B. Botta et al., *J. Am. Chem. Soc.* 123, 7658 (2002). © 2002, American Chemical Society.

3. CHIRAL MACROCYCLES CONTAINING METALS

Compared to covalently bonded organic counterparts, metal-organic supramolecules can be assembled with much ease and higher efficiency. Coordination-driven self-assembly of metallosupramolecular systems can be readily achieved by mixing appropriately designed multitopic ligands and metal ions with suitable binding geometries. Among many metal-organic supramolecular systems, the construction of molecular squares based on metallocorners with $\sim 90^\circ$ angles and linear bridging ligands has proven to be the most reliable strategy, as exemplified by successful design of numerous molecular squares based on the *cis*-[M(phosphine)₂]²⁺ corners ($M = \text{Pd}$ or Pt) by Leininger et al. [6], the *cis*-[M(en)]²⁺ corners ($M = \text{Pd}$ and Pt ; en is ethylenediamine) by Fujita [7], the *fac*-(CO)₃ReX corners ($X = \text{halide}$) by Hupp et al. [52, 53], and the M₂(carboxylate)₂ corners by Cotton et al. [54]. Some of these metallosupramolecular assemblies have shown promise for applications in host–guest recognition [55–57], inclusion [58, 59], catalysis [60, 61], and fluorescence sensing [62]. Over the past decade, there has been tremendous progress in the catalytic asymmetric synthesis of chiral compounds, both enzymatically and chemically. Rational design of chiral metallosupramolecular systems can thus lead to new enzyme-like chiral pockets and functionalities which may find important applications in chiral sensing and asymmetric catalysis. The progress toward these goals made over the past few years will be surveyed.

Three different approaches have thus far been utilized to construct chiral metalcycles: (1) introduction of metallocorners that are coordinated to chiral capping groups, (2) use of metal-based chirality owing to specific coordination arrangements, and (3) introduction of chiral bridging ligands. Among these, the third approach requires the most synthetic manipulations but also offers the versatility of fine-tuning the chiral pockets or functionalities for potential applications.

Oenyuk et al. [63] demonstrated the first strategy by using optically active metal complexes [M(*R*-BINAP)(OTf)₂]

[M = Pd or Pt, BINAP = 2,2'-bis(diphenylphosphino)-1,1'-binaphthalene] as a chiral building block for the formation of chiral molecular squares. When combined with bis(4-(4'-pyridyl)phenyl)iodonium triflate, heteronuclear optically active cyclic species **19a** and **19b** were obtained (Fig. 13). Since the analogous cycles with two triethylphosphines in place of each *R*-BINAP are achiral [6], molecular squares **24a** and **24b** are chiral due only to the chiral transition-metal auxiliary (BINAP) in the assembly. It is also interesting to note that the coordinated pyridine moieties exhibit restricted rotation around the metal-pyridyl linkage; the hydrogen atoms on the pyridine rings become diastereotopic. Both **24a** and **24b** possess D_2 symmetry, with one C_2 axis passing through the center of the binaphthyl rings and the other C_2 axis passing through the two iodine atoms.

Chiral tetranuclear molecular squares were readily synthesized when [M(*R*-BINAP)(OTf)₂] was treated with C_{2h} -symmetrical diaza ligands 2,6-diazaanthracene (DAA) in acetone. Only a single diastereomer was obtained as evidenced by a single signal in the ³¹P NMR spectrum. In contrast, when 2,6-diazaanthracene-9,10-dione was used in place of DAA (Fig. 14), the reaction mixture consisted of a dominant diastereomer of **25a** and **25b** in a d.e. of 81% and minor amounts of other diastereomers. These chiral molecular squares have also been characterized by electrospray mass spectrometry (MS).

Fan et al. [64] have also synthesized a family of interesting chiral molecular squares containing porphyrins by using *trans*-DPyDPP, 5,15-di(4'-pyridyl)porphyrin, **26**, as the linear modules, and *R*(+)-, *S*(-)-BINAP-Pd(II) as the angular units (Fig. 15). The rotation of the metal-pyridyl bonds in **27a-b** is restricted at room temperature but becomes unrestricted at elevated temperatures. The chirality of the metal corners thus promotes the formation of enantiomeric macrocycles with a puckered geometry. As expected, the porphyrin chromophores in the enantiopure metalocycles **27a** and **27b** show strong circular dichroism around 420 nm. Cooperative coupling of four excitons in **27a** and **27b** leads to Davydov splitting with a very high amplitude.

Coordination chemists have taken advantage of the intrinsic chirality of transition metal complexes with certain geometries for the construction of chiral supramolecular assemblies since Werner's time [65]. Recent work has shown that nonlinear optically active coordination networks can be crystal engineered using such an approach [66]. Zhang and co-workers [67] have investigated the assembly of chiral molecular squares using octahedral metal ions

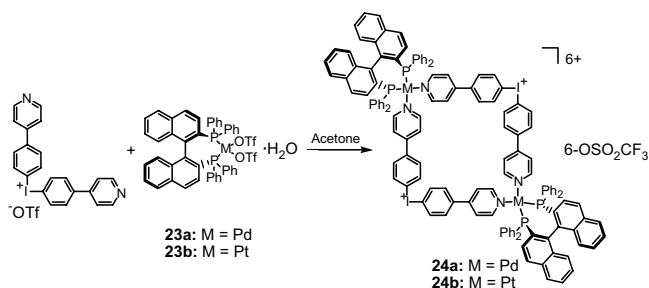


Figure 13. Hybrid chiral metalocycles. Reprinted with permission from [63], B. Oenyuk et al., *J. Am. Chem. Soc.* 118, 8221 (1996). © 1996, American Chemical Society.

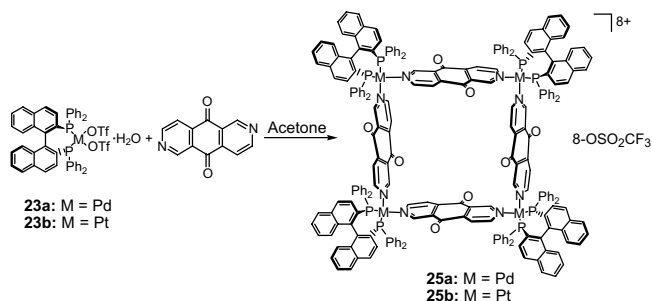


Figure 14. Chiral metalocycles with DAAD. Reprinted with permission from [63], B. Oenyuk et al., *J. Am. Chem. Soc.* 118, 8221 (1996). © 1996, American Chemical Society.

such as Co(II) and Mn(II). Unlike the square-planar Pt(II) or Pd(II) complexes, octahedral Co(II) or Mn(II) complexes with two chelating ligands are inherently chiral, and no chiral auxiliary ligands are required for the construction of chiral molecular squares. When the D_{2d} symmetric bridging ligand, tetraacetylene dianion (tae), was coordinated to octahedral Co(II) metalocorners that are capped with two chelating di-2-pyridylamine (dpa) ligands, the D_{2d} symmetry is reduced to pure rotational symmetries, and chiral molecular squares were obtained. Chiral molecular square Co₄(tae)₄(dpa)₄, **28**, was obtained in 15% yield and characterized by single crystal X-ray crystallography (Fig. 16). Each edge of the square (i.e., each pair of Co₂)

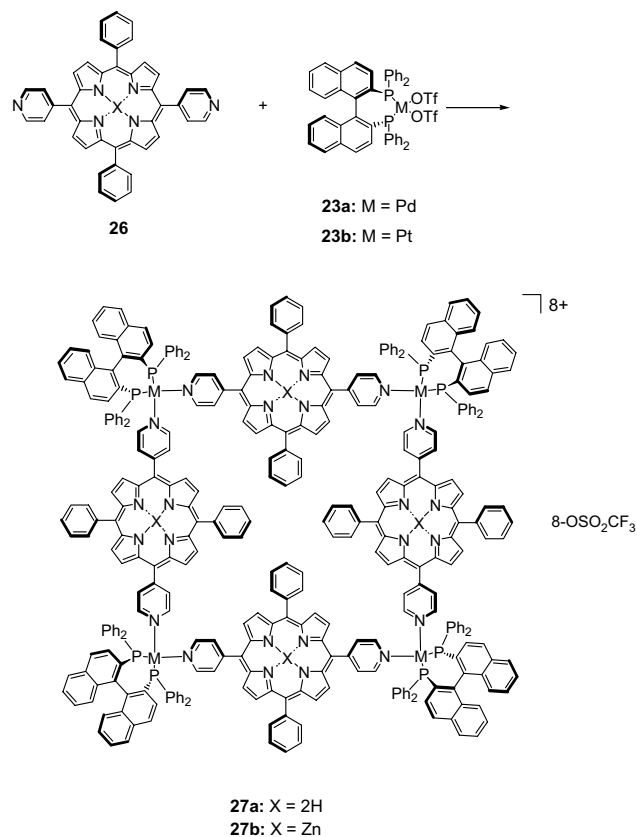


Figure 15. Synthesis of porphyrin-containing macrocycle. Reprinted with permission from [64], J. Fan et al., *J. Am. Chem. Soc.* 121, 2741 (1999). © 1999, American Chemical Society.

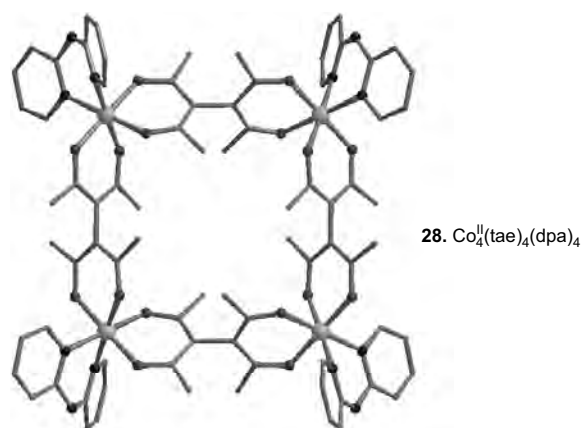


Figure 16. Structure of $\text{Co}_4^{\text{II}}(\text{tae})_4(\text{dpa})_4$. Reprinted with permission from [67], Y. Zhang et al., *J. Am. Chem. Soc.* 120, 9398 (1998). © 1998, American Chemical Society.

has a helical structure similar to that observed in $[\text{Co}_2(\text{tae})_2(\text{dpa})_2][(\text{O}_2\text{CCH}_3)_2(\text{H}_2\text{O})_2]$. The overall structure of **28** can therefore be described as a cyclic helicate (Fig. 16). Compound **28** is a rare example of structurally characterized molecular squares with a chiral structure in the solid state. The synthesis of **28** demonstrates that ligands with a $\sim 90^\circ$ twist between the binding sites can facilitate the formation of chiral molecular squares when octahedral metal ions are employed. The tae ligands in **28** also facilitate the ferromagnetic exchange between the Co(II) centers on the corners, and compound **28** is a weak ferromagnet.

The propeller-like arrangements of three chelating ligands around octahedral metal centers are also inherently chiral and have been used to introduce chirality to supramolecular assemblies at both local and global structural levels [68]. Ali and MacDonnell [69] demonstrated the use of intrinsic chirality at the kinetically inert octahedral metal center as a tool to direct the formation of molecular hexagons with diameters of 5.5 nm. The opposite absolute stereochemistry of the six vertex synthons $[(\text{bpy})\text{Ru}(\text{tpphz})_2]^{2+}$, **30a**, or $[(\text{bpy})\text{Os}(\text{tpphz})_2]^{2+}$, **30b** (Fig. 17), directs the formation of the ring structure and permits topospecific placement of different metals at unique symmetry sites within the ring. Three mixed-metal self-assembled systems were described, each containing six kinetically inert transition metal complexes (**29a** or **29b**) joined by six labile Pd(II) ions. The Ru_6Pd_6 , **30a**, Os_6Pd_6 , **30b**, and $\text{Ru}_3\text{Os}_3\text{Pd}_6$, **30c**, structures (Fig. 17) form due to the torsional restraints imposed by the stereochemistry of **29a** or **29b** along with the entropic factors which favor rings systems over polymeric structures. As seen in Figure 17, the metals alternate in a Ru–Pd, Os–Pd, and Ru–Pd–Os–Pd fashion for **30a**, **30b**, and **30c**, respectively. Compounds **30a** and **30b** are achiral due to the presence of both enantiomers of Ru(II) or Os(II) corner units, while compound **30c** is pseudo-*meso* due to the opposite handedness of the Ru(II) and Os(II) corners units. The formation of these mixed metal ring structures has been difficult to verify, due to the inability to obtain a satisfactory mass spectrum.

The preparation of chiral macrocyclic molecules typically requires the use of enantiopure building units or auxiliary ligands. The syntheses of macrocycles using racemic starting materials tend to result in complex diastereomeric

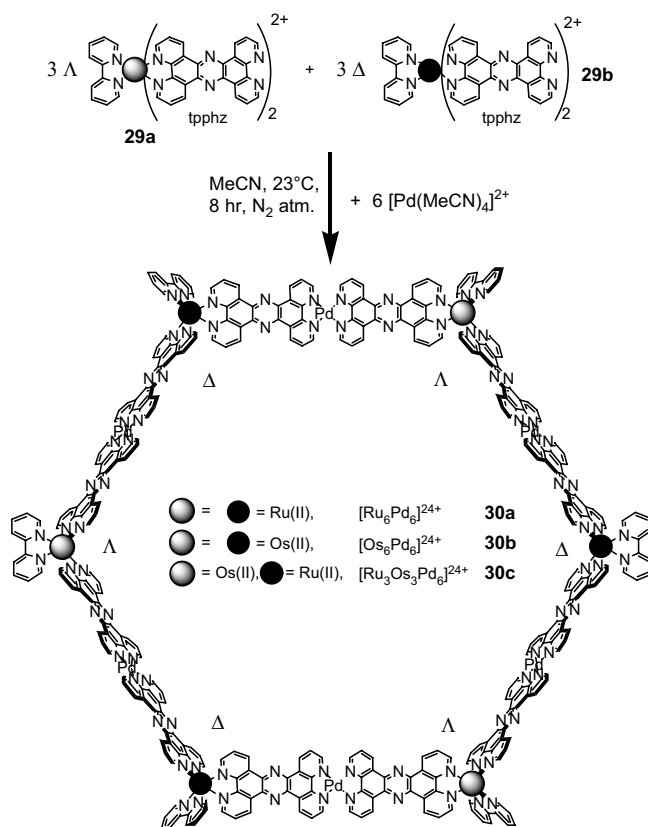


Figure 17. Synthesis of structure of mixed metal hexagons. Reprinted with permission from [69], M. M. Ali and F. A. MacDonnell, *J. Am. Chem. Soc.* 122, 11527 (2000). © 2000, American Chemical Society.

mixtures. Schafer and Tilley [70] have recently demonstrated efficient and high-yield diastereoselective synthetic routes to multigram quantities of BINOL containing macrocycles using zirconocene coupling procedures [71]. Dimeric macrocycle **32** was prepared from the known diyne **31** [72] as shown in Figure 18, using Negishi-type zirconocene coupling conditions [73]. Cyclodimerization of racemic compound **31** could lead to three stereoisomers of macrocycle **32**; however, only one pair of homochiral enantiomers (i.e., *SS* and *RR*) was obtained in this reaction. Enantiopure macrocycles were prepared from (*R*)-**31** and showed the same NMR spectra as the macrocycles obtained from racemic **31** and thus supported the assignment of racemic nature of dimeric macrocycle **32**. Such a diastereoselectivity was confirmed by single crystal X-ray crystallography. Macrocycle **32** has D_2 molecular symmetry and crystallizes as a racemic mixture of homochiral macrocycles. The naphthyl planes of each BINOL unit possess a large dihedral angle ($\sim 110^\circ$).

Racemic dyines **34** containing the enforced smaller dihedral angle by methylene bridges were also subjected to zirconocene coupling conditions to generate a larger macrocyclic structure, **35**, via zirconocene-mediated cyclotrimerization. The diastereoselective synthesis of homochiral macrocycles is once again achieved, and the product contained only a pair of homochiral enantiomers (i.e., *SSS* and *RRR*) (Fig. 19). In the solid state, the macrocycle adopts a highly folded geometry with pseudo C_2 molecular symmetry (Fig. 19).

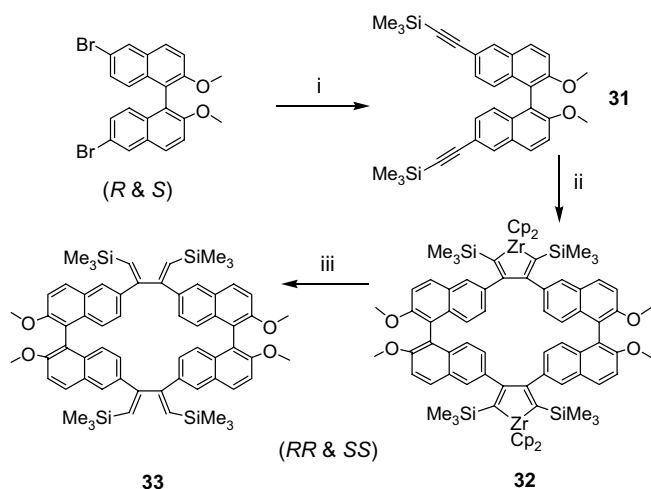


Figure 18. Diastereoselective synthesis of dimeric macrocycle and X-ray single crystal structures. (i) Me_3SiCCH , $\text{Pd}(\text{Ph}_3)_4$, CuI , $\text{NH}(\text{iPr})_2$, toluene, 80°C , 14 h; (ii) Cp_2ZrCl_2 , 2 equiv., $n\text{-BuLi}$, THF, -78°C to RT, 16 h; (iii) PhCO_2H , toluene, RT, 14 h. Reprinted with permission from [70], L. L. Schafer and T. D. Tilley, *J. Am. Chem. Soc.* 123, 2683 (2001). © 2001, American Chemical Society.

Kim and co-workers [74] have demonstrated the formation of an achiral macrocycle from racemic ligands using a ligand self-discrimination strategy in which one enantiopure ligand specifically senses its enantiomer to generate an achiral complex (Fig. 20). This 1,1'-binaphthol-containing ligand **38** was prepared by ester condensation of 1,1'-binaphthol and acid chloride of isonicotinic acid. Interestingly, ^1H NMR titration studies of $^{\text{rac}}\text{L}$ with $(\text{dppp})\text{Pd}(\text{OTf})_2$ **37a** in acetone- d_6 show a highly symmetric single set of signals at a 2:2 metal:ligand ratio, while ^1H NMR titrations of $^{\text{S}}\text{L}$ with $(\text{dppp})\text{Pd}(\text{OTf})_2$ **37a** show a complicated set of signals. These results imply that $^{\text{S}}\text{L}$ prefers to generate an achiral, heterodimeric complex exclusively with its enantiomer, rather than a homochiral complex.

Habereder et al. [75] reported unusual diastereoselective triangular cyclization from mesomeric starting materials.

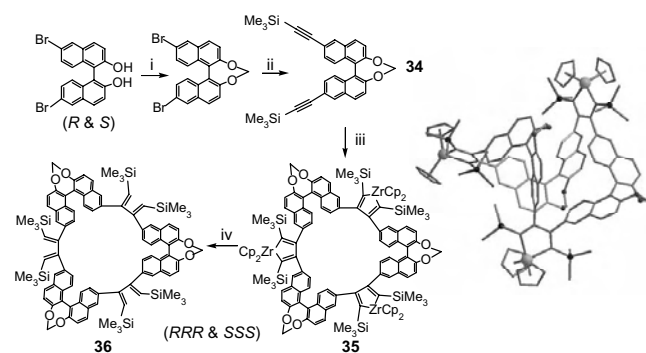


Figure 19. Synthesis of trimeric macrocycle and X-ray single crystal structure of macrocycle **35**. (i) CH_2I_2 , K_2CO_3 , DMF, 80°C , 16 h; (ii) Me_3SiCCH , $\text{Pd}(\text{PPh}_3)_4$, CuI , $\text{HN}(\text{iPr})_2$, toluene, 85°C , 14 h; (iii) Cp_2ZrCl_2 , 2 equiv., $n\text{-BuLi}$, THF, -78°C to RT, 4 h, 60°C , 8 h; (iv) PhCO_2H , toluene, RT, 16 h. Reprinted with permission from [71], S. S. H. Mao and T. D. Tilley, *J. Am. Chem. Soc.* 117, 5365 (1995). © 1995, American Chemical Society.

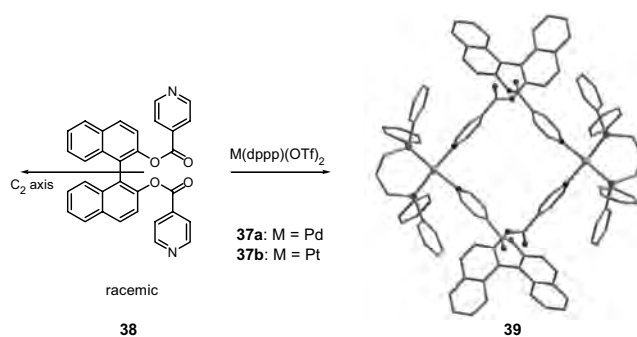


Figure 20. Self-discrimination of the racemic ligands in the self-assembly. Reprinted with permission from [74], T. W. Kim et al., *Chem. Commun.* 743 (2001). © 2001, Royal Society of Chemistry.

The heterocyclic bridging ligand is the dianion of 3-hydroxy-2-methyl-4(1H)-pyridone which is synthesized from 3-hydroxy-2-methyl-4-pyrone (maltol). When this ligand was treated with $(\text{Cp}^*)\text{Ir}(\text{III})$ **40a** or $(\eta^6\text{-cymene})\text{Ru}(\text{II})$ **40b** in the presence of one equivalent of base, its mesomeric form was formed (Fig. 21). The proton bound at the nitrogen atom becomes very acidic and the chlorine ligand is expected to be labile, thus providing the driving force for a base-induced cyclization (Fig. 21). Although the symmetry of supramolecule assembled from metal–ligand interaction depends on the geometry of the ligand and the metal, these complexes possess pseudo-octahedral geometry. Moreover, the bridging ligand acts as an O, O' -chelate and simultaneously coordinates through the nitrogen atom in position 4 to another metal atom and sits almost perpendicular to the cyclic plane. Interestingly, these macrocycles can regenerate their monomeric starting complexes by adding three equivalents of HCl. Therefore, this system demonstrates that macrocyclization can be induced and reversed by addition of appropriate amounts of base or acid, respectively (Fig. 22).

Although many chiral metallocycles have been constructed using all three approaches outlined earlier, none of them exhibit functionalities that are exploitable for enantioselective processes. Lee and Lin have recently demonstrated high-yield synthesis of chiral macrocycles based on *fac*- $\text{Re}(\text{CO})_3\text{Cl}$ corners with 90° angles and chiral linear bridging ligands via self-assembly (Fig. 23) [76]. The chiral ligands **42a–d** were synthesized in seven steps from BINOL with relatively high overall yield. BINOL was chosen as the backbone for the atropisomeric bridging ligands because it is well established that BINOL and derivatives provide outstanding asymmetric differentiation

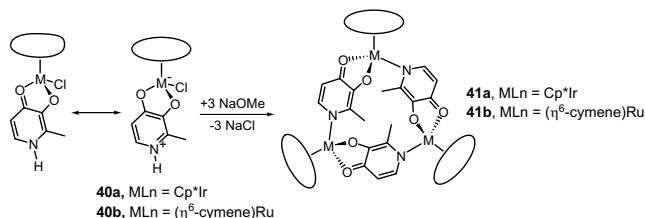


Figure 21. Mesomeric forms of starting materials and base-induced formation of chiral cycles. Reprinted with permission from [75], T. Habereder et al., *Angew. Chem., Int. Ed. Engl.* 38, 3225 (1999). © 1999, Wiley-VCH.

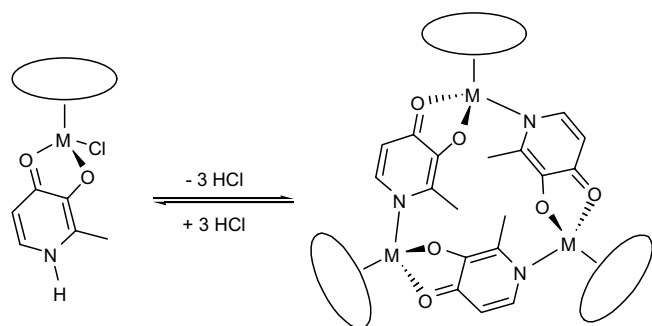


Figure 22. The assembly–disassembly process by addition of acid or base. Reprinted with permission from [75], T. Haberer et al., *Angew. Chem., Int. Ed. Engl.* 38, 3225 (1999). © 1999, Wiley–VCH.

properties and stable chiral configuration. Chiral macrocycle **43d** shows interesting enantioselective luminescence sensing behavior in THF. The fluorescence signal of enantiopure **43d** at 412 nm is efficiently quenched by both enantiomers of 2-amino-1-propanol, but at significantly different rates. For (*R*)-**43d**, the Stern–Völmer quenching constant K_{sv} is 7.35 M^{-1} in the presence of (*S*)-2-amino-1-propanol and 6.02 M^{-1} in the presence of (*R*)-2-amino-1-propanol. (*R*)-**43d** has an enantioselectivity factor $k_{sv}(R-S)/k_{sv}(R-R)$ of 1.22 for fluorescence quenching in favor of (*S*)-2-amino-1-propanol. The opposite trend in enantioselectivity was observed for the quenching of (*S*)-**43d** by 2-amino-1-propanol, which lends further support to a chirality-based luminescence-quenching selectivity between chiral metallo-cycle **43d** and 2-amino-1-propanol. It is interesting to note that no enantioselectivity was observed for the fluorescence quenching of **43d** by 1-amino-2-propanol, which supports the involvement of amino groups in the formation of a ground-state hydrogen-bonded complex and an excited-state proton-transfer complex. The greater distance of the amino group from the chiral center in 1-amino-2-propanol is responsible for its lack of fluorescence-quenching enantioselectivity. Control experiments show that fluorescence quenching of atropisomeric ligand **42d** by 2-amino-1-propanol does not exhibit enantioselectivity and thus demonstrates the importance of the supramolecular nature of the enantioselective process of **43d**. See Figure 24.

In order to design chiral macrocycles exhibiting favorable solubility in nonpolar solvents which are required for

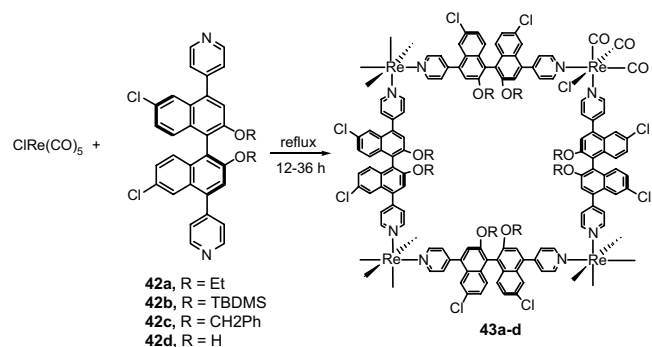


Figure 23. Synthesis of chiral macrocycles with Re corners. Reprinted with permission from [76], S. J. Lee and W. Lin, *J. Am. Chem. Soc.* 124, 4554 (2002). © 2002, American Chemical Society.

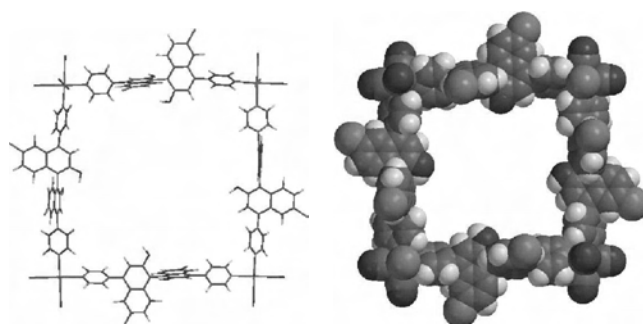


Figure 24. Energy-minimized structure of **43d**.

many asymmetric catalytic reactions, Lee et al. have taken advantage robust Pt–alkynyl linkages to construct a family of chiral molecular triangles [77]. Treatment of ligands **44a–c** with equal molar equivalents of *cis*-PtCl₂(PEt₃)₂ in the presence of CuI catalyst at room temperature generates chiral cycles **45a–c** in modest yields. Chiral cycle **45d** was obtained quantitatively by treating **45c** with TBAF in THF (Fig. 25). Compounds **45a–d** were characterized by ¹H, ¹³C{¹H}, and ³¹P{¹H} NMR spectroscopy, mass spectrometry, elemental analysis, and infrared (IR), ultraviolet-visible (UV-vis), and circular dichroism (CD) spectroscopies. In particular, CD spectra of **45a–d** exhibit an intense band at ~202 nm, in addition to three lower energy bands corresponding to naphthyl $\pi \rightarrow \pi^*$ transitions and two acetylenic $\pi \rightarrow \pi^*$ transitions (Fig. 26). The new CD band at ~202 nm can be assigned to the transitions associated with *cis*-Pt(PEt₃)₂ moieties. This result suggests that triethylphosphines on the Pt centers adopt a propeller-type arrangement (relative to the naphthyl groups), apparently steered by chiral binaphthyl moieties. Cycles **45a–d** exhibit enhanced lower energy CD signals over the free ligands **44a–d**, consistent with the presence of multiple ligands in each metallo-cycle. See Figure 27.

Chiral molecular triangle **45d** contains dihydroxy functionalities and was used for highly enantioselective catalytic

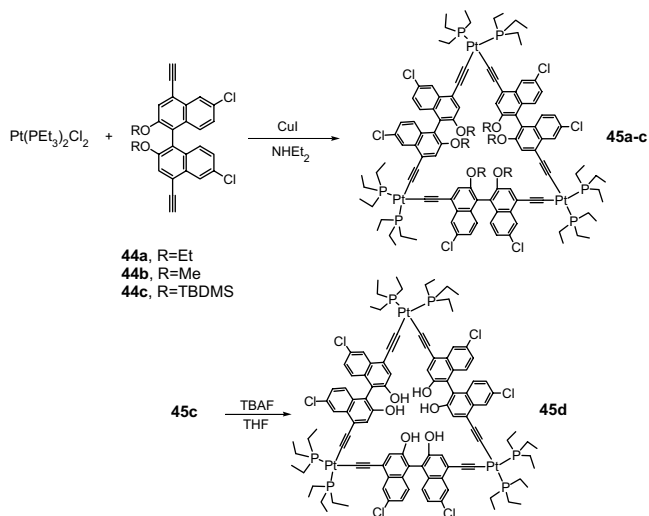


Figure 25. Synthesis of triangular chiral macrocycles. Reprinted with permission from [77], S. J. Lee et al., *J. Am. Chem. Soc.* 124, 12948 (2002). © 2002, American Chemical Society.

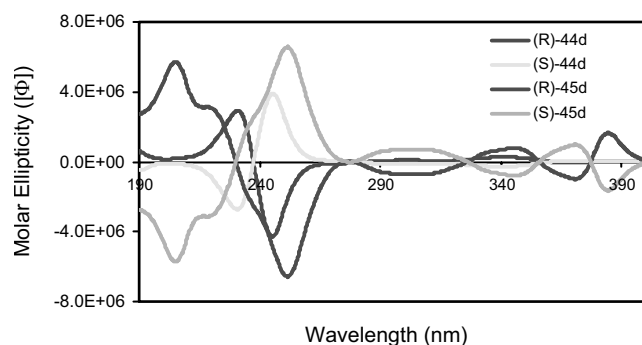
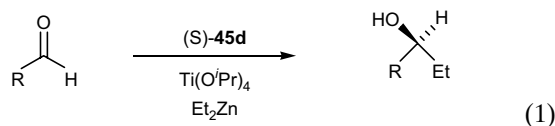


Figure 26. CD spectra of **44d** and **45d** in acetonitrile. Reprinted with permission from [77], S. J. Lee et al., *J. Am. Chem. Soc.* 124, 12948 (2002). © 2002, American Chemical Society.

diethylzinc additions to aromatic aldehydes [Eq. (1)]. With Ti(IV) complexes of **45d** as the catalyst, chiral secondary alcohols were obtained in greater than 95% yield and 89–92% e.e. for a wide range of aromatic aldehydes with varying steric demands and electronic properties (Table 1). In comparison, when free ligand **44d** was used instead of **45d**, a lower e.e. (80%) was obtained for the addition of diethylzinc to 1-naphthaldehyde. The broad substrate scope for catalytic diethylzinc additions using **45d** and $\text{Ti}(\text{O}^i\text{Pr})_4$ suggests that there is significant flexibility in the dihydroxy groups to accommodate aldehydes of various sizes.



In contrast to previously discussed chiral triangles, chiral dinuclear metallacyclophanes [*cis*-(PEt_3)₂Pt(**46**)₂], **47a–c**, were obtained when enantiomerically pure atropisomeric bis(acylenes) **46a–c** were treated with one equiv. of *cis*-Pt(PEt_3)₂Cl₂ in the presence of catalytic amounts of CuCl in diethylamine at room temperature [78]. Compounds **47a–c** were characterized by ¹H, ¹³C{¹H}, and ³¹P{¹H} NMR spectroscopy, HR-MS, elemental analysis, and IR, UV-Vis, and CD spectroscopies.

A single-crystal X-ray diffraction study on compound **47c** unambiguously demonstrated the formation of a chiral metallacyclophane. Compound **47c** crystallizes in chiral

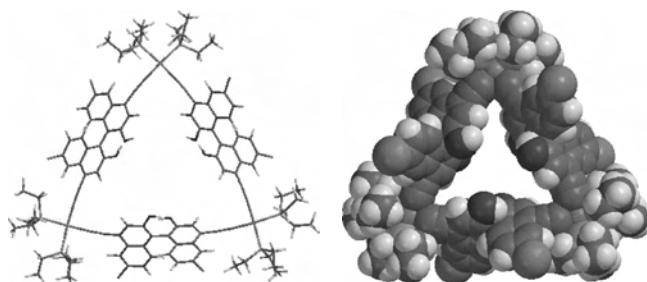


Figure 27. Energy-minimized structure of **45d**. Reprinted with permission from [77], S. J. Lee et al., *J. Am. Chem. Soc.* 124, 12948 (2002). © 2002, American Chemical Society.

Table 1. Diethylzinc additions to aldehydes catalyzed by Ti(IV) complexes of **40d**.

Entry	Aldehyde	Temp.	Conversion	e.e. (%)
1		RT	>95%	91
2		RT 0 °C	>95% >95%	91 92
3		RT	>95%	90
4		RT	>95%	91
5		RT	>95%	89
6		RT	>95%	90

monoclinic space group $P2_1$. Two *cis*-Pt(PEt_3)₂ units are linked by two enantiopure **46c** ligands to form a cyclic dinuclear structure (Fig. 28). Both Pt centers adopt slightly distorted square planar geometry with the *cis* angles around the Pt1 center ranging from 82.4(2) to 101.3(1)° and the *cis* angles around the Pt2 center ranging from 84.3(2) to 100.3(1)°. The rigid metallacyclophane structure of **47c** is characterized by very small dihedral angles between the naphthyl rings within each **47c** ligand (62.18 and 3.45°). See Figure 29.

As shown in Table 2, the Ti(IV) complexes of **47c** are excellent catalysts for the additions of diethylzinc to 1-naphthaldehyde with 94% e.e. and >95% conversion at 0 °C. The enantioselectivity has, however, dropped significantly when other smaller aromatic aldehydes were used as the substrates. This result differs from the performance of **45d** which has a very broad substrate scope. Such a difference is believed to be a direct consequence of the much more rigid structure of **47c**; the dihedral angles of naphthyl rings in the Ti(IV) catalyst cannot vary to accommodate aldehydes of various sizes to give high enantioselectivity. The chiral dihydroxy groups in **47c** thus differ from those of BINOL and may prove useful for mechanistic work due to their rigid structure.

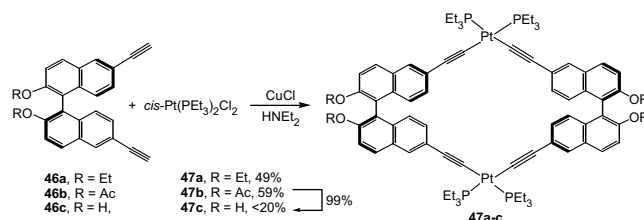


Figure 28. Chiral dinuclear metallacyclophanes. Reprinted with permission from [78], H. Jiang et al., *Chem. Commun.* 96 (2003). © 2003, Royal Society of Chemistry.

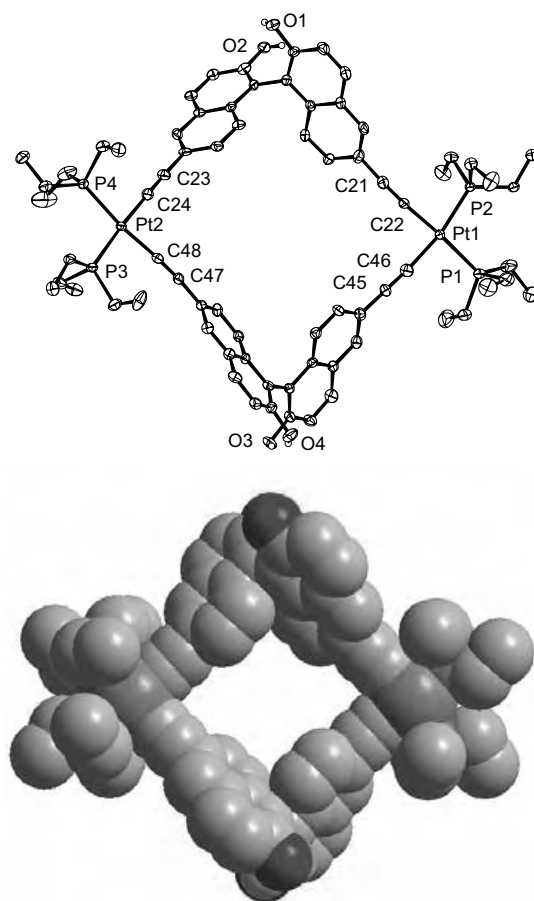
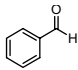
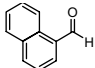
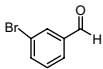
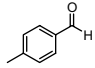
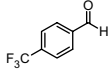
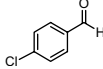


Figure 29. Top: ORTEP view of metallacyclophane **47c**. Bottom: A space-filling model of **47c**. Reprinted with permission from [78], H. Jiang et al., *Chem. Commun.* 96 (2003). © 2003, Royal Society of Chemistry.

Table 2. Diethylzinc additions to aldehydes catalyzed by Ti(IV) complexes of **47c**.

Aldehyde	Temp.	Time (h)	Conversion	e.e. (%)
	RT	16	>95%	77
	0 °C	16	>95%	84
	RT	16	>95%	91
	0 °C	16	>95%	94
	RT	16	>95%	75
	0 °C	16	>95%	78
	RT	16	>95%	77
	0 °C	40	~40%	78
	RT	16	>95%	76
	0 °C	40	~80%	77
	RT	16	>95%	75
	0 °C	16	>95%	78

4. CONCLUDING REMARKS

The examples illustrated in this chapter give testimony to our ability, through chemical manipulation, to create large chiral macrocycles that can potentially serve as mimics of natural enzyme systems. With properly designed building units, chiral macrocycles can be readily synthesized. In particular, through a judicious combination of multitopic bridging ligands and unsaturated metal centers, chiral metalocycles can be constructed with unprecedented predictability and ease. It is also possible to maintain the structural features of the chiral macrocycles and yet fine-tune their properties via a systematic modification of their constituent building units.

Recent work has clearly illustrated supramolecular functions of chiral metalocycles which are reminiscent of biological macromolecular systems. Future work will be directed toward the design and exploitation of such supramolecular functions in the areas of molecular recognition, host-guest interaction, chiral recognition, and catalysis. It can be expected that such research efforts will lead to new materials with desirable tunable properties and ultimately to the demonstration of nanoscale devices and molecular machinery [79, 80].

GLOSSARY

Asymmetric catalysis A catalytic reaction in which one enantiomer is produced in excess of the other.

Chiral A chiral object is not superimposable on its mirror image.

Enantiomer Two stereoisomers that are not superimposable images of each other.

Enantiomeric excess (ee) Percentage by which one enantiomer is in excess over the other in a mixture of two.

Macrocycle A cyclic (macro)molecule that has no end groups.

Metalocycle A macrocycle that contains metal centers in the cycle.

Self-assembly The spontaneous formation of molecules into covalently bonded, well-defined, stable structures.

Supramolecular chemistry The chemistry of the intermolecular bond, concerning the structure and functions of the entities formed by the association of two or more chemical species.

REFERENCES

1. G. F. Swiegers and T. J. Malefetse, *Chem. Rev.* 100, 3483 (2000).
2. D. S. Riley, *Chem. Rev.* 99, 2573 (1999).
3. B. Linton and A. D. Hamilton, *Chem. Rev.* 97, 1669 (1997).
4. C. J. Peterson, *J. Am. Chem. Soc.* 7017 (1967).
5. R. C. Helgeson, G. R. Weisman, J. L. Toner, T. L. Tarnowski, Y. Chao, J. M. Mayer, and D. J. Cram, *J. Am. Chem. Soc.* 4928 (1979).
6. S. Leininger, B. Olenyuk, and P. J. Stang, *Chem. Rev.* 100, 853 (2000).
7. M. Fujita, *Chem. Soc. Rev.* 27, 417 (1998).
8. D. S. Lawrence, T. Jiang, and M. Levett, *Chem. Rev.* 95, 2229 (1995).

9. G. M. Whitesides, E. E. Simanek, J. P. Methias, C. T. Ceto, D. N. Chin, M. Mammen, and D. M. Gordon, *Acc. Chem. Res.* 28, 37 (1995).
10. J. M. Canary and B. C. Gibb, "Progress in Inorganic Chemistry," Vol. 1, p. 45. Wiley, New York, 1997.
11. J.-M. Lehn, "Supramolecular Chemistry: Concepts and Perspectives." VCH, New York, 1995.
12. M. Fujita and K. Ogura, *Coord. Chem. Rev.* 148, 249 (1996).
13. P. J. Stang and B. Olenyuk, *Acc. Chem. Res.* 30, 502 (1997).
14. B. Olenyuk, A. Fechtenkötter, and P. J. Stang, *J. Chem. Soc. Dalton Trans.* 1707 (1998).
15. X. Chi, A. J. Guerin, R. A. Haycock, C. A. Hunter, and L. D. Sarson, *J. Chem. Soc. Chem. Commun.* 2563 (1995).
16. X. Chi, A. J. Guerin, R. A. Haycock, C. A. Hunter, and L. D. Sarson, *J. Chem. Soc. Chem. Commun.* 2567 (1995).
17. H. Zhao and W. Hua, *J. Org. Chem.* 65, 2933 (2000).
18. G. W. Gokel, J. M. Timko, and D. J. Cram, *J. Chem. Soc. Chem. Commun.* 394 (1975).
19. D. S. Lingenfelter, R. C. Helgeson, and D. J. Cram, *J. Org. Chem.* 46, 393 (1981).
20. S. P. Artz, M. P. deGrandpre, and D. J. Cram, *J. Org. Chem.* 50, 1486 (1985).
21. M. Newcomb, J. L. Toner, R. C. Helgeson, and D. J. Cram, *J. Am. Chem. Soc.* 101, 4941 (1979).
22. G. D. Y. Sogah and D. J. Cram, *J. Am. Chem. Soc.* 101, 3035 (1979).
23. J. M. Lehn and C. Sirlin, *J. Chem. Soc., Chem. Commun.* 949 (1978).
24. J. Sanchez-Quesada, M. P. Isler, and M. R. Ghadiri, *J. Am. Chem. Soc.* 124, 10004 (2002).
25. H. Rapaport, H. S. Kim, K. Kjaer, P. B. Howes, S. Cohen, J. Als-Nielsen, M. R. Ghadiri, L. Leiserowitz, and M. Lahav, *J. Am. Chem. Soc.* 121, 1186 (1999).
26. T. D. Clark, L. K. Buehler, and M. R. Ghadiri, *J. Am. Chem. Soc.* 120, 651 (1998).
27. J. D. Hartgerink, J. R. Granja, R. A. Milligan, and M. R. Ghadiri, *J. Am. Chem. Soc.* 118, 43 (1996).
28. S. L. Daubendiek, K. Ryan, and E. T. Kool, *J. Am. Chem. Soc.* 117, 7818 (1995).
29. D. Liu, S. L. Daubendiek, M. A. Zillman, K. Ryan, and K. T. Kool, *J. Am. Chem. Soc.* 118, 1587 (1996).
30. B. Kohler, V. Enkelmann, M. Oda, S. Pieraccini, G. S. Spada, and U. Scerf, *Chem. Eur. J.* 7, 3000 (2001).
31. N. Harada and K. Nakanishi, "Circular Dichroic Spectroscopy—Exciton Coupling in Organic Chemistry." Oxford Univ. Press, Oxford, 1983.
32. B. M. V. Langeveld-Voss, D. Deljonne, Z. Shuai, R. A. J. Janssen, S. C. J. Meskers, E. W. Meijer, and J.-L. Bredas, *Adv. Mater.* 10, 1343 (1998).
33. V. Prantsch, S. Ibach, and F. Vogtle, *J. Incl. Phenom. Macrocycl. Chem.* 33, 427 (1999).
34. G. W. Gokel, "Comprehensive Supramolecular Chemistry," Vol. 1, Molecular Recognition: Receptors for Cationic Guests. Pergamon, Oxford, 1996.
35. J. Jazwinski, J.-M. Lehn, R. Meric, J.-P. Vigneron, M. Cesario, J. Guilhaum, and C. Pascard, *Tetrahedron Lett.* 28, 3489 (1987).
36. R. Menif and A. E. Martell, *J. Chem. Soc., Chem. Commun.* 1521 (1989).
37. D. Chen and A. E. Martell, *Tetrahedron* 47, 6895 (1991).
38. P. Comba, A. Fath, T. W. Hambley, and D. T. Richens, *Angew. Chem., Int. Ed. Engl.* 34, 1883 (1995).
39. Y. Tian, J. Tong, G. Frenzen, and J.-Y. Sun, *J. Org. Chem.* 64, 1442 (1999).
40. M. R. Suissa, C. Romming, and J. Dale, *Chem. Eur. J.* 5, 3055 (1999).
41. J. E. Richman and T. J. Atkins, *J. Am. Chem. Soc.* 96, 2268 (1974).
42. J. Gawroński, H. Kobon, M. Kwit, and A. Katrusiak, *J. Org. Chem.* 65, 5768 (2000).
43. A. P. Marchand, M. Takhi, V. S. Kumar, K. Krishnudu, and B. Ganguly, *ARKIVOC* 3, 13 (2001).
44. D. L. An, T. Nakano, A. Orita, and J. Otera, *Angew. Chem., Int. Ed. Engl.* 41, 171 (2002).
45. S. Anderson, U. Neidlein, V. Gramlich, and F. Diederich, *Angew. Chem., Int. Ed. Engl.* 34, 1596 (1995).
46. U. Neidlein and F. Diederich, *Chem. Commun.* 1493 (1996).
47. J. Lin, H.-C. Zhang, and L. Pu, *Org. Lett.* 4, 3297 (2002).
48. R. A. Bissell, A. P. de Silva, H. Q. N. Gunaratna, P. L. M. Lynch, G. E. M. Maguire, C. P. McCoy, and K. R. A. S. Sandanayake, *Top. Curr. Chem.* 168, 223 (1993).
49. R. A. Bissell, A. P. de Silva, H. Q. N. Gunaratna, P. L. M. Lynch, G. E. M. Maguire, and K. R. A. S. Sandanayake, *Chem. Soc. Rev.* 21, 187 (1992).
50. A. W. Czarnik, *Acc. Chem. Res.* 27, 302 (1994).
51. B. Botta, M. Botta, A. Filippi, A. Tafi, G. D. Monache, and M. Speranza, *J. Am. Chem. Soc.* 123, 7658 (2002).
52. P. H. Dinolfo and J. T. Hupp, *Chem. Mater.* 13, 3113 (2001).
53. S. Benlanger, J. T. Hupp, I. A. Guzei, and A. L. Rheingold, *Coord. Chem. Rev.* 171, 221 (1998).
54. F. A. Cotton, C. Lin, and C. A. Murillo, *Acc. Chem. Res.* 34, 750 (2001).
55. R. V. Slone, D. I. Yoon, R. M. Calhoun, and J. T. Hupp, *J. Am. Chem. Soc.* 117, 11813 (1995).
56. M. Aoyagi, K. Biradha, and M. Fujita, *J. Am. Chem. Soc.* 121, 7457 (1999).
57. A. J. Lees and S. Sun, *J. Am. Chem. Soc.* 122, 8956 (2000).
58. M. Yoshizawa, T. Kusukawa, M. Fujita, and K. Yamaguchi, *J. Am. Chem. Soc.* 122, 6311 (2000).
59. M. Yoshizawa, T. Kusukawa, M. Fujita, S. Sakamoto, and K. Yamaguchi, *J. Am. Chem. Soc.* 123, 10454 (2001).
60. M. Fujita, Y. J. Kwon, S. Washizu, and K. Ogura, *J. Am. Chem. Soc.* 116, 1151 (1994).
61. J. Kang, G. Hilmersson, J. Santamaria, and J. Rebek, Jr., *J. Am. Chem. Soc.* 120, 3650 (1998).
62. M. Lahav, R. Gabai, A. N. Shipway, and I. Willner, *Chem. Commun.* 1937 (1999).
63. B. Oenyuk, J. A. Whiteford, and P. J. Stang, *J. Am. Chem. Soc.* 118, 8221 (1996).
64. J. Fan, J. A. Whitehold, B. Olenyuk, M. D. Levin, P. J. Stang, and E. B. Fleischer, *J. Am. Chem. Soc.* 121, 2741 (1999).
65. F. A. Cotton and G. Wilkinson, "Advanced Inorganic Chemistry," 5th ed. Wiley, New York 1988.
66. O. R. Evans and W. Lin, *Acc. Chem. Res.* 35, 511 (2002).
67. Y. Zhang, S. Wang, G. D. Enright, and S. R. Breeze, *J. Am. Chem. Soc.* 120, 9398 (1998).
68. F. R. Keene, *Coord. Chem. Rev.* 166, 121 (1997).
69. M. M. Ali and F. A. MacDonnell, *J. Am. Chem. Soc.* 122, 11527 (2000).
70. L. L. Schafer and T. D. Tilley, *J. Am. Chem. Soc.* 123, 2683 (2001).
71. S. S. H. Mao and T. D. Tilley, *J. Am. Chem. Soc.* 117, 5365 (1995).
72. K. Onitsuka, Y. Harada, F. Takei, and S. Takahashi, *Chem. Commun.* 643 (1998).
73. E. I. Negishi, F. E. Cederbaum, and T. Takahashi, *Tetrahedron Lett.* 27, 2829 (1986).
74. T. W. Kim, M. S. Lah, and J.-I. Hong, *Chem. Commun.* 743 (2001).
75. T. Haberer, M. Warchhold, H. Noth, and K. Severin, *Angew. Chem., Int. Ed. Engl.* 38, 3225 (1999).
76. S. J. Lee and W. Lin, *J. Am. Chem. Soc.* 124, 4554 (2002).
77. S. J. Lee, A. Hu, and W. Lin, *J. Am. Chem. Soc.* 124, 12948 (2002).
78. H. Jiang, A. Hu, and W. Lin, *Chem. Commun.* 96 (2003).
79. D. B. Amabilino and J. F. Stoddart, *Chem. Rev.* 95, 2727 (1995).
80. D. B. Amabilino, M. Asakawa, P. R. Aston, R. Ballardini, V. Balzani, M. Belohradsky, A. Credi, M. Higuchi, F. M. Raymo, T. Shimazu, J. F. Stoddart, M. Venturi, and K. Yase, *New J. Chem.* 22, 959 (1998).

